SPRINGER NATURE
Reference

Randall Allemang
Peter Avitabile
Editors

Handbook of Experimental Structural Dynamics

Springer

Handbook of Experimental Structural Dynamics

Randall Allemang • Peter Avitabile
Editors

Handbook of Experimental Structural Dynamics

With 667 Figures and 70 Tables

Springer

Editors

Randall Allemang
Mechanical and Materials Engineering
University of Cincinnati
Cincinnati, OH, USA

Peter Avitabile
Structural Dynamics and
Acoustic Systems
Laboratory, University
of Massachusetts
Lowell, Lowell, MA, USA

ISBN 978-1-4614-4546-3 ISBN 978-1-4614-4547-0 (eBook)
https://doi.org/10.1007/978-1-4614-4547-0

This Springer imprint is published by the registered company Springer Science+Business Media, LLC part of Springer Nature.
The registered company address is: 1 New York Plaza, New York, NY 10004, U.S.A.

Preface and Introduction

The purpose of the SEM Handbook of Experimental Structural Dynamics is to provide a summary/overview of information and reference material in the areas of analytical and experimental structural dynamics that are important to the Society of Experimental Mechanics. The topics covered in this Handbook all address the essential material that is germane to the International Modal Analysis Conference that has been held yearly for close to 40 years beginning in 1982.

This Handbook can be viewed as covering the macro topics of experimental mechanics while the traditional SEM Handbook of Experimental Solid Mechanics covers the micro topics of experimental mechanics. In past revisions of the SEM Handbook of Experimental Mechanics, all subject areas were contained in one single volume. Due to the expansions of topics, the Society decided to divide the material into two Handbooks with this Handbook consisting of two volumes.

The content of the SEM Handbook of Experimental Structural Dynamics primarily involves the areas of structural mechanics (statics and dynamics) that are served by the SEM International Modal Analysis Conference (IMAC) and covered by several Technical Divisions (TDs) or Focus Groups (FGs) of the Society. A few of the topics that will be included in this Handbook will come from TDs and FGs that are active in the SEM Annual Conference but were not included in the recently revised SEM Handbook of Experimental Solid Mechanics.

While the general topic of each chapter is defined by the chapter title, in all cases the content of the chapter reflects the experimental nature of the Handbook and the focus/content of the almost 40 years of science and technology representative of the IMAC Conference. Therefore, even a chapter like Finite Element Modeling reflects the experimental concerns/issues rather than a purely theoretical explanation of the methodology. Terminology and nomenclature are suggested (using the IMAC suggested nomenclature list) but not required due to overlapping standards of nomenclature used in different technical areas. The focus of the material is on proven methods and not simply a literature review. Some overlap between various chapters cannot be avoided for several chapters due to the inter-relationship of certain topics.

Each chapter generally involves a review of the important theory involved in the specific analytical and experimental methods as well as the specific science and technology that is involved. Additionally, though, each chapter covers the relevant practical needs of scientists and engineers who are new to the field involved. In most

cases both the pertinent theory and particularly the practical issues have not yet been presented formally in an academic textbook. Each chapter should be a 'must read' for someone new to the field or for someone returning to the field after an absence. The reference list in each chapter may not be all inclusive but does consist of the seminal papers and references for the area of the chapter.

While much of the material in this Handbook may be found scattered in a variety of different publications, this Handbook attempts to pull together all that material into one location to facilitate current and future research as this field moves forward.

June 2022

Randall Allemang
Peter Avitabile
Editors

Contents

Volume 1

Volume 2

About the Editors

Dr. Allemang is a Professor Emeritus and member of the faculty of the Mechanical Engineering Program in Mechanical and Materials Engineering, University of Cincinnati, where he currently also serves as Director of the Structural Dynamics Research Laboratory (UC-SDRL). Dr. Allemang has been actively involved in the area of experimental structural dynamics and modal analysis for over forty years, pioneering the use of multiple input, multiple output estimation of frequency response functions, developing the concept of cyclic averaging, formulating the modal assurance criterion (MAC) and the enhanced frequency response function and reformulating modal parameter estimation algorithms into the unified matrix (coefficient) polynomial approach (UMPA). Dr. Allemang has served on the Advisory Board for the International Modal Analysis Conference (1981-2015, Chairman, 1986-1995), on the Editorial Board of Sound and Vibration Magazine (1983-2017) and on the Scientific Committee of the ISMA Noise and Vibration Conference at the Katholieke University of Leuven, Belgium (1984-present). Dr. Allemang has also served on the Executive Board of the Society for Experimental Mechanics (SEM) from 1998-2006, including President for the Society during 2003-2004. Dr. Allemang is currently involved as Senior Collaborator for the AFRL Structural Sciences Center at WPAFB, working on the verification and validation (experimental quantification of margin and uncertainty) of experimental and analytical dynamic models and has been recognized by three professional societies as a Fellow (SEM, SAE and ASME). Dr. Allemang has also mentored two PhD graduates who went on to win Presidential Early Career Award for Scientists and Engineers (PECASE).

Dr. Peter Avitabile is a Professor Emeritus and member of the faculty at the University of Massachusetts Lowell (UML) in the Mechanical Engineering Department. He serves a Co-Director of the Structural Dynamics and Acoustic Systems Laboratory (SDASL) at UML.

Dr. Avitabile has over 4 decades of experience in design and analysis using FEM and experimental techniques. His main area of research is structural dynamics specializing in the areas of modeling, testing and correlation of analytical and experimental models along with advanced applications for developing structural dynamic models.

He is a Fellow of the Society for Experimental Mechanics (SEM), has received the DeMichele award (2004), has held numerous board and executive positions in the SEM Organization and the International Modal Analysis Community and served as President of SEM during 2016-2017.

Peter has contributed well over 300 technical papers in the area as well as his 17 year "Modal Space" article series in the Experimental Techniques magazine published by the Society for Experimental Mechanics. Pete has also published a book entitled "Modal Testing: A Practitioner's Guide" (Wiley 2017).

Contributors

Douglas E. Adams Vanderbilt University, Nashville, TN, USA

R. J. Allemang Structural Dynamics Research Laboratory, Mechanical and Materials Engineering, University of Cincinnati, Cincinnati, OH, USA

Matt Allen University of Wisconsin-Madison, Madison, WI, USA

Matthew S. Allen Department of Engineering Physics, University of Wisconsin, Madison, WI, USA

Raquel Almeida UNIDEMI, Department of Mechanical and Industrial Engineering, FCT NOVA – Faculty of Science and Technology, Universidade NOVA de Lisboa, Caparica, Portugal

Jerome Antoni Univ Lyon, INSA-Lyon, Villeurbanne, France

Peter Avitabile Structural Dynamics and Acoustic Systems Laboratory, University of Massachusetts Lowell, Lowell, MA, USA

Javad Baqersad Department of Mechanical Engineering, Kettering University, Flint, MI, USA

Andrew Barnard Mechanical Engineering-Engineering Mechanics Department, Michigan Technological University, Houghton, MI, USA

R. J. Barthorpe Dynamics Research Group, Department of Mechanical Engineering, University of Sheffield, Sheffield, UK

Raymond M. Bond Vanderbilt University, Nashville, TN, USA

Pietro Borghesani University of New South Wales, Sydney, NSW, Australia

Queensland University of Technology, Brisbane, QLD, Australia

Ruben Boroschek University of Chile, Santiago, Chile

Anders Brandt Department of Mechanical and Electrical Engineering, University of Southern Denmark, Odense, Denmark

Ralph Brillhart ATA Engineering, Inc., San Diego, CA, USA

D. L. Brown Structural Dynamics Research Laboratory, Mechanical and Materials Engineering, University of Cincinnati, Cincinnati, OH, USA

L. A. Bull Dynamics Research Group, Department of Mechanical Engineering, University of Sheffield, Sheffield, UK

Thomas Carne Sandia National Laboratories, Retired, Albuquerque, NM, USA

Paolo Castellini Università Politecnica delle Marche, Ancona, Italy

Paolo Chiariotti Università Politecnica delle Marche, Ancona, Italy

Robert Coppolino Measurement Analysis Corporation, Torrance, CA, USA

E. J. Cross Dynamics Research Group, Department of Mechanical Engineering, University of Sheffield, Sheffield, UK

N. Dervilis Dynamics Research Group, Department of Mechanical Engineering, University of Sheffield, Sheffield, UK

C. R. Farrar Engineering Institute, Los Alamos National Laboratory, Los Alamos, NM, USA

David Formenti BlackHawk Technology, Santa Cruz, CA, USA

Gary Foss The Boeing Company, Chicago, IL, USA

Michael I. Friswell College of Engineering, Swansea University, Swansea, UK

R. Fuentes Dynamics Research Group, Department of Mechanical Engineering, University of Sheffield, Sheffield, UK

P. A. Gardner Dynamics Research Group, Department of Mechanical Engineering, University of Sheffield, Sheffield, UK

Lothar Gaul Institut für Nichtlineare Mechanik, Universität Stuttgart, Stuttgart, Germany

Norman F. Hunter Thomas Paez Consulting, Albuquerque, NM, USA

Daniel Kammer University of Wisconsin – Madison, Madison, WI, USA

G. Kerschen Space Structures and Systems Laboratory, Department of Aerospace and Mechanical Engineering, University of Liège, Liege, Belgium

Michael Link Department of Civil and Environmental Engineering, University of Kassel, Kassel, Germany

Nuno Maia Department of Mechanical Engineering, LAETA/IDMEC/IST (Instituto Superior Tecnico), University of Lisbon, Lisbon, Portugal

Michael Mains University of Cincinnati, Cincinnati, OH, USA

Lothar Gaul: deceased.

Stefano Manzoni Department of Mechanical Engineering, Politecnico di Milano, Milan, Italy

Randall L. Mayes Sandia National Laboratories, Albuquerque, NM, USA

Jessica Meloy Pensar Development, Seattle, WA, USA

Janette J. Meyer School of Engineering, Vanderbilt University, Nashville, TN, USA

John E. Mottershead School of Engineering, University of Liverpool, Liverpool, UK

Kevin Napolitano ATA Engineering, Inc., San Diego, CA, USA

Christopher Niezrecki Department of Mechanical Engineering, University of Massachusetts Lowell, Lowell, MA, USA

Thomas L. Paez Thomas Paez Consulting, Albuquerque, NM, USA

A. W. Phillips Structural Dynamics Research Laboratory, Mechanical and Materials Engineering, University of Cincinnati, Cincinnati, OH, USA

Robert B. Randall University of New South Wales, Sydney, NSW, Australia

Christian Rembe TU Clausthal, Clausthal-Zellerfeld, Germany

Phillip L. Reu Sandia National Laboratories, Albuquerque, NM, USA

Mark Richardson Vibrant Technology, Inc., Centennial, CA, USA

Daniel Rixen Technische Universität München, Garching, Germany

T. J. Rogers Dynamics Research Group, Department of Mechanical Engineering, University of Sheffield, Sheffield, UK

Daniel P. Rohe Sandia National Laboratories, Albuquerque, NM, USA

Joao Pedro Santos Structural Monitoring Unit, National Laboratory for Civil Engineering, Lisboa, Portugal

Carsten Schedlinski ICS Engineering GmbH, Dreieich, Germany

André Schmidt Institut für Nichtlineare Mechanik, Universität Stuttgart, Stuttgart, Germany

H. Shi Dynamics Research Group, Department of Mechanical Engineering, University of Sheffield, Sheffield, UK

Tiago Silva UNIDEMI, Department of Mechanical and Industrial Engineering, FCT NOVA – Faculty of Science and Technology, Universidade NOVA de Lisboa, Caparica, Portugal

David O. Smallwood Thomas Paez Consulting, Albuquerque, NM, USA

António Urgueira UNIDEMI, Department of Mechanical and Industrial Engineering, FCT NOVA – Faculty of Science and Technology, Universidade NOVA de Lisboa, Caparica, Portugal

A. F. Vakakis Department of Mechanical Science and Engineering, University of Illinois at Urbana-Champaign, Champaign, IL, USA

Mark Valentino PCB Piezotronics, Inc., Depew, NY, USA

Chuck Van Karsen Mechanical Engineering-Engineering Mechanics Department, Michigan Technological University, Houghton, MI, USA

Patrick Walter Texas Christian University & PCB Piezotronics, Inc., Fort Worth, TX, USA

K. Worden Dynamics Research Group, Department of Mechanical Engineering, University of Sheffield, Sheffield, UK

Part I
Sensors and Measurements

Recent History of Experimental Structural Dynamics

1

R. J. Allemang

Contents

Abstract

This chapter on the recent history of experimental structural dynamics puts much of the Handbook in a historical perspective that begins with the development of digital data methodology and computerized data processing that began in

R. J. Allemang (✉)
Structural Dynamics Research Laboratory, Mechanical and Materials Engineering, University of Cincinnati, Cincinnati, OH, USA
e-mail: Randall.Allemang@UC.EDU

R. Allemang, P. Avitabile (eds.), *Handbook of Experimental Structural Dynamics*,
https://doi.org/10.1007/978-1-4614-4547-0_1

the mid-1960s. Experimental structural dynamics began much earlier with analog, single frequency data acquisition and mostly visual data processing that began in the 1800s with the rail and marine industries, particularly when the steam engine impacted those technologies. The analog, single frequency data acquisition methodology, continued in the automotive and the aircraft industries in the first half of the 1900s. This Handbook mostly chronicles data acquisition and processing methods that began more recently, in the mid-1960s, with the advent of the Fourier transform, analog to digital data conversion, and digital minicomputers to the present time period. The Handbook also discusses many methods and techniques in use during the 1960s and 1970s that utilize experimentally derived models, both linear and nonlinear, to calibrate and validate corresponding analytical models. Part of this discussion includes the issue of the varying dimensionality of the number of degrees of freedom (DOF) between experimental and analytical models. This chapter also discusses the researchers and educators that were part of the development of the experimental structural dynamics methodology in the 1960s to 1980s that led to the current technical state of the art. This discussion includes the identification of researchers and educators that were instrumental to the Society for Experimental Mechanics (SEM) in the development of this area of interest within the Society over the last 50 years.

Keywords

Experimental structural dynamics · Experimental modal analysis · Modal parameter estimation · Forced normal mode · Phase resonance · Phase separation · Sinusoidal input-output model · Frequency response function (FRF) Model · Damped complex exponential response model · General input-output model · Frequency response function (FRF) · Impulse response function (IRF) · IMAC Advisory Board · Handbook chapters and authors · Pioneers and contributors

Nomenclature

N_i	Number of inputs
N_o	Number of outputs
N_S	Short Dimension (min(N_i, N_o))
N_L	Long Dimension (max(N_i, N_o))
N_f	Number of spectral lines (frequencies)
N_e	Number of effective modal frequencies
N	Number of modal frequencies
$F_{\max}$	Maximum frequency (Hz)
ω_k	Frequency (rad/sec)
$\omega_{\max}$	Maximum frequency (rad/sec)
s_k	Generalized Frequency - Complex Valued (rad/sec)
λ_r	Complex modal frequency
T	Observation period (sec)

Δf	Frequency resolution (Hz)
s_i	Generalized frequency variable
m	Model order for denominator polynomial
n	Model order for numerator polynomial
$[\alpha]$	Denominator polynomial matrix coefficient
$[\beta]$	Numerator polynomial matrix coefficient
$[I]$	Identity matrix
$[M]$	Mass matrix
$[C]$	Damping matrix
$[C]$	Companion matrix (alternate usage)
$[K]$	Stiffness matrix
$[A]$	State space model matrix
$[B]$	State space model matrix
$[A]$	Controls model matrix
$[B]$	Controls model matrix
$[C]$	Controls model matrix
$[D]$	Controls model matrix
$[H(s)]$	Transfer function matrix. $(N_o \times N_i)$
$[H(\omega)]$	Frequency response function matrix. $(N_o \times N_i)$
A_{pqr}	Residue, output DOF p, input DOF q, mode r
$[T]$	Transformation matrix
$[U]$	Left singular vector matrix
$[\Sigma]$	Singular value matrix (diagonal)
$[\Lambda]$	Eigenvalue matrix (diagonal)
$[V]$	Right singular vector, or eigenvector, matrix

1 Introduction

The purpose of the SEM Handbook of Experimental Structural Dynamics is to provide a summary/overview of information and reference material in the areas of analytical and experimental structural dynamics that are important to the Society for Experimental Mechanics. The topics covered in this Handbook all address the essential material that is germane to the International Modal Analysis Conference that has been held annually for close to 40 years beginning in 1982.

This Handbook can be viewed as covering the macro topics of experimental mechanics, while the traditional SEM Handbook of Experimental Solid Mechanics covers the micro topics of experimental mechanics. In past revisions of the SEM Handbook of Experimental Mechanics, all subject areas were contained in one single volume. Due to the expansion of topics, the Society decided to divide the material into two volumes. The content of this SEM Handbook of Experimental Structural Dynamics primarily involves the areas of structural mechanics (statics and dynamics) that are served by the SEM International Modal Analysis Conference (IMAC) and are covered by several technical divisions (TDs) or focus groups (FGs) of the Society. A few of the topics that will be included in this Handbook will come from TDs and FGs that are active in the SEM Annual Conference but were not included in previous SEM handbooks and were not covered in the 2008 revision of the SEM Handbook of Experimental Solid Mechanics.

While the general topic of each chapter is defined by the chapter title, in all cases the content of the chapter reflects the experimental nature of the Handbook and the focus/content of the almost 40 years of science and technology representative of the IMAC Conference. Therefore, even a chapter like finite element modeling (FEM) reflects the experimental concerns/issues rather than a purely theoretical explanation of the FEM methodology. Terminology and nomenclature are suggested (using the IMAC suggested nomenclature list) but not required due to overlapping standards of nomenclature used in different technical areas. The focus of the material is on proven methods and not simply a literature review. Some overlap between various chapters cannot be avoided for several chapters due to the interrelationship of certain topics. Each chapter generally involves a review of the important theory involved in the specific analytical and experimental methods as well as the specific science and technology that is involved. Additionally, though, each chapter covers the relevant practical needs of scientists and engineers who are new to the field involved. In most cases both the pertinent theory and particularly the practical issues have not yet been presented formally in an academic textbook. Each chapter should be a "must read" for someone new to the field or for someone returning to the field after an absence. The reference list in each chapter may not be all inclusive but does consist of the seminal papers and references for the area of the chapter. While much of the material in this Handbook may be found scattered in a variety of different publications, this Handbook attempts to pull together all that material into one location to facilitate current and future research as this field moves forward.

2 Timeline History

Experimental structural dynamics is defined as estimating the dynamic properties of structures via estimation methods often involving the determination of modal properties of the structures (modal frequencies and damping factors, modal vectors, and modal scaling) from experimentally measured data in the time domain. The history of these methods goes back to the early 1900s or before in terms of visual or analog methods, mostly conducted with single frequency experiments. Most experimental methods prior to 1965 were limited by the sensors available to the time period in addition to the limits of analog measurement methods that used analog bandpass filters and single frequency methods.

By 1965, sensors to measure analog force and response were available, and computer-based data acquisition was becoming available to generate digital time data via analog to digital conversion (ADC) of analog voltage measurements. The fast Fourier transform (FFT) algorithm made processing of digital data in the frequency domain possible.

By 1985, several conferences with archived proceedings began to become available. The current experimental structural dynamics methods are covered in other chapters in this SEM Handbook. The discussion in this chapter will primarily focus on the period from 1965 to 1985 where publications and references are harder

to find. A relatively complete list of references that were available prior to 1982 is included in the first (1982) IMAC Conference proceedings [1].

3 Technology Developments

Prior to 1965 and the development of the fast Fourier transform (FFT) [2], only analog methods were available to measure experimental structural dynamics. Some sensors were developed using variable resistance potentiometers beginning in the 1850s. These sensors were often directly attached to moving structures with mechanical connections that involved friction and limitations of very low frequency. Sensors involving bonded strain gages (1930s) and piezoelectric sensors (1950s) were developed which made observations other than visual, mechanical, or resistance measurements possible. By the late 1960s, minicomputer data acquisition using ADCs made digital time domain measurements along with the associated digital frequency domain measurement possible.

Beginning in the early 1980s, computer workstation and personal computer (PC)-based data acquisition began to be available with increased processing speed, increased memory, and more flexible operating system environments. This time period also brought synchronous multiple channel data acquisition systems which made true multiple input, multiple output (MIMO) data acquisition a commonly used methodology. MIMO data acquisition also made the estimation of close or repeated modal frequencies possible for first time, and many multiple reference parameter estimation algorithms were developed over the next 20–30 years.

3.1 Sensors

For the purpose of discussion in this text, only sensors and sensor technologies that are capable of giving a measurable voltage signal proportional to load or motion will be discussed. Most of these sensor technologies are still in use today for specialized applications.

3.1.1 Resistance Technology

Linear and rotational resistance potentiometers originated somewhere around the mid-1850s. The rotational version was referred to as a rheostat by Sir Charles Wheatstone about that time. Displacement motion is measured by connecting the moving structure to the linear or rotational potentiometer so that resistance varies with the displacement motion. The resistance is used in a voltage divider electrical circuit to generate a voltage signal proportional to displacement. This technology is limited to very low frequency and relatively large displacements. This resistance technology is still used at the present time in automotive applications in the form of string potentiometers where a multi-turn rotational potentiometer has a string wound around the rotational axis of the potentiometer.

3.1.2 Bonded Strain Gage Technology

Bonded strain gage technology provided a revolution in the development of both load and response (mostly accelerometers) sensors. The bonded strain gage has a unique connection to the early creation of the Society for Experimental Mechanics. The Society for Experimental Mechanics (SEM) began as the New England Photoelasticity Conference in 1935. This led to the Society for Experimental Stress Analysis (SESA) founded in 1943. SESA had two foci at that time: photoelasticity and strain. Strain gages were developed somewhat independently by Edward Simmons, a graduate student working at the California Institute of Technology (CalTech), and by J. Hans Meier, a graduate student working at the Massachusetts Institute of Technology (MIT) for Professor Ruge. Both groups were awarded patents for their overlapping developments in 1941 which created a conflict. About the time SESA was founded, the bonded strain gage was of great commercial interest, and the company Baldwin-Southwark was able to get an agreement from both inventors in order to produce commercially available strain gages. J. Hans Meier stayed very active in the area of strain gage technology and SESA becoming president of the Society in 1951–1952. The SEM name change officially came about in 1985 [3].

The 1990 article by Peter Stein [4] gives a very complete history of the development of bonded stain gages and the early developments of sensor technology based upon bonded strain gages.

3.1.3 Piezoelectric Crystal Technology

In order to overcome some of the limitations of bonded strain gage technology in 1943, a number of companies and research groups began working on piezoelectric crystal technology. Early technology used ferroelectric ceramics (barium titanate) and quartz crystals, and these early designs required the development of charge amplifiers. These charge amplifier designs were used in both load and acceleration sensor designs yielding relatively flat frequency response characteristics to 10,000 Hz as opposed to flat frequency response characteristics to 200 Hz for bonded strain gage devices. While extremely useful in sensor designs, since the sensor signals are charge based, the capacitance of the cables connected to the sensors created some problems when different cable lengths were utilized (different capacitance). Also note that the piezoelectric crystal technology is limited at the low-frequency end of the usable sensor range due to the bleed off of the steady-state charge signal associated with DC and low-frequency signals.

A significant improvement in sensor designs for both load and response sensors came about as integrated circuit technology developed. A two wire field-effect transistor (FET) design allowed for the FET to be embedded in the sensor resulting in low noise, low impedance, voltage level designs. This technology is referred to as integrated circuit piezotronic (ICP®) or integrated electronics piezoelectric (IEPE).

Except for shock and very high frequency applications, the (ICP®) or (IEPE) designs are the most widely used technology for measuring both force and acceleration response at the present time. The 2007 article by Pat Walter [5] gives

a very complete history of the development of piezoelectric technology and its use in accelerometers. Also, please refer to the chapter in this Handbook entitled ▸ Chap. 2, "Sensors and Their Signal Conditioning for Dynamic Acceleration, Force, Pressure, and Sound Applications".

3.1.4 Inductance and Capacitance Technology

A number of displacement sensors, primarily used in the experimental rotational analysis area, are based upon inductance or capacitance technology. This sensor technology yields an output voltage proportional to the gap between the sensor and an object (normally ferrous material) and is used to measure very small displacements. The inductance technology essentially involves a very small eddy current device embedded in nonconductive resin that is placed in close proximity to a ferrous material. The output of the eddy current circuit is proportional to the gap between the probe and the ferrous material. This gives a response sensor that has a relatively flat frequency response beginning at 0 Hz. This eddy current, proximity probe (now referred to generically as an inductance sensor), began as a sensor developed in 1961, primarily for use in rotational systems by the Bentley Nevada Corporation. This sensor is often referred to as a Bentley probe based upon the original development.

3.1.5 Optical Technology

Two distinct optical sensor technologies have evolved over more recent years. The first optical technology is the use of laser Doppler velocimetry to measure velocity normal to the direction of the laser. While this technology was originally used for alignment of large equipment dating to the 1970s, measurement of velocity based upon a single beam laser dates to at least the early 1990s. Today this technology has been extended to large grids of velocity data using scanning lasers and to three dimension (3D) using multiple, aligned laser heads. Some laser systems use multiple beam lasers so that a grid of laser beams can give motion over a 4×4, 2×8, or 1×16 configuration. Laser-based optical technologies are obviously limited to measurements along the axis of the laser(s) and can be difficult maintaining resolution if large distances or if there is large displacement motion such as in free-free testing. Please refer to the chapter in this Handbook entitled ▸ Chap. 3, "Laser Doppler Vibrometry Measurements in Structural Dynamics" for more complete information.

The second optical technology is the more recent development of digital image correlation (DIC). This technology utilizes high-speed video cameras with extensive post processing of the frame by frame photogrammetry data to yield displacement data. Each frame of the high-speed video is correlated with successive frames, and feature extraction methodology is used to reduce the high resolution (1024×1024 pixels or greater) to a series of 8×8 pixels in a time stream. The centroids of these 8×8 pixels essentially serve as virtual displacement sensors. Much of this technology was developed for traditional static displacement and strain applications within SEM by Dr. Michael Sutton (another interesting aside is that Dr. Sutton has also recently served as president of SEM). Resolution of DIC technology is limited

to a number of pixels in each frame of the video (e.g., 1024 × 1024), the size of the pixels used to create a virtual displacement sensor (e.g., 8 × 8), and the optical frame physical size of the camera (e.g., 100 feet × 100 feet versus 1 inch × 1 inch). DIC can be very effective for relatively small objects but will become limited as the field of view is large. Note that the sampling frequency of the high-speed video cameras is a form of digital data acquisition, and anti-aliasing filtering can be an issue. For this reason, the maximum frequency of interest is often limited to one half of the video sampling frequency (framing rate). For complete details of applying DIC optical technology to the measurement of structural systems, please refer to the chapter in this Handbook entitled ▶ Chap. 8, "DIC and Photogrammetry for Structural Dynamic Analysis and High-Speed Testing".

Both methods of optical technology require placement of optical devices (lasers or high-speed cameras) in the region of the test article, with a primary orientation normal to the surface being measured. Objects that have significant 3D characteristics present more difficulty and require multiple optical systems or a number of different optical devices synchronized together. Both methods may require surface treatment (speckling or photoluminescence dots) to obtain optimal measurement conditions. Both methods are most easily applied to 1D or 2D measurement situations although 3D measurements are now gaining applications.

3.2 Data Acquisition

Analog data acquisition began with visual observations and gradually moved to various forms of strip chart recording. This was followed by oscilloscope time traces, which included two channel Lissajous patterns and analog voltage meters. All of these devices were made more useful via the use of analog signal filtering, especially narrow bandpass filtering. Included along this path was the development of hybrid real-time analyzers that implemented a discrete frequency methodology via time compression (or sometimes referred to as frequency shifting or heterodyne technology).

Digital data acquisition became the default methodology beginning in the late 1960s with the development of the FFT algorithm [2], the development of minicomputers that implemented the FFT algorithm in relatively real time and the development of analog to digital conversion (ADC) of continuous time data.

3.2.1 Analog Technology

Most analog methods before the 1960s used single-frequency excitation and the associated response with analog, bandpass filtering. If input and response channels were measured simultaneously, the two time domain signals could be presented on a two-channel oscilloscope in an X-Y format to generate a Lissajous pattern. This single pattern gave the input-response ratio between the two sinusoidal signals, and the major axis of the Lissajous ellipse gave the phase relationship. This was the beginning of the concept of the transfer function analyzer (TFA) developed by Spectral Dynamics [6].

The TFA used very slowly swept sine methodology with tracking narrow bandpass analog filters on each of two channels. The sine frequency was used to adjust the center frequency of narrow bandpass analog filters applied to both channels being measured. These two channels were compared using a Co-Quad meter to determine the coincident information in the two signals separately from the quadrature information between the two signals. Today, this information is referred to as the real and imaginary parts of the frequency response function (FRF) at one single frequency. The analog output of the Co and Quad meter was plotted as the frequency was slowly swept along to generate an analog version of the FRF.

A structural system with light to moderate damping required a very slowly swept sine to allow for structural system response to stabilize, frequency by frequency. The stabilization time required by the narrow bandpass analog filters also limit the speed at which the sine wave can be swept [6].

A short time later in the 1960s and early 1970s, a number of companies developed real-time analyzers (RTA), most notably Spectral Dynamics and Federal Scientific Corp [7]. The real-time analyzer had many names at that time that included time compression methodology that was based upon tape recorder playback at altered playback tape speeds. This was also referred to as frequency shifting or heterodyne technology. Most of these technologies involved only single channel analysis of measurement data but gave real-time analysis of measured data in terms of the frequency content. As with the TFA, the RTA generally had no data storage capability, and data was plotted to paper or captured with a photo [8].

3.2.2 Digital Technology

While the TFA and the RTA methodologies gave apparent frequency by frequency information, these technologies were at best considered hybrid technologies. Very useful at the time they were developed but soon to be mostly eclipsed by the true digital technologies. The digital technology depended on two major innovations: (1) development of ADCs and (2) implementation of the FFT algorithm. From a practical point of view, these two innovations arrived right when minicomputers were first becoming available. This made everything possible.

Analog to Digital Conversion Development of analog to digital conversion (ADC) hardware began in the 1960s once the need was identified by the potential use of the FFT algorithm. Most of the initial designs were based upon circuit board implementations of 8 bit ADCs. These circuit board designs gave way to potted modules and with the development of integrated circuits, true chip-based technology. Today, ADCs are rarely developed for measurement applications since audiovisual hardware uses six or more channels of 24 bit or higher ADCs on a single chip. Initial ADC designs were 8 bit and 10 bit ADCs giving 256–1024 levels of resolution over a voltage range (typically $+$V to $-$V). By 1980, most ADCs were 12–14 bit giving 4096–16384 levels of resolution over a voltage range. Today most ADCs are quite inexpensive and are based upon delta-sigma ADC designs that are popularized by current audio-video applications. These delta-sigma ADC designs are 24–40 bit equivalent designs, and some implementations use multiple ADCs to get even higher bit equivalent designs. Note that these higher bit designs allow a

single large voltage range (+V to −V) without the need for multiple voltage ranges and/or auto-ranging of the ADC.

Minicomputer FFT systems Many of the first implementations of the FFT algorithm occurred in physically large mainframe computers that were the basis for engineering and science computations in the 1960s. A few of these large mainframe computers were hybrid computers with an analog computer directly connected to the digital computer. For experimental studies that could be placed in this computing environment, these hybrid computers are where the potential of the FFT algorithm was unlocked. Some large mainframe computers used measured digital time data on magnetic tape as an operational methodology.

The implementation of the fast Fourier transform (FFT) in a minicomputer environment allowed for users in a wide variety of industries to begin to use the technology. The Hewlett Packard Company and Time Data Corporation (eventually purchased by General Radio) both developed minicomputer FFT systems at the end of the 1960s. These two implementations were similar: Hewlett Packard utilizing the HP minicomputer and Time Data utilizing the PDP minicomputer. Both of these initial implementations utilized from two to four channels of data acquisition with sampling frequencies of 50 KHz or above make them suitable for structural and most acoustic measurements. By the mid-1970s, a second wave of FFT analyzers was being developed by other manufacturers, and smaller, more portable, FFT analyzers were available.

Beginning in the late 1970s, multiplexed data acquisition was being implemented to allow for more channels of acquisition. However, the multiplexing sample rate induced a time delay, channel to channel, that limited multiple channel use to relatively low frequencies, acceptable for most structural dynamics applications. True multichannel, multiple input, multiple output (MIMO) capabilities became available around 1990.

Further perspectives concerning two of the companies (Brüel & Kjær [9, 10] and Spectral Dynamics [11]) involved in many of these developments have been recently published. Unfortunately no such historical look back at the early years at the Hewlett Packard Company and Time Data Corporation could be found.

A good perspective of the state of vibration equipment (shakers, test equipment, etc.) in the late 1960s can be found in articles by Tustin [12] and Bickel [7]. Welaratna [13] gave a summary of the development of hybrid and digital analyzers in his 1997 paper. A recent look back by Lang [14] also adds some detail to last 50 years of experimental equipment development.

4 Experimental Structural Dynamics Methods 1965–1985

In reviewing the literature in the area of experimental structural dynamics (experimental modal analysis), some sort of outline of the various techniques is helpful in

categorizing the different methods that have been developed over the last 55 years. Most of these methods began during the years 1965–1985.

4.1 Classification Methods

One approach is to group the methods according to whether one mode or multiple modes will be excited at one time. The terminology that is used for this is:

- Phase resonance (one mode excited, all other modes suppressed)
- Phase separation (all modes excited simultaneously)

At the current time, almost all experimental modal analyses would fall into the phase separation category. Phase resonance methods are used by an increasingly smaller group of aerospace testing activities.

A slightly more detailed approach, and the one that is used in the following text, is to group the methods according to the type of measured data that is acquired. When this approach is utilized, the relevant terminology is:

- Sinusoidal input-output model
- Frequency response function model
- Damped complex exponential response model
- General input-output model

A very common concept in comparing and contrasting experimental modal analysis methodologies that is often used in the literature is based upon the type of model that will be used in the modal parameter estimation stage that follows the acquisition of the data. The relevant nomenclature for this approach is:

- Parametric model (Unknowns have physical significance or meaning)
  - Modal model
  - [M], [C], [K] Model
- Nonparametric model (Unknowns are mathematical conveniences)
  - Polynomial model
  - Autoregressive moving-average (ARMA) model
  - [A], [B] Model
  - [A], [B], [C], [D] Model

Finally, the different experimental modal analysis approaches may be grouped according to the domain that the modal parameter estimation model will be formulated. The relevant nomenclature for this approach is:

- Time domain
- Frequency domain
- Spatial domain

Regardless of the approach used to organize or classify the different approaches to generating modal parameters from experimental data, the fundamental underlying theory is the same. The differences largely are a matter of logistics, user experience requirements, and numerical or compute limitations, rather than a fundamentally superior or inferior method.

4.2 Data Acquisition Classification

Over the past 50 years, at least four general categories of experimental structural dynamics methods, which are based upon the type of data that is acquired, can be identified as follows:

- Sinusoidal input-output model
- Frequency response function
- Damped complex exponential response (free decay and impulse response functions)
- General input-output model

Historically, the modal characteristics of mechanical systems have been estimated by techniques that fall into either the first or second category. The experimental modal analysis methods that fall into the last two categories are composite approaches that utilize elaborate parameter estimation algorithms based upon structural models. This section reviews and provides references for the initial work in each of these areas. Over the years from 1965 until the late 1980s. Methods developed from the late 1980s to present are covered in later chapters in this Handbook.

In order to evaluate and improve any approach to experimental modal analysis, the relative merits of all viable techniques must be well understood. To that goal, many articles have been written to try to compare and contrast the value of one method over another. Unfortunately, most of these comparisons have been heavily concerned with differences that are a function of specific implementations of the various techniques. These comparisons were also potentially biased by the expertise of the test engineers being restricted to only one of the areas of testing. Since each method involves very special testing awareness, this sort of analysis has limited value.

In the evaluation of experimental modal analysis methods, the differences in the theoretical approach are obviously of prime concern. Since most experimental modal analysis methods involve similar theoretical basis, the only significant areas of difference concern the concept of real versus complex modal vectors, the explicit measurement of the input, and the different numerical approaches used. The debate over the need to describe complex valued modes of vibration may never end. Certainly, the concept of a complex mode, since it contains a real mode as a special case, appears to be the most general case. Likewise, some experimental modal analysis methods do not require the measurement of the input. While this can be

advantageous at times where the implicit nature of the input is known or assumed, it seems prudent, where the input can be measured, to do so.

Beyond the direct theoretical differences, though, there are several key evaluation considerations which may or may not be a direct function of the theory. The availability of confidence factors, the potential for implementation, stability and precision of the solution algorithm, sensitivity to random and/or bias errors in the measured data, and the need for operator expertise may control the ability to estimate valid modal parameters. Specifically, through the knowledge of these aspects with respect to other experimental modal analysis methods, the use of each of the approaches may be enhanced due to this transfer of technology between the methods.

Generally, the methods that utilize frequency response function data, damped complex exponential response data, and/or general input-output data can all be explained using a *unified matrix polynomial approach (UMPA)*. Most modal parameter estimation algorithms can be reformulated into this consistent mathematical formulation with a corresponding set of definitions and unifying concepts [15].

Particularly, this matrix polynomial approach is used to unify the presentation with respect to current algorithms such as the least-squares complex exponential (LSCE), the polyreference time domain (PTD), Ibrahim time domain (ITD), eigensystem realization algorithm (ERA), rational fraction polynomial (RFP), polyreference frequency domain (PFD), and the complex mode indicator function (CMIF) methods. The unified matrix polynomial approach provides a common formulation that encourages a discussion of the similarities and differences of the commonly used methods as well as a discussion of the numerical characteristics. Complete details concerning all experimental structural dynamics methods in use today can be found in another Handbook chapter titled ▸ Chap. 10, "Experimental Modal Analysis Methods."

4.2.1 Sinusoidal Input-Output Method

Methods covered by this category involve excitation that consists of only one frequency during the observation period. While excitation involves only one frequency, the response will initially involve many frequencies due to the initiation of the excitation (transient). Even after this initial transient, the response may contain energy at more than one frequency due to the harmonic distortion of the excitation caused by system nonlinearities. This harmonic distortion is normally removed by filtering the response before the data is processed, leaving a single frequency of information in both the input and output signals.

The sinusoidal input/output methods require minimal data acquisition capabilities but generally involve more sophistication in the test setup or in the post-processing of the acquired data. Since only a single frequency is present in the input and output signals, analog time domain methods or, at most, small block size fast Fourier transform (FFT) methods can be used to determine signal amplitudes. Depending upon the approach used, this data will yield the modal parameters somewhat directly or will require considerable post-processing. In the forced normal mode approach, the configuration of the test setup (location and phasing of multiple

exciters) yields the modal parameters somewhat directly. In the forced response decomposition approach, the test setup is very general (and similar), but the modal parameters are found using an elaborate post-processing procedure.

Forced Normal Mode Excitation Method The forced normal mode excitation method of experimental modal analysis is the oldest approach to the estimation of dynamic structural parameters. This approach is the first method to use the application of multiple inputs in the estimation of modal parameters. Currently, this method is still used in the aerospace industry for ground vibration testing of aircraft structures. This method was originally outlined in an article by Lewis and Wrisley in 1950 [16] and begins with the matrix form of the differential equation for the system being tested, Equation 1.

$$[M]\ \{\ddot{x}(t)\}\ +\ [C]\ \{\dot{x}(t)\}\ +\ [K]\ \{x(t)\}\ =\ \{f(t)\} \tag{1}$$

Very simply stated, Lewis and Wrisley found that a number of exciters, utilizing a common frequency and monophase amplitudes, could be tuned to exactly balance the dissipative forces in a structure. This is represented by Equations 2 and 3 and occurs when the phase lag angle ϕ lags the input force by 90° at every response location.

$$\{f(t)\} = \{F\}\sin(\omega t) \qquad \{x(t)\} = \{X\}\sin(\omega t + \phi) \tag{2}$$

$$\{f(t)\} = [C]\,\{\dot{x}(t)\} \tag{3}$$

When the force balance is achieved, the differential equations of motion describing the structure can be reduced to the undamped homogeneous differential equations of motion at that particular frequency. This is represented by Equation 4

$$[M]\,\{\ddot{x}(t)\} + [K]\,\{x(t)\} = \{0\} \tag{4}$$

In order to more thoroughly explain this phenomena, De Veubeke published an article [17] which explains the theoretical basis for this testing in terms of characteristic phase lag theory. Further development of the practical application of this theory was enhanced by the concept of effective number of degrees of freedom by Trail-Nash [18].

This concept explains that the required number of exciters is a function of the effective number of degrees of freedom, not the total number of degrees of freedom. The effective number of degrees of freedom (N_e) is a function of modal density and damping. Finally, Asher utilized the determinant of the real part of the frequency response matrix to locate damped natural frequencies and determine the effective number of degrees of freedom [19]. Most of the work done since 1958 has been concerned with improvements in the implementation of the method, primarily the force appropriation [20, 21] using digital data and FFT data processing.

One of the most advanced implementations of this method involves approximately 500 channels of data acquisition and co/quad analysis equipment controlled from a minicomputer. Extensive tuning criteria are utilized as well as real-time animated displays of the modal vector as well as of the out of phase response. This can be particularly useful for optimum exciter location as well as force appropriation. Once a modal vector is tuned using a 90° phase lag angle criteria, the excitation frequency can be varied with no change in modal vector. Theoretically, this can be used as a check to determine whether the modal vector has been adequately tuned.

In addition to this potential confidence check, the excitation can be removed from the system once a modal vector is tuned. If the modal vector contains only responses due to a single mode of vibration, the exponential decay at all response positions should contain only the excitation frequency, and the envelope of exponential decay should give an accurate estimate of the system damping.

The forced normal mode excitation method works well in the presence of proportional damping but theoretically does not include the concept of complex modes of vibration nor the concept of repeated and multiple roots. (Proportional damping is a mathematical approach to the description of damping that states that the damping matrix resulting from whatever damping mechanism that is present is either proportional to the mass matrix, the stiffness matrix, or to some linear combination of the two.) Due to this theoretical limitation, the practical application of the 90° lag criteria is normally applied only to within plus or minus 10°. Likewise, added difficulty is encountered in evaluating the exponential decay purity as well as force appropriation. Much work has been done on automated tuning algorithms to alleviate this. These algorithms alter excitation magnitude and phase to try to achieve 90° phase lag criteria under severe impedance matching situations. Unfortunately, the location of the excitation cannot be evaluated automatically in this process.

Forced Response Decomposition Method The forced response decomposition method uses an array of exciters (multiple input) to excite the system into a forced response at a single frequency. While the magnitude of each input and the phasing between inputs may be chosen randomly or according to some particular regime, the inputs are held constant during the observation period. Therefore, after the initial transient decays, the response is a steady-state forced response of this system. A forced response vector is created by using all output points of interest simultaneously. This is represented by Equations 5 through 7.

$$[M]\ \{\ddot{x}(t)\} + [C]\ \{\dot{x}(t)\} + [K]\ \{x(t)\} = \{f(t)\} \tag{5}$$

$$\{f(t)\} = \{F\}\sin(\omega_k t) \tag{6}$$

$$\{x(t)\} = \{X\}\sin(\omega_k t - \phi_k) \tag{7}$$

The forced response vector that is generated, by definition based upon linear vibration theory, must be a linear superposition of the modal vectors of the system (expansion theorem). Since in a given frequency range of interest, N modal vectors will contribute to the response, the individual modal vectors cannot be determined from one forced response vector. If N or more independent forced response vectors can be generated, the N modal vectors can be determined. A large number of independent forced response vectors can be generated by two approaches. First of all, at a single frequency, many different input vectors can be generated with randomly chosen magnitudes and relative phasing. Each of these choices will yield a potentially independent forced response vector. Secondly, this process can be repeated for different frequencies which will, once again, yield potentially independent forced response vectors. Since the degree of independence among the forced response vectors is unknown and since the best estimate of the modal vectors is desired, many more forced response vectors, compared to the number of expected modal vectors (N), are acquired.

The post-processing of the forced response vectors involves using a singular value decomposition of the data spanned by the forced response vectors. If N_V forced response vectors are acquired (where $N_V \gg N$), the number of significant singular values in the $N_V \times N_V$ data space is an indication of the number of contributing modal vectors in the data. The singular vectors, associated with the significant singular values, provide a transformation matrix to transform the forced response vectors to modal vectors. Frequency and damping values are found in a second stage solution process. If frequency response functions or the input vectors required to force a specific normal mode are desired, these characteristics can be found at this time as well.

The forced response decomposition method, in one form or another, is currently receiving much research attention [22, 23].

While the methods have not been used commercially to this point, the methods are very attractive due to minimal data acquisition requirements (when the data acquisition has been specifically designed for this method) and due to sophisticated post-processing techniques which require minimal computational power (micro-computers or minicomputers).

4.2.2 Frequency Response Function Method

The frequency response function method of experimental modal analysis is the most commonly used approach to the estimation of modal parameters. This method originated as a testing technique as a result of the use of frequency response functions in the forced normal mode excitation method to determine natural frequencies and effective number of degrees of freedom. With the advent of the computer and minicomputer, the frequency response function method became a separate, viable technique [24, 25, 26].

In this method, frequency response functions are measured using excitation at single, or multiple, points. The relationships between the input ($F(\omega)$) and the response ($X(\omega)$) for both single and multiple inputs are shown in Equations 8 through 12.

Single Input Relationship

$$X_p = H_{pq}\ F_q \tag{8}$$

While Equation 8 could be used directly to estimate the FRF, averaged power spectra methods are normally used to reduce noise and get a best least-squares estimate if the FRF. This formulation is shown in Equation 9.

$$H_{pq} = \frac{G_{XF_{pq}}}{G_{FF_{qq}}} \tag{9}$$

Multiple Input Relationship

$$\begin{bmatrix} X_1 \\ X_2 \\ \cdot \\ \cdot \\ X_p \end{bmatrix}_{N_o \times 1} = \begin{bmatrix} H_{11} & \cdots\cdots & H_{1q} \\ H_{21} & & \cdot \\ \cdot & & \cdot \\ \cdot & & \cdot \\ H_{p1} & \cdots\cdots & H_{pq} \end{bmatrix}_{N_o \times N_i} \begin{bmatrix} F_1 \\ F_2 \\ \cdot \\ \cdot \\ F_q \end{bmatrix}_{N_i \times 1} \tag{10}$$

While Equation 10 represents the multiple input, multiple output (MIMO) relationship, averaged power spectra are used to estimate the FRF matrix, typically one row at a time. The MIMO estimation procedure utilizes an inverse of the $[G_{FF}]$ matrix. This places a numerical constraint on the $[G_{FF}]$ matrix. Details concerning the estimation of FRFs can be found in the Handbook chapter titled ▸ Chap. 6, "Frequency Response Function Estimation."

$$[H][G_{FF}] = [G_{XF}] \tag{11}$$

$$[H] = [G_{XF}][G_{FF}]^{-1} \tag{12}$$

If all or part of the elements of the frequency response matrix can be measured, each column will contain information which can be used to estimate modal vectors. Since the frequency response matrix is considered to be symmetric due to the Maxwell-Betti relations, each row will also contain the information needed to estimate modal vectors.

Often Equations 13 through 16 and Equation 17 are altered by an assumption of real modes, a specific damping mechanism, or known system poles. Under such assumptions, the estimation of the modal parameters may become simpler. Most current research and development in the area of the frequency response function method involves the modal parameter estimation algorithms that are related to the

time or frequency domain models equivalent to Equations 13 through 17. Much of this work involves algorithms that utilize as much of the redundant information within multiple rows and columns of the frequency response function matrix as possible.

Modal parameters are estimated from FRFs using a variety of modal parameter estimations today, but during the time period from 1965 to 1985, modal parameter estimation was limited to mostly single degree of freedom (SDOF), single reference methods. The time period from 1978 to 1985 was the beginning of multi-reference modal parameter estimation algorithms that are now widely used to process MIMO FRFs into modal parameters.

The frequency response functions are used as input data to modal parameter estimation algorithms that estimate modal parameters using a frequency domain model. Through the use of the fast Fourier transform, the Fourier transform of the frequency response function, the impulse response function, can be calculated for use in modal parameter estimation algorithms involving time domain models:

$$[H(\omega_i)]_{N_L \times N_S} = \sum_{r=1}^{N} \frac{[A_r]_{N_L \times N_S}}{j\omega_i - \lambda_r} + \frac{[A_r^*]_{N_L \times N_S}}{j\omega_i - \lambda_r^*} = \sum_{r=1}^{2N} \frac{[A_r]_{N_L \times N_S}}{j\omega_i - \lambda_r} \tag{13}$$

$$\left\{H_{pq}(\omega)\right\}_{N_L \times 1} = \sum_{r=1}^{2N} \frac{\left\{A_{pqr}\right\}_{N_L \times 1}}{j\omega - \lambda_r} \tag{14}$$

$$[\, H(\omega)\,]_{N_S \times N_L} = \sum_{r=1}^{2N} \frac{[\, A_r\,]_{N_S \times N_L}}{j\omega - \lambda_r} \tag{15}$$

Noting that

$$A_{pqr} = L_{pr}\psi_{qr} \tag{16}$$

When Equations 13 through 16 are applied to the estimation of modal vectors, the relationships between the references (known as the modal participation vectors ($[L]$)), and the complex valued modal frequencies, λ_r, are already known. This allows the equation to be rearranged to take this a priori information into account.

Most of the work over the last 25 years has focused on the measurement of multiple columns of the frequency response function matrix simultaneously. This work has involved establishing the numerical and excitation requirements for solving the relationship identified in Equation 10, developing alternate estimation algorithms and developing modal parameter estimation algorithms that are matched to this new data acquisition/estimation procedure. This work has revolutionized experimental modal analysis testing for several reasons. First of all, in order to be sure that all modal vectors have been found experimentally, a number of excitation (reference) points must be utilized, either one at a time or simultaneously. This

minimizes the possibility of exciting the system at or near a node of one of the modal vectors which would provide inaccurate estimates of that modal vector. Secondly, multiple columns (or rows) of the frequency response function matrix are necessary for the detection of repeated or pseudo-repeated (close) modal frequencies. The ability to measure, detect, and identify the presence of repeated or close modes was not generally possible prior to this research. Finally, the increased number of measurements per measurement cycle obtained using multiple inputs does not affect the time required to acquire frequency response function data adversely. Therefore, a more complete set of data, allowing for a more complete dynamic model of the system to be validated, is possible in the same measurement time.

4.2.3 Damped Complex Exponential Methods

The damped complex exponential response methods of experimental modal analysis are approaches that have received considerable attention in the 1970s. These methods are normally formulated to utilize data corresponding to the free decay of a system generated by the release of an initial condition but apply quite generally to impulse response function data as well. Since impulse response function data is scaled to include the forcing condition, use of this method on impulse response function data yields properly scaled modal parameters that can be used to calculate proper modal scaling (generalized mass and stiffness). This is not possible if free decay responses are used. Even so, the formulation of the impulse response function generally involves the computation of the frequency response function (FRF) via a fast Fourier transform (FFT), potentially introducing digital signal processing (DSP) bias errors such as leakage, which may degrade the estimation of the modal parameters.

In order to obtain estimates of the modal vectors, the damped complex exponential response functions, normally the impulse response functions, are used as input in a parameter estimation scheme based on one of Equation 17. Note that if the true damped complex exponential response function can be measured in the time domain, such as a free decay response, bias errors such as leakage will not be a problem since the fast Fourier transform is not used.

$$[h(t)]_{N_L \times N_S} = \sum_{r=1}^{N} [A_r]_{N_L \times N_S} e^{\lambda_r t} + [A_r^*]_{N_L \times N_S} e^{\lambda_r^* t} = \sum_{r=1}^{2N} [A_r]_{N_L \times N_S} e^{\lambda_r t} \tag{17}$$

While the current implementation of methods based upon damped complex exponentials is relatively recent, the basis of much of the work was formulated in the eighteenth century by Prony [27]. Currently, the three approaches, that are widely used, are the Ibrahim time domain (ITD) approach, the polyreference time domain (PTD) approach, and the eigensystem realization algorithm (ERA) approach. These methods are discussed briefly in the following sections as well as in detail in the Handbook chapter on ▸ Chap. 10, “Experimental Modal Analysis Methods”.

Ibrahim Time Domain (ITD) Approach One practical implementation of the damped complex exponential method is the Ibrahim time domain (ITD) method [28, 29] developed to extract the modal parameters from damped complex exponential response information. Digital free decay response data are measured at various points on the structure. If response data from all the selected measurement positions cannot be obtained simultaneously because of equipment restrictions, a common position is retained between measurement groups. A recurrence matrix is created from the free decay data, and the eigenvalues of this matrix are exponential functions of the poles of the system, from which the poles are easily computed. The eigenvectors of the recurrence matrix are response residues, from which the mode shapes are determined. The Ibrahim time domain method generates a matrix polynomial characteristic equation with matrix dimension equal to the number of response sensors (N_o) and low model order.

The damped complex exponential response method is rather straightforward in application if the necessary data acquisition hardware, computer facilities, and software are available. This approach computes the poles and residues based upon a specific initial vibration condition of the structure. A number of different initial conditions can be established, analogous to the practice of using several exciter positions in ordinary single input modal surveys, until all the important modes have been excited. All the modes cannot be established from one exciter position, and likewise all the modes cannot be determined from one initial condition.

Although this technique is based upon free decay data, the ITD method can also be used with operating inputs if the free decay is computed from the operating inputs by using *random-decrement averaging* or from measured auto- and cross-correlation functions. Again, it should be emphasized that this can only be done if there are no poles or zeros in the input spectrum in the frequency range of interest. An additional development by Ibrahim with respect to this technique is the concept of *modal confidence factor* [29].

The modal confidence factor is a complex number calculated for each identified mode of the structure, while undergoing an exponential decay form of vibration test. The modal confidence factor is based upon the modal deflection at a particular measurement point being related to the modal deflection at that same measurement point at any time earlier or later in the free decay response. Therefore, if modal vectors are estimated from exponential decay data and two separate estimates are calculated from sets of data taken some fixed time Δt apart, the relationship between the measured second estimate of the modal vector and the calculated estimate of the modal vector based upon the measured first estimate of the modal vector is defined as the modal confidence factor. The purpose of the modal confidence factor is to provide an indicator for determining whether an estimated modal vector is real or computational.

Polyreference Time Domain (PTD) Approach In 1979, a least-squares complex exponential (LSCE) algorithm was developed to utilize all measured impulse response function (IRF) data (or free decay data) to estimate a single set of modal frequencies [30]. Note that IRF data is commonly estimated from the inverse FFT

of the measured FRFs. While the LSCE method could utilize data from multiple references (inputs), the algorithm did not formulate the estimation problem in a matrix sense and only used a scalar coefficient polynomial solution. Most of the comments relative to the ITD approach can also be repeated with respect to the LSCE approach. Of particular importance, once again, is the desirability of acquiring all response data simultaneously to reduce time invariance problems.

A more complete MIMO implementation of the damped complex exponential approach to experimental modal analysis is the polyreference time domain (PTD) approach developed by Vold [31, 32, 33]. In contrast to the LSCE approach, the polyreference time domain approach utilizes all measured damped complex exponential information, from all references or initial conditions, simultaneously in the estimation of modal frequencies. Since multiple initial conditions or reference data is accounted for in the algorithm, the polyreference time domain method is the first estimation algorithm to be able to solve for closely spaced or repeated roots (matrix coefficient polynomial solution). Additionally, the PTD approach broke new ground in the estimation of a single modal coefficient for each measurement degree of freedom in the presence of multiple initial conditions or references. This characteristic is shared by the frequency response function method when the polyreference frequency domain (PFD) approach is used as the parameter estimation algorithm and with some of the approaches within the mathematical input-output model methods. The formulation of the algorithm such that constraints are included to account for redundant information is an advantage but requires that the total dataset be acquired so as to match this assumption. The data acquisition best matches the analysis procedure when all of the data can be acquired simultaneously. The polyreference time domain method generates a matrix polynomial characteristic equation with matrix dimension equal to the number of reference sensors (N_i for a multi-shaker test and N_o for a roving impact hammer test) and high model order.

While much of the work utilizing the polyreference approach is quite recent, the evaluation of the method based upon comparisons between experimentally measured and synthesized frequency response functions is quite impressive when compared to other modal parameter estimation approaches.

Eigensystem Realization Algorithm Approach The eigensystem realization algorithm (ERA) approach is another technique that is basically an extended version of the Ho-Kalman system realization algorithm [34, 35, 36]. The ERA algorithm was developed at NASA-Langley Research Center under an interdisciplinary effort involving structural dynamics and controls. This method is similar to the other damped complex exponential methods in that all involve solutions of a matrix eigenvalue problem. Since the ERA approach utilizes multiple reference data, the ERA approach is similar to the polyreference time domain (PTD) approach. This means that repeated roots can be identified with this approach as well as the polyreference time domain approach. Other significant attributes of this approach include the extensive use of accuracy indicators to assess effects of noise and nonlinearities as well as rank information provided by singular value decomposition techniques.

The ERA approach is based upon well-established realization (state-space) theory using the concepts of controllability and observability. The approach determines a complete state-space model based upon the important principles of minimal realization theory attributed to Ho and Kalman. The Ho-Kalman procedure uses a sequence of real matrices known as Markov parameters (impulse response functions) to construct a state-space representation of a linear system. The ERA approach begins with a block data matrix formulated from damped complex exponential functions, such as free decay responses. This block data matrix is similar to a general Hankel matrix and includes information from several initial conditions and a weighted set of damped complex exponential functions. The weighted set of functions means that points of interest or points with large response can be emphasized without loss of capability of the method. The state-space matrices are found from the block data matrix by factorization of the block data matrix using singular value decomposition. Based upon the rank evaluation of the block data matrix in this factorization procedure, a state-space set of matrices can be formulated based on the reduced order. In eigenvalues and eigenvectors of this reduced order, state-space model are then found. Accuracy indicators such as the rank of the block data matrix, modal amplitude coherence, modal phase collinearity, and data reconstruction are used to identify the final set of modal parameters. The eigensystem realization algorithm (ERA) generates a matrix polynomial characteristic equation with matrix dimension equal to the number of response sensors (N_o) and low model order.

The ERA approach is a recent method that demonstrates extensive use of accuracy indicators. Several studies comparing multiple reference algorithms indicate good agreement between all methods, but the identification of nonrealistic modal parameters is still a significant problem. The ERA approach, through the extensive development and use of accuracy indicators, attempts to deal with this part of the identification problem more completely than most other approaches. The accuracy indicators utilized in the ERA approach are already being applied to several other approaches with similar success. The primary limitation of this and other low- order methods is the amount of computer memory required to solve the problem for cases with a large number of response sensors.

4.2.4 Mathematical Input-Output Model Method

The experimental modal analysis methods that are included within the category of mathematical input-output model methods are those approaches that generally involve input and response data independently without the need for creating auto and cross moment functions. There is no other restriction with regard to time or frequency domain models, effective number of degrees of freedom, etc. On this basis, two approaches are currently in use that can be described in this fashion. First of all, the autoregressive moving average approach is a time domain formulation that utilizes a pole-zero model as the basis for the description of the system characteristics. While this model is appropriate, the model cannot be easily constrained to account for known system information. Additionally, although the current application of this technique does not involve multiple inputs, the theoretical background for the multiple input case is well developed.

The other approach currently in use involves a reduced structural matrix model for the basis of the description of the system characteristics. This model involves the reduced mass, stiffness, and damping matrices with regard to the measured degrees of freedom. This model easily accounts for constraints such as known elements in the mass, stiffness, and damping matrices or known characteristics of the distribution within the matrices such as symmetric or banded characteristics. This method also incorporates the multiple input case routinely as known terms in the forcing vector of the matrix differential equation that serves as the mathematical model. These two approaches to experimental modal analysis will be briefly described in the following paragraphs.

Autoregressive Moving Average Approach One approach to estimating the modal characteristics from time domain input-output data is the *autoregressive moving-average (ARMA)* procedure. This method has been applied to the determination of structural parameters by Gersch [37, 38, 39, 40, 41] and Pandit [42, 43]. With this technique the response data is assumed to be caused by a white random noise input to the structure. The technique computes the best statistical model of the system in terms of its poles (from the autoregressive part) and zeros (from the moving-average part), as well as statistical confidence factors on the parameters. It has been primarily used to estimate the characteristics of buildings being excited by wind forces. The data used in the computational process are the autocorrelation functions of the responses measured at various points on the structure. Since in the general case the inputs are not measured, the modal vectors are determined by referencing each response function to a single response to provide relative magnitude and phase information.

Paralleling the development of the FRF equations (Equations 8 and 10), a time domain model representing the relationship between a single response degree of freedom and a single input degree of freedom can be stated as follows:

$$\sum_{k=0}^{m} \alpha_k \; x\,(t_{i+k}) = \sum_{k=0}^{n} \beta_k \; f\,(t_{i+k}) \tag{18}$$

For the general multiple input, multiple output case:

$$\sum_{k=0}^{m} [\alpha_k]\,\{x\,(t_{i+k})\} = \sum_{k=0}^{n} [\beta_k]\,\{f\,(t_{i+k})\} \tag{19}$$

The above model, in the time domain, is also known as an autoregressive moving-average (ARMA(m,n)) model when developed from a set of discrete time equations in the time domain.

If the discussion is limited to the use of free decay or impulse response function data, the previous time domain equations can be simplified by noting that the forcing function can be assumed to be zero for all time greater than zero. If this is the case, the $[\beta_k]$ coefficients can be eliminated from the equations.

$$\sum_{k=0}^{m} [\alpha_k] [h\,(t_{i+k})] = 0 \tag{20}$$

Additional equations can be developed by repeating Equation 20 at different time shifts (initial times t_i) into the data until all data or a sufficient overdetermination factor is achieved. Note that at least one time shift is required in order to accurately estimate conjugate modal frequencies. More properly, this model is known as the autoregressive with eXogenous inputs (ARX(m,n)) model.

The solution for the autoregressive moving average coefficients proceeds in a two stage least-squares fashion in the Gersch solution. In the first stage a *long* autoregressive model is solved linearly by using the Yule-Walker equations. This process uses output covariance functions to determine the autoregressive coefficients based upon a determination of the order of the autoregressive model. The second stage involves setting up an equivalent moving average model for the output involving convolution of the impulse response function and the input function. This procedure also involves computations using covariance functions and results in the least- squares computation of the moving average coefficients. Since the solution for the autoregressive moving average coefficients, and thus the structural parameter estimates, are statistically based, statistical confidence factors, called coefficients of variation, for the natural frequencies and damping can be easily calculated. These coefficients represent the ratio of standard deviation of each parameter with respect to the actual parameter.

Note that if the response function $x(t)$ is replaced by the impulse response function $h(t)$ and the forcing function $f(t)$ is replaced by an impulsive force (unity at time 0, zero after time 0), the ARMA approach is essentially the same approach as the damped complex exponential response methods (PTD, ITD, ERA).

Reduced Structural Matrix Approach Over the period of time from 1965 to 1985, there has been increasing interest in being able to estimate reduced structural (mass, stiffness, and damping) matrices from experimental data. Most of these methods are based upon an indirect approach utilizing the estimated modal parameters to synthesize the reduced matrices.

An algorithm has been developed in Germany by Link and Vollan [44] which attempts to use frequency domain input and response data to directly estimate the reduced matrices. This method has been designated Identification of Structural System Parameters (ISSPA) [45]. Leuridan used this formulation as a starting point and has published results [46, 47, 48] using the same general approach for the estimation of modal parameters referred to as the direct system parameter identification (DSPI) method. Since modal parameters are found as a result of the solution of the eigenvalue problem using the reduced matrix estimations, the process of estimating the reduced matrices may represent the ultimate goal in experimental modal analysis. If this process could be correlated with a purely theoretical finite element approach, the engineering design cycle would be complete.

Since there are many more known pieces of information (input and output information at different times) than unknowns that must be estimated, the solution, then, is a function of the pseudo-inverse procedure chosen. Leuridan and Vold have evaluated pseudo-inverse numerical procedures utilizing the normal equations, least-squares approach, and the Householder reflections approach. Since the system matrix that results is often ill-conditioned, the Householder reflections approach yields more numerical precision for a given computational word size but at a sacrifice in speed.

Link and Vollan formulate the pseudo-inverse based upon a singular value decomposition procedure under the restriction that the rank of the data-dependent matrices is equal to the effective number of degrees of freedom. This effective number of degrees of freedom is dependent upon the number of theoretical system poles in the frequency range of interest, the accuracy of the measured data, and the computational precision of the computer with respect to the solution algorithm utilized.

Once the unknown elements of the mass, stiffness, and damping matrices are found, the modal parameters are estimated from the $[M]$, $[C]$, and $[K]$ matrices by way of a complex eigenvalue-eigenvector solution algorithm such as the QR algorithm.

A confidence or validity check of the frequencies, damping factors, and modal vectors can be performed using a back substitution procedure. The dynamic response is calculated and compared to the original measured response. The agreement between these responses is regarded as a measure of the accuracy of the estimated modal parameters.

This approach has not generated the anticipated results due to a number of reasons. First of all, regardless of the approach used, the solution for the reduced matrices is not unique. There are many combinations of matrix relationships that can be generated from the given set of estimated modal parameters. Second, the reduced frequency range of the modal parameter estimates means that the matrices will be weighted to represent an incomplete model. Third, the limitation of the precision of the modal parameter estimates as a result of commonly accepted experimental error tends to desensitize the process of estimating the reduced matrices. Finally, the problem of invalid modal parameter estimates will obviously result in invalid estimates of reduced matrices.

4.3 Summary

The modal parameter estimation classifications that are included in Sect. 4.2 are often presented in the literature as one of many modal parameter estimation methods summarized by the acronyms, titles, and references cited in Table 1. These modal parameter estimation methods are explained in more detail in ▸ Chap. 10, "Experimental Modal Analysis Methods."

Table 1 Acronyms – Experimental modal parameter estimation algorithms

Modal parameter estimation algorithms	
CEA	Complex exponential algorithm [49,30]
LSCE	Least-squares complex exponential [30]
PTD	Polyreference time domain [31,32]
ITD	Ibrahim time domain [28,50]
MRITD	Multiple reference Ibrahim time domain [51]
ERA	Eigensystem realization algorithm [34,35,52]
PFD	Polyreference frequency domain [53,54,55,56]
FDPI	Frequency domain direct parameter identification [55,56]
SFD	Simultaneous frequency domain [57]
MRFD	Multi-reference frequency domain [58]
RFP	Rational fraction polynomial [47,59,60]
OP	Orthogonal polynomial [60,61,62,63,64,65,66,67,68,69,70,71]
PLSCF	Polyreference least-squares complex frequency [72,73,74,75,76,77]
CMIF	Complex mode indication function [78]

5 Conferences

A number of conferences began during the time period shortly after experimental data acquisition and analysis hardware became available to serve both researchers and practitioners in the area of experimental structural dynamics. The notable conferences that began due to the experimental hardware becoming available were the International Seminar on Modal Analysis (ISMA) at the Katholieke University of Leuven (KUL) in Belgium, the International Modal Analysis Conference (IMAC) sponsored originally by Union College in Schenectady, New York, the SAE Noise and Vibration Conference (SAE-NVC), and the Shock and Vibration Symposium (SVS). These conferences continue to this day. Several other professional societies (ASME, AIAA, and the American Helicopter Society (AHS)) also began to have focused sessions on experimental structural dynamics topics after these four conferences led the way. All of the following conferences have archives of the conference papers available from the sponsors.

5.1 ISMA

The International Seminar on Modal Analysis (ISMA) began in 1975 at the KUL in Leuven, Belgium. Professor Raymond Snoeys of KUL together with Professor David Brown of the University of Cincinnati (UC) and a number of KUL graduate students developed a seminar for industry on the topic of modal analysis. Hewlett Packard assisted in inviting researchers from European companies and universities that were starting to use the data acquisition hardware who were interested in learning about the topic. Beginning in 1980, an ISMA conference was added, and

researchers were invited to submit papers on their research and topics of interest. This conference has been held biennially since that time. The 30th edition of the Biennial ISMA Conference on Noise and Vibration Engineering will be held in 2022 at KUL at the same time as the 2022 ISMA Seminar. Further details can be found at https://www.isma-isaac.be/.

5.2 IMAC

The International Modal Analysis Conference (IMAC) began with its first conference in 1982, organized by Dick DeMichele and Peter Juhl at Union College in Schenectady, New York. Dick and Peter solicited ideas and potential attendee lists from many researchers in the area of experimental modal analysis as well as from many of the companies involved in hardware development and/or use of the technology. During the years 1982–1986, the conference was sponsored by Union College followed by cosponsorship by Union College and the Society for Experimental Mechanics (SEM) during the years 1987–1991. Beginning in 1991, SEM assumed responsibility for the organization and management of IMAC, while Union College continued in the role of consulting partner until 1996. Dick DeMichele, a well-known researcher already a member of SEM, continued as IMAC technical director until 1995 as SEM began to take the lead on most management and organizational roles [3]. Today IMAC is one of two annual conferences sponsored by SEM where the organization and management of both conferences is under the technical divisions (TDs) and focus groups (FGs) of the Society. Further details about the next IMAC can be found at https://sem.org/imac.

5.3 Other Conferences

SAE-NVC In the 1980s, the Society of Automotive Engineering (SAE) began to notice an increase in publications in the noise and vibration areas. In response to this, the SAE developed the Noise and Vibration Conference (NVC) first held in Traverse City, Michigan. Due to the strong interest in automotive applications, the SAE-NVC held a biennial conference that advanced many applications in the area of experimental structural dynamics. Generally, this conference has been held biennially, in May or June, at locations in the midwestern region of the USA, close to the automotive industry (Traverse City, Grand Rapids, etc.), but the schedule has changed due to recent events. The next scheduled SAE-NVC is in September 2023. Further details about the next SAE-NVC can be found at https://www.sae.org/attend/nvh.

SVS The annual Shock and Vibration Symposium (SVS) is another forum for the structural dynamics and vibration community to present and discuss new developments and ongoing research. The Symposium was established in 1947 and typically includes both unclassified (unlimited and limited distribution) and

classified sessions. Topics covered at the symposium include shock-ship testing, water shock, weapons effects (air blast, ground shock, cratering, penetration) shock physics, earthquake engineering, structural dynamics, and shock and vibration instrumentation and experimental techniques. The next scheduled conference is the 91st Symposium, and it will be held in September 2023. Further details about the next SVS can be found at http://savecenter.org/symposium.html.

6 Publications and Books

There are a number of publications and books that have been heavily referenced by conference proceedings and journal publications over the past years. Some of these references are well-known, and some other important references are a bit obscure. The following are some of interest to those in the experimental structural dynamics area.

Sound and Vibration Magazine The Sound and Vibration Magazine began publication in 1967 specifically to serve practitioners and researchers in the sound and vibration industry. Jackson "Jack" Mowry served as the editor for this entire period. This magazine is notable in that (1) topical research articles, many in the area of experimental structural dynamics, were published throughout the more than 50 years of the magazine's existence, and (2) the magazine was made available to readers at no charge. The importance of the Sound and Vibration Magazine can not be overstated with respect to the dissemination of experimental structural dynamics information over the last 50 years.

The 50th anniversary issue was celebrated in January 2017. After 2017, the publication moved to bimonthly, and then, beginning in 2018, the magazine became part of Tech Science Press as a bimonthly and now as a quarterly, online journal. Past issues of Sound and Vibration Magazine can be found at *SandV.com* at no charge. The online version of the current Sound and Vibration can be found at *TechSciencePress.com*

Handbooks A number of handbooks have been published since the early 1990s that have attempted to collect and organize material pertinent to the area of experimental structural dynamics, much in the same way as this Handbook of Experimental Structural Dynamics is attempting. The following list of handbooks contains the most well-known, but the authors apologize for any that have been left out.

The oldest handbook that included a number of areas of interest to those in the experimental structural dynamics area is the Shock and Vibration Handbook, published in 1961, edited by C.M. Harris of Columbia University and C.E. Crede of the California Institute of Technology (CalTech). The chapter topic of Experimental Modal Analysis first appears in the 1988 Third Edition [79] and subsequent editions.

The First Edition of the SEM Handbook on Experimental Mechanics edited by A.S. Kobayashi and published in 1987 focused on experimental mechanics topics of

interest to the Society. This first edition of the Handbook and the subsequent second edition in 1994 also included a chapter topic of Experimental Modal Analysis [80].

The first handbook dedicated to the area of structural testing is the SEM Handbook on Structural Testing published in 1993 just as modern, digital methods were being applied to many areas of structural testing. The editors for this handbook, Reese and Kawahara, and many of the chapter authors were SEM members with strong affiliations with Sandia National Labs [81].

Government Reports A number of technical reports have provided initial research and information that is still useful background and reference material. It is notable that several of these reports eventually became textbooks that are still widely cited and used today.

A number of technical reports generated by USAF contracts beginning in 1965 provided the basis of much of the early digital signal processing methodology. Two of these early contracts were with Measurement Analysis Corporation, providing the numerical and statistical background of frequency response, coherence, and multiple coherence [82, 83]. Note that many of these concepts did not find their way into experimental hardware and software until the early to late 1970s. These concepts were in practice in the late 1970s and early 1980s and were subsequently documented in several later USAF contract reports [84, 85, 86, 87, 88, 89, 90].

A number of these same authors developed monographs for the Naval Research Laboratory as part of the US Department of Defense (DOD), Shock and Vibration Information Center's (SAVIAC) Shock and Vibration Monograph Series (SVM-1 through SVM-12) during the time period 1967–1986. Probably the most notable monograph in the series is SVM-3 by L.D. Enochson and R.K. Otnes [91].

A more recent contribution (1996) from a government agency is the Dynamic Test Agency Handbook from the Dynamic Testing Agency (DTA) in the UK [92]. The original DTA was set up in the late 1980s through a collaboration between industry and the UK's Department of Trade and Industry to disseminate best practice to the structural dynamic community. Its output was primarily biased toward the testing community not only to provide fundamental advice on how to implement effective testing but also to inform users on the analysis and interpretation of results. One of the objectives of the original group was to bring together test and analysis to exploit the complementary aspects of each approach. The Handbook was originally available only to the DTA members but now can be accessed via NAFEMS at https://www.nafems.org/community/working-groups/dynamics-working-groups/structural-dynamics/dta_handbook/.

Textbooks There are really only two or three textbooks that have been written that focus on experimental modal analysis. The first text was by Dr. David Ewins from Imperial College in 1984 [93]. This text is comprehensive for the year that it was written, but many contributions have been made from 1980 until now that were not included. A more recent text is a contribution by Dr. Peter Avitabile [94] that includes many of the advances particularly in MIMO methodology and experimentally based modeling of the last 25 years. Another recent text is from

Dr. Robert Coppolino from Measurement Analysis Corporation [95] that is a little more narrow in scope but adds much to the textbook publication arena to fill in the state of the art. Hopefully, this Handbook will be even more comprehensive and expansive and will provide the documentation of all important activities in experimental structural dynamics over the last 50–60 years.

Some other texts are notable starting with texts in the applied mathematics area. The oldest text concerns elementary matrix methods by Frazer, Duncan, and Collar from 1938 [96]. This text introduced the matrix operation methodology that moves higher-order polynomials to first order and allowed second-order differential equations to be written as first-order, eigenvalue form. Today, this is known as state-space methodology, and it is used in all higher-order, matrix coefficient polynomials used in MIMO modal parameter estimation methods.

Many methods in experimental modal analysis and in experimental modeling utilize eigenvalue-eigenvector methods that were first comprehensively discussed by Wilkinson in 1965 [97]. Other texts in the area of applied linear algebra were introduced about that time in the first edition textbook by Strang [98] somewhere around 1965.

One very notable series of textbooks in the applied digital signal processing area were authored by Julius Bendat and Allan Piersol beginning in 1966 [99]. This book was followed by several editions of a more detailed book by Bendat and Piersol in 1971 and 1986 [100,24]. It should be noted that the 1971 first edition is widely cited in the experimental structural dynamics area, but the second edition made important changes to concepts like partial coherence. A similar book to the 1971 first edition of Bendat and Piersol is the book by Otnes and Enochson. This book first appeared in 1972 [101] after appearing in print as part as the Naval Research Lab Monograph SVM-3 in 1968 [91]. All of these texts were extensively cited in early work in the experimental structural dynamics area.

Several current mechanical vibration textbooks have some documentation of vibration testing and the relationship to experimental structural dynamics. These are too numerous to reference here. However, the mechanical vibrations text by J.P. Den Hartog, first edition, published in 1934 was unique in that the text extensively documented experimental problems and applications [102] of that era. While obviously quite dated, the Den Hartog book is still enjoyable reading.

Dr. Roy Craig, Jr. authored a textbook [103] in 1982 that is one of the few textbooks to address many structural dynamic related topics. The text contains basic SDOF/MDOF vibration theory found in many vibration texts but also continues on with finite element modeling basics and expands into system modeling with component mode synthesis. In addition, the text includes very detailed material on all the generic numerical processing from static decomposition techniques to eigensolution techniques followed by propagation solution techniques rounding out all the numerical processing typically required. The text also contains basic information on experimental structural dynamic methods. Dr. Roy Craig, Jr. was an early IMAC participant, serving on the IMAC Advisory Board for many years.

7 Pioneers/Contributors

There are a large number of contributors to the area of experimental structural dynamics particularly from the mid-1960s to the mid-1980s when the ISMA and IMAC conferences began to flourish. Most of these contributors can be identified from the author and attendee list from IMAC and ISMA covering the time period from 1982 until now. Prior to 1982, a bibliography list of papers and references can be found as one of the papers in the first (1982) IMAC Conference proceedings [1]. This list of papers and authors includes most references prior to 1982 and is relatively comprehensive. Two other publications include discussion of early contributors **Pioneers of Shock and Vibration** [104] and **The Old and the New . . . A narrative on the history of the Society for Experimental Mechanics** [3]. These texts provide additional information for early researchers that is not limited to those involved in experimental structural dynamics. Certainly the authors of textbooks mentioned in the previous section would also be important contributors to the topic.

7.1 Pioneers: Experimental Structural Dynamics

There are two significant contributors to the field of experimental structural dynamics that would be on the list of pioneers for this field regardless of who is asked. This very short list would include Professor David L. Brown of the University of Cincinnati and Professor David J. Ewins of Imperial College. Both of these researchers started in the mid-1960s at their respective universities and took leading roles in the development of many aspects of the field of experimental structural dynamics as is known today. Simply doing a literature search during the time period of 1960 to the present day for these two authors would allow the reader to get a comprehensive idea of the field.

Dr. David L. Brown initially focused on the dynamics of machine tool cutting at the University of Cincinnati at a time when analytical methods (finite element methods) were just being developed. The only practical approach to understanding the dynamics of machine tools and the effect of machine tool dynamics on cutting was the emerging analog experimental modal analysis method based upon a slow swept sine estimation of frequency response functions (FRFs). This initial research work led Dr. Brown to the fast Fourier transform and developing general broadband approach to the estimation of frequency response functions (FRFs) utilizing digital minicomputers. That starting point led to improved FRF estimation methods and the development of single and multiple degree of freedom modal parameter estimation methods during the 1970s along with multiple input estimation of FRFs around 1980.

Dr. David J. Ewins followed a similar path at Imperial College where he ended up focusing on the experimental dynamic analysis of rotating turbo-machinery. This focus required specialized methods to understand and experimentally measure the

dynamics of many similar circular objects such as brakes, wheels, and the dynamics of circular complex structures involved in jet engines and turbines. Dr. Ewins first textbook [93] was the first to focus on experimental structural dynamics and the first text to document the measurement and parameter estimation methods that were becoming common practice and, to this point in time, were only presented in conference proceedings.

Both Dr. Brown and Dr. Ewins have distinguished themselves as first rate researchers, educators, and technologists. Both have presented the theoretical side of their research as well as the practical and applied experimental side of the research. Both Dr. Brown and Dr. Ewins became heavily involved internationally in giving applied short courses to industry on the experimental structural dynamic methods that they were pioneering. Once the IMAC Conference began, Dr. Brown and Dr. Ewins worked together on the modal analysis course given each year at IMAC in addition to their own experimental modal analysis courses. Both Dr. Brown and Dr. Ewins brought graduate student researchers with them to IMAC, and these graduate students have gone on to numerous professor positions and now bring a second and third generation of graduate student researchers to IMAC.

Both Dr. Brown and Dr. Ewins have received many awards from the technical community across many professional societies. Limiting the discussion to the Society for Experimental Mechanics (SEM), both Dr. Brown and Dr. Ewins served on the IMAC Advisory Board for the first 25 years as the IMAC Conference evolved. Dr. Ewins served as the chairman of the IMAC Advisory Board for the first 5 years. Both Dr. Brown and Dr. Ewins have received many awards from the Society for Experimental Mechanics including the SEM Fellow Award (2014), the M. M. Frocht Award (2002), and the D. J. DeMichele Award (1993) for Dr. Ewins and the SEM Fellow Award (2013), the William M. Murray Lecture (2006), the B.J. Lazan (1987), and the D.J. DeMichele Award (1992) for Dr. Brown. Both Dr. Brown and Dr. Ewins have been honored by giving two IMAC keynote speeches. Dr. Brown in the 1st (1982) and the 25th (2007) and Dr. Ewins (1984) in the 2nd and the 25th (2007).

7.2 Contributors: Handbook

Certainly the authors of chapters for this Handbook are important contributors to the field of experimental structural dynamics. The list is not limited to the authors of the chapters of this Handbook, but this is a good starting point (Table 2).

7.3 Contributors: SEM IMAC

The list of the SEM IMAC contributors is very long with 200–300 papers published in each IMAC since 1982. The best way to get a view of these contributors, particularly the first 20 years, is to acquire a DVD copy of all of the papers along with the Table of Conference for each IMAC Proceedings. This DVD is still available through the Society for Experimental Mechanics.

Table 2 Contributors to the Handbook of Experimental Structural Dynamics

Author	Affiliation	Topic
Randall J Allemang	University of Cincinnati-SDRL	History of Experimental Structural Mechanics
Peter Avitabile	University of Massachusetts Lowell	History of Experimental Structural Mechanics
Christopher Niezrecki	University of Massachusetts Lowell	DIC and Photogrammetry Measurements
Phillip L. Reu	Sandia National Laboratories	DIC and Photogrammetry Measurements
Javad Baqersad	Kettering University	DIC and Photogrammetry Measurements
Daniel P. Rohe	Sandia National Laboratories	DIC and Photogrammetry Measurements
Paolo Chiariotti	Università Politecnica delle Marche	Laser Doppler Vibrometry Measurements
Christian Rembe	Technical University Clausthal	Laser Doppler Vibrometry Measurements
Paolo Castellini	Università Politecnica delle Marche	Laser Doppler Vibrometry Measurements
Matthew S. Allen	University of Wisconsin-Madison	Laser Doppler Vibrometry Measurementss
Robert B. Randall	University of New South Wales	Applied Digital Signal Processing
Jerome Antoni	"University of Lyon, INSA-Lyon"	Applied Digital Signal Processing
Pietro Borghesani	University of New South Wales	Applied Digital Signal Processing
Anders Brandt	University of Southern Denmark	Spectral and Correlation Analysis Methods
Stefano Manzoni	Politecnico di Milano	Spectral and Correlation Analysis Methods
Allyn W. Phillips	University of Cincinnati-SDRL	Frequency Response Function Estimation
Randall J Allemang	University of Cincinnati-SDRL	Frequency Response Function Estimation
Thomas L. Paez	Sandia National Laboratories	Random Vibration and Mechanical Shock
Norm F. Hunter	Los Alamos National Laboratory	Random Vibration and Mechanical Shock
David Smallwood	Sandia National Laboratories	Random Vibration and Mechanical Shock
Mark Valentino	PCB Piezotronics, Inc."	Sensors and their Signal Conditioning for Dynamics
Patrick L. Walter	Texas Christian University	Sensors and their Signal Conditioning for Dynamics
Gary Foss	The Boeing Company	Sensors and their Signal Conditioning for Dynamics
Jessica Meloy	The Boeing Company	Sensors and their Signal Conditioning for Dynamics

(continued)

Table 2 (continued)

Author	Affiliation	Topic
Thomas Carne	Sandia National Laboratories	Design of Modal Tests
Ralph Brillhart	ATA Engineering, Inc.	Design of Modal Tests
Daniel Kammer	University of Wisconsin – Madison	Design of Modal Tests
Mr. Kevin Napolitano	ATA Engineering, Inc.	Design of Modal Tests
Randall J Allemang	University of Cincinnati-SDRL	Experimental Modal Parameter Evaluation Methods
Allyn W. Phillips	University of Cincinnati-SDRL	Experimental Modal Parameter Evaluation Methods
Carlos Ventura	University of British Columbia	Operating Modal Analysis Methods
Randall J Allemang	University of Cincinnati-SDRL	Experimental Modal Analysis Methods
David L. Brown	University of Cincinnati-SDRL	Experimental Modal Analysis Methods
Daniel Rixen	Technische Universität München	Substructuring and Component Mode Synthesis
Peter Avitabile	University of Massachusetts Lowell	Finite Element Model Correlation
Mike Mains	University of Cincinnati-SDRL	Finite Element Model Correlation
John E. Mottershead	University of Liverpool	Model Updating
Michael Link	University of Kassel	Model Updating
Michael I. Friswell	Swansea University	Model Updating
Carsten Schedlinski	ICS Engineering GmbH	Model Updating
Lothar Gaul	University of Stuttgart	Damping of Materials and Structures
Andre Schmidt	University of Stuttgart	Damping of Materials and Structures
Francois Hemez	Lawrence Livermore National Lab	Uncertainty Quantification: UQ & QMU
Kendra Lu Van Buren	Lawrence Livermore National Lab	Uncertainty Quantification: UQ & QMU
Janette J. Meyer	Vanderbilt University	Nonlinear System Analysis Methods
Raymond M. Bond	Vanderbilt University	Nonlinear System Analysis Methods
Douglas E. Adams	Vanderbilt University	Nonlinear System Analysis Methods
Keith Worden	University of Sheffield	Structural Health Monitoring, Damage Identification
Ramon Fuentes	Los Alamos National Laboratory	Structural Health Monitoring, Damage Identification
Charles R. Farrar	Los Alamos National Laboratory	Structural Health Monitoring, Damage Identification

(continued)

Table 2 (continued)

Author	Affiliation	Topic
Randall L. Mayes	Sandia National Laboratories	Experimental Dynamic Substructures
Matthew S. Allen	University of Wisconsin	Experimental Dynamic Substructures
Mark Richardson	Vibrant Technology, Inc.	Structural Dynamics Modification, Modal Modeling
David Formenti	Blackhawk Technology	Structural Dynamics Modification, Modal Modeling
Nuno Maia	University of Lisbon	Robust Response Models: Issues
António Urgueira	Universidade NOVA de Lisboa	Robust Response Models: Issues
Raquel Almeida	Universidade NOVA de Lisboa	Robust Response Models: Issues
Tiago Silva	Universidade NOVA de Lisboa	Robust Response Models: Issues
Gaetan Kerschen	University of Liège	Modal Analysis of Nonlinear Mechanical Systems
Alexander F. Vakakis	University of Illinois (UIUC)	Modal Analysis of Nonlinear Mechanical Systems
Peter Avitabile	University of Massachusetts Lowell	Linear Modal Substructuring, Nonlinear Connections
Jim De Clerck	Michigan Technological University	Automotive Structural Testing
Ruben Boroschek	University of Chile	Civil Structural Testing
Joao Pedro Santos	National Laboratory for Civil Engineering, Lisboa, Portugal	Civil Structural Testing
Robert Coppolino	Measurement Analysis Corporation	Aerospace Perspective for Modeling and Validation
Chuck Van Karsen	Michigan Technological University	Applied Math for Experimental Structural Dynamics
Andrew Barnard	Michigan Technological University	Applied Math for Experimental Structural Dynamics

Contributions to the Society and to IMAC take on many forms. One notable contribution to the Society for Experimental Mechanics is to serve on the executive board and/or as an officer of the Society. Three of the active researchers in the area of experimental structural dynamics have gone on to serve as president for the Society: Dr. Randall Allemang (2003–2004), Dr. Carlos Ventura (2012–2013), and Dr. Peter Avitabile (2016–2017).

In recognition of their contributions to the Society, a number of researchers in the area of experimental structural dynamics have been honored with the award of SEM Fellow. Those researchers are noted in the following table (Table 3).

Table 3 Recipients of the SEM Fellows Award

Recipient (Year)	Recipient (Year)	Recipient (Year)
Peter Avitabile (2022)	Randall Mayes (2022)	Douglas Adams (2021)
Charles Ferrar (2018)	Carlos Ventura (2018)	Dan Inman (2017)
David J. Ewins (2014)	David L. Brown (2013)	Randall J. Allemang (2010)

Table 4 Recipients of the D.J. DeMichele Award

Recipient (Year)	Recipient (Year)	Recipient (Year)
Jason Blough (2021)		
Scott Cogan (2020)	Ralph D. Brillhart (2019)	Charles D. Van Karsen (2018)
Mark Schiefer (2017)	Michael D. Todd (2016)	Randy Mayes (2015)
Keith Worden (2014)	Charles R. Farrar (2013)	Raj K. Singhal (2012)
Mark Richardson (2011)	François M. Hemez (2010)	Douglas E. Adams (2009)
Álvaro Cunha (2008)	Daniel J. Inman (2007)	William R. Shapton (2006)
James Lally (2005)	Peter Avitabile (2004)	Carlos E. Ventura (2003)
Roy R. Craig Jr. (2002)	Sam Ibrahim (2001)	Thomas G. Carne (2000)
Alfred L. Wicks (1999)	Randall Allemang (1998)	Kenneth G. McConnell (1997)
Nobuyuki Okubo (1996)	Larry D. Mitchell (1995)	Tzu Chuen Huang (1994)
David J. Ewins (1993)	David L. Brown (1992)	Bruno Piombo (1991)
Dominick J. DeMichele (1990)		

In addition, there is a specific Society award to recognize researchers and educators active in the structural dynamics area. This award is named after D.J. Dick DeMichele who led the effort to get IMAC started back in 1982. Those recipients are listed in the above table (Table 4).

Most of the researchers in the experimental structural dynamics have also been recognized by other organizations and/or professional societies too numerous to be included here.

7.3.1 IMAC Advisory Board

The original IMAC Advisory Board was established by Peter Juhl and Dr. Dick DeMichele as they interviewed many active researchers trying to determine the interest level for a new organization and conference centered on experimental structural dynamics. Both Mr. Juhl and Dr. DeMichele obtained input from many of the active researchers about the format and content of the potential conference. Many of the researchers listed as part of the original IMAC Advisory Board participated in this process in the 3–4 years before the first conference in 1982. Both Mr. Juhl and Dr. DeMichele were lecturers at Union College, and they involved Union College in the organization of the first few conferences as the primary sponsor (1982–1986). Gradually, there was a desire to have some sort of professional society affiliation, and the Society for Experimental Mechanics became the home of the conference after 1991 as the Society assumed the responsibility for organization and

Table 5 Members of the Original IMAC Advisory Board

Member	Affiliation
David J. Ewins	Imperial College of Science and Technology, England
Dominique Bonnecase	AS&I Rhone-Alpes, France
David L. Brown	University of Cincinnati-SDRL, USA
Dominick J. DeMichele	Union College/IMTS, USA
Keneth A. Galione	Society for Experimental Mechanics, Inc., USA
Arnold E.S. Gussin,	Union College, USA
Larry E.S. Mitchell	Virginia Polytechnic Institute, USA
Nobuyuki Okubo	Chuo University, Japan
Michael P. Pakstys	NKF Engineering Associates, Inc., USA
Anders Reveman	Tre Konsultar AB, Sweden
Mark H. Richardson	Structural Measurement Systems, Inc., USA
Paul Sas	Katholieke Universiteit Leuven, Blegium
Havard Vold,	Structural Dynamics Research Corporation, USA
Lingmi Zhang	Nanjing Aeronautical Institute, China
Cheng Yaodong	Zhejiang University, China
Randall J Allemang	University of Cincinnati-SDRL, USA

management of IMAC. Union College continued as a cosponsor with the Society from 1987 to 1991 and ceased any further involvement in 1996 (Table 5).

Dr. David Ewins was elected as the first chair of the IMAC Advisory Board and served from 1982 to 1987. Dr. Ewins was followed by Dr. Randall Allemang from 1987 to 1995 and by Dr. Mark Richardson from 1995 to 2015. Much of the growth of IMAC and the integration of the IMAC activity into the Society for Experimental Mechanics was the result of hard work by the original Advisory Board and the chairman during this time period along with the willingness of Union College to discontinue involvement after 1996. In recent years, the Advisory Board and chairman are now part of the Society administrative structure with regular changes in Advisory Board members and chairman.

8 Summary/Conclusions

This introductory chapter for the Handbook reviews the recent history of modern experimental structural dynamics methods and highlights the active researchers and educators involved in the developments. Modern experimental structural dynamics refers to the time period since digital computing, the fast Fourier transform, and analog to digital conversion of measured data became readily available, somewhere around the mid-1960s. The experimental methods introduced in this chapter are covered in great detail in other chapters of this Handbook along with advances that took place after 1975. This chapter simply represents the starting point that became the focus of activities within the Society for Experimental Mechanics since the mid-1980s.

References

1. Allemang RJ (1982) Experimental modal analysis bibliography. In: Proceedings, international modal analysis conference (IMAC), pp 714–726
2. Cooley JW, Tukey J (1965) An algorithm for the machine calculation of complex Fourier series. Math. Comput. 19(90):297
3. Sciammarella CA, Zimmerman KB (2018) The old and new . . . a narrative on the history of the society for experimental mechanics. Morgan and Claypool Publishers, San Rafael
4. Stein PK (1990) A brief history of bonded resistance strain gages from conception to commercialization. Exp. Tech. 14(5):13–20
5. Walter PL (2007) The history of the acccelerometer, 1920s–1996 – prologue and epilogue, 2006. Sound Vib Mag (SVM) 41(1):84–92
6. Keller AC (1969) Vector component techniques: a modern way to measure modes. Sound Vib Mag (SVM) 3(3):18–26
7. Bickel HJ (1971) Real time spectrum analysis. Sound Vib Mag (SVM) 5(3):14–20
8. Keller AC (1975) Real-time spectrum analysis of machinery dynamics. Sound Vib Mag (SVM) 9(4):40–48
9. Gade S, Herlufsen H (2017) 35 years of structural measurements at Brüel & Kjær. Sound Vib Mag (SVM) 51(1):26–30
10. Mowry J, Borring G (2012) Journey to greatness. The story of Brüel & Kjær. Acoustical Publications, Inc. Bay Village, OH, www.SandV.com
11. Keller T (2017) The making of a great company: how spectral dynamics came to be. Sound Vib Mag (SVM) 51(1):64–84
12. Tustin W (1969) Vibration test equipment. Sound Vib Equip 3(3):27–32
13. Welaratna S (1997) Thirty years of FFT analyzers. Sound Vib Mag (SVM) 31(1):5
14. Lang GF (2017) Historical snippets from our half century. Sound Vib Mag (SVM) 51(1):2–4
15. Allemang R, Brown D, Fladung W (1994) Modal parameter estimation: a unified matrix polynomial approach. In: Proceedings, international modal analysis conference (IMAC), pp 501–514
16. Lewis RC, Wrisley DL (1950) A system for the excitation of pure natural modes of complex structures. J Aeronaut Sci 17(11):705–722
17. De Veubeke BF (1956) A variational approach to pure mode excitation based on characteristic phase lag theory. AGARD, Report, vol 39, p 35
18. Trail-Nash RW (1958) On the excitation of pure natural modes in aircraft resonance testing. J Aeronaut Sci 25(12):775–778
19. Asher GW (1958) A method of normal mode excitation utilizing admittance measurements. In: Dynamics of aeroelasticity, Proceedings. Institute of the Aeronautical Sciences, pp 69–76
20. Stahle CV, Forlifer WR (1958) Ground vibration testing of complex structures. In: Flight flutter testing symposium, NASA-SP-, vol 385, pp 83–90
21. Stahle CV Jr (1962) Phase separation technique for ground vibration testing. Aerosp Eng 1962:8
22. DeBlauwe F (1991) Investigation of a parameter estimation algorithm for spatial sine testing. Doctoral Dissertation, University of Cincinnati, vol 117
23. Deblauwe F, Shih CY, Rost R, Brown DL (1987) Survey of parameter estimation algorithms applicable to spatial domain sine testing. In: Proceedings, international seminar on modal analysis (ISMA), vol 15
24. Bendat JS, Piersol AG (1986) Random data: analysis and measurement procedures, 2nd edn. Wiley-Interscience, New York
25. Napolitano KL (2016) Using singular value decomposition to estimate frequency response functions. Top Modal Anal Test 10:27–44
26. Allemang R, Patwardhan R, Kolluri M, Phillips A (2022) Frequency response function estimation techniques and the corresponding coherence functions: a review and update. Mech Syst Sig Process (MSSP) 162(1):108100

27. Prony R (1795) Essai Experimental et Analytique sur les Lois de la Dilatabilite des Fluides Elastiques et sur Celles de la Force Expansive de la Vapeur de l'eau et de la Vapeur de l'Alkool, a Differentes Temperatures. Journal de l' Ecole Polytechnique (Paris) 1(2):24–76
28. Ibrahim S, Mikulcik E (1977) A method for the direct identification of vibration parameters from the free response. Shock Vib Bull 47:183–198
29. Ibrahim S (1978) Modal confidence factor in vibration testing. Shock Vib Bull 48:65–75
30. Brown D, Allemang R, Zimmerman R, Mergeay M (1979) Parameter estimation techniques for modal analysis. SAE Paper Number 790221, SAE Trans 88:828–846
31. Vold H, Kundrat J, Rocklin T, Russell R (1982) A multi-input modal estimation algorithm for mini-computers. SAE Trans 91(1):815–821
32. Vold H and Rocklin T (1982) The numerical implementation of a multi-input modal estimation algorithm for mini-computers. In: Proceedings, international modal analysis conference (IMAC), pp 542–548
33. Vold H, Leuridan J (1982) A generalized frequency domain matrix estimation method for structural parameter identification. In: Proceedings, international seminar on modal analysis (ISMA)
34. Juang J-N, Pappa RS (1985) An eigensystem realization algorithm for modal parameter identification and model reduction. AIAA J Guid Control Dyn 8(4):620–627
35. Juang J (1987) Mathematical correlation of modal parameter identification methods via system realization theory. J Anal Exp Modal Anal 2(1):1–18
36. Juang JN, Pappa RS (1985) Effects of noise on ERA-identified modal parameters. AAS Paper, vol 23, No AAS-85-422
37. Gersch W (1970) Estimation of the auto regressive parameters of a mixed autoregressive moving-average time series. IEEE Trans Autom Control AC-15:583–588
38. Gersch W, Luo S (1972) Discrete time series synthesis of randomly excited structural system responses. J Acoust Soc Am 51(1):402–408
39. Gersch W, Sharpe DR (1973) Estimation of power spectra with finite-order autoregressive models. IEEE Trans Autom Control AC-18:367–369
40. Gersch W, Nielsen NN, Akaike H (1973) Maximum likelihood estimation of structural parameters from random vibration data. J Sound Vib (JSV) 31(3):295–308
41. Gersch W (1974) On the achievable accuracy of structural system parameter estimates. J Sound Vib (JSV) 34(1):63–79
42. Pandit SM (1977) Analysis of vibration records by data dependent systems. Shock Vib Bull (47), 161–174
43. Pandit SM, Suzuki H (1979) Application of data dependent systems to diagnostic vibration analysis. ASME Paper, No. 79-DET-7, p 9
44. Link M,and Vollan A (1978) Identification of structural system parameters from dynamic response data. Zeitschrift Fur Flugwissenschaften 2(3):165–174
45. Leuridan J (1981) Direct system parameter identification of mechanical structures with application to modal analysis. Master of Science Thesis, Department of Mechanical Engineering, University of Cincinnati, p 200
46. Leuridan J, Mergeay M, Vandeurzen U, Desanghere G (1984) Multiple input estimation of frequency response functions for experimental modal analysis: currently used method and some new developments. In: International seminar on modal analysis, p 34
47. Leuridan J (1984) Some direct parameter model identification methods applicable for multiple input modal analysis. Doctoral Dissertation, p 384+
48. Leuridan J, Brown D, Allemang R (1985) Time domain parameter identification methods for linear modal analysis: a unifying approach. ASME Paper Number 85-DET-90
49. Spitznogle F (1971) Improvements in the complex exponential signal analysis computational algorithm, Report Number U1-829401-5, Representation and Analysis of Sonar Signals, vol 1, p 37
50. Pappa R (1982) Some statistical performance characteristics of the ITD modal identification algorithm. AIAA Paper Number 82-0768, p 19

51. Fukuzono K (1986) Investigation of multiple-reference Ibrahim time domain modal parameter estimation technique. M. S. Thesis, p 220
52. Longman RW, Juang J-N (1989) Recursive form of the eigensystem realization algorithm for system identification. AIAA J Guid Control Dyn 12(5):647–652
53. Zhang L, Kanda H, Brown D, Allemang R (1985) A polyreference frequency domain method for modal parameter identification. ASME Paper No. 85-DET-106, p 8
54. Lembregts F, Leuridan J, Zhang L, Kanda H (1986) Multiple input modal analysis of frequency response functions based on direct parameter identification. In: Proceedings, international modal analysis conference (IMAC)
55. Lembregts F (1988) Frequency domain identification techniques for experimental multiple input modal analysis, Doctoral Dissertation
56. Lembregts F, Leuridan J, Van Brussel H (1989) Frequency domain direct parameter identification for modal analysis: state space formulation. Mech Syst Sig Process (MSSP) 4(1):65–76
57. Coppolino R (1981) A simultaneous frequency domain technique for estimation of modal parameters from measured data. SAE Paper No. 811046, vol 12
58. Craig R, Kurdila A, Kim HM (1990) State-space formulation of multi-shaker modal analysis. J Anal Exp Modal Anal 5(3):169–183
59. Natke H (1988) Updating computational models in the frequency domain based on measured data: a survey. Probab Eng Mech 3(1):28–35
60. Richardson M, Formenti D (1982) Parameter estimation from frequency response measurements using rational fraction polynomials. In: Proceedings, international modal analysis conference (IMAC), pp 167–182
61. Shih C, Tsuei Y, Allemang R, Brown D (1988) A frequency domain global parameter estimation method for multiple reference frequency response measurements. Mech Syst Sig Process (MSSP) 2(4):349–365
62. Shih C (1989) Investigation of numerical conditioning in the frequency domain modal parameter estimation methods. Doctoral Dissertation, p 127+
63. Van der Auweraer H, Leuridan J (1987) Multiple input orthogonal polynomial parameter estimation. Mech Syst Sig Processing (MSSP) 1(3):259–272
64. Van der Auweraer H, Snoeys R, Leuridan J (1986) A global frequency domain modal parameter estimation technique for mini-computers. ASME J Vib Acoust Stress Reliab Des 108
65. Vold H (1986) Orthogonal polynomials in the polyreference method. In: Proceedings, international seminar on modal analysis (ISMA)
66. Vold H, Shih CY (1988) On the numerical conditioning of some modal parameter estimation methods. In: Proceedings, international seminar on modal analysis. In: Proceedings, international seminar on modal analysis
67. Vold H (1990) Numerically robust frequency domain modal parameter estimation. Sound Vib Mag (SVM) 24(1):38–40
68. Vold H (1990) Statistics of the characteristic polynomial in modal analysis. In: Proceedings, international seminar on modal analysis (ISMA), pp 53–57
69. Vold H, Napolitano K, Hensley D, Richardson M (2008) Aliasing in modal parameter estimation, an historical look and new innovations. In: Proceedings, international modal analysis conference (IMAC), vol 16, pp 12–17
70. Fladung W, Vold H (2016) An improved implementation of the orthogonal polynomial modal parameter estimation algorithm using the orthogonal complement. In: Proceedings, international modal analysis conference (IMAC)
71. Fladung W, Vold H (2016) An orthogonal view of the polyreference least-squares complex frequency modal parameter estimation algorithm. In: Proceedings, international modal analysis conference (IMAC)
72. Van der Auweraer H, Guillaume P, Verboven P, Vanlanduit S (2001) Application of a fast-stabilizing frequency domain parameter estimation method. ASME J Dyn Syst Meas Control 123(4):651–658

73. Guillaume P, Verboven P, Vanlanduit S, Van der Auweraer H, Peeters B (2003) A polyreference implementation of the least-squares complex frequency domain estimator. In: Proceedings, international modal analysis conference (IMAC), p 12
74. Verboven P, Guillaume P, Cauberghe B, Parloo E, Vanlanduit S (2003) Stabilization charts and uncertainty bounds for frequency domain linear least squares estimators. In: Proceedings, international modal analysis conference (IMAC), pp 1–10
75. Verboven P, Cauberghe B, Vanlanduit S, Parloo E, Guillaume P (2004) The secret behind clear stabilization diagrams: the influence of the parameter constraint on the stability of the poles. In: Proceedings, society of experimental mechanics (SEM) annual conference, vol 17, pp 1–17
76. Verboven P (2002) Frequency domain system identification for modal analysis. Doctoral Dissertation
77. Cauberghe B (2004) Application of frequency domain system identification for experimental and operational modal analysis. Doctoral Dissertation, p 259
78. Shih C, Tsuei Y, Allemang R, Brown D (1988) Complex mode indication function and its application to spatial domain parameter estimation. Mech Syst Sig Process (MSSP) 2(4): 367–377
79. Harris CM, Piersol AG (eds) (2009) Shock and vibration handbook, 6th edn. McGraw-Hill, New York
80. Kobayashi A (ed) (1994) Handbook on experimental mechanics, 2nd edn. Prentice Hall
81. Reese RT, Kawahara WA (eds) (1993) Handbook on structural testing. Society of Experimental Mechanics/The Fairmont Press, Inc., Lilburn
82. Enochson LD, Goodman NR (1965) Gaussian approximations to the distribution of sample coherence, USAF Report AFFDL-TR-65-57, p 33
83. Goodman NR (1965) Measurement of matrix frequency response functions and multiple coherence functions, USAF Report AFFDL-TR-65-58, p 38
84. Allemang RJ, Brown DL, Rost RW (1984) Multiple input estimation of frequency response functions for experimental modal analysis, No. AFATL-TR-84-15
85. Allemang R, Brown D (1987) Volume I: Summary of technical work. Experimental modal analysis and dynamic component synthesis
86. Allemang R, Brown D (1987) Volume II: Measurement techniques for experimental modal analysis. Experimental modal analysis and dynamic component synthesis
87. Allemang R, Brown D (1987) Volume III: Modal parameter estimation. Experimental modal analysis and dynamic component synthesis
88. Allemang R, Brown D (1987) Volume IV: System modeling techniques. Experimental modal analysis and dynamic component synthesis
89. Allemang R, Brown D (1987) Volume V: Modal parameter estimation. Experimental modal analysis and dynamic component synthesis
90. Allemang R, Brown D (1987) Volume VI: Software users guide. Experimental modal analysis and dynamic component synthesis
91. Enochson L, Otnes R (1968) Programming and analysis for digital time series data SVM-3. In: The shock and vibration information center (SAVIAC)
92. Agency DT (ed) (1996) Dynamic test agency handbook, vols 0–9. Dynamic Testing Agency and Crown Publications
93. Ewins D (1984) Modal testing: theory and practice. Wiley, New York
94. Avitabile P (2017) Modal testing: a practitioner's guide. SEM and John Wiley & Sons Ltd., West Sussex
95. Coppolino RN (2019) The integrated test analysis process for structural dynamic systems. Morgan & Claypool Publishers, San Rafael
96. Frazer R, Duncan W, Collar A (1938) Elementary matrices (1965 Reprint). Cambridge University Press, London
97. Wilkinson JH (1965) The algebraic eigenvalue problem. Oxford University Press, Oxford
98. Strang G (2006) Linear algebra and its applications, 4th edn. Centage Learning, Boston

99. Bendat JS, Piersol AG (1966) Measurement and analysis of random data. Wiley, New York City, New York
100. Bendat JS, Piersol AG (1971) Random data: analysis and measurement procedures, 1st edn. Wiley-Interscience, New York
101. Otnes RK, Enochson L (1972) Digital time series analysis. Wiley, New York
102. Den Hartog J (1947) Mechanical vibrations, 3rd edn. McGraw-Hill Book Company, New York/London
103. Craig, R. Jr., Kurdila A (1982) Fundamentals of structural dynamics. Wiley, New York City, New York
104. Freeman M (1996) Pioneers of shock and vibration. SAVIAC/Booz-Allen and Hamilton Inc., Arlington

Sensors and Their Signal Conditioning for Dynamic Acceleration, Force, Pressure, and Sound Applications

2

Gary Foss, Jessica Meloy, Mark Valentino, and Patrick Walter

Contents

G. Foss
The Boeing Company, Chicago, IL, USA
e-mail: garyfoss3@comcast.net

J. Meloy
Pensar Development, Seattle, WA, USA
e-mail: jessica.meloy@pensardevelopment.com

M. Valentino (✉)
PCB Piezotronics, Inc., Depew, NY, USA
e-mail: mvalentino@pcb.com

P. Walter
Texas Christian University & PCB Piezotronics, Inc., Fort Worth, TX, USA
e-mail: p.walter@tcu.edu

R. Allemang, P. Avitabile (eds.), *Handbook of Experimental Structural Dynamics*,
https://doi.org/10.1007/978-1-4614-4547-0_33

Abstract

The continued demand for efficiency, reliability, and lower operating costs together with the general increase in awareness of the effects of vibration and noise in the workplace has demanded a better understanding of the causes and characteristics of the vibration of machines and structures in many industries. This, coupled with advances in transducer technology, electronics, and signal processing power, has led to a wealth of commercial products for performing structural dynamics measurements.

Structural dynamics is the response of a structural system to dynamically imposed loads. Undesirable responses can cause suboptimum performance or structural failure. Understanding the relationships between forces and responses may involve in-service operational measurements or the creation of simulated environments in the laboratory. Analytical modeling verified by experimental modal analysis is a frequently employed tool to understand and/or adjust structural dynamics before the introduction of a product into service.

Successful testing depends on the accurate measurement of the dynamic force and pressure loading encountered by the structure as well as the response of the structure. The common electromechanical transducers that are used for these measurements are pressure transducers and microphones, load cells or force transducers, strain gages, and accelerometers. The signals from these devices are amplified and filtered in a way that preserves their fidelity over the required bandwidth and amplitude levels. Proper use depends on wise selection, informed by the knowledge of the required data and the limitations of the products. This chapter provides a guide to the sensing technologies and electronics available to make these measurements and their use.

Keywords

Sensor · Sensing · Piezoelectric · Strain gage · Microphone · Force sensor · Pressure sensor · Impedance · Signal conditioning

1 Sensing Technologies

1.1 Piezoelectricity

Piezoelectricity is a transduction technology particularly applicable to transducers intended to measure time-varying force, pressure, and acceleration measurands. Just as the research focus since the 1960s has been on silicon technology (soon discussed), a similar effort existed in the 1920s through the 1950s on piezoelectric technology. Polycrystalline ceramics and quartz were the principal piezoelectric materials of focus during the latter part of this time span. The uses for piezoelectric materials continue to grow, although piezoelectric technology itself is now fairly mature.

Piezoelectricity is attributable to strain inducing a change in the shape of a crystal that possesses no center of charge symmetry. An electric charge results from this change in shape. Twenty-one of the 32 crystal classes lack this symmetry element, and crystals in all but one of these classes can exhibit piezoelectricity.

Quartz (Fig. 1) is a common piezoelectric material that exists in nature. Today, however, quartz is principally grown artificially. Quartz is highly stable, rugged, and linear and operates over a wide temperature range. It is typically the technology of choice for piezoelectric pressure transducers and compression type load cells. Tourmaline is another piezoelectric found in nature and is acquired through mining operations. It operates well in high-temperature applications and underwater explosions. In addition, some ferroelectric polycrystalline ceramic materials can be artificially manufactured to exhibit piezoelectricity. This latter group of materials is of particular interest since the manufacturing process can control their mechanical

Fig. 1 A boule of quartz

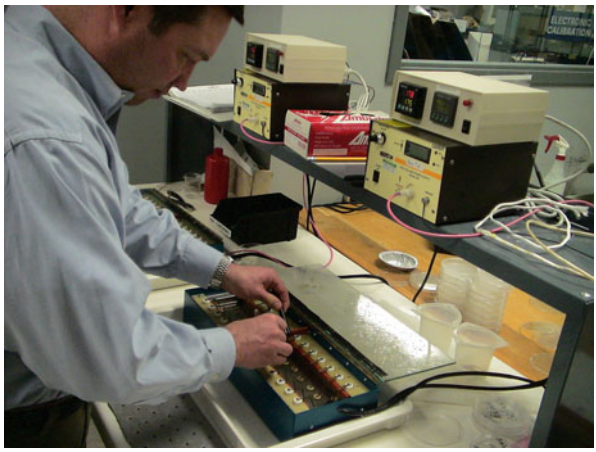

Fig. 2 Poling ceramics to effect piezoelectric properties. (Courtesy PCB Piezotronics)

and electrical properties. This manufacturing process consists of the weighing and proportioning of ceramic powders, calcining at high temperatures to produce a chemical combination of the ingredients, mixing in a ball mill to repowder the raw compound, adding a binder, granulating, compressing the powder into pellet form, and firing the pellets in a controlled atmosphere in a kiln. This firing transforms the pellets into ceramic elements. The elements are lapped and plated for subsequent polarization. A high-voltage field is applied across each pellet under controlled environmental conditions (Fig. 2). The minute crystal domains within the ceramic are forced to align themselves with the applied field, and this alignment is retained after the field is removed.

There are many important properties of piezoelectric materials. The piezoelectric constant for a material expresses the amount of charge generated per unit applied force or the deflection per unit applied voltage. Typical units are Coulombs/Newton (C/N) or meters/volt (m/v). The coupling coefficient provides the energy conversion efficiency of the piezoelectric material; a high value is desired. The dielectric constant determines the capacitance of the material. A piezoelectric transduction element is effectively a capacitor that produces a charge across its plates proportional to the force applied to it. The material resistivity must be high to keep the charge generated in the material from leaking off. The open-circuit voltage is the voltage generated at the output of the piezoelectric element per unit of applied force. Unlike silicon-based transducers, piezoelectric transducers do not have response to dc or 0 Hz.

The Curie temperature is the temperature above which the crystal lattice modifies its structure and the piezoelectric properties are lost. Good practice is to avoid transducer use at greater than 1/2 the Curie temperature.

The following table provides some electrical and mechanical properties for a few piezoelectric materials. These properties indicate why these materials are desirable for application as transduction elements.

	Young's modulus (c_{11}) (N/m^2)	Density (g/cm^3)	Piezoelectric constant (10^{-12}) (C/N)
Quartz	86.7 x 10^9	2.65	−2.3
Tourmaline	270 x 10^9	3.1	2.1
PZT-5A	121 x 10^9	0.75	374

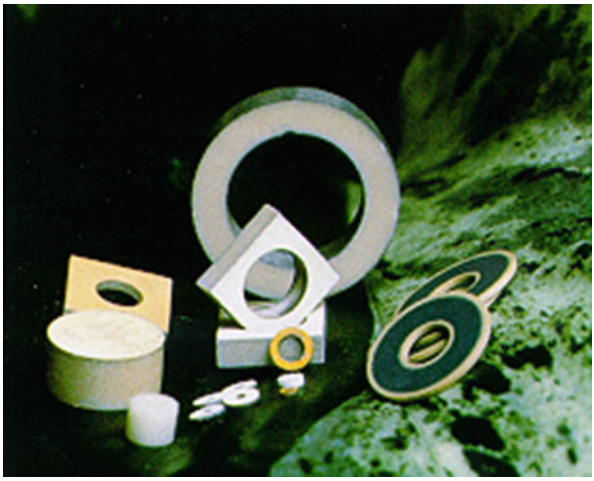

Fig. 3 Manufactured ceramic shapes

The moduli of elasticity of these materials are between 50% and 150% of the values for steel and silicon; they are quite stiff. Similarly, their modulus-to-density ratios are between 60% and 130% that of steel. If the properties of PZT 5A (lead zirconate titanate) are used as an example, the piezoelectric constant is 374 picocoulombs/Newton. It is apparent that a small force input to this ceramic material would result in a large electrical output signal. Therefore, these materials enable miniaturization of transducer design while still permitting operation over large amplitude ranges. Figure 3 illustrates various piezoelectric ceramic shapes dependent on application.

1.2 Metal Strain Gages

A strain gage is a device used to measure strain on the surface of an object. The most common type of strain gage consists of an insulated flexible backing on which a metal foil serpentine pattern is supported. The gage is attached to the object by a suitable adhesive for the application. As the object is deformed, the foil is also deformed, causing its electrical resistance to change. This resistance change, usually measured using a Wheatstone bridge, is related to the strain by the quantity known as the gage factor. Bonded metal foil strain gages (Fig. 4) are a mature technology. Their importance is routinely encountered in our daily lives every time that a weighing process occurs, the dynamic characteristics of a structural system are

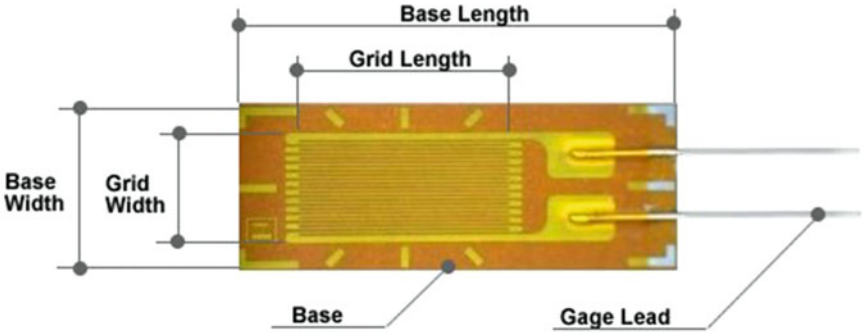

Fig. 4 Foil strain gage. (Courtesy of VPG Sensors)

assessed to monitor for material fatigue and structural design margin, the damaging resonant frequencies contained in a structure are identified, and much more.

The detailed history of the evolution of the strain gage is presented in reference [1]. On September 10, 1936, Ed Simmons, an electrical engineering graduate student at the California Institute of Technology, suggested using bonded wire to measure the dynamic forces generated by an impact testing machine. The professor with whom he was working, Dr. Gottfried Datwyler, bonded 40-gage, cotton-wrapped, insulated, constantan wire to a piece of clock spring with Glyptal cement. The spring was mounted as a cantilever beam, and the wire change in resistance was proven to be linear, repeatable, and hysteresis-free with applied strain. The bonded wire strain gage was born. The experimental work was completed and presented at an ASTM meeting in June 1938. Scant attention was given at this meeting to the strain gage development that supported the experimental work.

History: In 1938, at MIT, Prof. Arthur Ruge was working on a research contract with his graduate assistant Hans Meir to measure the stresses induced in water towers under earthquake conditions. On April 3, 1938, Prof. Ruge unwound wire from a precision resistor, bonded it to a test beam, and created a strain gage. The importance of this discovery was immediately apparent to Prof. Ruge. He and Mr. Meir spent the rest of their lives developing and commercializing the bonded strain gage and transducers based on its operating principle. During a patent search following the 1938 MIT discovery, Mr. Simmons' earlier work was uncovered. As a result, Simmons ultimately received patent number 2,292,549 on August 11, 1942, as the recognized inventor of the bonded resistance strain gage. Today the bonded wire strain gage has been replaced by foil-etched gages formed by printed circuit techniques. Currently the vast majority of strain gage applications associated with experimental stress analysis are performed using bonded metal foil strain gages. Their manufacture is as follows.

Construction: The two most common materials comprising metal foil gages are constantan (55% Cu 45% Ni) and karma (20% Cr 2.5% Al 2.5% Cu balance Ni). Both these materials offer (1) atypical resistance versus temperature behavior, (2) malleability sufficient to allow processing into foil less than 0.001 in (0.025 mm.)

thick, (3) ease of photochemical machining into accurate configurations, and (4) reasonable cost. Considering gage resistance-temperature behavior, it is desired that a strain gage eliminates false signals due to thermal expansion of the material on which it is mounted. If the increase in gage resistance due to thermal expansion of this material can be offset by a corresponding decrease in gage alloy resistivity, the result will be zero change and no false signal. In reality, a finished gage assembly includes its backing, sealant, and adhesive. All of these materials expand at their own rate and contribute to this false signal. Thermal coefficient of resistance (TCR) values required to achieve thermal compensation tend to range from −25 to +5 p.p.m./°C. These values are well within the capability of cold rolled constantan and karma. Optimum compensation is obtained by heat treatment of the two foils dependent on the material on which they are mounted. Figure 5 shows one typical thermal or false strain compensation that can be achieved by a given strain gage in a temperature range around room temperature.

Strain gage manufacturing involves first putting stringently manufactured alloys through a closely controlled melting process. Repeated stages of rolling result in a thin foil that is bonded to a backing film, acting as a carrier. The foil with the backing is then etched with photochemicals to form the desired gage geometry.

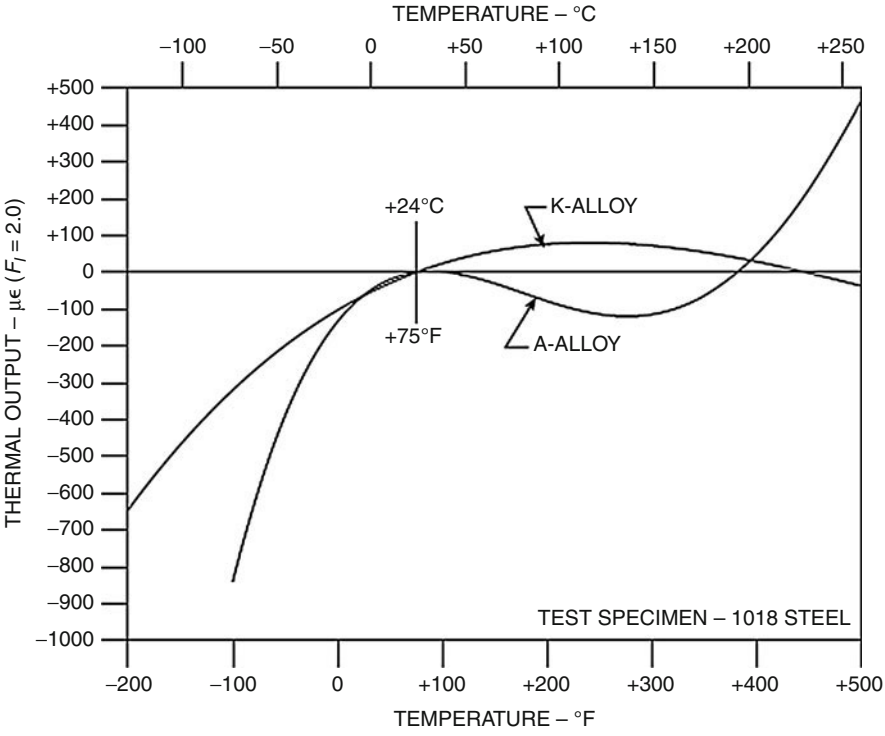

Fig. 5 Typical temperature compensation curves achievable with constantan (A) and karma (K) strain gage materials (courtesy of VPG Sensors)

Sheets of gages are then cut apart and packaged for sale. Reference [2] provides a detailed description of this process.

To build effective strain sensing circuits, one must be aware of the interaction between the gage and the surface of the flexure to which it is mounted. Mechanical aspects of this interaction include the influence of backing material, size, orientation, transverse sensitivity, distance from the surface, bonding, and installation.

***Backing material*:** The purpose of the backing material used in constructing strain gages is to provide support, dimensional stability, and mechanical protection for the grid element. The backing material acts as a spring in parallel with the parent material to which it is attached and can potentially modify mechanical behavior. In addition, the temperature operating range of the gage can be constrained by its backing material, typically polyimide. The standard temperature range for polyimide backed gages is from −100 to +350F. Special construction can extend this range from cryogenic to +500F. Some gages are encapsulated for chemical and mechanical protection as well as extended fatigue life. Special purpose metal gages can be welded. The frequency response of welded gages, due to uncertainties in dynamic response, is a subject area still requiring investigation.

***Size*:** The major factors to be considered in determining the size of strain gage to use are available space for gage mounting, strain gradient at the test location, and character of the material under test. The strain gage must be small enough to be compatible with its mounting location and the concentrated strain field. It must be large enough so that, on metals with large grain size, it measures average strain as opposed to local effects. Grid elements greater than 0.125 in. (3 mm.) generally have greater fatigue resistance.

***Transverse sensitivity and orientation*:** Strain gage transverse sensitivity and mounting orientation are concurrent considerations. Transverse sensitivity in strain gages is important due to the fact that part of the geometry of the gage grid is oriented in directions other than parallel to the principal gage sensing direction. Values of transverse sensitivities are provided with individual gages but typically vary between fractional and several percent. The position of the strain gage axis relative to the numerically larger principal strain on the surface to which it is mounted will have an influence on indicated strain.

***Distance from the surface*:** The grid element of a strain gage is separated from the structure under test by its backing material and cement. The grid then responds to strain at a location removed from its mounting surface. The strain on structures such as thin plates in bending can vary considerably from that measured by the strain gage.

***Bonding adhesives*:** Resistance strain gage performance is entirely dependent on the bond attaching it to the parent material. The grid element must have the strain transmitted to it undiminished by the bonding adhesive. Adhesive types break into categories depending on the manner of cure: one part or two part mixes and room or elevated temperature cure. Common strain gage adhesives are as follows:

Cyanoacrylate adhesives. Most widely used general-purpose one-part adhesive. Easiest to handle. Room temperature cures in under 1 min. Long-term temper-

ature range from -25F to +150F. Creep-free, fatigue-resistant bond with strain capability of 5% or more.

Epoxy adhesives. Useful over a temperature range from – 270 to +320 °C. Two classes are room temperature curing or thermal setting: both available with various organic fillers to optimize performance for individual test requirements.

Polyimide adhesives. For high performance applications, polyimide adhesives are a one-part thermal setting resin with a very thin, nearly creep-free bond layer. Temperature range for one product is from −450 to +700F and is achieved by step curing at four different temperatures.

Polyester adhesives. For rough or porous surfaces like concrete, mortar, and wood. Two-part, room temperature cure. Temperature range from −20 to +350F.

Ceramic adhesives. For high-temperature applications to 2000F. Gages must be free wire or foil. Single part elevated temperature cure.

Weldable strain gages are also available for spot welding to structures and components. They are ideal for applications where test or environmental conditions preclude clamping and curing an adhesively bonded gage.

1.3 Semiconductor, Piezoresistive, and MEMS Strain Gages

In the 1940s through the 1950s, it became recognized that, when geometrically distorted, the resistance change of semiconductor materials could also be correlated to strain [3]. The semiconductor strain gage became of interest because its sensitivity to strain was about 50 to 200 times that of metal gages. However, whether using p- or n-type silicon, gage sensitivity was discovered to be strongly influenced by both temperature and strain level. For this reason, semiconductor strain gages find principal application only in experimental stress analysis involving small strain differences at controlled temperatures. *Colloquially, the term "piezoresistive" strain gage is used synonymously with silicon or semiconductor strain gages.*

While not extensively used in experimental stress analysis work, because of their higher strain sensitivity, piezoresistive strain gages do find significant application in the construction of transducers (e.g., pressure, force, and acceleration) whose output can be thermally compensated. Piezoresistive transducers manufactured in the 1960s first used silicon strain gages fabricated from lightly doped ingots. These ingots were sliced with respect to the crystal axes of the silicon to form small bars or patterns which became gages. These gages were usually bonded directly to the transducer flexure. Since the late 1970s, there has been a continual evolution of microsensors into the market place. Piezoresistive transducers manufactured in this manner use silicon both as their flexural element and as their transduction element. The strain gages are diffused directly into the flexure. The most typical fabrication process has the following sequence of events: the single crystal silicon is grown; the ingot is trimmed, sliced, polished, and cleaned; diffusion of a dopant into a surface region of the parent silicon wafer is controlled by a deposited film; a photolithography process includes etching of the film at places defined in the

developing process, followed by removal of the photoresist; and isotropic and anisotropic wet chemicals are used for shaping the mechanical microstructure. Both the resultant stress distribution in the microstructure and the dopant control the piezoresistive coefficients of the silicon.

Electrical interconnection of various controlled surfaces formed in the silicon crystal as well as bonding pads is provided by thin film metallization. The silicon wafer is then separated into individual dies. The dies are bonded by various techniques into the transducer housing, and wire bonding connects the metalized pads to metal terminals in the transducer housing. Sensors fabricated in this manner are known as microelectromechanical systems (MEMS) transducers. While metal strain gage-based transducers typically provide 20 to 30 millivolts of unamplified full-scale signal, by comparison, MEMS resistance-based transducers produce 100–200 millivolts of unamplified signal. This provides a signal-to-noise advantage at low strain levels. MEMS transducer technology is rapidly expanding in commercial and military applications. Reference [4] provides an extensive chapter on strain gage-based transducers.

1.4 Piezoelectric Strain Gages

Strain within a piezoelectric material displaces electrical charges within the strained elements, and the charges accumulate on opposing electrode surfaces. Piezoelectric strain gages do not have response to zero Hz. Therefore, their application in experimental stress analysis is limited. However, modern gages have integral signal-conditioning electronics (ICP® or IEPE) that greatly enhance the measurement system's signal-to-noise ratio. Five volts of unamplified signal can be provided for 100 microstrain making these type gages very desirable for low-level, dynamic strain measurements (Fig. 6).

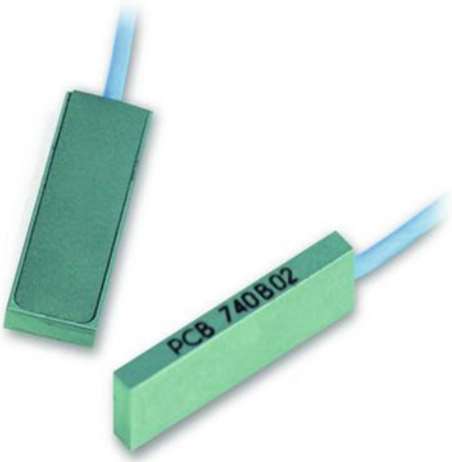

Fig. 6 Piezoelectric strain gage. (Courtesy PCB Piezotronics)

1.5 Capacitance

Both microphones and accelerometers can be constructed using the principle of changing capacitance. Microphones based on capacitance are usually called "condenser microphones."

Condenser microphones: Through the years there have been a number of different microphone designs used to measure sound, or unwanted sound commonly referred to as noise. Sound gets transmitted through either liquids, solids, or gasses as oscillations of pressure waves and can either be detected by the human ear (the audible range) or be in the form of infrasound or ultrasound. Infrasound represents sounds below the human hearing range, and ultrasound is above the designated human hearing range of 20 Hz to 20 kHz. Acoustics is the study of these waves. Microphones allow us the capability to measure these sounds. The most common test and measurement microphone for accurately measuring sound is the condenser style.

Construction: A condenser microphone is an electromechanical sensor that converts a change in capacitance into a measureable electrical voltage as discussed in reference [5]. The condenser microphone contains two parallel plates which are electrically isolated surfaces separated by a dielectric medium, which acts as an insulator. The dielectric for condenser microphones is air. The two parallel surfaces consist of a backplate and a diaphragm.

The backplate in a prepolarized microphone includes an electret material that stores a fixed embedded charge to provide a difference in electrical potential across the air gap. An externally polarized microphone uses a power supply to apply a voltage across the backplate-diaphragm gap. The diaphragm is a thin material stretched across the housing, which is maintained at a separate electrical potential from the backplate. When these two parallel surfaces are combined with the air dielectric, they form a capacitor with a very stable electrical charge.

Changes in pressure cause the diaphragm to deflect, causing variations in the gap between the diaphragm and the backplate, and the result is an oscillating electric field. As the distance between the microphone's diaphragm and stationary backplate changes, the capacitance changes proportionately to the sensitivity of the microphone and its air gap as shown in Fig. 7. An output voltage can then be obtained that represent the changes in sound or pressure waves that the diaphragm was exposed to (Fig. 8).

$$\mathrm{C} = \left(\frac{\mathrm{Q}_0}{\mathrm{E}_0 - \mathrm{e}}\right) = \left(\frac{\varepsilon \cdot \mathrm{A}}{\mathrm{D}_0 - \mathrm{d}}\right)$$

Where:

A = Area of capacitor plate
C = Instantaneous capacitance between plates
Do = Distance between plates at rest position
d = Displacement of moveable plate (diaphragm) from rest position
Eo = Polarization voltage

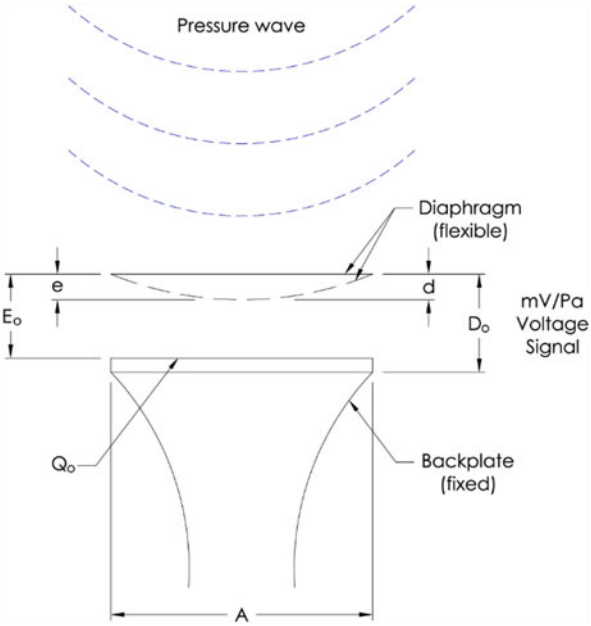

Fig. 7 Microphone Output. (Courtesy PCB Piezotronics)

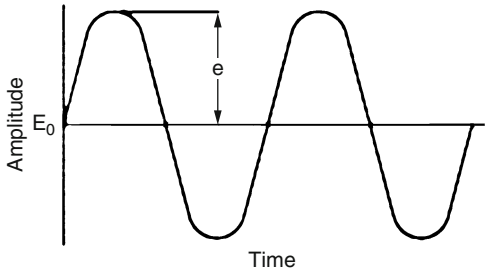

Fig. 8 Microphone output voltage superposed on polarization voltage (E_0)

e = Voltage change caused by plate displacement
Qo = Constant charge on plate capacitor
Epsilon = Dielectric constant of air

The primary components of a condenser microphone (seen in Fig. 9) consist of a diaphragm, a backplate, a body, an insulator, and grid cap. The diaphragm is a thin material and is tensioned to a desired amount which can either allow it to be very sensitive or be less sensitive. In general, high tension on the diaphragm will increase the high-frequency response capability and lower the sensitivity. Conversely, lower tension on the diaphragm will degrade the high-frequency response. Inherent noise is also tied to the sensitivity of the diaphragm. High sensitivity will provide lower inherent noise or high signal-to-noise ratio, while low sensitivity will have higher inherent noise. For enhanced low-frequency response, adjustments in both the venting design and the preamplifier design need to be incorporated. The preamplifier

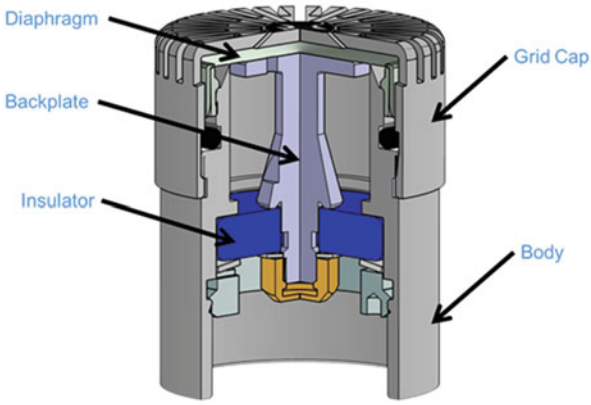

Fig. 9 Components of a condenser microphone

provides the impedance conversion required to drive the signals across the cable to the end devices.

The backplate is a metal component that may contain strategically placed holes in it to properly allow for the desired damping characteristics required for the specific microphone design. The damping is modified to meet the desired inherent noise and sound field design requirements. For example, critically damped systems will yield a smooth frequency response with a small roll-off. This is desired in pressure fields and diffuse field applications. An overdamped system is desired for free-field applications where a more significant roll-off is desired. The field response types and their intended applications are discussed later in this chapter.

The body, also called the housing, is the outer component that encapsulates the microphone and helps tension the diaphragm. Stress relieving the housing (along with the diaphragm) is one of the critical processes necessary to ensure long-term stability of the microphone. The insulator shields the backplate from the rest of the microphone and external components. The grid cap is a cover that protects the delicate diaphragm.

The above components are designed to allow a microphone to output a voltage that correlates to its desired amplitude and a frequency. The displacement of the microphone diaphragm provides the changes in the electrical field that represent the amplitude of the pressure exerted upon it. The oscillations of the diaphragm provide the frequency component. When multiple microphones are placed in a predetermined pattern (also called an array) and combined with the proper software and phase characteristics, they can be used to analyze particle velocity and the direction of sound, allowing this grouping of microphones to be an excellent choice for noise source location applications.

Condenser microphones are stable over time, temperature, and humidity and are the microphone of choice for precision sound level meters and many of today's test and measurement applications. The two most common design types desired for precision testing are externally polarized and prepolarized condenser microphones.

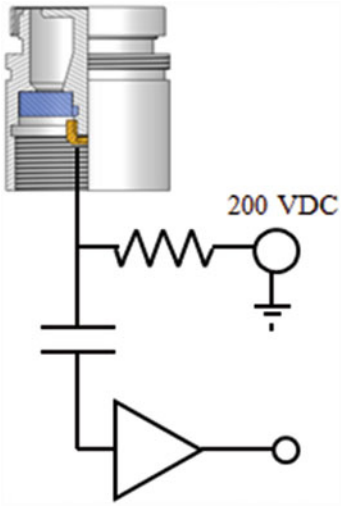

Fig. 10 Externally polarized microphone design

Externally polarized microphones: The externally polarized method of supplying the necessary voltage to the backplate is accomplished by applying a fixed 200 V via an external power supply (see Fig. 10). The electrical isolation between the backplate and the diaphragm provides a difference in electrical potential across the air gap, providing the basic requirements for the capacitor used to measure pressure waves exerted on the microphone [13].

The externally polarized design is the traditional method which was originally widely accepted by acousticians and test engineers. In addition to the 200 V power supply, the externally polarized models require multiconductor cabling and connectors. The most common is a seven-pin LEMO® connector. Most externally polarized microphone cartridges have the capability to reach temperatures of 150 °C without significant sensitivity loss. This temperature specification can be limited by the preamplifier operating temperature capability. The externally polarized design is easier to build and, prior to the technological advances of prepolarized electret microphones, offered better stability and noise floor specifications.

Electrets or prepolarized microphones: An electret or prepolarized design operates in a similar capacitance fashion. The difference between the externally polarized design and the electret or prepolarized design is that an electrical charge is embedded into a polymer material that sits on top of the backplate facing the diaphragm (see Fig. 11). This eliminates the need for an external 200 V power supply. With this new electret-based design, any 2–20 mA constant current supply, for example, ICP® power supplies (also called signal conditioners), can now be used to power the microphone.

The prepolarized design is a more modern design and allows for the use of cost-effective coaxial cables and BNC, 10–32, or SMB connectors. The combination of the cable savings and the use of signal conditioners in lieu of 200 V power supplies offer significant equipment savings. The prepolarized design is also better

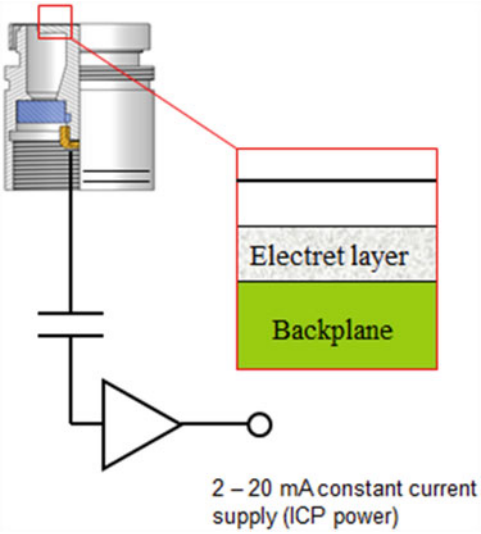

Fig. 11 Prepolarized or electret microphone design

for humid applications and for portability. The 2–20 mA power supply and coaxial cabling are the same power and cabling required by many other common test and measurement sensors such as accelerometers and piezoelectric pressure sensors. With a multichannel signal conditioner, setup time can be minimized, and multiple vibration and sound tests can be run within the same setup. This design is significantly growing in popularity due to its flexibility to be used with other sensors and the low-cost per-channel savings it offers. Data acquisition manufacturers have taken notice and are manufacturing a greater number of their products with the same 2–20 mA power built-in, making this electret prepolarized design even more portable and easy to use.

Capacitive accelerometers: *Capacitive accelerometers sense a change in electrical capacitance, with respect to acceleration, to vary the output of an energized circuit. Typically they* are structured with a mass loaded diaphragm that undergoes flexure in the presence of acceleration. Two fixed plates sandwich the diaphragm, creating two capacitors, each with an individual fixed plate and each sharing the diaphragm as a movable plate. The flexure causes a capacitance shift by altering the distance between two parallel plates, the diaphragm itself being one of the plates. *The two capacitors operate in an AC bridge circuit, along with two fixed capacitors, and alter the peak voltage generated by an oscillator when the structure undergoes acceleration. Detection circuits capture the peak voltage, which is then fed to a summing amplifier that processes the final output signal. One design is shown in* Fig. 12.

This type of mechanism creates a very stable, accurate measurement device, which is inherently insensitive to base strain and transverse acceleration effects. The design permits operation to DC acceleration and is ideal for low-amplitude, low-frequency requirements. Maximum useful frequency range depends on sensitivity:

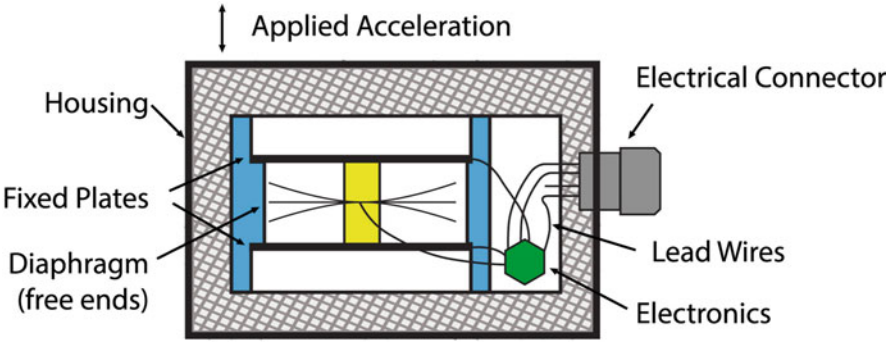

Fig. 12 Capacitive Accelerometer Design (courtesy PCB Piezotronics)

typical limit is between 300 and 1000 Hz. The DC response permits the measurement of tilt and orientation commonly required for consumer products such as game controllers and cellphones.

2 Sensor Dynamic Models

A transducer may be thought of as an energy conversion device. In the transducers being considered in this work, mechanical energy will be converted into electrical energy. The sensing technologies just described, when integrated into the structural flexures of transducers, enable this energy conversion to occur. Electromechanical transducers are able to measure pressure, force, and acceleration from fractional psi, pounds, and Gs, to greater than 100,000 units of these same measurands. When measuring the loads applied to or the response of structural systems via electromechanical transducers, the dynamic performance of these transducers must first be understood. Strain gages are unique in the fact that they can either be integrated into transducer flexures or used in a stand-alone configuration to measure structural response. For this reason, the dynamic response of the strain gage as a stand-alone element will first be considered.

2.1 Strain Gage

While often mounted on the flexures of electromechanical transducers, the basic dynamic response capability of the strain gage itself is considered here. It will be assumed that mounting variables such as adhesive bond thickness are controlled so that they do not influence gage frequency response. If these assumptions are satisfied, the strain gage can be shown to act as a spatial averaging device whose frequency response is a function of both its gage length and the sound velocity of

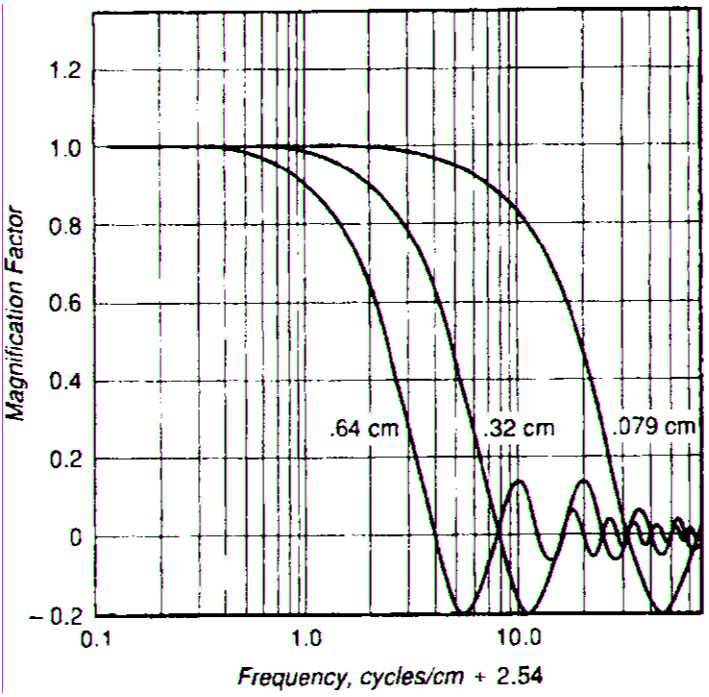

Fig. 13 Frequency response of a strain gage

the material on which it is mounted. Figure 13 portrays this relationship. Reference [6] discusses the analysis from which Fig. 13 is extracted.

As an example of using Fig. 13, we can see that a strain gage with a 0.32 cm gage length (1/8th of an inch) uniformly passes all frequencies to about 1.0/2.54 or 0.394 cycles/cm. The velocity of sound in steel is nominally 510,000 cm/sec. If we multiply 0.394 times 510,000, we get approximately 200,000 Hz as an upper frequency limit for "uniform" or "flat" frequency response for a 0.32 cm (1/8th inch) properly mounted strain gage. Thus, strain gages are capable of measuring structural response to very high frequencies.

2.2 Pressure, Force, and Acceleration Transducers

The simplified dynamic model of a pressure, force, or acceleration transducer is typically presented as in Fig. 14. Figure 15 shows equally simplified conceptual loading models. The farthest left item in Fig. 15 shows a piezoelectric element (red, the spring in every case) being compressed by an applied force on both its top and bottom. The central item in Fig. 15 shows the piezoelectric element being compressed on its top surface by a force attributable to an applied pressure load.

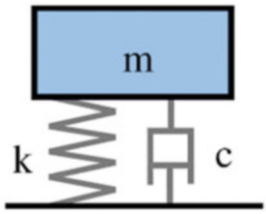

Fig. 14 Dynamic model of a pressure, force, or acceleration transducer

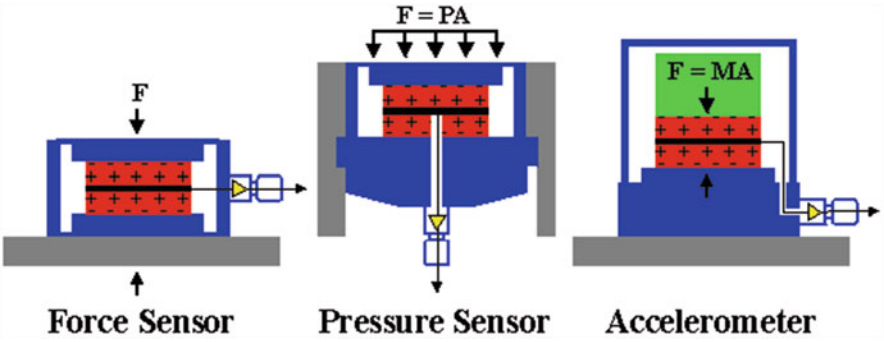

Fig. 15 Pictorial load models for piezoelectric transducers. (Courtesy PCB Piezotronics)

Fig. 16 Physical implementation (left to right) of piezoelectric force, pressure, and acceleration transducers. (Courtesy PCB Piezotronics)

The right item in Fig. 15 shows an inertial force being applied to the piezoelectric element attributable to base acceleration. Figure 16 shows an assortment of transducers representing the physical implementations of Fig. 14. As noted previously, piezoelectricity is just one of several sensing technologies that can be implemented in electromechanical transducers.

Figure 17 (left) illustrates strain gages mounted on a mechanical flexure to form an accelerometer. Figure 17 (right) shows, attributable to the miniaturization achievable with MEMS technology, how strain gage accelerometers (as well as capacitive) can be manufactured from silicon in extremely small sizes. For all of these examples, the frequency response characterization of the simplified dynamic model of Fig. 14 is presented in Fig. 18.

All piezoelectric sensors have very small values of damping (ζ = damping ratio ≈ 0.03). Focusing on the top set of curves in Fig. 18, it can be seen that the frequency

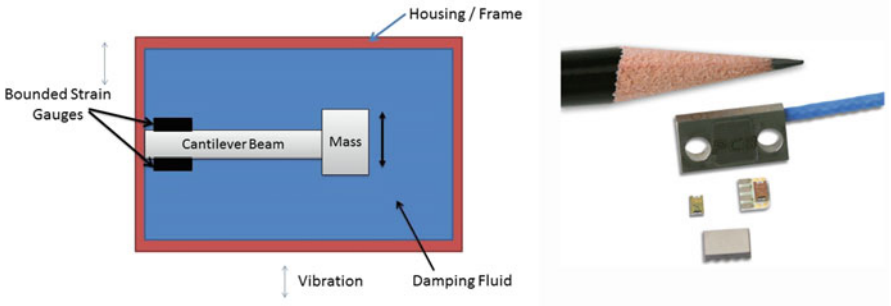

Fig. 17 Strain gage accelerometer (left) and physical implementation with MEMS technology (right). (Courtesy PCB Piezotronics)

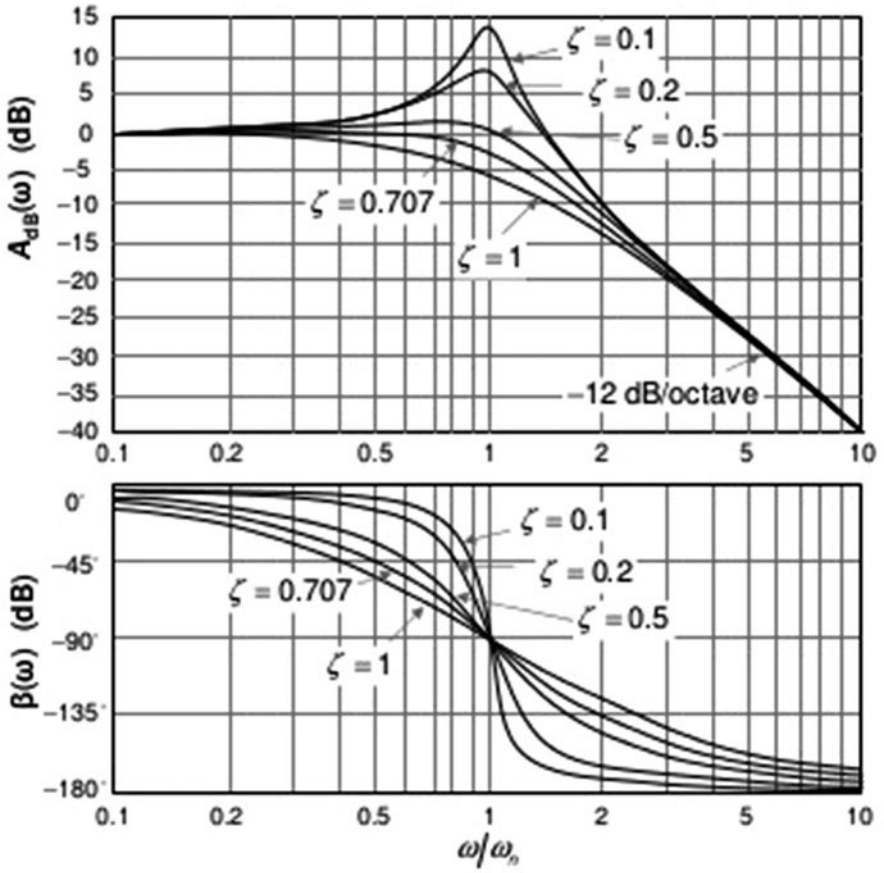

Fig. 18 Amplitude vs. normalized frequency response and simplified dynamic model for pressure, force, and acceleration transducers

content of signals measured by a transducer compatible with this model is replicated with fidelity to about 1/5th of the natural frequency ($\omega/\omega_n = 1$) of the transducer. The phase response (bottom set of curves) indicates that over this same range of response frequencies, essentially no phase shift is introduced by the transducer. For MEMS technology this same observation holds. Three exceptions should be noted:

(1) The electrical model of a piezoelectric transducer (force, pressure, and accelerometer) is that of a voltage source with a series capacitor. A transducer following this model cannot respond to 0 Hz (DC). The frequency response of a piezoelectric transducer is then uniform or "flat" over an intermediate band of frequencies. Its low-frequency limitation is attributable to the time constant of the associated electrical high-pass circuit, and its high-frequency constraint is attributable to the resonant frequency of the transduction element. See Fig. 19. By contrast, MEMS-based strain gage transducers do not have this low-frequency limitation.
(2) Some low G metal strain gage and MEMS-based sensing technology accelerometers have adequate flexure motion to enable mechanical damping of 0.7 to be incorporated into them. Formerly this damping was achieved with fluids, but with the technology of today, it is accomplished with a gaseous medium. Gases are preferred since their viscosity is essentially constant with temperature. A value of 0.7 damping optimizes the range of the accelerometers maximum "flat" frequency response and yields a nominally linear phase response vs. frequency.
(3) Force transducers respond according to the simplified model of Fig. 13 when impulsively loaded. However, in application most force transducers become physically integrated into a test stand. This test stand contains distributed mass

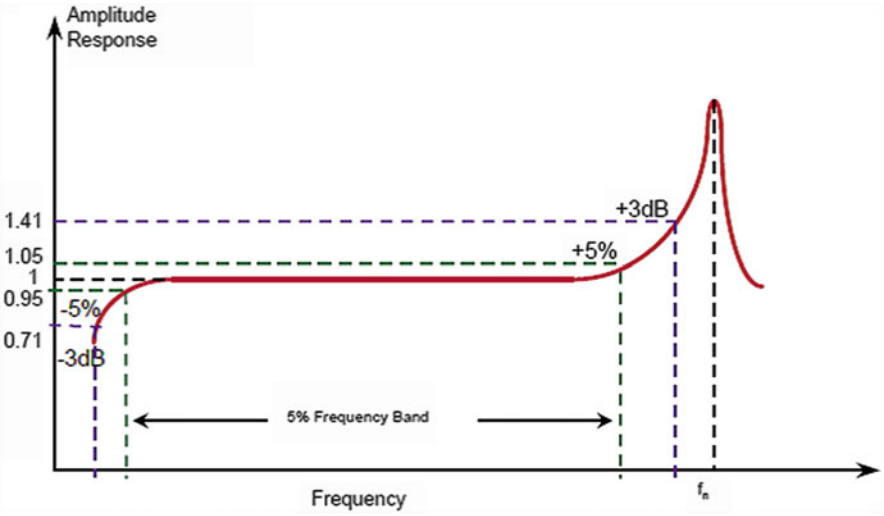

Fig. 19 Useful operating range of piezoelectric transducers. (Courtesy PCB Piezotronics)

and elasticity of differing materials and interfaces. *Thus, the force transducer becomes a structural part of the test stand and does not retain its individual identity. The signal output from the force transducer must then be analyzed as part of the structural response of the entire test stand.*

In general, the dynamic response of a piezoelectric transducer can be broken down into regions by frequency, shown in Fig. 19. A low-pass filter limits the low-frequency response. The useful range is customarily assumed to be between the frequency at which amplitude response is down 5% and extends to the frequency where the amplitude response is up 5% (at around 1/5 of resonant frequency). This would be defined as the 5% frequency band and is usually found on the vendor's specification sheet.

3 Sensor Selection and Use

3.1 Piezoelectric Accelerometers

A piezoelectric accelerometer is an electromechanical transducer that generates an electrical output when subjected to vibration or shock and is the most widely used motion measurement transducer to be found throughout industry. It is used in a variety of environments and applications to measure absolute vibration, directly as acceleration or integrated to provide velocity and displacement data. There are many different piezoelectric accelerometer types commercially available, all of which benefit from most of the following characteristics:

(1) Wide frequency range of operation
(2) Self-generating signal, built-in charge amplifier
(3) Linear over a wide dynamic range of operation
(4) Compact, with high output-to-mass ratio
(5) Robust and easy to install
(6) Operational in a wide variety of environmental conditions

A simple representation of a piezoelectric accelerometer was shown in Fig. 15 on the right. The mass element is connected to the mounting body via the piezoelectric material, which acts as a spring-damper and provides an electrical output proportional to the relative displacement of the mass element with respect to the mounting body. This is directly proportional to the acceleration experienced at the accelerometer mounting body. An amplifier may be added for the conversion of the charge signal to a low impedance voltage signal, hereafter referred to as IEPE.

Most accelerometers can be considered as base excited single-degree-of-freedom systems and are purposely designed to be sensitive in only one axis. The sensitivity of an accelerometer is the ratio of the electrical output charge (Coulombs) or voltage to the applied acceleration. This sensitivity is dependent on the inertia mass and the volume and characteristics of the piezoelectric material. With no internal charge

converter, the sensitivity is defined in units of picocoulombs/g (pC/g). With internal electronics, the sensitivity is specified in units of millivolts/g. Ideally the sensitivity of an accelerometer remains constant throughout its working frequency range.

The reference information for the selection of a piezoelectric accelerometer is the manufacturer's specification. From this specification, the user can match the accelerometer type to meet the requirements. These are the most important considerations:

(1) Physical size and weight
(2) Useable frequency range
(3) Acceleration limits and sensitivity
(4) Type of mount
(5) Base strain and cross-axis sensitivity
(6) Resonant frequency
(7) Connector position on the case
(8) Operating temperature and humidity

Piezoelectric accelerometers are available in packages ranging from less than 0.5 gram to thousands of grams. As a rule, the larger packages permit a larger sensing element which translates into higher sensitivity. As another rule, smaller sensing elements offer higher resonant frequency and therefore higher useful frequency range. Sensitivity should be chosen such that the expected test levels reach an appreciable portion of the full dynamic range. "Appreciable" could be defined as anywhere from 20% to 90%, depending on uncertainty of the test levels. Exceeding the full-scale range can lead to loss of data, so overestimating levels is safer than underestimation.

The lower-frequency limit of a piezoelectric accelerometer is marked by a decrease in sensitivity determined by the high-pass cutoff of the electronics. It may be as low as 0.2 Hz for larger high-sensitivity units and up to 5 Hz for ultraminiature or shock accelerometers. The upper frequency limit of a piezoelectric accelerometer is marked by an unacceptable increase in sensitivity due to the resonance behavior shown in Figs. 18 and 19. Full-scale acceleration limits of commercial accelerometers range from .5G to 100,000G.

There are a variety of established techniques for mounting an accelerometer to a structure. Each method has its benefits and disadvantages, and each affects the working upper frequency limit of measurement. The effect of mounting is to add an additional mechanical system consisting of a spring (the stud or adhesive), the mass of the entire accelerometer, and some additional damping. If this system resonance is lower than the crystal resonance, the upper useable frequency limit will be less than the vendor's specification.

The best mounting employs a stiff threaded stud supplemented with a thin layer of grease between smooth, flat mating surfaces. This will require a drilled and tapped hole and possibly a milled, flat surface on the test article (not always permitted). It will produce a mounted natural frequency that should be close to the accelerometer specification. The next best mounting is with a good quality adhesive such as epoxy,

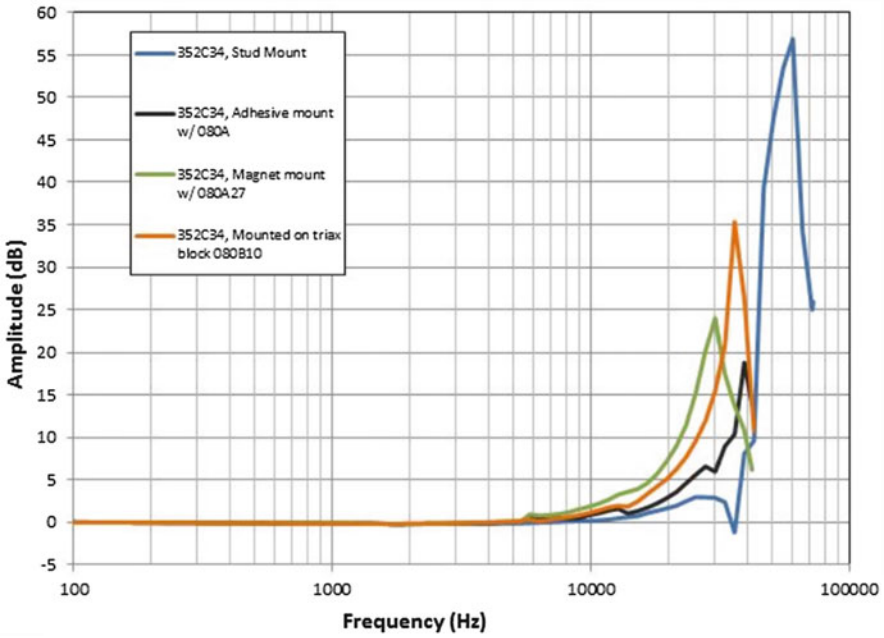

Fig. 20 Frequency response curves showing the effect of the type of various accelerometer mounts. (Courtesy PCB)

with properly cleaned and prepared mating surfaces. For room temperature, non-shock applications, cyanoacrylate adhesive is very quick to apply. For temporary mounting, a thin layer of beeswax offers attachment in seconds, with some sacrifice in frequency response. Another temporary method is double-sided tape, which further compromises frequency response. Figure 20 shows the frequency response of several mounting methods together with their characteristics and applications. The notable effect of mounting is to decrease the resonant frequency (and hence the 1/5 flatness limit) and increase the damping. Note that the use of a separate triaxial block also compromises the specification.

Base strain sensitivity is undesirable when accelerometers are mounted on thinner structures experiencing strain. The strain in the structure is transmitted to the crystal where it is indistinguishable from the measured acceleration. Large errors can result. The solution is to select an accelerometer with very small strain sensitivity or mount it through a block which attenuates the strain.

Large errors can also result if there is high-frequency energy in the structure capable of exciting the mounted transducer resonance. The high-frequency energy can be mechanically amplified, and the output can saturate the electronics. A check of the unfiltered transducer signal will show any output due to transducer resonance. Piezoelectric accelerometers are available (usually a special order) with built-in mechanical filters to mitigate this problem.

Some vendors offer a choice between a side connector and a top connector. The side connector is preferred for permanent applications, but some slack in the cable near the sensor should be provided for strain relief. A top connector makes troubleshooting easier, but the loop of cable should be fastened near the sensor so the cable motion doesn't cause an unwanted signal.

A typical temperature range for an IEPE accelerometer is from −60 to +250F. Special accelerometers are available for cryogenic applications to -320F. Higher temperatures can be achieved with charge accelerometers containing no internal electronics. For special applications such as engine testing, units are available for operation at 1200F.

For operation in high humidity or exposure to liquids, hermetically sealed units should be used, and a watertight connector should be employed.

Although piezoelectric accelerometers are generally robust, they are susceptible to damage if dropped. If the surface is hard, the acceleration levels experienced may exceed 1000 g, and permanent damage may be caused. It is prudent to protect a piezoelectric accelerometer with a rubber sleeve or boot, usually available from the vendor.

3.2 Force Sensors

Force transducers or force gages are most frequently used to measure dynamic forces and to determine frequency response functions of receptance, mobility, or inertance. There are two types commonly used in the dynamic testing field. The first is the piezoelectric force transducer, which is widely used for frequency response measurements where the frequency range of interest is wide but does not include the static load. The second type is the strain gage force transducer, which is more limited in frequency but does extend to DC. The force gage manufacturer's specification sheets provide all the information to enable the choice of force gage to be made for the more common applications.

The piezoelectric force gage operates using the same principle as the piezoelectric accelerometer but is in fact one stage simpler, as the deformation of the piezoelectric material is a direct result of the applied force which is being measured. Figure 15, left, shows a conceptual cross section of a typical piezoelectric force gage.

When a force is applied in the direction of sensitivity, the piezoelectric element is compressed and produces an electrical output proportional to the force transmitted through it. The transducer can measure both tensile and compressive forces, as its piezoelectric element is preloaded. A high overall stiffness ensures that it has a high resonant frequency and also minimal effect due to deformation. The sensitivity of a force gage is the ratio of the electrical output charge (Coulombs) or voltage to the applied force. This sensitivity is dependent on the configuration and characteristics of the piezoelectric material and is defined in units of picocoulombs/lb. (pC/lb) or millivolts/lb., depending on whether an internal IEPE preamplifier is used. Ideally the sensitivity of a force gage remains constant throughout its working frequency

and load range. If the preload is ever relaxed, the full-scale range in tension will no longer match the full-scale range in compression. During calibration, load cells should be checked for linearity in both tension and compression.

To minimize the error caused by the inertia properties of the case, the end of the transducer with the smallest mass should be connected to the surface where the force is to be measured. The frequency response of the system is dependent not only on the force gage but also on how it is mounted and the stiffness of the location at which is mounted. A typical upper frequency limit for a piezoelectric force transducer, stud mounted to a stiff foundation, will be of the order of several kHz.

3.3 Impedance Heads

A device which combines an accelerometer and a force transducer in one assembly for the purpose of point mobility measurement is traditionally called an "impedance head." The design is a combination based on the characteristics of both transducers. Although mechanical impedance is defined as the complex ratio of force to velocity taken at the same or different points in a mechanical system during simple harmonic motion, the main application of an impedance head is to measure point accelerance (acceleration/force). For lower frequencies of interest, the point accelerance is sufficiently estimated by simply mounting the two sensors in close proximity.

3.4 Pressure Measurements

Most machinery causes pressure disturbance in the environment in the form of acoustic noise, and many hydraulic or aerodynamic devices experience pressure fluctuations in their working fluids which are associated with mechanical vibrations, either as cause or effect. The range of pressures of interest is very large, ranging from a few tens of μPa to a few tens of Pa for environment acoustic measurements and from a few kPa to tens of MPa for measurements in the working fluids of machines. Transducers covering the first range of pressures for environmental acoustic measurements are classed as microphones. Those covering the second area are described as pressure transducers.

Condenser microphones: Condenser microphones are the standard type of microphone used for test and measurement and come in multiple sizes and response fields. The microphone size is referred to by its diameter, with the most common sizes being 1/8″ (3 mm), ¼″ (6 mm), ½″ (12 mm), and 1″ (25 mm) models. Smaller diameter microphones lend themselves better to high-pressure and high-frequency applications, while larger diameter microphones have a lower noise floor making them excellent choices for low sound pressure or low noise measurements.

For optimum accuracy, the microphone sensitivity should remain consistent (flat) over the desired frequency range and within its intended sound field and environment. Internal resonance frequencies determine the usable frequency range. Unlike accelerometers and pressure sensors, whose resonance frequency is beyond

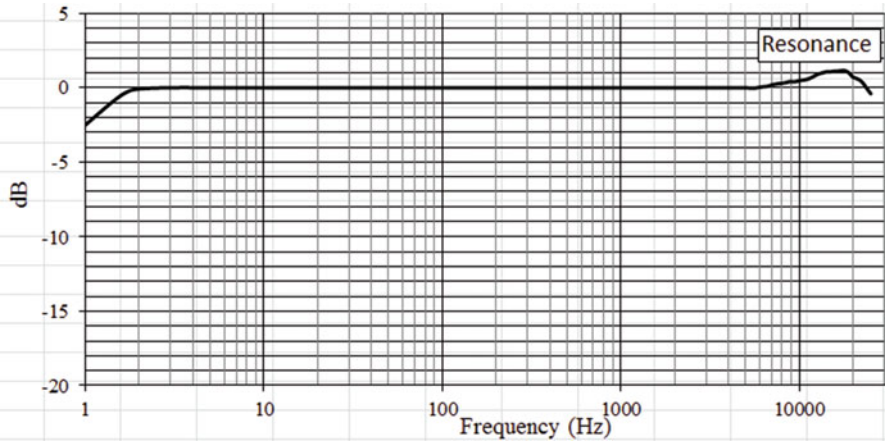

Fig. 21 Frequency response of a microphone. (Courtesy PCB Piezotronics)

the typical measuring capability, the microphone's resonance frequency is within the usable range. The microphone resonance is damped greater than a piezoelectric accelerometer, resulting in a minimal effect on the response. Figure 21 is an example of one response curve. This shows a resonance peak below 20 kHz which is typical for a ½″ high sensitivity condenser microphone. The effect of resonance on the sensitivity in this case is about +1db.

An object, when placed in a test area, can impact the measurement. Depending upon the mass of the object and the frequency value of the pressure wave, the microphone itself can negatively impact the measurement. The microphones own presence within the sound field can disturb the very pressure wave that it is attempting to accurately measure. With frequencies below 1 kHz, a ½″ diameter microphone (or smaller) will have a minimal impact on the sound. The wave size is too big to be affected significantly by the small microphone size. As the frequency increases (in Hertz), the microphone will have a greater impact and disturbance on the sound field, and it becomes more important to select the correct microphone design in order to achieve the most accurate test results. The goal is to measure the true sound as if the microphone was not present.

In order to compensate for the negative effect the microphone has on the sound field, manufacturers implement design changes to the diaphragms resonance and the damping of the microphone in order to tune the microphone and account for the impact of the microphone in the sound field. The three common condenser microphone designs that account for the different sound fields are free-field, random-incidence (also referred to as diffuse field), and pressure-response microphones.

Free-field microphone: The free-field microphone is the most common condenser microphone. It is designed to be used in an area that is open or free of reflections. Some examples of free-field environments are anechoic chambers that limit sound

Fig. 22 Free-field microphone

reflections, or outdoors in an open field or area which do not have objects located close enough to the microphone which can cause a reflection to be picked up by the microphone. A free-field microphone is optimized to have a flat frequency response with sound primarily coming from a single source facing the microphones diaphragm, and this style of microphone will compensate for its presence in the sound field. Free-field microphones can still pick up sounds coming from multiple directions, but the free-field microphone is optimized for a sound source arriving at zero degrees incidence. See Fig. 22.

Random-incidence microphone: A random-incidence (also called diffuse field) microphone is designed to measure sound coming from multiple directions. Examples of areas where a random-incidence microphone would be applied are reverberation chambers, or any room with hard surfaces located close by that will cause reflections, similar to music halls or industrial floor settings. This style of microphone is optimized to measure sound pressure which stems from multiple sources or reflections. See Fig. 23.The Random-incidence microphone will compensate for its own presence in the sound field.

Pressure microphone: A pressure microphone is designed to measure sound pressure in a similar application setting to that of a piezoelectric or ceramic pressure transducer. Examples of areas where a pressure microphone would be used would be inside a coupler or cavity or in a flush mounted wall or panel setup. This style of microphone is optimized for having a flat frequency response while taking measurements from uniform sound pressure. See Fig. 24. Since the pressure microphone is typically flush mounted, it is purposely designed to not compensate for its own presence in the sound field.

Microphone standards: Externally polarized and prepolarized microphones are governed by the same set of standards which ensure that both will work equally as well in most applications. The International Electrotechnical Commission (IEC) with input from the American National Standards Institute (ANSI) published the standard for test and measurement microphones. The IEC 61094–4 standard applies to precision "working-class" condenser microphones and dictates specifications for sensitivity, frequency, dynamic range, long-term stability, and coefficients for the effects of environmental factors such as humidity, temperature, and atmospheric pressure. The standard includes dimensional tolerances ensuring interchangeability among different manufacturers microphones.

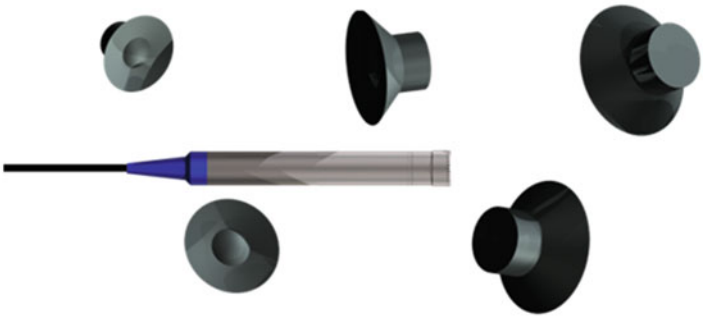

Fig. 23 Random-incidence microphone

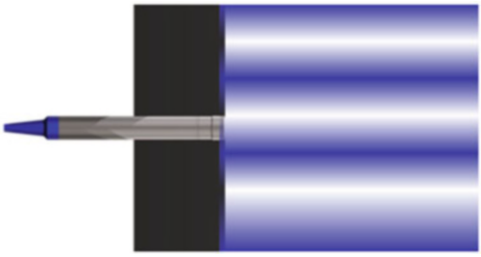

Fig. 24 Pressure microphone

Many condenser microphone applications involve either designing products to be more pleasing to the human ear or to assess the effects that sound has on the human ear to help preserve hearing. The human hearing range is 20 Hz to 20 kHz. Within this range, the human ear perceives sound differently depending upon the frequency and the loudness of the signal. In order to understand how sound is perceived by the ear, Fletcher and Munson performed a study in 1933. Equal loudness curves were generated to show the relationship between a measured sound and a perceived sound. Points were plotted to represent how loud a sound pressure level would have to be in decibels at different frequencies in order to equal that of a 1 kHz sound at the same loudness level in phons. It was found that the human ear is most sensitive at frequencies between 1 kHz and 6 kHz and naturally attenuates sound at other frequencies.

Weighting: ANSI incorporated this data into the S1.4 standard for sound level meters. Separate frequency weighting systems were established through the years. The IEC 61052 standard contained A-, B-, C-, and D-weightings. The A-weighting was established to represent how the human ear would perceive sound at low levels, 40 phons. Testing also verified that the human ear does not attenuate the sound as much when low frequencies are combined with higher-pressure levels. The B-, C-, and D-weightings are based on higher-pressure levels. Examples of higher SPL applications include gunshot testing, blast detection, or aircraft noise.

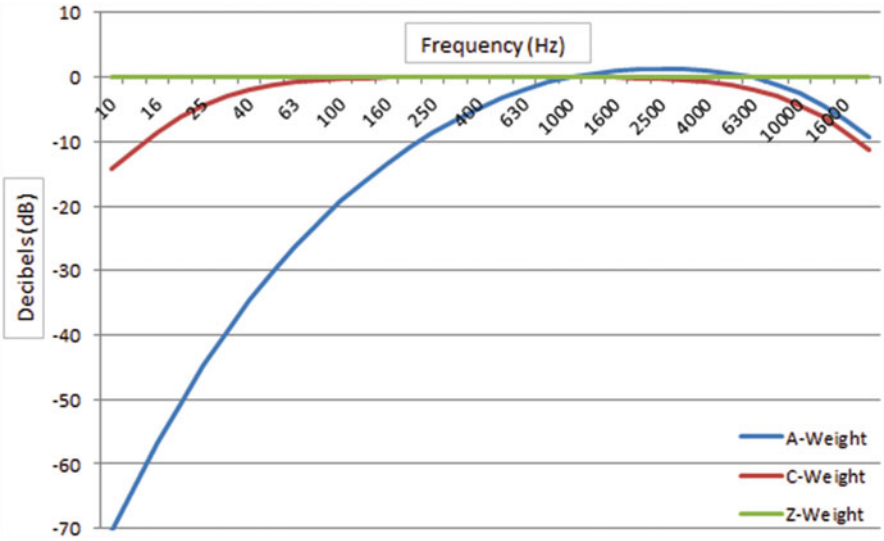

Fig. 25 Weighting curves

In 2003 IEC 61672 discontinued the use of the B- and D-weighting designations and added the Z-weighting scale designation which represented a flat or linear unweighted scale. Today's higher-quality sound level meters contain the A-, C-, and linear (Z)-weighting data, shown above in Fig. 25.

3.5 Pressure Transducers

Pressure transducers make a direct measurement of the force generated at an interface diaphragm between the working and reference fluids under the difference in pressure across the diaphragm. The rear of the diaphragm (reference side) may be vented to enable differential pressure measurements to be made or sealed for absolute pressure measurements. Strain gages are very commonly used as the transducing element and offer a response down to zero frequency, though piezoelectric transducers may also be used, especially in applications not requiring measurements to zero frequency.

It is good practice to check the calibration of a pressure transducer prior to use, and it is much more easily done with a strain gage pressure transducer, where static calibration can be made with a deadweight tester. For more demanding applications, the calibration should also be dynamic, using a reference transducer of known dynamic calibration over the frequency range of interest.

One common type of pressure transducer uses a diaphragm, often of stainless steel, with strain gages fixed to the face on the reference side. Another common type

uses a diaphragm constructed out of a single slice of silicon, with mechanical and electrical features produced by methods developed in the semiconductor industry. The silicon strain gages so formed give high sensitivity. These transducers tend to be rather temperature sensitive, and most are offered with built-in compensation to overcome this effect. It is possible to obtain pressure transducers with the primary interfacing electronics built-in, leading to very simple installation and signal conditioning.

The parameters which need to be determined by the user, possibly in consultation with the manufacturer, include:

(1) Pressure range, accuracy, and resolution required; whether overpressure can occur; and whether differential or absolute pressure is required
(2) Frequency range.
(3) Temperature range.
(4) Working fluid: some working fluids are chemically active, and the transducers should be of an appropriate material to resist attack.
(5) Whether there is separate or integral signal conditioning.
(6) Mounting method: the user should ensure that the mounting is of sufficient accuracy to avoid strain of the transducer when it is fitted; fitting strain can alter the calibration; and the zero offset is often very sensitive to fitting strain.
(7) Special environmental conditions, such as thermal or mechanical shock, exposure to high g levels, or vibration.

4 Sensor Systems

4.1 Sensor System Architecture

Generally, a sensor system can be broken into five functional blocks, as shown in Fig. 26. These five blocks do not necessarily represent five different physical items as multiple functions can be performed in the same package or by the same circuit. For example, an IEPE sensor combines the sensor element with an impedance converter (Fig. 26).

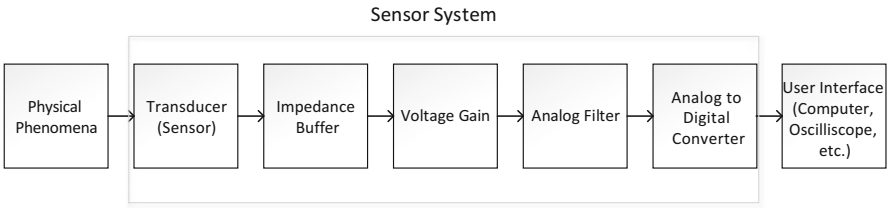

Fig. 26 Block diagram of a sensor system indicating the components required between a transducer and an end user

Transducer: This component of the sensor system is a measurement device or array of devices previously described.

Impedance buffer: This portion of a sensor system protects the sensor from any loading effects due to downstream circuitry. All data acquisition systems, amplifiers, filters, and other such systems have a finite input impedance that can be represented as a resistor in parallel with a capacitor, usually on the order of $10^6\Omega$ and 10^{-12}pF. A simplified example of the need for an impedance buffer is the measurement of a voltage drop across a resistor. The input impedance of a standard multimeter is approximately 1MΩ. Placing this impedance in parallel with a simple resistive divider consisting of R1 and R2 produces a reading on the multimeter as

$$V_{measured} = V_{source} * \frac{\frac{R_2 R_{meter}}{R_2 + R_{meter}}}{R_1 + \frac{R_2 R_{meter}}{R_2 + R_{meter}}}$$

When the resistance of the multimeter is much greater than the resistor R2, this reduces to the desired measurement of

$$V_{measured} = V_{source} * \frac{R_2}{R_1 + R_2}$$

As the value of R2 gets closer to the equivalent input resistance of the multimeter, the measurement is attenuated. An impedance buffer is designed with the sensor impedance in mind, eliminating or greatly reducing the attenuation due to long cable length or a low resistive load at the end of the cable.

Voltage gain: In most cases, data acquisition systems have a set range of full-scale inputs that can be measured by the system on the order of tens of millivolts to tens of volts. As previously discussed, the native output of many of the transducers described in this section is on the order of 10E-6 to 10E-3 V. In order to match the range of the data system to the output of the sensor, gain may be added. There are many higher-order effects that the introduction of gain can influence, such as phase shifts or other types of signal distortion. A carefully designed gain stage will allow for maximum measurement resolution with minimal loss of fidelity.

Filtering: Some level of filtering is always required on a digital data acquisition system in order to prevent aliasing. Aliasing is the contamination of a signal due to insufficient sample rate and will be discussed in a subsequent section. Beyond that, it may be desirable to have a filter in a sensor measurement system in order to reduce contamination of known noise sources, such as electromagnetic coupling from a motor drive or powerline noise. Again, there are phase and distortion effects that require careful design when implementing a filter.

Analog-to-digital converter: All instrumentation-based sensor systems end in a conversion to the digital domain. The approximation of a continuous time signal into a discretized series of values can be achieved through many different methods, all with differing accuracy, timing, and speed. The ultimate method which will be used to analyze the data will largely drive the requirements for analog-to-digital (A/D) conversion.

5 Signal Conditioning

The term "signal conditioning" refers to the analog electronic circuitry between the sensor and the A/D converter. It may combine impedance buffering, amplification (gain), and any filtering required to optimize performance of the analog-to-digital converter.

5.1 Types of Amplifiers

There are four basic kinds of amplifiers commonly used for dynamic signals, depending on sensor output type: one for single-ended voltage, one for a differential voltage, one for a charge, and one for constant current excitation, also called integrated circuit piezoelectric (ICP).

***Voltage amplifier*:** A voltage amplifier is a common immediate interface for a sensor. It is generally constructed using an operational amplifier (or op amp) which effectively isolates the sensor from the influence of downstream circuitry. This stage can also contain gain, which amplifies the sensor output. A schematic of a simple unity gain noninverting voltage amplifier is shown in Fig. 27 left. This specific type of voltage amplifier is commonly referred to as a buffer or voltage follower. An example of a voltage amplifier that inverts the signal and provides gain or attenuation is shown on the right. The output voltage will be determined by the ratio of the two resistors: $V_{out} = \frac{R_2}{R_1} V_{in}$.

***Charge amplifier*:** A charge amplifier is a current integrator that produces a voltage output proportional to the integrated value of the input current. The amplifier offsets the input charge using a feedback reference capacitor and produces an output voltage proportional to the total input charge flowing during a specified time period. A simple charge amplifier is shown in Fig. 28. The resistor Rfb can be used to set the DC operating point and limit the low-frequency response. Without it the amplifier output would drift either up or down to one of the supply voltages. "Gain" is not the best way of describing the transfer function because the output voltage will be

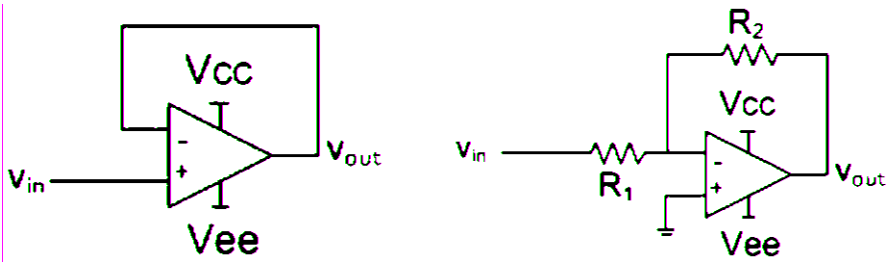

Fig. 27 Operational amplifier configurations

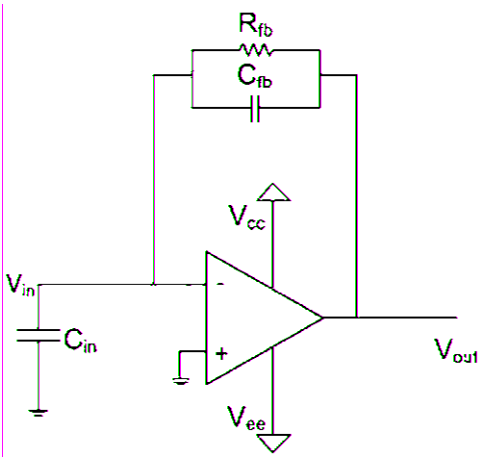

Fig. 28 Charge amplifier

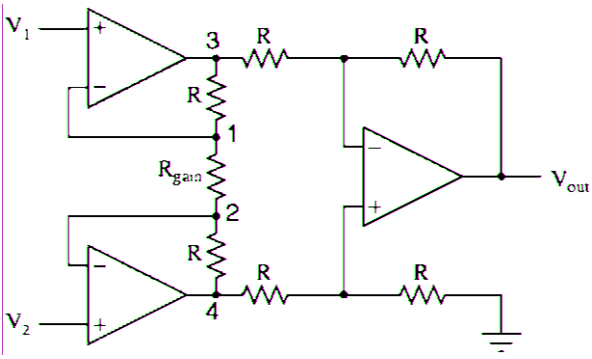

Fig. 29 Differential "instrumentation" amplifier

proportional to the transducer charge, Q, developed across CIN. The output will be $V_{out} = \frac{Q}{C_{fb}}$:

***Differential amplifier*:** A differential amplifier amplifies only the difference between two input voltages, suppressing any voltage common to the two inputs. This is frequently used for Wheatstone bridge circuits which have two mirrored outputs relative to a reference voltage. The circuit also cancels noise common to both inputs. A differential amplifier can be constructed from a single op amp, but a better design is shown in Fig. 29. If the R values are equal, the gain is $V_{out} = (V_2 - V_1)\left(1 + \frac{2R}{R_{gain}}\right)$. This configuration is commonly referred to as an "instrumentation amplifier."

***IEPE*:** "Integrated electronics piezoelectric" (IEPE) is a method by which two wires from the transducer to the signal conditioning conduct both the power and the superimposed signal. IEPE is very common for piezoelectric sensors and will be explained in some detail.

IEPE sensors offer many advantages over traditional charge output sensors, including:

(1) Fixed voltage sensitivity, independent of cable length or capacitance.
(2) Low output impedance (<100 ohms) allows signals to be transmitted over long cables through harsh environments with virtually no loss in signal quality.
(3) Two-wire system accommodates standard low-cost coaxial or other two-conductor cables.
(4) Intrinsic sensor self-test feature by monitoring sensor output bias voltage.
(5) Low per-channel cost.
(6) Direct operation into data acquisition instruments which incorporate IEPE power.

IEPE is achieved by providing a constant current excitation to the transducer and allowing the voltage to vary. The variations in this compliance voltage are the transducer output. Typical fixed currents for IEPE data systems are 2 mA, 4 mA, or 10 mA. This has been standardized so that the circuitry inside of the transducer package can condition the current excitation into the necessary voltage.

The constant current excitation is achieved by one of several methods. The simplest implementation uses a constant current diode to provide the excitation current. These diodes provide a deterministic current path that provides the rest of the circuitry a bias point to operate around. It is preferable to use one of these diodes instead of a transistor or resistor as the process variation associated with the diode production provides a more stable reference than a more complicated circuit. An example of an IEPE circuit using a diode is shown in Fig. 30.

There are a few constraints on IEPE circuit design that need to be considered. First, there is no DC component to the output of an IEPE system, since it is removed by the coupling capacitor. Additionally, as frequency increases, the ability of the IEPE circuit to drive a long cable is diminished. If an IEPE system is being evaluated for systems in the multi-kHz range, the cable type, cable length, and expected output voltage amplitude should be evaluated. A graph illustrating this design space is shown below. Most modern dynamic data systems have an option for powering an IEPE transducer. If the data system offers voltage input only, external IEPE signal conditioning must be used.

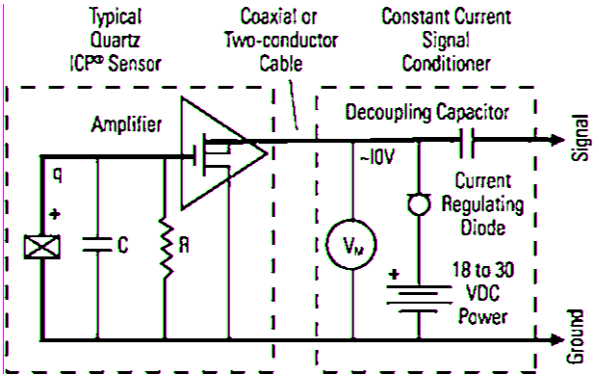

Fig. 30 IEPE transducer and signal conditioning (courtesy PCB Piezotronics)

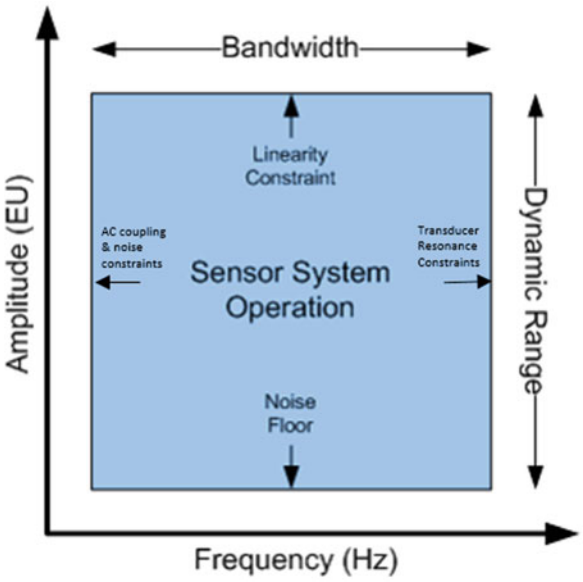

Fig. 31 IEPE sensor system operating space

Linearity: IEPE sensor systems are linear over a wide amplitude and frequency range. The limits of linearity are due to mechanical and/or electrical constraints. *The operating range may be thought of as the two-dimensional space shown in* Fig. 31.

Mechanical considerations: The mechanical structure within the sensor most often imposes a high-frequency limit on sensing systems. That is, the sensitivity begins to rise rapidly as the natural frequency of the sensor is approached:

$$\omega = \sqrt{\frac{k}{m}}$$

where ω = natural frequency

k = stiffness of sensing element

m = mass loading of the sensing element

This equation helps to explain why larger sensors with greater mass have a lower resonant frequency.

Electrical considerations: When acquiring low-frequency information, the constraints are:

(1) The transducer discharge time constant of the sensor crystal.
(2) The time constant of the coupling capacitor used in the signal conditioner. (If DC coupling is used, only #1 needs to be considered).

Either or both of these factors can set the low-frequency limit, and it is important that they are readily understood.

Transducer time constant: The transducer discharge time constant is the more important of the low-frequency limits, because it is fixed by the sensor design.

Consider the IEPE sensor shown previously in Fig. 30. While the sensing element will vary widely in physical configuration for the various types (and ranges) of pressure, force, and acceleration sensors, the basic theory of operation is similar for all. The sensing element, when acted upon by pressure, force, or acceleration, produces a quantity of charge proportional to the mechanical input. In quartz IEPE sensors, this charge accumulates in the total capacitance, Ctotal, which includes the capacitance of the sensing element, plus amplifier input capacitance and any additional stray capacitance. The result is a voltage according to the law of electrostatics: $\Delta V = \Delta q / C_{total}$. This voltage is then amplified by a MOSFET voltage amplifier to determine the final sensitivity of the sensor. In ceramic IEPE sensors, the charge from the crystal is typically used directly by an integrated charge amplifier. In this case, only the feedback capacitor (located between the input and output of the amplifier) determines the voltage output and consequently the sensitivity of the sensor. While the principle of operation is slightly different for quartz and ceramic sensors, the schematic (Fig. 30) indicates that both types of sensors are essentially resistor-capacitor (RC) circuits. The low-frequency cutoff of the sensor will be determined by

$$F_c = \frac{1}{2\pi RC}$$

where Fc is the cutoff frequency in Hz at 3db of attenuation, R is the internal sensor resistor value shown in Fig. 30, and C is the total capacitance as above.

Coupling capacitor time constant: If the constant current signal conditioner is DC-coupled, the low-frequency response of the system is determined only by the sensor time constant. However, since most IEPE signal conditioners are AC-coupled, the coupling capacitor may be the limiting factor for low-frequency measurements. For example, a typical AC-coupling capacitor might be 1 μF. Assuming a 1 megohm input impedance on the readout instrument, the coupling time constant is R times C or 1 second. If the transducer itself has a longer time constant, the coupling capacitor in the signal conditioning may limit the low-frequency response. To get the full lower limit on frequency range, the coupling time constant should be at least 10 times larger than the sensor time constant.

Some signal conditioners have a DC-coupled option. This is usually paired with an adjustment to remove the bias to zero volts in the amplifier. A DC-coupled output from a standard AC-coupled signal conditioner can be obtained by inserting a "T" connector in the transducer cable. The signal from the "T" connector contains the raw sensor data signal which includes the DC bias, typically 8 to 10 VDC. This bias can be removed by the readout instrument if it has an offset capability.

IEPE precautions: These measures should be followed to reduce risk of damage or failure in IEPE sensors:

(1) Do not apply more than 20 mA constant current to the sensors.
(2) Do not exceed 30 VDC supply voltage.
(3) Do not apply voltage without constant current protection.

(4) Do not subject standard sensors to temperatures above 250 °F (121 °C). Consult the vendor to discuss testing requirements in higher-temperature environments.
(5) Most IEPE sensors have an all-welded hermetic housing. However, due to certain design parameters, some models may be epoxy sealed. In such cases, humidity from moist environments may penetrate the housing and degrade the frequency range specification of the internal electronics. If this has occurred, the sensors can be restored by baking at 250 °F (121 °C) for 2 h to expel the contaminants.
(6) Many IEPE sensors are not shock-protected, and a drop on a hard surface can generate thousands of volts in the piezoelectric material. This will damage the internal amplifier. Care should be taken to avoid dropping IEPE devices.

IEPE cable length check: For coaxial cables, the cable capacitance and the circuit resistance form a low-pass filter. If cable length is greater than 100 feet, high-frequency response could be compromised. This can be checked with the equation above or solved using the nomograph below. The ordinate is the circuit resistance: roughly the maximum signal peak voltage divided by the supplied constant current, minus one milliamp to account for the quiescent power drawn by the internal electronics, or $R = \frac{V}{Ic-1}$. For example, if the IEPE current is 2 ma, R would be 5 volts divided by .002A–.001A or 5000 ohms. A 100-foot cable rated at 30pf/ft. would have a total capacitance of 3000pf. The ordinate value in the nomograph is scaled by 1000, so the intersection of 5.0 on the abscissa with the 3000 pf line would occur at 10.6 kHz. The recommended practice is to have this frequency be 1.5 to 2 times the maximum frequency of interest. If it is not, the constant current to the sensor should be increased (if possible) (Fig. 32).

5.2 Filters

A filter is a transmission path that alters a signal based on the frequency of that signal. A filter can alter both the magnitude and phase of the signal. The frequencies that pass through a filter without attenuation in magnitude are said to be in the passband of the filter. Frequencies which are attenuated by a filter are said to be in the stop band. The frequency or frequencies where the magnitude is attenuated to half of its original power (3 dB) is called the corner frequency or cutoff frequency. The rate at which attenuation increases with respect to frequency from the corner frequency toward the stop band is related to the number of poles or order of the filter. In general there are four typical filter implementations: low pass, high pass, band pass, or band stop (also called notch). In addition to magnitude alteration, phase is influenced by a filter. The overall phase shift due to a filter is related to the placement of the filter poles and overall order of the filter. Idealized responses of these filters are shown in Fig. 33 in the frequency domain.

These idealized responses are not achieved in practice but are approached as the filter model order is increased. Realistic filters have nonideal passband characteristics. The most common of these characteristics is pass-band and stop-band ripple. An illustration of this behavior is shown in Fig. 34.

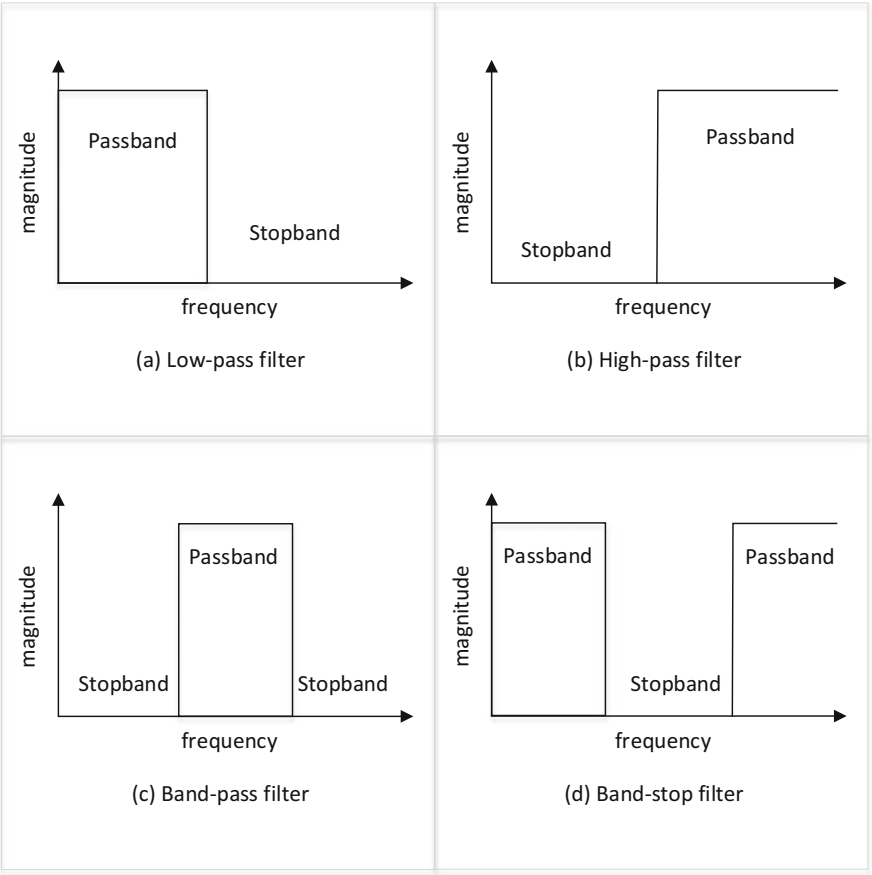

Fig. 32 Effect of cable length on IEPE signals. (Courtesy PCB Piezotronics)

In the time domain, there are two basic characterizations of a filter: the impulse response and the step response. The impulse response is defined as the output of a system due to an infinitely short, infinite magnitude input. The step response is the output of a system due to a step increase in the input. This is also the integral of an impulse response by definition. These tests can help determine the settling time, bandwidth, and time delay due to a filter.

Designing a filter requires creating a mathematical description of the desired frequency response and then implementing it in either the analog or digital domains. There are some closed form solutions that are commonly implemented in systems: Butterworth, Chebyshev, and Bessel. The trade-offs between these different filter designs are the amount of ripple in the pass band, the phase response, and the achievable filter roll-off. These characteristics are summarized in the following table (Fig. 35, Table 1):

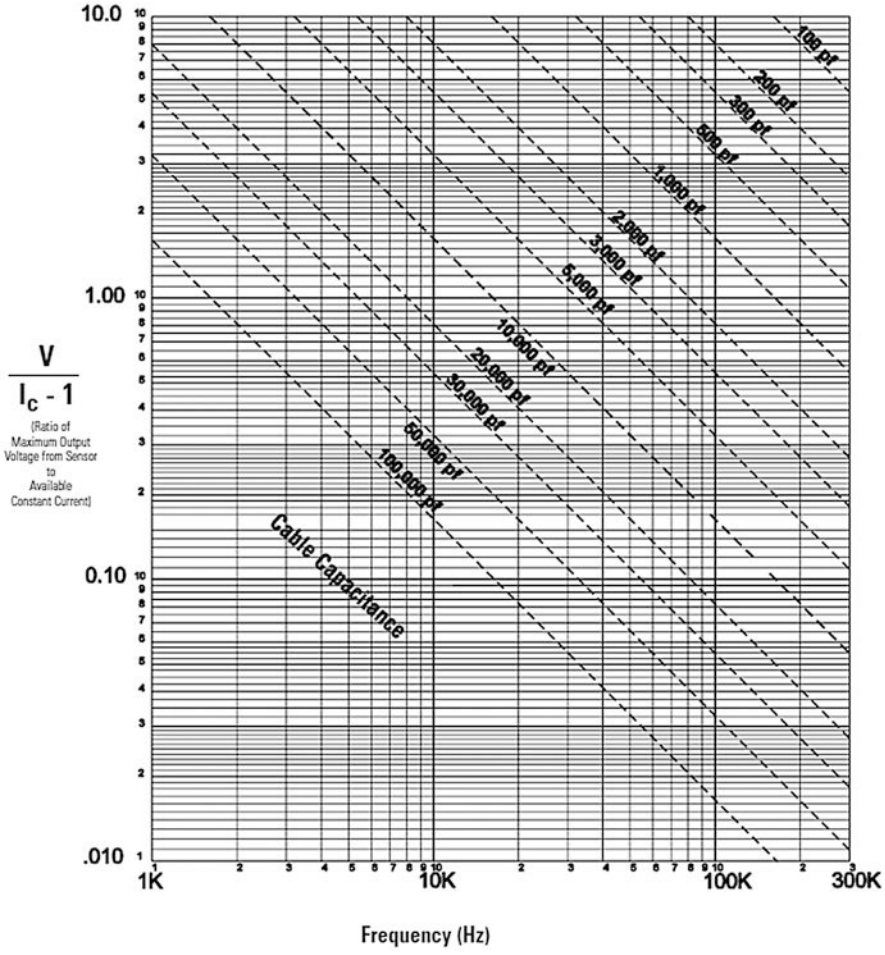

Fig. 33 Common idealized filter implementations

These systems can be implemented in the analog domain, while the signal is still a continuous time-varying voltage or in the digital domain as a mathematical function to alter digital data.

Analog filters: Analog filters are constructed using reactive circuit elements, which change impedance with frequency. For example, the impedance of a capacitor is Zc = 1/jwC. At DC, the impedance is infinite, while at high frequencies, the impedance approaches zero. Placing this capacitor into a voltage divider with a resistor, a simple filter can be created.

There are two types of analog filters: active and passive. A passive filter is composed of resistors, inductors, and capacitors and can only attenuate the signal. An active filter contains an operational amplifier. Some simple examples of filters

Fig. 34 Filter ripple

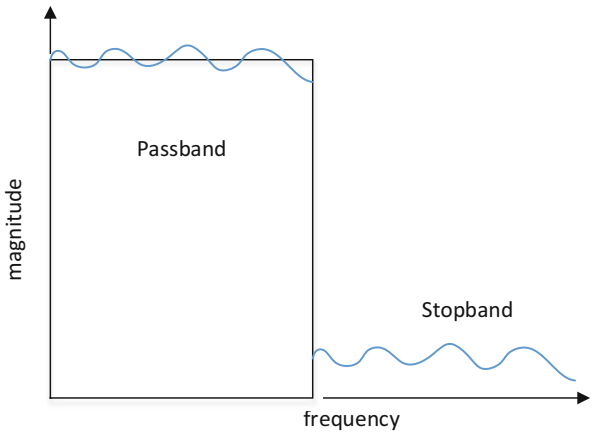

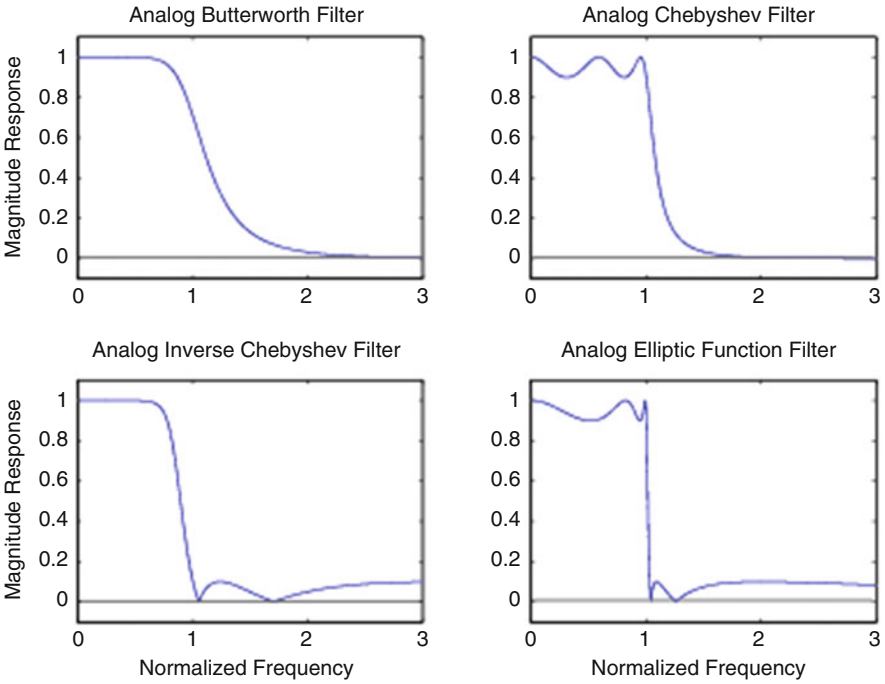

Fig. 35 Response characteristics of some filters in Table 1

are shown in Table 2; however, many detailed design manuals for active and passive filter design exist [7, 8].

Digital filters: Digital filters are algorithms that digitized data is passed through in order to manipulate the frequency content of the data. They are generally considered as more accurate as they do not rely on physical components that

Table 1 Common filter implementations

Filter type	Pass/stopband flatness	Roll-off	Phase response
Butterworth	No ripple	Slow roll-off	Phase change near corner
Chebyshev	High ripple	Sharp roll-off	Phase change near corner
Bessel	No ripple	Very slow roll-off	Linear phase

Table 2 Comparison of passive and active analog filters

Filter type	Passive example	Active example
Low pass	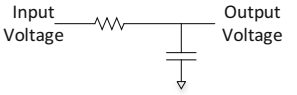	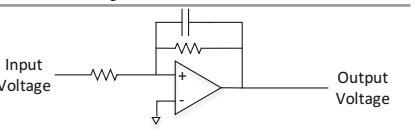
High pass	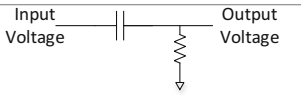	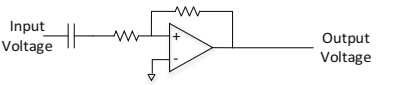
Band pass	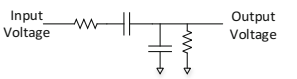	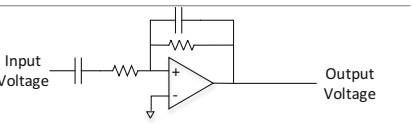
Band stop filter	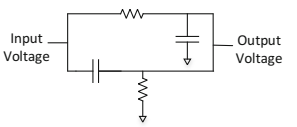	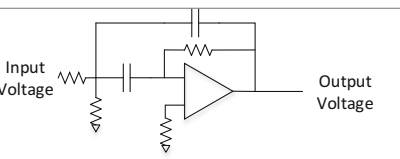

have finite tolerances and drift characteristics. Digital filters can be realized in a post-processing script on a host machine or on an in-line digital signal processor (DSP) chip. A DSP is a specialized microcontroller that operates at much higher speeds than the A/D converter. This allows a filtering algorithm to run and save a result before the next sample is taken. The speed of the A/D converter, speed of the DSP chip, and complexity of the filtering algorithm all influence overall bandwidth capability. Digital filters are described in terms of their impulse response and fall into one of two fundamental types: finite impulse response (FIR) and infinite impulse response (IIR).

FIR filters are used to implement virtually any frequency response with linear phase. The FIR filter uses a delay and weighted sum approach to alter the frequency content of the input data. The simplest version of an FIR filter is a moving average. A moving average is implemented when an output is represented by the average of the last N inputs, where N is the number of points for the moving average. Considering a sine wave input, if N corresponds to the total period of the sine wave, a moving average will produce zero output. The higher the order of the filter, the greater the

number of delay stages that are necessary and the faster the DSP needs to be relative to the data rate.

IIR filters are more analogous to analog filters producing amplitude and phase responses described by Butterworth, Chebyshev, Bessel, and others. They are represented by two-pole building blocks called bi-quads, which can be added in series to create higher-order filters. Designing an IIR filter begins with finding the transfer function of the desired filter response. That transfer function is then translated to the discrete, or z-domain, form and implemented in code on a DSP or in a post-processing algorithm. Computationally they are more complicated than FIR filters and therefore require additional computing power to implement.

5.3 Analog-to-Digital Conversion

An analog-to-digital converter (A/D converter) is a device that converts an analog voltage time history to a stream of digital values; see Fig. 26. In an extreme case, consider a simple comparator as shown in Fig. 36. This circuit will produce 5 V when the input voltage is above 2.5 V and will produce 0 V when the input voltage is below 2.5 V. As the input voltage changes, the comparator creates a series of digital pulses based on the input voltage. As a digital system is by definition a discrete-time system, this pulse train is recorded at a regular interval, or sample rate, to create a digital representation of the input analog signal. This simple example demonstrates the fundamental requirements for A/D converters.

More resolution can be obtained from a system which combines many of these comparators in parallel, all with a different reference to test the input voltage against. The resolution of an A/D converter is equal to the number of evenly spaced reference voltages, or "bits," that the signal can be compared to.

The maximum voltage that the A/D can resolve is set by the ceiling of this comparison system. The relationship between the maximum voltage an A/D converter can resolve and the minimum voltage it can resolve is called the dynamic

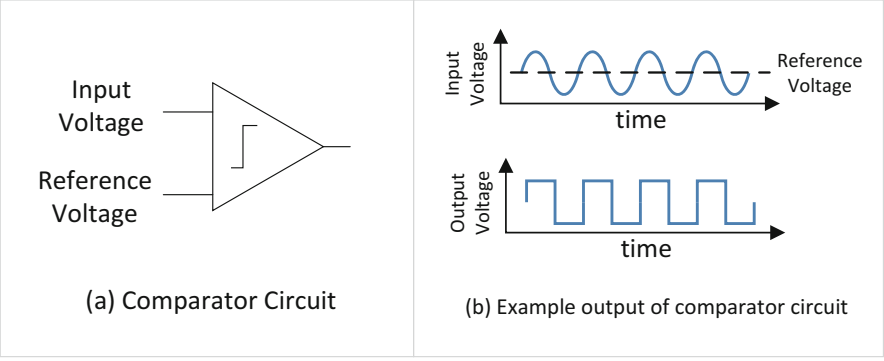

Fig. 36 Analog-to-digital conversion using a simple comparator

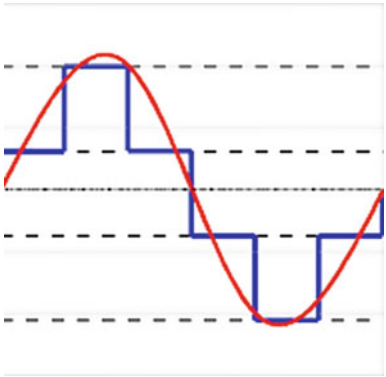

Fig. 37 Two-bit resolution with four quantization levels

range of the A/D converter. The minimum voltage step an A/D system can resolve is equal to the range divided by the number of discrete bits:

$$V_{bit} = (V_{max} - V_{min}) / 2^{total\ number\ of\ bits}$$

Figure 37 shows a simplified example of a sampled sine wave with two-bit resolution representing four discrete values. If a change in the analog voltage is smaller than the minimum resolvable voltage step, there may be no change in the digital output. This error in output is referred to as quantization error. If a transducer with a low-level voltage output is connected directly to an A/D converter, the signal change may not be large enough for the output to adequately represent the signal. This motivates designing an amplifier stage into a sensor system to match the expected signal levels to the dynamic range of the A/D converter.

Aliasing: In addition to considering the amplitude range of the signal being digitized, the rate of sampling is important. In order to properly represent the frequency content of a signal, the sample rate must be greater than twice the highest frequency being measured in order to satisfy the Nyquist criterion. If this rule is not followed, the resulting signal may be aliased. This can be demonstrated when a car wheel or propeller blade is shown in a movie or television show and appears to move backward. The frame rate of the camera recording the moving object is much slower than the rate at which it is moving, so the resulting image appears to move backward. In a data system, aliasing can be visualized as shown in Fig. 38. A higher frequency is misinterpreted as a lower frequency, due to an inadequate sample rate. This motivates the need for an analog filter stage prior to the A/D converter to ensure that no high-frequency content "folds back" into the digital data. These filers are referred to as anti-aliasing filters.

A/D converter types: There are many ways to implement an analog-to-digital converter, and as integrated circuit design improves and systems get faster and more accurate, the philosophy of A/D system design will continue to evolve. A few examples of A/D converters are briefly described here.

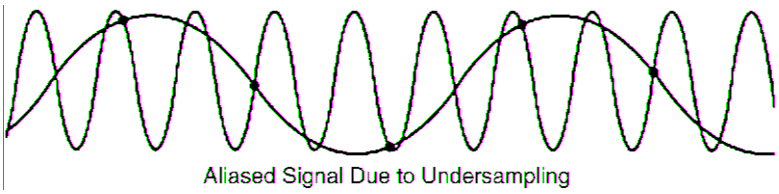

Fig. 38 Aliasing of a signal

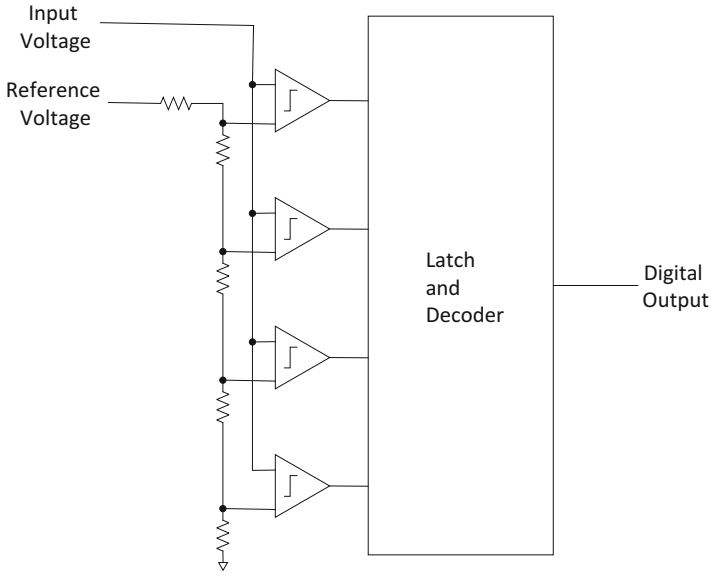

Fig. 39 Flash converter

Flash: The simplest type of A/D converter is the one described above. The flash A/D converter uses multiple comparators in parallel with incrementally different comparison voltages to determine a digital output. This is shown in Fig. 39. In general these types of A/D converters have high-power consumption and poor performance at high frequencies.

Subranging: Given the example of a flash A/D converter, imagine if a reference voltage could be adjusted to follow the input voltage. The resulting comparison voltages would have greater resolution as the dynamic range of the converter is maximized. A subranging A/D converter operates on this principle. As shown in Fig. 40, the subranging converter first digitizes the input signal and then uses a digital-to-analog converter to regenerate the analog voltage to use as a reference signal for a second stage of digitization. The final digital output is a combination of the original digitized value and the subranged value, producing an overall higher-resolution estimate. In order for this kind of converter to work, the A/D converters and digital-to-analog converter must have a higher number of bits than the expected

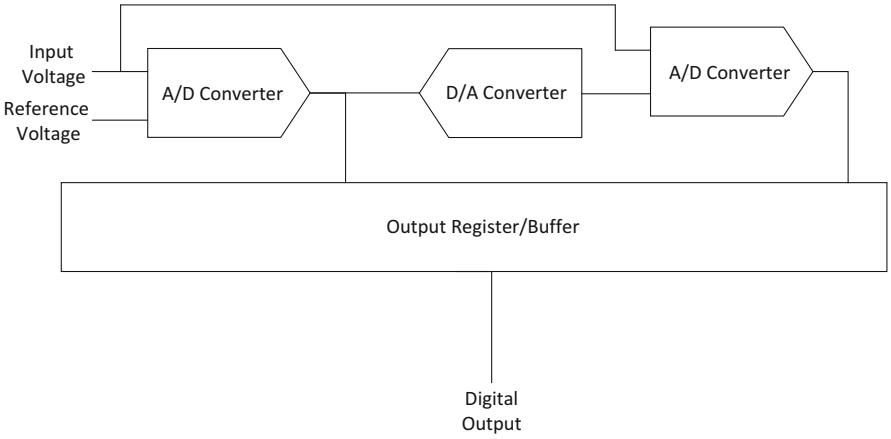

Fig. 40 Subranging converter

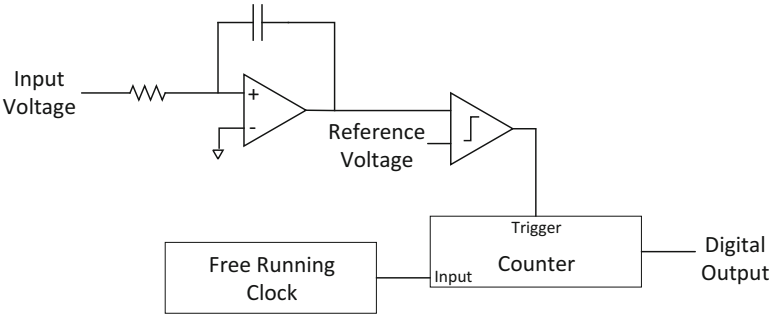

Fig. 41 Integrating converter

final answer. There are many methods by which the subranging estimation can occur beyond the simplest implementation of a series of flash converters. Many other references are available that describe these designs and the trade-offs between more complex designs and overall system accuracy (Datel) [7, 9].

Integrating: In an effort to increase accuracy over single counting topologies like flash or subranging A/D converters, integrating or multi-slope A/D converters were developed. As shown in Fig. 41, the integrating A/D converter applies an unknown analog input to an integrating circuit. The integrator builds charge until a known threshold is passed, triggered by the comparator. The input is then switched to a known reference voltage that is of opposite polarity, and the integrator output begins to decay. Both of these time periods of integration are counted. The resulting count generates the digital representation of the analog input voltage. The accuracy of this type of A/D converter is higher than previous design efforts; however, each digital step requires a substantial integration time to achieve that accuracy. Integrating

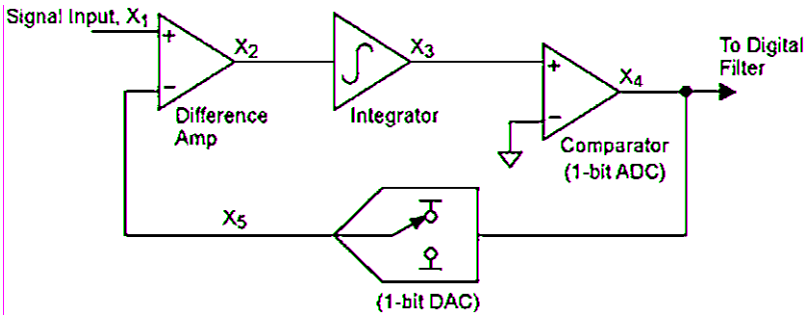

Fig. 42 Delta-sigma converter

A/D converters are still in use for low-frequency applications but have largely been replaced by delta-sigma converters for higher bandwidth systems [10].

Delta-sigma: A delta-sigma ($\Delta\Sigma$) converter is an extremely fast one-bit digitizer. The digitizer runs hundreds of times faster than the input signal, and the resulting one-bit data stream is digitally filtered by a process called decimation. The decimation process changes the effective sampling rate by several orders of magnitude. Another effect of the decimation process is that the underlying noise floor is shifted up in frequency. This makes delta-sigma converters well suited for low-frequency applications that require a low noise floor. Designing a delta-sigma converter requires expertise in both analog circuit design and digital signal processing techniques. There are many excellent sources that delve into the details of these systems [11, 12] The delta-sigma converter is currently the industry standard for analog-to-digital converters (Fig. 42).

6 Other Considerations

While the choice of transducer and data system usually gets the most thought, other aspects of installing a sensor system are equally important. There are many types of cabling and installation considerations. In this section some of these installation-related design considerations are discussed.

6.1 Grounding

Grounding is the establishment of a path of electrical conduction between a circuit and an arbitrary reference point. This point is usually at zero potential in reference to all other system voltages. It is dependent on the system and could be the earth, the test article, an equipment case, or a bus structure defined as “ground.” Ideally it would be the zero reference point for both power and data signals. Frequently in practice, separate circuit paths to ground are provided for power returns, digital

signals, and analog signals to minimize electromagnetic interference, which is visible in systems as background noise. In the case of low level, single-ended analog signals, it is important to establish a single-point ground. Because a remotely grounded transducer may be at a different potential than the first gain stage, the resulting "ground loop" could introduce background noise in the data. This influence can be removed by grounding the cable shield at one end only, usually at the input to the signal conditioning. For this to be achieved, the sensors must be electrically isolated. If this is not provided in the sensor packaging, electrically isolated studs and mounts should be used. For some applications it may be sufficient to apply aluminum "speed" tape to the test article, to which the sensors are adhesively attached. The transducer is effectively ground, isolated through several layers of nonconducting adhesive.

Electromagnetic noise: Noise may be added to the transducer signal because of the presence of an alternating magnetic field in the vicinity of the cable, such an electric motor or other running machinery. This causes electromagnetic induction in the cable and results in a corrupted measurement signal. Precautions against this effect include:

1. The rerouting of cables
2. The use of short cables
3. Shielding

Rerouting may be a cost-effective method of reducing electromagnetic noise, as long as the source of the noise is recognized. The use of shielded cable is a preventative method which is commonly used by test engineers, although it is practically impossible to eliminate powerline-related frequency influences. Shielding is achieved by surrounding the wire by a conductive surface, which maintains the enclosed area free from external fields.

Electrostatic noise: Noise may also arise from electrostatic fields close to cable runs. Precautions against this effect include:

1. The rerouting of cables
2. The use of short cables
3. Shielding
4. Lowering of line impedance

Electrostatic shielding has different requirements from electromagnetic screening. Electrostatic shielding provides a conducting surface for the termination of electrostatic flux lines and commonly consists of either copper mesh or aluminum foil. A good magnetic shield is usually a good electrostatic shield, but the converse is not always true.

Lowering of the line impedance is effective at reducing electrostatic noise but is not effective at reducing electromagnetic noise. Electrostatic noise is directly proportional to the circuit impedance.

6.2 Cabling

The most common method to achieve signal transmission is the use of electrical cables to connect directly between the transducer mounted on the vibrating structure and the signal-conditioning equipment. These electrical cables are extremely important elements in the total measurement system. The type of cable used varies with the particular application and may be well-shielded coaxial cables, which traverse long distances between a piezoelectric accelerometer and its charge amplification system, or, alternatively, may be short unshielded twisted wires connecting IEPE sensors to signal conditioning, or strain gage bridges to the balance and amplification system. The selection of a particular cable form will depend on:

(1) The application
(2) The type of transducer
(3) The cable length
(4) The severity of the environmental conditions

The cables may in some applications be far from the passive devices they are often.

considered to be and may attract additional voltage signals which have not originated from the transducer. There are several possible origins for these extraneous signals:

(1) Electromagnetic fields
(2) Electrostatic fields
(3) Ground loops
(4) Triboelectric effects

All of these influences add unwanted signals to the *true* signal and are, in general, referred to as noise.

6.3 Ground Loops

Ground loops are generally more important than electromagnetic induction and occur because the measuring device is not at the same potential as the remainder of the system, and thus a voltage drop is created along the length of the cable. It is also possible that there may be a potential difference between nominal “grounds” in a laboratory. This influence can be removed by grounding the cable shield at one end only.

The user should be aware that in an industrial environment, different electrical power points can have different ground potentials, and that this may cause problems when several units are interconnected. This problem may be overcome by running equipment from a power source with a common ground.

Fig. 43 Common transducer connectors for dynamic measurements

6.4 Triboelectric Effects

Triboelectric charges result when coaxial cable is subjected to distortion either from tension, compression, or bending motions. The loss mechanism is friction between the inner cables and outer screening which effectively *rubs off* the charge. This influence can be greatly reduced by routing the cable in a way that avoids flexing and distortion of the cable during testing. Low noise cable is also available which can reduce this effect even further. The influence of triboelectric effects can be reduced by:

1. Taping down the cable where it is in contact with stationary objects
2. Allowing strain relief cable loops where relative motion occurs
3. Transferring cable runs from vibrating structures at points with lower vibration levels

6.4.1 Connectors

Connectors are required to attach cables to transducers, amplifiers, analyzers, etc. They rely on metal-to-metal surface contact to pass the signal. Each connection is a possible point of signal loss or noise, and the number should be kept to a minimum. Connectors have particular problems in difficult environments such as high humidity, corrosive atmospheres, or underwater applications. Manufacturers supply adaptors to allow conversion between differing standards. The most Common transducer connectors for dynamic measurements are BNC, microdot, and LEMO, shown in Fig. 43.

7 Data Validation

In the measurement process, we wish for the accurate conversion of physical parameters into a stream of digital values, within the amplitude and frequency range of interest. Unfortunately, there are many ways for dynamic data signals to become corrupted or compromised. Signals should be checked for validity before proceeding

with detailed analysis operations. This validation can start with an inspection of the measured time histories to verify that the basic characteristics of the signal are consistent with the physical mechanisms producing the signal.

7.1 Examples

The following are examples of anomalies that can be observed in time domain signals. They include overloads, underloads, noise contamination, null data, electromagnetic interference, cable and connector-generated signals, cross talk, telemetry problems, sensor resonance and nonlinearity, insufficient or excessive signal bandwidth, sensor mounting, lack of sensor power, and sensor base strain sensitivity.

One of the most common errors in data acquisition is the failure to provide an adequate upper limit for the dynamic range, due to a sensitivity that is too high. This results in signal clipping and is shown in the first three figures for different types of signal (Figs. 44, 45, 46, 47, 48, 49, 50, 51, 52, 53, 54, 55, 56, 57, 58, 59, 60, 61, 62, and 63).

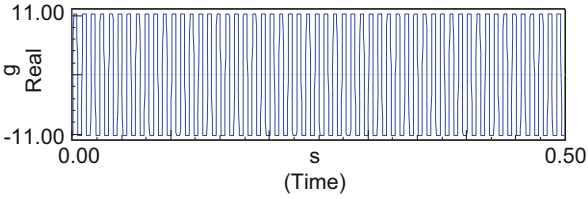

Fig. 44 Insufficient full-scale range results in clipping of a sine wave with both positive and negative peaks clipped. The limiting is readily apparent

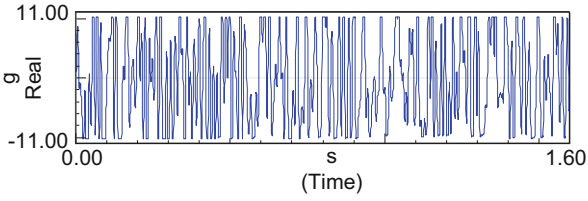

Fig. 45 Insufficient full-scale range results in clipping of a random signal. Clipped tops are visible but not as apparent as in Fig. 44

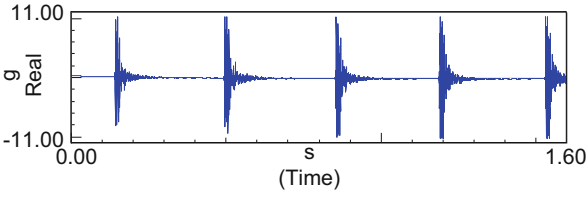

Fig. 46 Insufficient full-scale range results in clipping of a transient signal. Because of the short duration, clipping is difficult to detect

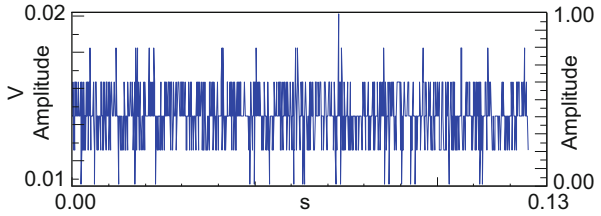

Fig. 47 Excessive full-scale range results in poor signal definition, shown here as bitnoise in the A/D converter. This could be due to insufficient gain or a defective transducer

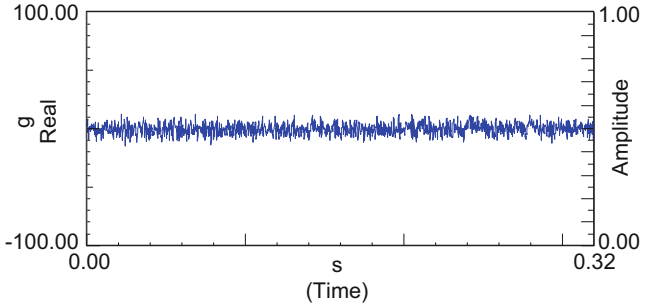

Fig. 48 Random noise can be expected in a data channel at some low level, originating in the sensor, signal conditioning, or environment. Whether this is an acceptable level depends on the full-scale level and how the noise compares to the signal of interest

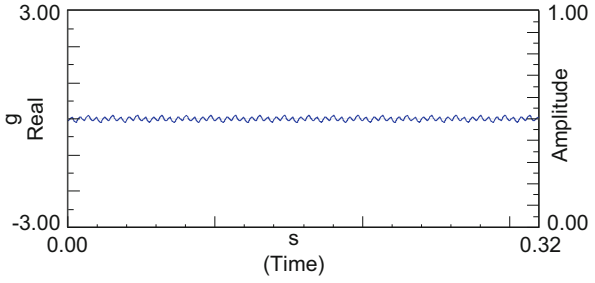

Fig. 49 Narrowband noise at multiples of 60 Hz can also be expected at some low level if the sensor and signal conditioning are not sufficiently shielded or isolated from the AC powerline. Ground loops are also a common cause of narrowband noise

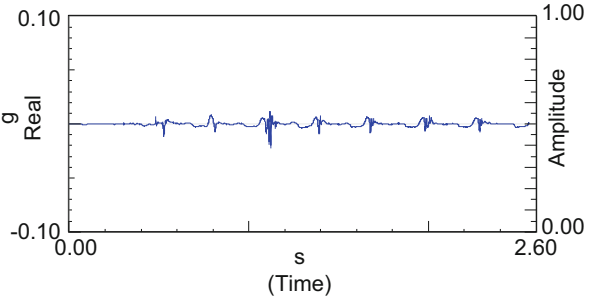

Fig. 50 Noise can be generated in a signal cable by sudden mechanical flexing, due to the triboelectric effect. This noise was created in an ICP accelerometer circuit by impacting the cable bundle against a hard surface

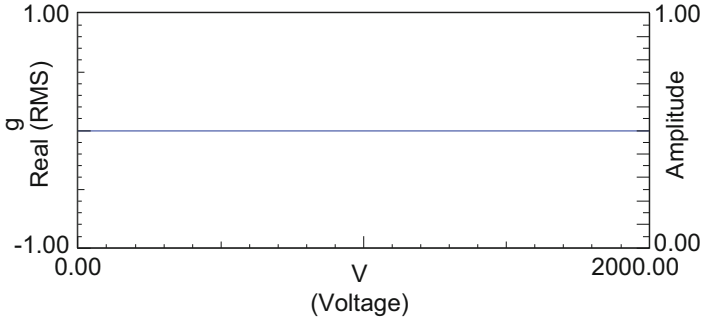

Fig. 51 Null data can indicate a problem. A stream of exactly zero values is unlikely in a physical measurement and probably indicates signal to range mismatch, A/D failure, or unintentional scaling by zero

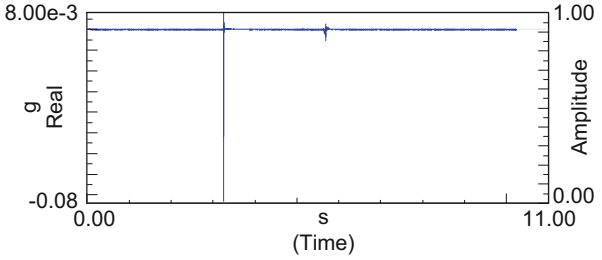

Fig. 52 Sometimes a test involves a nearby firing or actuation circuit with large momentary electrical currents. This can induce a pulse in sensor cables. In this case, an IEPE accelerometer signal appears to contain a large impulse, which is actually induced from a high current pulse through a nearby cable

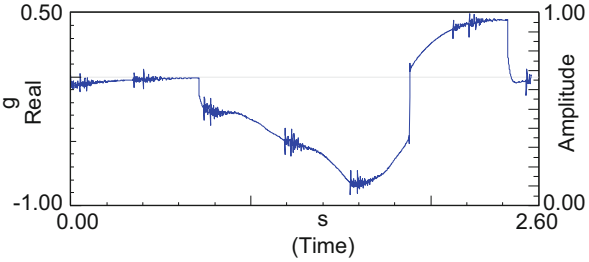

Fig. 53 RF interference created from a walkie-talkie keyed near the signal cable. The RF is rectified in the circuitry and appears at much lower frequencies. Sources of RF energy should not be in proximity to data cables

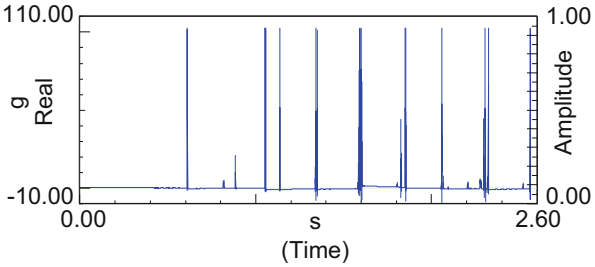

Fig. 54 The most common problem in instrumentation cabling is momentary interruption of the circuit from loose or dirty connectors, broken wires, or faulty solder joints. In IEPE circuitry this is characterized by short excursions to full scale and a small DC offset, while the circuit recovers from the electrical overload

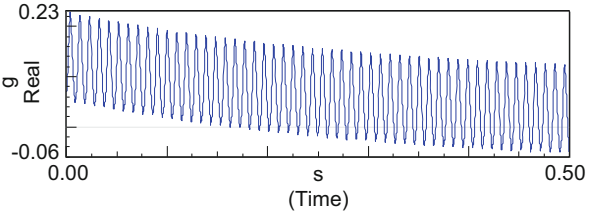

Fig. 55 In an AC-coupled circuit, it may take time after connections are made to reach equilibrium. Data should not be acquired until the spurious trend has settled. In some cases this may take several minutes

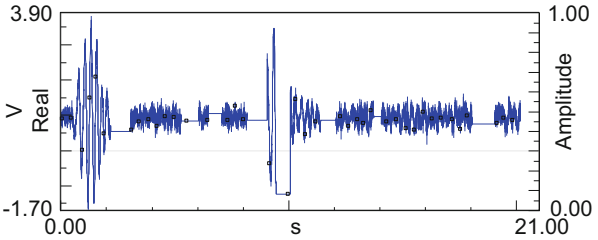

Fig. 56 In RF telemetry systems, dropouts can occur from temporary low signal levels due to poor antenna positioning or signal cancellation due to multiple RF paths. Typical behavior is the persistence of the last data value until the link is restored

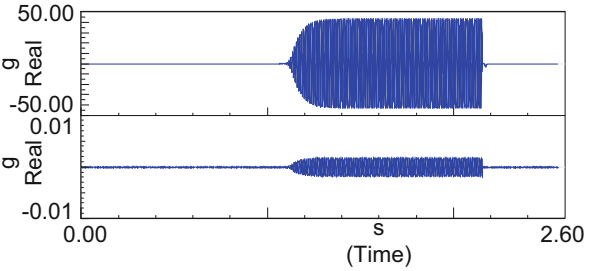

Fig. 57 The signals in a data system can couple between channels if there is not enough isolation and shielding. In this case a 50 g signal in channel 1 couples into an open circuit channel 2. This is called "cross talk." In this case, the attenuation is acceptably high, 80 db or more

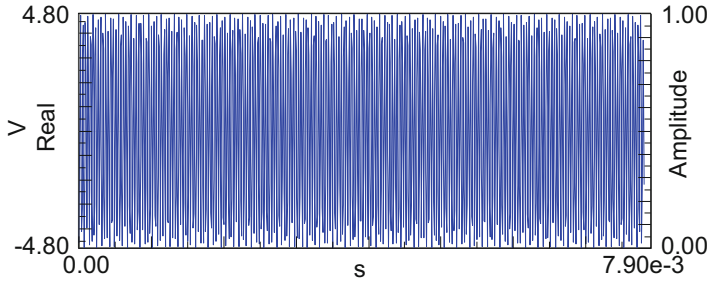

Fig. 58 If the energy received by the sensor is high enough in frequency, ringing of sensor components may result. In this case, the mass and piezoelectric crystal in an accelerometer are excited into resonance near full-scale amplitude, making identification of other frequencies problematic. This can only be observed by unfiltered viewing on a high bandwidth system such as an oscilloscope

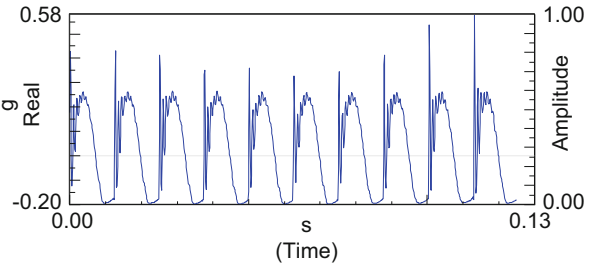

Fig. 59 Poor bonding of an accelerometer to a test article may result in nonlinear contact. In this case, the measured sinusoidal motion from a handheld calibrator should be a clean 100 Hz sine wave. A partially broken bond may result in small nonlinear impacts. This could also be caused by a loose mounting stud

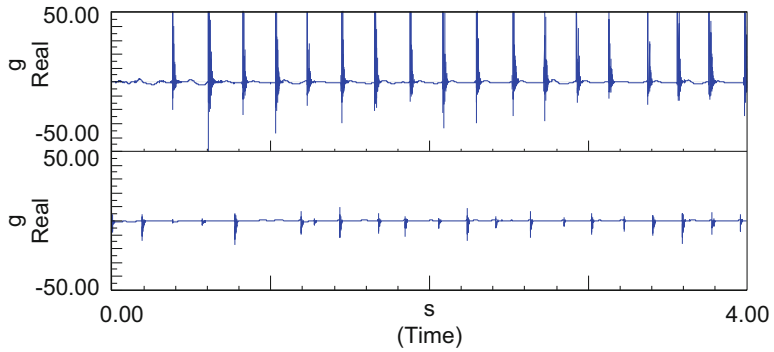

Fig. 60 IEPE accelerometers are powered internally by a constant current, typically supplied by the data system signal-conditioning circuitry. If the operator neglects to turn the IEPE power on, a weaker, uncalibrated, and likely distorted signal will still be output by the sensor. This could be mistaken for a real signal. The upper trace measures tapping on a powered accelerometer mounted to a beam; the lower trace is the same situation with the accelerometer unpowered

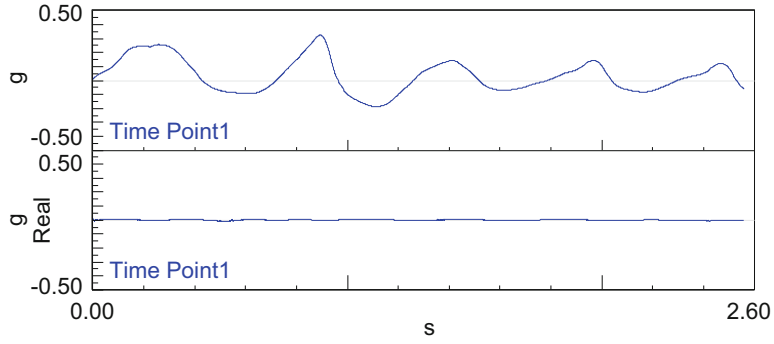

Fig. 61 Accelerometer base strain sensitivity. Upper figure shows accelerometer directly mounted to thin panel subjected to flexing. Lower figure shows same condition with an aluminum block inserted between the accelerometer and panel. The strain influence is greatly attenuated by the block

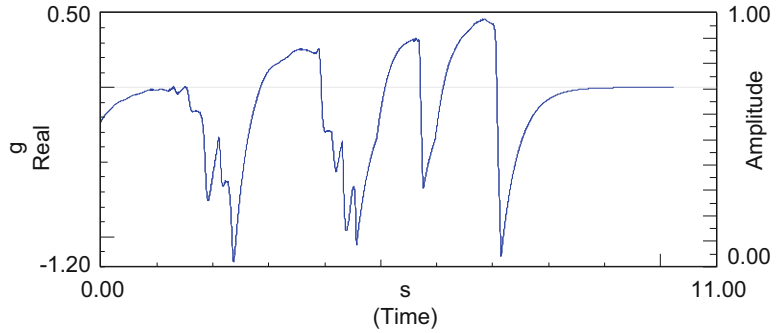

Fig. 62 Thermal drift. Some types of accelerometers are sensitive to small thermal changes in the environment. This output was caused by repeatedly waving a warm airstream source across a bare accelerometer case. Smaller effects can result from laboratory air turbulence or outdoor wind action on a sensor

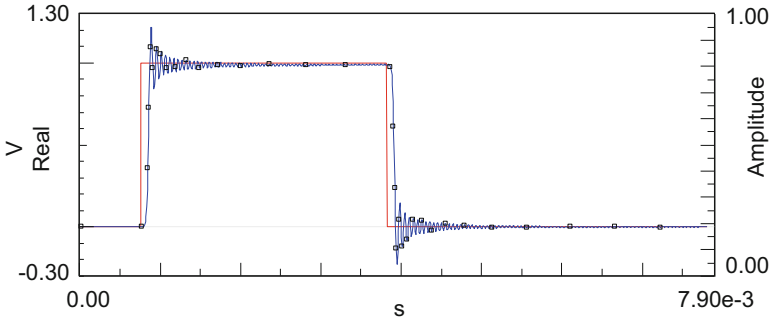

Fig. 63 A step input to a data system can make the anti-alias filter ring. The original signal is the red trace; the measured result is the blue trace. For analysis which focuses on time histories, the data system should employ an anti-alias filter which minimizes ringing and overshoot

References

1. Stein PK (1936) A banner year for strain gages and experimental stress analysis-an historical perspective. Exp Tech 30(1):23–41, (2006)
2. Robinson M (2006) Strain gage materials processing, metallurgy, and manufacture. Exp Tech 30(1):42–46
3. Semiconductor Strain Gage Handbook. Baldwin, Lima, Hamilton, Inc. (1973)
4. Mechanical Engineer's Handbook, 3rd Edition, Part 1, Instrumentation, Systems, Controls, and MEMS, Myer Kutz, editor, Chapter 3, Bridge Transducers, pages 69–130, Patrick L. Walter, Wiley, 2006 (originally printed: Instrumentation and Control, Wiley, 1990)
5. Cady WG (2018) Piezoelectricity: Volume One: An Introduction to the Theory and Applications of Electromechanical Phenomena in Crystals, ISBN-13:978046835129, Dover Publications
6. Walter PL (1980) Deriving the transfer function of spatial averaging transducers. ISA Trans 19(3). https://www.journals.elsevier.com/isa-transactions

7. Analog Devices (2008) Chapter 8: analog filters. In: Zumbahlen H (ed) Linear circuit design handbook
8. INTEGRATED M (n.d.) Analog filter design demystified. Retrieved from https://www.maximintegrated.com/en/app-notes/index.mvp/id/1795
9. Kester W (n.d.) Analog Devices MT-024 TUTORIAL. Retrieved from ADC Architectures V: Pipelined Subranging ADCs: http://www.analog.com/media/en/training-seminars/tutorials/MT-024.pdf
10. Kester W, Bryant J (n.d.) Analog Devices MT-027 tutorial. Retrieved from ADC Architectures VIII: Integrating ADCs: http://www.analog.com/media/en/training-seminars/tutorials/MT-027.pdf
11. Baker B (n.d.) Texas instruments incorporated: data acquisition. Retrieved from How delta-sigma ADCs work, Part I: http://www.ti.com/lit/an/slyt423/slyt423.pdf
12. Kester W (n.d.) Analog Devices MT-022. Retrieved from ADC Architectures III: Sigma-Delta ADC Basics: http://www.analog.com/media/en/training-seminars/tutorials/MT-022.pdf
13. Lawrenson C, Valentino M (2013) Microphone handbook. PCB Piezotronics
14. Himelblau H, Piersol AG, Wise JH (1994) Grundvig handbook for dynamic data acquisition and analysis. Institute of Environmental Sciences
15. Datel (n.d.) Application note. Retrieved from Subranging ADCs operate at High Speed with High Resolution: http://www.datel.com/data/ads/adc-an5.pdf
16. Maxim Integrated (n.d.) *Tutorial 1870*. Retrieved from Demystifying Delta-Sigma ADCs: https://www.maximintegrated.com/en/app-notes/index.mvp/id/1870
17. PCB Piezotronics (2009) General signal conditioning guide. https://www.pcb.com/techsupport/docs/pcb/PCB-G0001G-1209_Lowres.pdf

Laser Doppler Vibrometry Measurements in Structural Dynamics

3

Paolo Chiariotti, Christian Rembe, Paolo Castellini, and Matt Allen

Contents

P. Chiariotti · P. Castellini (✉)
Università Politecnica delle Marche, Ancona, Italy
e-mail: p.chiariotti@univpm.it; p.castellini@univpm.it

C. Rembe
TU Clausthal, Clausthal-Zellerfeld, Germany
e-mail: christian.rembe@tu-clausthal.de

M. Allen
University of Wisconsin-Madison, Madison, WI, USA
e-mail: matt.allen@wisc.edu

R. Allemang, P. Avitabile (eds.), *Handbook of Experimental Structural Dynamics*,
https://doi.org/10.1007/978-1-4614-4547-0_4

Abstract

Laser vibrometry is a powerful tool for measurement of vibration on a variety of structures. Lasers do not mass-load or otherwise change the dynamics of a structure, and so they have enabled measurements from surfaces that are too light, delicate, hot, etc. to allow conventional surface mounted sensors. The position of the measurement point can also be changed readily. Thus, laser vibrometry has also allowed acquisition of measurements over a dense grid of points, to more completely characterize a structure its deformation shapes, the evolution of stress waves, or the identification of structural damages than it might be feasible with other methods. The chapter is divided in two sections: the first one is intended to provide an insight about the theory behind laser Doppler vibrometry (LDV), while the second section aims at giving an overview of the different types of laser Doppler vibrometers that have been developed so far. The chapter is not intended to give a comprehensive discussion of laser Doppler vibrometry, but it provides sufficient details about potentials, issues, and best practice approaches for successfully exploiting such technique in structural dynamics testing. References are provided to direct the interested reader to more detailed information as well as to examples of application cases.

Keywords

Non-contact measurement · Laser Doppler vibrometry · Vibration analysis · Interferometry

Nomenclature

AEL	Accessible emission limits
A/D	Analog-to-digital converter
AOM	Acousto-optic modulator
BS	Beam splitter
CSLDV	Continuous-scan laser Doppler vibrometry
DAQ	Data acquisition
DOE	Diffractive optical element
DoF	Degree of freedom
FDM	Frequency demodulation
HPF	High-pass filter
I&Q	In-phase and quadrature signal
GUM	ISO Guide to the Expression of Uncertainty in Measurement
LDV	Laser Doppler vibrometer
LASER	Light amplification by stimulated emission of radiation
LPF	Low-pass filter
PBS	Polarized beam splitter
PDM	Phase demodulation
PID	Proportional-integrative-derivative controller
PLL	Phase-locked Loop

PD	Photodiode
QWP	Quarter-wave plate
RSSI	Received signal strength indication
SM	Self-mixing effect
SNR	Signal-to-noise ratio
THD	Total harmonic distortion
VCO	Voltage-controlled oscillator

1 Theory of Vibrometry

This section of the chapter aims at providing an insight about the theory behind laser vibrometry. It is not intended to give a comprehensive discussion of such subject; references are provided to direct the reader to more detailed information.

1.1 Lasers Sources and Doppler Effect

The acronym LASER, light amplification by stimulated emission of radiation, addresses a specific light source developed in the 1960s. Hence, the word LASER describes the emission of light, which is an electromagnetic radiation, by a mechanism called stimulated emission. Three main characteristics differentiate light emitted by a laser source from light emitted by other sources:

- Laser light is monochromatic (narrowband electromagnetic spectrum) and coherent (fixed phase relationship between the electric field values in time, different times, and space, different locations).
- Laser light is collimated (light is emitted as a low-divergence beam, i.e., the beam radius does not undergo significant modifications within moderate propagation distances).
- Laser light can be linearly polarized (the electric field oscillates in a direction – horizontal/vertical – perpendicular to the propagation direction in a stable way).

Anyone who has used a laser pointer is familiar with the first and second properties, which cause the laser to have a single color and the beam to spread little with distance. However, to truly understand vibration measurements with lasers, one must consider the properties of the beam more closely. The stimulated emission giving birth to the laser beam takes place into a resonance cavity, a cylindrical volume of lasing material put between two parallel mirrors, one of which is partly transparent to make it possible the exit of the laser beam. The resonating action of such optical cavity swamps out the random nature of the spontaneous emission and the light passing through the exit-end mirror will then have high spatial coherence. Indeed, because it is created in a cavity, both transverse modes (nodes on the cross section of the cavity) and longitudinal modes (nodes along the length of the cavity) do exist. The most important (and dominant) transverse mode

is the uniphase mode TEM_{00}. This mode induces the typical circular symmetry and Gaussian profile in the beam light intensity. Higher transversal modes can be suppressed by careful design. Longitudinal modes are directly related to the spectral characteristics of the laser. Let's reverse the perspective, and let L be the length of a given optical cavity (distance between the mirrors corrected for the refracting index of the lasing medium). The frequency gap Δf_m between two consecutive modes (m) is $c_n/2L$, where c_n represents the speed of light in the medium with refraction index n. This means that assuming a certain number of modes existing, it might happen that for certain L the spectral width of the laser light (frequency difference between the lowest and highest modes) is too small to be detected by common spectrometers and the laser appears to be monochromatic even if it is not single mode. When this happens (number of wavelengths within the laser length) such spread of frequencies induces a finite coherence length (length over which coherence degrades significantly). A truly single mode laser (true monochromatic laser) would have an indefinitely long coherence length. A typical laser that is utilized in the majority of commercially available vibrometers is a multi-mode helium-neon laser, in which at least two laser modes exist. The interference of two modes leads to a finite coherence length and thus causes the intensity of the optical signal to vary periodically along the optical path difference between the interfering beams. Such phenomena, which will be further explained in the section related to the backscatter issues, do induce alternating visibility maxima and minima and therefore might significantly influence the quality of the measurement.

The Doppler effect is a very well-known effect in physics. It is the key in laser Doppler vibrometry because it allows the possibility of directly relating the velocity of a target to a Doppler frequency shift in a beam of light. The Doppler effect for sound waves is a phenomenon that one can experience in everyday life, for example, when observing the sound of a passing automobile. As a sound source such as this moves toward a stationary observer, the number of wavefronts emitted by the source must be constant, but the travel distance decreases (assuming a constant sound propagation speed at Mach<1). Hence, the number of wavefronts impinging on the observer in the unit of time increases. Therefore, pitch of the sound seems to increase for the observer. This phenomenon can be well explained by the velocity superposition principle. In contrast, when considering light waves, the simple model of the velocity superposition that supports the understanding of the effect in the case of sound is not so straightforward. One can use a relativistic approach, which takes into account a transformation of space and time coordinates, as explained in [1]. However, recent studies on retardation effects in laser Doppler measurements [2] demonstrated that it is not necessary to consider relativistic effects in measurements of a two-beam interferometer, since the source and the observer are in the same reference frame. This condition is the one depicted in Fig. 1a.

This case might be considered as a double Doppler shift, one involving the source S and the moving object P and the other one involving the receiver O and the moving object. The frequency observed by P (f_P) can be expressed as

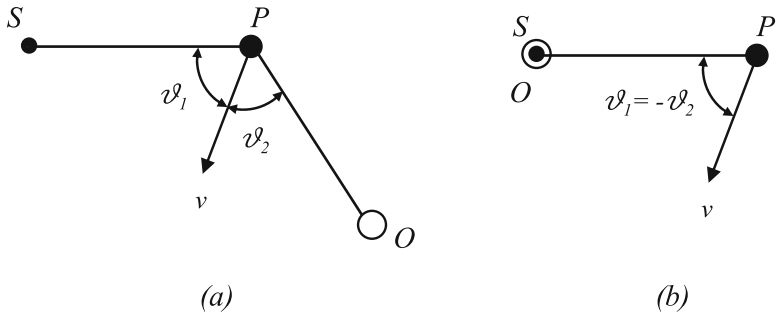

Fig. 1 Diagram for the calculation of the Doppler shift on scattering by a moving object *P*: source S and observer O in different locations (**a**); source S and observer O in the same location (**b**)

$$f_P = \frac{f}{\sqrt{\left(1 - v^2/c^2\right)}} \left(1 + \frac{v}{c} \cos \vartheta_1\right) \tag{1}$$

This holding, when the velocity is much less than the speed of light ($v < < c$), which is almost always the case in standard applications, it might be possible to expand in a power series in v/c and stop the expansion to the first order, so to obtain the Doppler shift (Δf) as shown below in Eq. (2). The equivalence $c = f\lambda$ and the prosthaphaeresis formulas were utilized to obtain the well-known expression for the Doppler shift.

$$\Delta f = f_O - f_P = \frac{f v}{c} (\cos \vartheta_1 + \cos \vartheta_2) = \frac{2v}{\lambda} \cos \frac{\vartheta_1 + \vartheta_2}{2} \cos \frac{\vartheta_1 - \vartheta_2}{2} \tag{2}$$

In most vibrometers, the source and the observer are located at the same place (backscatter configuration – Fig. 1b). The Doppler shift in such configuration can be expressed as reported in (3).

$$\Delta f = \frac{2v}{\lambda} \cos \vartheta \tag{3}$$

A vibrometer (Fig. 2) measures the motion of a target by exploiting the built-in interferometer capability, which resolves the phase of the back-reflected/backscattered light once the target is illuminated with coherent light. The motion is measured along the direction of the light ray because the illuminating and detecting rays have the same optical axis and polarization; thus the measurement can be considered to be a one-dimensional propagation problem where the electromagnetic wave equation simplifies to

$$\frac{\partial^2 E(x,t)}{\partial x^2} = \frac{1}{c_n^2(x,t)} \frac{\partial^2 E(x,t)}{\partial t^2}. \tag{4}$$

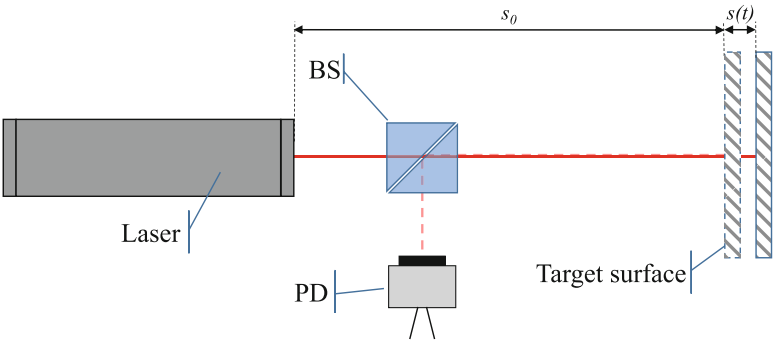

Fig. 2 Base optical configuration of a vibrometer with beam splitter (BS) and photodetector (PD)

In (4), $E(x,t)$ represents the norm of the linearly polarized electric field vector, $c_n(x,t) = c/n(x,t)$ is the speed of light in the medium having a refraction index $n(x,t)$, and c is the speed of light in vacuum. For $x = 0$ $E(x,t)$ results in $E(x,t)_{x=0} = E_0 \cos\ (2\pi ft)$.

For homogeneous media (no variation of n in space) and for an observation time t_m in which the time dependency of n can be neglected, if considering, for the target motion $s_t(t) = s_0 + s(t)$, the following conditions $|s_0| > > |s(t)|_{\max}$ and $|v(t)|_{\max} < < c_n$, and by defining s_d as the detector position, the Doppler shift, which represents the time derivative of the phase variation of the electric field of the light wave at the photodetector, to an approximation in the order v/c_n, with v instantaneous velocity of the target, can be expressed as

$$\Delta f_D = \frac{d\phi(t)}{dt} = k\frac{ds_{\text{opt}}(t)}{dt} \overset{n \approx const}{=} 2kn\frac{ds(t)}{dt} = 2knv(t) \tag{5}$$

where $k = 2\pi f/c$ is the wavenumber of the coherent light in vacuum and s_{opt} represents the optical path length. The Doppler shift is then generated through an optical path length variation. The interested reader might find more detailed information related to the mathematical derivation of (5) in [3].

1.2 From Interferometers to Vibrometers

1.2.1 Optical Homodyne and Heterodyne

The motion of the target induces a phase-modulation (and a frequency modulation at the same time) on the electric field of the measurement beam. This modulation is at optical frequencies (in the THz), and typical photodiodes cannot deal with this frequency directly; therefore optical beating has to be created by mixing the measurement beam with a reference beam (e.g., by using another coherent light

source of frequency f_2 and fixed phase relation or by exploiting a second laser mode of the same source). Independent of the mechanism that generates the beating, the mixing of the light waves takes place on the sensitive surface of a photodetector, a device that converts light intensity into an electric signal. Interference takes place properly (uniform over the full photodetector area) if interfering beams are well aligned and mode-matched. This has two major implications: their intensity profiles overlap, and their wavefronts have the same curvature on the detector. Photodetectors show a limited bandwidth; therefore they act as a low-pass filter (LPF) for optical frequencies. Saying that beating occurs on the surface of the photodetector means nothing else than a photocurrent is generated that is proportional to the intensity of light impinging on it. However, the photodetector is of significance only as a measurer of light intensity.

The output photocurrent $i_d(t)$ from the photodetector is proportional to light intensity $I(t)$, which depends on the square of the total electric field $E_d(t) = E_m \cos\ (2\pi f_1\ t - \varphi(t)) + E_r \cos\ (2\pi f_2 - \varphi_0)$, being E_r the amplitude of the reference beam, f_1 the frequency of the light source generating the measurement beam, $\varphi(t)$ the time varying phase containing the Doppler information, and φ_0 the initial phase difference between the two beams. Considering that the photodetector cannot. This holding, the photocurrent $i_d(t)$ from the photodetector can be expressed as in (6)

$$i_d(t) = A\ \left[\frac{1}{2}\left(E_m^2 + E_r^2\right) + E_m E_r \cos\ \ (2\pi\ (f_1 - f_2)\, t - \phi(t) + \phi_0)\right] \tag{6}$$

where $A = \frac{1}{2}\frac{G}{Z_0}$ is defined as amplification with conversion parameter $G = \eta q/h\nu$ and the impedance of free space $Z_0 = \frac{1}{\varepsilon_0\, c_0} \approx 120\ \pi\ \ \Omega$. Here, the parameters are the quantum efficiency η, the elementary electric charge q, the Planck constant h, the light frequency ν, the electric constant ε_0, and the speed of light c. The factor ½ takes the beam splitter into account always necessary to interfere two collimated beams without generating interference fringes. Obviously, a constructively interference requires destructive interference somewhere else to conserve the energy. The power of an electromagnetic wave is $P = \frac{\overline{E}^2}{Z_0}$ where $\overline{E}$denotes the mean electrical field for the time constant of the considered photodetector. The output thus contains a DC term, which is proportional to the total intensity and a beat frequency term that is proportional to the product of the amplitudes $E_m\ E_r$ (by a linear amplification A). The beat term can also be expressed as a function of the intensities of the two beams, i.e., as $\sqrt{I_m I_r}$.

An interferometer without frequency shift between reference and measurement beam is called homodyne interferometer. In a homodyne configuration, the current $i_d(t)$ is a direct function of the phase dependency, as shown in (7).

$$i_d(t) = A\left[\frac{1}{2}\left(E_m^2 + E_r^2\right) + E_m E_r \cos\ \ (\phi(t) - \phi_0)\right] \tag{7}$$

However, there are limitations due to the imperfect nature of real photodetectors. Homodyne vibrometers show high sensitivity to photo-receiver nonlinearity and susceptibility to electrical hum and noise, and the optical alignment is critical (in the motion direction configuration) as discussed in [4]. For such reasons a heterodyne-based optical arrangement, where a frequency shift is induced on one of the beams (typically the reference beam), is more typically adopted. This makes the frequency difference $|f_1 - f_2|$ equal to the frequency of the shifting device ($|f_c|$), which turns out to be the carrier for the phase modulation generated through the optical path length variation linked to the motion of the target. In a heterodyne configuration, the signal of the photodetector can therefore be expressed as in (8), where $0 < \varepsilon < 1$ defines the heterodyning efficiency (which considers degradation of the AC current for optical distortions and misalignment and depends on the light intensities, coherence, and polarization).

$$i_d(t) = A\left[\frac{1}{2}\left(E_m^2 + E_r^2\right) + \varepsilon E_m E_r \cos\ \left(2\pi f_c t - \phi(t) + \phi_0\right)\right] \tag{8}$$

In the next sections the beat signal will be computed for different interferometric configurations.

1.2.2 Michelson Interferometer

The Michelson interferometer configuration that had been implemented the most in commercial vibrometers is represented in Fig. 3. Such representation is far from the basic implementation of a Michelson interferometer, which presents only the central beam splitter, the mirror on the top and one photodetector (PD1). The importance of the configuration reported in Fig. 3, however, is related to the possibility of

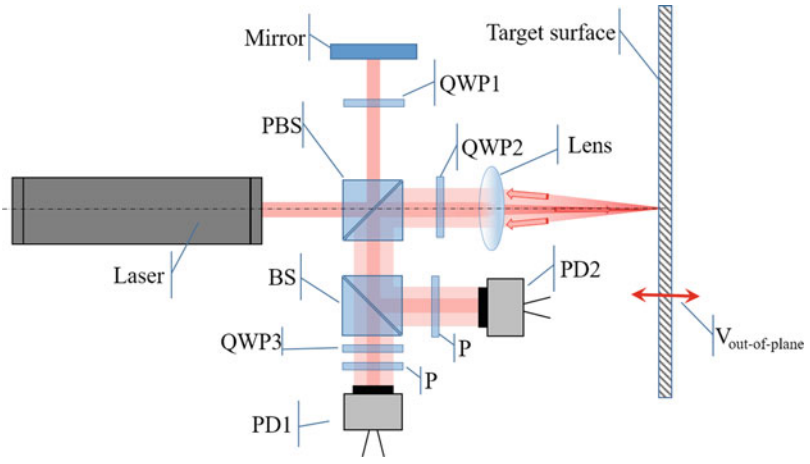

Fig. 3 Optical scheme of a vibrometer based on Michelson interferometer – two detectors configuration

solving the directional ambiguity that is characteristic of the basic configuration of Michelson interferometers.

The beam emitted by the laser source is split in two coherent parts at the polarizing beam splitter PBS. The polarizing beam splitter is utilized to split light efficiently to the photodetectors. One beam (reference beam) goes toward a reflecting mirror placed inside the vibrometer, passing through a quarter-wave plate (QWP1) that changes the polarization of the beam from linear to circular and vice versa after the reflection. The second beam (measurement beam) exits the vibrometers (before it passes through a quarter-wave plate – QWP2 – as well), interacts with the moving target, and is backscattered to the vibrometer. The second passage through the quarter-wave plate changes again the beam polarization from circular to linear. A non-polarizing beam splitter (BS) splits the two beams on the photodetectors PD1 and PD2, where interference between the beams takes place. A quarter-wave plate (QWP3) is placed on the line of sight of PD1, in order to obtain a signal in quadrature with the signal given by PD2 ($\pi/2$ out-of-phase). The laser beams at each photodetector are perpendicularly polarized; therefore a polarizer (P) is needed to obtain an optical beat. The signals coming out of the photodetectors in such an arrangement are called sine and cosine signals, or i_I and i_Q signal, where I stands for in-phase and Q stands for quadrature.

These two signals can be written in terms of light intensity as reported in (9).

$$\begin{aligned} i_I &= I_I \cos\left(\phi(t) + \phi_0\right) \\ i_O &= I_O \sin\left(\phi(t) + \phi_0\right) \end{aligned} \tag{9}$$

The velocity sign can then be found using (10).

$$\begin{cases} +v \Rightarrow i_I \propto +\cos, \quad i_O \propto +\sin \\ -v \Rightarrow i_I \propto +\cos, \quad i_O \propto -\sin \end{cases} \tag{10}$$

The relative phase of such signals contains information on the sign of f_D and thus on the sign of velocity v.

Advances in low-cost electronic devices have made it possible to tackle the issue of demodulation and direction ambiguity using, for instance, phase shifting approaches such as the one reported in Fig. 4.

By multiplying the signals coming out the photodetectors (I&Q signals), which carry the Doppler shift information ($\omega_D = 2\pi f_D$), respectively, with two carriers (ω_S) that are $\pi/2$ radians out of phase, and summing the resulting signals, a frequency modulated output that is sensitive to the target velocity can be obtained. This can then be passed to a standard demodulator to get the velocity information.

The phase shifting approach was a quite common approach in oldest vibrometers. Nowadays, the tendency is to digitize the I&Q signals and compute the phase with sign by an arctangent operation. This latter approach will be further detailed in the *demodulation of Doppler signals* section.

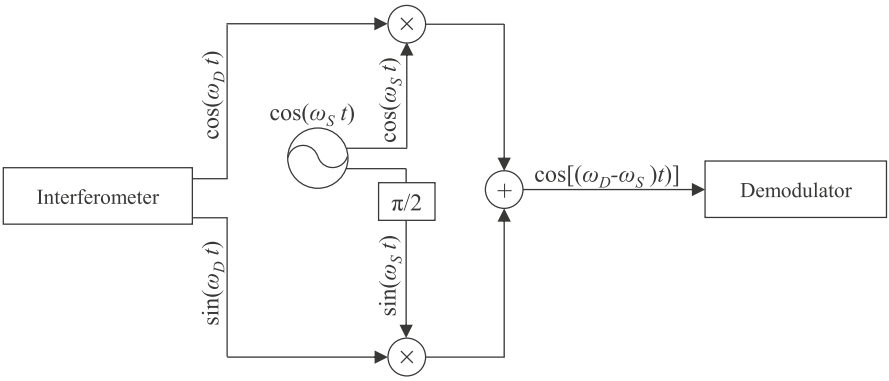

Fig. 4 Functional scheme of electronic phase shifting approach

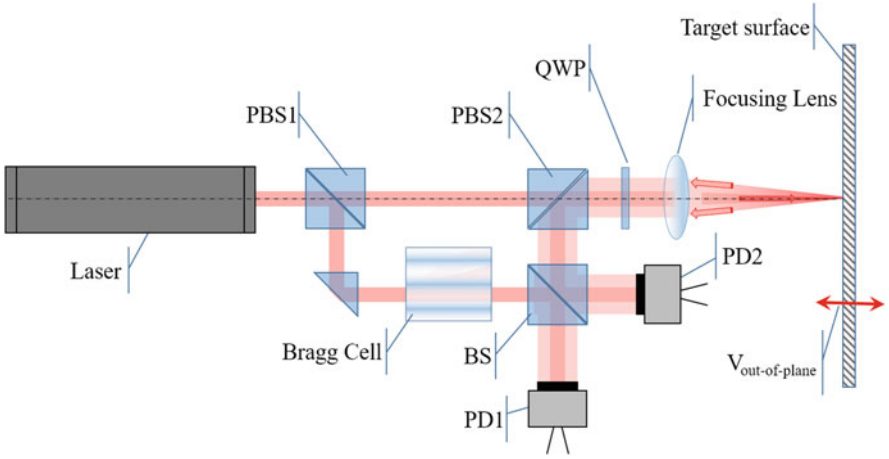

Fig. 5 Optical scheme of a vibrometer based on Mach-Zehnder interferometer

1.2.3 Mach-Zehnder Interferometer

The Mach-Zehnder (MZ) interferometer, based on a heterodyne configuration, is the most common scheme implemented in commercial vibrometers (Fig. 5). One of the advantages of the MZ interferometer is the ability it gives to address the sign ambiguity that was present in the Michelson configuration.

The most common solution employs a Bragg cell to produce a frequency shift $(f + f_B)$ in the reference beam. The Bragg cell is an acousto-optic modulator based on a vibrating transparent crystal that produces a travelling train of parallel plane acoustic wavefronts that move at a certain velocity across the crystal. The moving sound waves are generated by a piezoelectric actuator, driven by a voltage signal at frequency f_B, that is placed on one plane surface of the crystal. An acoustic absorber is mounted on the opposite side of the crystal, at a slanted angle, in order to avoid

acoustic reflections inside the crystal. The wave train acts as a moving diffraction grating, since the acoustic waves, pressure waves, induce a spatial modulation on the refraction index of the crystal (the index of refraction is related to the strain field in the crystal).

The quarter-wave plate (QWP) and polarizing beam splitter (PBS2) placed on the measurement beam path constitute an optical isolator that contribute in maximizing light intensity at the photodetectors and at preventing stray light from travelling toward the laser cavity. Interference takes place at the photodetector PD1 and will therefore produce a photocurrent (i_{PDI}) out of PD1 that can be expressed as in (11), where ε represents the heterodyning efficiency.

$$i_{PD1} = A\left[\frac{1}{2}\left(E_r^2 + E_m^2\right) + \varepsilon E_r E_m \cos\ \ (2\pi f_B\ t - \phi(t) + \phi_0)\right] \tag{11}$$

The Mach-Zehnder scheme makes it possible to implement a differential amplification scheme with the photodetectors. Such a configuration is useful to reject common mode noise. Indeed, the signals at PD1 and PD2 are π radians out of phase (the sign in the alternating component of Eq. (11) changes at the two PDs), because of energy conservation. The use of a differential transimpedance amplifier will then produce a low-passed-filtered signal at the amplifier output without DC component that can be expressed as in (12), where K represents the amplification of the transimpedance amplifier.

$$u_{AMP}(t) = K\ A\ \ \varepsilon\ E_r E_m \cos\ [2\pi f_B t - \phi(t) + \phi_0] \tag{12}$$

This configuration therefore provides a relevant improvement in terms of signal-to-noise ratio. Also, all of the DC components cancel, if they are equal to each other.

The term in (14) thus represents the heterodyne Doppler signal with a carrier frequency f_B and modulated phase angle $\varphi(t)$. The third term within the cosine function (φ_0) represents the starting phase. When the target moves undergoing a displacement $s(t)$, i.e., $s(t) = \hat{s} \cdot \sin\ \ (2\pi f_{\text{vibr}} t + \phi_s)$, the Doppler shift in Eq. (5) can be reformulated in terms of the modulated phase angle (13)

$$\phi(t) = \frac{4\pi \cdot s(t)}{\lambda} \quad = \quad \frac{4\pi \cdot \hat{s}}{\lambda} \cdot \sin\ \ (2\pi f_{\text{vibr}} t + \phi_s) \tag{13}$$

and frequency shift (14) with respect to the center frequency f_B.

$$\Delta f_D(t) = \frac{\Delta\omega}{2\pi} = \frac{d\phi(t)}{dt} = \frac{2 \cdot v(t)}{\lambda} \quad = \frac{2 \cdot \hat{v}}{\lambda} \cdot \cos\ \ (2\pi f_{\text{vibr}} t + \phi_s). \tag{14}$$

The terms $\frac{4\pi \cdot \hat{s}}{\lambda}$ and $\frac{2 \cdot \hat{v}}{\lambda}$, respectively, represent the phase deviation ($\Delta\varphi$) and the frequency deviation (Δf) of the modulated carrier. It is clear, then, that the instantaneous frequency of the heterodyne signal can resolve the sign of the velocity

vector as long as the condition $f_B > |\Delta f_D|$ is respected. Note that $f_{\text{extracted}} > f_B$ implies the target is moving toward the interferometer.

In standard HeNe vibrometers ($\lambda_{HeNe} \cong 632\,\text{nm}$), $f_B = 40$ MHz, therefore the maximum measureable peak velocity is about 10 m/s (as long as the vibration frequency does not exceed a few MHz). This value is usually sufficient in many applications; when it is not the case, a larger frequency shift, f_B, should be adopted. Indeed, acousto-optic modulators up to 80 MHz and more are commercially available.

A lens is also present in the scheme reported in Fig. 5. This allows the possibility of increasing the amount of light backscattered by diffusive surfaces.

1.2.4 Self-Mixing

The use of the self-mixing (SM) effect (also named optical-feedback interferometry, or less frequently, backscattered-modulation) for developing optical vibrometers has gained a large interest among researchers and producers of commercial systems over the years. This is mainly due to the clear advantages offered by the optical configuration of such systems. The first paper describing the use of "self-mixing" to measure velocity is from Rudd [5].

The SM vibrometer is based on reintroducing the laser radiation that is reflected back from the target directly into the laser cavity (this is usually avoided in traditional LDV). This configuration makes it possible to have a very compact optical setup and therefore to reduce manufacturing costs. In SM vibrometers, the interference process takes place directly inside the laser cavity (typically a laser diode cavity) due to the slight frequency difference between the frequency of the radiation emitted and the frequency of the Doppler-shifted backscattered radiation.

The interference signal is collected by a photodiode that is usually installed in the laser cavity for monitoring purposes. The SM interferometric configuration requires neither the presence of a reference arm nor discrete optical components; hence the setup, shown in Fig. 6, is extremely simple and inexpensive [6, 7].

The power emitted by the laser diode is amplitude-modulated by an interferometric waveform $F(\varphi)$ which is a periodic function of the back-injected field phase $\varphi = 2ks$, where $k = 2\pi/\lambda$ is the wavenumber and s is the distance from the laser diode to target. The power emitted by the laser diode can be written as

$$P(\phi) = P_0 [1 + mF(\phi)] \tag{15}$$

where P_0 is the power emitted by the unperturbed laser diode and m is a modulation index. The modulation index m and the shape of the interferometric function $F(\varphi)$ depend on the so-called feedback parameter C:

$$C = \frac{s_0}{\sqrt{A_{\text{opt}}}} \cdot \frac{\kappa\sqrt{1+\alpha^2}}{L_{\text{las}} n_{\text{las}}} \cdot \frac{1-R_2}{\sqrt{R_2}} \tag{16}$$

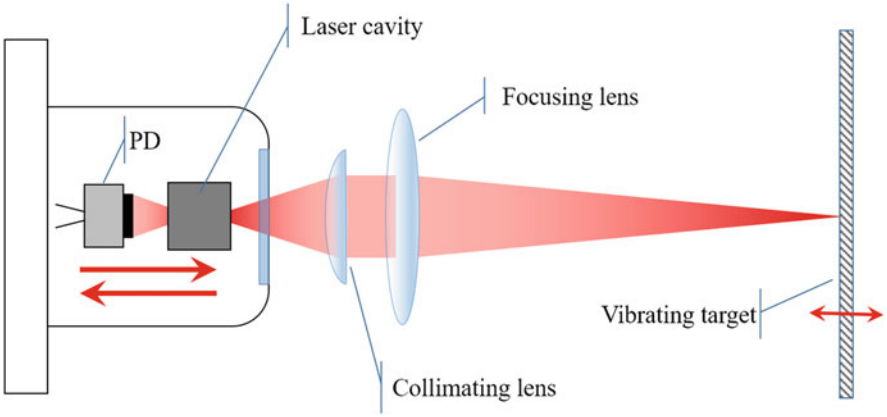

Fig. 6 Conceptual design of a self-mixing vibrometer

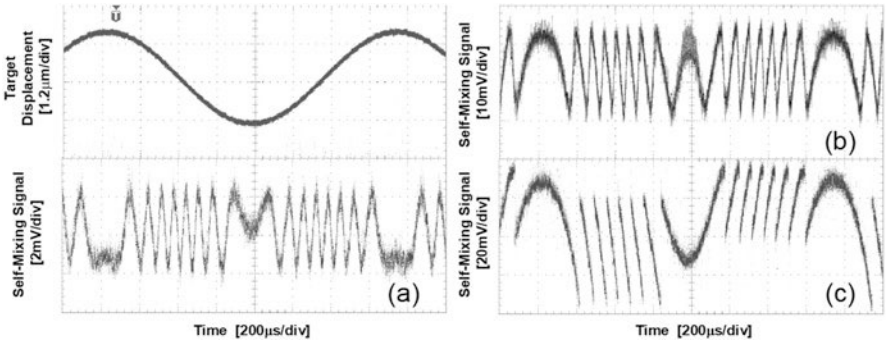

Fig. 7 SM interferometric signals for different optical feedback regimes. Upper-left displacement signal, (**a**) C < < 1, (**b**) C ≈ 1, (**c**) C > 1

where $A_{opt} > 1$ is the total roundtrip power attenuation in the external cavity; α (typ. $\alpha = 3$) is the laser diode linewidth enhancement factor; $\kappa < 1$ (typ. $\kappa = 0.5$), which accounts for a mismatch between the reflected and the lasing modes; L_{las} is the laser cavity length; n_{las} is the cavity refractive index; and R_2 is diode output facet power reflectivity.

The C parameter, which depends on both the amount of optical feedback and on the target distances_0, is of great importance, because it determines different feedback regimes. For $C << 1$ (weak feedback) the function $F(\varphi)$ is a cosine, just like the usual interferometric waveform. When C approaches unity, the function $F(\varphi)$ resembles a distorted cosine. For $C > 1$ (moderate feedback regime, which corresponds to usual optical attenuation and laser-to-target distance), the function $F(\varphi)$ becomes sawtooth-like and exhibits hysteresis. Examples of the waveforms obtained in the different feedback regimes are reported in Fig. 7.

An interesting solution to process the interferometric signal is to use an electronic feedback loop that acts on the laser diode injected current to achieve wavelength modulation. In this way the interferometric phase is locked to half-fringe, and an active phase-nulling technique makes it possible to obtain a wide dynamic range [8].

1.3 Demodulation of Doppler Signals

The modulated heterodyne signal from the optical interferometer in a heterodyne scheme usually shows a frequency range of 8 to 72 MHz (40 MHz Bragg cell + 10 m/s full scale for a HeNe laser). Different decoding schemes are needed for meeting these ranges. Furthermore, one can use phase demodulation (PDM) to obtain displacement measurements, while frequency demodulation (FDM) is utilized for velocity measurements (Fig. 8).

Frequency demodulation can be performed using the same technology developed for signal transmission as, for instance, radio-based chips. However, a more complex technique seems to be required for vibration applications. Indeed, in vibrometers demodulation is performed as a down mixing of the interference signal with the reference signal driving the Bragg cell. This down-mixed signal is then filtered depending on the frequency range chosen (the latter determining the sensitivity and linearity parameters of the down mixed signal), in order to obtain the velocity signal. To this basic structure, usually smarter filtering strategies (such as amplifiers, signal conditioners, tracking filters, Butterworth, etc.) are added, in order to improve the signal-to-noise ratio (SNR). Commercially available laser Doppler vibrometers (LDVs) use analog frequency demodulation to convert the Doppler frequency into an analog voltage proportional to the velocity of vibration. A widely used FM demodulation approach is based on the use of phase-locked loops (PLLs). The baseband signal, corresponding to the velocity signal, is extracted at the input of the voltage-controlled oscillator (VCO). On the one hand this approach makes it possible to achieve high linearity and resolution, with a good SNR; on the other hand, the bandwidth is quite limited, and this scheme is sensitive to signal dropouts.

The measurement of target displacement can be performed by counting interference fringes, as is typically utilized in the low frequency range of vibration,

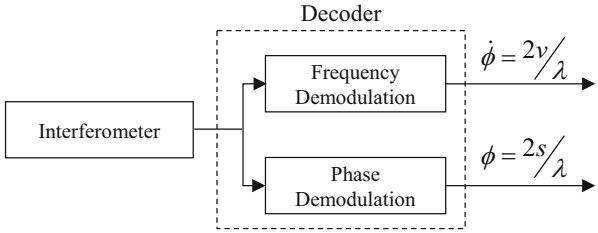

Fig. 8 Demodulation of Doppler signal

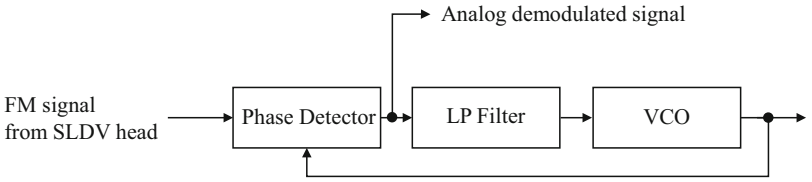

Fig. 9 FM demodulator based on PLL

or through phase decoding, as in the case of ultrasonic vibration up to 20 MHz. Such decoders work on the high-pass filtered signal (>50 kHz) in order to eliminate disturbing noise and utilize PLL circuits to detect the phase of the signal in a range of ±90 degrees. These limit the resolving capability to relatively small displacements (±λ/8 or about 150 nm peak to peak for a He-Ne Laser). In order to obtain an improvement in resolution, the interference signal is usually interpolated, and resolution down to λ/80 is obtained. In contrast, analog velocity decoders can be matched to a variety of processing requirements such as very high frequency, DC response, and high velocity range. These are still the preferred choices when it comes to measurements at high speeds (10 m/s or more) and high frequencies (Fig. 9).

The reader should be aware, however, that analog electronic components are sensitive to drift as well as aging, and there are certain limits in linearity. Moreover, these components must be calibrated in order to guarantee accurate measurements. Accuracy, repeatability, and traceability strongly depend on each component (amplifier, resistances, and capacitance) in the analog signal processing chain, with particular emphasis on the quality of phase and frequency demodulators. In addition, analog demodulation does not make it possible to adapt processing parameters to the actual signal characteristics, while thermal drift can induce modifications in settings.

All these aspects have induced LDV producers to move to digital demodulation, since digital demodulation can indeed overcome some of the problems and drawbacks of analog demodulators. In digital demodulation, the interference signal from the interferometer is digitized using analog-to-digital (A/D) converters operating at an adequate sampling rate. Computational algorithms then process the signal numerically. Data can be acquired for a defined time interval and then processed in offline mode, or, if the A/D converter is associated with a circular buffer, data can be continuously sampled and transferred to the processing unit for quasi-real-time demodulation. The main advantages of LDVs based on digital demodulation include minimal drift from calibration, amplitude resolution only limited by optical noise, sub-nanometer displacement resolution within the full velocity, and frequency range from DC up to the MHz range.

It is worth highlighting that digital vibrometers such as these have been accepted by the German Institute of Standards (PTB) for traceable calibrations according to the ISO 16063-11 standard. In fact, in digital decoding the repeatability in frequency demodulation is related only to the accuracy of the timing in the A/D conversion,

and this is a very stable parameter, easily verified with high accuracy. All that remains then are the algorithms implemented in the software, which are completely deterministic.

The main limitations of digital decoding are related to the very high sampling frequency and to the large storage required when vibration velocity increases in a heterodyne scheme. For this reason, digitally decoded vibrometers usually have a lower full-scale velocity range than the corresponding analog versions even though the interferometer is the same.

To overcome such problems the most common approach is the conversion of the heterodyne signal into an I&Q homodyne signal by quadrature mixing. An analog circuit mixes the Doppler signal with the signal from a Bragg-cell oscillator, to obtain Doppler signals in the baseband. Indeed, the RF carrier itself, introduced by the Bragg cell, does not contain any Doppler information and can be suppressed. Mixing is done with two reference signals, $\pi/2$radians out of phase to each other so as to obtain two quadrature signals, named I&Q as above. In this way the noise rejection capability of the heterodyne optical scheme is coupled with the advantage of using baseband signals (about 3 MHz for 1 m/s of range of HeNe laser), which require a less critical signal sampling. After the quadrature conversion, the two signals (I&Q) are sampled and further processing is performed as in the case of the homodyne interferometer. One of the most common demodulation algorithms is the arctangent phase demodulation.

The signal sampling and the data processing takes some time, and so it is no longer possible for the digital system to operate in real time as the analog systems do. Furthermore, the time delay caused by the digital demodulation can vary for different settings of the digital processor; this needs careful consideration when performing vibration measurements together with analog sensors as a reference (e.g., a load cell for modal analysis).

Digital demodulation also makes it easier to implement additional algorithms into the signal processing, such as dropout detection.

After demodulation, an output signal related to the vibration velocity can be made available to the user in different forms. It can be a digital signal with the samples stored in a mass memory or transferred to a PC through a digital line (e.g., a SPDIF or serial bus), or it can be converted to an analog signal. The first solution is conceptually simpler and more accurate, but it makes it difficult to synchronously acquire any other signals with standard data acquisition boards.

The interested reader might refer to [3, 4] for further information regarding demodulation of Doppler signal in vibrometers.

1.4 Noise and Resolution

Vibration amplitudes much smaller than the diameter of an atom can be relevant in a vibration spectrum. There are applications where picometer resolution is required as, for example, ultra-high-frequency (UHF) resonators. In the frequency regime above 100 MHz, the vibration amplitudes rarely exceed a nanometer. Resolution is

defined as the smallest detectable magnitude of the desired measurement quantity which, in the case of laser vibrometry, is the smallest detectable vibration amplitude in the examined vibration bandwidth. The root mean square amplitude of the noise is usually defined as a noise metric and depends on the bandwidth of the considered signal. The noise power depends linearly on the bandwidth for white photon shot-noise which results in white displacement noise. Therefore, the noise level of a laser vibrometer is usually defined in displacement per square root Hertz.

The significant noise sources of a laser vibrometer have to be analyzed in order to understand the limits of resolution [3]. This thermal-noise contribution $\bar{i}_{th}$ to the mean detector current $\bar{i}_D = \sqrt{\int \frac{i_D^2 dt}{T}}$ can be estimated with the following Equation

$$\overline{u}_{th}^2 = K^2 \frac{4\ k_B\ T\ B}{R_d} \tag{17}$$

with k_B the Boltzmann constant, $R_d$the detector load resistance, and B the bandwidth of the photodetector.

Besides such a technical noise source, the quantum nature of light defines the ultimate limitation for any interferometer. The light power cannot be constant since the light energy is transferred by quanta with energy $E = h\ f$. This effect leads to a mean square voltage noise of

$$\overline{u}_{sh}^2 = K^2\ G\eta\ q\ B\ \ (P_m + P_r) \tag{18}$$

by photon shot-noise with $P_m = \frac{\overline{E}_m^2}{2Z_0}$ the power of the measurement beam at a single photodetector and $P_r = \frac{\overline{E}_r^2}{2Z_0}$ the power of the reference beam at a single photodetector. The third noise contribution originates in the signal processing and decoding. For example, analog down mixing to a frequency band that is suitable for a certain analog-to-digital converter introduces phase noise from the reference oscillator. The analog digital conversion itself contributes digitization noise. Assuming a direct digitization without down-mixing of the heterodyne carrier signal with n bits would result in a quantization interval of $q = U_r/2^{n-1}$ which yields the mean square voltage noise contribution within the evaluated detector bandwidth B

$$\overline{u}_{qn}^2 = \frac{1}{12}\left(\frac{U_r}{2^{n-1}}\right)^2 \frac{2B}{f_S}, \tag{19}$$

where U_r is the full scale of the A/D-converter and f_S is the sampling frequency. Considering a full scale of $U_r = 4KG\varepsilon\sqrt{P_m P_r}$, Eq. (8) results in the noise contribution by quantization noise

$$\overline{u}_{qn}^2 = \frac{4\ (K\ G\ \varepsilon)^2 P_m P_r}{3 \cdot 2^{2\,n-1}} \frac{2B}{f_S} \tag{20}$$

However, as mentioned previously, the ultimate limit is defined by the photon shot-noise. It can be concluded from Eqs. (8) and (12) that the power of the heterodyne signal and the power of the shot-noise both depend linearly on the power of the reference light. The amplification of the interference signal by the reference light is called coherent amplification and is absolutely noise free as the shot-noise power increases by the same factor as the signal power. A properly designed photodetection in a laser Doppler vibrometer is, therefore, shot-noise limited by adjusting the reference light power to a level where the photon shot-noise exceeds the thermal noise. A controlled amplifier (limiter) usually amplifies the detector signal to a constant signal strength. Thus, it can be concluded that the quantization noise is full-scale and defined by Eq. (20). Usually, the noise level is defined by the decoder when the signal strength of the detector is maximum. The SNR of the shot-noise-limited detector signal is

$$SNR = \frac{2G\varepsilon^2 P_m P_r}{q\ B\ (P_m + P_r)} = \frac{2\eta\ \varepsilon^2\ P_m\ P_r}{h\ f\ B\ (P_m + P_r)} = \frac{2\ \lambda\ \eta\ \varepsilon^2 P_m\ P_r}{h\ c\ B\ (P_m + P_r)}. \quad (21)$$

To realize a shot-noise limited demodulated signal the SNR of the digitized carrier signal

$$SNR_{\text{dig}} = 3 \cdot 2^{2\,n-1} \cdot \frac{f_S}{2\ B} \quad (22)$$

needs to be higher than the shot-noise-limited SNR in Eq. (21). Heterodyne detection enables measuring always at the optimal sensitivity point of the fringe pattern. At this point it is

$$\overline{u}_S^2 = \left(2\,K G\varepsilon\ \overline{\phi}(t)\right)^2 P_m P_r = (8\pi\ K G\varepsilon\ \overline{s}(t)/\lambda\ )^2 P_m P_r = \frac{\left(8\pi\ K G\varepsilon\ \hat{s}/\lambda\ \right)^2}{2} P_m P_r. \quad (23)$$

The shot-noise limited resolution limit is reached at

$$\overline{u}_S^2 = \frac{\left(8\pi\ K G\varepsilon\ \hat{s}/\lambda\ \right)^2}{2} P_m P_r = \overline{u}_{sh}^2 = 2K^2\ G\ q\ B\ (P_m + P_r) \quad (24)$$

and results in a smallest resolvable displacement amplitude of

$$\hat{s}_{srda} = \frac{\lambda}{4\pi}\sqrt{\frac{qB\,(P_m + P_r)}{G\ \varepsilon^2\ P_m P_r}} = \frac{\lambda}{4\pi}\sqrt{\frac{h\ f\ B\,(P_m + P_r)}{\eta\ \varepsilon^2\ P_m P_r}} = \frac{\lambda}{2\pi \cdot \sqrt{SNR}}. \quad (25)$$

With (25) the noise-equivalent displacement amplitude is obtained in the order of a few femtometers per square root Hertz. To reach this resolution possible with the shot-noise-limited detector signal, it is required an effective bit resolution for a certain SNR in respect to Eqs. (21) and (22). Assuming 100 μW measurement

light and 1 mW reference light, a bandwidth of 1 MHz, a wave length of 1550 nm, a quantum efficiency of 0.8, and a heterodyning efficiency of 0.9, it is obtained a SNR of the analog photodetector signal of approximately 90 dB which corresponds to the SNR of approximately 14 effective bits. The resulting resolution would be approximately 6 pm or 6 fm/$\sqrt{\text{Hz}}$ for these numbers. Modern commercially available decoders achieve noise levels below 20 fm/$\sqrt{\text{Hz}}$. In this example, a shot-noise limited demodulation would require a minimum of 14 effective bits if the sampling rate is just high enough to fulfill the Nyquist-Shannon sampling theorem. Doubling the sampling rate corresponds to one more effective bit.

From Eq. (25) it can be concluded that low light-power levels have a proportional dependence of the displacement noise on the inverse of the square root of the measurement-light power. Consequently, a reduction of the detected measurement-light power by a factor of 100 increases the noise just by a factor of 10. Thus, even low detected light-power levels result in reasonable noise levels. For example, just 1 nW measurement light on the detector results in 10 MHz demodulation bandwidth still in a displacement resolution of approximately 5.5 nm. Therefore, laser Doppler vibrometry is a very robust technique for the analysis of structural dynamics.

1.5 Critical Aspects in Laser Vibrometry

1.5.1 Backscatter Issues

The amount of light collected by a vibrometer lens is of primary importance to obtain high-quality measurements. Laser Doppler vibrometers collect the light backscattered by the vibrating target to produce the interference with a reference wave. If light scattered back is insufficient (this condition implies low signal level), demodulation cannot work properly, and measurement results could be compromised. The signs and symptoms of inadequate light impinging on the photodetectors are, among others, high noise levels, signal dropouts, and sensor over-range conditions also for low vibration velocity. Two factors can induce this phenomenon: a laser-to-target distance close to a low coherence distance of the laser and the target surface characteristics.

The laser-to-target distance (stand-off distance) must be selected to avoid periodic minima of the laser coherence. Coherence due to relative interference is high when the difference of the optical path is an integer multiple of 2 L, where L represents the laser cavity length. For other optical path length differences, the coherence reduces. In case of low signal level, a simple repositioning in the range 5–10 cm can change significantly the signal level. The positions of low coherence can be easily determined if the laser system warms up.

The target surface roughness deeply influences the amount of light backscattered to the photodetectors. Mirror-like surfaces make it possible to get the highest amount of light impinging on the photodetector, with up to the 95% of light back reflected. However, mirror-like surfaces do need perfect parallelism between the normal-to-target surface and the incident beam. Such an ideal condition can be achieved in very few cases (vibration of hard disk drives, electronic devices) because alignment

is very critical. In standard applications, the surface tilting induced by the vibration of the target might be large enough to make the measurement useless even if the alignment were perfect.

It is clear that a rough surface is better suited for a LDV measurement, even though the surface roughness needs to be related to the wavelength of laser ($Ra << \lambda$, typical of very polished surfaces give rise to a mirror-like behavior, while very rough surfaces $Ra >> \lambda$ produce better scatter). On real rough surfaces, light scattering usually deviates from the ideal behavior (ideal diffuser). Indeed, a narrower scattering appears around the direction of specular reflection.

Surface scattering power could be maximized in several ways:

- Change of surface roughness (e.g., using sand paper)
- Use of white diffusive paints (e.g., spray developers utilized for crack analysis in non-destructive testing)
- Use of reflecting tapes (e.g., "cat-eyes" reflectors)

Reflecting tapes are made of microspheres (transparent polymers or glass) deposited on a tape. The microspheres act like microscopic multidirectional reflectors. In such a way they make it possible to increase diffusivity of light in space and to increase the amount of light backscattered to the LDV, also when the angle between the incident beam and the normal-to-target surface is large.

1.5.2 Speckle Noise

Speckle [9–13] is the optical effect that can be observed when a coherent light source, like a laser, interacts with a rough surface. It is due to the constructive and destructive interference of light wavelets diffused from different portions of the surface illuminated. Mirror-like surfaces are the only surfaces that would not exhibit a diffuse pattern.

Speckle exhibits a grainy pattern, apparently random, that is related to the surface characteristics and moves with it. As an example, when retroreflective tape is utilized, the resulting speckle pattern appears very bright, concentrated in a reduced solid angle, and geometrically periodic. The latter characteristic is related to the regular pattern of the microspheres fixed on the substrate of the tape. On a generic surface, the speckle pattern appears less regular. Another interesting example is the speckle pattern generated by a machined aluminum surface, i.e., a surface with spatially structured roughness. In such surface grooves induce diffusion in the direction orthogonal to the grooves themselves; indeed, microscopic grooves on the surface act as a diffraction grating and produce a fan-shaped diffuse pattern, with a superimposed speckle pattern (Fig. 10).

The front lens of a vibrometer collects part of the light diffused by the surface and focuses it on the photodiode, wherein interference and photoelectric conversion take place. Considering that:

- Speckle moves with the surface movement, different speckle reach the photodiode in the time

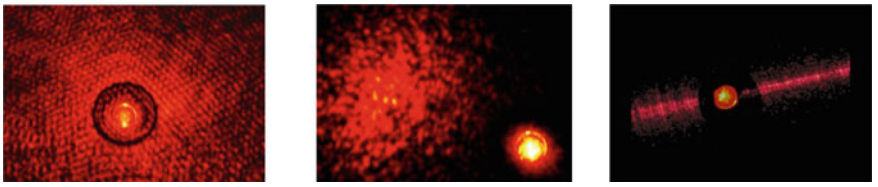

Cat-eye	Rough surface (extruded aluminum)	Tool-Machined aluminum

Fig. 10 Pictures of the diffuse light pattern from different surfaces

- Each speckle has its own amplitude and phase, which vary randomly from one speckle to the other
- Such variation is correlated to the spatial distribution of the light scattered

lateral movements of the speckle pattern with respect to the photodiode or evolutions in time of the speckle pattern induce time dependency in the amplitude and phase of the Doppler signal; as a consequence, the output signal of the vibrometer become amplitude and phase modulated, this causing the so-called speckle noise [14]. An example on how to practically deal with speckle noise can be found in [15].

As discussed previously, whenever the amplitude of the Doppler signal decreases too much, a so-called dropout takes place. While speckle-noise has received considerable attention from the scientific community, far less attention has been given to dropout noise. This is due, in part, to the fact that dropout noise can be reduced by improving the scattering characteristics of the target surface. However, dropout noise still remains an issue on varnished surfaces or enameled steel sheets, since dropout noise becomes pseudo-random in nature.

1.5.3 Measuring in Media and Through Windows

If the vibrating surface lies in a transparent medium having a refractive index (n_a) different from the one characterizing air in standard conditions (n), the laser wavelength of the beam crossing the medium changes. This is a matter of influence of the refractive index on the LDV sensitivity. Indeed, sensitivity changes, and the measured velocity should be corrected taking into account Eqs. (26) and (27).

$$n_a \cdot \sin\theta_a = n \cdot \sin\psi \tag{26}$$

$$v_{\text{real}} = \frac{v_{\text{meas}}}{\cos\psi} \cdot \frac{n_a}{n} \tag{27}$$

Such a condition can be met in several applications, as on objects operating immersed in liquids (e.g., water) or in air or gasses when the temperature changes significantly (e.g., combusting fluids [16]).

Other effects could occur when changes in the refractive index take place along the beam rather than on the target object itself. Since vibrometers are sensitive to changes in the optical path, and the change in the refraction index does change the optical path, the signal measured by the sensor will reproduce such variations. This effect is sometimes utilized to characterize air pressure variations induced by fluid-dynamic or acoustic effects [17].

It might happen that the target vibrating surface is not directly accessible. This is the case of structures operating in confined domains, where envelops are needed to limit high temperatures or pressure, chemical reactions, or simply operating fluids. In these cases [18], an optical access must be built in order to make it possible for the laser beam to reach the surface to be measured. Optical windows introduce a constant additional path length; however, they do not have any influence on the deviation of φ_m as when a medium change takes place.

Even then, optical windows should be managed carefully, since their use does present some issue:

- Optical windows could distort the wavefronts of the laser; the surface flatness should be very good, in the order of $\lambda/10$ or smaller, to avoid this.
- The LDV beam will be partially reflected at the optical window, with an intensity that can be larger than the intensity of the light backscattered from the target surface. If that light is collected by the front lens of the vibrometer, the beat signal produced by window reflection may be larger than the beat signal produced from the light scattered from the surface. In such a case, the demodulated signal represents the window vibration rather than the vibration of the target behind the window.
- The dimension of the optical window should be large enough to avoid any reduction in the scattered light that is collected by the LDV.

Some tricks have to be taken into account to correctly measure on targets lying behind optical windows. First of all, it is necessary to avoid perfect orthogonality between the laser beam and the optical window surface. Indeed, on the one hand, the first light reflection at the window reduces the light scattered by the target and collected by the vibrometer; on the other hand, the light reflected by the window does not reach the front lens of the vibrometer, thus avoiding disturbances. It is also good practice to keep the optical window out of the depth-of-field of the receiving optics. In cases where the window is close to the target, a possible solution might be to place the vibrometer close to the window and operate with a short focal length. This setup will limit the amount of reflected light collected by the LDV.

Windows must be optically neutral, usually made of BK7 fused silica glass, quartz glass, or sapphire windows. Birefringency induced by residual stresses, which could modify laser beam polarization, must be carefully avoided.

1.6 Signal Enhancement Approaches

1.6.1 Tracking Filter

Signal dropouts are generated by dark speckles impinging the receiving aperture of the LDV objective if the signal power is smaller than the noise in the demodulation bandwidth. Such dropouts can be rather short depending on the time the laser beam persists on the particular position. For surfaces with a fast replacement of the measurement positions, the dropouts can be quite short, even much shorter than the basis period of the vibration under investigation. In such a case, the information of the vibration is still completely available in the signal but might be distorted by the signal dropouts. In such cases it is preferable to filter the signal in order to remove spikes and noise. Such a filter is called a tracking filter.

Since modern vibrometers employ digital decoding techniques, tracking filters are realized nowadays in the digital domain. Two tracking filtering approaches can be distinguished: (1) methods which remove the noise from the demodulated signal by analyzing the demodulated signal and (2) methods which remove the noise by evaluating the original detector signal.

A signal dropout reduces in the first place the signal strength on the photodetector. After demodulation, the lower signal strength results in a higher noise level in the displacement or velocity signal. A power-controlled amplifier (limiter) amplifies the signal power to a certain level to provide a carrier signal with constant amplitude and, in addition, provides a control signal that is related to the signal strength and which is a voltage signal in a certain bandwidth. This signal is called received signal strength indication RSSI. Since a signal dropout is generated by a dark speckle , the signal strength is reduced, and the noise of the demodulated displacement or velocity signal is increased.

Method (1) detects the increase of the noise in the demodulated signal. Usually a dropout generates a spike in the velocity signal. Therefore, a threshold of maximum acceleration can be defined. In such a case the demodulated signal can be replaced by the last valid velocity value. This would correspond to a sample-hold approach. As soon as the acceleration is below the threshold and the velocity is within a reasonable deviation to the hold velocity value, the real-time velocity signal is again provided at the output. Such a simple approach generates buckles and hops in the output signal. A better approach is to use the available information and to continue the signal, for example, by holding also the derivative of the output signal.

Method (2) employs the fact that the signal strength corresponds directly to the information content and the noise level of the detected signal. Thus, the bandwidth of the output signal can be controlled with the signal strength. Such an approach would define a low-pass filter for the demodulated signal with a cutoff frequency which is monotonically dependent on the signal strength. In the most simple and common case the cutoff frequency of the output signal would depend linearly on the signal strength.

1.6.2 Diversity Combining

An advanced approach for speckle treatment has been explored at Polytec [19, 20] which is based on the basic concepts of signal combining. It has been demonstrated that this technique is suitable to treat effects from rapidly changing speckles. Here, the light scattered from the measurement spot is analyzed from different apertures usually with the same numerical aperture as the impinging beam. However, the optical setup for diversity is realized, the total scattered light power remains constant for a given surface reflectivity whatever roughness topography the surface may have. Therefore, the received power of two different channels is uncorrelated or in case of a directional scatter with only a few speckles rather anticorrelated.

In any event, the probability of receiving dark speckles in all detection channels at the same time is a much rarer event than receiving a dark speckle in just one detection channel. Thus, it can be concluded that a weighted sum of the demodulated signals of each channel

$$s_{\mathrm{com}}(t) = \sum_{i=}^{N} a_i\,(RSSI_i)\,s_i(t) \Big/ \sum_{i=}^{N} a_i\,(RSSI_i) \tag{28}$$

will result in a substantially improved combined signal. The weighting factors are strictly increasing functions from the current RSSI value of the *i*th channel. Therefore, the stronger the signal, the higher the weight of that channel.

Since the computation is performed in real time, the combined signal is slightly delayed but retains its full bandwidth. A signal dropout appears at a certain RSSI value in dependence on the demodulation bandwidth. A reduction of the probability for a dropout can be reduced by a factor of 30 with only 2 channels [19]. A factor above 2000 can be achieved with 4 channels [20]. The laser-speckle effect not only leads to signal dropouts; it also generates phase jumps at dark speckles. Since dark speckles are suppressed by diversity combining, velocity spikes at laterally moving objects are reduced, and, thus, phase noise by laser speckles is reduced dramatically.

1.7 Uncertainty and Calibration

Each measurement performed is affected by a certain value of inaccuracy: such inaccuracy is quantifiable by the uncertainty parameter, defined in the ISO Guide to the Expression of Uncertainty in Measurement (GUM) [21].

It is a common perception that laser Doppler vibrometers, due to their complexity, are measurement systems able to provide almost "uncertainty-free" data, in the sense that their accuracy is much higher than needed in the large majority of applications. However, this is misleading. Indeed, vibrometers are complex systems, even though they are apparently very user-friendly. Moreover, their tasks can be challenging, and therefore experienced users are needed. The apparent ease of use of such systems might induce the general user to underestimate the complexity of the application, thus leading to incorrect measurements. The complexity of the

instrument, together with the complexity of the application, causes stakeholders to have quite high expectations in terms of results and accuracy, which are expected to be reliable and to comply with given requirements.

Under controlled conditions vibrometers are very accurate measurement instruments. As a result, it can be difficult to assess their metrological performance, because the definition of procedures and setups that are able to stress such small uncertainties represents a difficult task [22].

An international standard (ISO 16063-41 [23]) for the calibration of laser vibrometers was recently published. Such standard is intended to define the instrumentation and the procedures to be adopted for calibrating laser vibrometers in the frequency range 0.4 Hz-50 kHz.

Calibration is, as usual, obtained by comparing the vibrometer to be calibrated with a reference sensor, in this case an interferometer of a national measurements and standards laboratory.

Specific interferometric systems have been developed in several national metrology institutes to obtain outstanding performances in laboratory conditions. Such primary standards have been established using primary calibration methods specified in the ISO standards [24].

Specification on each component must be as good as possible to improve the accuracy (Table 1). The laser must guarantee a known wavelength with a stability of 10^{-5} over a period of 2 years minimum within a temperature interval of (23 ± 5) °C. Usually a helium-neon laser should preferably be utilized. Under laboratory conditions (i.e., at an atmospheric pressure of 100 kPa, a temperature of 23 °C, and a relative humidity of 50%), the wavelength of a helium-neon laser is 0.63281 μm. In order to make it possible that both systems are measuring the same displacement, an optical arrangement is utilized that leads the two laser light beams to be parallel and operating to the same point. In general, digital techniques, according to ISO standards, make it possible an accurate and traceable demodulation. Such calibration procedures in national metrological institutes are at the highest level of the traceability chain, and reference vibrations are to be

Table 1 Metrological characteristics of state-of-the-art laser vibrometers

Specification	Laser vibrometer (state of the art)	Laser vibrometer standard (minimum requirements)
Total measurement range	0.1 μm/s to >10 m/s	1 μm/s to 0.1 m/s
Frequency range	0 Hz to >10 MHz	0.1 Hz to 20 kHz
Demodulation	Analog voltage	Digital data
Calibration uncertainty	1% to 2%	0.5%
Amplitude frequency response	±1% (20 Hz to 100 kHz)	±0.2% (0.1 Hz to 20 kHz)
Phase frequency response	<0.1 deg./kHz to >10 deg./kHz	Delay time specified
Harmonic distortions	< 1%THD	0.1%THD
SFDR	> 86 dB (per meas. Range)	100 dB (total)

measured with the smallest measurement uncertainties (mostly between 0.05% and 0.5%). Shakers have to be very accurate, ensuring uniaxial and purely sinusoidal motion. Disturbing quantities (e.g., harmonics from nonlinear distortion) act on the measuring instrument (laser vibrometer) and contribute to signal noise.

When a vibrometer is applied in the field in the real word, the complexity of the instrument can determine sneaky effects if the user do not have, or cannot have, the full control of the experimental conditions.

Aspects to be taken into account in the design of the experiment (DoE) are:

1. Surface diffusivity and signal level
2. Speckle noise
3. Coherence distance
4. Index of refraction of medium
   (a) Air temperature
   (b) Other media
5. Optical windows
6. Angle of incidence
7. In-plane motion
8. Tracking filter
9. Phase delays in digital decoding
10. Vibrations of vibrometer base

In some real-life cases, the vibrometer measurement uncertainty is less important with respect to the possibility of getting reliable result in difficult tasks; in such conditions measurement uncertainties between 5% and 20% (frequently 10%) are usually accepted.

Finally, when mode shapes must be observed, uncertainty in the measurement with scanning LDV is frequently not an issue. In fact, in such a case, the assessment of the absolute value of the vibration level is not needed, and only spatial distribution of vibration is of interest. In this case, the main requirement is that the amplitude and phase information in system remain stable in the short period.

1.8 Laser Safety and Standards

Whenever dealing with lasers, one should pay attention to safety [25]. In general, laser vibrometers do not pose severe laser safety problems, because they use almost low power level, but safety risks are still present. The level of risk for laser exposure is given by the irradiance parameter, i.e., the radiant flux received by a surface per unit area (W/m^2). For instance, considering the case of a 1 mW laser beam (collimated beam diameter 2 mm) impinging on area of the retina of $1.13\ 10^{-13}\ m^2$, the irradiance is about $16\ MW/m^2$.

Considering the power levels of typical vibrometers, possible damage by laser radiation concerns only the eyes. Effects on the eye are wavelength dependent, because radiation is absorbed by different parts of the eye versus wavelength. Visible

and near-infrared radiation (400–1400 nm range) is partially absorbed by aqueous humor and is transmitted through the eye and reaches the retina. Mid-infrared (1400 nm – 1 mm) and far-ultraviolet (180–315 nm) are absorbed by the cornea. Near-ultraviolet (315–400 nm) is absorbed by the lens. Far-infrared radiation can cause corneal burns, while ultraviolet radiation (UV-C and UV-B) can cause dermal photokeratitis. Corneal burns can be self-repaired through the regenerative process of the epithelium layer. Damages to the stroma can cause edema and collagen shrinkage with probable permanent impairment.

The classification of a laser product depends on the safety of the laser involved, and it is based on the concept of accessible emission limits (AEL – maximum power or energy that can be emitted in a specified wavelength range and exposure time that passes through a specified aperture stop at a specified distance). The reference document determining the classification of laser products is the IEC: 60825–1:2014 [26]. Such document is the revised version of [27] and aims at classifying laser products that emit radiation in the wavelength range 180 nm to 1 mm according to their degree of optical radiation hazard. Almost all commercial vibrometers do have usually an eye-safe laser class (typically 2, 2 M and 3R – the latter in microscope systems) in respect to the last IEC classification scheme.

2 Instrumentation, Measurement Issues, and Applications

This section of the chapter aims at giving an overview of the different types of laser Doppler vibrometers that have been developed so far. An insight into the working principles of each vibrometer configuration, together with references to application cases and best practice approaches, is also given.

2.1 Single-Point Vibrometers

The main difference between other single-point single-wavelength interferometers and the vibrometers considered here lies in the broad-bandwidth frequency-demodulations of the interference detector-signal, which was discussed in this chapter in the section *From Interferometers to Vibrometers*. As discussed above the analog photodetector signal is conditioned as two homodyne signals in quadrature or as single heterodyne carrier signal with, at least, twice the bandwidth. At next the conditioned detector signal is analog-digital converted and decoded by digital signal processing. With reference to Fig. 8, it should be clarified that the decoder can be separated in a second box or it can be integrated in the sensor housing with the interferometer. In addition to these basic components, the LDV has control and communication electronics and optical elements to focus the measurement laser-beam on the specimen.

A classical single point LDV with sensor head and separated controller is the OFV 500 with OFV 5000 controller from Polytec. This system is shown in Fig. 11a. An example of a LDV single-point sensor where the decoder is integrated with the

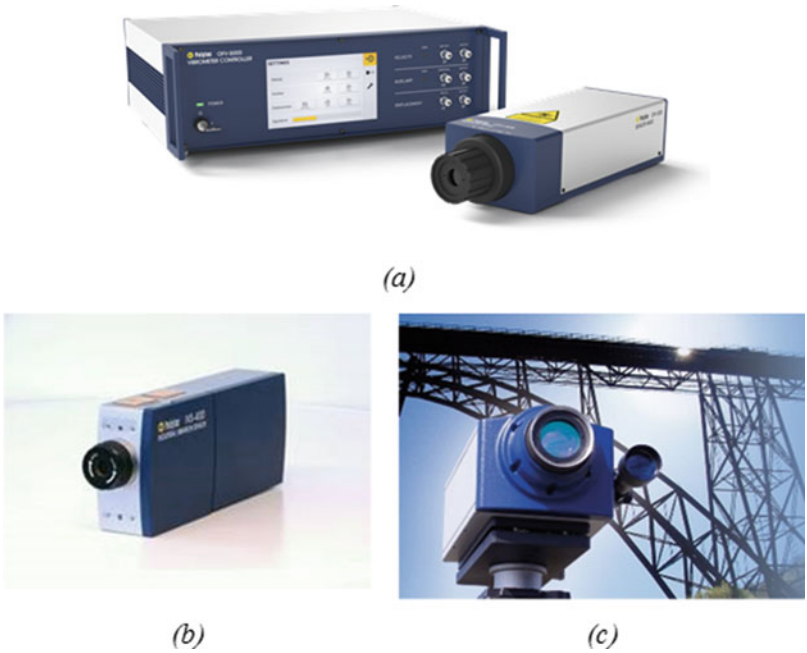

Fig. 11 Examples of single-point vibrometers: Polytec OFV 500 with the separated controller OFV 5000 (**a**); Compact Industry sensor Polytec IVS 400 (**b**); IR-vibrometer RSV-150 for highest resolutions over long working distances (**c**). (Courtesy Polytec)

interferometer in a compact sensor housing is the IVS 400 (see Fig. 11b), which has been designed by Polytec for industrial production monitoring. Historically, laser vibrometers have been equipped with a helium-neon gas laser. Such lasers need to be stabilized to realize a single-frequency operation. Since such stabilizations are expensive double longitudinal-mode lasers are typically installed. The interference between the two longitudinal modes generates variations of the signal strength in dependence on the working distance if accidentally two modes have close amplitudes. Usually, manufacturers call the position of possible minimum signal strengths visibility minima and the position of maximal signal strength visibility maxima and specify it in the manual. Vibrometers with helium-neon lasers are usually built with 1 mW measurement-light power and are classified as laser class 2 devices which corresponds to the class of laser pointers.

It can be seen from Eq. (22) that the SNR of the detector signal depends linearly on the wavelength. The higher the wavelength for the same measurement power, the higher the shot-noise-limited SNR of the heterodyne carrier signal due to the higher number of photons for long wavelengths. Therefore, it can be obtained a more robust behavior against signal-level variations for IR wavelengths. It can be concluded from Eq. (26) that the resolvable displacement amplitude increases with the square root of the wavelength. A favorable wavelength is the telecommunication

wavelength at 1550 nm. Here, erbium fiber lasers can be employed which are single-frequency, narrow-linewidth light sources that do not show visibility minima. In addition, laser light at 1550 nm does not penetrate the eye, and, therefore, sensors with below 10 mW laser power can be classified as laser class 1, which is absolutely eye safe. The higher possible laser power improves the SNR of an IR-vibrometer even further up to more than 160 dB/$\sqrt{}$Hz and allows even better amplitude-vibration resolutions as compared to a vibrometer with a HeNe-laser. However, these lasers are much more expensive than helium-neon lasers, and, therefore, this wavelength is currently mainly utilized for special applications. The better sensitivity makes an IR vibrometer of this type especially well-suited for long-distance measurements (e.g., measurements on bridges and buildings). An example is the RSV-150 from Polytec which is shown in Fig. 11c.

2.2 Optical Fiber Vibrometers

Sometimes measurement points are located at positions that are difficult to access. In this case, small optical probes are required. This demand can be achieved with optical fibers which are utilized to parcel the light from the interferometer to the optical probe. The fibers need to be realized as single-mode, polarization-maintaining fibers in order to prevent phase differences in different modes of the light field traveling through the fiber. Such phase variations would appear in multi-mode fibers. The polarization of the measurement light at the photodetector needs to be aligned in the same direction as the reference light in order to achieve maximum interference contrast. Perpendicular polarization states do not interfere at all. The interferometer can be assembled similar as the standard single-point vibrometer, but the measurement light is coupled into the fiber by a launcher. The launcher provides four mechanical degrees of freedom (two orthogonal displacements, two orthogonal angles) and an adjustable focus to align the impinging field distribution to the required single-mode field of the fiber. In addition, opto-mechanic means are necessary to align the polarization by either rotating the fiber in the launcher or to rotate the laser polarization at the launcher by half-wave plate. The probe at the fiber end has a miniature lens system to image the fiber exit on the specimen (corresponds to the best focus). Such a probe can be really small, and in some cases the probe consists of a gradient index lens with a few millimeter diameter. A fiber vibrometer with a multiplexer and IR-light from OptoMET is shown in Fig. 12.

2.3 Differential Vibrometers

The laser Doppler vibrometer measures the relative movement between sensor and specimen. Usually, this does not affect the measurement because the vibration amplitudes at the specimen at the investigated frequencies are much larger as the parasitic vibrations of the sensor. However, especially at low frequencies it is sometimes necessary to suppress influences of the sensor motion by differential

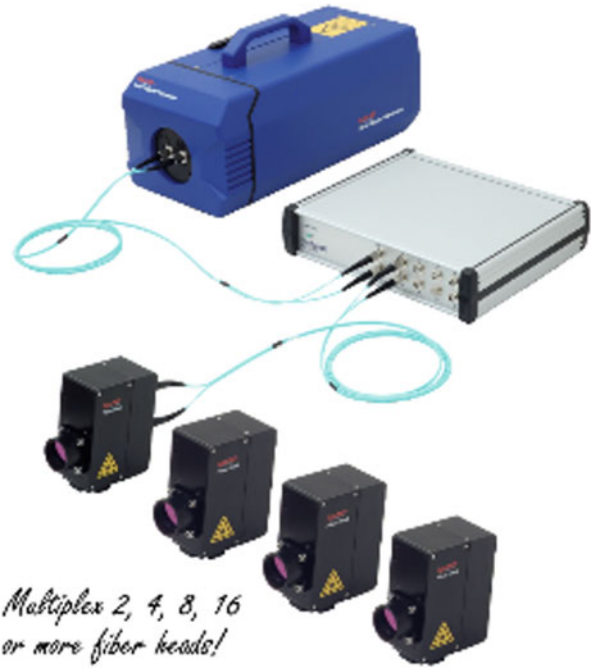

Fig. 12 Fiber technology allows flexible adjustment of the measurement spot and multiplexing to different probes with the dual-fiber vibrometer of OptoMET. (Courtesy OptoMET)

measurements. To measure the movement of a measurement point on the specimen relative to another surface point at any object, the reference beam is also coupled out of the interferometer, and the optical path length of the reference path is altered by the movement of the reference point. If both beams measure in the same direction, the alteration of the interference signal depends only on the relative path length between measurement and reference light. Differential vibrometers are often realized as optical fiber vibrometers in order to adjust the measurement positions of the two laser beams independently. An interesting application of differential vibrometers is reported in [28], wherein the vibrometer is utilized to assess the kinematics of poppet valves in a combustion engine. Differential measurements are especially important for measurement tasks on small structures with slow movements as, for example, MEMS mirrors; differential measurements are often realized in laser-vibrometer microscopes. Here, fiber vibrometers are also favorable because they can be more easily coupled into a confocal laser scanning microscope.

2.4 Rotational Vibrometers

Impinging two parallel laser beams with distance d on a rotating shaft, the sum of the frequency shifts depends only on the rotation speed if the two beams impinged on different sides of the shaft. This can be understood by Fig. 13.

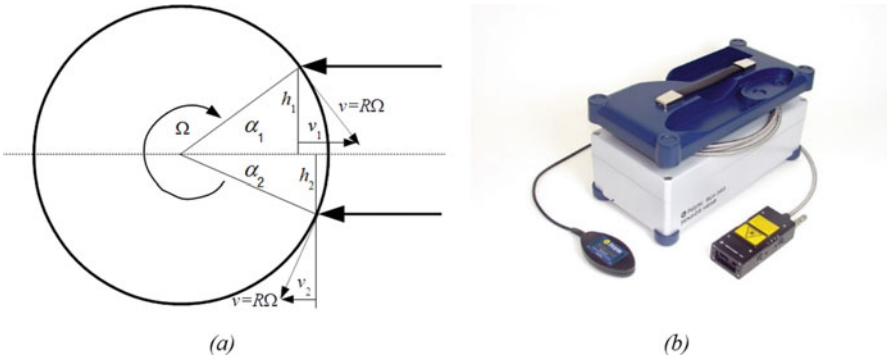

Fig. 13 Rotational vibrometer: working principle (**a**) and example of a commercial device (**b**) Courtesy of Polytec

Assuming a rotating cylinder the Doppler shifts f_D of the upper and lower beams can be expressed as in (29) and (30), respectively.

$$f_{D1} = \frac{2R\Omega \cdot \sin\alpha_1}{\lambda} = \frac{2\Omega \cdot h_1}{\lambda}. \tag{29}$$

$$f_{D2} = -\frac{2R\Omega \cdot \sin\alpha_2}{\lambda} = -\frac{2\Omega \cdot h_2}{\lambda}. \tag{30}$$

Thus the sum of both Doppler shifts result in the rotational speed

$$\Omega = \frac{(f_{D1} - f_{D2})\,\lambda}{2 \cdot d} \tag{31}$$

and reveals that the combined signal is proportional to the rotation velocity and the fixed beam distance, but it is independent on the exact positions of the laser beams. Therefore, a rotational vibrometer as it is shown in Fig. 13 is a flexible rotation speed meter. The rotational vibrometer is indeed a very powerful instrument for structural dynamics [29, 30]; however, particular attention should be given to its setup in order to obtain reliable results.

The measurement head must always be mounted in such a way that the plane containing the laser beams lies orthogonally to the rotation axis of the measurement object. If the angle of incidence is different from 90° degrees, the measurement results decrease in relation to the cosine functions.

The relative position of the two measurement beams with respect to the rotation axis also influences the quality of the results. Optimal results are achieved with a symmetrical position of the two beams, in particular for thin shafts. Indeed, if one beam hits the surface too tangentially, the scattering conditions become significantly worse. In addition, an asymmetrical alignment reduces also the available

measurement range, as the range is fixed for each interferometer whose output is mixed with opposite signs.

In many practical cases, the rotating body undergoes also bending or translational motion. In theory, an additional translational motion, overlapping both velocities on the two beams, does not influence the resulting Doppler frequency. When the vibrometer is correctly installed and its arms are perfectly balanced, the effect of the generic additional bending modes will also be null ($v_{1,\,\text{bend}} = v_{2,\,\text{bend}}$). On the contrary, if for some reasons a good balancing cannot be achieved, the rotational vibrometer becomes sensitive also to bending modes. Possible causes of a not perfect balancing ($v_{1,\,\text{bend}} \neq v_{2,\,\text{bend}}$) could be the following:

- Optical (e.g., the local reflection conditions are different for the two spots; the two beams are disposed highly asymmetrically with respect to the rotation axis), electrical, or hardware (e.g., differences in the two photodetectors) causes.
- Not perfect parallelism between the two measurement beams.
- The structure or the mode has a particular complex shape.

These problems are minimized when the vibrometer is measuring on a rotating shaft, while they become more important if a torsional modal analysis in steady conditions is performed. In fact, in this case the object vibrates and rotates on a steady condition and thus the terms ($\delta f_1 - \delta f_2$) and ($v_{1,\,\text{bend}} + v_{2,\,\text{bend}}$) are comparable. In this situation, because of the contribution of the above factors, the frequencies of the larger bending modes are recorded in the rotational velocity signal, as shown for a camshaft analysis in [31].

2.5 In-Plane Vibrometers

In-plane vibrometers (Fig. 14) have two laser beams which are focused on the same spot of the specimen and generate an interference pattern with fringe distance Δs in the intersection volume [32]. The angle between the two beams is ϕ. Light scattered from the intersection volume to the angle bisector has a modulation frequency (36) that is only proportional to the in-plane velocity.

$$v_{bisec} = \frac{v_{\text{in-plane}}}{\Delta s} = \frac{2 \cdot v_{\text{in-plane}} \cdot \sin\phi}{\lambda} \tag{32}$$

Such a system is not sensitive to out-of-plane displacements. Coherent application is not applicable to such an optical system, and the photodetector receives light scattered in the direction of the angle bisector.

In-plane vibrometers enable interesting applications in structural dynamics. However, some best practices should be taken into account. Among others, three main conditions should be satisfied:

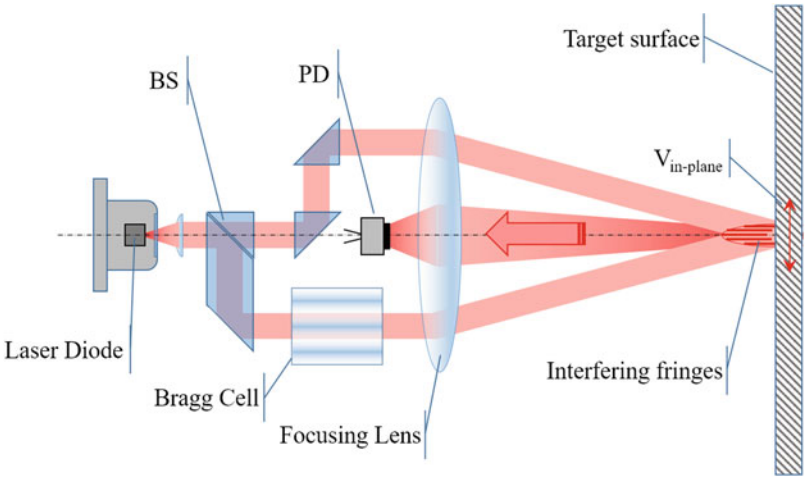

Fig. 14 Schematic representation of in-plane vibrometer

- The stand-off distance should make it possible to have the cross-point of the two laser beams lying on the target surface.
- The optical axis of the instrument should be directed perpendicular to the surface under test.
- The plane containing the two laser beams should also contain the desired velocity component.

The optical configuration of the vibrometers can induce a lower SNR with respect to vibrometers measuring out-of-plane vibrations. When measuring on highly reflective surfaces, better results might be found by tilting the laser head at a small angle (about 5°) around the axis of the velocity vector to be measured. This tilting avoids saturation of the photodetector from direct reflections. Once measurement uncertainty sources are taken into account [33], in-plane vibrometers can really be exploited in applications where out-of-plane vibrometers cannot be utilized (see, e.g., [34].).

2.6 Scanning Vibrometers

2.6.1 Step Scan Vibrometers (Single DoF)

The idea of a scanning LDV is based on the possibility to sequentially and automatically measure vibration at several points defined by the user and was invented in 1968 by Massey [35]. In this way, the time evolution of the phenomenon under analysis can be related to the spatial evolution of the same phenomenon. When performing a vibration test, this means obtaining operational deflection shapes of the structure.

Different solutions could be adopted to perform a scan, as the movement of the single-point vibrometer through a motorized traversing gear or the orientation of the laser beam by a couple of oscillating thick glasses. However, the most common solution involves the use of a pair of oscillating mirrors. The mirrors are usually moved by galvanometric motors. Typical rotation angles reached ranges between ±20 deg. Motors are driven by a closed loop controller that checks mirror position using an angular position sensor (usually a capacitive sensor). The system is also thermo-stabilized, for better accuracy. Apart from galvo-motors, other systems involving stepper motors or piezoelectric-driven motors can be found as well. However, the latter solutions are rarely implemented in commercially available scanning vibrometers.

The rotation axes of the two mirrors are orthogonal to each other. Such a configuration makes a two-direction scan possible. An example of such system is reported in Fig. 15. The focusing optics are sometimes installed after the oscillating mirrors to align laser beam and make it possible to scan with parallel beams (same incidence angle with respect to the normal to target surface).

In order to reduce the distance d_s between the two oscillating mirrors ($d_s \approx 30$ mm), and to better pack the whole scanning system, the axes of the mirrors are placed at an acute angle. In this way, even at smaller distances between the mirrors axes, the risk of ruining the mirrors at typical scanning angles reduces. Moreover, the instrument head is quite compact, and wide measurement grids can be

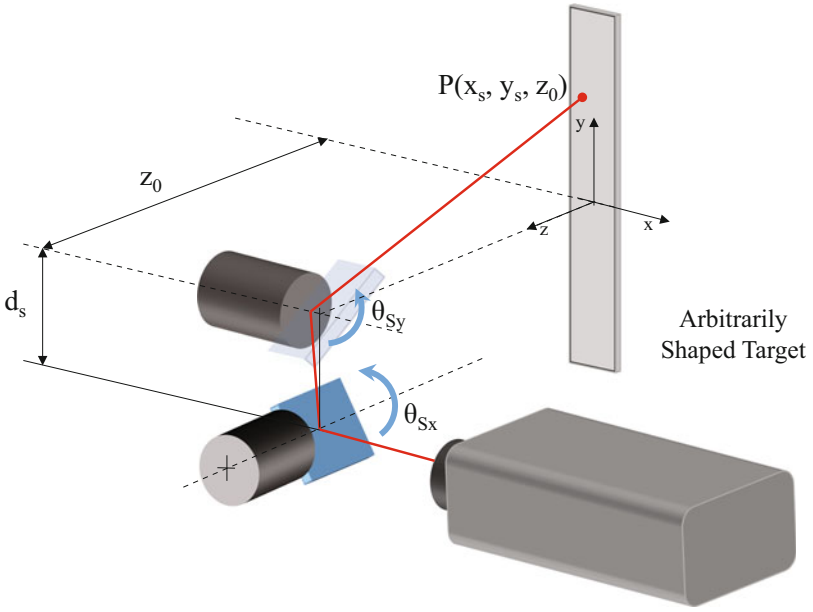

Fig. 15 Schematic representation of a double mirror scanning configuration

scanned once a proper laser to target distance (z_0) is set up. The main disadvantage of the double mirror configuration (without the focusing optics after the mirrors) has to be identified in the measuring of a vibration velocity that is a superposition of in-plane and out-of-plane components. Indeed, since the beam direction changes during the scan, different components are measured on different points. In case of pure out-of-plane motions, and when $P(x_s, y_s, z_0) = P(x_0, y_0, z_0)$ for ϑ_{sx}, ϑ_{sy} being in their "home" position (Fig. 15), the user can compensate for the angle incidence error. When this is not the case, the vibration velocity measured is sensitive to out-of-plane and in-plane components in a different way whenever the laser spot moves to a different point. All these aspects can be well understood referring to the modelling framework developed by Halkon and Rothberg [36].

A typical measurement procedure, involving a computer-controlled scanning systems to support the user, comprises the following steps:

- Focus the laser beam on the target surface
- Acquire the image of the object, for reporting the position of the grid on the object
- Align the camera coordinate with the grid coordinate
- Define the measurement grid
- Manage (if required) the excitation
- Manage the acquisition parameters and strategy
- Move the laser spot on each point of the grid (settling time of about <10 ms), for acquisition
- Acquire, for each measurement point, the vibrometer and the reference (or references) signals
- Post-process data and display results
- Store data

A mandatory requirement for performing a vibration test using step scanning vibrometry is the stationarity of the phenomenon under analysis. If this is not the case, repeatability of the phenomenon, under an adequate trigger condition, should be guaranteed at least. Whenever all these requirements are not met, scanning vibrometry cannot be utilized to assess the global vibration behavior of a structure, since vibration information on different points cannot be related to each other.

It is also good practice to have also a reference signal when performing a scan. Such reference signal, i.e., a signal given by a sensor measuring on the same position, plays the same role that a reference sensor (e.g., a load cell) plays in traditional modal analysis tests, that is:

- To verify that phenomena under analysis are stationary
- To obtain a phase reference among each point
- To calculate correlation functions (e.g., frequency response functions), if needed

2.6.2 Special Solutions

Continuous-Scan LDV

Continuous-scan laser Doppler vibrometry (CSLDV) can greatly accelerate modal testing by continuously sweeping the measuring laser over a structure, effectively capturing its response at hundreds of points along the laser path in one measurement. Scanning the laser can increase laser speckle noise, so this application seeks to find a balance between the additional spatial information that CSLDV provides (in a reduced time) with increasing speckle noise. CSLDV typically increases speckle noise, but it has been shown to decrease the noise in some cases [37]. A schematic of the CSLDV process is shown in Fig. 16, as well as a photograph from an actual CSLDV test from [38].

Continuous-scan vibrometry also changes the nature of the signals that are measured, so new methods are needed to process CSLDV measurements and extract the structure's modal natural frequencies, damping ratios and the mode shapes along the laser scan path. Among the first and probably, the most prolific is the method developed by Ewins, Stanbridge, Martarelli, and others, who modelled the operating deflection shape as a continuous polynomial function of the laser position. The recorded vibration shape using CSLDV was treated as being modulated by the moving laser position, which leads to sideband harmonics in the spectrum that are separated by the scan frequency. They showed that the amplitudes at those harmonics are related to the polynomial coefficients by a transformation matrix. Once the polynomial coefficients are extracted, the mode shapes can be reconstructed using the known laser path. This method is very effective and straightforward and has been used to reconstruct the mode shapes of a structure using sinusoidal [39],

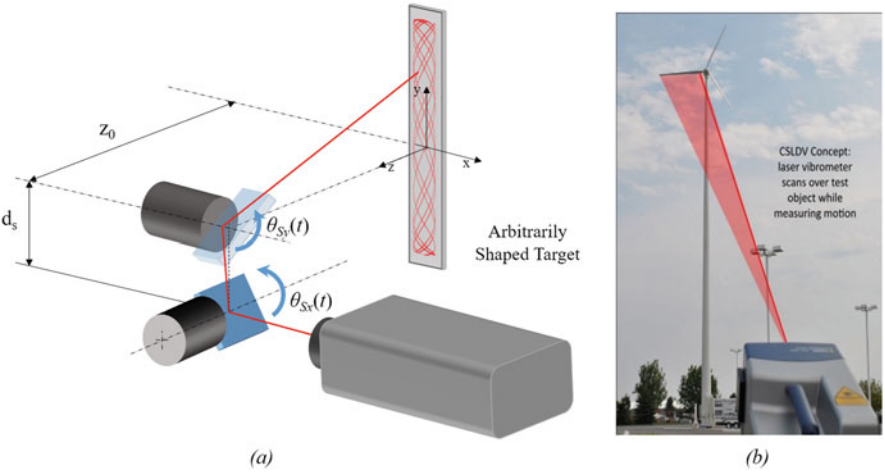

Fig. 16 Schematic representation of continuous-scan LDV using a double mirror configuration. (**a**) The laser sweeps continuously over the surface as the measurement is acquired. (**b**) Photograph from an actual CSLDV test on a wind turbine blade with the laser path artificially colored

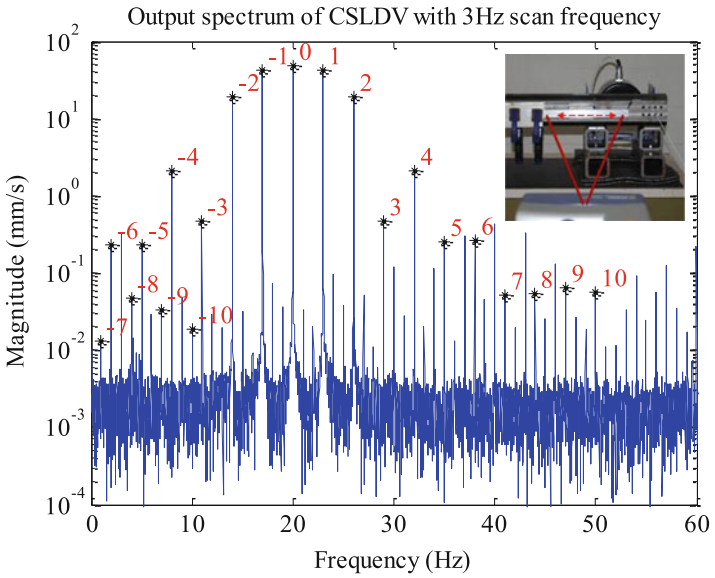

Fig. 17 Spectrum measured using CSLDV on a cantilever beam that is vibrating at 20 Hz. The laser is scanning at 3 Hz and so the measurement shows sideband harmonics at 20 ± 3 Hz. The side band amplitudes can be collected to estimate the mode shape using the method in [38]

impact [40], and pseudo-random excitation [41]. An application of the approach for the assessment of timing-belt dynamics in running condition is reported in [42]. If the operational shape along the laser path is complicated, then high-order polynomial coefficients may be necessary to accurately describe the shape. Hence, the precision of CSLDV is limited by the number of harmonics that stands out above the noise floor in the measured spectrum. An example is shown in Fig. 17.

The CSLDV methods mentioned so far are all tailored to a certain class of forcing input (e.g., sinusoidal has been most common) and require specialized post-processing to extract the natural frequencies and mode shapes from the measurements. Allen et al. proposed several alternatives that more closely resemble conventional modal analysis. In [43] they proposed the discrete "lifting" approach, in which the responses at the same location along the laser path are grouped together. The reorganized responses then appear to be from a set of pseudo transducers distributed along the scan path, and then standard routines can be used to curve fit the measurements and extract the mode shapes. However, each pseudo-sensor samples only once per scan period, and there is a constant time delay between the measurements at each point. As a result, according to the sampling theorem, all the modes of the system and their harmonics are aliased to the range from zero to half of the scan frequency. In [44] Allen et al. used the lifting approach to extract the natural frequencies and mass-normalized mode shapes of a free-free beam under impact excitation. They demonstrated that, ideally, one would choose the scan frequency

to be larger than twice the maximum frequency of interest, but often this is not possible. The maximum scan frequency is restricted by the mechanical scanners (up to 500 Hz), and the laser speckle noise also increases with the scan frequency. Instead, the scan frequency can be chosen to ensure that the modes do not overlap after being aliased to the band of half of the scan frequency. Therefore, the lifting approach is more suitable for measuring structures whose natural frequencies are only a few hundreds of Hertz or lower.

The most general approach for treating CSLDV measurements was presented in [37] and is based on the harmonic transfer function (HTF) concept developed by Wereley and Hall [45]. The HTF extends the transfer function concept to systems where the system parameters are periodic functions of time. In the case of CSLDV, the measurement point is a periodic function of time. This concept can also be used to address output only modal analysis, where the input is not measured but can be assumed to be broadband and random. For example, Yang and Allen used this approach in [38] to process the CSLDV measurements of a parked wind turbine that was excited by a light wind, as shown in Fig. 18. Detailed mode shapes were obtained from one 20-minute time record using a single laser; to obtain similar resolution with conventional stepped-scanning LDV, one would have needed two lasers and several hours to acquire the measurements.

Alternative use of CSLDV can be cited for vibro-acoustic applications [46], damage detection [47], and biomedical applications [48]. A multi-beam CSLDV approach was also proposed in [49] for landmine detection.

LDV Strategies on Rotating/Moving Structures

Scanning Laser Doppler Vibrometry with Optical Derotator

There are mirror or prism systems with an odd number of reflections which rotate the image when the optical system is rotated [50, 51]. For example, watching through a rotating Dove prism, one would see the image rotating with twice the rotation speed of the prism. A laser beam moves on a circle if the beams shine through a rotating Dove prism if the optical axis of the prism is absolutely coaxial to the rotation axis. To receive a standing image of a rotating object, the prism needs to rotate with exactly half the rotational speed of the specimen. In addition, the optical axis of the prism needs to intersect the rotational axis of the specimen on the specimen surface. Therefore, an optical derotator is well suited to measure on a rotating specimen with a scanning laser Doppler vibrometer if suitable degrees of freedom for alignment are available.

It has been demonstrated that rotations up to 12.000 revolutions per minute (rpm) of the prism can be achieved with standard electronic motors and motor controllers. It is necessary to realize a phase-locked loop between an encoder signal of the prism rotation and an encoder signal from the rotating object in order to synchronize both rotations. Thus, a controller is required capable implementing a digital phase control loop. Usually the control applies first a frequency control to synchronize the rotational speed of the prism to half the rotational speed of the object. Then the control parameters are adapted automatically in order to achieve

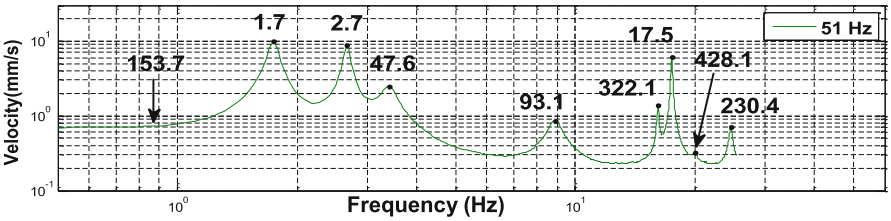

(a)

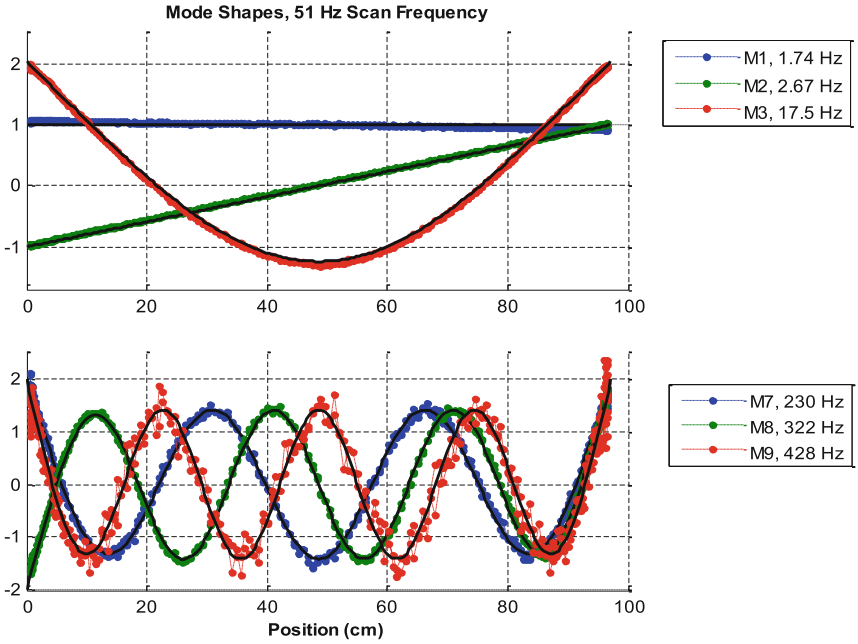

(b)

Fig. 18 Spectrum measured using CSLDV on free-free beam excited by an impulsive force. The lifting approach was used to expand the measurement to hundreds of pseudo-measurement points, and the average spectrum shown (**a**) reveals that each mode occurs at a single frequency, although aliased within the 25.5 Hz bandwidth. The mode shapes (**b**) can be extracted by curve fitting this set of measurements using standard LTI modal analysis algorithms, from [41]

a steady phase relation for a steady image of the rotating parts. Such a system can follow rotational accelerations up to 700 rpm/s.

Tracking Laser Doppler Vibrometry

Tracking laser Doppler vibrometry (TLDV) is basically conceived as an enhanced SLDV; it is aimed at enhancing common scanning LDV. The aim of TLDV is non-contact vibration testing on a point, or over a grid of points, fixed on a moving

target (i.e., Lagrangian approach) [52]. The system is based on a SLDV where the mirrors, conventionally utilized to scan the beam across a grid of static points, are now controlled to track the motion of an arbitrary moving structure, its trajectory being known.

In the case of rotating machinery, the trajectory to be followed can be measured using a position sensor, i.e., which can track the changes of the target angular position. For instance, in case a digital encoder is connected to the rotating shaft, the encoder signal provides the angular position and becomes the clock (i.e., it acts as the clock of the D/A converters of the acquisition system DAQ board which generates analog voltages to directly drive the LDV mirrors) to drive the mirrors so to track the position of a certain point during the target revolution.

In case the target trajectory is not a priori known, a closed loop approach can be utilized [53]. A camera, coaxial with the laser beam, observes the target (a bright spot on a dark background) position with respect to the laser beam and provides an "error" signal to a PID controller. The output of the controller feeds the scanning mirror, making possible a constant tracking of the target.

These architectures allow one to track each visible point on the moving structure; a complete grid of points, moving with the target, can therefore be explored, by taking sequential measurement on the different rotating points which are part of the grid [54] under steady conditions.

The tracking strategy has been applied in several kinds of rotating machinery, as helicopter rotor blades [55] and naval propeller blades [56].

A further evolution of the tracking concept is to be found in the use of continuous-scan LDV for assessing the vibration of a structure undergoing rigid body motion. Such concept, addressed in literature as Tracking CSLDV (TCSLDV), consists in performing a continuous scan over the target surface while tracking the target rigid body motion. A deeper insight into the method, given by application cases, can be found in [57–60].

2.6.3 3D Scanning Vibrometer

One of the most important applications of laser Doppler vibrometry is discrete 3D scanning [61]. Here, three laser beams impinge a measurement spot from three different linearly independent directions. Thus, such a system can obtain three linearly independent velocity components from a measurement spot. For every scanning vibrometer, the Doppler shift can be expressed by the vector formula

$$\delta f_i = \frac{1}{\pi} \cdot \vec{v} \cdot \vec{k}_i \tag{33}$$

with the wave vector $\vec{k}_i$ of the three components $k_{xi} = \vec{k}_i \vec{e}_x$, $k_{yi} = \vec{k}_i \vec{e}_y$, and $k_{zi} = \vec{k}_i \vec{e}_z$ in a Cartesian coordinate system. Thus, the velocity vector can be derived by the Equation

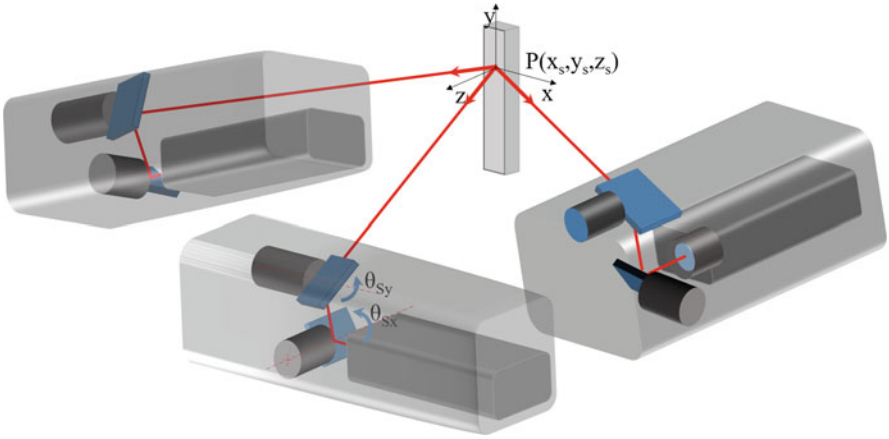

Fig. 19 3D scanning vibrometer

$$\vec{v} = \frac{1}{\pi} \begin{pmatrix} k_{x1} & k_{y1} & k_{z1} \\ k_{x2} & k_{y2} & k_{z2} \\ k_{x3} & k_{y3} & k_{z3} \end{pmatrix}^{-1} \cdot \begin{pmatrix} \delta f_1 \\ \delta f_2 \\ \delta f_3 \end{pmatrix}. \tag{34}$$

Thus, a 3D scanning vibrometer as it is shown in Fig. 19 makes possible the detection of broadband 3D vibration spectra at every measurement spot.

Complete 3D operational deflection shapes can be obtained by scanning the three beams over a surface and by receiving a reference signal of a periodic vibration to synchronize the measurements.

Geometry data of the measurement spots can be either imported in the user software or it can be measured with a time-of-flight measurement with a laser distance sensor integrated in the PSV-500.

A recently published solution [62] allows 3D measurements with just a single measurement beam by collecting light from three directions and evaluating the directional Doppler effect. This solution is especially well suited for small structures since the laser spot is just defined by the central impinging beam which can be focused with a microscope objective. A spot diameter of 3.3 μm has been demonstrated for 3D measurements.

2.7 Multi-beam

Scanning measurements are not possible if either a reference signal is not available or if the vibration is aperiodic or not repeatable. This is the case for events like operational vibrations during heating which is the case for any engine during startup or run-up. Other example applications are impacts, processes with strong friction (e.g., brakes), breaking structures, or explosions. Since the number of channels

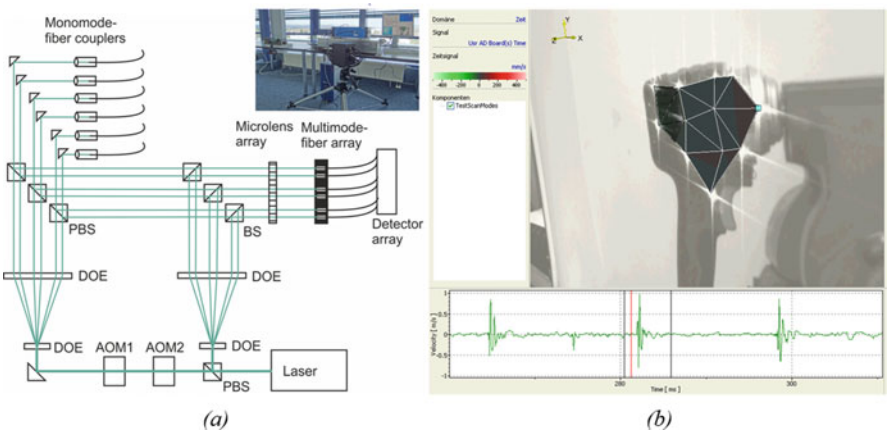

Fig. 20 12-channel, laser Doppler vibrometer realized as demonstrator in the corporation project Holovib funded by the BMBF under the grant number 13 N9338: (**a**) optical setup (**a**); (**b**) example of a measurement on an impact wrench (Courtesy Polytec)

is limited due to the high cost of a vibrometer, the flexible adjustment of the measurement is essential. Such a system, which is capable of adjusting an arbitrary measurement grid, has been demonstrated by Haist et al. [63]. The multichannel vibrometer has been realized as complex bulk-optics setup with holograms to split the laser light to multiple channels with homodyne [64] or heterodyne [65]. Fibers are employed to parcel the measurement light to flexible probes with adjustable objectives [45, 66, 67] (Fig. 20).

3 Conclusions

When it comes the necessity of avoiding contact sensors for measuring vibration response of structures (e.g., on lightweight, hot structures, etc.), laser Doppler vibrometry surely represents a target technique. Indeed, LDV has gained a relevant role within structural dynamics testing and is currently widely used in several application fields. However, as it happens with every measurement technique, LDV must be properly known to be properly exploited. The aim of this chapter was to provide the reader with the fundamentals of LDV (from interferometry basics, to laser safety) as well as with the main instrumentations, measurement issues, and applications involving this technique. The chapter was not intended to give a comprehensive picture of LDV, for which the interested reader is encouraged to go for the references reported, but can be considered to be a sufficiently detailed document enabling the experimenter to learn the potentials of this measurement approach and some “best practice” gathered from the experience gained by the authors during their careers.

References

1. Drain LE (1980) The laser Doppler technique. John Wiley & Sons Ltd, Chichester
2. Rembe C (2008) Retardation effects in Laser-Doppler Measurements. In: 8th International conference on vibration measurements by laser techniques, advances and applications, SPIE, vol 7098, p 13
3. Rembe C, Siegmund G, Steger H, Wörtge M (2006) Measuring MEMS in motion by laser-Doppler vibrometry. In: Osten W (ed) Optical inspection of microsystems, pp 245–292
4. Bauer M, Ritter F, Siegmund G (2002) High-precision laser vibrometers based on digital Doppler-signal processing. In: 5th International conference on vibration measurements by laser techniques, advances and applications, vol 4827. SPIE, pp 50–61
5. Rudd MJ (1968) A laser Doppler velocimeter employing the laser as a mixer-oscillator. J Phys E 1:723–726
6. Giuliani G, Norgia M, Donati S, Bosch T (2002) Laser diode self-mixing technique for sensing applications. J Opt A Pure Appl Opt 4:S283–S294
7. Scalise L, Yu Y, Giuliani G, Plantier G, Bosch T (2004) Self-mixing laser diode velocimetry: application to vibration and velocity measurement. IEEE Trans Instrum Meas 53(1): 223–232
8. Scalise L, Steenbergen W, de Mul F (2001) Self-mixing feedback in a laser diode for intra-arterial optical blood velocimetry. Appl Opt 40:4608–4615
9. Dainty JC (1975) Laser speckle and related phenomena. Springer, Berlin
10. Strean RF, Mitchell LD, Barker AJ (1998) Global noise characteristics of a laser Doppler vibrometer – I. theory. Opt Lasers Eng 30(2):127–139
11. Rothberg SJ, Baker JR, Halliwell NA (1998) Laser vibrometry: pseudo-vibrations. J Sound Vib 135(3):516–522
12. Rothberg S (2006) Numerical simulation of speckle noise in laser Vibrometry. Appl Opt 45(19):4523–4533
13. Martin P, Rothberg S (2009) Introducing speckle noise maps for laser vibrometry. J Optics Lasers in Engineering 47:431–442
14. Dräbenstedt A. (2007) Quantification of displacement and velocity noise in vibrometer measurements on transversely moving or rotating surfaces. In: Proceedings of SPIE 6616, Optical measurement systems for industrial inspection, vol 6616 (32). https://doi.org/10.1117/12.726115
15. Vass J, Smìd R, Randall RB, Sovka P, Cristalli C, Torcianti B (2008) Avoidance of speckle noise in laser vibrometry by the use of kurtosis ratio: application to mechanical fault diagnostics. Mech Syst Signal Process 22:647–671
16. Paone N, Revel GM (1998) Modelling and experimental analysis of the performance of a laser Doppler vibrometer used to measure surface vibrations through combustive flows. Opt Lasers Eng 30:163–178
17. Castellini P, Martarelli M, Tomasini EP (2013) Sub-sonic jet pressure fluctuation characterization by tomographic laser interferometry. Exp Fluids 54:12
18. Buligan G, Paone N, Revel GM, Tomasini EP (2003) The measurement of hermetic compressor valve motion by laser vibrometry, IMAC-2003, Kissimmee
19. Dräbenstedt A (2014) Diversity combining in laser Doppler vibrometry for improved signal reliability. AIP Conference, vol 1600, p 263
20. Rembe C, Dräbenstedt A (2015) Speckle-insensitive laser-Doppler vibrometry with adaptive optics and signal diversity. Sensor 2015, Erlangen, Deutschland, 19–21 May
21. Evaluation of measurement data – Guide to the expression of uncertainty in measurement, First edition September 2008 © JCGM 2008
22. Robinson DC, Serbyn MR, Payne BF (1987) A description of NBS calibration services in mechanical vibration and shock. NBS Technical Note:1232
23. ISO 16063-41:2011, Methods for the calibration of vibration and shock transducers – Part 41: Calibration of laser vibrometers

24. ISO 16063-15:2006, Methods for the calibration of vibration and shock transducers – Part 15: primary angular vibration calibration by laser interferometry. International Organization for Standardization (ISO), Geneva
25. Practical Laser Safety, 2nd edn. CRC Press. ISBN: 0824782402
26. IEC 60825-1:2014 – Safety of laser products Part 1: equipment classification and requirements
27. IEC 60825-1:2007 – Safety of laser products Part 1: equipment classification and re-quirements
28. Paone N, Santolini C, Tomasini EP (1994) Application of a laser Doppler vibrometer to evaluate engine poppet valve kinematics. In: XII International. Modal analysis conference, Hawaii
29. Hallowell NA (1996) The laser torsional vibrometer: a step forward in rotating machinery diagnostics. J Sound Vib 190(3):399–418
30. Lewin AC, Roth V, Siegmund G (1995) Measurement of rotational vibrations using a novel interferometric technique. Measurement 16(2):81–90
31. Revel GM, Tomasini EP (1999) Torsional Vibrations: a laser vibrometry approach. In: Vibration, noise & structural dynamics '99, Venezia, pp 448–453
32. van Netten SM (1988) Laser interferometer microscope for the measurement of nanometer vibrational displacements of a light-scattering microscopic object. J Acoust Soc Am 83: 1667–1674
33. Gasparetti M, Revel GM (1999) The influence of operating conditions on the accuracy of in-plane laser Doppler velocimetry measurements, measurement, vol 26. Elsevier Science Ltd., Oxford, pp 207–220. ISSN 0263-2241
34. Castellini P, Chiariotti P, Martarelli M, Tomasini EP (2013) Valvetrain motion measure-ments in firing conditions by laser Doppler vibrometer. In: IMAC XXXI International modal analysis conference, Hyatt Regency Orange County, Garden Grove
35. Massey GA (1968) An optical heterodyne ultrasonic image converter. IEEE Sonics Ultrasonics 56:2157–2161
36. Halkon BJ, Rothberg SJ (2003) Vibration measurement using continuous scanning laser Doppler vibrometry: theoretical velocity sensitivity analysis with applications. Meas Sci Technol 14:382–393
37. Yang S, Allen MS (2014) Harmonic transfer function to measure translational and rotational velocities with continuous-scan laser doppler vibrometry. ASME J Vib Acoust 136(2)
38. Yang S, Allen MS (2012) Output-only modal analysis using continuous-scan laser Doppler vibrometry and application to a 20 kW wind turbine. Mech Syst Signal Process 31:228–245
39. Stanbridge AB, Ewins DJ (1999) Modal testing using a scanning laser Doppler vibrometer. Mech Syst Signal Process 13(2):255–270
40. Ribichini, R et al. (2008) Impact testing with a continuously-scanning LDV. In: 26th International modal analysis conference (IMAC XXVI), Orlando
41. Di Maio D, Carloni G, Ewins DJ (2010) Simulation and validation of ODS measurements made using a continuous SLDV method on a beam excited by a pseudo random signal. In: 28th International modal analysis conference (IMAC XXVIII), Jacksonville
42. Chiariotti P, Martarelli M, Castellini P (2017) Exploiting continuous scanning laser Doppler vibrometry in timing belt dynamic characterization, 86, Part B, pp 66–81
43. Allen MS, Sracic MW (2010) A new method for processing impact excited continuous-scan laser Doppler vibrometer measurements. Mech Syst Signal Process 24:721–735
44. Yang S, Sracic MW, Allen MS (2012) Two algorithms for mass normalizing mode shapes from impact excited continuous-scan laser Doppler vibrometry. J Vib Acoust 134(2):021004
45. Wereley NM (1991) Analysis and control of linear periodically time varying systems. Department of Aeronautics and Astronautics, Massachusetts Institute of Technology, Cambridge
46. Chiariotti P, Martarelli M, Revel GM (2014) Exploiting continuous scanning laser Doppler vibrometry (CSLDV) in time domain correlation methods for noise source identification. Meas Sci Technol 25(7):075204 (13pp). https://doi.org/10.1088/0957-0233/25/7/075204
47. Chiariotti P, Martarelli M, Revel GM (2017) Delamination detection by multi-level wavelet processing of continuous scanning laser Doppler vibrometry data. Opt Lasers Eng 99:66–79

48. Salman M, Sabra KG (2011) Synchronized vibrations measurements at multiple locations using a single continuously scanning laser Doppler vibrometer. Applications to non-contact sensing of human body vibrations. J Acoust Soc Am 130(4):2394–2394
49. Aranchuk V, Lal AK, Zhang H, Hess CF, Sabatier JM (2004) Acoustic sensor for landmine detection using a continuously scanning multi-beam LDV, vol 5415. SPIE, Orlando, p 61
50. Boedecker S, Dräbenstedt A, Heller L, Kraft A, Leonhardt A, Pape C, Ristau S, Reithmei-er E, Rembe C (2006) Optical derotator for scanning vibrometer measurements on rotating objects, SPIE vol 6345, 63450M
51. Johansmann M, Fritzsche M, Schell J (2011) A new method for measurement of rotating objects utilizing laser Doppler vibrometry combined with an optical derotator with focus on automotive applications. SAE Technical Paper 2011-26-0043
52. Castellini P, Paone N (2000) Development of the tracking laser vibrometer: performance and uncertainty analysis. Rev Sci Instrum 71(12):4639
53. Castellini P, Tomasini EP (2004) Image-based tracking laser Doppler vibrometer. Rev Sci Instrum 75(1):222
54. Castellini P, Montanini R (2002) Automotive components vibration measurements by tracking laser Doppler vibrometry: advances in signal processing. Meas Sci Technol 13: 1266–1279
55. Fioretti A, Di Maio D, Ewins DJ, Castellini P, Tomasini EP (2010) Deflection shape re-contructions of a rotating five-blade helicopter rotor from SLDV measurements. In: 9th International conference on vibration measurements by laser and noncontact techniques & short course, Ancona
56. Castellini P, Santolini C (1998) Vibration measurements on blades of naval propeller rotating in water with tracking laser vibrometer. Measurement 24:43–54
57. Martarelli M, Castellini P, Santolini C, Tomasini EP (2011) Laser Doppler vibrometry on rotating structures in coast-down: resonance frequencies and operational deflection shape characterization. Meas Sci Technol 22:115106
58. Martarelli M, Castellini P (2012) Performance analysis of continuous tracking laser Doppler vibrometry applied to rotating structures in coast-down. Meas Sci Technol 23:065202. https://doi.org/10.1088/0957-0233/23/6/065202
59. Di Maio D, Ewins DJ (2010) Applications of continuous tracking SLDV measurement methods to axially symmetric rotating structures using different excitation methods. Mech Syst Signal Process 24(8):3013–3036
60. Gasparoni A, Allen MS, Yang MS, Sracic MW, Castellini P, Tomasini EP (2010) Experimental modal analysis on a rotating fan using tracking-CSLDV. In: 9th International conference on vibration measurements by laser and noncontact techniques & short course, Ancona, ISBN 978–0–7354-0801-2
61. Bendel K, Fischer M, Schüssler M (2004) Vibrational analysis of power tools using a novel three dimensional scanning vibrometer. In: Sixth International conference of vibration measurement by laser techniques, vol 5503. SPIE, pp 177–184
62. Rembe C, Kowarsch R, Ochs W, Dräbenstedt A, Giesen M, Winter M (2014) Optical 3D-vibrometer microscope with picometer-resolution in x, y, and z. Opt Eng 53(3):034108
63. Haist T, Lingel C, Osten W, Winter M, Giesen M, Ritter F, Sandfort K, Rembe C, Bendel K (2013) Multipoint vibrometry with dynamic and static holograms. Rev Sci Instrum 84:121701
64. Cupido E, Morel S, Smith D (2003) Multipoint laser Doppler vibrometer for transient analysis. In: IMAC-XXI: conference & exposition on structural dynamics, SEM
65. Lal AK, Hess C (2006) Array and matrix based laser Doppler vibrometers for measuring noise and vibration. Inter-Noise, Honolulu
66. Fu Y, Guo M, Phua PB (2011) Multipoint laser Doppler vibrometry with single detector: principles, implementations, and signal analyses. Appl Opt 50(10):1280–1288
67. Waz AT, Kaczmarek PR, Abranski KM (2009) Laser-fibre vibrometry at 1550 nm. Meas Sci Technol 20:105301

Applied Digital Signal Processing

4

Robert B. Randall, Jerome Antoni, and Pietro Borghesani

Contents

R. B. Randall (✉)
University of New South Wales, Sydney, NSW, Australia
e-mail: b.randall@unsw.edu.au

J. Antoni
Univ Lyon, INSA-Lyon, Villeurbanne, France
e-mail: jerome.antoni@insa-lyon.fr

P. Borghesani
University of New South Wales, Sydney, NSW, Australia

Queensland University of Technology, Brisbane, QLD, Australia
e-mail: p.borghesani@unsw.edu.au

R. Allemang, P. Avitabile (eds.), *Handbook of Experimental Structural Dynamics*,
https://doi.org/10.1007/978-1-4614-4547-0_6

Abstract

This chapter contains a broad discussion of digital signal processing techniques as applied to the solution of mechanical problems, primarily by analyzing the vibration responses of a machine or structure. Such responses are always a combination of a set of excitation functions and structural response or transfer functions, and the aim of the analyst is usually to separate them and learn their characteristics, for purposes such as structural analysis, primarily concerned with changes in the latter, and machine condition monitoring and diagnostics, primarily concerned with changes in the former, but possibly in both. Since a number of other chapters are mainly concerned with structural analysis, the reader is referred to those for some specialized treatments.

The chapter first introduces a number of idealized signal types, including their definitions and basic analysis methods, then gives a guide to the optimum choice of such models to apply in practical situations, such as for modal analysis and condition monitoring.

A very important section deals with the two types of blind separation required for complete analysis; first the separation of the various independent sources acting on the machine or structure, and then the identification of the different transfer functions by which the responses to these different sources are modified at the various measurement points. Topics include separation by filtering, blind extraction, blind deconvolution, and separation of responses to different sources, including those distinguished by different characteristics (e.g. deterministic or random), or by virtue of statistical independence.

There is a comprehensive discussion of analysis in different domains, or domain pairs, such as time, frequency, and joint time-frequency, but also the recognition that with variable speed machines, it is often best to represent "time" as rotation angle, with corresponding "frequency" in terms of harmonic order. A topic that has become much more important in recent years is the recognition that many machine signals are stochastic, but with random carrier signals that are modulated by deterministic modulation functions, usually linked to machine speed, which can be extracted and identified, even though seemingly hidden in normal signal representations. With constant speed machines, such signals are "cyclostationary", but with varying speed are termed "cyclo-non-stationary".

Most of these approaches are demonstrated by applying them to three quite different, but very important examples of machine diagnostics, namely for rolling element bearings, gears and reciprocating machines and engines.

Finally, a topic which is not widely known, cepstrum analysis, is presented in some detail, because of its very powerful properties in both source separation and structural analysis, with examples of application to machine diagnostics and modal analysis.

Keywords

Signal processing of mechanical signals · Vibration-based health monitoring · SHM · Denoising · Change detection · Change detection · Blind extraction · Blind separation · Cepstrum · Cepstral analysis · Cyclostationary signals · Angle-time cyclostationary signals · Cyclo-non-stationary signals

1 Overview

Rotating machine condition monitoring and traditional modal analysis have been among the earliest applications of vibration signal analysis. The traditional analytical modelling of such systems and related excitations originally led researchers and engineers to focus mainly on deterministic signals: periodic in the case of rotating machines and transient in the case of impact-test-based modal analysis (although experimental modal analysis has incorporated stationary random signals for many years). Despite being obviously in contrast with the randomness of all experimental signals, the deterministic framework has been successful for decades in these fields.

However, the further extension of the field of application of signal processing (e.g., operational modal analysis and diagnostics of complex systems) emphasized

the limits of the deterministic framework and the necessity for stochastic (in particular non-stationary stochastic) signal models and analysis techniques.

This chapter starts with a review of periodic and deterministic transient signals and the basic Fourier analysis tools to describe them. Then the most successful stochastic models for different families of signals are introduced, and finally advanced techniques for their analysis are discussed with examples.

2 Deterministic Signals and Traditional Fourier Analysis

Traditional vibration analysis models vibration signals as deterministic, i.e., mathematical functions whose value is determined and exactly predictable in the future. Two main classes of signals belong to the deterministic family:

- Periodic signals, which replicate the same waveform after a fixed period T:

$$x_T(t) = x_T\,(t + nT) \text{ with } n = 1, 2, \ldots \tag{1}$$

- Transient signals, whose energy is finite, i.e., with an event-like behaviour and decaying to zero in a sufficiently long time:

$$\int_{-\infty}^{\infty} |x(t)|^2 dt = a \text{ finite} \tag{2}$$

The first have dominated the field of rotating machine condition monitoring, where most excitations are modelled as periodic and often sinusoidal (e.g., unbalance) and systems are generally approximated as linear time invariant (LTI). The second have been at the basis of the traditional impact-test approach for modal analysis, where an LTI system is excited by an impulsive force.

2.1 Periodic Signals and Fourier Series

In the analysis of periodic vibration signals, the traditional Fourier series represents a strong and relatively simple methodology for the separation of vibration components due to different excitations and the identification of those induced by faults thanks to their a priori known frequencies (e.g., 1 per rev frequency of unbalance).

The Fourier series decomposes a periodic signal $x_T(t)$ (with period T) into a series of sinewaves with frequencies multiples of the fundamental frequency $1/T$, amplitude A_k, and phase (at time zero) ϕ_k.

$$x_T(t) = \sum_{k=0}^{\infty} A_k \cos\left(\frac{2\pi k}{T} t + \phi_k\right) \tag{3}$$

A more versatile form of the Fourier series uses the Euler identity to decompose the cosine functions of the previous equation into rotating complex exponentials:

$$x_T(t) = \sum_{k=-\infty}^{\infty} X_k e^{i\frac{2\pi k}{T}t} \tag{4}$$

where i is the imaginary unit.

In this case both the amplitude and phase information are retained in the complex coefficients X_k, with the condition that X_{-k} and X_k are a complex conjugate pair for real signals. They can be computed as:

$$X_k = \frac{1}{T}\int_0^T x_T(t) e^{-i\frac{2\pi k}{T}t} dt \tag{5}$$

2.2 Transient Signals and the Fourier Transform

Transient deterministic signals, such as dynamic responses of structures to impulsive excitations require an extension of the Fourier series. In this case the frequency decomposition of the signal is continuous rather than discrete:

$$x(t) = \int_{-\infty}^{\infty} X(f) e^{i2\pi f t} df \tag{6}$$

and the function $X(f)$ of $x(t)$ is obtained from:

$$X(f) = \int_{-\infty}^{\infty} x(t) e^{-i2\pi f t} dt \tag{7}$$

The transformations of Eqs. (6) and (7) are called, respectively, inverse Fourier transform and Fourier transform. Note that the spectrum of Eq. (7) has different dimensions from that in Eq. (5).

2.3 Discrete-Time Signals and Digital Implementation

Digital signal processing is performed after an analogue-to-digital conversion (ADC) of finite length signals. The ADC involves a discretization in the time domain, usually with a constant sample rate F_s (in samples per second). Signals become therefore time series, and an analogue vibration $x(t)$ is converted into a discrete-time signal by sampling only at constant time intervals, multiples of $\Delta t = 1/F_s$:

$$x[n] = x(n\Delta t) \tag{8}$$

Quantization (the discretization in the domain of values of the signal) is hereby not treated as it is usually a design issue, which, if properly dealt with, has negligible effect on the result of digital vibration signal analysis.

For periodic signals, the extension of Fourier series to discrete time is straightforward, given the correct selection of sampling rate and acquisition length. In this case a simple discretization of the time variable $t(t_n = n\Delta t)$ in Eq. (7) and the approximation of the integral with a Riemann sum produces:

$$X[k] = \frac{1}{N} \sum_{n=0}^{N-1} x[n] e^{-i2\pi \frac{nk}{N}} \tag{9}$$

The algorithm of Eq. (9) is referred to as the discrete Fourier transform (DFT). For a generic periodic signal $x_T(t)$ with period T, it can be demonstrated that the DFT coincides exactly with the continuous time coefficients X_k provided that the sampling rate F_s is an exact multiple of the fundamental frequency $f_0 = 1/T$ of the signal ($F_s = mf_0$ with m positive integer), with the additional condition of $F_s > 2nf_0$ ($m > 2n$), where n is the number of harmonics of the fundamental frequency present, and the signal is observed for an integer number of periods, i.e., $N\Delta t = pT$ with $p \in \mathbb{Z}^+$.

The inverse discrete Fourier transform (IDFT) allows exact transformation back to the time domain:

$$x[n] = \sum_{k=0}^{N-1} X[k] e^{i2\pi \frac{nk}{N}} \tag{10}$$

For transient signals, the discretization of time in Eq. (7) leads to the discrete-time Fourier transform (DTFT):

$$X(f) = \Delta t \sum_{n=-\infty}^{\infty} x[n] e^{-i2\pi f n \Delta t} \tag{11}$$

The expression of the DTFT is clearly impractical, given the finite length $n = 0, \ldots, N-1$ of all experimental signals. Therefore it is often approximated by a further discretization, in this case of the frequency variable f ($f_k = k\Delta f$). Taking $\Delta f = F_s/N$ reduces the DTFT to a simple DFT, in this case normalized with Δt:

$$X[k] = \Delta t \sum_{n=0}^{N-1} x[n] e^{-i2\pi \frac{nk}{N}} \tag{12}$$

The inversion is again performed with the IDFT, in this case normalized by F_s/N:

$$x[n] = \frac{F_s}{N} \sum_{k=0}^{N-1} X[k] \, e^{i2\pi \frac{nk}{N}} \tag{13}$$

The use of the DFT for both periodic and transient signals has led to a certain degree of freedom of terminology, with DFT and IDFT defined with different normalizations in different references (the product of the normalization coefficients of DFT and IDFT must in any case be $1/N$ to ensure identity when subsequently applying the direct and inverse transformation). In the most common software packages, the DFT is defined simply as:

$$X[k] = \sum_{n=0}^{N-1} x[n] \, e^{-i2\pi \frac{nk}{N}} \tag{14}$$

and normalization must be performed according to the application. Details of this are given below in Sect. 4.

3 Experimental Signals and Stochastic Signal Modelling

Owing to the imperfect nature of measured systems and measuring devices, and also the inherent stochastic nature of certain excitation signals, such as turbulent fluid flow in turbines, experimental signals are always characterized by a certain degree of unpredictability and therefore belong to the random signal family. These signals cannot be expressed by mathematical functions, but can only be described by their statistical properties.

3.1 Time-Varying Distributions: Ensemble Versus Time Quantities

In a generic stochastic model, any measured signal $x(t)$ is seen as a single realization of a (generally) time-varying distribution $\mathcal{D}_x(t)$. In a discrete-time perspective, this means that the *time-sample* $x[n] = x(n\Delta t)$ is one *ensemble sample* extracted from the distribution $\mathcal{D}_x(n\Delta t)$ while the next time-sample $x[n+1] = x((n+1)\Delta t)$ is a stochastic realization of a different distribution $\mathcal{D}_x((n+1)\Delta t)$. The probability that the two consecutive time-samples jointly take given values is similarly reflected by a joint distribution. The difference between time and ensemble domains is crucial in understanding the stochastic signal processing approach and at the basis of the sub-classification of random signals. In Fig. 1 this interpretation of stochastic signals is graphically explained with an example. Green lines show numerically defined distributions (in PDF terms), while the red circles (x_1) and blue crosses (x_2) represent two discrete-time signals obtained from the same time-varying

distributions. The two simultaneous samples $x_1(t_0)$ and $x_2(t_0)$ of the signals are two ensemble samples from the same ensemble-distribution $\mathcal{D}_x(t_0)$.

Information regarding structure or machine properties is often hidden within the two first statistical moments of the signal's time-varying distribution, the expected value $\mu_x(t)$ and the covariance function $C_x(t, \tau)$:

$$\mu_x(t) = \mathbb{E}\{x(t)\} \tag{15}$$

$$C_x(t, \tau) = \mathbb{E}\{[x(t) - \mu_x(t)] \cdot [x(t + \tau) - \mu_x(t + \tau)]\} \tag{16}$$

where the symbol $\mathbb{E}$ denotes the ensemble average in the population "produced" by distribution $\mathcal{D}_x$ in Eq. (15) and its joint version in Eq. (16).

In most practical applications, only one sample is available for each signal at each time instant (so in the case of Fig. 1, the measurement will either observe x_1 or x_2); thus the task of inferring properties of the two moments is in general arduous and must exploit assumptions on the time evolution of the distributions.

Some sub-classes of the random family have been identified as recurrent in structural and machine dynamics:

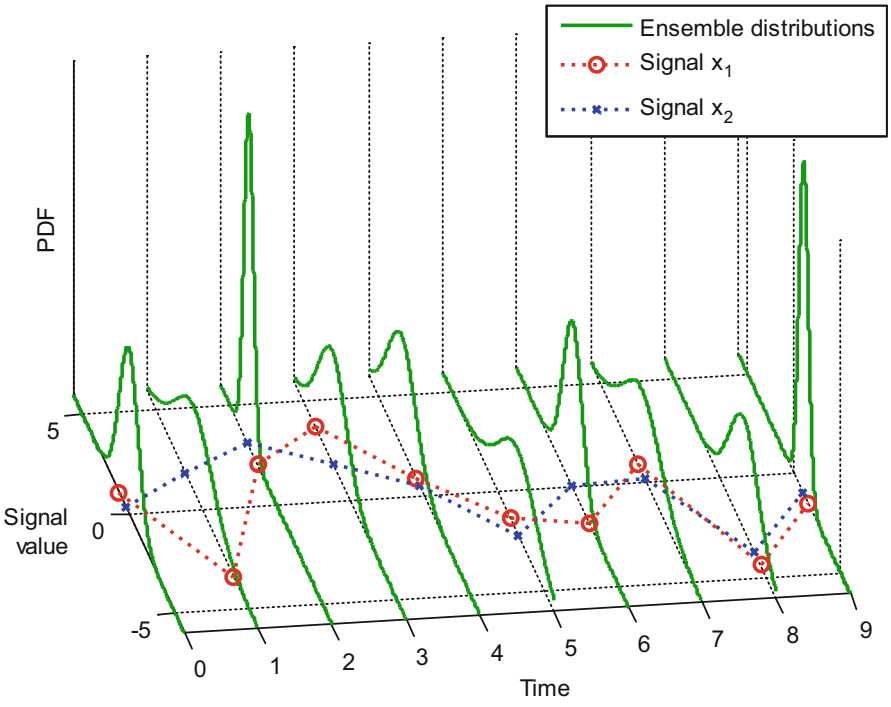

Fig. 1 Numerical example of a discrete-time signal obtained from a time-varying distribution

- *Stationary signals*, characterized by a time-constant distribution. In this case the ensemble moments can be estimated directly by the time moments, since every time sample is generated by the same distribution. Condition of convergence of the time moments to quantities that are identical for all measurements is a technical concept known as ergodicity.
- *Cyclostationary signals*, characterized by a periodic evolution of the statistical moments. In this case the ensemble moments can be estimated using periodic time subsets of the signal, exploiting the periodic recurrence of samples extracted from the same distribution. Condition of convergence of the time moments to quantities that are identical for all measurements is a technical concept known as cycloergodicity.
- *Transient random signals*, characterized by a finite energy and concentrated within a limited time window, usually triggered by a controllable event. In this case the ensemble moments can be obtained only by replicating experiments to obtain multiple realizations of the same time-evolving distribution.
- *Cyclo-non-stationary signals*, where many excitation forces are linked to machine speed. At constant speed they would be cyclostationary, but with varying speed the instantaneous frequency varies directly with the speed, and in general the instantaneous amplitude also varies with the speed.

The use of these sub-classes to model experimental signals in practice is variable and not consistent, even within the same engineering applications. This is mainly due to the fact that real signals often show hybrid and imperfect characteristics, and also often evidence a mixture of types rather than an affiliation to a single class, which allows assignment of their components to certain families only with a certain level of approximation. For this reason, the following sections will refer to these families as *models*, which are "unrigorously" applied to experimental signals to allow their description in a "rigorous" analytical framework. Therefore, the role of the engineer should often focus on the choice of the most suitable model for the signal, resulting in a series of available analytical tools whose mathematics has already been developed and validated by signal processing experts and statisticians. In order to understand the importance of this step, it is important to highlight the fact that the same analytical techniques are often applied in different signal models and that a proper implementation and interpretation of their outcomes is only ensured if considered in the selected modelling framework. In the rest of this section, some popular and effective signal models are introduced, while the following section will discuss typical engineering problems and their relationship with these models.

3.2 Stationary Signal Model

Stationary signals are characterized by time-constant stochastic properties, i.e., every sample of the signal $x(t)$ is generated from the same statistical distribution $\mathcal{D}_x$, which does not vary in time ($\mathcal{D}_x\,(t_1) = \mathcal{D}_x\,(t_2) = \mathcal{D}_x$). Therefore, the mean μ_x and the covariance function R_{xx} have the following properties:

$$\mu_x(t_1) = \mu_x(t_2) = \mu_x \text{ for each } t_1, t_2 \tag{17}$$

$$C_x(t_1, \tau) = C_x(t_2, \tau) = C_x(\tau) \text{ for each } t_1, t_2, \tau \tag{18}$$

Despite more stringent requirement for strict stationarity (full time-independent distribution), often the conditions on the first two moments of Eqs. (17) and (18) are considered sufficient for a de facto stationarity, labelled as "wide-sense stationarity" (WSS). A typical example of stationary signal modelling is encountered in OMA under the assumption of random excitation (e.g., wind, vehicle and pedestrian traffic, earthquake). This modelling is of course only valid if the time scale of the observation is chosen so that the excitation can be modelled as stationary. Measurement noise is also typically modelled as stationary. A stationary signal model is often a matter of convenience to simplify the analysis.

3.3 Cyclostationary Signal Model

Cyclostationary signals are non-stationary random signals characterized by periodic statistical properties. As for the strict definition of stationarity, strict cyclostationarity requires a periodicity of the full distribution generating the signal, but a "wide-sense cyclostationarity" (WSCS) only requires the first two moments to be periodic. For the sake of simplicity, WSCS signals are generally called "cyclostationary" (CS), implicitly recognizing the actual unfeasibility of testing for "strict cyclostationarity." Within CS signals a strong distinction is made between signals which show periodicity in their mean (first-order cyclostationary or CS1) and signals which have a periodic autocorrelation function (second-order cyclostationary or CS2). T-periodic CS1 signals have a periodic mean:

$$\mu_x(t) = \mu_x(t + T) \, \forall t \in \mathbb{R} \tag{19}$$

T-periodic CS2 signals have a periodic autocorrelation function:

$$C_x(t, \tau) = C_x(t + T, \tau) \forall t, \tau \in \mathbb{R} \tag{20}$$

This cyclic recurrence of statistical properties allows the extension of some characteristics of stationary signals to this class. In particular, if a cyclostationary signal is characterized by the cyclic period T, the subset of samples $\{x(t + kT), k \in \mathbb{Z}\}$ is a stationary process (for a fixed value of t):

$$\mu_x(t) = \mu_x(t + kT) \;\; k \in \mathbb{Z}, \forall t, \tau \in \mathbb{R} \tag{21}$$

$$C_x(t,\tau) = C_x(t+T,\tau)\ \ k \in \mathbb{Z},\ \forall t,\tau \in \mathbb{R} \tag{22}$$

CS1 and CS2 signals can be seen as a composition of a stationary random component $r(t)$ and a deterministic periodic signal $p_T(t)$. In particular, a pure CS1 signal x_{CS1} and a pure CS2 signal x_{CS2} can be modelled as:

$$x_{CS1}(t) = r(t) + p_T(t) \tag{23}$$

$$x_{CS2}(t) = r(t) \cdot p_T(t) \tag{24}$$

An example of this signal composition is given in Fig. 2.

Most signals from machines running at constant speed show cyclostationary behaviour and are generally composed of a mix of CS1 and CS2 components. Typical CS1 components are detectable in system responses to periodic excitations (e.g., unbalance in turbomachinery, dominant components in gearmesh-induced vibrations), while CS2 components arise in case of modulation/convolution of random phenomena by cyclic phenomena (e.g., bearing fault-induced vibrations, systems excited by pulsating random forces such as engine combustion). The

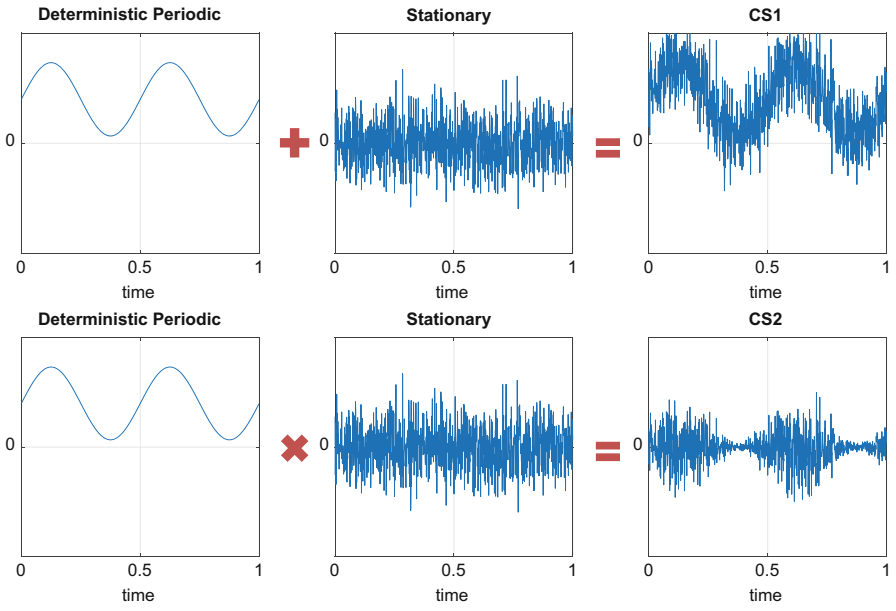

Fig. 2 Numerically generated examples of deterministic periodic, stationary random, CS1 and CS2 signals. CS1 is obtained by summation of stationary random and deterministic periodic CS2 by multiplication (amplitude modulation) of stationary random and deterministic periodic (positive only)

extraction/estimation of the periodic statistical properties is the main objective of cyclostationary analysis, both for CS1 and CS2 signals.

3.3.1 CS1 Model

In case of first-order cyclostationary signals (CS1), the identification of the periodic part consists of a separation of the two terms of the summation in Eq. (23) and a removal of the "noisy" part $r(t)$, which does not carry information on the fault. This is obtained by a series of methodologies which will be discussed in detail in Sect. 6.6.

3.3.2 CS2 Model

In the case of second-order cyclostationarity (CS2), the multiplication of Eq. (24) makes the random part $r(t)$ a relevant component of the fault symptom: i.e., in contrast to the CS1 case, the random part is the carrier of the information, and its properties are often of physical relevance to identify the source of the fault. To better understand the properties of CS2 signals, a further numerical example is produced in Fig. 3. Each of the four CS2 signals carries characteristics from both the stationary and periodic "parent signals." In particular the short-time behaviour is inherited from the "random parent": CS2 signals in rows (a) and (b) preserve the high correlation C_x over time lags τ longer than the examples of rows (c) and (d); i.e., the random short-term variability of the CS2 signals is "smoother" in (a, b) than in (c, d). On the other hand, the macroscopic behaviour of the signals is determined by the characteristic period of the "periodic parent": CS2 signals in rows (a) and (c) show a cyclic power modulation slower than those of rows (b) and (d).

In an intuitive acoustical example of CS2 sound, the short-term variability of the stationary random carrier $r(t)$ is reflected in the "pitch" of the sound, while the modulation introduced by $p_T(t)$ gives the rhythm with which the noise is reproducing.

3.4 Cyclo-non-stationarity

Here only a very brief introduction to cyclo-non-stationarity is given, but reference is made to a number of papers giving further detail. In particular, the description here is based largely on that in Ref. [1], which was one of the first to develop these ideas. As mentioned earlier, cyclo-non-stationary (CNS) signals are similar to cyclostationary (CS) signals except that the statistics, rather than being periodic, vary deterministically in a known way. The most common situation giving rise to this is where the machine speed, which gives periodic statistics when it is constant, varies as a known function of time, and this is the example used here, in Fig. 4 (from [1]), to demonstrate the general case.

Fig. 4a shows a typical CNS signal arising from an impulse occurring every revolution of a shaft, at the same rotation angle, and exciting an impulse response that is independent of the shaft speed (i.e., of the spacing between the impulses).

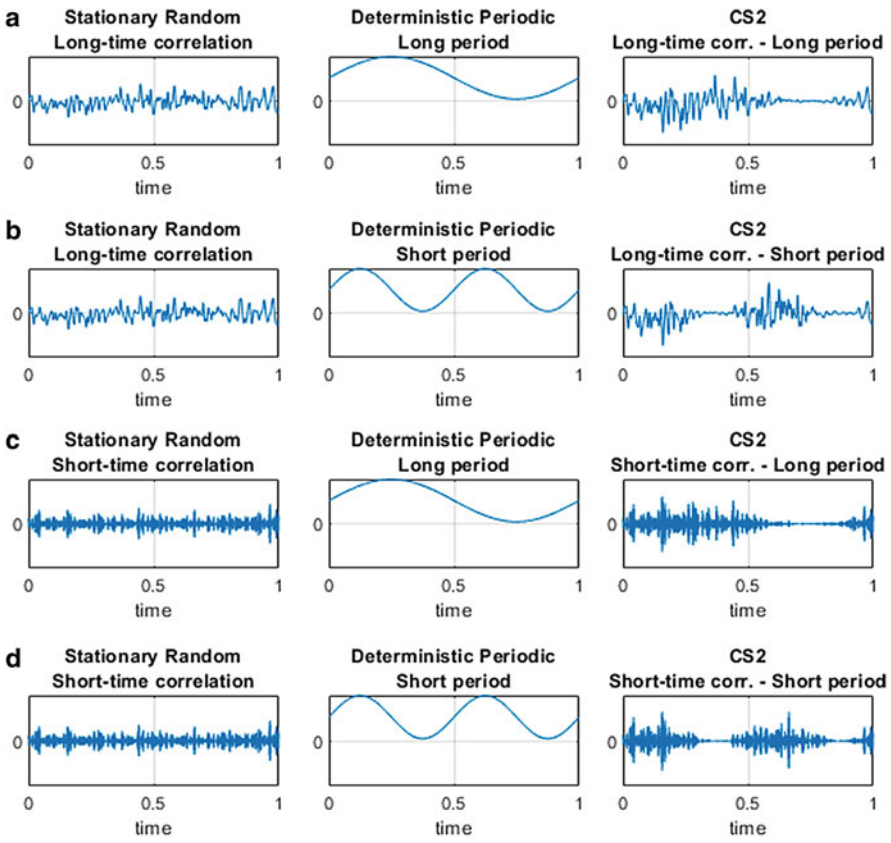

Fig. 3 Examples of different CS2 signals obtained from long-time (**a**, **b**) and short-time (**c**, **d**) correlation stationary noise and long (**a, c**) and short (**b**, **d**) period deterministic modulations

The rotation angle of the shaft is $\theta(t)$, and its variation with time must be known. Such a signal can be described by a Fourier series expansion:

$$x(t) = \sum_k c_k(t) e^{ik\theta(t)} \tag{25}$$

where the Fourier series coefficients (related to the impulse responses in this case) are time dependent and the complex exponentials (related to the impulses) are functions of angle.

It is shown in [1] that if the correlation length of the time-varying components is short with respect to the cycle duration, such signals are characterized as angle-time cyclostationary (AT-CS). If they are analyzed by standard CS methods, as shown in Fig. 4b where both time lag τ and cycle period are in time units, the time domain autocovariance function gives local autocorrelations non-uniformly spaced in time,

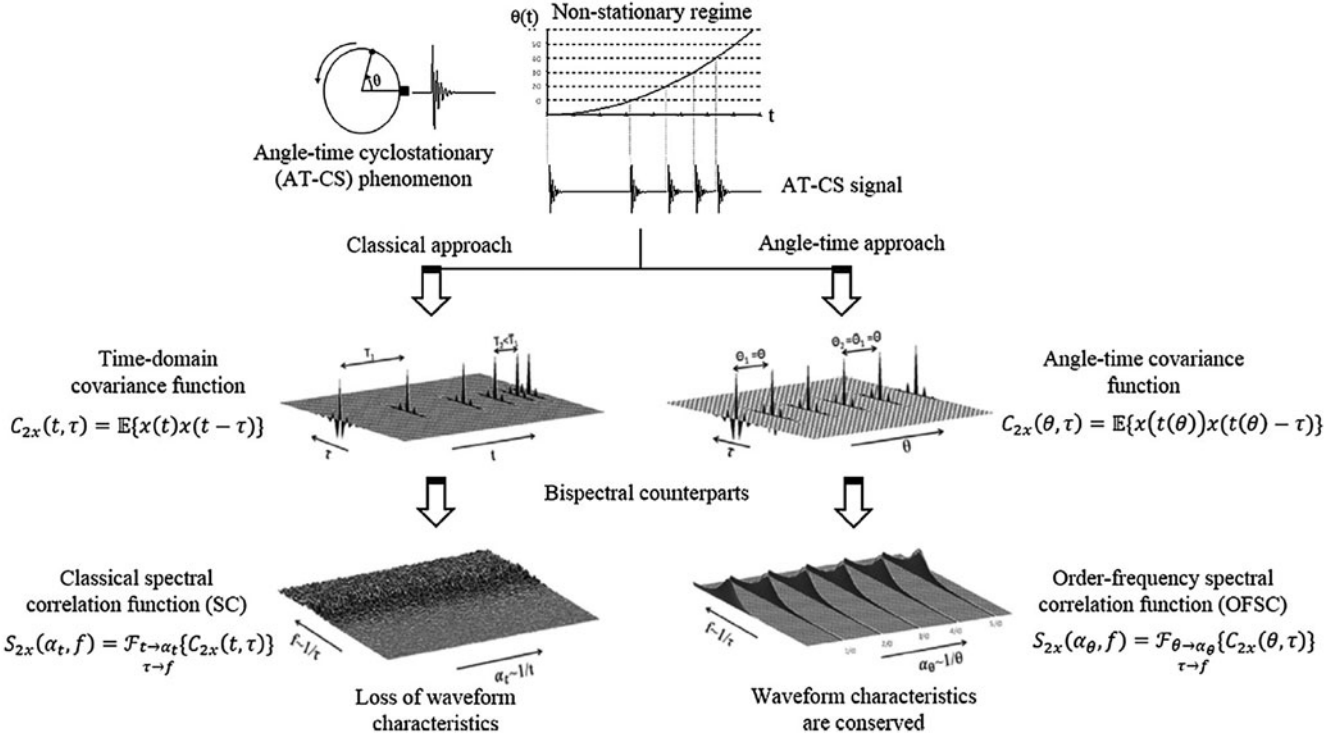

Fig. 4 Example of cyclo-non-stationarity and spectral correlation diagrams (from [1])

whereas if the cyclic period is in terms of angle (Fig. 4c), the angle-time covariance function in Eq. (26), defined as a function of position in angle, and time lag in time, gives uniformly spaced autocorrelations.

$$C_{2x}(\theta, t) = \mathbb{E}\{x(t(\theta))\, x(t(\theta) - \tau)\} \tag{26}$$

The resulting spectral correlation diagrams obtained by performing Fourier transforms in the lag and cyclic directions, respectively, give the results shown in Fig. 4d, e. The non-uniform spacing of the autocorrelation functions in Fig. 4b smears the classic spectral correlation (SC) in Fig. 4d whereas the periodic spacing in Fig. 4c means that the corresponding order-frequency spectral correlation (OFSC) in Fig. 4e has the frequency responses corresponding to the impulse responses located at the various orders of the basic cyclic periodicity. Thus, a complete separation has been made between the time-frequency nature of the impulse responses and the angle/order nature of the repetition rate defined by the machine speed.

Ref. [1] make reference to a number of applications of this CNS theory, while Ref. [2] give further insights and applications.

3.5 Transient Signal Model

Transient random signals are stochastic signals whose energy is mostly concentrated in a finite time window. Since the instantaneous power of a signal is defined as $\mathbb{E}\left\{x(t)^2\right\} = |\mu_x(t)|^2 + R_{xx}(t, 0)$, a signal cannot be both stationary and transient. Pure transient signals have a finite energy, resulting in the properties:

$$\int_{-\infty}^{+\infty} \mu_x(t)\, dt = a \text{ with } a \in \mathbb{R} \tag{27}$$

$$\int_{-\infty}^{+\infty} C_x(t, \tau)\, dt = p(\tau) \text{ with } p(\tau) \in \mathbb{R}, \quad \forall \tau \tag{28}$$

As for stationary signals, pure transients are rarely encountered in practice, where even a small background noise would by itself compromise the condition of finite energy. However, cases such as responses of damped structures to a single impulsive excitation (e.g., impact tests) can be generally modelled as transients, with $\mu_x(t)$ dominated by the impulse response of the structure. This modelling choice is often coupled with the application of a time-windowing function, forcing a long-term decay of the residual vibration signal.

4 Scaling and Dimensions for Various Versions of the Fourier Transform

It is not sufficiently widely realized that the different forms of the Fourier transform in general give frequency spectra with different dimensions and units, and this can give problems when attempting to represent the spectra of signals containing mixtures of different signal types.

Unless otherwise specified, in this chapter the word "spectrum" will be used to represent the result of an FFT analysis scaled in engineering units EU (i.e., scaled as for Fourier series and valid for discrete frequency components). In section 4 only, for consistency with other chapters, asterisk * is used to represent multiplication, but elsewhere it is used to represent convolution. If a signal also contains stationary random or transient components, these will not be scaled correctly in this "spectrum". A "power spectrum" will be the squared amplitude of a "spectrum", scaled in EU*EU, and will also only be valid for discrete frequency components. A "power spectral density" spectrum will have units of (EU * EU/Hz) and is only valid for the spectra of stationary random signals. If obtained from a "power spectrum", it must be divided by the effective bandwidth of each line in the FFT spectrum, which is the line spacing multiplied by a factor accounting for the noise bandwidth of any window used (e.g., it is 1.5 for a Hanning window). Scaling of log spectra in dB re r EU will be the same for spectra and power spectra, since it equals $10\log_{10}(\{|X|/r\}^2) = 20\log_{10}(|X|/r)$, where X is the spectrum value in EU and r is the dB reference value. For further details and the scaling of other signal types, such as transients, see the following sections.

4.1 Periodic and Quasi-periodic Signals

This category of signals is made up entirely of discrete frequency sinusoidal components. Periodic signals contain only components with frequencies that are integer multiples (harmonics) of a fundamental frequency, because after one period of the fundamental frequency, all harmonics have run through an integer number of cycles and their sum starts again with the same conditions, making them periodic with this period. Quasi-periodic signals have at least two frequencies without a lowest common multiple, so that no fundamental frequency can be found. In theory this means that the ratio of two frequencies must be an irrational number, but in practice quasi-periodic signals occur when there is a mixture of two or more periodic components from independent sources, such as the various rotors of an aero engine, connected only aerodynamically.

Both signal types can be analyzed using the Fourier series equations (3, 4, 5) with the proviso that for quasi-periodic signals, the limit should be taken in Eq. (5) as $T \to \infty$.

Since the integral is normalized by dividing by T (Eq. (5), this is the only form of the Fourier transform giving spectra with the same units and dimensions as the

original signal. The individual sinusoids have instantaneous "power" equal to the square of the instantaneous value, as does the sum of all components, and the mean power is the mean square value averaged over a period of the fundamental frequency or infinity. The signal strength is usually expressed in terms of its RMS (root mean square) value, the square root of the mean square value (power), as this has the same units as the original signal, and is independent of the phase relationships of the components.

The word "power" is used to describe the square of a measured parameter with units EU and is thus EU*EU. It can usually be related to physical power via some kind of dimensioned scaling constant. For example, for a resistive electrical circuit, with voltage V, current I, and resistance R, power $W = IV = I^2R = V^2/R$ since $V = IR$. Similarly, "energy" is used to describe the time integral of "power."

Parseval's theorem states that the total power (or energy, depending on the signal type) of a signal is the same whether integrated over all time or all frequency. For the Fourier series spectrum, the mean square value of the time signal is equal to the sum of squares of the amplitude of all spectrum components. For the two-sided spectrum of Eqs. (4, 5), the power is equally divided between positive and negative frequency components for each frequency, and $|X_k| = A_k/2$ so $|X_k|^2 + |X_{-k}|^2 = {A_k}^2/2$, the same as obtained for a single sinusoid in the time domain, since ${A_k}^2\cos^2(\omega t) = {A_k}^2\left({}^1\!/_2 + {}^1\!/_2\cos(2\omega t)\right)$, whose mean value is ${A_k}^2/2$.

The spectrum of squared amplitude values $|X_k|^2$ is called the power spectrum, and each discrete frequency component will have units EU · EU. If the DFT of Eq. (14) is used (e.g., the FFT in Matlab®), the result must be divided by N to give correct scaling, and the inverse transform (divided by N in Matlab®) must be multiplied by N.

4.2 Stationary Random Signals, Power Spectral Density (PSD)

For stationary random signals, the instantaneous power is still the squared value of the time signal, but now the spectrum is continuous. Parseval's theorem now states that the total power in the time domain (the mean square value) must be equal to the integral over all frequency of the squared amplitude of the spectrum, which thus must be a spectral density with units EU*EU/Hz. It is called the "power spectral density" or PSD. There is no direct form of the Fourier transform for stationary random signals, but if there were, the normalization of the integral would have to be by division by $\sqrt{T}$ (since the integral tends to a limit proportional to $\sqrt{T}$), giving a direct spectrum with units EU*$\sqrt{\text{s}}$, for which the amplitude squared spectrum would have units EU*EU*s or EU*EU/Hz. In fact the spectrum of a stationary random signal is usually obtained by Fourier transformation (Eq. 7) of the autocorrelation function with units EU*EU, once again giving a spectrum with units EU*EU*s or EU*EU/Hz. The autocorrelation function of a stationary random signal is a transient with finite length.

The power spectral density of stationary random signals can be estimated by averaging the squared amplitude spectra of records of length N obtained by FFT. If the FFT corresponds to Eq. (14), the power in each spectral line will be obtained by division by N^2, and if the weighting of each record is rectangular (i.e., no weighting), the PSD at each line (assumed constant over the interval) can be estimated by dividing by the bandwidth per line, F_s/N, altogether a division of the original squared values by NF_s. If other than a rectangular window is used, this estimate must also be divided by the relative bandwidth of the window (e.g., 1.5 for a Hanning window). This will give a PSD spectrum with the correct units of EU*EU/Hz.

Alternative ways of calculating PSD spectra are given in ▸ Chap. 5, "Introduction to Spectral and Correlation Analysis: Basic Measurements and Methods."

4.3 Deterministic Transient Signals, Energy Spectral Density (ESD)

Transient signals with units EU have a finite amount of energy, equal to the integral of their instantaneous power over all time, and having the units EU*EU*s. The application of the Fourier transform (Eq. (7)) to them gives a spectrum with the units EU*s, whose amplitude squared spectrum thus has the units EU*EU*s*s or EU*EU*s/Hz. This is known as "energy spectral density" or ESD.

In this case, Parseval's theorem states that the total integral over all time or all frequency of the squared amplitude is the same, and is equal to the total energy, with units EU*EU*s.

If the FFT is used as above, the power per line is estimated by dividing the squared amplitude values by N^2, once again converted to a spectral density by dividing by the line spacing (equivalent to multiplication by record length $T = N/F_s$) and then converted to energy (per record length) by multiplication again by $T = N/F_s$. Overall, this corresponds simply to division by ${F_s}^2$ and gives a result with units EU*EU*s/Hz.

Note that rectangular windowing is normally assumed here, as even though windows are sometimes used, they genuinely affect the energy and ESD in a non-predictable way, and cannot be easily compensated for.

5 Choosing the Right Model for an Experimental Signal

In order to assist the reader in the complex task of choosing the best model for a specific vibration analysis problem, it is useful to start from the identification of the information to be retrieved from the signal. The information available in a vibration signal usually relates to two key dynamical aspects: excitations and system response.

The extraction of selective information on the two aspects (always present in combination) is the aim of the main typologies of application in the field of vibration signal processing: modal analysis and condition monitoring. Modal analysis aims at identifying the characteristics of the system response (e.g., natural frequencies,

damping), thus "removing" the excitation-induced characteristics from the signal. Condition monitoring can focus either on the identification of variations of the system response indicative of specific damages in the structure, or on the detection of particular excitations arising from faults or malfunctions.

5.1 Modal Analysis

Analysis methods for conventional modal analysis, involving frequency response functions (FRFs), impulse response functions, etc., are well covered in specialist chapters dealing with these topics, for example, ▸ Chap. 6, "Frequency Response Function Estimation" and ▸ Chap. 11, "Experimental Modal Analysis Methods," with additional insights on signal processing given in ▸ Chap. 5, "Introduction to Spectral and Correlation Analysis: Basic Measurements and Methods."

Here we refer only to material not treated elsewhere, in particular cepstral methods of (operational) modal analysis, discussed briefly in Sect. 10.4. A historical survey of cepstral methods has recently been published [3].

5.2 Condition Monitoring for Rotating/Reciprocating Machines

Condition monitoring signals are often composed of a rich series of diverse components, each most suitably described by a different signal model. The complexity of machine signals is often the result of the presence of multiple rotating/reciprocating elements, each characterized by a different kinematic and dynamic behaviour. Typical signals are, for instance, composed of vibration components carrying information on multiple shafts, bearings, gears, combustion chambers, and fluid guide vanes/blades. In the case of rotating and reciprocating machines, faults or malfunctions in each part are usually associated with a specific set of frequencies related to the kinematics of the component itself. The cyclic nature of such kinematics and the resulting vibration components makes cyclostationary models the most suitable for this family of applications. The choice between CS1 and CS2 models is usually made considering the degree of randomness of the fault-related phenomenon and in particular whether the periodic component is additive or modulates random components. It is discussed in the following subsections for the most typical cases.

5.2.1 Typical Rotor Problems

Typical rotor problems, such as unbalance, misalignment, and gearmeshing, have excitations theoretically phase-locked to the rotation of the corresponding shaft. Slight non-linearities in the response (e.g., fluid film bearings) do not compromise the "periodicity" of the phenomenon, and simply result in the generation of higher harmonics in the vibration signal. Therefore, if the speed is constant, the only source of randomness is represented by measurement noise and other additive uncertainties (e.g., external sources of vibration). In this case, the expected value of the vibration

signal is highly periodic and characterized by a priori known frequencies related to the shaft speed, making CS1 the most suitable model. The most common CS1 tools used for the analysis of these signals are Fourier series and synchronous averaging. Both methods are meant to highlight the periodic content to the detriment of the random part.

The behaviour of flexible rotors suspended in fluid dynamic bearings and running at speeds above their first critical is quite complex and has been the subject of much specialized research over the years. It is not covered in much detail here, but the reader is referred to specialist publications on rotor dynamics.

5.2.2 Gear Faults

Gear faults have been studied over many years, and many diagnostic methods developed, but primarily for machines with almost constant speed. The vibration signals from meshing gears at almost constant speed are mainly deterministic, at least in the rotation angle domain, and with constant load, since particular pairs of teeth (even with faults on either or both) always mesh in the same way, and their response signals should be periodic with some period. On the other hand, for gear systems with several stages, and with so-called "hunting tooth" design (where the numbers of teeth on a meshing pair have no common factors), the period may be very long and the signal pseudo-random with that period. When the time scales of the analysis records are shorter than the pseudo-random period, the signals appear random, and can then be modelled as a mixture of CS1 and CS2, though usually with the CS1 dominant.

In any case the signal associated with a particular gear can usually be treated as CS1 and the dominant periodic part extracted using time synchronous averaging (TSA). If the TSA is done using the speed of a particular shaft for synchronization, the average will represent the gear(s) on this shaft, and the spectrum of the TSA signal will contain only harmonics of this shaft speed. If there is more than one gear mounted on the shaft, the harmonics coming from each will be present, but often these are widely spaced in frequency (very different numbers of teeth) and can largely be separated in the frequency domain. Another alternative for TSA is to make the average for a particular gearmesh, by making the average over records encompassing a number of toothmesh periods corresponding to the lowest common multiple of the numbers of teeth on each gear. The spectrum should then only contain the harmonics of the two gear speeds in that mesh, including the gearmesh frequency (and its harmonics) which is a common harmonic of both gear speeds.

TSA is primarily used for extracting information from the time signals, but as discussed in Sect. 9.2 further analysis can be performed such as removal of the regular toothmeshing patterns, so as to reveal local faults, and demodulation of the toothmesh frequency to detect sudden changes in both amplitude and phase of the meshing pattern.

The other main analysis technique for gears is frequency analysis, often supplemented by cepstrum analysis as discussed in Sect. 9.2. Gear faults can be roughly divided between uniformly distributed faults such as uniform wear and localized faults such as tooth root cracks and spalls on individual teeth or groups of teeth.

The first show up primarily as changes in the harmonics of the toothmesh frequency (often starting with the second harmonic, because wear tends to concentrate on either side of the pitch point where there is no sliding between teeth). Localized and non-uniformly distributed faults tend to show up in modulation sidebands around the toothmesh harmonics, with a spacing equal to the speed of the gear on which the fault is located. Because these sideband patterns can be complex, and mixed for the two gears, cepstrum analysis is a useful tool to separate and quantify them, as shown in Sect. 10.3.

With varying speed, new considerations arise in that the forcing functions vary directly with speed, whereas resonant responses are fixed in frequency. Order tracking (Sect. 8.1) compensates for frequency variation, but not, for example, for the amplitude variations caused by passage of gearmesh frequencies through resonances. A potential solution of this problem using cepstral methods is given in Sect. 10.3.

5.2.3 Bearing Faults

Bearing diagnostics is a widely explored yet challenging signal processing application. Most typical bearing faults are localized spalls on the bearing races caused by the surfacing of contact-fatigue sub-surface cracks [4]. Once in operation at constant speed, the rolling elements will subsequently impact on the race spall with approximate time regularity, made imperfect by the stochastic slip between rollers and races. Each roller-spall impact will trigger vibrations in the system at the natural frequencies of the structure (the case of a spalled rolling element results in an analogous signal, with a different cyclic periodicity). These vibration bursts are reproduced with regularity in the signal, as subsequent rollers impact with the spall, and their cyclic repetition is characterized by a known almost-period $1/BCF$, where the so-called bearing characteristic frequency (BCF) depends only on the shaft rotational speed, the geometry of the bearing, and the location of the spall (inner, outer race or roller). This signal model is expressed by the following equation:

$$s(t) = \sum\nolimits_i A_i h\left(t - i\frac{1}{BCF} - \tau_i\right) + n(t) \tag{29}$$

where $h(t)$ is the impulse response of the system characterized by a set of natural frequencies, τ_i is a small random delay/anticipation of the i-th impact due to slip between rollers and races, A_i is the amplitude of the i-th impact (usually random and in general variable with the rotation of the shaft), and $n(t)$ is background noise (Table 1).

A simple numerical simulation of this model is reproduced in Fig. 5, assuming a single degree of freedom $h(t)$, i.e., a single natural frequency f_n, and a constant A_i. In practice, the presence of multiple frequencies, the highly random behaviour of A_i, and the time variation of $h(t)$ with the rotation of the shaft increase the random behaviour of the signal, already ensured by the non-null random "jitter" τ_i. The second-order cyclostationary model is obviously the natural candidate to describe

Table 1 Bearing characteristic frequencies. f = shaft rotational freqeuncy, NR = number of rollers, PD = pitch diameter, RD = roller diameter, α = contact angle

Location of the fault	Bearing characteristic frequency	BCF expression
Inner race	Ball pass frequency inner race	$BPFI = NR\frac{f}{2}\left(1 + \frac{RD}{PD}\cos\alpha\right)$
Outer race	Ball pass frequency outer race	$BPFO = NR\frac{f}{2}\left(1 - \frac{RD}{PD}\cos\alpha\right)$
Roller	Ball spin frequency	$BSF = \frac{PD}{2RD}f\left(1 - \left(\frac{RD}{PD}\cos\alpha\right)^2\right)$
Cage	Fundamental train frequency	$FTF = \frac{f}{2}\left(1 - \frac{RD}{PD}\cos\alpha\right)$

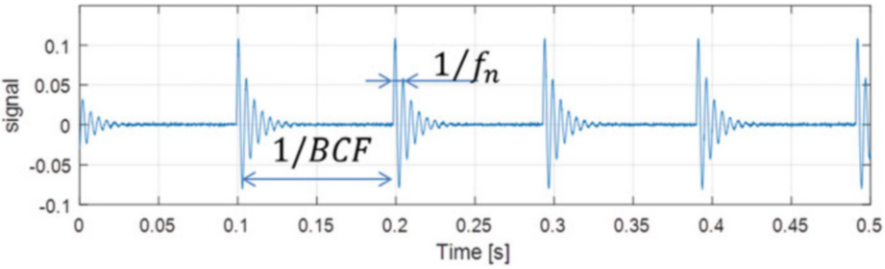

Fig. 5 Simplified numerical example of a faulty bearing vibration signal

this combination of random and cyclic nature of bearing signals, showing a power (i.e., second-order statistics) which cyclically varies in time.

Note that the random "jitter" model is not strictly correct, although it is a good approximation in most cases. In Refs. [5, 6] it is shown that the true random variable is not a jitter in the length of each period, but the actual period itself, meaning that the bearing signal is not truly cyclostationary, but has been termed "pseudo-cyclostationary." As shown in the same references, the differences for practical purposes are very small. In addition, the actual average period can deviate (usually by a few percentage points) from the theoretical values [7]. Finally, as for all rotating machines at variable speed (see Sect. 3.4), the most correct model if speed fluctuations are of non-negligible magnitude is a cyclo-non-stationary one [8].

5.2.4 Internal Combustion Engines

The signals from internal combustion (IC) engines, and in fact most reciprocating machines, are a series of impulsive events, for example, combustion, piston slap, bearing knock, and valves opening and closing, and a natural way to analyze them is by some form of time-frequency analysis. This is analogous to the way in which an experienced mechanic detects faults by ear, by hearing changes in both the cyclic patterns of the events, and in the frequency content of the events. Combustion events are cyclic but not exactly periodic, so the signals are a mixture of CS1 and CS2 cyclostationary components, with neither necessarily dominant.

Mechanical faults, such as piston slap and bearing knock, caused by increasing clearance between piston and cylinder, and in the bearings of the connecting rod, respectively, give impulsive impacts rather like rolling element bearing faults, with

some random variation in the spacing, and are therefore dominantly CS2. They can be analyzed in the same way as bearing faults, by envelope analysis.

Combustion faults such as misfires are a particular case where non-uniformity between the cylinders gives rise to fluctuating torques, and corresponding variations in the torsional vibration of the crankshaft. Very simple analysis of this torsional vibration is a powerful technique for detecting, diagnosing, and quantifying such faults. Rotational accelerations of the engine block are also sensitive to the combustion faults and can be used as an alternative, though not quite so simple, method.

Examples of a number of diagnostic methods for typical cases are given in Sect. 9.3.

6 Signal Extraction and Separation

6.1 General Introduction

One of the principal aims of signal processing is to extract information from non-ideal measurements. This is typically the case with vibration and acoustic signals which are composed of the responses to multiple sources of excitation together with possible instrumentation and environmental interferences. In many situations, the user will be interested in extracting or assessing a restricted fraction of the total information contained in the measurement – this formally defines the "signal" on the one hand and the "noise" on the other hand. The objective of signal extraction/separation is purposely to recover the signal part from the noise part. This general statement actually goes beyond classical filtering or denoising and embodies a collection of techniques which have been developed in various domains of applications. In health monitoring, signal extraction/separation is typically used to extricate symptomatic sources that can be further analyzed or controlled for diagnostic purposes. In structural dynamics, these techniques have also been successfully used to identify the different modal contributions of a system.

Formally, the issue may be described by the general equation:

$$y(t) = x_1(t) + \cdots + x_n(t) + n(t) \tag{30}$$

where $y(t)$ stands for the current measurement, $x_1(t), \ldots, x_n(t)$ for the components which constitute the informative part – or the "signal" – and $n(t)$ for the disturbance, or the "noise." It is generally accepted that "signal extraction" aims at isolating one of the components of interest, while "signal separation" aims at recovering simultaneously all the components in the decomposition of Eq. (30).

6.2 Signal Extraction

Signal extraction may be described as isolating one single component, say $x(t)$, from measurement $y(t)$:

$$y(t) = x(t) + n(t) \tag{31}$$

Note that, without loss of generality, other components which are not of interest have been relegated to the noise part. In signal extraction, component $x(t)$ is also referred to as the "signal of interest." In many instances and especially when dealing with vibration and acoustics, the objective is far from easy since the signal of interest may be completely masked by the noise. This is typically the case with incipient faults (such as in bearings) which are often characterized by a small signal-to-noise ratio.

Different strategies for signal extraction are envisioned depending on the available information and statistical properties of the components in Eq. (31).

6.3 Reference-Based Filtering

The ideal situation is when the component of interest is indirectly sensed by an extra measurement which returns a possibly filtered but noise-free image of it. This is described by the following set of equations:

$$\begin{cases} y(t) = x(t) + n(t) \\ r(t) = h(t) * x(t) \end{cases} \tag{32}$$

where $h(t)$ stands for a (unknown) linear filter, * for the convolution operation, and $r(t)$ for the "reference" on the source of interest. This scenario is typically encountered when there are several transmission paths for the source of interest, one of which can be singled out. Two classical solutions are provided by the Wiener and the Kalman filters. The Wiener filter assumes an unknown time-invariant filter $h(t)$ and returns an estimate of $x(t)$ by filtering $y(t)$ with the linear filter whose frequency gain is the ratio of the cross-spectrum $S_{xr}(f)$ to the autospectrum $S_r(f)$:

$$G(f) = \frac{S_{xr}(f)}{S_r(f)} \tag{33}$$

This is in all points similar to the H1 estimation of the frequency response functions as commonly practised in modal analysis. It is widely used for transfer path analysis (TPA) and dereverberation in acoustics. The Kalman filter is a model-based approach that accepts a time-varying filter but requires it to have a known state-space description (at least in its original formulation).

6.4 Filtration

The simplest situation in the case where no reference is available is when the two components in Eq. 31 have known and quasi-disjoint support sets in a specific domain. Signal extraction then boils down to denoising by filtering.

If support sets happen to be quasi-disjoint in the frequency domain, then linear filtering will obviously extract signal components with a degree of precision that directly depends on the overlap between the spectra of $x(t)$ and $n(t)$. Indeed, if $S_x(f)$ and $S_n(f)$ denote the energy/power spectra of $x(t)$ and $n(t)$, then the optimal separation filter (in the sense of minimizing the mean-square error) to be applied to $y(t)$ to extract $x(t)$ has frequency gain:

$$G(f) = \frac{S_x(f)}{S_x(f) + S_n(f)} \tag{34}$$

which is close to one when the signal-to-noise $S_x(f)/S_n(f)$ is high and close to zero when it is low.

Similar ideas can be transposed to other domains, sometimes with different filtering strategies. If component $x(t)$ has known and nearly disjoint support sets in time, then it can be simply extracted by time gating (or "windowing"), a practice largely used to filter out transients in reciprocating machine signals, for instance. In this case the optimal window is given by the exact counterpart of Eq. (34) in the time domain. The cepstrum liftering discussed in Sect. 10.2 is a special case where signals have disjoint supports in the cepstral domain.

More generally, signals may have overlapping time and spectral contents but are still separable in the joint time-frequency or time-scale domains. This has led to several new filtering strategies based on invertible time-frequency transforms (e.g., the Gabor transform) and the wavelet transforms which are direct generalizations of the former approaches. A simple example is the use of time-frequency masks to gate the signal components of interest in the time-frequency plane or of time-scale thresholds to clip out noise components in the wavelet transform.

6.5 Blind Extraction

Blind extraction basically aims at achieving a filtration of the signal of interest when prior information is available in the form of a statistical property that uniquely defines it and differentiates it from the noise part. This is similar to a marker which makes possible to track the presence of the signal even in strong background noise. As illustrated in Fig. 6, blind extraction consists in shaping a linear filter to be applied to $y(t)$ which maximizes the marker property of the output so that it resembles as much as much as possible the expected signal $x(t)$. Three markers commonly used with machine signals are i) periodicity, ii) impulsivity, and iii) cyclostationarity. Since the *blind extraction of periodic signals* is found particularly important, it is reviewed in a dedicated subsection. The blind extraction of impulsive and cyclostationary signals is briefly discussed hereafter.

6.5.1 Blind Extraction of Impulsive Signals

Impulsive signals pertain to the non-stationary class and usually refer to signals made of series of impulses or transients which may occur on a repetitive basis

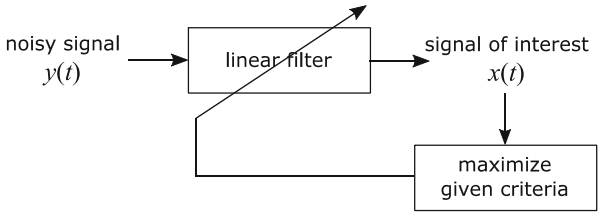

Fig. 6 Principle of blind extraction of a signal: a linear filter is blindly learned so as to extract a signal of which a given characteristic (e.g., impulsivity, cyclostationarity) is maximized

or not. They are often indicative of mechanical impacts, shocks, or sudden force variations in the system. In particular, they constitute symptomatic signatures of many incipient faults such as in gears and in bearings. Impulsive signals produce heavy-tailed histograms with a wider spread and more peaked in the middle than the Gaussian (given the same standard deviation). Therefore, impulsivity is often measured as departure from Gaussianity, for instance, by means of the kurtosis (which will take high positive values) or the entropy (various definitions are proposed in signal processing, which usually lead to a maximal value when the signal is Gaussian). The effect of (presumably Gaussian) additive noise on an impulsive signal is to progressively drive its original distribution to a Gaussian shape. Blind extraction explicitly exploits this fact in the reverse way: by automatically tuning a filter that maximizes a measure of impulsivity of the signal, additive noise is consequently removed as much as possible.

The direct approach which consists in learning a filter by maximizing the kurtosis (or by minimizing the entropy) leads to sophisticated optimization algorithms. A much simpler but suboptimal method is to test several filters in a dictionary (typically narrowband filters with different central frequencies and bandwidths) and to retain that one (or a combination of those ones) which maximizes the criterion. The Fast-Kurtogram proposes such a solution based on an efficient implementation by means of multirate filters.

6.5.2 Blind Extraction of Cyclostationary Signals

Cyclostationary signals have been introduced in Sect. 3.3. They represent an important class because many signals – especially from rotating machines – can be modelled as such. In principle, the blind extraction of cyclostationary signals follows exactly the same lines as for impulsive signals. In particular, the cyclostationary property of a signal is progressively attenuated by adding stationary noise so that, proceeding in the reverse sense, a blind extraction filter is learned such as to maximize a criterion of cyclostationarity. The absolute (or quadratic) sum of the cyclic correlations (i.e., the Fourier coefficients of the instantaneous autocorrelation function) or of the cyclic spectra (i.e., the Fourier transform of the cyclic correlations) is a good candidate to define indicators of cyclostationarity.

However, in the case of cyclostationary signals, the spectral correlation (the waterfall of all cyclic spectra represented as a two-variable function of the carrier

frequency f and the cyclic frequency α) provides a simple tool to visually identify the frequency bands where cyclostationarity is dominant and which are therefore eligible to design an extraction filter.

6.6 Blind Deconvolution

Blind deconvolution goes one step further than blind extraction by seeking to reconstruct the excitation source that produced the signal of interest. The problem reads:

$$y(t) = x(t) + n(t) = h(t) * s(t) + n(t) \tag{35}$$

where $s(t)$ is the excitation source to be recovered and $h(t)$ is an unknown linear filter such that $x(t) = h(t) * s(t)$. Note that the problem has no unique solution in general since it contains two unknowns for one noisy observation. It however represents the ultimate goal in many applications and especially in acoustics and vibration where the source of excitation is often the quantity of interest. In the diagnostics of machines, it gives access to the indirect measurement of the fault and therefore allows the assessment of its dimensions, severity, and of the remaining useful life. The blind deconvolution problem cannot be solved unless strong prior information on the excitation source is available. For instance, it often happens that incipient faults in rotating machines produce excitation forces which are well modelled by a series of delta functions (with possible random times of occurrence and magnitudes). This puts strong prior information on $s(t)$ in the form of a flat spectrum and a leptokurtic probability distribution (i.e., with a high kurtosis). The effect of the model of Eq. (35) is to transform this much contrasted source $s(t)$ into a diffuse signal $x(t) = h(t) * s(t)$ (the convolution has the effect of spreading the energy of the impulsive signal over the time axis and additive noise of making $y(t)$ more and more Gaussian). Blind deconvolution attempts to proceed in the reverse direction by seeking an inverse filter to be applied to $y(t)$ that maximizes the supposed characteristics of the source; the output of the inverse filter is then expected to resemble as much as possible the unknown source $s(t)$.

Popular criteria that are optimized to blindly deconvolve a white and impulsive excitation are the signal entropy, higher-order statistics (of which the kurtosis is a particular case), and the Lp (pseudo)-norms ($0 \leq p < 2$). If the excitation is impulsive and repetitive at the same time (e.g., synchronized on a rotating component), it is wise to maximize a measure of cyclostationarity. As shown in Sects. 10.3 and 10.4, the cepstrum sometimes deconvolves forcing and transfer functions.

6.7 Discrete-Random Separation

In vibration and acoustics, periodic and random signals often reflect phenomena of different origins. For instance, in rotating machines, strong periodic signals are

emitted by the shaft and gear rotations, while bearings contribute to producing random (though almost periodic) signals (because of random slip). Periodic and random vibrations may also be distinguished according to the scale of the physical phenomena they originate from, the former being more related to macro-phenomena and the latter to micro-phenomena. From another point of view, periodic signals relate to deterministic phenomena (i.e., which can be precisely described by equations) in contrast to random signals. For all these reasons, the separation of discrete and random components is of importance in many applications. If only the former components are of interest, the problem is also known as "harmonic (or line) enhancement." As seen in Sect. 2.1, the spectral signature of periodic signals is a series of discrete components (i.e., "harmonics"), while that of random signals is a continuous density. This provides good hope to achieve their separation.

Two scenarios must be considered: the case when the periods of the periodic components to be extracted are known and the more difficult situation when they are unknown.

6.7.1 Extraction of Periodic Signals with Known Periods: Synchronous Averaging

The scenario is described by a periodic signal of interest, $x_T(t) = x_T(t + T)$, in the model of Eq. (30). A natural solution to extract $x_T(t)$ from the noisy measurement $y(t)$ is from the synchronous average:

$$\hat{x}_T(t) = \frac{1}{K} \sum_{k=0}^{K-1} y\,(t + kT) \tag{36}$$

where K is the number of periods of $x_T(t)$ observed in $y(t)$. Since the average of Eq. (36) is synchronized on period T, it is constructive for the T-periodic component but destructive for the noise part. Obviously $\hat{x}_T(t)$ tends to $x_T(t)$ as the number of available periods K becomes large. The synchronous average of Eq. (36) has an equivalent interpretation in terms of a comb filter, a filter whose frequency gain is unity at multiples of the frequency $f = 1/T$ and which tends to zero (in inverse proportion to K) elsewhere.

In practice the application of synchronous averaging is rarely performed directly on the time domain sampled signal due to small speed fluctuations or slight imperfection in the selection of the sampling frequency. In fact, if the reference shaft speed is not perfectly constant and the sampling frequency is not its exact multiple, the time domain signal will not have the same number of samples per revolution, thus making impossible the application of the synchronous average. This issue is solved by the transformation of the signal from time to angular domain, thus obtaining a constant sample rate in samples/revolution. The process most commonly used for this purpose is *computed order tracking*, discussed in Sect. 8.1

6.7.2 Extraction of Periodic Signals with Unknown Periods

This scenario is a particular case of the blind extraction discussed in Sect. 6.5 and relies on the definition on a good marker that singles out a periodic signal (without

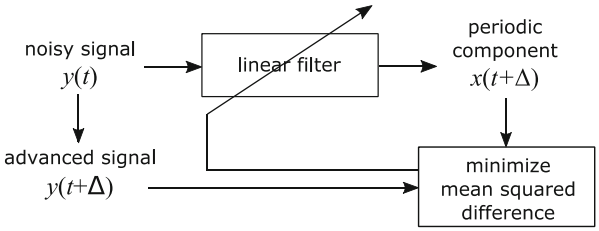

Fig. 7 Principle of the blind extraction of a periodic signal: a linear filter is learned that optimally (in the mean square sense) maps the signal to its advanced version, which naturally tunes itself into a comb filter

the knowledge of its period) from random noise. This is provided by the property of a periodic signal to be perfectly predictable in the future from its partial observation in the present in contrast to random noise which is not predictable farther than its correlation length. This means there exists a linear filter which exactly maps $x_T(t)$ to $x_T(t+\Delta)$ for any $\Delta > 0$. Such a filter can be constructed according to Eq. (33) where $x_T(t)$ is seen as the reference of $x_T(t+\Delta)$. Now, provided that the delay Δ is taken greater than the correlation length of noise $n(t)$, the filter will naturally tune itself into a comb filter with unit gain at the harmonic frequencies and zero gain elsewhere. Its application to measurement $y(t)$ will then return an estimate of all the periodic components it comprises, as illustrated in Fig. 7. One advantage of this approach (in addition to not requiring the knowledge of the periods) is that it can extract multiple periodic components at the same time without requiring their periods to be coded on an integer number of samples; however the corresponding comb filter is generally less sharp than the one obtained from the synchronous average (given an equivalent signal length).

6.8 Blind Source Separation

Blind source separation (BSS) is more stringent than signal extraction in that it tries to separate simultaneously all the components that make up the observed signal in Eq. (30). For this, the components are seen as the responses to a limited number of underlying sources – sometimes also called the "latent variables" – as illustrated in Fig. 8. The adjective "blind" indicates that the ambition is to achieve the separation without any reference signal or knowledge of the transfer functions that relate the underlying sources to their measured contributions.

BSS is a difficult problem which was first solved theoretically in the 1990s; since then, works on the subject have grown exponentially, initially in the field of telecommunications and more recently in other disciplines such as biology, physics, and mechanics.

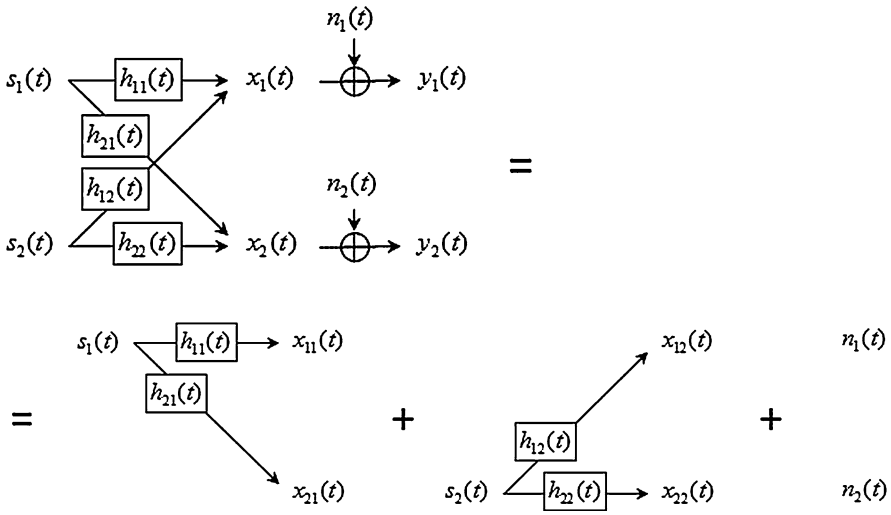

Fig. 8 Blind source separation is to recover the sources $s_i(t)$ s or their individual contributions $x_{ij}(t)$ from a set of simultaneous measurements $y_j(t)$

6.8.1 The Notion of a Source

To be a well-posed problem, BSS requires the notion of a source to be carefully defined. The physical understanding of a source is a signal linked to an excitation mechanism in the system under study; different sources refer to excitation mechanisms of different physical origins. In a rotating machine, for instance, sources will typically relate to excitations in the motor, in the gears, in the bearings, etc. Note that a source does not necessarily have a point-like nature; indeed, its exact spatial distribution is irrelevant as long as a model of the form of Eq. (35) holds.

From a statistical point of view, the fact the sources originate from different physical origins is reflected by their mutual independence. This means that the knowledge of one source does not help at all to predict the value of the other sources. Mutual independence implies in particular – but not only – that sources are mutually uncorrelated, i.e., their cross-spectra are all nil.

6.8.2 Problem Statement

The rationale behind BSS is that a set of measurements is produced by the superposition of the responses to a limited number of sources. The objective is to recover the original sources or, to a lesser extent, their individual contributions in the measurements. The contribution of a source is defined as the signal that would be measured as if all other sources were switched off. This is illustrated in Fig. 8 where BSS is interpreted like the decomposition of a multiple-input multiple-output (MIMO) system into a superposition of single-input multiple-output (SIMO) systems.

The difficulty in BSS is that all sources are necessarily operating concurrently and that only mixtures of their contributions can be observed. This is the situation typically encountered with machine signals, which are produced by a superposition of responses to multiple sources of excitation which are activated by the operation of the machines. The separation of competing sources usually requires multiple and simultaneous measurements.

The BSS problem can be formulated rather generally as:

$$\begin{cases} y_1(t) = \underbrace{h_{11}\{s_1(t)\}}_{x_{11}(t)} + \cdots + \underbrace{h_{1N}\{s_N(t)\}}_{x_{1N}(t)} + n_1(t) \\ \qquad\qquad\qquad\qquad \vdots \\ y_M(t) = \underbrace{h_{M1}\{s_1(t)\}}_{x_{M1}(t)} + \cdots + \underbrace{h_{MN}\{s_N(t)\}}_{x_{MN}(t)} + n_M(t) \end{cases} \tag{37}$$

where the $y_i(t)$'s, $i = 1, \ldots M$ refer to M simultaneous measurements, the $s_j(t)$'s, $j = 1, \ldots N$ to N competing sources, and the $n_i(t)$'s to additive noise. The operator $h_{ij}\{\ldots\}$ denotes the effect of the transfer on source $s_j(t)$ to measurement $y_i(t)$, which may take different forms as seen below. Equation (37) clearly indicates that the set of measurements is completely explained by a limited number of underlying sources whose contributions are shared by all channels plus possible additive noise which, by definition, is independent throughout the channels.

Depending on the applications, the objective of BSS is either to recover the original sources $s_j(t)$'s or solely their contributions $x_{ij}(t) = h_{ij}\{s_j(t)\}$'s. The second case is obviously less ambitious than the first one and is actually sufficient in many instances.

It is important to realize that all quantities are unknown in Eq. (35) except for the measurements, the $y_i(t)$'s. Due to the many unknowns to be solved, it is therefore advantageous to have the number M of measurements as large as possible as compared to the number N of sources. The *over-determined* case $M > N$ is recommended in the presence of significant additive noise. This justifies a major difference between signal extraction, which usually proceeds with a single channel, and BSS, which usually requires multiple simultaneous measurements.

6.8.3 Types of Mixture

The BSS problem strongly depends on the type of mixture described by Eq. (37). A fairly general configuration is when the operator $h_{ij}\{\ldots\}$ is a convolution, i.e., $x_{ij}(t) = h_{ij}(t) * s_j(t)$ – the so-called convolutive mixture – yet it is also the most difficult case to solve. The simplest configuration is when the operator $h_{ij}\{\ldots\}$ is a static gain, i.e., $x_{ij}(t) = h_{ij} \cdot s_j(t)$; this is the so-called linear instantaneous mixture which is conveniently expressed in matrix form as:

$$\mathbf{y}(t) = \mathbf{H}\,\mathbf{s}(t) + \mathbf{n}(t) \tag{38}$$

with $\mathbf{y}(t)$, $\mathbf{s}(t)$, and $\mathbf{n}(t)$ column vectors that contain the elements $y_i(t)$'s, $s_i(t)$'s, and $n_j(t)$'s, respectively, and $\mathbf{H}$ a matrix whose element (i,j) is h_{ij}.

It is noteworthy that the convolutive mixture can be transformed into an "instantaneous" mixture in the Fourier domain.

6.8.4 General Principles

Once the type of mixture has been specified, BSS proceeds in three steps: the design of a separation operator, the definition of a separation criterion, and the construction of an optimization algorithm. These steps are briefly reviewed in the case of the simple instantaneous mixture.

Separation Operator

The principle of BSS is to find a separation operator – a *separation matrix* $\mathbf{W}$ in the linear instantaneous mixture – such that

$$\hat{\mathbf{s}}(t) = \mathbf{W}\,\mathbf{y}(t) \tag{39}$$

returns an estimate $\hat{\mathbf{s}}(t)$ of the sources $\mathbf{s}(t)$. Note that $\mathbf{W}$ is generally not the (pseudo) inverse of $\mathbf{H}$ (i.e., such that $\mathbf{WH} = \mathbf{I}$, the identity matrix) since it will also try to reduce the effect of additive noise $\mathbf{n}(t)$ to some extent. It is important to note that the recovered sources are arbitrarily scaled and sorted. Indeed, since $\mathbf{H}$ is unknown, it can exchange any column and gain with $\mathbf{W}$ (e.g., $\mathbf{WH} = (k\ \mathbf{W})(k^{-1}\ \mathbf{H})$, thus leading to another separation matrix $k\ \mathbf{W}$ and another source estimate $k\hat{\mathbf{s}}(t)$). The unknown amplitude and sorting of the sources are fundamental indeterminacies of BSS. However, the former indeterminacy is actually fixed when estimating the contribution of a source. Once an estimate is available on a source $s_i(t)$, its contribution $x_{ij}(t)$ to the measurement $y_j(t)$ can be estimated from the reference-based approach of Sect. 6.3, i.e.:

$$\hat{x}_{ij}(t) = \frac{\left\langle y_j(t)\hat{s}_i(t)\right\rangle}{\left\langle \left|\hat{s}_i(t)\right|^2\right\rangle}\hat{s}_i(t) = \frac{\left\langle y_j(t)\mathbf{y}(t)^T\right\rangle \mathbf{w}_i^T}{\mathbf{w}_i\left\langle \mathbf{y}(t)\mathbf{y}(t)^T\right\rangle \mathbf{w}_i^T}\mathbf{w}_i\mathbf{y}(t) \tag{40}$$

where $\langle \ldots \rangle$ denotes the time-average operation, $\mathbf{w}_i$ the i-th row of matrix $\mathbf{W}$, and $\ldots^T$ the transpose of a vector. It is clear from Eq. (40) that contribution $\hat{x}_{ij}(t)$ is properly scaled, even if the estimated source $\hat{s}_i(t)$ is not. It is also noteworthy from this equation that BSS is to be interpreted as a spatial filter.

Separation Criteria

The main challenge of BSS is to blindly estimate the above separation operator from the output measurements only. Similarly to blind extraction and blind deconvolution previously discussed in Sects. 6.5 and 6.6, this requires strong a priori assumptions

about the statistical properties of the sources. The separation operator is thus sought so as to enforce recovered sources $\hat{\mathbf{s}}(t)$ with the expected properties. Some typical separation criteria are listed hereafter:

- Mutual decorrelation of the sources. Because of their statistical independence, sources are mutually uncorrelated, i.e., with zero cross-spectra. In contrast, correlation is introduced between the measured signals in Eq. (38) because of the mixture of sources. The idea of BSS is to design a separation matrix $\mathbf{W}$ that recovers sources whose correlation is minimized. This may be seen as an extension of principal component analysis to signals. The working assumption of this approach is that sources must have distinct spectra.
- Mutual decorrelation of cyclostationary sources. When sources are cyclostationary, they are also expected to have zero cyclic cross-spectra. This provides more constraints into the problem to better estimate the separation matrix, in particular in the presence of strong stationary background noise. This separation criterion is particularly well suited to machine signals which are often well described as cyclostationary.
- Mutual independence of sources. Going one step further, the idea is to enforce not only the source decorrelation but also their mutual independence. Here again independence is lost in the mixing in Eq. (38) and will not be recovered unless the correct separation matrix is found in Eq. (39). This is achieved by requiring some non-linear measure of statistical dependence, such as higher-order cross-correlations or cross-entropy, to be zero. Again this may be seen as a generalization of principal component analysis referred to as independent component analysis (ICA). The working assumption of this approach is that no more than one source in the mixture has a Gaussian probability distribution.
- Maximum kurtosis of sources. In the case of sources with an impulsive behaviour, their mixture tends to average out this characteristic. More generally, a mixture of leptokurtic sources (i.e., with high kurtosis) tends to become Gaussian (i.e., with zero kurtosis) by virtue of the central limit theorem of probabilities. Therefore, a separation matrix is sought that restores maximum kurtosis of the sources. Similar popular criteria have been devised based on minimizing measures of entropy.
- Intermittent sources. In some instances, the sources occur intermittently in the time domain so that there exist time intervals where only one source is active at a time. This makes possible to grasp this source as a reference and then estimate a separation matrix from classical reference-based techniques. Other approaches directly proceed with masks in the time-frequency domain.
- Sparse sources. Sparse sources are a generalization of intermittent sources which are described (or well approximated) by only a few non-zero coefficients in a given transformed domain, such as the Fourier or wavelet domains. The objective is to seek a separation matrix that effectively returns sources which can be represented as sparsely as possible.

Optimization Algorithm
Estimating a separation operator by enforcing a given statistical property of the sources is achieved by means of an optimization algorithm. Several toolboxes are nowadays available that implement the most popular BSS algorithms.

6.9 Blind Separation of Structural Modes

6.9.1 Context

A successful application of BSS in structural dynamics is for the separation of modal contributions from output-only data. The aim is to decompose a set of simultaneous measurements of a MIMO system into the individual contributions of underlying SIMO systems. When the sources are represented by the modal coordinates of a structure, BSS boils down to the separation of each modal contribution, that is, the response of the structure when only one mode is active. In other words, the response of a complex multiple-degree-of-freedom is then decomposed into the sum of responses of single-degree-of-freedom systems. This finds considerable interest in Operational Modal Analysis (OMA) where modal parameters can then easily be identified from single-degree-of-freedom responses, without controlling the excitation. The working assumption – which is common to all OMA approaches – is that the excitation to the structure is broadband enough so that its spectrum can be considered constant across the bandwidth of any modal resonance of interest. This assumption is found to apply reasonably well in several instances, in particular under ambient excitations where loading on the structure is produced by fluid-dynamic forces (wind, waves), natural seismic activity, traffic, etc.

As compared to other identification algorithms dedicated to OMA (e.g., stochastic subspace identification), BSS may be used as a useful pre-processing step or a substitute which instead allows the use of simple degree-of-freedom identification techniques.

6.9.2 Principle

The rationale beyond the application of BSS to OMA proceeds from the similarity between the linear instantaneous mixture of BSS (see Eq. (39)) and the modal expansion theorem which states that the response of a structure to any excitation can always be expanded into a linear combination of modes weighted by the modal coordinates. Namely, by denoting $\boldsymbol{\phi}_i$ the i-th mode shape (a vector), $q_i(t)$ the corresponding modal coordinate (a signal), and $\mathbf{y}(t)$ the vector that stacks the responses of the structure measured at different points,

$$\mathbf{y}(t) = \sum\nolimits_i \boldsymbol{\phi}_i q_i(t) + \mathbf{n}(t) \tag{41}$$

where $\mathbf{n}(t)$ stands for possible additive noise. This can be further cast in matrix form as:

$$\mathbf{y}(t) = \mathbf{\Phi}\mathbf{q}(t) + \mathbf{n}(t) \tag{42}$$

where matrix $\mathbf{\Phi}$ contains the active mode shapes in columns and $\mathbf{q}(t)$ stands for the vector of modal coordinates. Comparing Eq. 42 with Eq. (38), it is seen that the modal matrix $\mathbf{\Phi}$ plays the role of the mixing matrix $\mathbf{H}$ and the modal coordinates $\mathbf{q}(t)$ play the role of the sources $\mathbf{s}(t)$ in BSS. There is therefore good hope that BSS can be applied to Eq. (42) in order to estimate jointly the modal matrix $\mathbf{\Phi}$ and the modal coordinates $\mathbf{q}(t)$ from the output-only measurements $\mathbf{y}(t)$.

In order to do so, the assumptions of BSS must first be repeated. Section 6.8.4 introduced several separation criteria usually used in BSS. Among them, the criterion of mutual decorrelation of the modal coordinates has been found to apply generally well in the case of lightly damped structures with low modal density. The reason is that under these assumptions the spectra of the modal coordinates have nearly disjoint supports so that their mutual correlations are indeed very small. The extreme case is given by a conservative system where the modal coordinates then look like pure sines: they are therefore exactly uncorrelated as soon as they oscillate at different natural frequencies. In practice, the criteria of mutual decorrelation has been found to be quite robust even in the case of modal overlap factors slightly greater than one and damping factors on the order of 20%.

Several algorithms are conceivable to separate modal contributions based on their mutual decorrelation. A popular one is SOBI (second-order blind identification) which forces decorrelation at several time lags by jointly diagonalizing a set of correlation matrices. As explained in Sect. 6.8, the output of a BSS algorithm comprises the separation matrix $\mathbf{W}$ which, in the present context, provides an estimate of the inverse of the modal matrix $\mathbf{\Phi}$. Therefore mode shapes can be recovered in the columns of the inverse of the separation matrix, $\mathbf{W}^{-1}$. Similarly, application of the separation matrix to the measurements returns an estimate of the modal coordinates, $\hat{q}(t) = \mathbf{W}\mathbf{y}(t)$, from which global modal properties (natural frequencies and damping ratios) can be easily estimated by using single-degree-of-freedom techniques.

A necessary condition for this strategy is to have at disposal at least as many sensors as active modes to recover. If not satisfied from the onset, this condition can easily be forced by applying BSS in frequency bands that contain no more active modes than available sensors. A frequency domain version of BSS can be implemented on this basis which forces joint decorrelation at several frequency bins – i.e., nil cross-spectra – in a given frequency band.

6.9.3 Example of Application

The use of BSS for the separation of modal contributions is illustrated here on data provided in the Operational Modal Analysis Modal Parameter Estimation Round Robin organized at the IMAC XXVII 2011 conference. The structure under study is a scaled model of a wind turbine blade. The structure is fixed at the root and excited by means of random tapping for duration of about 5 min. The response is measured in all 3 directions at 16 locations at a sampling rate of 512 Hz. The power spectra

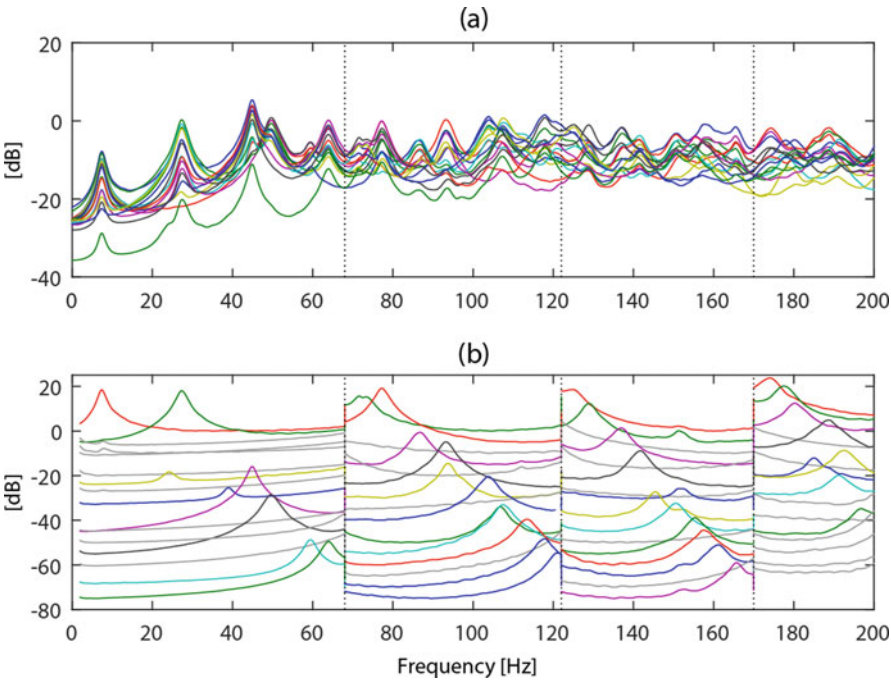

Fig. 9 (**a**) Power spectra vibration responses of a scaled wind turbine blade (16 channels). (**b**) Power spectra of separated modal responses in four sub-bands

of the 16 responses in the frequency range of interest up to 200 Hz are displayed in Fig. 9a. It is seen that apart from the first three or four modes which clearly pop up below 50 Hz, the structure quickly exhibits a "mid-frequency behaviour" with significant damping and a modal overlap factor that becomes greater than 1 above 100 Hz. As explained above, these observations depart to some extent from the theoretical assumptions of mutually uncorrelated sources used here as a criterion for BSS.

In order to cope with the large number of modes up to 200 Hz, the frequency band of interest is divided into 4 bands which are expected to contain less than 16 active modes each, so as to comply with the condition of having more sensors than modal contributions to recover. The power spectra of the separated modal coordinates in each band are displayed in Fig. 9b (here a frequency domain version of BSS based on mutual decorrelation has been used). It is seen that six dominant modes could be separated in the first band from 0 to 68 Hz, up to eight modes in the band from 68 Hz to 122 Hz (the last one in the band actually pertains to the next band), up to ten modes in the band from 122 Hz to 170 Hz and at least seven modes in the last band. It is remarkable that the algorithm has been able to achieve good separation not only in the first band characterized by a clean modal behaviour but also in the higher-frequency bands characterized by "mid-frequency behaviour."

Table 2 Identified modal parameters and modal overlap factors

Freq. (Hz)	Damp. (%)	MOF	Freq. (Hz)	Damp. (%)	MOF	Freq. (Hz)	Damp. (%)	MOF
7.33	1.19	1%	106.52	1.13	119%	155.50	0.85	77%
27.27	1.35	5%	107.64	0.91	56%	158.89	1.01	121%
38.94	1.71	15%	113.55	0.94	42%	160.81	0.85	80%
44.85	0.78	13%	117.76	0.89	57%	165.78	0.89	47%
49.73	1.38	19%	120.91	1.00	68%	173.46	0.99	58%
59.38	1.25	21%	124.90	1.09	68%	177.56	0.97	101%
63.90	1.22	17%	128.87	0.86	38%	180.29	1.22	125%
77.27	0.81	11%	136.73	0.87	37%	184.58	1.00	92%
86.46	1.04	22%	141.62	0.72	47%	188.35	1.10	114%
93.23	0.86	43%	145.41	0.70	48%	191.84	1.63	302%
93.91	0.91	33%	150.17	0.83	75%	192.50	0.96	121%
103.62	1.01	33%	152.07	0.75	86%	197.92	1.21	89%

From these separation results, the natural frequencies and damping ratios could be easily estimated by using single degree-of-freedom techniques (more advanced curve-fitting techniques or subspace algorithms could also be used at this stage). The values are displayed in Table 2, along with the estimated modal overlap factor. The recovered mode shapes finally made possible the identification of combinations of flexure and torsion of the wing.

7 Time-Frequency Representations

This material is based largely on the discussion in Ref. [9].

7.1 STFT

A relatively simple, but powerful, way of dividing up a signal in both time and frequency is to move a fixed window function, for example, a Hanning window, along a slowly varying time record, usually in overlapping steps, and record the autospectrum of the corresponding windowed time signal for each displacement of the window. This is illustrated in Fig. 10.

The formula for the Fourier spectrum of each windowed section is:

$$S(t, f) = \int_{-\infty}^{\infty} x(\tau)\, w(\tau - t) \exp(-i2\pi f \tau)\, d\tau \tag{43}$$

where the $H(t,f)$ in Fig. 10 is equal to $|S(t,f)|$, and if the squared amplitude spectrum is plotted, the diagram is usually called a "spectrogram." The window overlap

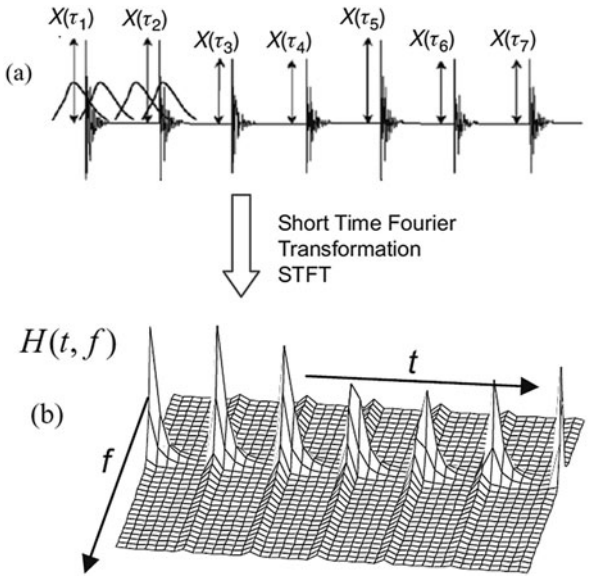

Fig. 10 Generation of STFT

is chosen to give a smooth visual transition and is smaller than the actual time resolution.

The length of weighting function $w(t)$ determines the frequency bandwidth and resolution of each spectrum and must therefore be chosen carefully. For example, in Fig. 10 it should be chosen to be shorter than the spacing of the impulse responses (IRs) dominating the signal, but longer than the individual IRs to give meaningful results, but this of course is data dependent. The product of resolution in time and resolution in frequency is a constant, this being one aspect of the Heisenberg uncertainly principle.

7.2 Wigner-Ville Distribution (WVD)

The Wigner-Ville distribution (WVD) seems to violate the uncertainty principle in appearing to give better resolution than the STFT, but suffers from interference components, with possible local negative values, between the actual components. The original Wigner distribution [10] was modified by Ville [11] who proposed the analysis of the corresponding analytic signal so as to eliminate interference between positive and negative frequency components. The WVD is one of the so-called Cohen's class of time-frequency distributions [12], most of which have been proposed to improve on the WVD in some way. Even the STFT falls into this class. Cohen's class may be represented by the formula:

$$C_x(t, f, \phi) = \mathcal{F}_{\tau \to f}\{R(t, \tau)\} \tag{44}$$

where $R(t, \tau)$ is a weighted autocorrelation-like function defined by:

$$R(t, \tau) = \int_{-\infty}^{\infty} x\left(u + \frac{\tau}{2}\right) x^*\left(u - \frac{\tau}{2}\right) \phi((t-u), \tau)\, du \tag{45}$$

and $\phi(u, \tau)$, with $\phi((t-u), \tau) = w(t-u-\tau/2)w(t-u+\tau/2)$ being a kernel function used to smooth the WVD (with $\phi((t-u), \tau) = \delta(t-u)$, the WVD is obtained). The "pseudo Wigner-Ville distribution" is a finite windowed version of the WVD, with $\phi((t-u), \tau)$ being a function of τ only, and the "smoothed pseudo Wigner-Ville distribution," with $\phi((t-u), \tau)$ being a separable function in $(t-u)$ and in τ, suppresses interference in both the time and frequency directions. The results of smoothing are data dependent but usually give better simultaneous resolution in the time and frequency directions than the STFT.

7.3 Wigner-Ville Spectrum (WVS)

For second-order cyclostationary signals (CS2), with no admixture of CS1 (i.e., after removal of periodic signals), it is possible to remove interference components by indirect averaging. A standard way of analyzing cyclostationary signals is to first generate a two-dimensional autocorrelation function, with lag time τ on one axis and cyclic time t on the other, according to the formula:

$$R_{xx}(t, \tau) = \mathbb{E}\left\{x(t + \tau/2)\, x^*(t - \tau/2)\right\} \tag{46}$$

where the difference from Eq. (45) is the ensemble averaging given by the expectation operator. As described in Ref. [13], this can be transformed in both time lag and cyclic time directions to give the spectral correlation diagram, to give a 3D diagram with normal frequency f on one axis and cyclic frequency α on the other. If the Fourier transformation is done first in the τ direction, the Wigner-Ville spectrum (WVS) is obtained, giving frequency distribution vs time t. Since the interference components have random phase for CS2 signals, they average to zero, so that the WVS has the same resolution as the WVD, but with interference components largely removed. This may appear to violate the uncertainty principle, but it should be kept in mind that much longer data records are required to perform the averaging. By contrast, averaging STFT diagrams does not improve resolution, but does smooth noise spectra.

Figure 11 compares the results of performing STFT, WVD and WVS on the vibration signal from a reciprocating compressor, with many separate events with different frequency contents occurring at different times (i.e. crank angles) in the compression cycle. This shows the improved resolution of the WVS compared with the STFT, without the interference components of the WVD.

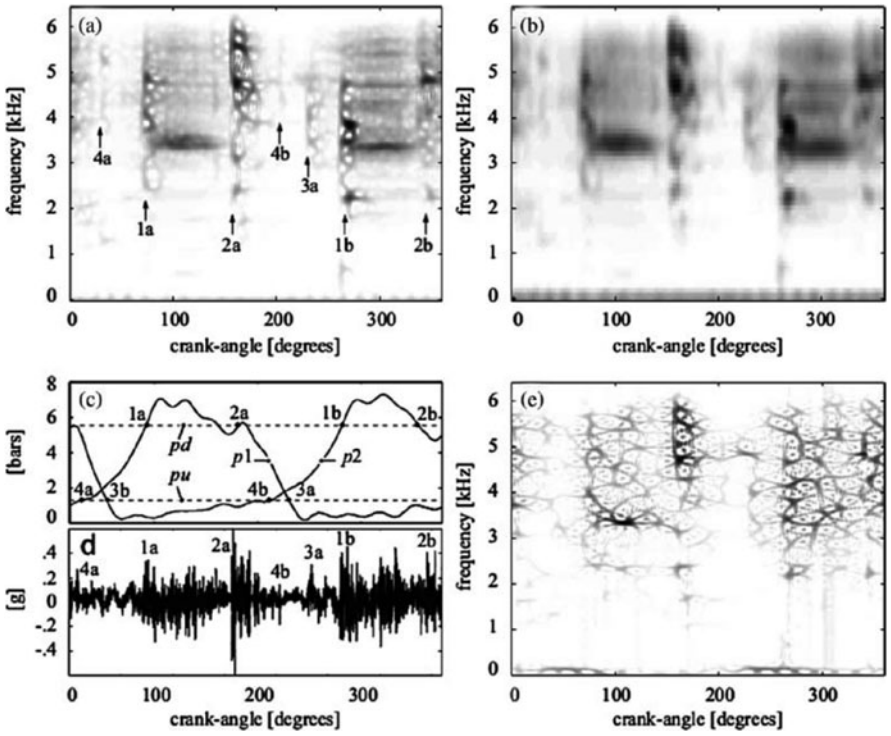

Fig. 11 Diagnostics of a reciprocating compressor. (**a**) WVS. (**b**) STFT. (**c**) Pressure on forward and backward strokes. (**d**) Accelerometer signal. (**e**) WVD for one cycle. (**a**) Forward stroke, (**b**) backward stroke. 1, 2, Opening, closing of discharge valve. 3, 4, Opening, closing of suction valve. (From [13])

7.4 Wavelets

Another approach to time-frequency analysis is to decompose the signal in terms of a family of "wavelets" which have a fixed shape but can be shifted and dilated in time. The formula for the wavelet transform is:

$$W(a;b) = \frac{1}{\sqrt{a}} \int_{-\infty}^{\infty} x(t)\psi^* \left(\frac{(t-b)}{a} \right) dt \tag{47}$$

where $\psi(t)$ is the mother wavelet, translated by b and dilated by factor a. Since this is a convolution, the wavelets can be considered as a set of impulse responses of filters.

7.4.1 Constant Percentage Bandwidth

Displacement by b results in a linear time axis, but scaling by a, often by factors of 2, tends to give an octave-based (constant percentage bandwidth) frequency scale, and the decomposition is known as time-scale rather than time-frequency.

Wavelets can be orthogonal or non-orthogonal, and continuous or discrete [14]. Examples of orthogonal wavelets are the Daubechies dilation wavelets [15], which are compact in the time domain but in principle infinite in the frequency domain. They tend to have irregular shapes in the time domain. Newland [14] describes complex harmonic wavelets, which are compact in the frequency domain but infinite in the time domain. They have the appearance of windowed sinusoids (harmonic functions) and are typically of one octave bandwidth, although they can be narrower. The advantage of complex wavelets is that the imaginary part of the wavelet is orthogonal to the real part (sine rather than cosine) and thus the overall result is not sensitive to the position (phasing) of the event being transformed (it may be centered on a zero crossing of the real part, but this would be a maximum of the imaginary part). The local sum of squares of the real and imaginary parts is a smooth function.

Wavelets are subject to the uncertainty principle, but because of the constant percentage frequency scale give a better time localization at high frequencies, and for that reason can be useful for detecting local events in a signal. Figure 12 shows the difference in time-frequency localization for STFT and (octave-based) wavelets, showing how the latter give fine time localization at some scales, whereas if this is chosen for the STFT, it detracts from frequency localization. In all cases the areas of the boxes are constant to comply with the uncertainty principle.

Many authors have described the use of wavelets for machine diagnostics, including detecting local faults in gears and bearings, and Ref. [16] provides a good summary.

Orthogonal wavelets are particularly useful for applications involving analysis/synthesis, but not so important for pure analysis, where the information is extracted directly from the wavelet diagram. For machine diagnostics, a very important class of wavelets are Morlet wavelets, where the mother wavelet is a cosine weighted with a Gaussian function. Complex Morlet wavelets exist, where the cosine is replaced by a complex exponential function, whose imaginary part is the Hilbert transform of the real part (sine rather than cosine). The advantage of the

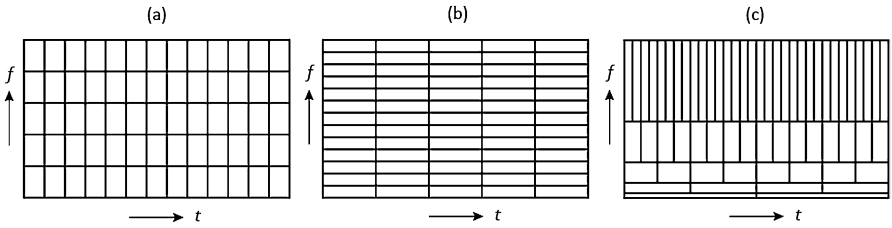

Fig. 12 Time-frequency paving of (**a**) the STFT with a fine time resolution, (**b**) the TFT with a fine frequency resolution, (**c**) the octave wavelet transform

Gaussian function is that its Fourier transform is also a Gaussian function, so the wavelet envelope is of the same form in both time and frequency domains.

A particular application involving analysis/synthesis is wavelet denoising, where all components in the wavelet diagram whose amplitude is below a certain threshold are considered to be noise. In so-called hard thresholding, all components thus defined as noise are set to zero, but the retained components are left unchanged. In "soft thresholding," the noise estimate (the threshold value) is subtracted from them also (symmetrical treatment of positive and negative values). Wavelet denoising is based on the original work of Donoho and Johnstone [17]. This type of denoising has the advantage that noise in time and scale directions is equally removed.

7.4.2 Wavelet Packets

Another way of considering wavelet decomposition at each scale is as a division into details and approximation components, by a highpass and lowpass filter, respectively. The shortest possible scale components (highest frequency) are obtained, for example, as the mean of adjacent pairs of samples (each frequency component requires at least two samples). When the shortest scale components are subtracted, the approximation contains all longer scale components, but this can again be decomposed into detail and approximation components at the next scale, and so on. This leads to the normal octave-based frequency scale of the wavelet transform. With wavelet packets, even the upper octave at each scale is separated by highpass and lowpass filters, so that a linear frequency axis is divided into 2, 4, 8, 16, and other bands, resulting in a constant bandwidth frequency resolution at each scale. It could be said that wavelet packets are equivalent to a series of STFTs with time window lengths changing in 2:1 steps. Thus, there seems little justification for them in machine diagnostics.

Much of the extensive theory developed for the wavelet transform can be carried over to wavelet packets.

8 Specialized Analysis

8.1 Order Analysis

Many machine vibration signals can be considered phase-locked with the rotation of a reference shaft. If small speed fluctuations of the shaft occur, the signals will be cyclostationary in the angular domain of the shaft, rather than in time domain. For instance, a CS1 vibration signal $x(t)$ of this type will show a periodic expected value in the shaft angular domain θ, rather than in time domain:

$$\mathbb{E}\{x(\theta)\} = \mathbb{E}\{x(\theta + 2k\pi)\} \tag{48}$$

Fourier analysis is therefore much more effective on these signals if performed in the angular domain. Resulting spectral quantities are therefore defined in the shaft-order domain Ω rather than the traditional Hertz-frequency domain f. Orders are

expressed in times-per-revolution of the reference shaft used for the definition of the angular domain θ. The following subsections will describe some methodology to obtain the transformations $t \rightarrow \theta$ and $f \rightarrow \Omega$.

Synchronous averaging is only meaningful if carried out in the shaft angular domain, as practised over several decades for gear diagnostics.

8.1.1 Computed Order Tracking

Computed order tracking is aimed at transforming the signal from time to angular domain. This procedure is often found as a preliminary step of synchronous averaging algorithms (see dedicated section), in order to ensure a uniform number of samples for every revolution of the reference shaft. Order tracking implements a series of interpolations on the shaft rotation measurement (often a 1 $\times$ rev tachometer) and on the vibration signal resulting in a resampled vibration signal whose sample rate is defined (and constant) in the angular domain of the shaft, rather than in time. The first interpolation works on each shaft rotation k and estimates the times $t_k[m]$ at which the shaft is in the uniformly spaced angular positions $2\pi m/P$ (P the new sample rate in samples per shaft revolution). Considering a 1 $\times$ rev tachometer and a piecewise-linear approach interpolation, this operation can be written as:

$$t_k\,[m] = t'_k + \left(t'_{k+1} - t'_k\right) \frac{m}{P} \tag{49}$$

where t'_k is the k th 1 $\times$ rev tacho reference pulse and $t_k[m]$ is therefore estimating the times corresponding to the angle $2\pi k + 2\pi m/P$. A uniformly angular resampled signal (i.e., order tracked) can be obtained by a second interpolation of the original signal $x(n\Delta t)$ at the times $t_k[m]$:

$$\widetilde{x}\,(r\,\Delta\alpha) = \widetilde{x}\left(2\pi\left(k + \frac{m}{P}\right)\right) \approx x\,(t_k\,[m]) \tag{50}$$

McFadden [18] showed that cubic spline interpolation is considerably better than linear interpolation from two considerations:

1. The interpolation gives a lowpass filtration of components approaching half the sampling frequency, and cubic spline cuts off at a higher frequency than linear, which in turn cuts off higher than quadratic interpolation.
2. Some aliasing of high-order sidelobes is unavoidable but is much lower for cubic spline than quadratic interpolation, which in turn is better than linear.

8.2 Second-Order Cyclostationary Indicators

Cyclostationary signals are characterized by a periodic non-stationarity. Detection of the presence and quantification of cyclostationarity is of interest in several applications, either because it is symptomatic of a particular phenomenon

(e.g., a mechanical fault) or because it allows advanced processing (e.g., signal extraction/separation – see related subsections). In many instances, cyclostationarity cannot be revealed by classical signal processing tools and thus requires specific approaches. This is in particular the case for second-order cyclostationary signals, a wide class of considerable practical interest characterized by a periodic autocovariance function (see Sect. 3.3.2).

An illustrative example of a second-order cyclostationary signal is provided by a (zero-mean) stationary random noise, $r(t)$, modulated by a periodic envelope, $p_T(t) = p_T(t + T)$ (example already introduced in the Sect. 3.3.2):

$$x(t) = p_T(t)r(t) \tag{51}$$

Both the frequency characteristics of random carrier and those of the modulating signal are therefore inherited by the CS2 signal. Figure 13 reports an example of the hybrid nature of CS2 signals.

- On a ***short-time scale***, the effect of the PSD of the random carrier $r(t)$ is reproduced: low frequency in case of Fig. 13 (a) and high frequency in case of Fig. 13 (b).
- On a ***long-time scale***, the period/frequency of the periodic signal $p_T(t)$ is reproduced in the cyclic flow of power of the signal: higher frequency in case of Fig. 13 (a) and lower frequency in case of Fig. 13 (b).

This double-frequency characterization of CS2 signals is critical in their separation and identification. The frequency axis of the short-time PSD characteristic is usually described by the symbol f and referred to as *spectral frequency* (associated to the properties of the random parent signal $r(t)$), while the long-term periodicity in the signal's power inherited from the modulating signal $p_T(t)$ is usually described by the symbol α and referred to as *cyclic frequency*.

Comparing Fig. 13a, b and Fig. 3b, c, it is possible to intuitively recognize the correspondence between the cyclic frequency α and the time variable t in the autocorrelation function $C(t, \tau)$ and the equivalent relationship τ-f. An example of such CS2 signal is the random vibration of a flexible shaft modulated by its rotation (α linked to shaft rotational speed). In this case the signal will also show specific f characteristics, depending on the shaft resonances. Moreover, as in most practical cases, an additional stationary noise $n(t)$ will be present (e.g., to reflect the presence of other vibration sources).

$$y(t) = p_T(t)r(t) + n(t) \tag{52}$$

This model well describes also the typical vibrations obtained from a faulty rolling element bearing: with the characteristic spectral frequency (f) corresponding to the structural resonances excited by each impact of the rolling elements with the fault and the phenomenological cyclic frequencies (α) linked to the time lag between subsequent impacts (see simplified numerical example of Fig. 14).

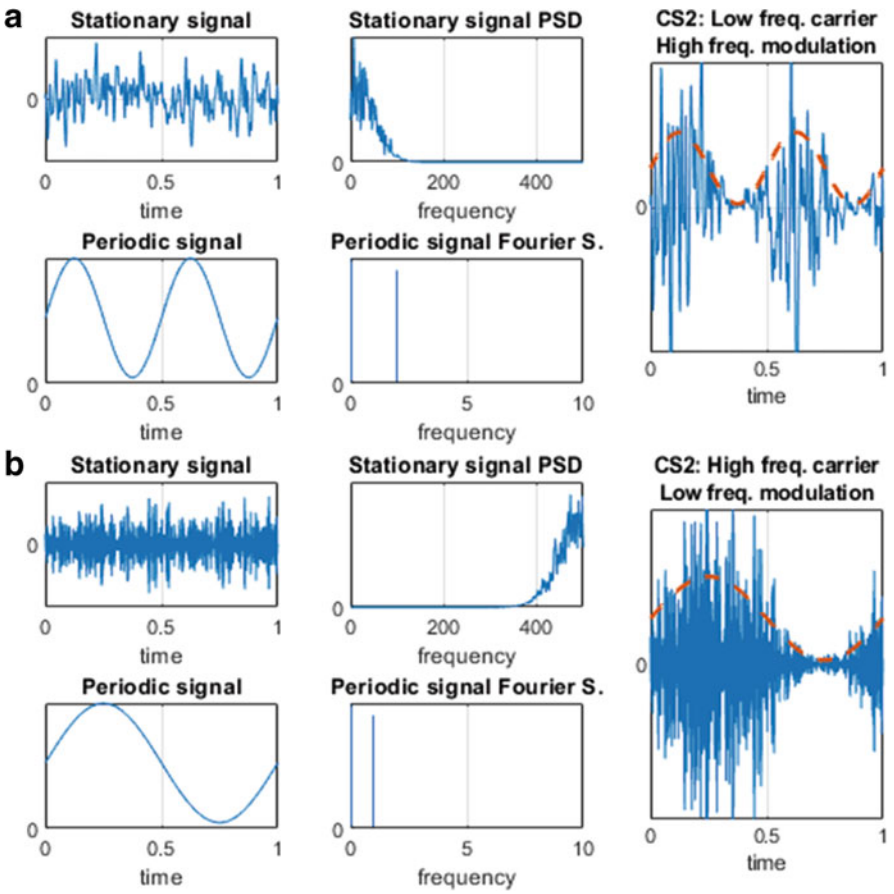

Fig. 13 Two numerical examples of CS2 signals generated by multiplying a random stationary carrier and a periodic modulating signal: (**a**) random carrier with low-frequency PSD ($f_a = 0 - 100$ Hz) and mono-harmonic modulation frequency $\alpha_a = 2$ Hz, (**b**) random carrier with high-frequency PSD ($f_a = 400 - 500$ Hz) and mono-harmonic modulation frequency $\alpha_a = 1$ Hz

Figure 15 displays one realization of another CS2 signal in time domain (a) and the same signal with the addition of stationary background noise (b). The corresponding power spectral densities are shown in Fig. 16 (a). A few observations are noteworthy. Signal $x(t)$ clearly evidences a random behaviour, yet with a periodic modulation; this may be interpreted as a periodic flow of its energy along the time axis with cyclic frequency α. At the same time, the presence of this "hidden periodicity" (additional α-axis) is completely missed in the classical power spectral density (see Fig. 16 (a)) which essentially reflects the continuous distribution of the random carrier (f-axis description) and the absence in the signal of any *additive* sinusoid. Besides, the presence of cyclostationarity is not detectable in the noisy

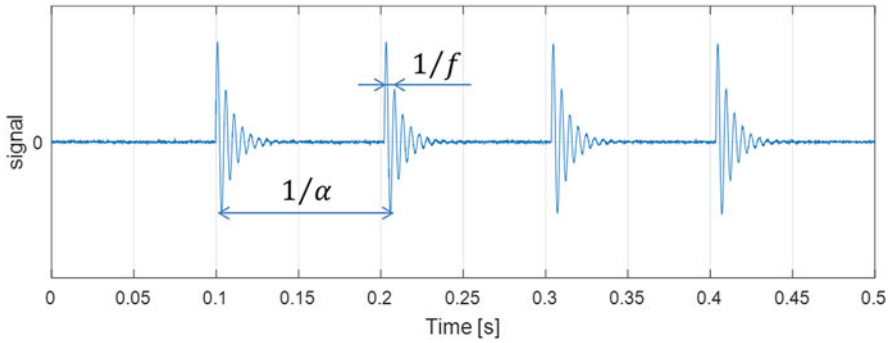

Fig. 14 Simplified numerically generated bearing signal

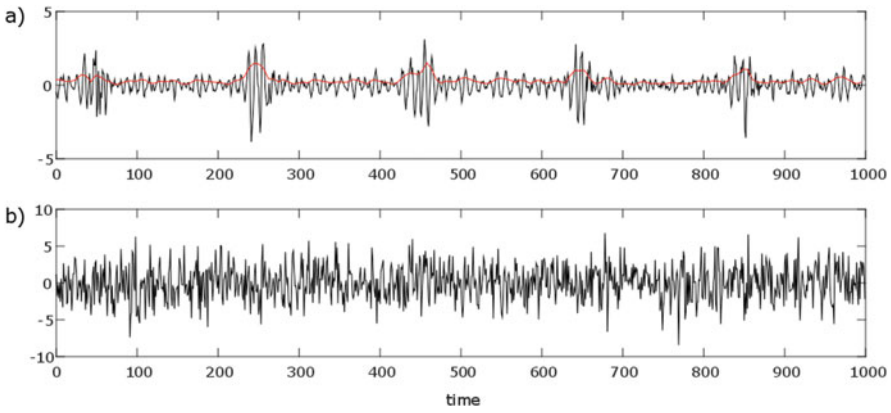

Fig. 15 (**a**) Realization of a second-order cyclostationary signal (sampling frequency $F_s = 1$ Hz) made of a narrowband stationary random carrier modulated by a periodic amplitude. The signal envelope (magnitude of the analytical signal after bandpass filtering in band $[0.05F_s\ 0.15F_s]$) is displayed in red. (**b**) Same signal after addition of stationary random noise (SNR = -9 dB). Note that the cyclostationary behaviour of the signal is completely masked in (**b**)

version of the signal, even in the time domain. This asks for the use of specific CS2 tools, which will be investigated in the following sections.

8.3 The Envelope Spectrum

The idea of the squared envelope spectrum is to reveal the presence of a periodic flow of energy in a cyclostationary signal. The flow of energy is estimated by computing the squared envelope of the signal, which is then Fourier transformed to evidence a harmonic structure.

As exemplified by Fig. 15, it is important to carefully select the frequency band that carries the periodic modulation in order to extract it from additive noise which

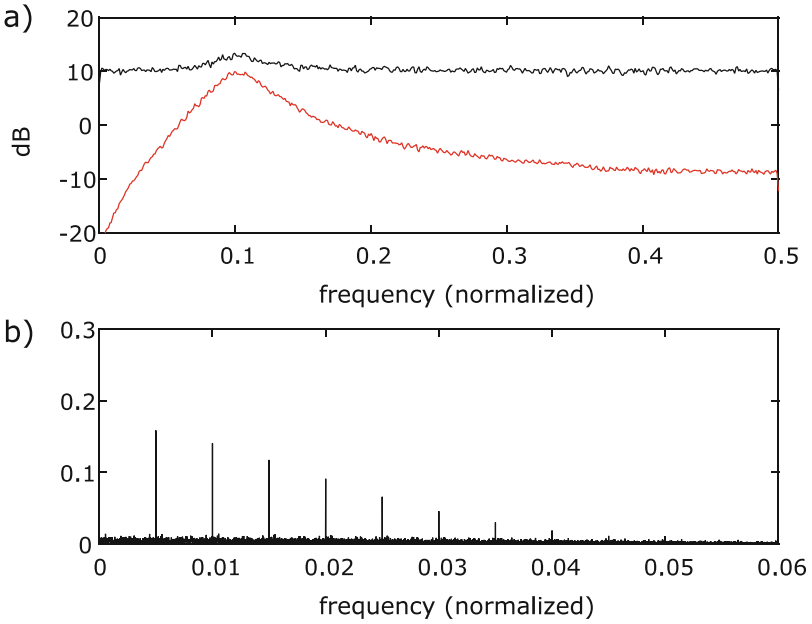

Fig. 16 (**a**) Power spectral density of signals in Fig. 15a (red curve) and in Fig. 15b (black curve) (frequency resolution $= 5 \times 10^{-4}$Hz). (**b**) Squared envelope spectrum of signal in Fig. 1b after bandpass filtering in band $[0.05F_s\ 0.15F_s]$ (frequency resolution $= 1 \times 10^{-5}$Hz). In contrast to the power spectral density which displays a continuous distribution, the squared envelope spectrum clearly reveals a harmonic structure. Note that correctly bandpass filtering the signal in the band where the SNR is maximized is crucial

may possibly mask it otherwise. This is achieved by a preliminary bandpass filtering of the signal. The squared envelope is then conveniently computed as the squared magnitude of the analytic signal. The algorithm to compute the squared envelope spectrum is summarized in Fig. 17. Its application to the signal of the previous subsection is illustrated in Fig. 16b. It is seen that cyclostationarity is easily detected even though it was barely visible in the time domain due to the presence of strong additive noise.

It is eventually remarkable to notice that the key point of the squared envelope spectrum is to introduce a quadratic non-linearity: squaring a second-order cyclostationary signal produces additive sinusoids which can then be detected and quantified by classical spectral analysis.

8.4 The Cyclic Modulation Spectrum

The success of the squared envelope spectrum largely depends on correctly selecting the frequency band where to demodulate the signal. When the latter is not known, its selection by trial and error may be a tedious and hazardous task. A simple solution

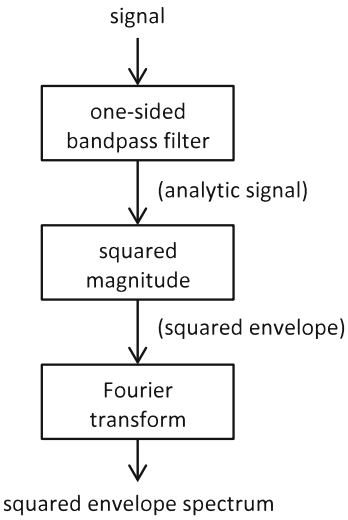

Fig. 17 Steps for computing the squared envelope spectrum

is to display a cascade of squared envelope spectra at the output of a filter bank that decomposes the signal into a set of sub-band components [19]. This defines the cyclic modulation spectrum, which is displayed as function of the modulation frequency α – also called cyclic frequency – and the carrier frequency f, also called spectral frequency. A simple interpretation of the cyclic modulation spectrum (and an efficient computational approach) is actually as the Fourier transform of the spectrogram (the squared magnitude of the short-time Fourier transform) along the time variable (see Fig. 18).

A significant value of the cyclic modulation spectrum at a given pair (α, f) thus indicates the presence of a periodic flow of energy with frequency α in the frequency band centered at f. In the case of a broadband cyclostationary signal, the cyclic modulation spectrum evidences a symptomatic set of vertical lines at discrete values of the modulation frequency and continuous values of the carrier frequency. Following a numerical example analogous to Figs. 3 and 13, the CMS of a CS2 signal $x_{CS2}(t)$ composed by the product of a stationary random carrier $r(t)$ and a periodic modulation $p_T(t)$ is reported in Fig. 19f. In this case the peak at $\alpha = 4$ Hz and $f = 0 - 100$ Hz shows a second-order cyclostationary component whose energy is mainly concentrated in the 0–100 Hz band and cyclically fluctuates with a frequency of 4 Hz. As clearly visible comparing Fig. 19b, c, d, this CMS peak shows:

- An f-axis content which corresponds to the PSD of the carrier $r(t)$
- An α-axis content which corresponds to the Fourier series of the squared periodic modulation $|p(t)|^2$

The same concepts are illustrated for the more complex signal of Fig. 15b in Fig. 20a. In this case, the presence of cyclostationarity is clearly evident in

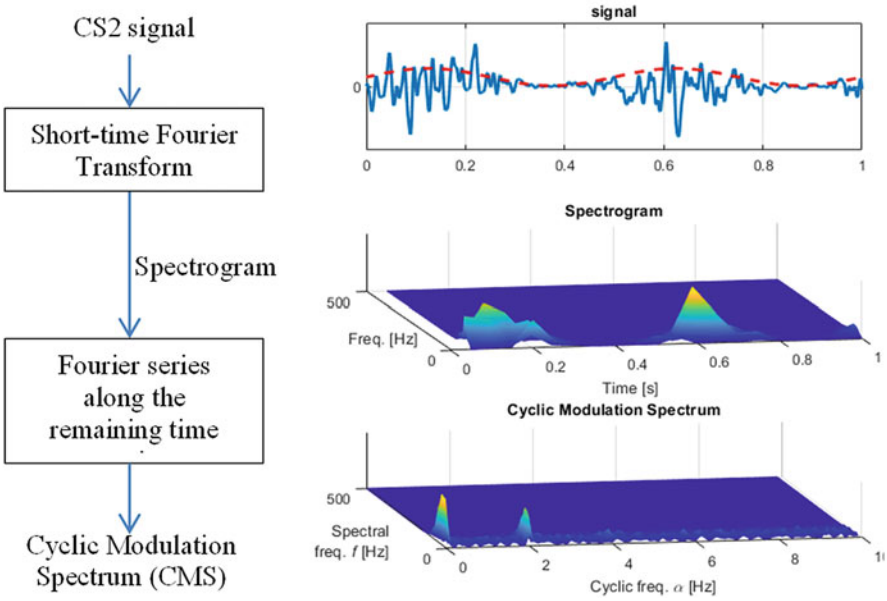

Fig. 18 (Left) Schematics of the procedure to calculate the CMS using the spectrogram, (right) corresponding initial intermediate and final results for a numerically generated CS2 signal

the frequency band from 0.05 Hz to 0.15 Hz which carries the modulation and with cyclic frequency at 1/200 Hz. The number of cyclic harmonics reflects the "roughness" (non-sinusoidal characteristic) of the modulation, and, as explained in Sect. 3.3.2, it is actually related to the time domain of the signal.

One limitation of the cyclic modulation spectrum – and thus of the squared envelope spectrum – is that it cannot detect modulations that are faster than the bandwidth set in the filter bank: fast modulations will require a filter bank with large bands, thus with a coarse spectral resolution; in contrast, a fine spectral resolution in the cyclic modulation spectrum implies slow modulations. This is a direct consequence of the uncertainty principle of time-frequency analysis.

This has consequences in practice. For instance, when trying to detect a bearing fault, the expected signal is in the form of a series of repetitive transients with mean period T_0 (as explained in 5.2.3, this signal is close to cyclostationary rather than periodic due to random fluctuation in the period and possibly in the amplitude). The bandwidth of the cyclic modulation spectrum should then be set large enough so as to include the "hidden harmonics" of the fault, that is, larger than $1/T_0$.

8.5 The Spectral Correlation Density

The limitation inherent to the cyclic modulation spectrum can be bypassed by defining the spectral correlation density, a fundamental tool of second-order cyclo-

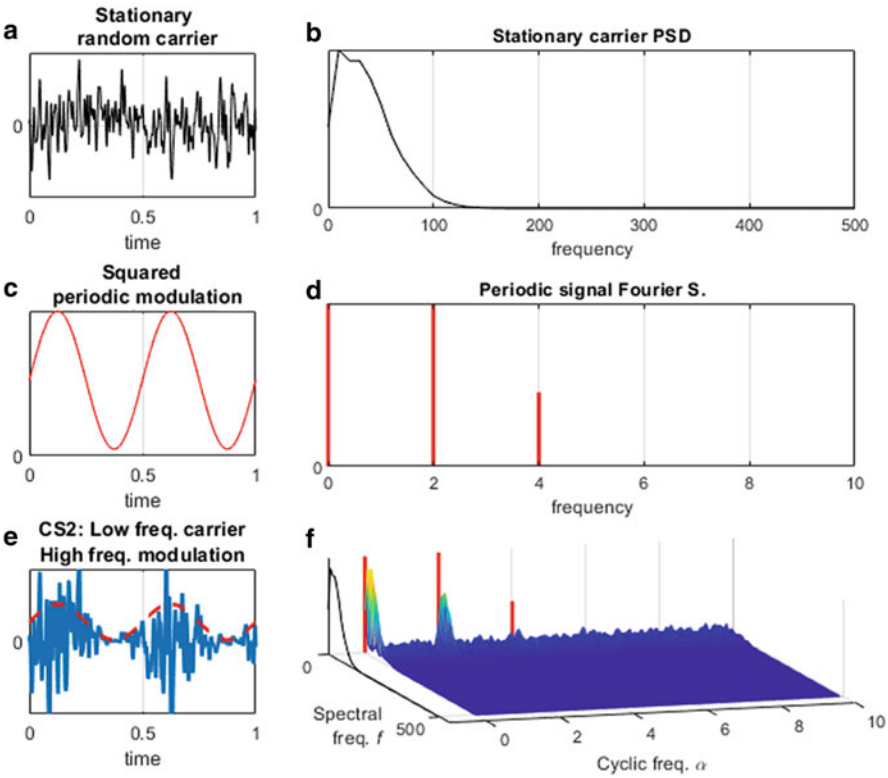

Fig. 19 Relationship between the cyclic modulation spectrum of a numerically generated CS2 signal with the spectral characteristics of its random carrier and modulating periodic signal. (**a**) Stationary carrier $r(t)$, (**b**) PSD of the carrier $PSD_r(f)$, (**c**) squared value of periodic modulation $p_T(t)$ (red), (**d**) Fourier series of the squared modulation $\mathcal{F}\left\{|p_t(t)|^2\right\}$, (**e**) CS2 signal $x_{CS2}(t) = r(t)p_T(t)$ (blue) and modulation $p_T(t)$ (red dashed), (**f**) CMS of $x_{CS2}(t)$ (surface plot) in comparison with $PSD_r(f)$ (black dotted) and $\mathcal{F}\left\{|p_t(t)|^2\right\}$ (red dotted)

stationary processes. The introduction of the spectral correlation density requires a more formal approach, based on the covariance function of the signal. As mentioned in Sect. 3.3.2, the covariance function of a second-order cyclostationary signal is a periodic function of time (see Eq. (22)); taking the example of Sect. 3.3.2, it writes:

$$C_x(t,\tau) = m(t)m(t+\tau)\, C_\varepsilon(\tau) = C_x(t+T,\tau) \tag{53}$$

The squared envelope spectrum and its extended version, the cyclic modulation spectrum, essentially investigates the periodicity of $C_x(t,0)$ (after filtration in frequency bands), which reflects the flow of energy as a function of time. The spectral correlation density considers the complete covariance function (not only for $\tau = 0$) through the double Fourier transform.

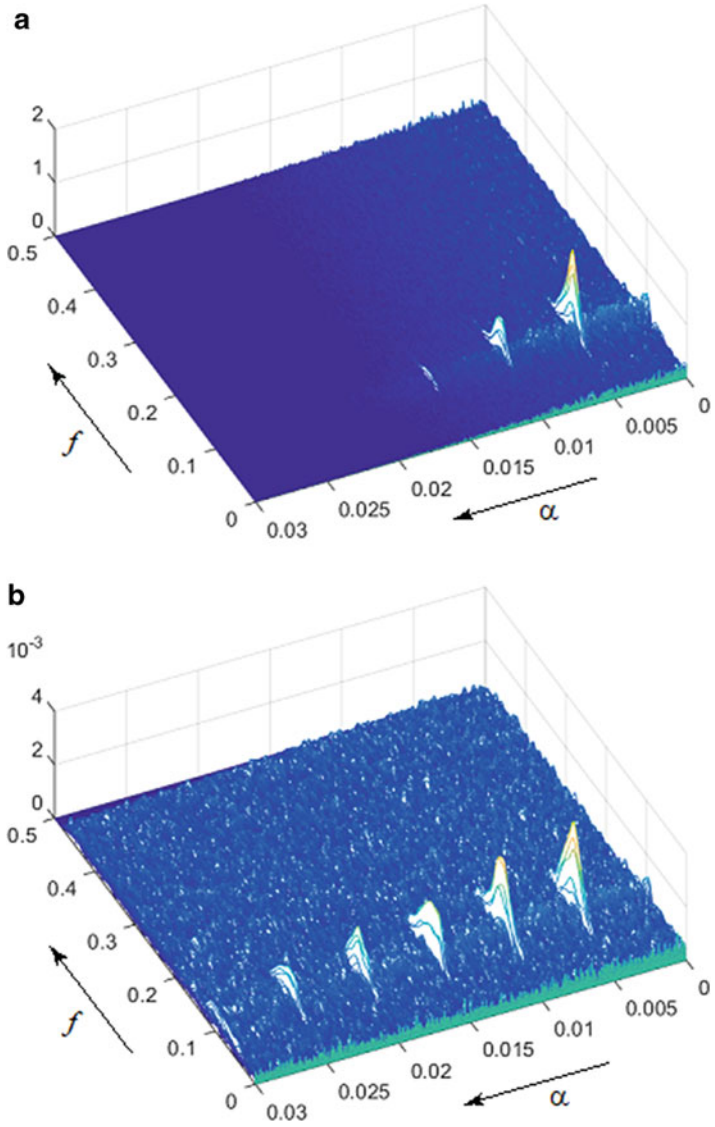

Fig. 20 (**a**) Cyclic modulation spectrum and (**b**) spectral coherence density of signal in Fig. 13 (**b**) (frequency resolution $\Delta f = 8 \times 10^{-3}$Hz; cyclic frequency resolution $= 1 \times 10^{-5}$Hz). The cyclic modulation spectrum has a cyclic frequency range on the order of Δf (a strong attenuation is seen after 2 Δf), whereas the spectral coherence density has no such limitation. The spectral coherence density is normalized between 0 and 1 and usually shows a better contrast. The presence of cyclostationarity is evidenced in the band [$0.05F_s$;$0.15F_s$] and with a fundamental cyclic frequency of 1/200 Hz

$$S_x(\alpha, f) = \mathcal{F}_{t\to\alpha}\mathcal{F}_{\tau\to f}\{C_x(t,\tau)\} \tag{54}$$

According to the t-periodicity of $C_x(t,\tau)$, the spectral correlation density of a second-order cyclostationary signal is expected to be discrete in the cyclic frequency and continuous in the spectral frequency. The relationship between the two frequency axes and the two time domain variables is crucial in understanding the properties of CS2 signals and their bispectral representation. Referring to the acoustic example already mentioned in Sect. 3.3.2, the characteristic high-energy f band(s) of the signal corresponds to the "pitch" of a CS2 sound, while the characteristic α frequency (or frequencies) indicates the rhythm with which the sound is repeated. Note also that the spectral correlation density at $\alpha = 0$ is equivalent to the power spectral density of the signal, $S_x(f)$ (as it indicates the "t-average" component of $C_x(t,\tau)$). As a consequence, the contribution of stationary noise is also completely and only confined to $\alpha = 0$. Interestingly, the spectral correlation density can be equivalently defined by means of the Fourier transform $X_D(f)$ of the signal on a time interval of duration D:

$$S_x(\alpha, f) = \lim_{D\to\infty}\frac{1}{D}\mathbb{E}\left\{X_D(f)X_D^*(f-\alpha)\right\} \tag{55}$$

(where $\mathbb{E}$ stands for the expectation operator and * for the conjugation) which provides a practical algorithm of estimation. This definition gives evidence that spectral components spaced apart by the modulation frequency are correlated. In other words, although the spectrum of a cyclostationary signal does not give evidence of harmonics in general, the presence of hidden periodicities in it manifests itself by a correlation of its spectral components. Therefore, a natural tool to quantify cyclostationarity is the spectral coherence density (in all points similar to a correlation coefficient):

$$\gamma_x(\alpha, f) = \frac{S_x(\alpha, f)}{\sqrt{S_x(f)S_x(f-\alpha)}} \tag{56}$$

which returns a measure between 0 and 1. The spectral coherence density is particularly useful to disclose weak cyclostationary signals in the presence of strong coloured noise because it is independent of the actual magnitude of the signal and, when coming to estimation issues, its variance is constant in the whole (α, f) plane.

Refs. [20, 21], respectively, detail the theoretical foundation and efficient implementation of a fast algorithm for the calculation of the spectral correlation.

8.6 The Relationship Between Kurtosis, Envelope, and CS2 Indicators

The bispectral CS2 indicators described in the previous section expose the full nature of CS2 signals: while α "sets the tempo" of the long-term cyclic pulsation of

energy, the f-axis describes the velocity of the short-term random signal variation constituting the signal power itself.

The traditional squared envelope spectrum (calculated with a broad pass-band) is actually equivalent to an f-integral estimation of the spectral correlation, i.e., the SES is representing the cumulated effect of a series of horizontal (α-parallel) slices of the spectral correlation $S_x(\alpha,f)$:

$$SES_x\left(\alpha;\, f_{\text{low}},\, f_{\text{high}}\right) \approx \int_{f_{\text{low}}}^{f_{\text{high}}} S_x\left(\alpha,\, f\right) df \tag{57}$$

where $SES_x(\alpha;f_{\text{low}},f_{\text{high}})$ represents the squared envelope spectrum obtained after bandpass filtering with pass-band $[f_{\text{low}},f_{\text{high}}]$. Any peak in the squared envelope spectrum $SES_x(\alpha;f_{\text{low}},f_{\text{high}})$ will therefore represent an (α-)periodicity in the cyclic flow of energy carried by frequencies within the range $[f_{\text{low}},f_{\text{high}}]$. This sheds some light on the true cyclostationary meaning of envelope analysis: the explicit α-axis represents periodicity in the second-order moment of the signal (power, autocorrelation), while the implicit dependency on f (through the preliminary bandpass filtering operation) reflects the τ-dependecy of the second-order moment $C_x(t,\tau)$. When choosing a filter for the envelope analysis operation, the pass-band therefore defines the components of the signal whose energy pulsation is analyzed. In the example of Fig. 20, the best envelope analysis result (clearest peak at $\alpha = 0.005\ F_s$) is thus obtained using the bandpass filter 0.05–0.15 F_s before enveloping, since this band is the one whose energy is actually fluctuating with a period of $2000/F_s$.

This relationship can be further extended to kurtosis by integrating the squared envelope spectrum over the remaining α-axis [22]. In fact, using Parseval's theorem it is possible to demonstrate that for a zero-mean signal $x(t)$:

$$\sum\nolimits_{\alpha} SES_x\left(\alpha\right) = {RMS_x}^4 \cdot \kappa_x \tag{58}$$

where $SES_x(\alpha)$ is the SES calculated using the full band (no bandpass filtering) and RMS_x and κ_x are the RMS and (sample) kurtosis of the signal. Moreover, since the fourth power of the RMS is equivalent to the null cyclic frequency SES, the (sample) kurtosis is equivalent to:

$$\kappa_x = \frac{\sum_{\alpha} SES_x\left(\alpha\right)}{SES_x(0)} \tag{59}$$

This equivalence allows a cyclostationary interpretation of the kurtosis, which is equivalent to the sum of all the different α-contributions of the full f-spectrum SES, normalized by the signal's power. Since the SES of Eq. (57) is performed using the raw signal, it is equivalent to a full-band integration of the spectral correlation, and consequently the (sample) kurtosis is equivalent to a full (α, f)-plane integration of the spectral correlation. These results show how kurtosis, envelope analysis,

and advanced spectral correlation estimators are all aiming, with different levels of specificity, at the identification of the cyclic variation of the autocorrelation function (and power) characteristic of CS2 signals.

The strong relationship between CS2 and fourth-order statistics highlights an unwanted sensitivity of CS2 indicators to impulsive noise, which has been shown to potentially mask CS2 components [23]. A series of techniques have been proposed to deal with this issue, usually including fractional-order or logarithmic transformations of the envelope [24, 25].

9 Typical Diagnostic Examples

In this section a number of examples are given which draw on combinations of techniques introduced in earlier sections. They demonstrate the wide diversity of problems that can arise in machine diagnostics, and how they can be tackled.

9.1 Rolling Element Bearings

The first example illustrates a case where the speed of the machine is constant, but the bearing signal is completely masked by stronger signals from gears, right up until just before failure. The example was first published in [26], but most details are repeated in [27]. A series of signals were taken from a helicopter gearbox test rig at DSTO (Defence Science and Technology Organisation), Melbourne, Australia, as it was run to failure. The signals were analyzed blind to detect the source of the failure(s). Direct comparison of raw time signals and their spectra could detect no change from the start to finish of the test. The time signal just before failure is shown in Fig. 21a and has a kurtosis of -0.61, effectively the same as Gaussian noise. The analysis procedure first applied was linear prediction, as a means of removing the discrete frequency components from the gears and leaving the bearing signal in the residual. The kurtosis increased from -0.61 to 2.2, but primarily because some modulation was now apparent at the rate of the planet pass frequency; the bearing signal was not detectable. A wavelet kurtogram was then used to determine the optimum band for demodulation, and that is shown in Fig. 21b. By filtering the residual signal with the optimum band (1/12-octave centered on 18.8 kHz), the kurtosis increased to 14.1, and the bearing fault impulses can now be seen in Fig. 21c.

Frequency analysis of the squared envelope of the processed signal in Fig. 21c in two different frequency ranges gave the envelope spectra in Fig. 22.

The harmonics in Fig. 22a at 9.83 Hz corresponded to the cage frequency (relative to the load zone) of the planet gear bearings in the planetary section of the gearbox. This indicates a fault travelling at cage speed, and this is often a sign of faulty rollers, though often accompanied with components at the roller spin frequency (not found in this case). When the gearbox was dismantled, three

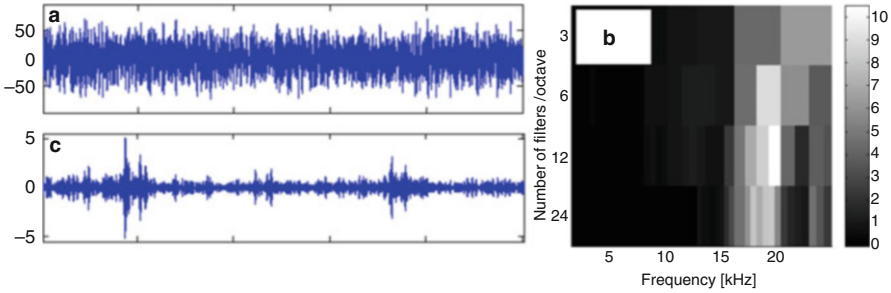

Fig. 21 Signal processing stages for a bearing fault in a helicopter gearbox (from [26]). (**a**) Original signal, kurtosis −0.61. (**b**) Wavelet kurtogram. (**c**) Processed signal, kurtosis 14.1

adjacent rollers in one bearing were found to have some spalling, and this group was apparently modulating the signals as they passed through the load zone.

The harmonics in Fig. 22b at 117.7 Hz corresponded to the inner race fault frequency in the same planet gear bearings, and when the faulty bearing was dismantled, severe spalling was found in the inner race of one planet bearing. It should be noted that with planet bearings, it is the inner race that is fixed with respect to the load direction, so no modulation sidebands were expected or found.

Even though this result is from near the end of life, the trend of the kurtosis of the processed signal showed that the faults could have been detected about 30 h before the end of a 160 h test.

9.2 Gears

A standard way of analyzing gear signals is to start with TSA (time synchronous averaging), which in general extracts the signal for each gear from the total signal, including those of other gears. Even when the gearbox is running at nominally constant speed, it is necessary to first carry out order tracking and resampling of the signal, to ensure that there are an integer number of samples per rotation of the gear, and a fixed starting phase (e.g., the exact time of a once-per-rev tacho pulse, which may occur between two of the original samples). Even though the order tracking removes speed variations, it is generally still necessary to resample for each successive shaft speed so as to satisfy the requirement of a fixed number of samples per rev.

The TSA result will generally allow visualization of the vibration response of each tooth on the gearmeshing with the mating gear, and changes can often be recognized in both amplitude and variability. The regular gearmeshing pattern can however disguise some local disturbances, so a standard method of revealing these is to remove that pattern by two alternative basic procedures:

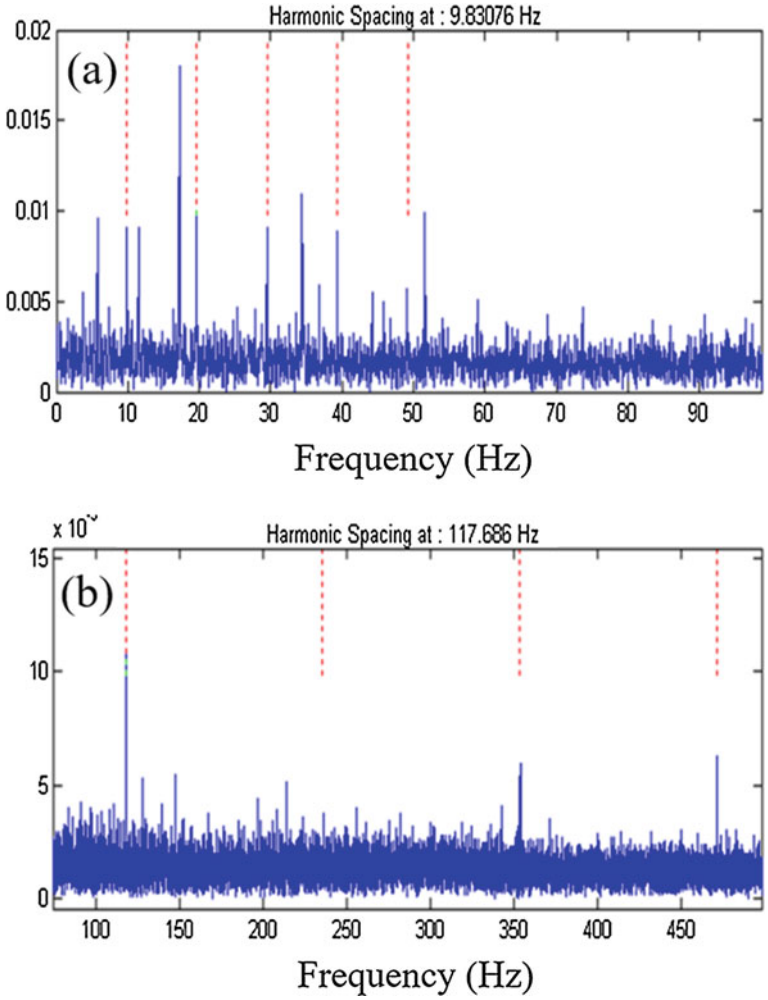

Fig. 22 Envelope spectra in two different frequency ranges (from [26]). (**a**) Low frequency, showing a series of harmonics of 9.83 Hz. (**b**) High frequency, showing a series of harmonics of 117.7 Hz

- Remove harmonics of the gearmeshing frequency in the frequency domain and transform back to the time domain. Since the primary aim is to detect local faults on the gears, it has been found advisable to remove slow modulations as well by removing one or even two pairs of sidebands around each harmonic as well. Since only the information of one gear is left in the TSA signal, these sidebands will also be harmonics of the rotational speed of the gear.
- Use linear prediction to predict and subtract the regular toothmeshing pattern, but leave the unpredictable sudden changes which deviate from this pattern.

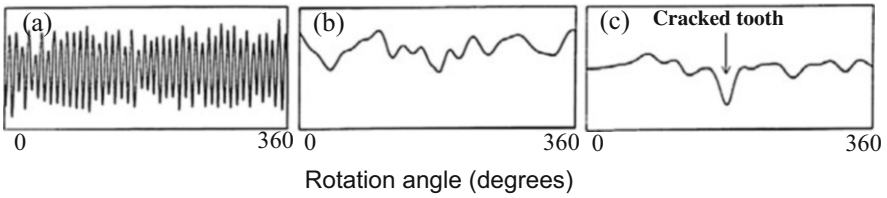

Fig. 23 Amplitude and phase demodulation of a gearmesh signal (from [28]). (**a**) Original TSA signal. (**b**) Amplitude demodulation. (**c**) Phase demodulation

The linear prediction filter can be adjusted to remove slow changes but retain sudden ones.

The following example is one where the TSA signal did not immediately reveal a fault, and neither did the residual after removing the toothmesh signal.

The actual fault was a tooth root crack in a gear in a helicopter gearbox, and the method proposed to reveal it in [28] consisted in performing a demodulation of the toothmesh component, both amplitude and phase demodulation. Figure 23 shows the original TSA signal and the results of amplitude and phase demodulation of the (second harmonic of) gearmesh frequency. The second harmonic was demodulated because it was stronger than the first.

Even though the TSA signal is not completely uniform, there is no definite indication of a fault, and the same applies to the amplitude modulation signal. The phase modulation signal does however reveal a sudden deviation in one location, which corresponded to the location of the tooth root crack. At a later stage in the development, the amplitude modulation signal also revealed the crack, but the phase deviation was the first indication. Note that this method only works when the fault manifests itself within the maximum frequency band for demodulation, which corresponds to the gearmesh frequency. In this case the demodulation band was from 1.5 to 2.5 times the gearmesh frequency. In [29] a case is reported where a tooth root crack on a very slow component in a wind turbine gearbox (gearmesh frequency 30 Hz) manifested itself most strongly around 11 kHz, and was not detectable by either synchronous averaging or toothmesh demodulation. It could, however, be detected using spectral kurtosis.

Further examples of gear diagnostics using the cepstrum are given in Sect. 10.3.

9.3 Reciprocating Machines and Engines

Since reciprocating machine signals tend to be a series of impulsive events, and thus vary rapidly in both time and frequency, even at constant speed, a common way of analyzing them is by some form of time-frequency analysis (TFA). A large component is usually second-order cyclostationary, since individual combustion cycles have considerable random variation but repeat cyclically. This means that a

very powerful form of TFA is the Wigner-Ville spectrum (see Fig. 11), where cross terms are eliminated for CS2 components, and better simultaneous time-frequency resolution is possible than by a normal spectrogram (better than the uncertainty principle, by virtue of the extra data required for averaging).

There are a couple of other fault types, however, which can be diagnosed by relatively simple techniques, but enhanced considerably by using simulation models of the machine.

The first is combustion faults in internal combustion (IC) engines, which can be detected by changes in torsional vibrations. The latter can be measured very simply by frequency demodulation of a shaft encoder signal, and that can be as simple as a tooth-pass signal from a proximity probe detecting passage of the teeth on the engine flywheel. For engines with a rigid crankshaft (lowest torsional resonance frequency above a number of times the engine firing frequency), this is very straightforward as the torsional acceleration from a given torque pulse is independent of the cylinder from which it originates and insensitive to speed. However, as shown in [30], a relatively simple torsional vibration model of a flexible crankshaft can be made with lumped parameters and then updated using a small number of actual measurements. Waveforms are very sensitive to actual natural frequencies, so the model updating involved allowing the natural frequencies and damping to adjust to give optimal matching of the waveforms, while using the analytical eigenvectors (mode shapes) from the simple analytical model. This was successful on two nominally identical engines with quite different waveforms. Figure 24 compares the simulated waveform with the measured one for one engine.

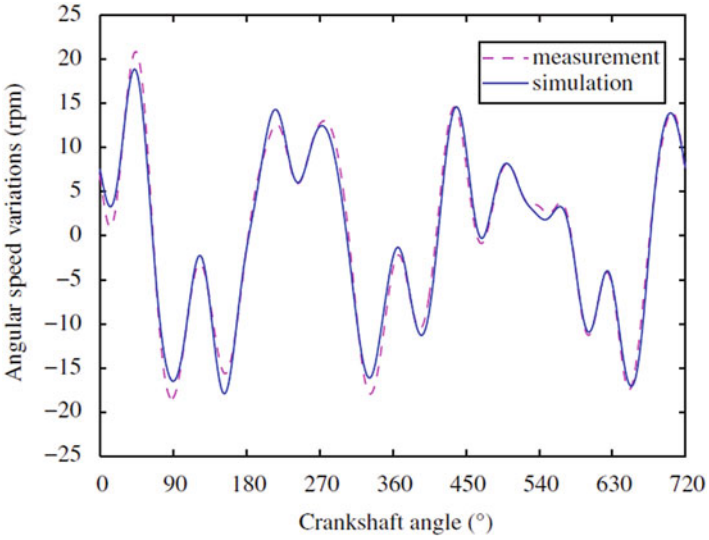

Fig. 24 Simulation of the angular speed variations at the crankshaft free end (continuous line) compared to the actual measurement (dashed line). (Courtesy M. Desbazeille)

Very little "faulty" data was available, but an artificial neural network (ANN) trained on outputs from this simulation model was able to detect the two faults fed to it.

Reference [31] used a similar principle to train neural networks for a much wider range of combustion faults purely using simulated data, but the engine was smaller and had a rigid crankshaft. On the other hand, another simulation model was also generated to simulate the rotational motions of the engine on its supports due to the same combustion faults, and this has similar characteristics to the torsional model of the flexible crankshaft, since the engine mounting resonances were constant and within the frequency excitation range of the combustion faults, meaning that responses varied with the faulty cylinder and engine speed. The ANNs trained purely on simulated data in both cases were 100% successful in diagnosing the fault severity and location.

The same principles were used to train ANNs to diagnose mechanical faults (piston slap, bearing knock) in the same IC engine and were also 100% successful [32, 33]. For the mechanical faults, the features used to train the ANNs were the amplitude and phase of various harmonics of the cycle frequency of the engine, measured on the squared envelope of an optimally filtered band, quite analogous to bearing faults (since these signals were CS2).

10 Cepstrum

10.1 Background and Definitions

The cepstrum was first proposed in 1963 [34], being defined as the "power spectrum of the log power spectrum." The original application was to the detection of echo delay times, it being much less sensitive than the autocorrelation function (inverse Fourier transform of the power spectrum) to the color of the signal. The reason for the definition was apparently that it was published 2 years before the FFT (though with a common author, Tukey) and so software was readily available for power spectra (via the autocorrelation function) but not for complex Fourier transforms. Shortly after the publication of the FFT, the "power cepstrum" was redefined as the inverse Fourier transform of the log power spectrum, which meant that it was reversible to the (log) power spectrum after editing in the cepstrum. At about the same time, work by Oppenheim and Schafer led to the definition of the "complex cepstrum," which retains the phase information in the log spectrum, so that it is reversible to a time function after editing in the cepstrum. This can only be done for spectra whose phase can be unwrapped to a continuous function of frequency. Given a signal $x(t)$, most important definitions are now as follows:

Complex cepstrum:

$$C_c(\tau) = \mathcal{F}^{-1}\{\log(\mathcal{F}\{x(t)\})\} = \mathcal{F}^{-1}\{\log(A_x(f)) + i\phi_x(f)\} \tag{60}$$

where $A_x(f)$ and $\phi_x(f)$ are, respectively, the amplitude and phase of the discrete Fourier transform of the signal $x(t)$:

$$\mathcal{F}\{x(t)\} = A_x(f) \cdot e^{i\phi_x(f)} \tag{61}$$

Power cepstrum:

$$C_c(\tau) = \mathcal{F}^{-1}\{\log(S_x(f))\} = \mathcal{F}^{-1}\left\{\log\left(|\mathcal{F}\{x(t)\}|^2\right)\right\} = \mathcal{F}^{-1}\{2\log(A_x(f))\} \tag{62}$$

The so-called real cepstrum is sometimes defined by setting the phase term in Eq. (60) to zero, which is seen to be a scaled version of Eq. (62).

In the original paper [34], the authors coined the word "cepstrum" by reversing the first syllable of "spectrum," the justification being that it was a "spectrum of a spectrum" (although the autocorrelation is also a spectrum of a spectrum, just without the log transformation). Similarly, the word "quefrency" was obtained from "frequency," and the authors also suggested a number of other terms, including "rahmonic" from "harmonic" and "lifter" from "filter," and these four terms are still used in the cepstrum literature. Note that because the original cepstrum was not reversible, a lifter had to be applied as a convolutive filter to the log spectrum, but it is now applied as a window in the cepstrum.

Using z-transforms to replace Fourier transforms for digitized signals, Oppenheim and Schafer showed [35] that the complex cepstrum of a general transfer function

$$H(z) = \frac{B\prod_{i=1}^{M_i}\left(1 - a_i z^{-1}\right)\prod_{i=1}^{M_0}\left(1 - b_i z\right)}{\prod_{i=1}^{N_i}\left(1 - c_i z^{-1}\right)\prod_{i=1}^{N_0}\left(1 - d_i z\right)} \tag{63}$$

could be expressed in terms of its poles and zeros in the z-plane as:

$$\begin{aligned} C_h(n) &= \log(B) \quad , \quad n = 0 \\ C_h(n) &= -\sum_i \frac{a_i^n}{n} + \sum \frac{c_i^n}{n} \quad , \quad n > 0 \\ C_h(n) &= \sum_i \frac{b_i^n}{n} - \sum \frac{d_i^n}{n} \quad , \quad n < 0 \end{aligned} \tag{64}$$

where the c_i and a_i are poles and zeros inside the unit circle, respectively, and the d_i and b_i are the (reciprocals of the) poles and zeros outside the unit circle, respectively. Since the cepstrum of minimum phase functions is thus causal, the log amplitude and phase of the log spectrum are related by a Hilbert transform, meaning that the phase does not have to be measured or unwrapped, and the complex cepstrum can be obtained from the real cepstrum by setting negative quefrency components to zero and doubling positive quefrency components. Many simple mechanical transfer functions are minimum phase, and it is shown in [36] that the cepstrum of each pole term can be expressed as:

$$C_{sdof}(n) = \frac{c^n}{n} + \frac{c^{*n}}{n} = \frac{|c|^n}{n}\left(e^{in\arg(c)} + e^{-in\arg(c)}\right) = 2\frac{e^{-\sigma n\Delta t}}{n}\cos\left(n\arg(c)\right) \tag{65}$$

where Δt is time sample spacing (so that $t = n\Delta t$) and σ is the damping constant corresponding to the exponential decay $|c|^n$. Zeros have the same form, but negative, and maximum phase zeros are similar but at negative quefrency. Maximum phase poles are not viable for stable systems.

The cepstrum thus has at least three useful properties for analysis of mechanical systems:

- Echoes give a periodic structure to the log spectrum (log amplitude and phase), resulting in discrete rahmonics (spaced at the echo delay time) in the cepstrum. This was the original application and allows accurate measurement of the delay time, and even echo removal.
- Periodic structures in the log spectrum, such as families of equally spaced harmonics and sidebands, also give corresponding rahmonics in the cepstrum (of which the first two or three are the most important), facilitating detection and evaluation of such families and accurate measurement of their spacing.
- For single-input multiple-output (SIMO) systems, the output at each response point is a convolution in the time domain, a product in the frequency spectrum, a sum in the log spectrum and equally a sum in the cepstrum, often allowing separation of forcing and transfer functions in the response cepstrum. Multiple-input multiple-output (MIMO) responses have to be separated into a sum of SIMOs, e.g., by blind source separation, before this cepstral separation can be applied.

Exploitation of these properties is demonstrated in the following sections.

10.2 Cepstrum Liftering

Liftering (editing) in the cepstrum is done for four primary purposes:

- To remove uniformly spaced rahmonics in the cepstrum with a (comb) notch lifter, so as to remove the corresponding families of harmonics or sidebands in the (log) spectrum. Note that there must be a minimum of about eight uniformly spaced components in the spectrum for there to be distinct rahmonics in the cepstrum.
- To apply an exponential weighting to the cepstrum as a “shortpass” lifter to emphasize the modal characteristics of the transfer path (while adding a small known amount of damping to each mode), at the same time as removing many forcing functions and disturbances at higher quefrency.

- Possibly by subtraction of this modally weighted part of the cepstrum, to retain the part of the signal dominated by higher quefrency forcing functions, with suppression of modal information. So-called cepstral pre-whitening is an extreme example of this where all cepstrum components except that at zero quefrency are set to zero to make the spectrum completely white. This not only removes modal information but also sets discrete frequency components to a fixed level throughout the spectrum.
- To apply a "longpass" lifter at quefrencies below the modal ones, to remove the effects of broadband excitations (impulsive or broadband random) at even lower quefrencies, and to further enhance the modal characteristics in the absence of higher quefrency excitations.

10.2.1 Comb Notch Lifter

As described in [37], there are two types of comb notch lifters, depending on the way in which the rahmonics deviate from the ideal of a series of delta functions, which would only be the case if the corresponding families of harmonics/sidebands had uniform strength over the whole of the (two-sided) log spectrum, with the sampling frequency being an integer multiple of the harmonic/sideband spacing. For Type 1, the width of the notch remains constant over the whole range of quefrency, while for Type 2, the width increases in proportion to quefrency. The first applies where there is a fixed windowing of the spectral components or amplitude modulation, while the second applies when the width of the spectral components increases with frequency, as caused by small random frequency modulation of a basic periodicity. Note that removal of such components cannot be achieved by synchronous averaging, which assumes that all harmonics are discrete frequencies.

Figure 25 shows how a Type 1 lifter can be applied to the complex cepstrum to remove echoes from a time signal, even when these overlap. This is made easier by the fact that the cepstrum of the basic signal (in this case an SDOF response) is shorter than the impulse response itself (Eq. (65)).

Figure 26 shows an example where a series of groups of sidebands spaced at 120 Hz (around non-commensurate carrier frequencies) have been removed by a Type 1 lifter (with notch width $\pm 15\%$ of the rahmonic spacing). This is another case where synchronous averaging cannot be used because it only removes harmonics. The width of the notch was determined by trial and error but corresponds to the reciprocal of the average number of sidebands in each group (6–8). Note that the lifter was applied to the real cepstrum in this case, but time signals can be regenerated for each record by combining the modified amplitude spectrum with the original phase spectrum [36].

Further examples are given in Sects. 10.3 and 10.4.

10.2.2 Exponential Lifter

Since every pole (and zero) has the basic form of Eq. (65), it can be seen that multiplying the cepstrum of a response signal by an exponential window $e^{-\sigma_0 t}$ will add (constant) damping σ_0 rad/s to every pole (and zero) term. This can in principle be compensated for in the same way as an exponential window applied to

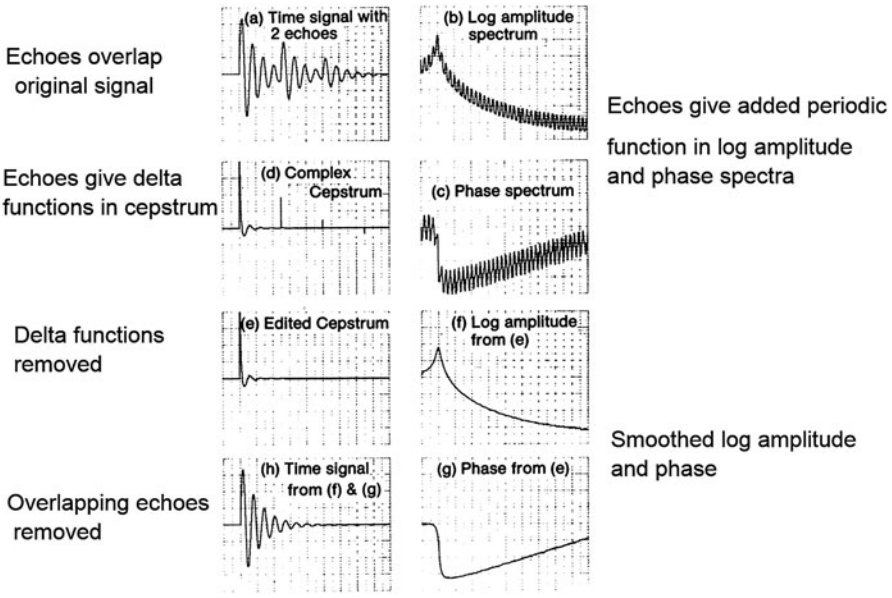

Fig. 25 Echo removal using a notch lifter in the complex cepstrum. (Courtesy Brüel&Kjær)

the response to a hammer blow in modal analysis, but is not limited to transients. It can be applied to each record of a continuous signal, once again in the real cepstrum but with regeneration of time signals using the original phase spectrum of each record.

Figure 27 shows the application of this approach to a signal from a gas turbine, with excitation by multiple harmonics of the various shaft speeds. It is seen that most of these are at high quefrency, and removed by the exponential lifter, so that the liftered spectrum is dominated by the modal information of the dominant transfer paths. The time constant of the lifter was made approximately equal to that of the lowest frequency mode at around 2 kHz, with corresponding decreasing effect on higher-frequency modes.

Further examples are given in Sects. 10.3 and 10.4.

10.2.3 Modal Suppression

If the residual cepstrum after subtraction of an exponentially windowed cepstrum is used, it will be dominated by the high quefrency excitation components such as shaft harmonics arising from gears, etc. and will be unaffected by the passage of such components through resonances. This is useful for variable speed machines as demonstrated in Sect. 10.3. Cepstrum pre-whitening was first done using the cepstrum but can equally be achieved by dividing the (complex) spectrum of each record by its modulus, without using the cepstrum. Even though discrete frequency components are reduced to the same strength as adjacent noise, phase-

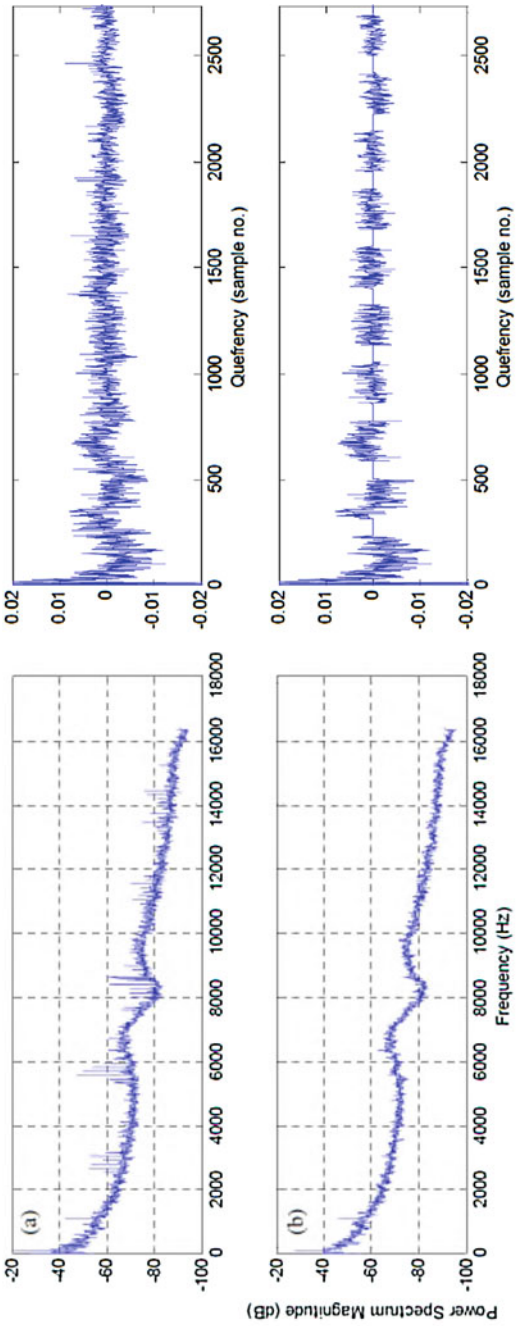

Fig. 26 Removal of groups of sidebands by notch lifter in real cepstrum. (From [37])

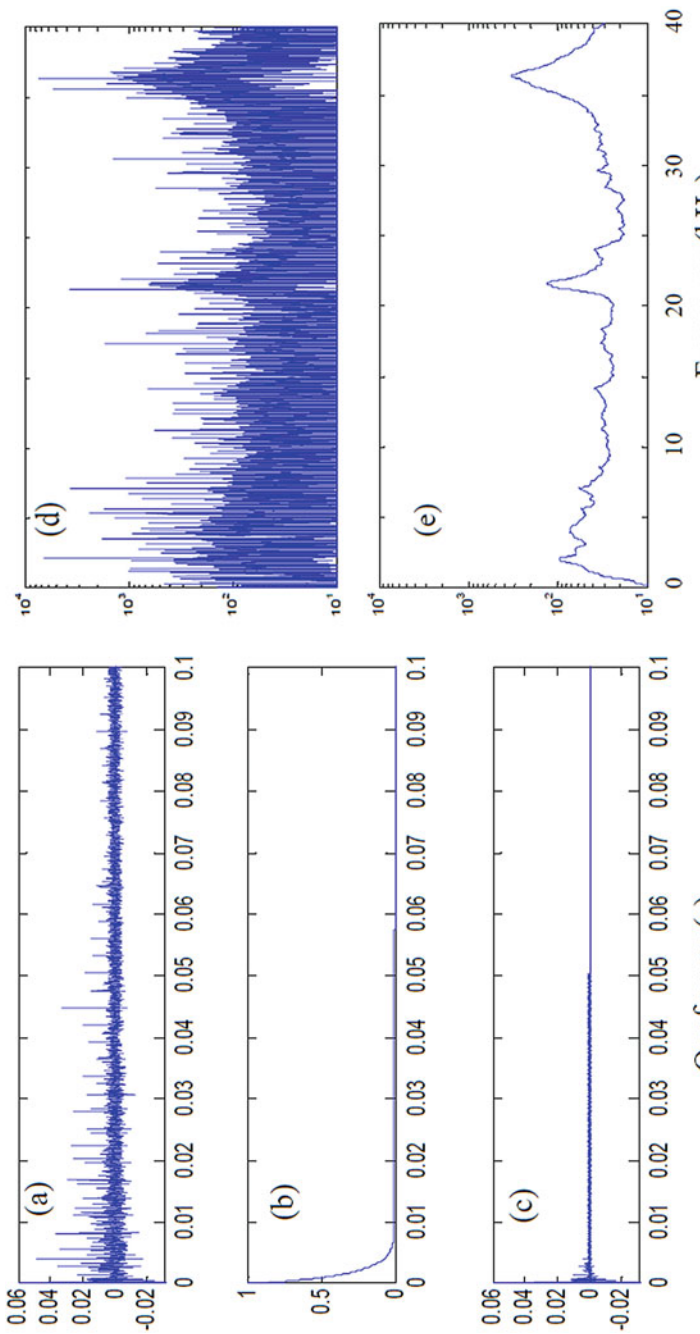

Fig. 27 Use of an exponential shortpass lifter to enhance modal information (from [36]). (**a**) Full cepstrum (of (**d**)). (**b**) Exponential lifter. (**c**) Liftered cepstrum. (**d**) Original spectrum. (**e**) Liftered spectrum

coherent harmonics and sidebands in a particular frequency band can make that band dominant in terms of impulsiveness of time signals, with uniform weighting over all frequency and no masking by particular resonances. Cepstral pre-whitening has also been found valuable for variable speed machines as shown in Sect. 10.3.3.

10.2.4 Longpass Lifter

If an impulse such as a hammer blow is appreciably shorter than the period of an excited natural frequency, its cepstrum will also be shorter, and the cepstrum of the response will be dominated by the modal properties for all quefrencies above that of the excitation. In an equivalent way, if the bandwidth of a broadband random excitation is appreciably broader than the 3 dB bandwidth of a mode, its cepstrum will be shorter and not interfere with the cepstrum of the modal properties. A "longpass lifter" can then be applied in the cepstrum of the response to remove the excitation without greatly affecting the cepstrum of the structural transfer function. This condition is often described as the log spectrum being relatively "smooth and flat," although it may still be far from white, in particular on a linear amplitude scale. The longpass liftered cepstrum can then be curve-fitted for the modal properties of the transfer function, as described in Sect. 10.4.

10.3 Cepstrum for Machine Diagnostics

Machine diagnostics, or condition monitoring, is based on the analysis of machine vibration responses, to determine any change in condition. Most often, such changes are indicated by changes in the forcing functions, such as unbalance, misalignment, gearmeshing forces, and impacts caused by bearing faults, but occasionally the change in condition is because of a change in the structural properties, such as a developing crack, and the cepstrum can be useful for separating these two possibilities, as well as assisting diagnosis by giving accurate indications of forcing and response frequencies, as expanded in the following sections.

Reference [36] is an extensive survey and history of the uses of cepstrum analysis for machine diagnostics.

10.3.1 Changes due to Forcing Functions

Many faults in machine components, such as gears, give rise to series of impulsive responses which give large numbers of harmonics in the frequency domain and quite often families of sidebands due to modulation by these impulsive forces. Gear faults can be divided into those which are uniform, such as uniform wear spread over all teeth, and those which give deviations around the mean errors, such as local tooth root cracks and spalls. The former give changes in a small number of harmonics of the toothmesh frequency and are best detected in the spectrum, while the latter give the sidebands which complicate the spectrum and are best detected and evaluated using the cepstrum. Figure 28 (from [37]) shows an example where (log) spectra and cepstra are compared for a gearbox before and after a deterioration giving both distributed wear and local spalls. The gearbox is a multi-stage wind turbine

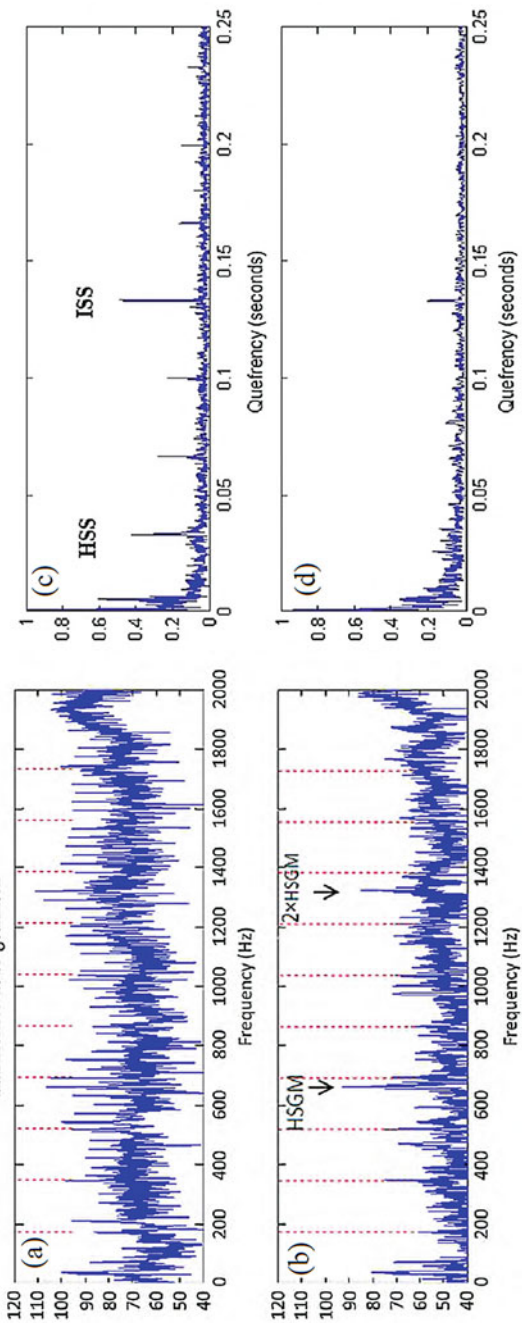

Fig. 28 Comparison of spectra and cepstra for a gear set in original and deteriorated condition. (**a**, **b**) Spectra. (**c**, **d**) Cepstra. (**b**, **d**). (Original (from [37]))

gearbox, with an overall ratio of about 100, but careful choice of the spectrum frequency range allows individual gear sets to be examined by centering on their mesh frequencies.

Comparing the spectra in Fig. 28a, b, it is seen that there has been a considerable increase in the harmonics of the high-speed gearmesh (HSGM), in particular of the second which has increased from 80 to nearly 110 dB. There has also been a considerable increase of all the harmonics of the intermediate shaft (IS) gearmesh (highlighted by the harmonic cursor). This indicates uniformly distributed wear. The spectrum of Fig. 28a, however, is complicated by the growth in multiple sidebands, mainly spaced at the speed of the high-speed shaft (HSS) around the harmonics of the HSGM. Comparing the cepstra in Fig. 28c, d gives a much clearer picture of the sideband structures, where spacings at both the HSS and ISS are apparent in deteriorated condition. Localized spalls were found on the HSS gear, which greatly increased the sidebands with this spacing. This situation is complicated by the very poor design of this gear set with an exact 4:1 ratio (88:22 teeth), and the two sets of sidebands would be even better separated in the more normal case of a hunting tooth design.

Figure 29 demonstrates the use of a comb notch lifter to remove one set of sidebands to make the diagnosis clearer. Despite the exact 4:1 ratio, which meant that every fourth rahmonic of the HSS coincided with a rahmonic of the ISS, the remaining rahmonics of HSS were removed by a specially designed notch lifter (Fig. 29b), and the effect on the spectrum can be seen by comparing Fig. 29c, d. All HSS harmonics (including sidebands) have been removed from the spectrum, leaving only the harmonics of the ISS, including those corresponding to the ISGM, highlighted by a harmonic cursor. It is now evident that these do not form a sideband structure around the gearmesh harmonics, meaning that the wear on this gear set is uniform rather than localized. This was confirmed by inspection and ascribed partly to the fact that this gear set was hunting tooth (23:82, with no common factors). This means that an incipient fault on one tooth is smeared over all teeth on the mating gear (and vice versa).

It was shown in [37] that the separation by this means gave a somewhat better result than synchronous averaging, which was implemented by dividing the SA for the IS shaft into the four revolutions of the HS shaft, averaging them, and then subtracting the repeated average from the original. Moreover, the SA required initial order tracking, not required for the cepstral liftering.

10.3.2 Changes due to Structural Response

In condition monitoring it is important to know whether a change in the response is due to a change in the forcing function or a change in the structural dynamic properties, and the cepstrum provides a simple way of doing this. For example, an increase in the second harmonic of a gearmeshing frequency would normally be taken as indicating an increase in uniform wear. However, it is possible that a resonance frequency, originally above the toothmesh harmonic, has decreased because of a growing crack in the shaft or casing and now amplifies it without any change in the forcing function. The prognosis would be completely different.

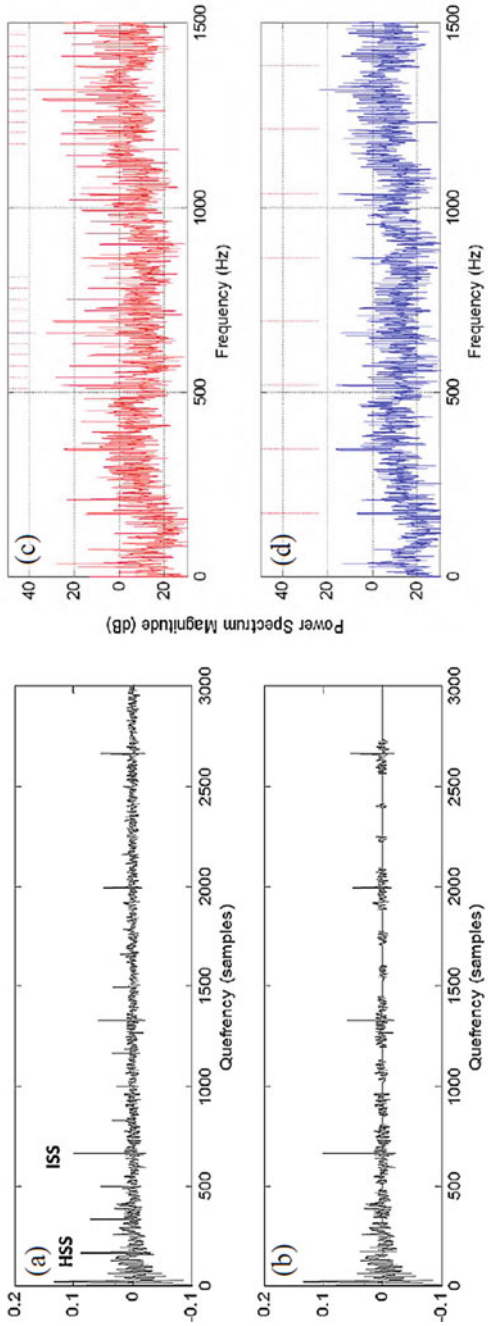

Fig. 29 Removing the effects of the HSS by comb liftering in the cepstrum. (**a**, **b**) Cepstra. (**c**, **d**) Spectra. (**a**, **c**) Unmodified. (**b**, **d**) Liftered. (From [37])

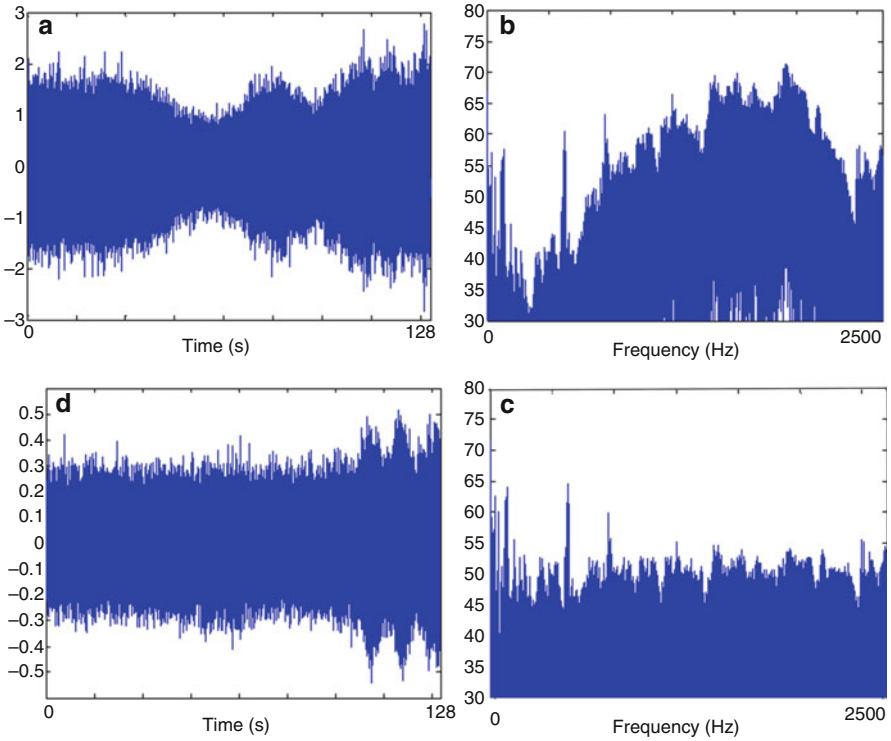

Fig. 30 Suppression of modal information in a variable speed gearbox. (**a**) Original time record, (**b**) log spectrum, (**c**) liftered spectrum after suppression of modal information, (**d**) regenerated time signal lowpass filtered above 3×GM frequency. (From [38])

Applying an exponential shortpass lifter, as in Fig. 30, it is possible to obtain a spectrum showing the modal frequencies very clearly and thus to see if they have changed over time. In complicated cases it would even be possible to curve-fit the natural frequencies using the methods described in Sect. 10.4.

The separation of the modal information like this can also be used for other purposes, such as to enhance or suppress its effects, in particular with variable speed machines. Bearing fault information is often carried by resonances, so it could be an advantage to weight the spectrum with the modal shape before performing order analysis (which smears modal frequencies in the shaft angle domain), the latter being necessary to identify the order-related bearing fault frequencies. This reduces at the same time the disturbing influence of unrelated shaft orders. The exact opposite is the case for gear diagnostics, where the diagnostic information is usually in forcing functions directly related to shaft speed. Order analysis removes frequency modulation, allowing components to be identified on an order scale, but does not remove amplitude modulation, such as might be given by gearmesh

frequencies passing through resonances. Synchronous averaging of amplitude-modulated signals is no longer meaningful.

Figure 30 (from [38]) shows an example of a signal from a wind turbine gearbox over a period where the speed varied over a range of 30%. The raw signal in 6(a) shows considerable amplitude variation with speed, and even after order tracking, the amount of amplitude variation was unchanged.

The dB spectrum in (b) has a basic modal structure which has been removed in (c) by subtracting its cepstrum from that of the total signal. The order-related components now protrude from a basically flat base noise spectrum. Regenerating the liftered time signal corresponding to (c) (using the original phase spectrum) gives the result shown in (d), This signal was lowpass filtered below the third harmonic of the highest gearmesh frequency in order to concentrate on information relating to the gear signals. It is seen to be roughly stationary over most of its length, indicating that the effect of gearmesh harmonics passing through resonances has largely been suppressed. The reason for the localized amplitude modulation near the end of the record is not known but suspected to be caused by acceleration/deceleration as the speed varied more rapidly here. This would change the forcing function independent of the transfer function. Even so it would be possible to choose a section with little amplitude variation in order to perform synchronous averaging. In this case there was no known fault.

10.3.3 Example of Cepstrum Pre-whitening for the Diagnostic of Rolling Element Bearings in Variable Speed Conditions

An effective example of application of cepstrum pre-whitening is obtained in the field of bearing diagnostics. The example reported in this section is obtained on a bearing diagnostics test rig installed in the laboratories of the Queensland University of Technology, Brisbane (Australia) [23]. A long shaft between the test bearing and the gearbox ensures that the vibrations recorded on the gearbox (Acc#1) and on the test bearing (Acc#2) are almost entirely uncoupled, so that vibratory effects of the gearbox scarcely affect the bearing and vice versa. A faulty bearing (outer race spall) was installed on the main shaft, with a theoretical bearing pass frequency outer of approximately 4.85 times the rotational speed of the shaft (Fig. 31).

In order to show the effectiveness of the cepstrum pre-whitening procedure, vibration measurements were taken with the two accelerometers during a speed transient (from 1.2 Hz to 2.4 in 50 s) and summed together, so as to reproduce the effect of a typical hybrid gearbox-bearing signal (Fig. 32).

The raw signal DFT and SES of the composite signal (Acc#1 + Acc#2) were of course of scarce usefulness, given the smearing of the bearing fault symptoms along the frequency axis, due to the high variations of the shaft speed (see Fig. 33a, b). The signal was therefore subject to a two-step procedure of order tracking-synchronous averaging and cepstrum pre-whitening.

The order tracking and synchronous averaging was aimed at transforming the signal to the angular domain and then removing the shaft-synchronous components (i.e., the harmonics of the shaft speed). The signal's DFT (Fig. 33c) still showed

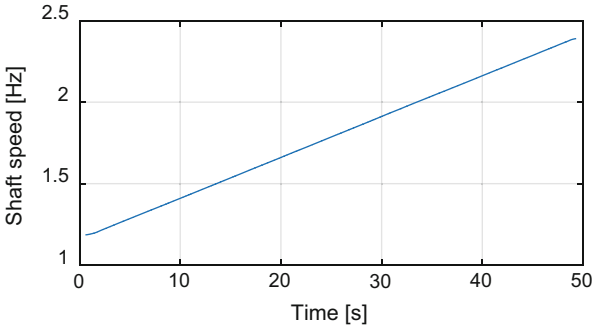

Fig. 31 Speed profile during the acquisition

strong spectral components resulting in a "noisy" SES (Fig. 33d) which did not clearly allow the identification of the BPFO component.

The final step of cepstral pre-whitening allowed to reduce this effect, by flattening the signal's spectrum (Fig. 33e) and therefore highlighting the information carried by the phase of the spectrum. Therefore, the SES of the pre-whitened signal clearly showed a peak in proximity of the theoretical BPFO (Fig. 33f).

To verify that the peak was actually representing the bearing fault frequency, the SES obtained with the two-step pre-whitening method is compared in Fig. 34 with the SES of the signal Acc#2 collected directly on the accelerometer (no effect of the gearbox).

10.4 Cepstrum for Modal Analysis

Because of its possibility of separating forcing and transfer functions in response signals, the cepstrum has the potential to be used for operational modal analysis (OMA) in two ways:

1. As a complete stand-alone procedure
2. As a pre-processing technique for other OMA procedures

A full description of these procedures has recently been published in [3] and only a summary is given here.

10.4.1 Full OMA Procedure

In contrast to some other OMA procedures, the cepstrum can retrieve both poles and zeros in transfer functions which thus gives some of the information contained in the residues of the different poles, as shown below.

The first step is to curve-fit the auto spectrum of the response for its poles and zeros. If the excitation is impulsive and single input, with little extraneous noise, this might be done directly, as described in the original publication [39].

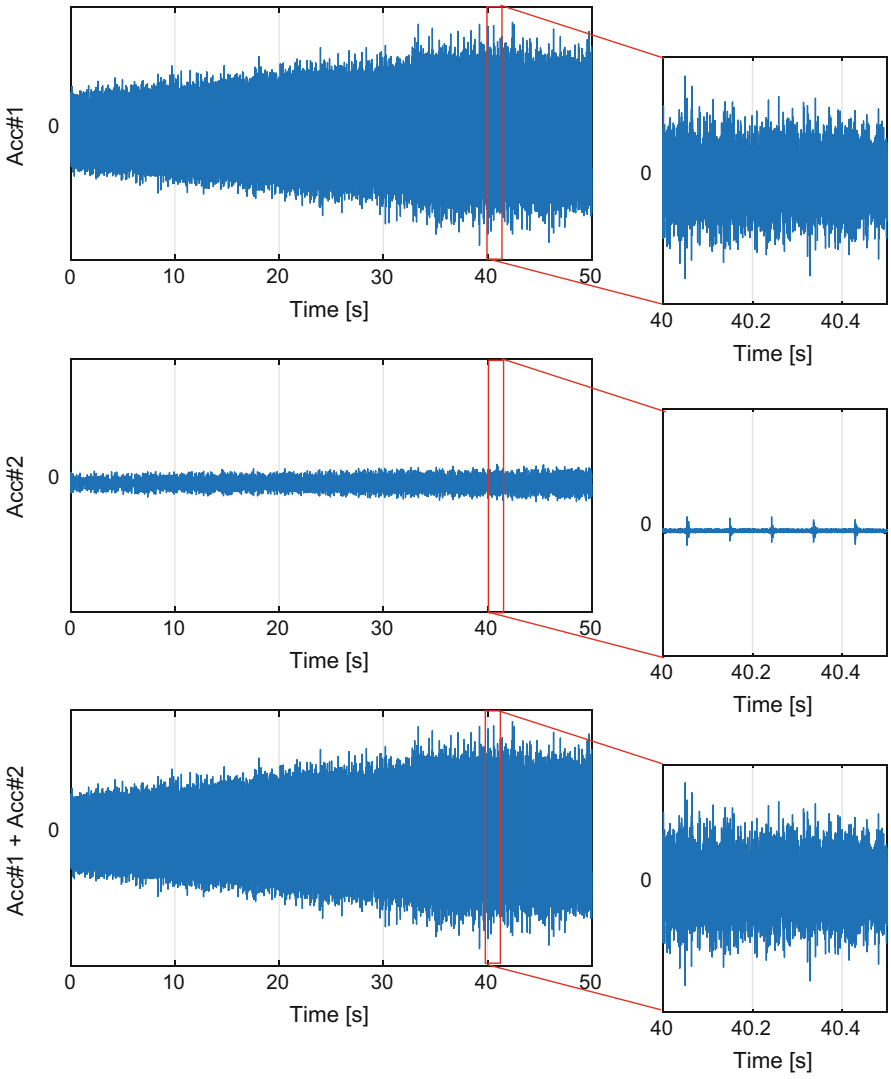

Fig. 32 Experimental signals measured by the gearbox accelerometer (Acc#1, top), the bearing accelerometer (Acc#2, middle), and composite signal obtained by superposition of Acc#1 and Acc#2 (bottom). The axes are to scale

Most recently [3], it has been shown that the zeros can be obtained more accurately from transmissibilities rather than response autospectra, with the advantages that noise, which otherwise disguises zeros, is removed by averaging and, for SIMO situations, that the transmissibilities are independent of the forcing function, as long as it is broadband.

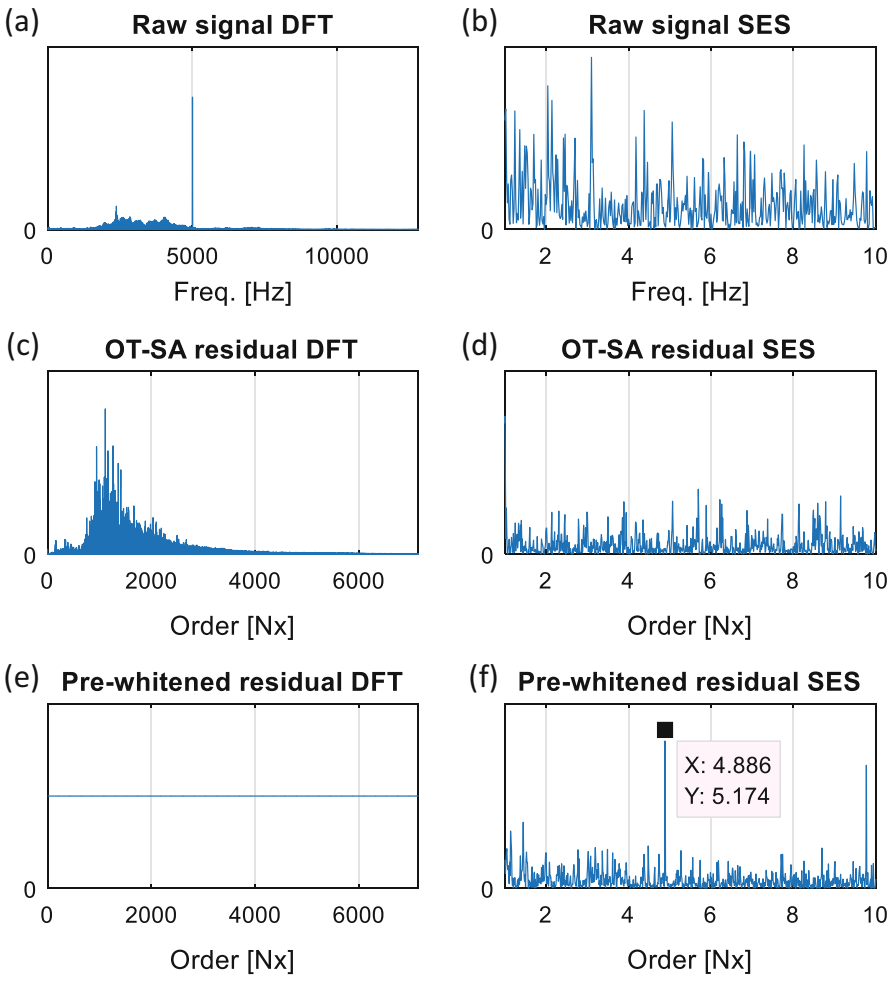

Fig. 33 (**a**, **b**) DFT and SES of the raw signal, (**c**, **d**) DFT and SES of the residual after order tracking ad synchronous averaging (OT-SA), (**e**, **f**) DFT and SES after OT-SA and cepstrum pre-whitening

If the frequency response function (FRF) is regenerated using only the identified in-band poles and zeros, there are two missing pieces of information:

- An equalization curve is required to compensate for the effects of out-of-band poles and zeros. This is dependent mainly on the relative number of poles and zeros, however, and only weakly on their exact placement.
- An overall scaling factor, since this is mixed with the forcing function at zero quefrency.

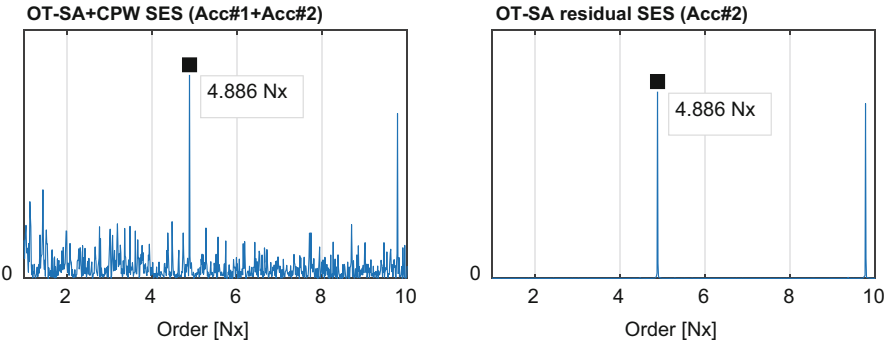

Fig. 34 Comparison between SES obtained after OT-SA and CPW from the composite signal Acc#1 + Acc#2 (left) with the SES of the bearing accelerometer signal Acc#2 (only OT-SA is applied)

In [40] it was shown that the equalization curve could be found using "phantom zeros" in a similar manner to the rational fraction polynomial technique [41], which also used a pole-zero model. More recently it has been shown that it can more easily be found by smoothing the dB difference between the FRF generated on the basis of the in-band poles and zeros, and a reference FRF, which can either be from an earlier measurement, an EMA measurement, or from a finite element (FE) model of the structure. As mentioned, the equalization curve is insensitive to small changes such as a slow change in condition, or in-service operating conditions. The smoothing is required because of differences in actual positions of poles and zeros between the updated and reference FRFs, giving peak notches in the difference curves. It has recently been shown that the smoothing is best achieved by polynomial curve-fitting, making sure that the regenerated curves include the negative (and zero) frequency poles and zeros derived from the inferred support conditions and measured positive frequency poles and zeros [3]. Such a smoothed equalization curve can also correct for absolute scaling if the reference FRF is also correctly scaled. For example, an FE model of a free-free structure can easily be arranged to have correct rigid body inertial properties, which determine the zero frequency values of FRFs, and even for constrained structures, whose zero frequency values are determined by static stiffness, the FE model can be updated to give agreement on the first couple of elastic modes and will then be accurate at zero frequency.

Figure 35 (from [42]) shows an example of the application of such an equalization process to the OMA of a free-free beam excited by a shaker with a pink noise excitation, the pink color having no influence on the equalization process. A comparison is made between a driving point FRF, with the same number of poles and zeros, and an end-to-end FRF with no zeros. In the former case, little equalization is required because of the balance of numbers of poles and zeros out-of-band, whereas the absence of zeros in the second case requires a maximum of equalization. Note that only five of the six modes were curve-fitted. This example

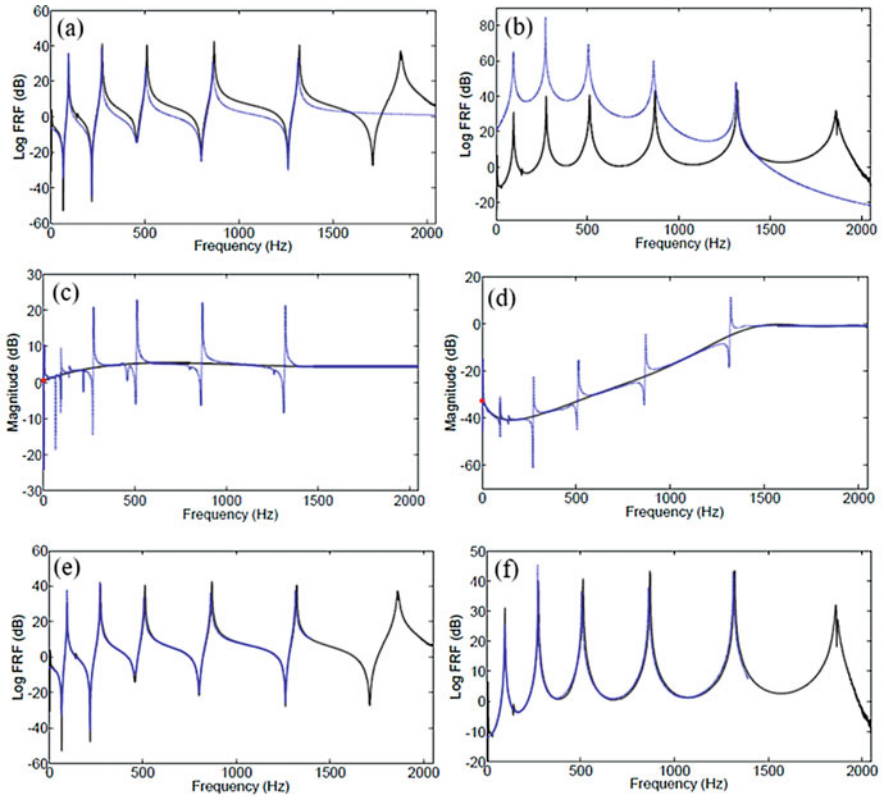

Fig. 35 Regeneration of FRFs using an equalization and scaling curve. (**a**, **c**, **e**) Driving point measurement. (**b**, **d**, **f**) End-to-end measurement. (**a**, **b**) Regenerated FRF (blue) from in-band poles and zeros vs reference (black). (**c**, **d**) Unsmoothed difference curve vs polynomially smoothed equalization curves. (**e**, **f**) True (measured) FRF (black) vs equalized estimate (blue) for five modes. (From [42])

used only the positive frequency poles and zeros, but it is shown in [3] that a better result is achieved by including the negative frequency components.

Normally, for OMA the spectrum will be contaminated by extraneous components, such as discrete frequencies, and it will be an advantage to suppress these by applying a notch comb lifter, an exponential shortpass lifter, or both, beforehand.

In the general MIMO case, it would in principle be necessary to separate the response to a single source by BSS methods. A particular case of this where the cepstrum has advantages over other methods is where there is only one CS2 source with a particular cyclic frequency, as described in [43]. The practical case proposed there is a diesel railcar, where the excitation from the combustion is broadband but cyclic at the engine firing frequency. It is shown in [43] that the cepstrum of the cyclic spectrum at the cyclic frequency contains only the structural path information

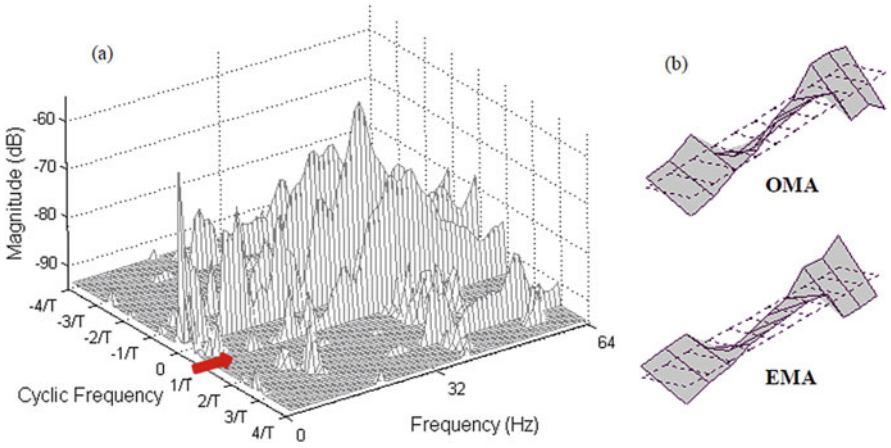

Fig. 36 (**a**) Spectral correlation of railcar body excited by a CS2 force (**b**) resulting OMA mode shape from curve-fitting such cyclic spectra for the indicated cyclic frequency (compared with EMA mode shape). (From [43])

from that particular source to each response point. This was illustrated by exciting the car by a shaker using a CS2 force signal (burst random), which was measured and used for experimental modal analysis (EMA) at the same time. Figure 36 shows the spectral correlation of the response, and the cyclic spectrum at the excitation frequency is highlighted. The figure also shows one of the extracted mode shapes (of the floor) obtained both by OMA and EMA. The two estimates compare very well.

However, it is likely only in specialized situations, such as the very complex excitation signals from rotating machines, that the cepstral method of modal analysis would have advantages over the conventional OMA methods.

10.4.2 Cepstral Pre-processing for Other OMA Procedures

There is thought to be considerably more potential for using cepstral methods for pre-processing response signals prior to OMA, in order to enhance the modal part of the response and remove other disturbances such as extraneous discrete frequency excitations. In a case such as illustrated in Fig. 27, it is obvious that the application of a simple exponential shortpass lifter has removed almost everything except the modal properties of the transfer paths, equivalent to a white excitation.

When there are only a small number of periodic contaminating components to remove, it has been shown that they can be isolated by synchronous averaging (SA) and then subtracted [44]. In principle this requires transformation to the angle/order domain for the removal, followed by transformation back to the time domain for the modal analysis, although if speed variation is very small, the difference between the frequency and order axes is primarily one of scaling. In [44] it was shown that a combination of a comb notch lifter and exponential shortpass lifter was able to achieve a similar result to the SA method, in removing the harmonics of rotor

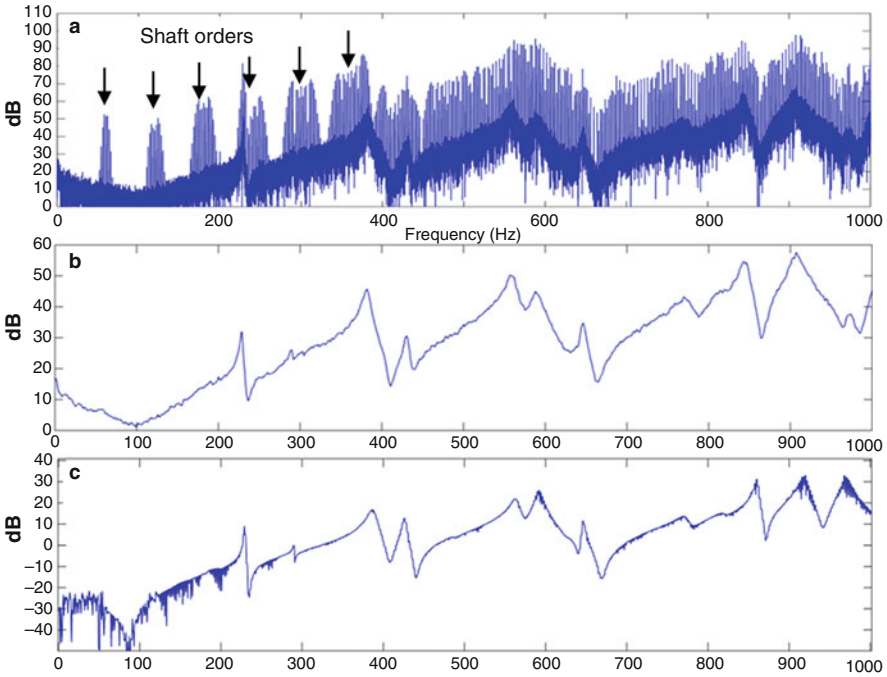

Fig. 37 Use of an exponential lifter for OMA of responses to a simulated gear signal with speed variation ±5%. (**a**) Response autospectrum. (**b**) Corresponding exponentially liftered spectrum. (**c**) FRF obtained using the measured force. (From [45])

frequency from response measurement on a helicopter in steady flight, except that the fundamental rotor frequency was interpreted as a mode. The time constant of the exponential lifter could not be reduced enough to make it less than the rotor period. The cepstral method could be done without order tracking however.

As soon as the speed varies a little more, there is likely to be amplitude modulation which cannot be removed by SA, and then the cepstral method is superior. In [45] it is shown that in a signal simulating the response to gearmeshing in a gearbox with speed varying by ±5% (but with simultaneous low-level broadband noise excitation), the application of a simple exponential lifter resulted in a response spectrum very similar to the equivalent FRF, and a group of signals treated in this way gave a very similar OMA result to that obtained when the gearbox casing was excited by a pure broadband noise signal. Figure 37 shows a typical result from this paper. Later improvements on this approach are shown in [3].

References

1. Abboud D, Baudin S, Antoni J, Rémond D, Eltabach M, Sauvage O (2016) The spectral analysis of cyclo-non-stationary signals. Mech Syst Signal Process 75:280–300

2. Abboud D, Antoni J (2017) Order-frequency analysis of machine signals. Mech Syst Signal Process 87:229–258
3. Randall RB, Antoni J, Smith WA (2019) A survey of the application of the cepstrum to structural modal analysis. Mech Syst Signal Process 118:716–741
4. Ferreira JLA, Balthazar JC, Araujo APN (2003) An investigation of rail bearing reliability under real conditions of use. Eng Fail Anal 10(6):745–758
5. Antoni J, Randall RB (2002) Differential diagnosis of gear and bearing faults. J Vib Acoust 124:165–171
6. Antoni J, Randall RB (2003) A stochastic model for simulation and diagnostics of rolling element bearings with localized faults. J Vib Acoust 125(3):282–289
7. Pennacchi P, Borghesani P, Ricci R, Chatterton S (2011) An experimental based assessment of the deviation of the bearing characteristic frequencies. In: 6th international conference acoustic and vibratory surveillance methods and diagnostic techniques
8. Borghesani P, Ricci R, Chatterton S, Pennacchi P (2013) A new procedure for using envelope analysis for rolling element bearing diagnostics in variable operating conditions. Mech Syst Signal Process 38(1):23–35
9. Randall RB (2011) Vibration-based condition monitoring: industrial, aerospace and automotive applications. Wiley, Chichester
10. Wigner E (1932) On the quantum correction for thermodynamic equilibrium. Phys Rev 40:479–760
11. Ville J (1948) Theorie et applications de la notion de signal analytique. Cables Transmissions 2:61–74
12. Cohen L (1995) Time frequency analysis theory and applications. Prentice Hall, Englewood Cliffs
13. Antoni J (2007) Cyclic spectral analysis in practice. Mech Syst Signal Process 21(2):597–630
14. Newland DE (2008) Wavelet analysis of vibration signals, Chapter 49. In: Handbook of noise and vibration control. Wiley, New York
15. Daubechies I (1990) The wavelet transform, time-frequency localization and signal analysis. IEEE Trans Inf Theory 36(5):961–1005
16. Peng ZK, Chu FL (2004) Application of the wavelet transform in machine condition monitoring and fault diagnostics: a review with bibliography. Mech Syst Signal Process 18: 199–221
17. Donoho DL, Johnstone JM (1994) Ideal spatial adaptation by wavelet shrinkage. Biometrika 81:425–455
18. McFadden PD (1989) Interpolation techniques for time domain averaging of gear vibration. Mech Syst Signal Process 3(1):87–97
19. Antoni J, Hanson D (2012) Detection of surface ships from interception of cyclostationary signature with the cyclic modulation coherence. IEEE J Ocean Eng 37(3):478–493
20. Antoni J, Xin G, Hamzaoui N (2017) Fast computation of the spectral correlation. Mech Syst Signal Process 92:248–277
21. Borghesani P, Antoni J (2018) A faster algorithm for the calculation of the fast spectral correlation. Mech Syst Signal Process 111:113–118, Oct
22. Borghesani P, Pennacchi P, Chatterton S (2014) The relationship between kurtosis- and envelope-based indexes for the diagnostic of rolling element bearings. Mech Syst Signal Process 43(1–2):25–43
23. Borghesani P, Shahriar MR (2016) Cyclostationary analysis with logarithmic variance stabilisation. Mech Syst Signal Process 70–71:51–72
24. Borghesani P, Antoni J (2017) CS2 analysis in presence of non-Gaussian background noise – effect on traditional estimators and resilience of log-envelope indicators. Mech Syst Signal Process 90:378–398
25. Antoni J, Borghesani P (2019) A statistical methodology for the design of condition indicators. Mech Syst Signal Process 114:290–327
26. Sawalhi N, Randall RB (2007) Semi-automated bearing diagnostics -three case studies. In: Proceedings of COMADEM 2007, Faro, Portugal

27. Randall RB, Antoni J (2011) Rolling element bearing diagnostics – a tutorial. Mech Syst Signal Process 25:485–520
28. McFadden PD (1986) Detecting fatigue cracks in gears by amplitude and phase demodulation of the meshing vibration. J Vib Acoust Stress Reliab Des 108:165–170
29. Barszcz T, Randall RB (2009) Application of spectral kurtosis for detection of a tooth crack in the planetary gear of a wind turbine. Mech Syst Signal Process 23(4):1352–1365
30. Desbazeille M, Randall RB, Guillet F, El Badaoui M, Hoisnard C (2010) Model-based diagnosis of large diesel engines based on angular speed variations of the crankshaft. Mech Syst Signal Process 24:1529–1541
31. Chen J, Randall RB (2015) Improved automated diagnosis of misfire in internal combustion engines based on simulation models. Mech Syst Signal Process 64–65:58–83
32. Chen J, Randall RB, Peeters B (2016) Advanced diagnostic system for piston slap faults in IC engines, based on the non-stationary characteristics of the vibration signals. Mech Syst Signal Process 75:434–454
33. Chen J, Randall RB (2016) Intelligent diagnosis of bearing knock faults in internal combustion engines using vibration simulation. Mech Mach Theory 104:161–176
34. Bogert BP, Healy MJR, Tukey JW (1963) The quefrency alanysis of time series for echoes: cepstrum, pseudo-autocovariance, cross-cepstrum and saphe cracking. In: Rosenblatt M (ed) Time series analysis, pp 209–243
35. Oppenheim AV, Schafer RW, Buck JR (1999) Discrete-time signal processing solutions. In: Discrete time signals and systems. Prentice Hall, Upper Saddle River
36. Randall RB (2017) A history of cepstrum analysis and its application to mechanical problems. Mech Syst Signal Process 97:3–19
37. Randall RB, Sawalhi N Cepstral removal of periodic spectral components from time signals. In: Proceedings of CMMNO 2013. Springer, Ferrara
38. Randall R, Smith W, Coats M Gear diagnostics under widely varying speed conditions. In: CMMNO 2014. INSA, Lyon
39. Gao Y, Randall RB (1996) Determination of frequency response functions from response measurements – I. extraction of poles and zeros from response cepstra. Mech Syst Signal Process 10(3):293–317
40. Gao Y, Randall RB (1996) Determination of frequency response functions from response measurements – II. Regeneration of frequency response functions from poles and zeros. Mech Syst Signal Process 10(3):319–340
41. Richardson M, Formenti D (1985) Global curve fitting of frequency response measurements using the rational fraction polynomial method. In: Proceedings of the IMAC III
42. Smith WA, Randall RB (2016) Cepstrum-based operational modal analysis revisited: a discussion on pole–zero models and the regeneration of frequency response functions. Mech Syst Signal Process 79:30–46
43. Hanson D, Randall RB, Antoni J, Waters TP, Thompson DJ, Ford RAJ (2007) Cyclostationarity and the cepstrum for operational modal analysis of MIMO systems-Part I: modal parameter identification. Mech Syst Signal Process 21(6):2441–2458
44. Randall RB, Peeters B, Antoni J, Manzato S (2012) New cepstral methods of signal pre-processing for operational modal analysis. In: Proceedings of the international conference on noise and vibration engineering (ISMA 2012), Leuven, Belgium
45. Randall RB, Coats MD, Smith WA (2016) Repressing the effects of variable speed harmonic orders in operational modal analysis. Mech Syst Signal Process 79:3–15

Introduction to Spectral and Correlation Analysis: Basic Measurements and Methods

5

Anders Brandt and Stefano Manzoni

Contents

A. Brandt (✉)
Department of Mechanical and Electrical Engineering, University of Southern Denmark, Odense, Denmark
e-mail: abra@sdu.dk

S. Manzoni
Department of Mechanical Engineering, Politecnico di Milano, Milan, Italy
e-mail: stefano.manzoni@polimi.it

R. Allemang, P. Avitabile (eds.), *Handbook of Experimental Structural Dynamics*,
https://doi.org/10.1007/978-1-4614-4547-0_7

Abstract

Spectral analysis is one of the most important tools used in experimental structural dynamics. This can be partly explained by the fact that the output of a linear system in the frequency domain, at each frequency, is equal to the product of the input spectrum at that frequency and the frequency response at the same frequency. For random vibrations, correlation functions and their frequency counterparts, spectral densities, are the tools used to describe the frequency content of the vibrations. In this chapter, we start by briefly describing the essential properties of linear systems. After this, we describe the three classes of signals: periodic, random, and transient signals, and for each signal class, we define a spectrum to describe its frequency content. We then go on to describe the discrete Fourier transform, DFT, since this is by far the most common tool to compute spectra, by the fast Fourier transform (FFT) algorithm. In this context, leakage and time windowing are explained, after which we go into detail on how to compute the spectra for each type of signal. Two different methods are described: Welch's method, based on averaging several shorter DFT blocks, and the periodogram-based method which relies on making one, long DFT and then averaging adjacent frequency bins. Finally, also correlation function estimates are described using the same two techniques.

Keywords

Fourier transform · Spectrum analysis · Linear spectrum · Spectral density · Correlation function

1 Introduction

Spectral analysis is one of the most important tools in experimental structural dynamics. This is for a very simple reason; the response of a linear system at a particular frequency is only dependent on the input at that frequency and the frequency response at the same frequency, as we will discuss in Sect. 1.1. Spectra are thus very important functions, and the spectra of periodic, random, and periodic functions will be presented in Sect. 2. Finding a solution to a vibration problem often boils down to finding at what frequency the problem occurs and then finding the structure's dynamics (defined by the *frequency response functions*, FRFs) and/or the loads, at this frequency.

Correlation functions are other important measurement functions, particularly for operational modal analysis (OMA). Correlation functions are closely related to spectra; more precisely they are inverse Fourier transforms of the spectral density functions. As we will see in Sect. 2.2.1, correlation functions are closely related with *impulse response functions* (IRFs) and can essentially be treated as such functions when extracting modal parameters in OMA.

The contents of the present chapter are mostly textbook stuff. It is not so easy to find easily readable books on applied signal analysis aimed for mechanical or civil

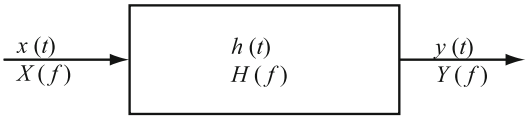

Fig. 1 Illustration of single-input/single-output linear system with input signal (e.g., force) $x(t)$ and output signal (response, e.g., acceleration) $y(t)$

engineers. There are, however, a few books that can be recommended; for general reading, see [8, 5, 2], for more in-depth analysis of random signals, there are rather a few books, for example [1, 7, 11], and also see the chapter on Random and Shock Testing. A more specialized book on spectrum analysis that can be recommended is [9].

1.1 Properties of Linear Systems

The simplest linear system, depicted in Fig. 1, has an input $x(t)$ and an output (or response) $y(t)$. The system can, for example, describe the linear relationship between the force input in a particular point and the response acceleration in another point on a structure. The linear system can be characterized by its frequency response function (FRF), $H(f)$, which is defined by

$$H(f) = \frac{Y(f)}{X(f)} \tag{1}$$

where $X(f)$ and $Y(f)$ are the Fourier transforms of the input and response signals, respectively. We can rewrite the equation as $Y(f) = X(f) \cdot H(f)$ which clearly shows that at a particular frequency, f, the response is only dependent on the input and the frequency response at that particular frequency. Thus, knowing the spectra $X(f)$ and $Y(f)$ are partial steps toward the description of the system in terms of FRFs. It should be pointed out here that Eq. (1) is only conceptual and should not be used in practice. To estimate FRFs, rather one of the methods described in the chapter "Structural Measurements – FRF" should be used.

1.2 Common Applications in Experimental Structural Dynamics

The basic measurements we will describe in the present chapter are common to many applications in the field of experimental structural dynamics. Some of the most common applications will be mentioned here, together with the typical spectra and other functions associated with them.

Operating deflection shape measurements, ODS, is a very common application for troubleshooting vibration problems. ODSs may be based on any spectral functions that contain amplitude and phase information, e.g., cross-spectra, or even FRFs.

Measurements of FRFs for *experimental modal analysis measurements*, EMA, will be covered in the chapter on FRF measurements. Here, it is sufficient to explain that EMA is usually based on measurements of input forces and responses in some form (velocity or acceleration signals, typically). The frequency response functions between force(s) and response(s) are then estimated from the spectra of the force and response signals that we present in the present chapter.

Operational modal analysis measurements, OMA, are often, although not always, based on correlation functions (sometimes also called covariance functions). If correlation functions are used, OMA is sometimes referred to as *NeXT*, [6].

2 Signal Classes and Their Spectra

Now that we have established the need to experimentally obtain spectra, we will have to discuss how this can be done for different types of signals. This is necessary, as different signals have spectra with different properties. The main types of signals in this respect can be divided into three *signal classes*

- periodic signals,
- random signals, and
- transient signals

Each of these types of signals needs to be described by its own type of spectrum as we will describe in the following.

2.1 Periodic Signals

Periodic signals, or signals that can, at least, be approximated as periodic, occur in applications where there are rotating or reciprocating parts, for example, turbines and combustion engines. For periodic signals, we know from Fourier series theory that they can be described as a discrete sum of harmonics. Furthermore, for vibration signals we know they have to be zero mean, so in the following, we assume all signals are zero mean. It is good practice to always remove means of all measured vibration signals after data acquisition. Any such periodic signal, $x_p(t)$, with period T_p seconds, can be written as the Fourier series

$$x_p(t) = \sum_{k=1}^{\infty} a_k \cos\left(\frac{2\pi kt}{T_p}\right) + b_k \sin\left(\frac{2\pi kt}{T_p}\right) \tag{2}$$

where the Fourier coefficients a_k and b_k can be computed by

$$a_k = \frac{2}{T_p} \int_{t_0}^{t_0+T_p} x_p(t) \cos\left(\frac{2\pi k}{T_p} t\right) dt \quad k = 1, 2, \ldots \tag{3}$$

and

$$b_k = \frac{2}{T_p} \int_{t_0}^{t_0+T_p} x_p(t) \sin\left(\frac{2\pi k}{T_p} t\right) dt \quad k = 1, 2, \ldots \tag{4}$$

for an arbitrary starting point t_0.

Instead of the Fourier series presented in Eq. (2), the *complex Fourier Series* is often used, particularly since it is more closely related to the discrete Fourier transform; see Sect. 3.2. The complex Fourier series is thus defined by

$$x_p(t) = \sum_{k=-\infty}^{\infty} c_k e^{\frac{j2\pi k}{T_p} t} \tag{5}$$

where the coefficients c_k are given by

$$\begin{aligned} c_0 &= \frac{a_0}{2} \\ c_k &= \frac{1}{2}(a_k - jb_k) = \frac{1}{T_p} \int_{t_0}^{t_0+T_p} x_p(t) e^{-\frac{j2\pi k}{T_p} t} dt \end{aligned} \tag{6}$$

and $c_0 = 0$ since we assume no mean. The complex Fourier coefficients, c_k, can easily be shown (for real signals $x_p(t)$) to be such that $\mathrm{Re}(c_{-k}) = \mathrm{Re}(c_k)$ and $\mathrm{Im}(c_{-k}) = -\mathrm{Im}(c_{-k})$. The negative values of k in Eq. (5) can be interpreted as negative frequencies, which will be discussed more in Sect. 2.4.

The Fourier series, real or complex, show that a periodic signal only contains discrete frequencies, $f_k = k/T_p$. For physical signals, furthermore, the higher frequencies will vanish, resulting in finite sums in Eqs. (2) and (5).

2.2 Random Signals

Random signals occur when the forces originate in some random phenomenon, for example, wind loads, traffic loads, or the loads from the road surface acting on road vehicles. For random signals, or with a fancier name, *stochastic processes*, we need to use a rather different description of the spectral content. First, random signals have continuous spectra, as opposed to the discrete spectra of periodic signals. This means that the spectra of random signals must be described in terms of *density functions*. Before exploring this, however, we need to deal with the random (stochastic) nature of the signals, by defining the correlation functions.

2.2.1 Correlation Functions

A random signal is *stationary* if its mean, variance, and higher-order moments are constant in time. It is, further, *ergodic* if its statistical values (mean, variance, etc.) can be replaced by *time averages*. In engineering applications, a signal which is stationary can normally be regarded also to be ergodic. It should, however, be stressed that most signals are not stationary, at least not over any particularly long time. Stationarity is often something that needs to be investigated or controlled by experimental design.

For two stationary and ergodic random signals, $x(t)$ and $y(t)$, we define the cross-correlation, $R_{yx}(\tau)$, by

$$R_{yx}(\tau) = \mathrm{E}\left[y(t)x(t-\tau)\right] \tag{7}$$

where E denotes the expectation value. It should be noted that the cross-correlation function is equal to the signal $y(t)$ convolved by $x(-t)$. For a single signal, $x(t)$, the autocorrelation is a special case of the cross-correlation between the signal and itself, i.e.:

$$R_{xx}(\tau) = \mathrm{E}\left[x(t)x(t-\tau)\right] \tag{8}$$

$R_{yx}(\tau)$ thus tells if there is correlation (relationship) between the signal $y(t)$ and a shifted version of $x(t)$ shifted τ seconds. Periodic signals thus have periodic correlation functions, with period $\tau = T_p$. For random signals, the correlation function is usually an oscillating function with a maximum at, say, τ_0 and which decays as $\pm(\tau - \tau_0)$ increases. For our purposes it can be of interest to look at two different correlation functions, depicted in Fig. 2. In Fig. 2a, the autocorrelation of a bandlimited random signal with 1 Hz bandwidth is plotted. It can be seen that the autocorrelation function is of $\sin(x)/x$ type. In Fig. 2b, the cross-correlation between the input and output of a single-degree-of-freedom (SDOF) system with undamped natural frequency 1 Hz and relative damping of 1% is shown. Here it can be seen that the cross-correlation resembles the impulse response function, for positive lags τ. Actually, the positive lags in cross-correlation functions include the same information about the system as the impulse response, which is why it can be used for OMA parameter extraction; see the chapter on Operational Modal Analysis Methods.

2.2.2 Spectral Density Functions

The spectral density of a random signal is defined by the so-called Wiener-Khinchin(-Einstein) relationship, as the Fourier transform of the correlation function. Thus, the Fourier transform of an autocorrelation is referred to as a power spectral density, (PSD) function, or sometimes an autospectral density (ASD) function, thus defined by

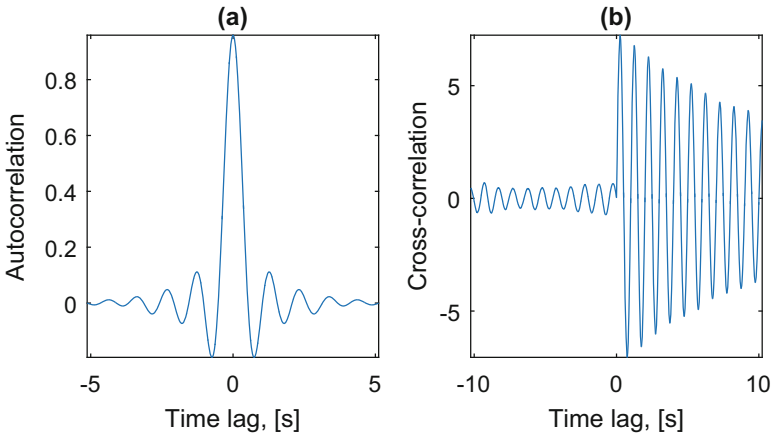

Fig. 2 Example correlation functions: in (**a**) autocorrelation function of bandlimited noise with 1 Hz bandwidth and in (**b**) cross-correlation function between the input and output of a single-degree-of-freedom (SDOF) mechanical system with undamped natural frequency of 1 Hz and relative damping of 1%. It can be seen that the cross-correlation in (**b**) is similar to an impulse response function, for positive lags τ

$$S_{xx}(f) = \int_{-\infty}^{\infty} R_{xx}(\tau) e^{-j2\pi f\tau} d\tau \tag{9}$$

The Fourier transform of a cross-correlation function, on the other hand, is referred to as a cross-spectral density (CSD) function

$$S_{yx}(f) = \int_{-\infty}^{\infty} R_{yx}(\tau) e^{-j2\pi f\tau} d\tau \tag{10}$$

An example of a PSD of a velocity signal measured on a bridge is shown in Fig. 3.

The units of a PSD are the measured unit squared per Hz, for example, $(\mathrm{m/s^2})^2/\mathrm{Hz}$ if acceleration in metric (SI) units are used. This unit reflects the fact that a PSD displays the *distribution* of the power of the signal, over frequency. The area under the PSD between two frequencies thus equal the mean square (square of the RMS level) of the signal in that frequency range.

It should be noted that the PSD is a real-valued, and positive, function, whereas the CSD is complex-valued (i.e., includes phase information).

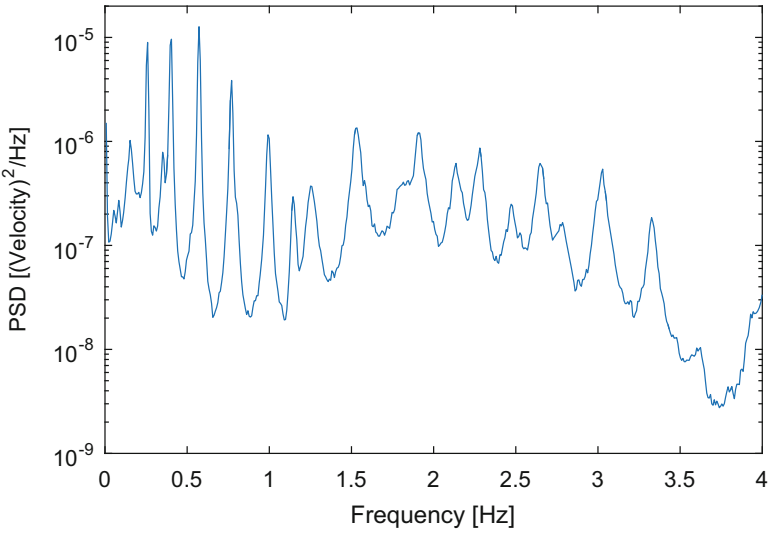

Fig. 3 Example power spectral density (PSD) of a velocity signal measured on a bridge

2.3 Transient Signals

A transient signal is a finite signal with limited duration. Examples of transient signals are responses to pyroshock testing, for example, the sound of a car door closing. Transient signals are usually, but not always, deterministic. An example of a nondeterministic transient signal is a burst random signal; see the chapter on FRF measurements. If we restrict the discussion here to deterministic transient signals, then an appropriate spectrum of the signal is the direct, continuous Fourier transform. The spectrum of a transient, deterministic, signal, $x(t)$, is thus

$$X(f) = \int_{-\infty}^{\infty} x(t) e^{-j2\pi f t} dt. \tag{11}$$

The units of the transient spectrum of an acceleration in SI units are thus [m/s$^2\cdot$ s] which can also be represented as [(m/s^2)/Hz]. Often, the *energy spectral density* function (ESD) is used instead of the straight Fourier transform. The ESD is equal to the magnitude squared of the spectrum $X(f)$.

2.4 Double-Sided Versus Single-Sided Spectra

The Fourier transform results in double-sided functions. The PSDs and transient spectra in the previous sections are therefore double-sided, i.e., they contain both

negative and positive frequencies. The negative frequencies are a result of the symmetry of the Fourier transform, and thus half the "energy" of the signal is distributed on the negative frequency axis and the other half on the positive. For practical use, this is not very convenient, so the spectra found in real life are usually single-sided spectra. For random signals, we thus get the single-sided PSD, for example, which is computed by discarding all negative frequencies and multiplying all the positive frequencies (not the 0 frequency!) by a factor 2. The single-sided PSD is denoted $G_{xx}(f)$ to distinguish it from the double-sided version.

3 Frequency Analysis

In this section we will first describe a basic principle of spectrum analysis as it is fundamental to the understanding of the spectra we are going to cover in Sect. 3.1. We will then describe the discrete Fourier transform (DFT) in some detail, since it is the tool most often used for spectrum estimation in structural dynamics applications.

3.1 Spectrum Analysis Principle

There are two main groups of methods for spectrum analysis, either *parametric* or *nonparametric* methods. The parametric methods rely on some a priori knowledge about the spectrum to be estimated, e.g., that it is produced by a Gaussian, white random force that has passed a structure having eight modes. The nonparametric methods do not require any such knowledge but give a spectrum estimate without any assumption. Experience has shown that the parametric methods usually perform poorly on vibration signals, so what is used in practice, with only rare exceptions, are the nonparametric methods.

The most common nonparametric methods for spectrum estimation in the field of structural dynamics are octave (and $1/n$ octave) analysis, DFT/FFT-based estimates, and wavelet spectra. It is very important to realize that *all nonparametric methods rely on the same principle*, which we will now outline.

The principle of nonparametric spectrum estimation is schematically illustrated in Fig. 4. The picture illustrates that each frequency in the estimated spectrum is the result of a calculation of the RMS level of the output of a bandpass filter with a particular center frequency, f_c, and bandwidth, B (often alternatively denoted by Δf). It is important to understand that *all* nonparametric methods for spectrum analysis rely on this simple principle. The only thing that can differ between the methods is the properties of the bandpass filter: the center frequency, bandwidth, and shape. In octave and $1/n$ octave analysis, the center frequencies and bandwidths increase exponentially with frequency. This is often called *constant relative bandwidth* because $\Delta f/f_c$ is kept constant. DFT/FFT-based spectra typically have fixed frequency increment and bandwidth, although we will see in Sect. 5.2 that this is not necessary. Wavelet spectra, finally, usually have constant relative bandwidth.

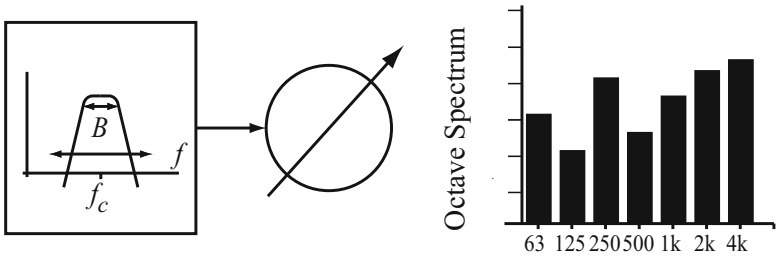

Fig. 4 Principle for spectrum analysis. The content at each discrete frequency, where the estimated spectrum contains information, is the result of the RMS evaluation of the output of a bandpass filter

Since DFT/FFT-based spectrum analysis is by far the most common in structural dynamics, we will limit the discussion here to those types of estimates.

3.2 The Discrete Fourier Transform (DFT)

The discrete Fourier transform (DFT) is the most common tool used to compute discrete spectra of measured signals. The *fast Fourier transform* (FFT) is an *algorithm* that computes the DFT much faster than the direct formula implies. The output of the FFT is thus the DFT, and for that reason, it is sufficient to discuss the DFT and its properties here.

The DFT, $X(k)$, at discrete frequencies k, of a signal $x(n)$ sampled with N samples (which we call the *blocksize*), is

$$X(k) = \sum_{n=0}^{N-1} x(n) e^{-j2\pi kn/N} \quad k = 0, 1, \ldots, N-1 \tag{12}$$

with the inverse discrete Fourier transform, the IDFT, defined by

$$x(n) = \frac{1}{N} \sum_{k=0}^{N-1} X(k) e^{j2\pi kn/N} \quad n = 0, 1, \ldots, N-1 \tag{13}$$

In order to understand the DFT, first of all the complex exponential $e^{-j2\pi kn/N}$ can be expanded to $\cos(2\pi kn/N) - jsin(2\pi kn/N)$. The DFT at frequency k is thus obtained by multiplying the signal $x(n)$ by a cosine and a sine and sum each of these products to produce the real part and imaginary part of the DFT, respectively. It is easily seen that the exponential is a cosine and sine with k periods during the measurement time $N \cdot \Delta t$, since the ratio n/N goes from 0 to 1 when n goes from 0 to N. The first frequency, $k = 1$, which is also the frequency increment of the DFT output, is thus $\Delta f = 1/(N\Delta t) = f_s/N$. This means that $k = N$ corresponds to the

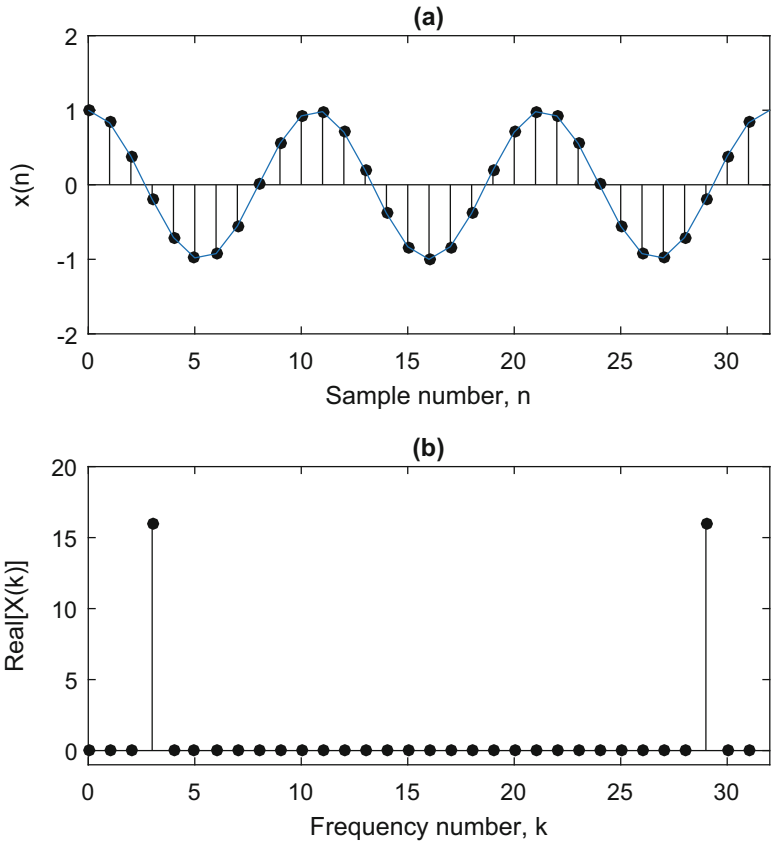

Fig. 5 Time signal in (**a**) and corresponding DFT result in (**b**). The signal is a cosine, periodic with three periods within the time window, and sampled with $N = 32$ samples. The DFT result is entirely real-valued, because the cosine is an even function, and the peak is located on frequency bin $k = 3$ because the cosine contains three periods in the time window

sampling frequency, and thus $k = N/2$ corresponds to half the sampling frequency, known as the *Nyquist* frequency. It should also be noted that the measurement time $N\Delta t$ is actually one sampling distance longer than the actual time it takes to acquire the N samples. It is apparent why this is so in the upper plot of Fig. 5, where the last sample is one sample short of the periodicity of the cosine plotted.

In Fig. 5 the result of a DFT computation of a cosine with three periods within the time window is shown. First of all, in the figure it is clear that the peaks in the DFT are not immediately (at least seemingly) related to the amplitude of the cosine; the DFT output is unscaled, as can be clearly seen from the value $X(0) = \sum x(n)$, not the mean of the signal as it "should" be. Furthermore, since a cosine is an even function, only the multiplication with the cosine in the complex exponential will result in a nonzero sum. Thus the result of the DFT of the cosine is real-valued, and therefore the imaginary part of $X(k)$ is not plotted in the figure.

Since the cosine in Fig. 5 contains three periods within the time window, the peak in the spectrum $X(k)$ occurs at $k = 3$. It can also be seen that the values for $k = N/2 + 1, N/2 + 2, \ldots, N - 1$ are the negative frequencies, translated to the right. Therefore, after computing the DFT, we usually discard all frequencies above $k = N/2$. For a block size of 1024 samples, for example, 513 values in the DFT result should be kept. Due to the symmetry of the DFT, the discarded frequencies can easily be computed by procedures that can be found in any textbook on the topic.

A summary of the most important properties of the DFT are:

1. The DFT result $X(k)$ is periodic with period N
2. The DFT is symmetric such that $\mathrm{Re}[X(-k)] = \mathrm{Re}[X(k)]$ and $\mathrm{Im}[X(-k)] = -\mathrm{Im}[X(k)]$ (even real part, odd imaginary part)
3. The real part of $X(k)$ is the DFT of the even part of $x(n)$, and the imaginary part of $X(k)$ is the DFT of the odd part of $x(n)$
4. The DFT is unscaled, which can be seen from $X(0) = \sum x(n)$, which is not the mean but the sum of the signals. Thus, the DFT needs some scaling, which we will address in the following sections.

3.2.1 Leakage and Windowing

Leakage is a phenomenon caused by the truncation in time that occurs for continuous signals which are not periodic in N, when we limit the calculation of the DFT to N samples. If a continuous signal is measured during a limited time $T = N\Delta t$, then the time truncation corresponds to multiplying the continuous time signal by a *rectangular time window*

$$w(t) = \begin{cases} 1, & |t| \leq T/2 \\ 0, & |t| > T/2 \end{cases} \tag{14}$$

Since multiplication in the time domain corresponds to convolution in the frequency domain, the result of the truncation of the measurement time is that the true spectrum of the signal $x(t)$ is convolved with the spectrum of the time window, $W(f)$. It is therefore essential to understand the properties of the spectrum (Fourier transform) of the time window. This is illustrated in Fig. 6, where the time and frequency domain plots of three common windows are shown: the rectangular, Hanning, and flattop windows. The frequency axis of the spectra is showing number of frequency increment (bins), Δf. In the frequency domain, all windows have a main lobe (the center lobe) and side lobes. What differs between the window spectra is essentially the width of the main lobe and the height and falloff rate of the side lobes, and there is a trade-off between the two, the broader the main lobe, the lower the side lobes.

The rectangular window, in Fig. 6b, has the narrowest main lobe of only ± 1 frequency bin and the highest side lobes, the highest being approximately -18 dB relative to the main lobe. The falloff rate of the rectangular window is very small

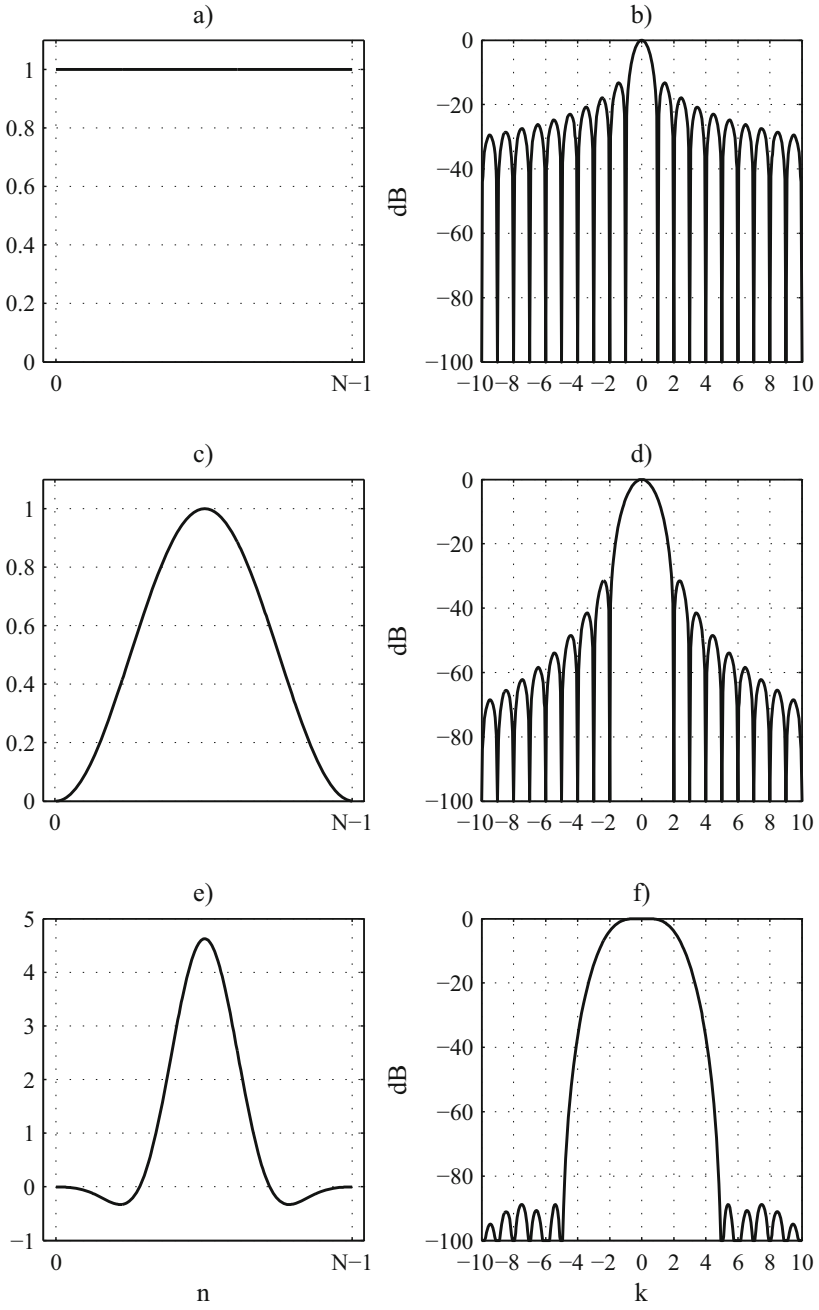

Fig. 6 Some common time windows in time and frequency domain. In (**a**) and (**b**), time and frequency domain representations of the rectangular window; in (**c**) and (**d**), the same for the Hanning window and in (**e**) and (**f**) for the flattop window. It can be seen that the rectangular window has a narrow main lobe and high side lobes, compared to the Hanning and flattop windows. It can also be noted that a wider main lobe results in lower side lobes

(6 dB/octave). The Hanning window, in Fig. 6d, has a main lobe of ±2 frequency bins, and the first side lobe is approximately −32 dB under the main lobe, and the falloff rate is considerably faster than for the rectangular window (18 dB/octave). The flattop window, finally, has a very broad mainlobe, ±5 frequency bins, very low side lobes, approximately −90 dB below the main lobe.

Consider now the convolution of one of the window spectra and an actual spectrum of a structure with a resonance. Remember that the "ideal" convolution is that of a δ-function, i.e., convolving with a δ-function results in the function it is convolved with. The wider the main lobe is, the more *smearing* there will be in the resulting spectrum. The higher the side lobes are, the more contribution there will be at a particular frequency, from frequencies far away from that frequency. A good all-round window for random signals and spectra that exhibit resonance peaks is the Hanning window, which is therefore the standard window used for random signals and spectral density estimates. The flattop window is good for periodic signals, with well-separated harmonics. The rectangular window, finally, should only be used when the measured signal does not have any leakage, i.e., transients that are entirely captured by the N samples of the DFT or signals that are periodic inside the N samples.

The maximum amplitude error caused by leakage when estimating the DFT of a sine is approximately −40% for the rectangular window, −16% for Hanning window, and −0.1% for the flattop window.

3.2.2 Cyclic Convolution and Zero Padding

Cyclic convolution is a phenomenon due to the periodicity of the DFT which is important to understand in many cases of applying the DFT, for example, for filtering purposes. We know from continuous Fourier transform theory that multiplication in the frequency domain corresponds to convolution in the time domain. But this is not immediately true for the DFT, since it is periodic in both time domain and frequency domain. This is easy to show with an example.

Example 1. Consider the discrete sequence (signal)

$x(n) = [1 \quad 1 \quad 1 \quad 1]$.
The true convolution of this sequence is clearly
$y(n) = [1 \quad 2 \quad 3 \quad 4 \quad 3 \quad 2 \quad 1]$.
But try the following, for example, in MATLAB:

```
» x=[1 1 1 1];
» y = ifft(fft(x).*fft(x);
```

and the result will show

```
ans = 4 4 4 4
```

□

This result is an effect of the cyclic nature of the DFT. For each shift in the convolution, the sample(s) shifted out to the right are appearing on the left side. Thus, for each value, the convolution result is the sum of the sequence

[1 1 1 1]

multiplied by itself and summed. The solution to this is *zero padding*. If we add as many zeros to the original sequence as it is long, we get the following result, again illustrated by an example in MATLAB.

Example 2. Now, include zero padding in the sequence x, with as many zeros as the length of x

```
» x=[1 1 1 1 0 0 0 0];
» y = ifft(fft(x).*fft(x);
```

and the result will show

```
ans = 1 2 3 4 3 2 1 0
```

□

which is clearly the correct result!

Zero padding should be used for proper results, whenever a convolution in the time domain is computed by a multiplication in the frequency domain. Thus, it should always be used when any kind of filtering operation is computed in the frequency domain. We will also use it to compute correlation functions in Sects. 4.5 and 5.3.

3.2.3 Window Scaling Factors

The time windows obviously remove part of the windowed signal, and this causes the DFT of the windowed signal having lower values than the DFT of the unwindowed signal. Luckily, this can be compensated for, however, we need to discuss two different compensations, depending on what result we want.

If, in the first instance, we apply a window to a periodic signal and we want the DFT of the windowed signal to show correct peak values (i.e., peaks corresponding to the amplitude of the harmonic at the frequency bin k), then we need to find an *amplitude correction factor* (ACF). We denote this factor A_w, and it can readily be found. Assume that we have a complex sine with amplitude A, coinciding with frequency bin k_0, which can then be written as

$$x(n) = Ae^{j2\pi k_0 n/N}, n = 0, 1, \ldots, N-1 \tag{15}$$

If we compute the DFT of this sine windowed by window $w(n)$, divided by N (because we saw in Sect. 3.2 that the DFT has to be scaled by N), we obtain

$$X(k) = \frac{1}{N} \sum_{n=0}^{N-1} w(n) A e^{-j2\pi k_0 n/N} e^{j2\pi kn/N} \tag{16}$$

All of the values of $X(k)$ will be zero, except the value for $X(k_0)$ which will be

$$X(k_0) = \frac{A}{N} \sum_{n=0}^{N-1} w(n) \tag{17}$$

Since we want this frequency bin to equal A, then we have that the window amplitude correction factor, A_w, is

$$A_w = \frac{N}{\sum_{n=0}^{N-1} w(n)} \tag{18}$$

so that $A_w \cdot \mathrm{DFT}\,[w(n)x(n)]$ produces the correct amplitude A.

In the second instance, we will later see that often, instead of wanting a peak to be properly scaled, we wish for the sum of the (square of) values of the DFT to be correct. This factor is a little more complicated to deduce, and we therefore refer to [1, 2] for a deduction. Here, it is sufficient to define the *normalized equivalent bandwidth*, B_{en}, of a window $w(n)$ by

$$B_{en} = \frac{N \sum_{n=0}^{N-1} w^2(n)}{\left[\sum_{n=0}^{N-1} w(n)\right]^2} \tag{19}$$

This factor is exactly 1.5 for the Hanning window and will be used in Sect. 4.3.

4 Block-Based Spectrum and Correlation Estimation

In this section we will look at estimators for the theoretical spectra that were presented in Sect. 2. We thus assume that we have a discrete time signal, $x(n)$, equal to the continuous signal $x(t)$ sampled at the equidistant sampling instances $t_n = n \cdot \Delta t$, where the sampling increment is the reciprocal of the sampling frequency, f_s, i.e., $\Delta t = 1/f_s$. We further assume that we have sampled L samples of the signal $x(n)$.

There are two different principles for spectrum and correlation estimation using the DFT/FFT: either the time signal is divided into smaller segments, for which windowed DFTs are computed and averaged in the frequency domain, or one, large

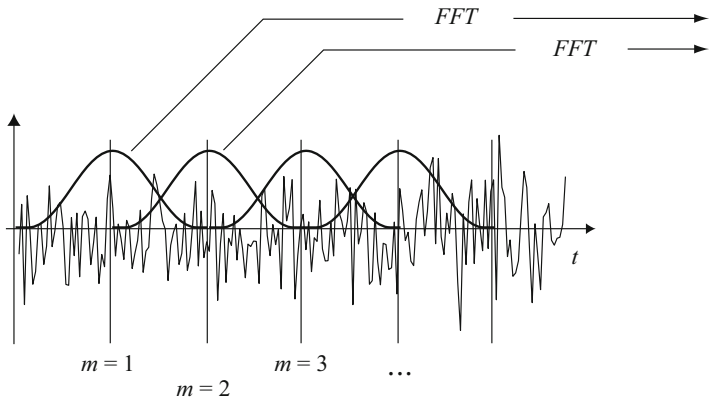

Fig. 7 Schematic illustration of Welch's method for spectrum and correlation function estimation. The data are divided into a number of, possibly overlapping, segments, each of which is windowed, after which the DFT is computed (by FFT) whereafter averaging is done in the frequency domain

DFT is computed using the entire time signal. The former method is referred to as Welch's method after [10] and the latter as a periodogram method, or sometimes Daniell's method, after [4]. In this section we will present Welch's method for computation of both spectral density estimates and correlation function estimates. This method is usually the only method implemented in commercial systems for structural dynamics, although, as we will see in Sect. 5, there can sometimes be reasons for choosing the periodogram-based methods.

The principle of Welch's method is illustrated schematically in Fig. 7. The data are divided into M blocks of length N samples (the block size). The M segments can be overlapped; see Sect. 4.3. For each segment, a time window is applied, the DFT calculated, and averaging is then performed in the frequency domain, as we will show in the next subsections.

In Sect. 3 we mentioned that the spectral density of a signal is the Fourier transform of the correlation function. This is not a very practical solution for computing spectra, however, since correlation functions are computationally intense. The spectrum estimators are based on computing the FFT because it is considerably faster than the direct DFT. Therefore, we need to see how to use the FFT/DFT to obtain the Fourier transform of the correlation function. This can relatively easily be seen, if we consider Eq. (7), where it was shown that the cross-correlation $R_{yx}(\tau)$ essentially corresponds to the convolution of the signal $y(t)$ by the signal $x(-t)$ (it actually corresponds to the convolution divided by the number of samples, as there is an expectation value in Eq. (7)). We can now use the Fourier transform pair of $x(-t)$, which is $X^*(f)$. Thus, the cross-spectral density between signals x and y is proportional to

$$S_{yx}(f) = \mathscr{F}\left[R_{yx}(\tau)\right] \propto Y(f)X^*(f) \tag{20}$$

where $\mathscr{F}[\,]$ denotes the Fourier transform. To complete the equation, and to compute the estimators by using the DFT, we need some scaling that we will address below.

4.1 The Linear (RMS) Spectrum

We are now ready to address the spectrum estimator best suited for dealing with periodic signals, without significant noise. Such signals can, for example, be vibrations on a reciprocating engine or on power generators. The spectrum estimator is the so-called *linear spectrum* or *RMS spectrum*. This estimator, which we denote $X_L(k)$, is the square root of the *autopower spectrum*. The reason for using the intermediate autopower spectrum is that if averaging is necessary to reduce the variance of the estimate due to noise, then this averaging has to be applied to squared spectral components, in order for the average to be a mean square average. This is necessary because we always want the averaging result to display true RMS levels.

The autopower spectrum is produced by dividing the signal $x(n)$ with length L samples, into M blocks of length N that we denote $x_m(n)$, (if L is not an integer number of blocks with length N, we simply discard the last few samples of the signal). Each of the M blocks is windowed, the DFT of the windowed block is computed, and the DFT results are averaged, frequency by frequency. An intermediate step is thus to compute the DFT of the windowed block number $m = 1, 2, \ldots, M$, of $x(n)$ that we denote $X_{w,m}$ and which equals

$$X_{w,m}(k) = \sum_{n=0}^{N} w(n)x_m(n)e^{-j2\pi kn/N} \quad k = 0, 1, \cdots, N/2 \tag{21}$$

where $w(n)$ is the time window. Note that we discard the upper half of the DFT blocks, i.e., the negative frequencies in the definition of $X_{w,m}$. We can now define the autopower spectrum of the signal x, by

$$\hat{A}_{xx}(k) = \frac{S_A}{M}\sum_{m=1}^{M} X_{w,m}(k)X^*_{w,m}(k) = \frac{S_A}{M}\sum_{m=1}^{M}|X(k)|^2 \tag{22}$$

where S_A is a scaling constant to produce peaks in $A_{yx}(k)$ equal to the square of the RMS level of the corresponding harmonic component in the signal. The scaling constant is

$$S_A = \begin{cases} \dfrac{2A_w^2}{N^2}, & k \neq 0 \\ \dfrac{A_w^2}{N^2}, & k = 0 \end{cases} \tag{23}$$

where A_w is the window amplitude scaling factor from Eq. (18).

After we have estimated the autopower spectrum, the linear (RMS) spectrum can be computed, as the square root of A_{xx}

$$\hat{X}_L(k) = \sqrt{\hat{A}_{xx}(k)} \tag{24}$$

A peak in the linear spectrum is thus interpreted as the RMS level of a harmonic component at that frequency. Note that the linear spectrum does not have any phase.

The choice of scaling the linear spectrum to the RMS level of the harmonics is, of course, not mandatory, although we certainly recommend it. In some fields it is common to also scale linear spectra to the amplitude of the harmonics. Therefore, it is important to include the scaling in the units of the plot, by specifying, e.g., "[m/s^2 RMS]" if the measured signal was acceleration in the SI unit of m/s^2.

We are now ready to apply the linear spectrum to a real signal. The parameters we need to consider are listed in Table 1. One setting is not listed in the table; the bandwidth (highest frequency) of the measurement naturally needs to be chosen. This is a setting that should normally be chosen based on some knowledge about the signal to be measured, such as the RPM of the engine and how many harmonics are required. Alternatively, one may try a high-frequency setting and, after looking at the obtained spectrum, gradually reduce the bandwidth until the spectrum shows a sufficient amount of higher frequencies for the purpose of the measurement.

To select the settings for the linear spectrum estimator, the time window is usually set based on taste. A flattop window is sometimes preferred, as it guarantees that the RMS levels of harmonic components are accurately determined (to within 0.1%). On the other hand, due to the wide main lobe of the flattop window, some users prefer the Hanning window and accept the error in RMS readings of up to −16%, which, in many cases in vibration applications, is certainly negligible. An appropriate number of averages usually has to be found by a trial and error procedure. If the RMS levels change significantly for repeated measurements without averaging, the number of averages can be increased until stable RMS levels are obtained. This usually requires a small number of averages, typically between

Table 1 Typically used settings for block-based spectrum estimators. Low number of averages are typically 5–20; high can be 50–500

Spectrum type	Window	Number of averages	Overlap, %	Block size, N
Linear spectrum	**Flattop**, Hanning	Low	**0**–50	Large enough to obtain a line spectrum
PSD, CSD	Hanning	High	50	Large enough to avoid bias
ESD	Rectangular	No*	No	Large enough to capture entire transient

*For transients, triggered acquisition can be used with averaging, for example, for impact testing, see the chapter on FRF measurements

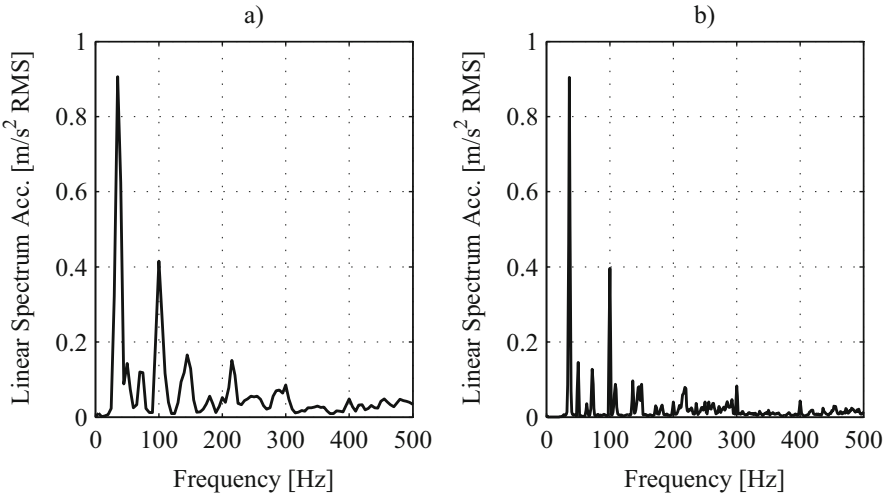

Fig. 8 Example of linear spectrum estimates with two different block sizes; in (**a**) a frequency increment of 5 Hz has been used; in (**b**) the fre8quency increment is 1.25 Hz. It is clear in (**a**) that the frequency increment is not small enough to allow the spectrum to reach zero between the peaks, whereas in (**b**) the peaks are distinct, and thus the spectrum is an appropriate line spectrum as expected for a periodic signal

5 and 20. For periodic signals, overlap is often not used, although 50% can be advantageously used to speed up the measurement. See more about averaging in Sect. 4.3.

The last setting in Table 1 is the most important to set correctly. The block size should be set such that a line spectrum is obtained, i.e., that the spectrum reaches zero between every peak. If this is not the case, the frequency increment is too large. The recommended procedure to find the optimal block size is thus to make repeated measurement, starting with a small block size that does not create a line spectrum, and then increase the block size until a line spectrum is obtained. This procedure is illustrated in Fig. 8 where two linear spectra of the same signal, the acceleration measured on a fan, are shown.

4.2 The Phase Spectrum

Sometimes, for periodic signals, a phase relative to some reference signal (a tachometer signal or another response signal) is required, for example, for *operating deflection shape* (ODS) measurements. There is really only one way to obtain such a phase, and that is from a cross-spectrum. The *phase spectrum* is an "artificial" spectrum where the linear spectrum is added a phase from the cross-spectrum between the response signal and some reference signal. Assume we have a reference signal $x(t)$ and a response signal $y(t)$ for which we wish to have the linear spectrum

with reference to $x(t)$. For this purpose, first the cross-power spectrum $\hat{A}_{yx}(k)$ is estimated by

$$\hat{A}_{yx}(k) = \frac{S_A}{M} \sum_{m=1}^{M} Y_{w,m}(k) X^*_{w,m}(k) \tag{25}$$

and the linear spectrum, $\hat{Y}_L(k)$, is estimated by Eqs. (22) and (24). The phase spectrum $\hat{Y}_{px}$ is then constructed from these two spectra as

$$\hat{Y}_{px}(k) = \hat{Y}_L(k) e^{j \arg[\hat{A}_{yx}(k)]} \tag{26}$$

where arg[ ] denotes the phase in radians. Each spectral line of the phase spectrum will thus contain the RMS level of the signal y and the phase of y related to the reference x at that frequency. This allows software to pick amplitude and phase information for animation of ODSs.

4.3 Welch's PSD and CSD Estimates

Welch's method for PSD estimation relies on the same procedure as the method for estimating autopower spectra we discussed in Sect. 4.1. Similarly to Eq. 22, we thus define the PSD estimate, $\hat{G}_{xx}(k)$ as

$$\hat{G}_{xx}(k) = \frac{S_P}{M} \sum_{m=1}^{M} X_{w,m}(k) X^*_{w,m}(k) = \frac{S_P}{M} \sum_{m=1}^{M} \left| X_{w,m}(k) \right|^2 \tag{27}$$

where S_P is a scaling constant to produce spectral density scaling, such that the area under the estimate $\hat{G}_{xx}(k)$ equals the mean square of the signal $x(t)$. The scaling constant is

$$S_P = \frac{S_A}{B_{en} \Delta f} \tag{28}$$

where S_A is the RMS scaling constant for autopower spectrum defined by Eq. (23) and B_{en} is the normalized equivalent noise bandwidth defined by Eq. (19). Similarly the cross-spectral density estimate between two signals, $x(t)$ and $y(t)$, is defined by

$$G_{yx}(k) = \frac{S_P}{M} \sum_{m=1}^{M} Y_{w,m}(k) X^*_{w,m}(k) \tag{29}$$

The PSD estimate in Eq. (27) is rather different from the estimate of the autopower spectrum, since the signal, $x(t)$, is assumed to be random. Thus, the spectral density is continuous, and there will be two errors in the estimate: a bias error and a random error. The bias error is a result of a continuous spectrum being

estimated by a discrete estimator and can be eliminated if necessary, by making the frequency increment, Δf small enough, i.e., by using a block size, N, which is large enough. This can be achieved by a similar approach as that described for obtaining an appropriate frequency increment for the linear spectrum estimate, at the end of Sect. 4.1.

The random error of a PSD estimate is defined by the standard deviation of the difference between the estimated and true PSDs. Usually we talk about the normalized random error, ε_r, which is the mentioned standard deviation divided by the true value of the PSD or

$$\varepsilon_r\left[\hat{G}_{xx}\right] = \frac{\sqrt{\mathrm{E}\left[(\hat{G}_{xx} - G_{xx})^2\right]}}{G_{xx}} \tag{30}$$

The random error is independent of frequency and is reduced as the number of averages is increased. Usually 50% overlap is recommended for PSD estimation, as this gives a significantly lower (almost half) random error, for a given measurement time. Although rather complicated in detail, the random error of a Welch PSD estimate is an effect of the time window, the overlap, and the number of averages. For space reasons we refer to [2,10] for a thorough treatment. It is sufficient here to refer to Fig. 9 which shows the random error as a function of the number of averages used, when the PSD is estimated by Welch method, a Hanning window, and 50%

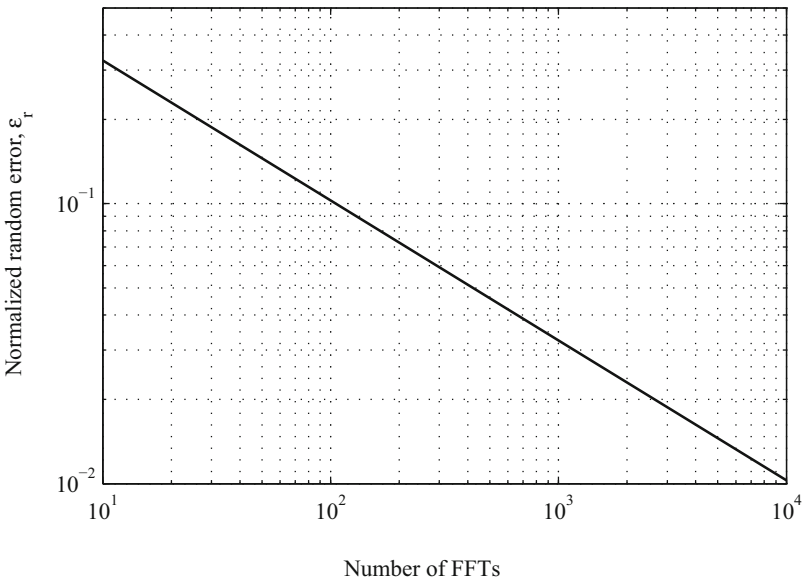

Fig. 9 Random error of Welch PSD estimate estimated using Hanning window and 50% overlap, as a function of the number of averages used for the estimate

overlap processing. As is evident from this plot, many averages are needed to obtain a small random error; for an error of 5%, for example, 400 averages are needed. With 50% overlap, that means that the data have to contain 200 non-overlapped blocks.

In Table 1, in the row for PSD estimates, the recommended measurement system settings for a PSD estimate are shown. A Hanning window should always be used together with 50% overlap (slightly more overlap can be used, but hardly pays off as it results in very slightly lower random error). The number of averages normally has to be high, which means, say, between 50 and 500 averages. Most important, however, is that the block size is made large enough to eliminate the bias error, at least in cases where the PSD is going to be used for further processing, for example, for modal parameter extraction.

4.4 Energy Spectral Density Estimates

The *energy spectral density* (ESD) function is usually used as the preferred spectrum for (deterministic) transient signals. As we described in Sect. 2.3, the ESD is the magnitude squared of the Fourier transform of the transient. Although the ESD is not, strictly speaking, a block-based estimate, we still describe it here, as it is usually found alongside the linear spectrum and PSD estimates in commercial software for vibration analysis.

The ESD estimate $\mathscr{G}_{xx}(k)$ of the transient captured in $x(n)$ of length L, is therefore rather straightforwardly defined by

$$\mathscr{G}_{xx}(k) = \left| \Delta t \cdot \sum_{n=0}^{L-1} x(n) e^{-j2\pi kn/L} \right|^2 \tag{31}$$

where it should be especially noted that we do not use any time window. The typical measurement system settings for an ESD measurement are listed in the last line in Table 1.

4.5 Welch's Correlation Function Estimates

To estimate correlation functions, the most common estimator used in commercial measurement systems is Welch's estimator. It is very important, however, to note that the correlation function should not be estimated as the inverse DFT of a PSD estimated by the procedure described in Sect. 4.3 as this will lead to a distorted (biased) estimate, not suitable for parameter extraction of modal parameters, for example. To see how to estimate the correlation function properly, we refer back to the definition. A direct calculation of the cross-correlation of two random time signals $x(t)$ and $y(t)$ as by Eq. (7) is

$$R_{yx}(\tau) = \mathrm{E}[y(t)x(t-\tau)] = \frac{1}{T}\int_{-T/2}^{T/2} y(t)x(t-\tau)dt \tag{32}$$

It is easily realized that this estimator will lead to a biased estimator, because we divide by T, the length of the signal $x(t)$, whereas for any lag $\tau \neq 0$, there will actually only be overlapping data that can be multiplied together of length $T - \tau$. Thus we obtain the *unbiased cross-correlation estimator* by

$$R_{yx}(\tau) = \mathrm{E}[y(t)x(t-\tau)] = \frac{1}{T-|\tau|}\int_{-T/2}^{T/2} y(t)x(t-\tau)dt \tag{33}$$

and for a single signal, $x(t)$, as mentioned previously, the autocorrelation is obtained by replacing $y(t)$ by $x(t)$.

Since, for structural dynamics applications, we are usually only interested in the nonnegative lags $\tau \geq 0$, we will limit the discussion here to those lags. To find an appropriate discrete estimator for the time integral in Eq. (33), we start by observing that the discrete correlation function should be equal to the convolution of $x(n)$ by $x(n-m)$, weighted by $1/(N-m)$ where we let m denote the discrete lag, in number of samples, and N is the block size of the DFT. This is thus equal to a multiplication in the frequency domain, of $X(f)$ by its complex conjugate $X^*(f)$. But, *it is very important to use zero padding in the computation of the DFT*, $X(f)$, to obtain the intermediate spectra (DFT results) $X_{m,z}$ and $Y_{m,z}$, in order to avoid cyclic convolution effects. If the data contains N samples, then it should be zero padded by N zeros, prior to the DFT calculation.

Furthermore, using Welch's approach, we use a block size, N, much smaller than the total length L, thus averaging M DFT results in the frequency domain. We denote the resulting, temporary, PSD estimate by $\hat{S}^C_{yx}$ and obtain it by

$$\hat{S}^C_{yx}(k) = \frac{1}{M}\sum_{m=1}^{M} Y_{m,z}(k)X^*_{m,z}(k) \tag{34}$$

The next step is to calculate and properly scale the inverse DFT (IDFT) of $\hat{S}^C_{yx}(k)$ which results in the unbiased estimate of the cross-correlation function

$$\hat{R}_{yx}(m) = \frac{1}{2N(N-m)}\sum_{k=0}^{2N-1} \hat{S}^C_{yx}(k)e^{j2\pi km/(2N)}, \quad m = 0, 1, \ldots m_{\max} < N/2 \tag{35}$$

where the factor $2N$ in the denominator belongs to the inverse DFT. It is not necessary to apply overlap processing to compute $\hat{S}^C_{yx}(k)$, since it does not significantly contribute to a reduced random error in the correlation estimate.

5 Periodogram-Based Spectrum and Correlation Estimation

In this section we introduce the alternative to the block-based technique (Welch's method) for computing spectra and correlation functions. The methods we will discuss are based on making only one, large DFT/FFT of each measurement signal, followed by some processing and scaling to produce reliable estimates. Although this requires more memory in the computer, with modern computers and measurement systems, this is rarely a drawback, and as we will see, there are some reasons for sometimes choosing the periodogram-based methods instead of the block-based.

5.1 The Periodogram

The (auto)periodogram of a signal $x(n)$ is defined as the magnitude squared of the DFT of the signal, $X(l)$, scaled by the length, L,

$$\hat{P}_{xx}(l) = \frac{\Delta t}{L}\left|\sum_{n=0}^{L-1} x(n)e^{-j2\pi ln/N}\right|^2 \tag{36}$$

We could, of course, also define a cross-periodogram, if we have an additional signal $y(n)$ (where $x(n)$ is considered the reference) by

$$\hat{P}_{yx}(l) = \frac{\Delta t}{L}\left(\sum_{n=0}^{L-1} y(n)e^{-j2\pi ln/N}\right)\left(\sum_{n=0}^{L-1} x(n)e^{-j2\pi ln/N}\right)^* \tag{37}$$

where * denotes complex conjugation. Note that we have used the symbol l to denote the discrete frequency of the periodogram. This is to distinguish this, usually much finer, frequency index from the frequency index of the estimates using Welch's estimate, for the discussion in Sect. 5.2.

The periodogram in Eq. (36) is an estimator for spectral density but a rather poor such estimator, as can be seen in Fig. 10a, b where periodograms of white Gaussian noise are plotted, based on $L = 512$ samples in (a) and $L = 4096$ samples in (b). The periodogram is an *inconsistent* estimator, in that it does not approach the true PSD with increasing length L. On the contrary, as can be seen in the figure, it behaves more and more wildly the more data it is based on. On the right-hand side of Fig. 10, in (c) and (d), similar periodograms but of a signal containing a periodic signal plus random noise are plotted. As can be seen in the plots, with more data, the periodic components stand out of the noise. Thus, the periodogram is a good estimator for finding sines hidden in noise, although there is a lot of leakage. This can easily be avoided by applying a flattop window to the data before computing the periodogram, however, thus computing a *windowed periodogram*.

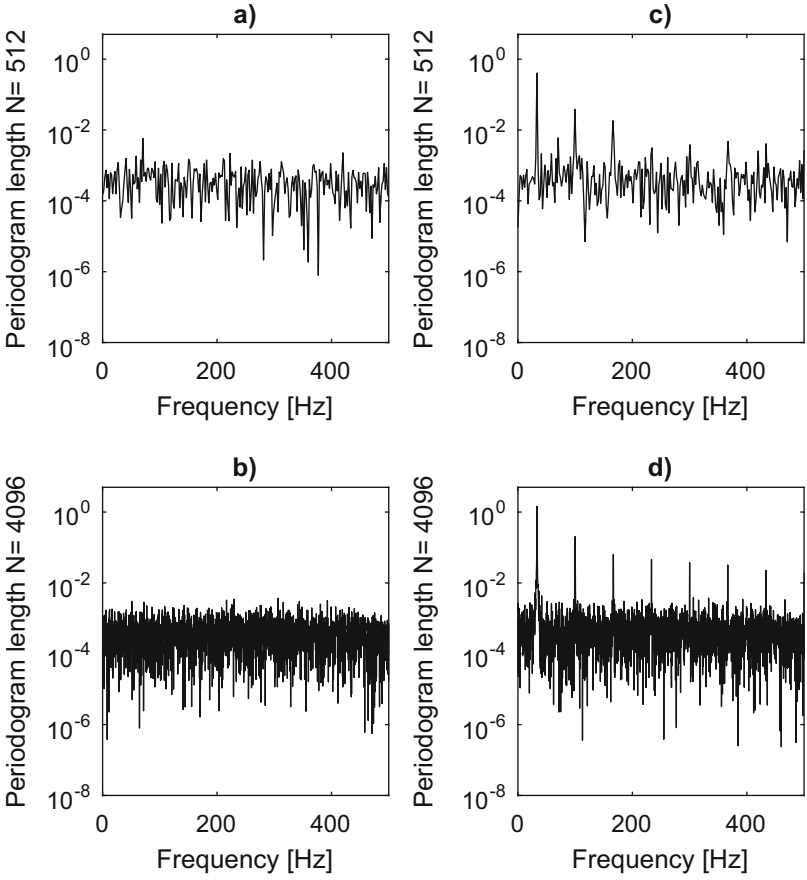

Fig. 10 Periodogram plots of random signal (left) and a periodic signal with noise (right). In (**a**) and (**b**), periodograms of the same random signal are shown, with data length of $N = 512$ in (**a**) and $N = 4096$ in (**b**) and in (**c**) and (**d**), similarly for periodograms of a periodic signal with noise

5.2 The Smoothed Periodogram PSD Estimate

An alternative to the PSD estimate by Welch's method, which can offer some advantages, is the so-called smoothed periodogram or sometimes the Daniell method. This estimate is obtained by smoothing (averaging) the periodogram in Eq. (36) around each frequency where an estimate is wanted. If we, for example, choose the same frequencies, $k \cdot fs/N, k = 0, 1, \ldots N/2$ that Welch's estimate would yield, then the smoothed autoperiodogram estimator is

$$\hat{G}_{xx}^{SP}(k) = \frac{2}{(L_s + 1)} \sum_{l=k \cdot D - L_s/2}^{k \cdot D + L_s/2} \hat{P}_{xx}(l) \quad k = 1, 2, \ldots \tag{38}$$

and similarly for the cross-periodogram estimator. The factor 2 in the numerator in Eq. (38) is due to scaling for a single-sided PSD, $\hat{G}_{xx}^{SP}(k)$, as the periodogram $\hat{P}_{xx}(l)$ is double-sided. We have assumed L_s is an even number, and the variable D is the number of frequency bins l between each target frequency k. The straight average in Eq. (38) can be replaced by weighted averaging, but it turns out to give very little difference in the properties of the resulting estimates.

We will illustrate the smoothed periodogram estimator with an example.

Example 3. Assume we have data $x(n)$ with length $L = 100 \cdot N$ and $N = 1024$, the block size we use with Welch's method, and with a sampling frequency of 1024 Hz. This would yield frequencies for Welch's estimate at $k\Delta f = kf_s/N = k \cdot 1\,\text{Hz}$. If we, for the sake of a direct comparison, assume that we do not use any overlap processing, Welch's method would result in 100 averages.

The corresponding smoothed periodogram estimator would be obtained by selecting the same frequencies $f_k = k\Delta f$ for the resulting spectrum and setting $L_s = 100$, the same as the number of averages used for Welch's estimate. Since the frequency increment of the periodogram is $f_s/L = f_s/(L_s N) = \Delta f/L_s = 1/100$ in this case, then obviously $D = L_s = 100$. So, each frequency bin k in the Welch's estimate corresponds to the frequency bins $l = kD$ in the periodogram. At each of these latter bins, the periodogram is averaged over ± 50 bins. □

The smoothed periodogram computed as described above is similar to Welch's estimate, in terms of its bias and random errors. It requires a much larger FFT than Welch's method but only one, as opposed to 100 FFTs of the Welch estimate in our example. Welch's estimate has the advantage of requiring much less memory, but the computation speed for the periodogram estimate is similar to that for Welch's estimate for typical data lengths in structural dynamics applications. There are, furthermore, at least two advantages that can make the smoothed periodogram PSD estimator a preferred estimator:

- harmonics can easily be removed using the periodogram; see Sect. 5.4
- the smoothed periodogram estimate can easily be computed using constant relative bandwidth, $\Delta f/f_k$ by letting D and L_s grow exponentially with frequency

5.3 The Periodogram Correlation Estimate

The periodogram can also be used to compute the correlation functions, as described in [3]. This is actually a more straightforward way than using Welch's method as described in Sect. 4.5. To obtain correlation functions without effects of cyclic correlation, L zeros have to be added to the time signal of length L, prior to computing the periodogram. In addition, we do not use the scaling by the time increment and data length, as in Eq. (36), but instead use the magnitude square of the DFT, without scaling. A straightforward computation of the cross-correlation

estimate, $\hat{R}_{yx}(\tau)$, is thus obtained by first computing the zero-padded DFTs to be the $2L$ length FFTs to obtain $X_z(l)$ and $Y_z(l)$. Then the unbiased cross-correlation estimate for positive lags, m, is obtained by the inverse DFT, divided by $L-m$, i.e.:

$$\hat{R}^P_{yx}(m) = \frac{1}{(2L(L-m))} \sum_{l=0}^{2L-1} Y_z(l) X_z^*(l) e^{j2\pi ml/(2L)} = \frac{1}{L-m} \text{IDFT}\left[Y_z X_z^*\right] \tag{39}$$

The autocorrelation $R_{xx}(m)$ is obtained by replacing Y_z in the equation by X_z. Normally we are only interested in a number of lags $m \ll L$, so the large part of the IDFT in Eq. (39) can be discarded. This estimator requires a long DFT (FFT) to be computed, but for most data lengths typically used for OMA, for example, modern computers have sufficient performance that this estimate is computed in a similar amount of time compared to the Welch's estimate (and sometimes even faster). It should be noted that the correlation function estimate in Eq. (39) is identical to the direct time domain computation, as well as the computation by Welch's method.

5.4 Dealing with Harmonics in Correlation Functions

Harmonics in the response signals is a large problem in applications of OMA on, for example, wind power mills, ships, and power generators, since it violates the assumptions for OMA. The periodogram offers a relatively easy way to remove the harmonics in such cases which is particularly attractive if spectral densities or correlation functions are going to be computed as described in Sects. 5.2 or 5.3. As shown in Fig. 10, harmonics stand out from the periodogram; the longer the data length, the more they stand out. Thus, after computing the long DFTs, $Y_r(l)$, $r = 1, 2, \ldots, N_r$ for N_r responses used for OMA (see the chapter on OMA), each auto and cross-periodogram is produced. The harmonics will typically only appear as single, or very few, frequency bins in these periodograms and can easily be edited away, by replacing them by linear interpolation between the remaining frequency bins on the left- and right-hand sides. After this, the periodograms are either smoothed, to produce PSDs and CSDs, or inverse Fourier transformed, to produce auto- and cross-correlation functions. More information of this may be found in [3].

6 Summary

In this chapter we have described the basic properties of spectra and correlation functions and how these functions should be estimated. When calculating and interpreting spectra, it is important to consider what type of signal is at hand, a

periodic, a random, or a transient signal. The most important results presented in the chapter are the following.

A periodic signal should be described by a *linear spectrum*, also called *RMS spectrum*, as described in Sect. 4.1. This spectrum should be scaled so that a peak value in the spectrum corresponds to the RMS level of a harmonic component at the frequency. The units of this spectrum, if the measured unit is EU (engineering units), are [EU RMS], for example, [m/s^2 RMS] for an acceleration signal. For the linear spectrum, a time window has to be selected, as described in Sect. 4.1. Some recommendations for settings can be found in Table 1.

A random signal should be represented by a *power spectral density* (PSD) spectrum, which is interpreted such that the area under the PSD is the mean square value (the square of the RMS) of the signal. PSDs may be estimated in two different ways; in Sect. 4.3 we described how to do it with the Welch estimator (dividing the signal into a number of segments, which are processed and averaged in the frequency domain). Another method for estimating a PSD is the periodogram method described in Sect. 5.2 which is based on one DFT (FFT) being computed on the entire measured signal. The units of the PSD are [EU^2/Hz], for example, [(m/s^2)^2/Hz] for an acceleration signal. For the PSD, a Hanning window is recommended. For further recommendations, see Table 1.

A transient signal is most often represented by the *energy spectral density* (ESD) spectrum, computed from a DFT (FFT) of the entire transient signal. The area under the ESD is interpreted as the energy of the transient and has units of [EU^2/Hz $\cdot$ s]. The estimator is described in Sect. 2.3. For an ESD, no time window should be used; see Table 1.

Correlation functions of random signals are mostly used for operational modal analysis. Again, there are two ways to compute these functions in the frequency domain: one block-based method (Welch's method) and one method based on a periodogram. How to estimate these functions are described in Sects. 4.5 and 5.3, respectively.

References

1. Bendat JS, Piersol AG (2010) Random data: analysis and measurement procedures, 4th edn. Wiley Interscience, Hoboken
2. Brandt A (2011) Noise and vibration analysis – signal analysis and experimental procedures. Wiley, Chichester
3. Brandt A (2019) A signal processing framework for operational modal analysis in time and frequency domain. Mech Syst Signal Process 115:380–393
4. Daniell PJ (1946) Discussion of 'on the theoretical specification and sampling properties of autocorrelated time-series'. J R Stat Soc 8(suppl.)(1):88–90
5. de Silva CW (2006) Vibration: fundamentals and practice, 2nd edn. CRC Press, Boca Raton, Florida
6. James GH, Carne TG, Lauffer JP (1995) The natural excitation technique (next) for modal parameter extraction from operating structures. Modal Anal Int J Anal Exp Modal Anal 10(4):260–277

7. Newland DE (2005) An introduction to random vibrations, spectral, and wavelet analysis, 3rd edn. Dover Publications Inc., Mineola/New York
8. Shin K, Hammond J (2008) Fundamental of signal processing for sound and vibration engineers. Wiley, Chichester
9. Stoica P, Moses R (2005) Spectral analysis of signals. Prentice Hall, Upper Saddle River
10. Welch PD (1967) The use of fast Fourier transform for the estimation of power spectra: a method based on time averaging over short, modified periodograms. IEEE Trans Audio Electroacoust AU-15(2):70–73
11. Wirsching PH, Paez TL, Ortiz H (1995) Random vibrations: theory and practice. Wiley Interscience, New York, NY

Frequency Response Function Estimation

6

A. W. Phillips and R. J. Allemang

Contents

A. W. Phillips (✉) · R. J. Allemang
Structural Dynamics Research Laboratory, Mechanical and Materials Engineering, University of Cincinnati, Cincinnati, OH, USA
e-mail: Allyn.Phillips@UC.EDU; Randall.Allemang@UC.EDU

R. Allemang, P. Avitabile (eds.), *Handbook of Experimental Structural Dynamics*,
https://doi.org/10.1007/978-1-4614-4547-0_8

Abstract

For current approaches to experimental modal analysis, the frequency response function is the most important measurement to be made. This chapter develops the frequency response function from the perspective of experimentally measured system excitations and responses. Experimental measurement and numerical processing techniques are presented that allow minimization of the impact of measurement noise and signal processing errors.

Keywords

Multiple input frequency response function · Ordinary coherence · Multiple coherence · Conditioned coherence · Spectral averaging · Selective excitation

Nomenclature

N	Number of degrees of freedom
N_i	Number of inputs
N_o	Number of outputs
N_s	Number of spectral lines (frequencies)
$F_{\max}$	Maximum frequency (Hz)
ω	Frequency (rad/s)
Δf	Frequency resolution (Hz)
T	Observation period (s)
λ	Complex eigenvalue
$\{V\}$	Complex eigenvector
$[H(s)]$	Transfer function matrix
$[H(\omega)]$	Frequency response function matrix
$\{X(\omega)\}$	Response vector
η	Noise on response
$\{F(\omega)\}$	Excitation vector
υ	Noise on excitation
$[G_{FF}]$	Input-input power spectral matrix
$[G_{XF}]$	Output-input cross power spectral matrix
$[G_{XX}]$	Output-output power spectral matrix
O_{COH}	Ordinary coherence
M_{COH}	Multiple coherence
P_{COH}	Partial coherence
C_{COH}	Cumulative coherence
F_{COH}	Fractional coherence
V_{COH}	Virtual coherence
SVD	Singular value decomposition
ED	Eigenvalue decomposition
CD	Cholesky decomposition

1 Introduction

For current approaches to experimental modal analysis, the frequency response function is the most important measurement to be made. When estimating frequency response functions, a measurement model is needed that will allow the frequency

response function to be estimated from measured input and output data in the presence of noise (errors). Some of the errors are:

- Digital signal processing errors
  - Leakage
  - Aliasing
- Noise
  - Equipment problem (power supply noise)
  - Cabling problems (RFI, EMI)
  - Rattles, cable motion
- Calibration (operator error)
  - Complete system calibration
  - Transducer calibration

Since the frequency response function can be expressed in terms of system properties of mass, stiffness, and damping, it is reasonable to conclude that in most realistic structures, the frequency response functions are considered to be constants just like mass, stiffness, and damping. This concept means that when formulating the frequency response function using H_1, H_2, or H_v algorithms, the estimate of frequency response is intrinsically unique, as long as the system is linear and the noise can be minimized or eliminated. The estimate of frequency response is valid whether the input is stationary, nonstationary, or deterministic. Therefore, several important points to remember before estimating frequency response functions are as follows:

- The system (with the boundary conditions for that test) determines the frequency response functions for the given input/output locations.
- It is important to eliminate or at least minimize all errors (aliasing, leakage, noise, calibration, etc.) when collecting data.
- If all noise terms are identically zero, the assumption concerning the source/location of the noise does not matter ($H_1 = H_2 = H_v = H_s = H$). Therefore, concentrate on eliminating the source of the noise.
- Since modal parameters are computed from estimated frequency response functions, the modal parameters are only as accurate as the estimated frequency response functions.

There are at least four different testing configurations that can be compared. These different testing conditions are largely a function of the number of acquisition channels or excitation sources that are available to the test engineer. In general, the best testing situation is the multiple input/multiple output (MIMO) configuration since the data is collected in the shortest possible time with the fewest changes in the test conditions.

- Single input/single output (SISO)
  - Only option if two-channel data acquisition system.

  - Longest testing time. Roving inputs. Roving outputs.
  - Time invariance problems between measurements.
- Single input/multiple output (SIMO)
  - Multiple channel system (three or more). (One ADC channel for each response signal to be measured plus one ADC channel for an input signal.)
  - Shorter testing time than SISO. Transducers not necessarily moved.
  - Consistent frequency and damping for data acquired simultaneously.
  - Time invariance problems between measurements from different inputs.
- Multiple input/single output (MISO)
  - Multiple channel system required (three or more.). (One ADC channel for each input signal to be measured plus one ADC channel for a response signal.)
  - Long testing time. Roving response transducer.
  - More than one input location per measurement cycle.
  - Detects repeated roots. Maxwell reciprocity checks are possible.
  - Time invariance problems between measurements from different responses are possible.
- Multiple input/multiple output. (MIMO)
  - Multiple channel system (up to 512 channels). Increased setup time. Large amount of data to be stored and organized.
  - Shortest testing time.
  - Consistent frequency and damping for all data acquired simultaneously.
  - Detects repeated roots. Maxwell reciprocity checks are possible.
  - Best overall testing scheme.

2 Frequency Response Function Development

In this chapter, frequency response functions are developed from experimentally measured input-output (force-response) relationships. However, prior to that development, it is advantageous to show the relationship to a lumped parameter mass, damping, and stiffness (M,C,K) model and the system transfer function matrix.

The transfer function representation of a general multiple degree of freedom system can be formulated by starting with the differential equation of motion in terms of mass, stiffness, and damping matrices:

$$[M]\{\ddot{x}(t)\} + [C]\{\dot{x}(t)\} + [K]\{x(t)\} = \{f(t)\} \tag{1}$$

Taking the Laplace transform of Equation 1, assuming all initial conditions are zero, yields:

$$\Big[[M]s^2 + [C]s + [K]\Big]\{X(s)\} = \{F(s)\} \tag{2}$$

Letting:

$$[B(s)] = \left[[M]s^2 + [C]s + [K]\right] \tag{3}$$

Then Equation 2 becomes:

$$[B(s)]\{X(s)\} = \{F(s)\} \tag{4}$$

where $[B(s)]$ is referred to as the *impedance matrix* or just the *system matrix*.

Premultiplying Equation 4 by $[B(s)]^{-1}$ yields:

$$[B(s)]^{-1}\{F(s)\} = \{X(s)\} \tag{5}$$

Defining:

$$[H(s)] = [B(s)]^{-1} \tag{6}$$

Then:

$$[H(s)]\{F(s)\} = \{X(s)\} \tag{7}$$

Equation 7 relates the system response $\{X(s)\}$ to the system forcing functions $\{F(s)\}$ through the matrix $[H(s)]$. The matrix $[H(s)]$ is generally referred to as the *transfer function matrix*.

By observing the partitioned nature of the matrix equations and evaluating the equation for a single output response $X_p(s)$:

$$\sum_{q=1}^{N} H_{pq}(s) F_q(s) = X_p(s) \tag{8}$$

the familiar relationships for the transfer function (output over input) are obtained by evaluating for a single input excitation $F_q(s)$ with all other inputs zero $F_k(s) = 0$: $k \neq q$:

$$H_{pq}(s) = \frac{X_p(s)}{F_q(s)} \tag{9}$$

- p is the output degree of freedom (physical location and orientation).
- q is the input degree of freedom (physical location and orientation).

Thus, $H_{pq}(s)$ is the transfer function which would be measured by exciting the system with $F_q(s)$ and measuring the response $X_p(s)$. Unfortunately, it is not possible to measure $F(s)$ and $X(s)$ directly.

However, since s is a general frequency variable ($s = \sigma + j\omega$ with units of rad/s), by evaluating the transfer function matrix at $s = j\omega$, the *frequency response function matrix* results:

$$H(\omega) = \left[-\omega^2 [M] + j\omega [C] + [K]\right]^{-1} \tag{10}$$

Therefore, measuring a column of the frequency response function matrix $[H(\omega)]$ can be accomplished by using a single, fixed input (exciter system) with a roving response, and measuring a row can be accomplished by using a roving input (hammer) and a single fixed response:

$$H_{pq}(\omega) = \frac{X_p(\omega)}{F_q(\omega)} \tag{11}$$

It should be reiterated that the subscript notation of p or q refers to both a physical location and also direction or orientation.

3 Frequency Response Function Estimation

Frequency response functions are normally used to describe the input-output (force-response) relationships of any system. Most often, the system is assumed to be linear and time invariant although this is not a necessary part of the definition. In the cases where assumptions of linearity and time invariance are not valid, the measurement of frequency response functions is also dependent upon the independent variables of time and input. In this way, a conditional frequency response function is measured as a function of other independent variables in addition to frequency. Note that the different possible formulations listed in Table 1 can all be considered frequency response functions since each of these formulations can be numerically manipulated (synthetic differentiation, integration, etc.) into the equivalent displacement over force relationship. This assumes that initial conditions can be ignored.

Table 1 Frequency response function formulations

Receptance	$\frac{Acceleration}{Force}$
Effective Mass	$\frac{Force}{Acceleration}$
Mobility	$\frac{Velocity}{Force}$
Impedance	$\frac{Force}{Velocity}$
Dynamic Compliance	$\frac{Displacement}{Force}$
Dynamic Stiffness	$\frac{Force}{Displacement}$

The estimation of the frequency response function depends upon the transformation of data from the time to frequency domain. The Fourier transform is used for this computation. Unfortunately, though the integral Fourier transform definition requires time histories from negative infinity to positive infinity, since this is not possible experimentally, the computation is performed digitally using a *fast Fourier transform (FFT)* algorithm which is based upon only a limited time history. In this way, the theoretical advantages of the Fourier transform can be implemented in a digital computation scheme. The frequency response functions satisfy the following single and multiple input relationships:

Single Input Relationship:

$$X_p = H_{pq}\ F_q \tag{12}$$

Multiple Input Relationship:

$$\begin{bmatrix} X_1 \\ X_2 \\ \cdot \\ \cdot \\ X_p \end{bmatrix}_{N_o \times 1} = \begin{bmatrix} H_{11} & \cdots\cdots & H_{1q} \\ H_{21} & & \cdot \\ \cdot & & \cdot \\ \cdot & & \cdot \\ H_{p1} & \cdots\cdots & H_{pq} \end{bmatrix}_{N_o \times N_i} \begin{bmatrix} F_1 \\ F_2 \\ \cdot \\ \cdot \\ F_q \end{bmatrix}_{N_i \times 1} \tag{13}$$

An example of a two-input, two-output case for Equation 13 is shown in Equation 14 and Fig. 1.

$$\begin{bmatrix} X_1 \\ X_2 \end{bmatrix} = \begin{bmatrix} H_{11} & H_{12} \\ H_{21} & H_{22} \end{bmatrix} \begin{bmatrix} F_1 \\ F_2 \end{bmatrix} \tag{14}$$

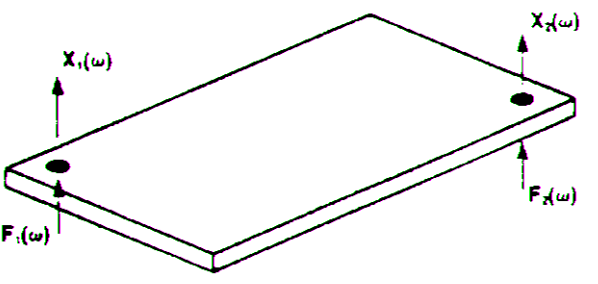

Fig. 1 Two-input, two-output FRF concept

3.1 Noise/Error Minimization

The most reasonable, and most common, approach to the estimation of frequency response functions is by the use of *least squares* (LS) or *total least squares* (TLS) techniques [1, 2, 3, 4, 5]. This is a standard technique for estimating parameters in the presence of noise. Least squares methods minimize the square of the magnitude error and, thus, compute the *best* estimate of the magnitude of the frequency response function but have little effect on the phase of the frequency response function. The primary difference in the algorithms used to estimate frequency response functions is in the assumption of where the noise enters the measurement problem. The different assumptions of the source of the error is noted graphically in Fig. 2.

Three algorithms, referred to as the H_1, H_2, and H_v algorithms, are commonly available for estimating frequency response functions. Table 2 summarizes this characteristic for the three methods that are widely used.

Consider the case of N_i inputs and N_o outputs measured during a modal test. Based upon the assumed location of the noise entering the estimation process, Equations 15, 16, and 17 represent the corresponding model for the H_1, H_2, and H_v estimation procedures.

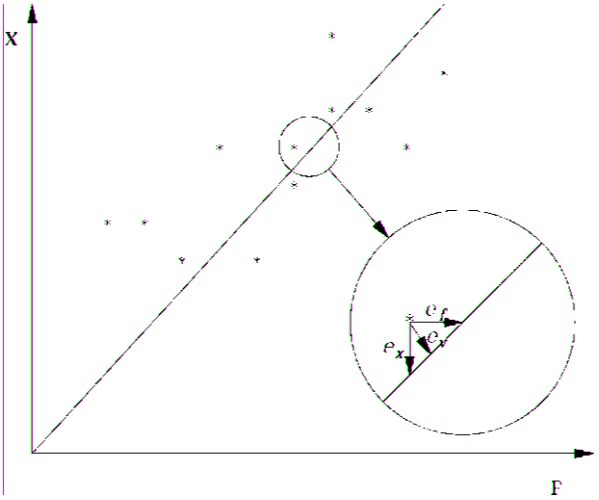

Fig. 2 Least squares concept

Table 2 Summary of frequency response function estimation models

Frequency response function models			
Technique	Solution	Assumed location of noise	
	Method	Force inputs	Response
H_1	LS	No noise	Noise
H_2	LS	Noise	No noise
H_v	TLS	Noise	Noise

H_1 **Technique:**

$$[H]_{N_o \times N_i} \{F\}_{N_i \times 1} = \{X\}_{N_o \times 1} - \{\eta\}_{N_o \times 1} \tag{15}$$

H_2 **Technique:**

$$[H]_{N_o \times N_i} \left\{ \{F\}_{N_i \times 1} - \{\upsilon\}_{N_i \times 1} \right\} = \{X\}_{N_o \times 1} \tag{16}$$

H_v **Technique:**

$$[H]_{N_o \times N_i} \left\{ \{F\}_{N_i \times 1} - \{\upsilon\}_{N_i \times 1} \right\} = \{X\}_{N_o \times 1} - \{\eta\}_{N_o \times 1} \tag{17}$$

Note that while not necessarily obvious yet, in all methods, the inversion of a matrix will be involved. Therefore, the inputs (references) that are used must not be fully correlated so that the inverse will exist. Extensive evaluation tools (using eigenvalue decomposition) have been developed in order to detect and avoid this condition [6, 7].

3.2 Single Input FRF Estimation

Figure 3 represents the model of the measurement situation for a single input, single output frequency response function measurement.

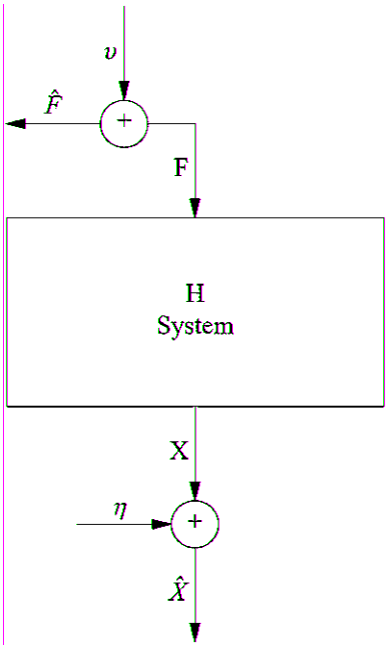

Fig. 3 System model: single input

With reference to Fig. 3 for a case involving only one input and one output (input location q and response location p), the equation that is used to represent the input-output relationship is:

$$\hat{X}_p - \eta_p = H_{pq}(\hat{F}_q - \upsilon_q) \tag{18}$$

where:

- $F = \hat{F} - \upsilon$ = actual input
- $X = \hat{X} - \eta$ = actual output
- $\hat{X}$ = spectrum of the $p-th$ output, measured
- $\hat{F}$ = spectrum of the $q-th$ input, measured
- H = frequency response function
- υ = Spectrum of the noise part of the input
- η = Spectrum of the noise part of the output
- X = Spectrum of the $p-th$ output, theoretical
- F = Spectrum of the $q-th$ input, theoretical

If $\upsilon = \eta = 0$, the theoretical (expected) frequency response function of the system is estimated. If $\eta \neq 0$ and/or $\upsilon \neq 0$, a least squares method is used to estimate a *best* frequency response function, in the presence of noise.

In order to develop an estimation of the frequency response function, a number of averages N_{avg} are used to minimize the random errors (variance). This can be easily accomplished through the use of intermediate measurement of the auto and cross power spectra. The estimate of the auto and cross power spectra for the model in Fig. 3 can be defined as follows. Note that each function is a function of frequency.

Auto Power Spectra:

$$G_{FF_{qq}} = \sum_{1}^{N_{\text{avg}}} F_q \; F_q^* \tag{19}$$

$$G_{XX_{pp}} = \sum_{1}^{N_{\text{avg}}} X_p X_p^* \tag{20}$$

Cross Power Spectra:

$$G_{XF_{pq}} = \sum_{1}^{N_{\text{avg}}} X_p F_q^* \tag{21}$$

$$G_{FX_{qp}} = \sum_{1}^{N_{\text{avg}}} F_q X_p^* \tag{22}$$

where:

- F^* = complex conjugate of $F(\omega)$
- X^* = complex conjugate of $X(\omega)$

3.2.1 H_1 Algorithm: Minimize Noise on Output (η)

The most common formulation of the frequency response function, often referred to as the H_1 algorithm, tends to minimize the noise on the output. This formulation is shown in Equation 23.

$$H_{pq} = \frac{G_{XF_{pq}}}{G_{FF_{qq}}} \tag{23}$$

Note that recently an FRF development based upon a Cholesky decomposition has been developed [8]. This formulation is equivalent to the H_1 formulation.

3.2.2 H_2 Algorithm: Minimize Noise on Input (υ)

Another formulation of the frequency response function, often referred to as the H_2 algorithm, tends to minimize the noise on the input. This formulation is shown in Equation 24.

$$H_{pq} = \frac{G_{XX_{pp}}}{G_{FX_{qp}}} \tag{24}$$

In the H_2 formulation, an auto power spectrum is divided by a cross power spectrum. This can be a problem since the cross power spectrum can theoretically be zero at one or more frequencies. In both formulations, the phase information is preserved in the cross power spectrum term.

3.2.3 H_v Algorithm: Minimize Noise on Input and Output (η and υ)

Rather than assuming that the noise is solely on the input or output, the noise can be assumed to be on both the input and output. This results in a vector least squares solution that is found via an eigenvalue decomposition. This approach to estimating the frequency response function is referred to as the H_v algorithm.

The eigenvalue solution is used to find the optimal least squares solution of two linear equations represented by the H_1 algorithm and the H_2 algorithm.

The H_1 algorithm can be rewritten as:

$$G_{FF_{qq}} H_{pq} - G_{XF_{pq}} = 0 \tag{25}$$

The H_2 algorithm can be rewritten as:

$$G_{FX_{qq}} H_{pq} - G_{XX_{pq}} = 0 \tag{26}$$

Combining these two representations for H_{pq} in a matrix equation:

$$\begin{bmatrix} G_{FF_{qq}} & G_{XF_{pq}} \\ G_{FX_{qp}} & G_{XX_{pp}} \end{bmatrix}_{2\times 2} \begin{Bmatrix} H_{pq} \\ -1 \end{Bmatrix}_{2\times 1} = \begin{Bmatrix} 0 \\ 0 \end{Bmatrix}_{2\times 1} \tag{27}$$

Recognizing that in the presence of noise, the right hand side of the above equation will not be equal to zero. Replacing the right hand side by a noise vector $\{\epsilon\}$ with the following form:

$$\begin{Bmatrix} \varepsilon_1 \\ \varepsilon_2 \end{Bmatrix}_{2\times 1} = \lambda \begin{Bmatrix} H_{pq} \\ -1 \end{Bmatrix}_{2\times 1} \tag{28}$$

$$\begin{bmatrix} G_{FF_{qq}} & G_{XF_{pq}} \\ G_{FX_{qp}} & G_{XX_{pp}} \end{bmatrix}_{2\times 2} \begin{Bmatrix} H_{pq} \\ -1 \end{Bmatrix}_{2\times 1} = \lambda \begin{Bmatrix} H_{pq} \\ -1 \end{Bmatrix}_{2\times 1} \tag{29}$$

This is a recognizable eigenvalue equation. The solution associated with the smallest eigenvalue will give an eigenvector, when normalized as above, that will estimated the optimal value for H_{pq}.

Therefore, the solution for H_{pq} using the H_v algorithm is found by the eigenvalue decomposition of a matrix of power spectra. For the single input case, the following matrix involving the auto and cross power spectra can be defined:

$$\left[G_{FFX_p}\right] = \begin{bmatrix} G_{FF_{qq}} & G_{XF_{pq}} \\ G_{FX_{qp}} & G_{XX_{pp}} \end{bmatrix}_{2\times 2} \tag{30}$$

The solution for H_{pq} is found by the eigenvalue decomposition of the $[G_{FFX_p}]$ matrix as follows:

$$\left[G_{FFX_p}\right] = [V]\,\lceil\Lambda\rfloor\,[V]^H \tag{31}$$

where:

- $\lceil\Lambda\rfloor$ = *diagonal matrix of eigenvalues*

Solution for the H_{pq} matrix is found from the eigenvector associated with the smallest (minimum) eigenvalue ($\lambda_{\min}$). The size of the eigenvalue problem is second order resulting in finding the roots of a quadratic equation. This eigenvalue solution must be repeated for each frequency, and the complete solution process must be repeated for each response point X_p.

Note that the eigenvalue decomposition does not necessarily yield the eigenvalues in any particular order so the smallest or minimum eigenvalue must be found and is not generally the first or last eigenvalue. However, since the decomposition matrix $[G_{FFX}]$ is Hermitian, the eigenvalues should be real valued (and, while not required, the eigenvectors can be scaled to be orthonormal as shown in Equation 31.)

Also note that the noises on the input and output are assumed proportional to the eigenvector scaling. Other forms of scaling are possible by altering the above equation giving rise to the definition of H_s.

Alternately, the solution for H_{pq} is found by the eigenvalue decomposition of the following matrix of auto and cross power spectra:

$$\left[G_{XFF_p}\right] = \begin{bmatrix} G_{XX_{pp}} & G_{FX_{qp}} \\ G_{XF_{pq}} & G_{FF_{qq}} \end{bmatrix}_{2\times 2} \tag{32}$$

$$\left[G_{XFF_p}\right] = [V]\lceil\Lambda\rfloor[V]^H \tag{33}$$

where:

- $\lceil\Lambda\rfloor$ = *diagonal matrix of eigenvalues*

The solution for H_{pq} is again found from the eigenvector associated with the smallest (minimum) eigenvalue ($\lambda_{\min}$).

The frequency response function is found from the normalized eigenvector associated with the smallest eigenvalue. If $[G_{FFX_p}]$ is used, the eigenvector associated with the smallest eigenvalue must be normalized as follows:

$$\{V\}_{\lambda_{\min}} = \begin{Bmatrix} H_{pq} \\ -1 \end{Bmatrix} \tag{34}$$

If $[G_{XFF_p}]$ is used, the eigenvector associated with the smallest eigenvalue must be normalized as follows:

$$\{V\}_{\lambda_{\min}} = \begin{Bmatrix} -1 \\ H_{pq} \end{Bmatrix} \tag{35}$$

One important consideration of the three formulations for frequency response function estimation is the behavior of each formulation in the presence of a bias error such as leakage. In all cases, the estimate differs from the expected value particularly in the region of a resonance (magnitude maxima) or antiresonance (magnitude minima). For example, H_1 tends to underestimate the value at resonance, while H_2 tends to overestimate the value at resonance. The H_v algorithm gives an answer that is bounded by the H_1 and H_2 values for the single input case. The different approaches are based upon minimizing the magnitude of the error but have no effect on the phase characteristics.

There are a number of formulations for the H_v estimation of the FRFs that appear to be different. Note that there are several decompositions of the $[G_{FFX}]$ and $[G_{XFF}]$ matrices, including SVD and ED, that have been used in the development of H_v. The original, historical presentation/development used the eigenvalue decomposition as presented in this chapter.

3.2.4 Ordinary Coherence

In addition to the attractiveness of H_1, H_2, and H_v in terms of the minimization of the error, the availability of auto and cross power spectra allows the determination of other important functions. The quantity γ^2_{pq} is called the scalar or *ordinary coherence function* and is a frequency-dependent, real value between zero and one. The ordinary coherence function indicates the degree of correlation in a frequency response function. If the coherence is equal to one at any specific frequency, the system is said to have perfect correlation at that frequency. In other words, the measured response power is linearly related to the measured input power (or by sources which are coherent with the measured input power). A coherence value less than unity at any frequency indicates that the measured response power is greater than that due to the measured input. This is due to some extraneous noise also contributing to the output power. It should be emphasized, however, that low coherence does not necessarily imply poor estimates of the frequency response function but simply means that more averaging is needed for a statistically reliable result. Note that the coherence will not necessarily improve (i.e., get closer to one) unless the noise is eliminated, but the variance will mean that the FRF answer will be statistically better. The ordinary coherence function is computed as follows:

$$O_{COH_{pq}} = \gamma^2_{pq} = \frac{\left|G_{XF_{pq}}\right|^2}{G_{FF_{qq}} G_{XX_{pp}}} = \frac{G_{XF_{pq}} G_{FX_{qp}}}{G_{FF_{qq}} G_{XX_{pp}}} \tag{36}$$

When the coherence is zero, the output is totally uncorrelated to the measured input suggesting that the response is due to other unmeasured sources. In general, then, the coherence can be a measure of the degree of noise contamination in a measurement. Thus, with more averaging, the estimate of coherence may contain less variance, therefore giving a better estimate of the noise energy in a measured signal. This is not the case, though, if the low coherence is due to bias errors such as nonlinearities, multiple unmeasured inputs, or leakage. A typical ordinary coherence function is shown in Fig. 4 together with the corresponding frequency response function magnitude. In Fig. 4, the frequencies where the coherence is lowest are often the same frequencies where the frequency response function is at a maxima in magnitude or at a minima in magnitude. This is often an indication of leakage since the frequency response function is most sensitive to the leakage error at the lightly damped peaks corresponding to the maxima. At the minima, where there is little response from the system, the leakage error, even though it is small, may still be significant.

Note that while the above development of ordinary coherence is historical and was based upon the H_1 FRF algorithm, this definition is also valid for both the H_2 and H_v FRF algorithms.

In all of these cases, the estimated coherence function will approach, in the limit, the expected value of coherence at each frequency, dependent upon the type of noise present in the structure and measurement system. Note that with more averaging, the estimated value of coherence will not increase; the estimated value of coherence

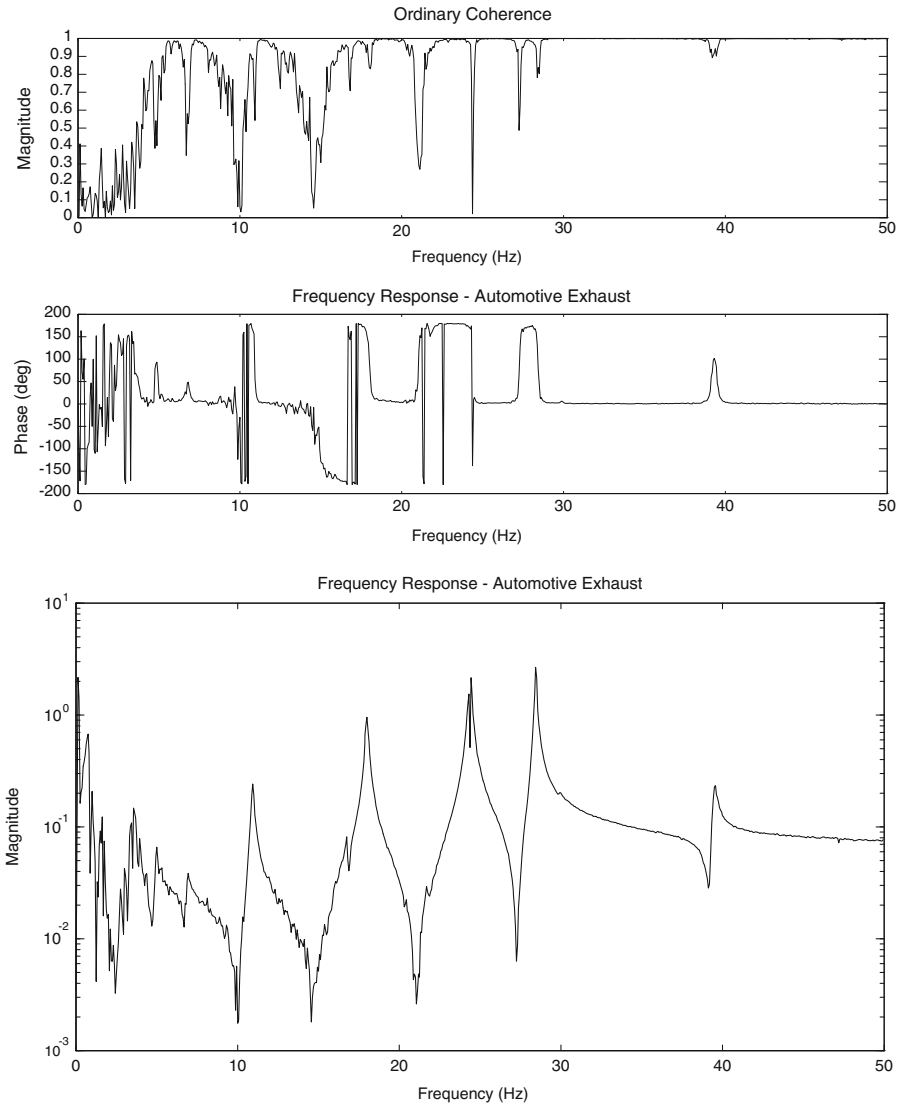

Fig. 4 Ordinary coherence function and frequency response function

always approaches the expected value from the upper side. This is described in Table 3 [1].

Note that a high value of coherence (0.9) after 16 averages has approximately the same possible variance of the frequency response function as a low value of coherence (0.3) after 256 averages.

Two special cases of low coherence are worth particular mention. The first situation occurs when a *leakage error* occurs in one or both of the input and output

Table 3 Ordinary coherence relationship – averaging ($\pm|H|$ dB, $\pm\phi°$)

Measured value	Number of averages of coherence function				
	16	32	64	128	256
0.2	+5.2 dB	+3.8 dB	+2.8 dB	+2.1 dB	+1.5 dB
	−14.6 dB	−7.1 dB	−4.2 dB	−2.7 dB	−1.8 dB
	(±54°)	(±34°)	(±23°)	(±16°)	(±11°)
0.3	+4.2 dB	+3.1 dB	+2.2 dB	+1.6 dB	+1.2 dB
	−8.4 dB	−4.8 dB	−3.0 dB	−2.0 dB	−1.4 dB
	(±38°)	(±25°)	(±17°)	(±12°)	(±8°)
0.4	+3.5 dB	+2.6 dB	+1.8 dB	+1.3 dB	+1.0 dB
	−6.0 dB	−3.6 dB	−2.3 dB	−1.6 dB	−1.1 dB
	(±30°)	(±20°)	(±14°)	(±10°)	(±7°)
0.5	+3.0 dB	+2.1 dB	+1.5 dB	+1.1 dB	+0.8 dB
	−4.5 dB	−2.8 dB	−1.9 dB	−1.3 dB	−0.9 dB
	(±24°)	(±16°)	(±11°)	(±8°)	(±5°)
0.6	+2.5 dB	+1.8 dB	+1.3 dB	+0.9 dB	+0.7 dB
	−3.5 dB	−2.2 dB	−1.5 dB	−1.0 dB	−0.7 dB
	(±19°)	(±13°)	(±9°)	(±6°)	(±4°)
0.7	+2.1 dB	+1.5 dB	+1.0 dB	+0.7 dB	+0.5 dB
	−2.7 dB	−1.7 dB	−1.2 dB	−0.8 dB	−0.6 dB
	(±15°)	(±10°)	(±7°)	(±5°)	(±4°)
0.8	+1.6 dB	+1.1 dB	+0.8 dB	+0.6 dB	+0.4 dB
	−2.0 dB	−1.3 dB	−0.9 dB	−0.6 dB	−0.4 dB
	(±12°)	(±8°)	(±6°)	(±4°)	(±3°)
0.9	+1.1 dB	+0.8 dB	+0.5 dB	+0.4 dB	+0.3 dB
	−1.3 dB	−0.8 dB	−0.6 dB	−0.4 dB	−0.3 dB
	(±8°)	(±5°)	(±4°)	(±3°)	(±2°)

90% confidence limits on the measurement of the amplitude $|H|$ and phase ϕ of transfer functions, as a function of the measured value of coherence and the number of averages

measurements. This causes the coherence in the area of the peaks of the frequency response to be less than unity. This error can be reduced by the use of weighting functions or by cyclic averaging. The second situation occurs when a significant *propagation time delay* occurs between the input and output as may be the case with acoustic measurements. If a propagation delay of length t is compared to a sample function length of T, a low estimate of coherence will be estimated as a function of the ratio t/T. This propagation delay causes a bias error in the frequency response and should be removed prior to computation if possible. Coherence will be explained in more detail in Sect. 3.4 once the concept of multiple inputs is discussed.

3.3 Multiple Input FRF Estimation

Multiple input estimation of frequency response functions is desirable for several reasons. The principal advantage is the increase in the accuracy of estimates of the

frequency response functions. During single input excitation of a system, there may exist large differences in the amplitudes of vibratory motion at various locations because of the dissipation of the excitation power within the structure. This is especially true when the structure has heavy damping. Small nonlinearities in the structure will consequently cause errors in the measurement of the response. With multiple input excitation, the vibratory amplitudes across the structure typically will be more uniform, with a consequent decrease in the effect of nonlinearities.

A second reason for improved accuracy is the increase in consistency of the frequency response functions compared to the single input method. When a number of exciter systems are used, the elements from columns of the frequency response function matrix corresponding to those exciter locations are being determined simultaneously. With the single input method, each column is determined independently, and it is possible for small errors of measurement due to nonlinearities and time-dependent system characteristics to cause a change in resonance frequencies, damping, or mode shapes among the measurements in the several columns. This is particularly important for the polyreference modal parameter estimation algorithms that use frequency response functions from multiple columns or rows of the frequency response function matrix simultaneously.

An additional, significant advantage of the multiple input excitation is a reduction of the test time. In general, using multiple input estimation of frequency response functions, frequency response functions are obtained for all input locations in approximately the same time as required for acquiring a set of frequency response functions for one of the input locations, using a single input estimation method.

Another potential advantage of the simultaneous measurement of a number of columns or rows of the frequency response function matrix is the ability to use a linear combination of frequency response functions in the same row of the matrix in order to enhance specific modes of the system. This technique is analogous to the forced normal mode excitation experimental modal analysis in which a structure is excited by a forcing vector which is proportional to the modal vector of interest. For this analysis, the coefficients of a preliminary experimental modal analysis are used to weight the frequency response functions, so that the sum emphasizes the modal vector that is sought. The revised set of conditioned frequency response functions is analyzed to improve the accuracy of the modal vector. A simple example of this approach for a structure with approximate geometrical symmetry would be to excite at two symmetric locations. The sum of the two frequency response functions at a specific response location should enhance the symmetric modes. Likewise, the difference of the two functions should enhance the antisymmetric modes.

3.3.1 Multiple Input Versus Single Input

Advantages:

- Better energy distribution reduces nonlinearities at input location.
- Better energy distribution excites the structure more evenly.
- Data collected simultaneously has consistent frequency and damping information which is consistent with parameter estimation algorithms.

- Advances in hardware/software have kept data collection time the same for single input/multiple output. More measurements per measurement cycle.
- Multiple input data permits the detection of repeated or closely spaced roots.

Disadvantages:

- Inputs must not be correlated.
- More equipment required.

The theoretical basis of multiple input frequency response function analysis is well documented in a number of sources [1, 2, 3, 9, 10, 11, 12, 13, 14, 15, 16, 17, 18, 19, 20]. While much had been written about multiple input theory, the application of multiple input theory to experimental modal analysis apparently had not been seriously investigated prior to 1980 [9, 10, 11, 12, 13, 14, 15, 16, 17, 18, 19, 20]. It also needs to be noted that this application of multiple input, multiple output (MIMO) theory represents a very special case of multiple input, multiple output data analysis. For this case, everything about the inputs is known or can be controlled. The number of inputs, the location of the inputs, and the characteristics of the inputs are controlled by the test procedure. For the general case, none of these characteristics may be known.

Consider the case of N_i inputs and N_o outputs measured during a modal test on a dynamic system as shown in Fig. 5. The model assumed for the dynamics is:

$$\hat{X}_p - \eta_p = \sum_{q=1}^{N_i} H_{pq} * (\hat{F}_q - \upsilon_q) \tag{37}$$

where:

- $F = \hat{F} - \upsilon$ = actual input
- $X = \hat{X} - \eta$ = actual output
- $\hat{X}_p$ = spectrum of the $p-th$ output, measured
- $\hat{F}_q$ = spectrum of the $q-th$ input, measured
- H_{pq} = frequency response function of output p with respect to input q
- υ_q = spectrum of the noise part of the input
- η_p = spectrum of the noise part of the output
- X_p = spectrum of the $p-th$ output, theoretical
- F_q = spectrum of the $q-th$ input, theoretical

In order to develop an estimation of the frequency response function for the multiple input case, a number of averages N_{avg} will be used to minimize the random errors (variance). This can be easily accomplished through use of intermediate measurement of the auto and cross power spectra as defined in Equations 19, 20, 21 and 22. Additional matrices, constructed from the auto and cross power spectra need to be defined as follows. Note that each function and, therefore, each resulting matrix is a function of frequency.

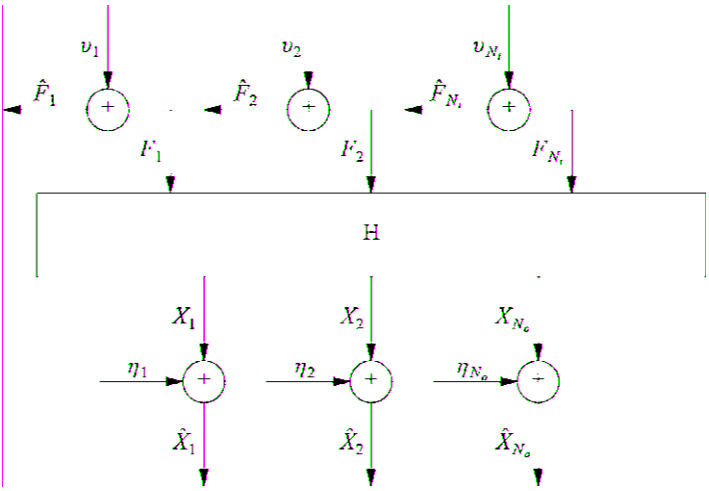

Fig. 5 System model: multiple inputs

Input/Output Cross Spectra Matrix:

$$[G_{XF}] = \{X\}\{F\}^H = \begin{Bmatrix} X_1 \\ X_2 \\ \cdot \\ \cdot \\ X_{N_o} \end{Bmatrix} \begin{bmatrix} F_1^* & F_2^* \cdots F_{N_i}^* \end{bmatrix} = \begin{bmatrix} G_{XF_{11}} & \cdots & G_{XF_{1N_i}} \\ \cdot & \cdot & \cdot \\ \cdot & \cdot & \cdot \\ G_{XF_{N_o1}} & \cdots & G_{XF_{N_oN_i}} \end{bmatrix} \tag{38}$$

Input Cross Spectra Matrix:

$$[G_{FF}] = \{F\}\{F\}^H = \begin{Bmatrix} F_1 \\ F_2 \\ \cdot \\ \cdot \\ F_{N_i} \end{Bmatrix} \begin{bmatrix} F_1^* & F_2^* \cdots F_{N_i}^* \end{bmatrix} = \begin{bmatrix} G_{FF_{11}} & \cdots & G_{FF_{1N_i}} \\ \cdot & \cdot & \cdot \\ \cdot & \cdot & \cdot \\ G_{FF_{N_i1}} & \cdots & G_{FF_{N_iN_i}} \end{bmatrix} \tag{39}$$

The frequency response functions can now be estimated for the three algorithms as follows:

3.3.2 H_1 Algorithm: Minimize Noise on Output (η)

$$[H]_{N_o \times N_i} \{F\}_{N_i \times 1} = \{X\}_{N_o \times 1} - \{\eta\}_{N_o \times 1} \tag{40}$$

$$[H]\{F\}\{F\}^H = \{X\}\{F\}^H - \{\eta\}\{F\}^H \tag{41}$$

Since the noise vector $\{\eta\}$ is assumed to be independent of the excitation force vector $\{F\}$, thus with averaging, the $\{\eta\}\{F\}^H$ cross term approaches zero:

$$[H]_{N_o \times N_i} \{F\}_{N_i \times 1} \{F\}^H_{1 \times N_i} = \{X\}_{N_o \times 1} \{F\}^H_{1 \times N_i} \tag{42}$$

The above relationship can be concisely stated as:

$$[H][G_{FF}] = [G_{XF}] \tag{43}$$

$$[H] = [G_{XF}][G_{FF}]^{-1} \tag{44}$$

where:

- $[\ ]^H$ = complex conjugate transpose (Hermitian matrix)

In the experimental procedure, the input and response signals are measured, and the averaged cross spectra and auto spectra necessary to create the $[G_{XF}]$ and $[G_{FF}]$ matrices are computed. If the computation of ordinary, multiple, or partial coherence functions will be required, then the diagonal elements of the output cross spectrum matrix $[G_{XX}]$ must be computed also. Note that Equation 44 involves a matrix inverse or equivalent numerical procedure on the $[G_{FF}]$ matrix. This will only be possible when the number of averages is equal to or greater than the number of inputs.

Equation 43 is valid regardless of whether the various inputs are correlated. Unfortunately, there are a number of situations where the input cross spectrum matrix $[G_{FF}]$ may be singular for specific frequencies or frequency intervals. When this happens, the inverse of $[G_{FF}]$ will not exist, and Equation 44 cannot be used to solve for the frequency response function at those frequencies or in those frequency intervals. A computational procedure that solves Equation 44 for $[H]$ should therefore monitor the rank of the matrix $[G_{FF}]$ that is to be inverted and desirably provide direction on how to alter the input signals or the use of the available data when a problem exists. The current approach for evaluating whether the inputs are sufficiently uncorrelated at each frequency involves determining the principal/virtual forces using principal component analysis [7]. This will be covered later in Sect. 3.5.

Note that recently an FRF development based upon a Cholesky decomposition has been developed [8]. This formulation is equivalent to the H_1 formulation.

3.3.3 H_2 Algorithm: Minimize Noise on Input (v)

$$[H]_{N_o \times N_i} \left\{\{F\}_{N_i \times 1} - \{v\}_{N_i \times 1}\right\} = \{X\}_{N_o \times 1} \tag{45}$$

$$[H]\ \{\{F\} - \{v\}\}\ \{X\}^H = \{X\}\ \{X\}^H \tag{46}$$

Since the noise vector $\{\upsilon\}$ is assumed to be independent of the response vector $\{X\}$, thus with averaging, the $\{\upsilon\}\{X\}^H$ cross term approaches zero:

$$[H]_{N_o \times N_i} \{F\}_{N_i \times 1} \{X\}^H_{1 \times N_o} = \{X\}_{N_o \times 1} \{X\}^H_{1 \times N_o} \tag{47}$$

One problem with using the H_2 algorithm is that the solution for $[H]$ can only be found directly using an inverse when the number of inputs N_i and number of outputs N_o are equal. Then:

$$[H][G_{XF}] = [G_{XX}] \tag{48}$$

$$[H] = [G_{XX}][G_{XF}]^{-1} \tag{49}$$

3.3.4 H_v Algorithm: Minimize Noise on Input and Output (υ and η)

$$[H]_{N_o \times N_i} \left\{ \{F\}_{N_i \times 1} - \{\upsilon\}_{N_i \times 1} \right\} = \{X\}_{N_o \times 1} - \{\eta\}_{N_o \times 1} \tag{50}$$

$$[H] \{ \{F\} - \{\upsilon\} \} = \{X\} - \{\eta\} \tag{51}$$

The solution for $[H]$ is found by the eigenvalue decomposition of one of the following two matrices:

$$\left[G_{FFX_p}\right] = \begin{bmatrix} [G_{FF}] & \left[G_{XF_q}\right] \\ \left[G_{FX_p}\right] & \left[G_{XX_p}\right] \end{bmatrix}_{(N_i+1)\times(N_i+1)} \tag{52}$$

$$\left[G_{XFF_p}\right] = \begin{bmatrix} \left[G_{XX_p}\right] & \left[G_{FX_p}\right] \\ \left[G_{XF_q}\right] & [G_{FF}] \end{bmatrix}_{(N_i+1)\times(N_i+1)} \tag{53}$$

Therefore, the eigenvalue decomposition would be:

$$\left[G_{FFX_p}\right] = [V]\lceil\Lambda\rfloor[V]^H \tag{54}$$

Or:

$$\left[G_{XFF_p}\right] = [V]\lceil\Lambda\rfloor[V]^H \tag{55}$$

where:

- $\lceil\Lambda\rfloor$ = *diagonal matrix of eigenvalues*

Solution for the $p-th$ row of the $[H]$ matrix is found from the eigenvector associated with the smallest (minimum) eigenvalue. Note that the size of the eigenvalue problem is $N_i + 1$ and that the eigenvalue solution must be repeated for each frequency. Note also that the complete solution process must be repeated for each response point X_p.

The frequency response functions associated with a single output p and all inputs are found by normalizing the eigenvector associated with the smallest eigenvalue. If $[G_{FFX_p}]$ is used, the eigenvector associated with the smallest eigenvalue must be normalized as follows:

$$\{V\}_{\lambda_{\min}} = \begin{Bmatrix} H_{p1} \\ H_{p2} \\ . \\ . \\ H_{pN_i} \\ -1 \end{Bmatrix} \tag{56}$$

If $[G_{XFF_p}]$ is used, the eigenvector associated with the smallest eigenvalue must be normalized as follows:

$$\{V\}_{\lambda_{\min}} = \begin{Bmatrix} -1 \\ H_{p1} \\ H_{p2} \\ . \\ . \\ H_{pN_i} \end{Bmatrix} \tag{57}$$

Note that there are several decompositions of the $[G_{FFX}]$ or $[G_{XFF}]$ matrices, including SVD and ED, that have been used in the development of H_v. The original, historical presentation/development used the eigenvalue decomposition as presented in this chapter.

Recent developments have shown that there is an alternative formulation, H_{svd}, which gives equivalent results to the presented H_v form [21].

3.4 Coherence: Ordinary, Multiple, and Conditioned

The concept of the coherence function, as defined for single input measurement (Sect. 3.2.4), needs to be expanded to include the variety of additional relationships that are possible for multiple inputs.

3.4.1 Ordinary Coherence

Ordinary coherence is defined in this general sense as the correlation coefficient describing the linear relationship between any two spectra. This is consistent with the ordinary coherence function that is defined for single input, single output measurements. Great care must be taken in the interpretation of ordinary coherence when more than one input is present. The ordinary coherence of an output with respect to an input can be much less than unity even though the linear relationship between inputs and outputs is valid, because of the influence of the other inputs.

The ordinary coherence function can be formulated in terms of the elements of the matrices defined previously. The ordinary coherence function between the pth output and the qth input can be computed from the following formula:

Ordinary Coherence Function

$$O_{COH_{pq}} = \gamma_{pq}^2 = \frac{\left|G_{XF_{pq}}\right|^2}{G_{FF_{qq}} G_{XX_{pp}}} \tag{58}$$

where:

- $G_{XX_{pp}}$ = *auto power spectrum of the output* p
- $G_{FF_{qq}}$ = *auto power spectrum of the input* q
- $G_{XF_{pq}}$ = *cross power spectrum between output* p *and input* q

3.4.2 Multiple Coherence

Multiple coherence is defined as the correlation coefficient describing the linear relationship between an output and all known inputs. There is a multiple coherence function for every output. Multiple coherence can be used to evaluate the importance of unknown contributions to each output. These unknown contributions can be measurement noise, nonlinearities, or unknown inputs. Particularly, as in the evaluation of ordinary coherence, a low value of multiple coherence near a resonance will often mean that the *leakage* error is present in the frequency response function. Unlike the ordinary coherence function, a low value of multiple coherence is not expected at antiresonances. The antiresonances for different input and the same response locations do not occur at the same frequency. Though one response signal may have a poor signal-to-noise ratio at its antiresonance, other inputs will not have at the same frequency.

The formulation of the equations for the multiple coherence functions can be simplified from the normal computational approach to the following equation.

Multiple Coherence Function:

$$M_{COH_p} = \frac{\{G_{XF}\}\left[G_{FF}\right]^{-1}\{G_{FX}\}^T}{G_{XX_{pp}}} \tag{59}$$

Frequently, the multiple coherence is expressed in various references in terms of the computed or estimated frequency response functions as in Equation 60.

$$M_{COH_p} = \sum_{q=1}^{N_i} \sum_{t=1}^{N_i} \frac{H_{pq} G_{FF_{qt}} H_{pt}^*}{G_{XX_{pp}}} \tag{60}$$

where:

- H_{pq} = frequency response function for output p and input q
- H_{pt} = frequency response function for output p and input t
- $G_{FF_{qt}}$ = cross power spectrum between input q and input t
- $G_{XX_{pp}}$ = auto power spectrum of output p

However, what is not necessarily obvious is that the formulation expressed in Equation 60 is only valid if the frequency response is computed using the H_1 estimator, and therefore, Equation 60 should generally be avoided.

If the multiple coherence of the $p-th$ output is near unity, then the $p-th$ output is well predicted from the set of inputs using the least squares frequency response functions.

It should be noted that there is only one multiple coherence definition, Equation 59, which is always correct; however, the multiple coherence can also be computed or estimated from conditioned coherences as shown in the following section.

3.4.3 Conditioned Coherence

An important feature, characteristic, or premise of coherence in general is that it identifies either the individual contribution of an input to an output (as in ordinary coherence) or the collective input contribution to an output (as in multiple coherence). In addition, its value must be bounded 0 to 1. [22]

Historically, the conditioned coherence, called *partial coherence*, was defined as the ordinary coherence between a conditioned output and another conditioned output, between a conditioned input and another conditioned input, or between a conditioned input and a conditioned output. The output and input are conditioned by removing contributions from other input(s). The removal of the effects of the other input(s) is formulated on a linear least squares basis. The order of removal of the inputs during *conditioning* has a definite effect upon the partial coherence if some of the inputs are mutually correlated. Thus, there will be a partial coherence function for every input/output, input/input, and output/output combination for all permutations of conditioning.

Unfortunately, this variability in the order of conditioning for the partial coherence, especially with respect to outputs, has limited its value and applicability to experimental FRF estimation because the combination of these coherences for a given output do not add up to be the multiple coherence for that output.

However, recent reformulations of the partial coherence where conditioning is restricted to the input-input G_{FF} matrix and the order of conditioning is determined by the relative importance or significance of the input contributor to the output have proved valuable. Particularly, since when appropriately conditioned, the partial coherence can be computed using a traditional ordinary coherence calculation, and the combination of these conditioned coherences (partial coherences in this case) for a given output does add up to be the multiple coherence for that output.

Table 4 Summary of conditioned coherence models

Conditioned coherence models		
Name	Conditioning	Reference DOF
Partial coherence	CD	Physical
Cumulative coherence	CD	Physical
Fractional coherence	SVD	Virtual
Virtual coherence	SVD or ED	Virtual

In the following sections, two different classes of conditioned coherences are developed, the principal difference between them being the type of conditioning applied to the G_{FF} matrix: the first which results in coherence functions which can be referenced back to physical input degrees of freedom and the second which results in coherence functions which correspond to the virtual input degrees of freedom which are found by principal component analysis (Sect. 3.5). A comparison of the characteristics of the conditioned coherences is presented in Table 4.

While the individual coherence functions identified by these methods cannot be compared between methods, for both approaches, the functions can be summed to yield the traditional multiple coherence function defined in Sect. 3.4.2.

Conditioned Coherences Which Retain Physical Source Reference

The following two coherence formulations retain the connection to a physical source reference. The order and value of the individual coherence components are not necessarily the same, but each still sums to give the multiple coherence.

Partial Coherence

Thus, one way to study the linear correlation of the output with one of the inputs in a MISO/MIMO system is to calculate the corresponding partial coherence by arranging the inputs in a predetermined order, usually based on their significance. They are then sequentially *conditioned* so that each new input is completely uncorrelated from its preceding inputs. Once the order has been determined, the partial coherence of the output with the first force is obviously the same as the corresponding ordinary coherence. For the second force, the conditioned input auto power is found as shown in Equation 63.

$$G_{F_2F_2.F_1} = G_{F_2F_2} - \left[\frac{G_{F_2F_1}}{G_{F_1F_1}}\right] G_{F_1F_2} \tag{61}$$

$$G_{F_2F_2.F_1} = G_{F_2F_2} - \left[\frac{G_{F_2F_1}}{G_{F_1F_1}}\right] G_{F_1F_2} \tag{62}$$

$$G_{F_2F_2.F_1} = [1 - \gamma^2_{F_1F_2}] G_{F_2F_2} \tag{63}$$

The subscript on the left hand side signifies that the auto power computed for the second input in this fashion does not have any correlation with the first input. Each subsequent input is conditioned in the same way, and the partial coherence

of the output with any arbitrary conditioned input can be computed as shown in Equation 64.

$$P_{COH_{pq}} = \gamma^2_{F_q X_p . F_{q-1}!} = \frac{|G_{F_q X_p . F_{q-1}!}|^2}{G_{F_q F_q . F_{q-1}!} G_{X_p X_p}} \tag{64}$$

The term $F_{q-1}!$ signifies that the uncorrelation takes place from input 1 through $q-1$ to find the conditioned input q. Adding the partial coherences for all the inputs results in the corresponding multiple coherence. The above formulation was shown in [23] which is the fourth edition of this textbook. (In the first two editions, the output term in the denominator on the right hand side used a conditioned output spectrum for normalization instead. When a conditioned output spectrum is used, the sum of the conditioned coherences is not the same as the corresponding multiple coherence. This disambiguation is necessary, as several follow-up works [24, 8] that made use of the older editions of the textbook as reference include the latter development which is inconsistent.)

Note that the corresponding set of partial coherences is dependent on the ordering of the inputs chosen.

Cumulative Coherence

In [8], a use of Cholesky decomposition is demonstrated to obtain the conditioned inputs efficiently. In [25], the input auto power matrix is decomposed into a lower triangular matrix L and a diagonal matrix C multiplied to the former's Hermitian as shown in Equation 65. Here, the diagonal matrix C is representative of the conditioned inputs.

$$G_{FF} = L_{FC}\, C\, L^H_{FC} \tag{65}$$

A relation between the output spectra with the conditioned input spectra can be computed as described in Equation 66.

$$L_{XC} = G_{XF}[L^H_{FC}]^{-1} G^{-1}_{CC} \tag{66}$$

The cross spectrum between the output and the conditioned inputs can then be found as:

$$G_{XC} = L_{XC}\, G_{CC}\, L^H_{XC} \tag{67}$$

The output-by-output cumulative coherence can then be found as shown in Equation 68.

$$C_{COH_{pq}} = \gamma^2_{F_q X_p . F_{q-1}!} = \frac{|G_{C_q X_p}|^2}{G_{C_q C_q} G_{X_p X_p}} \tag{68}$$

The corresponding set of cumulative coherences is dependent on the ordering of the inputs chosen. A variant of this concept that includes restoring force terms representing any nonlinear functional terms that describe the system behavior was developed in [26] also named cumulative coherence.

Conditioned Coherences Which Utilize Virtual Source Reference

The following two coherence formulations do not retain the connection to a physical source reference. Instead, they resolve the coherence to virtual source inputs. While the order of the virtual sources is not necessarily the same between the two formulations, each still sums to give the multiple coherence.

Fractional Coherence

Instead of depending on some a priori knowledge of the significance of the inputs, a singular value decomposition [8] of the input auto power matrix allows for the computation of the partial dependency of the output with the virtual forces thus obtained. This metric does not retain the spatial information and always orders the resulting virtual forces in the order of their significance and is, therefore, independent of the ordering of the inputs chosen. In the same vein as the Cholesky decomposition shown at the end of previous section, the relation between the output and the virtual forces can be used to find the corresponding fractional coherence as shown in Equation 71.

$$G_{FF} = U_{FS}\, G_{SS}\, U_{FS}^{H} \tag{69}$$

$$G_{XS} = G_{XF} \left[U_{FS}^{H} \right]^{-1} G_{SS}^{-1} \tag{70}$$

$$F_{COH_{pq}} = \gamma^2_{F_q X_p . F_{q-1}!} = \frac{|G_{S_q X_p}|^2}{G_{S_q S_q} G_{X_p X_p}} \tag{71}$$

The discussion regarding the disambiguation of the normalization factor presented for partial coherence holds true here as well. If the fractional coherence is computed as presented, it can be added up to compute the corresponding multiple coherence.

Virtual Coherence

As a coherence computed in conjunction with, or as a correspondence to, the virtual forces (or principal components) defined in Sect. 3.5, the *virtual coherence* can be computed using either singular value decomposition [27] or eigenvalue decomposition [28].

$$G_{FF} = \Psi_{FV}\, G_{VV}\, \Psi_{FV}^{H} \tag{72}$$

$$G_{XV} = G_{XF} [\Psi_{FV}^{H}]^{-1} G_{VV}^{-1} \tag{73}$$

$$V_{COH_{pq}} = \gamma^2_{F_q X_p . F_{q-1}!} = \frac{|G_{V_q X_p}|^2}{G_{V_q V_q} G_{X_p X_p}} \tag{74}$$

If the virtual coherence is computed as presented, it can be added up to compute the corresponding multiple coherence.

In summary, all the conditioned coherence formulations presented utilize some form of orthogonal conditioning basis and as a result are consistent with the fundamental coherence premise presented: bounded 0 to 1 and sum to be the multiple coherence.

Two DOF Illustration

To begin to understand the size of the problem involved, start with the two-input, one-output case (Fig. 6).

$$\hat{X}_p \; - \; \eta_p \; = \; H_{p1} \; F_1 \; + \; H_{p2} \; F_2 \tag{75}$$

If more than one output is measured, the equations become:

$$\{X_p\} \; [F_1^* \; F_2^*] \; = \; [H_{p1} \;\; H_{p2}] \begin{Bmatrix} F_1 \\ F_2 \end{Bmatrix} \; [F_1^* \; F_2^*] \tag{76}$$

Therefore, for input locations 1 and 2, each output is used with the two inputs to compute two frequency response functions. Therefore, there will be $2 \times N_o$ frequency response functions to be computed:

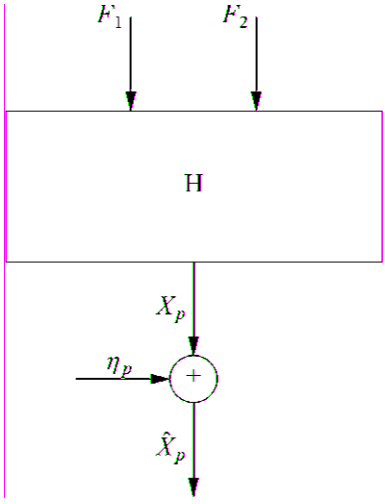

Fig. 6 Two-input, one-output model

$$\begin{bmatrix} H_{11} & H_{12} \\ H_{21} & H_{22} \\ H_{31} & H_{32} \\ \cdot & \cdot \\ \cdot & \cdot \\ H_{N_o1} & H_{N_o2} \end{bmatrix} = \begin{bmatrix} G_{XF_{11}} & G_{XF_{12}} \\ G_{XF_{21}} & G_{XF_{22}} \\ G_{XF_{31}} & G_{XF_{32}} \\ \cdot & \cdot \\ \cdot & \cdot \\ G_{XF_{No1}} & G_{XF_{No2}} \end{bmatrix} \begin{bmatrix} G_{FF_{11}} & G_{FF_{12}} \\ G_{FF_{21}} & G_{FF_{22}} \end{bmatrix}^{-1} \tag{77}$$

For each output location, one formulation of the equations to be solved can be developed by replacing the inverse of the $[G_{FF}]$ matrix with the equivalent adjoint of the $[G_{FF}]$ matrix divided by the determinant of the $[G_{FF}]$ matrix. In this way, it is clear that the frequency response functions can be found as long as the determinant of the $[G_{FF}]$ matrix is not zero:

$$H_{p1} = \frac{G_{XF_{p1}} G_{FF_{22}} - G_{XF_{p2}} G_{FF_{21}}}{\det[G_{FF}]} \tag{78}$$

$$H_{p2} = \frac{G_{XF_{p2}} G_{FF_{11}} - G_{XF_{p1}} G_{FF_{12}}}{\det[G_{FF}]} \tag{79}$$

where:

- $\det[G_{FF}]$ = determinant of $[G_{FF}]$ matrix
- $\det[G_{FF}] = G_{FF_{11}} G_{FF_{22}} - G_{FF_{21}} G_{FF_{12}}$

For the two-input, one-output case, several possible coherence functions can be formulated. While the ordinary coherence between the output and each input can be formulated, these coherence functions may not provide useful information due to the possible interaction between the two forces.

Ordinary coherence (output p and Input 1):

$$O_{COH_{p1}} = \frac{\left|G_{XF_{p1}}\right|^2}{G_{FF_{11}} G_{XX_{pp}}} \tag{80}$$

Ordinary coherence (output p and input 2):

$$O_{COH_{p2}} = \frac{\left|G_{XF_{p2}}\right|^2}{G_{FF_{22}} G_{XX_{pp}}} \tag{81}$$

The ordinary coherence between the two inputs is a useful function since this is a measure of whether the forces are correlated. If the forces are perfectly correlated at a frequency, the inverse of the $[G_{FF}]$ matrix will not exist, and the frequency response functions cannot be estimated at that frequency. In this case, the ordinary coherence between the two forces cannot be unity, although values from 0.0 to 0.99

are theoretically acceptable. The limit is determined by the accuracy of the measured data and the numerical precision of the computation.

Ordinary Coherence (Input 1 and Input 2):

$$O_{COH_{12}} = \frac{\left|G_{FF_{12}}\right|^2}{G_{FF_{11}} G_{FF_{22}}} \tag{82}$$

Multiple coherence is always a good measure of whether the output response is caused by the combination of the measured inputs. Multiple coherence is used in multiple input situations in the same way that ordinary coherence is used in the single input situations.

Multiple Coherence

$$M_{COH_p} = \frac{\{G_{XF}\}\,[G_{FF}]^{-1}\,\{G_{FX}\}^T}{G_{XX_{pp}}} \tag{83}$$

Summary of Methods

H_1 **Technique:**

- Underestimates amplitude at resonances. Causes damping to be overestimated.
- Underestimates amplitude at antiresonances.

H_2 **Technique:**

- Overestimates amplitude at resonances. Causes damping to be underestimated.
- Overestimates amplitude at antiresonances.

H_v **Technique:**

- Best estimate of amplitude at resonances. Causes damping to be estimated best.
- Best estimate of amplitude at antiresonances.
- Phase characteristics not altered.

3.5 Multiple Input Force Analysis/Evaluation

Of the variety of situations that can cause difficulties in the computation of the frequency response functions, the highest potential for trouble is the case of coherent inputs. If two of the inputs are fully coherent at one of the analysis frequencies, then there are no unique frequency response functions associated with those inputs at that analysis frequency. Unfortunately, there are a number of situations where the input cross spectrum matrix $[G_{FF}]$ may be singular at specific frequencies or frequency intervals. When this happens, the inverse of $[G_{FF}]$ will not exist, and Equation 44 cannot be used to solve for the frequency response function at those frequencies

or in those frequency intervals. First, one of the input autospectra may be zero in amplitude over some frequency interval. When this occurs, then all of the cross spectra in the same row and column in the input cross spectrum matrix $[G_{FF}]$ will also be zero over that frequency interval. Consequently, the input cross spectrum matrix $[G_{FF}]$ will be singular over that frequency interval. Second, two or more of the input signals may be fully coherent over some frequency interval. Although the signals used as inputs to the exciter systems must be uncorrelated random inputs, the response of the structure at resonance, combined with the inability to completely isolate the exciter systems from this response, results in the ordinary or conditioned partial coherence functions with values other than zero, particularly at the system poles. For example, for the two-input case, as long as the coherence function between the inputs is not unity at these frequencies, Equation 44 can be solved uniquely for the frequency response functions.

Note that the auto and cross spectra involved in the calculation of the multiple input case for the estimation of frequency response functions should be computed from analog time data that has been digitized *simultaneously*. If data is not processed in this manner, many more averages are required to reduce the variance on each individual auto and cross spectrum, and the efficiency of the multiple input approach to the estimation of frequency response functions will not be as attractive. Finally, numerical problems, which cause the computation of the inverse to be inexact, may be present. This can happen when an autospectrum is near zero in amplitude, when the cross spectra have large dynamic range with respect to the precision of the computer, or when the matrix is ill-conditioned because of nearly redundant input signals.

Due to the form of the equations that must be solved to compute frequency response functions in the presence of multiple inputs, special care must be taken to assure that the input spectrum matrix is not singular. Therefore, techniques have been investigated to evaluate the form of the input spectrum matrix before taking any data. Singular, in this case, implies that:

- Input forces may not be coherent at any frequency.
  - Independent, uncorrelated noise sources must be used (random, random transient, periodic random).
  - The impedance of the structure at the input locations may tend to correlate the inputs at resonance.
- There are no zeros in the input spectrum matrix.

3.5.1 Ordinary and Partial Coherence Functions

The historical approach that was used to try to evaluate the correlation between the forces utilized ordinary and partial coherence functions. The ordinary coherence function measures the degree of linear dependence (or correlation) between the spectra of two signals. The partial coherence function measures the degree of linear dependence between the spectra of two signals, after eliminating, in a least squares sense, the contribution of some other signals. Both functions can be used in a systematic procedure to verify that the forces are not correlated or that the input

cross spectra matrix $[G_{FF}]$ is not singular. For cases involving more than two inputs, this approach is very difficult and requires considerable judgment. In reality, only the ordinary coherence function, for the case of two inputs, is still used.

$$O_{COH_{ik}} = \frac{\left|G_{FF_{ik}}\right|^2}{G_{FF_{ii}} G_{FF_{kk}}} \tag{84}$$

where:

- $G_{FF_{ik}}$ = cross power spectrum between inputs i and k
- $G_{FF_{ii}}$ = auto power spectrum of input i
- $G_{FF_{kk}}$ = auto power spectrum of input k

3.5.2 Principal/Virtual Input Forces (Virtual Forces)

The current approach used to determine correlated inputs involves utilizing principal component analysis to determine the number of contributing forces to the $[G_{FF}]$ matrix. In this approach, the matrix that must be evaluated is:

$$[G_{FF}] = \begin{bmatrix} G_{FF_{11}} & \cdots & G_{FF_{1N_i}} \\ \cdot & & \cdot \\ \cdot & & \cdot \\ \cdot & & \cdot \\ G_{FF_{N_i1}} & \cdots & G_{FF_{N_iN_i}} \end{bmatrix} \tag{85}$$

where:

- $G_{FF_{ik}} = G_{FF_{ki}}{}^*$ (Hermitian matrix)
- $G_{FF_{ik}} = \sum F_i F_k^*$
- G_{FF} is the power spectrum of a given input.

Principal component analysis involves a singular value or eigenvalue decomposition of the $[G_{FF}]$ matrix [7]. Since the eigenvectors of such a decomposition are unitary, the eigenvalues should all be of approximately the same size if each of the inputs is contributing. If one of the eigenvalues is much smaller at a particular frequency, one of the inputs is not present, or one of the inputs is correlated with the other input(s):

$$[G_{FF}] = [V] \lceil \Lambda \rfloor [V]^H \tag{86}$$

$\lceil \Lambda \rfloor$ represents the eigenvalues of the $[G_{FF}]$ matrix. If any of the eigenvalues of the $[G_{FF}]$ matrix are zero or insignificant, then the $[G_{FF}]$ matrix is singular. Therefore, for a three-input test, the $[G_{FF}]$ matrix should have three eigenvalues at each frequency. (The number of eigenvalues is the number of uncorrelated inputs.)

This concept is shown graphically in Fig. 7 for the auto power spectra for a three-input case. It is difficult to determine if the inputs are mutually correlated from these plots. Figure 8 shows the principal force plots for the same case. At the frequencies where the third principal/virtual force drops (lowest curve), this indicates that the inputs are mutually correlated at those frequencies. This is not apparent from Fig. 7.

3.5.3 Optimum Number Of Inputs

The location and number of inputs have a direct effect on the quality of frequency response functions that are estimated. This is an area that has not been researched completely and is still being reviewed. It is clear that beyond some number of inputs, the return from the investment of more equipment, in the form of inputs, is not warranted. Some considerations are:

- Two at symmetric locations. Frequency response functions can be added or subtracted to enhance in-phase or out-of-phase modes.
- To excite as many modes as possible in one test configuration.
  - Two vertical and one horizontal on a car.
  - One on each wing and one on each horizontal stabilizer, all symmetric, on an aircraft structure.
- To excite *operating* conditions.

4 Averaging

The averaging of signals is normally viewed as a summation or weighted summation process where each sample function has a common abscissa. Normally, the designation of *history* is given to sample functions with the abscissa of absolute time, and the designation of *spectra* is given to sample functions with the abscissa of absolute frequency. The spectra are normally generated by Fourier transforming the corresponding history. In order to generalize and consolidate the concept of signal averaging as much as possible, the case of relative time can also be considered. In this way, *relative history* can be discussed with units of the appropriate event rather than seconds, and a *relative spectrum* will be the corresponding Fourier transform with units of cycles per event. This concept of signal averaging is used widely in structural signature analysis where the event is a revolution. This kind of approach simplifies the application of many other concepts of signal relationships such as Shannon sampling theorem and Rayleigh criterion of frequency resolution.

4.1 General Averaging Methods

When comparing data taken with different equipment, care must be taken to be certain that the averaging is being performed the same way. The terminology with

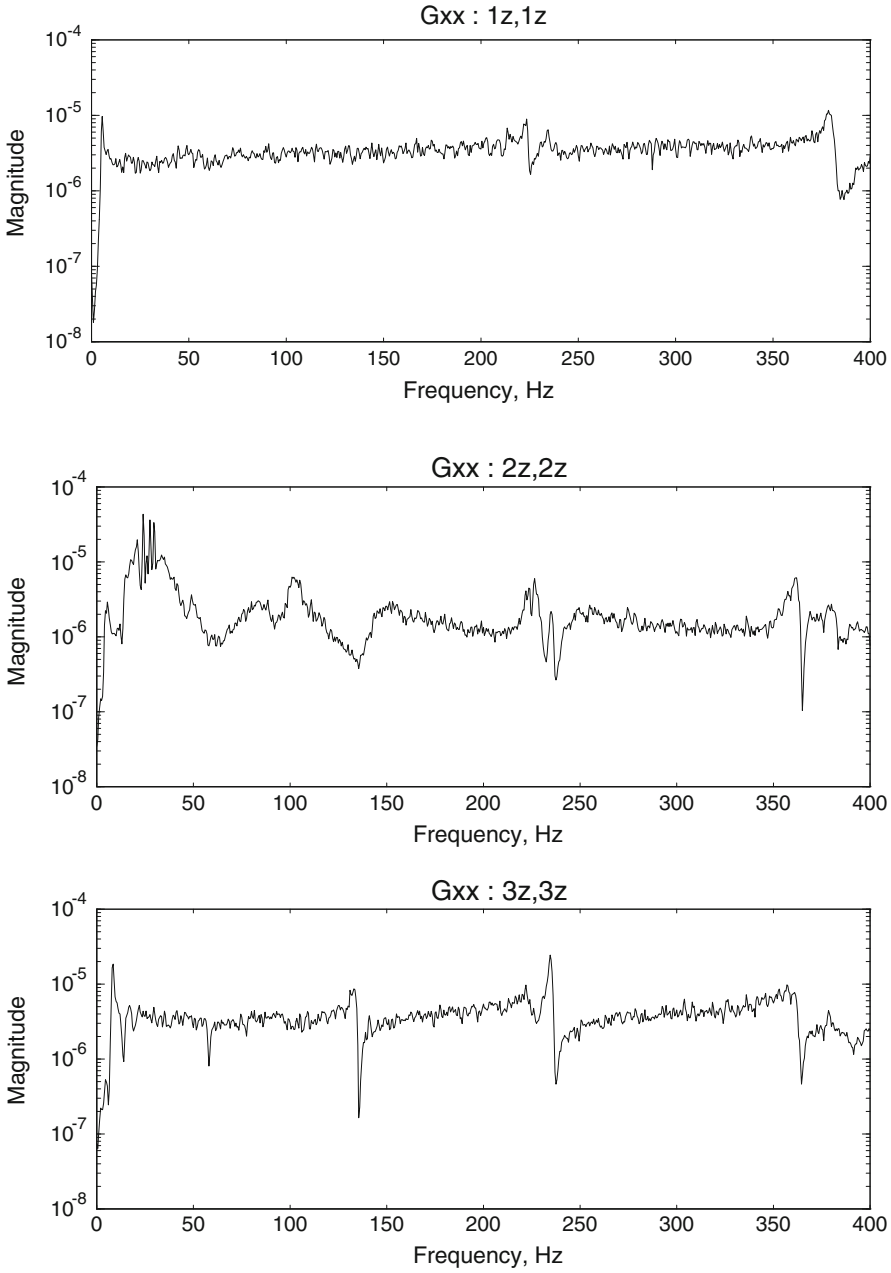

Fig. 7 Auto power spectrum of input forces

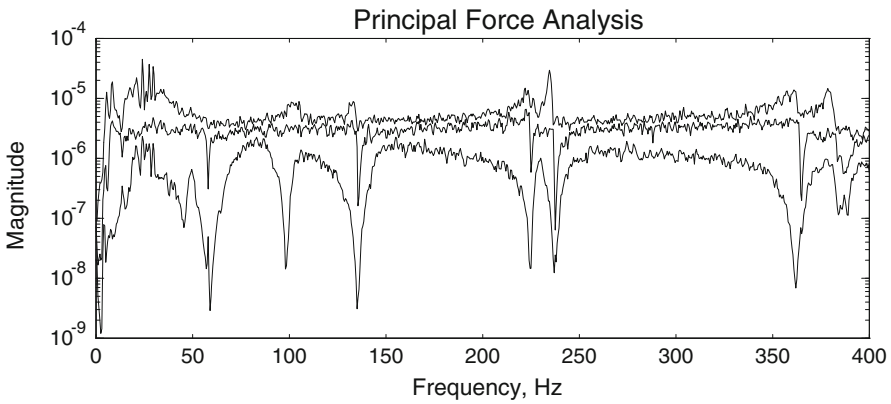

Fig. 8 Principal (virtual) force spectrum

regard to averaging is not always the same, so some sort of evaluation may be required using test cases to be certain that the same form of averaging is being used.

4.1.1 Linear Averaging

Linear averaging is the simplest form of averaging and is what most people think of as averaging. Essentially, linear averaging is simply trying to find the mean value in a set of numbers. Since measurements deal with information at different times or frequencies, linear averaging refers to finding the mean value at each time or frequency over a number of ensembles or averages. Linear averaging is fundamentally calculated with the following formula:

$$\bar{x}(t)_{N_{\text{avg}}} = \frac{\sum_{i=1}^{N_{\text{avg}}} x(t)_i}{N_{\text{avg}}} \tag{87}$$

$$\bar{X}(\omega)_{N_{\text{avg}}} = \frac{\sum_{i=1}^{N_{\text{avg}}} X(\omega)_i}{N_{\text{avg}}} \tag{88}$$

Linear averaging is useful primarily when some form of initial trigger is available in order for information that is synchronized with the trigger to be emphasized. Note that if no trigger is available and the averages are collected in a free run data acquisition mode, the phasing of any dynamic signals will be random from ensemble to ensemble. With a large number of averages, only the DC signal content will be preserved. Note that linear averaging gives the same result whether implemented in the time or frequency domain. Linear averaging is normally implemented in the frequency domain.

If some sort of initializing trigger is available, the averaged data reduce the noise and enhance the signal, giving an improved signal-to-noise ratio (SNR). The variance is reduced a function of $\frac{1}{\sqrt{N_{\text{avg}}}}$. This means that to reduce the variance to 10 percent of the variance on a single average, 100 averages must be taken.

The terminology *time averaging* refers to a special case of linear averaging when the trigger of each average is synchronized with a specific position of a rotating shaft (e.g., top dead center) in the time domain. In this case, each ensemble will have a fixed number of rotations in the time history, and each data point in the time history will be collected when the rotating system is in the same position as long as the speed of rotation is constant. If the data is sampled at fixed intervals during the rotation (e.g., by utilizing an encoder to give 32 samples per revolution), the fixed speed is not required. The processing of data for this situation requires further consideration and will not be presented here.

4.1.2 Magnitude Averaging

Magnitude, or amplitude, averaging involves finding the mean value of the absolute values of the data at each time or frequency. While this form of averaging is not very common, it has been used in some older digital signal analyzers. This form of averaging has generally been replaced by RMS averaging in most current digital signal analyzers. Magnitude averaging and RMS averaging will give nearly identical results if there is little dynamic range in the data being averaged. Since the absolute value is formed, the phasing provided by an initial trigger is not required for magnitude averaging. However, magnitude averaging does not improve the signal-to-noise ratio (SNR) since the noise magnitude accumulates in the same way as the signal magnitude. Therefore, magnitude averaging does not reduce the variance in the data with averages in the same way as linear averaging. Magnitude averaging is fundamentally calculated with the following formula:

$$\bar{x}(t)_{N_{\text{avg}}} = \frac{\sum_{i=1}^{N_{\text{avg}}} \sqrt{x(t)_i \times x(t)_i}}{N_{\text{avg}}} \tag{89}$$

$$\bar{X}(\omega)_{N_{\text{avg}}} = \frac{\sum_{i=1}^{N_{\text{avg}}} \sqrt{X(\omega)_i \times X(\omega)_i{}^*}}{N_{\text{avg}}} \tag{90}$$

Magnitude averaging is generally not a concern unless historical data or data acquisition procedures are involved. This can be a concern if data or data acquisition procedures are specified, particularly in patents or other historical documents. Note that magnitude averaging does not give the same result whether implemented in the time or frequency domain. Magnitude averaging is normally implemented in the frequency domain.

4.1.3 Root Mean Square (RMS) Averaging

Root mean square (RMS) averaging is commonly used in many digital signal analyzers and is the basis for estimating frequency response and coherence functions from auto and cross power spectra. RMS averaging refers to the computational procedure involving the mean squared value of the data at each time or frequency. This is useful for determining the power, or energy, in the data which may contain positive and negative values and/or real and complex values. Since the squared value is formed, the phasing provided by an initial trigger is not required for RMS averaging. However, RMS averaging does not improve the signal-to-noise ratio (SNR) since the noise power accumulates in the same way as the signal power. Therefore, RMS averaging does not reduce the variance in the data with averages in the same way as linear averaging. In the estimation of the frequency response function, the variance error is reduced by choosing the FRF estimation algorithm based upon the location of the noise in the inputs and outputs. Magnitude averaging and RMS averaging will give nearly identical results if there is little dynamic range in the data being averaged. RMS averaging is fundamentally calculated with the following formula:

$$\bar{x}(t)_{N_{\text{avg}}} = \sqrt{\frac{\sum_{i=1}^{N_{\text{avg}}} x(t)_i \times x(t)_i}{N_{\text{avg}}}} \tag{91}$$

$$\bar{X}(\omega)_{N_{\text{avg}}} = \sqrt{\frac{\sum_{i=1}^{N_{\text{avg}}} X(\omega)_i \times X(\omega)_i{}^*}{N_{\text{avg}}}} \tag{92}$$

Note that in the above equations, the units on the averaged data are the same as the units of each average. Frequently, digital signal analyzers show the resulting averaged data with units squared. This is simply indicating that the averaged data is being displayed without the square root. This is simply a display issue and the user can choose between units and units squared. Note that RMS averaging does not give the same result whether implemented in the time or frequency domain. RMS averaging is normally implemented in the frequency domain.

As a simple example of the difference between linear, magnitude, and RMS averaging, Table 5 indicates the problem.

4.1.4 Exponential Averaging

Exponential averaging weights new data differently (typically more heavily) than old data. This is useful for tracking time-varying characteristics in the data (not used in data for experimental modal analysis). The weighting is generally dependent on the number of averages chosen for the exponential averaging (typically a power of 2, either 4 or 8). Once the exponential averaging is started, the averaging continues until it is stopped (it does not stop after the number of averages selected; the

Table 5 Comparison of averaging methods

Ensemble	Linear	Magnitude	RMS
1	2	2	4
2	3	3	9
3	4	4	16
4	−2	2	4
5	−3	3	9
6	−4	4	16
Total	0	18	58
Average	0	3.000	3.109

number of averages determines the weighting or *forgetting* factor). For the first few averages, linear and exponential averaging is nearly the same. Exponential averaging is fundamentally calculated with the following formula:

$$\bar{X}(\omega)_{N_{\text{avg}}} = (1 - 2^{-N_{\text{avg}}})\ \bar{X}(\omega)_{N_{\text{avg}-1}} + 2^{-N_{\text{avg}}}\ X(\omega)_i \tag{93}$$

4.1.5 Stable Averaging

Stable averaging is not really a separate form of averaging but refers to a display characteristic. If the averaging process is stopped before N_{avg} are reached, stable averaging always shows the display information with the appropriate correction for the number of averages. Stable averaging means that the above equations are reformulated in a recursive form so that the displayed can be updated, average by average, so that the amplitude of the data is correct regardless of when the average is stopped. The recursive form of the averaging equations weights old and new data records appropriately to yield the appropriate arithmetic mean for the current number of averages.

4.1.6 Peak Hold

Peak hold data collection is often included in the averaging selection of a digital signal analyzer. Peak hold, as the name indicates, is not really a form of averaging since only the peak value is retained at each time or frequency and no arithmetic mean (in the common understanding of the term) is formed. Normally, the peak magnitude or peak RMS information is retained over a number of ensembles. This data collection approach is very useful for identifying the maxima that occur during transients or general time-varying events.

4.2 Estimation of Frequency Response Functions

The process of signal averaging as it applies to frequency response function estimation involves linear averaging of auto and cross power spectra. This is a bit

confusing since the general averaging concepts always are explained in terms of a single data signal. With frequency response function estimation, there are a number of input and output signals that are all initiated (triggered) at the same start time for each average and are all sampled at the same time. The reduction of noise on the frequency response function estimates depends upon the noise model that is used to describe where the noise enters the measurements, on the inputs, on the outputs, or both. Based upon the noise model, the FRF estimation algorithm will reduce the random noise according to a least squared error procedure. Note that since the least squared error procedure minimizes the squared error by eliminating the phase information, these procedures will affect the magnitude but not the phase.

It is important to realize that while the frequency response function is assumed to be unique, the auto and cross power spectra used to estimate the FRF are not unique unless the input is stationary and a sufficiently large number of averages are taken. Generally, this is never the case. This is not a concern, however, since the desired information is the frequency response function not auto and cross power spectra. After a reasonable number of averages (5–100), the auto and cross power spectra may still appear to be noisy. Some of the *noise* is due to random or bias errors in the data, and some of the noise is simply due to the uneven excitation that occurs with transient or random input(s) to the system being tested. The uneven excitation in the auto and cross spectra is consistent between the input and output power spectra (related by the FRF) and will cancel when the frequency response function is estimated. The random portion of the noise will be minimized due to the least squared error estimation of the frequency response function. The bias portion of the noise will not generally be eliminated. Therefore, it is critical that bias errors, such as leakage, be eliminated if possible.

The triggering issues relative to averaging of auto and cross power spectra that will be used to estimate FRFs required some additional terminology in order to clarify the measurement procedure. One of the two forms of linear averaging, asynchronous and synchronous averaging, is always used to estimate FRFs depending upon the type of excitation. Additionally, cyclic averaging, a special case of time domain linear averaging, may be used when leakage is a serious problem in conjunction with traditional averaging methods (asynchronous or synchronous averaging). Cyclic averaging reduces the leakage bias error by digitally filtering the data to eliminate the frequency information that cannot be described by the FFT (only integer multiples of Δf are retained) prior to the application of the FFT. Cyclic averaging can always be used, together with asynchronous or synchronous averaging, to reduce both the leakage error and the random errors.

Since the Fourier transform is a linear function, there is no theoretical difference between the use of time or frequency domain data when averaging. Practically, though, synchronous and asynchronous averaging is normally performed in the frequency domain and cyclic averaging is normally performed in the time domain. Therefore, these three classifications primarily refer to the initial trigger and sampling relationships between averages and ensembles while collecting the auto

and cross power spectra used to estimate frequency response functions. This will be explained further in the following sections.

4.2.1 Asynchronous Signal Averaging

The asynchronous classification of linear signal averaging of the auto and cross power spectra represents the case where no known relationship exists each average. The FRF is correctly estimated solely on the basis of the uniqueness of the frequency response function [29, 30]. In this case, the auto and cross power spectra (least squares) approach to the estimate of frequency response must be used since no other way of preserving phase and improving the estimate is available. In this situation, the trigger to initiate each average takes place in a random fashion dependent only upon the data acquisition equipment timing. The triggering is said to be in a free run mode.

4.2.2 Synchronous Signal Averaging

The synchronous classification of linear signal averaging adds the additional constraint that each average must be initiated with respect to a specific trigger condition (often the magnitude and slope of the excitation) [31, 32]. This means that the frequency response function could be formed as $X(\omega)_{Navg}$ divided by $F(\omega)_{Navg}$ since phase is preserved. Even so, linear averaging of the auto and cross power spectra is still the preferred FRF estimation method due to the reduction of variance and the ability to estimate the ordinary coherence function. The ability to synchronize the initiation of digitization for each average allows for use of nonstationary or deterministic inputs with a resulting increased signal-to-noise ratio.

The synchronization takes place as a function of a trigger signal occurring in the input (internally) or in some event related to the input (externally). An example of an internal trigger would be the case where an impulsive input is used to estimate the frequency response. Each average would be initiated when the input reached a certain amplitude and slope. A similar example of an external trigger would be the case where the impulsive excitation to a speaker is used to trigger the estimate of frequency response between two microphones in the sound field. Again, each average would be initiated when the trigger signal reached a certain amplitude and slope.

4.2.3 Cyclic Signal Averaging

The cyclic classification of signal averaging involves a special case of linear averaging with the added constraint that the digitization is coherent between averages [31, 33, 32, 34]. This means that the exact time between each average is used to enhance the signal averaging process. Rather than trying to keep track of elapsed time between averages, the normal procedure is to allow no time to elapse between successive averages. This simple averaging procedure results in a digital comb filter in the frequency domain, with the teeth (passbands) of the comb at frequency increments that are integer multiples of the $\Delta f = 1/T$ relationship.

The result is an attenuation of the spectrum between the teeth not possible with other forms of averaging. Cyclic signal averaging is generally performed in the time domain and is coupled with asynchronous or synchronous averaging procedures in the frequency domain.

This form of signal averaging is very useful for filtering periodic components from a noisy signal since the teeth of the filter are positioned at harmonics of the frequency of the sampling reference signal. This is of particular importance in applications where it is desirable to extract signals connected with various rotating members. This same form of signal averaging is particularly useful for reducing leakage during frequency response measurements.

A very common application of cyclic signal averaging is in the area of analysis of rotating structures. In such an application, the peaks of the comb filter are positioned to match the fundamental and harmonic frequencies of a particular rotating shaft or component. This is particularly powerful, since in one measurement it is possible to enhance all of the possible frequencies generated by the rotating member from a given data signal. With a zoom Fourier transform type of approach, one shaft frequency at a time can be examined depending upon the zoom power necessary to extract the shaft frequencies from the surrounding noise.

The application of cyclic averaging to the estimation of frequency response functions can be easily observed by noting the effects of cyclic averaging on a single frequency sinusoid. Figures 9 and 10 represent the cyclic averaging of a sinusoid that is periodic with respect to the observation time period T. Figures 11 and 12 represent the cyclic averaging of a sinusoid that is aperiodic with respect to the observation time period T. By comparing Figs. 10, 11, and 12, the attenuation of the nonperiodic signal can be clearly observed.

Theory of Cyclic Averaging

In the application of cyclic averaging to frequency response function estimates, the corresponding fundamental and harmonic frequencies that are enhanced are

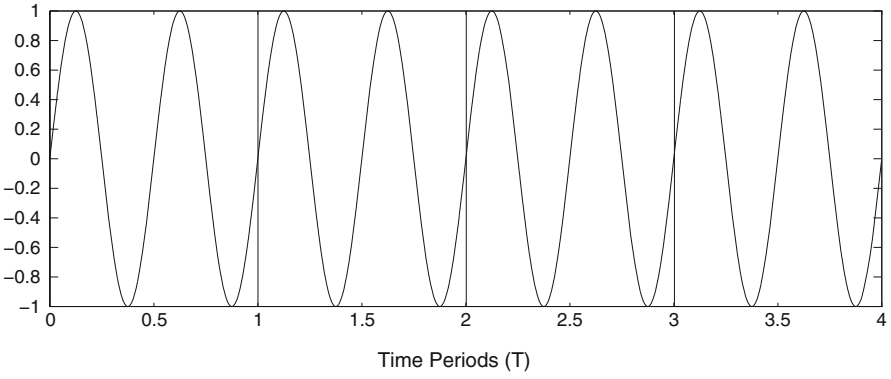

Fig. 9 Contiguous time records (periodic signal)

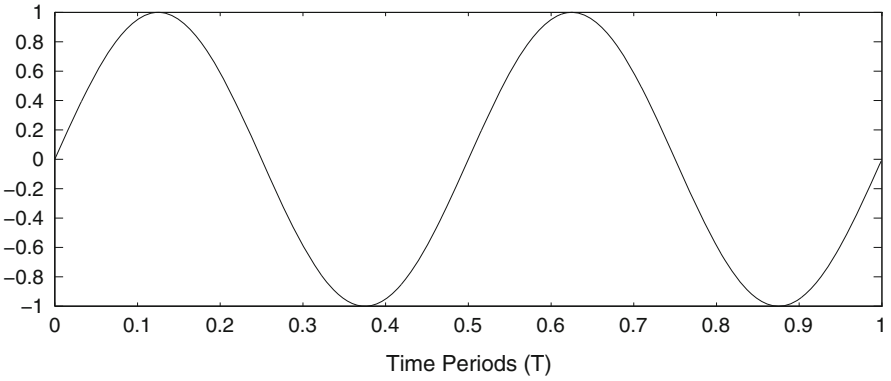

Fig. 10 Averaged time records (periodic signal)

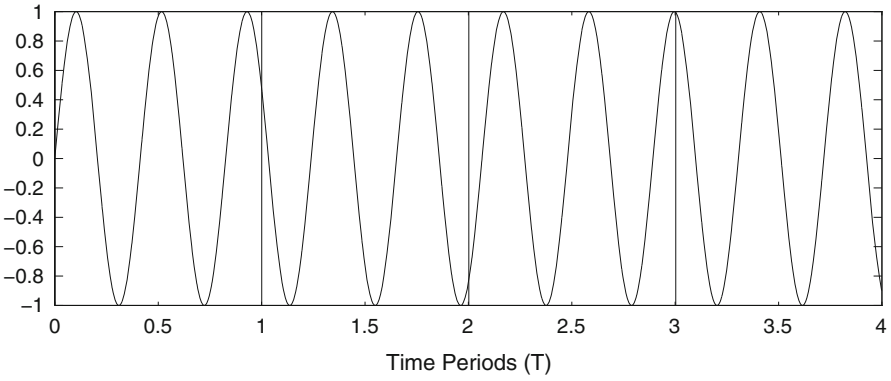

Fig. 11 Contiguous time records (nonperiodic signal)

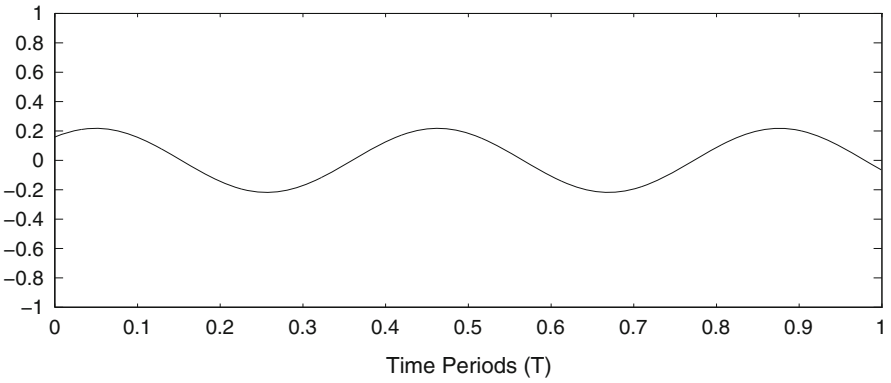

Fig. 12 Averaged time records (nonperiodic signal)

the frequencies that occur at the integer multiples of Δf. In this case, the spectra between each Δf is reduced with an associated reduction of the bias error called *leakage*.

The first observation to be noted is the relationship between the Fourier transform of a history and the Fourier transform of a time shifted history. In the averaging case, each history will be of some finite time length T which is the observation period of the data. Note that this time period of observation T determines the fundamental frequency resolution Δf of the spectra via the Rayleigh Criteria ($\Delta f = \frac{1}{T}$).

The Fourier transform of a history is given by:

$$X(\omega) = \int_{-\infty}^{+\infty} x(t)\, e^{-j\omega t}\, dt \tag{94}$$

Using the time shift theorem of the Fourier transform, the Fourier transform of the same history that has been shifted in time by an amount t_0 is [35]:

$$X(\omega)\, e^{-j\,\omega\, t_0} = \int_{-\infty}^{+\infty} x(t + t_0)\, e^{-j\omega t}\, dt \tag{95}$$

For the case of a discrete Fourier transform, each frequency in the spectra is assumed to be an integer multiple of the fundamental frequency $\Delta f = \frac{1}{T}$. Making this substitution in Equation 95 ($\omega = k\, \frac{2\pi}{T}$ with k as an integer) yields:

$$X(\omega)\, e^{-j\, n\, \frac{2\pi}{T}\, t_0} = \int_{-\infty}^{+\infty} x(t + t_0)\, e^{-j\omega t}\, dt \tag{96}$$

Note that in Equation 96, the correction for the cases where $t_0 = N\ T$ with N is an integer will be a unit magnitude with zero phase. Therefore, if each history that is cyclic averaged occurs at a time shift, with respect to the initial average, that is an integer multiple of the observation period T, then the correction due to the time shift does not affect the frequency domain characteristics of the averaged result. All further discussion will assume that the time shift t_0 will be an integer multiple of the basic observation period T.

The signal averaging algorithm for histories averaged with a boxcar or uniform window is:

$$\bar{x}(t) = \frac{1}{N_c} \sum_{i=0}^{N_c - 1} x_i(t) \tag{97}$$

where:

- N_a number of asynchronous averages
- N_c number of cyclic averages

For the case where $x(t)$ is continuous over the time period $N_c T$, the complex Fourier coefficients of the cyclic averaged time history become:

$$C_k = \frac{1}{T} \int_0^T \bar{x}(t)\, e^{-j\omega_k t}\, dt \tag{98}$$

$$C_k = \frac{1}{T} \int_0^T \frac{1}{N_c} \sum_{i=0}^{N_c - 1} x_i(t)\, e^{-j\omega_k t}\, dt \tag{99}$$

Finally:

$$C_k = \frac{1}{N_c\, T} \int_0^T \sum_{i=0}^{N_c - 1} x_i(t)\, e^{-j\omega_k t}\, dt \tag{100}$$

Since $x(t)$ is a continuous function, the sum of the integrals can be replaced with an integral evaluated from 0 to $N_c\ T$ over the original function $x(t)$. Therefore:

$$C_k = \frac{1}{N_c\, T} \int_0^{N_c\, T} x(t)\, e^{-j\omega_k t}\, dt \tag{101}$$

The above equation indicates that the Fourier coefficients of the cyclic averaged history (which are spaced at $\Delta f = \frac{1}{T}$) are the same Fourier coefficients from the original history (which are spaced at $\Delta f = N_c\ T$). Note that the number of Fourier coefficients for the cyclic averaged history will be $\frac{1}{N_c}$ the number of coefficients of the original history since the number and size of the frequency spacing change by this factor. Also note that Parseval's theorem, concerning the energy representation of each Fourier coefficient, is not preserved by the cyclic averaging process since the frequency information not related to the harmonics of $\Delta f = \frac{1}{T}$ is removed [35].

The approach used to understand the frequency domain effects of windows on digital data can be used to understand the effect of cyclic averaging [36, 37]. Since cyclic averaging yields the Fourier coefficients of an effectively larger observation time ($N_c\ T$ compared to T), the effect of cyclic averaging results in an effective frequency domain window characteristic that is a result of this longer observation time. However, the Δf axis needs to be adjusted to account for the actual frequencies that occur in the cyclic averaged spectra.

Figure 13 shows the two-sided frequency domain characteristic of the cyclic averaged ($N_c = 4$) case with a uniform window. Likewise, Fig. 14 shows the two-sided frequency domain characteristic of the cyclic averaged ($N_c = 4$) case with

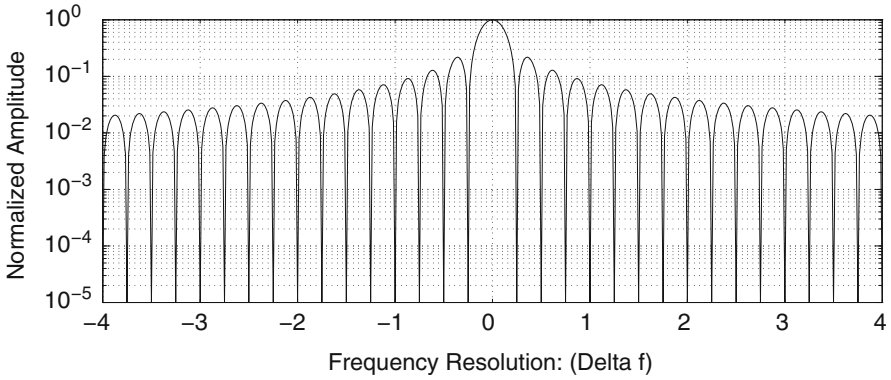

Fig. 13 Cyclic averaging ($N_c = 4$) with uniform window

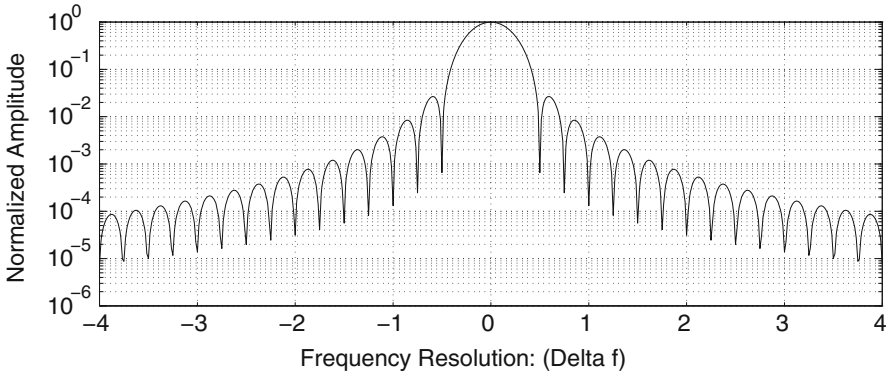

Fig. 14 Cyclic averaging ($N_c = 4$) with Hanning window

a Hanning window. Further detail of these characteristics is given in Figs. 15, 16, 17, 18, 19, and 20. Figures 15, 16, and 17 show the cyclic averaging effect in the frequency domain for the cases of 1, 2, and 4 averages with a uniform window applied to the data. Figure 15 essentially represents no cyclic averaging and is the familiar characteristic of a uniform window [36, 37]. Figures 16 and 17 show how cyclic averaging effects this window characteristic with respect to the $\Delta f = \frac{1}{T}$ frequency spacing. Figures 18, 19, and 20 show the cyclic averaging effect in the frequency domain for the cases of 1, 2, and 4 averages with a Hanning window applied to the original contiguous data. Figure 18 essentially represents no cyclic averaging and is the familiar characteristic of a Hanning window [36,37]. Figures 19 and 20 show how cyclic averaging effects this window characteristic with respect to the $\Delta f = \frac{1}{T}$ frequency spacing.

These figures demonstrate the effectiveness of cyclic averaging in rejecting nonharmonic frequencies. Practically, these figures also demonstrate that based upon effectiveness or the limitations of the dynamic range of the measured data,

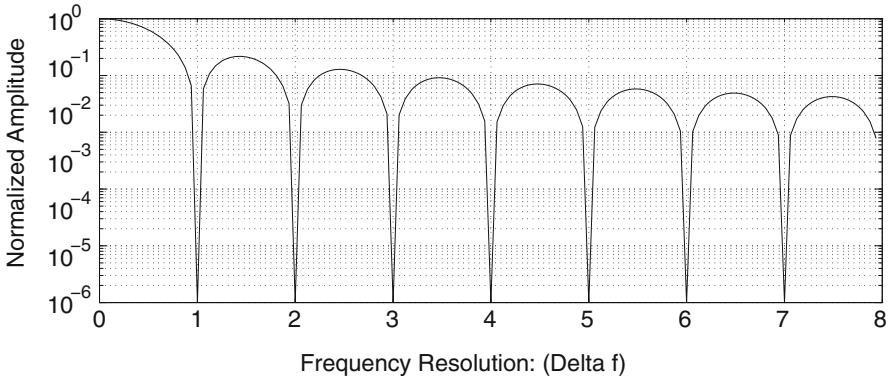

Fig. 15 Uniform window characteristics

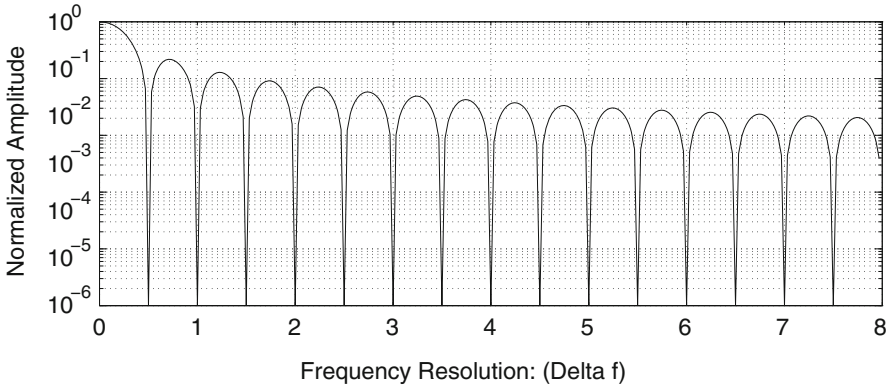

Fig. 16 Cyclic averaging ($N_c = 2$) with uniform window

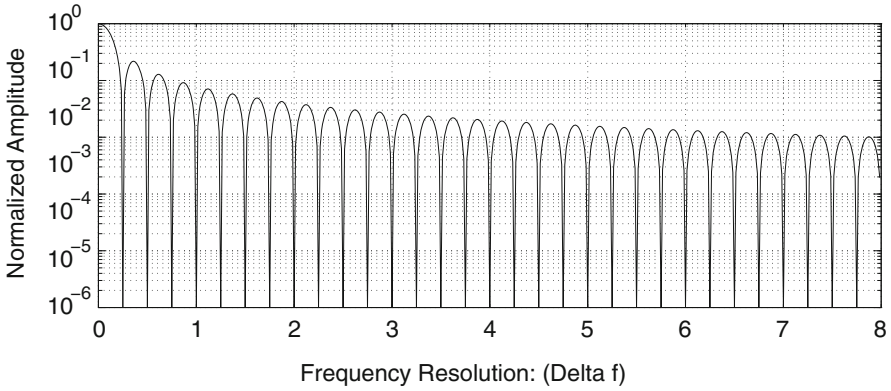

Fig. 17 Cyclic averaging ($N_c = 4$) with uniform window

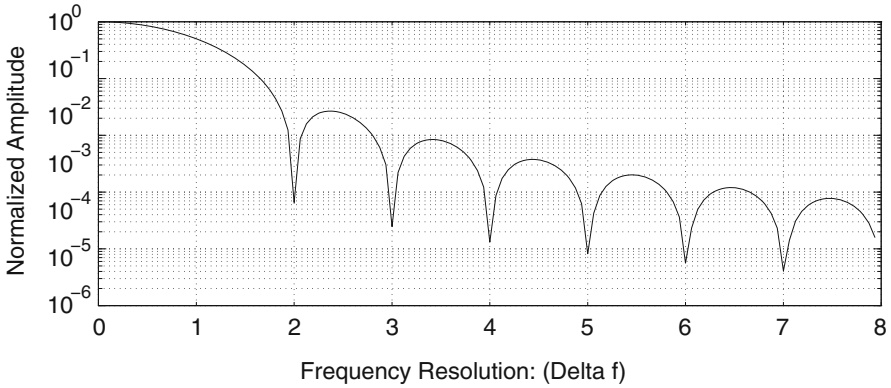

Fig. 18 Hanning window characteristics

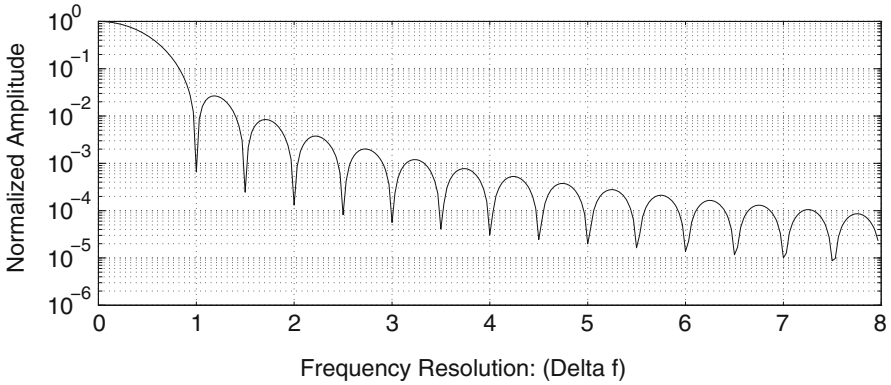

Fig. 19 Cyclic averaging ($N_c = 2$) with Hanning window

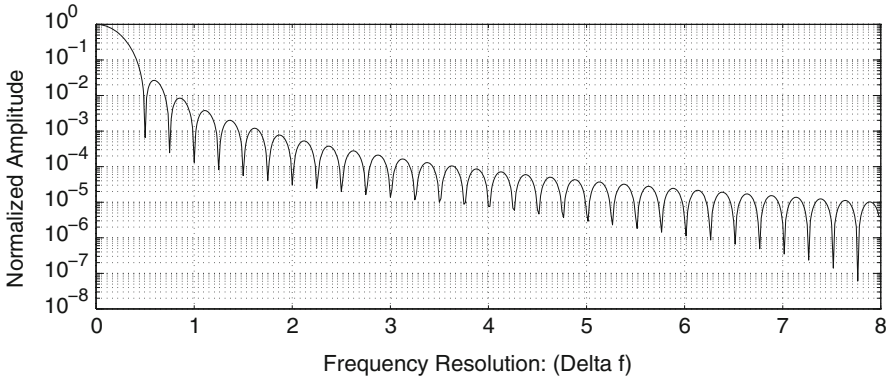

Fig. 20 Cyclic averaging ($N_c = 4$) with Hanning window

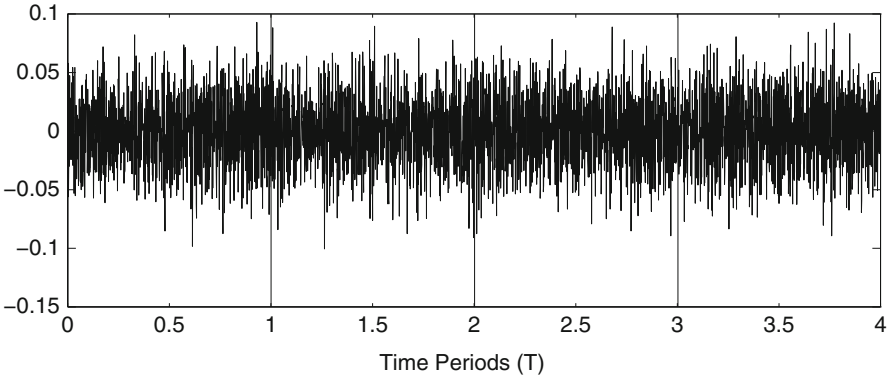

Fig. 21 Contiguous time records

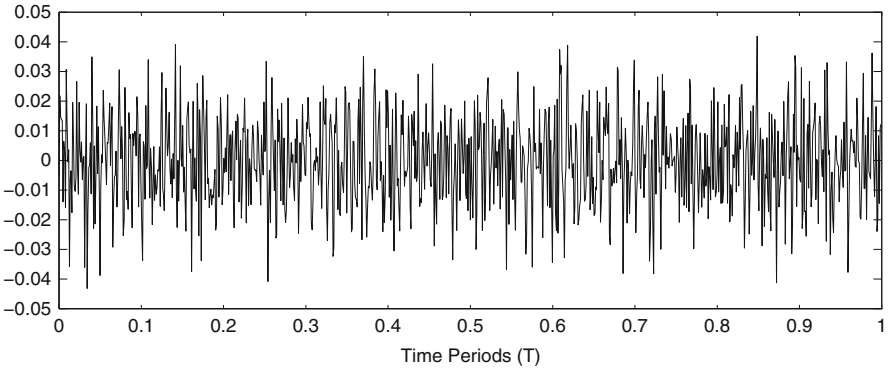

Fig. 22 Averaged time records

a maximum of 16 to 32 averages is recommended. Realistically, four to eight cyclic averages together with a Hanning window provide a dramatic improvement in the FRF estimate.

The results of cyclic averaging of a general random signal with the application of a uniform window are shown in Figs. 21 and 22. Likewise, the results of cyclic averaging of a general random signal with the application of a Hanning window are shown in Figs. 23 and 24.

Practical Example

The implementation of cyclic signal averaging to frequency response function (FRF) estimation is not easily applicable to many existing discrete Fourier transform analyzers. The reason for this is that the user is not given control of the time data acquisition such that the cyclic averaging requirements can be met. However, many users currently are acquiring data with personal computer (PC) data acquisition boards or the VXI-based data acquisition boards where control of the time data

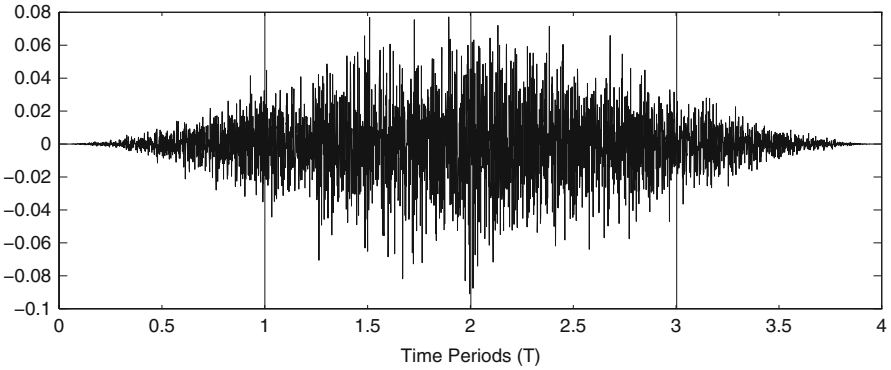

Fig. 23 Contiguous time records with Hanning window

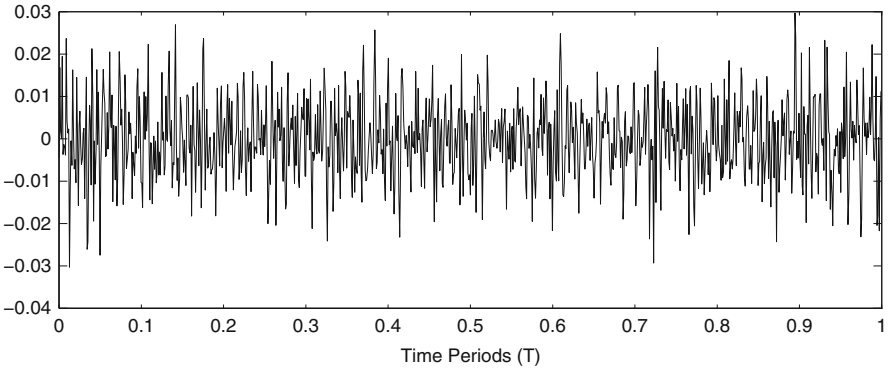

Fig. 24 Averaged time records with Hanning window

acquisition is more available to the user. In this environment, cyclic averaging is simple to implement by acquiring long data records and breaking the long data record into N_c contiguous time records which can be cyclic averaged.

The cyclic averaged inputs and outputs are normally computed by simply summing successive time records. The important requirement of the successive time records is that no data is lost. Therefore, these successive time records could be laid end to end to create the original longer time data record ($N_c\ T$). The cyclic averaged records are then created by simply adding each time record of length T together in a block mode.

While the basic approach to cyclic averaging involves using the data weighted uniformly over the total sample time $N_c\ T$, the benefits that can be gained by using weighting functions can also be applied. The application of a Hanning window to the successive time records before the summation occurs yields an even greater reduction of the bias error. Therefore, for frequency response function measurements, Hanning weighted signal averaging should drastically reduce the

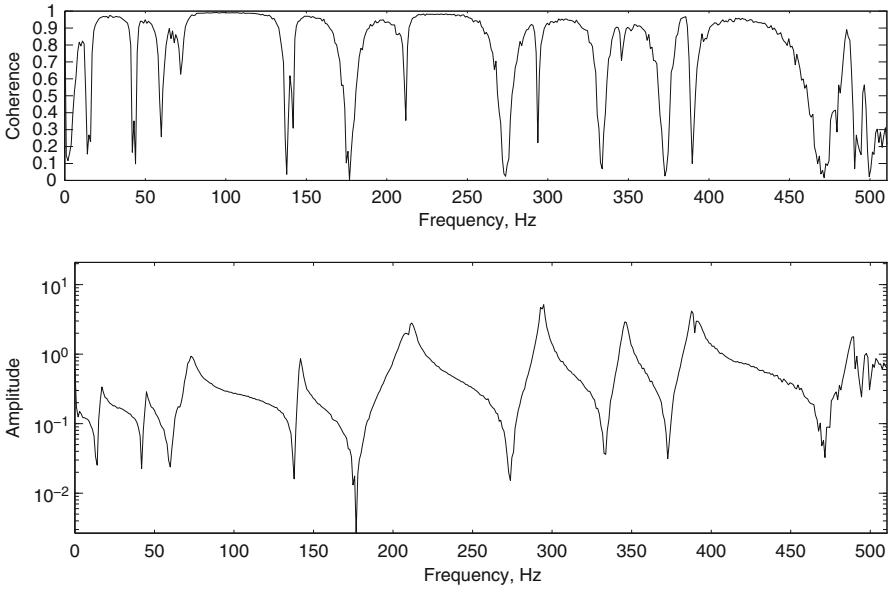

Fig. 25 Case I: asynchronous averaging

leakage errors which can exist when using broadband random excitation techniques to measure frequency response.

In Figs. 25, 26, 27, and 28, four different measurement cases are documented for the same FRF measurement. This data was acquired as typical data from a lightly damped, cantilever beam. Each figure shows the amplitude of an FRF with the associated ordinary coherence function shown as a measurement quality indicator. In each case, the H_1 FRF estimation algorithm was used; only the windowing and the number of asynchronous (N_a) and the number of cyclic (N_c) averages were changed. The four cases are as follows:

- Case I: The FRF is computed from 64 asynchronous averages ($N_a = 64$). A uniform window (no additional window) is applied to the data. This is an unacceptable measurement and represents poor measurement procedure.
- Case II: The FRF is computed from 64 asynchronous averages ($N_a = 64$). A Hanning window is applied to the data. This is a marginally acceptable measurement and represents a common measurement procedure.
- Case III: The FRF is computed from 4 cyclic averages ($N_c = 4$) and 16 asynchronous averages ($N_a = 16$). A uniform window (no additional window) is applied to the data. This is a marginally acceptable measurement and compares reasonably to Case II.
- Case IV: The FRF is computed from 4 cyclic averages ($N_c = 4$) and 16 asynchronous averages ($N_a = 16$). A Hanning window is applied to the data. This is a good measurement. Note particularly the increase in the FRF amplitude at the peak frequency locations compared to the three previous cases.

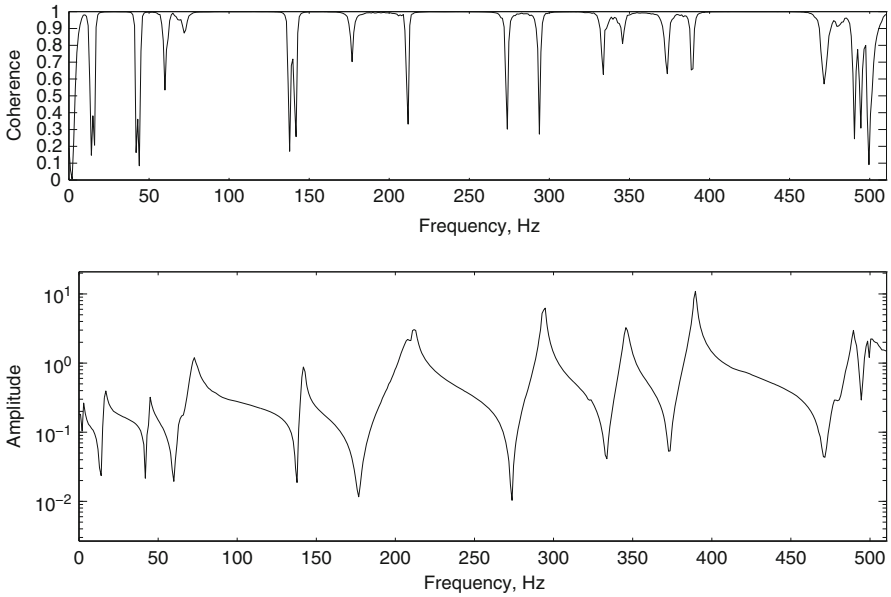

Fig. 26 Case II: asynchronous averaging with Hanning window

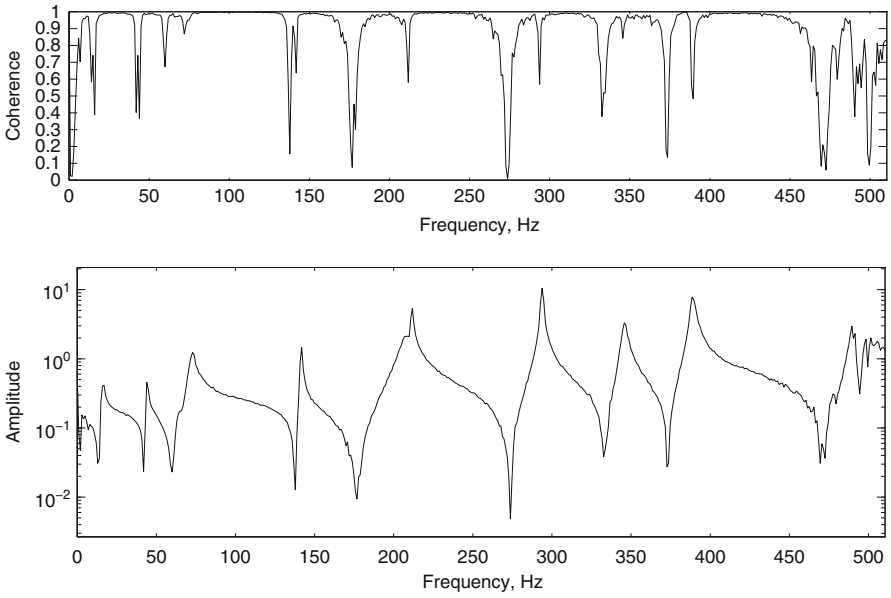

Fig. 27 Case III: cyclic averaging

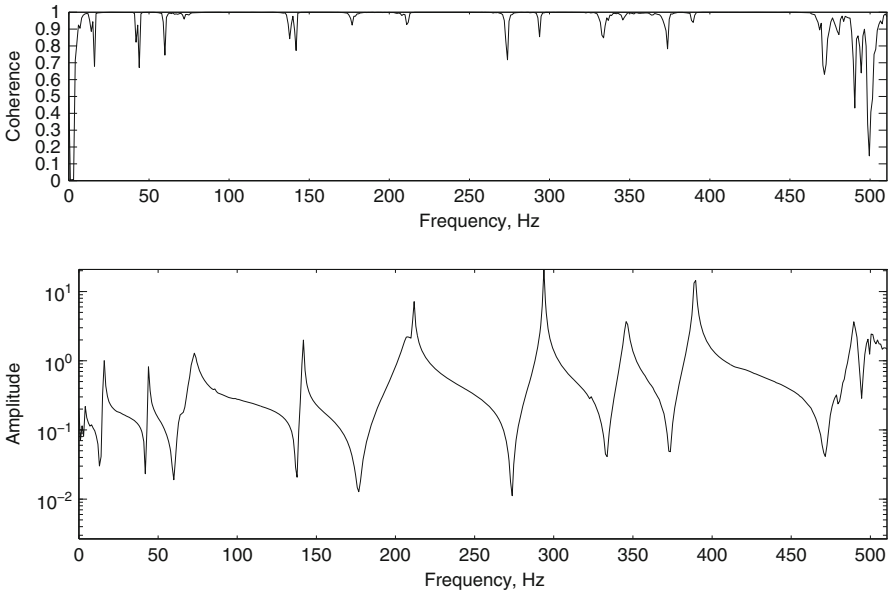

Fig. 28 Case IV: cyclic averaging with Hanning window

The value of N_c indicates the number of cyclic time records averaged together, and N_a is the number of asynchronous auto and cross spectrum averages: a total of N_c N_a time records were sampled. This is done so that, statistically, the same amount of independent information is available in each averaging case. *Note that in this example, the data for these cases was acquired only once. Each case results from processing the original time data differently.*

Clearly, the measurement using cyclic averaging with the Hanning window (Fig. 28) shows a significant reduction of the bias error. An interesting point is that the data near the antiresonance is also drastically improved due to the sharp roll off of the line shape of the Hanning weighted averaging.

Cyclic averaging is a powerful digital signal processing tool that minimizes the leakage error when FRF measurements are being estimated. While existing discrete Fourier analyzers may not be able to include cyclic averaging for the FRF estimation case, computer-based data acquisition common to personal computer or workstation systems generally permits the user to apply cyclic averaging together with asynchronous or synchronous averaging to effectively minimize both random errors and the leakage bias error.

4.3 Special Types of Signal Averaging

There are at least two common averaging techniques that use histories which may or may not overlap. In both cases, the averaging techniques involve processing random data histories in order to enhance the data.

4.3.1 Overlap Processing

The first case is that of overlap processing. Overlap processing involves using individual sample histories which are not totally independent from one another. The dependence that occurs results from each successive history starting before the previous history ends. For the general case where the time data is not weighted in any fashion, it should be obvious that this averaging procedure does not involve any new data and, therefore, statistically does not improve the estimation process. In the special case where weighting functions are involved, this technique can utilize data that is otherwise ignored. Figure 29a is an example of a data record that has been weighted to reduce the leakage error using a Hanning weighting function. The data prior to 20 percent of each sample period and after 80 percent of each sample period

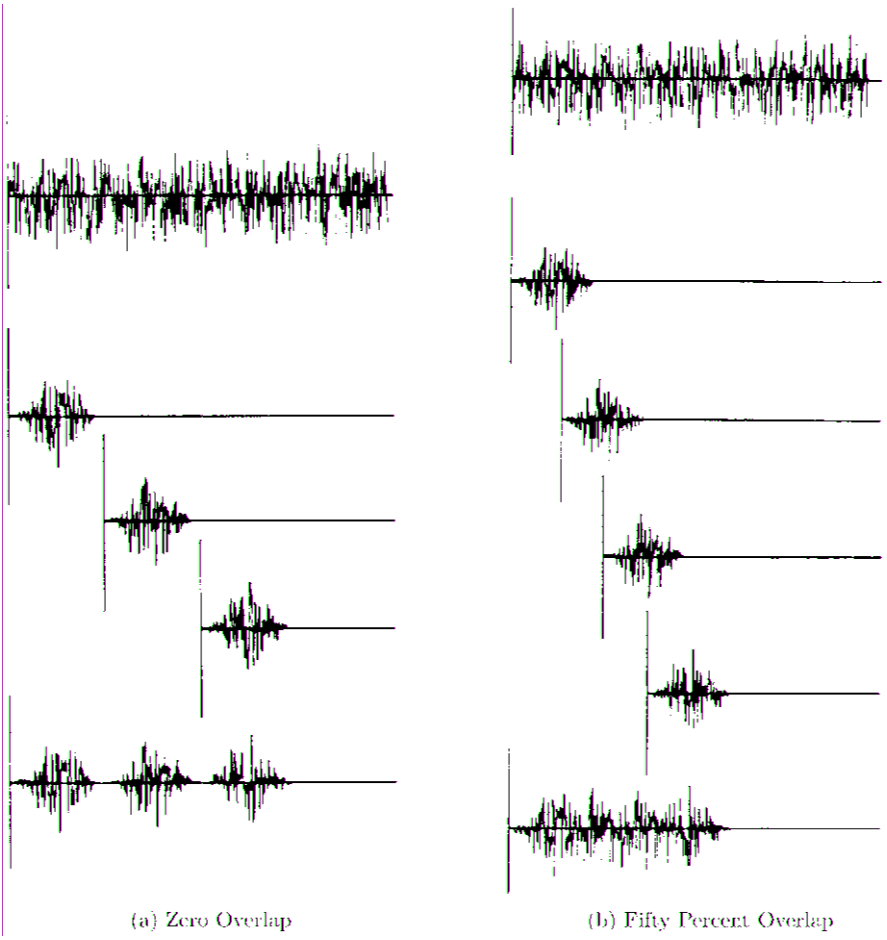

Fig. 29 Overlap processing. (**a**) Zero overlap. (**b**) Fifty percent overlap

is nearly eliminated by the Hanning window used. Using an overlap factor of at least 20–30 percent as in Fig. 29b involves this data once again in the averaging process.

The second case involving overlapping histories is that of random decrement analysis [31, 33, 29, 32, 34]. This process involves the overlapping of histories in order to enhance the deterministic portion of the random record. In general, the random response data can be considered to be made up of two parts: a deterministic part and a random part. Averaging in the time domain, the random part can be reduced if a trigger signal with respect to the information of interest exists. In the previous discussions, this trigger signal has been a function of the input (asynchronous or synchronous averaging) or of the sampling frequency (cyclic averaging). More generally, though, the trigger function can be any function with characteristics related to the response history. Specifically, then, the random decrement technique utilizes the assumption that the deterministic part of the random response signal itself contains free decay step and impulse response functions and can be used as the trigger function. Therefore, by starting each history at a specific value and slope of the random response function, characteristics related to the deterministic portion of the history will be enhanced.

4.3.2 Random Decrement

There are three specific cases of random decrement averaging that represent the limiting results of its use. The first case occurs when each starting value is chosen when the random response history reaches a specific constant level with alternating slopes for each successive starting value. The random decrement history for this case becomes the free decay step response function. An example of this case for the first few averages is shown in Fig. 30.

The second case occurs when each starting value is chosen when the random response history crosses the zero axis with positive slope. The random decrement history for this case becomes the free decay positive impulse response function.

The third case occurs when each starting value is chosen when the random response history crosses zero with negative slope. The random decrement history for this case becomes the free decay negative impulse response function.

Therefore, in each of these cases, the random decrement technique acts like a notched digital filter with pass bands at the poles of the trigger function. This tends to eliminate spectral components not coherent with the trigger function.

If a secondary function is utilized as the trigger function, only the history related to the poles of the secondary function will be enhanced by this technique. If the trigger function is sinusoidal, the random decrement history will contain information related only to that sinusoid. Likewise, if the trigger function is white noise, the random decrement history will be a unit impulse function at time zero. One useful example of this concept was investigated for conditioning random response histories so that information unrelated to the theoretical input history is removed. In this situation, the theoretical input history serves as the trigger function. The random decrement history formed on the basis of this trigger function represents the random response function that would be formed if the theoretical input history were truly the system input.

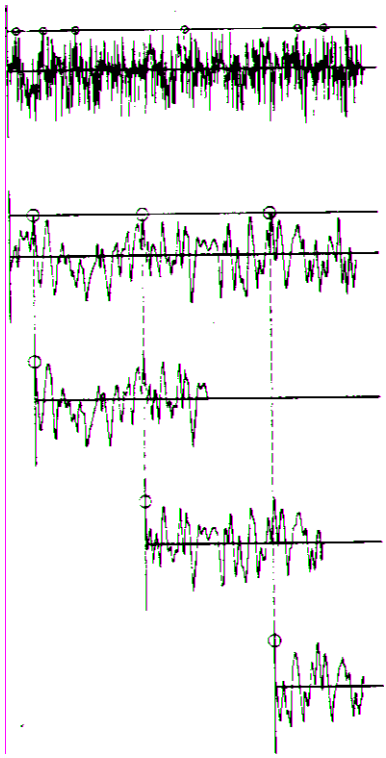

Fig. 30 Random decrement averaging

In reality, the measured input history may vary due to noise, impedance mismatch, and many other factors. However, the success of the technique is highly dependent upon the identification of the precise trigger timing. The default uncertainty of $\pm\Delta T$ in the timing of the actual trigger event means that the procedure will take a very long time to converge, if at all. Thus, it is necessary to over sample the data by a factor of 10X to 100X and then down sample to the desired sampling rate, in order to make sure that the start of each average (ensemble) is more precise and allow for more rapid convergence.

5 Excitation

Excitation includes any form of input that is used to create a response in a mechanical system. This can include environmental or operational inputs as well as the controlled force input(s) that are used in a vibration or modal analysis test. In general, the following discussion will be limited to the force inputs that can be measured and/or controlled in some rigorous way. With respect to frequency response function measurements to be used in experimental modal analysis, the excitation normally is applied using shakers or with impact devices (hammers). For

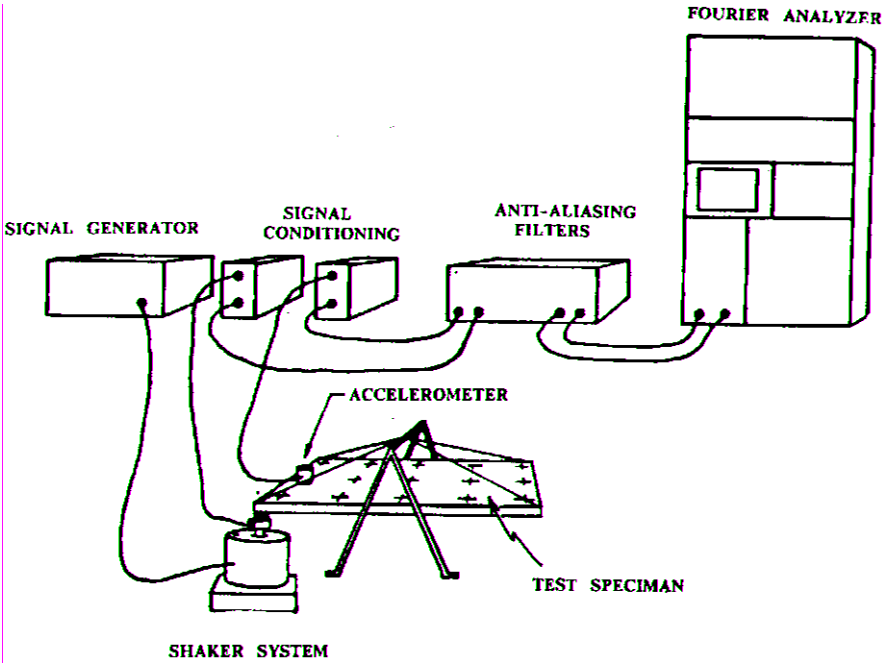

Fig. 31 Typical test configuration: shaker

those excitation signals that require the use of a shaker, Fig. 31 shows a typical test configuration, while Fig. 32 shows a typical test configuration when an impact form of excitation is to be used.

Single and multiple input estimation of frequency response functions (FRFs) via shaker excitation has become the mainstay of most mechanical structure measurements, particularly in the automotive and aircraft industries. While there are appropriate occasions for the use of deterministic excitation signals (sinusoids), the majority of these measurements are made using broadband (random) excitation signals. These signals work well for moderate to heavily damped mechanical structures which exhibit linear characteristics. When the mechanical structures are very lightly damped, care must be taken to minimize the leakage error so that accurate frequency response function (FRF) data can be estimated in the vicinity of the modal frequencies of the system. Frequently, when random excitation methods are compared to deterministic methods (sinusoids), the comparisons are questionable since proper procedures for eliminating the leakage error have not been followed.

Historically, a number of random excitation signals have been utilized, together with appropriate digital signal processing techniques [1, 2, 3, 35, 38], to obtain accurate FRF data. The most common random signal that is used in this situation is the pure random signal together with a Hanning window. This signal is normally

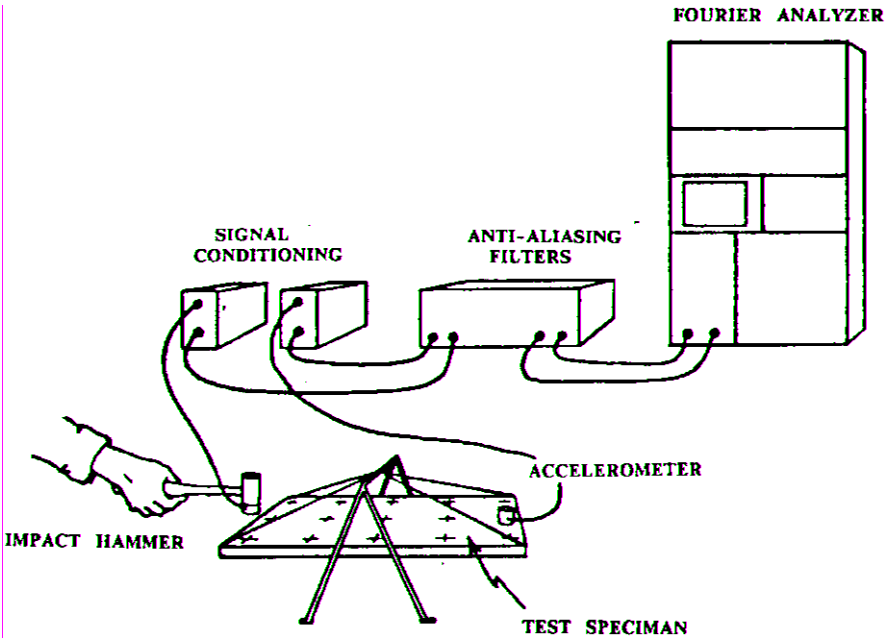

Fig. 32 Typical test configuration: impact hammer

generated by the data acquisition system utilizing built-in random signal generator(s) or via external random signal generator(s). While this approach does not eliminate the source of leakage and the effect of applying the Hanning window must be considered, this approach is normally considered as a baseline random excitation method for estimating FRF measurements since this method is available with almost any data acquisition system.

Other forms of random signals (pseudorandom, periodic random, burst random, etc.) utilize more control or frequency shaping of the excitation signal(s) and generally require digital-to-analog (DAC) converter(s). For this reason, some of these alternate methods are infrequently available and therefore not used. This is unfortunate since these methods often yield a superior FRF measurement in less total testing time.

When FRFs are measured on lightly damped systems, great care must be taken to eliminate the leakage error. Regardless of the type of excitation signal hardware involved (random signal generator or DAC), there are random excitation methods that can nearly eliminate the leakage error. In some cases, one approach will be superior on the basis of minimizing the total test time, but on the basis of accurate, leakage-free FRFs, one of the methods will always work if test time can be sacrificed. Note that these alternate forms of random excitation focus on eliminating the source of leakage by customizing the random signal to match the requirements of fast Fourier transform (FFT) that is used in converting from the

time to frequency domain. The FFT requires that the time domain signal must either be totally observed in the observation period (T) or be periodic in the observation period (T). For leakage-free FRF measurements, all of the input and output signals must match one of these two requirements. Burst random excitation is an attempt to match the first requirement; pseudorandom and periodic random excitations are attempts to match the second requirement.

5.1 Excitation Assumptions

The primary assumption concerning the excitation of a linear structure is that the excitation is observable. Whenever the excitation is measured, this assumption simply implies that the measured characteristic properly describes the actual input characteristics. For the case of multiple inputs, the different inputs must often be uncorrelated for the computational procedures to yield a solution. In most cases, this means only that the multiple inputs must not be perfectly correlated at any frequency. As long as the excitation is measured, the validity of these limited assumptions can be evaluated.

Currently, there are a number of techniques that can be used to estimate modal characteristics from response measurements with no measurement of the excitation. If this approach is used, the excitation assumptions are much more imposing. Obviously, if the excitation is not measured, estimates of modal scaling (modal mass, modal A, residues, etc.) cannot be generated. Even under the assumption that the estimation of these parameters is not required, all of these techniques have one further restriction: an assumption has to be made concerning the characteristics of the excitation of the system. Usually, one assumes that the autospectrum of the excitation signal is sufficiently smooth over the frequency interval of interest.

In particular, the following assumptions about the excitation signal can be used:

- The excitation is impulsive. The autospectrum of a short pulse (time duration much smaller than the period of the greatest frequency of interest) is nearly uniform, or constant in amplitude, and largely independent of the shape of the pulse.
- The excitation is white noise. White noise has an autospectrum that is uniform over the bandwidth of the signal.
- The excitation signal is a step. A step signal has an autospectrum that decreases in amplitude in proportion to the reciprocal of frequency. The step signal can be viewed as the integral of an impulsive signal.
- There is no excitation. This is called the free response or free decay situation. The structure is excited to a condition of nonzero displacement, or nonzero velocity, or both. Then the excitation is removed, and the response is measured during free decay. This kind of response can be modeled as the response of the structure to an excitation signal that is a linear combination of impulsive and step signals.

When the excitation autospectrum is uniform, the autospectrum of the response signal is proportional to the square of the modulus of the frequency response function. Using the notation of a pole-zero model, the poles of the response spectrum are the poles of the frequency response, which are the parameters of the system resonances. If the autospectrum is not uniform, then the excitation spectrum can be modeled as an analytic function to a precision comparable to typical experimental error in the measurement of spectra. In this model, the excitation spectrum has poles that account for the nonuniformity of the spectrum amplitude. The response signal, therefore, can be modeled by a spectrum that contains zeros at the zeros of the excitation and the zeros of the frequency response and contains poles at the poles of the excitation and at the poles of the frequency response. It is obviously important that the force spectrum should have no poles or zeros which coincide with poles of the frequency response.

For transient inputs, such as an impact or step relaxation, the assumption of smooth excitation spectra is generally true, but for operating inputs or inputs generated by an exciter system, care must be taken to insure the input force spectrum is smooth. This is especially true for tests performed using a hydraulic or an electromechanical exciter, because the system being analyzed may *load* the exciter system (the structure's impedance is so low that the desired force level cannot be achieved within the constraint of small motion), and this causes a nonuniformity in the input force spectrum.

To determine the characteristics of the system from the response, it is necessary that the response have the same poles as the frequency response or that the analysis process corrects for the zeros and poles of the excitation. If the force input spectrum has a zero in the frequency range of interest, the pole location measured from the response spectrum will not match that of the frequency response. This potential problem is demonstrated in Fig. 33 for the typical case of shaker excitation. The top figure is the magnitude of the frequency response function. The middle figure is the auto power spectrum of the input, and the lower figure is the auto power spectrum of the response. Note that the estimates of modal parameters that would be derived from the auto power spectrum of the response would be quite different from those derived from the frequency response function.

Presently, there is a great deal of interest in determining modal parameters from measured response data taken on operating systems (e.g., turbulent flow over an airfoil, road inputs to automobiles, and environmental inputs to proposed large space structures). For these cases, care must be taken not to confuse poles that are system resonances with those that exist in the output spectrum due to unmeasured inputs.

In general, the poles of the response include those of the frequency response and of the input spectrum. Therefore, if the force is not measured, it is not possible without some prior knowledge about the input to determine if the poles of the response are truly system characteristics. If no poles or zeros exist in the force spectrum in the frequency range of interest, then any poles in the response in this range must be a result of the system characteristics. Obviously, when the excitation can be measured, it is prudent to do so.

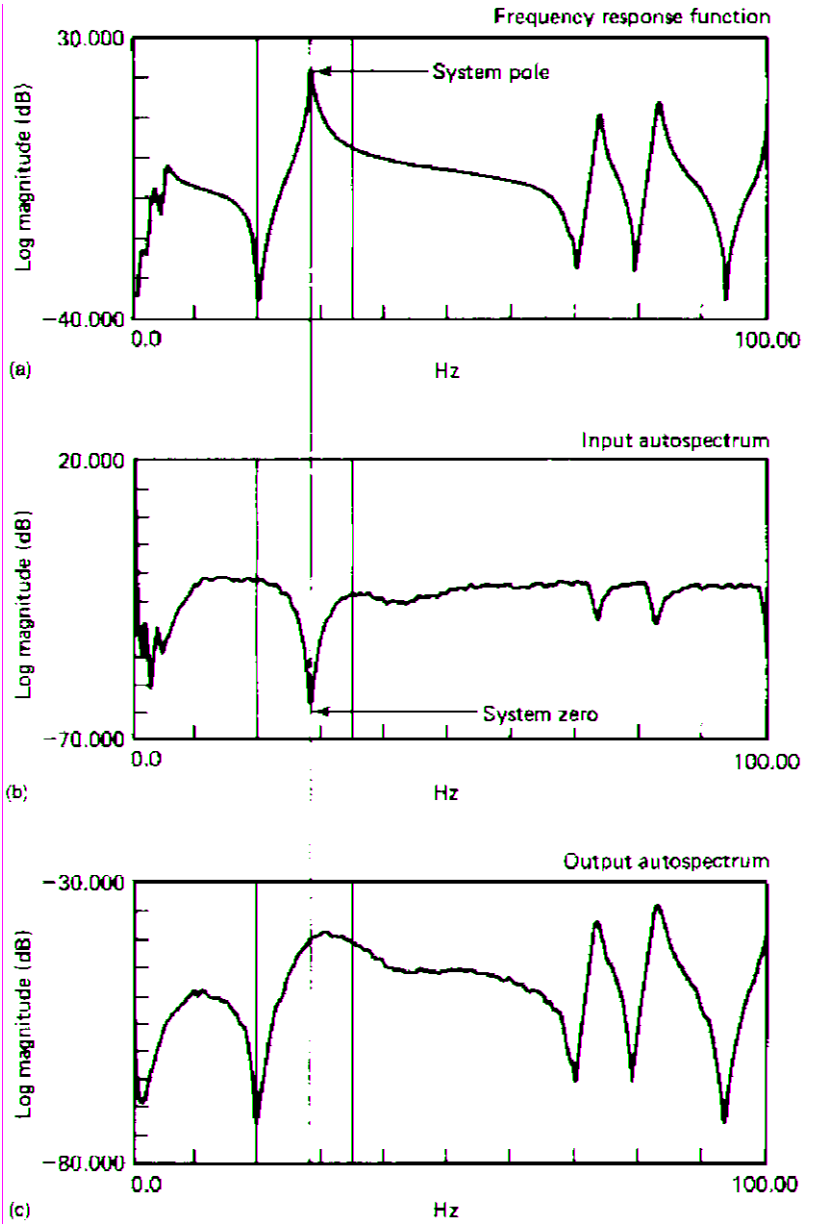

Fig. 33 Input spectrum example

5.2 Excitation Terminology and Nomenclature

Historically, a number of terminology and nomenclature issues have not been rigorously defined when excitation methods have been described.

The following terminology is important to the explanation of different excitation methods together with the associated digital signal processing requirements.

5.2.1 Signal Type

Signal type refers to the basic form of the signal, such as random, impact, sinusoidal, or chirp.

5.2.2 Frequency Shaping

Frequency shaping refers to any frequency domain constraint or characteristic that is applied to the specific signal type. With respect to random excitation, a common frequency shaping is pseudorandom. Other frequency shaping is commonly applied to sinusoids and chirps via the rate at which the change of frequency and/or amplitude occurs. Impact excitation is commonly frequency-shaped by controlling the tip characteristic of the hammer.

5.2.3 Contiguous Blocks

The number of contiguous blocks of excitation that takes place without the associated input and output data being acquired is referred to as the delay blocks (N_d). This is normally associated with an excitation technique that is periodic in nature. The delay blocks are needed in order to give the transient response to any start or change in the periodic excitation to decay out of the response signal(s) so that both the input(s) and output(s) are periodic with respect to any observation period (T). It is this requirement that makes swept sinusoidal excitation methods (analog swept or digitally stepped) so time-consuming, particularly on lightly damped systems. Each delay block is equal in length to the observation period (T), and the number of delay blocks is normally chosen as an integer. The number of delay blocks does not have to be an integer for all excitation methods but, for the purposes of this paper and in common usage, is normally chosen as an integer. The delay blocks are not recorded and are not used in the estimation of the FRFs.

5.2.4 Capture Blocks

The number of capture blocks refers to the number of contiguous blocks of time data (excitation (input) and response (output)) that are recorded or captured for each average (N_c). The number of capture blocks is also the number of cyclic averages that will be used to reduce the leakage error. Each group of contiguous capture blocks (N_c) is used as the time domain data contributing to one power spectral average that contributes to the estimate of the FRF measurements.

5.2.5 Window Function

The window function refers to the digital signal processing, time domain window that is applied to the capture blocks. The application of the window function to the capture blocks is on the basis of the group of contiguous capture blocks, not on each capture block.

5.2.6 Ensemble or Average

The term ensemble (or average) refers to the total collection of contiguous time blocks that contribute to each power spectral average. The total time of each ensemble is equal to the sum of the number of delay blocks (N_d) plus the number of capture blocks (N_c) times the observation period (T) which is the same for all delay and capture blocks. The number of averages (N_{avg}) refers to the number of these contiguous collections of time blocks and is, therefore, the same as the number of power spectral averages. The number of capture blocks can also be thought of as the number of cyclic averages (N_c). Cyclic signal averaging is often used with excitation characteristics in order to better match the time domain input and output signals to the requirements of the FFT prior to the application of the FFT. Cyclic signal averaging essentially digitally comb filters the time domain data to reduce the amount of information in the data that is not periodic with the observation period (T). This type of averaging reduces the effects of the leakage error. As long as the N_c successive blocks of data are contiguous, the blocks of time domain data can be averaged together, with or without windows, to achieve the benefit of leakage reduction [39,40].

5.2.7 Excitation Signal

If the excitation signal is repeated for each delay and capture block, the signal is referred to as periodic. This classification is consistent with the definition of a periodic function and includes typical examples of sinusoids and chirps as well as a random signal that is repeated on the basis of the observation period (T). The periodic classification does not define whether the same signal is repeated for each successive group of contiguous delay and capture blocks.

5.2.8 Burst Length

Burst length is the percentage (0% to 100%) of the average or ensemble time that the excitation signal is present. Burst length is normally adjusted in order to achieve a signal that is a totally observed transient. The decay of the signal is a function of the system damping and the characteristics of the excitation hardware. Burst length can be defined as the percentage of the total number of contiguous delay and capture blocks or of a percentage of just the capture blocks. For the purpose of this paper, the burst length refers to the percentage of the total number of contiguous delay and capture blocks.

5.2.9 Power Spectral Average

The number of power spectral averages (N_{avg} or N_a) is the number of auto and cross spectra that are averaged together to estimate the FRF measurements. The actual

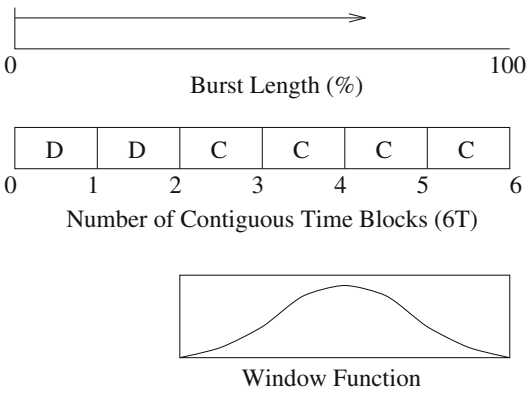

Fig. 34 Total contiguous time per power spectral average (ensemble)

amount of test time contributing to each power spectral average is a function of the number of contiguous delay and capture blocks. The purpose of power spectral averages is to eliminate the noise that is random with respect to the averaging procedure in order to reduce the variance on the resulting FRF estimate. This type of averaging does not reduce the effects of bias errors like the leakage error.

5.2.10 Excitation Terminology Illustration

In order to clarify the preceding terminology, Fig. 34 is a schematic representation of the number of contiguous blocks of time domain data contributing to one power spectral average. In this example, the two blocks marked *D* represent delay blocks, and the four blocks marked *C* represent capture blocks. The total time for each power spectral average is, therefore, six contiguous blocks of time data ($6 \times T$ seconds of data).

5.3 Classification of Excitation

Inputs that can be used to excite a system in order to determine frequency response functions (FRFs) belong to one of the two classifications, random or deterministic [4, 5, 7].

The first classification is that of a random signal. Signals of this form can only be defined by their statistical properties over some time period. Any subset of the total time period is unique, and no explicit mathematical relationship can be formulated to describe the signal. Random signals can be further classified as stationary or nonstationary. Stationary random signals are a special case where the statistical properties of the random signals do not vary with respect to translations with time. Finally, stationary random signals can be classified as ergodic or non-ergodic. A stationary random signal is ergodic when a time average on any particular subset of the signal is the same for any arbitrary subset of the random signal. All random signals which are commonly used as input signals fall into the category of ergodic, stationary random signals.

The second classification of inputs which can be used to excite a system in order to determine frequency response functions is that of a deterministic signal. Signals of this form can be represented in an explicit mathematical relationship. Deterministic signals are further divided into periodic and nonperiodic classifications. The most common inputs in the periodic deterministic signal designation are sinusoidal in nature, while the most common inputs in the nonperiodic deterministic designation are transient in form.

The choice of input to be used to excite a system in order to determine frequency response functions depends upon the characteristics of the system, upon the characteristics of the modal parameter estimation, and upon the expected utilization of the data. The characterization of the system is primarily concerned with the linearity of the system. As long as the system is linear, all input forms should give the same expected value. Naturally, though, all real systems have some degree of nonlinearity. Deterministic input signals result in frequency response functions that are dependent upon the signal level and type. A set of frequency response functions for different signal levels can be used to document the nonlinear characteristics of the system. Random input signals, in the presence of nonlinearities, result in a frequency response function that represents the best linear representation of the nonlinear characteristics for a given RMS level of random signal input. For systems with small nonlinearities, the use of a random input will not differ greatly from the use of a deterministic input.

The characterization of the modal parameter estimation is primarily concerned with the type of mathematical model being used to represent the frequency response function. Generally, the model is a linear summation based upon the modal parameters of the system. Unless the mathematical representation of all nonlinearities is known, the parameter estimation process cannot properly weight the frequency response function data to include nonlinear effects. For this reason, random input signals are prevalently used to obtain the best linear estimate of the frequency response function when a parameter estimation process using a linear model is to be utilized.

The expected utilization of the data is concerned with the degree of detailed information required by any post-processing task. For experimental modal analysis, this can range from implicit modal vectors needed for troubleshooting to explicit modal vectors used in an orthogonality check. As more detail is required, input signals, both random and deterministic, will need to match the system characteristics and parameter estimation characteristics more closely. In all possible uses of frequency response function data, the conflicting requirements of the need for accuracy, equipment availability, testing time, and testing cost will normally reduce the possible choices of input signal.

With respect to the reduction of the variance and bias errors of the frequency response function, random or deterministic signals can be utilized most effectively if the signals are periodic with respect to the sample period or totally observable with respect to the sample period. If either of these criteria are satisfied, regardless of signal type, the predominant bias error, leakage, will be minimized. If these criteria are not satisfied, the leakage error may become significant. In either case,

the variance error will be a function of the signal-to-noise ratio and the amount of averaging.

5.4 Random Excitation Methods

Random signals are widely utilized for general single input and multiple input shaker testing when evaluating structures that are essentially linear. Signals of this form can only be defined by their statistical properties over some time period. Any subset of the total time period is unique, and no explicit mathematical relationship can be formulated to describe the signal. Random signals can be further classified as stationary or nonstationary. Stationary random signals are a special case where the statistical properties of the random signals do not vary with respect to translations with time. Finally, stationary random signals can be classified as ergodic or non-ergodic. A stationary random signal is ergodic when a time average on any particular subset of the signal is the same for any arbitrary subset of the random signal. All random signals which are commonly used as input signals fall into the category of ergodic, stationary random signals.

Many signals are appropriate for use in experimental modal analysis. Some of the most commonly used random signals, used with single and multiple input shaker testing, are described in the following sections.

5.4.1 Pure Random Signal

The pure random signal is an ergodic, stationary random signal which has a Gaussian probability distribution. In general, the frequency content of the signal contains energy at all frequencies (not just integer multiples of the FFT frequency increment ($\Delta f = 1/T$)). This characteristic is shown in Fig. 35. This is undesirable since the frequency information between the FFT frequencies is the cause of the leakage error. The pure random signal may be filtered ($F_{\min}$ to $F_{\max}$) to include only information in a frequency band of interest. The measured input spectrum of the pure random signal, as with all random signals, will be altered by any impedance mismatch between the system and the exciter. The number of power spectral averages used in the pure random excitation approach is a function of the reduction of the variance error and the need to have a significant number of averages to be certain that all frequencies have been adequately excited.

5.4.2 Pseudorandom Signal

The pseudorandom signal is an ergodic, stationary random signal consisting of energy content only at integer multiples of the FFT frequency increment (Δf). The frequency spectrum of this signal is shaped to have a constant amplitude with random phase. This characteristic is shown in Fig. 36. If sufficient delay time is allowed in the measurement procedure for any transient response to the initiation of the signal to decay (number of delay blocks), the resultant input and output histories are periodic with respect to the sample period. The number of power spectral averages used in the pseudorandom excitation approach is a function of

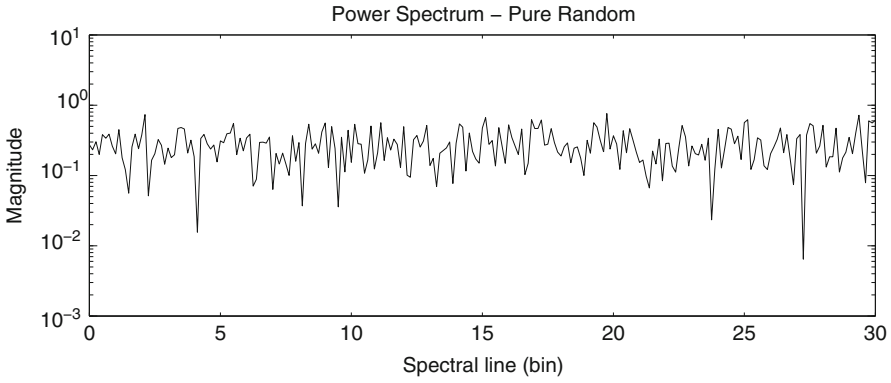

Fig. 35 Signal energy content – pure random

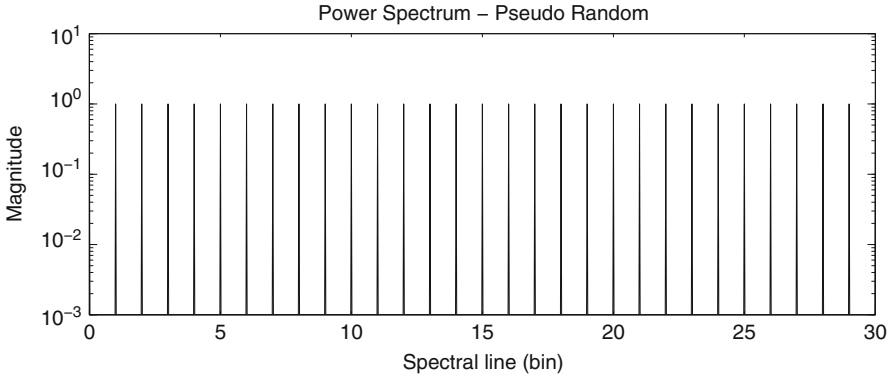

Fig. 36 Signal energy content – pseudorandom

the reduction of the variance error. In a noise-free environment, only one average (per input) may be necessary.

5.4.3 Periodic Random Signal

The periodic random signal is an ergodic, stationary random signal consisting only of integer multiples of the FFT frequency increment. The frequency spectrum of this signal has random amplitude and random phase distribution. This characteristic is shown in Fig. 37. For each average, input signals are created with random amplitude and random phase. The system is excited with these inputs in a repetitive cycle until the transient response to the change in excitation signal decays (number of delay blocks). The input and response histories should then be periodic with respect to the observation time (T) and are recorded as one power spectral average in the total process. With each new average, a new history, random with respect to previous input signals, is generated so that the resulting measurement will be completely randomized. The number of power spectral averages used in the periodic random

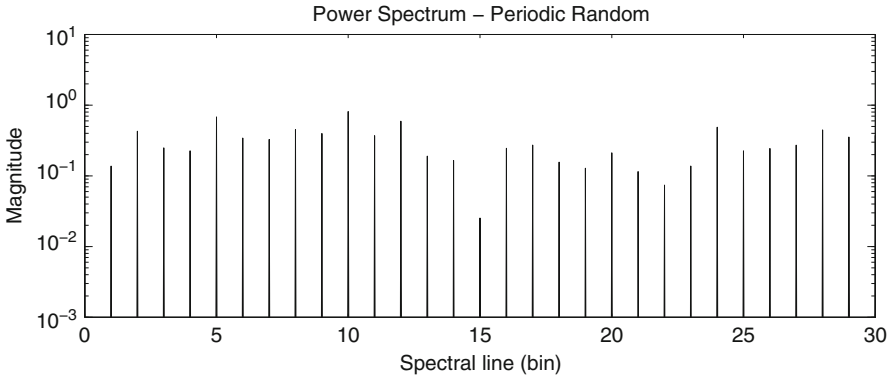

Fig. 37 Signal energy content – periodic random

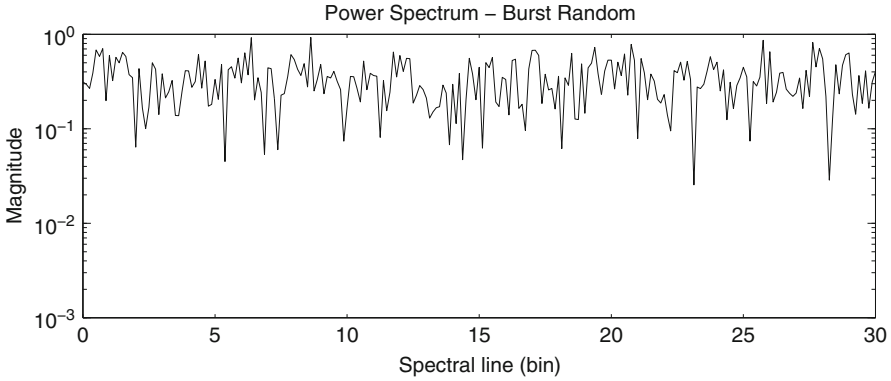

Fig. 38 Signal energy content – burst random

excitation approach is a function of the reduction of the variance error and the need to have a significant number of averages to be certain that all frequencies have been adequately excited.

5.4.4 Burst Random Signal

The burst random signal is neither a completely transient deterministic signal nor a completely ergodic, stationary random signal but contains properties of both signal types. The frequency spectrum of this signal has random amplitude and random phase distribution and contains energy throughout the frequency spectrum. This characteristic is shown in Fig. 38. The difference between this signal and the random signal is that the random transient history is truncated to zero after some percentage of the observation time (T). Normally, an acceptable percentage is 50–80 percent. The measurement procedure duplicates the random procedure but without the need to utilize a window to reduce the leakage problem as long as both the input and output decay to zero in the observation time (T).

The burst length (0–100%) is chosen so that the response history decays to zero within the observation time (T). For moderate to heavily damped systems, the response history will decay to zero very quickly due to the damping provided by the system being tested. These systems do not cause a leakage error in the first place.

For lightly damped cases, burst random will force the response to decay to zero in the observation time (T) primarily due to the exciter system characteristics. Exciter systems, particularly electromagnetic, attempt to match the excitation signal to some physical characteristic of the exciter. Typically, this means that the displacement, velocity, or acceleration of the armature of the shaker will attempt to match the excitation signal. (Note that this is normally an open-loop control process; no attempt is made to exactly match the excitation signal.) Electromagnetic shaker systems work either in a voltage or current feedback configuration in order to control the shaker according to the desired input signal. *Voltage feedback* refers to the type of amplifier in the exciter system that attempt to match the voltage supplied to the shaker to the excitation signal. This effectively means that the displacement of the armature will follow the excitation signal. Therefore, if a zero voltage signal is sent to the exciter system, the exciter will attempt to prevent the armature from moving. This damping force, provided by the exciter/amplifier system, is often overlooked in the analysis of the characteristics of this signal type. Since this measured input, although not part of the generated signal, includes the variation of the input during the decay of the response history, the input and response histories are totally observable within the sample period, and the system damping that will be computed from the measured FRF data is unaffected. *Current feedback* refers to the type of amplifier in the exciter system that attempts to match the current supplied to the shaker to the excitation signal. This effectively means that the acceleration of the armature will follow the excitation signal. Therefore, if a zero voltage signal is sent to the exciter system, the exciter will allow the armature to move, preventing any force to be applied by the exciter system. The characteristic of a voltage feedback exciter system for a burst random excitation is shown in the following figures. Note the difference between the desired burst random signal and the actual force measured (Figs. 39, 40, and 41).

For very lightly damped systems, the burst length may have to be shortened below 20 percent. This may yield an unacceptable signal-to-noise ratio (SNR). The number of power spectral averages used in the burst random excitation approach is a function of the reduction of the variance error and the need to have a significant number of averages to be certain that all frequencies have been adequately excited plus the exciter/amplifier system trying to maintain the input at zero (voltage feedback amplifier in the excitation system).

5.4.5 Slow Random Signal

The slow random signal is an ergodic, stationary random signal consisting only of integer multiples of the FFT frequency increment. This signal behaves just like the pseudorandom signal but without the frequency shaping of the amplitude. The slow random signal is generated by cyclic averaging a random signal in order to produce digitally comb filtered excitation signal(s) with the proper characteristics.

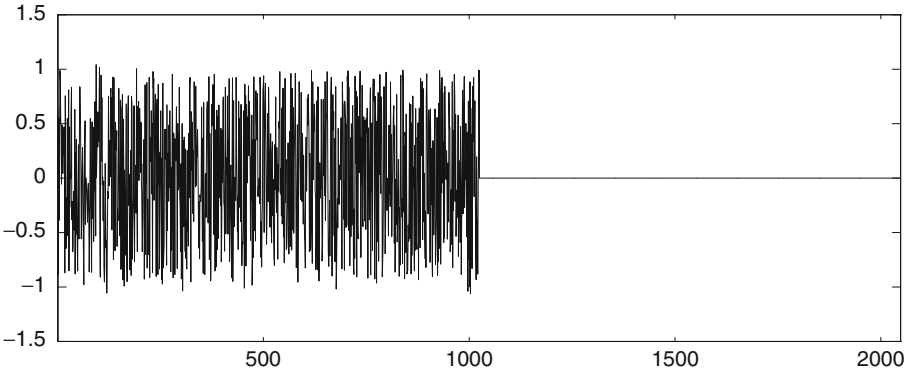

Fig. 39 Burst random – signal to shaker

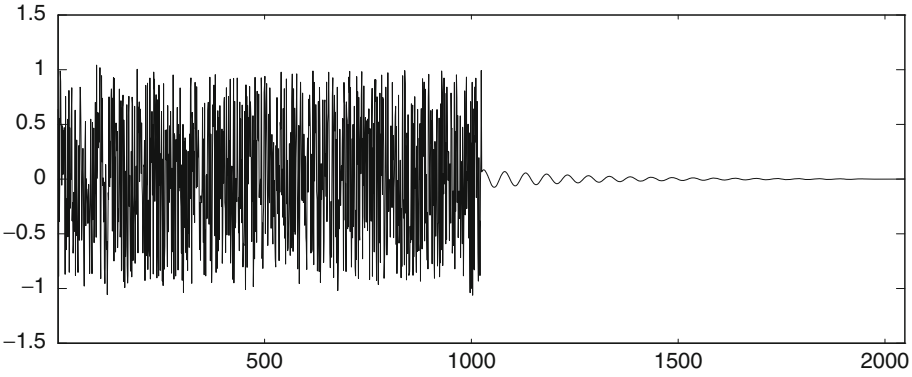

Fig. 40 Burst random – signal from load cell (voltage feedback)

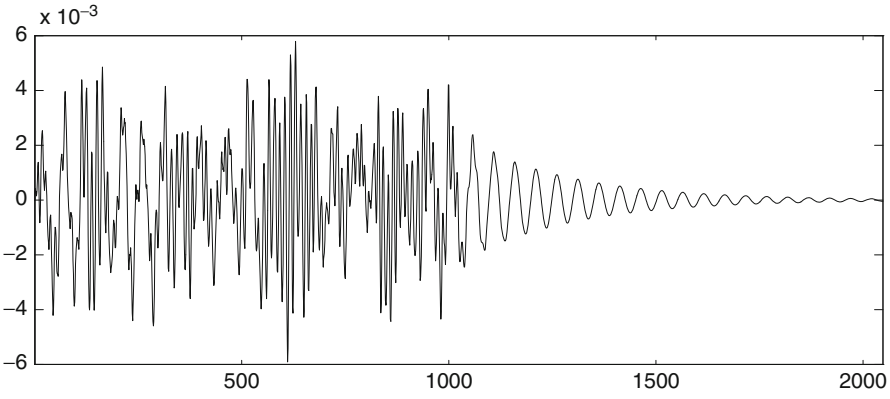

Fig. 41 Burst random – signal from accelerometer

5.4.6 MOOZ Random Signal

The MOOZ random signal is an ergodic, stationary random signal consisting only of integer multiples of the FFT frequency increment band limited to the frequency band of a ZOOM fast Fourier transform (FFT)($F_{\min}$ to $F_{\max}$). The MOOZ (ZOOM spelled backward) random signal requires synchronization between the data acquisition and the digital-to-analog converter (DAC). The MOOZ random signal is essentially a slow random excitation signal adjusted to accommodate the frequencies of a ZOOM FFT.

The relationships between delay blocks and averages for some of the most commonly used random excitation methods are shown in Fig. 42.

5.4.7 Hybrid Random Signal

Several random excitation methods have recently been demonstrated that are hybrid methods involving combinations of burst random and pseudorandom and burst random and periodic random together with cyclic averaging.

Figure 43 shows the energy content of a hybrid excitation method that combines pseudorandom with burst random. This excitation signal would be combined with cyclic averaging.

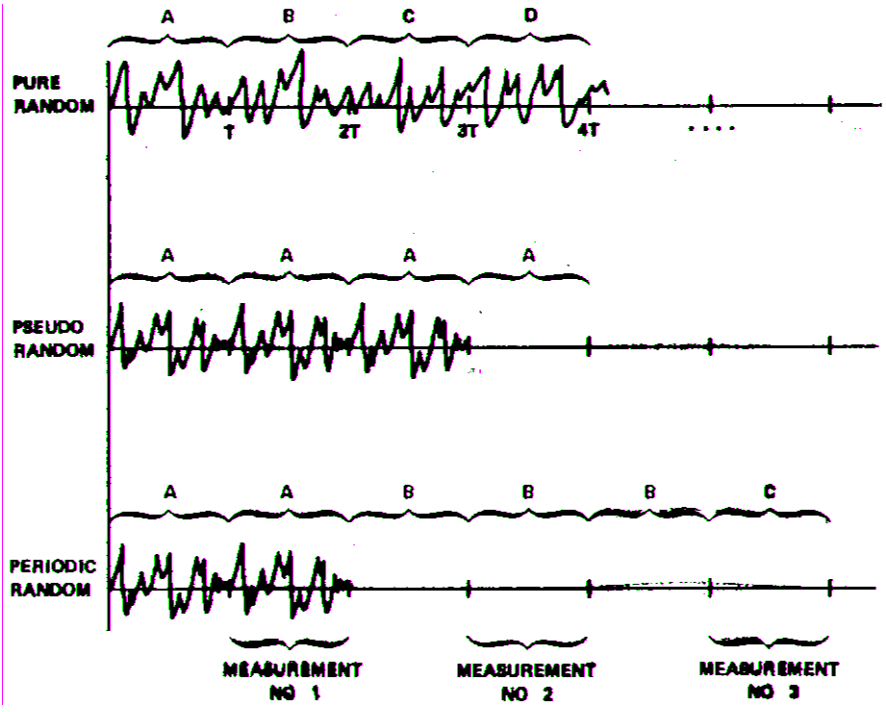

Fig. 42 Excitation characteristics

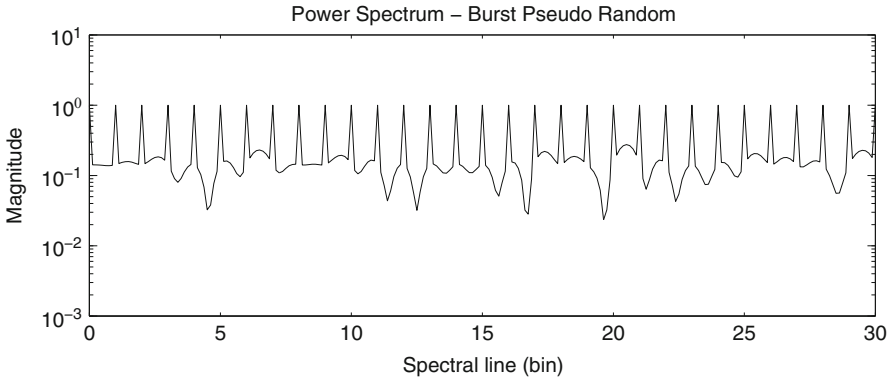

Fig. 43 Signal energy content – burst pseudorandom

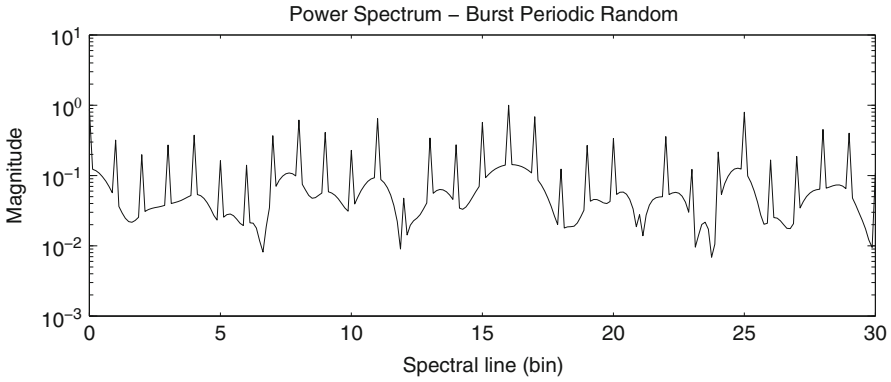

Fig. 44 Signal energy content – burst periodic random

Figure 44 shows the energy content of a hybrid excitation method that combines periodic random with burst random. This excitation signal would be combined with cyclic averaging.

5.5 Deterministic Excitation Methods

Deterministic signals can be characterized directly by mathematical formula, and the characteristic of the excitation signal can be computed for any instance in time. While this is true for the theoretical signal sent to the exciter, it is only approximately true for the actual excitation signal due to the amplifier/shaker/structure interaction that is a function of the impedances of these electromechanical systems. Deterministic signals can, nevertheless, be controlled more precisely and are frequently utilized in the characterization of nonlinear systems for this reason.

5.5.1 Slow Swept Sine Signal

The slow swept sine signal is a periodic deterministic signal with a frequency that is an integer multiple of the FFT frequency increment. Sufficient time is allowed in the measurement procedure for any transient response to the changes in frequency to decay so that the resultant input and response histories will be periodic with respect to the sample period. Therefore, the total time needed to compute an entire frequency response function will be a function of the number of frequency increments required and the system damping.

5.5.2 Periodic Chirp Signal

The periodic chirp is a deterministic signal where a sinusoid is rapidly swept from $F_{\min}$ to $F_{\max}$ within a single observation period (T). This signal is then repeated in a periodic fashion. While this signal is not random in characteristic, it is often included in discussions of random excitation since it has similar properties as pseudorandom (Figs. 45 and 46).

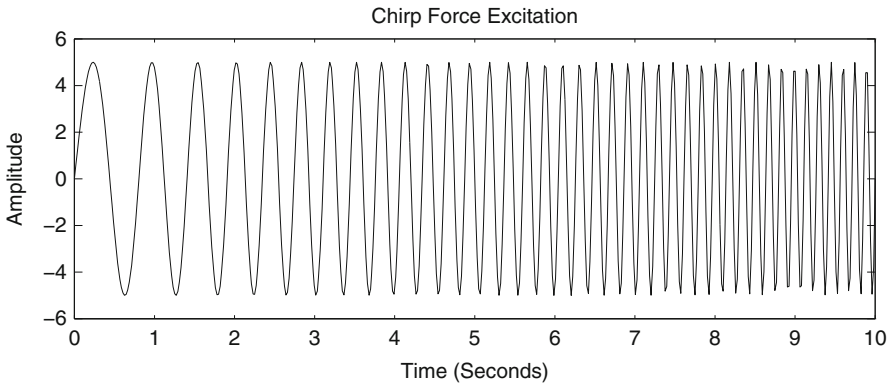

Fig. 45 Typical chirp signal – time domain

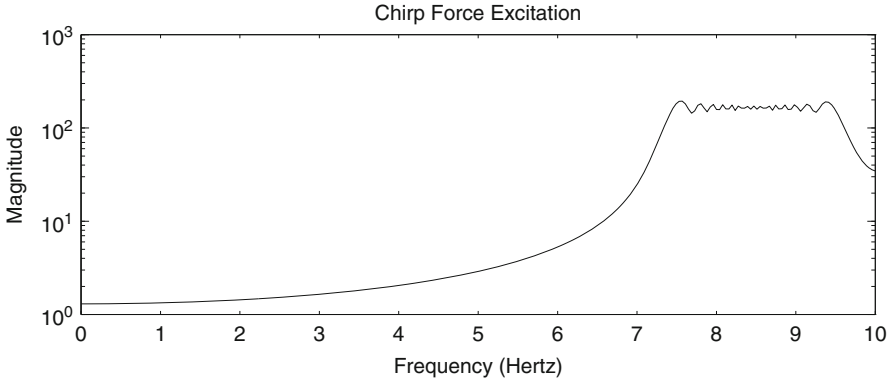

Fig. 46 Typical chirp signal – frequency domain

5.5.3 Impact Signal

The impact signal is a transient deterministic signal which is formed by applying an input pulse to a system lasting only a very small part of the sample period. The width, height, and shape of this pulse will determine the usable spectrum of the impact. Briefly, the width of the pulse will determine the frequency spectrum, while the height and shape of the pulse will control the level of the spectrum. Impact signals have proven to be quite popular due to the freedom of applying the input with some form of an instrumented hammer. While the concept is straightforward, the effective utilization of an impact signal is very involved [29,41,42].

Impact Testing

Impact testing is an attempt to match the input and output data to the requirement of the discrete or fast Fourier transform that the data be a totally observed transient in the observation time (T). While the impact is almost always totally observable, the response for lightly damped systems may not be. Special windows are often used for impact testing that accommodate the characteristics of the transient input and the response of the system to a transient input.

Impact excitation is widely used due to the minimal equipment required, portability and low cost of the impact devices, and broad applicability to both small-, medium-, and large-size structures. However, impact testing also suffers from limitations imposed by the human control of the impact. Repeatability and consistency of the impact (force and direction) cannot be guaranteed, particularly as the test becomes long and repetitious. Care must be taken to ensure that the impact and response are not too small and not too large (overload) and that there is only one impact per observation period.

When impact testing is used, windows are generally required on both the force and response data in order to minimize different errors. The force window is used to eliminate the signal coming from the impact device after the short-duration impact is over. This eliminates electrical noise and spurious output from the hammer during data acquisition that is caused by motion of the impact device that does not put force into the system. The response (exponential) window is used to force the response closer to zero by the end of the observation period (T) and should be used carefully. If the response is already near zero at time T, no response window should be added. To be theoretically correct and to allow for the effects of this response window to be accounted for, the decay rate of the exponential must be recorded, and the same window should also be applied to the input data, in addition to the force window.

Force Window

Force windows are used to improve the signal-to-noise problem caused by the noise on the input channel measured after the impact is completed. Note that the exponential window used on the response should also be applied to the input in addition to the force window (Fig. 47).

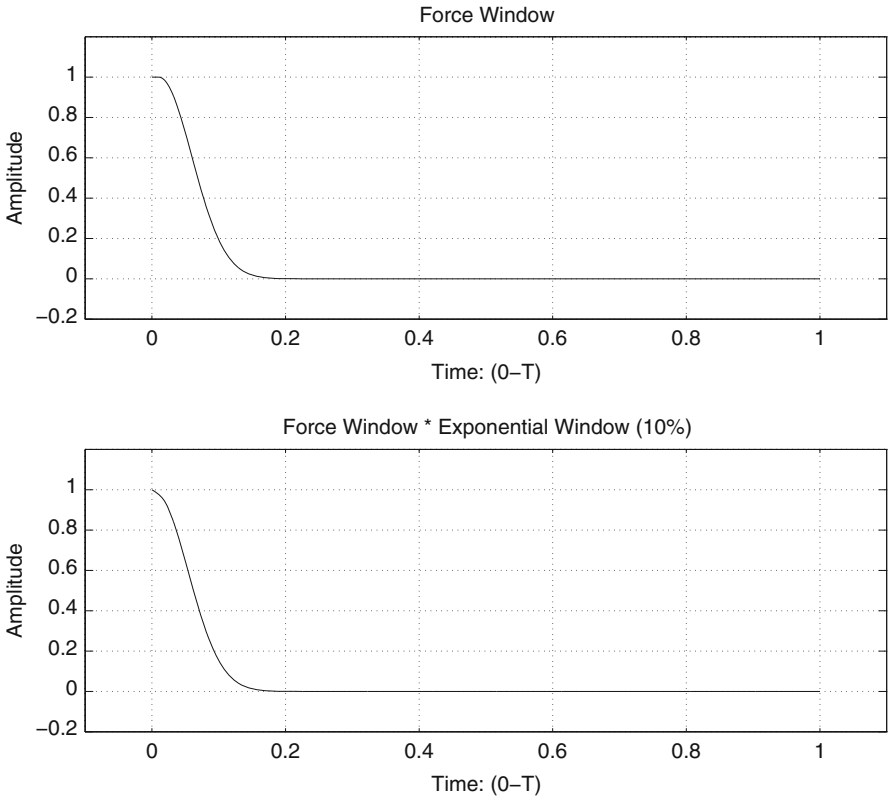

Fig. 47 Typical force windows

Response (Exponential) Window

Response (exponential) windows are used to minimize the leakage error for lightly damped systems by attenuating the response so that it decays to zero within the observation period. Normally, for lightly damped systems, a window that attenuates to 1–5 percent at the end of the response is appropriate. For heavily damped systems, a window that is similar to the decay of the system will attenuate any noise (Fig. 48).

Response (Exponential) Window Correction

The windows that are added to the force and response signals must be corrected. Primarily, the response (exponential) window may add significant damping to the resultant frequency response function. This can only be corrected after the modal damping for each mode is found:

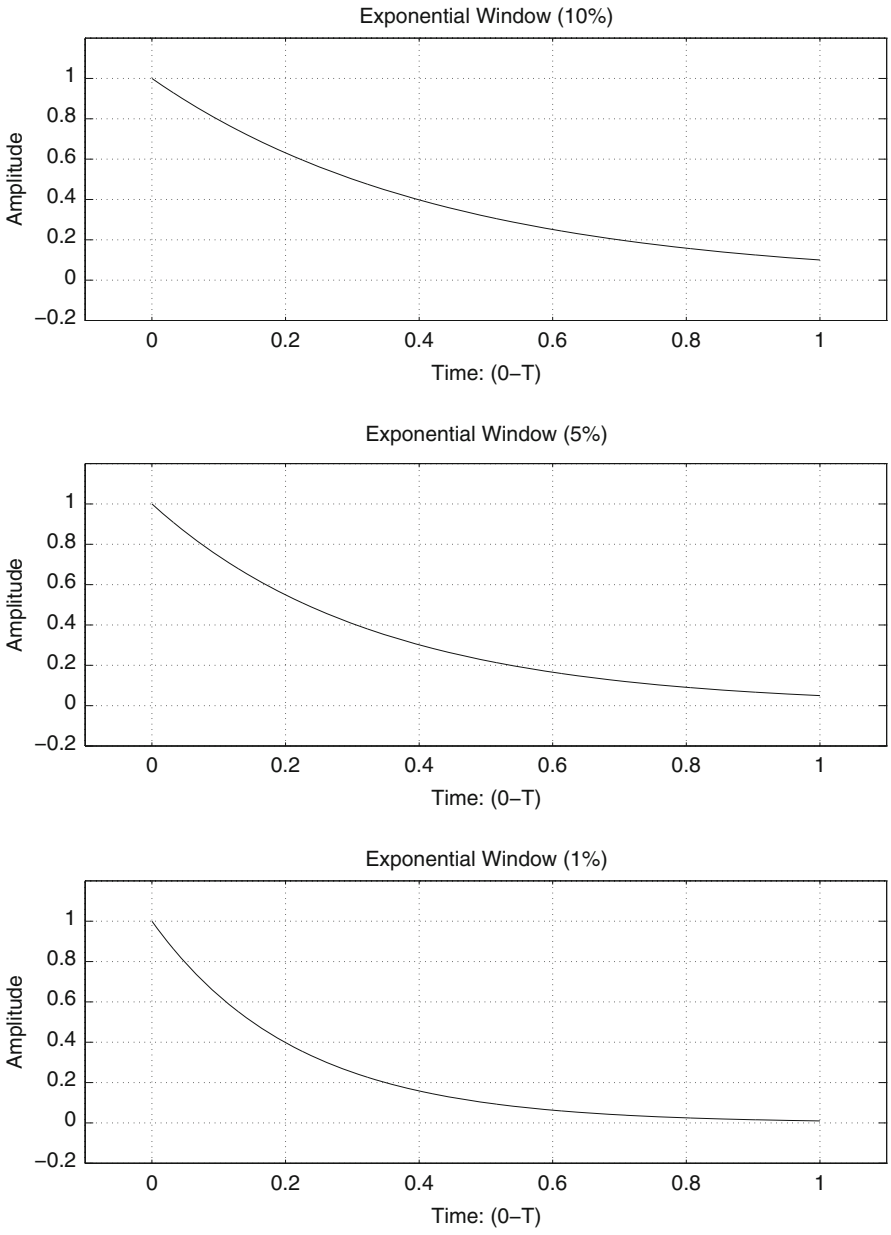

Fig. 48 Typical response windows

- $h_{pq}(t) = \sum_{r=1}^{2N} A_{pqr}\, e^{\lambda_r t}$
- $e^{\beta t} h_{pq}(t) = e^{\beta t} \sum_{r=1}^{2N} A_{pqr}\, e^{\lambda_r t}$
- $e^{\beta t} h_{pq}(t) = \sum_{r=1}^{2N} A_{pqr}\, e^{\beta t} e^{\lambda_r t}$
- $e^{\beta t} h_{pq}(t) = \sum_{r=1}^{2N} A_{pqr}\, e^{(\lambda_r + \beta) t} = \sum_{r=1}^{2N} A_{pqr}\, e^{\hat{\lambda}_r t}$
- $\hat{\lambda}_r = \hat{\sigma}_r + j\,\hat{\omega}_r = (\sigma_r + \beta) + j\,\omega_r$
- $\hat{\sigma}_r = \sigma_r + \beta$
- $\sigma_r = \hat{\sigma}_r - \beta$
- $\omega_r = \hat{\omega}_r$

5.5.4 Step Relaxation Signal

The step relaxation signal is a transient deterministic signal which is formed by releasing a previously applied static input. The sample period begins at the instant that the release occurs. This signal is normally generated by the application of a static force through a cable. The cable is then cut or allowed to release through a shear pin arrangement [43].

5.5.5 Summary of Excitation Signal Characteristics

Table 6 summarizes the advantages and disadvantages for the most commonly used excitation signals.

5.6 Excitation Example: H-Frame

The following example presents a single FRF measurement on an H-frame test structure in a test lab environment as a representative example. The configuration of the test involved two shaker locations (inputs) and eight response accelerometers (outputs). The test results are representative of all data taken on the H-frame structure. This H-frame test structure is very lightly damped and has been the subject of many previous studies. For all FRF measurement cases, the same test configuration was used. Sensors were installed and left in place; no additions or changes were made to the test configuration other than altering the excitation, averaging, and digital signal processing parameters. Therefore, any changes in the FRF measurements are assumed to be due to the change in measurement technique and not due to a test setup variation. The test results were repeated to be certain that the results are representative.

All FRF measurements are estimated using the H_1 estimation algorithm using 1024 spectral (frequency) lines of information. The frequency bandwidth is from 0 to 250 hertz for the 1024 spectral lines; only the first 80% of the spectral lines

Table 6 Summary of excitation signals

Excitation signal characteristics								
	Steady -state sine	Pure random	Pseudo random	Periodic random	Fast sine	Impact	Burst sine	Burst random
Minimize leakage	No	No	Yes	Yes	Yes	Yes	Yes	Yes
Signal-to-noise ratio	Very high	Fair	Fair	Fair	High	Low	High	Fair
RMS-to-peak ratio	High	Fair	Fair	Fair	High	Low	High	Fair
Test measurement time	Very long	Good	Very short	Fair	Fair	Very short	Very short	Very short
Controlled frequency content	Yes	Yes[a]	Yes[a]	Yes[a]	Yes[a]	No	Yes[a]	Yes[a]
Controlled amplitude content	Yes	No	Yes[a]	No	Yes[a]	No	Yes[a]	No
Removes distortion	No	Yes	No	Yes	No	No	No	Yes
Characterize nonlinearity	Yes	No	No	No	Yes	No	Yes	No

[a]Special hardware required

(0 to 200 Hertz) are displayed in order to exclude the data affected by the anti-aliasing filters.

The FRF data is plotted with phase above log magnitude. The log magnitude portion of the plot also contains the relevant multiple coherence plotted on a linear scale in the background. The log magnitude scaling is annotated on the left side of the plot, and the multiple coherence scaling is annotated on the right side of the plot.

Fourteen representative cases were measured on this structure. The relevant excitation and digital signal processing characteristics of each case are shown in Table 7.

Case 1 (Fig. 49) is considered a baseline case since this a very popular method for making an FRF measurement and it can be easily made on all data acquisition equipment. However, it is clear that in this measurement situation, there is a significant drop in the multiple coherence function at frequencies consistent with the peaks in the FRF measurement. This characteristic drop in multiple (or ordinary) coherence is often an indication of a leakage problem. This can be confirmed if a leakage reduction method reduces or eliminates the problem when the measurement is repeated. In all subsequent cases, the test configuration was not altered in any way – data was acquired simply using different excitation, averaging, and digital signal processing combinations.

Case 2 (Fig. 50) demonstrates an improvement over Case 1 when the same total measurement time is used, but cyclic averaging is used to reduce the leakage error. Case 3 (Fig. 51) further demonstrates that burst random with cyclic averaging

Table 7 Test cases – excitation/averaging/DSP parameters

Case	Signal type	Frequency shaping	Periodic function	Burst length	Window function	N_d	N_c	N_{avg}	Total blocks
Case 1	Random	No	No	No	Hanning	0	1	20	20
Case 2	Random	No	No	No	Hanning	0	5	4	20
Case 3	Random	No	No	Yes (75%)	Uniform	0	5	4	20
Case 4	Random	Pseudo	No	No	Uniform	4	1	4	20
Case 5	Random	No	Yes	No	Uniform	4	1	4	20
Case 6	Random	Pseudo	No	No	Uniform	3	1	5	20
Case 7	Random	No	Yes	No	Uniform	3	1	5	20
Case 8	Random	Pseudo	No	Yes (75%)	Uniform	0	5	4	20
Case 9	Random	No	Yes	Yes (75%)	Uniform	0	5	4	20
Case 10	Random	No	No	Yes (75%)	Uniform	0	8	12	20
Case 11	Random	No	No	No	Hanning	0	1	96	96
Case 12	Random	No	No	No	Hanning	0	8	12	96
Case 13	Random	Pseudo	No	No	Uniform	3	2	4	20
Case 14	Random	No	Yes	No	Uniform	3	2	4	20

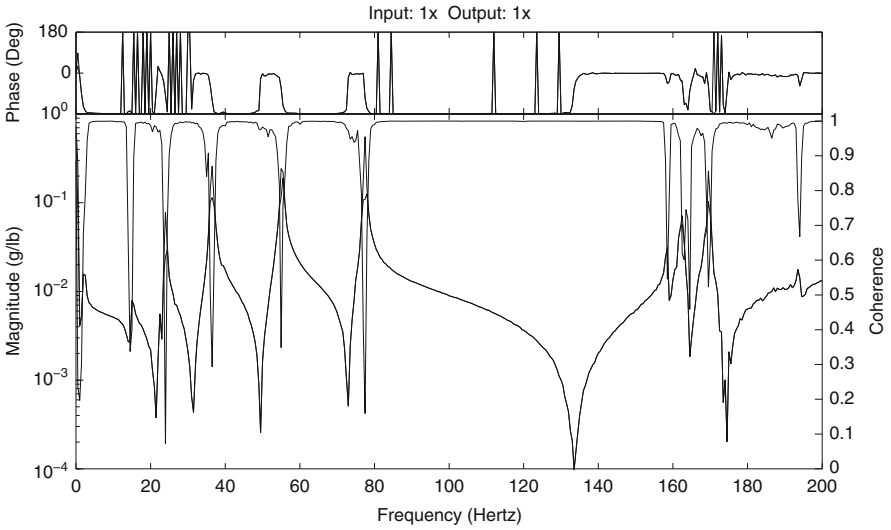

Fig. 49 Case 1: random excitation with Hanning window

improves the measurement further. Again the total measurement time remains the same.

Cases 4 through 7 (Figs. 52, 53, 54, and 55) demonstrate the quality of FRF measurements that can be achieved with pseudorandom and periodic random excitation methods with very few power spectral averages.

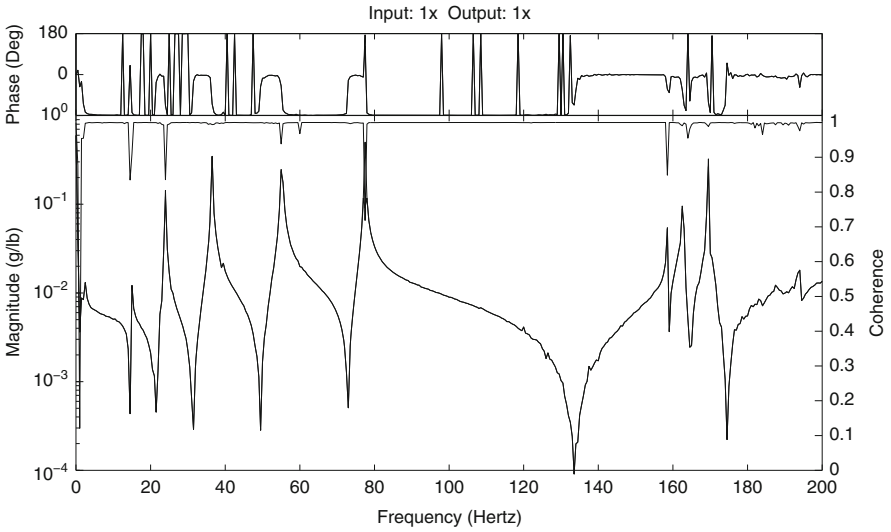

Fig. 50 Case 2: Random excitation with Hanning window and cyclic averaging

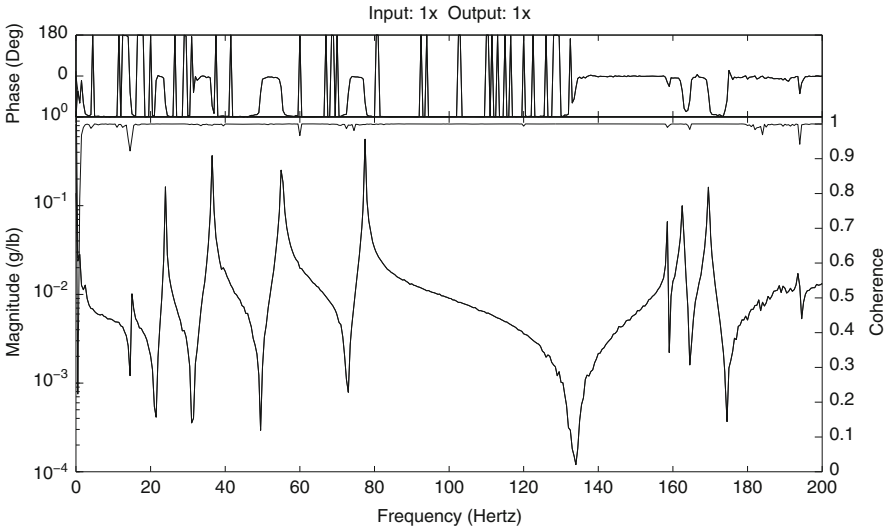

Fig. 51 Case 3: Burst random excitation with cyclic averaging

Cases 8 and 9 (Figs. 56 and 57) are hybrid techniques involving the combination of burst random with pseudorandom and periodic random excitation together with cyclic averaging.

Case 10 (Fig. 58) demonstrates that Case 3 can be marginally improved with more averages, both cyclic and power spectral averages. However, Case 11 (Fig. 59)

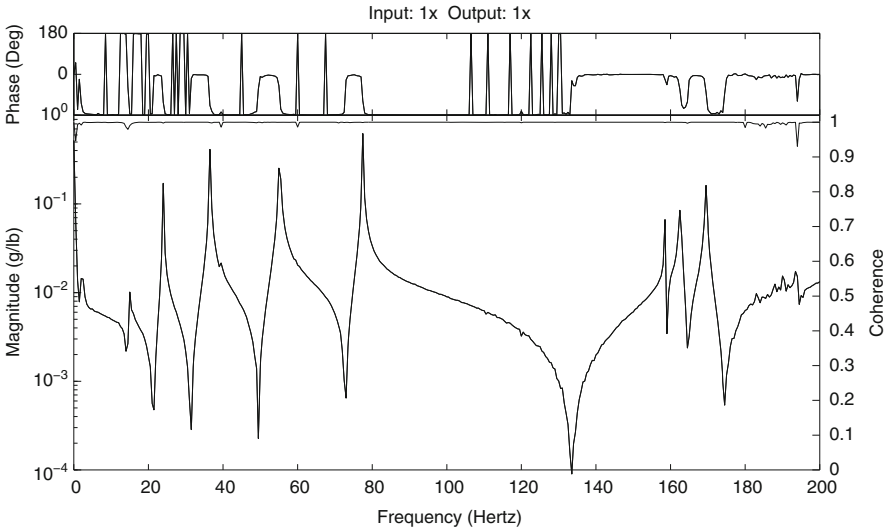

Fig. 52 Case 4: Pseudorandom excitation

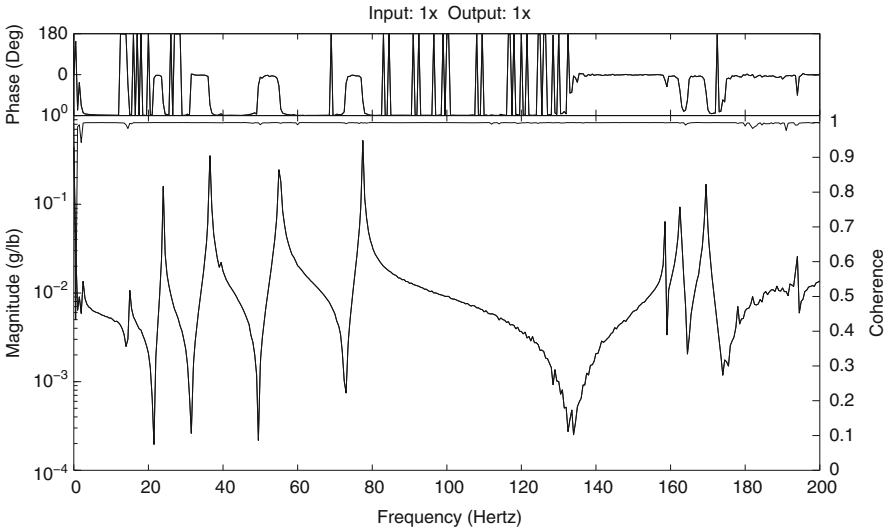

Fig. 53 Case 5: Periodic random excitation

demonstrates that Case 1 (random with Hanning window) cannot be improved by adding power spectral averages. This is a popular misconception that adding power spectral averages will improve the FRF estimate. This is clearly not true for this case.

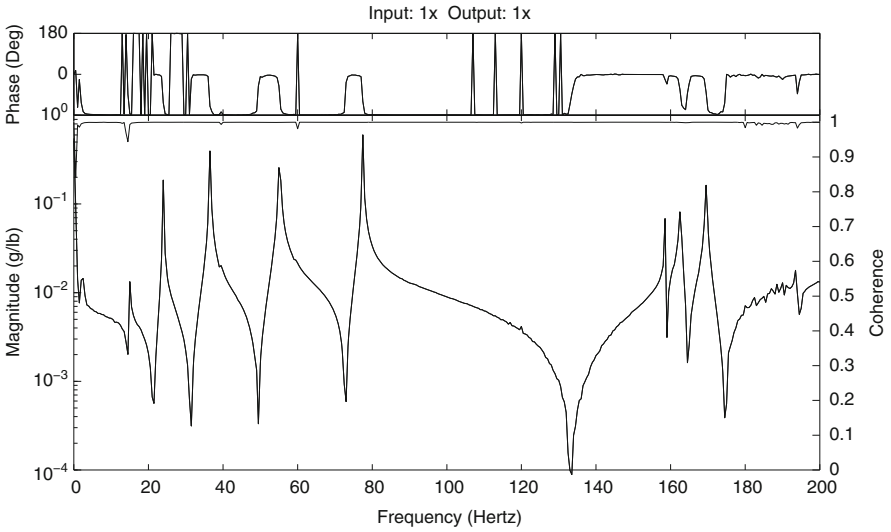

Fig. 54 Case 6: Pseudorandom excitation

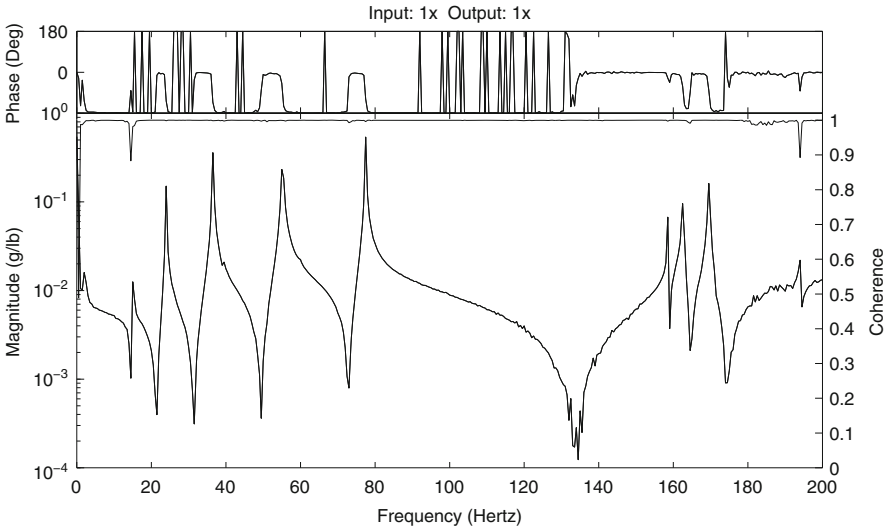

Fig. 55 Case 7: periodic random excitation

Case 12 (Fig. 60) demonstrates that additional cyclic averages, together with power spectral averages, are an improvement over Case 2, but the improvement is not significant considering the additional measurement time.

Finally, Cases 13 and 14 (Figs. 61 and 62) demonstrate that when pseudorandom and periodic random excitation is coupled with cyclic averaging, a nearly perfect

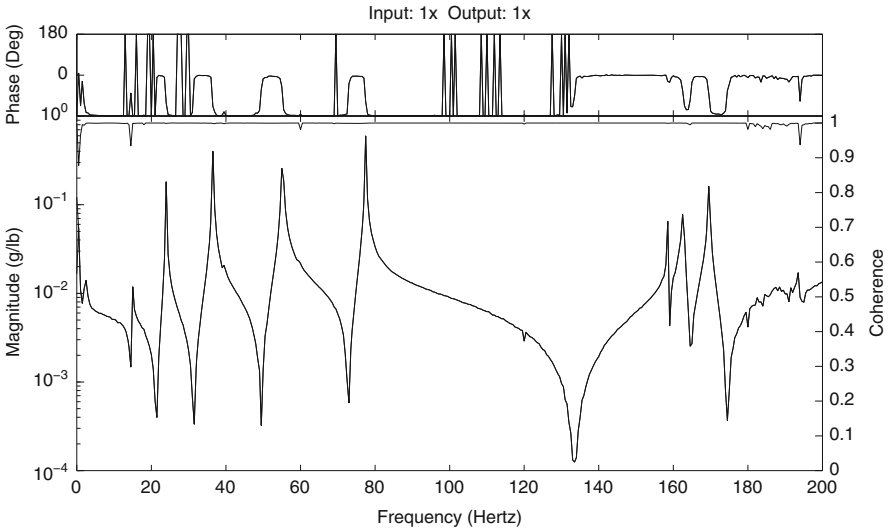

Fig. 56 Case 8: Burst pseudorandom excitation with cyclic averaging

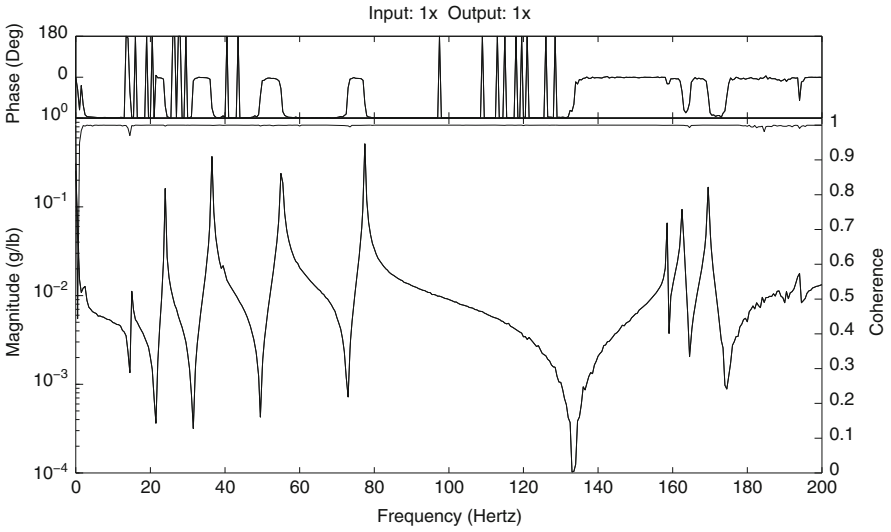

Fig. 57 Case 9: burst periodic random excitation with cyclic averaging

FRF measurement results. Note also that in almost every case where high-quality FRF measurements have been achieved, window functions are not required, so correction for the window characteristics is unnecessary.

It is clear that in many of the measurement cases, the multiple coherence can be improved dramatically using simple excitation, averaging, and digital signal

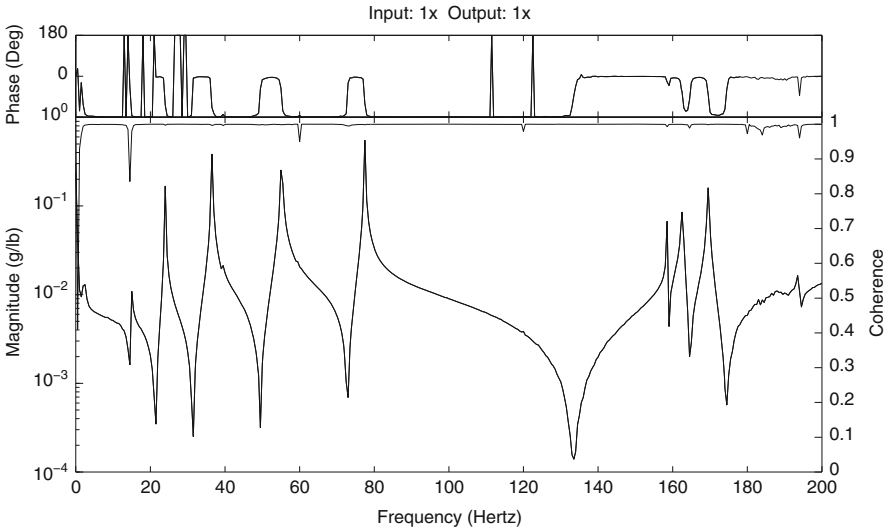

Fig. 58 Case 10: burst random excitation with cyclic averaging

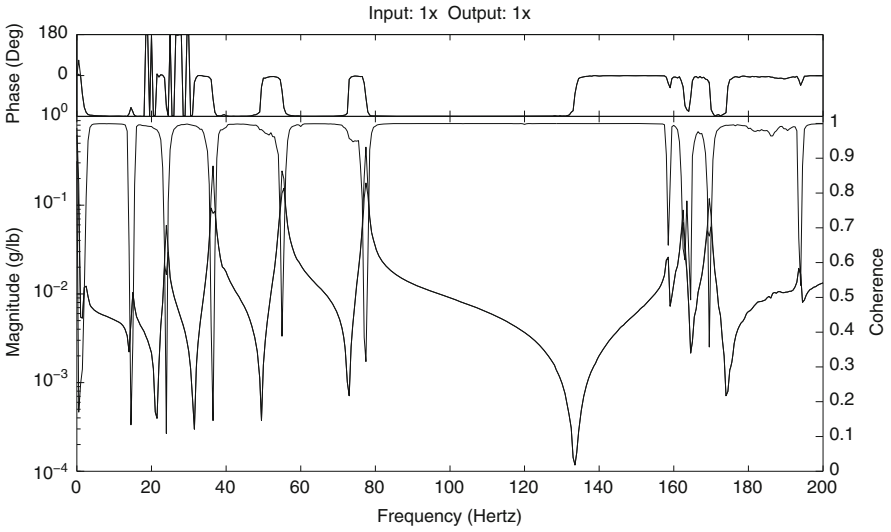

Fig. 59 Case 11: random excitation with Hanning window

processing methods. Note that as the multiple coherence improves, dramatic changes in the FRF magnitude accompany the improvement (factors of 2 to more than 10). When estimating modal parameters, the frequency and mode shape would probably be estimated reasonably in all cases. However, the damping and modal scaling would be distorted (overestimating damping and underestimating modal

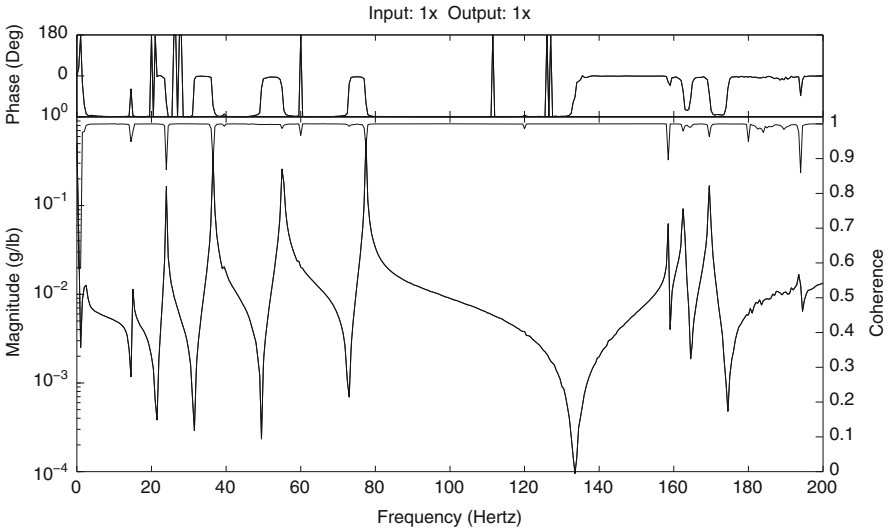

Fig. 60 Case 12: random excitation with Hanning window and cyclic averaging

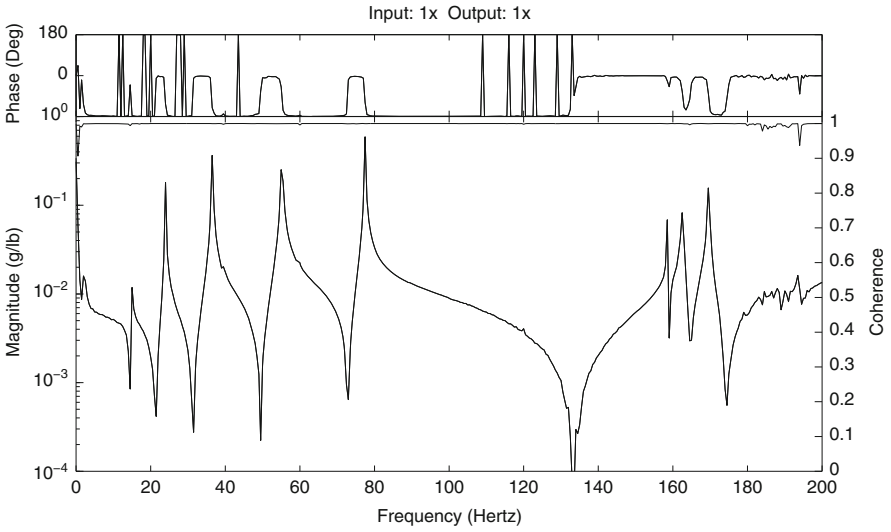

Fig. 61 Case 13: pseudorandom excitation with cyclic averaging

scaling). Using these results for model prediction or FE correction would bias the predicted results.

The most important conclusion that can be drawn from the results of this measurement exercise on a lightly damped mechanical system is that accurate data is an indirect function of measurement time or number of averages but is a direct

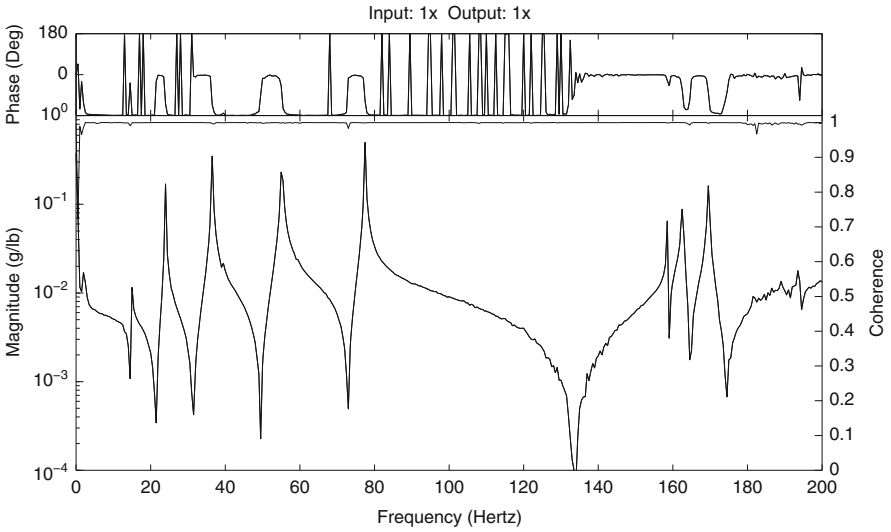

Fig. 62 Case 14: periodic random excitation with cyclic averaging

function of measurement technique. The leakage problem associated with utilizing fast Fourier transform (FFT) methodology to estimate frequency response functions on a mechanical system with light damping is a serious problem that can be managed with proper measurement techniques, like periodic and pseudorandom excitation or cyclic averaging with burst random excitation. Hybrid techniques demonstrated in this paper clearly show that a number of measurement techniques are acceptable, but some commonly used techniques are clearly unacceptable.

It is also important to note that while ordinary/multiple coherence can indicate a variety of input/output problems, a drop in the ordinary/multiple coherence function, at the same frequency as a lightly damped peak in the frequency response function, is often a direct indicator of a leakage problem. Frequently, comparisons are made between results obtained with narrowband (sinusoid) excitation and broadband (random) excitation when the ordinary/multiple coherence function clearly indicates a potential leakage problem. It is important that good measurement technique be an integral part of such comparisons.

6 Structural Testing Conditions

The test condition for any modal analysis test involves several environmental factors as well as appropriate boundary conditions. First of all, temperature, humidity, vacuum, and gravity effects must be properly considered to match with previous analysis models or to allow the experimentally determined model to properly reflect the system.

In addition to the environmental concerns, the boundary conditions of the system under test are very important. Traditionally, modal analysis tests have been performed under the assumption that the test boundary conditions can be made to conform to one of four conditions:

- Free-free boundary conditions (impedance is zero)
- Fixed boundary conditions (impedance is infinite)
- Operating boundary conditions (impedance is correct)
- Arbitrary boundary conditions (impedance is known).

It should be obvious that except in very special situations, none of these boundary conditions can be practically achieved. Instead, practical guidelines are normally used to evaluate the appropriateness of the chosen boundary conditions. For example, if a free-free boundary is chosen, the desired frequency of the highest rigid body mode should be a factor of ten below the first deformation mode of the system under test. Likewise, for the fixed boundary test, the desired interface stiffness should be a factor of ten greater than the local stiffness of the system under test. While either of these practical guidelines can be achieved for small test objects, a large class of flight vehicle systems cannot be acceptably tested in either configuration. Arguments have been made that the impedance of a support system can be defined (via test and/or analysis) and the effects of such a support system can be eliminated from the measured data. This technique is theoretically sound, but due to the significant dynamics in the support system and limited measurement dynamics, this approach has not been uniformly applicable.

In response to this problem, many alternate structural testing concepts have been proposed and are under current evaluation. Active, or combinations of active and passive, suspension systems are being evaluated, particularly for application to very flexible space structures. Active inert gas suspension systems have been used in the past for the testing of smaller commercial and military aircraft, and, in general, such approaches are formulated to better match the requirements of a free-free boundary condition.

Another alternate test procedure is to define a series of relatively conventional tests with various boundary conditions. The various boundary conditions are chosen in such a way that each perturbed boundary condition can be accurately modeled (e.g., the addition of a large mass at interface boundaries). Therefore, as the experimental model is acquired for each configuration and used to validate and correct the associated analytical model, the underlying model will be validated and corrected accordingly. This procedure has the added benefit of adding the influence of modes of vibration that would normally occur above the maximum frequency of the test into the validation of the model. For example, the inertial effect of the addition of a mass at an interface will cause a downward shift in frequency of any mode that is active at the interface (modes that are not affected by the interface dynamics will not be shifted). Since this shift is measured and the analytical model can accurately define the dynamics of the added mass, any inaccuracy in

the analytical prediction of the frequency shifts as well as the corresponding effects on the modal vectors will be due to the lack of fidelity of the underlying analytical model.

Recently, other researchers have proposed multiple configurations of test conditions as a methodology of utilizing practical test configurations in the testing of flight vehicle systems. In a related research area, work is progressing on using constrained testing together with direct parameter estimation methods to define the characteristics of the unconstrained structure. In this test procedure, the excitation forces and the constraint forces are measured together with appropriate response information. The direct parameter estimation method produces a general matrix model that describes the unconstrained (free-free) structural system. All of these newer methods will increase the cost (time, financial, technical) of performing structural tests with the attendant incremental increase in the accuracy of the test results.

7 Practical Measurement Considerations

There are several factors that contribute to the quality of actual measured frequency response function estimates. Some of the most common sources of error are due to measurement mistakes. With a proper measurement approach, most of this type of error, such as overloading the input, extraneous signal pickup via ground loops, strong electric or magnetic fields nearby, etc., can be avoided. Violation of test assumptions is often the source of another inaccuracy and can be viewed as a measurement mistake. For example, frequency response and coherence functions have been defined as parameters of a linear system. Nonlinearities will generally shift energy from one frequency to many new frequencies, in a way which may be difficult to recognize. The result will be a distortion in the estimates of the system parameters, which may not be apparent unless the excitation is changed. One way to reduce the effect of nonlinearities is to randomize these contributions by choosing a randomly different input signal for each of the n measurements. Subsequent averaging will reduce these contributions in the same manner that random noise is reduced. Another example involves control of the system input. One of the most obvious requirements is to excite the system with energy at all frequencies for which measurements are expected. It is important to be sure that the input signal spectrum does not have *holes* where little energy exist. Otherwise, coherence will be very low, and the variance on the frequency response function will be large.

Assuming that the system is linear, the excitation is proper, and obvious measurement mistakes are avoided, some amount of error (noise) will be present in the measurement process. Five different approaches can be used to reduce the error involved in frequency response function measurements in current fast Fourier transform (FFT) analyzers. First of all, the use of *different frequency response function estimation algorithms* (H_v compared to H_1) will reduce the effect of the leakage error on the estimation of the frequency response function computation.

The use of *averaging* can significantly reduce errors of both variance and bias and is probably the most general technique in the reduction of errors in frequency response function measurement. *Selective excitation* is often used to verify nonlinearities or randomize characteristics. In this way, bias errors due to system sources can be reduced or controlled. The *increase of frequency resolution* through the zoom fast Fourier transform can improve the frequency response function estimate primarily by reduction of the leakage bias error due to the use of a longer time sample. The zoom fast Fourier transform by itself is a linear process and does not involve any specific error reduction characteristics compared to a baseband fast Fourier transform (FFT). Finally, the *use of weighting functions (windows)* is widespread, and much has been written about their value [1, 2, 3, 44, 45]. Primarily, weighting functions compensate for the bias error (leakage) caused by the analysis procedure.

8 Summary

The quality of results in modern experimental modal analysis is highly dependent upon the quality and accuracy of the measured frequency response functions (FRF). In this chapter, several different methods of computing the FRFs have been presented. If there is no noise in the measurement process, then all perform equally well. The differences between them lie in how the noise enters the system and how the measurement errors are handled. These issues hold true regardless of whether the measurements are single input or multiple input.

In addition, a number of different coherence formulations (measurement quality metrics) have been presented. Under the basic premise that a coherence function provides essentially explained output variation relative to the total output variation, there are several coherence forms that, while not identical to one another, provide comparable information. The differences are primarily in the ordering of the functions and the ordering or assumed relative significance of the inputs. Of crucial importance is that in the newer formulations, the functions sum to given the traditional multiple coherence, thus while the underlying individual functions may be different, they do provide essentially equivalent information.

Further influencing the quality of experimentally measured FRFs is the process by which the data blocks are accumulated and averaged. Several different averaging mechanisms were presented by which the effect of noise, in various forms and of various origins, might be minimized.

Finally, the effect of measurement technique, particularly excitation choices, on the measured FRFs was presented. As shown (Sect. 5.6), there are a great variety of traditional and hybrid excitation techniques to address many different testing scenarios. The proper use of which can mitigate, and essentially eliminate, one of the most prevalent measurement errors, leakage.

In summary, through proper choice of selective excitation, averaging choices, and FRF formulation, coupled with coherence indicators, it is possible to make quality measurements suitable for use in modern parameter identification schemes.

References

1. Bendat JS, Piersol AG (1971) Random data: analysis and measurement procedures. Wiley, New York
2. Bendat JS, Piersol AG (1980) Engineering applications of correlation and spectral analysis. Wiley, New York
3. Otnes RK, Enochson L (1972) Digital time series analysis. Wiley, New York
4. Strang G (1988) Linear algebra and its applications, 3rd edn. Harcourt Brace Jovanovich Publishers, San Diego
5. Lawson CL, Hanson RJ (1974) Solving least squares problems. Prentice-Hall, Inc., Englewood Cliffs
6. Wilkinson JH (1965) The algebraic eigenvalue problem. Oxford University Press, Oxford
7. Jolliffe IT (1986) Principal component analysis. Springer, New York
8. Smallwood DO (1996) Matrix methods for estimating the coherence functions from estimates of the cross-spectral density matrix. Shock Vib 3:237–247
9. Allemang RJ (1980) Investigation of some multiple input/output frequency response function experimental modal analysis techniques. Doctor of Philosophy Dissertation, Mechanical Engineering Department, University of Cincinnati
10. Allemang RJ, Rost RW, Brown DL (1982) Dual input estimation of frequency response functions for experimental modal analysis of aircraft structures. In: Proceedings, international modal analysis conference (IMAC), pp 333–340
11. Carbon GD, Brown DL, Allemang RJ (1982) Application of dual input excitation techniques to the modal testing of commercial aircraft. In: Proceedings, international modal analysis conference (IMAC), pp 559–565
12. Allemang RJ, Brown DL, Rost RW (1982) Dual input estimation of frequency response functions for experimental modal analysis of automotive structures, SAE Paper Number 820193
13. Allemang RJ, Brown DL, Rost RW (1984) Multiple input estimation of frequency response functions for experimental modal analysis. U.S. Air Force Report Number AFATL-TR-84-15, 185pp
14. Allemang RJ, Brown DL, Rost RW (1987) Measurement techniques for experimental modal analysis, experimental modal analysis and dynamic component synthesis, USAF Technical Report, Contract Number F33615-83-C-3218, AFWAL-TR-87-3069, vol 2
15. Cobb RE, Mitchell LD (1988) A method for the unbiased estimate of system FRFs in the presence of multiple correlated inputs. J Anal Exp Modal Anal 3:123–128
16. Mitchell LD, Cobb RE, Deel JC, Luk YW (1988) An unbiased frequency response function estimator. J Anal Exp Modal Anal 3:12–19
17. Vold H, Crowley J, Rocklin G (1985) A comparison of H1, H2 and Hv frequency response functions. In: Proceedings, international modal analysis conference (IMAC), pp 272–278
18. Rost R, Leuridan J (1985) A comparison of least squares and total least squares for multiple input estimation of frequency response functions, ASME Paper Number 83-DET-105, 6pp
19. Rost R, Leuridan J (1985) Multiple input estimation of frequency response functions: diagnostic techniques for the excitation, ASME Paper Number 83-DET-107, 5pp
20. Leuridan J, De Vis D, Van der Auweraer H, Lembregts F (1986) A comparison of some frequency response function measurement techniques. In: Proceedings, international seminar on modal analysis (ISMA), 11pp
21. Napolitano KL (2016) Using singular value decomposition to estimate frequency response functions. In: Proceedings, international modal analysis conference (IMAC), pp 27–43
22. Patwardhan RS (2020) Frequency response and coherence function estimation methods. Master of Science Thesis, University of Cincinnati, 73pp
23. Bendat JS, Piersol AG (2011) Random data: analysis and measurement procedures, 4th edn. Wiley, New York

24. Potter RW (1977) Matrix formulation of multiple and partial coherence. J Acoust Soc Am 66:776–781
25. Coppolino RN (2000) Manual: ITAP Toolbox; User's Guide, Measurement Analysis Corporation
26. Richards CM, Singh R (1999) Feasibility of identifying non-linear vibratory systems consisting of unknown polynomial forms. J Sound Vib 220:413–450
27. (2016) Manual: Functions; LMS Test.Lab, Siemens Industry Software
28. Price SM, Bernhard RJ (1986) Virtual coherence: a digital signal processing technique for incoherent source identification. In: Proceedings, international modal analysis conference (IMAC), 4pp
29. Phillips AW, Allemang RJ, Zucker AT (1998) An overview of MIMO FRF excitation/averaging techniques. In: Proceedings, international seminar on modal analysis (ISMA), vol 1, no. 12
30. Phillips AW, Zucker AT, Allemang RJ (1999) A comparison of MIMO FRF excitation/averaging techniques on heavily and lightly damped structures. In: Proceedings, international modal analysis conference (IMAC), 10pp
31. Fladung WA, Zucker AT, Phillips AW, Allemang RJ (1999) Using cyclic averaging with impact testing. In: Proceedings, international modal analysis conference (IMAC), 7pp
32. Allemang RJ, Phillips AW (1998) A new excitation method: combining burst random excitation with cyclic averaging. In: Proceedings, international modal analysis conference (IMAC), pp 891–899
33. Phillips AW, Zucker AT, Allemang RJ (1999) Frequency resolution effects on FRF estimation: cyclic averaging vs large block size. In: Proceedings, international modal analysis conference (IMAC), 14pp
34. Allemang RJ, Phillips AW (1996) Cyclic averaging for frequency response function estimation. In: Proceedings, international modal analysis conference (IMAC), pp 415–422
35. Hsu HP (1970) Fourier analysis. Simon and Schuster, New York
36. Cole HA J (1971) Failure detection of a space shuttle wing flutter model by random decrement, NASA TM X-62, 041, May 1971
37. Cole HA (1973) On-line failure detection and damping measurement of aerospace structures by random decrement signatures, NASA CR-2205, Mar 1973
38. Dally JW, Riley WF, McConnell KG (1984) Instrumentation for engineering measurements. Wiley, New York
39. Akaike H (1965) On the statistic estimation of the frequency response function of a system having multiple inputs. Ann Inst Stat Math 17:185–210
40. Carter G, Knapp C, Nuttall A (1973) Estimation of the magnitude-squared coherence function via overlapped fast fourier transform processing. IEEE Trans Audio Electroacoust 21:337–344
41. Halvorsen WG, Brown DL (1977) Impulse technique for structural frequency response testing. Sound Vib Mag 8–21, Nov 1977
42. Van Karsen C (1987) A survey of excitation techniques for frequency response function measurement. Master of Science Thesis, University of Cincinnati, 81pp
43. Stenger G (1979) Step relaxation method for structural dynamic excitation. Master of Science Thesis, Department of Mechanical Engineering, University of Cincinnati, 54pp
44. Coleman AD, Driskill TC, Anderson JB, Brown DL (1988) A mass additive technique for modal testing as applied to the space shuttle ASTRO-1 payload. In: Proceedings, international modal analysis conference (IMAC), pp 154–159
45. Kuo C-P, Wada BK (1989) Multiple boundary condition test (MBCT): identification with mode shapes, NASA JPL Report, NPO-17574

Random Vibration and Mechanical Shock

7

Thomas L. Paez, Norman F. Hunter, and David O. Smallwood

Contents

Abstract

All physical systems are exposed to structural dynamic environments, including random vibration or mechanical shock, or both. These environments can cause structural or component failure. The capability to analyze dynamic response is critical not only for purposes of response prediction and design, but also for specification of random vibration and shock tests. This chapter develops

T. L. Paez (✉) · N. F. Hunter · D. O. Smallwood
Thomas Paez Consulting, Albuquerque, NM, USA
e-mail: hunter@swflora.com

R. Allemang, P. Avitabile (eds.), *Handbook of Experimental Structural Dynamics*,
https://doi.org/10.1007/978-1-4614-4547-0_9

the ideas and the mathematics underlying the structural dynamics of linear single-degree-of-freedom and multiple-degree-of-freedom structures, random processes, random vibration, mechanical shock, random vibration testing, and mechanical shock testing. Examples are provided and many recommendations are given for the performance of random vibration and shock tests.

Keywords

Random vibration · Mechanical shock · Structural dynamics · Single-degree-of-freedom structure · Multiple-degree-of-freedom structure · Expected value function · Autocorrelation function · Spectral density function · Shock response spectrum · Random vibration control · Transient control

Nomenclature

In general, bold letters denote vectors and matrices, and non-bold letters denote scalar quantities. Dots denote differentiation with respect to time.

a	Acceleration
A	Amplitude, Fourier transform of acceleration
Bw	Bandwidth
c	Viscous damping coefficient
d	Displacement
Db	Decibels
D_f	RMS duration of a function of frequency
D_t	RMS duration of a function of time
e	Estimation error
E	Energy of a shock
$E[\bullet]$	Expectation
f	Frequency (in *Hertz*), a function
$\hat{g}$	One-sided spectral density estimator
G	One-sided spectral density
h	Impulse response function
H	Frequency response function
k	Stiffness coefficient
m	Mass
m_i	A temporal moment
M	Number of modes retained in modal analysis
N	Number of averages used to form spectral density estimate
q	Force
$\boldsymbol{Q}$	Fourier transform of $\boldsymbol{q}$
RMS	Root mean square
S	Shock response spectrum
S_r	Sample rate
v	Velocity
x	Absolute displacement
X	Fourier transform of x
y	A function
Y	Fourier transform of y
z	A function
Z	Fourier transform of z

$\{X(t)\}$	Random process
x_b	Base excitation
z	Relative displacement
$\boldsymbol{\gamma}$	Modal coordinates
γ^2	Coherence
$\boldsymbol{\Gamma}$	Fourier transform of $\boldsymbol{\gamma}$
ζ	Damping factor, A decay rate
θ	Fourier transform of force
ξ	Fourier transform of displacement
μ	Mean
$\boldsymbol{\varphi}$	Matrix of mode shapes
ω	Frequency (in *radians/second*)
ω_n	Natural frequency (in *radians/second*)
ω_d	Damped natural frequency (in *radians/second*)

1 Introduction

Mechanical systems are universally exposed to random vibration and mechanical shock environments, and sometimes, those environments are important enough to merit consideration during system modeling or testing. This chapter has three parts: Section 2 reviews the mathematical foundations of structural dynamics, mechanical shock, and random vibration. Section 3 introduces the ideas of random vibration testing. Section 4 introduces the ideas of mechanical shock testing.

2 Mathematical Foundations of Structural Dynamics

Because mechanical shock and random vibration environments can cause structures to fail, it is critical to understand the behaviors of structures that are dynamically excited. The principles of mechanics can be used to approximately model the behaviors of mechanical systems. This section summarizes the equations governing structural dynamic behaviors of linear systems and the solutions to those equations (Because space is limited, the behaviors of nonlinear systems are not considered here.), random vibration, and mechanical shock. Section 2.1 presents the equations governing motion of single-degree-of-freedom (SDOF) structures and their solutions. Section 2.2 generalizes the governing equations and their solutions to the case of multiple-degree-of-freedom (MDOF) structures. Section 2.3 presents the idea of the random process as a representation of a mechanical excitation. It continues to describe the spectral density as the fundamental characteristic of a stationary random process. In Sect. 2.4, the fundamental relation of random vibration is written and described. Section 2.5 presents the idea of mechanical shock as the application of transient excitation to a structure and computation of structural response. The important idea of shock response spectrum (SRS) is introduced, as well as the framework in which it is applied to the specification of shock tests.

2.1 Single-Degree-of-Freedom Structures

The response of a linear structure is unique; that is, when a specific excitation is applied to a structure, there is one and only one response that the structure executes. This fact arises from the characteristics of linear differential equations [1]. That unique response can, however, be obtained and expressed in different ways. The theory of structural dynamics can express the equations governing motion and their solutions in both the time and frequency domains; under different circumstances, each means of expression is preferable to the other. The following two subsections present, first, results obtained in the time domain and then results obtained in the frequency domain.

2.1.1 Structural Dynamics in the Time Domain

The single-degree-of-freedom (SDOF) structure idealization represents the most basic of oscillatory systems. The idealization is shown in Fig. 1. The structure consists of a rigid mass m that is constrained to move along a single coordinate; the absolute displacement of the mass is x. The mass is attached to an immobile reference via a linear spring with constant stiffness k and a linear, viscous damper with constant c. The force applied directly to the mass is $q(t)$, $-\infty < t < \infty$. The force may be known over a finite or semi-infinite time interval, only; when that is so, the response may be evaluated over that interval, and into the infinite future, if desired. When the time at which the response commences is finite, then the initial conditions of the system at the start of the response must be specified in order to evaluate the response.

Newton's second law can be used to write the equation governing motion of the SDOF structure. (Ref. [2], for example, has a more detailed development of the equations and solutions to follow.) It is:

$$m\ddot{x} + c\dot{x} + kx = q(t) \qquad -\infty < t < \infty \tag{1}$$

where dots denote differentiation with respect to time. We consider a transformed version of the equation, one in which both sides are divided by the mass m:

$$\ddot{x} + 2\zeta\omega_n\dot{x} + \omega_n^2 x = \frac{q(t)}{m} \qquad -\infty < t < \infty \tag{2}$$

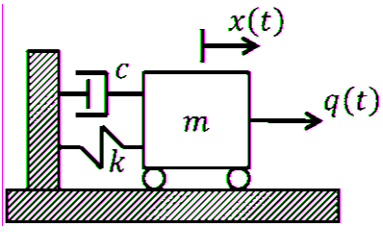

Fig. 1 The fixed-base, force-excited single-degree-of-freedom structure

where $\omega_n = \sqrt{k/m} > 0$ is the structure's natural frequency (in *radians/second*), and $\zeta = c/(2m\omega_n) \in (0, 1]$ is its damping factor. The meanings of these parameters will become clear, in a moment.

The solution to the equation of motion has two parts: the homogeneous solution and the particular solution. The former defines the response of the structure to initial conditions, in the absence of a forcing function. The latter defines the response of the structure to the forcing function, only. The superposition of the two solution parts forms the response to both initial conditions and applied force.

The homogeneous solution is obtained by solving Equation (1) when $q(t) = 0$, and initial conditions, $x(0) = x_0$, and $\dot{x}(0) = v_0$, are specified. (Here, we have specified the initial conditions at time $t = 0$. The solution can easily be written for the case where the initial conditions are specified at the arbitrary time, $t = t_0$.) For lack of space in this chapter, we will not provide a detailed development of the method for obtaining the homogeneous solution. Rather, we simply note that the displacement and velocity responses to the initial conditions are:

$$x_h(t) = e^{-\zeta\omega_n t}\left[x_0 \cos(\omega_d t) + \frac{\zeta\omega_n x_0 + v_0}{\omega_d}\sin(\omega_d t)\right] \qquad t \geq 0$$

$$\dot{x}_h(t) = e^{-\zeta\omega_n t}\left[v_0 \cos(\omega_d t) - \frac{\omega_n x_0 + \zeta v_0}{\sqrt{1-\zeta^2}}\sin(\omega_d t)\right] \qquad t \geq 0 \tag{3}$$

where $\omega_d = \omega_n\sqrt{1-\zeta^2}$ is the damped natural frequency of the SDOF structure. The results clarify the terminology of ω_n and ζ. The damped natural frequency is the circular frequency of motion of the response when the response results from initial conditions, only. The damping factor is required to occupy the interval $(0, 1]$ for structures to exhibit oscillatory response, but it usually is quite small, in the range $(0.002, 0.100]$. Monolithic structures (i.e., structures with no joints, like a steel bar) that are free-in-space may have dampings as low as a fraction of 1 percent; structures composed of many parts connected by mechanical joints or concrete structures excited to high levels may have dampings up to several percent, or even 10 percent. Because realistic damping factors are near zero, $\omega_d \cong \omega_n$.

The particular solution to the equation of motion is the response of the SDOF structure to the forcing function $q(t)$. For a linear structure that response is unique, but it may be expressed in several different ways. We start with the time domain expression for forced response. Again, because there is not room, here, to develop the response expression, we simply write it for absolute displacement:

$$x(t) = \int_0^t h_{xq}(t-\tau)\, q(\tau)\, d\tau \qquad t \geq 0 \tag{4}$$

where $h_{xq}(t)$, $t \geq 0$ is the impulse response function (IRF) of absolute displacement response to force excitation; the subscripts indicate the response followed by the

input of interest. This response expression is written for an input that starts at time $t = 0$; however, it can be written for any starting time, including $t \to -\infty$. When the start time of the response is not zero, then the lower limit on the integral must be changed to the start time. The form of Equation (4) is known as a convolution integral.

The feature that makes the convolution integral an appropriate form for the expression of a particular measure of response is the IRF. The reader can confirm the mathematical expression for the IRF by substituting the convolution integral of Equation (4) into Equation (2). He or she would obtain a second order differential equation in $h_{xq}(t)$ whose solution is:

$$h_{xq}(t) = \frac{e^{-\zeta \omega_n t}}{m\omega_d} \sin(\omega_d t) \qquad t \geq 0 \tag{5}$$

A heuristic approach to the solution of Equation (2) would show that Equation (4) is its proper solution where the IRF is the first of Equations (3) with $x_0 = 0$ and $v_0 = 1/m$. The IRF of a causal system (i.e., a system that responds to an input only at the time of, and after the input has been applied) must always be zero for $t < 0$. Because of that, the upper limit on the integral of Equation (4) can be made ∞.

The IRFs of other measures of force-excited response can be written, as well. For example, the IRF of absolute velocity response to force excitation for SDOF structures is:

$$h_{\dot{x}q}(t) = \frac{e^{-\zeta \omega_n t}}{m} \left[\cos(\omega_d t) - \frac{\zeta}{\sqrt{1-\zeta^2}} \sin(\omega_d t) \right] \qquad t \geq 0 \tag{6}$$

Recognize that this is simply the derivative of Equation (5) with respect to time. When this IRF is used in a convolution integral, like Equation (4), with the force, $q(t)$, the integral yields the absolute velocity response.

So far, we have considered the structure of Fig. 1, governed by Equation (2). There is another important application, namely, the base-excited structure. Figure 2 shows an SDOF structure that is excited by forces transmitted to the mass through the spring and damper that attach the mass to its base. The enforced displacement of

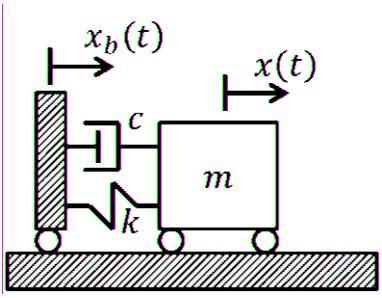

Fig. 2 SDOF structure excited at its base

the base is $x_b(t)$, $-\infty < t < \infty$. (As with externally applied force, base excitation can be applied over a finite or semi-infinite time interval.) We assume that at least two derivatives of the enforced base displacement exist; that is, there are a velocity and an acceleration that correspond to the base displacement.

Define the relative displacement of the mass $z(t) = x(t) - x_b(t)$. The equation governing relative motion of the SDOF system is:

$$m\ddot{z} + c\dot{z} + kz = -m\ddot{x}_b \qquad -\infty < t < \infty \tag{7}$$

The form is identical to Equation (1). We usually consider the normalized version of the equation where both sides are divided by the mass m:

$$\ddot{z} + 2\zeta\omega_n\dot{z} + \omega_n^2 z = -\ddot{x}_b \qquad -\infty < t < \infty \tag{8}$$

Because of the similarity of Equation (8) to Equation (2), the homogeneous solution for $z(t)$ is identical to Equations (3) for displacement and velocity.

Further, the particular solution to Equation (8) takes the same form as the particular solution to Equation (2), a convolution integral. When we use $-\ddot{x}_b(t)$ in place of $q(t)/m$ in Equation (4), we obtain the relative displacement response excited by a base acceleration input. We modify the factors in the integrand, slightly, to obtain:

$$z(t) = \int_0^t h_{z\ddot{x}_b}(t-\tau)\,\ddot{x}_b(\tau)\,d\tau \qquad -\infty < t < \infty \tag{9}$$

where the IRF of relative displacement response to base acceleration input is:

$$h_{z\ddot{x}_b}(t) = -\frac{e^{-\zeta\omega_n t}}{\omega_d}\sin(\omega_d t) \qquad t \geq 0 \tag{10}$$

Likewise, we can obtain the IRF of relative velocity response to base acceleration input. It is:

$$h_{\dot{z}\ddot{x}_b}(t) = -e^{-\zeta\omega_n t}\left[\cos(\omega_d t) - \frac{\zeta}{\sqrt{1-\zeta^2}}\sin(\omega_d t)\right] \qquad t \geq 0 \tag{11}$$

When we use $h_{\dot{z}\ddot{x}_b}(t)$ in a convolution integral with the base acceleration $\ddot{x}_b(t)$, the result is the relative velocity response of the SDOF structure.

During experimental applications of mechanical shock and random vibration, many excitation and response quantities can be measured, including accelerations, strains, velocities, and relative displacements. However, for reasons related to practicality and economics, the quantity most frequently measured is the absolute acceleration at a point on a structure in a particular direction. Therefore, we are interested in expressing the acceleration response to an acceleration input. When

we rearrange the definition of relative displacement and take its second derivative, we obtain:

$$\ddot{x}(t) = \ddot{z}(t) + \ddot{x}_b(t) \qquad t \geq 0 \tag{12}$$

Rearrange Equation (8) and use this expression in it to show:

$$\ddot{x}(t) = -\omega_n^2 z(t) - 2\zeta\omega_n \dot{z}(t) \qquad t \geq 0 \tag{13}$$

Finally, substitute the appropriate convolution integrals for $z(t)$ and $\dot{z}(t)$, combine integrands and simplify to obtain:

$$\ddot{x}(t) = \int_0^t h_{\ddot{x}\ddot{x}_b}(t-\tau)\,\ddot{x}_b(t)d\tau \qquad t \geq 0 \tag{14}$$

where the IRF for absolute acceleration response to base acceleration input is:

$$h_{\ddot{x}\ddot{x}_b}(t) = \omega_n e^{-\zeta\omega_n t}\left[\frac{\left(1-2\zeta^2\right)}{\sqrt{1-\zeta^2}}\sin\left(\omega_d t\right) + 2\zeta\cos\left(\omega_d t\right)\right] \qquad t \geq 0 \tag{15}$$

The expression in Equation (15) can be used in Equation (14) to compute the acceleration response of a linear, SDOF structure.

2.1.2 Structural Dynamics in the Frequency Domain

We are often most interested in the temporal behavior of structures and use the approach of Sect. 2.1.1 to express responses. However, interpretation of structural behavior is best accomplished in the frequency domain. Further, numerical analysis of structural response is more efficient in the frequency domain, and the classical analysis of random vibration depends on the frequency domain interpretation of structural behavior.

Several approaches lead to the solution of the problems of linear structural dynamics in the frequency domain [3]. We pursue the solution of this section by taking the Fourier transform of each term in Equation (2):

$$\left[\left(\omega_n^2 - \omega^2\right) + 2\zeta\omega_n i\omega\right]\xi_0(\omega) = \frac{1}{m}\theta(\omega) \qquad -\infty < \omega < \infty \tag{16}$$

where $i = \sqrt{-1}$ is the imaginary unit, and $\xi_0(\omega)$ and $\theta(\omega)$ are the Fourier transforms of $x(t)$ and $q(t)$, respectively, defined as:

$$\begin{aligned} \xi_0(\omega) &= \int_{-\infty}^{\infty} x(t)e^{-i\omega t}dt \\ \theta(\omega) &= \int_{-\infty}^{\infty} q(t)e^{-i\omega t}dt \qquad -\infty < \omega < \infty \end{aligned} \tag{17}$$

The "0" subscript on $\xi_0(\omega)$ indicates that it is the Fourier transform of the zeroth derivative of the function $x(t)$. The Fourier transforms of $\ddot{x}(t)$ and $\dot{x}(t)$ are $-\omega^2\xi_0(\omega)$ and $i\omega\xi_0(\omega)$, respectively.

Fourier transformation converts the differential relation of Equation (2) into an algebraic relation. Equation (16) can be solved to obtain:

$$\xi_0(\omega) = \frac{1}{m\left[\left(\omega_n^2 - \omega^2\right) + 2\zeta\omega_n i\omega\right]}\theta(\omega) \qquad -\infty < \omega < \infty \tag{18}$$

The coefficient on the right is known as the force input/absolute displacement output, frequency response function (FRF), and is denoted as:

$$H_{xq}(\omega) = \frac{1}{m\left[\left(\omega_n^2 - \omega^2\right) + 2\zeta\omega_n i\omega\right]} \qquad -\infty < \omega < \infty \tag{19}$$

The FRF is a fundamental descriptor of the behavior of a linear structure (SDOF in this case). If the structure governed by Equation (2) were excited by the purely harmonic input $q(t) = Qe^{i\omega t}$, it would excite the purely harmonic response $H_{xq}(\omega)Qe^{i\omega t}$; the response would be amplified by the amount $|H_{xq}(\omega)|$ and its phase would be modified by the amount $phase[H_{xq}(\omega)] = tan^{-1}(Im[H_{xq}(\omega)]/\, Re\,[H_{xq}(\omega)])$.

When we use Equation (19) in Equation (18), we obtain the concise expression:

$$\xi_0(\omega) = H_{xq}(\omega)\,\theta(\omega) \qquad -\infty < \omega < \infty \tag{20}$$

Figure 3 shows a normalized version of $H_{xq}(\omega)$ for $\omega \geq 0$, and for several values of damping factor ζ, in terms of its modulus and phase. As the damping factor diminishes, the amplification reflected by the FRF increases at the natural frequency of the SDOF structure. The phase passes through $-\pi/2$ at $\omega/\omega_n = 1$.

Because Equation (20) represents the Fourier transform of the absolute displacement response, and because the Fourier transform is invertible, the absolute displacement response can be obtained in the time domain through inversion of Equation (20):

$$x(t) = \frac{1}{2\pi}\int_{-\infty}^{\infty} H_{xq}(\omega)\,\theta(\omega)\,e^{i\omega t}\,d\omega \qquad -\infty < t < \infty \tag{21}$$

For some excitations $q(t)$, $-\infty < t < \infty$, this computation might be carried out in closed form. However, when $q(t)$ is known over a finite time interval and at equally spaced, discrete times, the computation can be carried out numerically, using the fast Fourier transform (FFT) [4]. $H_{xq}(\omega)$ can be evaluated at discrete frequencies using Equation (19). The product in the integrand of Equation (21) can be formed. Then the inverse Fourier transform of Equation (21) can be approximated using FFT. This sequence of operations is much more efficient than the numerical approximation of the convolution integral.

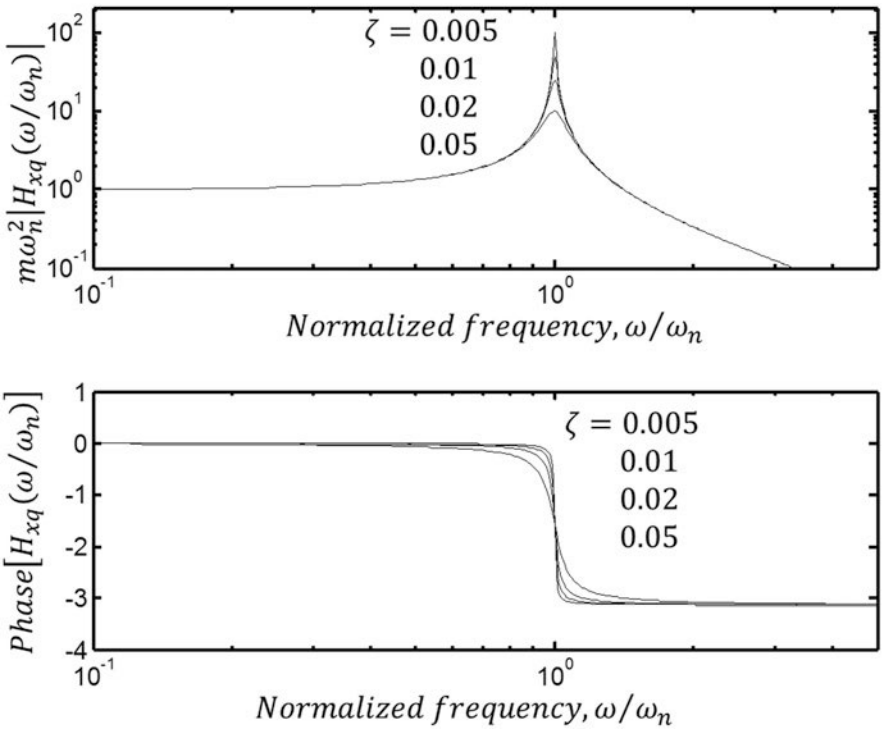

Fig. 3 Modulus (top) and phase (bottom) of force input/absolute displacement output FRF of an SDOF structure

Leibniz's rule [5] can be used with Equation (21) to obtain velocity and acceleration responses, and this leads to expressions for the force input – absolute velocity, and absolute acceleration FRFs:

$$H_{\dot{x}q}(\omega) = \frac{i\omega}{m\left[\left(\omega_n^2 - \omega^2\right) + 2\zeta\omega_n i\omega\right]} \qquad -\infty < \omega < \infty \tag{22}$$

$$H_{\ddot{x}q}(\omega) = \frac{-\omega^2}{m\left[\left(\omega_n^2 - \omega^2\right) + 2\zeta\omega_n i\omega\right]} \qquad -\infty < \omega < \infty \tag{23}$$

The time domain velocity and acceleration responses are:

$$\dot{x}(t) = \frac{1}{2\pi}\int_{-\infty}^{\infty} H_{\dot{x}q}(\omega)\,\theta(\omega)\,e^{i\omega t}d\omega \qquad -\infty < t < \infty \tag{24}$$

$$\ddot{x}(t) = \frac{1}{2\pi}\int_{-\infty}^{\infty} H_{\ddot{x}q}(\omega)\,\theta(\omega)\,e^{i\omega t}d\omega \qquad -\infty < t < \infty \tag{25}$$

When we Fourier transform the two equations, above, we obtain:

$$\xi_1(\omega) = H_{\dot{x}q}(\omega)\,\theta(\omega) \qquad -\infty < \omega < \infty \tag{26}$$

$$\xi_2(\omega) = H_{\ddot{x}q}(\omega)\,\theta(\omega) \qquad -\infty < \omega < \infty \tag{27}$$

where the subscripts "1" and "2," on the left indicate that $\xi_1(\omega)$ and $\xi_2(\omega)$ are the Fourier transforms of the first and second derivatives of $x(t)$, respectively. These two equations and Equation (20) serve as the frequency domain relation between force and the measures of response of an SDOF structure.

We can follow the procedure used to obtain the FRFs for a force-excited structure to establish the FRFs for the responses of a base-excited structure. The preliminary analysis would consider Equation (8) and obtain FRFs of relative displacement, velocity, and acceleration to an enforced base excitation. The FRFs are $H_{z\ddot{x}_b}(\omega)$, $H_{\dot{z}\ddot{x}_b}(\omega)$, and $H_{\ddot{z}\ddot{x}_b}(\omega)$, $-\infty < \omega < \infty$, respectively, where base acceleration is the input. Then the relation $z(t) = x(t) - x_b(t)$ could be used to solve for the absolute displacement $x(t)$. The first and second derivatives of the expression can be evaluated and then Fourier transformed to obtain the FRFs of absolute displacement, velocity, and acceleration to enforced base excitation. The base acceleration input/absolute acceleration response FRF is:

$$H_{\ddot{x}\ddot{x}_b}(\omega) = \frac{\omega_n^2 + 2i\zeta\omega_n\omega}{\left(\omega_n^2 - \omega^2\right) + 2i\zeta\omega_n\omega} \qquad -\infty < \omega < \infty \tag{28}$$

The graph of this FRF, when normalized, is similar to the graphs in Fig. 3.

By analogy with Equation (27), the Fourier transform of the absolute acceleration response to base acceleration input is:

$$\xi_2(\omega) = H_{\ddot{x}\ddot{x}_b}(\omega)\,\xi_{b2}(\omega) \qquad -\infty < \omega < \infty \tag{29}$$

where $\xi_{b2}(\omega)$, $-\infty < \omega < \infty$ is the Fourier transform of the base acceleration. This is the frequency domain relation between base acceleration input and absolute acceleration response. The acceleration response in the time domain is:

$$\ddot{x}(t) = \frac{1}{2\pi}\int_{-\infty}^{\infty} H_{\ddot{x}\ddot{x}_b}(\omega)\,\xi_{b2}(\omega)\,e^{i\omega t}d\omega \qquad -\infty < t < \infty \tag{30}$$

This expression provides the time domain, absolute acceleration response in terms of the Fourier transform of the base acceleration input and the structure FRF.

Example 1 Computation of SDOF Structure Response in the Frequency Domain

An input applied at its base is used to excite an SDOF structure with natural frequency $\omega_n = (2\pi)100$ *rad/sec* and damping factor $\zeta = 0.02$. The time-domain

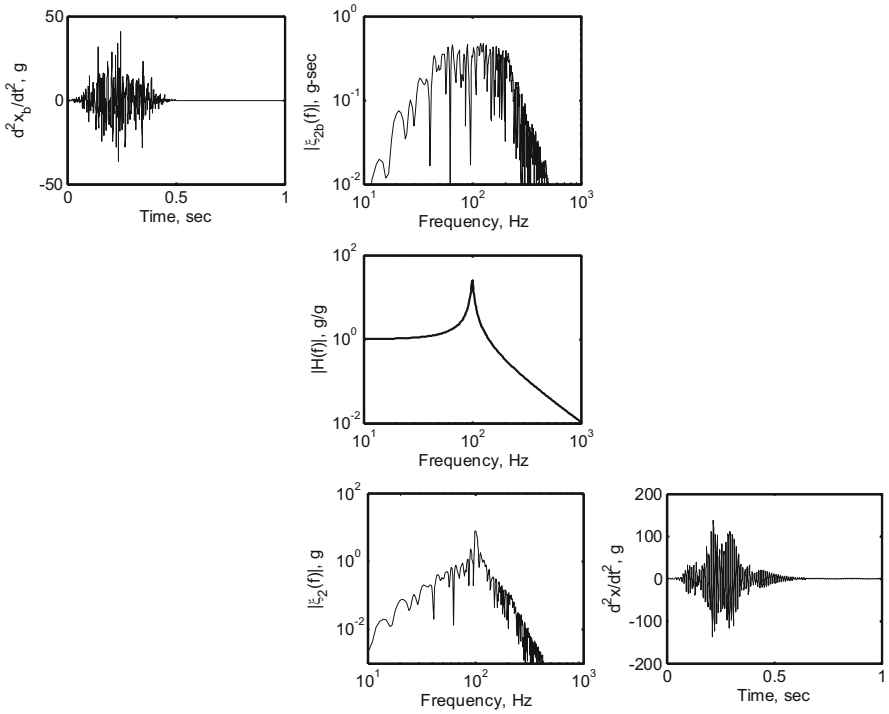

Fig. 4 Graphic showing the sequence of operations involved in computation of linear structure response in the frequency domain

input is shown on the top left in Fig. 4; it is sampled at a rate of 2048 *samples/sec* (i.e., $\Delta t = 4.88 \times 10^{-4} sec$). We compute the absolute acceleration response in the frequency domain. The modulus of the DFT of the input is shown at top center in the figure at frequencies $f_k = k\Delta f$, $k = 0, \ldots, 1024$; $\Delta f = 1\ Hz$. (All DFT moduli are plotted at these frequencies. The phase is erratic and provides little intuition regarding the structural response. The phase of the structural response is the sum of the phases of the input and the FRF.) The modulus of the FRF of absolute acceleration response to base acceleration input is shown in the center of the figure. The modulus of the product of the input and the FRF is shown at bottom center; this is the response DFT. The inverse DFT of the response DFT is shown at bottom right; of course, computation of the inverse DFT requires use of the phase as well as the modulus of the response DFT. Within numerical round-off, this is the result that would be obtained via numerical convolution.

2.2 Multiple-Degree-of-Freedom Structures

The developments of Sect. 2.1 consider the responses of SDOF structures in the time and frequency domains. Many real structures can be modeled, approximately, as SDOF; however, most real structures are spatially continuous and reflect more complex behavior. This section presents (without development) the equations governing motion of more complex, more realistic structures and presents their solutions.

2.2.1 Structural Dynamics in the Time and Frequency Domains

It is beyond the scope of this chapter to develop the methodology for analyzing complex structures; however, the equations that govern the behavior of linear continuous structures can be approximated with simultaneous, linear, ordinary differential equations (ODE) [6]. Those equations describe what are known as multiple-degree-of-freedom (MDOF) models. Finite element (FE) codes [6] develop such models for specific structures, and solve the governing equations to establish MDOF structure responses. Figure 5 shows, at left, the schematic of a (two-dimensional) continuous structure. The idea behind FE modeling is that the continuous structure is divided into *elements*; the schematic on the right in Fig. 5 shows the idea. Equations that describe the equilibrium of each element are developed, and the collection of elements is combined and connected to obtain a set of simultaneous equations approximately governing the equilibrium of the overall structure. The modeler may be interested in predicting motions at the location and in the directions indicated by (x_i, x_{i+1}, x_{i+2}). When a model provides the capacity to execute those motions, it is said to have those degrees-of-freedom (DOF). Indeed, the model has DOF associated with all permissible motions at the *nodes* of the model; we consider the nodes as the points where elements connect. (The motions are translations or rotations and are referred to as generalized motions.)

The idea behind a dynamic model is that it can be used to approximate responses $(\boldsymbol{x}, \dot{\boldsymbol{x}}, \ddot{\boldsymbol{x}})$ at all DOF and at all times of interest. Dots denote differentiation with

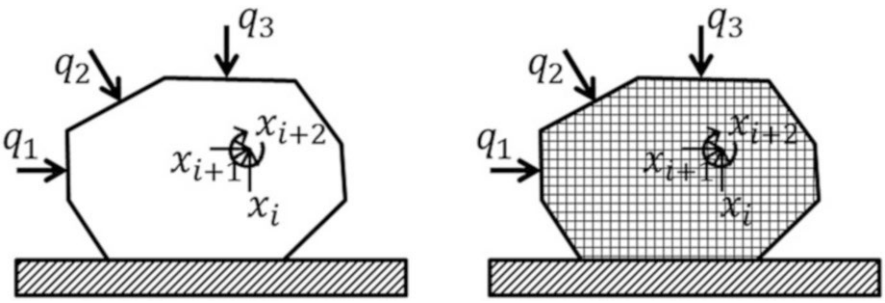

Fig. 5 Schematic of a continuous structure (left) and its spatially discretized approximation (right)

respect to time. $\boldsymbol{x}$ denotes displacements at the model DOF; $\dot{\boldsymbol{x}}$ denotes velocities; $\ddot{\boldsymbol{x}}$ denotes accelerations. When the model has N DOF, then each of the vectors $(\boldsymbol{x}, \dot{\boldsymbol{x}}, \ddot{\boldsymbol{x}})$ has dimension $N \times 1$.

During the analysis of dynamic response, one or more externally applied forces, $q_i(t)$, $i = 1, 2, \ldots, -\infty < t < \infty$, may be specified. (The forces may alternately be applied over a finite or semi-infinite time interval.) The forces can be collected into the $N \times 1$ vector, $\boldsymbol{q}(t)$, $-\infty < t < \infty$. There is a force in $\boldsymbol{q}(t)$ for each model DOF; some or all the $q_i(t)$ in $\boldsymbol{q}(t)$ may be zero. The forces are generalized in the sense that they may be translational or rotational, depending on the DOFs they excite.

Given information on the geometry of a structure, the material properties of its various parts, and its boundary conditions, an FE code establishes the mass matrix $\boldsymbol{m}$ of a structure to describe its inertial properties and the stiffness matrix $\boldsymbol{k}$ of a structure to describe its stiffness. Both the mass and stiffness matrices have dimension $N \times N$. The matrix equation governing motion of a linear MDOF structure is:

$$\boldsymbol{m}\ddot{\boldsymbol{x}} + \boldsymbol{c}\dot{\boldsymbol{x}} + \boldsymbol{k}\boldsymbol{x} = \boldsymbol{q}(t) \qquad -\infty < t < \infty \tag{31}$$

The $N \times N$ matrix $\boldsymbol{c}$ is the matrix of viscous damping coefficients; it is usually specified based on experimental data or an understanding of typical dissipative behavior of a class of structures.

Within the framework of FE analysis, there are multiple approaches to solving the governing Equation (31). For example, when the force excitations are specified at the discrete times $t_j = j\Delta t$, $= 0, 1, \ldots$, with $\Delta t > 0$ a time increment, the forces might be denoted $\boldsymbol{q}_j = \boldsymbol{q}(t_j)$, $j = 0, 1, \ldots$. Equation (31) can be solved, approximately, at all the structural DOF and at all times to obtain the responses $\left(\boldsymbol{x}_j, \dot{\boldsymbol{x}}_j, \ddot{\boldsymbol{x}}_j\right) = \left(\boldsymbol{x}\left(t_j\right), \dot{\boldsymbol{x}}\left(t_j\right), \ddot{\boldsymbol{x}}\left(t_j\right)\right)$, $j = 0, 1, \ldots$. However, that approach does not provide the most efficient method for obtaining responses. The more common method for analyzing response involves modal analysis, and the modes of a structure also characterize the MDOF structure.

Modal analysis starts by considering the eigenvalue problem associated with the undamped, unforced form of the equation of motion:

$$\boldsymbol{m}\ddot{\boldsymbol{x}} + \boldsymbol{k}\boldsymbol{x} = \boldsymbol{0} \tag{32}$$

Solution of the eigenvalue problem obtained from Equation (32) yields a collection of up to N eigenvectors $\boldsymbol{v}_k$, $k = 1, \ldots, N$ and corresponding modal frequencies ω_k, $k = 1, \ldots, N$. These have physical meaning: There are certain frequencies ω_k, where, in free, undamped vibration, a linear structure will execute harmonic motion while maintaining a constant shape $\boldsymbol{v}_k$. The eigenvectors are referred to as mode shapes. The mode shapes and modal frequencies are approximated via iterative procedures, and, typically, the lowest M modes, only, are approximated. (Typically, especially in the case where the model is large $M \ll N$.) The analyst typically chooses M so that $\omega_M \cong \omega_{Max}$ where ω_{Max} is the highest frequency where the input $\boldsymbol{q}(t)$ has substantial signal content.

Each mode shape can be normalized using $\boldsymbol{\varphi}_k = b_k \boldsymbol{v}_k$, so that:

$$\boldsymbol{\varphi}_k^T \boldsymbol{m} \boldsymbol{\varphi}_k = 1 \qquad k = 1, \ldots, M \tag{33}$$

When the normalization of Equation (33) is established, it is also true that:

$$\boldsymbol{\varphi}_k^T \boldsymbol{k} \boldsymbol{\varphi}_k = \omega_k^2 \qquad k = 1, \ldots, M \tag{34}$$

Further, the following relations hold:

$$\boldsymbol{\varphi}_k^T \boldsymbol{m} \boldsymbol{\varphi}_r = 0 \qquad k \neq r \qquad \boldsymbol{\varphi}_k^T \boldsymbol{k} \boldsymbol{\varphi}_r = 0 \qquad k \neq r \tag{35}$$

The mode shapes with the properties in Equations (33) through (35) are referred to as ortho-normal. When the modal vectors are gathered into an $N \times M$ matrix $\boldsymbol{\varphi}$ whose columns are the $\boldsymbol{\varphi}_k$, $k = 1, \ldots, M$, then:

$$\boldsymbol{\varphi}^T \boldsymbol{m} \boldsymbol{\varphi} = \boldsymbol{I} \qquad \boldsymbol{\varphi}^T \boldsymbol{k} \boldsymbol{\varphi} = \boldsymbol{\omega}^2 \tag{36}$$

where $\boldsymbol{I}$ is the $M \times M$ identity matrix and $\boldsymbol{\omega}^2$ is the diagonal $M \times M$ matrix with elements ω_k^2, $k = 1, \ldots, M$. Typically, we also assume that:

$$\boldsymbol{\varphi}^T \boldsymbol{c} \boldsymbol{\varphi} = 2\boldsymbol{\zeta} \boldsymbol{\omega} \tag{37}$$

where $\boldsymbol{\zeta}$ is the diagonal $M \times M$ matrix with elements ζ_k, $k = 1, \ldots, M$. ($\boldsymbol{c}$ can be constructed so that Equation (37) holds, or if $\boldsymbol{c}$ is constructed so that Equation (37) does not hold, we might ignore the off-diagonal terms.)

In view of Equations (36) and (37), we can define the transformation $\boldsymbol{x} = \boldsymbol{\varphi}\, \boldsymbol{\gamma}$ and use it in Equation (31). The $M \times 1$ vector $\boldsymbol{\gamma}(t)$ includes the modal coordinates of motion. We then pre-multiply the result by $\boldsymbol{\varphi}^T$ to obtain:

$$\boldsymbol{I} \ddot{\boldsymbol{\gamma}} + 2\boldsymbol{\zeta} \boldsymbol{\omega} \dot{\boldsymbol{\gamma}} + \boldsymbol{\omega}^2 \boldsymbol{\gamma} = \boldsymbol{\varphi}^T \boldsymbol{q}(t) \qquad -\infty < t < \infty \tag{38}$$

Because the coefficient matrices on the left are all diagonal, Equation (38) represents a sequence of M second order ODEs like Equation (2), each governing the motion of an SDOF structure. Therefore, the effect of modal analysis is to reduce the governing Equation (31) to a set of M equations, each one describing the behavior of one mode. The k^{th} modal equation is:

$$\ddot{\gamma}_k + 2\zeta_k \omega_k \dot{\gamma}_k + \omega_k^2 \gamma_k = \left(\boldsymbol{\varphi}^T \boldsymbol{q}(t) \right)_k = q_{\text{mod},k}(t) \; k = 1, \ldots, M, -\infty < t < \infty \tag{39}$$

where $(\boldsymbol{\varphi}^T \boldsymbol{q}(t))_k = q_{mod,\,k}(t)$ is the kth element in the $M \times 1$ column vector $\boldsymbol{\varphi}^T \boldsymbol{q}(t)$. It is the kth modal excitation.

The time-domain solution to Equation (39) was developed in Sect. 2.1.1. One form of it is:

$$\gamma_k(t) = \int_{-\infty}^{\infty} h_{\gamma_k q}(t-\tau)\, q_{\text{mod},k}(\tau)\, d\tau \qquad k = 1, \ldots, M, -\infty < t < \infty \quad (40)$$

where $h_{\gamma_k q}(t), t \geq 0$ is the force input/absolute displacement response IRF of an SDOF structure. As shown in Sect. 2.1.1, expressions for the force-excited absolute velocity and acceleration responses can also be obtained. As well, expressions for the base-excited relative motion and absolute motion responses can be developed.

When the $\gamma_k(t)$, $k = 1, \ldots, M$ of Equation (40) are used to construct the vector $\boldsymbol{\gamma}(t)$, we obtain:

$$\boldsymbol{\gamma}(t) = \int_0^t \boldsymbol{h}_{\gamma q}(t-\tau)\, \boldsymbol{\varphi}^T \boldsymbol{q}(\tau)\, d\tau \qquad -\infty < t < \infty \quad (41)$$

where $\boldsymbol{h}_{\gamma q}(t), t \geq 0$ is the $M \times M$, diagonal matrix of modal IRFs for the structure. Finally, we obtain the response in physical coordinates by using the definition of modal coordinates:

$$\boldsymbol{x}(t) = \boldsymbol{\varphi}\boldsymbol{\gamma}(t) = \int_0^t \boldsymbol{\varphi}\boldsymbol{h}_{\gamma q}(t-\tau)\, \boldsymbol{\varphi}^T \boldsymbol{q}(\tau)\, d\tau \qquad -\infty < t < \infty \quad (42)$$

The leading triplet of terms inside the integrand is the matrix of IRFs of the physical system; therefore, we write:

$$\boldsymbol{h}_{xq}(t) = \boldsymbol{\varphi}\boldsymbol{h}_{\gamma q}(t)\boldsymbol{\varphi}^T \qquad t \geq 0 \quad (43)$$

The $i^{\text{th}} - row$, $j^{\text{th}} - column$ element of $\boldsymbol{h}_{xq}$ is interpreted as the absolute displacement response of the structure at DOF i to a force impulse applied at DOF j. The dimension of $\boldsymbol{h}_{xq}$ is $N \times N$, but we rarely compute the entire matrix of functions. Rather, the elements of $\boldsymbol{h}_{xq}$ can be computed one-at-a-time, and they usually are computed in this manner. For example, it makes no sense to compute the $i^{\text{th}} - row$, $j^{\text{th}} - column$ element of $\boldsymbol{h}_{xq}$ for columns j corresponding to rows in $\boldsymbol{q}$ where the input is zero; so those elements are always skipped. Likewise, we are normally interested, only, in evaluating the response at certain DOF; so we evaluate the IRF at those rows i only.

Section 2.1.2 developed the method for solving the equation governing motion of SDOF structures in the frequency domain. Equation (39) can be solved using that method to obtain the response in the frequency domain of the kth structural mode. That solution is the Fourier transform of the solution written in Equation (40):

$$\Gamma_k(\omega) = H_{\gamma_k q}(\omega)\, Q_{\text{mod},k}(\omega) \qquad k = 1, \ldots, M, -\infty < \omega < \infty \quad (44)$$

where $H_{\gamma_k q}(\omega)$ is the FRF of the k^{th} structural mode, the Fourier transform of $h_{\gamma_k q}(t)$, and $Q_{mod,\,k}(\omega)$ is the Fourier transform of $q_{mod,\,k}(t)$. The $M \times 1$ vector of absolute, modal displacement responses can be constructed with Equation (44) to obtain:

$$\boldsymbol{\Gamma}(\omega) = \boldsymbol{H}_{\gamma q}(\omega)\,\boldsymbol{\varphi}^T\,\boldsymbol{Q}(\omega) \qquad -\infty < \omega < \infty \tag{45}$$

where $\boldsymbol{Q}(\omega)$ is the Fourier transform of $\boldsymbol{q}(t)$, and $\boldsymbol{H}_{\gamma q}(\omega)$ is the $M \times M$, diagonal matrix of modal FRFs, the Fourier transform of $\boldsymbol{h}_{\gamma q}(t)$.

The Fourier transform of the vector of physical responses can be denoted $\boldsymbol{X}(\omega)$, $-\infty < \omega < \infty$, and it can be recovered by using the definition of the modal coordinates:

$$\boldsymbol{X}(\omega) = \boldsymbol{\varphi}\boldsymbol{\Gamma}(\omega) = \boldsymbol{\varphi}\boldsymbol{H}_{\gamma q}(\omega)\,\boldsymbol{\varphi}^T\,\boldsymbol{Q}(\omega) \qquad -\infty < \omega < \infty \tag{46}$$

We recognize the leading triplet on the right as the matrix of FRFs of the physical structure; therefore, we write:

$$\boldsymbol{H}(\omega) = \boldsymbol{\varphi}\boldsymbol{H}_{\gamma q}(\omega)\,\boldsymbol{\varphi}^T \qquad -\infty < \omega < \infty \tag{47}$$

$\boldsymbol{H}(\omega)$ has dimension $N \times N$, and its $i^{\text{th}} - row, j^{\text{th}} - column$ element is complex-valued. When the excitation $e^{i\omega t}$ is input at DOF j (and all other inputs are zero), then the response at DOF i is the $i\text{th} - row, j^{\text{th}} - column$ element of $\boldsymbol{H}(\omega)$ times $e^{i\omega t}$, i.e., $H_{ij}(\omega)e^{i\omega t}$. The magnitude $|H_{ij}(\omega)|$ describes the amplification or diminishment of the response over the input; the phase of $H_{ij}(\omega)$ describes the phase lag between the input and the response. Of course, only those FRFs of interest in a given analysis need be established with Equation (47).

Equation (47) indicates that the matrix of FRFs of a linear structure is a superposition of its modal FRFs. Each modal FRF is a function that amplifies the response motion at its modal frequency. Therefore, the magnitude of each function in $\boldsymbol{H}(\omega)$ reflects a sequence of peaks at the structural modes and troughs between the peaks. The relative magnitudes of the peaks depend on the relative amplitudes of the elements in the columns of the modal matrix $\boldsymbol{\varphi}$.

The matrix FRF developed in Equation (47) relates input forces to response motions. The specific form of $\boldsymbol{H}(\omega)$ depends on what measure of response motion is to be established. The base excitation input/structural motion output FRF could be established as well. The FRFs developed here could also be expressed as a function of cyclic frequency $\boldsymbol{H}(f), f \geq 0$.

2.3 Random Processes

The bases for the study of random vibration are the theories of random processes and structural dynamics. Some ideas of structural dynamics have been outlined in Sects. 2.1 and 2.2. Here, we introduce some ideas from the theory of random processes.

There are multiple ways to define a random process, but it suits our purposes to think of a random process as an abstract collection including an infinite number of continuous-valued oscillatory signals. Denote the signals $x_j(t)$, $j = 1, 2, \ldots, -\infty < t < \infty$. The collection of signals is the ensemble of the random process. When we measure a signal from a random source, it is a member of the ensemble, and we are said to draw a realization from the random process. Typically, in the practice of random vibration, we measure input excitations and responses of mechanical systems. Five finite-duration segments of structural response random process realizations are shown in Fig. 6. The independent variable of the random process whose realizations are shown is continuous time; this is the random process parameter. The ordinate has a measure of interest like acceleration, velocity, or displacement; the signals shown in Fig. 6 are accelerations in units of g's.

When the signals in the ensemble of a random process are in a random steady-state, then the random process is said to be stationary. In principle, the signals in the ensemble cover the interval $(-\infty, \infty)$, but, of course, in practice, no real source maintains a steady-state for infinite time. When the realizations of a random process maintain a steady-state for a time period that is large compared to the fundamental period of the structure under consideration, then the excitation and response random processes can be considered approximately stationary. For example, a store carried on an aircraft wing might have a fundamental frequency of $f_1 = 50\ Hz$ and a

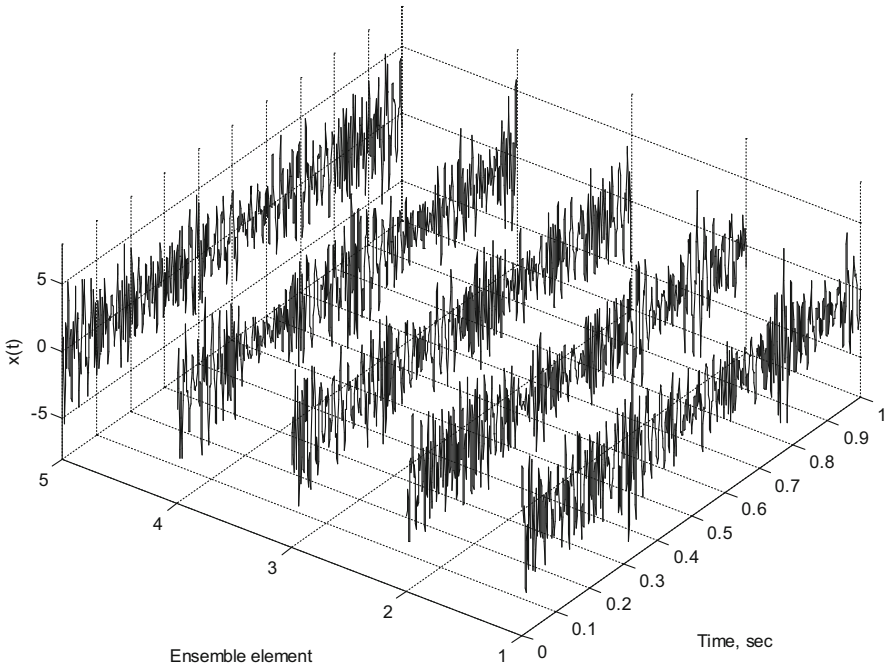

Fig. 6 Five realizations of a response random process

corresponding fundamental period of $T_1 = 1/f_1 = 0.02$ *sec*. When that system is excited in a random steady state for 2 *sec* or more, then the excitation and response might be considered stationary.

A stationary random process is often denoted as $\{X(t), -\infty < t < \infty\}$. The average or expected value of a random process is denoted as $E[X(t)], -\infty < t < \infty$; this defines the average of all members of the ensemble at time t:

$$E[X(t)] = \lim_{n\to\infty} \frac{1}{n} \sum_{j=1}^{n} x_j(t) \qquad -\infty < t < \infty \tag{48}$$

The conditions for weak stationarity of a random process are (1) that is has an expected value that is constant as a function of time, i.e., $E[X(t)] = E[X] = \mu_X$, and (2) that it possesses a frequency-domain decomposition known as the spectral density. (When the expected value of an excitation random process is non-zero, we usually consider the oscillatory portion, only, of the random process and evaluate the response to the mean separately. This is how we treat random excitations in the following.) The spectral density of a random process can be defined in several equivalent ways; we provide an intuitive description of the one-sided spectral density that is a function of cyclic frequency $f, f \geq 0$. The spectral density of the random process $\{X(t)\}$ is denoted $G_{XX}(f), f \geq 0$. To describe the spectral density, we define the random process $\{X(t;f, \Delta f)\}$ as a filtered version of $\{X(t)\}$ with signal content in the frequency interval $[f,f + \Delta f]$, only [3]. The realizations of $\{X(t;f, \Delta f)\}$ can be denoted $x_j(t;f, \Delta f), j = 1, 2, \ldots$. The area under the spectral density curve over the interval $[f,f + \Delta f]$ is defined as:

$$\int_f^{f+\Delta f} G_{XX}(u)du = \lim_{n\to\infty} \frac{1}{n} \sum_{j=1}^{n} x_j^2(t; f, \Delta f) \tag{49}$$

where the quantity on the right is the mean square of a realization of the filtered random process. This defines the spectral density implicitly. The definition of the spectral density can be converted into a time-average in which the spectral density can be obtained from a single (infinite duration) random process realization. In order for this to hold, the stationary random process must be ergodic; that is, any realization of the random process must be representative of all the others.

When we denote the mean square of the random process $\{X(t)\}$ as σ_X^2 (a constant), then the definition in Equation (49) implies:

$$\sigma_X^2 = \int_0^{\infty} G_{XX}(f)df \tag{50}$$

That is, the area under the spectral density curve equals the mean square of the random process. Because the area under $G_{XX}(f), f \geq 0$ is a mean square, which cannot be negative, the function $G_{XX}(f)$ must be non-negative. Further, the

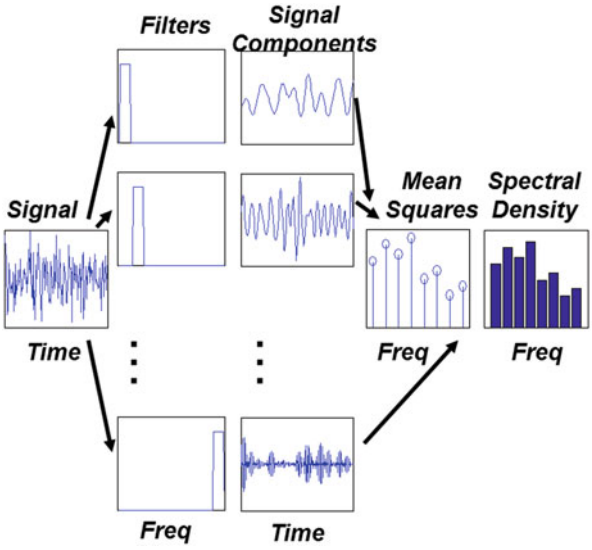

Fig. 7 A graphic interpretation of spectral density

amplitudes of the spectral density reveal how the mean square signal content of a random process is distributed with frequency.

A graphic interpretation of the spectral density function is provided in Fig. 7. The fundamental idea is that a random signal (first column) can be filtered (second column) into a sequence of components (third column) with independent signal content. The mean square of each component (fourth column) can be established and plotted as a function of the center frequency of the filter. Each mean square can be divided by the filter bandwidth to obtain the spectral density (fifth column). Until the advent of digital analysis and control, spectral density was actually estimated in the manner described in Fig. 7.

There is another important measure of the behavior of stationary random process pairs known as the cross-spectral density [7]. The spectral density, described in the previous equations, is also referred to as the autospectral density. The autospectral density characterizes the mean square signal content of a random process in the frequency domain. That is, it describes the signal content of a quadratic form of a random process. The cross-spectral density describes the simultaneous signal content of a pair of different random processes $\{X(t), -\infty < t < \infty\}$ and $\{Y(t), -\infty < t < \infty\}$; it is based on a quadratic form of the two random processes. It is denoted as $G_{XY}(f)$, $f \geq 0$, and it is generally a complex function. When the two random processes are strongly correlated (either positively or negatively, see reference [7]) at a given frequency f, then the magnitude of $G_{XY}(f)$ is great; otherwise, the magnitude of $G_{XY}(f)$ is small. The phase of $G_{XY}(f)$ measures the average phase difference between the phases of the random processes $\{X(t)\}$ and $\{Y(t)\}$.

The units of autospectral density are the units of the random process, squared, per unit of frequency. For example, when a random process has units of $g's$ and the frequency measure of interest is Hz, then the spectral density units are g^2/Hz.

2.4 Random Vibration

The mathematical theory of random vibration has been developed over the course of the last century (approximately); the first paper on the subject was written by Einstein [8]. (Reference [8] is reprinted in Reference [9].). The idea that enables treatment of random vibration with modern techniques is the spectral density, and that was developed by Wiener in [10]. When a linear, stable, deterministic structure is excited by one or more stationary random inputs, the responses at all DOF on the structure converge to stationary random processes. When the responses reach the stationary state, both the inputs and the responses possess auto- and cross-spectral densities.

Consider a structure with the $N_{out} \times N_{in}$ matrix FRF $\boldsymbol{H}(f), f \geq 0$; assume that $\boldsymbol{H}(f)$ is a force input/motion output FRF. The N_{out} rows of the FRF correspond to DOF where we desire the response of the structure; the N_{in} columns of the FRF correspond to DOF where there are force inputs. The matrix form of the fundamental relation of random vibration (a descriptive name specified by Crandall [11, 12]) is:

$$\boldsymbol{G}_{\boldsymbol{XX}}(f) = \boldsymbol{H}(f)\boldsymbol{G}_{\boldsymbol{QQ}}(f)\left[\boldsymbol{H}^*(f)\right]^T \qquad f \geq 0 \tag{51}$$

where $\boldsymbol{G}_{\boldsymbol{QQ}}(f), f \geq 0$ is the matrix of one-sided spectral densities of the stationary, vector random force excitation $\{\boldsymbol{Q}(t)\}$. The vector of random input forces is $\boldsymbol{Q}(t) = \left(Q_1(t), \ldots, Q_{N_{in}}(t)\right)^T$; the elements on the right are scalar, stationary, force random processes. The matrix $\boldsymbol{G}_{\boldsymbol{QQ}}(f)$ has dimension $N_{in} \times N_{in}$. Its diagonal terms are the autospectral densities of the elements of $\{\boldsymbol{Q}(t)\}$, and its off-diagonal terms are the cross-spectral densities between pairs of the elements in $\{\boldsymbol{Q}(t)\}$. $\boldsymbol{G}_{\boldsymbol{XX}}(f)$ is the $N_{out} \times N_{out}$ matrix of one-sided spectral densities of the stationary, vector random response motions $\{\boldsymbol{X}(t)\}$. The elements of $\{\boldsymbol{X}(t)\}$ and $\boldsymbol{G}_{\boldsymbol{XX}}(f)$ are described in terms analogous to the description of the random force input.

When the input is a base excitation applied in one direction, only, then the dimension of the FRF is $N_{out} \times 1$. The spectral density of the excitation is, in this case, a scalar. The matrix, fundamental relation of random vibration takes the form:

$$\boldsymbol{G}_{\ddot{\boldsymbol{X}}\ddot{\boldsymbol{X}}}(f) = G_{\ddot{X}_b\ddot{X}_b}(f)\boldsymbol{H}_{\ddot{\boldsymbol{X}}\ddot{X}_b}(f)\left[\boldsymbol{H}^*_{\ddot{\boldsymbol{X}}\ddot{X}_b}(f)\right]^T \qquad f \geq 0 \tag{52}$$

In this particular case, the relation is written for a base acceleration input and an absolute acceleration output. This is the idealized form that might be used, for example, for computation of the behavior of a structure excited on a shaker in the laboratory. (It is an idealization because, in the laboratory, base excitation usually has inputs in three directions and rotations about three axes. When those

additional inputs are known, then expressions like the one in Equation (52) can be superimposed to obtain predictions of response spectral densities.)

The fundamental relation of random vibration for the single-input/single-output (SISO) case is a special case of Equation (51). When stationary, random force input to a structure is applied at one location, only, its spectral density can be denoted as $G_{QQ}(f), f \geq 0$. When we are interested in assessing the response spectral density at one location, only, then the response spectral density can be denoted as $G_{XX}(f)$, $f \geq 0$. The relation between excitation and response spectral densities is:

$$G_{XX}(f) = |H(f)|^2 G_{QQ}(f) \qquad f \geq 0 \tag{53}$$

Because the magnitude of the FRF, $|H(f)|$, of an MDOF structure displays a sequence of peaks at structural modes, this relation implies that if there is mean square signal content in the stationary random force input at a modal frequency, then that input is amplified in the spectral density of the response. The response spectral density is not amplified, and may be diminished, between modes.

Example 2 Random Vibration of an MDOF Structure

The structure shown in Fig. 8 is a simple, spring-mass structure that has a series configuration. All masses are equal with $m = 8.64 \times 10^{-4}\ lb - sec^2/in$. The stiffnesses are equal with $k = 250\ lb/in$. The damping constants are equal with $c = 7.50 \times 10^{-3}\ lb - sec/in$. These parameters yield modal frequencies of $[38.1, 106.8, 154.3]\ Hz$ and damping factors of $[0.020, 0.016, 0.019]$. The structure is excited at its base with a zero-mean, stationary random input; the input spectral density is shown in Fig. 9. The input root-mean-square (RMS) is 2.29 g.

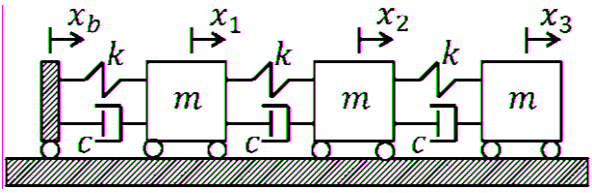

Fig. 8 Simple spring-mass structure

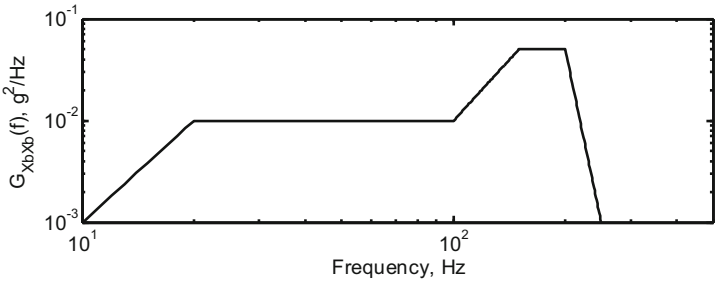

Fig. 9 Spectral density of the base input applied to the structure of Fig. 8

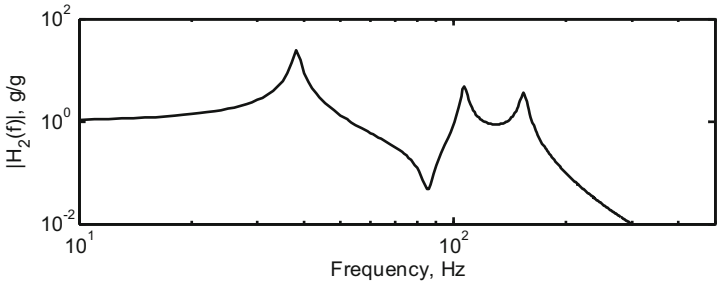

Fig. 10 Modulus of the FRF for acceleration output at DOF 2 to base acceleration input

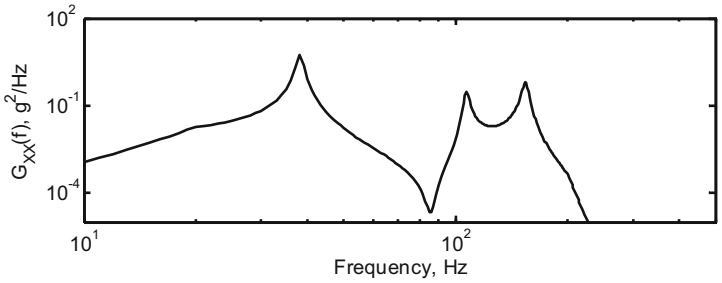

Fig. 11 Spectral density at DOF 2 of the structure shown in Fig. 8 excited by the base-excitation with spectral density shown in Fig. 9

The base acceleration input/absolute acceleration output FRF was computed for the structure using the approach that led to Equation (47), but for a base-excited structure. Then Equation (52) was used to compute response spectral densities at the structural DOF. Figure 10 shows the modulus of the FRF. The spectral density of absolute acceleration response at DOF 2 is shown in Fig. 11. The RMS of the response is 4.64 *g*. Of course, because the structure has three DOF, there are three peaks in the response spectral density, and they occur at the modal frequencies of the structure. As long as the stationary random excitation has signal content at the modal frequencies of the structure and response is measured at structural locations where there are not nodes in mode shapes, peaks will occur at structural modes in the response spectral density.

The theory of random vibration has many applications. To understand the applications, we note that three items of information are involved in analysis of stationary random vibration, namely, excitation spectral density, structure FRF, and response spectral density. When two of the three pieces of information are available, then, in principle, the third can be estimated. However, estimation of excitation spectral density from the other two pieces of information requires, in some cases, substantial caution.

2.5 Mechanical Shock

Computation of structural response to mechanical shock follows the approach developed in Sects. 2.1 and 2.2 when the structure under consideration is modeled as linear. When a shock input is known, then one of the approaches to response computation can be used to establish the desired measure of response. However, if we were to limit our comments to this simple statement, we would omit the fundamental measure of mechanical shock used in the laboratory and in analysis, today. That measure is the shock response spectrum (SRS). The SRS aims to be a measure of the severity – or damage-causing capability – of a shock. Its definition and characteristics are developed in more detail in [13].

The SRS of a shock motion (usually analyzed for measured acceleration) is defined as a frequency spectrum of peak responses excited in linear SDOF structures by the shock motion. Let $\ddot{x}_b(t), t \geq 0$ denote a mechanical shock. Assume that it is applied at the base of an SDOF structure with natural frequency $\omega_n = 2\pi f_n$ and damping factor ζ and that it excites the absolute acceleration response $\ddot{x}(t), t \geq 0$. The peak in the absolute value of the acceleration defines one ordinate in the SRS, $S_\zeta(f), f > 0$, of $\ddot{x}_b(t), t \geq 0$:

$$S_\zeta\left(f_n\right) = \max_{t \geq 0} |\ddot{x}(t)| \tag{54}$$

By repeating this computation for SDOF systems whose natural frequencies cover a range of frequencies $[f_0, f_{max}]$, we develop the entire SRS, $S_\zeta(f)$, $f_0 \leq f \leq f_{max}$, of $\ddot{x}_b(t), t \geq 0$. This form of the SRS is known as the absolute acceleration maximax SRS; absolute acceleration because $\ddot{x}(t), t \geq 0$ is an absolute acceleration; maximax because it considers the maximum value of the absolute response over all time. Other forms of the SRS can also be defined for alternate measures of response, like displacement or velocity, or even for built-up measures of response like $\omega_n\, x(t)$, known as the pseudo-velocity. Of course, the response depends on the damping factor of the SDOF structure involved in the SRS computation; that dependence is denoted by the "ζ" subscript on the SRS.

Example 3 Some SRS
Compute the absolute acceleration maximax SRS of:

$$\ddot{x}_b(t) = \begin{cases} \frac{1}{2}\left[1 - \cos\left(2\pi t / T\right)\right] & 0 \leq t \leq T \\ 0 & t > T \end{cases} \tag{55}$$

The shock signal $\ddot{x}_b(t)$, a classical pulse known as a haversine, is shown on the left in Fig. 12. Its SRS is shown on the right.

The SRS of Fig. 12 shows a feature of all absolute acceleration maximax SRS. They asymptotically approach the peak value of the time domain signal at high frequencies.

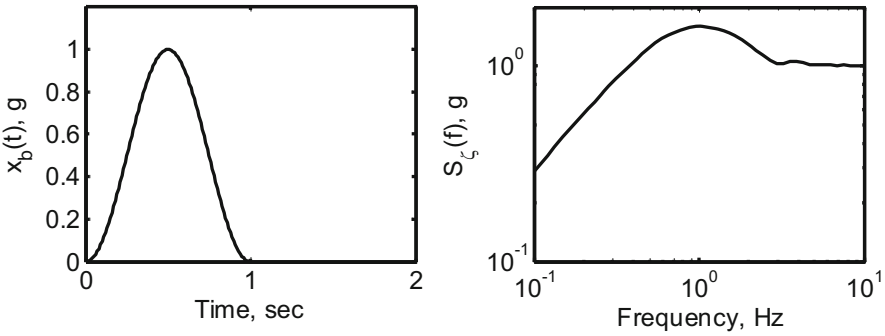

Fig. 12 Haversine shock pulse (left) and its SRS (right)

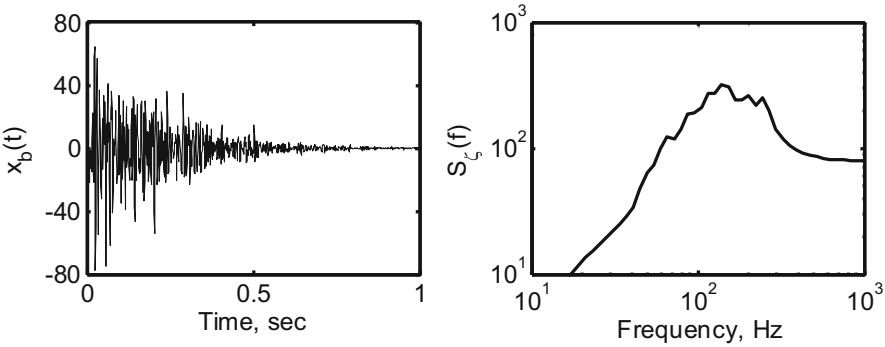

Fig. 13 An oscillatory shock pulse (left) and its SRS (right)

Now compute the absolute acceleration maximax SRS of the shock shown on the left in Fig. 13. This is known as an oscillatory shock, and may be the type measured in practice. The SRS is shown on the right of Fig. 13.

The two shocks and their SRS, shown in Example 3, help to explain why the SRS was developed in the first place (in the 1930s). Sometimes our laboratory test equipment is not capable of reproducing shocks like the one shown on the left in Fig. 13, yet we might have equipment capable of producing shocks like the one on the left in Fig. 12; in instances like these, we need a method for establishing an "equivalence" between two types of shock.

The method of shock response spectra specifies that if two shocks have "equivalent" SRS, then the severities of the two shocks are equivalent. This holds even when the shock time histories are dissimilar. The method of SRS permits replacement of an oscillatory shock with a shock that has a classical pulse shape (or with another oscillatory shock). This is useful when it is desired to obtain a test shock to represent a collection of shocks measured in the field.

Example 4 Application of the Method of SRS
In this example, we find a haversine test shock that is equivalent, in the SRS sense, to the shock shown on the left in Fig. 13. To accomplish this task, we note that [13] there are amplitude and time/frequency scaling laws that apply to all SRS. Because the SRS is simply the responses of a sequence of linear SDOF structures to a shock, the amplitude of every SRS scales linearly in the vertical direction; i.e., as the amplitude of a shock is doubled, the amplitude of its SRS is doubled. Further, for the same reason, when the duration of a shock is lengthened/shortened, then the SRS shifts downward/upward along the frequency axis in proportion to the lengthening/shortening of the shock signal.

Note that the peak in the SRS on the right in Fig. 13 occurs at an amplitude of 319 g and the peak in the SRS of the unit haversine on the right in Figure 12 is 1.59 g. Then a haversine with amplitude of $200 = 319/1.59$ is called for. Further, the peak in the SRS of the oscillatory pulse occurs at frequency 139 Hz, and the peak in the SRS of the haversine occurs at 1 Hz. Then a haversine with duration $0.0072 = 1/139$ is called for.

The test haversine is shown on the right in Fig. 14, and its SRS is shown with the SRS of the oscillatory pulse on the left side of the figure.

The SRS of the test pulse is not a perfect match for the SRS of the oscillatory pulse, but it cannot be because the time histories of the shocks are so far apart. Indeed, to make the test pulse conservative with respect to the oscillatory pulse, we normally enforce conservatism in the SRS "match." The amplitude of the test pulse is greater than the amplitude of the oscillatory shock on the left in Fig. 13. This relation is typical; the SRS of classical pulses "equivalent" to oscillatory pulses tend to be greater.

Of course, there are many caveats to the use of the method of SRS for specification of test pulses; among the most important is that analysts and testers are

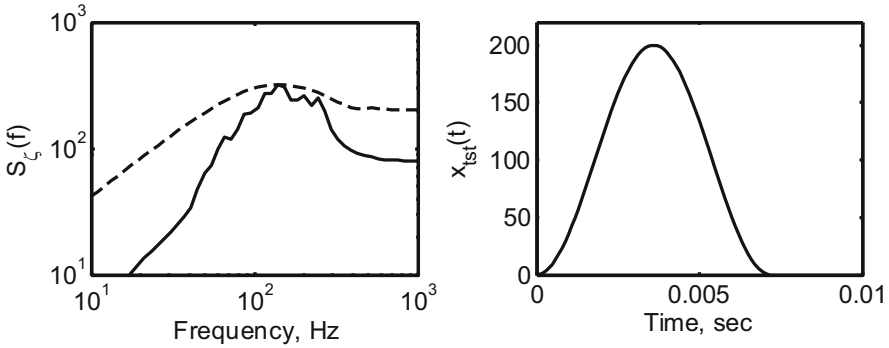

Fig. 14 SRS of the oscillatory pulse from Example 3 and the SRS of a test pulse (left) and the time history of the classical pulse (right)

encouraged to specify test with a duration that is comparable to or shorter than the field-measured shock. This tends to assure that some devious method of establishing a test pulse that is much lower than the oscillatory pulse and yet has an SRS that is correctly specified cannot be developed.

The ideas of SRS and mechanical shock testing will be amplified in Sect. 4.

3 Random Vibration Testing

Vibration tests form a critical component of the environmental testing sequence. The test structure, or test item, is exposed to a combination of oscillatory forces in the laboratory for a specified time period. This laboratory testing simulates exposure to a similar field environment. Such field vibration environments are induced by road transportation, by aerodynamics, by propulsion systems, in shipboard environments and sometimes by operation of the equipment itself. Vibration testing was historically conducted using the most basic from of excitation, the sinusoidal waveform $a(t) = A_0\ sin\ (2\pi ft)$. Here A_0 is the amplitude f is the frequency and t is time.

Vibration amplitude is typically displayed in $g's$, where one g is the nominal acceleration of earth's gravity, 386.4 in/sec^2 or 9.806 $meters/sec^2$. Vibration amplitudes may also be quantified in terms of velocity or displacement. Tradition favors acceleration because acceleration measurements are readily conducted using piezoelectric accelerometers. Note that, as frequency increases, the peak velocities and displacements which correspond to constant peak acceleration are defined by:

$$a(t) = A_0 \sin(2\pi f t)$$

$$v(t) = \frac{A_0 g}{2\pi f} \cos(2\pi f t)$$

$$d(t) = \frac{A_0 g}{4\pi^2 f^2} \sin(2\pi f t) \tag{56}$$

Typical vibration tests cover some portion of the frequency range from 1 Hz to 5000 Hz. For tests on an electrodynamic vibration machine, a typical test uses frequencies from 10 Hz to 2000 Hz. At 10 Hz, 1 g corresponds to 0.2 *inches* peak-to-peak displacement. At 2000 Hz, 1 g corresponds to 5 *microinches* peak-to-peak. In general, lower frequencies imply higher velocities and displacements. Of course pure sinusoidal testing is unusual today, but it remains true that lower frequency vibrations, whatever their complex spectral content, imply greater velocities and displacements.

Random vibration testing supplanted sinusoidal tests for two reasons, first because random tests are much more realistic, and second because improved test

technology allowed random vibration tests to be conducted expeditiously. The advent of digital vibration control technology in the 1970s enhanced random vibration test capabilities enormously.

Random vibration testing is a broad topic, encompassing the theory of random processes (Sect. 2.3), practical test specification, differences between field and laboratory tests, over-testing concerns, test setup, instrumentation, test conduct, data analysis, and test reports.

Section 3.1 briefly reviews random processes, illustrates the autospectral density (also referred to as the autospectrum), and shows some typical random process realizations. Section 3.2 considers the essential differences between field and laboratory tests with emphasis on boundary conditions and the problems involved in test specification. Section 3.3 outlines the components of a random vibration test in a block diagram format. Section 3.4 covers that major portion of a test, setup and instrumentation. Section 3.5 describes test conduct.

3.1 Random Processes and the Autospectral Density

Section 2.3 provides a brief introduction to the theory of random processes. From a practical testing standpoint, three features of a random signal are important: the time history, the autospectrum, and the probability density [14]. The time history is the time evolution of the random signal. The autospectrum is an estimate of the normalized average squared magnitude of the frequency content as a function of frequency, and the probability density is an estimate of the distribution of signal magnitudes. A typical random vibration might expose a test item to an input acceleration of 5 g' *s RMS* (*Root mean squared*) over a frequency range from 20 *Hz* to 2000 *Hz* for 10 *minutes*. Figure 15 illustrates a typical realization of a time history, the corresponding autospectrum, and the probability density function. The time history is a typical broadband random signal. The autospectrum estimate is computed from the average magnitude of the frequency lines in discrete Fourier transforms (DFT) of successive blocks of the time history data [7]. (The estimate is erratic because it is based on finite data.) The normalized estimation error is approximately:

$$e = \frac{1}{\sqrt{2N}} = \text{estimation error}$$

$$N = \text{Number of averages used to form estimate} = \text{Blocks of data} \tag{57}$$

In the example shown in Fig. 15, a total of 62, 1024 point data blocks are averaged, so the expected error is about $e = 0.09$. This is consistent with the variation in the estimated autospectrum, which shows about 10% variation about a mean value of 0.0005 g^2/Hz. Autospectra are typically displayed on log-log plots.

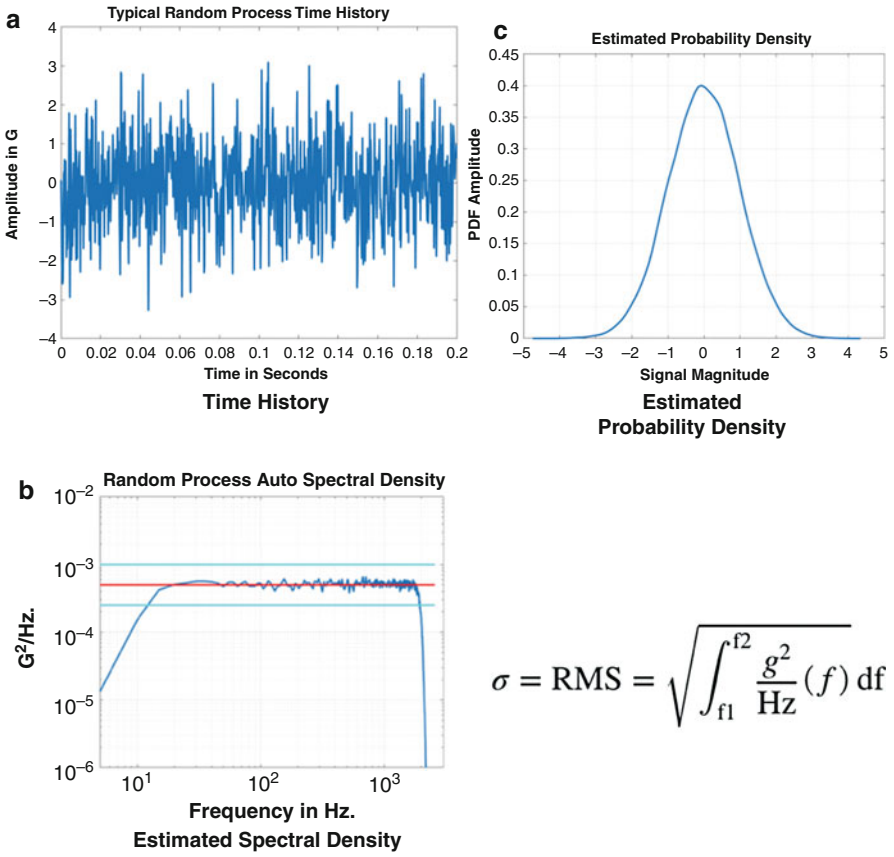

Fig. 15 Field tests and laboratory tests – implications for test specification

The desired test level is indicated by the red reference line. Tolerance bands of $+/-3$ *Db* are shown by the cyan lines in Fig. 15. The definition of a decibel is:

$$\begin{aligned} Db &= 20\log_{10}R \ \text{(Ratio of two amplitudes)} \\ Db &= 10\log_{10}R \ \text{(Ratio of powers)} \end{aligned} \tag{58}$$

where R is a ratio of two quantities, the denominator is a reference, and the numerator is said to be *Db* above or below the reference. Since the autospectrum is a squared quantity, the power ratio formula is used. Hence, 6 *Db* corresponds to about 4 times the reference level and 3 *Db* to twice the reference level on the g^2/Hz scale in Fig. 15. In Fig. 15, for example, the reference line is 0.0005 g^2/Hz. The lower -3 *Db* tolerance line is at half this value, 0.00025 g^2/Hz, and the upper $+3$ *Db* tolerance line is at twice 0.0005 g^2/Hz or 0.001 g^2/Hz. The root mean square

(RMS) value corresponding to the upper +3 *Db* line is the square root of the g^2/Hz level, or approximately $\sqrt{2} \times 1.013\ g$.

The probability density illustrated in Fig. 15c is typical for Gaussian random noise. Lower amplitudes are more probable than higher amplitudes. The signal is symmetric about the mean of zero. Magnitudes greater than about three times the RMS value are improbable, so the typical peak value of Gaussian random noise is often very roughly stated as +/− three times the RMS level.

A vibration test in the laboratory attempts to replicate the field environment. Such replication means that a component failure in the laboratory should replicate a similar failure in the field. Further, analytical models developed from laboratory test measurements should represent field conditions and field loads. Even so, field and laboratory conditions may differ substantially, as illustrated in Fig. 16.

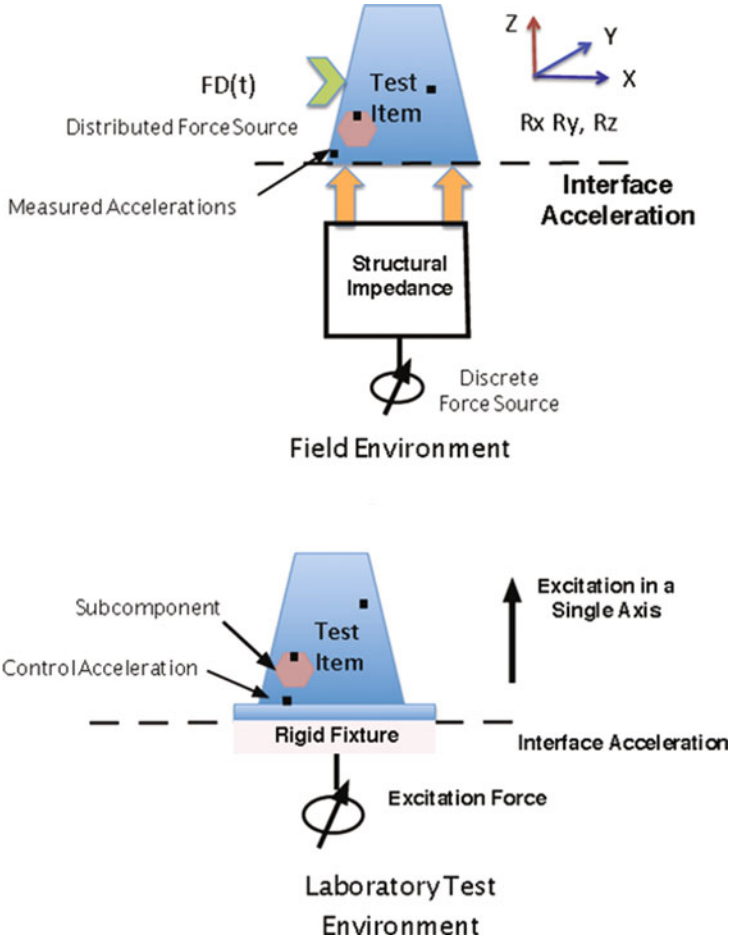

Fig. 16 Test item in field (top, **a**) and laboratory (bottom, **b**)

In the field, Fig. 16a, the test item is potentially excited by a suite of forces, some of which travel from a relatively discrete source through a supporting structure to the test body and some of which may be distributed. Acoustic and aerodynamic forces are examples of distributed forces. The forces act simultaneously in six degrees of freedom, x, y, z translations, and rotations about x, y, z axes. The dynamic loads on the test body are the result of a complex combination of the structural characteristics of the test item, the mechanical impedance of the support structure, and the excitation forces.

A conceptual laboratory environment is illustrated in Fig. 16b. The test item, attached to a fixture, is excited by a vibration machine. The force path is through the fixture interface into the test item. Distributed forces are not generally replicated. Further, the fixture mechanical impedance differs from the field structure. In the laboratory, the fixture is usually very rigid while in the field the structure is often moderately flexible. In the laboratory, the input control is usually at the fixture-test item interface where the field acceleration autospectrum is reproduced. Up to a point, this is reasonable. However, in the field, test item resonances produce notches in the acceleration spectrum at the control point. In the laboratory, the control spectrum is an approximation to the complex field measurement. For conservatism, this is usually accomplished by enveloping the measured field spectrum, thus eliminating the notches and yielding some level of over-test.

In the field then, test item resonances reduce acceleration levels at some frequencies. In the laboratory, test item resonances do not reduce control acceleration levels because the vibration machine, acting with large force capability through a rigid fixture, keeps the control acceleration spectra at the requested, enveloped, level. This results in a substantial over-test at resonant test item resonant frequencies.

The over-testing issue has been recognized for many years. Several approaches address the issue. One approach uses measurements of interface force in field and laboratory. With combined force-acceleration control, the interface acceleration is a function of required force, which mitigates the over-testing issue. This can work well, but force measurements are often hard to implement in the laboratory and are simply not available in the field.

A second approach to mitigate the over-testing issue is widely implemented. In this scheme, the interface acceleration spectrum is notched at frequencies where measured test item responses exceed field levels. This mitigates the over-testing issue. Even so, it is evident that, across the test item, the range of acceleration values experienced is quite different in field and laboratory environments, although the laboratory environment in some sense approximates the field environment.

In the field, the test body experiences excitation in six degrees of freedom. These are translations in the x, y, z directions, and the corresponding rotations about the x, y, z axes. In the laboratory, accelerations are usually applied sequentially in x, y, z axes. Clearly the test body responds quite differently in the multiaxis field environment than in the single axis laboratory environment. A further complication is that, in general, rotational environments are only rarely simulated in the laboratory. Recent advances in multi-shaker, multi-axis testing allow six degree of freedom excitation, but to date these are fairly complex and expensive to implement.

Research continues and some form of six degree of freedom excitation will likely become common in future vibration tests.

In summary, then, current vibration tests expose a test item to random acceleration with a specified spectral density, sequentially, in each of three orthogonal axes. The spectrum is usually different for each axis. To mitigate over-testing, the spectral response may be limited in certain frequency bands at some response locations.

3.2 Random Test Control Loop

A random vibration test exposes the test item to an acceleration time history. This time history is a realization of a Gaussian random process with a specified autospectral density. The desired spectral density is typically specified by a set of straight lines on a log-log scale. The electrodynamic vibration machine and power amplifier, when operating properly, are reasonably well approximated by a set of linear differential equations. The combined dynamics of the power amplifier, vibration machine, and test item result in a complicated spectral response at the control point. In each frequency band, the system dynamics modify the gain and phase characteristics of the voltage drive signal. This is compactly expressed in the frequency response function (FRF) graph in Fig. 17, which illustrates the acceleration response as a function of a constant voltage at each frequency. Below about 5 *Hz*, the illustrated FRF is inaccurate. In any case, below 5 *Hz*, small accelerations can exceed the maximum vibration machine displacement of between 1 and 3 *inches* peak-to-peak. 1 *g* peak at 3 *Hz* corresponds to a peak-to-peak displacement of 2 *inches*. Between about 5 *Hz* and 100 *Hz*, the velocity response

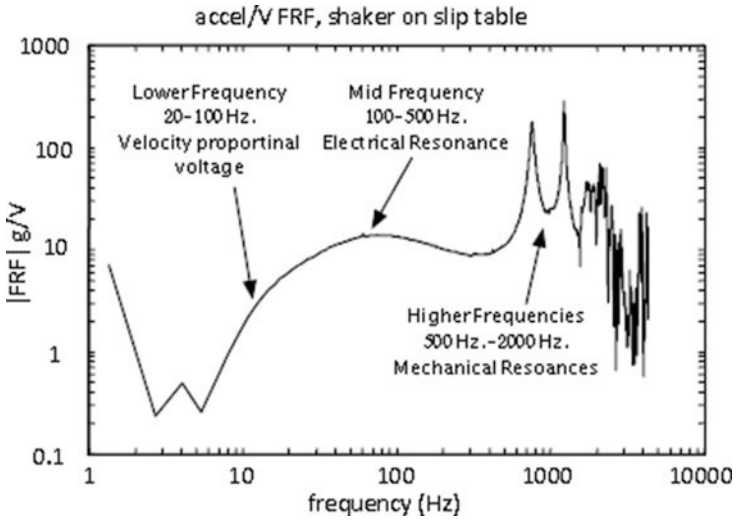

Fig. 17 Typical control acceleration/voltage drive FRF

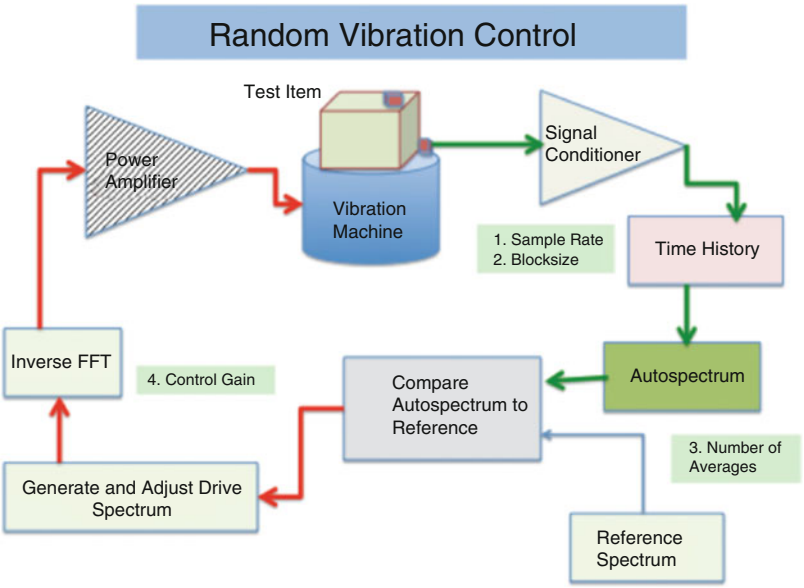

Fig. 18 Closed-loop scheme used to control random vibration test

is proportional to applied voltage, so the acceleration response increases linearly as a function of frequency. Above 100 Hz, the acceleration response is governed by the electrical resonance of the shaker armature-power amplifier system combined with the mechanical dynamics of the test item. Above about 500 Hz, the effects of test item and fixture resonances dominate the acceleration response.

To produce a flat acceleration spectrum, the voltage applied to the power amplifier must have the inverse of the frequency response function of Fig. 17. This is accomplished using a closed loop control system like that illustrated in Fig. 18.

Historically, random vibration control was accomplished by passing a random signal with a flat spectral density through a set of analog band pass filters. The composite signal, the sum of the filter outputs, was applied to a power amplifier driving the vibration machine. With the advent of digital vibration control in the 1970s, the analog filters were replaced by digital filters defined by the fast Fourier transform (FFT). (The FFT is an efficient implementation of the DFT.) Using the FFT a filter is effectively located at each discrete frequency line. Given a time series sampled at a rate S_r, the time record is typically broken into N blocks, each containing $n - points$; an FFT is performed on each block. Denote the blocks x_{jm}, $j = 0, \ldots, n-1$, $m = 1, \ldots, N$; within each block, the measurements are made at times $t_j = j/S_r$, $j = 0, \ldots, n-1$. Denote the DFTs of the blocks of random process realizations A_{km}, $k = 0, \ldots, n-1$, $m = 1, \ldots, N$. Within a constant, the DFT represents the Fourier transform at frequency $f_k = k\Delta f$, $k = 0, \ldots, n-1$, where $\Delta f = 1/(n\Delta t)$. Because the DFT is symmetric, the autospectrum is computed using the frequency lines $k = 0, \ldots, n/2$. The spectral density estimate is the

scaled average of the squared magnitudes of the FFT values from each block. The autospectrum estimator is:

$$\hat{g}\left(f_k\right) = \frac{2}{NnS_r} \sum_{k=1}^{N} |A_{km}|^2 \; k = 0, \ldots, n/2 \tag{60}$$

In commercially available vibration control systems, typical sample rates range from 2.56 to 4 times the highest control frequency. For example, for a test bandwidth of 2 KHz, the sample rate ranges from 5120 to 8000 Hz. Block lengths are traditionally a power of 2. For a block length of 4096 points, there are 20,489 spectral lines spaced 1.25 Hz apart.

The known response autospectrum is compared to the desired, or reference autospectrum. The drive voltage spectrum defines the normalized, squared magnitude of each frequency line in the drive voltage. If the response is too low at the control point, then the drive voltage spectrum is increased at that frequency line, and conversely if the response spectrum is high. To generate the drive voltage time history, the phase of each frequency component is randomized and an inverse FFT performed to generate a block of drive voltage. In practice, to prevent discontinuities at block boundaries, a time windowing and overlap algorithm is used to combine adjacent blocks.

The entire system in Fig. 18 runs in closed loop, with drive voltage continually applied to the power amplifier and continuous autospectral measurements computed from the time history response.

When a test is started at low level, drive voltage with a flat spectrum is applied to the power amplifier. The control loop steadily modifies the drive voltage spectrum until the response spectrum is within the desired bounds. These bounds are typically $+/-3\ Db$. The test level is then increased in steps until the full test level is reached. At each step, a drive voltage magnitude correction is performed on the drive spectra at each frequency line. Thus, ideally, the spectrum is just as specified at the full test level.

If acceleration limits are desired, the limit autospectrum, derived from some response accelerometer on the test item, is computed and compared to the desired limit. If the limit is exceeded, the drive voltage in the affected bandwidth is decreased until the response spectral density is within the desired limit. This "notches" the spectrum at the control point.

3.3 Test Setup and Instrumentation

The most time-consuming part of a random vibration test is almost always the test setup and instrumentation. Each test is unique, but there is a common thread. Table 1 provides a general guide to test setup and conduct.

Table 1 Test setup

Step	Designation	Comments
1	Instrument test unit	
2	Bolt fixture and test unit to vibration table	
3	Connect instrumentation to signal conditioning.	
4	Set sensitivity	
5	Setup control system test profile(s)	
6	Check sensitivity and control profiles	
7	Check that control transducer is in the test axis	

Comments:

1. For optimum results, the test operator should follow a procedure, but not blindly, and check each step in the process.
2. The test operator should check that the fixture attaches properly to the vibration table and the test unit.
3. Instrument the test unit, typically with accelerometers. Use a robust adhesive that is not prone to failure. Document the location of each transducer with text and photos. Develop a chart listing transducer locations and sensitivities. Ensure that the transducers are not inadvertently grounded to the test item. Grounding tends to introduce excessive 60 Hz noise due to ground loops. Secure cable attachments to the transducers. In some cases, the cable connection may be fixed with adhesives. Two common problems causing signal loss in vibration tests are failure of transducer mounting and poor cable connections. These both can occur during the test and may be difficult to remedy.
4. Bolt the test unit to the vibration table. Ensure that the power amplifier is not active. Over-testing has occurred in those (fortunately rare) cases where the power was applied to the shaker during setup and an inadvertent signal resulted in shocks or vibration applied to a partially mounted test system.
5. Torque all mounting bolts. Double check that all bolts are properly torqued. A relatively common problem in test setup is the failure to properly torque all bolts. One loose bolt can chatter, contaminating the test signals with accelerations caused by impacts. These signals are usually high amplitude, high frequency pulses.
6. Systematically connect all instrumentation to the signal conditioning system. Document the connection order. Set and check all transducer sensitivity values. Use a standard, documented output sensitivity. This sensitivity defines the voltage signal corresponding to a given acceleration value. An example sensitivity might be 25 *mv*/*g*, meaning that 25 *mv* corresponds to 1 *g*. For a system with 10 *volts* full scale, this means a full scale acceleration level of 400 *g*. Setting the sensitivity is a balancing act. Set a value that keeps the expected signals as large as possible, but well below the system full scale range. For many vibration tests, sensitivities ranging from 10 *mv*/*g* to 100 *mv*/*g* are optimal.

7. Set up the control system. This means defining the maximum test frequency, the desired spectrum, the number of frequency lines, and the control channel or channels. Control may be defined by a single channel, but it may also be defined by the average of the spectral density at several locations, or by a combination of control and limit channels. Define the test duration and the initial test level. A typical initial test level is 12 *Db* below the full level test. The RMS acceleration at -12 *Db* is one-quarter that of full level and the corresponding spectral density, in g^2/Hz, is one-sixteenth of full level.
8. Traditionally control autospectral values are defined using straight line segments on a log-log plot. An example of a flat spectrum is shown in Fig. 4. Once the autospectrum is input, check that the RMS level computed by the control system matches the expected RMS value of the reference spectrum. Also check that the displacement, velocity, and acceleration values estimated by the control system for the desired reference spectrum are within the vibration machine capabilities. This is somewhat problematic in many cases. Displacement is computed from the lower frequency components present in the reference autospectrum and is usually an accurate estimate. A peak-to-peak estimated displacement significantly less than the vibration machine capability is a good sign. Velocity estimates are also usually good. A problem arises with acceleration limits since the actual acceleration achieved is a function of the combined effects of the acceleration/voltage frequency response function of the combination of test item and vibration machine. This may be available prior to testing. A rough estimate can be made by dividing the vibration machine force capability by the total test item plus fixture mass. For example, consider a vibration machine with a force rating of 24,000 *lb* RMS. Suppose the armature weight is 100 *lb*, the fixturing is 200 *lb*, and the test unit is 100 *lb*. Estimated maximum RMS *g* is then $24{,}000/400 = 60$ *g*. In practice, this is a pretty rough estimate, but does provide some guidance.

With the instrumentation complete and the control system setup, the next step is conducting the test.

3.4 Conducting a Random Vibration Test

Conducting the random vibration test requires attention and vigilance. Even if one has conducted hundreds of tests, it is important to treat each new test as a new experience. While different vibration controllers have their own unique features, the testing procedure for all is similar. Table 2 lists the typical sequence of steps involved in test conduct. The most crucial item is the integrity of the control loop. Common problems include incorrect transducer sensitivity and transducer orientation. If the control system is set for a 100 *mv*/*g* sensitivity and the actual transducer/instrumentation system sensitivity is 25 *mv*/*g*, then the controller will, to achieve a 1 *g* response, increase the drive voltage until the 100 *mv* signal is reached. This is then an overtest since the true level is $100/25 = 4$ *g*. There are a couple of

Table 2 Conducting a random vibration test

Step	Designation	Comments
1	Start power amplifier and set gain	Gain appropriate for test level
2	Check control loop integrity	Control signal as expected, drive voltage reasonable
3	Initiate data recording	
4	Start test at low level	Levels of in axis channels consistent
5	Check instrumentation responses	All channels show reasonable response
6	Sanity check on responses	Frequency response function of in-axis channels unity at low frequency
7	Increase test level	
8	Stabilize at full level	
9	Conduct test for required duration	Continue to check control and response spectra and time signals
10	Reduce gain	
11	Shut down power amplifier	
12	Review test data	Recorded? Reasonable?

ways to minimize this problem. First, double check sensitivity settings. Second, have a "level check" transducer installed whose sensitivity is set to a constant value for all tests. Compare the level check and control transducer levels at lower frequencies where the test system approaches rigid body motion. They should be approximately equal.

Another insidious problem in the control loop occurs when the control transducer is inadvertently mounted in the wrong axis. This is especially easy to accomplish when a triaxial control accelerometer is used. If, for example, the test item is driven in the *x axis*, but the *y axis* is set up to read the control signal, then the measured control is really the off-axis motion. The controller then applies a very large drive voltage to make the off-axis response equal to the desired control level. This is a huge over-test! Fortunately, the loop integrity check integral to startup of most control systems will often read "open control loop" and thus avoid this problem. Sometimes the cross motion excited by the loop check drive voltage is sufficient to pass the loop check. Then the over-test occurs. There are a ways to minimize this problem. First, double check the control accelerometer orientation. Second, for critical tests, utilize a backup control accelerometer and set the control system to control on the maximum of the two acceleration signals. Then, if one accelerometer is incorrectly oriented, the control will, for most frequencies, be done using the correctly oriented accelerometer. Once control is achieved, a sanity check confirms accelerometer orientation and the controller can be set to control on the desired control channel.

Be ready to abort the test if anything untoward occurs, like violent shaker motion. The control autospectrum is often initially poor but should rapidly approximate the desired spectral response. Check that the control and level check spectra are in reasonable agreement (say, within 10%, $+/-1$ *Db*) at lower frequencies. This

means that the autospectra nearly overlap. If these do not agree, it may indicate problems with one of the accelerometers or instrumentation problems. "Lower frequencies" usually mean frequencies from about 10– 30 *Hz*. In this frequency range, most test systems respond nearly as rigid bodies and consequently all in-axis accelerations are similar.

Observe the responses on all of the instrumentation channels. All channels should have detectable random acceleration values. It is most unusual for a viable channel not to show some response to random excitation. In-axis channels should, like the level check channel, respond such that the low frequency autospectra overlay the control autospectra. If any channels fail to respond, troubleshoot the instrumentation system to isolate the issue.

Systematically increase the test level until full level is achieved. This is often done in steps. For example, the test might be started at -12 *Db* and levels increased in steps to -9 *Db*, -6 *Db*, -3 *Db*, and finally to full level. Once at full level, the test is conducted for the desired duration. Continually monitor the test responses. It is important to focus on the test, even with durations of hours. Failure to concentrate on the test can lead to problems that could have been corrected but, undetected, compromise the test. For example, if averaging or limiting is part of the test control, loss of a limit acceleration channel could mean an over-test. Control systems are designed to detect loss of signal, but this feature is by no means perfect.

4 Shock Testing on Shakers

Shock (transient vibration) testing became practical on electrodynamic and electrohydraulic shakers in the late 1960s, as evidenced by a paper of Favour and LeBrun [15]. The methods used have matured in the past decades, and several commercial software packages are now available. In spite of the basic simplicity of the technique, serious problems can arise. These are often due to nonlinearities that can hamper successful tests. The purpose of this chapter is to review the basic methods and explain why the tests don't always work.

Shock testing conducted on shakers can be divided into two basic classes. The first is reproduction of classical shock waveforms. By classical waveforms, we mean such shapes as a terminal-peak sawtooth or a haversine, the first application of shock testing on shakers. However, it was quickly realized that shakers had inherent limitations that prevented faithful reproduction of these waveforms. Several methods evolved to modify the classical waveforms so that they could be reproduced on a shaker. Reproduction of classical waveforms has serious limitations because of the velocity and displacement limits of the shakers. Except in special circumstances, it is not recommended that classical shock testing be performed on shakers and this method will not be further discussed. Shakers are better suited for reproducing oscillatory waveforms of the type that are suitable for shock testing. It was also realized that oscillatory shock environments are better simulated with an oscillatory shock than with a classical shock test, like a drop test.

The most common method for measuring severity of a shock is the shock-response spectrum (SRS, Sect. 2.5). This led to methods for preforming shock tests on shakers: synthesizing a waveform to match an SRS and reproducing the synthesized waveform on the shaker. The success of the test was the matching of the SRS and not the faithful reproduction of the time history. There are several varieties of the SRS, and there are many time histories that have essentially the same SRS. The variations in the definition of the SRS will be discussed and the most common methods to synthesize a shock time history to match an SRS will be reviewed.

The most common methods used today divide synthesis and reproduction into separate phases of the test. This section is organized to reflect such division. In some commercial software packages for shock testing on shakers, this separation is not always apparent to the user.

4.1 Time History Synthesis

The ideas and limitations of time history synthesis are covered in this section.

4.1.1 Basic Shaker Limitations

Before starting the discussion of shock testing on shakers, we should consider characteristics and limitations of shakers and their effect on the types of waveforms we can reproduce.

Initial and final acceleration and velocity must be zero for electrodynamic and electrohydraulic exciters. As with any testing machine, the maximum attainable values of acceleration and velocity are limited by the design of the machine and its power source. Flexures in electrodynamic exciters generate restoring forces that return the exciter table to its original position (defined as zero). This is not a requirement for electrohydraulic systems; however, by imposing this limitation, we can take advantage of both the forward and return portion of the stroke to generate the required transient.

The maximum acceleration that can be achieved is limited by two factors: the physical strength of the shaker armature (the manufacturer supplies this information) and the current and voltage capabilities of the power amplifier, combined with the complex electrical impedance of the shaker with the test item attached. Voltage and current being supplied by the amplifiers should be monitored. If peak voltage and current capabilities of the amplifier (set by the manufacturer) exceed preset maximum values, protection circuits shut down the amplifier. The acceleration limit of a particular transient waveform reproduced on a shaker/power amplifier, with a test item in place, is dependent on the system and is difficult to predict. Usually a lowlevel test is run and the peak current and voltage are observed to determine this limit. Another trick is to run a full-level transient through the power amplifier with the shaker field off. This can be used to determine whether the amplifier will dump without exposing the test item to a potentially damaging transient.

The peak-velocity capability of a shaker is determined by the voltage and current drawn during the transient test. The usual velocity limits specified for a shaker are

determined by steady-state cooling requirements and may not be representative for transient testing. As for acceleration, the manufacturer sets velocity limits. Experiments to test the transient limits can also be useful. The displacement limits are usually rigidly determined by the shaker design.

4.1.2 Classification of Waveforms

Velocity and displacement requirements for a waveform are related to the initial slope of the magnitude of the Fourier-spectrum of the waveform. This can be seen by noting that velocity and acceleration are the first and second derivatives of the displacement, respectively. Hence, the Fourier spectrum of velocity and acceleration can be found from the displacement Fourier spectrum to within a constant by multiplying by the frequency and the frequency squared, respectively. The SRS at moderately low frequencies is dominated by the residual spectrum. Since the undamped residual-shock spectrum and the Fourier spectrum are related, we would expect the initial slope of a lightly damped SRS also to be related to velocity and displacement requirements of a waveform. Many field measurements of the SRS of oscillatory shocks are corrupted at the lowest frequencies resulting in an incorrect slope of the SRS at low frequencies, suggesting a larger required velocity than realistically possible. The slope of the required SRS for transient testing on shakers should be carefully monitored to make sure the resulting synthesized waveforms can be reproduced on the shaker.

4.1.3 Matching a Required Shock Response Spectrum

The concept of the SRS [13] is deeply ingrained in dynamic testing. We will not develop the concept here except to say that the shock spectrum is a measure of the peak response of a single-degree-of-freedom system to a given input, plotted as a function of the natural frequency of the system. The shock spectrum is probably the most used, misunderstood, and abused concept in dynamic testing. It is a useful concept, and many shock environments are described and specified in terms of their shock spectra. As a result, a large effort has been made to synthesize waveforms that have some specified shock spectrum. At the outset, we note that this synthesis is not unique; that is, many waveforms exist that have essentially the same shock spectrum. It is not clear that all waveforms with the same shock spectrum will produce an equivalent test or produce the same damage to a test structure. Test engineers should have several waveforms available that will produce similar spectra so they can pick the one that best satisfies test requirements. Listed below are some of the many supplements to the shock spectrum that have been suggested to restrict the class of waveforms that can be used for a particular test. None has been universally accepted.

Limit the duration of the transient. It has been suggested that limits could be placed on the minimum and maximum allowable durations for the transient. It is felt that if the shock spectrum is matched and the duration is comparable to the field environment, the “damage” should be the same. For complex waveforms, careful attention should be given to “defining” the duration: STD-MIL-STD-810 suggests this method. This is the method favored by the author.

Require the shock spectrum to be matched at two different values of damping. Because damping is the least-known parameter in many systems, it is felt that if the shock spectrum is matched at two different values of damping (for example, a Q of 5 and 25), the resulting transient should be a reasonable simulation for all values of damping. However, it is very difficult to find a transient that will match a shock spectrum at two values of damping except for a limited class of functions. In fact, it is not even clear that a solution always exists. It is true, however, that a solution can exist. An example is the set of shock spectra with different damping values for a known time history. But if those spectra are modified (for example, smoothed, raised in level, or enveloped), it is not clear that a solution will still exist.

Specify the allowable ratios of the peak shock response and the peak input level. Encourage the use of oscillatory-type input as opposed to a single pulse (for example, a half-sine) input. Specifically exclude certain methods.

4.1.4 Time History Synthesis Using Oscillatory Waveforms

Several methods have been developed to synthesize a time history that will match a specified SRS. These methods have many similarities, and all are iterative to converge to a satisfactory solution. One method will be discussed in detail and the others more briefly since the basic procedures are the same for all. We will first discuss using sums of exponentially decaying sinusoids, then several variations of decaying sinusoids. Another method is WAVSYN (also called wavelets, [16]). The basic waveform of a WAVSYN pulse is an odd number of half sine waves windowed with a half sine. Other techniques, which include shaker optimized cosines (SHOC, not used much anymore), fast sine sweeps (not recommended), modulated random noise (frequently used), modification of field-time histories (used in the seismic industry), and least-favorable responses, are discussed in [17].

Sums of Decaying Sinusoids

It has been recognized for years that many field environments can be adequately represented by sums of decaying sinusoids [18, 19]. For example, the response of a structure to an impulsive load is the impulse response of the structure, which can be represented as a sum of decaying sinusoids. A component mounted on that structure will see this impulse response as an input.

The basic waveform for an exponentially decaying sinusoid is given by

$$a(t) = Ae^{-\zeta\omega t}\sin\omega t \ (\omega t) \qquad t \geq 0 \tag{61}$$

Figure 19 is a plot of the basic waveform. The waveform has three parameters that can be used to change its shock spectrum: the amplitude (A), to raise and lower the entire curve; the frequency (ω), to change the location of the peak in the curve; and the decay rate (ζ), to change the shape of the curve. Note that the decay rate is a parameter of the waveform and is not related to the fraction of critical damping used to compute the shock spectrum. By forming a sum of the basic waveforms, each

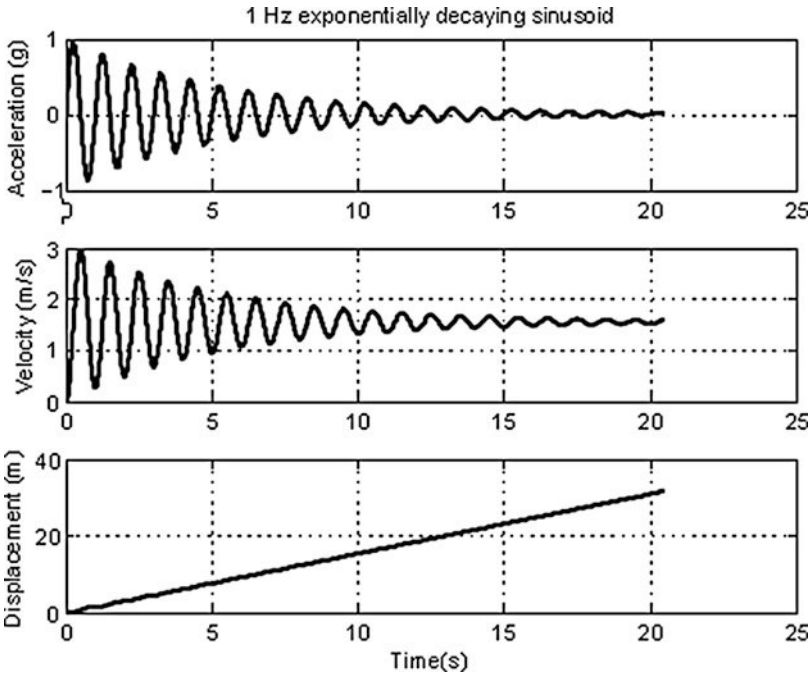

Fig. 19 Exponentially decaying sinusoidal acceleration and corresponding velocity and displacement

with different amplitude, decay rate, and frequency, we should be able to synthesize a waveform with almost any shock-response spectrum.

However, this waveform does not meet the requirements for a zero-velocity and zero-displacement change. If an attempt is made to reproduce this waveform, it will be distorted by the shaker system, removing the velocity and displacement change. Because the exact distortion will be a function of the shaker, it is difficult to predict the velocity and displacement requirements for the test.

Several modifications have been suggested to remove the objectionable velocity and displacements. Nelson and Prasthofer [19] suggested velocity and displacement compensation by adding two exponential pulses and a phase shift to the basic waveform.

$$x(t) = A\omega a^2 K_a e^{-at} + A\omega b^2 K_b e^{-bt} + A\left(c^2 + \omega^2\right) K_c e^{-ct} \sin\left(\omega t + \varphi_a\right)$$

$$K_a = 1/\left\{(a-b)\left[(c-a)^2 + \omega^2\right]\right\}$$

$$K_b = 1/\left\{(b-a)\left[(c-b)^2 + \omega^2\right]\right\}$$

$$K_c = 1/\sqrt{\left[(c-b)^2 + \omega^2\right]\left[(c-a)^2 + \omega^2\right]}$$

$$\varphi_a = \tan^{-1}\left(\frac{-2c\omega}{c^2-\omega^2}\right) - \tan^{-1}\left(\frac{\omega}{a-c}\right) - \tan^{-1}\left(\frac{\omega}{b-c}\right) \tag{62}$$

The first two terms are added for velocity and displacement compensation. The phase shift $\boldsymbol{\varphi}_a$ is added to force the initial values to zero. Considerations in the Laplace domain led to the above form. With this method, each individual component is compensated. Fisher and Posehn [20] derived a different method to accomplish the same objective (an initial and final acceleration, velocity, and displacement of zero). They called the method ZERD (zero residual displacement).

A third method [18] is to add a highly-damped, low-frequency, delayed, exponentially decaying sinusoid to compensate for velocity and displacement, CEDS (compensated, exponentially decaying sinusoids). This method has the advantage of correctly compensating for velocity and displacement when the acceleration waveform is truncated. As a result, lower values of decay rates can be used than for either Nelson's or Fisher's method. The time history of a single compensated component using (1 Hz, 1 g amplitude, 3% damping, 0 delay, is shown as Figure (EXPScTH.pdf). The compensated waveform is shown in Fig. 20. The SRS of the un-compensated and compensated waveforms is shown in Fig. 21.

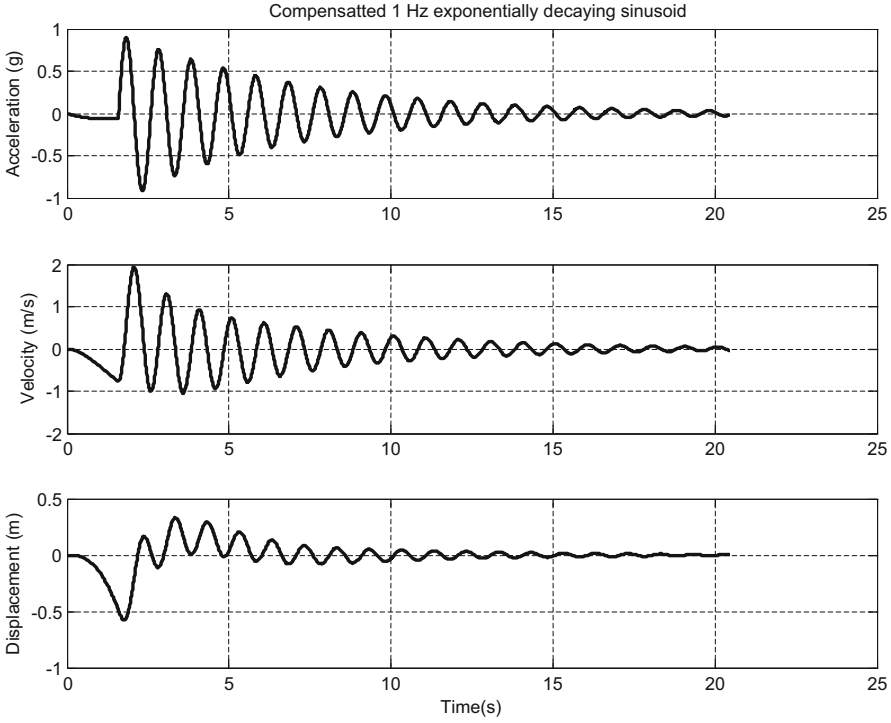

Fig. 20 A compensated, exponentially decaying sinusoid

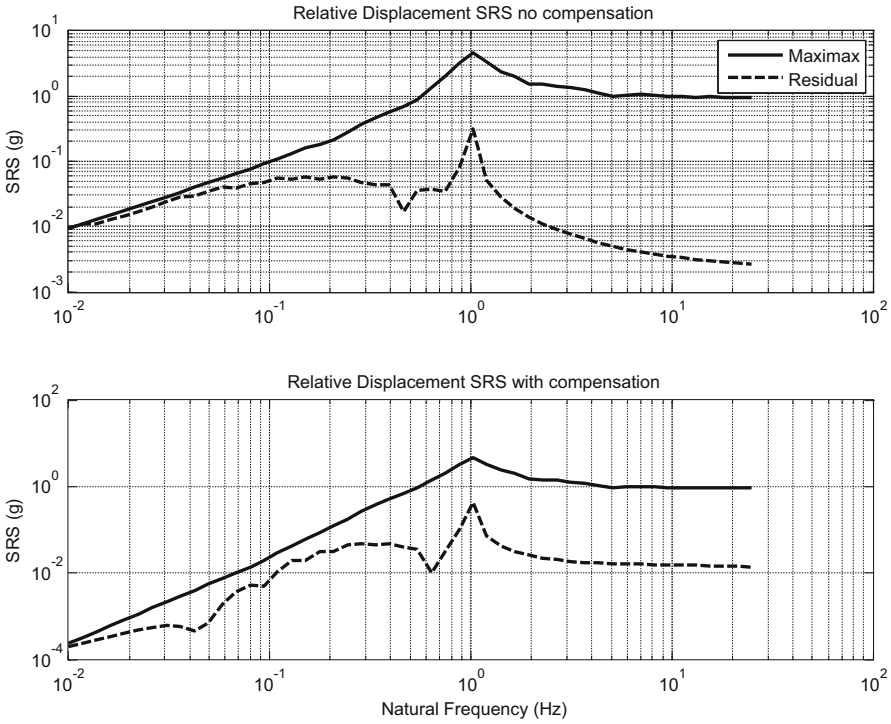

Fig. 21 SRS of uncompensated and compensated exponentially decaying sinusoids

Each of the three previous methods should give similar results. They are all based on exponentially decaying sinusoids (Figure 20) and have three free parameters for each component: amplitude, frequency, and decay rate. A fourth parameter, delay, is usually included. The delay is used to change the start time of a component. In this way, the components can be delayed with respect to each other and with respect to the start of the data frame.

It is probable that all three methods are still being used in some software packages. We will illustrate matching an SRS using Smallwood's method.

The iteration used is straightforward:

1. The shock pulse is a sum of indexed terms, each of which mimics Equation (61).
2. The amplitude of each component is changed a small amount, but not allowed to change sign.
3. The effect on the shock spectrum at the component's frequency is calculated.
4. A linear extrapolation of the amplitudes to produce the desired shock spectrum is then made.
5. For stability, at each iteration only a user-specified fraction of the correction is made.

The sample rate of 10,000 samples/second was used. English units were used with $g = 386.088$ *in*/*sec*^{2}. The SRS was the absolute acceleration model, with 12 *natural frequencies*/*octave*. The frequency of the compensating pulse was 40 *Hz*. The resulting acceleration waveform was 1024 *points* long. The frequencies of the decaying sinusoids are spaced at 1/3 *octaves* from 100 to 2000 *Hz* rounded to 2 significant digits.

The reference SRS has the break points provided in Table 3.

The decay rates were set so the components decay three time constants at the end of the pulse. The component delays were all set to zero. The initial amplitudes of the components were set to 1 and then iterated to the final amplitudes.

The final results are provided in Table 4.

The last component (15) is the compensating pulse to force the final velocity and displacement to zero.

Figure 22 shows the acceleration, velocity, displacement, and SRS of the final result.

Table 3 Break points for reference SRS

Frequency (*Hz*)	*SRS* (*g*)
100	10
1000	1000
1500	2000
2000	2000
10,000	1600

Table 4 Components in the sum of compensated, exponentially decaying sinusoids

Index(*k*)	*Freq.*(*Hz*)	*Ampl.*(*g*)	*Decay Rate*(ζ)	*Delay*(*sec*)	*Reqd. SRS*(*g*)	*Actual SRS*(*g*)	*Percenterror*
1	100	1	0.047	0	10	10.69	6.9
2	130	−2.44	0.036	0	16.9	16.78	−0.7
3	160	2.6	0.029	0	25.6	24.64	−3.7
4	200	−4	0.023	0	40	41.06	−2.6
5	250	6.2	0.019	0	62.5	61.42	−1.7
6	320	−11.45	0.015	0	102.4	99.75	−2.6
7	400	13.08	0.012	0	160	165.2	3.2
8	500	−25	0.009	0	250	248.7	−0.5
9	630	32.91	0.007	0	396.9	395.7	−0.3
10	800	−52.22	0.006	0	640	633.7	−1
11	1000	85	0.005	0	1000	1003	0.3
12	1300	−127.7	0.004	0	1566	1581	1
13	1600	194.3	0.003	0	2000	2016	0.8
14	2000	−176.5	0.002	0	2000	2069	3.5
15	40	2.71	1	−0.004	0.01	1.64	0

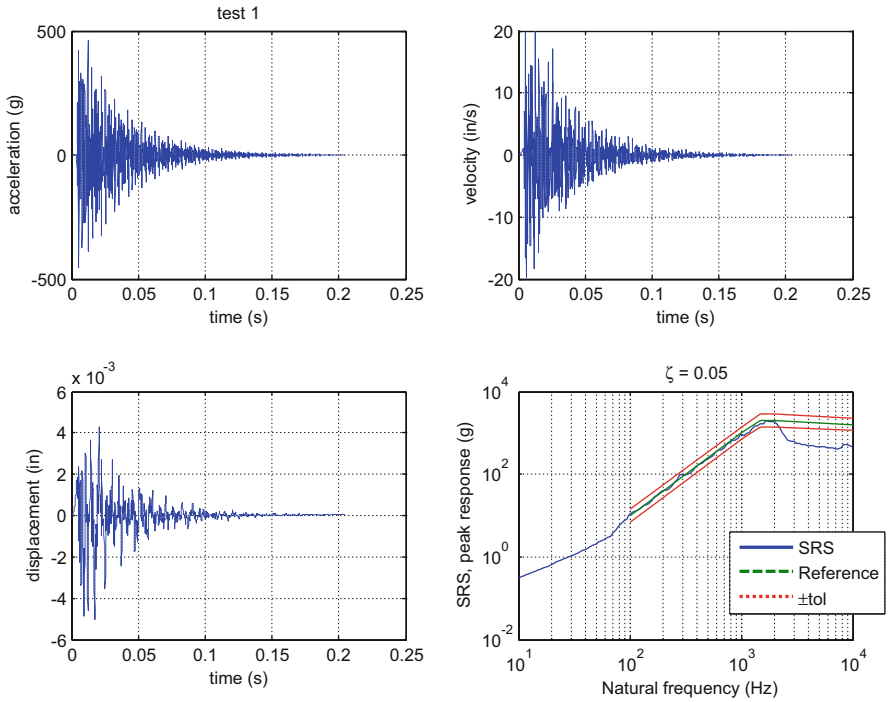

Fig. 22 Acceleration (top left), velocity (top right), displacement (bottom left), and SRS (bottom right) of the example

4.1.5 Problems with Synthesis

When any of the above-mentioned methods are used, problems are sometimes encountered. Some of these problems are now discussed.

Iteration will not converge – The components of the synthesized waveform are assumed to be independent from each other during iterations when in fact they are not. If the components are too close together, the damping is too large, or if the slope of the shock spectrum is too large, a solution may not exist. A small increase in the amplitude of one component can sometimes reduce the shock spectrum at that frequency because of the interaction between adjacent components. The absolute amplitude of a component cannot be reduced to less than zero even if the shock spectrum is high at that frequency; the component amplitude must not be allowed to go through zero. Changing the sign of the component amplitude will not, in general, lower the shock spectrum. The iteration software must be carefully written to avoid problems of convergence when these anomalies occur.

If the shock spectrum at high frequencies is less than the spectrum at some other frequency, a solution may not exist because the peak amplitude required to achieve the correct spectrum at the lower frequency may be larger than the required spectrum at the high frequencies. Remember that the shock spectrum at high frequencies will

approach the value of the peak acceleration. If convergence is a problem, you must determine why. Suggested solutions include: lowering the decay rates; reducing the number of components; changing the component frequencies; and changing the signs of the amplitudes of some of the components.

The spectrum matches at the component frequencies but is too low between the frequencies – To solve this problem, the number of components can be increased, placing the frequencies of the added components near the low places in the spectrum. The decay rates can be increased, filling in the low spots. The sign of the component amplitudes can be changed; however, the components interact in unpredictable ways when the sign of one of two nearby components is changed.

The spectrum matches at the component frequencies but is too high between some frequencies – You can lower the decay rates for components near the problem, change the sign of the amplitude of one of the nearby components, or drop a component.

The resulting waveform is not within the shaker capabilities – If the acceleration is too high, you must look for ways to reduce the peak acceleration. Delays of some of the components will sometimes work, as will changing the signs of some of the component amplitudes. A different waveform type could give a lower peak input. Lowering the decay rates will allow more resonant buildup during SRS computation, resulting in lower peak inputs. Sometimes, the frequency range over which the spectrum is matched will have to be narrowed to achieve an acceptable peak acceleration. If the velocity is too large, the low-frequency components are usually the cause, and a compromise at the low frequencies is sometimes required. A large displacement is also usually caused by the low-frequency components. A different waveform will have different velocity and displacement requirements; a change of waveforms sometimes helps. If compromises required to achieve a waveform within the shaker capabilities are not acceptable, the test should be moved to some other shock facility.

Historically, field shock spectra are often incorrectly high at low frequencies. Incorrect algorithms have been and are being used. Small errors in the zero line or waveform truncation can cause big errors in the low-frequency end of the shock spectrum. The SRS of a field environment that involves a very small velocity change should roll off between 12 and 18 *dB*/*octave* at low frequencies. Specifications that require large velocity changes should be questioned: Is a large-velocity change part of the environment being simulated? If a large-velocity change is involved, is a shaker the appropriate place for the test?

4.2 Time History Reproduction

The idea and limitations of time history reproduction are covered in this section.

4.2.1 Classical Theory

Time history reproduction on shakers rests on the Fourier transform theory. More specifically the discrete Fourier transform (DFT). A complete discussion of the theory is given in several standard texts [13].

In this section, a lower-case variable is generally a function of time, and its Fourier transform (or DFT) is given by the corresponding upper-case variable.

An important theorem connected to the Fourier transform relates the Fourier transforms of functions involved in a convolution (see Sect. 2.1.2). Let $x(t)$, $y(t)$, $z(t)$, $-\infty < t < \infty$ be functions of time, and let $X(\omega)$, $Y(\omega)$, $Z(\omega)$, $-\infty < \omega < \infty$ be their respective Fourier transforms. If the convolution:

$$z(t) = x(t) * y(t) = \int_{-\infty}^{\infty} x(\tau)\, y(t-\tau)\, d\tau \quad -\infty < t < \infty \tag{63}$$

is defined, then:

$$Z(\omega) = X(\omega)\, Y(\omega) \quad -\infty < \omega < \infty \tag{64}$$

These equations state that a multiplication in the frequency domain is equivalent to a convolution in the time domain. The former equation is important because it can be shown that for a single-input/single-output linear system, the output can be found from the convolution of the system's input and the impulse response of the system (for example, Equation (20)). The Fourier transform of the impulse response function is called the system frequency response function (FRF). Therefore, the Fourier transform of the output can be found from the product of the FRF and the Fourier transform of the input.

The shaker's transient control problem is a variation of the classical convolution problem. In our case, if we can determine the frequency response function, the required shaker drive (the input) can be determined from the desired output and the measured FRF:

$$X(\omega) = \frac{Y(\omega)}{H(\omega)} \quad -\infty < \omega < \infty \tag{65}$$

This class of problems is called deconvolution and presents more problems than convolution, as will be explained later.

The continuous Fourier transform is never calculated when testing on shakers. The FFT (fast Fourier transform) is used, which is an algorithm for computing the DFT. The differences and similarities between the DFT and the continuous transform are discussed in several texts [21, 22]. The three basic problems caused by using the DFT are aliasing, circular convolution, and leakage.

Aliasing is caused by using an inadequate sampling rate. High frequencies appear as low frequencies; therefore, analog, anti-aliasing filters should always be used. Filters with linear phase in the frequency band of interest should be used to

measure the response of the system. It is not essential to use linear phase filters with the drive waveforms.

Circular convolution is caused by the implicit assumption of periodic waveforms in the DFT. The convolution of two waveforms results in a waveform that has duration equal to the sum of the durations of the two individual waveforms. This can be seen by looking at the equation that defines a convolution. We will perform convolutions by taking the product of two DFTs. The two original time histories must contain enough zeros in the frame to assure that the convolved sequence will fit into the data block. If this is not done, circular convolution errors result.

Leakage arises because of the periodic assumption of a DFT. A DFT of length N assumes that the $(N + 1)^{st}$ point in the data sequence is the same as the first point. If this is not true, a discontinuity exists at the frame boundary. Extra frequencies will be generated to match this discontinuity; this is called leakage. Discontinuities in the derivatives at the frame boundary also cause leakage. If we multiply the original time history by a window to eliminate the discontinuity at the frame boundary, we are still performing a convolution in the frequency domain of the window and the original time history. This will smear the original frequencies over the bandwidth of the window. Leakage will be reduced but not eliminated. Leakage and the effects of windows are important because of the methods discussed later to measure the FRF.

4.2.2 Duration of a Transient Waveform

The i^{th} temporal moment of the function $f(t)$, $-\infty < t < \infty$ about a is defined as

$$m_i(a) = \int_{-\infty}^{\infty} (t-a)^i f^2(t) dt \; i = 0, 1, \ldots \tag{66}$$

The zero moment is called the energy (E) and is independent of a. The value of a, which makes the first moment zero, is called the centroid (τ). The square root of the second moment about the centroid (τ) normalized by the energy E is called the RMS duration [13] D_t.

$$D_t^2 = \frac{m_2(\tau)}{E} = \frac{1}{E}\int_{-\infty}^{\infty} (t-\tau)^2 [f(t)]^2 dt \tag{67}$$

The RMS duration is a convenient way to define the duration of a transient.

One of the flaws of transient testing using the SRS is that there are no restrictions on the duration of the waveform. It is not clear that waveforms with the same SRS but with different durations have the same damage potential. One way to avoid this issue is to specify the duration, with tolerances, of the test waveform.

There is an interesting relationship between the RMS duration and the RMS bandwidth of a transient. The RMS bandwidth of the Fourier transform of $f(t)$, namely $F(f)$, is computed about its centroid, c, and is defined as:

$$D_f^2 = \frac{2}{E}\int_0^\infty (f-c)^2 |F(f)|^2 df \tag{68}$$

The product of the RMS bandwidth and the RMS duration must satisfy the inequality:

$$D_f D_t \geq \frac{1}{4\pi} = 0.0796 \tag{69}$$

This implies that we cannot have a transient with a short duration and a narrow bandwidth.

4.2.3 Measurement of the System Frequency Response Function

The first step in reproducing a transient is to measure the FRF. Figure 23 outlines the basic procedure. A low-level calibration waveform is applied to the shaker with the test item attached. It is usually essential to have the test item mounted because the dynamic loading of the test item can greatly influence the FRF. Many forms of a calibration waveform can be used (Table 5). The only strong requirement is that the waveform has nonzero frequency content at all frequencies of interest. The RMS level of the waveform should be large with respect to the RMS noise in the system to maximize the signal-to-noise ratio. However, consideration must be made to assure the calibration procedure is not more damaging than the test waveform.

The first waveform used was an exponential, decaying pulse [15]. This waveform has good frequency content. The frequency content is flat to a cutoff frequency defined by the decay rate of the exponential and then gently rolls off. The faster the waveform decays (the shorter the pulse), the wider the frequency content of the pulse. A short pulse degrades the signal-to-noise ratio as the average value of the pulse over the whole data frame decreases. Thus, a conflict arises: a short pulse

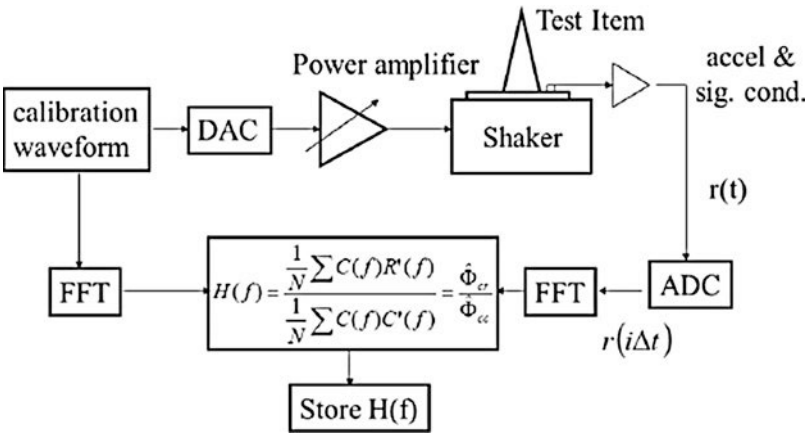

Fig. 23 Basic procedure for obtaining the FRF

Table 5 Waveforms that can be used for system identification

TYPE	S/N	Frequency content	Noise rejection
Fast sine sweeps	Good	Good	Fair
Random burst	Good	Good	Good
Exponential decaying pulse	Poor	Good	Poor
Reference waveform	Fair	Poor	Fair/poor

has better frequency content but increases the noise in the FRFs. The same pulse is repeated for averaging; therefore, this wave form cannot reject nonlinearities.

The next waveform used was a fast sine sweep. This waveform had a better signal-to-noise ratio but still could not reject nonlinearities. To prevent leakage, the sine sweep must be short enough for the response to decay before the end of the frame.

Another frequently tried waveform uses the reference waveform as the calibration pulse. This is often a poor choice because the reference waveform may have near zeros in its frequency content.

Another popular transient waveform is a random burst. The burst is usually re-randomized between averages to reject nonlinearities. To prevent leakage errors, the burst must be short enough for the response to decay before the end of the frame.

Steady-state excitation is also used. Steadystate random excitation is popular. This waveform has a good signal-to-noise ratio and can reject nonlinearities. However, a window has to be used to prevent leakage, causing a smearing of the frequency lines and distorting the FRF.

Pseudo-random can be used. It is usually defined as a waveform that appears to be random, but is really one period of a very complicated periodic signal. If a pseudo-random signal is repeatedly output and the period of the digitized waveform is the same as the pseudo-random period, it is not necessary to window the data to prevent leakage. The estimate of the FRF is thus not biased by the window. The signal-to-noise ratio is good and, while uncorrelated related noise is rejected, nonlinearities are not.

The Fourier transforms of the calibration waveform $C(\omega)$ and the system response $R(\omega)$ are calculated. In the simplest form, the FRF is estimated by taking the ratio of these transforms. The FRF is then stored for later use. In practice, the FRF that is found from the ratio of the transforms of a single calibration pulse tends to be noisy and is of limited use. Some averaging is usually required to produce a satisfactory FRF. A convenient form for estimating the FRF when averaging is given by:

$$H_2(\omega) = \frac{G_{cr}(\omega)}{G_{cc}(\omega)} \tag{70}$$

where $G_{cr}(\omega) = Ave[C^*(\omega)R(\omega)]$, the cross-spectrum between the input and output, and

$G_{cc}(\omega) = Ave[C^*(\omega)C(\omega)]$, the auto(power) spectrum of the input

For one average, this formulation reduces to the simple form:

$$H_2(\omega) = \frac{G_{cr}(\omega)}{G_{cc}(\omega)} = \frac{C^*(\omega) R(\omega)}{C^*(\omega) C(\omega)} = \frac{R(\omega)}{C(\omega)} \tag{71}$$

Another advantage of using the above formulation is the availability of the coherence function. The coherence is a measure of the quality of the linear FRF estimate. The magnitude of the FRF can be found from

$$|H_2(\omega)|^2 = \frac{G_{cr} G_{cr}^*}{G_{cc} G_{cc}} \tag{72}$$

For a noise free linear system, another estimate of the FRF is given by

$$|H_1(\omega)|^2 = \frac{G_{rr}(\omega)}{G_{cc}(\omega)} \tag{73}$$

where $G_{rr}(\omega) =$ the autospectrum of the response.

The coherence is defined as

$$\gamma^2(\omega) = \frac{G_{cr} G_{cr}^*}{G_{cc} G_{rr}} = \frac{|H_2(\omega)|^2}{|H_1(\omega)|^2} \tag{74}$$

A coherence of less than one indicates the presence of uncorrelated response. Thus, a coherence of almost one indicates a linear system with little noise. The coherence will drop when nonlinearities are present in the system if the excitation is varied in some random way between data frames. If both input and output are deterministic, the coherence will stay almost at one even if the system is nonlinear. To detect nonlinearities, the phase relationships between different frequency components must change from one excitation pulse to the next.

These equations illustrate why it is important that the input waveform have a non-zero frequency content at all frequencies of interest. If the Fourier spectrum is near zero at any frequency, the FRF will be the ratio of two small numbers, resulting in a poorly defined value at that frequency.

The formulation above can reject uncorrelated noise from the estimate of the FRF. If the system is nonlinear, the formulation will reject the nonlinearities if the input waveform is varied in some random way between averages.

The level that should be used to determine the FRF is never clear. A high level is desired to minimize effects of the assumption of linearity between the calibration level and the test level. This is particularly important with electrohydraulic shakers because these shakers are nonlinear. However, if the level is too high, the calibration pulse to determine the FRF can be more damaging than the actual test. Some of

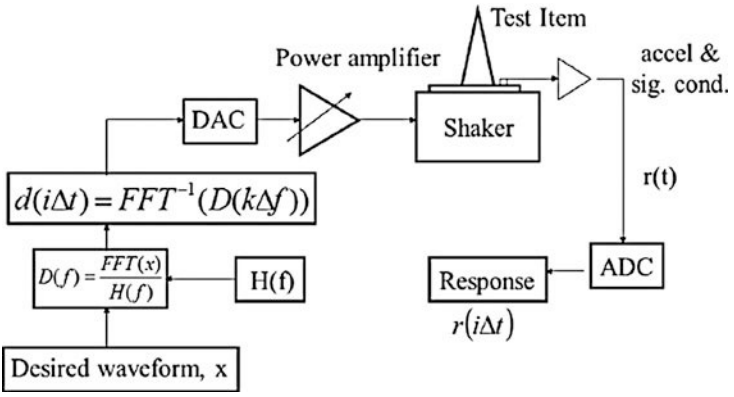

Fig. 24 Procedure for performing a shock test

the waveforms require a long excitation time of the test item. Periodic random is an example. The test time as well as the level must then be considered.

Also, the excitation used to determine the FRF is frequently broader in frequency content and has a higher RMS-to-peak ratio than the test pulse. The customer should always be aware of the requirement to excite the system to determine the FRF, and the levels used should be agreed on.

The system FRF $H(\omega)$ is estimated from the input and response of the system to the calibration waveform. The drive waveform $x(t)$ required to reproduce the desired waveform $y(t)$ is then computed in the frequency domain using:

$$X(\omega) = Y(\omega) / H(\omega) \tag{75}$$

Careful attention must be used when preforming this calculation to avoid the errors discussed above. Many times it is necessary to window the impulse response of the FRF inverse to prevent leakage.

The computed drive waveform is then used to drive the shaker, and the result is observed in Fig. 24. Typically several reduced level transients are output to determine if the results are satisfactory before the full level test is performed. The FRF and the computed drive may be updated during this phase.

Often the success of the test is measured by the SRS of the control accelerometer, and not the exact reproduction of the desired waveform.

4.2.4 Why Things Do Not Always Work

Deconvolution is not easily and accurately accomplished; many times it is ill-conditioned, and a good solution is difficult. The software needs a bag of tricks to help make things as easy as possible. If the FRF has zeros or notches at any frequency, they become maximums when the FRF is inverted. If these notches

are noisy (random amplitude and phase errors), the noise is amplified. The noise causes ripple in the amplitude and phase of the FRF, which tends to spread the time history of the inverse impulse response (IIR) as the RMS duration discussion illustrated earlier. Typically, the FRFs found in the test laboratory do have poorly defined notches. The FRF tends to roll off at low frequencies, resulting in a notch at zero frequency. Often the high frequencies in the FRF have several very noisy notches. Even if the desired waveform does not have much energy content at the high frequencies, the computed pulse will, because of the noisy FRF at the high frequencies. The system is trying to say that if the FRF is poorly defined in a notch, a large, poorly defined input is required to achieve the desired response at that frequency.

4.2.5 Why Things Do Not Always Work, an Extreme Example

The desired waveform (a sum of exponentially decaying sinusoids) is shown in Fig. 25. A measured FRF is shown in Fig. 26. The resulting reproduced waveform is shown in Fig. 27. The result is satisfactory. A noisy notch is introduced into the FRF (Fig. 28). The desired waveform along with the simulated reproduced waveform is shown as Fig. 29. As can be seen, any resemblance to the desired waveform is coincidental.

4.2.6 Improving Your Chances for a Good Test

Several things can be done to improve your chances of a good test (if your software will let you). Always preview the FRF before running the test. A little experience will frequently identify a bad FRF. Preview the drive waveform. Again, experience will indicate problems before, rather than after, the test. Delete part of the FRF. Often a band of frequencies (usually the high frequencies) will have little effect on the resulting drive. If the drive at these frequencies is poorly defined, they can be deleted. For example, consider the case of a desired waveform composed of exponentially decaying sinusoids, with a highest frequency component of 1000 *Hz*.

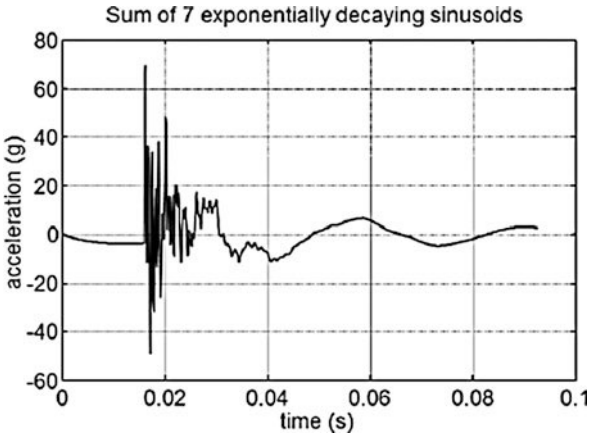

Fig. 25 Desired time history

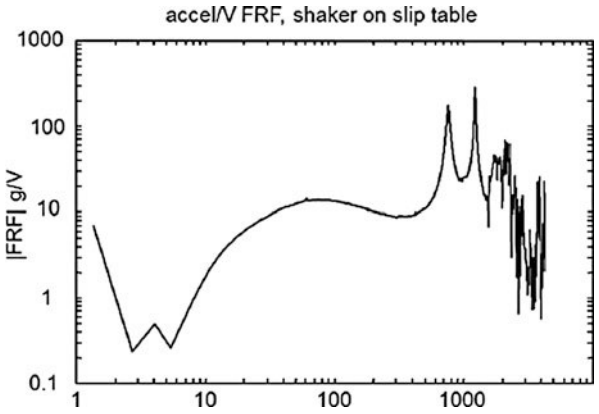

Fig. 26 FRF based on accurate measurements

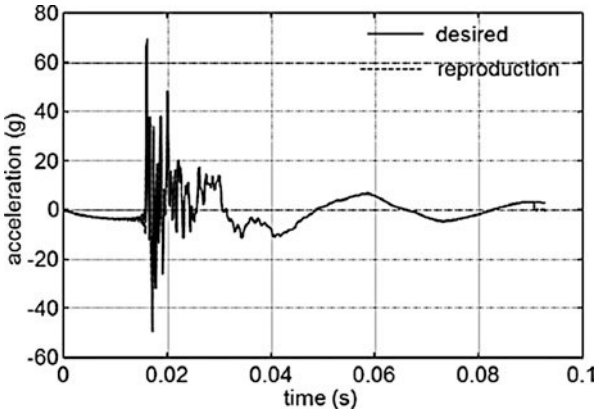

Fig. 27 Test time history obtained during accurate analysis

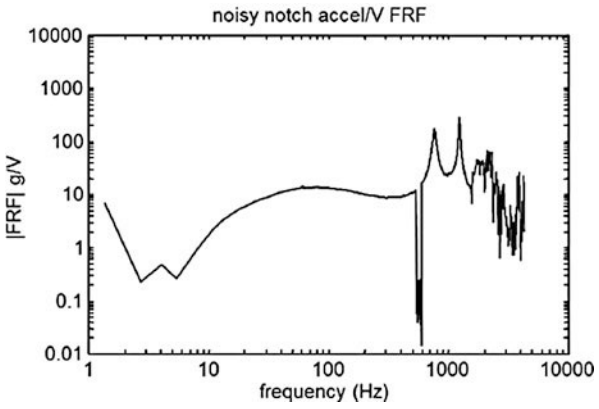

Fig. 28 FRF with noisy notch

Assume that a sample rate of 10,000 *samples*/*sec* was used. The FRF could be calculated to 5000 *Hz* in some systems. The frequencies above 1500 *Hz* are not necessary for good reproduction of the waveform. If a noisy FRF is causing a

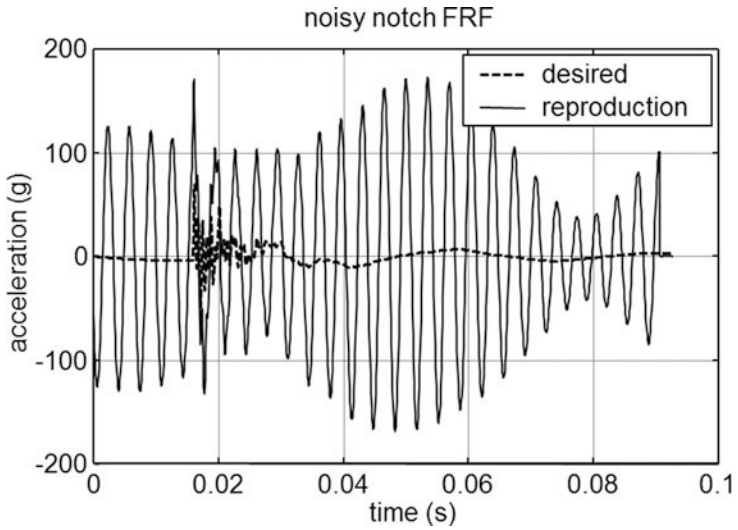

Fig. 29 Test time history obtained using FRF with noisy notch

problem, the FRF could be deleted above 1500 Hz. This example also indicates how an ideal notch (deleted frequency lines) can sometimes have less effect than a noisy notch.

Multiply the inverse FRF by the coherence; some authors have called this function H_2. The modified FRF will deemphasize those frequencies where the uncertainty is the greatest.

Smooth the FRF; a Hanning smoothing in the frequency domain often gives good results.

Some of the transient control packages in use offer an option of correcting the drive, based on an error signal derived from the difference between the actual return waveform and the desired waveform. These options frequently do not work very well because the error (the difference between the actual return waveform and the desired waveform) can be divided into two parts. The first is deterministic – the part for which an identical input will produce the same output. This part is created by two factors. The estimated FRF may not be the true FRF but contains some errors and nonlinearities. This factor can be corrected by dividing the Fourier transform of the error by the FRF and then transforming the correction to the time domain and subtracting it from the drive waveform. For stability, sometimes only a fraction of the correction is used. The correction should produce a response equal and opposite to the error, thus canceling the error. However, part of the error is not deterministic. We have seen how this error can be amplified by the deconvolution process. The correction calculated will not improve this error, but will make it worse. After a few iterations the error can grow enough to dominate the response.

Another iteration method uses the drive waveform and the response of the control point to update the FRF. In concept, multiple applications of the test waveform

will improve the FRF, and the difference between the desired waveform and the actual shaker response at the control point should be reduced. In practice, the drive waveform will usually have notches in the frequency domain. These notches result in poor estimates of the FRF, and the error between the desired and actual waveforms will degenerate instead of improving.

The frequency content of the waveform can be changed to improve the estimate of the FRF. For example, the lower frequencies are often difficult to measure because of the low response at low frequencies. Additional energy in the calibration pulse can improve the results. The mechanical setup can also be improved. Joints that open or slip can cause problems. If these joints are part of the setup, they can be improved.

The control accelerometer can be moved since its location is often poorly defined. For example, the control could be specified on a flange; moving it a few inches can result in significantly different responses in the kilohertz frequency ranges.

The largest cause of poor results in transient testing on shakers is nonlinearities. Some of the most common forms of nonlinearities follow:

Rattling loose parts – The FRF is sensitive to amplitude and the response is nonsymmetrical. For example, when the input is <1 *g*, the FRF looks normal. When the input exceeds this amount, the nonlinearities become apparent. The only solution to this problem is to remove the loose parts.

Gapping joints – The FRF will be sensitive to amplitude, but the input level required is not necessarily 1 *g*, for the loose-part problem. It can vary depending on the load required to open the joint. Typically, the FRF will look normal because the levels used to measure the FRF were not high enough to open the joint. When the test is run at low levels, the results are good. But at some higher level, the waveform reproduction looks good part-way into the transient; however, it then breaks up, showing increased high-frequency content from impacts as the joint closes. Little can be done except to tighten the joint. If the joint is within the test item, the test engineer frequently cannot change the joint preload.

Sliding joints – This is similar to the gapping joint except that the joint slides instead of opening. The sliding joint chatters or impacts when the shear gaps close. The symptoms are also similar to the gapping problem.

4.3 Conclusion

This section should provide the reader with some insight into the strengths and weaknesses of transient testing on shakers. The insight should provide users of transient software packages with a better understanding of their test results and give them ideas for improving lessthan-ideal tests. The customers of dynamic testing services can use the insight to understand that a poor test is not always due to the test methods but can also be due to the less than ideal capriciousness of Mother Nature. The methods assume linear systems; the shakers are usually almost linear; but the test items are sometimes very nonlinear.

5 Closure

Practically all real-world structures are subjected to random vibration and mechanical shock environments during their design lives. The time domain and frequency domain analyses in Sect. 2 illustrate methods for estimating structural responses to applied dynamic loads. For either single- or multiple-degree-of-freedom systems, the analytical approach uses differential equations to estimate response time histories and the Fourier transforms of response time histories. Each mode of a multiple degree of freedom structural response is governed by the equations for a single-degree-of-freedom structure. In the field where a system is excited by forces derived from transportation, aerodynamic or other environments, the analytical methods provide a useful, robust means of estimating dynamic behavior based on first principles.

From the experimental perspective outlined in Sect. 3, strains, displacements, velocities, and accelerations are measured variables. The contrasting conditions characteristic of field and laboratory tests are noted. Laboratory modal and vibration tests measure dynamic responses under controlled conditions.

In field or laboratory, in analysis and experiment, time history responses, spectra, and modes are basic features of the dynamics. For approximately linear systems, exposed to non-destructive environments, the analytical and experimental results are reasonably comparable, especially at frequencies corresponding to the lower eigenvalues (modes). Four major sources of difference between analytical and experimental results are:

1. The difficulty of properly defining the numerical functions governing damping
2. Problems specifying the actual characteristics of physical joints
3. The inevitable presence of some amount of nonlinearity
4. The statistical nature of the prosperities of nominally identical physical structures

The analytical model often provides an excellent approximation to the measured physical response, but its utility is far reaching because it also provides a way of thinking about and quantifying the basic principles underlying the often exceedingly complex temporal responses of real systems.

From a testing standpoint, many vibration environments, whether field or laboratory, deal with as noted in Sect. 3. Section 4 dealt with mechanical shock, another common field environment. The same analysis concepts of spectra, frequency response functions, modes, temporal responses, and frequency domain response apply to both random vibration and mechanical shock. Analytically the approaches to response estimation are quite similar. Experimentally, for shock tests a specific response waveform is the desired response. For random tests, the autospectral density characterizes the desired response. Of course, shock spectrum applies almost exclusively to shock tests.

In general, the less averaging involved in the measure considered the more problematic the comparison between analytical and experimental results. Autospectral responses and lower frequency mode frequencies and shapes are often very

comparable. In contrast comparisons of temporal response are a best vaguely similar.

Analytical first principles models and experimental test results are mirror aspects of the same phenomena. Both address the forces and accompanying strains to which real systems are exposed. The intelligent use of both is essential to full understanding of structural dynamics.

New developments continue in both analysis and experiment. The very substantial increase in computational power in the past three decades means that first principles models can now deal with finer physical features and can be applied to a range of statistically similar systems. In the experimental world, new testing procedures like multi-shaker and multi-axis tests do a better job of approximating the real field environment. In both venues, there is a real need for new ways of viewing nonlinear behavior and the statistical nature of real structures. The time is ripe for the emergence of new measures to supplement the tried and true spectral analysis, shock spectra, frequency response, and modal characterizations.

References

1. Murphy GM (2011) Ordinary differential equations and their solutions. Dover Publications, Mineola
2. Inman DJ (2000) Engineering vibration, 2nd edn. Prentice Hall, Upper Saddle River
3. James JF (2011) A student's guide to Fourier transforms: with applications in physics and engineering, 3rd edn. Cambridge University Press, Cambridge, UK
4. Bendat JS, Piersol AG (2010) Random data, analysis and measurement procedures, fourth edition. Wiley, New York
5. Abramowitz M, Stegun I (2014) Handbook of mathematical functions with formulas, graphs, and mathematical tables. National Bureau of Standards, Applied Mathematics series 55. U.S. Government Printing Office, Washington, DC
6. Bathe K-J (1996) Finite element procedures. Prentice Hall, Upper Saddle River
7. Wirsching PH, Paez TL, Ortiz K (1995) Random vibrations, theory and practice. Dover Publications, Mineola
8. Einstein A (1905) On the movement of small particles suspended in a stationary liquid demanded by the molecular kinetic theory of heat. Annalen der Pyhsik 17:549. Also, reprinted in Einstein [9]
9. Einstein A (1956) Investigations on the theory of the Brownian movement. Dover Publications, New York, Edited by R. Furth
10. Wiener N (1930) Generalized harmonic analysis. Acta Math 55:118
11. Crandall S (1958) Statistical properties of response to random vibration, Chapter 4. In: Crandall S (ed) Random vibration. Technology Press of MIT and Wiley, New York
12. Crandall S (ed) (1958) Random vibration. Technology Press of MIT and Wiley, New York
13. Piersol AG, Paez TL (2010) Harris' shock and vibration handbook, 6th edn. McGraw-Hill, New York. (See Chapter 8)
14. Ang AH-S, Tang WH (2006) Probability concepts in engineering: emphasis on applications to civil and environmental engineering, 2nd edn. Wiley, New York
15. Favour JD, LeBrun JD, Young JP (1969) Transient waveform control of electrodynamic test equipment. In: Shock and vibration bulletin 40. Shock and Vibration Exchange, Arvonia
16. Yang RC (1970) Safeguard BDM system – development of a waveform synthesis technique, SAG-64. Ralph M. Parsons, New York

17. Smallwood DO (1975) Time history synthesis for shock testing on shakers. In: Seminar on understanding digital control and analysis in vibration test systems, Part II. A Publication of the S&V Information Center, Shock and Vibration Exchange, Arvonia, pp 23–42
18. Smallwood DO, Nord AR (1974) Matching shock spectra with sums of decaying sinusoids compensated for shaker velocity and displacement limitations. In: Shock and vibration bulletin 44, Part 3. Shock and Vibration Information Center, Naval Research Laboratory, Washington, DC, pp 43–56
19. Nelson DB, Prasthofer PH (1974) A case for damped oscillatory excitation as a natural pyrotechnic shock simulation. In: Shock and vibration bulletin 44, Part 3. Shock and Vibration Exchange, Arvonia, pp 57–71
20. Fisher DK, Posehn MR (1977) Digital control system for a multiple-actuator shaker. In: Shock and vibration bulletin 47, Part 3. Shock and Vibration Exchange, Arvonia, pp 79–96
21. Stearns SD (1975) Digital signal analysis. Hayden Book Company, Rochelle Park
22. Rabiner LR, Gold B (1975) Theory and application of digital signal processing. Prentice-Hall, Englewood Cliffs

DIC and Photogrammetry for Structural Dynamic Analysis and High-Speed Testing

8

Christopher Niezrecki, Phillip L. Reu, Javad Baqersad, and Daniel P. Rohe

Contents

Sandia National Laboratories is a multimission laboratory managed and operated by National Technology and Engineering Solutions of Sandia, LLC, a wholly owned subsidiary of Honeywell International Inc., for the U.S. Department of Energy's National Nuclear Security Administration under contract DE-NA0003525.

C. Niezrecki (✉)
Department of Mechanical Engineering, University of Massachusetts Lowell, Lowell, MA, USA
e-mail: Christopher_niezrecki@uml.edu

P. L. Reu · D. P. Rohe
Sandia National Laboratories, Albuquerque, NM, USA
e-mail: plreu@sandia.gov; dprohe@sandia.gov

J. Baqersad
Department of Mechanical Engineering, Kettering University, Flint, MI, USA
e-mail: jbaqersad@kettering.edu

R. Allemang, P. Avitabile (eds.), *Handbook of Experimental Structural Dynamics*,
https://doi.org/10.1007/978-1-4614-4547-0_3

Abstract

This chapter provides an overview and some important considerations to be made when making optical and stereophotogrammetry measurements on structures for dynamic applications. In particular, the chapter focuses on leveraging

those measurements to perform digital image correlation (DIC) to extract dynamic parameters (e.g., strain, deflection, operating shapes, and mode shapes). Structural dynamic testing and analysis in the context of performing optical measurements is described. Information on optical high rate testing is also presented along with lessons learned and best practices.

Keywords

Stereophotogrammetry · Digital image correlation · High-speed testing · Structural dynamics · Modal analysis

1 Introduction and Relation to Prior Related Work on DIC and Point Tracking

Photogrammetry is a method of identifying geometry, displacement, and deformation of objects using photographs or digital images. This non-contacting measurement approach was initially used aerially in order to create maps. The fundamental approach in photogrammetry involves correlating an object's dimensions to its dimensions within a photograph (see Fig. 1). With advances in digital cameras and computing systems, the accuracy of the photogrammetry technique has improved significantly. These advances have allowed engineers and scientists to use close-range photogrammetry for laboratory measurements with a very high degree of precision. Recently, photogrammetry has received particular attention due to its nonintrusive, noncontact measurement capabilities and its robustness for in situ measurements. This technique provides accurate full-field geometrical measurement

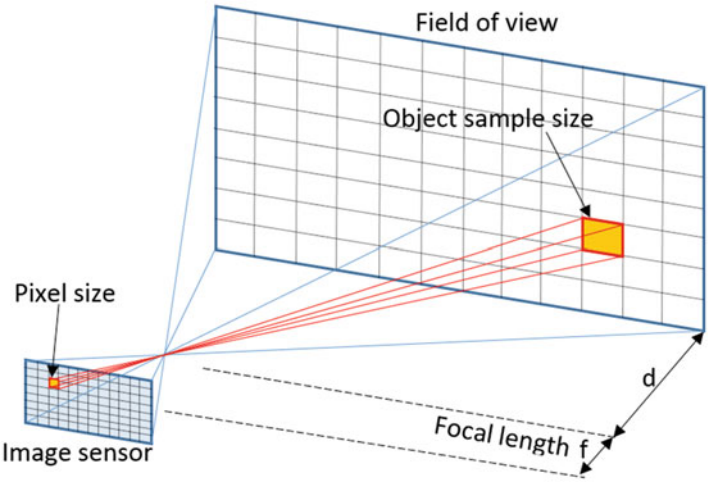

Fig. 1 The fundamentals of photogrammetry showing how the sensor size and pixel size can be correlated to the field of view (FOV) and object sample size, respectively

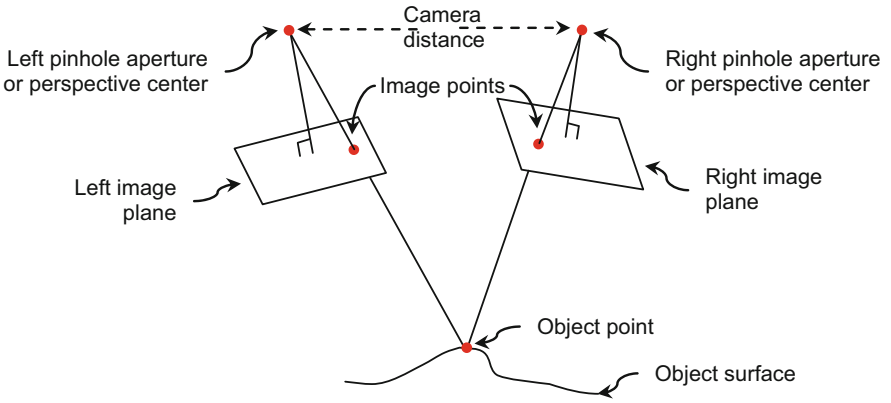

Fig. 2 A schematic of the stereophotogrammetry technique showing the two cameras and how the location of a point is identified using stereo-triangulation [27]

results as well as graphically meaningful images and videos of structural shape, motion, deformation, and strain.

The background of the photogrammetry technique goes back to Leonardo da Vinci who studied the perspective concept [15]. A single camera can measure the displacement of objects in a two-dimensional (2D) planar motion. However, three-dimensional (3D) measurements are performed using stereo or multiple cameras. In the 1900s, Pulfrich and Fourcade were among the pioneers who studied the analytical aspects of the stereovision for 3D measurement [15]. A triangulation technique using a ray-tracing process is used to determine the coordinates of the features in the test structure (see Fig. 2). In the 1980s, Peters and Ranson developed a technique to use the photogrammetry technique to measure the deformations of objects. They proposed an approach to measure the 2D deformation of a structure by measuring the displacement of points on the surface of a structure [52]. This new technique was later expanded to measure full-field strain on structures and was called digital image correlation (DIC) [38]. Using this technique, a single camera can measure the displacement of objects in a 2D plane. The DIC approach has been widely used in solid mechanics to measure semi-static deformations. With current advances in camera technology, cameras are able to record high-speed phenomena. Thus, researchers have started to use this technology to measure vibrations and transient phenomena in structures [7].

1.1 Photogrammetry Techniques

Point-tracking, DIC, and target-less approaches are three common photogrammetry techniques used in structural dynamics.

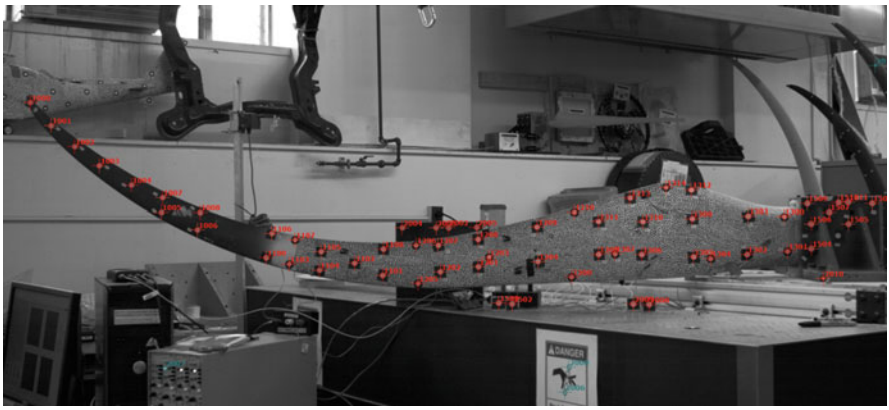

Fig. 3 An image showing optical targets mounted to a single wind turbine blade; the optical targets are identified by using a point tracking technique [16]

1.1.1 Point Tracking

The point tracking technique uses cameras to identify discrete points mounted to a structure. For this method, a series of optical targets (usually high contrast circular points) are mounted to the structure. Depending on the type of target finding algorithms, software programs may suggest using a specific type of target for optimal measurement. For circular optical targets, the centers of the targets are found using an ellipse finding algorithm, and the coordinates of the points in space are identified using a triangulation technique. 3D point tracking (3DPT) determines the displacements of the targets by tracking the optical targets at different time stages and comparing the coordinates to the reference stage (usually the first stage). Therefore, only the displacement of the targets at a handful of points can be measured by using the 3DPT method (see Fig. 3). The size of these optical targets is usually greater than eight pixels as a rule of thumb.

1.1.2 Digital Image Correlation (DIC)

DIC is another technique for image-based optical measurement. This technique works based on detecting gray-scale variations of a contiguous pattern. A high-contrast speckle pattern with dot sizes of 3–7 pixels is applied to the surface of the structure (the speckle size can be made much bigger for modal testing when global mode shapes of the structure are desirable and local deformations are not of interest); for more information interested readers are referred to the "iDIC Good Practice Guide" [28]. After surface preparation, a series of pictures is recorded from the object under deformation. In every digital picture, a specific gray-level is assigned to each pixel. Tracking a single pixel in several digital photographs recorded during the deformation is impossible because many pixels might have a similar gray-level. However, a neighborhood of pixels (i.e., subset or facet) can create a unique light intensity variation that can be used to track a point on the surface of a structure. The red rectangles in Fig. 4a show the location of the subsets.

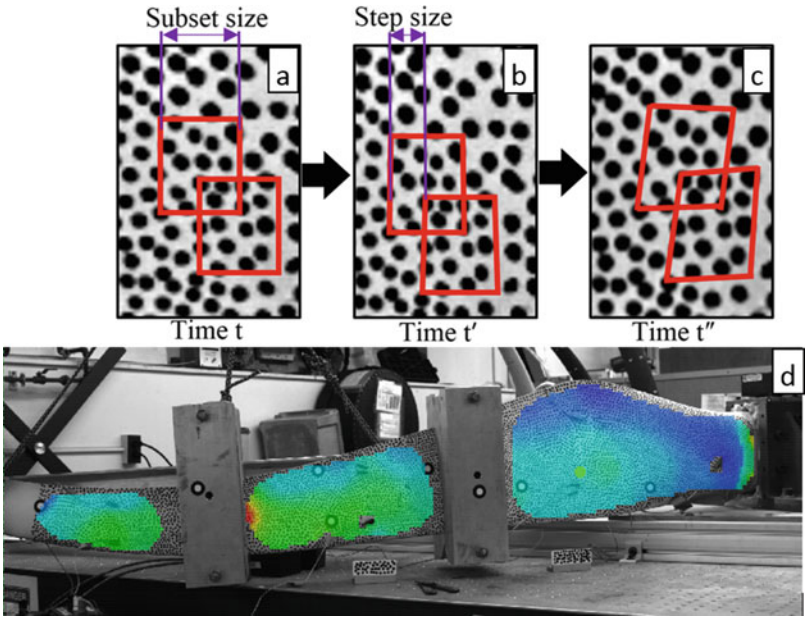

Fig. 4 (**a**) An image showing overlapping subsets (facets) and the subset size; (**b**) and (**c**) images showing how DIC tracks the subsets after deformation; (**d**) a photo showing the patterned area of a wind turbine blade; with the computed strain of the blade overlaid on the patterned blade surface

To be effective, a subset must contain several gray-level variations and its length and width is usually five times larger than speckle size (15–25 pixels for speckle size of 3–5 pixels). The distance between these facets is called step size. The step is usually selected as 3/4 of the subset size but can have a wide range of values. DIC achieves spatially distributed measurement by creating an array of overlapping (or nonoverlapping) subsets over the total area of interest and correlating each subset to the subset in the undeformed structure. In the photo taken from the deformed model, a subset with the highest values of similarity to the reference subset is set as the new deformed subset (see Fig. 4b, c).

Correlating the deformed subset to the undeformed subset can be performed using mathematical correlation functions. Equation 1 shows a sample 2D correlation function used to identify the possible matches of subsets in the deformed photos to a reference subset in the original photos using least square minimization [90].

$$C\left(x, y, u, v\right) = \sum_{i,j=-n/2}^{n/2} \left(I\left(x+i, y+j\right) - I^{*}\left(x+u+i, y+v+j\right)\right)^{2} \quad (1)$$

In this equation, C is the correlation function, which is a function of the reference pixel coordinate (x,y) and displacement (u, v). I and I^{*} are related to the image before

and after motion, respectively. The differences between pixels in a subset after the motion and before the motion are summed on the entire subset (n = subset size). The minimum value of the correlation function (C) shows that a correct deformed subset has been identified and can be tracked. It should be noted that Eq. 1 is a sample correlation equation and DIC packages might use other correlation functions to identify the optimum correlation values.

To perform a DIC analysis, usually an initial start point is manually defined in the reference image (or images for a stereo system). Afterwards, the remainder of the field of view (FOV) that is visible to both cameras is covered by an array of subsets. After finding the deformed subsets, the displacement of each subset is calculated. The full-field strain can be computed using continuum mechanics equations (strain = $\nabla Displacement$). This calculation is usually performed using triangular meshes and applying linear or spline strain computations. It should be noted that DIC can only identify the strain in the tangential plane of the surface unless volumetric DIC is performed (e.g., Digital Volume Correlation using CAT or MRI scans).

1.1.3 Target-Less Approaches

Computer vision has enabled researchers to identify deformations of an object using features within the object or at the edges of the object. This approach does not need patterning or mounting of optical targets. This is an emerging approach and has been used in structural dynamics. In this approach, edge detection, pattern matching, and blob detection algorithms are used to identify the areas that may be tracked. This technique has been used to measure deformations of a traffic signal structure [9], a cylindrical structure [73], and a solar array mounted to a space station [24] in addition to other applications. It should be noted that the non-target approaches have approximate resolutions of fractions of pixels (e.g., edge detection = 0.5 pixels and circular fiducials = 0.02 pixels) while DIC has been shown to have better resolution (DIC patterns for in-plane measurements = 0.01 pixels) [81, 85].

1.2 DIC Hardware

A photogrammetry system consists of several components (1) camera (s) to record photos, (2) camera tripods, camera bar or stands to hold the cameras in fixed positions, (3) a controller to start the measurement and to synchronize the cameras, and (4) a computer to possibly record and process the data.

Charged coupled device (CCD) digital cameras, CMOS cameras, and infrared cameras have been used to record images. For a 3D measurement, at least two cameras are required. The pair of cameras needs to be held in fixed positions with respect to each other during the measurement. The relative displacement of the cameras during a measurement in laboratory conditions should ideally be less than sub-micron [54]. Thus, strong stands with high stiffness are typically used. When high-magnification lenses are used, vibration isolation is required to prevent image

blurring. Synchronizing the cameras can be performed using a control box. Current high-speed cameras are able to synchronize using their built-in control system.

1.3 DIC Software

Currently, many software packages for DIC and point tracking are available. Most of the commercial software programs have been integrated with their associated cameras and are capable of controlling the cameras and calibrating them. They are also equipped with post-processing features such as rigid-body correction, coordinate transformation, and result presentation. Nowadays, 2D DIC versions of software packages are available at no charge. A list of some of the software packages used for photogrammetry along with their capabilities is shown in Table 1.

1.4 Patterning

For a DIC measurement, a random or nonuniform speckle pattern needs to be applied to the surface of the test object. This pattern should deform with the object during testing without affecting the mechanical integrity of the host structure. Thus, special attention must be paid to choose a flexible pattern for the test cases in which large deformation occurs. The pattern must also be thin enough to prevent adding stiffness or mass to the test object. The paint for the pattern should be matte (flat or non-glossy) in order to prevent reflection; using a reflective background for the pattern would reduce the accuracy of the measurement. It should be noted that using a dark background and white dots or the opposite would lead to similar accuracy level in the results. More information about patterning in DIC can be found in Reu [61, 62] and IDIC [28] and is discussed further in Sect. 16.

1.5 Calibration

A calibration process for the photogrammetric cameras needs to be performed before each measurement series. The objective of the calibration process is to identify the intrinsic (focal length, image center, distortion, skew) and extrinsic (camera pair's relative position) parameters, and the scale of the units. Prior to calibration, a measurement volume is determined. This volume should be large enough to fit the object before and during motion or deformation. Care should be taken to ensure that the test structure fills as much of the FOV as possible, so that the entire sensor resolution can be effectively used to record the area of interest.

Camera calibration is usually performed using bundle adjustment [84], which is a robust process commonly used in commercial DIC packages. In this calibration process, a series of photos are taken of a pattern or an array of optical targets (fiducials) applied to a rigid calibration object that is placed in different positions/orientations. There is no need for a knowledge of the calibration object, but the distance between

Table 1 An example of some DIC and point tracking software packages as of 2018[a]

Software name	Company	Country of origin	Capabilities	Website
Aramis/ Pontos	GOM	Germany	2D and 3D DIC, 3DPT, FFT calculator	www.gom.com
Correli	LMT Cachan and Airbus	France	2D and 3D DIC, FFT calculator	www.correli-stc.com
DICe	Sandia National Lab	USA	2D DIC	https://dice.sandia.gov
DPA	AICON	Germany	3DPT	http://aicon3d.com/
Limess	Limess	Germany	2D and 3D DIC	www.limess.com
MatchID	MatchID	Belgium	2D and 3D DIC	http://matchidmbc.be
	The Catholic University of America	USA	2D and 3D DIC	www.opticist.org
Ncorr	Georgia Institute of Technology	USA	2D DIC	www.ncorr.com
Q-400	Dantec Dynamics	Germany	2D and 3D DIC, FFT calculator, operating shape extraction (using Scilab)	www.dantecdynamics.com
Strain Master	LaVision	Germany	2D and 3D DIC	www.lavision.de/en
TEMA Motion /TEMA DIC	Imagesystems	Sweden	3D PT, 2D and 3D DIC, and FFT calculator	www.imagesystems.se
VIC-3D	Correlated Solutions	USA	2D and 3D DIC, FFT calculator, operating shape extraction	www.correlatedsolutions.com
ProAnalyst	Xcitex	USA	2D and 3D point tracking	http://www.xcitex.com

[a]Note: The authors attempted to prepare a comprehensive list, but some vendors may have been unknowingly omitted and over time it is likely that additional software packages will become available

the reference points must not change during the calibration. This pattern can include coded targets, uncoded targets, or a combination of each. The optical targets are typically recognized by the two cameras using an ellipse finder algorithm. The location of the targets is identified in the software using a triangulation algorithm. A minimum of two scale bars (measurements between two points in the calibration pattern) is needed to be introduced to the software to finalize the calibration. The calibrating parameters are extracted using a least-square minimization approach. The calibration results from the DIC software packages are usually a residual from the calibration (a comparison between what the extracted points are and what the

model shows after minimization) for the measurement volume. The test structure must remain in this measurement volume in order to extract accurate results.

After calibration, a DIC system can stay calibrated as long as the camera's relative position is unchanged even if both cameras are moved. The parameters that can cause a loss in calibration include: movement of the cameras with respect to each other, zooming or refocusing of the lenses, and changes in temperature. The epipolar line status in calibration can be examined with a correlation check using static photos. In this pretest, a handful of stereo-photos are taken from the test object. An arbitrary point in the first image is selected. The ability of the camera system to locate the corresponding point in the second image of the stereo system shows how accurate the camera calibration is. If this epipolar constraint is violated, the software should give a warning or an error to show that the measurement is not accurate. The noise floor of the measurement also can be monitored using these photos. If all the parameters stay fixed, it has been shown that the system can maintain the calibration for days. It should be noted that when camera calibration can be readily performed, the system should be re-calibrated before each measurement.

Commercial calibration objects for photogrammetry are usually made in the shape of either panels or crosses (see Fig. 5). These objects are able to calibrate FOVs in limited ranges. However, in many experiments, the desired FOV that needs to be calibrated exceeds the size of available calibration objects. Extended calibration and large-area calibration are two approaches to calibrate large fields of view.

One example of an extended calibration process uses a standard calibration object to calibrate a FOV larger than the calibration object. The normal calibration procedure involves recording a series of photos from the calibration panel in different orientations and at different distances away from the cameras. The extended calibration is performed after performing a normal calibration. A series of extra pictures is taken from the calibration panel placed close to the edges of the larger FOV in order to cover the whole FOV. Taking photos on the edges of the

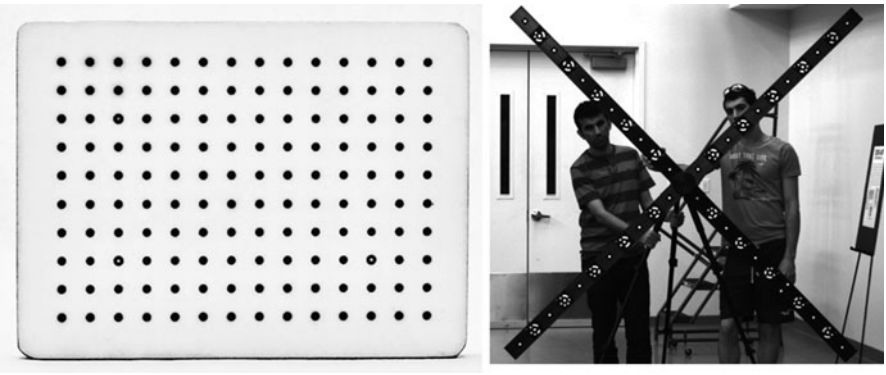

Fig. 5 A sample calibration panel (left) and a calibration cross (right)

extended FOV helps to accurately identify the distortion of the lenses near the edges and corners of the FOV [2].

Another approach to calibrate large areas uses large area calibration. In this approach, there is no need for a calibration panel or object that is the same scale as the FOV. Instead, a series of coded targets and uncoded targets are mounted to a fixed structure [53]. Several photos are recorded from the targets with the cameras located in different locations and orientations. The final photo is taken when the cameras are fixed in the final position. Some software packages use a DIC speckle pattern for calibration and establish a scale bar between two points. At least two scale bars (the displacement of two targets measured by a tape measure or another device) are introduced to the software. For example, for a measurement on a rotor with large rotations and deformations, distances between two targets along a blade can be assumed to be fixed (in the non-rotating state) and used to calibrate the cameras and monitor the calibration status.

1.6 Measurement and Applications

After the cameras are calibrated, the measurement can be triggered using a control unit. The DIC system can be synchronized with other machines that provide a trigger signal (e.g., a mechanical testing machine or stroboscope). The reference image is usually taken of the undeformed object or at some initial point in time. However, if the undeformed shape of the object is not available, a photograph of the deformed structure might be used as the reference. The other photographs are compared to the reference to extract relative displacement, deformation, or strain.

The photogrammetry system has wide areas of applications including: material testing, finite-element model validation, strain computation, component testing, bioengineering, structural health monitoring, crash analysis, metal forming, and vibration measurement. The applications vary from nanometers in scanning electron microscopes [79] to hundreds of meters as in the case of wind turbines [49].

2 Overview of Modal Testing and Requirements

An important aspect of experimental modal analysis is to derive the modal parameters of the test article (i.e., natural frequencies, damping ratios, and mode shapes) from the measured test data. These parameters are intrinsic properties of the test article and its boundary conditions, and as such they are often of interest for model validation and updating. If an analyst can match natural frequencies and mode shapes between their model and experiment, a good deal of confidence is gained in that model. Additionally, in many situations the damping of a system cannot be computed analytically, so the analyst may rely on experimental estimates of the damping ratio for their model. In addition to model validation, modal parameters derived from experiments can be useful for other situations such as instrumentation placement [33], force reconstruction [10], or experimental substructuring [86].

Modal tests are often designed to approximate a free boundary condition for the part, using soft bungee cords or foam to support the test article. This facilitates easier comparison with an analytical model of the test article, because it is often easier to quantify and model the effect of a few soft springs on the dynamics of the test article than a potentially complicated interface to the ground, which may require tuning bolt stiffness, contact patches, and other parameters.

To perform a traditional modal test, the test article is excited, and the responses to the excitation are measured. Historically, accelerometers mounted to the test article's surface have been used to measure the responses, although these have the disadvantage of adding mass to the test article that can alter its dynamics. More recently, methods such as laser Doppler vibrometry [17] and 3D DIC or 3D point tracking [27, 45, 88] have enabled noncontact, full-field measurement of the response of the test article. The considerations listed in this chapter will focus on the capabilities and important considerations when modal testing is performed using a DIC approach.

The most common types of excitation used for experimental modal analysis are impact testing using an instrumented hammer or shaker testing using an electrodynamic shaker attached to a force transducer. Alternatively, operational or output-only modal analysis is a testing strategy that attempts to identify modal parameters of the system without a measured excitation force. Here the system may be excited by its natural operating conditions (e.g., a wind turbine being excited by the wind), or a more novel excitation method such as focused or unfocused acoustic pressure and magnetic excitation [29]. For the most accurate results, however, the forces used to excite the structure must be measured by a calibrated force transducer, and that force input should be used to compute the frequency response functions from which the modal parameters can be estimated.

2.1 Frequency Response Function Measurement Considerations

In analytical modal analysis, the natural frequencies and mode shapes can be found from the eigensolution of the general eigenvalue problem formed by the mass and stiffness matrices of the structure. For experimental modal analysis, no such matrices exist a priori. The modal parameters will, therefore, be estimated from the test data.

For experimental modal analysis the frequency response function (FRF) $\mathbf{H}(\omega)$, which relates the input force spectra $\mathbf{F}(\omega)$ to the output displacement spectra $\mathbf{X}(\omega)$ (or velocity or acceleration) at each frequency line ω, is of key importance. For standard modal test hardware and software packages, FRF creation is generally integrated into the software and performed automatically for the test engineer based on specified parameters. However, since DIC is a relatively new technology in structural dynamics testing, FRF computation capabilities may not be included in the software, and the test engineer may need to create FRFs externally. The structural dynamic input-output relation is governed by:

$$\mathbf{X}(\omega) = \mathbf{H}(\omega)\,\mathbf{F}(\omega)$$

Through modal substitution, it can be shown that the FRF values depend on the modal parameters of the system,

$$\mathbf{H}(\omega) = \sum_{k=1}^{N_{modes}} \frac{\{\Phi\}_k \{\Phi\}_k^T}{\omega_k^2 + 2i\zeta_k\omega_k\omega - \omega^2} = \sum_{k=1}^{N_{modes}} \frac{\mathbf{A}_k}{i\omega - \lambda_k} + \frac{\mathbf{A}_k^*}{i\omega - \lambda_k^*}$$

where ω_k, ζ_k, and $\{\Phi\}_k$ are the natural frequency, damping ratio, and mass-normalized mode shape vector for the mode k, and λ_k and $\mathbf{A}_k$ are the system poles and residues, respectively. The asterisk operator denotes the complex conjugate. Therefore, if the FRF matrix $\mathbf{H}$ is known, modal parameters can be fit to that data using various strategies.

Because we cannot measure the frequency response functions directly, they must be estimated from the time domain data measured by the data acquisition system. For DIC measurements, this is often a displacement time history at each measurement point supplemented with one or more force time histories measuring the excitation applied to the test article. The time domain data is then transformed into frequency domain data via the Fourier Transform, and cross power spectra GXF_{jk} and GFX_{jk} and auto power spectra GFF_{jj} and GXX_{jj} can be computed:

$$GXF_{jk} = \sum_{l=1}^{N_{avg}} X_j F_k^* \qquad GFX_{jk} = \sum_{l=1}^{N_{avg}} F_j X_k^*$$

$$GFF_{jj} = \sum_{l=1}^{N_{avg}} F_j F_j^* \qquad GXX_{jj} = \sum_{l=1}^{N_{avg}} X_j X_j^*$$

To reduce the noise in the computed power spectra, several sets of data are typically measured, and the resulting spectra are averaged. This averaging smooths out some of the random errors inherent in any measured signal. The frequency response functions are then computed from the power spectra. Several formulations are available depending on where the noise is expected in the measurement.

Estimator	Formulation	Reduces noise on:
H_1	$H_{ij} = \frac{GXF_{ij}}{GFF_{jj}}$	Outputs/responses
H_2	$H_{ij} = \frac{GXX_{ii}}{GFX_{ji}}$	Inputs/forces

Note that for multiple-input, multiple-output (MIMO) cases, *GFX*, and *GFF* will be matrices that will need to be inverted. This limits the H_2 estimator because it

requires that GFX be square, meaning the number of inputs must equal the number of outputs. Many other FRF estimators exist in the literature, for example, the H_V [41], H_c [42], and H_s [89] estimators, and each have their own strengths and weaknesses.

2.2 Fourier Transformation and Leakage Considerations

The signals measured with DIC or other data acquisition systems will be discretely sampled and have finite length. These signals are then transformed into the frequency domain via a discrete Fourier transform (DFT). Due to the nature of the DFT, the measured signals must either be fully contained within the measurement window (i.e., go to zero at the beginning and end of the measurement frame) or consist of only signals that are periodic in the measurement frame length.

If the signal is not periodic or the transient is not completely captured within the measurement time frame, a bias error commonly referred to as leakage may occur, resulting in the frequency content of a particular sinusoid being smeared across many frequency bins in the DFT. Figures 6 and 7 show two examples of this phenomenon. Note that the frequency resolution in this example is quite low which exacerbates the effects of leakage; this was done to more clearly illustrate the effects. Effects of leakage may not be as severe in a typical application.

Leakage can generally be reduced by increasing the frequency resolution of the FFT (which effectively lengthens the measurement frame), and may also be improved with averaging. However, with DIC measurements, the camera memory

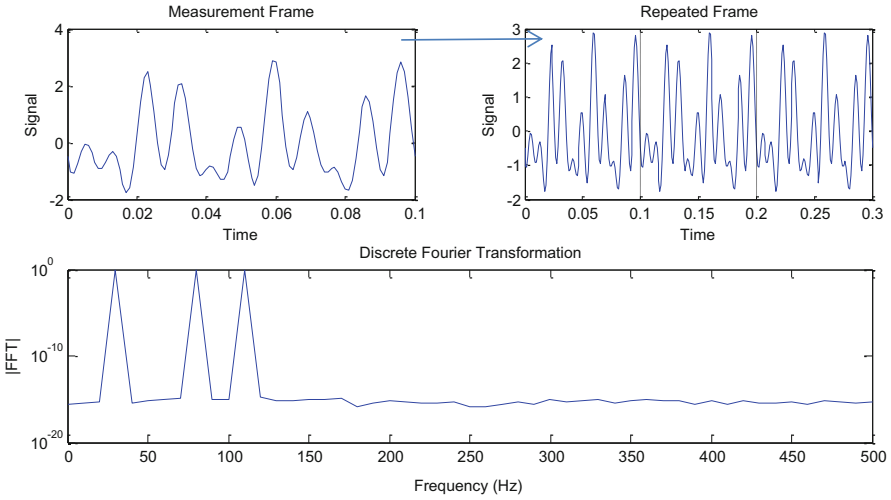

Fig. 6 Signal made from unit-amplitude sine waves at 30, 80, and 110 Hz with random phases. The signal is periodic in the measurement frame, and no leakage occurs

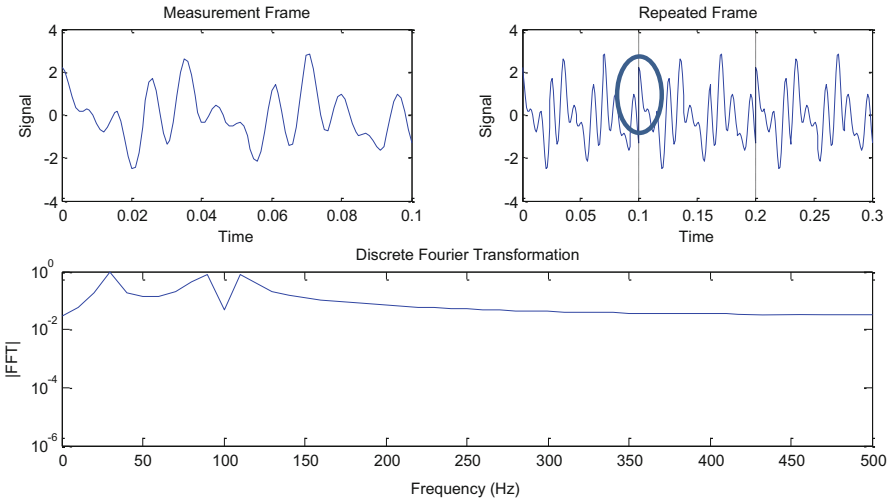

Fig. 7 Signal made from unit-amplitude sine waves at 28.1, 86.9, and 112.5 Hz with random phases. The signal is not periodic in the measurement frame, and significant leakage is seen in the frequency domain spectra

may be limited; thus simply measuring for a longer duration may not be an option. One common method to reduce the effects of leakage (but not eliminate it entirely) is to apply a window or weighting function to the time data before computing spectra. This can improve the spectra quality; however, we note that applying a window does affect the results. The window function should be viewed as a last resort when other methods to reduce leakage such as increasing the frequency resolution, averaging, or applying a more periodic excitation are not feasible. A common window for random vibration testing is the Hann or Hanning window. Figure 8 shows the results of applying a Hann window (red curve) to the time signal, and the resulting improvement in the estimation of the amplitudes of the sine waves.

When to use a window is sometimes obvious, for example, when shaker-testing using pure random signal, as there is no guarantee that the signal will be periodic within the measurement frame. Other times, for example when impact testing, it may not be obvious if the response to the impact will decay within the measurement frame. Previewing the data is then advantageous to ensure that the transient is entirely contained in the measurement frame. However, DIC does not provide a practical way to preview the data to iterate on measurement parameters such as exponential window properties or frame length due to the time required to download images from the camera and then process them into time histories. We suggest supplementing the DIC measurement with another measurement technique, an accelerometer or single point laser Doppler vibrometer, from which data can be compared and evaluated more quickly.

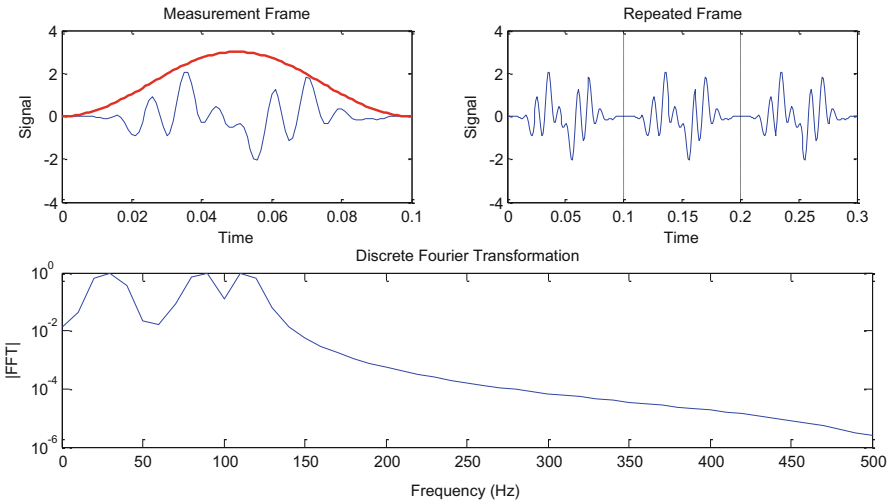

Fig. 8 Signal from Fig. 7 with Hann window applied. The Hann window forces the signal to zero at the start and end of the measurement frame, so that it can be repeated without discontinuity. The estimates of the sine wave amplitudes are significantly improved, but the estimated frequency of each of the sine waves become less precise

2.3 Curve Fitting Considerations

With the FRFs created, modal parameters can be estimated and fit to the data. There are a number of different strategies and algorithms used (for more detail, interested readers are encouraged to refer to ▶ Chap. 11, "Experimental Modal Parameter Evaluation Methods"). When fitting modes to the data, it is important to understand what data the mode fitting software is expecting. For example, because of the popularity of accelerometers for measuring modal response, many software packages expect *Receptance* or *Accelerance* FRFs which relate the acceleration at response points to forces at the inputs. Because the output from DIC measurements is not acceleration but displacement, the data may need to be converted to acceleration frequency response functions if required by the curve fitting software. This differentiation can easily be performed in the frequency domain simply by multiplying all displacement FRFs by $-\omega^2$ at each frequency line, where ω is the angular frequency (in radians per second) of that frequency line.

An additional consideration to make when curve fitting DIC data is that in general many more degrees of freedom (DoF) (or data points) are measured during a DIC test than during a standard modal test using accelerometers. Software packages used to analyze standard modal test data seldom need to handle more than a few hundred degrees of freedom, while high-resolution DIC may measure 1000 points or more during a given test. Code that runs sufficiently fast for standard testing conditions may not be optimized for the large volume of data supplied by DIC, so analysis time may suffer, especially if any iteration on the curve fitter settings is necessary. The

DIC data may need to be decimated or spatially averaged and down sampled to a manageable size to improve turnaround time in this case.

3 The Distinction Between Operating Shapes and Mode Shapes

In modal analysis, the common parameters of interest include natural frequencies, damping ratios, and mode shapes. The mode shapes are very valuable because they form a "basis" for the deflections that the part undergoes and can be visualized and animated to create an intuitive picture of how the structure vibrates. Closely related, but not the same, are operating deflection shapes, often called "operating shapes" or "deflection shapes." These shapes are more general in that they are any shape that a structure may take as it vibrates during an arbitrary excitation (e.g., single frequency, multiple frequencies, or broadband). Operating shapes are often formed from a row or column of the FRF matrix corresponding to a given frequency line, and are often animated by applying the magnitude and phase of the FRF to a deflection of the corresponding node in a display model.

Confusion often arises between the two terms because operating shapes can appear very similar to mode shapes, especially at frequency lines in the vicinity of a mode if the modes are well-spaced in frequency. This often occurs when performing a rudimentary form of curve-fitting called peak-picking, where the analyst estimates the natural frequency and mode shape from an FRF at a single frequency line that is a local maximum in the FRF curve. Though the shape values extracted from the FRFs may approximate a mode shape if the modes are spaced appropriately, the shape at any given frequency line is actually a summation of many mode shapes (though it is possible that a single mode dominates the summation).

We illustrate this point with an example. A free mass-spring system with four degrees of freedom has natural frequencies, damping ratios, and mass-normalized mode shapes shown in Tables 2 and 3. Figure 9 shows the FRFs of this system from an input at DoF 4. From Fig. 9 it can be seen that the two modes are closely spaced and the third is fairly far from the other two. Drawn on the figure are each mode's contribution to the FRFs. Table 4 compares the actual values of the mode shapes used to create the FRFs in Fig. 9 to the deflection shape constructed from the imaginary part of the FRFs at the peak. These values have been normalized to unit length.

Table 2 Natural frequencies and damping ratios for the example problem

Mode	Natural frequency (Hz)	Damping ratio (%)
Rigid body (RB) mode	0	0
1	14.6	1.5
2	15.3	1.5
3	19.7	1.5

Table 3 Mass-normalized mode shapes for the example problem

	RB mode	Mode 1	Mode 2	Mode 3
DoF 1	−0.4264	0.6559	0.5222	0.3395
DoF 2	−0.4264	0.1893	−0.5222	−0.0980
DoF 3	−0.4264	−0.6187	0.0000	0.6598
DoF 4	−0.4264	−0.2772	0.3482	−0.5355

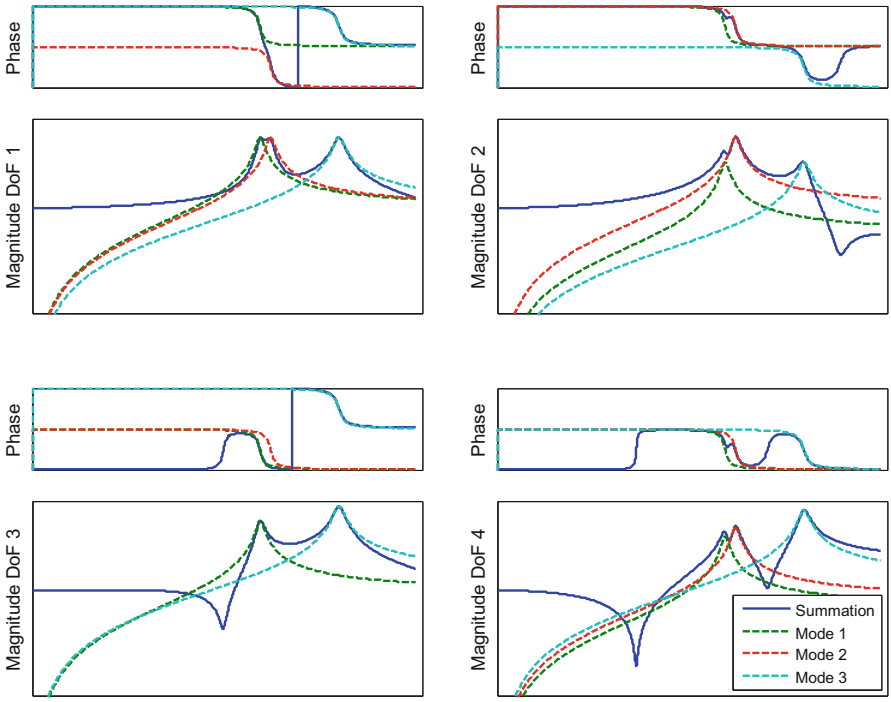

Fig. 9 FRF of acceleration with respect to force showing three modes with each mode's contribution to the FRF superposed on the figure

Table 4 Mode shapes versus peak-picked deflection shapes normalized to unit length

	Mode 1		Mode 2		Mode 3	
	Mode shape	Defl. shape	Mode shape	Defl. shape	Mode shape	Defl. shape
DoF #1	0.6817	0.6258	0.6396	−0.5782	0.3689	0.3686
DoF #2	0.1968	0.2663	−0.6396	0.6681	−0.1065	−0.1045
DoF #3	−0.6431	−0.65	0	−0.0615	0.7169	0.7159
DoF #4	−0.2881	−0.339	0.4264	−0.4643	−0.5819	−0.5836

Notice that the deflection shape near the peak corresponding to Mode 3 is actually a very good approximation for the mode shape. This is because Mode 3 is sufficiently far away from other modes so that the contributions from those modes are several orders of magnitude lower than the contributions from Mode 3. Similarly,

it can be seen that the operating deflection shapes from the closely spaced modes do not approximate the mode shapes as well because the tails of neighboring modes are still a significant fraction of the peak of the mode of interest. Note that for all three modes, the deflection shapes would not be scaled properly, and therefore would not be able to be used in computations such as substructuring or modal effective mass; however, they may still be adequate for providing a qualitative understanding of the mode shapes.

4 DIC Measurement Resolution in Relation to Structural Dynamic Testing/Modal Analysis

Prior to embarking on a measurement campaign or test using DIC or point tracking for modal analysis or structural dynamic testing, it is important to consider the measurement resolution of the sensors being used. As with any sensor, the minimum measurable quantity is limited by the physics of the sensing element and the associated external influences that contribute to additive noise. For a given set of cameras, one of the most important considerations that influences the resolution of the measurement is the FOV. As the FOV increases, the measurement resolution will decrease proportionally. Likewise, DIC is a displacement measurement and a practitioner needs to be careful that the minimum structural motion of interest is sufficiently large to obtain a useful measurement. This topic is discussed in detail in Sects. 5 and 6. Lastly, there are many factors that influence and contribute to noise in the measurement (e.g., calibration, atmospheric turbulence, lighting and glare, patterning, post-processing choices). Many factors that influence noise are presented in Sect. 10.

5 DIC Measurement Range in the Context of Structural Motion and Frequency

For typical structural dynamic measurement, accelerometers are used to measure acceleration and laser vibrometers are used to measure velocity. However, for DIC or point tracking measurements made in conjunction with stereo-photogrammetry, the measurand is displacement. This presents some benefits as well as challenges in order to extract a useful measurement. The most common structural dynamic measurement that most engineers are familiar with utilize accelerometers and the harmonic acceleration, velocity, and displacement can be respectively expressed as:

$$a(t) = Ae^{i\omega t}$$

$$v(t) = \frac{1}{i\omega} Ae^{i\omega t}$$

$$x(t) = \frac{-1}{\omega^2} A e^{i\omega t}$$

where A, ω, *and* t represent the acceleration amplitude, angular frequency, and the time, respectively. Compared to the acceleration amplitude, the displacement amplitude is decreased to the second power as the frequency is increased. This effect results in DIC being less effective for measuring a structure's vibration at higher frequencies because the motion of the structure may fall below the noise floor of the measurement. Conversely, as the frequency is reduced (e.g., <∼50 Hz) accelerometer measurements can have diminished sensitivity and laser vibrometers are poor at measuring low-frequency vibration especially when the amplitude of vibration is very large (e.g., > a few centimeters). Therefore, for structural dynamic measurement compared to other measurement approaches, DIC performs best in applications when the operating frequencies are relatively low, and the displacements are large. However, the useful frequency range is very much dependent on the size of the FOV, the camera resolution (i.e., pixel count), and the camera sample rate. As the FOV decreases, the DIC measurement resolution will improve extending the measurable frequency range.

6 Analysis in the Temporal Versus Frequency Domains

The smallest time-domain displacement that a DIC system can resolve is approximately 0.01 pixels [81] at the detector, meaning the smallest physical displacement measurable is dependent on the FOV and the camera resolution. Given the typically low level of vibration used when modal testing (especially at high frequencies), it may seem that DIC measurement techniques may not be adequate to capture the corresponding responses. However, preliminary results indicate that processing results in the frequency domain reveal that inherent measurement noise is reduced compared to time domain processing of data. This is likely due to the displacement noise being spread over multiple frequency bins, but the reason is still under investigation by the research community.

Figure 10 shows an example measurement taken where due to the FOV of the cameras, 0.01 pixels corresponds to approximately 2 μm of out-of-plane displacement [68]. However, it can be seen that the frequency domain noise floor is significantly lower than the time-domain noise floor (approximately 10 nm) and modes of the system are still visible in this spectrum.

7 Identifying the Number of Images Needed

The determination of the number of images/samples needed for a particular modal measurement is a function of the measurement bandwidth and number of frequency lines required, as well as the number of averages required to reduce the noise in the measured data. For DIC, there can be a great deal of overhead involved in processing

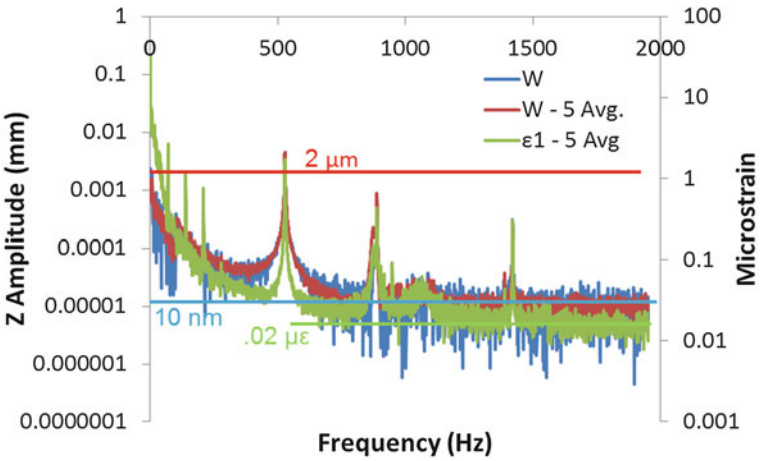

Fig. 10 Example test data showing the typical noise floor for a time-domain DIC measurement, as well as acquired data displayed in the frequency domain [68]. Note the extremely low strain noise floor. 0.02 $\mu\varepsilon$

the images recorded in a test, and the memory of the camera may be limited to a certain number of images (see Fig. 30 in Sect. 16). Therefore, it is often important to optimize the test to minimize the number of images required while still achieving good data.

7.1 Sampling Theory Relationships

Sampling theory defines a number of relationships between time-domain parameters of the measurements such as sample time T, sampling frequency f_{sample}, time between samples Δt, and number of samples N, and frequency domain parameters such as maximum frequency F_{max} of interest, frequency bin spacing Δf:

$$f_{sample} = \frac{1}{\Delta t} = 2 \times F_{max} \qquad T = \frac{1}{\Delta f}$$

$$f_{sample} = \frac{N}{T} = N\Delta f$$

We note that many data acquisition systems sample at a rate higher than $2 \times F_{max}$ in order to provide additional bandwidth for anti-aliasing filters to help reduce the contamination caused by higher frequency content. For DIC, it may be advantageous to sample at a higher rate as well: though DIC generally does not have anti-aliasing filters, displacement magnitudes do tend to decrease naturally as the frequency increases [11], and this extra bandwidth may allow any aliased frequency content

to negligibly influence the true spectrum. If the signal is adequately oversampled, it may be possible to use a digital anti-aliasing filter, though oversampling will result in more images to download and process. It is therefore better to control the input such that there is no frequency content above the bandwidth of interest (see Sect. 8.2 for additional details).

7.2 Selecting Proper Sampling Parameters

Selecting the sampling parameters of the system may be an iterative process. For example, the damping of a lightly damped system might drive the measurement time required to capture the entire transient response to an impact excitation, but the damping will generally not be known a priori, so the initial measurement may not be long enough. Due to the processing overhead associated with DIC measurements, it may be advantageous to set up the sampling parameters using another measurement technique such as an accelerometer or single point laser Doppler vibrometer. This can also help the user prevent aliasing. Shortening the time spent on each iteration will allow the test engineer to more rapidly identify the appropriate sampling parameters.

Many different properties of the test may determine what sampling parameters should be used. Damping is perhaps the property of a test article that is least understood, but it is often the most critical for setting up sampling parameters. If a mode is lightly damped, the corresponding peak in an FRF will be very sharp, and it may require closely spaced frequency bins to adequately resolve the peak (Δf will be small). The equations in Sect. 7.1 indicate that the measurement time T will grow large, and if a certain bandwidth is required for the test, the number of samples N will correspondingly grow large.

Similarly, in the time domain, especially for impact testing, the damping directly affects the time it takes for the responses of the part to decay. If the decay time is long, the test engineer may increase the testing time T, and for a given frequency bandwidth this will involve increasing the number of samples N. Alternatively, the test engineer may utilize a window function (e.g., exponential window) to help damp out the response by the end of the measurement.

Another test parameter that can significantly influence the number of images required is the number of averages. Averaging is utilized when constructing FRFs from time domain data. By averaging data, noise is reduced in the measured transfer functions at the expense of longer testing times and more samples. Because of the overhead involved with processing DIC measurements, it is advantageous to utilize an excitation technique that does not require a large number of averages.

7.3 Dealing with Long Sampling Requirements

While high-speed cameras record very quickly to their internal memory, transfer off of the camera to a computer for processing can take a significant amount of time.

This can create a severe testing bottleneck if long-running tests are recorded. For a traditional modal test, the continuity of the test is often not a significant concern, and while tedious, pausing the testing every handful of averages to download the camera memory onto an external data storage and processing system will not prevent a successful test. However, one must use care to maintain the boundary conditions of the test, which are more likely to change over a long-running test. For example, bungee cords that support the part in a free-free boundary condition may sag (due to stress relaxation), and this sagging may cross-load a shaker stinger causing a stiffening effect that can cause natural frequencies to shift significantly; inconsistent data such as this can impede curve fitting efforts.

A more significant concern arises for more general structural dynamics and vibration testing, perhaps on a shaker table, where the environment is to be a specific spectrum profile for a specific amount of time. A test like this might need to run to completion in order to satisfy some requirement, for example a fatigue life test may run until a component fails, and this leaves no time to download data off of the camera. The utility of DIC for this type of measurement may need to be evaluated on a case-by-case basis.

If the excitation profile is stationary over the period of the test, one or more DIC measurements taken during the test might be considered representative of the response to the applied excitation. If the excitation is transient, the DIC system may not be able to record all of the various portions of the test. The test engineer may need to pick which portions are measured, for example, if one portion of the excitation profile is expected to be more damaging to the component under test.

8 Sources of Measurement Error and Best Practices

8.1 Modes of the Stereo System Hardware and iIts Measurement Effect

All mechanical structures that have stiffness, mass, and finite boundary conditions, when excited will have standing waves that are referred to as modes of the system. The specific modes (e.g., bending, in-plane, torsional) are dependent on the unique structural geometry and the boundary conditions. One of the fundamental assumptions for DIC testing is that once a camera pair is calibrated, the cameras' relative position should not change. For DIC testing, the cameras are typically placed on an aluminum or steel camera bar that can exhibit modal vibration influencing the measurement. Several things should be considered by the practitioner: (1) although the rigid body motion of the camera bar can be compensated for during post-processing, it is generally best to keep them fixed in space and eliminate all vibration that is transmitted to the camera bar mounts or to the tripods supporting the camera pair; (2) the tester needs to be aware of the vibrational modes of the camera bar and avoid structural modes that coincide with the external excitation through the flanking path from the excitation source. A list of natural frequencies and mode shapes of common structures can be found in [13]; (3) for some cameras,

a cooling fan is located within the camera and the cameras themselves can be the source of mechanical excitation. If possible, the camera bar should be designed such that the modes of the camera bar or tripod are not coincident with the blade passage frequency of the fan and its harmonics. If possible, the camera cooling fans need to be off during the measurement and if the practitioner is concerned about self-excitation, a measurement can be made on a stationary object to help quantify the measurement errors.

8.2 Aliasing

8.2.1 Description of Temporal Aliasing for Image Processing

When conventional data acquisition is performed using typical sampling hardware (e.g., A/D converters), anti-aliasing filters are applied to the input signal to eliminate aliasing (see Sect. 7.1). The filters eliminate frequency content past the Nyquist frequency and therefore the sample rate is typically 2.56 times the desired bandwidth for many data acquisition systems. The anti-aliasing filters reduce the amplitude of the higher frequency content and prevent the influence of higher frequency signals to fold about the Nyquist frequency into the lower frequency spectrum. Unfortunately, when most cameras sample data, there is no simple way to filter out structural motion that has frequency content above the Nyquist frequency (half the sample rate). For image processing, no robust anti-aliasing filters currently exist. However, as described in Sect. 5, as the frequency of a structure's motion increases, the displacements will decrease. Therefore, in practice the higher frequency displacements are measured by the camera but their relative magnitude is typically negligible. As a rule of thumb, the sample rate of the cameras should be at a minimum higher than the twice the highest frequency of interest (bandwidth) and any displacements occurring past half the camera sample rate should be very small or below the noise floor of the DIC system. A single point laser vibrometer or accelerometer can be used in this case to ensure there is negligible motion above the Nyquist frequency of the cameras.

8.2.2 Mitigating Aliasing with a Single Point Measurement

To identify if aliasing is present in the optical measurements, the following approach can be taken. A single point laser Doppler vibrometer or accelerometer sampling at a higher frequency will help the test engineer determine if there is any frequency content in the optically sampled images above the bandwidth of interest that may alias and contaminate the data.

8.3 Artificial Aliasing to Enhance Measurement

Digital camera technology has gone through rapid advancement in the last three decades and has been built on a $\sim$ hundred years of film camera motion picture

evolution. Some of the lessons learned from prior generations can be adapted to DIC measurement to enhance structural dynamic measurement and are now discussed.

8.3.1 Stroboscope Lights and High-Speed Measurements

Dynamic motion events (rigid body or structural dynamic) have the potential to have blurred images and may require cameras to be triggered in correspondence with the motion at a frame rate that is less than the frequency of operation. A short shutter time does not allow enough light to be recorded by the camera's pixel array under normal lighting conditions. A stroboscope solves both the problems of needing a sufficient amount of light in a short shutter time because a quick and bright flash will both illuminate the object over a brief moment in time preventing motion blur. A stroboscope can be used for events which require maximum illumination with the shortest shutter time since the flash duration of a strobe is often less than the smallest possible shutter time of a camera. Cameras can be triggered from the stroboscope external pulse signal, off of a voltage signal from a variety of sensors, or from a function generator if the precise frequency of a cyclic event is known.

Strobe lights require less power to illuminate a test object compared to typical lights. For example, a 2 kW generator can provide the power for LED strobe lights to illuminate a 2.5 MW utility-scale wind turbine [49]. These lights can be synchronized with the camera shutter trigger mechanism so that they only work for short intervals of time. In general, if at all possible, strobe times should be longer than the exposure time (e.g., ∼twice the shutter time duration). Other benefit of using a strobe light is a saving in energy consumption because of the discontinuous power output and the reduced heating of the test specimen as opposed to continuously illuminated lighting. More discussion of strobe lighting for high-speed applications can be found in Sects. 16.9 and 16.10.

As an example, a bench test was designed to determine if measurements could be made on a rotating blade using the DIC approach [26]. The test object used was a variable speed commercially available desk fan with three blades. A speckle pattern was applied to the surfaces of the blades and the hub, and a Tenma 72-7601 stroboscope was used. The cameras and the stroboscope were simultaneously triggered by a pulse from a function generator. The setup is shown in Fig. 11. The stroboscope allows for an intense flash of light which is less than that of the minimum shutter time of the cameras and had a flash duration of approximately 60 microseconds. The desk fan was rotated at a speed of 18 Hz (1080 RPM). The fastest possible camera speed is 12 fps. In order to record the shape of the fan at all rotation angles, the stroboscope and cameras were triggered at a rate of 8.96 Hz. This translates to one image taken every 363.25 degrees of actual fan rotation.

From the captured images (an example is shown in Fig. 12a), a rendering of the fan's surface at one point in time can be created (see Fig. 12b). Three complete rotations of the fan blades were captured where approximately 40 image pairs were taken of each rotation. Surface displacements were calculated by subtracting the measured surface shape of the fan in a static condition from the measurements of the fan made while the blades were rotating. The measurements can be de-

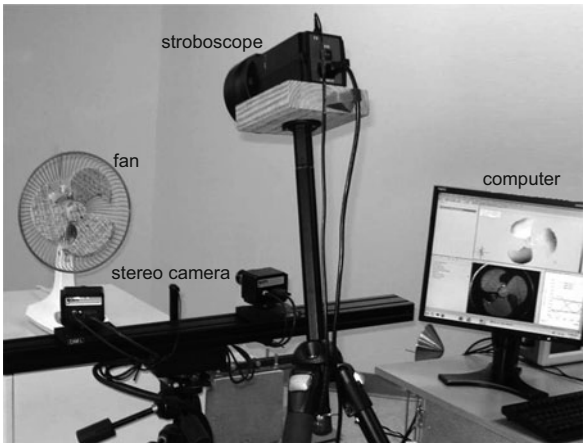

Fig. 11 Experimental setup showing the use of DIC and a stroboscope for measuring the shape of a rotating fan [26]

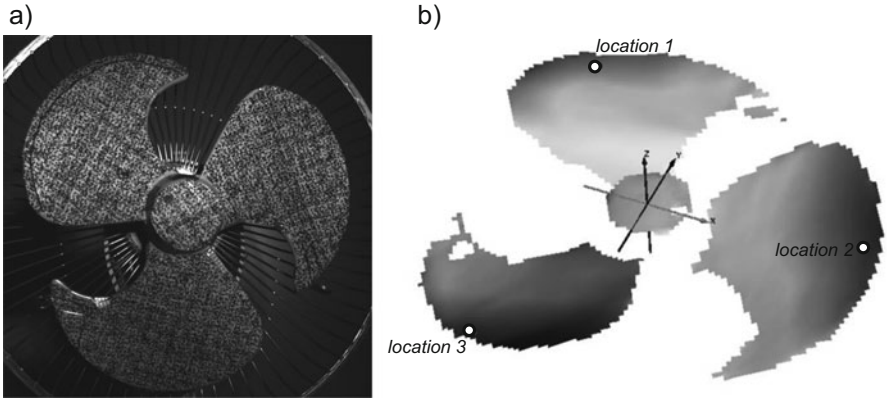

Fig. 12 (**a**) One of the images captured by DIC using the stroboscope technique to capture the position of the rotating fan blades; (**b**) rendering of the fan blades using the data captured while the blades were rotating with the location of three points whose displacements were plotted as a function of rotation angle [26]

rotated allowing them to be displayed in a rotating coordinate system. One point on each blade was chosen to demonstrate the cyclic displacements of the fan blades. Displacement in the out-of-plane direction at the chosen point locations are plotted as a function of the angle of the fan for approximately three full cycles of the fan (see Fig. 13). These plots show that the fan had a rigid body displacement of approximately 3.5 mm during operation as compared to its initial position. Moreover, the results indicate that two of the points are moving approximately in phase with each other while the third point is moving essentially out of phase.

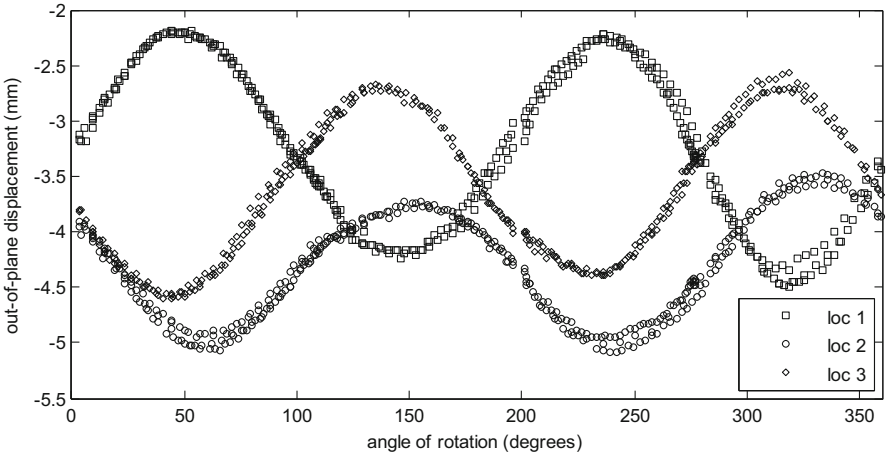

Fig. 13 Measured displacements of the points shown in Fig. 12b as a function of rotation angle [26]

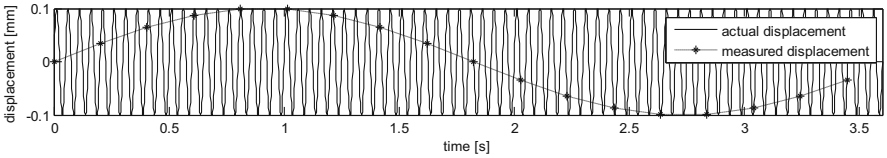

Fig. 14 Example of how low-frequency measurements can be made to capture a high-frequency periodic structural motion

8.3.2 Phase Stepping

Generally speaking, aliasing should be avoided for dynamic measurements. However, when a structure is moving in a periodic manner, aliasing can be exploited to enable the use of low-speed cameras to measure the motion of a structure whose operating frequency exceeds the sample rate of the cameras. The term "phase-stepping" refers to a measurement in which the time period of the camera shutter opening (or image sample) is an integer number of periods of the periodic structural vibration plus a small additional time duration. For each image sample the time duration between image samples is increased a slight amount or phase-stepped so that the cameras record the motion of the structure throughout its periodic oscillation. An example of a phase-stepped measurement to capture a high-speed cyclic event with a low-speed camera is shown in Fig. 14.

As an example, a test was conducted on a base-upright structure in which forced normal mode testing was conducted to drive the structure at resonance (26 Hz) [88]. Shakers were mounted near the base of the upright, as shown in Fig. 15. The camera pair then captured a series of images throughout several cycles using a phase-stepping approach. Figure 15 shows an example of the motion captured at the 8 measurement points for the 26 Hz structural mode using 3D point-tracking

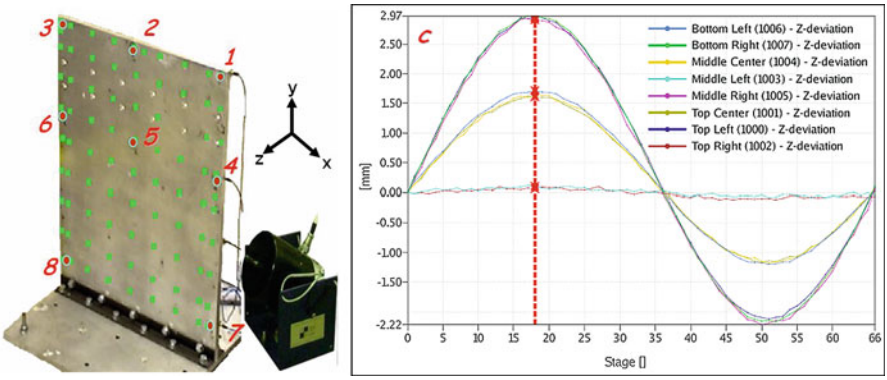

Fig. 15 Base-upright structure with shaker orientation and measurement points (left) and sample output of point-tracking obtained using phase-stepping (right) [88]

measurements with the cameras sampling at ~11 fps. Note that each signal is in-phase, which is to be expected when measuring what is essentially the first bending mode of the structure. The three points along the top of the upright are moving at roughly the same amplitude while those along the midline are moving in phase with approximately half the amplitude as the top points. Likewise, the bottom measurement points display very little motion since they are located near the root of the upright portion of the structure.

8.4 Lighting Requirements, Shutter Time, and Lens Adjustment

8.4.1 Lens Adjustment

Camera lenses need to be adjusted before every measurement in order to provide a proper focal length, focus, aperture, and shutter speed. The focal length is the distance between the optical center and image sensor (see Fig. 1). The focal length can determine the dimensions of the FOV (b) by using the equation below.

$$b = s\frac{d}{f} \tag{2}$$

In this equation, s, f, and d represent the sensor size, the focal length, and the distance between the camera and the object, respectively (see Fig. 1). Longer focal length lenses (e.g., telephoto lenses) provide an equivalent FOV at greater standoff than a shorter focal length lens. When using these lenses, special attention must be paid to the camera fixtures because any camera movement is greatly magnified. On the other hand, for some measurements, there might be a space limitation, and the cameras must be installed close to the object (e.g., measurement inside a wind tunnel). For these measurements, short focal length lenses (e.g., 10 or 12 mm lenses) can be used to provide a wider FOV. However, using very short focal length lenses

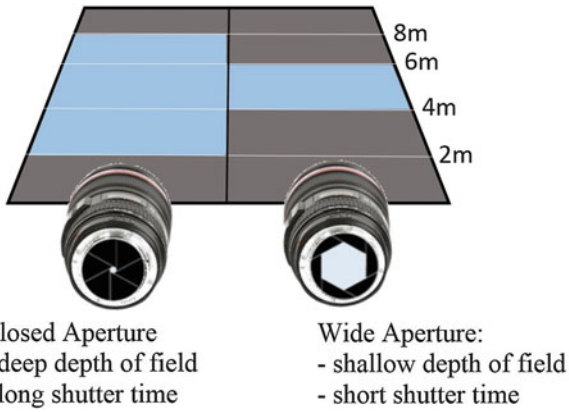

Fig. 16 Effects of aperture on the FOV; smaller aperture size can increase the depth of field

(wide angle lenses) can significantly increase distortions in the images particularly when the sample has large translations in the images. Fixed focal length lenses are more common in photogrammetry than zoom lenses because they create fewer optical distortions in the photos.

The depth of field of photographs is critical when large rigid body motions occur. The depth of field is affected by three parameters: (1) focal length – the shorter the focal length, the deeper depth of field; (2) distance from the object to the camera – the closer to the camera, the shallower depth of field; and (3) aperture – the smaller the aperture (f/stop), the deeper depth of field you will have.

The relationship between the aperture size, shutter speed, and depth of field is graphically shown in Fig. 16. The aperture specifies the amount of light that is transmitted to the sensor. A wider aperture allows more light to enter the camera box and sensor; thus, it would need a shorter shutter time. However, using a wide aperture would also create a shallow depth of field. On the other hand, when a smaller aperture (a large f-stop) is used, a longer shutter time or more light is needed to allow enough light to transmit to the sensor. This setup creates a deeper depth of field. Selecting a proper aperture size depends on the lighting condition in the test space, the required shutter speed, and the distance that the object is moving away or toward the cameras. When measuring large rigid body motions, a higher f-stop (a smaller opening of the lens) allows one to track the object while the subject is still in focus; however, extra illumination might be necessary.

It should also be noted that when the aperture is wide open, the cameras are very sensitive to focus. Thus, one should focus the cameras when the aperture is wide open. Afterwards, the aperture can be closed to the desired aperture size.

8.4.2 Blurring

In dynamic conditions, moving objects may create blurring effects (see Fig. 17). In other words, the shutter time sometimes is not negligible with respect to the velocity of the targets. The shutter time must be fast enough to prevent image smearing. When an object has a velocity of v (mm/s) and the movement is recorded using

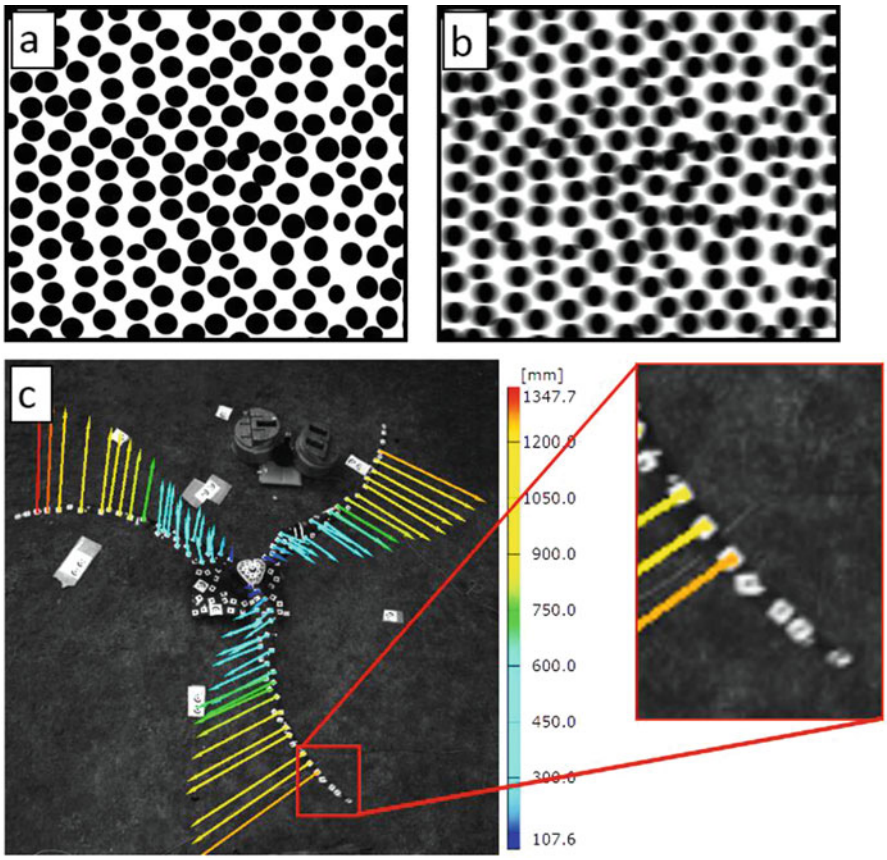

Fig. 17 (**a**) An image showing a pattern that has no blurring, (**b**) the same photo when it contains blurring because of horizontal movement, (**c**) a photograph showing that the photogrammetry software cannot identify some optical targets due to high blur of the targets near the tip of the blades [8]

a lens with an image magnification of k (pixel/mm), the displacement during the exposure time of t is calculated as:

$$w(pixel) = k.v.t \tag{3}$$

As an example, for an object with an in-plane velocity of 10 m/s, which can be seen in rotating structures, and the exposure time of 8 microseconds, and image magnification of 7 pixel/mm, the displacement during the exposure is 0.48 pixel of motion during the image capture. This corresponds to a very large motion that

creates blurry photos. The displacement during exposure time value should ideally be very small to create focused photos. It is important to note that for point tracking, ellipse finding algorithms can still find the center of the moving circular optical targets with reasonable accuracy even when the images are slightly blurry. It should be noted that the blurring is more critical for dot targets than speckle patterns. Also, change in the blur is more critical than the absolute blur value. More discussion about blurring is found in Sects. 10.1 and 16.

8.4.3 Lighting

Uniform illumination of the test object is a crucial part of generating high-quality, high-contrast photographs with minimum noise. Lighting might be required because of the high frame rates used for vibration measurements and the small apertures used for increased depth of field. A high contrast between the pattern/optical target and the background is critical for accurate measurements. Diffuse lighting leads to uniform illumination. Thus, when appropriate, sunlight can be used for illumination. Indoor measurements need to be performed using several lights or strobe lights to create a uniform illumination. Uniform lighting can also be provided using photography shades. Halogen lights have been conventionally used but LED lights have recently been more popular. The LED lights require less power and provide light with less heat than using a halogen light.

For DIC patterns, a flat or matte paint can be easily illuminated with a uniform light. Illuminating a gloss paint is very challenging because of reflections that create highlights in the photos. However, for point tracking measurements on large test objects in dark environments, using retro-reflective targets and a lighting system can limit the background light required. Researchers have suggested using monochromatic lights to reduce the effects of radiations from tests object at high temperatures [18] and to perform measurements in varying ambient light [51].

8.4.4 Heating Effects Due to Lighting

During an experiment, the lighting system can increase the temperature of the object. This temperature increase can be detected by touching the specimen or using infrared thermometer. The heat may change the material property of the structure or induce artificial strain due to thermal expansion. Furthermore, the heat waves may influence the camera sensors. This is more critical when the specimen is patterned with a dark background. Thus, proper measures, such as using a fan or switching off the lights (when not used), should be adopted. LED lights generate less heat and are becoming the more popular choice for illuminating a test object. More discussion about heating effects is found in Sect. 10.1.

Additional discussion of lighting, strobe lights, and heating effects is provided in the section on DIC for High-rate Testing located at the end of this chapter (see Sect. 16).

9 Excitation Strategies for Modal Testing and Application to DIC Measurements

9.1 Impact Testing

Impact testing is widely used in experimental modal analysis and is performed with an instrumented modal hammer. It is generally quick to set up compared to shaker testing: no shaker alignment needs to be performed and no amplifiers are needed for excitation signals. There is some additional effort involved when hammer testing in that a trigger needs to be set so the data acquisition system (cameras for DIC and whatever additional data acquisition system will measure the hammer input) records at the correct time.

For impact testing, there are few parameters that are controllable. The test engineer can generally control the force applied when impacting, though perhaps with a lesser degree of precision due to human factors involved. The mass of the hammer and the stiffness of the tip can also be varied and will both influence the length of the impact and thus control the frequency content of the impact. A more massive hammer will generally remain in contact with the part for a longer period of time, resulting in a wider pulse which has lower frequency content. Similarly, a softer hammer tip will also result in the hammer remaining in contact with the part for a longer period of time. Conversely, utilizing a lightweight hammer with a very stiff tip will result in a very short impact pulse and therefore higher frequency content imparted to the test article. Figure 18 shows three hammer hits with varying pulse widths and corresponding frequency content imparted to the structure.

The hammer spectra shown in Fig. 18 clearly demonstrate that there is not a sharp cut-off in the frequency content exciting test article. This means that modes outside the bandwidth of interest may be excited by the hammer impact if the spectrum is not tuned correctly. This is especially important for DIC measurements which have limited options for dealing with frequency domain aliasing: out-of-band modes may alias down into the bandwidth of interest and contaminate the data. When impact testing with DIC, it is strongly suggested that the hammer tip and mass be tuned so that the hammer input spectrum rolls off sufficiently past the frequency band of interest, but within the sampling rate of the cameras.

9.2 Shaker Testing

Shaker testing is advantageous to hammer testing in that the test engineer can often specify the exact signal sent to the shaker, and therefore can appropriately tune the force spectrum that the component receives. Additionally, shaker testing can often provide inputs at multiple locations on the test article which can shorten the testing time (MIMO) compared to exciting each location sequentially. However, shakers have some disadvantages compared to impact testing. The shaker is physically attached to the test article, which can change the dynamics of the system due to mass

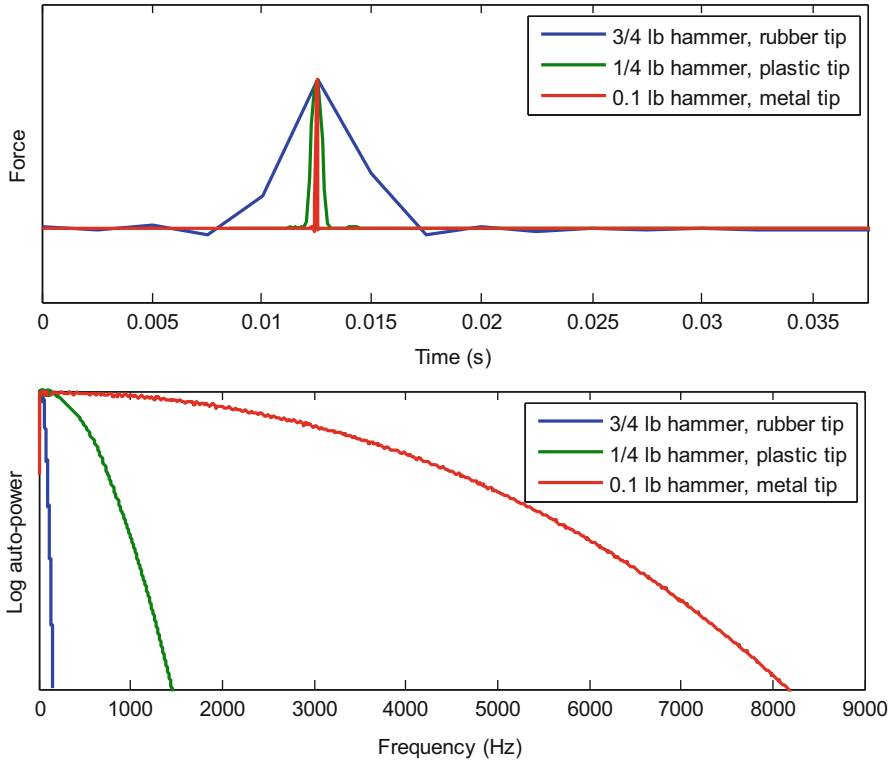

Fig. 18 Normalized force-time histories and auto-power spectra from three hits from different modal hammers

loading and can also introduce spurious modes of the stinger and shaker hardware if they couple with the dynamics of the system.

9.2.1 Sine Excitation

One of the simplest signals that can be supplied to a shaker is a single sinusoid. This signal excites the system at a single frequency, and if the test article is sufficiently linear, it will respond at that frequency as well. Sine testing provides the highest signal-to-noise ratio of any excitation technique, but that signal is limited to only one spectral line. A sine dwell excitation can provide large deformations at a resonant frequency; this can make it easier for a DIC system to capture the mode shape.

9.2.2 Swept Sine/Chirp Excitation

A slowly sweeping or stepped sine excitation can be used to measure responses frequency line by frequency line, but one must be careful to allow sufficient time between measurements for any transients due to the change in frequency to die

out. This type of testing results in long testing times and long acquisition periods, resulting in a potentially large number of DIC images which would then need to be downloaded and processed. The measurement may need to be paused and the images downloaded if the camera memory is not sufficient. Using a chirp input is similar to sine testing in that the signal is deterministic. However, instead of measuring one frequency line per measurement frame, the sinusoid sweeps from a starting frequency to an ending frequency over the course of the measurement frame. A chirp excitation is typically quick and generally provides very high signal-to-noise ratios and FRFs with high coherence.

9.2.3 Pure Random Excitation

Pure random excitation is generally implemented as a stationary random signal with a Gaussian probability distribution. Because it is random, there is generally frequency content over the entire bandwidth, not just the discrete frequency lines in the FFT: the signal is not periodic within the measurement frame. Leakage is a concern for this excitation method so windows are generally necessary. Pure random excitation can be advantageous in systems where nonlinearities are present if the test engineer wishes to obtain a linear representation of the system for a specified level of excitation. Often a large number of averages are required to ensure that all frequencies are adequately excited. This can be a disadvantage for DIC measurements due to the large number of images that would need to be downloaded and processed. The measurement may need to be paused and the images downloaded if the camera memory is not sufficient.

9.2.4 Pseudo Random Excitation

Pseudo random excitation is a sum of sinusoids with constant amplitude and randomized phase having frequencies equivalent to the discrete frequency values in the FFT. If enough delay cycles are run for the startup transients to die out, pseudo random excitation is then periodic in the measurement frame so it does not suffer from leakage: no window is necessary. Because there is a constant amplitude at each frequency line, this input strategy can use fewer averages than a pure random excitation, making it more attractive for a DIC measurement. The downside of the pseudo random excitation occurs for significantly nonlinear systems where the distortion caused by those nonlinearities will not be removed: the excitation level at each frequency line is constant, so the nonlinear effects are not averaged over a range of amplitudes, as they are in a pure random input.

9.2.5 Periodic Random Excitation

Periodic random excitation is similar to pseudo random in that the frequency content is tailored to the discrete frequency values in the FFT, but instead of only randomizing the phases of the frequency content, the amplitudes are also randomized. If enough delay cycles are run for the startup transients to die out, periodic random excitation is periodic in the measurement frame, so similar to

pseudo random excitation, it should not require any windowing. However, like the pure random excitation, a large number of averages are required to ensure that all frequencies are adequately excited. This can be a disadvantage for DIC measurements due to the large number of images that would need to be downloaded and processed. The measurement may need to be paused and the images downloaded if the camera memory is not sufficient.

9.2.6 Burst Random

The burst random excitation is a transient random signal that after a specified percentage of the measurement frame is set to zero. When the signal to the shaker cuts off, the structure then rings down and the responses as well as the forces applied to the structure decay to zero. If this entire transient is captured within the measurement frame, no window is needed to reduce leakage, but if the transient dies out to quickly in the measurement frame, the signal-to-noise ratio may be reduced. Similar to pure random excitation, a large number of averages are required to ensure that all frequencies are adequately excited. This can be a disadvantage for DIC measurements due to the large number of images that would need to be downloaded and processed. The measurement may need to be paused and the images downloaded if the camera memory is not sufficient.

9.3 Recommended Inputs for DIC Testing

Because of the large amount of data gathered per sample when using DIC, the number of samples that can be taken before the cameras need to have their memories dumped to a computer may be limited. For this reason, excitation techniques requiring many measurement samples may be difficult or time-consuming to perform. Impact testing and pseudo random excitation are two good candidates for excitation that can be used that generally require few averages. Additionally, because pseudo random is periodic in the measurement frame, low-speed cameras could potentially be used to measure relatively high frequency content if the triggering is set up appropriately (see Sect. 8.3.2 on phase-stepping).

However, none of these signals can be applied blindly. In impact testing the frequency content is not easily controllable; the test engineer may have only a handful of hammers and hammer tips to choose from to tune the frequency content of the impact. Improper frequency content in the impact can lead to serious issues such as frequency domain aliasing. Additionally, due to its transient nature, impact testing tends to have a poorer signal-to-noise ratio than the shaker inputs that last the entire measurement frame. A low-level modal test attempting to linearly excite a structure may already require a low-level force, and the tail end of the response decay may not be resolvable or may be very noisy. Pseudo random testing will not adequately remove the distortion from the test article due to nonlinearities, so if a system is not sufficiently linear, it may not be a good excitation strategy.

10 DIC and Photogrammetry Measurement Range and Noise Floor

Similar to other measurement systems, DIC results are subjected to bias and noise. Bias is the systematic deviation of the results from correct values while noise is random and has a zero mean. Proper setup and calibration can significantly reduce the bias. On the other hand, noise can be minimized but never removed.

As a rule of thumb, with current camera technology, the nominal noise floor for the displacement measured with DIC in the time domain is as low as 1% of the object sample size (see Fig. 1) for in-plane and 3% for out of plane motions [88]. For example, if the pixel within in the image spans 1 mm of the FOV, the in-plane and out-of-plane displacement will have a resolution of no better than ~0.01 mm and ~ 0.03 mm, respectively. A well-calibrated DIC system can also measure strain with a noise floor as low as 5 microstrain [65] but more typical results are on order of 50 microstrain. It should be noted that by using proper data processing techniques, better accuracies than the nominal noise floors can be reached. The parameters that influence the noise can be categorized as "pre-measurement" and "post-measurement parameters." A list of these parameters is shown in Table 5.

10.1 Pre-measurement Parameters

10.1.1 Camera Setup and Calibration

The camera type and setup can change the accuracy of the DIC system. Using high-resolution cameras can improve the accuracy of DIC for measuring displacements (because it increases the resolution of the obtained images). However, strain accuracy stays constant when the camera resolution changes. Using high-speed cameras that can provide the proper frame rate to capture the vibrations can affect the noise floor [20]. For a stereo camera system, the cameras should be synchronized

Table 5 Parameters that affect the noise floor of DIC

Pre-measurement parameters	Post measurement parameters
Camera calibration	Subset size
Camera resolution and sample size	Subset step
Camera angle	Shape function
Shutter speed and sample motion	Strain calculation size
Camera synchronization	Filtering
Illumination	
Speckle pattern size	
Speckle pattern density	
Aliasing	
Air turbulence	
Thermal radiation	

to within a small fraction of the exposure time. The camera calibration can also affect the accuracy of the DIC measurement. Selecting a proper calibration volume and calibrating the entire space helps to ensure that the cameras are accurately calibrated (see Sect. 1).

10.1.2 Blurring

Due to the fast motion of objects in vibrating structures, blurring can be one of the sources of uncertainty in dynamic measurements. Selecting a proper shutter speed (see Sect. 8.4) with minimum image blurring can improve the accuracy of the system. The graphs shown in Fig. 19 can be used to quantify the uncertainty of DIC due to blurring. The results are extracted by adding motion blur in the form of Gaussian noise to the images. In this figure, w (x-axis) is defined as the length of the path covered by a target during the exposure time (see Eq. 3 in Sect. 8.4). The y-axis shows the mean and standard deviation of displacement and strain uncertainty of the DIC system. As can be seen, the uncertainty significantly increases when the imposed motion blur increases.

It should be noted that blurring creates more uncertainty when there is a change in blur amount. For example, the velocity of the object due to the impact made by a modal impact hammer changes rapidly and the blur is different between before and

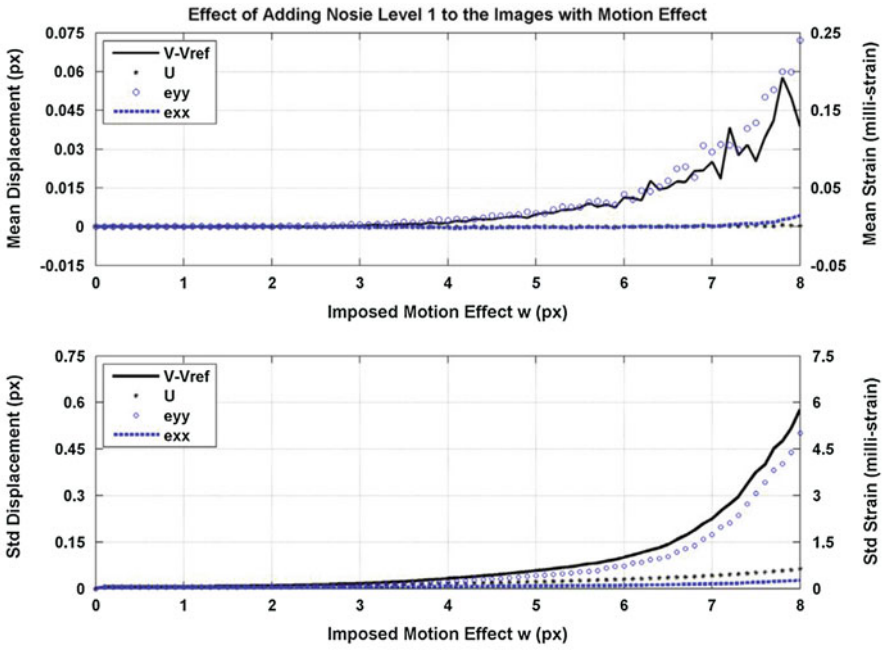

Fig. 19 Mean and standard deviation of displacement in case of rigid motion with zero displacement after adding Gaussian Noise (V and eyy are the displacement and strain in the direction of motion and U and exx are in the orthogonal direction, respectively) [90]

after impact. However, with shaker testing – the blur stays approximately constant during the entire event.

An image pre-processing technique has been suggested to minimize the effects of blurring in dynamic applications [91]. In this approach, a blurry target can be compared to the original target in the reference frame to identify the mathematical function that can convert the original target to the blurry target. When this part of the blur is identified, the pure displacement can be measured with higher accuracy. This technique can reduce the bias error and the uncertainty of measurements in dynamic applications of DIC.

10.1.3 Speckle Pattern and Target Shape

The DIC speckle pattern is another parameter that can influence its accuracy. A proper speckle size (3–7 pixels) and contrast can improve the accuracy of the results. Using soft-edge speckles has shown better results than sharp-edged speckles [62]. The soft-edge pattern can be generated by using inkjet printers, sharpies, stochastic sprays, rollers, pattern brushes, or pattering stencils. Printed adhesive mask foils are also used to create patterns. Post filtering of the images can also create soft edges for the pattern. It should be noted that contrast is the most important factor for patterning and should be optimized – even if the speckle edge is sharp. On the other hand, images can be post-processed to create soft-edge speckles.

Optical targets used for point tracking may have different shapes (e.g., square, circle, or ellipse). It has been shown that some point tracking algorithms are more accurate using sharp angles targets (e.g., square shape targets) [20].

10.1.4 Camera Angle

The shooting angle of the cameras and the stereo angle can also affect the accuracy of DIC measurement. To obtain a high accuracy for in-plane displacement and strain measurement, the cameras need to shoot perpendicular to the object surface. For 3D measurements, the minimum stereo angle between cameras should be ~11 degrees to satisfy triangulation requirement. However, a larger stereo angle (e.g., ~35 degrees) can result in a better out-of-plane displacement accuracy. Thus, selecting an appropriate stereo angle depends on whether out-of-plane displacement or in-plane displacement and strain is desired. It should also be noted that the larger stereo angle may cause difficulties when curved objects and objects with complex geometries are tested. In these cases, the two cameras might not have line of sight on all areas of the object.

The stereo angle is very critical for the cameras with wide-angle lenses. Figure 20 shows captured images using 8-mm and 75-mm lenses when they are placed in narrow and wide stereo angles. The uncertainty of the stereo-correlation is shown with the red squares (i.e., Matching Error in Fig. 20). The green region is captured using the 75-mm lenses and the blue region is recorded using the 8-mm lenses. The green and blue lines intersecting with rays of light represent the sensor planes for the 75-mm and 8-mm lenses, respectively. As can be seen, the wide angle lenses move the sensor plane toward the cameras; this can increase the effects of matching error. Figure 20 shows that the out-of-plane error for the cameras used with wide

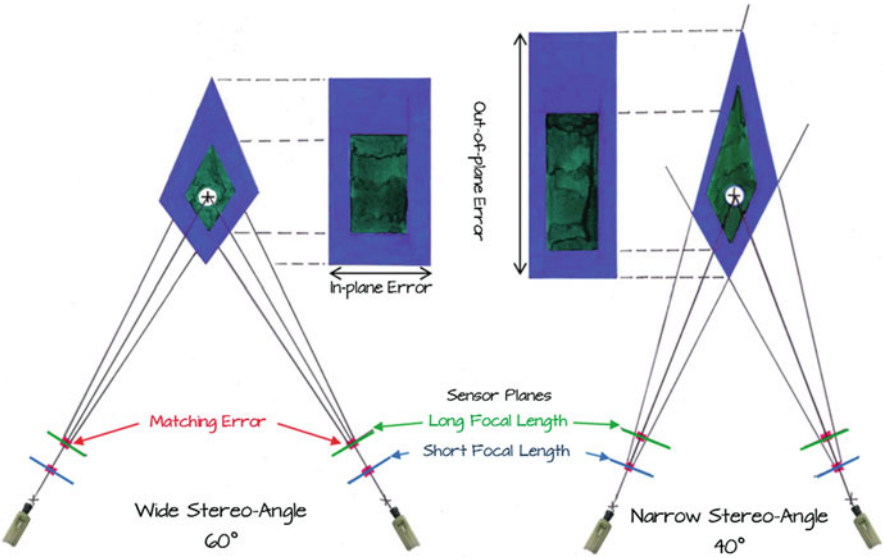

Fig. 20 Uncertainty as a function of stereo angle and focal length [56]. The figure shows the uncertainty in DIC when a 75-mm (results shown in green) and an 8-mm (results shown in blue) lenses are both used in narrow and wide stereo angles

stereo angle is smaller than the when the cameras are mounted with narrow stereo-angle. Thus, it is best to use wide-angle lenses with wide stereo angles to reduce the matching error (minimum stereo angle of 25 degrees). Furthermore, because distortion increases on the corners of the lenses, noise is highest in the image boundaries. Thus, to have less distortion when wide-angle lenses or small stereo angles are used, it is recommended to set the area of interest near the optical axis (center of the images).

10.1.5 Air Turbulence

The air turbulence and thermal fluctuations can also increase the uncertainty of DIC measurements [32]. Camera fans can create turbulence in the air and motions in cameras which are sources of noise; using cooled cameras that do not have fans significantly reduces the noise floor. It should be noted that the air turbulence is less problematic in the frequency domain because usually it is distributed in the 1 to 50 Hz range. On the other hand, the lighting system can heat up the cameras and specimen. As such, the lighting system should be installed at a higher-level position with respect to the cameras and as far from the cameras as possible. It has also been shown that air turbulence for experiments at elevated temperatures can also distort the images. Using a fan during measurement or testing in a vacuum are two suggested approaches to reduce the noise in these cases [81]. Under no circumstances should the lights be placed directly below or in front of the cameras as

the thermal convective turbulence in the air will cause air density variations leading to light refractions and distortions in the images taken.

10.2 Image Correlation and Data Processing Parameters

The image correlation parameters can effectively influence the accuracy of DIC. A subset should include an adequate number of grayscale variations. The spatial resolution (i.e., the spacing between each of the data points) of DIC is directly related to the step size. Similar to finite-element analysis, one may use subsets of small sizes to extract more accurate results with finer resolution. In order to use smaller subsets, the speckle sizes must also be small so that the small subset can contain enough grayscale variations to perform accurate correlation. Another approach to improve the spatial resolution of DIC is to increase overlapping parts of subsets up to 50% of the subset size (using smaller subset steps). However, this also increases the computation time.

The displacement and strain measured by DIC will virtually always contain some noise. The noise can be reduced using low-pass filters and spatial filtering. A median or Gaussian spatial filter is usually used to serve this purpose (median is best when outliers exist in the data median while Gaussian can reduce the noise). In this approach, the median value in a matrix of unfiltered data around a point is assigned to this point. The size of this matrix can be adjusted based on the measurement. Because strain is related to the spatial derivative of displacement values, it contains more noise than displacement. A suggested filter size of seven, with a count of three to measure strain, is used as a default in some software packages to reduce the noise in strain data. Furthermore, the computation size specifies the number of data points that are used in the strain calculations (it defines the virtual strain-gage size) [63]. For more information interested readers are referred to the "iDIC Good Practice Guide" [28].

10.2.1 Data Processing Parameters

Postprocessing techniques for DIC data can significantly influence the accuracy. In quasi-static configuration, several photos can be acquired from the object in a single position and the results are averaged to reduce the noise. However, this is not possible for vibration measurement. The results of DIC in the time domain are dependent on the noise floor of a DIC system. This noise floor might not be low enough considering small magnitudes of displacements and strain for vibrating structures. However, the noise in DIC results can be assumed as Gaussian noise. Therefore, when the results are transferred to the frequency domain, the noise is quite evenly spread on the entire bandwidth. On the other hand, the response of the structure in the frequency domain is concentrated at a few resonant frequencies. Therefore, higher accuracies can be achieved when the data is processed in the frequency domain (see Sect. 6).

Researchers have also used finite-element smoothing and the least-square method to improve the accuracy of the DIC system [39, 50]. In dynamic conditions, a

linear combination of the mode shapes can be used to smooth and expand the measured data and reduce the noise [5, 6]. Similar to conventional modal analysis measurements that need several averages for a single measurement, an averaging approach on the final results can be used to reduce the noise floor [25].

11 Strain Mode Shapes

Conventional modal analysis techniques use accelerometers to measure the response of a structure and eventually extract displacement mode shapes of the structure. However, in many applications such as damage prognosis, durability and fatigue analysis, and structural health monitoring, strain data can be a better representative of the structure performance and many of these structures are monitored using strain-gages. Strain mode shapes have recently received more attention and some modal software packages (e.g., LMS) have added strain mode shape modules. For these types of measurements, strain-gages are used to measure strain at a few locations, and modal analysis is performed on the strain data to identify the modes. Strain mode shapes can be extracted using numerical and finite-element models. DIC offers new capabilities to extract full-field strain mode shapes with no need to develop a finite-element model.

To extract the equations for strain mode shapes, we start with displacement mode shapes. Equation 4 shows the basic theory of modal analysis. This theory states that the response of a structure to excitations can be expressed as a linear combination of the mode shapes.

$$u(t) = \sum_{i=1}^{n} \left(p_i(t) \{\phi\}_i \right) \tag{4}$$

In this equation, u is the response of the structure, and $\{\varnothing\}_i$ is the i-th displacement mode shape, while $p_i(t)$ shows the contribution of each mode in the response. Using the theory of elasticity, the strain in the x-direction can be calculated as:

$$\varepsilon_x = \frac{\partial u}{\partial x} \tag{5}$$

A similar equation exists between the displacement and strain mode shapes.

$$\{\psi\}_i = \frac{\partial \{\phi\}_i}{\partial x} \tag{6}$$

where $\{\psi\}_i$ shows the i-th strain mode shape. It can be shown that the strain response of a structure (ε) can also be represented using a linear combination of its strain mode shapes.

$$\varepsilon(t) = \sum_{i=1}^{n} p_i(t)\{\psi\}_i \tag{7}$$

The contribution of each mode in the response depends on the excitation force (F).

$$p_i = \Lambda_i^{-1}\{\phi\}_i F, \text{ and } \Lambda_i = -m_i\omega_i^2 + jc_i\omega_i + k_i \tag{8}$$

In this equation, m_i, c_i, k_i, and ω_i, respectively represent, mass, stiffness, damping, and natural frequency associated with a mode of structure. The equations for the Strain Frequency Response Function $[H^{\varepsilon}]$ are:

$$\left[H^{\varepsilon}\right] = \begin{bmatrix} H_{11}^{\varepsilon} & H_{12}^{\varepsilon} & \dots & H_{1n}^{\varepsilon} \\ H_{21}^{\varepsilon} & H_{22}^{\varepsilon} & \dots & H_{2n}^{\varepsilon} \\ \vdots & \vdots & \vdots & \vdots \\ H_{m1}^{\varepsilon} & H_{m2}^{\varepsilon} & \dots & H_{mn}^{\varepsilon} \end{bmatrix} = \sum_{i=1}^{n} \Lambda_i^{-1} \cdot \begin{bmatrix} \psi_{1i}\phi_{1i} & \psi_{1i}\phi_{2i} & \dots & \psi_{1i}\phi_{ni} \\ \psi_{2i}\phi_{1i} & \psi_{2i}\phi_{2i} & \dots & \psi_{2i}\phi_{ni} \\ \vdots & \vdots & \vdots & \vdots \\ \psi_{mi}\phi_{1i} & \psi_{mi}\phi_{2i} & \dots & \psi_{mi}\phi_{ni} \end{bmatrix} \tag{9}$$

In this equation, m and n represent the number of strain sensors and excitation points, respectively. The strain frequency response function matrix (SFRF) contains information about both strain and displacement mode shapes. Eq. 9 shows that unlike an FRF matrix, an SFRF matrix is not symmetric. Any column of the SFRF matrix represents unscaled strain mode shapes of the structure (mode shapes multiplied by a constant number) [21]. A column of this matrix is extracted by exciting the structure at a single location and using multiple strain sensors to record the response. Using a roving modal impact hammer with a single strain sensor results in a row of the SFRF matrix (an unscaled displacement mode shape). It should be noted that for an operational modal analysis, the excitation force is not measured; thus, unscaled strain mode shapes are extracted.

Both strain-gages and DIC can measure SFRF of a specimen. SFRF can be extracted using a test with strain-gages mounted to the structure. However, these modes may not be graphically shown because the results are discrete strain values at a few locations. On the other hand, a DIC system can present both the full-field displacement and strain mode shapes with a graphical interface.

Many equations and relationships used for displacement mode shapes can also be applied to strain mode shapes. For example, modal reductions/expansion techniques have conventionally been used for correlation purposes or for real-time monitoring of structures [5]. The System Equivalent Reduction and Expansion Process [47] is a technique that uses displacement mode shapes to reduce or expand the displacement data. It has been shown that strain data can also be reduced/expanded using strain mode shapes [4, 12]. This technique can be applied when the full-field strain data for an operating system needs to be monitored while only a few strain-gages can be mounted to the sample (e.g., wind turbine blades or helicopter rotors). The

strain mode shapes for the expansion can be extracted using a numerical model. Developing an accurate finite-element model can be very challenging. On the other hand, DIC enables us to extract strain mode shapes without any need to develop a finite-element model. Using this approach, the strain mode shapes for a structure can be extracted in a testing facility. An in situ measurement can be performed using a limited set of strain-gages or fiber optic sensors. The limited set of measurements can be expanded using the strain mode shapes to extract full-field results.

12 Projected Patterns Pros and Cons

12.1 Projected Speckle Patterns

In order to perform DIC or point tracking measurement, a pattern or optical targets must be placed onto the surface of interest in order to track changes in deformation and strain. Without a pattern that is adhered to the structure, it is still possible to obtain a shape measurement over time but not mechanical strain. Several static shape measurements using projected patterns were successfully performed to measure bridge spalling [46] (see Fig. 21) and railroad tie deflection [69]. For structural dynamic measurement, it is possible to measure the shape of the structure of interest at each image sample. In order to determine the structural deflection, the shape needs to be compared to some reference state at an instance in time. Again, it is not possible to determine strain directly because the projected pattern will not respond to changes in mechanical strain.

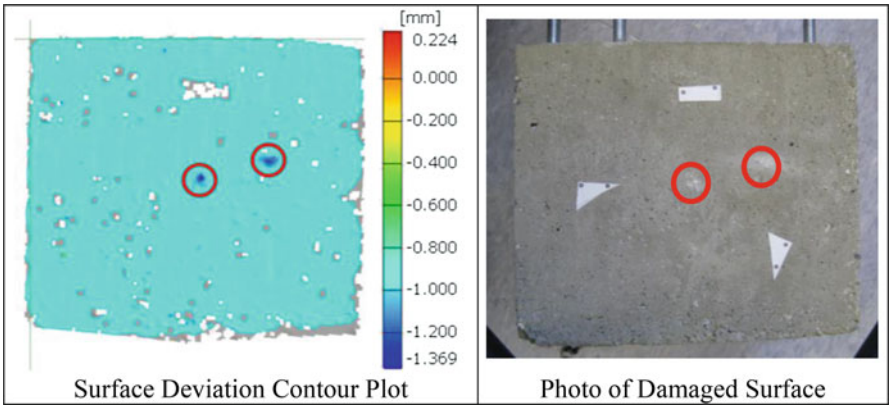

Fig. 21 Contour plot of deviation between damaged and undamaged bridge surfaces, and photograph of damaged surface; red circles denote the locations of induced damage [46]

12.2 Deflectometry

Deflectometry is another measurement technique that can be used to investigate modal shapes with high-speed cameras. It uses a mirror finish on the surface to reflect a grid pattern to the camera. By analyzing the motion of the grid image, the local slope of the surface can be measured. Extremely sensitive measurements of the slope are possible because of the magnification effect of the reflected grid. For more information, see Surrel et al. [77].

13 Rotating Optical Measurements

Measuring the dynamics of rotating structures has been a challenge due to wiring and data transmission issues. However, the noncontact capability of photogrammetry makes it useful for measuring the dynamics of rotating structures. Furthermore, this technique is not sensitive to large displacements and rotations. This makes photogrammetry very desirable for monitoring the dynamics of rotating structures.

Optical targets can be readily mounted to the structure; thus, point tracking has been frequently used to measure the dynamics of rotating structures [35, 37, 49]. Another advantage of using point tracking is the similarity of the data from 3DPT to conventional measurement systems (e.g., accelerometers). The measured data in the time domain can be transferred to a modal software package such as LMS, for further processing and for the extraction of the mode shapes. Many modal packages have special tools for analyzing dynamics of rotating structures. This is usually performed by organizing data in MATLAB and creating Universal File Format (UFF) files that can then be used as inputs to modal analysis packages.

13.1 Frequency of Measurement, Duration, and Shutter Time

Measuring the vibrations of rotating structures usually needs high-speed cameras due to the fast displacements that occur at the tip of the rotors and the high frequency vibrations. The frame rate of cameras should be adjusted based on the desired information. As a rule of thumb, the frame rate of the cameras should be set to approximately 20–30 times the rotation frequency, but is dependent on the frequency range of the modes of interest. In order to perform an effective operational modal analysis on the data, the measurement duration should be 200 times greater than the period of the lowest order modes in the data. However, for high-damping cases, this number might be greater than 200 [48]. Similar to vibration measurements, the phase stepping technique can be used when low-speed cameras are used for measurements in rotating structures [26] (see Sect. 8.3.2).

The shutter time for the cameras needs to be based on the speed at the tip of the blades. The tips of the rotor travel tangentially faster than the rest of the rotor, and the targets and pattern at the tip of the blades are more prone to blurring. It should be noted that a small amount of blurring might be visible when the rotation speed

is constant. In these cases, one of the images with a blurred pattern can be selected as the reference image; the rest of the photos will likely contain the same amount of smearing.

13.2 Camera Setup

A single stereo system can be used to measure the vibrations of a rotor. To measure the vibrations of a rotating structure, a stereo camera can be installed above, below, or in front of the rotor (see Fig. 22a) in order to cover full the motion over the entire rotation. In some measurements, it might not be possible to locate the cameras in front of the rotor. When the cameras are located underneath the rotor, a single stereo system can only cover an azimuth angle of the entire rotation. However, this measured data can also be used for operational modal analysis and for the extraction of the mode shapes of single blades.

Another approach involves mounting several stereo systems to record a complete rotation or large azimuth angles. This technique was used to measure the dynamics of a helicopter's rotor in a wind tunnel [1]. In this measurement, cameras were placed underneath the helicopter. Each camera pair would only cover a quarter of the rotation; thus, eight cameras were used to cover a complete rotation.

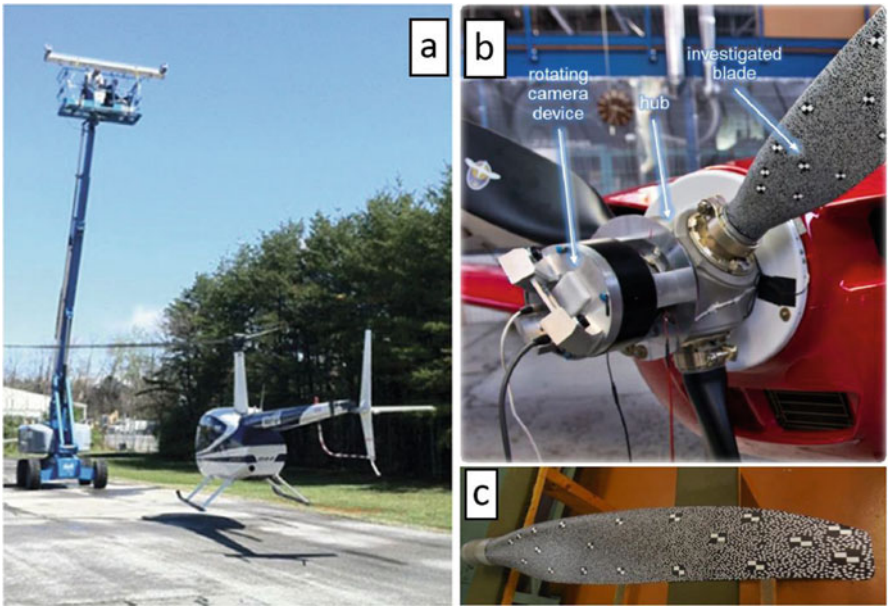

Fig. 22 (**a**) A photogrammetric measurement on a hovering helicopter when the cameras are looking from the top of the rotor [37], (**b**) a DIC measurement on a rotor when the cameras are mounted to the rotor and rotates with it, (**c**) progressively patterned blade used for the case with rotating blade [76]

Another approach for measuring the dynamics of a rotating structure is to use cameras that rotate with the blades (see Fig. 22b). These cameras need to have their own batteries and can be controlled by means of a wireless system. If the cameras are installed very close to the rotor with a high inclination angle, the patterns close to the cameras might appear very large while the points far from the sensor are very small in the images. This issue can be resolved by using a special type of cauliflower pattern, or a pattern that increases its size when moving away from the center along with elliptical optical targets (Fig. 22c). Researchers have used a tachometer as well as a laser sensor to synchronize the cameras and strobes with the rotation speed [75]. By using this approach, images can be recorded at exactly the same angle in each rotation to perform a more consistent measurement.

13.3 Rigid Body Correction

Rigid body correction is a technique to extract actual deformations of a structure from measured displacements. If a group of optical targets attached to a structure is translating or rotating together, the flexible deformation of the structure is calculated by subtracting the rigid body motion of the entire structure from the measured displacement. Rigid body correction in fact changes the coordinate system from the camera to the rotor. A set of points (minimum of three) that are ideally fixed with respect to each other during the test are considered as reference points to perform a rigid body correction. For the rigid body correction, the measured displacements of all points or facets are subtracted by the reference points' translation and/or rotation. This method is very useful when the deformations of blades in a rotating turbine are desirable. The out-of-plane measurement is very small compared to the rigid body displacement of the entire structure during rotation. In this case, the displacement of the structure that is caused by rotation of the turbine might not be desirable. Using the points on the hub, the measured displacement can be de-rotated and the actual deformation of the blades can be extracted [36]. If the hub is not fixed, an "instrumentation pod" can be attached to the rotor to add a few points that are fixed with respect to each other.

Identifying the rotation plane (or surface) and rotation center is critical for processing the data for rotating structures. The center of rotation is usually extracted using the trajectory of markers. If a circle is fit to this path, the center of the circle is the center of rotation. Using more targets in this process can result in a more accurate estimate of the center of the circle.

13.4 Mode Extraction Challenges and Effects of Harmonics

Analyzing rotating data to extract mode shapes for rotating structures are challenging endeavors. These challenges also exist when other techniques are used for measurement. An important factor that hampers the processing of data for rotating structures is that these structures are not usually in a steady state, and their

dynamics may change during operation. Having a steady-state system is one of the assumptions used in operational modal analysis. The support stiffness for a rotor may change during operation based on the blade's azimuth angle. Furthermore, aerodynamic effects may also vary during measurement.

Aeroelastic damping is another factor that makes the dynamic measurement of the rotating structures challenging. The aerodynamic damping can be as high as 10% to 30% of critical damping while for most of the structures the structural damping is less than 1% [48]. This high aerodynamic damping does not allow for the accurate extraction of the structural modes and can mask the structural damping.

The effects of harmonics of rotation speed on the dynamics of rotating structures are significant. In the operational modal analysis, there is an assumption that the input of the system has a Gaussian distribution to excite all resonant frequencies of the structure. The excitations due to the harmonics of rotation speed violate this assumption. Many of these harmonics might coincide with the resonant frequencies of the system; thus, it might be difficult to verify the mode shapes. The rotating data modified by harmonics can be analyzed using multiple approaches. One technique is to measure the operating data with different rotating speeds. This can show the structural modes that are likely to be inherent in the results (if the centrifugal effects are negligible) compared to harmonics of the rotation speed, which are very dependent on the rotation speeds. Other approaches are based on using harmonic filters. These filters remove the effects of harmonics on the data. There are many OMA approaches that can identify the modal parameters when the system is influenced by harmonics [43] and some modal analysis packages are equipped with harmonic removal tools.

14 Some Experimental Case Studies

14.1 Comparison bBetween 3D Scanning Laser Doppler Vibrometry and 3D Stereo-DIC

Some of the first quantitative comparisons of test/analysis/correlation of data measured using the DIC approach to traditional accelerometers, a scanning laser vibrometer, and a finite element model were presented by Helfrick et al. The results indicated that all three approaches correlated well with the finite element model and provided validation for the DIC approach for full-field vibration measurement [3, 27]. Another related work obtained frequency response function measurements for a vibrating structure using 3DPT while simultaneously validating the shape of the two optically based measurements to the two other traditional vibration measurements as well as to a finite element model [88] (see Fig. 23).

In Reu et al. [68], a comparison between 3D Scanning Laser Doppler Vibrometry (3D SLDV) and 3D Stereo DIC was performed using a modal test on a small plate structure as a test problem (shown in Fig. 24). Both systems allow full-field measurements over a surface and have the ability to compute strains; however, the systems use vastly different methods to measure responses of the test article.

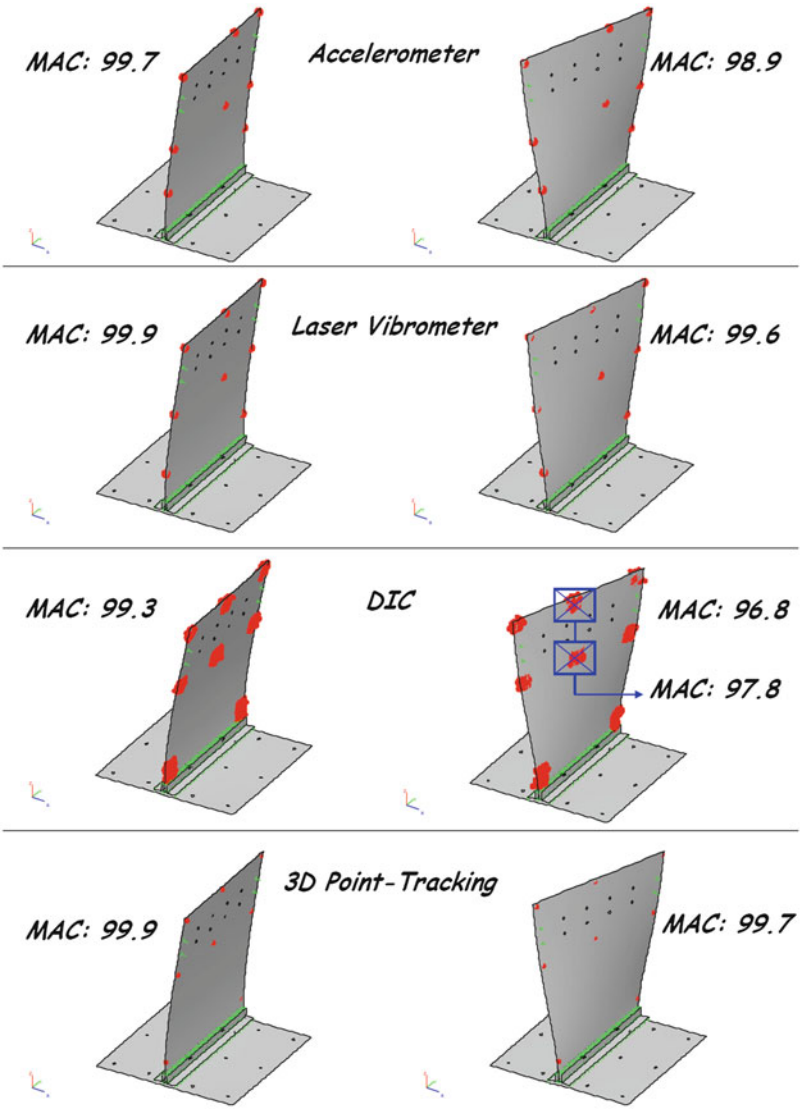

Fig. 23 Correlation of the mode shapes predicted by the FEM to the various sensing methods, for modes 1 (26 Hz) and 3 (78 Hz) of a base-upright structure from Fig. 15 [88]

The authors of that work sought to determine each system's advantages and disadvantages.

For the test, the DIC system and 3D SLDV system were set to sample at 3906.25 Hz. About 1600 frequency lines were measured with a frequency resolution of 0.977 Hz. Because pseudo random excitation was supplied to the shaker, only five frames were measured and averaged to form frequency response functions.

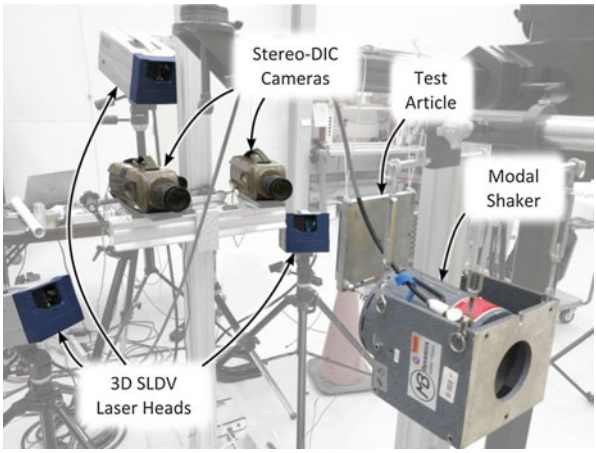

Fig. 24 Experimental setup for a comparison of 3D SLDV and 3D DIC

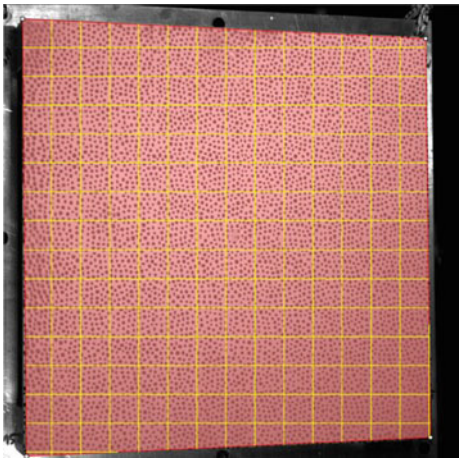

Fig. 25 Overlay of the subset (facet) size on the speckle pattern over the entire plate. Note that in the solution there was an overlap of approximately ½ the subset size

Note that this is the maximum number of averages that could be recorded with the DIC cameras used for this test. The DIC system measured 715 points on the surface of the test article (see Fig. 25), and the 3D SLDV system measured 545 (see Fig. 26). Because the 3D SLDV scans point sequentially, the 3D SLDV measurement took significantly longer than the DIC measurement which measures all points simultaneously. However, due to the significant download and processing time involved to turn DIC images into time histories, the time difference between the two measurements ended up being negligible.

Both the DIC and 3D SLDV data needed to be transformed to accelerations via frequency domain differentiation before curve fitting could be performed. There was good agreement between the modal parameters extracted from the measured data. Table 6 and Fig. 27 show the natural frequencies and mode shapes. It should be noted that the speckle patterned surface, which was necessary for the DIC measurement, was not optimal for the 3D LDV system, since dark surfaces do not

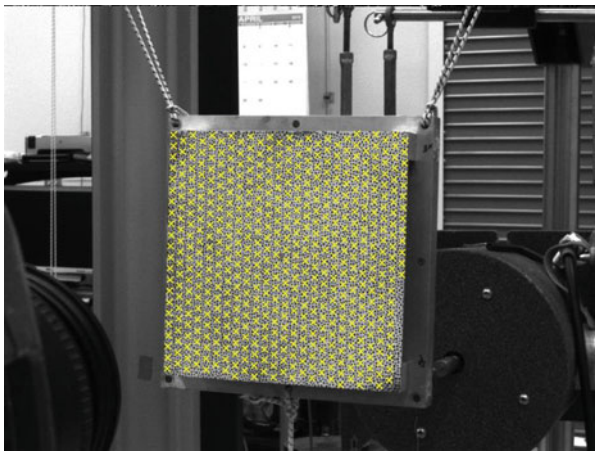

Fig. 26 Measurement point locations for the 3D SLDV system

Table 6 Comparison of modal parameters extracted from the test data

Mode	Frequency (Hz)			Damping (%)		
	DIC	LDV	LDV w/RET	DIC	LDV	LDV w/RET
1	529.4	529.5	524.8	0.042	0.042	0.104
2	883.0	883.1	875.0	0.022	0.024	0.095
3	891.7	891.7	883.3	0.015	0.026	0.098
4	948.3	948.4	938.8	0.019	0.019	0.071
5	1420.1	1420.4	1406.6	0.015	0.020	0.096

return adequate light to the laser head for a good measurement signal. Therefore the 3D SLDV shapes have some erroneous points. These errors disappeared when retroreflective tape (RET) was applied to the surface of the test article, but application of the tape required taking down the test article, so some of the natural frequencies and damping ratios have shifted slightly due to small changes in the test setup. Strain shapes computed from a sine dwell test at the natural frequencies were also compared between the two tests, and are shown in Fig. 28.

In this test it was shown that the DIC and 3D SLDV can achieve similar results for traditional modal testing. FRFs measured with the 3D SLDV were significantly less noisy (see e.g., Fig. 29), but it seemed that the DIC strain computation algorithms were more robust. Table 7 shows a comparison between the two measurement methods for the various test parameters performed in this example. A broader comparison between measurement approaches is shown in Table 8.

15 DIC Comparison to Traditional Modal Analysis Sensing

Traditionally, modal analysis has been performed by using modal impact hammers to excite the structure and by using accelerometers to record the response. Strain-

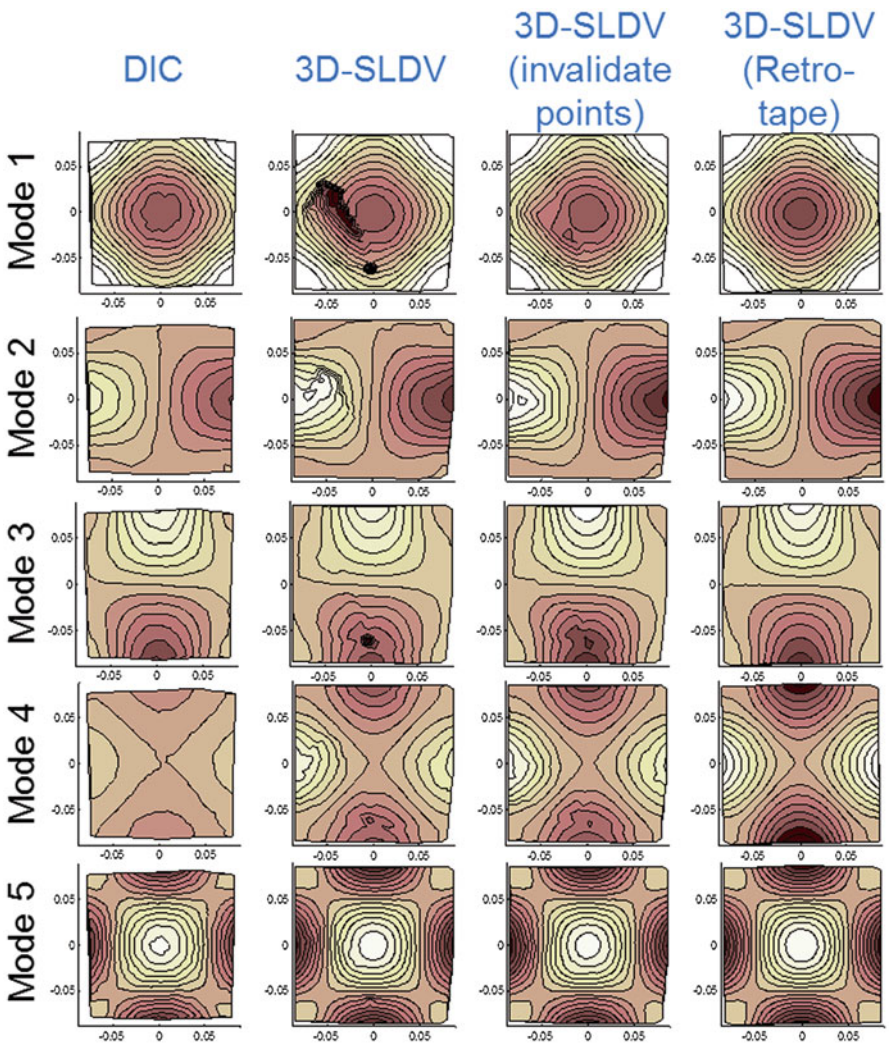

Fig. 27 Mode shapes for out-of-plane motion for the DIC and different SLDV measurement approaches

gages, LVDTs, and other contact-based measurement systems have been used to measure the response of the structure. All of these sensors measure the response at discrete locations and need instrumentation for data transmission. Fiber optic sensors have been recently used to measure vibration to monitor structural health. However, they need to be integrated into the structure in the manufacturing stage and are only capable of one-dimensional measurement. Optical measurement techniques are used in structural dynamics due to their non-contact features. These

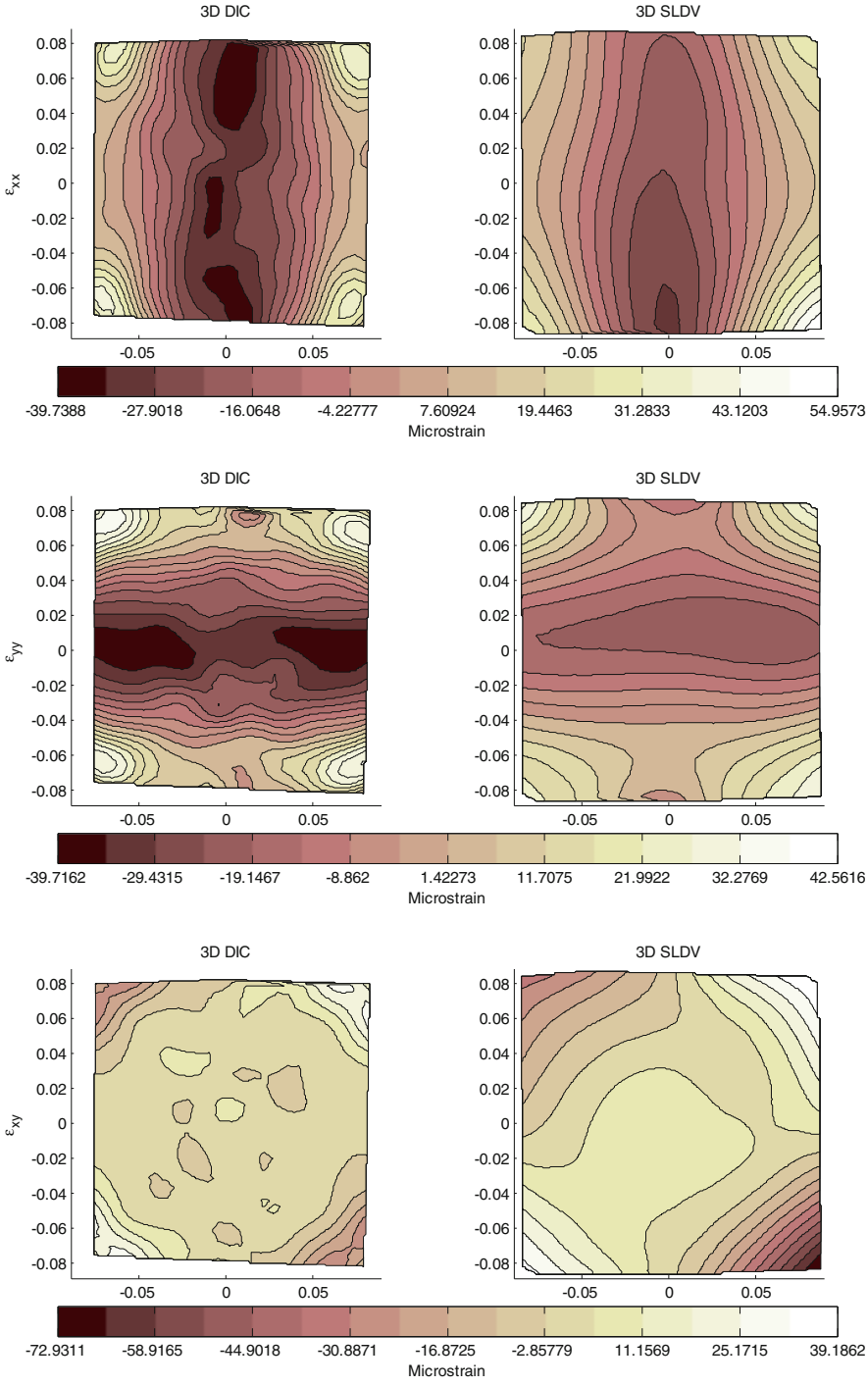

Fig. 28 Strain from a sine-dwell test at 530 Hz for both SLDV (25-mm filter) and DIC. Top is ε_{xx}, middle is ε_{yy}, and bottom is ε_{xy}

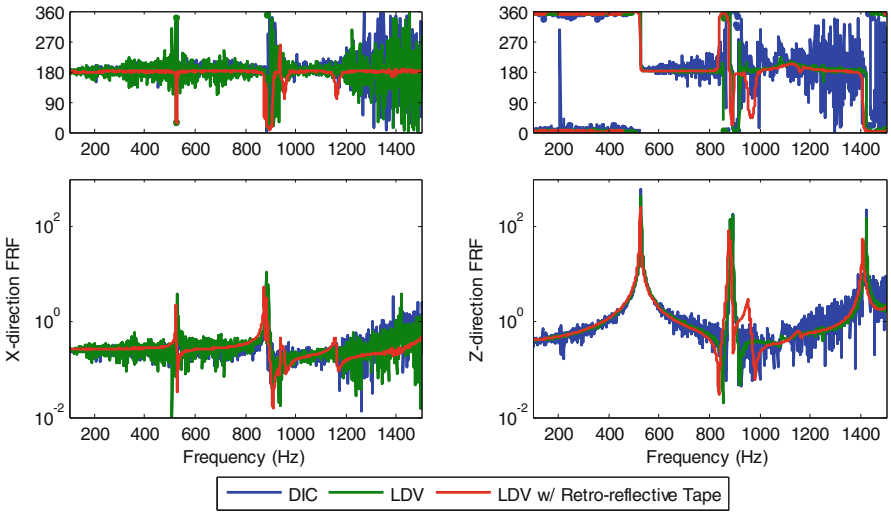

Fig. 29 Noise floor comparison between DIC and LDV; phase (top) and magnitude (bottom). The z-direction corresponds to an out-of-plane measurement, while the x-direction corresponds to an in-plane measurement

Table 7 Comparison between LDV and DIC for the tests performed by Reu et al. [68]

Comparison metric	LDV	DIC
Cost	≈$650 k	≈$350 k ✓
Setup time	2 h	2 h
Acquisition time	Hours	Seconds ✓
Analysis time	Seconds ✓	Hours
Disp. resolution	≈ picometers ✓	≈ nanometers
Strain resolution	?	5 microstrain ✓
Strain calculation	Integrated – but researchy	Seamlessly integrated ✓
Anti-aliasing	Included ✓	Not possible at the moment
Data volume	Small (Mbytes) includes only frequency data	Large (Gbytes) but includes time history
Software	Designed for structural dynamics testing ✓	In its infancy

optical techniques include pattern interferometry, laser Doppler vibrometry, and photogrammetry.

The interferometry technique measures vibrations of structures by using an interference fringe pattern created by superposing two coherent light patterns and measuring the displacement between them. Electronic Speckle Pattern Interferometry (ESPI) and Digital Speckle Shearography (DSS) use the phase-shift between the references and reflect beam waves in order to measure the vibrations of a structure.

Table 8 A comparison between different dynamic measurement techniques

Point-wise sensors (accelerometers, strain-gages, and LVDTs)	Interferometry techniques (ESPI, DSS)	Laser Doppler vibrometer	Photogrammetry and DIC
Needs wiring; may induce mass or stiffness loading	Noncontact	Noncontact	Noncontact
Easy to obtain transfer functions	Needs post processing to obtain transfer functions	Easy to obtain transfer functions	Needs post processing to obtain transfer functions
Has anti-aliasing filter	No anti-aliasing filter	Has anti-aliasing filter	No anti-aliasing filter
Sensitivity for each point depends on the transducer	Sensitive; sensitivity goes down as the fringe gets larger	Very sensitive; sensitivity is related to frequency shift measurement	Sensitive; sensitivity improves as the field of view gets smaller
Wide frequency range	Better for low-frequency measurements	Very wide frequency range	Better for low-frequency measurements
Not sensitive to rigid body motions	Calibration is highly sensitive (for ESPI) and sensitive (for DSS) to changes in setup	Alignment/calibration are highly sensitive to changes in setup conditions and rigid body motions	Calibration is less sensitive to changes in setup condition and rigid body motions
Inexpensive	Expensive	Very expensive	Very expensive/expensive depending on camera requirements for the application
Low special resolution	High spatial resolution	High spatial resolution	High spatial resolution (DIC)
Due to sensitivity issues, it is very challenging to extract both rigid body modes and flexible modes using one type of transducer	Hard to extract rigid body modes Applicable for simpler spatial deformation patterns and not applicable for highly flexible structures	Hard to extract rigid body modes Applicable for simpler spatial deformation patterns and not appropriate for very high deflections or deformations	Easy to extract rigid body modes Appropriate to be used for highly flexible structure Very accurate for spatially complex deformations
Very fast measurement unless roving hammer or sensor techniques are employed	Very fast measurement	Very time-consuming measurement	Very fast measurement
Very fast data processing	Fast data processing	Very fast data processing	Time-consuming data processing (DIC); fast data processing (PT)

(continued)

Table 8 (continued)

Can be real-time	Can be real-time	Can be real-time	Usually works off-line
Small data volume	Large data volume	Small data volume	Large data volume
Depending on the type of the sensor, only measures displacement, acceleration, or strain	Measures both displacement and strain	Measures velocity; can measure strain with additional post-processing	Measures displacement (DIC and PT) and strain is readily obtained for DIC;
Difficult to use for rotating structures due to wiring	Difficult to use for rotating structures	Difficult to use for rotating structures	Very appropriate to use for rotating structures

They can perform fast, real-time, and accurate dynamic measurements, but they are sensitive to ambient vibrations.

Similar to the other interferometry techniques, a Laser Doppler Vibrometer (LDV) compares the reference beam and the beam reflected from the object. However, an LDV measures the frequency shift between the reference and reflected beam waves. The Scanning Laser Doppler Vibrometer (SLDV) is frequently used for full-field vibration measurements. The laser vibrometer typically records data sequentially, has a wide frequency range, and can measure very high frequency vibrations. However, laser vibrometer measurements are very time-consuming and the results might not be consistent because during the measurement the structure or the excitation may change. Furthermore, the laser vibrometer is very sensitive to large motions and cannot effectively measure structural dynamics when a large rigid body motion occurs.

Photogrammetry is a noncontact measurement approach that has a distributed sensing capability allowing for spatially simultaneous measurement. This technique can measure the true dynamics of structures without adding mass or stiffness effects. Photogrammetry can be used for in situ measurements and in testing conditions in which none of the interferometry techniques can operate. Photogrammetry is also able to measure large deformations and rotations. A comparison between commonly used dynamic measurement techniques is shown in Table 8.

16 DIC for High Rate Testing

The flexibility of DIC and the incredible improvement in high-speed imaging have opened a new world of research and have opened up a range of experiments that were heretofore inconceivable. However, the move into high-rate DIC testing is not as simple as replacing traditional machine vision cameras with their more expensive cousins. There are a number of complications that need to be addressed before working in this regime. These complications and potential pitfalls are the subject of this section.

16.1 Definition of High-Rate Testing

For the purposes of this chapter, it is assumed that high-rate testing is any experiment that requires frame rates that are approximately 2-kHz and above. This includes the modal testing [11, 22, 68, 72, 87] covered in the previous sections, as well as Hopkinson bar testing [44, 70], drop tables, explosive loading [23, 71, 74, 83], crash testing [14], and the like. Each of these examples includes complications that may be unique, but generally there are similar hurdles in setting up a DIC experiment for these types of tests, and include:

1. Camera selection for high-speed testing
2. 2D versus stereo-DIC: What do I choose and why?
3. The testing environment and its complications
4. Unique camera calibration situations
5. Lighting for high-rate testing
6. Camera synchronization
7. Patterning, painting and speckling

In addition to these considerations – it is also important to consider all of the traditional rules of DIC testing that are covered elsewhere in this volume, including: image correlation algorithms, speckle attributes, camera calibration, and so forth. For more information about DIC for shape and deformation measurement and best practices for testing readers can refer to Sutton [78] and IDIC [28]. We discuss in this section the *unique* problems associated with high-speed (HS) and ultra-high-speed (UHS) DIC testing.

16.2 High-Rate Camera Selection

The high-speed camera market has expanded significantly since 2005. The number of vendors, the frame rate, and record time have all been improving very rapidly. While the cost of these cameras remains relatively high, the increased competition in the market segment has held prices in check and it is hoped that they will become even more affordable in the future. Figure 30 contains a market survey of the existing high-speed cameras as of 2016, and for interest can be compared with the original chart published in 2008 [66]. The cameras can be broken into two groups: HS and UHS cameras. HS cameras have a single detector that is read out into HS on-board memory. They have a fundamental frame rate limited by the throughput of the detector to the memory. Because the memory rate (GBit/second) is fixed, to increase the frame-rate, the resolution of the camera needs to be decreased. Therefore, at rates above approximately 100 KHz in the current cameras, the usable number of pixels becomes very small. The UHS cameras use a variety of techniques to avoid this problem, and older generation UHS cameras use beam-splitters or rotating mirrors to distribute the image onto different detectors, which are then read out slowly.

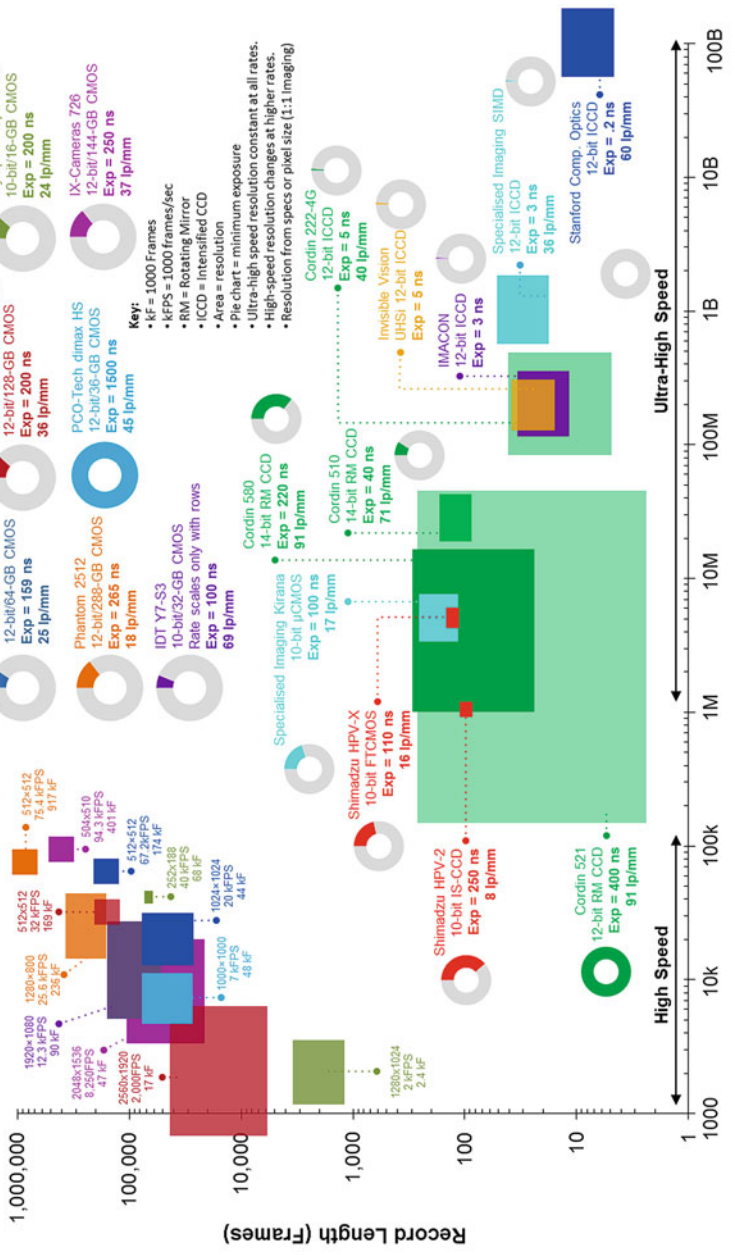

Fig. 30 High-speed testing camera survey. Highest frame rate and resolution; for a circa 2008 version see [66]

These camera types have the drawback of a limited number of images available, usually 16 or less, and have a complicated optical path making them difficult to use for 2D-DIC and nearly impossible for stereo-DIC. For a review of these cameras and their pitfalls, a paper by Tiwari is an excellent source of information [82]. Fortunately for DIC, a new UHS detector architecture has arrived that includes a single detector with fixed resolution at all frame rates *and* a reasonable record time. The first such camera was the Shimadzu HPV series of cameras, followed by the improved HPV-X and a competitor in the Specialised-Imaging Kirana camera. The importance of the single-chip architecture of the camera for stereo-DIC cannot be overstated. Before this advancement, stereo-DIC was virtually impossible at a MHz or higher frame capture rate.

16.3 2D Versus 3D Stereo-DIC

Because of the camera cost, the decision to do 2D DIC may be a hard budget requirement. However, if the UHS camera rates needed are not available in the single detector architecture (e.g., greater than 5 MHz), or if an intensified camera is needed, 2D may also be a practical requirement. 2D-DIC places some fundamental and important limitations on the experimental setup that must be heeded. These requirements include having a flat specimen *and* the sample must remain in the same plane during the entire test. The first requirement is often easy to meet in material testing with traditional dog-bone samples, but meeting the second requirement (i.e., remaining in plane) is extremely difficult to ensure with nearly any practical DIC setup. The pitfalls and errors associated with out-of-plane motion are covered in Sutton et al. [80] where the strain error is found to be directly related to the out-of-plane motion divided by the sample stand-off distance. A few simple calculations should suffice to convince one that even small motions (sub-mm) will lead to unacceptably large strain errors. However, the math immediately suggests a solution to this problem: Increase the sample stand-off. This can be accomplished by either using a long focal length lens or better by using a bi-telecentric lens. A bi-telecentric lens only accepts light rays arriving along the axis of the lens and therefore has fixed magnification. This increases the "effective" stand-off significantly reducing the out-of-plane errors. However, this advantage is problematic in terms of flexibility because the lens then also has a fixed sample size it can image and a fixed standoff distance, making the lens dedicated for a particular type of experiment. The bi-telecentric lens is often large, as the lens has to be the size of the FOV. However, they are the most practical approach to helping eliminate out-of-plane errors and their use is strongly encouraged in situations when stereo-DIC is not practical.

16.4 Environmental Concerns

The test environment for HS and UHS testing is often dynamic and highly energetic. Because of this there are often unique requirements of the experimental setup, including eliminating camera motion and protecting the camera.

16.5 Camera Motion

Highly energetic testing, out-door testing, and vibration and shock testing are all environments where the cameras are likely to move. This is far more problematic at the high-speed regimes, where the acquisition rates are in the kHz, as the modal frequencies of the stereo-rig are likely to overlap with the frequency content of the test in question [11]. If modal testing is being done as described in the previous sections, the frequency domain can be used to isolate the camera motion error; however, for most other testing, the data must remain in the time-domain. In this case, the camera motion will be an added error source that must be considered. In the MHz acquisition realm, the cameras do not have time to move appreciably before the experiment is over and camera motion is generally not a problem.

The first approach is to mitigate the camera motion by careful camera mounting that is rigid and/or isolated from the experiment. It is particularly important that the mounting of the stereo-pair hold the two cameras rigid relative to each other, because the motion of the entire stereo-rig is a rigid-body-motion of the test item and may often be removed from the data relatively easily (e.g., by performing rigid body correction or calculating the strain on the sample). However, relative motion of the stereo-pair leads to issues with the triangulation and will lead to bias errors in the results. The first approach to mitigation is to move the cameras far enough away that the shock from the experiment will be delayed in reaching the cameras until after the data of interest has been captured. Often this is either impractical or inherently impossible, in which case the camera motion must either be accounted for in the uncertainty analysis and/or removed from the images [40]. Both of these techniques require that there be a "stationary" speckle pattern somewhere in the FOV that can be used to track the motion of the cameras.

The strategy of moving the cameras further from the test sample must be pursued with caution. The longer the focal length of the lens, the greater the stand-off from the sample; however, this comes with two important downsides, including increased influence of "heat waves" and an amplified effect of camera motion. The heat wave effect is caused by imaging through air that has variable index of refraction along the optical path. The longer the path, the more likely there is to be a problem. In HS imaging, refraction issues can come from simple environmental effects, such as unevenly heated air, or from the experiment itself, with a shock wave due to detonation for example. Again, these errors are more problematic in the kHz imaging regime because the frequency content of the heated air may be of the same order as the experiment. In the MHz regime, the heated air is stationary relative to the experiment and will not cause problems. This is not true of shock waves, which will be at a high enough rate to cause issues. The use of long focal length lenses for either camera protection, mitigation of camera motion, or limiting out-of-plane errors in 2D has the negative effect of amplifying a number of errors. This can be visualized by considering the viewing angle subtended by a single pixel on the detector (see Fig. 31). With a long focal length lens, this angle will be much smaller than with a short focal length for an equivalent FOV. Therefore, even small camera motions will be amplified when using a long focal length lens. That is, a

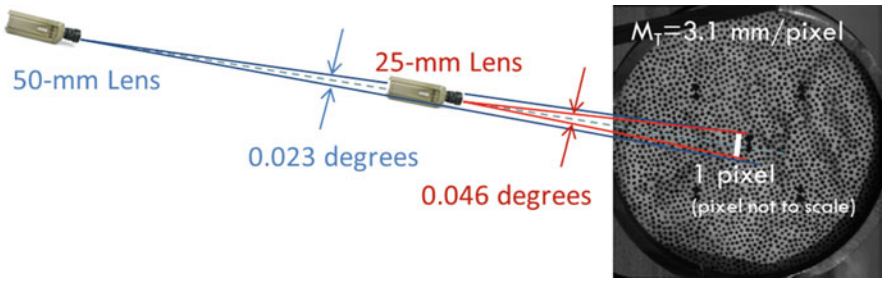

Fig. 31 Camera motion illustration. For 20-μm pixels focused at infinity. Pixel on object not to scale

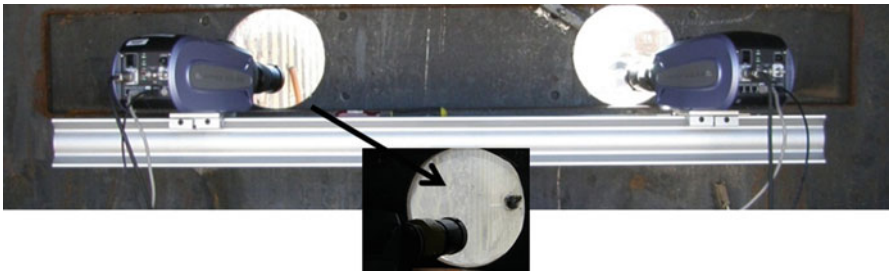

Fig. 32 Camera protection using Lexan and heavy steel plates

small motion of the camera will cause the camera pixel to travel a larger distance across the sample surface than for a shorter focal length lens.

16.6 Camera Protection

The first approach to protecting the camera was traditionally to move the camera a long distance from the test item and use a long telephoto lens. However, this comes with the important downsides of increased index of refraction issues and increased camera motion errors. It is therefore typically better to avoid using lenses longer than 150 mm and provide other methods of protecting the equipment. Two choices include optical grade Lexan (bullet proof glass) and first-surface mirrors. Both of these options provide good camera protection but at the cost of introducing optical distortions into the measurement that are difficult to correct. At a minimum, these added errors should be quantified and included in the uncertainty estimates (see the following extended noise floor section).

For direct viewing of the sample, an optical grade Lexan can be used that provides very good camera protection (see Fig. 32). The thickness of the Lexan will need to be minimized, without compromising the protection because thicker material will have larger distortions. Thick Lexan or glass will also cause imaging problems and cause problems with focusing the lens if longer focal length lenses are

used. This can be somewhat mitigated by using a smaller aperture, but at the cost of needing more light on the sample to compensate. If the shockwave is going to impact on the Lexan before the experiment is over, flexing of the viewport should also be considered. The typical rule of thumb is to put as little distance between the camera and the sample as is safely possible.

A safer option, although optically somewhat more complicated, is to use mirrors. This allows the cameras to not be directly in the path of the hazard, while allowing an inexpensive component to be sacrificed on each test. Mirrors of good optical quality are generally inexpensive and easily obtained. Mounting of the mirrors must be done with some care, as any added bending or lack of flatness will cause issues with the calibration and triangulation. The other consideration with using mirrors is that there is another component in the optical path that must be held in position and stationary. This is often hard to do because the mirrors will need to be placed away from the cameras and independent of them. As noted previously with the camera motion, this is less of a problem during the test if the cameras are running at MHz frequencies, but will definitely cause issues during the calibration, which acquires the images slowly, and will result in a lower quality calibration. The same issue will occur between the calibration time and the actual test, where it is likely that there will be relative motion between the mirrors and the cameras. Some DIC codes allow for an extrinsic parameter calibration correction. To do this more accurately, a known dimension is required on the sample itself to provide scale. As a best practice, it is good to provide some fiducials (or targets) on the surface with known dimensions for correcting the calibration using the reference frame of the test image series.

A final important note for using mirrors is that the images must be flipped to correct for the left/right switch of viewing through a mirror. This can easily be automated with many after market software packages including MATLAB, LabVIEW, Python, etc. and is built into many HS camera control software packages.

16.7 Extended Noise Floor Measurements

A very useful, and indeed required technique when using Lexan or mirrors, is to do what is called an "extended noise floor" measurement (see [28]). This is accomplished by having a sample with a known shape (flat can be used, or maybe better a curved surface of known radius) and translating the sample through the measurement volume. Five to ten images that span the expected range of motion of the sample where accurate DIC results are desired should be taken. Then, the extended noise floor images using the DIC software can be analyzed and the rigid body motion from the results can be removed (most DIC software provides a function to do this). Any changes from the original shape are a result of uncorrected distortions in the optical system, and the residual noise is the estimated measurement resolution. This quick and intuitive top-down uncertainty approach should be done on all experiments.

16.8 Camera Calibration

Camera calibration is often more difficult when doing HS and UHS DIC because the optical system is usually more complicated due to camera protection, mirrors, Lexan, and long focal length lenses. Because of this, a reduced calibration accuracy can be expected, and care should be taken to understand the effect of this on the final results, by using an extended noise floor measurement for example.

16.9 Lighting Techniques

As with the camera technologies, lighting has improved exponentially over the last decade. The introduction of high-intensity LED lights, strobed LED lights, and commercial strobe lights is incredibly helpful for HS imaging. We look at the pros and cons of these light sources in this section.

Strobe lights will provide more light over a shorter period of time that can be synchronized with the camera framing. This is helpful for minimizing the heat coming from the light source while maximizing the efficiency of the lights. Additionally, most HS cameras have an output specifically designed for triggering strobes synchronously with the camera framing. There can be limits though on the strobe rate that can be obtained and they will not work with the higher frame rates of the newer UHS cameras.

High-intensity LED lights are another viable solution. The increased brightness of these lights together with the improved sensitivity of the modern HS cameras makes LED lights easy to use and an excellent solution for all but the shortest exposures.

Flash lamps have traditionally been the preferred lighting source for ultra-high-speed imaging. These lamps discharge a high voltage into a gas which provides a short duration (milliseconds) pulse of high intensity light and are often a good solution for UHS imaging. Flash lamps will require pre-triggering of the lamps to provide time for the lights to reach full intensity before imaging. Norman D24 flash lamps are a commercial solution that provides adequate illumination of modest FOV at up to 5 MHz.

A last class of pulsed lights includes the CAVILUX or SI-LUX incoherent laser illumination. They provide very short duration pulses (50 ns) with high power and can pulse up to the MHz range. Even though they are laser driven, they are incoherent so they do not create laser speckle. Unfortunately, applicable FOVs are only up to 10's of millimeters.

"Diffuse" light is the optimum for all DIC imaging [55]. Highlights and shadows are to be avoided at all costs. This often means that diffusers, polarizers or indirect lighting will be needed to flatten and improve the light. These techniques work by removing any path for the light to go directly from the light source to the camera. The problem with this for HS and UHS imaging is that you need a lot of light and all of these techniques "waste" a large amount of the light. Therefore,

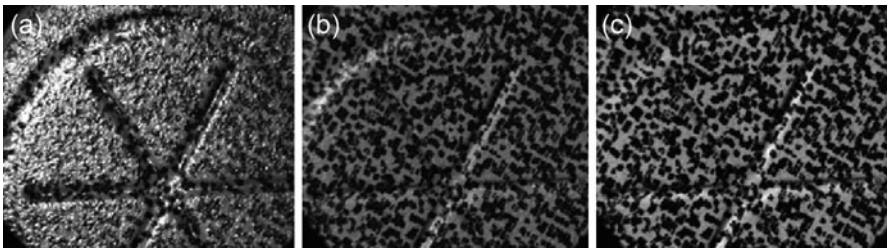

Fig. 33 (**a**) Specular reflections from light source, compromising DIC in those regions. (**b**) Polarizers installed but not correctly aligned. (**c**) Correctly aligned polarizers cleaning up the lighting for ideal DIC images [19]

to obtain adequate intensity, the lights are nearly always aimed directly at the object. Choosing "flat" paint and using polarizers are two solutions that will help in obtaining quality images using direct illumination.

16.9.1 Polarization

When lighting high-speed experiments, diffuse light is often very difficult to achieve because of the required intensity for the short exposures. One helpful possibility is the use of cross-polarization techniques [19, 34]. This removes specular or reflective highlights from the surface because the linearly polarized light from the source maintains its polarization during specular reflection, but loses its polarization with diffuse reflection. A cross-polarizer on the camera then eliminates the specular reflections and removes the highlights from the image. An example of this from a stereomicroscope UHS experiment is shown in Fig. 33. While this technique is a quick and easy way to clean up the images and simplifies the lighting, it should be noted that the cross-polarization technique will result in a loss of approximately 2–3 f-stops of light. That is, four to eight times the amount of light or a similar increase in exposure time to obtain the same contrast in the image will be needed.

16.9.2 Motion Blur

Traditional thinking in DIC was that motion blur was always a problem and should be minimized to below the DIC displacement resolution of approximately 0.01 pixels. This criterion is overly restrictive and can be hard to meet in many high-speed applications, where exposures cannot be made short enough to completely eliminate motion blur. Current research [90] indicates that motion blur is acceptable if the average position of the object will be calculated and for many applications this is acceptable. It should be noted, however, that there are two types of motion blur: constant and varying. If the motion blur is constant, that is, the velocity of the object remains fairly constant over the test period, the blurred speckles will appear the same in all images and there will be no correlation problems. However, if the velocity is varying, say in an impact test, the blurred and unblurred image segments may be so dissimilar that decorrelation results. At this point, the analysis will need to be done in an incremental mode, or a new reference image chosen after the impact event

where the blur has been eliminated or changes drastically. The ideal situation is to remove all blur if possible, or certainly keep it subpixel, but if that is not possible, DIC can still be performed.

16.10 Camera Synchronization

An assumption for stereo-DIC is that the images were taken at the same moment, that is, they are synchronized. With most HS cameras, we cannot assume exact synchronization, even when being run in a "synced" mode (FSync for example in the Phantom cameras). The sync error is caused by the timing architecture of the camera, due to delays between the camera syncing pulse and when the frame is actually taken. Fortunately, most manufacturers also supply a strobe signal that is synchronous with the framing. This signal should be inspected with an oscilloscope to ensure that both cameras are acquiring their images at exactly the same time. Because of the variability in the delay, the camera software provides the option to include a frame delay to achieve camera synchronization. When the correct delay has been determined it is possible to synchronize the cameras to within the internal timing frequency of the camera, usually in the 10's of nanoseconds. By taking the velocity of the sample multiplied by the timing error, you can calculate the relative motion of the sample between the two stereo frames. For nearly all mechanical experiments, the nanosecond synchronization of the cameras is more than adequate. If the cameras are not synchronized, a bias error will occur in the data. More information on this topic can be found in Reu and Miller [67].

16.10.1 IRIG (Inter-Range Instrumentation Group) Timing

Most HS cameras also provide synchronization with each other as well as other data acquisition systems IRIG-B [30] timecode via the timing signals received from Global Positioning System (GPS) satellites. Specially designed receivers convert Coordinate Universal Time (UTC) data in to various IRIG timecodes in both digital and amplitude modulated formats. The IRIG-B timecode [31] is the most common format and is typically connected to each instrument (e.g., camera, data recorder, oscilloscope) using the amplitude modulated version, especially when distributing the signal at a distance greater than 50 m.

A few benefits of using a common timing signal such as IRIG-B are: (a) synchronization between asynchronous data recorders and cameras, (b) introduction of a known time scale, and (c) ability to coordinate results captured from instruments separated by very large distances (kilometers).

16.11 Painting Techniques

For nearly all DIC tests it is required that the sample surface be painted and speckled to provide a high contrast pattern that moves with the underlying surface. High-rate DIC imposes the same constraints on the speckles as traditional DIC and these are

covered in [58–62, 64, 81]. The ideal speckles as outlined in these documents are at least 3-pixels in size and have an even distribution across the surface. The DIC technique requires that a region of the speckle pattern be analyzed in the subset or facet, and this region must contain 3-speckles (significant gray level variations) as a rule of thumb. To have the highest spatial resolution then, the speckles must be carefully applied to meet these rules, without being too large or too small. Beyond these general rules for all DIC, there are a few other considerations for high rate testing:

1. Very careful attention should be paid to the surface preparation. The surface should be cleaned and prepared to receive the paint according to the manufacturer's recommendations. This involves having a clean and grease-free surface.
2. Use an appropriate paint. A flat white or black paint for the first coat should be used. There are also "primer" paints that are made to specifically bond with different metals. These will often adhere better than a cheap spray paint. Some examples include Rust-Oleum™ and SEM brand paints.
3. The painted surface should be "fresh." That is, you should test the sample within 24 hours or less of painting. Paint that has cured too long becomes brittle and will fail, coming off the surface leaving nothing to track.

The last point raises an important consideration: We are assuming that the paint surface is following the contour of the substrate surface and it is important to be sure to investigate whether this is true in your experiment. Another approach is to not use a painted surface. This can work in situations where the sample itself contains contrast within it that is of an appropriate scale and contrast for DIC. Unfortunately, having structure or test panel that already has an appropriate pattern is very rare.

16.12 Conclusion

HS and UHS DIC follow all of the same rules as for quasi-static testing, with a few important added challenges. Most of the complications are not due to the cameras, which behave image wise very similarly to traditional machine vision cameras, but more because of experimental issues derived from the test itself. Most high rate DIC testing is performed in "highly" dynamic events where camera motion and camera protection are required. Even with these problems, nearly always the most difficult aspect is speckling and lighting the sample. Obtaining enough light that is well distributed and diffused can take practice and time to set up. Timing and triggering the cameras with the experiment are also problematic for UHS experiments, as there is a limited record time available to take the data. Tight triggering synchronization is nearly always required to have the event of interest within the camera memory. The final difficulty is cost. Camera equipment is expensive and unfortunately there are no easy substitution;, however as technology advances, camera costs are continually becoming cheaper with higher resolution and improved frame capture rate.

Best practices for HS and UHS DIC testing include acquiring high contrast images with a well-calibrated DIC system taking into account the possibly compromised optical path and any issues with motion or timing. Because of these complications, it is strongly encouraged that efforts be made to ensure that adequate consideration is given to the uncertainty. Uncertainty recommendations and information are found in Reu [57, 65].

References

1. Abrego AI, Olson LE, Romander EA, Barrows DA, Burner AW (2012) Blade displacement measurement technique applied to a full-scale rotor test. American Helicopter Society 68th annual forum proceedings, Fort Worth, 1–3 May 2012
2. Aramis – User Manual-Software; Aramis v6.1 and higher, 2018. https://www.gom.com
3. Avitabile P, Niezrecki C, Helfrick M, Warren CP, Pingle P (2010) Noncontact measurement techniques for model correlation. Sound and Vibration Magazine, January, pp 8–12
4. Baqersad J, Bharadwaj K (2018) Strain reduction expansion approach. Mech Syst Signal Process 101:156–167. https://doi.org/10.1016/j.ymssp.2017.08.023
5. Baqersad J, Niezrecki C, Avitabile P (2015a) Full-field dynamic strain prediction on a wind turbine using displacements of optical targets measured by stereophotogrammetry. Mech Syst Signal Process 62:284–295. https://doi.org/10.1016/j.ymssp.2015.03.021
6. Baqersad J, Niezrecki C, Avitabile P (2015b) Extracting full-field dynamic strain on a wind turbine rotor subjected to arbitrary excitations using 3D point tracking and a modal expansion technique. J Sound Vib 352:16–29. https://doi.org/10.1016/j.jsv.2015.04.026
7. Baqersad J, Poozesh P, Niezrecki C, Avitabile P (2016a) Photogrammetry and optical methods in structural dynamics – a review. Mech Syst Signal Process. https://doi.org/10.1016/j.ymssp.2016.02.011
8. Baqersad J, Poozesh P, Niezrecki C, Avitabile P (2016b) A noncontacting approach for full-field strain monitoring of rotating structures. J Vib Acoust 138:031008. https://doi.org/10.1115/1.4032721
9. Bartilson DT, Wieghaus KT, Hurlebaus S (2015) Target-less computer vision for traffic signal structure vibration studies. Mech Syst Signal Process 60–61:571–582. https://doi.org/10.1016/j.ymssp.2015.01.005
10. Bateman VI, Mayes RL, Carne TG (1997) Comparison of force reconstruction methods for a lumped mass beam. Shock Vib 4(4):231–239
11. Beberniss TJ, Ehrhardt DA (2017) High-speed 3D digital image correlation vibration measurement: recent advances and noted limitations. Mech Syst Signal Process 86:38–48
12. Bharadwaj K, Baqersad J, Poozesh P (2016) Modal expansion using strain mode shapes. In: IMAC XXXV, Garden Grove
13. Blevins RD (1979) Formulas for natural frequency and mode shape. Van Nostrand Reinhold. ISBN 10: 0442207107/ISBN 13: 9780442207106
14. Burguete RL, Lampeas G, Mottershead JE, Patterson EA, Pipino A, Siebert T, Wang W (2013) Analysis of displacement fields from a high-speed impact using shape descriptors. J Strain Anal Eng Design
15. Burtch R (2004) History of photogrammetry. Notes of the Center for Photogrammetric Training
16. Carr J, Baqersad J, Niezrecki C, Avitabile P (2015) Full-field dynamic strain on wind turbine blade using digital image correlation techniques and limited sets of measured data from photogrammetric targets. Exp Tech. https://doi.org/10.1111/ext.12129
17. Castellini P, Martarelli M, Tomasini EP (2006) Laser Doppler vibrometry: development of advanced solutions answering to technology's needs. Mech Syst Signal Process 20(6):1265–1285

18. Chen X, Xu N, Yang L, Xiang D (2012) High temperature displacement and strain measurement using a monochromatic light illuminated stereo digital image correlation system. Meas Sci Technol 23:125603
19. Cooper MA, Skaggs MN, Reu PL (2016) High-speed stereomicroscope digital image correlation of rupture disc behavior. In: Advancement of optical methods in experimental mechanics, vol 3. Springer, Cham, pp 19–26
20. D'Emilia G, Razzè L, Zappa E (2013) Uncertainty analysis of high frequency image-based vibration measurements. Measurement 46:2630–2637. https://doi.org/10.1016/j.measurement.2013.04.075
21. dos Santos F, Peeters B, Lau J, Desmet W, Góes L (2014) An overview of experimental strain-based modal analysis methods. In: Proceedings of the international conference on noise and vibration engineering (ISMA), Leuven
22. Ehrhardt DA, Yang S, Beberniss TJ, Allen MS (2014) Mode shape comparison using continuous-scan laser Doppler vibrometry and high speed 3D digital image correlation. In: Special topics in structural dynamics, vol 6. Springer, Cham, pp 321–331
23. Gagliardi FC, Cunningham B (2010) The use of digital image correlation in explosive experiments. In: 14th Annual detonation symposium, Coeur d'Alene, 11–16 April 2010
24. Gilbert MG, Welch SS, Pappa RS, Demeo ME (1997) STS-74/Mir photogrammetric appendage structural dynamics experiment preliminary data analysis. In: Proceedings of the 1997 38th AIAA/ASME/ASCE/AHS/ASC structures, structural dynamics, and materials conference. Part 4 (of 4), 7–10 April 1997. AIAA, Kissimmee, pp 566–576
25. Ha NS, Vang HM, Goo NS (2015) Modal analysis using digital image correlation technique: an application to artificial wing mimicking beetle's hind wing. Exp Mech 55:989–998. https://doi.org/10.1007/s11340-015-9987-2
26. Helfrick MN, Pingle P, Niezrecki C, Avitabile P (2009) Optical non-contacting vibration measurement of rotating turbine blades. In: 27th Conference and exposition on structural dynamics 2009, IMAC XXVII, 9–12 February 2009. Springer/Society for Experimental Mechanics (SEM), New York
27. Helfrick MN, Niezrecki C, Avitabile P, Schmidt T (2011) 3D digital image correlation methods for full-field vibration measurement. Mech Syst Signal Process 25:917–927. https://doi.org/10.1016/j.ymssp.2010.08.013
28. IDIC (2018) iDIC good practice guide. International Digital Image Correlation Society website. www.idics.org. Accessed 2018
29. Ind P (2004) The non-intrusive modal testing of delicate and critical structures. PhD thesis, Imperial College of Science, Technology & Medicine, University of London, London
30. IRIG (2018a) Inter-Range Instrumentation Group. https://en.wikipedia.org/wiki/Inter-Range_Instrumentation_Group. Accessed 2018
31. IRIG (2018b) Time code. Accessed 2018. https://en.wikipedia.org/wiki/IRIG_timecode
32. Jones EMC, Reu PL (2017) Distortion of digital image correlation (DIC) displacements and strains from heat waves. Exp Mech. https://doi.org/10.1007/s11340-017-0354-3
33. Kammer DC (Mar 1991) Sensor placement for on-orbit modal identification and correlation of large space structures. J Guid Control Dyn 14:251–259
34. LePage WS, Daly SH, Shaw JA (2016) Cross polarization for improved digital image correlation. Exp Mech 56:1–17
35. Lundstrom T, Baqersad J, Niezrecki C, Avitabile P (2012) Using high-speed stereophotogrammetry techniques to extract shape information from wind turbine/rotor operating data. In: 30th IMAC, a conference on structural dynamics, 30 January 2012–2 February 2012. Springer New York/Jacksonville, pp 269–275. https://doi.org/10.1007/978-1-4614-2419-2_26
36. Lundstrom T, Niezrecki C, Avitabile P (2013) Appropriate rigid body correction of stereophotogrammetry measurements made on rotating systems. Exp Tech. https://doi.org/10.1111/ext.12030
37. Lundstrom T, Baqersad J, Niezrecki C (2015) Monitoring the dynamics of a helicopter main rotor with high-speed stereophotogrammetry. Exp Tech. https://doi.org/10.1111/ext.12127

38. Luo PF, Chao YJ, Sutton MA, Peters WH III (1993) Accurate measurement of three-dimensional deformations in deformable and rigid bodies using computer vision. Exp Mech 33:123–132
39. Meng LB, Jin GC, Yao XF (2007) Application of iteration and finite element smoothing technique for displacement and strain measurement of digital speckle correlation. Opt Lasers Eng 45:57–63. https://doi.org/10.1016/j.optlaseng.2006.04.012
40. Miller TJ, Schreier HW, Reu P (2007) High-speed DIC data analysis from a shaking camera system. Society for Experimental Mechanics, Springfield
41. Mitchell LD (1982) Improved methods for the FFT calculation of the frequency response function. J Mech Des 104:277–279
42. Mitchell LD, Deel JC (1987) An unbiased frequency response function estimator. In Proceedings of the 5th international modal analysis conference, London
43. Mohanty P, Rixen DJ (2004) Operational modal analysis in the presence of harmonic excitation. J Sound Vib 270:93–109
44. Moulart R, Pierron F, Hallett SR, Wisnom MR (2011) Full-field strain measurement and identification of composites moduli at high strain rate with the virtual fields method. Exp Mech 51(4):509–536
45. Niezrecki C, Avitable P, Warren C, Pingle P, Helfrick M (2010) A review of digital image correlation applied to structural dynamics. In: Proceedings of the 9th international conference on vibration measurements by laser and noncontact techniques, Ancona, 22–25 June 2010
46. Nonis C, Niezrecki C, Yu T, Ahmed S, Su C, Schmidt T (2013) Implementation of digital image correlation for structural health monitoring of bridges. In: Proceedings of 9th international workshop on structural health monitoring, Stanford/Palo Alto, 10–12 September 2013
47. O'Callahan J, Avitabile P, Riemer R (1989) System equivalent reduction expansion process (SEREP). In: Proceedings of the 7th international modal analysis conference, Union College Schnectady, pp 29–37
48. Ozbek M, Rixen DJ (2013) Operational modal analysis of a 2.5 MW wind turbine using optical measurement techniques and strain gauges. Wind Energy 16:367–381. https://doi.org/10.1002/we.1493
49. Ozbek M, Rixen DJ, Erne O, Sanow G (2010) Feasibility of monitoring large wind turbines using photogrammetry. Energy 35:4802–4811. https://doi.org/10.1016/j.energy.2010.09.008
50. Pan B, Asundi A, Xie H, Gao J (2009) Digital image correlation using iterative least squares and pointwise least squares for displacement field and strain field measurements. Opt Lasers Eng 47:865–874. https://doi.org/10.1016/j.optlaseng.2008.10.014
51. Pan B, Wu D, Xia Y (2012) An active imaging digital image correlation method for deformation measurement insensitive to ambient light. Opt Laser Technol 44:204–209. https://doi.org/10.1016/j.optlastec.2011.06.019
52. Peters WH, Ranson WF (1982) Digital imaging techniques in experimental stress analysis. Opt Eng 21:213427. https://doi.org/10.1117/12.7972925
53. Poozesh P, Baqersad J, Niezrecki C, Avitabile P, Harvey E, Yarala R (2016) Large-area photogrammetry based testing of wind turbine blades. Mech Syst Signal Process. https://doi.org/10.1016/j.ymssp.2016.07.021
54. Reu P (2012) Stereo-rig design: creating the stereo-rig layout – part 1. Exp Tech 36:3–4. https://doi.org/10.1111/j.1747-1567.2012.00871.x
55. Reu P (2013a) Stereo-rig design: lighting – part 5. Exp Tech 37(3):1–2
56. Reu P (2013b) Stereo-rig design: stereo-angle selection – part 4. Exp Tech 37:1–2. https://doi.org/10.1111/ext.12006
57. Reu P (2013c) A study of the influence of calibration uncertainty on the global uncertainty for digital image correlation using a Monte Carlo approach. Exp Mech 53(9):1661–1680
58. Reu P (2014a) All about speckles: aliasing. Exp Tech 38(5):1–3
59. Reu P (2014b) Speckles and their relationship to the digital camera. Exp Tech 38(4):1–2
60. Reu P (2014c) All about speckles: speckle size measurement. Exp Tech 38(6):1–2
61. Reu P (2015a) All about speckles: contrast. Exp Tech 39(1):1–2

62. Reu P (2015b) All about speckles: edge sharpness. Exp Tech 39:1–2. https://doi.org/10.1111/ext.12139
63. Reu P (2015c) Virtual strain gage size study. Exp Tech 39:1–3. https://doi.org/10.1111/ext.12172
64. Reu P (2015d) All about speckles: speckle density. Exp Tech 39(3):1–2
65. Reu P (2016) A realistic error budget for two dimension digital image correlation. In: Jin H et al (eds) Advancement of optical methods in experimental mechanics, vol 3. Proceedings of the 2015 annual conference on experimental and applied mechanics. Springer International Publishing, Cham, pp 189–193
66. Reu PL, Miller TJ (2008) The application of high-speed digital image correlation. J Strain Anal Eng Des 43(8):673–688
67. Reu P, Miller TJ (2009) Synchronization errors in high-speed digital image correlation. Society for Experimental Mechanics, Bethel
68. Reu PL, Rohe DP, Jacobs LD (2017) Comparison of DIC and LDV for practical vibration and modal measurements. Mech Syst Signal Process 86:2–16
69. Sabato A, Niezrecki C (2017) Feasibility of digital image correlation for railroad tie inspection and ballast support assessment. Measurement 103. https://doi.org/10.1016/j.measurement.2017.02.024
70. Schmidt T, Tyson J (2009) 3D and 2D high speed image correlation for dynamic testing. Society for Experimental Mechanics Annual Meeting, Albuquerque
71. Schmidt T, Tyson J, Galanulis K, Revilock D, Melis M (2005) Full-field dynamic deformation and strain measurements using high-speed digital cameras. In: 26th International congress on high speed photography and photonics, vol 5580, pp 174–185
72. Siebert T, Wang WZ, Mottershead JE, Pipino A (2011) Application of high speed image correlation for measurement of mode shapes of a car bonnet. Appl Mech Mater 70:45–50
73. Son K-S, Jeon H-S, Park J-H, Park JW (2015) Vibration displacement measurement technology for cylindrical structures using camera images. Nucl Eng Technol 47:488–499. https://doi.org/10.1016/j.net.2015.01.011
74. Spranghers K, Vasilakos I, Lecompte D, Sol H, Vantomme J (2012) Full-field deformation measurements of aluminum plates under free air blast loading. Exp Mech 52(9):1371–1384
75. Stasicki B, Boden F (2009) Application of high-speed videography for in-flight deformation measurements of aircraft propellers. In: 28th International congress on high-speed imaging and photonics, 9–14 November 2008. SPIE, Canberra. https://doi.org/10.1117/12.822046
76. Stasicki B, Boden F (2015) In-flight measurements of aircraft propeller deformation by means of an autarkic fast rotating imaging system. In: International conference on experimental mechanics 2014, ICEM 2014, 15–17 November 2014. SPIE, Singapore. https://doi.org/10.1117/12.2081393
77. Surrel Y, Fournier N, Grédiac M, Paris P-A (1999) Phase-stepped deflectometry applied to shape measurement of bent plates. Exp Mech 39(1):66–70. https://doi.org/10.1007/BF02329303
78. Sutton MA (2008) Digital image correlation for shape and deformation measurements, Chapter 20. In: Handbook of experimental solid mechanics. Springer Science+Business Media, New York, pp 565–600. ISBN: 978-0-387-26883-5
79. Sutton MA, Li N, Garcia D, Cornille N, Orteu JJ, McNeill SR, Schreier HW, Li X (2006) Metrology in a scanning electron microscope: theoretical developments and experimental validation. Meas Sci Technol 17:2613
80. Sutton MA, Yan JH, Tiwari V, Schreier HW, Orteu JJ (2008) The effect of out-of-plane motion on 2D and 3D digital image correlation measurements. Opt Lasers Eng 46(10):746–757
81. Sutton MA, Orteu JJ, Schreier H (2009) Image correlation for shape, motion and deformation measurements: basic concepts, theory and applications. Springer Science+Business Media, New York
82. Tiwari V, Sutton MA, McNeill SR (2007) Assessment of high speed imaging systems for 2D and 3D deformation measurements: methodology development and validation. Exp Mech 47(4):561–579

83. Tiwari V, Sutton MA, McNeill SR, Xu S, Deng X, Fourney WL, Bretall D (2009) Application of 3D image correlation for full-field transient plate deformation measurements during blast loading. Int J Impact Eng 36(6):862–874
84. Triggs B, McLauchlan PF, Hartley RI, Fitzgibbon AW (1999) Bundle adjustment – a modern synthesis. In: International workshop on vision algorithms. Springer, London, pp 298–372
85. Valley MT, Shields RW, Reed JM (2004) TrackEye tracking algorithm characterization. In: Target-in-the-loop: atmospheric tracking, imaging, and compensation. International Society for Optics and Photonics, pp 179–189
86. Voormeeren SN, van der Valk PLC, Rixen DJ (2011) Generalized method for assembly and reduction of component models for dynamic substructuring. AIAA J 49(5):1010–1020
87. Wang W, Mottershead JE, Siebert T, Pipino A (2012) Frequency response functions of shape features from full-field vibration measurements using digital image correlation. Mech Syst Signal Process 28:333–347
88. Warren C, Niezrecki C, Avitabile P, Pingle P (2011) Comparison of FRF measurements and mode shapes determined using optically image based, laser, and accelerometer measurements. Mech Syst Signal Process 25:2191–2202. https://doi.org/10.1016/j.ymssp.2011.01.018
89. Wicks A, Vold H (1986) The Hs frequency response function estimator. In Proceedings of the 4th international modal analysis conference
90. Zappa E, Mazzoleni P, Matinmanesh A (2014a) Uncertainty assessment of digital image correlation method in dynamic applications. Opt Lasers Eng 56:140–151. https://doi.org/10.1016/j.optlaseng.2013.12.016
91. Zappa E, Matinmanesh A, Mazzoleni P (2014b) Evaluation and improvement of digital image correlation uncertainty in dynamic conditions. Opt Lasers Eng 59:82–92. https://doi.org/10.1016/j.optlaseng.2014.03.007

Part II
Modal Model Development

Design of Modal Tests

9

Thomas Carne, Ralph Brillhart, Daniel Kammer, and Kevin Napolitano

Contents

T. Carne (✉)
Sandia National Laboratories, Retired, Albuquerque, NM, USA
e-mail: tgcarne@bresnan.net

R. Brillhart · K. Napolitano
ATA Engineering, Inc., San Diego, CA, USA
e-mail: ralph.brillhart@ata-e.com; kevin.napolitano@ata-e.com

D. Kammer
University of Wisconsin – Madison, Madison, WI, USA
e-mail: daniel.kammer@wisc.edu

R. Allemang, P. Avitabile (eds.), *Handbook of Experimental Structural Dynamics*,
https://doi.org/10.1007/978-1-4614-4547-0_11

Abstract

This chapter examines a number of issues that require consideration when a modal test is being planned or designed. As with any engineering procedure, a modal test needs to be designed; otherwise, objectives may not be fulfilled or time and effort may be poorly used. The issues discussed in this chapter include the purpose of the test, excitation considerations, response measurements, support conditions, measurement quality criteria, and considerations for model validation. When a modal test is to be performed to validate a finite element model, one needs to design the test so that the resulting measurements will provide the data required for the correlation of modeling results with those from the test. From a correlation perspective, one would like to select the response locations to allow a definitive, one-to-one correspondence between the measured modes and the predicted modes. Further, the excitation must be designed to excite all the modes of interest at a sufficient level so that the modal estimation algorithms can accurately extract the modal parameters.

Keywords

Test design · Test plan · Support conditions · Free boundary conditions · Model validation · Modal kinetic energy · Effective independence · Min-Mac · Cross-orthogonality · TAMs

Acronyms

DOFs	Degrees of freedom
FFT	Fast Fourier transform
ω	Frequency (radian/sec)
FEM	Finite element model
m	Mass element of a 2 DOF system
k_t	True stiffness of structure
k_s	Stiffness of the support
c_t	True damping coefficient
c_s	Damping coefficient of the support
c_m	Measured damping coefficient
ω_t	True frequency of structure
ω_s	Frequency due to supports only
ω_m	Measured frequency of structure
ζ_t	True modal damping
ζ_s	Modal damping of support system
ζ_m	Measured modal damping
γ_t	True structural modal damping
γ_s	Structural damping of supports
γ_m	Measured structural modal damping
$\Delta\omega$	Change in frequency due to support
ϕ^j	value of mass-normalized mode shape at position j
ψ	Mode shape of interest
C_s	Damping matrix of support system
TAM	Test-analysis model
ϕ_i	The i^{th} mass-normalized mode shape

ke_{ij}	The contribution of the j^{th} DOF to the i^{th} mode generalized mass
KE	The fractional importance of each FEM DOF to the modal mass
ke_i	Column vector containing contribution of DOF j to the kinetic energy of the i^{th} mode
EfI	Effective independence sensor selection
y_s	Response at sensor locations
ϕ_{fs}	Matrix of FEM target mode shapes partitioned to sensor DOFs
q	Target modal response
w	The sensor noise
Q	Fisher information matrix, FIM
G	A matrix whose columns sum to the eigenvalues of FIM Q
Ψ	Eigenvectors
λ	Eigenvalue matrix
F_E	Matrix representing fractional contribution of i^{th} sensor to the j^{th} information matrix eigenvalue
E_D	Effective independence distribution
$\{1\}_n$	A column vector of 1's length n
Min-Mac	Minimizing MACs-based sensor selection
MAC_{ij}	Modal assurance criterion between mode shape vectors i and j
φ_i	Mode shape vector for i^{th} mode
Φ	Mode shape matrix, existing set of sensors
ψ	Mode shape matrix, remaining set of sensors
a_{ij}	Elements of $A = \Phi^T \Phi$
$(MAC_{ij})_{+k}$	MAC value between modes i and j with added DOF k
O_{12}	Orthogonality between modes 1 and 2

1 Introduction

One might ask, why would one design a test? You can design hardware or a manufacturing process, but you just perform a test. However, a test costs time and resources, just as any other process or hardware, and there are expectations of the information that will be measured or estimated from the test data, so the test requires a similar level of attention. Obviously, if the test will be a one-hour procedure to measure the frequency of the first mode, there may be little reason to spend much time on test planning or design. But suppose you are testing a satellite whose current value is 50 million dollars, and every day spent testing is costing the project 25,000 dollars. Further, if the measured results will be used to validate or modify the finite model that will be used to validate coupled loads, the design of the modal test clearly requires careful consideration taking into account the test issues discussed in this chapter.

In designing a modal test, the first issue that must be clarified is the purpose of the test. There are many possible purposes – such as model validation, diagnosis, troubleshooting, structural modification, comparison with operating conditions, design input, or control system evaluation – and one particular design will not satisfy them all. Additionally, the test design from a previous program may not necessarily fulfill the requirements for a new and different purpose. The second issue is identifying who has a vested interest in the results of the test. This may not be at all clear when the modal test is first conceived. The finite element modeler, controls

person, vibration test engineer, hardware owner, management personnel – all of these individuals may have preconceived ideas about what results the modal test will provide. To be successful, one needs a clear understanding of both the purpose of the test and the expectations of interested individuals. With a full understanding of all the desired outputs, one can think about the implications for the test design. These might include the number of modes to be measured, the frequency range of interest, what excitation is best, and what response measurements are required.

Of course, there are always constraints on any engineering process, including the costs, human resource time, test article availability, modal analysis tools, data acquisition hardware, and so on. However, with a well-conceived test design, the various constraints and conflicts can be evaluated based on the expected output of the test. Professor Carlos Ventura of The University of British Columbia proposed a mnemonic for the key elements of test design: SMART, for Specific, Measurable objectives, Agreed, Realistic, and Time constraint. These five items comprise a general list of aspects to be considered; the more specific considerations and some of their consequences are addressed more thoroughly in sections below.

2 Excitation Techniques

Just as there are many types of disturbances or excitations of structures in nature, there are a number of types of excitations that can, and should, be considered in designing a modal survey of a structure. Historically, early modal testing was conducted with periodic, harmonic (sinusoidal) excitation, which led to observations that were readily understood. However, as modal testing methods evolved, it has become clear that there are various different excitation methods that lend themselves to excellent modal tests without any sacrifice in the clear definition of the modal behavior. As a result, modal test design should include an appropriate assessment of the type or multiple types of excitation to be employed for the best chance of success. The following discussion provides insight into excitation technique selection and how it is important for developing a successful modal test design.

2.1 General Considerations

In selecting an appropriate excitation type, early consideration should be given to the structure that will be tested and the overriding objectives of the test. The ultimate data quality from the modal test is highly dependent on the excitation approach used. Keep in mind that it is common that a single excitation technique will not be adequate or sufficient, and the use of multiple types of excitation can provide better insight into the structural behavior. This is particularly true when the structure will be subjected to different excitation environments in service. As such, just as qualification testing of structures might employ random vibration, sinusoidal vibration, and shock environments, modal testing can often be most effectively conducted using a combination of excitation types.

2.1.1 Frequency Range

The modal test frequency range of interest is typically a parameter that is quantified at the early stages of modal test preparation. It is often selected based on a finite element model (FEM) which is used to predict the natural frequencies and mode shapes of interest. In addition, the expected excitation environment can be used to help in selecting an appropriate modal test excitation type and frequency range. In preparation for any modal test, there should be accommodations to allow frequency range adjustments as needed during the test once data becomes available. Initial investigations with an expanded frequency range may be conducted, followed by detailed testing after frequency range adjustments are made.

Launch vehicles are typically exposed to random (both vibration and acoustic environments) and some harmonic excitation sources. Similarly, satellites and launch vehicle payloads are exposed to the launch vehicle environment types as well as harmonic tones once they are "on-orbit." Automotive vehicles experience a variety of harmonic inputs as well as random and shock environments transmitted through their suspensions.

The modal test frequency range of interest is often the result of an evaluation of which modes of the structure have "significant" modal mass, which in turn can produce loads on the structure or its interfaces which will be important in the operational environment.

In the aerospace industry, slightly different objectives can be used to select the frequency range of interest. For aircraft, the modes that can develop significant dynamic loads as well as those that may result in dynamic instability, or flutter, define the frequency range of interest. For large aircraft, this frequency range can be quite low – often below 30 Hz. Modest-sized aircraft typically exhibit higher frequencies, and the range of interest might well be above 100 Hz. Drones and other smaller aircraft may yield frequencies of interest upward of 500 Hz. Very small components (engine turbine blades, for example) may have frequencies of interest in the kilohertz range. Giving appropriate consideration to actual environments, performance behavior required, and possible model predictions will lead to successful modal testing.

2.1.2 Excitation Level

The next consideration involves identifying the proper excitation level to make sure that the modes of the structure will be well excited and that all modes of interest can be characterized. The magnitude of the excitation required in a modal test can be affected by the amount of damping or energy dissipation in the structure and can also be influenced greatly by the size of the test structure and the number and types of excitation sources. Large structures with light or modest damping might be easily excited using only modest excitation levels; for example, wind turbine blades and towers, which typically are lightly damped, can be excited with only a few hundred pounds of excitation force.

Of course, the excitation type and frequency range of interest also affects the amount of force required. Impulsive excitation such as step relaxation can focus the frequency content at low frequencies, and peak forces may be thousands of

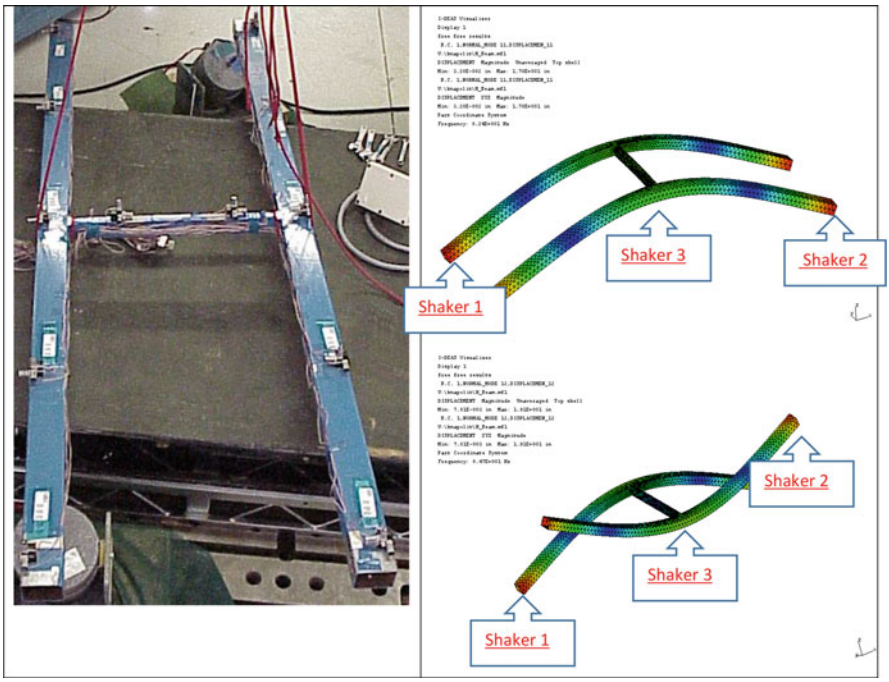

Fig. 1 Good shaker location selection is important for successful modal testing

pounds. On the other hand, impulsive excitation using small load-cell-instrumented hammers can provide frequency content covering high frequencies using small to large force levels.

Excitation level requirements are strongly influenced by the excitation location on the structure and the direction. To excite a mode, locations that have good modal participation need to be selected. As seen in Fig. 1, during testing of an H-frame, shaker 1 and shaker 2 do a good job of exciting both modes of interest, but shaker 3 only excites one of the two modes. This does not mean that locations of high modal displacement need to be selected; locations with lower response can be used effectively by increasing the excitation input level, as seen in Fig. 2.

The excitation levels can also be described differently depending on the excitation type [14]. Peak force might be used to assess impact and step relaxation, whereas peak and root-mean-square (RMS) might be used to describe the input from random and sine excitation signals.

Excitation levels can be constrained in a modal test by the structural limitations of the test article, but damage to the test article can be avoided by selecting structural locations that can withstand a wide range of excitation levels, or excitation level limits might be imposed to ensure that no damage is done. Mechanical fuses and software limit controls might be implemented to limit the maximum excitation levels. Hardware can also be added to the structure to spread the load over a larger

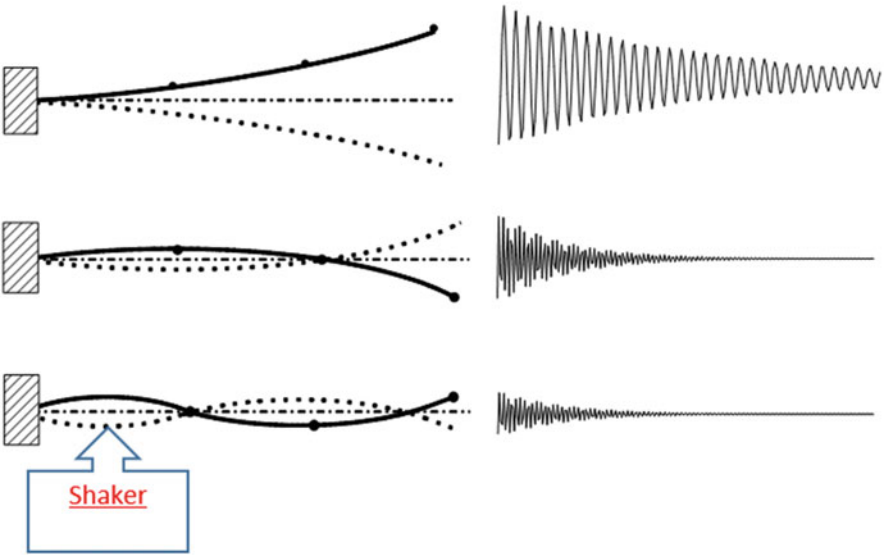

Fig. 2 Excitation at highest modal displacement locations is not required

area and lower the local pressure to reduce the chance of damage. Peak force levels that occur in impact testing may need to be evaluated to determine whether there is any likelihood of local structural damage.

2.1.3 Linearity of Structure

Many modal tests require an investigation of linearity . These linearity tests require a range of excitation levels to be applied. Multiple excitation levels might be applied as a matter of course in any modal test so that the test program can define how linearly the structure behaves within the excitation range applied. Linearity can of course be dependent on the excitation level and type – almost any structure will exhibit nonlinearity at significant enough excitation levels. The intent in the modal test is to provide engineering information to help characterize this so that the importance of any nonlinearity can be determined and computer modeling efforts can take this information into account. In almost all modal test programs, the linearity should be investigated using multiple levels or multiple types of excitation with the intent of observing how the behavior changes.

If the modal test article is highly nonlinear, the test should investigate this to make sure that the behavior is well documented. An example of this is an aircraft control surface, which is expected to have a nonlinear response. Characterization of this behavior is important to fully understand how the system will behave in operation and is critical to making control system interaction and flutter predictions. Controlled tests using excitation level variations should be used in these cases to document the type of nonlinear behavior that can be expected. Excitation levels required for this type of testing should be evaluated prior to the test to ensure

that expected levels can be achieved and that the test structure can be adequately exercised. Automotive vehicle suspensions also typically exhibit a high degree of nonlinear behavior due to the types of springs or geometric behavior and dampers.

2.1.4 Damping of Structure

Structural damping has a key influence on the excitation levels required in the modal test program. The damping may also vary with excitation level, so using variable excitation levels can help define this effect. The type of damping present will influence the behavior observed. Most modal evaluations treat damping as though it is distributed and can be characterized as equivalent viscous damping; since this is not always the case, a series of tests can be planned to provide a better understanding of the behavior. Damping may be distributed or discrete, viscous or hysteretic, and targeted modal testing can help evaluate the damping characteristics.

During selection of shaker locations using a simulation study, a parametric study of estimated damping levels should be applied to allow reasonable estimation of the required test excitation levels. The expected damping levels should be selected from historical data when possible; similar structures provide reasonable damping ranges that can be used in this process. When similar structural data is not available, a range of damping values can be used to perform a parametric evaluation.

2.1.5 Simulation of Operational Loads

The types (random, sinusoidal, transient) of operational loads should be used in the appropriate selection and definition of the excitation used for a modal test. In some cases, the operational loading environment or an approximation can, and should, be used in the modal test; the magnitude of the environment may limit the actual excitation selected, but the spectrum applied can mimic the operational environment. This is clearly not always the case, as an operating environment may be discrete frequency tones, and modal testing is used to quantify the overall structural dynamic characteristics. The modal test engineer must therefore use judgment in selecting whether the operational environment is applicable to the modal test.

Shaping the frequency spectrum to more closely match the operating conditions can be very useful in obtaining modal properties that closely match what will be observed in service, as it can allow the magnitude of the excitation levels to be adjusted to higher levels in frequency bands than might be achieved if a flat force spectrum were applied.

2.2 Artificial Input

In discussing the excitation applied to a system to generate responses, a distinction should be made between artificial inputs and natural or operational inputs. Natural inputs are generally considered those that occur in nature; for example, they could be wind, seismic, or traffic. Operational inputs are the excitation resulting from operating the system. An example of operational inputs could be aerodynamic

input on a flying aircraft or input from a rocket motor burning its fuel. Natural and operational inputs can be somewhat related. In contrast, artificial inputs are specifically designed and controlled excitations applied to the structure to measure the resulting responses and then extract information about the structure's modal parameters. Examples include a random force applied by an attached shaker, an acoustic input from speakers, or a short transient force. These inputs and their advantages and disadvantages for use in modal testing are discussed in the following sections, starting with a discussion of artificial inputs.

2.2.1 Impulsive Inputs

Impulsive or transient excitation is an input of short duration relative to the measured time record, in contrast to random or sine inputs. The versatility of transient excitation techniques provides several advantages over typical vibration shaker input: it enables quick diagnostics of structures with short setup times, the input frequency spectrum is generally flat and can range from less than ten hertz to a million hertz, and high-amplitude inputs are achievable as well. Finally, the scalability of transient excitation is quite good; tested structures can range from a fraction of a centimeter to hundreds of meters. Impulsive excitation can consist of much more than hammer impacts, although that is by far the most common approach to apply a short-duration input: the excitation could also include projectile impacts, explosive inputs, step relaxation, or many other short-duration inputs. For a more complete description of various transient excitations, see Carne and Stasiunas [9].

Impact Inputs

The most commonly used method of transient excitation for modal testing is the impact hammer. The idea of exciting a structure with an impact hammer is actually very simple: one strikes the structure at a particular location and in a particular direction with an impact hammer. The impact hammer, which is instrumented with a force transducer located behind the tip, measures the force used to excite the structure. Figure 3 shows a small impact hammer with an integral load cell being used to apply a transient forcing function to a test article. The force input and corresponding responses are then used to compute the frequency response functions (FRFs) [7, 24]. The response to a hammer impact is an approximation of the impulse response function, although in actual applications, the impact is not assumed to be instantaneous but is measured and transformed into the frequency domain and used to compute the FRFs. An example force transient and corresponding frequency content is shown in Fig. 4.

The most important issue when utilizing impact hammer excitation is the choice of hammer mass and tip stiffness. These parameters determine the impact duration, which consequently determines the frequency content of the input. When impacting the test structure, the input frequency content should be sufficient to excite only the modes in the frequency range of interest. Exciting the structure above the frequency range of interest should be avoided, as the undesired response will fill the dynamic range of the measurement system and more than likely obscure the desired

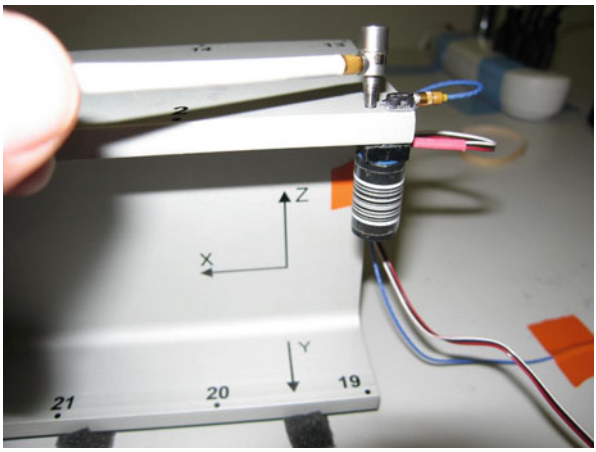

Fig. 3 Impact hammer with integral load cell to measure the applied force

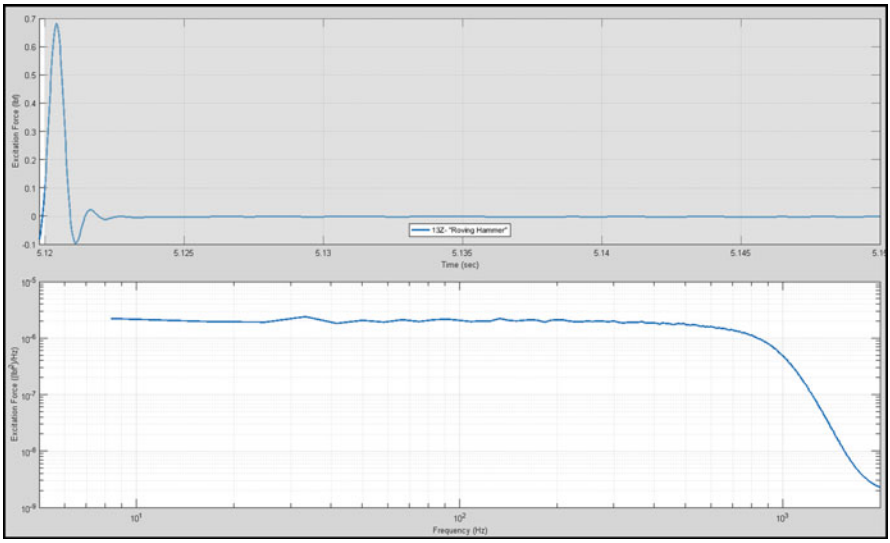

Fig. 4 Impact hammer force transient (upper) and spectral content (lower)

information. Therefore, an estimate of the desired frequency range of interest is important in the test design process.

Hammer impact testing has some distinct advantages. The input spectrum from the impact is flat out to the roll-off frequency, typically with no holes in the spectrum. The technique can be very efficient and portable compared to aligning and moving shakers and their associated control systems. Relatively small numbers of averages – as low as three to six – are sufficient to reduce noise in the calculated FRFs. Finally, for lightly damped, linear test structures, hammer impact testing can result in very high-quality FRFs.

Step Inputs

Step relaxation is a very powerful, but seldom used, excitation technique for formal modal analysis, although it is used extensively for informal tests. A step relaxation input is basically a pluck to the structure: an initial deformation is enforced upon a test structure and then rapidly released. Every time a guitar string or cantilever beam is plucked, the step relaxation technique is performed. In contrast to impact excitations, which have very flat Fourier spectra out to their roll-off frequency, the Fourier spectrum of the step input rolls off similar to $1/\omega$. Consequently, step input is extremely well suited to use with low-frequency systems [9].

Applying a step input to a structure is simple in design. Typically, a wire or string is attached to the test structure, with the free end anchored to the ground and tensioned, enforcing the required deformation. An example schematic of such an arrangement is shown in Fig. 5, and a simple gravity load release mechanism is shown in Fig. 6. Once preloaded, the wire is abruptly released or cut, resulting in step input excitation. In a test of a wind turbine, a 2-cm-diameter steel cable was used to provide a deformation to a 110-meter-tall wind turbine. For release, explosive cutters were used on the cable [10].

One requirement of step relaxation is the use of a force transducer as an element of the mechanism that applies the enforced deformation. This input force must be measured to compute the input–output FRF. Furthermore, the transducer needs to have a frequency response down to DC if it is to monitor the applied static force. A major advantage of step relaxation is that it is basically a noncontact excitation method; after the enforced deformation is released, there is no attachment

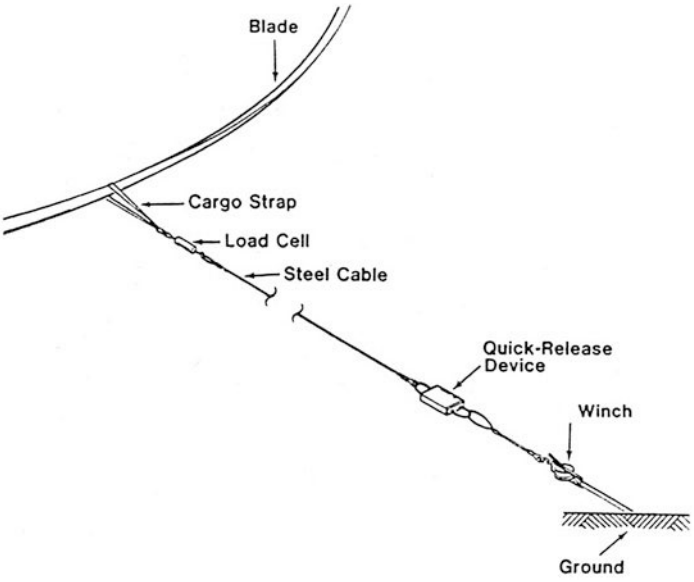

Fig. 5 Step relaxation hardware arrangement

Fig. 6 Gravity loaded quick release step relaxation system

to the excitation system. Step relaxation also scales very easily to large or small structures.

Applying step relaxation results in a unique signal processing issue. The force from a step input is ideally a classic step function, with a constant force beginning in the past and then suddenly dropping to zero within the test acquisition window as seen in Fig. 7. The data processing issue lies in using the Fast Fourier transform (FFT) to process the input-force time-domain signal: to the FFT, the step input appears to be a square wave, which results in very large holes or zeros in the input spectrum as seen in Fig. 8. This situation makes the original input step force unsuitable for typical FRF calculation. This signal processing issue can be solved easily but requires a bit of forethought: if both the original step input and the resulting responses are passed through matched high-pass filters with a low cut-off frequency, perhaps at 0.3 Hz (e.g., using an AC coupling circuit), the input step function converts to a negative spike, similar to an impact test as seen in Fig. 9. The resulting FFT, seen in Fig. 10, is very well behaved and is consequently easy to use for FRF computation and the averaging of repeated tests. Despite the drastic change in the time-domain signal caused by filtering the step, the resulting frequency content will be unchanged above 0.3 Hz. In fact, this representation of the force signal is compatible with all signal processing techniques used for impact testing including force windows, negative exponential windows, and pre-triggering.

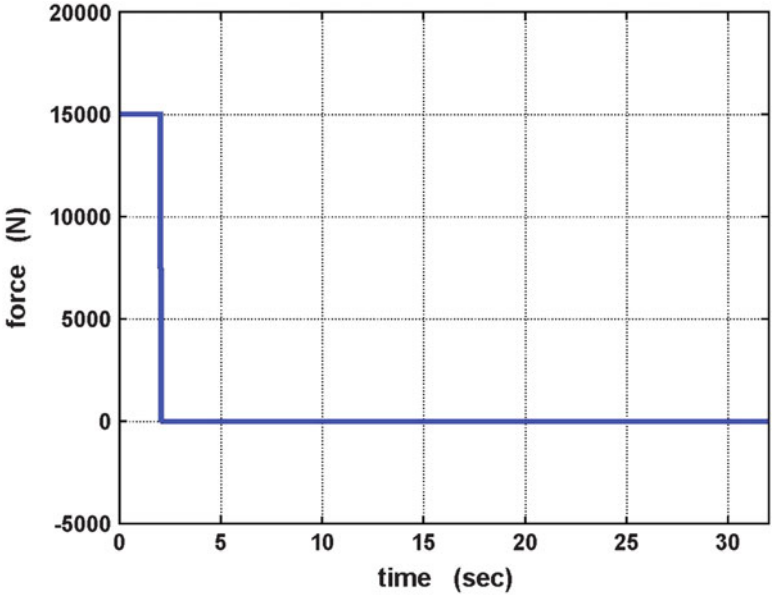

Fig. 7 Step relaxation force transient

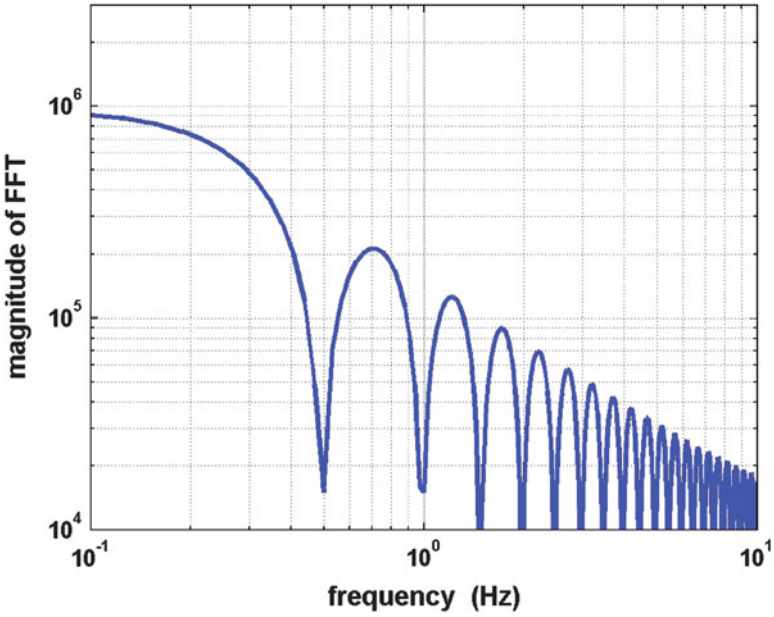

Fig. 8 FFT of step relaxation transient force

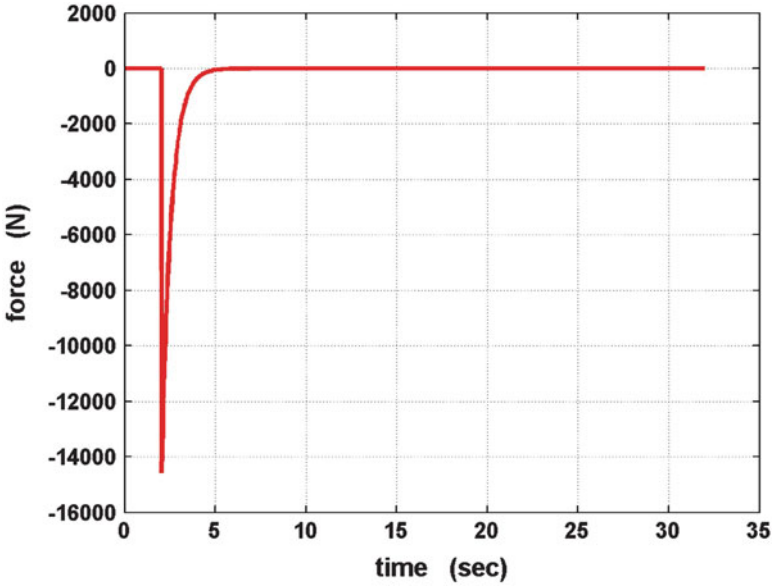

Fig. 9 Step relaxation transient force after filter application

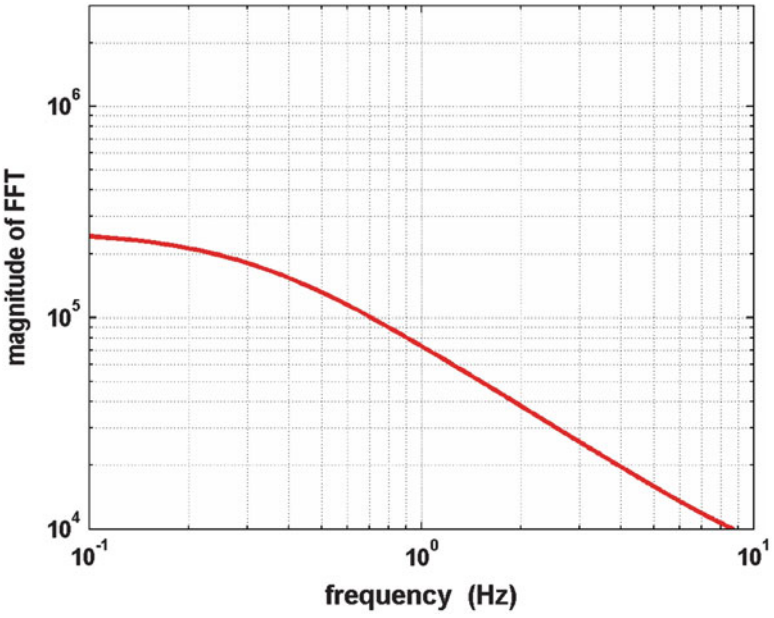

Fig. 10 FFT of step relaxation transient force after filter application

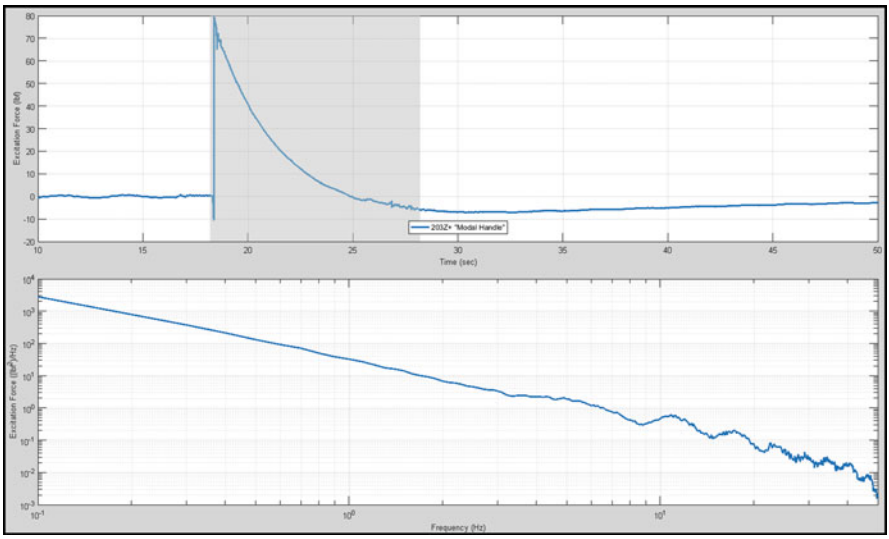

Fig. 11 Step relaxation transient force using piezoelectric load cell transducer

Another approach which does not require additional filtering involves the use of a piezoelectric load sensor. These sensors do not exhibit the static load and only yield the transient load when the preload is released. This results in a waveform and frequency content as shown in Fig. 11, which can be used directly in computing the desired FRF. Combining both types of load cells (static and dynamic) in the test design allows for optimal signal processing using this excitation technique.

In summary, step relaxation results in an input spectrum whose magnitude is proportional to $1/\omega$, making this technique particularly applicable to low-frequency structures. As with impact testing, step inputs work best with lightly damped, linear structures; the input does not work well for structures with significant nonlinearities or slipping joints. Scalability is possible with step relaxation, enabling excitation for small or massive structures, but the technique is particularly useful for the testing of large structures due to the ability to apply significant forces with a pre-tensioned cable. Finally, the FRFs measured from step relaxation can be of very high quality with very little noise.

Damping and Nonlinearities

In many cases, impulsive excitation works quite well, resulting in high-quality measured FRFs. One feature that enables the measurement of quality FRFs is low damping and inherent linearity. With high damping, the response due to the impact is quickly diminished, reducing the information available in the response

measurement. Highly damped structures can be difficult to test utilizing impacts or step relaxation, although good results can still be obtained under certain conditions.

Significant structural damping may indicate nonlinearities in the structure as well. For example, a common cause of high damping in structures is joint interaction or joint sliding, which is one source of nonlinear behavior in structures. In this case, the application of impulsive inputs is not advisable. In fact, even small nonlinearities can result in poor FRF measurements when impulsive inputs are used, as the input excites the structure initially to high response levels and then the response damps down to very low levels, resulting in data from multiple structural states all in one FRF measurement. This can create very confusing data, with the observed modal frequencies varying within one data sample. For structures with significant nonlinear behavior, random excitation or sine testing, provided with a shaker, will yield the best results for the linear model of the system. Random excitation is discussed in a subsequent section.

2.2.2 Controlled Inputs

The most common type of controlled excitation source is a modal shaker. Usually modal shakers are voice coil actuators that impart a measured force on a structure that is proportional to the provided electrical signal. An electromagnetic (electrodynamic) shaker as shown in Fig. 12 is coupled to the structure using a mechanical stinger rod and a load cell to measure the applied excitation force. However, the actuator can also be hydraulic, pneumatic, piezoelectric, or another actuator type that imparts a force appropriate for the type of structure and objectives of the test. Selection of the type and size of shaker is dependent on the structure

Fig. 12 Electromagnetic shaker attached to the test article with a mechanical stinger rod

size, required excitation force, frequency range of interest, number of excitation locations, as well as other factors such as power requirements. Inputs can also be acoustic using speakers (another voice coil actuator which is coupled to the structure through an acoustic media), or even accelerations such as those provided by vibration tables. The inputs imparted to the test article can be deterministic or random. Deterministic signals are those that can be described at any point in time by a mathematical function [2], whereas random signals cannot. Examples of deterministic signals include sinusoidal dwells, stepped sine, sinusoidal sweeps, and pseudo-random. Examples of random signals include burst random, periodic random, and true random signals.

Stepped-sine excitation is a special case of sinusoidal excitation which dwells at discrete frequencies for some amount of time while data is collected. The sine frequency is then stepped to the next frequency. Both the amount of time spent at each frequency and the frequency spacing can be selected during the test planning process, and they can also be adjusted during the test. The sinusoidal signal used to drive the structure is controlled in amplitude and phase by each excitation actuator.

Sinusoidal sweeps, which can consist of a long sweep or a "chirp," involve continuously changing the sinusoidal frequency of an input over a frequency range. The difference between a chirp and a long sweep is the amount of time the sweep lasts. A chirp is defined here as a sweep that lasts less than a frame of data. A long sweep is a sweep that lasts over all frames of data.

The total amount of time required using stepped-sine is dependent on the frequency range being covered, the frequency spacing or resolution, the dwell time, and the number of excitation phase combinations to be used. These parameters can be evaluated during test planning to assess the total time required using this method. In general, stepped-sine excitation is considered a somewhat slow method, particularly when high frequency resolution is required. However, it can be quite effective when performing detailed testing covering small frequency ranges and can provide high-resolution FRFs to allow detailed focus on a particular mode or modes of interest.

2.2.3 Multiple Inputs

There are two major considerations that should drive the definition of the inputs for a modal survey:

- The input must be able to excite the modes (at least a subset of modes)
- The combined inputs must be able to uniquely excite all the modes of interest (this is related to mode independence and force appropriation)

Multiple inputs are typically used in modal testing to ensure that a good distribution of energy to the system is achieved. It is also important to develop a set of FRFs that provides either a full or partial matrix which can be used to describe the structural behavior. Multiple inputs allow development of the multi-reference FRFs needed for parameter estimation, such as the well-known Polyreference parameter estimation tools. Multiple inputs are not limited to shakers. Various

impact excitation techniques have been employed (Multiple Reference Impact Testing – MRIT) to develop FRF matrices that can be used in multi-reference parameter estimation techniques. Further, single-input excitation techniques can be used (and were for many years) to develop a partial FRF matrix for multi-reference parameter estimation by simply moving the excitation input to a number of locations on the structure. However, in most cases – and what is of most concern – the implementation of multiple, simultaneous inputs to the test article will yield a more consistent modal characterization and better energy distribution through the structure.

The number of excitation sources or inputs used in a modal test is often a matter of convenience as well as availability. However, there are specific considerations that must be taken into account in determining the number of excitation sources to be used in a modal test. Single inputs can be used to develop a set of multiple-input FRFs. However, except in the case of stationary, linear structures, there is a likelihood that the FRFs will not be consistent due to the changes in time and physical boundary conditions. It is better to configure all inputs simultaneously so that a consistent data set is obtained in the test. The capacity of any shakers to be used and where they can be attached to the structure should be considered as part of the planning process.

One key consideration in setting the number of excitation sources is whether the inputs are linearly independent. This is required so that the reference auto-spectral matrix, S_{XX}, can be inverted in developing the desired FRFs. For random input signals, the number of frames of test data must be greater than the number of inputs used. For deterministic input signals, the number of phasing cases between the different input signals must be greater than or equal to the number of exciters.

2.3 Natural or Operational Inputs

In contrast to the artificial excitations discussed above, there are natural or operational excitations that can be considered as a viable excitation to a structure for measuring its modal parameters. In some cases, a structure can be so immense that it is very difficult to apply an adequate artificial excitation; examples include large wind turbines, buildings, and bridges. Frequently for structures that have been assembled in their operational environment, there exists substantial natural excitation and responses that would interfere with an artificial excitation test. Generally, natural inputs are those existing in the environment, such as wind, seismic inputs, and vehicular or foot traffic. Somewhat contrasting to natural inputs are the operational inputs that result from operating the system or structure. Examples here would be a *rotating* wind turbine, a *flying* aircraft, or a *moving* vehicle on a road surface. The two terms – natural and operational inputs – are frequently interchanged with the currently more common term "operational modal analysis."

The use of natural inputs for wind turbine testing was first introduced at the 1988 International Modal Analysis Conference (IMAC) [11], and the concept of operational modal analysis (OMA) followed quickly. Numerous improvements

and refinements and the theoretical grounding have been subsequently published. James et al. [19] discussed the theoretical development of the NExT (Natural Excitation Technique) approach for using natural inputs for modal analysis. In that development, it was shown that the cross-correlation functions arising from broadband random inputs can be represented as a sum of decaying sinusoids of the same form as the impulse response functions. This was a significant development as it revealed that any modal extraction algorithm that uses impulse response functions could be used to extract modal parameters from the cross-correlation functions. Various time-domain extraction algorithms have been used to estimate the measured modal parameters, including ERA and Polyreference. In practice, cross-correlations can be much noisier than FRFs due to the lack of noise cancellation that is obtained in computing FRFs. Consequently, it is recommended that many more averages be used than one would use to compute FRFs; 100–200 averages is not an unreasonable number.

There have been a tremendous number of modal analysis applications using natural or operational inputs – including wind turbines, bridges, buildings, monuments, stadiums, aircraft, rockets, vehicles, and other civil structures – and there is even a biannual conference, the International Operational Modal Analysis Conference (IOMAC), dedicated to applications and developments in OMA.

3 Response Measurements

3.1 Transducers

To measure structural responses, one clearly requires some sort of transducer that will create an electrical signal proportional to the response being observed . Ninety percent of modal tests use accelerometers with specific characteristics chosen depending on the size, weight, geometry, and other properties of the structure under test. Other chapters in this handbook discuss in detail various characteristics one must consider in selecting an accelerometer. However, there are many applications in which accelerometers are not the best choice for response measurement. In those cases, one needs to be aware of the other means that can be used to measure responses.

High-output strain gauges might serve well as a transducer when weight or temperature is a particular concern. Strain gauges do not have the cross-axis sensitivity that accelerometers do, and they can be geometrically combined to sense only axial strain or bending strains. Velocity probes, interferometry devices, or displacement gauges might also have application for a particular object under test. Interferometry can be particularly effective for objects of extremely low mass, such as micromechanical systems, or any object where contact needs to be avoided or frequencies are extremely high. Additionally, active materials attached to the structure could act as a strain gauge or a force transducer in some applications.

3.2 Number of Degrees of Freedom to Measure

Clearly, when a modal test is designed, the number of response degrees of freedom (DOFs) needs to be considered. By measuring more responses, one obtains more detail; however, the number of measured responses also increases the cost and complexity of the test. These considerations are discussed more in Sects. 3.4 and 6, which discusses requirements for model validation. However, just because one *can* measure 300 responses in a test does not mean that one *should*. One needs to be conscious of the costs and time involved in the installation and operation of the sensors as well.

One aspect that needs to be decided is the number of DOFs to be measured at each location. For some structures, one DOF is just fine; but others may require two or three – or one may even need to measure rotations as well as translations. If a high-fidelity model is available, some responses can be inferred or computed using the model, such that they do not need to be explicitly measured. Again, further discussion of the number of DOFs and which DOFs are required for modal validation is included in Sect. 6.

3.3 Acquisition Methods

Independent of the types of transducers used in conducting the modal test, a key consideration to be addressed before starting the instrumentation is how the sensors will be installed and how many will be used or collected at a time. The number of sensors available for installation can provide an upper limit here, as can the number of input channels on the data acquisition system. However, potential measurement effects should be taken into account regardless of the approach taken. There are primarily four approaches which can be taken when acquiring the modal data.

- Simultaneous collection of all channels with all sensors installed
- Sequential collection of all channels with all sensors installed
- Sequential collection of channels with roving sensors
- Sequential collection of channels with roving input, using reciprocity

In the ideal case, all sensors should be installed and measured simultaneously using a high-performance, high-channel data acquisition system. This ensures that a consistent data set is acquired using the same data acquisition conditions and with the same excitation inputs. Of course, this means that the sensors and data collection system must be matched for the total number of channels; if the test involves measuring 100 sensors, the data system used must be able to collect all 100 sensors and the excitation input signals simultaneously. This can be a problem if the data collection system does not have enough channels to acquire all of the sensors, or if there are not enough sensors to be installed at every desired measurement location. This is true whether the sensor types are accelerometers or lasers or some other

type. The reason this is so important is that if all test measurements are not made simultaneously, structural variations may occur and may change the modal behavior. These changes in the modal behavior then make parameter estimation difficult if not impossible. For example, an airplane being tested was instrumented with over 100 sensors, but the data system could only collect a subset (16 channels) of these at one time. Since the sensors had to be collected in subsets, the measurements were spread out over some time, during which there were thermal effects that caused the aircraft structure to expand, yielding inconsistent sensor orientation and modal behavior over time. Even though the excitation input was essentially the same for each subset of the measurements, the structural changes resulted in a poorly defined set of FRFs, which made modal parameter extraction much more difficult.

Nonetheless, there are many cases where it is not possible to make all of the measurements simultaneously, and roving accelerometer and laser vibrometer measurements are common methods used to make FRF measurements in these cases. If this approach is to be used, attention must be paid to keeping the test article as consistent as possible throughout the measurement cycle. If accelerometers are being moved (roved), mass simulators should be installed at all locations to represent the physical accelerometer mass at each measurement location. These masses can be removed as the sensors are installed and then reinstalled when the sensors are moved to another location. In all cases, even with laser measurements, the environment around the test article should be well controlled. This includes temperature and humidity controls as well as things like environmental noise. This may mean utilizing a special facility to house the test article. The same considerations should be applied when deciding to use a roving hammer with a few fixed sensor measurements. With this approach, the roving input is applied at all of the measurement points of interest and reciprocity of the FRF measurements is used in development of the FRF matrix. The number of locations to be measured and thus the amount of time required to do so may have an effect on how consistent the structure remains during the test.

Many different approaches can be used in collecting the test measurements. With careful planning of the approach to be used and control of the test article, the test should yield a consistent set of test data. The amount of time required for the testing activity will also be strongly influenced by the approach selected. If multiple test configurations will be required, roving techniques will typically require considerably more time due to the setup required, even though the initial setup time may be less. In general, if more than one test configuration will be studied, it will require less overall time to install all sensors at the beginning of the testing than would be taken using a roving technique. Of course, the total number of sensors to be installed will also need to be evaluated.

3.4 Geometry Definition

Assignment of sensors to specific measurement locations on the test article structure are important to allow mode shape visualization and for comparisons to FEM

predictions. This geometric or physical placement of the sensors is an important step in the planning and setup phase of conducting a modal test. When FEMs are available, geometry can be extracted from the model. But since these models are often simplifications of the real structure, the actual geometry may be different. The test engineer should ask how important this geometry is and determine the amount of effort that should go into defining specific measurement locations.

Many modal tests are performed without any prior knowledge or geometric information from FEMs or geometry models. In these cases, the geometry of the structure can be measured where the sensors are installed. Or geometric assumptions can be made to define measurement locations and then validated as the sensors are placed. This is often the case when modal testing is performed as part of a troubleshooting effort and measurement selection is defined as the testing effort progresses.

3.4.1 Accuracy of Location Measurements

When measuring where the modal test sensors are to be installed on a structure, an important question that arises is what accuracy is required for the location measurements. There is no specific answer to this question, but it is important to consider the modes of interest and whether the geometry measurement accuracy will influence the ability to quantify the shapes being measured. A way of demonstrating this is to consider the measurement of a sinusoidal waveform. If the wavelength being considered is shorter than the accuracy of the measurement location, then there will be a high degree of uncertainty associated with the corresponding shape. Of course, this will vary greatly depending on the structure under test and the frequency range of interest; accuracy of ± 1 inch on a Boeing 747 aircraft would have much less impact than on a Cessna 172 aircraft.

During preparations for a modal test, the expected mode shape wavelengths and frequency range should be evaluated to determine whether placement accuracy of the sensors will have an influence on the accuracy of the mode shapes, as the answer may influence the method used to make the measurements. Laser systems are available now which can accurately measure the physical locations of the sensors (before or after installation). On the other hand, a simple tape measure can enable good geometry accuracy, provided there are well-defined reference points on the structure.

3.4.2 Layout and Documentation

Much of the layout for sensor placement can be planned before the test. The geometry definition, if made available prior to the test, can be used to develop methods to quickly locate the sensor placement on the structure. There are many methods that can be used in laying out the measurement locations on the test article structure. New methods enable accurate measurement of the locations where sensors will be installed. For instance, a laser tracking system can be used to define locations that are visible from outside of the test structure; for interior locations, other methods must be used to properly verify where measurements are to be made. Structural landmarks can often be used as reference points or physical locations

where sensors might be installed; these might be apparent as structural seams, weld lines, rivet lines, mold lines, and so on. As new methods such as 3-D printing become more widely used, however, some of these physical attributes that can be used for geometric definition may become less predominant, and new geometry definition methods may need to be employed.

If geometry is developed during the test planning stage, this information can be entered into the laser tracking system with appropriate reference to allow automated sensor placement. Laser systems can also be used to measure or validate sensor placement even when prior geometry is not available. Similarly, optical methods such as photogrammetry can be used to record where sensors are located.

Many test articles can be laid out for the measurement locations using simple tape measures. Good reference points should be identified from which measurements can be made. Since sensors are typically placed on the exterior surface of the test article, the surface geometry is taken to correspond to models or drawings that define the surface. Measurements along the surface then define the location where sensors are to be placed.

Templates can also be used as a reliable method to define where measurements are to be made. Preliminary geometry can be located on the template for accurate placement, and then the template can be aligned to reference positions on the test article to show where sensors are to be placed.

As locations are identified, it is a good approach to mark the sensor installation location before the sensor is installed. Since some surfaces are sensitive and marking the surface may not be desired, tape can be placed on the surface and the location marked on the tape. The sensor can then be attached to the tape at the marked location. It is important to consider the frequency range of interest and the mass of the sensor being installed when using tape, since the attachment method can affect the measurements made. An approach that has minimal effect on the expected measurement should be selected.

The measurements of geometry should be documented showing three-DOF coordinates in the appropriate coordinate systems. If a local coordinate system is used, those measurements should be recorded along with any transformed coordinates, such as global coordinates.

3.4.3 Test Display Model

A test display model is an important tool for conducting a modal test and evaluating the quality of the data as the test proceeds. This model, in its simplest form, is a geometric 3-D representation of where the test measurements are being made. Nodes (which are analogous to geometry grids and finite element nodes) are used to define the locations on the structure where sensors are located. Connective elements between the measurement nodes can be made using line traces or by employing various finite element types (typically linear beams, triangular and quadrilateral shells, etc.) to yield a 3-D display that is analogous to the test article. As measurements are made, they are directly associated with the display nodes and directions. The test display model, in addition to allowing the visualization of the mode shapes, allows visual comparisons to be made with a FEM as shown in Fig. 13.

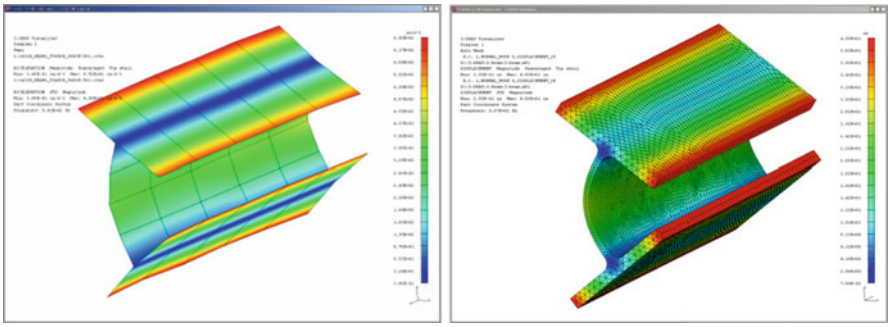

Fig. 13 A test display model (left) is important for mode shape visualization

The test display model can be expanded beyond the sensor measurement locations to provide improved mode shape displays and animation. During preparation for the test, if a FEM is available, model-based transformations should be considered; these enable the test measurement DOFs to be expanded to other unmeasured locations, which provide improved visualization of mode shapes. While it is not a necessary step, this process can provide better interpretation of modal behavior without changing any of the original measurement data. In some cases, it is also possible to use a variety of constraint equations, such as rigid body behavior, to compute shape behavior where measurements were not made in the test. Care should be taken when using these approaches, however, as the physical structure may behave differently than the assumed constraint equations.

In the extreme case, modal results from test can simply be expanded to the full FEM, which can then be used for visualization. While this might be done for some simpler models, detailed FEMs can require significant time to convert and display, thus limiting the effectiveness of this approach for evaluation of test results during the performance of the test. Also, any errors in the model can lead to distorted mode shape information in the expansion of the test data. It may prove more effective to use this method at the completion of the testing while model updates are being performed.

4 Support Conditions

There is a maxim used in the aerospace industry which applies to many types of testing, and certainly to modal testing: “Test Like You Fly.” This has many meanings, but in modal testing, it is meant to imply that the test article should be representative of the flight hardware and the boundary condition should be representative of the way the article will be constrained when it is in service. Interestingly, this can lead to multiple tests, each with different boundary conditions: a satellite has a constrained boundary condition when it is being launched and delivered to orbit, yet it has a free boundary condition when it is in service.

However, most satellite modal tests are conducted with a fixed or constrained boundary condition, since that is the condition for which large loads can develop at the boundary as experienced during launch. Similarly, components mounted on a satellite have a constrained boundary condition and would typically be tested with a fixed condition boundary.

On the other hand, aircraft and land vehicles are operated in either a free or a softly suspended condition, and modal tests conducted in that configuration should be considered first. Aircraft are most often tested with low-frequency suspensions intended to approximate a free-flight boundary condition and isolate the aircraft rigid body modes from the aircraft flexible modes. Automobiles are typically tested using their actual suspension systems, which properly capture the rigid body vehicle suspension modes along with the suspension characteristics.

With all these considerations, if one is performing a modal test to validate a FEM, either the model must include the support conditions from the test or the test must adequately approximate the boundary conditions imposed by the model. This requires coordination between the modal test design and the modeling effort. In any case, it is virtually impossible to achieve either a totally free boundary condition or a completely fixed boundary condition. Consequently, suspension development for a modal test must take into account the expected changes to the test article behavior to achieve a suspension system that meets the objectives of the test. The effectiveness of the suspension, whether fixed or free, can be evaluated through parametric studies performed prior to the test using FEMs, if available. Designing the test with suspension components imposed also ensures that the appropriate support locations are included in the model if suspension elements may need to be adjusted for model updating.

4.1 Approximating Free Boundary Conditions, and the Resulting Compromises

When modal testing a structure for the purpose of model validation, free boundary conditions are frequently approximated in the lab to compare with free boundary condition analyses. Free conditions are used because they are normally easy to simulate analytically and easier to approximate experimentally than boundary conditions with fixed conditions. However, the free conditions can only be approximated in the lab because the structure must be supported in some manner. To properly design the modal test, one needs to be able to quantify the effects of the support conditions on both the measured modal frequencies and damping factors. As will be shown, the measured modal damping is significantly more sensitive to the support system (stiffness and damping) than the measured modal frequency. There are simple formulas that can be used to predict the effect on the measured modal parameters given the support stiffness and damping.

Historically, there has been concern for support stiffness and its effect on measured modal frequencies. As early as 1955, Bisplinghoff et al. [4] discuss the effects of support stiffness and mass on measured modal frequencies. Wolf [33]

discusses the effects of support stiffness with regard to modal testing of automotive bodies. He reports that the rule of thumb to simulate free boundary conditions is to design the support system so that the rigid body modes – that is, the modes that would be at zero frequency except for the support conditions – are no more than one-tenth the frequency of the lowest elastic mode. But it is seldom possible to achieve this separation for vehicle tests, with test engineers frequently using a 1:3 to 1:5 separation ratio between the rigid body modes and the lowest elastic mode. Wolf [33] shows that such stiff supports can lead to significant errors in the measured modal frequencies. Ewins [16], in the test planning chapter of his second edition of *Modal Testing*, briefly discusses the issue of the location of suspensions for free boundary conditions. More recently, Brillhart and Hunt [6] presented an exposition of many of the practical difficulties involved in designing good fixtures for a modal test, and Avitabile [3] briefly discusses this issue in a "back to basics" article.

Many authors have subsequently added to this topic, and Carne et al. [12] developed relatively simple formulas for predicting the effect of support stiffness and damping on the measured modal frequencies and modal dampings. They applied these techniques to the testing of a wind turbine blade in the freely supported condition. The formulas presented here are taken from Carne et al. [13].

Perhaps the best way to develop an understanding of the effects of support conditions is to examine the very simple two-DOF system. Let us consider a simple model, pictured in Fig. 14, of an unconstrained structure (free boundary conditions), consisting of two masses connected by a linear spring and a viscous damper with motion restricted to a single direction.

This system could be support in several ways, but let us add a support system symmetrically as diagrammed in Fig. 15. Here, k_t and c_t designate the true stiffness and damping of the structure, and k_s and c_s designate the added support stiffness and damping. Using the symmetry, the modal parameters of the supported system can be solved by inspection. There are two modes for this system, $\phi_1 = [1\ 1]^T$, and $\phi_2 = [1\ -1]^T$. The first mode is referred to as the support mode or the rigid body mode because there is no deformation in the original structure (Fig. 14), only deformation of the support system. The second mode is the elastic mode because it involves elastic deformation of the original structure as well as the support system. The undamped natural frequencies for the two modes are

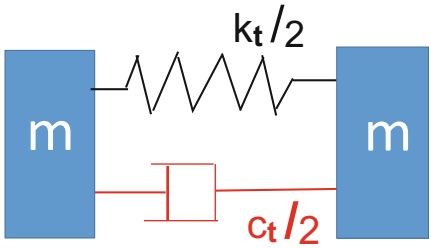

Fig. 14 Freely supported two-degree-of-freedom system

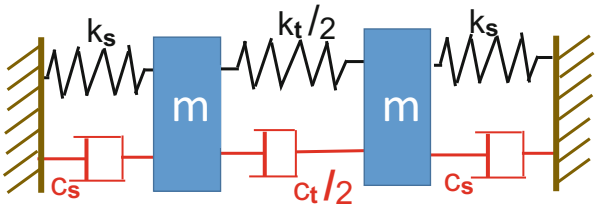

Fig. 15 Two-degree-of-freedom system with added support stiffness and damping

$$\omega_s = \sqrt{k_s/m} \qquad \omega_m = \sqrt{(k_t + k_s)/m} \tag{1}$$

where ω_s indicates the rigid body mode due to the support system, and ω_m indicates the measured frequency of the elastic mode, which includes the support. Similarly, the damping factors can be derived from inspection and are

$$\zeta_s = c_s/2m\omega_s \qquad \zeta_m = (c_s + c_t)/2m\omega_m \tag{2}$$

Now define symbols for the true natural frequency and damping factor of the structure, if it had no supports, as

$$\omega_t = \sqrt{k_t/m} \tag{3a}$$

$$\zeta_t = c_t/2m\omega_t. \tag{3b}$$

Combining Eqs. (1) and (3a), a very simple, and easily remembered, expression results, relating the measured frequency, ω_m, to the true frequency, ω_t, and the support frequency, ω_s:

$$\omega_m^2 = \omega_t^2 + \omega_s^2 \tag{4}$$

Or the true frequency can be expressed as

$$\omega_t = \omega_m \left[1 - \frac{\omega_s^2}{\omega_m^2}\right]^{1/2} \tag{5}$$

And if $\omega_s/\omega_m << 1.0$, then

$$\frac{\Delta\omega}{\omega_m} = \frac{\omega_m - \omega_t}{\omega_m} \cong \frac{1}{2}\left(\frac{\omega_s}{\omega_m}\right)^2 \tag{6}$$

From Eq. (6), it is easy to see the effect of added support stiffness on the measured frequency of the test item. If the support stiffness is such that the ratio

of the rigid body frequency, ω_s, to the measured frequency, ω_m, is 1:10, the true frequency would be approximately one half of 1% different from the measured frequency, so the 1:10 ratio is a good rule of thumb for most applications for reasonable accuracy. If the ratio were 1:3, the error would be over 5%, which generally would be unacceptable.

However, this is just a rule of thumb. For example, envision freely supporting a horizontal beam with two vertical, soft bungee cords and then measuring the first bending mode of the beam. If the supports are attached at the extreme ends of the beam, the supports would have a much greater effect on that modal frequency. In fact, the effect would be four times greater than that shown in Eq. (5). One would need to insert a multiplier of 4.0 in front of the ${\omega^2}_s$ term. In contrast, if the supports are attached at the node points of the bending mode, the supports would have zero effect on that particular modal frequency.

Let us now turn our attention to the measured damping ratio. Following the example of the frequency analysis above, combining Eqs. (2) and (3b), another simple formula relating the damping factors results.

$$\zeta_m \omega_m = \zeta_t \omega_t + \zeta_s \omega_s \tag{7}$$

The above expression can now be solved for the true damping ratio in terms of the measured and rigid body damping ratios.

$$\zeta_t = \zeta_m \frac{\omega_m}{\omega_t} \left[1 - \frac{\omega_s}{\omega_m} \frac{\zeta_s}{\zeta_m} \right] \tag{8}$$

This expression has similarities to that for the frequencies, Eq. (5), except that the frequency ratio inside the brackets is no longer squared, and it is also multiplied by the ratio of the damping ratios. If there is a frequency ratio of 1:10, as the rule of thumb suggests, and if the support and measured damping ratios, ζ_s and ζ_m, are equal, there would be a 10% error if the true damping were assumed equal to the measured damping.

However, suppose there is a moderately damped structure and the frequency ratio is still 1:10, but the support damping is 5% and the measured damping is 1%. Now the ratio of dampings in the bracket is 5.0, and it has a large effect. The true damping would only be 0.5%, so one would have 100% error if one assumed the measured damping to be equal to the true damping. Lastly, let us now consider the case in which the frequency ratio is 1:3. If the true damping ratio is again 0.5% and the support damping ratio is 5%, the measured damping ratio would be 2.59%, resulting in 400% error if one assumed the measured damping to be equal to the true damping.

From these examples and Eq. (8), one can see that the situation for the measured damping ratios is significantly different from that for the measured modal frequencies. Assuming the true damping ratio is the same as the measured damping ratio can result in huge errors as compared to those for the frequencies. Unfortunately, most FEMs do not include damping, so one cannot validate a damping model with test

data and then remove the support damping. Frequently, test-derived modal damping is used in the model to create the damping model.

There is one saving factor in the measurement of modal damping. The viscous damping model (one that is independent of frequency) is frequently not a good model for support structures such as bungee cords and airbags. A discussion of damping models is beyond the scope of this present work, but many authors would model the damping as structural damping or solid damping, at least in part. See, for example [30]. Using structural damping model, then, the typically measured viscous damping factor, ζ, at the resonant frequency is approximately equal to $\gamma/2$ [25]. And Eq. (8), which relates the viscous damping factors, would be modified for structural damping models instead of viscous damping models. The measured structural damping coefficient, γ_m, can be expressed as a weighted sum of the support damping, γ_s, and the true damping, γ_t, as

$$\gamma_m = \frac{k_s \gamma_s + k_t \gamma_t}{k_t + k_s} \tag{9}$$

Note that structural damping elements do not add in the same way viscous damping elements do. Dividing the numerator and denominator of the fraction in Eq. (9) by the mass, we obtain a relationship similar in form to Eq. (8), but significantly different due to the squares on the frequencies:

$$\omega_m^2 \gamma_m = \omega_s^2 \gamma_s + \omega_t^2 \gamma_t \tag{10}$$

This expression can be solved for the true structural damping in terms of the measured and support damping coefficients:

$$\gamma_t = \gamma_m \frac{\omega_m^2}{\omega_t^2} \left[1 - \frac{\omega_s^2}{\omega_m^2} \frac{\gamma_s}{\gamma_m} \right] \tag{11}$$

This Eq. (11) is much more forgiving of the support system damping than Eq. (8), due to the squares on the frequency ratio. Also, recall that the viscous damping factor, ζ, at the resonant frequency is approximately equal to $\gamma/2$. So, for example, suppose again there is a moderately damped structure and the support frequency to measured frequency ratio is still 1:10, but the structural support damping is five times that of the structural measured damping: the measured damping would contain only a 5% error compared to the true damping. In the extreme case when the frequency ratio is 1:3 and the support damping is five times that of the measured structure, the measured damping is 50% in error and would be unacceptable, but not nearly as bad as the viscous damping model. Even for the structural damping model, one can still vastly overestimate the modal damping in a structure if the true damping is small. So for applications with low damping in the structure, one must be particularly attentive to the added support damping, regardless of the damping model.

The discussion, up to this point, has examined the very simple two-DOF model as diagrammed in Fig. 15. The two-DOF model is very useful as it can be analyzed exactly and is very helpful for creating intuition and very simple formulas. As Winston Churchill once said, "Out of intense complexities, intense simplicities emerge." That is the beauty of the two-DOF system. However, the multi-DOF problem is the concern for most modal testing. Typically, the most concern is with the lowest mode of the dynamic system because it will be most affected by the support system, so one might think that the two-DOF model should be sufficient. Frequently, that is true. However, with a multi-DOF system, the placement of the supports relative to the mode shape can be accounted for, and that can be a very important aspect of the support problem. This aspect was mentioned in the previous section with the example of the softly supported beam, where the frequency shift depends whether the supports are attached at the beam ends or the nodes of the first mode: if the supports are attached at the beam extremities, the effect of the support conditions is four times more than the two-DOF formulas provided; and if they are attached at the nodes of the mode, the effects are reduced to zero.

The derivation for the multi-DOF system is somewhat more complicated than that for the two-DOF system, so only the final formulas are included in this text. For the full derivation, refer to [12]. Referring back to Eq. (6), a similar result can be derived for the multi-DOF system. The change in the frequency, $\Delta\omega$, due to the added support stiffness, Δk_{ii}, is given by the formula below:

$$\Delta\omega \cong \frac{1}{2\omega_t}\left(\varphi^i\right)^2 \Delta k_{ii} \tag{12}$$

where the change in frequency, $\Delta\omega$, is the difference between the measured and true frequencies. Δk_{ii} is the added or support stiffness at point i on the structure, and ϕ^i is the value of the mass-normalized mode shape at position i. This formula for the change in frequency is quite simple, and it is straightforward to evaluate using the stiffness of the support system and the value of the mode shape at the attachment position. With more than one support element, one would simply add the contributions from the elements, including rotational constraints, if any. Comparing Eq. (12) with Eq. (6), one can reduce Eq. (12) to be exactly the same as Eq. (6), keeping in mind that the mode shape in Eq. (12) has been mass normalized and there are two added support stiffnesses. Also note that ω_t is in the denominator on the right-hand side of Eq. (12), so at higher modal frequencies, $\Delta\omega/\omega_t$ varies proportionally as $(1/\omega_t)^2$.

Turn now to the issue of damping in a multi-DOF softly supported structure. For the support damping, the situation is more complicated than for the modal frequency because one will typically not have an analytical model of the damping in the structure, in contrast to the stiffness of the support system. But the issue is the same as for the stiffness: given a measurement of the damping for a particular mode, how can we determine the change in that modal damping due to the support system? It has been shown [12] that an approximation to the change in modal damping can be computed if the support system makes a negligible change to the mode shape

of the structure. Further, the mode shape components at the support connections for *mass-normalized* mode shapes are required, as well a damping model for the support system. From the analysis of the complex eigenvalue equation, the result for the measured damping is

$$\zeta_m \omega_m = \zeta_t \omega_t + \frac{\psi' C_s \psi}{2} \tag{13}$$

which is very similar to Eq. (7) derived for the single-DOF system. Here, the contribution due to the support damping has just been generalized to include the mode shapes. C_s is the damping matrix for the support system, and ψ is the mass-normalize mode shape for the particular mode of interest. ψ' is the transpose of the column vector ψ. Solving for ζ_t, results in

$$\zeta_t = \zeta_m \frac{\omega_m}{\omega_t} \left[1 - \frac{\psi' C_s \psi}{2 \omega_m \zeta_m} \right] \tag{14}$$

This formula for the true damping ratio, as the frequency formula in Eq. (12), is a fairly simple expression. Given the measured modal damping, the measured modal frequency, the components of the mass-normalized mode shape at the support DOFs, and the damping model, the true damping ratio of the unsupported structure can be calculated. Equation (14) can also be compared to Eq. (8) for the single-DOF case. Again, these equations are very similar, and Eq. (14) reduces to Eq. (8) for the single-DOF case.

Equation (14) reveals some important features, just as Eq. (8) did. Because the quantity in the brackets is the difference between one and a positive number, the difference between the true damping ratio and the measured damping ratio can be significant if the last term in the brackets is not close to zero. In conclusion, when attempting to simulate a free body in the lab for modal testing, one must be careful that the supposedly soft support system does not significantly affect the measured modal frequency or the measured modal damping. Highly damped support systems can significantly affect the measured damping.

4.2 Suspension System Design, Low Spring Rates

When free boundary conditions are desired, the most common means to achieve this is to design a system that provides a low spring rate in all six DOFs of the structure. However, "low spring rate" is a relative phrase. For a structure with modes of interest in the hundreds of hertz, a spring rate that provides rigid body modes below 20 Hz may be quite acceptable, whereas for a structure with modes below 10 Hz, it might be desirable to have a suspension system yield rigid body modes below 1 Hz. This can be a difficult design goal and is often a challenge for large aircraft. As a result, the suspension systems used may not yield any pure rigid body modes and the lowest modes may reveal coupled behavior between the desired rigid body modes and the flexible body modes.

The design goal in developing a low-frequency suspension system is to achieve good isolation between the six-DOF rigid body modes and the first flexible modes of the structure. If these frequencies are too close together, the suspension system modes will influence the responses in the flexible modes of the system, and in extreme cases they will couple, combining rigid body and flexible body behavior in the mode shapes.

Some simple evaluation of desired isolation frequency, required spring rates, and the capability to support the test article weight can help in the suspension design process. In a single-mass case, the static spring force $F = W = Kx = Ma$, and the natural frequency $f_n = \left(\frac{1}{2\pi}\right)\sqrt{\frac{K}{M}}$. This helps define the ratio between K and M, which can yield the desired frequency and show the static deflection requirements for a linear spring. A good rule of thumb is that static deflection, x, is equal to $10/f_n^2$ in inches.

The suspension design can be evaluated using a rigid body model of the test article with appropriate suspension system attachment locations. After adjustments are made to the spring rates to achieve the suspension frequencies, the suspension spring rates can be applied to a flexible model of the structure and further analysis completed.

For many test articles, good suspension system isolation can be achieved by using rubber bands or bungee cord to support the test article. If a single-point support location can be identified, such a system allows five DOFs of the suspension system to be characterized by pendulum behavior, which can yield very low frequencies. The spring rate of the bungee then defines the sixth DOF suspension frequency, which can be adjusted while accommodating the static weight of the article.

Other test articles can be placed on a suspension system made of foam. This is often done when the test article is light weight and the flexible frequencies are quite high. Many new composite structures can be characterized in this fashion. A foam suspension provides good isolation between the rigid body modes and the flexible body modes so that they do not exhibit coupled behavior.

Large aircraft present a variety of suspension challenges. It is difficult to achieve low spring rates with the capacity to carry this large weight and still achieve a sufficiently low suspension frequency. Often the first flexible mode of a large aircraft is near 1 Hz, making suspension isolation difficult. As a result, the suspensions used are often the aircraft landing gear tires. This is analogous to the tires for automotive vehicles, and these cannot typically achieve the low spring rates desired. Suspension system effects can be accounted for in these cases by using FEMs that include the suspension system or by making accurate modal models, which can be used to subtract the suspension system's influence.

4.3 Constrained Support, Built-In, and Other Boundary Conditions

FEMs are effective in providing estimates of completely fixed boundary conditions. These models can be used to plan for the test and perform parametric studies of

the influence of the planned constraint method. Also the model can include any flexibility in future updates.

In cases where a constrained or fixed boundary condition is desired, it is often difficult to achieve a completely fixed condition for actual hardware. Instead, the intent is to develop a boundary condition stiff enough to achieve constraint loads similar to those that would be imposed by a fixed boundary condition. This may be achieved by attaching the test article to a plate or mass that is much larger than the test article. Unfortunately, in many cases, the selected mass may not be large enough to impose a truly fixed base condition. In these cases, a model of the boundary condition and supporting hardware should be included in the FEM.

The boundary condition should be validated by making measurements around the base of the test article to ensure that there is no unexpected motion or excessive participation in the structural test modes. In some cases, the interface loads at the connection between the test article and the boundary constraint can be made to validate the actual interface loads imposed.

4.4 Operating Environments

In planning for the type of boundary condition to be used in a modal test, the operating environment should be strongly considered. The structure's operating environment will influence the modal behavior of the structure, and it is important to capture those effects in the test boundary condition to make sure that similar modal behavior is developed. This will ensure that the strain energy in the test structure is similar to that observed in the operating environment. Since free and fixed boundary conditions can completely alter the modal parameters (including the shapes) of the test article, the strain energy distribution will be substantially different. Therefore, the test boundary condition should be carefully considered in planning for the modal test.

5 Measurement Quality Criteria

There are numerous quality checks that should be planned for in conducting a modal test. These checks will help ensure high-quality FRF measurements so that accurate modal models can be achieved. The quality checks should be performed at various stages over the course of the modal test, and they should be included in test planning and procedure documents to verify that they are properly completed.

During test performance, validation that measurement sensors are providing proper, clean signals is important to all subsequent data processing. All data channels can be assessed visually for signs of problems with connections or signal conditioning. These visual checks can be accomplished by examining the time-domain responses and evaluating the FFT signals. All channels should be reviewed.

All time-domain data should be stored for further review. While storing all time-domain responses was not practical in the past due to storage constraints and data processing capabilities, this is now easily accomplished. Storing all time-domain

data allows many data quality checks to be performed immediately after measuring the data to determine whether more data should be acquired. It also allows the data to be processed using alternative processing techniques, which can also prove useful in the evaluation of data quality.

The review of time-domain data should include an assessment of fundamental statistics, including the peak-to-RMS ratio for the measured data. The peak-to-RMS ratio can provide insight into whether any channel of data experienced intermittent signals or "spikes" during acquisition, as can be caused by loose cables, connections, or structural rattles. Assessing this behavior for each channel allows problems to be identified and corrected before further data is collected.

Review of the time-domain waveforms can also be done to identify when any channel clipping may have occurred. Channel clipping may occur if the signal levels are too high for the data acquisition system input configuration; in this case, the setup can be corrected. Clipping or saturation may also occur in the sensor if the electronics voltage levels are exceeded. This can occur if a sensor is used whose sensitivity is too high for the response levels observed. Changes to the instrumentation or the excitation input levels may be required to account for these issues. Conversely, if the excitation levels are too low, or the sensors have low sensitivity, or the data system input voltage range is set too high, the data may exhibit signs of digitization bit noise. Once the reason for the bit noise is identified, corrections can be made before further testing proceeds.

Following review of time-domain signals, results of data processing can be evaluated using frequency-domain data. Plotting the auto spectra of all channels together can help identify any channels that appear to be out of range of all the other channels, as this can be indicative of a calibration issue or a channel ranging issue.

Coherence is also a standard quality metric that is applied to data channels to evaluate whether the response measured resulted primarily from the applied excitation input. Ranking data channels using overall coherence allows channels with poor coherence to be flagged for further review. Additionally, weight coherence can be computed to bias results toward those channels with low response levels, and order ranking again can be used to identify channels that may need further review.

Drive point reciprocity should be reviewed to assess all excitation inputs and identify any input issues. For these reciprocity comparisons, response measurements must be made at each of the input locations in the same direction as the input, yielding drive point FRFs. Drive point FRFs and drive point reciprocity FRFs help confirm that all shakers are performing properly and yielding high-quality FRFs. At the same time, the power spectra of the force signals should be compared to verify that the excitation levels and frequency range of interest are being achieved.

As the data quality checks are completed and all data channels are confirmed to be operating properly, further quality checks of the modal survey can be conducted by adjusting excitation input levels to check for structural linearity. This check is not so much a check of data quality as a check of the structural behavior observed, and it can also indicate whether high excitation levels result in excessive amounts of noise due to structural rattles.

6 Modal Tests for Model Validation

When a modal test is to be performed for purposes of validating an analytic or finite element model, one needs to design the test so that the resulting measurements will provide the required data for validating or updating the model. There are three key issues to consider in the design of a model validation test: the number and location of response sensors; the number, location, and orientation of the inputs; and the criteria that will be used to judge the validity of the model. Typically, one compares the modal frequencies and mode shapes from the model with those of the test. However, for example, one may want to compare particularly important FRFs, or examine the cross orthogonality between the test mode shapes and the analytical mode shapes [5]. This latter criterion is described more thoroughly in Sect. 6.1.4.

Regardless of the validation criteria, if agreement between the model and the test is not acceptable, uncertain structural parameters may need to be identified and adjusted to improve the agreement. One must measure quantities that are affected by these uncertain parameters, whether the quantities are frequencies, components of the modal vector, rotations, strains, gradients, damping, or other factors. Frequently, it is the uncertain structural parameters one wishes to identify in the modal test. For example, if there were uncertainty about the stiffness of a bolted joint connecting two elements of the structure, one would want to choose instrumentation that would reveal the relative motions across the joint so that a comparison with the model could be conducted. Due to these considerations, one must design the test so as to be relatively certain of making the appropriate measurements, but one should also keep in mind the effort required for testing and avoid making more measurements than necessary.

Fortunately, if validating the model is our objective, then the model is typically available, and it can be used as a tool in the design process. As mentioned above, two of the key issues are sensors and inputs. Regarding the sensors, the number, direction, and location must be chosen so that a correspondence between the analysis and the measured mode shapes can be obtained. One cannot assume that the numerical order of the modes measured in the test will align with those from the analysis, so being able to differentiate between mode shapes is critical, and all the mode shape vectors must be relatively independent; otherwise, differentiation will be very difficult. Consequently, the inner products between all the shape vectors need to be relatively small. The discussion that follows in Sect. 6.1 addresses only the first issue – the response sensors – with a review of various approaches for selecting an optimal set of measurement locations and directions.

Regarding the input excitation, the various approaches to developing an adequate excitation design are discussed in Sect. 6.2. For all the approaches, the primary requirement is that an excitation must be designed so that all the target modes are excited to the degree that they are fairly easily (and thus accurately) identified and estimated from the measurements. However, this brings up another issue, that of the target modes. As part of the design process, one must determine the number and the character of the target modes. In some tests and analyses, one may be concerned with only a few modes that dominate the dynamic behavior. In other tests, one

may need to examine many modes to characterize all the important dynamics of the structure.

One more issue involved in the design of any modal test is the ability to visualize the mode shapes once they have been estimated. This is most important for the test engineer so that he or she can visualize the shapes and ascertain the accuracy of the mode shape estimation. All too frequently, a sensor will have the wrong direction, position, or polarity associated with it, but the visualization of the shapes will frequently resolve these issues. Consequently, in selecting a set of measurement locations, one needs to start with a visualization or intuition set. Then, locations can be added to that set to optimize the design requirement, as discussed in the sections below.

6.1 Selecting Response Locations

FEMs in general contain many more DOFs than could ever be instrumented with accelerometers during a modal test. Therefore, a subset of DOFs must be selected for measurement in the test. The selection of these DOFs must be based on the figure of merit for the modal survey test. In many cases, the figure of merit may be mode shape visualization or the ability to identify and quantify sources of compliance of a load path in the model, such as compliance across joints. In these cases, manual selection of a preliminary set of response locations may be very useful. In cases where the figure of merit includes a mathematical objective function, such as mode shape independence, automated methods are useful to supplement the manual selection.

Automated procedures for selecting appropriate accelerometer locations are most often required in the cases of complex structures or when only a small number of accelerometers are available. In any case, it is important to remember that automatic sensor placement techniques can never totally supplant engineering judgment. The test and analysis engineers must still be proactive in the placement of sensors; the DOFs from an automatically selected sensor set must be further studied to determine whether the set makes sense and whether any DOF has been included at which it is physically impossible to place a sensor. Also, rotational DOFs are usually not included in the sensor set unless there exists a large mass with a large rotational inertia, because rotational acceleration cannot easily be measured.

Goals in selection of the test response DOFs are as follows:

1. Ability to visualize all unique target mode shapes
2. Ensuring the independence of the mode shapes evaluated at those response DOFs, that is, small shape-vector inner-products
3. Identifying responses at key structural locations and joints where needed

6.1.1 Modal Kinetic Energy

The first automatic technique that is discussed, modal kinetic energy, is for use with the static reduction method [17]. See, for example, Shah and Udwadia [29], Udwadia and Garba [31], and Salama et al. [28]. For an accurate static test-analysis

model (TAM), we must retain in the sensor set all the DOFs that have large deformations in the target modes or possess a lot of mass. In addition, the sensor set should be somewhat evenly distributed over the structure. The sensor DOFs must render the sensor partition of the FEM target modes linearly independent or the TAM will not predict all the target modes. Assuming that each target mode of interest is mass normalized, the FEM mode shapes satisfy the relation $\phi_i^T M \phi_i = 1.0$, and we need to determine the fractional contribution of each candidate sensor DOF to the modal generalized mass. Let us consider just the i^{th} mode. The contribution of the j^{th} DOF to this i^{th} mode generalized mass is given by

$$ke_{ij} = \phi_{ij} \sum_{k=1}^{n} M_{jk} \phi_{ik} = \phi_{ij} M_j \phi_i \tag{15}$$

in which ϕ_{ij} is the j^{th} row of the i^{th} target FEM mode shape corresponding to the j^{th} DOF, M_{jk} is the entry in the j^{th} row and k^{th} column of the FEM mass matrix, M_j is the j^{th} row of the FEM mass matrix, and n is number of FEM DOFs. This contribution is a fractional one because if the value is computed for each FEM DOF and summed over all the DOFs, the total must naturally be 1.0, corresponding to the value of the i^{th} generalized mass.

Using the above computation, one can generate a column vector ke_i for each mode shape listing the contribution of each DOF. Ultimately, one wants a single measure of importance for each DOF over all the target modes. Note that modal kinetic energy gives us no information as to the importance of one mode with respect to another, so we will treat them all equally. One way of coming up with a single measure of goodness is to average each DOF's importance over all the target modes:

$$KE = \frac{1}{n_m} \sum_{i=1}^{n_m} ke_i \tag{16}$$

where ke_i is a column vector containing the contribution of each of the degrees of freedom j to the kinetic energy of the i^{th} mode.

The vector *KE* provides a listing of the fractional importance of each FEM DOF. This vector can then be sorted from high to low. This computation is usually performed for a large candidate set of sensor DOFs. The modal kinetic energy is then used to either truncate the low-energy DOFs all at once, or one candidate sensor at a time can be deleted. At each iteration, the lowest-energy candidate sensor is deleted from the candidate sensor set. That DOF is statically reduced out of the mass matrix, and then the kinetic energy distribution is recomputed and sorted.

6.1.2 Effective Independence

The modal kinetic energy approach to sensor placement is dictated by the requirements of the accurate use of the static reduction technique for TAM generation. In contrast, the Effective Independence (*EfI*) technique [20] approaches the sensor

placement problem from the standpoint of a structural dynamicist who must use the modal parameters identified during a modal test to perform test-analysis correlation [18] and FEM updating. It is vital that the targeted test mode shapes are linearly or spatially independent. As in the case of modal kinetic energy, the sensor placement process begins by designating a large set of candidate sensor locations from which the smaller final sensor configuration will be selected. The modal kinetic energy distribution, presented in Eq. (16), can be used to help determine a good candidate sensor set.

The objective of the *EfI* sensor placement strategy is to select sensor locations that render the FEM target mode shape partitions as linearly independent as possible while at the same time retaining as much information as possible about the target modal responses within the sensor data. Independence of the target mode partitions is required such that the test data can be used in test-analysis correlation as mentioned previously. The sensor placement problem can be alternatively cast in the form of a state estimation problem. The target mode independence requirement implies that at any time t, the sensor output can be sampled and the target modal response can be estimated. A static Fisher model is assumed for the output equation of the form

$$y_s = \phi_{fs} q + w \tag{17}$$

in which y_s is the response at the sensor locations, ϕ_{fs} is the matrix of FEM target mode shapes partitioned to the sensor degrees of freedom, q is the target modal response, and w is the sensor noise. It can be shown that the best estimate of the modal response is obtained by minimizing the error covariance matrix, which is equivalent to maximizing the Fisher information matrix (FIM). Therefore, the sensors should be placed such that the FIM is maximized in the appropriate matrix norm. Details can be found in Kammer [20].

Assuming we know nothing a priori about the sensor noise, the corresponding FIM is given by

$$Q = \phi_{fs}^T \phi_{fs} \tag{18}$$

Maximization of the FIM determinant has been a commonly used criterion for optimal parameter estimation. It is suggested here that maximization of the information matrix determinant is also appropriate for optimal sensor placement. The form of the information matrix presented in Eq. (18) indicates that if the target modal partitions are not linearly independent, the determinant will be zero. Therefore, maximizing the information matrix determinant will maximize the spatial independence of the target modal partitions as desired. It will also maximize the signal strength of the target modal responses in the sensor output, which is very desirable in the presence of noise. Thus, for the purpose of sensor placement using a state estimation formulation, the determinant is the appropriate measure of the size of the FIM.

The *EfI* method approaches the problem by determining how much each sensor location contributes to the eigenvalues of the FIM. For n_m target modes, the positive definite and symmetric information matrix possesses a set of n_m orthonormal eigenvectors and positive eigenvalues λ. The eigenvectors represent orthogonal unit directions in an n_m -dimensional identification space. In the matrix G formed by the product

$$G = \left[\phi_{fs}\Psi\right]^{\wedge 2} \tag{19}$$

in which the symbol $^{\wedge 2}$ indicates a term-by-term multiplication, each row contains the squares of the components of the corresponding row of ϕ_{fs} in terms of the coordinates defined by the eigenvectors Ψ. Each column of matrix G sums to the corresponding eigenvalue of FIM Q. Therefore, the i^{th} term in the j^{th} column of G represents the contribution of the i^{th} sensor location to the j^{th} eigenvalue of Q. Normalizing G by post-multiplying by the inverse of the eigenvalue matrix produces

$$F_E = \left[\phi_{fs}\Psi\right]^{\wedge 2}\lambda^{-1} \tag{20}$$

where now the directions in identification space are all of equal importance and the ij^{th} term in F_E represents the fractional contribution of the i^{th} sensor location to the j^{th} information matrix eigenvalue. Adding the terms within the rows of F_E produces an n_c dimensional vector called the Effective Independence Distribution, which is given by

$$E_D = \left[\phi_{fs}\Psi\right]^{\wedge 2}\lambda^{-1}\{1\}_{n_m} \tag{21}$$

in which $\{1\}_{n_m}$ is a column vector of 1's of dimension n_m. The sum of the terms in column vector E_D is n_m, which is the rank of the FIM and the target modal partition ϕ_{fs}. It can be shown that individual values E_{Di} of vector E_D satisfy the relation $0 \leq E_{Di} \leq 1.0$, where a value of 0.0 indicates that the i^{th} sensor contributes nothing to the linear independence of the target modes or even their observability, and a value of 1.0 indicates that the corresponding sensor is absolutely vital to the independence of the target modes and thus cannot be deleted from the candidate set.

As mentioned previously, the initial candidate sensor set is selected such that ϕ_{fs} is full column rank implying that Q is positive definite. Entries in vector E_D are sorted by magnitude, and the lowest-ranked sensor is deleted from the candidate set. Remaining sensor locations are then ranked and sorted again. In an iterative fashion, the initial candidate set of sensor locations is rapidly reduced to the number allotted for the modal test. It is important to note that candidate sensor locations must be deleted in an iterative fashion and not all at once to obtain the desired number, because as sensor locations are deleted, their *EfI* value E_{Di} changes such that the sum of the *EfI* distribution vector E_D remains at n_m. Therefore, deletion of large numbers of sensors in one iteration may lead to the removal of a vital sensor location, resulting in the loss of linear independence of the target mode partitions.

As suggested, the determinant is the appropriate measure of the size of the FIM for the state estimation problem in Eq. (17) and thus also the sensor placement problem for modal identification. It is a direct measure of the amount of target modal response information contained in the sensor data, and it can be used to determine the goodness of one sensor set with respect to another. It can be shown that the *EfI* of the i^{th} sensor location E_{Di} represents the fractional change in the determinant of the FIM when the corresponding sensor location is removed from the candidate set [27]. It is important to note that whenever a sensor is removed from the candidate sensor set, the determinant decreases. When the lowest-ranked sensor is removed at each iteration, the remaining sensor locations produce the largest possible FIM determinant. Therefore, even though the *EfI* method of sensor placement is suboptimal due to its iterative nature, it tends to maintain the determinant of the FIM, which leads to a smaller error covariance matrix and better estimates of the target modal response.

As an example, consider sensor placement for a simple unconstrained beam representation of a large space structure with a concentrated mass at the midpoint equal to three quarters of the mass of the beam itself. The finite element representation, illustrated in Fig. 16, was constructed using 22 grid points and 21 elements. Each grid possesses a transverse and a rotational DOF. The first ten mode shapes and frequencies were computed, which include two rigid body modes and eight elastic modes. The first seven elastic mode shapes were selected as target modes to be identified during a modal test. All 22 transverse displacement DOFs were considered in an initial candidate sensor set. Figure 17 presents each of the initial 22 sensor locations' fractional contributions to the target mode independence; this is essentially a ranking of the importance of prospective sensor locations to the

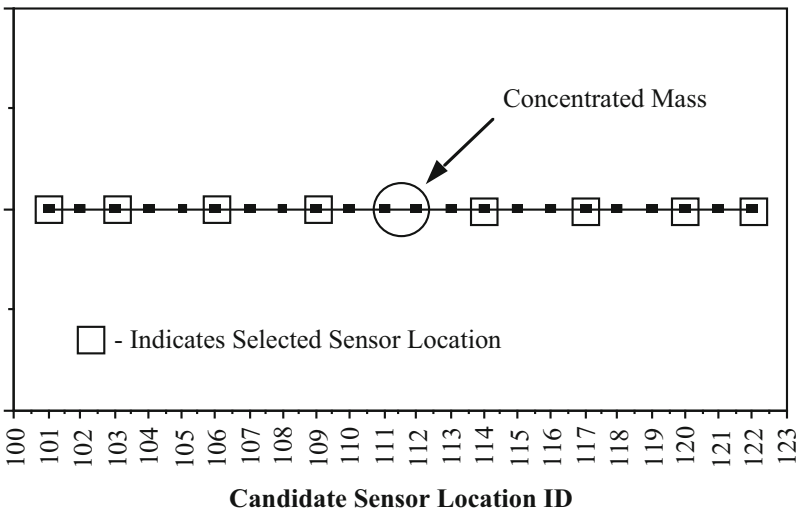

Fig. 16 Simple beam model with central concentrated mass

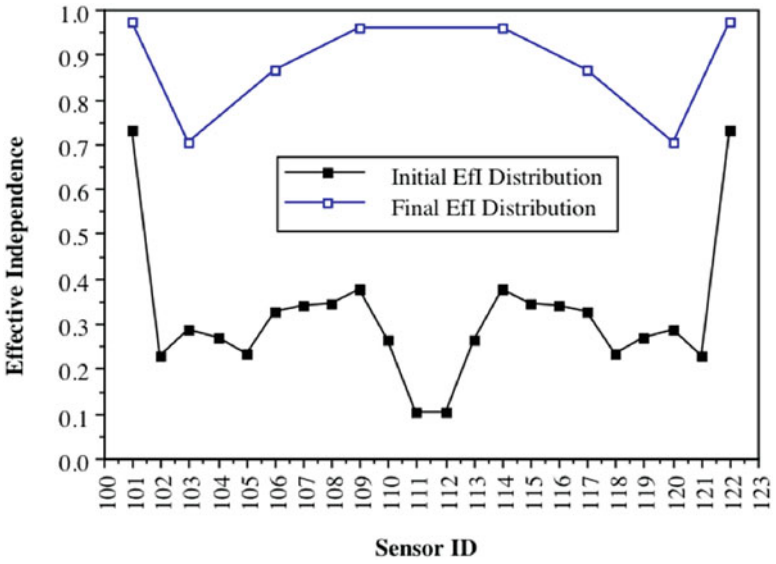

Fig. 17 Fractional contribution of sensor locations to linear independence

success of the modal survey. As expected for this case, the beam endpoints are the most important locations. Note, however, that none of the locations is vital to independence for the initial set.

Fourteen iterations were used to reduce the initial candidate sensor set to a final configuration of eight sensors which maintains the determinant of the FIM and the linear independence of the target modes. The eight selected sensor locations are illustrated in Fig. 16, and the corresponding *EfI* distribution for the selected configuration is pictured in Fig. 17. Note that the *EfI* values for the sensor locations in the final configuration are larger than their initial values in the original candidate set; as sensors are deleted, the remaining locations become more important and, in some cases, the relative importance of sensors changes. For instance, in the initial *EfI* distribution, sensor 116 was more important that sensor 120; however, as sensors were deleted, location 120 surpassed 116 in importance and was selected for the final configuration while 116 was deleted.

The *EfI* method for sensor placement has another advantage in that the distribution for the final configuration indicates the cost of losing a sensor. This information can be used to place backup sensors when necessary, such as in on-orbit modal identification. The *EfI* technique of sensor placement provides sensor configurations that produce independent target mode partitions that an analyst can use to perform test-analysis correlation and then model updating. It has also been shown that this approach to sensor placement enhances the actual identification of the target modes during a modal survey [21]. The method can also be extended to include DOF mass weighting [23] and the placement of triaxial sensors [22].

6.1.3 Min-MAC

The Min-MAC approach to sensor selection is quite straightforward [8]: response sensor locations and directions are simply chosen to minimize the off-diagonal elements of the modal assurance criterion (MAC) matrix [1, 15]. To easily distinguish one mode shape vector from another, the inner product between the two vectors, normalized by the vector lengths, must be relatively small. The normalized inner product is merely the cosine of the angle between the vectors. If the cosine is near ± 1, the vectors are close to parallel; if the cosine is small, the vectors are very independent and easily distinguishable. The commonly used MAC matrix can be utilized to evaluate the square of the cosine between the shape vectors as given below.

$$MAC_{ij} = \frac{\left(\varphi_i^H \varphi_j\right)^2}{\left(\varphi_i^H \varphi_i\right)\left(\varphi_j^H \varphi_j\right)} \tag{22}$$

where φ_i and φ_j are the mode shape vectors for the i^{th} and j^{th} modes. The superscript H indicates the Hermitian of the vector or just the complex-conjugate transpose. For real vectors obtained from a FEM, the Hermitian reduces merely to the transpose, and the MAC is simply computed using vector transposes as a real quantity. By examining the off-diagonal terms in the MAC matrix, using modal vectors computed from a detailed FEM, that are evaluated (or partitioned) only at a reduced set of DOFs, we can determine whether a set of sensors at those DOFs will be a good design for obtaining independence of the vectors. Thus, our design criterion is to require all the off-diagonal elements of the MAC matrix to be relatively small.

The MAC matrix uses an identity-weighting matrix (not the mass matrix), so one should not expect the off-diagonal terms to be zero, which implies orthogonality. Orthogonality of the vectors is not necessary; their MAC values need only be small (e.g., 0.2) so that vectors are easily distinguishable. Mathematically, any MAC value less than 1 would reveal two unique independent vectors. However, the MAC values between the test vectors must be small because when the analysis shape vectors are aligned or compared with the test shape vectors with the MAC computation as a guide, the test-analysis cross-MAC values may actually not be near unity if there is significant error in the FEM or significant experimental error in the measurement or estimation of the shape vectors.

In the introduction to this section, the visualization or intuition set was discussed. This set of response locations and directions is important for enabling the test engineer to visualize the deformed mode shapes and identify any measurement errors and to characterize the various modes. This visualization set is then used to initialize the selection process in Min-MAC. For a complex multidimensional structure like a satellite or car body, one might use only triaxial sensors in the visualization set. This allows the shapes to be immediately visualized without depending upon any transformation based on the model to fill in the omitted DOFs for a full three-dimensional visualization. This does increase the number of sensors used, but it significantly increases the robustness of the design for visualization.

Alternatively, one can intuitively select single-direction sensors, which will still reveal the fundamental shapes of the measured modes.

After the small visualization set has been defined, a procedure is used to add one sensor at a time, choosing from the DOFs remaining in the FEM to reduce the off-diagonal MAC values to an acceptable magnitude. This procedure is described subsequently. However, this approach is in significant contrast to many other design techniques. Here, the sensor set in initialized using a small visualization set and additional DOFs are added one at a time, whereas other approaches start with the entire set of available DOFs and attempt to reduce that number to a manageable set. It will be subsequently shown that there is a tremendous numerical advantage in starting small and increasing rather than starting with a large set of DOFs and paring down: with this procedure, a very large FEM can be used without computational difficulties or excessive time required.

This numerical procedure is next described in detail. As discussed earlier, the goal of this technique for sensor selection is to reduce the magnitude of off-diagonal elements of the MAC matrix by adding one sensor at a time to the initial set or the current set. Thus, a method is required for evaluating the effect of adding a single additional sensor on the MAC matrix.

Let $\Phi(n \times m)$ and $\Psi(p \times m)$ denote the mode shape matrices for the existing set and the remaining set of DOFs from the FEM, respectively, where n is the number of DOFs in the current set, p is the number of remaining DOFs from which to select, and m is the number of modes. The MAC value between modes i and j is

$$MAC_{ij} = \frac{{a_{ij}}^2}{a_{ii}a_{jj}} \tag{23}$$

where a_{ij} are the elements of $A = \Phi^{\mathrm{T}}\Phi$. When a new response is added to the Φ from the Ψ, for instance row k of Ψ, the MAC value between modes i and j with the added DOF k becomes

$$\left(MAC_{ij}\right)_{+k} = \frac{\left(a_{ij} + \psi_{ki}\psi_{kj}\right)^2}{\left(a_{ii} + \psi_{ki}\psi_{ki}\right)\left(a_{jj} + \psi_{kj}\psi_{kj}\right)} \tag{24}$$

Examination of Eq. (24) shows that evaluating a candidate sensor only requires five multiplications, three additions, and one division per MAC matrix element. The simplicity of this equation makes it possible to efficiently evaluate the influence of a large number of candidate DOFs on the MAC matrix.

After a response DOF is chosen to be added to the existing set, the matrices Φ, Ψ, and A are updated to reflect the changes. One can then continue this process for evaluating candidate DOFs. Of all the DOFs available, the DOF leading to the smallest maximum above-diagonal MAC value in the entire matrix is then included. This method requires the use of Eq. (24) $m(m-1)p/2$ times for each added sensor. Of course, one can limit the range of p to be a subset of all available DOFs in the

FEM; realistically, one might choose 1000 or so candidate DOFs from the entire FEM to be considered for sensor placement.

To illustrate the use of Min-MAC technique, an example application is described below for which the technique was applied to an automotive body structure. As previously described, an initial visualization sensor set was selected based on intuition. For the car body, 34 nodes were selected with all three DOFs, as triaxial sensors were to be used for the modal test, creating an initial set of 102 DOFs. This is more than one would ordinarily use, but it did provide excellent visualization. Now using the FEM, the 11 mode shape vectors with the lowest frequencies were partitioned down to these 102 DOFs, and the MAC matrix was formed to determine the off-diagonal values. (The diagonal values of the self-MAC are unity, of course, in contrast to a cross-MAC between the FEM modes and the test modes.) Table 1 shows the full MAC matrix (11 by 11), which is symmetric, for the shapes using this initial visualization set of DOFs. In this matrix, one can see that two of the off-diagonal elements are fairly large. In particular, element (3,5) has a value of 0.51 and element (5,7) has a value of 0.60. This is an unacceptable design, as mode shapes 5 and 7 will appear similar, as will mode shapes 3 and 5. An estimated test mode shape could easily have a MAC value of 0.5 with both modes 5 and 7, and there would be no way of determining the correspondence between the test and analysis modes.

Now, the Min-MAC algorithm is applied using the analysis mode shapes from the FEM to reduce the off-diagonal MAC values by adding one DOF at a time. The result of adding DOFs to the existing set is shown in Table 2.

Table 1 MAC matrix for initial set based on mode visualization and intuition

Mode Number	1	2	3	4	5	6	7	8	9	10	11
1	1.00	0.01	1.00	0.00	0.00	0.16	0.00	0.00	0.02	0.00	0.01
2		1.00	0.00	0.00	0.00	0.00	0.00	0.00	0.01	0.00	0.00
3			1.00	0.16	0.51	0.00	0.25	0.02	0.00	0.01	0.00
4				1.00	0.21	0.00	0.00	0.21	0.00	0.00	0.00
5					1.00	0.00	0.60	0.23	0.00	0.09	0.05
6		Symmetric values				1.00	0.00	0.00	0.14	0.06	0.10
7							1.00	0.00	0.00	0.24	0.15
8								1.00	0.00	0.10	0.06
9									1.00	0.00	0.00
10										1.00	0.04
11											1.00

Table 2 Maximum off-diagonal MAC values for the added sensors

Added sensors	0	1	2	3	4	5	6	7	8	9	10
Largest MAC values	0.598	0.232	0.203	0.185	0.175	0.179	0.163	0.159	0.157	0.152	0.149

Notice that with ten additional DOFs (or sensors), the maximum off-diagonal MAC value has been reduced to below 0.15. There were actually four MAC values of 0.15 with this design. For purposes of comparison, the MAC matrix using all the DOFs in the entire FEM was computed. The maximum off-diagonal MAC value was 0.12 – virtually the same as the design with just 112 sensors.

In conclusion, the Min-MAC procedure for selecting sensors is initialized with a small intuition or visualization set, and then sensors are added to reduce the off-diagonal MAC elements. This procedure addresses both the visualization and the vector correspondence issues. The procedure is very efficient numerically, as it starts with a small set and adds sensors one at a time, and it confers a tremendous numerical advantage that can be used when computing off-diagonal MAC elements, given you already have the MAC matrix for the vectors with one less component included in the vectors. With this procedure, one can evaluate an extremely large set of DOFs from a FEM without difficulty and directly obtain a sensor set that reduces the off-diagonal MAC elements.

6.1.4 Aerospace Cross-Orthogonality; TAMs

It is important to establish the goals and instrumentation response locations during the test planning stage when the test mode shapes will be used to help validate a FEM. The test mode shapes can be most successful and easily compared to those of the FEM when a TAM is developed from the FEM during test preparation. This TAM provides the specific DOFs that will be compared between the test and analysis modal models. In the test planning activity, this TAM can be used to determine how many DOFs or response measurements are needed and where they need to be located to meet the comparison goals that will be applied. This determination of DOFs establishes the FEM mass matrix that will be used in orthogonality and cross-orthogonality comparisons, as well as the partitioned analysis mode shapes to be used in the cross-orthogonality checks [5].

The possible success of the test sensor set is evaluated by using the full FEM mode shapes, partitioned to the test DOFs, and computing the pseudo-orthogonality relative to the TAM mass matrix. The pseudo-orthogonality can be computed with the mode shapes unnormalized and then normalized for a unit diagonal orthogonality matrix, just as would be done during the test. These computations allow assessment of whether all of the system mass has been captured at the test DOFs and whether the test DOFs provide an independent set of modes. The modes acquired from the partitioned FEM shapes are checked for orthogonality using the TAM analytical mass matrix. The orthogonality matrix $[O_{12}]$ is computed from the following matrix product.

$$[O_{12}] = [\Phi_1]^T [M_{AA}] [\Phi_2] \tag{25}$$

When checking the DOFs for orthogonality as would be obtained in the test, the terms $[\varphi_1]$ and $[\varphi_2]$ are mode shape matrices (normalized to $[M_{AA}]$ to produce 1.0 on the $[O_{12}]$ diagonal), and $[M_{AA}]$ is the TAM analytical mass matrix. The pseudo-

orthogonality of the partitioned FEM mode shapes relative to the TAM mass matrix is computed from Eq. (25) with $[\varphi_1] = [\varphi_2]$.

It is important to note that the DOFs preserved in the mass matrix match the DOFs of the analysis TAM, which also match the response locations to be used in the test. Proper selection of these DOFs is important to the ability to achieve good orthogonality. A good set of DOFs for the TAM does not require that three DOFs be measured at each test node described; instead, it is usually more effective to distribute the response measurements around the structure with measurements at key locations that have high mass weighting. Sometimes these will yield three-DOF measurements at individual points, but usually numerous locations will be developed with one-DOF and two-DOF responses. In this way, pretest evaluation of the selected DOFs and resulting possible orthogonality results help in defining the most effective response measurement set for the test.

6.2 Selecting Input Locations, Directions, and Number

Good test planning should include taking steps to identify the specific locations, number, and directions of the inputs to be used in the modal test. Evaluation and selection of input locations can involve engineering judgment; however, more rigorous selection steps can and should be taken particularly when a FEM is available for pretest planning. This selection is an important step in the test planning effort as using a good set of input locations can strongly influence the quality of the modal test data.

6.2.1 General Guidelines

Candidate sets of possible input locations can be assembled by reviewing locations that are accessible and show acceptable modal participation. These candidate locations can supplement the other measurement DOFs that have been defined for the test; however, the input locations are often co-located with other measurement locations. Alignment with the local and global coordinate systems is not required, and it is frequently beneficial to use inputs that are not aligned with any of the coordinate directions. Inputs need to be defined in number and orientation such that the most modes are effectively excited. It is not necessary to use locations that are part of the measurement set or part of the test display model. However, drive point accelerometers co-located and aligned with the input directions should always be installed, as doing so ensures that reciprocity comparisons can be made during data quality checks.

In general, the number and locations of exciters should be selected so as to be able to excite all modes of interest. If possible, they should be placed at stiff points on the structure that are designed to carry static loads so that the vibration energy can be distributed throughout the structure. Using multiple input locations increases the likelihood of exciting all of the modes. Pretest planning with the FEM can help

in identifying the appropriate locations: FRFs can be computed to reveal whether a location is predicted to excite many of the modes.

It is also important that expected response levels be acceptable. Again, response levels can be predicted using the FEM. This does require some assumptions of the amount of damping in the structure, but this can be reasonably estimated based on other test articles, where available, and other engineering information. Predicted response levels can be used to match sensor measurement capabilities and sensitivities to ensure that proper modal signal levels can be observed.

6.2.2 Selection of Locations

It is possible to select modal input locations using ad hoc approaches simply by looking at the structure and estimating which locations might be effective for exciting the structure, and these input locations can often be selected with regard to convenience. However, it is usually best to perform some evaluation of the drive point FRFs to assess whether input locations selected in this fashion will provide acceptable results.

As an initial step, impact testing approaches can be used to assess input locations when shakers are going to be installed. Measuring the drive point FRFs using hammer impacts will show whether acceptable FRFs can be obtained from the specific locations and specific directions evaluated, and numerous drive points can be evaluated and compared. From these, the best locations can be selected with an appropriate number of locations that indicate excitation of all modes in the frequency range of interest.

A valuable tool for selecting the input locations is the mode-indicator function (MIF) [8, 26, 32]. This tool can be used whether the input locations are identified analytically using the FEM or experimentally using the measured results from a candidate input. The FRFs are used to compute the MIFs associated with each input location, which allows assessment of whether all modes of interest are excited. With MIFs computed using FRFs from the FEM, an automated procedure can be developed to identify an acceptable set of input locations and directions. Minimum criteria of the MIF can be defined and evaluated across all of the possible input locations, and candidate inputs can then be selected to determine the best combinations of input locations and directions.

6.3 Planning the Criteria for "Test Exit"

Specific goals and test evaluation metrics should be included in the test planning for a modal test. These provide tools to assess whether sufficient testing has been completed to meet the overall objectives of the test. Test objectives are not always the same, so they need to be clearly stated during the planning stage. There are numerous objectives that can be listed in terms of the modal parameters to be identified, such as the following:

- Mode independence checks
  - Modal Assurance Criteria (MAC)
    - Criteria for specific off-diagonal values
    - Criteria applied to only specified target modes
  - Orthogonality
    - Mass weighting derived from FEM TAM
    - Criteria to achieve specific off-diagonal values
    - Criteria applied to only specified target modes; effective mass weighting is often used
- Mode completeness
  - All target modes identified
  - Comparison to analysis target modes
    - MAC
    - Orthogonality
    - Root Sum Square of orthogonality terms

The target modes can be defined a number of ways, such as the following:

- All modes within a specified frequency range
- First *n* modes
- Modes defined using various criteria such as effective mass weighting

Establishing specific goals and metrics to be used in assessing the modal results during test planning enables a clear evaluation path to be used in checking the modal results. Some or all of these criteria may be applied depending on the overriding reason for conducting the modal test. In cases where simple exploratory testing is being performed, it may be sufficient to identify the first three flexible structural modes, for example, without any other criteria. This criterion seems rather simple but may serve the purpose of the test program. An even simpler criterion might be to identify the first three *frequencies*, with no mode shapes. While this might seem an oversimplification, it too may satisfy the test objectives in certain cases.

In most cases, however, the criteria applied are more extensive and require an assessment of the modal parameters extracted from the test. MAC is often used as a tool to check test mode shapes, particularly when an analysis model is not available for comparison. Even if the model is available, cross-MAC might be a good check if the model has not been used to develop a TAM and corresponding mass matrix, as it helps in assessing whether the test mode shapes are comparable to those predicted by analysis for both frequency and shape.

Orthogonality provides a more complete and rigorous assessment of the test mode shapes than simply looking at MAC. This is particularly true for aerospace structures where the mass normalization of the mode shapes helps ensure that the modes' mass-weighted behavior is checked, since the mass of the elements in the mode shapes can skew the overall comparisons. Small, lightweight components can have large mode shape coefficients, which cause mode shapes to appear similar even though they do not produce substantial loads. Orthogonality (test results against

themselves) and cross-orthogonality (test versus analysis) are typical criteria applied in detailed aerospace modal tests. For orthogonality, mass weighting is applied to provide unit diagonal terms, and then the off-diagonal terms are evaluated to see whether there is any shape coupling. Typical criteria are 10% or less for all off-diagonal terms for all target modes.

As a result of test shape normalization, cross-orthogonality does not yield a unit diagonal matrix. Instead, the terms closest to 100% provide an indication of similarity between test and analysis shapes. Since differences between the model and the physical test structure can result in various combinations of modal behavior and shapes, it is often necessary to also check for the Root Sum Square of the cross-orthogonality terms to determine whether various combinations of extracted test shape behavior match those predicted by analysis.

In summary, developing an appropriate list of test criteria during the test planning effort ensures that the right tools are in place for conducting these final checks to ensure that the test has been successfully completed. Evaluating the criteria before the test is started enables a good understanding of the methods that will be used to assess test result quality and to determine when testing can be considered complete.

7 Closure

In conclusion, planning or designing a modal test is just as important as the data collection or the data analysis. One needs to clearly identify the objectives of the test and the stake holders; then develop a test design that supports the realization of those objectives. When a modal test is to be performed to validate a finite element model, one needs to design the test so that the resulting measurements will provide the data required for the correlation of modeling results with those from the test. From a correlation perspective, one needs to select the response locations to allow a definitive, one-to-one correspondence between the measured modes and the predicted modes. Further, the excitation must be designed to excite all the modes of interest at a sufficient level so that the modal estimation algorithms can accurately extract the modal parameters.

References

1. Allemang RJ, Brown DL (1982) A correlations coefficient for modal vector analysis. In: Proceedings of the 1st international modal analysis conference, pp 110–116
2. Avitabile P (1998) Which shaker excitation is best? Is there any difference? SEM Experimental Techniques. https://www.uml.edu/docs/dec98_tcm18-189813.pdf
3. Avitabile P (2006) Modal space, back to basics. Exp Tech 30(3):19–20
4. Bisplinghoff RL, Ashley H, Halfman RL (1955) Aeroelasticity. Addison-Wesley Publishing Company, Cambridge, MA, pp 771–779
5. Blelloch PA (1992) Direct correlation of test-analysis cross-orthogonality. In: Proceedings of the 10th international modal analysis conference, pp 999–1003

6. Brillhart R, Hunt D (2005) Lessons learned in modal testing—part 1: the pitfalls, pratfalls, and downfalls of fixturing. Exp Tech 29(6):58–61
7. Brown DL, Allemang RJ, Phillips AW (2015) Forty years of use and abuse of impact testing: a practical guide to making good FRF measurements. In: De Clerck J (ed) Experimental techniques, rotating machinery, and acoustics, vol 8. Conference proceedings of the society for experimental mechanics series
8. Carne TG, Dohrmann CR (1995) A modal test design strategy for model correlation. In: Proceedings of the 13th international modal analysis conference, pp 927–933
9. Carne TG, Stasiunas EC (2006) Lessons learned in modal testing—part 3: transient excitation for modal testing, more than just hammer impacts. Exp Tech:69–79
10. Carne TG, Lauffer JP, Gomez AJ (1988a) Modal testing of a very flexible 110m wind turbine structure. In: Proceedings of the 6th international modal analysis conference, pp 845–855
11. Carne TG, Lauffer JP, Gomez AJ (1988b) Modal testing of an immense flexible structure using natural and artificial excitation. Int J Anal Exp Modal Anal 3(4):117–122
12. Carne TG, Griffith DT, Casias ME (2007a) Support conditions for free boundary-condition modal testing. In: Proceedings of the 25th international modal analysis conference
13. Carne TG, Griffith DT, Casias ME (2007b) Support conditions for experimental modal analysis. Sound and Vibration Magazine, pp 10–15
14. Deiters T, Hunt D, Osborne E (1994) A comparison of excitation methods to the Taurus vehicle modal test. In: Proceedings of the 12th international modal analysis conference
15. Ewins DJ (1984) Modal testing: theory and practice. Wiley, New York, p 225
16. Ewins DJ (2000) Modal testing: theory and practice and application, 2nd edn. Research Studies Press, Letchworth
17. Guyan RJ (1965) Reduction of mass and stiffness matrices. AIAA J 3:380
18. Hasselman TK, Coppolino RN, Zimmerman DZ (2000) Criteria for modeling accuracy – a state-of-the-practice survey. In: Proceedings of the 18th international modal analysis conference
19. James GH, Carne TG, Lauffer JP (1995) The natural excitation technique (NExT) for modal parameter extraction from operating wind turbines. Int J Anal Exp Modal Anal 10(4):260–277
20. Kammer DC (1991) Sensor placement for on-orbit modal identification and correlation of large space structures. J Guid Control Dyn 14:251–259
21. Kammer DC (1996) Optimal sensor placement for modal identification using system-realization methods. J Guid Control Dyn 19(3):729–731
22. Kammer DC (2004) Optimal placement of triaxial accelerometers for modal vibration tests. Mech Syst Signal Process 18:29–41
23. Kammer DC, Peck J (2008) Mass weighting for sensor placement using sensor set expansion techniques. Mech Syst Signal Process 22:1515–1525
24. Klosterman AL (1971) On the experimental determination and use of modal representations of dynamic characteristics. Doctor of philosophy dissertation, Department of Mechanical Engineering, University of Cincinnati
25. Maia NMM, Silva JMM (1997) Theoretical and experimental modal analysis. Research Studies Press, Baldock, p 32
26. Napolitano, KL , Blelloch PA (2003) Automated selection of shaker locations for modal tests. In: Proceedings of the 21st international modal analysis conference on structural dynamics
27. Poston WL, Tolson RH (1992) Maximizing the determinant of the information matrix with the effective independence method. J Guid Control Dyn 15:1513–1514
28. Salama M, Rose T, Farga J (1987) Optimal placement of excitation and sensors for verification of large dynamical systems. In: Proceedings of the 28th AIAA/ASME structure, structural dynamics, and material conference, pp 1024–1031
29. Shah PC, Udwadia FE (1978) Methodology for optimal sensor locations for identification of dynamic systems. J Appl Mech 45:188–196
30. Slater JC, Belvin WK, Inman DJ (1993) A survey of modern methods for modeling frequency dependent damping in finite element models. In: Proceedings of the 11th international modal analysis conference, pp 1508–1512

31. Udwadia FE, Garba JA (1985) Optimal sensor locations for structural identification. In: JPL Proceedings of the workshop on identification and control of flexible space structures, pp 247–261
32. Williams R, Crowley J, Vold H (1985) The multivariate mode Indicator function in modal analysis. In: Proceedings of the international modal analysis conference, pp 66–70
33. Wolf JA Jr (1984) The influence of mounting stiffness on frequencies measured in a vibration test. SAE Paper 840480, Society of Automotive Engineers

Experimental Modal Analysis Methods

10

R. J. Allemang and D. L. Brown

Contents

R. J. Allemang (✉) · D. L. Brown
Structural Dynamics Research Laboratory, Mechanical and Materials Engineering, University of Cincinnati, Cincinnati, OH, USA
e-mail: randall.allemang@uc.edu; david.l.brown@uc.edu

R. Allemang, P. Avitabile (eds.), *Handbook of Experimental Structural Dynamics*,
https://doi.org/10.1007/978-1-4614-4547-0_36

Abstract

This chapter provides the basis and background of all experimental modal analysis (EMA) methods that have been developed over the last fifty years. In this context, modal parameters refer to complex valued modal frequencies, complex valued modal vectors and complex valued modal scaling. The chapter focusses on modal parameter estimation (MPE) methods that have been or are commercially available but includes many related MPE methods that have been developed and presented in research journals and articles as well. The methods are mostly based upon experimentally measured frequency response function (FRF) or impulse response function (IRF) data. MPE methods that are fundamentally single input, single output (SISO) methods finding one single mode are included through modern multiple input, multiple output (MIMO) methods that find all modal parameters for all modes simultaneously (in one or two passes). Discussion includes the theoretical background of all methods along with the kernel equations for each method. The mathematical development utilizes a central concept of matrix coefficient polynomials that provide the basis of the unified matrix polynomial approach (UMPA). Basic definitions are included as concepts are developed and a complete set of historical references is provided.

Keywords

Modal parameter estimation · Experimental modal analysis · Modal parameter estimation methods · SDOF methods · MDOF methods · Polynomial models · Unified matrix coefficient polynomial approach (UMPA) · Partial fraction models · Residue and residual estimation · Complex z mapping

Nomenclature

N_i = Number of inputs
N_o = Number of outputs
N_S = Short dimension ($\min(N_i, N_o)$)
N_L = Long dimension ($\max(N_i, N_o)$)
N_f = Number of frequencies (spectral lines)
N_t = Number of times
N_e = Number of effective modal frequencies
N = Number of modal frequencies
F_{max} = Maximum frequency (Hz)
ω_i = Frequency (rad/sec)
ω_{max} = Maximum frequency (rad/sec)
Δf = Frequency resolution (Hz)
λ_r = Complex modal frequency
T = Observation period (sec)
s_i = Generalized frequency variable
m = Model order for denominator polynomial
n = Model order for numerator polynomial
A_{pqr} = Residue, output DOF p, input DOF q, mode r

$R_{I_{pq}}$ = Residual inertia, output DOF p, input DOF q
$R_{F_{pq}}$ = Residual flexibility, output DOF p, input DOF q
$[C]$ = Companion matrix
$[\alpha]$ = Denominator polynomial matrix coefficient
$[\beta]$ = Numerator polynomial matrix coefficient
$[I]$ = Identity matrix
$[H(\omega_i)]$ = Frequency response function matrix. $(N_o \times N_i)$
$[T]$ = Transformation matrix
$[U]$ = Left singular vector matrix
$[\Sigma]$ = Singular value matrix (diagonal)
$[\Lambda]$ = Eigenvalue matrix (diagonal)
$[V]$ = Right singular vector, or eigenvector, matrix
MPE-1 = First stage of modal parameter estimation
MPE-2 = Second stage of modal parameter estimation

1 Introduction

Experimental modal analysis is the process of determining the modal parameters of a structural system (frequencies, damping factors, modal vectors, and modal scaling values) from experimental input-output data, normally frequency response functions (FRFs) or impulse response functions (IRFs). This is in contrast to **analytical modal analysis** where the modal parameters are found from a theoretical, continuous, or discrete model of the structural system. This could be a closed form solution for simple structures or, more commonly, a discrete model like a finite element model for structural systems with more complex geometry. Analytical modal analysis generally does not include damping factors as part of the solution. Finally, **operational modal analysis (OMA)**, sometimes called **response-only modal analysis**, attempts to determine modal parameters from data taken without measured inputs. The inputs come from natural excitation (wind, waves, traffic, etc.) or from the operational inputs provided to a structural system. Operational modal analysis gives a subset of modal parameters that depends upon whether the unmeasured inputs excite the modal parameters and may mix modal parameters with forced vibration information. Since operational modal analysis does not measure the inputs, modal scaling cannot be determined without additional testing. Operational modal analysis is the subject of the "Operational Modal Analysis Methods" chapter in this Handbook. The following discussion is concerned with experimental modal analysis. Analytical and operational modal analysis is covered in other related material.

One important continuing focus of experimental modal analysis is the presentation of modal parameter estimation algorithms in a single, consistent mathematical formulation with a corresponding set of definitions and unifying concepts [1, 2, 3, 4, 5, 6]. In particular, a matrix coefficient polynomial approach can be used to unify the presentation with respect to current algorithms such as the least-squares complex exponential (LSCE), polyreference time domain (PTD), polyreference least-squares complex frequency (LSCF), Ibrahim time domain (ITD), Eigensystem realization algorithm (ERA), rational fraction polynomial (RFP), orthogonal polynomials

(OP), polyreference frequency domain (PFD), and the complex mode indication function (CMIF) methods. Using this unified matrix polynomial approach (UMPA) encourages a discussion of the similarities and differences of the commonly used methods, as well as a discussion of the numerical characteristics. Some of the different numerical methods that are used in different methods are the least squares (LS), total least squares (TLS), double least squares (DLS), and singular value decomposition (SVD) methods (to take advantage of redundant measurement data) and the eigenvalue and singular value decomposition transformation methods (to reduce the effective size of the resulting eigenvalue-eigenvector problem).

The unified matrix polynomial approach (UMPA) is an attempt to place most commonly used experimental modal parameter estimation algorithms within a single educational framework. The goal of the UMPA presentation is to highlight the similarity between the different algorithms rather than differences. This approach does not attempt to explain the detailed development of the authors who originated each method but attempts to present a common framework so that different algorithms can be easily compared and contrasted.

2 Modal Parameter Estimation: Background

Modal parameter estimation is a special case of system identification where the a priori model of the system is known to be in the form of modal parameters. Over the past 40 years, a number of algorithms have been developed to estimate modal parameters from measured multiple input, multiple output (MIMO), frequency response function (FRF), or impulse response function (IRF) data. While most of these individual algorithms, summarized in Table 1, are well understood, the comparison of one algorithm to another has become one of the thrusts of current research in this area. Comparison of the different algorithms is possible when the algorithms are reformulated using a common mathematical structure.

This reformulation attempts to characterize different classes of modal parameter estimation techniques in terms of the structure of the underlying matrix coefficient polynomials rather than the physically based models used historically. Since the modal parameter estimation process involves a greatly overdetermined problem (more data than independent equations), this reformulation is helpful in understanding the different numerical characteristics of each algorithm and, therefore, the slightly different estimates of modal parameters that each algorithm yields. As a part of this reformulation of the algorithms, the development of a conceptual understanding of modal parameter estimation technology has emerged. This understanding involves the ability to conceptualize the measured data in terms of the concept of characteristic space, the data domain (time, frequency, spatial), the dimension of the measured data, the evaluation of the order of the problem, the condensation of the data, and a common parameter estimation theory that can serve as the basis for developing any of the algorithms in use today. The following sections review these concepts as applied to the current modal parameter estimation methodology.

Table 1 Acronyms – experimental modal parameter estimation algorithms

Modal parameter estimation algorithms	
CEA	Complex exponential algorithm [7, 8]
LSCE	Least-squares complex exponential [8]
PTD	Polyreference time domain [9, 10]
ITD	Ibrahim time domain [11, 12]
MRITD	Multiple reference Ibrahim time domain [13]
ERA	Eigensystem realization algorithm [14, 15, 16]
PFD	Polyreference frequency domain [17, 18, 19, 20]
FDPI	Frequency domain direct parameter identification [19, 20]
SFD	Simultaneous frequency domain [21]
MRFD	Multi-reference frequency domain [22]
RFP	Rational fraction polynomial [23, 24, 25]
OP	Orthogonal polynomial [25, 26, 27, 28, 29, 30, 31, 32, 33, 34, 35, 36]
PLSCF	Polyreference least-squares complex frequency [37, 38, 39, 40, 41, 42]
CMIF	Complex mode indication function [43]

2.1 Assumptions, Definitions, and Concepts

A number of assumptions, basic definitions, and general concepts are essential to understanding the experimental modal analysis process. Since there is considerable history in the development of modal parameter estimation methodology, it is helpful to provide a structure that provides a common basis for all modal parameter estimation algorithms. Some of these definitions and concepts are briefly introduced in the following subsections.

2.1.1 Assumptions

By its very nature, modal analysis is one way to describe the dynamic characteristics of a structural system. For modal analysis to be considered, there are several assumptions involved. Generally, the structural system is assumed to be *linear*, *time invariant*, and *reciprocal*. Other assumptions can be involved but are not a requirement. An example would be *proportional* or Rayleigh damping which restricts the form of the modal vectors that are found.

2.1.2 Definition: Modal Parameters

While some situations do not require all modal parameters, a complete set of modal parameters is needed if a complete model of the input-output relationships is desired. Modal parameters include the complex valued modal frequencies (λ_r), the associated complex valued modal vectors ($\{\psi_r\}$), and the complex valued modal scaling (Modal A_r). Note that the complex valued modal frequencies are of the form ($\lambda_r = \sigma_r + j\omega_r$) where σ_r is the damping factor and ω_r is the damped natural frequency for the $r - th$ mode. Additionally, most current multiple input, multiple output (MIMO) algorithms estimate modal participation (weighting) vectors ($\{L_r\}$) and residue vectors ($\{A_r\}$) as part of the overall process of estimating the complex

valued modal vectors. Modal participation vectors are a result of MIMO modal parameter estimation algorithms and relate how well each modal vector is excited from each of the reference locations included in the measured data. The combination of the modal participation vector ($\{L_r\}$), the modal vector ($\{\psi_r\}$), and the Modal A (M_{A_r}) for a given mode yields the residue matrix ($[A_r]$) for that mode.

In general, modal parameters are considered to be global properties of the system. The concept of global modal parameters simply means that there is only one answer for each modal parameter and that the modal parameter estimation solution procedure enforces this constraint. Most of the current modal parameter estimation algorithms estimate the modal frequencies and damping in a global sense but very few estimate the modal vectors in a global sense. This is due to various modal vector scaling normalization methods which, together with the modal scaling value, give equivalent results but not unique, mathematical values.

Modal Vector Normalization

While there is a unique answer for the modal frequencies, the complex valued modal vectors represent the relative pattern of motion associated with each complex valued modal frequency. This relative pattern results from a rank-deficient system of equations where the modal vector is found via an eigenvalue-eigenvector solution. The complex valued modal vectors, together with the modal scaling, represent the unique characteristic for each modal vector. For this reason, the normalization of the complex valued modal vector is important when modal vectors or the associated modal scaling values are compared numerically.

While there are a number of acceptable normalization schemes for modal vectors, *choosing the largest element in each complex valued modal vector equal to unity* is the most common and most useful in a physical sense. This method of normalization will be used in all following discussions. Recognizing that an arbitrarily scaled modal vector is complex valued means that the largest element will in general be complex valued. When the arbitrarily scaled modal vector is divided (normalized) by the largest element, this will force all elements of the scaled modal vector to be bounded by the complex unit circle and, for most cases, to lie along the real axis of the unit circle.

2.1.3 Definition: Degrees of Freedom (DOFs)

Degrees of freedom (DOFs) refer to the physical location and direction of all of the potential inputs to, or outputs from, a structural system. For the theoretical problem, the number of inputs and the number of outputs are always the same and are equal to the number of modal parameter sets of information (typically designated N) that will be found. The general notation that is often used involves inputs in the form of forces and outputs in the form of displacements, velocities, and/or accelerations. The generalized concept of inputs and outputs could be used to represent translational or rotational outputs (or their derivatives) or translational or rotational inputs.

In an experimental sense, the DOFs are where the input and output sensors are located (physical location and direction). Today that includes response measurements from scanning laser vibrometers and digital image correlation (DIC) photogrammetry methods. Equation 1 is a representation of an FRF where the output DOF utilizes the notation p and the input DOF utilizes the notation q. Note that the X and F notation represents the output and input in a general way and does not imply displacement or force.

$$H_{pq}(\omega) = \frac{X_p(\omega)}{F_q(\omega)} \tag{1}$$

- p is the output degree of freedom (physical location and orientation).
- q is the input degree of freedom (physical location and orientation).

For the experimental case, the number of input DOFs (N_i) and output DOFs (N_o) is not the same and in general cannot be directly linked to the N sets of modal parameters that will be estimated.

2.1.4 Concept: Experimental Modal Parameter Estimation

Experimental modal parameter estimation involves estimating the modal parameters of a structural system from measured input-output data. The experimental approach originally involved methods that are referred to as phase resonance methods using sinusoidal excitation (narrowband) and mode by mode tuning with a forcing vector to balance the damping effect, assuming the modal vectors are normal modes. These methods gave way to phase separation methods that involve a range of frequency information (broadband) where the effects of several modes are separated using mathematical models for the experimental data. Most current modal parameter estimation are phase separation methods, based upon the measured data being the frequency response function or the equivalent impulse response function, typically found by inverse Fourier transforming the frequency response function.

The current approach is to use numerical techniques to separate the contributions of individual modes of vibration in measurements such as frequency response functions. The concept involves estimating the individual single degree of freedom (SDOF) contributions to the multiple degree of freedom (MDOF) measurement. Then, the modal parameters are found from the SDOF contributions.

$$[H(\omega_i)]_{N_L \times N_S} = \sum_{r=1}^{N} \frac{[A_r]_{N_L \times N_S}}{j\omega_i - \lambda_r} + \frac{[A_r^*]_{N_L \times N_S}}{j\omega_i - \lambda_r^*} = \sum_{r=1}^{2N} \frac{[A_r]_{N_L \times N_S}}{j\omega_i - \lambda_r} \tag{2}$$

Equation 2 represents a mathematical problem that, at first observation, is nonlinear in terms of the unknown modal parameters. Once the modal frequencies (λ_r) are known, the mathematical problem is linear with respect to the remaining unknown modal parameters ($[A_r]$). For this reason, the numerical solution in many modal parameter estimation (MPE) algorithms frequently involves two linear stages that utilize least-squares (LS) solution methods. Typically, the modal frequencies and modal participation vectors are found in a first stage (MPE-1), and residues, modal vectors, and modal scaling are determined in a second stage (MPE-2). This concept, involving a summation of partial fraction terms, is represented mathematically in Eq. 2 and graphically in Fig. 1.

While the model stated in Eq. 2 is fundamental to the linear superposition of individual SDOF contributions, this model is normally limited to being used as the basis for estimating the residues A_{pqr} once the modal frequencies (λ_r) are known. Based upon the speed and memory of modern personal computers, these two stages are often executed together giving the appearance of a single stage solution.

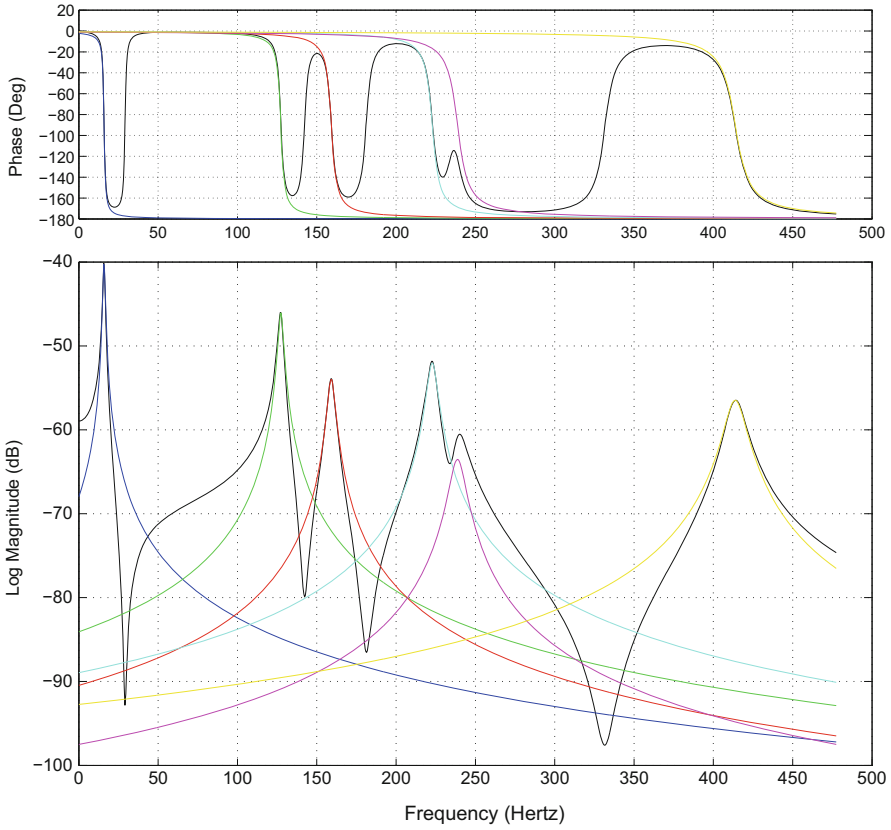

Fig. 1 MDOF – superposition of SDOF (positive frequency poles)

Equation 2 can be represented in the time domain in terms of impulse response functions in a similar summation form as shown in Eq. 3:

$$[h(t_i)]_{N_L \times N_S} = \sum_{r=1}^{N} [A_r]_{N_L \times N_S} e^{\lambda_r t_i} + [A_r^*]_{N_L \times N_S} e^{\lambda_r^* t_i} = \sum_{r=1}^{2N} [A_r]_{N_L \times N_S} e^{\lambda_r t_i} \tag{3}$$

2.1.5 Concept: Data Domain

Modal parameters can be estimated from a variety of different measurements that exist as discrete data in different data domains (time and/or frequency). These measurements can include free decays, forced responses, power spectra, covariance, frequency response functions (FRFs), or impulse response functions (IRFs). These measurements can be processed one at a time or in partial or complete sets simultaneously. The measurements can be generated with no measured inputs, a single measured input, or multiple measured inputs. The data can be measured individually or simultaneously. There is a tremendous variation in the types of measurements and in the types of constraints that can be placed upon the testing procedures used to acquire this data. For most measurement situations, FRFs are utilized in the frequency domain, and IRFs are utilized in the time domain. When IRFs are utilized, they are generally formed from the inverse Fourier transform of the measured FRFs. For the purpose of the following discussions, force-displacement data is considered the basis for the equations recognizing that force-displacement data can be numerically synthesized from measured force-acceleration data or force-velocity data.

2.1.6 Concept: Characteristic Space

From a conceptual viewpoint, the measurement space of a modal identification problem can be visualized as occupying a volume with the coordinate axes defined in terms of the three sets of characteristics. Two axes of the conceptual volume correspond to spatial information and the third axis to temporal information. The spatial axes are in terms of the input and output degrees of freedom (DOF) of the system. The temporal axis is either time or frequency depending upon the domain of the measurements. These three axes define a 3D volume which is referred to as the Characteristic Space (Figs. 2, 3, and 4).

This space or volume represents all possible measurement data. This conceptual representation is very useful in understanding what data subspace has been measured. Also, this conceptual representation is very useful in recognizing how the data is organized and utilized with respect to different modal parameter estimation algorithms (3D volume to stacked 2D matrices). Information parallel to one axis consists of a superposition of the characteristics defined by that axis. The other two characteristics determine the scaling of each term in the superposition.

Any structural testing procedure measures a subspace of the total possible data available. Modal parameter estimation algorithms may then use all of this subspace or may choose to further limit the data to a more restrictive subspace via sieving

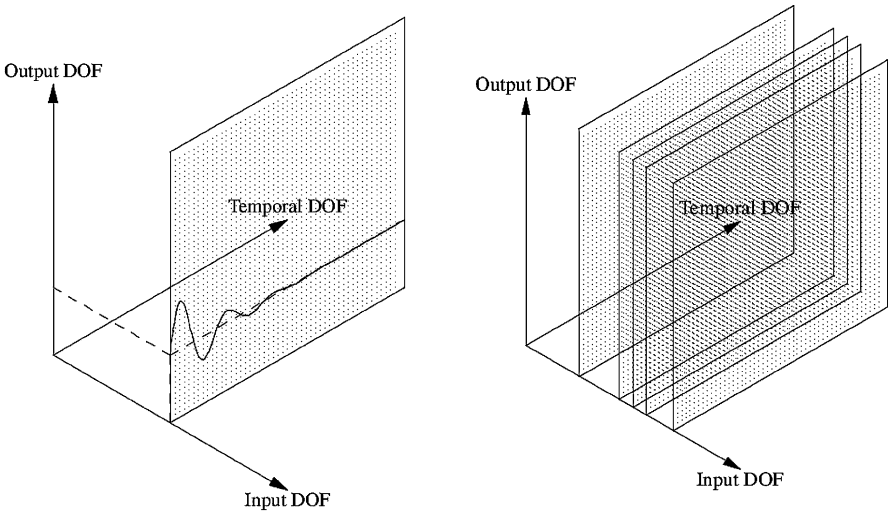

(a) Single Input Reference (b) Multiple Input References

Fig. 2 Characteristic space: columns of measurements. (**a**) Single input reference. (**b**) Multiple input references

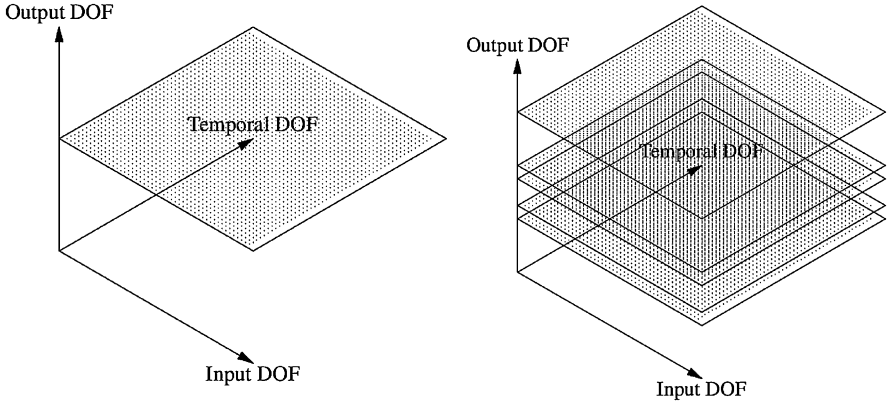

(a) Single Output Reference (b) Multiple Output References

Fig. 3 Characteristic space: rows of measurements. (**a**) Single output reference. (**b**) Multiple output references

and/or filtering. It is theoretically possible to estimate the characteristics of the total space by measuring any subspace which samples all three characteristics. Measurement data spaces involving many planes of measured data are the best possible modal identification situations since the data subspace includes contributions from temporal and spatial characteristics. The particular subspace which is measured and the weighting of the data within the subspace in an algorithm are the main

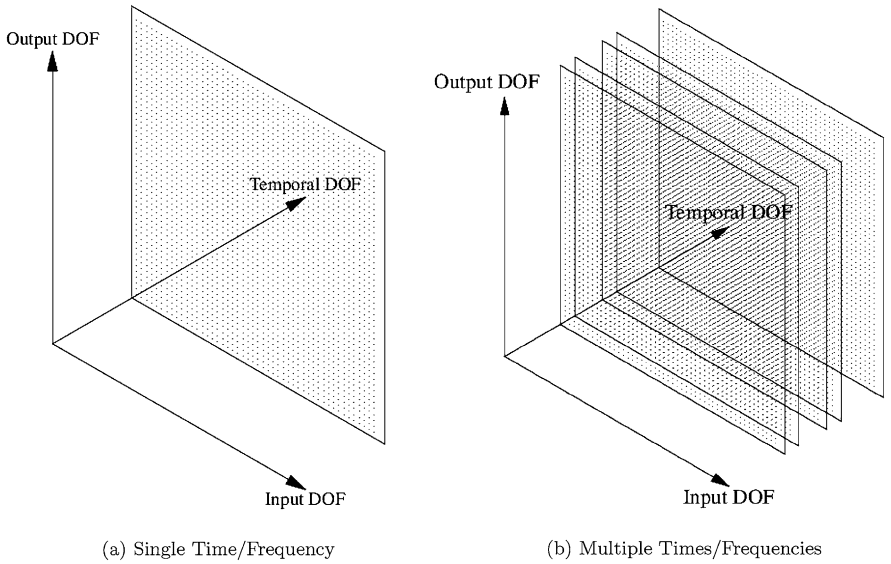

Fig. 4 Characteristic space: times/frequencies of measurements. (**a**) Single time/frequency. (**b**) Multiple times/frequencies

differences between the various modal identification procedures which have been developed.

It should be obvious that the data which defines the subspace needs to be acquired in a consistent measurement process in order for the algorithms to estimate accurate modal parameters. This fact has triggered the need to measure all of the data simultaneously and has led to recent advancements in data acquisition, digital signal processing, and instrumentation designed to facilitate this measurement problem.

While it is not always obvious, most modal parameter estimation methods assume that the measured data includes one or more pairs of matched input and output DOFs in what is commonly referred to as driving point FRFs.

2.1.7 Concept: Data Dimensionality

In the following discussion, the use of notation involving the number of input degrees of freedom (DOFs), (N_i), and the number of output DOFs, (N_o), is replaced by an alternate notation. Since the FRF matrix is always assumed to be reciprocal, it is more important to note the smaller and larger of the number of DOFs with respect to the inputs and outputs when the data is utilized by modern MIMO modal parameter estimation algorithms. For this reason, the dimension that is larger is referred to as the long dimension, (N_L), and the dimension that is smaller is referred to as the short dimension, (N_S). The short dimension is often referred to as the number of references, and the long dimension is often referred to as the number of responses. The dimension of the third axis (temporal axis) is either the number of frequencies (N_f) or the number of times (N_t).

2.1.8 Concept: Generalized Frequency

In the following development, all frequency domain models will be presented as a function of the generalized frequency variable s. This variable is a general complex valued variable that is most often thought of as $s = j\omega$, representing the independent frequency variable associated with the FRF. There are several other scaled or mapped versions of the generalized frequency variable s which are useful for minimizing the numerical conditioning associated with different frequency domain MPE algorithms.

$$H_{pq}(\omega_i) = \frac{X_p(\omega_i)}{F_q(\omega_i)} = \frac{\beta_n(s_i)^n + \beta_{n-1}(s_i)^{n-1} + \cdots + \beta_1(s_i)^1 + \beta_0(s_i)^0}{\alpha_m(s_i)^m + \alpha_{m-1}(s_i)^{m-1} + \cdots + \alpha_1(s_i)^1 + \alpha_0(s_i)^0} \tag{4}$$

One example is a simple scaled version of s where $s = \frac{j\omega}{\omega_{\max}}$. When the generalized frequency variable is scaled or mapped in this fashion, any frequency estimate that results must be corrected accordingly. This concept will be explained further in the section on high-order, frequency domain algorithms.

2.1.9 Concept: Kernel Equations

Each experimental modal parameter estimation method has a basic equation that is repeated for different powers or subspaces of the independent variable (t, s, ω, z) to get additional sets of solutions. The base equation for each method is referred to as the kernel equation. Consistency between the different sets of solutions is one common method of determining the most likely modal parameters in the data.

2.1.10 Concept: Overdetermined Linear Models

Most current modal parameter estimation methods utilize linear models, sometimes in several successive solution steps, that have more equations than unknowns in each solution step. This will be true for simple SDOF models as well as complicated MIMO MDOF models. The number of equations is larger than the unknowns since an equation can be formed at each measured frequency or time, while the number of unknowns is limited to a function of the number of modal parameters N. The overdetermination factor is the ratio of the number of equations to the number of unknowns. The overdetermination factor can easily be a number greater than 2-5.

Overdetermined sets of linear equations are most often solved using least-squares (LS) techniques, particularly when the noise on the data is expected to be random. The least-squares solution will yield the best solution in the presence of random noise. With respect to the estimation of frequency response functions (FRFs) as the measured data for most modal parameter estimation, this means that bias errors on the FRF data are much more concerning than the random errors.

2.1.11 Concept: General (Two-Stage) Solution Procedure

Most modern modal parameter estimation (MPE) algorithms are implemented in two stages that each involves the solution of overdetermined linear equations. The first stage, referred in this text as MPE-1, is where the modal frequencies (λ_r) are estimated along with associated modal weighting vectors ($\{L_r\}$). The second stage,

referred in this text as MPE-2, is where the modal vectors ($\{\psi_r\}$) and modal scaling are estimated. These two stages can generally be briefly summarized as follows:

- MPE-1: Utilize measured FRF or IRF data with a matrix coefficient, polynomial model to find multiple estimates of the modal parameters. Select the best set of modal frequencies and modal participation vectors. This stage is often performed in two fundamental steps: (1) solve a set of overdetermined linear equations and (2) solve for the roots of a polynomial.
- MPE-2: Utilize measured FRF or IRF data, with selected complex valued modal frequencies and modal participation vectors to find complex valued modal vectors from an overdetermined set of linear equations.

Additional steps are often added to the above procedure to enhance the numerical solution. This concept will be described in greater detail in a later section.

2.1.12 Concept: Equation Normalization

Many of the overdetermined sets of linear equations involve a null space problem in which the right-hand side (RHS) of the equation is zero or null. In these cases, the unknown coefficients of the equation are non-unique but can be found by choosing one of the coefficients, typically, equal to the identity matrix. The numerical solution of the overdetermined sets of linear equations will yield different answers depending on which coefficient is chosen. While theoretical data would yield only one answer, experimental data will have random and bias noise, and this noise is what yields somewhat different answers. Historically, two solutions have been used in these cases, setting the lead coefficient and the last coefficient to the identity matrix to give two answers that bracket the solution. This is true for both frequency domain methods and time domain methods. This choice of choosing a coefficient to be the identity is referred to as equation normalization.

$$\sum_{k=0}^{m}\left[[\alpha_k](s_i)^k\right][H(\omega_i)] = \sum_{k=0}^{n}\left[[\beta_k](s_i)^k\right][I] \tag{5}$$

Equation 5 is an example of such a null space (rank deficient) equation. The unknowns in the equation are the $[\alpha]$ and $[\beta]$ coefficients. Since every term has an unknown coefficient matrix, the equation can be pre-multiplied by the inverse of any one of the $[\alpha]$ coefficients to derive a solvable (full rank) base equation.

Lowest $[\alpha_0]$ Normalization: $[\alpha_0] = [I]$

$$\sum_{k=1}^{m}\left[[\alpha_k](s_i)^k\right][H(\omega_i)] - \sum_{k=0}^{n}\left[[\beta_k](s_i)^k\right][I] = -\left[[\alpha_0](s_i)^0\right][H(\omega_i)] \tag{6}$$

Highest $[\alpha_m]$ Normalization: $[\alpha_m] = [I]$

$$\sum_{k=0}^{m-1}\left[[\alpha_k](s_i)^k\right][H(\omega_i)] - \sum_{k=0}^{n}\left[[\beta_k](s_i)^k\right][I] = -\left[[\alpha_m](s_i)^m\right][H(\omega_i)] \tag{7}$$

It is important to note that this equation normalization must occur in the initial step of choosing the base equation. Then the unknown coefficients are solved in an overdetermined set of these linear equations. It is not sufficient to manipulate the final solution of polynomial coefficients into a different normalized form. The difference that equation normalization provides is determined by the LS solution for the coefficients [39,41].

2.2 Analytical Models

While analytical models can be continuous, represented in closed form, in terms of time and/or frequency, most analytical models of structures are discrete, represented by mass [M], damping [C], and stiffness [K] matrices in a second-order system of equations. An equivalent discrete analytical model in terms of [A] and [B] matrices in a first-order model provides a more direct relationship to the modal parameters found in experimental approaches.

2.2.1 [M] [C] [K] Models

Generally, most structures are more complicated than the single degree of freedom mass, spring, and damper system. The general case for a multiple degree of freedom system will be used to show how the frequency response functions of a structure are related to the modal vectors of that structure.

$$[M]\ \{\ddot{x}(t)\} + [C]\ \{\dot{x}(t)\} + [K]\ \{x(t)\} = \{f(t)\} \tag{8}$$

$$\Big[\ [M]\ s^2 + [C]\ s + [K]\Big]\ \{X(s)\} = \{F(s)\} \tag{9}$$

The transfer function representation of a general multiple degree of freedom system can be formulated by starting with generalized frequency domain equation of motion in terms of mass, stiffness, and damping matrices.

$$\Big[[M]\,s^2 + [C]\,s + [K]\Big]\,\{X\,(s)\} = \{F\,(s)\} \tag{10}$$

$$\Big[[M]\,s^2 + [C]\,s + [K]\Big]\,\{X\,(s)\} = [B\,(s)]\,\{X\,(s)\} = \{F\,(s)\} \tag{11}$$

where $[B\,(s)] = \Big[[M]\,s^2 + [C]\,s + [K]\Big]$ and $[B\,(s)]$ is referred to as the system impedance matrix or just the system matrix. Pre-multiplying both sides of the previous equation by $[B\,(s)]^{-1}$ yields:

$$[B\,(s)]^{-1}\,\{F\,(s)\} = [H\,(s)]\,\{F\,(s)\} = \{X\,(s)\} \tag{12}$$

where $[H\,(s)] = [B\,(s)]^{-1}$ and is referred to as the transfer function matrix. By evaluating the transfer function matrix at $s = j\omega$, the frequency response function matrix results.

$$[H(\omega)] = \left[-\omega^2 [M] + j\omega [C] + [K]\right]^{-1} \tag{13}$$

2.2.2 [A] [B] Models

A more general representation of the matrix model can be formed from the [M] [C] [K] model. This model is in the form of a first-order differential equation utilizing matrices that are combinations of the [M] [C] [K] matrices and is more desirable due to its direct relationship to the generalized eigenvalue-eigenvector form. This methodology is often referred to as a state space expansion due to its final form. However, this methodology was documented in the 1930s by Frazer, Duncan, and Collar [44] to put the [M] [C] [K] model into Hamilton's dynamical equations and has since been put in this final form by others [45, 46]. This development begins with the [M] [C] [K] differential equation:

$$[M]\ \{\ddot{x}(t)\} + [C]\ \{\dot{x}(t)\} + [K]\ \{x(t)\} = \{f(t)\} \tag{14}$$

This system of equations can be augmented by the following identity:

$$[M]\ \{\dot{x}(t)\} - [M]\ \{\dot{x}(t)\} = \{0\} \tag{15}$$

The two above equations can be combined as follows to yield a new system of $2N$ equations in a classical eigenvalue solution form.

$$\begin{bmatrix} [0] & [M] \\ [M] & [C] \end{bmatrix} \begin{Bmatrix} \ddot{x}(t) \\ \dot{x}(t) \end{Bmatrix} + \begin{bmatrix} -[M] & [0] \\ [0] & [K] \end{bmatrix} \begin{Bmatrix} \dot{x}(t) \\ x(t) \end{Bmatrix} = \begin{Bmatrix} 0 \\ f(t) \end{Bmatrix} \tag{16}$$

$$[A]\ \{\dot{y}(t)\} + [B]\ \{y(t)\} = \left\{f'(t)\right\} \tag{17}$$

where

- $[A] = \begin{bmatrix} [0] & [M] \\ [M] & [C] \end{bmatrix} \quad [B] = \begin{bmatrix} -[M] & [0] \\ [0] & [K] \end{bmatrix} \quad \{y(t)\} = \begin{Bmatrix} \dot{x}(t) \\ x(t) \end{Bmatrix}$

The generalized frequency domain equation is therefore:

$$[[A]\, s + [B]]\ \{Y(s)\} = \left\{F'(s)\right\} \tag{18}$$

The advantage of representing the [M], [C], [K] model in the [A], [B] form is that the equation becomes a first-order problem that can be solved with standard eigenvalue-eigenvector solution methods. This form gives diagonalized matrices when the weighted orthogonality concept is applied, similar to the diagonalized matrices when the weighted orthogonality concept is considered for the undamped and proportionally damped cases.

Also note that the well-known *Hamilton's dynamical equations* result when Eqs. 14 and 15 are first pre-multiplied by the inverse of the mass matrix.

$$\begin{bmatrix} [0] & [I] \\ [I] & [M]^{-1}[C] \end{bmatrix} \begin{Bmatrix} \ddot{x}(t) \\ \dot{x}(t) \end{Bmatrix} + \begin{bmatrix} -[I] & [0] \\ [0] & [M]^{-1}[K] \end{bmatrix} \begin{Bmatrix} \dot{x}(t) \\ x(t) \end{Bmatrix} = \begin{Bmatrix} 0 \\ [M]^{-1}\{f(t)\} \end{Bmatrix} \tag{19}$$

Note that Eq. 19 is just a normalized form of Eq. 16.

2.2.3 [A] [B] [C] [D] Models

Another theoretical methodology that is used by some researchers to determine modal parameters is based upon a system identification approach that involves a four matrix form. The model uses input-output data and a MIMO state space process that includes inputs, outputs, noise on the inputs, noise on the outputs, and noise on the state.

$$\{\dot{y}(t)\} = [A]\ \{y(t)\}\ +\ [B]\ \{f(t)\} \tag{20}$$

$$\{x(t)\} = [C]\{y(t)\}\ +\ [D]\ \{f(t)\} \tag{21}$$

This time domain approach is commonly used in control theory, system identification modeling. With respect to the [M], [C], [K] model, the [A] matrix in the above equation is proportion to the [A] matrix in Eq. 19, but the other matrices are not directly related to any other matrices defined in the previous sections [47,48,49,50]. This method has been adapted to utilize frequency domain data in the form of frequency response functions using an algorithm referred to as N4SID.

This method, however, is not commonly used by any commercial algorithms and will not be discussed further in this text.

2.2.4 Eigen-Solutions, Orthogonality and Modal Scaling

The modal parameters for analytical models can be found directly from the homogeneous form of Eq. 10 or from Eq. 18 using a number of numerical methods. Both equations represent a rank-deficient system of equations where the complex valued frequencies are found first, followed by a solution for the complex valued modal vectors. This is complicated for a generally damped system of more than two or three degrees of freedom. However, the general solution of any size problem can be easily found using eigenvalue-eigenvector methods when the [A] [B] matrix model is used. Any specialized form of damping, including undamped and proportionally damped models, is likewise found using this approach.

The solution of the homogeneous equation for the [A] [B] matrix model yields the complex valued natural frequencies (eigenvalues) and complex valued modal vectors (eigenvectors) once an augmented $2N$ equation system is formed. Note that in this mathematical form, the complex valued eigenvalues will directly yield the

complex valued modal frequencies, while the complex valued modal vectors will be found from the $2N$ eigenvectors, which are each $2N$ in length. Rearranging the homogeneous form of Eq. 18 puts the equation into a standard generalized eigenvalue problem form.

$$[B] \ \{Y(s)\} \ = \ -s \ [A] \ \ \{Y(s)\} \tag{22}$$

$$\begin{bmatrix} -[M] & [0] \\ [0] & [K] \end{bmatrix} \{Y(s)\} \ = \ -\lambda \begin{bmatrix} [0] & [M] \\ [M] & [C] \end{bmatrix} \{Y(s)\} \tag{23}$$

where

- $\{Y(s)\} \ = \begin{Bmatrix} \lambda \{X(s)\} \\ \{X(s)\} \end{Bmatrix}$

The standard form of the eigenvalue-eigenvector solution method can cause some confusion since the standard mathematical notation is similar to, but different from, Eq. 18 as follows:

$$\left[\tilde{A}\right] \{Y(s)\} \ = \ \lambda \ [I] \ \{Y(s)\} \tag{24}$$

$$\left[\tilde{A}\right] \{Y(s)\} \ = \ \lambda \ \left[\tilde{B}\right] \{Y(s)\} \tag{25}$$

Note that the $[\tilde{A}]$ and $[\tilde{B}]$ matrices in Eq. 25 are in different positions in the equation compared to the $[A]$ and $[B]$ matrices in Eq. 22. Also note the difference in the eigenvector notation.

The $2N$ eigenvalues give the $2N$ complex valued modal frequencies, which result in N complex conjugate pairs of complex valued modal frequencies. The exact form of the eigenvectors can be seen from the associated modal matrix for the $2N \times 2N$ equation system. Note that the notation $\{\phi\}$ is used for an eigenvector in the $2N \times 2N$ equation system and that the notation $\{\psi\}$ is used for the modal vector of the $N \times N$ equation system.

The modal matrix or modal state matrix $[\phi]$ for this generally damped system can be represented as follows:

$$[\phi] \ = \ \left[\ \{\phi\}_1 \{\phi\}_2 \{\phi\}_3 ... \{\phi\}_r ... \{\phi\}_{2N} \ \right] \tag{26}$$

$$[\phi] = \begin{bmatrix} \lambda_1 \{\psi\}_1 & \lambda_2 \{\psi\}_2 & \lambda_3 \{\psi\}_3 & ... & \lambda_r \{\psi\}_r & ... & \lambda_{2N} \{\psi\}_{2N} \\ \{\psi\}_1 & \{\psi\}_2 & \{\psi\}_3 & ... & \{\psi\}_r & ... & \{\psi\}_{2N} \end{bmatrix} \tag{27}$$

Note that this matrix involves the $N \times 2N$ matrix of modal vectors in the lower half of the matrix and the $N \times 2N$ matrix of the modal vectors, each modified by the appropriate complex valued modal frequency, in the upper half of this matrix.

These sub-matrices are not square since both the modal vector and the complex conjugate of the modal vector are involved. Also note that the upper half of this matrix is often viewed as the derivative of the lower half of the matrix (each upper vector is the derivative of the corresponding lower vector). Finally, each column with information associated with one modal vector is often described as a state vector.

Orthogonality

Since the [A] and [B] matrices form an eigenvalue problem, the associated eigenvectors are weighted orthogonal with respect to these matrices.

$$[\phi]^T\,[A]\,[\phi] = \lceil M_A \rfloor \tag{28}$$

$$[\phi]^T\,[B]\,[\phi] = \lceil M_B \rfloor \tag{29}$$

Weighted orthogonality means that the $[M_A]$ and $[M_B]$ matrices are diagonal with scaling terms, for each of the associated 2N modal eigenvectors, on the diagonal. The characteristics (magnitude and phase) of the scaling terms will depend on how the eigenvectors are normalized/scaled.

Note that for the generally damped problem, the weighted orthogonality concept will not extend to the mass and stiffness matrices and the lower half of the eigenvector matrix noted in Eq. 25 even when the 2N eigenvectors are reduced to the N modal vectors associated with the N positive modal frequencies.

$$[\psi]^T\,[M]\,[\psi] \neq \left\lceil \tilde{M} \right\rfloor \tag{30}$$

$$[\psi]^T\,[K]\,[\psi] \neq \left\lceil \tilde{K} \right\rfloor \tag{31}$$

If, and only if, the damping matrix represents some form of proportional damping (which includes no damping as a trivial case), then the weighted orthogonality concept will extend to the mass and stiffness matrices.

$$[\psi]^T\,[M]\,[\psi] = \left\lceil \tilde{M} \right\rfloor \tag{32}$$

$$[\psi]^T\,[K]\,[\psi] = \left\lceil \tilde{K} \right\rfloor \tag{33}$$

Modal Scaling

When weighted orthogonality applies, the diagonal terms become what is referred to as modal scaling. For the generally damped problem, the terms on the diagonal of the $[M_A]$ and $[M_B]$ matrices are defined as the Modal A (M_{A_r}) and Modal B (M_{B_r}) scaling terms, for each of the associated 2N modal eigenvectors.

Note that the actual value of the Modal A (M_{Ar}) and Modal B (M_{Br}) terms will depend upon the normalization/scaling of the eigenvectors.

$$\{\phi_r\}^T\ [A]\ \{\phi\} = M_{Ar} \tag{34}$$

$$\{\phi_r\}^T\ [B]\ \{\phi\} = M_{Br} \tag{35}$$

Since modal vectors are often compared and modal scaling is sometimes compared, a standardized scaling of the modal vectors is desirable. Unfortunately, this has not been done to this point in time. For several reasons, scaling each modal vector such that each modal vector is dominantly real valued and such that the largest coefficient in each modal vector is unity length, works optimally most of the time. Note, however, this means that the complete eigenvector will need to be scaled so that the modal vector, the lower half of the eigenvector, takes on these characteristics.

When the damping matrix does represent proportional damping, then the weighted orthogonality concept extends to the mass, damping and stiffness matrices.

$$\{\psi_r\}^T\,[M]\,\{\psi_r\} = \tilde{M}_r \tag{36}$$

$$\{\psi_r\}^T\,[C]\,\{\psi_r\} = \tilde{C}_r \tag{37}$$

$$\{\psi_r\}^T\,[K]\,\{\psi_r\} = \tilde{K}_r \tag{38}$$

Note that in Eqs. 36 through 38, the modal mass ($\tilde{M}_r$), modal damping ($\tilde{C}_r$), and modal stiffness ($\tilde{K}_r$) definitions are sometimes referred to as generalized mass, damping, and stiffness. Like Modal A and Modal B, these modal scaling terms are sensitive to the normalization/scaling of the modal vectors. In all cases, the normalization and scaling of the modal vectors relate to the force-displacement model.

2.3 Experimental Models

Experimental models are used to directly relate to the measured data that is estimated in the time and frequency domains. These models are generally physics-based models that originate from the general [M] [C] [K] models but are represented in frequency response function (FRF), impulse response function (IRF), or general polynomial matrix models that utilize the relationships between input and output data in either the frequency or time domains. The general polynomial matrix model can be directly related to the measured FRF and IRF models and are most often the core of modern modal parameter estimation (MPE) methods. The following models can also be applied to measured power spectra data (frequency domain) or measured covariance data (time domain), but direct scaling is not possible if input and output data is not included. While this idea is very useful, it will not be explored further in this text.

2.3.1 Polynomial Models

Frequency Domain

Rather than using a physically based mathematical model, the common characteristics of different modal parameter estimation algorithms can be more readily identified by using a matrix coefficient polynomial model. One way of understanding the basis of this model can be developed from the polynomial model used historically for the frequency response function. Note the nomenclature in the following equations regarding measured frequency ω_i and generalized frequency s_i. Measured input and response data are always functions of measured frequency, but the generalized frequency variable used in the model may be altered to improve the numerical conditioning. This will become important in a later discussion of generalized frequency involving normalized frequency, orthogonal polynomials, and complex Z mapping.

$$H_{pq}(\omega_i) = \frac{X_p(\omega_i)}{F_q(\omega_i)} = \frac{\beta_n(s_i)^n + \beta_{n-1}(s_i)^{n-1} + \cdots + \beta_1(s_i)^1 + \beta_0(s_i)^0}{\alpha_m(s_i)^m + \alpha_{m-1}(s_i)^{m-1} + \cdots + \alpha_1(s_i)^1 + \alpha_0(s_i)^0} \tag{39}$$

This can be rewritten:

$$H_{pq}(\omega_i) = \frac{X_p(\omega_i)}{F_q(\omega_i)} = \frac{\sum_{k=0}^{n} \beta_k(s_i)^k}{\sum_{k=0}^{m} \alpha_k(s_i)^k} \tag{40}$$

Further rearranging yields the following equation that is linear in the unknown α and β terms:

$$\sum_{k=0}^{m} \alpha_k(s_i)^k X_p(\omega_i) = \sum_{k=0}^{n} \beta_k(s_i)^k F_q(\omega_i) \tag{41}$$

This model can be generalized to represent the general multiple input, multiple output case as follows:

$$\sum_{k=0}^{m} (s_i)^k [\alpha_k] \{X_p(\omega_i)\} = \sum_{k=0}^{n} (s_i)^k [\beta_k] \{F_q(\omega_i)\} \tag{42}$$

Note that the size of the coefficient matrices $[\alpha_k]$ will normally be $N_S \times N_S$ or $N_L \times N_L$ and the size of the coefficient matrices $[\beta_k]$ will normally be $N_S \times N_L$ or $N_L \times N_S$ when the equations are developed from experimental data.

Rather than developing the basic model in terms of force and response information, the models can be stated in terms of power spectra or frequency response information. First, post multiply both sides of the equation by $\{F\}^H$:

$$\sum_{k=0}^{m} (s_i)^k [\alpha_k] \left\{X_p(\omega_i)\right\} \left\{F_q(\omega_i)\right\}^H = \sum_{k=0}^{n} (s_i)^k [\beta_k] \left\{F_q(\omega_i)\right\} \left\{F_q(\omega_i)\right\}^H \tag{43}$$

Now recognize that the product of $\{X(\omega_i)\}\{F(\omega_i)\}^H$ is the output-input cross-spectra matrix ($[G_{XF}(\omega_i)]$) for one ensemble and $\{F(\omega_i)\}\{F(\omega_i)\}^H$ is the input-input cross-spectra matrix ($[G_{FF}(\omega_i)]$) for one ensemble. With a number of ensembles (averages), these matrices are the common matrices used to estimate the FRFs in a MIMO case. This yields the following cross-spectra model:

$$\sum_{k=0}^{m} (s_i)^k [\alpha_k] [G_{XF}(\omega_i)] = \sum_{k=0}^{n} (s_i)^k [\beta_k] [G_{FF}(\omega_i)] \tag{44}$$

The previous cross-spectra model can be reformulated to utilize frequency response function (FRF) data by post multiplying both sides of the equation by $[G_{FF}(\omega_i)]^{-1}$:

$$\sum_{k=0}^{m} (s_i)^k [\alpha_k] [G_{XF}(\omega_i)] [G_{FF}(\omega_i)]^{-1} = \sum_{k=0}^{n} (s_i)^k [\beta_k] [G_{FF}(\omega_i)] [G_{FF}(\omega_i)]^{-1} \tag{45}$$

Therefore, the multiple input, multiple output FRF model is:

$$\sum_{k=0}^{m} (s_i)^k [\alpha_k] [H(\omega_i)] = \sum_{k=0}^{n} (s_i)^k [\beta_k] [I] \tag{46}$$

Additional equations can be developed by repeating Eq. 46 at many frequencies (ω_i) until all data or a sufficient overdetermination factor is achieved. Note that both positive and negative frequencies are required in order to accurately estimate conjugate modal frequencies.

In terms of sampled data, the frequency domain matrix polynomial coefficients result from a set of linear equations (repeated application of Eq. 46 where each equation is formulated by choosing a different frequency from the FRF data. From a numerical perspective, Eq. 46 is generally not well-formed, and the condition number associated with this system of equations will be extreme when the model order (m) exceeds five or six. This issue will require special consideration in order to obtain reasonable answers for the modal frequencies. This is discussed further in Sect. 5.2.

Once the alpha ($[\alpha]$) and beta ($[\beta]$) coefficients have been found, the modal frequencies can be found from the roots of the alpha ($[\alpha]$) matrix coefficient polynomial.

$$\sum_{k=0}^{m} [\alpha_k] s^k = 0 \tag{47}$$

The roots of this matrix coefficient polynomial are in terms of the generalized frequency variable s and will be the complex modal frequencies (λ_r) directly.

Time Domain

Paralleling the development of Eqs. 39 through 46, a time domain model representing the relationship between a single response degree of freedom and a single input degree of freedom can be stated as follows:

$$\sum_{k=0}^{m} \alpha_k \; x\,(t_{i+k}) = \sum_{k=0}^{n} \beta_k \; f\,(t_{i+k}) \tag{48}$$

For the general multiple input, multiple output case:

$$\sum_{k=0}^{m} [\alpha_k]\,\{x\,(t_{i+k})\} = \sum_{k=0}^{n} [\beta_k]\,\{f\,(t_{i+k})\} \tag{49}$$

The above model, in the time domain, is also known as an autoregressive-moving-average (ARMA(m,n)) model when developed from a set of discrete time equations in the time domain. More properly, this model is known as the autoregressive with exogenous inputs (ARX(m,n)) model.

If the discussion is limited to the use of free decay or impulse response function data, the previous time domain equations can be simplified by noting that the forcing function can be assumed to be zero for all time greater than zero. If this is the case, the $[\beta_k]$ coefficients can be eliminated from the equations.

$$\sum_{k=0}^{m} [\alpha_k]\,[h\,(t_{i+k})] = 0 \tag{50}$$

Additional equations can be developed by repeating Eq. 50 at different time shifts (initial times t_i) into the data until all data or a sufficient overdetermination factor is achieved. Note that at least one time shift is required in order to accurately estimate conjugate modal frequencies.

In terms of sampled data, the time domain matrix polynomial coefficients result from a set of linear equations (repeated application of Eq. 50 where each equation is formulated by choosing various distinct initial times. From a numerical perspective, Eq. 50 is generally well-formed, and the condition number associated with this system of equations will not be extreme even for high order (m).

In contrast, the frequency domain matrix polynomial developed in Eqs. 39 through 46 results from a set of linear equations (repeated application of Eq. 46) where each equation is formulated at one of the frequencies of the measured FRF data. This distinction is important to note since the roots of the matrix characteristic equation formulated in the time domain are in a mapped complex z domain (z_r), which is similar but not identical to the z-domain familiar to control theory. Once the

alpha ([α]) coefficients have been found, the roots of a polynomial in the complex z domain can be found since all of the measured time domain data utilize the same Δt spacing.

$$\sum_{k=0}^{m} [\alpha_k]\, z^k = 0 \tag{51}$$

Equation 51 is developed from the fixed time spacing (Δt) and derivative relationships associated with discrete time data. It is important to note that this development is theoretically exact and no approximations are involved.

These mapped complex z values (z_r) must be converted back to the generalized frequency domain (λ_r), while the roots of the matrix characteristic equation formulated in the frequency domain (λ_r) are already in the desired domain [1,2,3]. Note also that the roots that are estimated in the time domain are limited to maximum values determined by the Shannon sampling theorem relationship (due to the discrete time steps).

$$z_r = e^{\lambda_r \Delta t} \qquad \lambda_r = \sigma_r + j\,\omega_r \tag{52}$$

$$\sigma_r = Re\left[\frac{\ln z_r}{\Delta t}\right] \qquad \omega_r = Im\left[\frac{\ln z_r}{\Delta t}\right] \tag{53}$$

In light of the above discussion, it is now apparent that the general matrix coefficient polynomial model is a way in which most modal parameter estimation methods, both for the time and for the frequency domain, generate functionally similar matrix coefficient polynomial models. In this way, all of these methods can be viewed in a similar framework. For that reason, the **unified matrix polynomial approach (UMPA)** terminology is used to describe both domains since the time domain, autoregressive-moving average (ARMA) terminology is already connected with only the time domain.

For the **frequency domain** data case, this yields:

$$\left|[\alpha_m]\, s^m + [\alpha_{m-1}]\, s^{m-1} + [\alpha_{m-2}]\, s^{m-2} + \cdots\cdots\cdots + [\alpha_0]\right| = 0 \tag{54}$$

For the **time domain** data case, this yields:

$$\left|[\alpha_m]\, z^m + [\alpha_{m-1}]\, z^{m-1} + [\alpha_{m-2}]\, z^{m-2} + \cdots\cdots\cdots + [\alpha_0]\right| = 0 \tag{55}$$

Once the matrix coefficients ([α]) have been found, the modal frequencies can be found from the roots of the associated matrix coefficient polynomial. Originally, this was accomplished by forming a companion matrix from the matrix coefficients and using an eigenvalue solution method on the companion matrix. Most modern matrix solution packages now use the matrix coefficients directly in a root solving algorithm (e.g., *polyeig* in Matlab®) where the algorithm forms the companion matrix and then solves the associated eigenvalue problem.

2.3.2 Companion Matrix

Once the matrix coefficients ($[\alpha]$) have been found, the modal frequencies (λ_r or z_r) can be found using a number of numerical techniques. While in certain numerical situations, other numerical approaches may be more robust, a companion matrix approach yields a consistent concept for understanding the process. Therefore, the roots of the matrix characteristic equation can be found as the eigenvalues of the associated companion matrix. The companion matrix can be formulated in one of several ways.

Highest $[\alpha]$ Matrix Normalization:

One common formulation for finding the modal frequencies from a matrix coefficient polynomial comes from the eigenvalue solution of a companion matrix formed from the normalization of the highest order $[\alpha]_m$ coefficient matrix to the identity matrix $[I]$ yielding the following companion matrix:

$$[C] = \begin{bmatrix} -[\alpha]_{m-1} & -[\alpha]_{m-2} & \cdots\cdots\cdots & -[\alpha]_1 & -[\alpha]_0 \\ [I] & [0] & \cdots\cdots\cdots & [0] & [0] \\ [0] & [I] & \cdots\cdots\cdots & [0] & [0] \\ [0] & [0] & \cdots\cdots\cdots & [0] & [0] \\ \cdots & \cdots & \cdots\cdots\cdots & \cdots & \cdots \\ \cdots & \cdots & \cdots\cdots\cdots & \cdots & \cdots \\ \cdots & \cdots & \cdots\cdots\cdots & \cdots & \cdots \\ [0] & [0] & \cdots\cdots\cdots & [0] & [0] \\ [0] & [0] & \cdots\cdots\cdots & [0] & [0] \\ [0] & [0] & \cdots\cdots\cdots & [I] & [0] \end{bmatrix} \tag{56}$$

Note again that the numerical characteristics of the eigenvalue solution of the companion matrix will be different for low-order cases compared to high-order cases for a given data set. The companion matrix can be used in the following eigenvalue formulation to determine the modal frequencies for the original matrix coefficient equation:

$$[C]\{X\} = \lambda\ [I]\ \{X\} \tag{57}$$

$$[I] = \begin{bmatrix} [I] & [0] & \cdots\cdots\cdots & [0] & [0] \\ [0] & [I] & \cdots\cdots\cdots & [0] & [0] \\ [0] & [0] & \cdots\cdots\cdots & [0] & [0] \\ \cdots & \cdots & \cdots\cdots\cdots & \cdots & \cdots \\ \cdots & \cdots & \cdots\cdots\cdots & \cdots & \cdots \\ \cdots & \cdots & \cdots\cdots\cdots & \cdots & \cdots \\ [0] & [0] & \cdots\cdots\cdots & [0] & [0] \\ [0] & [0] & \cdots\cdots\cdots & [I] & [0] \\ [0] & [0] & \cdots\cdots\cdots & [0] & [I] \end{bmatrix} \tag{58}$$

Lowest $[\alpha]$ Matrix Normalization:

Another common formulation for finding the modal frequencies from a matrix coefficient polynomial comes from the eigenvalue solution of a companion matrix formed from the normalization of the lowest-order $[\alpha]_0$ coefficient matrix to the identity matrix $[I]$ yielding the following companion matrix:

$$[C] = \begin{bmatrix} -[\alpha]_{m-1} & -[\alpha]_{m-2} & \cdots\cdots\cdots & -[\alpha]_1 & -[I] \\ [I] & [0] & \cdots\cdots\cdots & [0] & [0] \\ [0] & [I] & \cdots\cdots\cdots & [0] & [0] \\ [0] & [0] & \cdots\cdots\cdots & [0] & [0] \\ \cdots & \cdots & \cdots\cdots\cdots & \cdots & \cdots \\ \cdots & \cdots & \cdots\cdots\cdots & \cdots & \cdots \\ \cdots & \cdots & \cdots\cdots\cdots & \cdots & \cdots \\ [0] & [0] & \cdots\cdots\cdots & [0] & [0] \\ [0] & [0] & \cdots\cdots\cdots & [0] & [0] \\ [0] & [0] & \cdots\cdots\cdots & [I] & [0] \end{bmatrix} \tag{59}$$

Note again that the numerical characteristics of the eigenvalue solution of the companion matrix will be different for low-order cases compared to high-order cases for a given data set. The companion matrix can be used in the following eigenvalue formulation to determine the modal frequencies for the original matrix coefficient equation:

$$\left[\tilde{I}\right] = \begin{bmatrix} [\alpha]_m & [0] & \cdots\cdots\cdots & [0] & [0] \\ [0] & [I] & \cdots\cdots\cdots & [0] & [0] \\ [0] & [0] & \cdots\cdots\cdots & [0] & [0] \\ \cdots & \cdots & \cdots\cdots\cdots & \cdots & \cdots \\ \cdots & \cdots & \cdots\cdots\cdots & \cdots & \cdots \\ \cdots & \cdots & \cdots\cdots\cdots & \cdots & \cdots \\ [0] & [0] & \cdots\cdots\cdots & [0] & [0] \\ [0] & [0] & \cdots\cdots\cdots & [I] & [0] \\ [0] & [0] & \cdots\cdots\cdots & [0] & [I] \end{bmatrix} \tag{60}$$

$$[C]\{X\} = \lambda \left[\tilde{I}\right] \{X\} \tag{61}$$

The eigenvectors that can be found from the eigenvalue-eigenvector solution utilizing the companion matrix may, or may not, be useful in terms of modal parameters. The eigenvector that is found, associated with each eigenvalue, is of length model order m times matrix coefficient size, N_S or N_L. In fact, the unique (meaningful) portion of the eigenvector is of length equal to the size of the coefficient matrices, N_S or N_L, and is repeated in the eigenvector m times. For each repetition, the unique portion of the eigenvector is repeated, multiplied by a different complex scalar which is a successively larger, integer power of the associated modal

frequency. Therefore, the eigenvectors of the companion matrix have the following form:

$$\{\phi\}_r \propto \left\{ \begin{array}{c} \lambda_r^{m-1}\{\psi\}_r \\ \cdot \\ \cdot \\ \cdot \\ \lambda_r^{2}\{\psi\}_r \\ \lambda_r^{1}\{\psi\}_r \\ \lambda_r^{0}\{\psi\}_r \end{array} \right\}_r \propto \left\{ \begin{array}{c} z_r^{m-1}\{\psi\}_r \\ \cdot \\ \cdot \\ \cdot \\ z_r^{2}\{\psi\}_r \\ z_r^{1}\{\psi\}_r \\ z_r^{0}\{\psi\}_r \end{array} \right\}_r \tag{62}$$

These vectors are often referred to as m-th order state vectors. Note that the z_r mapped version of the λ_r is commonly used to avoid numerical problems with weighting that occurs when high frequencies are involved. Note that, unless the size of the coefficient matrices is at least as large as the number of measurement degrees of freedom, only a partial set of modal coefficients, the modal participation coefficients (L_{qr}) will be found. For the case involving scalar polynomial coefficients, no meaningful modal coefficients will be found.

If the size of the coefficient matrices (N_S), and therefore the modal participation vector ($\{L_r\}$), is less than the largest spatial dimension of the problem (N_L), then the modal vectors are typically found in the second stage solution (MPE-2) process using one of Eqs. 63 through 68. Even if the complete modal vector ($\{\psi\}$) of the system is found from the eigenvectors of the companion matrix approach, the modal scaling and modal participation vectors for each modal frequency are normally found in this second stage formulation.

2.3.3 Partial Fraction Models: Residues and Residuals

Residues

The following sections review the relevant theoretical concepts and equations required for discussing the estimation of final scaled modal vectors. The final scaled modal vectors are often derived from the residues of the partial fraction model of the MIMO FRF data matrix [6]. Alternatively, the final scaled modal vectors can be estimated as a vector proportional to the residue vector with associated modal scaling, such as Modal A (M_{A_r}).

Residues from Single Reference FRFs

The equations that relate the complex modal frequencies, complex valued residues, and complex valued modal vectors to the single reference FRF data are well-known and are restated in the following equations for discussion purposes [6, 51]:

$$H_{pq}(\omega) = \sum_{r=1}^{N} \frac{A_{pqr}}{j\omega - \lambda_r} + \frac{A^*_{pqr}}{j\omega - \lambda^*_r} \tag{63}$$

$$\left\{H_{pq}(\omega)\right\}_{N_L \times 1} = \sum_{r=1}^{N} \frac{\left\{A_{pqr}\right\}_{N_L \times 1}}{j\omega - \lambda_r} + \frac{\left\{A^*_{pqr}\right\}_{N_L \times 1}}{j\omega - \lambda^*_r} \tag{64}$$

The above equations represent a partial fraction, residue model for the force-displacement FRF relationships. At the point where modal vectors are estimated, the FRF measurements, the measured frequencies, and the complex valued modal frequencies, λ_r, are known. The above model assumes that the residues (the numerator terms) occur in complex conjugate pairs. This model is often generalized as follows:

$$H_{pq}(\omega) = \sum_{r=1}^{2N} \frac{A_{pqr}}{j\omega - \lambda_r} \tag{65}$$

$$\left\{H_{pq}(\omega)\right\}_{N_L \times 1} = \sum_{r=1}^{2N} \frac{\left\{A_{pqr}\right\}_{N_L \times 1}}{j\omega - \lambda_r} \tag{66}$$

In the above equations, no assumption is made regarding the complex conjugate pair relationship among the residues. Once the residues are estimated, the estimates are evaluated to determine if there are complex conjugate pairs as a measure of quality.

Residues from Multiple Reference FRFs

Likewise, the equations that relate the complex modal frequencies, complex valued modal participation vectors, complex valued modal vectors, and complex valued residues in the multiple reference and multi-input, multi-output (MIMO) FRF data situation are well-known and are restated in the following equations for discussion purposes [6, 52]:

$$[H(\omega)]_{N_S \times N_L} = \sum_{r=1}^{2N} \frac{[A_r]_{N_S \times N_L}}{j\omega - \lambda_r} \tag{67}$$

The above equation is the natural extension of the single reference, partial fraction residue model in the previous section. When this equation is applied to the estimation of modal vectors, the relationships between the references (known as the modal participation vectors ($[L]$)) and the complex valued modal frequencies, λ_r, are already known. This allows the equation to be rearranged to take this a-priori information into account.

$$[\![H(\omega)]\!]_{N_S \times N_L \times N_f} = [L]_{N_S \times 2N} [\![\Lambda(\omega)]\!]_{2N \times 2N \times N_f} [\psi]^T_{2N \times N_L} \tag{68}$$

Noting that:

$$A_{pqr} = L_{pr} \psi_{qr} \tag{69}$$

In the above equation, note that an unconventional format is used to clarify the structure of the equation. The double bracket notation $[\![\ ]\!]$ is used to note that the term within the brackets is repeated across all frequencies (N_f). This makes the matrix products ambiguous since a matrix product between a 2D and a 3D matrix is not uniquely defined. This will be explained further in a later section.

Also in the above equations, note that the columns of the $[\![H(\omega)]\!]$ matrix are uncoupled as are the columns of the $[\psi]$ matrix. This allows this equation to be implemented for N_S FRFs, associated with one response DOF. This solution then proceeds for each of the N_L response DOFs, one at a time as in the single reference situation.

In all equations to this point in the chapter, it should be noted that the residues should be purely imaginary for a normal mode case (proportional damping) utilizing displacement over force FRF data. For the anticipated normal mode situation, there is no constraint on the numerical characteristics of either the modal participation coefficient or the modal vector coefficient individually as long as the product of these two terms yields the correct residue characteristic.

Residues from IRFs

Most current modal parameter estimation algorithms utilize frequency or impulse response functions as the data, or known information, to solve for modal parameters. If the data is utilized in the form of impulse response functions, a damped complex exponential model is appropriate. Impulse response functions are rarely directly measured but are calculated from associated frequency response functions via the inverse FFT algorithm.

The damped complex exponential model is essentially the Fourier or Laplace transform of the partial fraction models already discussed. Since the damped complex exponential model is numerically well-formed, this model has also been used extensively. In terms of the same notation used previously, the damped complex exponential model can be formed as either a summation of terms or product of terms, just as the partial fraction model is formed in the frequency domain.

The general equation that can be used to represent the relationship between the measured impulse response function matrix and the modal parameters is shown as a summation of terms in Eq. 70 or, in the equivalent matrix product form, in Eqs. 71 and 72.

$$[h(t)]_{N_L \times N_S} = \sum_{r=1}^{N} [A_r]_{N_L \times N_S} e^{\lambda_r t} + [A_r^*]_{N_L \times N_S} e^{\lambda_r^* t}$$

$$= \sum_{r=1}^{2N} [A_r]_{N_L \times N_S} e^{\lambda_r t} \tag{70}$$

$$[\![h(t)]\!]_{N_L \times N_S \times N_t} = [\psi]\, e^{\lambda_r t}]\!]_{2N \times 2N \times N_t} [L]^T_{2N \times N_S} \tag{71}$$

$$[\![h(t)]\!]^T_{N_S \times N_L \times N_t} = [L]\, e^{\lambda_r t}]\!]_{2N \times 2N \times N_t} [\psi\ ]^T{}_{2N \times N_L} \tag{72}$$

Again noting that:

$$A_{pqr} = L_{pr} \psi_{qr} \tag{73}$$

Many modal parameter estimation algorithms have been originally formulated from Eqs. 63 through 73. However, a more general development for all algorithms is based upon relating the above equations to a general matrix coefficient polynomial model.

Residuals from FRFs

Continuous systems have an infinite number of degrees of freedom but, in general, only a finite number of modes can be used to describe the dynamic behavior of a system. The theoretical number of degrees of freedom can be reduced by using a finite frequency range. Therefore, for example, the frequency response can be broken up into three partial sums, each covering the modal contribution corresponding to modes located in the frequency ranges. Note how the mode at 2.2 Hertz affects the modes below and above in the frequency range plotted in Fig. 5.

In the frequency range of interest, the modal parameters can be estimated to be consistent with Eq. 63. For a situation where modes below and above the frequency range of interest cannot be ignored, residual terms can be included to account for the effect that these modes will have when estimating modal parameters within the frequency range of interest. In this case, Eq. 63 can be rewritten for a single frequency response function as:

$$H_{pq}(\omega) = R_{F_{pq}} + \sum_{r=1}^{N} \frac{A_{pqr}}{j\omega - \lambda_r} + \frac{A^*_{pqr}}{j\omega - \lambda^*_r} + \frac{R_{I_{pq}}}{(j\omega)^2} \tag{74}$$

where

- $R_{F_{pq}}$ = Residual flexibility
- $R_{I_{pq}}$ = Residual inertia

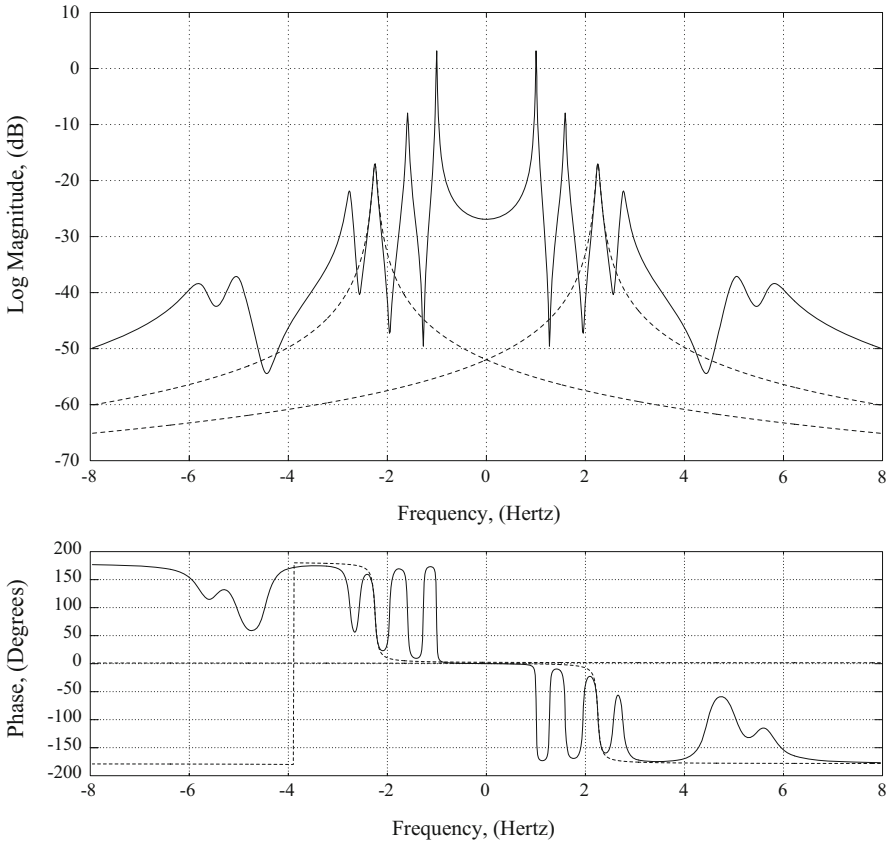

Fig. 5 Residual effects on FRF frequency band

The oldest and simplest approach is to include two frequency domain terms to account for the inertia effect of lower frequency modes of vibration, below the minimum frequency, and the stiffness effect of higher frequency modes of vibration, above the maximum frequency. These two terms are referred to as residual inertia ($R_{I_{pq}}$) and residual flexibility ($R_{F_{pq}}$).

Note that using the form of the above equation, residual flexibility ($R_{F_{pq}}$) should be a positive constant, and residual inertia ($R_{I_{pq}}$) should be a positive constant representing the magnitude of the second-order frequency term (Fig. 6).

The lower residual is a term reflecting the inertia or mass of the lower modes and is an inverse function of the frequency squared. The upper residual is a term reflecting the flexibility of the upper modes and is constant with frequency. In many cases the lower residual term is called the inertia restraint.

Residuals are a function of each individual frequency response function measurement and are not global properties of the frequency response function matrix. Therefore, residuals cannot be estimated unless the frequency response function has been measured.

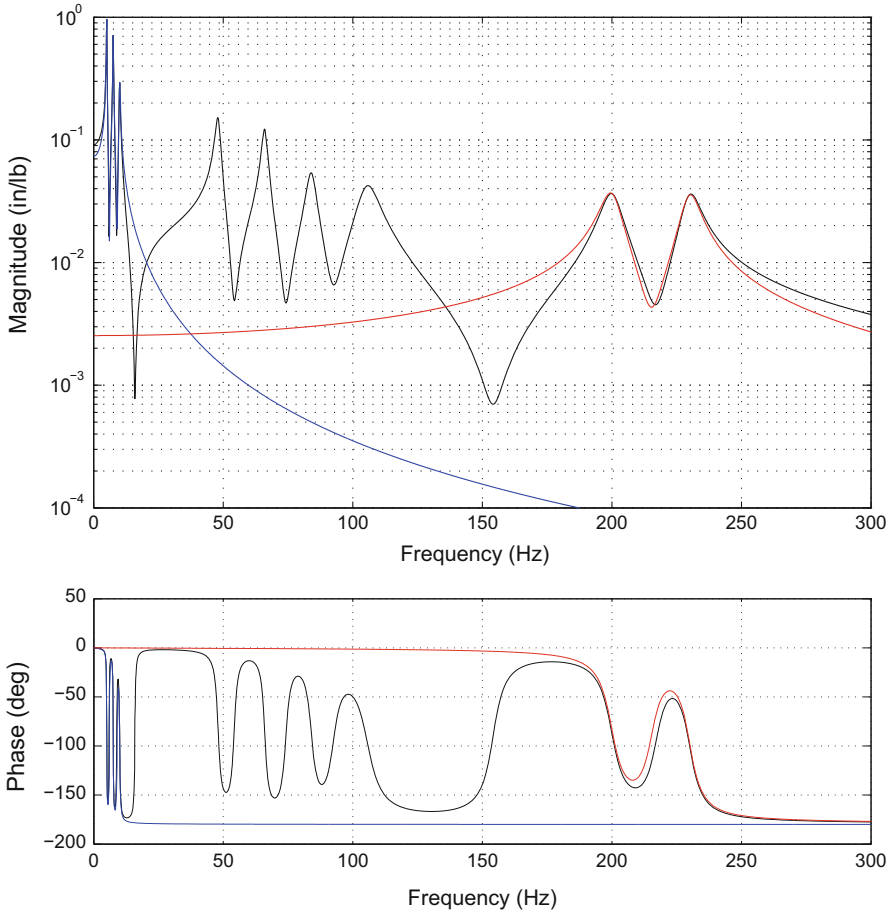

Fig. 6 Influence of residuals on nearby modes

Note that in this common formulation of residuals, both terms are real valued quantities. Also note that in general this is a simplification: the residual effects of modes below and/or above the frequency range of interest cannot be completely represented by such simple relationships.

In this case, the form of the residual is based upon a physical concept of how the system poles below and above the frequency range of interest will affect the data in the range of interest. As the system poles below and above the range of interest are located in the proximity of the boundaries, these effects are not the simple real valued quantities noted in Eq. 74.

In these cases, residual modes may be included in the model to partially account for these effects. When this is done, the modal parameters that are associated with these residual poles have no physical significance but may be required in order to compensate for strong dynamic influences from outside the frequency range of

interest. Using the same argument, the lower and upper residuals can take on any mathematical form that is convenient as long as the lack of physical significance is understood. Mathematically, power functions of frequency (zero, first, and second order) are commonly used within such a limitation. In general, the use of residuals is confined to frequency response function models. This is primarily due to the difficulty of formulating a reasonable mathematical model and solution procedure in the time domain for the general case that includes residuals.

The above models do not show additional mathematical terms, referred to as residuals, that account for the influence of modes with modal frequencies outside of the range of the frequencies used in the modal parameter estimation, or even outside the frequency range of the FRF measurements. This approach can be generalized to a set of five or more frequency domain, polynomial terms that are mathematical in structure but simply an extension of the residual inertia and flexibility concept. This approach better accounts for modes with frequencies above and below the maximum and minimum frequency of interest for cases where the modal frequencies are close to the frequency boundaries.

$$H_{pq}(\omega) = R_{F_{pq}} + R_{1_{pq}}(j\omega) + R_{2_{pq}}(j\omega)^2 + \sum_{r=1}^{N} \frac{A_{pqr}}{j\omega - \lambda_r} + \frac{A^*_{pqr}}{j\omega - \lambda^*_r} + \frac{R_{3_{pq}}}{(j\omega)} + \frac{R_{I_{pq}}}{(j\omega)^2} \qquad (75)$$

The above two approaches to estimating residuals are most often a part of the LS and WLS solutions. The concept is that the addition of residuals reduces the contamination of the modal vectors that are estimated from the modes with frequencies outside the frequency band of interest.

Another form of residuals is to allow extra computational poles (terms that have the same form as complex modal frequencies) to augment the physical complex modal frequencies that have been identified. These additional terms are of similar mathematical structure to the physical complex modal frequencies and are easy to implement in the solution procedure. Again the concept is that these additional computational terms allow the modal vectors to be estimated with less influence or contamination from modes that are nearby in frequency or even noise within the frequency band of interest. These computational poles may take on any complex valued frequency value and are found from the modal parameter estimation process. In normal situations, these poles are not included as physical, complex modal frequencies since they do not satisfy requirements of complex modal frequencies (consistency of estimates, realistic damping or frequency, etc.).

In all cases, the value of the residuals are of little practical value except to improve the estimates of the modal vectors. The residual information is generally not retained after the modal vectors have been estimated.

2.3.4 Modal Vectors and Modal Scaling from Residues

The modal vectors are most often determined by normalizing the residues. There are a number of normalization methods that can be used. Once the modal vectors are

determined, the modal scaling can be determined. The modal vector normalization is up to the user but most commonly is chosen to give modal vectors that are dominantly real valued (close to normal modes). The choice of normalization may also consider how the comparable modal vectors from analytical methods have been normalized. For this reason, it is common to choose the modal vector normalization such that the realities of experimental estimation of the modal vectors (noting that the residues will not be perfectly imaginary valued) are considered. One example of a useful normalization is to choose to make the largest modal coefficient in each modal vector unity.

$$\{\psi_r\}_{N_L \times 1} = \frac{\{A_{pqr}\}_{N_L \times 1}}{\max(A_{pqr})} \tag{76}$$

In the above equation, the residue vector is divided by the residue with the largest complex magnitude, mode by mode. This yields a modal vector that will generally be dominantly real valued and limited in magnitude to plus/minus unity.

The modal A scaling term (M_{A_r}) can then be found to provide the absolute scaling associated with this modal vector normalization/scaling. *Note that if the normalization/scaling of this modal vector is the same as that used for an analytical solution, then the modal A scaling terms are comparable.*

$$A_{pqr} = \frac{\psi_{pr}\,\psi_{qr}}{M_{A_r}} \qquad M_{A_r} = \frac{\psi_{pr}\,\psi_{qr}}{A_{pqr}} \tag{77}$$

If the modal vector is completely real valued, the modal mass scaling term (M_r) can be estimated.

$$A_{pqr} = \frac{\psi_{pr}\,\psi_{qr}}{j2\omega_r M_r} \qquad M_r = \frac{\psi_{pr}\,\psi_{qr}}{j2\omega_r A_{pqr}} \tag{78}$$

Note that if the normalization/scaling of this modal vector is the same as that used for an analytical solution, then the modal mass scaling terms are comparable.

Finally, from the above equations, *modal mass* can be estimated from *modal A* as long as the modal vector is a normal (real valued) mode.

$$M_r = \frac{M_{A_r}}{j2\omega_r} \tag{79}$$

If the modal vector is not a real valued normal mode, the modal vector can be normalized to an equivalent real valued normal mode and Eq. 78 can be used. Alternatively, an *effective modal mass* can be estimated from Eq. 80 as long as the modal vector is dominantly real valued.

$$\|M_r\| = \|\frac{M_{A_r}}{j2\omega_r}\| \tag{80}$$

2.3.5 Other Experimental Model Methods

There are several other models and methods that researchers use to solve for, or enhance, modal parameter estimates up through methods that are used to solve for data originating from a nonlinear system. Many times, these techniques are used to improve modal parameter estimates that originated with data that has noticeable noise. One method would be a maximum likelihood method [53, 54, 55, 56, 56] that begins with a modal parameter solution from one of the methods discussed here, integrating a procedure that can allow one or more of the modal parameters to be varied to improve the comparison between measured data and synthesized data. Another method that would be applied to input-output data that has expected nonlinear characteristics is the time domain NARMAX methods or the frequency domain reverse path methods. These methods are not covered in any further detail in this text.

3 Single Degree of Freedom Methods

3.1 SDOF Algorithms: Overview

For any real system, the use of single degree of freedom algorithms to estimate modal parameters is always an approximation since any realistic structural system will have many degrees of freedom. Nevertheless, in cases where the modes are not close in frequency and do not affect one another significantly, single degree of freedom algorithms are very effective. Specifically, single degree of freedom algorithms are quick, rarely involving much mathematical manipulation of the data, and give sufficiently accurate results for most modal parameter requirements. Naturally, most multiple degree of freedom algorithms can be constrained to estimate only a single degree of freedom at a time if further mathematical accuracy is desired.

3.2 Operating Vector (Peak-Pick) Estimation

Technically, when many single degree of freedom approaches are used to estimate modal parameters, sufficient simplifying assumptions are made such that the results may not be modal parameters in a rigorous sense. In these cases, the results are often referred to as *operating vectors* or *operating deflection shapes (ODS)* rather than modal vectors. This term refers to the fact that if the structural system is excited at this frequency, the resulting motion will be a linear combination of the modal vectors rather than a single modal vector. If one mode is dominant, then the operating vector will be approximately equal to the modal vector. Modal parameters can be estimated, but, generally, methods that use a model and several frequencies are preferred. The term *operating deflection shapes (ODS)* is generally used when data other than FRFs, such as cross power spectra (CPS), is the experimentally measured data.

The most commonly used single degree of freedom algorithms involve using the information at a single frequency as an estimate of the modal vector. These methods have historically been referred to as *peak-pick methods*. Figure 7 is an example of using the information at the peak frequency location (positive or negative peak in the imaginary part of the X/F frequency response functions) as an estimate of the modal vectors of a simple beam.

Summary: Operating (Peak-Pick) Vector Methods

- Methods are simple, approximate methods
- Modal frequency
  - Peak in imaginary part of FRF
  - Zero crossing in real part of FRF
  - Peak in magnitude or log magnitude of FRF
- Modal damping: half-power method
- Residue: SDOF equation
  - Complex qmplitude of FRF
  - Imaginary part of FRF – X/F or A/F
  - Real part of FRF – V/F
  - Magnitude of FRF (+/− sign depending on phase angle)
- Separation of close modes is generally not possible
- No residuals

If modal parameters are desired, the approximate relationships that are used in these cases are represented in the following two equations.

$$H_{pq}(\omega_r) \approx \frac{A_{pqr}}{j\omega_r - \lambda_r} + \frac{A^*_{pqr}}{j\omega_r - \lambda^*_r} \tag{81}$$

$$H_{pq}(\omega_r) \approx \frac{A_{pqr}}{-\sigma_r} \qquad A_{pqr} \approx -\sigma_r H_{pq}(\omega_r) \tag{82}$$

For these less complicated methods, the damped natural frequencies (ω_r) are estimated by observing the maxima in the frequency response functions. The damping factors (σ_r) are estimated using half-power methods [45]. The residues (A_{pqr}) are then estimated from Eq. 82 using the frequency response function data at the damped natural frequency.

Figures 8, 9, and 10 show frequency response function measurements in different formats to emphasize that the data can be determined in several ways. Note the characteristics of the FRF data, in each format, in the frequency range around the damped natural frequency (ω_r).

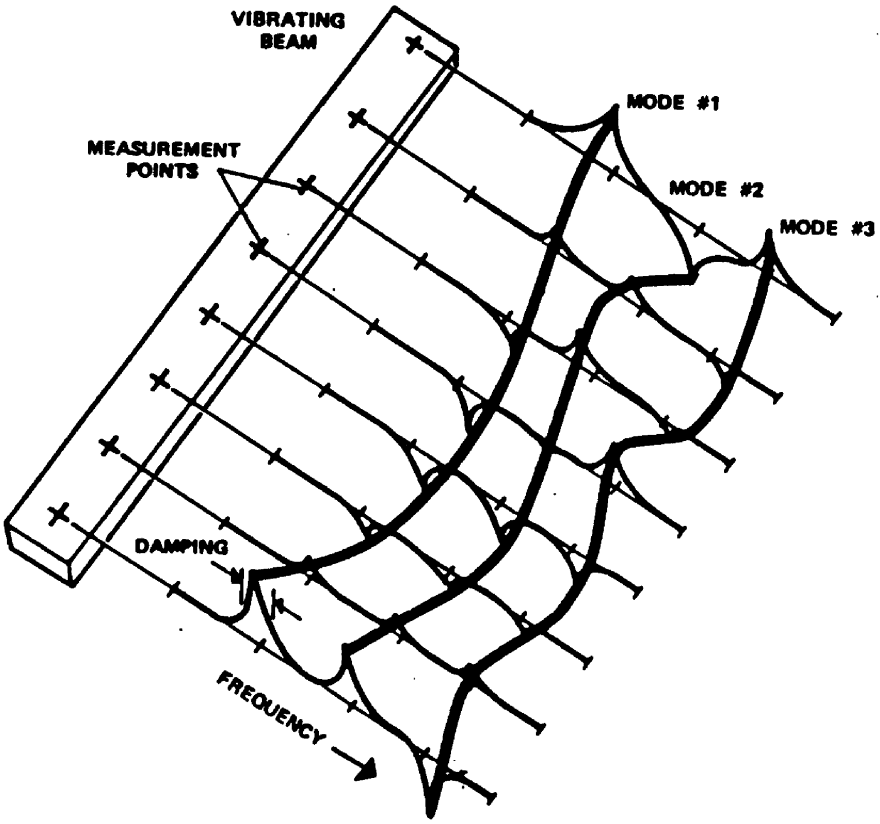

Fig. 7 Modal vectors from the imaginary part of the FRF

The damped natural frequency ω_r is estimated in one of three ways:

- The frequency where the magnitude of the FRF reaches a maximum
- The frequency where the real part of the FRF crosses zero
- The frequency where the imaginary part of the FRF reaches a relative minima (or maxima)

Of these three methods, the last approach gives the most reliable results under all conditions.

Once the damped natural frequency ω_r has been estimated, the real part of the modal frequency, the damping factor σ_r, can be estimated. The damping factor σ_r can be estimated by using the half-power bandwidth method or possibly the log decrement method.

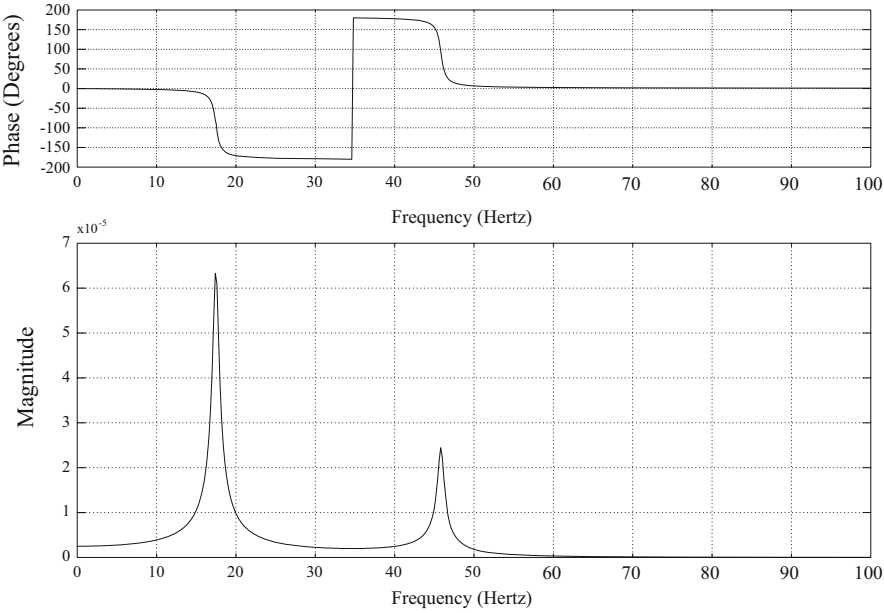

Fig. 8 Single degree of freedom method – magnitude/phase

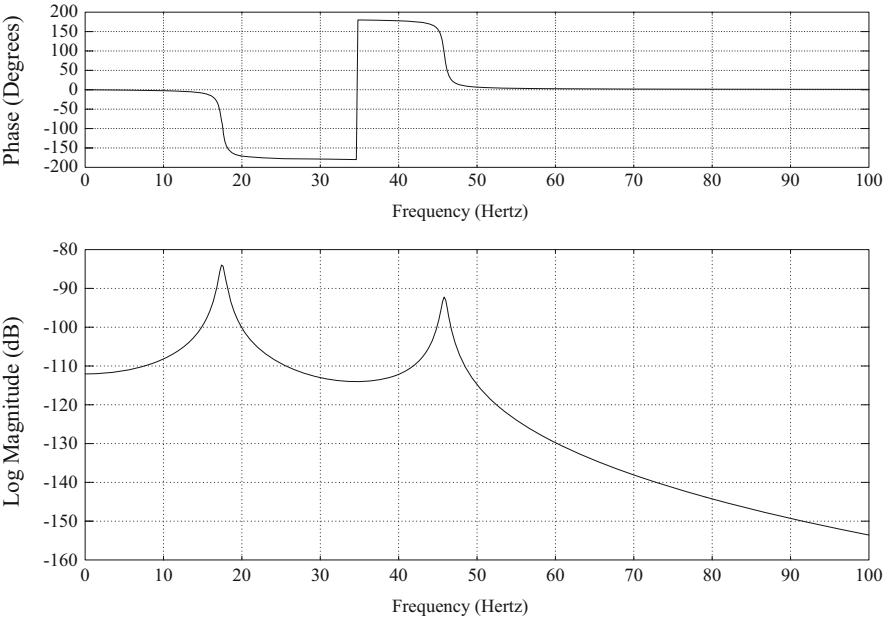

Fig. 9 Single degree of freedom method – log magnitude/phase

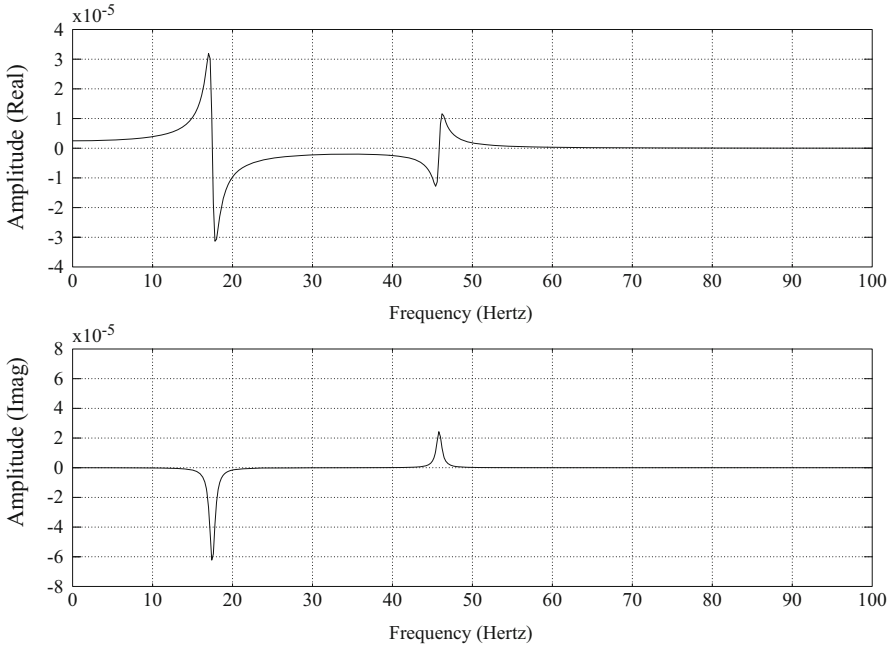

Fig. 10 Single degree of freedom method – real/imaginary

3.2.1 Half-Power Bandwidth Method

The half-power bandwidth method [45] is a frequency domain method that can give good results if only one mode is present in the frequency domain data and sufficient frequency resolution is available. For lightly damped situations, failure to meet this second criteria is quite common and can lead to significant error.

This method uses the data from the FRF in the region of the damped natural frequency to estimate the fraction of critical damping. Note that as long as the modes are separated in frequency, each mode can be treated as a SDOF. If this is the case, the fraction of critical damping can be found from the following formula:

$$\zeta_r = \frac{{\omega_b}^2 - {\omega_a}^2}{(2\,\omega_r)^2} \tag{83}$$

In the above equation, ω_r is the damped natural frequency as previously estimated. ω_a is the frequency, below ω_r, where the magnitude is 0.707 of the peak magnitude of the FRF. This corresponds to a half-power point. ω_b is the frequency, above ω_r, where the magnitude is 0.707 of the peak magnitude of the FRF. This also corresponds to a half-power point. These half-power points are also referred to as the -3 dB points, relative to the dB value at the peak.

For lightly damped systems, the above equation can be approximated by the following:

$$\zeta_r \approx \frac{\omega_b - \omega_a}{(2\,\omega_r)} \tag{84}$$

Once ζ_r is estimated, the damping factor σ_r can be estimated from the following equation.

$$\sigma_r = -\zeta_r\,\Omega_r \tag{85}$$

Again, assuming that the system is lightly damped, $\Omega_r \approx \omega_r$, the damping factor can be estimated from the following equation:

$$\sigma_r \approx -\zeta_r\,\omega_r \tag{86}$$

Figure 11 shows the frequency region around a damped natural frequency where no other nearby modes are present. The half-power bandwidth method can be applied to this data to estimate damping, but the lack of frequency resolution near the peak will mean that the true "full-power" amplitude cannot be observed. Therefore, the frequencies associated with the half-power amplitudes will not be found accurately. The fraction of critical damping will not be accurately found for this case.

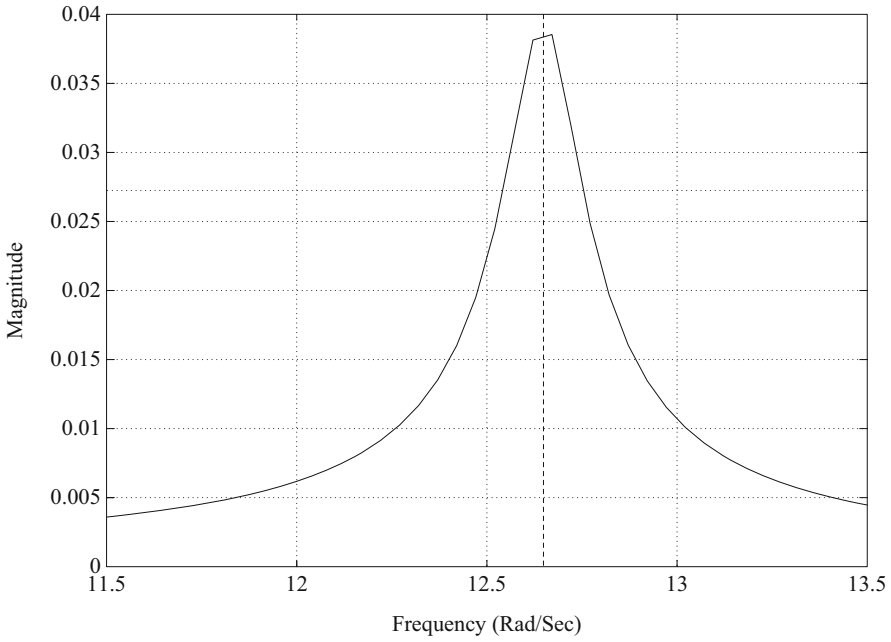

Fig. 11 SDOF FRF: magnitude plot with poor frequency resolution

Note that while this approach can yield reasonable results, most of the partial fraction methods discussed in upcoming Sects. 3.4 through 3.7 give superior results using the same data without the frequency resolution issues.

3.2.2 Logarithmic Decrement Method

An alternate approach to estimating the damping is from the time domain response using the log decrement method [45]. This method is rarely used since it will be difficult to obtain the time response of one mode when many modes are present. Nevertheless, the log decrement will be presented for completeness.

If time domain data for one mode of vibration can be obtained, looking like the free decay response in Fig. 12, the *log decrement*, defined as δ, can be found from two successive peak amplitudes in the following relationship:

$$\delta = \log_e\left(\frac{x(t_n)}{x(t_{n+T})}\right) = ln\left(\frac{x(t_n)}{x(t_{n+T})}\right) \tag{87}$$

where T is the length of one period of the oscillation.

The log decrement value can be used to estimate the fraction of critical damping:

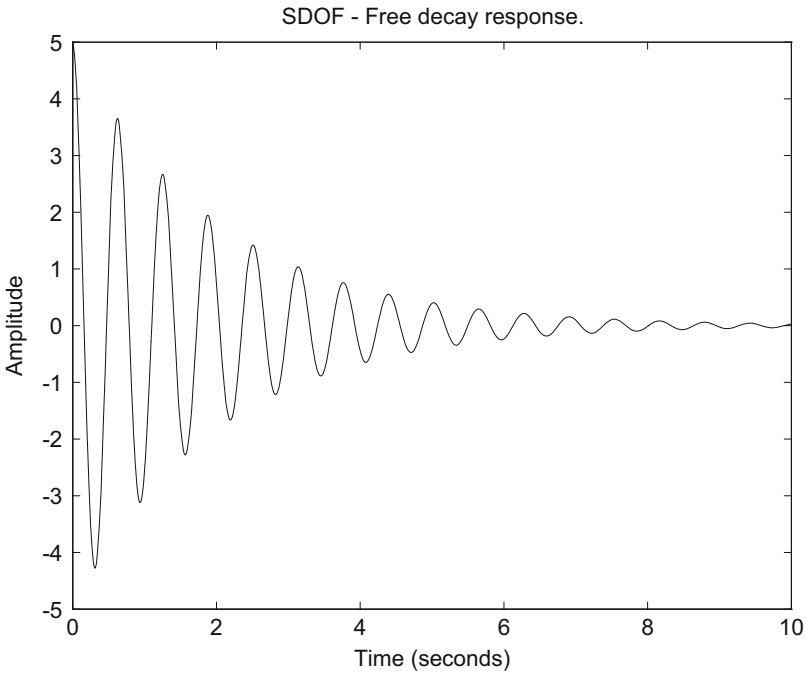

Fig. 12 SDOF Time Domain: free decay response

$$\delta = \frac{2\pi\zeta}{\sqrt{1-\zeta^2}} \approx 2\pi\zeta \quad for \ \zeta \ll 0.1 \tag{88}$$

Note that the damped natural frequency ω_r can be found from the time of one period of this oscillatory response as:

Note that while this approach can yield reasonable results, most of the partial fraction methods discussed in the upcoming Sects. 3.4 through 3.7 give superior results without the frequency resolution limitation, using the same data.

3.3 Complex Plot (Circle Fit) Method

The Circle Fit method is based upon a technique first reported by Kennedy and Pancu in 1947 [57]. This method utilizes the concept that the data curve in the vicinity of a modal frequency looks circular. In fact, the diameter of the circle is used to estimate the residue once the damping factor is estimated. More importantly, though, Kennedy and Pancu noted that the distance along the curve between data points at equidistant frequency maximized in the neighborhood of the modal frequency. In this way, the circle fit method was the first method to detect closely spaced modes.

This method can give erroneous answers when the modal coefficient is near zero. This occurs essentially because when the mode does not exist in a particular frequency response function (either the input or response degree of freedom is at a node of the mode), the remaining data in the frequency range of the mode will be strongly affected by the next higher or lower mode. Therefore, the diameter of the circle that will be estimated will be a function of the modal coefficient for the next higher or lower mode. This can be detected visually but is somewhat difficult to detect automatically.

Summary: Complex Plot – Circle Fit Method

- Simple historical method (Kennedy and Pancu, 1947)
- Modal frequency: frequency where largest spacing between data points occurs (frequency at bottom or top of complex plot)
- Modal damping: half-power method
- Residue: SDOF equation
  - Diameter of the circle $\approx \frac{A_{pqr}}{-\sigma_r}$
- Separation of close modes possible
- Residuals possible
  - Center of the circle not on axis
- Complex modal coefficients
- Problem: Error when modal coefficient should be zero

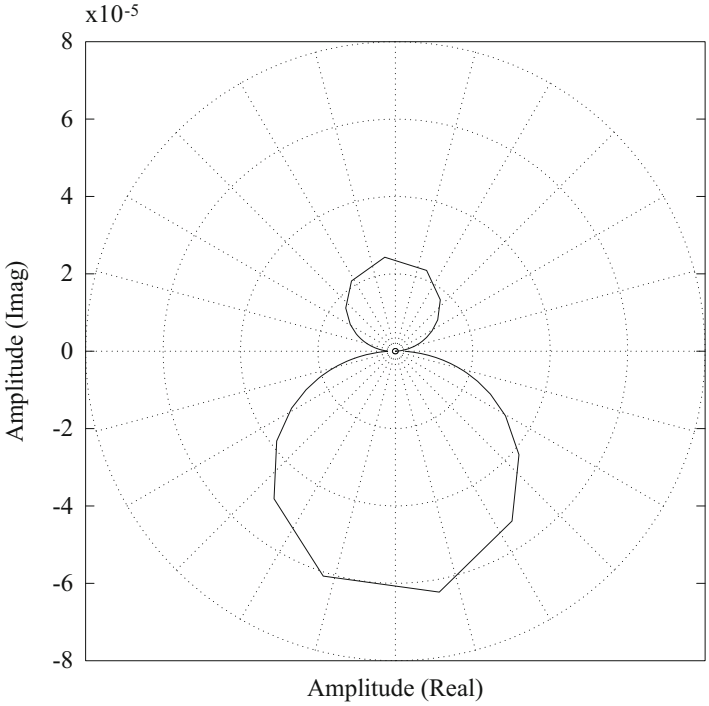

Fig. 13 SDOF FRF Complex Plot: real versus imaginary

The approximate relationship that is used in this case is represented in the following equation (Fig. 13).

$$H_{pq}(\omega_r) \approx R_{pq} + \frac{A_{pqr}}{j\omega_r - \lambda_r} + \frac{A^*_{pqr}}{j\omega_r - \lambda^*_r} \tag{89}$$

General equation of a circle

$$x^2 + y^2 + a\,x + b\,y + c = 0 \tag{90}$$

$$a\,x + b\,y + c = -x^2 - y^2 \tag{91}$$

Center of circle

$$x_c = -\frac{a}{2} \qquad y_c = -\frac{b}{2} \tag{92}$$

Radius of circle

$$Radius = \left(\left(\frac{a}{2}\right)^2 + \left(\frac{b}{2}\right)^2 - c \right)^{0.5} \tag{93}$$

Data points for circle

$$x_i = Real(H_{pq}(\omega_i)) \qquad y_i = Imag(H_{pq}(\omega_i)) \tag{94}$$

Direct solution (three data points)

$$a\,x_1 + b\,y_1 + c = -x_1^2 - y_1^2 \tag{95}$$

$$a\,x_2 + b\,y_2 + c = -x_2^2 - y_2^2 \tag{96}$$

$$a\,x_3 + b\,y_3 + c = -x_3^2 - y_3^2 \tag{97}$$

$$\begin{bmatrix} x_1 & y_1 & 1 \\ x_2 & y_2 & 1 \\ x_3 & y_3 & 1 \end{bmatrix} \begin{Bmatrix} a \\ b \\ c \end{Bmatrix} = \begin{Bmatrix} -x_1^2 - y_1^2 \\ -x_2^2 - y_2^2 \\ -x_3^2 - y_3^2 \end{Bmatrix} \qquad or \qquad [T] \begin{Bmatrix} a \\ b \\ c \end{Bmatrix} = \{S\} \tag{98}$$

$$\begin{Bmatrix} a \\ b \\ c \end{Bmatrix} = [T]^{-1}\,\{S\} \tag{99}$$

Least-squares solution (more than three data points)

$$\begin{bmatrix} x_1 & y_1 & 1 \\ x_2 & y_2 & 1 \\ x_3 & y_3 & 1 \\ x_4 & y_4 & 1 \\ \cdots & \cdots & \cdots \\ x_n & y_n & 1 \end{bmatrix} \begin{Bmatrix} a \\ b \\ c \end{Bmatrix} = \begin{Bmatrix} -x_1^2 - y_1^2 \\ -x_2^2 - y_2^2 \\ -x_3^2 - y_3^2 \\ -x_4^2 - y_4^2 \\ \cdots \\ -x_n^2 - y_n^2 \end{Bmatrix} \qquad or \qquad [T] \begin{Bmatrix} a \\ b \\ c \end{Bmatrix} = \{S\} \tag{100}$$

$$[T]^T\,[T] \begin{Bmatrix} a \\ b \\ c \end{Bmatrix} = [T]^T\,\{S\} \tag{101}$$

$$\begin{Bmatrix} a \\ b \\ c \end{Bmatrix} = \Big[[T]^T\,[T]\Big]^{-1} [T]^T\,\{S\} \tag{102}$$

3.4 Two-Point Finite Difference Formulation

The difference method formulations are simple methods that are based upon comparing adjacent frequency information in the vicinity of a resonance frequency [58]. When a ratio of this information, together with information from the derivative of the frequency response function at the same frequencies, is formed, a reasonable estimation of the modal frequency and residue for each mode can be determined under the assumption that modes are not too close together. This method can give erroneous answers when the modal coefficient is near zero. This problem can be detected by comparing the predicted modal frequency to the frequency range of the data used in the finite difference algorithm. As long as the predicted modal frequency lies within the frequency band, the estimate of the residue (modal coefficient) should be valid.

Summary: Finite Difference Method

- Common method implemented on many two channel digital signal processing analyzers.
- Solves for both modal frequency (λ_r) and residue (A_{pqr}).
- Uses the frequency response function information at two frequencies in the vicinity of a single mode.
- Several combinations of two frequencies can be used and the results averaged.
- Approximate method (ignores complex conjugate contribution).
- No residuals.
- Problem: Error when modal coefficient should be zero.

The approximate relationships that are used in this case is represented in the following three equations. The frequencies noted in these relationships are as follows: ω_1 is a frequency near the damped natural frequency ω_r, and ω_p is the peak frequency close to the damped natural frequency ω_r.

$$H_{pq}(\omega_1) \approx \frac{A_{pqr}}{j\omega_1 - \lambda_r} \tag{103}$$

$$H_{pq}(\omega_p) \approx \frac{A_{pqr}}{j\omega_p - \lambda_r} \tag{104}$$

The finite difference relationships are formulated as follows:

$$\Delta_1 = H_{pq}(\omega_p) - H_{pq}(\omega_1) \approx \frac{A_{pqr}(j\omega_1 - j\omega_p)}{(j\omega_1 - \lambda_r)(j\omega_p - \lambda_r)} \tag{105}$$

$$\Delta_2 = j\omega_p H_{pq}(\omega_p) - j\omega_1 H_{pq}(\omega_1) \approx \frac{A_{pqr}(j\omega_1 - j\omega_p)\lambda_r}{(j\omega_1 - \lambda_r)(j\omega_p - \lambda_r)} \quad (106)$$

$$\Delta_3 = j(\omega_1 - \omega_p) H_{pq}(\omega_1) H_{pq}(\omega_p) \approx \frac{j(\omega_1 - \omega_p) A_{pqr} A_{pqr}}{(j\omega_1 - \lambda_r)(j\omega_p - \lambda_r)} \quad (107)$$

Modal frequency (λ_r)

$$\lambda_r \approx \frac{\Delta_2}{\Delta_1} = \frac{j\omega_p H_{pq}(\omega_p) - j\omega_1 H_{pq}(\omega_1)}{H_{pq}(\omega_p) - H_{pq}(\omega_1)} \quad (108)$$

Residue (A_{pqr})

$$A_{pqr} \approx \frac{\Delta_3}{\Delta_1} = \frac{j(\omega_1 - \omega_p) H_{pq}(\omega_1) H_{pq}(\omega_p)}{H_{pq}(\omega_p) - H_{pq}(\omega_1)} \quad (109)$$

Least-Squares Solution

Since both of the equations that are used to estimate modal frequency λ_r and residue A_{pqr} are linear equations, a least-squares solution can be formed by using other frequency response function data in the vicinity of the resonance. For this case, additional equations can be developed using $H_{pq}(\omega_2)$ or $H_{pq}(\omega_3)$ in the above equations instead of $H_{pq}(\omega_1)$. Starting with Eqs. 108 and 109 for any frequency (ω_1) in the vicinity of the peak frequency (ω_p) (rearranging Eqs. 108 and 109 slightly):

$$(H_{pq}(\omega_p) - H_{pq}(\omega_1))\,\lambda_r = j\omega_p H_{pq}(\omega_p) - j\omega_1 H_{pq}(\omega_1) \quad (110)$$

$$(H_{pq}(\omega_p) - H_{pq}(\omega_1))\,A_{pqr} = j(\omega_1 - \omega_p) H_{pq}(\omega_1) H_{pq}(\omega_p) \quad (111)$$

Two more equations, involving the same two unknowns, can now be written for any other frequency in the vicinity of the peak frequency (ω_p). Putting these equations into matrix form yields:

$$\begin{Bmatrix} H_{pq}(\omega_p) - H_{pq}(\omega_1) \\ H_{pq}(\omega_p) - H_{pq}(\omega_2) \\ H_{pq}(\omega_p) - H_{pq}(\omega_3) \\ \cdots \\ H_{pq}(\omega_p) - H_{pq}(\omega_s) \end{Bmatrix}_{N_s \times 1} \{\lambda_r\}_{1\times 1} = \begin{Bmatrix} j\omega_p H_{pq}(\omega_p) - j\omega_1 H_{pq}(\omega_1) \\ j\omega_p H_{pq}(\omega_p) - j\omega_2 H_{pq}(\omega_2) \\ j\omega_p H_{pq}(\omega_p) - j\omega_3 H_{pq}(\omega_3) \\ \cdots \\ j\omega_p H_{pq}(\omega_p) - j\omega_s H_{pq}(\omega_s) \end{Bmatrix}_{N_s \times 1} \quad (112)$$

$$\begin{Bmatrix} H_{pq}(\omega_p) - H_{pq}(\omega_1) \\ H_{pq}(\omega_p) - H_{pq}(\omega_2) \\ H_{pq}(\omega_p) - H_{pq}(\omega_3) \\ \cdots \\ H_{pq}(\omega_p) - H_{pq}(\omega_s) \end{Bmatrix}_{N_s \times 1} \quad \{A_{pqr}\}_{1\times 1} = \begin{Bmatrix} j(\omega_p - \omega_1) H_{pq}(\omega_p) & H_{pq}(\omega_1) \\ j(\omega_p - \omega_2) H_{pq}(\omega_p) & H_{pq}(\omega_2) \\ j(\omega_p - \omega_3) H_{pq}(\omega_p) & H_{pq}(\omega_3) \\ \cdots & \\ j(\omega_p - \omega_s) H_{pq}(\omega_p) & H_{pq}(\omega_s) \end{Bmatrix}_{N_s \times 1} \tag{113}$$

The above equations represent overdetermined sets of linear equations that can be solved using any pseudoinverse or normal equations approach.

3.5 Least-Squares (Local) SDOF Method

The least-squares local SDOF formulations are simple methods that are based upon using an SDOF model in the vicinity of a resonance frequency [58]. A reasonable estimation of the modal frequency and residue for each mode can be determined under the assumption that modes are not too close together. This method can give erroneous answers when the modal coefficient is near zero. This problem can be detected by comparing the predicted modal frequency to the frequency range of the data used in the algorithm. As long as the predicted modal frequency lies within the frequency band, the estimate of the residue (modal coefficient) should be valid.

Summary: Least-Squares (Local) SDOF Method

- Common method implemented on many two channel digital signal processing analyzers.
- Solves for both modal frequency (λ_r) and residue (A_{pqr}).
- Uses the frequency response function information in the vicinity of a single mode.
- Approximate method (ignores complex conjugate contribution).
- No residuals.
- Problem: Error when modal coefficient should be zero.

The approximate relationship that is used in this case is represented in the following equation. The frequency ω_1 is a frequency near the damped natural frequency ω_r.

$$H_{pq}(\omega_1) \approx \frac{A_{pqr}}{j\omega_1 - \lambda_r} \tag{114}$$

$$H_{pq}(\omega_1)\,(j\omega_1 - \lambda_r) \;=\; A_{pqr} \tag{115}$$

$$H_{pq}(\omega_1)\,\lambda_r \;+\; A_{pqr} \;=\; (j\omega_1) H_{pq}(\omega_1) \tag{116}$$

Repeating the above equation for several frequencies in the vicinity of the peak frequency:

$$\begin{bmatrix} H_{pq}(\omega_1) & 1 \\ H_{pq}(\omega_2) & 1 \\ H_{pq}(\omega_3) & 1 \\ H_{pq}(\omega_p) & 1 \\ \cdots & \cdots \\ H_{pq}(\omega_s) & 1 \end{bmatrix}_{N_s \times 2} \begin{Bmatrix} \lambda_r \\ A_{pqr} \end{Bmatrix}_{2\times 1} = \begin{Bmatrix} (j\omega_1) H_{pq}(\omega_1) \\ (j\omega_2) H_{pq}(\omega_2) \\ (j\omega_3) H_{pq}(\omega_3) \\ (j\omega_p) H_{pq}(\omega_p) \\ \cdots \\ (j\omega_s) H_{pq}(\omega_s) \end{Bmatrix}_{N_s \times 1} \tag{117}$$

The above equation again represents an overdetermined set of linear equations that can be solved using any pseudoinverse or normal equation approach.

3.6 Least-Squares (Global) SDOF Method

The least-squares, global SDOF formulations are simple methods that are based upon using an SDOF model in the vicinity of a resonance frequency for all measurements in a row or column of the FRF matrix [58]. A reasonable estimation of the modal frequency and residue for each mode can be determined under the assumption that modes are not too close together. This method can give erroneous results for a specific residue when the modal coefficient is near zero.

Summary: Least-Squares (Global) SDOF Method

- Solves for both modal frequency (λ_r) and residue (A_{pqr}).
- Uses the frequency response function information in the vicinity of a single mode.
- Approximate method (ignores complex conjugate contribution).
- No residuals.
- Problem: Error when modal coefficient should be zero still possible but normally avoided.

The approximate relationship that is used in this case begins with the result of the least-squares local SDOF method.

$$\begin{bmatrix} H_{pq}(\omega_1) & 1 \\ H_{pq}(\omega_2) & 1 \\ H_{pq}(\omega_3) & 1 \\ H_{pq}(\omega_p) & 1 \\ \cdots & \cdots \\ H_{pq}(\omega_s) & 1 \end{bmatrix}_{N_s \times 2} \begin{Bmatrix} \lambda_r \\ A_{pqr} \end{Bmatrix}_{2\times 1} = \begin{Bmatrix} (j\omega_1) H_{pq}(\omega_1) \\ (j\omega_2) H_{pq}(\omega_2) \\ (j\omega_3) H_{pq}(\omega_3) \\ (j\omega_p) H_{pq}(\omega_p) \\ \cdots \\ (j\omega_s) H_{pq}(\omega_s) \end{Bmatrix}_{N_s \times 1} \tag{118}$$

Note that the above equation can be written for each measurement in a column or row of the frequency response function matrix. When this is done, the modal frequency (λ_r) is the same for each measurement, while the residue (A_{pqr}) changes with each measurement. This is described by the matrix version of the above equation:

$$\begin{bmatrix} \{H_{pq}(\omega_1)\} & [I] \\ \{H_{pq}(\omega_2)\} & [I] \\ \{H_{pq}(\omega_3)\} & [I] \\ \{H_{pq}(\omega_p)\} & [I] \\ \cdots & \cdots \\ \{H_{pq}(\omega_s)\} & [I] \end{bmatrix}_{N_o N_s \times 2} \begin{Bmatrix} \lambda_r \\ \{A_{pqr}\} \end{Bmatrix}_{N_o+1 \times 1} = \begin{Bmatrix} (j\omega_1)\{H_{pq}(\omega_1)\} \\ (j\omega_2)\{H_{pq}(\omega_2)\} \\ (j\omega_3)\{H_{pq}(\omega_3)\} \\ (j\omega_p)\{H_{pq}(\omega_p)\} \\ \cdots \\ (j\omega_s)\{H_{pq}(\omega_s)\} \end{Bmatrix}_{N_o N_s \times 1} \tag{119}$$

In the above equation, the size of the frequency response function column ($H_{pq}(\omega_1)$) determines the number of residues that will be estimated as well as the size of the identity matrix. The above equation again represents an overdetermined set of linear equations that can be solved using any pseudoinverse or normal equations approach.

3.7 Other SDOF Methods

There are numerous other SDOF methods that may yield improved results when special conditions exist. One example would be when errors in the data require special attention like the case where the FRF data has frequency shift errors due to sensor mass loading. In this case, any kind of least squares estimate of the modal frequency across all FRFs, as with the previous least-squares (global) SDOF method, will yield compromised answers.

Some errors that are mostly random, or even systematic, bias errors from modes that are close in frequency, can be minimized by adding residuals to the SDOF model. The least-squares (global) SDOF method can be improved with the addition of residuals [59, 60] to account more completely for the nearby modes.

4 Multiple Degree of Freedom Methods

Modern multiple degree of freedom (MDOF) methods normally will include the general case of solving for multiple modal parameters that represent all measurements in a multiple input, multiple output (MIMO) set of data. While some of these methods may have originated as single measurement or single reference methods, all have been generalized to include those cases as a subset of the total method.

All methods utilize a kernel equation in the time or frequency domain with square matrix coefficients that are used to find modal frequencies based upon the size (dimension) of the square matrix coefficient and the model order.

4.1 General (Two-Stage) Solution Procedure

Based upon Eqs. 41 through 46 and Eqs. 47 through 50, most modern modal identification algorithms can be outlined briefly as in Sect. 2.1.11. This two stage procedure can be elaborated as follows:

- MPE-1: Utilize measured FRF or IRF data with a matrix coefficient, polynomial model to find multiple estimates of the modal parameters. Select the best set of modal frequencies and modal participation vectors.
  - Choose polynomial or subspace order (m).
  - Load measured data into over-determined linear equation form.
  - Solve for unknown matrix coefficients ($[\alpha_k]$).
    * Add sufficient block kernel equations (for different starting times or frequencies) until there are more block kernel equations than there are block unknowns ($[\alpha_k]$).
    * Solve for matrix coefficients ($[\alpha_k]$) in a least squares (LS) sense.
  - Solve for complex valued modal frequencies for (λ_r or z_r)
    * Formulate companion matrix.
    * Obtain eigenvalues of companion matrix. (λ_r or z_r).
      · Time Domain: convert eigenvalues from (λ_r or z_r).
      · Frequency Domain: compensate for generalized frequency.
    * Obtain modal participation vectors (L_{qr}) or modal vectors (ψ_r) from eigenvectors of the companion matrix, normalize as needed
  - Iterate over different polynomial orders or subspace orders in the kernel equation to get multiple estimates of the modal parameters.
  - Select one set of complex valued modal frequencies, with associated participation vectors, from the multiple sets. Manual or automated selection methods can be used.
- MPE-2: Utilize measured FRF or IRF data, with selected complex valued modal frequencies and modal participation vectors, to find complex valued modal vectors and modal scaling from an overdetermined set of linear equations.
  - Solve for modal vectors using a weighted least squares solution method involving the fixed set of modal frequencies and modal participation (weighting) vectors. Solution process often involves the estimation of residues.
  - Find modal vectors and modal scaling from Equations 75 through 79.
  - Normalize modal vectors as needed.
  - Solve for modal scaling associated with normalized modal vectors.

4.1.1 Consistency Diagrams

The MPE-1 stage is generally repeated for different matrix coefficient dimensions, model order, and/or equation normalizations to find statistically consistent sets of modal parameter results (sometimes referred to as clusters). Different kernel equations can also be combined to provide a statistical set of answers across all methods. Normally, 20 to 40 solution iterations are combined in a single diagram referred to as a consistency diagram. The consistency diagram shows the consistent

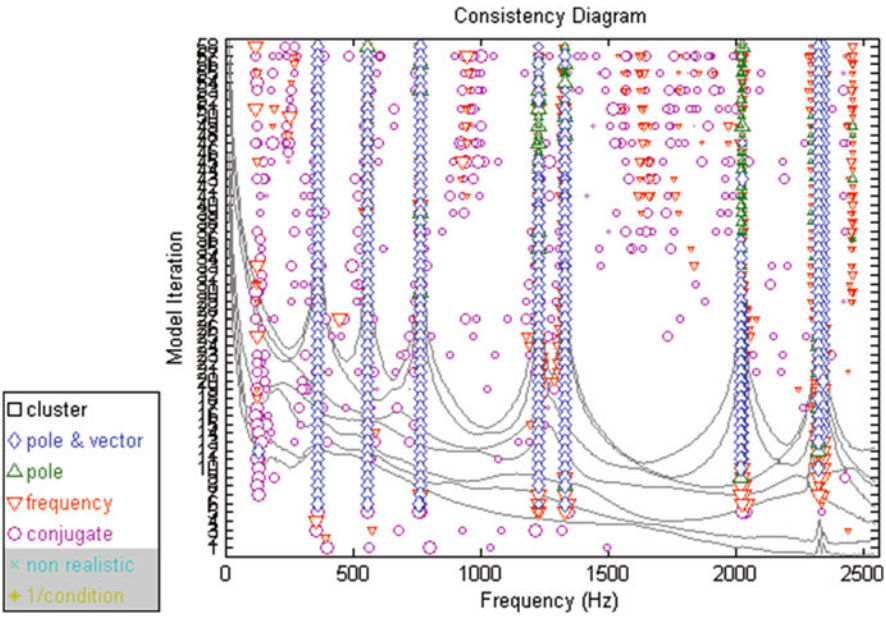

Fig. 14 Consistency diagram example

modal parameter results via a set of symbols denoting consistency in: modal frequency, modal frequency and damping, and modal frequency, damping and vectors. Historically, the consistency diagram was referred to as a stability diagram. Figure 14 is an example of a consistency diagram. More examples and further explanation of such validation methods are given in ▶ Chap. 11, "Experimental Modal Parameter Evaluation Methods" of this Handbook.

Once the final choice of modal frequency, modal damping, modal participation vectors, and modal scaling is found from the consistency diagram or other validation methods, the MPE-2 stage is implemented with the known information to determine the final scaled modal vectors.

4.2 Current MPE Methods

Using the concepts developed in the previous section, the most commonly used modal identification methods can be summarized as shown in Table 2. The high-order model is typically used for those cases where the system is under-sampled in the spatial domain. For example, the limiting case is when only one measurement is made on the structure. For this case, the left-hand side of the general linear equation corresponds to a scalar polynomial equation with the order equal to or greater than the number of desired modal frequencies.

Table 2 Modal vector estimation methods: overview

	Domain		Matrix polynomial order			Coefficients	
Algorithm	Time	Freq	Zero	Low	High	Scalar	Matrix
Complex exponential algorithm (CEA)	•				•	•	
Least-squares complex exponential (LSCE)	•				•	•	
Polyreference time domain (PTD)	•				•		$N_S \times N_S$
Ibrahim time domain (ITD)	•			•			$N_L \times N_L$
Multiple reference Ibrahim time domain (MRITD)	•			•			$N_L \times N_L$
Eigensystem realization algorithm (ERA)	•			•			$N_L \times N_L$
Polyreference frequency domain (PFD)		•		•			$N_L \times N_L$
Simultaneous frequency domain (SFD)		•		•			$N_L \times N_L$
Multi-reference frequency domain (MRFD)		•		•			$N_L \times N_L$
Rational fraction polynomial (RFP)		•			•	•	$N_S \times N_S$
Orthogonal polynomial (OP)		•			•	•	$N_S \times N_S$
Polyreference least-squares complex frequency (PLSCF)		•			•	•	$N_S \times N_S$
Complex mode indication function (CMIF)		•	•				$N_L \times N_S$

The low-order model is used for those cases where the spatial information is complete. In other words, the number of physical coordinates (N_L) is greater than the number of desired (positive) modal frequencies (N). For this case, the order (m) of the left-hand side of the general linear equation, Eq. 46 or 50, is equal to two.

The zero-order model corresponds to a cases where the temporal information is neglected and only the spatial information is used. These methods directly estimate the eigenvectors as a first step. In general, these methods are programmed to process data at a single temporal condition or variable. In this case, the method is essentially equivalent to the single degree of freedom (SDOF) methods which have been used with frequency response functions. In others words, the zeroth-order matrix polynomial model compared to the higher-order matrix polynomial models is similar to the comparison between the SDOF and MDOF methods used historically in modal parameter estimation.

Modal parameter estimation algorithms are similar in more ways than they are different. Fundamentally, all algorithms can be developed beginning with a linear, constant coefficient, symmetric matrix model involving mass, damping, and stiffness. The common goal in all algorithms, therefore, is the development of a charac-

teristic matrix coefficient equation that describes a linear, time invariant, reciprocal mechanical system consistent with this theoretical background. This is the rationale behind using the **Unified Matrix Polynomial Approach** as the educational basis for demonstrating this common kernel for all modal parameter estimation algorithms [1,2,3,4,5,6]. The following sections discuss the similarity of the kernel equations common to all widely used modal parameter estimation algorithms.

4.3 Kernel Equations: Time Domain Algorithms

The following are the kernel equations for low- to high-order time domain algorithms. While both first- and second-order kernel equations are included to be consistent with historical development, research has shown that the two approaches, first order and second order, give exactly the same values in the estimated coefficient matrices when exactly the same data is utilized [61].

4.3.1 High-Order Methods

Summary: High-Order Time Domain Methods
Typical algorithms

- Complex exponential (CE)
- Least-squares complex exponential (LSCE)
- Polyreference time domain (PTD)

General linear equation formulation

- Model order ($m \geq 2N/N_S$) where N is the number of desired positive frequency roots
- Number of roots ($m \times N_S$)
- Data matrix size ($N_S \times N_L$)
- Alpha coefficient matrix size ($N_S \times N_S$)

Kernel equation: high-order coefficient normalization

$$\left[\,[\alpha_0]\;[\alpha_1]\cdots[\alpha_{m-1}]\,\right]_{N_S\times mN_S}\begin{bmatrix}[h(t_{i+0})]\\ [h(t_{i+1})]\\ \cdots\\ [h(t_{i+m-1})]\end{bmatrix}_{mN_S\times N_L}=-\Big[[h(t_{i+m})]\Big]_{N_S\times N_L} \tag{120}$$

Kernel equation: zero-order coefficient normalization

$$\left[[\alpha_1]\ [\alpha_2] \cdots [\alpha_m] \right]_{N_S \times mN_S} \begin{bmatrix} [h(t_{i+1})] \\ [h(t_{i+2})] \\ \cdots \\ [h(t_{i+m})] \end{bmatrix}_{mN_S \times N_L} = -\Big[[h(t_{i+0})] \Big]_{N_S \times N_L} \tag{121}$$

4.3.2 Low-Order Methods: First Order

Summary: Low-Order (First) Time Domain Methods
Typical algorithms

- Ibrahim time domain (ITD)
- Multiple reference time domain (MRITD)
- Eigensystem realization algorithm (ERA)

General linear equation formulation

- Model order ($m = 1$)
- Number of roots ($1 \times 2N_L$)
- Data matrix size ($N_L \times N_S$)
- Alpha coefficient matrix size ($2N_L \times 2N_L$)

Kernel equation: high-order coefficient normalization

$$[[\alpha_0]]_{2N_L \times 2N_L} \begin{bmatrix} [h(t_{i+0})] \\ [h(t_{i+1})] \end{bmatrix}_{2N_L \times N_S} = -\begin{bmatrix} [h(t_{i+1})] \\ [h(t_{i+2})] \end{bmatrix}_{2N_L \times N_S} \tag{122}$$

Kernel equation: zero-order coefficient normalization

$$[[\alpha_1]]_{2N_L \times 2N_L} \begin{bmatrix} [h(t_{i+1})] \\ [h(t_{i+2})] \end{bmatrix}_{2N_L \times N_S} = -\begin{bmatrix} [h(t_{i+0})] \\ [h(t_{i+1})] \end{bmatrix}_{2N_L \times N_S} \tag{123}$$

4.3.3 Low-Order Methods: Second Order

Summary: Low-Order (Second) Time Domain Methods
Typical algorithms

- Time domain equivalent to polyreference frequency domain

General linear equation formulation

- Model order ($m = 2$)
- Number of roots ($2 \times N_L$)
- Data matrix size ($N_L \times N_S$)
- Matrix coefficients ($N_L \times N_L$)

Kernel equation: high-order coefficient normalization

$$\left[[\alpha_0]\ [\alpha_1] \right]_{N_L \times 2N_L} \begin{bmatrix} [h(t_{i+0})] \\ [h(t_{i+1})] \end{bmatrix}_{2N_L \times N_S} = -\Big[[h(t_{i+2})] \Big]_{N_L \times N_S} \tag{124}$$

Kernel equation: zero-order coefficient normalization

$$\left[[\alpha_1]\ [\alpha_2] \right]_{N_L \times 2N_L} \begin{bmatrix} [h(t_{i+1})] \\ [h(t_{i+2})] \end{bmatrix}_{2N_L \times N_S} = -\Big[[h(t_{i+0})] \Big]_{N_L \times N_S} \tag{125}$$

4.4 Kernel Equations: Frequency Domain Algorithms

The following are the kernel equations for low- to high-order frequency domain algorithms. While both first- and second-order kernel equations are included to be consistent with historical development, research has shown that the two approaches, first order and second order, give exactly the same values in the estimated coefficient matrices when exactly the same data is utilized [61].

4.4.1 Generalized Frequency

High-order, frequency domain (rational fraction polynomial) methods all have distinctive numerical problems that make the solution process problematic. Low-order, frequency domain (rational fraction polynomial) methods do not have this numerical problem.

The numerical problem associated with high-order, frequency domain methods can be highlighted by looking at the characteristics of the data matrix involved in estimating the matrix coefficients. These matrices involve power polynomials that are functions of increasing powers of the frequency, typically $s_i = j\omega_i$. These

matrices are of the Van der Monde form and are known to be ill-conditioned for cases involving wide frequency ranges and high-ordered models.

Van der Monde Matrix Form:

$$\begin{bmatrix} (s_1)^0 & (s_1)^1 & (s_1)^2 & \cdots & (s_1)^m \\ (s_2)^0 & (s_2)^1 & (s_2)^2 & \cdots & (s_2)^m \\ (s_3)^0 & (s_3)^1 & (s_3)^2 & \cdots & (s_3)^m \\ \cdots & \cdots & \cdots & \cdots & \cdots \\ (s_i)^0 & (s_i)^1 & (s_i)^2 & \cdots & (s_i)^m \end{bmatrix} \quad or \quad \begin{bmatrix} (s_1)^m & (s_2)^m & (s_3)^m & \cdots & (s_i)^m \\ \cdots & \cdots & \cdots & \cdots & \cdots \\ (s_1)^2 & (s_2)^2 & (s_3)^2 & \cdots & (s_i)^2 \\ (s_1)^1 & (s_2)^1 & (s_3)^1 & \cdots & (s_i)^1 \\ (s_1)^0 & (s_2)^0 & (s_3)^0 & \cdots & (s_i)^0 \end{bmatrix} \tag{126}$$

The above two matrices are just transposes of one another; both have the same ill-conditioning, and both are still considered Van der Monde matrix forms. The matrix on the right will be used in upcoming graphical examples.

The ill-conditioned characteristic of matrices that are of the Van der Monde form can be reduced, but not eliminated, by the following:

- Minimizing the frequency range of the data
- Minimizing the order of the model
- Normalizing the frequency range of the data (-1,1) or (-2,2)
- Use of orthogonal polynomials
- Use of complex z mapping

The last three methods involved the concept of **generalized frequency** where the actual FRF complex data is not altered in any way but is remapped to a new generalized or virtual frequency which eliminates or reduces the ill-conditioning caused by the weighting of the FRF data by the physical frequency ($s_i = j\omega_i$) in the linear equations. These concepts are explained further in Sect. 5.2. Note that the use of generalized frequency concepts does not change the kernel equation for the high-order, frequency domain but does improve the solution as different frequency weighting appears in the kernel equation.

4.4.2 High-Order Methods

Summary: High-Order Frequency Domain Methods
Typical algorithms

- Rational fraction polynomial (RFP)
- Orthogonal polynomial (OP)
- Polyreference least-squares complex frequency (PLSCF)

(continued)

General linear equation formulation

- Model order ($m \geq 2N/N_S$) where N is the number of desired positive frequency roots
- Number of roots ($m \times N_S$)
- Data matrix size ($N_S \times N_L$)
- Alpha coefficient matrix size ($N_S \times N_S$)

Kernel equation: high-order coefficient normalization

$$\left[[\alpha_0]\ [\alpha_1] \cdots [\alpha_{m-1}]\ [\beta_0]\ [\beta_1] \cdots [\beta_n] \right]_{N_S \times (mN_S + (n+1)N_L)} \times \begin{bmatrix} (s_i)^0[H(\omega_i)] \\ (s_i)^1[H(\omega_i)] \\ \cdots \\ (s_i)^{m-1}[H(\omega_i)] \\ -(s_i)^0[I] \\ -(s_i)^1[I] \\ \cdots \\ -(s_i)^n[I] \end{bmatrix}_{(mN_S + (n+1)N_L) \times N_L} = -(s_i)^m[H(\omega_i)]_{N_S \times N_L} \tag{127}$$

Kernel equation: zero-order coefficient normalization

$$\left[[\alpha_1]\ [\alpha_2] \cdots [\alpha_m]\ [\beta_0]\ [\beta_1] \cdots [\beta_n] \right]_{N_i \times mN_i + (n+1)N_o} \times \begin{bmatrix} (s_i)^1[H(\omega_i)] \\ (s_i)^2[H(\omega_i)] \\ \cdots \\ (s_i)^m[H(\omega_i)] \\ -(s_i)^0[I] \\ -(s_i)^1[I] \\ \cdots \\ -(s_i)^n[I] \end{bmatrix}_{mN_i + (n+1)N_o \times N_o} = -(s_i)^0[H(\omega_i)]_{N_i \times N_o} \tag{128}$$

4.4.3 Low-Order Methods: First Order

Summary: Low-Order (First) Frequency Domain Methods
Typical algorithms

- Simultaneous frequency domain (SFD)
- Multiple reference simultaneous frequency domain (MRSFD)
- Frequency domain equivalent to ITD, MRITD, ERA

General linear equation formulation

- Model order ($m = 1$)
- Number of roots ($1 \times 2N_L$)
- Data matrix size ($N_L \times N_S$)
- Alpha coefficient matrix size ($2N_L \times 2N_L$)

Kernel equation: high-order coefficient normalization

$$\left[[\alpha_0]\ [\beta_0]\right]_{2N_o \times (2N_o+2N_i)} \left[\begin{bmatrix} (s_i)^0[H(\omega_i)] \\ (s_i)^1[H(\omega_i)] \end{bmatrix} \begin{bmatrix} -(s_i)^0[I] \\ -(s_i)^1[I] \end{bmatrix}\right]_{(2N_o+2N_i)\times N_i} = -\begin{bmatrix} (s_i)^1[H(\omega_i)] \\ (s_i)^2[H(\omega_i)] \end{bmatrix}_{2N_o \times N_i} \tag{129}$$

Kernel equation: zero-order coefficient normalization

$$\left[[\alpha_1]\ [\beta_0]\right]_{2N_o \times (2N_o+2N_i)} \left[\begin{bmatrix} (s_i)^1[H(\omega_i)] \\ (s_i)^2[H(\omega_i)] \end{bmatrix} \begin{bmatrix} -(s_i)^0[I] \\ -(s_i)^1[I] \end{bmatrix}\right]_{(2N_o+2N_i)\times N_i} = -\begin{bmatrix} (s_i)^0[H(\omega_i)] \\ (s_i)^1[H(\omega_i)] \end{bmatrix}_{2N_o \times N_i} \tag{130}$$

4.4.4 Low-Order Methods: Second Order

Summary: Low-Order (Second) Frequency Domain Methods
Typical algorithms

- Polyreference frequency domain (PFD)
- Frequency domain direct parameter identification (FDPI)

General linear equation formulation

- Model order ($m = 2$)
- Number of roots ($2 \times N_L$)
- Data matrix size ($N_L \times N_S$)
- Alpha coefficient matrix size ($N_L \times N_L$)

Kernel equation: high-order coefficient normalization

$$\left[[\alpha_0]\ [\alpha_1]\ [\beta_0]\ [\beta_1] \right]_{N_o \times (2N_o + 2N_i)} \begin{bmatrix} (s_i)^0[H(\omega_i)] \\ (s_i)^1[H(\omega_i)] \\ -(s_i)^0[I] \\ -(s_i)^1[I] \end{bmatrix}_{(2N_o+2N_i) \times N_i} = -(s_i)^2[H(\omega_i)]_{N_o \times N_i} \quad (131)$$

Kernel equation: zero-order coefficient normalization

$$\left[[\alpha_1]\ [\alpha_2]\ [\beta_0]\ [\beta_1] \right]_{N_o \times (2N_o + 2N_i)} \begin{bmatrix} (s_i)^1[H(\omega_i)] \\ (s_i)^2[H(\omega_i)] \\ -(s_i)^0[I] \\ -(s_i)^1[I] \end{bmatrix}_{(2N_o+2N_i) \times N_i} = -(s_i)^0[H(\omega_i)]_{N_o \times N_i} \quad (132)$$

4.5 Residue (Modal Vector) Estimation

Modal vectors are normally found directly when a weighted least-squares solution is utilized, where the weighting comes from the modal participation vectors found in the first stage of the modal parameter estimation (MPE-1). This is the case for most multiple reference methods. If residues are desired to complete a partial fraction model, they can be found from combinations of the modal participation vector coefficients and the modal vector coefficients.

For the single reference case, residues are first found directly, and then the modal vectors are found by normalizing the residue vectors. Then the modal scaling can be estimated.

Historically, residues and modal vectors were found with both time and frequency domain estimations. Since it is easiest to involve residuals in frequency domain methods, only frequency domain methods are utilized in most solution procedures today.

As residues or modal vectors are estimated, the number (N) of modal frequencies and modal participation vectors are already known. This means that the solution procedure will always involve a least squares (LS), weighted least squares (WLS) or total least-squares (TLS) approach.

4.5.1 Time Domain Methods

Time domain estimation (single reference)

$$\begin{Bmatrix} h_{pq}(t_1) \\ h_{pq}(t_2) \\ h_{pq}(t_3) \\ \cdots \\ h_{pq}(t_{N_t}) \end{Bmatrix}_{N_t \times 1} = \begin{bmatrix} e^{\lambda_1 t_1} & e^{\lambda_2 t_1} & e^{\lambda_3 t_1} & \cdots & e^{\lambda_{2N} t_1} \\ e^{\lambda_1 t_2} & e^{\lambda_2 t_2} & e^{\lambda_3 t_2} & \cdots & e^{\lambda_{2N} t_2} \\ e^{\lambda_1 t_3} & e^{\lambda_2 t_3} & e^{\lambda_3 t_3} & \cdots & e^{\lambda_{2N} t_3} \\ \cdots & \cdots & \cdots & \cdots & \cdots \\ e^{\lambda_1 t_{N_t}} & e^{\lambda_2 t_{N_t}} & e^{\lambda_3 t_{N_t}} & \cdots & e^{\lambda_{2N} t_{N_t}} \end{bmatrix}_{N_t \times 2N} \begin{Bmatrix} A_{pq1} \\ A_{pq2} \\ A_{pq3} \\ \cdots \\ A_{pq2N} \end{Bmatrix}_{2N \times 1} \tag{133}$$

where

- N_t = Number of time points
- N = Number of modal frequencies (positive and negative)
- $N_t \geq 2N$

Time domain estimation (multiple references)

$$\{h(t_i)\}^T{}_{N_i \times 1} = [L]_{N_i \times 2N} \left\lceil e^{\lambda_r t_i} \right\rfloor_{2N \times 2N} \{\psi\}^T{}_{2N \times 1} \tag{134}$$

where

- N_t = Number of time points
- N = Number of modal frequencies (positive and negative)
- $N_t \geq 2N$

Above equation is repeated N_t times

$$\left\{h_{pq}(t_i)\right\} = \begin{Bmatrix} h_{p1}(t_i) \\ h_{p2}(t_i) \\ h_{p3}(t_i) \\ \cdots \\ h_{pq}(t_i) \end{Bmatrix} \qquad \left\lceil e^{\lambda t_i} \right\rfloor = \begin{bmatrix} e^{\lambda_1 t_i} & 0 & 0 & \cdots & 0 \\ 0 & e^{\lambda_2 t_i} & 0 & \cdots & 0 \\ 0 & 0 & e^{\lambda_3 t_i} & \cdots & 0 \\ \cdots & \cdots & \cdots & \cdots & \cdots \\ 0 & 0 & 0 & \cdots & e^{\lambda_{2N} t_i} \end{bmatrix} \tag{135}$$

The residues are calculated from the modal participation vector coefficients (L) and the modal coefficients (ψ); ($A_{pqr} = L_{qr}\psi_{pr}$). Note that if one column q of the modal participation matrix ($[L]$) is normalized to unity, the modal coefficients that are found will be equal to the residues for that reference (A_{pqr}).

$$\left[\psi_{pr}\right] = \begin{Bmatrix} \psi_{p1} \\ \psi_{p2} \\ \psi_{p3} \\ \cdots \\ \psi_{p2N} \end{Bmatrix} \qquad \left[L_{rq}\right] = \begin{bmatrix} L_{11} & L_{12} & L_{13} & \cdots & L_{12N} \\ L_{21} & L_{22} & L_{23} & \cdots & L_{22N} \\ L_{31} & L_{32} & L_{33} & \cdots & L_{32N} \\ \cdots & \cdots & \cdots & \cdots & \cdots \\ L_{N_i1} & L_{N_i2} & L_{N_i3} & \cdots & L_{N_i2N} \end{bmatrix} \tag{136}$$

4.5.2 Frequency Domain Methods

Frequency domain estimation (Single Reference with Residuals)

$$\left\{H_{pq}(\omega)\right\}_{N_s\times 1} = \left[\frac{1}{j\omega - \lambda_r}\right]_{N_s\times(2N+2)} \left\{A_{pqr}\right\}_{(2N+2)\times 1} \tag{137}$$

where

- N_s = Number of spectral lines (frequency points)
- N = Number of modal frequencies (positive and negative)
- $N_s \geq 2N + 2$

$$\left[\frac{1}{j\omega - \lambda_r}\right] = \begin{bmatrix} \frac{1}{j\omega_1-\lambda_1} & \frac{1}{j\omega_1-\lambda_2} & \frac{1}{j\omega_1-\lambda_3} & \cdots & \frac{1}{j\omega_1-\lambda_{2N}} & \frac{-1}{\omega_1^2} & 1 \\ \frac{1}{j\omega_2-\lambda_1} & \frac{1}{j\omega_2-\lambda_2} & \frac{1}{j\omega_2-\lambda_3} & \cdots & \frac{1}{j\omega_2-\lambda_{2N}} & \frac{-1}{\omega_2^2} & 1 \\ \frac{1}{j\omega_3-\lambda_1} & \frac{1}{j\omega_3-\lambda_2} & \frac{1}{j\omega_3-\lambda_3} & \cdots & \frac{1}{j\omega_3-\lambda_{2N}} & \frac{-1}{\omega_3^2} & 1 \\ \cdots & \cdots & \cdots & \cdots & \cdots & \cdots & \cdots \\ \frac{1}{j\omega_{N_s}-\lambda_1} & \frac{1}{j\omega_{N_s}-\lambda_2} & \frac{1}{j\omega_{N_s}-\lambda_3} & \cdots & \frac{1}{j\omega_{N_s}-\lambda_{2N}} & \frac{-1}{\omega_{N_s}^2} & 1 \end{bmatrix} \tag{138}$$

$$\left\{A_{pqr}\right\} = \begin{Bmatrix} A_{pq1} \\ A_{pq2} \\ A_{pq3} \\ \cdots \\ A_{pq2N} \\ R_{I_{pq}} \\ R_{F_{pq}} \end{Bmatrix} \qquad \left\{H_{pq}(\omega)\right\} = \begin{Bmatrix} H_{pq}(\omega_1) \\ H_{pq}(\omega_2) \\ H_{pq}(\omega_3) \\ \cdots \\ H_{pq}(\omega_{N_s}) \end{Bmatrix} \tag{139}$$

Frequency domain estimation (multiple references)

$$\{H(\omega_i)\}^T{}_{N_i\times 1} = [L]_{N_i\times 2N} \left[\frac{1}{j\omega_i - \lambda_r}\right]_{2N\times 2N} \{\psi\}^T{}_{2N\times 1} \tag{140}$$

where

- N_s = Number of spectral lines (frequency points)
- N = Number of modal frequencies (positive and negative)
- $N_s \geq 2N$
- Above equation is repeated N_s times

$$\left\{H_{pq}(\omega_i)\right\} = \begin{Bmatrix} H_{p1}(\omega_i) \\ H_{p2}(\omega_i) \\ H_{p3}(\omega_i) \\ \cdots \\ H_{pq}(\omega_i) \end{Bmatrix} \tag{141}$$

$$\left[\frac{1}{j\omega_i - \lambda_r}\right] = \begin{bmatrix} \frac{1}{j\omega_i - \lambda_1} & 0 & 0 & \cdots & 0 \\ 0 & \frac{1}{j\omega_i - \lambda_2} & 0 & \cdots & 0 \\ 0 & 0 & \frac{1}{j\omega_i - \lambda_3} & \cdots & 0 \\ \cdots & \cdots & \cdots & \cdots & \cdots \\ 0 & 0 & 0 & \cdots & \frac{1}{j\omega_i - \lambda_{2N}} \end{bmatrix} \tag{142}$$

The residues are calculated from the modal participation vector coefficients (L) and the modal coefficients (ψ); ($A_{pqr} = L_{qr}\psi_{pr}$). Note that if one column q of the modal participation matrix ($[L]$) is normalized to unity, the modal coefficients that are found will be equal to the residues for that reference A_{pqr}.

$$\left[\psi_{pr}\right] = \begin{Bmatrix} \psi_{p1} \\ \psi_{p2} \\ \psi_{p3} \\ \cdots \\ \psi_{p2N} \end{Bmatrix} \qquad \left[L_{rq}\right] = \begin{bmatrix} L_{11} & L_{12} & L_{13} & \cdots & L_{12N} \\ L_{21} & L_{22} & L_{23} & \cdots & L_{22N} \\ L_{31} & L_{32} & L_{33} & \cdots & L_{32N} \\ \cdots & \cdots & \cdots & \cdots & \cdots \\ L_{N_i1} & L_{N_i2} & L_{N_i3} & \cdots & L_{N_i2N} \end{bmatrix} \tag{143}$$

The details of how the data is positioned into the MIMO FRF model for the estimation of modal vectors often require a little manipulation to see the matrix conformal relationships. The following development expands each term so that the overdetermined linear equation is easier to visualize.

The primary equation used for multiple reference modal vector estimation can be restated as:

$$[\![H(\omega)]\!]_{N_S \times N_L \times N_f} = [L]_{N_S \times 2N} \, [\![\Lambda(\omega)]\!]_{2N \times 2N \times N_f} \, [\psi]^T{}_{2N \times N_L} \tag{144}$$

where

$$[\![H(\omega)]\!] = \begin{bmatrix} [H(\omega_1)] \\ [H(\omega_2)] \\ [H(\omega_3)] \\ \cdots \\ [H(\omega_{N_f})] \end{bmatrix}_{N_S N_f \times N_L} \qquad [L][\![\Lambda(\omega)]\!] = \begin{bmatrix} [L][\Lambda(\omega_1)] \\ [L][\Lambda(\omega_2)] \\ [L][\Lambda(\omega_3)] \\ \cdots \\ [L][\Lambda(\omega_{N_f})] \end{bmatrix}_{N_S N_f \times 2N} \tag{145}$$

The modal participation matrix ($[L]$) is of the following form:

$$[L] = \begin{bmatrix} L_{1,1} & L_{2,1} & L_{3,1} & \cdots & L_{2N,1} \\ L_{1,2} & L_{2,2} & L_{3,2} & \cdots & L_{2N,2} \\ L_{1,3} & L_{2,3} & L_{3,3} & \cdots & L_{2N,3} \\ \cdots & \cdots & \cdots & \cdots & \cdots \\ L_{1,N_S} & L_{2,N_S} & L_{3,N_S} & \cdots & L_{2N,N_S} \end{bmatrix} \tag{146}$$

Note that in the above notation, the modal participation vectors span the row space with each column representing the participation information for another mode. The modal vector matrix ($[\psi]$) is of the following form:

$$[\psi]^T = \begin{bmatrix} \psi_{1,2} & \psi_{1,2} & \psi_{1,3} & \cdots & \psi_{1,N_L} \\ \psi_{2,1} & \psi_{2,2} & \psi_{2,3} & \cdots & \psi_{2,N_L} \\ \psi_{3,1} & \psi_{3,2} & \psi_{3,3} & \cdots & \psi_{3,N_L} \\ \cdots & \cdots & \cdots & \cdots & \cdots \\ \psi_{2N,1} & \psi_{2N,2} & \psi_{2N,3} & \cdots & \psi_{2N,N_L} \end{bmatrix} \tag{147}$$

Note that in the above notation, the transpose of the modal vector matrix span the column space with each row representing another mode. Note that the notation for both the $[L]$ and the $[\psi]$ matrices is consistent with the academic definition of a modal matrix, but the solution method is actually finding the $[\psi]^T$ matrix.

The diagonal $[\Lambda(\omega_i)]$, at each frequency, is of the following form:

$$\lceil \Lambda(\omega_i) \rfloor = \begin{bmatrix} \frac{1}{j\omega_i - \lambda_1} & & & & \\ & \frac{1}{j\omega_i - \lambda_2} i2 & & & \\ & & \frac{1}{j\omega_i - \lambda_3} i3 & & \\ & & & \ddots & \\ & & & & \frac{1}{j\omega_i - \lambda_{2N}} \end{bmatrix} \tag{148}$$

Finally, the combined matrix of the $[L]$ matrix and the $[\Lambda]$ matrix can be formed at each frequency:

$$[L]\ [\Lambda(\omega_i)] = \begin{bmatrix} \frac{L_{1,1}}{j\omega_i - \lambda_i} & \frac{L_{2,1}}{j\omega_i - \lambda_1} & \frac{L_{3,1}}{j\omega_i - \lambda_1} & \cdots & \frac{L_{2N,1}}{j\omega_i - \lambda_1} \\ \frac{L_{1,2}}{j\omega_i - \lambda_2} & \frac{L_{2,2}}{j\omega_i - \lambda_2} & \frac{L_{3,2}}{j\omega_i - \lambda_2} & \cdots & \frac{L_{2N,2}}{j\omega_i - \lambda_2} \\ \frac{L_{1,3}}{j\omega_i - \lambda_3} & \frac{L_{2,3}}{j\omega_i - \lambda_3} & \frac{L_{3,3}}{j\omega_i - \lambda_3} & \cdots & \frac{L_{2N,3}}{j\omega_i - \lambda_3} \\ \cdots & \cdots & \cdots & \cdots & \cdots \\ \frac{L_{1,N_S}}{j\omega_i - \lambda_{N_S}} & \frac{L_{2,N_S}}{j\omega_i - \lambda_{N_S}} & \frac{L_{3,N_S}}{j\omega_i - \lambda_{N_S}} & \cdots & \frac{L_{2N,N_S}}{j\omega_i - \lambda_{N_S}} \end{bmatrix} \quad (149)$$

This combined matrix can now be stacked vertically so that the row space matches the row space of the $[\![H(\omega)]\!]$ matrix, as in Eq. 144. Now the solution for the modal vectors can be found by multiplying both sides of Eq. 144 by the pseudoinverse of the $[L]\,[\![\Lambda(\omega)]\!]$ matrix.

Note that in the above development, if the short dimension (N_S) of the FRF matrix is one, the matrix in Eq. 144 will be the same as the matrix in Eq. 146.

5 Differences in MPE Algorithms

Modal parameter estimation algorithms typically give slightly different estimates of modal parameters due to the way the FRF data is weighted and processed in the computation of the matrix coefficients. Some of the most common variations are discussed in the following sections.

5.1 Polynomial Coefficient Estimation

The polynomial coefficients that are used to define the matrix polynomial characteristic equation are always found from an overdetermined set of block linear equations. The answers for the modal parameters will always change if any degree of overdetermination is changed. These changes will often be small if the overdetermination factor is four or more. The method of solving for the polynomial coefficients when forming an overdetermined problem can also be changed. Originally and historically, the approach was to form the direct solution by pre-multiplying the equation with its transpose. Currently, this type of overdetermined problem is generally solved with a singular value decomposition (SVD) approach. Any of these differences in the implementation of the solution procedure will involve small changes in ultimate estimate of the modal parameters. If the dynamic range of the data in the overdetermined equations becomes very large, the impact on the modal parameter estimates could become significant.

5.2 Generalized Frequency

The fundamental problem with using a high-order, frequency domain method (e.g., rational fraction polynomial) can be highlighted by looking at the characteristics of the data matrix involved in estimating the matrix coefficients. These matrices involve power polynomials that are functions of increasing powers of the frequency, typically $s_i = j\omega_i$. These matrices are of the Van der Monde form and are known to be ill-conditioned for cases involving wide frequency ranges and high-ordered models.

Van der Monde matrix form:

$$\begin{bmatrix} (s_1)^0 & (s_1)^1 & (s_1)^2 & \cdots & (s_1)^{2N-1} \\ (s_2)^0 & (s_2)^1 & (s_2)^2 & \cdots & (s_2)^{2N-1} \\ (s_3)^0 & (s_3)^1 & (s_3)^2 & \cdots & (s_3)^{2N-1} \\ \cdots & \cdots & \cdots & \cdots & \cdots \\ (s_i)^0 & (s_i)^1 & (s_i)^2 & \cdots & (s_i)^{2N-1} \end{bmatrix} \tag{150}$$

The ill-conditioning problem can be best understood by evaluating the condition number of the Van der Monde matrix. The condition number measures the sensitivity of the solution of linear equations to errors, or small amounts of noise, in the data. The condition number gives an indication of the accuracy of the results from matrix inversion and/or linear equation solution. The condition number for a matrix is computed by taking the ratio of the largest singular value to the smallest singular value. A good condition number is a small number close to unity; a bad condition number is a large number. For the theoretical case of a singular matrix, the condition number is infinite.

As mentioned in Sect. 4.4.1, the ill-conditioned characteristic of matrices that are of the Van der Monde form can be reduced, but not eliminated, by the following:

- Minimizing the frequency range of the data
- Minimizing the order of the model
- Normalizing the frequency range of the data (-1,1) or (-2,2)
- Use of orthogonal polynomials
- Use of complex z mapping

The last three methods involved the concept of generalized frequency where the actual FRF complex data is not altered in any way but is remapped to a new generalized or virtual frequency which eliminates or reduces the ill-conditioning caused by the weighting of the FRF data by the physical frequency ($s_i = j\omega_i$) in the linear equations. These concepts are briefly explained in the following sections.

5.2.1 Normalized Frequency

The simplest method of using the generalized frequency concept is to normalize the power polynomials by utilizing the following equation:

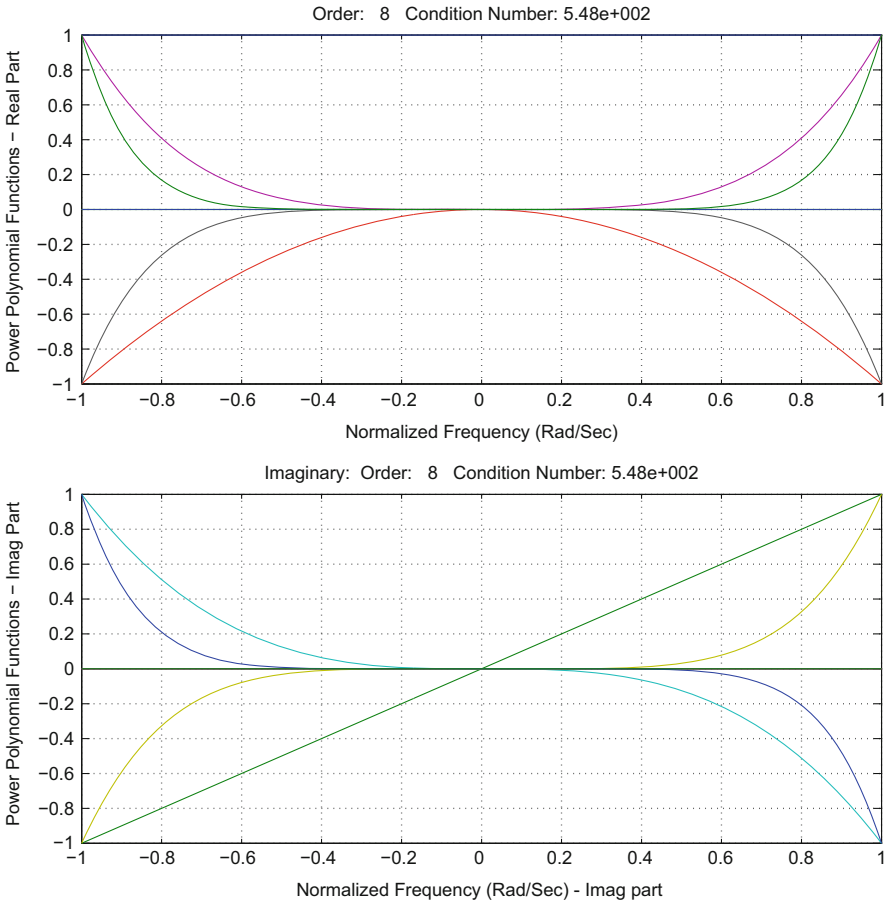

Fig. 15 Van der Monde matrix – normalized frequency – orders 0–8

$$s_i = j * (\omega_i / \omega_{\max}) \tag{151}$$

This gives a generalized frequency variable that is bounded by (-1,1) with much better numerical conditioning than utilizing the raw frequency range ($-\omega_{\max}$,$\omega_{\max}$). When the modal frequencies are estimated, the corrected modal frequencies must be determined by multiplying by the normalizing frequency ($\omega_{\max}$). All frequency domain algorithms, at a minimum, will use some form of this frequency normalization. The graphical plot of this Van der Monde matrix for orders 0 through 8 is shown in Fig. 15.

5.2.2 Orthogonal Polynomials

In the past, the only way to avoid the numerical problems inherent in the frequency domain methods (Van der Monde matrix), even when normalized frequencies are

implemented, is to use a transformation from power polynomials to orthogonal polynomials [25, 26, 28, 29, 30, 31, 32, 33, 36]. Any power polynomial series can be represented by an equivalent number of terms in an orthogonal polynomial series. Several orthogonal polynomials have been applied to the ill-conditioning problem, such as Forsythe polynomials [25] and Chebyshev polynomials [26, 27]. The orthogonal polynomial concept is represented by the following relationship.

$$\sum_{k=0}^{m} (s_i)^k \alpha_k = \sum_{k=0}^{m} P_k(s_i)\gamma_k \tag{152}$$

The orthogonal polynomial series can be formed by the following relationships:

$$P_0(s_i) = 1.0 \tag{153}$$

$$P_j(s_i^*) = P_j^*(s_i) \tag{154}$$

$$P_{n+1}(s_i) = a_n\, s_i\, P_n(s_i) - \sum_{k=0}^{n} b_{n,k}\, P_k(s_i) \tag{155}$$

This orthogonal polynomial series can be formulated in matrix form by utilizing two weighting matrices involving the coefficients a_n and $b_{n,k}$ as follows:

$$[W_a] = \begin{bmatrix} a_n & 0 & 0 & \cdots & 0 \\ 0 & a_{n-1} & 0 & \cdots & 0 \\ 0 & 0 & a_{n-2} & \cdots & 0 \\ \cdots & \cdots & \cdots & \cdots & \cdots \\ 0 & 0 & 0 & \cdots & a_0 \end{bmatrix} \quad [W_b] = \begin{bmatrix} b_{n,n} & b_{n,n-1} & b_{n,n-2} & \cdots & b_{n,0} \\ 0 & b_{n-1,n-1} & b_{n-1,n-2} & \cdots & b_{n-1,0} \\ 0 & 0 & b_{n-2,n-2} & \cdots & b_{n-2,0} \\ \cdots & \cdots & \cdots & \cdots & \cdots \\ 0 & 0 & 0 & \cdots & b_{0,0} \end{bmatrix} \tag{156}$$

Different orthogonal polynomials are generated using different weighting coefficients and are orthogonal over different ranges. For example, Forsythe orthogonal polynomials are orthogonal over the (-2,2) range, while Chebyshev orthogonal polynomials are orthogonal over the (-1,1) range. In the orthogonal polynomial approach, the original complex valued FRF data is used together with the orthogonal polynomial coefficients $P_k(s_i)$ in place of the generalized frequency $(s_i)^k$ where s_i is the properly normalized generalized frequency (e.g., Eq. 152). The unknown matrix coefficients of the matrix orthogonal polynomial (γ_k) are substituted in place of the original matrix coefficients (α_k). These matrix orthogonal polynomial coefficients are then loaded in the companion matrix ($[C]$) as before.

When this orthogonal polynomial transformation is used to generate a new generalized frequency, the corrected modal frequencies are determined from a generalized form of the companion matrix solution. The companion matrix ($[C]$) is determined in the same way as always, but the solution for the modal frequencies is found from the following equation (note that the following form originates from a high-order coefficient normalization):

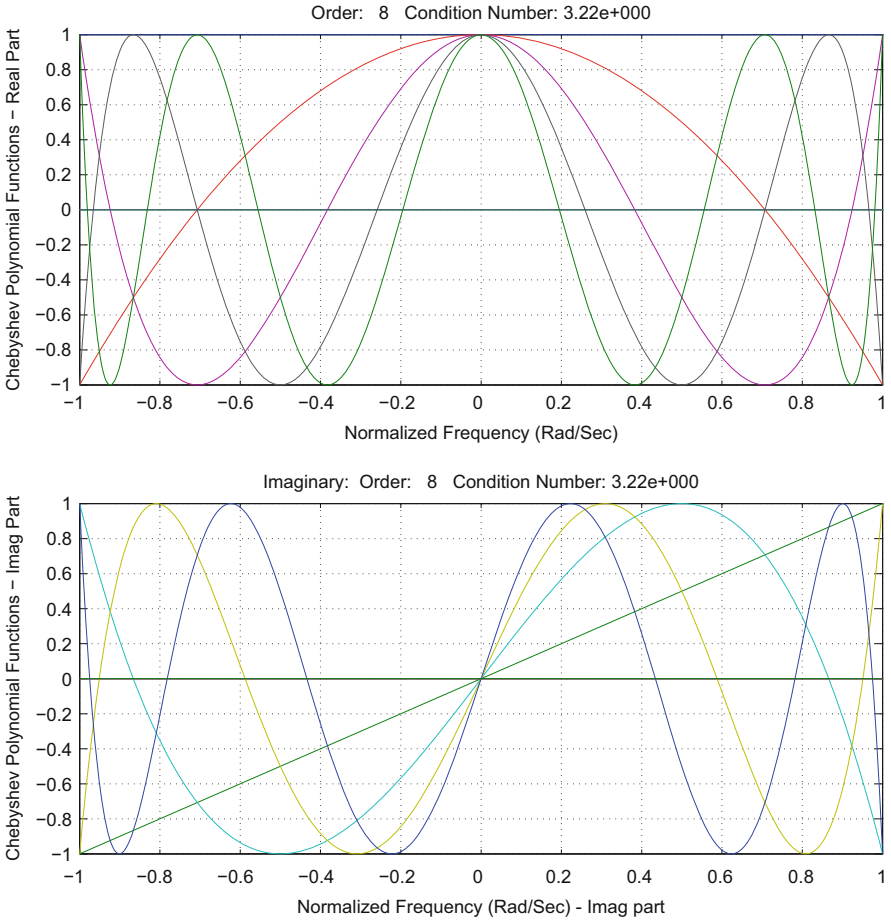

Fig. 16 Van der Monde matrix – Chebyshev orthogonal polynomials – orders 0–8

$$[[C] + [W_b]]\{X\} = \lambda [W_a]\{X\} \tag{157}$$

The above equation can also be formed for the low-order coefficient normalization using the same process as that shown in Eqs. 56 through 61.

The graphical plot of the Van der Monde matrix for orders 0 through 8 for a set of Chebyshev orthogonal polynomials is shown in Fig. 16.

Discrete Orthogonal Polynomials

Most orthogonal polynomial methods are based upon continuous polynomials. Since the measurements are made at discrete frequencies, this means that the orthogonality is approximate. Discrete orthogonal polynomials are based upon the discrete frequencies involved and provide a more exact orthogonality with added

accuracy. Both continuous and discrete orthogonal polynomials are summarized in a recent publication [35].

5.2.3 Complex Z Mapping

The important contribution behind the development of the polyreference LSCF [37, 38, 39, 40, 41, 42] method is the recognition of a new method of frequency mapping. The generalized frequency in this approach is a trigonometric mapping function (complex z) that has superior numerical conditioning to orthogonal polynomials without the added complication of solving a generalized companion matrix eigenvalue problem. This approach can be applied to any frequency domain method, low-order frequency domain methods, as well as high-order frequency domain methods, although the numerical advantage is not as profound for the low-order methods.

The basic complex Z mapping function, in the nomenclature of this presentation, is as follows:

$$s_i = z_i = e^{j*\pi*(\omega_i/\omega_{\max})} = e^{j*\omega_i*\Delta t} \tag{158}$$

$$s_i^m = z_i^m = e^{j*\pi*m*(\omega_i/\omega_{\max})} \tag{159}$$

This mapping function maps the positive frequency range to the positive unit circle in the complex plane and the negative frequency range to the negative unit circle in the complex plane. This is graphically represented in Fig. 17.

This effectively yields a real part of the mapping functions which are cosine terms and an imaginary part which are sin functions. Since sin and cos functions

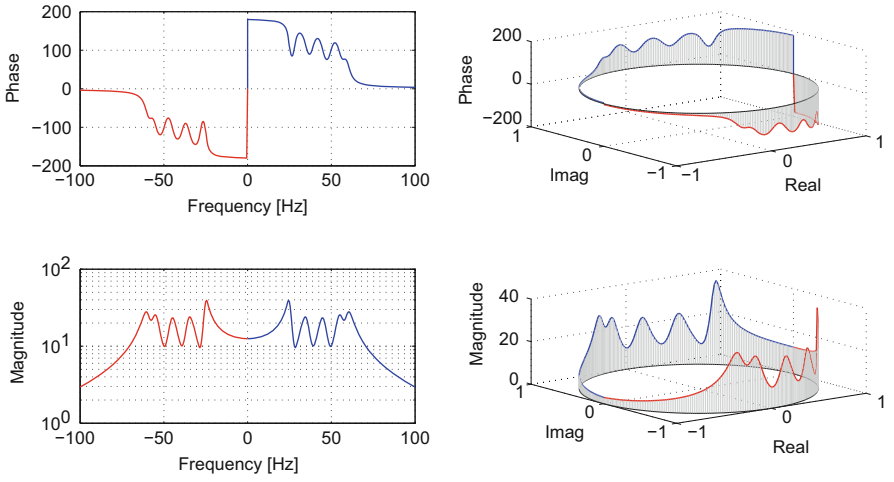

Fig. 17 Mapping the frequency response function onto the unit circle in the complex plane

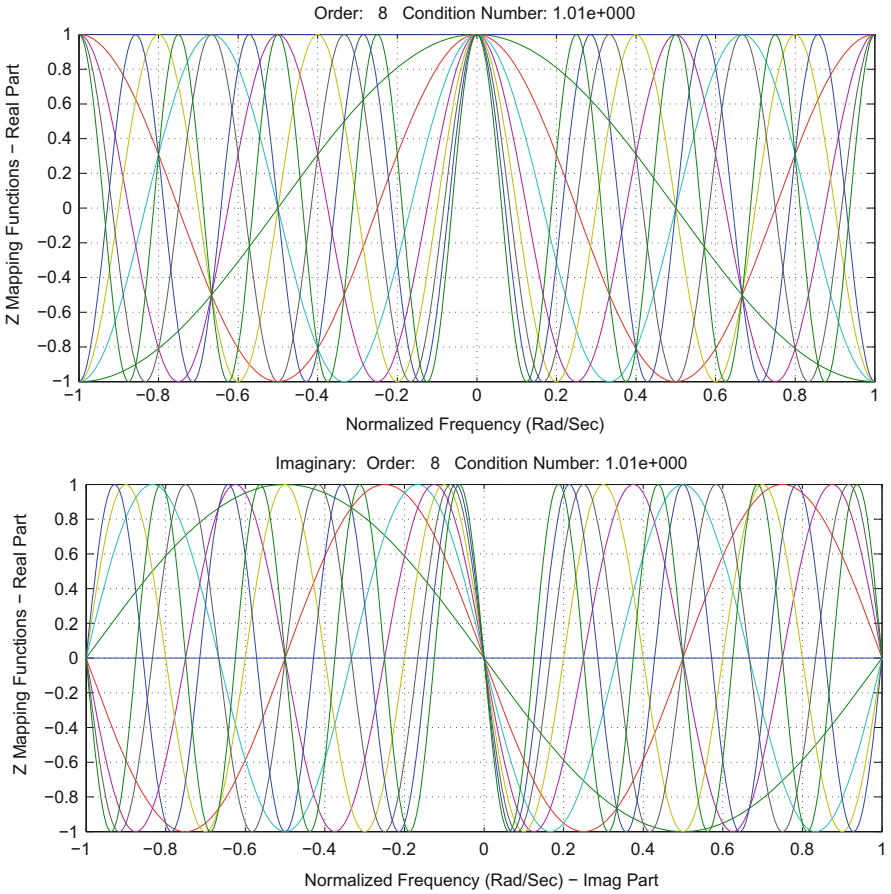

Fig. 18 Van der Monde matrix – complex Z mapped frequency – orders 0–8

at different frequencies are mathematically orthogonal, the numerical conditioning of this mapping function is quite good. The graphical plot of this Van der Monde matrix for orders 0 through 8 is shown in Fig. 18. The condition number for this example matrix is 1.01 (Fig. 18) compared to a condition number of 548 for the normalized frequency example (Fig. 15).

5.3 Data Sieving/Filtering/Decimation

For almost all cases of modal identification, a large amount of redundancy or overdetermination exists. This means that the number of equations available compared to the number required to form an exactly determined solution, defined as the overdetermination factor, will be quite large. Beyond some value of overde-

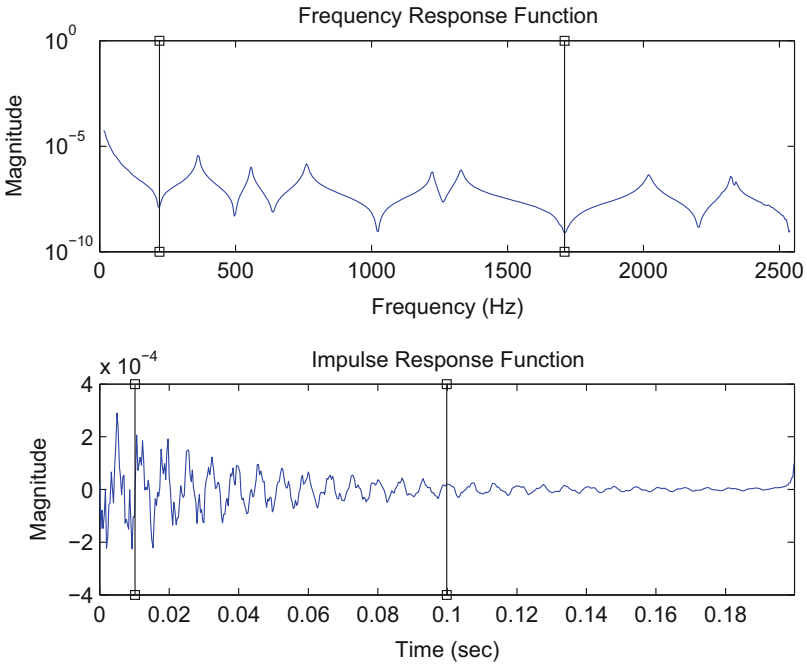

Fig. 19 Filtering example

termination factor, the additional equations contribute little to the result but may add significantly to the noise and, thus, to the solution time. For this reason, the data space is often filtered (limited within minimum and maximum temporal axis values), sieved (limited to prescribed input DOFs and/or output DOFs) and/or decimated (limited number of equations from the allowable temporal data) in order to obtain a reasonable result in the minimum time. The above figure is an example of choosing a frequency band of the frequency response function (filtering) and working with the inverse FFT of that frequency banded data in the time domain impulse response function (Fig. 19).

5.4 Coefficient Condensation (Virtual DOFs)

For the low-order modal identification algorithms (model order 2), the number of physical coordinates (typically N_L), which dictates the size of the coefficient matrices ($[\alpha_k]$), is often much larger than the number of desired modal frequencies (N). For this situation, the numerical solution procedure is constrained to solve for N_L or $2N_L$ modal frequencies. This can be very time consuming and is unnecessary. One simple approach to reducing the size of the coefficient matrices is to sieve the physical DOFs to temporarily reduce the dimension of N_L. Beyond excluding all

physical DOFs in a direction or those that are part of a subcomponent, this is difficult to do in an effective manner that will retain the correct information from the FRF data matrix.

The number of physical coordinates (N_L) can be reduced to a more reasonable size ($N_e \approx N$ or $N_e \approx 2N$) by using a decomposition transformation from physical coordinates (N_L) to the approximate number of effective modal frequencies (N_e). These resulting N_e transformed coordinates are sometimes referred to as virtual DOFs. Currently, singular value decompositions (SVD) or eigenvalue decompositions (ED) are used to condense the spatial information while preserving the principal modal information prior to formulating the linear equation solution for unknown matrix coefficients [19, 62, 63].

It is important to understand that the ED and SVD transformations yield a mathematical (linear) transformation that, in general, contains complex valued vectors as part of the transformation matrix, $[T]$. Conceptually, the transformation will work well when these vectors are estimates of the modal vectors of the system, normally a situation where the vectors can be scaled to real valued vectors. Essentially, this means that the target goal of the transformation is a transformation from physical space to modal space. As the modal density increases and/or as the level of damping increases, the ED and SVD methods give erroneous results, if the complete $[H]$ matrix is used. Generally, superior results will be obtained when the imaginary part of the $[H]$ matrix is used in the ED or SVD transformation, thus forcing a real valued transformation matrix, $[T]$. Another option is to load both the real and imaginary portions of the complex data into a real matrix which will also force a real valued transformation matrix [64].

In order to form a consistency diagram using virtual DOFs, several approaches can be used. In most cases, when the long dimension is large, results from different subspaces can be combined in a consistency diagram to look for statistically significant results. This is normally done by using a subspace of dimension two and then successively increasing the size of the subspace to some limit that will give 30 to 40 solution iterations up to the limit of N modal frequencies (30-40). The largest subspace size is roughly equal to the number of desired modal frequencies. An alternate approach is to choose a relatively small size for the dimension of the subspace and then using model order iteration, beginning with model order 2 up to a model order that will yield the number of required modal frequencies.

$$[H'] = [T]\,[H] \tag{160}$$

where

- $[H']$ is the transformed (virtual or condensed) frequency response function matrix.
- $[T]$ is the transformation matrix.
- $[H]$ is the original FRF matrix.

The difference between the two techniques lies in the method of finding the transformation matrix, $[T]$. Once $[H]$ has been condensed, however, the parameter estimation procedure is the same as for the full data set. Because the data eliminated from the parameter estimation process ideally corresponds to the noise in the data, the poles of the condensed data are the same as the poles of the full data set. However, the participation factors calculated from the condensed data may need to be expanded back into the full space.

$$\begin{aligned} [H'] &= [T]\,[H] \\ [\Psi] &= [T]^T\,[\Psi'] \end{aligned} \tag{161}$$

where

- $[\Psi]$ is the full-space participation matrix.
- $[\Psi']$ is the condensed-space participation matrix.

While linear decomposition methods known as eigenvalue decomposition (ED) and singular value decomposition (SVD) are most often used to find the transformation matrix ($[T]$), a number of other methods have been developed in various areas of mathematics and science that find linear orthogonal subspaces of a data matrix. These methods are now grouped into a class of decomposition methods referred to as principal component analysis [65].

5.4.1 Eigenvalue Decomposition

In the eigenvalue decomposition method, the $[T]$ matrix is composed of the eigenvectors corresponding to the N_e largest eigenvalues of the power spectrum of the FRF matrix as follows:

$$[H(\omega)]_{N_L \times N_S N_f} [H(\omega)]^H_{N_S N_f \times N_L} = [V]\,\lceil\Lambda\rfloor\,[V]^H \tag{162}$$

The eigenvalues and eigenvectors are then found, and the $[T]$ matrix is constructed from the eigenvectors corresponding to the N_e largest eigenvalues:

$$[T]_{N_e \times N_L} = \left[\{v_1\}\{v_2\}\cdots\{v_k\}\cdots\left\{v_{N_e}\right\}\right]^T \tag{163}$$

where

- $\{v_k\}$ is the $N_L \times 1$ eigenvector corresponding to the $k-th$ eigenvalue.

This technique may be adapted for condensing on the input space, as well. The power spectrum matrix is again found, but the FRF matrix must be reshaped (transposed) so that it is an $N_S \times N_L$ matrix for each spectral line:

$$[H(\omega)]_{N_S \times N_L N_f} [H(\omega)]^H_{N_L N_f \times N_S} = [V]\,\lceil\Lambda\rfloor\,[V]^H \tag{164}$$

The eigenvalues and eigenvectors are again found as before, and the transformation matrix $[T]$ becomes:

$$[T]_{N_e \times N_S} = \left[\{v_1\}\{v_2\}\cdots\{v_k\}\cdots\left\{v_{N_e}\right\}\right]^T \tag{165}$$

where

- $\{v_k\}$ is the $N_S \times 1$ eigenvector corresponding to the $k-th$ eigenvalue.

5.4.2 Singular Value Decomposition

The singular value decomposition condensation technique is similar to the eigenvalue-based technique but operates on the FRF matrix directly instead of the power spectrum of the FRF matrix. The basis for this technique is the singular value decomposition [66, 64] by which the matrix $[H]$ is broken down into three component parts, $[U]$, $[\Sigma]$, and $[V]$:

$$[H]_{N_L \times N_S N_f} = [U]_{N_L \times N_L} \lceil \Sigma \rfloor_{N_L \times N_L} [V]^H_{N_L \times N_S N_f} \tag{166}$$

The left-singular vectors corresponding to the N_e largest singular values are the first N_e columns of $[U]$. These become the transformation matrix $[T]$:

$$[T]_{N_e \times N_L} = \left[\{u_1\}\{u_2\}\cdots\{u_k\}\cdots\left\{u_{N_e}\right\}\right]^T \tag{167}$$

where

- $\{u_k\}$ is the $k-th$ column of $[U]$, which corresponds to the $k-th$ singular value.

This technique may also be adapted for condensing the input space, as long as the FRF matrix $[H]$ is reshaped (transposed) to an $N_S \times N_L$ matrix at each spectral line. The SVD operation then becomes:

$$[H]_{N_S \times N_L N_f} = [U]_{N_S \times N_S} \lceil \Sigma \rfloor_{N_S \times N_S} [V]^H_{N_S \times N_L N_f} \tag{168}$$

The transformation matrix $[T]$ is still composed of the left singular vectors corresponding to the N_e largest singular values,

$$[T]_{N_e \times N_i} = \left[\{u_1\}\{u_2\}\cdots\{u_k\}\cdots\left\{u_{N_e}\right\}\right]^T \tag{169}$$

where

- $\{u_k\}$ is again the $k-th$ column of $[U]$, which corresponds to the $k-th$ singular value.

5.4.3 Virtual FRFs

One way of visualizing the effects of condensation on the FRF matrix is formulating the condensed frequency response functions based on the reduced dimension of the virtual DOFs. These FRFs are referred to as virtual FRFs or principal response functions [64,67]. For a given decomposition, the virtual FRFs represent a subspace of the full FRF matrix space. Using Eq. 160 for a given subspace, typically between two and some fraction of the long dimension, the following figures represent virtual FRFs for all of the subspaces above and below the chosen subspace. Note that the short dimension remains the same for each subspace.

Figure 20 represents the virtual FRFs for a specific decomposition of the long dimension of the FRF matrix. Note that the dynamics in the data are clearly shown and that, therefore, the use of this decomposition (subspace) will give good results for the estimated modal frequency information.

Figure 21 represents the virtual FRFs for all of the decompositions of the long dimension of the FRF matrix that are more dominant than those shown in Fig. 20. Again note that the dynamics of the data are clearly shown. The use of any of the decompositions (subspaces) in these sets of virtual FRFs will give good results.

Figure 22 represents the virtual FRFs for all of the decompositions of the long dimension of the FRF matrix that are less dominant than those shown in Fig. 20. Again note that the dynamics of the data are clearly shown in a few of these virtual

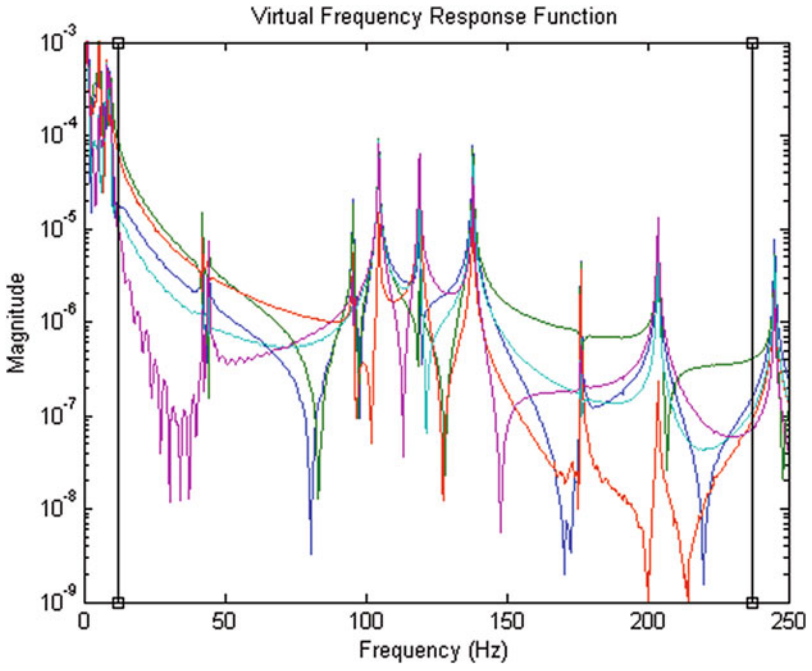

Fig. 20 Virtual FRFs at a specific SVD

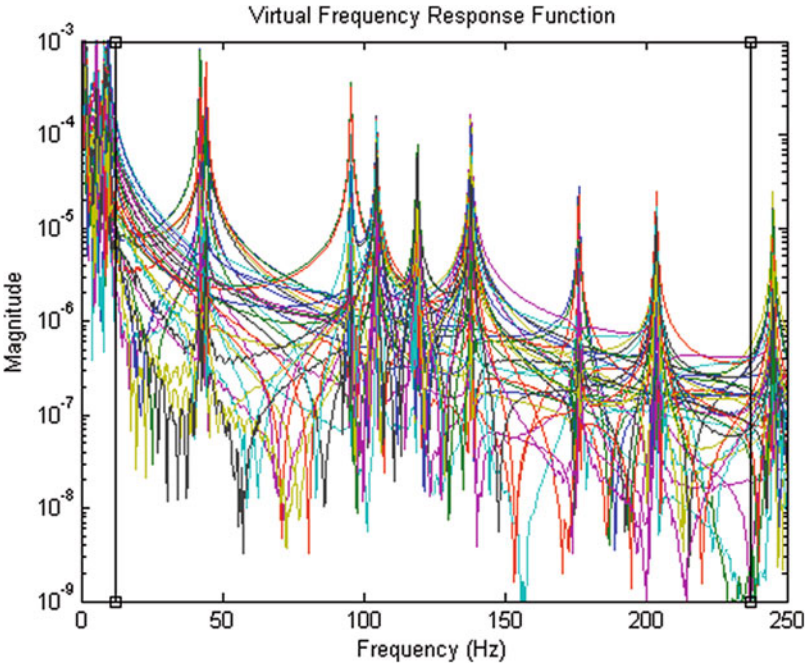

Fig. 21 Virtual FRFs at smaller SVD dimensions

FRFs. Most of the virtual FRFs in these subspaces represent the noise on the FRF data. The use of most of the decompositions (subspaces) in these sets of virtual FRFs will give poor results.

5.5 Equation Condensation

Equation condensation methods are used to reduce the number of equations generated from measured data to more closely match the number of unknowns in the modal parameter estimation algorithms. There are a large number of condensation algorithms available. Based upon the modal parameter estimation algorithms in use today, the three types of algorithms most often used are:

- Least squares: Least squares (LS), weighted least squares (WLS), total least squares (TLS), or double least squares (DLS) is used to minimize the squared error between the measured data and the estimation model.
- Transformations: The measured data is reduced by approximating the data by the superposition of a limited (reduced) set of independent vectors. The number of significant, independent vectors is chosen equal to the maximum number modes that are expected in the measured data. This set of vectors is used to approximate

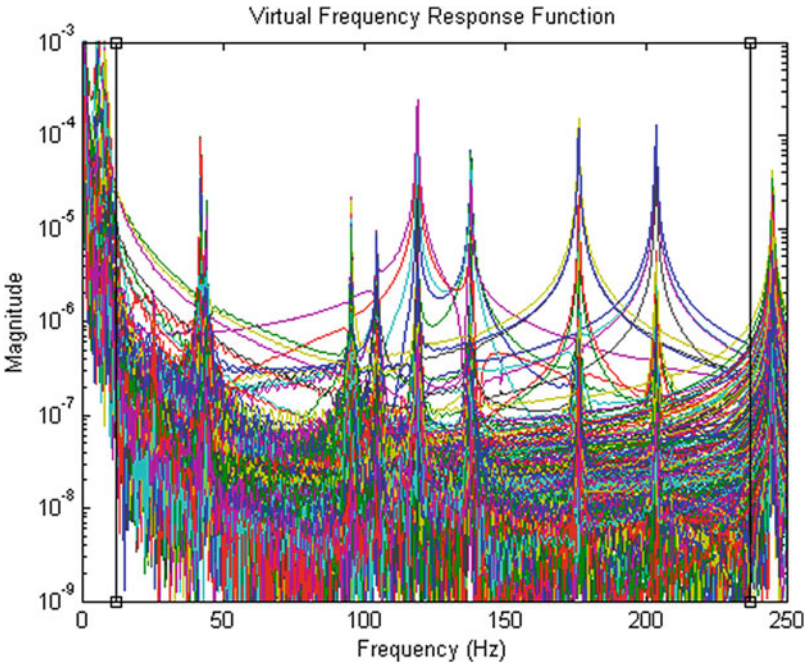

Fig. 22 Virtual FRFs at larger SVD dimensions

the measured data and used as input to the parameter estimation procedures. Singular value decomposition (SVD) is an example of one of the more popular transformation methods.

- Coherent averaging: Coherent averaging is another popular method for reducing the data. In the coherent averaging method, the data is weighted by performing a dot product between the data and a weighting vector (spatial filter). Information in the data which is not coherent with the weighting vectors is averaged out of the data.

The least squares and the transformation procedures tend to weight those modes of vibration which are well excited. This can be a problem when trying to extract modes which are not well excited. The solution is to use a weighting function for condensation which tends to enhance the mode of interest. This can be accomplished in a number of ways:

- In the time domain, a spatial filter or a coherent averaging process can be used to filter the response to enhance a particular mode or set of modes.
- In the frequency domain, the data can be enhanced in the same manner as the time domain plus the data can be additionally enhanced by weighting the data in a frequency band near the natural frequency of the mode of interest.

Obviously, the type of equation condensation method that is utilized in a modal identification algorithm has a significant influence on the results.

6 Summary

Experimental modal analysis methods are probably one of the most misunderstood aspects of the experimental modal analysis process. Since most modal parameter estimation methods are mathematically intimidating, many users do not fully understand the ramifications of the decisions made during the measurement stages as well as later in the modal parameter estimation process. Ideally, by consolidating the conceptual approach and unifying the theoretical development of modal identification algorithms, increased understanding, with respect to general advantages and disadvantages of different algorithms, can be achieved. This sort of overview of modal parameter estimation methods can be used simply as a guide toward further study and understanding of the details of the individual modal identification algorithms.

The two-stage modal parameter estimation process can be updated further to include some of the details discussed in previous sections.

- MPE-1: Utilize measured FRF or IRF data with a matrix coefficient, polynomial model to find multiple estimates of the modal parameters. Select the best set of modal frequencies and modal participation vectors.
  - Choose polynomial or subspace order (m).
  - Load measured data into over-determined linear equation form.
  - Solve for unknown matrix coefficients ($[\alpha_k]$) Least squares (LS) approach.
  - Solve for complex valued modal frequencies for (λ_r or z_r) Companion matrix approach.
  - Iterate over different polynomial orders or subspace orders in the kernel equation to get multiple estimates of the modal parameters.
  - Select one set of complex valued modal frequencies, with associated participation vectors, from the multiple sets. Manual or automated selection methods can be used.
- MPE-2: Utilize measured FRF or IRF data, with selected complex valued modal frequencies and modal participation vectors, to find complex valued modal vectors and modal scaling from an overdetermined set of linear equations.
  - Solve for modal vectors using a weighted least squares solution method involving the fixed set of modal frequencies and modal participation (weighting) vectors. Solution process often involves the estimation of residues.
  - Find modal vectors and modal scaling from Equations 75 through 79.
  - Normalize modal vectors as needed.
  - Solve for modal scaling associated with normalized modal vectors.

Experimental modal methods will continue to evolve to add information that can be gleaned from the redundancy in the MIMO data. One obvious addition will be

the inclusion of more statistical information for the measured modal parameters. This will help in the quantification of margin and uncertainty (QMU) for the modal parameters, important in verification and validation evaluations. ▶ Chap. 11, "Experimental Modal Parameter Evaluation Methods" in this Handbook explains many of the current methods used to evaluate and validate the modal parameters estimated in this chapter.

Work will continue on several topics that are not viewed as complete topics, including situations that cannot be adequately solved today. For example, specific attention is being given to methodology needed to estimate modal parameters for heavily damped systems, particularly systems with significant modal density. Generally systems with high modal density (structures with many coupled panels) are difficult to both model and test. Work is ongoing on autonomous methods and methods that begin to evaluate nonlinearities, including both nonlinear signal processing issues as well as nonlinear structure issues.

References

1. Leuridan J, Brown D, Allemang R (1985) Time domain parameter identification methods for linear modal analysis: a unifying approach, ASME paper number 85-DET-90
2. Allemang RJ, Brown D (1987) Volume III: modal parameter estimation, USAF report: AFWAL-TR-87-3069, Experimental modal analysis and dynamic component synthesis, no. 3, pp 130
3. Allemang R, Brown D, Fladung W (1994) Modal parameter estimation: a unified matrix polynomial approach. In: Proceedings, International Modal Analysis Conference (IMAC), pp 501–514
4. Allemang R, Brown D (1996) A unified matrix polynomial approach to modal identification, pp 379–390, Mar 1996
5. Allemang R, Brown D (1998) A unified matrix polynomial approach to modal identification. J Sound Vib 211(3):301–322
6. Allemang R, Phillips A (2004) The unified matrix polynomial approach to understanding modal parameter estimation: an update. In: Proceedings, International Seminar on Modal Analysis (ISMA)
7. Spitznogle F (1971) Improvements in the complex exponential signal analysis computational algorithm, Report number U1-829401-5, Representation and analysis of sonar signals, vol 1, pp 37
8. Brown D, Allemang R, Zimmerman R, Mergeay M (1979) Parameter estimation techniques for modal analysis. SAE Trans 88:828–846. SAE paper number 790221
9. Vold H, Rocklin T (1982) The numerical implementation of a multi-input modal estimation algorithm for mini-computers. In: Proceedings, International Modal Analysis Conference (IMAC), pp 542–548
10. Vold H, Kundrat J, Rocklin T, Russell R (1982) A multi-input modal estimation algorithm for mini-computers. SAE Trans 91(1):815–821
11. Ibrahim S, Mikulcik E (1977) A method for the direct identification of vibration parameters from the free response. Shock Vib Bull 47:183–198
12. Pappa R (1982) Some statistical performance characteristics of the ITD modal identification algorithm, AIAA paper number 82-0768, p 19
13. Fukuzono K (1986) Investigation of multiple-reference Ibrahim time domain modal parameter estimation technique, M. S. thesis, p 220

14. Juang J, Pappa R (1985) An eigensystem realization algorithm for modal parameter identification and model reduction. AIAA J Guid Control Dyn 8(4):620–627
15. Juang J (1987) Mathematical correlation of modal parameter identification methods via system realization theory. J Anal Exp Modal Anal 2(1):1–18
16. Longman RW, Juang J-N (1989) Recursive form of the eigensystem realization algorithm for system identification. AIAA J Guid Control Dyn 12(5):647–652
17. Zhang L, Kanda H, Brown D, Allemang R (1985) A polyreference frequency domain method for modal parameter identification, ASME paper No. 85-DET-106, vol 8, pp 8+
18. Lembregts F, Leuridan J, Zhang L, Kanda H (1986) Multiple input modal analysis of frequency response functions based on direct parameter identification. In: Proceedings, International Modal Analysis Conference (IMAC)
19. Lembregts F (1988) Frequency domain identification techniques for experimental multiple input modal analysis, Doctoral dissertation, Katholieke University of Leuven, Belgium, vol 213
20. Lembregts F, Leuridan J, Van Brussel H (1989) Frequency domain direct parameter identification for modal analysis: state space formulation. Mech Syst Signal Process (MSSP) 4(1): 65–76
21. Coppolino R (1981) A simultaneous frequency domain technique for estimation of modal parameters from measured data, SAE paper No. 811046, vol 12
22. Craig R, Kurdila A, Kim HM (1990) State-space formulation of multi-shaker modal analysis. J Anal Exp Modal Anal 5(3):169–183
23. Leuridan J (1984) Some direct parameter model identification methods applicable for multiple input modal analysis, Doctoral dissertation, vol 384, pp 384+
24. Natke H (1988) Updating computational models in the frequency domain based on measured data: a survey. Probab Eng Mech 3(1):28–35
25. Richardson M, Formenti D (1982) Parameter estimation from frequency response measurements using rational fraction polynomials. In: Proceedings, International Modal Analysis Conference (IMAC), pp 167–182
26. Shih C, Tsuei Y, Allemang R, Brown D (1988) A frequency domain global parameter estimation method for multiple reference frequency response measurements. Mech Syst Signal Process (MSSP) 2(4):349–365
27. Shih C (1989) Investigation of numerical conditioning in the frequency domain modal parameter estimation methods, Doctoral dissertation, vol 127, pp 127+
28. Van der Auweraer H, Leuridan J (1987) Multiple input orthogonal polynomial parameter estimation. Mech Syst Signal Process (MSSP) 1(3):259–272
29. Van der Auweraer H, Snoeys R, Leuridan JM (1986) A global frequency domain modal parameter estimation technique for mini-computers. ASME J Vib Acoust Stress Reliab Des 10
30. Vold H (1986) Orthogonal polynomials in the polyreference method. In: Proceedings, International Seminar on Modal Analysis (ISMA)
31. Vold H, Shih CY (1988) Numerical sensitivity of the characteristic polynomial. In: Proceedings, International Seminar on Modal Analysis (ISMA)
32. Vold H (1990) Numerically robust frequency domain modal parameter estimation. Sound Vib Mag (SVM) 24(1):38–40
33. Vold H (1990) Statistics of the characteristic polynomial in modal analysis. In: Proceedings, International Seminar on Modal Analysis (ISMA), pp 53–57
34. Vold H, Napolitano K, Hensley D, Richardson M (2008) Aliasing in modal parameter estimation, an historical look and new innovations. In: Proceedings, International Modal Analysis Conference (IMAC), vol 16, pp 12–17
35. Fladung W, Vold H (2016) An improved implementation of the orthogonal polynomial modal parameter estimation algorithm using the orthogonal complement. In: Proceedings, International Modal Analysis Conference (IMAC)
36. Fladung W, Vold H (2016) An orthogonal view of the polyreference least-squares complex frequency modal parameter estimation algorithm. In: Proceedings, International Modal Analysis Conference (IMAC)

37. Van der Auweraer H, Guillaume P, Verboven P, Vanlanduit S (2001) Application of a fast-stabilizing frequency domain parameter estimation method. ASME J Dyn Syst Meas Control 123(4):651–658
38. Guillaume P, Verboven P, Vanlanduit S, Van der Auweraer H, Peeters B (2003) A polyreference implementation of the least-squares complex frequency domain estimator. In: Proceedings, International Modal Analysis Conference (IMAC), p 12
39. Verboven P, Guillaume P, Cauberghe B, Parloo E, Vanlanduit S (2003) Stabilization charts and uncertainty bounds for frequency domain linear least squares estimators. In: Proceedings, International Modal Analysis Conference (IMAC), pp 1–10
40. Verboven P, Cauberghe B, Vanlanduit S, Parloo E, Guillaume P (2004) The secret behind clear stabilization diagrams: the influence of the parameter constraint on the stability of the poles. In: Proceedings, Society of Experimental Mechanics (SEM) Annual Conference, vol 17, pp 1–17
41. Verboven P (2002) Frequency domain system identification for modal analysis, Doctoral dissertation
42. Cauberghe B (2004) Application of frequency domain system identification for experimental and operational modal analysis, Doctoral dissertation, p 259
43. Shih C, Tsuei Y, Allemang R, Brown D (1988) Complex mode indication function and its application to spatial domain parameter estimation. Mech Syst Signal Process (MSSP) 2(4):367–377
44. Frazer R, Duncan W, Collar A (1938) Elementary matrices (1965 Reprint). Cambridge University Press, Cambridge
45. Tse F, Morse I, Hinkle R (1978) Mechanical vibrations, theory and applications, 2nd edn. Allyn and Bacon, Inc., Boston
46. SDRC (unknown) (1974) Structural dynamics theory, structural dynamics research corporation
47. Ljung L (1987) System identification: theory for the user. Prentice-Hall, Inc., Englewood Cliffs
48. van Overschee P, De Moor B (1996) Subspace identification of linear systems: theory, implementation, applications. Springer Publishing, Cham
49. McKelvey T, Akcay H, Ljung L (1996) Subspace-based multivariable system identification from frequency response data. IEEE Trans Autom Control 41(7):960–979
50. Vakilzadeh M, Yaghoubi V, McKelvey T, Abrahamsson T, Ljung L (2015) Experimental design for improved frequency domain subspace system identification of continuous-time systems. IFAC PapersOnLine 48(28):886–891
51. Allemang R, Phillips A (2014) Spatial information in autonomous modal parameter estimation. Shock Vib J 2014:1–18. Special ICEDYN Issue
52. Allemang R (2003) The modal assurance criterion (MAC): twenty years of use and abuse. Sound Vib Mag (SVM) 37(8):14–23
53. Cauberghe B, Guillaume P, Verboven P, Parloo E, Vanlanduit S (2004) A poly-reference implementation of the maximum likelihood complex frequency-domain estimator and some industrial applications. In: Proceedings, International Modal Analysis Conference (IMAC), p 12
54. De Troyer T, Guillaume P, Pintelon R, Vanlanduit S (2009) Fast calculation of confidence intervals on parameter estimates of least-squares frequency-domain estimators. Mech Syst Signal Process (MSSP) 23:261–273
55. El-Kafafy M, Accardo G, Peeters B, Janssens K, De Troyer T, Guillaume P (2015) A fast maximum likelihood-based estimation of a modal model. In: Proceedings, International Modal Analysis Conference (IMAC), pp 133–156
56. El-Kafafy M, Peeters B, Guillaume P, De Troyer T (2016) Constrained maximum likelihood modal parameter identification applied to structural dynamics. Mech Syst Signal Process (MSSP) 72–73:567–589
57. Kennedy C, Pancu C (1947) Use of vectors in vibration measurement and analysis. J Aeronaut Sci 14:603–625
58. Phillips A, Allemang R (1996) Single degree-of-freedom modal parameter estimation algorithms. In: Proceedings, International Modal Analysis Conference (IMAC)
59. Fladung W (1994) Multiple reference impact testing, MS thesis, University of Cincinnati

60. Fladung W, Phillips A, Allemang R (2003) Application of a generalized residual model to frequency domain parameter estimation. J Sound Vib (JSV) 262:677–705
61. Allemang R, Phillips A, Brown D (2011) Combined state order and model order formulations in the unified matrix polynomial method (UMPA). In: Proceedings, International Modal Analysis Conference (IMAC)
62. Dippery KD, Phillips AW, Allemang RJ (1996) Spectral decimation in low-order frequency domain modal parameter estimation. J Modal Anal 11:145–154
63. Phillips A, Allemang R (2004) The impact of measurement condensation and modal participation vector normalization on the estimation of modal vectors and scaling. In: Proceedings, International Modal Analysis Conference (IMAC), p 12
64. Dippery K, Phillips A, Allemang R (1996) An SVD condensation of the spatial domain in modal parameter estimation. Int J Exp Anal Modal Anal 11
65. Jolliffe IT (1986) Principal component analysis. Springer, New York and Inc
66. Strang G (2006) Linear algebra and its applications, 4th edn. Cengage Learning
67. Pickrel CR (1996) Numerical assessment of test data using SVD. In: Proceedings, International Modal Analysis Conference (IMAC), Oct 1996

Experimental Modal Parameter Evaluation Methods

11

R. J. Allemang and A. W. Phillips

Contents

Abstract

Modern experimental modal analysis (EMA) methods provide a number of modal parameter solutions based upon different models, different model orders

R. J. Allemang (✉) · A. W. Phillips
Structural Dynamics Research Laboratory, Mechanical and Materials Engineering, University of Cincinnati, Cincinnati, OH, USA
e-mail: Randall.Allemang@UC.EDU; Allyn.Phillips@UC.EDU

R. Allemang, P. Avitabile (eds.), *Handbook of Experimental Structural Dynamics*,
https://doi.org/10.1007/978-1-4614-4547-0_12

and different numerical processing of the redundant data and/or results. Evaluation of the modal parameter solutions provides a way of obtaining a single unique set of modal parameters that best represents the measured experimental data. The early portion of this chapter is a review of some of the experimental modal analysis (EMA) methods covered in detail in Chap. 10, "Experimental Modal Analysis Methods" in this handbook. This is followed by presenting a number of numerical tools that are used in connection with the EMA methods to evaluate and validate the number of modal parameters that can be estimated from a multiple input, multiple output (MIMO) set of measured data. Some tools like complex and multivariate mode indication functions (CMIF and MvMIF) can be used to determine the model order and/or number of modal frequencies that can be estimated from the experimental data. These tools can be applied independent of the EMA method that is used and are particularly useful when close or repeated modal frequencies are present in the experimental data. Additionally, various consistency diagrams, pole surface plots and modal parameter clustering methods are defined that become part of, and enhance, the EMA method used to estimate the modal parameters. Finally, the last portion of this chapter overviews methods that are primarily post processing tools to evaluate and validate the modal parameters that have been estimated. Methods include techniques for normalizing, conditioning and presenting the modal vectors, like the modal vector complexity plot (MVCP) along with techniques for using the estimated modal vectors to estimate other functions like the enhanced frequency response function (eFRF) which can be used to validate the physical validity of the estimated modal vectors. Orthogonality of modal vectors along with consistency of modal vectors, as measured by the modal assurance criterion (MAC), also falls into this category of evaluation and validation tools that are applied after the modal parameters have been estimated. The chapter finishes with a brief example of how several of the evaluation and validation tools can be combined into an autonomous modal parameter estimation method.

Keywords

Experimental modal analysis · Modal parameter evaluation · Modal parameter validation · Modal assurance criterion · Enhanced frequency response function (eFRF) · Complex mode indication function (CMIF) · Multivariate mode indication function (MvMIF) · Consistency diagram · Pole surface diagram · Autonomous modal parameter estimation

Nomenclature

N_i	=	Number of inputs
N_o	=	Number of outputs
N_S	=	Short dimension ($\min(N_i, N_o)$)
N_L	=	Long dimension ($\max(N_i, N_o)$)
N_f	=	Number of spectral lines (frequencies)

N_e =	Number of effective modal frequencies
N =	Number of modal frequencies
F_{max} =	Maximum frequency (Hz)
ω_i =	Frequency (rad/sec)
ω_{max} =	Maximum frequency (rad/sec)
Δf =	Frequency resolution (Hz)
λ_r =	Complex modal frequency
T =	Observation period (sec)
s_i =	Generalized frequency variable
m =	Model order for denominator polynomial
n =	Model order for numerator polynomial
A_{pqr} =	Residue, output DOF p, input DOF q, mode r
$R_{I_{pq}}$ =	Residual inertia, output DOF p, input DOF q
$R_{F_{pq}}$ =	Residual flexibility, output DOF p, input DOF q
$[C]$ =	Companion matrix
$[\alpha]$ =	Denominator polynomial matrix coefficient
$[\beta]$ =	Numerator polynomial matrix coefficient
$[I]$ =	Identity matrix
$[H(\omega_i)]$ =	Frequency response function matrix. ($N_o \times N_i$)
$[T]$ =	Transformation matrix
$[U]$ =	Left singular vector matrix
$[\Sigma]$ =	Singular value matrix (diagonal)
$[\Lambda]$ =	Eigenvalue matrix (diagonal)
$[V]$ =	Right singular vector, or eigenvector, matrix
MPE-1 =	First stage of modal parameter estimation
MPE-2 =	Second stage of modal parameter estimation

1 Introduction

Experimental modal analysis is the process of determining the modal parameters of a structural system (frequencies, damping factors, modal vectors, and modal scaling values) from experimental input-output data, normally frequency response functions (FRFs) or impulse response functions (IRFs). This is in contrast to *analytical modal analysis* where the modal parameters are found from a theoretical (continuous, or discrete) model of the structural system. This could be a closed-form solution for simple structures or, more commonly, a discrete model like a finite element model for structural systems with more complex geometry. Analytical modal analysis generally does not include damping factors as part of the solution. Finally, operational modal analysis (OMA), sometimes called response-only modal analysis, attempts to determine modal parameters from data taken without measured inputs. The inputs come from natural excitation (wind, waves, traffic, etc.) or from the operational inputs provided to a structural system. Operational modal analysis gives a subset of modal parameters that depends upon whether the unmeasured inputs excite the modal parameters and may mix modal parameters with forced vibration

information. Since operation modal analysis does not measure the inputs, modal scaling cannot be determined without additional testing. Operational modal analysis is the subject of the chapter "Operational Modal Analysis" in this handbook. The following discussion is concerned with experimental modal analysis. Analytical and operational modal analysis is covered in other related material.

One important continuing focus of experimental modal analysis is the presentation of modal parameter estimation algorithms in a single, consistent mathematical formulation with a corresponding set of definitions and unifying concepts [1, 2, 3, 4, 5, 6]. In particular, a matrix coefficient polynomial approach can be used to unify the presentation with respect to current algorithms such as the least squares complex exponential (LSCE), polyreference time domain (PTD), polyreference least squares complex frequency (LSCF), Ibrahim time domain (ITD), Eigensystem realization algorithm (ERA), rational fraction polynomial (RFP), orthogonal polynomials (OP), polyreference frequency domain (PFD), and the complex mode indication function (CMIF) methods. Using this *unified matrix polynomial approach* (UMPA) encourages a discussion of the similarities and differences of the commonly used methods, as well as a discussion of the numerical characteristics. Some of the different numerical methods that are used in different methods are the least squares (LS), total least squares (TLS), double least squares (DLS), and singular value decomposition (SVD) methods (to take advantage of redundant measurement data) and the eigenvalue and singular value decomposition transformation methods (to reduce the effective size of the resulting eigenvalue-eigenvector problem).

The unified matrix polynomial approach (UMPA) is an attempt to place most commonly used experimental modal parameter estimation algorithms within a single educational framework. The goal of the UMPA presentation is to highlight the similarity between the different algorithms rather than differences. This approach does not attempt to explain the detailed development of the authors who originated each method but attempts to present a common framework so that different algorithms can be easily compared and contrasted.

2 Background: Modal Parameter Estimation Methods

Modal parameter estimation is a special case of system identification where the a priori model of the system is known to be in the form of modal parameters. Over the past 40 years, a number of algorithms have been developed to estimate modal parameters from measured multiple input, multiple output (MIMO) frequency response function (FRF) or impulse response function (IRF) data. While most of these individual algorithms, summarized in Table 1, are well understood, the comparison of one algorithm to another has become one of the thrusts of current research in this area. Comparison of the different algorithms is possible when the algorithms are reformulated using a common mathematical structure.

This reformulation attempts to characterize different classes of modal parameter estimation techniques in terms of the structure of the underlying matrix polynomials

Table 1 Acronyms – experimental modal parameter estimation Algorithms

Modal parameter estimation algorithms	
CEA	Complex exponential algorithm [7, 8]
LSCE	Least squares complex exponential [8]
PTD	Polyreference time domain [9, 10]
ITD	Ibrahim time domain [11, 12]
MRITD	Multiple Reference Ibrahim Time Domain [13]
ERA	Eigensystem realization algorithm [14, 15, 16]
PFD	Polyreference frequency domain [17, 18, 19, 20]
FDPI	Frequency Domain Direct Parameter Identification [19, 20]
SFD	Simultaneous frequency domain [21]
MRFD	Multi-reference frequency domain [22]
RFP	Rational fraction polynomial [23, 24, 25]
OP	Orthogonal polynomial [25, 26, 27, 28, 29, 30, 31, 32, 33, 34, 35, 36]
PLSCF	Polyreference least squares complex frequency [37, 38, 39, 40, 41, 42]
CMIF	Complex mode indication function [43]

rather than the physically based models used historically. Since the modal parameter estimation process involves a greatly overdetermined problem (more data than independent equations), this reformulation is helpful in understanding the different numerical characteristics of each algorithm and, therefore, the slightly different estimates of modal parameters that each algorithm yields. As a part of this reformulation of the algorithms, the development of a conceptual understanding of modal parameter estimation technology has emerged. This understanding involves the ability to conceptualize the measured data in terms of the concept of characteristic space, the data domain (time, frequency, spatial), the dimension of the measured data, the evaluation of the order of the problem, the condensation of the data, and a common parameter estimation theory that can serve as the basis for developing any of the algorithms in use today. The following sections review these concepts as applied to the current modal parameter estimation methodology.

2.1 Assumptions, Definitions, and Concepts

A number of assumptions, basic definitions, and general concepts are essential to understanding the experimental modal analysis process. Since there is considerable history in the development of modal parameter estimation methodology, it is helpful to provide a structure that provides a common basis for all modal parameter estimation algorithms. Some of these definitions and concepts are briefly introduced in the following subsections.

2.1.1 Assumptions

By its very nature, modal analysis is one way to describe the dynamic characteristics of a structural system. For modal analysis to be considered, there are several assumptions involved. Generally, the structural system is assumed to be *linear*, *time invariant*, and *reciprocal*. Other assumptions can be involved but are not a requirement. An example would be proportional or Rayleigh damping which restricts the form of the modal vectors that are found.

2.1.2 Definition: Modal Parameters

While some situations do not require all modal parameters, a complete set of modal parameters is needed if a complete model of the input-output relationships is desired. Modal parameters include the complex-valued modal frequencies (λ_r), the associated complex-valued modal vectors (ψ_r), and the complex-valued modal scaling (modal A_r). Note that the complex-valued modal frequencies are of the form ($\lambda_r = \sigma_r + j\omega_r$) where σ_r is the damping factor and ω_r is the damped natural frequency for the $r - th$ mode. Additionally, most current multiple input, multiple output (MIMO) algorithms estimate modal participation (weighting) vectors and (L_r) and residue vectors (A_r) as part of the overall process of estimating the complex-valued modal vectors. Modal participation vectors are a result of MIMO modal parameter estimation algorithms and relate how well each modal vector is excited from each of the reference locations included in the measured data. The combination of the modal participation vector (L_r), the modal vector (ψ_r), and the modal A (M_{Ar}) for a given mode yields the residue matrix ($[A]_r$) for that mode.

In general, modal parameters are considered to be global properties of the system. The concept of global modal parameters simply means that there is only one answer for each modal parameter and that the modal parameter estimation solution procedure enforces this constraint. Most of the current modal parameter estimation algorithms estimate the modal frequencies and damping in a global sense, but very few estimate the modal vectors in a global sense. This is due to various modal vector scaling normalization methods which, together with the modal scaling value, give equivalent results but not unique, mathematical values.

Modal Vector Normalization

While there is a unique answer for the modal frequencies, the complex-valued modal vectors represent the relative pattern of motion associated with each complex-valued modal frequency. This relative pattern results from a rank-deficient system of equations where the modal vector is found via an eigenvalue-eigenvector solution. The complex-valued modal vectors, together with the modal scaling, represent the unique characteristic for each modal vector. For this reason, the normalization of the complex-valued modal vector is important when modal vectors, or the associated modal scaling values, are compared numerically.

While there are a number of acceptable normalization schemes for modal vectors, *choosing the largest element in each complex-valued modal vector equal to unity* is the most common and most useful in a physical sense. This method of normalization

will be used in all following discussions. Recognizing that an arbitrarily scaled modal vector is complex valued means that the largest element will in general be complex valued. When the arbitrarily scaled modal vector is divided (normalized) by the largest element, this will force all elements of the scaled modal vector to be bounded by the complex unit circle and, for most cases, to lie along the real axis of the unit circle.

2.1.3 Definition: Degrees of Freedom (DOFs)

Degrees of freedom (DOFs) refer to the physical location and direction of all of the potential inputs to, or outputs from, a structural system. For the theoretical problem, the number of inputs and the number of outputs are always the same and are equal to the number of modal parameter sets of information (typically designated N) that will be found. The general notation that is often used involves inputs in the form of forces and outputs in the form of displacements, velocities, and/or accelerations. The generalized concept of inputs and outputs could be used to represent translational or rotational outputs (or their derivatives) or translational or rotational inputs.

In an experimental sense, the DOFs are where the input and output sensors are located (physical location and direction). Today that includes response measurements from scanning laser vibrometers and digital image correlation (DIC) photogrammetry methods. Equation 1 is a representation of an FRF where the output DOF utilizes the notation p and the input DOF utilizes the notation q. Note that the X and F notation represents the output and input in a general way and does not imply displacement or force.

$$H_{pq}(\omega) = \frac{X_p(\omega)}{F_q(\omega)} \tag{1}$$

- p is the output degree of freedom (physical location and orientation).
- q is the input degree of freedom (physical location and orientation).

For the experimental case, the number of input DOFs (N_i) and output DOFs (N_o) is not the same and in general cannot be directly linked to the N sets of modal parameters that will be estimated.

2.1.4 Concept: Experimental Modal Parameter Estimation

Experimental modal parameter estimation involves estimating the modal parameters of a structural system from measured input-output data. The experimental approach originally involved methods that are referred to as *phase resonance* using sinusoidal excitation (narrowband) and mode by mode tuning with a forcing vector to balance the damping affect assuming the modal vectors are normal modes. These methods gave way to *phase separation* methods that involve a range of frequency information (broadband) where the effects of several modes are separated using mathematical models for the experimental data. Most current modal parameter estimation is phase separation methods, based upon the measured data being the frequency response

function or the equivalent impulse response function, typically found by inverse Fourier transforming the frequency response function.

The current approach is to use numerical techniques to separate the contributions of individual modes of vibration in measurements such as frequency response functions. The concept involves estimating the individual single degree of freedom (SDOF) contributions to the multiple degree of freedom (MDOF) measurement. Then, the modal parameters are found from the SDOF contributions.

$$[H(\omega_i)]_{N_L \times N_S} = \sum_{r=1}^{N} \frac{[A_r]_{N_L \times N_S}}{j\omega_i - \lambda_r} + \frac{[A_r^*]_{N_L \times N_S}}{j\omega_i - \lambda_r^*} = \sum_{r=1}^{2N} \frac{[A_r]_{N_L \times N_S}}{j\omega_i - \lambda_r} \tag{2}$$

Equation 2 represents a mathematical problem that, at first observation, is nonlinear in terms of the unknown modal parameters. Once the modal frequencies (λ_r) are known, the mathematical problem is linear with respect to the remaining unknown modal parameters ($[A_r]$). For this reason, the numerical solution in many modal parameter estimation (MPE) algorithms frequently involves two linear stages that utilize least squares (LS) solution methods. Typically, the modal frequencies and modal participation vectors are found in a first stage (MPE-1), and residues, modal vectors, and modal scaling are determined in a second stage (MPE-2). This concept, involving a summation of partial fraction terms, is represented mathematically in Eq. 2 and graphically in Fig. 1.

While the model stated in Eq. 2 is fundamental to the linear superposition of individual SDOF contributions, this model is normally limited to being used as the basis for estimating the residues A_{pqr} once the modal frequencies (λ_r) are known. Based upon the speed and memory of modern personal computers, these two stages are often executed together giving the appearance of a single stage solution.

Equation 2 can be represented in the time domain in terms of impulse response functions in a similar summation form as shown in Eq. 3:

$$[h(t_i)]_{N_L \times N_S} = \sum_{r=1}^{N} [A_r]_{N_L \times N_S} e^{\lambda_r t_i} + [A_r^*]_{N_L \times N_S} e^{\lambda_r^* t_i} = \sum_{r=1}^{2N} [A_r]_{N_L \times N_S} e^{\lambda_r t_i} \tag{3}$$

2.1.5 Concept: Experimental Modal Parameter Methods

Using the concepts developed in the previous section, the most commonly used modal identification methods can be summarized as shown in Table 2. The high-order model is typically used for those cases where the system is under-sampled in the spatial domain. For example, the limiting case is when only one measurement is made on the structure. For this case, the left-hand side of the general linear equation corresponds to a scalar polynomial equation with the order equal to or greater than the number of desired modal frequencies.

The low-order model is used for those cases where the spatial information is complete. In other words, the number of physical coordinates (N_L) is greater than

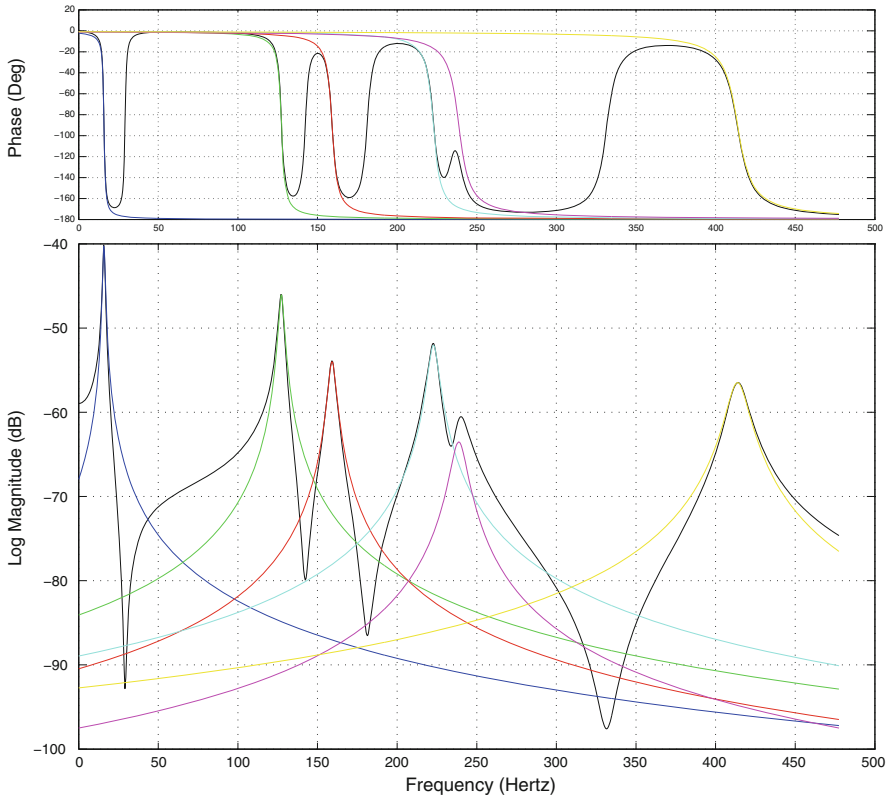

Fig. 1 MDOF – superposition of SDOF (positive frequency poles)

the number of desired (positive) modal frequencies (N). For this case, the order (m) of the left-hand side of the general linear equation, Eqs. 5 or 6, is equal to two.

The zero-order model corresponds to cases where the temporal information is neglected and only the spatial information is used. These methods directly estimate the eigenvectors as a first step. In general, these methods are programmed to process data at a single temporal condition or variable. In this case, the method is essentially equivalent to the single degree of freedom (SDOF) methods which have been used with frequency response functions. In other words, the zeroth-order matrix polynomial model compared to the higher-order matrix polynomial models is similar to the comparison between the SDOF and MDOF methods used historically in modal parameter estimation.

Modal parameter estimation algorithms are similar in more ways than they are different. Fundamentally, all algorithms can be developed beginning with a linear, constant coefficient, symmetric matrix model involving mass, damping, and stiffness. The common goal in all algorithms, therefore, is the development of

Table 2 Modal vector estimation methods: overview

	Domain		Matrix polynomial order			Coefficients	
Algorithm	Time	Freq	Zero	Low	High	Scalar	Matrix
Complex exponential algorithm (CEA)	•				•	•	
Least squares complex exponential (LSCE)	•				•	•	
Polyreference time domain (PTD)	•				•		$N_S \times N_S$
Ibrahim time domain (ITD)	•			•			$N_L \times N_L$
Multi-reference Ibrahim time domain (MRITD)	•			•			$N_L \times N_L$
Eigensystem realization algorithm (ERA)	•			•			$N_L \times N_L$
Polyreference frequency domain (PFD)		•		•			$N_L \times N_L$
Simultaneous frequency domain (SFD)		•		•			$N_L \times N_L$
Multi-reference frequency domain (MRFD)		•		•			$N_L \times N_L$
Rational fraction polynomial (RFP)		•			•	•	$N_S \times N_S$
Orthogonal polynomial (OP)		•			•	•	$N_S \times N_S$
Polyreference least squares complex frequency (PLSCF)		•			•	•	$N_S \times N_S$
Complex mode indication function (CMIF)		•	•				$N_L \times N_S$

a characteristic matrix coefficient equation that describes a linear, time-invariant, reciprocal mechanical system consistent with this theoretical background. This is the rationale behind using the unified matrix polynomial approach as the educational basis for demonstrating this common kernel for all modal parameter estimation algorithms [1,2,3,4,5,6]. The following sections discuss the similarity of the kernel equations common to all widely used modal parameter estimation algorithms.

2.1.6 Concept: Data Domain

Modal parameters can be estimated from a variety of different measurements that exist as discrete data in different data domains (time and/or frequency). These measurements can include free decays, forced responses, power spectra, covariance, frequency response functions (FRFs), or impulse response functions (IRFs). These measurements can be processed one at a time or in partial or complete sets simultaneously. The measurements can be generated with no measured inputs, a single measured input, or multiple measured inputs. The data can be measured individually or simultaneously. There is a tremendous variation in the types of measurements and in the types of constraints that can be placed upon the testing procedures used

to acquire this data. For most measurement situations, FRFs are utilized in the frequency domain, and IRFs are utilized in the time domain. When IRFs are utilized, they are generally formed from the inverse Fourier transform of the measured FRFs. For the purpose of the following discussions, force-displacement data is considered the basis for the equations recognizing that force-displacement data can be numerically synthesized from measured force-acceleration data or force-velocity data.

2.1.7 Concept: Characteristic Space

From a conceptual viewpoint, the measurement space of a modal identification problem can be visualized as occupying a volume with the coordinate axes defined in terms of the three sets of characteristics. Two axes of the conceptual volume correspond to spatial information and the third axis to temporal information. The spatial axes are in terms of the input and output degrees of freedom (DOF) of the system. The temporal axis is either time or frequency depending upon the domain of the measurements. These three axes define a 3D volume which is referred to as the characteristic space.

This space or volume represents all possible measurement data. This conceptual representation is very useful in understanding what data subspace has been measured. Also, this conceptual representation is very useful in recognizing how the data is organized and utilized with respect to different modal parameter estimation algorithms (3D volume to stacked 2D matrices). Information parallel to one axis consists of a superposition of the characteristics defined by that axis. The other two characteristics determine the scaling of each term in the superposition.

Any structural testing procedure measures a subspace of the total possible data available. Modal parameter estimation algorithms may then use all of this subspace or may choose to further limit the data to a more restrictive subspace via sieving and/or filtering. It is theoretically possible to estimate the characteristics of the total space by measuring any subspace which samples all three characteristics. Measurement data spaces involving many planes of measured data are the best possible modal identification situations since the data subspace includes contributions from temporal and spatial characteristics. The particular subspace which is measured and the weighting of the data within the subspace in an algorithm are the main differences between the various modal identification procedures which have been developed.

It should be obvious that the data which defines the subspace needs to be acquired in a consistent measurement process in order for the algorithms to estimate accurate modal parameters. This fact has triggered the need to measure all of the data simultaneously and has led to recent advancements in data acquisition, digital signal processing, and instrumentation designed to facilitate this measurement problem.

While it is not always obvious, most modal parameter estimation methods assume that the measured data includes one or more pairs of matched input and output DOFs in what is commonly referred to as driving point FRFs.

2.1.8 Concept: Data Dimensionality

In the following discussion, the use of notation involving the number of input degrees of freedom (DOFs), (N_i), and the number of output DOFs, (N_o), is replaced by an alternate notation. Since the FRF matrix is always assumed to be reciprocal, it is more important to note the smaller and larger of the number of DOFs with respect to the inputs and outputs when the data is utilized by modern MIMO modal parameter estimation algorithms. For this reason, the dimension that is larger is referred to as the long dimension, (N_L), and the dimension that is smaller is referred to as the short dimension, (N_S). The short dimension is often referred to as the number of references, and the long dimension is often referred to as the number of responses. The dimension of the third axis (temporal axis) is either the number of frequencies (N_f) or the number of times (N_t).

2.1.9 Concept: Generalized Frequency

In the following development, all frequency domain models will be presented as a function of the generalized frequency variable s. This variable is a general complex-valued variable that is most often thought of as $s = j\omega$, representing the independent frequency variable associated with the FRF. There are several other scaled or mapped versions of the generalized frequency variable s which are useful for minimizing the numerical conditioning associated with different frequency domain MPE algorithms.

$$H_{pq}(\omega_i) = \frac{X_p(\omega_i)}{F_q(\omega_i)} = \frac{\beta_n (s_i)^n + \beta_{n-1}(s_i)^{n-1} + \cdots + \beta_1 (s_i)^1 + \beta_0 (s_i)^0}{\alpha_m (s_i)^m + \alpha_{m-1}(s_i)^{m-1} + \cdots + \alpha_1 (s_i)^1 + \alpha_0 (s_i)^0} \quad (4)$$

One example is a simple scaled version of s where $s = \frac{j\omega}{\omega_{max}}$. When the generalized frequency variable is scaled or mapped in this fashion, any frequency estimate that results must be corrected accordingly. This concept will be explained further in the section on high-order, frequency domain algorithms.

2.1.10 Concept: Kernel Equations

Each experimental modal parameter estimation method has a basic equation that is repeated for different model orders (m) powers or subspaces of the independent variable (t, s, ω, z) to get additional sets of solutions. The base equation for each method is referred to as the kernel equation. Consistency between the different sets of solutions is one common method of determining the most likely modal parameters in the data.

Frequency Domain

$$\sum_{k=0}^{m} (s_i)^k [\alpha_k] [H(\omega_i)] = \sum_{k=0}^{n} (s_i)^k [\beta_k] [I] \quad (5)$$

Additional equations can be developed by repeating Eq. 5 at many frequencies (ω_i) until all data or a sufficient overdetermination factor is achieved. Note that

both positive and negative frequencies are required in order to accurately estimate conjugate modal frequencies.

In terms of sampled data, the frequency domain matrix polynomial coefficients result from a set of linear equations (repeated application of Eq. 5) where each equation is formulated by choosing a different frequency from the FRF data. From a numerical perspective, Eq. 5 is generally not well-formed, and the condition number associated with this system of equations will be extreme when the model order (m) exceeds five or six. This issue will require special consideration in order to obtain reasonable answers for the modal frequencies. This has been discussed further in Section 5.2.3 of the ▸ Chap. 10, "Experimental Modal Analysis Methods" in this handbook. This approach involves mapping the generalized frequency s_i to the z independent variable z_i as noted in the two following equations:

$$s_i = z_i = e^{j*\pi*(\omega_i/\omega_{max})} = e^{j*\omega_i*\Delta t} \tag{6}$$

$$s_i^m = z_i^m = e^{j*\pi*m*(\omega_i/\omega_{max})} \tag{7}$$

Once the alpha $[\alpha]$ and beta $[\beta]$ coefficients have been found, the modal frequencies can be found from the roots of the alpha $[\alpha]$ matrix coefficient polynomial.

$$\sum_{k=0}^{m} [\alpha_k] s^k = 0 \tag{8}$$

The roots of this matrix coefficient polynomial are in terms of the generalized frequency variable s and will be the complex modal frequencies (λ_r) directly.

Time Domain

If the discussion is limited to the use of free decay or impulse response function data, the previous time domain equations can be simplified by noting that the forcing function can be assumed to be zero for all time greater than zero. If this is the case, the $[\beta_k]$ coefficients can be eliminated from the equations.

$$\sum_{k=0}^{m} [\alpha_k] [h\,(t_{i+k})] = 0 \tag{9}$$

Additional equations can be developed by repeating Eq. 9 at different time shifts (initial times t_i) into the data until all data or a sufficient overdetermination factor is achieved. Note that at least one time shift is required in order to accurately estimate conjugate modal frequencies.

In terms of sampled data, the time domain matrix polynomial coefficients result from a set of linear equations (repeated application of Eq. 6) where each equation is formulated by choosing various distinct initial times. From a numerical perspective,

Eq. 6 is generally well-formed, and the condition number associated with this system of equations will not be extreme even for high order (m).

In contrast, the frequency domain matrix polynomial developed in Eqs. 3 through 5 results from a set of linear equations (repeated application of Eq. 4) where each equation is formulated at one of the frequencies of the measured FRF data. This distinction is important to note since the roots of the matrix characteristic equation formulated in the time domain are in a mapped complex z domain (z_r), which is similar but not identical to the z-domain familiar to control theory. Once the alpha [α] coefficients have been found, the roots of a polynomial in the complex z domain can be found since all of the measured time domain data utilize the same Δt spacing.

$$\sum_{k=0}^{m} [\alpha_k] z^k = 0 \tag{10}$$

Equation 10 is developed from the fixed time spacing (Δt) and derivative relationships associated with discrete time data. It is important to note that this development is theoretically exact and no approximations are involved.

2.1.11 Concept: Overdetermined Linear Models

Most current modal parameter estimation utilizes linear models, sometimes in several successive solution steps, that have more equations than unknowns in each solution step. This will be true for simple SDOF models as well as complicated MIMO MDOF models. The number of equations is larger than the unknowns since an equation can be formed at each measured frequency or time while the number of unknowns is limited to a function of the number of modal parameters N. The overdetermination factor is the ratio of the number of equations to the number of unknowns. The overdetermination factor can easily be a number greater than 2–5.

Overdetermined sets of linear equations are most often solved using least squares (LS) techniques, particularly when the noise on the data is expected to be random. The least squares solution will yield the best solution in the presence of random noise. With respect to the estimation of frequency response functions (FRFs) as the measured data for most modal parameter estimation, this means that bias errors on the FRF data is much more concerning than the random errors.

2.1.12 Concept: General (Two-Stage) Solution Procedure

Most modern modal parameter estimation (MPE) algorithms are implemented in two stages that each involves the solution of overdetermined linear equations. The first stage, referred in this text as MPE-1, is where the modal frequencies (λ_r) are estimated along with associated modal weighting vectors (L_r). The second stage, referred in this text as MPE-2, is where the modal vectors (ψ_r) and modal scaling are estimated. These two stages can generally be briefly summarized as follows:

- MPE-1: Utilize measured FRF or IRF data with a matrix coefficient, polynomial model to find multiple estimates of the modal parameters. Select the best set of modal frequencies and modal participation vectors. This stage is often performed in two fundamental steps: (1) Solve a set of overdetermined linear equations, and (2) solve for the roots of a polynomial.
  - Choose polynomial or subspace order (m)
  - Solve for unknown matrix coefficients (α_k)
    * Add sufficient block kernel equations (for different starting times or frequencies) until there are more block kernel equations than there are block unknowns ($[\alpha_k]$).
    * If using a frequency domain method, utilize one or more of the generalized frequency approaches to improve the numerical conditioning.
    * Solve for matrix coefficients ($[\alpha_k]$) in a least squares (LS) sense.
    * Solve for complex-valued modal frequencies for (λ_r or z_r) utilizing the eigenvalues from an eigenvalue-eigenvector solution method to solve the matrix coefficient polynomial (companion matrix approach).
    * If time domain methods have been used, correct from z_r to λ_r
    * If generalized frequency methods have been used, correct for the frequency conversion.
    * Using the eigenvectors from the above eigenvalue-eigenvector solution as modal participation (weighting) vectors L_{qr}. Normalize as needed.
  - Iterate over different polynomial orders or subspace orders in the kernel equation to get multiple estimates of the modal parameters.
  - Select one set of complex-valued modal frequencies, with associated participation vectors, from the multiple sets. Manual or automated selection methods can be used.
- MPE-2: Utilize measured FRF or IRF data, with selected complex-valued modal frequencies and modal participation vectors, to find complex-valued modal vectors from an overdetermined set of linear equations.
  - Solve for modal vectors or residues using a weighted least squares solution method involving the fixed set of modal frequencies and modal participation (weighting) vectors.
  - Normalize modal vectors as needed.
  - Solve for modal scaling associated with normalized modal vectors and previous modal participation vectors.

2.1.13 Concept: Equation Normalization

Many of the overdetermined sets of linear equations involve a null space problem in which the right-hand side (RHS) of the equation is zero or null. In these cases, the unknown coefficients of the equation are non-unique but can be found by choosing one of the coefficients, typically, equal to the identity matrix. The numerical solution of the overdetermined sets of linear equations will yield different answers depending on which coefficient is chosen. While theoretical data would yield only one answer,

experimental data will have random and bias noise, and this noise is what yields somewhat different answers. Historically, two solutions have been used in these cases, setting the lead coefficient and the last coefficient to the identity matrix to give two answers that bracket the solution. This is true for both frequency domain methods and time domain methods. This choice of choosing a coefficient to be the identity is referred to as *equation normalization*.

$$\sum_{k=0}^{m}\left[[\alpha_k](s_i)^k\right][H(\omega_i)] = \sum_{k=0}^{n}\left[[\beta_k](s_i)^k\right][I] \tag{11}$$

Equation 11 is an example of such a null space (rank deficient) equation. The unknowns in the equation are the $[\alpha]$ and $[\beta]$ coefficients. Since every term has an unknown coefficient matrix, the equation can be pre-multiplied by the inverse of any one of the $[\alpha]$ coefficients to derive a solvable (full rank) base equation.

Lowest $[\alpha_0]$ **Normalization** $[\alpha_0] = [I]$

$$\sum_{k=1}^{m}\left[[\alpha_k](s_i)^k\right][H(\omega_i)] - \sum_{k=0}^{n}\left[[\beta_k](s_i)^k\right][I] = -\left[[\alpha_0](s_i)^0\right][H(\omega_i)] \tag{12}$$

Highest $[\alpha_m]$ **Normalization** $[\alpha_m] = [I]$

$$\sum_{k=0}^{m-1}\left[[\alpha_k](s_i)^k\right][H(\omega_i)] - \sum_{k=0}^{n}\left[[\beta_k](s_i)^k\right][I] = -\left[[\alpha_m](s_i)^m\right][H(\omega_i)] \tag{13}$$

It is important to note that this equation normalization must occur in the initial step of choosing the base equation. Then the unknown coefficients are solved in an overdetermined set of these linear equations. It is not sufficient to manipulate the final solution of polynomial coefficients into a different normalized form. The difference that equation normalization provides is determined by the least squares solution for the coefficients [39, 41].

2.1.14 Concept: Modal Vectors, Modal Scaling, Residues

The modal vectors are most often determined by normalizing the residues. There are a number of normalization methods that can be used. Once the modal vectors are determined, the modal scaling can be determined. The modal vector normalization is up to the user but most commonly is chosen to give modal vectors that are dominantly real valued (close to normal modes). The choice of normalization may also consider how the comparable modal vectors from analytical methods have been normalized. For this reason, it is common to choose the modal vector normalization such that the realities of experimental estimation of the modal vectors (noting that the residues will not be perfectly imaginary valued) are considered. One example

of a useful normalization is to choose to make the largest modal coefficient in each modal vector unity.

$$\{\psi_r\}_{N_L \times 1} = \frac{\{A_{pqr}\}_{N_L \times 1}}{max(A_{pqr})} \tag{14}$$

In the above equation, the residue vector is divided by the residue with the largest complex magnitude, mode by mode. This yields a modal vector that will generally be dominantly real valued and limited in magnitude to plus/minus unity.

The modal A scaling term (M_{A_r}) can then be found to provide the absolute scaling associated with this modal vector normalization/scaling. *Note that if the normalization/scaling of this modal vector is the same as that used for an analytical solution, then the modal A scaling terms are comparable.*

$$A_{pqr} = \frac{\psi_{pr}\,\psi_{qr}}{M_{A_r}} \qquad M_{A_r} = \frac{\psi_{pr}\,\psi_{qr}}{A_{pqr}} \tag{15}$$

If the modal vector is completely real valued, the modal mass scaling term (M_r) can be estimated.

$$A_{pqr} = \frac{\psi_{pr}\,\psi_{qr}}{j2\omega_r M_r} \qquad M_r = \frac{\psi_{pr}\,\psi_{qr}}{j2\omega_r A_{pqr}} \tag{16}$$

Note that if the normalization/scaling of this modal vector is the same as that used for an analytical solution, then the modal mass scaling terms are comparable.

Finally, from the above equations, modal mass can be estimated from modal A as long as the modal vector is a normal (real-valued) mode.

$$M_r = \frac{M_{A_r}}{j2\omega_r} \tag{17}$$

If the modal vector is not a real-valued normal mode, the modal vector can be normalized to an equivalent real-valued normal mode, and Eq. 17 can be used. Alternatively, an effective modal mass can be estimated from Eq. 18 as long as the modal vector is dominantly real valued.

$$\|M_r\| = \|\frac{M_{A_r}}{j2\omega_r}\| \tag{18}$$

3 Modal Frequency Evaluation/Validation Tools

3.1 Model Order Relationships

From a theoretical consideration, the number of characteristic values (number of modal frequencies, number of roots, number of poles, etc.) that can be determined depends upon the size of the matrix coefficients involved in the model and the order of the polynomial terms in the model. The characteristic matrix polynomial equation, Eq. 5 or Eq. 9, has a model order of m, and the number of modal frequencies or roots that will be found from this characteristic matrix polynomial equation will be m times the size of the coefficient matrices $[\alpha]$.

For a given algorithm, the size of the matrix coefficients is normally fixed; therefore, determining the model order is directly linked to estimating N, the number of modal frequencies that are of interest in the measured data. As has always been the case, an estimate for the minimum number of modal frequencies can be easily found by counting the number of peaks in the frequency response function in the frequency band of analysis. This is a minimum estimate of N since the frequency response function measurement may be at a node of one or more modes of the system, repeated roots may exist, and/or the frequency resolution of the measurement may be too coarse to observe modes that are closely spaced in frequency. Several measurements can be observed, and a tabulation of peaks existing in any or all measurements can be used as a more accurate minimum estimate of N.

3.2 Auto Moment Functions

A more automated procedure for including the peaks that are present in several frequency response functions is to observe the summation of frequency response function power (Fig. 2). This function represents the auto power or auto moment of the frequency response functions summed over a number of response measurements and is normally formulated as follows for the p-th reference:

$$H_{power-p}(\omega) = \sum_{q=1}^{N_L} H_{pq}(\omega) H_{pq}{}^{*}(\omega) \tag{19}$$

Note in the above figure that the mode slightly above 500 Hz is not well observed. If all FRFs from all N_S references are included, all the modes are observed as in Fig. 3.

$$H_{power}(\omega) = \sum_{p=1}^{N_S} \sum_{q=1}^{N_L} H_{pq}(\omega) H_{pq}{}^{*}(\omega) \tag{20}$$

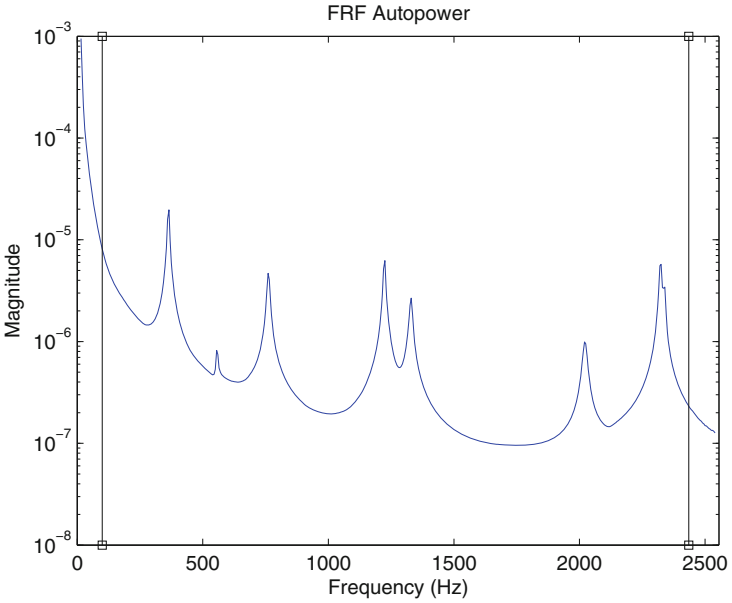

Fig. 2 Auto moment function-FRFs from reference p

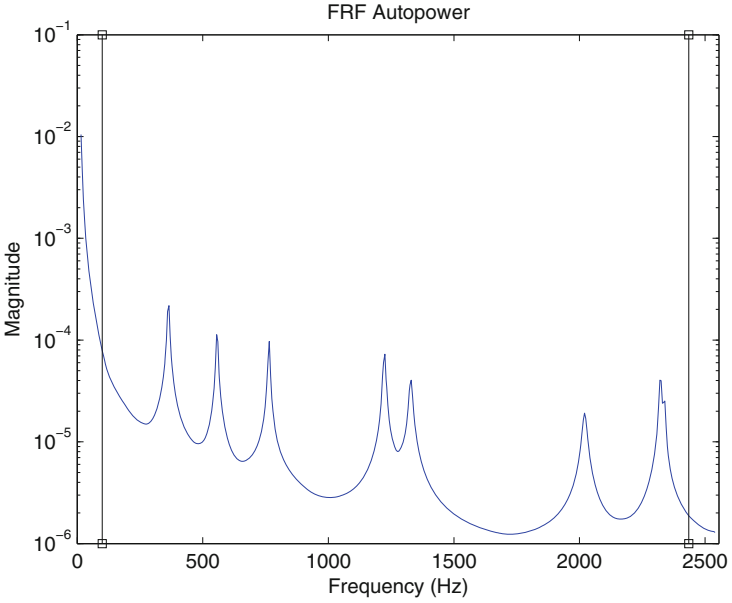

Fig. 3 Auto moment function-FRFs from all references

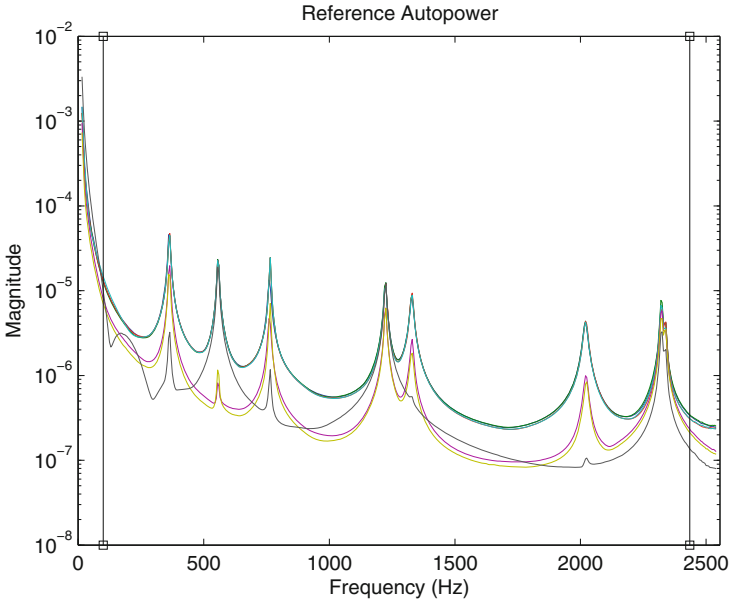

Fig. 4 Auto moment function-FRFs from all references

The above figure, however, does not indicate which modes are observed from the different references. If the above figure is plotted reference by reference, the figure provides more discernible information regarding which modes are well excited by each reference (Fig. 4).

These simple techniques are extremely useful but do not provide an accurate estimate of model order when repeated roots exist or when modes are closely spaced in frequency. The above figure is found from FRFs of a circular object where numerous repeated modal frequencies exist. Note that this plot looks very much like a complex mode indication function (CMIF) for the FRF data but does not discriminate close modes properly. The CMIF is explained in Sect. 3.3.1. For these reasons, an appropriate estimate of the order of the model (function of the number of modes) is of prime concern and is the single most important problem in modal parameter estimation. A CMIF plot or the equivalent will be needed to properly determine the order of the model required.

In order to determine a reasonable estimate of the model order for a set of representative data, a number of techniques have been developed as guides or aids to the user. Much of the user interaction involved in modal parameter estimation involves the use of these tools. Most of the techniques that have been developed allow the user to establish a maximum model order to be evaluated (in many cases, this is set by the limits of the algorithm or the computer memory). Data is acquired based upon an assumption that the model order is equal to this maximum. In a sequential fashion, this data is evaluated to determine if a model order less than

the maximum will describe the data sufficiently. This is the point that the user's judgment and the use of various evaluation aids become important. Some of the commonly used techniques are mode indication functions, consistency (stability or stabilization) diagrams, and pole surface density plots.

3.3 Mode Indication Functions

Mode indication functions (MIF) are normally real valued, frequency domain functions that exhibit local minima or maxima at the natural frequencies of the modes. One mode indication function can be plotted for each reference available in the measured data. The primary mode indication function will exhibit a local minimum or maximum at each of the natural frequencies of the system under test. The secondary mode indication function will exhibit a local minimum or maximum at repeated or pseudo repeated roots of order two or more. Further mode indication functions yield local minima or maxima for successively higher orders of repeated or pseudo repeated roots of the system under test.

3.3.1 Complex Mode Indication Function

An algorithm based on singular value decomposition (SVD) methods applied to multiple reference FRF measurements, identified as the complex mode indication function (CMIF), was first developed for traditional FRF data in order to identify the proper number of modal frequencies, particularly when there are closely spaced or repeated modal frequencies [43]. Unlike the multivariate mode indication function (MvMIF), which indicates the existence of normal (real-valued) modes, CMIF indicates the existence of real-valued or complex-valued modes and the relative magnitude of each mode. Furthermore, MvMIF yields a set of force patterns that can best excite the normal (real-valued) mode, while CMIF yields the corresponding mode shape and modal participation vector.

The CMIF is defined as the economical singular values, computed from the FRF matrix at each spectral line. The CMIF is the plot of these singular values on a log magnitude scale as a function of frequency. The peaks detected in the CMIF plot indicate the existence of modes, and the corresponding frequencies of these peaks give the damped natural frequencies for each mode. In the application of CMIF to traditional modal parameter estimation algorithms, the number of modes detected in the CMIF determines the minimum number of degrees of freedom of the system equation for the algorithm. A number of additional degrees of freedom may be needed to take care of residual effects and noise contamination.

$$[H(\omega)] = [U(\omega)]\lceil \Sigma(\omega) \rfloor [V(\omega)]^H \tag{21}$$

Most often, the number of input points (reference points), N_i, is less than the number of response points, N_o. In Eq. 21, if the number of effective modes is less

than or equal to the smaller dimension of the FRF matrix, i.e., $N_e \leq N_i$, the singular value decomposition leads to approximate mode shapes (left singular vectors) and approximate modal participation factors (right singular vectors). The singular value is then equivalent to the the scaling factor Q_r divided by the difference between the discrete frequency and the modal frequency $j\omega - \lambda_r$. For a given mode, since the scaling factor is a constant, the closer the modal frequency is to the discrete frequency, the larger the singular value will be. Therefore, the damped natural frequency is approximately the frequency at which the maximum magnitude of the singular value occurs. If different modes are compared, the stronger the modal contribution (larger residue value), the larger the singular value will be. The peak in the CMIF indicates the location on the frequency axis that is nearest to the pole. The frequency is the estimated damped natural frequency, to within the accuracy of the frequency resolution Δf (Fig. 5).

Since the mode shapes that contribute to each peak do not change much around each peak, several adjacent spectral lines from the FRF matrix can be used simultaneously for a better estimation of mode shapes. By including several spectral lines of data in the singular value decomposition calculation, the effect of the leakage error can be minimized. If only the quadrature (imaginary) part of the FRF matrix (for force-displacement or force-acceleration FRFs) is used in CMIF, the singular values will be much more distinct. Note that if force-velocity FRFs are used (as in laser-based response measurements), the coincident (real) part of the FRF is used (Fig. 6).

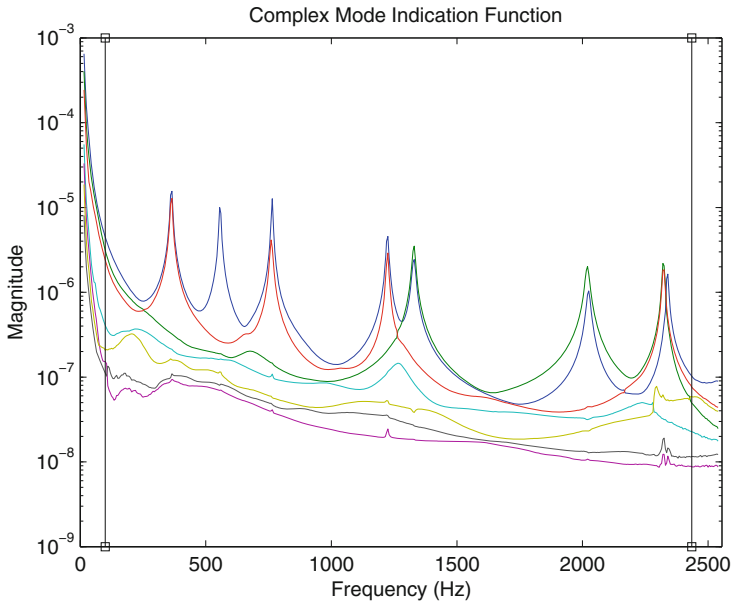

Fig. 5 Complex mode indication function (CMIF)

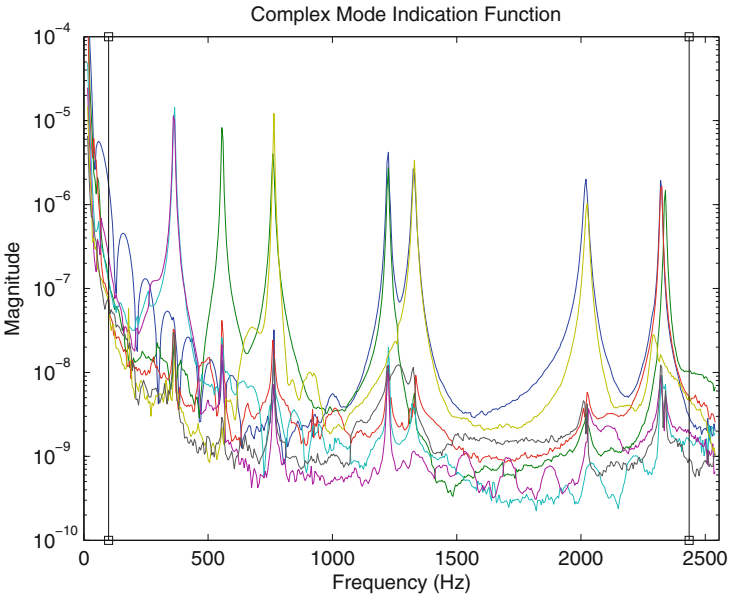

Fig. 6 Quadrature complex mode indication function (CMIF)

3.3.2 Multivariate Mode Indication Function

The multivariate mode indication function (MvMIF) is based upon finding a force vector F that will excite a normal mode at each frequency in the frequency range of interest [44]. If a normal mode can be excited at a particular frequency, the response to such a force vector will exhibit the 90° phase lag characteristic. Therefore, the real part of the response will be as small as possible particularly when compared to the imaginary part or the total response. In order to evaluate this possibility, a minimization problem can be formulated as follows:

$$\underset{||F||=1}{min} \frac{\{F\}^T [H_{Real}]^T [H_{Real}] \{F\}}{\{F\}^T \left([H_{Real}]^T [H_{Real}] + [H_{Imag}]^T [H_{Imag}] \right) \{F\}} = \lambda \tag{22}$$

This minimization problem is similar to a Rayleigh quotient, and it can be shown that the solution to the problem is found by finding the smallest eigenvalue λ_{min} and the corresponding eigenvector $\{F\}_{min}$ of the following problem:

$$[H_{Real}]^T [H_{Real}] \{F\} = \lambda \left([H_{Real}]^T [H_{Real}] + [H_{Imag}]^T [H_{Imag}] \right) \{F\} \tag{23}$$

The above eigenvalue problem is formulated at each frequency in the frequency range of interest. Note that the result of the matrix product $[H_{Real}]^T [H_{Real}]$ and $[H_{Imag}]^T [H_{Imag}]$ in each case is a square, real-valued matrix of size equal to the

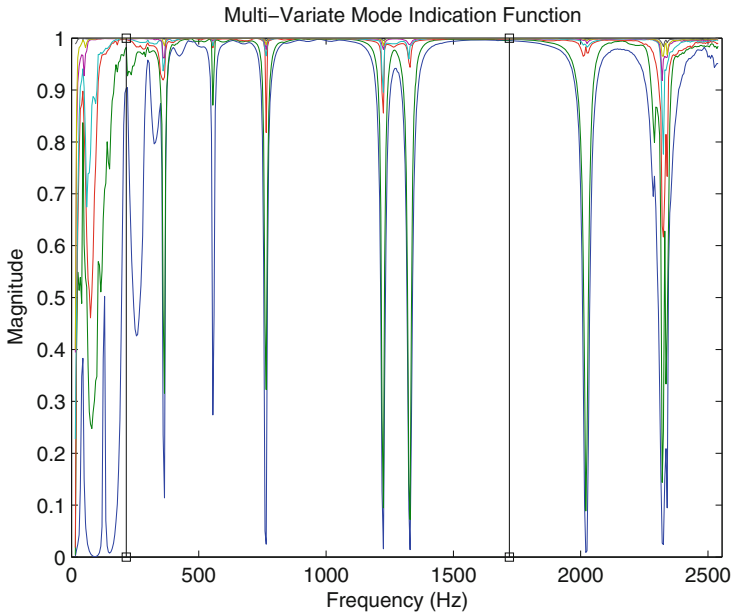

Fig. 7 Multivariate mode indication function (MvMIF)

number of references in the measured data $N_i \times N_i$. The resulting plot of a mode indication function for a seven reference case can be seen in Fig. 7.

3.4 Consistency Diagrams

One of the most common methods for determining the number of modes present in the measurement data is the use of consistency diagrams, formerly referred to as stability or stabilization diagrams. The consistency diagram is developed by successively computing different model solutions (utilizing different model orders for the characteristic polynomial, different normalization methods for the characteristic matrix coefficient polynomial, different equation condensation methods, and/or different algorithms) and involves tracking the estimates of frequency, damping, and possibly modal participation vectors as a function of model solution iteration. Symbols are used to identify consistency characteristics between the modal parameter solutions found in each iteration, comparing the estimates to those found in the previous iteration. Normally, the consistency levels are evaluated sequentially beginning with whether (1) the modal parameter estimates are physically reasonable (damping), (2) the modal parameters are found as conjugate pairs, (3) the frequency estimates are consistent, (4) the frequency and damping estimates are consistent, and (5) the frequency, damping, and modal participation vectors are consistent. Consistency at each level is defined by a user tolerance that defines how close

statistically that the estimates, from one model iteration to the next, must be to be classified as consistent. Note that when modal participation vectors are compared, the modal assurance criterion (MAC) is utilized (see Sect. 4.5 for more specific information).

As the number of model solution iterations is increased, more and more modal frequencies are estimated, but, hopefully, the estimates of the physical modal parameters will be consistently determined as the correct model parameters are found. Ideally, the nonphysical (computational) modes will not be estimated in a consistent way during this process and can be sorted out of the modal parameter data set more easily. Note that inconsistencies (frequency shifts, leakage errors, etc.) in the measured data set will obscure this consistency and render the diagram difficult to use. Normally, a tolerance, in percentage, is given for the consistency of each of the modal parameters that are being evaluated.

Figures 8 through 9 demonstrate two different presentations of consistency diagrams based upon two common normalizations of the characteristic matrix coefficient polynomial, omitting the lower-level consistencies associated with conjugate only poles and frequency only consistency in Fig. 9. The omission of the lower-level consistencies results in a clear consistency diagram. In all of the following figures, the MIMO FRF data was estimated from an impact test with seven reference accelerometers and a frequency resolution of 5 Hz ($\Delta f = 5$ Hz.). For these cases, the polyreference time domain (PTD) algorithm was used, but the results shown are typical for all algorithms evaluated. In all figures, a CMIF plot is plotted on the consistency diagram in the background for reference.

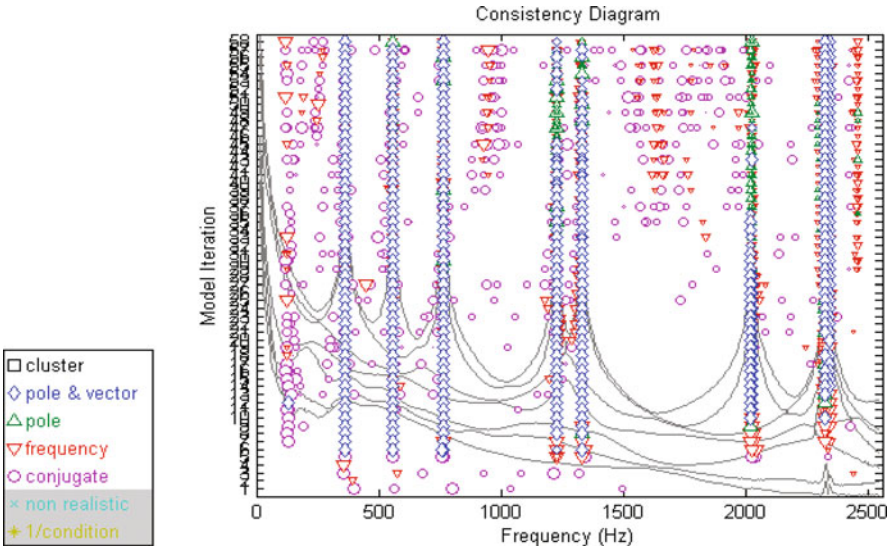

Fig. 8 Consistency diagram – max order 30 – both normalizations

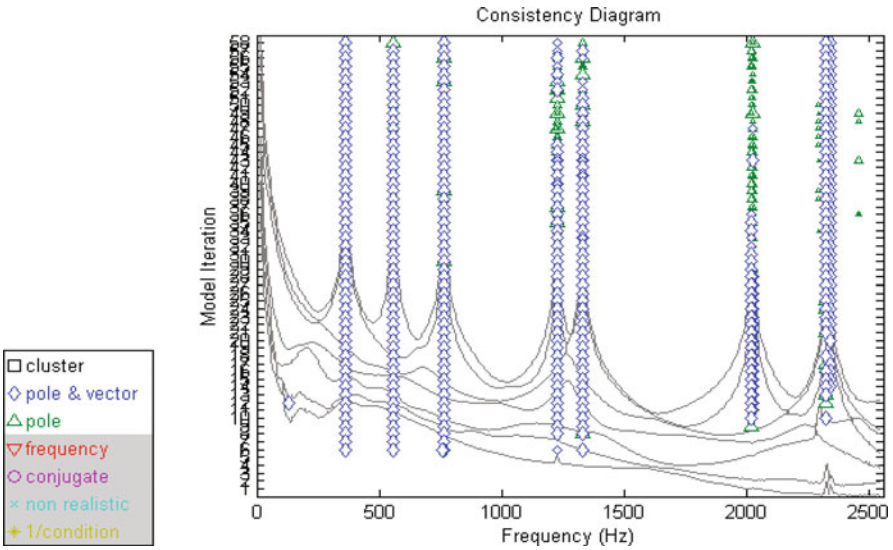

Fig. 9 Consistency diagram – max order 30 – both normalizations, clear

If only model order is evaluated from iteration to iteration, research [40] has shown that the correct choice of normalization of the characteristic matrix coefficient polynomial (lowest order coefficient normalized to unity) has a distinct effect on producing clear consistency diagrams. However, the biggest effect comes from the solutions that are excluded, or included, based upon the tolerance levels and consistency evaluations that are in the associated consistency diagram. Figure 9 compared to Fig. 8 distinctly shows that a clear consistency diagram is achieved when the lowest levels of consistency evaluation are excluded.

Note that the only difference between Figs. 8 and 9 is the omission of the lower-level consistency evaluations (omitting conjugate pair evaluation and frequency consistency evaluation). Figure 9 clearly shows the benefits of a clear consistency diagram. Similar results are obtained when the tolerance levels are changed for some of the consistency evaluations.

Note that in Figs. 8 and 9, the icons used to represent consistency form a vertical line, referred to as a trail, which helps identify valid results. Also note that the trails in these figures are often so close together as to be viewed as a single trail when more than one trail is actually present. When the consistency diagram is viewed interactively, the frequency scale can be expanded to make this evident. This is the case for these figures which involve FRF data from a circular plate with very close modal frequencies, well within the frequency resolution (Δf = 5 Hz). Most of the trails in these consistency diagrams represent two or more very close modal frequencies.

3.4.1 Alternate Consistency Diagram

Another version of a consistency diagram has been developed to overcome some of the sequential nature of the consistency evaluation. The process is the same as in the more common consistency diagram, but the evaluation from one order iteration to the next is what is changed. The modal frequency and damping is combined with the modal participation vector estimate to form a state vector, sometimes referred to as a pole-weighted vector. Then the state vectors from one iteration to the next are evaluated via the modal assurance criterion (MAC) of the state vectors. The modal assurance criterion (MAC) and the state vector concept are explained in more detail in Sect. 4.5. The result of this change in presentation is shown in Fig. 10 which represents the same information as that in Fig. 8.

3.5 Pole Surface Consistency Plots

One common problem with consistency diagrams is that consistency is estimated based upon a statistical comparison to the previous model solution iteration, evaluating the different levels of consistency in sequential order. While this works in most cases, it will sometimes yield a consistency diagram that is difficult to interpret. Furthermore, if model iterations from different algorithms are combined in one consistency diagram, the sequential nature of the consistency diagram can pose interpretation problems. In this case, since different model characteristics are being evaluated at the same time, the order that the model solution iterations are presented may affect the presentation of consistency (or stability). In general,

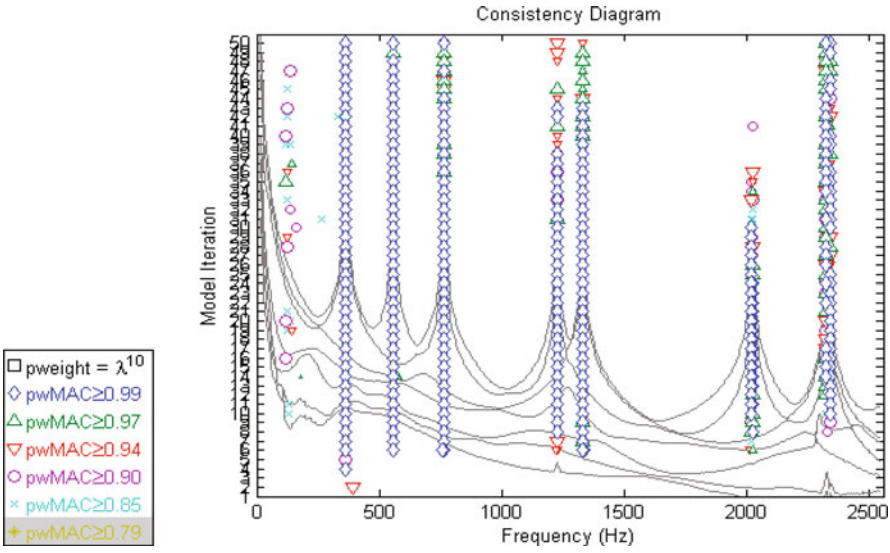

Fig. 10 Consistency diagram – max order 30 – both normalizations

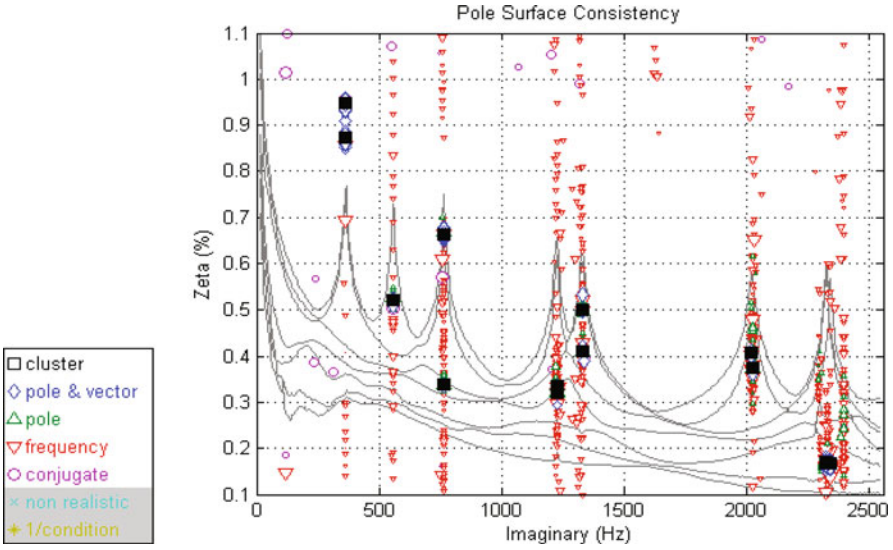

Fig. 11 Pole surface consistency – max order 30 – both normalizations

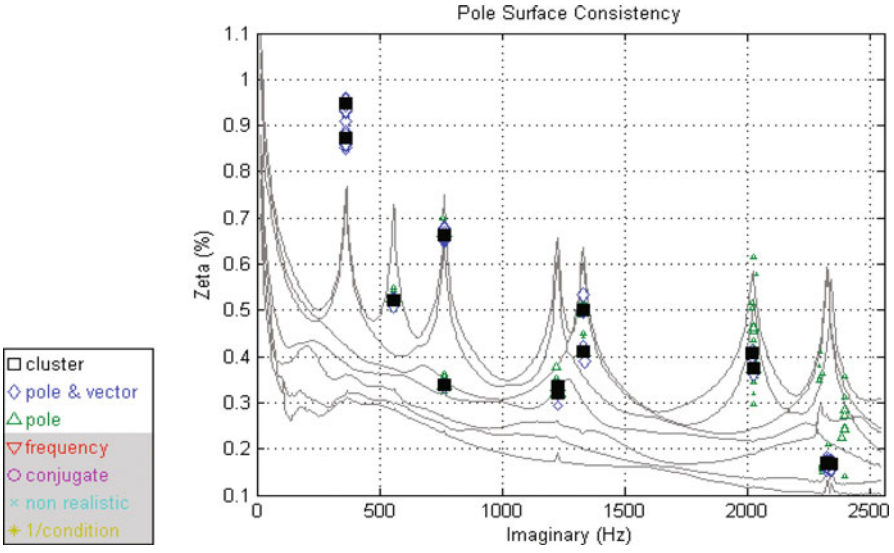

Fig. 12 Pole surface consistency – max order 30 – both normalizations, clear

a clearer estimate of the modal frequencies will be determined by plotting the consistency (or density) of poles found from all model solution iterations, presented in the second quadrant of the complex plane [45]. Figures 11, 12, and 13 represent pole surface consistency plots for the same previous two consistency diagrams. Note

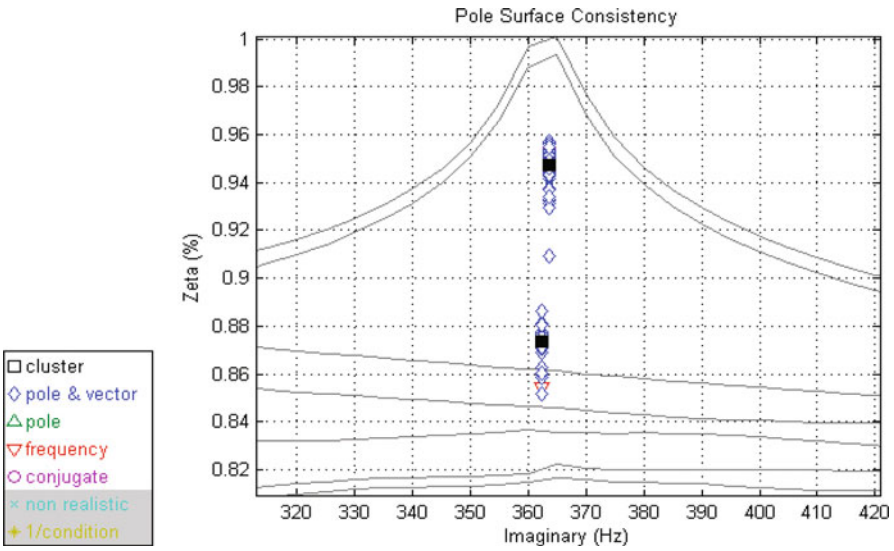

Fig. 13 Pole surface consistency – max order 30 – both normalizations

that a black square represents the statistical solution for the one modal parameter set that best represents the associated cluster of modal parameters.

3.6 Modal Parameter Clustering

The modal parameter clusters shown in Figs. 11, 12, and 13 can be grouped together based on the closeness of the modal frequencies and damping along with the similarity in the associated modal participation vectors or associated state vector form of the modal participation vectors (see Sect. 4.5.3). Once grouped in this fashion, the modal parameter cluster can be autonomously identified, and statistics can be estimated to quantify the variance in the modal parameters found from the associated consistency diagram.

The two modal parameter clusters represented in Fig. 13 are individually shown in Figs. 14 and 15. The rectangular box and associated circle represent one sigma of standard deviation in the modal frequency pole in terms of frequency units of Hertz. All of the identified solutions in the figure have been used to identify the best answer for modal frequency and establish the statistics, modal frequency by modal frequency. Note that in both of these figures, 54 modal frequency estimates from the consistency diagram trail have been utilized. The vertical axis in these figures has been converted from fraction of critical damping to damping in units of Hertz to allow the standard deviation to have square aspect ratio.

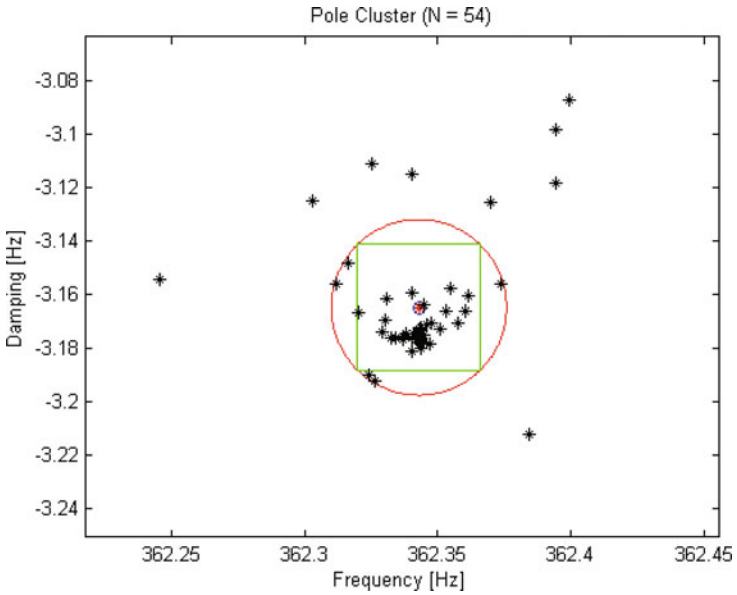

Fig. 14 Modal parameter cluster – 362.3 Hz

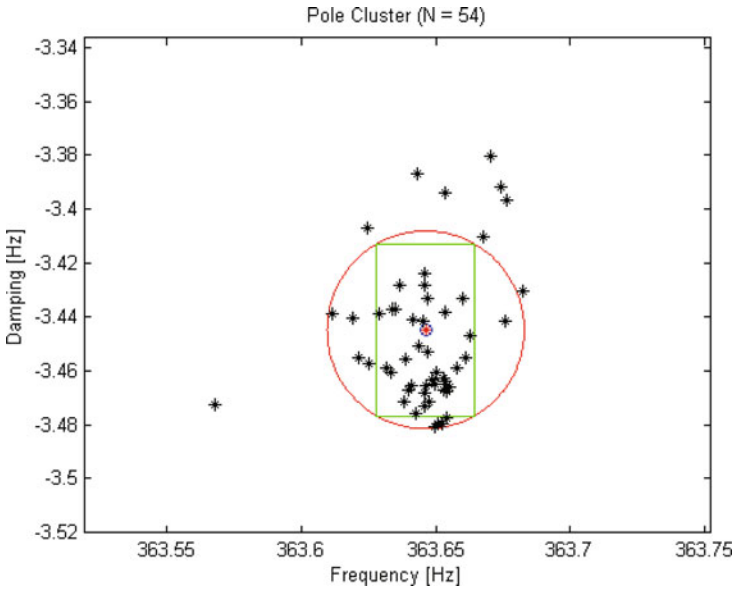

Fig. 15 Modal parameter cluster – 363.6 Hz

Please note that the identified modal frequency and damping information is very consistent within a cluster despite the frequency resolution of the FRF data being 5 Hz.

4 Modal Vector Evaluation/Validation Tools

4.1 Modal Vector Conditioning

Vector conditioning generally applies to the three vectors (modal participation vectors, residue vectors, and modal vectors) that are estimated as part of any modal parameter estimation method. Vector conditioning involves methods that are designed to improve the final modal vector estimates and may vary from user to user and may be available at different levels in commercial software. In general, vector conditioning, first and foremost, is designed to remove potential contamination from the final modal vector estimates.

Vector conditioning begins with the recognition that the modal participation vector is the result of an eigenvalue problem where the eigenvectors are arbitrarily scaled and even a normal mode might be represented as a set of real-valued numbers modified by a complex-valued scalar. This means that some sort of normalization is needed to remove the complex-valued scalar. Furthermore, if some sort of real normalization is desirable (to match up well with, e.g., an undamped, analytical model), the understanding of the contamination that is being removed is a prerequisite to any procedure. Random contamination may simply be ignored, smoothed, or averaged out, but if the contamination is related to a bias from nearby modes, it may indicate that the modal parameter estimation may need further evaluation or that more data from additional reference DOFs is required.

4.1.1 Vector Normalization

Vector conditioning begins with some form of normalization. Normalization can simply mean that each vector will be normalized with respect to one element within the vector. This is often done as is shown in Eq. 24 where the residue vector is divided by the largest element within the residue vector.

$$\{\psi_r\}_{N_L \times 1} = \frac{\{A_{pqr}\}_{N_L \times 1}}{max(A_{pqr})} \qquad A_{pqr} = \frac{\psi_{pr}\ \psi_{qr}}{M_{A_r}} \tag{24}$$

The meaning of largest in this sense is that the magnitude of the complex-valued element of the vector is the maximum absolute value found within the vector but the division occurs on a complex-valued basis. This means that the largest element of the normalized vector will be unity. In general, though, the normalized vector will still be complex valued at all other positions in the normalized vector. Other normalization choices are possible (unity vector length, etc.), but dividing by the maximum provides a simple and reliable method. This approach will also yield modal scaling values that can be more directly related to the physical properties of the system.

Normalization as defined above can be applied to either the modal participation vectors or the modal vectors. Since the residue vectors have physical meaning and

units, normalization is generally not applied except to estimate the modal vector from the residue vector.

4.1.2 Real Normalization

Once a vector has been normalized to be dominantly real valued, the vector can be limited to only real values if desired. This limitation can be a simple truncation (delete imaginary parts) or some other procedure that preserves the complex magnitude with the appropriate 0 or 180 degree phase. The complex-valued vectors should always be evaluated, visually or numerically, before any real normalization is performed to be certain the process does not have unintended consequences.

In the case of modal participation vectors, while these vectors are theoretically proportional to the final modal vectors at the included DOFs, their function in the modal parameter estimation process is one of weighting the least squares solution in the second stage of modal parameter estimation (MPE-2). Performing a real normalization of the modal participation vectors has been found to be beneficial always and does not affect the final modal vector estimates adversely [46].

4.1.3 Central Axis Rotation

The normalization described in the previous section guarantees that one element in the vector will become unity but the vector itself may statistically not be best aligned with the real axis. A statistical estimate of the central axis of the vector can be performed to make sure that the mean phase of the vector is along the real axis. This is in addition to making sure that the largest magnitude in this statistical solution is unity (in a complex magnitude sense).

In order to establish a uniform procedure for normalizing vectors that are related to modal vectors (modal vectors, modal participation vectors, residue vectors), each potentially complex-valued vector must first be rotated to an orientation where the dominant information of the vector in complex space is aligned with the real axis. This is required since the complex-valued vector is generally the result of the solution of an eigenvalue-eigenvector problem involving the complex-valued MIMO FRF data as stated above.

Given an original modal vector for mode r, a central axis rotation method is utilized to determine the dominant axes. These dominant axes can be identified via the singular value decomposition of the relationship between the real part, $\{\psi_R\}_r$, and the imaginary part, $\{\psi_I\}_r$, of the vector for mode r as follows:

$$[U, \Sigma, V] = SVD\left(\left[\{\psi_I\}_r \{\psi_R\}_r\right]^T \left[\{\psi_I\}_r \{\psi_R\}_r\right]\right) \tag{25}$$

Recognize that this decomposition is an attempt to locate the two dominant axes of a 2D ellipse that encompasses the modal vector data in the complex plane. Following the decomposition, the central axis angle is estimated using the true (four-quadrant) arctangent of the right singular vector relationship. Note that, regardless of the number of DOF positions represented in the modal vector, the right

singular vector matrix will always be two by two in dimension representing the 2D characteristics of the ellipse.

$$\bar{\phi}_r \;=\; \tan^{-1}\left(\frac{V_{22}}{-V_{12}}\right) \tag{26}$$

After identifying the central axis angle, the original complex-valued modal vector is rotated by multiplying by the complex rotational phasor.

$$\left\{\hat{\psi}\right\}_r \;=\; \left(\cos\left(\bar{\phi}_r\right) \;-\; j\;\sin\left(\bar{\phi}_r\right)\right)\;\{\psi\}_r \tag{27}$$

This rotation, followed by a normalization by the magnitude of the maximum element in the resulting vector, results in a normalization procedure that assures that the resulting vector is dominantly real, with a maximum value of unity, based upon all of the vector information, rather than a single DOF that is chosen arbitrarily (e.g., rather than selecting the DOF associated with the largest modal vector coefficient).

4.1.4 Vector Complexity

Vector complexity is often defined in terms of mean phase deviation (MPD) as an indication of how the phase deviates from 0 and/or 180 degrees. This definition allows some ambiguity in what is meant by a complex mode. It may simply mean that the elements of the estimated modal vector contain complex values. For this case, the elements of the modal vector may be rotated by an angle in the complex plane but are otherwise co-linear. Or it may mean that the modal vector contains complex values that cannot be made real by a simple complex phasor rotation. For this case, the modal coefficients are not all co-linear in the complex plane. For this development, it is the second definition that is used. Note that if the central axis rotation procedure is performed, the mean phase will always be zero degree.

The mean phase deviation (MPD_r) for modal vector r has been defined historically as a number between zero and unity where zero represents a real-valued modal vector (normal mode) and where unity represents a complex-valued modal vector with no recognizable dominant real or imaginary characteristic, once an attempt has been made to rotate the vector to a dominant central axis position. This fraction is often multiplied by 100 to represent the percentage of complex-valued modal vector characteristics. In terms of the definitions utilized in the previous section, assuming that the modal vector has already been rotated to its most dominant real orientation, the MPD_r is defined as the norm of the imaginary part of the rotated vector divided by the norm of the real part of the rotated vector, as shown in Eq. 28. Thus, the MPD_r gives a dispersion ratio around the central axis of the rotated modal vector bounded between zero and one.

Mean Phase Deviation (MPD_r)

$$MPD_r = \frac{\left\| \left\{ \hat{\psi}_I \right\}_r \right\|}{\left\| \left\{ \hat{\psi}_R \right\}_r \right\|} \tag{28}$$

Once the MPD_r is defined in terms of the fraction between zero and unity, the associated mean phase correlation (MPC_r) for modal vector r is defined as in Eq. 29.

Mean Phase Correlation (MPC_r)

$$MPC_r = 1 - MPD_r \tag{29}$$

The mean phase correlation can then be interpreted as an indicator of normalcy, from a purely normal mode (1.0) to a purely complex mode (0.0).

4.1.5 Modal Vector Complexity Plots

A modal vector complexity plot (MVCP) is often used to represent the characteristics of modal vectors with respect to MPC and vector complexity. The vectors in this presentation are always scaled to a maximum value of unity. Figure 16 is an example of such a plot.

For these case studies, the entire frequency range from 220 to 2500 Hz was fit by the RFP-Z algorithm and the ERA algorithm using traditional complex-valued participation vector weighting as well as real-valued participation vector weighting. For most cases, the complete set of modal participation vectors was utilized although two cases show the deficiencies of single-reference approaches. One case with two references shows the power of multiple reference modal parameter estimation. The CSSAMI autonomous modal parameter estimation procedure [47] was utilized to remove user bias from the selected results.

Case 6

This modal vector complexity plot (MVCP) demonstrates that, while most of the modes appear to have been fit for residues in the MPE-2 stage reasonably well, simply converting the complex-valued participation to real does not guarantee the quality of fit. The three modes between 2320 and 2340 Hz represent a repeated root pair and an additional close mode. The MPC values show that the fit for two of the modes retains significant modal complexity that is not anticipated in this structure.

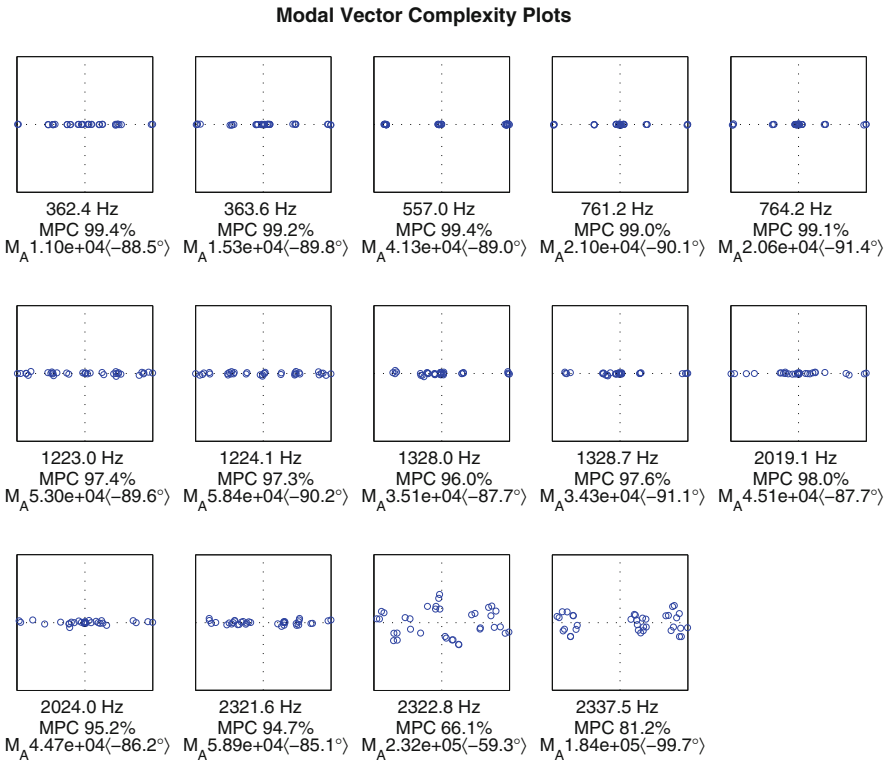

Fig. 16 Case 6: Modal vector complexity plot, multiple references, all DOFs, ERA method

Case 8

The data for this modal vector complexity plot (MVCP) is identical to Case 6 with the addition of reprocessing the normalized eigenvector from the ERA method to residue scaling and then performing the central axis rotation and decimation of the long dimension N_L vectors to the short dimension N_S. This is followed by real normalization of the short dimension participation vectors ($[L]$) which yields a very physical, realistic result. The improvement on the estimation can be noted for the last two modes (Fig. 17).

Case 10

This modal vector complexity plot (MVCP) shows a comparable result to Case 8 even though a short dimension MPE algorithm is utilized. Case 10 shows that reprocessing the normalized eigenvector from the RFP-Z method to residue scaling and then performing the central axis rotation, followed by real normalization of the short dimension participation vectors ($[L]$), yields a very physical, realistic result. This result has a slight improvement in the MPC value for the last two modes (Fig. 18).

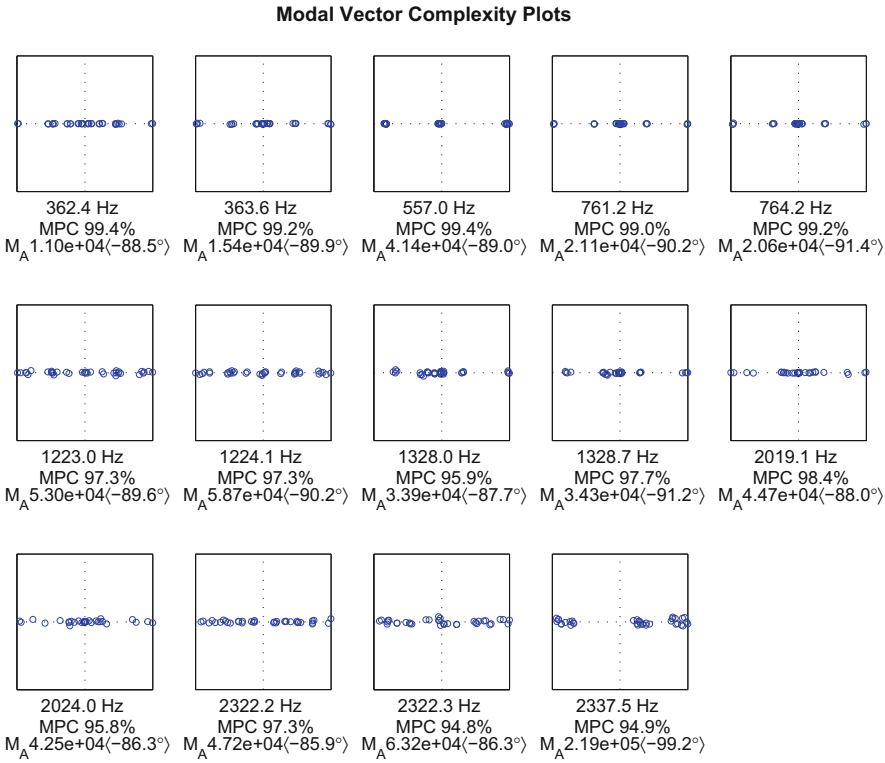

Fig. 17 Case 8: Modal vector complexity plot, multiple references, all DOFs, ERA method

4.2 Modal Vector Validation: eFRF

A virtual measurement, known as the enhanced frequency response function (eFRF), can be used to identify the modal frequencies and scaling of a single degree of freedom characteristic that is associated with each peak in the CMIF [43]. If only one peak is dominant in the eFRF, this can be used as a validation of the particular modal vector. The eFRF is developed based upon the concept of physical to modal coordinate transformation and is used to manipulate frequency response functions so as to enhance a particular mode of vibration. The left singular vectors, associated with the peaks in the CMIF, are used as an estimate of the modal filter which accomplishes this.

4.2.1 eFRF: Theoretical Definition

Starting with the basic FRF partial fraction equation:

$$H_{pq}(\omega) = \sum_{r=1}^{2N} \frac{A_{pqr}}{(j\omega - \lambda_r)} = \sum_{r=1}^{2N} \frac{Q_r \psi_{pr} \psi_{qr}}{(j\omega - \lambda_r)} \tag{30}$$

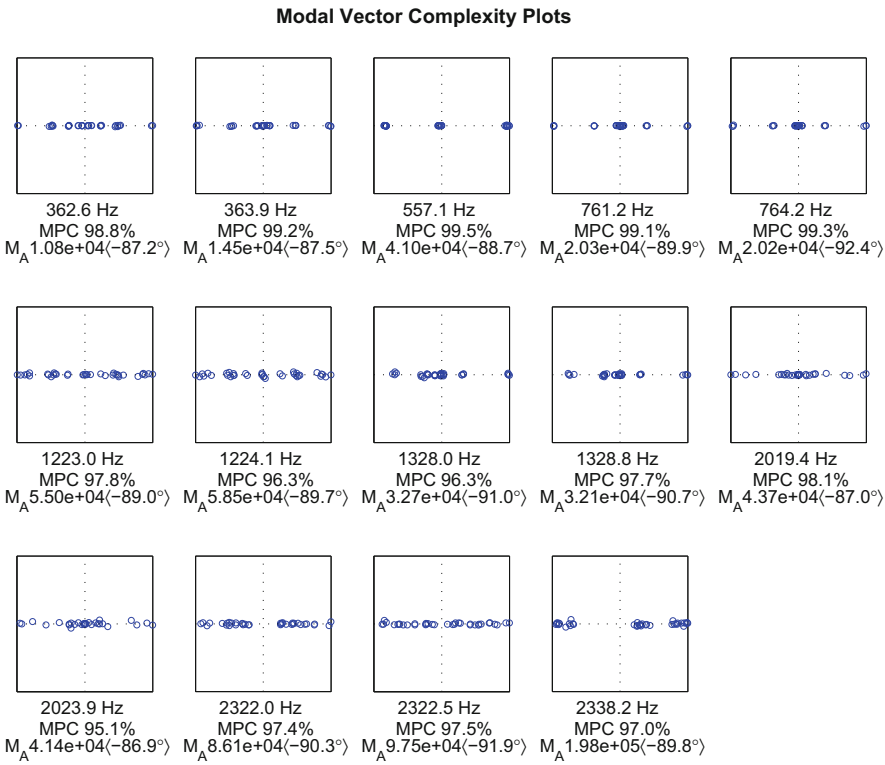

Fig. 18 Case 10: Modal vector complexity plot, multiple references, all DOFs, RFP-Z method

Noting that the scaling term Q_r can represent either modal A or modal mass scaling, the FRF relationship can be redefined:

$$H_{pq}(\omega) = \sum_{r=1}^{2N} \psi_{pr} \frac{Q_r \psi_{qr}}{(j\omega - \lambda_r)} \tag{31}$$

The enhanced frequency response function ($eFRF_r(\omega)$) for mode r can now be defined:

$$eFRF_r(\omega) = \frac{Q_r \psi_{qr}}{(j\omega - \lambda_r)} \tag{32}$$

The eFRF has only to do with the reference location q and is constant for a given column of the FRF matrix. The FRF model for a column of FRFs can be rewritten as:

$$\left\{H_{pq}(\omega)\right\} \;=\; \sum_{r=1}^{2N} \left\{\psi_{pr}\right\} \frac{Q_r \psi_{qr}}{(j\omega - \lambda_r)} \;=\; \sum_{r=1}^{2N} \left\{\psi_{pr}\right\} eFRF_r(\omega) \tag{33}$$

4.2.2 eFRF: Historical Development

The eFRF can be formulated from measured frequency response function data in the following manner:

$$\{\psi_{sr}\}^T [M] \left\{H_{pq}(\omega)\right\} \;=\; \sum_{r=1}^{2N} \{\psi_{sr}\}^T [M] \left\{\psi_{pr}\right\} \frac{Q_r \psi_{qr}}{(j\omega - \lambda_r)} \;=\; M_s \frac{Q_s \psi_{qs}}{(j\omega - \lambda_s)} \tag{34}$$

$$\{\psi_{sr}\}^T [M] \left\{H_{pq}(\omega)\right\} \;=\; M_s \;\; eFRF_s(\omega) \tag{35}$$

The last equation indicates that an estimate of the modal mass scaling (M_s) is needed to develop the enhanced frequency response function as well as a mass matrix whose dimension has been reduced to the DOFs of the FRF column of measurements. In many situations, when the mass distribution is adequately represented by the measured degrees of freedom (good spatial representation), the modal vector can be used directly to estimate an eFRF that is proportional to within a complex constant representing the mass scaling.

$$\{\psi_{sr}\}^T \left\{H_{pq}(\omega)\right\} \approx eFRF_s(\omega) \tag{36}$$

In reality, the goal of the eFRF is to allow a simple SDOF modal parameter estimation algorithm to be used to estimate modal frequency and scaling from the eFRF. If other modes are still observable in the eFRF, these modes can be handled with residuals in the modal parameter estimation. The fact that the resultant eFRF looks dominantly like an SDOF FRF is used as a validation that the modal vector ψ_r is correct.

4.2.3 eFRF: FRF SVD Development

The above estimation of the eFRF was used in the original development [48] which was based upon orthogonality. The original modal vectors used in the eFRF estimation were simply quadrature FRF estimates taken from the FRF measurements (SDOF estimate). Modal vectors from any modal parameter estimation algorithm can be used.

Subsequently, the eFRF was revised to take advantage of the singular vectors of the FRF matrix which changes the formulation so that it is based upon the linear expansion theorem. This simplifies some of the scaling issues and does not require a reduced mass matrix to get properly scaled eFRFs. In the newer technique, utilized in the following examples, the left and right singular vectors, associated with the singular values of the FRF matrix (found at the peaks of the CMIF), are used as in the following equations. The frequency response function matrix is assumed to

have been corrected for transducer orientation. Although this is not required for the computation of damped natural frequency and damping, this will simplify the phasing issues associated with the eFRFs and any modal scaling estimation.

The singular value decomposition (SVD) of the measured FRF matrix can be represented as:

$$[H(\omega)] = [U(\omega)][\Sigma(\omega)][V(\omega)]^H \tag{37}$$

Note that the dimensions of the FRF matrix are assumed to be $N_L \times N_S$ at each frequency. Using lower case notation to represent the individual left and right singular vectors, the eFRF can be represented by:

$$eFRF_r(\omega) = \alpha \{u_r\}^T [H(\omega)] \{v_r\} \tag{38}$$

The eFRF is typically used, together with single degree of freedom (SDOF) modal parameter estimation methods, to estimate the frequency and damping of the associated modal frequency. The validation of the modal vector is based upon whether the associated eFRF is dominantly an SDOF function. In order for the eFRF to also be used to estimate the modal scaling (modal mass and/or modal A), the correct scaling (correct magnitude and phase) of the eFRF must be accounted for (the complex-valued scaling term α in the above equation). Since the left and right singular vectors in the singular value decomposition are unitary and scaled consistently as a set, both left and right singular vectors must be involved to preserve the physical characteristics of the eFRF.

For the general case, where the modal vector used in the eFRF is estimated from the left singular vector associated with a peak in the singular values in the CMIF plot, the eFRF is scaled by utilizing the values of the left and right singular vectors, associated with the significant singular value, at the driving point locations. Note that it is probable that v may not be a strict subset of u; in this case a scale factor must be estimated from the common subset of the input/output degrees of freedom (i.e., the driving point degrees of freedom). Complete details of the development can be found in [49].

Figure 19 shows the eFRF for one of the modes around 360 Hz. The modal vector used for the enhancement (weighted averaging) was a complex-valued estimate of the modal vector. The result is clearly very close to a SDOF FRF plot with small deviations around the frequencies where other modes were present in the data.

Figure 20 shows the eFRF for the same mode around 360 Hz. The modal vector used for the enhancement (weighted averaging) was a real-valued estimate of the modal vector. The result is clearly very close to an SDOF FRF plot with small deviations around the frequencies where other modes were present in the data. Some small differences are noted in the modal parameters when compared to Fig. 19. Both figures clearly validate that the modal vectors are appropriate for this set of FRF data.

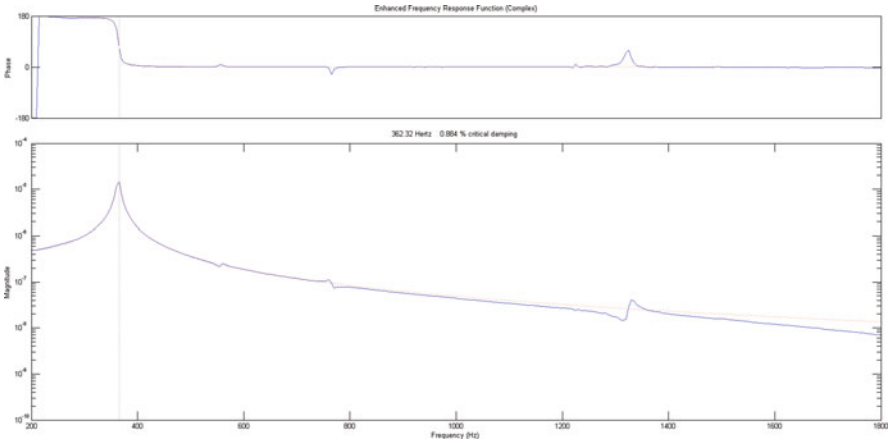

Fig. 19 Enhanced FRF – complex-valued modal vector (362.32 Hertz 0.884 % critical damping)

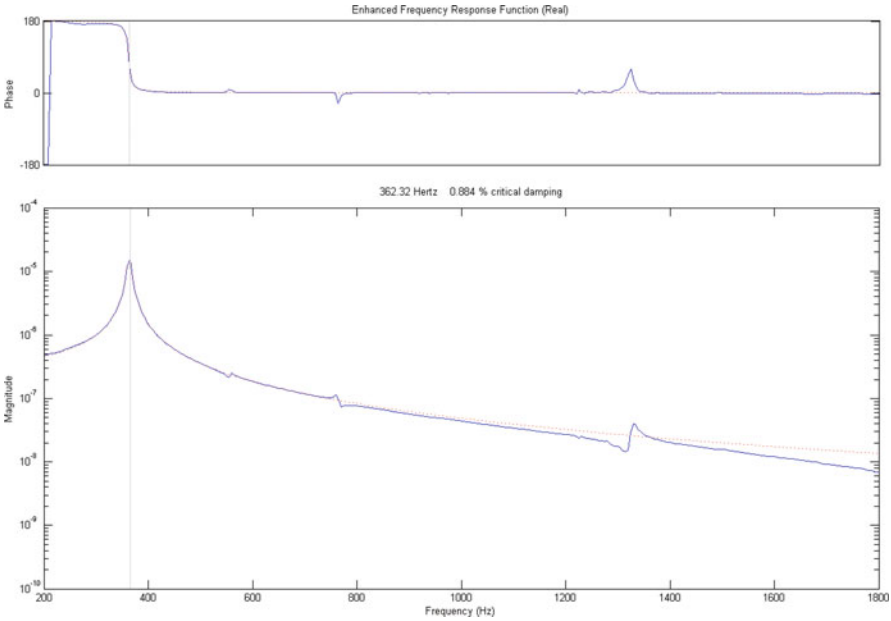

Fig. 20 Enhanced FRF – real-valued modal vector (362.32 Hertz 0.884 % critical damping)

Figures 21 and 22 show the eFRF results for two very closely spaced modal frequencies in the FRF data. The modal parameter information for the two eFRFs is notably different, and the two modal vectors are validated for this FRF data set. Note that the frequency resolution in the FRF data is 5 Hz, so the SVD information that is the basis of the left and right singular vectors is likewise limited to 5 Hz

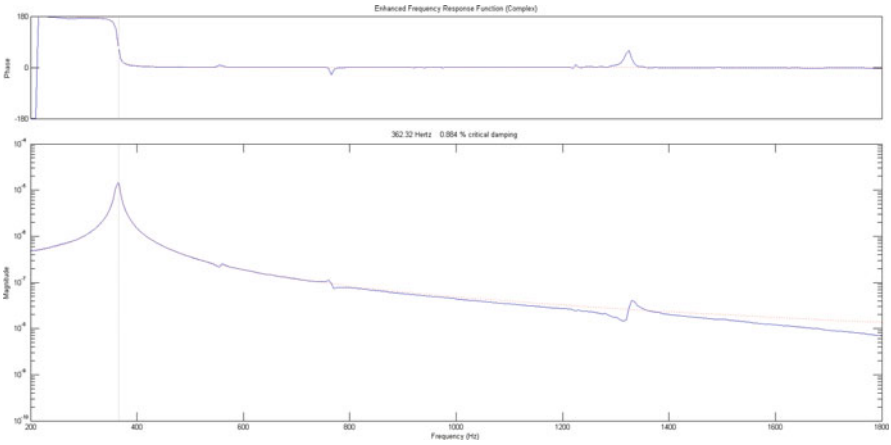

Fig. 21 Enhanced FRF – Repeated Modal Frequency 1 (362.32 Hertz 0.884 % critical damping)

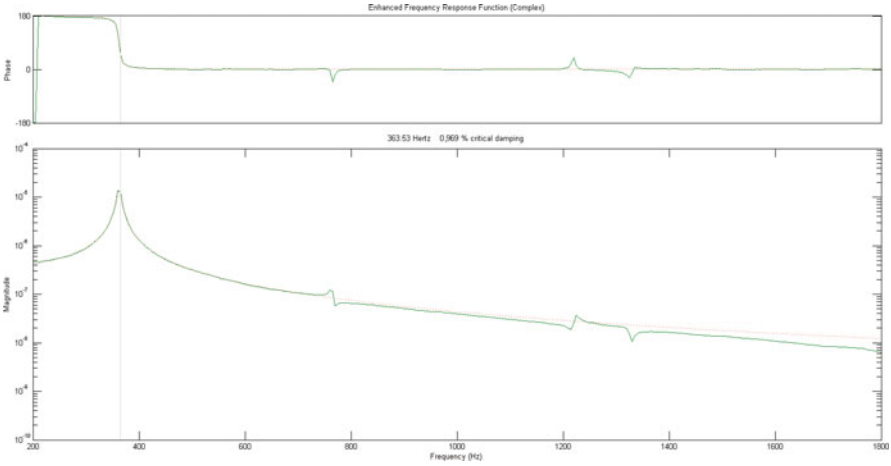

Fig. 22 Enhanced FRF – Repeated Modal Frequency 2 (363.53 Hertz 0.569 % critical damping)

resolution. Nevertheless, the SDOF modal parameter estimation method is clearly able to estimate modal frequencies within the 5 Hz resolution. These results compare favorably with modal parameter estimation results from polyreference algorithms.

The concept of an enhanced frequency response function (eFRF) can be used anytime a column/row of FRF data is available along with an estimate of a modal vector.

4.3 Weighted Modal Vector Orthogonality

The primary method that has historically been used to validate an experimental modal model involves a weighted orthogonality check comparing measured modal vectors, analytical modal vectors, and an appropriately sized, square weighting matrix. The size of the square weighting matrix must match the length and spatial dimension (in terms of DOFs) of the analytical and experimental modal vectors and is generally formed from an estimated mass or stiffness matrix. A common approach uses analytical modal vectors together with experimental modal vectors and the appropriately sized mass or stiffness matrix. This latter comparison is normally referred to as a pseudo orthogonality check (POC).

In the traditional weighted orthogonality check, the modal vectors are used together with a mass matrix, normally derived from a finite element model, to evaluate orthogonality of the modal vectors. In the pseudo orthogonality check, the experimental modal vectors are used together with a mass matrix, normally derived from a finite element model, and the analytical modal vectors, normally derived from the same finite element model, to evaluate orthogonality between the experimental and analytical modal vectors.

The experimental and analytical modal vectors are scaled so that the diagonal terms of the modal mass matrix are unity. With this form of scaling, the off-diagonal values in the modal mass matrix are expected to be less than 0.1 (10 percent of the diagonal terms). Theoretically, for the case of proportional damping, each modal vector of a system will be orthogonal to all other modal vectors of that system when weighted by the mass, stiffness, or damping matrix. In practice, these matrices are made available by way of a finite element analysis, and normally the mass matrix is considered to be the most accurate. For this reason, any further discussion of weighted orthogonality will be made with respect to mass matrix weighting. As a result, the weighted orthogonality relations can be stated as follows:

4.3.1 Weighted Orthogonality of Modal Vectors

For r $\neq$ s:

$$\{\psi_r\}^T [M] \{\psi_s\} = 0 \tag{39}$$

For r = s:

$$\{\psi_r\}^T [M] \{\psi_s\} = M_r \tag{40}$$

$$\frac{\{\psi_r\}^T}{\sqrt{M_r}} \Big[M\Big] \frac{\{\psi_s\}}{\sqrt{M_r}} = 1.0 \tag{41}$$

Weighted cross orthogonality refers to Eq. 39, which means that the vectors have no projection on each other in the dimensionality of the modal vector space.

4.4 Weighted Pseudo Orthogonality of Modal Vectors

Weighted pseudo orthogonality refers to the case where one side of Eqs. 39 through 41 is replaced by experimental modal vectors. Note that this process involves making sure that the dimensionality of the analytical modal vectors, the experimental modal vectors, and the mass matrix is the same and the DOFs utilized are consistent.

Experimentally, the result of zero for the weighted pseudo cross orthogonality calculations ($r \neq s$) (Eq. 39) can rarely be achieved, but values up to one tenth of the magnitude of the generalized mass of each mode are considered to be acceptable. It is a common procedure to form the modal vectors into a normalized set of mode shape vectors with respect to the mass matrix weighting. The accepted criterion in the aerospace industry, where this confidence check is made most often, is for all of the generalized mass terms to be unity and all weighted pseudo cross orthogonality terms to be less than 0.1. Often, even under this criteria, an attempt is made to adjust the modal vectors so that the weighted pseudo cross orthogonality conditions are satisfied.

Note that, in general, experimental modal vectors are not always real valued and Eqs. 39 through 41 are developed based upon normal (real-valued) modal vectors. This complication has to be resolved by a process of real normalization of the measured modal vectors prior to utilizing Eqs. 39 through 41 or by applying an equivalent procedure involving the state-space form of the weighted orthogonality relationship.

In Eqs. 40 and 41, the mass matrix must be an $N_L \times N_L$ matrix corresponding to the measurement locations on the structure. This means that the finite element mass matrix must be modified from whatever size and distribution of grid locations required in the finite element analysis to the $N_L \times N_L$ square matrix corresponding to the measurement locations. This normally involves some sort of reduction algorithm as well as interpolation of grid locations to match the measurement situation [50, 51, 52, 53, 54, 55, 56].

When Eqs. 39 is not sufficiently satisfied, one (or more) of three situations may exist. First, the modal vectors can be invalid. This can be due to measurement errors or problems with the modal parameter estimation algorithms. This is a very common assumption and many times contributes to the problem. Second, the mass matrix can be invalid. Since the mass matrix does not always represent the actual physical properties of the system when it is built or assembled, this probably contributes significantly to the problem. Third, the reduction of the mass matrix can be invalid [50, 51, 52, 53, 54, 55]. This can certainly be a realistic problem and cause severe errors. The most obvious example of this situation would be when a relatively large amount of mass is reduced to a measurement location that is highly flexible, such as the center of an unsupported panel. In such a situation, the measurement location is weighted very heavily in the orthogonality calculation of Eqs. 39 but may represent only incidental motion of the overall modal vector. In all probability, all three situations contribute to the failure of orthogonality or pseudo orthogonality criteria on occasion. When the orthogonality conditions are not satisfied, this result

does not indicate where the problem originates. From an experimental point of view, it is important to try to develop methods that indicate confidence that the modal vector is, or is not, part of this problem.

4.5 Modal Vector Consistency

Since any evaluation of weighted orthogonality requires an appropriately sized weighting matrix and real-valued modal vectors, these two conditions pose problems as they are not often met by experimentally measured data. Beginning around 1975, the experimental focus changed to estimating a MIMO FRF set of data where redundancy of the modal parameters, reference by reference, was expected. Since a MIMO FRF set of data will have an estimate of the modal parameters for each reference in the MIMO set, evaluating the redundancy, or consistency, became desirable. Consistency in the MIMO FRF data set means that the modal parameters are the same from each references. Consistency therefore means that the complex-valued modal frequencies are expected to be the same and the modal vectors are the same to within a complex-valued constant (same shape with different scaling). Eventually, MIMO MPE methods became available that took advantage of this concept to estimate a single set of modal parameters directly from MIMO FRF data.

Consistency, with respect to modal vectors, means that the vectors associated with the same modal frequency from different references should always be linearly related. This problem was a familiar least squares estimate of the linear complex-valued scaling constant with an associated squared correlation coefficient that directly paralleled the least squares estimate of the FRF with the associated ordinary coherence function. The scaling constant is referred to as the modal scale factor (MSF), and the squared correlation coefficient is referred to as the modal assurance criterion (MAC).

The development of the modal assurance criterion [48, 57, 58] came about due to the focus on modal vector consistency (linearity) as opposed to modal vector orthogonality. The fact that modal vectors estimated from different references are expected to be the same to within a complex-valued scaling constant revealed a consistency methodology that could easily be explored experimentally, independent of analytical methods and associated weighting matrices.

The development of the modal assurance criterion has led to a number of similar assurance criteria used in the area of experimental and analytical structural dynamics. It is important to recognize the mathematical similarity of these varied criteria in order to be certain that conclusions be correctly drawn from what is essentially a squared, linear regression correlation coefficient. The modal assurance criterion is a statistical indicator, just like ordinary coherence associated with FRF estimation, which can be very powerful when used correctly but very misleading when used incorrectly. In Sect. 4.5.4, other similar assurance criteria are identified although the list is not intended to be comprehensive. Typical uses of the modal assurance criterion are discussed, and, finally, typical abuses are identified.

4.5.1 Modal Vector Linearity or Consistency

When the modal assurance criterion was originally developed, MIMO modal parameter estimation was just beginning to be developed. Therefore, when MIMO FRF data was acquired, the primary benefit was to make sure a complete set of modal parameters was estimated. The big concern was that if a reference was too close to a nodal position in a modal vector, that mode would be missed or estimated poorly. If redundant modal vectors were estimated from the references, an average of the modal vectors could improve the modal vector estimate.

The function of the modal scale factor (MSF) is to provide a means of normalizing all estimates of the same modal vector, taking into account magnitude and phase differences. Once two different modal vector estimates are scaled similarly, elements of each vector can be averaged (with or without weighting), differenced, or sorted to provide a best estimate of the modal vector or to provide an indication of the type of error vector superimposed on the modal vector. In terms of modern, multiple reference modal parameter estimation algorithms, the modal scale factor is a normalized estimate of the modal participation factor between two references for a specific mode of vibration. The function of the modal assurance criterion (MAC) is to provide a measure of consistency (degree of linearity) between estimates of a modal vector. This provides an additional confidence factor in the evaluation of a modal vector from different excitation (reference) locations or different modal parameter estimation algorithms. The modal scale factor and the modal assurance criterion also provide a method of easily comparing estimates of modal vectors originating from different sources. The modal vectors from a finite element analysis can be compared and contrasted with those determined experimentally as well as modal vectors determined by way of different experimental or modal parameter estimation methods. In this approach, methods can be compared and contrasted in order to evaluate the mutual consistency of different procedures rather than estimating the modal vectors specifically. If an analytical and an experimental vector are deemed consistent or similar, the analytical modal vector, together with the modal scale factor, can be used to complete the experimental modal vector if some degrees of freedom could not be measured.

The modal scale factor is defined, according to this approach, as follows:

$$MSF_{cdr} = \frac{\sum_{q=1}^{N_L} \psi_{cqr} \psi_{dqr}^*}{\sum_{q=1}^{N_L} \psi_{dqr} \psi_{dqr}^*} = \frac{\{\psi_{cr}\}^T \left\{\psi_{dr}^*\right\}}{\{\psi_{dr}\}^T \left\{\psi_{dr}^*\right\}} \tag{42}$$

Since the modal vectors are in general complex valued, this is also equivalent to:

$$MSF_{cdr} = \frac{\{\psi_{dr}\}^H \{\psi_{cr}\}}{\{\psi_{dr}\}^H \{\psi_{dr}\}} \tag{43}$$

Equations 42 and 43 imply that the modal vector d is the reference to which the modal vector c is compared. In the general case, modal vector c can be considered to be made of two parts. The first part is the part linearly correlated with modal vector d. The second part is the part that is not linearly correlated with modal vector d and is made up of contamination from other modal vectors and of any random contribution. This error vector is considered to be noise.

The modal assurance criterion is defined as a squared, scalar correlation coefficient constant, bounded zero to one, relating the degree of consistency (linearity) between one modal vector and another reference modal vector as follows:

Consistency of Modal Vectors

$$MAC_{cdr} = \frac{\left| \sum_{q=1}^{N_L} \psi_{cqr} \psi_{dqr}^* \right|^2}{\sum_{q=1}^{N_L} \psi_{cqr} \psi_{cqr}^* \sum_{q=1}^{N_L} \psi_{dqr} \psi_{dqr}^*} = \frac{\left| \{\psi_{cr}\}^T \left\{\psi_{dr}^*\right\} \right|^2}{\{\psi_{cr}\}^T \left\{\psi_{cr}^*\right\} \{\psi_{dr}\}^T \left\{\psi_{dr}^*\right\}} \tag{44}$$

Since the modal vectors are complex valued, the modal assurance criterion is a real-valued scalar equivalent to:

$$MAC_{cdr} = \frac{\left| \{\psi_{dr}\}^H \{\psi_{cr}\} \right|^2}{\{\psi_{dr}\}^H \{\psi_{dr}\} \{\psi_{cr}\}^H \{\psi_{cr}\}} = \frac{\{\psi_{dr}\}^H \{\psi_{cr}\} \{\psi_{cr}\}^H \{\psi_{dr}\}}{\{\psi_{dr}\}^H \{\psi_{dr}\} \{\psi_{cr}\}^H \{\psi_{cr}\}} \tag{45}$$

Note that the definition of MAC involves the Hermitian (conjugate transpose) of the associated modal vectors. A frequent error is made when the Hermitian is replaced by the transpose. If all the vectors involved are real valued, no error is generated. However, when any of the vectors are complex valued, the MAC will be estimated incorrectly. The proper approach is to always use the Hermitian (conjugate transpose).

The modal assurance criterion takes on values from zero, representing no consistent correspondence, to one, representing a consistent correspondence. In this manner, if the modal vectors under consideration truly exhibit a consistent, linear relationship, the modal assurance criterion should approach unity, and the value of the modal scale factor can be considered to be reasonable. Note that, unlike the orthogonality calculations, the modal assurance criterion is normalized by the magnitude of the vectors and, thus, is bounded between zero and one.

The modal assurance criterion can only indicate consistency, not validity or orthogonality. If the same errors, random or bias, exist in all modal vector estimates, this is not delineated by the modal assurance criterion. Invalid assumptions are normally the cause of this sort of potential error. Even though the modal assurance criterion is unity, the assumptions involving the system or the modal parameter estimation techniques are not necessarily correct. The assumptions may cause

consistent errors in all modal vectors under all test conditions verified by the modal assurance criterion.

Modal Assurance Criterion (MAC) Zero

If the modal assurance criterion has a value near zero, this is an indication that the modal vectors are not consistent. This can be due to any of the following reasons:

- The system is non-stationary. This can occur if the system is nonlinear, and two data sets have been acquired at different times or excitation levels. System nonlinearities will appear differently in frequency response functions generated from different exciter positions or excitation signals. The modal parameter estimation algorithms will also not handle the different nonlinear characteristics in a consistent manner.
- There is noise on the reference modal vector. This case is the same as noise on the input of a frequency response function measurement. No amount of signal processing can remove this type of error.
- The modal parameter estimation is invalid. The frequency response function measurements may contain no errors, but the modal parameter estimation may not be consistent with the data.
- The modal vectors are from linearly unrelated mode shape vectors. Hopefully, since the different modal vector estimates are from different excitation positions, this measure of inconsistency will imply that the modal vectors are orthogonal.

Obviously, if the first three reasons can be eliminated, the modal assurance criterion can be interpreted in a similar way as an orthogonality calculation.

Modal Assurance Criterion (MAC) Unity

If the modal assurance criterion has a value near unity, this is an indication that the modal vectors are consistent. This does not necessarily mean that they are correct. The modal vectors can be consistent for any of the following reasons:

- The modal vectors have been incompletely measured. This situation can occur whenever too few response stations have been included in the experimental determination of the modal vector.
- The modal vectors are the result of a forced excitation other than the desired input. This would be the situation if, during the measurement of the frequency response function, a rotating piece of equipment with an unbalance is present in the system being tested.
- The modal vectors are primarily coherent noise. Since the reference modal vector may be arbitrarily chosen, this modal vector may not be one of the true modal vectors of the system. It could simply be a random noise vector or a vector reflecting the bias in the modal parameter estimation algorithm. In any case, the modal assurance criterion will only reflect a consistent (linear) relationship to the reference modal vector.

- The modal vectors represent the same modal vector with different arbitrary scaling. If the two modal vectors being compared have the same expected value when normalized, the two modal vectors should differ only by the complex-valued scale factor which is a function of the common modal coefficients between the rows or columns.

Therefore, if the first three reasons can be eliminated, the modal assurance criterion indicates that the modal scale factor is the complex constant relating the modal vectors and that the modal scale factor can be used to average, difference, or sort the modal vectors.

Under the constraints mentioned previously, the modal assurance criterion can be applied in many different ways. The modal assurance criterion can be used to verify or correlate an experimental modal vector with respect to a theoretical modal vector (eigenvector). This can be done by computing the modal assurance criterion between N_e modal vectors estimated from experimental data and N_a modal vectors estimated from a finite element analysis evaluated at common stations. This process results in a $N_e \times N_a$ rectangular modal assurance criterion matrix with values that approach unity whenever an experimental modal vector and an analytical modal vector are consistently related.

Once the modal assurance criterion establishes that two vectors represent the same information, the vectors can be averaged, differenced, or sorted to determine the best single estimate or the potential source of contamination using the modal scale factor. Since the modal scale factor is a complex scalar that allows two vectors to be phased the same and normalized to the same mean value, these vectors can be subtracted to evaluate whether the error is random or biased. If the error appears to be random and the modal assurance criterion is high, the modal vectors can be averaged, using the modal scale factor, to improve the estimate of a modal vector. If the error appears to be biased or skewed, the error pattern often gives an indication that the error originates due to the location of the excitation or due to an inadequate modal parameter estimation process. Based upon partial but overlapping measurement of two columns of the frequency response function matrix, modal vectors can be sorted, assuming the modal assurance function indicates consistency, into a complete estimate of each modal vector at all measurement stations.

The modal assurance criterion can be used to evaluate modal parameter estimation methods if a set of analytical frequency response functions with realistic levels of random and bias errors is generated and used in common to a variety of modal parameter estimation methods. In this way, agreement between existing methods can be established, and new modal parameter estimation methods can be checked for characteristics that are consistent with accepted procedures. Additionally, this approach can be used to evaluate the characteristics of each modal parameter estimation method in the presence of varying levels of random and bias error.

The concept of consistency in the estimate of modal vectors from separate testing constraints is important considering the potential of multiple estimates of the same modal vector from numerous input configurations and modal parameter estimation algorithms. The computation of the modal scale factor and modal assurance criterion

results in a complex scalar and a correlation coefficient which does not depend on weighting information outside the testing environment. Since the modal scale factor and modal assurance criterion are computed analogous to the frequency response function and coherence function, both the advantages and limitations of the computation procedure are well understood. These characteristics, as well as others, provide a useful tool in the processing of experimental modal vectors. Typical presentations of the modal assurance criterion are shown in Figs. 23 and 24.

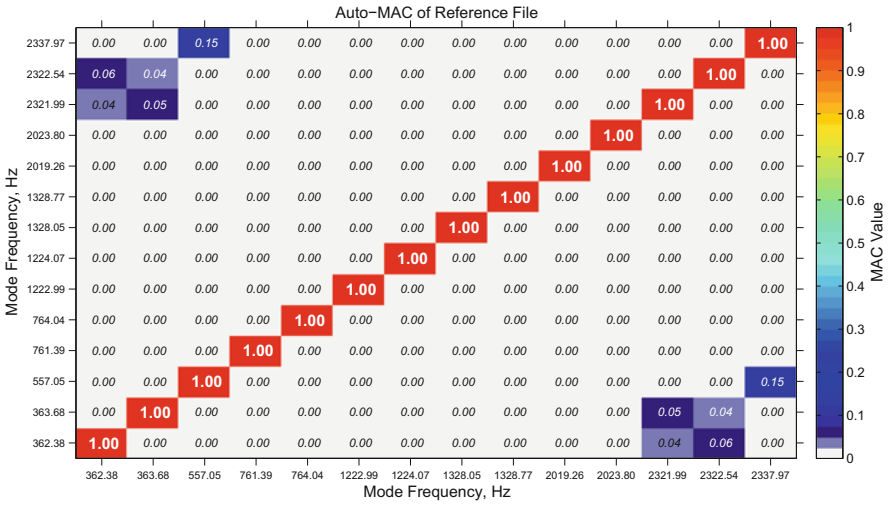

Fig. 23 Modal assurance criterion

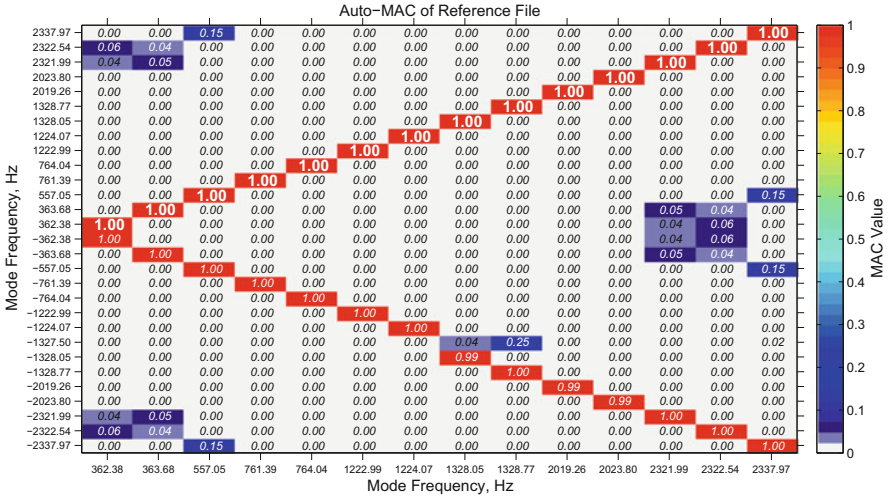

Fig. 24 Modal assurance criterion – conjugate modal vectors

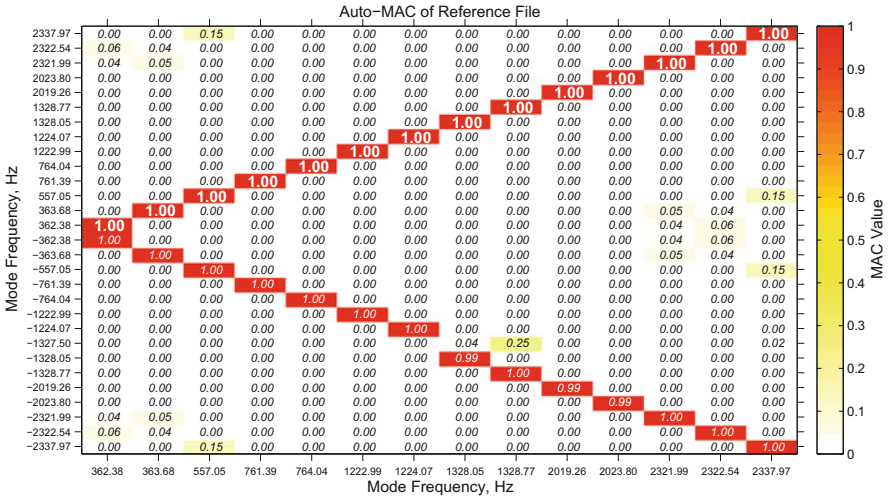

Fig. 25 Modal assurance criterion

Figure 24 shows a variation in the presentation to include both the comparison between the modal vectors associated with the positive frequencies and themselves and also with the modal vectors associated with the conjugate modal (negative) frequencies. This can be useful if the conjugate modal parameters are estimated independently. Users have found that a good MAC value between the positive and negative frequency modal vectors is a quality check on the estimated modal parameters. Note that the upper diagonal in Fig. 24 theoretically must have MAC values equal to 1.0 but this is not the case for the lower diagonal comparing modal vectors to their conjugate counterparts.

Note that Fig. 25 uses a different colorbar as compared to Figs. 23 and 24 to visually downplay the similarity between different modal vectors.

4.5.2 Cross Modal Assurance Criterion (Cross MAC)

Rather than comparing a set of modal vectors to themselves to look for cross-contamination between modal vectors, two different sets of modal vectors can be compared. This is useful when comparing experimental results to analytical results, or when comparing different experimental results. Unlike the case when comparing a modal vector set to itself, the cross MAC does not necessarily yield unity along the diagonals and may not find a common modal vector between the two modal vector sets. This is common when comparing analytical modal vector sets to experimental modal vector sets. This is very useful when the modal frequencies occur in different numerical order between the analytical (e.g., FEA) and the experimental modal vector sets of data.

Figure 26 is a cross MAC between two modal vectors sets generated with different modal parameter estimation (MPE) algorithms, PTD on the x-axis and

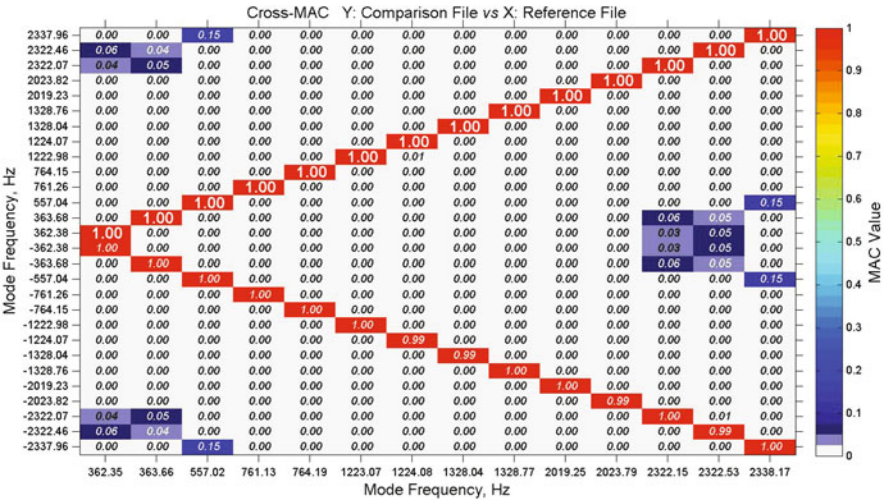

Fig. 26 Modal assurance criterion

RFP-Z on the y-axis. It is clear in this cross MAC that the two different MPE methods give nearly identical modal vector results.

4.5.3 Pole-Weighted or State Vector MAC

Since the modal assurance criterion (MAC) is based upon the sensor degrees of freedom (DOFs), there can be insufficient spatial information to describe similar modal vectors adequately. This can lead to a situation where the MAC value between different modal vectors is higher than it should. This is referred to as **spatial aliasing**. Spatial aliasing can be seen in each of Figs. 23, 24, 25, and 26.

This problem can be somewhat minimized by replacing the modal vector in the MAC equation by its equivalent state vector of model order m. This is referred to as a pole-weighted MAC or state vector MAC.

$$\{\phi\}_r = \begin{Bmatrix} \lambda_r^m\{\psi\}_r \\ \cdot \\ \cdot \\ \cdot \\ \lambda_r^2\{\psi\}_r \\ \lambda_r^1\{\psi\}_r \\ \lambda_r^0\{\psi\}_r \end{Bmatrix}_r \quad or \quad \{\phi\}_r = \begin{Bmatrix} z_r^m\{\psi\}_r \\ \cdot \\ \cdot \\ \cdot \\ z_r^2\{\psi\}_r \\ z_r^1\{\psi\}_r \\ z_r^0\{\psi\}_r \end{Bmatrix}_r \tag{46}$$

The second form of the state vector given in Eq. 46 is preferred for numerical reasons. The state vector can be visualized in the graphical plots shown in Figs. 27 and 28.

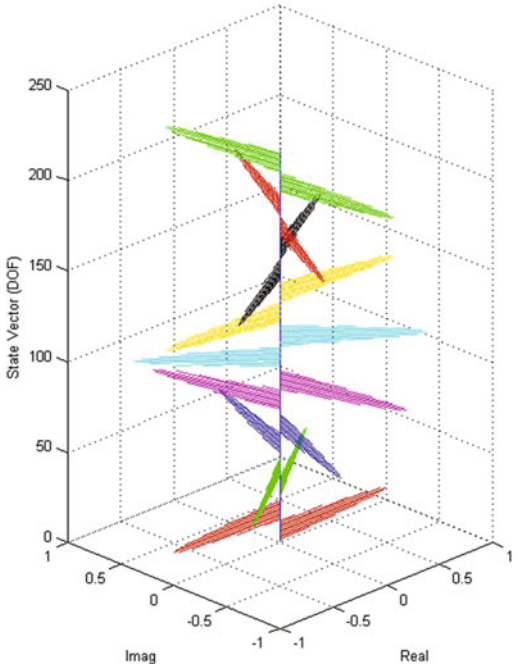

Fig. 27 Modal assurance criterion

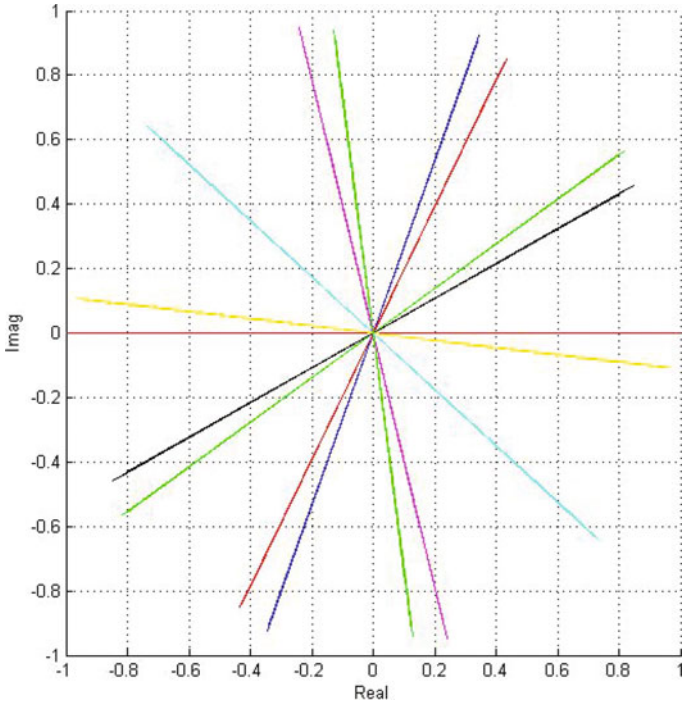

Fig. 28 State vector modal assurance criterion

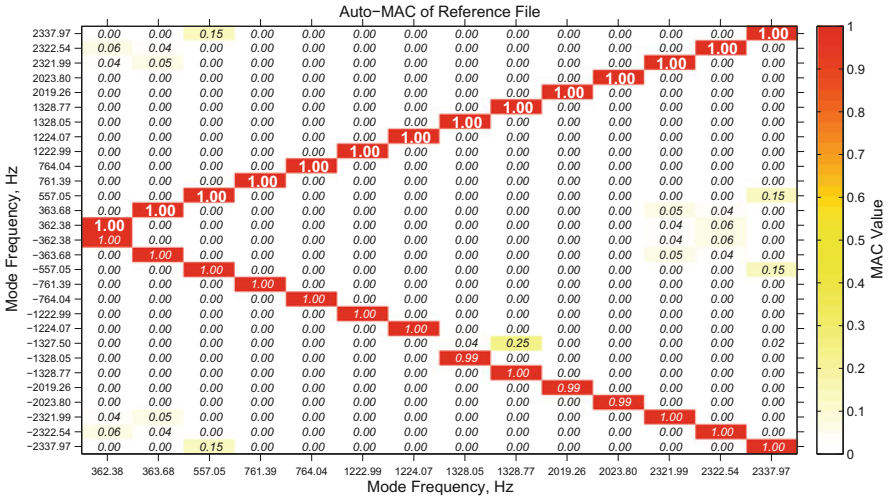

Fig. 29 Modal assurance criterion (no weighting or pole weight = 1)

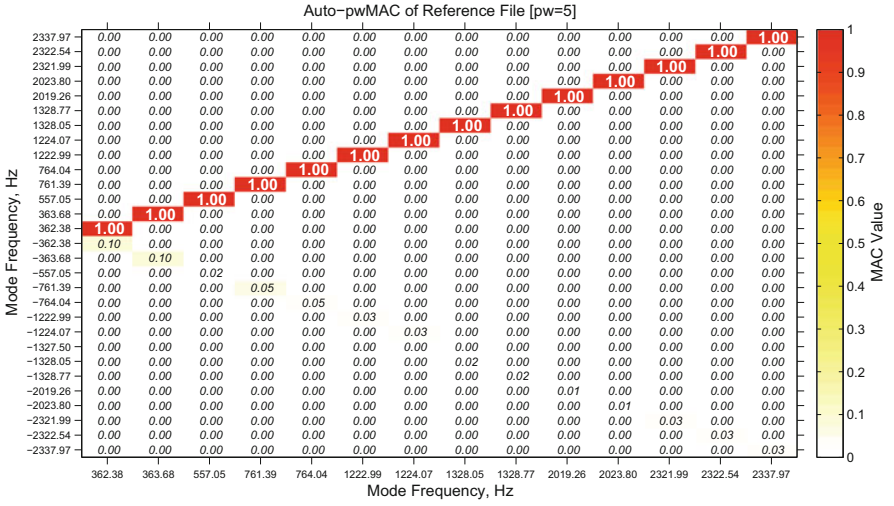

Fig. 30 State vector modal assurance criterion (pole weight = 5)

The MAC results compared to the state vector MAC results are shown in Figs. 29 and 30.

4.5.4 Other Similar Assurance Criteria

The following brief discussion highlights assurance criteria that utilize the same linear, least squares computation approach to the analysis (projection) of two vector spaces as the modal assurance criterion. The equations for each assurance criterion

are not repeated unless there is a significant computational difference that needs to be clarified or highlighted. This list is by no means comprehensive, nor is it in any particular order of importance but includes most of the frequently cited assurance criterion found in the literature.

Weighted Modal Analysis Criterion (WMAC)

A number of authors have utilized a weighted modal assurance criterion (WMAC) without developing a special designation for this case. WMAC is proposed for these cases. The purpose of the weighting matrix is to recognize that MAC is not sensitive to mass or stiffness distribution, just sensor distribution, and to adjust the modal assurance criterion to weight the degrees of freedom in the modal vectors accordingly. In this case, the WMAC becomes a unity normalized weighted orthogonality, or weighted pseudo orthogonality, check where the desirable result for a set of modal vectors would be ones along the diagonal (associated with the same modal vectors) and zeros off diagonal (associated with different modal vectors) regardless of the scaling of the individual modal vectors. Note that the weighting matrix is normally found by first estimating the modal assurance criterion and then using the MAC values to define the weighting matrix.

Partial Modal Analysis Criterion (PMAC)

The partial modal assurance criterion (PMAC) [59] is developed as a spatially limited version of the modal assurance criterion where a subset of the complete modal vector is used in the calculation. The subset is chosen based upon the user's interest and may reflect only a certain dominant sensor direction (X, Y, and/or Z) or only the degrees of freedom from a component of the complete modal vector.

Modal Assurance Criterion Square Root (MACSR)

The square root of the modal assurance criterion (MACSR) [60] is developed to be more consistent with the orthogonality and pseudo orthogonality calculations using an identity weighting matrix. Essentially, this approach utilizes the square root of the MAC calculation which tends to highlight the cross terms (off-diagonal) which are generally the MAC values that are very small.

Scaled Modal Assurance Criterion (SMAC)

The scaled modal assurance criterion (SMAC) [61] is essentially a weighted modal assurance criteria (WMAC) where the weighting matrix is chosen to balance the scaling of translational and rotational degrees of freedom included in the modal vectors. This development is needed whenever different data types (with different engineering units) are included in the same modal vector to normalize the magnitude differences in the vectors. This is required since the modal assurance criterion minimizes the squared error and is dominated by the larger values.

Modal Assurance Criterion Using Reciprocal Vectors (MACRV)

A reciprocal modal vector is defined as the mathematical vector that, when transposed and pre-multiplied times a specific modal vector, yields unity. When

the same computation is performed with this reciprocal modal vector and any other modal vector or any other reciprocal modal vector, the result is zero. The reciprocal modal vector can be thought of as a product of the modal vector and the unknown weighting matrix that will produce a perfect orthogonality result. Reciprocal modal vectors are computed directly from measured frequency response functions and the experimental modal vectors and are, therefore, experimentally based. The modal assurance criterion using reciprocal modal vectors (MACRV) [62] is the comparison of reciprocal modal vectors with analytical modal vectors in what is very similar to a pseudo orthogonality check (POC). The reciprocal modal vectors are utilized in controls applications as modal filters, and the MACRV serves as a check of the mode isolation provided by each reciprocal modal vector compared to analytical modes expected.

Modal Assurance Criterion with Frequency Scales (FMAC)

Another extension of the modal assurance criterion is the addition of frequency scaling to the modal assurance criterion [63, 64]. This extension of MAC offers a means of displaying simultaneously the mode shape correlation, the degree of spatial aliasing, and the frequency comparison in a single plot. This development is particularly useful in model correlation applications (model updating, assessment of parameter variation, etc.)

Coordinate Modal Assurance Criterion (COMAC)

An extension of the modal assurance criterion is the coordinate modal assurance criterion (COMAC) [65]. The COMAC attempts to identify which measurement degrees of freedom contribute negatively to a low value of MAC. The COMAC is calculated over a set of mode pairs, analytical versus analytical, experimental versus experimental, or experimental versus analytical. The two modal vectors in each mode pair represents the same modal vector, but the set of mode pairs represents all modes of interest in a given frequency range. For two sets of modes that are to be compared, there will be a value of COMAC computed for each (measurement) degree of freedom. The coordinate modal assurance criterion (COMAC) is calculated using the following approach, once the mode pairs have been identified with MAC or some other approach:

$$COMAC_q = \frac{\sum_{r=1}^{L} \left|\psi_{qr}\phi_{qr}\right|^2}{\sum_{r=1}^{L} \psi_{qr}\psi_{qr}^* \sum_{r=1}^{L} \phi_{qr}\phi_{qr}^*} \tag{47}$$

Note that the above formulation assumes that there is a match for every modal vector in the two sets and the modal vectors are renumbered accordingly so that the matching modal vectors have the same subscript. Only those modes that match between the two sets are included in the computation.

Enhanced Coordinate Modal Assurance Criterion (ECOMAC)
One common problem with experimental modal vectors is the potential problem of calibration scaling errors and/or sensor orientation mistakes. The enhanced coordinate modal assurance criterion (ECOMAC) [66] was developed to extend the COMAC computation to be more aware of typical experimental errors that occur in defining modal vectors such as sensor scaling mistakes and sensor orientation (plus or minus sign) errors.

Mutual Correspondence Criterion (MCC)
The mutual correspondence criterion (MCC) [67] is the modal assurance criterion applied to vectors that do not originate as modal vectors but as vector measures of acoustic information (velocity, pressure, intensity, etc.). The equation in this formulation utilizes a transpose and will only correctly apply to real-valued vectors.

Modal Correlation Coefficient (MCC)
One of the natural limitations of a least squares-based correlation coefficient like the modal assurance criterion is that it is relatively insensitive to small changes in magnitude, position by position, in the vector comparisons. The modal correlation coefficient (MCC) [68, 69] is a modification of MAC that attempts to provide a more sensitive indicator. This approach is particularly important when using modal vectors in damage detection situations where the magnitude changes of the modal vectors being measured are minimal.

Inverse Modal Assurance Criterion (IMAC)
An alternative approach to increasing the sensitivity of the modal assurance criterion to small mode shape changes is the inverse modal assurance criterion (IMAC) [70]. This approach uses essentially the same computational scheme as MAC but utilizes the inverse of the modal coefficients. Therefore, small modal coefficients become significant in the least squares-based correlation coefficient computation. Naturally, this computation suffers from the possibility that a modal coefficient could be numerically zero.

Frequency Response Assurance Criterion (FRAC)
Any two frequency response functions representing the same input-output relationship can be compared using a technique known as the frequency response assurance criterion (FRAC) [71]. The simplest example is a validation procedure that compares the FRF data synthesized from the modal model with the measured FRF data. The basic assumption is that the measured frequency response function and the synthesized frequency response function should be linearly related (unity scaling coefficient) at all frequencies. Naturally, the FRFs can be compared over the full or partial frequency range of the FRFs as long as the same discrete frequencies are used in the comparison. This approach has been utilized in the modal parameter estimation process for a number of years under various designations (parameter estimation correlation coefficient (PMAC) [59], synthesis correlation coefficient (SCC) [2,72], and response vector assurance criterion (RVAC) [73]). This procedure

is particularly effective as a modal parameter estimation validation procedure if the measured data was not part of the data used to estimate the modal parameters. This serves as an independent check of the modal parameter estimation process.

$$FRAC_{pq} = \frac{\left| \sum_{\omega=\omega_1}^{\omega_2} H_{pq}(\omega) \hat{H}^*_{pq}(\omega) \right|^2}{\sum_{\omega=\omega_1}^{\omega_2} H_{pq}(\omega) H_{pq}{}^*(\omega) \sum_{\omega=\omega_1}^{\omega_2} \hat{H}_{pq}(\omega) \hat{H}^*_{pq}(\omega)} \tag{48}$$

Complex Correlation Coefficient (CCF)
A significant variation in the frequency response assurance criterion is the complex correlation coefficient (CCF) [73] which is computed without squaring the numerator term, thus, yielding a complex-valued coefficient. The magnitude of the coefficient is the same as the FRAC computation, but the phase describes any systematic phase lag or lead that is present between the two FRFs. In situations where analytical and experimental FRFs are compared, the CCF will detect the common problem of a constant phase shift that might be due to experimental signal conditioning problems, etc.

Frequency Domain Assurance Criterion (FDAC)
A similar variation in the frequency response assurance criterion is the frequency domain assurance criterion (FDAC) [74] which is a FRAC type of calculation evaluated with different frequency shifts. Since the difference in impedance (FRF) model updating is often an FRF that is in question due to frequencies of resonances or anti-resonances, the FDAC is formulated to identify this problem. A related criterion, the modal FRF assurance criterion (MFAC) [74], combines analytical modal vectors with measured frequency response functions (FRFs) in an extension of FRAC and FDAC that weights or filters the FRF data based upon the expected, analytical modal vectors.

Coordinate Orthogonality Check (CORTHOG)
The coordinate orthogonality check (CORTHOG) [75] is a normalized error measure between the pseudo orthogonality calculation, comparing measured to analytical modal vectors, and the analytical orthogonality calculation, comparing analytical to analytical modal vectors. Several different normalizing or scaling methods are used with this calculation.

4.5.5 Uses of the Modal Assurance Criterion

Most of the potential uses of the modal assurance criterion are well-known, but a few may be more subtle. A partial list of the most typical uses that have been reported in the literature is as follows:

- Validation of experimental modal models
- Correlation with analytical modal models (mode pairing)

- Correlation with operating response vectors
- Mapping matrix between analytical and experimental modal models
- Modal vector error analysis
- Modal vector averaging
- Experimental modal vector completion and/or expansion
- Weighting for model updating algorithms
- Modal vector consistency/stability in modal parameter estimation algorithms
- Repeated and pseudo repeated root detection
- Structural fault/damage detection
- Quality control evaluations
- Optimal sensor placement

4.5.6 Misuse/Abuse of the Modal Assurance Criterion

Many of the alternate formulations of the modal assurance criterion were developed to address some of the shortcomings of the original modal assurance criterion formulation. When users utilize the original modal assurance criterion in these situations, a poor result will often follow. For the purposes of this discussion, this is referred to as misuse or abuse. The misuse or abuse of the modal assurance criterion generally results due to one of the five issues. These issues can be summarized as:

- The modal analysis criterion is not an orthogonality check.
- The wrong mathematical formulation for the modal assurance criterion is used.
- The modal assurance criterion is sensitive to large values (wild points?) and insensitive to small values.
- The number of elements in the modal vectors (space) is small.
- The modal vectors have been zero padded at unmeasured DOFs.

5 Autonomous Modal Parameter Estimation

Autonomous modal parameter estimation often involves sorting a large number of possible solutions to develop one consistent estimate of the modal parameters (frequency, damping, modal vector, and modal scaling). Once the final, consistent estimate of modal parameters is established, this estimate can be compared to related solutions from the larger set of solutions to develop statistical attributes for the final, consistent set of modal parameters. These attributes include sample size, standard deviation, and other familiar variance estimates. New variance estimates can be introduced to categorize the modal vector solution. These modal vector statistics are based upon the residual contributions in a set of correlated modal vectors that are used to estimate a single modal vector.

5.1 Current Approaches

The interest in automatic modal parameter estimation methods has been documented in the literature since at least the mid-1960s when the primary modal method was the analog, force appropriation method [76, 77, 78]. Following that early work, there has been a continuing interest in autonomous methods [79, 80, 81, 82, 83, 84, 85, 86, 87, 88, 89, 90, 91, 92, 93, 94, 95, 96, 97] that, in most cases, have been procedures that are formulated based upon a specific modal parameter estimation algorithm like the Eigensystem realization algorithm (ERA), the polyreference time domain (PTD) algorithm or more recently the polyreference least squares complex frequency (PLSCF) algorithm, or the commercial version of the PLSCF, the PolyMAX method.

Each of these past procedures has shown some promise but has not yet been widely adopted. In many cases, the procedure focused on a single modal parameter estimation algorithm and did not develop a general procedure. Most of the past procedural methods focused on pole density but depended on limited modal vector data to identify correlated solutions. Many of these current and past methods are commercially developed, and, due to proprietary concerns, details of the autonomous procedure may not be provided.

Currently, due to increased computational speed and larger availability of memory, procedural methods can be developed that were beyond the computational scope of available hardware only a few years ago. These methods do not require any initial manual evaluation of the solution sets and rely upon correlation of the vector space of thousands of potential solutions as the primary identification tool. With the addition to any modal parameter estimation algorithm of the concept of pole-weighted state vector, the length, and therefore sensitivity, of the extended vectors provides an additional tool that appears to be very useful.

The larger question concerning autonomous modal parameter estimation is the intended user. Is the autonomous modal parameter estimation procedure expected to give results sufficiently robust for the novice user? This implies that the user could have no experience with modal analysis and, therefore, have no experiential judgment to use in assessing the quality of the results. The use of the term *wizard* is very common in the commercial autonomous methods, and this description implies that this is the desired situation. In contrast, the user could be very knowledgeable in the theory and experienced in the practice of extracting modal parameters from experimental data. For this case, the autonomous modal parameter estimation procedure is simply an efficient mechanism for sorting a very large number of solutions into a final set of solutions that satisfies a set of criteria and thresholds that are acceptable to the user. Statistical parameters are often part of the solution of these autonomous methods so that users can make judgments concerning the quality of the results. Such statistical parameters are designed to give all users additional information that will allow both experienced and novice users to successfully identify the modal parameters, within the limits of the information provided by the measured data.

5.2 Common Statistical Subspace Autonomous Mode Identification (CSSAMI)

One autonomous modal parameter estimation (MPE) method that is somewhat general and can be applied to any MPE method that generates a consistency diagram or something similar is the Common Statistical Subspace Autonomous Mode Identification (CSSAMI) method [47, 98, 99]. The reader is directed to these references in order to get an overview of one methodology and to view application results for several cases using that methodology.

As a brief summary, the CSSAMI methods begin by forming an m-th order state vector associated with every solution represented in consistency diagram. The user does not need to define which solutions to use. Note that a number of MPE methods can be included in one consistency diagram using techniques noted in [100, 101]. Thus, the number of possible modal parameter solution sets can be in the thousands. All of the state vectors are combined in a single matrix, and a state vector (pole-weighted) MAC is computed between each state vector and all others. A threshold of some value for the state vector MAC is used to find groups of solution sets that represent the same modal vector. Note that this approach sorts all common state vectors together with separate groups of solutions for modal frequencies and conjugate modal frequencies.

Each group of state vectors that represents a common state vector, determined by the MAC threshold, is then subjected to a singular value decomposition (SVD) to find the dominant state vector characteristic for the group as well as checking statistics to determine if more than one state vector is present. The zeroth-order portion of the dominant state vector, compared to the first-order portion of the dominant state vector, is then used to determine the modal frequency and the modal vector. Statistics are computed and assigned to each state vector group to monitor how well the autonomous MPE procedure meets the criteria. Criteria are represented by a small number of thresholds at different points in the procedure.

During the development of any new autonomous modal parameter estimation procedure, it becomes obvious that, since a large number of possible solutions are being evaluated, this development was a natural way to introduce statistical evaluations into the modal analysis estimation process.

Note that much of the background of the CSSAMI method is based upon the unified matrix polynomial algorithm (UMPA) described in a number of papers [3, 4, 5, 6, 102, 101]. However, any modal parameter estimation method can utilize the process outlined in the CSSAMI method.

6 Summary

Modal parameter estimation is probably one of the most misunderstood aspects of the experimental modal analysis process. The methods reviewed in this chapter serve as tools for estimating valid modal parameters from the various modal

parameter estimation (MPE) algorithms available. These MPE algorithms were summarized in ▸ Chap. 10, "Experimental Modal Analysis Methods" in this handbook. Since most modal parameter estimation methods are mathematically intimidating, many users do not fully understand the ramifications of the decisions made during the measurement stages as well as later in the modal parameter estimation process. Tools presented in this chapter aid the user in validating the modal parameters estimated from the different algorithms. Much of the basis for the newer autonomous MPE methods utilizes the tools presented in this chapter.

Over the last 40 years, the modal assurance criterion and the consistency diagram have been the primary tools used by most users and are available in all modal parameter estimation software. The modal assurance criterion has demonstrated how a simple statistical concept can become an extremely useful tool in the field of experimental modal analysis and structural dynamics. The use of the modal assurance criterion (MAC), and the development and use of a significant number of related criteria, has been remarkable and is most likely due to the overall simplicity of the concept. The consistency diagram was developed around the same time as the modal assurance criterion and is widely used, providing a mechanism for evaluating very large sets of modal parameter estimates. The consistency diagram is also very simple and is just a repeated solution procedure over a range of modal parameter algorithm model orders.

Certainly, in the next few years, the increased use of other statistical methods and further development of singular value/vector decomposition methods are related technical areas that will generate useful tools in this area. Currently, many users are utilizing more statistical approaches to understand the meaning and bounds of experimental modal parameters [45, 103, 104, 105, 106, 107]. This approach extends again to the modal assurance criterion as well as to the consistency diagram. Examples are the bootstrap and jackknife approaches [105,106,107] to the evaluation of the mean and standard deviation of discrete sets of experimental data. These approaches remove and/or replace portions of the computation (bootstrap uses replicative resampling; jackknife uses sequential elimination) to evaluate the bounds or limits on the MAC values. In this way, the sensitivity of any statistical computation can be more effectively evaluated than with the current single number indicating the degree of linearity between two modal vectors that are being compared.

References

1. Leuridan J, Brown D, Allemang R (1985) Time domain parameter identification methods for linear modal analysis: a unifying approach. ASME Paper Number 85-DET-90
2. Allemang RJ, Brown, D (1987) Volume III: modal parameter estimation. USAF Report: AFWAL-TR-87-3069. Experimental modal analysis and dynamic component synthesis, no 3, pp 130
3. Allemang R, Brown, D, Fladung W (1994) Modal parameter estimation: a unified matrix polynomial approach. In: Proceedings, International Modal Analysis Conference (IMAC), pp 501–514

4. Allemang R, Brown D (1996) A unified matrix polynomial approach to modal identification, Allied Publishers Limited pp 379–390
5. Allemang R, Brown D (1998) A unified matrix polynomial approach to modal identification. J Sound Vib 211(3):301–322
6. Allemang, R, Phillips A (2004) The unified matrix polynomial approach to understanding modal parameter estimation: an update. In: Proceedings, International Seminar on Modal Analysis (ISMA)
7. Spitznogle F (1971) Improvements in the complex exponential signal analysis computational algorithm. Report Number U1-829401-5, Representation and Analysis of Sonar Signals, vol 1, pp 37
8. Brown D, Allemang R, Zimmerman, R, Mergeay M (1979) Parameter estimation techniques for modal analysis. SAE Paper Number 790221, SAE Transactions, vol 88, pp 828–846
9. Vold, H, Rocklin T (1982) The numerical implementation of a multi-input modal estimation algorithm for mini-computers. In: Proceedings, International Modal Analysis Conference (IMAC), pp 542–548
10. Vold H, Kundrat J, Rocklin, T, Russell R (1982) A multi-input modal estimation algorithm for mini-computers. SAE Trans 91(1):815–821
11. Ibrahim, S, Mikulcik E (1977) A method for the direct identification of vibration parameters from the free response. Shock Vib Bull 47:183–198
12. Pappa R (1982) Some statistical performance characteristics of the ITD modal identification algorithm. AIAA Paper Number 82-0768, p 19
13. Fukuzono K (1986) Investigation of multiple-reference ibrahim time domain modal parameter estimation technique. M. S. Thesis, p 220
14. Juang, J, Pappa R (1985) An eigensystem realization algorithm for modal parameter identification and model reduction. AIAA J Guid Control Dyn 8(4):620–627
15. Juang J (1987) Mathematical correlation of modal parameter identification methods via system realization theory. J Anal Exp Modal Anal 2(1):1–18
16. Longman RW, Juang J-N (1989) Recursive form of the eigensystem realization algorithm for system identification. AIAA J Guid Control Dyn 12(5):647–652
17. Zhang L, Kanda H, Brown, D, Allemang R (1985) A polyreference frequency domain method for modal parameter identification. ASME Paper No. 85-DET-106, vol 8, pp 8+
18. Lembregts F, Leuridan J, Zhang, L, Kanda H (1986) Multiple input modal analysis of frequency response functions based on direct parameter identification. In: Proceedings, International Modal Analysis Conference (IMAC)
19. Lembregts F (1988) Frequency domain identification techniques for experimental multiple input modal analysis. Doctoral Dissertation, Katholieke University of Leuven, Belgium, vol 213
20. Lembregts F, Leuridan, J, Van Brussel H (1989) Frequency domain direct parameter identification for modal analysis: state space formulation. Mech Syst Signal Process 4(1):65–76
21. Coppolino R (1981) A simultaneous frequency domain technique for estimation of modal parameters from measured data. SAE Paper No. 811046, vol 12
22. Craig R, Kurdila A, Kim HM (1990) State-space formulation of multi-shaker modal analysis. J Anal Exp Modal Anal 5(3):169–183
23. Leuridan J (1984) Some direct parameter model identification methods applicable for multiple input modal analysis. Doctoral Dissertation, vol 384, pp 384+
24. Natke H (1988) Updating computational models in the frequency domain based on measured data: a survey. Probab Eng Mech 3(1):28–35
25. Richardson, M, Formenti D (1982) Parameter estimation from frequency response measurements using rational fraction polynomials. In: Proceedings, International Modal Analysis Conference (IMAC), pp 167–182
26. Shih C, Tsuei Y, Allemang, R, Brown D (1988) A frequency domain global parameter estimation method for multiple reference frequency response measurements. Mech Syst Signal Process (MSSP) 2(4):349–365

27. Shih C (1989) Investigation of numerical conditioning in the frequency domain modal parameter estimation methods, Doctoral Dissertation, vol 127, pp 127+
28. Van der Auweraer, H, Leuridan J (1987) Multiple input orthogonal polynomial parameter estimation. Mech Syst Signal Process (MSSP) 1(3):259–272
29. Van der Auweraer H, Snoeys R, Leuridan JM (1986) A Global frequency domain modal parameter estimation technique for mini-computers. ASME J Vib Acoust Stress Reliab Des 10, vol 11
30. Vold H (1986) Orthogonal polynomials in the polyreference method. In: Proceedings, International Seminar on Modal Analysis (ISMA-11)
31. Vold, H, Shih CY (1988) Numerical sensitivity of the characteristic polynomial. In: Proceedings, International Seminar on Modal Analysis (ISMA-13)
32. Vold H (1990) Numerically robust frequency domain modal parameter estimation. Sound Vib Mag (SVM) 24(1):38–40
33. Vold H (1990) Statistics of the characteristic polynomial in modal analysis. In: Proceedings, International Seminar on Modal Analysis (ISMA), pp 53–57
34. Vold H, Napolitano K, Hensley, D, Richardson M (2008) Aliasing in modal parameter estimation, an historical look and new innovations. In: Proceedings, International Modal Analysis Conference (IMAC), vol 16, pp 12–17
35. Fladung, W, Vold H (2016) An improved implementation of the orthogonal polynomial modal parameter estimation algorithm using the orthogonal complement. In: Proceedings, International Modal Analysis Conference (IMAC)
36. Fladung, W, Vold H (2016) An Orthogonal view of the polyreference least-squares complex frequency modal parameter estimation algorithm. In: Proceedings, International Modal Analysis Conference (IMAC)
37. Van der Auweraer H, Guillaume P, Verboven, P, Vanlanduit S (2001) Application of a fast-stabilizing frequency domain parameter estimation method. ASME J Dyn Syst Meas Control 123(4):651–658
38. Guillaume P, Verboven P, Vanlanduit S, der Auweraer V H and Peeters B (2003) A polyreference implementation of the least-squares complex frequency domain estimator. In: Proceedings, International Modal Analysis Conference (IMAC), p 12
39. Verboven P, Guillaume P, Cauberghe B, Parloo, E, Vanlanduit S (2003) Stabilization charts and uncertainty bounds for frequency domain linear least squares estimators. In: Proceedings, International Modal Analysis Conference (IMAC), pp 1–10
40. Verboven P, Cauberghe B, Vanlanduit S, Parloo, E, Guillaume P (2004) The secret behind clear stabilization diagrams: the influence of the parameter constraint on the stability of the poles. In: Proceedings, Society of Experimental Mechanics (SEM) Annual Conference, vol 17, pp 1–17
41. Verboven P (2002) Frequency domain system identification for modal analysis. Doctoral Dissertation
42. Cauberghe B (2004) Application of frequency domain system identification for experimental and operational modal analysis. Doctoral Dissertation, p 259
43. Shih C, Tsuei Y, Allemang, R, Brown D (1988) Complex mode indication function and its application to spatial domain parameter estimation. Mech Syst Signal Process (MSSP) 2(4):367–377
44. Williams R, Crowley, J, Vold H (1985) The multivariable mode indicator function in modal analysis. In: Proceedings, International Modal Analysis Conference (IMAC), pp 66–70
45. Phillips AW, Allemang RJ, Pickrel CR (1997) Clustering of modal frequency estimates from different solution sets. In: Proceedings, International Modal Analysis Conference (IMAC), pp 1053–1063
46. Phillips, A, Allemang R (2014) Normalization of experimental modal vectors to remove modal vector contamination. In: Proceedings, International Modal Analysis Conference (IMAC), p 12
47. Phillips A, Allemang, R, Brown D (2011) Autonomous modal parameter estimation: methodology. In: Proceedings, International Modal Analysis Conference (IMAC), p 22

48. Allemang R (1980) Investigation of some multiple input/output frequency response function experimental modal analysis techniques. Doctoral Dissertation, pp 141–214
49. Phillips, A, Allemang R (1998) The enhanced frequency response function (eFRF): scaling and other issues. In: Proceedings, International Seminar on Modal Analysis (ISMA)
50. Guyan R (1965) Reduction of stiffness and mass matrices. AIAA J 3(2):380
51. Irons B (1965) Structural eigenvalue problems: elimination of unwanted variables. AIAA J 3(5):961–962
52. Downs B (1979) Accurate reduction of stiffness and mass matrices for vibration analysis and a rationale for selecting master degrees of freedom. ASME Paper Number 79-DET-18, p 5
53. Sowers J (1978) Condensation of free body mass matrices using flexibility coefficients. AIAA J 16(3):272–273
54. O'Callahan J, Avitabile, P, Riemer R (1989) System equivalent reduction expansion process (SEREP). In: Proceedings, International Modal Analysis Conference (IMAC), pp 29–37
55. Kammer D (1987) Test analysis model development using an exact modal reduction. J Anal Exp Modal Anal 2(4):174–179
56. Kammer D (1990) Sensor placement for on-orbit modal identification and correlation of large space structures. In: Proceedings, American Control Conference, pp 2984–2990
57. Allemang, R, Brown D (1982) A correlation coefficient for modal vector analysis. In: Proceedings, International Modal Analysis Conference (IMAC), pp 110–116
58. Allemang R (2002) The modal assurance criterion (MAC): twenty years of use and abuse. In: Proceedings, International Modal Analysis Conference (IMAC), pp 397–405
59. Heylen W (1990) Extensions of the modal assurance criterion. J Vib Acoust (JVA) 112:468–472
60. O'Callahan J (1998) Correlation considerations – Part 4 (Modal vector correlation techniques). In: Proceedings, International Modal Analysis Conference (IMAC), pp 197–206
61. Brechlin E, Bendel, K, Keiper W (1998) A New Scaled Modal Assurance Criterion for Eigenmodes Containing Rotational Degrees of Freedom. In: Proceedings, International Seminar on Modal Analysis (ISMA), vol ISMA23, pp 7
62. Wei J, Wang, W, Allemang R (1990) Model correlation and orthogonality criteria based on reciprocal modal vectors. In: Proceedings, SAE Noise and Vibration Conference, pp 607–616
63. Fotsch, D, Ewins D (2000) Applications of MAC in the frequency domain. In: Proceedings, International Modal Analysis Conference (IMAC), pp 1225–1231
64. Fotsch, D, Ewins D (2001) Further Applicatios of the FMAC. In: Proceedings, International Modal Analysis Conference (IMAC), pp 635–639
65. Lieven, N, Ewins D (1988) Spatial correlation of mode shapes, the coordinate modal assurance criterion (COMAC). In: Proceedings, International Modal Analysis Conference (IMAC), pp 690–695
66. Hunt D (1992) Application of an enhanced coordinate modal assurance criterion (ECOMAC). In: Proceedings, International Modal Analysis Conference (IMAC), pp 66–71
67. Milecek S (1994) The use of modal assurance criterion extended. In: Proceedings, International Modal Analysis Conference (IMAC), pp 363–369
68. Samman M (1996) A modal correlation coefficient (MCC) for detection of kinks in mode shapes. ASME J Vib Acoust 118(2):271–272
69. Samman M (1997) Structural damage detection using the modal correlation coefficient (MCC). In: Proceedings, International Modal Analysis Conference (IMAC), pp 627–630
70. Mitchell L (2001) Increasing the sensitivity of the modal assurance criteria to small mode shape changes: the IMAC. In: Proceedings, International Modal Analysis Conference (IMAC), pp 64–69
71. Heylen, W, Lammens S (1996) FRAC: a consistent way of comparing frequency response functions. In: Proceedings, International Conference on Identification in Engineering, Swansea, pp 48–57
72. Allemang R (1990) Vibrations: experimental modal analysis, UC-SDRL-CN-20-263-663/664, pp 7-1–7-2

73. Van der Auweraer H, Iadevaia M, Emborg U, Gustavsson M, Tengzelius, U, Horlin N (1998) Linking test and analysis results in the medium frequency range using principal field shapes. In: Proceedings, International Seminar on Modal Analysis (ISMA), p 8
74. Pascual R, Golinval, J, Razeto M (1997) A Frequency domain correlation technique for model correlation and updating. In: Proceedings, International Modal Analysis Conference (IMAC), pp 587–592
75. Avitabile, P, Pechinsky F (1994) Coordinate orthogonality check (CORTHOG). In: Proceedings, International Modal Analysis Conference (IMAC), pp 753–760
76. Hawkins F (1965) An automatic resonance testing technique for exciting normal modes of comples structures. In: Symposium IUTAM, Recent Progress in the Mechanics of Linear Vibrations, pp 37–41
77. Hawkins F J. (1967) GRAMPA – an automatic technique for exciting the principal modes of vibration of complex structures. Royal Aircraft Establishment, vol RAE-TR-67-211
78. Taylor GA, Gaukroger, D, Skingle C (1967) MAMA – a semi-automatic technique for exciting the principal modes of vibration of complex structures. Aeronautical Research Council, vol ARC-R/M-3590, pp 20
79. Takahashi, K, Furusawa M (1987) Development of automatic modal analysis. In: Proceedings, International Modal Analysis Conference (IMAC), pp 686–692
80. Yam Y, Bayard D, Hadaegh F, Mettler E, Milman M and Scheid R (1989) Autonomous frequency domain identification: theory and experiment. NASA JPL Report JPL Publication 89-8, p 204
81. Lim T, Cabell, R, Silcox R (1996) On-line identification of modal parameters using artificial neural networks. J Vib Acoust (JVA) 118(4):649–656
82. Pappa R, Woodard S E, Juang J (1997) A benchmark problem for development of autonomous structural modal identification. In: Proceedings, International Modal Analysis Conference (IMAC), pp 1071–1077
83. Pappa R, James, G, Zimmerman D (1998) Autonomous modal identification of the space shuttle tail rudder. J Spacecr Rocket 35(2):163–169
84. Chhipwadia K, Zimmerman, D, James III G (1999) Evolving autonomous modal parameter estimation. In: Proceedings, International Modal Analysis Conference (IMAC), pp 819–825
85. James III G, Zimmerman, D, Chhipwadia K (1999) Application of autonomous modal identification to traditional and ambient data sets. In: Proceedings, International Modal Analysis Conference (IMAC), pp 840–845
86. Vanlanduit S, Verboven P, Schoukens, J, Guillaume P (2001) An automatic frequency domain modal parameter estimation algorithm. In: Proceedings, International Conference on Structural System Identification, pp 637–646
87. Verboven P, Parloo E, Guillame, P, Overmeire M (2001) Autonomous modal parameter estimation based on a statistical frequency domain maximum likelihood approach. In: Proceedings, International Modal Analysis Conference (IMAC), pp 1511–1517
88. Verboven P, Parloo E, Guillaume, P, Van Overmeire M (2002) Autonomous structural health monitoring, part i: modal parameter estimation and tracking. Mech Syst Signal Process (MSSP) 16(4):637–657
89. Parloo E, Verboven P, Guillaume, P, Van Overmeire M (2002) Autonomous structural health monitoring – Part II: vibration-based in-operation damage assessment. Mech Syst Signal Process (MSSP) 16(4):659–675
90. Vanlanduit S, Verboven P, Guillaume, P, Schoukens J (2003) An automatic frequency domain modal parameter estimation algorithm. J Sound Vib (JSV) 265:647–661
91. Lanslots J, Rodiers, B, Peeters B (2004) Automated Pole-Selection: Proof-of-Concept and Validation. In: Proceedings, International Seminar on Modal Analysis (ISMA)
92. Mevel L, Sam, A, Goursat M (2004) Blind modal identification for large aircrafts. In: Proceedings, International Modal Analysis Conference (IMAC), p 8
93. Lau J, Lanslots J, Peeters, B, der Auweraer V (2007) Automatic modal analysis: reality or myth?. In: Proceedings, International Modal Analysis Conference (IMAC), p 10

94. Liu J, Ying H, Shen, S, Dong S (2007) The function of modal important index in autonomous modal analysis. In: Proceedings, International Modal Analysis Conference (IMAC), p 6
95. Mohanty P, Reynolds, P, Pavic A (2007) Automatic interpretation of stability plots for analysis of a non-stationary structure. In: Proceedings, International Modal Analysis Conference (IMAC), p 7
96. Poncelet F, Kerschen, G, Golinval J (2008) Operational modal analysis using second-order blind identification. In: Proceedings, International Modal Analysis Conference (IMAC), p 7
97. Rainieri C, Fabbrocino, G, Cosenza E (2009) Fully automated OMA: an opportunity for smart SHM systems. In: Proceedings, International Modal Analysis Conference (IMAC), p 9
98. Allemang R, Phillips, A, Brown D (2011) Autonomous modal parameter estimation: statistical considerations. In: Proceedings, International Modal Analysis Conference (IMAC), p 17
99. Brown D, Allemang, R, Phillips A (2011) Autonomous modal parameter estimation: application examples. In: Proceedings, International Modal Analysis Conference (IMAC), p 17
100. Phillips A, Allemang, R, Pickrel C (1998) Estimating modal parameters from different solution sets. In: Proceedings, International Modal Analysis Conference (IMAC), p 10
101. Allemang, R, Phillips A (2014) Spatial Information in Autonomous Modal Parameter Estimation, Shock and Vibration Journal: Special ICEDYN Issue, pp 1–18
102. Allemang R, Phillips, A, Brown D (2011) Combined state order and model order formulations in the unified matrix polynomial method (UMPA). In: Proceedings, International Modal Analysis Conference (IMAC)
103. DeClerck, J, Avitabile P (1996) Development of several new tools for modal pre-test evaluation. In: Proceedings, International Modal Analysis Conference (IMAC), pp 1272–1277
104. Cafeo J, Lust, R, Meireis U (2000) Uncertainty in Mode Shape Data and its Influence on the Comparison of Test and Analysis Models. In: Proceedings, International Modal Analysis Conference (IMAC), pp 349–355
105. Paez, T, Hunter N (1998) Fundamental concepts of the bootstrap for statistical analysis of mechanical systems. Exp Tech 21(3):35–38
106. Hunter, N, Paez T (1998) Applications of the bootstrap for mechanical system analysis. Exp Tech 21(4):34–37
107. Efron, B, Gong G (1983) A leisurely look at the bootstrap, the jackknife and cross-validation. Am Stat 37(1):36–48

Damping of Materials and Structures

12

Lothar Gaul and André Schmidt

Contents

Lothar Gaul: deceased.

L. Gaul
Institut für Nichtlineare Mechanik, Universität Stuttgart, Stuttgart, Germany
e-mail: lothar.gaul@iam.uni-stuttgart.de

A. Schmidt (✉)
Institut für Nichtlineare Mechanik, Universität Stuttgart, Stuttgart, Germany
e-mail: schmidt@inm.uni-stuttgart.de

R. Allemang, P. Avitabile (eds.), *Handbook of Experimental Structural Dynamics*,
https://doi.org/10.1007/978-1-4614-4547-0_19

Abstract

Damping is a phenomenon that can be observed in connection with all kind of materials: solid, liquid, or gaseous. Any kind of time-dependent change in stresses or strains of the material results in a loss of mechanical energy, which in most cases is transformed into thermal energy. However, all the other mechanisms such as the conversion into electrical energy or any kind of radiation over the system's boundaries play a role. Typical observations that can be made in connection with damping are the occurrence of creep and relaxation processes or hysteresis curves in the case of cyclic loadings. The overall damping is influenced by a variety of mechanisms, especially for structures assembled from different components.

No matter whether the presence of damping is sought or should be avoided in technical applications, for any kind of tuning or optimization of a system under consideration, a basic understanding of the underlying physics is needed. This is especially true if calculations or simulations have to be run in order to predict the dynamical behavior of a system.

This chapter intends to introduce the reader into the subject and provide an extensive overview on the different aspects of damping regarding the fundamentals, mathematical, and numerical models as well as experimental techniques for the detection of damping properties. It shall give an overview of the state of knowledge and experience gathered in various fields of application and research. For further information, the reader is referred to various publications and textbooks whenever needed. This chapter is organized as follows: Sect. 1 provides an extensive overview on the topic, the classification of damping phenomena, and some remarks on computer-based programs. Section 2 refers to the damping of solids, while Sect. 3 extends the view on structures assembled from different components. Section 4 deals with different mathematical models toward the description of damping and relevant numerical approaches. Experimental techniques for the detection of the damping parameters needed for calculations are described in Sect. 5. This includes possible instrumentation as well as analytical methods. Finally, in Sect. 6, an application of the whole subject

covering the detection of damping properties, its mathematical representation, and parameter identification along with a numerical simulation is presented as an example. Conclusions from this chapter are drawn in Sect. 7.

Keywords

Damping · Creep · Relaxation · Hysteresis · Dissipation · Experimental techniques · Joints · Assemblies · Finite element method · Boundary element method · Rheological models · Fractional derivatives

Nomenclature

α	Order of derivative
β	Order of derivative
$\boldsymbol{\Phi}$	Matrix of eigenvectors
$\boldsymbol{B}$	Spatial derivatives of matrix of shape functions
$\boldsymbol{H}$	Matrix of shape functions
$\boldsymbol{K}$	Stiffness matrix
$\boldsymbol{M}$	Mass matrix
$\boldsymbol{u}$	Relative displacement vector
χ	Material loss factor
$\dot{\gamma}$	Shear speed
γ	Pure shear distortion
κ	Curvature
λ	Wavelength
ν	Poisson's ratio, order of derivative
ω_0	Natural frequency
ω_d	Natural damped frequency
$\Psi(t)$	shift function
ρ	Mass density
σ	Normal stress
τ	shear stress
$\underline{\boldsymbol{\sigma}}$	Complex stress
$\underline{\boldsymbol{\varepsilon}}$	Complex strain
$\underline{\boldsymbol{E}}$	Complex elastic modulus
$\underline{\boldsymbol{G}}$	Complex shear modulus
$\underline{\boldsymbol{K}}$	Complex bulk modulus
ε	Strain
Ω	Angular frequency
ϑ	damping ratio
ζ	Angular phase difference
E	Young's modulus, spring constant
e	Deviatoric strain
$E(t)$	Relaxation function
E'	Storage modulus

E''	Loss modulus
F	Force
H_k	Coulomb element
i	Unit imaginary number
$J(t)$	Creep compliance function
$K(t)$	Decay function
P	Active power
p	Spring-pot coefficient
R_k	damping constant
So	Sommerfeld number
T	Temperature, time interval
t	Time
U	Potential energy
V	Volume
W	Mechanical work
W_D	dissipated mechanical energy

1 Classification and Survey

1.1 Introduction

All dynamic processes in mechanic systems are more or less damped. Consequently, damping is highly relevant in those fields of technology and applied physics which deal with dynamics and vibrations. These include

- machine-, building-, and structural dynamics,
- system dynamics,
- control engineering, and
- technical acoustics,

because damping in these cases often has a considerable effect on the time history, intensity, or even the existence of vibrations. Important applications are:

- transient vibrations (transient effects associated with the onset or decay of vibrations, shock-induced vibrations, reverberation effects)
- resonance vibrations (unavoidable with random excitation)
- wave propagation
- dynamic-stability problems

Accordingly, a multitude of scientific publications dealing with damping, or taking it into account at least, are found in technical literature. Due to different theory approaches, objects, and task definitions in the applications listed above, the designations, the characterization of damping, the experimental techniques, and the analytical and numerical methods are not harmonized.

The dynamic behavior of damped structures can, in special cases, be calculated using generally valid material laws for inelastic materials based on continuum mechanics taking into account boundary effects (e.g., joints). In general, this approach is too elaborate or expensive or not at all practicable. In most cases, therefore, phenomenological equivalent systems or mathematical models tailored to the task definition are used which are only valid assuming a special state of stresses and/or a special time history. Harmonic (sinusoidal) time histories are a preferred special case where complex quantities describe the elastic and damping properties. These depend on a number of parameters: material data, rate of deformation, frequency, temperature, number of load cycles, etc. In the case of nonlinear behavior, there is also a dependence on the amplitude.

For certain problems, it is sufficient to state, for one deformation cycle, the energy dissipated in a unit volume or within the system, or the energy released into the environment at the system boundaries, often related to a conveniently chosen elastic energy in a unit volume or in the system as a whole. However, in structural dynamics, the use of modal damping ratios has proven useful, which do no longer contain detailed information about the damping.

1.2 The Notion of Damping

Damping in mechanical systems is understood to be the irreversible transition of mechanical energy into other forms of energy as found in time-dependent processes. Damping is mostly associated with the change of mechanical energy into thermal energy. Damping can also be caused by releasing energy into a surrounding medium. Electromagnetic and piezoelectric energy conversion can also give rise to damping if the energy converted is not returned to the mechanical system.

1.3 Classification of Damping Phenomena

The physical causes of damping are multifarious. In addition to friction, wave propagation or flow effects, other possible causes are phase transitions in materials or energy conversion by piezoelectric, magnetostrictive or electromechanical processes.

Forces associated with damping are non-conservative. They can be internal or external forces. If both action and reaction forces in a free body diagram are effective within the system boundaries, the effect is said to be an internal damping effect. Whereas if the reaction force is effective outside the system boundaries, the effect is an external damping effect.

Examples of internal damping are:

- material damping due to nonelastic material behavior
- friction between components, e.g., in slide ways, gears, etc.

- conversion of mechanical vibration energy into electrical energy by means of the piezoelectric effect and dissipation due to dielectric losses

Examples of external damping are:

- friction against the surrounding medium
- airborne-sound radiation into the environment
- structureborne-sound radiation into the ground

Phenomenological contributions of damping to a mechanical system:

- **Material damping**
  The energy dissipation within a material, due to deformation and/or displacement, is called material damping. Its physical causes are, in essence:
  For solids:
  – heat flows induced by deformation (thermomechanical coupling)
  – slip effects
  – microplastic deformations
  – diffusion processes
  For fluids:
  – viscos flow losses
- **Contact-surface damping**: relative motion, friction
  Contact-surface damping is caused by relative motions in the contact surfaces of joined components such as screwed, riveted, and clamped joints. The physical causes are:
  – friction due to relative motions in the contact surface
  – pumping losses in the enclosed medium due to relative motion in a direction normal to the contact surface (e.g., gas pumping)

Structural damping refers to the following cases:

- damping in guides This includes energy dissipation in longitudinal guides (e.g., slides) and circular guides (e.g., journal bearings)
- electromechanical damping. Electromechanical damping can be caused by piezoelectric, magnetostrictive, or electromagnetic effects
- energy release to the surrounding medium. This includes causes such as air, fluid, and bedding damping.

1.4 Notes on Modern, Computer-Based Analytical and Measurement Programs

Whereas the mass and stiffness matrices of relatively complex structures can be readily determined nowadays using three-dimensional CAD drawings, automatic

grid generation, and subsequent FEM analysis, an appropriate calculation model cannot usually be established with sufficiently precise information on damping. More precise damping parameters can be determined experimentally.

"Experimental Modal Analysis" (EMA) has become established as the suitable tool worldwide. It uses measured frequency-response curves between appropriately chosen excitation points and measuring points and modern curve-fitting techniques for identifying the modal parameters: natural frequencies, eigenmodes, and modal damping ratios. In the case of simple structures, the system can be excited by means of a hammer impact. In the case of complex components and considerable damping, excitation using one or several exciters has proven convenient, allowing to control exciter amplitudes and energy distribution for selected frequency ranges. The system response is often measured by means of piezoelectric accelerometers or laser-optical sensors.

Modern measurement and analytical systems offer the possibility to identify discrete damping couplings provided that the substructures have been separately investigated beforehand.

Link modules allow to establish the connection between the results of experimental modal analysis and the calculated FEM analysis (e.g., matching of nodal points and coordinate axes through interpolation).

Quality criteria such as MAC (Modal Assurance Criterion) compare the relations (such as orthogonality) between the eigenmodes found in terms of the scalar product of the eigenvectors. Additional normalization using the mass or stiffness matrix allows a quantitative assessment.

After model updating on the modal level, including damping ratios determined by experiment, operation vibrations can be calculated for any load function. The simulation model which was developed step by step can thus be verified under practical conditions.

2 Damping of Solids

2.1 Physical Phenomena

It is observed experimentally that solid materials do not exhibit behavior as predicted by a model of ideal elasticity. Such materials are therefore referred to as inelastic. The two standard tests depicted in Fig. 1 illustrate the typical characteristics of inelastic material behavior. When the material is subjected to a step-like change in stress as shown in the following Eq. (1), it responds by time-dependent creep, $\varepsilon(t)$. If the strain, on the other hand, is kept constant after a step-like change in strain shown in Eq. (2), the stress, $\sigma(t)$, will decrease due to reordering at the atomic, molecular, crystalline, and intercrystalline levels. This is known as recovery or relaxation.

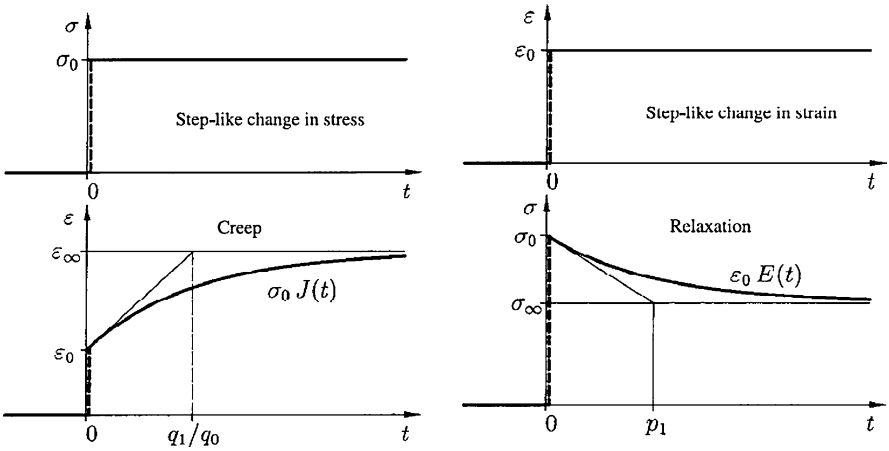

Fig. 1 Creep and relaxation behavior (source: VDI guideline 3830)

$$\sigma(t) = \sigma_0 1(\mathrm{t}) \tag{1}$$

$$\varepsilon(t) = \varepsilon_0 1(\mathrm{t}) \tag{2}$$

In case of harmonic stressing of the material, inelastic behavior manifests itself in the form of a loss of usable mechanical energy (hysteresis). Figure 2 shows two such hysteresis cycles.

The mechanical energy dissipated due to damping effects per unit volume during one cycle of period T_p and also in the case of arbitrary time history, which affects the damping can be expressed as follows:

$$W_D = \oint \sigma \mathrm{d}\varepsilon = \oint^{T_p} \sigma(t)\dot{\varepsilon}(t)\mathrm{d}t. \tag{3}$$

The material loss factor is a relative damping characteristic defined by:

$$\chi = \frac{W_{Dh}}{2\pi U_{\mathrm{ref}}}. \tag{4}$$

where W_{Dh} is the damping work per unit volume per cycle in case of a harmonic strain curve, and U_{ref} is the reference energy per unit volume at maximum strain ($\hat{\varepsilon}$) shown as an area in Fig. 2. In the linear case, Fig. 2, U_{ref} is the maximum stored potential energy $U_{\max}$ per unit volume. The material loss factor depends to a great extent on the amplitude and the time period, i.e., $\chi : \chi = \chi(T_p, \hat{\varepsilon})$

For a component, the loss factor is defined by analogy to Eq. (4):

$$\chi_S = \frac{W_{Sh}}{2\pi U_{\mathrm{S}}}. \tag{5}$$

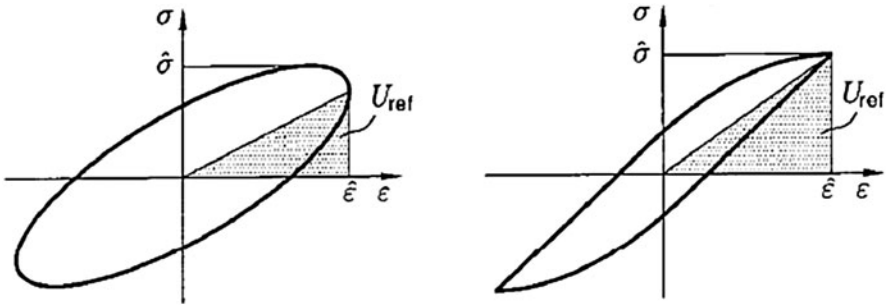

Fig. 2 Stress-Strain curves, cyclic loading, hysteresis loops for linear and nonlinear materials (source: VDI guideline 3830)

The straightforward description of the characteristic damping work per cycle has the following shortcomings:

- The characteristic can only be given for harmonic stresses or distortions and only for hysteresis curves without sub-loops.
- The damping work does not contain any information on the rigidity of the material.

2.2 Linear Models

A viscoelastic model is the easiest manner in which a linear inelastic material may be described. The behavior can be characterized by employing a network of massless springs and dampers, known as rheological models. The most fundamental configuration is a 3-parameter model; it allows to describe the results of the standard tests as per Fig. 1. A better conformity to the curves can be achieved by using several combinations of the said models. However, this leads to difficulties when model parameters are required to be associated with experimental behavior.

2.2.1 Three-Parameter Models

Figure 3 shows two possible configurations of springs and dampers in a 3-parameter model for solids. Other spring and damper configurations in 3-parameter models describe the behavior of fluids.

For model (a) in Fig. 3, E_{0a}, E_{1a}, and R_{1a} are the parameters of the springs and the damper, ε is the total strain, and ε_{1a} is the spring excursion. For equilibrium, we have:

$$\sigma = E_{0a}\varepsilon + E_{1a}\varepsilon_{1a} \tag{6}$$

$$E_{1a}\varepsilon_{1a} = R_{1a}(\dot{\varepsilon} - \dot{\varepsilon}_{1a}). \tag{7}$$

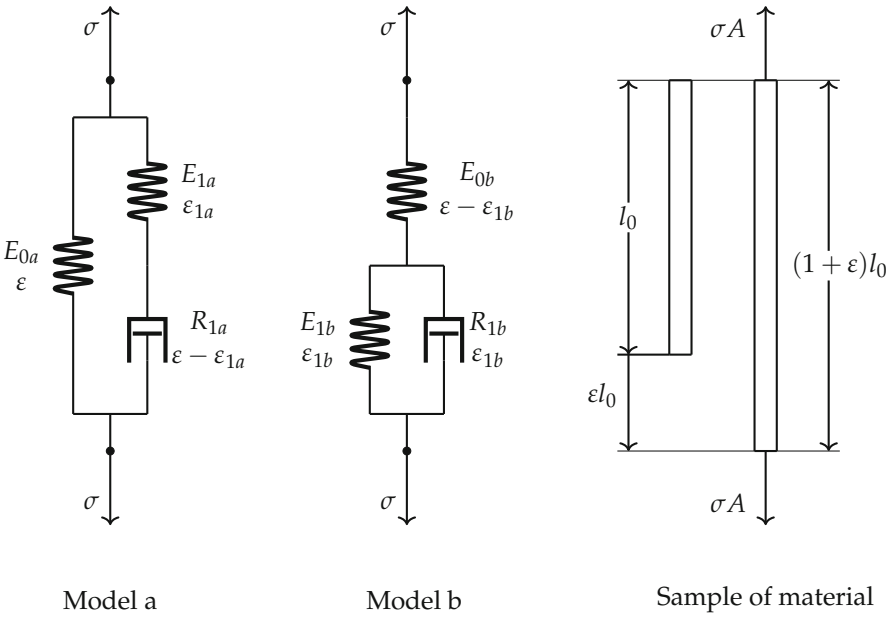

Fig. 3 Three-parameter models for linear inelastic materials

The equilibrium conditions in Fig. 3 lead to the respective viscoelastic material law:

$$\sigma + p_1\dot{\sigma} = q_0\varepsilon + q_1\dot{\varepsilon} \tag{8}$$

where,

$$p_1 = \frac{R_{1a}}{E_{1a}} \tag{9}$$

$$q_0 = E_{0a} \tag{10}$$

$$q_1 = R_{1a}\frac{E_{0a} + E_{1a}}{E_{1a}}. \tag{11}$$

Considering model (b) in Fig. 3 using subscript "b" we have,

$$p_1 = \frac{R_{1b}}{E_{0b} + E_{1b}} \tag{12}$$

$$q_0 = \frac{E_{1b}E_{0b}}{E_{0b} + E_{1b}} \tag{13}$$

$$q_1 = \frac{R_{1b}E_{0b}}{E_{0b} + E_{1b}}. \tag{14}$$

2.2.2 Three-Parameter Models in the Standard Test

Considering Fig. 1 when subjected to a creep test the three-parameter model behaves by responding with a strain as follows:

$$\varepsilon(t) = \sigma_0 J(t) \tag{15}$$

where,

$$J(t) = \frac{1}{q_0}\left[1 - \left(1 - \frac{p_1 q_0}{q_1}\right)e^{-\frac{q_0}{q_1}t}\right] \tag{16}$$

is known as the creep compliance.

Furthermore, considering a relaxation test in the context of Fig. 1, we have the stress response:

$$\sigma(t) = \varepsilon_0 E(t) \tag{17}$$

where,

$$E(t) = \left[q_0 - \left(q_0 - \frac{q_1}{p_1}\right)e^{-\frac{1}{p_1}t}\right] \tag{18}$$

is the relaxation function.

It can be inferred from Fig. 1 that both 3-parameter models, as depicted in Fig. 4, will initially respond to a step-like change in stress and will then, subsequently exhibit asymptotically elastic behavior:

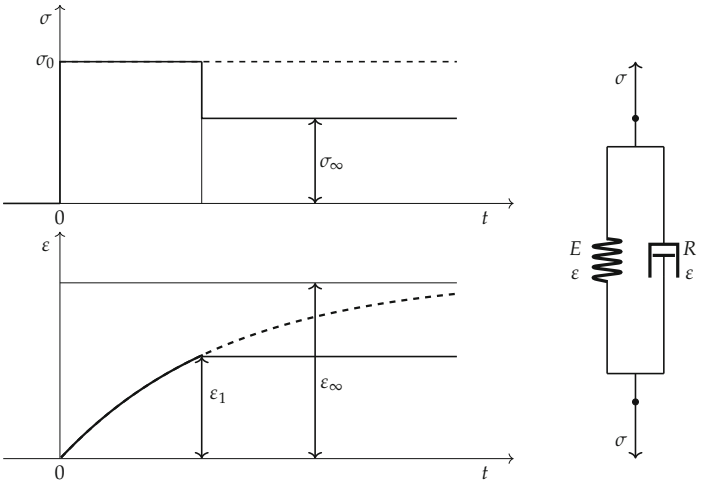

Fig. 4 Standard Test on the Kelvin-Voigt 2 parameter model

$$\varepsilon_0 = \varepsilon(0^+) = \sigma_0 \frac{p_1}{q_1} = \frac{\sigma_0}{E_0} \tag{19}$$

and

$$\lim_{t\to\infty} \varepsilon(t) = \frac{\sigma_0}{q_0} = \frac{\sigma_0}{E_\infty} \tag{20}$$

where $E_0 = E(0^+)$ denotes the initial modulus and $E_\infty = E(\infty)$ is the equilibrium modulus. As long as the strain is held constant, the material will continue to relax up until the point when $\sigma_\infty = \varepsilon_0 E_\infty \leq \sigma_0 = \varepsilon_0 E_0$. This can be seen in Fig. 1 above.

Figure 4 above graphically shows the temporal stress and strain relations in the two parameter Kelvin-Voigt model for comparison purposes. Also, the material law as per Eq. (8) has the following factors in this case:

$$p_1 = 0 \tag{21}$$

$$q_0 = E \tag{22}$$

$$q_1 = R. \tag{23}$$

The creep compliance and relaxation functions $J(t)$ and $E(t)$ are given by the following relations:

$$J(t) = \frac{1}{q_0}\left(1 - e^{-\frac{q_0}{q_1}t}\right) \tag{24}$$

$$E(t) = q_0. \tag{25}$$

The two-parameter model does not allow for a spontaneous elastic strain $\varepsilon_0 \neq 0$. However, the relaxation process is spontaneous with an initial modulus of $E_0 \to \infty$.

2.2.3 N-Parameter Model

A more accurate description of the actual system behavior can be achieved by modifying models described previously to incorporate more parameters. This of course, entails more effort.

Figure 5 shows a rheological N-parameter model for a given material. For a given set of parameters, E_0, E_k and $R_k (k = 1, \ldots, K = (N-1)/2)$ of N springs and dampers, equilibrium requires that the total strain ε and the spring extensions ε_k satisfy the following relation in the model:

$$\sigma = E_0\, \varepsilon + \sum_{k=1}^{K} E_k\, \varepsilon_k \tag{26}$$

and at the nodes between the springs and dampers

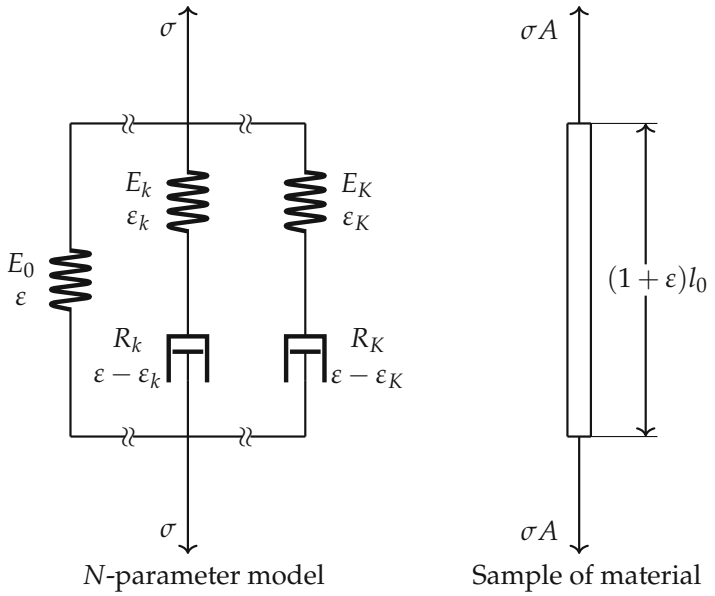

Fig. 5 Rheological model of viscoelastic material behavior

$$E_k\,\varepsilon_k = R_k\,(\dot{\varepsilon} - \dot{\varepsilon}_k). \tag{27}$$

From the point of view of continuum mechanics, the material behavior is characterized using two variables, viz., the external variable ε and the internal variables ε_k. The internal variables ε_k satisfy the relaxation equations given by Eq. (27). We can now eliminate the internal strains ε_k and then differentiate with respect to time, t, yields the material law as shown below:

$$\sigma + p_1\,\dot{\sigma} + \ldots\, p_m\,\sigma^{(m)} = q_0\,\varepsilon + q_1\,\dot{\varepsilon} + \ldots + q_n\,\varepsilon^{(n)} \tag{28}$$

where $m = n = \dfrac{N-1}{2}$.

2.2.4 Operator Notation

Other rheological models have different orders $m \neq n$ of the derivatives in the associated material equations. When using the differential operators

$$P = \sum_{k=0}^{m} p_k \frac{\mathrm{d}^k}{\mathrm{d}t^k} \qquad\qquad Q = \sum_{k=0}^{n} q_k \frac{\mathrm{d}^k}{\mathrm{d}t^k} \tag{29}$$

Equation (28) in the generalized form is given below:

$$P\,\sigma = Q\,\varepsilon. \tag{30}$$

A more generalized form of the above equation replaces the integer-order time derivatives by fractional-order derivatives:

$$P = \sum_{k=0}^{m} p_k \frac{\mathrm{d}^{\alpha_k}}{\mathrm{d}t^{\alpha_k}} \qquad\qquad Q = \sum_{k=0}^{n} q_k \frac{\mathrm{d}^{\beta_k}}{\mathrm{d}t^{\beta_k}} \tag{31}$$

where $\alpha_k \in R_0^+$ and $\beta_k \in R_0^+$, [1, 36, 54]. The definition of a fractional-order derivative is as given below:

$$\frac{\mathrm{d}^{\alpha} x(t)}{\mathrm{d}t^{\alpha}} = \frac{1}{\Gamma(n-\alpha)} \frac{\mathrm{d}^{n}}{\mathrm{d}t^{n}} \int_0^t \frac{x(t-\tau)}{\tau^{\alpha-n+1}}\,\mathrm{d}\tau \tag{32}$$

where

$$n \in N, n-\alpha > 0 \qquad\qquad \Gamma(1-\alpha) = \int_0^{\infty} e^{-x} x^{-\alpha} \mathrm{dx}. \tag{33}$$

The gamma term in Eq. (33) is called *Gamma Function*.

2.2.5 Creep and Relaxation

Substituting the integrals of the relaxation equations in Eq. (27) for the internal strains, ε_k, in Eq. (26) results in a description of the material behavior by means of the so-called *memory integrals*. Applying the boundary condition $\varepsilon_k(-\infty) = 0$, the integrals are given by

$$\varepsilon_k(t) = \int_0^{\infty} e^{-\frac{\tau}{T_k}}\,\dot{\varepsilon}(t-\tau)\mathrm{d}\tau. \tag{34}$$

The quantity $T_k = R_k/E_k$ is the relaxation time corresponding to the k^{th} spring-damper element. At this point, the material equation can be obtained by inserting Eq. (34) into Eq. (26). This yields:

$$\sigma(t) = E_{(\infty)}\,\varepsilon(t) + \int_0^{\infty} \tilde{E}(\tau)\dot{\varepsilon}(t-\tau)\mathrm{d}\tau \tag{35}$$

where the function $\tilde{E}(\tau)$ is given by:

$$\tilde{E}(\tau) = \sum_{k-1}^{K} E_k\, e^{-\frac{\tau}{T_k}}. \tag{36}$$

Equation (36) describes the monotonous fading of the *material memory* for the past deformation events, $\varepsilon(t)$. $\tilde{E}(\tau)$ shows asymptotic behavior, i.e., $\lim_{t\to\infty} \tilde{E}(\tau) = 0$. Equation (35) also describes relaxation of the stress $\sigma(t)$ after a step-like change in strain, $\varepsilon(t) = \varepsilon_0\, 1(t)$ according to the equation:

$$\sigma(t) = (E_{(\infty)} + \tilde{E}(t))\varepsilon_0 = E(t)\,\varepsilon_0. \tag{37}$$

It can be seen from the above figure that the material parameters $E_{(\infty)}$, E_k, R_k can be determined from measured relaxation function $E(t)$. Equation (35) may be expressed as a *relaxation type* equation by utilizing the relaxation function $E(t)$ as follows:

$$\sigma(t) = \int_{-\infty}^{t} E(t-\tau)\,\dot{\varepsilon}(\tau)\,\mathrm{d}\tau. \tag{38}$$

Also on the other hand, solving the equation for strain yields a *creep type* material law given by the following equation:

$$\varepsilon(t) = \int_{-\infty}^{t} J(t-\tau)\,\dot{\sigma}(\tau)\,\mathrm{d}\tau. \tag{39}$$

The creep function $J(t)$ describes creep after a step-like change in stress, $\sigma(t) = \sigma_0 1(t)$, as shown in Fig. 6. The creep and relaxation functions $J(t)$ and $E(t)$ are related to each other via the following linear integral relation:

$$\frac{\mathrm{d}}{\mathrm{d}t}\int_0^t J(t-\tau)\,E(\tau)\,\mathrm{d}\tau = 1. \tag{40}$$

If the strain is initially zero, i.e., $\varepsilon(t) = 0$ for $t < 0$ we can rewrite Eq. (38) as follows:

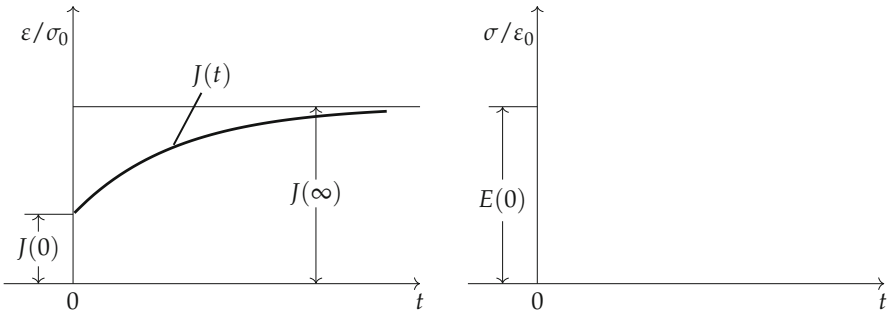

Fig. 6 Creep and Relaxation Functions

$$\sigma(t) = E(t)\,\varepsilon(0) + \int_0^t E(t-\tau)\,\dot{\varepsilon}(\tau)\,\mathrm{d}\tau. \tag{41}$$

Also, a consequence of Eq. (39) is that for $\sigma(t) = 0$ and for $t < 0$

$$\varepsilon(t) = J(t)\,\sigma(0) + \int_0^t J(t-\tau)\,\dot{\sigma}(\tau)\,\mathrm{d}\tau. \tag{42}$$

2.2.6 Harmonic Stress and Strain Function

When the strain is harmonic and time dependent:

$$\varepsilon(t) = \hat{\varepsilon}\,\cos(\Omega t + \varphi_{0\varepsilon}) = \mathrm{Re}\left\{\underline{\hat{\varepsilon}}\,e^{i\Omega t}\right\} \tag{43}$$

the material equation, i.e., Eq. (38) yields the following phase-shifted expression for steady-state stress:

$$\sigma(t) = \hat{\sigma}\,\cos(\Omega t + \varphi_{0\sigma}) = \mathrm{Re}\left\{\underline{\hat{\sigma}}\,e^{i\Omega t}\right\} \tag{44}$$

with the complex amplitudes $\underline{\hat{\varepsilon}} = \hat{\varepsilon}\;e^{i\varphi_{0\varepsilon}}$ and $\underline{\hat{\sigma}} = \hat{\sigma}\;e^{i\varphi_{0\sigma}}$. It is now possible to define a complex modulus. The real part is denoted as $E'(\Omega)$ and is called the *storage modulus*. The imaginary part on the other hand is known as the *loss modulus*, and is denoted by the $E''(\Omega)$. Therefore, we have:

$$\underline{E}(\Omega) = E'(\Omega) + i\,E''(\Omega). \tag{45}$$

The relation between the complex stress and strain is given by the following relation:

$$\underline{\hat{\sigma}} = \underline{E}(\Omega)\,\underline{\hat{\varepsilon}}. \tag{46}$$

Equation (38) can be utilized to obtain a relation between the complex modulus, $\underline{E}(\Omega)$ and the relaxation function, $E(t)$. For this, we use the approach of Eq. (44):

$$E'(\Omega) = E_0 + \Omega\int_0^\infty \tilde{E}(\tau)\;\sin\Omega\tau\,\mathrm{d}\tau \qquad E''(\Omega) = \Omega\int_0^\infty \tilde{E}(\tau)\cos\Omega\tau\,\mathrm{d}\tau. \tag{47}$$

The complex modulus can also be formulated using the so-called *loss factor*, $\chi(\Omega)$

$$\chi(\Omega) = \frac{E''(\Omega)}{E'(\Omega)}. \tag{48}$$

The complex modulus thereby is given by the following expression:

$$\underline{E}(\Omega) = E'(\Omega)\,[1 + i\,\chi(\Omega)]. \tag{49}$$

Equation (43) into Eq. (49) results in the expression:

$$\chi(\Omega) = \tan\delta(\Omega) \tag{50}$$

where $\delta(\Omega)$ is essentially the phase difference between the stress and the strain: $\delta(\Omega) = \varphi_{0\sigma} - \varphi_{0\varepsilon}$. The rheological model shown in Fig. 5 comprises the storage and the loss modulus as per the following relations:

$$E'(\Omega) = E_0 + \sum_{k=1}^{K} E_k \frac{\Omega^2 {T_k}^2}{1 + \Omega^2 {T_k}^2} \tag{51}$$

and

$$E''(\Omega) = \sum_{k=1}^{K} E_k \frac{\Omega T_k}{1 + \Omega^2 {T_k}^2}. \tag{52}$$

In the case of a low-frequency harmonic process, an approximation for the complex modulus can be used, which is given as follows and is equivalent to the 2-parameter Kelvin-Voigt model shown in Fig. 4:

$$\underline{E}(\Omega) = E_0 + i\Omega R \qquad \text{with} \quad R = \sum_{k=1}^{K} R_k. \tag{53}$$

The damping work per unit volume per cycle is given by:

$$W_{Dh}(\Omega) = \pi E''(\Omega)\hat{\varepsilon}^2 = \pi\chi(\Omega)E'(\Omega)\hat{\varepsilon}^2 = \pi\chi(\Omega)\frac{E'(\Omega)}{|\underline{E}(\Omega)|^2}\,\hat{\sigma}^2. \tag{54}$$

With the exception of the normalizing constant $\pi\hat{\varepsilon}^2$, the loss modulus $E''(\Omega)$ and the damping work per unit volume per cycle $W_{dh}(\Omega)$, are identical.

The frequency dependence of the measured damping work under harmonic excitation can be approximated in a given frequency range by appropriate choice of the model parameters, E_0, E_k, and R_k.

The storage and loss moduli are shown in Fig. 7 for the 3-parameter model (E_0, E_1, and R_1) and the 2-parameter Kelvin-Voigt model. Figure 8 shows the characteristics in the hysteresis curve, assuming a linear-viscoelastic material.

2.2.7 Three-Dimensional Stress State

Analogous to the 1-D case, the mathematical and rheological models may be extended to the three-dimensional stress state. The symmetric stress tensor (σ_{jl})

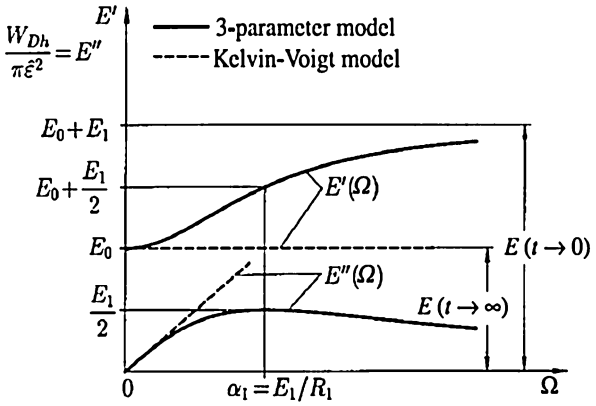

Fig. 7 Storage and loss moduli of the 3-parameter model and the 2-parameter Kelvin-Voigt model (source: VDI guideline 3830)

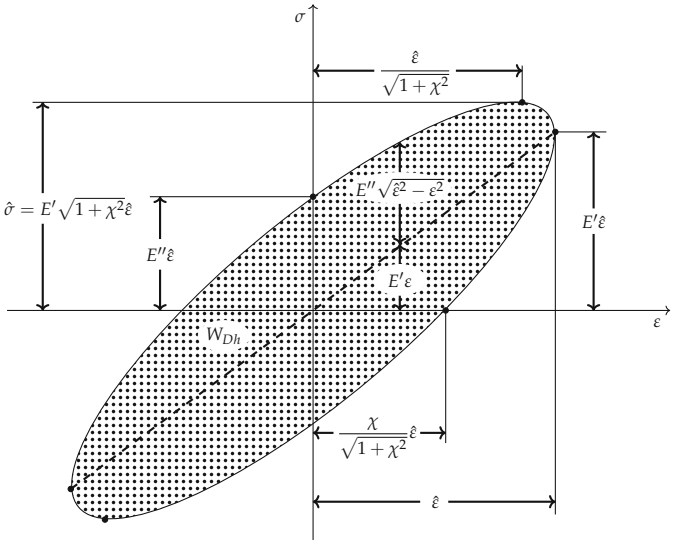

Fig. 8 Hysteresis characteristics for linear viscoelastic material behavior

can be considered to be comprised of a spherically symmetric, i.e., hydrostatic component ($s\,\delta_{jl}$)and the stress deviator (s_{jl})

$$\begin{pmatrix} \sigma_{11} & \sigma_{12} & \sigma_{13} \\ \sigma_{21} & \sigma_{22} & \sigma_{23} \\ \sigma_{31} & \sigma_{32} & \sigma_{33} \end{pmatrix} = s \begin{pmatrix} 1 & 0 & 0 \\ 0 & 1 & 0 \\ 0 & 0 & 1 \end{pmatrix} + \begin{pmatrix} s_{11} & s_{12} & s_{13} \\ s_{21} & s_{22} & s_{23} \\ s_{31} & s_{32} & s_{33} \end{pmatrix} \tag{55}$$

where the mean stress s is:

$$s = \frac{1}{3}\,(\sigma_{11} + \sigma_{22} + \sigma_{33}) \tag{56}$$

Analogous to the stress, the strain tensor (ε_{jl}):

$$\begin{pmatrix} \varepsilon_{11} & \varepsilon_{12} & \varepsilon_{13} \\ \varepsilon_{21} & \varepsilon_{22} & \varepsilon_{23} \\ \varepsilon_{31} & \varepsilon_{32} & \varepsilon_{33} \end{pmatrix} = e \begin{pmatrix} 1 & 0 & 0 \\ 0 & 1 & 0 \\ 0 & 0 & 1 \end{pmatrix} + \begin{pmatrix} e_{11} & e_{12} & e_{13} \\ e_{21} & e_{22} & e_{23} \\ e_{31} & e_{32} & e_{33} \end{pmatrix} \tag{57}$$

with the mean strain, as with stress given by the relation,

$$e = \frac{1}{3}(\varepsilon_{11} + \varepsilon_{22} + \varepsilon_{33}). \tag{58}$$

The strain deviator (e_{jl}) characterizes the deformation in the system. The volume dilatation, i.e., the change in volume is $3e$. It is to be noted that only five of the six deviator coordinates are independent in each case. This is a result of the condition that

$$s_{11} + s_{22} + s_{33} = 0 \qquad \text{and} \qquad e_{11} + e_{22} + e_{33} = 0. \tag{59}$$

Using the differential operator, the following statements are true for the case of isotropic materials:

- for the deviator components ($j, l = 1, 2, 3$)

$$P_1\, s_{jl} = Q_1\, e_{jl} \tag{60}$$

- and for the mean stress and mean strain

$$P_2\, s = Q_2\, e. \tag{61}$$

For integer time derivatives, the differential operators are defined as follows:

$$P_1 = \sum_{k=0}^{m_1} p_{1k}\, \frac{\mathrm{d}^k}{\mathrm{d}t^k} \qquad\qquad Q_1 = \sum_{k=0}^{n_1} q_{1k}\, \frac{\mathrm{d}^k}{\mathrm{d}t^k} \tag{62}$$

$$P_2 = \sum_{k=0}^{m_2} p_{2k}\, \frac{\mathrm{d}^k}{\mathrm{d}t^k} \qquad\qquad Q_2 = \sum_{k=0}^{n_2} q_{2k}\, \frac{\mathrm{d}^k}{\mathrm{d}t^k}. \tag{63}$$

As for fractional derivatives,

$$P_1 = \sum_{k=0}^{m_1} p_{1k} \frac{\mathrm{d}^{\alpha_{1k}}}{\mathrm{d}t^{\alpha_{1k}}} \qquad Q_1 = \sum_{k=0}^{n_1} q_{1k} \frac{\mathrm{d}^{\beta_{1k}}}{\mathrm{d}t^{\beta_{1k}}} \tag{64}$$

$$P_2 = \sum_{k=0}^{m_2} p_{2k} \frac{\mathrm{d}^{\alpha_{2k}}}{\mathrm{d}t^{\alpha_{2k}}} \qquad Q_2 = \sum_{k=0}^{n_2} q_{2k} \frac{\mathrm{d}^{\beta_{2k}}}{\mathrm{d}t^{\beta_{2k}}}. \tag{65}$$

Because of isotropy, P_1 and Q_1 are identical for all deviator coordinates, and all quantities s_{jl} have the same relaxation times, T_k. From Eq. (60), we can see that simulation of the material model requires a unified rheological model for the six deviator coordinates. In addition to this, an additional model is required for volume dilatation as per Eq. (61).

Three cases are relevant:

(a) For *elastic materials* with shear modulus G, bulk modulus K, and Poisson's ratio ν, the differential operators reduce to constant factors:

$$P_1 = P_2 = 1 \tag{66a}$$

$$Q_1 = 2G \tag{66b}$$

$$Q_2 = 3K = G\,\frac{2(1+\nu)}{1-2\nu}. \tag{66c}$$

(b) In case of *elastic volume* change, energy is lost via deformations. However, there are no losses due to change in volume. Here

$$P_2 = 1 \tag{67a}$$

$$Q_2 = 3K. \tag{67b}$$

(c) When stress is *mono-axial*, the operators P and Q in Eq. (29) are related to P_1, Q_1, P_2, and Q_2 as follows:

$$P = P_2\,Q_1 + 2Q_2P_1 \qquad \text{and} \tag{68a}$$

$$Q = 3\,Q_2Q_1. \tag{68b}$$

When written down in terms of memory integrals, the material equations of the *relaxation type* are as given below:

$$s_{jl}(t) = \int_{-\infty}^{t} E_1(t-\tau)\dot{e}_{jl}(\tau)\,\mathrm{d}\tau \quad \text{for} \quad j,l = 1,2,3 \tag{69a}$$

$$s(t) = \int_{-\infty}^{t} E_2(t-\tau)\dot{e}(\tau)\mathrm{d}\tau \tag{69b}$$

where $E_1(t)$ and $E_2(t)$ are the memory functions. If we solve for strains, we obtain the material equations of *creep type*:

$$e_{jl}(t) = \int_{-\infty}^{t} J_1(t-\tau)\dot{s}_{jl}(\tau)\,\mathrm{d}\tau \quad \text{for} \quad j,l = 1,2,3 \tag{70a}$$

$$e(t) = \int_{-\infty}^{t} J_2(t-\tau)\dot{s}(\tau)\mathrm{d}\tau \tag{70b}$$

where $J_1(t)$ and $J_2(t)$ are the creep functions.

In case of harmonic time histories:

$$s_{jl}(t) = Re(\underline{\hat{s}}_{jl}\, e^{i\Omega t}) \quad \text{for} \quad j,l = 1,2,3 \tag{71a}$$

$$e_{jl}(t) = Re(\underline{\hat{e}}_{jl}\, e^{i\Omega t}) \quad \text{for} \quad j,l = 1,2,3 \tag{71b}$$

$$s(t) = Re(\underline{\hat{s}}\, e^{i\Omega t}) \tag{71c}$$

$$e(t) = Re(\underline{\hat{e}}\, e^{i\Omega t}) \tag{71d}$$

the *complex shear modulus*

$$\underline{G}(\Omega) = G'(\Omega) + iG''(\Omega) \tag{72}$$

relates the complex deviator amplitudes, $\underline{\hat{s}}_{jl}$ and $\underline{\hat{e}}_{jl}$ as follows

$$\underline{\hat{s}}_{jl} = 2\underline{G}(\Omega)\,\underline{\hat{e}}_{jl} \quad \text{for} \quad j,l = 1,2,3 \tag{73}$$

and the *complex bulk modulus*

$$\underline{K}(\Omega) = K'(\Omega) + iK''(\Omega) \tag{74}$$

relates the complex amplitudes $\underline{\hat{s}}$ and $\underline{\hat{e}}$ of the mean stress and strain, respectively

$$\underline{\hat{s}} = 3\underline{K}\,(\Omega)\,\underline{\hat{e}}. \tag{75}$$

Using the Equations (61) through (65) in Eq. (59), the relation between the modulli $G'(\Omega)$, $G''(\Omega)$, $K'(\Omega)$, $K''(\Omega)$, and the memory functions $E_1(t)$ and $E_2(t)$ can be deduced as follows:

$$G'(\Omega) = \frac{1}{2}E_1(\infty) + \frac{\Omega}{2}\int_0^{\infty}[E_1(\tau) - E_1(\infty)]\sin\Omega\tau\,\mathrm{d}\tau \tag{76a}$$

$$G''(\Omega) = \frac{\Omega}{2}\int_0^{\infty}[E_1(\tau) - E_1(\infty)]\cos\Omega\tau\,\mathrm{d}\tau \tag{76b}$$

$$K'(\Omega) = \frac{1}{3}E_2(\infty) + \frac{\Omega}{3}\int_0^\infty [E_2(\tau) - E_2(\infty)] \sin \Omega\tau \, \mathrm{d}\tau \tag{76c}$$

$$K''(\Omega) = \frac{\Omega}{3}\int_0^\infty [E_2(\tau) - E_2(\infty)] \cos \Omega\tau \, \mathrm{d}\tau. \tag{76d}$$

It thus implies that

$$\chi_1(\Omega) = \frac{G''(\Omega)}{G'(\Omega)} \qquad \text{and} \qquad \chi_2(\Omega) = \frac{K''(\Omega)}{K'(\Omega)} \tag{77}$$

are the loss factors for deviatoric deformations and changes in volume.

2.2.8 Temperature Dependence of Viscoelastic Material Properties

Up until now, we discussed isothermal visco-elastic changes of state or neglected temperature dependence of material properties when dealing with non-isothermal phenomena. Material properties of thermoplastics are highly temperature dependent especially near the glass transition temperature.

Creep and relaxation test under conditions of varying temperature show similar dependencies of mechanical properties. This can be seen in Fig. 9, shown below:

Storage modulus E' and the material loss factor χ are also temperature dependent as evident form Fig. 10. The short-term domain in Fig. 11 and the respective high-frequency domain in Fig. 10 pertain to the vitreous state. The rubbery state in the long-term and low-frequency domain is marked by a borderline of a narrow temperature range around the glass transition temperature T_g. T_g is a reference quantity. Its corresponding quantity in the frequency axis is ω_g. As evident from

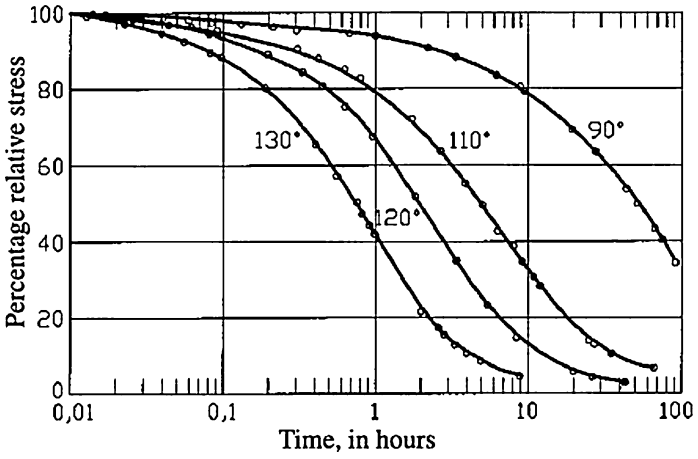

Fig. 9 Stress relaxation of a rubber material (Vulcollan A) at four temperatures (source: VDI guideline 3830)

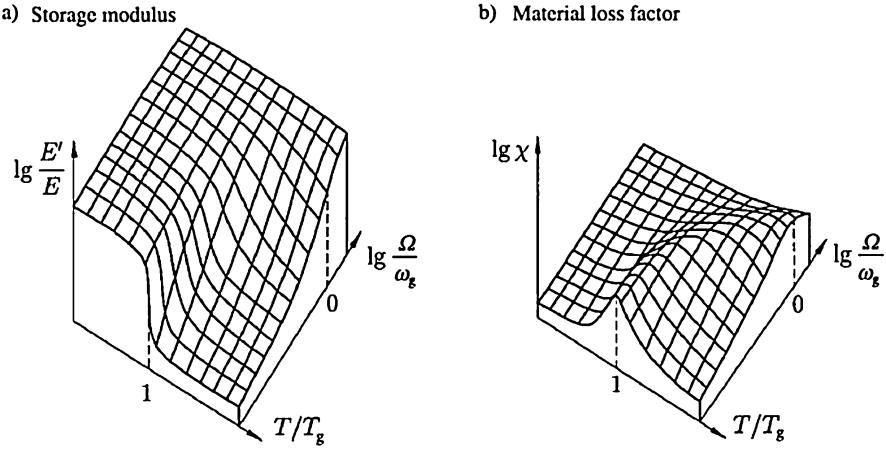

Fig. 10 Examples of the temperature and frequency dependence of storage modulus and material loss factor (source: VDI guideline 3830)

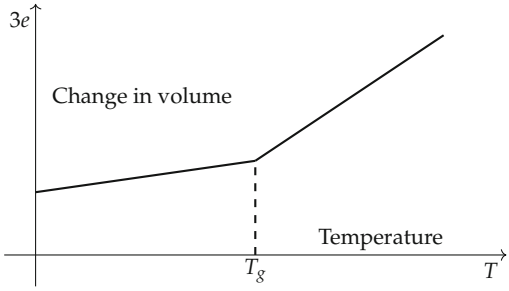

Fig. 11 Change in volume as a function of temperature

Fig. 11, the glass transition temperature is mostly determined via the change in volume.

2.2.9 Thermo-Rhoelogical Simple Materials

Experiments show [8, 26] that a wide range of viscoelastic materials exhibit a *thermo-rheological simple* behavior [55, 56]. The relaxation function, $E(t, T_0)$ and Creep function, $J(t, T_0)$ at a given reference temperature, T_0, meet the below mentioned conditions:

$$E(t, T) = E(t\varphi(T), T_0) \quad \text{and} \tag{78a}$$

$$J(t, T) = J(t\varphi(T), T_0). \tag{78b}$$

This means that the material functions for the temperature T are obtained from those at the temperature T_0 by substituting the reduced time, $t\varphi(T)$, for the time t. The *shift function* $\varphi(T)$ accounting for the time distortion fulfills the conditions:

$$\varphi(T_0) = 1 \quad \text{and} \quad \frac{\mathrm{d}\varphi(T)}{\mathrm{d}T} > 0. \tag{79}$$

This material property must be determined experimentally. The temperature-dependent complex moduli $\underline{E}(\Omega, T)$ at temperature T result from the moduli $\underline{E}(\Omega, T_0)$ at the reference temperature T_0 by substituting $\Omega/\varphi(T)$ for Ω. The frequency shift function $a(T)$, therefore, is the reciprocal of the time shift function $\varphi(T)$.

Time and frequency shifts will not change the asymptotic values of the mechanical material properties but will affect the transition range. A simple approach for the time shift function $\varphi(T)$ is given as [26]:

$$\log \varphi(T) = \frac{C_1(T - T_0)}{C_2 + (T - T_0)}. \tag{80}$$

This function is called the WLF function after the names of Williams, Landel, and Ferry. It is often used with numerical values (Fig. 12).

$$\log \varphi(T) = \frac{8.86(T - T_0)}{101.5K + (T - T_0)} \qquad \text{where} \quad T_0 \approx T_g + 50K. \tag{81}$$

More details can be found in the literature, see, e.g., [26, 12]

2.3 Nonlinear Models

Under conditions of large deformations, all materials show nonlinear behavior, and the stresses and strains cannot be related to each other by linear equations and also superposition principle fails to apply [21, 36].

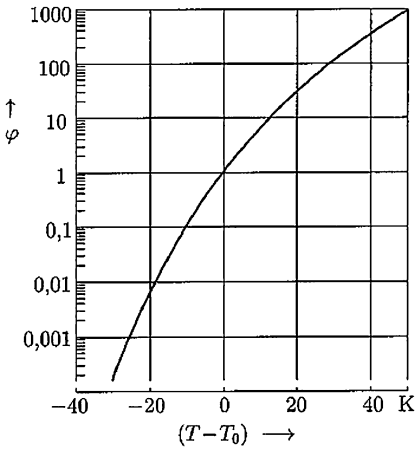

Fig. 12 Time shift function (WLF function) (source: VDI guideline 3830)

Mathematical models of continuum mechanics exist. It allows conditions of triaxial stress states and also arbitrary time histories. They result in nonlinear material laws in the form of an expansion of Equations (69) and (70) and Equations (38) and (39), respectively. Series expansions of the memory function terms lead to sums of simple and multiple integrals which are of little practical use as they hardly find any application in vibration problems [46].

In addition, rheological models or calculation models exist, each with a limited range of application. The parameters pertaining to these models are identified in measured results such as hysteresis curves, memory, or creep functions. This chapter will give examples of such models, which apply to the uniaxial stress condition.

2.3.1 Models for Static Hysteresis

The hysteresis curve of many materials (mostly metals), when subjected to harmonic tensile strain $\varepsilon(t) = \hat{\varepsilon}\cos(\Omega t + \varphi_{0\varepsilon})$, will have the distorted shape shown in Fig. 2. In case the stress amplitude exceeds about 1/20 of the fatigue strength under alternating stress, the shape of the hysteresis curve and the damping work per unit volume have almost no dependence on frequency, $W_{Dh} = W_{Dh}(\hat{\varepsilon})$ and therefore called *static hysteresis* or *velocity independent behavior*. While damping work W_{Dh} per unit volume for linear-viscoelasticity is proportional to $\hat{\varepsilon}^2$, under nonlinearity, this is not the case.

Point-Symmetrical Hysteresis Without Reversal Points

If the hysteresis curve measured under harmonic strain is point symmetrical and has no reversal points, the Masing model as shown in Fig. 13 can be used. This is the simplest model for such an application. It consists of massless linear spring elements and massless Coulomb friction elements.

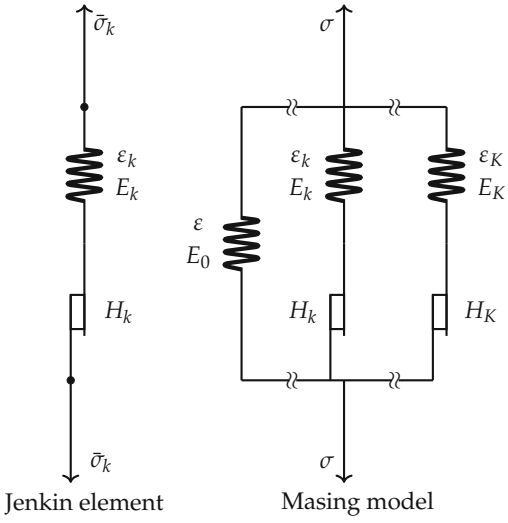

Fig. 13 Phenomenological model for static hysteresis

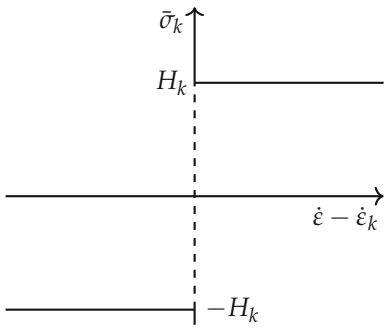

Fig. 14 Characteristic of the kth Coulomb element

A combination of one linear spring and a Coulomb element in series is termed as a Jenkins element. Each Coulomb element transmits a "stress" $\bar{\sigma}_k$ whose magnitude is H_k or less. Refer Fig. 14

The total stress is given by:

$$\sigma = E_0\,\varepsilon + \sum_{k=1}^{K} \bar{\sigma}_k. \tag{82}$$

If the kth Coulomb element slips, in that case:

$$\bar{\sigma}_k = H_k \operatorname{sgn} \dot{\varepsilon} \quad \text{and} \quad \dot{\varepsilon_k} = 0 \tag{83}$$

The end of the slip phase is marked by the change of sign of the strain velocity, $\dot{\varepsilon}$ and then the kth element sticks. If ε^+ and $\dot{\varepsilon}^+$ denote the strain and strain time derivative, immediately at the beginning of the stick range, then the following can be written:

$$\bar{\sigma}_k = E_k\,(\varepsilon - \varepsilon^+) - H_k \operatorname{sgn} \dot{\varepsilon}^+ \quad \text{and} \quad \dot{\varepsilon}_k = \dot{\varepsilon} \tag{84}$$

as long as $|\bar{\sigma}_k| = H_k$. The next slip phase starts when, $|\bar{\sigma}_k| = H_k$ with $|\varepsilon|$ growing at that point in time. The stress-strain curves of the overall model consist of piecewise linear polygon lines.

Figure 15 shows the hysteresis curve for a strain $\varepsilon(t) = \hat{\varepsilon} \cos(\Omega t + \varphi_{0\varepsilon})$ in the steady state which, depending on the initial conditions, is only reached after an instationary phase. In this case, only the Coulomb element with parameter ratios

$$\frac{H_k}{E_k} < \hat{\varepsilon} \tag{85}$$

dissipate energy; the others always stick. The damping work per unit volume per period, W_{Dh}, is:

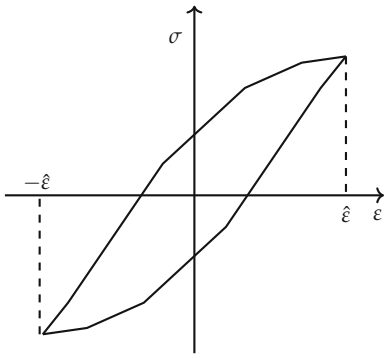

Fig. 15 Qualitative representation of the hysteresis of the Masing model shown in Fig. 13 assuming harmonic strain

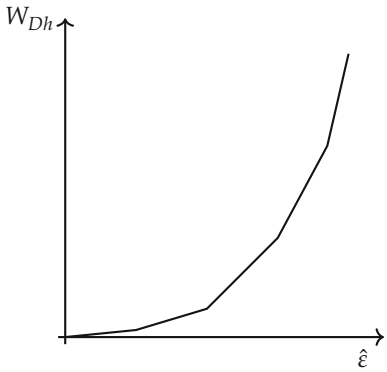

Fig. 16 Qualitative curve of loss work, W_{Dh}, as a function of the strain amplitude, $\hat{\varepsilon}$, under harmonic strain

$$W_{Dh}\,(\hat{\varepsilon}) = \sum_{k=1}^{k^*} 4\,H_k\,(\hat{\varepsilon} - \frac{H_k}{E_k}). \tag{86}$$

Contributions to the above sum only come from elements that fulfill the condition in Eq. (85). The function $W_{Dh}\,(\hat{\varepsilon})$ forms a polygon line linking the nodes $\hat{\varepsilon} = H_k/E_k, k = 1, \ldots, k^*$. As the number of elements increases, the quality of the approximation improves (Fig. 16).

The Masing model, however, has two disadvantages: stiffness discontinuities and the need to distinguish between phases of slip and stick.

Nonetheless, we can modify the model. The modification replaces Eqs. (83) and (84), while retaining Eq. (82), by evolution equations for the internal variables [5].

$$\dot{\bar{\sigma}}_k = E_0\,\dot{\varepsilon}\left(1 - \frac{1}{2}(1 + \operatorname{sgn}(\dot{\varepsilon}\,\bar{\sigma}_k))\left|\frac{\bar{\sigma}_k}{H_k}\right|^m\right). \tag{87}$$

In the above equation, m is always a positive value. As m increases the quality of approximation of Eqs. (83) and (84) improve.

The curvilinear method [43] for pure shear distortion, γ, separates the shear stress, τ, into a linear part $G\gamma$, and a frictional part, τ_R:

$$\tau = G\gamma + \tau_R. \tag{88}$$

After each reversal point, γ_U, of the strain, the frictional part, τ_R, is approximated using the two model parameters R and ρ, by the following equation:

$$\tau_R = R \operatorname{sgn} \dot{\gamma} \ln(1 + \rho|\gamma(t) - \gamma_U|). \tag{89}$$

This method dispenses with the integration of evolution equations. Instead, the reversal points, γ_{Ui}, of the distortion, i.e., the zero crossings of $\dot{\gamma}$, must be determined over and over, and the part τ_R must be determined by consecutive appending of line elements.

General Shape of Hysteresis Curves

The characterization of the behavior of materials whose hysteresis curves have reversal points, or which are unsymmetrical, requires more general models. One possible method consists in the generalization of Eqs. (82) and (87) [5]:

$$\sigma = E(\varepsilon)\varepsilon + \sum_{k=1}^{K} \bar{\sigma}_k \tag{90a}$$

$$\dot{\bar{\sigma}}_k = \dot{\varepsilon} \left(A_k(\varepsilon) - (\beta_k + \alpha_k \operatorname{sgn}(\dot{\varepsilon}\, \bar{\sigma}_k)) \left| \frac{\bar{\sigma}_k}{H_k(\varepsilon)} \right|^m \right). \tag{90b}$$

The calculation model contains distortion dependent stiffnesses, $E(\varepsilon) > 0$, $A_k(\varepsilon) > 0$ and stick forces $H_k(\varepsilon)$ as well as the real constants α_k, β_k, and m. This ensures a good potential for matching to measured results.

2.3.2 Models for Nonlinear Viscoelasticity

There are a deviation from the elliptical shape of the hysteresis curve of a viscoelastic solid subjected to a tensile test with harmonic strains and large amplitudes, $\hat{\varepsilon}$, see Fig. 17.

In the general case, the resulting hysteresis curve will not even be a closed loop. Where closed hysteresis loops exist, the damping work, W_{Dh}, depends on the angular frequency, Ω, and the strain amplitude, $\hat{\varepsilon}$, i.e., $W_{Dh} = W_{Dh}(\Omega, \hat{\varepsilon})$. The loss work per period for a viscoelastic solid is:

$$\lim_{\Omega \to 0} W_{Dh}(\Omega, \hat{\varepsilon}) = 0. \tag{91}$$

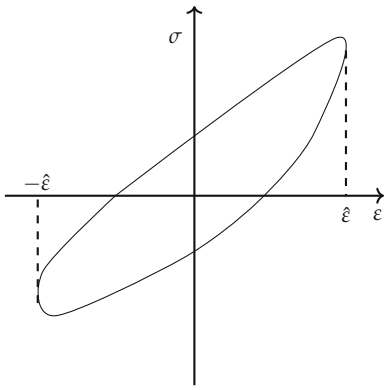

Fig. 17 Stress Strain curve of a nonlinear viscoelastic material under harmonic strain

The following models apply to arbitrary time histories of monoaxial stress conditions and are a modification of the integral distortion laws used in the theory of linear viscoelasticity [54, 60]:

If the longitudinal strain, $\varepsilon(t)$, is given:

$$\sigma(t) = \int_0^t \left[h_0(\varepsilon(\tau))E_0 + h_1(\varepsilon(\tau)) \sum_{k=1}^{K} E_k e^{-\frac{t-\tau}{\tau_k}} \right] \frac{\mathrm{d}\varepsilon(\tau)}{\mathrm{d}\tau} \mathrm{d}\tau \tag{92}$$

where E_0 and E_k are constant material parameters having the dimension of Young's moduli, τ_k are the discrete relaxation times, and h_0 and h_1 are the strain dependent nonlinearity functions. If the longitudinal stress, $\sigma(t)$, is given:

$$\varepsilon(t) = \int_0^t \left[g_0(\sigma(\tau))J_0 + g_1(\sigma(\tau)) \sum_{k=1}^{K} J_k \left(1 - e^{-\frac{t-\tau}{\tau_k}}\right) \right] \frac{\mathrm{d}\sigma(\tau)}{\mathrm{d}\tau} \mathrm{d}\tau \tag{93}$$

where J_0 and J_k are constant material parameters, τ_k are the discrete relaxation times, and g_0 and g_1 are the stress-dependent nonlinearity functions. Equations (92) and (93) encompass the special case of linear viscoelasticity for $h_0 = h_1 = 1$, and $g_0 = g_1 = 1$.

2.3.3 Models for Static Hysteresis and Viscoelasticity

The models in Sect. 2.3 are two limiting cases of nonlinear material behavior. In general, the characteristics of static hysteresis emerge at the same time as the dependence on distortion velocity, as the effects of different damping mechanisms are superimposed. In this case, the hysteresis curves measured in tensile tests under harmonic strain, $\varepsilon(t) = \hat{\varepsilon} \cos(\Omega t + \varphi_{0\varepsilon})$, will have peaks, and the area and shape of the hysteresis curve changes with the angular frequency Ω as shown in Fig. 18. Filled polymers such as technical rubber materials show this behavior.

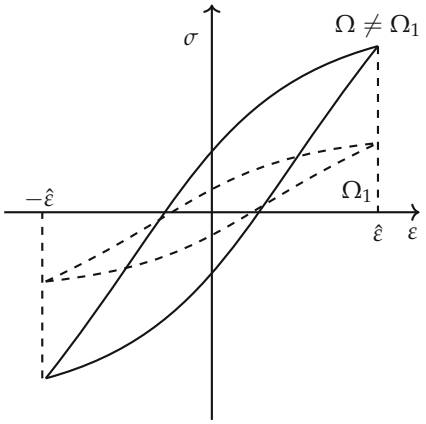

Fig. 18 Hysteresis curves of a material exhibiting static hysteresis and frequency-dependent damping under harmonic strain

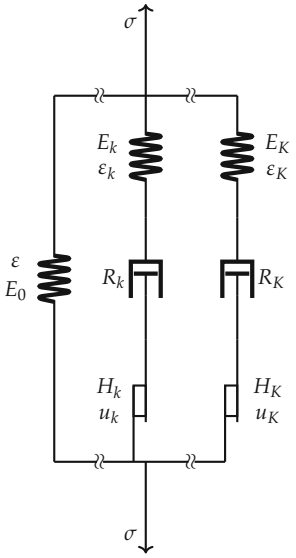

Fig. 19 Rheological model of nonlinear material behavior

Rheological Models

Filled polymers may be described by Rheological models combining velocity-dependent behavior and velocity-independent behavior. The resulting combination models comprise Coulomb elements, springs, and dampers in varying configurations depending on the material and the load condition, see Fig. 19 [42]. If $\bar{\sigma}_k$ denotes the partial stress transmitted along the line consisting of Coulomb element H_k, damper R_k, and spring E_k, the total stress is:

$$\sigma = E_0\,\varepsilon + \sum_{k=1}^{K} \bar{\sigma}_k. \tag{94}$$

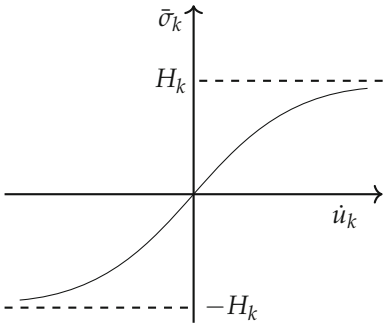

Fig. 20 Dependence of the frictional stress, $\bar{\sigma}_k$, on the distortion velocity, $\dot{u}_k$

Distinctions between the cases of stick and slip for the kth Coulomb element can be avoided by using the approximation:

$$\bar{\sigma}_k = \frac{2\,H_k}{\pi}\,\arctan\frac{\dot{u}_k}{v_k} \tag{95}$$

for the dependence of the frictional stress $\bar{\sigma}_k$ on the distortion velocity of the Coulomb element, with the sufficiently small reference velocity $v_k > 0$ (Fig. 20). From Eq. (95), follow the evolution equations for the internal variables u_k:

$$\dot{u}_k = v_k \tan\frac{\pi}{2}\frac{\bar{\sigma}_k}{H_k} \qquad \text{for} \quad k = 1, \ldots, K. \tag{96}$$

Taking into account the characteristic curves of the damper R_k and the spring E_k, and Eq. (96), the evolution equations for the partial stresses result as:

$$\dot{\bar{\sigma}}_k = E_k\left(\dot{\varepsilon} - \frac{\bar{\sigma}_k}{R_k}\right) - E_k\,v_k\,\tan\frac{\pi\,\bar{\sigma}_k}{2\,H_k} \tag{97a}$$

$$\text{for} \quad k = 1, \ldots, K. \tag{97b}$$

The above equations, viz., (94), (96), and (97) describe the material behavior for the superposition of viscoelasticity and static hysteresis.

Mathematical Model

The following mathematical model is an updated version of the "curvilinear method" of Sect. 2.3 [43], assuming that the linear elastic part, $G\gamma(t)$, remains unchanged and the frictional part, τ_R, is replaced by a relaxing viscoelastic part τ_v:

$$\tau(t) = G\gamma(t) + \tau_v(t). \tag{98}$$

The following applies to the relaxing, viscoelastic part:

$$\tau_v(t) = \int_{-\infty}^{t} \frac{R\rho\,\dot{\gamma}(s)}{1+\rho|\gamma(s)-\gamma_U|} K(t-s)\mathrm{d}s \tag{99}$$

where γ_U is the shear stress in the preceding reversal point of the distortion direction, R and ρ are the constant material parameters, and $K(t)$ is the decay function.

3 Damping of Assemblies

In this chapter, we will deal with the effects of damping on assembled structures and the mathematical models used to it. We will review *material damping* as discussed in Sect. 2 and move further to *damping of components and assemblies*

A *component* can be defined as the smallest coherent, jointless unit of an assembly. Components that have a positive fit yield *laminated components (or composites)*. An *assembly* on the other hand is "composed" of components, e.g. a clamped, bolted or screwed connection. A machine or system is in turn formed via various assemblies, or an assembly could be a system in itself. But this is a matter of definition.

In this chapter, we will also consider the following special damping effects:

- damping in joints between components and assemblies
- damping due to fluids surrounding the oscillator
- damping by local displacements of liquids between components

The damping properties are "assembled" in a hierarchical fashion beginning with the material and moving up via components eventually to the assembly. The description takes into account the possibilities of measuring damping characteristics, i.e.,

- We accomplish this in the time domain by analyzing the time histories for linear deformation (material) laws, majorly by an assessment of the amplitude decay of damped vibrations.
- In the frequency domain, we use relations between the input and output quantities.
- We can also determine the energy dissipation, particularly for steady state vibrations.

3.1 From Material Description to Complete Homogeneous Component

If material properties are uniform over the entire volume, it is called homogeneous. The damper model chosen will have the same parameters, for any element and any point in the component. However, stress and distortion conditions are position dependent in a component – as opposed to differentially small volume elements.

For example, beams, shafts, plates, and shells. As per Eqs. (100) and (101), the loss factor of a component χ_S and loss factor for the material will differ. For χ_S, we integrate the damping energy over the volume of the component, V, and divide by the maximum stored potential energy, U_S, of the vibration:

$$\chi_S = \frac{\int_V W_D(x, y, z)\mathrm{d}V}{2\pi \int_V U(x, y, z)\mathrm{d}V} = \frac{W_S}{2\pi U_S}. \tag{100}$$

Here, W_D is the damping energy per unit volume and cycle. Displacements are assumed to have a harmonic time history. U is the potential energy per unit volume at the point of maximum excursion. Using the loss factor of the material χ:

$$\chi = \frac{W_D}{2\pi U}. \tag{101}$$

This leads to the loss factor of the component:

$$\chi_S = \frac{\int_V \chi\ U\,\mathrm{d}V}{\int_V U\,\mathrm{d}V}. \tag{102}$$

Within a given zone, the specific damping energy and the stress amplitude, $\hat{\sigma}$ can be related as in the following power law:

$$W_D = J\left(\frac{\hat{\sigma}}{\hat{\sigma_0}}\right)^n. \tag{103}$$

J and n are real material parameters determined via experiments for a given reference stress, cf. Lazan [45]. Also, if the effect of stress is understood, the damping afforded by the component can be obtained from the specific damping energy, W_D as shown below:

$$W_D = W_D(\hat{\sigma}). \tag{104}$$

One can deduce from Eq. (103): therefore that the damping energy per period of the component is as follows:

$$W_S = \int_V W_D\mathrm{d}V = \int_V J\left(\frac{\hat{\sigma}}{\hat{\sigma_0}}\right)^n \mathrm{d}V. \tag{105}$$

Example. Beam with one end fixed and a mass on the other end, in steady-state vibration in its fundamental mode (Fig. 21):

In the above, we will neglect the mass of the beam. It follows that $\hat{M}_y(x) = \hat{F}x$, where $\hat{F}$ is the amplitude of force at $x = 0$. Therefore the position-dependent normal stress amplitude is, then:

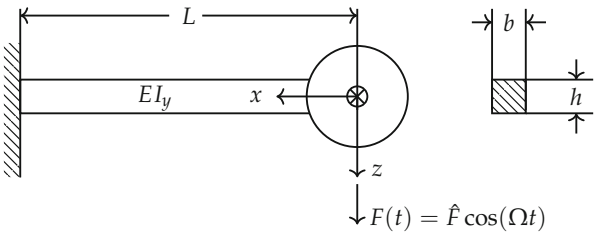

Fig. 21 Beam exposed to forced vibration

$$\hat{\sigma_x}(x,z) = \frac{\hat{F}x}{I_y} z. \tag{106}$$

The damping energy is:

$$W_s = 2J \int_{x=0}^{L} \int_{z=0}^{h/2} \left(\frac{\hat{F}x}{I_y} \frac{z}{\hat{\sigma_0}} \right)^n b \, \mathrm{d}x \, \mathrm{d}z \tag{107a}$$

$$W_s = J \left(\frac{\hat{F} L h}{2 I_y \hat{\sigma_0}} \right)^n \frac{b \, L \, h}{(n+1)^2}. \tag{107b}$$

Here we have the bending stiffness at the fixed end as the reference quantity:

$$\hat{\sigma_0} = \hat{\sigma_L} = \left(\frac{\hat{F} \, L \, h}{2 I_y} \right). \tag{108}$$

The volume V and the damping energy of the component W_S are as follows:

$$V = b \, L \, h \tag{109}$$

$$W_S = \frac{J \, V}{(n+1)^2}. \tag{110}$$

The maximum deformation energy can be expressed as:

$$U_s = \int_{x=0}^{L} \frac{\hat{M_y}^2(x)}{2 E I_y} \mathrm{d}x = \int_{x=0}^{L} \frac{(\hat{F}x)^2}{2 E I_y} \mathrm{d}x \tag{111a}$$

$$U_s = \frac{\hat{F}^2 L^3}{6 E I_y} = \frac{V \hat{\sigma}_L^2}{18 \, E}. \tag{111b}$$

If we now use Eq. (100) i.e., the definition of loss factor, we have:

$$\chi_S = \frac{9}{\pi} \frac{J\,E}{(n+1)^2}\,\hat{\sigma}_L^{-2}. \tag{112}$$

3.2 Laminated Components

Laminated components are essentially composites comprising homogeneous components. Each component typically has different material properties, and no relative motion is permitted between these components. If at all any relative motion is possible, it needs to be accounted for. This is dealt with in the next section.

Calculation of the loss factor, χ_s, in laminates as in Eq. (100) is:

$$\chi_s = \frac{\sum_i \int_{V_i} W_{Di}(x, y, z)\mathrm{d}V_i}{2\pi \sum_i \int_{V_i} U_i(x, y, z)\mathrm{d}V_i} = \frac{W_s}{2\pi U_s}. \tag{113}$$

Analogous to the previous section, displacement is assumed to have a harmonic time history.

3.3 Damping in Joints

Compared to Material damping, damping at the contact surfaces of joints such as rivets, joints or shrink fits, etc. is greater. It occurs mainly due to the relative motion of the mating surfaces, micro-slip being one of the mechanisms. Micro slip is the interfacial slip of small areas. With an increase in tangential loading or the decrease in contact pressure, a transition occurs from micro to macro level slip. This means that the entire face of the joint now has relative motion. Coulomb's Law promises an approximation for macro-slip. Apart from this, a surface normal relative motion is also possible. This is mainly associated with elastoplastic deformation at the rough surfaces [16].

The above mechanisms have a combined effect at the joints and thereby result in nonlinearity. However, there are cases where nonlinearity is not of significant importance, viz., where "pumping losses" as in gas pumping are the dominant factor. This is described in Sect. 3.5. There is a strong relation coupling between the dissipation mechanisms and the contact pressure, surface condition of mating surfaces, and the mating materials.

If the wavelength of the vibrations of a joined component is shorter or similar to the joint dimensions, an FEM simulation can allow for inferences about the transmission characteristics of the joints in the structure [18,67]. This is particularly true in the case of large surface joints and for high-frequency phenomena.

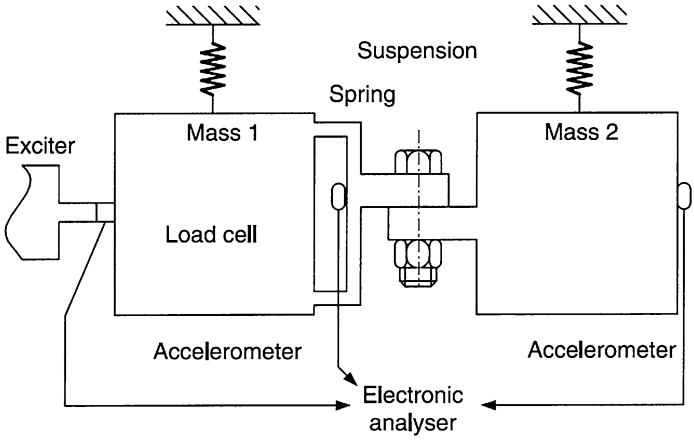

Fig. 22 Measurement of longitudinal force and relative displacement at an isolated bolted lay joint as described in [29] (source: VDI guideline 3830)

Alternatively, if the wavelength of the vibration is much larger than the joint dimensions, local modeling is possible. One can experimentally investigate individual joints and in a phenomenological manner, develop a mechanical model of the combined effects [52]. Figure 22 shows one such experimental setup. It is a set-up for testing a lay joint loaded in the longitudinal direction [29]. The joint is a bolted lay joint between two masses. The bending compliance of the beam inserted between the left and right mass causes a system capable of vibrating, which, for identifying the parameters, is investigated under resonance conditions. This allows creating large periodic longitudinal forces and easy measurement of the friction hysteresis in the joint.

It is found from experiments that for a given harmonic load, force/displacement hysteresis are more or less frequency independent (Sect. 2.3). It is the stress and strain amplitudes that majorly influence the shape of the hysteresis. They have peaks at the zeros of the velocity, which is a hint toward Coulomb friction as shown in Fig. 23.

Transmission behavior of joints may be described in many ways.

3.3.1 Description by a Functional Equation

Frictional hysteresis can be described by the theory of viscoplasticity [62]. By means of a transform of the variables, an ordinary differential equation is obtained [31], where the first time derivative of the force $\dot{F}$ is a function of the relative displacement u, the relative velocity $\dot{u}$, and the force F and is given as per the following relation. The equation holds true for longitudinal and transverse forces and thereby also moments:

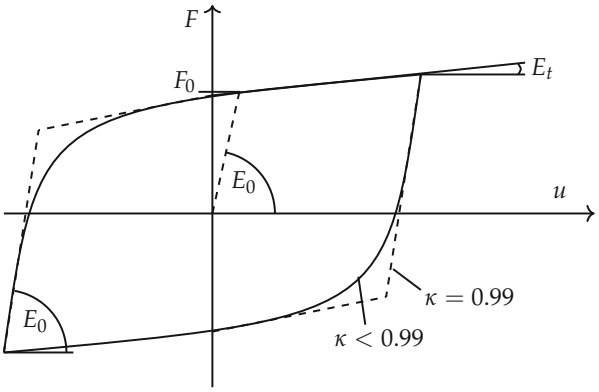

Fig. 23 Joint hysteresis with the parameters of the Valanis model as described in [30]

$$\dot{F}(u, \dot{u}, F) = \frac{E_0 \dot{u} \left[1 + \frac{\lambda}{E_0} \operatorname{sgn} \dot{u} (E_t u - F)\right]}{1 + \kappa \frac{\lambda}{E_0} \operatorname{sgn} \dot{u} (E_t u - F)}. \tag{114}$$

The above equation consists of four parameters. Static stiffness E_0 which characterizes behavior without slip, the sliding stiffness, E_t, a dimensionless parameter κ to denote the curvature of transition from E_0 to E_t:

$$0 \leq \kappa < 1. \tag{115}$$

The parameter λ is determined as per the following equation:

$$\lambda = \frac{E_0}{F_0 \left(1 - \kappa \frac{E_t}{E_0}\right)}. \tag{116}$$

Here F_0 is the equivalent limit of static friction. It characterizes the force at which the transition from stiffness E_0 to stiffness E_t occurs. The parameters E_0, E_t, κ, and F_0 can be located on the hysteresis curve is shown in Fig. 23. $\kappa = 1$ denotes the trivial case of linear elastic behavior and therefore is not included in the inequality (115). The mathematical model, i.e., Eq. (114), does not distinguish between static and dynamic friction and therefore can be easily integrated into dynamic systems where rate-independent friction forces must be considered [29, 30].

3.3.2 Description in Terms of Springs and Coulomb Elements

Another method is to use models comprising springs and Coulomb elements [45]. The transmission behavior can be characterized for any arbitrary load history using the material models. This was already discussed in Sect. 3.1. Figure 24 shows as to how one could accommodate a joint model into a bar structure. Figure 25 shows the

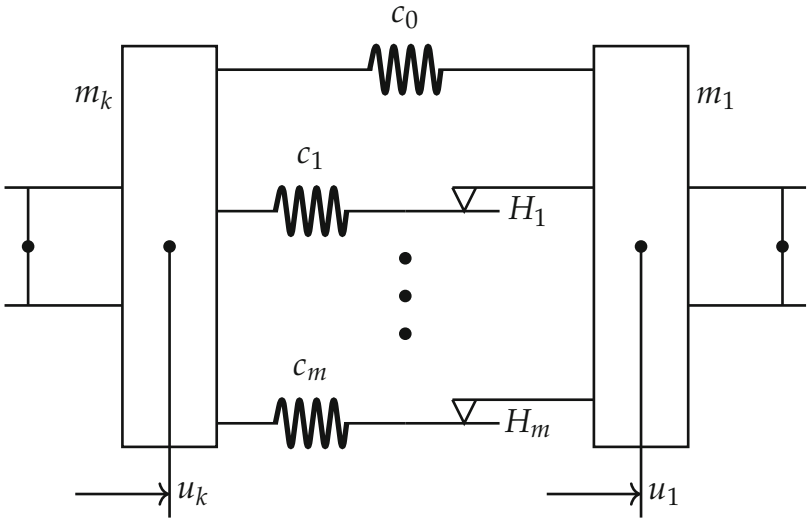

Fig. 24 Nonlinear joint model with flange masses

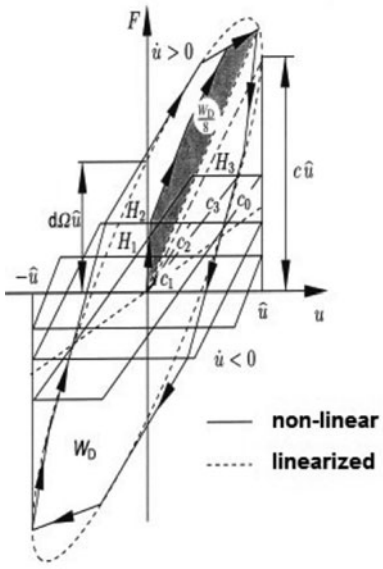

Fig. 25 Hysteresis loop of a joint model with seven parameters (source: VDI guideline 3830)

hysteresis for cyclic relative displacements, u, with the velocity zero crossings at $\hat{u}$ and $-\hat{u}$ for a seven-parameter model. As in Eq. (86), the loss energy per cycle, W_D is determined as a function of $\hat{u}$:

In contrast to an equivalent discrete model, the dependence of the loss energy W_D on the relative displacement amplitude, $\hat{u}$ is not approximated by a polygon

line as in Fig. 16. We use here Eq. (104) via a smooth curve such as:

$$W_D(\hat{u}) = 4H\hat{u}^m \tag{117}$$

where H and m are real parameters in the continuous equivalent model as per [52] and [58]:

In [28], we can see the integration of a joint model into a structure discretized by the FEM using a bar as an example. In case the dimensions of the joint prevent representing it as a single local model, several such models can be arranged along a line or in a surface [67].

If one encounters weak nonlinearities, additional effort is required for numerical computation of structural dynamics. Nonlinear joints may be included by reduction via equivalent linearization. Joint models with linear springs and viscous dampers with experimentally determined parameters ignore nonlinearities and static hysteresis [64].

3.3.3 Description in Terms of Equivalent Spring and Equivalent Damper

In the frequency domain, using equivalent spring stiffness and damping coefficients is one of the options to describe linearized stationary periodical transmission behavior of joints. It is based on the analysis of an experimental hysteresis curve measured under harmonic relative displacement, $f(u)$ and $g(u)$ being functions related to loading and unloading. The longitudinal force is given by:

$$F = \frac{1}{2}\left[f(u) + g(u)\right] + \frac{1}{2}\left[f(u) - g(u)\right]\operatorname{sgn}\dot{u}. \tag{118}$$

Using harmonic balance method, the equivalent spring stiffness and damping coefficient can be determined as follows [18]:

$$c(\Omega, \hat{u}) = \frac{1}{\pi\hat{u}}\int_0^{2\pi} F(\hat{u}\cos\Omega t, -\hat{u}\Omega\sin\Omega t)\cos\Omega t\,\mathrm{d}(\Omega t) \tag{119}$$

$$d(\Omega, \hat{u}) = \frac{1}{\pi\hat{u}\Omega}\int_0^{2\pi} F(\hat{u}\cos\Omega t, -\hat{u}\Omega\sin\Omega t)\sin\Omega t\,\mathrm{d}(\Omega t). \tag{120}$$

The elliptical hysteresis loop of the linearized longitudinal force with the complex stiffness $\underline{c}(\Omega, \hat{u}) = c(\Omega, \hat{u}) + i\Omega d(\Omega, \hat{u})$ can be compared to the hysteresis polygon of the nonlinear model. Usually, the nonlinear amplitude and the frequency dependence of the parameters of the equivalent system requires iterative solutions of the nonlinear algebraic functions of the dynamic transmission behavior [27].

Using an equivalent linearization of the joint model of Fig. 24, $\alpha_i = \arccos(1 - 2H_i/c_i\hat{u})$, we get the spring stiffness as:

$$c(\Omega, \hat{u}) = c_0 + \sum_{i=1}^{m} \frac{c_i}{\pi} \left(\alpha_i - \frac{\sin 2\alpha}{2} \right). \tag{121}$$

Also, the equivalent damping coefficient is:

$$d(\Omega, \hat{u}) = \sum_{i=1}^{m} \frac{c_i}{2\pi\Omega} (1 - \cos 2\alpha_i). \tag{122}$$

Implementation of the above joint model in a discretized structures can be found in [53].

3.3.4 Description Using Finite Element Models

One could also use FEM to model the joint. Convenient optimization of damping of joints or comparing different variants is possible as these changes are easier to implement in a numerical simulation than in an experiment.

To obtain good predictions, physically reasonable contact formulae are needed that describe macro- and micro-slip behavior. By taking into account the rough surfaces and deformation behavior, such formulae can be achieved. This kind of detailed modeling requires a large amount of effort, and therefore, statistical averaging methods are used [65]. Based on a description of the rough surface as a random process, relations for the elastoplastic behavior of the roughnesses are obtained as averages over the contact surface [66].

Outputs from these relations such as load dependent contact stiffnesses in the normal and tangential directions or limit of static friction can be used as input parameters in FEM models to obtain a realistic joint behavior [32].

3.4 Damping Due to Fluids

3.4.1 Interaction Between a Structure and the Surrounding Medium

Excursions normal to the surface of a vibrating structure cause displacements in the surrounding medium which, in turn, acts back on the structure, exerting a pressure on the surface. The normal velocity and the pressure variations are related via the Kirchhoff-Helmholtz integral. For harmonic vibrations in a loss-free medium, we have:

$$\underline{p}(\boldsymbol{r}, t) = \underline{\hat{p}}(\boldsymbol{r}) e^{i\Omega t} \tag{123}$$

where $\boldsymbol{r}$ is a position vector specifying a particular point in space. Also, the normal velocity is given by:

$$\underline{v}_n(\boldsymbol{r}_S, t) = \underline{\hat{v}}(\boldsymbol{r}_S) e^{i\Omega t} \tag{124}$$

where $\boldsymbol{r}_S$ is the position vector of a point on the surface of the vibrating structure. $\underline{\hat{p}}(\boldsymbol{r})$ is given by the following integral:

$$\underline{\hat{p}}(\boldsymbol{r}) = \frac{1}{4\pi} \int_S \left[\underline{\hat{p}}(\boldsymbol{r}_S) \frac{\partial}{\partial n} \left(\frac{e^{-ikR}}{R} \right) + i\Omega\rho \underline{\hat{v}}_n(\boldsymbol{r}_S) \frac{e^{-ikR}}{R} \right] \mathrm{d}S \tag{125}$$

where the pressure amplitude, $\underline{\hat{p}}(\boldsymbol{r}_S)$, at the surface of the structure, is determined by substituting on $\underline{\hat{p}}(\boldsymbol{r})$ the left-hand side of Eq. (125) by $\underline{\hat{p}}(\boldsymbol{r}_S)$ and solving the integral. However, this involves high computational costs. Equation (125) shows:

$R = \lvert \boldsymbol{r} - \boldsymbol{r}_s \rvert$	distance between the structure surface and the point under consideration in the medium
ρ	density of the medium
$k = \Omega/c = 2\pi/\lambda$	angular wavenumber of the medium
$\partial/\partial \boldsymbol{n}$	spatial derivative in the surface normal direction
S	total surface area of boundary surfaces of the medium

- Pressure amplitudes in the medium and at the surface depend on the normal velocities of all points of the surface.
- Pressure variations and normal velocities in general do not vary in phase.

An often made assumption that $p(\boldsymbol{r}_S, t)$ and $v_n(\boldsymbol{r}_S, t)$ are proportional is in contradiction to Eq. (125). The following assumes a linear, infinite, and loss-free medium. The theoretical basis of the structure surrounding medium are found in [23, 25, 40].

3.4.2 Radiation Efficiency, Logarithmic Radiation Efficiency, and Radiation Loss Factor

The radiation behavior of bodies and structures, as per technical acoustics [22, 24], is characterized by the *radiation efficiency*:

$$\sigma = \frac{P_S}{\rho c A \bar{v}^2} \tag{126}$$

or the *logarithmic radiation efficiency* given by

$$\sigma' = 10 \ \log \sigma \ \mathrm{dB} \tag{127}$$

P_S	sound power radiated
c and ρ	speed of sound in, and density of, the medium
A	total area of radiating surface
$\tilde{v}$	root mean square of the vibration velocity normal to the surface, time-averaged over the area

In cases where the *acoustic wavelength* is much smaller than the dimensions of say, a plate vibrating in phase:

$$\lambda = \frac{2\pi c}{\Omega} = \frac{c}{f} \tag{128}$$

the radiation efficiency is $\sigma = 1$. The vibration frequency and the vibration mode significantly affect the radiation efficiency. The energy radiated by a vibrating structure per cycle (harmonic with angular frequency of Ω)

$$W_S = \frac{2\pi\ P_{Sh}}{\Omega} = \frac{2\pi\sigma\rho c A\bar{v}^2}{\Omega}. \tag{129}$$

Also the radiation loss factor is given by the following equation [22]:

$$\chi_S = \frac{W_S}{2\pi U_S} = \frac{P_S}{\Omega U_S}. \tag{130}$$

In this equation, U_S is the vibration energy of the structure as shown in Eq. (113). Vibration energy of the surrounding however is not taken into account in this equation. χ_S plus the loss factors due to other damping mechanisms give the complete loss factor.

3.4.3 Elementary Radiators

This section deals with some idealized vibrating systems which one could use to estimate power and radiation efficiency of real systems.

Monopole or Zero-Order Spherical Radiator (Breathing Sphere)

It is essentially a sphere with a fixed center and an oscillating radius $r(t) = r_0 + \triangle r(t)$ where r_0 is the mean position about which the oscillation occurs. The surface velocity, $v_S = d(\triangle r)/dt$, is assumed to be known. A spherically symmetrical sound field is created around the radiator. A harmonic velocity:

$$\underline{v}_S = \hat{v}_S e^{i\Omega t} \tag{131}$$

induces a pressure variation on the surface, which is given by:

$$\underline{p}_S = \underline{\hat{p}}_S e^{i\Omega t}. \tag{132}$$

Here the complex amplitude is given by:

$$\underline{\hat{p}}_S = i\rho c\hat{v}_S \frac{(2\pi r_0/\lambda)}{1 + i(2\pi r_0/\lambda)} \tag{133}$$

where λ is the acoustic wavelength as described in Eq. (128). As $\hat{v}^2 = \hat{v}_S^2/2$, the expression for sound power is:

$$P_S = 4\pi {r_0}^2 \rho c \tilde{v}^2 \frac{(2\pi r_0/\lambda)^2}{1 + (2\pi r_0/\lambda)^2} \tag{134}$$

and the radiation efficiency as:

$$\sigma = \frac{(2\pi r_0/\lambda)^2}{1 + (2\pi r_0/\lambda)}. \tag{135}$$

As can be seen from Fig. 26, the only quantity that affects the magnitude of the logarithmic radiation efficiency is the ratio $(2\pi r_0/\lambda)$. The following borderline cases can be seen:

1. $(2\pi r_0/\lambda) << 1$ (very low frequencies)

$$P_S \approx 4\pi {r_0}^2 \rho c \tilde{v}^2 (2\pi r_0/\lambda)^2 \tag{136a}$$

$$\sigma \approx (2\pi r_0/\lambda)^2. \tag{136b}$$

2. $(2\pi r_0/\lambda) >> 1$ (very high frequencies)

$$P_S \approx 4\pi {r_0}^2 \rho c \tilde{v}^2 \tag{137a}$$

$$\sigma \approx 1. \tag{137b}$$

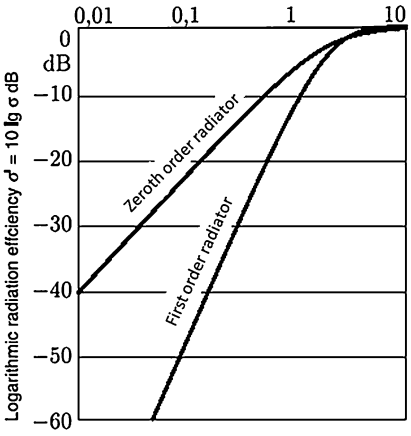

Fig. 26 Logarithmic radiation efficiencies, σ', of spherical radiators as a function of the ratio $(2\pi r_0/\lambda)$ (source: VDI guideline 3830)

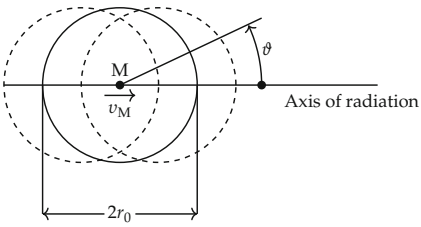

Fig. 27 First-order spherical radiator

Dipole or First-Order Radiator (Vibrating Rigid Sphere)

As can be seen from Fig. 27, a rigid sphere with radius r_0 with center M moves harmonically on a straight line with a velocity $\underline{v}_M = \hat{v}_M e^{i\Omega t}$. The surface normal velocity of the surface elements v_S depends on the reaction angle ϑ given by the relation:

$$\underline{v}_S = \hat{v}_M \cos\vartheta e^{i\Omega t} \tag{138}$$

and the sound power is as follows:

$$P_S = 4\pi {r_0}^2 \rho c \frac{\tilde{v}_M^2}{3} \frac{(2\pi r_0/\lambda)^4}{4 + (2\pi r_0/\lambda)^4}. \tag{139}$$

In the above equation, $\tilde{v}_M$ is the root mean square (RMS) value of the vibration velocity of the sphere. The relation between $\tilde{v}_S^2$ averaged over the surface and $\tilde{v}_M^2$ is:

$$\tilde{v}_S^2 = \frac{1}{4\pi {r_0}^2} \int_S \tilde{v}_M^2 \cos^2\vartheta \, \mathrm{d}S \tag{140a}$$

$$\tilde{v}_S^2 = \frac{1}{2}\tilde{v}_M^2 \int_0^\pi \sin\vartheta \cos^2\vartheta \, \mathrm{d}\vartheta = \frac{1}{3}\tilde{v}_M^2. \tag{140b}$$

The above result in conjunction with the sound power, i.e., Eq. (139) can be used with Eq. (126) that the radiation efficiency is:

$$\sigma = \frac{(2\pi r_0/\lambda)^4}{4 + (2\pi r_0/\lambda)^4} \tag{141}$$

which depends only on the ratio $(2\pi r_0/\lambda)$ as seen in Fig. 26. Yet again, we observe the following cases:

1. $(2\pi r_0/\lambda) << 1$ (very low frequencies)

$$P_S \approx 4\pi {r_0}^2 \rho c \frac{\tilde{v_M}^2}{12} \tag{142a}$$

$$\sigma \approx \frac{1}{4}(2\pi r_0/\lambda)^4. \tag{142b}$$

2. $(2\pi r_0/\lambda) >> 1$ (very high frequencies)

$$P_S \approx 4\pi {r_0}^2 \rho c \frac{\tilde{v_M}^2}{3} \tag{143a}$$

$$\sigma \approx 1. \tag{143b}$$

Plane Radiator (Piston) [24]

A rigid plane with a surface normal velocity v_K can be idealized as a piston. In this case, the precise form of the surface does not matter. Only the surface area A_K is of interest which can be given by its mean radius:

$$r_K = \sqrt{A_K/\pi}. \tag{144}$$

The following two differentiations can be made here:

- $(2\pi r_K/\lambda) << 1$ (low frequency)
  If one side of the radiator is *acoustically screened* such that there is no acoustic short circuiting of the front and rear of the radiator surface – for harmonic vibrations, $\underline{v}_K = \hat{v}_K e^{i\Omega t}$ the sound power is given by:

$$P_S \approx A_K \rho c \tilde{v}_K^2 \frac{1}{2} \left(\frac{2\pi r_K}{\lambda}\right)^2. \tag{145}$$

  This can be used in cases of in-phase vibration of multiple membranes or plates that are supported over the entire perimeter. In such cases, we use $\tilde{v}_K^2$ in place of $\tilde{v}^2$ and the radiation efficiency turns out as:

$$\sigma \approx \frac{1}{2} \left(\frac{2\pi r_K}{\lambda}\right)^2. \tag{146}$$

  However, due to short circuiting in radiators without acoustic screening, both radiation efficiency and sound power are diminished as seen below:

$$P_S \approx A_K \rho c \tilde{v}_K^2 \frac{1}{24} \left(\frac{2\pi r_K}{\lambda}\right)^4 \tag{147a}$$

$$\sigma \approx \frac{1}{24} \left(\frac{2\pi r_K}{\lambda}\right)^4. \tag{147b}$$

- $(2\pi r_K/\lambda) >> 1$ (high frequency)
  In this case, acoustic short circuits play no role and

$$P_S \approx A_K \rho c \tilde{v}_K^2 \tag{148a}$$

$$\sigma \approx 1. \tag{148b}$$

3.4.4 Damping of Bending Vibrations of Plates

Radiation loss Factor of Homogeneous, Constant Thickness Plates

For a homogeneous plate with density ρ_p, thickness h, and surface area A_p the vibration energy is given by:

$$U_S = \rho_p h A_p \tilde{v}^2 \tag{149}$$

and the loss factor

$$\chi_S = \frac{\sigma}{2\pi} \frac{\rho}{\rho_p} \frac{c}{fh}. \tag{150}$$

Infinite Homogeneous Plate of Constant Thickness

We consider a thin plate which has, in its undeformed state, its center plane in the x, y plane. The equation of motion neglecting the

- shear deformation and rotational inertia (Kirchhoff's theory of a plate)
- internal damping
- interaction with the surrounding medium

is given by:

$$B' \left(\frac{\partial^4 w}{\partial x^4} + 2 \frac{\partial^4 w}{\partial x^2 \partial y^2} + \frac{\partial^4 w}{\partial y^4} \right) + m'' \frac{\partial^2 w}{\partial t^2} = 0 \tag{151}$$

w	Deflection of the plate center plane along the z direction
$B' = \dfrac{Eh^3}{12(1-\upsilon^2)}$	bending stiffness of the plate
h	Plate thickness
E, υ	Young's modulus, Poisson's ratio
ρ_p	Density of plate material
$m'' = \rho_p h$	Plate mass per unit area

For a harmonic plane bending wave propagating in the x direction:

$$w = \hat{w} \cos(\Omega t - k_B x) \tag{152}$$

the wavenumber follows from the Eq. (150):

$$k_B = \sqrt{\Omega} \sqrt[4]{\frac{m''}{B'}}. \tag{153}$$

This directly gives us the wavelength:

$$\lambda_B = \frac{2\pi}{\sqrt{\Omega}} \sqrt[4]{\frac{B'}{m''}}. \tag{154}$$

Here we introduce a term *cut-off frequency* or *coincidence frequency* denoted by ω_g or f_g. At this frequency, the acoustic wavelength equals the bending wavelength. Therefore from Eq. (153):

$$\omega_g = c^2 \sqrt[4]{\frac{m''}{B'}} \tag{155a}$$

$$f_g = \frac{c^2}{2\pi} \sqrt[4]{\frac{m''}{B'}}. \tag{155b}$$

As the plate thickness increases, the cut-off frequency decreases (Fig. 28).

$$\sigma = 0 \qquad \text{for} \quad f < f_g \tag{156a}$$

$$\sigma = [1 - (f_g/f)]^{-0.5} \qquad \text{for} \quad f > f_g. \tag{156b}$$

This can also be represented in terms of angular wavenumbers, k_B and $k = \omega/c$

$$\sigma = 0 \qquad \text{for} \quad k < k_B \tag{157a}$$

$$\sigma = [1 - (k_B/k)^2]^{-0.5} \qquad \text{for} \quad k > k_B. \tag{157b}$$

A graphical illustration of Eqs. (155) and (156) is given in Fig. 29 where

$$\sigma \approx 1 \quad \text{for} \quad f >> f_g \quad \text{or} \quad k >> k_B \tag{158}$$

In case of infinite plates, there is no radiation for frequencies $f < f_g$, and the vibrations in the medium decay very quickly as distance from the plate increases.

Homogeneous Rectangular Plate of Constant Thickness

Apart from the ration of f/f_g or k/k_g, the radiation efficiencies also depend on:

- the geometry
- the vibration mode
- the boundary conditions of the sound field outside the plate

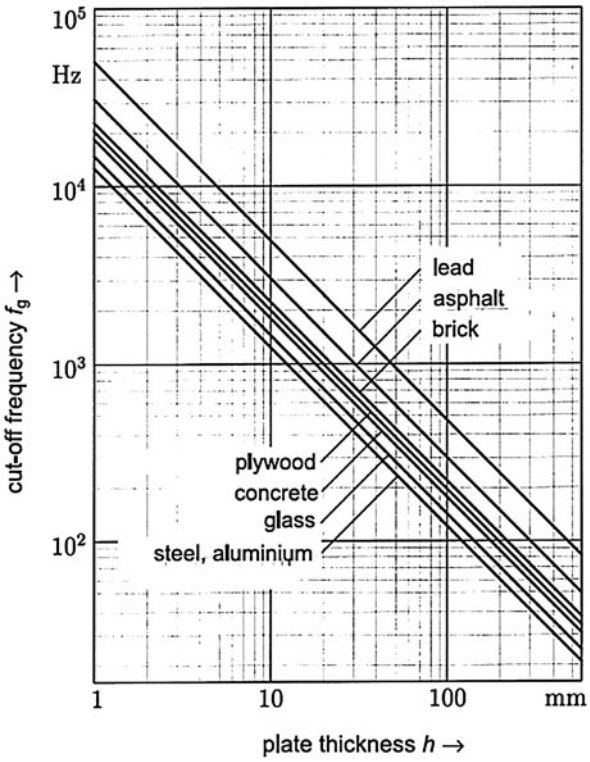

Fig. 28 Cut-off frequencies, f_g, as a function of the plate thickness, h, for radiation into air under normal conditions by plates, as per [22] (source: VDI guideline 3830)

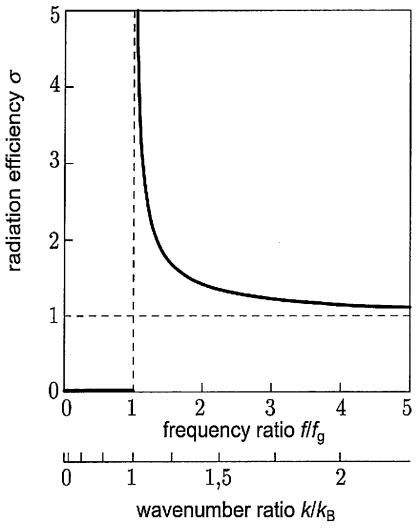

Fig. 29 Radiation efficiency of an infinite plate as a function of the frequency ratio f/f_g or of the wavenumber ratio k/k_B (source: VDI guideline 3830)

Eigenmodes of bending vibrations are important and have two qualitative differences compared to the infinite plate:

1. For $f = f_g$ the radiation efficiency remains finite.
2. Even if the frequency is less than the cut-off frequency f_g, radiation occurs and therefore damping takes place.

Also, for all eigenmodes:

$$\sigma \approx 1 \quad \text{for} \quad f >> f_g \quad (k << k_B). \tag{159}$$

Rectangular Plates Supported on All Sides

For rectangular plates fitted in an infinite acoustic screen as in Fig. 30, there is extensive numerical information available [37,63]. The eigenmodes, $w_{m,n}$ of a plate jointed on all sides having side lengths a and b, are of the type:

$$w_{m,n} = \hat{w}_{m,n} \sin\left(m\pi\frac{x}{a}\right) \sin\left(n\pi\frac{y}{b}\right) \quad m = 1, 2, 3 \ldots; \; n = 1, 2, 3 \ldots. \tag{160}$$

In the range $k < k_B$ $(f < f_g)$, radiation efficiencies vary strongly as a function of the mode number (m, n) and the aspect ration b/a of the rectangular plate. As Fig. 31 shows the results calculated for a square plate demonstrating the effect of mode numbers m, n on the radiation efficiency, $\sigma_{m,n}$. Similarly, Fig. 32 illustrates the effect of the aspect ratio b/a of a rectangular plate for (1,1) and (2,2) modes. When the vibration mode numbers are odd, the radiation efficiency is the highest and on the other hand, lowest when they are even. Mode (1,1), which is the fundamental mode, has the highest radiation efficiency among all others. For a given value of

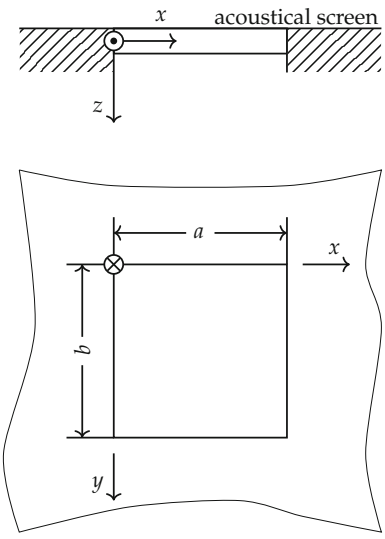

Fig. 30 Rectangular plate fitted in an infinite acoustical screen

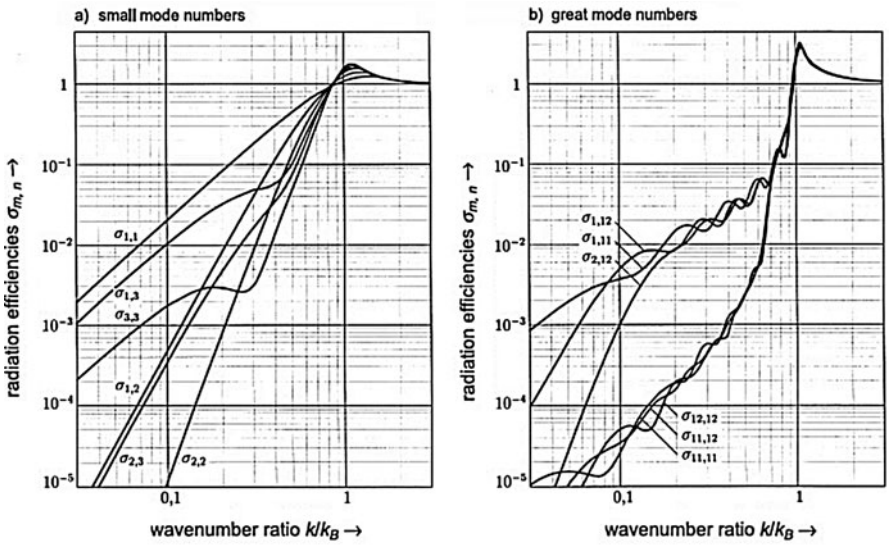

Fig. 31 Radiation efficiencies, $\sigma_{m,n}$, of the eigenmodes $w_{m,n}$ of a square plate supported on all sides, as a function of the wavenumber ratio k/k_B, as per [63] (source: VDI guideline 3830)

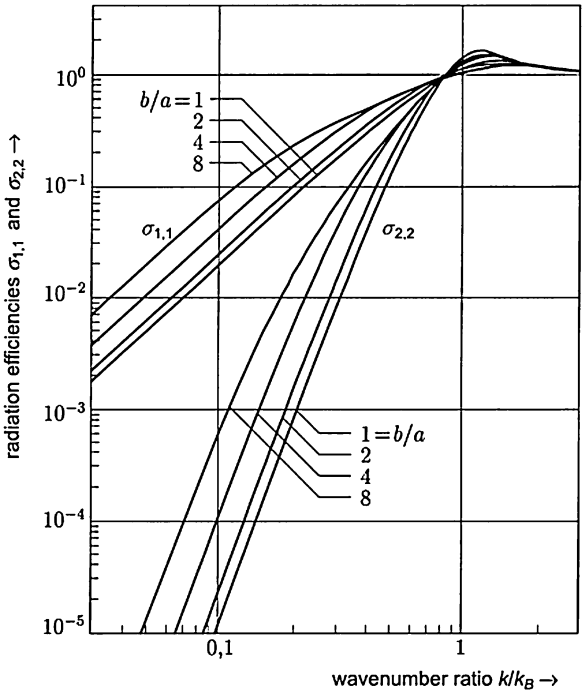

Fig. 32 Radiation efficiencies, $\sigma_{1,1}$ and $\sigma_{2,2}$, of the eigenmodes $w_{1,1}$ and $w_{2,2}$ of a rectangular plate supported on all sides, for selected aspect ratios b/a, as a function of the wavenumber ratio k/k_B, as per [63] (source: VDI guideline 3830)

(m,n) and k/k_B, vibration modes whose nodal lines (approximately) enclose square areas radiate little sound; the more the ratio *na/mb* deviates from unity, the more intense the radiation from the plate. This can also be seen in [63].

Other Boundary Conditions

As per the investigations by *Gomperts* [37] for more general boundary conditions, radiation efficiency can increase or decrease under stronger restraint to fixed plate edges.

For a specific eigenmode, a simple analytical expression for radiation efficiency cannot be given. However, average modal logarithmic radiation efficiencies as a function of the frequency, f can be estimated via the diagram developed by *Holmer* and *Ver* [39], see Fig. 33. An average is taken over the eigenmodes with eigen frequencies in a frequency band centered around the frequency f. This is a problem as the applicability of the diagram is then limited. It is applicable in cases with broadband excitation forces exciting several resonances at the same time, if the responses of the eigenmodes are then summed up.

At frequencies below the cut-off frequency, the plate edges are the main contributor to sound radiation and therefore, damping. As an assumption in rigid and infinite acoustic screens, we consider prevention of flow of the surrounding medium around the plate edges. With no screen, acoustic short circuit occurs and therefore reduces sound radiation and damping.

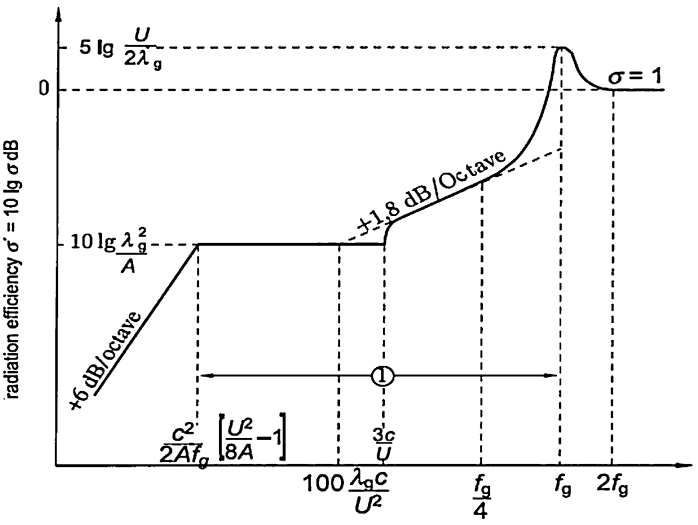

Fig. 33 Theoretical mean values for the logarithmic radiation efficiencies of eigenmodes of rectangular plates (having surface area A and perimeter length U) in a rigid acoustical screen; $\lambda_g = c/f_g$ is the wavelength at the cut-off frequency as per [39]. In the range (1), add 3 dB if edges are fixed (source: VDI guideline 3830)

Ribbed Plates

Stiffening ribs on thin plates effectively act like the subdivision of the total area into many sub-areas. They act as internal edges and thus increases the radiation efficiency below the cut-off frequency. If the total length of the ribs is L and U is the perimeter of the plate, then, Maidanik [48] recommended to increase the radiation efficiency in this range by a factor of $1 + (2L/U)$.

3.4.5 Damping of Vibrating Pipes

We consider here homogeneous, cylindrical pipes with constant cross sections.

Infinite Regular Cylindrical Pipe

The radial velocity of the surface v of an infinite regular cylindrical pipe with outer radius a as shown in Fig. 34 due to a harmonic wave in axial direction, expressed in cylindrical coordinates is as follows:

$$v_n(\varphi, z, t) = \underline{\hat{v}}_n \cos n\varphi \exp[i(\Omega t - k_z z)] \quad n = 0, 1, 2 \ldots . \tag{161}$$

Figure 35 shows pipe deformations in the lowest three-mode numbers:

- $n = 0$: breathing
- $n = 1$: bending
- $n = 2$: ovalizing

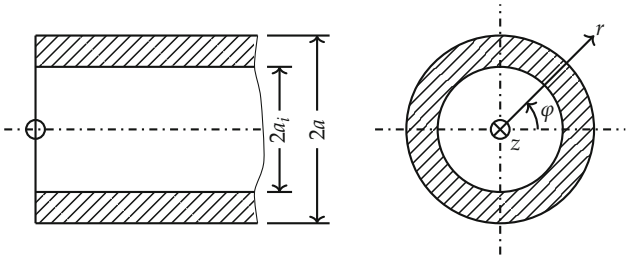

Fig. 34 Regular-cylindrical pipe; dimensions and cylindrical coordinate system

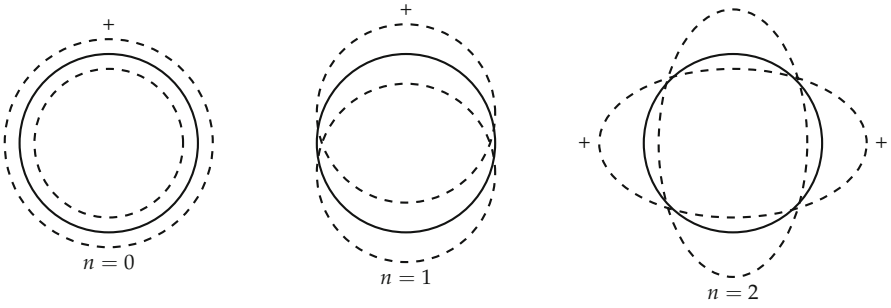

Fig. 35 First eigenmodes of a pipe

The infinite tube will only radiate sound if the axial wavenumber k_z is less than the acoustical wavenumber k, $k_z < k$ [23]. The mode number n has a strong influence on the radiation behavior. In the limiting case where $k_z a << ka << 1$, the radiated sound power per unit length is governed by the following:

$$P_0{}' = \frac{1}{2}\pi^2 a(\rho c)(ka)|\underline{\hat{v}}_0|^2 \qquad n = 0 \tag{162a}$$

$$P_1{}' = \frac{1}{4}\pi^2 a(\rho c)(ka)^3|\underline{\hat{v}}_1|^2 \qquad n = 1 \tag{162b}$$

$$P_2{}' = \frac{1}{32}\pi^2 a(\rho c)(ka)^5|\underline{\hat{v}}_2|^2 \qquad n = 2. \tag{162c}$$

In the entire range $ka < 1$ in a uniformly vibrating pipe ($k_z = 0$) as shown in Fig. 36 - as n increases, the sound radiation decreases. ka here, is the ratio of pipe perimeter to acoustical wavelength. In addition to this, to avoid acoustic short circuits at the surface, the following condition is required:

$$k_z{}^2 + (n/a)^2 < k^2. \tag{163}$$

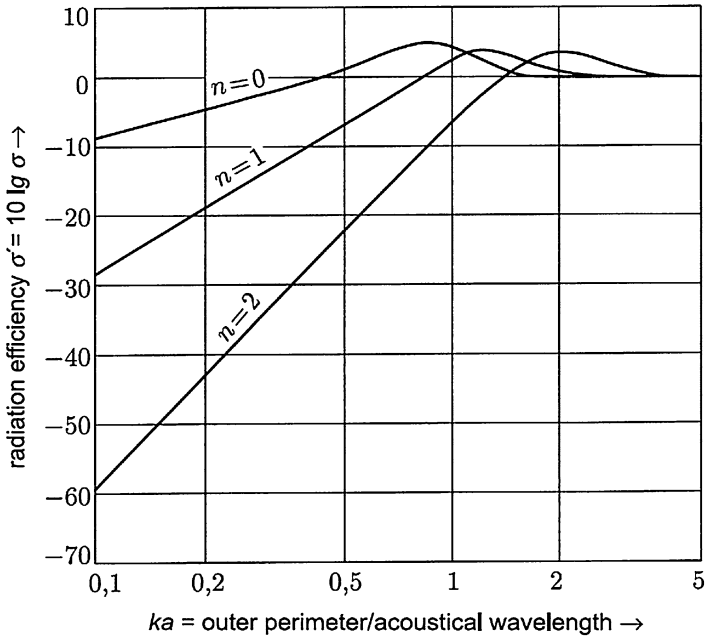

Fig. 36 Radiation efficiency, σ', of a uniformly vibrating, regular cylinder as a function of the ratio ka = outer perimeter/acoustical wavelength, as per [23] (source: VDI guideline 3830)

This is analogous to the requirement of infinite plates that $k_B < k$. This means that for a given value of n, cylinders with large outer radius can fulfill the criteria in Eq. (162), while ones with small outer radius cannot. For efficient radiation in case of *bending vibrations* of regular cylinders ($n = 1$), the following must be assured:

$$(k^2 - {k_z}^2)\, a^2 > 1 \tag{164}$$

where k_z is the axial wavenumber of bending vibrations given by

$$k_z = \sqrt[4]{\frac{4\rho_r \Omega^2}{E({a^2} + {a_i}^2)}} \tag{165}$$

where ρ_r is the density of the pipe and a_i is the inner radius.

Bending Vibrations of Long Regular Cylindrical Pipes

As evident from the discussion, so far we know that the finite length of long regular cylinders only has an effect far below the cut-off frequency. Also this was true if the pipes are poor radiators anyway. This provides enough reason to neglect boundary conditions and calculate radiation loss factor only in an approximate manner [41] as shown in Fig. 37.

Bending Vibrations of Long Pipes with Elliptical or Rectangular Cross Section

For rotationally nonsymmetric cross sections, several geometrical parameters influence the radiation behavior. In case of elliptical cross sections, Fig. 38 shows that the radiation loss factor for a range of semiaxes ratios, ($0.1 < a/b < 10$),

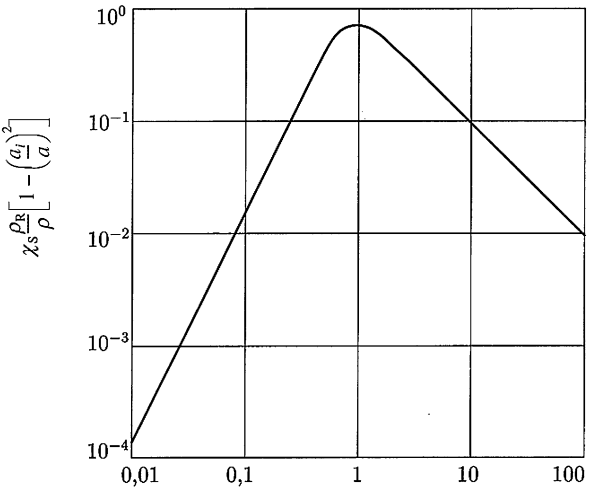

Fig. 37 Diagram for estimating the radiation loss factor, χ_S, of long regular cylindrical pipes in accordance with [41] (source: VDI guideline 3830)

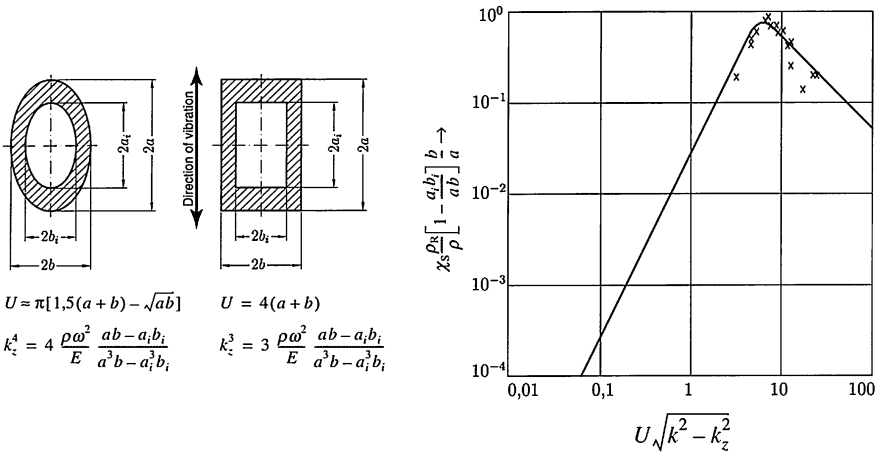

Fig. 38 Diagram for approximate determination of the radiation loss factor, χ_S, of long pipes with elliptical and rectangular cross sections, as per [41]. x: calculation results for rectangular cross sections with various aspect ratios (source: VDI guideline 3830)

approximately lies on a curve. An acceptable estimate of the radiation loss factor for rectangular cross sections with various aspect ratios also fit into this diagram [15].

3.4.6 References to Nonlinearities

In bending vibrations of strip specimens, considerable nonlinearity of air damping, increasing with the vibration amplitude, is observed. This is, as used for measurements of material damping refer [13, 14]. Having said that, nonlinearities can also occur in other cases.

3.5 Damping by Displacement

3.5.1 Damping by Air Displacement

In screwed on or riveted plates and stiffeners, there are gaps that will open and close. This will result in the so-called gas pumping and involves suction and ejection of air as shown in Fig. 39. As per the experiments in [20, 49], this will contribute significantly to the total damping in a frequency range far above the lowest eigenfrequency.

Known theoretical models cannot predict the magnitude of such damping. Extensive experimentation on the decay of vibrations nonetheless allows the estimation of loss factors for vibration frequencies in a given one-third octave band [20, 61]. Typical dynamic loads do not entail any nonlinearity.

For plates without stiffeners, damping depends on the wavelength λ_B of the harmonic bending waves. The longitudinal wave velocity for a homogeneous plate with thickness h, density ρ, Young's modulus E, and Poisson's ratio ν is given by:

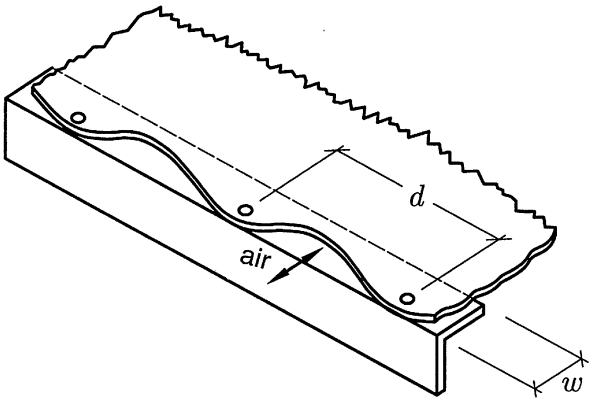

Fig. 39 Damping by air displacement in plates with stiffeners (source: VDI guideline 3830)

$$c_L = \sqrt{\frac{E}{\rho}}. \tag{166}$$

For steel, aluminum, titanium, and magnesium, $c_L \approx 5100\text{m/s}$. Additionally, we also have the relation:

$$\lambda_B = \frac{\sqrt{\pi}}{\sqrt[4]{3(1-\nu^2)}}\sqrt{\frac{hc_L}{f}}. \tag{167}$$

The bending wavelength may also be expressed in terms of the absorption coefficient and the loss factor [38]:

$$\chi = \gamma \frac{L\lambda_B}{\pi^2 A}. \tag{168}$$

The absorption coefficient γ has roughly a linear behavior with respect to the width of the overlap w. Other influencing factors are the ratio of spacing d between the fixing points, to bending wavelength λ_B and on the ambient pressure p. Figure 40 shows recommended values ("*modified*"- γ_{m0}) of the absorption coefficient. Figure 41 shows the dependence of absorption factors.

The following can be used for conversion purposes to other conditions:

$$f_m = f\left(\frac{d}{d_0}\right)^2 \frac{h_0}{h}\frac{c_{L0}}{c_L} \tag{169}$$

and

$$\gamma = \gamma_m \frac{w}{w_0}. \tag{170}$$

If there are many joints, the following summation needs to be employed to find the loss factor of the entire component:

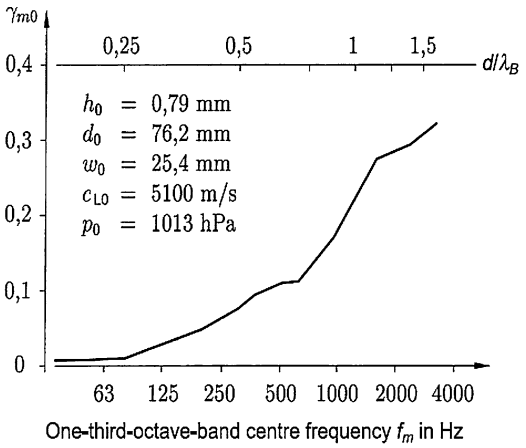

Fig. 40 Average value of the modified absorption coefficient γ_{m0} as a function of the modified one-third-octave band center frequency f_m or of the ratio d/λ_B, as per [20] (source: VDI guideline 3830)

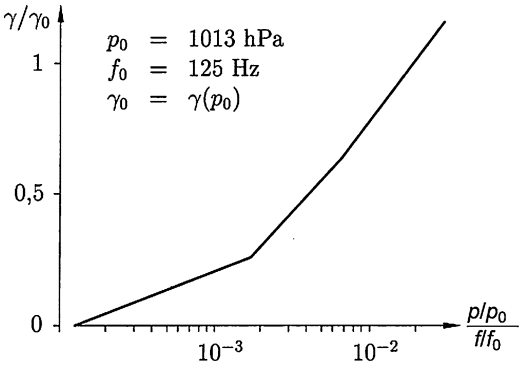

Fig. 41 Dependence of the absorption coefficient, γ, on the ambient pressure, p, as per [20] (source: VDI guideline 3830)

$$\chi_S = \frac{\lambda_B}{\pi^2 A} \Sigma \gamma_n L_n. \tag{171}$$

3.5.2 Journal Bearings, Squeeze Film Dampers

In journal bearings and squeeze film dampers, the damping effect results from the buildup of pressure as a consequence of displacement flows. The resulting damping force is proportional to the vibration velocity and progressively increases with the eccentricity of the journal, in plain journal bearings and radial dampers. As an approximation, total carrying force for a given static eccentricity is linearized, and therefore, the damping force can be expressed in terms of damping constants.

Journal Bearings

Figure 42 shows a plain journal bearing. As per simple bearing theory [44], the relative eccentricity, $\varepsilon = e/\delta$, and the angle α depend on the Sommerfeld number and on the ratio of the widths, B/D:

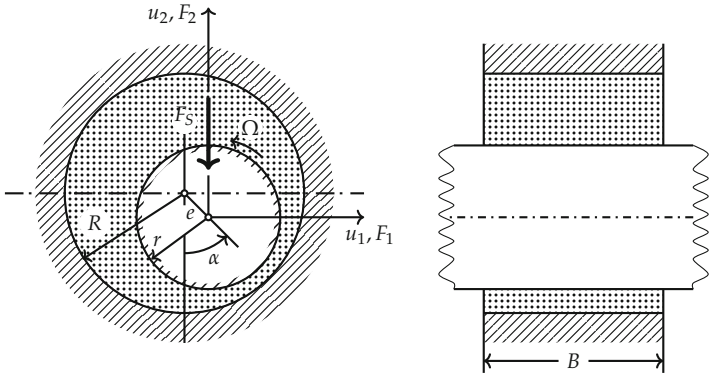

Fig. 42 Circular Bearing

$$So = \frac{F_S \Psi^2}{B D \eta \Omega} \tag{172}$$

where

η	dynamic viscosity
$D = 2R$	bearing diameter
B	bearing width
r	journal radius
$\delta = R - r$	bearing play
$\Psi = \delta / R$	relative bearing play
e	journal eccentricity
$\varepsilon = e/\delta$	relative eccentricity
F_S	static bearing force
α	attitude angle
Ω	angular velocity of rotor

If the journal executes small amplitude transverse movements, $u_1(t)$ and $u_2(t)$, around the equilibrium position determined by the static bearing force, F_S, the components of the resulting additional force are approximately linear functions of the movements:

$$\Delta F_1(t) = k_{11} u_1 + k_{12} u_2 + d_{11} \dot{u}_1 + d_{12} \dot{u}_2 \tag{173a}$$

$$\Delta F_2(t) = k_{21} u_1 + k_{22} u_2 + d_{21} \dot{u}_1 + d_{22} \dot{u}_2. \tag{173b}$$

In the above equations, k and d are the stiffness and damping coefficients of the oil film. Nondimensional coefficients for stiffness and damping are:

$$\gamma_{ik} = k_{ik}\frac{\delta}{F_S} \qquad \beta_{ik} = d_{ik}\frac{\delta\Omega}{F_S}. \tag{174}$$

A more detailed tabulations can be found in [33, 47, 59] and DIN 31 657-1. For $B/D < 0.3$ analytical expressions for γ_{ik} and β_{ik} can be found [50]. Dependence of γ_{ik} and β_{ik} are shown in Figs. 43 and 44. In case of large journal amplitudes or large dynamic amplitudes a nonlinear approach needs to be taken to adequately describe the vibration behavior. In practice, static bearing loads and the excitation forces acting on the rotor are given, and the vibration movements of rotor and journal are investigated. Rotor movements can be known via the solution to Reynolds equation. The forces $F_1(t)$ and $F_2(t)$ can be calculated via an iterative procedure [19, 34].

3.5.3 Squeeze Film Dampers

The working principle of squeeze film dampers is shown in Fig. 45. The design details of the squeeze film dampers can be seen in Fig. 1 of [35] and [57]. Squeeze film bearings can be considered as journals with a nonrotating journal with the

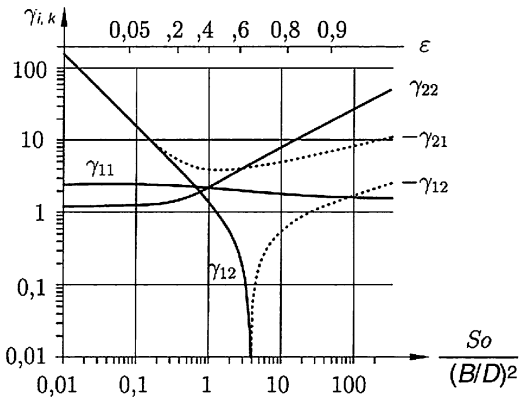

Fig. 43 Relative stiffness coefficients of the short circular bearing (source: VDI guideline 3830)

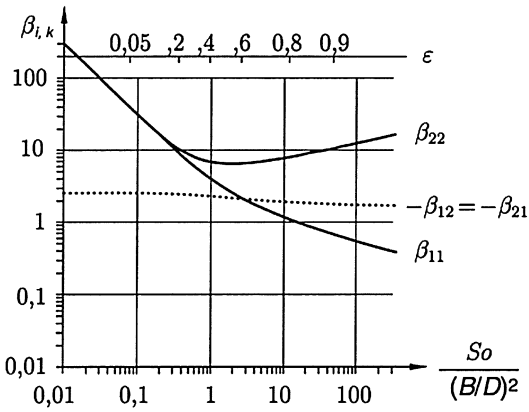

Fig. 44 Relative damping coefficients of the short circular bearing (source: VDI guideline 3830)

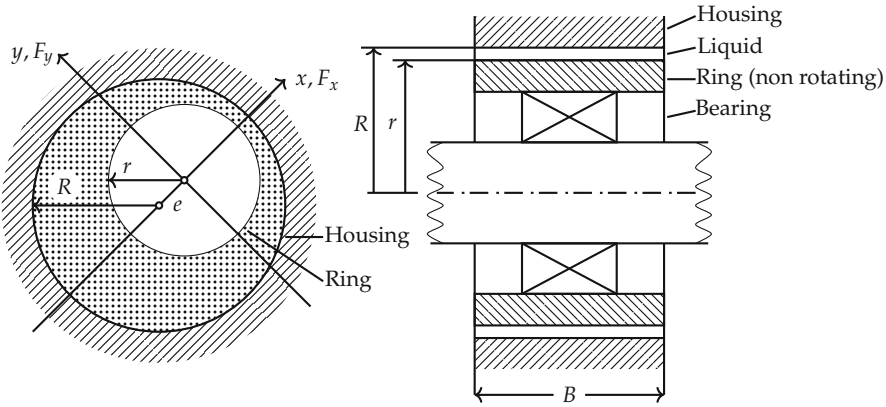

Fig. 45 Squeeze film damper

medium in the gap. Using a linear approximation we may write:

$$F_x(t) = d_x \dot{x} \tag{175a}$$

$$F_y(t) = d_y \dot{y}. \tag{175b}$$

The above is valid even for an eccentric position. As opposed to a journal bearing squeeze film dampers are open at the sides and have no pockets and have no coupling terms in the principle frame of reference. For a regular cylindrical design and centric position $d_x = d_y$:

$$d_x = \frac{2B\eta}{\Psi^3}\beta_x^*, \qquad d_y = \frac{2B\eta}{\Psi^3}\beta_y^*. \tag{176}$$

Using Eq. (176) the damping coefficients d_x, d_y can be calculated. The dependence of β_x^*, β_y^* on eccentricity and the ratio of widths B/D are shown in Figs. 46 and 47. For high vibration velocities, inertial characteristics must also be taken into account [57]. As expected from Eq. (175), until the load limit, the vibration velocity amplitude will increase linearly after which cavitation will occur in the squeeze film leading to reduced damping performance or even complete failure. Load limits may be altered by changing the static oil pressure in the damper.

3.6 Assemblies

In assemblies, many components are joined together between which energy dissipation can occur due to relative motion. The total loss factor can be given as follows:

$$\chi_S = \frac{\Sigma_i W_{Di} + \Sigma_j W_{DFj} + \Sigma_k W_{DAk}}{2\pi U_{ges}}. \tag{177}$$

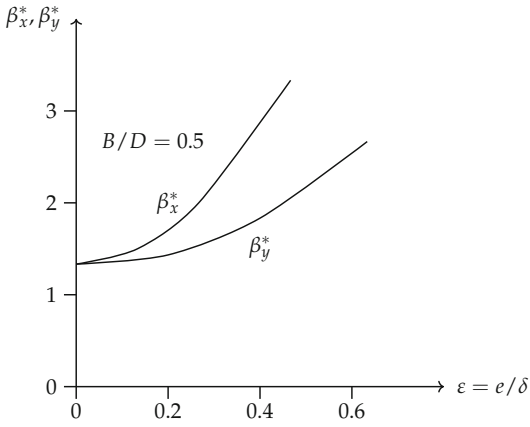

Fig. 46 Relative damping coefficients of a squeeze film damper as a function of relative eccentricity, as per [35]

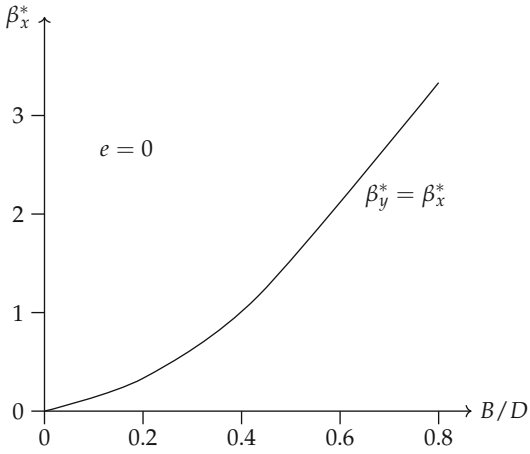

Fig. 47 Relative damping coefficients of a squeeze film damper as a function of relative eccentricity, as per [35]

In the above equation the following dissipation energies occur:

- component damping W_D
- joint damping W_{DF}
- external damping W_{DA}

A synthetic determination of χ_S is problematic and can only be successful in simple cases. The loss factor corresponding to the rth eigen vibration is calculated via a weighted summation [17]:

$$\chi_S^{(r)} = \frac{\sum_{j=1}^{N} \chi_{Sj}\, U_j^{(r)}}{\sum_{j=1}^{N} U_j^{(r)}}. \tag{178}$$

4 Models for Damped Structures

In Sects. 2.1 through 2.3, we dealt with deformations in structures as a whole and also deformations on the surface. It is clear that the usability of a particular model is subject to the problem formulation. In the models presented below, we assume linear damping. In light of what was said in the earlier paragraph, the linearity condition should be checked ascertained in case of application.

4.1 Basic Model

A standard model in vibration engineering is the 1-DOF oscillator. This may be used to model oscillatory systems such as mechanical, electrical, acoustic, or fluidic systems. In a mechanical system, there is the exchange of energy from potential energy to kinetic energy. Due to damping effects, energy is dissipated, and the free vibrations decay. In case of an externally applied force, there is also a phase-shift between excitation and response resulting in hysteresis. The governing equation of the model, see Fig. 48, is as follows:

$$m\ddot{u} + d\dot{u} + ku = F(t) \tag{179}$$

where,

u	displacement at time t
$F(t)$	external force
m	mass
k	spring stiffness
d	damping coefficient

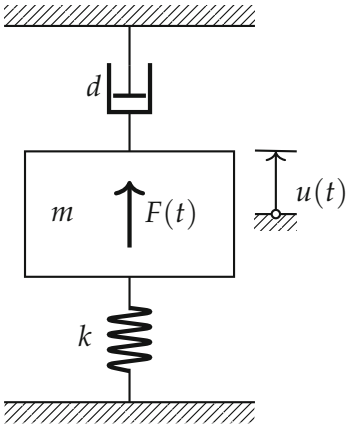

Fig. 48 Mechanical system with translatory vibrations

4.1.1 Free Vibrations with F(t) = 0

With a natural frequency of:

$$\omega_0 = \sqrt{\frac{k}{m}} \tag{180}$$

damping ratio,

$$\vartheta = \frac{d}{2\sqrt{km}} \tag{181}$$

the natural angular frequency ω_d of the damped system,

$$\omega_d = \omega_0 \sqrt{1 - \vartheta^2} \tag{182}$$

the decay coefficient,

$$\delta = \vartheta \omega_0 \tag{183}$$

and the abbreviation

$$\omega_d^* = \omega_0 \sqrt{\vartheta^2 - 1} \tag{184}$$

the time dependent solution of the free vibrator with $F(t) = 0$ and initial conditions $u(0) = u_0$ and $\dot{u}(0) = v_0$:

- for $0 \leq \vartheta < 1$:

$$u(t) = e^{-\delta t} \left[u_0 \cos \omega_d t + \frac{\delta u_0 + v_0}{\omega_d} \sin \omega_d t \right] \tag{185a}$$

$$u(t) = e^{-\delta t} \hat{u} \sin(\omega_d t + \varphi) \tag{185b}$$

where,

$$\hat{u} = \sqrt{u_0^2 + \left(\frac{\delta u_0 + v_0}{\omega_d} \right)^2} \tag{185c}$$

$$\tan \varphi = \frac{u_0 \omega_d}{\delta u_0 + v_0} \tag{185d}$$

- for $\vartheta = 1$:

$$u(t) = e^{-\omega_0 t} [u_0 (1 + \omega_0 t) + v_0 t] \tag{186}$$

- for $\vartheta > 1$:

$$u(t) = e^{-\delta t}\left[u_0 \cosh \omega_d^* t + \frac{\delta u_0 + v_0}{\omega_d^*} \sin \omega_d^* t\right]. \tag{187}$$

When no damping is present the above equations reduce to harmonic vibrations with angular velocity ω_0. When damping is very high, i.e., $\vartheta \geq 1$ the time history curve passes through a zero at most, once.

The most common case in engineering is when damping is weak, i.e., $\vartheta < 1$, there is a succession of zero crossings at a time interval of:

$$T_d = \frac{2\pi}{\omega_d} > T_0 = \frac{2\pi}{\omega_d}. \tag{188}$$

The amplitude decay occurs on a logarithmic scale as given below:

$$\Lambda = \ln \frac{u(t)}{u(t + T_d)} = \delta T_d = 2\pi \frac{\vartheta}{\sqrt{1 - \vartheta^2}}. \tag{189}$$

If damping is very weak:

$$\Lambda = 2\pi\vartheta. \tag{190}$$

4.1.2 Forced Vibrations Where F(t)≠0

If the external force is a harmonic excitation force:

$$F(t) = \hat{F} \cos(\Omega t) \tag{191}$$

the displacement can be written as:

$$u(t) = \hat{u} \cos(\Omega t - \zeta) \tag{192}$$

where,

$$\hat{u} = \frac{\hat{F}}{k} \alpha(\eta, \vartheta). \tag{193}$$

In the above equation, α is the frequency-dependent amplitude with the amplitude-frequency characteristic

$$\alpha(\eta, \vartheta) = \frac{1}{\sqrt{(1 - \eta^2)^2 + (2\vartheta\eta)^2}} \tag{194}$$

where the frequency ratio is:

$$\eta = \frac{\Omega}{\omega_0}. \tag{195}$$

ζ is the angle of lag and is given by:

$$\tan\zeta = \frac{2\vartheta\,\eta}{1-\eta^2} \qquad \text{where, } 0 \le \zeta < \pi. \tag{196}$$

Dissipation of energy by the damper can be computed using:

$$W_{Dh} = \pi\, d\, \Omega\, \hat{u}^2. \tag{197}$$

Using the term for loss factor Sect. 3.1, we get:

$$U_{\max} = \frac{1}{2} k \hat{u}^2 \tag{198}$$

$$\chi = \frac{W_{Dh}}{2\pi\, U_{\max}} = \frac{d\,\Omega}{k}. \tag{199}$$

In case of resonance $\Omega = \omega_0$ or $\eta = 1$ results in:

$$\chi_0 = \frac{d\,\omega_0}{k} = 2\vartheta. \tag{200}$$

In complex notation:

$$F(t) = \hat{F}\cos(\Omega t + \gamma) = \mathrm{Re}[\underline{\hat{F}}\, e^{i\Omega t}] \tag{201}$$

$$u(t) = \hat{u}\cos(\Omega t + \beta) = \mathrm{Re}[\underline{\hat{u}}\, e^{i\Omega t}]. \tag{202}$$

$\underline{\hat{F}}$ and $\underline{\hat{u}}$ are complex amplitudes as can be seen from Fig. 49:

$$\underline{\hat{F}} = \hat{F} e^{i\gamma} \tag{203}$$

$$\underline{\hat{u}} = \hat{u} e^{i\beta}. \tag{204}$$

Therefore, the angular phase difference can be given by:

$$\zeta = \gamma - \beta. \tag{205}$$

In complex notation, the following frequency responses occur:

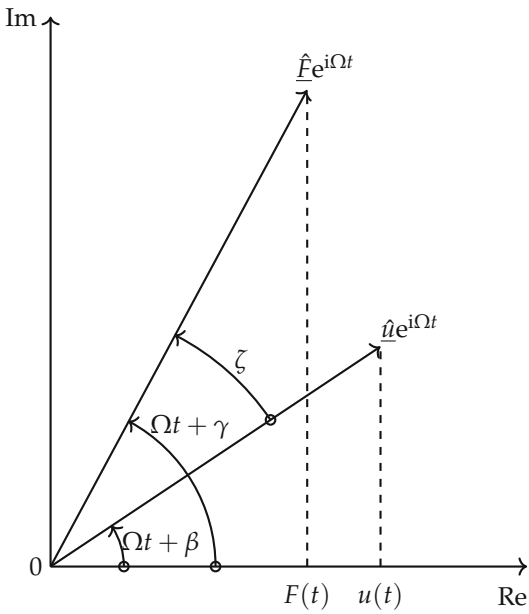

Fig. 49 Forced harmonic vibration on the complex plane. The pointers rotate at the angular velocity Ω.

4.1.3 Dynamic Compliance (Receptance)

$$\frac{\hat{\underline{u}}}{\hat{\underline{F}}} = \frac{\alpha}{k} e^{-i\zeta} = \frac{1}{k} \frac{1}{(1-\eta^2) + i2\vartheta\eta} \tag{206a}$$

$$\frac{\hat{\underline{u}}}{\hat{\underline{F}}} = \frac{1}{k} \left[\frac{1-\eta^2}{(1-\eta^2)^2 + (2\vartheta\eta)^2} + i \frac{-2\vartheta\eta}{(1-\eta^2)^2 + (2\vartheta\eta)^2} \right] \tag{206b}$$

4.1.4 Dynamic Stiffness

$$\frac{\hat{\underline{F}}}{\hat{\underline{u}}} = \frac{k}{\alpha} e^{i\zeta} = k[(1-\eta^2) + i2\vartheta\eta] \tag{207}$$

4.1.5 Mobility (Admittance)

$$\frac{\hat{\dot{\underline{u}}}}{\hat{\underline{F}}} = i\,\Omega \frac{\hat{\underline{u}}}{\hat{\underline{F}}} = i\Omega \frac{\alpha}{k} e^{-i\zeta} \tag{208a}$$

$$\frac{\hat{\dot{\underline{u}}}}{\hat{\underline{F}}} = \frac{\eta}{\sqrt{km}} \left[\frac{2\vartheta\eta}{(1-\eta^2) + (2\vartheta\eta)^2} + i \frac{1-\eta^2}{(1-\eta^2) + (2\vartheta\eta)^2} \right] \tag{208b}$$

4.1.6 Mechanical Impedance

$$\frac{\underline{\hat{F}}}{\underline{\hat{\dot{u}}}} = \frac{\underline{\hat{F}}}{i\Omega\underline{\hat{u}}} = \frac{k}{i\Omega\alpha}e^{i\zeta} = d\frac{2\vartheta\eta - i(1-\eta^2)}{2\vartheta\eta} \tag{209}$$

4.1.7 Accelerance

$$\frac{\underline{\hat{\ddot{u}}}}{\underline{\hat{F}}} = -\Omega^2\frac{\underline{\hat{u}}}{\underline{\hat{F}}} = -\Omega^2\frac{\alpha}{k}e^{-i\zeta} \tag{210a}$$

$$\frac{\underline{\hat{\ddot{u}}}}{\underline{\hat{F}}} = -\frac{\eta^2}{m}\left[\frac{1-\eta^2}{(1-\eta^2)^2+(2\vartheta\eta)^2} + i\frac{2\vartheta\eta}{(1-\eta^2)+(2\vartheta\eta)^2}\right] \tag{210b}$$

4.1.8 Dynamic Mass or Inertance

$$\frac{\hat{F}}{\underline{\hat{\ddot{u}}}} = -\frac{1}{\Omega^2}\frac{\hat{F}}{\underline{\hat{u}}} = -m\frac{1}{\eta^2\alpha}e^{i\zeta} = -m\frac{(1-\eta^2)+i2\vartheta\eta}{\eta^2} \tag{211}$$

It is possible to represent complex frequency responses in the form of:

- Amplitude and phase frequency response
- Real- and imaginary-part frequency response
- Locus diagram in the complex plane
- Logarithmic plotting in the Bode diagram

4.2 Structures with a Finite Number of Degrees of Freedom

For a finite element or boundary element implementation, we discretize the domain so as to have a finite number of degrees of freedom. Damping can be accounted for in the following ways:

- viscoelastic material behavior
- structural damping with given frequency dependence
- local energy dissipation

With the help of special damping matrices and nodal transformation, equations of motion can be decoupled and solved. If such decoupling is not reflective of the actual system, coupling effects need to be incorporated. If decoupling is not possible, bimodal calculation [75] needs to be carried out.

4.2.1 N-Parameter Model for Viscoelastic Material Behavior

In a discretized domain, let the displacement vector be $\boldsymbol{u} = \{u_1, u_2, \ldots u_n\}^T$. Assuming linear behavior and no damping, the equation of motion is given by:

$$\boldsymbol{M}\ddot{\boldsymbol{u}} + \boldsymbol{K}\boldsymbol{u} = \boldsymbol{f}(t) \tag{212}$$

Here $\boldsymbol{M}$ is the symmetrical, positive definite mass matrix, and $\boldsymbol{K}$ is the symmetrical, positive definite or semi-definite elastic stiffness matrix. $\boldsymbol{K}$ and $\boldsymbol{f}(t)$ may be determined using a finite element model with $\boldsymbol{u_e}(t)$ as the nodal displacements and $\boldsymbol{N}(x, y, z)$ as the trial or shape functions, we obtain the displacement vector as:

$$\boldsymbol{v}(x, y, z, t) = \boldsymbol{N}(x, y, z)\, \boldsymbol{u_e}(t). \tag{213}$$

The strain vector:

$$\boldsymbol{\varepsilon} = \{\varepsilon_{xy}, \varepsilon_{yz}, \varepsilon_{zx}, \varepsilon_{xx}, \varepsilon_{yy}, \varepsilon_{zz}\}^T \tag{214}$$

can be obtained via a differential operator $\boldsymbol{C}$ as shown below:

$$\boldsymbol{C} = \begin{pmatrix} \frac{1}{2}\frac{\partial}{\partial y} & \frac{1}{2}\frac{\partial}{\partial x} & 0 \\ 0 & \frac{1}{2}\frac{\partial}{\partial z} & \frac{1}{2}\frac{\partial}{\partial y} \\ \frac{1}{2}\frac{\partial}{\partial z} & 0 & \frac{1}{2}\frac{\partial}{\partial x} \\ \frac{\partial}{\partial x} & 0 & 0 \\ 0 & \frac{\partial}{\partial y} & 0 \\ 0 & 0 & \frac{\partial}{\partial z} \end{pmatrix} \tag{215}$$

$$\boldsymbol{\varepsilon} = \boldsymbol{C}\, \boldsymbol{v} = \boldsymbol{C}\, \boldsymbol{N}\, \boldsymbol{u_e} = \boldsymbol{C_N}\, \boldsymbol{u_e} \tag{216}$$

The elemental stiffness matrix is given by [68, 79]:

$$\boldsymbol{K_e} = \int_V \boldsymbol{C_N^T}\, \boldsymbol{E}\, \boldsymbol{C_N}\, \boldsymbol{dV}. \tag{217}$$

Stress and strain are related by:

$$\boldsymbol{\sigma} = \boldsymbol{E}\, \boldsymbol{\varepsilon}. \tag{218}$$

The global stiffness matrix $\boldsymbol{K}$ is obtained by assembling the element stiffness matrices $\boldsymbol{K_e}$ which link the nodal degrees of freedom to the nodal forces $\boldsymbol{f_e}$:

$$\boldsymbol{K_e}\,\boldsymbol{u_e} = \boldsymbol{f_e}. \tag{219}$$

The case of viscoelasticity is treated by means of the correspondence principle. Starting point are the constitutive equations of the homogeneous isotropic continuum in the form:

$$\boldsymbol{\sigma} = [2G\boldsymbol{E_G} + 3K\boldsymbol{E_K}]\boldsymbol{\varepsilon} \tag{220}$$

where,

$$\boldsymbol{\sigma} = \begin{pmatrix} \sigma_{xy} \\ \sigma_{yz} \\ \sigma_{zx} \\ \sigma_{xx} \\ \sigma_{yy} \\ \sigma_{zz} \end{pmatrix} \quad \boldsymbol{E_G} = \begin{pmatrix} 1 & 0 & 0 & 0 & 0 & 0 \\ & 1 & 0 & 0 & 0 & 0 \\ & & 1 & 0 & 0 & 0 \\ & & & \frac{2}{3} & \frac{1}{3} & \frac{1}{3} \\ & & & & \frac{2}{3} & \frac{1}{3} \\ (\text{symm}) & & & & & \frac{2}{3} \end{pmatrix} \quad \boldsymbol{E_K} = \begin{pmatrix} 0 & 0 & 0 & 0 & 0 & 0 \\ & 0 & 0 & 0 & 0 & 0 \\ & & 0 & 0 & 0 & 0 \\ & & & \frac{1}{3} & \frac{1}{3} & \frac{1}{3} \\ & & & & \frac{1}{3} & \frac{1}{3} \\ & & & & & \frac{1}{3} \end{pmatrix}. \tag{221}$$

Differential Operator Formulation

It should be noted here that the elastic constitutive law as shown in Eq. (220) is related to the viscoelastic constitutive law in the differential operator formulation as shown in Sect. 2.2.7. Shear modulus G and the bulk modulus K have the following relations:

$$G = \frac{1}{2}\left(\frac{Q_1}{P_1}\right) \tag{222}$$

$$K = \frac{1}{3}\left(\frac{Q_2}{P_2}\right). \tag{223}$$

To avoid undefined divisions, we multiply by $P_1 P_2$ and obtain the following:

$$P_1 P_2 \boldsymbol{\sigma}(t) = (\boldsymbol{E_G} Q_1 P_2 + E_K Q_2 P_1)\,\varepsilon(t). \tag{224}$$

Replacing stiffness matrix $2G\boldsymbol{E_G} + 3K\boldsymbol{E_K}$ by the operator $\boldsymbol{E_G} Q_1 P_2 + \boldsymbol{E_K} Q_2 P_1$ gives us the system of differential equations:

$$(\boldsymbol{K_G} Q_1 P_2 + \boldsymbol{K_K} Q_2 P_1)\,\mathbf{u_e} = P_1 P_2\,\boldsymbol{f_e} \tag{225}$$

where,

$$\boldsymbol{K_G} = \int_V \boldsymbol{C}_N^T \boldsymbol{E_G} \boldsymbol{C_N} \mathrm{d}V \tag{226a}$$

$$\boldsymbol{K_K} = \int_V \boldsymbol{C}_N^T \boldsymbol{E_K} \boldsymbol{C_N} \mathrm{d}V. \tag{226b}$$

On the elemental level therefore, the equation of motion, in differential form, is written as:

$$\boldsymbol{M_e} P_1 P_2 \boldsymbol{u_e} + (\boldsymbol{K_G} Q_1 P_2 + \boldsymbol{K_K} Q_2 P_1) \boldsymbol{u_e} = P_1 P_2 \boldsymbol{f_e}. \tag{227}$$

4.2.2 Memory Integral Formulation

The memory integral formulation as shown in Sect. 2.2.5 for the constitutive law in the case of uniaxial loading corresponds to the elastic constitutive law as per Eq. (220):

$$\boldsymbol{\sigma}(t) = [2G_0 \boldsymbol{E_G} + 3K_0 \boldsymbol{E_K}] \boldsymbol{\varepsilon}(t) + \int_0^\infty [2\tilde{G}(\tau) \boldsymbol{E_G} + 3\tilde{K}(\tau) \boldsymbol{E_K}] \dot{\boldsymbol{\varepsilon}}(t-\tau) \mathrm{d}\tau. \tag{228}$$

The shear and compression relaxation functions are given as below, respectively,

$$G(t) = G_0 + \tilde{G}(t) \tag{229}$$

$$K(t) = K_0 + \tilde{K}(t). \tag{230}$$

Using the constitutive law as in Eq. (228) and the matrices in Eqs. (226), Eq. (219) yields:

$$[2G_0 \boldsymbol{K_G} + 3K_0 \boldsymbol{K_K}] \boldsymbol{u_e} + \int_0^\infty [2\tilde{G}(\tau) \boldsymbol{K_G} + 3\tilde{K}(\tau) \boldsymbol{K_K}] \dot{\boldsymbol{u}}_{\boldsymbol{e}}(t-\tau) \mathrm{d}\tau = \boldsymbol{f_e}. \tag{231}$$

Finally, the finite element equation of motion may be expressed as an integro-differential equation:

$$\boldsymbol{M_e} \ddot{\boldsymbol{u}}_{\boldsymbol{e}} + [2G_0 \boldsymbol{K_G} + 3K_0 \boldsymbol{K_K}] \boldsymbol{u_e} + \int_0^\infty [2\tilde{G}(\tau) \boldsymbol{K_G} + 3\tilde{K}(\tau) \boldsymbol{K_K}] \dot{\boldsymbol{u}}_{\boldsymbol{e}}(t-\tau) \mathrm{d}\tau = \boldsymbol{f_e}(t). \tag{232}$$

In the literature solutions from the difference operator formulation can be found. Methods for determining $\boldsymbol{u}(t)$ primarily use:

- numerical integration
- finite time elements
- integral transformations (Laplace, Fourier)

- modal analysis
- matrix functions

Integration of the viscoelastic constitutive equations in order to determine the stress states can be found in the references [69, 76].

4.2.3 2-Parameter Model According to Kelvin-Voigt, Viscous Damping

The equation of motion for the 2-parameter Kelvin-Voigt model is given by:

$$\boldsymbol{M\ddot{u} + D\dot{u} + Ku = f}(t). \tag{233}$$

For the solutions to and the properties of displacements $\boldsymbol{u}(t)$ as given in Eq. (233) under free and forced vibrations can be found in the references [75, 78].
By means of the modal transformation:

$$\boldsymbol{u = \Phi q} \tag{234}$$

we can achieve a decoupling of the n equations of motion from Eq. (233). This is applicable however, only in cases when the following relation holds (commutative property of the system of equations):

$$\boldsymbol{K\,M^{-1}\,D = D\,M^{-1}\,K}. \tag{235}$$

$\boldsymbol{\Phi}$ is an $(n \times n)$ modal matrix given by $\boldsymbol{\Phi} = [\boldsymbol{u_1} \ldots \boldsymbol{u_i} \ldots \boldsymbol{u_n}]$ where $\boldsymbol{u_i}$ are the eigenvectors of the undamped system ($\boldsymbol{D} = \boldsymbol{0}$ in Eq. (233)). The diagonalization condition leads to the decoupled equations as given below:

$$\mathrm{diag}(m_i)\,\ddot{\boldsymbol{q}} + \mathrm{diag}(d_i)\,\dot{\boldsymbol{q}} + \mathrm{diag}(k_i)\,\boldsymbol{q} = \boldsymbol{g} \tag{236}$$

with the following diagonal matrices:

$$\begin{aligned}
\mathrm{diag}(m_i) &= \boldsymbol{\Phi^T\,M\,\Phi} \text{ of the modal masses } m_i \\
\mathrm{diag}(d_i) &= \boldsymbol{\Phi^T\,D\,\Phi} \text{ of the modal damping coefficients } d_i \\
\mathrm{diag}(k_i) &= \boldsymbol{\Phi^T\,K\,\Phi} \text{ of the modal stiffness coefficients } k_i
\end{aligned}$$

and the modal forces $\boldsymbol{g} = \boldsymbol{\Phi^T\,f}$. Real eigenvectors can be scaled arbitrarily. In practical applications, often the quantitively largest component of the eigenvector is set equal to one, while for theoretical studies, the modal masses are frequently set such that $m_i = 1\,\forall\,i$. From this, since $\omega_i^2 = k_i/m_i$, the corresponding modal stiffness $k_i = \omega_i^2$ follows.

In the case where there is Rayleigh-type damping, the damping matrix can be split into a mass proportional and stiffness proportional parts:

$$\boldsymbol{D} = a_0\,\boldsymbol{M} + a_1\,\boldsymbol{K}. \tag{237}$$

For a more general case refer [70, 71]. As in the case referring to Eq. (237), the modal damping ratios:

$$\vartheta_i = \frac{d_i}{2\sqrt{k_t\, m_t}} \tag{238}$$

assigned to the damping coefficients b_i satisfy the relation:

$$\vartheta_i = \frac{1}{2}\left(\frac{a_0}{\omega_t} + a_1\omega_t\right). \tag{239}$$

Here $\omega_t = \sqrt{k_t/m_t}$ is the natural undamped angular frequency. a_0 and a_1 can be calculated from Eq. (240) where ϑ_n and ϑ_m are determined experimentally:

$$\begin{pmatrix} a_0 \\ a_1 \end{pmatrix} = 2\frac{\omega_m\omega_n}{\omega_n^2 - \omega_m^2} \begin{pmatrix} \omega_n & -\omega_m \\ -\dfrac{1}{\omega_n} & \dfrac{1}{\omega_m} \end{pmatrix} \begin{pmatrix} \vartheta_m \\ \vartheta_n \end{pmatrix}. \tag{240}$$

This means that the damping ratios of the remaining eigenforms will have the frequency dependence of Eq. (239), which is shown in Fig. 50. In the case of more than two known damping ratios, one should determine the parameters in Eq. (237) by matching.

When modal dampings are known, $\boldsymbol{D}$ can be calculated from:

$$\boldsymbol{D} = \boldsymbol{\Phi}^{-T}\,\mathrm{diag}(d_i)\boldsymbol{\Phi}^{-1} = \boldsymbol{M}\left(\sum_{i=1}^{n}\frac{2\vartheta_t\,\omega_t}{m_t}\boldsymbol{u}_t\,\boldsymbol{u}_t^T\right)\boldsymbol{M}. \tag{241}$$

When modal decoupling is not possible, Eq. (233) must be used. The damping matrix can be calculated from Eqs. (237) and (241). If $\boldsymbol{D}$ does not satisfy diagonalization condition as in Eq. (235) secondary diagonal elements $d_{ij}^*(i \neq j)$ will occur signifying the so-called *Damping coupling*. This is further discussed in the literature, refer [77, 78].

When component damping is predominant, the diagonalization condition as in Eq. (235) is warranted, but care should be taken not to ignore coupling from discrete dampers. If there is no diagonalization, the eigenvectors of the damped system are complex. A decoupling of the first-order system assigned to Eq. (233):

$$\boldsymbol{A_1}\dot{\boldsymbol{z}} + \boldsymbol{A_0}\boldsymbol{z} = \boldsymbol{b}(t) \tag{242a}$$

where,

$$\boldsymbol{z} = \begin{pmatrix} \boldsymbol{u} \\ \dot{\boldsymbol{u}} \end{pmatrix} \qquad \boldsymbol{b}(t) = \begin{pmatrix} \boldsymbol{f} \\ \boldsymbol{0} \end{pmatrix} \tag{242b}$$

$$\boldsymbol{A_1} = \begin{pmatrix} \mathbf{D} & \mathbf{M} \\ \mathbf{M} & \mathbf{0} \end{pmatrix} \qquad \boldsymbol{A_1} = \begin{pmatrix} \mathbf{K} & \mathbf{0} \\ \mathbf{0} & -\mathbf{M} \end{pmatrix} \tag{242c}$$

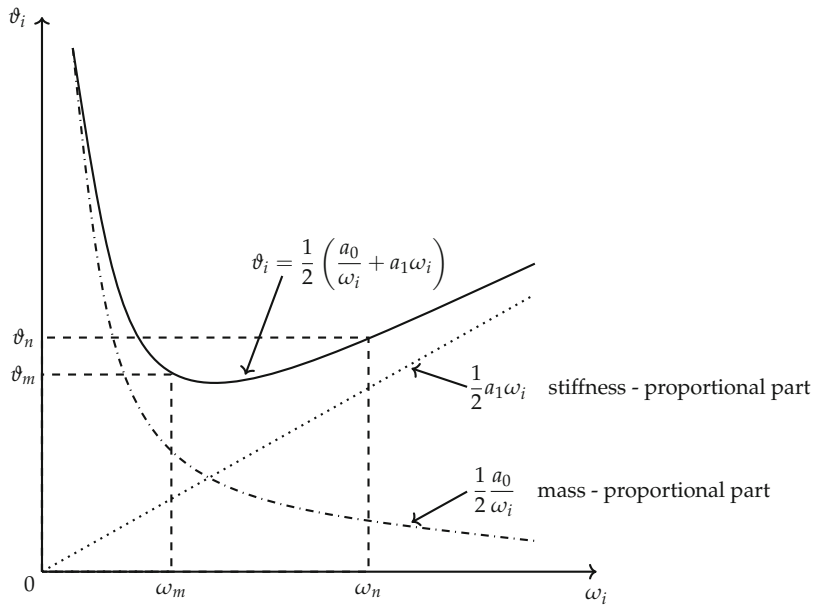

Fig. 50 Connection of damping ratio and associated natural angular frequencies with Rayleigh damping

can always be performed by a bimodal transformation with the right-hand and left-hand eigenvectors of the corresponding eigenvalue problems $\boldsymbol{A}_1\dot{\boldsymbol{z}} + \boldsymbol{A}_1\boldsymbol{z} = \boldsymbol{0}$ and $\boldsymbol{A}_1^T\dot{\boldsymbol{z}} + \boldsymbol{A}_0^T\boldsymbol{z} = \boldsymbol{0}$. Further reference to this can be found in [75, 80].

4.2.4 Damping with Given Frequency Dependence

The complex modulus can be represented in terms of the frequency-dependent damping coefficients R as:

$$\underline{E}(\Omega) = E + i\Omega R. \tag{243}$$

This is the representation of the Kelvin-Voigt model as discussed in Sect. 2. Refer Fig. 51.

The member loss factors $\chi(\Omega)$ can be determined as follows:

$$\chi(\Omega) = \frac{R|\Omega|}{E} > 0 \tag{244}$$

and

$$\underline{E}(\Omega) = E[1 + i\chi(\Omega)\operatorname{sgn}\Omega]. \tag{245}$$

Regardless of the experimentally determined damping coefficients $R(\Omega)$, Eq. (246) can be used. However, as $\chi(\Omega)$ will not be proportional to Ω, one can no longer use

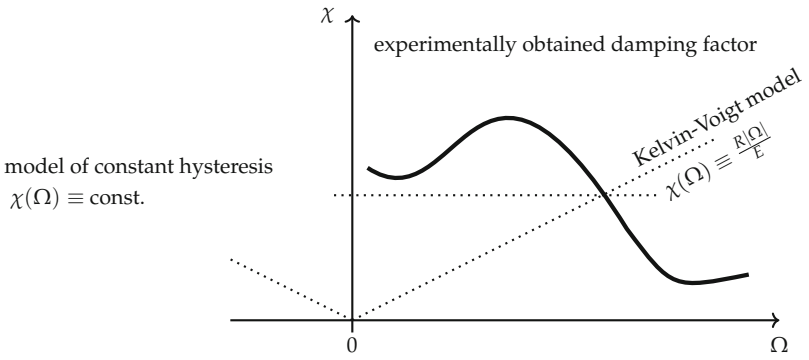

Fig. 51 Frequency dependence of the loss factors

the rheological model. Equation (246) only applies within the frequency range – in other words, to Fourier-transformed state variables:

$$\boldsymbol{U}(i\Omega) = \int_{-\infty}^{\infty} \boldsymbol{u}(t)\ e^{i\Omega t}\mathrm{d}t \tag{246}$$

or to the steady state of a harmonic motion (248)

$$\boldsymbol{u}(t) = \mathrm{Re}(\underline{\hat{\boldsymbol{u}}}\, e^{i\Omega t}). \tag{247}$$

4.2.5 Calculation of Viscoelastic Components by the Boundary Element Method

The boundary element method can be used especially for 3D problems involving compact members. Using the formulations mentioned in Sect. 2.2.7, BEM may be formulated for viscoelastic problems. The BEM reduces the problem dimension by one as calculation is done on the basis of the boundary integral equation.

The problem shown in Fig. 53 describes a viscoelastic domain Ω^* with the boundary Γ, where a mixed boundary value problem is formulated with displacements $\bar{u}_i$ prescribed on Γ_u and tractions $\bar{p}_i$ prescribed on Γ_p. Initial conditions also apply to displacements and velocities.

With the finite element method, trial functions in the element are selected which do not exactly satisfy the field equations. In contrast, the boundary element method uses weighting functions which satisfy the field equations exactly in the domain. At the boundary, approximations are formulated.

In BEM, the fundamental solution is used as weighting functions which are exact solutions of the field equations of an elastic/viscoelastic unbounded space (full space) at a field point $\boldsymbol{x}$ with a single load acting at load point $\boldsymbol{\xi}$. This acts either harmonically time dependent and spatially as a Dirac delta function (the solution in the frequency range of the Fourier transformation, or in the steady state with

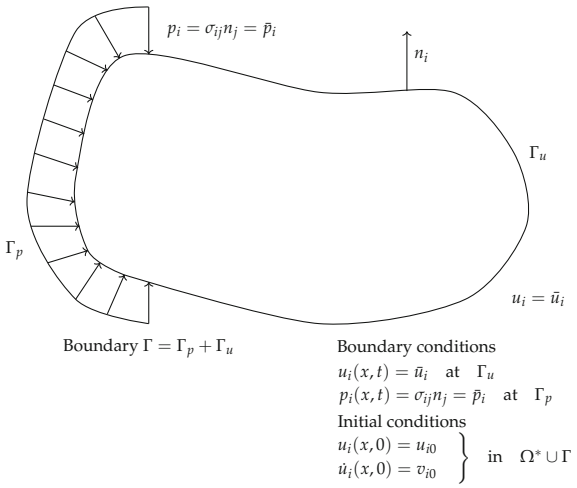

Fig. 52 Region and boundary of a continuum with initial and boundary conditions

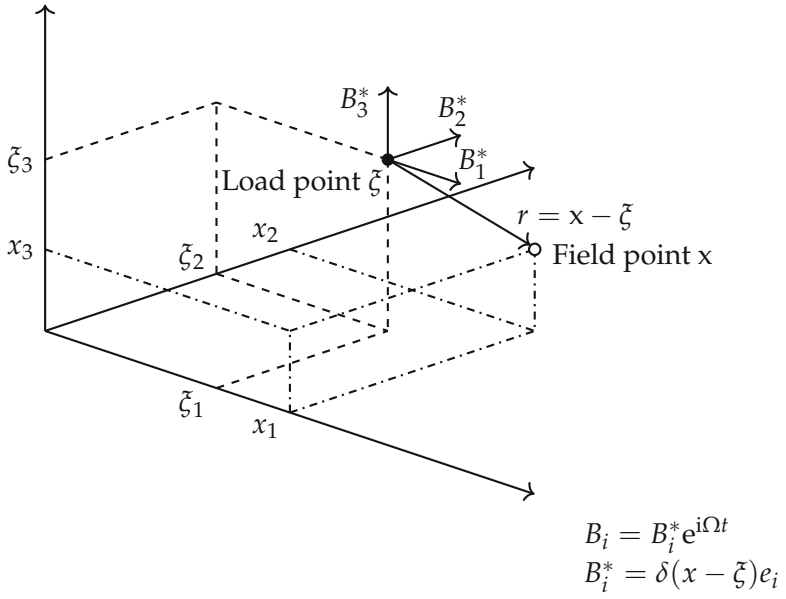

Fig. 53 Load application and geometry for the fundamental solution

harmonic motion, is independent of the initial conditions) or as a spatial and Dirac impulse (we will not treat here the solution in the time domain; see [73]).

Coordinate B_i^* of the load (body force) in the i direction at the source or load point $\boldsymbol{x}$ gives rise to the stress vector coordinates $P_{ji}^*(\boldsymbol{x}, \boldsymbol{\xi}, \Omega)$ and the displacement vector coordinates U_{ij}^* $(\boldsymbol{x}, \boldsymbol{\xi}, \Omega)$ in the j direction at the receiver or field point $\boldsymbol{x}$ (as shown in Fig. 53).

The fundamental solution of the viscoelastic full space satisfies the constitutive equations in Sect. 2.2.7 discussed in Sect. 2. In the fundamental solution of the displacement field $U_{ij}^*(x_i, \xi)$ in the frequency range, the complex moduli of shear $G(i\,\Omega)$ and compression $K(i\,\Omega)$ and the distance $r = |\boldsymbol{x} - \boldsymbol{\xi}|$ are contained in the functions Ψ and κ (see [72, 81]).

$$U_{ij}^*(\boldsymbol{x}, \boldsymbol{\xi}, \Omega) = \frac{1}{4\pi \underline{G}} \left(\Psi \delta_{ij} - \kappa \frac{\partial r}{\partial x_i} \frac{\partial r}{\partial x_j} \right) \tag{248}$$

As per Maxwell and Betti's theorem, the work associated with P_i, B_i, and U_{ij}^* must equal to the work associated with B_i^*, P_{ji}^*, and U_i. With no body forces, we have the equation:

$$U_i(\boldsymbol{\xi}) = \int_\Gamma [(P_j(\boldsymbol{x}) U_{ij}^*(\boldsymbol{x}, \boldsymbol{\xi})) - P_{ij}^*(\boldsymbol{x}, \boldsymbol{\xi}) U_j(\boldsymbol{x})] \mathrm{d}\Gamma \tag{249}$$

Referring to Fig. 52, the boundary values $\bar{U}_t$ at Γ_u and $\bar{P}_t$ at Γ_p are known. In the direct formulation of the BEM, the unknown displacement field U_i and the stress field P_i at the boundary are determined from a boundary integral equation which is derived from the integral Eq. (249) by relocating the load point $\boldsymbol{\xi}$ (see Fig. 53) from a point within the region to the boundary. If the solution fields U_i and P_i on the boundary are known, then it will be possible to calculate from Eq. (249) the displacement field at any point in the interior of the domain.

For a numerical solution apart from the geometry of the component boundary, displacements and stress fields must be approximated. For this purpose, the boundary is discretised into the so-called *boundary elements* within which the approximation is done using the isoparametric concept. Refer Figs. 54 and 55 and [72] for a more detailed discussion. For each load point, we get two or three equations depending whether the problem is two or three dimensional, respectively. These are then numerically integrated using say, the Gauss Quadrature.

Due to the usage of approximations, the boundary integral equations are not completely satisfied. This results in a defect or *residual*. According to the method of weighted residuals, this residual must disappear when weighted with a function and integrated over the boundary. If we chose each node to be a load point –

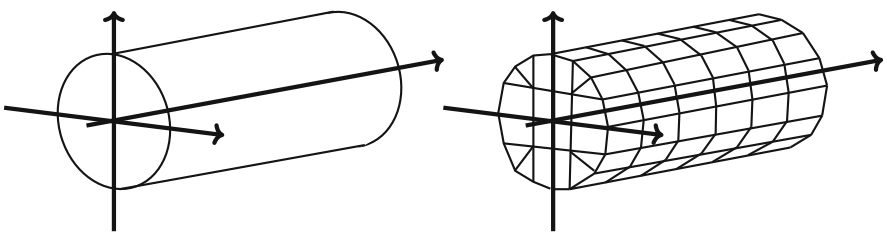

Fig. 54 Discretisation of a surface into boundary elements

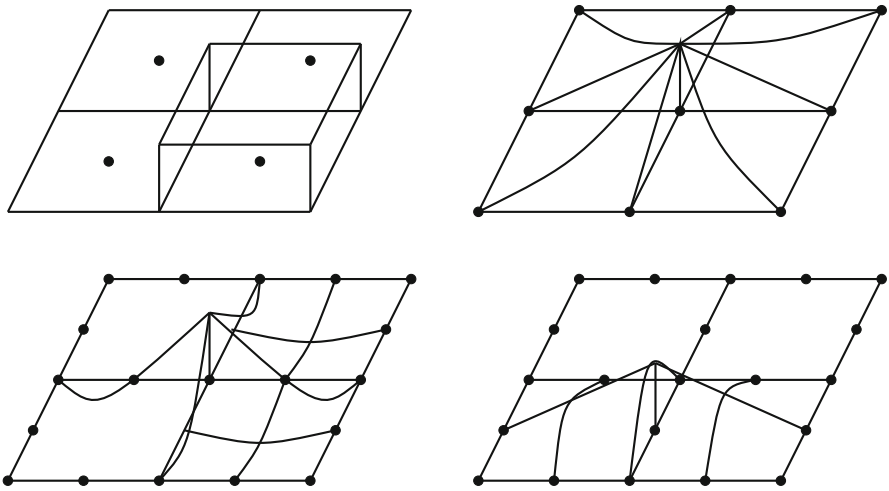

Fig. 55 Two-dimensional trial functions for boundary variables and geometry, The points represent nodes

the number of equations is the same as the number of unknowns. The solution results in boundary displacements and stress. These can be calculated using the constitutive laws. Using inverse Fourier transform, one can convert the frequency domain solution to one in the time domain [74].

5 Experimental Techniques for the Determination of Damping Characteristics

5.1 Experimental Techniques

5.1.1 Basic Procedures

Many of the variables that constitute the mathematical description of materials, components or systems require experimental determination. The excitation and corresponding response are measured and linked or an energy balance is applied. Material properties are determined from component or system level experimentation.

If the nonlinearity of the system and the damping is small, a linear viscoelastic model is a reasonable approximation. However, the diverse approximations in conjunction with measurement errors have a cumulative effect on the end result and thus give rise to a great deal of scatter in the results of identified damping measures.

5.1.2 External Damping

Damping measurement is influenced by the loss of mechanical energy due to external factors *(external damping)*. The following are some of these factors:

- ambient air
- bearing points
- losses due to clamping
- parts of the measure instrument itself

In measurement of cases with low damping special care must be taken to avoid external damping.

5.1.3 Applicability of Results

Factors influencing the damping characteristics can be classified into three categories:

- material parameters such as chemical composition and cross-linking in polymers and anisotropies induced via manufacturing processes such as heat treatment
- mechanical loads and deformations such as the magnitude of the deformations or the damage history
- ambient influences and test conditions

Measured damping characteristics are highly specific to testing conditions, and therefore global application is problematic especially in the case of nonlinear damping.

5.2 Experimental Techniques and Types of Apparatus

5.2.1 Survey of Experimental Techniques

With powerful computers, these days, complex numerical identification algorithms can be used. This section however deals with fundamental evaluation methods which make possible a fast estimation of parameters and checking of the numerical results. There is a diverse array of applications of damping and its measurement that can be converted from one to the other via calculation. Evaluation of measurement results in order to determine damping characteristic values can be made easier if experimental techniques are used which come close to the operational conditions which apply in the real world.

For example, in solids, determination of *creep* or *relaxation functions*, is done via a *creep* or *relaxation tests*, respectively. In the case of fluids, evaluation of flow behavior is also required. For a more detailed discussion, refer [94].

5.2.2 Quasi-Static Methods for the Determination of Material Properties

Quasi-static methods include the creep and relaxation tests for solids and the determination of its viscosity in the case of fluid. Loads and displacements are measured temporally, while stress and strain are determined by geometry factors called c_{geom}. Creep and relaxation functions can be determined by following the guidelines based on Sect. 2.

5.2.3 Experimental Determination of Damping in Solid Bodies with a Low Shear Modulus

Materials with a shear modulus in the range of $0.1\,\mathrm{N/mm^2} \leq G \leq 100\,\mathrm{N/mm^2}$ create some issues regarding external damping, but this can be overcome by using sufficiently rigid testing equipment. Specimens used to determine damping characteristics from creep tests are usually simple shear specimens, tension specimens, and torsion specimens with a rectangular cross-section as shown in Fig. 56.

The following equations for converting measured loads (forces F and torsional moments M_T) and deformations (extensions Δl and torsions $\Delta\varphi$) into stresses (σ and τ) and distortions (elongations ε and slip angle γ) apply to these.

$$\text{Shear specimen}: \quad \frac{\tau}{\gamma} = \frac{1}{c_{\text{geom}}}\frac{F}{\Delta l} \quad \text{where} \quad c_{\text{geom}} = \frac{bl_0}{a} \tag{250a}$$

$$\text{Tension specimen}: \quad \frac{\sigma}{\epsilon} = \frac{1}{c_{\text{geom}}}\frac{F}{\Delta l} \quad \text{where} \quad c_{\text{geom}} = \frac{ba}{l_0} \tag{250b}$$

$$\text{Torsion specimen}: \quad \frac{\tau}{\gamma} = \frac{1}{c_{\text{geom}}}\frac{M_T}{\Delta\varphi} \quad \text{where} \quad c_{\text{geom}} = \frac{ba^3c_1}{l_0}. \tag{250c}$$

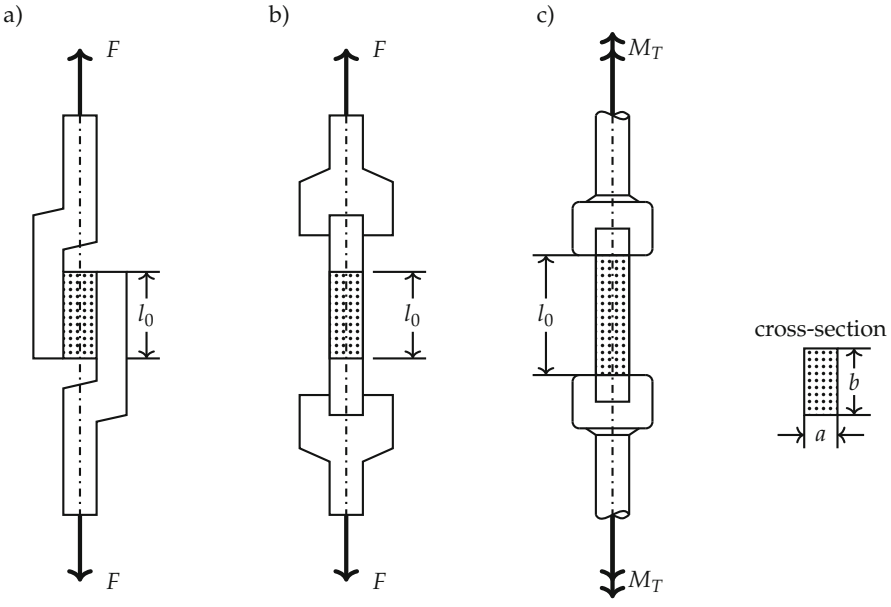

Fig. 56 Solid specimens for creep and relaxation tests (**a**) Specimen under pure shear (in central longitudinal cross-section) (**b**) Specimen with evenly distributed tensile stress (outside the clamping zone) (**c**) Torsional specimen with rectangular cross-section (inhomogeneous distribution of the shear stress and cross-sectional camber)

For a more detailed description of the methodology for tests on the above mentioned specimens, refer [94].

5.2.4 Experimental Determination of Damping in Solid Bodies with a High Shear Modulus

For specimens of high stiffness, testing machines with high stiffness are required. Such machines for creep and stress relaxation under torsion have been developed. Further reading can be done in [85]. Solids whose viscoelastic behavior can be reproduced by a Kelvin-Voigt model as a parallel arrangement of spring and damper only exhibit signs of creep and negative creep but not of relaxation as shown in Fig. 57. Basic equations with regard to storage modulus E' and damping coefficient R are:

$$E' = \frac{\sigma_\infty}{\varepsilon_0} \qquad R = \frac{\sigma_0}{(\mathrm{d}\varepsilon/\mathrm{d}t)_{t=0}}. \tag{251}$$

5.2.5 Experimental Determination of Damping in Viscous Liquids

The standardized measurement equipment used for determining the dynamic viscosity $\eta(T, \dot{\gamma})$ of Newtonian liquids is the flow viscosimeter, where, T is the temperature and $\dot{\gamma}$ is the shear speed given by $\dot{\gamma} = \mathrm{d}v/\mathrm{d}h$. Many different types

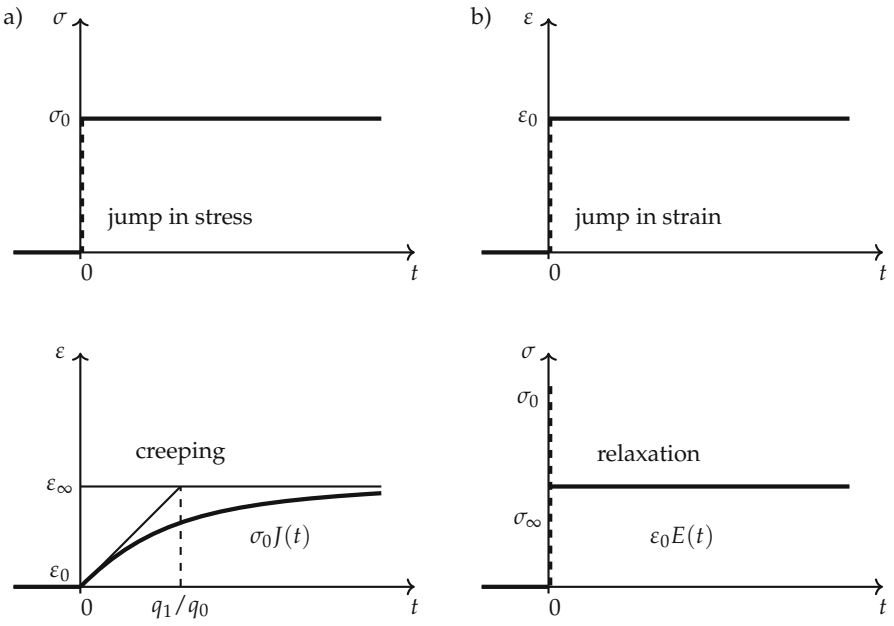

Fig. 57 Stress and strain plotted against time in the creep test and in the relaxation test with tension specimens (ideal curve with Kelvin-Voigt model) (**a**) Creep Test (**b**) Relaxation Test

of viscosimeters are available – a few rotational viscosimeters are shown in Fig. 58. Major equations involved in the experimental set up are as follows:

$$\eta = \frac{\tau}{\dot{\gamma}} = \frac{1}{c_{\text{geom}}} \frac{M_T}{\dot{\varphi}}. \tag{252}$$

For a cone plate viscosimeter shown in Fig. 58a:

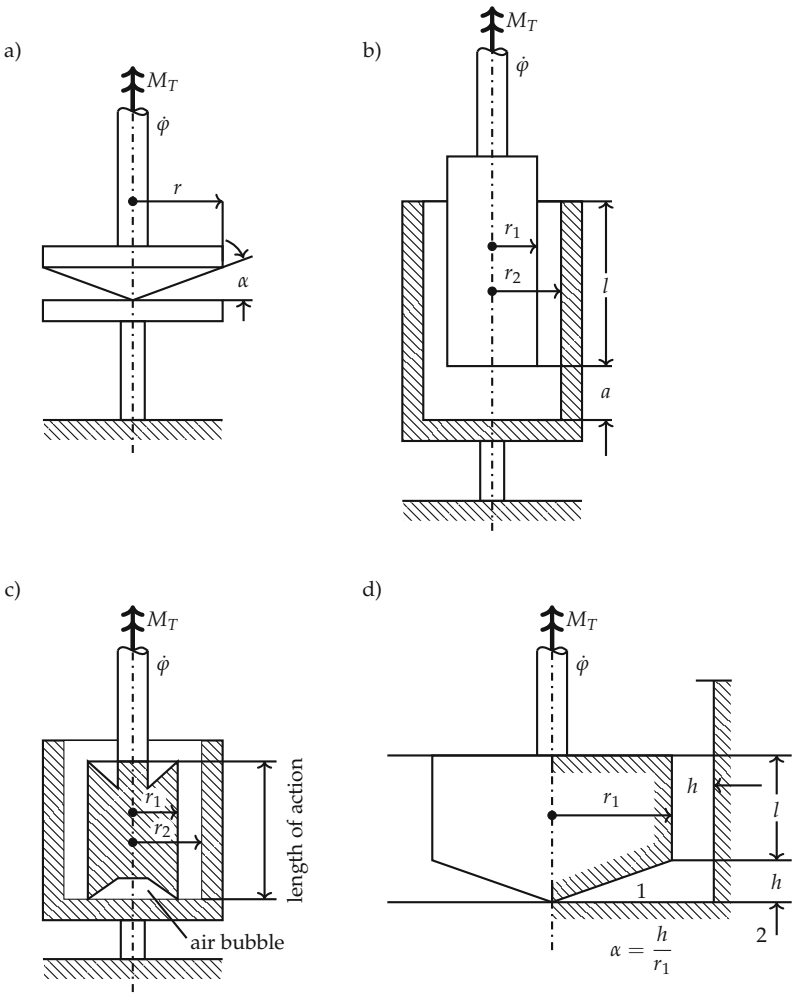

Fig. 58 Types of rotation viscosimeters (**a**) Cone-plate viscometer (**b**) Simple shear flow between coaxial cylinders (Couette flow) (**c**) Shear flow between coaxial cylinders with flat end faces (**d**) Shear flow between coaxial cylinders and between cone end face and plate ($h \ll r_1$)

$$c_{\text{geom}} = \frac{2\pi r^3}{3a}. \tag{253}$$

For the Couette flow shown in Fig. 58b (exact only for Newtonian liquids) this equation applies:

$$c_{\text{geom}} = \frac{4\pi/(r_1 r_2)^2}{r_2^2 - r_1^2}. \tag{254}$$

In the case of the viscosimeter shown in Fig. 58c, Eq. (254) corresponds to Fig. 58b provided corrections for the ultimate effect of the internal cylinder are included.

Corresponding to Fig. 58d, we have:

$$c_{\text{geom}} = \frac{2\pi r_1^3 \, l \left(1 + \frac{1}{3} r_1 / l\right)}{h}. \tag{255}$$

The following referencing have a detailed discussion on the above mentioned topics: DIN 1342-3, DIN 53018-1 and -2, DIN 51563, DIN 53017, and DIN 53018, [85] and [94].

With silicone oils or melts, it is recommended, as a way of checking the test results, that the so-called reduced viscosity $\eta(T, \dot{\gamma})/\eta_0$ where $\eta_0 = \eta(T, 0)$ be formed and plotted against the reduced shear speed $\dot{\gamma}\eta_0$. In a graph of this kind, the measured values of silicone oils of different characteristic viscosities $\nu_{sn} = \eta_{s0}/\rho$ and temperatures T will lie on approximately the same curve (Fig. 59).

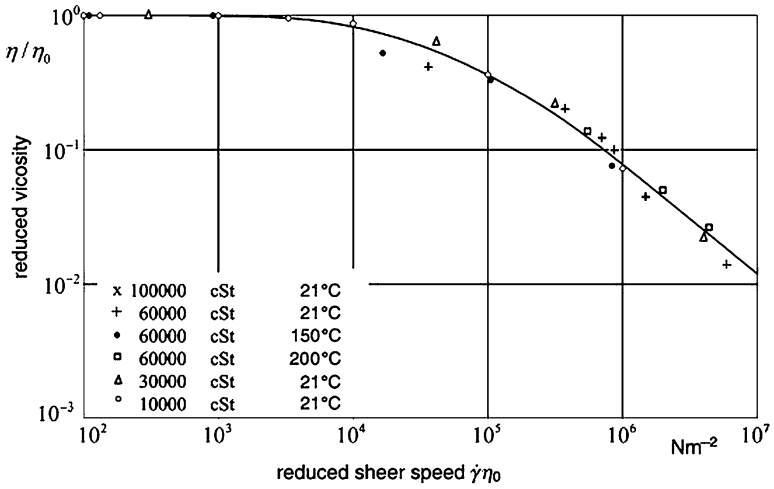

Fig. 59 Reduced viscosity as a function of reduced shear speed (Note: $1cSt = 10^{-6}\text{m}^2/\text{s}$) (source: VDI guideline 3830)

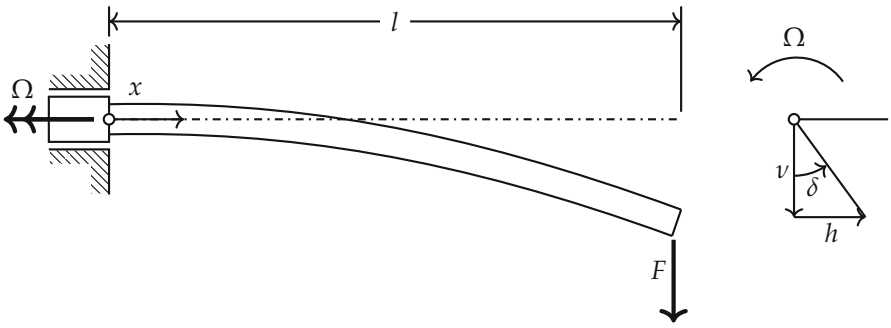

Fig. 60 Method of rotating bending

5.2.6 Determination of Damping in Uniformly Rotating Specimens

In rotating, rotationally symmetrical and homogeneous specimens, constant forces with constant direction generate harmonically changing stresses within the component. This means that on the basis of measured, time-independent forces and deformations, it is possible to deduce the material characteristic values for harmonic time responses. During the test, a test rod of circular cross-section with fixed diameter d_0 is used which is clamped at one end [83], rotated at the constant angular velocity Ω, and loaded with the constant, directionally true force F (Fig. 60).

Here, we have two displacements, v due to the applied force and h resulting from material damping. The resultant displacement therefore depends on the rotational velocity Ω. For viscous absorption and with the stress strain equation $\sigma = E\varepsilon + R\dot{\varepsilon}$ for the displacement components, the following equations apply where the axial area moment of inertia: $I = \pi d_0^4/64$:

$$v(\Omega) = \frac{F\ l^3}{3EI}\frac{1}{[1+(R\Omega/E)^2]} \tag{256a}$$

$$h(\Omega) = \frac{F\ l^3}{3EI}\frac{R\Omega/E}{[1+(R\Omega/E)^2]}. \tag{256b}$$

From Eqs. (256)

$$E = \frac{F\ l^3}{3\,vI[1+(h/v)^2]} \tag{257a}$$

$$R = \frac{h}{\Omega v}E \tag{257b}$$

where the storage modulus $E' = E$ and the loss modulus $E'' = Eh/v$. The angle δ follows the following relation:

$$\tan\delta = X = \frac{h}{v}. \tag{258}$$

For a detailed explanation with regard to other material types and loading patterns, refer [94].

5.2.7 Determination of Damping in the Case of Free Vibrations with One Degree of Freedom

In a free vibration test, the magnitude of the damping is determined in the form of the logarithmic decrements Λ of the time-decreasing vibration amplitude $A(t)$ or the peak-to-valley value $A^*(t)$. In the case of flexural beams supported on bearings which are free of damping, the free-vibration test is carried out in a vacuum; torsional vibrations are, however, applied by preference. Figures 61 and 62 show the arrangements used for standardized torsional vibration devices. As per Fig. 63, the measured variables are the maximum torsional vibration deflections A_n in the points of maximum excursion or the oscillation peak-to-valley values A_n^*. The procedural details which need to be observed when carrying out a torsional vibration test and related calculations are summarized in DIN EN ISO 6721-2, DIN 1311-2. Important equations are summarized below.

$$\Lambda = \ln\left(\frac{A_{n-1}}{A_n}\right) \approx \ln\left(\frac{A_{n-1}^*}{A_n^*}\right). \tag{259}$$

For the damping ratio

$$\vartheta = \frac{\Lambda}{\sqrt{4\pi^2 + \Lambda^2}}. \tag{260}$$

For weak damping i.e. $\vartheta \ll 1$ we also have $\vartheta \approx \Lambda/(2\pi)$ and therefore

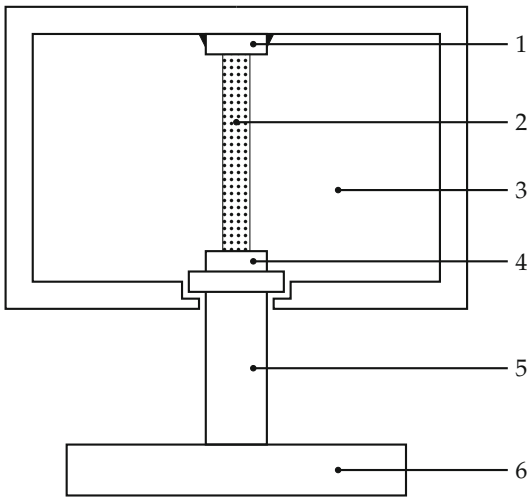

Fig. 61 Torsional vibration apparatus as per DIN EN ISO 6721-2, Method A (1) Upper fixed clamping point (2) Specimen (3) Heating chamber (4) Lower moving clamping point (5) Connection rod (rigid) (6) Inertial element

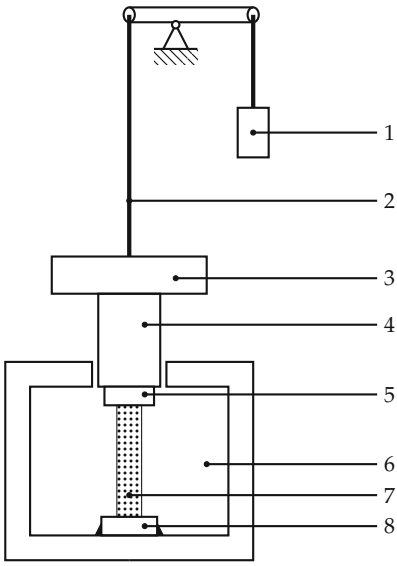

Fig. 62 Torsional vibration apparatus as per DIN EN ISO 6721-2, Method B (1) Counterweight to compensate for vibration body weight (2) Flexible wire with low torsional stiffness (3) Inertial element (4) Connection rod (rigid) (5) Upper moving clamping point (6) Tempering chamber (7) Specimen (8) Lower fixed clamping point

$$\Lambda = \frac{1}{m} \ln \left(\frac{A_n}{A_{n+m}} \right). \tag{261}$$

In case the system behavior is non-linear then $\Lambda_n^* = \Lambda(A_n^*)$. For procedure B,

$$\Lambda = \frac{f_B \Lambda_B - f_0 \Lambda_0}{\sqrt{f_B^2 - f_0^2 + \frac{f_0 \Lambda_0}{2\pi^2}(f_B \Lambda_B - f_0 \Lambda_0)}}. \tag{262}$$

Here variables Λ_0 and f_0 relate to a test not using specimens, variables Λ_B and f_B relate to a test with a wire and specimen. Note that care must be taken to account for the logarithmic dependence of Λ in case of non linear viscous damping. Free vibration tests under flexural stress can in principle be carried out using freely suspended or beams clamped at one end or both ends (Fig. 64). For specific advantages, disadvantages and further related reading refer [94].

5.2.8 Determination of Damping via Specification of Harmonic Deformations

Here, the testing apparatus forces onto the specimen undergoing harmonic displacements of amplitude $\hat{s}$ with a mean displacement s_m. The set up can be seen in Fig. 65. The deformation enforced is $s \approx s_m + \hat{s} \sin \Omega t$. The force F is measured at a specified s which has a steady component F_m and harmonics with whole number multiples of the angular frequency Ω. It has the form:

$$F_1 = \hat{F}_1 \sin(\Omega t + \delta_G). \tag{263}$$

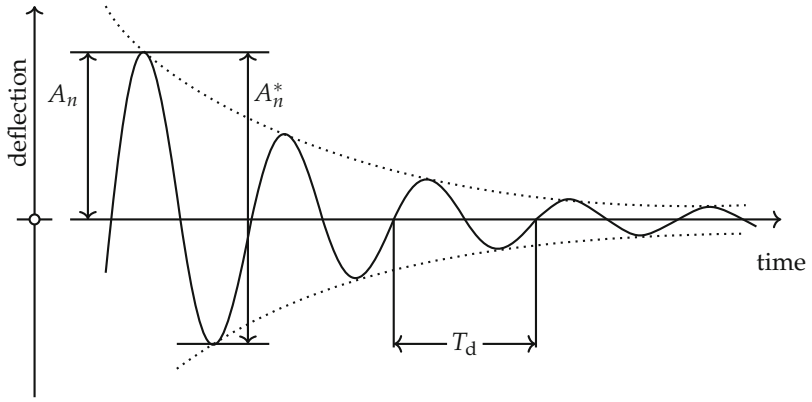

Fig. 63 Time curve for oscillatory deflection with damped free vibrations

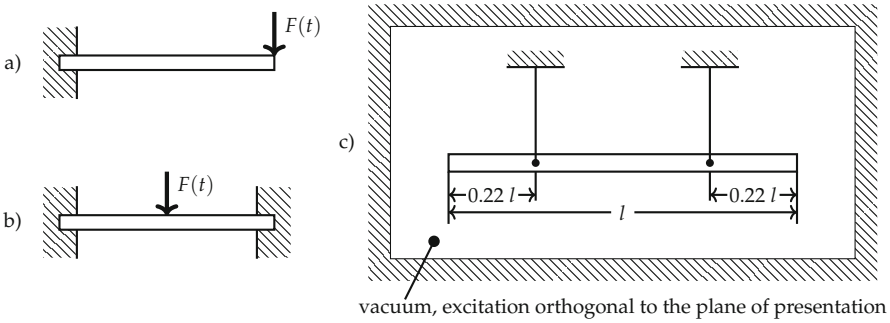

Fig. 64 Bearing supports for flexural rods for decay tests

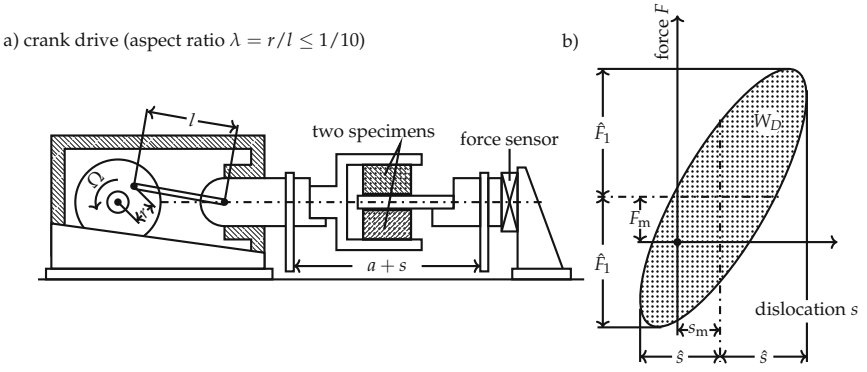

Fig. 65 Shear test with approximate harmonic forced drive (**a**) Test apparatus (**b**) Force-deformation diagram

For cross section and thickness, A_0 and L_0, respectively – the complex shear modulus is

$$|\underline{G}(\Omega, \hat{s})| = \frac{\hat{F}_1 L_0}{2 A_0 \hat{s}}. \tag{264}$$

Also, energy loss per cycle is given by:

$$W_s = \pi \hat{F}_1 \hat{s} \sin \delta_G. \tag{265}$$

From this, the loss factor results as $\chi_G = \tan \delta_G$. $|\underline{E}|$ and χ_E are determined using the strain specimen although this is limited to low frequencies.

5.2.9 Measurement of the Oscillation Amplitude in Vicinity of Resonance (Determination of Halfwidth Value)

If a system only has one degree of freedom or if the natural frequency of one eigenform differs notedly enough from the adjacent, the resonance test for determining damping parameters is the most commonly used method in the frequency range of 20 Hz to 1 kHz.

The damping of a separated degree of freedom can be obtained from the resonance curve by means of the "half-width value" [82] $(\Omega_0 - \Omega_u)$ where care is taken to ensure that resonance maximum is included in the resonance curve. Errors may occur especially if steady state is not achieved or, when the measurement is done if no frequency sampling point coincides with the resonance frequency. In the case of a resonance curve of the vibration velocity resulting from force or spring excitation as shown in Fig. 66, double the damping ratio is expressed as below:

$$2\,\vartheta = \frac{1}{2}\left[\left(\frac{\Omega_0}{\omega_0} - \frac{\omega_0}{\Omega_0}\right) - \left(\frac{\Omega_u}{\omega_0} - \frac{\omega_0}{\Omega_u}\right)\right]. \tag{266}$$

Due to the symmetry, $\Omega_0/\omega_0 = \omega_0/\Omega_u$ the damping ratio is given by the relation:

$$\vartheta = \frac{\Omega_0 - \Omega_u}{2\omega_0} = \frac{1}{2}(\eta_0 - \eta_u). \tag{267}$$

Given above is a basic outline of the idea. Further possibilities, interpretations, and procedures can be found in [94].

5.2.10 Measurement of Amplitudes and Phase Angles

In case a real system can be sufficiently approximated by a 1 DOF oscillator, the following possibilities exist for the determination of the damping ratio. Figure 67 shows the Nyquist curve for the displacement amplitude $\underline{\hat{u}}(\Omega)$. Ω_a and Ω_b are the excitation frequencies at which the tangent to the Nyquist curve is parallel with the imaginary axis. With this, in theory, the damping ration is expressed as:

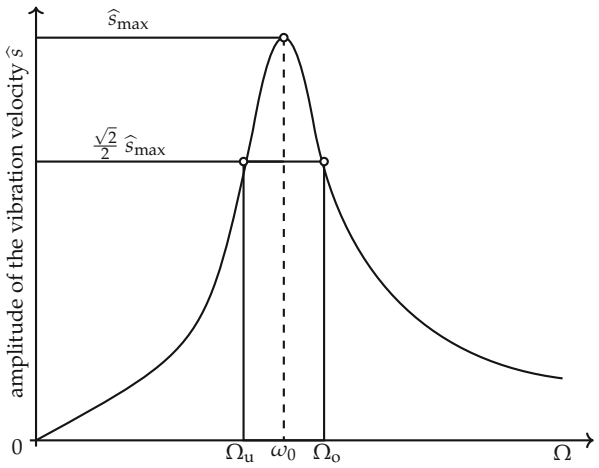

Fig. 66 Amplitude of the vibration velocity with spring or force excitation with resonance maximum and "half-value ordinates" as well as the corresponding angular frequencies Ω_0, Ω_u and ω_0

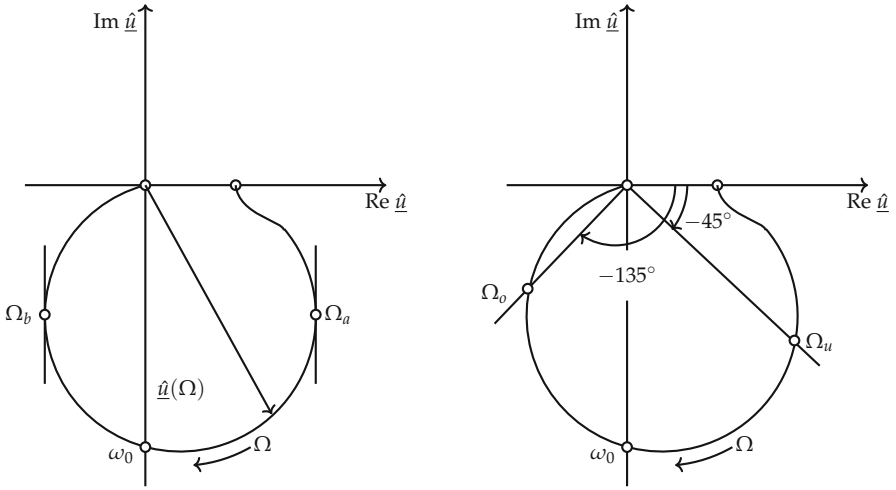

Fig. 67 Nyquist curve of the displacement amplitude with spring force excitation

$$\vartheta = \frac{1}{2}\frac{\Omega_b^2 - \Omega_a^2}{\Omega_b^2 + \Omega_a^2} \tag{268}$$

where Ω_u is the excitation frequency at the intersection of the $-45°$ line and the Nyquist curve and Ω_0 the excitation frequency at the intersection with the $-135°$ line. From this we have, the damping ratio as:

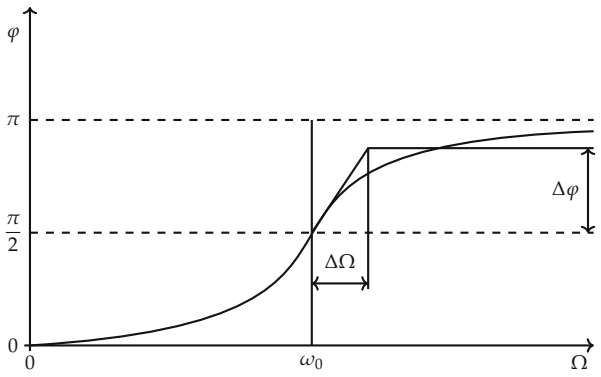

Fig. 68 Phase frequency response with force or displacement excitation

$$\vartheta = \frac{1}{2}\left(\frac{1}{\eta_u} - \eta_u\right) = \frac{1}{2}\left(\frac{\omega_0}{\Omega_u} - \frac{\Omega_u}{\omega_0}\right) \tag{269}$$

and

$$\vartheta = \frac{1}{2}\left(\eta_0 - \frac{1}{\eta_0}\right) = \frac{1}{2}\left(\frac{\Omega_0}{\omega_0} - \frac{\omega_0}{\Omega_0}\right). \tag{270}$$

Another possibility to determine damping is to use the phase frequency response. When $\Omega = \omega_0$:

$$\frac{\mathrm{d}\,\varphi}{\mathrm{d}\,\Omega} = \frac{1}{\omega_0 \vartheta} \tag{271}$$

and as per Fig. 68 we have:

$$\vartheta = \frac{1}{\omega_0}\frac{\Delta\Omega}{\Delta\varphi}. \tag{272}$$

Refer [94] for details about the assumption and applicability of the above mentioned procedure.

5.2.11 Determination of Damping via Thermal Energy Balances

Irreversible deformational work in most cases results in production of measurable heat. Satisfactory results can be obtained for quasi-stationary temperature states. Older studies [86] used specimens immersed in flowing water in the vibration test with measurements of inlet and outlet water temperatures. However, there still remained a large number of potential sources of errors in integral heat quantity determination for the material regions under load.

5.2.12 Energy Balances at the Subsystem Boundaries of Multicomponent Systems

Here, we have the assumption that in the subsystem as shown in Fig. 69 for which the damping is to be measured, the force F can be applied in a harmonic manner and also measured (also the oscillatory moment M_T) along with the displacements u (also the angle of oscillation φ). So we have:

$$u_1 = \hat{u}_1 \cos \Omega t \tag{273a}$$

$$u_2 = \hat{u}_2 \cos(\Omega t - \beta) \tag{273b}$$

$$F_1 = \hat{F}_1 \cos(\Omega t + \delta_1) \tag{273c}$$

$$F_2 = \hat{F}_2 \cos(\Omega t - \beta + \delta_2). \tag{273d}$$

Active power applied at boundary 1 is given as

$$P_1 = \frac{1}{2} \Omega \hat{F}_1 \hat{u}_1 \sin \delta_1 \tag{274}$$

and the active power transmitted at boundary 2

$$P_2 = \frac{1}{2} \Omega \hat{F}_2 \hat{u}_2 \sin \delta_2. \tag{275}$$

Therefore, the energy lost in 1 cycle

$$\Delta W_S = \pi (\hat{F}_1 \hat{u}_1 \sin \delta_1 - \hat{F}_2 \hat{u}_2 \sin \delta_2). \tag{276}$$

Ignoring the inertial forces, the amplitude of the displacement difference is:

$$\Delta \hat{s} = \sqrt{\hat{u}_1^2 + \hat{u}_2^2 - 2 \hat{u}_1 \hat{u}_2 \cos \beta}. \tag{277}$$

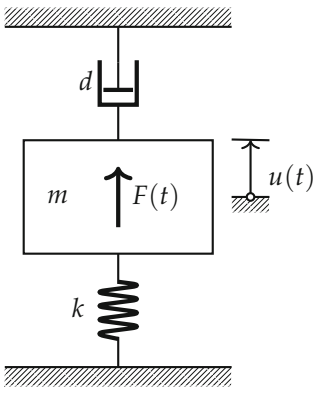

Fig. 69 Subsystem within a multipart total system

The loss angle can be calculated from:

$$\Delta W_S = \pi \hat{F} \Delta \hat{s} \sin \delta. \tag{278}$$

5.2.13 Force and Displacement Measurements at Subsystem Boundaries

Any energy dissipating element is usually a part of a larger system, and its corresponding parameters can be measured without knowing the parameters of the entire system. The structure can be referred in Fig. 70. From the motion equations or directly from a consideration of the complex dynamic stiffness in the subsystem, we obtain the two relations:

$$\underline{\hat{F}} + m_1 \Omega^2 \underline{\hat{u}}_1 + (k + i d\Omega)(\underline{\hat{u}}_2 - \underline{\hat{u}}_1) = \underline{0} \tag{279}$$

$$(k + i d\Omega)(\underline{\hat{u}}_2 - \underline{\hat{u}}_1) - m_2 \Omega^2 \underline{\hat{u}}_2 = \underline{0}. \tag{280}$$

Parameters k and d can be obtained from the complex force and/or displacement amplitudes [82]. For the four complex amplitudes $\underline{\hat{F}}$, $\underline{\hat{u}}_1$, $\underline{\hat{u}}_2$ and $\underline{\hat{w}}$, it must be possible to measure the ratio of any two in quantity and phase. The other complex amplitudes can be eliminated from the two equations (279) and (280). Depending on which variables are measured, formulations can be made for k and d. Further to this, force and distortion amplitudes can also be measured. For a detailed treatment of this, refer [94].

5.3 Special Experimental Techniques for Determining Damping Under Difficult Conditions

5.3.1 Systems with High Damping

In structures where damping is very high, resonance vibration tests may not be accurate enough. This is especially true if stiffness and damping depend on the frequency of excitation or if the excitation force is not large enough to produce sufficiently large oscillations. In such a case, a known damping-free spring with

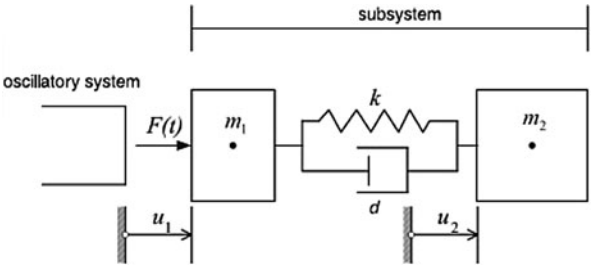

Fig. 70 Subsystem (m_1, m_2) with in-line spring damper element (source: VDI guideline 3830)

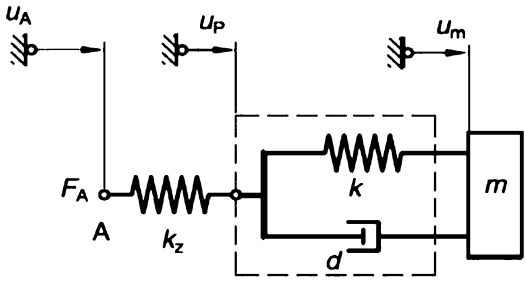

Fig. 71 Reduction in the effective damping due to an additional spring k_z connected in series (source: VDI guideline 3830)

real stiffness k_z can, as shown in Fig. 71, be connected in series with the damped specimen with complex stiffness $k + id\Omega$. The stiffness and the damping coefficient can be determined from the measured complex frequency response of the expanded system. $u_A(t)$, $u_m(t)$, $u_P(t)$ have the following relations between them:

$$k(u_m - u_P) + d(\dot{u}_m - \dot{u}_P) = k_z(u_P - u_A) \tag{281a}$$

$$m\ddot{u}_m = -k_z(u_P - u_A). \tag{281b}$$

For the complex amplitudes $\underline{\hat{u}}_A$, $\underline{\hat{u}}_P$, $\underline{\hat{u}}_m$ the following relations hold:

$$u_A = \mathrm{Re}\{\underline{\hat{u}}_A e^{i\Omega t}\} \quad u_P = \mathrm{Re}\{\underline{\hat{u}}_P e^{i\Omega t}\} \quad u_m = \mathrm{Re}\{\underline{\hat{u}}_m e^{i\Omega t}\} \tag{282}$$

$$(k_z + k + id\Omega)\underline{\hat{u}}_P = (k + id\Omega)\underline{\hat{u}}_m + k_z\underline{\hat{u}}_A \tag{283a}$$

$$k_z\underline{\hat{u}}_P = m\Omega^2\underline{\hat{u}}_m + k_z\underline{\hat{u}}_A. \tag{283b}$$

Elimination of $\underline{\hat{u}}_P$ leads to the complex stiffness

$$(k + id\Omega) = \frac{(\underline{\hat{u}}_m/\underline{\hat{u}}_A)m\Omega^2}{(\underline{\hat{u}}_m/\underline{\hat{u}}_A)(1 - m\Omega^2/k_z) - 1}. \tag{284}$$

Separating the real and imaginary part, stiffness and damping can be found which needs to be determined for every frequency of interest Ω.

This method assumes that the mass m and the stiffness k_z of the additional spring are known. These parameters can be determined experimentally beforehand, with the aid, for example, of a resonance test which does not include the specimen to be tested. The resonance frequency of the entire arrangement can be suitably chosen by selection of mass m. If the stiffness k and damping coefficient d of the specimen are required as a function of the frequency Ω, tests should be carried out with different excitation frequencies and, if necessary, with different additional springs. If k and d can be regarded as frequency independent, taking measurements at different excitation frequencies will minimize random error creating influences.

5.3.2 Flexural Vibrations of Lamellar Specimens

In the field of acoustics, complex moduli or loss factors of elastomers are of much interest in the frequency range of 10 Hz or higher. Flexural vibrations of lamellar specimen with an assumption of the Euler Bernoulli beam theory can be useful for parameter identification [89]. The thickness h must be small as compared to the distance between the adjacent nodes a_k, i.e., $h \leq a_k/6$. The following have proved useful as boundary conditions:

- rigid clamp at on end, the other end unrestrained
- rigid clamps at both ends
- both ends unrestrained

Homogeneous Strips

Homogeneous strips are used for measuring the complex modulus of materials which, having a modulus of elasticity of $E > 5\,\mathrm{e9\,N/m^2}$, are so stiff that the natural frequencies of the strips fall within the frequency range in which the modulus is to be determined. Which measurement technique to use will depend on the magnitude of the loss factor. Some possibilities are:

- resonance test
- free-vibration test

Laminated Strips

For materials which are relatively soft and/or exhibit very heavy damping lamnated strips may be used. For this purpose, stiff and comparatively damping-free strips are bonded together as shown in Fig. 72. A detailed mathematical representation of the above mentioned subheadings can be found in [94].

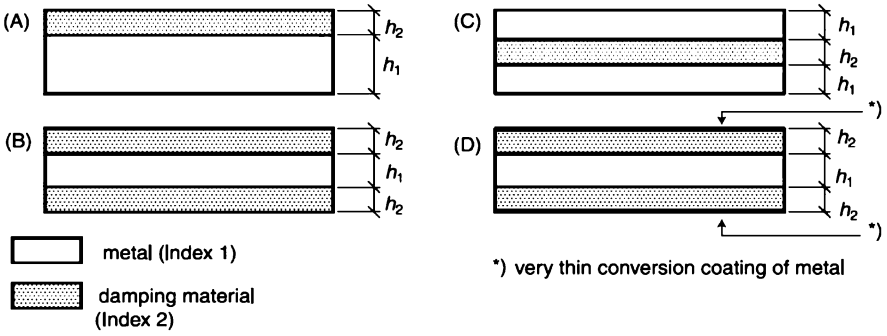

Fig. 72 Examples of cross-sections of layered strips (**a**) two layers (topmost beam [92]) (**b**) three layers, symmetrical (Nashif beam [89]) (**c**) and (**d**) sandwich arrangements (source: VDI guideline 3830)

5.3.3 Longitudinal Waves in Bars

Complex moduli of elasticity can also be determined from longitudinal oscillations in bars. The method involving progressive, damped extensional waves [88] is less advantageous in practical terms – the resonance method is more suitable. One end of the bar is excited; the other end is unrestrained [87] or bears a rigid mass [91]. The complex transfer function between the exciting force and the longitudinal movement supplies the information for identifying the complex modulus.

5.4 Experimental Modal Analysis

Real mechanical problems are problems in continua which are approximated to N (sufficiently large) pointwise degrees of freedom – collocation points. Mathematical formulations exist that describe phenomena of this equivalent model. The model parameters are adjusted so that it gives the best approximation to the real-world problem evaluated in terms of a specific error criterion [84, 90].

5.4.1 Discrete Equivalent Model

In the equation of motion:

$$\boldsymbol{M}\ddot{\boldsymbol{u}} + \boldsymbol{D}\dot{\boldsymbol{u}} + \boldsymbol{K}\boldsymbol{u} = \boldsymbol{f}(t) \tag{285}$$

where $\boldsymbol{u}$ and $\boldsymbol{f}$ are vectors of displacements and excitations at the collocation points. $\boldsymbol{M}$, $\boldsymbol{D}$ and $\boldsymbol{K}$ are the symmetrical, positively (semi-) definite mass, damping and stiffness matrices of the equivalent model. Apart from the symmetry, also,

$$\boldsymbol{K}\boldsymbol{M}^{-1}\boldsymbol{D} = \boldsymbol{D}\boldsymbol{M}^{-1}\boldsymbol{K}. \tag{286}$$

The frequency range Equation (285) reads:

$$\underline{\hat{\boldsymbol{u}}}(i\Omega) = \underline{\boldsymbol{H}}(i\Omega)\ \underline{\hat{\boldsymbol{f}}}(i\Omega) \tag{287}$$

$\underline{\boldsymbol{H}}(i\Omega)$ is the matrix of transfer functions that contains the complex frequency-dependent compliances $\underline{\boldsymbol{H}}_{ln}$ which links the complex Fourier spectra $\underline{\hat{\boldsymbol{f}}}(i\Omega)$ and $\underline{\hat{\boldsymbol{u}}}(i\Omega)$. The Fourier spectrum of a transformable time function is defined by:

$$F\{x\} = \underline{X}(i\Omega) = \int_{-\infty}^{\infty} x(t) e^{-i\Omega t}\,\mathrm{d}t. \tag{288}$$

Eq. (287) also applies in particular even to harmonic excitation and vibratory response:

$$\boldsymbol{f} = \mathrm{Re}\,[\underline{\hat{\boldsymbol{f}}} e^{i\Omega t}] \qquad \text{and} \qquad \boldsymbol{u} = \mathrm{Re}\,[\underline{\hat{\boldsymbol{u}}} e^{i\Omega t}] \tag{289}$$

The assumptions Eqs. (285) and (286) make it possible for the elements of the matrix of the transfer function to be expressed by the N real eigenvectors $\boldsymbol{u}_j$ of the associated undamped system $\underline{\boldsymbol{H}}(i\Omega)$:

$$\boldsymbol{M}\ddot{\boldsymbol{u}} + \boldsymbol{K}\boldsymbol{u} = \boldsymbol{0} \tag{290}$$

and the modal characteristics

$$\underline{H}_{ln} = \sum_{l=j}^{N} \frac{u_{jl}u_{jn}}{k_j - m_j\Omega^2 + i\Omega d_j} = \underline{H}_{nl} \tag{291}$$

where

$m_j = \boldsymbol{u}_j^T \boldsymbol{M}\boldsymbol{u}_j$	are the modal masses
$d_j = \boldsymbol{u}_j^T \boldsymbol{D}\boldsymbol{u}_j$	are the modal damping coefficients
$k_j = \boldsymbol{u}_j^T \boldsymbol{K}\boldsymbol{u}_j$	are the modal stiffnesses

with natural angular frequency $\omega_j = \sqrt{k_j/m_j}$ and modal damping ratios $\vartheta_j = d_j/(2m_j\omega_j)$ we have

$$\underline{H}_{ln} = \sum_{j=l}^{N} \frac{u_{jl}u_{jn}/m_j}{\omega_j^2 - \Omega^2 + i2\vartheta_j\omega_j\Omega} = \underline{H}_{nl}. \tag{292}$$

In experimental modal analysis, a distinction is drawn between time and frequency range evaluations. Time-domain procedures fall back on measured impulse responses; frequency-domain procedures on measured transfer functions. Both types of approach are equivalent from the theoretical point of view since impulse responses $h_{ln}(t)$ and transfer functions $\underline{H}_{ln}(i\Omega)$ are Fourier transform pairs:

$$\underline{H}_{ln}(i\Omega) = F^{-1}\{h_{ln}(t)\} \quad \Leftrightarrow \quad h_{ln}(t) = F\{\underline{H}_{ln}(i\Omega)\}. \tag{293}$$

The following section will therefore be restricted to dealing with the frequency domain.

5.4.2 Basic Principles in the Measurement of Complex Frequency Responses

Due to symmetry, the matrix of transfer functions is also symmetric – which means that the excitation and the response measurement points can be interchanged. Also, a column or a row of the matrix of the transfer functions already contains all eigenvalues. Therefore, measurement of N transfer functions is sufficient (instead of N^2). For this purpose, the structure is either

- excited only at one point n and the responses measured at all N response points
- successively excited at all N collocation points and the response measured only at one and the same point n

The mathematical procedure describing this process in detail can be found in [94].

5.4.3 Evaluation of Measured Frequency Responses at an Isolated Resonance Point

The following methods exclude closely adjacent natural frequencies and evaluate the frequency response in each case in the vicinity of an isolated resonance frequency $\omega_{Gr} \approx \omega_r$ (SDOF identification method). The damping ratio ϑ_r must on the one hand be small enough (approximately $\vartheta \leq 0.1$) for the influence of the r-th eigenform in the frequency response to dominate at the resonance point. On the other hand, it should not be so small that accurate measurements are not possible.

Idealization as Vibrator with One Degree of Freedom

A simple method completely ignores the eigenforms $j \neq r$ at ω_{Gr} chooses the approximation of a system with one DOF. Therefore, in Eq. (292), only:

$$\underline{H}_{lnr} = \frac{u_{rl} u_{rn}/m_r}{\omega_r^2 - \Omega^2 + i2\vartheta_r \omega_r \Omega} = \underline{H}_{ln} \tag{294}$$

is taken into account (Fig. 73).

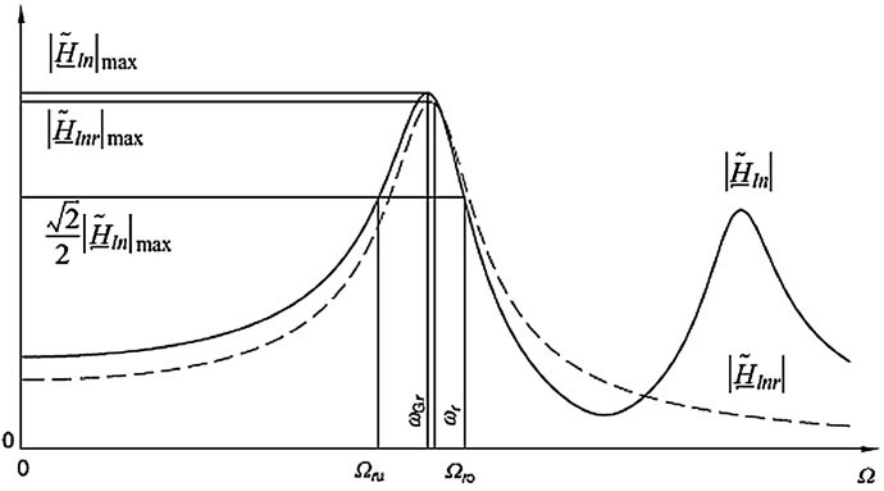

Fig. 73 Value of the frequency response of a vibrating system in the environment of the natural frequency ω_r (source: VDI guideline 3830)

Approximative Inclusion of the Other Degrees of Freedom

The sum in Eq. (292) can be split into $\underline{H}_{lnr}$ as in Eq. (294) and the component covering other eigenforms where $j \neq r$

$$\underline{A}_{lnr}(i\Omega) = \sum_{j=l,\, j\neq r} \frac{u_{jl} u_{jn}/m_j}{\omega_j^2 - \Omega^2 + i2\vartheta_j \omega_j \Omega}. \tag{295}$$

Thus, we have:

$$\underline{\tilde{H}}_{ln}(i\Omega) = \underline{\tilde{H}}_{lnr}(i\Omega) + \underline{\tilde{A}}_{lnr}(i\Omega). \tag{296}$$

Here only a short description of the basic idea of the above two subheadings is covered. Refer [94] for an exhaustive guideline.

5.4.4 Approximation of Measured Frequency Responses in an Interval with Several Resonance Points

The above mentioned methods are not applicable in many cases such as when resonance frequencies lie close to each other. The accuracy obtained is not sufficient if the measured frequency response has several resonance points within a frequency interval. Cases of this call for methods which simultaneously take into account the dynamic behavior of several natural modes of vibration – so-called MDOF (multiple degree of freedom) methods. Many methods for such phenomenon have already been developed [84, 90]. Here a brief outline of a select few methods is presented. A common assumption will be that there exist multiple natural frequencies ω_j where $j \in [J_1, J_2]$.

Incomplete Equivalent Model

Instead of the incomplete frequency response:

$$\underline{H}_{ln}(i\Omega) = \sum_{j=J_1}^{J_2} \frac{u_{jl} u_{jn}/m_j}{\omega_j^2 - \Omega^2 + i2\vartheta_j \omega_j \Omega} \tag{297}$$

a better approximation

$$\underline{H}_{ln}(i\Omega) = \sum_{j=J_1}^{J_2} \frac{u_{jl} u_{jn}/m_j}{\omega_j^2 - \Omega^2 + i2\vartheta_j \omega_j \Omega} + \frac{1}{K_{ln}} - \frac{1}{M_{ln}\Omega^2} \tag{298}$$

with the constants K_{ln} and M_{ln} is used for the equivalent model. This approximation covers all modal DOF where $\omega_j > \omega_{J_2}$.

Generalization of the Method for Isolated Resonance Points

The accuracy of the method can be improved by incorporating a corrected frequency response to cover isolated resonance points:

$$\underline{\tilde{H}}_{nr}^{\mathrm{cor}}(i\Omega) = \underline{\tilde{H}}_{ln}(i\Omega) - \left[\sum_{j=J_1, j\neq r}^{J_2} \frac{u_{jl}u_{jn}/m_j}{\omega_j^2 - \Omega^2 + i2\vartheta_j\omega_j\Omega} + \frac{1}{K_{ln}} - \frac{1}{M_{ln}\Omega^2} \right]. \tag{299}$$

General Approximation of the Frequency Response

The general approximation fits the frequency response $\underline{H}_{ln}(i\Omega)$ of the computational model to the measured frequency response $\underline{H}_{ln}(i\Omega)$. The values $\underline{\tilde{H}}_{ln}(i\Omega_p)$ at the frequencies Ω_p where $p = 1, \ldots, P$ are known from measurement. For the equivalent model the following applies at these points:

$$\underline{H}_{ln}(i\Omega_p) = \sum_{j=J_1}^{J_2} \frac{u_{jl}u_{jn}/m_j}{\omega_j^2 - \Omega_p^2 + i2\vartheta_j\omega_j\Omega_p} + \frac{1}{K_{ln}} - \frac{1}{M_{ln}\Omega_p^2}. \tag{300}$$

In an iterative manner, the quantities K_{ln}, M_{ln}, ω_j, ϑ_j, and $u_{jl}u_{jn}/(2\vartheta_j k_j)$ are determined $\forall j \in [J_1, J_2]$. Then the error is determined and minimized as per the following equations:

$$e_p = |\underline{\tilde{H}}_{ln}(i\Omega_p) - \underline{H}_{ln}(i\Omega_p)|^2 \tag{301}$$

$$e = \sum_{p=1}^{P} w_p e_p \tag{302}$$

$$\frac{\partial e}{\partial x} = 0 \qquad \rightarrow \qquad K_{ln},\ M_{ln},\ \omega_j,\ \vartheta_j\ u_{jl}u_{jn}/(2\vartheta_j k_j). \tag{303}$$

5.5 Experimental Techniques for Measuring Soil Damping

Soil damping is composed of the material damping of the ground and the energy extraction due to wave radiation (*geometric damping*). As there are no methods to determine energy extraction due to wave radiation, total soil damping and material damping are separately defined. Here, a brief outline of testing methods is given. For a more detailed description refer [94]. Among individual tests, boundary conditions should be ensured to be the same as material damping parameters greatly depend on the

- deformation amplitude
- mean hydrostatic pressure
- density
- void ratio
- load cycles

Geometric damping, on the other hand, depends only on the frequency and is calculated as a difference between total and material damping.

Measurement techniques broadly fall into the category of either *seismic*, where the propagation of an impulse or equivalent signals is employed or *stationary* methods, where a wave source is used to generate a standing wave field.

In the field, the following methods are suitable for determining soil damping:

- cross-hole measurement
- Rayleigh wave dispersion measurement
- measurement with model foundations

Laboratory measurement techniques for determining the material damping of soil samples are limited to the analysis of stationary vibrations using the:

- triaxi apparatus
- resonant column apparatus
- simple shear apparatus
- ring shear apparatus

In these experiments, care should be taken to remove soil samples such that the mechanical properties of the subsoil are unchanged. Hydrostatic pressure can be simulated in the test equipment.

6 Application of Fractional Calculus to Viscoelastically Damped Structures in the Finite Element Method

All materials show some amount of material damping. Under time periodic or Heaviside stress/strain loads – hysteresis or creep/relaxation responses can be observed, respectively. Damping in the case of many rubbers and polymers can be high and as a result may not be ignored, while material modeling. Material damping may be modeled by differential operators or hereditary integral viscoelastic constitutive equations. It is generally sufficient to use a linear stress-strain relationship – which is often realized via linear sprin and viscous dashpots. These result in constitutive equations of integer-order differential operator type. However, when applied to large time or frequency intervals, these models are cumbersome. Thermodynamically consistent and more robust models can be formulated using *fractional derivatives*. Refer [95,96,97,98,99,101]. An implementation of fractional constitutive equations into finite element and parameter identification is given in [103, 105]. Boundary element implementations can be found in [100, 100].

6.1 Grünwald Definition of Fractional Derivatives

Using backward difference, the first (integer order) derivative is given by:

$$\frac{\mathrm{d}^1 f(t)}{\mathrm{d}t^1} = \lim_{\Delta t \to 0} \frac{1}{\Delta t}[f(t) - f(t - \Delta t)]. \tag{304}$$

By the same rule, we may define any integer-order derivative by the following relation:

$$\frac{\mathrm{d}^n f(t)}{\mathrm{d}t^n} = \lim_{\Delta t \to 0} \left[\frac{1}{(\Delta t)^n} \sum_{j=0}^{n} (-1)^j \binom{n}{j} f(t - j\Delta t) \right] \tag{305}$$

where $\binom{n}{j}$ are binomial coefficients. If we replace the time step Δt by a fraction $\frac{t}{N}$ with $N = 1, 2, 3\ldots$, we can rewrite the above equation as:

$$\frac{\mathrm{d}^n f(t)}{\mathrm{d}t^n} = \lim_{N \to \infty} \left[\left(\frac{t}{N} \right)^{-n} \sum_{j=0}^{N-1} (-1)^j \binom{n}{j} f(t - j\frac{t}{N}) \right] \tag{306}$$

with the condition that

$$\binom{n}{j} = 0 \quad \text{for} \quad j > n. \tag{307}$$

A detailed treatment of the above equation can be found in [102, 104]. In order to deduce a formulation that is valid for any real-order derivative, we use the extended definition of the binomial coefficient:

$$\binom{a}{j} = \begin{cases} \dfrac{a(a-1)(a-2)\ldots(a-j+1)}{j} & \text{for} \quad j > 0 \\ 1 & \text{for} \quad j = 0 \end{cases} \tag{308}$$

where a is a real number and j is a natural number. For $j > 0$ therefore:

$$\begin{aligned} (-1)^j \binom{n}{j} &= (-1)^j \frac{\overbrace{n(n-1)(n-2)\ldots(n-j+2)(n-j+1)}^{j \text{ factors}}}{j!} \\ &= \frac{(j-n-1)(j-n-2)\ldots(-n+1)(-n)}{j!} \\ &= \binom{j-n-1}{j} \\ &\equiv \frac{\Gamma(j-n)}{\Gamma(-n)\Gamma(j+1)} \end{aligned} \tag{309}$$

such that Γ is the gamma function. Using the above equation in Eq. (306), we have:

$$\frac{\mathrm{d}^n f(t)}{\mathrm{d}t^n} = \lim_{N\to\infty}\left[\left(\frac{t}{N}\right)^{-n}\sum_{j=0}^{N-1}\frac{\Gamma(j-n)}{\Gamma(-n)\Gamma(j+1)}f(t-j\frac{t}{N})\right], \qquad n>0. \tag{310}$$

If we assume now, n to be any real number ν, we obtain the Grünwald definition of fractional derivatives and integrals given by:

$$\frac{\mathrm{d}^\nu f(t)}{\mathrm{d}t^\nu} = \lim_{N\to\infty}\left[\left(\frac{t}{N}\right)^{-\nu}\sum_{j=0}^{N-1}A_{j+1}f(t-j\frac{t}{N})\right] \tag{311}$$

where

$$A_{j+1} = \frac{\Gamma(j-\nu)}{\Gamma(-\nu)\Gamma(j+1)} \tag{312}$$

are the so-called Grünwald coefficients. Here, as long as ν is not a positive integer, A_{j+1} is nonzero. If, e.g., $\nu=-1$, then $A_{j+1}=1$ for all j, according to the Riemann sum for integer-order integration. If ν is a natural number n, only the first $n+1$ Grünwald coefficients A_{j+1} are nonzero, indicating a local operator. Conversely, fractional derivatives are non-local operators if ν is a positive non-integer. The limits of the summation here are the terminal values. The lower limit $j=0$ corresponds to $A_1 f(t)$, and the upper limit $j=N-1$ corresponds to $A_N f(t-\frac{(N-1)t}{N}) = A_N f(\frac{t}{N})$. Thus, the interval (0; t] is divided into N sections of equal size. Here, we always assume the lower terminal to be 0. As in differential operator notation, we may write:

$${}_0D_t^\nu f(t) = \frac{\mathrm{d}^\nu f(t)}{\mathrm{d}t^\nu} = \lim_{N\to\infty}\left[\left(\frac{t}{N}\right)^{-\nu}\sum_{j=0}^{N-1}A_{j+1}f(t-j\frac{t}{N})\right] = D^\nu. \tag{313}$$

6.2 Numerical Calculation of Fractional Derivatives

Approximate numerical evaluations can be done by replacing the infinite by a finite sum:

$$D^\nu f(t) \approx \left(\frac{t}{N}\right)^{-\nu}\sum_{j=0}^{N-1}A_{j+1}f(t-j\frac{t}{N}). \tag{314}$$

For reasons of numerical stability, calculation of A_{j+1} is carried out using the following recursive relationship:

$$A_{j+1} = \frac{\Gamma(j-\nu)}{\Gamma(-\nu)\Gamma(j+1)} = \frac{j-1-\nu}{j}\frac{\Gamma(j-1-\nu)}{\Gamma(-\nu)\Gamma(j)} = \frac{j-1-\nu}{j}A_j. \quad (315)$$

It is also possible to show that:

$$\lim_{j\to\infty} |A_{j+1}| = 0. \quad (316)$$

With growing j, the values A_{j+1} are weighting function values that are situated further in the past. This is why the influence of the past is faded out as time elapses, which is attributed to the "fading memory" property. We use here, a time integration scheme with fractional derivatives being evaluated at each increment. The time-discrete function values $f(t - j\frac{t}{N})$ that are needed to evaluate the fractional derivative are then computed from the history of the time integration. Also, time step for the fractional derivative is set equal to the time step size for the time integration. This means that in the beginning of the evaluation ($N = 1$), there are no history values to be taken into account. But as time elapses, the calculation of the fractional derivative slows down as it has to take more and more history data into account. Also, as a result of more history data, storage requirements increase. Shown below are three concepts that may be used to accelerate the computational process and reduce the storage requirements.

Concept 1. Due to the property of fading memory, the history data beyond a given point in time is not of much significance and therefore motivate the truncation of Eq. (314) such that:

$$D^{\nu} f(t) \approx \left(\frac{t}{N}\right)^{-\nu} \sum_{j=0}^{N_l} A_{j+1} f(t - j\frac{t}{N}), \qquad N_l > N - 1. \quad (317)$$

We see that only N_l sample points of the past are taken into consideration. Therefore, computational time and storage requirement first increase and then remain constant for rest of the time integration.

Concept 2. Another alternative is to choose time steps for fractional derivatives as a multiple of the time step for time integration.

$$\frac{t}{N} = c\Delta t, \qquad c > 1. \quad (318)$$

If $c = 2$ then compared to the number of evaluations for the time integration, the number of evaluations for the fractional derivatives is half and consequently, also the storage requirements. It is to be noted that the accuracy of the fractional derivatives drops as higher values of c is chosen. However, stronger requirements exist on Δt than on the time step for fractional derivatives; refer [103]. Therefore $c = 2$ is a reasonable compromise.

Concept 3. In this case, we approximate newer history with high resolution while the older one with lower resolution. We start with Eq. (314) and use the recursive relation as in Eq. (315). Therefore, at time t_0, we have:

$$\begin{aligned} D^{\nu} f(t) \approx \left(\frac{t_0}{N}\right)^{-\nu} \Bigg[\sum_{j=0}^{i} A_{j+1} f_j + A_{i+2} \Bigg(f_{i+1} + \frac{i-\nu+1}{i+2} f_{1+2} \\ + \frac{(i-\nu+1)(i-\nu+2)}{(i+2)(i+3)} f_{i+3} + \dots \Bigg) \Bigg] \\ \stackrel{!}{=} \left(\frac{t_0}{N}\right)^{-\nu} \Bigg[\sum_{j=0}^{i} A_{j+1} f_j + A_{i+2} T_{i+1} \Bigg] . \end{aligned} \tag{319}$$

In the above equation, f_j is the abbreviation for $f(t_0 - j\frac{t_0}{N})$. Also, T_{i+1} represents the whole interval as *one* contribution to the factional derivative as shown in Fig. 74. Keeping the upper and lower limit constant for the time integration part (i = const.)- n time increments later, i.e., at time $t_0 + n\Delta t$ the fractional derivative has the form:

$$\begin{aligned} D^{\nu} f(t) \approx \left(\frac{t_0}{N}\right)^{-\nu} \Bigg[\sum_{j=0}^{i+n} A_{j+1} f_{j-n} + A_{i+n+2} \Bigg(f_{i+1} + \frac{i+n-\nu+1}{i+n+2} f_{i+2} \\ + \frac{(i+n-\nu+1)(i+n-\nu+2)}{(i+n+2)(i+n+3)} f_{i+3} + \dots \Bigg) \Bigg] \\ = \left(\frac{t_0}{N}\right)^{-\nu} \Bigg[\sum_{j=0}^{i+n} A_{j+1} f_{j-n} + A_{i+n+2} T_{i+n+1} \Bigg] . \end{aligned} \tag{320}$$

For viscoelastic problems, ν is positive. For $i > \nu - 1$, the value of all weighting factors in T range between 0 and 1. In addition, all weighting factors tend to unity for increasing elapsed time, while at the same time, the weighting factor A_{i+n+2} tends to zero (fades out). We can approximate the time dependent quantity T_{i+n+1} as we know the starting value T_{i+1} at time t_0, the value R_∞ for $t \to \infty$, and the unity function $f^1 = 1$. Thus, we have:

Fig. 74 Time axis; definition of the interval

$$T_{i+n+1} = T_{i+1} + \frac{T^{\mathbf{1}}_{i+n+1} - T^{\mathbf{1}}_{i+1}}{T^{\mathbf{1}}_{\infty} - T^{\mathbf{1}}_{i+1}} (T_\infty - T_{i+1}) \stackrel{!}{=} T_{i+1} + w_{i+n+1} (T_\infty - T_{i+1}). \quad (321)$$

The bold face indices on the upper right indicate that the value is calculated using the unity function.

This concept is especially beneficial in methods utilizing spatial discretization such as FEM. In the following section, we will calculate the fractional derivative of stresses and strains – the fractional derivatives are needed for all nodal displacements and the stresses at all integration points. Weighting factors w are calculated once for each increment as it depends only on time. For each nodal displacement and stress state at each integration point, only the values of T_{i+1} and T_∞ have to be calculated and stored in order to approximate the influence of the time interval under consideration on the fractional derivative. Also, when we have large numbers of time increments, many intervals can be setup successively.

The quality of Approximation (Eq. (321)) is demonstrated by applying it to three different functions:

$$f_1(t) = 1 \qquad f_2(t) = at \qquad f_3(t) = \sin(\pi a t) \qquad \text{where} \quad a = \frac{1}{s} \quad (322)$$

and comparing it to Eq. (314). Figure 75 shows the comparison. The time step used is $\frac{t_0}{N} = \Delta t = 0.05s$ $i = 20$ time increments, and the order of the derivative is $\nu = 0.5$. The value of T is then computed for the next 500 time increments. Values from Eqs. (320) and (321) are depicted as solid and dashed lines, respectively.

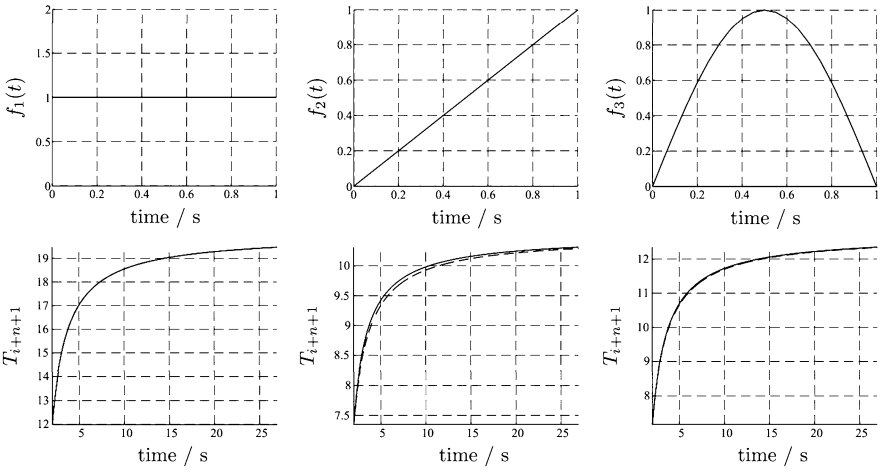

Fig. 75 Approximation of fractional derivatives using concept C

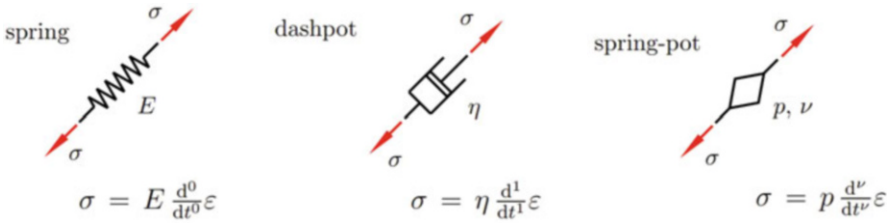

Fig. 76 Rheological elements of viscoelasticity

6.3 Fractional-Order Constitutive Equations

The constitutive equations of linear viscoelastic can be deducend from rheological models consisting of springs and 'spring-pots' (Fig. 76). The stress-strain relation of the latter may be written as:

$$\sigma = pD^{\nu}\varepsilon. \tag{323}$$

In the above equation, if $\nu = 0$, we get a spring with stiffness p. On the other hand, for $\nu = 1$ we obtain a dashpot with viscosity p. This means a fractional derivative denotes a material behavior between that of a spring and a dashpot. This is denoted as a *Rhombus* and was first introduced by Koeller [101]. The hybrid element is called a "spring pot". By replacing the dashpots in rheological models by spring-pots, fractional rheological models are derived. Application to the 5-parameter model (two Maxwell elements and a spring in parallel) results in the "fractional 5-parameter model," see Fig. 77. The constitutive equation is given by:

$$\begin{aligned}
&\sigma + \frac{p_1}{E_1} D^{\nu_1}\sigma + \frac{p_2}{E_2} D^{\nu_2}\sigma + \frac{p_1\, p_2}{E_1\, E_2} D^{\nu_1+\nu_2}\sigma \\
&= E_0\varepsilon + p_1 \frac{E_0 + E_1}{E_1} D^{\nu_1}\varepsilon + p_2 \frac{E_0 + E_2}{E_2} D^{\nu_2}\varepsilon \\
&+ p_1\, p_2 \frac{E_0 + E_1 + E_2}{E_1\, E_2} D^{\nu_1+\nu_2}\varepsilon.
\end{aligned} \tag{324}$$

Here, all fractional order initial conditions are assumed to be zero referring to a material that is totally relaxed at $t = 0$. A three-dimensional extension to Eq. (324) can be referred to in [105].

6.4 Finite Element Formulation and Implementation

The displacement-type formulation of the FEM is given by:

$$\boldsymbol{u} = \boldsymbol{H}\hat{\boldsymbol{u}} \tag{325}$$

Fig. 77 5-parameter model

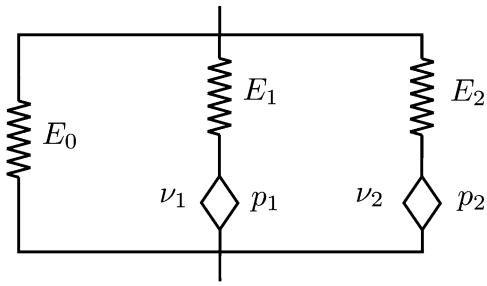

where $\boldsymbol{u}$ denotes the displacement field of an element, $\hat{\boldsymbol{u}}$ is the vector of the nodal displacements, and $\boldsymbol{H}$ is the matrix of shape functions. The strain is given by:

$$\boldsymbol{\varepsilon} = \boldsymbol{B}\hat{\boldsymbol{u}}. \tag{326}$$

The matrix $\boldsymbol{B}$ consists of the spatial derivatives of $\boldsymbol{H}$. From the principle of virtual work, we have the equation of motion as:

$$\int_R \boldsymbol{B}^{\boldsymbol{T}}\boldsymbol{\sigma}\ \mathrm{d}R + \boldsymbol{M}\ddot{\hat{\boldsymbol{u}}} = \boldsymbol{r} \tag{327}$$

where R is the region in which the element is defined, and $\boldsymbol{r}$ defines the external and the body forces. $\boldsymbol{M}$ is the consistent mass matrix given by the relation:

$$\boldsymbol{M} = \int_R \boldsymbol{H}^{\boldsymbol{T}}\rho\boldsymbol{H}\ \mathrm{d}R. \tag{328}$$

Here ρ is the mass density of the material. For convenience and readability $\hat{\cdot}$ notation is dropped, and the equation of motion at time t (as upper left index) is given by:

$$\int_V \boldsymbol{B}^{\boldsymbol{T}}\ {}^t\boldsymbol{\sigma}\ \mathrm{d}R + \boldsymbol{M}\ {}^t\ddot{\boldsymbol{u}} = {}^t\boldsymbol{r}. \tag{329}$$

${}^t\boldsymbol{\sigma}$ is the stress vector derived from Eq. (324). If we apply the time discrete Grünwaldian fractional derivatives to Eq. (324), we obtain:

$$
{}^{t}\boldsymbol{\sigma} = \left[1 + \frac{p_1}{E_1} A_1^{(\nu_1)} \left(\frac{t}{N}\right)^{-\nu_1} + \frac{p_2}{E_2} A_1^{(\nu_2)} \left(\frac{t}{N}\right)^{-\nu_2} + \frac{p_1\, p_2}{E_1\, E_2} A_1^{(\nu_1+\nu_2)} \left(\frac{t}{N}\right)^{-\nu_1-\nu_2} \right]^{-1} \cdot
$$

$$
\left[E_0 {}^{t}\boldsymbol{\varepsilon} + p_1 \frac{E_0 + E_1}{E_1} \left(\frac{t}{N}\right)^{-\nu_1} \sum_{j=0}^{N} A_{j+1}^{(\nu_1)\, t - j\frac{t}{N}} \boldsymbol{\varepsilon} + p_2 \frac{E_0 + E_2}{E_2} \left(\frac{t}{N}\right)^{-\nu_2} \right.
$$

$$
\sum_{j=0}^{N} A_{j+1}^{(\nu_2)\, t - j\frac{t}{N}} \boldsymbol{\varepsilon} + p_1\, p_2 \frac{E_0 + E_1 + E_2}{E_1\, E_2} \left(\frac{t}{N}\right)^{-\nu_1-\nu_2} \sum_{j=0}^{N} A_{j+1}^{(\nu_1+\nu_2)\, t - j\frac{t}{N}} \boldsymbol{\varepsilon}
$$

$$
- \frac{p_1}{E_1} \left(\frac{t}{N}\right)^{-\nu_1} \sum_{j=1}^{N} A_{j+1}^{(\nu_1)\, t - j\frac{t}{n}} \boldsymbol{\sigma} - \frac{p_2}{E_2} \left(\frac{t}{N}\right)^{-\nu_2} \sum_{j=1}^{N} A_{j+1}^{(\nu_2)\, t - j\frac{t}{N}} \boldsymbol{\sigma}
$$

$$
\left. - \frac{p_1\, p_2}{E_1\, E_2} \left(\frac{t}{N}\right)^{-\nu_1-\nu_2} \sum_{j=1}^{N} A_{j+1}^{(\nu_1+\nu_2) t - j\frac{t}{N}} \boldsymbol{\sigma} \right] . \tag{330}
$$

In Eq. (330), the upper-right indices in brackets indicate the dependence of the Grünwald coefficients on the order of respective fractional derivative. Note, Eq. (330) depends on the actual strain, the strain history, and the stress history. If we insert Eq. (330) into Eq. (329) and replace the strains $\boldsymbol{\varepsilon}$ by Eq. (326), the resulting equation of motion can be transformed into:

$$
\boldsymbol{M}\, {}^{t}\ddot{\boldsymbol{u}} + \boldsymbol{K}^{*t}\boldsymbol{u} = {}^{t}\boldsymbol{r}^{*} \tag{331}
$$

where $\boldsymbol{K}^{*}$ and $\boldsymbol{r}^{*}$ are the modified stiffness matrix and the modified force vector, respectively. Further reference to this can be seen in [105]. Regarding the form of Eq. (331), it can be solved with any elastic FE solver in conjunction with either implicit and explicit integration schemes.

6.5 Parameter Identification: A Case Study with $Delrin^{TM}$

Here, a parameter identification for the polymer $Delrin^{TM}$ is carried out in the time domain and in the frequency domain simultaneously. The time-dependent behavior is given in terms of the creep modulus E_c in the range from 10 s up to 10,000 h. Besides the measurements of the manufacturer, own measurements have been carried out to cover the short time period smaller than 360 s. In addition, free decay tests of a cantilever made of $Delrin^{TM}$ have been carried out at 12 different frequencies in the range from 50 Hz up to 500 Hz. The oscillations were measured by a laser vibrometer, and the frequency-dependent complex modulus was calculated.

The fractional 5-parameter model as shown in Fig. 77 has seven material properties which are determined by a least-squares fit method. While the complex modulus of the fractional rheological models can be calculated analytically [105],

E_0	E_1	E_2	p_1	p_2	ν_1	ν_2
$58.534\ \frac{\mathrm{N}}{\mathrm{mm}^2}$	$2760.8\ \frac{\mathrm{N}}{\mathrm{mm}^2}$	$2967.7\ \frac{\mathrm{N}}{\mathrm{mm}^2}$	$24.797\ \frac{\mathrm{N}}{\mathrm{mm}^2}\,\mathrm{s}^{\nu_1}$	$62\,510\ \frac{\mathrm{N}}{\mathrm{mm}^2}\,\mathrm{s}^{\nu_2}$	0.19911	0.24991

Fig. 78 Identified parameters in the time and frequency domain

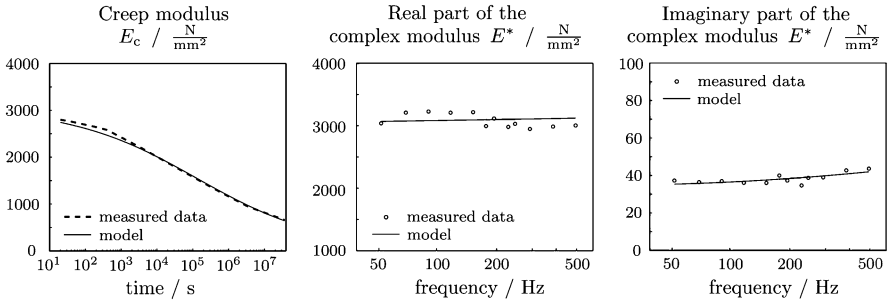

Fig. 79 Comparison between measured data and fractional 5-parameter model

the time-dependent behavior is evaluated by numerical time integration in each iteration step. The material parameters are given in Fig. 78, while the time- and frequency-dependent material behavior is compared to the measurements in Fig. 79.

6.6 Finite Element Calculations and Comparison of the Different Concepts

A finite element implementation is realized via 8-noded isoparametric brick elements in MARC. Numerical and computational costs are reduced by using concepts 1, 2, and 3 as described in Sect. 6.2.

As an example, the free decay of a cantilever made of $Delrin^{TM}$ is calculated, where the identified fractional 5-parameter model is used. The FE model is shown in Fig. 80. At the left side, fixed displacement type of boundary conditions is applied to the first two rows of nodes in order to model the fixed support. The free length of the cantilever is 100 mm, while its cross-section measures 2.2 mm $\times$ 10 mm. The model is initially at rest and in the first increment; a steady force in y-direction is applied to the last row of nodes at the right-hand side. Thus, an oscillation about the position of equilibrium is excited, while the position of equilibrium moves with time due to material creep. Since the height of the model has no influence on either the vibration and then creep, only one row of elements is modeled. The calculation is continued for 2000 time increments of 0.001 s using the Newmark integration method without numerical damping. Calculations are performed with the "original" approximation of fractional derivatives Eq. (314) as the "reference calculation" and with the concepts 1, 2, and 3. The results of the decaying oscillation can be compared to the respective measurements, while the superposed creep behavior can be compared to the theoretical curve from numerical integration.

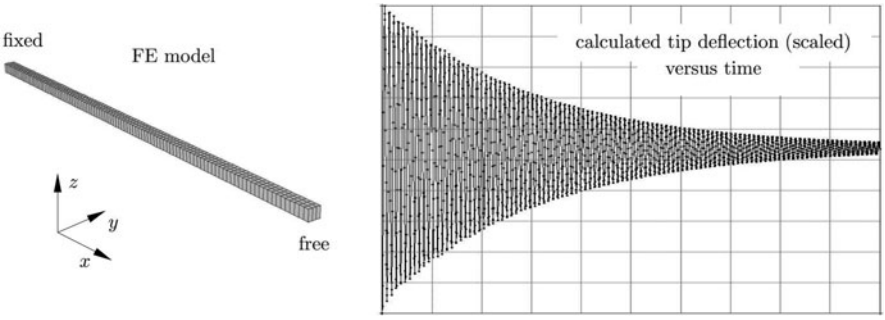

Fig. 80 FE model and calculated tip deflection

	ref. calculation	concept A	concept B	concept C
parameters	—	$N_\ell = 250$	$c = 2$	$i = 50$, length of intervals: $200\ \frac{t}{N}$
relative cpu-time	100 %	24.43 %	26.60 %	24.70 %
relative memory	100 %	18.56 %	53.88 %	26.25 %

Fig. 81 Computational requirements for the different concepts

Fig. 82 Creep behavior of the cantilever

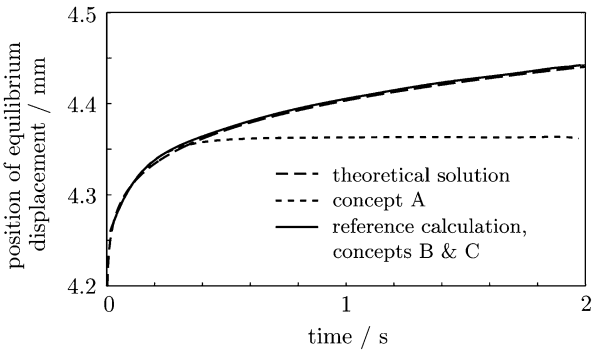

The CPU time needed and the storage requirements are summarized in the table labeled Fig. 81. The creep behavior shows significant deviation when different concepts are compared with each other. The equilibrium state is available from the calculation by means of values of each two consecutive maxima and a polynomial is fitted. This is depicted in Fig. 82. While concepts 2 and 3 show very good agreement to the theoretical calculations, concept 1 does not. The reason for this is that only the most recent part of the history information is considered. After N_l time increments, the errors accumulate during time integration.

Thus, from the above results, it can be inferred that for pure oscillations, concepts 1 and 3 result in considerable saving on the computational requirements while being both stable and accurate. Concept 2, on the other hand, is susceptible to numerical instability consequently giving rise to inaccuracies after a few hundred time increments. Having said that, concept 1 performs badly when the creep

behavior is examined. Concept 3, therefore, is the only candidate providing an advantage in computational requirements without compromising on accuracy.

7 Conclusion

The term "damping" indicates the loss of mechanical energy of a system beyond its physical boundaries. In most cases, damping implies the conversion of mechanical energy into heat energy; however, other mechanisms such as the transformation into electric energy by piezoelectric materials, propagating waves through the system's boundaries, or radiation into surrounding media may also cause energy losses. This chapter mainly dealt with damping effects of materials and assembled structures by means of phenomenological effects, modeling aspects, and experimental techniques.

The measurement and modeling of damping are challenging tasks that are still current research topics. As long as the material damping has to be determined, the damping properties are mainly linear resulting in somewhat simple damping models which do not have to account for any local effects. Additionally, a variety of techniques are available to accurately determine the amount of damping depending on the desired parameters such as frequency or temperature. Special materials, such as rubbers or plastics, show an extensive dependency on the temperature, which might be modeled using a temperature-frequency shift function that holds for thermal-rheologically simple materials. Therefore, instead of measuring the frequency-dependent damping properties over a broad frequency range, one can restrict to a limited frequency band which is used for different temperatures and results in a master curve, consequently covering an extremely broad range. As long as the amount of damping is equally distributed within the material under consideration, a modal analysis leads to complex eigenvalues indicating the presence of damping but real-valued eigenmodes.

As soon as the damping properties of a structure assembled from different components are considered, its occurrence and extent usually are mainly influenced by its joints instead of the respective material damping. In fact, the amount of material damping typically ranges between 1% and 10% relative to the overall loss of energy. In contrast to material damping, dissipative effects in the assembled structures mainly occur locally which consequently leads to complex eigenmodes. Thus, respective damping models must account for the location of the underlying damping effects. In addition, linearity is not fulfilled anymore, and the applicability of linear techniques such as the modal analysis must be verified carefully. The physical background of the nonlinearities is given by the occurrence of macro slip in the interface of the different components. As long as the contact pressure of all joints is large enough to guarantee the exclusive existence of micro slip for a given load level, the assumption of linearity is justified. However, the contact pressure of most interfaces to high extent depends on the distance between the origin of the contact force (e.g., the location of bolts, rivets, weld points). As a consequence, regions of micro slip and macro slip exist in parallel whereupon their extension changes with the current load level. Therefore, respective mechanical models have

to be solved in the time domain making use of suitable friction models resulting in a high computational effort. A general problem for the detection of damping values of assembled structures is given by the lack of reproducibility. After disassembling and reassembling a structure under consideration, its damping properties in general show a substantial deviation.

Technical Standards

DIN 1311-1: 2000-02 Schwingungen und schwingungsfähige Systeme – Teil 1: Grundbegriffe, Einteilung ((Mechanical) vibrations, oscillation and vibration systems – Part 1: Basic concepts, survey). Berlin: Beuth Verlag

DIN 1311-2: 2002-08 Schwingungen und schwingungsfähige Systeme – Teil 2: Lineare, zeitinvariante schwingungsfähige Systeme mit einem Freiheitsgrad ((Mechanical) vibrations, oscillations and vibration systems - Part 2: lineartime-invariant vibration systems with single degree of freedom). Berlin: Beuth Verlag

DIN 1311-3: 2000-02 Schwingungen und schwingungsfähige Systeme – Teil 3: Lineare, zeitinvariante schwingungsfähige Systeme mit endlich vielen Freiheitsgraden ((Mechanical) vibrations, oscillation and vibration systems – Part 3: linear time-invariant vibration systems with a finite number of degrees of freedom). Berlin: Beuth Verlag

DIN 1311-4: 1974-02 Schwingungslehre – Schwingende Kontinua, Wellen (Vibration; vibrating continua, waves). Berlin: Beuth Verlag

DIN 5487: 1988-07 Fourier-, Laplace- und Z-Transformation – Zeichen und Begriffe (Fourier-, Laplace- and Z-transformation; symbols and concepts). Berlin: Beuth Verlag

DIN 13 342: 1976-07 Nicht-newtonsche Flüssigkeiten – Begriffe, Stoffgesetze (Non-newtonian liquids; concepts, rheological equations). Berlin: Beuth Verlag

DIN 13 343: 1994-04 Linear-viskoelastische Stoffe – Begriffe, Stoffgesetze, Grundfunktionen (linear viscoelastic materials; concepts, constitutive equations, basic functions). Berlin: Beuth Verlag

DIN 51 563: 1976-12 Prüfung von Mineralölen und verwandten Stoffen – Bestimmung des Viskosität-Temperatur-Verhaltens – Richtungskonstante m (Testing of Mineral Oils and Related Materials; Determination of Viscosity Temperature Relation; Slope m). Berlin: Beuth Verlag

DIN 53 017: 1993-11 Viskosimetrie – Bestimmung des Temperaturkoeffizienten der Viskosität von Flüssigkeiten (Viscosimetry; determination of the temperature coefficient of viscosity of liquids). Berlin: Beuth Verlag

DIN 53 018-1: 1976-03 Viskosimetrie – Messung der dynamischen Viskosität newtonscher Flüssigkeiten mit Rotationsviskosimetern – Teil 1: Grundlagen (Viscosimetry; Measurement of the Dynamic Viscosity of Newtonian Fluids with Rotational Viscosimeters; Part 1: Principles). Berlin: Beuth Verlag

DIN 53 018-2: 1976-03 Viskosimetrie – Messung der dynamischen Viskosität newtonscher Flüssigkeiten mit Rotationsviskosimetern – Teil 2: Fehlerquellen und Korrektionen bei Zylinder-Rotationsviskosimetern (Viscosimetry; Measurement of

the Dynamic Viscosity of Newtonian fluids with Rotational Viscosimeters; Part 2: Sources of Errors and Corrections concerning Cylinder; Rotation Viscosimeters). Berlin: Beuth Verlag

DIN 53 019-1: 1980-05 Viskosimetrie – Messung von Viskositäten und Fließkurven mit Rotationsviskosimetern mit Standardgeometrie – Teil 1: Normalausführung (Viscosimetry; Determination of viscosities and flow curves using standard design rotary viscosimeters with a standard geometry measuring system). Berlin: Beuth Verlag

DIN 53 019-2: 2001-02 Viskosimetrie – Messung von Viskositäten und Fließkurven mit Rotationsviskosimetern mit Standardgeometrie – Teil 2: Viskosimeterkalibrierung und Ermittlung der Messunsicherheit (Viscosimetry – Measurement of viscosities and flow curves by means of rotation viscosimeters – Part 2: Viscosimeter calibration and determination of the uncertainty of measurement). Berlin: Beuth Verlag

DIN 53 513: 1990-03 Prüfung von Kautschuk und Elastomeren – Bestimmung der viskoelastischen Eigenschaften von Elastomeren bei erzwungenen Schwingungen außerhalb der Resonanz (Determination of the viscoelastic properties of elastomers on exposure to forced vibration at non-resonant frequencies). Berlin: Beuth Verlag

DIN 53 535: 1982-03 Prüfung von Kautschuk und Elastomeren – Grundlagen für dynamische Prüfverfahren (Testing of rubber; general requirements for dynamic testing). Berlin: Beuth Verlag

DIN EN ISO 6721-1: 2003-01 Kunststoffe – Bestimmung dynamisch- mechanischer Eigenschaften – Teil 1: Allgemeine Grundlagen (ISO 6721-1:2001). Deutsche Fassung der EN ISO 6721-1:2002 (Plastics – Determination of dynamic mechanical properties – Part 1: General principles (ISO 6721-1:2001); German version EN ISO 6721-1:2002). Berlin: Beuth Verlag

DIN EN ISO 6721-2: 1996-12 Kunststoffe – Bestimmung dynamisch- mechanischer Eigenschaften – Teil 2: Torsionspendel-Verfahren. (ISO 6721-2:1994) Deutsche Fassung der EN ISO 6721-2:1996 (Plastics – Determination of dynamic mechanical properties – Part 2: Torsion-pendulum method (ISO 6721-2:1994, including Technical Corrigendum 1:1995); German version EN ISO 6721-2:1996). Berlin: Beuth Verlag

DIN EN ISO 6721-3: 1996-12 Kunststoffe – Bestimmung dynamisch- mechanischer Eigenschaften – Teil 3: Biegeschwingung, Resonanzkurven- Verfahren. (ISO 6721-3:1994) Deutsche Fassung der EN ISO 6721-3:1996 (Plastics – Determination of dynamic mechanical properties – Part 3: Flexural vibration; resonance-curve (ISO 6721-3:1994, including Technical Corrigendum 1:1995); German version EN ISO 6721-3:1996). Berlin: Beuth Verlag

ISO/DIS 18 437-2: 2003-04 Mechanical Vibration and shock – Characterisation of the dynamic mechanical properties of resilient materials – Part 2: Resonance method

ISO/DIS 18 437-3: 2003-04 Mechanical Vibration and shock – Characterisation of the dynamic mechanical properties of resilient materials – Part 3: Single cantilever beam method

ISO/DIS 18 437-4 Mechanical Vibration and shock – Characterisation of the dynamic mechanical properties of resilient materials – Part 4: Impedance method

VDI Richtlinie 3830 Blatt 1: 2004-08 Werkstoff- und Bauteildämpfung – Einteilung und Übersicht (Part 1: Damping of materials and members – Classification and survey). Berlin: Beuth Verlag

VDI Richtlinie 3830 Blatt 2: 2004-10 Werkstoff- und Bauteildämpfung – Dämpfung in festen Werkstoffen (Part 2: Damping of materials and members – Damping of solids). Berlin: Beuth Verlag

VDI Richtlinie 3830 Blatt 3: 2004-07 Werkstoff- und Bauteildämpfung – Dämpfung von Baugruppen (Part 3: Damping of materials and members – Damping of assemblies). Berlin: Beuth Verlag

VDI Richtlinie 3830 Blatt 4: 2005-05 Werkstoff- und Bauteildämpfung – Modelle für gedämpfte Strukturen (Part 4: Damping of materials and members – Models for damped structures). Berlin: Beuth Verlag

VDI Richtlinie 3830 Blatt 5: 2005-11 Werkstoff- und Bauteildämpfung – Versuchstechniken zur Ermittlung von Dämpfungskenngrößen (Part 5: Damping of materials and members – Experimental techniques for the determination of damping characteristics). Berlin: Beuth Verlag

VDI Richtlinie 3833 Blatt 1: 2003-12 Schwingungsdämpfer und Schwingungstilger – Schwingu- ngsdämpfer – Begriffe, Kenngrößen, Realisierung, Anwendung (Dynamic damper and dynamic vibration absorber – Dynamic damper – Terms, characteristics implementation, application). Berlin: Beuth Verlag

VDI Richtlinie 3833 Blatt 2 (Entwurf): 2004-04 Schwingungstilger und Schwingungsdämpfer – Schwingungstilger und Schwingungstilgung (Dynamic damper and dynamic vibration absorber – Dynamic vibration absorber and dynamic vibration absorption). Berlin: Beuth Verlag

References

1. Bagley RL, Torvik PJ (1986) On the fractional calculus model of viscoelastic behavior. J Rheol 30(1):133–155
2. Christensen RM (1971) Theory of viscoelasticity – an introduction. Academic Press, New York/San Francisco/London
3. Ferry JD (1980) Viscoelastic properties of polymers. J. Wiley & Sons, New York/ London
4. Göldner H (1978) Übungsbuch der höheren Fertigkeitslehre, Elastizitätstheorie – Plastizitätstheorie – Viskoelastizitätstheorie. Physik-Verlag, Weinheim
5. Kolsch H (1993) Schwingungsdämpfung durch statische Hysterese; Modellierung von Bauteilen, Parameteridentifikation, Schwingungsberechnungen. Fortschr.-Ber. VDI Reihe 11 Nr. 190. Düsseldorf: VDI Verlag
6. Kümmlee H (1986) Ein Verfahren zur Vorhersage des nichtlinearen Steifigkeits- und Dämpfungsverhaltens sowie der Erwärmung drehelastischer Gummikupplungen bei stationärem Betrieb. Fortschr.-Ber. VDI Reihe 1 Nr. 136. VDI Verlag, Düsseldorf
7. Lambertz S (1995) Spannungs-Dehnungsverhalten technischer Gummiwerkstoffe. Antriebstechnisches Kolloquium ATK'95, S 1–35
8. Leaderman H (1943) Elastic and creep properties of filamentous materials and other high polymers. Textile Foundation, Washington, p 175

9. Lockett FJ (1972) Nonlinear viscoelastic solids. Academic Press, New York
10. Schapery RA (1969) On the characterization of nonlinear viscoelastic materials. Polym Eng Sci 9(4):295–310
11. Steiner H (1997) Untersuchungen zum nichtlinear-viskoelastischen Materialverhalten von Kunststoffen. Herbert Utz Verlag Wissenschaft, München
12. Tobolsky AV (1960) Properties and structure of polymers. J. Wiley & Sons, New York/London
13. Adams RD, Bacon DGC (1973) Measurement of the flexural damping capacity and dynamic Young's modulus of metals and reinforced plastics. J Phys D Appl Phys 6:27–41
14. Baker WE, Woolam WE, Young D (1967) Air and internal damping of thin cantilever beams. Int J Mech Soc 9:743–766
15. Barr ADS, Johnston RA (1969) Acoustic and internal damping of uniform beams. J Mech Eng Soc 11(2):117–127
16. Beards CF (1981) The damping of structural vibration by controlled interfacial slip in joints. ASME Paper, No. 81-DET-86, pp 1–5
17. Beck CJ, Ikegami R, Johnson DW, Walker WJ (1985) Application of viscoelastic passive damping to satellite equipment support structures. J Vib Acoust Stress Reliab Des 107(4): 367–374
18. Bohlen S, Gaul L (1984) Zum nichtlinearen Übertragungsverhalten von Fügestellen. ZAMM 64:T45–T48
19. Butenschön HJ (1986) Das hydrodynamische, zylindrische Gleitlager endlicher Breite unter instationärer Belastung. Diss. TH Karlsruhe
20. Carbonell JR, Ungar EE (1966) On panel vibration damping due to structural joints. AIAA J 4(8):1385–1390
21. Christensen RM (1971) Theory of viscoelasticity – an introduction. Academic Press, New York/San Francisco,London
22. Cremer L, Heckl M (1996) Körperschall, 2. Auflage. Springer, Berlin
23. Fahy F (1985) Sound and structural vibration; radiation, transmission and response. Academic Press, London
24. Fallen M, Henn H, Sinambri GR (1984) Ingenieurakustik. F. Vieweg & Sohn, Wiesbaden, Braunschweig
25. Feit D, Junger MC (1972) Sound, structures and their interaction. MIT Press, Cambridge
26. Ferry JD (1980) Viscoelastic properties of polymers. J. Wiley and Sons, New York/London
27. Gaul L (1981) Zur Dämmung und Dämpfung von Biegewellen an Fügestellen. Ing Archiv 51:101–110
28. Gaul L (1983) Zum Einfluss von Schraub-, Niet- und Klemmverbindungen auf die Dynamik von Maschinen und Strukturen. In: Maschinenbau FB (Hrsg) Festschrift 10 Jahre Hochschule der Bundeswehr Hamburg. Fachbereich Maschinenbau, S 49–58
29. Gaul L, Lenz J (1997) nonlinear dynamics of structures assembled with bolted joints. Acta Mech 125:169–181
30. Gaul L, Lenz J, Sachau D (1998) Active damping of space structures by contact pressure control in joints. Mech Struct Mach 26:81–100
31. Gaul L, Lenz J, Willner K (1994) Modellbildung des dynamischen Übertragungsverhaltens von Fügestellen. Techn. Report, Arbeitsbericht zum DFG-Projekt Az. Ga209/11-1
32. Gaul L, Willner K (1995) A penalty approach for contact description by FEM based on interface physics. In: Proceedings of CONMEC'95, Ferrara, pp 257–264
33. Glienicke J (1966) Feder-Dämpfungskonstanten von Gleitlagern für Turbomaschinen und deren Einfluss auf das Schwingungsverhalten eines einfachen Rotors. Dissertation, Technische Hochschule Karlsruhe, Karlsruhe
34. Glienicke J (1993) Nichtlineare Schwingungen allgemeiner gleitgelagerter Rotoren. VDI-Berichte, Nr 1082. VDI Verlag, Düsseldorf, S 299–316
35. Glienicke J, Schwer M (1985) Kennlinien realer Quetschöldämpfer. Konstruktion 37(8): 301–308
36. Göldner H (1978) Übungsbuch der höheren Festigkeitslehre, Elastizitä tstheorie – Plastizitäts-theorie – Viskoelastizitätstheorie. Physik-Verlag, Weinheim

37. Gomperts MC (1977) Sound radiation from baffled, thin, rectangular plates. Acustica 37(2):93–102
38. Heckl M (1962) Measurement of absorption coefficients on plates. J Acoust Soc Am 34(6):803–806
39. Holmer CI, Vér IL (1971) Interaction of sound waves with solid structures. In: Beranek LL (ed) Noise and vibration control, pp 270–361. McGraw-Hill Book Company, New York
40. Ingard KU, Morse PM (1968) Theoretical acoustics. McGraw-Hill Book Company, New York
41. Jeyapalan RK, Richards EJ, Wescott MW (1979) On the prediction of impact noise; Part II: ringing noise. J Sound Vib 65(3):417–451
42. Kümmlee H (1986) Ein Verfahren zur Vorhersage des nichtlinearen Steifigkeits- und Dämpfungsverhaltens sowie der Erwä rmung drehelastischer Gummikupplungen bei stationärem Betrieb. Fortschr.-Ber. VDI Reihe 1, Nr 136. VDI Verlag, Düsseldorf
43. Lambertz S (1995) Spannungs-Dehnungsverhalten technischer Gummiwerkstoffe. Antriebstechnisches Kolloquium ATK '95, S 1–35
44. Lang OR, Steinhilper W (1978) Gleitlager. Springer, Berlin/Heidelberg/New York
45. Lazan BJ (1968) Damping of materials and members in structural mechanics. Pergamon Press, Oxford
46. Lockett FJ (1972) Nonlinear viscoelastic solids. Academic Press, New York
47. Lund JW (1979) Evaluation of stiffness and damping coefficients of fluid-film bearings. Shock Vibration Digest 11(1):5–10
48. Maidanik G (1962) Response of ribbed panels to reverberant acoustic fields. J Acoust Soc Am 34(6):809–826
49. Maidanik G (1966) Energy dissipation associated with gas-pumping in structural joints. J Acoust Soc Am 40(5):1064–1072
50. Merker H-J (1981) Über den nichtlinearen Einfluss von Gleitlagern auf die Schwingungen von Rotoren. Fortschr.-Ber. VDI Z, Reihe 11, VDI-Forschungsheft, Nr 40. VDI Verlag, Düsseldorf
51. Morland LW, Lee EH (1960) Stress analysis for linear viscoelastic materials with temperature variation. Trans Soc Rheol 4:233
52. Ottl D (1981) Schwingungen mechanischer Systeme mit Strukturdämpfung. VDI-Forschungsheft, Nr 603. VDI Verlag, Düsseldorf
53. Petersmann N (1986) Substrukturtechnik und Kondensation bei der Schwingungsanalyse. Fortschr.-Berichte VDI Reihe 11, Nr 6. VDI Verlag, Düsseldorf
54. Schapery RA (1969) On the characterization of nonlinear viscoelastic materials. Polym Eng Sci 9(4):295–310
55. Schwarzl F, Staverman AJ (1952) Time-temperature dependence of linear viscoelastic behavior. J Appl Phys 23:838–843
56. Schwarzl FR (1990) Polymermechanik. Springer, Berlin
57. Schwer M (1986) Eigenschaften von Quetschöldämpfern. Diss. TH Karlsruhe. TH Karlsruhe
58. Siegl G (1981) Das Biegeschwingungsverhalten von Rotoren, die mit Blechpaketen besetzt sind. Diss. TU Berlin. TU Berlin
59. Someya T (1989) Journal-bearing handbook. Springer, Berlin
60. Steiner H (1997) Untersuchungen zum nichtlinear- viskoelastischen Materialverhalten von Kunststoffen. Herbert Utz Verlag Wissenschaft, München
61. Ungar EE (1980) Damping of panels due to ambient air. In: Torvik PJ (ed) Damping applications in vibration control, vol. 38, pp 73–81. American Society of Mechanical Engineers, New York
62. Valanis K (1971) A theory of viscoplasticity without a yield surface. Arch Mech 23(4):517–551
63. Wallace CE (1972) Radiation resistance of a rectangular panel. J Acoust Soc Am 51(3): 946–952
64. Weck M, Petuelli G (1981) Steifigkeits- und Dä mpfungskennwerte verschraubter Fügestellen. Konstruktion 33:241–245
65. Willner K (1995) Ein statistisches Modell für den Kontakt metallischer Körper. Diss. Univ. der Bundeswehr Hamburg, Univ. der Bundeswehr Hamburg

66. Willner K (1997) Elasto-plastic contact of rough surfaces. In: Aliabadi M, Samartin A (ed) Computational methods in contact mechanics III. Computational Mechanics Publications, Madrid
67. Wissbrock H (1985) Untersuchungen zur Fugendämpfung zusammengesetzter Bauteile. Fortschr.-Berichte VDI Reihe 11, Nr 68. VDI Verlag, Düsseldorf
68. Bathe KJ (1996) Finite element procedures. Prentice-Hall, New Jersey
69. Carpenter WM (1972) Viscoelastic stress analysis. Int J Numer Methods Eng 4:357–366
70. Caughey TK (1962) Vibration of dynamic systems with linear hysteretic damping. In: Proceedings of the fourth U.S. National Congress of Applied Mechanics 1, pp 87–97
71. Caughey TK, O'Kelly ME (1965) Classical normal modes in damped linear dynamic systems. J Appl Mech E 32:583–588
72. Gaul L, Fiedler C (1997) Methode der Randelemente in Statik und Dynamik. Friedrich Vieweg & Sohn, Braunschweig/Wiesbaden
73. Gaul L, Schanz M (1999) A comparative study of three boundary element approaches to calculate the transient response of viscoelastic solids with unbounded domains. Comput Methods Appl Mech Eng 179:11–123
74. Gaul L, Wirnitzer J (1999) Calculation of transient wave propagation problems in semi-infinite media by BEM in frequency domain. In: Proceedings of the 13th International Conference on Boundary Element Technology (BETECH99), Las Vegas, pp 185–194
75. Krämer E (1984) Maschinendynamik. Springer, Berlin
76. Krings W (1976) Beitrag zur Finiten Element Methode bei linearem, viskoelastischem Stoffverhalten. Mitteilungen aus dem Institut für Mechanik der Ruhr-Universität Bochum, Nr 3, Bochum
77. Link, M (1984) Finite Elemente in der Statik und Dynamik. Teubner-Verlag, Stuttgart
78. Natke HG (1992) Einführung in Theorie und Praxis der Zeitreihen-und Modalanalyse. 3. Auflage. Vieweg-Verlag, Braunschweig
79. Zienkiewicz OC (1984) Methode der Finiten Elemente, 2. Auflage. Carl Hanser Verlag, München/Wien
80. Zurmühl R, Falk S (1974) Matrizen und ihre Anwendungen, 6. Auflage. Springer-Verlag, Berlin
81. Gaul L, Kögl M, Wagner M (2003) Boundary element methods for engineers and scientists. An introductory course with advanced topics. Springer, Berlin
82. Broede, J (1983) Experimentelle Untersuchungen und analytische Betrachtungen zur Deutung der Drehschwingungs-Eigendä mpfung in Kolbenmaschinen-Triebwerken. Dissertation, Technische Universität Berlin, Berlin
83. Dubbel (1990) Taschenbuch für den Maschinenbau, 17. Auflage. Springer, Berlin
84. Ewins DJ (1989) Modal testing: theory and practice, 5. Auflage. John Wiley & Sons, London/New York
85. Ferry JD (1980) Viscoelastic properties of polymers. J. Wiley and Sons, London/New York
86. Lehr, E (1925) Die Abkürzungsverfahren zur Ermittlung der Schwingungsfestigkeit von Materialien. Dissertation, Technische Hochschule Stuttgart, Stuttgart
87. Madigosky W (1984) Improved extensional modulus measurements for polymers and metal matrix composites. In: Rogers L (ed) Proceedings Vibration damping 1984 Workshop Proceedings, Nr. AFWAL-TR-84-3064 in Q1–Q12
88. Madigosky, WM, Lee GF (1979) Automated dynamic Youngs's modulus and loss factor measurements. J Acoust Soc Am 66(2):345–349
89. Nashif AD (1967) New method for determining damping properties of viscoelastic materials. Shock Vib Bull 36(Part 4):37–47
90. Natke HG (1992) Einführung in Theorie und Praxis der Zeitreihen-und Modalanalyse, 3. Auflage. Vieweg-Verlag, Braunschweig
91. Norris DM, Young W-C (1970) Complex- modulus measurement by longitudinal testing. Exp Mech 10:93–96

92. Oberst H, Frankenfeld K (1952) Über die Dämpfung der Biegeschwingungen dünner Bleche durch festhaftende Beläge. Acustica 2, Akustische Beihefte, Heft 4, S 181–194
93. Pourabdolrahim R (1979) Entwicklung und systematische Untersuchung einer Drehschwingungsprüfmaschine für umlaufende Maschinenelemente. Dissertation, Technische Universität Berlin, Berlin
94. Verein Deutscher Ingenieure: damping of materials and members – Experimental techniques for the determination of damping characteristics. VDI 3830 Blatt 5:2005–2011
95. Bagley RL, Torvik PJ (1979) A generalized derivative model for an elastomer damper. Shock Vib Bull 49:135–143
96. Bagley RL, Torvik PJ (1983) Fractional calculus – a different approach to the analysis of viscoelastically damped structures. AIAA J 21(5):741–748
97. Bagley RL, Torvik PJ (1983) A theoretical basis for the application of fractional calculus to viscoelasticity. J Rheol 27(3):201–210
98. Bagley RL, Torvik PJ (1986) On the fractional calculus model of viscoelastic behavior. J Rheol 30(1):133–155
99. Caputo M, Mainardi F (1971) Linear models of dissipation in anelastic solids. Rivista del Nuovo Cimento 1(2):161–198
100. Gaul L (1999) The influence of damping on waves and vibrations. Mech Syst Signal Process 13(1):1–30
101. Koeller RC (1984) Application of fractional calculus to the theory of viscoelasticity. J Appl Mech 51:299–307
102. Oldham KB, Spanier J (1974) The fractional calculus. Academic Press, New York/London
103. Padovan J (1987) Computational algorithms for FE formulations involving fractional operators. Comput Mech 2:271–287
104. Podlubny I (1999) Fractional differential equations. Academic Press, San Diego/London
105. Schmidt A, Gaul L (2001) FE implementation of viscoelastic constitutive stress-strain relations involving fractional time derivatives. In: Constitutive Models for Rubber II. A.A.Balkema Publishers, Tokyo, S 79–89

Modal Analysis of Nonlinear Mechanical Systems

13

G. Kerschen and A. F. Vakakis

Contents

Abstract

The objective of this chapter is to introduce nonlinear normal modes (NNMs) to structural dynamicists who are not acquainted with them. Specifically, this chapter describes how the concept of modes can be extended to the nonlinear

G. Kerschen (✉)
Space Structures and Systems Laboratory, Department of Aerospace and Mechanical Engineering, University of Liège, Liege, Belgium
e-mail: g.kerschen@uliege.be

A. F. Vakakis
Department of Mechanical Science and Engineering, University of Illinois at Urbana-Champaign, Champaign, IL, USA
e-mail: avakakis@illinois.edu

R. Allemang, P. Avitabile (eds.), *Handbook of Experimental Structural Dynamics*,
https://doi.org/10.1007/978-1-4614-4547-0_35

case. It also describes, in simple terms, the fundamental properties of NNMs, including frequency-energy dependence, harmonics, bifurcation, and stability.

Keywords

Nonlinearity · Vibration modes · Natural frequencies

1 Nonlinear Normal Modes: A Brief Historical Perspective

The concept of a normal mode is central in the theory of linear vibrating systems. Besides their obvious physical interpretation, the linear normal modes (LNMs) have interesting mathematical properties. They can be used to decouple the governing equations of motion; i.e., a linear system vibrates as if it were made of independent oscillators governed by the eigensolutions. Two important properties that directly result from this decoupling are:

1. *Invariance*: if the motion is initiated on one specific LNM, the remaining LNMs remain quiescent for all time.
2. *Modal superposition*: free and forced oscillations can conveniently be expressed as linear combinations of individual LNM motions.

In addition, LNMs are relevant dynamical features that can be exploited for various purposes including model reduction (e.g., substructuring techniques [1]), experimental modal analysis [2], finite element model updating [3], and structural health monitoring [4].

Clearly, though, linearity is an idealization, an exception to the rule; nonlinearity is a frequent occurrence in real-life applications [5]. For instance, in an aircraft, besides nonlinear fluid-structure interaction, typical nonlinearities include backlash and friction in control surfaces, hardening nonlinearities in engine-to-pylon connections, saturation effects in hydraulic actuators, plus any underlying distributed nonlinearity in the structure. Furthermore, the next generations of aircraft are using materials such as glass-fiber or carbon-fiber composites to a greater extent for structural weight reduction. These materials entail new challenges for performance prediction, because they exhibit a structural behavior deviating significantly from linearity. Their increased use also creates more interfaces between different materials, which are further sources of nonlinear behavior.

Any attempt to apply traditional linear analysis to nonlinear systems results, at best, in a suboptimal design. Thus, there is a need for efficient, analytically rigorous, broadly applicable analysis techniques for nonlinear structural dynamics. In this context, nonlinear normal modes (NNMs) offer a solid theoretical and mathematical tool for interpreting a wide class of nonlinear dynamical phenomena, yet they have a clear and simple conceptual relation to the LNMs, with which practicing structural engineers are familiar.

NNMs were pioneered in the 1960s thanks to the seminal work of Rosenberg [6, 7, 8]. They were further studied in the 1970s by Rand [9, 10, 11] and Manevitch

and Mikhlin [12]. They were regarded as a theoretical curiosity until the beginning of the 1990s when they were given a new impetus through the efforts of Vakakis et al. [13, 14, 15, 16, 17, 18] and Shaw and Pierre [19, 20, 21, 22]. Since then, a large body of literature has addressed, with notable success, the qualitative and quantitative analysis of nonlinear phenomena using NNMs (see, e.g., [23, 24, 25, 26, 27, 28, 29, 30, 31, 32, 33, 34, 35, 36, 37, 38, 39, 40, 41, 42, 43]).

However, most structural engineers still view NNMs as a concept that is foreign to them. There are at least two reasons supporting this statement:

1. Nonlinear systems can exhibit extremely complex behaviors which linear systems cannot. These phenomena include jumps, bifurcations; saturation; subharmonic, superharmonic, and internal resonances; resonance captures; limit cycles; modal interactions; and chaos.
2. NNMs have two important limitations compared to their linear counterpart. First and foremost, the principle of superposition, which is the cornerstone of linear theory, does not apply to nonlinear systems. Second, the lack of orthogonality relations satisfied by the NNMs complicates their exploitation as bases for order reduction of the nonlinear dynamics.

The objective of the present chapter is thus to describe, in simple terms, the fundamental properties of NNMs, including frequency-energy dependence, harmonics, bifurcation, and stability. The chapter is organized as follows. In the next section, the two main definitions of NNMs are provided. In addition, their fundamental properties are described, and their representation in a frequency-energy plot is introduced. In Sect. 3, the different means of computing the NNMs are briefly reviewed and assessed. The potential applications of NNMs to "linear" and nonlinear modal analysis and nonlinear model reduction are then discussed in Sect. 4.

2 Nonlinear Normal Modes: What Are They?

To illustrate the different concepts, a two-degree-of-freedom (2DOF) system with a cubic stiffness is chosen. The system is depicted in Fig. 1, and its motion is governed by the equations

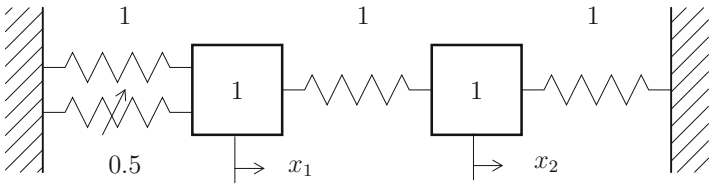

Fig. 1 Schematic representation of the 2DOF system example

$$\ddot{x}_1 + (2x_1 - x_2) + 0.5\,x_1^3 = 0$$
$$\ddot{x}_2 + (2x_2 - x_1) = 0 \tag{1}$$

For comparison purposes, the underlying linear system

$$\ddot{x}_1 + (2x_1 - x_2) = 0$$
$$\ddot{x}_2 + (2x_2 - x_1) = 0 \tag{2}$$

is also considered in this study. The time series corresponding to in-phase and out-of-phase normal mode motions of the linear system (2) are depicted in Fig. 2. Motion in the configuration space (i.e., in the plane of the displacements $x_1(t)$ and $x_2(t)$) is given in Fig. 3. Obviously, LNM motions correspond to straight lines in this plane.

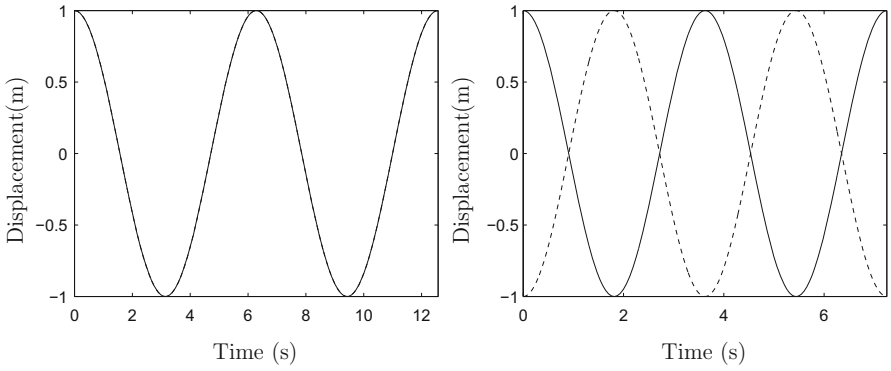

Fig. 2 Time series of LNM motions of system (2) (——: $x_1(t)$; – – –: $x_2(t)$). Left plot: in-phase LNM ($[x_1(0)\ x_2(0)\ \dot{x}_1(0)\ \dot{x}_2(0)] = [1\ 1\ 0\ 0]$); right plot: out-of-phase LNM ($[x_1(0)\ x_2(0)\ \dot{x}_1(0)\ \dot{x}_2(0)] = [1\ -1\ 0\ 0]$)

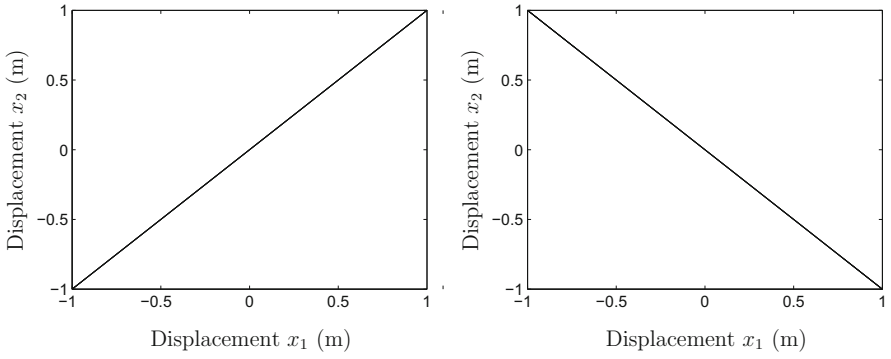

Fig. 3 LNM motions of system (2) in the configuration space. Left plot: in-phase LNM; right plot: out-of-phase LNM

2.1 Definition of a Nonlinear Normal Mode

There exist two main definitions of the NNMs in the literature, due to Rosenberg [6,7,8] and Shaw and Pierre [19,20,21,22]. We note that a new, interesting definition has been proposed recently [44], but it is not discussed herein.

2.1.1 Rosenberg's Definition

During the normal mode motion of a linear conservative system, each system component moves with the same frequency and with a fixed ratio among the displacements of the components. Targeting a straightforward nonlinear extension of the LNM concept, Rosenberg defined an NNM as a *vibration in unison* of the system (i.e., a synchronous oscillation). This definition requires that all material points of the system reach their extreme values and pass through zero simultaneously and allows all displacements to be expressed in terms of a single reference displacement.

For illustration, time series corresponding to the free response to specific initial conditions of system (1) are depicted in Fig. 4. These time series correspond to synchronous motion, and, hence, to NNM motions according to Rosenberg's definition. The associated modal shapes in Fig. 5 are curves, resulting from the nonlinear relationship between the coordinates during the periodic motion. These curved NNMs, termed nonsimilar NNMs by Rosenberg, are generic in nonlinear systems, and their existence certainly complicates the concept of orthogonality between modes. When special spatial symmetries exist, the NNMs may degenerate into (energy-invariant) straight modal lines (see [14] and Sect. 2.2.3).

At first glance, Rosenberg's definition may appear restrictive in two cases:

1. This definition, as such, cannot be easily extended to nonconservative systems.
2. In the presence of modal interactions (i.e., when two NNMs interact), some coordinates may have a dominant frequency component different than that of

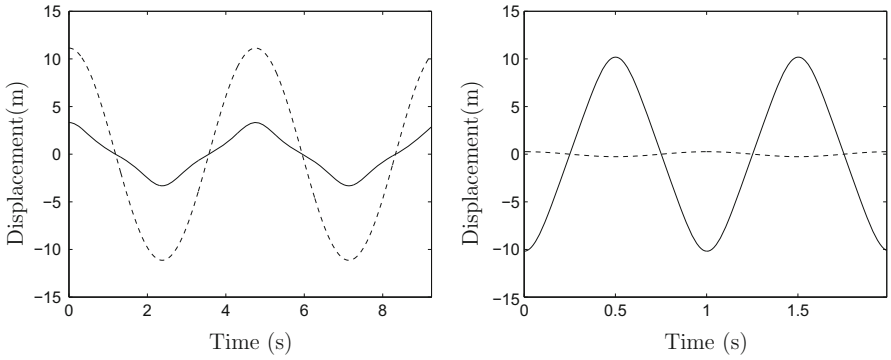

Fig. 4 Time series of NNM motions of system (1) (——: $x_1(t)$; − − −: $x_2(t)$). Left plot: in-phase NNM ($[x_1(0)\ x_2(0)\ \dot{x}_1(0)\ \dot{x}_2(0)] = [3.319\ 11.134\ 0\ 0]$); right plot: out-of-phase NNM ($[x_1(0)\ x_2(0)\ \dot{x}_1(0)\ \dot{x}_2(0)] = [-10.188\ 0.262\ 0\ 0]$)

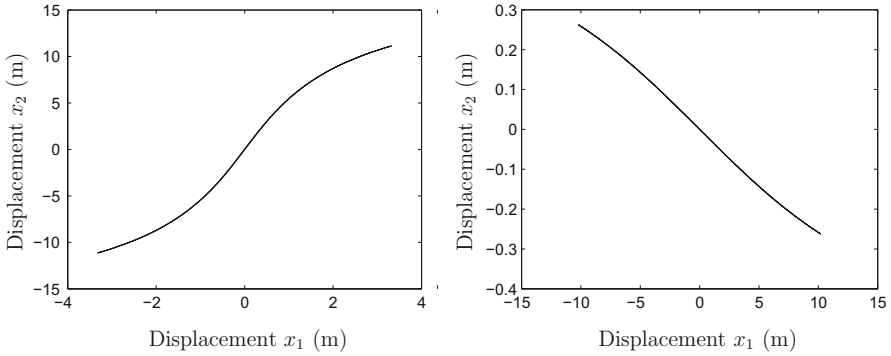

Fig. 5 NNM motions of system (1) in the configuration space. Left plot: in-phase NNM; right plot: out-of-phase NNM

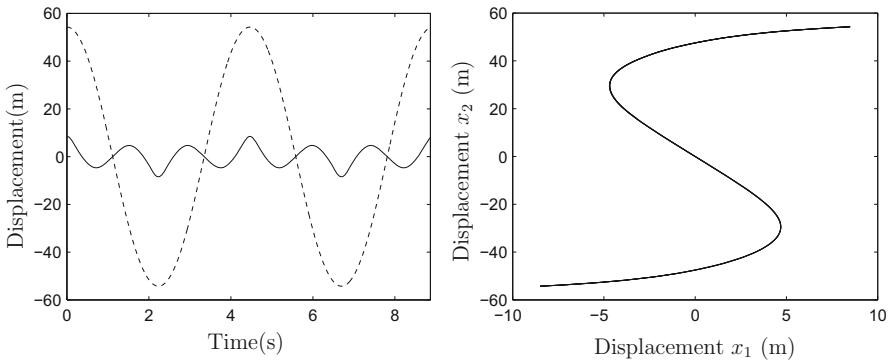

Fig. 6 Internally resonant NNM (3:1 internal resonance; $[x_1(0)\ x_2(0)\ \dot{x}_1(0)\ \dot{x}_2(0)] = [8.476\ 54.263\ 0\ 0]$). Left plot: time series (——: $x_1(t)$; − − −: $x_2(t)$); right plot: configuration space

the other coordinates. In this case, the system may no longer be synchronous. This is illustrated in Fig. 6 for a 3:1 internally resonant NNM of system (1).

However, these two limitations can be circumvented. On the one hand, the damped dynamics can often be interpreted based on the topological structure of the NNMs of the underlying undamped system. The concept of periodic motion was also extended to damped systems in [45]. On the other hand, realizing that the motion is still periodic in the presence of modal interactions, Rosenberg's definition can be extended to *a (non-necessarily synchronous) periodic motion of the system*, as proposed in [29]. This extended definition is particularly attractive when targeting a numerical computation of the NNMs. It enables the nonlinear modes to be effectively computed using algorithms for the continuation of periodic solutions, which are really quite sophisticated and advanced.

2.1.2 The Invariant Manifold Approach

Shaw and Pierre proposed a generalization of Rosenberg's definition that provides a direct and elegant extension of the NNM concept to damped systems. Based on geometric arguments and inspired by the center manifold technique, they defined an NNM as a two-dimensional invariant manifold, i.e., an invariant surface, in phase space. Such a manifold is invariant under the flow (i.e., orbits that start out in the manifold remain in it for all time), which extends the invariance property of LNMs to nonlinear systems. In order to parametrize the manifold, a single pair of state variables (i.e., both the displacement and the velocity) are chosen as master coordinates, the remaining variables being functionally related to the chosen pair. Therefore, the system behaves like a nonlinear single-DOF system on the manifold.

Geometrically, LNMs are represented by planes in phase space, and NNMs are two-dimensional surfaces that are tangent to them at the equilibrium point. For illustration, the manifolds corresponding to in-phase and out-of-phase NNMs motions of system (1) are given in Fig. 7.

2.2 Fundamental Properties

NNMs have intrinsic properties that are fundamentally different from those of LNMs. They are reviewed and illustrated in what follows.

2.2.1 Frequency-Energy Dependence

One typical dynamical feature of nonlinear systems is the frequency-energy dependence of their oscillations. One important consequence is that the frequency response functions (FRFs) of nonlinear systems are no longer invariant. For illustration, the (unscaled) FRFs of system

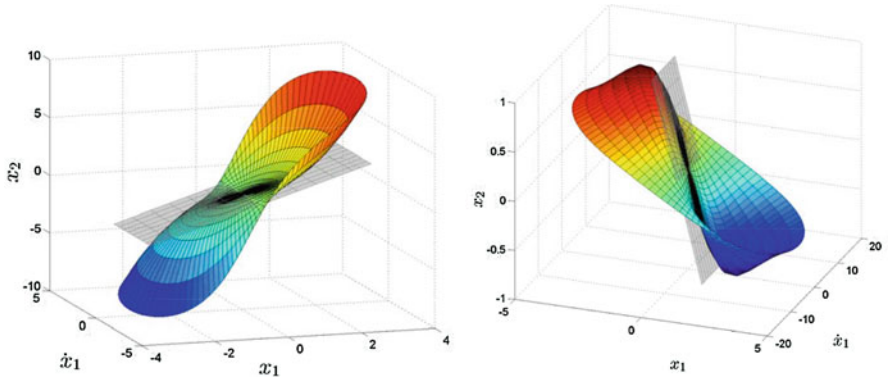

Fig. 7 Two-dimensional invariant manifolds of system (1) with the corresponding LNMs. Left plot: in-phase LNM and NNM; right plot: out-of-phase LNM and NNM

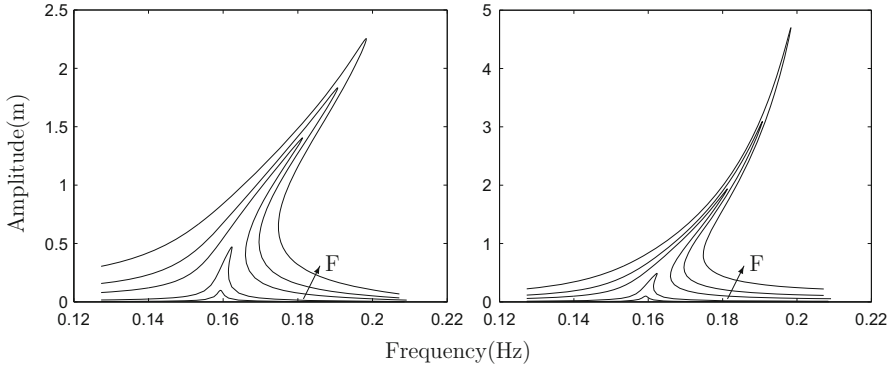

Fig. 8 Nonlinear frequency response functions close to the first resonant frequency (5 different forcing amplitudes: 0.002N, 0.01N, 0.05N, 0.1N, 0.2N). Left plot: x_1; right plot: x_2

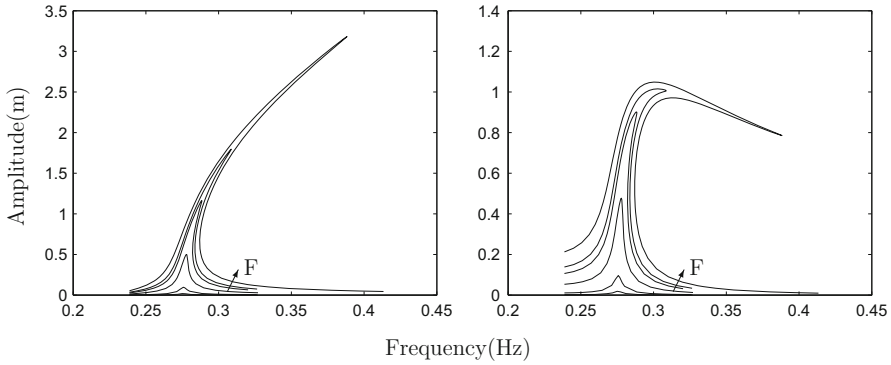

Fig. 9 Nonlinear frequency response functions close to the second resonant frequency (5 different forcing amplitudes: 0.002N, 0.01N, 0.05N, 0.1N, 0.2N). Left plot: x_1; right plot: x_2

$$\begin{aligned} \ddot{x}_1 + (0.02\dot{x}_1 - 0.01\dot{x}_2) + (2x_1 - x_2) + 0.5\,x_1^3 &= F\cos\omega t \\ \ddot{x}_2 + (0.02\dot{x}_2 - 0.01\dot{x}_1) + (2x_2 - x_1) &= 0 \end{aligned} \tag{3}$$

are depicted in Figs. 8 and 9 for F varying between 0.002 N and 0.2 N.

The modal shapes and frequencies of oscillation of NNMs also depend on the total energy in the system. In contrast to linear theory, this energy dependence prevents the direct separation of space and time in the governing equations of motion, which complicates the analytical calculation of the NNMs.

Returning to the undamped system (1), Fig. 10 shows the time series, the configuration space, the power spectral density (PSD), and two-dimensional projections of the phase space of three in-phase NNM motions of increasing energies. The NNM motion at low energy resembles that of the in-phase LNM of the underlying linear system (2). The modal shape is a straight line, there is one main harmonic

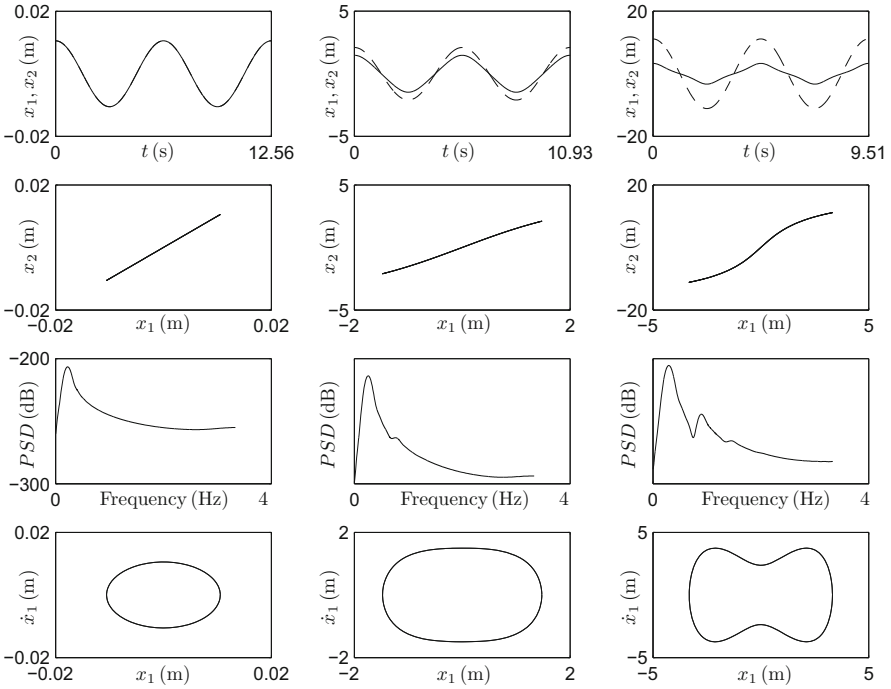

Fig. 10 Frequency-energy dependence of NNMs. From left to right: low- ($[x_1(0)\ x_2(0)\ \dot{x}_1(0)\ \dot{x}_2(0)] = [0.105\ 0.105\ 0\ 0]$), moderate- ($[x_1(0)\ x_2(0)\ \dot{x}_1(0)\ \dot{x}_2(0)] = [1.476\ 2.100\ 0\ 0]$) and high- ($[x_1(0)\ x_2(0)\ \dot{x}_1(0)\ \dot{x}_2(0)] = [3.319\ 11.134\ 0\ 0]$) energy in-phase NNMs. From top to bottom: time series (——: $x_1(t)$; − − −: $x_2(t)$); configuration space; power spectral density of $x_1(t)$; two-dimensional projections of the phase space

component in the system response, and the motion in phase space is a circle. For the motion at moderate energy, the NNM is now a curve, and the presence of two harmonic components can be detected. A clear departure from the LNM (harmonic) motion is observed. At high energy, this is even more visible. For instance, the motion in phase space is a strongly deformed ellipse. When moving from the low- to the high-energy NNM, the motion period decreases from 6.28 s to 4.755 s, due to the hardening characteristic of the cubic spring. Another noticeable characteristic of the NNMs is that the modes at higher energies are not the geometric continuation of those at lower energies. For illustration, Fig. 11 superposes the three-in-phase NNMs in the configuration space.

To further illustrate the frequency-energy dependence of the NNMs, the harmonic balance method can be applied to system: (1). This method expresses the periodic motion of a system by means of a finite Fourier series. For simplicity, a series with a single harmonic component is considered

$$x_1(t) = A\cos\omega t, \quad x_2(t) = B\cos\omega t \tag{4}$$

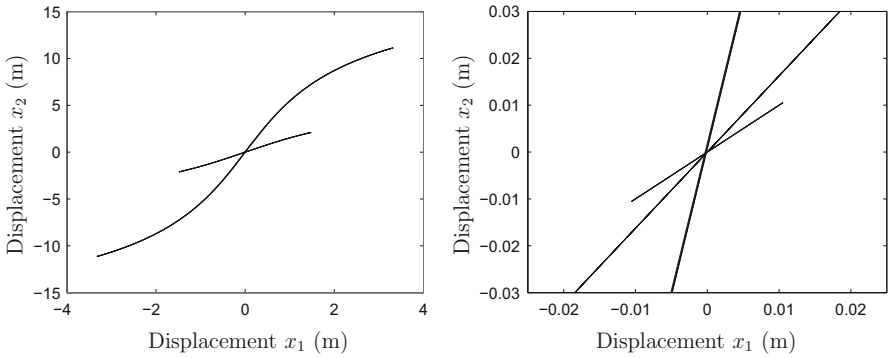

Fig. 11 Superposition of low-, moderate- and high-energy NNM motions in the configuration space. The right plot is a close-up of the left plot

This expression is plugged into the equations of motion (1). Expanding $\cos^3 \omega t$ in terms of $\cos \omega t$ and $\cos 3\omega t$, and balancing all the coefficients of the $\cos \omega t$ terms yields

$$\begin{aligned} -A\omega^2 + (2A - B) + 0.5\,\frac{3A^3}{4} &= 0 \\ -B\omega^2 + (2B - A) &= 0 \end{aligned} \tag{5}$$

Analytic expressions for coefficients A and B are then readily obtained

$$A = \pm\sqrt{\frac{8(\omega^2 - 3)(\omega^2 - 1)}{3(\omega^2 - 2)}} \tag{6}$$

$$B = \frac{A}{2 - \omega^2} \tag{7}$$

The square root exists in the two frequency intervals

$$\omega_1 \in [1, \sqrt{2}] \quad \text{and} \quad \omega_2 \in [\sqrt{3}, +\infty] \tag{8}$$

noting that $\omega = 1$ rad/s and $\omega = \sqrt{3}$ rad/s are the two natural frequencies of the underlying linear system (2). In the first (second) frequency interval, B has the same (opposite) sign as A; an in-phase (out-of-phase) NNM motion is observed for initial conditions $[x_1(0)\ x_2(0)\ \dot{x}_1(0)\ \dot{x}_2(0)] = [A\ B\ 0\ 0]$).

The (conserved) total energy during the free response of system (1) is

$$\text{Total Energy} = \text{Kinetic Energy} + \text{Potential Energy} = \frac{A^2}{2} + \frac{(B - A)^2}{2} + \frac{B^2}{2} + 0.5\,\frac{A^4}{4} \tag{9}$$

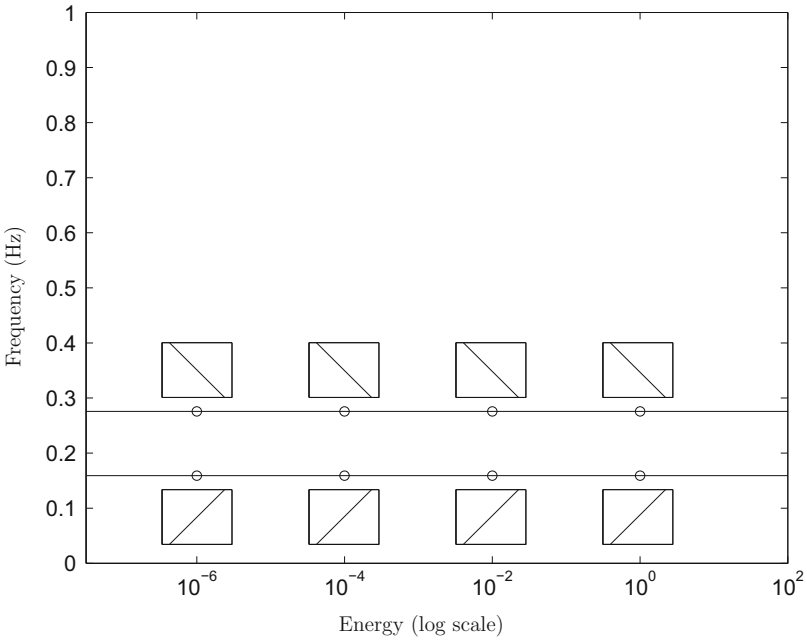

Fig. 12 Frequency-energy plot of system (2). LNM motions depicted in the configuration space are inset

which, according to equations (6) and (7), demonstrates the frequency-energy dependence of NNM motions.

An appropriate graphical depiction of the NNMs is a *frequency-energy plot* (FEP). An NNM is represented by a point in the FEP, which is drawn at a frequency corresponding to the minimal period of the periodic motion and at an energy equal to the conserved total energy during the motion. A branch, represented by a solid line, is a family of NNM motions possessing the same qualitative features (e.g., the in-phase NNM motions of a 2DOF system).

As a point of comparison, the FEP of the linear system (2) is shown in Fig. 12. Because the modal parameters of a linear system do not depend on energy, this FEP comprises two horizontal lines at the two natural frequencies of the system. The LNM motions represented in the configuration space are inset and are also unaltered by the energy level.

The FEP of the nonlinear system (1) was computed using the method proposed in [46]; it is shown in Fig. 13. The backbone of the plot is formed by two branches, which represent in-phase ($S11+$) and out-of-phase ($S11-$) synchronous NNMs. The letter S refers to symmetric periodic solutions for which the displacements and velocities of the system at half period are equal but with an opposite sign to those at time $t = 0$. As shown in the next section, unsymmetric periodic solutions may also be encountered and are denoted by a letter U. The indices in the notations are used

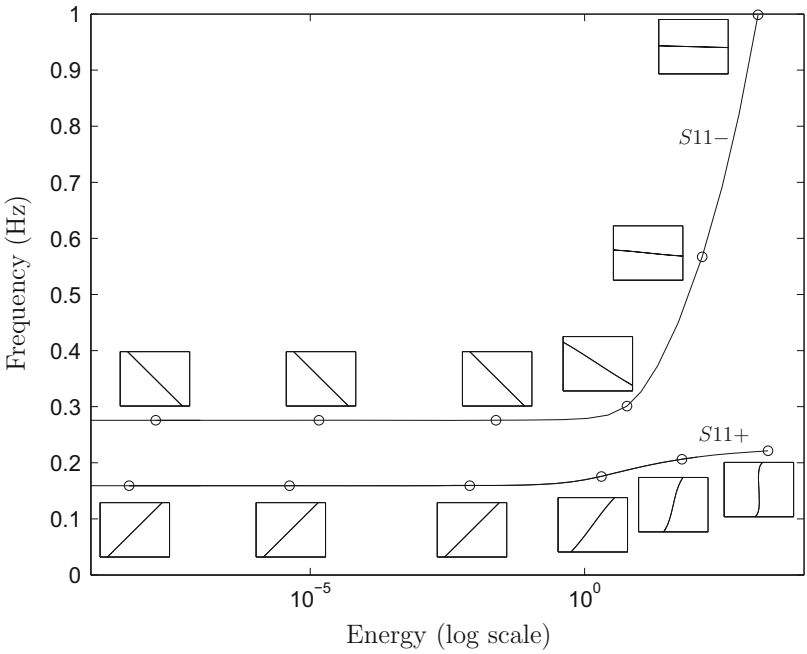

Fig. 13 Frequency-energy plot of system (1). NNM motions depicted in the configuration space are inset. The horizontal and vertical axes in these plots are the displacements of the first and second DOFs, respectively; the aspect ratio is set so that increments on the horizontal and vertical axes are equal in size to indicate whether or not the motion is localized to a particular DOF

to mention that the two masses vibrate with the same dominant frequency. The FEP clearly shows that the nonlinear modal parameters have a strong dependence on the total energy in the system:

1. The frequency of both the in-phase and out-of-phase NNMs increases with the energy level, which reveals the hardening characteristic of the system.
2. The modal curves change for increasing energies. The in-phase NNM tends to localize to the second DOF (i.e., it resembles a vertical curve), whereas the out-of-phase NNM localizes to the first DOF (i.e., it resembles an horizontal curve).

The comparison between Figs. 12 and 13 also reveals that NNMs have a clear and simple conceptual relation to the LNMs.

2.2.2 Modal Interactions: Internally Resonant Nonlinear Normal Modes

Another salient feature of nonlinear systems is that NNMs may interact during a general motion of the system. Nonlinear modal interactions have been studied extensively in the literature (see, e.g., the monograph [47]). A case of particular interest is

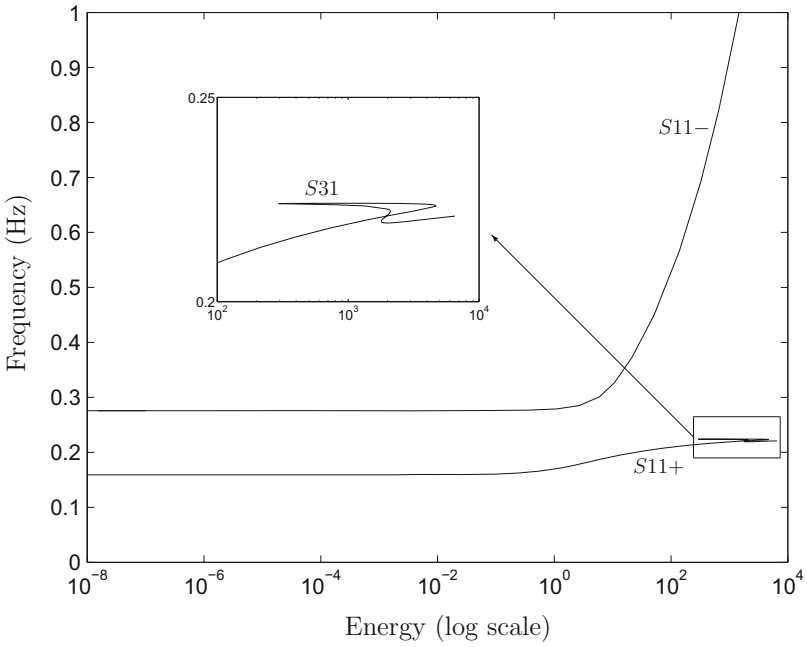

Fig. 14 Frequency-energy plot of system (1) featuring a 3:1 internal resonance between the in-phase and out-of-phase NNMs

when the linear natural frequencies are commensurate or nearly commensurate. An energy exchange between the different modes involved may therefore be observed during the internal resonance. For instance, exciting a high-frequency mode may produce a large-amplitude response in a low-frequency mode. Vibration absorbers exploiting these energy transfers have been studied in [48].

The FEP in Fig. 13 does not seem to feature internally resonant NNMs. However, when carrying out the NNM computation at higher energy levels, Fig. 14 shows that another branch of periodic solutions, termed a tongue, emanates from the backbone branch $S11+$. On this tongue, denoted $S31$, there is a 3:1 internal resonance/modal interaction between the in-phase and out-of-phase NNMs.

Surprisingly, the ratio of the linear natural frequencies of system (1) is $\sqrt{3}$. Due to energy dependence, a 3:1 ratio between the two frequencies can still be realized, because the frequency of the in-phase NNM increases less rapidly than that of the out-of-phase NNM. This shows that NNMs can be interact without necessarily having commensurate linear natural frequencies.

To better illustrate the resonance mechanism, the branch $S11-$ is represented in the FEP of Fig. 15 at the third of its frequency. This is relevant, because a periodic solution of period T is also periodic with period $3T$, and the resulting branch is therefore denoted $S33-$. It turns out that a smooth transition from $S11+$ to $S33-$ occurs on tongue $S31$. This transition is also depicted in Fig. 16 where the evolution

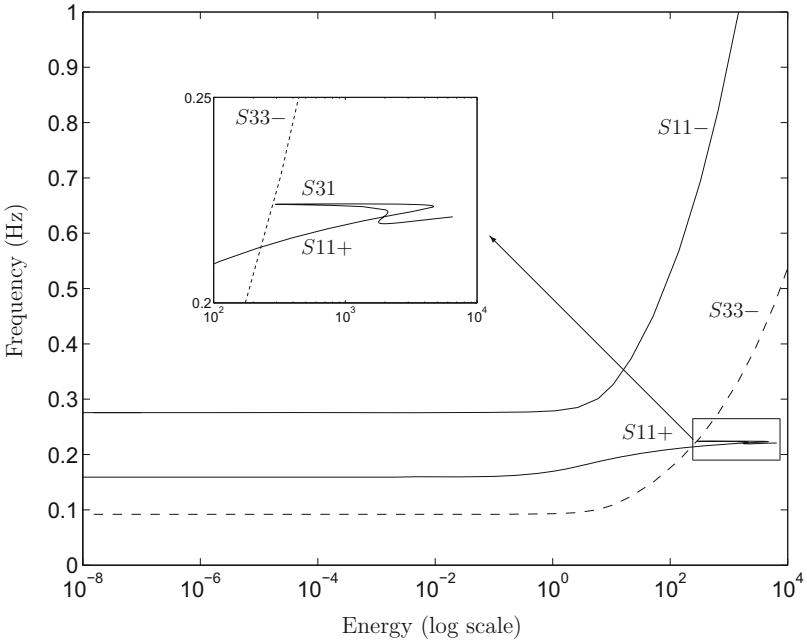

Fig. 15 Frequency-energy plot of system (1). − − −: $S33-$, that is $S11-$ represented at the third of its dominant frequency

of the configuration space and of the Fourier coefficients is shown for several points on $S31$ or in its vicinity. Starting from NNM (a), an in-phase motion characterized by two perceptible harmonic components is observed. From (a) to (d), the relative importance of the third harmonics grows, as clearly confirmed by the motion in the configuration space. Moving from (d) to (e) corresponds to a drastic qualitative change in the dynamics. Firstly, the first harmonics has completely disappeared for both oscillators. Secondly, the signs of the coefficients of the third harmonics are opposite. Overall, this means that an out-of phase motion with a three times as large frequency is realized. Eventually, through a 3:1 internal resonance, the motion ends up on $S33-$ or, equivalently, on $S11-$. From (f) to (h), the relative importance of the third harmonics diminishes, and a motion qualitatively similar to that at (a) is observed. However, the configuration space of NNM (h) reveals the presence of a fifth harmonics, which is a precursor to the gradual development of tongue $S51$.

This indicates that other resonance scenarios exist in this seemingly simple system. The frequency of the out-of-phase NNM motions on $S11-$ steadily increases for increasing energies, whereas the NNM motions on $S11+$ have their frequency asymptotically approaching a value close to $\sqrt{3}$ rad/s. Following this reasoning, we expect the existence of a countable infinity of internal resonance cases (e.g., 2:1, 4:1, 5:1, etc.). To confirm this conjecture, additional tongues were computed numerically and are represented in Fig. 17. These tongues emanate from

$S11+$ and coalesce into $S11-$ following a mechanism similar to that described above (Fig. 16). To illustrate the rich dynamics, a few representative modal shapes of system (1) are depicted in Fig. 18.

We note that interactions between NNMs were observed in real-world structures [49,50,51,52].

2.2.3 Mode Bifurcations and Stability

A third fundamental property of NNMs is that their number may exceed the number of DOFs of the system. Due to mode bifurcations, not all NNMs can be regarded as nonlinear continuation of normal modes of linear systems [17]. Internally resonant NNMs are one example. Another possible example corresponds to the NNM bifurcations of the system

$$\begin{aligned} \ddot{x}_1 + x_1 + x_1^3 + K(x_1 - x_2)^3 &= 0 \\ \ddot{x}_2 + x_2 + x_2^3 + K(x_2 - x_1)^3 &= 0 \end{aligned} \tag{10}$$

for variations of the coupling spring K [14]. This system possesses similar NNMs that obey to the relation $x_2(t) = cx_1(t)$. Eliminating x_2 from equations (10) yields

$$\begin{aligned} \ddot{x}_1 + x_1 + \left[1 + K(1-c)^3\right] x_1^3 &= 0 \\ \ddot{x}_1 + x_1 - \frac{1}{c}\left[K(1-c)^3 + c^3\right] x_1^3 &= 0 \end{aligned} \tag{11}$$

Because both equations must lead to the same solution, it follows

$$K(1+c)(c-1)^3 = c(1-c^2), \quad c \neq 0 \tag{12}$$

Equation (12) means that system (10) always possesses two modes characterized by $c = \pm 1$ that are direct extension of the LNMs. However, this system can possess two additional similar NNMs that cannot be captured using linearization procedures. At $K = 0.25$, these NNMs bifurcate from the out-of-phase mode, as shown in Fig. 19.

Another important characteristic of NNMs is that they can be stable or unstable, which is in contrast to linear theory where all modes are neutrally stable. In this context, instability means that small perturbations of the initial conditions that generate the NNM motion lead to the elimination of the mode oscillation. Therefore, unstable NNMs are not physically realizable. The NNM stability analysis can be performed numerically or analytically. In Fig. 20, stability is computed numerically through the eigenvalues of the monodromy matrix. In other studies, analytical results are obtained through Floquet theory after adding small perturbations to the periodic solutions. For a detailed stability analysis of the NNMs, the reader can refer to [14,16,17,53,54].

Bifurcations and stability are interrelated concepts, because a change in stability occurs through a bifurcation. For instance, the bifurcation in system (10) generates a

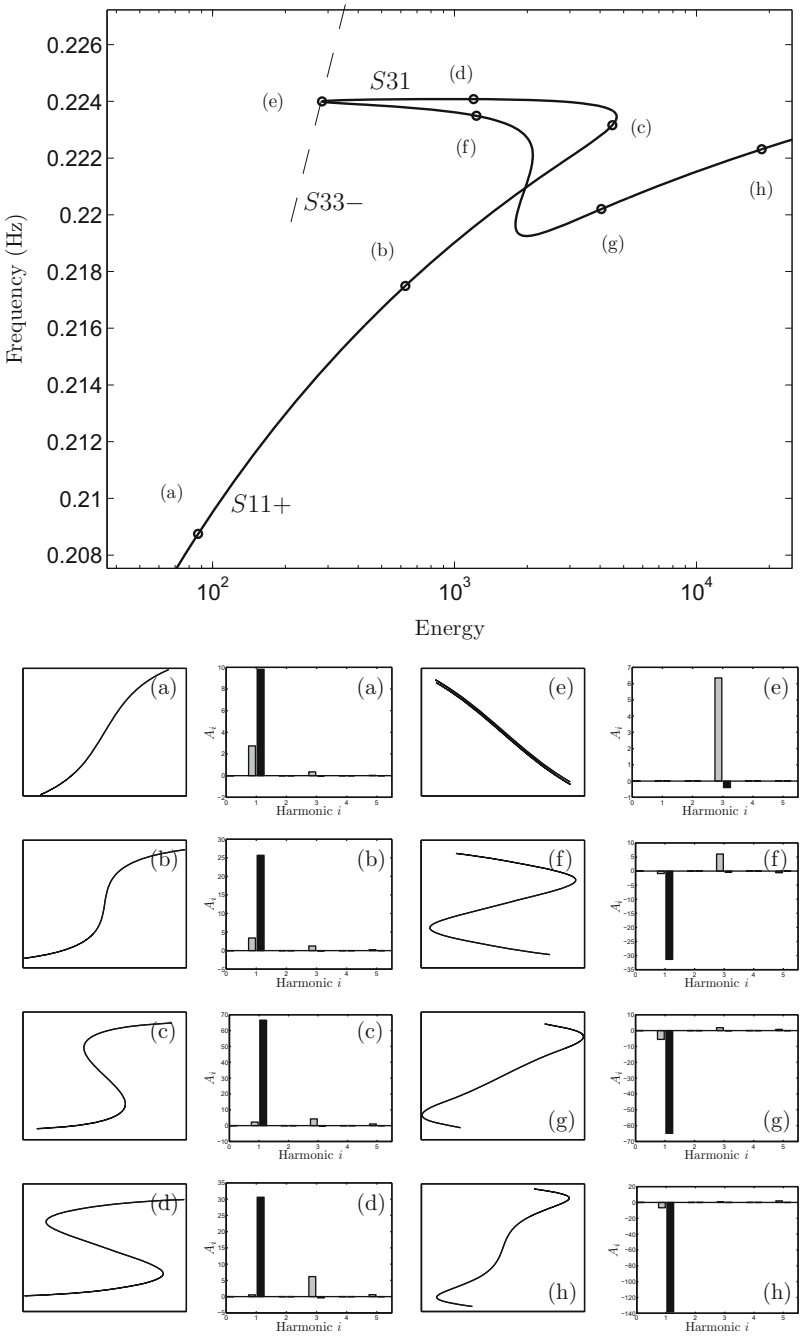

Fig. 16 (Continued)

pair of stable/unstable NNMs (Fig. 19). Returning to system (1), another illustration of NNM stability is shown in the FEP of Fig. 20. When the tongue $U21$ bifurcates from $S11+$, the NNMs on this latter branch lose stability. A detailed description of this tongue and the related dynamical mechanisms (e.g., symmetry-breaking bifurcation) is beyond the scope of this paper. This figure also shows that stability can be lost when a turning point is encountered.

3 Nonlinear Normal Modes: How to Compute Them?

Different methods for computing NNMs of discrete and continuous systems are briefly described in this section. They are classified in two categories, according to whether the computation relies on analytical or numerical methods.

3.1 Analytical Techniques

Rosenberg was the first to develop constructive techniques for computing NNMs of discrete conservative oscillators. The book by Vakakis et al. [17] summarizes the developments until the 1990s. In what follows, two techniques directly inspired by the two NNM definitions discussed previously are briefly reviewed.

3.1.1 An Energy-Based Formulation

This formulation relies on Rosenberg's work [8] and expresses an NNM as a modal curve in the configuration space. It was further developed by Manevitch and Mikhlin for discrete conservative oscillators [12] and exploited in a few other studies [15,17]. To illustrate the method, it is applied to system (1)

$$\begin{aligned} \ddot{x}_1 + (2x_1 - x_2) + 0.5\,x_1^3 &= 0 \\ \ddot{x}_2 + (2x_2 - x_1) &= 0 \end{aligned} \tag{13}$$

When the system vibrates along an NNM, the displacement x_2 is linked to x_1 through the expression of the modal curve $\hat{x}_2$

$$x_2 = \hat{x}_2(x_1) \tag{14}$$

The objective of the method is to eliminate the time derivatives from the equations of motion (13). To compute the second time derivative of x_2, relation (14) is differentiated twice using the chain rule

Fig. 16 Internally resonant NNMs (3:1 resonance). Top plot: close-up of the tongue $S31$ in the frequency-energy plot. Bottom plots: configuration space (horizontal axis: x_1; vertical axis: x_2) and Fourier coefficients of a series containing cosine terms only (grey: x_1; black: x_2)

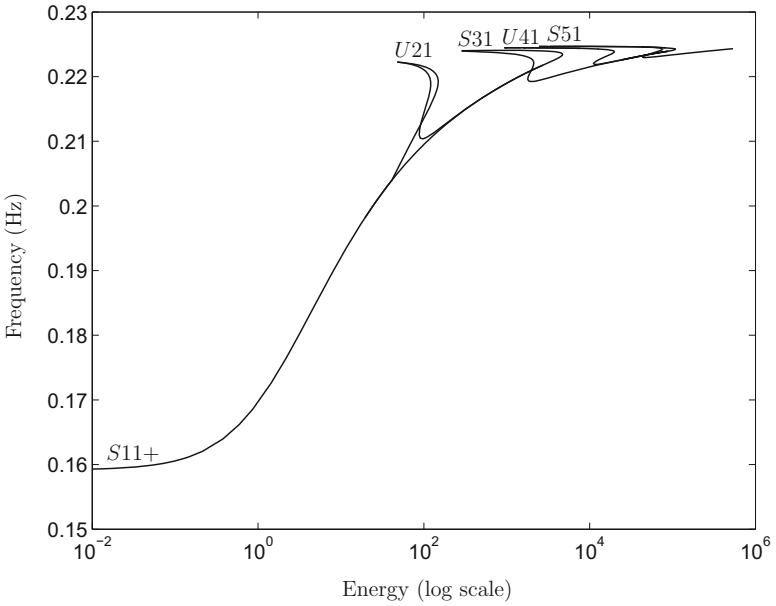

Fig. 17 Close-up of $S11+$ at higher energy levels

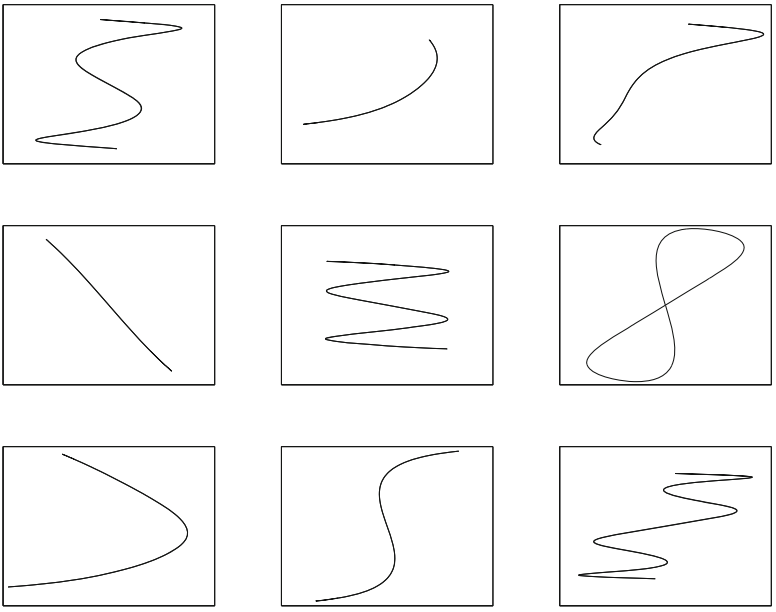

Fig. 18 A few representative NNMs of system (1) in the configuration space

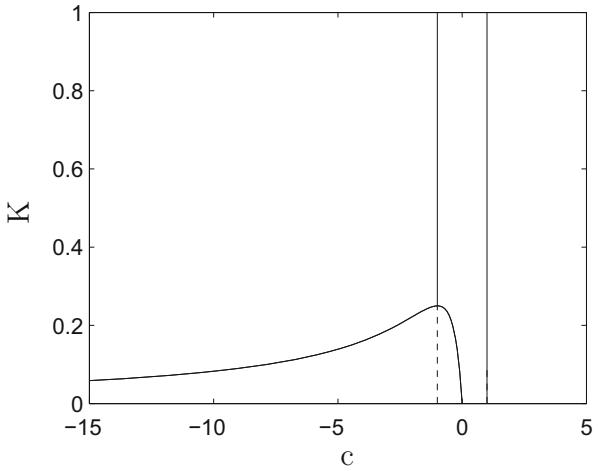

Fig. 19 NNM bifurcations of system (10) [14] (——: stable NNMs; − − −: unstable NNMs)

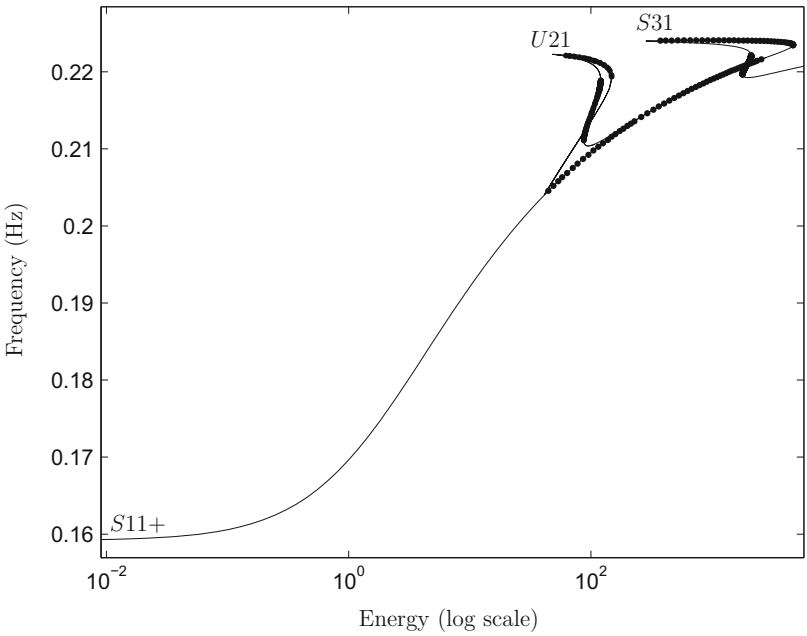

Fig. 20 Close-up of $S11+$ with stability results (——: stable NNMs; • • •: unstable NNMs)

$$\ddot{x}_2 = \hat{x}_2'' \dot{x}_1^2 + \hat{x}_2' \ddot{x}_1 \tag{15}$$

where prime denotes differentiation with respect to x_1. This expression involves the second time derivative of x_1, which is readily obtained from the equations of motion

$$\ddot{x}_1 = -2x_1 + \hat{x}_2 - 0.5x_1^3 \tag{16}$$

It then remains to compute the first time derivative of x_1 appearing in equation (15). To this end, a first integral of motion expressing explicitly the conservation of energy during the motion is written by multiplying equation (16) by $\dot{x}_1$ and integrating

$$\dot{x}_1^2 = 2\int_0^{\dot{x}_1} \dot{x}_1 \, \mathrm{d}\dot{x}_1 = -2\int_{X_1}^{x_1} \left[2u - \hat{x}_2(u) + 0.5u^3\right] \mathrm{d}u \tag{17}$$

where X_1 is the maximum amplitude attained by x_1; i.e., when $\dot{x}_1 = 0$. The derivatives are substituted into the second of equations (13), which yields the equation governing the modal curve:

$$\hat{x}_2'' \left\{-2\int_{X_1}^{x_1} \left[2u - \hat{x}_2(u) + 0.5u^3\right] \mathrm{d}u\right\} + \hat{x}_2' \left[-2x_1 + \hat{x}_2 - 0.5x_1^3\right] + (2\hat{x}_2 - x_1) = 0 \tag{18}$$

Because the coefficient of the highest derivative vanishes when $x_1 = X_1$, this functional equation is singular at the maximum equipotential surface. It must therefore be supplemented by a boundary condition

$$\left\{\hat{x}_2' \left[-2x_1 + \hat{x}_2 - 0.5x_1^3\right] + (2\hat{x}_2 - x_1)\right\}_{x_1 = X_1} = 0 \tag{19}$$

which expresses that the nonlinear mode intersects orthogonally the maximum equipotential surface in the configuration space. Equation (18) does not depend on the time variable, and its solution is amenable to a power series expansion:

$$\hat{x}_2(x_1) = \hat{x}_2^{(0)}(x_1) + \epsilon \hat{x}_2^{(1)}(x_1) + \epsilon^2 \hat{x}_2^{(2)}(x_1) + O(\epsilon^3) \tag{20}$$

This formulation was extended to undamped continuous systems in [16]. The displacement of any point of the system is expressed in terms of a single reference displacement $x_0(t) = x(s_0, t)$ by the functional relation

$$x(s, t) = X\left[s, x_0(t)\right] \tag{21}$$

where s is the spatial coordinate and X is a modal function characterizing the considered NNM. Then, an integral equation expressing the conservation of energy during the motion is used in conjunction with equation (21) to eliminate the time derivatives from the equations of motion. Eventually, the equation governing the modal function X is obtained and is solved using power series.

In the presence of internal resonances, the folding of the NNMs in the configuration space may result in multivalued relationship among the various coordinates (see Fig. 6). This was nicely addressed in [55] by considering NNMs in an appropriately defined modal space.

3.1.2 The Invariant Manifold Approach

The invariant manifold approach [19, 20, 21, 22] is similar in spirit to the energy-based formulation. The difference with the previous approach is that a pair of state variables (i.e., both the displacement and the velocity) are chosen as master coordinates, the remaining variables being functionally related to the chosen pair:

$$x(s,t) = X_1\left[s, x_0(t), \dot{x}_0(t)\right] \quad \text{and} \quad \dot{x}(s,t) = X_2\left[s, x_0(t), \dot{x}_0(t)\right] \tag{22}$$

These relations define a two-dimensional invariant manifold in phase space. By taking the time derivative of these constraint equations and using the chain rule differentiation, the explicit time dependence from the equations of motion can be eliminated. Eventually, this yields a set of partial differential equations governing the modal functions X_1 and X_2. These equations are as difficult to solve as the original problem, but the solution can be approximated using power series.

For systems with internal resonances, a multi-mode invariant manifold is considered in [56] to account for the influence of several modes. For instance, when two modes are resonant, the master coordinates comprise two pairs of state variables, and the resulting invariant manifold is four-dimensional.

3.2 Numerical Techniques

One of the first approaches was proposed by Slater in [57]. Based on Rosenberg's definition, the procedure integrates directly the governing equations of motion over one period using numerical algorithms (e.g., Runge-Kutta and Newmark). It comprises two steps:

1. An isolated periodic solution corresponding to a specific energy level is computed by modifying iteratively the initial conditions governing the free response of the system. This is carried out using optimization algorithms that minimize a periodicity condition (i.e., a cost function representing the lack of periodicity of the current iterate).
2. Low-energy modal curves and the corresponding periods of oscillation are first computed, taking the normal modes and natural frequencies of the underlying linear system as initial guesses. The energy is then gradually increased with the previously computed NNM as an initial guess for the next NNM.

This step-wise type of continuation of periodic solutions is called sequential continuation. A more advanced continuation scheme, i.e., pseudo-arclength continuation, was used in [46] and led to the development of a computationally effective

method for the calculation of NNMs. Another sophisticated continuation method is the so-called asymptotic-numerical method [58]. It is a semi-analytical technique that is based on a power series expansion of the unknowns parameterized by a control parameter. It is utilized to follow the NNM branches in conjunction with the harmonic balance method in [59] or with finite difference methods in [60].

3.3 Assessment of the Different Methodologies

Analytical methodologies have the advantage that NNMs can be constructed symbolically, which is certainly useful for gaining insight into the dynamics and for performing parametric studies. Among other things, they clearly highlight the frequency-energy dependence of the NNMs. The fundamental drawbacks of these techniques is that (i) they are quite analytically involved and require a careful treatment in the presence of internal resonances; (ii) the resultant dynamics are only accurate for small-amplitude motions; and (iii) the upper bound for these motions is not known a priori.

In this context, numerical methods have certainly the potential to make nonlinear modal analysis more accessible to the practicing structural engineer. Most of them provide an *exact* solution to the NNM calculation. But their key advantage is that they can calculate NNMs of real-world structures in strongly nonlinear regimes of motion. For instance, pseudo-arclength continuation was exploited in [50, 52] to compute NNMs of real-world spacecraft and aircraft, respectively, and in [37] for structures with distributed nonlinearity.

4 Nonlinear Normal Modes: Why Are They Useful?

The objective of this section is to describe several applications where NNMs represent a useful framework for the structural dynamicist. Specifically, we highlight how useful the NNMs are for modal analysis and system identification and how they may be exploited in conjunction with time-frequency analysis in order to extend the existing linear methodologies [2]. Nonlinear model reduction is also briefly discussed.

4.1 "Linear" Modal Analysis

Modal analysis and testing of linear mechanical structures has been developed over the past 40–50 years, and the techniques available today are mature and advanced [2]. Clearly, though, linearity is an idealization, an exception to the rule; nonlinearity is a frequent occurrence in real-life applications. In the presence of nonlinear phenomena, the structural dynamicist should therefore ask the question: *can I still use the linear modes ?* Obviously, the answer depends on the type of the nonlinearity and on the excitation level.

In this context, we believe that the computation of the NNMs and their representation in a FEP is a robust and accurate tool to decide whether or not the

linear framework is still applicable. It can be used to determine which modes (and to what extent) are sensitive to the nonlinearity. Going back to Fig. 13, it is clear that, until an energy of 10^{-1}, the mode shapes and natural frequencies are unaffected by the nonlinearity and can safely be used. Beyond this critical energy level, both the in-phase and out-of-phase modes show a significant departure from the LNMs and become dependent on the total energy in the system.

As another example, the FEP of system

$$\begin{aligned} \ddot{x}_1 + (2x_1 - x_2) &= 0 \\ \ddot{x}_2 + (2x_2 - x_1 - x_3) + 0.5\,x_2^3 &= 0 \\ \ddot{x}_3 + (2x_3 - x_2) &= 0 \end{aligned} \tag{23}$$

is depicted in Fig. 21. The linear modal parameters remain unchanged until approximately an energy of 10^{-1}. Another interesting finding is that the nonlinearity has no influence either on the frequency or on the mode shape of the second mode.

4.2 Nonlinear Modal Analysis

When it is certain that the system is excited in the nonlinear range, the linear framework should be abandoned in favor of a nonlinear modal analysis. Any attempt

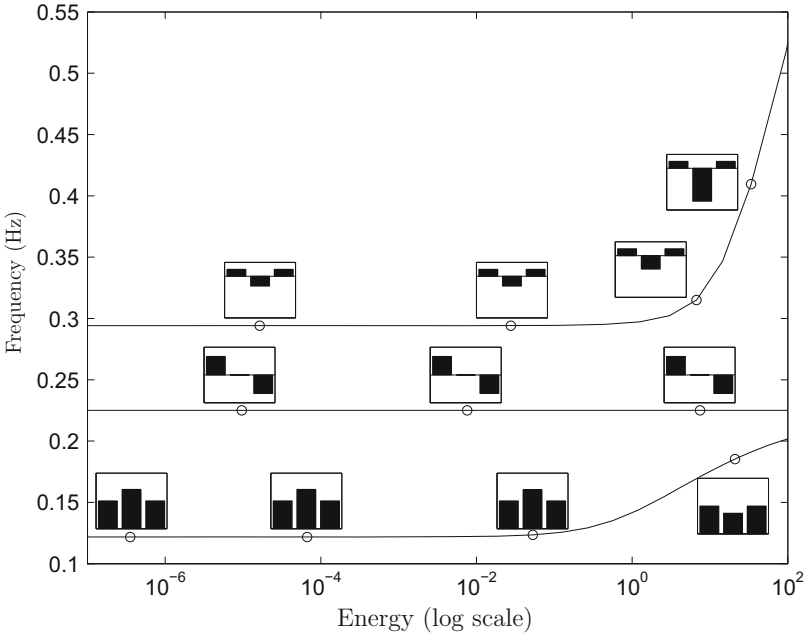

Fig. 21 Frequency-energy plot of system (23). NNMs represented by bar graphs are inset; they are given in terms of the initial displacements that realize the periodic motion (with zero initial velocities assumed)

to apply traditional linear analysis in this context results, at best, in a suboptimal design.

Considering again system (1) as a first example, its FEP in Fig. 13 greatly helps to understand how the modal curves deform under the action of the nonlinearity. The in-phase NNM tends to localize to the second DOF, whereas the out-of-phase NNM localizes to the first DOF. Regarding the corresponding frequency of oscillation, both modes are characterized by a hardening behavior due to the presence of the cubic spring.

As a second example, a planar cantilever beam discretized by 20 finite elements and with a cubic spring at the free end is now considered (see Table 1 for the geometrical and mechanical properties). This models a real nonlinear beam that was used as a benchmark for nonlinear system identification during the European action COST F3 [61]. The first two modes are plotted in the FEPs of Figs. 22 and 23, respectively. Considering the same energy level, the first modal curve seems somewhat more affected by the nonlinearity compared to the second modal curve. Their frequencies of oscillation undergo a strong increase with increasing energy levels. The FEPs also highlight the presence of two tongues, revealing the existence of internal resonances. The tongue in Fig. 22 corresponds to a 5:1 internal resonance between the first and second modes of the beam. When the energy gradually increases along the tongue, a smooth transition from the first mode to the second mode occurs following a dynamical mechanism similar to that described in Sect. 2.2.2. Similarly, a 5:1 internal resonance between the second and fourth modes is observed in Fig. 23. These internal resonances occur despite that the linear natural frequencies are not commensurate, as also discussed in Sect. 2.2.2.

These two examples demonstrate that such a nonlinear modal analysis is an important tool for thoroughly understanding the system's vibratory response in the nonlinear regime. Clearly, this cannot be achieved using linearization procedures. However, because the general motion of a nonlinear system cannot be expressed as a superposition of individual NNM motions and because the modes in all these figures are computed based on the underlying undamped system, the practical utility of the nonlinear modal analysis might appear, at first, questionable.

A first motivation to compute and exploit the NNMs is that forced resonances in nonlinear systems occur in their neighborhoods. The knowledge of the NNMs can therefore provide valuable insight into the structure of the resonances, a feature of considerable engineering importance [17]. For illustration, system (3) is considered. In Figs. 24 and 25, the backbone of the FEP of Fig. 13 is superposed to the nonlinear frequency response functions of Fig. 8 and 9. It can be observed that the backbone of the FEP traces the locus of the frequency response peaks for both the in-phase

Table 1 Geometrical and mechanical properties of the planar cantilever beam

Length (m)	Width (m)	Thickness (m)	Young's modulus (N/m^2)	Density (kg/m^3)	Nonlinear coeff. (N/m^3)
0.7	0.014	0.014	2.05e11	7800	$6\,10^9$

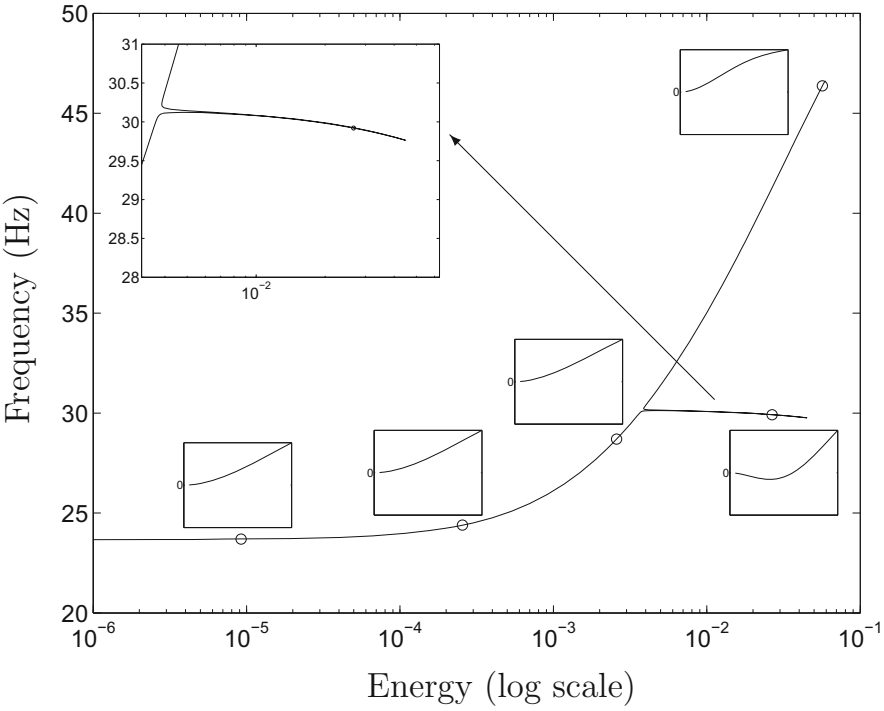

Fig. 22 Frequency-energy plot of the cantilever beam; close-up of the first mode

and out-of-phase modes. Furthermore, Fig. 26 compares the forced response of the system close to the first resonance (for $F = 0.1$, see the square in Fig. 24) to the free response of the corresponding point of the backbone. An excellent agreement is obtained between the two types of motion.

A second motivation is that the damped dynamics closely follows the NNMs of the underlying undamped system. To demonstrate this, a time-frequency analysis method, the continuous wavelet transform (CWT) is used. The CWT can track the temporal evolution of the instantaneous frequencies, which makes it an effective tool for analyzing nonlinear signals. The usual representation of the transform is to plot its modulus as a function of time and frequency in a three-dimensional or contour plot. To use the CWT in conjunction with the FEP, a different representation is proposed herein. The CWT is represented in a frequency-energy plot by substituting the instantaneous energy in the system for time.

The free response of system

$$\begin{aligned} \ddot{x}_1 + 0.03\dot{x}_1 + (2x_1 - x_2) + 0.5\,x_1^3 &= 0 \\ \ddot{x}_2 + 0.01\dot{x}_2 + (2x_2 - x_1) &= 0 \end{aligned} \tag{24}$$

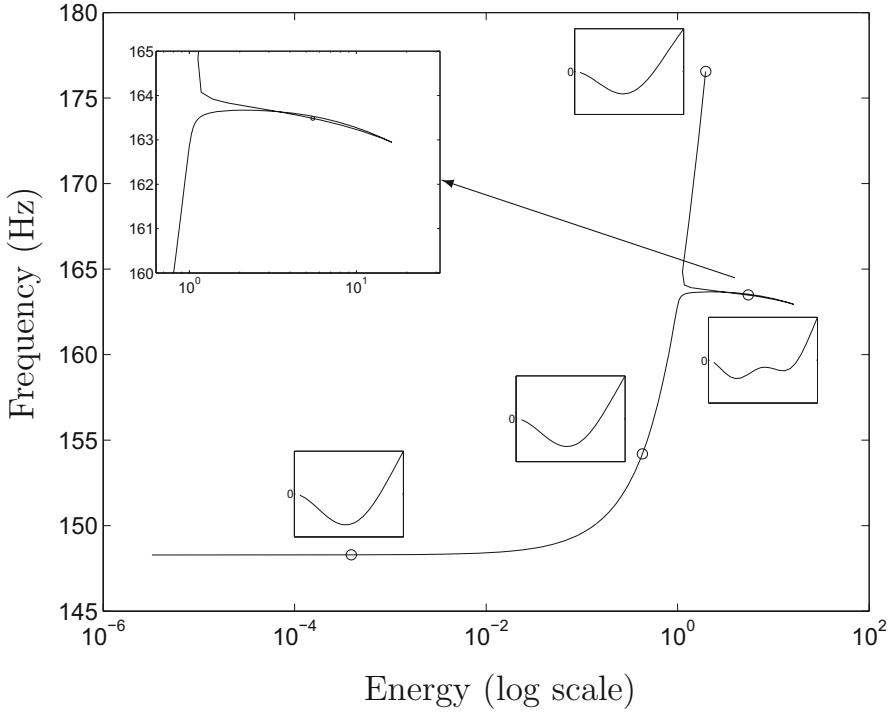

Fig. 23 Frequency-energy plot of the cantilever beam; close-up of the second mode

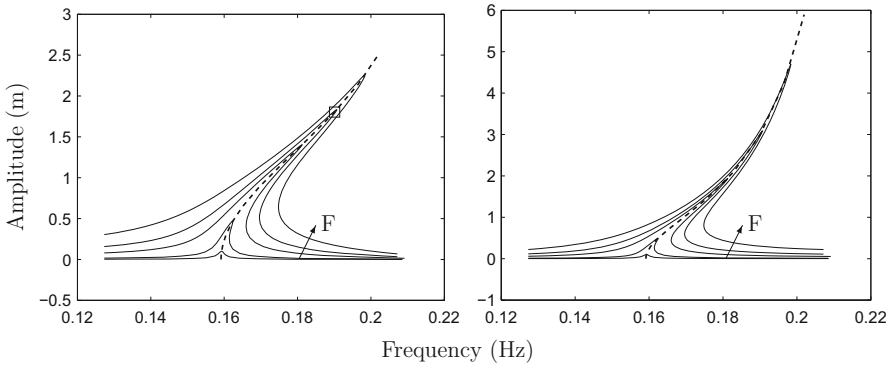

Fig. 24 Nonlinear frequency response functions close to the first resonant frequency (5 different forcing amplitudes: 0.002N, 0.01N, 0.05N, 0.1N, 0.2N). The dashed line is the backbone $S11+$ of the frequency-energy plot. Left plot: x_1; right plot: x_2

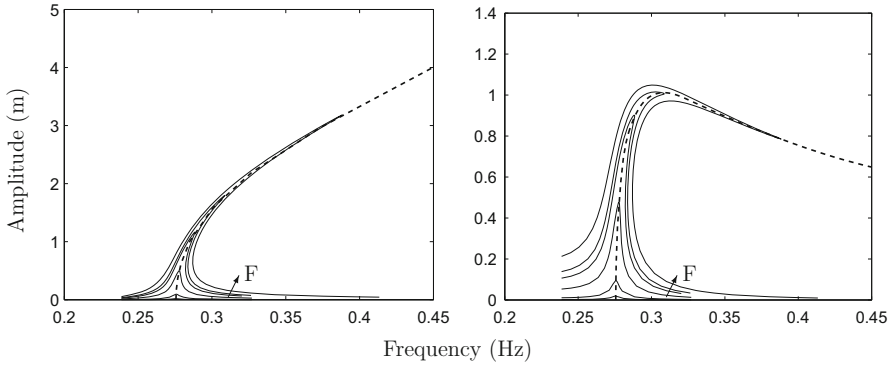

Fig. 25 Nonlinear frequency response functions close to the second resonant frequency (5 different forcing amplitudes: 0.002N, 0.01N, 0.05N, 0.1N, 0.2N). The dashed line is the backbone $S11-$ of the frequency-energy plot. Left plot: x_1; right plot: x_2

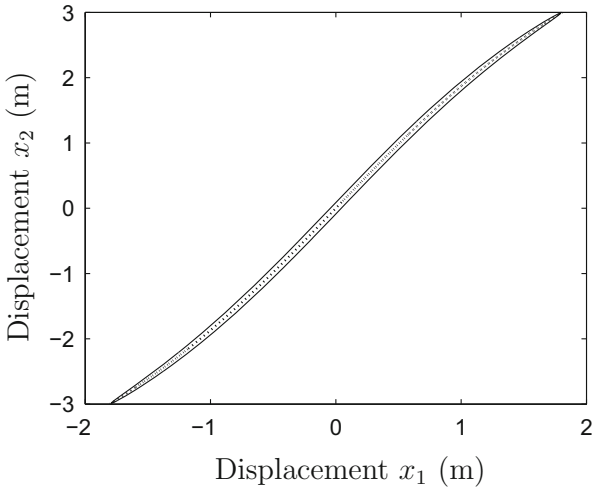

Fig. 26 Free ($F = 0$) and forced responses ($F = 0.1$) of system (3) in the configuration space. ——: forced response; - - -: free response

is depicted in Figs. 27 and 28 for an excitation of an in-phase and out-of-phase NNM, respectively. The left plot is the theoretical FEP that is the FEP computed from the equations of motion. The right plot is the "experimental" FEP, calculated directly from the time series: (i) the backbone is provided by the CWT, and (ii) the modal curves are obtained by representing the time series in the configuration space for one oscillation around a specific energy level. For comparison, the theoretical backbone is represented by a solid line in the experimental FEP. A perfect agreement is obtained between the two FEPs, which shows that the undamped NNMs are

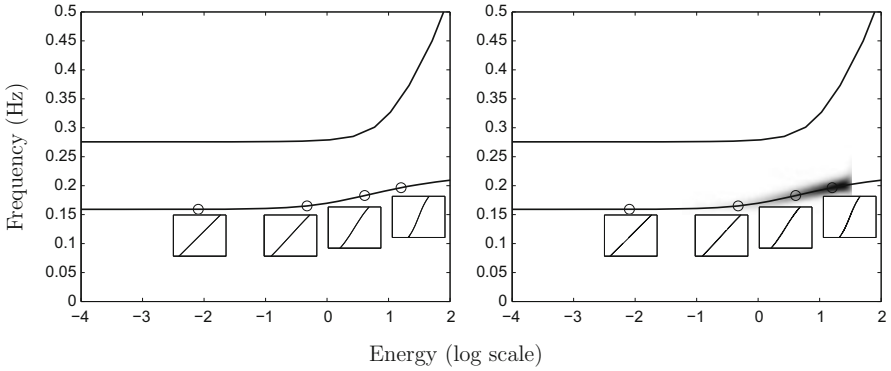

Fig. 27 Frequency-energy plot of system (1). Left plot: theoretical FEP; right plot: experimental FEP for an excitation of an in-phase NNM ($[x_1(0)\ x_2(0)\ \dot{x}_1(0)\ \dot{x}_2(0)] = [2.500\ 5.895\ 0\ 0]$)

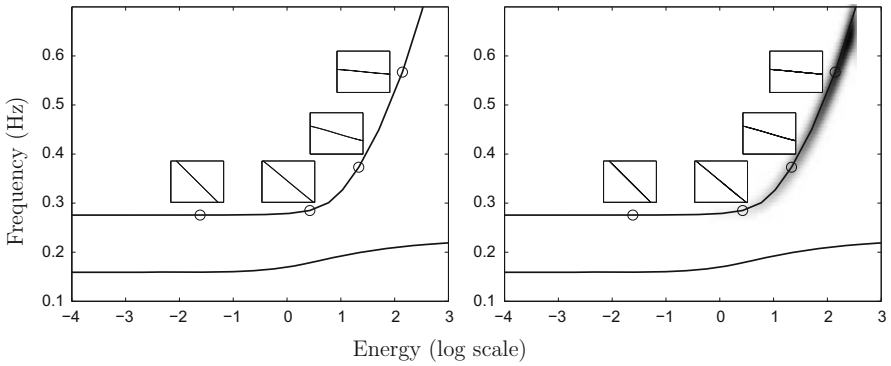

Fig. 28 Frequency-energy plot of system (1). Left plot: theoretical plot; right plot: experimental plot for an excitation of an out-of-phase NNM ($[x_1(0)\ x_2(0)\ \dot{x}_1(0)\ \dot{x}_2(0)] = [-6.842\ 0.389\ 0\ 0]$)

attractors for the damped trajectories. In the present case, the modal damping ratios are 1% and 0.6%, but we note that this result holds for higher damping ratios.

The combined use of the FEP and the CWT represents a suitable framework for developing a nonlinear system identification method, which could be viewed as a practical nonlinear analog of experimental modal analysis.

4.3 Reduced-Order Modeling

In a recent series of works [31, 62, 63, 64], it was shown that NNMs can provide effective bases for constructing reduced-order models of the dynamics of discrete and continuous nonlinear oscillators.

Specifically, Touzé et al. performed a comparative study of reduced-order models of large-amplitude vibrations of shell structures of different configurations using either LNMs or NNMs [64]. They showed that one or two NNMs were sufficient for accurately capturing the shell dynamics, and even the bifurcation structure of the

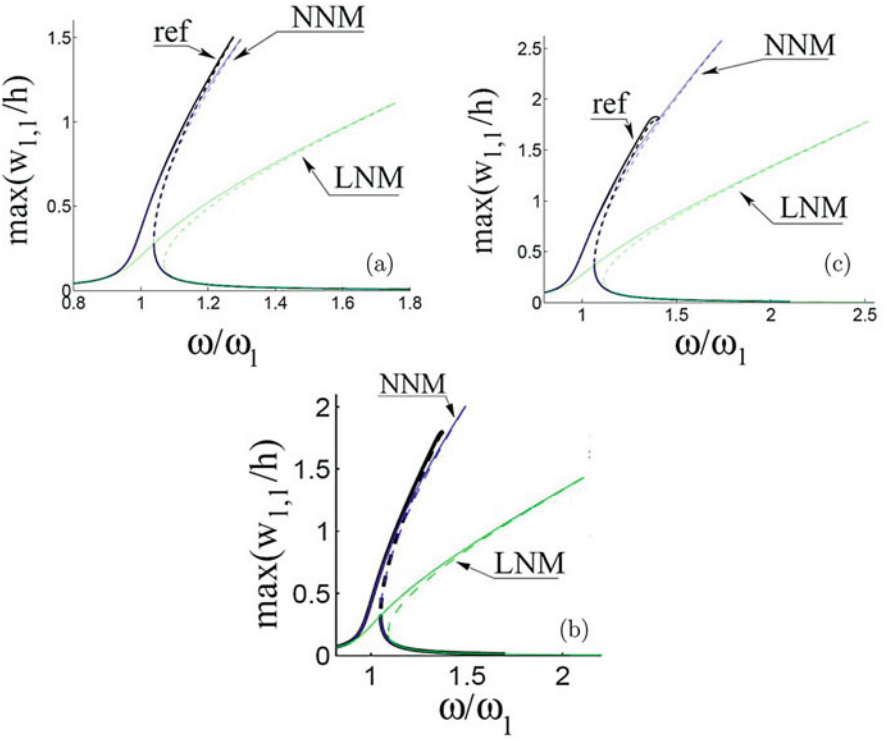

Fig. 29 Frequency response curve of an hyperbolic paraboloid panel: reference (exact) computational solution compared to reduced-order models based on the leading LNM and NNM for varying forcing amplitudes. (**a**) 2.84N; (**b**) 4.37N and (**c**) 6.66N. (Taken from Touze et al. [64])

dynamics that resulted from the nonlinear interaction of two shell modes in internal resonance. By contrast, multiple linear modes were necessary to achieve the same accuracy. For illustration, a specific application taken from [64] is shown in Fig. 29. It depicts the frequency response curve of the nondimensionalized amplitude of the transverse displacement of a hyperbolic paraboloid panel under harmonic excitation. The harmonic excitation is applied at the center of the panel, and its frequency is in the vicinity of the first eigenfrequency. Comparing the reference (exact) computational solution to reduced-order models obtained using the leading NNM and LNM, respectively, the accuracy of the NNM-based model and its superiority over the LNM-based model are established. In this example, 15 LNMs were required to obtain results of similar accuracy.

These results demonstrate that NNMs hold promise for low-order reduction of structural models with many DOFs (e.g., finite element computational models). Even though NNMs do not possess orthogonality properties (as do the LNMs), the resulting models are still expected to be much more accurate compared to their linear counterpart.

5 Closure

To robustly and accurately model nonlinearity in realistic vibrating structures is one of the greatest challenges in structural engineering. In this context, NNMs have a clear conceptual relation to the linear normal modes, yet they can highlight nonlinear phenomena that are unexpected (and unexplainable) from a linear viewpoint.

By combining algorithms for the numerical calculation of NNMs with a signal processing tool such as the wavelet transform and with a relevant graphical depiction such as the frequency-energy plot, the damped dynamics of a nonlinear system can be interpreted based on NNMs. These tools should help extend experimental modal analysis, which is well-established for linear systems, to a practical nonlinear analog. An experimental illustration of the NNM concept can be found in [65].

References

1. Craig R, Bampton M (1968) Coupling of substructures for dynamic analysis. AIAA J 6:1313–1319
2. Ewins DJ (2000) Modal testing: theory, practice and application, 2nd edn. Research Studies Press LTD, Hertfordshire
3. Friswell MI, Mottershead JE (1995) Finite element model updating in structural dynamics. Kluwer Academic Publishers, London
4. Doebling SW, Farrar CR, Prime MB, Shevitz DW (1996) Damage identification and health monitoring of structural and mechanical systems from changes in their vibration characteristics: a literature review, Los Alamos National Laboratory Report LA-13070-MS
5. Kerschen G, Worden K, Vakakis AF, Golinval JC (2006) Past, present and future of nonlinear system identification in structural dynamics. Mech Syst Signal Process 20:505–592
6. Rosenberg RM (1960) Normal modes of nonlinear dual-mode systems. J Appl Mech 27: 263–268
7. Rosenberg RM (1962) The normal modes of nonlinear n-degree-of-freedom systems. J Appl Mech 29:7–14
8. Rosenberg RM (1966) On nonlinear vibrations of systems with many degrees of freedom. Adv Appl Mech 9:155–242
9. Rand R (1971) Nonlinear normal modes in two-degree-of-freedom systems. Journal of Applied Mechanics 38:561.
10. Rand R (1971) A higher-order approximation for nonlinear normal modes in two-degree-of-freedom systems. Int J Nonlinear Mech 6:545–547
11. Rand R (1974) A direct method for nonlinear normal modes. Int J Nonlinear Mech 9:363–368
12. Manevitch LI, Mikhlin YV (1972) On periodic solutions close to rectilinear normal vibration modes. PMM 36:1051–1058
13. Vakakis AF (1990) Analysis and identification of linear and nonlinear normal modes in vibrating systems. Ph.D. Dissertation, California Institute of Technology
14. Caughey TK, Vakakis AF, Sivo JM (1990) Analytical study of similar normal modes and their bifurcations in a class of strongly nonlinear systems. Int J Nonlinear Mech 25:521–533
15. Vakakis AF (1992) Non-similar normal oscillations in a strongly non-linear discrete system. J Sound Vib 159:341–361
16. King ME, Vakakis AF (1994) An energy-based formulation for computing nonlinear normal-modes in undamped continuous systems. J Sound Vib 116:332–340
17. Vakakis AF, Manevitch LI, Mikhlin YV, Pilipchuk VN, Zevin AA (1996) Normal modes and localization in nonlinear systems. John Wiley & Sons, New York

18. Vakakis AF (1997) Non-linear normal modes and their applications in vibration theory: an overview. Mech Syst Signal Process 11:3–22
19. Shaw SW, Pierre C (1991) Non-linear normal modes and invariant manifolds. J Sound Vib 150:170–173
20. Shaw SW, Pierre C (1992) On nonlinear normal modes. ASME Winter Annual Meeting
21. Shaw SW, Pierre C (1993) Normal modes for non-linear vibratory systems. J Sound Vib 164:85–124
22. Shaw SW, Pierre C (1994) Normal modes of vibration for non-linear continuous systems. J Sound Vib 169:319–347
23. Jezequel L, Lamarque CH (1991) Analysis of nonlinear dynamic systems by the normal form theory. J Sound Vib 149:429–459
24. Yabuno H, Nayfeh AH (2001) Nonlinear normal modes of a parametrically excited cantilever beam. Nonlinear Dyn 25:65–77
25. Xie WC, Lee HP, Lim SP (2003) Nonlinear dynamic analysis of MEMS switches by nonlinear modal analysis. Nonlinear Dyn 31:243–256
26. Mazzilli CEN, Soares MES, Baracho Neto GP (2004) Non-linear normal modes of a simply supported beam: continuous system and finite-element models. Comput Struct 82: 2683–2691
27. Gendelman OV (2004) Bifurcations of nonlinear normal modes of linear oscillator with strongly nonlinear damped attachment. Nonlinear Dyn 37:115–128
28. Lacarbonara W, Camillacci R (2004) Nonlinear normal modes of structural systems via asymptotic approach. Int J Solids Struct 41:5565–5594
29. Lee YS, Kerschen G, Vakakis AF, Panagopoulos PN, Bergman LA, McFarland DM (2005) Complicated dynamics of a linear oscillator with a light, essentially nonlinear attachment. Physica D 204:41–69
30. Dick AJ, Balachandran B, Mote CD (2006) Nonlinear vibration modes in micro-resonator arrays. In: Smart Structures and Materials 2006: Modeling, Signal Processing, and Control, Proceedings of the SPIE, vol 6166, pp 206–217
31. Touzé C, Amabili M (2006) Nonlinear normal modes for damped geometrically nonlinear systems: Application to reduced-order modelling of harmonically forced structures. J Sound Vib 298:958–981
32. Srinil N, Rega G (2007) Two-to-one resonant multi-modal dynamics of horizontal/inclined cables. Part II: Internal resonance activation, reduced-order models and nonlinear normal modes. Nonlinear Dyn 48:253–274
33. Lenci S, Rega G (2007) Dimension reduction of homoclinic orbits of buckled beams via the non-linear normal modes technique. Int J Nonlinear Mech 42:515–528
34. Lacarbonara W, Paolone A, Vestroni F (2007) Non-linear modal properties of non-shallow cables. Int J Nonlinear Mech 42:542–554
35. Cochelin B, Vergez C (2009) A high order purely frequency-based harmonic balance formulation for continuation of periodic solutions. J Sound Vib 324:243–262
36. Laxalde D, Thouverez F, Complex non-linear modal analysis for mechanical systems: application to turbomachinery bladings with friction interfaces. J Sound Vib 322 (2009), 1009–1025.
37. Kuether RJ, Allen MS (2014) A numerical approach to directly compute nonlinear normal modes of geometrically nonlinear finite element models. Mech Syst Signal Process 46:1–15
38. Hill TL, Cammarano A, Neild SA, Wagg DJ (2015) Interpreting the forced responses of a two-degree-of-freedom nonlinear oscillator using backbone curves. J Sound Vib 349: 276–288
39. Renson L, A. Gonzalez-Buelga, Barton DAW, Neild SA, Robust identification of backbone curves using control-based continuation. Journal of Sound and Vibration 367 (2016), 145–158.
40. Hill TL, Cammarano A, Neild SA, Barton DAW (2017) Identifying the significance of nonlinear normal modes. Proc R Soc A 473:20160789

41. Scheel M, Peter S, Leine RI, Krack M (2018) A phase resonance approach for modal testing of structures with nonlinear dissipation. J Sound Vib 435:56–73
42. Ribeiro P, Thomas O (2017) Nonlinear modes of vibration and internal resonances in nonlocal beams. J Comput Nonlinear Dyn 12:031017
43. Song M, Renson L, Noel JP, Moaveni B, Kerschen G (2018) Bayesian model updating of nonlinear systems using nonlinear normal modes. Struct Control Health Monit 25:e2258
44. Haller G, Ponsioen S (2016) Nonlinear normal modes and spectral submanifolds: existence, uniqueness and use in model reduction. Nonlinear Dyn 86:1493–1534
45. Krack M (2015) Nonlinear modal analysis of nonconservative systems: extension of the periodic motion concept. Comput Struct 154:59–71
46. Peeters M, Viguié R, Sérandour G, Kerschen G, Golinval JC (2009) Nonlinear normal modes, Part II: toward a practical computation using numerical continuation. Mech Syst Signal Process 23:170–194
47. Nayfeh AH (2000) Nonlinear interactions: analytical, computational and experimental methods. Wiley-Interscience, New York
48. SS. Oueini, Chin CM, Nayfeh AH (1999) Dynamics of a cubic nonlinear vibration absorber. Nonlinear Dyn 20:283–295
49. Noel JP, Renson L, Kerschen G (2014) Complex dynamics of a nonlinear aerospace structure: experimental identification and modal interactions. J Sound Vib 333:2588–2607
50. Renson L, Noel JP, Kerschen G (2015) Complex dynamics of a nonlinear aerospace structure: numerical continuation and normal modes. Nonlinear Dyn 79:1293–1309
51. Claeys M, Sinou JJ, Lambelin JP, Todeschini R (2016) Modal interactions due to friction in the nonlinear vibration response of the "Harmony" test structure: experiments and simulations. J Sound Vib 376:131–148
52. Kerschen G, Peeters M, Golinval JC, Stephan C (2013) Nonlinear modal analysis of a full-scale aircraft. AIAA J Aircr 50:1409–1419
53. Pak CH (2006) Synge's concept of stability applied to non-linear normal modes. Int J Nonlinear Mech 41:657–664
54. Recktenwald G, Rand R (2007) Stability of strongly nonlinear normal modes. Commun Nonlinear Sci Numer Simul 12:1128–1132
55. King ME, Vakakis AF (1995) An energy-based approach to computing resonant nonlinear normal modes. J Appl Mech 63:810–819
56. Boivin N, Pierre C, Shaw SW (1995) Non-linear modal analysis of structural systems featuring internal resonances. J Sound Vib 182:336–341
57. Slater JC (1996) A numerical method for determining nonlinear normal modes. Nonlinear Dyn 10:19–30
58. Cochelin B, Damil N, Potier-Ferry M (1994) Asymptotic numerical methods and Padé approximants for nonlinear elastic structures. Int J Numer Methods Eng 37:1187–1213
59. Pérignon F (2004) Vibration forcées de structures minces, élastiques, non-linéaires. Ph.D. Thesis, Université de la Méditerrané, Marseille
60. Arquier R, Bellizzi S, Bouc R, Cochelin B (2006) Two methods for the computation of nonlinear modes of vibrating systems at large amplitudes. Comput Struct 84:1565–1576
61. Thouverez F (2003) Presentation of the ECL benchmark. Mech Syst Signal Process 17: 195–202
62. Pesheck E (2000) Reduced-order modeling of nonlinear structural systems using nonlinear normal modes and invariant manifolds. Ph.D. Thesis, University of Michigan, Ann Arbor
63. Touzé C, Thomas O, Chaigne A (2004) Hardening/softening behaviour in non-linear oscillations of structural systems using non-linear normal modes. J Sound Vib 273:77–101
64. C. Touzé, Amabili M, Thomas O (2007) Reduced-order models for large-amplitude vibrations of shells including in-plane inertia. In: Proceedings of the EUROMECH Colloquium on Geometrically Nonlinear Vibrations, Porto
65. Peeters M, Kerschen G, Golinval JC (2011) Modal testing of nonlinear vibrating structures based on nonlinear normal modes: experimental demonstration. Mech Syst Signal Process 25:1227–1247

Part III
Analytical/Experimental Modeling Applications

Substructuring Concepts and Component Mode Synthesis

14

Daniel Rixen

Contents

Abstract

In this chapter, the basic principle of model reduction for linear models in structural dynamics is explained. In particular, the principle of substructuring is outlined following different common approaches.

Keywords

Model reduction · Representation modes · Component dynamics

D. Rixen (✉)
Technische Universität München, Garching, Germany
e-mail: rixen@tum.de

R. Allemang, P. Avitabile (eds.), *Handbook of Experimental Structural Dynamics*,
https://doi.org/10.1007/978-1-4614-4547-0_16

1 Model Reduction: General Concepts

1.1 Reduction by Projection

Often, a finite element model is first built for static analysis in order to assess static deformations and stress levels which might be concentrated around small features of the structure (stress concentration areas). Therefore, it is very common to find static models that have a very refined mesh, hence a high number of degrees of freedom (typically up to several millions). Such very large static models can be solved by means of efficient solvers, but when it comes to computing free vibration modes, harmonic responses and/or transient responses, it is required to solve many static-like problems (i.e., in the inverse iterations of the eigensolvers or in the time-stepping loop) and the computing time required is often unacceptable.

Fortunately, for most dynamical problems, such highly refined meshes are not needed to capture the interesting dynamic behavior. For instance, if we want to compute the fundamental modes, we know that the first free vibration modes have a rather smooth deformation and thus a coarser mesh would be sufficient to compute these modes. Similarly, when computing the dynamic response to external loads which are no shocks (i.e., which have no high spectral content compared to the eigenfrequency spectrum of the structure), a coarse mesh yields in most cases accurate results. In summary, *using a coarser representation of the displacement field in the dynamic model is often acceptable in terms of accuracy and is required in order to perform dynamic analyses in a reasonable time.*

The structural analyst should thus in principle build two models, one for the static simulations, one for the dynamic analysis. Knowing that building a model is a significant part of the entire study, it would be very useful to device a procedure that reduces the size of the dynamic problem without modifying the mesh grid.

Such procedures indeed exist and are known as *reduction methods.* Similarly to the way one approximates continuous fields by a set of shape functions in a Rayleigh–Ritz approach (e.g., in Finite Elements), the driving idea in reduction techniques is to replace the degrees of freedom (DOF) by a set of global variables representing the amplitudes of possible displacement modes:

$$\mathbf{u}(t) \simeq \mathbf{T}\mathbf{q}(t) \tag{1}$$

where $\mathbf{u}$ are all the n DOF of the system, $\mathbf{T}$ a reduction matrix of dimension $n \times r$, $r < n$, and $\mathbf{q}$ of dimension $r \times 1$ is a set of reduced generalized degrees of freedom. The columns of $\mathbf{T}$ define possible displacement shapes for the DOF $\mathbf{u}$, and $\mathbf{q}$ are the corresponding amplitude.

In general, replacing $\mathbf{u}$ by Eq. (1), only an approximate solution can be found and the accuracy of the approximation will depend on how well the assumed modes in $\mathbf{T}$ can represent the exact solution. Introducing Eq. (1) in the linear dynamic equation of motion of the structure

$$\mathbf{M}\ddot{\mathbf{u}} + \mathbf{C}\dot{\mathbf{u}} + \mathbf{K}\mathbf{u} = \mathbf{f}(t) \tag{2}$$

one obtains

$$\mathbf{MT}\ddot{\mathbf{q}} + \mathbf{CT}\dot{\mathbf{q}} + \mathbf{KT}\dot{\mathbf{q}} = \mathbf{f}(t) + \mathbf{r} \tag{3}$$

where $\mathbf{r}$ is a residual force that is a remainder for the dynamic equilibrium equation; since the reduction subspace $\mathbf{T}$ can in general not represent the exact solution, there will always be an equilibrium error, whatever the choice of $\mathbf{q}$. Indeed, one now has only r unknowns $\mathbf{q}$ to satisfy $n > r$ equations. Then following the idea of virtual work, one requires that the reduced DOF $\mathbf{q}$ be chosen such that the residual force $\mathbf{r}$ does not contribute to the dynamics in the representation space $\mathbf{T}$ or, in other words, that the residual force does not produce any work for the possible shapes of motion contained in $\mathbf{T}$:

$$\mathbf{T}^T\mathbf{r} = 0. \tag{4}$$

With this condition, we can find the equations to determine $\mathbf{q}$ by projecting the dynamic equilibrium equations (3) onto the subspace $\mathbf{T}$:

$$\mathbf{T}^T\mathbf{MT}\ddot{\mathbf{q}} + \mathbf{T}^T\mathbf{CT}\dot{\mathbf{q}} + \mathbf{T}^T\mathbf{KTq} = \mathbf{T}^T\mathbf{f} \tag{5}$$

which is usually written as

$$\tilde{\mathbf{M}}\ddot{\mathbf{q}} + \tilde{\mathbf{C}}\dot{\mathbf{q}} + \tilde{\mathbf{K}}\mathbf{q} = \tilde{\mathbf{f}} \tag{6}$$

where the tilde superscript indicates that the matrices and vectors pertain now to a representation in a reduced space.

After having solved the reduced problem (6) for $\mathbf{q}$, one can build the solution $\mathbf{u}$ for the physical DOF by substituting in Eq. (1). The residual force $\mathbf{r}$ for the full problem can be computed by substitution in the original problem (3); it provides a way to monitor, a posteriori, the error on the equilibrium.

In what follows, we will drop the damping term in order to clarify the presentation. Reduction of the damping matrix, in particular for substructure reduction, is discussed in Refs. [15, 16] and the references therein.

1.2 The Guyan–Irons Method

The cornerstone of every reduction method consists in finding a representation space $\mathbf{T}$ of the solution that allows finding a good approximation and that can be obtained with a computational cost significantly smaller than the one involved in solving the full problem. One very common way to find a reasonably good representation space was proposed in 1965 by Guyan [18] and Irons [23], as described next.

Let us consider the matrix equation that governs the system dynamics (2). To reduce the size of matrices $\mathbf{K}$ and $\mathbf{M}$, let us eliminate a subset of DOF. The eliminated (condensed) and remaining DOF are written, respectively, $\mathbf{u}_1$ and $\mathbf{u}_2$.

Assuming that no forces are applied on $\mathbf{u}_1$, the equation can be partitioned as follows:

$$\begin{bmatrix} \mathbf{M}_{22} & \mathbf{M}_{21} \\ \mathbf{M}_{12} & \mathbf{M}_{11} \end{bmatrix} \begin{bmatrix} \ddot{\mathbf{u}}_2 \\ \ddot{\mathbf{u}}_1 \end{bmatrix} + \begin{bmatrix} \mathbf{K}_{22} & \mathbf{K}_{21} \\ \mathbf{K}_{12} & \mathbf{K}_{11} \end{bmatrix} \begin{bmatrix} \mathbf{u}_2 \\ \mathbf{u}_1 \end{bmatrix} = \begin{bmatrix} \mathbf{f}_2 \\ \mathbf{0} \end{bmatrix} \tag{7}$$

or

$$\mathbf{M}_{22}\ddot{\mathbf{u}}_2 + \mathbf{M}_{21}\ddot{\mathbf{u}}_1 + \mathbf{K}_{22}\mathbf{u}_2 + \mathbf{K}_{21}\mathbf{u}_1 = \mathbf{f}_2 \tag{8}$$

$$\mathbf{M}_{12}\ddot{\mathbf{u}}_2 + \mathbf{M}_{11}\ddot{\mathbf{u}}_1 + \mathbf{K}_{12}\mathbf{u}_2 + \mathbf{K}_{11}\mathbf{u}_1 = \mathbf{0}. \tag{9}$$

One may imagine separating the condensed coordinate $\mathbf{u}_1$ into two contributions

$$\mathbf{u}_1 = \mathbf{u}_{1,stat} + \mathbf{u}_{1,dyn} \tag{10}$$

with the "static" part deduced from

$$\mathbf{u}_{1,stat} = -\mathbf{K}_{11}^{-1}\mathbf{K}_{12}\mathbf{u}_2. \tag{11}$$

This is obtained by neglecting the inertia forces in Eq. (9).

The static condensation algorithm consists in neglecting $\mathbf{u}_{1,dyn}$ and in building the reduction

$$\begin{bmatrix} \mathbf{u}_2 \\ \mathbf{u}_1 \end{bmatrix} = \mathbf{T}^{GI}\ \mathbf{u}_2 = \begin{bmatrix} \mathbf{I} \\ \mathbf{S} \end{bmatrix} \mathbf{u}_2 \tag{12}$$

where $\mathbf{T}^{GI}$ stands for the Guyan–Irons reduction matrix and where

$$\mathbf{S} = -\mathbf{K}_{11}^{-1}\mathbf{K}_{12} \tag{13}$$

is the static condensation matrix, the columns of which contain the so-called *static modes* representing the static response of $\mathbf{u}_1$ for unit $\mathbf{u}_2$ displacements. In other words, they represent the static deformation induced on $\mathbf{u}_1$ when a unit displacement is given to one of the DOFs $\mathbf{u}_2$. The retained DOFs $\mathbf{u}_2$ are sometimes called "master DOFs" whereas the condensed ones, $\mathbf{u}_1$, are often called "slave DOFs" since they are statically enslaved to $\mathbf{u}_2$.

The reduced matrices are then

$$\mathbf{K}^{GI} = \mathbf{T}^T\mathbf{K}\mathbf{T} = \mathbf{K}_{22} - \mathbf{K}_{21}\mathbf{K}_{11}^{-1}\mathbf{K}_{12} \tag{14}$$

$$\mathbf{M}^{GI} = \mathbf{T}^T\mathbf{M}\mathbf{T} = \mathbf{M}_{22} - \mathbf{M}_{21}\mathbf{K}_{11}^{-1}\mathbf{K}_{12} - \mathbf{K}_{21}\mathbf{K}_{11}^{-1}\mathbf{M}_{12} + \mathbf{K}_{21}\mathbf{K}_{11}^{-1}\mathbf{M}_{11}\mathbf{K}_{11}^{-1}\mathbf{K}_{12}. \tag{15}$$

We observe that the reduced stiffness matrix is the stiffness matrix statically condensed on $\mathbf{u}_2$. The reduced mass matrix is the mass matrix associated to $\mathbf{u}_2$ and augmented by the inertia of $\mathbf{u}_1$ assumed to respond quasi-statically.

The dynamic problem is then reduced to

$$\mathbf{M}^{GI}\ddot{\mathbf{u}}_2 + \mathbf{K}^{GI}\mathbf{u}_2 + \mathbf{f}_2^{GI}. \tag{16}$$

If the static condensation algorithm is applied to static problems, the exact solution is found. But when applied to dynamic problems, an approximation is introduced by neglecting the dynamic response of the interior of the substructure and thereby assuming that all condensed DoFS $\mathbf{u}_1$ respond quasistatically to the $\mathbf{u}_2$ displacements. The validity of the condensation algorithm thus depends on the extent to which the correction $\mathbf{u}_{1,dyn}$ is negligible. It is possible to show (see, for instance, Ref. [13]) that the static condensation technique is valid if

$$\omega^2 = \mu_1^2 \tag{17}$$

where ω is the highest eigenfrequency that one wants to compute for the complete structure and μ_1 is the lowest eigenfrequency of the structure when $\mathbf{u}_2$ are clamped. The complete analysis allows to show that static condensation always leads to overestimating the eigenvalues compared to the full model. This is natural if we recall that a model obtained by applying consistently a Rayleigh–Ritz approach is always stiffer due to the restrictions imposed to the model by the discretization field (see, for instance, Ref. [13]).

The algorithm described above is very frequently used in the context of finite element structural analysis. Although originally proposed independently by Guyan and Irons, it is commonly known as the Guyan reduction method. In commercial codes, this method is often implemented and used to reduce the complexity of the problem when no substructuring approach is used. The choice of an appropriate set of master DOF $\mathbf{u}_2$ is sometimes done automatically by the software. One simple heuristics consists in ranking the DOFs $\mathbf{u}$ according to their individual pseudo-frequency computed by the ratio of the diagonals of the stiffness and mass matrices, namely, for a DOF k, $v_k^2 = K_{kk}/M_{kk}$, and choosing as master DOF $\mathbf{u}_2$ the ones with the lowest v_i^2.

1.3 Model Reduction Through Substructuring

A very interesting way of applying reduction technique is found by applying the following procedure:

1. Define subparts of the structure, called *substructures*. These substructures correspond for instance to parts of the model that are analyzed and designed by

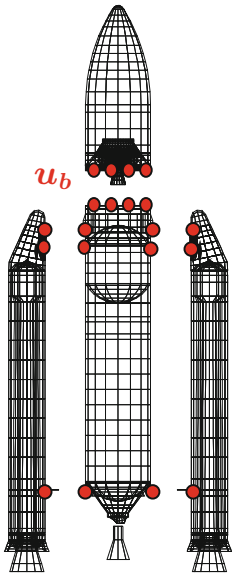

Fig. 1 Example of a substructured system. The red nodes suggest the location of interface nodes between subcomponents. (Courtesy of ESA/ESTEC)

different teams. For an aircraft, this might be the wings, fuselage, stabilizers, and tail. For a launcher system, it could be different stages of the rocket and the payload (see the schematic in Fig. 1). For a vehicle, one could define as substructures the engine block, the accessories, the suspension, and the car body. We will denote every substructure by $\Omega^{(s)}$. The stiffness and mass matrices corresponding to the nonassembled substructures will be denoted by $\mathbf{K}^{(s)}$ and $\mathbf{M}^{(s)}$, respectively. The DOF per substructure are denoted as $\mathbf{u}^{(s)}$.

2. For every subpart, define a reduction matrix $\mathbf{T}^{(s)}$ that retains at least the DOF on the interface boundary, called $\mathbf{u}_b^{(s)}$, such that

$$\mathbf{u}^{(s)} = \mathbf{T}^{(s)} \begin{bmatrix} \mathbf{u}_b^{(s)} \\ \boldsymbol{\zeta}^{(s)} \end{bmatrix} \tag{18}$$

where $\boldsymbol{\zeta}^{(s)}$ are generalized degrees of freedom denoting the amplitudes of representation modes additional to the ones governed by $\mathbf{u}_b^{(s)}$. The substructures are now seen as macroelements (also called *superelement*) whose stiffness and mass matrices are given by

$$\tilde{\mathbf{K}}^{(s)} = \mathbf{T}^{(s)^T} \mathbf{K}^{(s)} \mathbf{T}^{(s)} \qquad \tilde{\mathbf{M}}^{(s)} = \mathbf{T}^{(s)^T} \mathbf{M}^{(s)} \mathbf{T}^{(s)}. \tag{19}$$

These reduced matrices of the substructures can easily be shared between different design teams. Such methods are sometimes called *component mode synthesis* or CMS.

3. The interface boundary degrees of freedom $\mathbf{u}_b^{(s)}$ are assembled on the interface of the substructures exactly as if one would assemble the macroelement.

   If one first assumes that the entire reduction of a substructure is performed by keeping only the interface DOF $\mathbf{u}_b^{(s)}$ (i.e., no additional reduced DOF $\boldsymbol{\zeta}^{(s)}$ per substructure), one can resort to the method of Guyan–Irons (see previous section) where the interface DOF are the master DOF (previously called $\mathbf{u}_2^{(s)}$ when the Guayn–Irons reduction was applied to a nondecomposed problem). With a simple Guyan–Irons reduction on the interface DOF of the substructures, the dynamics of the DOF inside the substructures is neglected, which could be a crude assumption if the eigenfrequencies of the substructures fixed on the interface are not small (see criteria (17)). Hence additional information about the substructure vibrations should be added to the reduction basis as explained in the next section.

2 Numerical Techniques for Model Reduction of Substructures

2.1 The Hurty/Craig–Bampton Method

The substructure reduction method discussed in this section is one of the most commonly used substructuring technique in engineering practice. It was proposed by Roy Craig in 1968 [6], writing in a more intuitive form ideas previously published by Hurty [22]. Hence, although most commonly known as the Craig–Bampton method, we will call it the *Hurty/Craig–Bampton* method.

The FE discretized system of equations of motion for a substructure reads

$$\mathbf{M}^{(s)}\ddot{\mathbf{u}}^{(s)} + \mathbf{K}^{(s)}\mathbf{u}^{(s)} = \mathbf{f}^{(s)}, \tag{20}$$

where $\mathbf{M}^{(s)}$ and $\mathbf{K}^{(s)}$ are the mass and stiffness matrices, respectively, $\mathbf{u}^{(s)}$ is the displacement vector, $\mathbf{f}^{(s)}$ is the forcing vector, and the superscript s denotes the sth substructure. The substructure equations of motion are partitioned into interior and boundary (or interface) DOF (denoted by subscripts i and b, respectively) as

$$\begin{bmatrix} \mathbf{M}_{ii}^{(s)} & \mathbf{M}_{ib}^{(s)} \\ \mathbf{M}_{bi}^{(s)} & \mathbf{M}_{bb}^{(s)} \end{bmatrix} \begin{Bmatrix} \ddot{\mathbf{u}}_i^{(s)} \\ \ddot{\mathbf{u}}_b^{(s)} \end{Bmatrix} + \begin{bmatrix} \mathbf{K}_{ii}^{(s)} & \mathbf{K}_{ib}^{(s)} \\ \mathbf{K}_{bi}^{(s)} & \mathbf{K}_{bb}^{(s)} \end{bmatrix} \begin{Bmatrix} \mathbf{u}_i^{(s)} \\ \mathbf{u}_b^{(s)} \end{Bmatrix} = \begin{Bmatrix} \mathbf{0} \\ \mathbf{f}_b^{(s)} \end{Bmatrix} \tag{21}$$

where the subscripts b and i are indexes referring to the boundary and internal component of the matrices and vectors.

The representation modes are formed by computing the static response of the interior of the substructure when one interface DOF is given a unit displacement and all the other DOF are held fixed. The set of interface static modes for the entire interface is expressed as

$$\boldsymbol{\Psi}^{(s)} = \begin{bmatrix} -\mathbf{K}_{ii}^{(s)^{-1}} \mathbf{K}_{ib}^{(s)} \\ \mathbf{I} \end{bmatrix}. \tag{22}$$

The resulting basis $\boldsymbol{\Psi}^{(s)}$ is used to statically eliminate all interface DOF from the model, retaining only the boundary DOF. The resulting reduced system is usually of small size since only boundary DOF are remaining unknowns. As mentioned earlier, these static modes can be seen as a specific case of Guyan–Iron modes (see previous section) for the case where the master DOFs are chosen on the interface.

In order to capture the dynamics of the system, the static modes are augmented with a set of dynamic modes which are obtained by fixing the interface DOF and solving the following eigenvalue problem

$$\left(\mathbf{K}_{ii}^{(s)} - \omega_r^2 \mathbf{M}_{ii}^{(s)}\right) \boldsymbol{\phi}_{i,r}^{(s)} = 0. \tag{23}$$

The eigenvectors obtained from this equation are referred to as fixed-interface modes. A truncated set of m of these mass-normalized eigenvectors are collected into a fixed-interface mode matrix

$$\boldsymbol{\Phi}^{(s)} = \begin{bmatrix} \boldsymbol{\phi}_{i,1}^{(s)}, \ldots, \boldsymbol{\phi}_{i,m}^{(s)} \\ \mathbf{0} \end{bmatrix} = \begin{bmatrix} \boldsymbol{\Phi}_i^{(s)} \\ \mathbf{0} \end{bmatrix}. \tag{24}$$

These modes provide a normal basis for the interior DOF of the substructure. The fixed-interface modes and the interface static modes are combined to form the HCB reduction matrix as

$$\mathbf{T}^{(s)\mathrm{HCB}} = \left[\boldsymbol{\Phi}^{(s)} \boldsymbol{\Psi}^{(s)}\right], \tag{25}$$

which provides a transformation from the substructure physical DOF to the HCB generalized DOF,

$$\begin{bmatrix} \mathbf{u}_i^{(s)} \\ \mathbf{u}_b^{(s)} \end{bmatrix} \approx \mathbf{T}^{\mathrm{HCB}^{(s)}} \begin{bmatrix} \mathbf{q}_i^{(s)} \\ \mathbf{u}_b^{(s)} \end{bmatrix}, \tag{26}$$

where $\mathbf{q}_i^{(s)}$ represents the modal coordinate vector associated with the fixed-interface modes. The meaning of the static modes and of the fixed interface modes as used in the HCB method is illustrated in Fig. 2.

The uncoupled substructure reduced mass and stiffness matrices are now formed by applying the HCB transformation to these matrices as

$$\mathbf{M}^{(s)\mathrm{HCB}} \left(\mathbf{T}^{(s)\mathrm{HCB}}\right)^T \mathbf{M}^{(s)} \mathbf{T}^{(s)\mathrm{HCB}}, \quad \mathbf{K}^{(s)\mathrm{HCB}} = \left(\mathbf{T}^{(s)\mathrm{HCB}}\right)^T \mathbf{K}^{(s)} \mathbf{T}^{(s)\mathrm{HCB}}. \tag{27}$$

which, using Eq. (25), are given by

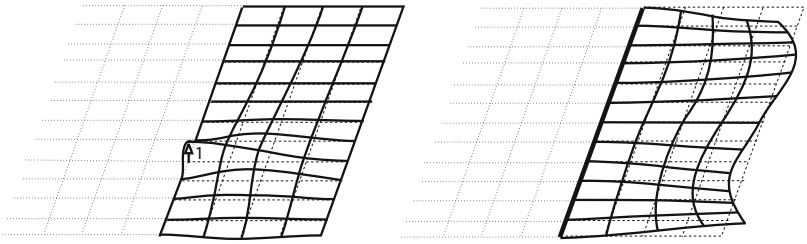

Fig. 2 Static modes and internal vibration modes of a substructure

$$\mathbf{K}^{(s)\mathrm{HCB}} = \begin{bmatrix} \boldsymbol{\Omega}_m^{(s)^2} & \mathbf{0} \\ \mathbf{0} & \tilde{\mathbf{K}}_{bb}^{(s)} \end{bmatrix} \quad \text{and} \quad \mathbf{M}^{(s)\mathrm{HCB}} = \begin{bmatrix} \mathbf{I} & \tilde{\mathbf{M}}_{ib}^{(s)} \\ \tilde{\mathbf{M}}_{bi}^{(s)} & \tilde{\mathbf{M}}_{bb}^{(s)} \end{bmatrix} \tag{28}$$

with $\boldsymbol{\Omega}_m^{(s)^2}$ the diagonal matrix of the eigenfrequencies of the fixed interface modes and with the full submatrices

$$\tilde{\mathbf{K}}_{bb}^{(s)} = \mathbf{K}_{bb}^{(s)} - \mathbf{K}_{bi}^{(s)} \mathbf{K}_{bb}^{(s)^{-1}} \mathbf{K}_{bi}^{(s)} \tag{29}$$

$$\begin{aligned} \tilde{\mathbf{M}}_{bb}^{(s)} = \mathbf{M}_{bb}^{(s)} &- \mathbf{M}_{bi}^{(s)} \mathbf{K}_{ii}^{(s)^{-1}} \mathbf{K}_{ib}^{(s)} - \mathbf{K}_{bi}^{(s)} \mathbf{K}_{ii}^{(s)^{-1}} \mathbf{M}_{ib}^{(s)} \\ &+ \mathbf{K}_{bi}^{(s)} \mathbf{K}_{ii}^{(s)^{-1}} \mathbf{M}_{ii}^{(s)} \mathbf{K}_{ii}^{(s)^{-1}} \mathbf{K}_{ib}^{(s)} \end{aligned} \tag{30}$$

$$\underline{\tilde{\mathbf{M}}}_{ib} = \boldsymbol{\Phi}^{(s)^T} \left(\mathbf{M}_{ib}^{(s)} - \mathbf{M}_{ii}^{(s)} \mathbf{K}_{ii}^{(s)^{-1}} \mathbf{K}_{ib}^{(s)} \right) = \tilde{\mathbf{M}}_{bi}^T. \tag{31}$$

The HCB reduced order models are typically coupled using a primal assembly by defining a transformation between the uncoupled and coupled DOF that selects the substructure boundary DOF from a unique global set of boundary DOF. This assembly is very similar to the assembly of finite elements, except that now macroelements with many nodes (the interface nodes) are assembled, the internal DOFs $\mathbf{q}_i^{(s)}$ remaining unassembled.

The choice of the number of fixed interface modes kept in the reduction basis for each substructure can be made based on different criteria:

- A criterion often used in practice is based on the eigenfrequencies of the kept modes. Typically, one chooses all fixed interface modes having an eigenfrequency lower than 1.8 or 2 times the highest frequency of interest in the assembly.
- One can also choose the fixed interface modes based on how easily they can be excited through the support, for instance by defining a measure of the interface reaction force associated to a mode. Following a similar reasoning, one evaluates how complete the basis of the fixed interface modes needs to be by specifying

how much of the mass of the substructure must be represented in its reduced matrix. This can be evaluated using the concept of effective modal mass (see, for instance, Ref. [13]).

- The number of modes can also be chosen based on a posteriori error estimators [24], later reformulated in a less mathematical form and used for adaptive selection strategies in Ref. [41].

2.2 Substructure Reduction Using Free Interface Modes

The discussion in this section is based on the overview in Ref. [14].

Considering the equation of motion of substructure s,

$$\mathbf{M}^{(s)}\ddot{\mathbf{u}}^{(s)} + \mathbf{C}^{(s)}\dot{\mathbf{u}}^{(s)} + \mathbf{K}^{(s)}\mathbf{u}^{(s)} = \mathbf{f}^{(s)} + \mathbf{g}^{(s)}. \tag{32}$$

every substructure can be seen as being excited by the interface connection forces and the external forces (contrary to the paradigm underlying the HCM method, where the substructures are considered as being excited by interface displacements).

This indicates that the displacements of each substructure $\mathbf{u}^{(s)}$ can be expressed in terms of local static solutions $\mathbf{u}_{stat}^{(s)}$ and in terms of eigenmodes associated to the entire substructure matrices $\mathbf{K}^{(s)}$ and $\mathbf{M}^{(s)}$ (hence the free interface modes):

$$\mathbf{u}^{(s)} = \mathbf{u}_{stat}^{(s)} + \sum_{j=1}^{n^{(s)}-r^{(s)}} \boldsymbol{\theta}_j^{(s)} \eta_j^{(s)} \tag{33}$$

where $n^{(s)}$ and $r^{(s)}$ are the number of DOF and of rigid body modes for substructure s, and where the free interface modes are solutions of the eigenvalue problem

$$\left(\mathbf{K}^{(s)} - \omega_j^{(s)^2}\mathbf{M}^{(s)}\right)\boldsymbol{\theta}_j^{(s)} = \mathbf{0}. \tag{34}$$

The static solution is written as follows (assuming no external forces are applied for simplicity):

$$\mathbf{u}_{stat}^{(s)} = -\mathbf{K}^{(s)^+}\mathbf{g}^{(s)} + \sum_{j=1}^{r^{(s)}} \mathbf{r}_j^{(s)}\alpha_j^{(s)}. \tag{35}$$

The static solution arises from solving Eq. (32) under the assumption that there are no inertia forces and no external forces acting on the substructure. The notation $\mathbf{K}^{(s)^+}$ denotes the inverse of $\mathbf{K}^{(s)}$ when there are enough boundary conditions to prevent the substructure with a free interface from floating [32]. If a substructure is floating, $\mathbf{K}^{(s)^+}$ is the generalized inverse of $\mathbf{K}^{(s)}$ and $\mathbf{r}_j^{(s)}$ are the rigid body modes

of s (see, for instance, Ref. [13] on how to compute a generalized inverse and the rigid body modes).

If only a limited number of free interface modes are used for the substructure dynamics equations (33), and (35) result in the approximation

$$\mathbf{u}^{(s)} \approx -\mathbf{K}^{(s)^+}\mathbf{B}^{(s)^T}\boldsymbol{\lambda} + \mathbf{R}^{(s)}\boldsymbol{\alpha}^{(s)} + \boldsymbol{\Theta}^{(s)}\boldsymbol{\eta}^{(s)}. \tag{36}$$

The vector $\boldsymbol{\alpha}^{(s)}$ contains the amplitudes of the rigid body modes and the vector $\boldsymbol{\eta}^{(s)}$ contains the amplitudes of the retained $n_\theta^{(s)}$ local free interface modes eigenmodes. The matrices $\mathbf{R}^{(s)}$ and $\boldsymbol{\Theta}^{(s)}$ contain all rigid body modes and the retained eigenmodes.

Since a part of the subspace spanned by $\boldsymbol{\Theta}^{(s)}$ is already included in $\mathbf{K}^{(s)^+}$, the residual flexibility matrix $\mathbf{G}_r^{(s)}$ can be used instead of $\mathbf{K}^{(s)^+}$, which is defined by

$$\mathbf{G}_r^{(s)} = \sum_{j=n_\theta^{(s)}+1}^{n^{(s)}-r^{(s)}} \frac{\boldsymbol{\theta}_j^{(s)}\boldsymbol{\theta}_j^{(s)^T}}{\omega_j^{(s)^2}} = \mathbf{K}^{(s)^+} - \sum_{j=1}^{n_\theta^{(s)}} \frac{\boldsymbol{\theta}_j^{(s)}\boldsymbol{\theta}_j^{(s)^T}}{\omega_j^{(s)^2}}. \tag{37}$$

Note that, by construction, $\mathbf{G}_r^{(s)} = \mathbf{G}_r^{(s)^T}$, and it is computed using the second equality in Eq. (37). For further properties of $\mathbf{G}_r^{(s)}$ see, for instance, Ref. [32]. As a result, the approximation of one substructure writes

$$\mathbf{u}^{(s)} \approx \underbrace{\left[\mathbf{R}^{(s)}\boldsymbol{\Theta}^{(s)}\mathbf{G}_r^{(s)}\mathbf{A}^{(s)^T}\right]}_{\mathbf{T}_1^{(s)}} \begin{bmatrix} \boldsymbol{\alpha}^{(s)} \\ \boldsymbol{\eta}^{(s)} \\ \boldsymbol{g}_b^{(s)} \end{bmatrix}. \tag{38}$$

$\mathbf{G}_r^{(s)}\mathbf{A}^{(s)^T}$ is the matrix containing the residual flexibility attachment modes of substructure s, since the Boolean localization matrix $\mathbf{A}^{(s)^T}$ simply picks the columns of $\mathbf{G}_r^{(s)}$ associated to the boundary DOF. In other words,

$$\mathbf{A}^{(s)^T} g_b^{(s)} = \begin{bmatrix} \mathbf{0} \\ \mathbf{g}_b^{(s)} \end{bmatrix} = \mathbf{g}^{(s)}.$$

The approximation (38) can now be used to reduce the substructure DOF. Using the orthogonality properties of the modes in Eq. (38), the equation of motion of one substructure becomes

$$\mathbf{M}_{free}^{(s)} \begin{bmatrix} \ddot{\boldsymbol{\alpha}}^{(s)} \\ \ddot{\boldsymbol{\eta}}^{(s)} \\ \ddot{\mathbf{g}}_b^{(s)} \end{bmatrix} + \mathbf{K}_{free}^{(s)} \begin{bmatrix} \boldsymbol{\alpha}^{(s)} \\ \boldsymbol{\eta}^{(s)} \\ \mathbf{g}_b^{(s)} \end{bmatrix} = \mathbf{T}_1^{(s)^T} \left(\mathbf{f}^{(s)} + \mathbf{g}^{(s)}\right) \tag{39}$$

with the matrices

$$\mathbf{K}_{free}^{(s)} = \mathbf{T}_1^{(s)^T} \mathbf{K}^{(s)} \mathbf{T}_1^{(s)} = \begin{bmatrix} \mathbf{0} & \mathbf{0} & \mathbf{0} \\ \mathbf{0} & \boldsymbol{\Omega}^{(s)^2} & \mathbf{0} \\ \mathbf{0} & \mathbf{0} & \mathbf{G}_{r,bb}^{(s)} \end{bmatrix} \tag{40}$$

where

$$\mathbf{G}_{r,bb}^{(s)} = \mathbf{A}^{(s)} \mathbf{G}_r^{(s)} \mathbf{A}^{(s)^T} \tag{41}$$

and

$$\mathbf{M}_{free}^{(s)} = \mathbf{T}_1^{(s)^T} \mathbf{M}^{(s)} \mathbf{T}_1^{(s)} = \begin{bmatrix} \mathbf{I} & \mathbf{0} & \mathbf{0} \\ \mathbf{0} & \mathbf{I} & \mathbf{0} \\ \mathbf{0} & \mathbf{0} & \mathbf{M}_{r,bb}^{(s)} \end{bmatrix}. \tag{42}$$

where

$$\mathbf{M}_{r,bb}^{(s)} = \mathbf{A}^{(s)} \mathbf{G}_r^{(s)} \mathbf{M}^{(s)} \mathbf{G}_r^{(s)} \mathbf{A}^{(s)^T}. \tag{43}$$

$\mathbf{G}_{r,bb}^{(s)}$ is the residual flexibility and $\mathbf{M}_{r,bb}^{(s)}$ is the interface inertia associated to the residual flexibility related to the boundary DOF, respectively, and $\boldsymbol{\Omega}^{(s)}$ being a diagonal matrix containing the retained $n_\theta^{(s)}$ eigenvalues $\omega_j^{(s)}$.

2.2.1 Rubin Method (RM)

The Rubin method was proposed in 1975 in Ref. [35] and, with the definitions above, can be explained in a simple manner following the derivation proposed in Ref. [30] as explained next.

In order to assemble in a primal manner the substructure equation of motion (39) in the global system, a second transformation is applied by the RM. The force DOF $\mathbf{g}_b^{(s)}$ are transformed back to the boundary displacements $\mathbf{u}_b^{(s)}$ using Eq. (38):

$$\mathbf{u}_b^{(s)} = \mathbf{A}^{(s)} \mathbf{u}^{(s)} = \mathbf{R}_b^{(s)} \boldsymbol{\alpha}^{(s)} + \boldsymbol{\Theta}_b^{(s)} \boldsymbol{\eta}^{(s)} + \mathbf{G}_{r,bb}^{(s)} \mathbf{g}_b^{(s)} \tag{44}$$

$\mathbf{R}_b^{(s)}$ and $\boldsymbol{\Theta}_b^{(s)}$ are the subparts of $\mathbf{R}^{(s)}$ and $\boldsymbol{\Theta}^{(s)}$ related to the boundary DOF, respectively. From this equation, the interface force DOF can be solved as

$$\mathbf{g}_b^{(s)} = \mathbf{K}_{r,bb}^{(s)} \left(\mathbf{u}_b^{(s)} - \mathbf{R}_b^{(s)} \boldsymbol{\alpha}^{(s)} - \boldsymbol{\Theta}_b^{(s)} \boldsymbol{\eta}^{(s)} \right) \tag{45}$$

with $\mathbf{K}_{r,bb}^{(s)} = \mathbf{G}_{r,bb}^{(s)^{-1}}$. The transformation matrix $\mathbf{T}_2^{(s)}$ from force DOF $\mathbf{g}_b^{(s)}$ back to the boundary displacements $\mathbf{u}_b^{(s)}$ leaving $\boldsymbol{\alpha}^{(s)}$ and $\boldsymbol{\eta}^{(s)}$ unchanged writes then

$$\mathbf{T}_2^{(s)} = \begin{bmatrix} \mathbf{I} & \mathbf{0} & \mathbf{0} \\ \mathbf{0} & \mathbf{I} & \mathbf{0} \\ -\mathbf{K}_{r,bb}^{(s)}\mathbf{R}_b^{(s)} & -\mathbf{K}_{r,bb}^{(s)}\boldsymbol{\Theta}_b^{(s)} & \mathbf{K}_{r,bb}^{(s)} \end{bmatrix}. \tag{46}$$

The RM approximation for one substructure writes therefore

$$\mathbf{u}^{(s)} = \mathbf{T}_R^{(s)} \begin{bmatrix} \boldsymbol{\alpha}^{(s)} \\ \boldsymbol{\eta}^{(s)} \\ \mathbf{u}_b^{(s)} \end{bmatrix} \quad \text{where} \quad \mathbf{T}_R^{(s)} = \mathbf{T}_1^{(s)}\mathbf{T}_2^{(s)} \tag{47}$$

Application of this transformation to the matrices of Eqs. (42) and (40) gives the RM reduced matrices of one substructure:

$$\mathbf{K}_{red,R}^{(s)} = \mathbf{T}_2^{(s)^T}\mathbf{K}_{free}^{(s)}\mathbf{T}_2^{(s)} = \mathbf{T}_R^{(s)^T}\mathbf{K}^{(s)}\mathbf{T}_R^{(s)} \tag{48}$$

$$\mathbf{M}_{red,R}^{(s)} = \mathbf{T}_2^{(s)^T}\mathbf{M}_{free}^{(s)}\mathbf{T}_2^{(s)} = \mathbf{T}_R^{(s)^T}\mathbf{M}^{(s)}\mathbf{T}_R^{(s)} \tag{49}$$

These matrices can be directly assembled using primal assembly to get the RM reduced matrices $\mathbf{K}_{red,R}$ and $\mathbf{M}_{red,R}$ of the global system. The RM applies the reduction matrix $\mathbf{T}_R^{(s)}$ consistently to the mass and stiffness matrix resulting in a true Rayleigh–Ritz method as was observed in Ref. [10].

2.2.2 MacNeal Method (MNM)

The MNM [29] is nearly identical to the RM except for a small change. First, we will derive the preliminary MNM reduced matrices $\tilde{\mathbf{K}}_{red,MN}^{(s)}$ and $\tilde{\mathbf{M}}_{red,MN}^{(s)}$ following the derivation of the RM to show the similarities between these two methods. The reduced stiffness matrix of both the RM and the MNM are identical (given in Eq. (48))

$$\tilde{\mathbf{K}}_{red,MN}^{(s)} = \mathbf{K}_{red,R}^{(s)} \tag{50}$$

but the MNM reduced mass matrix $\tilde{\mathbf{M}}_{red,MN}^{(s)}$ is obtained differently. The residual mass term $\mathbf{M}_{r,bb}^{(s)}$ of the matrix $\mathbf{M}_{free}^{(s)}$ in Eq. (42) is neglected, resulting in a modified matrix [40].

$$\mathbf{M}_{free,MN}^{(s)} = \begin{bmatrix} \mathbf{I} & \mathbf{0} & \mathbf{0} \\ \mathbf{0} & \mathbf{I} & \mathbf{0} \\ \mathbf{0} & \mathbf{0} & \mathbf{0} \end{bmatrix}. \tag{51}$$

The MNM reduced mass matrix writes now

$$\tilde{\mathbf{M}}_{red,MN}^{(s)} = \mathbf{T}_2^{(s)^T}\mathbf{M}_{free,MN}^{(s)}\mathbf{T}_2^{(s)} = \mathbf{M}_{free,MN}^{(s)}. \tag{52}$$

This gives in fact inconsistent equations of motion since the mass and stiffness matrices are not reduced with the same basis. The assembly of the MNM reduced matrices $\tilde{\mathbf{K}}^{(s)}_{red,MN}$ and $\tilde{\mathbf{M}}^{(s)}_{red,MN}$ in the global system proceeds in the same manner as for the RM. Observing that the boundary DOF $\mathbf{u}_b$ have no associated inertia in Eq. (52), those DOF can be condensed out of the equation of motion of the assembled problem and the final MNM reduced matrices $\mathbf{K}_{red,MN}$ and $\mathbf{M}_{red,MN}$ are obtained [29]. Thus, the size of the assembled MNM system is reduced further by the number of DOF of $\mathbf{u}_b$.

2.2.3 Dual Craig–Bampton Method (DCBM)

The reduction transformation (Eq. 38) can also be used directly, without transforming $\mathbf{g}^{(s)}_b$ in interface DOF (as done in Eq. (45) for the RM or for the MNM), if one considers the dually assembled problem. The dual assembly of the full (original) problem writes

$$\begin{bmatrix} \ddots & \mathbf{0} & \vdots \\ \mathbf{0} & \mathbf{M}^{(s)} & 0 \\ & & \ddots \\ \dots & \mathbf{0} & \dots \mathbf{0} \end{bmatrix} \begin{bmatrix} \vdots \\ \ddot{\mathbf{u}}^{(s)} \\ \vdots \\ \ddot{\boldsymbol{\lambda}} \end{bmatrix} + \begin{bmatrix} \ddots & \mathbf{0} & \vdots \\ \mathbf{0} & \mathbf{K}^{(s)} & \mathbf{B}^{(s)^T} \\ & & \ddots \\ \dots \mathbf{B}^{(s)} & \dots & \mathbf{0} \end{bmatrix} \begin{bmatrix} \vdots \\ \mathbf{u}^{(s)} \\ \vdots \\ \boldsymbol{\lambda} \end{bmatrix} = \begin{bmatrix} \vdots \\ \mathbf{f}^{(s)} \\ \vdots \\ \mathbf{0} \end{bmatrix}. \tag{53}$$

Here, the compatibility constraints between the substructures are written explicitly and are enforced using Lagrange multipliers $\boldsymbol{\lambda}$. Those Lagrange multipliers can be interpreted as the internal force intensities that are required between matching interface nodes in order to assemble them. The matrices $\mathbf{B}^{(s)}$ are signed Boolean matrices that express the compatibility condition between interface DOFs. For a more detailed discussion on the dual assembly and its formulation, see for instance [26, 32, 39].

Comparing the equations of motion of the substructures in Eq. (53) with the formulation used earlier in Eq. (32), it is clear that

$$\mathbf{g}^{(s)} = \mathbf{A}^{(s)^T} \mathbf{g}^{(s)}_b = -\mathbf{B}^{(s)^T} \boldsymbol{\lambda}. \tag{54}$$

Assembling all substructures N in a dual fashion, the entire problem unknowns can consequently be approximated by rewriting Eq. (38) as

$$\begin{bmatrix} \mathbf{u} \\ \boldsymbol{\lambda} \end{bmatrix} \approx \mathbf{T}_{DCB} \begin{bmatrix} \boldsymbol{\alpha}^{(1)} \\ \boldsymbol{\eta}^{(1)} \\ \vdots \\ \boldsymbol{\alpha}^{(N)} \\ \boldsymbol{\eta}^{(N)} \\ \boldsymbol{\lambda} \end{bmatrix} \tag{55}$$

with the DCBM reduction matrix $\mathbf{T}_{DCB}$:

$$\mathbf{T}_{DCB} = \begin{bmatrix} \mathbf{R}^{(1)} & \boldsymbol{\Theta}^{(1)} & & \mathbf{0} & \mathbf{0} & -\mathbf{G}_r^{(1)}\mathbf{B}^{(1)^T} \\ & & \ddots \; \ddots & & & \vdots \\ \mathbf{0} & \mathbf{0} & & \mathbf{R}^{(N)} & \boldsymbol{\Theta}^{(N)} & -\mathbf{G}_r^{(N)}\mathbf{B}^{(N)^T} \\ \mathbf{0} & \mathbf{0} & & \mathbf{0} & \mathbf{0} & \mathbf{I} \end{bmatrix}. \tag{56}$$

The reduced form of the dynamic equations of the dual assembled system (53) is then found as

$$\mathbf{M}_{red,DCB} \begin{bmatrix} \ddot{\boldsymbol{\alpha}}^{(1)} \\ \ddot{\boldsymbol{\eta}}^{(1)} \\ \vdots \\ \ddot{\boldsymbol{\alpha}}^{(N)} \\ \ddot{\boldsymbol{\eta}}^{(N)} \\ \ddot{\boldsymbol{\lambda}} \end{bmatrix} + \mathbf{K}_{red,DCB} \begin{bmatrix} \boldsymbol{\alpha}^{(1)} \\ \boldsymbol{\eta}^{(1)} \\ \vdots \\ \boldsymbol{\alpha}^{(N)} \\ \boldsymbol{\eta}^{(N)} \\ \boldsymbol{\lambda} \end{bmatrix} = \mathbf{T}_{DCB}^T \mathbf{f} \tag{57}$$

with the DCBM reduced mass and stiffness matrix

$$\mathbf{M}_{red,DCB} = \mathbf{T}_{DCB}^T \begin{bmatrix} \mathbf{M} & \mathbf{0} \\ \mathbf{0} & \mathbf{0} \end{bmatrix} \mathbf{T}_{DCB} = \begin{bmatrix} \mathbf{I} & \mathbf{0} \\ \mathbf{0} & \mathbf{M}_r \end{bmatrix} \tag{58}$$

$$\mathbf{K}_{red,DCB} = \mathbf{T}_{DCB}^T \begin{bmatrix} \mathbf{K} & \mathbf{B}^T \\ \mathbf{B} & \mathbf{0} \end{bmatrix} \mathbf{T}_{DCB} \tag{59}$$

with

$$\mathbf{M}_r = \sum_{s=1}^{N} \mathbf{B}^{(s)} \mathbf{G}_r^{(s)} \mathbf{M}^{(s)} \mathbf{G}_r^{(s)} \mathbf{B}^{(s)^T}. \tag{60}$$

$\mathbf{M}_{red,DCB}$ and $\mathbf{K}_{red,DCB}$ are diagonal for the parts related to the different substructures. The coupling between the substructures is only achieved by the rows and columns related to $\boldsymbol{\lambda}$. The DCBM applies the reduction matrix $\mathbf{T}_{DCB}$ consistently to the mass and stiffness matrix resulting in a true Rayleigh–Ritz method.

The DCBM enforces only a weak compatibility between the substructures and does not enforce a strong displacement compatibility between the interfaces compared to many other common reduction methods [32]. Considering the system of Eqs. (53) and (32) multiplied by the reduction matrix $\mathbf{T}_{DCB}^T$, the last row of Eq. (57) results from

$$\begin{bmatrix} \mathbf{M}^{(1)}\ddot{\mathbf{u}}^{(1)} + \mathbf{K}^{(1)}\mathbf{u}^{(1)} + \mathbf{B}^{(1)^T}\boldsymbol{\lambda} = \mathbf{f}^{(1)} \\ \vdots \\ \mathbf{M}^{(N)}\ddot{\mathbf{u}}^{(N)} + \mathbf{K}^{(N)}\mathbf{u}^{(N)} + \mathbf{B}^{(N)^T}\boldsymbol{\lambda} = \mathbf{f}^{(N)} \\ \sum_{s=1}^{N} \mathbf{B}^{(s)}\mathbf{u}^{(s)} = \mathbf{0} \end{bmatrix} \tag{61}$$

multiplied from left by the last row of $\mathbf{T}_{DCB}^T$ which is

$$\left[-\mathbf{B}^{(1)}\mathbf{G}_e^{(1)} \cdots - \mathbf{B}^{(N)}\mathbf{G}_r^{(N)}\mathbf{I}\right]. \tag{62}$$

Replacing the strong interface compatibility condition of Eq. (53) by the weak form according to the multiplication of Eq. (61) by Eq. (62) can be interpreted as follows. Denote $\Delta\mathbf{f}^{(s)}$ the residual forces of substructure s resulting from the weak satisfaction of the local equilibrium of the substructure approximating the dynamics by a small number of free interface normal modes. Name $\Delta\mathbf{u}^{(s)} = \mathbf{G}_r^{(s)}\Delta\mathbf{f}^{(s)}$ the displacements these residual force $\Delta\mathbf{f}^{(d)}$ would create locally. Then the weak interface compatibility condition (Eqs. 61 and 62) states that a compatibility error (i.e., an interface displacement jump) equal to the incompatibility of $\Delta\mathbf{u}^{(s)}$ is permitted [32].

The fact that a weak interface compatibility is allowed in the DCBM implies that the infinite eigenvalues related to the Lagrange multipliers $\boldsymbol{\lambda}$ in the nonreduced problem (53) are now becoming finite and negative [34]. In practice those negative eigensolutions will appear only in the higher eigenvalue spectrum if the reduction space is rich enough [34]. Nevertheless, the reduction basis has to be selected with care avoiding potential nonphysical effects of the possibly occurring negative eigenvalues. Using the dually reduced problem can nevertheless be used for time integration as shown in Ref. [17] when using an appropriate modal superposition.

If $\mathbf{M}_r$ in Eq. (58) is neglected, strong interface compatibility is enforced again and the DCBM reduced system with $\mathbf{M}_r = \mathbf{0}$ is equivalent to the MNM [32]. Then static condensation can be applied again to remove $\boldsymbol{\lambda}$ (as it was done for $\mathbf{u}_b$ at the end of the derivation of the MNM) from the assembled system since no mass is associated to them.

2.3 Numerical Examples of Different Substructure Reduction Techniques

The Benfield truss [8] of Fig. 3 is used to compare the results obtainable by the HCB, the MNM, the RM, and the DCBM. The planar truss consists of 2 substructures having uniform bay section whereas all members have constant area and uniform stiffness and mass properties. The left component consists of 5 equal bays and has a total of 18 joints and the right component consists of 4 equal bays and has a total of 15 joints [8]. The lowest eigenfrequencies ω of

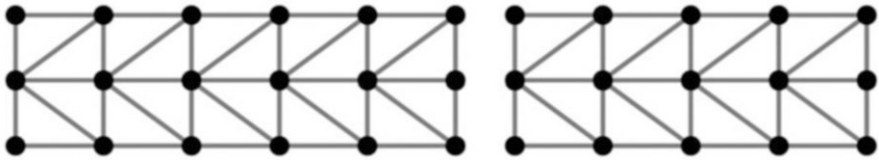

Fig. 3 Benfield truss [8]

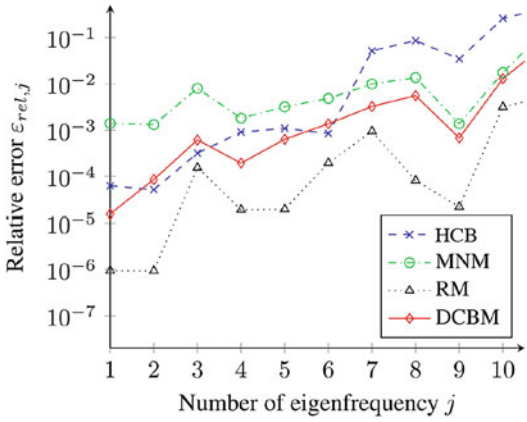

Fig. 4 Relative error $\varepsilon_{rel,j}$ of eigenfrequency j using five normal modes per substructure for the approximation of the lowest eigenfrequencies of the Benfield truss

the entire structure shall be approximated by the different methods. The relative error $\varepsilon_{rel,j} = \mid \omega_{red,j} - \omega_{full,j} \mid / \omega_{full,j}$ of the j-th eigenfrequency is used as a criterion to assess the accuracy of the different methods. Thereby, $\omega_{full,j}$ is the j-th eigenfrequency of the full (nonreduced) system and $\omega_{red,j}$ represents the j-th eigenfrequency of the reduced system obtained by each method.

Using five elastic (fixed or free interface normal modes) per substructure, the resulting relative errors ε_{rel} are depicted in the semilog graph in Fig. 4. Since all methods give the correct rigid body modes, only the relative errors of the elastic modes are plotted. All methods give a relative error less than 1% for the first six eigenfrequencies. Comparing the free interface methods for this example, the RM performs always better than the DCB and the DCB performs again always better as the MNM. The HCB and the DCB result in similar frequency errors.

The sparsity pattern of the reduced stiffness matrix $\mathbf{K}_{red}$ and reduced mass matrix $\mathbf{M}_{red}$ of the HCB (Fig. 5), the MNM (Fig. 6), the RM (Fig. 7), and the DCB (Fig. 8), respectively, illustrate the differences of the assembled reduced structures. Both the reduced stiffness matrix $\mathbf{K}_{red}$ and the reduced mass matrix $\mathbf{M}_{red}$ applying the HCB and the DCB, respectively, have only diagonal entries for the subparts of each substructure. On the one hand, the coupling between the substructures using the HCB is entirely achieved by the last rows and last columns in the mass matrix $\mathbf{M}_{red,CB}$ (Fig. 5b) and the remaining part is diagonal [6]. On the other hand, the coupling applying the DCB is entirely achieved by the last rows and last columns in the stiffness matrix $\mathbf{K}_{red,DCB}$ (Fig. 8a) and again the remaining part is diagonal

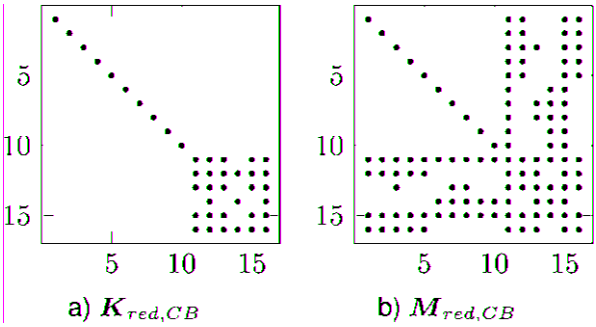

Fig. 5 Sparsity pattern of the reduced matrices applying the HCB using five normal modes per substructure

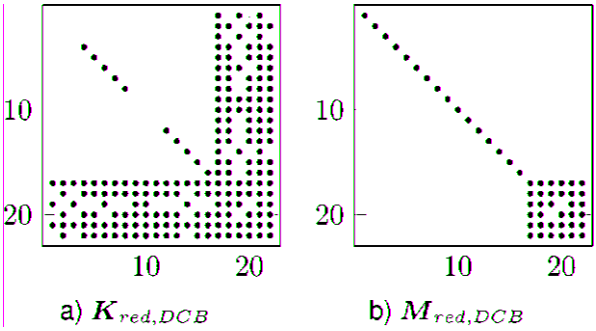

Fig. 6 Sparsity pattern of the reduced matrices applying the MNM using five normal modes per substructure

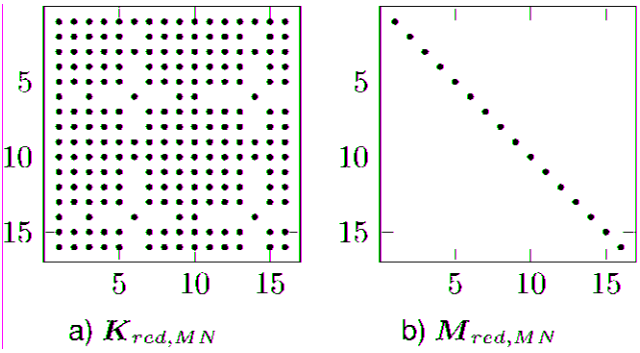

Fig. 7 Sparsity pattern of the reduced matrices applying the RM using five normal modes per substructure

[32]. The corresponding degrees of freedoms are either the interface displacements $\mathbf{u}_b$ or the interface forces $\boldsymbol{\lambda}$ but no direct coupling between the modal parameters of adjacent substructures occurs which ensures the sparse structure.

In contrast, the sparsity pattern of stiffness matrix $\mathbf{K}_{red}$ and the reduced mass matrix $\mathbf{M}_{red}$ obtained but the MNM and the RM, respectively, show full matrices. The MNM gives indeed an entirely diagonal reduced mass matrix $\mathbf{M}_{red,MN}$ (Fig. 6b) but causes always a full coupling between all DOF of all substructures via the reduced stiffness matrix $\mathbf{K}_{red,MN}$ (Fig. 6a). This makes the reusability of reduced

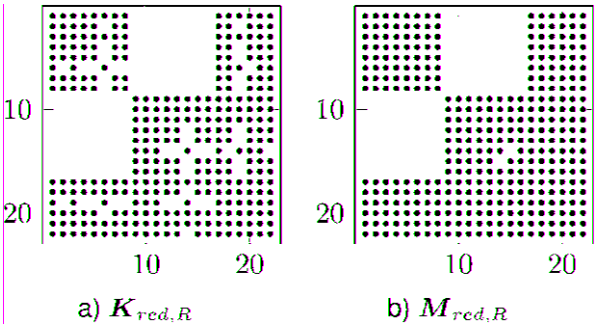

Fig. 8 Sparsity pattern of the reduced matrices applying the DCB using five normal modes per substructure

Table 1 Number n of nonzero elements in the reduced matrices obtained by the different methods for the Benfield truss using five normal modes per substructure

	HCB	MNM	RM	DCB
n in $\boldsymbol{K}_{red}$	40	216	314	196
n in $\mathbf{M}_{red}$	118	16	354	50
n_{total}	158	232	668	246

models obtained by the MNM very inefficient and therefore nearly impossible from a practical point of view. The RM also causes a coupling between the substructures via interface displacements $\mathbf{u}_b$ in the reduced stiffness matrix $\mathbf{K}_{red,R}$ (Fig. 7a) as well as in the reduced mass $\mathbf{M}_{red,R}$ (Fig. 7b). Moreover, all DOF belonging to one reduced substructure are coupled with all other DOF of the same substructure which is why the reduced matrices of the RM are full for the substructure blocks and not diagonal.

This result concerning the sparsity of the reduced matrices is outlined in Table 1 which shows the number n of nonzero elements in the reduced matrices $\mathbf{K}_{red}$ and $\mathbf{M}_{red}$, and the sum n_{total} of both obtained by the different methods for this example. The reduced matrices of the HCB, the MNM, and the DCB contain a similar number of entries while the RM causes even for such a simple example a remarkable high number of entries. The number of entries of the MNM are comparable to the HCB and the DCB but will increase significantly if the number of substructures is increased since $\mathbf{K}_{red}$ will always be completely full.

2.4 Other Reduction Techniques for Substructures

In the previous sections, we have outlined the classical substructure reduction methods (or component mode synthesis) using either free or fixed interface modes.

Other methods are not outlined here, like for instance the Craig–Chang approach which uses also free interface modes, but computes the interface forces from a global (assembled) problem [10].

Many other variants of CMS methods were published over the last years and they can be classified as follows:

- **Loaded Interface Modes:** Some authors have proposed to compute the quasistatic modes around a central frequency [36] or to use vibration modes with an impedance attached to the interface. In certain cases, such modifications can improve the accuracy of the reduced model.
- **Modal Truncation Augmentation and Moment Matching:** The vibration modes used for instance in the HCB or in the RM approaches are not specifically tuned for the excitations coming through the interface, whereas the static modes are. It is possible to enrich the static modes with higher-order static contribution computed over a Krylov series. This leads to a method originally called modal truncation augmentation (or MTA) [12] and was generalized to higher orders corrections in the HCB in Ref. [31]. Later, techniques called moment matching [38], that basically used the same ideas as MTAs, were applied for model reduction mainly in the control community (see, for instance, Refs. [2, 20, 37]). The idea of MTA was also applied for the DCBM [25, 33].
- **Balanced Truncation:** In the control community, reduction is seen from the point of view of controllability and observability. This leads to representation modes derived from so-called Grammians that were used for reducing substructure models in Refs. [20, 37].
- **Mixed Methods:** Several combined methods were, where different types of vectors (attachment modes and static modes were combined). One of the most commonly used in major finite element software (although not cited much in the community, maybe because the explanations in the publication are poor) is the one from Herting [19]. Note also that it is possible to mix primal and dual assembly for different DOF on an interface (which can be advantageous depending on the stiffness ratios across the interface) [40].
- Finally, let us mention that methods have been proposed where the reduction is performed in an iterative manner, computing the residual force on the full model after a reduction (see Eq. (3)) and enriching the reduction base with, for instance, the static response of the substructures to that residual force [5, 7].

3 Interface Reduction with the Hurty/Craig–Bampton Method: Characteristic Constraint Modes

3.1 Interface Reduction Approaches

While the number of degrees of freedom in a model may be reduced dramatically using substructuring techniques such as the Hurty/Craig–Bampton (HCB) method, that method retains all of the DOF at the interfaces between substructures, and so the

resulting model may still be unacceptably large. Furthermore, since the minimum timestep for time integration is limited by the distance between the two closest nodes, the HCB model may still be almost as expensive to integrate as the original model. Several methods have been proposed over the years to address this problem, and while none has been widely implemented as has the HCB method, they do seem to be effective in many scenarios. This section presents a brief review of methods for interface reduction. For further details and a comparison of each method on the W-bracket, see, for instance, the review in Ref. [27].

Craig and Chang [11] seem to have been the first to propose methods to reduce the interface DOF, presenting three methods in 1977. However, they do not appear to have been used subsequently until Castanier et al. [9] rediscovered the modal method by applying a secondary eigenvalue analysis on the interface partition of the assembled CMS model and obtaining what they called the characteristic constraint (CC) modes. The assembled, system-level HCB matrices were used to compute these modes, so this method is referred to as the system-level characteristic constraint (S-CC) mode method. While the method is effective, it is often undesirable to have to assemble the system before reduction and so this has inspired the investigation of other methods that perform the reduction before assembly.

Hong et al. [21] subsequently proposed an interface reduction technique that performs an eigenvalue analysis on the HCB interface DOF prior to assembly. They then concatenate the shapes obtained for each interface and enforce compatibility between the local-level characteristic constraint (L-CC) modes obtained from each interface. This method is referred to in Ref. [27] as the "exact compatibility L-CC method," because it is possible to enforce exact compatibility using that method. However, in practice some of the shapes are typically truncated and there is some level of approximation.

Alternatively, Kuether et al. [28] proposed a method that weakens the compatibility at the interface. The L-CC modes are combined to minimize the compatibility error between connecting substructure interfaces. Aoyama et al. [3] presented a method similar to S-CC except that each interface is assembled and then reduced separately. Balmès [4] explored a CMS basis that defined arbitrary interface deformations to describe a set of generalized DOF along an interface. A few other less commonly known methods are reviewed in Ref. [27].

In the next section, the method based on so-called system-level characteristic constraint (S-CC) modes is shortly described.

3.2 System-Level Characteristic Constraint (S-CC) Modes

As done by Craig and Chang [11], and detailed by Castanier et al. [9], the HCB models for all subcomponents are first assembled, the interface partition of the assembled system is extracted and then an eigenvalue analysis is performed

$$\left(\mathbf{K}_{bb}^{\mathrm{HCB}} - \omega_r^2 \mathbf{M}_{bb}^{\mathrm{HCB}}\right) \boldsymbol{\phi}_r^{\text{S-CC}} = \mathbf{0}. \tag{63}$$

The eigenvectors obtained are called S-CC modes and the first n vectors are collected into a matrix

$$\boldsymbol{\Phi}^{\text{S-CC}} = \left[\boldsymbol{\phi}_1^{\text{S-CC}}, \ldots, \boldsymbol{\phi}_n^{\text{S-CC}}\right]. \tag{64}$$

The matrix $\boldsymbol{\Phi}^{\text{S-CC}}$ is used to replace the interface DOF of the HCB model into amplitudes of the S-CC modes

$$\mathbf{u}_b \approx \boldsymbol{\Phi}^{\text{S-CC}} \mathbf{q}_b. \tag{65}$$

The S-CC reduced mass (and similarly stiffness) matrices are obtained by pre- and post multiplying the assembled HCB matrices in Eq. (28) with the S-CC transformation matrix to obtain

$$\mathbf{M}^{\text{S-CC}} = \begin{bmatrix} \mathbf{I} & \mathbf{0} \\ \mathbf{0} & \boldsymbol{\Phi}^{\text{S-CC}} \end{bmatrix}^{\text{T}} \begin{bmatrix} \mathbf{M}_{ii}^{\text{HCB}} & \mathbf{M}_{ib}^{\text{HCB}} \\ \mathbf{M}_{bi}^{\text{HCB}} & \mathbf{M}_{bb}^{\text{HCB}} \end{bmatrix} \begin{bmatrix} \mathbf{I} & \mathbf{0} \\ \mathbf{0} & \boldsymbol{\Phi}^{\text{S-CC}} \end{bmatrix}. \tag{66}$$

This reduces the size of the interface partition of the HCB model from the number of physical DOF on the interface to the number of S-CC modes in the truncated eigenvector set $n_{\boldsymbol{\Phi}_b}$. It is interesting to note that static reduction modes were also proposed for the interface of a dual Criag–Bampton model in Ref. [34].

References

1. Allen MS, Rixen D, van der Seijs M, Tiso P, Abrahamsson T, Mayes TL (2020) Substructuring in engineering dynamics. In: CISM international centre for mechanical sciences. Vol 594. Springer
2. Antoulas AC (2005) Approximation of large-scale dynamical systems. Society for Industrial and Applied Mathematics, Philadelphia
3. Aoyama Y, Yagawa G (2001) Component mode synthesis for large-scale structural eigenanalysis. Comput Struct 79(6):605–615
4. Balmès E (1996) Use of generalized interface degrees of freedom in component mode synthesis. In: Proceedings of the 14th international modal analysis conference, 1
5. Balmès E (1997) Modèles expérimentaux complets et modèles analytiques réduits en dynamiquedes structures. PhD thesis, Université Pierre et Marie Curie, Paris VI, ONERA, Directions des Structure, DRET/AC
6. Bampton MCC, Craig JRR (1968) Coupling of substructures for dynamic analyses. AIAA J 6(7):1313–1319
7. Bathe KJ, Dong J (2014) Component mode synthesis with subspace iterations for controlled accuracy of frequency and mode shape solutions. Comput Struct 139:28–32
8. Benfield W, Hruda R (1971) Vibration analysis of structures by component mode substitution. AIAA J 9(7):1255–1261
9. Castanier MP, Tan YC, Pierre C (2001) Characteristic constraint modes for component mode synthesis. AIAA J 39(6):1182–1187
10. Craig RR, Chang CJ (1977) On the use of attachment modes in substructure coupling for dynamics analysis. In: 18st structures, structural dynamics and material conference. AIAA/ASME, San Diego, pp 89–99

11. Craig RR Jr, Chang CJ (1977) Substructure coupling for dynamic analysis and testing. Report, National Aeronautics and Space Administration
12. Dickens JM, Stroeve A (2000) Modal truncation vectors for reduced dynamic substructure models. In: 41st AIAA/ASME/ASCE/AHS/ASC structures, structural dynamics, and materials conference and exhibit, Atlanta
13. Géradin M, Rixen D (2015) Mechanical vibrations. Theory and application to structural dynamics, 3rd edn. Wiley, Chichester
14. Gruber FM, Rixen DJ (2016) Evaluation of substructure reduction techniques with fixed and free interfaces. Stroj Vestn–J Mech E 62(7–8):452–462
15. Gruber F, Rixen D (2018) A comparison of Craig-Bampton approaches for systems with arbitrary viscous damping in dynamic substructuring. In: IMAC-XXXVI: international modal analysis conference, Orlando. Society for Experimental Mechanics, Bethel
16. Gruber FM, Rixen DJ (2018) Dual Craig-Bampton component mode synthesis method for model order reduction of nonclassically damped linear systems. Mech Syst Signal Process 111:678–698
17. Gruber FM, Gille M, Rixen DJ (2019) A strategy to stabilize the transient analysis and increase the approximation accuracy of dual Craig-Bampton reduced systems. Finite Elem Anal Des 160:32–45
18. Guyan R (1965) Reduction of mass and stiffness matrices. AIAA J 3(2):380
19. Herting D (1985) A general purpose, multi-stage, component modal synthesis method. Finite Elem Anal Des 1(2):153–164
20. Holzwarth P, Eberhard P (2015) SVD-based improvements for component mode synthesis in elastic multibody systems. Eur J Mech A Solids 49:408–418
21. Hong SK, Epureanu BI, Castanier MP (2013) Next-generation parametric reduced-order models. Mech Syst Signal Process 37(1–2):403–421
22. Hurty WC (1965) Dynamic analysis of structural systems using component modes. AIAA J 3(4):678–685
23. Irons B (1965) Structural eigenvalue problems – elimination of unwanted variables. AIAA J 3(5):961–962
24. Jakobsson H, Bengzon F, Larson MG (2011) Adaptive component mode synthesis in linear elasticity. Int J Numer Methods Eng 86:829–844
25. Kim JH, Kim J, Lee PS (2017) Improving the accuracy of the dual Craig-Bampton method. Comput Struct 191:22–32
26. Klerk DD, Rixen DJ, Voormeeren SN (2008) General framework for dynamic substructuring: history, review and classification of techniques. AIAA J 46(5):1169–1181
27. Krattiger D, Wu L, Zacharczuk M, Buck M, Kuether RJ, Allen MS, Tiso P, Brake MRW (2019) Interface reduction for Hurty/Craig-Bampton substructured models: review and improvement. Mech Syst Signal Process 114:579–603
28. Kuether RJ, Allen MS, Hollkamp JJ (2017) Modal substructuring of geometrically nonlinear finite element models with interface reduction. AIAA J 55(5):1695–1706
29. MacNeal RH (1971) Special issue on structural dynamics: a hybrid method of component mode synthesis. Comput Struct 1(4):581–601
30. Martinez D, Carne T, Gregory D, Miller A (1984) Combined experimental/analytical modelling using component mode synthesis. In: 25th structures, structural dynamics and materials conference, pp 140–152
31. Rixen D (2002) High order static correction modes for component mode synthesis. In: Fifth world Congress on computational mechanics, Vienna
32. Rixen D (2004) A dual Craig-Bampton method for dynamic substructuring. J Comput Appl Math 168(1–2):383–391
33. Rixen DJ (2009) Dual Craig-Bampton with enrichment to avoid spurious modes. In: IMACXXVII: international modal analysis conference, Orlando. Society for Experimental Mechanics, Bethel

34. Rixen DJ (2011) Interface reduction in the dual Craig-Bampton method based on dual interface modes. In: IMAC-XXIX: international modal analysis conference, Jacksonville. Society for Experimental Mechanics, Bethel
35. Rubin S (1975) Improved component-mode representation for structural dynamic analysis. AIAA J 13(8):995–1006
36. Shyu WH, Ma ZD, Hulbert GM (1997) A new component mode synthesis method: quasi-static mode compensation. Finite Elem Anal Des 24(4):197–298
37. Stoev J, Möhring J (2010) Hybrid reduction of non-symmetric mimo systems. In: Paul Sas et al. (ed) ISMA. KU Leuven, Leuven
38. Su TJ, Craig R (1991) Model reduction and control of flexible structures using Krylov vectors. J Guid Control Dyn 14(2):260–267
39. Voormeeren S (2012) Dynamic substructuring methodologies for integrated dynamic analysis of wind turbines. PhD thesis, Delft University of Technology, Delft
40. Voormeeren SN, van der Valk PLC, Rixen DJ (2011) Generalized methodology for assembly and reduction of component models for dynamic substructuring. AIAA J 49:1010–1020
41. Voormeeren S, Nortier B, Rixen D (2013) Error estimation and adaptive model reduction applied to offshore wind turbine modeling. In: IMAC-XXXI: international modal analysis conference, error estimation and adaptive model reduction applied to offshore wind turbine modeling. Society for Experimental Mechanics, Bethel

Finite Element Model Correlation

15

Peter Avitabile and Michael Mains

Contents

Abstract

Correlation of a finite element model with test data is commonly performed. In order to perform these correlation studies, the finite element model may require reduction due to the large size of the model, or the test data may be expanded to the size of the finite element model. Model reduction and model expansion techniques are presented first. Correlation tools typically deployed are then presented. Some additional commentary related to the test data and the correlation process is also provided to give insight into some of the issues that must be faced.

P. Avitabile (✉)
Structural Dynamics and Acoustic Systems Laboratory, University of Massachusetts Lowell, Lowell, MA, USA
e-mail: peter_avitabile@uml.edu

M. Mains
University of Cincinnati, Cincinnati, OH, USA
e-mail: mainsml@ucmail.uc.edu

R. Allemang, P. Avitabile (eds.), *Handbook of Experimental Structural Dynamics*,
https://doi.org/10.1007/978-1-4614-4547-0_17

Keywords

Correlation · Modal correlation · Vector correlation · Orthogonality · Cross orthogonality · Pseudo orthogonality · Model reduction · Reduced order model · Vector expansion

Acronyms

FEM	Finite element model
EMA	Experimental modal analysis
SEREP	System equivalent reduction expansion process
IRS	Improved reduced system
MAC	Modal assurance criteria
CoMAC	Coordinate modal assurance criteria
POC	Pseudo orthogonality check
CORTHOG	Coordinate orthogonality check
FRAC	Frequency response assurance criteria
RVAC	Response vector assurance criteria
MACCO	Modal assurance criteria contribution
FRF	Frequency response function
DOF	Degree of freedom
NDOF	Full set of "n" finite element DOF
ADOF	Reduced set of "a" test DOF
DDOF	Remaining set of "d" deleted or omitted DOF

Nomenclature

Matrix

[M]	Analytical mass matrix
[C]	Analytical damping matrix
[K]	Analytical stiffness matrix
[U]	Analytical modal matrix
[I]	Diagonal modal mass matrix
$[\Omega^2]$	Diagonal modal stiffness matrix
[T]	Transformation matrix
[E]	Experimental modal vectors
[D]	Dynamic matrix

Vector

$\{\ddot{x}\}$	Acceleration
$\{\dot{x}\}$	Velocity
{x}	Displacement
{F}	Force
{p}	Modal displacement
{u}	Modal vector
$\{e_i\}$	ith experimental modal vector
$\{u_j\}$	jth analytical modal vector

Scalars

e_k	kth degree of freedom of the experimental modal vector
u_p	pth degree of freedom of the analytical modal vector

Subscript

n	Full set of finite element DOF
a	Tested set of experimental DOF (also master/active DOF)
d	Deleted (omitted) set of DOF
S	Static condensation
I	IRS condensation
f	Dynamic condensation
U	SEREP condensation
H	Hybrid condensation
k,p	Degree of freedom identifiers
i,j	Mode identifiers

Superscript

T	Transpose
g	Generalized inverse
−1	Standard inverse
*	Conjugate

1 Introduction/Background

Correlation of a finite element model with test data is commonly performed to identify the suitability of the model for response predictions. This may be required contractually or performed to improve the overall system performance based on design requirements or internally generated specifications to assure good modeling techniques are utilized in the design and analysis process.

The finite element model is typically very large with many degrees of freedom, whereas the test data acquired typically has very few degrees of freedom. This mismatch then requires that the finite element model be reduced to the size of the test model or the test data expanded to the size of the finite element model; both of these can introduce errors in the correlation process. Model reduction and expansion techniques commonly employed are presented. The typical correlation tools often deployed are also presented.

The biggest problem to overcome in the correlation of vectors is the model reduction and vector expansion process which can have a direct effect on the results depending on the particular techniques utilized. One other difficulty is that all of the correlation tools may provide some indication of discrepancies and hint to where problems may exist, but it must be clearly understood that the test data and the finite element model can both have deficiencies, so the correlation tools may provide conflicting results and may not always provide the same overall indication of the model adequacy based on the measured data. In fact, there can be cases where the test data (which is not perfect by any means) has errors, and this complicates the correlation process. The user of any of these correlations tools must be very careful in any conclusion obtained from each tool. Engineering judgment and a clear understanding of both the finite element modeling theories and experimental testing approaches is of paramount importance in any correlation analysis.

Some of the relevant theory is presented for model reduction and model expansion along with the commonly used correlation tools. The references are provided at the end of this section to assist the reader in finding additional information related to this and are provided in a bibliography for the different tools and techniques.

2 Theory

The basic matrix equation of motion is generally written as

$$[M_n]\{\ddot{x}_n\} + [C_n]\{\dot{x}_n\} + [K_n]\{x_n\} = \{F_n(t)\} \tag{1}$$

where the [M], [C], and [K] are the mass, damping, and stiffness matrices of the system and {F} is the vector of applied forces on the system and {x} is the vector of displacements of the system (with appropriate derivatives of velocity and acceleration); the subscript "n" denotes the full dimensionality of the set of equations. Assuming that the damping matrix is proportional to either the mass or stiffness matrix (which is often assumed to be the case), the eigensolution can be written as

$$[[K_n] - \lambda[M_n]]\{x_n\} = \{0\} \tag{2}$$

with ω_i $\{u_i\}$ as the resulting eigenvalue and eigenvector, respectively. The eigenvectors can be arranged in column fashion to form the modal matrix [U]. Using this notation and noting the eigenvalues can be assembled into a diagonal matrix, the eigen problem can be restated as

$$[K_n][U_n] = [M_n][U_n]\left[\Omega^2\right] \tag{3}$$

where

$$\begin{bmatrix} \ddots & & \\ & \Omega^2 & \\ & & \ddots \end{bmatrix} = \begin{bmatrix} \omega_1^2 & & \\ & \omega_2^2 & \\ & & \ddots \end{bmatrix} \quad \text{and} \quad [U] = [\{u_1\} \ \{u_2\} \ \cdots] \tag{4}$$

Using the modal matrix, a transformation can be made from physical space to modal space using the relationship:

$$\{x\} = [U]\{p\} = \left[\{u_1\}\ \{u_2\} \cdots\right] \begin{Bmatrix} p_1 \\ p_2 \\ \vdots \end{Bmatrix} \tag{5}$$

Substituting Eq. (5) into the equation of motion in Eq. (1) and premultiplying by the transpose of the projection operator to put the equations into normal form give

the standard modal space representation:

$$[U_n]^T [M_n] [U_n] \{\ddot{p}_n\} + [U_n]^T [K_n] [U_n] \{p_n\} = [U_n]^T \{F_n(t)\} \tag{6}$$

Due to the orthogonality of the modal vectors with respect to the system mass and stiffness matrices, the highly coupled set of physical mass, damping (proportionality assumed), and stiffness matrices become uncoupled in modal space to form the modal mass, modal damping (with proportional damping shown for completeness), and modal stiffness of the system in modal space given as

$$\begin{bmatrix} \overline{m}_1 & & \\ & \overline{m}_2 & \\ & & \ddots \end{bmatrix} \begin{Bmatrix} \ddot{p}_1 \\ \ddot{p}_2 \\ \vdots \end{Bmatrix} + \begin{bmatrix} \overline{c}_1 & & \\ & \overline{c}_2 & \\ & & \ddots \end{bmatrix} \begin{Bmatrix} \dot{p}_1 \\ \dot{p}_2 \\ \vdots \end{Bmatrix} + \begin{bmatrix} \overline{k}_1 & & \\ & \overline{k}_2 & \\ & & \ddots \end{bmatrix} \begin{Bmatrix} p_1 \\ p_2 \\ \vdots \end{Bmatrix} = \begin{Bmatrix} \{u_1\}^T \{F\} \\ \{u_2\}^T \{F\} \\ \vdots \end{Bmatrix} \tag{7}$$

or as

$$\begin{bmatrix} & & \\ & \overline{M} & \\ & & \end{bmatrix} \{\ddot{p}\} + \begin{bmatrix} & & \\ & \overline{C} & \\ & & \end{bmatrix} \{\dot{p}\} + \begin{bmatrix} & & \\ & \overline{K} & \\ & & \end{bmatrix} \{p\} = [U]^T \{F\} \tag{8}$$

where the bar overscore denotes modal space.

When the mode shapes are scaled to unit modal mass, this relationship reduces to

$$[I_n] \{\ddot{p}_n\} + [\Omega_n] \{p_n\} = [U_n]^T \{F_n(t)\} \tag{9}$$

It is important to note that the diagonal modal mass matrix is given as

$$[U_n]^T [M_n] [U_n] = [I] \tag{10}$$

and the diagonal modal stiffness matrix is given as

$$[U_n]^T [K_n] [U_n] = \left[\Omega^2\right] \tag{11}$$

(Note: Subscript "n" here denotes normalized and elsewhere denotes size of matrix.)

2.1 Model Reduction

This section presents some of the basic approaches to the reduction of finite element models. Model reduction is typically performed to obtain a reduced model for other structural dynamic applications such as forced response analysis, system modeling, and component model synthesis techniques. However, for this work, model reduction is specifically used to form a mapping between the very large set of finite element degrees of freedom and the relatively small set of tested degrees of freedom necessary for model correlation studies.

Most reduction or condensation techniques affect the dynamic character of the resulting reduced model. Model reduction is performed for a number of reasons, but the technique is used primarily as a mapping technique. A schematic of the reduction process is shown in Fig. 1.

In general a relationship between the full set of analytical or finite element DOF and the reduced set of active or condensed DOF can be written as

$$\{x_n\} = \begin{Bmatrix} x_a \\ x_d \end{Bmatrix} = [T]\{x_a\} \tag{12}$$

The "n" subscript denotes the full set of analytical DOFs, the "a" subscript denotes the active set of DOF (sometimes referred to as master DOF and for correlation studies referred to as test DOF), and the subscript "d" denotes the deleted DOF (sometimes referred to as embedded or omitted DOF); the [T] transformation relates the transformation between these two sets of DOFs.

The reduced mass matrix and reduced stiffness matrix can be expressed as

$$[M_a] = [T]^T [M_n][T] \tag{13}$$

and

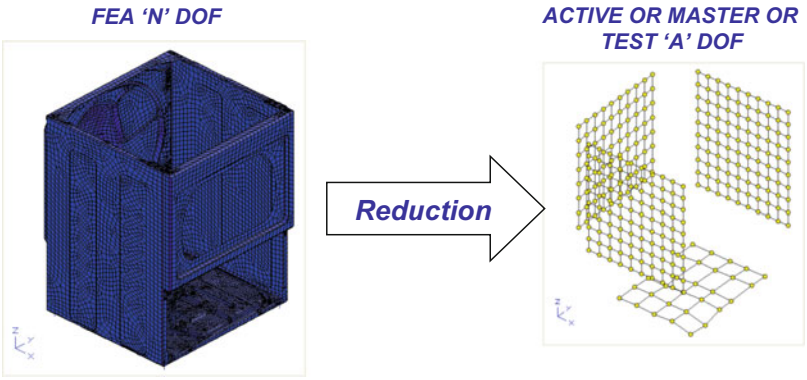

Fig. 1 Schematic of reduction process

$$[K_a] = [T]^T [K_n] [T] \tag{14}$$

Using these new mass and stiffness matrices in "a" space, the equation of motion becomes

$$[M_a] \{\ddot{x}_a\} + [K_a] \{x_a\} = \{F_a(t)\} \tag{15}$$

with a corresponding eigensolution given by

$$[[K_a] - \lambda [M_a]] \{x_a\} = \{0\} \tag{16}$$

Depending on the reduction scheme utilized, the eigenvalues of the reduced system will generally be greater than, or at most equal to, the eigenvalues of the full system.

2.1.1 Guyan Reduction

For a static system, the equation of motion can be written in partitioned form as

$$\begin{bmatrix} [K_{aa}] & [K_{ad}] \\ [K_{da}] & [K_{dd}] \end{bmatrix} \begin{Bmatrix} x_a \\ x_d \end{Bmatrix} = \begin{Bmatrix} F_a \\ F_d \end{Bmatrix} \tag{17}$$

Again the "a" subscript denotes the master or active set of DOF, and the "d" subscript denotes the embedded or deleted DOF. Assuming that the forces on the deleted DOF are zero, the equations can be partitioned and manipulated to obtain the equation written in terms of the active DOF as

$$[K_{aa}] \{x_a\} + [K_{ad}] [K_{dd}]^{-1} [K_{da}] \{x_a\} = \{F_a\} \tag{18}$$

Therefore, a relationship is available relating the active DOF to the full set of DOF as

$$\{x_n\} = \begin{bmatrix} [I] \\ -[K_{dd}]^{-1} \quad [K_{da}] \end{bmatrix} \{x_a\} \quad = \quad [T_s] \quad \{x_a\} \tag{19}$$

Using this transformation matrix, the reduced system stiffness matrix can be written as

$$\left[K_a^G\right] = [T_s]^T [K_n] [T_s] \tag{20}$$

This transformation is exact in the static sense. Guyan [1]/Irons [2] proposed that the same system transformation matrix used to modify the stiffness matrix be used to modify the system mass matrix:

$$\left[M_a^G\right] = [T_s]^T [M_n] [T_s] \tag{21}$$

This transformation attempts to convert the system mass to the set of active DOFs. However, because this technique is based solely on the static stiffness of the system, there is no guarantee that the reduced matrix will be accurate for dynamic applications. The solution of the reduced problem will contain eigenvalues and eigenvectors that are similar to the eigenvalues and eigenvectors of the full system model. The degree of similarity is heavily dependent on the selection of the set of "a" DOF – both the total number of DOF and the distribution of the DOF. In general, the relative difference increases as the mode number increases with the lower-order modes generally having less discrepancy than the higher-order modes.

2.1.2 Improved Reduced System (IRS)

As an extension of the Guyan reduction process, the improved reduced system (IRS) [3] attempts to account for some of the effects of the deleted DOFs that cause distortion in the Guyan reduction process. The development is based on the fact that the static structural model containing distributed forces can be condensed producing a reduced system and solution. The displacements of the reduced system are then expanded and adjusted for the deleted forces producing an exact statistical solution of the complete system. A first-order approximation of the eigensystem is formed using a Guyan/Irons reduced model approach which is based on the static condensation process with no adjustment for the deleted distributed inertia forces. The modal vectors of the approximate solution can be adjusted in a similar fashion as in the static solution to produce an improved set of eigenvectors. Finally, an estimate of the transformation matrix from full space to reduced space can be formed for the IRS system. The resulting transformation equation is summarized as

$$[T_i] = \begin{bmatrix} [I] \\ [t_s] \end{bmatrix} + [t_i] \tag{22}$$

where

$$\begin{aligned} [t_s] &= -[K_{dd}]^{-1} \ [K_{da}] \\ [t_i] &= \begin{bmatrix} [0] & [0] \\ [0] & \left[K_{dd}^{-1}\right] \end{bmatrix} [M_n] [T_s] [M_a]^{-1} [K_a] \end{aligned} \tag{23}$$

The IRS technique generally produces a better reduced eigensystem when compared with the Guyan/Irons approach, because an estimate of the inertia associated with the deleted DOF is developed as part of the reduction process. The IRS technique has also been deployed in an iterative fashion to further improve the reduced matrices.

2.1.3 Dynamic Condensation

A dynamic implementation of the Guyan reduction process is the dynamic condensation [4] process which is often used in correlation studies, particularly for expansion of mode shapes. A shift value, f, is introduced into the set of equations describing the dynamic system, thus

$$[[K_n] - (\lambda - f)[M_n]]\{x_n\} = \{0\} \tag{24}$$

and rearrange terms to group the constant shift frequency term f times the mass matrix with the stiffness matrix to yield

$$[[[K_n] + f[M_n]] - \lambda[M_n]]\{x_n\} = \{0\} \tag{25}$$

Now let

$$[D_n] = [K_n] + f[M_n] \tag{26}$$

Using the same approach in Guyan condensation, these equations can be written for the active DOF as

$$[D_{aa}]\{x_a\} + [D_{ad}][D_{dd}]^{-1}[D_{da}]\{x_a\} = \{F_a\} \tag{27}$$

Therefore, the relationship between the active DOFs and the full set of analytical DOFs can be written as

$$\{x_n\} = \begin{bmatrix} [I] \\ -[D_{dd}]^{-1} \quad [D_{da}] \end{bmatrix}\{x_a\} = [T_f] \quad \{x_a\} \tag{28}$$

So the reduced mass and stiffness matrices can be written as

$$\left[M_a^f\right] = [T_f]^T[M_n][T_f] \tag{29}$$

$$\left[K_a^f\right] = [T_f]^T[K_n][T_f] \tag{30}$$

Due to the formulation of the dynamic condensation process, the eigensolution of the reduced matrices will result in one eigenvalue which will correspond to the shift value used for the reduction process. If the shift value happens to correspond exactly to one of the eigenvalues of the system, then this eigenvalue will be preserved accurately in the reduced model and will also produce an expanded eigenvector which will be exactly the same as the corresponding eigenvector from the full finite element model relating to the shifted eigenvalue. None of the other eigenvalues will correspond exactly to any of the eigenvalues of the full system.

2.1.4 System Equivalent Reduction Expansion Process (SEREP)

As done with the other reduction schemes, there is a relationship between the tested or active "a" DOF and the deleted "d" DOF which can be written in general form as

$$\{x_n\} = \begin{Bmatrix} x_a \\ x_d \end{Bmatrix} = [T]\{x_a\} \tag{31}$$

The modal transformation in Eq. (5) can be rewritten using this notation as

$$\{x_n\} = \begin{Bmatrix} x_a \\ x_d \end{Bmatrix} = \begin{bmatrix} U_a \\ U_d \end{bmatrix}\{p\} \tag{32}$$

Note that the modal matrix can also be partitioned into the "a" active and "d" deleted set of DOF. Looking at just the relationship for the "a" set of DOF, then

$$\{x_a\} = [U_a]\{p\} \tag{33}$$

The inverse specification of this equation involves a generalized inverse because the number of unknowns is not equal to the number of equations that need to be solved. There are two possible solutions to this situation:

- When the number of equations "a" are greater than or equal to the number of solution variables "m" (an overspecification of the system)
- When the number of equations "a" are less than the number of solution variables "m" (an underspecification of the system)

Least squares solution

$$\begin{aligned} \{x_a\} &= [U_a]\{p\} \\ [U_a]^T\{x_a\} &= [U_a]^T[U_a]\{p\} \\ \left([U_a]^T[U_a]\right)^{-1}[U_a]^T\{x_a\} &= \left([U_a]^T[U_a]\right)^{-1}[U_a]^T[U_a]\{p\} \\ \{p\} &= \left([U_a]^T[U_a]\right)^{-1}[U_a]^T\{x_a\} = [U_a]^g\{x_a\} \end{aligned}$$

Average solution

$$\{p\} = [U_a]^T\left([U_a]^T[U_a]\right)^{-1}\{x_a\} = [U_a]^g\{x_a\}$$

For most structural dynamic applications in dynamic testing, the least squares solution is used because the number of master DOF (or tested DOF) is far greater than the number of modes in the system and then the generalized inverse is

$$\{p\} = \left([U_a]^T [U_a]\right)^{-1} [U_a]^T \{x_a\} = [U_a]^g \{x_a\} \tag{34}$$

This equation for the modal displacement can be substituted into the modal transformation equation to give

$$\{x_n\} = [U_n] [U_a]^g \{x_a\} = [T_U] \{x_a\} \tag{35}$$

where

$$[T_U] = [U_n] [U_a]^g \tag{36}$$

This is the SEREP [5] transformation matrix that is used for either the reduction of the finite element mass and stiffness matrices or the expansion of the measured experimental modal vectors. The system equivalent reduction expansion process (SEREP) relies on a finite element model or analytical model from which an eigensolution is obtained for developing the mapping between the full set of "n" finite element DOF and the reduced set of "a" DOF. The eigensolution of the full set of system matrices yields a set of modal vectors which can be partitioned into those degrees of freedom that correspond to the active set of "a" DOF and the inactive set of "d" DOF. This is shown pictorially in Fig. 2. (Note that it is not required to have a sequential set of modes for the SEREP reduction process.)

Using this SEREP transformation matrix, the reduced mass and stiffness matrices can then be written as

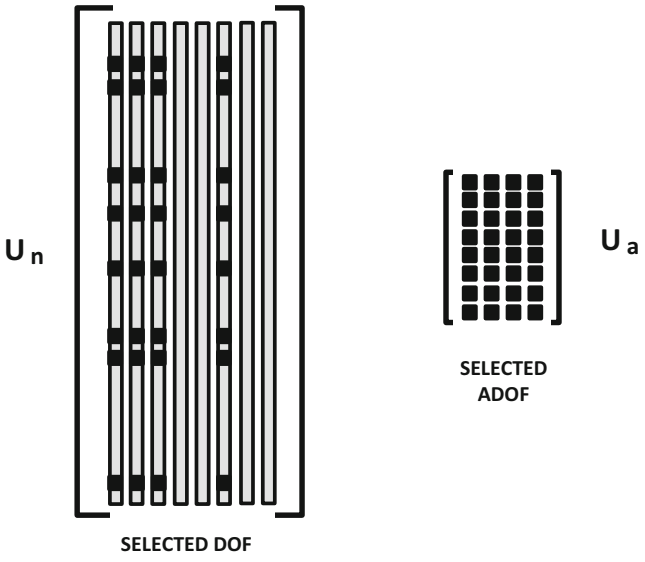

Fig. 2 Schematic of U_a partition of U_n

$$\begin{aligned}\left[M_a^S\right] &= [T_U]^T \ [M_n] \ [T_U] \\ \left[K_a^S\right] &= [T_U]^T \ [K_n] \ [T_U]\end{aligned} \tag{37}$$

The equation of motion for the "a" set of DOF can be written as

$$\left[M_a^S\right]\{\ddot{x}_a\} + \left[K_a^S\right]\{x_a\} = \{F_a\,(t)\} \tag{38}$$

Substituting in the SEREP transformation matrix in Eq. (36) into the reduced mass matrix in Eq. (37) gives

$$[M_a] = [U_a]^{g^T}[U_n]^T\,[M_n]\,[U_n]\,[U_a]^g \tag{39}$$

From mass orthogonality in Eq. (10), Eq. (39) can be written for the reduced mass as

$$[M_a] = [U_a]^{g^T}[U_a]^g \tag{40}$$

Note that the original system mass matrix is not needed in order to compute the reduced mass matrix. Similarly for the reduced stiffness matrix, the SEREP transformation matrix can be substituted into the reduced stiffness matrix in Eq. (37) to give

$$[K_a] = [U_a]^{g^T}[U_n]^T\,[K_n]\,[U_n]\,[U_a]^g \tag{41}$$

From stiffness orthogonality in Eqs. (11) and (41) can be written for the reduced stiffness matrix as

$$[K_a] = [U_a]^{g^T}\left[\Omega^2\right][U_a]^g \tag{42}$$

Note that the original system stiffness matrix is not needed in order to compute the reduced stiffness matrix.

While the size of these reduced mass and stiffness matrices is "a" by "a," the rank of the reduced matrices is only "m." Therefore, use of these matrices must be done with caution. Due to this rank deficiency, an alternate form of the SEREP reduction process which invokes an exact solution can be obtained by using a = m for the reduction.

2.1.5 Modal TAM

The modal TAM is very similar to SEREP, except that the a-set modes are unmodified (not smoothed). This is accomplished by realizing there is a direct representation of $\{x_a\}$ like we see in Guyan reduction, IRS, and dynamic condensation:

$$\{x_a\} = [I]\{x_a\} \tag{43}$$

The next observation is to look at the lower partition of Eq. (32) given as

$$\{x_d\} = [U_d]\{p\} \tag{43}$$

and substituting Eq. (34) into Eq. (43) providing the relationship between the a-set and d-set DOFs as

$$\{x_d\} = [U_d][U_a]^g\{x_a\} \tag{44}$$

Referring back to Eq. (32), the modal TAM is written as

$$\{x_n\} = \begin{Bmatrix} x_a \\ x_d \end{Bmatrix} = \begin{bmatrix} [I] \\ [U_d][U_a]^g \end{bmatrix}\{x_a\} = [T_M]\{x_a\} \tag{45}$$

where

$$[T_M] = \begin{bmatrix} [I] \\ [U_d][U_a]^g \end{bmatrix} \tag{46}$$

When using this transform to reduce mass and stiffness matrices, "m" is typically less than "a", resulting in rank deficient matrices, but retaining the full accuracy of the original "m" FEM modes in frequency and full mode shape accuracy. When this transform is used for test shape expansion the modes at the a-set are unmodified.

As the number of modes are increased, and the a-set is well chosen, then SEREP and Modal TAM become equivalent. This occurs when and if

$$[U_a][U_a]^g = [I] \tag{47}$$

2.1.6 Hybrid

Another method for reducing of the system matrices utilizes the exactness of the SEREP or modal TAM process and overcomes the rank deficiency by incorporating the effects of Guyan condensation into the process and is referred to as the hybrid reduction [6] technique and is formulated as

$$[T_H] = [T_s] + [[T_M] - [T_S]][P] \tag{48}$$

The reduced matrices of the hybrid TAM are not rank deficient with the eigenvalue decomposition giving the mode shapes and natural frequencies that the modal TAM would provide for the m target modes included in the aforementioned modal TAM plus the additional information that the Guyan reduction would provide for the remaining model order (a-set minus the target modes (a-m)). The projector matrix [*P*] is given in both its oblique and orthogonal forms as

Table 1 Summary of hybrid TAM combinations

Hybrid	Projector	TAM combinations	
1	Oblique	Modal	Guyan
2	Orthogonal	Modal	Guyan
3	Oblique	SEREP	Guyan
4	Orthogonal	SEREP	Guyan
5	Oblique	Modal	IRS
6	Orthogonal	Modal	IRS
7	Oblique	SEREP	IRS
8	Orthogonal	SEREP	IRS

$$\left[P_{\text{oblique}}\right] = [U_a]\,[U_a]^T[T_M]^T\,[M]\,[T_M] \tag{49}$$

$$[P_{\text{ortho}}] = [U_a]\,[U_a]^g \tag{50}$$

Observation shows that in addition to the oblique and orthogonal forms of the hybrid TAM, SEREP can be substituted for the modal TAM, and IRS can be used instead of the Guyan TAM. Table 1 summarizes the eight different hybrid TAM combinations that are possible.

$$[T_H] = [T_s] + [[T_M] - [T_S]]\,[P]$$

$$[T_H] = [T_s] + [[T_U] - [T_S]]\,[P]$$

$$[T_H] = [T_I] + [[T_M] - [T_I]]\,[P]$$

$$[T_H] = [T_I] + [[T_U] - [T_I]]\,[P]$$

2.2 Model Expansion (Vector Expansion)

Experimental mode shapes only exist at the DOF associated with the test points ("a" DOF). Because the mass and stiffness matrices are described at the full set of finite element DOFs ("n" DOF), the system mass and stiffness matrices need to be reduced to the set of experimental DOF for correlation studies. However, there is also a need to expand the measured experimental mode shape over the full set of finite element DOF for further correlation studies. Therefore, expansion techniques are necessary for other studies. A schematic of the expansion process is shown in Fig. 3.

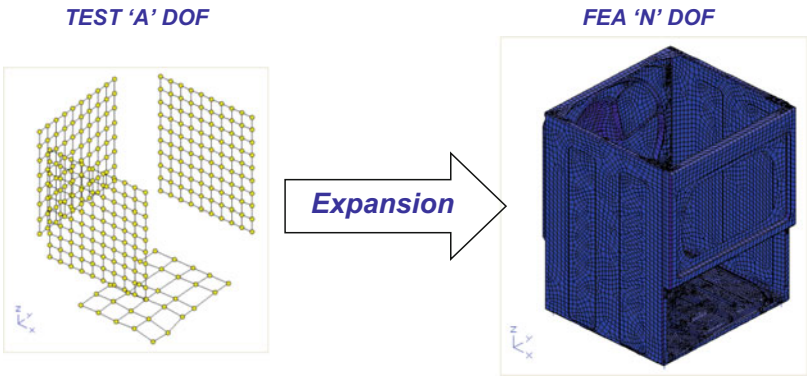

Fig. 3 Schematic of the expansion process

Early expansion techniques evolved around using spline fits and polynomial expansion based on geometry and measured data. While in concept they are useful, in practice, using these approaches for general structural systems is not feasible. Most expansion techniques utilized today involve the use of the finite element model as a mechanism to complete the unmeasured DOF from the experimental modal model. In essence, the finite element model is used as a high-order polynomial curve fitter to estimate the experimental mode shapes at the deleted DOF. The majority of the expansion techniques use the model reduction transformation matrix as an expansion mechanism.

Recall that the basic relationship relating the "a" DOF to the "n" DOF is given by

$$\{x_n\} = \begin{Bmatrix} x_a \\ x_d \end{Bmatrix} = [T] \quad \{x_a\} \tag{51}$$

Using this expansion concept along with measured experimental modal data, then

$$[E_n] = \begin{bmatrix} E_a \\ E_d \end{bmatrix} = [T]\,[E_a] \tag{52}$$

The measured experimental modal vectors at "a" DOF are expanded over all the finite element "n" DOF using the transformation matrix [T]. This transformation matrix will take on various forms depending on which technique is utilized.

At times, the expansion is broken down into two parts, namely, completion and smoothing. The completion of the mode shape refers to unmeasured DOFs which are obtained in the expansion process. The smoothing of the mode shape refers to the possible least squares fitting of the measured DOF. There are differences of opinion as to whether or not smoothing should be performed, and there is no clear answer on this. On one hand, the data measured is what was measured, and many

feel that this should not be manipulated in the expansion process. On the other hand, the measured data is clearly never perfect and does have variance which is why smoothing might be performed. One additional concern when using unsmoothed data is that there is a mathematical inequity between the measured data and the completed data that can have an effect on the correlation results.

Each of the reduction techniques discussed above is also useful for expansion.

2.2.1 Guyan Expansion

The Guyan expansion technique uses the static condensation transformation matrix to expand the measured DOF over all the finite element DOF. The expansion is given by

$$[E_n] = \begin{bmatrix} E_a \\ E_n \end{bmatrix} = [T_s]\,[E_a] = \begin{bmatrix} [I] \\ -[K_{dd}]^{-1}\ [K_{da}] \end{bmatrix} [E_a] \tag{53}$$

Of course, the Guyan condensation process will not produce acceptable results unless there are sufficient DOF to describe the mass of the system (as previously discussed in the reduction section). If sufficient DOFs are available, then the Guyan process will produce reasonably good results but will never produce exact results because the inherent formulation of the reduction matrix is approximate. The Guyan reduction process is still widely used for model reduction applications due to its long historical background but is not widely used for expansion of mode shapes because other more accurate techniques have been developed.

2.2.2 Improved Reduced System (IRS)

The IRS expansion technique uses the static condensation transformation matrix along with adjustment terms to compensate for the inertia associated with the deleted DOF to expand the measured DOF over all the finite element DOF. The expansion is given by

$$\begin{aligned} [E_n] &= \begin{bmatrix} E_a \\ E_d \end{bmatrix} = [T_i]\,[E_a] \\ &= \left[\begin{bmatrix} [I] \\ -[K_{dd}]^{-1}\ [K_{da}] \end{bmatrix} + \begin{bmatrix} 0 & 0 \\ 0 & K_{dd}^{-1} \end{bmatrix} [M_n]\,[T_s]\,[M_a]^{-1}\,[K_a] \right] [E_a] \end{aligned} \tag{54}$$

Of course, the IRS technique will improve on the Guyan expansion process, but will not produce acceptable results unless there are sufficient DOFs to describe the mass of the system (as previously discussed in the reduction section 2.1). If sufficient DOFs are available, then the IRS process will produce reasonably good results (which are improved over the Guyan results) but will never produce exact results because the inherent formulation of the reduction matrices is approximate.

2.2.3 Dynamic Expansion

The dynamic expansion technique is very similar to the static expansion process except that the stiffness matrix is modified to include the effects of the mass of the system at a particular frequency. This is accomplished by adding an adjustment term of the reference frequency times the system mass to the stiffness matrix as was shown in the development of the model reduction equations. In essence, this matrix is exact for this one particular frequency, and the transformation matrix will be exact in regard to expanding a mode shape at that particular frequency. Of course, the shift frequency must correspond to one of the eigenvalues of the system. The expansion is given by

$$[E_n] = \begin{bmatrix} E_a \\ E_d \end{bmatrix} = [T_f] \quad [E_a] = \begin{bmatrix} [I] \\ -[D_{dd}]^{-1} \quad [D_{da}] \end{bmatrix} [E_a] \tag{55}$$

The dynamic expansion process will produce exact results for one frequency and only one frequency. Providing that the shift frequency corresponds exactly to one of the eigenvalues of the system, then the expansion will produce an exact mode shape for this one eigenvalue. If additional eigenvectors need to be expanded, then separate shift values need to be processed. While many matrices need to be processed for each eigenvector that needs to be expanded, the exactness of the process warrants the additional processing.

2.2.4 System Equivalent Reduction Expansion Process (SEREP)

The SEREP expansion technique uses the SEREP transformation matrix to expand the measured DOF over all the finite element DOF. The expansion is given by

$$[E_n] = \begin{bmatrix} E_a \\ E_d \end{bmatrix} = [T_U]\,[E_a] = [U_n]\,[U_a]^g\,[E_a] = \begin{bmatrix} U_a \\ U_d \end{bmatrix} [U_a]^g\,[E_a] \tag{56}$$

Notice that the "a" DOF may be changed as seen by the upper partition of this equation:

$$[E_a]' = [U_a]\,[U_a]^g\,[E_a] \tag{57}$$

and that the deleted DOFs are estimated by

$$[E_d] = [U_d]\,[U_a]^g\,[E_a] \tag{58}$$

When the "a" DOFs are expanded, there is the possibility that the initially measured DOF may be modified by the expansion process. This is referred to as smoothing of the measured DOF. This occurs because the SEREP process is based on a generalized inverse using a least squares error minimization. Therefore, the measured data is smoothed as part of the process. While much controversy exists over whether or not to smooth the actual measured data, this is the proper way

to process the data, from a mathematical standpoint. Otherwise, a mathematical mismatch exists in the expanded vector between the "a" DOF and the "d" DOF.

2.2.5 Modal

The modal TAM expansion technique uses the modal TAM transformation matrix to expand the measured DOF over all the finite element DOF. The expansion is given by

$$[E_n] = \begin{bmatrix} E_a \\ E_d \end{bmatrix} = [T_M]\,[E_a] = \begin{bmatrix} [I] \\ [U_d]\,[U_a]^g \end{bmatrix} [E_a] \tag{59}$$

Notice that the "a" DOFs are unchanged as seen by the upper partition of this equation and the deleted DOFs are estimated in the same manner as the SEREP process.

2.2.6 Hybrid

The Hybrid TAM expansion technique uses a combination of the SEREP or modal TAM and Guyan or IRS transformation matrix to expand the measured DOF over all the finite element DOF. The expansion is given by

$$[E_n] = \begin{bmatrix} E_a \\ E_d \end{bmatrix} = [T_H]\,[E_a] = [[T_s] + [[T_M] - [T_S]]\,[P]]\,[E_a] \tag{60}$$

2.2.7 Model Reduction Considerations for Sensor Locations

The transformation matrices need to be understood when selecting DOF for measurement locations. This is an important consideration because there may be a limited budget for measurements on the structure to be made or portions of the structure, which are dynamically active, may not be instrumented. Typically, the transformation matrices are not plotted or reviewed, and there is useful information to be seen in these matrices.

In order to illustrate some of the typical transformation matrix characteristics, two simple academic structures are shown. The first structure has a very well distributed set of "a" DOF for a two-beam system where there is modal energy in each of the beams but distributed differently for each system model (as is typically seen in any practical structure). For this structure, there are four DOFs on the upper beam and eight DOFs on the lower beam which is a proper distribution for the modes of this structure. The mode shapes are shown in Fig. 4 for reference for the first several modes. The Guyan, IRS, and SEREP transformation matrices are plotted in a 3D plot in Fig. 5. Notice that there is very little difference between the different transformation matrices and that IRS slightly adjusts Guyan and SEREP provides the most accurate representation for the matrix. Note that all of the system frequencies and mode shapes are represented well with SEREP producing the exact frequencies and mode shapes for the system; Guyan provides good estimates of the

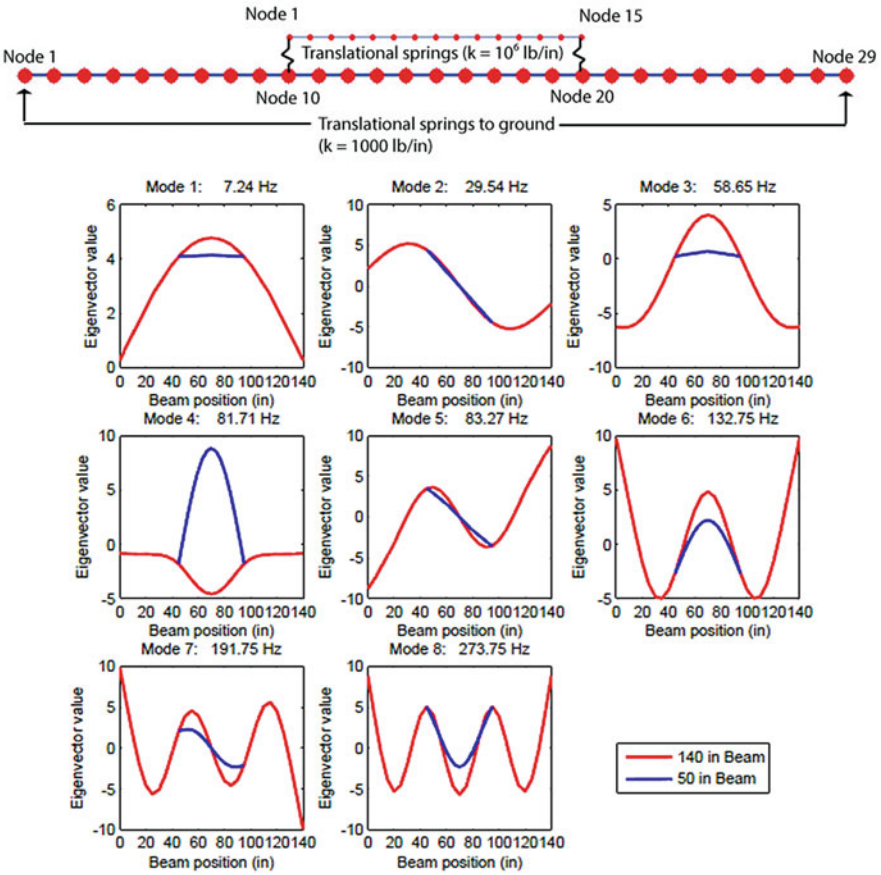

Fig. 4 Schematic showing mode shapes for two-beam system

frequencies and mode shapes and IRS improves on Guyan, but neither has the exact representation of the full system captured in the reduced model.

Now in the second case, the DOFs are only distributed on the lower beam which contains most of the modal information, but no DOFs are distributed on the upper beam which only has a few dynamically important modes for the system. The DOF may not be distributed to the upper beam because it may be inaccessible for instrumentation, it may not be considered as one of the important target modes of the system, and there may be a lack of instrumentation budget for enough sensors, or a number of other reasons. But the important item is that the portion of the structure is not included in the reduction process; essentially an inadequate number of transducer measurement locations have been identified. The Guyan, IRS, and SEREP transformation matrices are plotted in a 3D plot in Fig. 6. Notice that the SEREP transformation matrix is substantially different than the Guyan and IRS matrices. Remember that the SEREP process is exact and the transformation matrix

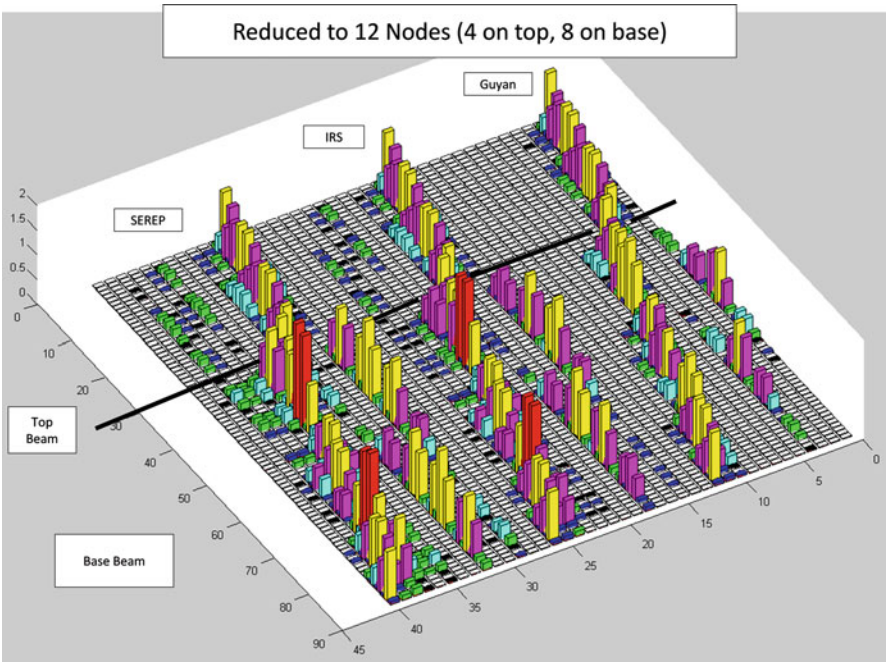

Fig. 5 Transformation matrix [T] shown for Guyan, IRS, and SEREP for a well-selected set of DOF showing similarity in the project matrix

for SEREP accurately illustrates the true transformation needed to accommodate the poor selection of DOF for this reduced model. Notice that the Guyan and IRS transformation matrices appear similar indicating that IRS can only make useful adjustments to the Guyan model based on the starting DOF used for Guyan reduction. Both the Guyan and IRS transformation matrices are not adequate to map the system accurately with the DOF selected.

2.3 Test Data Considerations

There must be serious consideration given to the data that is measured and to be used for the correlation process. All too often this is overlooked by the finite element or correlation engineer performing the analysis with the assumption that the test engineer has done an extensive evaluation of the data collected; this should have been done but may not have been evaluated with the degree and depth needed when performing correlation. Certainly, this is a critical step in the process, but only a few of the more important considerations can be provided here.

In actuality, a detailed pretest analysis really needs to be performed prior to actually starting the data collection. Issues related to target mode selection and sensor placement are of critical concern. For target mode selection, many tools

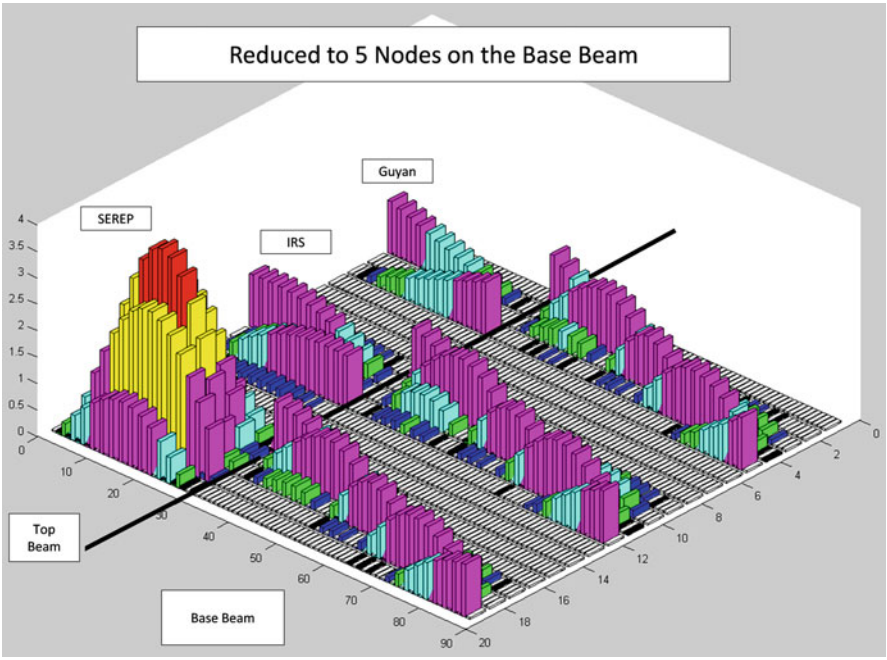

Fig. 6 Transformation matrix [T] shown for Guyan, IRS, and SEREP for a poorly selected set of DOF showing dissimilarity in the project matrix

such as effective modal mass, kinetic energy fraction, and mode participation need to be evaluated for the test. As for sensor placement, many tools such as modal displacement method, nodal kinetic energy, and sensor identification (effective independence and MAC contribution) are commonly used.

But from the practical side, there are many test data issues that are often missed, overlooked, or not clearly understood by the test engineer or the analyst performing the correlation. There are always the considerations for time invariance, linearity, reciprocity, repeatability, and measurement adequacy to name a few that can distort measured data as well as quantization, frequency resolution, leakage, and windows. Table 2 lists a few other general concerns for measured data.

Beyond the measurement aspects, the excitation utilized can also have an effect on the measurement adequacy. Techniques such as burst random, pseudorandom, sine chirp, and digital stepped sine to name a few of the more popular techniques commonly used are very important to the success of the data extracted.

The actual setup of the test can have an impact on the results that are extracted from the test data collected. Issues related to simple items such as the boundary conditions used for the test setup can have an effect on the modes extracted. It is imperative that the finite element model be constructed in a fashion that attempts to replicate the actual test setup conditions so as to maintain a proper representation of the boundary conditions as much as possible. All too often the finite element model

Table 2 Instrumentation considerations

Test instrumentation – amplifiers/filters
• Calibration • Magnitude and phase distortion • Magnitude and phase mismatch
Test instrumentation – transducer mounting
• Accuracy • Repeatability • Local effects
Test instrumentation – transducers
• Calibration • Magnitude and phase distortion • Mass loading effects/stiffening effects • Sensitivity to environment • Cross axis sensitivity

is constructed with either a free-free or fully built-in condition which is impossible to achieve in any test that is performed.

Often times there are never enough measurement transducers to provide the proper amount of tested DOF to assure a good representation of the modes of the system. In larger tests, there may need to be a multiple-input multiple-output data collection performed. When too few shakers (or only one shaker) are used, the data collection must be repeated several times with subsets of the total number of multiple shakers deployed. This measurement scenario is usually not acceptable, and data inconsistencies may exist due to test setup changes and the time required to collect the entire data set when the test environment cannot be guaranteed to remain constant. Too few accelerometers can result in missed (or poorly understood) modes and may be inappropriate for the reduced model comparison using Guyan and IRS techniques. Many times more effective measurement points are attempted by roving accelerometers around the structure, but this can potentially cause mass loading effects which can completely distort the experimental data extracted. Even when using dummy masses at all measurement locations, the time required to remap channels often results in a staggering in time when the data is collected and the test environment may not be stable enough to accommodate these minor changes. The most critical item is that the test data needs to be collected simultaneously in a consistent fashion so that the data reduction requirements are not violated; often this is unknown to the analyst when receiving data.

But one prevailing statement can be made which is not often understood by so many that are involved in these test-analysis correlation studies.

All the measured degrees of freedom are not measured with the same accuracy for each mode of the system. This means that for a correlation study, a certain set of degrees of freedom may be measured very accurately for one particular mode and be measured very inaccurately for another mode. This raises the question as to whether to use all the degrees of

(continued)

freedom when correlating each mode of the system and is a critically important item to understand when undertaking a test-analysis correlation study.

2.4 Vector Correlation

The tools available for correlation can generally be broken down into global assessment (vector based) or local assessment (DOF based). Each of the techniques is identified below. Each generally has some metric, but the actual value of acceptability is not an exact value. The specific level of acceptance is very dependent on the design specification and intent of the correlation study. However, in some industries, there are specific contractual values that must be achieved, but this does not necessarily translate to all industries and applications. But often times due to the lack of understanding of what specific target values are needed, many often revert to use of some of these industry-mandated values, but there is no specific requirement or need to do so. The level of correlation needed should really be dictated by the design specification and overall system level performance necessary to achieve the stated goals or design objectives.

2.4.1 Modal Assurance Criteria (MAC)

The modal assurance criteria [7] (MAC) is an extremely useful technique which gives a first indication of the level of correlation that exists between the analytical and experimental modal vectors. The MAC, for real valued vectors, is given by

$$\mathrm{MAC}_{ij} = \frac{\{u_i\}^H \{e_j\} \{e_j\}^H \{u_i\}}{\{u_i\}^H \{u_i\} \{e_j\}^H \{e_j\}} \tag{61}$$

While the original MAC is written using complex notation, the MAC is generally used with real normal vectors when utilized in finite element correlations.

In this formulation, the values of MAC range between "0.0" and "1.0," where "0.0" indicates that there is little or no correlation between the vectors and "1.0" indicates that there is a high degree of similarity between the modal vectors. MAC is ideal for identifying those analytical modes corresponding to experimental modes, and it is very useful when identifying mode switching. MAC is very sensitive to the DOFs that are largest in value and is very insensitive to very small DOF in the mode shape vector. Mass weighting is not used in this formulation, which has the advantage that mass reduction is not needed. A typical schematic for a MAC matrix is shown in Fig. 7.

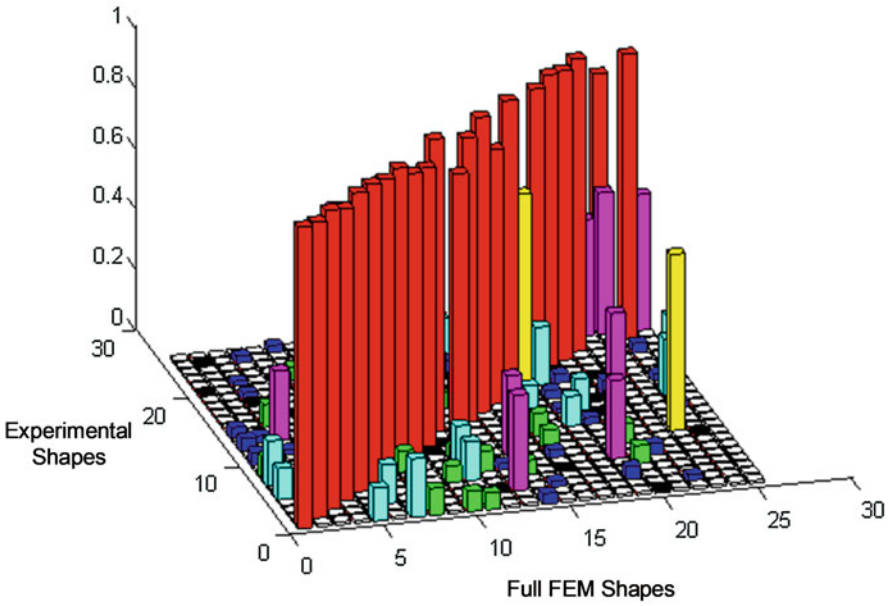

Fig. 7 Typical modal assurance criteria matrix

2.4.2 Orthogonality Checks

Two orthogonality checks [8] are often made when evaluating vector correlation – the cross orthogonality check and the pseudo orthogonality check. The obvious hurdle to overcome is whether to reduce the finite element mass and stiffness matrices to the set of tested DOF or to expand the measured experimental modal vectors to the full space of the finite element model. Alternately, some combination of both reduction and expansion, in order to compute the orthogonality, could be used. A schematic of the reduction and expansion process for correlation is shown in Fig. 8 along with an orthogonality matrix.

The cross orthogonality check is an orthogonality check where the modal vector matrices are obtained from the experimentally measured modal data:

$$\text{CROSS} = [\text{E}]^{\text{T}} [\text{M}] [\text{E}] \stackrel{?}{=} [\text{I}] \tag{62}$$

The pseudo orthogonality check is essentially an orthogonality check where one of the modal vector matrices is replaced with the experimentally measured modal data:

$$\text{POC} = [\text{U}]^{\text{T}} [\text{M}] [\text{E}] \stackrel{?}{=} [\text{I}] \tag{63}$$

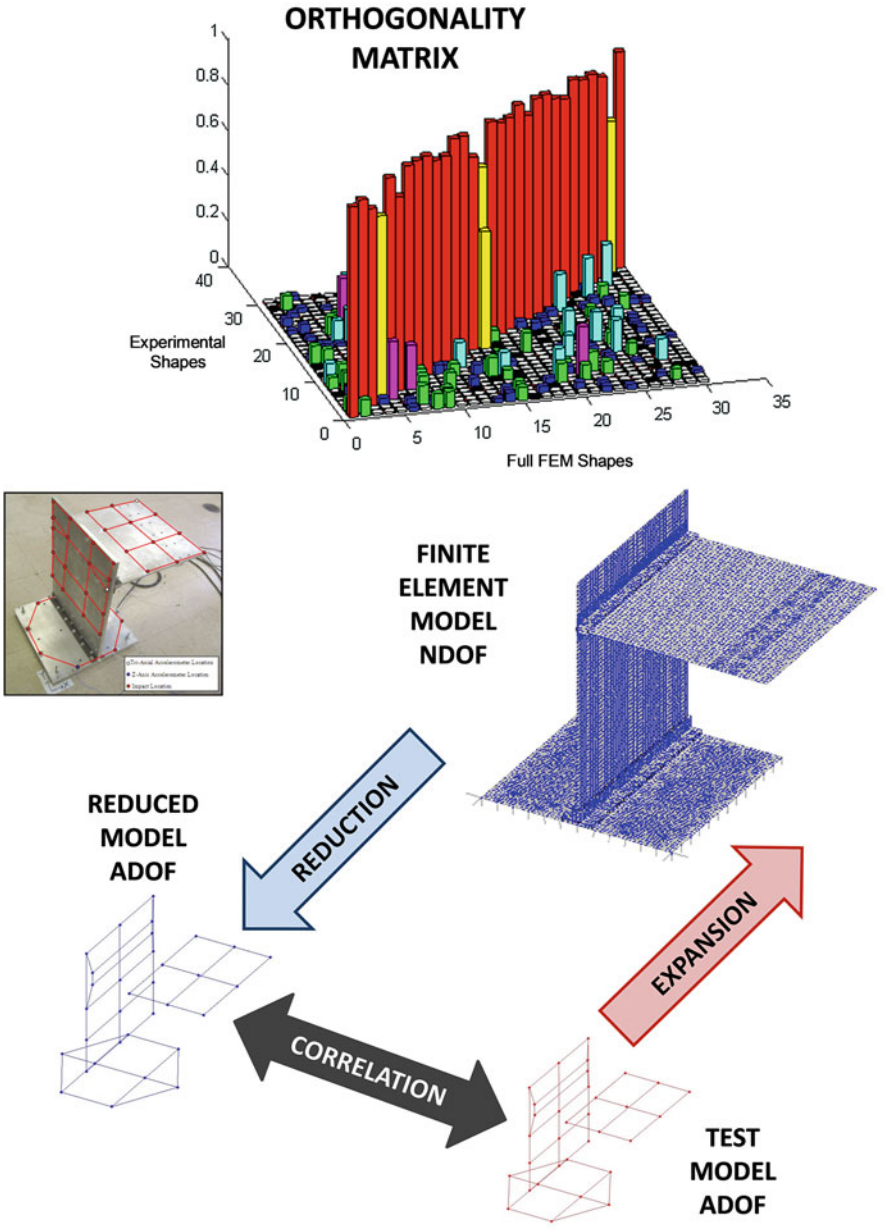

Fig. 8 Overall schematic of the model reduction/expansion process for correlation

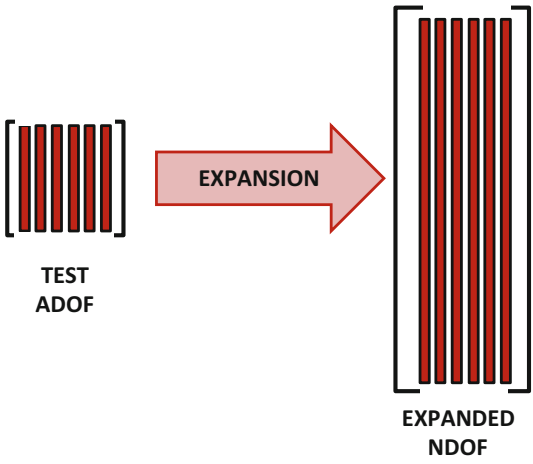

Fig. 9 Schematic of expansion for orthogonality checks

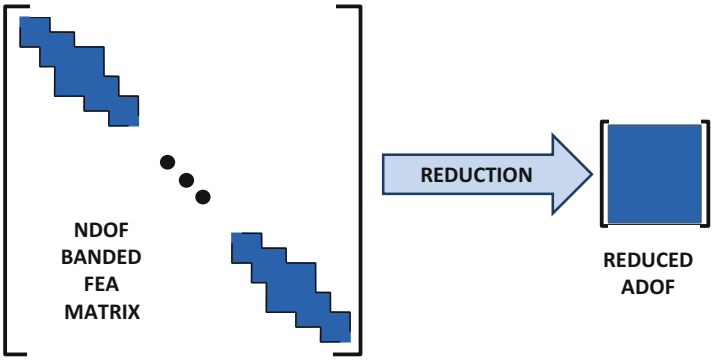

Fig. 10 Schematic of reduction for orthogonality checks

As mentioned above, in order to accomplish this triple product, the matrices must conform. Therefore, either the system mass matrix must be reduced to the set of tested DOF (and corresponding "a" DOF from the test model), or the experimentally measured modal vectors must be expanded to the full space of the finite element model. This is schematically shown in Figs. 9 and 10. Of course, the results of either of these checks will be dependent on the type of reduction, or expansion, utilized, except for the SEREP process which preserves the dynamics of the system in the reduced model.

In reviewing the results of the cross orthogonality check and the pseudo orthogonality check, there are similarities that exist because one check basically uses the experimentally measured vectors twice in the computation of orthogonality,

and, therefore, the resulting terms are larger. However, there is no benefit of using these vectors twice in the cross orthogonality check, and no additional insight is gained in this process. Thus, there is no benefit in using the cross orthogonality check rather than the pseudo orthogonality check for general orthogonality using the usual model reduction and expansion processes such as Guyan and IRS. However, when using the SEREP process, there are significant computational benefits to be gained when using the pseudo orthogonality check.

In all of the reduction/expansion techniques, there is some numerical processing necessary to either reduce the mass matrix or expand the experimental modal vectors. Due to its formulation, the SEREP process has some very important characteristics. The POC at the set of tested "a" DOF is exactly equal to the POC at the full set of "n" DOF. Also, the POC can be performed without the use of any system matrices:

$$[U_a]^T [M_a] [E_a] = [U_n]^T [M_n] [E_n] = [U_a]^g [E_a] \tag{64}$$

First, the pseudo orthogonality check will provide exactly the same results whether the check is done at the full space of the finite element model or at the reduced space of the test model. Therefore, the computation is most efficiently performed in the reduced space of the test model. Second, tremendous computational and procedural benefits are obtained for the pseudo orthogonality check using the SEREP process because the mass matrix is not needed for this computation [9].

2.4.3 Coordinate Modal Assurance Criteria (CoMAC)

The coordinate modal assurance criteria [10] follows the same formulation as MAC in that a correlation coefficient is developed to determine the degree of correspondence that exists for a particular DOF over a set of correlated mode pairs. CoMAC is useful in determining how well correlated each individual DOF may be over a set of modes and provides some insight into where discrepancies may exist:

$$\text{CoMAC}\,(k) = \frac{\left[\sum_{c=1}^{m} \left| u_k^{(c)} \cdot e_k^{(c)} \right| \right]^2}{\sum_{c=1}^{m} \left(u_k^{(c)} \right)^2 \cdot \sum_{c=1}^{m} \left(e_k^{(c)} \right)^2} \tag{65}$$

However, without mass scaling to properly weight the DOFs, at times it is difficult to determine the degree of correlation that exists. Another drawback of the CoMAC is that it can only be used for correlated mode pairs. This implies that only the diagonal related terms of the MAC correlation matrix can be assessed (once the vectors are arranged in proper correlated order if necessary). The CoMAC is shown schematically in Fig. 11. Of course it is important to mention that there

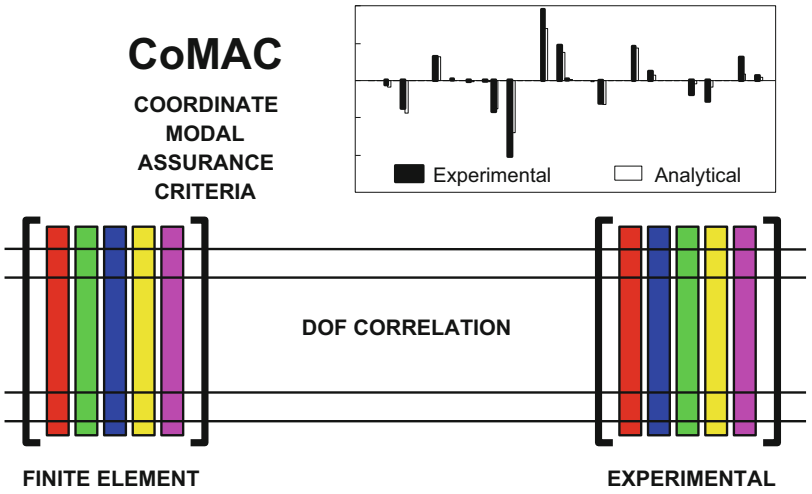

Fig. 11 Schematic of CoMAC for vector correlation

are variations of this CoMAC formulation such as the enhanced CoMAC [11] and modulus difference.

2.4.4 Frequency Response Assurance Criteria (FRAC)

The frequency response assurance criteria evaluates each DOF based on the FRF comparison of the analytical and experimentally derived functions. The formulation is very similar to the MAC function and has a similar interpretation. The FRAC is given by

$$\text{FRAC}\,(\beta) = \frac{\left(\{h_{\text{test}}\}\,\{h_{\text{fem}}\,(\beta)\}^*\right)^2}{\left(\{h_{\text{test}}\}\,\{h_{\text{test}}\}^*\right)\left(\{h_{\text{fem}}\,(\beta)\}\,\{h_{\text{fem}}\,(\beta)\}^*\right)} \tag{66}$$

The FRAC is a useful tool for evaluating FRFs. However, the main drawback is that the analytical model FRF may have similar shape characteristics but differ slightly in frequency which can cause significantly low FRAC values. Therefore, the function is constructed with a shifting function to allow for some frequency adjustment due to global stiffness differences. The FRAC is mainly used for correlation in frequency response-based model updating studies. One critical concern is the damping selected for the development of the finite element FRF which will have an effect on the results. The FRAC is shown schematically in Fig. 12.

2.4.5 Response Vector Assurance Criteria (RVAC)

A companion to the FRAC is the response vector assurance criteria (RVAC) which compares a specific spectral line of the FRF for the analytical and experimental

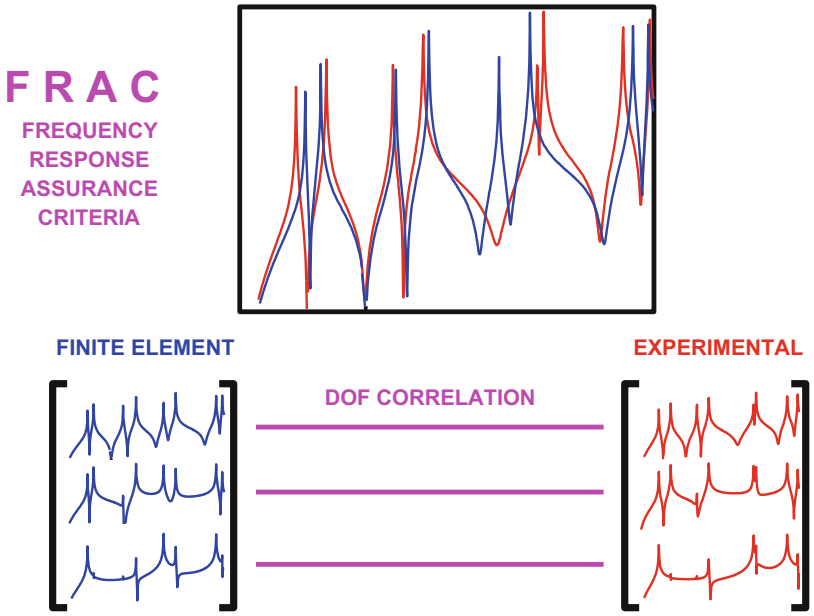

Fig. 12 Schematic of FRAC for vector correlation

FRF for a number of measurement points. Essentially, RVAC is a MAC correlation technique for the analytical and experimental vectors (approximated using a peak pick technique) and is given as

$$\text{RVAC}\,(\omega) = \text{MAC}\,(\{\text{E}_{\text{test}}\,(\omega)\}\,,\{\text{U}_{\text{fem}}\,(\omega\beta)\}) \tag{67}$$

The RVAC is shown schematically in Fig. 13.

2.4.6 Test Response Assurance Criteria (TRAC)

Another correlation sometimes used is the test response assurance criteria (TRAC) which is another variant of MAC that is used to compare time responses from a finite element model and measured time response data. It follows the same interpretation as MAC and is given as

$$\text{TRAC} = \frac{\left[\{\text{X}_{\text{n1}}\}^{\text{T}}\ \{\text{X}_{\text{n2}}\}\right]^2}{\left[\{\text{X}_{\text{n1}}\}^{\text{T}}\ \{\text{X}_{\text{n1}}\}\right]\ \left[\{\text{X}_{\text{n2}}\}^{\text{T}}\ \{\text{X}_{\text{n2}}\}\right]} \tag{68}$$

The TRAC is schematically shown in Fig. 14a along with a MAC to illustrate the two tools often used in correlation studies; Fig. 14b shows the two traces plotted

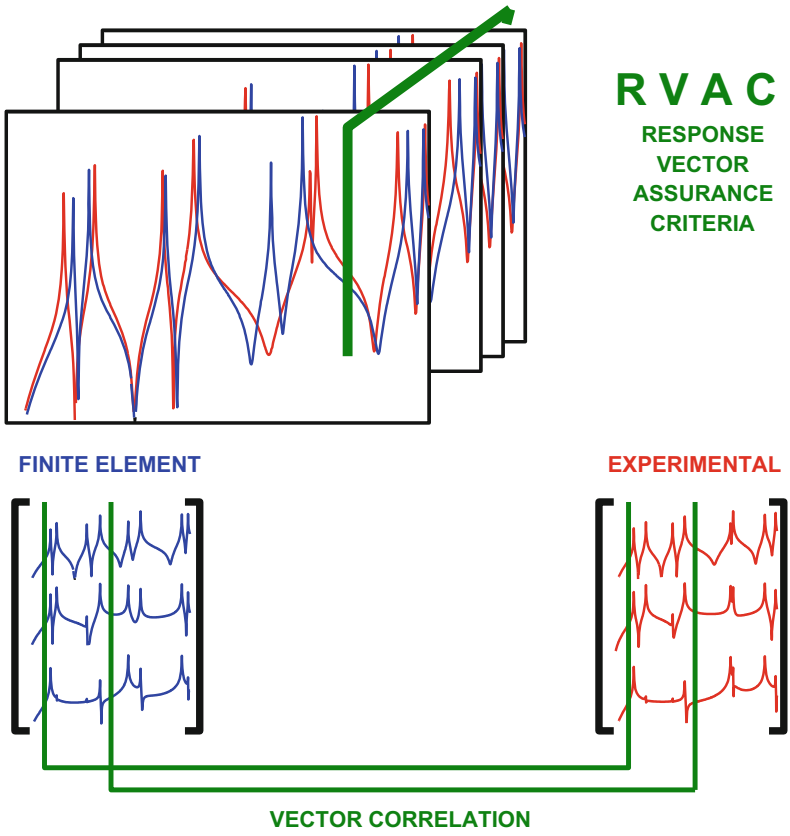

Fig. 13 Schematic of RVAC for vector correlation

against each other and illustrates that the TRAC (and MAC) are really nothing more than the R^2 value from a regression analysis.

2.4.7 CORTHOG

The coordinate orthogonality check [12] (CORTHOG) is a mass scaled degree of freedom correlation that is conceptually similar to CoMAC but can be used for checking any mode pair and not just correlated mode pairs. But the most important feature for CORTHOG is the fact that mass scaling is included in the formulation.

The simplest statement summarizing the coordinate orthogonality check is as follows: The coordinate orthogonality check is simply the comparison of what should

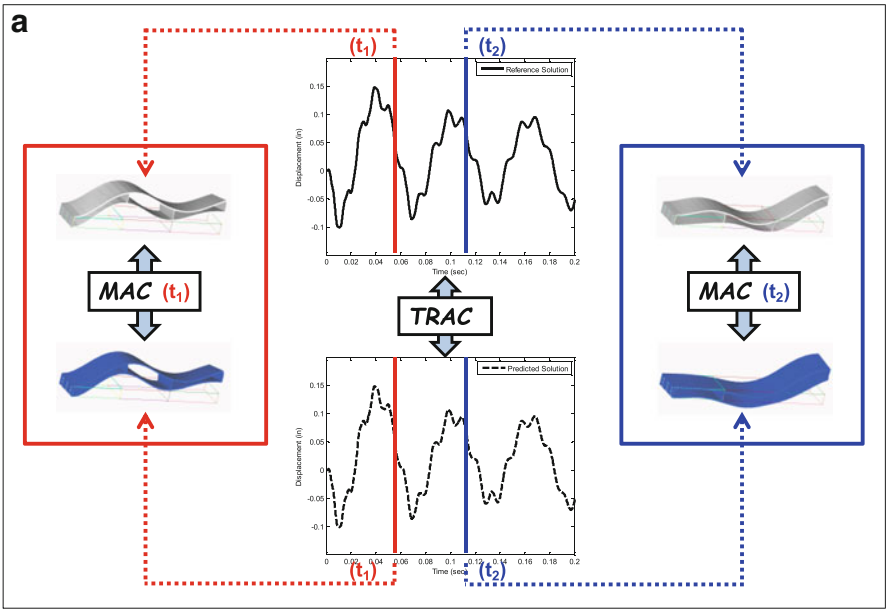

Fig. 14 (**a**, **b**) Schematic of the TRAC and MAC correlation tools

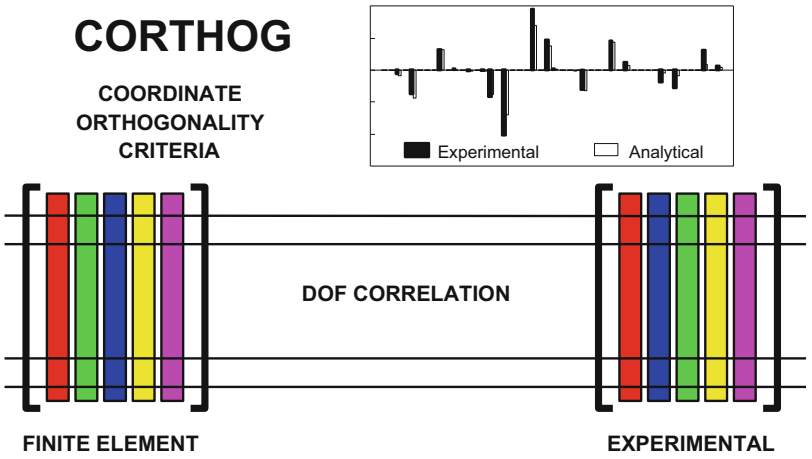

Fig. 15 Schematic of the coordinate orthogonality check

have been obtained analytically for each degree of freedom in an orthogonality check to what was actually obtained for each degree of freedom in a POC from test.

While many different formulations exist, the most basic form is the simple difference given as

$$\text{CORTHOG}_{ij}^{k} = \sum_{l=1}^{m} e_{ki} m_{kl} u_{lj} - u_{ki} m_{kl} u_{lj} \tag{69}$$

The CORTHOG is schematically shown in Fig. 15.

If the SEREP process is used for the formulation, then the CORTHOG can be very easily computed without the system mass matrix. Remember that the orthogonality can be written as

$$\text{ORT} = \; [U_n]^T [M_n] [U_n] = [U_a]^T [M_a] [U_a] = [U_a]^g \; [U_a] \tag{70}$$

and the pseudo orthogonality check can be written as

$$\text{POC} = [U_n]^T [M_n] [E_n] = [U_a]^T [M_a] [E_a] = [U_a]^g \; [E_a] \tag{71}$$

Therefore, for any particular mode pair, the CORTHOG can be written as shown schematically in Fig. 16.

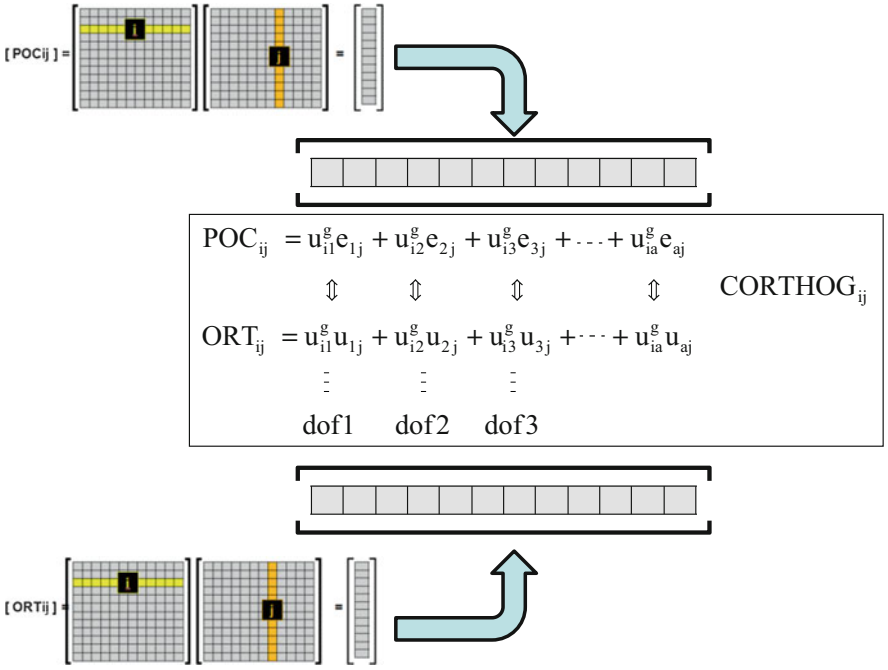

Fig. 16 Schematic of efficient coordinate orthogonality check computation

3 Closing Remarks

Any or all of these correlation tools can be used to help identify the similarities or differences that exist between the finite element model and the measured data. While in some industries (i.e., aerospace) there may be specific target values to achieve to meet contractual requirements, there really is no hard and fast rule as to acceptable levels of correlation. This really should be customized for particular applications based on design specification needs for a particular design and intended function (in the same way that tolerancing on a mechanical part will vary depending on how the part mates to other parts where some tolerances need to be much tighter than others depending on the design). It is also very important to note that some tools may provide better information for certain applications and other tools may be more useful for different applications.

For reference, some typical MAC and orthogonality are shown for a few academic structures to illustrate the use of these tools as seen in Fig. 17.

Correlation of Wing FEA Model and Test Data along with MAC Matrix.

FEA Flexible Mode Number	Experimental Flexible Mode Number	FEA Frequency (Hz)	Experimental Frequency (Hz)	Frequency % Difference	MAC Value (%)	15 Mode POC Value
1	1	87.87	90.63	-3.14	99.6	1.013
2	2	141.94	148.60	-4.69	99.2	1.026
3	3	219.27	228.83	-4.36	99.7	1.078
4	4	243.55	253.30	-4.00	99.5	1.048
5	5	411.43	427.25	-3.85	98.5	0.992
6	6	430.80	446.72	-3.70	97.7	1.056
7	7	506.55	528.47	-4.33	96.9	0.989
8	8	549.54	568.15	-3.39	99.0	0.958
9	9	681.00	673.10	1.16	93.8	1.022
10	10	749.30	783.14	-4.52	98.8	0.993

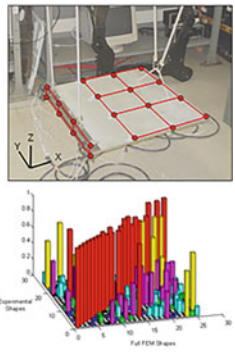

Correlation of Upright FEA Model and Test Data along with MAC Matrix.

FEA Mode Number	Experimental Mode Number	FEA Frequencies (Hz)	Experimental Frequencies (Hz)	Frequency % Difference	MAC Value (%)	20 Mode POC Value
1	1	26.03	26.17	-0.54	99.8	1.071
2	2	70.70	67.34	4.75	98.5	0.973
3	3	77.69	75.89	2.32	99.3	1.033
4	4	108.80	104.48	3.97	97.1	1.073
5	5	158.01	161.55	-2.24	98.9	1.048
6	6	269.88	270.00	-0.04	98.9	1.019
7	7	304.40	299.93	1.47	96.5	1.024
8	8	350.45	354.60	-1.18	98.5	0.979
9	9	419.36	419.22	0.03	94.3	0.483
10	10	457.13	482.15	-5.47	92.7	0.836
11	12	541.29	547.84	-1.21	96.6	0.995
12	11	563.47	538.20	4.48	86.3	0.785
13	13	777.29	771.76	0.71	90.3	1.002
14	14	779.61	791.18	-1.48	97.7	0.944
15	15	862.76	871.90	-1.06	84.3	0.795

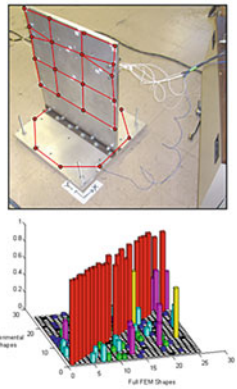

Correlation of Assembly Test-Data and FEA Model along with MAC Matrix.

Mode Number	(Fig. A4) FEA Freq. (Hz)	Experimental Frequencies (Hz)	Frequency % Difference	MAC Value	20 Mode POC Value
1	13.06	13.29	-1.76	98.8	0.993
2	25.2	26.03	-3.29	99.1	1.055
3	28.55	28.57	-0.07	99.1	1.075
4	53.41	52.36	1.97	98.6	1.019
5	70.25	72.28	-2.89	99.4	0.983
6	96.12	93.5	2.73	99.1	1.033
7	141.63	145.81	-2.95	99.1	1.052
8	185.54	191.72	-3.33	98.6	1.010
9	218.57	226.33	-3.55	97.3	0.998
10	231.27	237.02	-2.49	93.4	1.015

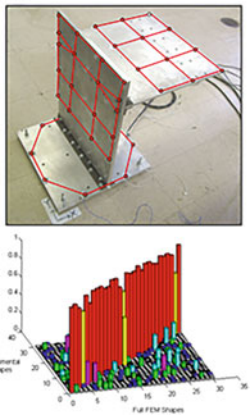

Fig. 17 Correlation of FEA model and test data along with MAC matrix and orthogonality check for two components (top and middle) used to form an assembly (bottom)

References

1. Guyan, R.J., "Reduction of Stiffness and Mass Matrices", AIAA Journal, Vol. 3, No 2, 1965, p. 380
2. Irons, B, "Structural Eigenvalue Problems: Elimination of Unwanted Variables", AIAA Journal, Vol 3, No 5, 1965,, pp. 961–962
3. O'Callahan,J.C., "A Procedure for an Improved Reduced System (IRS)", Seventh International Modal Analysis Conference, Las Vegas, Nevada, February 1989, pp. 17–21
4. Paz, M, "Dynamic Condensation", AIAA Journal, Vol22, No 5, May 1984, pp. 724–727
5. O'Callahan,J.C., Avitabile, P., Riemer,R., "System Equivalent Reduction Expansion Process", Seventh International Modal Analysis Conference, Las Vegas, Nevada, February 1989, pp. 29–37
6. Kammer,D.C., "A Hybrid Approach to Test Analysis Model Development for Large Space Structures", Journal of Acoustics and Vibrations,Vol 113, No 3, July 1991, pp. 325–332
7. Allemang,R.J. and Brown,D.L., "A Correlation Coefficient for Modal Vector Analysis", First International Modal Analysis Conference, Orlando, Florida, November 1982, pp. 110–116
8. Avitabile, P., O'Callahan,J.C., Milani,J. "Model Correlation and Orthogonality Criteria", Sixth International Modal Analysis Conference, Orlando, Florida, February 1988, pp. 1039–1047
9. Avitabile, P., O'Callahan,J., "Mass and Stiffness Orthogonality Checks without a Mass or Stiffness Matrix", Thirteenth International Modal Analysis Conference, Nashville, Tenn, February 1995, pp. 1515–1519
10. Lieven,N.A.J., Ewins,D.J., "Spatial Correlation of Mode Shapes, the Coordinate Modal Assurance Criteria (COMAC)", Sixth International Modal Analysis Conference, Orlando, Florida, February 1988, pp. 690–695
11. Hunt,D., "Application of an Enhanced Coordinate Modal Assurance Criterion", Tenth International Modal Analysis Conference, San Diego, California, February, 1992, pp. 66–71
12. Pechinsky,F., Avitabile, P., "Evaluation of DOF Correlation using the Coordinate Orthogonality Check", Thirteenth International Modal Analysis Conference, Nashville, Tennessee, February 1995, pp. 1313–1320

Bibliography

13. Allemang,R.J. and Brown,D.L., "A Correlation Coefficient for Modal Vector Analysis", First International Modal Analysis Conference, Orlando, Florida, November 1982, pp. 110–116
14. Avitabile,P., O'Callahan,J.C., Milani,J. "Model Correlation and Orthogonality Criteria", Sixth International Modal Analysis Conference, Orlando, Florida, February 1988, pp. 1039–1047
15. Avitabile,P., Li,P., Foster,T., Effects of DOF Selection on Orthogonality using Reduced System Matrices", Eleventh International Modal Analysis Conference, Orlando, Florida, February 1992, pp. 1073–1078
16. Avitabile,P., Pechinsky,F., O'Callahan, J.C., "Study of Modal Vector Correlation using Various Techniques for Model Reduction", Tenth International Modal Analysis Conference, San Diego, California, February, 1992, pp. 572–583
17. Avitabile,P., O'Callahan,J., "Mass and Stiffness Orthogonality Checks without a Mass or Stiffness Matrix", Thirteenth International Modal Analysis Conference, Nashville, Tenn, February 1995, pp. 1515–1519
18. Avitabile, P., Modal Model Correlation, University of Massachusetts Lowell, Copyright TX 4764-126 (1998 Dissertation)
19. Baker, M, "Review of Test/Analysis Correlation Methods and Criteria for Validation of Finite Element Models for Dynamic Analysis", Tenth International Modal Analysis Conference, San Diego, February 1992, pp. 984–990
20. Blades, EL, Craig, RR, "A Craig-Bampton Test-Analysis Model", Fifteenth International Modal Analysis Conference, Orlando, Florida, February 1997, pp. 1386–1391

21. Blaschke,PG, Bosch,R, Ewins, D, "The MAC Revisited and Updated", Fifteenth International Modal Analysis Conference, Orlando, Florida, February 1997147–154
22. Blelloch, PA, "Direct Correlation of Test-Analysis Cross-Orthogonality", Tenth International Modal Analysis Conference, San Diego, February 1992, pp. 998–1002
23. Blelloch,P., "Shape- and Matrix Based Sensor Selection Algorithms", Twenty-First International Modal Analysis Conference, Orlando, FL, February 2003
24. Brillhart, RD, Kammer, DC, "Evaluation of Optimal Modal Sensor Placement Using a System Realization Method", Twelfth International Modal Analysis Conference, Honolulu, Hawaii, February 1994, pp. 1401–1407
25. Carne,T.G., Dohrmann,C.R., "A Modal Test Design Strategy for Model Correlation, Thirteenth International Modal Analysis Conference, Nashville, Tennessee, February 1995, pp. 927–933
26. Chung, Y.T., Sernaker M.L., "Assessment of Target Mode Selection Criteria for Payload Modal Survey", 12th IMAC, 1994, Honolulu, Hawaii, pp. 272–279.
27. DeClerck,J.P., Avitabile,P., Development of Several New Tools for Pre-Test Modal Evaluation", Fourteenth International Modal Analysis Conference, Dearborn, Mich-igan, February 1996, pp. 1272–1277
28. Flanigan, CC, Hunt, DL, "Integration of Pretest Analysis and Model Correlation Methods for Modal Surveys", Eleventh International Modal Analysis Conference, Orlando, Florida, February 1993, pp. 444–448
29. Flanigan C. C. and Hunt D. L., 1993, "Integration of Pretest Analysis and Model Correlation Methods for Modal Surveys", Eleventh International Modal Analysis Conference, Orlando, FL, February 1993, pp. 444–448.
30. Flanigan, CC, Freymiller, JE, "Using Dynamic Expansion to Improve Test-Analysis Correlation", Twelfth International Modal Analysis Conference, Honolulu, Hawaii, February 1994, pp. 198–204
31. Foster,T., "Evaluation of DOF Selection for Modal Vector Correlation and Expansion Studies", Masters Thesis, University of Massachusetts Lowell, Lowell, Massachusetts, July 1993
32. Freed,A.M., Flannigan,C.C., "A Comparison of Test Analysis Model Reduction Methods", Eighth International Modal Analysis Conference, Orlando, Florida, February 1990, pp. 1344–1351
33. Friswell, MI, Garvey, SD, Penny, JET, "Model Reduction Using an Iterated IRS Technique", 5th International Conference on Recent Advances in Structural Dynamics, Southhampton, UK, July 1994, pp. 879–889
34. Goh, EL, Mottershead, JE, "On the Model Reduction Techniques for Finite Element Model Updating", NAFEMS/DTA International Conference on Structural Dynamics, Modeling, Test, Analysis and Correlation, Milton Keynes, July 1993, pp. 421–432
35. Gordis, J, "An Analysis of the Improved Reduced System (IRS) Model Reduction Procedure", Tenth International Modal Analysis Conference, San Diego, February 1992, pp. 471–479
36. Guyan, R.J., "Reduction of Stiffness and Mass Matrices", AIAA Journal, Vol. 3, No 2, 1965, p. 380
37. Gysin, HP, "Comparison of Expansion Method for FE Modeling Error Localization", Eighth International Modal Analysis Conference, Orlando, Florida, February 1990, pp. 195–204
38. Gysin, HP, "Expansion: The Achilles Heel of Fe Model Updating", Proceedings of the 15th International Seminar on Modal Analysis, September 1990, pp. 919–937
39. Hemez, FM, Farhat, C, "Comparing, Mode Shape Expansion Methods for Test-Analysis Correlation", Twelfth International Modal Analysis Conference, Honolulu, Hawaii, February 1994, pp. 1560–1567
40. Humbad, NG, Mallick, S, "Modal Comparison Criteria", Fifth International Modal Analysis Conference, London, England, February 1987, pp. 1191–1197
41. Hunt, DL, Peterson, EL, Vold, H, Williams, R, "Optimal Selection of Excitation Methods for Enhanced Modal Testing", AIAA paper, No. 84–1068, AIAA Dynamics Conference, Palm Springs, California, May 1984, pp. 549–553
42. Hunt,D., "Application of an Enhanced Coordinate Modal Assurance Criterion", Tenth International Modal Analysis Conference, San Diego, California, February, 1992, pp. 66–71

43. Imamovic, N, Ewins, D, "Optimization of Excitation DOF Selection for Modal Tests", Fifteenth International Modal Analysis Conference, Orlando, Florida, February 1997, pp. 1945–1951
44. Imregum, M, Ewins, D, "An Investigation into Mode Shape Expansion Techniques", Eleventh International Modal Analysis Conference, Orlando, Florida, February 1993, pp. 168–175
45. Irons, B, "Structural Eigenvalue Problems: Elimination of Unwanted Variables", AIAA Journal, Vol 3, No 5, 1965,, pp. 961–962
46. Irons, B, "Structural Eigenvalue Problems: Elimination of Unwanted Variables", AIAA Journal, Vol 3, No 5, 1965, pp. 961–962
47. J.O'Callahan, C.M.Chou, I.W.Lieu, "Determination of Rotational Degrees of Freedom for Moment Transfers in Structural Modifications", Third International Modal Analysis Conference, Orlando, Florida, January 1985, pp. 465–470
48. J.O'Callahan, P.Avitabile, R.Madden, I.W.Lieu, "An Efficient Method of Determining Rotational Degrees of Freedom from Analytical and Experimental Modal Data", Fourth International Modal Analysis Conference, Los Angeles, California, February 1986, pp. 50–58
49. J.O'Callahan, "Comparison of Reduced Model Concepts", Eighth International Modal Analysis Conference, Orlando, Florida, January 1990, pp. 422–430
50. Kammer, DC, "Test-Analysis Model Development Using the Exact Modal Reduction", The International Journal of Analytical and Experimental Modal Analysis, Oct 1987, pp. 174–179
51. Kammer,D.C., "A Hybrid Approach to Test Analysis Model Development for Large Space Structures", Journal of Acoustics and Vibrations, Vol 113, No 3, July 1991, pp. 325–332
52. Kammer D. C., "Sensor Placement for On-orbit Modal Identification and Correlation of Large Space Structures." Journal of Guidance, Control and Dynamics, V. 15. No. 2. pp. 251–259, 1991.
53. Kammer, DC, Triller, MJ, "Efficient Sensor Placement on On-Orbit Modal Identification of Sequentially Assembled Large Space Structures", Tenth International Modal Analysis Conference, San Diego, February 1992, pp. 954–964
54. Kammer, DC, "Effects of Noise on Sensor Placement for On-Orbit Modal Identification of Large Space Structures:, Journal of Dynamic System, Measurement and Control, Vol 114, September 1992, pp. 436–443
55. Kammer, DC, "Effects of Noise on Sensor Placement for On-Orbit Modal Identifi-cation of Large Space Structures:, Journal of Dynamic System, Measurement and Control, Vol 114, September 1992, pp. 436–443
56. Kammer D. C., Cessna J, Kostuch A., "An Effective Mass Measure for Selecting Free-Free Target Modes", Twenty-Third International Modal Analysis Conference, Orlando, FL, February 2005.
57. Kidder, RL, "Reduction of Structure Frequency Equations", AIAA, Vol 11, No 6, June 1973, p. 892
58. Kientzy,D., Richardson,M., Blakely,K., "Using Finite Element Data to Setup Modal Tests", Sound & Vibration, June 1989
59. Lallement,G. et al., "Optimal Selection of the Measured Degrees of Freedom and Application to a Method of Parameter Correlation", Ninth International Modal Analysis Conference, San Diego, California, 1991.
60. Lang,G.F., "Including Rotational Terms in a Modal Model...An Experimental Prelude", Sound & Vibration, November 1989
61. Larson C. B.. Zimmerman D. C.. and Marek, E. L., "A Comparison of Modal Test Planning Techniques: Excitation and Sensor Placement Using the NASA 8-Bay Truss", Twelfth International Modal Analysis Conference, Honolulu, HI, February 1994, pp. 205–211.
62. Larson C. B., Zimmerman D. C., and Marek, E. L., "A Comparative Study of Metrics for Modal Pretest Sensor and Actuator Selection Using the JPL/MPI Testbed Truss", Proceedings of the AIAA Dynamic Specialists Conference, Hilton Head, SC, 1994.
63. Levine-West, MB, Kissil, A, Milman, M, "Evaluation of Mode Shape Expansion Techniques on the Micro-precision Interferometer Truss", Twelfth International Modal Analysis Conference, Honolulu, Hawaii, February 1994, pp. 212–218

64. Lieven, NAJ, Ewins, D, "Expansion of Modal Data for Correlation", Eighth International Modal Analysis Conference, Orlando, Florida, February 1990, pp. 605–609
65. Lieven,N.A.J., Ewins,D.J., "Spatial Correlation of Mode Shapes, the Coordinate Modal Assurance Criteria (COMAC)", Sixth International Modal Analysis Conference, Orlando, Florida, February 1988, pp. 690–695
66. Lipkins, J., Vandeurzen, U., "The Use of Smoothing Techniques for Structural Modification Applications", Proceedings of the 12th International Seminar on Modal Analysis, Leuven Belgium, 1987, S1–3
67. Mains, M.L., "Orthogonality for Modal Vector Correlation: The Effects of Removing Degrees-of-Freedom", Thirty-first International Modal Analysis Conference, Orange County, California, 2013.
68. Mains, M.L., "Orthogonality for Modal Vector Correlation: The Effects of Removing Degrees-of-Freedom", Thirty-first International Modal Analysis Conference, Orange County, California, 2013.
69. Mains, M.L., "Orthogonality for Modal Vector Correlation: The Effects of Removing Degrees-of-Freedom", Thirty-first International Modal Analysis Conference, Orange County, California, 2013.
70. Mains, M, Vold, H, "Investigation of the Effects of Transducer Cross-Sensitivity and Misalignment Error on Modal Vector Correlation", Thirteenth International Modal Analysis Conference, Nashville, Tennessee, February 1995, pp. 1048–1056
71. Mains, M.L., "Orthogonality for Modal Vector Correlation: The Effects of Removing Degrees-of-Freedom", Thirty-first International Modal Analysis Conference, Orange County, California, 2013.
72. O'Callahan, JC, Lieu, IW, Chou, CM, "Determination of Rotational Degrees of Freedom for Moment Transfers in Structural Modifications", Third International Modal Analysis Conference, Orlando, Florida, February 1985, pp. 465–470
73. O'Callahan,J.C., "A Procedure for an Improved Reduced System (IRS)", Seventh International Modal Analysis Conference, Las Vegas, Nevada, February 1989, pp. 17–21
74. O'Callahan,J.C., Avitabile,P., Riemer,R., "System Equivalent Reduction Expansion Process", Seventh International Modal Analysis Conference, Las Vegas, Nevada, February 1989, pp. 29–37
75. O'Callahan, JC, "Comparison of Reduced Model Concepts", Eighth International Modal Analysis Conference, Orlando, Florida, February 1990, pp. 422–430
76. O'Callahan, JC, Li, P, "A Non-Smoothing SEREP Process for Modal Vector Expansion", Twelfth International Modal Analysis Conference, Honolulu, Hawaii, February 1994, pp. 232–238
77. O'Callahan, JC, Li, P, "An Automatic Selection of Reduced Degrees of Freedom", Twelfth International Modal Analysis Conference, Honolulu, Hawaii, February 1994, pp. 481–485
78. O'Callahan, JC, Li, P, "An Automatic Selection of Reduced Degrees of Freedom", Twelfth International Modal Analysis Conference, Honolulu, Hawaii, February 1994, pp. 481–485
79. O'Callahan, JC, Li, P, "The Effects of Modal Vector Expansion on Finite Element Model Updating", Thirteenth International Modal Analysis Conference, Nashville, Tennessee, February 1995, pp. 599–607
80. O'Callahan, JC, "Development of a General Pseudo Orthogonality Correlation Procedure", Thirteenth International Modal Analysis Conference, Nashville, Tennessee, February 1995, pp. 1013–1021
81. Park, YS, Kim, HB, "Sensor Placement Guide for Model Comparison and Improvement", Fourteenth International Modal Analysis Conference, Dearborn, Michigan, February 1996, pp. 404–409
82. Paz, M, "Dynamic Condensation", AIAA Journal, Vol22, No 5, May 1984, pp. 724–727
83. P.Avitabile, J.O'Callahan, E.Pan, "Effects of Various Model Reduction Techniques on Computed Response", Seventh International Modal Analysis Conference, Las Vegas, Nevada, February 1989, pp. 777–785

84. P.Avitabile, J.O'Callahan, J.Milani, "Comparison of System Characteristics Using Various Model Reduction Techniques", Seventh International Modal Analysis Conference, Las Vegas, Nevada, February 1989, pp. 1109–1115
85. P.Avitabile, Modal Model Correlation, University of Massachusetts Lowell, Copyright TX 4-764-126 (1998 Dissertation)
86. P.Avitabile, J.O'Callahan, C.M.Chou, V.Kalkunte, "Expansion of Rotational Degrees of Freedom for Structural Dynamic Modification", Fifth International Modal Analysis Conference, London, England, April 1987, pp. 950–955
87. P.Avitabile, Modal Model Correlation, University of Massachusetts Lowell, Copyright TX 4-764-126 (1998 Dissertation)
88. P.Avitabile, T.Foster, J.O'Callahan, "Comparison of Reduction vs. Expansion for Orthogonality Checks", Twelfth International Modal Analysis Conference, Honolulu, Hawaii, January 1994, pp. 225–231
89. P.Avitabile, Modal Model Correlation, University of Massachusetts Lowell, Copyright TX 4-764-126 (1998 Dissertation)
90. P.Avitabile, Modal Model Correlation, University of Massachusetts Lowell, Copyright TX 4-764-126 (1998 Dissertation)
91. Pechinsky,F., Avitabile,P., Coordinate Orthogonality Check (CORTHOG)", Twelfth International Modal Analysis Conference, Honolulu, Hawaii, February 1993, pp. 753–760
92. Pechinsky,F., Avitabile,P., "Evaluation of DOF Correlation using the Coordinate Orthogonality Check", Thirteenth International Modal Analysis Conference, Nashville, Tennessee, February 1995, pp. 1313–1320
93. Penny, JET, Friswell, MI, Garvey, SD, "The Automatic Choice of Measurement Locations for Dynamic Testing", Tenth International Modal Analysis Conference, San Diego, February 1992, pp. 30–36
94. Penny,JE, Friswell,MI, Garvey,SD, "The Automatic Choice of Meas-urement Location for Dynamic Testing", Tenth International Modal Analysis Conference, San Diego, CA, February 1992.
95. Pickrel C. R., "A Practical Approach to Modal Pretest Design", Mechanical Systems and Signal Processing, Vol. 13. No. 2, pp. 271–295, 1999.
96. Roy, N, Girard, A, Bugeat, LP, "Expansion of Experimental Mode Shapes - An Improvement of the Projection Technique", Eleventh International Modal Analysis Conference, Orlando, Florida, February 1993, pp. 152–158
97. Schedlinski, C, Link, M, "An Approach to Optimal Pick-up and Exciter Placement", Fourteenth International Modal Analysis Conference, Dearborn, Michigan, February 1996, pp. 376–382
98. Urgueira, A, Lieven, NAJ, Ewins, D, "A Generalized Reduction Method for Modal Testing", Eighth International Modal Analysis Conference, Orlando, Florida, February 1990, pp. 222–227
99. Yap Keng C., Zimmerman D.C., "Optimal Sensor Placement for Dynamic Model Correlation", Eighteenth International Modal Analysis Conference, San Antonio, TX, February 2000.

Model Updating

16

John E. Mottershead, Michael Link, Michael I. Friswell, and Carsten Schedlinski

Contents

J. E. Mottershead (✉)
School of Engineering, University of Liverpool, Liverpool, UK
e-mail: j.e.mottershead@liverpool.ac.uk

M. Link
Department of Civil and Environmental Engineering, University of Kassel, Kassel, Germany
e-mail: link@uni-kassel.de

M. I. Friswell
College of Engineering, Swansea University, Swansea, UK
e-mail: M.I.Friswell@swansea.ac.uk

C. Schedlinski
ICS Engineering GmbH, Dreieich, Germany
e-mail: sched@ics-engineering.com

R. Allemang, P. Avitabile (eds.), *Handbook of Experimental Structural Dynamics*,
https://doi.org/10.1007/978-1-4614-4547-0_18

Abstract

The term "model updating" describes the process of adjusting the parameters of a finite element model in order that its predictions, in terms of eigenvalues and eigenvectors, are in agreement with measurements obtained by modal testing. The sensitivity method described in this chapter has been implemented numerous times in commercial codes and applied successfully in industry. It has become a mature technology in regular use in the automotive and aerospace industries worldwide. However, there are various subtleties surrounding the application of model updating that are discussed here for the benefit of potential users. Firstly there must be an awareness of the frequency range in which the updated model is to be applied. The available data is generally insufficient to define the system parameters without the use of additional information provided by regularization. And the choice of parameters is of critical importance: it is not only a matter of choosing sensitive parameters; they should also be chosen as part of an engineering understanding of the dynamics of the system. Careful choice of parameters, together with regularization, will lead to validated models that predict the behavior of the system beyond the scope of the original test data.

Keywords

Model updating · Sensitivity · Parameterization · Regularization · Stochastic model updating · Validation

Nomenclature

$\mathbf{f}$	Vector of forces
$\mathbf{x}$	Displacement vector
$\mathbf{z}$	Vector of outputs
$\mathbf{C}$	Damping matrix
$\mathbf{G}$	Matrix of sensitivities
$\mathbf{H}$	Matrix of frequency response functions
$\mathbf{K}$	Stiffness matrix
$\mathbf{M}$	Mass matrix
$\mathbf{P}$	Matrix of stiffness-matrix eigenvalues
$\mathbf{W}$	Weighting matrix
λ	Eigenvalue
$\boldsymbol{\theta}$	Vector of parameters

φ	Eigenvector
$\boldsymbol{\Psi}$	Matrix of stiffness-matrix eigenvectors
$Cov(\bullet, \bullet)$	Covariance matrix
$(\bar{\bullet})$	Mean

1 Introduction

Modern and highly sophisticated finite element (FE) procedures are available for structural analysis, yet practical application often reveals considerable discrepancy between analytical prediction and test results. The way to reduce this discrepancy is to modify the modeling assumptions and parameters until the correlation of analytical predictions and experimental results satisfies practical requirements. Classically, this is achieved by a trial-and-error approach, which is generally time-consuming and may not be feasible in some cases. Thus computational procedures have been developed to update the parameters of analytical models using test data. In particular, modal data (natural frequencies and mode shapes) extracted from measured frequency response data have found broad application as a target for model parameter adjustment. This procedure was described in detail by Natke [52] and by the present authors [20, 45, 49] and in recent years has developed into a mature technology applied successfully for the correction of industrial-scale FE models.

One of the first attempts to address the problem of updating or "correcting" finite element models by using vibration measurements was made by Collins, Hart, Hasselman, and Kennedy [11]. This paper has since proven to be extraordinarily influential in providing the common basis for modern model updating codes and techniques using the sensitivity method and probabilistic model updating – including Bayesian model updating. A review of model updating methods was carried out by Mottershead and Friswell [45], and this was followed by the research monograph *Finite Element Model Updating in Structural Dynamics* [20]. In the review paper, the techniques were separated into two categories: Lagrange multiplier methods and penalty function methods. The penalty methods were then divided according to the type of data used: natural frequencies and mode shapes or frequency response functions (FRFs). The research monograph gives more detail. The Lagrange multiplier methods are called direct methods: they have the advantage that closed-form solutions are often available, but their disadvantages include (i) lack of physical meaning of the updated model, (ii) failure to represent known connectivities, and (iii) the need for model reduction or eigenvector expansion techniques because of the mismatch of dimensions between the FE model and the measurements. Various approaches were tried to overcome these problems, including Kenigsbuch and Halevi [35] and Smith [63], both of which appeared in a special issue of *Mechanical Systems and Signal Processing* on model updating. Yuen [71] developed a direct method suitable for use with incomplete modal measurements. Formulation as an inverse eigenvalue problem also leads to direct model updating solutions [69], with quadratic orthogonality constraints [13] and

model structure preservation [68]. In active vibration control, the concept of assigning certain chosen poles while the other poles of the system remain unchanged can be attractive in many applications because instability due to spillover is made impossible. The same principle was applied to model updating by Carvalho et al. [10], Mao and Dai [42], and Kuo and Datta [38] to prevent the occurrence of spurious modes.

The penalty function methods in the review paper [45] are called iterative methods in the research monograph [20]. They are also known as sensitivity methods and sometimes called model-based methods. An important part of the sensitivity method is the parameterization of the finite element model and regularization of the ill-conditioned updating equations [3, 21, 22, 47]. Further contributions include Hua et al. [31] who developed an adaptive procedure for adjusting the regularization parameter between Newton iterations. Webber et al. [67] addressed the problem of linear regularization and Newton iterations affecting each other in an undesirable way. Their approach includes nonlinear updating algorithms with consistent regularization of the updating parameters relative to an a priori estimate using line search and stopping criteria together with generalized cross-validation for estimating the optimal regularization parameter. Goulet et al. [26] proposed a model parameterization method based on model falsification – i.e., on the principle that in science, data cannot truly validate a hypothesis; it can only be used to falsify it. A space of possible models (a combination of parameters) was then generated, and an error-domain falsification procedure was used to reject instances that have unlikely differences (residuals) between predictions and measurements. Wang et al. [66] carried out nonlinear model updating in the frequency domain by a sensitivity-based approach that firstly localized and characterized discrete nonlinearities before identifying the nonlinear parameters using a semi-analytical output residual. A tutorial on the sensitivity method in model updating was presented by Mottershead et al. [49].

The area of greatest research activity in very recent times has been in the development of probabilistic (and non-probabilistic) methods for uncertainty quantification in model updating, reviewed in detail by Simoen et al. [62] covering sensitivity, Bayesian, interval, and fuzzy methods, and with particular emphasis on damage detection. Among many notable contributions, Jacquelin et al. [33] introduced a direct method using random matrix theory. Adhikari and Friswell [1] represented randomized beam-bending properties using the Karhunen-Loève expansion. Goller et al. [24] proposed a robust method using multidimensional Gaussian kernel density functions in the case of insufficient data, thereby enabling the quantification of design insensitivity. Mthembu et al. [50] used Bayesian evidence for model selection, essentially selection from a finite set of candidate parameter groups based on plausibility. Batou [7] considered uncertainty in the placement and orientation of sensors and actuators, optimizing the sensitivity of measured data and the robustness of updating parameters.

A distinction should be made regarding the interpretation of uncertainty. Epistemic uncertainty can be reduced by applying additional data. This applies, for example, to the case in model updating when measurements are noisy and the

parameters are distinct but are estimated using probabilistic methods in terms of mean values and covariances. The standard deviations may be used as a measure of confidence in the estimated means. The other viewpoint on uncertainty is the frequentist one, known as aleatory uncertainty, which is irreducible, and represents, for example, the distribution on the depth of a finite set of nominally identical beams. In this case the distribution on the depths of the beams is physically meaningful, as well as being useful to a designer wishing to understand the variation in performance resulting from the distribution. Bayesian approaches are inherently epistemic. Early examples include Beck and Katafygiotis [8] and Katafygiotis and Beck [34], whereby experimental data is used to progressively revise the updating parameters expressed by a posterior probability density function. One problem with the Bayesian approach has been the requirement for large computation, now largely overcome as demonstrated by Goller et al. [25] using parallelization of the updating code together with the transitional (Markov chain Monte Carlo) MCMC algorithm, which identifies parameter regions with the highest posterior probability. Behmanesh et al. [9] used a hierarchical Bayesian method to account for inherent variability due to temperature changes, temperature gradient, wind speed, and traffic flow in civil engineering structures. The reader is referred to Yuen [70] for a detailed exposition of Bayesian inference in model updating.

Mares et al. [43] and Mottershead et al. [48] were the first to use the term *stochastic model updating*. Hua et al. [30] and Khodaparast et al. [36] developed efficient perturbation methods, applicable to the aleatory (frequentist) problem of multiple, nominally identical test structures. Govers and Link [27] extended the classical sensitivity-based model updating procedure for the determination of parameter mean values and covariances; similar to the perturbation approach, this technique was based on an assumption of small variability. It was demonstrated very convincingly using data obtained by repeated disassembly and reassembly of the DRL AIRMOD structure [28]. Hua et al. [32] developed a reliability index to assess the quality of a model updated using a perturbation approach. A thorough comparison of sensitivity and Bayesian methods using test data from the AIRMOD structure was given by Patelli et al. [54]. Au [5] considered the connections between the Bayesian and frequentist approaches and concluded that results obtained by the two methods were very similar in the case of little or no modeling error.

Uncertainty quantification without the restriction of small variability generally demands multiple runs of deterministic finite element code, and the expense of doing so has led to the extensive use of surrogate models. The simplest of these are polynomial input-output response surfaces, as described, for example, by Fang et al. [16] with Monte Carlo simulation (MCS) and significance evaluation using analysis of variance (ANOVA). Zhang et al. [72] used the polynomial chaos expansion as a surrogate as well as an evolutionary MCMC algorithm where a population of chains is updated by mutation to avoid being trapped in local basins of attraction. Non-probabilistic methods have also been applied in model updating. Khodaparast et al. [37] used a Kriging model in interval updating to construct a bounding hypercube over the space of parameter uncertainty. This has the advantage of generating not merely a fitted surrogate but the most probable input-output representation that

reproduces the finite element model exactly at the training points. Fang et al. [17] developed an interval response surface by removing the interaction terms from a second-order polynomial response surface and completing the square. This had the advantage, not only of efficiency, but also it also avoided the overestimation frequently encountered with interval arithmetic.

This chapter provides a basic introduction to the most important procedures of computational model updating and includes simple tutorial examples to reinforce the reader's understanding together with a typical model updating example taken from the automotive industry, in Sect. 6.

2 Parameter Estimation

Parameter updating techniques aim to fit the parameters of a given initial analytical model in such a way that the model behavior corresponds as closely as possible to the measured behavior. The resulting parameters represent estimated values rather than true values since the test data are unavoidably polluted by unknown random and systematic errors. Also the mathematical structure of the initial analysis is not unique depending on the idealizations made by the analyst for the real structure. The residuals containing the test/analysis differences may be formed by force and response equation errors, by eigenfrequency and mode shape errors, and by frequency response errors.

The first step in parameter estimation is the definition of a residual containing the difference between analytical and measured structural behavior

$$\boldsymbol{\varepsilon}_z = \mathbf{z}_m - \mathbf{z}\left(\boldsymbol{\theta}\right) \tag{1}$$

where $\mathbf{z}_m$ denotes the measurement. The analytical prediction is $\mathbf{z}(\boldsymbol{\theta})$ and $\boldsymbol{\theta}$ represents the parameters to be updated. The analytical predictions are calculated from the equation of motion in the frequency domain:

$$\mathbf{f} = \mathbf{Z}\left(\mathrm{i}\omega\right)\mathbf{x}; \quad \mathbf{Z}\left(\mathrm{i}\omega, \boldsymbol{\theta}\right) = \left[-\omega^2\mathbf{M}\left(\boldsymbol{\theta}\right) + \mathrm{i}\omega\mathbf{C}\left(\boldsymbol{\theta}\right) + \mathbf{K}\left(\boldsymbol{\theta}\right)\right] \tag{2}$$

where $\mathbf{Z} \in \mathbb{C}^{N \times N}$ is the dynamic stiffness matrix, with the finite element mass matrix $\mathbf{M}$, the damping matrix $\mathbf{C}$, and the stiffness matrix $\mathbf{K}$. The excitation frequency is denoted by ω, the excitation force vector is $\mathbf{f}$, and $\mathrm{i} = \sqrt{-1}$.

Typically the eigenvalue λ and the mode shape φ are used as the analytical predictions. These are calculated from the undamped eigenvalue problem $[-\lambda\ \mathbf{M}(\boldsymbol{\theta}) + \mathbf{K}(\boldsymbol{\theta})]\varphi = \mathbf{0}$ while the complex frequency response functions $\mathbf{H}(\omega) = \mathbf{Z}^{-1}$ may be determined by inversion of Eq. (2).

The objective is to minimize

$$J(\boldsymbol{\theta}) = \boldsymbol{\varepsilon}_z^T \mathbf{W}_\varepsilon \boldsymbol{\varepsilon}_z = \boldsymbol{\varepsilon}_z^T \mathbf{W}_v^T \mathbf{W}_v \boldsymbol{\varepsilon}_z \tag{3}$$

where the symmetric weighting matrix $\mathbf{W}_\varepsilon$ has been included to account for the importance of each individual term in the residual vector. $\mathbf{W}_\varepsilon$ is difficult to estimate, although at the very least this weighting should include scaling to equalize the effect of amplitude and a reasonable choice is $\mathbf{W}_\varepsilon = [\text{diag}(\mathbf{z}_m)]^{-2}$. In general the model response vector $\mathbf{z}(\boldsymbol{\theta})$ represents a nonlinear function of the parameters resulting in a nonlinear minimization problem. One of the techniques to solve this nonlinear optimization problem is to expand the model response vector into a Taylor series about the current parameter estimate, $\boldsymbol{\theta} = \boldsymbol{\theta}_i$, truncated after the linear term and leading to the linearized expression:

$$\boldsymbol{\varepsilon}_z \approx \mathbf{r}_i - \mathbf{G}_i \ (\boldsymbol{\theta} - \boldsymbol{\theta}_i) = \mathbf{z}_m - \mathbf{z}_i - \mathbf{G}_i \ \Delta\boldsymbol{\theta}_i \tag{4}$$

where $\mathbf{r}_i = \mathbf{z}_m - \mathbf{z}_i$ denotes the residual, the difference between the measured and analytically predicted outputs, $\mathbf{z}_m$ and $\mathbf{z}_i = \mathbf{z}(\boldsymbol{\theta}_i)$, at the ith iteration. The sensitivity matrix $\mathbf{G}_i$ is given by

$$\mathbf{G}_i = \left[\frac{\partial z_j}{\partial \theta_k}\right]_{\boldsymbol{\theta}=\boldsymbol{\theta}_i} \tag{5}$$

where $j = 1, 2, \ldots, q$ denotes the output data points and $k = 1, 2, \ldots, p$ is the parameter index. The sensitivity matrix $\mathbf{G}_i$ is computed at the current value of the complete vector of parameters $\boldsymbol{\theta} = \boldsymbol{\theta}_i$. The error, $\boldsymbol{\varepsilon}_z$, is assumed to be small for parameter $\boldsymbol{\theta}$ in the vicinity of $\boldsymbol{\theta}_i$.

The minimization $\partial J/\partial \Delta\boldsymbol{\theta}_i = 0$ of the weighted objective function (3) together with Eq. (4) yields the linear equation system:

$$\mathbf{W}_v \mathbf{G}_i \Delta\boldsymbol{\theta}_i = \mathbf{W}_v \mathbf{r}_i \tag{6}$$

which at each iteration step i is solved for $\Delta\boldsymbol{\theta}_i$ and the model is then updated to give

$$\boldsymbol{\theta}_{i+1} = \boldsymbol{\theta}_i + \Delta\boldsymbol{\theta}_i . \tag{7}$$

This procedure continues until consecutive estimates $\boldsymbol{\theta}_i$ and $\boldsymbol{\theta}_{i+1}$ are sufficiently converged.

The case when fewer measurements than parameters are available in Eq. (6) ($q < p$) leads to an underdetermined system, whose solution is not unique. Indeed, if $\text{rank}(\mathbf{G}_i) = q$ and $\mathbf{r}_i \in \text{range}(\mathbf{G}_i)$, then the model is able to reproduce the measurements, i.e., $\boldsymbol{\varepsilon}_z = \mathbf{0}$. Even if a minimum norm or a minimum parameter change solution is selected, the resulting parameters will in general not retain their physical meaning. In parameter updating the number of measurements should always be made larger than the number of parameters ($q > p$) which yields overdetermined

equation systems. A very effective way of choosing suitable parameters is by the subset selection described by Lallement and Piranda [39] and Friswell et al. [21]. The data should of course be sensitive to the selected parameters, which must be justified by physical understanding of the structure and the test arrangement. For the overdetermined case, the solution of Eq. (6) with respect to $\Delta\boldsymbol{\theta}_i$ gives an improved parameter estimate as

$$\Delta\boldsymbol{\theta}_i = \left[\mathbf{G}_i^T \mathbf{W}_{\boldsymbol{\varepsilon}} \mathbf{G}_i\right]^{-1} \mathbf{G}_i^T \mathbf{W}_{\boldsymbol{\varepsilon}} \mathbf{r}_i. \tag{8}$$

Even in the overdetermined case, the condition of the sensitivity matrix $\mathbf{G}$ plays an important role for the accuracy and the uniqueness of the solution. A fundamental requirement to obtain a solution is that rank $\left[\mathbf{G}_i^T \mathbf{W}_{\boldsymbol{\varepsilon}} \mathbf{G}_i\right] = p$.

3 Modeling Errors and Measurement Inaccuracy

Model updating is essentially a process of adjusting certain parameters of the finite element model. The user should be aware of numerous sources of modeling error and make necessary adjustments particularly those aspects of the model that cannot the corrected by changing the values of selected model updating parameters. Examples of such errors, listed in categories (1) and (2) below, are related to the mathematical structure of the model and generally referred to as *model structure errors*. These errors cannot be eliminated by model updating and should be eliminated or reduced by careful interrogation of the model before the application of model updating techniques. The errors listed under category (3) are typical of those that can be corrected by model updating:

1. Idealization errors resulting from the assumptions made to characterize the mechanical behavior of the physical structure. Such errors typically arise from:
   - Simplifications of the structure, for example, when a plate is treated like a beam, which might or might not be erroneous depending on the length-to-width ratio of the plate and the frequency range to be covered.
   - Inaccurate assignment of mass properties, for example, when distributed masses are modeled with too few lumped masses or when rotational inertia is disregarded.
   - When the finite element formulation neglects particular properties, for example, when the influence of transverse shear deformation or warping due to torsion in beam elements is neglected.
   - Errors in the connectivity of the mesh, i.e., some elements are not connected or are connected to a wrong node.
   - Erroneous modeling of boundary conditions, for example, when an elastic foundation is assumed to be rigid.

- Erroneous modeling of joints, for example, when an elastic connection is assumed to be rigid (clamped) or when an eccentricity of a beam or a plate connection is omitted from the model.
- Erroneous assumptions for the external loads.
- Erroneous geometrical shape assumptions.
- A nonlinear structure assumed to behave linearly.

2. Discretization errors introduced by numerical methods such as those inherent in the finite element method, for example:
   - Discretization errors when the finite element mesh is too coarse so that the modal data in the frequency of interest is not fully converged.
   - Truncation errors in order reduction methods such as static condensation.
   - Poor convergence and apparent stiffness increase due to element shape sensitivity.
3. Erroneous assumptions for model parameters, for example:
   - Material parameters such as Young's modulus or mass density
   - Cross section properties of beams such as area moments of inertia
   - Shell/plate thicknesses
   - Spring stiffnesses
   - Nonstructural mass

When the model includes idealization and discretization errors, it may only be updated in the sense that the deviations between test and analysis are minimized. The same happens when the selected correction parameters are not consistent with the real source and the location of the error. The parameters in such cases may lose their physical meaning after updating. A typical result of updating such *inconsistent* models is that they may be capable of reproducing the test data but may not be useful to predict the system behavior beyond the frequency range used in the updating. Similarly, they may not be able to predict the effects of structural modifications or to serve as a substructure model to be assembled as part of a model of the overall structure.

The aim of all structural analyses to predict the structural response can only be achieved if all three kinds of modeling errors are minimized with respect to the given purpose of the structural analysis. Models that fulfil these requirements shall be called *validated models*. Model quality must therefore be assessed in three steps:

Step 1: Assessment of idealization and numerical method errors (model structure errors) prior to parameter updating.

Step 2: Correlation of analytical model predictions and test results and selection of correction parameters.

Step 3: Assessment of model quality after parameter updating. Since a unique solution cannot be expected, this requirement must be related to the intended purpose for which the model is used, for example:

- To predict the system behavior to types of load or response other than those used in the test
- To predict the system behavior beyond the frequency range and/or at degrees of freedom other than those used for updating
- To predict the effects of structural modifications
- To check if the model, when used as a substructure within an assembled complete structure, will improve the response of the whole model

The validation of updated finite element models is discussed in more detail in Sect. 9.

4 Sensitivity Analysis

In practice, the first step is the definition of a residual. In this section we consider the following residuals, representing probably the most widely used techniques: real eigenvalues, real mode shapes, and the frequency-domain displacement residual.

A comprehensive selection of these and other residuals with special consideration of statistically based weighting and the statistical properties of the parameter estimates is given by Natke et al. [53].

4.1 Undamped Eigenvalue Residual

The linearized undamped eigenvalue residuals are defined by the differences between the vector of measured eigenvalues $\boldsymbol{\lambda}_m$ and their analytical counterparts $\boldsymbol{\lambda}(\boldsymbol{\theta})$, which being undamped are entirely real. The eigenvalues in this case are defined as the squares of the system natural frequencies, $\lambda_j = \omega_j^2, \quad j = 1, 2, \ldots,$ at the linearization point, "*i*." Thus the eigenvalue residual and sensitivity are given by Eqs. (4), (5), and (6) when $\mathbf{z}(\boldsymbol{\theta}) = \boldsymbol{\lambda}(\boldsymbol{\theta})$; $\mathbf{z}_m = \boldsymbol{\lambda}_m$. It is necessary to ensure that the analytical and measured eigenvalues correspond to the same physical mode. This process, usually referred to as *mode pairing*, may be achieved by carrying out a modal correlation using the modal assurance criterion (MAC) [20]. Special care has to be taken for systems with repeated roots (e.g., axisymmetric systems) where arbitrary combination of mode shapes (analytically and experimentally) may cause significant degradation of MAC values. To overcome this, a general method for transforming analytical eigenvectors is, for instance, described in Schedlinski and Staples [58], which allows for an easy and especially automated compensation of the effect.

The terms in the sensitivity matrix may be determined analytically [18] by differentiation of the undamped eigenvalue equation:

$$\frac{\partial \lambda_j}{\partial \theta_k} = \boldsymbol{\varphi}_j^T \left[-\lambda_j \frac{\partial \mathbf{M}}{\partial \theta_k} + \frac{\partial \mathbf{K}}{\partial \theta_k} \right] \boldsymbol{\varphi}_j \tag{9}$$

where $\mathbf{M}$, $\mathbf{K} \in \Re^{N \times N}$ are the finite element mass and stiffness matrices, respectively, and φ_j is the jth mass normalized mode shape. It is seen that only the jth eigenvalue and eigenvector are needed to calculate all the jth eigenvalue sensitivities. As well as the analytical approach to calculating the sensitivity matrix terms, it is also possible to obtain numerical approximations by the simple procedure of perturbing the parameters in turn by a suitably small quantity and determining numerically the change in the predicted eigenvalues and eigenvectors. Although efficient procedures exist in finite element codes such as MSC.NASTRAN, there is a considerable advantage in using analytically determined sensitivities when large-scale structures are to be updated.

4.2 Undamped Mode-Shape Residual

The linearized undamped mode-shape residuals are the differences between the measured mode shapes at a restricted number of degrees of freedom corresponding to the location of sensors and the analytical mode shapes at the same coordinates. The differences are determined at $N_m < N$ measured degrees of freedom. Thus the mode-shape residual and sensitivity are given by Eqs. (4), (5), and (6) when $\mathbf{z} = \varphi(\boldsymbol{\theta})$; $\mathbf{z}_m = \varphi_m$, where the vectors $\varphi(\boldsymbol{\theta})$ and φ_m may contain many concatenated vectors of the different analytical and measured mode shapes, respectively. The analytical and experimental mode shapes should be normalized in the same way.

The determination of mode-shape sensitivities is a significant computational task, and several approaches are available. In this chapter we consider only the method of Fox and Kapoor [18]. The method, based on expanding the gradients into a weighted sum of the eigenvectors, is widely used due to its simplicity of implementation:

$$\frac{\partial \boldsymbol{\varphi}_j}{\partial \theta_k} = \sum_{h=1}^{H} a_{jkh} \boldsymbol{\varphi}_h; \quad H \leq N \tag{10}$$

which, after substitution of Eq. (10) into the derivative of the eigenvalue equation, produces the factor a_{jkh} in the form:

$$a_{jkh} = \frac{\boldsymbol{\varphi}_h^T \left(-\lambda_j \frac{\partial \mathbf{M}}{\partial \theta_k} + \frac{\partial \mathbf{K}}{\partial \theta_k} \right) \boldsymbol{\varphi}_j}{\left(\lambda_j - \lambda_h \right)}; \quad h \neq j \tag{11}$$

and

$$a_{jkj} = -\frac{1}{2} \boldsymbol{\varphi}_j^T \left(\frac{\partial \mathbf{M}}{\partial \theta_k} \right) \boldsymbol{\varphi}_j. \tag{12}$$

This expansion is exact if $H{=}N$ modes are used. For $H < N$ the expansion represents an approximation depending on the number of modal terms. Corrections

to this approach have been investigated by several authors. Equations (10) and (11) show that the expansion contains large factors a_{jkh} for neighboring eigenvalues $\lambda_j \approx \lambda_h$ that can cause convergence problems. Nelson's method [20] has the advantage that only the mode shape of interest is required but can be very time-consuming in the case of large-scale finite element models. The antiresonance residual may be used as an alternative to the undamped mode-shape residual, as was considered by D'Ambrogio and Fregolent [12].

4.3 Frequency-Domain Displacement Response Residual

The frequency response error linearized at $\boldsymbol{\theta}$ is obtained from the differences of the measured and the analytical frequency response at the measured degrees of freedom $n_m < n$. The analytical frequency response is given by

$$\mathbf{x}(\omega, \boldsymbol{\theta}) = \mathbf{H}(\omega, \boldsymbol{\theta})\, \mathbf{f}_m(\omega) \tag{13}$$

at those degrees of freedom that coincide with the measured ones.

The sensitivity matrix $\mathbf{G}_r$ of the frequency response may be obtained by using the identity

$$\partial \mathbf{H}/\partial \theta_k = -\mathbf{H}\,(\partial \mathbf{Z}/\partial \theta_k)\,\mathbf{H} \tag{14}$$

where

$$\mathbf{H}(\omega) = \mathbf{Z}^{-1} = \left[-\omega^2 \mathbf{M} + \mathrm{i}\omega \mathbf{C} + \mathbf{K}\right]^{-1}. \tag{15}$$

Thus,

$$\begin{aligned} \mathbf{G}_r &= \frac{\partial \mathbf{x}}{\partial \theta_k} \\ &= -\mathbf{H}(\omega, \boldsymbol{\theta}) \left[-\omega^2 \frac{\partial \mathbf{M}}{\partial \theta_k} + \mathrm{i}\omega \frac{\partial \mathbf{C}}{\partial \theta_k} + \frac{\partial \mathbf{K}}{\partial \theta_k}\right] \mathbf{x}(\omega, \boldsymbol{\theta}); \quad k = 1, 2, \ldots, p. \end{aligned} \tag{16}$$

The frequency response function matrix $\mathbf{H}(\omega, \boldsymbol{\theta}) = \left[-\omega^2 \mathbf{M}(\boldsymbol{\theta}) + \mathrm{i}\omega \mathbf{C}(\boldsymbol{\theta}) + \right.$ $\left. + \mathbf{K}(\boldsymbol{\theta})\right]^{-1}$ may be expressed either by

$$\mathbf{H}(\omega, \boldsymbol{\theta}) = \sum_{j=1}^{q} \boldsymbol{\varphi}_j \boldsymbol{\varphi}_j^T / \left(\omega_j^2 - \omega^2 + \mathrm{i}2\omega\omega_j \zeta_j\right) \tag{17}$$

in the case of proportional or modal damping or by

$$\mathbf{H}\left(\omega, \boldsymbol{\theta}_{(i)}\right) = \sum_{j=1}^{2q} \boldsymbol{\psi}_j \boldsymbol{\psi}_j^T / \left(\mathrm{i}\omega - \eta_j\right) \tag{18}$$

for the general case of nonproportional damping where η_j and $\boldsymbol{\psi}_j$ denote the complex eigenvalues and eigenvectors. In both cases q represents the number of modes included in the sum, and the terms in the eigenvectors are those corresponding to the measured coordinates.

One problem with the frequency response formulation is the measured, and analytical FRF peaks do not coincide leading to large frequency-domain displacement errors. This problem is particularly pronounced when close modes cross over each other such that the orders of the test and analytical modes are different. A possible solution is to firstly update the **M** and **K** matrices using a different residual. The peaks then become closely aligned, and the frequency-domain displacement response residual can be used to update the damping matrix **C**. This approach is described in more detail in Sect. 9.

5 Regularization

The treatment of ill-conditioned, noisy systems of equations is a problem central to finite element model updating [3, 22, 51, 65]. Such equations often arise in the correction of finite element models by using vibration measurements. The classical weighted least squares method described above can be extended in cases where it is difficult to obtain a convergent solution because of an ill-conditioned sensitivity matrix. The objective function, Eq. (3), is extended by the requirement that the parameter changes $\Delta\boldsymbol{\theta}$ should be minimized, to give

$$J\left(\boldsymbol{\theta}\right) = \boldsymbol{\varepsilon}_z^T \mathbf{W}_\varepsilon \boldsymbol{\varepsilon}_z + \mu^2 \Delta\boldsymbol{\theta}_i^T \mathbf{W}_\theta \Delta\boldsymbol{\theta}_i. \tag{19}$$

The parameter weighting matrix $\mathbf{W}_\theta$ should be chosen to reflect the uncertainty in the initial parameter estimates [44, 55, 67]. This may be formally related to Bayesian methods, where the optimum matrices $\mathbf{W}_\varepsilon$ and $\mathbf{W}_\theta$ are the inverse of the output and parameter variances, respectively [11, 19]. However, the variance of the initial parameter estimates are rarely known in practice, and an alternative given by Link (1993) relates the choice of weighting matrix, $\mathbf{W}_\theta$, to the inverse of the squared sensitivity matrix according to

$$\mathbf{W}_\theta = \frac{\text{mean}\left(\text{diag}\left(\boldsymbol{\Gamma}\right)\right)}{\text{mean}\left(\text{diag}\left(\boldsymbol{\Gamma}^{-1}\right)\right)} \boldsymbol{\Gamma}^{-1}; \tag{20}$$

$$\boldsymbol{\Gamma} = \text{diag}\left[\mathbf{G}_i^T \mathbf{W}_\varepsilon \mathbf{G}_i\right]. \tag{21}$$

This definition allows the parameter changes to be constrained according to their sensitivity. In consequence the parameters remain unchanged if their sensitivity approaches zero. $\mathbf{W}_\theta = \mathbf{I}$ represents the classical Tikhonov regularization [64] used to solve ill-conditioned systems of equations.

Equation (3) is easily extended to penalize differences between the updated parameters and the corresponding initial estimates or to penalize differences between nominally identical parameters [3, 22]. For example, in an experimental frame structure, a number of "T" joints may exist that are nominally identical. Due to manufacturing tolerances, the parameters of these joints will be slightly different, although these differences should be small. Therefore a side constraint is placed on the parameters, so that both the residual and the differences between nominally identical parameters are minimized.

Minimizing J in Eq. (19) gives the solution

$$\Delta\boldsymbol{\theta}_i = \underbrace{\left[\mathbf{G}_i^T\mathbf{W}_\varepsilon\mathbf{G}_i + \mu^2\mathbf{W}_\theta\right]^{-1}\mathbf{G}_i^T\mathbf{W}_\varepsilon}_{\mathbf{T}_i}\mathbf{r}_i = \mathbf{T}_i\mathbf{r}_i \tag{22}$$

where $\mathbf{T}_i$ is the generalized pseudo-inverse of the sensitivity matrix.

The question remains how to choose the regularization parameter μ that provides a balance between the measurement residual, $J_\varepsilon(\boldsymbol{\theta}) = \boldsymbol{\varepsilon}^T\mathbf{W}_\varepsilon\boldsymbol{\varepsilon}$, and the side constraint (or parameter change), $J_\theta\,(\boldsymbol{\theta}) = \Delta\boldsymbol{\theta}_i^T\mathbf{W}_\theta\Delta\boldsymbol{\theta}_i$. Link [40] suggested that the factor μ^2 lies in the range between 0 (no regularization) and 0.3. High μ values are used if there are many insensitive parameters, and the matrix $\mathbf{G}_i^T\mathbf{W}_\varepsilon\mathbf{G}_i$ is strongly ill-conditioned. If ill-conditioning is not too strong, $\mu^2 = 0.05$. The higher the value of μ, the higher is the necessary number of iteration steps to achieve convergence.

This regularization approach is very closely related to the optimization of multiple objective functions. From Eq. (19) it is clear that the residual and side constraint are functions of μ: $J_\varepsilon(\boldsymbol{\mu})$ and $J_\theta(\boldsymbol{\mu})$. The way in which these two terms are balanced depends on the size of the regularization parameter μ. If μ is too small, then the problem will be too close to the original ill-posed problem, but if μ is too large, then the problem solved will have little connection with the original problem. A useful approach is to plot the norm of the side constraint, $\sqrt{J_\theta\,(\boldsymbol{\mu})}$, against the norm of the residual, $\sqrt{J_\varepsilon\,(\boldsymbol{\mu})}$, for different values of μ. For multi-objective function optimization, this is called the Pareto front and in regularization is called the L-curve. Hansen [29] showed that the norm of the side constraint is a monotonically decreasing function of the norm of the residual. He pointed out that for a reasonable signal-to-noise ratio and the satisfaction of the Picard condition, the curve is approximately vertical for $\mu < \mu_{opt}$ and soon becomes a horizontal line when $\mu > \mu_{opt}$, with a corner near the optimal regularization parameter μ_{opt}. The curve is called the L-curve because of this behavior. The optimum value of the regularization parameter, μ_{opt}, corresponds to the point with maximum curvature at the corner of the log-log plot of the L-curve. This point represents a balance between confidence in the measurements and the analyst's intuition.

One difficulty in model updating is that the relationship between the parameters and the measurements is nonlinear and the estimation problem is solved by constructing the linearized model and iterating until convergence. At each iteration regularization may be applied, although often the corner of the L-curve disappears as the iterations progress [65], and thus the value of the regularization parameter is difficult to determine. Hence, it is often convenient to set the regularization parameter at the first iteration and retain this value until convergence.

5.1 Example: Two Degree-of-Freedom Statically Loaded System

We now consider the two degree-of-freedom static example shown in Fig. 1. In the initial model, the spring constants are all 1 N/m, so that $k_1 = k_2 = k_3 = 1$N/m. The *measured* data are taken from a system with $k_1 = 1.2$N/m, $k_2 = 0.8$N/m, and $k_3 = 1.0$N/m. The purpose of the example is to show how the stiffness correction may be determined from measured static displacements u_1 and u_2. Two cases will be considered, namely, the underdetermined and overdetermined cases.

The updating equation is formulated using a force residual which is obtained by introducing the measured displacement response into the equation of motion (2). In the static load case, $\omega = 0$, this results in an analytical force vector $\mathbf{f}(\boldsymbol{\theta}) = \mathbf{K}(\boldsymbol{\theta})\mathbf{u}_m$ which for the example of Fig. 1 is given by

$$\mathbf{f} = \begin{pmatrix} f_1 \\ f_2 \end{pmatrix} = \begin{bmatrix} k_1 + k_2 & -k_2 \\ -k_2 & k_2 + k_3 \end{bmatrix} \begin{pmatrix} u_{m1} \\ u_{m2} \end{pmatrix}.$$

The residual defined in Eq. (1) is then calculated from

$$\boldsymbol{\varepsilon}_z \approx \mathbf{f}_m - \mathbf{f} - \mathbf{G}\Delta\boldsymbol{\theta} \tag{23}$$

where $\mathbf{f}_m$ denotes the measured force vector and $\mathbf{G} = \begin{bmatrix} \frac{\partial f_1}{\partial k_1} & \frac{\partial f_1}{\partial k_2} & \frac{\partial f_1}{\partial k_3} \\ \frac{\partial f_2}{\partial k_1} & \frac{\partial f_2}{\partial k_2} & \frac{\partial f_2}{\partial k_3} \end{bmatrix} = \begin{bmatrix} u_{m1} & u_{m1} - u_{m2} & 0 \\ 0 & -u_{m1} + u_{m2} & u_{m2} \end{bmatrix}$ is the sensitivity matrix. This latter matrix doesn't depend

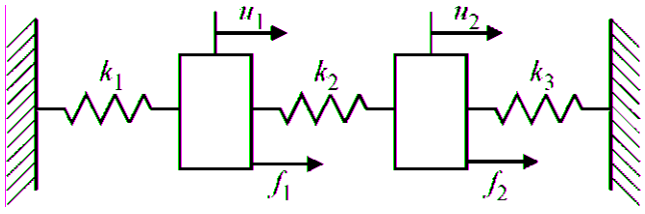

Fig. 1 Two degree-of-freedom discrete example

on the current stiffness value so that there is no iteration necessary in this simple case. Thus the updating Eq. (23) is of the same form as Eq. (4).

Case 1: Underdetermined System

Suppose that the force applied to the springs is $\mathbf{f}_{m1} = [\ 1\ \ 0\ ]^T$ and the measured static deflection is $\mathbf{u}_{m1} = \left\{ \begin{matrix} 0.60811 \\ 0.27027 \end{matrix} \right\}$. The vector of stiffness changes that reproduces the measured displacement, for the minimum norm of the stiffness change, may be obtained as $\Delta k_1 = 0.1398$, $\Delta k_2 = -0.0916$, and $\Delta k_3 = 0.1354$. Figure 2 shows the results obtained by including the side constraint of minimum stiffness change, for various values of regularization parameter, μ. In this case the matrix $\mathbf{G}$ is not ill-conditioned, and hence the side constraint yields a solution that is a weighted average of the minimum norm solution and the zero change solution, as shown by the smooth variation in the spring stiffnesses with μ in Fig. 2. This is also the reason the residual plot does not have the L-curve shape. Note also that the simulated stiffness change is never recovered by the estimation procedure.

Case 2: Overdetermined System

Suppose that a second force, $\mathbf{f}_{m2} = [\ 0\ \ 1\ ]^T$, is applied to the springs, giving the measured static deflection of $\mathbf{u}_{m2} = \left\{ \begin{matrix} 0.27027 \\ 0.67568 \end{matrix} \right\}$. If this data is combined with the data for the first load case $\mathbf{f}_{m1} = [\ 1\ \ 0\ ]^T$, then the estimation is overdetermined. Since there is no noise or modeling errors, the exact spring stiffnesses are obtained: $\Delta k_1 = 0.2$, $\Delta k_2 = -0.2$, and $\Delta k_3 = 0.0$.

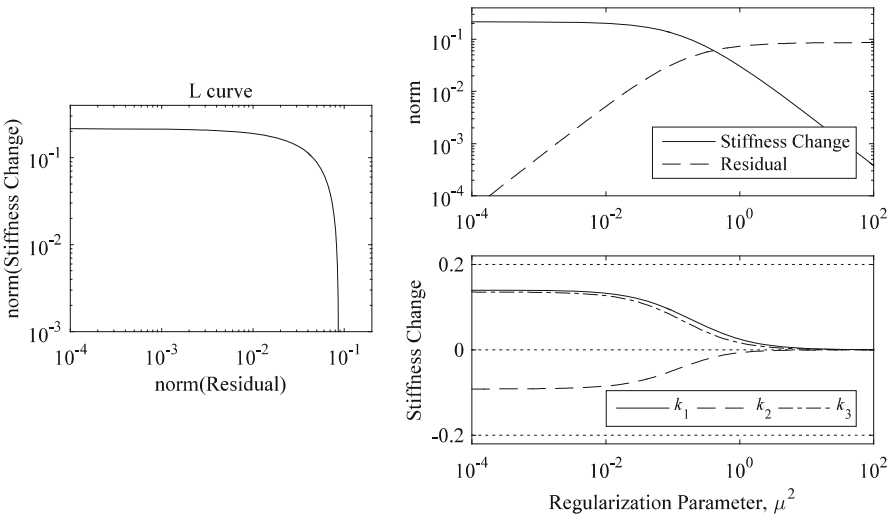

Fig. 2 The estimation results for the underdetermined case. Dotted lines represent the simulated stiffness change. (Reproduced by kind permission of Elsevier)

Regularization is most useful when the coefficient matrix is relatively ill-conditioned and noise is present. In this simple example, ill-conditioning is obtained by considering measurements taken at two force levels, namely, $\mathbf{f}_{m1} = [\ 1\ \ 0\ ]^T$ and $\mathbf{f}_{m3} = [\ 1.05\ \ 0\ ]^T$. The exact "measured" displacement for $\mathbf{f}_{m3}$ is $\mathbf{u}_{m3} = \begin{Bmatrix} 0.63851 \\ 0.28378 \end{Bmatrix}$. Noise is added to the measurements: $\begin{Bmatrix} -0.0002 \\ 0.0003 \end{Bmatrix}$ to $\mathbf{u}_{m1}$ and $\begin{Bmatrix} 0.0010 \\ -0.0002 \end{Bmatrix}$ to $\mathbf{u}_{m3}$. Figure 3 shows the results obtained by including the side constraint of minimum stiffness change, for various values of regularization parameter, μ. The L-curve now has the classical shape, with a defined corner. For low values of regularization parameter, the estimation is clearly ill-conditioned leading to large estimated stiffness changes. The condition number of $\mathbf{G}$ in this example is 880. At the corner of the L-curve, the stiffness changes are approximately those obtained from the minimum norm solution for the underdetermined case. For a regularization parameter slightly less than that at the corner of the L-curve, the stiffness changes are very close to those simulated, although this is impossible to determine solely from the estimated results. Figure 4 shows the results when using the parameter weighting matrix given by Eqs. (19), (20), and (21). Although similar to the results of Fig. 3, the updated parameters at the corner of the L-curve are now much closer to the simulated values, as shown in Table 1.

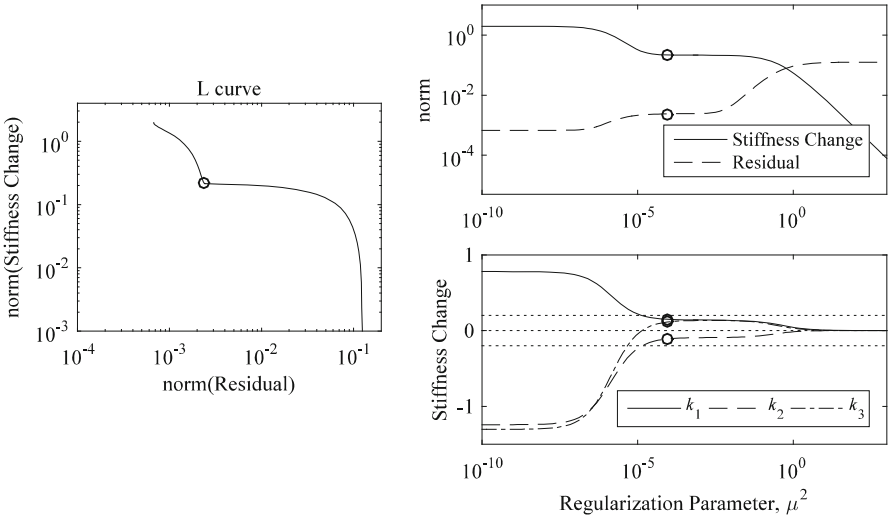

Fig. 3 The estimation results for the overdetermined case with the minimum norm parameter change. Dotted lines represent the simulated stiffness change. Circles denote the corner of the L-curve and the associated values of residuals and stiffness changes. (Reproduced by kind permission of Elsevier)

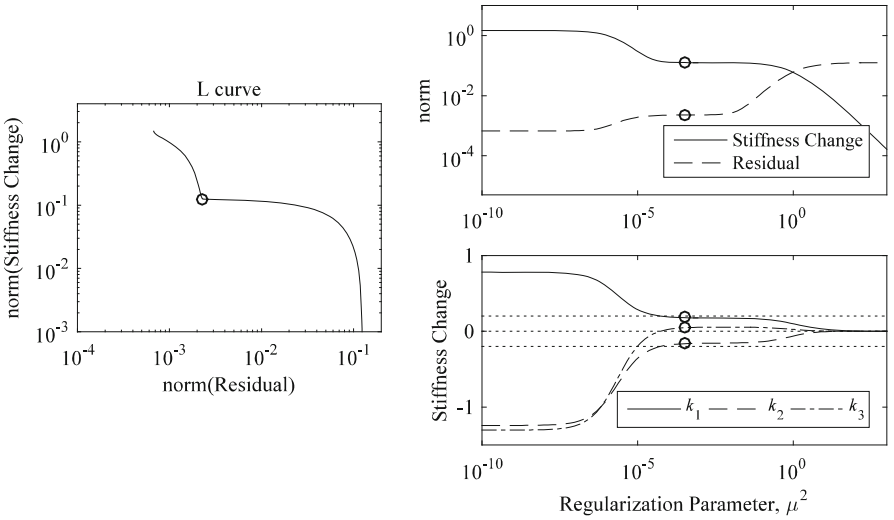

Fig. 4 The estimation results for the overdetermined case with parameter weighting matrix given by Eq. (20). Dotted lines represent the simulated stiffness change. Circles denote the corner of the L-curve and the associated values of residuals and stiffness changes. (Reproduced by kind permission of Elsevier)

Table 1 Updated parameter estimates for the overdetermined two degree-of-freedom static example

	μ	k_1(N/m)	k_2(N/m)	k_3(N/m)
No regularization	0	1.779	−0.243	−0.304
L-curve corner, Fig. 3	0.0093	1.149	0.889	1.112
L-curve corner, Fig. 4	0.0179	1.179	0.836	1.046
"Exact"		1.200	0.800	1.000

Examples of regularization using experimental data may be found in the literature. Examples include Link [40] on a five degree-of-freedom laboratory test structure using Eq. (22) and Ahmadian et al. [3] who used the L-curve to determine the regularization parameter for the experimental frame structure, mentioned previously, with nominally identical welded joints.

6 Parameterization

The amount of information that can be obtained from vibration test data is limited, and therefore taking more measurements in the same frequency range won't necessarily result in more information. Neither will the additional measurements allow more parameters to be estimated necessarily. The number of parameters should be considerably smaller than the number of measurements. The objective should be that

the model updating problem will be overdetermined. Often the resulting equations are ill-conditioned, and it is then necessary to apply additional information in the form of a side constraint by regularization as described previously. The parameters should be justified by physical understanding of the structure under test and the test setup. Ideally the chosen parameters should have a physical meaning directly, but this is not always possible in practice. Equivalent models and their parameters often lead to improved models when "physical" parameters cannot be found. The data should be sensitive to small changes in the parameters. Difficult features, such as joints, may be made more or less sensitive by choosing different types of parameters. A study that includes several different parameterizations of the same joint in a space frame structure is described by Mottershead et al. [47].

When choosing parameters it is always advisable to try to understand the behavior of the structure globally and locally in those regions where local modeling inaccuracies might be responsible for discrepancies in predictions. For example, close study of finite element mode shapes is able to reveal the motion of joints at each of the measured natural frequencies. Parameters can then be chosen that influence this motion and their significance in model updating easily confirmed by sensitivity analysis and subset selection. In regions of high strain energy, one would usually choose stiffness parameters, whereas mass parameters would be useful in regions of high kinetic energy. Stiffness is generally more difficult to model than mass, and it is therefore more likely that errors in stiffness modeling are responsible for inaccurate predictions than mass errors. Damping is in many respects a special case. Whereas finite element mass and stiffness matrices may be readily derived from variational or energy principles, similar derivations for damping are generally not available. Joints and boundary conditions are particularly difficult to model closely. In principle it is possible to design tests that increase the sensitivity of chosen parameters, but this is extremely difficult to achieve in practice.

6.1 Mass, Damping, and Stiffness Matrix Multipliers

Probably the simplest parameters for model updating are nondimensional scalar multipliers applied at the element or substructure level. The updated model takes the form

$$\mathbf{M} = \mathbf{M}_0 + \alpha_1 \mathbf{M}_1 + \cdots + \alpha_r \mathbf{M}_r + \cdots + \alpha_R \mathbf{M}_R \tag{24}$$

$$\mathbf{C} = \mathbf{C}_0 + \beta_1 \mathbf{C}_1 + \cdots + \beta_s \mathbf{C}_s + \cdots + \beta_S \mathbf{C}_S \tag{25}$$

$$\mathbf{K} = \mathbf{K}_0 + \gamma_1 \mathbf{K}_1 + \cdots + \gamma_u \mathbf{K}_u + \cdots + \gamma_U \mathbf{K}_U \tag{26}$$

where in this case U stiffness parameters, S damping parameters, and R mass parameters are chosen for updating. The subscript "0" denotes the analytical model before updating. Of course the parameters α_r, β_s, or γ_u may be applied to more

than just one element. In this way the parameters may be applied to substructures, when those elements sharing the same updating parameter are connected, or there may be elements dispersed through the mesh that for some physical reason are to be updated in the same way. One reason why different parts of the structure might be updated using the same parameter would be the sensitivity of the eigenvalues, (and eigenvectors) in the frequency range of interest to small changes in the parameters is very similar. In that case separating the elements whose changes have a similar effect would be a bad choice, possibly leading to ill-conditioning of the sensitivity matrix.

It is a good practice to scale the updating equations so that the parameters α_1, $\ldots$, α_r, $\ldots$, α_R, β_1, $\ldots$, β_s, $\ldots$, β_S, and γ_1, $\ldots$, γ_u, $\ldots$, γ_U take similar numerical values. One way to do this is by dividing the parameter correction by the initial parameter values, which is done implicitly in Eqs. (24), (25), and (26). Returning to the specific discussion of matrix multiplier parameters, it is seen that the terms $\frac{\partial \mathbf{M}}{\partial \alpha_r}$, $\frac{\partial \mathbf{C}}{\partial \beta_s}$, $\frac{\partial \mathbf{K}}{\partial \gamma_u}$ are simply the r^{th} element mass matrix, $\mathbf{M}_r$; s^{th} element damping matrix, $\mathbf{C}_s$; and the u^{th} element stiffness matrix, $\mathbf{K}_u$, a fact which makes the computation of the various sensitivities especially simple.

6.2 Material Properties, Thicknesses, and Sectional Properties

The most common material property parameters are Young's modulus and mass density, identical to the γ_u and α_r above since the element stiffness and mass matrices are linear in E and ρ.

In the case of a beam having a rectangular cross section, the element matrices are

$$\mathbf{K}^e = \frac{EI}{l^3}\begin{bmatrix} 12 & 6l & -12 & 6l \\ 6l & 4l^2 & -6l & 2l^2 \\ -12 & -6l & 12 & -6l \\ 6l & 2l^2 & -6l & 4l^2 \end{bmatrix}, \quad I = \frac{bt^3}{12} \tag{27}$$

and

$$\mathbf{M}^e = \frac{\rho Al}{420}\begin{bmatrix} 156 & 22l & 54 & -13l \\ 22l & 4l^2 & 13l & -3l^2 \\ 54 & 13l & 156 & -22l \\ -13l & -3l^2 & -22l & 4l^2 \end{bmatrix}, \quad A = bt \tag{28}$$

where l denotes the element length and the breadth and thickness of the cross section are denoted by t and b, respectively. Young's modulus and mass density are represented by E and ρ.

The choice of parameters E and I independently would lead to redundancy and ill-conditioning since they lead to identical eigenvalue sensitivities (except for a scaling factor). I and A independently would be a difficult choice to justify

physically. But, both $\mathbf{K}^e$ and $\mathbf{M}^e$ depend upon b and t, so that the choice of these two parameters would allow the correction of a beam cross section meaningfully. Other useful parameters include the thicknesses and dimensions of thin-walled sections and plate thicknesses.

The material parameters, thicknesses, and cross-sectional dimensions tend to be powerful updating parameters because they often apply throughout a finite element mesh affecting a large number of elements. Thus a small change in these parameters often affects the natural frequencies very considerably.

6.3 Offset Nodes

Joints and boundary conditions are difficult to represent accurately, and it is in these regions of the model that assumptions are often made. Probably the most common assumption is that the connection made at a joint or boundary is rigid when in fact there is flexibility. The problem of introducing flexibility into joints and boundaries assumed to be rigid can be tackled in a number of different ways, all resulting in equivalent models with parameters that cannot be justified on physical grounds. However, the dynamic behavior of the model and its physical usefulness will most definitely be improved by this approach.

One approach, useful in many applications, is to make use of offset finite element nodes and to use the offset dimensions to correct the model [46]. Lengthening or shortening an offset dimension usually corresponds to making the joint more flexible or to stiffening it, and in this way it is possible to reconcile the modification with engineering understanding of the structure.

6.3.1 Example: Parameterization of a "T" Joint

The "T" joint under consideration is shown in Fig. 5. It consists of three elements, two horizontal elements and one vertical element, each of which is inextensible so that $x_1 = x_4$, $x_2 = x_5$ and $y_3 = y_6$.

The shaded region may be considered rigid in which case the degrees of freedom at nodes 1, 2, and 3 are referred to node $3'$ according to the connection matrix:

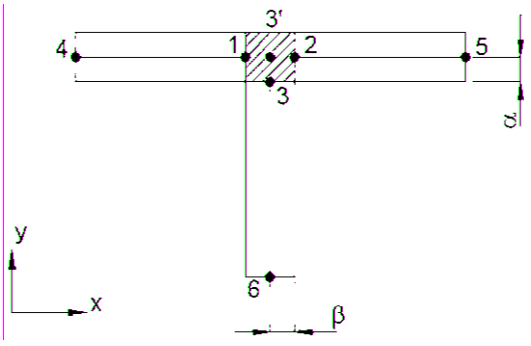

Fig. 5 "T" joint. (Reproduced by kind permission of Elsevier)

$$\begin{Bmatrix} y_1 \\ \vartheta_1 \\ y_2 \\ \vartheta_2 \\ x_3 \\ \vartheta_3 \\ y_4 \\ \vartheta_4 \\ y_5 \\ \vartheta_5 \\ x_6 \\ \vartheta_6 \end{Bmatrix} = \begin{bmatrix} 1 & -\beta & & & & & & & & & & \\ & 1 & & & & & & & & & & \\ 1 & \beta & & & & & & & & & & \\ & 1 & & & & & & & & & & \\ 1 & \alpha & & & & & & & & & & \\ & 1 & & & & & & & & & & \\ & & 1 & & & & & & & & & \\ & & & 1 & & & & & & & & \\ & & & & 1 & & & & & & & \\ & & & & & 1 & & & & & & \\ & & & & & & 1 & & & & & \\ & & & & & & & 1 & & & & \\ & & & & & & & & 1 & & & \\ & & & & & & & & & 1 & & \\ & & & & & & & & & & 1 & \end{bmatrix} \begin{Bmatrix} x_{3'} \\ y_{3'} \\ \vartheta_{3'} \\ y_4 \\ \vartheta_4 \\ y_5 \\ \vartheta_5 \\ x_6 \\ \vartheta_6 \end{Bmatrix}. \tag{29}$$

Construction of the overall stiffness matrix of the "T" joint by the usual methods results in a matrix that contains the offsets α and β. If the overall dimensions of the joint remain unchanged, then increasing the offsets causes the joint to become stiffer while reducing them makes the joint more flexible. Parameters such as α and β have been found to be extremely effective in the correction of inaccurately modeled joints.

6.4 Generic Elements

Generic elements offer perhaps the most sophisticated and most general way to parameterize a finite element model [2, 4, 23]. The basic idea is to change the element formulation within the limitations imposed by the number of nodes and the degrees of freedom available. A number of different methods are available, based either on eigenvalue decomposition or the application of constraints (not discussed in the present chapter). Whichever of the different methods are chosen, generic elements are applied at the element (or substructure) level.

Quite often the mass matrix is considered to be accurate, and only the stiffness matrix needs to be updated. Then an eigenvalue decomposition of the stiffness may be carried out:

$$\mathbf{K}^e = \boldsymbol{\Psi} \begin{bmatrix} \mathbf{0} & \mathbf{0} \\ \mathbf{0} & \mathbf{P} \end{bmatrix} \boldsymbol{\Psi}^T \tag{30}$$

where the matrix of eigenvectors is orthogonal, since $\mathbf{K}^e$ is a real symmetric matrix:

$$\boldsymbol{\Psi}^T \boldsymbol{\Psi} = \mathbf{I}. \tag{31}$$

The eigenvalues and eigenvectors of the stiffness matrix are not the same as those of the element's generalized eigenvalue problem, $(\mathbf{K}^e - \lambda_j \mathbf{M}^e)\,\varphi_j = 0$,

$j = 1, 2, 3, \ldots$. Each eigenvalue can be thought of as a spring coefficient for a deflection defined by its eigenvector.

A new matrix of eigenvectors may be introduced:

$$\hat{\boldsymbol{\Psi}} = \boldsymbol{\Psi}\mathbf{S} \tag{32}$$

so that a new stiffness matrix may be written as

$$\hat{\mathbf{K}}^e = \boldsymbol{\Psi}\boldsymbol{\kappa}\boldsymbol{\Psi}^T; \quad \boldsymbol{\kappa} = \mathbf{S}\begin{bmatrix} \mathbf{0} & \mathbf{0} \\ \mathbf{0} & \mathbf{P} \end{bmatrix}\mathbf{S}^T, \tag{33}$$

and from Eqs. (31) and (32), it is apparent that $\mathbf{S}$ is an orthogonal matrix.

It seems at first that the number of updating parameters might be quite large, but the number can be reduced very considerably by applying engineering judgment. For example, the first two stiffness eigenvalues might be very sensitive parameters for many of the lower vibration modes of the complete structure. In this case only the first two diagonal terms, p_1, p_2, would be chosen. Otherwise modifying the terms of $\boldsymbol{\kappa}$ will lead to changes in both the stiffness eigenvalues and eigenvectors.

6.4.1 Example: Eigenvalue Decomposition of a Beam Element

A beam element stiffness matrix with the properties, $EI = 1$ and $l = 1$, can be written as

$$\mathbf{K}^e = \begin{bmatrix} 12 & 6 & -12 & 6 \\ 6 & 4 & -6 & 2 \\ -12 & -6 & 12 & -6 \\ 6 & 2 & -6 & 4 \end{bmatrix}$$

and possesses eigenvalues 0, 0, 2, 30 (with units of stiffness) and eigenvectors

$$\boldsymbol{\Psi} = \begin{bmatrix} 1 & 1/2 & 0 & 2/\sqrt{10} \\ 0 & -1 & 1/\sqrt{2} & 1/\sqrt{10} \\ 1 & -1/2 & 0 & -2/\sqrt{10} \\ 0 & -1 & -1/\sqrt{2} & 1/\sqrt{10} \end{bmatrix}.$$

The rigid body modes describe pure translation and pure rotation about the center of mass of the beam. Since $\mathbf{K}^e = \sum_{j=1}^{2} \boldsymbol{\psi}_{j+2}^T p_j \boldsymbol{\psi}_{j+2}$, it is seen that $\mathbf{K}^e \in \Re^{4\times 4}$ is a rank 2 matrix, so that only the strain "modes" contribute to the stiffness of the beam element. The rigid body modes of $(\mathbf{K}^e - p_j\,\mathbf{I})$ are the same as the rigid body modes of $(\mathbf{K}^e - \lambda_j\,\mathbf{M}^e)$ so that the mass matrix has no influence on the rigid body modes, which span the null space of the element stiffness matrix.

6.4.2 Example: Generic Element Parameters for a Pinned-Pinned Beam

The eigenvectors of the stiffness matrix formed from two uniform beam elements with pinned ends are shown in Fig. 6. The first and third are symmetric, whereas the second and fourth modes are antisymmetric.

To select modifications to all the eigenvalues but only the symmetric eigenvectors, the matrix $\mathbf{S}$ is chosen so that

$$\mathbf{S} = \begin{bmatrix} s_{11} & & s_{13} & \\ & 1 & & \\ s_{31} & & s_{33} & \\ & & & 1 \end{bmatrix}$$

$$\text{and } \mathbf{W} = \mathbf{S}^T\mathbf{P}\mathbf{S} = \begin{bmatrix} \left(s_{11}^2 p_1 + s_{31}^2 p_3\right) & 0 & \left(s_{11}s_{13}p_1 + s_{31}s_{33}p_3\right) & 0 \\ 0 & p_2 & 0 & 0 \\ \left(s_{13}s_{11}p_1 + s_{33}s_{31}p_3\right) & 0 & \left(s_{13}^2 p_1 + s_{33}^2 p_3\right) & 0 \\ 0 & 0 & 0 & p_4 \end{bmatrix}.$$

The element stiffness matrix can be reconstructed as

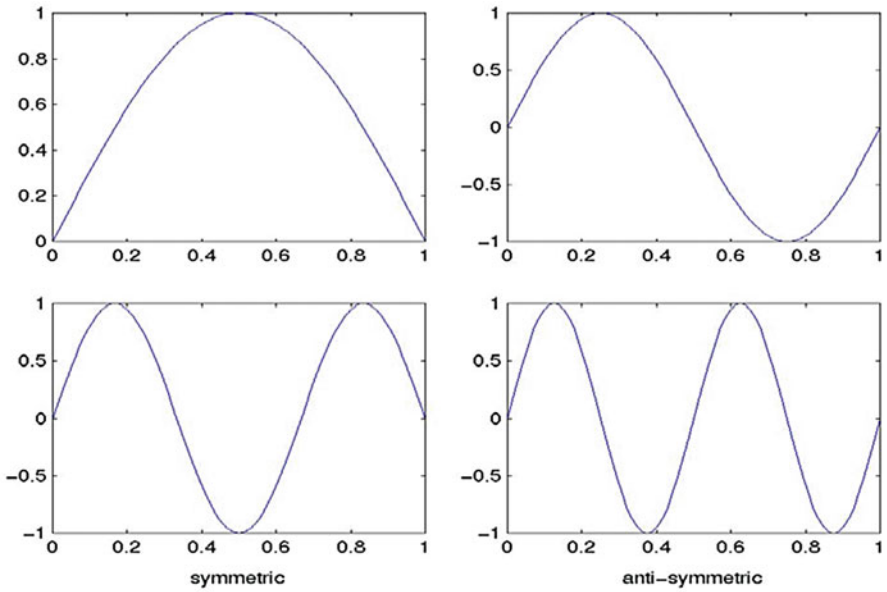

Fig. 6 Mode shapes of the pinned-pinned beam. (Reproduced by kind permission of Elsevier)

$$\mathbf{K}^e = \begin{bmatrix} \boldsymbol{\psi}_1 & \boldsymbol{\psi}_2 & \boldsymbol{\psi}_3 & \boldsymbol{\psi}_4 \end{bmatrix} \begin{bmatrix} \kappa_{11} & 0 & \kappa_{13} & 0 \\ 0 & \kappa_{22} & 0 & 0 \\ \kappa_{31} & 0 & \kappa_{33} & 0 \\ 0 & 0 & 0 & \kappa_{44} \end{bmatrix} \begin{bmatrix} \boldsymbol{\psi}_1^T \\ \boldsymbol{\psi}_2^T \\ \boldsymbol{\psi}_3^T \\ \boldsymbol{\psi}_4^T \end{bmatrix},$$ and there are five updating parameters, κ_{11}, $\kappa_{13} = \kappa_{31}$, κ_{22}, κ_{33}, and κ_{44}.

6.4.3 Example: Updating a System of Three Beams with Offset Central Span

We consider the system of three beams connected in-line but with the axis of the central beam offset from the axes of the two outer beams as shown in Fig. 7. The breadth of all three beams is 0.2 m, and the material is steel ($E = 210$ GN/m^2, $\rho = 7860$ kg/m^3). The system is represented by a finite element model consisting of ten beam elements as indicated in the figure with rigidly fixed ends. Each node has three degrees of freedom, axial and transverse displacements and a rotation about the third axis. The fourth and seventh elements have offset nodes at the left-hand and right-hand ends, respectively.

The connection matrix defining the offset node at the fourth element is given by

$$\begin{bmatrix} 1 & 0 & a \\ 0 & 1 & 0 \\ 0 & 0 & 1 \end{bmatrix}.$$

In the first case, a finite element model with initial parameters $E_0 = 180$ GN/m^2 and $a_0 = 0.015$ m is updated using the correct choice of parameters. Updating is carried out using the standard Moore-Penrose pseudo-inverse based on convergence of the first five natural frequencies. It is seen from Fig. 8 that exact convergence to the true solution is obtained in two iterations.

In the second case, the finite element model is corrected using generic element parameters. This time the finite element mass matrix is correct, but in the stiffness

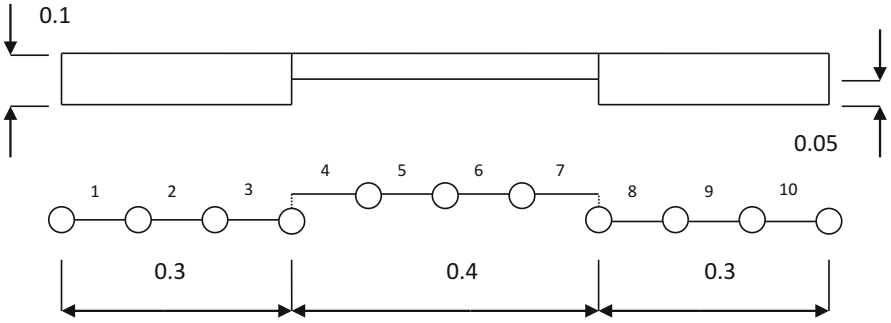

Fig. 7 System of three beams with offset central span (dimensions in meters). (Reproduced by kind permission of Elsevier)

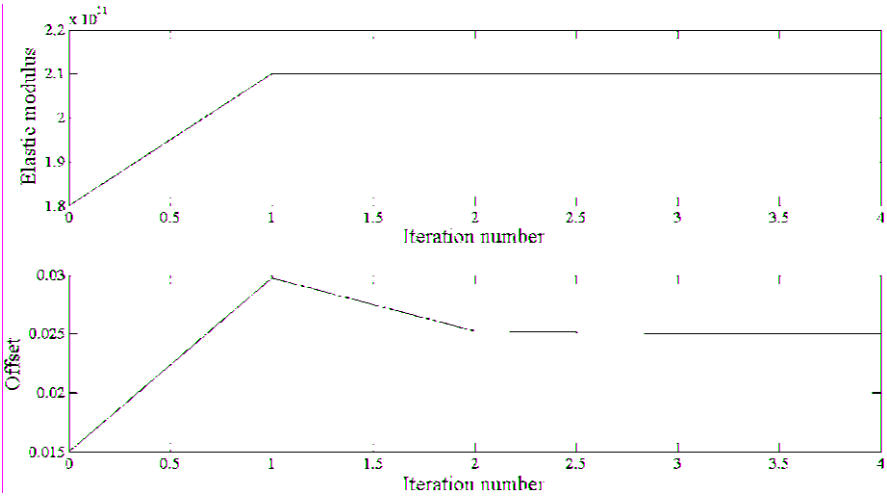

Fig. 8 Parameter convergence – E and a. (Reproduced by kind permission of Elsevier)

matrix, the offset is initially given by 0.8 of its true value. The elastic modulus is correct. The generic element is formed from the group of elements, 3, 4, 7, 8, at the junctions between the thick and thin beam sections. The stiffness matrices from elements 3 and 4 are uncoupled from elements 7 and 8, but each pair of elements has identical eigenvalues. Therefore the eigenvalues of the generic element stiffness matrix occur in pairs. It is found that the first natural frequency of the beam is not very sensitive to the generic element parameters, which represent (shape) stiffnesses at the junctions – well away from the most strained portion of the beam in the middle. The second and third natural frequencies are very sensitive, and the fourth mode is axial and therefore insensitive. A single generic element parameter is not sufficient to produce good results, but in Figs. 9 and 10 results are shown from two updating parameters κ_{11}, κ_{22}. It is seen that the second and third natural frequencies converge correctly after approximately 20 iterations when the parameters κ_{11}, κ_{22} are fully converged.

Updating was achieved using the weighted (regularized) updating Eq. (22) using the first ten natural frequencies. The second and third diagonal terms of $\mathbf{W}_\varepsilon$ were given by values of 13,000 with the remaining diagonal terms set to unity (off-diagonal terms set to zero), $\mathbf{W}_\theta = \text{diag}\left(250\ 50\right)$. It is seen that the generic element parameters are able to provide an updated model that accurately reproduces the dynamic behavior of the offset beam (in the frequency range considered) even though the updated model lacks physically meaning. Nevertheless, such a model may be meaningful within the updating frequency range.

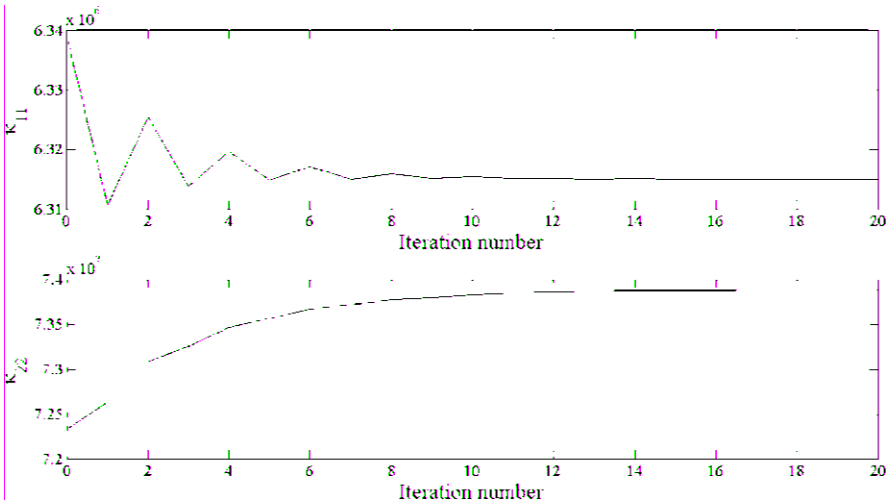

Fig. 9 Parameter convergence – κ_{11}, κ_{22}. (Reproduced by kind permission of Elsevier)

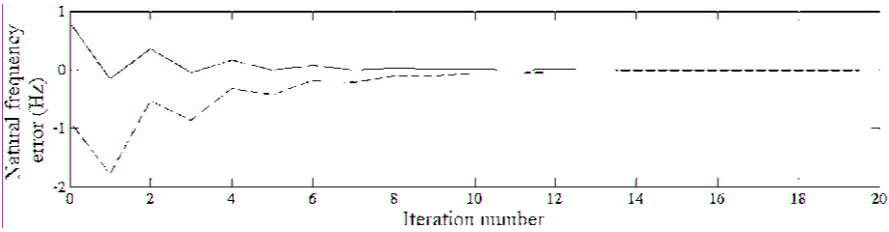

Fig. 10 Convergence of natural frequencies – generic element parameters. (Reproduced by kind permission of Elsevier)

7 Stochastic Model Updating

The stochastic model updating problem may be expressed as

$$\left(\mathbf{z}^e - \overline{\mathbf{z}}^e\right) = \overline{\mathbf{G}}_j \left(\boldsymbol{\theta} - \overline{\boldsymbol{\theta}}\right)_{j+1} + \boldsymbol{\varepsilon}_{j+1} \tag{34}$$

by the assumption of small perturbation about the mean. In Eq. (34) the over-bar denotes the mean; $\mathbf{z}^e, \overline{\mathbf{z}}^e$ are experimentally measured outputs, typically natural frequencies and mode-shape terms; $\boldsymbol{\theta}_{j+1}$ is the $(j+1)^{th}$ estimate of parameter distribution to be determined, with mean $\overline{\boldsymbol{\theta}}_{j+1}$. The mean sensitivity matrix is

denoted by $\overline{\mathbf{G}}_j = \mathbf{G}\left(\overline{\boldsymbol{\theta}}_j\right)$, and $\boldsymbol{\varepsilon}_{j+1}$ represents errors introduced from various sources including inaccuracy of the model and measurement imprecision.

Model updating of the means is a deterministic problem given by

$$\overline{\boldsymbol{\theta}}_{j+1} = \overline{\boldsymbol{\theta}}_j + \overline{\mathbf{T}}_j \left(\overline{\mathbf{z}}^e - \overline{\mathbf{z}}_j^a \left(\overline{\boldsymbol{\theta}}_j\right)\right) \tag{35}$$

where $\overline{\mathbf{z}}_j^a \left(\overline{\boldsymbol{\theta}}_j\right)$ is the predicted output of the model at the j^{th} iteration. The transformation matrix $\overline{\mathbf{T}}_j$ is the generalized pseudo-inverse of the sensitivity matrix $\overline{\mathbf{G}}_j$:

$$\overline{\mathbf{T}}_j = \left(\overline{\mathbf{G}}_j^T \mathbf{W}_\varepsilon \overline{\mathbf{G}}_j + \mathbf{W}_\theta\right)^{-1} \overline{\mathbf{G}}_j^T \mathbf{W}_\varepsilon, \tag{36}$$

and $\mathbf{W}_\varepsilon$ and $\mathbf{W}_\vartheta$ are weighting matrices, to allow for regularization of ill-posed sensitivity equations (see Eq. (22) in Sect. 5).

It is seen from Eq. (34) that the matrix of output covariances is given by

$$Cov\left(\Delta\mathbf{z}^e, \Delta\mathbf{z}^e\right) = \overline{\mathbf{G}}_j Cov\left(\Delta\boldsymbol{\theta}_{j+1}, \Delta\boldsymbol{\theta}_{j+1}\right) \overline{\mathbf{G}}_j^T + Cov\left(\boldsymbol{\varepsilon}_{j+1}, \boldsymbol{\varepsilon}_{j+1}\right) \tag{37}$$

$$\Delta\mathbf{z}^e = \mathbf{z}^e - \overline{\mathbf{z}}^e; \quad \Delta\boldsymbol{\theta} = \boldsymbol{\theta} - \overline{\boldsymbol{\theta}}_j. \tag{38}$$

Then, if the error covariances are deemed to be small, an estimate of the parameter covariances may be obtained by inversion, using Eq. (36) to obtain

$$Cov\left(\Delta\boldsymbol{\theta}_{j+1}, \Delta\boldsymbol{\theta}_{j+1}\right) = \overline{\mathbf{T}}_j Cov\left(\Delta\mathbf{z}^e, \Delta\mathbf{z}^e\right) \overline{\mathbf{T}}_j^T. \tag{39}$$

Equation (39) allows for the computation of $Cov(\Delta\boldsymbol{\theta}_{j+1}, \Delta\boldsymbol{\theta}_{j+1})$ using only the transformation matrix, $\overline{\mathbf{T}}_j$, obtained at the final step of deterministic updating of the means and the measured output covariance. It avoids expensive forward propagation of uncertainty through the model required by alternative approaches. It was shown [61] that Eq. (39) may be developed straightforwardly from expressions given previously by Haddad Khodaparast et al. [36]:

$$\begin{aligned} Cov\left(\Delta\boldsymbol{\theta}_{j+1}, \Delta\boldsymbol{\theta}_{j+1}\right) = {} & Cov\left(\Delta\boldsymbol{\theta}_j, \Delta\boldsymbol{\theta}_j\right) - Cov\left(\Delta\boldsymbol{\theta}_j, \Delta\mathbf{z}_j\right) \overline{\mathbf{T}}_j^T \\ & - \overline{\mathbf{T}}_j Cov\left(\Delta\mathbf{z}_j, \Delta\boldsymbol{\theta}_j\right) + \overline{\mathbf{T}}_j Cov\left(\Delta\mathbf{z}_j, \Delta\mathbf{z}_j\right) \overline{\mathbf{T}}_j^T \\ & + \overline{\mathbf{T}}_j Cov\left(\Delta\mathbf{z}^e, \Delta\mathbf{z}^e\right) \overline{\mathbf{T}}_j^T \end{aligned} \tag{40}$$

and Govers and Link [27]

$$Cov\left(\Delta\boldsymbol{\theta}_{j+1}, \Delta\boldsymbol{\theta}_{j+1}\right) = Cov\left(\Delta\boldsymbol{\theta}_j, \Delta\boldsymbol{\theta}_j\right) + \overline{\mathbf{T}}_j Cov\left(\Delta\mathbf{z}^e, \Delta\mathbf{z}^e\right)\overline{\mathbf{T}}_j^T - \overline{\mathbf{T}}_j Cov\left(\Delta\mathbf{z}_j, \Delta\mathbf{z}_j\right)\overline{\mathbf{T}}_j^T. \tag{41}$$

7.1 Example: Stochastic Model Updating of a Three Degree-of-Freedom System

The example considered is the three degree-of-freedom mass-spring system shown in Fig. 11.

The nominal values of the parameters of the "experimental" system are $m_i = 1.0\,\text{kg}$ $(i = 1, 2, 3)$, $k_i = 1.0\text{N/m}$ $(i = 1, 2, \ldots, 5)$, and $k_6 = 3.0\text{N/m}$. The erroneous random parameters are assumed to have Gaussian distributions with mean values, $\mu_{k_1} = \mu_{k_2} = \mu_{k_5} = 2.0$ N/m, and standard deviations $\sigma_{k_1} = \sigma_{k_2} = \sigma_{k_5} = 0.3$ N/m. The true mean values are the nominal values with standard deviations $\sigma_{k_1} = \sigma_{k_2} = \sigma_{k_5} = 0.2$ N/m (20% of the true mean values). Parameters k_1, k_2, and k_5 are assumed to be independent.

Case 1 – Consistent Set of Updating Parameters

This example comprises a consistent updating problem where three uncertain stiffnesses, k_1, k_2, k_5, are deemed to be responsible for observed variability in the three natural frequencies of the system. Eqs. (39) and (40) were applied, and the initial cloud of predicted natural frequencies was made to converge upon the cloud of "measured" natural frequencies as shown in Fig. 12. The measured data consisted of 30 separate measurement points (30 points in the three-dimensional space of the natural frequencies), and the predictions were represented by 1000 points, needed for forward propagation by Latin hypercube sampling (LHS) with imposed correlation from a normal distribution $\boldsymbol{\theta}_j \in N_n\left(\overline{\boldsymbol{\theta}}_j, Cov\left(\boldsymbol{\theta}_j, \boldsymbol{\theta}_j\right)\right)$, in order to determine $\Delta\mathbf{z}_j$ from $\Delta\boldsymbol{\theta}_j$.

Figure 12 shows the results produced by the two methods, where it is apparent that the updated covariance ellipses from the two solutions are almost indistinguish-

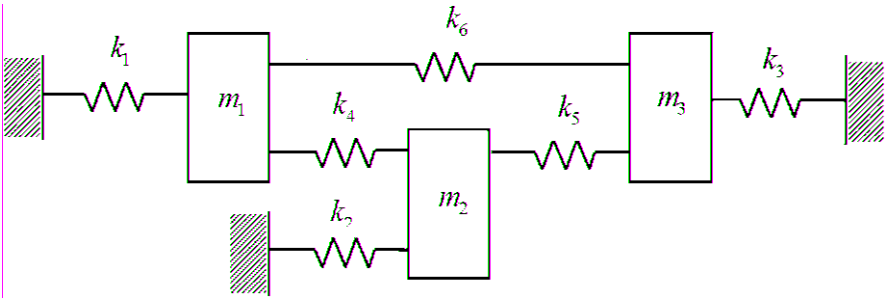

Fig. 11 Three degree-of-freedom mass-spring example

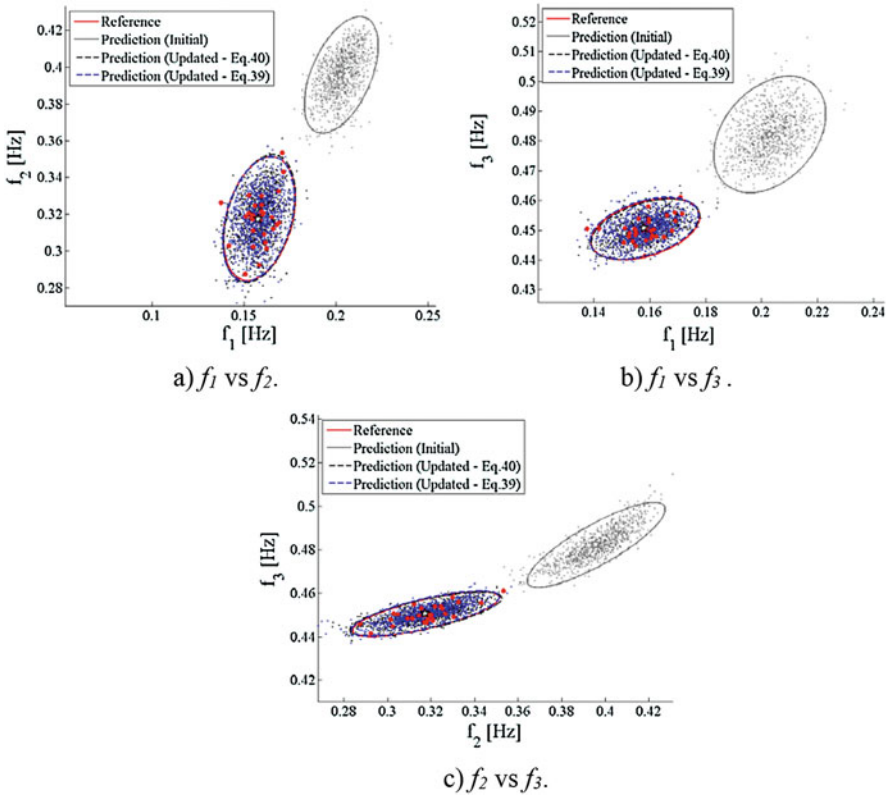

Fig. 12 Frequency scatter plots (Case 1). (Reproduced by kind permission of Elsevier)

able from each other or from the covariance ellipse of the "measured" data. Note that the covariance ellipses on the scatter plots encompass 95% of the data (two-sigma ellipses).

Typical convergence characteristics are shown in Fig. 13, and the updated parameter values are given in Table 2. The adopted convergence criterion was that the deviation of the predicted eigenfrequencies with respect to the reference ones should be less than a specified tolerance.

The CPU times shown in Table 2 are determined with respect to the solution from Eq. (39). It is seen that for this particular three degree-of-freedom problem, calculation of the parameter covariance matrix is approximately 300 times faster by Eq. (39) than by Eq. (40).

Case 2 – Inconsistent Updating Parameter Set

Case 2 presents an example of an inconsistent updating problem where the updating parameter set does not include all the uncertain parameters responsible for the

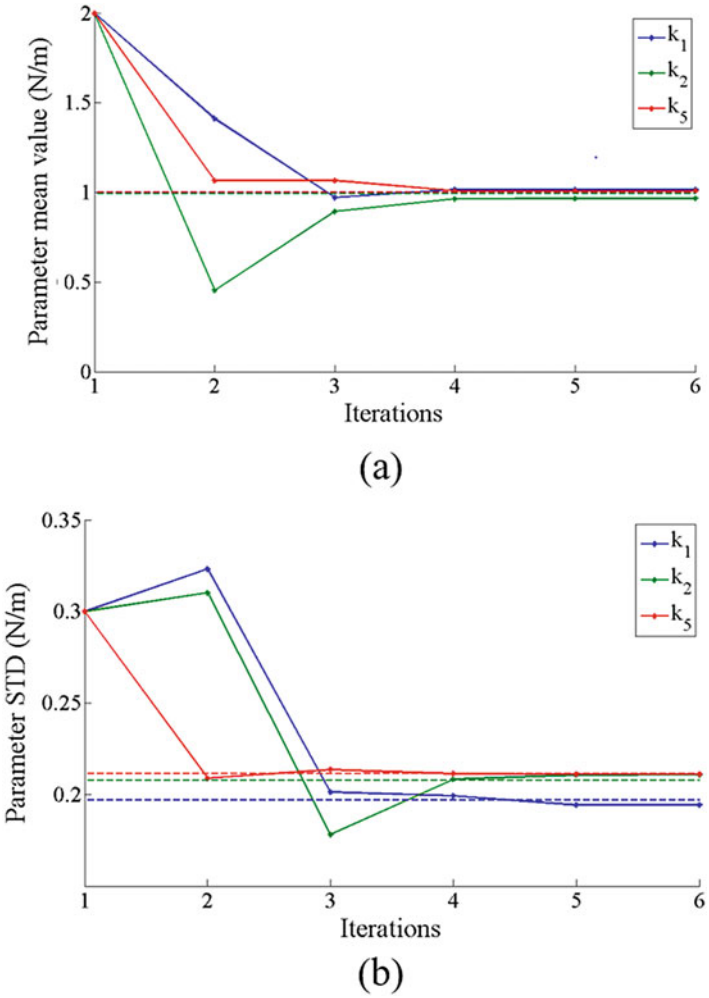

Fig. 13 Convergence plots (Case 1): (**a**) Mean values of the estimates and (**b**) standard deviation of the estimates (dash-dotted line: reference values). (Reproduced by kind permission of Elsevier)

observed variability in the reference responses. As in the previous cases, the reference data were produced with randomized k_1, k_2 and k_5, while the updating parameter set is composed of k_1, k_2, and k_6, i.e., the uncertain k_5 is not included in the updating parameter set. In this case regularization was applied with $\mathbf{W}_\theta = \mathbf{I}$, $\mathbf{W}_\varepsilon = 0.1 \times \mathbf{I}$.

Figures 14 and 15 show the results of the updating process. The scatter plots of Fig. 14 show that the output means are reconstructed faithfully, but the choice of an inconsistent set of updating parameters has resulted in large errors in the reconstructed covariance ellipses. The updating parameters k_1, k_2, k_6 are fully

Table 2 Parameters and eigenfrequencies values

	Reference 30 obs.	Initial (error %)	Updated (error %) Eq. (40) 1000 obs.	Updated (error %) Eq. (39)
$\overline{k_1}$ [N/m]	1.001	2.0 (99.73)	1.001 (−0.03)	1.014 (1.26)
$\overline{k_2}$ [N/m]	0.992	2.0 (101.55)	0.993 (0.06)	0.966 (−2.68)
$\overline{k_5}$ [N/m]	1.001	2.0 (99.84)	1.001 (−0.02)	1.008 (0.69)
σ_{k_1} [N/m]	0.197	0.3 (52.59)	0.194 (−1.59)	0.194 (−1.36)
σ_{k_2} [N/m]	0.208	0.3 (44.58)	0.213 (2.35)	0.211 (1.40)
σ_{k_5} [N/m]	0.211	0.3 (41.94)	0.211 (−0.05)	0.211 (−0.11)
f_1 [Hz]	0.1586	0.2030 (28.02)	0.1586 (−0.00)	0.1586 (−0.00)
f_2 [Hz]	0.3180	0.3960 (24.54)	0.3180 (−0.00)	0.3180 (−0.00)
f_3 [Hz]	0.4505	0.4823 (7.06)	0.4505 (−0.00)	0.4505 (0.00)
# Iterations	–	–	9	6
CPU time ratio	–	–	∼300	1

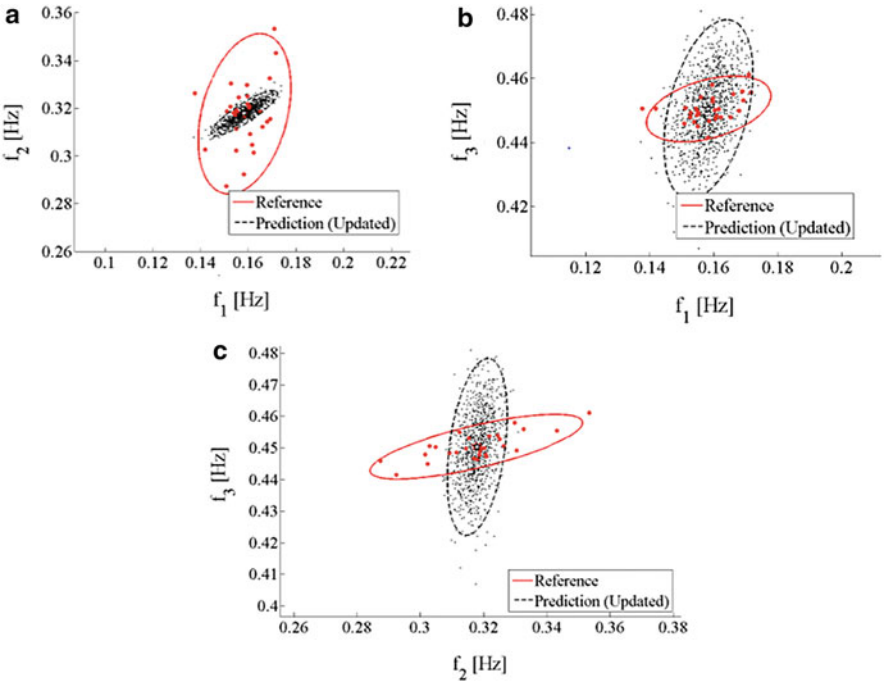

Fig. 14 Frequency scatter plots (Case 2 – Eq. (39)). (Reproduced by kind permission of Elsevier)

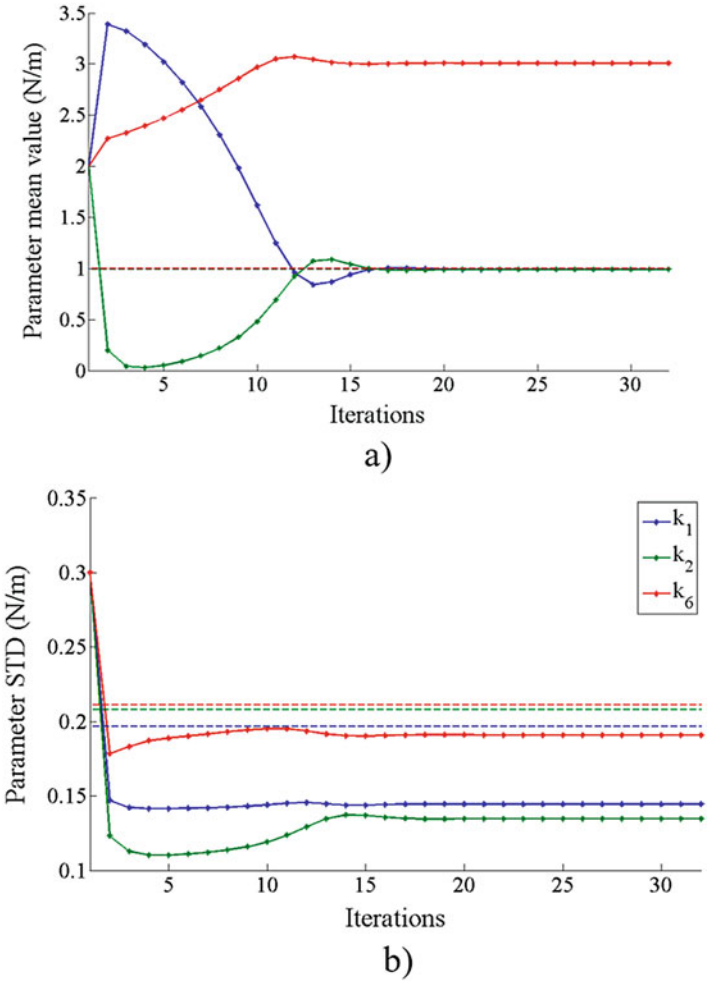

Fig. 15 Convergence plots (Case 2 – Eq. (39)): (**a**) Mean values of the estimates and (**b**) standard deviation of the estimates (dash-dotted line: reference values). (Reproduced by kind permission of Elsevier)

converged after 30 iterations as shown in Fig. 15. This result demonstrates that the selection of updating parameters on the basis of reconstructing the output means is not sufficient to ensure that the output covariances will be well reconstructed.

The inconsistent parameter problem was addressed by Silva et al. [61] who showed how the updated parameters should be selected based on the scaled covariances of the outputs and a scaled sensitivity matrix, with columns g_{θ_k} corresponding to candidate parameters θ_k. Based on an assumption that the updating parameters are mutually independent and independent of measurement noise, the output covariance

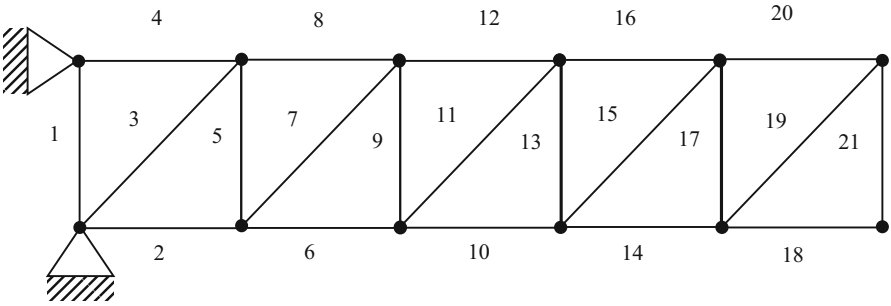

Fig. 16 Pin-jointed truss. (Reproduced by kind permission of Elsevier)

matrix was shown to be given by a sum of rank 1 matrices with each term associated exclusively with a single parameter. The cosine distance between the column g_{θ_k} and its projection g'_{θ_k} on the hypersurface defined by the range of the matrix of output covariances was used. A cosine distance of zero (or close to zero) is an indicator of a correctly chosen updating parameter.

7.2 Example: Parameter Selection for Stochastic Model Updating

The pin-jointed truss shown in Fig. 16 has overall dimensions 5 m × 1 m and is composed of 21 elements in total, each with a stiffness matrix given by

$$\mathbf{K} = k_i \begin{bmatrix} 1 & -1 \\ -1 & 1 \end{bmatrix}; \quad i = 1, 2, \ldots, 21.$$

The five diagonal bars of nominal stiffness $\frac{EA}{L} = 1.485 \times 10^8$ N/m are each randomized for updating. The true mean value of each is equal to the nominal stiffness, and the standard deviations are given by $\sigma_{k_j} = 0.135\mu_{k_j}$, $j = 3, 7, 11, 15, 19$. For the purposes of parameter selection, the initial estimates of all the mean stiffnesses, k_i, $i = 1, 2, \ldots, 21$, are considered to be 70% of the reference values, and the standard deviations are given by $\sigma_{k_j} = 0.27\mu_{k_3}$.

Parameter selection results are shown in Figs. 17, 18, 19, and 20. It is seen that the correct parameters for updating are recognized correctly in each case of different numbers of outputs.

It can be seen from the figures that the first bar element k_1 has zero cosine distance. This happens because the boundary condition prevents any extension or compression of k_1, so that all the outputs are insensitive to it. When the constraints are removed, so the truss is in the free-free condition, the cosine distance corresponding to parameter k_1 becomes finite as shown in Fig. 21.

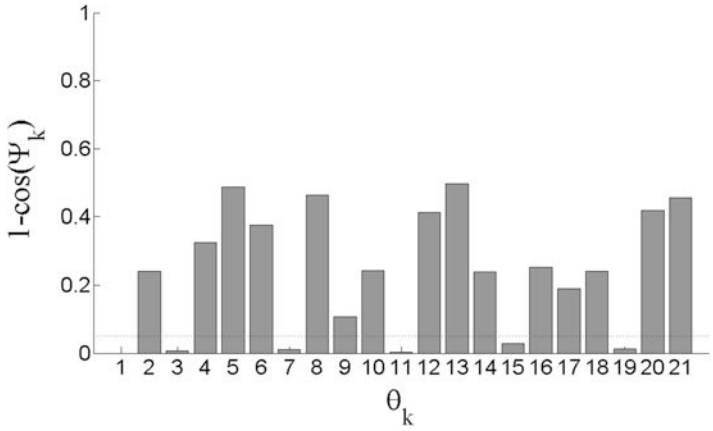

Fig. 17 Cosine distance – first ten eigenvalues. (Reproduced by kind permission of Elsevier)

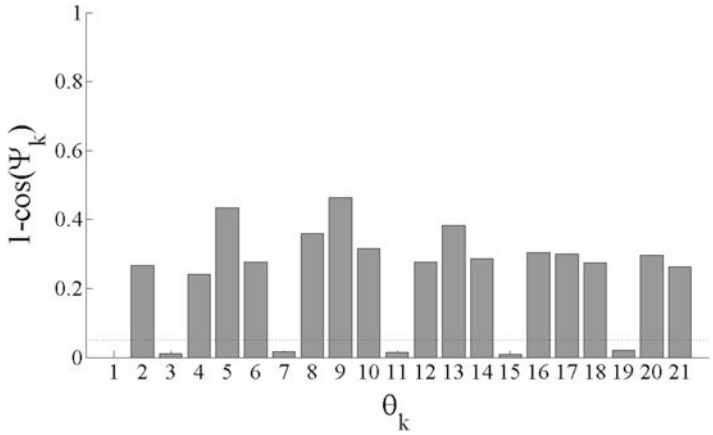

Fig. 18 Cosine distance – first 15 eigenvalues. (Reproduced by kind permission of Elsevier)

8 Validation of Updated Models

Basic requirements for model validation were formulated in Sect. 3. It was explained that even when comparisons of experimental modal analysis results with analytical predictions show satisfactory agreement this does not automatically mean that the updated model is capable of predicting the structural response for other loading and/or boundary conditions or for other structural configurations. In the following some findings are reported from a benchmark study defined within the European COST Action F3 on "Structural Dynamics" and described

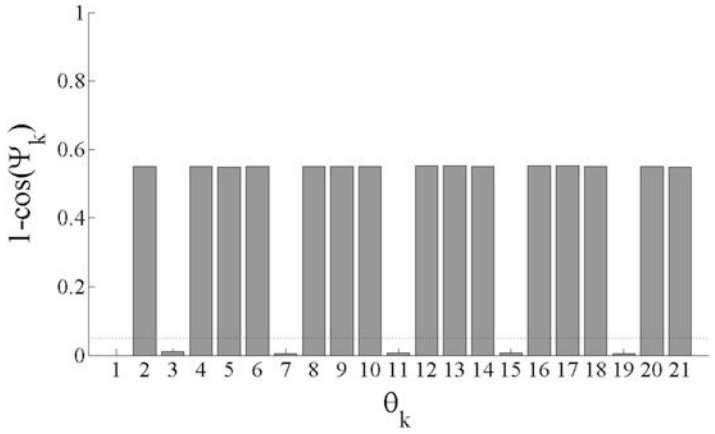

Fig. 19 Cosine distance – all eigenvalues. (Reproduced by kind permission of Elsevier)

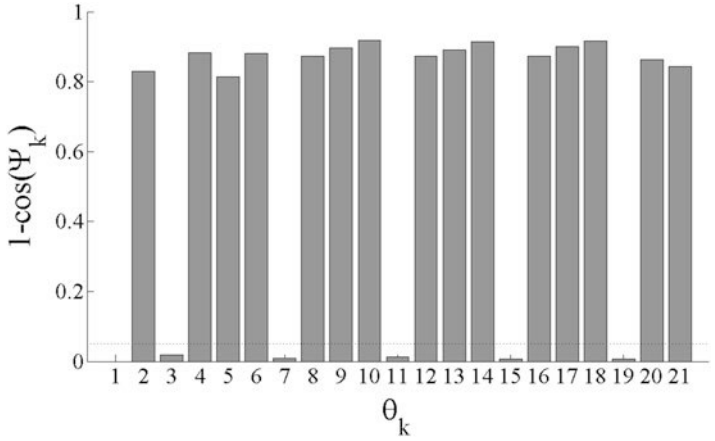

Fig. 20 Cosine distance – all eigenvalues and eigenvectors. (Reproduced by kind permission of Elsevier)

in [14]. The study was aimed at investigating the quality of updated models under real practical conditions where neither the modeling assumptions nor the assumptions for updating were unique but defined differently by the participants of the benchmark. The study should show if the expected non-uniqueness of the results due to different computational methods, different structural idealizations, and different parameter sets could be tolerated with regard to the intended purpose. The following requirements for a validated model were defined:

1. The model must be capable of predicting the experimental modal data and/or the frequency response functions (FRFs) within the active frequency range and

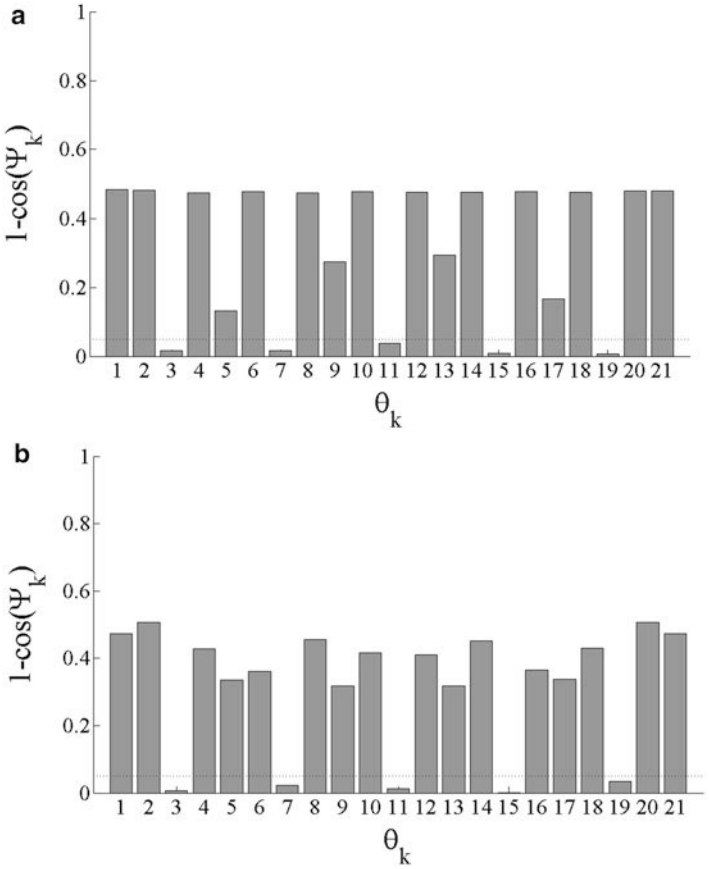

Fig. 21 (**a**) Cosine distance – free-free condition – first ten eigenvalues. (**b**) Cosine distance – free-free condition – first 20 eigenvalues. (Reproduced by kind permission of Elsevier)

within certain accuracy limits, of course. The term active frequency range was related to the frequency range used for computational model updating (CMU). The above criterion represents a minimum requirement which does not yet say much about the prediction quality of the model. The prediction quality should therefore be checked using the following additional criteria:

2. Prediction of the eigenfrequencies and modes beyond the active frequency range.
3. Prediction of the modal data and/or FRFs of a modified structure. For the benchmark structure, two structural modifications were considered consisting of additional masses fixed at two different locations as shown in Fig. 22.

The participants were allowed to generate any initial FE model that they found suitable.

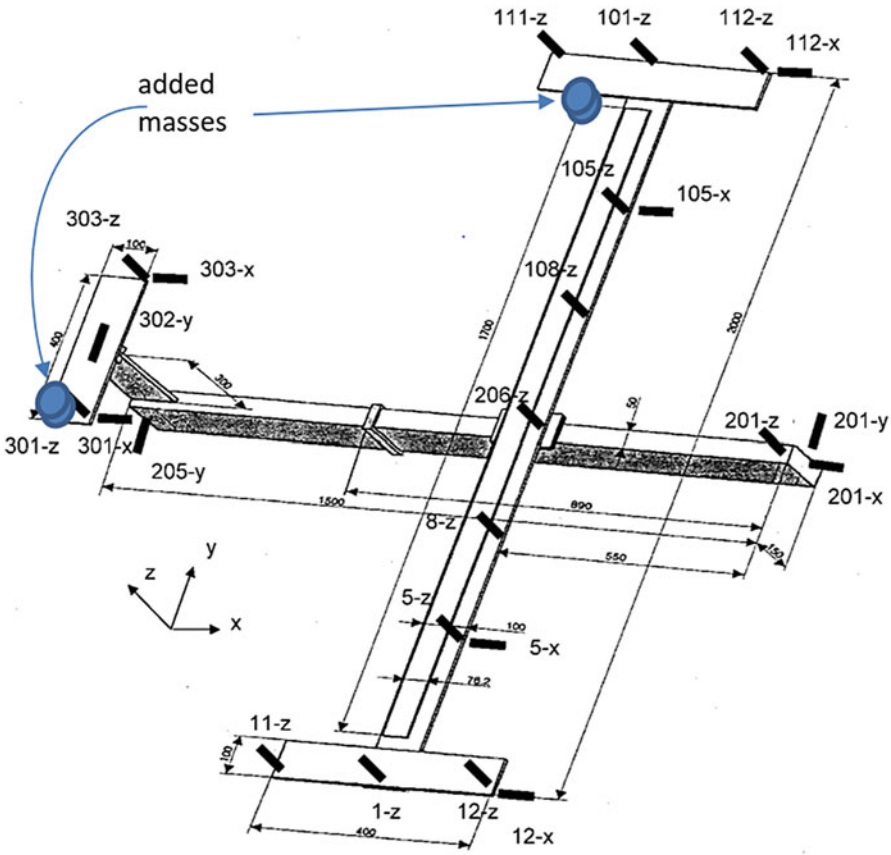

Fig. 22 Geometry and accelerometer location

8.1 Benchmark Data

The benchmark structure was a laboratory structure built to simulate the dynamic behavior of an aeroplane. The structure was initially built for a benchmark study on experimental modal analysis conducted by the Structures and Materials Action Group (SM-AG19) of the Group for Aeronautical Research and Technology in EURope (GARTEUR) [6, 14, 15, 41]. The test bed was designed and manufactured by ONERA, France. Figure 22 shows the test structure geometry and the location of the measured degrees of freedom. The overall length of the structure was 1.5 m, the wing span was 2.0 m, and the overall mass was 44 kg. The material used was aluminum. In order to increase the damping, a $1.1 \times 76.2 \times 1700\ \text{mm}^3$ viscoelastic constraining layer was bonded to the wings. The modal test data for up to 14 modes for the unmodified and also for the two mass-modified structures were provided for the participants. Further details are described in Link and Friswell [41].

8.2 Summary of Model Validation Results

The methods applied by the benchmark participants could be classified according to:

1. The type of test/analysis residuals
2. The type of FE model (beam or shell elements)
3. The type and number of updating parameters

Very different choices were made by the participants. The model validation was essentially performed in two steps:

(a) Initial model tuning: This step included updating the parameters of the initial model of the unmodified structure and to check if the model was capable of predicting the experimental modal data within the active frequency range (criterion 1). Some participants extended the checks with respect to the passive frequency range (criterion 2).
(b) Check of prediction capability concerning the modified structures (criterion 3).

Since all the participants used different residuals for their objective function to be minimized, and different types of structural idealization (beam or plate elements), it was difficult to make recommendations on what residual and what parameter choice were the best. It was necessary to carefully select the parameters describing the connections, particularly when beam models were used. The most important issue was to find an appropriate parameter set. With this requirement fulfilled, good prediction results were found, even with the simple eigenfrequency residual. Looking at the great variety of parameters, it became obvious that even though the parameters might be called physical or geometric (like Young's modulus or a beam offset), they must be interpreted as non-unique equivalent parameters describing lumped stiffness and mass properties. It was interesting to note that good prediction capabilities of the updated models were achieved in many different ways. In principle it was found that the higher the requirement needed to meet the structure's intended purpose, the greater are the number of above validation criteria that must to be satisfied.

9 Industrial Example Problem

The updating and validation of large-scale finite element models is a challenging task because of the high degree of complexity of today's mechanical systems and the number of candidate updating parameters potentially involved. In order to succeed, a systematic approach should be adopted as shown in Fig. 23.

A bottom-up strategy has proven to be very effective especially when the overall system is composed of many interconnected components. This requires the step-by-step approach shown in Fig. 24, starting with single components (*component*

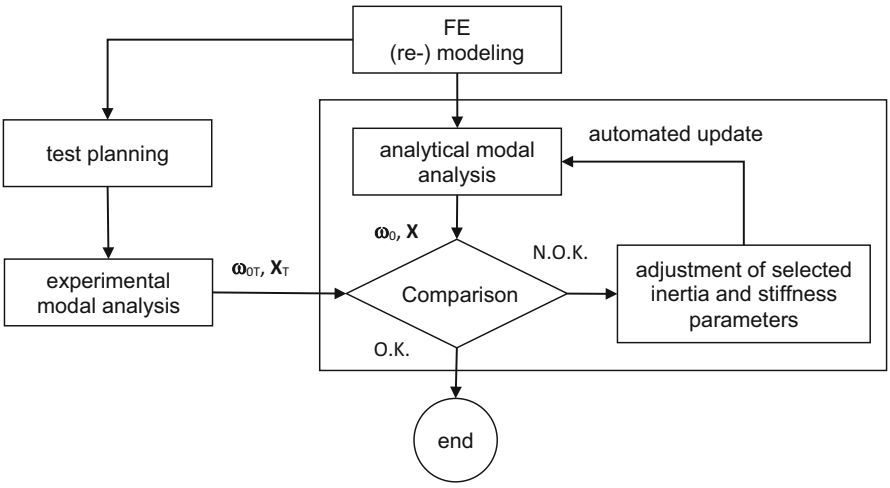

Fig. 23 Model validation strategy

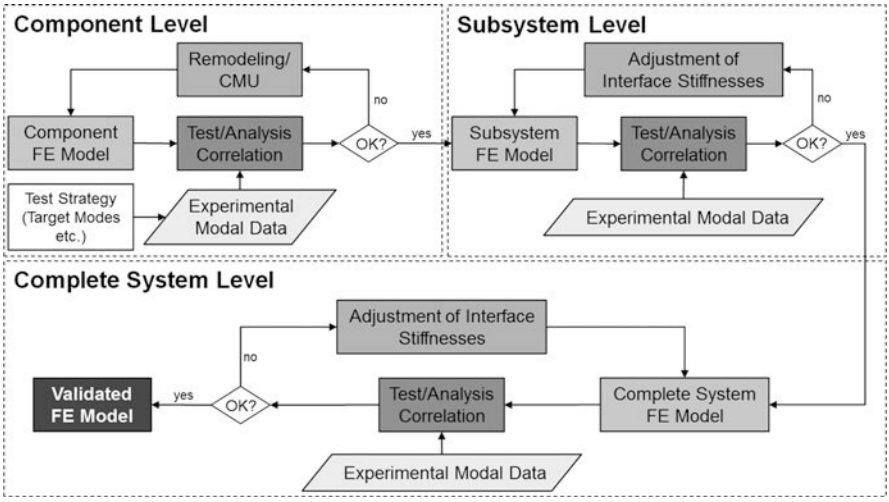

Fig. 24 Bottom-up strategy

level) over subassemblies (*subsystem level*) until the complete system is obtained (*complete system level*). Then model updating and validation become feasible as demonstrated, for example, in Schedlinski and Staples [58], Schedlinski et al. [59, 60], and Schedlinski [56], and in the automotive example described below.

It is usually assumed that all deviations of the analysis from test data are due entirely to uncertainties in the finite element model. There are however test uncertainties too (e.g., exact mounting conditions, signal analysis related errors,

observability and controllability, data analysis, nonlinearities) which must be kept as small as possible.

Test planning makes use of the finite element model, which not only enables the design of the test but also considerably simplifies the later correlation with the analytical results. Test planning should cover the following aspects:

- Boundary conditions (fixed, free, flexible)
- Target modes (frequency range, local and global modes)
- Measurement degrees of freedom (MDOFs)
  - Assessment of required measurement information
  - Selection of sensor locations based on FE model, accessibility, and visualization of modes
  - Unique mode shape recognition using the auto-MAC
- Excitation
  - Assessment of suitable excitation points
  - Selection, e.g., based on analytical Mode Indicator Functions (MIF)
  - Frequency resolution

For test planning and computational model update, several commercial software tools are readily available capable of handling large-scale finite element models. Typical parameters for model updating are described in Sect. 6.

It has proven to be effective to update inertia and stiffness properties first, e.g., based on eigenvalue and eigenvector residuals. After successful updating of these parameters, damping parameters can be adjusted by minimizing the deviations in the resonance regions between measured and simulated FRFs.

A common difficulty in computational model updating is the selection of updating parameters. A necessary condition, but not a sufficient one, is that the parameters should be sensitive. Subset selection methods based on comparing the columns of the sensitivity matrix to the vector of residuals can also be helpful. However, engineering understanding of the physical structure and the finite element model is almost always the most important factor. In particular, close inspection of mode shapes to recognize parameters for updating in highly strained regions is a skill that the practitioner should aim to develop for great advantage in model updating.

9.1 Automotive Example Problem

In the following the automotive exhaust system shown in Fig. 25 shall be updated and validated with particular focus on global vibration behavior and damping. Special attention will be paid to the modeling of interface stiffnesses and damping using the bottom-up strategy introduced above. The identification of local damping parameters will be carried out at every validation step. One important aspect of this procedure is that the properties of the individual joints can be developed separately.

Fig. 25 Complete automotive exhaust system with shaker excitation

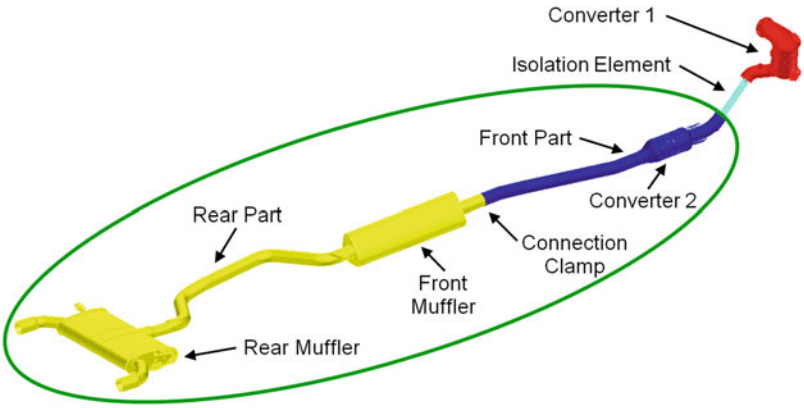

Fig. 26 Components and subsystems of the exhaust system

For the bottom-up concept, the exhaust system needs to be separated into a number of components, subsystems, and subassemblies. Figure 26 shows the chosen subsystems:

At the component level:

- Converter 1
- Isolation element
- Front part including converter 2
- Rear part with mufflers

At the subassembly and system levels:

- Assembly of rear and front part (outlined in green in Fig. 26)
- Complete system

Each component and each (sub-) assembly are first subjected to an experimental modal analysis. Frequency response functions are experimentally determined, and eigenfrequencies and eigenvectors are identified. Model updating is then carried out step by step starting at the component level and leading eventually to the overall system. The bottom-up procedure has several advantages:

- Structural modeling deficiencies of components can be located more easily and resolved.
- The number of candidate parameters at each validation step can be kept low, which improves convergence and uniqueness of the updating process, and favors the finding of physically meaningful results.
- For the validation of the (sub-) assemblies, the main focus can be set on the interfaces (joints) between the constituent components, where generally the largest modeling uncertainties exist.
- The separate consideration of joints allows the identification of individual joint parameters (stiffness and damping).

In what follows, the bottom-up process is demonstrated on the rear part of the exhaust system at the component level. Then the rear and front parts (*Assembly I*, encircled in Fig. 26) are considered at the subassembly level.

9.1.1 Component Level

The agreement of finite element eigenfrequencies and eigenvectors with data determined from experimental modal tests for each component is checked and, if necessary, improved by adjusting mass distributions as well as local stiffnesses by remodeling and model updating. Frequency deviations and MAC values serve as evaluation criteria for the achieved quality of the finite element model.

Figure 27 and Table 3 show the initial correlation, i.e., the MAC matrix as well as the MAC values and frequency deviations. The first six eigenvectors exhibit promising MAC values greater than 80%, but there are two large frequency deviations of more than 4%.

As the first step, the masses of the finite element model and of the physical part are compared and reviewed. The total masses match sufficiently well. If large deviations had been found, the mass of the finite element model could be adjusted either globally or locally via the densities of the materials or by (additional) mass elements representing single local masses. At the second step, local stiffnesses of the finite element model are updated, typically shell thicknesses and Young's moduli. Preferably model areas are selected for update which either exhibit a certain degree of modeling uncertainty or are especially sensitive to parameter changes.

The already mapped eigenvectors of the rear part of the exhaust system represent global bending modes, characterizing the global vibration behavior of the overall setup. Since the bending modes are primarily influenced by the stiffness of the tube between the two mufflers, the modulus of elasticity of the pipe is chosen as the update parameter. Eigenvectors that were not paired are basically local vibration modes of the mufflers with limited influence on the global dynamic behavior of the

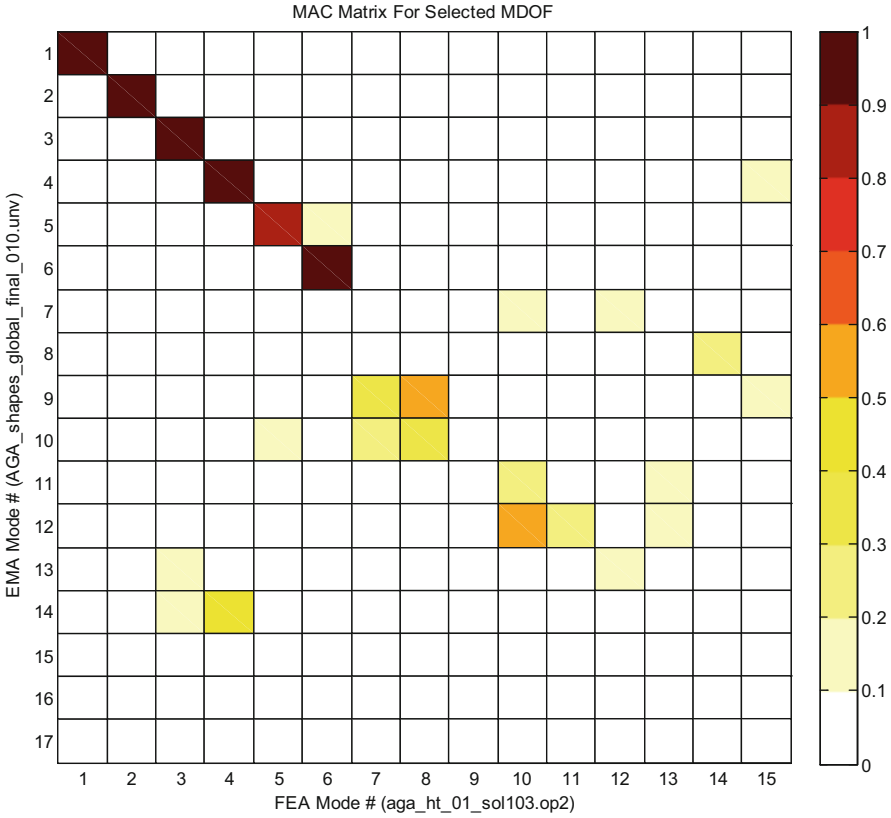

Fig. 27 Initial MAC matrix for the rear part of the exhaust system

Table 3 Initial correlation for the rear part of the exhaust system

No.	EMA	FEA	EMA [Hz]	FEA [Hz]	Dev. [%]	MAC [%]
1	1	7	12.67	12.88	1.70	96.98
2	2	8	22.72	23.99	5.59	93.55
3	3	9	33.74	35.29	4.59	95.65
4	4	10	49.52	50.06	1.10	95.99
5	5	11	61.37	61.28	−0.14	83.27
6	6	12	69.94	70.27	0.46	92.92
7	9	14	173.35	169.54	−2.19	57.83
8	12	16	282.53	260.21	−7.90	52.64
30%	Upper limit of frequency deviations					
50%	Lower limit for MAC values					

overall setup. Therefore, proper representation of these local modes is rated as less important.

The actual model update is carried out using the dedicated model validation software ICS.sysval [57] that makes special use of the MSC.Nastran structural optimization capabilities (SOL200). The software allows for a direct use of Nastran models and thus is capable of handling industrial size finite element models.

The quality of the updated rear part of the exhaust system is presented in Fig. 28 and Table 4. The MAC values are improved by the changes applied to the model, and the relative frequency deviations are, except for one eigenfrequency, now below 3%. This result can be regarded as good with respect to the goal of validating the global vibration behavior of the complete exhaust system.

After the successful adaptation of mass and stiffness, the updating process concentrates on the damping. For this purpose damping must be defined in the finite element model locally, e.g., as structural damping for individual materials or parts of the model or as discrete viscous damping, e.g., for joints.

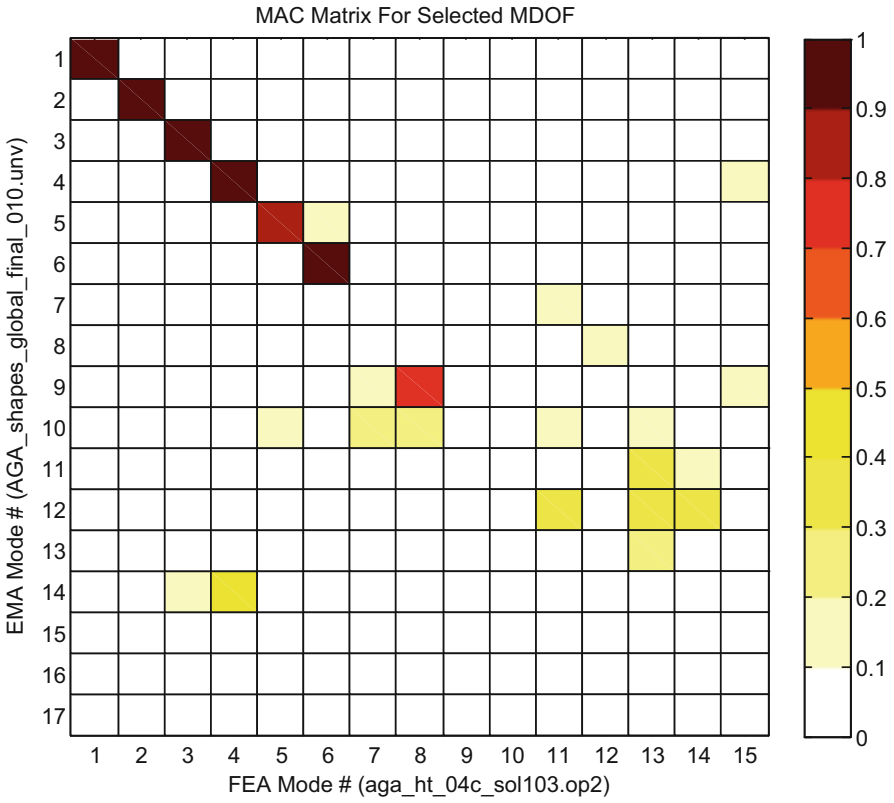

Fig. 28 MAC matrix after model update for the rear part of the exhaust system

Table 4 Correlation after model update for the rear part of the exhaust system

No.	EMA	FEA	EMA [Hz]	FEA [Hz]	Dev. [%]	MAC [%]
1	1	1	12.67	12.45	−1.71	96.97
2	2	2	22.72	23.38	2.87	94.07
3	3	3	33.74	34.20	1.37	96.42
4	4	4	49.52	49.87	0.71	96.18
5	5	5	61.37	60.23	−1.86	88.67
6	6	6	69.94	68.60	−1.91	94.34
7	9	8	173.35	167.25	−3.52	73.13
30%	Upper limit of frequency deviations					
50%	Lower limit for MAC values					

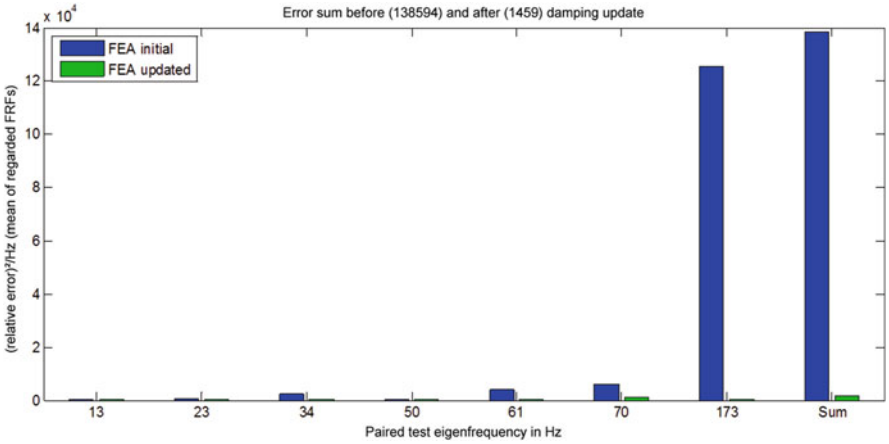

Fig. 29 Error sums before (FEA initial, left) and after (FEA updated, right) damping update for the rear part of the exhaust system

The evaluation of the finite element model in terms of damping is based on the frequency-domain displacement residual. The non-paired eigenfrequencies of the local modes are disregarded. By adjusting the damping, the differences between the analytical and measured FRF peaks are minimized at the paired eigenfrequencies. During the model update process, the convergence should be checked for different damping seed values manually selected based on user experience. By cataloging identified damping values for typical cases, a knowledge database can be obtained for material and joint damping that may be used for future modeling tasks.

For the rear part of the exhaust system, structural damping of materials (muffler housings, acoustic wool in mufflers, and connecting tube) was selected as update parameters. Figure 29 shows the individual error sums before (left bars) and after (right bars) updating the damping, as well the total sum for all paired measured eigenfrequencies (the pair of bars to the extreme right). Figure 30 shows a measured FRF next to its counterpart calculated with the finite element model before and after

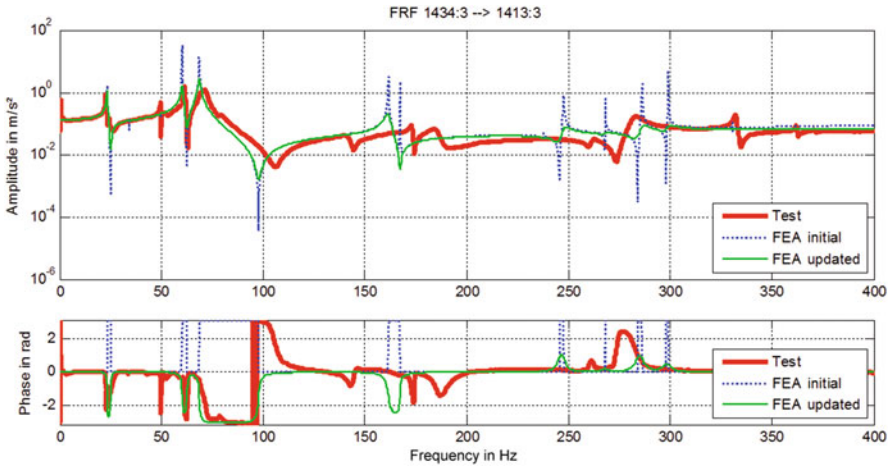

Fig. 30 Example of FRFs before (FEA initial) and after (FEA updated) damping update for the rear part of the exhaust system

damping updating. The reduction of the error sums due to the damping update and the significantly improved match of the FRFs in the resonance areas are clearly visible.

9.1.2 Subassembly Level

After successful model updating of all components with respect to mass, stiffness, and damping, the joints within the assemblies can be updated. The approach is similar to that taken with the components: first the overall mass is checked and, if necessary, adjusted; second the stiffnesses of the joints are assessed based on relative frequency deviations and MAC values and if necessary updated. Then, in the third step, the joint damping is updated based on the deviations of the calculated FRFs from their measured counterparts.

In the case of *Assembly I* of the exhaust system (consisting of the rear and the front part), the clamped joint is represented in the finite element model by a completely modeled clamp assembly. For model updating Young's modulus and structural damping of the clamp material are chosen as updating parameters. Alternatively, a spring/viscous damper element representation of the clamp could have been considered.

Figure 31 and Table 5 show the MAC matrix and the correlation table after stiffness update of the clamp. For *Assembly I* 12 global vibration modes can be paired with high or very high MAC values. The relative frequency deviations are below 3% for the first eight natural frequencies. Figure 32 shows a FRF from the test, as well as its FE-generated counterpart before and after damping updating. Again, the updating of damping significantly reduces the deviations in the resonance regions between calculation and test.

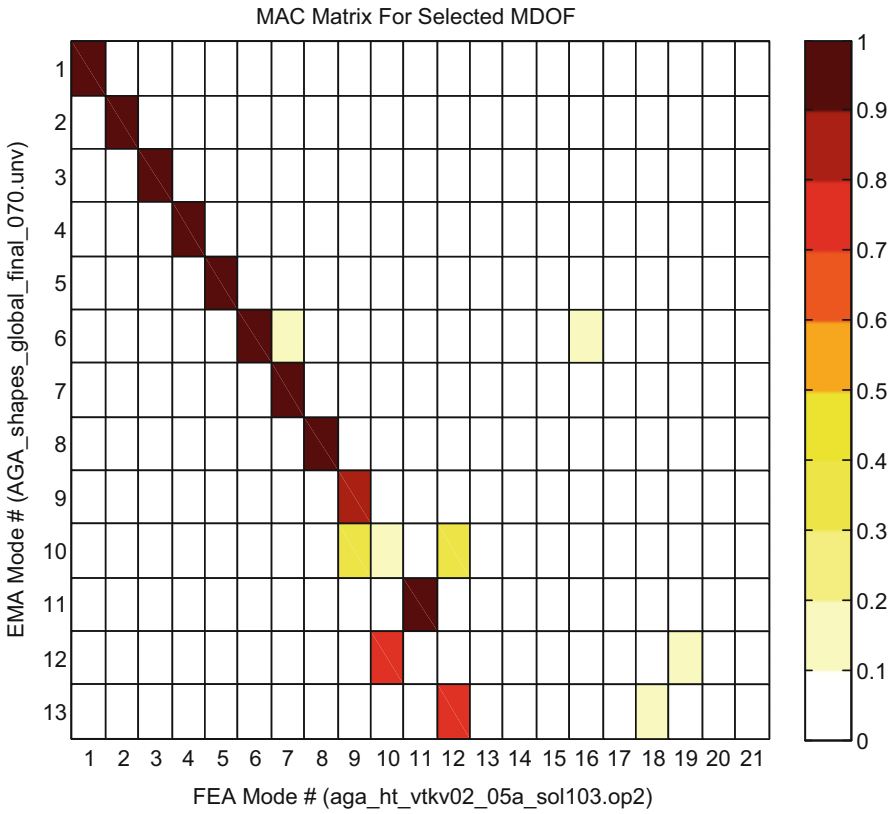

Fig. 31 MAC matrix after model update for *Assembly I*

10 Conclusions

This chapter describes the complete procedure for finite element model updating by the sensitivity method. It begins with the general formulation of an objective function and linearization of the output in terms of parameters, thereby permitting parameter estimation by iteration. After the separate treatment of systematic errors, typically model structure errors, the procedure consists essentially of defining a residual, describing the finite element discrepancy with respect to test data, such as eigenfrequencies, modes shapes, or frequency response functions. The resulting equations are generally ill-conditioned and require regularization by the application of side constraints. The corner of the L-curve defines an optimal value of the regularization parameter that maximizes the condition of the combined system of updating equations and side constraints. The selection of updating parameters is a

Table 5 Correlation after model update for *Assembly I*

No.	EMA	FEA	EMA [Hz]	FEA [Hz]	Dev. [%]	MAC [%]
1	1	1	7.53	7.46	−0.88	97.81
2	2	2	10.55	10.62	0.71	95.68
3	3	3	23.70	23.77	0.28	94.23
4	4	4	31.79	32.01	0.71	91.12
5	5	5	42.28	41.75	−1.25	95.02
6	6	6	53.48	53.77	0.55	93.27
7	7	7	61.71	60.37	−2.17	95.81
8	8	8	69.33	70.14	1.17	94.46
9	9	9	128.42	136.66	6.41	83.50
10	11	11	162.16	169.27	4.38	90.63
11	12	10	173.73	166.22	−4.32	77.50
12	13	12	195.36	184.26	−5.69	72.69
30%	Upper limit of frequency deviations					
50%	Lower limit for MAC values					

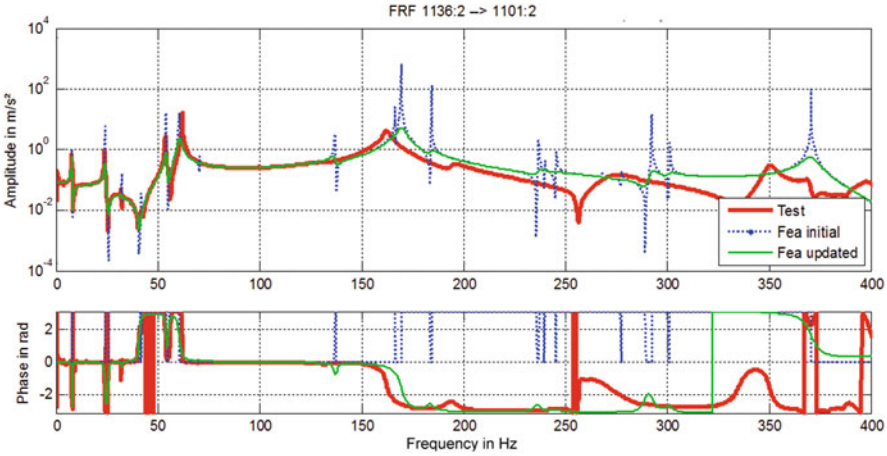

Fig. 32 Example of FRFs before and after damping updating for *Assembly I*

crucial step requiring deep understanding of the physical test structure and the finite element model. Numerous parametrization techniques are described. Stochastic model updating is capable of determining the statistics (means and covariances) of updating parameters responsible for observed output variability in nominally identical test structures. Updated models are usually said to be validated when demonstrated to be capable of predicting the behavior of the physical system under different conditions from those used in the updating process. Numerical examples are used throughout to illustrate the main points.

Finally, an industrial example, that of an automotive exhaust system, representative of many multicomponent engineering assemblies, is described. The bottom-up strategy is adopted, whereby the standard process of mass and stiffness updating is improved by carrying out additional updating of damping parameters. This leads to a significantly improved match between calculated and measured FRFs. The highlighted procedure for damping update is in particular important for nonmetallic materials such as catalyst ceramics and for joints, where reliable damping parameters are not readily available. The validated finite element model of the assembly matches the measured eigenfrequencies, eigenvectors, and FRFs much better than the initial model, while realistic damping estimates are obtained, thereby highlighting the potential of the model updating and model validation procedures.

Acknowledgments The content and images presented for the automotive example problem are published with the kind permission of the Volkswagen AG, Germany.

References

1. Adhikari S, Friswell MI (2010) Distributed parameter model updating using the Karhunen-Loève expansion. Mech Syst Signal Process 24:326–339
2. Ahmadian H, Gladwell GML, Ismail F (1997) Parameter selection strategies in finite element model updating. ASME J Vib Acoust 119:37–45
3. Ahmadian H, Mottershead JE, Friswell MI (1998) Regularisation methods for finite element model updating. Mech Syst Signal Process 12(1):47–64
4. Ahmadian H, Mottershead JE, Friswell MI (2002) Physical realisation of generic element parameters in model updating. Trans Am Soc Mech Eng J Vib Acoust 124(4):628–632
5. Au SK (2012) Connecting Bayesian and frequentist quantification of parameter uncertainty in system identification. Mech Syst Signal Process 29:328–342
6. Balmes E (1997) Garteur Group on Ground Vibration Testing – results from the tests of a single structure by 12 laboratories in Europe. Proceedings of the International Modal Analysis Conference IMAC XV, Orlando, pp 1346–1352
7. Batou A (2015) Model updating in structural dynamics – uncertainties on the position and orientation of sensors and actuators. J Sound Vib 354:47–64
8. Beck JL, Katafygiotis L (1998) Updating models and their uncertainties. I: Bayesian statistical framework. J Eng Mech 124(4):445–461
9. Behmanesh I, Moaveni B, Lombaert G, Papadimitriou C (2015) Hierarchical Bayesian model updating for structural identification. Mech Syst Signal Process 64–65:360–376
10. Carvalho J, Datta BN, Gupta A, Lagadapati M (2007) A direct method for model updating with incomplete measured data and without spurious modes. Mech Syst Signal Process 21:2715–2731
11. Collins JD, Hart GC, Hasselman TK, Kennedy B (1974) Statistical identification of structures. AIAA J 12(2):185–190
12. D'Ambrogio W, Fregolent A (2000) The use of antiresonances for robust model updating. J Sound Vib 236:227–243
13. Datta BN, Deng S, Sokolov VO, Sarkissian DR (2009) An optimization technique for damped model updating with measured data satisfying quadratic orthogonality constraints. Mech Syst Signal Process 23:1759–1772
14. Degener M (1997) Ground vibration results from the tests of an aircraft model performed as part of an European round robin exercise. Proceedings of the CEAS international forum on aeroelasticity and structural dynamics, Rome

15. Degener M, Hermes H (1996) Ground vibration test and finite element analysis of the GARTEUR SM-AG19 testbed. Deutsche Forschungsanstalt für Luft- und Raumfahrt e V Institut für Aeroelastik, IB 232-96 J 08
16. Fang SE, Ren WX, Perera R (2012) A stochastic model updating method for parameter variability quantification based on response surface models and Monte-Carlo simulation. Mech Syst Signal Process 33:83–96
17. Fang SE, Zhang QH, Ren WX (2015) An interval model updating strategy using interval response surface models. Mech Syst Signal Process 60–61:909–927
18. Fox R, Kapoor M (1968) Rate of change of eigenvalues and eigenvectors. AIAA J 6:2426–2429
19. Friswell MI (1989) The adjustment of structural parameters using a minimum variance estimator. Mech Syst Signal Process 3(2):143–155
20. Friswell MI, Mottershead JE (1995) Finite element model updating in structural dynamics. Kluwer Academic Publishers, Dordrecht
21. Friswell MI, Mottershead JE, Ahmadian H (1998) Combining subset selection and parameter constraints in model updating. Trans Am Soc Mech Eng J Vib Acoust 120(4):854–859
22. Friswell MI, Mottershead JE, Ahmadian H (2001) Finite element model updating using experimental test data: parameterisation and regularisation. R Soc Philos Trans Math Phys Eng Sci 359:169–186
23. Gladwell GML, Ahmadian H (1995) Generic element matrices suitable for finite element model updating. Mech Syst Signal Process 9(6):601–614
24. Goller B, Pradlwarter HJ, Schuëller GI (2009) Robust model updating with insufficient data. Comput Methods Appl Mech Eng 198:3096–3104
25. Goller B, Broggi M, Calvi A, Schuëller GI (2011) A stochastic model updating technique for complex aerospace structures. Finite Elem Anal Des 47:739–752
26. Goulet J-A, Michel C, Smith IFC (2013) Hybrid probabilities and error domain structural identification using ambient vibration monitoring. Mech Syst Signal Process 37:199–212
27. Govers Y, Link M (2010) Stochastic model updating – covariance matrix adjustment from uncertain experimental modal data. Mech Syst Signal Process 24(3):696–706
28. Govers Y, Link M (2012) Using stochastic experimental modal data for identifying stochastic finite element parameters of the AIRMOD benchmark structure. Proceedings of the international conference on noise and vibration engineering, USD2012, Leuven, Belgium, pp 4697–4715
29. Hansen PC (1994) Regularisation tools: a MATLAB package for analysis and solution of discrete ill-posed problems. Numer Algorithms 6:1–35
30. Hua XG, Ni YQ, Chen ZQ, Ko JM (2008) An improved perturbation method for stochastic finite element model updating. Int J Numer Methods Eng 73:1845–1864
31. Hua XG, Ni YQ, Ko JM (2009) Adaptive regularisation parameter optimization in output-error-based finite element model updating. Mech Syst Signal Process 23:563–579
32. Hua XG, Wen Q, Ni YQ, Chen ZQ (2017) Assessment of stochastically updated finite element models using reliability indicator. Mech Syst Signal Process 82:217–229
33. Jacquelin E, Adhikari S, Friswell MI (2012) A second-moment approach for direct probabilistic model updating in structural dynamics. Mech Syst Signal Process 29:262–283
34. Katafygiotis L, Beck JL (1998) Updating models and their uncertainties. II: model identifiability. J Eng Mech 124(4):463–467
35. Kenigsbuch R, Halevi Y (1998) Model updating in structural dynamics: a generalised reference basis approach. Mech Syst Signal Process 12(1):75–90
36. Khodaparast HH, Mottershead JE, Friswell MI (2008) Perturbation methods for the estimation of parameter variability in stochastic model updating. Mech Syst Signal Process 22(8):1751–1773
37. Khodaparast HH, Mottershead JE, Badcock KJ (2011) Interval model updating with irreducible uncertainty using the Kriging predictor. Mech Syst Signal Process 25(4):1204–1226
38. Kuo Y-C, Datta BN (2012) Quadratic model updating with no spillover and incomplete measured data: existence and computation of solution. Linear Algebra Appl 436:2480–2493

39. Lallement G, Piranda J (1990) Localisation methods for parameter updating of finite element models in elastodynamics. IMAC IIX, Orlando, pp 579–585
40. Link M (1999) Updating of analytical models – basic procedures and extensions. In: Silva JMM, Maia NMM (eds) Modal analysis and testing. Kluwer Academic Publishers, Dordrecht, pp 281–304
41. Link M, Friswell MI (2003) Working group 1: generation of validated structural dynamic models- results of a benchmark study Utilising the GARTEUR SM-AG19 test-bed. In: Golinval J-C, Link M (eds) COST action F3 "structural dynamics" (1997–2001)- an European co-operation in the field of science and technology. Mechanical Systems & Signal Processing, vol 17, no (1), pp 9–20
42. Mao X, Dai H (2012) Finite element model updating with positive definiteness and no spillover. Mech Syst Signal Process 28:387–398
43. Mares C, Mottershead JE, Friswell MI (2006) Stochastic model updating: part 1- theory and simulated examples. Mech Syst Signal Process 20(7):1674–1695
44. Mottershead JE, Foster CD (1991) On the treatment of ill-conditioning in spatial parameter estimation from measured vibration data. Mech Syst Signal Process 5(2):139–154
45. Mottershead JE, Friswell MI (1993) Model updating in structural dynamics: a survey. J Sound Vib 167(2):347–375
46. Mottershead JE, Friswell MI, Ng GHT, Brandon JA (1996) Geometric parameters for finite element model updating of joints and constraints. Mech Syst Signal Process 10(2):171–182
47. Mottershead JE, Mares C, Friswell MI, James S (2000) Selection and updating of parameters for an aluminium space-frame model. Mech Syst Signal Process 14(6):923–944
48. Mottershead JE, Mares C, James S, Friswell MI (2006) Stochastic model updating: part 2- application to a set of physical structures. Mech Syst Signal Process 20(8):2171–2185
49. Mottershead JE, Link M, Friswell MI (2011) The sensitivity method in finite element model updating: a tutorial. Mech Syst Signal Process 25(7):2275–2296
50. Mthembu L, Marwala T, Friswell MI, Adhikari S (2011) Model selection in finite element model updating using the Bayesian evidence statistic. Mech Syst Signal Process 25:2399–2412
51. Natke HG (1991) On regularization methods applied to the error localization of mathematical models. Proc Int Modal Analysis Conf IMAC IX, Florence, pp 70–73
52. Natke HG (2004) Einführung in Theorie und Praxis der Zeitreihen und Modalanalyse. Vieweg Verlag, Braunschweig/Wiesbaden
53. Natke HG, Lallement G, Cottin N (1995) Properties of various residuals within updating of mathematical models. Inverse Prob Eng 1:329–348
54. Patelli E, Govers Y, Broggi M, Martins Gomes H, Link M, Mottershead JE (2017) Sensitivity or Bayesian model updating: a comparison of techniques using the DLR AIRMOD test data. Arch Appl Mech 87(5):905–925
55. Prells U (1996) A regularisation method for the linear error localisation of models of elastomechanical systems. Inverse Prob Eng 3:197–217
56. Schedlinski C (2012) Finite element model validation of a large spinning facility. Proceedings, ISMA 2012, Leuven
57. Schedlinski C (2018) ICS.sysval product description. http://www.ics-engineering.com
58. Schedlinski C, Staples B (2004) Computational model updating of axisymmetric systems. Proceedings of the noise and vibration engineering conference, ISMA 2004, Leuven
59. Schedlinski C, et al (2004) Experimental modal analysis and computational model updating of a body in white. Proceedings of the noise and vibration engineering conference, ISMA 2004, Leuven
60. Schedlinski C, et al (2008) Computational model updating of structural damping and acoustic absorption for coupled fluid-structure-analyses of passenger cars. Proceedings of the Noise and Vibration Engineering Conference, ISMA 2008, Leuven
61. Silva T, Maia NMM, Link M, Mottershead JE (2016) Parameter selection and covariance updating. Mech Syst Signal Process 70–71:269–283
62. Simoen E, De Roeck G, Lombaert G (2015) Dealing with uncertainty in model updating for damage assessment: a review. Mech Syst Signal Process 56–57:123–149

63. Smith SW (1998) Iterative matrix approximation for model updating. Mech Syst Signal Process 12(1):187–202
64. Tikhonov AN, Arsenin VY (1977) Solutions of ill-posed problems. Wiley, New York
65. Titurus B, Friswell MI (2008) Regularization in model updating. Int J Numer Methods Eng 75(4):440–478
66. Wang X, Hill TL, Neild SA, Shaw AD, Khodaparast HH, Friswell MI (2018) Model updating strategy for structures with localized nonlinearities using frequency response measurements. Mech Syst Signal Process 100:940–961
67. Webber B, Paultre P, Proulx J (2009) Consistent regularisation of nonlinear model updating for damage identification. Mech Syst Signal Process 23:1965–1985
68. Xie D (2011) A numerical method of structure-preserving model updating problem and its perturbation theory. Appl Math Comput 217:6364–6371
69. Yuan Y (2009) A symmetric inverse eigenvalue problem in structural dynamic model updating. Appl Math Comput 213:516–521
70. Yuen K-V (2010) Bayesian methods for structural dynamics and civil engineering. Wiley, Singapore
71. Yuen K-V (2012) Updating large models for mechanical systems using incomplete modal measurement. Mech Syst Signal Process 28:297–308
72. Zhang EL, Feissel P, Antoni J (2011) A comprehensive Bayesian approach for model updating and quantification of modelling errors. Probab Eng Mech 26:550–560

Nonlinear System Analysis Methods

17

Janette J. Meyer, Raymond M. Bond, and Douglas E. Adams

Contents

J. J. Meyer
School of Engineering, Vanderbilt University, Nashville, TN, USA
e-mail: janette.j.meyer@vanderbilt.edu

R. M. Bond · D. E. Adams (✉)
Vanderbilt University, Nashville, TN, USA
e-mail: ray.bond@vanderbilt.edu; douglas.adams@vanderbilt.edu

R. Allemang, P. Avitabile (eds.), *Handbook of Experimental Structural Dynamics*,
https://doi.org/10.1007/978-1-4614-4547-0_22

Abstract

Practical techniques for experimentally detecting and characterizing system nonlinearities are demonstrated through a test bed consisting of a composite panel, both with and without a disbond, undergoing an electrodynamic shaker excitation. Techniques for detecting and characterizing system nonlinearities are applied to force and response data collected from this test bed, and then models are identified for those nonlinearities. Both time and frequency domain techniques are utilized, and the underlying theory and experimental requirements for each technique are discussed. References to the literature are provided throughout the chapter for more in-depth discussion of the techniques.

Keywords

Nonlinearity · Coherence · FRF distortion · Higher-order FRFs · Hilbert transform · Restoring force · Vibro-acoustic modulation · NARMAX · Direct parameter estimation · Reverse path · NIFO

Nomenclature

$x(t)$	Time domain response
$f(t)$	Time domain input
$X(\omega)$	Frequency domain response
$F(\omega)$	Frequency domain input
ω, Ω	Frequency
$G_{xf}(\omega)$	Average cross-spectral density
$G_{xx}(\omega)$, $G_{ff}(\omega)$	Average auto-spectral densities
$H(\omega)$	Frequency response function (FRF)
$H_n(\omega)$	nth order FRF
m, k, c; $[M]$, $[K]$, $[C]$	Linear mass, stiffness, damping
$[B(\omega)]$	inverse of the FRF matrix
$f_i(\{x\}, \{\dot{x}\}$	Functional form of the i^{th} nonlinearity
$[A_i]$	Coefficients of nonlinear model terms

1 Introduction

Nonlinearities abound in structural dynamic systems. While idealized linear stiffness and damping representations are effective for characterizing many structures, a wide range of materials, joints, or loading scenarios present stiffness or damping characteristics which change significantly based on the amplitude or direction of the response. This dependence of the stiffness or damping on the response is a hallmark of a nonlinear structural dynamic system. Some materials have inherent nonlinear stiffness and damping characteristics. For instance, most elastomeric isolators provide a stiffness that varies with the relative displacement that is experienced

across the isolator. Joints can also exhibit nonlinear characteristics because the internal forces imposed by the joint on a structural assembly vary with the relative motion across the joint. Backlash, which is a form of hysteresis, is an example of this type of nonlinear behavior introduced by bolted joints. Other sources of nonlinear stiffness include structural members that are preloaded in compression, which allows for buckling as the structure dynamically responds. Nonlinear damping is common as well, and it can, in some cases, result in dynamic phenomena that would be impossible in linear systems. For instance, in cases where fluid-structure interaction injects a type of nonlinear damping, sustained steady-state oscillations can be present in the absence of a cyclic forcing function. Even sensors and data acquisition systems can introduce nonlinear effects in experimental measurements as in the case of clipping of a measurement or operating the sensor outside its linear calibration range.

Because there are many possible sources of nonlinearity, it is fortunate for the experimentalist that there are many tools available for system identification of these nonlinearities. There are nonlinear analysis methods based in the time domain and methods based in the frequency domain, methods that use sinusoidal excitations and methods that use random excitations, and so on. This chapter does not discuss every possible method for analyzing experimental structural dynamic data but, rather, presents a set of representative methods applied to an experimental test bed. Through these examples, we will illustrate how these methods work, how the methods are similar, and how the methods are different in terms of the data and signal processing techniques required. These examples are meant to illustrate a set of considerations that an experimentalist might evaluate when selecting the best method for nonlinear system identification – comprised of detecting nonlinearity, characterizing nonlinearity, and estimating the parameters in a nonlinear model of a nonlinear structural dynamic system – in a particular application.

Despite the wide range of methods that are available for nonlinear system identification, there are a number of common considerations when implementing any of these methods. Some of these recommended "best practices" in nonlinear system identification include the following:

- When the option is available, acquire time histories, and do not perform any averaging of the data upfront. This practice is recommended because nonlinearity is often masked through the averaging process. Likewise, the experimentalist should keep in mind that both correlated and uncorrelated noise that appears on the excitation and response measurements can change the nonlinear technique that is most suitable for a particular experiment. This is because noise in the excitation measurement is filtered by input nonlinearities (e.g., $u^2(t)$ where $u(t)$ denotes an excitation time history) whereas noise in the response measurement is filtered by output nonlinearities (e.g., $x^3(t)$ where $x(t)$ denotes a response time history).
- In order to fully observe both modal (or linear) response characteristics and nonlinear characteristics that accompany these modal responses, the sampling frequency should be set high enough to ensure that the effects of aliasing do

not inhibit the nonlinear analysis process. A higher sampling frequency than needed for a corresponding linear system may be required because nonlinearities introduce additional response characteristics that are nonlinear functions of the modal responses (e.g., harmonics, modulation).

- The correct forcing function must be selected depending on the nonlinear system identification approaches that are chosen. For example, when the experimentalist seeks to detect bifurcation in the steady-state dynamic response amplitude, a slow swept sinusoidal excitation is recommended because these excitations provide experimental data that can be analyzed to detect and track the dynamic response through a bifurcation. Several theoretical studies for validation of test results are also facilitated through the use of sinusoidal excitations.
- It is recommended that the measurement degrees of freedom be selected in the experiment in order to fully observe the parts of the system that are thought to potentially exhibit localized nonlinearities. For example, it is recommended that response measurements on both sides of a mechanical joint be used to fully observe the relative motion across the joint.
- When designing the experiment and selecting the test parameters, the experimentalist should keep in mind that all aspects of the system, such as the stiffness and damping as well as the steady-state response, can depend on the initial conditions and the amplitude of the excitation and response. For example, one commonly employed method for studying these dependencies is to select different amplitudes of excitation for different tests in order to selectively expose nonlinear behaviors in the locations of the structural system.

In the remainder of this chapter, an experimental test bed that will be used to apply a number of nonlinear experimental identification method is first described. Then, various methods for the detection, characterization, and parameter estimation of nonlinear systems are summarized and applied to this experimental test bed. For each of these methods, the underlying theory that connects nonlinear phenomena to the corresponding nonlinear identification approach is also discussed. Some of the advantages and drawbacks of these techniques are described along the way to provide the experimentalist with guidance on selecting the most appropriate methods for a particular application.

2 Experimental Setup

Figure 1 shows the experimental setup used to demonstrate many of the nonlinear analysis methods described below. The same experimental setup will be used to demonstrate the application of the methods presented here in order to allow the reader to better compare and contrast the methods. The test specimen used were sandwich composite panels each comprised of two fiberglass face sheets bonded to an aluminum honeycomb core. Two panels of the same size were used during

testing, both measuring about 20 cm by 20 cm. The first panel was unmodified after fabrication, while a portion of the face sheet of the second panel was separated from the core using a razor blade. The purpose of this modification was to introduce a significant nonlinearity into the structure. The disbond between the face sheet and core creates a nonlinear stiffness because the interface between the core and the face sheet has zero stiffness in tension but significant stiffness in compression. During testing, the edges of two sides of the panel were clamped to steel blocks using aluminum beams screwed to the blocks, as shown in Fig. 1. Foam tape was used between the beam and the panel and between the panel and the steel block to prevent rattling, which is a common source of nonlinearities in experimental setups. Screws were tightened using a torque wrench to provide consistent boundary conditions.

Several different excitation methods and waveforms were used throughout testing to accommodate the requirements of the different analysis methods. The main excitation source was an electrodynamic shaker (SmartShaker K2007E01) with a carbon fiber stinger attached to the back side of the panel. Single frequency sine waves, sine sweeps, stepped sine, and random inputs were used. In addition to shaker inputs, an instrumented impact hammer (PCB 086C03) was used to provide impulsive inputs to the panel. Finally, a piezoelectric stack actuator (PI P-010.10P) was used for high-frequency, sinusoidal excitation. Input forces from the shaker and the actuator were measured using force sensors (PCB 288D01 and PCB 208C03). Figure 2 shows the shaker and piezo-actuator force sensors attached to the test structure.

Three different measurement systems were used to measure the response of the panels. The three-dimensional scanning laser vibrometer (Polytec PSV-400-3D) shown in Fig. 3 was used to measure the surface velocity of the panel. A one-dimensional laser displacement sensor (Keyence LK-H157) was used to measure the displacement of the panel. And, a single axis accelerometer (PCB 352C22) was used

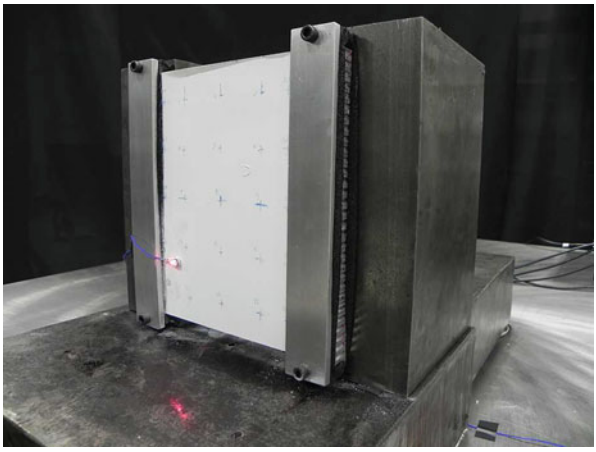

Fig. 1 Test specimen and fixture

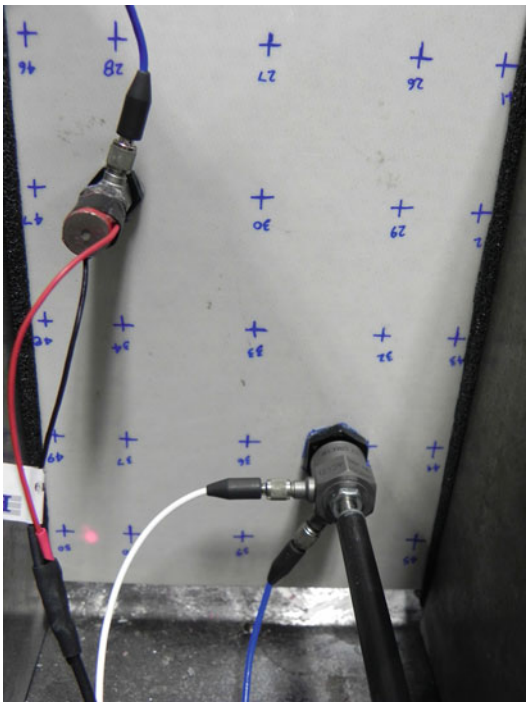

Fig. 2 Force sensors used to measure input from the stack actuator (top left) and shaker (bottom right)

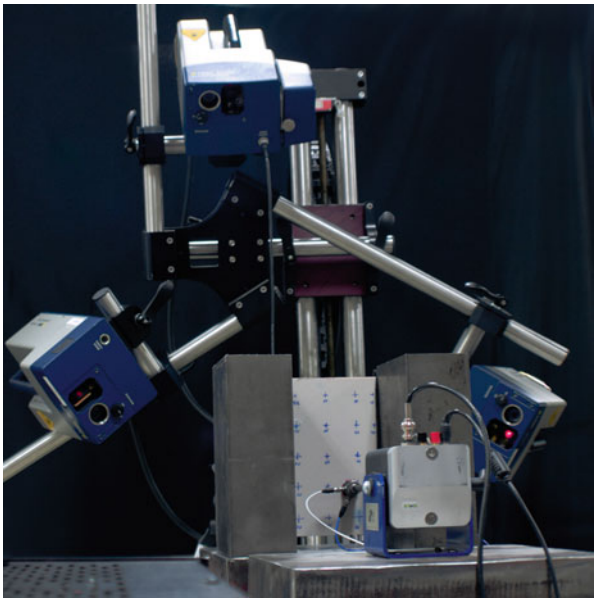

Fig. 3 Laser vibrometer used to measure response of the panels

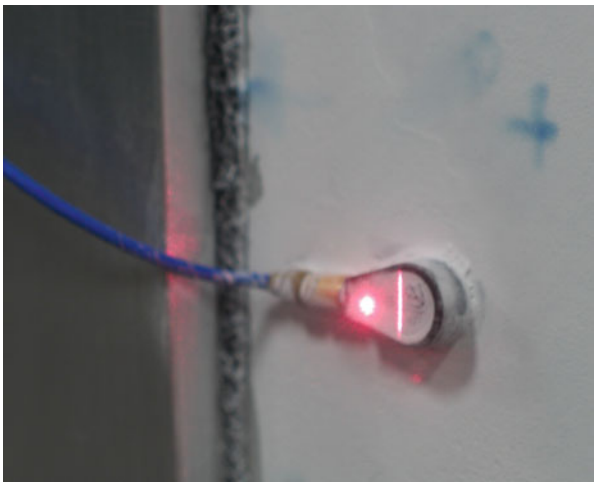

Fig. 4 Accelerometer, three co-located lasers from the vibrometer (red dot), and displacement laser (line)

Table 1 Analysis methods

Detection and characterization	Modeling
Coherence	NARMAX
FRF distortion	Direct parameter estimation
Higher-order FRFs	Reverse path
Hilbert transform (Time)	NIFO
Hilbert transform (Freq.)	
Restoring force	
Vibro-acoustic modulation	

to measure the acceleration of the panel. For most tests, only the laser vibrometer was used to measure the response. In some tests, the response of the panel was measured simultaneously using all three measurement systems, as shown in Fig. 4. Table 1 lists the analysis methods presented in the remainder of the chapter.

3 Methods for Nonlinear Characterization

3.1 Coherence

Perhaps the most straight forward to apply but least conclusive test for nonlinear behavior is examining the coherence of a set of measured input and output data when performing a modal test to estimate frequency response functions (FRFs) for a system. Coherence is typically calculated during the course of a test, so it is a convenient first check for symptoms of structural nonlinearities. Careful interpretation must be used when trying to identify nonlinearities through coherence, because low coherence can be caused by a number of other factors, and a nonlinear system may

show high coherence if all input data is consistent and the system is linearizable at typical input levels.

To review, coherence is a measure of the quality of fit for a linear FRF estimated using a set of input/output measurements [2]. For a system with response $x(t)$ and input $f(t)$, the coherence function, $\gamma_{xf}^2(\omega)$, is a function of average cross-spectral density ($G_{xf}(\omega)$) and auto-spectral densities ($G_{xx}(\omega)$,$G_{ff}(\omega)$):

$$\gamma_{xf}^2(\omega) = \frac{|G_{xf}(\omega)|^2}{G_{xx}(\omega)G_{ff}(\omega)} \tag{1}$$

where ω is the frequency.

For the theoretical case where the system is linear and there is no error or noise in the measurements, the coherence is unity for all frequencies. In real-world measurements of linear systems, the coherence is typically high at frequencies which are well excited with a high signal to noise ratio (SNR). Coherence is typically low for a linear system at anti-resonances or other frequencies where the response amplitude is low, and the SNR is therefore lower.

Low coherence values at frequencies that have poor SNR are to be expected even for linear systems (e.g., at anti-resonances or outside the excitation bandwidth) and should not be confused with an indication of nonlinearity. However, if the coherence is low at frequencies where peaks in the FRF appear and the response amplitude is reasonably high, nonlinearities are one possible explanation. Several other explanations for low coherence should be ruled out before drawing any conclusions about the linearity of the system. For instance, peaks in the FRF with low coherence could be explained by a narrowband input to the system which is not being measured, clipping or saturation of the response signal, or low forcing amplitude at that frequency, causing a peak as a result of a near divide by zero situation. If, however, low coherence is observed where there is a high response amplitude without any other evident sources of error, nonlinearity is a possible cause. Another indication of possible nonlinearities is peaks with low coherence at integer multiples of a linear modal frequency or an excitation frequency. These trends are not definitive, however, so if the coherence of the measurements indicates the possibility of structural nonlinearities, further characterization of these potential nonlinearities is warranted.

3.1.1 Example: Undamaged Panel Versus Panel with Disbond

The coherence of modal impact measurements for each of the panels described in Sect. 2 were determined from data acquired during testing. In this example, measurements from a test that used an impact force and a measured acceleration were used. However, any type of measured output can be used. The choice of input can also vary, as long as the force spans the frequency range of interest. Impacts, sine sweeps, and random excitation are all viable choices.

Each panel was impacted five times at a selected point using an instrumented impact hammer which measures the input force, and the response of the panel was

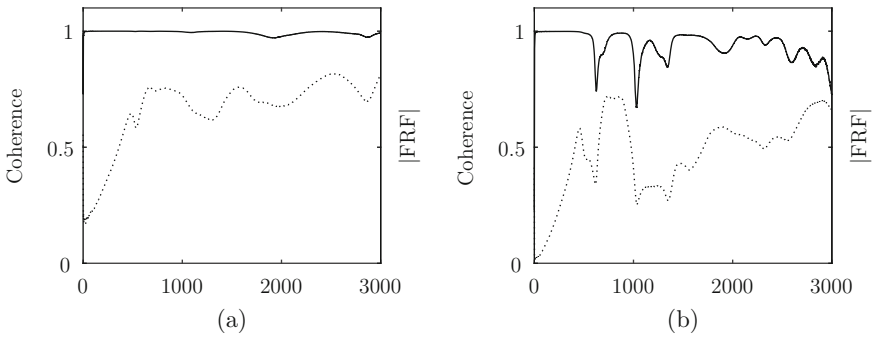

Fig. 5 Coherence (——) and corresponding FRF (- - -) determined from impact testing. (**a**) Undamaged panel. (**b**) Panel with disbond

measured using an accelerometer. Average cross-spectral and auto-spectral densities were calculated from the five data sets, which were then substituted into Eq. 1 to calculate the coherence. Figure 5 shows the results. The value of the coherence of the undamaged panel (solid line) is nearly one across the frequency range excited by the impact, with the exception of anti-resonances (e.g., 2 kHz) seen in the FRF (dotted line). The coherence of the panel with the disbond shows significant deviation from unity at several frequencies. Several dips (e.g., 600 Hz and 1 kHz) correspond to anti-resonances. However, other deviations (e.g., 1.9 kHz) correspond to peaks in the FRF. Because it is known a priori that this panel contains a disbond, these deviations can be attributed to the nonlinearities associated with the disbond. If the condition of the panel was unknown ahead of time or if no undamaged panel was available for comparison, further testing would be needed to confirm the cause of the reduction in coherence.

3.2 Frequency Response Function Distortion

The principle of superposition is fundamental to many of the methods that are used in linear system analysis. As a consequence of superposition, amplifying an input signal by some factor results in the output increasing by the same factor. Nonlinear systems tend to violate this principle, and the resulting effects can be used to detect the presence of structural nonlinearities. The frequency response function (FRF) of a dynamic system describes the amplitude and phase of the output relative to the input in the steady state. The FRF of a linear system is independent of the input amplitude. If inputs of different amplitudes are used to estimate the FRF of a linear system, the FRF will remain the same in the absence of measurement error. Many nonlinear systems, on the other hand, exhibit amplitude dependent nonlinearities, so the FRFs estimated from two different amplitude inputs tend to differ. This behavior can be used to observe and detect nonlinearities by exciting the system at different amplitudes and comparing the estimated FRFs.

Harmonic distortion is a concept related to FRF distortion. Harmonic distortion is the phenomenon exhibited by many nonlinear systems in which the system responds at harmonics of an input frequency. In a linear system, the system responds only at the frequencies excited by the input, but nonlinear systems do not in general obey this rule. By exciting the system with a single frequency and observing the output spectrum, the presence of harmonics of the forcing frequency can be a good indicator of nonlinear behavior.

3.2.1 Example: Undamaged Panel Versus Panel with Disbond

The response of the undamaged panel to a sine sweep generated by the shaker was measured using the 3D laser vibrometer described in Sect. 2. Twenty repetitions of the sweep were performed in order to determine the average auto- and cross-spectral density functions, and the FRF ($H(\omega)$) associated with the input, $f(t)$, and output, $x(t)$, was estimated using the H_1 estimator:

$$H(\omega) = \frac{G_{fx}(\omega)}{G_{ff}(\omega)}. \tag{2}$$

The sweep was repeated at a higher amplitude and a second FRF was estimated. Figure 6a shows the two FRFs. There is little variation between the two FRFs estimated from inputs of different amplitudes, which suggests the system is behaving as a linear system. The same testing and analysis were performed on the panel with the disbond. Unlike the undamaged panel, the response of the damaged panel shows significant amplitude dependence. The high and low FRFs shown in Fig. 6b have noticeable discrepancies, suggesting that the system is nonlinear.

Although a sine sweep excitation and a velocity measurement were used in this example, any excitation method and output measurement that can be used to estimate a system's FRF is a valid choice to perform FRF distortion analysis.

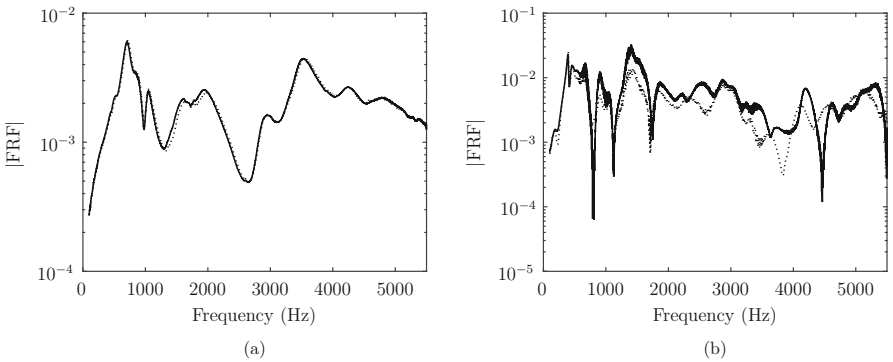

Fig. 6 FRFs determined from low (- - -) and high (——) amplitude inputs. (**a**) Undamaged panel. (**b**) Panel with disbond

3.3 Higher-Order FRFs

Higher-order frequency response functions (FRFs) are a generalization of first-order FRFs which are capable of characterizing nonlinearity in a system's response. In their most general form, higher-order FRFs express a system's response to multi-frequency excitations. The order of the FRF indicates the number of simultaneous frequency components used in the input signal. The complexity of data acquisition, visualization, and analysis increases dramatically with increasing order. To fully determine the higher-order FRF matrices, all possible combinations of excitation frequencies must be applied. Data visualization is challenging beyond second-order FRFs because more than three dimensions are required (first-order FRFs require two dimensions, second-order FRFs require three dimensions, etc.). For these reasons, a simplification is often made to make the method more practical. As developed in [13], a single frequency excitation can be used to determine the diagonal components of the higher-order FRFs, thus simplifying data acquisition and interpretation. The FRFs are called diagonal because they are evaluated along an n-dimensional line of equal frequencies. Some information about a system's response to certain combinations of excitation frequencies is lost with this simplification, but the trade-off in terms of time efficiency is typically justified. Visualization of the diagonal components of each higher-order FRF requires only two dimensions, where the system's response is plotted against the nth multiple of the excitation frequency. By determining the system's response at multiples of the excitation frequency, the type of nonlinearity present in the system can be identified.

Higher-order FRFs are derived from the Volterra model. For a nonlinear system excited by a single frequency excitation ($f(t) = F\mathrm{e}^{j\omega t}$), the relationship between the input, $f(t)$, and output, $x(t)$, is expressed as

$$x(t)=F\mathrm{e}^{j\omega t}\int_{-\infty}^{\infty} h_1(\tau_1)\mathrm{e}^{-\omega\tau_1}\mathrm{d}\tau_1+F^2\mathrm{e}^{j2\omega t}\iint_{-\infty}^{\infty} h_2(\tau_2,\tau_2)\mathrm{e}^{-j2\omega\tau_2}\mathrm{d}\tau_2\mathrm{d}\tau_2+\ldots$$
$$+F^n\mathrm{e}^{jn\omega t}\int_{-\infty}^{\infty}\ldots\int_{-\infty}^{\infty} h_n(\tau_n,\ldots,\tau_n)\mathrm{e}^{-jn\omega\tau_n}\mathrm{d}\tau_n\ldots\mathrm{d}\tau_n. \quad (3)$$

where $h(t)$ is the impulse response of the system. Rewriting in terms of Fourier transforms gives

$$x(t) = H_1(j\omega)F\mathrm{e}^{j\omega t} + H_2(j\omega, j\omega)F^2\mathrm{e}^{j2\omega t} + \cdots + H_n(j\omega,\ldots,\omega)F^n\mathrm{e}^{jn\omega t}. \quad (4)$$

where $H_n(j\omega)$ is the nth order FRF. It is assumed that the nonlinearity can be expressed in polynomial form; thus this method is not applicable for non-polynomial nonlinearities such as hysteretic damping, etc. In addition, the derivation assumes a complex input of the form $f(t) = \mathrm{e}^{j\omega t}$. This assumption is necessary for the real quantity $x(t)$ on the left-hand side of Eq. 4 to equal the sum of the complex

values on the right-hand side. In practice, this input is unrealizable, and a purely real sinusoidal excitation is typically used instead. Changing the form of the input can have consequences, however. For a nonlinear system, when a purely real excitation is used, extra terms are produced which contaminate the theoretical FRF. The source of these extra terms can be understood by recalling the complex form of a sinusoidal input

$$F\cos(\omega t) = \frac{F}{2}(\mathrm{e}^{j\omega t} + \mathrm{e}^{-j\omega t}). \tag{5}$$

In a linear system, the two exponential components in Eq. 5 can be considered separately, and superposition can be applied. The theoretical FRF can be determined based on applying Eq. 4 for each of the two inputs. For a nonlinear system, superposition cannot be assumed, and the entire right-hand side of Eq. 5 must be substituted for $F\mathrm{e}^{j\omega t}$ in Eq. 4. This substitution reveals the source of the extra terms. For example, when formulating the second-order term, the right-hand side of Eq. 5 is squared, resulting in a $(\frac{F}{2})^2$ term in addition to the exponential terms. The additional terms are said to "contaminate" the FRF. This contamination is unavoidable when testing a system experimentally.

The term higher-order transfer function may be used to indicate that experimental results will differ from the theoretical higher-order FRF. Equations for the higher-order transfer functions are similar to the equations for the theoretical higher-order FRFs except that they contain the contaminating terms mentioned above. Written in terms of the Fourier transforms of the input ($F(j\omega)$) and output ($X(j\omega)$), the theoretical higher-order FRFs are

$$\begin{aligned} H_1(j\omega) &= \frac{X(j\omega)}{F(j\omega)} \\ H_2(j\omega, j\omega) &= \frac{2X(j2\omega)}{F(j\omega)^2} \\ &\vdots \\ H_n(j\omega, \ldots, j\omega) &= \frac{2^{n-1}X(jn\omega)}{F(j\omega)^n}. \end{aligned} \tag{6}$$

When estimating higher-order FRFs experimentally, the above equations are typically used, and the extra terms are not identified. For example, when estimating the first-order FRF, $H_1{}^*$, where * indicates an estimation based on experimental data, to a first approximation, the standard equation for the linear FRF is used:

$$H_1{}^*(j\omega) = H_1(j\omega) + O(Y(j\omega))^2. \tag{7}$$

This equation acknowledges the presence of the extra terms by including $O(Y(j\omega))^2$, and the terms themselves are ignored in the calculations.

The experimental procedure for acquiring the data necessary to estimate a system's higher-order FRFs is based on a stepped sine excitation. First, the frequency range of interest should be determined by using a sine sweep or impact test to identify the relevant natural frequencies of the system. Then, the range of the stepped sine excitation is identified by selecting the lowest frequency to be no more than one third the lowest natural frequency of interest and the highest frequency to be greater than the highest frequency of interest. The one third factor was used here because FRFs up to third order are typically estimated. In general, if an nth-order FRF is to be estimated, the lowest frequency used in the stepped sine input should be chosen to be $1/n$ times the lowest natural frequency of interest. The frequency increment used in the stepped sine depends on the desired frequency resolution of the estimated higher-order FRF and, more practically, on the amount of time available for the test. Multiple data sets at each frequency of the stepped sine input should be acquired to allow for averaging. Alternatively, a single time history can be acquired that is long enough to be subdivided for averaging in the data post-processing phase. The measurement should be designed such that only the steady-state response, rather than the transient response, of the system is measured and an integer number of cycles is acquired to reduce leakage and ensure that the resulting frequency vector contains the excitation frequency. Note that these requirements can be enforced either when acquiring data or in the data processing after acquisition.

Input and output measurements are acquired at each of the frequencies of the stepped sine. A force transducer should be used to measure the input force of the actuator or shaker. Response measurements (displacement, velocity, or acceleration) can be made with any appropriate sensor. The first step in the data processing procedure is to calculate the force and response spectra via the discrete Fourier transform (DFT). Next, at each frequency step, Ω_i, in the stepped sine input, the amplitude and phase of the response spectrum at the first n harmonics of the excitation frequency(Ω_i, $2\Omega_i$, $3\Omega_i$,..., $n\Omega_i$) are determined. Only the amplitude and phase of the force spectrum at the excitation frequency (Ω_i) are recorded. These values are then used in Eq. 6 to estimate the higher-order FRFs of the system.

3.3.1 Example: Panel with Disbond

A stepped sine input was applied to the panel with the disbond, and the response was measured with an accelerometer near the location of the disbond. The measured acceleration and force data were processed as described above, and the diagonal components of the first-, second-, and third-order FRFs were estimated using Eq. 6. Figure 7 shows the amplitudes of the estimated FRFs. The first-order FRF matches well with an FRF estimated from a sine sweep (not shown). The peak near 410 Hz corresponds to a natural frequency of the panel, and based on the width of the peak, this is a highly damped mode. The second-order FRF can be used to detect non-symmetric nonlinearities, i.e., nonlinearities that cause a response at two times the excitation frequency. If a non-symmetric nonlinearity is present, a peak at half the natural frequency identified in the first-order FRF should be present. This peak would be present because when the structure is excited at half the natural

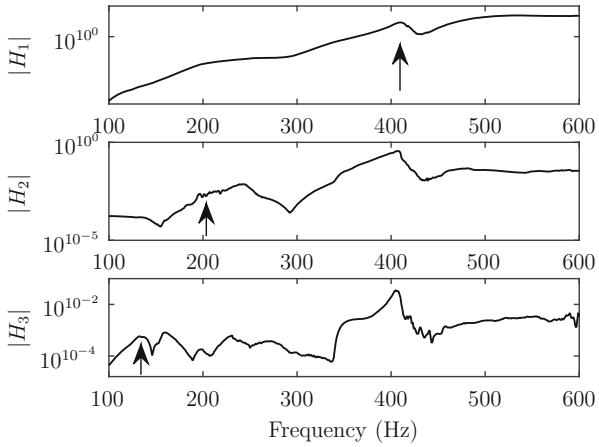

Fig. 7 First (H_1), second (H_2), and third (H_3) order FRFs estimated for the panel with disbond

frequency, the nonlinearity causes a response at twice the excitation frequency, which corresponds to the natural frequency and results in a resonant-like response. In Fig. 7, no clear peak is present, although a wide area of increased response can be observed between 180 and 300 Hz. The third-order FRF can be used to identify symmetric (e.g., cubic) nonlinearities that cause a response at three times the excitation frequency. Peaks at one third the excitation frequency are a result of the nonlinear response coinciding with the natural frequency. In Fig. 7, a peak is observed near 136 Hz, which is about one third of the 410 Hz natural frequency identified in the first-order FRF. Other peaks are also present in the third-order FRF which do not correspond to natural frequencies of the panel. Because the panel is highly damped, the peaks in the first-order FRF that correspond to the panel's natural frequencies are not very distinct. That makes this method less effective at characterizing the nonlinearities in the panel. Lightly damped system are better candidates for the application of this method.

3.4 Hilbert Transform in the Time Domain

One common characteristic of nonlinear system responses is an amplitude dependent period of oscillation. The swinging pendulum is the most famous example of this behavior. For a linear system, the instantaneous frequency will remain constant and independent of time, but for some nonlinear systems, the instantaneous frequency is a function of the response amplitude, and that relationship can be identified using the Hilbert transform along with associated signal processing techniques which are required to limit the signal to the response due to a single mode of vibration. By tracking the changes in frequency with amplitude, the nonlinearity in a system can often be detected, classified, and located. The plot of amplitude

versus frequency is called the system backbone and is the main by-product of Hilbert transform time domain techniques. The Hilbert transform can be used with free response data to estimate the instantaneous frequency and instantaneous amplitude, which can be used to show the system backbone and characterize nonlinear behavior in a system. The Hilbert transform is used to shift all frequency components of a signal by $\pm\pi/2$ rad, and the combination of the original signal and the phase shifted signal can be used to estimate the instantaneous frequency and amplitude of the signal. For a linear system, the instantaneous frequency will remain constant and independent of time, but for some nonlinear systems, the instantaneous frequency is a function of the response amplitude, and that relationship can be identified using the Hilbert transform along with associated signal processing techniques which are required to limit the signal to the response due to a single mode of vibration.

To apply time domain-based Hilbert transform analysis to experimental data, the free response (i.e., impulse response) of the system should first be estimated. The free response can be estimated from the frequency response function (FRF) of the system determined using an impulsive force, such as the force from the impact of a modal impact hammer, by taking the inverse Fourier transform of the FRF. Alternatively, the free response of the system can be measured directly if it is possible to give the system non-zero initial conditions (e.g., a pendulum being released from a horizontal position). Once the free response of the system, $x(t)$, is determined, an "analytical" signal, $X(t)$, is formed according to

$$X(t) = x(t) - j\tilde{x}(t) \tag{8}$$

where $\tilde{x}(t)$ is the Hilbert transform of $x(t)$. An analytic signal is a signal whose imaginary part is equal to the Hilbert transform of the real part. (See [9] for a description of the theory of analytical signals in the context of Hilbert transforms for vibration analysis.) Equation 8 can be written in polar form as

$$X(t) = A(t)\mathrm{e}^{j\psi(t)} \tag{9}$$

where

$$\begin{aligned} A(t) &= \sqrt{x^2(t) + \tilde{x}^2(t)} \\ \psi(t) &= \tan^{-1}\left(\frac{\tilde{x}(t)}{ix(t)}\right), \end{aligned} \tag{10}$$

and $A(t)$ is called the instantaneous amplitude (or envelope) and $\psi(t)$ is called the instantaneous phase. The instantaneous frequency, $\omega(t)$, can be found by numerically differentiating the instantaneous phase. The backbone curve can be generated by plotting the instantaneous amplitude (A) versus the instantaneous frequency (ω). Curvature in the backbone curve indicates nonlinearity in the system.

This time domain analysis based on the Hilbert transform is most effective on lightly damped, single degree of freedom systems. When applying this method to

multi-degree of freedom systems, filtering must be applied in order to remove all but one of the modes from the data. Results from systems with closely spaced and/or highly coupled modes can be inconclusive. In addition to filtering the measured data, filtering is necessary to smooth the instantaneous frequency.

Hilbert transform-based analysis can also be used to perform parameter estimation to determine the stiffness and damping characteristics of a system. Two methods, one using the free response of a system [7] and one using the forced response of a system [8], were developed that generate a force-displacement curve that can be used to identify the nonlinear stiffness in the system and a force-velocity curve that can be used to identity the nonlinear damping in the system. As with the analysis presented above, lightly damped single degree of freedom systems are the best candidates for this analysis.

3.5 Hilbert Transform in the Frequency Domain

The Hilbert transform can also be used to identify nonlinear systems in the frequency domain by checking whether the frequency response functions (FRFs) of the system are invariant under the Hilbert transform. For linear systems, the FRF is invariant under the Hilbert transform, but nonlinear systems do not necessarily share that property. As presented in [14], linear systems are causal, meaning their impulse response functions are always zero for $t < 0$. The Hilbert transform acts as an identity transformation (i.e., the output equals the input) on causal functions. Therefore, the following relationships hold for a linear system:

$$\begin{aligned} \mathcal{H}\{\mathrm{Im}(H(\omega))\} &= \mathrm{Re}(H(\omega)) \\ \mathcal{H}\{\mathrm{Re}(H(\omega))\} &= -\mathrm{Im}(H(\omega)) \end{aligned} \tag{11}$$

where $\mathcal{H}\{\cdot\}$ is the Hilbert transform and H is an FRF.

Nonlinear systems (that are also minimum phase systems) are also causal in the sense that the response never precedes the input. However, due to the data processing procedure used to calculate the Hilbert transform, nonlinear systems can exhibit "artificial" non-causality where the impulse response function is not always zero for $t < 0$. The non-causality is a result of imposing evenness and oddness conditions while converting one-sided FRFs to double-sided FRFs and then taking the inverse Fourier transform. In terms of Hilbert transform analysis, the result of this non-causality is that the relationships in Eq. 11 do not hold. Therefore, the violation of these equalities can be used to identify the presence of nonlinearity in a system.

One potential drawback to this method is that in order to detect nonlinearity in a system, a linear version of the system is required for comparison. The linearized version of the system can be achieved either by using a separate specimen that is known to be identical to the specimen being tested (e.g., the unmodified panel used in the previous examples) or, if possible, by acquiring data from the specimen at a low enough amplitude such that the nonlinearities are not excited. In either case, the

only data required to apply this method are FRFs from the linearized system and the (potentially) nonlinear system. Care should be taken to ensure that the suspected nonlinearities in the system are sufficiently excited during the data acquisition process. Once the FRFs have been estimated, the equalities in Eq. 11 are checked by plotting the real and imaginary parts of each FRF against the transformed imaginary and real parts. If significant deviation from the linearized system is observed, then the system can be identified as nonlinear.

Complications can arise when determining the Hilbert transform of the real and imaginary components of the FRF, however, because the Hilbert transform is an integration over all frequencies, and the experimentally estimated FRFs are naturally band limited. Several correction approaches are outlined in [14]; however many are most effective for lightly damped systems. Therefore, this technique is not generally appropriate for heavily damped systems.

3.6 Restoring Force Method

The restoring force method is a non-parametric approach for characterizing nonlinearities in a system. The derivation of the restoring force is based on a straightforward rearrangement of Newton's second law of motion. By simultaneously measuring a structure's displacement, velocity, and acceleration, the so-called restoring force can be determined and plotted as a function of displacement and velocity. The nonlinearities in the system can be visualized and characterized through this restoring force surface. The equation of motion for a single degree of freedom, linear mass, spring, and damper system is

$$m\ddot{x} + c\dot{x} + kx = f(t) \tag{12}$$

where x is the displacement of mass, m, c is the damping coefficient, k is the stiffness coefficient, $f(t)$ is an applied force, and dots indicate time derivatives. To extend this equation to a system with arbitrary nonlinearities, Eq. 12 can be rewritten as

$$m\ddot{x} + f_{RF}(x, \dot{x}) = f(t), \tag{13}$$

where $f_{RF}(x, \dot{x})$ is called the restoring force and represents the internal force that counters the system's applied and inertial forces. The restoring force can be determined by measuring the system's acceleration, mass, and the applied force using

$$f_{RF}(x, \dot{x}) = f(t) - m\ddot{x}. \tag{14}$$

To determine how this force relates to the system's displacement and velocity, the displacement and velocity must be determined either by direct measurement or by integration of the measured acceleration. The restoring force is plotted as a

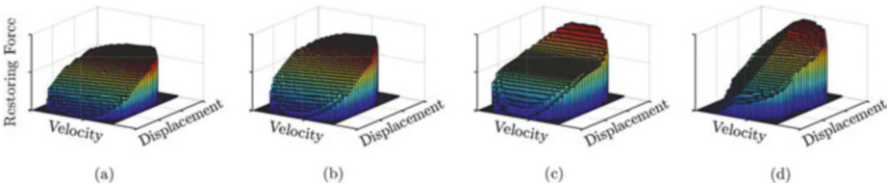

Fig. 8 Ideal restoring force surfaces. (**a**) Linear. (**b**) Quadratic stiffness. (**c**) Cubic stiffness. (**d**) Bilinear damping

surface over the displacement-velocity plane, and the shape of the surface is used to determine the nature of the system's nonlinearities. Figure 8 shows ideal restoring force surfaces for a linear system, a system with a quadratic stiffness nonlinearity, a system with a cubic stiffness nonlinearity, and a system with bi-linear damping. The nonlinearity can be characterized by observing the trends of the surface in the force-displacement plane for stiffness nonlinearities and the force-velocity plane for damping nonlinearities. Once the type/types of nonlinearity is/are determined, the $f_{RS}(x, \dot{x})$ term in Eq. 13 can be replaced with an algebraic expression for the nonlinear force (e.g., μx^2 for quadratic stiffness) and a least-squares curve-fitting can be applied to the data to determine the nonlinear parameter(s).

The design of experiment is particularly important when acquiring data for the restoring force method. The first consideration is whether a single degree of freedom system can be assumed. The restoring force method can be extended to systems with multiple degrees of freedom systems, but, to do so requires the use of modal vectors, which can change with amplitude in a nonlinear system. In some cases, a multi-degree of freedom system can be tested in a fixture which isolates the mode of interest or restricts the motion of the structure such that the assumption of a single degree of freedom system is a valid simplification. Alternatively, if the mode of interest is well-separated from other modes of the multi-degree of freedom system, the input excitation can be designed to excite only the mode of interest.

The second consideration when designing the experiment to acquire data for the restoring force method is the type of excitation to use. The excitation force must sufficiently excite the nonlinearity and, importantly, must result in sufficient coverage of the displacement-velocity plane. The former requirement informs the selection of the input amplitude, while the latter informs the choice of signal type. For example, the restoring force in response to a steady-state, periodic excitation is typically a single closed trajectory in the displacement-velocity plane. Therefore, this type of excitation does not provide sufficient coverage of the displacement-velocity plane to generate a complete restoring force surface. It is possible to improve the coverage of the plane by using periodic inputs at multiple amplitudes, but, in most cases, a better choice of inputs is a random signal. A discussion of the effectiveness of other types of inputs for generating restoring force surfaces can be found in [15].

The final consideration is what physical states to measure. The restoring force method requires time histories for the displacement, velocity, and acceleration of the system. In the example below, all three of these quantities are measured simultaneously to avoid the need to integrate or differentiate measurements to estimate unknown states. Direct measurement avoids the many numerical issues involved in estimating unknown states, but in many cases, simultaneously measuring displacement, velocity, and acceleration is not an option. In those cases, numerical integration and/or differentiation is required to estimate states that are not directly measured. In all cases, a force transducer should be used to measure the input force.

3.6.1 Example: Panel with Disbond

The restoring force method was applied to the damaged panel at the location of the disbond. The panel was excited with a band-limited random force using the electromagnetic shaker. The input signal was generated by filtering white noise to limit the bandwidth of excitation to frequencies in the vicinity of one mode of the panel in order to better fit the single degree of freedom assumption. The acceleration, velocity, and displacement of a chosen point were simultaneously measured using an accelerometer, a laser velocimeter, and a laser displacement transducer, as shown in Fig. 4. The ability to measure all three of these quantities simultaneously eliminated the need for numerical integration or differentiation. The input force and response time histories were measured for 300 s in this case, but comparable results could have been obtained using shorter time histories.

The restoring force surface was generated by plotting the calculated restoring force against displacement and velocity divided into finite ranges. The restoring force was calculated using Eq. 14. In general, if a single degree of freedom system is assumed, the total mass of the system begin tested can be used. The ranges of displacement and velocity measurements were then determined and divided into 50 increments of equal length. These increments were used to divide the displacement-velocity plane into a grid of equally sized squares. Restoring forces for measurements corresponding to $(x, \dot{x})$ pairs in each square are averaged to form the restoring force surface over the 50×50 grid. Figure 9a shows the restoring force surface for this experiment using a 3D bar plot.

The random input data used in this experiment provided good coverage of the displacement-velocity plane. In the event that there are holes in the surface due to lack of data within a given square of the plane, a longer acquisition time or a change in excitation signal may address the problem. Alternatively, the surface could be discretized using larger displacement and velocity intervals to construct the surface. To determine whether nonlinearities are present in the system (at the chosen force amplitude), the contours of the surface are analyzed. In this case, the slope of the surface tends to change at the lower and higher displacement ranges. A representative profile view of the force-displacement plane is shown in Fig. 9b. This nonlinear trend in the displacement-force plane indicates that a stiffness nonlinearity is present. Figure 9c shows a representative view of the force-velocity plane. The trend in this plane appears more linear. It cannot, however, be concluded that nonlinear damping is not present in the system. These results could indicate

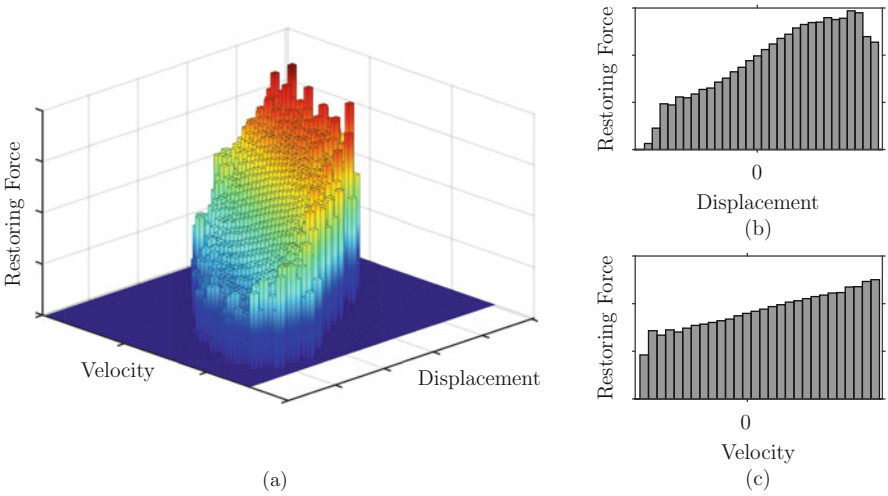

Fig. 9 (**a**) Restoring force surface for the panel with face sheet disbond. Representative profiles of the restoring force surface (**b**) in the force-displacement plane and (**c**) in the force-velocity plane

that the nonlinearity was not being excited. Overall, these results clearly show the presence of nonlinear stiffness in the panel, which is consistent with expectations based on the asymmetric stiffness at the location of the disbond.

3.7 Vibro-Acoustic Modulation

The vibro-acoustic modulation (VAM) method uses two or more simultaneous excitation forces to detect nonlinearity in a system. Because the principle of superposition does not hold for nonlinear systems, interactions between these multiple inputs are a useful indication of nonlinearity. The principle of superposition states that the response of a linear system to a multi-frequency excitation is equal to the sum of the responses of the system excited at each individual frequency. When excited by a multi-frequency signal, a nonlinear system may respond at additional frequencies, which are not present in the input, including integer multiples of the excitation frequencies (as described in Sect. 3.2) and frequencies which are linear combinations of the excitation frequencies. The amplitude and frequency of these response components can be used to characterize the nonlinearities in the system [6].

To apply VAM, a structure is excited by a signal of the form

$$f(t) = \cos(\Omega_1 t) + \cos(\Omega_2 t) \tag{15}$$

where Ω_1 is chosen to be at or near a low-frequency mode of the structure. The purpose of this signal, called the pumping signal, is to excite the nonlinearity in the system. Ω_2 is chosen to be much greater than Ω_1 and, if possible, in a frequency

range in which the structure's response is not strongly influenced by its linear modes. Nonlinearities cause the high-frequency signal, called the probing signal, to be modulated by the low-frequency response. For example, consider a single degree of freedom system with a quadratic nonlinearity. The equation of motion is

$$m\ddot{x} + c\dot{x} + kx + k_{sq}x^2 = f(t). \tag{16}$$

When excited by the force given in Eq. 15, the steady-state response of the structure will contain terms of the form

$$\cos(\Omega_1 t)\cos(\Omega_2 t) = \frac{1}{2}\left\{\cos\Big((\Omega_2 + \Omega_1)t\Big) + \cos\Big((\Omega_2 - \Omega_1)t\Big)\right\} \tag{17}$$

due to the quadratic term. These terms represent the modulated part of the response, where the system responds at the probing frequency (Ω_2) plus and minus the pumping frequency (Ω_1). For a cubic nonlinearity, the response will contain terms of the form $\cos((\Omega_2 + 2\Omega_1)t)$ and $\cos((\Omega_2 - 2\Omega_1)t)$. In general, nonlinearities that can be expressed as polynomial functions of the system response result in modulation at frequencies that are linear combinations of the pumping and probing frequencies.

To identify the presence of nonlinearity in a structure, its response to a multi-frequency excitation is measured and its response spectrum is determined. The response is analyzed (visually) to determine if peaks are present at the probing frequency plus and minus some multiple of the pumping frequency. These peaks are called sidebands. The frequencies at which the sidebands occur may indicate the order of the nonlinearity (i.e., quadratic, cubic, etc.) and the amplitude may indicate the strength of the nonlinearity, where a larger amplitude indicates a stronger nonlinearity. However, underlying linear effects, such as a strong modal response at or near the modulation frequencies, can affect sideband characteristics [10]. Care must be taken when drawing conclusions about the nature of the nonlinearity indicated by the sidebands.

When applying VAM, the forces used are typically single frequency sinusoidal inputs, as described above. However, the low-frequency sinusoidal input can be replaced with an impulsive force, such as from a modal impact hammer. When this substitution is made, the method is referred to as Impact Modulation (IM). In IM, rather than the probing signal being modulated by only one low-frequency component, it is modulated by every natural frequency excited by the impact that excites the system's nonlinearities. In some cases, IM is more convenient to implement because a modal impact hammer requires much less instrumentation and setup than a low-frequency shaker.

3.7.1 Example: Undamaged Panel Versus Panel with Disbond

VAM was applied to both the undamaged panel and the damaged panel. During each test, a panel was excited simultaneously by a low-frequency sinusoidal force generated by the modal shaker and a high-frequency sinusoidal force generated by

the smaller piezoelectric actuator, as shown in Fig. 2. The frequency of the pumping signal was chosen to be 453 Hz, which is near a natural frequency of the panels (determined by a sine sweep test). The probing signal was chosen to be 15 kHz, which is well outside the range where the panel has strong modal responses. The response of each panel was measured using the laser vibrometer; however, any type of response measurement could have been used. Only the response data was used in the analysis. Time data was acquired for 1.28 s at a sampling rate of 51.2 kHz. The sampling rate was chosen to be greater than twice the probing frequency plus five times the pumping frequency to ensure that all sidebands of interest would be in the usable frequency range. Time histories were transformed into the frequency domain via the DFT. Twenty spectra were acquired and averaged. In some cases, averaging may not be appropriate because it may make the presence of the nonlinearity less evident. Figure 10 shows the results for both the undamaged (solid black) and modified (dotted red) panel. The large peak at 15 kHz corresponds to the probing frequency. For the panel modified with a simulated disbond, sidebands at the probing frequency plus and minus one, two, and three times the pumping frequency can be clearly seen. A fourth sideband on the left and a fifth sideband on the right of the probing frequency can also be seen. The presence of these sidebands indicates nonlinearity in the system. The spectrum of the undamaged panel also shows sidebands, although their amplitudes are significantly smaller than those of the modified panel.

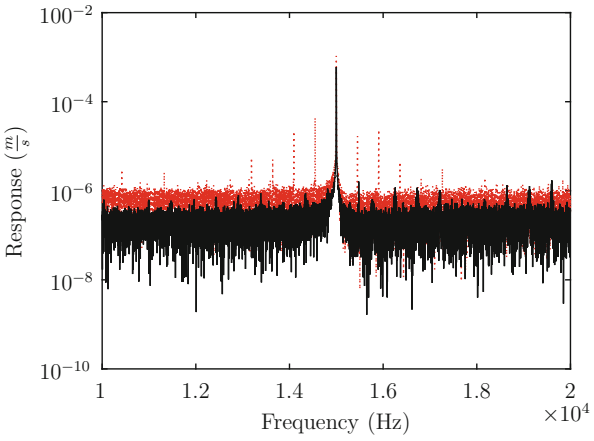

Fig. 10 Response spectra for the undamaged panel (——) and panel with disbond (- - -) determined from vibro-acoustic modulation testing

4 Methods for Parameter Estimation

4.1 Nonlinear Autoregressive Moving Average with Exogenous Inputs (NARMAX)

NARMAX, meaning Nonlinear Autoregressive Moving Average with eXogenous inputs, refers to both a type of discrete time model and an associated parameter estimation approach [5]. The NARMAX approach is attractive because it is both very general and widely applicable to nonlinear parameter estimation. Unlike some other methods, this technique does not require the form of the nonlinearity to be assumed, although an understanding of the mechanism of nonlinearity can be useful in formulating the model. To understand the NARMAX model, it is useful to start by building from related discrete time linear models. For example, consider a single degree of freedom mass-spring-damper system, with the equation of motion $m\ddot{x}(t) + c\dot{x}(t) + kx(t) = f(t)$, where $x(t)$ is the displacement of the mass, $f(t)$ is the applied force, and m, c, and k are the mass, damping, and stiffness, respectively. Approximating the first derivative of displacement using the backward difference approximation and the second derivative with the second-order central difference approximation, the equation of motion can be transformed into a discrete time equivalent. The discrete time equation of motion at time $t = (i-1)\Delta_t$, where $\Delta_t = 1/f_s$, f_s is the sampling frequency, and $x_i = x(i\Delta_t)$ is as follows:

$$mf_s^2(x_i - 2x_{i-1} + x_{i-2}) + cf_s(x_{i-1} - x_{i-2}) + kx_{i-1} = f_{i-1} \tag{18}$$

Grouping each lagged output, the response at time $t = i\Delta_t$ can be expressed as a weighted sum of the response and force at earlier times:

$$x_i = b_1 f_{i-1} + a_1 x_{i-1} + a_2 x_{i-2} \tag{19}$$

where the a_i and b_i are the coefficients to be estimated.

This model is called an ARX model, meaning that it is an autoregressive model, i.e., the response is a function of itself at earlier times, with exogenous inputs. If the system is nonlinear, this model needs to be extended to include nonlinear terms. Adding a cubic damping term to the mass spring damper system from above is a good example of how the number of coefficients needed to model a nonlinear system drastically increases relative to the linear equivalent. Starting from the equation of motion $m\ddot{x}(t) + c\dot{x}(t) + c_3\dot{x}(t)^3 + kx(t) = f(t)$, and following the same approach as above, the discrete time equivalent would be

$$mf_s^2(x_i - 2x_{i-1} + x_{i-2}) + cf_s(x_{i-1} - x_{i-2}) + c_3 f_s^3(x_{i-1} - x_{i-2})^3 + kx_{i-1} = f_{i-1} \tag{20}$$

After expanding the cubic term, Eq. 20 becomes

$$mf_s^2(x_i - 2x_{i-1} + x_{i-2}) + cf_s(x_{i-1} - x_{i-2}) + c_3 f_s^3(x_{i-1}^3 - 3x_{i-1}^2 x_{i-2} + 3x_{i-1}x_{i-2}^2 - x_{i-2}^3) + kx_{i-1} = f_{i-1} \tag{21}$$

After grouping terms and defining coefficients as before, the response at time $t = i\Delta_t$ can be written as

$$x_i = b_1 f_{i-1} + a_1 x_{i-1} + a_2 x_{i-2} + a_3 x_{i-1}^3 + a_4 x_{i-1}^2 x_{i-2} + a_5 x_{i-1} x_{i-2}^2 + a_6 x_{i-2}^3 \tag{22}$$

Equation 22 shows that by adding a single cubic damping nonlinearity, this NARX model (Nonlinear ARX model) has four additional coefficients that must be estimated. The large number of coefficients that can be needed to model the system is one of the most significant practical differences of nonlinear discrete time models as compared to linear counterparts. When the type of nonlinearity is not known, coefficients for all combinations of lagged input and responses are possible.

The number of unknown terms increases even more when noise is considered. The effects of noise on nonlinear systems are more complex than they are for linear systems. Because superposition does not hold for nonlinear systems, even simple additive noise on the output measurement can result in cross product terms in the model where noise is multiplied by the response or input. In the nonlinear damping example above, if the measured response (x') is $x' = x + e$, where x is the true response, e is a random noise term, the finite equation of motion can be written by substituting $x_i = x_i' - e_i$. Substituting this expression into just one of the four nonlinear terms in (22), $a_4 x_{i-1}^2 x_{i-2}$, shows how the additive noise on the response can cause numerous cross product terms to arise:

$$\begin{aligned} a_4 x_{i-1}^2 x_{i-2} &= a_4(x_{i-1}'^2 - 2x_{i-1}' e_{i-1} + e_{i-1}^2)(x_{i-2}' - e_{i-2}) \\ &= a_4(x_{i-1}'^2 x_{i-2}' - 2x_{i-1}' x_{i-2}' e_{i-1} + x_{i-2}' e_{i-1}^2 - x_{i-1}'^2 e_{i-2} - 2x_{i-1}' e_{i-1} e_{i-2} + e_{i-1}^2 e_{i-2}). \end{aligned}$$

As illustrated in this example, even additive noise on the response can cause complex noise terms mixed with response terms. For this reason, noise terms need to be included in the model formulation from the beginning in order to produce an unbiased estimate of model parameters. The inclusion of these error terms is the distinction between a NARX model and a NARMAX model. In general terms, the recurrence relation for a NARMAX model is as follows:

$$x_i = F(x_{i-1}, \ldots, x_{i-n_o}; f_{i-1}, \ldots, f_{i-n_i}; e_{i-1}, \ldots, e_{i-n_e}) \tag{23}$$

where $F(\ldots)$ is some nonlinear function and n_o, n_i, and n_e are the number of time delays included for the output, input, and error terms, respectively. Traditionally, $F(\ldots)$ is a polynomial function of up to order n_p, denoted as $F^{(n_p)}(\ldots)$, although

other forms of the nonlinear recurrence relation are possible and have been shown to be effective. Although the recurrence relation is nonlinear, it remains linear in the parameters, so coefficients can be estimated using linear least-squares techniques.

The rudimentary solution approach would be to select a model order and number of time delays and then estimate all of the model coefficients at once to produce a model. This approach might accurately represent the data that were used in the estimate, but the model is unlikely to represent the system well in general or accurately predict the output given a different input. Furthermore, the number of coefficients which would need to be estimated would be much larger than for a linear model. For instance, even if only one time delay was used on the input and output, three time delays were used for the error term, and a cubic polynomial recurrence relation were used, there would be 56 coefficients in total to estimate because all combinations of the input, output, and noise terms of different powers would have an associated coefficient.

Rather than trying to estimate every coefficient at once, a better approach is to use only as many terms as is necessary to reach an acceptable fit. This is accomplished by using an orthogonal least squares approach to evaluate the significance of each term, estimating that term and then iteratively continuing until an acceptable quality of fit is achieved. Once the parameters have been estimated, the model can be evaluated for validity, used to predict the output of the system, or be used for further analysis of the underlying dynamics of the system.

4.1.1 Example: Panel with Disbond

The damaged panel was tested in order to identify a NARMAX model which captures the nonlinear dynamics of the structure. Displacement data was acquired via the laser displacement transducer for a point near the disbond, while the panel was being excited by the modal shaker applying band-limited random force. The magnitude of the RMS (root mean square) amplitude of the force was chosen to be large enough to excite the nonlinearity in the panel. The applied force was measured using the force sensor mounted between the panel and the shaker's stinger, as shown in Fig. 2. The length of the time histories acquired was arbitrarily chosen to be 3 s. The number of samples acquired during data acquisition determines how over-determined the parameter estimation problem is. The measurement duration should be long enough to ensure that the nonlinear response is captured. When in doubt, acquiring long time histories which can be truncated in post processing is a good practice.

The NARMAX model was formulated by first choosing the maximum number of lags to allow for the input, output, and error terms. In this case, $n_i = n_o = n_e = 2$ was chosen. The choice of two lags was reasonable because displacement was measured and the equations of motions for the physical system are second order. If quantities other than displacement are measured or if the model fit is poor with the initial choice of n_i, n_o, and n_e, additional time delays could be used to improve the model fit. The other key parameter that needs to be specified in order to formulate the NARMAX model is the maximum order of the nonlinearity,

n_p, for polynomial nonlinear functions. As demonstrated above, increasing the polynomial order increases the number of unknown coefficients significantly. Prior knowledge about the nature of the nonlinearity (perhaps gained as a result of applying one of the characterization methods described previously) can be used to inform the order choice. If the model form is unknown, the polynomial order can be chosen heuristically. For this example, the order was chosen to be 3, meaning that all first-, second-, and third-order polynomials formed by the factors x_{i-1}, x_{i-2}, f_{i-1}, f_{i-2}, e_{i-1}, and e_{i-2} are potential terms in the model. Note that non-polynomial nonlinearities can also be assumed. Many software packages (e.g., MATLAB) have built-in functions that support the use of wavelets, neural networks, etc.

With the model form established, there are several possible choices for estimating the model coefficients. One option is to use a brute-force approach to solve for every possible coefficient, regardless of the significance to the total response. Again, commercial software packages such as MATLAB support this type of approach. Alternatively, an orthogonal least-squares approach can be used to identify and estimate terms which are significant. For this application, the orthogonal least-squares approach, described in [4], was used. In the orthogonal least-squares approach, noise-related terms are estimated by assuming e is a zero-mean, random (uncorrelated) time series. The result of the orthogonal least-squares solution approach is a subset of terms from the assumed model that sufficiently model the system's response. Note that failure to include noise in the model can lead to biased parameter estimates. This bias often results in the model being able to predict the system's response to the type of input used in the estimation process well, but not being able to accurately predict the system's response to inputs of different amplitudes and/or types.

Figure 11 shows the one-step ahead model predictions for both a random input (using a different data set than the one used for parameter estimation) and a sine sweep. There is good agreement between the measured response (solid black line) and the predicted response (dotted red line) in both cases. One-step ahead predictions, in which the system output is predicted using the estimated parameters and measured data, are the least stringent of the model validation techniques. More stringent techniques include model predicted output, in which the output is generated using only the measured inputs, and correlation tests, as described in [14]. Model validation is important in order to ensure that the model has captured the system's dynamics, and not simply fit an erroneous model to a single set of data. If the latter is true, the model will be useless to predict the system's response to inputs other than the one used for the parameter estimation.

4.2 Direct Parameter Estimation

Direct parameter estimation is a time domain method for estimating mass, damping, and stiffness parameters for both linear and nonlinear systems based on experimental measurements [11]. The equations of motion must be defined based on a lumped parameter model of the system, so for nonlinear systems, the form of the

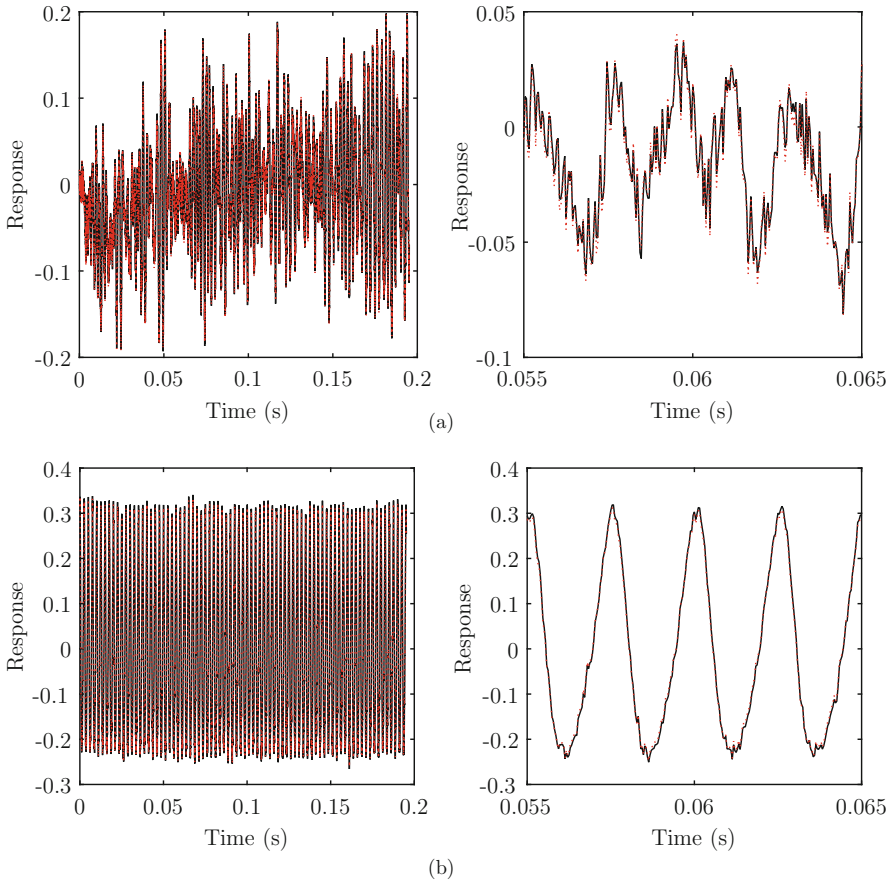

Fig. 11 Measured response (——) and one-step ahead predictions (- - -) from NARMAX model using (**a**) a random input and (**b**) a sinusoidal input

nonlinearity must be explicitly assumed. An overdetermined set of equations based on the equation of motion is generated using the measured force, displacement, velocity, and acceleration time histories. A least-squares method can be used to estimate the parameter matrices. The estimated parameters can then be used with the underlying equation of motion to simulate the system's response for validation purposes.

In practice, the first step in applying direct parameter estimation is to formulate the equations of motion of the system, including any nonlinear terms. In general, the equations take the form

$$[M]\{\ddot{x}\} + [C]\{\dot{x}\} + [K]\{x\} + \sum_i f_i(\{x\}, \{\dot{x}\}) = \{f(t)\} \tag{24}$$

where f_i is the functional form of the i^{th} nonlinearity included in the model. An important requirement in model formulation is to explicitly express the form of the nonlinearity (or nonlinearities). For example, when testing a structure with bolted interfaces, quadratic (i.e., non-symmetric) stiffness elements of the form $k_{sq}\Delta x^2$ may be included to account for micro-impacts that occur between the overlapping surfaces. It may also be appropriate to include nonlinear damping terms. There is no general rule for determining the type or types of nonlinearities to include, but techniques such as restoring force surfaces can be useful in selecting an appropriate form for the nonlinearity. Ultimately, the validity of the assumed model can be checked using a procedure described below.

After the equations of motion have been established, the system parameters are estimated by solving an overdetermined system of equations. This set of equations is generated by repeating Eq. 24 for a select number of points in time. The equations are populated using measured time histories of the displacements, velocities, accelerations, and applied force. Ideally, each of these quantities should be measured simultaneously. Alternatively, one state can be measured and the others estimated using an appropriate numerical integration or differentiation scheme. Once formulated, the system of equations is solved using a least-squares algorithm.

To check the validity of the chosen model, the parameters determined from the least-squares calculation are used with Eq. 24 to simulate the system response to the force $f(t)$. The simulated response is compared with the measured response (i.e., displacement, velocity, and/or acceleration). A close match between the measured and simulated response indicates that the chosen model captures the dynamics of the system. Conversely, large discrepancies indicate that the assumed form of the model is inadequate, and the equations of motion need to be revised.

4.3 Reverse Path

The reverse path method is a frequency domain method that can be used to decompose a system's response into an underlying linear system and an uncorrelated nonlinear system. This decomposition allows unbiased estimates of the linear parameters of the system along with estimates for the nonlinear parameters. Bias in linear parameters will usually occur if the parameters are estimated directly from nonlinear dynamic response measurements without taking into account the nonlinearity. The bias occurs because the frequency response functions (FRFs) contain information about both the linear and nonlinear parts of the system. The goal of the reverse path method is to separate the linear and nonlinear components of the system response so that the linear parameters can be estimated without "contamination" from the nonlinearities in the system.

The reverse path method was initially proposed in [3] for single degree of freedom systems and was extended to multi-degree of freedom systems in [12]. The multi-degree of freedom approach is typically referred to as conditioned reverse path because the approach is based on conditioned spectra and FRFs, which will

be defined below. Consider the system with N degrees of freedom defined by the equations of motion

$$[M]\{\ddot{x}(t)\} + [C]\{\dot{x}(t)\} + [K]\{x(t)\} + \sum_{i=1}^{N_n}[A_i]\{x_{ni}(t)\} = \{f(t)\} \tag{25}$$

where $[M]$,$[C]$, and $[K]$ are the NxN (linear) mass, damping, and stiffness matrices, $x(t)$ is the Nx1 displacement vector, $f(t)$ is the Nx1 vector of input forces, and $x_{ni}(t)$ is a q_ix1 vector that contains the nonlinear function(s) that describes the i^{th} type of nonlinearity. There are N_n types of nonlinearities (e.g., cubic stiffness, quadratic damping, etc.). The i^{th} type of nonlinearity occurs at q_i different locations within the system. $[A_i]$ is an Nxq_i matrix containing the coefficients of the corresponding nonlinear function vector ($\{x_{ni}(t)\}$). Note that each of the x_n vectors can be different sizes. Accordingly, each of the $[A_i]$ matrices can be different sizes to match the length of $\{x_{ni}\}$.

For example, consider a system that has one cubic and one quadratic spring between two degrees of freedom and a second cubic spring between two other degrees of freedom. In this example, $N_n = 2$ because there are two types of nonlinearities (cubic stiffness and quadratic stiffness). Arbitrarily taking the cubic stiffness to be the first nonlinearity ($i = 1$), $q_1 = 2$ because there are two separate cubic stiffness nonlinearities. Because the quadratic stiffness occurs at only one location, q_2 is equal to 1.

To formulate the reverse path form of Eq. 25, the Fourier transform of the equation is taken, and the terms are rearranged such that the force appears on the left-hand side of the equation:

$$\{F(\omega)\} = [B(\omega)]\{X(\omega)\} + \sum_{i=1}^{N_n}[A_i]\{X_{ni}(\omega)\} \tag{26}$$

where $[B] = -\omega^2[M] + j\omega[C] + [K]$. Note that $[B]$ is the reciprocal of the frequency response matrix, $[H]$. By placing the force on the left-hand side and the internal forces of the system on the right-hand side, the standard "path" of the system has been reversed: applied forces are now outputs, and response vectors $\{X\}$ and $\{X_{ni}\}$ are now inputs. As will be shown below, this formulation allows for the system to be recast in terms of uncorrelated inputs, which allows the underlying linear system to be distinguished from the nonlinear portion of the system.

Extracting the linear portion of the response is a recursive procedure. First, the portion of the total response that is correlated to the first nonlinear response is removed. Then, the portion of the remaining response that is correlated to the second nonlinearity is removed. This process continues until the portion of the remaining response that is correlated with the last nonlinearity is removed. The remaining response is uncorrelated with the system's nonlinearities and is thus assumed to be the linear portion of the total response. The portion of the force that is

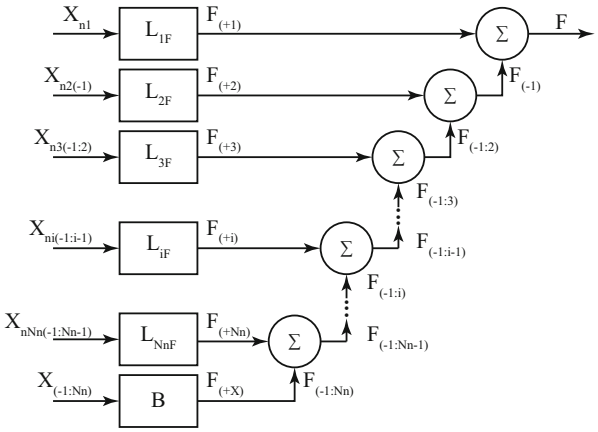

Fig. 12 Conditioned reverse path system model with uncorrelated inputs

uncorrelated with the nonlinearities in the system can be similarly identified. Figure 12 shows the reverse path model with uncorrelated inputs and outputs. Subscripts in parentheses are used to denote whether the quantity is correlated (+) or uncorrelated (−) with the response indicated. For quantities uncorrelated with more than one response, colon notation is used to identify all the uncorrelated responses. For example, $X_{n3(-1:2)}$ indicates the portion of the third nonlinear response vector that is uncorrelated with the first and second nonlinear response vectors. For each uncorrelated input, a frequency response matrix $[L_{iF}]$ relates the input to the portion of the force that is correlated with that nonlinearity. After the effect of each nonlinearity in the system is removed, the remaining response $(X_{(-1:N_n)})$ and force $(F_{(+X)} = F_{(-1:N_n)})$ can be used to estimate the linear frequency response matrix, and linear parameters can be estimated using any linear parameter estimation technique. The nonlinear parameters can be estimated recursively as will be shown below.

In practice, instead of working with the response and force spectra directly, power spectral density (PSD) matrices are used in a recursive algorithm in order to extract the linear system. The outputs of the algorithm are the conditioned PSD matrices necessary to estimate the linear frequency response matrix. Typically, either the H_1 or H_2 estimator is used, and therefore the required quantities are $G_{FF(-1:N_n)}$ and $G_{FX(-1:N_n)}$ for the H_1 estimator and $G_{XF(-1:N_n)}$ and $G_{XX(-1:N_n)}$ for the H_2 estimator. Because the measured response(s) and force(s) are processed to remove nonlinear components (i.e., conditioned) before being used to estimate the FRF, the result is called the "conditioned" estimate. Calculating the conditioned estimates begins by finding the "unconditioned" PSD matrices, which are calculated directly from the measured data. The unconditioned PSD matrices are calculated by the standard formula

$$G_{PQ} = \frac{2}{T} E[P^* Q^T] \tag{27}$$

where P and Q can each be any one of the quantities $\{X\}$,$\{F\}$, or $\{X_{ni}\}$, T is the total acquisition time, $E[\cdot]$ is the expected value (indicating that the mean of multiple averages should be used in the calculation), $(\cdot)^*$ is the complex conjugate, and $(\cdot)^T$ is the transpose. The algorithm starts by calculating the unconditioned PSD matrices G_{XX}, G_{XF}, G_{FF}, and for $i, j = 1, 2, \ldots, N_n$, $G_{X_{ni}X_{ni}}$, $G_{X_{ni}X_{nj}}$, $G_{X_{ni}X}$, and $G_{X_{ni}F}$.

Next, the conditioned PSD matrices are calculated recursively. In each step of the recursion, the portions of the spectra that are correlated with the rth nonlinearity are removed. Starting with $r = 1$, the conditioned PSD matrices, $G_{X_{ni}X_{nj}(-1:r)}$, are calculated using

$$\begin{aligned}[G_{X_{ni}X_{nj}(-1:r)}] = [G_{X_{ni}X_{nj}(-1:r-1)}] \\ - [G_{X_{ni}X_{nr}(-1:r-1)}][G_{X_{nr}X_{nr}(-1:r-1)}]^{-1}[G_{X_{nr}X_{nj}(-1:r-1)}]\end{aligned} \tag{28}$$

where $r < i, j$ and $[G_{ij(-1:0)}]$ refers to the unconditioned PSD matrix. To find conditioned PSD matrices involving X or F ($G_{XX(-1:r)}$, $G_{XF(-1:r)}$, $G_{X_{ni}X(-1:r)}$, etc.), the subscripts i and/or j are replaced with X or F in Eq. 28. The recursion to calculate the conditioned PSD matrices continues until $r = N_n$. Then the linear frequency response matrix is estimated using either of the following:

$$\begin{aligned} H_1 \text{ estimator:} \quad & H^T = [G^{-1}_{FF(-1:N_n)}][G_{FX(-1:N_n)}] \\ H_2 \text{ estimator:} \quad & H^T = [G^{-1}_{XF(-1:N_n)}][G_{XX(-1:N_n)}]. \end{aligned} \tag{29}$$

The final step in the conditioned reverse path analysis is to estimate the nonlinear parameters of the system, which are contained in the $[A_i]$ matrices. A formula for the $[A_i]$ matrices based on the conditioned PSD matrices can be derived from Eq. 26 by transposing the equation, pre-multiplying by $\{X^*_{ni(-1:i-1)}\}$ and taking $(2/T)E[\cdot]$, which yields

$$[G_{X_{ni}F(-1:i-1)}] = [G_{X_{ni}X(-1:i-1)}][B]^T + \sum_{j=1}^{N_n} [G_{X_{ni}X_{nj}(-1:i-1)}][A_j]^T. \tag{30}$$

Note that in the summation, $[G_{X_{ni}X_{nj}(-1:i-1)}] = 0$ when $j < i$ because the i^{th} nonlinear function vector is uncorrelated with the nonlinear function vectors 1 through $i - 1$. By pre-multiplying Eq. 30 by $G^{-1}_{X_{ni}X_{ni}(-1:i-1)}$, post-multiplying by $[H]^T$, and noting that the first term in the summation becomes $[A_i^T]$, the following equation from which the nonlinear parameters can be determined is derived:

$$[A_i]^T[H]^T = [G^{-1}_{X_{ni}X_{ni}(-1:i-1)}]\Big([G_{X_{ni}F(-1:i-1)}][H]^T - [G_{X_{ni}X(-1:i-1)}] - \sum_{j=i+1}^{N_n}[G_{X_{ni}X_{nj}(-1:i-1)}][A_j]^T[H]^T\Big). \quad (31)$$

Because $[A_i]$ is unknown, the left-hand side should be multiplied out symbolically. The estimation process begins by identifying $[A_{N_n}]$ and continues backwards to $[A_1]$. The values of the parameters in each $[A_i]$ matrix are frequency dependent, and, assuming the parameters are constants, their true values can be estimated by taking the spectral mean.

4.3.1 Example: Panel with Disbond

Conditioned reverse path analysis was applied to the damaged panel. Time histories of the response to a band limited random excitation were acquired using a laser displacement transducer. The input force was applied using the modal shaker and was measured using a force transducer. Twenty data sets, each 3 seconds long, were acquired as the panel was excited by band limited random excitation. The input force was generated by filtering Gaussian white noise with a low-pass filter having a cutoff frequency of 5 kHz, which was selected based on the frequency range in which the modes of interest occurred. Measurements were transformed from the time domain into the frequency domain via the DFT. No averaging of the data is performed prior to applying the reverse path analysis. The choice to measure displacement was made to avoid having to perform numerical differentiation in order to calculate the nonlinear function vectors.

A single, cubic stiffness nonlinearity that depends only on the displacement at a point measured near the disbond was assumed. Therefore, $N = 1, \{X\} = X, N_n = 1$, $[A_1] = \mu$, where μ is the coefficient of the cubic stiffness, $\{X_{n1}\} = \mathcal{F}[x(t)^3]$ (where $\mathcal{F}$ is the Fourier transform), and $\{F\} = F$. Data was assembled into a single $3 \times N_f \times N_{\text{ave}}$ matrix, where N_f is the number of frequency points in the spectra and N_{ave} is the number of data sets acquired. In general, the first N columns will be the response spectra, the next N_u columns will be the force spectra (where N_u is the number of inputs used), and the last N_n columns will be the spectra of the nonlinear function vectors. This assembly simplifies the coding required to calculate the unconditioned and conditioned spectra. Iterative loops were used to calculate the unconditioned PSD matrices according to Eq. 27. Expected values were found by averaging the PSD matrices from each of the twenty data sets. Next, iterative loops were used to find the conditioned PSD matrices according to Eq. 28.

Once the conditioned PSD matrices were determined, an estimate for the linear FRF was made using the H_2 estimator in Eq. 29. Figure 13 shows the estimate (dashed blue line) along with the FRF of the nonlinear system (solid black line) found by estimating the FRF directly from the measured data (i.e., with no conditioning). For reference, the FRF determined from a low amplitude sine sweep is shown (red dotted line), which is meant to represent the linear FRF of the panel.

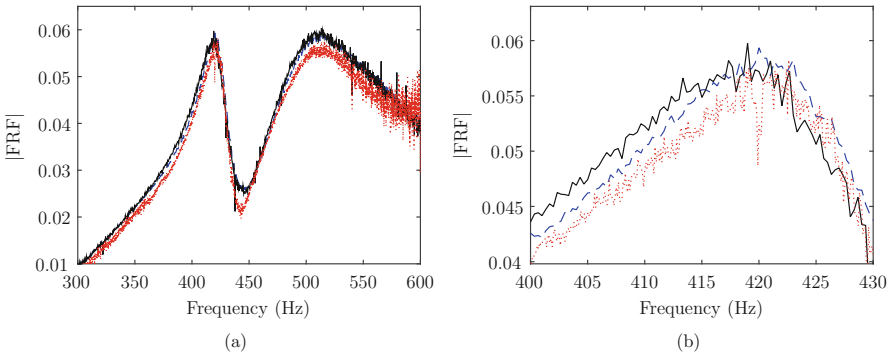

Fig. 13 Magnitudes of FRFs of the panel with disbond: FRF of the nonlinear system (——), FRF of the underlying linear system estimated using the conditioned reverse path method (— — —), and FRF of the panel excited by a low amplitude sine sweep (- - -). Figure (**b**) zooms in on the peak near 420 Hz

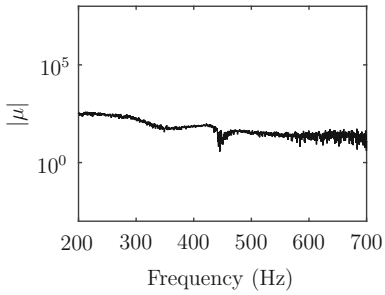

Fig. 14 The nonlinear parameter μ as a function of frequency from conditioned reverse path analysis

The linear FRF estimated by the conditioned reverse path analysis shows good agreement with the FRF determined in the selected frequency range from the low amplitude sine sweep.

The last step in the analysis was to estimate the nonlinear coefficient, $\mu(\omega)$, which is the only element in the $[A_1]$ matrix, using Eq. 31. Figure 14 shows the μ as a function of frequency. Because the parameter is assumed to be a constant, the estimated value is found by taking the mean over the frequency range of interest.

4.4 Nonlinear Identification Through Feedback of the Outputs (NIFO)

The nonlinear identification through feedback of the outputs (NIFO) technique is a frequency domain nonlinear system identification technique which utilizes spatial information to estimate nonlinear parameters in a simple solution approach [1]. If the location and form of the nonlinearity is understood, this technique can readily estimate the nonlinear parameters and separate the linear and nonlinear dynamics.

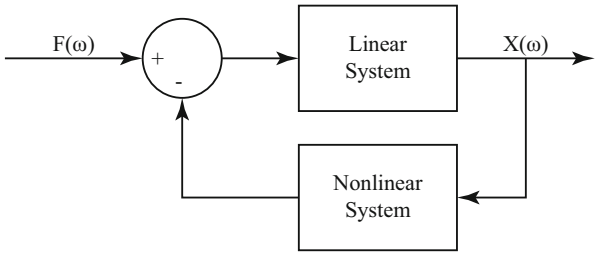

Fig. 15 Nonlinear feedback system diagram

The formulation of the nonlinear system in this approach is an underlying linear system with a nonlinear feedback loop. This idea is represented in Fig. 15.

The advantage to this formulation is that the overall response can be considered as a multiple-input system, with the inputs to the system being a combination of true forcing functions and nonlinear functions of the outputs. Furthermore, the portion of the response due to the nonlinearity is a function of the underlying linear frequency response function. In this form, the coefficient of the nonlinearity can be identified in a single step along with the frequency response of the underlying system. For a system with N_i measured inputs, N_o measured outputs, N_{avg} data sets, and N_n nonlinearities, the response of the system, $\{X(\omega)\}$, can be expressed in terms of the linear frequency response matrix, $[H_L(\omega)]$, the coefficients of nonlinearities, $\mu_n(\omega)$, the vectors that describes the degree of freedom at which the i^{th} nonlinear force is acting, $\{B_{ni}\}$, the vector of forcing functions, $\{F(\omega)\}$, and the nonlinear displacement associated with the i^{th} nonlinearity, $\{X_{ni}(\omega)\}$ as

$$[X(\omega)]_{N_o \text{x} 1} = \left[[H_L(\omega)]\ [H_L(\omega)]\mu_1(\omega)\{B_{n1}\}\ \ldots\ [H_L(\omega)]\mu_{N_n}(\omega)\{B_{nN_n}\}\right]_{(N_o \text{x}(N_i+N_n))} \times \begin{bmatrix} \{F(\omega)\}_{N_i \text{x} 1} \\ -\{X_n(\omega)\}_{N_n \text{x} 1} \end{bmatrix}_{((N_i+N_n)\text{x}1)}. \tag{32}$$

Equation 32 is the same form as a multi-input, multi-output (MIMO) frequency response function (FRF) relationship, where there are N_o output measurements and $N_i + N_n$ input measurements, with the only difference being that N_n of these inputs are a function of the system response. To simplify notation, the FRF matrix above can be renamed as

$$[H_{NL}] = [[H_L]\ [H_L]\mu_1\{B_{n1}\}\ \ldots\ [H_L(\omega)]\mu_{N_n}(\omega)\{B_{nN_n}\}],$$

and the rightmost vector $\{F_{NL}\} = [\{F\},\ -\{X_n\}]^T$. Making these substitutions, Eq. 32 becomes

$$[X]_{N_o \text{x} 1} = \left[H_{NL}\right]_{(N_o \text{x}(N_i+N_n))} \left[F_{NL}\right]_{((N_i+N_n)\text{x}1)} \tag{33}$$

Treating $\{F_{NL}\}$ as a standard forcing vector and $[H_{NL}]$ as a standard FRF matrix, $[H_{NL}]$ can be estimated using standard MIMO FRF estimation techniques. In this case, the H_2 FRF estimator considering several data sets is used. Once the matrix $[H_{NL}]$ is estimated, the underlying linear frequency response function matrix and the coefficient of nonlinearity can be found in a single step. The first N_i columns of $[H_{NL}]$ are $[H_L]$, and the last N_n columns are equal to the product $[H_L]\mu_i\{B_{ni}\}$, $i = 1..N_n$.

The strength of this technique is the simplicity with which it decouples the system's linear and nonlinear response characteristics if the location and form of the nonlinearity is well understood. Unlike methods such as the conditioned reverse path method, estimation of the linear system and the nonlinear parameters are accomplished simultaneously. The simple solution approach makes NIFO an attractive method for multi-degree of freedom systems with known nonlinearities.

4.4.1 Example: Panel with Disbond

NIFO analysis was applied to the damaged panel using measured displacement data at a point that coincided with the location of the disbond and force measurements from the impedance head on the shaker used to excite the panel. Twenty data sets, each 3 seconds long, were acquired as the panel was excited by band limited random excitation. The input force was generated by filtering Gaussian white noise with a low-pass filter with a cutoff frequency of 5 kHz, which was selected based on the frequency range in which the modes of interest occurred. In this example, only one input and one output location were used. However, the NIFO formulation easily accommodates the addition of more input and/or output locations.

The first step in formulating the NIFO analysis is to identify the location(s) and type(s) of nonlinearity (ies). In this example, a cubic stiffness nonlinearity that depends only on the displacement measured at the location of the disbond is assumed. Therefore, $N_n = 1$, $\{X_n(\omega)\} = X_{n1}(\omega) = \mathcal{F}[x(t)^3]$ (where $\mathcal{F}$ is the Fourier transform), μ_1 is the coefficient of X_{n1}, and $\{B_{n1}\} = 1$. If multiple output (i.e., measurement) locations had been used, zeros would be added to the B vector in all the rows except the row corresponding to the location of the nonlinearity. In the case that a nonlinearity is assumed that acts between two output locations, the B vector contains a one in the row corresponding to one of the locations, a negative one in the row corresponding to the second location, and zeros in all other rows.

After determining the form and location of the nonlinearity, $X(\omega)$ and $F(\omega)$ were calculated by transforming the measured time histories into frequency spectra via the DFT. Then, $X_n(\omega)$ was calculated by transforming $x(t)^3$ into the frequency domain via the DFT. These quantities were used in Eq. 33 in order to solve for $[H_{NL}(\omega)]$. Figure 16 shows a comparison of FRF estimates of the system. The solid black line shows the FRF estimated from the measured input/output data. This is typically referred to as the FRF of the nonlinear system. The dashed blue line shows $H_L(\omega)$, the estimate of the FRF of the underlying linear system. For comparison, the red dotted line is an FRF determined from a sine sweep performed at a low amplitude, which estimates the linear FRF. The linear FRF ($H_L(\omega)$) estimated from

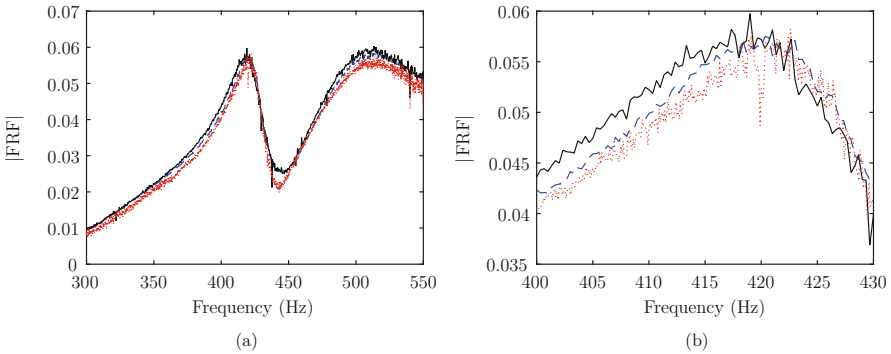

Fig. 16 Magnitudes of FRFs of the panel with disbond: FRF of the nonlinear system (——), FRF of the underlying linear system estimated using the NIFO method (— — —), and FRF of the panel excited by a low amplitude sine sweep (- - -). Figure (**b**) zooms in on the peak near 420 Hz

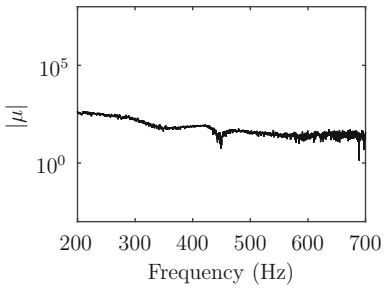

Fig. 17 The nonlinear parameter μ as a function of frequency from NIFO analysis

the NIFO analysis shows good agreement with the FRF determined from the low amplitude sine sweep.

Finally, $\mu_1(\omega)$ was determined from the second column of $[H_{NL}]$. Figure 17 shows the parameter as a function of frequency. The parameter is assumed to be a constant, so the estimate would be determined by taking the mean over the frequency range of interest.

5 Summary

The nonlinear analysis methods presented in this chapter are a representative subset of the methods available to the experimentalist for detecting, characterizing, and modeling a system's nonlinear dynamics. Table 2 summarizes the requirements to implement each method. The principles demonstrated here provide a fundamental basis upon which most nonlinear analysis approaches, including methods not presented here, are derived. These principles and guidelines provide a powerful toolbox for moving beyond linear systems analysis and experimentally characterizing nonlinear dynamic structures.

Table 2 Summary of nonlinear analysis methods

Methods for detection and characterization			
Method	Output data required	Excitation required	Comments
Coherence	FRF using any type of data	Random, sine sweep, impact, etc.	
FRF distortion	FRF using any type of data	Random, sine sweep, impact, etc.	Must acquire data at multiple input levels
Higher-order FRFs	Any output type (response spectra required)	Stepped sine from Ω_1 to Ω_2	For nth order FRF, $\Omega_1 \leq {}^1/_n$ lowest modal frequency of interest; $\Omega_2 >$ highest modal frequency of interest
Hilbert transform (time domain)	Any output type (acquire time histories)	Impact	Other inputs can be used, but a forced response necessitates an estimate of the system's mass
Hilbert transform (frequency domain)	FRF using any type of data	Random, sine sweep, impact, etc.	
Restoring forces	Displacement, velocity, and acceleration (acquire time histories)	Random, multi-amplitude sinusoids	Non-measured outputs can be estimated by numerically integrating and/or differentiating measured outputs input must generate outputs that densely cover the displacement-velocity plane.
Vibro-acoustic modulation	Any output type (response spectra required)	Low-frequency sinusoid and high-frequency sinusoidal	Low-frequency signal should be chosen to match a natural frequency low-frequency force can be replaced by an impact.
Methods for modeling			
NARMAX	Any output type (acquire time histories)	Random	Other input types may also be acceptable.
Direct parameter estimation	Displacement, velocity, and acceleration (acquire time histories)	Random	Non-measured outputs can be estimated by numerically integrating and/or differentiating measured outputs other input types may also be acceptable.
Conditioned reverse path	Displacement. Velocity only if damping nonlinearity is assumed (response spectra required).	Random, sine sweep	Form of nonlinearity must be assumed a priori
NIFO	Displacement. Velocity only if damping nonlinearity is assumed (response spectra required).	Random, sine sweep	Form of nonlinearity must be assumed a priori

References

1. Adams D, Allemang R (2000) A frequency domain method for estimating the parameters of a non-linear structural dynamic model through feedback. Mech Syst Signal Process 14(4):637–656
2. Bendat JS, Piersol AG (1980) Engineering applications of correlation and spectral analysis. Wiley-Interscience, New York, p 315
3. Bendat J, Palo P, Coppolino R (1992) A general identification technique for nonlinear differential equations of motion. Probab Eng Mech 7(1):43–61
4. Billings S, Tsang K (1989) Spectral analysis for non-linear systems, part I: parametric non-linear spectral analysis. Mech Syst Signal Process 3(4):319–339
5. Chen S, Billings SA (1989) Representations of non-linear systems: the narmax model. Int J Control 49(3):1013–1032
6. Donskoy D, Sutin A, Ekimov A (2001) Nonlinear acoustic interaction on contact interfaces and its use for nondestructive testing. NDT & E Int 34(4):231–238
7. Feldman M (1994) Non-linear system vibration analysis using hilbert transform–I. Free vibration analysis method 'Freevib'. Mech Syst Signal Process 8(2):119–127
8. Feldman M (1994) Non-linear system vibration analysis using hilbert transform–II. Forced vibration analysis method 'Forcevib'. Mech Syst Signal Process 8(3):309–318
9. Feldman M (2011) Hilbert transform in vibration analysis. Mech Syst Signal Process 25(3):735–802
10. Meyer JJ, Adams DE (2015) Theoretical and experimental evidence for using impact modulation to assess bolted joints. Nonlinear Dyn 81(1–2):103–117
11. Mohammad K, Worden K, Tomlinson G (1992) Direct parameter estimation for linear and non-linear structures. J Sound Vib 152(3):471–499
12. Richards C, Singh R (1998) Identification of multi-degree-of-freedom non-linear systems under random excitations by the reverse path spectral method. J Sound Vib 213(4):673–708
13. Storer D, Tomlinson G (1993) Recent developments in the measurement and interpretation of higher order transfer functions from non-linear structures. Mech Syst Signal Process 7(2):173–189
14. Tomlinson G, Worden K (2000) Nonlinearity in structural dynamics: detection, identification and modelling. Boca Rotan, CRC Press. https://doi.org/10.1201/9780429138331
15. Worden K (1990) Data processing and experiment design for the restoring force surface method, part II: choice of excitation signal. Mech Syst Signal Process 4(4):321–344

Structural Health Monitoring and Damage Identification

18

R. Fuentes, E. J. Cross, P. A. Gardner, L. A. Bull, T. J. Rogers, R. J. Barthorpe, H. Shi, N. Dervilis, C. R. Farrar, and K. Worden

Contents

R. Fuentes · E. J. Cross · P. A. Gardner · L. A. Bull · T. J. Rogers · R. J. Barthorpe · H. Shi
N. Dervilis · K. Worden (✉)
Dynamics Research Group, Department of Mechanical Engineering, University of Sheffield, Sheffield, UK
e-mail: ramon.fuentes@sheffield.ac.uk; k.worden@sheffield.ac.uk

C. R. Farrar
Engineering Institute, Los Alamos National Laboratory, Los Alamos, NM, USA

R. Allemang, P. Avitabile (eds.), *Handbook of Experimental Structural Dynamics*,
https://doi.org/10.1007/978-1-4614-4547-0_23

Abstract

Structural dynamics is fundamentally concerned with the design, operation, and understanding of physical structures. A significant concern in the management of these, often very high-value, assets, is their state of health. When a structure sustains damage, this can have an extremely negative effect on its availability, and this will have serious implications for profitability and also the safety of any human operators or occupants. It is therefore important to implement some means of monitoring structural health so that incipient damage can be detected and remedial actions can be taken before negative consequences occur. The pertinent damage identification methodology for engineering structures is *Structural Health Monitoring* (SHM). This chapter presents an overview of SHM, with particular reference to implementations based on monitoring structural vibrations and waves. The main philosophy under discussion here is *data-based* SHM, where diagnostics are based on the interpretation of measured data directly, without recourse to physics-based models. The main technologies for carrying out data-based SHM are statistical pattern recognition and machine learning, and the chapter gives some background on these methods and provides some case studies to illustrate their use. One of the main approaches to damage detection is *novelty detection*, where one develops a statistical model of measured features from the undamaged structure of interest, and monitors subsequent data to see if there are deviations from the model, indicative of damage. A serious problem with this approach is that it is prone to false alarms if there are benign changes to the data, like operational or environmental variations. Such benign changes – referred to here as *confounding influences*, need to be compensated for, if the SHM system is to be reliable and error-free (as far as possible). The chapter considers how confounding influences arise, and how they can be removed in the data-driven context by *data normalization.* Finally, the chapter concludes with some discussion of how physics-based models can still have a potentially useful role in data-driven SHM.

Keywords

Structural Health Monitoring (SHM) · Data-based and model-based SHM · Statistical pattern recognition · Machine learning · Confounding influences · Data normalization

1 Introduction

1.1 Motivation and Definition of SHM

In brief, *Structural Health Monitoring* (SHM) is any automated monitoring practice that seeks to assess the condition or health of a structure. In terms of a more formal definition, one might adopt: "SHM is the process of implementing a damage identification strategy for aerospace, civil and mechanical engineering infrastructure, where damage is defined as changes to the material and/or geometric properties of these systems, including changes to the boundary conditions and system connectivity, which adversely affect the systems performance" [1, 2].

The origins of SHM in the context of engineering can arguably be traced back as far as the time when tap-testing for fault detection became common, although the field did not really become established in research communities until the 1980s, when considerable interest was generated in the structural assessment of oil rigs, and later in aerospace structures and their health [3]. SHM has now established itself as a popular and still growing research field, which is more and more becoming a focus in terms of structural asset management within the engineering community. As Wenzel has observed [4], bridges (which are arguably the paradigm for critical infrastructure) have always been monitored, with this activity varying between visual inspection and continuous monitoring with dense sensor networks.

At its heart, SHM has significant aspirations that, once achieved, will hugely benefit society; it strives toward an ideal where one is able to monitor (in an automated fashion) a structure in such a way that any damage introduced, or any growth of inherent faults, would be immediately detectable, or detectable in time to plan and apply remedial actions which have minimal impact on operation. Furthermore, after detection, it is desirable that any fault could be located and its severity inferred so that decisions on remedial actions are optimal. These global objectives for SHM are formalized in Rytter's hierarchy [5], which classifies these aims into "levels" of increasing difficulty as follows:

Level 1 (DETECTION): The method gives a qualitative indication that damage might be present in the structure.
Level 2 (LOCALIZATION): The method gives information about the probable position of the damage.
Level 3 (CLASSIFICATION): The method indicates what type of damage is present.
Level 3 (ASSESSMENT): The method gives an estimate of the extent of the damage.
Level 4 (PREDICTION): The method offers information about the safety of the structure, for example, estimates a residual life.

At this point, it is perhaps important to stress what SHM *is not*; for disambiguation, it is important to discuss the differences between SHM and related fields associated with damage identification (a more detailed discussion can be found

in [6]). Although tap-testing was mentioned earlier in terms of the origins of SHM, the example more properly belongs to the field of *Non-Destructive Testing/Evaluation* (NDT/NDE). NDE/NDT concerns the assessment of a structure or component's health through (offline) non-damaging procedures; examples of tools commonly used for NDE are: x-ray, electron microscopy, measurement of acoustic emissions, and full scale vibration tests. In fact, all of these techniques supplement SHM technology; however, NDE is distinguished by its application as one-off planned events, often applied to preestablished small areas of a structure where the presence of damage is suspected. This is fundamentally different to SHM where monitoring is usually intended to be continuous and global, and is usually understood to require permanently installed sensors. In the future, it is likely that NDE inspection will form the basis for distinguishing between structural health and performance anomalies where this cannot be accomplished automatically. It is therefore true to say that NDE may be incorporated as part of an SHM system, but not vice versa. Another field related to SHM is *Condition Monitoring* (CM). CM usually concerns the health of rotating machinery; it has seen been widely applied and in some areas, accepted as part of everyday industrial practice. Its comparative success (in terms of industrial uptake) relative to SHM can be attributed to a number of simplifying factors: machinery often operates in a controlled environment, and it is usually easy to access and is typically on a small scale. Importantly, rotating machinery often have well-defined dynamic responses for particular fault categories, which makes fault detection and identification a more easily attainable goal than it perhaps is for SHM [7].

1.2 Statistical Pattern Recognition Approach to SHM

There are potentially many ways to organize a discussion of SHM. The approach here follows [8], in defining the SHM process in terms of a four-step statistical pattern recognition paradigm. This following four-step process includes [2]:

1. Operational evaluation
2. Data acquisition, normalization, and cleansing
3. Feature selection and information condensation
4. Statistical model development for feature discrimination

All studies in the fields of SHM and CM address some parts of this paradigm, but the number of studies that address all portions of the paradigm is very limited.

1.2.1 Operational Evaluation

Operational Evaluation (OE) attempts to answer four questions regarding the implementation of an SHM capability.

1. What are the life-safety and/or economic justifications for performing SHM?
2. How is damage defined for the system being investigated and, for multiple damage possibilities, which cases are of the most concern?

3. What are the conditions, both operational and environmental, under which the system to be monitored functions?
4. What are the limitations on acquiring data in the operational environment?

OE thus attempts to set the limitations on what will be monitored and how the monitoring will be accomplished; it attempts to tailor the SHM process to features that are unique to the system being monitored and tries to exploit unique features of the damage that is to be detected.

1.2.2 Data Acquisition, Normalization, and Cleansing

The data acquisition part of the SHM process involves selecting the excitation methods, the sensor types, number and locations, and the data acquisition/storage/transmittal hardware. Again, this process will be application specific. Cost (time/effort) will play a major role in making these decisions. The frequency with which the data should be collected is another consideration that must be addressed.

As data can be measured under varying conditions, the ability to normalize the data becomes very important in the SHM process. *Data normalization* is the process of separating changes in sensor readings caused by damage from those caused by varying operational and environmental conditions, which are benign and must not raise an alarm. Where environmental or operational variations are an issue, one may need to normalize the data in some temporal fashion to facilitate the comparison of data measured at different points in an environmental or operational cycle. Sources of variability in the data acquisition process and with the system being monitored need to be identified and minimized. In general, not all of such sources can be eliminated; therefore, it is necessary to make the appropriate measurements such that these sources can be statistically quantified. Variability can arise from changing environmental and test conditions, changes in the data reduction process and unit-to-unit inconsistencies [2]. Section 5 of this chapter provides a more in-depth discussion of the various methods available for dealing with environmental and operational changes.

Data cleansing is the process of selectively choosing data to pass on to, or reject from, the feature selection process. The data cleansing process is usually based on the knowledge gained by individuals directly involved with the data acquisition. For example, an inspection of the test setup may reveal that a sensor was loosely mounted, and, hence, based on the judgment of the individuals performing the measurement, this set of data or the data from that particular sensor may be selectively deleted from the feature selection process. Signal processing techniques such as filtering and resampling can also be thought of as data cleansing procedures.

1.2.3 Feature Extraction and Information Condensation

The part of the SHM process that usually receives most attention in the technical literature is the identification of data features that allow one to distinguish between the undamaged and damaged structure. As such, numerous articles have been devoted to the feature extraction portion of SHM [9, 10, 11, 12]. Inherent in this feature

selection process is the condensation of the data. The best features for damage identification are usually application specific. One of the most common feature extraction methods is based on correlating measured system response quantities, such as vibration amplitude or frequency, with the first-hand observations of the degrading system. Another method of developing features for damage identification is to apply engineered flaws – *proxies* – similar to ones expected in actual operating conditions, to systems and develop an initial understanding of the parameters that are sensitive to the expected damage [13, 14].

The flawed system can also be used to validate that the diagnostic measurements are sensitive enough to distinguish between features identified from the undamaged and damaged system. The use of analytical tools such as experimentally validated finite element models can be a great asset in this process. In many cases, the analytical tools are used to perform numerical experiments where the flaws are introduced through computer simulation. Damage accumulation testing, during which significant structural components of the system under study are degraded by subjecting them to realistic loading conditions, can also be used to identify appropriate features. This process may involve induced damage testing, fatigue testing, corrosion growth, or temperature cycling to accumulate certain types of damage in an accelerated fashion. Insight into the appropriate features can be gained from several types of analytical and experimental studies as described above, and is usually the result of information obtained from some combination of these studies.

The operational implementation and diagnostic measurement technologies needed to perform SHM produce more data than traditional uses of structural dynamics information. A condensation of the data is advantageous and necessary when comparisons of many feature sets obtained over the lifetime of the structure are envisioned. Also, because data will be acquired from a structure over an extended period of time and in an operational environment [2], robust data reduction techniques must be developed to retain feature sensitivity to the structural changes of interest in the presence of environmental and operational variability. To further aid in the extraction and recording of the high-quality data needed to perform SHM, the statistical significance of the features should be characterized and used in the condensation process. A discussion of some of the most popular damage-sensitive features is provided in Sect. 2 of this chapter, while Sect. 3 discusses some of the more advanced techniques that can be applied to problems such as data compression and recursive and online estimation of features.

1.2.4 Statistical Model Development

The final part of the SHM process is the development of statistical models for discrimination between features from the undamaged and damaged structures. Statistical model development is concerned with implementing algorithms that operate on the extracted features to qualify/quantify the damage state of the structure. The algorithms usually fall into three categories. When data are available from both the undamaged and damaged structure, the algorithms fall into the general class referred to as *supervised learning*. Classification and regression analysis are categories of supervised learning algorithms. *Unsupervised learning* refers to

algorithms that are applied to data only containing examples from the undamaged structure; outlier or novelty detectors are the primary forms of algorithms applied in unsupervised learning applications. All of the algorithms implicitly or explicitly analyze probability distributions of the measured or derived features to enhance the damage identification process.

The damage identification of a system can be described as a five-step process along the lines of Rytter's hierarchy as discussed above. The answers to the questions posed represent increasing knowledge of the damage state. When applied in an unsupervised learning mode, statistical models are typically used to answer questions regarding the existence and location of damage. When applied in a supervised learning mode and coupled with analytical models, the statistical procedures can be used to better determine the type of damage, the extent of damage and remaining useful life of the structure (Although prognosis is distinguished from the other SHM problems, in that it cannot be accomplished in a data-based fashion alone, physics-based models of the relevant damage mechanisms and processes are required.). The statistical models are also used to minimize false indications of damage. False indications of damage fall into two categories: (i) false-positive damage indication (indication of damage when none is present) and (ii) false-negative damage indication (no indication of damage when damage is present). Errors of the first type are undesirable, as they will cause unnecessary downtime and consequent loss of revenue, as well as loss of confidence in the monitoring system. More importantly, there are clear safety issues if misclassifications of the second type occur. Many pattern recognition algorithms allow one to weigh one type of error above the other; this weighting may be one of the factors decided at the operational evaluation [2] stage. Reviews that focus on the statistical modeling portion of the SHM process include [15, 16, 17, 18].

1.3 Fundamental Axioms of SHM

In terms of practical progress toward the aims and objectives of SHM, a great deal of experience and knowledge has already been gained. Reflecting on work in the field and the lessons learned over the years, a number of fundamental "axioms" have been formulated [19]:

Axiom I: All materials have inherent flaws or defects.

Axiom II: The assessment of damage requires a comparison between two system states.

Axiom III: Identifying the existence and location of damage can be done in an unsupervised learning mode, but identifying the type of damage present and the damage severity can generally only be done in a supervised learning mode.

Axiom IVa: Sensors cannot measure damage. Feature extraction through signal processing and statistical classification are necessary to convert sensor data into damage information.

Axiom IVb: Without intelligent feature extraction, the more sensitive a measurement is to damage, the more sensitive it is to changing operational and environmental conditions.

Axiom V: The length and time scales associated with damage initiation and evolution dictate the required properties of the SHM sensing system.

Axiom VI: There is a trade-off between the sensitivity to damage of an algorithm and its noise rejection capability.

Axiom VII: The size of damage that can be detected from changes in system dynamics is inversely proportional to the frequency range of excitation.

The axioms are intended to help to specify an SHM system in practice. They were originally proposed with the intention of stimulating discussion; however, despite the fact that the original paper has been cited many times, there has been very little dissent. In 2010, an Axiom VIII was proposed: "Damage increases the complexity of the structure" [20]. The new axiom appears to be a little more nuanced than the others and has generated interesting research on the nature of complexity as an indicator of health.

Where there has been some critical discussion, concerns Axiom II, with a number of authors arguing that "baseline-free" SHM is possible. The counterargument here is that the "baseline-free" methods are always carried out with respect to some idealization, whether this is a model or a conceptualization, and the "comparison" in the Axiom is thus implicitly present.

The axioms have greater or lesser importance, depending on the specific SHM context, for example, Axiom III provides some interesting points for discussion in the context of civil infrastructure SHM. Because only the lowest global modes are generally excited in practice for say a bridge, the modes will usually involve large-scale coherent motions. If the structure has a dense sensor network, a breakdown in correlations between neighboring sensors may give information about the location of damage. This fact means that localization of damage could be possible despite the fact that data from damage states are not available. Severity of damage could also be inferred from the extent of the breakdown of correlation. Another possibility is that within the highly heterogeneous structure that is a bridge, changes in local modes, for example, those of cables, may also allow some localization of damage.

Although one could discuss each axiom in turn, the section will conclude here with some comments on Axiom V. Axiom V is the reason why operational evaluation is a critical stage in the development of any SHM system. The design of the sensor system must be tailored to the time and length scales on which one expects damage to accumulate. In the context of certain aerospace alloys, a critical crack size smaller than a millimeter means that confident detection of the crack almost immediately after initiation is critical. In the context of civil infrastructure, it will usually be the case that damage will accumulate on longer time scales and will have a greater spatial extent before catastrophic failure would occur. Even so, these anticipated time and length scales must be considered very carefully in the specification for the monitoring system; because civil structures are so much larger, for confident detection sensor densities may well need to be relatively high.

1.4 Historical Overview

A detailed historical overview definitely falls outside the scope of this chapter, but it is worth pointing out some of the key developments over the last 40 years. Specific references are not cited, instead the reader is referred to [3, 16, 7] and [2] for more detailed summaries of this subject.

To date, the most successful application of SHM technology has been for CM of rotating machinery [7], as this is particularly well suited to the data-driven paradigm. Often this pattern recognition is performed only in a qualitative manner based on a visual comparison of features such as frequency spectra obtained from the system at different times. For rotating machinery systems, the approximate damage location is generally known, making a single-channel fast Fourier transform analyzer sufficient for most periodic monitoring activities. Typical damage that can be identified includes loose or damaged bearings, misaligned shafts, and chipped gear teeth. The success of CM is due in part to: (i) minimal operational and environmental variability associated with this type of monitoring, (ii) well-defined damage types that occur at known locations, (iii) large databases that include data from damaged systems, (iv) well-established correlation between damage and features extracted from the measured data, and (v) clear and quantifiable economic benefits that this technology can provide. These factors have allowed this application of SHM to make the transition from a research topic to industry practice several decades ago, resulting in comprehensive condition management systems such as Health and Usage Monitoring Systems (HUMS), which are new standard in modern rotary-wing aircraft.

During the 1970s and 1980s, the oil industry made considerable efforts to develop vibration-based damage identification methods for offshore platforms. This damage identification problem is fundamentally different from that of rotating machinery because the damage location is unknown and the majority of the structure is not readily accessible for measurement. A common methodology adopted by this industry was to simulate candidate damage scenarios with numerical models, examine the changes in resonance frequencies that were produced by these simulated changes, and correlate these changes with those measured on a platform. A number of very practical problems were encountered which prevented the adaptation of this technology, and efforts at further developing it for offshore platforms were largely abandoned in the early 1980s. The aerospace community began to study the use of vibration-based damage identification during the late 1970s and early 1980s in conjunction with the development of the space shuttle. This work has continued with current applications being investigated for the National Aeronautics and Space Administration's (NASA) space station and future reusable launch vehicle designs.

Since the mid-1990s, studies of damage identification for composite materials have been motivated by the development of a composite fuel tank for a reusable launch vehicle. The failure mechanisms, such as delamination caused by debris impacts, and corresponding material response for composite fuel tanks are significantly different to those associated with metallic structures. Moreover, the

composite fuel tank problem presents challenges because the sensing systems must not provide a spark source. This challenge has led to the development of SHM based on fiber-optic sensing systems. Reference [21] provides a more detailed discussion of SHM applied to aerospace structures.

The civil engineering community has studied vibration-based damage assessment of bridge structures and buildings since the early 1980s. Modal properties and quantities derived from them, such as mode shape curvatures and dynamic flexibility matrix indices, have been the primary features used to identify damage in bridge structures. Environmental and operating condition variability presents significant challenges to the bridge monitoring application. The physical size of the structure also presents many practical challenges for vibration-based damage assessment. Regulatory requirements in Asian countries, which mandate that the companies that construct the bridges periodically certify their structural health, are driving current research and commercial development of bridge SHM systems. The reviews of the technical literature presented by [3] and [22] show an increasing number of research studies related to damage identification. These studies identify many technical challenges to the adaptation of SHM that are common to all applications of this technology. These challenges include the development of methods to optimally define the number and location of the sensors; identification of the features sensitive to small damage levels; the ability to discriminate changes in these features caused by damage from those caused by changing environmental and/or test conditions; the development of statistical methods to discriminate features from undamaged and damaged structures; and performance of comparative studies of different damage identification methods applied to common datasets. These topics are currently the focus of various research efforts by many industries including: defense, civil infrastructure, automotive, and semiconductor manufacturing where multidisciplinary approaches are being used to advance the current capabilities of SHM and CM.

2 SHM Data and Damage-Sensitive Features

This section will provide a general overview of the types of dynamic response data typically used in SHM: vibration, acoustic emission (AE) and ultrasound, together with the basic signal processing required to extract damage-sensitive features often used in these contexts. Note that in the interest of focusing on the conceptual above the mathematical, a lot of detail will be skipped; in particular, with respect to the mathematics behind the signal processing context such as sampling and windowing. For these details, the reader is encouraged to consult other excellent dedicated signal processing texts such as the classic [23] or sections elsewhere in this book. The focus of this section is to give an overview of the breadth of damage-sensitive features and how they relate to the damage process across different scales and domains.

2.1 Vibration

Vibration-based SHM is now a very popular technique for assessing the state of an engineering system, with a significant part of SHM research and industrial applications being devoted to using vibration measurements to infer the presence and location of damage; this development dates back to the 1990s [3].

In SHM, vibration monitoring is based on the premise that an adverse change to the structure will cause a change in the dynamic response, which should be quantifiable using vibration measurements [19]. This change in the dynamics often manifests itself in changes to measurable parameters such as mode shapes, natural frequencies, or damping. Damage alters the structural response in ways that can be captured through a range of damage-sensitive features. Vibration data can cover a wide range of frequencies, and this is application dependent. Structures that vibrate at very low frequencies include most civil infrastructure, such as bridges, buildings, and stadia, as well as offshore oil rigs and wind turbines. The excitation source for most civil structures tends to be its own environment. Wind, traffic loading, and earth movement are common excitation sources in civil infrastructure. In wind turbines, the low-frequency loading comes predominantly from the aerodynamic loading caused by the rotation of the blades, and the effects that blades have on each other. This loading tends to be transmitted through the main driven shaft into the gearbox and subsequently into the tower.

In the aerospace industry, loading and natural frequencies tend to lie at higher values. In rotary wing aircraft, the main excitation source, coming from blade rotation, tends to be low-to-medium frequency, in the 2–50 Hz range, where the loading is almost purely harmonic. Fixed-wing aircraft tend to be excited by a number of sources, but the excitation tends to be broadband, and is typically approximated by Gaussian white noise, or other colored noise for analysis purposes. The excitation sources in fixed wing aircraft come predominantly from aerodynamic loads, such as buffeting, friction, and gusts. The frequency ranges involved in this can range from medium frequency narrowband buffeting in the 50–1000 Hz range, to much higher-frequency broadband noise involving noise up to several kiloHertz.

There is a strong overlap between SHM and machine CM. As discussed in Sect. 1.2, CM is now a mature field given the fact that the dynamics of rotating machinery are fairly well understood and such systems normally operate in controlled environments and loading conditions. For example, a wide variety of bearing and gearbox faults in gear and bearing components can be often easily classified as they manifest themselves in specific frequency bands. There are many similarities between the types of features that are sensitive to damage in both domains. Hence, much of the discussions that will follow regarding damage-sensitive features also apply to the field of CM.

2.1.1 Ways to Measure Vibration

The piezoelectric accelerometer is arguably the most popular and practical instrument for measuring vibration. The shapes and sizes vary according to application

and cost, but they all generally rely on the same principle – that of converting a mechanical acceleration into an electrical signal through the piezoelectric effect. An alternative method for measuring vibration is a laser vibrometer. Laser vibrometry relies on the Doppler effect on the reflection of a laser beam on a moving surface, to measure velocity normal to a surface. This technique solves some of the main drawbacks of accelerometers. Being noncontact, it does not add mass to the system and does not require a mounting point. Furthermore, large areas of a structure can be scanned with minimal setup; this can save large amounts of test time compared with setting up accelerometers, if the channel count is high. The main drawbacks of laser vibrometry are the fact that the surface has to be reflective and in the line of sight, and the laser setup is more suitable for laboratory than operational environments.

When measuring displacement, the most popular tool is the strain gauge. The basic working principle of a strain gauge is that as a material strains, its electrical resistance will change accordingly and one can measure this change by passing an electric current through it. There are many classes of strain gauges, but most of them constitute a wire or a metallic filament that is bonded to the surface of the structure.

2.1.2 Damage-Sensitive Features from Vibration

- To what degree is the excitation source known and can it be measured?
- What is the nature of the dynamic response (stationary, periodic, stochastic, transient)?
- How many dimensions (DOFs) are being measured?
- What type of damage is one interested in finding? Is there any prior knowledge regarding? Where this might manifest itself?

By far the most important factor that dictates which features might be useful for damage detection purposes and what further processing must be carried downstream is whether or not the excitation can be measured. This point is of fundamental importance, given that the input excitation has a direct impact on the output dynamic response. If the premise for detecting damage is based on spotting a change in the dynamic response, the best way to distinguish whether a change is the result of damage or a change in excitation is to measure the excitation. In the discussion that follows, the various different damage-sensitive features will be analyzed in terms of the points above.

As such, the raw dynamic response data constitute a damage-sensitive feature, although it is not always a particularly good one. One reason for this is that in most cases, a time-history is highly redundant in terms of its information content. This fact results in higher dimensions in the feature vectors, which is in fact problematic for the machine learning techniques further downstream. It is useful to use transformations of the raw data into domains that are low dimensional, so they summarize the data well, are fast to compute, and of course, also sensitive to damage. It is also often the case that one will choose a feature that has a clear physical interpretation, so that besides being useful for the purposes of automatically detecting damage using a machine learning algorithm, one can also understand the damage mechanism. To this end, Fourier analysis, which transforms signals from the

time to the frequency domain, is one of the most useful and widespread techniques, so a fair amount of attention will be devoted here to features derived from the Fourier transform.

Throughout this section, examples will be drawn from an investigation originally carried out in [24].

Features Based on Signal Statistics

Basic signal statistics constitute the simplest forms of damage sensitive features. This includes the mean, mean-square, variance, skewness, kurtosis, and root-mean-squared (RMS). Damage has been long known to manifest itself in changes in these values. Damage introduces changes to the dynamical system that governs the output measurements. For example, plasticity induced by a growing crack could alter the damping of a structure, which would lead to a change in the total energy transfer between input excitation and observed strain/acceleration. This energy change could be directly observed in all the statistics that measure overall spread such as peak amplitudes, RMS, and variance. Damage causes changes in the natural frequencies of the system, and if the system is being excited at a constant frequency, damage will lead to a change in spread and energy-measuring statistics too.

The higher-order moments, skewness, and kurtosis have also found uses in damage detection. Kurtosis effectively provides as measure of how non-Gaussian a signal is. A structural crack may result in an additional impact-like response as it opens and closes during oscillation cycles, and this may become evident in the kurtosis. In a similar way, the effect of a crack could be described by a bilinear stiffness model, where the material stiffens up as the crack closes and loses stiffness as it opens. These effects generate two different dynamic behaviors in the up and down strokes of oscillation cycles which will be evident in a skewed probability distribution of the raw signals.

Basic statistics offer a simple way of deriving damage-sensitive quantities with relatively minimal computational complexity. On the other hand, one must bear in mind that changes in these features can easily be caused by changing operational and environmental effects. Changing excitation amplitudes and frequencies will easily cause similar changes to these features as will damage. The same is true for changing material properties from changes in temperature and humidity.

Auto and Cross-Correlations

The correlation function is a similarity measure over time, which is a particularly useful concept in the analysis of signals. An *autocorrelation function,* $\delta_{xx}(\tau)$, of a signal *x(t)* is a self-similarity measure, defined by,

$$\delta_{xx}(\tau) = E\left[x(t+\tau)\, x(t)\right] \tag{1}$$

It is essentially a measure of how much a signal looks like itself when shifted in time by an amount τ. It is a useful damage-sensitive feature as it provides a normalization of the time axis (to the time-shift), so that one could effectively compare several autocorrelation feature vectors like-for-like. One could not do this

with a raw time history unless it was perfectly synchronized to a specific event, such as an impulse or the phase of a periodic excitation source. The autocorrelation function also highlights periodicity in waveforms, which will be evident as strong peaks in $\delta_{xx}(\tau)$. If one has two different stationary random processes *x(t)* and *y(t)* (usually the input and output of a system), one can define the cross-correlation functions,

$$\delta_{yx}(\tau) = E\left[y(t+\tau)\, x(t)\right] \tag{2}$$

$$\delta_{xy}(\tau) = E\left[x(t+\tau)\, y(t)\right] \tag{3}$$

In a sense $\delta_{yx}(\tau)$ detects causal relationships between signals; often these are the input and output to some system under investigation or test. In SHM, the auto- and cross-correlation functions are useful in a variety of contexts, often as damage-sensitive features themselves, but also serving as essential steps in the computation of other features, such as power spectra and coherence functions. In the context of vibration monitoring, the cross-correlation has been used extensively as a damage-sensitive feature [25, 26, 27]; its use in SHM extends to applications in Acoustic Emissions and ultrasound monitoring [28, 29, 30], the uses of which are discussed below in the respective sections. An important point to bear in mind when computing a cross-correlation function is its normalization. This is not discussed here but the reader is referred to any standard signal processing book for this.

Frequency Spectra

Transforming vibration signals into the frequency domain is undoubtedly a powerful approach to understanding vibration waveforms. The frequency spectrum of a discrete signal, derived using a discrete Fourier transform (DFT) is defined as (The nomenclature of spectra is quite precise, in that account should really be taken as to whether a spectrum represents power or power density, etc. The distinction is represented in the units of the object of interest, and should take account of the effects of windowing, etc. In this chapter, spectra are only discussed in terms of their usage as features for SHM, and their absolute scales are not relevant. For this reason, the discussion may be a little cavalier in places, concerning units and scales.),

$$X_n = \sum_{r=0}^{N-1} x_i e^{-i\frac{2\pi n}{N}r} \tag{4}$$

where n defines the spectral line index, corresponding to a specific frequency bin, and r represents the time index of waveform x. Performing this sum has a computational complexity of $O(N^2)$, which is fairly prohibitive for practical computation. This high computational cost led to the development of the fast Fourier transform (FFT) algorithm, which reduced the computational complexity of computing X_n to $O(N\ log\ N)$. The FFT has been singled out as one of the most important algorithmic developments of the *twentieth* century [31], and it has

enabled widespread application of Fourier analysis across a multitude of disciplines, including structural dynamics and SHM. Moving to the frequency domain is a particularly useful way of interpreting the output of a system as the amplitude and phase information is broken down into distinct bands associated with each response frequency. The output of a DFT/FFT can be readily interpreted as the amplitude contribution of each individual sine tone to the total signal. It is very effective when used in outputs of harmonically excited structures, but less so when the excitation is broadband and stochastic. A common function derived from the Fourier transform that is used to examine the output of a stochastic excitation in the frequency domain is the *power spectral density* (PSD). An example of a PSD is given in Figure 1c for undamaged and damaged class datasets. The PSD defines the relative distribution of power over a given frequency bandwidth. Any change in natural frequency, damping ratio, and input excitation will lead to a change in the shape of the PSD, thus making it a useful damage-sensitive feature.

The definition for the power spectrum follows conveniently from that of the autocorrelation of Eq. (2) (not shown here in detail). Taking the Fourier transform of $\tau(xy)$ yields the convenient form,

$$\begin{aligned} F\left[\tau(xy)\right] &= X(\omega)\, X(\omega)^* \\ S_{xx} &= X(\omega)^2 \end{aligned} \tag{5}$$

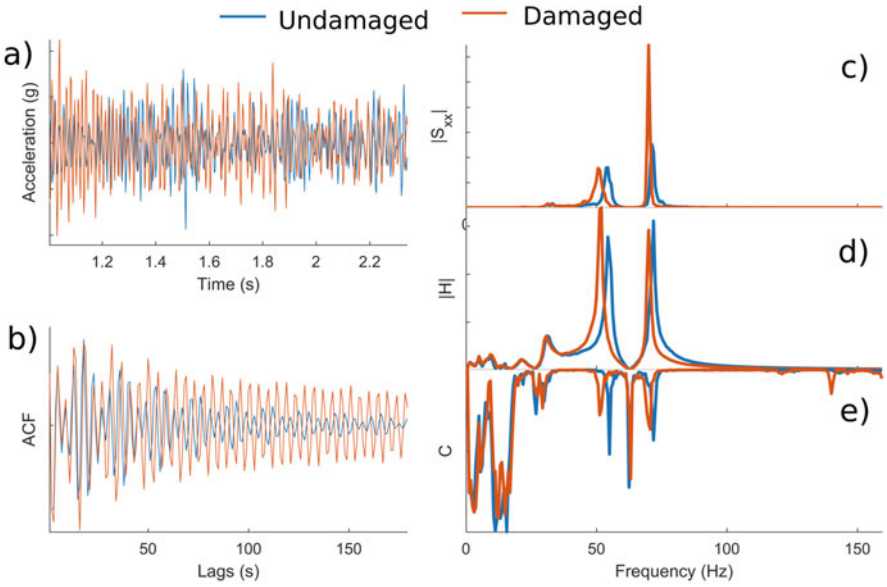

Fig. 1 Damaged and undamaged features from the five-story LANL test structure: (**a**) raw acceleration, (**b**) autocorrelation function, (**c**) PSD, (**d**) FRF, and (**e**) coherence.

which defines the power spectrum as the square-modulus of the Fourier transforms of *x(t)*. Similarly, the Fourier transform of the cross-correlation function leads to the definition of the cross-spectral power S_{xy}, which becomes handy in the computation of other features. Note that a power spectrum is an output-only measure and is therefore also sensitive to changes in the input excitation, so one would have to take this into account. If a measurement of the input excitation is available, the *Frequency Response Function* (FRF) naturally takes this into account, as by definition an FRF is a ratio between inputs and outputs in a system. The FRF has been identified as a useful damage-sensitive feature since the early days of SHM [32, 33, 34, 35, 36]. An FRF can be built as a ratio of acceleration, displacement, velocity, and combinations thereof. An example of an FRF on undamaged and damaged states is given in Fig. 1d. Mathematically, the FRF is defined as a ratio of inputs,

$$H(\omega) = \frac{S_{yx}}{S_{xx}} \tag{6}$$

Note that the cross-spectral density is used in the above computation; this is required in order to recover the phase information of the FRF. An amplitude-only estimate can be obtained from,

$$|H(\omega)|^2 = \frac{S_{yy}}{S_{xx}} \tag{7}$$

While the FRF is invariant under changes in input excitation, it is not invariant under the changing physics imposed by changing operational and environmental variables, such as that in mass and stiffness estimates arising from different temperatures and usage cases. More often than not, an FRF is a damage-sensitive feature found in laboratory environments, where one has the luxury of measuring and potentially controlling input loads. While in some industries it is possible to measure an input load in operation, there are many instances where measuring an input load is simply not possible, especially when wave or wind loading are involved, and one must resort to using other damage-sensitive features such as the PSD, and let the machine learning model the changes in loading conditions. Some of this will be discussed in more detail in Sect. 4.

2.1.3 Coherence

The next in line of useful features derived in the frequency domain is the **coherence function**. Coherence is a measure of how linearly related the output of a system is related to the input of a system; it thus provides an indication of whether nonlinearities have developed in a system, and nonlinear behavior can often be an indicator of the presence of damage. The coherence function takes values between zero and one, with unity indicating perfect linear correlation between input and output. The coherence function, γ^2, can be explained as a fraction of the output power (of signal y) that can linearly correlate to the input power (of signal x) and can be written as,

$$\gamma^2(\omega) = 1 - \frac{S_{mm}(\omega)}{S_{yy}(\omega)} \tag{8}$$

While the coherence function can be a useful damage-sensitive feature, care must be taken so as to capture effects associated to the breakdown of linearity, and not artifacts of the testing strategy or the signal processing. As an example, a white-masking effect could be introduced in the input-output relationship for lightly damped systems when multiple datasets are averaged, and some of the results in the current average contain transient responses that have not died out, hence appearing to be uncorrelated. The coherence function is shown in Figure 1e, for damaged and undamaged class datasets.

Time-Frequency Analysis

While frequency domain analyses carried out through Fourier transform methods are well suited for signals of a purely periodic nature, they largely fail to correctly characterize transient signals. This is due to the nature of the Fourier transform itself; it works by fitting infinitely long sinusoids to finite signals, and this introduces issues. One of the most popular ways of dealing with this problem is by pre-multiplying the vibration signal by a window function that reduces the effects of the signal edges. The obvious downside is that any information contained in those edges would be attenuated. The Short Time Fourier Transform (STFT) deals with this problem by splitting the signal into overlapping windows, and applying a windowed FFT on each signal segment. The resulting vector of frequency spectra for each window can then be used as features in a statistical inference algorithm. The particular case where the windowing function is Gaussian leads to the Gabor transform, which was used extensively before the generalization to the STFT.

The STFT can be particularly useful for extracting features from a system that is continuously changing, either from inherent complexities of the system such as nonlinearities, or changes in its environment and operation. An example of an STFT applied to a synthetic nonlinear oscillator is illustrated in Fig. 2. The features from this example will be used to illustrate dimensionality reduction and novelty detection in Sect. 4.

The discrete Fourier transform of a signal over a finite time window of size N will yield a complex vector of size N, of which only $N/2$ vectors are typically independent, given that the DFT is defined over negative and positive frequencies. There is an inherent relationship between the frequency resolution and the time resolution. Large STFT windows lead to higher frequency resolution. However, because the DFT/FFT applied within each window gives fundamentally a stationary distribution, large windows imply a loss of time resolution. Therefore, there is an inherent trade-off between frequency and time resolution in the STFT. This trade-off is illustrated in Fig. 3a. If one desires high frequency resolution, a large window must be used, but this will result in a loss of time resolution and vice versa. This is a problem, given that typically one requires higher frequency resolutions and less time resolution to analyze slow moving (low-frequency) processes, and high

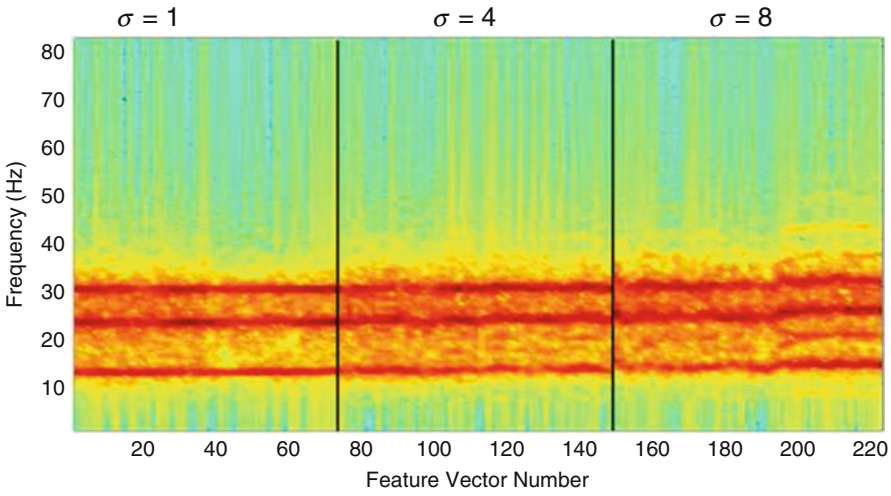

Fig. 2 Feature vectors comprising of amplitude spectra, derived using an STFT from the acceleration response of a simulated nonlinear 3-DOF system excited with white noise at increasing loads. Note the natural frequency increases slightly at different levels, and harmonics are evident at the highest loading

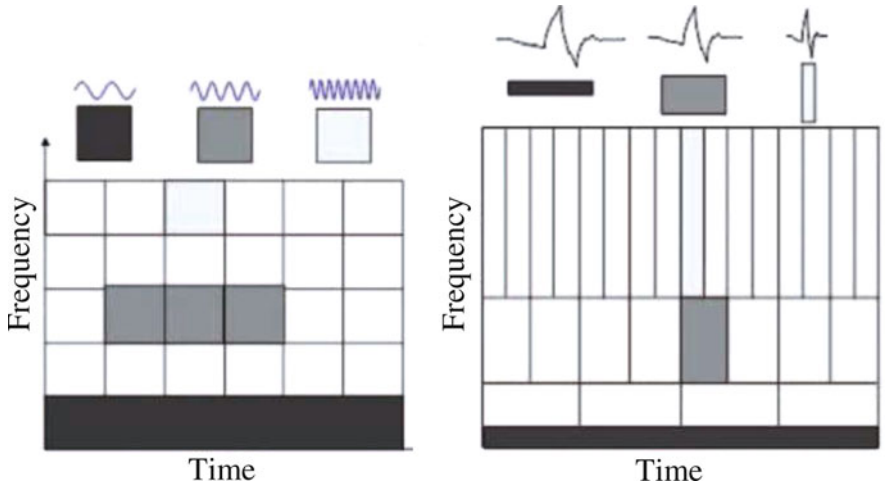

Fig. 3 Illustration of time-frequency resolution trade-off performed by (**a**) short time Fourier transform (STFT) and (**b**) discrete wavelet transform. (Figure from [38])

time resolution with less frequency resolution for fast-evolving processes (usually at higher frequencies). The STFT does not cater for both of these needs.

Time-Scale Analysis

The wavelet transform fixes some of the shortcomings of the STFT when applied to transient signals. Wavelet analysis is broadly divided into two classes: continuous and discrete. The continuous wavelet transform (CWT) of a signal *x(t)* is defined as its convolution with a wavelet function $\psi(a, t)$,

$$c(a,b) = \frac{1}{|a|^{1/2}} \int_{-\infty}^{\infty} x(t)\psi\left(\frac{t-b}{a}\right) dt \tag{9}$$

where a and b are scale and translation parameters, respectively. As an example of a simple analyzing mother wavelet ψ, take the complex Morlet wavelet, defined as a wave windowed by a Gaussian,

$$\psi(t) = (\pi C)^{-0.5} e^{-t^2/B} e^{2\pi i C t} \tag{10}$$

where B and C are bandwidth and center-frequency parameters, respectively.

The idea of the CWT is to perform this convolution between *x(t)* and ψ at varying scales and translations of the mother wavelet. In principle, it is a similar procedure to the STFT, except that the basis function is transient, which can better represent transient signals. The scale of the mother wavelet will be related to a physical frequency; low scales correspond to high frequencies and high scales to low frequencies.

Some care should be exercised when using a CWT as an SHM feature, as the transform naturally leads to redundant information. Using a CWT, one can analyze the energy of a signal at any arbitrary scale (frequency) and discrete time point. This arbitrary resolution makes it an excellent tool for the visualization of transient signals. However, for analysis purposes, the CWT can result in a very inefficient transform if care is not taken to select appropriate scales that provide useful information about the signal. The CWT has found some use in the field of machine CM, given its ability to tune into very specific frequencies [37]. In this context, it is often used in conjunction with a Hilbert transform.

An alternative to the CWT is the discrete wavelet transform (DWT). The names of these two transforms may be misleading as both operate on discrete data, but the CWT operates on a continuous space of scales, while the DWT operates on a discrete grid. The DWT is designed to overcome the redundancy issues of the CWT; it does so by specifying a mother wavelet that produces a half-band filter. In effect, the DWT splits the signal into approximation *(cA)* and detail coefficients *(cD)*. The approximations contain the low-frequency part of the signal, and the details contain the high frequencies. There is also a decimation step, so that the number of points in *x(t)* equals the sum of the number of points in *cA* and *cD*. The idea is to represent a signal in two bands, with equal numbers of points.

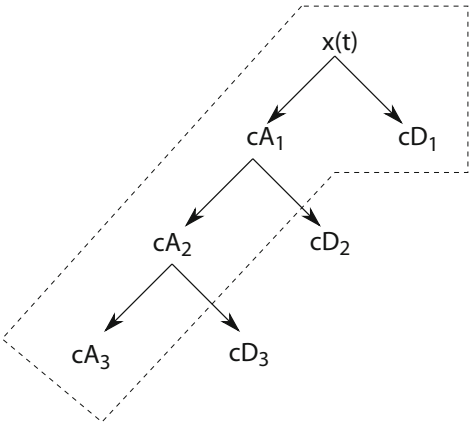

Fig. 4 Illustration of a multilevel wavelet decomposition down to three levels. The wavelet coefficients inside the dashed area fully define *x(t)*

The time frequency trade-off occurs when one applies the DWT recursively, in a tree. The multilevel wavelet decomposition is a DWT designed to split the signal *x(t)* into sets of *cA* and *cD* that represent all the frequencies in the signal, but with the right time resolution. The tree is illustrated in Fig. 4. The DWT is applied recursively to all the approximation coefficients, cA_i. Each approximation coefficient thus represents half of the frequency spectrum of the coefficients one level above, but with half the number of points. Thus, this decomposition results in each coefficient representing a frequency band at the appropriate sample rate for that band. This is significant, as it allows low-frequency data to be represented at a low rate, and the opposite for high frequency data. The area enclosed by the dashed region in Fig. 4, represents the entire spectrum of the signal. The multiresolution approach of the multilevel DWT is a natural trade-off between time and frequency resolution, compared with the STFT. This point is illustrated in Fig. 3. It is possible to apply an inverse DWT that perfectly reconstructs the original signal from these coefficients.

The value of this multiresolution analysis to SHM is great; in particular, for applications where the data are of a transient nature, or contain dynamics at different scales, and one requires to extract features that represent each scale succinctly. The use of wavelets in the SHM literature is quite popular now. Both the DWT and CWT require the use of a basis function to perform the wavelet decomposition. A lot of studies, in the SHM literature, have focused on finding suitable bases for particular SHM problems.

Time Series Models

Time series models provide a means for extracting features, and forecasting time series, purely in the time domain. Arguably the most popular time series model is the linear autoregressive (AR) formulation, which views a signal *y(t)* as a linear function of its previous *p* values,

$$y_t = \sum_{i=1}^{p} a_i y_{t-i} + \eta \tag{11}$$

where $\theta_{AR} = \{a_1, \ldots a_k\}$ are autoregressive coefficients, which effectively encode a spectral representation of *y(t)*, and η is a noise term. This form is essentially a linear regression problem on lagged versions of the signal, so the AR coefficients can be estimated with ordinary least squares (OLS) regression. Just as in the case of a frequency domain representation, these coefficients can highlight a change in the dynamics, and so have been extensively studied as damage-sensitive features [39, 3, 40, 41, 42]. Figure 5 illustrates the AR coefficients of a three-DOF mass-spring-damper system with and without damage.

Time series models distinguish themselves from spectral models since they can be used as predictors, and this can be readily exploited by SHM algorithms. A prediction is a one (or multiple) step-ahead forecast of where the signal will be in the future, so one could use the model/prediction residual, ϵ, as a damage-sensitive feature. The premise is that a change in the underlying dynamics would cause a change in the "true" AR coefficients of the system; any predictions on this, using a baseline undamaged AR model, will result in an increased model discrepancy, ϵ.

Most of the early studies into the use of autoregression focus purely on the damage detection and localization problem with no external influences [3, 42]. However, attention has shifted toward SHM under changing environmental and operational conditions. An example of an AR feature vector resulting from a

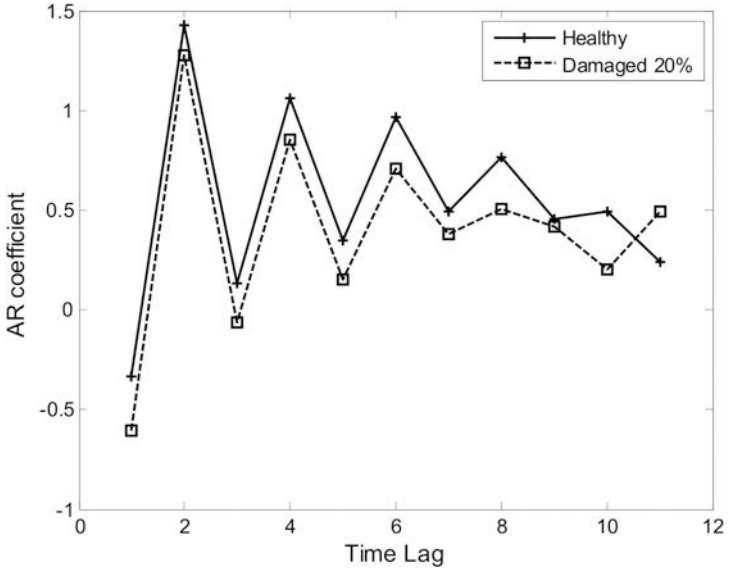

Fig. 5 Illustration of AR coefficients from an undamaged and damaged system, where damage is represented by a stiffness reduction on a three-DOF mass-spring-damper system

synthetic undamaged and damaged three-DOF mass-spring-damper system is given in Fig. 5. In this case, the damage was introduced through a 20% stiffness reduction in one of the springs.

Extensions of the linear AR model exist to account for *Moving Average* (MA) terms. For example, a linear mass-spring-damper system excited by unknown Gaussian noise can be captured by an ARMA model. These forms can be extended to account for external or eXogenous inputs (ARMAX) [43]. However, a linear AR, ARMA, or ARMAX model would fail to model nonlinear dynamics, and thus some further extension of this model is required if the system in question behaves nonlinearly. If the nonlinear parametric form of the underlying system is known, then this should be used. One of the most general models is the Nonlinear Autoregressive Model with eXogenous inputs (NARMAX) [44, 45]. The exogenous or MA terms can be dropped if it is appropriate for the application. The functional mapping between a signal $y(t)$ and its lagged values $y(t - p)$ for a NARMAX model can really be anything from nonlinear multinomials to more complex Neural Network [46] or other nonparametric forms such as radial basis function networks or Gaussian Process regression [47, 48].

The essence of time series models from an SHM perspective is to capture the dynamics of the process and use these to make predictions about the model. Whether the model is linear or nonlinear, parametric or nonparametric, is a modeling choice and it is the topic of system identification. It is no surprise that there is an abundance of these methods in the SHM literature, given that the time-domain system identification is a rather mature subject. In the use of the NARX model, for example, all that is required is a suitable nonlinear regression method between x_t and the p lagged values. Regression methods can be categorized into parametric and nonparametric. This results in either of two distinct models in their approach to modeling the dynamics, often known as white and black-box models. White-box models are often parametric, and they are distinguished by the relative ease by which one can recover the underlying parameters of the equations of motion that generated the data. This freedom gives not only the ability to predict the signal output but also yields some insight into the physics. On the other hand, black-box models are associated with nonparametric regression methods such as artificial neural networks (ANN), support vector machines (SVM), radial basis function (RBF) networks, relevance vector machines (RVM), and Gaussian processes (GP). These methods can all be used in the context of NARX models.

Modal Analysis-Based Features

The topic of damage-sensitive features derived for SHM applications extends far beyond the scope of this small section, so the focus will be on providing the reader with a very general overview of the topic. More thorough discussions can be found in [1]. Modal analysis falls under the general category of system identification techniques, and there are various ways of performing modal testing to extract the modes. Experimental modal analysis (EMA) is now a mature field, used in industry primarily to understand and evaluate structural dynamics with the purpose

of avoiding certain resonance frequencies, managing structural damping to control fatigue life, and to validate and update finite element models (FEM) [49].

The usefulness of modal analysis in damage detection and localization problems has been identified a long time ago [50, 51, 52]. Early studies have focused on examining the link between modal parameters and the structural degradation process. Natural frequencies extracted through EMA have been identified as a primary feature, as they will tend to decrease as the structure is degraded [50]. The curvature of mode shapes has also been identified as a feature that is useful for localizing damage [51]. Furthermore, FEM model updating techniques have also been explored as a means of detecting and locating damage [53].

One of the key aspects of EMA is that input excitations to the system are available for modeling and analysis. This is of relevance as extracting modal parameters involves finding a set of parameters for the system equations of motion that agree in some way with the data being measured. This is termed *system identification*, and it is (now) relatively simple to do this using frequency response functions (FRFs), which measure the input-output relationship between the forcing and the acceleration response. Modal parameter estimation is often done by finding a set of analytical FRFs that provide a good fit to the measured FRFs.

In order to compute an FRF, a measurement of the input force is normally required. However, this input loading may be very difficult to measure in most practical engineering applications, which is the main reason why EMA is usually confined to laboratory settings. Methods have been developed to estimate modal parameters without the need for the measurement of input loads, and they are classed as operational modal analysis (OMA). One of the most popular techniques for doing this is *Stochastic Subspace Identification* (SSI) [54], which fits a state-space model to the vibration response of the system. One of the key assumptions of this method (and most OMA methods) is that the loading can be approximated by white Gaussian noise. Section 3 will discuss the state-space methodology often used in OMA in more detail.

2.2 Acoustic Emissions (AE)

Acoustic emissions (AE) are high-frequency stress waves that are released from a material when the internal structure undergoes a change. These waves are often recorded as bursts, and can be generated by processes such as friction, corrosion, stress, and growing cracks. Because the application of stress leads to the generation of AE, this is a popular technique in NDT for assessing the loading history of a structure, thanks to the Kaiser effect [55]. Kaiser discovered, in the 1950s [55], that a structure will emit AE if loaded up to a stress that it has not been loaded to before. Any subsequent application of stress will result in much reduced AE levels.

It is worth establishing some contrast between what is classed as structural vibration, and AE. Physically, they are similar phenomena, but the excitation source

and frequency are much different. In theory, structural vibration can go up to any arbitrarily high frequency, but practical constraints limit vibration analysis to the tens of kilohertz range. Unless a structure is unreasonably stiff and lightweight, its first few natural frequencies will lie within the 0–10 kHz range. Mechanical excitation within this frequency range tends to be associated with environmental loads, shock, and rotational motion. This is thus classed as structural vibration.

Going into the tens of kiloHertz range, one finds that natural mechanical excitation arise from completely different sources. To generate a wave at this frequency, an impulse would have to be much shorter than the average impulse used, for example, in modal hammer testing. Micro-cracks tend to generate very short impulses, sending mechanical stress waves across the material, and this is what is referred to as AE. When generated from material dislocation, AE can be observed as discrete bursts, or as is referred to in the AE literature as *hits*. Figure 6 illustrates a series of AE hits generated from a yielding steel sample (taken from [56]).

A lot of research followed on from Kaiser's original thesis, and it is now a well-understood fact that stress causes AE. This fact is particularly useful given that a crack introduces a discontinuity in a material, and therefore cause stress concentration. On the other hand, crack-growth estimation methods rely heavily on stress concentration factors to estimate residual life. There is a strong link between AE and crack growth; this has been made a long time ago [57]. The strain energy release rate from a crack can manifest itself as stress waves. This quantity is thus well correlated to the count of discrete AE hits and their energy.

There are two key advantages of AE over vibration; the first is that damage can often be identified at a much earlier stage, owing to the fact that micro-cracks will generate AE before an appreciable change in the vibratory response appears. A further advantage of AE is that the source of damage can be located accurately with relative ease. If multiple sensors are used, the time-of-flight difference between different sensors can be used to find the spatial location of the acoustic source. If the geometry of the material is simple and the material properties isotropic, then all that is required is the wave propagation speed and a triangulation scheme. If the geometry is complex, a look-up table approach has been suggested [58] called Delta-*t* mapping. Another, better method based on Gaussian Process regression has

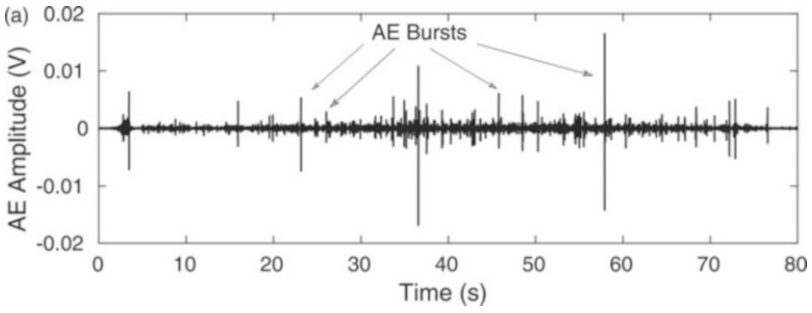

Fig. 6 Illustration of AE bursts, generated from a yielding steel sample [56]

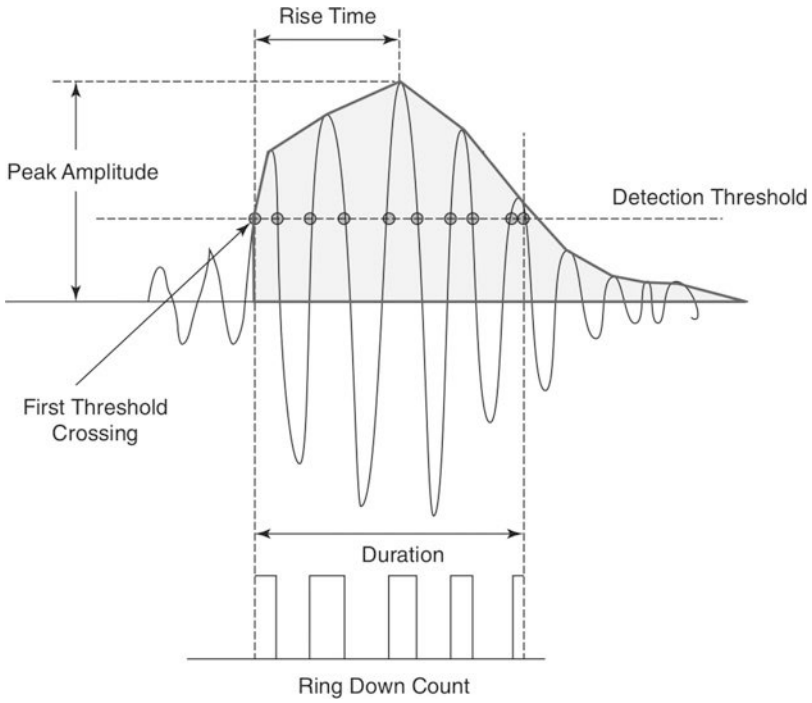

Fig. 7 Typical damage-sensitive features used in the analysis of AE signals [1]

been suggested in [59]. Both of these methods require an example dataset of time of arrivals with known source locations.

AE is often analyzed in terms of features derived from the transient bursts that are characteristic of energy release in solids. Features that are important involve those that quantify the level of energy in the burst, how fast it rises and decays, and its peak amplitude. These basic features are illustrated in Fig. 7. Note that these AE bursts are often defined by their exceedance above a threshold value which is often formed using an order statistic, or a simple maxima over the background noise floor. However, the choice of threshold has a big effect on the resulting features, and a simplistic threshold may under- or overestimate important quantities such as rise-time or accurate wave time-of-arrival differences for localization purposes. In this case, more advanced onset estimation techniques such as [60] are recommended.

2.3 Guided Waves

While AE is a passive technique, where one listens to the response of the material to stress and other material effects, it is also possible to excite the material with a pulse and listen to the response. This is the principle of ultrasound testing, which is

predominantly an NDT technique, where a pulse is sent across the thickness of the material, generating bulk waves, and listening to the reflection of that pulse. This principle of A, B, and C scans is built around mapping of ultrasonic time of flight across and between surfaces. The use is widespread in nondestructive evaluation of engineering structures, but it is not strictly an SHM technique as there are practical impediments to its implementation in that context.

Guided waves present a solution to this problem. These waves are guided by the boundaries of the medium in which they propagate. Unlike compression and shear waves, analytical solutions for wave propagation in these cases involve consideration of the boundary conditions of the medium. If one considers the problem of only one boundary condition (a surface), this leads to Rayleigh waves [61]. One of the key aspects of Raleigh waves comes from the fact that they propagate along a surface. Their geometrical amplitude attenuation is thus proportional to $1/\sqrt{R}$. In contrast, the amplitude of bulk waves decreases with $1/R$, as the wavefront propagates as a sphere. More interesting wave modes arise if there are two bounding surfaces (a plate). The analytical solution of wave propagation in these cases leads to the popular Lamb waves [62]. These are wave modes where both of the bounding surfaces of the plate interact with each other to create either symmetric or antisymmetric modes. These are illustrated in Fig. 8. The interesting thing about Lamb waves is that they are *dispersive*; their propagation speed depends on the frequency-thickness product. Many more Lamb wave modes exist if one keeps increasing the frequency. Figure 9 shows the dispersion curves for symmetric and antisymmetric modes in an aluminum plate.

Beyond being inherently interesting, there are some very practical implications to the (rather condensed) discussion above. The first is that a discontinuity such as a crack, or delamination of a composite medium will scatter and reflect Lamb waves. It is thus possible to monitor the integrity of a structure by generating Lamb waves and monitoring the response at various points in the structure. This fits well with the machine learning approach to structural damage identification; if the response changes, scattering or reflection is likely to have been the cause.

The second practical point is the frequency-thickness product. To efficiently use Lamb wave propagation for SHM, one needs to be able to both generate a pulse at the right frequency and acquire the resulting waveform. Working with one particular

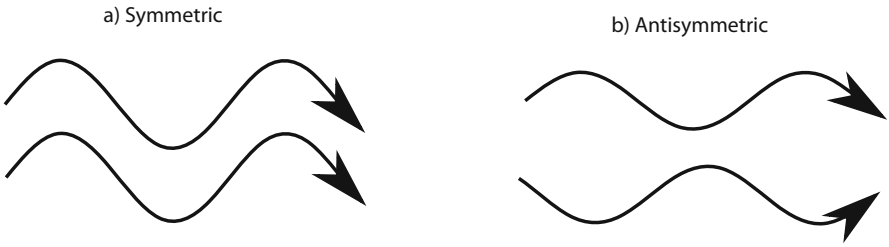

Fig. 8 Illustration of lamb waves showing (**a**) symmetric and (**b**) antisymmetric modes

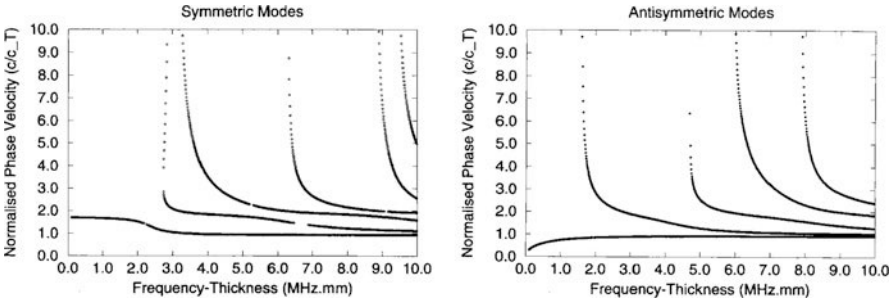

Fig. 9 Dispersion curves for symmetric and antisymmetric lamb wave modes in aluminum [63]

mode is thus desirable. The problem is that at high ωd, the propagation speeds of different modes become very similar and are thus hard to separate from each other. This task is usually straightforward at low ωd where the modes are very clearly separated. A typical piezoelectric transducer will have resonances in the range of 10 kHz to 10 MHz, which restricts the usable plate thickness to no more than a few centimeters, in most common engineering materials.

One of the key disadvantages in implementing guided-wave techniques in practice lies with the sensors. In transmission and reception, a piezoelectric transducer is normally used to convert a mechanical waveform into an electrical signal, and vice versa. The problem is that piezoelectric sensors are also very sensitive to temperature changes, so it is often difficult to establish a baseline condition under temperature fluctuations. Some studies suggest that the problem renders guided waves an impractical technique [64], and that the solution is to increase the number of sensors. However, this may not be a practical engineering solution in problems where a large sensor array would imply extra power (these sensors can use pulses of 100 V), and space may not be available. Aerospace applications are one such case. The signal processing solution has been suggested by Cross [65], where the use of cointegration as a means of removing environmental trends in SHM data is demonstrated with Lamb wave data under changing temperature. An example of this is given in Sect. 5.

2.4 Performance, Operational, and Environmental Parameters

Performance metrics, in this context, refer to data that do not relate directly to the dynamic response, but could help explain certain characteristics of the response itself. It is generally good practice to collect any associated operational and environmental parameters that affect the structural dynamics, such as temperatures, pressures, humidity, and other performance indicators. In some cases, these may be enough to identify certain types of damage and faults. For example, in the case of

wind turbines, various types of faults have been identified by modeling the power output, and more specifically, how this varies with wind speed [66].

3 Advanced Topics in Signal Processing and Feature Extraction

There are certain instances where one may wish to adopt more advanced techniques for the computation and estimation of damage-sensitive features. This section will discuss two such instances; the first is when one is faced with the problem of having to deal with large quantities of SHM data to a point where considering the problem of data compression becomes necessary. The second example is the case where one may need to perform SHM in an online manner, and so the features must be computed recursively as data is gathered. This section will discuss some solutions to these problems, focusing on the most recently developed methods.

Dealing with Large Quantities of Data: Compressive Sensing
Currently, one of the gold standards in data compression is the discrete wavelet transform, discussed in Sect. 2 and already used extensively in data compression tasks for SHM [1, 67, 68]. However, these traditional approaches to data compression can be computationally costly, and could be restrictive in SHM applications where computational power might be limited, such as with wireless sensor nodes. Recently, the field of compressive sensing (CS) [69] has challenged the traditional Nyquist-Shannon sampling theorem, and promises to allow one to infer information from much higher frequencies, using only a limited number of time domain samples. These ideas have the potential to bring huge advantages to the field of SHM where they have already begun to see some applications [70, 71].

The general goal of compressive sensing is to acquire a signal using a much smaller number of measurements than that required by the Nyquist-Shannon sampling theorem. It is now a well-established principle that a signal could be efficiently compressed, or coded, using a basis such as discrete cosine transform (DCT), Fourier transform, or wavelets (if the signal contains strong transients). This statement assumes that one has some knowledge of which coefficients in the representative basis play an important role in the signal.

However, there is a drawback to this approach, since the entire signal must be acquired for it to be then transformed into a sparse domain. This presents two issues: data storage and processing. Storing an ultrasound dataset before it is compressed can be a challenge given the very high sample rates, and the potentially large scanning areas required by a high-resolution C-scan. Subsequently transforming these large quantities of data into a compressed domain such as the wavelet domain can also be computationally time consuming.

Compressive sensing solves this problem by using a combination of ideas, with two basic underlying assumptions. The first is that the signal has a sparse representation in some domain. The second is that some knowledge of what

this domain may be is available. At the center of CS is the concept of using l_1-regularised regression to find a coefficient set from a base dictionary that is sparse. The following sections describe in more detail the essence of sparsity in the context of ultrasonic NDT, the use of l_1-regularized regression, and the use of dictionaries; these are all standard techniques in the field of CS.

A signal, x, with a high number of (time-domain) measurements n, is sparse in a transform domain if a very small number of coefficients, $m \ll n$, in the domain are sufficient to accurately represent the signal. Such a transform could be represented as,

$$x = \Psi \boldsymbol{\beta} \tag{12}$$

where Ψ is a basis function set, or dictionary, and $\boldsymbol{\beta}$ is the coefficient vector that represents the signal in the transform domain (note that in this chapter all vectors are assumed to be column vectors unless otherwise specified). A good example of a sparse representation would be a sinusoid at a fixed frequency, which may contain a high number of points in the time domain, but may be fully represented by one complex coefficient in the Fourier domain.

There is particular interest in the problem of dimensionality reduction, for the purposes of algorithm design, in SHM and many other areas; this is also central to the idea of CS and so it is worth a brief discussion. A way of "compressing" a dataset is to project the n-dimensional measurement vector x to a lower, m-dimensional space using a linear or nonlinear transformation. One popular approach is to use transformations, such as principal component analysis (PCA), independent component analysis (ICA), or factor analysis. Such a linear transformation could be written down as,

$$z = \Phi x \tag{13}$$

where z is now a low-dimensional representation of x. An interesting projection results if the rotation matrix, Φ, is set to be a random matrix. Johnson and Lindenstrauss [72] have shown that if Φ is distributed according to a Gaussian, or Bernoulli distribution, this linear dimensionality reduction preserves, with low error, certain features of x, such as pairwise distances. This random matrix transform is a key ingredient in the formulation of the CS problem.

In order for the compressed version of x, through the random transformation of (13), to be of immediate practical use, there needs to be an algorithm that is able to recover the original measurement. This is where the *Least absolute shrinkage and selection operator* (Lasso) comes into play. The Lasso solves the classical linear regression problem of $\mathbf{X}\boldsymbol{\beta} = y$, where $\mathbf{X}$ is a matrix with column-wise vectors of inputs, y is an output, and $\boldsymbol{\beta}$ holds the regression coefficients. The Lasso encourages sparse solutions for $\boldsymbol{\beta}$ through a penalty term based on an l_1 norm [73]. The optimization problem can be formulated as,

$$\text{minimize} : \left\{ \frac{1}{2N} \| y - \mathbf{X}\boldsymbol{\beta} \|_2^2 + \lambda \| \boldsymbol{\beta} \|_1 \right\} \tag{14}$$

The l_1 penalty is regularized by the term λ. A general l_q penalty could be computed using the sum $\|\boldsymbol{\beta}\| = \sum_{j=1}^{N} |\boldsymbol{\beta}|^q$, and the Lasso is the special case when $q = 1$. This constraint ensures that the optimization problem remains convex [73]. If $q = 0$, the resulting constraint would yield a subset selection problem that is non-convex and combinatorially hard, thus not computationally efficient. The Lasso is thus an attractive method for recovering sparse solutions in high dimensions while maintaining efficient computation.

The regularization parameter, λ, dictates the degree of sparsity in the solution. A high value of λ encourages a low number of nonzero coefficients, and vice versa. Therefore, an appropriate value of λ needs to be chosen for each problem in particular. The authors of the Lasso suggest using cross-validation [73] in order to estimate the best (Cross-validation involves iteratively holding out subsets of the available training data as test sets, in order to assess generalization performance and avoid model over-fitting.).

This brings the discussion of CS to the last step [69], which is concerned with finding a sparse set of coefficients $\boldsymbol{\beta}$ that best describe the random matrix projection Φx (the compressed signal representation). This is where the power of the Lasso is unleashed. What is available to the regression problem is not the full signal, but rather a projection of it through Φ. The coefficient set can be inferred if the basis dictionary is also projected through the sensing matrix to yield the following regression problem,

$$\Phi \Psi \boldsymbol{\beta} = \Phi x \tag{15}$$

where, as before, Φ is a random matrix projection, Ψ is a basis function set, and x is the (uncompressed n-dimensional) signal of interest. The Lasso minimization of (14) can now be used in order to obtain a sparse solution for $\boldsymbol{\beta}$.

Other reconstruction algorithms can also be used. In [74], a probabilistic reconstruction method is used to reconstructed randomly compressed ultrasound sequences. In this case, the reconstruction is also able to provide confidence bounds on the accuracy of the reconstructed signal. An example of an original and reconstructed ultrasound pulse, sampling significantly below the Nyquist rate is illustrated in Fig. 10.

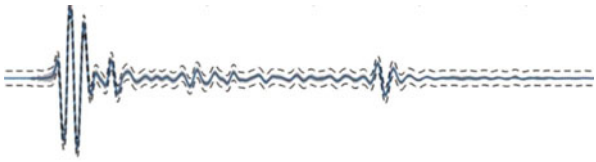

Fig. 10 Illustration of an original and reconstructed ultrasound pulse using compressive sensing, and the probabilistic reconstruction scheme in [74]

Recursive Estimation in the Linear Case: Kalman Filtering

Recursive estimation is an important topic in SHM, as it allows for the online estimation of damage-sensitive features as well as online estimation of unknown quantities of interest that cannot be measured directly, such as loading conditions. This section will review the basic principles of recursive estimation in the simplest case, when the dynamics of the system are linear, or when one is solving for features derived from a linear operator.

This section will be followed by a discussion of the recursive estimation problem in the more difficult nonlinear case.

When monitoring a dynamical system, one is often restricted to making measurements that do not necessarily measure the state of the system directly, but are related to the underlying process driving those measurements through some function. A *state-space* model provides a solution to this type of problem; it models the observations y_t as some function of the underlying dynamics of $\mathbf{x}_t$. If the relationship between $\mathbf{x}$ and $\mathbf{y}$ is linear, then this can be represented by the standard linear state-space formulation,

$$\begin{aligned} \mathbf{x}_t &= \mathbf{A}\mathbf{x}_{t-1} + \mathbf{w}_t\mathbf{w}_t \sim \mathcal{N}(0, \mathbf{Q}) \\ \mathbf{y}_t &= \mathbf{C}\mathbf{x}_t + \mathbf{v}_t\mathbf{v}_t \sim \mathcal{N}(0, \mathbf{R}) \end{aligned} \tag{16}$$

where $\mathbf{C}$ represents the linear function linking observations to underlying dynamics, and $\mathbf{A}$ represents the linear dynamics – the time evolution of $\mathbf{x}$. The observation model and the dynamics are both modeled with white Gaussian noises, $\mathbf{v}_t$ and $\boldsymbol{w}_t$, with zero mean, and covariance matrices $\mathbf{R}$ and $\mathbf{Q}$, respectively (Standard linear state-space models also include additive terms to account for control inputs. These are omitted here for simplicity.). State-space models have applications spanning various areas of science and engineering, and are now implemented in other fields such as financial-time series modeling; they are useful whenever one makes use of measurements that can be somehow related to the underlying state of a system, and those measurements are corrupted by noise. It is easy to relate this picture to a structural dynamics context. An MDOF linear vibrating system can be described by a linear superposition of SDOF systems; this is the foundation of modal analysis. The underlying driving functions are the SDOF oscillators, each of which has a characteristic natural frequency, and they are related to a physical location on the structure via a mode shape. Any good structural dynamics textbook will contain methods for representing MDOF systems in state-space form [75]. There may be more than one valid state-space representation of a system and one must adopt the one that is most suitable to the problem at hand. In SHM, there could be two different contexts where one might seek a state-space representation:

1. The state vector $\mathbf{x}$ represents the parameters of a model, and one is interested in estimating those parameters, as they evolve through time.
2. The state vector $\mathbf{x}$ represents some hidden variables that better model the underlying linear dynamics of a set of measurements $\mathbf{y}$.

In the first case, the state-space modeling approach is cast as a parameter identification problem. In this case, a state-space model could be seen as an alternative view to the popular recursive least squares (RLS) algorithm, which essentially solves the standard ordinary least squares problem, point by point. In this interpretation of state-space models, the state vector will usually have some direct physical meaning, and it will often be easy to interpret the results. In the second interpretation, the meaning of $\mathbf{x}$ can be more subtle; in fact, it does not necessarily need to have physical meaning at all. In this interpretation, if one possesses a physical model of the structure being considered (say, via a finite element model or an analytical model), then $\mathbf{C}$ and $\mathbf{A}$ can be derived, and one is interested in inferring the state $\mathbf{x}$ and in monitoring the residuals $\boldsymbol{v}_t$ and $\boldsymbol{w}_t$. An estimate of $\mathbf{A}$ and $\mathbf{C}$ that correctly describes the measured data is therefore required, and can be obtained via the popular stochastic subspace (SSI) methods or via the expectation maximization (EM) algorithms.

Even though in both cases, $\mathbf{x}_t$ represents something fundamentally different, both have useful SHM applications, and most importantly, both require a method for providing an estimate for $\mathbf{x}_t$. If linear Gaussian assumptions are made, the Kalman filter algorithm provides an efficient and intuitive solution for the inference problem, and so it is applicable to both the parameter estimation, and the latent variable approach to implementing state-space models for feature extraction or direct novelty detection in SHM.

3.1 Inference via the Kalman Filter

The key point of the state-space model is that the observations are modeled as independent of each other, and dependent only on the state vector at time t, while the state vector is dependent on all previous values on the Markov chain. There are two important conditional probability relationships at play: the probability of the observation vector given the state vector $p(\mathbf{y}_t|\mathbf{x}_t)$, and the probability of the state vector given the same state vector at a previous point in time $p(\mathbf{x}_t|\mathbf{x}_{t-1})$. If these two densities are assumed to be linear Gaussian, they can be written down as,

$$p\left(\mathbf{x}_t|\,\mathbf{x}_{t-1}\right) = \mathcal{N}\left(\mathbf{x}_t|\,\mathbf{A}\mathbf{x}_{t-1}, \mathbf{Q}\right) \tag{17}$$

$$p\left(\mathbf{y}_t|\,\mathbf{x}_t\right) = \mathcal{N}\left(\mathbf{y}_t|\,\mathbf{C}\mathbf{x}_t, \mathbf{R}\right) \tag{18}$$

The main interest is in estimating the unknown state vector, $\mathbf{x}_t$. Because $\mathbf{x}_t$ is not observed, the true state of the system will never be known, but a probability density can be estimated, and if Gaussianity is assumed on the residuals of the dynamics of the state, the distribution is fully specified by the mean and variance of the state vector at every point in time. There are three probability distributions for $\mathbf{x}_t$ of interest, and they are commonly referred to (in the statistical time series communities) as prediction, filtering, and smoothing, where each of them compute the following conditional probabilities:

1. Prediction: Probability of state vector, $\mathbf{x}_t$ at time t given observations up to time $t-1$, $p(\mathbf{x}_t|\mathbf{y}_1, \ldots, \mathbf{y}_{t-1})$.
2. Filtering: Probability of state vector, $\mathbf{x}_t$ given observations up to time t $p(\mathbf{x}_t|\mathbf{y}_1, \ldots, \mathbf{y}_t)$.
3. Smoothing: Probability of state vector, $\mathbf{x}_t$ given *all* the observations available $p(\mathbf{x}_t|\mathbf{y}_1, \ldots, \mathbf{y}_T)$.

For the state-space model, the filtering distribution can be shown to be,

$$p\left(\mathbf{x}_t \,|\, \mathbf{y}_{1:t}\right) \propto \int_{x_{t-1}} p\left(\mathbf{y}_t \,|\, \mathbf{x}_t\right) p\left(\mathbf{x}_t \,|\, \mathbf{x}_{t-1}\right) p\left(\mathbf{x}_{t-1} \,|\, \mathbf{y}_{1:t-1}\right) \tag{19}$$

So far, this does not assume linearity or Gaussianity; one is free to model the conditional probabilities inside equation (19) with any arbitrarily complex distribution. However, the assumption of linearity and Gaussianity simplifies things significantly because of Gaussian identities; the product of two Gaussians is itself a Gaussian, and the integral of a Gaussian is Gaussian too. These properties are what make the representation of the conditional densities as Gaussians (equations (17) and (18)) so efficient. The Kalman filter algorithm effectively solves equation (19) for the linear Gaussian case. The Kalman algorithm involves two steps, a time update and a measurement update. In the first case, the Gaussian mean and variance of the state vector is propagated forward using the physical model to generate a state prediction. The measurement-update step then takes in new measurements and computes the filtered state vector, $\mathbf{x}_t^t$ in light of the measurements gathered at time t. This procedure effectively uses Bayes' rule to shrink the uncertainty of the state, given the measurements. More details about the algorithm can be found in [76].

3.1.1 Inference for Parameter Identification

The Kalman filter is similar in nature to the recursive least squares (RLS) algorithm. RLS has been extensively investigated in the structural dynamics community as a method for identifying system parameters in real-time [77, 78, 49, 79]. For example, a sequential or recursive form for a linear AR parameter estimate (such as the one described by Eq. (11)), mapping y_t (note it is one-dimensional) to its lagged version, can be described by letting the state-space vector $\mathbf{x_t}$ be the AR parameter vector $\mathbf{a}$,

$$\mathbf{x}_t = \mathbf{x}_{t-1} - K_t \left(y_t \mathbf{x}_t - y_t\right) \tag{20}$$

where K_t is a function of the filtered variance, υ_t, at time index $(t-1)$, which represents the confidence in the state vector (in this case the parameters),

$$K_t = \upsilon_{t-1} y_t \left(1 + \upsilon_{t-1} y_t^2\right)^{-1} \tag{21}$$

and the update to the variance is,

$$\upsilon_t = \upsilon_{t-1} - \upsilon_{t-1}^2 x_t^2 \left(1 + \upsilon_{t-1} y_t^2\right)^{-1} \tag{22}$$

These recursive parameter estimates can be shown to give the same solution to the AR parameter estimation problem that OLS provides, once all the time steps have been processed. The equations above show the RLS parameter updates for a single variable case, but the generalization to a multivariate form is essentially a matrix version of equations (20), (21), and (22). This version is in fact provided by the Kalman filter recursions. Using the Kalman filter recursions, RLS can effectively be achieved for a variety of problems. The state vector $\mathbf{x}_t$ represents the parameters, and the observation matrix $\mathbf{C}$ would represent the observations. The state transition matrix $\mathbf{A}$ can have different forms, but a popular choice is to set it to the identity matrix; this assumes that the parameters follow a random walk, the volatility of which is provided by the state-transition noise model, $\mathbf{w}_t \sim \mathcal{N}(0, \mathbf{Q})$. Different choices of the state transition matrix could put different constraints on the parameter updates. One could solve for a variety of problems through a careful choice of $\mathbf{C}$ and $\mathbf{A}$. An application of interest in SHM is to estimate the AR coefficient vector recursively. This could be modeled by setting the observation matrix $\boldsymbol{C}_t$ in every Kalman filter recursion to be the lags of the signal of interest y. In other words, the observation matrix varies with time, and is,

$$\mathbf{C}_t = \left\{y_{t-1}, \ldots, y_{t-p}\right\} \tag{23}$$

for an AR model with p lags. Because $\mathbf{A}$ is defined as an identity matrix, the state transition reduces to specifying that the AR parameters should be close to the previous ones in time, to within a specified variance,

$$\mathrm{x}_t = \mathrm{x}_{t-1} + \mathrm{w} \tag{24}$$

As an illustration of this approach, Fig. 11 shows the fit of an AR model with 40 lags to the response of the second mass of a three-DOF nonlinear system, while it undergoes a step change in the response due to a cubic nonlinearity. Note that the estimates for both the AR parameters $(\mathbf{x_t})$ and their variances, $\mathbf{w}$ change as the system changes its dynamics. It is useful to be able to infer parameters in real-time, and as will be pointed out in Sect. 4, these could be used as features in novelty detection based on static data.

It should be noted that the filtering distribution can be used directly on the raw measurement vectors from a system in order to carry out novelty detection, but this use falls outside the scope of this chapter; more details can be found in [18].

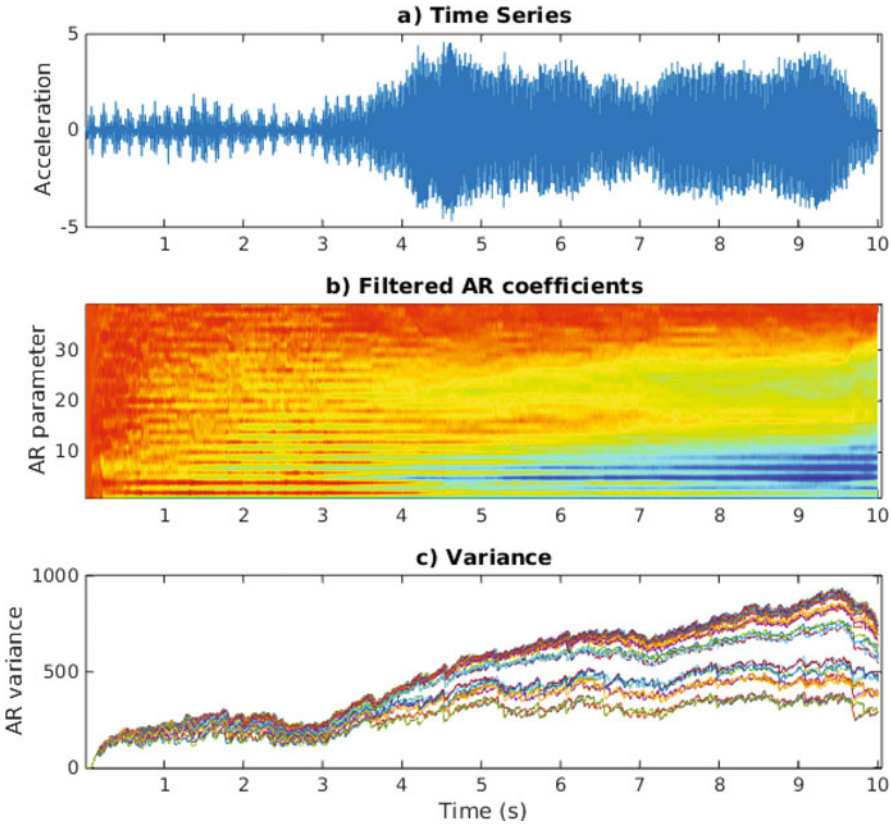

Fig. 11 Sequential estimation of AR parameters using a Kalman filter (**a**) shows the response of a nonlinear three-DOF system to white noise, with a step change in response, (**b**) shows the state vector $\mathbf{x}_t$, containing the AR parameters, and (**c**) shows the variance of each dimension of $\mathbf{x}_t$

3.2 Recursive Estimation in the Nonlinear Case

The linear Bayesian filtering equations shown in the previous section cover a wide class of models which can be very expressive, which includes all linear multi degree-of-freedom systems encountered in dynamics. However, many real-world systems are nonlinear and using the linear formulations may yield suboptimal performance and, in the worst case, fail to capture the dynamics of the system altogether. Nonlinear recursive Bayesian estimation is not straightforward. The complication arises from the solution to the integral of equation (19), which often does not admit a closed-form solution in instances when the dynamics ($p(\mathrm{x}_t|\mathrm{x}_{t-1})$) are nonlinear and/or non-Gaussian. The Kalman filter presents a solution for these two integrals in the special case when the dynamics are linear and the noise is assumed to be Gaussian, but in the absence of closed-form solutions one must resort to approximations which offer solutions to these equations.

This section will give a brief overview of the different approximations available that are relevant to SHM, but it is not intended as an in-depth review of the topic. The first approach to address prediction in nonlinear systems is often linearization. The Extended Kalman Filter (EKF) is the most popular linearization of nonlinear state-space models [80, 76, 81]. The EKF linearizes the system using a first-order Taylor series approximation, through a Jacobian of the nonlinear functions and forming transition and observation functions based on this. The EKF has been adopted widely within the SHM community as a tool to deal with nonlinear systems.

By far the most common application of this model is when the EKF is used to estimate parameters of a model, via a state augmentation approach. In this case, based on the estimates of the parameters found, inference is made about the condition of the structure when considering changes in the values of the parameters. Examples of the state-augmentation approach to parameter estimation can be seen in [82, 83, 84, 85, 86].

The EKF is known to be ineffective when the nonlinearity in the model is not weak, that is, it cannot be well approximated (locally) by a linear model with minor correction. Most importantly, the EKF is known to provide a bad approximation to the propagation of arbitrary complex distributions through the nonlinear transition functions. Even though the EKF is easy to implement, it often results in poor performance. The Unscented Kalman Filter (UKF) [87, 88, 76] was designed to remove the shortcomings of the EKF; it makes use of the *unscented transform* which is a method for Gaussianizing the nonlinear transformation of a probability distribution by means of a set of *sigma points*, and these deterministic points from the previous distribution are propagated through the nonlinear transition and used to estimate the mean and covariance of a Gaussian that best describes their distribution following the transformation. The UKF has been reported to outperform the EKF in various instances [89, 90, 91, 92]. These results are supported by the work in [93] which focuses on application of the UKF to a structural dynamics identification problem. The UKF has been used in many similar ways to the EKF within structural dynamics [94, 95, 96, 97]. A key advantage of the UKF over an EKF approach is that one does not have to derive and compute the Jacobian of the system.

While the UKF provides an improvement over the EKF in terms of the accuracy with which it will propagate the state densities, and is computationally very efficient, it is based on a heuristic and cannot guarantee even an approximate solution. Ultimately, the best approximations can often be achieved using sequential Monte Carlo (SMC) methods [98, 76]. These algorithms are a subset of the Monte Carlo approach to approximating probability distributions. In an SMC setting, an explicit evolving relationship between the distributions it exploited, that is, a sequence of probability distributions through time is modeled. The benefit of using SMC as opposed to either the EKF or UKF is that it is flexible enough to handle fully nonlinear, non-Gaussian models without resorting to linearization at any point. The trade-off is an increase in computational time.

The SMC algorithm consists of three basic steps: propagation, weighting, and resampling. SMC is useful for estimating a sequence of probability distributions, and one such sequence is shown in Fig. 12. SMC is most applicable when modeling

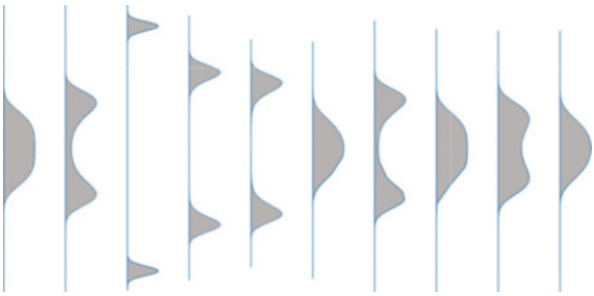

Fig. 12 A sequence of probability distributions to be estimated using an SMC scheme, for example, the latent states of an SSM representing the displacement and velocity of a nonlinear oscillator

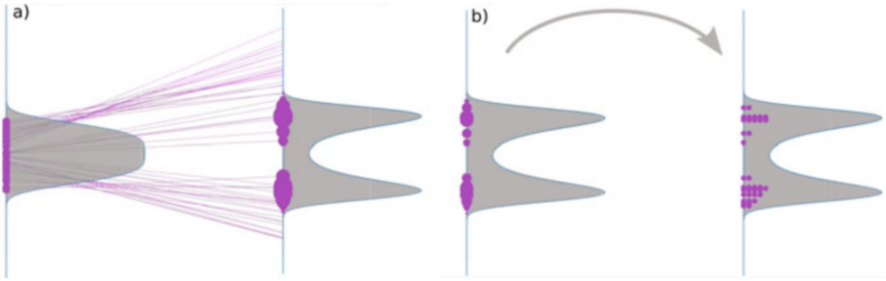

Fig. 13 (**a**) The propagation and weighting of particles from the first two steps of the sequence shown in 12, (**b**) Re-sampling of weighted particles following their propagation and weighting

nonlinear systems where the noise (process or observation) is non-Gaussian. Importantly, there exist results to prove convergence of the SMC estimation of the distributions toward the true distributions [99, 100]. There exist several variations on the SMC formulation, the simplest one being the Bootstrap Particle Filter introduced by [101]; here, this will be the focus of the explanation, but it should be noted that it is often possible to construct more efficient filters, for example, the Auxiliary Particle Filter [102].

The first step of the implementing the particle filter is to propagate a set of particles, each with a weight *1/N* (for N particles), through $f_\theta\ (x_t\ |x_{t-1},\ u_{t-1})$. This step defines both the functional form of the transition – for example, the equations that propagate a Duffing oscillator through time from t to $t+1$ – and the process noise model. In this way, values for the particles at $t+1$ can be sampled given the positions of the particles at time t and any control inputs applied u_{t-1}.

In Fig. 13a, the weights of the particles are represented by the sizes of the dots on their locations. On the left, the set of equally weighted particles is seen, that is, all the dots are the same size. The propagation of these particles is shown using the lines which indicate their position (on the right) after passing through the transition density. The next step is to calculate the weighting of the particles in their new positions at time $t+1$. This must be done via a weighting function which, in the bootstrap filter, is defined as equal to the likelihood given the observation model.

This procedure enables the estimation of the probability density over x_t, via an importance sampling approach. However, as can be seen in Fig. 13a, this can

result in a large number of particles ending up having very low weights. These particles contribute little information to understanding the distribution of interest. In an ideal case, each of the particles should contribute equally to understanding this distribution, this occurs when all the particles have an equal weight. In order to ensure that, before every propagation step, the particles are equally weighted. The particles are resampled according to their importance weights. The simplest manner in which to do this is to resample the particles based on a multinomial resampling procedure where the probabilities in the multinomial distribution are given by the normalized importance weights. The basic premise of the resampling procedure is to remove particles with low weights and to replace them with copies of particles with higher weights. Alternatively, it is possible to employ residual, stratified, or systematic resampling methods [103, 104] which can be more efficient, although this will not be discussed here specifically.

Within SHM, the particle filter is being used for the modeling of nonlinear dynamical systems [94, 105, 106, 107, 108, 109]. Again, the most common application of these models is in the attempted recursive estimation of system parameters. In addition to this point, the flexibility of an SMC scheme allows this to occur even when the dynamics of the system are nonlinear. The efficacy of the SMC approach when compared to an EKF is discussed in [110], with reference to its application in structural dynamics and SHM. In conclusion, it should be noted that, firstly, the SMC approach to handling nonlinearity in an SSM setting should be considered the *gold-standard* when compared to either the EKF or UKF. Secondly, care should be taken when using these models for recursive parameter estimation to ensure that the transition model for the parameters does not bias their solutions. It should also be noted that there is no guarantee that these recursive estimation methods will converge to the true posteriors over the parameters; therefore, it is worth considering that the use of a particle MCMC scheme may be a more appropriate tool for parameter estimation [111].

4 Statistical Pattern Recognition for Damage Identification

The preceding sections have discussed various methods for extracting damage-sensitive features from data that are measured from a structural or mechanical system. As discussed, the analysis of these features should, in theory, allow for the discrimination between the observations that relate to the normal operating condition(s) and those that relate to damage. This section is concerned with statistical analysis of these features, in order to inform damage identification.

4.1 Pattern Recognition for Feature Discrimination

It is generally accepted that pattern recognition theory offers a natural framework to address the feature discrimination problem [17]. Following this approach, *machine learning* algorithms have the potential to predict which groups of measured data

relate to different operating conditions; for example, is the system operating normally, under extreme temperatures, or, most critically, is the system damaged?

Feature discrimination can be formalized using Rytter's hierarchy [5], as discussed in Sect. 1.2, specifically levels I–III. The first level, *damage detection*, is typically addressed using *outlier analysis*, which utilizes the idea of *novelty detection* algorithms. The concept of novelty detection can be considered as a form of *unsupervised learning*; an introduction is provided in Sect. 4.3.

Damage assessment and classification (levels II and III) are more difficult, as the algorithms require more information in order to make informed predictions, which is often unavailable. Generally speaking, *supervised learning* is applied in an attempt to classify and assess any features that might relate to damage; an example of supervised learning is provided in Sect. 4.5.

4.2 Data-Driven Models in SHM: Learning and Prediction

When categorizing the measured data, $\mathbf{x}$, from a system or structure, algorithms (or "machines") can be used to *learn* which diagnostic labels, y, are associated with certain patterns within the input data (Note that for the remainder of this section, the notation $\mathbf{x}$ will be used to refer to a multivariate measurement vector of observations.). Therefore, a dataset must be available (in some form) in order to *train* the algorithm. The process of learning from a subset of training data can be defined in various ways. In the context of SHM, a visual introduction is provided.

4.2.1 Acoustic Emission Dataset

An acoustic emission (AE) dataset – collected by Pullin et al. at Cardiff University [112] – is used to demonstrate statistical pattern recognition in the context of SHM. These data were recorded during experiments in which a box-girder of a bridge was exposed to cyclic loading from 0.1 to 85 kN [1]; details of the test procedure can be found in [112, 113, 114]. Briefly, the AE burst signals were extracted from the background noise of the measured data by setting a threshold based on the mean and six standard deviations; an example of a burst signal is shown in Fig. 7. A total of 91 AE burst signals were identified from the measured data.

The object of this dataset is to distinguish between different AE sources, particularly those relating to crack growth, as this information might help to inform damage detection, classification and prognosis. There are various ways to implement machine learning in order to analyze the observed data. Time series analysis could be applied to the burst signals directly, to learn a function in the time domain and monitor the behavior of the signals [113]. In this example, however, and in agreement with existing work [112], features are extracted from the burst signals in the hope that they are sensitive to damage. The features used in this case are those discussed in Sect. 2 for AE data; specifically, these are *rise time*, *peak amplitude*, *duration*, and *ring-down count* [1].

Each AE burst, which represents an observation of the monitored system, is represented by four features. In order to visualize these data, and to aid discussion,

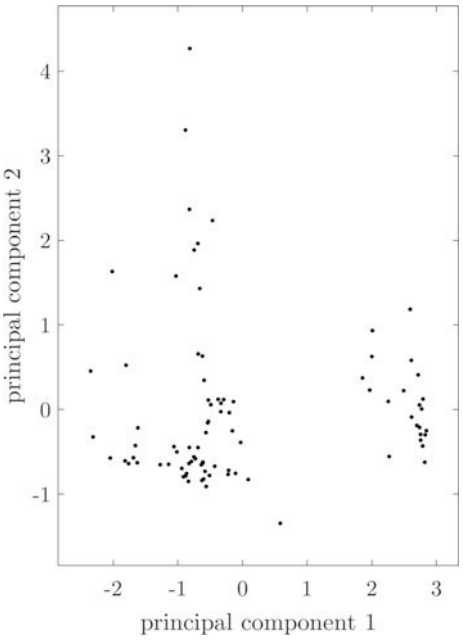

Fig. 14 PCA feature space for the 91 AE burst signals projected onto two dimensions such that the variance is maximized

dimension reduction is applied to represent each observation in two dimensions, such that $\mathbf{x} \in \mathbb{R}^2$; linear PCA is applied [115]. PCA can be interpreted such that the resulting features (or principal components) are a linear sum of the features that define the original data. Furthermore, the projection of the data is such that the variation has been maximized. The first two principal component scores are plotted in Fig. 14, which allows for visualization of the 91 AE burst signals, as they are represented in two dimensions. The goal of pattern recognition algorithms is to classify these observations according to the condition of the structure that generated each AE signal.

4.3 Outlier Analysis for Damage Identification

Novelty detection algorithms that utilize outlier analysis have been used extensively for damage detection in practical applications of structural health monitoring (SHM) [116, 117, 114]. The problem is to identify, from the measured data, if a machine or structure has deviated from the normal condition, that is, if the data are novel [116].

In an engineering context, outliers can be suitably defined for *novelty detection* as:

> Data that deviate so much from other observations, as to arouse suspicions that they were generated by some different mechanism. [118]

Specifically, outlying data should indicate a significant change in the underlying physics of the system, rather than benign fluctuations in measurement noise. Although this description is conceptually simple, detecting informative outliers from noisy engineering data is a nontrivial task.

4.3.1 Statistical Outlier Analysis

Parametric statistical approaches assume that the measured data can be represented by some d-dimensional random vector, $\mathbf{X}$, where each feature, $\mathbf{X}_i$, can be considered a random variable $\mathbf{X} \in \mathbb{R}^d \therefore \mathbf{X} = \{\mathbf{X}_1, \ldots, \mathbf{X}_d\}$. The random vector $\mathbf{X}$ is assumed to be defined by some probability distribution function (pdf) f, such that $\mathbf{X} \sim f$. Using these assumptions, the parameters of f can be estimated from the available data, and a *discordancy test* can be used as a measure of novelty [119, 116].

Typically, the normal condition data are assumed to be multivariate Gaussian-distributed, defined by the mean vector $\boldsymbol{\mu}$ and covariance matrix $\boldsymbol{\Sigma}$ (i.e., location and scatter), such that $f = \mathcal{N}(\mu, \boldsymbol{\Sigma})$ [1]. The parameters can be then estimated through the sample mean and covariance, $\left(\hat{\boldsymbol{\mu}}, \hat{\boldsymbol{\Sigma}}\right)$, to provide a maximum-likelihood estimate of the distribution f. To illustrate this concept, a subset of the AE data is assumed to define a class which is considered as the *normal* data. In this case, these are the AE bursts due to *frictional processes* away from the crack [113], shown by the red $\times\bullet$ markers in Fig. 15. In theory, any observations that are generated by an alternative mechanism (in this case, *crack-related events* [113]) can be considered as outliers.

The maximum likelihood estimate of f for the normal data is illustrated in Fig. 15a; this is defined by the sample mean and covariance $\left(\hat{\boldsymbol{\mu}}, \hat{\boldsymbol{\Sigma}}\right)$ from the training data ($\times$). Visually, it is anticipated that any novel data, that is, crack-related signals, should appear significantly different to the training data. With this in mind, an appropriate measure of discordancy is the Mahalanobis squared-distance (MSD) [114, 116]. The MSD can be interpreted as a covariance-weighted squared-Euclidean-distance from the sample mean $\hat{\boldsymbol{\mu}}$ of the normal data – if the covariance is equal to the identity they become synonymous [115],

$$MSD_i = \left(\mathbf{x}_i - \hat{\boldsymbol{\mu}}\right)^\top \hat{\boldsymbol{\Sigma}}^{-1} \left(\mathbf{x}_i - \hat{\boldsymbol{\mu}}\right), \tag{25}$$

where $\mathbf{x}_i$ is the potential outlying observation, such that $\mathbf{x}_i \in \mathbf{X}$.

A critical MSD value, or threshold, must be defined in order to classify data as normal or novel. The definition of this threshold proves to be nontrivial, thus, it is approximated in various ways. When assuming Gaussian-distributed features, the outliers can be seen as Chi-squared distributed, and the relevant critical values can be used to define a threshold [119, 120, 121]. An issue with this technique, however, is that it assumes a specific form of the data distribution; additionally, it is based on the asymptotic distribution of distance measures [120]. Alternatively, extreme value statistical theory [122] can be used to define the threshold; this approach has less strict assumptions regarding the distribution of the data, and as a result, the method should generalize across various datasets. In this example, however, a simple Monte

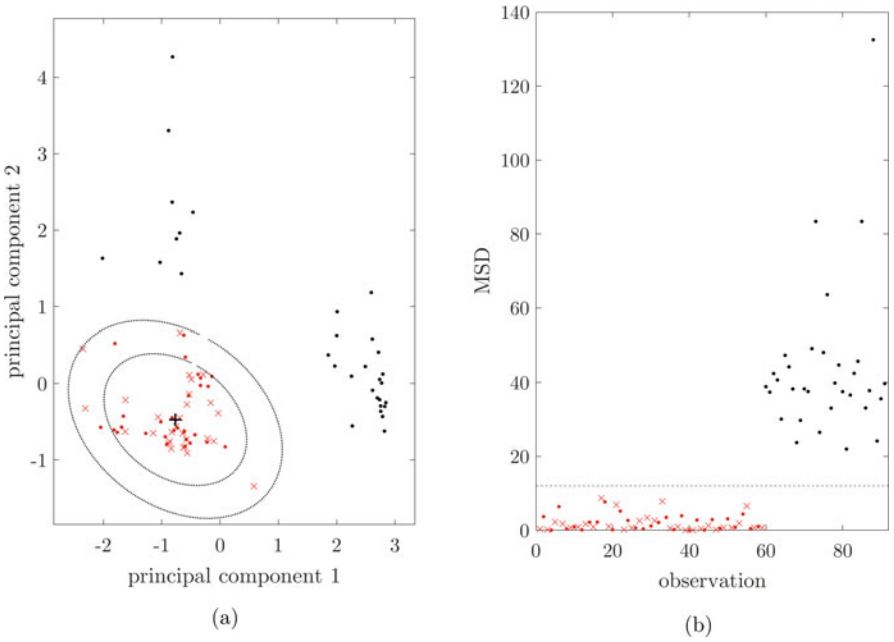

Fig. 15 Standard MSD outlier analysis with the AE dataset. The training and validation sets are shown by × and • markers, respectively: (**a**) Observations in the feature space. The maximum likelihood estimate of f is shown by the sample mean (+) and covariance (dotted lines represent two and three standard deviations), (**b**) the MSD for each of the 91 burst signals

Carlo (MC) sampling technique is used to define a threshold [116]. This method assumes Gaussian-distributed features, and represents a 99% confidence bound for a dataset with the same dimensions as the training set. For further details of the MC sampling regime, the reader is referred to [116].

The corresponding MSD for each observation in the AE data is shown in Fig. 15b. As this is a maximum-likelihood estimate, the model risks overtraining; therefore, it is critical to ensure that the model will generalize when applied to new data through validation. A detailed discussion of validation techniques can be found in [115]; however, in this simple example, a distinct validation set is used to ensure generalization, shown by the red • markers in Fig. 15. As expected, the normal condition data, relating to frictional processes, have a low discordancy for the training and validation sets; this supports the assumption that these data are sampled from the same underlying distribution, f. On the other hand, the crack-related AE signals show higher measures of discordancy, suggesting they were generated by some alternative and novel mechanism.

4.3.2 Outlier Analysis as One-Class Classifiers

Traditionally in SHM, outlier analysis is referred to as unsupervised learning [1]. This is true in the sense that the data labels, y, are not used explicitly with the

input data, $\mathbf{x}$, to learn a predictive model; instead, the model is built using the input data alone. However, in the *exclusive* setting (which has been demonstrated in the AE example), the training data can be assumed to represent the normal condition only [116], that is, one class of data. Considering this implicit labeling, it can be useful to consider outlier analysis and novelty detection tools techniques as *one-class classifiers* [123]; in other words, the measurements are either from the normal class (inlying) or they are not (outlying).

4.4 The Problem of Inclusive Outliers: Robust Outlier Analysis

As discussed, the previous example considered exclusive outlier analysis, such that a set of data can be assumed to be representative of the normal condition. While this is often valid for practical applications of SHM (e.g., the initial measurements from a system should represent the undamaged structure) there are scenarios where outliers can be hidden within the training data [116, 117]. Typically, these outlying data are referred to as *inclusive* outliers, and their presence can contaminate the parameter estimates $\left(\hat{\boldsymbol{\mu}}, \hat{\boldsymbol{\Sigma}}\right)$. In the context of SHM, the inclusive problem can occur when data are recorded over a range of operational and damage conditions without descriptive labeling (unsupervised learning). For example, when considering the AE data, this occurs when the *normal* condition data, shown by red markers in Fig. 15a, are undefined.

If inclusive outliers are not considered when defining a model for novelty detection, they can significantly influence the parameter estimates of f, leading to *masking* or *swamping* effects [124]. Masking is caused by inclusive outliers that lead to an increased covariance, $\hat{\boldsymbol{\Sigma}}$; thus, these outliers can mask the detection of future anomalies (leading to false negatives). Alternatively, outliers can shift the model location $\hat{\boldsymbol{\mu}}$, leading to swamping, causing normal data to appear as outlying (false positives) [124]. An example of masking with the AE data is shown in Fig. 16; in this example, almost all of the crack-related data appear as inlying, which is clearly uninformative.

4.4.1 The Minimum Covariance Determinant

Outlier tools that utilize robust statistics [125, 119, 120, 121] look to account for, and expose, inclusive outliers that are hidden within the dataset. Robust statistical methods were introduced into the field of engineering/SHM in [117]. Roughly speaking, these algorithms accurately estimate f by finding which h-subset of observations, H, (from the available data) have been generated by the normal condition, such that the size of the set (cardinality) is $|H| = h$. The optimal h-subset can then be used to determine robust estimates of $\hat{\boldsymbol{\mu}}$ and $\hat{\boldsymbol{\Sigma}}$.

In the existing literature, two typical ways to define H consider the minimum volume enclosing ellipsoid (MVEE) [121] or minimum covariance determinant (MCD) [120]. The MVEE approach defines H by searching for the smallest-volume ellipsoid that encapsulates h observations in the feature space. Alternatively,

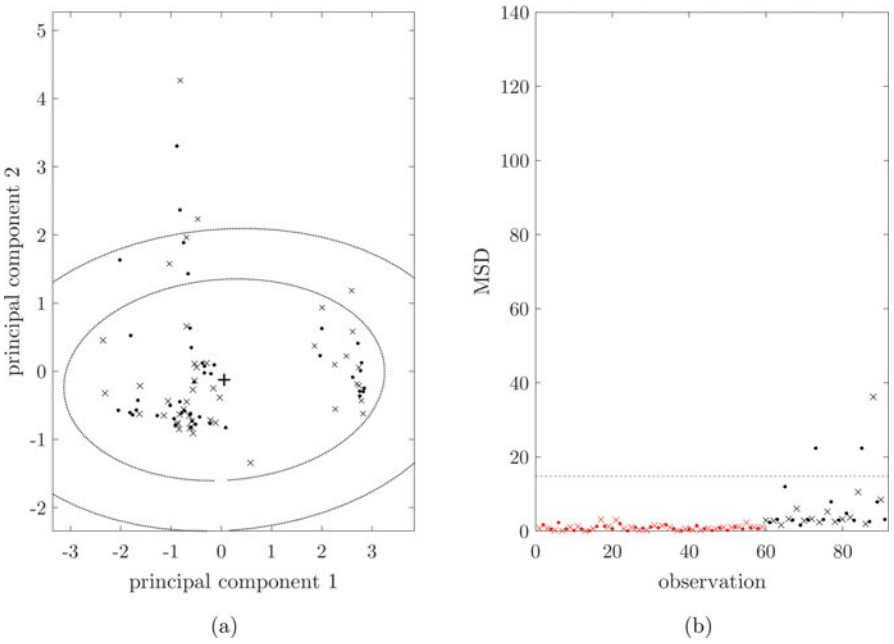

Fig. 16 The problem of inclusive outliers when using standard MSD outlier analysis: (**a**) Observations in the feature space. The maximum likelihood estimate of f is shown by the sample mean (+) and covariance (dotted lines represent two and three-sigma), (**b**) the MSD for each of the 91 burst signals

MCD methods define H as the subset whose covariance matrix has the minimum determinant. Both definitions can be interpreted as a way to describe the (majority) h-subset that is the most concentrated in the feature space [121]. Intuitively, this group is assumed to be generated by the same underlying mechanism, f.

The fast-MCD algorithm is applied to the AE data for demonstration; for further details relating to the search method used to approximate the optimal h-subset, refer to [125]. Figure 17 illustrates how the AE burst signals corresponding to crack-related events are successfully flagged as outliers, despite these inclusive outlying data being hidden within the training set. The robust approximation of the normal condition distribution, f, is shown in Fig. 17a, and the associated MSD for each observation is shown in Fig. 17b.

4.5 Probabilistic Classification through Supervised Learning

Often it is necessary to classify data into multiple groups, rather than simply *inlying* or *outlying* (one-class classifiers). For multi-class classification, each observation, $\mathbf{x}_i$, is associated with a label, $\mathbf{y}_i$, which categorizes the observations into K groups,

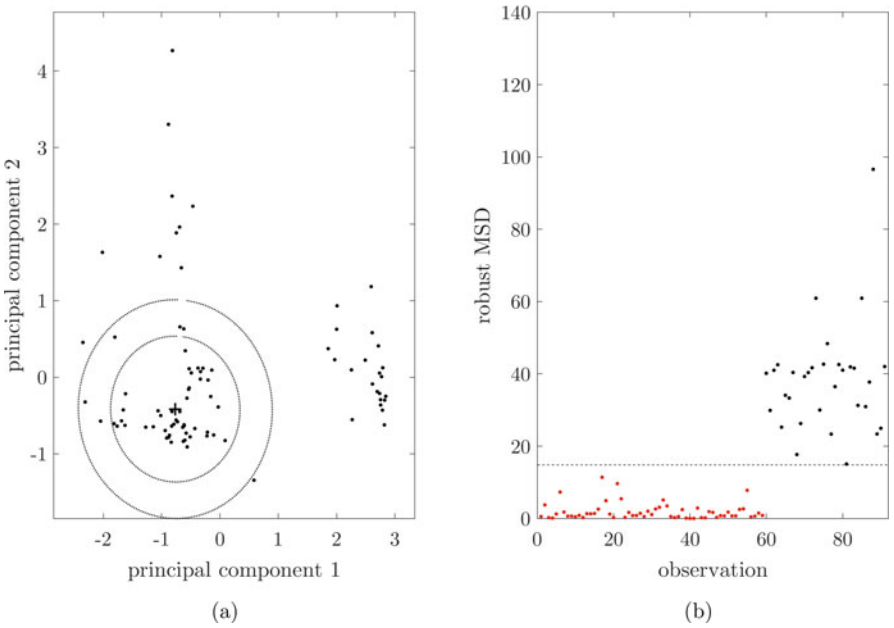

Fig. 17 Outlier analysis using the robust MCD algorithm: (**a**) Observations in the feature space. The maximum likelihood estimate of f is shown by *robust* estimates of the mean (+) and covariance (dotted lines represent two- and three-sigma), (**b**) the robust MSD for each of the 91 burst signals

such that $\mathbf{y}_i \in \{1, \ldots, K\}$. Predictive class labels for unseen observations can then be used to inform the SHM strategy.

In the context of the AE data, the 91 observations can be approximately split into three classes, such that a group of observations are associated with [113]:

- Class 1 – frictional processes away from the crack (clamping in the experimental setup)
- Class 2 – crack-related events (crack extension and crack-face rubbing)
- Class 3 – crack-related events at a distance from the sensor

This labeled dataset is illustrated in Fig. 18. Continuing with the parametric, statistical approach, it is useful to assume that the measured data can be represented by some random variable, $\mathbf{X}$; however, for the multiclass problem, it makes sense to consider $\mathbf{X}$ as a *mixture of Gaussians*, or a Gaussian mixture model (GMM). Following this approach, each of the K classes can be defined by its own Gaussian distribution, f_y,

$$x \,|\, y \sim \mathcal{N}\left(\boldsymbol{\mu}_y, \boldsymbol{\Sigma}_y\right), \tag{26}$$

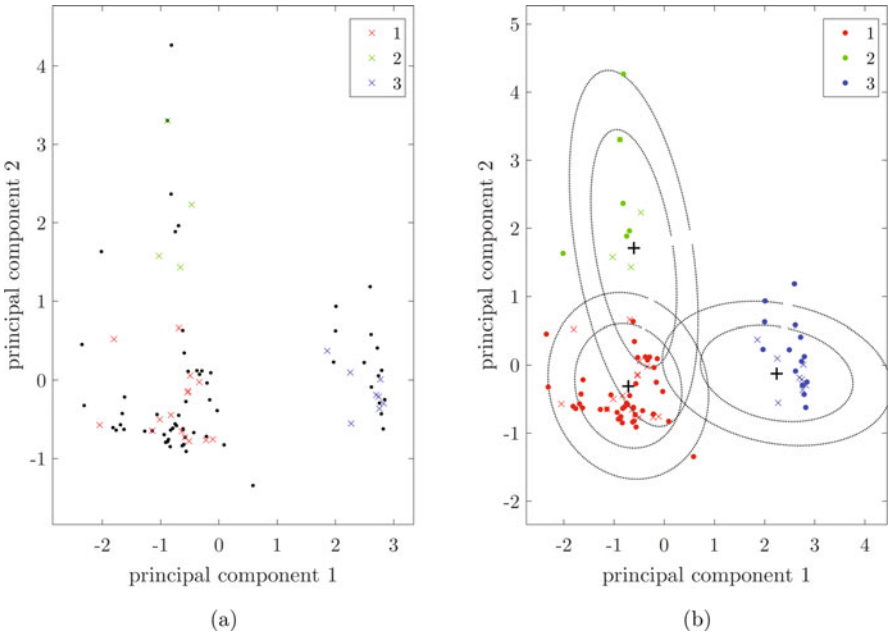

Fig. 18 Multiclass classification of the AE data: (**a**) Observations in the feature space, illustrating the training set (× markers) and the test set (• markers), (**b**) model predictions; the maximum a posteriori (MAP) estimate of f is shown by the MAP of the mean (+) and covariance (dotted lines represent two- and three-sigma)

$$\therefore, p\left(x|\,\mathbf{Y}=y\right)=\mathcal{N}\left(\boldsymbol{\mu}_y,\boldsymbol{\Sigma}_y\right)=f_y \tag{27}$$

A distinct pair of parameters $(\boldsymbol{\mu}_y, \boldsymbol{\Sigma}_y)$ are used to define the distribution of $\mathbf{X}$ for each of the K classes; note, for the AE data, $K = 3$.

Furthermore, it is useful to consider that the label space can be defined by some random variable, $\mathbf{Y}$. In this case, as the labels are discrete, $\mathbf{Y}$ is assumed to be categorically distributed; for more details behind this intuition, the reader is referred to [126],

$$y\sim Cat\left(\lambda\right), \tag{28}$$

where $\lambda = \{\lambda_1, \ldots, \lambda_K\}$ are the *mixing proportions* for each class $y \in \mathbf{Y}$, such that,

$$p(y)=\lambda_y=P\left(\mathbf{Y}=y\right)\forall y\in\mathbf{Y}. \tag{29}$$

A maximum likelihood approach can be used to approximate the parameters $\{\boldsymbol{\mu}_y, \boldsymbol{\Sigma}_y, \lambda_y\}$ of the distributions $p(x|y)$ and $p(y)$ (as in the outlier analysis example). However, in order to improve model generalization, and to avoid validation procedures,

a Bayesian approach is adopted to estimate the parameters of the mixture model. This involves considering the parameters to be random variables themselves, and incorporating a prior belief over the parameter estimates to prevent overtraining, particularly with small datasets. For details explaining the Bayesian approach to statistical modeling, the reader is referred to [126].

Having approximated the parameters of the mixture model, a generative Bayes' classifier can be defined to predict the probability of a label $y \in \mathbf{Y}$ for unseen observation $\hat{\mathrm{x}}$ [126],

$$p\left(y|\,\hat{\mathbf{x}}\right) = \frac{p\left(\hat{\mathbf{x}}|\,y\right)p(y)}{p\left(\hat{\mathbf{x}}\right)}, \tag{30}$$

Note: this generative model is a Baye's classifier; however, it is *not* a fully Bayesian method. For this to be the case, the full posterior distribution over each label estimate *p(y|x)* would have to be defined analytically or approximated. For more information on fully Bayesian models, the reader is directed to [127, 126].

As $p\left(\hat{\mathbf{x}}\right)$ is a normalizing constant (to ensure the integral of the pdf $p\left(y|\,\hat{\mathbf{x}}\right)$ is one), the predicted label, $\hat{y}$, can be defined as the most likely label given the observation $\hat{\mathbf{x}}$,

$$\hat{y} = \text{argmax}\left[p\left(\hat{\mathbf{x}}|\,y\right)\ p(y)\right] \tag{31}$$

The resulting multiclass classification for the AE data is shown in Fig. 18. A random sample of 30% of the total data is used to train the algorithm ($\times$ markers), while the model predicts the label for the remaining 70% (• markers).

4.6 The Problem of Feature Dimensionality

In SHM, the measured data are often high-dimensional (e.g., vibration observations). As a result, even large volumes of data records can be sparse in their feature space, leading to a poor representation of the distribution of data, and insufficient information to build a reliable model. This phenomenon is referred to as the *curse of dimensionality* [128, 115].

In the context of outlier analysis, the distance measures (used to define outliers) can lose their meaning for sparse data in high dimensions [128]; specifically, it has been shown that the magnitude of the distances between any pair of observations can become similar [128]. In this case, any observation might be considered as a potential outlier.

To combat issues of dimensionality, feature selection tools look to identify a low-dimensional subset of variables from the measured data that are sensitive to damage [1]. These low-dimensional data can then be used to build pattern recognition models. Sensitivity analysis [1] of variables over the input data can help identify

representative features objectively [129]. Alternatively, the use of genetic algorithms (GA) has been shown to provide promising results when applied to vibration data [130].

Dimension reduction techniques offer another method for data compression, while retaining as much information as possible from the full feature space. Linear PCA is typically used, which has been demonstrated with the AE data example. Alternatively, nonlinear variations include kernel-PCA [126] and auto-encoder networks [131]. When applying these techniques, the resulting features can be interpreted such that variation within the available data is maximized. While these methods are highly effective, a feature projection which maximizes variance is not necessarily indicative of damage, as any major changes in the data might relate to environmental conditions or other permissible variations during operation. With this is mind, engineering judgment, along with prior knowledge of the type of data and the application, is required during signal processing to ensure sensible and informative features are extracted from the measured data.

4.7 Outstanding Challenges in Data-Driven SHM

One of the most significant challenges for data-based SHM is a lack of data [132]. For example, in order to define a complete labeled dataset for an engineering structure, the system must be measured across all operational and damage conditions, while the structure is regularly inspected by an engineer to annotate the measured data. Additionally, the dataset recorded from one structure is not necessarily relevant to another (nominally) identical one. Therefore, traditional supervised learning of expensive systems (such as aerospace or civil structures) is clearly impractical and infeasible. Currently, this fact forces a dependence on unsupervised techniques in many practical applications, specifically, novelty detection. An alternative approach, however, is to utilize novel learning strategies for SHM, which can make use of datasets with limited information or annotation. These tools are emerging technologies in the SHM literature, including semi-supervised and active learning [132, 133].

5 SHM in Changing Environmental and Operational Conditions

This section discusses how the influence of changing environmental and operational conditions can be problematic when attempting to infer structural condition from monitoring data.

As previously alluded to, the effect of changing environmental and operational conditions on a structure is an important issue in SHM, and has been identified as a key concern to the research community [134]. This interest arises from the inconvenient fact that measured responses from a structure that demonstrate sensitivity to damage or structural degradation, will, in general, also exhibit sensitivity

to any change in operational and environmental conditions [19]. In these cases, the confounding effects of the environmental and operational variation must be accounted for in some way before a reliable measure of structural condition can be inferred. The problem is often referred to as the *data normalization problem* within the SHM community [16].

In the SHM literature, undoubtedly the most commonly occurring discussion of confounding influences on damage-sensitive features that arises from the sensitivity of structural response to temperature. For civil infrastructure, for example, temperature is generally considered to be the dominant environmental factor affecting the normal dynamic response, due to its effect on the stiffness of structural components, and also its potential effect on the boundary conditions of a structure (for instance from the freezing of foundations etc.). Historically, many studies have found fluctuations in modal frequencies to be correlated with ambient temperature, although different mechanisms have been used to explain this, see for example [135, 136, 137, 138]. Cornwell et al. [136] suggested that the thermal gradient across the deck of the Alamosa Canyon Bridge drives the observed fluctuations in modal frequency. In colder climates, significant shifts in frequency between above and below freezing temperatures have been attributed to an increase in stiffness explained by the Young's modulus of the asphalt on the deck at colder temperatures [137]. In this case, the modal frequencies of the Z24 bridge deck (Switzerland) were observed to have a bilinear relationship with temperature. A similar behavior has also been observed in a steel truss footbridge in the USA [139]. More recently, Xu et al. [140] showed that the displacement of the Tsing Ma Bridge deck was linearly related to the changes of ambient temperature, after conducting a 6-year monitoring campaign. While investigating the thermal effects on the Zhenjiang Bay Bridge (a cable-stayed bridge with a 480 m main span) in China, Cao et al. discovered that the effect of temperature differed across the structure and that the temperature in the concrete lagged 5–6 h behind the measured ambient air temperature [141]. Similarly the monitoring campaign of the Tamar Suspension Bridge in the UK revealed that the structural temperature lagged 10–60 min behind air temperature depending on which part of the bridge was measured [142].

Besides temperature, the importance of other environmental and operational conditions has also been considered. Wind-induced vibration is a critical factor for the design and maintenance of tall and slender structures like wind turbines, skyscrapers, and long-span bridges. A suspension bridge in Japan was tested by Mahmoud et al. [143]; they found that the natural frequencies, mode shapes, and damping ratios were all related to the variations in the ambient wind. Cross et al. [144] observed that the modal frequencies of the Tamar Bridge in the UK were not significantly correlated to wind speed unless the wind speed exceeded 25 mph, when a modal frequency dependency on the amplitude of deck vibration could be observed. The effect of humidity alongside temperature has also been studied. In [145], the effect of humidity and temperature on the modal parameters of a reinforced concrete slab was investigated; it was found that increased humidity effectively adds mass to a structure and, therefore, has a strong negative correlation with modal frequency.

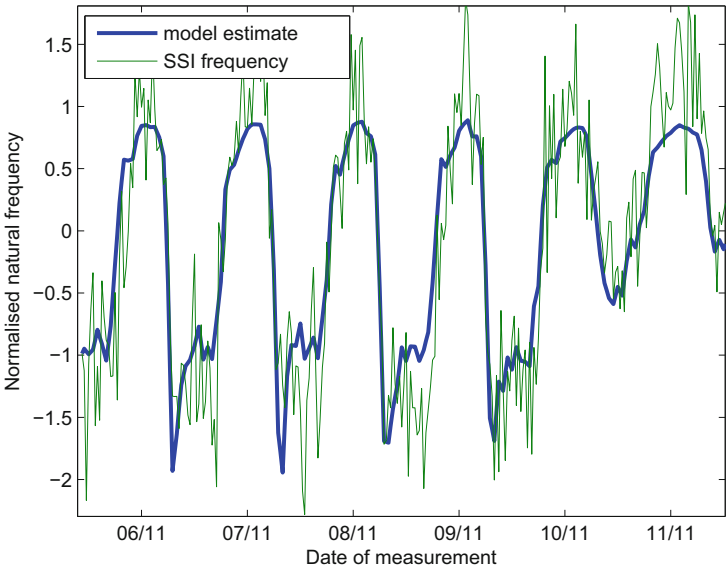

Fig. 19 Linear regression model of first deck modal frequency of the Tamar Bridge, with traffic loading input only [144]

Operational conditions in SHM can be considered to be a broad terminology that may include factors like traffic loading, flight conditions, operating speed, and payloads, which may vary with time, resulting in significant influences on the response and dynamic properties of structures of interest. The effect of traffic loading is of particular interest for bridges, where the modal properties of bridge decks have been found to be more or less influenced depending on the mass of the traffic relative to that of the structure itself. For example, the effect of traffic loading has been addressed in [146], where, for long-span bridges, the influence of traffic loading on the structure's modal frequencies was considered negligible due to the fact that the mass of a single vehicle is very small in comparison to the mass of the "superstructure." For the Tamar Suspension Bridge, the fundamental modal frequency of the deck has been shown to vary linearly with the estimated instantaneous traffic load. Figure 19 shows how a simple linear regression model with traffic load as an input can reproduce the variation of the fundamental modal frequency of the deck [144].

5.1 Removing Confounding Influences

A review of the relevant literature reveals a number of potential options explored for dealing with the problem of operational or environmentally induced variations in structural response. Perhaps the most common approach has been to attempt

to model the monitored parameters or damage sensitive features in question with respect to those environmental/operational factors considered to be driving its/their variation [147, 148, 149, 139, 150, 151, 152, 137, 153]. If a model can predict the value of a damage-sensitive feature given the conditions affecting it, the error of the model could be suitable as a robust indicator of structural condition. Often these approaches have employed a simple regression of the damage-sensitive feature (normally modal frequencies) onto measured structural temperature [148, 149, 139, 137, 153]. More complex approaches for regression have also been explored [150, 151, 152], where modal parameters of the Ting Kau bridge, Hong Kong, have been regressed onto measured temperature using support vector machines, principal component analysis, and neural networks. In a very similar vein, tracking the correlation between the measured strain of a harbor wall and temperature has been explored in [147].

For complex relationships between measurands, where it might be beneficial to model their functional relationship in distinct regimes, an alternative approach has been suggested that combines Classification and Regression Trees (CART) with a nonlinear regression model (particularly Gaussian process (CP) regression in this case) [154]. A treed-GP partitions the input domain into different regimes (leaves) using a Bayesian CART algorithm and employs a different GP in each regime. The GP can also be extended to the heteroscedastic context (the variance of the noise is time dependent); see for example [155].

In the approaches described thus far, the main limiting factor is that the changing environmental and operational conditions have to be identified and accurately measured. While this may be feasible where only one or two environmental or operational factors are important, such as temperature, where multiple factors affect the features of interest, a substantial monitoring campaign will then become necessary.

Other approaches, which do not rely on measurements of the environmental/operational conditions being available, have also been explored. A simple potential solution to the problem is to use a long span of response data to define the normal condition of a system, an idea explored in [156]. This could be, for example, data collected over a whole year, where all ranges of environmental/operational conditions have occurred. New measurements may then be compared in some way with the defined normal condition. Evidently this approach requires storage of a large amount of data, and a further drawback is that using a large normal condition set may reduce feature sensitivity to damage [153]. This issue was explored in the context of damage detection in composite panels in [157].

A number of other studies employ what may be described as *projection methods* or *latent variable models* [158], which, without measurement of the changing environment, attempt to capture the variation in the feature data caused by it. PCA has been used in a number of studies to re-express multivariate SHM feature data with a new set of orthogonal coordinate axes [159, 160]. The assumption employed in these studies is that the high-variance signatures of changes induced by environmental and operational conditions in SHM features will be trapped in the higher variance principal components. In [159], this assumption is exploited by discarding the

higher-variance principal components and projecting temperature-dependent data onto the minor components which constitute a temperature-independent feature set. In [160], only the higher-variance principal components are retained and used as a model to predict/reconstruct the feature data. This idea of linear projection and trapping of environmental variation was also independently proposed through the use of factor analysis (FA), which is a very similar algorithm to PCA [161]. In the next section the use of *cointegration*, an alternative projection method introduced by a subset of the authors of this chapter, will be introduced and demonstrated. The idea behind cointegration is to exploit the fact that some monitored variables will share common trends induced by the changing environment; where variables bear a linear relationship, these common trends can be removed by via a simple linear combination of the variables themselves.

Although such approaches have proven very useful in some applications, it has been shown that nonlinearity can hamper the effectiveness of employing the projection methods discussed above [162]. In [163], a remedy to problems introduced by nonlinearity was to cluster feature data into several (linear) regions and then employ PCA separately to each region. An auto-associative neural network, which may be said to be equivalent to nonlinear PCA, is used in [164] for data normalization of features extracted from an autoregressive type model. An auto-associative neural network (nonlinearly) maps its inputs onto themselves. The premise of using them for data normalization is that, if the network is trained on data from an undamaged structural condition, it will learn the effect of latent variation on the features input to the network. It is then expected that the network error will increase if damage occurs. Dervilis et al. [165] proposed to improve the robustness and efficiency of AANNs by adopting an auto-associator using a radial basis function (RBF). The main difference between a traditional multilayer perceptron (MLP) network and RBF network is that, instead of representing the nonlinear transfer function with the scalar products of the input vector and the weight vector, the RBF network adopts a nonlinear function of the distance (Euclidean distance in this case) between them, which is hugely advantageous because an RBF network does not require a cumbersome nonlinear optimization for the model parameters. The RBF network was examined with an experimental case study to detect damage in a wind turbine and was proved to be a fast online damage detection algorithm. Shi et al. introduce nonlinear cointegration for SHM in [166, 167], also discussed in the next section.

Along similar lines, a new approach for data normalization has recently emerged, where, for multiple sensor arrays, Gaussian Process regression is used to predict the measurement of each single sensor from the measurements of all other sensors in the network [161]. Given suitable training data from different environmental and operational conditions, the GP should be able to accurately predict structural response at each sensor if the structure continues to operate in a similar way as in the period where the training data were recorded. In a similar way to the regression techniques, the GP regression model error is used as an indicator of abnormal structural response.

A final alternative, rather than treating the management of EOVs as a regression task, is to manage these changes as a classification task. That is, to separate the

behavior of the system into discrete regimes based upon the current environmental or operational state. This approach has been explored in the literature; in [18] in the context of mixture modeling and in [168], where an online clustering approach detects, and subsequently is used to classify, emerging behavioral regimes.

5.2 Linear and Nonlinear Cointegration

Where measurements of changing environmental and operational conditions are not readily available, projection methods, as discussed above, have proven to be useful for removing their influences from damage-sensitive features. This section briefly introduces and demonstrates the idea of cointegration for removal of trends from SHM data, as one of the most promising of these methods (the bias of the authors should not go unnoted here). The full details of the theory can be found in [169].

Cointegration originates from the field of econometrics and is, in fact, a *property* of nonstationary time series. Informally speaking, two or more nonstationary time series are cointegrated if some linear combination of them is stationary. Economists traditionally test for cointegration between various econometric time series as a means of determining whether there is a statistically significant relationship between them. Although engineers may well be interested in problems of a similar nature, it is the stationary linear combination created during the cointegration process that is of practical interest here. If a number of variables from some process under investigation are cointegrated, the stationary linear combination of them found during the cointegration process will be purged of all common trends in the original datasets, leaving a residual equivalent to the long-run dynamic equilibrium of the process. For measurements from structural monitoring campaigns, it is likely that the nonstationarity in each variable will originate from the same cause, such as a temperature changes. This means that cointegration can be used to remove the common trends in the measured variables originating from confounding influences.

As an example, Fig. 20 shows 2 months' worth of measurements of deck and tower displacement of the Tamar Bridge (with any gaps in the record removed). These measurements were taken by the Vibration Engineering Section at the University of Exeter using a total position station (TPS); more details can be found in [170]. In the figure, one can see an oscillatory trend and a large mean shift occurring over a longer time period. The oscillatory trend is a daily trend induced by temperature variation, the mean shift is also temperature induced and occurs as the season changes and the environment gets colder [171]. Figure 21 shows these variables under a linear combination established using just 3 days' worth of data. The combination remains stationary for the duration of the period and one can clearly see that the seasonal trend visible in Fig. 20 has been purged.

For use in SHM, if the dataset used to establish this combination is representative of the normal condition of the structure, the linear combination can be used as a diagnostic tool by projecting all new data onto it. In the event that the residual becomes nonstationary, the structure can be said to have departed from its normal condition, or be damaged – if damage sensitive features make up the linear

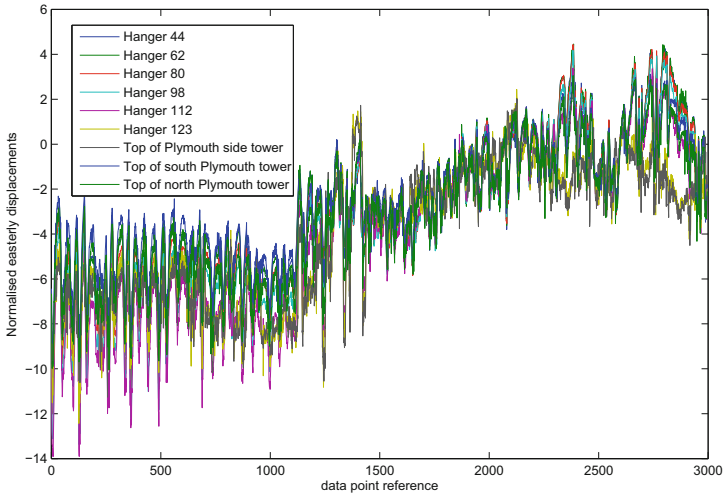

Fig. 20 TPS measurements of the Tamar Bridge deck and tower displacements

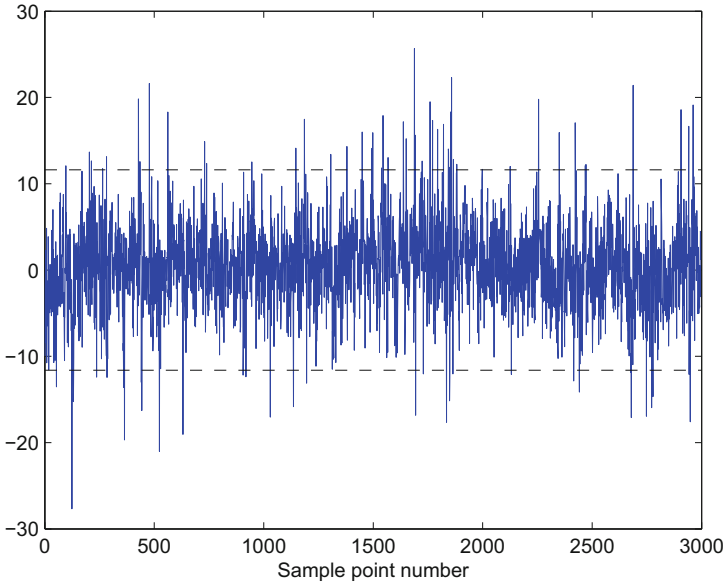

Fig. 21 Linear combination of variables shown in Fig. 20, along with error bars at plus and minus three standard deviations of the combination, added to act as a statistical process control chart

combination. In the following, a formal definition of cointegration is provided along with a brief overview of how the most stationary combination of variables of interest may be found.

Definition A set of nonstationary variables, say $\mathbf{y}_i$, are cointegrated if some linear combination $\mathbf{z}_i$ of them is stationary,

$$\mathbf{z}_i = \boldsymbol{\beta}^T \mathbf{y}_i. \tag{32}$$

If some $\boldsymbol{\beta}$ can be found such that $\mathbf{z}_i$ is stationary, then $\boldsymbol{\beta}$ is called the *cointegrating vector*. If $\boldsymbol{y}_i$ includes a total of n variables, there may be as many as $n - 1$ linearly independent cointegrating vectors.

Some constraints fall on the nonstationary variables in $\mathbf{y}_i$ if they are to be cointegrated; they must share common trends and they must also be "integrated" to the same order. A nonstationary time series, y, is integrated order d, denoted $y \sim I(d)$ if, after differencing the series d times, it becomes stationary. In essence, each time series must have the same degree of nonstationarity. For the purposes of SHM, the intent would be to use monitored variables that are cointegrated and find a cointegrating vector that will create a stationary residual sequence suitable to be used as a damage-sensitive feature. While it is likely that variables measured from the same structure will share common trends, this cannot be said of the order of integration of each monitored variable; this should be ascertained before any attempt is made to find the cointegrating vector. This is commonly achieved by using the *Augmented Dickey Fuller test*, which is a *unit root test* [172, 173].

Once it has been ascertained to what order all process variables of interest are integrated to, it remains to find the cointegrating vector that will result in the most stationary combination of them. There are two common approaches for this in econometrics; the first is the Engle-Granger two step estimation procedure [174], often employed when there are only two process variables included in the analysis; the second is the Johansen procedure [175], a more complex maximum-likelihood multivariate estimation procedure. The Johansen procedure is typically chosen when attempting to combine SHM variables. A quick outline of the theory behind finding the cointegrating vector will be briefly described below, but readers are referred to [169] for more detail.

Finding the Cointegration Vector

The Johansen procedure uses a maximum-likelihood approach to estimate the parameters of a *Vector Error-Correction Model* (VECM) of the variables under consideration. A VECM takes the form,

$$\Delta \mathbf{y}_i = \boldsymbol{\Pi} \mathbf{y}_{i-1} + \sum_{j=1}^{p-1} \mathbf{B}_j \Delta \mathbf{y}_{i-j} + \phi D(t) + \varepsilon_i, \tag{33}$$

where $\mathbf{y}_i$ denotes an n-vector including all n variables to be analyzed, with the subscript i relating to time, $i = 1, \ldots N$, p represents the model order, or the number

of lags to be included in the model, and ε_i is a normally distributed noise process; $\varepsilon_i \sim \mathcal{N}(0, \mathbf{\Sigma})$. A term to describe a deterministic trend $\mathbf{D}(t)$ can also been included.

If the variables $\mathbf{y}_i$ are cointegrated, then with the correct parameter choice, $\Delta\mathbf{y}_i$ will be stationary. It is shown in [175] that (roughly) a sufficient condition for a cointegrating vector to exist is that the matrix $\mathbf{\Pi}$ should be rank-deficient. Suppose, that the $n \times n$ matrix $[\Pi]$ has rank $n - r$, then a basic theorem of linear algebra asserts that it will admit a decomposition $\mathbf{\Pi} = \boldsymbol{\alpha}\boldsymbol{\beta}^T$ where $\boldsymbol{\alpha}$ and $\boldsymbol{\beta}$ are both $n \times r$ in dimension. It transpires that the columns of $\boldsymbol{\beta}$ are (up to a linear transformation) the desired cointegrating vectors. In principle then, construction of the cointegrating vectors looks fairly straightforward; one constructs a VECM, then once the matrix $\mathbf{\Pi}$ is found, its decomposition leads directly to $\boldsymbol{\beta}$. Unfortunately, things are not quite so straightforward; because $\mathbf{\Pi}$ is rank-deficient, standard least-squares regression procedures cannot be applied to the parameter estimation problem. A more complex reduced-rank regression approach is required; this can be summarized in terms of the Johansen procedure, detailed in references [169, 175].

5.2.1 Using Cointegration for SHM

Figures 20 and 21 showed how a temperature trend could be purged from measurements of bridge deck and tower displacement using cointegration. As the bridge is in a healthy state and performs well, another example is used here to illustrate how cointegration can be helpful for damage detection. In [157], a dataset from a Lamb wave inspection of a composite plate in a damaged and undamaged state is used. In the experiment, which was carried out under the Brite-Euram project DAMASCOS (BE97 4213), the panel was subjected to a fluctuating temperature in an environmental chamber; details of the experimental procedure can be found in [176]. For the example shown here, the features extracted for damage detection were the amplitude of 20 spectral lines from the area around the peak of the frequency spectrum. A time history of these spectral line amplitudes is plotted in Fig. 22. Here one can see that the features fluctuate throughout the test. Separated by the thick vertical lines, one can also see three regimes, the first is when the temperature in the environmental chamber is held steady, the second when the temperature is fluctuated periodically, the third is when damage was introduced with the temperature change continuing. The challenge is to be able to automatically detect the introduction of the damage.

In this example, a training data period used to establish the most stationary cointegrating vector was selected as data points 1000–2000 in Fig. 22; this includes 355 data points from the steady temperature regime and data from the fluctuating temperature regime. The selection of the training data for cointegration essentially establishes the "normal condition" for the structure. All remaining data are projected onto the cointegrating vector found from the training dataset and the stationarity of the resulting combination/residual assessed. If the residual becomes nonstationary, this indicates that the relationship between the variables combined has changed. Figure 23 shows all of the feature data projected onto the most stationary linear combination of the training data found via the Johansen procedure. Here, one can see that the residual has successfully been purged of the temperature trends visible in

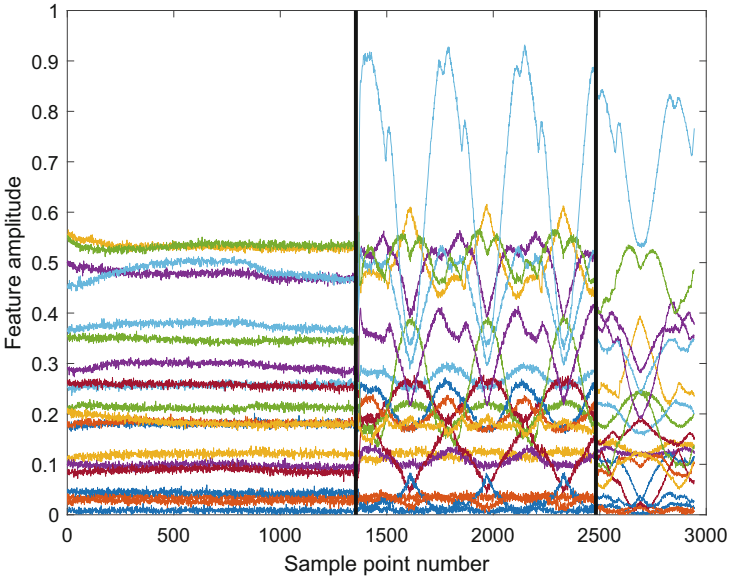

Fig. 22 Time history of 20 dimensional feature from a Lamb wave inspection of a composite plate

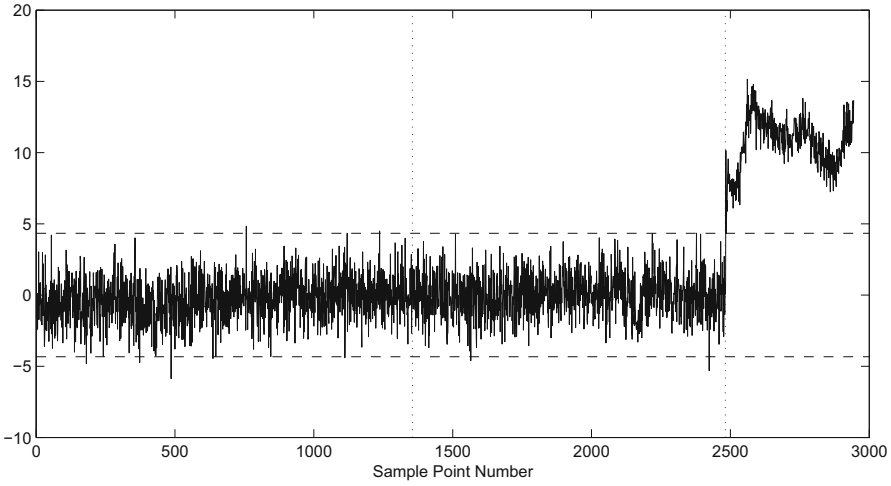

Fig. 23 Cointegrated signal (linear combination of 20 spectral lines)

the original data and that, on the introduction of damage, a large mean shift is visible and detected by control chart limits (which were set at three standard deviations of the residual in the training period). For more details and for a comparison between cointegration and a PCA-based projection method, interested readers are referred to [157].

5.3 Nonlinear Cointegration

In the previous section, the power of the cointegration method for removing environmental trends from damage-sensitive features was demonstrated. This has been shown to work well in a number of situations; it is limited, however, by its linear nature. The method is only valid where the variables of interest are linearly related during their normal condition. Alternative approaches must be sought where variables are nonlinearly related in an undamaged condition. An example of this comes from the famous Z24 benchmark dataset; here, the extracted modal frequencies have a nonlinear relationship which can be attributed to the change in the structure when sub-zero temperatures were experienced.

In this case a *nonlinear* combination of response variables is needed to remove unwanted environmental and operational trends. A number of possibilities for nonlinear cointegration for SHM are explored in [162]. Figure 24 is an example of just one of these approaches. Here the modal frequencies of the Z24 bridge have been nonlinearly combined using GP Regression. Here the second modal frequency

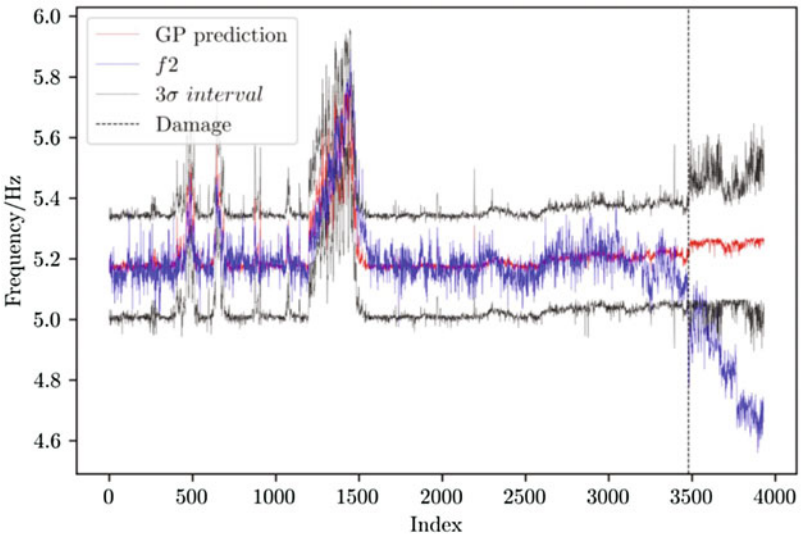

Fig. 24 Nonlinear cointegration of the Z24 deck modal frequencies; the vertical dotted line indicates the time at which damage was introduced into the structure

has been chosen as a target for the regression, where the model inputs are the remaining modal frequencies. One can see that the GP regression, established using datapoints from the undamaged condition, is able to predict the large trends induced by cold temperatures but remains unchanged after the introduction of damage. The model error would now be a good candidate for a damage-sensitive feature that has been purged of its temperature dependency.

6 Physics-Based Models in SHM

This section provides an overview of methodologies that utilize physics-based models in order to perform damage state inferences. Traditionally this category has been defined as model-driven (or physics-based) as these approaches use some form of physical law-based model, unlike data-driven techniques [19, 177, 178, 179]. In a historical context, this category referred solely to approaches that combined physics-based models with inverse techniques. These methods then posed the problem of SHM as inferring (or "updating") a set of model parameters using operational data, leading to decisions about structural integrity, based on the interpretation of these "updated" model parameter values [180, 10]. Herein, these methods are classed as *inverse model-driven.* However, another subdivision exists within the general model-driven category, known as *forward model-driven.* These approaches seek to integrate the physics and data-based techniques, in which physics-based models provide some level of training data or labels to traditional data-driven approaches [181, 182]. The focus of this section is on outlining the two philosophies, providing a review of methodologies, and highlighting outstanding challenges.

6.1 Inverse Model-Driven SHM

Inverse model-driven methods make decisions about structural integrity using "updated" model parameters inferred from in-service data. The application of these methods often involves the construction of a high-fidelity model of the structure, for which structural condition decisions are to be made, typically in the form of an FEA model. The assumption is that the model is a satisfactory representation of the structure, such that changes in the data due to damage will correspond to changes in a defined model parameter set.

There are two main procedures for updating a model in order to make health decisions; the first is a two-step process, where initially the model is calibrated so that it more accurately represents the structure in question. This is generally performed by model updating, based on in-service data of the undamaged condition. In the second stage, new in-service monitoring data from an unknown structural condition is used to update the model again. After the update, changes in the inferred model parameters from the baseline calibration are used to perform damage identification [183]. The second stage is to match response deviations between the undamaged state and the unknown state of the structure. These two procedures

can be used to perform damage identification at levels 1–4 of Rytters hierarchy. Prognosis may also be achievable because an updated physics-based model is generated through the inverse model-driven procedure [184].

SHM via an inverse model-driven approach relies on model updating or parameter estimation methods. *Model updating* refers to techniques where certain model parameters are adjusted such that the residual between observational data and model predictions is minimized [185]. This task is broadly attempted in two general approaches: direct methods, where structural matrices are updated to reproduce measured data, and sensitivity methods, where errors between predictions and observations, are minimized via changing a set of defined parameters [185, 186]. Commonly in SHM, sensitivity-based techniques are selected over direct approaches; this is because attempting to update full structural matrices within a direct approach often leads to a lack of control over the updated matrix values, leading to inferred parameters with little physical meaning.

Initial development of model updating methodologies approached the problem from a deterministic view, for example, the well-established iterative sensitivity-based method [187]. Such techniques approached the problem of model updating using optimization technologies, whereby a cost function is developed, typically in a least-squares formulation, and parameter steps made via sensitivity matrices [188, 187]. However, these approaches require regularization due to the problem of model updating being ill-posed [10]. These deterministic methods also have difficulties in handling variability and uncertainties that are present, for example, from environmental conditions, parametric variability, and model-form uncertainties. For these reasons, alternative frameworks for approaching model updating have been developed.

Two popular philosophical approaches for handling uncertainties within model updating are *fuzzy* and *Bayesian* methods [189]. Fuzzy techniques are non-probabilistic approaches that transform uncertainties into fuzzy inputs, that is, as a fuzzy number – a quantity that is characterized by a membership function – and then perform multiple optimization problems [190]. Fuzzy model updating technologies assume that the fuzzy input variables are independent and equally likely, which will result in the worst-case range of parameters being inferred. Bayesian methods, per contra, take a probabilistic view of parameter estimation, using Bayes' theorem to update model parameters and their uncertainties. In certain scenarios, these methods contain inherent model regularization contained within the marginal likelihood, sometimes referred to as the Bayesian Occam's razor [191]. Beck and Katafygiotis provide a review of Bayesian model updating [192, 193]. Nonetheless, most of the current model updating methodologies fail to account for uncertainties associated with model form errors, known as *model discrepancy.* Failure to consider this form of uncertainty will often lead to bias in the estimated parameters, and therefore incorrect health statements in an inverse model-driven context.

Inverse model-driven technologies suffer from several challenges when implemented as part of an SHM strategy. Firstly, the type and number of parameters to

use must be selected [194, 195]. In scenarios where damage is unknown, as is often the case, this can lead to an especially large number of parameters. Parametrization becomes increasingly challenging as model fidelity increases, where there are a large number of potential parameter sets. Another difficulty is that of interpreting the updated parameters to make a decision about the structure's health. This problem can be especially difficult when parameters affect structural stiffness, as multiple phenomena influence changes in stiffness. An accurate understanding of the physics must inform whether updated parameters are no longer physically meaningful rather than altered by the presence of damage, and constraints placed on the updating process when this is the case. As mentioned, variability and uncertainties within the "target" data must be handled as part of the updating process. Moreover, these issues are confounded by the problem that a solution, or a unique stable solution, for the inverse approach cannot always be achieved due to ill-conditioning. These non-identifiability issues become of increasing concern when the parameter values are being used for health diagnostics, as repeats of the update may lead to different conclusions.

6.2 Forward Model-Driven SHM

Forward model-driven techniques utilize physics-based models in a forward manner, whereby their predictions form training data, in a supervised-learning context, or a labeling method, in a semi-supervised procedure [181, 182]. Health decisions are subsequently made based on the inferred classifier using standard data-driven techniques. These classifiers can be trained using models alone, or a combination of model outputs and data. The main motivation for this class of methods is in improving the lack of available damage state data problem, by generating it from physics-based models, and removing issues associated with interpreting health states from updated model parameters.

Forward model-driven methods are comprised of two main components: generating representative damage state features from computer models, and using those predictions to train machine learning or pattern recognition approaches. The second component, well studied within the data-driven category of SHM, has been demonstrated to be effective when labeled damage state data are available. Within a forward model-driven approach, these techniques generally remain mathematically and algorithmically the same, with the only difference arising from the source of training data, that is, computer model-based predictions. Consequently, the major challenges in establishing a forward model-driven strategy are in developing methodologies and technologies that achieve the objective of the first component, namely the generation of representative damage-state features from computer models.

Few examples of forward model-driven approaches exist within the literature. FEA models have been used to generate features for ANNs in performing damage identification in bridges [196, 197]. Satpal et al. implemented a combined model

updating and SVM approach, where model predictions trained the classifier [198], with Hariri-Ardebili and Pourkamali-Anaraki applying a similar methodology to concrete dams [199]. Most of these approaches utilize deterministic FEA model outputs, with a few adding arbitrary noise terms to replicate variability, while others propagate "known" parameter uncertainties through Monte Carlo realizations. None of these methods consider model form errors, and either do not attempt to validate their models or implement full-system damage state data in the validation process.

Generating representative predictions from computer models means addressing several key challenges and will provide improvements to the existing forward model-driven literature. Firstly, there must be a method for determining whether computer model predictions of health states are representative of those obtained operationally. This requires the definition of what a valid computer model prediction *is* within the forward model-driven context. In order to develop this definition an understanding of how these predictions are used within classification methods must be established. In a data-driven framework, features extracted from operational data are often employed in training decision bounds that capture the expected behavior of the particular damage feature under each damage scenario in the training set. This requirement means that health state data generated from computer model predictions must capture the inherent variability and progression of the health state in question. A computer model will therefore be valid if its predictions generate statistical distributions of health states that are statistically similar to those from observations.

Secondly, generating statistically representative predictions will involve some level of calibration and a validation procedure. Unfortunately, both these processes require data from the real-world structure, leaving the conundrum of how to calibrate and validate the computer model given that structural condition data is neither feasible to obtain nor cost-effective in the majority of applications. If this question is not addressed, forward model-driven approaches simply become an expensive and demanding way to perform substandard data-driven SHM, introducing further approximations and modeling challenges. One solution to this problem is the division of the structure in question, and hence the computer model, into a set of components – sub-assembly, etc. – for which obtaining health state data is feasible and economically viable. In this scenario a full system, such as an aeroplane, is divided into various subsystems, for example, wing panels, riveted joints, landing gear assemblies, and coupons, where each subsystem can be tested with damage types that are expected to be likely causes of failure in the full-system. Small-scale test strategies can then be developed, or existing certification tests used to collect datasets that can be implemented in calibrating and validating the set of computer models. The usefulness of forward model-driven technologies rest on the ability to utilize and integrate these subsystem datasets into calibrated and validated subsystem level computer models, which, when propagated through to the full system, via an algebra of computer models and uncertainty management, produce valid, that is, statistically representative predictions, which have required no full-system health state data. Obviously this is an incredibly ambitious goal; nonetheless

methods such as multilevel uncertainty integration strategies offer techniques for undertaking such a challenge [200, 201, 202].

Thirdly, procedures for calibrating computer models naturally have to involve mechanisms for handling multiple sources of uncertainty, especially those from model form errors, known as model discrepancy [203, 204, 205]. Statistically representative predictions will not often be achievable without capturing observational variability, along with parameter uncertainties and accounting for any functional model discrepancy – the differences between computer model outputs and observational data. At the point of writing, forward-model driven SHM is still a developing field, but one which, by addressing these challenges could become a solution to some of the key difficulties facing SHM, such as the scarcity of training data.

7 Summary

This chapter has presented a general overview of data-driven SHM, placing a focus on signal processing and statistical learning techniques. The process of SHM, which largely follows Rytters' hierarchy of detection, localization, classification, assessment, and prediction, has been outlined in terms of its various components. The chapter has placed a strong emphasis on the detection stage; even this first stage presents some difficult challenges and requires an appropriate combination of operational evaluation, feature engineering, and machine learning algorithms to succeed. Today, one of the key challenges in SHM is dealing with the confounding influence of operational and environmental trends in SHM data. The chapter has presented an overview of the techniques available to deal with this challenge, focusing on removal of the confounding influences, as well as their identification through techniques such as robust statistics. Another problem of interest in SHM is the use of physical models to aid in the damage identification process. Physical and phenomenological models often provide a level of insight into the system dynamics that cannot be achieved with purely data-driven models. However, physics-based models often fail to accurately predict the output of complex systems, or handle operational and environmental changes. The last section of this chapter has discussed the progress that has been made in using physical models in SHM.

7.1 Applications

For a long time, SHM has been confined to laboratory experiments and demonstrations. However, the field is beginning to make a transition toward real-world applications, within both the private and public sectors, with a plethora of applications materializing the usage of such monitoring systems. A significant number of structures undergo routine inspections and maintenance in order to ensure structural stability of the system. The costs of these routine inspections could be significantly reduced if these inspections are shown to be unnecessary when a structure continues to be healthy, and this could be indicated automatically by implementing an SHM

system. SHM could offer robust and online monitoring and necessary maintenance or repairs could be addressed based on this technology. A very bold and strong branch of industry in which SHM takes flesh is the offshore wind industry. A good very recent example research initiative is provided by the "New Partnership in Offshore Wind" – a UK Engineering and Physical Research Council (EPSRC) Prosperity Partnership. This proposal brings together two major industrial players: Siemens-Gamesa Renewable Energy and Ørsted, with world-leading academic researchers in a £7.64 M, 5-year program in order to address fundamental research challenges that will help to reduce the levelized cost of electricity (LCoE) from offshore wind and to support UK supply chain growth. SHM is one of the core interests in this major project.

Another (historically) major player in SHM applications is the offshore oil and gas industry, where a platform may undergo routine maintenance or emergency component replacement, which, in turn, would be an economic and environmental drawback. Industries such as energy and aerospace have always been keen on life extension of critical components beyond the originally designed fatigue life. Applications of SHM systems are arising in additive manufacturing, biological systems, telescopy, and even in monitoring of advanced infrastructure such as accelerators. A good example of where this could be critical was highlighted in the failure that occurred in the £5bn CERN Large Hadron Collider in September 2008 [206]. That problem delayed the restart of the experiment at a critical point. SHM technology has the potential to benefit all sectors of industry concerned with monitoring key infrastructure (consider the most recent events concerning the Morandi Bridge in Genova, Italy). SHM provides the potential to move from time-based inspection and maintenance into condition-based maintenance approaches. The basic philosophy behind the condition-based maintenance is that a holistic and robust sensor network will monitor the system and via smart measurement processing will alert the operator about potential system abnormalities.

References

1. Farrar C, Worden K (2012) Structural health monitoring: a machine learning perspective. Wiley, Hoboken
2. Farrar CR, Worden K (2007) An introduction to structural health monitoring. R Soc Philos Trans Math Phys Eng Sci 365:303–315
3. Doebling S, Farrar C, Prime M, Shevitz D (1996) Damage identification and health monitoring of structural and mechanical systems from changes in their vibration characteristics: a literature review. Technical report. Los Alamos National Laboratories, Los Alamos
4. Wenzel H (2009) The character of SHM in civil engineering. In: Boiler C, Chang F-K, Fujino Y (eds) Encyclopedia of structural health monitoring. Wiley, Chichester, pp 2031–2037
5. Rytter A (1993) Vibrational based inspection of civil engineering structures. PhD thesis, Department of Building Technology and Structural Engineering, Aalborg University
6. Worden K, Dulieu-Barton J (2004) Damage identification in systems and structures. Int J Struct Health Monit 3:85–98
7. Randall R (2011) Vibration-based condition monitoring: industrial, aerospace and automotive applications. Wiley-Blackwell, Chichester

8. Farrar C, Doebling S, Nix D (2001) Vibration-based structural damage identification. Philos Trans R Soc A Math Phys Eng Sci 359(1778):131–149
9. Fassois S, Sakellariou J (2007) Time-series methods for fault detection and identification in vibrating structures. Philos Trans R Soc A Math Phys Eng Sci 365(1851):411–448
10. Friswell M (2007) Damage identification using inverse methods. Philos Trans R Soc A Math Phys Eng Sci 365:393–410
11. Mal A, Banerjee S, Ricci F (2007) An automated damage identification technique based on vibration and wave propagation data. Philos Trans R Soc A Math Phys Eng Sci 365:479–491
12. Staszewski W, Robertson A (2007) Time-frequency and time-scale analyses for structural health monitoring. Philos Trans R Soc A Math Phys Eng Sci 365:449–477
13. Papatheou E, Manson G, Barthorpe R, Worden K (2010) The use of pseudo-faults for novelty detection in SHM. J Sound Vib 329:2349–2366
14. Papatheou E, Manson G, Barthorpe RJ, Worden K (2014) The use of pseudo-faults for damage location in SHM: an experimental investigation on a Piper Tomahawk aircraft wing. J Sound Vib 333:971–990
15. Hayton P, Utete S, King D, King S, Anuzis P, Tarassenko L (2007) Static and dynamic novelty detection methods for jet engine health monitoring. Philos Trans R Soc A Math Phys Eng Sci 365(1851):493–514
16. Sohn H (2007) Effects of environmental and operational variability on structural health monitoring. Philos Trans R Soc A Math Phys Eng Sci 365:539
17. Worden K, Manson G (2006) The application of machine learning to structural health monitoring. Philos Trans R Soc A Math Phys Eng Sci 365(1851):515–537
18. Fuentes R (2017) On Bayesian networks for structural health and condition monitoring. PhD thesis, University of Sheffield
19. Worden K, Manson G (2007) The application of machine learning to structural health monitoring. Philos Trans R Soc A Math Phys Eng Sci 365(1851):515–537
20. Farrar C, Worden K, Park G (2010) Complexity: a new axiom for structural health monitoring? In Proceedings of 5th European workshop on structural health monitoring, Sorrento, pp 882–888
21. Boiler C, Buderath M (feb 2007) Fatigue in aerostructures - where structural health monitoring can contribute to a complex subject. Philos Trans R Soc A Math Phys Eng Sci 365:561–587
22. Sohn H, Farrar CR, Hemez F, Czarnecki J (1996) A review of structural health monitoring literature 1996–2001, Technical report. Los Alamos National Laboratory, Los Alamos
23. Oppenheim AV, Schaffer RW (1975) Digital signal processing. Prentice-Hall, Englewood Cliffe
24. Figueiredo E, Park G, Figueiras J, Farrar CR, Worden K (2009) Structural health monitoring algorithm comparisons using standard data sets: LANL report LA-14393, Technical report. Los Alamos National Laboratory, Los Alamos
25. Sohn H, Farrar C, Hunter N, Worden K (2001) Structural health monitoring using statistical pattern recognition techniques. ASME J Dyn Meas Syst Control 123:706–711
26. Yang Z, Yu Z, Sun H (oct 2007) On the cross correlation function amplitude vector and its application to structural damage detection. Mech Syst Signal Process 21:2918–2932
27. Wang L, Yang Z, Waters T (nov 2010) Structural damage detection using cross correlation functions of vibration response. J Sound Vib 329:5070–5086
28. Ng CT, Veidt M (2009) A Lamb-wave-based technique for damage detection in composite laminates. Smart Mater Struct 18:074006
29. Michaels JE (2008) Detection, localization and characterization of damage in plates with an in situ array of spatially distributed ultrasonic sensors. Smart Mater Struct 17:035035
30. Michaels J, Michaels T (2005) Detection of structural damage from the local temporal coherence of diffuse ultrasonic signals. IEEE Trans Ultrason Ferroelectr Freq Control 52:1769–1782
31. Dongarra J, Sullivan F (2000) Guest editors introduction to the top 10 algorithms. Comput Sci Eng 2:22–23

32. Salawu O (1997) Detection of structural damage through changes in frequency: a review. Eng Struct 19:718–723
33. Sampaio R, Maia N, Silva J (1999) Damage detection using the frequency-response-function curvature method. J Sound Vib 226:1029–1042
34. Kessler SS, Spearing S, Atalla MJ, Cesnik CE, Soutis C (2002) Damage detection in composite materials using frequency response methods. Compos Part B 33:87–95
35. Owolabi G, Swamidas A, Seshadri R (2003) Crack detection in beams using changes in frequencies and amplitudes of frequency response functions. J Sound Vib 265:1–22
36. Maia N, Silva J, ALMAS E, Sampaio R (2003) Damage detection in structures: from mode shape to frequency response function methods. Mech Syst Signal Process 17:489–498
37. Peng Z, Chu F (2004) Application of the wavelet transform in machine condition monitoring and fault diagnostics: a review with bibliography. Mech Syst Signal Process 18:199–221
38. Taha MMR (2006) Wavelet transform for structural health monitoring: a compendium of uses and features. Struct Health Monit 5(3):267–295
39. Nair KK, Kiremidjian AS, Law KH (2006) Time series-based damage detection and localization algorithm with application to the ASCE benchmark structure. J Sound Vib 291: 349–368
40. Krishnan Nair K, Kiremidjian AS (2007) Time series based structural damage detection algorithm using Gaussian mixtures modeling. J Dyn Syst Meas Control 129(3):285
41. Yao R, Pakzad SN (2012) Autoregressive statistical pattern recognition algorithms for damage detection in civil structures. Mech Syst Signal Process 31:355–368
42. Lu Y, Gao F (2005) A novel time-domain auto-regressive model for structural damage diagnosis. J Sound Vib 283(3–5):1031–1049
43. Shumway RH, Stoffer DS (2011) Time series analysis and its applications. Springer, New York
44. Chen S, Billings S a, Cowan CFN, Grant PM (1990) Practical identification of NARMAX models using radial basis functions. Int J Control 52(769892610):1327–1350
45. Billings S (2013) Nonlinear system identification NARMAX methods in the time, frequency, and spatio-temporal domains. Wiley, Chichester
46. Bishop C (2006) Pattern recognition and machine learning. Springer, New York
47. Rasmussen C, Williams C (2006) Gaussian processes for machine learning, vol 38. The MIT Press, Cambridge, MA
48. Worden K, Manson G, Cross EJ (2014) On Gaussian process NARX models and their higher-order frequency response functions. In: Solving computationally expensive engineering problems. Springer, Cham, pp 315–335
49. Mottershead J, Friswell M (1993) Model updating in structural dynamics: a survey. J Sound Vib 167(2):347–375
50. Cawley P, Adams RD (1979) The location of defects in structures from measurements of natural frequencies. J Strain Anal Eng Des 14:49–57
51. Pandey A, Biswas M, Samman M (1991) Damage detection from changes in curvature mode shapes. J Sound Vib 145(2):321–332
52. Hearn G, Testa RB (1991) Modal analysis for damage detection in structures. J Struct Eng 117(10):3042–3063
53. Jaishi B, Ren W-X (2006) Damage detection by finite element model updating using modal flexibility residual. J Sound Vib 290(1–2):369–387
54. Peeters B, De Roeck G (1999) Reference-based stochastic subspace identification for output-only modal analysis. Mech Syst Signal Process 13(6):855–878
55. Kaiser J (1950) Untersuchungen über das auftreten von geräuschen heim Zugversuch. PhD thesis, Technical University of Munich (TUM)
56. Fuentes R, Howard TP, Marshall MB, Cross EJ, Dwyer-Joyce RS (2016) Observations on acoustic emissions from a line contact compressed into the plastic region. Proc Inst Mech Eng J Eng Tribol 230(11):1371–1376
57. Baram J, Rosen M (1979) Fatigue life prediction by distribution analysis of acoustic emission signals. Mater Sci Eng 41(1):25–30

58. Baxter MG, Pullin R, Holford KM, Evans SL (2007) Delta T source location for acoustic emission. Mech Syst Signal Process 21(3):1512–1520
59. Hensman J, Mills R, Pierce SG, Worden K, Eaton M (2010) Locating acoustic emission sources in complex structures using Gaussian processes. Mech Syst Signal Process 24(1):211–223
60. Kurz JH, Grosse CU, Reinhardt HW (2005) Strategies for reliable automatic onset time picking of acoustic emissions and of ultrasound signals in concrete. Ultrasonics 43(7):538–546
61. Rayleigh L (1884) On waves propagating along the plane surface of an elastic solid. Proc Lond Math Soc 17:4–11
62. Lamb H (1917) On waves in an elastic plate. Proc R Soc Series A 93:93–114
63. Worden K (2001) Rayleigh and Lamb waves – basic principles. Strain 37:167–172
64. Croxford A, Wilcox P, Drinkwater B, Konstantinidis G (2007) Strategies for guided-wave structural health monitoring. Proc R Soc A Math Phys Eng Sci 463(2087):2961–2981
65. Cross E, Worden K (2011) Approaches to nonlinear cointegration with a view towards applications in SHM. In: Proceedings of 8th international conference on damage assessment – DAMAS 2011, Oxford, UK
66. Papatheou E, Dervilis N, Maguire A, Antoniadou I, Worden K (2015) A performance monitoring approach for the novel Lillgrund offshore wind farm. IEEE Trans Ind Electron 46(c):1–1
67. Zhang Y, Li J (2006) Wavelet-based vibration sensor data compression technique for civil infrastructure condition monitoring. J Comput Civ Eng 20:390–399
68. Staszewski W, Tomlinson G, Boiler C (2004) Health monitoring of aerospace structures, Smart Sensor Technologies and Signal Processing. Wiley, Hoboken
69. Candès E (2006) Compressive sampling. In: Proceedings of the international congress of mathematicians Madrid, August 22–30, 2006. European Mathematical Society Publishing House, Zurich, pp 1433–1452
70. Yuequan Bao Y, Beck JL, Li HH (2011) Compressive sampling for accelerometer signals in structural health monitoring. Struct Health Monit Int J 10:235–246
71. Mascareñas D, Cattaneo A, Theiler J, Farrar C (2013) Compressed sensing techniques for detecting damage in structures. Struct Health Monit Int J 12:325–338
72. Johnson WB, Lindenstrauss J (1984) Extensions of Lipschitz mappings into a Hilbert space. Contemp Math 26:189–206
73. Tibshirani R (1996) Regression selection and shrinkage via the lasso. J R Stat Soc B 58(1):267–288
74. Fuentes R, Mineo C, Pierce SG, Worden K, Cross EJ (2019) A probabilistic compressive sensing framework with applications to ultrasound signal processing. Mech Syst Signal Process 117:383–402
75. Rao SS (2010) Mechanical vibrations, 5th edn. Prentice Hall, Upper Saddle River
76. Särkkä S (2013) Bayesian filtering and smoothing. Cambridge University Press, Cambridge
77. Caravani P, Watson ML, Thomson WT (1977) Recursive least-squares time domain identification of structural parameters. J Appl Mech 44:135
78. Paleologu C, Benesty J, Ciochia S (2008) A robust variable forgetting factor recursive least-squares algorithm for system identification. IEEE Signal Proc Lett 15(3):597–600
79. Cooper J, Worden K (2000) On-line physical parameter estimation with adaptive forgetting factors. Mech Syst Signal Proc 14:705–730
80. Jazwinski AH (1970) Stochastic processes and filtering theory, vol 64. Academic, New York
81. Grewal MS, Andrews AP (2001) Kalman filtering: theory and practice. Wiley, Hoboken
82. Yang J, Lin S, Huang H, Zhou L (2006) An adaptive extended Kalman filter for structural damage identification. Struct Control Health Monit 13:849–867
83. Pan S, Yang J, Huang H (2007) An adaptive extended Kalman filter for structural damage identification II: unknown inputs. Struct Control Health Monit 14:497–521
84. Zhou L, Wu S, Yang JN (2008) Experimental study of an adaptive extended Kalman filter for structural damage identification. J Infrastruct Syst 14(1):42–51

85. Corigliano A, Mariani S (2004) Parameter identification in explicit structural dynamics: performance of the extended Kalman filter. Comput Methods Appl Mech Eng 193(36–38): 3807–3835
86. Mariani S, Corigliano A (2005) Impact induced composite delamination: state and parameter identification via joint and dual extended Kalman filters. Comput Methods Appl Mech Eng 194(50–52):5242–5272
87. Julier SJ, Uhlmann JK, Durrant-Whyte HF (1995) A new approach for filtering nonlinear systems. In: American control conference, proceedings of the 1995, vol 3. IEEE, pp 1628–1632
88. Julier SJ, Uhlmann JK (1997) New extension of the Kalman filter to nonlinear systems. In: Signal processing, sensor fusion, and target recognition VI, vol 3068. International Society for Optics and Photonics, pp 182–194
89. Wan EA, Van Der Merwe R (2000) The unscented Kalman filter for nonlinear estimation. In: Adaptive systems for signal processing, communications, and control symposium 2000. AS-SPCC. The IEEE 2000. IEEE, pp 153–158
90. LaViola JJ (2003) A comparison of unscented and extended Kalman filtering for estimating quaternion motion. In: American control conference, 2003. Proceedings of the 2003, vol 3. IEEE, pp 2435–2440
91. St-Pierre M, Gingras D (2004) Comparison between the unscented Kalman filter and the extended Kalman filter for the position estimation module of an integrated navigation information system. In: IEEE intelligent vehicles symposium. CiteSeerX, pp 831–835
92. Gustafsson F, Hendeby G (2012) Some relations between extended and unscented Kalman filters. IEEE Trans Signal Process 60(2):545–555
93. Wu M, Smyth AW (2007) Application of the unscented Kalman filter for real-time nonlinear structural system identification. Struct Control Health Monitor 14(7):971–990
94. Chatzi EN, Smyth AW (2009) The unscented Kalman filter and particle filter methods for nonlinear structural system identification with non-collocated heterogeneous sensing. Struct Control Health Monitor 16(1):99–123
95. Eftekhar Azam S, Ghisi A, Mariani S (2012) Parallelized sigma-point Kalman filtering for structural dynamics. Comput Struct 92-93:193–205
96. Mariani S, Ghisi A (2007) Unscented Kalman filtering for nonlinear structural dynamics. Nonlinear Dyn 49(1–2):131–150
97. Xie Z, Feng J (2012) Real-time nonlinear structural system identification via iterated unscented Kalman filter. Mech Syst Signal Process 28:309–322
98. Doucet A, Johansen AM (2009) A tutorial on particle filtering and smoothing: fifteen years later. Handb Nonlin Filter 12(656–704):3
99. Crisan D, Doucet A (2002) A survey of convergence results on particle filtering methods for practitioners. IEEE Trans Signal Process 50(3):736–746
100. Hu X-L, Schön T, Ljung L (2008) A basic convergence result for particle filtering. IEEE Trans Signal Process 56(4):1337–1348
101. Gordon NJ, Salmond DJ, Smith AF (1993) Novel approach to nonlinear/non-Gaussian Bayesian state estimation. IEE Proc F (Radar Signal Proc) 140(2):107–113
102. Pitt MK, Shephard N (1999) Filtering via simulation: auxiliary particle filters. J Am Stat Assoc 94(446):590–599
103. Douc R, Cappé O (2005) Comparison of resampling schemes for particle filtering. In: Image and signal processing and analysis, 2005. ISPA 2005. Proceedings of the 4th international symposium on. IEEE, pp 64–69
104. Hoi JD, Schon TB, Gustafsson F (2006) On resampling algorithms for particle filters. In: Nonlinear statistical signal processing workshop, 2006 IEEE. IEEE, pp 79–82
105. Chatzi E, Smyth A (2013) Particle filter scheme with mutation for the estimation of time-invariant parameters in structural health monitoring applications. Struct Control Health Monit 20:1081–1095
106. Corbetta M, Sbarufatti C, Manes A, Giglio M (2013) Stochastic definition of state-space equation for particle filtering algorithms. Chem Eng Trans:1–6

107. Corbetta M, Sbarufatti C, Giglio M, Todd MD (2018) Optimization of nonlinear, non-Gaussian Bayesian filtering for diagnosis and prognosis of monotonic degradation processes. Mech Syst Signal Process 104:305–322
108. Sbarufatti C, Corbetta M, Giglio M, Cadini F (2017) Adaptive prognosis of lithium-ion batteries based on the combination of particle filters and radial basis function neural networks. J Power Sources 344:128–140
109. Xue S, Tang H, Xie Q (2009) Structural damage detection using auxiliary particle filtering method. Struct Health Monit 8(2):101–112
110. Ching J, Beck JL, Porter KA (2006) Bayesian state and parameter estimation of uncertain dynamical systems. Probabilist Eng Mech 21(1):81–96
111. Andrieu C, Doucet A, Holenstein R (2010) Particle Markov chain Monte Carlo methods. J R Stat Soc B Stat Methodol 72(3):269–342
112. Rippengill S, Worden K, Holford KM, Pullin R (2003) Automatic classification of acoustic emission patterns. Strain 39:31–41
113. Manson G, Worden K, Holford K, Pullin R (2001) Visualisation and dimension reduction of acoustic emission data for damage detection. J Intell Mater Syst Struct 12:529–536
114. Farrar CR, Worden K (2012) Structural health monitoring: a machine learning perspective. Wiley, Hoboken
115. Bishop CM (2006) Pattern recognition and machine learning. Springer, Berlin
116. Worden K, Manson G, Fieller NR (2000) Damage detection using outlier analysis. J Sound Vib 229(3):647–667
117. Dervilis N, Cross E, Barthorpe R, Worden K (2014) Robust methods of inclusive outlier analysis for structural health monitoring. J Sound Vib 333(20):5181–5195
118. Hawkins DM (1980) Identification of outliers. Springer, Dordrecht
119. Rousseeuw PJ, Leroy AM (2005) Robust regression and outlier detection. Wiley, New York
120. Hubert M, Debruyne M (2010) Minimum covariance determinant. Wiley Interdiscip Rev Comput Stat 2(1):36–43
121. Van Aelst S, Rousseeuw P (2009) Minimum volume ellipsoid. Wiley Interdiscip Rev Comput Stat 1(1):71–82
122. Papatheou E, Dervilis N, Maguire AE, Campos C, Antoniadou I, Worden K (2017) Performance monitoring of a wind turbine using extreme function theory. Renew Energy 113:1490–1502
123. Moya MM, Koch MW, Hostetler LD (1993) One-class classifier networks for target recognition applications. Proc World Congr Neural Netw:359–367
124. Zimek A, Gaudet M, Campello RJ, Sander J (2013) Subsampling for efficient and effective unsupervised outlier detection ensembles. In: Proceedings of the 19th ACM SIGKDD international conference on knowledge discovery and data mining. ACM, pp 428–436
125. Rousseeuw PJ, Driessen KV (1999) A fast algorithm for the minimum covariance determinant estimator. Technometrics 41(3):212–223
126. Murphy KP (2012) Machine learning: a probabilistic perspective. MIT Press, Cambridge, MA
127. Gelman A, Carlin J, Rubin D, Vehtari A, Dunson D, Stern H (2013) Bayesian data analysis, 3rd edn. CRC Press, New York
128. Beyer K, Goldstein J, Ramakrishnan R, Shaft U (1999) When is "nearest neighbor" meaningful? In: Database theory – ICDT'99. Springer, Berlin/Heidelberg, pp 217–235
129. Manson G, Worden K, Allman D (2003) Experimental validation of a structural health monitoring methodology: part III. Damage location on an aircraft wing. J Sound Vib 259(2):365–385
130. Worden K, Manson G, Hilson G, Pierce S (2008) Genetic optimisation of a neural damage locator. J Sound Vib 309(3):529–544
131. Dervilis N (2013) A machine learning approach to structural health monitoring with a view towards wind turbines. PhD thesis, University of Sheffield
132. Bull L, Worden K, Manson G, Dervilis N (2018) Active learning for semi-supervised structural health monitoring. J Sound Vib 437:373–388

133. Rogers TJ, Worden K, Fuentes R, Dervilis N, Tygesen UT, Cross EJ (2019) A Bayesian non-parametric clustering approach for semi-supervised structural health monitoring. Mech Syst Signal Process 119:100–119
134. Farrar C, Sohn H, Worden K (2001) Data normalization: a key for structural health monitoring, technical report. Los Alamos National Laboratory, Los Alamos
135. Alampalli S (2000) Effects of testing, analysis, damage, and environment on modal parameters. Mech Syst Signal Process 14(1):63–74
136. Cornwell P, Farrar CR, Doebling SW, Sohn H (1999) Environmental variability of modal properties. Exp Tech 23(6):45–48
137. Peeters B, Roeck GD (2001) One-year monitoring of the Z24-bridge: environmental effects versus damage events. Earthq Eng Struct Dyn 30:149–171
138. Sohn H, Dzwonczyk M, Straser EG, Kiremidjian AS, Law KH, Meng T (1999) An experimental study of temperature effect on modal parameters of the Alamosa canyon bridge. Earthq Eng Struct Dyn 28(8):879–897
139. Moser P, Moaveni B (2011) Environmental effects on the identified natural frequencies of the Dowling hall footbridge. Mech Syst Signal Process 25(7):2336–2357
140. Xu Y, Chen B, Ng C, Wong K, Chan W (2010) Monitoring temperature effect on a long suspension bridge. Struct Control Health Monit 17(6):632–653
141. Cao Y, Yim J, Zhao Y, Wang ML (2011) Temperature effects on cable stayed bridge using health monitoring system: a case study. Struct Health Monit 10(5):523–537
142. de Battista N, Brownjohn JM, Tan HP, Koo K-Y (2015) Measuring and modelling the thermal performance of the Tamar suspension bridge using a wireless sensor network. Struct Infrastruct Eng 11(2):176–193
143. Mahmoud M, Abe M, Fujino Y (2001) Analysis of suspension bridge by ambient vibration measurement using time domain method and its application to health monitoring. In: Proceedings of the international modal analysis conference-IMAC, vol 1. Society for Experimental Mechanics, pp 504–510
144. Cross E, Koo K-Y, Brownjohn J, Worden K (2013) Long-term monitoring and data analysis of the Tamar bridge. Mech Syst Signal Process 35:16–34
145. Xia Y, Hao H, Zanardo G, Deeks A (2006) Long term vibration monitoring of an rc slab: temperature and humidity effect. Eng Struct 28(3):441–452
146. Kim C-Y, Jung D-S, Kim N-S, Kwon S-D, Feng MQ (2003) Effect of vehicle weight on natural frequencies of bridges measured from traffic-induced vibration. Earthq Eng Eng Vib 2(1):109–115
147. Lanata F, Schoefs F (2011) Multi-algorithm approach for identification of structural behavior of complex structures under cyclic environmental loading. Struct Health Monit 11: 51–67
148. Sohn H, Dzwonczyk M, Straser E, Law K, Meng T, Kiremidjian A (1998) Adaptive modeling of environmental effects in modal parameters for damage detection in civil structures. In: Smart systems for bridges, structures, and highways, pp 127–138
149. Moaveni B, He X, Conte J, Fraser M, Elgamal A (2009) Uncertainty analysis of Voigt bridge modal parameters due to changing environmental condition. In: Proceedings of international conference on modal analysis (IMAC-XXVII)
150. Ni Y, Hua X, Fan K, Ko J (2005) Correlating modal properties with temperature using long-term monitoring data and support vector machine technique. Eng Struct 27(12):1762–1773
151. Hua X, Ni Y, Ko J, Wong K (2007) Modeling of temperature–frequency correlation using combined principal component analysis and support vector regression technique. J Comput Civ Eng 21:122
152. Ni Y, Zhou H, Ko J (2009) Generalization capability of neural network models for temperature-frequency correlation using monitoring data. J Struct Eng 135(10):1290–1300
153. Worden K, Sohn H, Farrar C (2002) Novelty detection in a changing environment: regression and interpolation approaches. J Sound Vib 258(4):741–761
154. Worden K, Cross E (2018) On switching response surface models, with applications to the structural health monitoring of bridges. Mech Syst Signal Process 98:139–156

155. Dervilis N, Shi H, Worden K, Cross E (2016) Exploring environmental and operational variations in SHM data using heteroscedastic Gaussian processes. In: Dynamics of civil structures, vol 2. Springer, New York, pp 145–153
156. Surace C, Worden K (1997) Some aspects of novelty detection methods. In: Proceedings of the third international conference on modern practice in stress and vibration analysis, Dublin
157. Cross E, Manson G, Worden K, Pierce S (2012) Features for damage detection with insensitivity to environmental and operational variations. Proc R Soci A rspa20120031
158. Kullaa J (2011) Distinguishing between sensor fault, structural damage, and environmental or operational effects in structural health monitoring. Mech Syst Signal Process 25(8):1–8
159. Manson G (2002) Identifying damage sensitive, environment insensitive features for damage detection. In: Proceedings of the IES conference
160. Yan A, Kerschen G, De Boe P, Golinval J (2005) Structural damage diagnosis under varying environmental conditions part I: a linear analysis. Mech Syst Signal Process 19(4):847–864
161. Kullaa J (2004) Structural health monitoring under variable environmental or operational conditions. In: Proceedings of the 2nd European workshop on structural health monitoring
162. Shi H (2018) On nonlinear cointegration methods for structural health monitoring. PhD thesis, University of Sheffield
163. Yan A-M, Kerschen G, Boe PD, Golinval J-C (2005) Structural damage diagnosis under varying environmental conditions part II: local PCA for non-linear cases. Mech Syst Signal Process 19:865–880
164. Sohn H, Worden K, Farrar C (2002) Statistical damage classification under changing environmental and operational conditions. J Intell Mater Syst Struct 13(9):561
165. Dervilis N, Choi M, Taylor S, Barthorpe R, Park G, Farrar C, Worden K (2014) On damage diagnosis for a wind turbine blade using pattern recognition. J Sound Vib 333(6):1833–1850
166. Shi H, Worden K, Cross E (2016) A nonlinear cointegration approach with applications to structural health monitoring. In: Journal of Physics: Conference Series, vol 744, IOP Publishing, p 012025
167. Shi H, Worden K, Cross E (2018) A regime-switching cointegration approach for removing environmental and operational variations in structural health monitoring. Mech Syst Signal Process 103:381–397
168. Rogers T, Worden K, Fuentes R, Dervilis N, Tygesen U, Cross E (2019) A Bayesian non-parametric clustering approach for semi-supervised structural health monitoring. Mech Syst Signal Process 119:100–119
169. Cross EJ, Worden K, Chen Q (2011) Cointegration: a novel approach for the removal of environmental trends in structural health monitoring data. Proc R Soc Lond A Math Phys Eng Sci 467:2712–2732
170. Koo K-Y, Brownjohn J, List D, Cole R (2013) Structural health monitoring of the Tamar suspension bridge. Struct Control Health Monit 20(4):609–625
171. Cross E (2012) On structural health monitoring in changing environmental and operational conditions. PhD thesis, University of Sheffield
172. Dickey D, Fuller W (1979) Distribution of the estimators for autoregressive time series with a unit root. J Am Stat Assoc 74:427–431
173. Dickey D, Fuller W (1981) Likelihood ratio statistics for autoregressive time series with a unit root. Econometrica 49(4):1057–1072
174. Engle R, Granger C Cointegration and error correction: representation, estimation and testing. Econometrica 55(2):251–276
175. Johansen S (1988) Statistical analysis of cointegration vectors. J Econ Dyn Control 12(2–3): 231–254
176. Pierce SG, Dong F, Atherton K, Culshaw B, Worden K, Manson G, Monnier T, Guy P, Baboux J-C, Assad J et al (2001) Damage assessment in smart composite structures: the Damascos program. In: Smart structures and materials 2001: smart structures and integrated systems, vol 4327. International Society for Optics and Photonics, Bellingham, pp 223–234
177. Fan W, Qiao P (2011) Vibration-based damage identification methods: a review and comparative study. Struct Health Monit 10(1):83–111

178. Farrar C, Worden K (2013) Structural health monitoring: a machine learning perspective. Wiley, Chichester
179. Vagnoli M, Remenyte-Prescott R, Andrews J (2018) Railway bridge structural health monitoring and fault detection: state-of-the-art methods and future challenges. Struct Health Monit 17(4):971–1007
180. Friswell MI, Mottershead JE (2001) Inverse methods in structural health monitoring. Key Eng Mater 204–205:201–210
181. Barthorpe RJ (2011) On model- and data-based approaches to structural health monitoring. PhD thesis, University of Sheffield
182. Gardner P, Lord C, Barthorpe RJ (2018) A probabilistic framework for forward model-driven SHM. In: European Workshop on Structural Health Monitoring (EWHSM), pp 1–13
183. Gorl E, Link M (2003) Damage identification using changes of Eigen frequencies and mode shapes. Mech Syst Signal Process 17(1):103–110
184. Farrar CR, Lieven NA (2007) Damage prognosis: The future of structural health monitoring. Philos Trans R Soc A Math Phys Eng Sci 365:623–632
185. Friswell M, Mottershead J (1995) Finite element model updating in structural dynamics. Springer, New York
186. Friswell MI, Mottershead JE (2001) Physical understanding of structures by model updating. In: Proceedings of international conference on structural system identification, pp 81–96
187. Mottershead JE, Link M, Friswell MI (2011) The sensitivity method in finite element model updating: a tutorial. Mech Syst Signal Process 25(7):2275–2296
188. Jaishi B, Ren W-X (2005) Structural finite element model updating using ambient vibration test results. J Struct Eng 131(4):617–628
189. Simoen E, De Roeck G, Lombaert G (2015) Dealing with uncertainty in model updating for damage assessment: a review. Mech Syst Signal Process 56:123–149
190. Haag T, Carvajal González S, Hanss M (2012) Model validation and selection based on inverse fuzzy arithmetic. Mech Syst Signal Process 32:116–134
191. Rasmussen C, Ghahramani Z (2001) Occam's razor. In: Advances in neural information processing systems 13: proceedings of the 2000 conference, p 294
192. Beck JL, Katafygiotis LS (1998) Updating models and their uncertainties. I: Bayesian statistical framework. J Eng Mech 124(4):455–461
193. Katafygiotis LS, Beck JL (1998) Updating models and their uncertainties. II: model identifiability. J Eng Mech 124(4):463–467
194. Friswell MI, Penny JET, Garvey SD (1997) Parameter subset selection in damage location. Inverse Probl Eng 5(3):189–215
195. Friswell MI, Mottershead JE, Ahmadian H (1998) Combining subset selection and parameter constraints in model updating. J Vib Acoust Trans ASME 120:854–859
196. Ko JM, Sun ZG, Ni YQ (2002) Multi-stage identification scheme for detecting damage in cable-stayed Kap Shui Mun bridge. Eng Struct 24(7):857–868
197. Lee JJ, Lee JW, Yi JH, Yun CB, Jung HY (2005) Neural networks-based damage detection for bridges considering errors in baseline finite element models. J Sound Vib 280(3–5): 555–578
198. Satpal SB, Guha A, Banerjee S (2016) Damage identification in aluminum beams using support vector machine: numerical and experimental studies. Struct Control Health Monit 23:446–457
199. Hariri-Ardebili MA, Pourkamali-Anaraki F (2018) Support vector machine based reliability analysis of concrete dams. Soil Dyn Earthq Eng 104:276–295
200. Nagel JB, Sudret B (2016) A unified framework for multilevel uncertainty quantification in Bayesian inverse problems. Probabilistic Engineering Mechanics 43:68–84
201. Li C, Mahadevan S (2016) Role of calibration, validation, and relevance in multilevel uncertainty integration. Reliab Eng Syst Saf 148:32–43
202. Gardner P, Lord C, Barthorpe RJ (2018) A multi-level uncertainty integration strategy for forward model-driven SHM. In: Proceedings of the international conference on noise and vibration engineering, pp 3681–3692

203. Kennedy MC, O'Hagan A (2001) Bayesian calibration of computer models. J R Stat Soc B Stat Methodol 63(3):425–464
204. Gardner P, Lord C, Barthorpe RJ (2017) Bayesian calibration and bias correction for forward model-driven SHM. In: Proceedings of the 11th international workshop on structural health monitoring, pp 2019–2027
205. Gardner P, Lord C, Barthorpe RJ (2018) Bayesian history matching for forward model-driven structural health monitoring. In: Proceedings of IMAC XXXVI
206. Fault shuts large hadron collider for two months. The Guardian 2017

Experimental Dynamic Substructures

19

Randall L. Mayes and Matthew S. Allen

Contents

R. Mayes (✉)
Sandia National Laboratories, Albuquerque, NM, USA
e-mail: rajnd75@msn.com

M. Allen
Department of Engineering Physics, University of Wisconsin, Madison, WI, USA
e-mail: msallen@engr.wisc.edu

R. Allemang, P. Avitabile (eds.), *Handbook of Experimental Structural Dynamics*,
https://doi.org/10.1007/978-1-4614-4547-0_24

Abstract

This chapter deals with experimental dynamic substructures which are reduced order models that can be coupled with each other or with finite element derived substructures to estimate the system response of the coupled substructures. A unifying theoretical framework in the physical, modal or frequency domain is reviewed with examples. The major issues that have hindered experimental based substructures are addressed. An example is demonstrated with the transmission simulator method that overcomes the major historical difficulties. Guidelines for the transmission simulator design are presented.

Keywords

Experimental dynamic substructuring · Component mode synthesis · Frequency based substructures · Transmission simulator · Experimental models · Reduced order models

Nomenclature

FRF	Frequency response function
RMS	Root mean square
DOF	Degree of freedom
g	Connection force at a single connection DOF
u	Physical displacement of a single DOF
ω	Frequency in radians per second
$\mathbf{B}$	Matrix associated with compatibility of connected DOF
$\mathbf{L}$	Matrix associated with equilibrium forces of connected DOF
$\mathbf{Y}$	Frequency response function matrix
$\mathbf{\Phi}$	Mode shape matrix
$\overline{\mathbf{u}}$	Vector of displacements
$\overline{\mathbf{g}}$	Vector of connection forces
$\overline{\mathbf{q}}$	Vector of non-redundant connection DOF (physical or generalized coordinates)
$\overline{\xi}$	Vector of generalized modal DOF
†	Superscript indicating the Moore-Penrose pseudo-inverse of a matrix

1 Introduction

An experimental dynamic substructure is an experimentally derived model of some convenient portion of a structure. The substructure can only capture the response of the subsystem in a finite frequency band. The model input and response is generally defined only for locations where sensors obtain information on the subsystem. All the substructures of a system can be combined to simulate the full system response over a finite frequency band. Figure 1 shows an example using the SEM substructuring testbed, in which a substructure from a finite element model is combined with an experimental substructure to obtain the full system response.

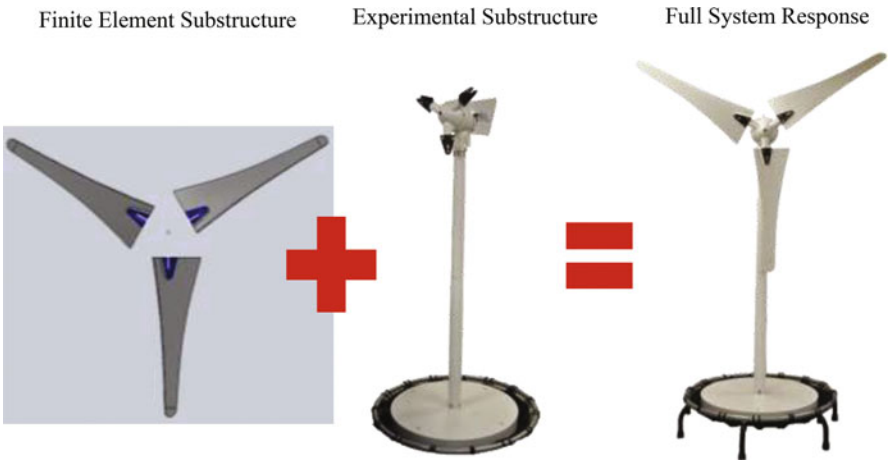

Fig. 1 Substructures from FE and experiment combined to obtain full system response of SEM testbed

Analytical substructures have been used for decades. Usually they are reduced order models of the subsystems derived from finite element models of the subsystems. Because they are reduced order models, when they are combined to simulate the response of the full system, they often reduce the computational burden by many orders of magnitude compared to the full system finite element model.

In addition to their computational advantage, substructures can be developed and shared by different organizations to obtain full system response. Important local dynamics can often be observed in the substructure alone that might be masked in the full system model response.

Experimental substructures share some of the advantages above and in some cases may provide a cheaper or more accurate solution than can be obtained from first principles models. If hardware is available, an experimental substructure may be extracted from an appropriate experiment.

While the experimental dynamic substructuring concept has been around for decades, early attempts revealed that accurate experimental substructures can be difficult to obtain because of several challenges that will be addressed in this chapter. Since about 2005, new approaches have been developed which are overcoming many of these challenges. Most of the work has been with linear substructures.

2 Experimental Substructure Technology

Over the years, many different substructure technologies have developed. Some approaches utilize physical degrees of freedom (DOF), generalized DOF, frequency response or impedance functions, and even state space formulations. These different

representations used to be considered almost different technologies, but they are actually related. Here we utilize a general framework [1] since this terminology shows the relationship between different approaches. The general framework matrix definitions will be clearly illustrated with simple models to show how two substructures can be combined to represent the full system in the physical, modal, and frequency domains.

2.1 Connecting Substructures with Compatibility and/or Equilibrium Equations

Whether substructuring is analytical or experimental, it is required that compatibility and force equilibrium be enforced between the boundaries of the substructures to simulate full system response. If we consider two substructures formulated with their physical DOF, compatibility can be expressed for any two connected DOF as

$$u^1 - u^2 = 0 \tag{1}$$

where u represents the scalar displacement of the connection DOF and the superscript denotes the substructure. This forces these two DOF to have the same displacement. In the general framework, all the compatibility equations can be written as a matrix equation as

$$\mathbf{B}\overline{\mathbf{u}} = \mathbf{0} \tag{2}$$

where the $\mathbf{B}$ matrix typically contains either -1, 0, or 1 in all its elements.

Force equilibrium for any two connected DOF can be expressed as

$$g^1 + g^2 = 0 \tag{3}$$

where the g values represent the amplitude of the equal and opposite connection forces on each substructure. In the general framework, another matrix equation can describe all the equilibrium equations for all connection forces as

$$\mathbf{L}^{\mathrm{T}}\overline{\mathbf{g}} = \mathbf{0} \tag{4}$$

where $\mathbf{L}$ is another Boolean matrix with either 0 or 1 in all its elements and superscript T denotes the matrix transpose.

A special property relates $\mathbf{B}$ and $\mathbf{L}$ which helps establish relationship between substructuring approaches that emphasize either compatibility or equilibrium. This can be derived by using the so-called primal form of substructuring to eliminate redundant DOF. Mathematically this is stated

$$\bar{\mathbf{u}} = \mathbf{L}\bar{\mathbf{q}} \tag{5}$$

where $\mathbf{q}$ is a subset of $\mathbf{u}$ that eliminates redundant attached DOF. Combining Eqs. (2) and (5) gives

$$\mathbf{BL}\bar{\mathbf{q}} = \mathbf{0}. \tag{6}$$

Since the vector $\mathbf{q}$ can have an infinite number of solutions depending on the excitation forces applied to the system, it is required that

$$\mathbf{BL} = \mathbf{0} \tag{7}$$

enforcing the rows of $\mathbf{B}$ to be orthogonal to the columns of $\mathbf{L}$. This property is sometimes stated that $\mathbf{L}$ is in the null space of $\mathbf{B}$. Many linear algebra tools have a programmed function that finds the null space of another matrix. (For example, in MATLAB L = null(B) can be used to find $\mathbf{L}$.) Hence, one knows $\mathbf{L}$ if $\mathbf{B}$ has been established, or vice versa.

The principles of displacement compatibility and force equilibrium between the boundary DOF of connected substructures are foundational to all substructuring technologies. The $\mathbf{B}$ and $\mathbf{L}$ matrices are found in every substructuring approach in the general framework, showing how the different approaches are related. In the next sections, we will demonstrate these principles for substructures in the physical, modal, and frequency domains to connect two simple substructures.

2.2 Connecting Substructures in the Physical Domain

Consider the two substructures in Fig. 2, which consist of two masses and a spring with the values given in Table 1. The goal is to connect DOF u_2 to u_3 to get response of the full system.

Compatibility to combine these two substructures would be written with the boundary DOF as

$$u_2 - u_3 = 0 \tag{8}$$

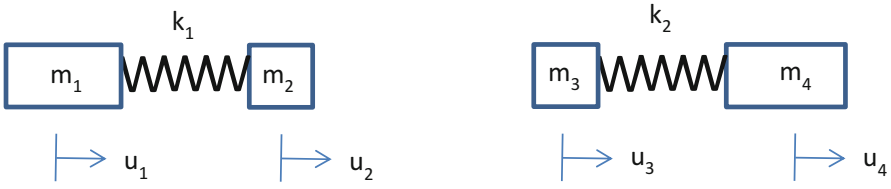

Fig. 2 Two simple substructures – constrain displacement of m_2 to displacement of m_3 to get full system response

Table 1 Mass and stiffness for two substructures

m1 = 1	k1 = 1.317e5
m2 = 0.7	k2 = 5.1681e4
m3 = 0.1	
m4 = 1	

which can be put into the form of Eq. (2) as

$$\mathbf{B}\bar{\mathbf{u}} = [0 \;\; 1 \;\; -1 \;\; 0] \begin{Bmatrix} u_1 \\ u_2 \\ u_3 \\ u_4 \end{Bmatrix} = 0 \tag{9}$$

which is sometimes called the constraint equation. Here there is only one constraint, so **B** has only one row, but normally there are several constraints. Construct a Boolean **L** matrix to eliminate u_3. This would conform to Eq. (5) as

$$\begin{gathered} \bar{\mathbf{u}} = \mathbf{L}\bar{\mathbf{q}} \\ \begin{Bmatrix} u_1 \\ u_2 \\ u_3 \\ u_4 \end{Bmatrix} = \begin{bmatrix} 1 & 0 & 0 \\ 0 & 1 & 0 \\ 0 & 1 & 0 \\ 0 & 0 & 1 \end{bmatrix} \begin{Bmatrix} u_1 \\ u_2 \\ u_4 \end{Bmatrix} \end{gathered} \tag{10}$$

so that the reduced **q** vector now contains only u_1, u_2, and u_4 (since $u_3 = u_4$). By Eq. (4), **L** should provide force equilibrium as

$$\mathbf{L}^{\mathrm{T}}\bar{\mathbf{g}} = \begin{bmatrix} 1 & 0 & 0 & 0 \\ 0 & 1 & 1 & 0 \\ 0 & 0 & 0 & 1 \end{bmatrix} \begin{Bmatrix} g_1 \\ g_2 \\ g_3 \\ g_4 \end{Bmatrix} = \begin{Bmatrix} 0 \\ 0 \\ 0 \end{Bmatrix} \tag{11}$$

which specifies that the constraint forces on mass 1 and 4, g_1 and g_4, $= 0$ and the constraint forces on mass 2 and 3 must be equal and opposite, $g_2 + g_3 = 0$. One can also check to see that **L** is in the null space of **B** according to Eq. (7) so that the constraint, Eq. (6), is still satisfied. The equations of motion can be written in a block diagonal form as

$$\begin{bmatrix} \mathbf{M^1} & \mathbf{0} \\ \mathbf{0} & \mathbf{M^2} \end{bmatrix} \begin{Bmatrix} \ddot{\bar{\mathbf{u}}}^1 \\ \ddot{\bar{\mathbf{u}}}^2 \end{Bmatrix} + \begin{bmatrix} \mathbf{K^1} & \mathbf{0} \\ \mathbf{0} & \mathbf{K^2} \end{bmatrix} \begin{Bmatrix} \bar{\mathbf{u}}^1 \\ \bar{\mathbf{u}}^2 \end{Bmatrix} = \begin{Bmatrix} \bar{\mathbf{f}}^1 \\ \bar{\mathbf{f}}^2 \end{Bmatrix} + \begin{Bmatrix} \bar{\mathbf{g}}^1 \\ \bar{\mathbf{g}}^2 \end{Bmatrix} \tag{12}$$

with the superscripts representing the values associated with the two different substructures, and the **f** vectors represent the external forces. Damping could easily be included, but we neglect these terms to save space when all elements

of the matrices are written in the examples below. This is in the dual form which includes all DOF for both substructures. To obtain the primal form which eliminates redundant (connected) DOF, substitute for the **u** vector from Eq. (10) and premultiply by $\mathbf{L}^{\mathrm{T}}$ to get

$$\mathbf{L}^{\mathrm{T}}\begin{bmatrix}\mathbf{M^1} & \mathbf{0}\\ \mathbf{0} & \mathbf{M^2}\end{bmatrix}\mathbf{L}\ddot{\overline{\mathbf{q}}}+\mathbf{L}^{\mathrm{T}}\begin{bmatrix}\mathbf{K^1} & \mathbf{0}\\ \mathbf{0} & \mathbf{K^2}\end{bmatrix}\mathbf{L}\overline{\mathbf{q}}=\mathbf{L}^{\mathrm{T}}\begin{Bmatrix}\vec{\mathbf{f}}^{\mathbf{1}}\\ \vec{\mathbf{f}}^{\mathbf{2}}\end{Bmatrix}+\mathbf{L}^{\mathrm{T}}\begin{Bmatrix}\vec{\mathbf{g}}^{\mathbf{1}}\\ \vec{\mathbf{g}}^{\mathbf{2}}\end{Bmatrix} \tag{13}$$

which can be expanded with our values for **L**, **q**, and the two substructures as

$$\begin{bmatrix}1&0&0&0\\0&1&1&0\\0&0&0&1\end{bmatrix}\begin{bmatrix}m_1&0&0&0\\0&m_2&0&0\\0&0&m_3&0\\0&0&0&m_4\end{bmatrix}\begin{bmatrix}1&0&0\\0&1&0\\0&1&0\\0&0&1\end{bmatrix}\begin{Bmatrix}\ddot{u}_1\\ \ddot{u}_2\\ \ddot{u}_4\end{Bmatrix}+$$
$$\begin{bmatrix}1&0&0&0\\0&1&1&0\\0&0&0&1\end{bmatrix}\begin{bmatrix}k_1&-k_1&0&0\\-k_1&k_1&0&0\\0&0&k_2&-k_2\\0&0&-k_2&k_2\end{bmatrix}\begin{bmatrix}1&0&0\\0&1&0\\0&1&0\\0&0&1\end{bmatrix}\begin{Bmatrix}u_1\\ u_2\\ u_4\end{Bmatrix}=\begin{bmatrix}1&0&0&0\\0&1&1&0\\0&0&0&1\end{bmatrix}\begin{Bmatrix}f_1\\ f_2\\ f_3\\ f_4\end{Bmatrix}+\begin{bmatrix}0\\0\\0\end{bmatrix} \tag{14}$$

which now represents the primal form of the full system with the substructures attached. Note the far right-hand term goes to zero in accordance with Eq. (11), because the internal connection forces are in equilibrium. Completing the multiplication gives

$$\begin{bmatrix}m_1&0&0\\0&(m_2+m_3)&0\\0&0&m_4\end{bmatrix}\begin{Bmatrix}\ddot{u}_1\\ \ddot{u}_2\\ \ddot{u}_4\end{Bmatrix}+\begin{bmatrix}k_1&-k_1&0\\-k_1&(k_1+k_2)&-k_2\\0&-k_2&k_2\end{bmatrix}\begin{Bmatrix}u_1\\ u_2\\ u_4\end{Bmatrix}=\begin{Bmatrix}f_1\\ f_2+f_3\\ f_4\end{Bmatrix} \tag{15}$$

which provides the coupled system equations of motion in the physical domain, without the redundant DOF u_3. The matrices that come from compatibility and equilibrium, **B** and $\mathbf{L}^T$, are used in various ways in the physical, modal, and frequency domains for various methods of substructuring. Because of the various formulations and methods to minimize the experimental errors in experimental substructuring, the form of **B** and **L** may be modified, but there is always some enforcement of compatibility and equilibrium. Solving the eigenvalue problem from Eq. (15) gives natural frequencies and mass-normalized mode shapes of the assembled system that are listed in Table 2.

Table 2 Mode shapes for coupled physical system

u_1	−0.5976	−0.5699	−0.5639
$u_2 = u_3$	−0.5976	−0.2695	0.9057
u_4	−0.5976	0.7855	−0.1606
Frequency (Hz)	0	41.93	93.23

2.3 Connecting Substructures in the Modal Domain: Component Mode Synthesis

There are multiple linear substructure formulations in the modal domain. Each formulation approximates the motion with a (usually) reduced number of DOF pertaining to shape functions that can be superimposed to approximate the actual. Typical types of shapes associated with the DOF might include vibration mode shapes with free boundary conditions, mode shapes with constraints at the interface, or static deflection shapes with constraints. Component Mode Synthesis (CMS) is the general class of this type of substructuring. It is used in analytical substructures, but is a very common approach for experimental substructures since modal DOF and mode shapes are extracted from a modal test. Because mode shapes are orthogonal with respect to the mass and stiffness matrices, the modal mass and stiffness matrices have the nice property of being diagonal or uncoupled.

The example from the previous section using two substructures will be utilized again to illustrate the concepts, but now we shall assume that substructure 1 is derived from a FE model and substructure 2 is derived from a modal test with free boundary conditions. Both substructures will be described in terms of their free modal DOF and free mode shapes. Analytical substructure 1 is derived from an eigenvalue analysis, and the experimental substructure 2 is obtained from a modal test.

One decision that is made early in the CMS process is what is the frequency band for the analytical eigenvalue analysis for the first substructure and for the modal test of the second substructure. Here we assume that 100 Hz is chosen as the highest frequency for which modes will be calculated or extracted for both substructures. CMS always provides an approximate solution, which assumes the effects of modes above the cutoff frequency (100 Hz for this example) are not of great importance. The error associated with neglecting higher-frequency modes is called modal truncation error. Performing the eigenvalue analysis on substructure 1 and a modal test on softly suspended substructure 2 with accelerometers on m_3 and m_4, we obtain the frequency and mode shape information in Tables 3 and 4. The mode shapes are mass-normalized, i.e., $\overline{\mathbf{\Phi}}_r^{\mathrm{T}}\mathbf{M}\overline{\mathbf{\Phi}}_r = 1$ for every mode r derived from the analysis. Note that the modal test did not extract the elastic mode, because it was above the chosen bandwidth of 100 Hz. We will consider the effect of using only the rigid body mode for substructure 2 in this example.

Table 3 Frequencies of substructures

Mode #	Analytical substructure 1 frequency (Hz)	Experimental substructure 2 frequency (Hz)
1	0	0
2	90.00	Above 100 Hz

Table 4 Mass-normalized mode shapes for two substructures

	Analytical mode #	1	2	Experimental mode #	1
DOF	u_1	0.767	−0.642	u_3	0.954
DOF	u_2	0.767	0.917	u_4	0.954

To derive the **B** and **L** compatibility and equilibrium matrices in the modal domain, start with the physical DOF of Eq. (9) which is repeated here as

$$\mathbf{B}\overline{\mathbf{u}} = \begin{bmatrix} 0 & 1 & -1 & 0 \end{bmatrix} \begin{Bmatrix} u_1 \\ u_2 \\ u_3 \\ u_4 \end{Bmatrix} = 0 \tag{16}$$

but the modal estimate of these DOF is

$$\begin{Bmatrix} u_1 \\ u_2 \\ u_3 \\ u_4 \end{Bmatrix} = \begin{bmatrix} \mathbf{\Phi}^1 & 0 \\ 0 & \mathbf{\Phi}^2 \end{bmatrix} \begin{Bmatrix} \overline{\xi}^1 \\ \overline{\xi}^2 \end{Bmatrix} \tag{17}$$

where the superscripts denote the substructure, $\mathbf{\Phi}$ are the free mode shapes at the analytical or measured DOF, and ξ are the generalized modal DOF. Insert the mode shapes from Table 4 and Eq. (17) into Eq. (16) to get

$$\mathbf{B}\overline{\mathbf{u}} = \begin{bmatrix} 0 & 1 & -1 & 0 \end{bmatrix} \begin{bmatrix} 0.767 & -0.642 & 0 \\ 0.767 & 0.917 & 0 \\ 0 & 0 & 0.954 \\ 0 & 0 & 0.954 \end{bmatrix} \begin{Bmatrix} \xi_1^1 \\ \xi_2^1 \\ \xi_1^2 \end{Bmatrix} = 0 \tag{18}$$

Combining the first and second matrices gives a new constraint matrix denoted $\mathbf{B}_m$ that is not Boolean yielding

$$\mathbf{B}_m\overline{\boldsymbol{\xi}} = \begin{bmatrix} 0.767 & 0.917 & -0.954 \end{bmatrix} \begin{Bmatrix} \xi_1^1 \\ \xi_2^1 \\ \xi_1^2 \end{Bmatrix} = 0 \tag{19}$$

which is the modal constraint equation. One finds a modified version of the $\mathbf{L}_m$ matrix as the null of $\mathbf{B}_m$ from a matrix algebra program as

$$\mathbf{L}_m = \begin{bmatrix} -0.5996 & 0.6237 \\ 0.7606 & 0.2491 \\ 0.2491 & 0.7409 \end{bmatrix} \tag{20}$$

which is no longer Boolean. Analogous to the physical domain Eq. (10), one has

$$\begin{Bmatrix} \xi_1^1 \\ \xi_2^1 \\ \xi_1^2 \end{Bmatrix} = \mathbf{L}_m \bar{\mathbf{q}} \tag{21}$$

where the $\mathbf{q}$ vector has only two DOF. In the modal domain, the equations of motion for the two substructures are

$$\begin{bmatrix} \mathbf{I^1} & \mathbf{0} \\ \mathbf{0} & \mathbf{I^2} \end{bmatrix} \begin{Bmatrix} \ddot{\bar{\boldsymbol{\xi}}}^{\mathbf{1}} \\ \ddot{\bar{\boldsymbol{\xi}}}^{\mathbf{2}} \end{Bmatrix} + \begin{bmatrix} \left[\boldsymbol{\omega}^2\right]^1 & \mathbf{0} \\ \mathbf{0} & \left[\boldsymbol{\omega}^2\right]^2 \end{bmatrix} \begin{Bmatrix} \bar{\boldsymbol{\xi}}^{\mathbf{1}} \\ \bar{\boldsymbol{\xi}}^{\mathbf{2}} \end{Bmatrix} = \begin{Bmatrix} \boldsymbol{\Phi}^{1\mathrm{T}} \bar{\mathbf{f}}^{\mathbf{1}} \\ \boldsymbol{\Phi}^{2\mathrm{T}} \bar{\mathbf{f}}^{\mathbf{2}} \end{Bmatrix} + \begin{Bmatrix} \boldsymbol{\Phi}^{1\mathrm{T}} \bar{\mathbf{g}}^{\mathbf{1}} \\ \boldsymbol{\Phi}^{2\mathrm{T}} \bar{\mathbf{g}}^{\mathbf{2}} \end{Bmatrix} \tag{22}$$

where the physical DOF u are replaced by Eq. (17) and the first substructure (first row of Eq. (12)) is premultiplied by $\boldsymbol{\Phi}^{1\mathrm{T}}$. The second substructure is characterized from the frequencies and mode shapes of the test. Here mode shapes are mass normalized to give the identity mass matrix, and the stiffness matrix is the circular frequency squared for each mode. Analogous to the primal method in the physical domain, one premultiplies by $\mathbf{L}_m^{\mathrm{T}}$ and substitutes Eq. (21) in for the modal ξ DOF to obtain

$$\begin{aligned} \mathbf{L}_m^{\mathrm{T}} \begin{bmatrix} \mathbf{I^1} & \mathbf{0} \\ \mathbf{0} & \mathbf{I^2} \end{bmatrix} \mathbf{L}_m \begin{Bmatrix} \ddot{q}_1 \\ \ddot{q}_2 \end{Bmatrix} + \mathbf{L}_m^{\mathrm{T}} \begin{bmatrix} \left[\boldsymbol{\omega}^2\right]^1 & \mathbf{0} \\ \mathbf{0} & \left[\boldsymbol{\omega}^2\right]^2 \end{bmatrix} \mathbf{L}_m \begin{Bmatrix} q_1 \\ q_2 \end{Bmatrix} \\ = \mathbf{L}_m^{\mathrm{T}} \begin{Bmatrix} \boldsymbol{\Phi}^{1\mathrm{T}} \bar{\mathbf{f}}^{\mathbf{1}} \\ \boldsymbol{\Phi}^{2\mathrm{T}} \bar{\mathbf{f}}^{\mathbf{2}} \end{Bmatrix} + \mathbf{L}_m^{T} \begin{Bmatrix} \boldsymbol{\Phi}^{1\mathrm{T}} \bar{\mathbf{g}}^{\mathbf{1}} \\ \boldsymbol{\Phi}^{2\mathrm{T}} \bar{\mathbf{g}}^{\mathbf{2}} \end{Bmatrix} \end{aligned} \tag{23}$$

and the far right-hand term goes to zero analogous to the physical Eq. (11). Putting in the numbers obtained from Eq. (20) and the circular frequencies squared derived from Table 3 gives

$$\begin{bmatrix} 1 & \mathbf{0} \\ \mathbf{0} & 1 \end{bmatrix} \begin{Bmatrix} \ddot{q}_1 \\ \ddot{q}_2 \end{Bmatrix} + 1.0e5 \begin{bmatrix} 1.8501 & -0.6056 \\ -0.6056 & 0.1983 \end{bmatrix} \begin{Bmatrix} q_1 \\ q_2 \end{Bmatrix}$$

$$= \begin{bmatrix} -0.9479 & 0.2374 & 0.2374 & 0.2374 \\ -0.3185 & -0.7065 & -0.7065 & -0.7065 \end{bmatrix} \begin{Bmatrix} f_1 \\ f_2 \\ f_3 \\ f_4 \end{Bmatrix} \tag{24}$$

Solving the eigenvalue problem from the left-hand side of Eq. (24) gives estimates for the natural frequencies of the assembly, which are 0 and 72.03 Hz. This is over 70% error for the first elastic modal frequency compared to the full physical system model. Comparing the CMS elastic mode shape to the true shape of the full physical system model in Table 5 also shows some significant error. DOF 2, 3, and 4 are all the same since only a rigid shape for substructure 2 was utilized in the modal model (since no elastic modes were available below the chosen cutoff frequency).

This provides a gross illustration of a typical modal truncation problem encountered when utilizing free mode shapes as the basis vectors for experimental CMS. The lower-frequency free modes in the testable frequency range of the experimental substructure may not strain the experimental substructure like the fully coupled system does.

Now consider a modified experiment where experimental substructure 2 is modified by attaching a fixture (mass of 0.2) to DOF u_3 that will cause the experimental substructure first elastic mode to drop down to 75.3 Hz which is below the cutoff frequency. Now two modes are included in the experimental substructure. However, the assembly now has the additional mass of the fixture, which is not part of the assembly of interest. To address this, one can simply add a third substructure and subtract its effect. The equations that set up this modified fixture test are given below, with substructure 3 representing the fixture mass.

Table 5 First elastic mode shape comparison

	Mode 2 full physical system	Mode 2 truncated CMS
u_1	−0.5699	−0.8018
$u_2 = u_3$	−0.2695	0.4454
u_4	0.7855	0.4454

$$\begin{bmatrix} \mathbf{I}^1 & 0 & 0 \\ 0 & \mathbf{I}^2 & 0 \\ 0 & 0 & -\mathbf{I}^3 \end{bmatrix} \begin{Bmatrix} \ddot{\bar{\boldsymbol{\xi}}}^1 \\ \ddot{\bar{\boldsymbol{\xi}}}^2 \\ \ddot{\bar{\boldsymbol{\xi}}}^3 \end{Bmatrix} + \begin{bmatrix} \left[\backslash \boldsymbol{\omega}^2 \backslash\right]^1 & 0 & 0 \\ 0 & \left[\backslash \boldsymbol{\omega}^2 \backslash\right]^2 & 0 \\ 0 & 0 & \left[\backslash -\boldsymbol{\omega}^2 \backslash\right]^3 \end{bmatrix} \begin{Bmatrix} \bar{\boldsymbol{\xi}}^1 \\ \bar{\boldsymbol{\xi}}^2 \\ \bar{\boldsymbol{\xi}}^3 \end{Bmatrix} = \begin{Bmatrix} \boldsymbol{\Phi}^{1^T} \bar{\mathbf{f}}^1 \\ \boldsymbol{\Phi}^{2^T} \bar{\mathbf{f}}^2 \\ \boldsymbol{\Phi}^{3^T} \bar{\mathbf{f}}^3 \end{Bmatrix} + \begin{Bmatrix} \boldsymbol{\Phi}^{1^T} \bar{\mathbf{g}}^1 \\ \boldsymbol{\Phi}^{2^T} \bar{\mathbf{g}}^2 \\ \boldsymbol{\Phi}^{3^T} \bar{\mathbf{g}}^3 \end{Bmatrix} \tag{25}$$

After inserting the mode shapes, the constraint equation becomes

$$\mathbf{B}\bar{\mathbf{u}} = \mathbf{B}\boldsymbol{\Phi}\bar{\boldsymbol{\xi}}$$

$$= \mathbf{B}_m \bar{\boldsymbol{\xi}} = \begin{bmatrix} -0.7670 & 0.9167 & 0.8771 & 1.6013 & 0.0000000 \\ 0.0000 & 0.0000 & -.8771 & -1.6013 & -2.2361 \end{bmatrix} \begin{Bmatrix} \eta_1^1 \\ \eta_2^1 \\ \eta_1^2 \\ \eta_2^2 \\ \eta_1^3 \end{Bmatrix} = \begin{Bmatrix} 0 \\ 0 \\ 0 \\ 0 \\ 0 \end{Bmatrix} \tag{26}$$

and one can then find the null space of $\mathbf{B}_m$ to obtain

$$\mathbf{L}_m^{\mathrm{T}} \bar{\mathbf{g}}_m = \begin{bmatrix} 0.4310 & 0.0386 & 0.8469 & -0.2796 & -0.1320 \\ 0.7868 & 0.0705 & -0.2796 & 0.4896 & -0.2410 \\ 0.1536 & 0.8651 & -0.1777 & -0.3244 & 0.3020 \end{bmatrix} \begin{Bmatrix} g_{m1}^1 \\ g_{m2}^1 \\ g_{m1}^2 \\ g_{m1}^2 \\ g_{m1}^3 \end{Bmatrix} = \begin{Bmatrix} 0 \\ 0 \\ 0 \end{Bmatrix} \tag{27}$$

When one does this, the answers are exactly the same as the full physical system. Other advantages of adding a fixture will be discussed later. Note several things here. In this case, $\mathbf{L}_m$ was determined from a matrix algebra program as the null space of $\mathbf{B}_m$. The $\mathbf{g}_m$ vector is the far right-hand term of Eq. (25). Five DOF are contained in the equation of motion, two modes for substructures 1 and 2 and one rigid body mode with 0 frequency for the fixture, substructure 3. Two constraints are applied to couple substructures 1 and 2 and to couple substructures 2 and 3. When one substitutes $\mathbf{L}_m \bar{\mathbf{q}}$ into Eq. (25) and premultiplies by $\mathbf{L}_m^{\mathrm{T}}$, the five-DOF problem is reduced by the two constraints to a three-DOF problem. The far right-hand term of Eq. (25) also goes to zero. Note the subtraction of the stiffness and mass of substructure 3 in the equation of motion. To summarize the use of the primal formulation with either physical or generalized DOF, one needs the equation of motion, some form of the constraint $\mathbf{B}$ from which $\mathbf{L}$ is derived, and then the equation of motion can be modified to eliminate redundant DOF using the $\mathbf{L}$ matrix.

2.4 Connecting Substructures in the Frequency Domain: Frequency-Based Substructuring

Frequency-based substructuring (FBS) is generally developed with the dual formulation, where all DOF on each substructure are retained in the solution. The equation of motion is formulated with a focus on the equilibrium forces where

$$\bar{\mathbf{g}} = -\mathbf{B}^{\mathrm{T}}\overline{\boldsymbol{\lambda}} \tag{28}$$

which automatically satisfies equilibrium Eq. (11) since $\mathbf{L}^{\mathrm{T}}\,\mathbf{B}^{\mathrm{T}} = 0$ because $\mathbf{B}^{\mathrm{T}}$ is in the null space of $\mathbf{L}^{\mathrm{T}}$. $\overline{\boldsymbol{\lambda}}$ is a vector of Lagrange multipliers corresponding to the interface force magnitudes. The equation of motion is rearranged slightly with each substructure block diagonal with the stiffness and mass matrices as

$$\mathbf{M}\ddot{\bar{\mathbf{u}}} + \mathbf{K}\bar{\mathbf{u}} + \mathbf{B}^{T}\overline{\boldsymbol{\lambda}} = \bar{\mathbf{f}}. \tag{29}$$

The mass, stiffness (and damping) matrices correspond to the impedance. Generally measurements are gathered in terms of frequency response functions, which are the inverse of impedance. Using $\mathbf{Y}$ as the frequency response function (FRF), receptance matrix yields

$$\mathbf{Y}^{-1}\bar{\mathbf{u}} + \mathbf{B}^{\mathrm{T}}\overline{\boldsymbol{\lambda}} = \bar{\mathbf{f}}. \tag{30}$$

Repeating the constraint equation

$$\mathbf{B}\bar{\mathbf{u}} = \mathbf{0} \tag{9}$$

and using it with Eq. (30), one can eliminate $\overline{\boldsymbol{\lambda}}$ and obtain a long result as

$$\bar{\mathbf{u}} = \left[\mathbf{Y} - \mathbf{Y}\mathbf{B}^{\mathrm{T}}\left(\mathbf{B}\mathbf{Y}\mathbf{B}^{\mathrm{T}}\right)^{-1}\mathbf{B}\mathbf{Y}\right]\bar{\mathbf{f}} \tag{31}$$

which still retains all DOF from each substructure. This provides response of every possible output from every possible input. Many times only a few rows are of interest. Two convenient subsets of this large matrix will be given here and demonstrated with the example problem. Suppose one desires the response at a point on substructure 2 due to a local force on the substructure 1. This can be extracted from Eq. (31) as

$$\mathbf{Y}_{ri} = \mathbf{Y}^{2}_{rc}\left(\mathbf{Y}^{2}_{cc} + \mathbf{Y}^{1}_{cc}\right)^{-1}\mathbf{Y}^{1}_{ci} \tag{32}$$

where subscript r is a response DOF, subscript i is the input force DOF, and subscript c implies all the connection DOF, and the superscripts denote FRFs for the particular substructure by itself. If, for example, there were 9 connection DOF, the size of the

$\mathbf{Y}_{cc}$ matrix for each substructure would be 9x9 for every frequency line. Of course, the connection DOF must be in the same order in each substructure matrix.

Now consider the example problem from Fig. 2. Choosing f_1 as the input and u_4 as the output for this case and noting that the connection DOF on substructure 1 is 2 while the connection DOF on substructure 2 is 3 gives

$$Y_{41} = Y_{43}(Y_{33} + Y_{22})^{-1} Y_{21} \tag{33}$$

The other common problem is to obtain a response on the same substructure as the force, which can be written generally as

$$\mathbf{Y}_{ri} = \mathbf{Y}^1_{ri} - \mathbf{Y}^1_{rc}\left(\mathbf{Y}^2_{cc} + \mathbf{Y}^1_{cc}\right)^{-1} \mathbf{Y}^1_{ci} \tag{34}$$

where this assumes the force and input are both on substructure 1. For the example problem, choosing f_1 and u_1 as input and response yields

$$Y_{11} = Y^1_{11} - Y^1_{12}\left(Y^2_{33} + Y^1_{22}\right)^{-1} Y^1_{21}. \tag{35}$$

Equations (32) and (34) can be applied to many problems.

For an example, Eq. (33) is selected. We could obtain the analytical substructure 1 FRFs with either a direct FRF calculation or superposition of modal FRF solutions from the FE model. Damping is usually included. We could obtain the experimental substructure 2 FRFs by measuring response of both u_3 and u_4 due to input on the connection DOF u_3 in a "free" boundary condition modal test. Y_{43} could be obtained by reciprocity with Y_{34}. Deriving the acceleration/force FRFs from all the free modes of vibration of each substructure yields the FRF magnitudes given in Fig. 3. Note that the resonant frequency for substructure 2 is outside the 100 Hz bandwidth, but the effect of the elastic resonance is captured in the "tails" of the 120 Hz mode visible in the 100 Hz band.

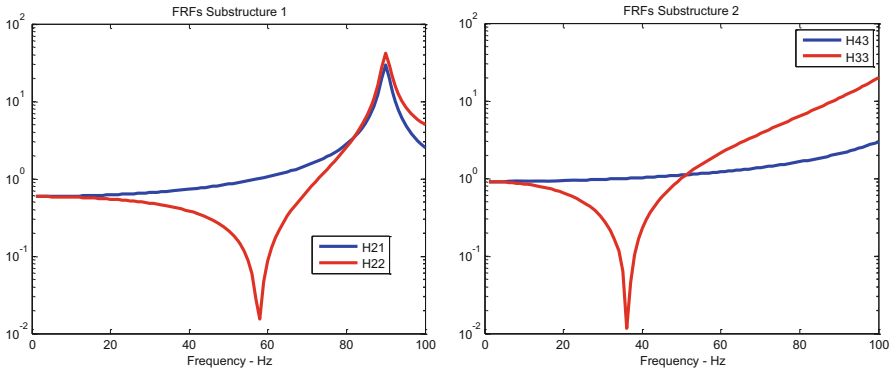

Fig. 3 FRFs for substructures 1 and 2 (not connected)

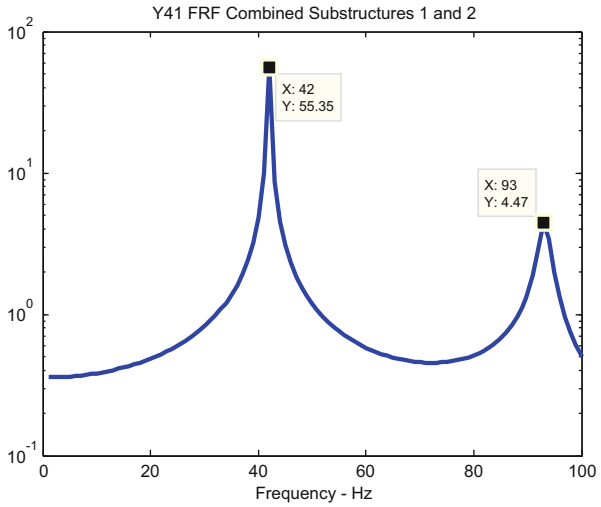

Fig. 4 FRF response at u_4 due to force at u_1

In Fig. 4 is given the response of u_4 due to the force on u_1 with the substructures coupled using Eq. (33). The new frequencies near 42 and 93 Hz match the full system response that one would compute with the full assembly equations of motion. The clear advantage of the FBS is that even if the resonances of higher modes are not captured, their information is still captured in the residual effects or "tails" of the resonances. Given this advantage, why not use FBS all the time? Some of the difficulties of experimental substructuring will be addressed in the next section.

3 Dealing with Experimental Difficulties

The two substructure example used in Sect. 2 is instructive, but it only illustrated one of the several difficulties encountered in experimental substructures: that difficulty was the effect of modal truncation shown in the CMS method. The lumped mass system with only one connection DOF per substructure is not representative of most substructures of interest.

3.1 Common Experimental Difficulties

The general framework [1] enumerates several of the experimental difficulties to which we add a few others including

1. Measuring rigid body modes
2. Modal fitting of nonlinear response

3. Mass errors introduced by sensors
4. Modal truncation errors
5. Measuring rotational DOF motion and forces
6. Continuity of the attachment interface
7. Difficulty in mounting sensors at connection points
8. Dynamic effects in the joints
9. Experimental errors

Mitigation strategies for each of these difficulties are provided below.

3.1.1 Measuring Rigid Body Modes

For free substructures, the most important modes to extract properly are often not the elastic modes, but the rigid body modes. One can have all the elastic modes represented perfectly and still obtain erroneous results. One way to understand the importance of rigid body modes is to consider the real part of acceleration/force FRFs. The natural frequency of a SDOF system is determined by the frequency at which the FRF real part goes to zero. When many modes of two substructures are active, the way the FRF real parts sum to zero determines where the natural frequencies of the connected system will be. The effect of the rigid body modes is entirely on the real part in the FRFs. If one eliminates or has poor estimates of the rigid body modes, this drastically changes the estimates of the frequencies at which the real parts will sum to zero. Usually the rigid body mode shapes can be estimated from mass properties of the structure. These may be either measured or obtained from a solid model. A good check on rigid body mode shapes is to synthesize FRFs at all the measurement DOF using only the rigid body mode shapes. Then compare the real part of the measured FRFs at low frequency to the synthesized FRFs. If there are large differences, something is probably wrong, and the substructuring effort will fail.

Consider again the two substructure example in Fig. 2. The mass line of the accelerance FRFs will be $(\mathrm{m3} + \mathrm{m4})^{-1} = 0.909$. The magnitude of the mass lines and the true FRFs are plotted in Fig. 5 and show agreement at low frequency. If there were error in the rigid body mode shapes, this plot would indicate a mismatch at low frequency.

3.1.2 Modal Fitting of Nonlinear Response

If one has to fit the modal frequency, damping, and shapes as in the experimental CMS approach, inaccuracies in the fitting can create large errors in the model. As an example, some algorithms extract the frequency and damping and then use those in a separate step to fit the mode shapes. If the damping estimate is off by a factor of 2, then the residue calculation (which leads to the mode shape) will compensate by a factor of 2 for the damping error in order to fit the FRFs. In many mode shape fitting algorithms, the drive point mode shape is used to determine the modal mass scaling for all the shapes. If the drive point response is very weak for a certain mode, large errors in the scaling can result. Large errors in mode shape create large errors in the CMS substructure model. A nonlinear response will often make it difficult to obtain

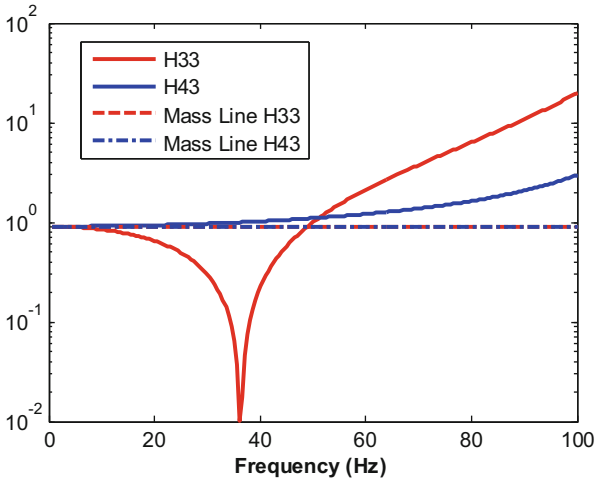

Fig. 5 FRFs for substructure 2 compared with mass line for rigid body mode shapes

accurate modal parameters and shapes. Therefore, fitting at low excitation levels is usually the best method to obtain FRFs fit the linear model form. There are some exceptions to this general rule.

3.1.3 Mass Errors Introduced by Sensors

When performing an experiment with a shaker, the force sensor is mounted to the substructure. Significant errors can be introduced if the load cell mass is significant with respect to the test article. Even in the designed direction of force measurement of the sensor, roughly half of the mass of the load cell is not accounted for in the FRF measurement. The mass of the sensor in the lateral (or shearing) directions is not corrected at all in the FRF measurement. Examples have been observed in which the load cell causes a 10% downward shift in the modal frequency (which is roughly 20% increase in modal mass!). For light or small structures, this makes an impact hammer a better approach. Impact hammers can also excite a structure to higher frequencies than typical modal shakers. Shakers are desirable to produce linearized FRFs using random input, but beware of mass loading effects of load cells. A good check is to remove the load cell and impact the structure with a hammer to see if the impact FRFs overlay well with the shaker and load cell FRFs. Mass loading can also be experienced from accelerometers, but most testers are aware of this. Mass loading from the load cell is more often overlooked.

The next six difficulties to be addressed were largely responsible for the failures that were experienced in the early decades of experimental dynamic substructuring. They can all be, at least partially, mitigated by proper testing with a fixture (later called a transmission simulator) attached at the interface. This approach will be described later.

3.1.4 Modal Truncation Errors

All modal methods of model reduction are only accurate in a limited frequency band. Even then, some mode shape bases are better than others, giving accurate results over a wider bandwidth for a similar number of modal DOF. For example, the Craig-Bampton shapes (fixed boundary mode shapes plus static constraint shapes) usually provide a better basis than free mode shapes given a certain frequency band. However, measuring fixed base shapes and static constraint shapes is usually unfeasible because 1. no fixed base exists in practice and 2. measuring static constraint shapes is unfeasible in most laboratories. Generally free modes are measured since this is easily accomplished with soft supports such as bungee cords. However, free tests put no strain at the boundary locations which is very different from the connected boundary condition that is of interest. When free modes are used, the resulting modal truncation errors can theoretically be corrected by adding the residual flexibility as in the Rubin and Craig-Chang methods. Residual flexibilities can theoretically be extracted from the FRFs of a free modal test. This becomes very demanding if there are many connection DOF since one must theoretically have a drive point at every connection DOF, including the rotations. It is beyond the state of the art to apply moments and measure rotations on systems with a significant number of connection DOF. As was shown in the CMS example of Sect. 2.3, one way to deal with out-of-band modes is to bring them down in frequency into the band by attaching a rigid fixture. The fixture approach to be described later enhances the result, but modal truncation error will increase with increase in frequency.

3.1.5 Measuring Rotational DOF Motion and Forces

Most load cells and motion sensors measure translational motion. Measuring moments and rotations usually requires much larger, more expensive sensors that are more difficult to attach to a test structure and may cause huge mass loading as discussed previously. Some progress is being made in sensing rotational motion, but little progress has been made on applying and measuring moments except for very specific applications. In most substructuring applications, the effects of moments and rotations cannot be neglected without causing significant errors. Some efforts have been attempted to obtain rotations by differencing translation measurements and dividing by the distance between them. This can be effective for a small number of connection DOF. For more general cases, the transmission simulator approach with the CMS method to be discussed later addresses this need.

One great difficulty of the pure FBS method using raw measured FRFs is measurement of all the drive point FRFs if there are many connection DOF. This is certainly impractical if there are rotational connection DOF. Since there are frequently many connection DOF, it can often prove impractical even if only the translation connection DOF need to be measured. Therefore, large numbers of connection DOF or rotation connection DOF make the raw FRF approach quite difficult.

3.1.6 Continuity of the Attachment Interface

As shown in the compatibility theory, substructuring compatibility equations focus on very discrete attachment locations. Many attachments are not discrete but are continuous, such as a bolted flange which has large areas in contact. Usually such attachments are over-simplified to discrete locations with little knowledge of the error this may induce. The transmission simulator approach to be discussed can address this challenge as well.

3.1.7 Difficulty in Mounting Sensors at Connection Locations

Many times one cannot even attach a sensor at the location of the connection DOF. For example, a small shoulder or a large threaded joint or a bolt hole can provide difficult mounting conditions. Use of the transmission simulator approach to be described later does not require sensors to be mounted at the precise connection location.

3.1.8 Dynamic Effects in the Joints

One difficulty with traditional substructuring is that it perfectly enforces compatibility at the attachment locations, when in the real hardware, there is actually compliance in the joint connection. The joint is also a significant source of energy dissipation. Testing with the transmission simulator, to be addressed later, captures both joint compliance and damping.

3.1.9 Experimental Errors

The examples given previously show that substructuring theory works very well with perfect data. However, experimental measurements always have both random (noise) and bias (sensitivity) errors. This tends to provide difficulty, especially in multiple connection applications. Typical accelerometers are considered calibrated if their sensitivity is within 3–5% error at every frequency in the usable range. If there is a 5% error in displacement at one location and a negative 5% error in another location, the internal forces to correct for the false incompatibility can cause huge errors. This incompatibility creates very ill-conditioned substructure matrices when substructures are assembled at the physical connection DOF. Ill-conditioning in either stiffness/mass or FRF matrices often manifests itself with spurious non-physical modes. Traditionally, one way to overcome such problems is to instrument more than necessary to provide least squares fitting through experimental data. Another mitigating strategy is to weaken the constraint. The transmission simulator approach in the next section takes advantage of both of these strategies.

3.2 The Transmission Simulator Approach to Mitigate Traditional Experimental Difficulties

The difficulties 4–9 listed above can be mitigated by the transmission simulator approach. The transmission simulator approach does require some additional

upfront preparation, but it eliminates or mitigates the most grievous difficulties that can cause experimental substructures to fail. The mitigation of difficulties will be listed along with the transmission simulator features in the description that follows. A transmission simulator consists of two entities, an instrumented physical fixture and a mathematical model of the fixture (usually a FE model). The fixture is fabricated to mate to the experimental substructure exactly like the next assembly will fit. The fixture should emulate the impedance of the nearest portion of the next assembly. Some "features" may be included on the fixture for attaching sensors or imparting various input forces. The FE model of the fixture is utilized to determine where sensors should be placed and loads applied in the experimental substructure test. A chosen number of free modes, usually going slightly beyond the frequency bandwidth of interest, are chosen to represent the fixture motion, so it is possible to represent both rigid and elastic motion with the approach. The fixture is then instrumented with enough sensors to capture the mode shapes so that all shapes are linearly independent on the sensor set. Usually the number of sensors is 1.5 to 2 times the number of free modes chosen to take advantage of least squares fitting of the experimental data (difficulty 9). The sensors are placed at convenient locations on the fixture. They do not have to be placed at the actual connection locations. The FE model of the fixture is used to convert all the measured motions to the modal DOF of the fixture. The modal DOF inherently capture the rotational motion and translational motion at connection DOF that are difficult to measure directly (difficulties 5 and 7). In addition the modal DOF of the fixture approximate the motion at the connection for continuous interfaces (difficulty 6). Because the fixture is mounted to the substructure in the test with the same type of joint that will be in the assembled system, the compliance and damping in the joint is captured in the substructure model (difficulty 8). The mass of the fixture also helps bring modes down into the testable bandwidth as demonstrated in the example in Sect. 2.3 (difficulty 4). If the chosen mode shapes span the space of the actual connection motion, the transmission simulator approach will be accurate. To the extent the chosen mode shapes do not span the space of the connection motion, inaccuracy (a form of modal truncation error) will be introduced in the connected substructures model. However, the mode shapes of the transmission simulator generally improve the connection shape bases a great deal over free modes without the fixture (difficulty 4).

3.3 An Example Using the Transmission Simulator Approach

Consider the hardware shown in Fig. 6. A FE substructure of the cylinder will be coupled with an experimental model of the plate/beam at the eight bolted locations to produce full system response. The transmission simulator, shown in Fig. 7, is a ring with tabs on it to allow for exciting the experiment in the tangential direction.

In this problem, the model of the transmission simulator was "welded" into the FE model of the cylinder. Then the experimental substructure with transmission simulator was coupled to the cylinder, and two transmission simulators were

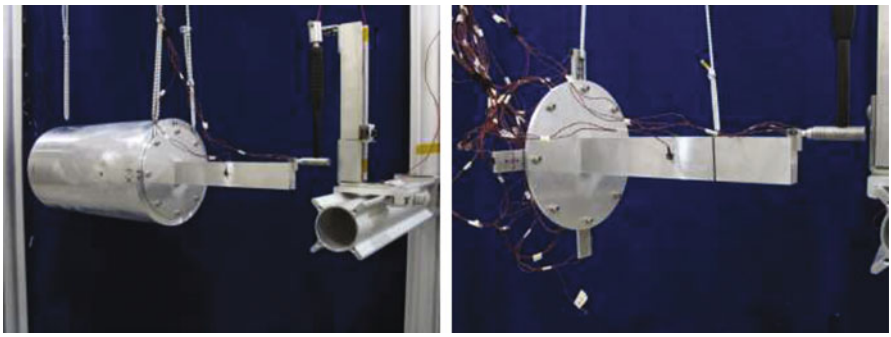

Fig. 6 Full system assembled for cylinder with plate/beam – experimental substructure at right

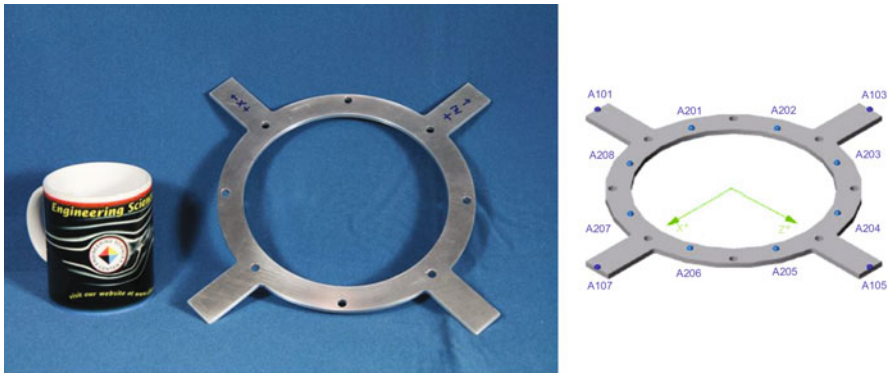

Fig. 7 Transmission simulator – triaxial accelerometer locations shown at right

subtracted to produce full system response. In hindsight, the authors believe that even better results could be obtained if the tabs on the transmission simulator were shorter, so the tab modes would have been above the testable frequency band.

Measurements were made on the end of the beam (Fig. 6) so that drive point response for an axial input on the end of the beam in the assembled system was developed with the transmission simulator method using FBS coupling. The FRFs for the experimental substructure were developed from analytical rigid body mode shapes and measured modes of the experiment to 4,000 Hz so they do not include residual effects of modes above 4,000 Hz. FRFs for the cylinder were calculated from 100 modes of the FE model of the cylinder. The resulting coupled FRF out to 2,000 Hz is shown in Fig. 8.

Since the plate/beam substructure was fairly simple, a FE model was generated for it. The FE model matched test data frequencies for the plate/beam alone quite well. A virtual test was then performed on the FE model of the plate and beam, and a virtual experimental model *without* the transmission simulator was generated from 21 modes (all the free modes to 4,000 Hz). The CMS free mode models were coupled at all 48 connection DOF (24 rotations and 24 translations) to the 100 mode

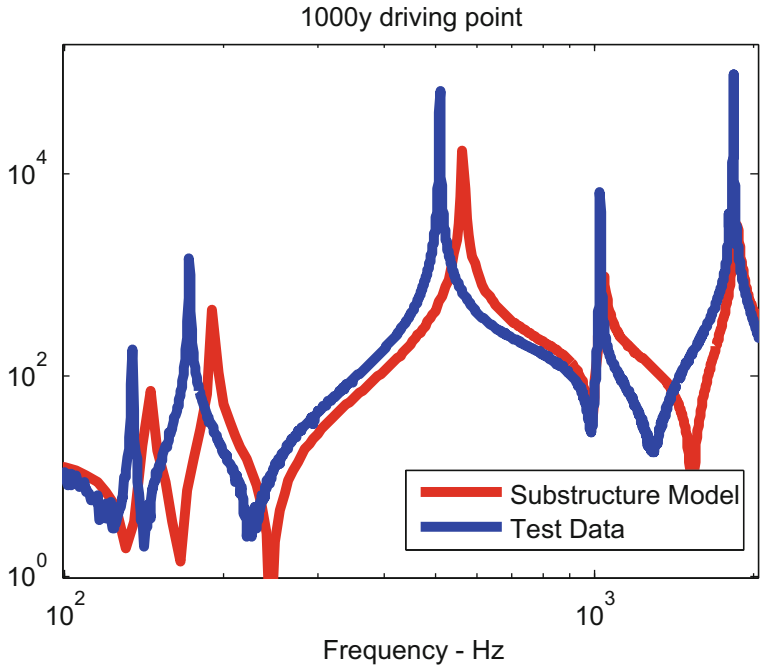

Fig. 8 FBS coupled analytical and experimental substructures versus test data

free mode model of the cylinder. The result is shown in Fig. 9. The FRF errors are pretty drastic, similar to the example CMS problem without the fixture given in Sect. 2.3. It is difficult to even establish correspondence of the resonances between the test data and substructure result. Many more free modes above 4,000 Hz (which might be quite difficult to extract) would need to be included in the experimental substructure to improve the CMS result. The result using the transmission simulator fixture in Fig. 8 is clearly more useable, and no rotational measurements were required.

3.4 Transmission Simulator Theory

Transmission simulator (TS) theory is developed with its own version of the **B** and **L** matrices and at least one additional substructure, the instrumented fixture, or transmission simulator [2]. We will consider the theory in light of the goal of coupling an experimental substructure to a FE substructure.

3.4.1 Preparation to Implement Transmission Simulator Theory

Before the measurement process for the experimental substructure is undertaken, the fixture is fabricated, and a model of the fixture is generated, usually with

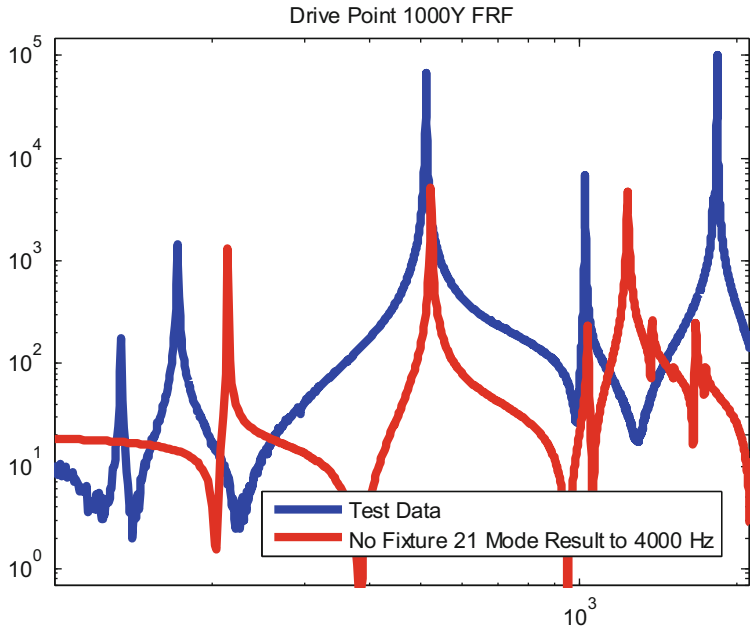

Fig. 9 FBS coupled model with virtual experimental model computed for 24 translations and 24 rotations with all free modes out to 4,000 Hz and no transmission simulator – a demonstration of free modes modal truncation error with no fixture

FE software. The FE model of the fixture, or transmission simulator, is used to calculate modes out significantly beyond the frequency of interest at many candidate measurement DOF, e.g., a factor of 10 more DOF than the required number of sensors. Then a number of retained modes will be selected that are deemed to be able to span the space of the connection motion. Usually modes past the frequency of interest are retained. The candidate measurement DOF are all chosen at locations where sensors can easily be installed. Then an algorithm is used to reduce the number of sensor DOF down from the candidate set to about 1.5 to 2 times the number of retained modes. Various approaches can suffice for this, such as the effective independence method [3], min-mac [4], or optimizing to obtain a condition number of the mode shape matrix that is no more than 3.5–5 [5]. This is important since the TS mode shape matrix must be inverted for this method, and ill-conditioning of the mode shape matrix can ruin the results. Once the sensor locations are established, one usually identifies force input locations that will excite all free modes of the TS well. One must have a drive point response sensor co-located with each force input. If all of the measurement DOF are physically located so they are in contact with DOF on the FE model, only one TS is required. If some DOF are not physically in contact with the FE substructure as nodes A10X on the tabs in Fig. 6, then one needs to attach the TS model to the FE model at all DOF where the TS and FE model occupy the same space. See Fig. 10 which has the TS bonded

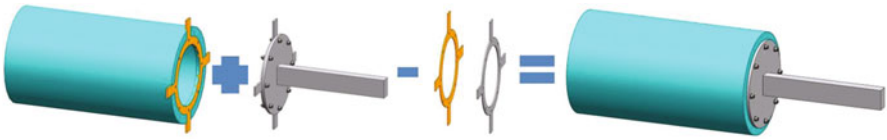

Fig. 10 Substructuring example using transmission simulator

in with the FE model. For development of the theory, assume this is the case. This means that two TS will need to be subtracted (one from each substructure). With this information in hand, one can now develop the compatibility equations and apply them to the appropriate equations of motion.

3.4.2 Transmission Simulator Method Using CMS

The TS method enforces the motion of the TS to be the same on the FE substructure and the experimental structure at the measurement DOF on the TS, but the constraint is weakened using the free modes of the TS as a basis. Consequently, the measured DOF, as opposed to the actual connection DOF, will be utilized in establishing compatibility. This allows one to use easy to instrument locations on the TS as opposed to requiring the measurement at all connection DOF which provides a great advantage. It also allows us to approximate connections even if the connection is not discrete but continuous. Since we have a FE substructure with a TS attached to it, an experimental substructure with TS, and a TS substructure, one can write for the physical DOF

$$\begin{aligned} \bar{\mathbf{u}}_{meas}^{FE} - \bar{\mathbf{u}}_{meas}^{\exp} &= 0 \\ \bar{\mathbf{u}}_{meas}^{\exp} - \bar{\mathbf{u}}_{meas}^{TS} &= 0 \end{aligned} \tag{36}$$

where subscript *meas* denotes the measurement DOF ***on the TS***. Building the B matrix for these DOF gives

$$\mathbf{B}\bar{\mathbf{u}}_{meas} = \begin{bmatrix} I & -I & 0 \\ 0 & I & -I \end{bmatrix} \begin{Bmatrix} \bar{\mathbf{u}}_{meas}^{FE} \\ \bar{\mathbf{u}}_{meas}^{\exp} \\ \bar{\mathbf{u}}_{meas}^{TS} \end{Bmatrix} = 0 \tag{37}$$

but in the CMS approach the displacements are expressed as a function of the mode shapes as follows.

$$\mathbf{B}\boldsymbol{\Phi}\bar{\mathbf{u}}_{meas} = \begin{bmatrix} I & -I & 0 \\ 0 & I & -I \end{bmatrix} \begin{bmatrix} \boldsymbol{\Phi}_{meas}^{FE} & 0 & 0 \\ 0 & \boldsymbol{\Phi}_{meas}^{\exp} & 0 \\ 0 & 0 & \boldsymbol{\Phi}_{meas}^{TS} \end{bmatrix} \begin{Bmatrix} \bar{\boldsymbol{\xi}}^{FE} \\ \bar{\boldsymbol{\xi}}^{\exp} \\ \bar{\boldsymbol{\xi}}^{TS} \end{Bmatrix} = 0 \tag{38}$$

The mathematical key to the TS is to premultiply each set of constraints by the pseudo-inverse of the retained TS mode shapes as

$$\mathbf{B}_{mTS}\bar{\boldsymbol{\xi}}_{meas} = \begin{bmatrix} \boldsymbol{\Phi}_{meas}^{TS\dagger} & 0 \\ 0 & \boldsymbol{\Phi}_{meas}^{TS\dagger} \end{bmatrix} \begin{bmatrix} I & -I & 0 \\ 0 & I & -I \end{bmatrix} \begin{bmatrix} \boldsymbol{\Phi}_{meas}^{FE} & 0 & 0 \\ 0 & \boldsymbol{\Phi}_{meas}^{\exp} & 0 \\ 0 & 0 & \boldsymbol{\Phi}_{meas}^{TS} \end{bmatrix} \begin{Bmatrix} \bar{\boldsymbol{\xi}}^{FE} \\ \bar{\boldsymbol{\xi}}^{\exp} \\ \bar{\boldsymbol{\xi}}^{TS} \end{Bmatrix}$$
$$= \begin{bmatrix} \boldsymbol{\Phi}_{meas}^{TS\dagger}\boldsymbol{\Phi}_{meas}^{FE} & -\boldsymbol{\Phi}_{meas}^{TS\dagger}\boldsymbol{\Phi}_{meas}^{\exp} & 0 \\ 0 & \boldsymbol{\Phi}_{meas}^{TS\dagger}\boldsymbol{\Phi}_{meas}^{\exp} & -I \end{bmatrix} \begin{Bmatrix} \bar{\boldsymbol{\xi}}^{FE} \\ \bar{\boldsymbol{\xi}}^{\exp} \\ \bar{\boldsymbol{\xi}}^{TS} \end{Bmatrix} = 0 \tag{39}$$

which projects the constraint onto the mode shapes of the TS. To the extent that the mode shapes of the TS span the true motion, this will provide a good approximation. Since there are fewer retained modes in the TS than the number of measured DOF, this reduces the number of constraints which weakens the constraint. The constraint can only be satisfied in a least squares sense instead of an absolute sense, i.e., Eqs. (37) and (38) will not be perfectly satisfied, and the physical displacements at the physical connection DOF will not match precisely. The advantage of this is that it does not force the substructuring problem to enforce compatibility for the experimental errors in the measured data (e.g., the 3–5% sensitivity errors of accelerometers). This improves the conditioning of the matrices tremendously and eliminates most of the spurious modes that would be obtained if one utilized compatibility Eq. (38) which would enforce the measured motion with its errors to satisfy compatibility. The related $\mathbf{L}_{mTS}$ matrix is just the null matrix of $\mathbf{B}_{mTS}$. The block diagonal modal equations of motion start with

$$\begin{bmatrix} \mathbf{I}^{FE} & 0 & 0 \\ 0 & \mathbf{I}^{\exp} & 0 \\ 0 & 0 & -2\mathbf{I}^{TS} \end{bmatrix} \begin{Bmatrix} \ddot{\bar{\boldsymbol{\xi}}}^{FE} \\ \ddot{\bar{\boldsymbol{\xi}}}^{\exp} \\ \ddot{\bar{\boldsymbol{\xi}}}^{TS} \end{Bmatrix} + \begin{bmatrix} \boldsymbol{\omega}^{2FE} & 0 & 0 \\ 0 & \boldsymbol{\omega}^{2\exp} & 0 \\ 0 & 0 & -2\boldsymbol{\omega}^{2TS} \end{bmatrix} \begin{Bmatrix} \bar{\boldsymbol{\xi}}^{FE} \\ \bar{\boldsymbol{\xi}}^{FE} \\ \bar{\boldsymbol{\xi}}^{FE} \end{Bmatrix}$$
$$= \begin{Bmatrix} \boldsymbol{\Phi}^{FE^{\mathrm{T}}}\bar{\mathbf{f}}^{FE} \\ \boldsymbol{\Phi}^{\exp^{\mathrm{T}}}\bar{\mathbf{f}}^{\exp} \\ \boldsymbol{\Phi}^{TS^{\mathrm{T}}}\bar{\mathbf{f}}^{TS} \end{Bmatrix} + \begin{Bmatrix} \boldsymbol{\Phi}^{FE^{\mathrm{T}}}\bar{\mathbf{g}}^{FE} \\ \boldsymbol{\Phi}^{\exp^{\mathrm{T}}}\bar{\mathbf{g}}^{\exp} \\ \boldsymbol{\Phi}^{TS^{\mathrm{T}}}\bar{\mathbf{g}}^{TS} \end{Bmatrix} \tag{40}$$

where one can see that two TS models are being subtracted in the mass and stiffness (and also damping if it is included). Analogous to Eq. (21)

$$\begin{Bmatrix} \bar{\boldsymbol{\xi}}^{FE} \\ \bar{\boldsymbol{\xi}}^{\exp} \\ \bar{\boldsymbol{\xi}}^{TS} \end{Bmatrix} = \mathbf{L}_{mTS}\bar{\mathbf{q}} \tag{41}$$

which one substitutes into Eq. (40) and premultiplies by transpose of $\mathbf{L}_{mTS}$ to obtain a result that has the same form as was seen in examples previously,

$$\mathbf{L}_{mTS}^{\mathrm{T}} \begin{bmatrix} \mathbf{I}^{FE} & 0 & 0 \\ 0 & \mathbf{I}^{\exp} & 0 \\ 0 & 0 & -2\mathbf{I}^{TS} \end{bmatrix} \mathbf{L}_{mTS} \ddot{\bar{\mathbf{q}}} + \mathbf{L}_{mTS}^{\mathrm{T}} \begin{bmatrix} \boldsymbol{\omega}^{2FE} & 0 & 0 \\ 0 & \boldsymbol{\omega}^{2\exp} & 0 \\ 0 & 0 & -2\boldsymbol{\omega}^{2TS} \end{bmatrix} \mathbf{L}_{mTS} \bar{\mathbf{q}} = \mathbf{L}_{mTS}^{\mathrm{T}} \begin{Bmatrix} \boldsymbol{\Phi}^{FE\mathrm{T}} \bar{\mathbf{f}}^{FE} \\ \boldsymbol{\Phi}^{\exp\mathrm{T}} \bar{\mathbf{f}}^{\exp} \\ \boldsymbol{\Phi}^{TS\mathrm{T}} \bar{\mathbf{f}}^{TS} \end{Bmatrix} \tag{42}$$

where the far right-hand term of Eq. (40) goes to zero because of the equilibrium condition, similar to Eqs. (11) and (14). New frequencies and eigenvectors are obtained by solving the eigenvalue problem of the left side. If those eigenvectors are given in matrix $\boldsymbol{\Gamma}$, the new motion will be

$$\bar{\mathbf{u}} = \boldsymbol{\Phi}\bar{\boldsymbol{\xi}} = \boldsymbol{\Phi}\mathbf{L}_{mTS}\bar{\mathbf{q}} = \boldsymbol{\Phi}\mathbf{L}_{mTS}\boldsymbol{\Gamma}\bar{\mathbf{p}} \tag{43}$$

so the new mode shapes are formed as $\boldsymbol{\Phi}\mathbf{L}_{mTS}\,\boldsymbol{\Gamma}$. The number of constraint equations in Eq. (39) is 2* N_{TS}, where N_{TS} is the number of retained modes for the TS. The total number of modes obtained by solving the eigenvalue problem of Eq. (42) is $N_{FE} + N_{exp} + N_{TS} - N_{constraints} = N_{FE} + N_{exp} - N_{TS}$.

3.4.3 Transmission Simulator Method Using FBS

For FBS, consider just attaching two substructures, the FE and the experimental substructures. (For brevity, subtracting the TS is not shown in the example below; subtraction could be done in a second step.) Compatibility begins with physical DOF equation as

$$\mathbf{B}\bar{\mathbf{u}}_{meas} = \begin{bmatrix} I & -I \end{bmatrix} \begin{Bmatrix} \bar{\mathbf{u}}_{meas}^{FE} \\ \bar{\mathbf{u}}_{meas}^{\exp} \end{Bmatrix} = 0 \tag{44}$$

and premultiply by the pseudo-inverse of the TS mode shape matrix at the measured DOF to get a new $\mathbf{B}$ matrix as

$$\mathbf{B}_{FBS,TS}\bar{\mathbf{u}}_{meas} = \boldsymbol{\Phi}_{meas}^{TS+} \begin{bmatrix} I & -I \end{bmatrix} \begin{Bmatrix} \bar{\mathbf{u}}_{meas}^{FE} \\ \bar{\mathbf{u}}_{meas}^{\exp} \end{Bmatrix} = \begin{bmatrix} \boldsymbol{\Phi}_{meas}^{TS+} & -\boldsymbol{\Phi}_{meas}^{TS+} \end{bmatrix} \begin{Bmatrix} \bar{\mathbf{u}}_{meas}^{FE} \\ \bar{\mathbf{u}}_{meas}^{\exp} \end{Bmatrix} = 0. \tag{45}$$

$\mathbf{B}_{FBS,TS}$ can be substituted directly into FBS Eq. (31) for the traditional $\mathbf{B}$ matrix. Eq. (31) is repeated here as

$$\bar{\mathbf{u}} = \left[\mathbf{Y} - \mathbf{Y}\mathbf{B}^{\mathrm{T}}\left(\mathbf{B}\mathbf{Y}\mathbf{B}^{\mathrm{T}}\right)^{-1}\mathbf{B}\mathbf{Y}\right]\bar{\mathbf{f}}. \tag{31}$$

To show how this would work in the subset of equations that cover many situations, first consider Eq. (32) where the force is applied to the FE substructure and the response is on the experimental substructure. The classical FBS equation is

$$\mathbf{Y}_{ri} = \mathbf{Y}_{rc}^{\exp}\left(\mathbf{Y}_{cc}^{\exp} + \mathbf{Y}_{cc}^{FE}\right)^{-1}\mathbf{Y}_{ci}^{FE} \tag{46}$$

where the exp and FE superscripts have replaced the substructure numbers. With the TS approach using the FE and EXP substructures, with $\mathbf{B}_{FBS\_TS}$ the form is

$$\mathbf{Y}_{ri} = \mathbf{Y}_{rc}^{\exp}\boldsymbol{\Phi}_{c}^{TS+\mathrm{T}}\left(\boldsymbol{\Phi}_{c}^{TS+}\mathbf{Y}_{cc}^{\exp}\boldsymbol{\Phi}_{c}^{TS+\mathrm{T}} + \boldsymbol{\Phi}_{c}^{TS+}\mathbf{Y}_{cc}^{FE}\boldsymbol{\Phi}_{c}^{TS+\mathrm{T}}\right)^{-1}\boldsymbol{\Phi}_{c}^{TS+}\mathbf{Y}_{ci}^{FE} \tag{47}$$

where all the c DOF are actually the measured DOF (i.e., $\boldsymbol{\Phi}_{c}^{TS+\mathrm{T}} = \boldsymbol{\Phi}_{meas}^{TS+}$). If one looks at the kernel for the connection DOF in the parentheses which must be inverted, the matrix has been reduced in size from the number of measurement DOF on the TS to the number of modes of the TS. This has the effect weakening the constraint, which reduces the ill-conditioning of the kernel for inversion. If the force is applied to the FE substructure and measured on the FE substructure, the traditional Eq. (34) is repeated here as

$$\mathbf{Y}_{ri} = \mathbf{Y}_{ri}^{FE} - \mathbf{Y}_{rc}^{FE}\left(\mathbf{Y}_{cc}^{\exp} + \mathbf{Y}_{cc}^{FE}\right)^{-1}\mathbf{Y}_{ci}^{FE} \tag{48}$$

where the number superscripts have been replaced by the appropriate substructure name. The TS version of Eq. (34) for our example is

$$\mathbf{Y}_{ri} = \mathbf{Y}_{ri}^{FE} - \mathbf{Y}_{rc}^{FE}\boldsymbol{\Phi}_{c}^{TS+\mathrm{T}}\left(\boldsymbol{\Phi}_{c}^{TS+}\mathbf{Y}_{cc}^{\exp}\boldsymbol{\Phi}_{c}^{TS+\mathrm{T}} + \boldsymbol{\Phi}_{c}^{TS+}\mathbf{Y}_{cc}^{FE}\boldsymbol{\Phi}_{c}^{TS+\mathrm{T}}\right)^{-1}\boldsymbol{\Phi}_{c}^{TS+}\mathbf{Y}_{ci}^{FE} \tag{49}$$

where the c DOF are the measured DOF.

3.5 Practical Guidance Using the Transmission Simulator Approach

There are several practical guidelines to using the TS approach which deserve mention here.

1. The TS fixture should be designed to be as simple as possible to fabricate and model. Furthermore, it is best if the fixture can be fabricated from one piece

of material to eliminate the uncertainty and nonlinearity of joints on the fixture dynamics.
2. Fabricate the fixture of the same material and with the same interface geometry as the assembly it is replacing to capture the joint compliance and dissipation as realistically as possible.
3. The fixture should capture the local impedance of the assembly it is replacing. This allows the joint to be excited realistically. The mass of the fixture will help bring modes down in frequency into the testable bandwidth. It is best to err on the side of making the fixture too stiff, rather than too flexible.
4. Cautiously add features to help obtain difficult measurements. In the example, tabs were added to allow accelerometer and force input locations that would be difficult to obtain on a pure ring. However, in the example, the tabs were too long, so that they had their own modes without much motion of the rest of the fixture. This actually degrades the results with the method. (In hindsight, shorter tabs would have improved results in the example.) Avoid features that result in repeated roots for the fixture modes. Add features that cause each natural frequency to be distinct. Add features that provide force input locations that will improve the excitation of poorly excited modes of the TS.

In addition, several guidelines are worth mentioning that are not specifically related to the TS approach.

1. Reduce the frequency bandwidth to the minimum required for the problem requirements. All substructuring methods suffer from modal truncation errors at some frequency. As one increases the bandwidth and adds more shapes to the bases, the possibility that the bases are insufficient to represent high-frequency motion increases. Many substructuring results have failed in an attempt to obtain a result for a much larger bandwidth than was truly required.
2. Where forces will be applied, a drive point motion sensor should be located perfectly co-linear with the input force. Either apply the force on the surface directly opposite of the sensor, or build a cap to put over the sensor, so that the force input may be co-linear with the motion sensor. (This is required for proper mode shape scaling in the CMS method or connection drive point measurements in FBS substructuring.)
3. Use low-level force inputs to minimize nonlinear response and improve the capability for fitting the modal parameters. (In most cases, low-level excitation will not excite nonlinear response as much as high-level excitation. There are some exceptions.)
4. Utilize hammer force inputs to a. minimize mass distortion due to shaker load cell mass and b. increase the frequency bandwidth of excitation over what can typically be obtained with shakers. If the substructure is massive, the mass of the load cell and frequency capability of the shaker may not be hindrances, so shakers may be a very good option.
5. When using CMS, make sure FRFs synthesized from the modal parameters reproduce the test FRFs adequately. For free substructures, the low-frequency

real part of the FRFs (mass line) should match to show that the analytical rigid body mode shapes are accurate. The elastic resonance amplitudes should match to show that the frequency/damping/mode shape/modal mass was extracted properly. Especially look to see that responses match for FRFs from references that were NOT used to extract the shapes. If they do not match, the drive point mode shape from the original reference may not have been extracted accurately.

6. To minimize the number of input references, FBS may be performed with FRFs accurately synthesized from modal parameters. The advantage of this is that one does not have to have a drive point FRF at every connection DOF. One only needs to use enough drive points to extract all the modes in the desired bandwidth. This approach helps eliminate experimental noise from the measurements. The disadvantage is that it cannot capture the residual effects of out-of-band modes.
7. Be aware of accuracy limitations of a coupled substructure model. The frequencies of the coupled model are usually most accurate in terms of percentage error. Usually, the mode shapes are less accurate, and the damping is the least accurate.

References

1. De Klerk D, Rixen DJ, Voormeeren SN (2008) General framework for dynamic substructuring: History, review, and classification of techniques. AIAA J 46(5):1169–1181
2. Allen MS, Mayes RL, Bergman EJ (2010) Experimental modal substructuring to couple and uncouple substructures with flexible fixtures and multi-point connections. J Sound Vib 329:4891–4906
3. Kammer DC (1991) Sensor placement for on-orbit modal identification and correlation of large space structures. J Guid Control Dyn 14:251–259
4. Carne TG, Dohrmann CR (1995) A modal test design strategy for model correlation. In: 13th international modal analysis conference, Nashville, pp 927–933
5. Bergman EJ, Allen MS, Kammer DC, Mayes RL (2010) Probabilistic investigation of sensitivities of advanced test-analysis model correlation methods. J Sound Vib 329:2516–2531

Structural Dynamics Modification and Modal Modeling

20

Mark Richardson and David Formenti

Contents

M. Richardson (✉)
Vibrant Technology, Inc., Centennial, CA, USA
e-mail: mark.richardson@vibetech.com

D. Formenti
BlackHawk Technology, Santa Cruz, CA, USA
e-mail: formenti@blkhawk.com

R. Allemang, P. Avitabile (eds.), *Handbook of Experimental Structural Dynamics*,
https://doi.org/10.1007/978-1-4614-4547-0_25

Abstract

The structural dynamics modification (SDM) method, also called eigenvalue modification, was first commercialized in the earlier 1980s by a software company founded by the authors. It has proved to be a useful engineering tool for providing a quick look at the influence of physical modifications to a mechanical structure on its modes of vibration.

SDM can be used with experimental mode shapes as well as analytical mode shapes. It provides meaningful results even when used with a few mode shapes and combined experimental and analytical mode shape data. This chapter also provides background information on the many details to be considered when acquiring experimental mode shapes. Finally, the example provided shows that SDM gives very accurate results when both translational and rotational joint stiffnesses are used to model the attachment of a rib stiffener to a plate.

Keywords

Frequency response function (FRF) · Experimental modal analysis mode shape (EMA mode shape) · Finite element analysis mode shape (FEA mode shape) · Operational modal analysis mode shape (OMA mode shape) · Unit modal mass mode shape (UMM mode shape) · Hybrid mode shape (combined EMA & FEA mode shape data)

1 Modal Models

SDM is unique in that it works directly with a modal model of the structure, either an Experimental **Modal Analysis (EMA)** modal model, a **Finite Element Analysis (FEA)** modal model, or a **Hybrid** modal model consisting of both EMA and FEA modal parameters. EMA mode shapes are obtained from experimental data, and FEA mode shapes are obtained from an analytical finite element computer model.

A **modal model** consists of a set of *scaled mode shapes*. In this chapter the mode shapes used in a modal model are scaled to **Unit Modal Masses**, called **UMM mode shapes**. FEA mode shapes are commonly scaled to **UMM mode shapes** using the mass matrix of the FEA model. In this chapter, it will be shown how EMA mode shapes can also be scaled to **UMM mode shapes** without using a mass matrix.

A modal model preserves the mass, damping, and stiffness properties of a mechanical structure and is used by SDM to represent the dynamic properties of the unmodified structure.

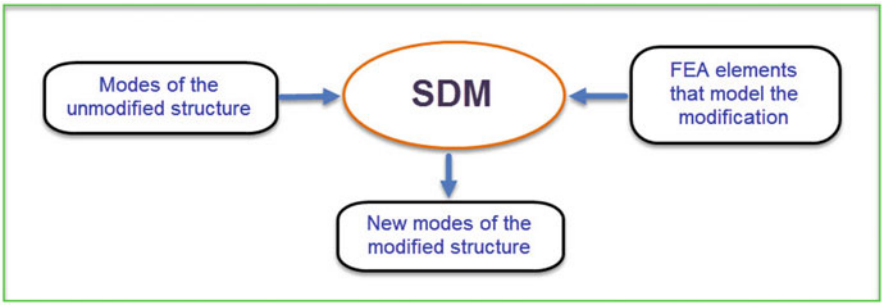

Fig. 1 SDM input-output diagram

2 Design Modifications

Once the dynamic properties of an unmodified structure are defined in the form of its modal model, SDM can be used to predict the dynamic effects of mechanical design modifications to the structure. These modifications can be as simple as *additions to* or *removals of* point masses, linear springs, or linear dampers, or more complex modifications can be modeled using FEA elements such as rod and beam elements, plate elements (membranes), and solid elements such as prisms, tetrahedrons, and brick elements.

SDM is computationally very efficient because it solves an eigenvalue problem in *modal space*. In contrast, FEA mode shapes are obtained by solving an eigenvalue problem in *physical space*.

Another advantage of SDM is that the modal model of the unmodified structure must only contain data for the DOFs (points and directions) *where the modification elements are attached* to a geometric model of the structure. SDM then provides a new modal model of the modified structure, as depicted in Fig. 1.

3 Eigenvalue Modification

A variety of numerical methods have been developed over the years which only require a modal model to represent the dynamics of an unmodified structure. Among the more traditional methods for performing these calculations are *modal synthesis*, the *Lagrange multiplier* method, and *diakoptics*. However, the *local eigenvalue modification* technique, developed primarily through the work of Weissenburger, Pomazal, Hallquist, and Snyder [1], is the technique commonly used by the SDM method today.

All of the early development work on SDM was done primarily with analytical FEA mode shapes. The primary objective was to provide a faster means of investigating physical changes to a structure without having to solve a much larger eigenvalue problem. FEA mode shapes are obtained by solving the problem in

physical coordinates, whereas SDM solves a much smaller eigenvalue problem in modal coordinates.

In 1979, Structural Measurement Systems (SMS) began using the local eigenvalue modification method together with an EMA modal model derived from a modal test [2–5]. The computational efficiency of this method made it very attractive for use in a laboratory on a desktop calculator or computer. More importantly, it gave reasonably accurate results using only a small number of EMA mode shapes in the modal model of the unmodified structure.

A modal model with only a few mode shapes in it is called a *truncated modal model*. Regardless of whether EMA or FEA mode shapes are used, *truncated modal model*s have been shown to adequately characterize the dynamics of a structure. The effects of using truncated modal models were investigated in [2, 3].

The fundamental calculation of SDM is the solution of an eigenvalue problem. The solution is computationally efficient because a small dimensional eigenvalue problem is solved. Computational speed is virtually independent of the number of DOFs in the modal model. Hence, large modifications involving many DOFs are handled as efficiently as smaller modifications.

The SDM computational process is straightforward. All physical modifications are converted into appropriate changes to the mass, stiffness, and damping matrices of the equations of motion, in the same manner as an FEA model is constructed. These modification matrices are then transformed to modal coordinates using the mode shapes of the modal model of the unmodified structure. The resulting transformed modifications are then added to the modal properties of the unmodified structure, and these new equations are solved for the new modes of the modified structure.

To illustrate this process, if there were 1000 DOFs in an FEA model, solving for its FEA mode shapes requires the solution of an eigenvalue problem with mass and stiffness matrices of the size 1000 by 1000 [6–8]. By contrast, if the dynamics of an unmodified structure is represented with a modal model consisting of ten mode shapes, new mode shapes resulting from a structural modification are found by solving an eigenvalue problem with transformed mass and stiffness matrices of the size 10 by 10.

The size of the eigenvalue problem in modal space is independent of the number of structural modifications made to the structure. Many modification elements can be attached to a 3D geometric model of the structure, and the SDM solution time does not significantly increase.

SDM requires two inputs:

1. A modal model that adequately represents the dynamics of the unmodified structure
2. Finite elements attached to a geometric model of the structure that characterize the structural modifications

With these inputs, SDM calculates a new modal model that represents the dynamics of the modified structure. It will also be shown in later examples that

SDM obtains results that are very comparable to those obtained from an FEA eigensolution.

4 Measurement Chain to Obtain an EMA Modal Model

If a modal model containing EMA mode shapes is used with SDM, the accuracy of the mode shapes will directly influence the accuracy of the results calculated with the SDM method. To understand the potential errors that can occur in an EMA modal model, it is important to review the steps in the *measurement chain* required to obtain EMA mode shapes.

Three major steps are commonly used to obtain an EMA modal model:

1. Acquire experimental vibration data from the test article.
2. Calculate a set of frequency response functions (FRFs) from the vibration data.
3. Curve fit the FRFs to estimate the EMA mode shapes of the test article.

4.1 Critical Issues in the Measurement Chain

Following is a list of issues to consider in implementing a measurement chain:

1. Nonlinearity of the test structure dynamics
2. Boundary conditions of the test structure
3. Excitation technique
4. Force and response sensors
5. Sensor mounting
6. Sensor calibration
7. Sensor cabling
8. Signal acquisition and conditioning
9. Spectrum analysis
10. FRF calculation
11. FRF curve fitting
12. Creating an EMA modal model

All of these issues involve assumptions that can impact the accuracy of the EMA modal model and ultimately the accuracy of the SDM results. Only a few of these critical issues will be addressed here, namely, sensors, sensor mounting, sensor calibration, FRF calculation, and FRF curve fitting.

4.2 Calculating FRFs from Experimental Vibration Data

To create an EMA modal model, a set of calibrated inertial FRF measurements is required. These frequency domain measurements are unique in that they involve

subjecting the test structure to a known measurable force while simultaneously measuring the structural response(s) due to the force. The structural response is measured either as acceleration, velocity, or displacement using sensors that are either mounted on the surface or are non-contacting but still measure the surface vibration.

An FRF is a special case of a Transfer Function. A Transfer Function is a frequency domain relationship between any type of input signal and any type of output signal. An FRF defines the dynamic relationship between the excitation force applied to a structure at a specific location in a specific direction and the resulting response motion at another specific location in a specific direction. The force input point and direction and the response point and direction are referred to as the degrees of freedom (or DOFs) of the FRF.

An FRF is also called a *cross-channel measurement*. It requires the *simultaneous acquisition* of both the excitation force and one of its resultant responses. This means that at least a two-channel data acquisition system or spectrum analyzer is required to measure the signals required to calculate an FRF. The force (input) and the response (output) signals must also be *simultaneously acquired*, meaning that both channels of data are amplified, filtered, and sampled without introducing any artificial phase difference between the two signals.

4.3 Sensing Force and Motion

The excitation force is typically measured with a load cell. The analog signal from the load cell is fed into one of the channels of the data acquisition system. The response is measured either with an accelerometer, laser vibrometer, displacement probe, or another sensor that can measure the surface vibration. Accelerometers are most often used today because of their availability, relatively low cost, and variety of sizes and sensitivities. The important characteristics of both the load cell and accelerometer are:

1. Sensitivity
2. Usable amplitude range
3. Usable frequency range
4. Transverse sensitivity
5. Mounting method

4.4 Sensitivity Flatness

The most common type of sensor today is referred to as an IEPE/CCLD/ICP/Delta tron/Isotron style of sensor. This type of sensor requires a 2–10 milliamp current supply, typically supplied by the data acquisition system, and has a built-in charge amplifier and other signal conditioning. It also has a fixed sensitivity. Typical sensitivities are 10mv/lb. or 100mv/g.

The ideal frequency spectrum for any sensor is a *"flat magnitude"* over its usable frequency range. The documented sensitivity of most sensors is typically given at a fixed frequency (such as 100 Hz, 159.2 Hz, or 250 Hz) and is referred to as its 0 dB level.

The sensitivity of an accelerometer is specified in units of mv/g or mv/(m/sˆ2) with a *typical accuracy of +/−5%* at a specific frequency. The frequency spectrum of all sensors is *not perfectly flat*, meaning that its sensitivity varies somewhat over its usable frequency range. The response amplitude of an ICP accelerometer typically *rolls off* at low frequencies and *rises* at the high end of its usable frequency range. This specification is the ***flatness*** of the sensor, with a *typical variance of +/−10% to +/−15%*.

All of this equates to a possible error in the sensitivity of the force or response sensor over its usable frequency range. This means that the amplitude of an FRF might be in error by the amount that the sensitivity changes over its measured frequency range.

4.5 Transverse Sensitivity

Adding to its flatness error is the *transverse sensitivity* of a sensor. Both force and vibration have a direction associated with them. That is, a force or motion is defined at a point in a specific direction.

A uniaxial (single axis) transducer should only output a signal due to force or motion in the direction of its sensitive axis. Ideally, any force or motion that is not along its sensitive axis should not yield an output signal, but this is not the case with most sensors.

All sensors have a documented specification called *transverse sensitivity* or *cross axis sensitivity*. Transverse sensitivity specifies how much of the sensor output is due to a force or motion that is sensed from a direction *other than the measurement axis* of the sensor. Transverse sensitivity is typically *less than 5%* of the sensitivity of the measurement axis. For example, if an accelerometer has a sensitivity of 100mv/g, its transverse sensitivity might be 5%, or about 5mv/g. Therefore, 1 g of motion in a direction other than the sensitive axis of an accelerometer might add 5mv (or 0.05 g) to its output signal.

4.6 Sensor Linearity

Another area affecting the accuracy of an FRF is the *linearity* of each sensor output signal relative to the actual force or vibration. If a sensor output signal were plotted as a function of its input force or vibration, all its output values should *lie on a straight line*. Any values that do not lie on a straight line are an indication of the *nonlinearity* of the sensor. The *nonlinearity* specification is *typically less than 1%* over the usable frequency range of a sensor.

As the amplitude of the measured signal becomes larger than the specified input amplitude range of the sensor, the signal will ultimately *cause an overload* in the internal amplifier of the sensor. This overload results in a *clipped output signal* from the sensor. A *clipped output signal* is the reason why it is very important to measure amplitudes that are within the specified amplitude range of a sensor.

4.7 Sensor Mounting

Attaching a sensor to the surface of the test article is also of critical importance. The function of a sensor is to *"transduce"* a physical quantity, for example, the acceleration of the surface at a point in a direction. Therefore, it is important to attach the sensor to a surface so that it will accurately transduce the surface motion over the frequency range of interest.

Mounting materials and techniques also have a usable frequency range just like the sensor itself. It is very important to choose an appropriate mounting technique so that the surface motion over the desired frequency range is not affected by the mounting material of method. The use of *magnets*, *tape*, *putty*, **glue**, or *contact cement* is convenient for attaching sensors to surfaces. But attaching a sensor using a *threaded stud* is the most reliable method, with the widest frequency range.

4.8 Leakage Error

Another error associated with the FRF calculation is a result of the FFT algorithm itself. The FFT algorithm is used to calculate the Digital Fourier Transform (DFT) of the force and response signals. These DFTs are then used to calculate an FRF.

4.9 Finite Length Sampling Window

The FFT algorithm assumes that the time domain window of acquired digital data (called the *sampling window*) *completely contains* the acquired signal. If an acquired signal is not fully captured within its sampling window, the DFT of the signal will contain *leakage error*.

4.10 Leakage-Free Spectrum

The spectrum of an acquired signal will be *leakage-free* if one of the following conditions is satisfied.

1. If a signal is *periodic* (like a *sine wave*), then it must make *one or more complete cycles* within the sampled window.

2. If a signal is *not periodic*, then it must be *completely contained* within the sampled window.

If an acquired signal does not meet one of the above conditions, there will be errors in its DFT and errors in the FRF that is calculated using the DFT. Leakage error causes both amplitude and frequency errors in a DFT and in a FRF that uses the DFT.

4.11 Leakage-Free Signals

Leakage is eliminated by using testing signals that meet one of the two conditions stated above. During impact testing, if the impulsive force and the impulse response signals are both completely contained within their sampling windows, *leakage-free FRFs* will be calculated using those signals.

During shaker testing, if a Burst Random or a Burst Chirp (fast swept sine) shaker signal is used to excite the structure, *leakage-free FRFs* can be calculated using those signals. A Burst Random or Burst Chirp signal is terminated prior to the end of its sampling window so that both the force and structural response signals are *completely contained* within their sampling windows.

4.12 Reduced Leakage

If one of the two leakage-free conditions cannot be met by the acquired force and response signals, then leakage errors *can be minimized* in their spectra by applying an appropriate time domain window to the sampled signal before it is transformed using the FFT. A *Hanning window* is typically applied to pure (continuous) random signals. Pure random signals are *never completely contained* within their sampling windows. Using a Hanning window prior to transforming them with the FFT will minimize leakage in their frequency spectrum.

4.13 Linear Versus Nonlinear Dynamics

Both EMA and FEA modal models are defined as solutions to a set of *linear differential equations.* Using a modal model assumes that *the linear dynamic behavior* of the test article can be *adequately described using these equations*. However, many real-world structures may not exhibit linear dynamic motion.

Real-world structures can have dynamic behavior ranging from *linear* to *slightly nonlinear* to *severely nonlinear*. If the test article is in fact undergoing nonlinear motion, significant errors will occur when attempting to extract modal parameters from a set of FRFs which are based on a linear dynamic model.

4.14 Random Excitation and Spectrum Averaging

To reduce the effects of nonlinear behavior, random excitation combined with signal post-processing must be applied to the acquired data. The goal is to yield a set of *linear FRF estimates* to represent the dynamics of the structure subject to a certain force level.

This common method for testing a nonlinear structure is to excite it with one or more shakers using random excitation signals. If these signals continually vary over time, the random excitation will excite the nonlinear behavior of the structure in a random fashion.

Each time a nonlinear signal is transformed using the FFT, the nonlinear components of the signal will appear as *random noise* spread over the frequency range of the DFT. If multiple DFTs of the response of a randomly excited structure are *averaged together*, the nonlinear components (random noise) will be *"averaged out"* of the average DFT, leaving only the *linear resonant response peaks*.

4.15 Curve Fitting FRFs

The first step of an *FRF-based EMA* is to calculate a set of FRFs that accurately represent the linear dynamics of the test article over a frequency range of interest. The second step is to curve fit the FRFs using a *linear parametric model* of an FRF. The unknown parameters of the FRF model are the modal parameters of the structure. The goal of these two steps is to obtain an *accurate EMA modal model*.

If the test article has a high modal density including either *closely coupled modes* (two modes represented by one resonance peak) or *repeated roots* (two modes with the same frequency but different mode shapes), extracting an accurate EMA modal model from the FRFs can be challenging.

The linear parametric curve fitting model is a *summation of contributions from all modes* at each frequency sample of the FRFs. This model is commonly curve fit to the FRF data using a *least-squared-error* method. This broadband curve fitting approach also assumes that all resonances of interest have been adequately excited over the frequency span of the FRFs.

A wide variety of FRF-based curve fitting methods are commercially available today. All FRF-based curve fitting methods assume that the FRFs adequately represent the linear dynamics of the test article and are leakage-free.

4.16 Modal Models and SDM

SDM will give accurate results when an accurate modal model of the unmodified structure is used. The modal model can contain EMA mode shapes, FEA mode shapes, Hybrid mode shapes consisting of both EMA and FEA modal parameters, or a mixture of all three types of mode shapes.

The advantage of SDM is that with a reasonably accurate modal model of the unmodified structure, numerous structural modifications can be quickly explored. This could include exploring alternate boundary conditions which are difficult to model with an FEA model.

Later in this chapter, a Hybrid modal model containing both translational and rotational DOFs will be used with SDM to model the attachment of a RIB stiffener to an aluminum plate. The new mode shapes calculated by SDM will then be compared with both FEA and EMA mode shapes of the plate with the RIB attached to it.

5 Structural Dynamic Models

The dynamic behavior of a mechanical structure can be modeled either with a set of differential equations in the time domain or with an equivalent set of algebraic equations in the frequency domain. Once the equations of motion have been created, they can be used to calculate mode shapes and to calculate structural responses to static loads or dynamic forces.

The dynamic response of most structures usually includes *resonance-assisted vibration.* Dynamic resonance-assisted response levels can *far exceed* the deformation levels due to static loads. Resonance-assisted vibration is often the cause of noisy operation, uncontrollable behavior, premature wear out of parts such as bearings, and unexpected material failure due to cyclic fatigue.

5.1 Structural Resonances

Two or more spatial deformations assembled into a vector format are called an Operating Deflection Shape (or ODS).

A mode of vibration is a mathematical representation of a structural resonance. An ODS is a *summation of mode shapes*.

Each mode is represented by its natural frequency (its modal frequency), a damping decay constant (the decay rate of a resonance when forces are removed from the structure), and its spatially distributed amplitude levels (its mode shape). These three modal properties (frequency, damping, and mode shape) provide a *complete mathematical representation* of each structural resonance. A mode shape is the contribution of a resonance to the overall deformation (the ODS) on the surface of a structure at each location in each direction.

It is shown later that both the time and frequency domain equations of motion can be represented solely in terms of modal parameters. This powerful conclusion means that a set of modal parameters can be used to *completely represent the linear dynamics* of a structure.

When properly scaled, a set of mode shapes is called a *modal model*. The complete dynamic properties of the structure are represented by its modal model.

SDM uses the *modal model* of the *unmodified* structure together with the FEA elements that represent structural modifications as inputs and calculates a *new modal model* for the modified structure.

5.2 Truncated Modal Model

All EMA and FEA modal models contain mode shapes for a *finite number of modes*. An EMA modal model contains a finite number of mode shapes that were obtained by curve fitting a set of FRFs that span a *limited frequency range*. An FEA modal model also contains a finite number of mode shapes that are defined for a *limited range of frequencies*. Therefore, both EMA and FEA modal models represent a *truncated (approximate) dynamic model* of a structure.

Except for so-called lumped parameter systems (like a mass on a spring), all real-world structures have an *infinite number of resonances*. But SDM still provides usable results because of the following property.

The dynamic response of most structures *is dominated* by the excitation of their *low frequency modes*.

When using the SDM method, *all the low frequency modes* should be included in the modal model. In order to account for the higher frequency modes that have been left out of the truncated modal model, it is also important to include several modes *above the highest frequency mode* of interest in the modal model.

5.3 Sub-structuring

To solve a sub-structuring problem, where one structure is mounted on or attached to another using FEA elements, the free-body dynamics (the *six rigid-body modes*) of the structure to be mounted on the other must also be included in its modal model. This will be illustrated by the example later in this chapter.

5.4 Rotational DOFs

Another potential source of error in using SDM is that certain modifications require mode shapes with both translational and rotational DOFs. Normally only translational motions are acquired experimentally, and therefore the resulting FRFs and mode shapes only have translational DOFs. If a modal model does not contain rotational DOFs, accurate modifications that involve torsional stiffnesses and/or rotary inertia effects cannot be accurately modeled.

FEA mode shapes derived from *rod, beam, and plate (membrane) elements* have rotational DOFs included in them. When rotational stiffness and inertia are important, FEA mode shapes with rotational DOFs in them can be used in a Hybrid modal model as input to SDM. Later in this chapter, SDM will be used to model

the attachment of a RIB stiffener to a plate structure. Mode shapes with rotational DOFs and spring elements with rotational stiffness will be used to correctly model the joint stiffness between the RIB and the plate.

6 Time Domain Dynamic Model

Modes of vibration are defined by assuming that the dynamic behavior of a mechanical structure or system *can be adequately described* by a set of time domain differential equations. These equations are a statement of *Newton's second law* **(F = Ma)**. They represent a *force balance* between the internal inertial (mass), dissipative (damping), and restoring (stiffness) forces and the external forces acting on the structure. This force balance is written as a set of linear differential equations:

$$[\mathbf{M}]\{\ddot{\mathbf{x}}(\mathbf{t})\} + [\mathbf{C}]\{\dot{\mathbf{x}}(\mathbf{t})\} + [\mathbf{K}]\{\mathbf{x}(\mathbf{t})\} = \{\mathbf{f}(\mathbf{t})\} \tag{1}$$

where

$[\mathbf{M}]$ ← Mass matrix (**n** by **n**)
$[\mathbf{C}]$ ← Damping matrix (**n** by **n**)
$[\mathbf{K}]$ ← Stiffness matrix (**n** by **n**)
$\{\ddot{\mathbf{x}}(\mathbf{t})\}$ ← Accelerations (**n**-vector)
$\{\dot{\mathbf{x}}(\mathbf{t})\}$ ← Velocities (**n**-vector)
$\{\mathbf{x}(\mathbf{t})\}$ ← Displacements (**n**-vector)
$\{\mathbf{f}(\mathbf{t})\}$ ← Externally applied forces (**n**-vector)

These differential equations describe the *dynamics between n-discrete points and directions* or *n-degrees of freedom (DOFs)* of a structure. To adequately describe its dynamic behavior, enough equations can be created involving as many DOFs as necessary. Even though equations could be created between an infinite number of DOFs, in a practical sense, only a finite number of DOFs is ever used, but they could still number in the hundreds of thousands.

Notice that the damping force is *proportional to velocity*. This is a model for *viscous damping*. Different damping models are addressed later in this chapter.

6.1 Finite Element Analysis (FEA)

Finite element analysis (FEA) is used to generate the coefficient matrices of the time domain differential equations written above. The mass and stiffness matrices are generated from the physical and material properties of the structure. Material properties include the *modulus of elasticity*, *inertia*, and *Poisson's ratio* (or *"squeezability"*).

Damping properties are not easily modeled for real-world structures. Hence the damping force term is usually left out of an FEA model. Even without damping,

the mass and stiffness terms are enough to model resonant vibration; hence, the equations of motion can be solved for modal parameters.

6.2 FEA Modes

The *homogeneous* form of the differential equations, where the external forces on the right-hand side are zero, can be solved for mode shapes and their corresponding natural frequencies. This is called an *eigen-solution.* Each natural frequency is an *eigenvalue*, and each mode shape is an *eigenvector*. The analytical mode shapes are referred to as **FEA mode shapes**. The transformation of the equations of motion (1) into modal coordinates is covered later in this chapter.

7 Frequency Domain Dynamic Model

In the frequency domain, the dynamics of a mechanical structure or system are represented by a set of linear algebraic equations, in a form called a *Transfer Function* model or *MIMO (Multiple Input Multiple Output) model.* This model contains Transfer Functions between all combinations of *input and response DOF pairs*:

$$\{\mathbf{X}(\mathbf{s})\} = [\mathbf{H}(\mathbf{s})]\{\ \mathbf{F}(\mathbf{s})\}\ (\mathbf{n} - \text{vector}) \tag{2}$$

where

s ← Laplace variable (complex frequency)
[**H**(**s**)] ← Transfer Function matrix (**n** by **n**)
{**X**(**s**)} ← Laplace transform of displacements (**n**-vector)
{**F**(**s**)} ← Laplace transform of externally applied forces (**n**-vector)

This model is also a complete description of the *dynamics between n-DOFs* of a structure. Equations can be created between as many DOF pairs of the structure as necessary to adequately describe its dynamic behavior over a frequency range of interest. Like the time domain differential Eq. (1), these Eq. (2) are finite dimensional.

8 Parametric Models Used for Curve Fitting

Curve fitting is a numerical process by which an analytical FRF model is matched to experimental FRF data in a manner that *minimizes the squared error* between the experimental data and the analytical curve fitting model. The purpose of curve fitting is to estimate the unknown modal parameters of the curve fitting model. More

precisely, the modal frequency, damping, and mode shape of each resonance in the frequency range of the FRFs are estimated by curve fitting an analytical model to a set of FRFs.

8.1 Rational Fraction Polynomial Model

The Transfer Function matrix in Eq. (2) can also be expressed analytically as a ratio of two polynomials. This is called a *rational fraction polynomial matrix form* of the Transfer Function matrix. Expressed in terms of **m**-modes, the denominator polynomial has (**2 m + 1**) terms, and each numerator polynomial has (**2 m**) terms:

$$[\mathbf{H}(\mathbf{s})] = \frac{[\mathbf{b_0}]\,\mathbf{s^{2m-1}} + [\mathbf{b_1}]\,\mathbf{s^{2m-2}} + [\mathbf{b_2}]\,\mathbf{s^{2m-3}} + \cdots + [\mathbf{b_{2m-1}}]}{\mathbf{a_0 s^{2m}} + \mathbf{a_1 s^{2m-1}} + \mathbf{a_2 s^{2m-2}} + \cdots + \mathbf{a_{2m}}} \ (\mathbf{n}\ \text{by}\ \mathbf{n}) \quad (3)$$

where

m= number of modes in the analytical curve fitting model
$\mathbf{a_0\ s^{2m}} + \mathbf{a_1\ s^{2m-1}} + \mathbf{a_2\ s^{2m-2}} + \ldots + \mathbf{a_{2m}}$ ← the characteristic polynomial
$\mathbf{a_0, a_1, a_2, \ldots, a_{2m}}$ ← real-valued coefficients
$[\mathbf{b_0}]\mathbf{s^{2m-1}} + [\mathbf{b_1}]\mathbf{s^{2m-2}} + [\mathbf{b_2}]\mathbf{s^{2m-3}} + \ldots + [\mathbf{b_{2m-1}}]$ ← numerator polynomial matrix (**n** by **n**)
$[\mathbf{b_0}], [\mathbf{b_1}], [\mathbf{b_2}], \ldots, [\mathbf{b_{2m-1}}]$ ← real-valued coefficient matrices (**n** by **n**)

Each Transfer Function in the (**n** by **n**) matrix has a *unique numerator polynomial* (**n** by **n**) matrix and the *same denominator polynomial*, called the *characteristic polynomial*.

8.2 Partial Fraction Expansion Model

The Transfer Function matrix in Eq. (2) can also be expressed in *partial fraction expansion form*. When expressed as shown in Eqs. (4) and (5), any Transfer Function value *at any frequency* is a *summation of terms*, each term *called the resonance curve of a mode of vibration*:

$$[\mathbf{H}(\mathbf{s})] = \sum_{\mathbf{k=1}}^{\mathbf{m}} \frac{[\mathbf{r_k}]}{\mathbf{2j}\ (\mathbf{s} - \mathbf{p_k})} - \frac{\left[\mathbf{r_k^*}\right]}{\mathbf{2j}\ \left(\mathbf{s} - \mathbf{p_k^*}\right)} \quad (4)$$

or

$$[\mathbf{H}(\mathbf{s})] = \sum_{\mathbf{k=1}}^{\mathbf{m}} \frac{\mathbf{A_k}\,\{\mathbf{u_k}\}\,\{\mathbf{u_k}\}^{\mathbf{t}}}{\mathbf{2j}\ (\mathbf{s} - \mathbf{p_k})} - \frac{\mathbf{A_k^*}\left\{\mathbf{u_k^*}\right\}\left\{\mathbf{u_k^*}\right\}^{\mathbf{t}}}{\mathbf{2j}\ \left(\mathbf{s} - \mathbf{p_k^*}\right)} \quad (5)$$

where

$\mathbf{m}$= number of modes of vibration
$[\mathbf{r_k}] \leftarrow$ Residue matrix for the k^{th} mode ($\mathbf{n}$ by $\mathbf{n}$)
$\mathbf{p_k} = -\boldsymbol{\sigma_k} + \mathbf{j}\boldsymbol{\omega_k} \leftarrow$ Pole location for the k^{th} mode
$\boldsymbol{\sigma_k} \leftarrow$ Damping decay of the k^{th} mode
$\boldsymbol{\omega_k} \leftarrow$ Damped natural frequency of the k^{th} mode
$\{\mathbf{u_k}\} \leftarrow$ Mode shape for the k^{th} mode ($\mathbf{n}$-vector)
$\mathbf{A_k} \leftarrow$ Scaling constant for the k^{th} mode
t – denotes the transposed vector

Figure 2 shows a Transfer Function for a single resonance, plotted over *half of the s-plane*.

8.3 Experimental FRFs

An FRF is defined as the *values of a Transfer Function along the jω-axis* in the s-plane.

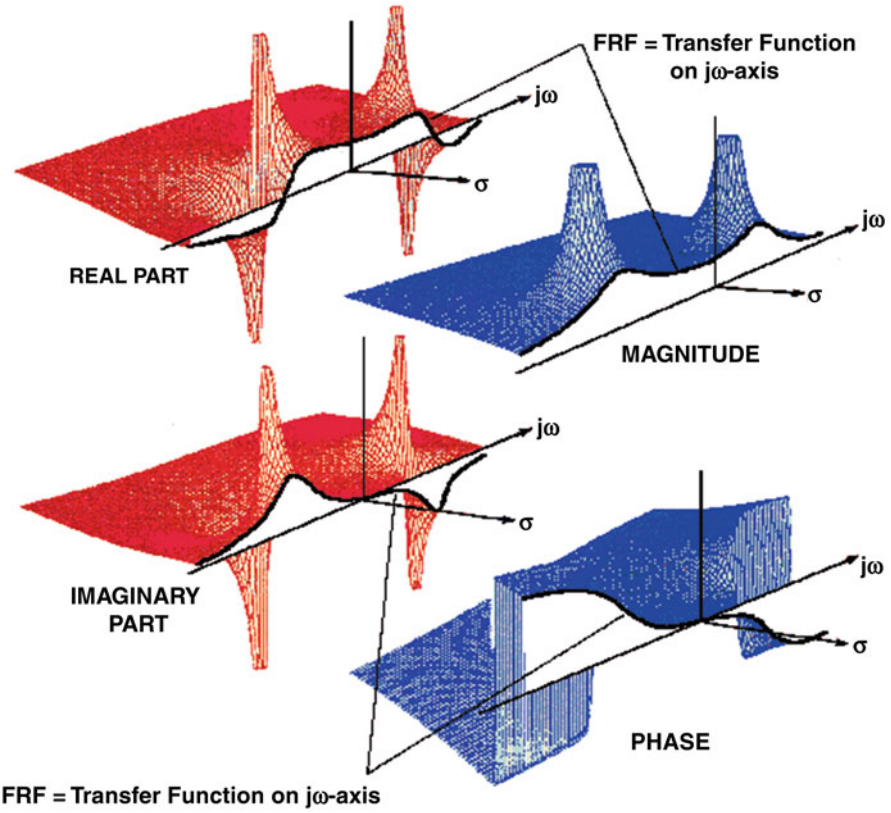

Fig. 2 Transfer Function and FRF of a single resonance

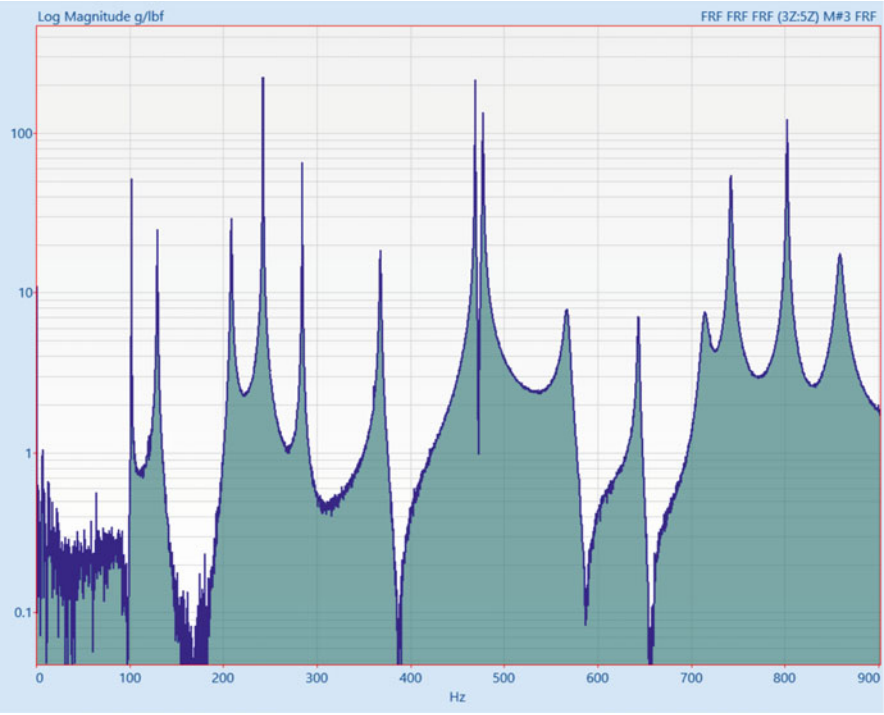

Fig. 3 Log magnitude of an experimental FRF

An experimental FRF can be calculated from acquired experimental data if *each excitation force* and *all responses caused by that force* are *simultaneously acquired*. Figure 3 shows the magnitude and phase of a typical experimental FRF.

9 FRF-Based Curve Fitting

Curve fitting is commonly done using a *least-squared-error algorithm* which minimizes the difference between an analytical FRF model and the experimental data. The outcome of *FRF-based curve fitting* is a pole estimate (frequency and damping) and a mode shape (a *row or column of residue estimates* in the residue matrix) for each resonance that is represented in the experimental FRF data.

All forms of the curve fitting model, Eqs. (3), (4), and (5), are used by different curve fitting algorithms. If the rational fraction polynomial model (3) is used, its numerator and denominator polynomial coefficients are determined during curve fitting. These polynomial coefficients are further processed numerically to extract the frequency, damping, and mode shape of each resonance represented in the FRFs.

9.1 Modal Frequency and Damping

Modal frequency and damping are calculated as the *roots of the characteristic polynomial*. The denominators of all three curve fitting models (3), (4), and (5) contain the same characteristic polynomial. Therefore, *global estimates* of modal frequency and damping are normally obtained by curve fitting an entire set of FRFs.

Another property resulting from the common denominator of the FRFs is that the *resonance peak for each* mode will occur at the *same frequency* in each FRF. Mass loading effects can occur when the response sensors add a significant amount of mass relative to the mass of the test structure. If the sensors are moved from one point to another during a test, some resonance peaks will occur at a different frequency in certain FRFs. When mass loading of this type occurs, a *local polynomial curve fitter*, which estimates frequency, damping, and residue for each mode in each FRF, will provide better results.

9.2 Modal Residue

The modal residue, or FRF numerator, *is unique for each mode and each FRF*.

A modal residue is the *magnitude (or strength)* of a mode in an FRF. A *row or column* of residues in the residue matrix *defines the mode shape* of a mode.

The relationship between residues and mode shapes is shown in the numerators of the two curve fitting models (4) and (5).

Figure 4 shows an analytical curve fitting function overlaid on the log magnitude of an experimental FRF.

If the partial fraction expansion model (5) is used, the pole (frequency and damping) and residues for each mode are explicitly determined during the curve

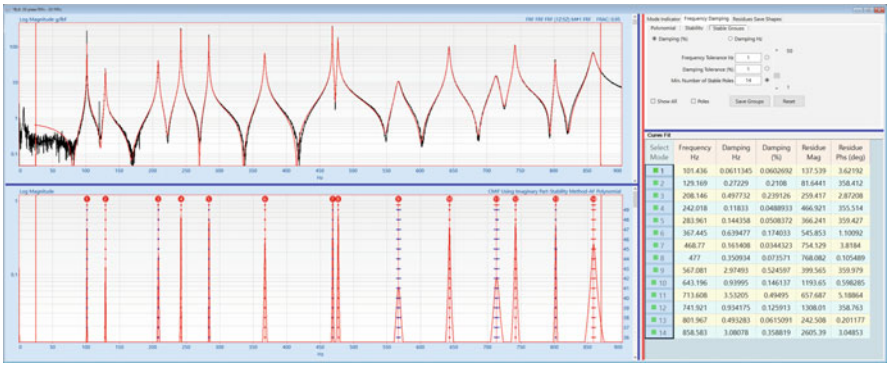

Fig. 4 Curve of an experimental FRF

fitting process. To achieve more numerical stability, curve fitting can be divided into two curve fitting steps.

1. Estimate frequency and damping (global or local estimates).
2. Estimate residues using the frequency and damping estimates.

10 Transformed Equations of Motion

Since the differential equations of motion (1) are linear, they can be transformed to the frequency domain using the Laplace transform without loss of any information. In the Laplace (complex frequency) domain, the equations have the form:

$$\mathbf{s^2}\,[\mathbf{M}]\,\{\mathbf{X}\,(\mathbf{s})\} + \mathbf{s}\,[\mathbf{C}]\,\{\mathbf{X}\,(\mathbf{s})\} + [\mathbf{K}]\,\{\mathbf{X}\,(\mathbf{s})\} = \{\mathbf{F}\,(\mathbf{s})\} + \{\mathbf{ICs}\} \tag{7}$$

where

$\{\mathbf{ICs}\} \leftarrow$ vector of initial conditions (**n**-vector)
$\{\mathbf{X}(\mathbf{s})\} \leftarrow$ Laplace transforms of displacements (**n**-vector)
$\{\mathbf{F}(\mathbf{s})\} \leftarrow$ Laplace transforms of applied forces (**n**-vector)

All physical properties of the structure are preserved in the left-hand side of the equations, while the applied forces and initial conditions {ICs} are contained on the right-hand side. The initial conditions can be treated as a special form of the applied forces and hence will be dropped from consideration without loss of generality in the following development.

The equations of motion can be further simplified:

$$[\mathbf{B}\,(\mathbf{s})]\,\{\mathbf{X}\,(\mathbf{s})\} = \{\mathbf{F}\,(\mathbf{s})\}\ \ (\mathbf{n} - \text{vector}) \tag{8}$$

where

$$[\mathbf{B}\,(\mathbf{s})] = \mathbf{s^2}\,[\mathbf{M}] + \mathbf{s}\,[\mathbf{C}] + [\mathbf{K}] \leftarrow \text{system matrix}\ \ (\mathbf{n}\ \text{by}\ \mathbf{n}) \tag{9}$$

Equation (8) shows that any linear dynamic system has *three basic parts*: applied forces (*inputs*), responses to those forces (*outputs*), and the dynamic system represented by its *system matrix* **[B(s)]**.

11 Dynamic Model in Modal Coordinates

The modal parameters of a structure are the solutions to the homogeneous equations of motion. That is, when $\{\mathbf{F(s)}\} = \{\mathbf{0}\}$, the solutions to Eq. (8) are complex valued eigenvalues and eigenvectors. The eigenvalues occur in complex conjugate

pairs $\left(p_k, p_k^*\right)$. The eigenvalues are the solutions (or roots) of the characteristic polynomial, which is derived from the following determinant equation:

$$\det\left[\mathbf{B}\left(\mathbf{s}\right)\right] = 0 \tag{10}$$

The eigenvalues (or *poles*) of the system are:

$$p_k = -\sigma_k + j\omega_k, \quad \mathbf{k} = 1, \ldots \mathbf{m}$$

$$p_k^* = -\sigma_k - j\omega_k, \quad \mathbf{k} = 1, \ldots \mathbf{m}$$

$\mathbf{m}$ = number of modes
$p_k = -\sigma_k + j\omega_k \leftarrow$ pole for the k^{th} mode
$p_k^* = -\sigma_k - j\omega_k \leftarrow$ conjugate pole for the k^{th} mode
$\sigma_k \leftarrow$ damping of the k^{th}mode
$\omega_k \leftarrow$ damped natural frequency of the k^{th} mode, $\mathbf{k = 1,} \ldots \mathbf{m}$.

Each eigenvalue has a corresponding eigenvector, and hence the eigenvectors also occur in complex conjugate pairs, $\left(\{u_k\}, \left\{u_k^*\right\}\right)$.

Each *complex eigenvalue* (also called a *pole*) contains the modal frequency and damping. Each corresponding *complex eigenvector* is the mode shape.

Each eigenvector pair is a solution to the algebraic equations:

$$\left[\mathbf{B}\left(\mathbf{p_k}\right)\right]\left\{\mathbf{u_k}\right\} = \{\mathbf{0}\} \ \mathbf{k} = 1, \ldots \mathrm{m} \ (\mathbf{n} - \text{vector}) \tag{11}$$

$$\left[\mathbf{B}\left(\mathbf{p_k^*}\right)\right]\left\{\mathbf{u_k^*}\right\} = \{\mathbf{0}\} \ \mathbf{k} = 1, \ldots \mathbf{m} \ (\mathbf{n} - \text{vector}) \tag{12}$$

The eigenvectors (or *mode shapes*) can be assembled into a matrix:

$$\begin{aligned}[\mathbf{U}] = \left[\{\mathbf{u}_1\}, \{\mathbf{u}_2\}, \ldots, \{\mathbf{u_m}\}, \left\{\mathbf{u}_1^*\right\}, \left\{\mathbf{u}_2^*\right\}, \ldots, \left\{\mathbf{u_m^*}\right\}\right] \\ \leftarrow \text{mode shape matrix } (\mathbf{n} \text{ by } \mathbf{2\ m})\end{aligned} \tag{13}$$

This transformation of the equations of motion means that all vibration can be represented in terms of modal parameters.

Fundamental Law of Modal Analysis: All vibration is a *summation of mode shapes*.

Using the ($\mathbf{n}$ by $\mathbf{2\ m}$) mode shape matrix **[U]**, the time domain response of a structure $\{\mathbf{x(t)}\}$ is related to its response in modal coordinates $\{\mathbf{z(t)}\}$ by:

$$\{\mathbf{x}(\mathbf{t})\} = [\mathbf{U}]\{\mathbf{z}(\mathbf{t})\} \ (\mathbf{n} - \text{vector}) \tag{14}$$

Applying the Laplace transform to Eq. (14) stated gives:

$$\{\mathbf{X}(\mathbf{s})\} = [\mathbf{U}]\{\mathbf{Z}(\mathbf{s})\}$$

where

$\{\mathbf{Z}(\mathbf{s})\} \leftarrow$ Laplace transform of displacements in modal coordinates $(\mathbf{2m} - \text{vector})$

Applying this transformation to Eq. (8) gives:

$$\left[\mathbf{s}^2[\mathbf{M}][\mathbf{U}] + \mathbf{s}[\mathbf{C}][\mathbf{U}] + [\mathbf{K}][\mathbf{U}]\right]\{\mathbf{Z}(\mathbf{s})\} = \{\mathbf{F}(\mathbf{s})\} \ (\mathbf{n} - \text{vector}) \tag{15}$$

Pre-multiplying Eq. (15) by the *transposed conjugate* of the mode shape matrix ($[\mathbf{U}]^{\mathbf{t}}$) gives:

$$\left[\mathbf{s}^2[\mathbf{U}]^{\mathbf{t}}[\mathbf{M}][\mathbf{U}] + \mathbf{s}[\mathbf{U}]^{\mathbf{t}}[\mathbf{C}][\mathbf{U}] + [\mathbf{U}]^{\mathbf{t}}[\mathbf{K}][\mathbf{U}]\right]\{\mathbf{Z}(\mathbf{s})\} = [\mathbf{U}]^{\mathbf{t}}\{\mathbf{F}(\mathbf{s})\} \ (\mathbf{2\,m} \text{ by } \mathbf{2\,m}) \tag{16}$$

Three new matrices can now be defined:

$$[\mathbf{m}] = [\mathbf{U}]^{\mathbf{t}}[\mathbf{M}][\mathbf{U}] \leftarrow \text{modal mass matrix} \ (\mathbf{2\,m} \text{ by } \mathbf{2\,m}) \tag{17}$$

$$[\mathbf{c}] = [\mathbf{U}]^{\mathbf{t}}[\mathbf{C}][\mathbf{U}] \leftarrow \text{modal damping matrix} \ (\mathbf{2\,m} \text{ by } \mathbf{2\,m}) \tag{18}$$

$$[\mathbf{k}] = [\mathbf{U}]^{\mathbf{t}}[\mathbf{K}][\mathbf{U}] \leftarrow \text{modal stiffness matrix} \ (\mathbf{2\,m} \text{ by } \mathbf{2\,m}) \tag{19}$$

The equations of motion *transformed into modal coordinates* now become:

$$\left[\mathbf{s}^2[\mathbf{m}] + \mathbf{s}[\mathbf{c}] + [\mathbf{k}]\right]\{\mathbf{Z}(\mathbf{s})\} = [\mathbf{U}]^{\mathbf{t}}\{\mathbf{F}(\mathbf{s})\} \ (\mathbf{2\,m} \text{ by } \mathbf{2\,m}) \tag{20}$$

11.1 Damping Models

In Eq. (1), the damping of the structure was modeled with a linear viscous force term which is proportional to surface velocity (1). This is called a **non-proportional damping** model. **Non-proportional damping** is the most commonly used damping model, unless there is a known physical reason for using a different damping model.

If the structure model has **no damping** ($[\mathbf{C}] = \mathbf{0}$), then it can be shown that the modal mass and stiffness matrices are *diagonal matrices* and the equations of motion in modal coordinates (20) are *uncoupled*.

Table 1 Damping models

Damping	Mode shapes	Modal matrices
None	Normal	Diagonal (m by m)
Non-proportional	Complex	Non-diagonal (2 m by 2 m)
Proportional	Normal	Diagonal (m by m)
Light	Almost normal	Almost diagonal (m by m)

If damping is modeled with a *proportional damping matrix* ($[C] = \alpha[M] + \beta[K]$), where α & β are proportionality constants, this is called a **proportional damping** model. With proportional damping, the modal mass, damping, and stiffness matrices are *diagonal matrices*, and the equations of motion in modal coordinates (20) are *again uncoupled*.

11.2 Lightly Damped Structures

When they vibrate, all real-world structures have *several damping mechanisms* which dissipate their vibration energy. On earth, the surrounding air always provides one damping mechanism. After all excitation forces are removed, all structural vibration will be damped out by the damping mechanisms.

A structure is assumed to be **lightly damped** if its *damping forces are significantly less* than its internal mass (inertial) and stiffness (restoring) forces.

If a structure exhibits troublesome resonance-assisted vibration, it is usually because it is lightly damped. A common way to define a lightly damped structure is as follows:

> A structure is called lightly damped if its modes have *less than 10% of critical damping*.

If a structure is lightly damping, then it can be shown that its modal mass, damping, and stiffness matrices in Eq. (20) are *approximately diagonal matrices*. Furthermore, its mode shapes can be shown to be approximately *normal* (or *real-valued*). In this case, the **2m**-equation (20) are redundant and can be replaced to **m**-equations, one corresponding to each mode.

The damping cases are summarized as follows (Table 1).

12 Scaling Mode Shapes to Unit Modal Masses

Mode shapes are called "*shapes*" because they are *unique in shape*, but not in value. In other words, the mode shape vector $\{\mathbf{u_k}\}$ for each mode (**k**) does not have unique values. The "*shape*" of $\{\mathbf{u_k}\}$ is unique, but its shape values are arbitrary.

Another way of saying this is that the ratio of any two mode shape components is unique. A mode shape is also called an *eigenvector*, meaning that its "*shape*" is unique, but its values are arbitrary. Therefore, a mode shape can be arbitrarily scaled using any scale factor.

Curve fitting a set of *un-calibrated FRFs* will yield *un-scaled mode shapes*; hence, they are *not a modal model* and cannot be used with SDM.

12.1 Modal Mass Matrix

SDM requires a modal model to describe the dynamics of the unmodified structure. In order to accurately model the structural dynamics, the mode shapes of the modal model must be scaled to preserve the mass, stiffness, and damping properties of the structure. SDM requires mode shapes which are scaled so that the *modal masses are one or unity*. These are called UMM mode shapes.

When the mass matrix is post-multiplied by the mode shape matrix and pre-multiplied by its transpose, the result is the diagonal matrix shown in Eq. (21). *This is a definition of modal mass*:

$$[\mathbf{U}]^{\mathrm{t}}\,[\mathbf{M}]\,[\mathbf{U}] = \begin{bmatrix} \ddots & & \\ & \mathbf{m} & \\ & & \ddots \end{bmatrix} = \begin{bmatrix} \ddots & & \\ & \frac{\mathbf{1}}{\mathbf{A\omega}} & \\ & & \ddots \end{bmatrix} \tag{21}$$

where

$[\mathbf{M}]$ ← mass matrix (**n** by **n**)
$[\mathbf{U}] = [\{\mathbf{u}_1\}, \{\mathbf{u}_2\}, \ldots, \{\mathbf{u_m}\}]$ ← mode shape matrix (**n** by **m**)

$$\begin{bmatrix} \ddots & & \\ & \mathbf{m} & \\ & & \ddots \end{bmatrix} = \begin{bmatrix} \ddots & & \\ & \frac{\mathbf{1}}{\mathbf{A\omega}} & \\ & & \ddots \end{bmatrix} \leftarrow \text{modal mass matrix } (\mathbf{m} \text{ by } \mathbf{m})$$

The modal mass of each mode (**k**) is a diagonal element of the modal mass matrix:

$$\mathbf{m_k} = \frac{1}{\mathbf{A_k \omega_k}} \leftarrow \text{modal mass } \mathbf{k} = \mathbf{1}, \ldots, \mathbf{m} \tag{22}$$

$\mathbf{p_k} = -\boldsymbol{\sigma}_\mathbf{k} + \mathbf{j}\boldsymbol{\omega}_\mathbf{k}$ ← pole location for the k$^{\text{th}}$mode
$\boldsymbol{\omega}_\mathbf{k}$ ← damped natural frequency of the k$^{\text{th}}$ mode
$\mathbf{A_k}$ ← scaling constant for the k$^{\text{th}}$ mode

12.2 Modal Stiffness Matrix

When the stiffness matrix is post-multiplied by the mode shape matrix and pre-multiplied by its transpose, the result is a diagonal matrix, shown in Eq. (23). *This is a definition of modal stiffness*:

$$[\mathbf{U}]^{t}\,[\mathbf{K}]\,[\mathbf{U}] = \begin{bmatrix} \ddots & & \\ & \mathbf{k} & \\ & & \ddots \end{bmatrix} = \begin{bmatrix} \ddots & & \\ & \frac{\sigma^2+\omega^2}{A\omega} & \\ & & \ddots \end{bmatrix} \tag{23}$$

where

$[\mathbf{K}]$ ← stiffness matrix. (**n** by **n**)

$\begin{bmatrix} \ddots & & \\ & \mathbf{k} & \\ & & \ddots \end{bmatrix} = \begin{bmatrix} \ddots & & \\ & \frac{\sigma^2+\omega^2}{A\omega} & \\ & & \ddots \end{bmatrix}$ = modal stiffness matrix (**m** by **m**)

The modal stiffness of each mode (**k**) is a diagonal element of the modal stiffness matrix:

$$\mathbf{k_k} = \frac{\sigma_k^2 + \omega_k^2}{\mathbf{A_k}\,\omega_k} \leftarrow \text{modal stiffness} \qquad \mathbf{k} = \mathbf{1}, \ldots, \mathbf{m} \tag{24}$$

where

σ_k ← modal damping of the k^{th} mode

12.3 Modal Damping Matrix

When the damping matrix is post-multiplied by the mode shape matrix and pre-multiplied by its transpose, the result is a diagonal matrix, shown in Eq. (25). *This is a definition of modal damping*:

$$[\mathbf{U}]^{t}\,[\mathbf{C}]\,[\mathbf{U}] = \begin{bmatrix} \ddots & & \\ & \mathbf{c} & \\ & & \ddots \end{bmatrix} = \begin{bmatrix} \ddots & & \\ & \frac{2\sigma}{A\omega} & \\ & & \ddots \end{bmatrix} \tag{25}$$

where

$[\mathbf{C}]$ ← damping matrix (**n** by **n**)

$$\begin{bmatrix} \ddots & & \\ & \mathbf{c} & \\ & & \ddots \end{bmatrix} = \begin{bmatrix} \ddots & & \\ & \frac{2\sigma}{A\omega} & \\ & & \ddots \end{bmatrix} = \text{modal damping matrix } (\mathbf{m} \text{ by } \mathbf{m})$$

The modal damping of each mode (**k**) is a diagonal element of the modal damping matrix:

$$\mathbf{c_k} = \frac{2\sigma_\mathbf{k}}{\mathbf{A_k}\omega_\mathbf{k}} \leftarrow \text{modal damping} \quad \mathbf{k} = \mathbf{1}, \ldots, \mathbf{m} \tag{26}$$

12.4 Unit Modal Masses

Each of the modal mass, stiffness, and damping matrix diagonal elements (22), (24), and (26) includes a *scaling constant* ($\mathbf{A_k}$). This constant is necessary because the *mode shapes are not unique* in value and therefore can be arbitrarily scaled.

One of the common ways to scale mode shapes is to scale them so that the modal masses are *"one"* or *"unity."* Normally, if a mass matrix [**M**] were available, the mode vectors would simply be scaled such that when the triple product $[\mathbf{U}]^t[\mathbf{M}][\mathbf{U}]$ was formed, the resulting modal mass matrix would be an *identity matrix*.

13 SDM Dynamic Model

The local eigenvalue modification process used by SDM requires a **modal model** of the *unmodified* structure. The modal model consists of the modal frequency, modal damping (optional), and mode shape of each mode in the model.

The dynamic model for the *unmodified* structure was given in Eq. (1). Similarly, the dynamic model for the *modified* structure is written:

$$[\mathbf{M} + \mathbf{\Delta M}]\{\ddot{\mathbf{x}}(\mathbf{t})\} + [\mathbf{C} + \mathbf{\Delta C}]\{\dot{\mathbf{x}}(\mathbf{t})\} + [\mathbf{K} + \mathbf{\Delta K}]\{\mathbf{x}(\mathbf{t})\} = \{\mathbf{f}(\mathbf{t})\} \tag{27}$$

where

$[\mathbf{\Delta M}]$ ← matrix of mass modifications (**n** by **n**)
$[\mathbf{\Delta C}]$ ← matrix of damping modifications (**n** by **n**)
$[\mathbf{\Delta K}]$ ← matrix of stiffness modifications (**n** by **n**)

14 SDM Equations Using UMM Mode Shapes

Unit Modal Mass (UMM) scaling is normally done on FEA mode shapes because the mass matrix is available for scaling them. However, when EMA mode shapes are extracted from experimental FRFs, no mass matrix is available for scaling the mode shapes to yield Unit Modal Masses.

The mode shapes are eigenvectors and hence *have no unique values*, but if they are scaled so that the modal mass matrix is an *identity matrix*, the equations of motion in modal coordinates (20) become:

$$\left[\mathbf{s^2}\,[\mathbf{I}] + \mathbf{s}\,[\mathbf{2\sigma}] + \left[\mathbf{\Omega^2}\right]\right]\{\mathbf{Z}\,(\mathbf{s})\} = [\mathbf{U}]^{\mathbf{t}}\,\{\mathbf{F}\,(\mathbf{s})\}\ \ (\mathbf{m} - \text{vector}) \tag{28}$$

where

$[\mathbf{I}]$ ← identity modal mass matrix (**m** by **m**)
$[\mathbf{2\sigma}]$ ← diagonal modal damping matrix (**m** by **m**)
$[\mathbf{\Omega^2}]$ ← diagonal modal frequency matrix (**m** by **m**)
$[\mathbf{\Omega^2}] = [\sigma^2 + \omega^2]$

In Eq. (28), the complete dynamics of the *unmodified* structure is represented by modal frequencies, modal damping, and mode shapes that are *scaled to unit modal masses*. All mass, stiffness, and damping properties of the *unmodified* structure are preserved in the *modal model* that consists of UMM mode shapes.

Using the UMM mode shapes, the equations of motion (27) for the *modified* structure can be transformed to modal coordinates:

$$\left[\mathbf{s^2}\,[\mathbf{m}] + \mathbf{s}\,[\mathbf{c}] + [\mathbf{k}]\right]\{\mathbf{Z}\,(\mathbf{s})\} = [\mathbf{U}]^{\mathbf{t}}\,\{\mathbf{F}\,(\mathbf{s})\}\,(\mathbf{m} - \text{vector}) \tag{29}$$

where

$$[\mathbf{m}] = [\mathbf{I}] + [\mathbf{U}]^{\mathbf{t}}\,[\mathbf{\Delta M}]\,[\mathbf{U}]\ \ (\mathbf{m}\text{ by }\mathbf{m}) \tag{30}$$

$$[\mathbf{c}] = [2\sigma] + [\mathbf{U}]^{\mathbf{t}}\,[\mathbf{\Delta C}]\,[\mathbf{U}]\ \ (\mathbf{m}\text{ by }\mathbf{m}) \tag{31}$$

$$[\mathbf{k}] = \left[\mathbf{\Omega}^2\right] + [\mathbf{U}]^{\mathbf{t}}\,[\mathbf{\Delta K}]\,[\mathbf{U}]\ \ (\mathbf{m}\text{ by }\mathbf{m}) \tag{32}$$

For a lightly damped structure, the mode shapes are *almost real-valued* so the mode shape matrix has dimension (**n** by **m**).

The homogeneous form of Eq. (29) is solved by the SDM method to find the modal properties of the modified structure.

Using the approach of Hallquist et al. [2], an additional transformation of the modification matrices [ΔM],[ΔC], and [ΔK] is made which results in a reformulation of the eigenvalue problem in modification space. For a single modification, this problem becomes a scalar eigenvalue problem, which can be solved quickly and efficiently. The drawback to making one modification at a time, however, is that if many modifications are required, computation time can become significant and errors will accumulate.

A more practical approach is to solve the homogeneous form of Eq. (29) directly. This is still a *relatively small* (**m** by **m**) eigenvalue problem which can include as many structural modifications as desired, but only needs to be solved once.

Equations (30) to (32) also indicate another advantage of SDM:

Only the mode shape components where the *modification elements are attached* to the structure model are required.

This means that only mode shape data for those DOFs *where the modification elements are attached* to the structure is necessary for SDM.

15 Scaling Residues to UMM Mode Shapes

Without a mass matrix, EMA mode shapes can be scaled to Unit Modal Masses by using the relationship between residues and mode shapes.

Residues are related to mode shapes by equating the numerators of curve fitting models (4) and (5):

$$[\mathbf{r}(\mathbf{k})] = \mathbf{A_k}\{\mathbf{u_k}\}\{\mathbf{u_k}\}^{\mathbf{t}} \; \mathbf{k} = \mathbf{1}, \ldots, \mathbf{m} \tag{33}$$

where

[**r**(**k**)] ← residue matrix for the mode **(k)** (**n** by **n**)

Residues are the numerators of the Transfer Function matrix in Eq. (4) when it is written in partial fraction form. For convenience, Eq. (4) is rewritten here:

$$[\mathbf{H}(\mathbf{s})] = \sum_{\mathbf{k=1}}^{\mathbf{m}} \frac{[\mathbf{r}(\mathbf{k})]}{\mathbf{2j}\ (\mathbf{s} - \mathbf{p_k})} - \frac{[\mathbf{r}(\mathbf{k})]^*}{\mathbf{2j}\ \left(\mathbf{s} - \mathbf{p_k^*}\right)} \tag{34}$$

* – denotes the *complex conjugate*

Residues have engineering units associated with them and hence *have unique values*. FRFs have units of (**motion/force**), and the FRF denominators have units

of Hz or (**radians/second**). Therefore, the residues in the numerator have units of (**motion/force-seconds**).

Equation (34) can be written for the $\mathbf{j^{th}}$ **column** (or **row**) of the residue matrix and for mode (**k**) as:

$$\begin{Bmatrix} \mathbf{r_{1j}(k)} \\ \mathbf{r_{2j}(k)} \\ \cdot \\ \cdot \\ \mathbf{r_{jj}(k)} \\ \cdot \\ \mathbf{r_{nj}(k)} \end{Bmatrix} = \mathbf{A_k} \begin{Bmatrix} \mathbf{u_{1k}u_{jk}} \\ \mathbf{u_{2k}u_{jk}} \\ \cdot \\ \cdot \\ \mathbf{(u_{jk})^2} \\ \cdot \\ \mathbf{u_{nk}u_{nk}} \end{Bmatrix} = \mathbf{A_k u_{jk}} \begin{Bmatrix} \mathbf{u_{1k}} \\ \mathbf{u_{2k}} \\ \cdot \\ \cdot \\ \mathbf{u_{jk}} \\ \cdot \\ \mathbf{u_{nk}} \end{Bmatrix} \mathbf{k = 1, \ldots, m} \tag{35}$$

Unique **Variable** **Variable**

This relationship states that *residues have unique values* and preserve the physical properties of the structure, but *mode shapes do not have unique values* and therefore can be scaled in any manner.

The scaling constant $\mathbf{A_k}$ must be chosen so that Eq. (35) remains valid. Either the value of $\mathbf{A_k}$ can be chosen first and the mode shapes scaled accordingly, or the mode shapes can be scaled first and $\mathbf{A_k}$ calculated so that Eq. (35) is still satisfied.

To obtain UMM mode shapes, simply set the *modal mass equal to one* and solve Eq. (22) for $\mathbf{A_k}$:

$$\mathbf{A_k} = \frac{1}{\boldsymbol{\omega_k}} \quad \mathbf{k = 1, \ldots, m} \tag{36}$$

15.1 Driving Point FRF Measurement

Mode shapes scaled to Unit Modal Mass (**UMM mode shapes**) are obtained from the $\mathbf{j^{th}}$ column (or row) of the residue matrix by substituting Eq. (36) into Eq. (35):

$$\begin{Bmatrix} \mathbf{u_{1k}} \\ \mathbf{u_{2k}} \\ \cdot \\ \cdot \\ \cdot \\ \mathbf{u_{nk}} \end{Bmatrix} = \frac{1}{\mathbf{A_k u_{jk}}} \begin{Bmatrix} \mathbf{r_{1j}(k)} \\ \mathbf{r_{2j}(k)} \\ \cdot \\ \cdot \\ \cdot \\ \mathbf{r_{nj}(k)} \end{Bmatrix} = \sqrt{\frac{\boldsymbol{\omega_k}}{\mathbf{r_{jj}(k)}}} \begin{Bmatrix} \mathbf{r_{1j}(k)} \\ \mathbf{r_{2j}(k)} \\ \cdot \\ \cdot \\ \cdot \\ \mathbf{r_{nj}(k)} \end{Bmatrix} \mathbf{k = 1, \ldots, m} \tag{37}$$

15.2 UMM Mode Shape

The *driving point residue* $\mathbf{r_{jj}(k)}$ (where *row index* **j** equals *column index* **j**) plays an important role in this scaling process. The driving point residue for each mode (**k**) is required in Eq. (37) for scaling mode shapes to UMM. Driving point residues are obtained by curve fitting a *driving point FRF*.

A *drive point FRF* is any measurement where the excitation force DOF is the same as the response DOF.

15.3 Triangular FRF Measurements

In some cases, it is difficult or even impossible to make a good driving point FRF measurement. In those cases, an alternative set of measurements can be made from which to create UMM mode shapes. From Eq. (37) the following equation can be written:

$$\mathbf{u_{jk}} = \sqrt{\frac{\mathbf{r_{jp}\,(k)}\ \ \mathbf{r_{jq}\,(k)}}{\mathbf{A_k}\ \ \mathbf{r_{pq}\,(k)}}}\ \mathbf{k = 1, \ldots, m} \tag{38}$$

Equation (38) can be substituted for $\mathbf{u_{jk}}$ in Eq. (37) to calculate UMM mode shapes. To calculate a starting component $\mathbf{u_{jk}}$, three FRFs are required ($\mathbf{FRF_{jp}}$, $\mathbf{FRF_{jq}}$, $\mathbf{FRF_{pq}}$). **DOF(j)** is the (fixed) reference for the $\mathbf{j^{th}}$ column (or row) of FRF measurements, so the two measurements $\mathbf{FRF_{jp}}$ and $\mathbf{FRF_{jp}}$ would normally be made. In addition, one extra measurement $\mathbf{FRF_{pq}}$ is also required in order to obtain the three residues required by Eq. (38). Since the FRFs ($\mathbf{FRF_{jp}}$, $\mathbf{FRF_{jq}}$, $\mathbf{FRF_{pq}}$) form a triangle of *off-diagonal FRFs* in the FRF matrix, they are called a **triangular FRF measurement**. Eq. (38) leads to the following conclusion:

A set of triangular FRF measurements which do not include driving point FRFs can be curve fit and their residues used to create **UMM mode shapes**

16 Integrating Residues to Displacement Units

Vibration measurements are commonly made using either accelerometers that measure acceleration responses or vibrometers that measure velocity responses. Excitation forces are typically measured with a load cell. Therefore, FRFs calculated for experimental data will have units of either (**acceleration/force**) or (**velocity/force**)

Modal residues always have the units of the FRF multiplied by (**radians/second**).

- Residues extracted from FRFs with units of (**acceleration/force**) will have units of (**acceleration/force-seconds**).
- Residues extracted from FRFs with units of (**velocity/force**) will have units of (**velocity/force-seconds**).
- Residues extracted from FRFs with units of (**displacement/force**) will have units of (**displacement/force-seconds**).

Since the modal mass, stiffness, and damping Eqs. (21), (23), and (25) assume **units of (displacement/force)**, residues with units of (**acceleration/force-seconds**) or (**velocity/force-seconds**) must be "*integrated*" to units of (**displacement/force-seconds**) before scaling them to UMM mode shapes.

Integration of a time domain function has an equivalent operation in the frequency domain. Integration of a Transfer Function is done by dividing it by the Laplace variable(**s**):

$$[\mathbf{H_d}\,(\mathbf{s})] = \frac{[\mathbf{H_v}\,(\mathbf{s})]}{\mathbf{s}} = \frac{[\mathbf{H_a}\,(\mathbf{s})]}{\mathbf{s^2}} \tag{39}$$

where

$[\mathbf{H_d}(\mathbf{s})]$= transfer matrix in (**displacement/force**) units
$[\mathbf{H_v}(\mathbf{s})]$= transfer matrix in (**velocity/force**) units
$[\mathbf{H_a}(\mathbf{s})]$= transfer matrix in (**acceleration/force**) units

Since residues are the result of the partial fraction expansion form of an FRF, residues can be "*integrated*" directly using the formula:

$$[\mathbf{r_d}\,(\mathbf{k})] = \frac{[\mathbf{r_v}\,(\mathbf{k})]}{\mathbf{p_k}} = \frac{[\mathbf{r_a}\,(\mathbf{k})]}{(\mathbf{p_k})^2}\mathbf{k} = \mathbf{1}, \ldots, \mathbf{m} \tag{40}$$

where

$[\mathbf{r_d}(\mathbf{k})]\leftarrow$ residue matrix in (**displacement/force**) units
$[\mathbf{r_v}(\mathbf{k})] \leftarrow$ residue matrix in (**velocity/force**) units
$[\mathbf{r_a}(\mathbf{k})] \leftarrow$ residue matrix in (**acceleration/force**) units
$\mathbf{p_k} = -\boldsymbol{\sigma_k} + \mathbf{j}\boldsymbol{\omega_k} \leftarrow$ pole location for the $\mathbf{k^{th}}$ mode

If *light damping is assumed* and the *mode shapes are real-valued*, Eq. (40) can be simplified to

$$[\mathbf{r_d}\,(\mathbf{k})] = \mathbf{F_k} \quad [\mathbf{r_v}\,(\mathbf{k})] = (\mathbf{F_k})^2 \quad [\mathbf{r_a}\,(\mathbf{k})] \tag{41}$$

Table 2 Residue scale factors

To change Transfer Function units		Multiply residues by
From	To	
$\frac{\textbf{ACCELERATION}}{\textbf{FORCE}}$	$\frac{\textbf{DISPLACEMENT}}{\textbf{FORCE}}$	$\mathbf{F^2}$
$\frac{\textbf{VELOCITY}}{\textbf{FORCE}}$	$\frac{\textbf{DISPLACEMENT}}{\textbf{FORCE}}$	$\mathbf{F}$

where

$$\mathbf{F_k} \cong \frac{\omega_k}{\left(\sigma_k^2 + \omega_k^2\right)} \quad \mathbf{k = 1, \ldots, m} \tag{42}$$

Equations (41) and (42) are summarized in the following Table 2 where $\mathbf{F} \cong \frac{\omega}{(\sigma^2+\omega^2)}$ (**seconds**)

17 Effective Mass

A useful question to ask is:

"At one of its DOFs, what is the effective mass of a structure at one of its resonant frequencies?"

Another way to ask the question is:

"At one of its DOFs, if a structure were treated like an SDOF mass-spring-damper what is its effective mass , effective stiffness & effective damping?"

The answer to those questions follows from a further use of the modal mass, stiffness, and damping Eqs. (21), (23), and (25) and the definition **UMM mode shapes**.

It has already been shown that residues with units of (**displacement/force-seconds**) can be scaled to UMM mode shapes. One further assumption is necessary to define the effective mass at a DOF.

18 Diagonal Mass Matrix

If the mass matrix [**M**] is assumed to be a *diagonal matrix*, then pre-multiplying and post-multiplying it by UMM mode shapes changes Eq. (21) to:

$$\sum_{\mathbf{j=1}}^{\mathbf{n}} \mathbf{mass_j}\left(\mathbf{u_{jk}}\right)^2 = \mathbf{1} \quad \mathbf{k = 1, \ldots, m} \tag{43}$$

where

$\mathbf{mass_j} \leftarrow \mathbf{j^{th}}$ diagonal element of the mass matrix
$\mathbf{u_{jk}} \leftarrow \mathbf{j^{th}}$ component of the UMM mode shape (**k**)

If the structure is viewed as a mass-spring-damper at DOF(**j**), the *effective mass* at the *frequency of* mode (**k**) at DOF(**j**) is determined from Eq. (43) as:

$$\textbf{effective mass}_\mathbf{j} = \frac{\mathbf{1}}{\left(\mathbf{u_{jk}}\right)^2} \; \mathbf{j = 1, \ldots, n} \tag{44}$$

If each DOF(**j**) is treated a driving point, Eq. (37) can be used to write the mode shape component $\mathbf{u_{jk}}$ in terms of the modal frequency $\boldsymbol{\omega_k}$ and driving point residue $\mathbf{r_{jj}(k)}$:

$$\mathbf{u_{jk}} = \sqrt{\boldsymbol{\omega_k} \mathbf{r_{jj}}\,(\mathbf{k})} \; \mathbf{j = 1, \ldots, n} \tag{45}$$

Substituting Eq. (45) into Eq. (44) gives another expression for the effective mass at the frequency of mode (**k**):

$$\textbf{effective mass}_\mathbf{j} = \frac{\mathbf{1}}{\boldsymbol{\omega_k} \mathbf{r_{jj}}\,(\mathbf{k})} \quad \mathbf{j = 1, \ldots, n} \tag{46}$$

18.1 Checking the Engineering Units

Assuming that the driving point residue $\mathbf{r_{jj}(k)}$ has units of *(displacement/force-seconds)* as discussed earlier, and the modal frequency $\boldsymbol{\omega_k}$ has units of *(radians/second)*, then the effective mass would have units of (**force-sec^2/ displacement**), which are units of mass.

Using the **effective mass**, the **effective stiffness and damping** of the structure can be calculated using Eqs. (29) and (31).

19 Effective Mass Example

Suppose that we have the following data for a single mode of vibration:

$$\textbf{Frequency} = \mathbf{10.0\ Hz}.$$

$$\textbf{Damping} = \mathbf{1.0}\%$$

$$\textbf{Residue vector} = \left\{ \begin{array}{c} -0.1 \\ +2.0 \\ +0.5 \end{array} \right\}$$

Also, suppose that the FRF measurements that were curve fit to obtain this data have units of (**Gs/Lbf**). Also assume that the driving point is at the second DOF of the residue vector, and therefore driving point residue is equal to 2.0.

Converting the frequency and damping into units of **radians/second**:

$$\textbf{Frequency} = 62.83\ \textbf{Rad/Sec}$$

$$\textbf{Damping} = 0.628\ \textbf{Rad/Sec}$$

The residues always carry the units of the FRF measurement multiplied by (**radians/second**). For this example, the units of the residues are:

$$\textbf{Residue units} \rightarrow \textbf{Gs/ (Lbf - Sec)} \rightarrow 386.4\ \textbf{Inches/}\left(\textbf{Lbf - Sec}^3\right)$$

In these units, the residues become:

$$\textbf{Residue vector} = \left\{ \begin{array}{c} -38.64 \\ +772.8 \\ +193.2 \end{array} \right\}\ \textbf{Inches/}\left(\textbf{Lbf - Sec}^3\right)$$

Since the modal mass, stiffness, and damping Eqs. (21), (23), and (25) assume units of (**displacement/force**), the above residues with units of (**acceleration/force**) must be converted to (**displacement/force**) units. This is done by using the appropriate scale factor from Table 2. For this example:

$$\mathbf{F^2} \cong \left(\frac{1}{62.83}\right)^2 = 0.000253\ \left(\textbf{Seconds}^2\right)$$

Multiplying the residues by $\mathbf{F^2}$gives:

$$\textbf{Residue Vector} = \left\{ \begin{array}{c} -0.00977 \\ +0.1955 \\ +0.0488 \end{array} \right\}\ \textbf{Inches/ (Lbf - Sec)}$$

Using Eq. (37) the **residue mode shape** must be multiplied by the following scale factor to obtain a UMM mode shape:

$$\mathbf{SF} = \sqrt{\frac{\omega}{r_{jj}}} = \sqrt{\frac{62.83}{+0.1955}} = 17.927$$

Therefore,

$$\textbf{UMM Mode Shape} = \left\{ \begin{array}{c} -0.175 \\ +3.505 \\ +0.875 \end{array} \right\} \textbf{Inches/ (Lbf} - \textbf{Sec)}$$

Using Eq. (44), the **effective mass** at the driving point is:

$$\textbf{effective mass} = \frac{1}{(u_2)^2} = \frac{1}{(3.505)^2} = 0.0814\textbf{Lbf} - \sec^2/\textbf{in}.$$

Or, using Eq. (46), the **effective mass** at the driving point is:

$$\textbf{effective mass} = \frac{1}{\omega\, r_{22}} = \frac{1}{(62.83)\,(0.1955)} = 0.0814\textbf{Lbf} - \sec^2/\textbf{in}.$$

20 SDM Example

In this example, SDM will be used to model the attachment of a RIB stiffener to an aluminum plate. The new mode shapes obtained from SDM will be compared with the FEA mode shapes of the plate with the RIB attached and with the EMA mode shapes obtained from an impact test of the actual plate with the RIB attached. Mode shapes will be compared in three cases.

1. **EMA versus FEA** mode shapes of the plate *without the RIB*
2. **SDM versus FEA** mode shapes of the plate *with the RIB attached*
3. **SDM versus EMA** mode shapes of the plate *with the RIB attached*

The plate and RIB are shown in Fig. 5. The dimensions of the plate are 20 in (508 mm) by 25 in (635 mm) by 3/8 in (9.525 mm) thick. The dimensions of the RIB are 3 in (76.2 mm) by 25 in (635 mm) by 3/8 inches (9.525 mm) thick.

Two roving impact modal tests were conducted on the plate, one before and one after the RIB stiffener was attached to the plate. FRFs were calculated from the impact force and the acceleration response only in the vertical (Z-axis) direction.

20.1 Cap Screw Stiffnesses

The RIB stiffener was attached to the plate with five cap screws, shown in Fig. 5b. When the RIB is attached to the plate, *translational and torsional forces* are applied between the two substructures along the length of the plate centerline where they are attached together. Both *translational and torsional stiffness forces* must be modeled in order to represent the real-world plate with the RIB stiffener attached.

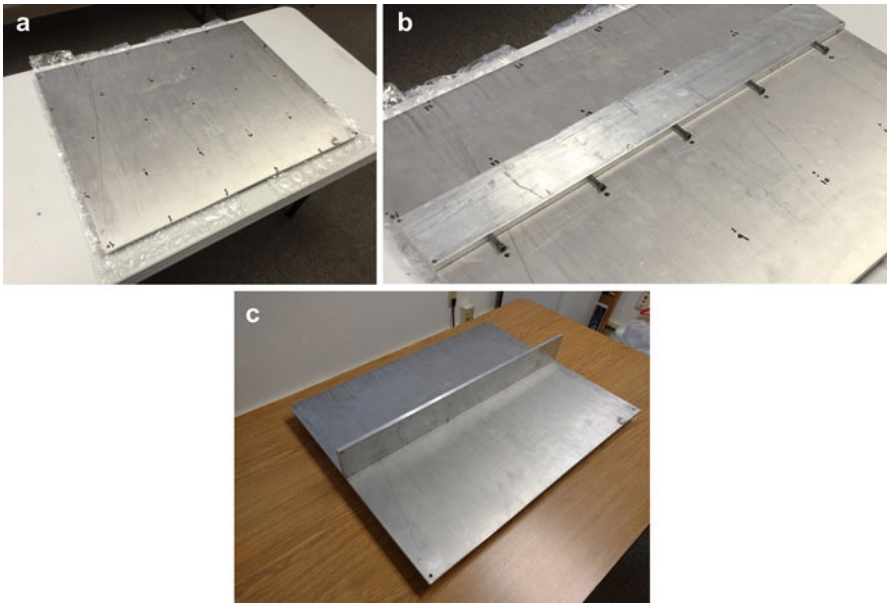

Fig. 5 (**a**) Aluminum plate. (**b**) RIB and cap screws. (**c**) Plate and RIB attached

The joint stiffness was modeled using **six-DOF springs** located at the five cap screw locations, as shown in Fig. 6. Each six-DOF FEA spring model contains *three translational* **DOFs** and *three rotational* **DOFs**. The six-DOF FEA springs were given large stiffness values to model a tight fastening of RIB to the plate using the cap screws.

- Translational stiffness: *1 × E6 lbs/in* (*1.75E+05 N/mm*)
- Torsional stiffness: *1 × E6 in-lbs/degree* (*1.75E+05 mm-N/degree*)

21 EMA Mode Shapes of the Plate

FRFs were calculated from data acquired while impacting the plate in the vertical direction, at each of the 30 points shown in Fig. 7. The plate was supported on bubble wrap laying on top of a table as shown in Fig. 5. A fixed reference accelerometer was attached to the plate. (The location of the reference accelerometer is arbitrary.)

The EMA modal parameters were estimated by curve fitting the 30 FRFs calculated from the roving impact test data. EMA mode shapes for 14 modes were obtained by curve fitting the FRFs, each mode shape having 30 DOFs (1Z through 30Z). A curve fit on one of the FRFs is shown in Fig. 4.

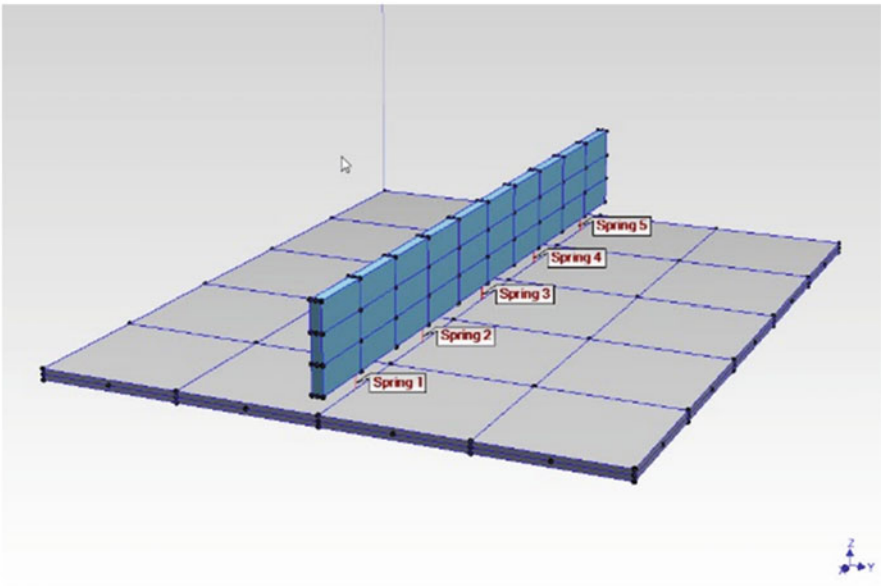

Fig. 6 FEA springs modeling the cap screws

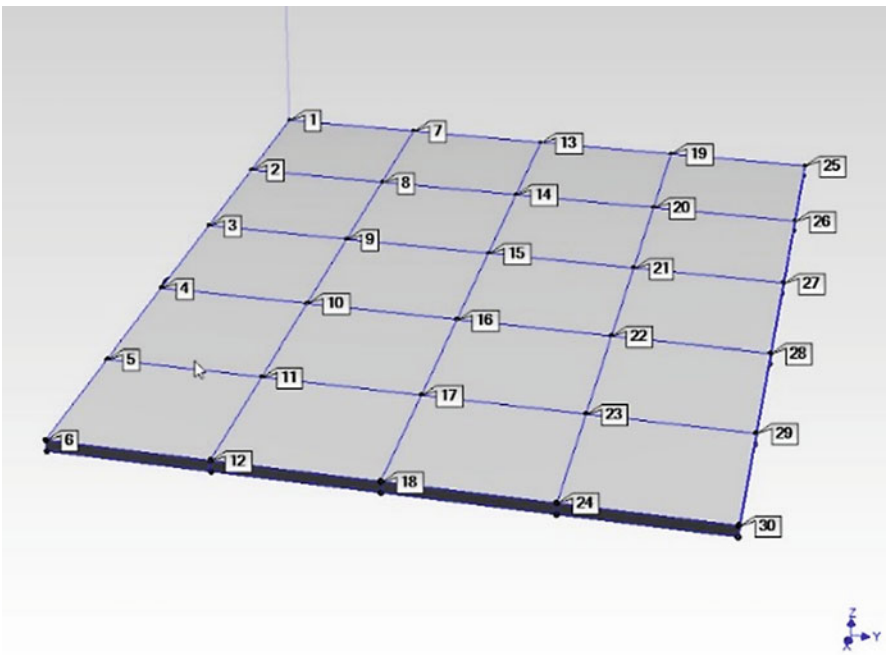

Fig. 7 Impact test points

22 FEA Mode Shapes of the Plate

An FEA model of the plate was constructed using *80 FEA plate (membrane) elements*. The following properties of the aluminum material in the plate were used:

1. **Young's modulus of elasticity**: 1E7 lbf/inˆ2 (6.895E4 N/mmˆ2)
2. **Density**: 0.101 lbm/inˆ3 (2.796E-6 kg/mmˆ3)
3. **Poisson's ratio**: 0.33
4. **Plate thickness**: 0.375 in (9.525 mm)

The FEA model shown in Fig. 9 has 99 points (or nodes). The eigen-solution included the first 20 FEA modes, **6 rigid-body mode shapes** and **14 flexible-body mode shapes**. Each FEA mode shape has **594 DOFs** (3 translational and 3 rotational DOFs at each point). The FEA mode shapes were scaled to UMM mode shapes; hence, they constitute a *modal model* of the plate (Fig. 8).

22.1 Mode Shape Comparison

The Modal Assurance Criterion (**MAC**) values between each EMA mode shape and each **flexible-body** FEA mode shape are displayed in the bar chart in Fig. 9.

MAC is a measure of the co-linearity of two mode shapes. The following rule of thumb is commonly used with MAC

- MAC = 1.00 → two shapes are the same (they lie on the same straight line)
- MAC > = 0.90 → two shapes are similar
- MAC < = 0.90 → two shapes are different

The diagonal MAC bars in Fig. 9 indicate that each flexible-body EMA mode shape *closely matched one-for-one* with the each flexible-body FEA mode shape. The *worst-case pair* of matching mode shapes is the first pair with **MAC = 0.97**.

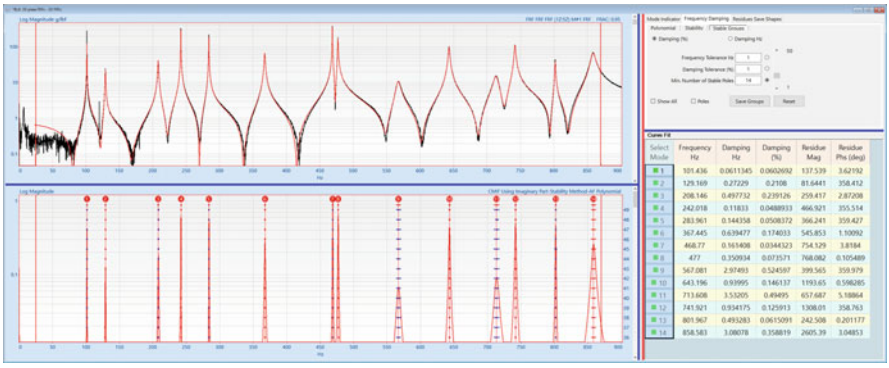

Fig. 8 Curve of an experimental FRF

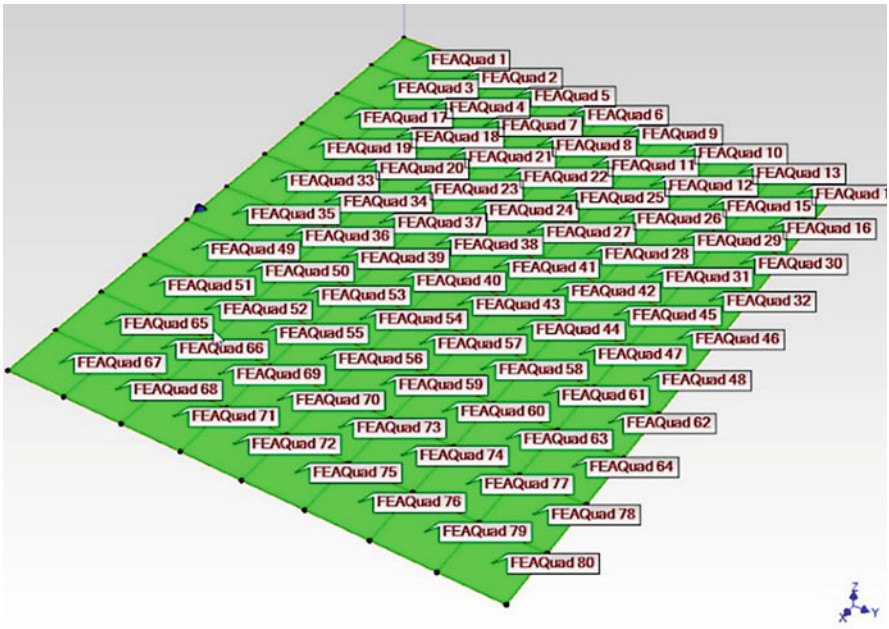

Fig. 9 FEA model with FEA Quads

22.2 Modal Frequency Comparison

The modal frequencies of the matching FEA and EMA mode pairs are listed in Table 3. Each EMA modal frequency is *higher* than the frequency of its corresponding FEA mode. The pair with the highest difference is different by 100 Hz.

The frequency differences indicate that the stiffness of the actual aluminum plate *is greater than* the stiffness of the FEA model. These frequency differences could be reduced by *increasing the modulus of elasticity* or *increasing the thickness* of the FEA plate elements. However, since the EMA and FEA modes shapes are closely matched, the EMA frequency and damping can be combined with the FEA mode shapes to provide a more accurate modal model of the plate.

22.3 Hybrid Modal Model

In most cases, EMA mode shapes will not have as many DOFs in them as FEA mode shapes. But in most all cases, EMA mode shapes will have more accurate modal frequencies than FEA mode shapes. Also, EMA mode shapes always have non-zero modal damping, whereas FEA mode shapes typically have no damping.

Table 3 FEA versus EMA modes – plate without RIB

Shape pair	FEA frequency (Hz)	EMA frequency (Hz)	EMA damping (Hz)	MAC
1	91.4	102	0.031	0.968
2	115	129	0.250	0.991
3	190	208	0.458	0.990
4	217	242	0.107	0.993
5	251	284	0.106	0.984
6	332	367	0.642	0.985
7	412	469	0.159	0.975
8	424	477	0.339	0.985
9	496	567	3.130	0.991
10	564	643	0.936	0.991
11	626	714	3.680	0.984
12	654	742	0.923	0.987
13	689	802	0.443	0.983
14	757	859	3.090	0.984

If a pair of EMA and FEA mode shapes is highly correlated (their MAC value is *close to 1.0*), a Hybrid mode shape can be created by replacing the frequency and damping of each FEA mode shape with the frequency and damping of its *closely matching* EMA mode shape.

In a *Hybrid mode shape,* the frequency and damping of each FEA mode shape is replaced with the frequency and damping of its *closely matching* EMA mode shape.

In Fig. 10 and Table 3, each FEA mode shape has a *high MAC value* with a corresponding EMA mode shape. Therefore, a Hybrid modal model of the plate can be created by replacing the modal frequency and damping of each FEA mode shape with the modal frequency and damping of its closely matching EMA mode shape.

A *Hybrid modal model* has several advantages for modeling the dynamics of an *unmodified* structure with SDM

- Its modal frequencies and damping are more realistic.
- It can have DOFs at locations where EMA data was not acquired.
- Its mode shapes can include *rotational* **DOFs** which are not typically included in EMA mode shapes.
- FEA mode shapes are typically scaled to UMM mode shapes.

22.4 RIB FEA Model

An FEA model of the RIB in a free-free condition (no fixed boundaries) was created using 30 FEA quad plate elements. The FEA RIB model is shown in Fig. 11.

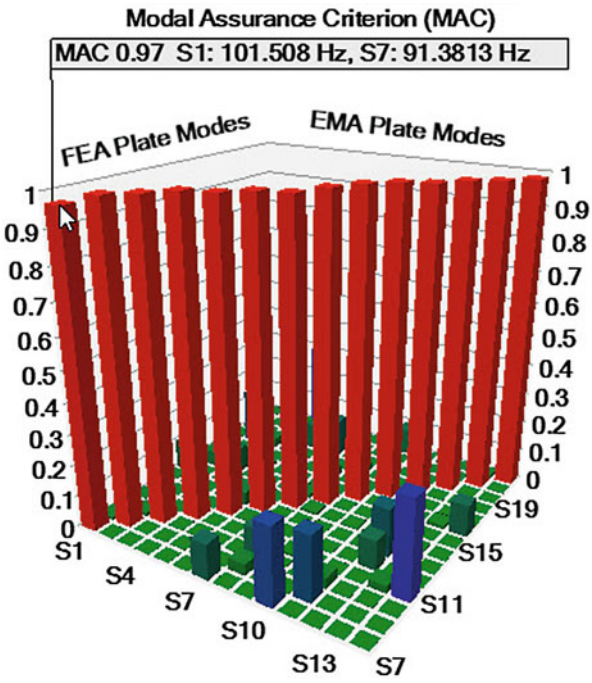

Fig. 10 MAC between FEA and EMA mode shapes

The frequencies of the first 16 FEA modes of the RIB are listed in Table 4. Because it has free-free boundary conditions, the *first six modes* of the FEA model are *rigid-body* **mode shapes** with zero "**0**" frequency. These FEA mode shapes are UMM mode shapes, so they constitute a modal model of the RIB.

22.5 RIB Impact Test

The RIB was impact tested to obtain its EMA modal frequencies and damping, but not its mode shapes. The RIB was only impacted once, and the resulting FRF was curve fit to obtain its EMA modal frequencies and damping. The curve fit of the FRF measurement is shown in Fig. 12, and the resulting EMA frequencies and damping are listed in Table 4.

22.6 Hybrid Modal Model of the RIB

We have already seen that pairs of the EMA and FEA mode shapes of the plate are *strongly correlated* based upon their *high MAC values*. The only significant difference between the EMA and FEA mode shapes was their modal frequencies, and each EMA mode also has modal damping, while the FEA mode shapes do not.

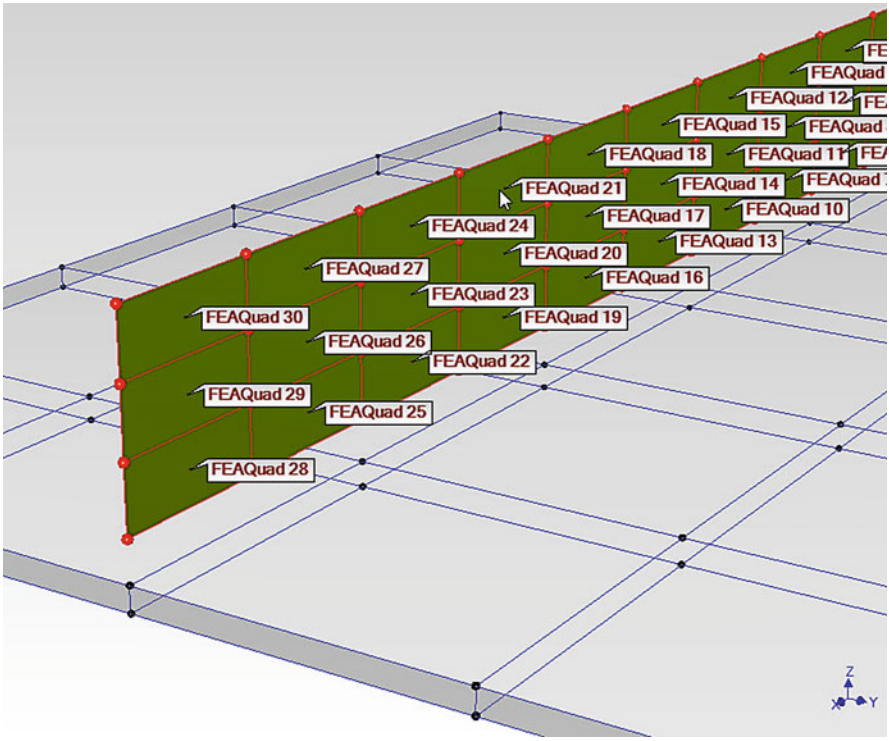

Fig. 11 FEA RIB model

Table 4 FEA versus EMA RIB frequencies

Shape pair	FEA frequency (Hz)	EMA frequency (Hz)	EMA damping (Hz)
1	0.0		
2	0.0		
3	0.0		
4	0.0		
5	0.0		
6	0.0		
7	117.0	121.0	0.78
8	315.0	330.0	0.72
9	521.0	582.0	0.89
10	607.0	646.0	2.49
11	987.0	1.07E+03	3.86
12	1.07E+03	1.18E+03	1.24
13	1.45E+03	1.60E+03	8.72
14	1.67E+03	1.79E+03	2.55
15	1.99E+03	2.24E+03	3.92
16	2.32E+03	2.44E+03	2.97

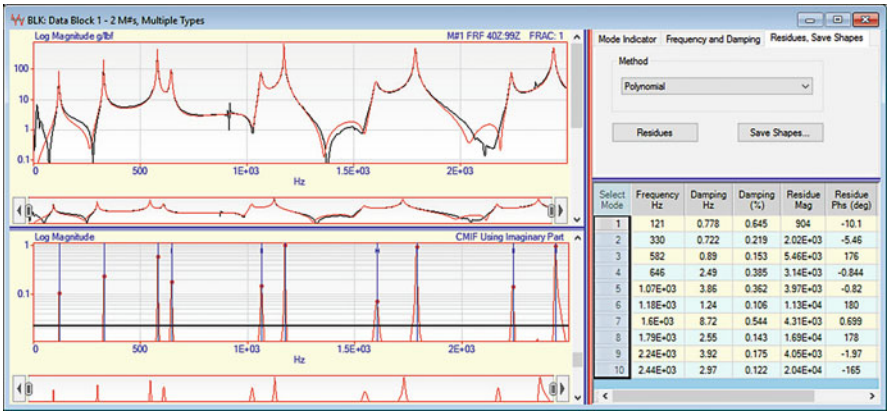

Fig. 12 Curve fit of a RIB FRF

Before it is attached to the plate, the RIB is a free body in space. It is essential that the *rigid-body modes* of the RIB be included in its modal model to correctly model its free-body dynamics. Rigid-body modes are typically not measured experimentally, but they are included in the FEA mode shapes.

A RIB **hybrid modal model** was created by replacing the frequency and damping of each FEA mode shape with the EMA modal frequency and damping from its closely matching EMA mode shape. The six rigid-body FEA mode shapes were also retained in the hybrid modal model to define the free-body dynamics of the RIB.

23 Substructure Modal Model

In order to model the RIB attached to the plate using SDM, the Hybrid modal model of the RIB was added to the Hybrid modal model of the plate to create a modal model for the entire *unmodified* structure. This is called a *substructure modal model*.

Figure 13 shows how the points on the RIB are *numbered differently* than the points on the plate. This ensures that the DOFs of the RIB modes are *uniquely numbered* compared to the DOFs of the plate modes.

23.1 Block Diagonal Format

When the modal model of the RIB is added to the modal model of the plate, the unique numbering of the points on the plate and RIB creates a modal model in *block diagonal format*. In block diagonal format, the DOFs of the RIB mode shapes are *zero valued* for DOFs on the plate, and likewise the DOFs of the plate mode shapes are *zero valued* for the DOFs of the RIB.

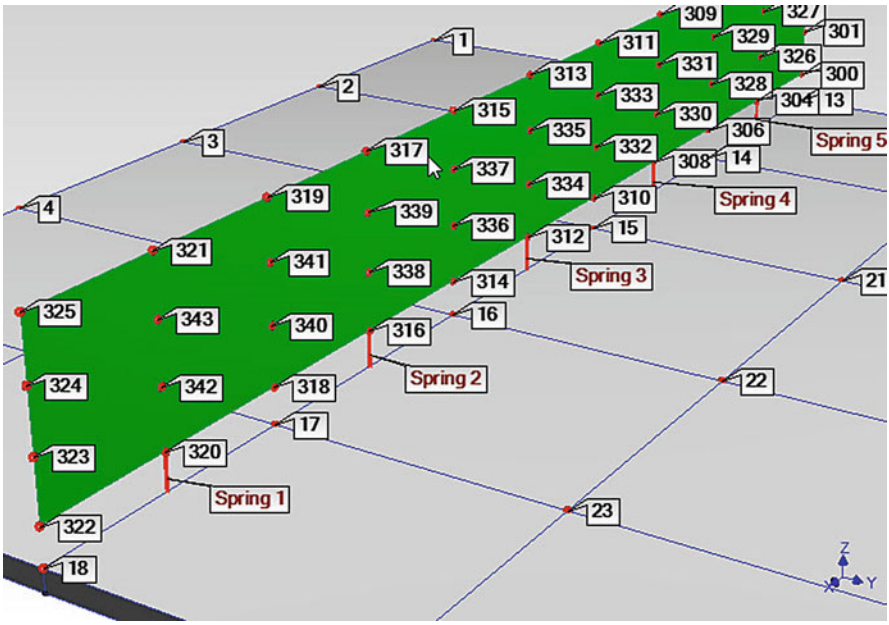

Fig. 13 Point numbers of the plate and RIB

The *plate modal model* contains 14 modes with 594 DOFs (297 translational and 297 rotational DOFs) in each mode shape. The *RIB modal model* contains 16 modes with 264 DOFs (132 translational and 132 rotational DOFs) in each mode shape. Therefore, the *substructure modal model* contains 30 modes and 858 DOFs (429 translational and 429 rotational DOFs) in each mode shape.

24 Calculating New Modes with SDM

The five FEA springs shown in Fig. 13 were used by SDM to model the five cap screws that attach the RIB to the plate. These springs were used together with the *substructure modal model* for the unmodified structure as inputs to SDM.

Even though the mode shapes in the substructure modal model have 858 DOFs in them, only the mode shape DOFs at the attachment points of the FEA springs are used by SDM to calculate the new frequencies and damping of the plate with the RIB attached. Following that, all 858 DOFs of the unmodified mode shapes are used to calculate the new mode shapes of the modified structure.

25 SDM Versus FEA Modes: Plate and RIB

An FEA model consisting of the 80 quad plate elements of the plate, 30 quad plate elements of the RIB, and the 5 springs was also solved using an FEA eigen-solver. The SDM and FEA results are compared in Table 5.

Table 5 SDM modes versus FEA modes – plate with RIB

Shape pair	FEA frequency (Hz)	SDM frequency (Hz)	SDM damping (Hz)	MAC
1	96.0	108.2	0.035	1.00
2	170.5	187.6	0.369	0.99
3	222.6	253.3	0.118	0.98
4	232.7	311.5	0.293	0.92
5	245.1	351.7	0.104	0.98
6	415.0	479.2	0.171	0.98
7	423.0	521.3	0.713	0.91
8	459.1	537.4	2.770	0.95
9	530.7	619.1	0.863	0.91
10	596.0	1412.0	3.185	0.63

The *first nine pairs of mode shapes* in Table 5 have MAC values *greater than 0.90*, indicating a *strong correlation* between those SDM and FEA mode shapes. The FEA modal frequencies are lower than the SDM frequencies for those *first nine mode shape pairs*.

It will be shown later in **FEA Model Updating** how SDM can be used to find more realistic material properties for the FEA model so that its modal frequencies more closely match the EMA frequencies.

25.1 SDM Mode Shapes

Figure 14 is a display of the first ten SDM mode shapes. Five of the ten mode shapes *clearly reflect the torsional coupling* between the RIB and the plate. All ten mode shapes show the intended effect of the RIB stiffener on the plate.

All bending of the plate along its centerline *has been eliminated* by attaching the RIB to it.

Both the RIB and plate are flexing together in unison, both being influenced by the torsional stiffness created by the 6-DOF springs that modeled the cap screws.

Attaching the RIB to the plate has created new modes with mode shapes that *did not exist before the modification*. This confirms the law stated earlier.

Fundamental Law of Modal Analysis: All vibration is a *summation of mode shapes*

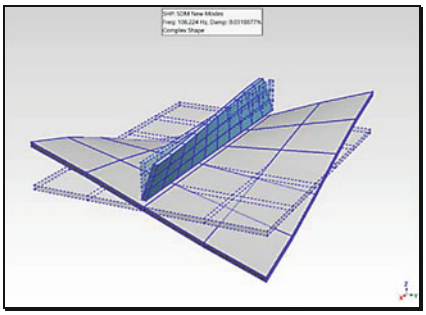

SDM Mode Shape 1

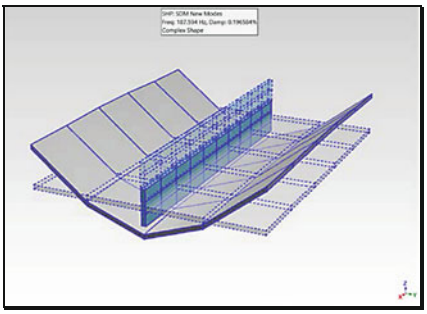

SDM Mode Shape 2

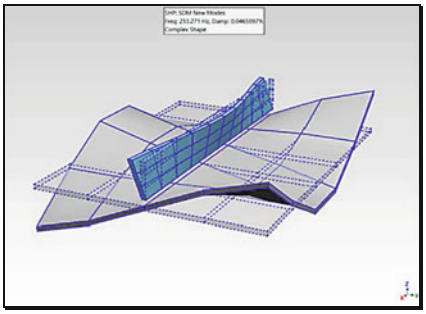

SDM Mode Shape 3

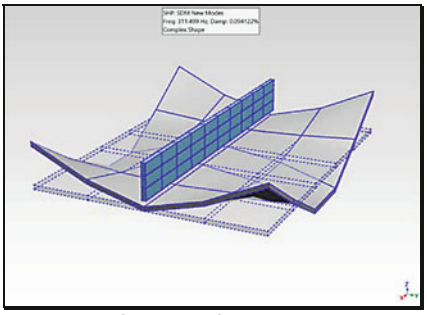

SDM Mode Shape 4

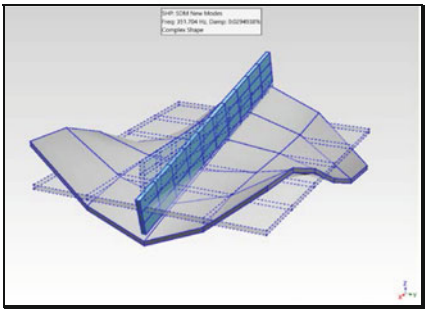

SDM Mode Shape 5

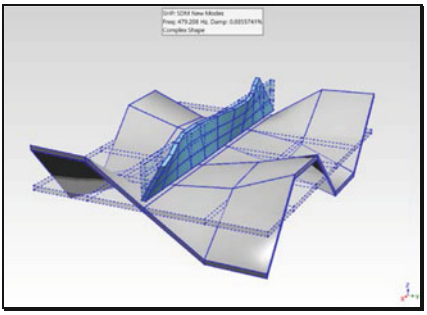

SDM Mode Shape 6

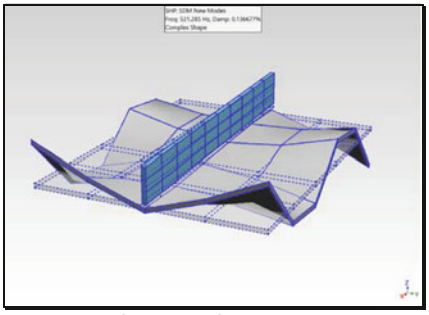

SDM Mode Shape 7

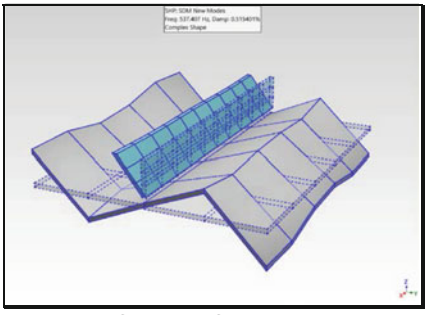

SDM Mode Shape 8

Fig. 14 SDM mode shapes

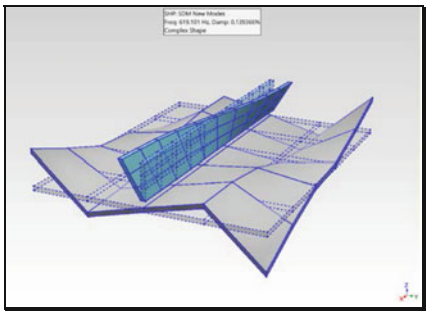

SDM Mode Shape 9

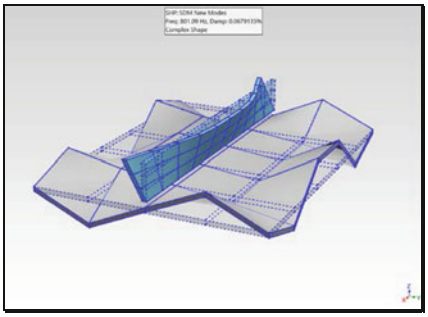

SDM Mode Shape 10

Fig. 14 continued

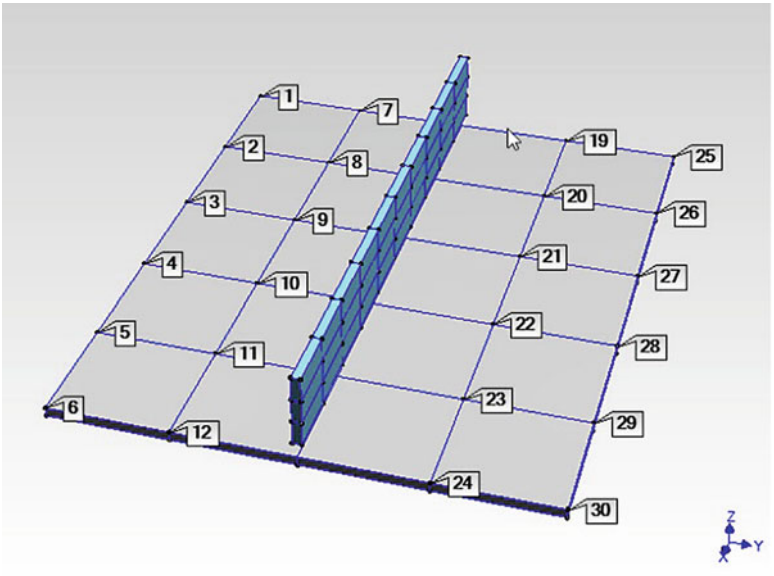

Fig. 15 Impact points on plate with RIB

26 SDM Versus EMA Modes: Plate and RIB

To compare the SDM mode shapes with EMA mode shapes, the plate with the RIB attached was impact tested using a roving impact hammer. The plate was impacted at 24 points on the plate in the **(vertical) Z-direction**, as shown in Fig. 15. This provided enough EMA mode shape data for comparison with the SDM mode shapes.

A driving point FRF measurement is not required since the EMA mode shapes do not require UMM scaling to compare them with SDM mode shapes using MAC.

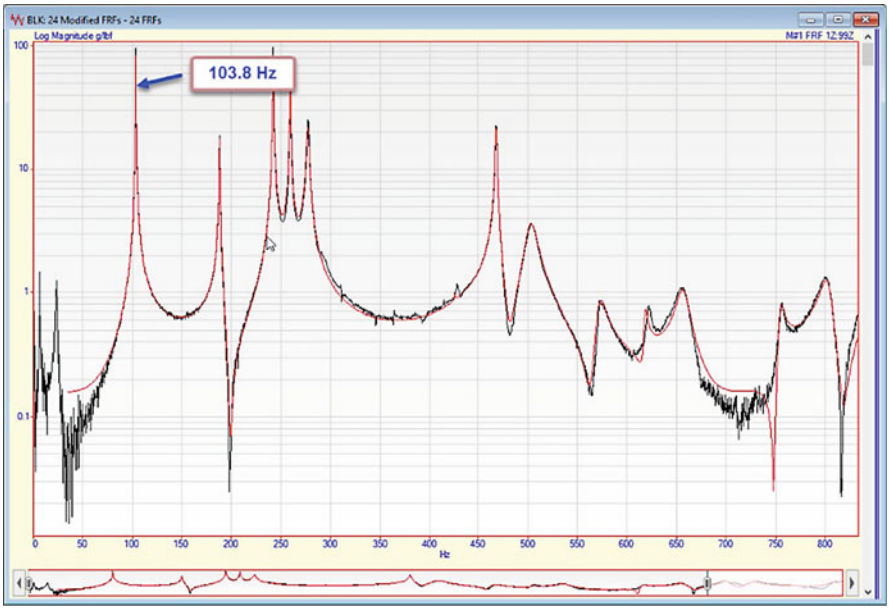

Fig. 16 Curve fit of an FRF from the plate with RIB

The curve fit of a typical FRF from the impact test is shown in Fig. 16. The 24 FRFs were curve fit to extract the EMA mode shapes for the modified plate.

27 Conclusions

In Table 6, the modal frequencies of the *first three* SDM modes agree closely with the frequencies of the first three EMA modes. In Table 6, the *first eight* SDM mode shapes agree closely with the first eight EMA mode shapes, all having MAC values *close to 1.0*.

The *close agreement* between the *first eight* mode shapes from all three cases, SDM, FEA, and EMA, verifies that the joint stiffness provided by the five cap screws was correctly modeled in SDM using 6-DOF springs and mode shapes with rotational DOFs in them. This example has demonstrated that even with the use of a *truncated modal model* containing relatively few mode shapes, SDM provides realistic and useful results.

Several options could be explored to obtain closer agreement between the SDM, FEA, and EMA mode shapes:

1. Add more FEA springs between the RIB and the plate to model the stiffness forces between the two substructures.

Table 6 EMA versus SDM modes for the plate and RIB

Shape pair	EMA frequency (Hz)	EMA damping (Hz)	SDM frequency (Hz)	SDM damping (Hz)	MAC
1	103.8	0.142	108.2	0.034	0.99
2	188.5	0.377	187.6	0.369	0.99
3	242.5	0.254	253.3	0.118	0.99
4	277.8	0.941	311.5	0.293	0.98
5	259.8	0.254	351.7	0.104	0.97
6	468.6	0.710	479.2	0.171	0.98
7	504.1	6.202	521.3	0.713	0.97
8	572.5	1.877	537.4	2.770	0.97
9	620.3	0.818	619.1	0.865	0.85
10	803.3	6.070	801.1	0.544	0.86

2. Use more FEA quad plate elements for the plate and RIB. Increasing the mesh of nodes for the plate elements usually provides more accurate FEA mode shapes.
3. Include more modes in the modal model of the *unmodified* plate and RIB. Extra modes will provide a more complete dynamic model of the two substructures as input to SDM.

28 Modeling a Tuned Vibration Absorber with SDM

Another use of SDM is to model the addition of tuned mass-spring-damper vibration absorbers to a structure. A tuned vibration absorber is designed to absorb some of the vibration energy in the structure so that one of its modes of vibration will absorb less energy and hence the structure will vibrate with less overall amplitude.

A tuned absorber is used to *suppress resonant vibration* in a structure. The primary effect of adding a tuned absorber is to *replace one of its resonances* with *two lower amplitude resonances*.

The mass and stiffness of the tuned absorber are chosen so that its natural frequency is *"close to"* the resonant frequency of a structural resonance to be suppressed. Ideally, the absorber should be attached to the structure at a point and in a direction where the magnitude of the resonance is large, near an *anti-node* of its mode shape. The absorber will have no effect if attached at a *node* of the mode shape, where its magnitude is zero.

SDM models the attachment of a tuned absorber to a structure by solving a substructuring problem like the one in the previous plate and RIB example. A tuned absorber is modeled by attaching an FEA mass to the structure using an FEA spring and FEA damper. SDM solves for the new modes of the structure with the tuned vibration absorber attached.

To begin the design, a mass must be chosen for the tuned absorber. The following rule should be used in choosing an absorber mass.

Rule of Thumb: The mass of a tuned absorber should not exceed **10%** of the mass of the structure.

After the mass has been chosen, the frequency of the structural mode to be suppressed together with the mass of the absorber will determine the stiffness of the spring required to attach the absorber to the structure. These three values are related to one another by the formula:

$$\mathbf{k} = \mathbf{m}\,\boldsymbol{\omega}^2 \tag{47}$$

where

$\mathbf{m} \leftarrow$ tuned absorber mass
$\boldsymbol{\omega} \leftarrow$ frequency of the structural mode to be suppressed
$\mathbf{k} \leftarrow$ tuned absorber stiffness

Adding a damper is optional. If a damper is added between the absorber mass and the structure, its damping value must also be chosen. A realistic damping value of a *few percent of critical damping* is calculated using the following formulas.

$$\mathbf{k} = \mathbf{m}\left(\boldsymbol{\omega}^2 + \boldsymbol{\sigma}^2\right) \tag{48}$$

where
$\boldsymbol{\sigma} = \frac{\boldsymbol{\omega}}{\sqrt{1-\%^2}} \leftarrow$ damping decay constant
$\% \leftarrow$ percent of critical damping

The mode shape of the unattached tuned absorber is simply the UMM rigid-body mode shape of the mass substructure in free space. In order to use SDM to model a tuned absorber, two more steps are necessary:

1. The free-free mode shape of the tuned absorber must be added in *block diagonal format* to the mode shapes of the unmodified structure. The block diagonal format was explained in the previous plate and RIB example.
2. The attachment DOF (point and direction) of the tuned absorber must be defined. A geometric model of the structure is usually required for this.

29 Adding a Tuned Absorber to the Plate and RIB

SDM will be used to model the attachment of a tuned vibration absorber to one corner of the flat aluminum plate used in the previous example. The absorber will be designed to suppress the amplitude of the high-Q resonance at 108 Hz, shown in the **blue FRF magnitude** plot in Fig. 17.

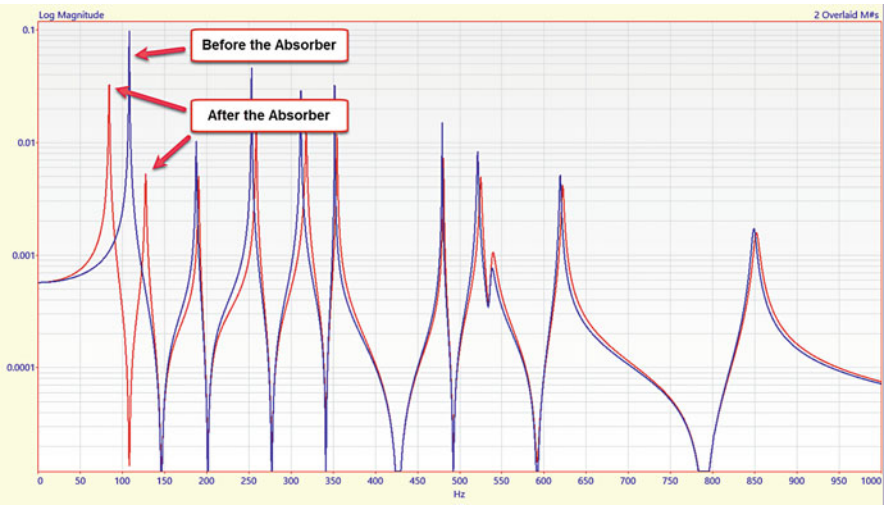

Fig. 17 Synthesized FRFs (1Z:1Z) before and after absorber

The plate and RIB weighs about **21.3 lbm** (**9.7 kg**). For this example, the absorber weight is chosen as **0.5 lbm** (**0.23 kg**). In order to absorb energy from the plate and RIB at 108 Hz, the attachment spring stiffness must be chosen so that the absorber will resonate at 108 Hz.

The absorber parameters are:

Mass: **0.5 lbm** (**0.23 kg**)
Stiffness: **586.6 lbf/in** (**104.8 N/mm**)
Damping: **0.5%**

Only the modal model data of the unmodified plate and RIB at **DOF 1Z** is required. Since the mass will be attached to the plate and RIB as a substructure, the mode shape of the free-body mass is added to the mode shapes of the unmodified plate and RIB in *block diagonal format*, explained in the previous example.

To model the tuned absorber, the modal model for the *unmodified* plate and RIB substructure together with a modal model and the spring and damper of the absorber are used as inputs to SDM. SDM then solves for the new modes of the plate and RIB with the absorber mass attached by the spring and damper to one corner of the plate (DOF 1Z).

Figure 17 shows the log magnitudes of two overlaid driving point FRFs of the plate and RIB at DOF 1Z, before (blue) and after (red) the tuned absorber was attached to the plate. These overlaid FRFs clearly show that the resonant frequency at 108 Hz has been removed from the plate and RIB and replaced with two new resonances, one at 84 Hz and the other at 128 Hz. The two new modes also have lower Q's (less amplitude) than the Q of the mode they replaced.

Table 7 Modes before and after tuned absorber attached at 1Z

Shape pair	Before TA frequency (Hz)	Before TA damping (Hz)	After TA frequency (Hz)	After TA damping (Hz)	MAC
1	108.2	0.0345	84.3	0.149	0.96
2	108.2	0.0345	127.6	0.333	0.93
3	187.6	0.369	190.4	0.422	0.99
4	253.3	0.118	258.7	0.250	0.98
5	311.5	0.293	317.9	0.488	0.98
6	351.7	0.104	354.4	0.217	0.99
7	479.2	0.171	480.7	0.239	1.00
8	521.3	0.713	524.9	0.924	0.97
9	537.4	2.77	538.7	2.808	0.98
10	619.1	0.863	622.1	1.055	1.00
11	801.1	0.544	801.1	0.544	1.00

The MAC values in Table 7 show that the two new mode shapes are *essentially the same* as the mode shape of the original 108 Hz mode. Notice also that the tuned absorber had *very little effect* on the other resonances of the structure.

Figure 18 shows how the tuned absorber mass moves with respect to the plate. In Fig. 18a. the tuned absorber is *moving in-phase* with the plate below it. In Fig.18b. it is *moving out-of-phase* with the plate below it. (An animated picture shows this relative motion more clearly.)

30 Modal Sensitivity Analysis

It is well-known that the *modal properties* of a structure *are very sensitive* to changes in its physical properties.

Because of its computational speed, SDM can be used to quickly solve for the modal parameters of *thousands* of potential modifications to a structure. The calculation and ordering of multiple SDM solutions from best to worst is called **Modal Sensitivity Analysis**.

30.1 EMA Modes of the Plate and RIB

In a previous example, SDM was used to model the attachment of a RIB stiffener to the aluminum plate shown in Fig. 5a–c. To validate the SDM mode shapes using experimental data, the plate with the RIB attached was tested with a roving impact hammer test.

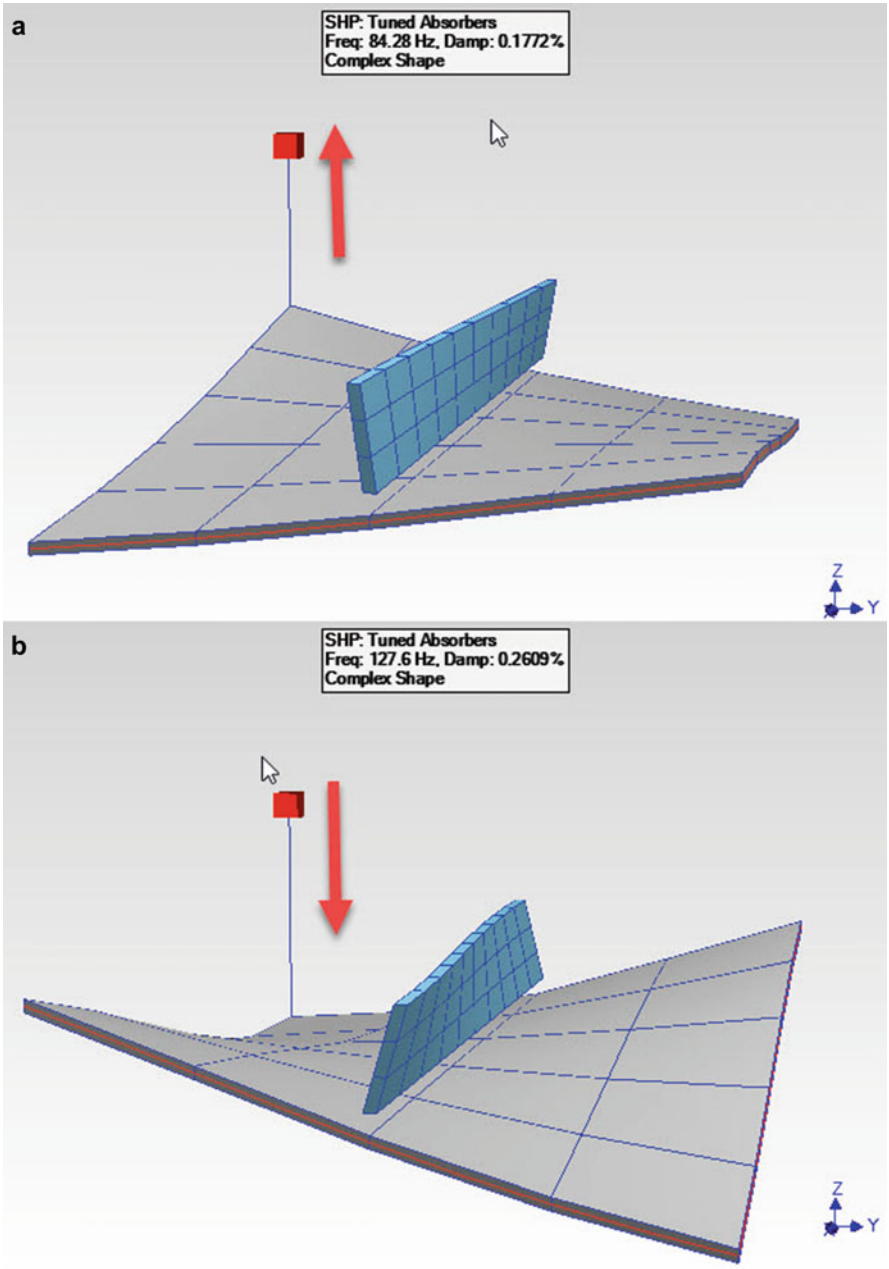

Fig. 18 (**a**) Absorber in-phase with the 84 Hz mode. (**b**) Absorber out-of-phase with the 128 Hz mode

Table 8 EMA versus SDM modes for the plate with RIB

Shape pair	EMA frequency (Hz)	EMA damping (Hz)	SDM frequency (Hz)	SDM damping (Hz)	MAC
1	103.8	0.144	108.2	0.0345	1.00
2	188.5	0.360	187.6	0.369	0.99
3	242.5	0.262	253.3	0.118	0.99
4	259.7	0.378	311.5	0.293	0.98
5	277.4	1.164	351.7	0.104	0.97
6	468.6	0.760	479.2	0.171	0.98
7	503.6	6.035	521.3	0.713	0.97
8	572.6	4.953	537.4	2.77	0.98
9	618.8	1.828	619.1	0.863	0.87
10	657.5	6.541	801.1	0.544	0,95

The plate was impacted at 24 points on the plate in the **(vertical) Z-direction** to gather enough data to uniquely define the EMA mode shapes for comparison with the SDM mode shapes. In Table 8, the first eight EMA and SDM mode shape pairs have MAC values *close to 1.0*, indicating that they are *closely matched.* But the EMA and SDM modal frequencies *are all different* from one another.

30.2 Using SDM to Explore Joint Stiffnesses

The first mode of the plate and RIB involves *twisting of both the plate and RIB*, as shown in Fig. 14. The mode shape is influenced by both the *translational* and *rotational* stiffness of the spring stiffeners used to attach the RIB to the plate.

Using the Hybrid modal model containing the mode shapes of the plate without the RIB attached, SDM can be used to quickly calculate the modes of the plate and RIB using *many different* translational and rotational stiffnesses of the springs used to attach the RIB to the plate. These solutions are then ordered from best to worst. **Modal Sensitivity Analysis** can be performed by calculating and ordering multiple SDM solutions.

30.3 Current Versus Target Frequency

A **Modal Sensitivity** window is set up in Fig. 19a to perform sensitivity calculations on the plate and RIB. The window contains two spreadsheets. The frequencies of the 30 modes of the *unmodified* plate and RIB substructures are listed in the **Current Frequency** column of the upper spreadsheet. This modal model contains 14 mode shapes of the plate without the RIB attached and 16 free-body mode shapes of the RIB. The mode shapes are sorted according to frequency, beginning with the rigid-body mode shapes of the RIB.

a

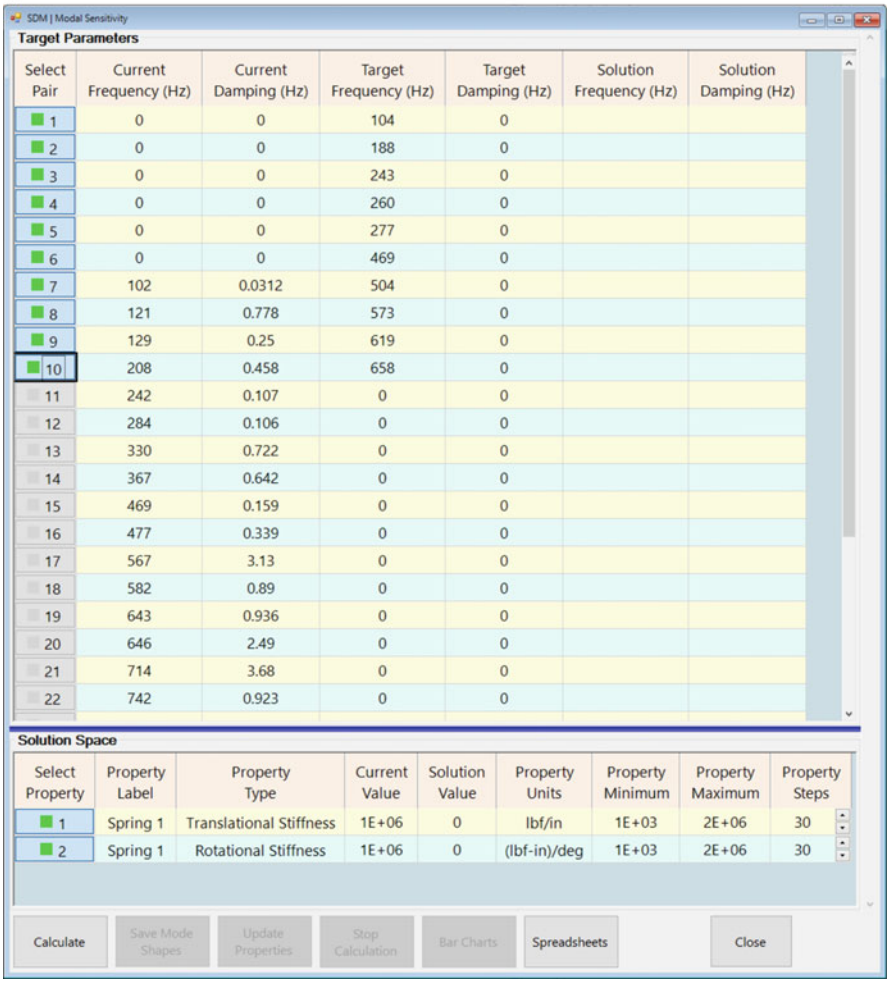

Fig. 19 (**a**) Modal sensitivity setup for 2500 solutions

The **EMA** modal frequencies of the plate and RIB are listed in the **Target Frequency** column in the upper spreadsheet. These frequencies are used for ranking the SDM solutions from best to worst.

Ten **Shape Pairs** have been selected in the upper spreadsheet. The **Selected Pairs** are used to order the solutions from best to worst. The best solution is the one which minimizes the difference between each **Solution Frequency** and each **Target Frequency**.

b

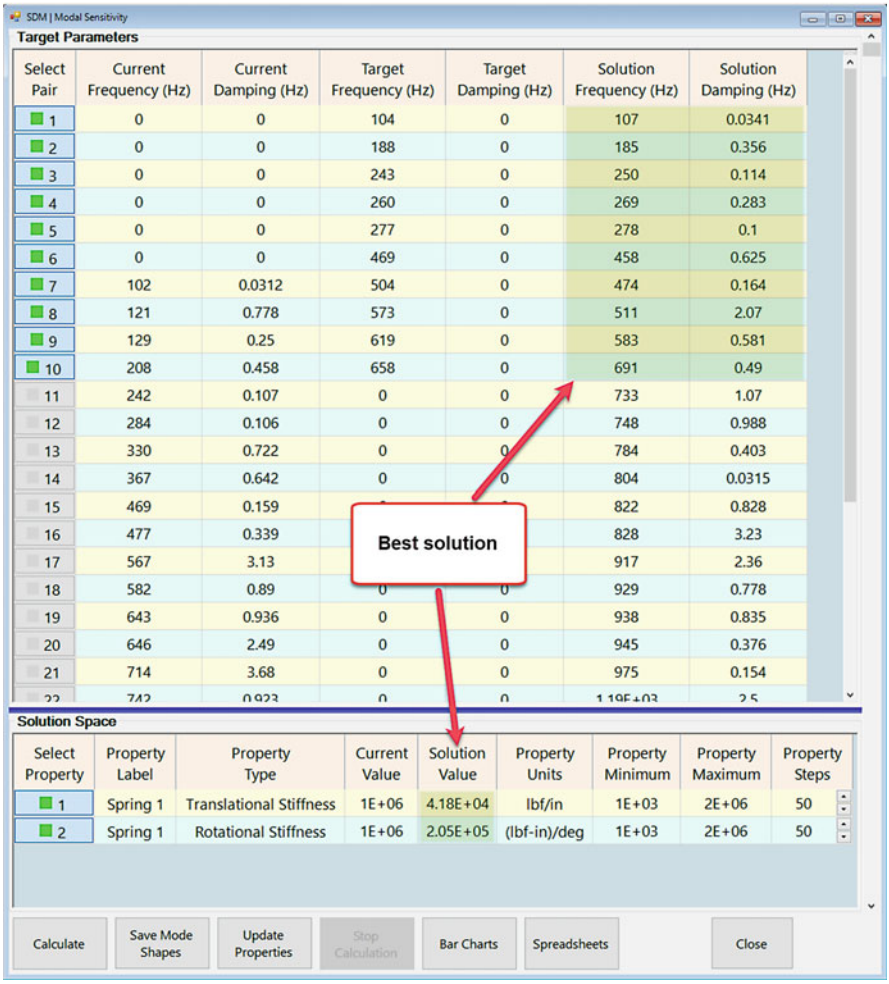

Fig. 19 (**b**) Best solution with eight shape pairs selected

30.4 Solution Space

In Table 8, the first EMA mode shape (at 103.8 Hz) has a lower frequency than the first SDM mode shape (at 108.2 Hz). Therefore, the best Modal Sensitivity solution should require *less stiffnesses* than the stiffnesses (**1,000,000**) used to attach the RIB to the plate.

The lower spreadsheet defines ranges of stiffness values for the translational and rotational stiffnesses of the five FEA springs. Each stiffness has a range of *50 Steps* (or values) in its solution space. Each SDM solution will use a stiffness value from

the **Minimum Property** (**1000**) to the **Maximum Property** (**2,000,000**) of each stiffener. The solution space has 50 steps × 50 steps = *2500 stiffness values* in it. SDM will solve for new modes using all combinations of stiffness values in the solution space of the two stiffeners.

Figure 19b shows the Modal Sensitivity window after 2500 solutions have been calculated and ordered from best to worst. The modal frequencies of the best solution are displayed in the **Solution Frequency** column of the upper spreadsheet. The damping values are displayed in the **Solution Damping** column.

The stiffness values used to calculate the best solution are displayed in the lower spreadsheet. The *translational* stiffness used to calculate the best solution is **4.18 E04 lbf/in**. The *rotational* stiffness used to calculate the best solution is **2.05 E05 (lbf-in)/deg**. *Much less* translational and rotational stiffness of the five spring stiffeners was required to *closely match* the frequencies of the first eight EMA modes of the plate and RIB.

31 FEA Modal Updating

Because of its computational speed, SDM can be used to quickly evaluate thousands of modifications to the physical properties of an FEA model. In Table 3 their MAC values indicate that each FEA mode shape of the plate *closely matches* with an EMA mode shape, but each FEA modal frequency *is less than* the EMA frequency of its matching mode shape.

The physical properties used for the plate elements in the FEA model of the aluminum plate were:

1. **Young's modulus of elasticity:** 1E07 lbf/inˆ2 (6.895E4 N/mmˆ2)
2. **Density:** 0.101 lbm/inˆ3 (2.796E-6 kg/mmˆ3)
3. **Poisson's ratio:** 0.33
4. **Plate thickness:** 0.375 in (9.525 mm)

The plate is made from 6061-T651 aluminum. A more accurate handbook value for the density of this alloy of aluminum is **0.0975 lbm/inˆ3** (**2.966E-6 kg/mmˆ3**). In addition, the quad plate elements were given a nominal thickness of **0.375 in** (**9.525 mm**). Plate stiffness is *very sensitive* to its thickness!

Error in the density or thickness of the elements in the FEA plate model could be the reason why the frequency of each FEA mode shape was *less than* the frequency of its corresponding EMA mode shape.

An **FEA Modal Updating** window is set up in Fig. 20a to perform SDM calculations using multiple density and thickness values. The **FEA Frequency** of each of the 14 FEA mode shapes of the plate is listed in the upper spreadsheet. Each EMA frequency is listed as a **Target Frequency**.

All 14 mode **Shape Pairs** are selected, meaning that each **Solution Frequency** will be compared with each **Target Frequency** to order the solutions from best to

a

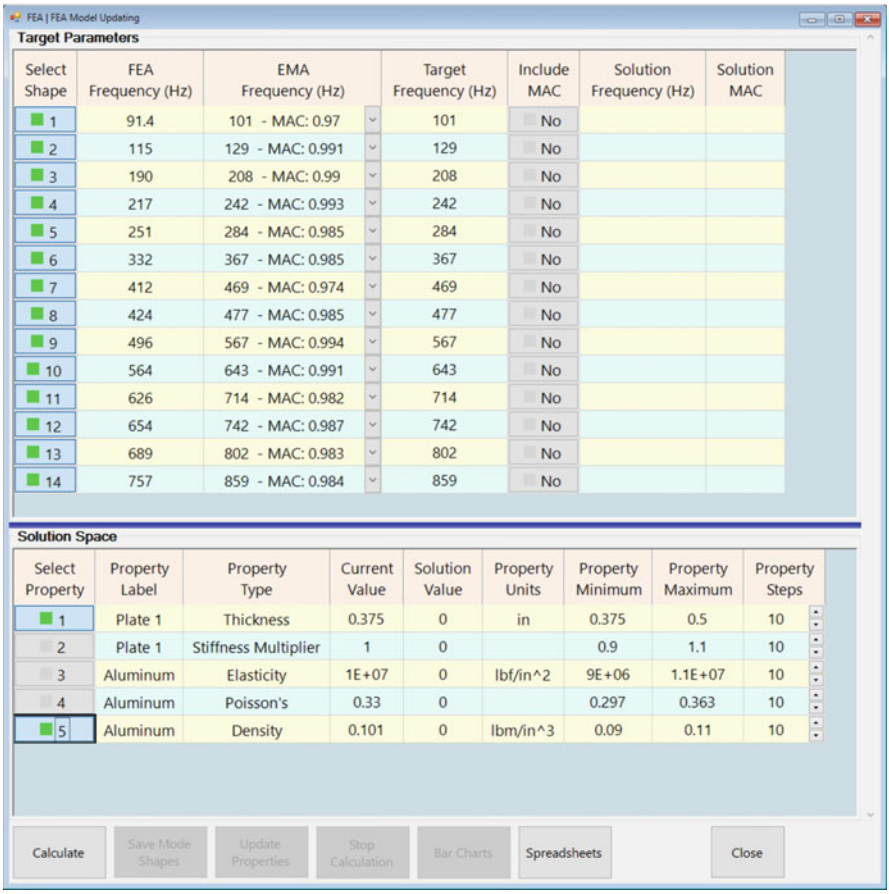

Fig. 20 (**a**) Setup for 100 FEA model updating solutions

worst. The best solution is the one which minimizes the difference between each **Solution Frequency** and each **Target Frequency**.

The **Solution Space** is defined in the lower spreadsheet. The plate thickness and density are selected, and each has **10 Property Steps** (or values) between its **Property Minimum** and **Property Maximum**. Solutions will be calculated over a solution space of *100 property values*, using all combinations of 10 different thicknesses and 10 different densities.

The properties of the *original* FEA model are required in order to update those properties.

b

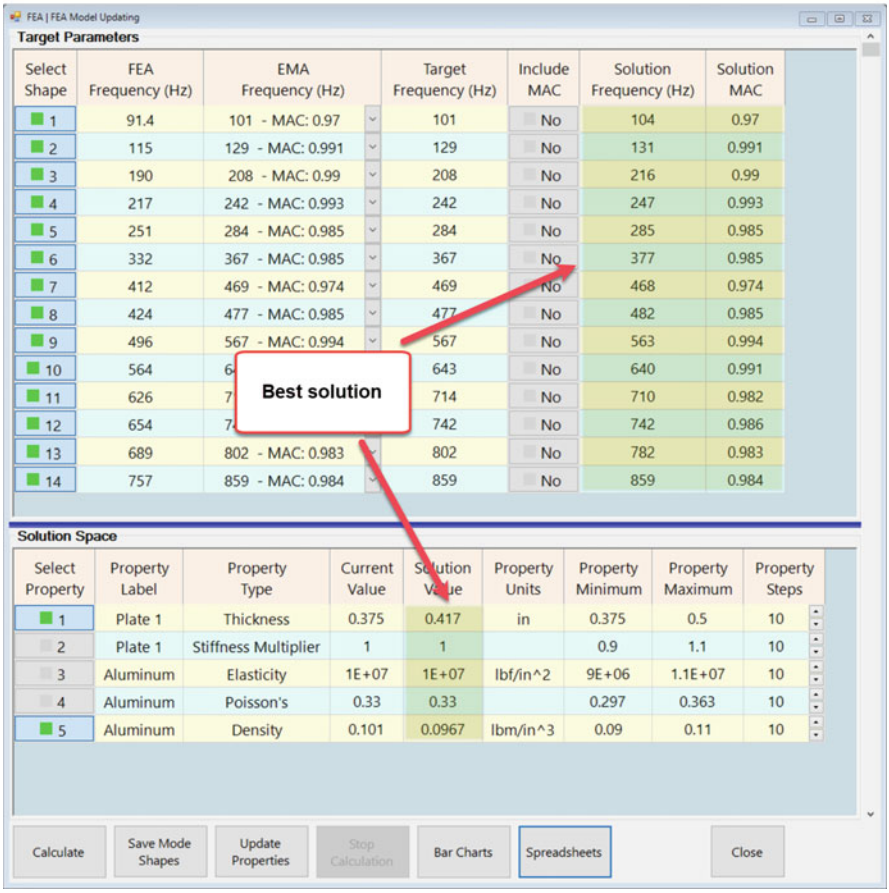

Fig. 20 (**b**) Best solution for updating density and thickness

To perform FEA Model Updating, the properties of the *unmodified* model must be removed from the mass and stiffness matrices before the new properties can be added.

Figure 20b shows the Model Updating window after 100 solutions have been calculated and ordered from best to worst. For all 14 Shape Pairs, each **Solution Frequency** *closely matches* each **Target Frequency**. The **Solution MAC** between each **Shape Pair** also indicates that the mode shapes of all 14 mode shapes were not changed by updating the density and thickness.

The updated density (**0.0967**) more closely matches the handbook density for 6061-T651 aluminum. The updated thickness (**0.417 in.**) is more than the thickness originally used, but it resulted in new modal frequencies that *more closely matched* the experimental frequencies.

32 Difference Between Modal Sensitivity and FEA Model Updating

In order to calculate the new modes of a modified structure, SDM only requires a **modal model** of the *unmodified* structure together with FEA elements. For Modal Sensitivity Analysis, the properties of modification elements are used. For FEA Modal Updating, the properties of FEA elements are used.

In **Modal Sensitivity Analysis**, multiple SDM solutions are calculated over a solution space of modification element properties, and the solutions are ordered from best to worst based on how closely the Solution frequency and damping of each selected Shape Pair match Target modal frequency and damping.
In **FEA Model Updating**, multiple SDM solutions are calculated over a solution space of FEA model properties, and the solutions are ordered from best to worst based on how closely the Solution frequency and mode shape of each selected Shape Pair match Target modal frequency and mode shape values.

Whether SDM is used for Modal Sensitivity or FEA Model Updating studies, *thousands of potential property changes* can be quickly evaluated and sorted from best to worst based on how close a Solution is to Target values. In these applications, SDM is very useful for *"closing the gap"* between analytical and experimental results.

References

1. Hallquist J (1974) Modification and synthesis of large dynamic structural systems. PhD dissertation, Michigan Technological University
2. Formenti D, Welaratna S (1980) Structural dynamics modification – an extension to modal analysis. SAE paper no. 811043
3. Structural Measurement Systems, Inc. An introduction to the structural dynamics modification system. Technical note no.1, February 1980
4. Ramsey K, Firmin A (1982) Experimental modal analysis structural modifications and FEM analysis – combining forces on a desktop computer. First IMAC proceedings, Orlando, 8–10
5. Wallack P, Skoog P, Richardson MH (1988) Simultaneous structural dynamics modification S^2DM). Proceedings of 6th IMAC, Kissimmee
6. Bathe KJ, Wilson EL (1976) Numerical methods in finite element analysis. Prentice Hall, Inc, Englewood Cliffs
7. Yang TY (1986) Finite element structural analysis. Prentice Hall, Inc, Englewood Cliffs
8. McGuire W, Gallagher RH (1979) Matrix structural analysis. Wiley, New York

Toward Robust Response Models: Theoretical and Experimental Issues

21

Nuno Maia, António Urgueira, Raquel Almeida, and Tiago Silva

Contents

N. Maia (✉)
Department of Mechanical Engineering, LAETA/IDMEC/IST (Instituto Superior Tecnico), University of Lisbon, Lisbon, Portugal
e-mail: nuno.manuel.maia@tecnico.ulisboa.pt

A. Urgueira · R. Almeida · T. Silva
UNIDEMI, Department of Mechanical and Industrial Engineering, FCT NOVA – Faculty of Science and Technology, Universidade NOVA de Lisboa, Caparica, Portugal

R. Allemang, P. Avitabile (eds.), *Handbook of Experimental Structural Dynamics*,
https://doi.org/10.1007/978-1-4614-4547-0_26

Abstract

The purpose of building a reliable response model requires awareness and understanding of the theoretical and practical problems and pitfalls that may be encountered along the process. Those issues have to deal with many different aspects of structural dynamics that will be tackled in this chapter. First of all, it is necessary to frame the problem in the context of structural dynamics and modal analysis; then, it is crucial to discuss the substructuring/coupling problem, especially when facing a very complex structure, which needs to be studied by parts. This leads us inevitably to the difficult task of measuring angular responses, that is, to measure the response at rotational degrees of freedom. A comprehensive discussion on this matter is given here.

Not only due to the lack of information regarding rotational measurements, a constant issue is the incompleteness of the experimental data and its expansion to the numerical model size or the condensation/reduction of the numerical model to the experimental one. A significant discussion on this subject is also given in this chapter.

Finally, the more recently developed transmissibility theory for N degrees of freedom allows for the estimation of unmeasured frequency response functions, contributing to the building of robust response models.

Keywords

Response model · Coupling · Rotational measurements · Expansion/Reduction techniques · Transmissibility · FRF estimation

1 Introduction

1.1 Foreword

The dynamic analysis of real structures is, in general, a complex matter that can be approached from various points of view, depending essentially on the purpose of the study and ultimately on the computational resources available. In any case, it may be also constrained by the complexity of the structure itself, which may prevent an easy numerical modeling, if that is the case, or an easy access when it comes to experimental testing. Sometimes, one may "simply" wish to evaluate the condition of the structure to detect any malfunctioning or damage progression, through the direct measurement of the output response, other times one wishes to know the response at one coordinate due to an applied force at another coordinate. There are cases, however, where it is important to have a model of the structure that can reproduce, as accurately as possible, its effective behavior in practice. Such a model may have just a few degrees-of-freedom or many thousands, depending once more on the objectives of the study. The main advantage of having a good model representing the dynamics of the structure is that one can use it to predict what will happen if a modification is made – like adding mass, stiffness, or damping at

some coordinates – or what will be the consequence of coupling a new substructure, without having to go through a series of experimental testing, which tends to be costly and time-consuming.

There are essentially two options when it comes to build a model: the experimental approach and the theoretical approach. Most researchers working on the experimental side tend to select a model that incorporates the information directly available from tests. On the other hand, the theoretical models are constructed in order to incorporate the spatial distributed properties.

In this chapter, devoted to the response (or impedance) modeling, one shall address its relation with respect to other modeling approaches, its advantages, disadvantages or limitations, referring also to some topics that are directly connected, like associated coupling techniques, the measurement of rotational degrees of freedom, incompleteness of the models, leading to reduction or expansion issues, and estimation of unmeasured responses.

1.2 Classification of the Models

Essential to the communication among different organizations and research groups is the terminology and format used to describe the dynamic properties of a system or subsystem model, be it theoretically or experimentally derived. In what follows, the three different model formats are described.

1.2.1 The Spatial Model

Any structure can be modeled numerically, in a more or less accurately way; this is often accomplished using the finite element method, where one ends up with a description of the model in terms of mass, stiffness, and damping matrices. It is known as the spatial model. The dynamic equilibrium equation is given by:

$$\boldsymbol{M}\ddot{\boldsymbol{x}} + \boldsymbol{C}\dot{\boldsymbol{x}} + \boldsymbol{K}\boldsymbol{x} = \boldsymbol{f} \tag{1}$$

where $\boldsymbol{M}$, $\boldsymbol{K}$, and $\boldsymbol{C}$ are matrices of order N (the number of degrees of freedom) representing the mass, stiffness, and viscous damping, respectively. In such a numerical model the damping is often neglected, as it requires experimental information to be taken into consideration. This can be a reasonable option to start with when the damping is really low. As a common alternative, one may assume a Rayleigh (proportional) type of damping, where the damping matrix is directly proportional to the stiffness and/or mass matrices, although some constants still have to be evaluated experimentally. In any case, it will be necessary to "tune" the model so that it represents the reality as close as possible, undergoing a refinement process involving some kind of comparison with real experimental data; such a process is known as model updating.

1.2.2 The Response Model

Sometimes, due to the complexity of the structure, it may not be so easy to build a numerical or analytical model and it is preferable to excite the structure with forces at some locations and measure the responses at those or other locations. By doing so, a series of the so-called frequency response functions (FRFs) can be grouped together to build a matrix, where each element is an FRF relating the response at coordinate *i* to the force at coordinate *j*, expressed as:

$$H_{ij}(\omega) = \frac{X_i(\omega)}{F_j(\omega)} \tag{2}$$

provided that all other forces are zero.

One has, therefore, the FRF matrix $\boldsymbol{H}$ representing the response model.

By taking into account all the degrees of freedom, one may write:

$$\boldsymbol{X} = \boldsymbol{H}\boldsymbol{F} \tag{3}$$

Ideally, if all the dofs can be measured and excited, one can write the inverse relation

$$\boldsymbol{F} = \boldsymbol{Z}\boldsymbol{X} \tag{4}$$

where $\boldsymbol{Z} = \boldsymbol{H}^{-1}$ is the dynamic stiffness matrix. In practice, this is not the case, as one can only measure a reduced number of dofs, one may end up with a reduced or condensed $\boldsymbol{Z}$ matrix. This will be discussed in Sect. 4.

Apparently, one might think that it would be indifferent to measured $\boldsymbol{Z}$ or $\boldsymbol{H}$. However, that is not the case, as each element Z_{ij} represents the force applied at dof *i* when dof *j* responds with a unit displacement and all the remaining dofs other than *j* do not move, that is, numerous dofs would have to be constrained to have no motion, which is not possible, or at least impractical. This is not the case with the FRF matrix $\boldsymbol{H}$, as each element H_{ij} represents the response at dof *i* due to a unit force at dof *j*, provided that all other forces are zero. Moreover, a measured FRF matrix at one stage of the design can be later expanded by simply performing new measurements at additional coordinates to form new rows and columns without modifying any existing elements. This is not the case whenever a dynamic stiffness matrix needs to be expanded, since all the existing elements would have to be re-measured after the new constraints had been imposed to the structure (assuming this could be somehow accomplished in practice).

Concluding, in practice, the response model is build based upon the measurement of FRFs, which can be in terms of displacement, velocity, or acceleration. Due to the wide use of accelerometers to acquire responses, the FRFs are often measured in terms of accelerations, that is, accelerance FRFs.

1.2.3 The Modal Model

It may also happen that some parts of the structure be modeled using the spatial model and other parts using the response model. In the "middle" stands the modal model, based on the so-called modal properties, constituted by the natural frequencies ω_r, mode shapes $\boldsymbol{\phi}_r$, and damping ratios ξ_r. In some applications it may be convenient to have the structure described in such terms. In contrast with the other two kinds of models, the modal model is not directly obtained from the structure; it is deduced from either the spatial model, solving a generalized eigenproblem, or the response model, using a modal identification technique.

1.2.4 Relation Among the Models

The three models are, of course, interrelated. From (1), assuming harmonic excitation, it follows that

$$\left(\boldsymbol{K} - \omega^2 \boldsymbol{M} + i\omega \boldsymbol{C}\right) \boldsymbol{X} = \boldsymbol{F} \tag{5}$$

Comparing Eqs. (3), (4), and (5), one concludes that the spatial and response models are related in the following way:

$$\boldsymbol{H}(\omega) = \boldsymbol{Z}^{-1}(\omega) = \left(\boldsymbol{K} - \omega^2 \boldsymbol{M} + i\omega \boldsymbol{C}\right)^{-1} \tag{6}$$

To relate the response and modal models one has to use the orthogonality conditions. Let $\boldsymbol{\phi}$ be the mass-normalized mode shape matrix. Assuming proportional damping, as it is usual to do when modeling with the finite element method, the orthogonality conditions are:

$$\begin{aligned} \boldsymbol{\phi}^T \boldsymbol{M} \boldsymbol{\phi} &= \boldsymbol{I} \\ \boldsymbol{\phi}^T \boldsymbol{K} \boldsymbol{\phi} &= \mathbf{diag}\left(\omega_r^2\right) \\ \boldsymbol{\phi}^T \boldsymbol{C} \boldsymbol{\phi} &= \mathbf{diag}\left(2\xi_r \omega_r\right) \end{aligned} \tag{7}$$

from which one can deduce the three matrices:

$$\begin{aligned} \boldsymbol{M} &= \boldsymbol{\phi}^{-T} \boldsymbol{\phi}^{-1} \\ \boldsymbol{K} &= \boldsymbol{\phi}^{-T} \mathbf{diag}\left(\omega_r^2\right) \boldsymbol{\phi}^{-1} \\ \boldsymbol{C} &= \boldsymbol{\phi}^{-T} \mathbf{diag}\left(2\xi_r \omega_r\right) \boldsymbol{\phi}^{-1} \end{aligned} \tag{8}$$

Substituting (8) in (6), inverting and pre- and post-multiplying by $\boldsymbol{\phi}^T$ and $\boldsymbol{\phi}$, respectively, yields:

$$\boldsymbol{\phi}^T \boldsymbol{H}^{-1} \boldsymbol{\phi} = \mathbf{diag}\left(\omega_n^2 - \omega^2 + i2\xi_r \omega \omega_r\right) \tag{9}$$

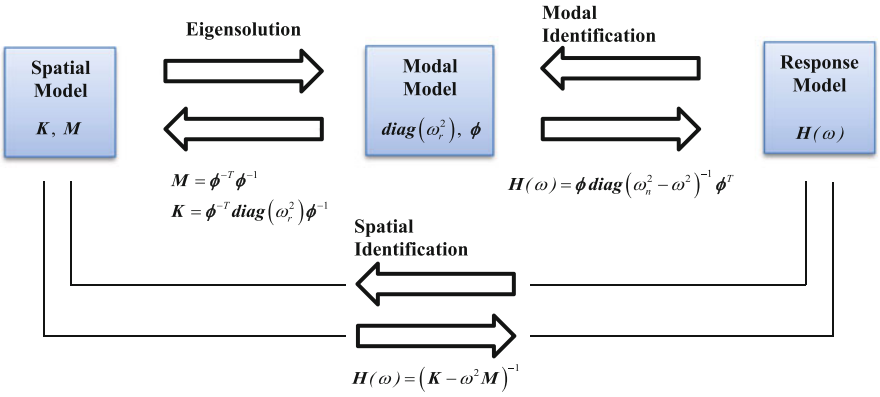

Fig. 1 Interrelation among the three dynamic models for an undamped model

and thus,

$$\boldsymbol{H}(\omega) = \boldsymbol{\phi}\left(\mathbf{diag}\left(\omega_n^2 - \omega^2 + i2\xi_r\omega\omega_r\right)\right)^{-1}\boldsymbol{\phi}^T \tag{10}$$

Provided that the models are complete, that is, that one has the information from all the degrees of freedom, one can easily go from one model to the other. From the spatial model to the modal model one has to solve a generalized complex eigenproblem to obtain the complex natural frequencies (which include the information about damping) and the mode shapes. The inverse process simply implies the application of Eq. (8). Going from the response model to the modal model requires a modal identification process, whereas the opposite operation is much easier, just involving the use of Eq. (10). Figure 1 illustrates the interrelation among the three models, for the undamped case (for clarity of exposition). The incompleteness of the models will be addressed in Sect. 4.

2 Coupling/Uncoupling Techniques

2.1 Coupling

The basic principle inherent to the coupling philosophy is the assumption that the whole (complex) structure is formed by different substructures (or components), each of them being first analyzed individually and independently from the others. This is the idea underlying the nowadays well-known "substructuring," or "coupling" approaches for solving static and dynamic problems.

The order of the matrices used to formulate the equations of motion of the assembled structure depends either on the number of coordinates (connection and interior ones) or on the number of kept modes pertaining to each component model.

One can say that two groups of coupling techniques emerge from the large variety of methods that have been used in different fields of research and industry, classified as:

- *Impedance* coupling techniques, which benefit from the reduction performed on the subsystem models in terms of *coordinates*
- *Modal* coupling techniques, which are suitable for the use of reduced models in terms of *modes*

The former group deals primarily with the coupling of subsystems whose models are described either by their spatial or response properties. The first of these types of models is used extensively in the finite element method, but is rarely used in cases involving experimental modeling. Although response models can be obtained by theoretical analysis, they mostly constitute the raw data available from modal tests. The techniques forming the latter group are applied in those situations where the component models are described by their modal properties – modal models. This type of model is easily generated from an eigensolution, if a theoretical tool such as the finite element method is used, or they can be derived from an identification process carried out on measured FRF data.

Depending on whether spatial or response component models are used directly as input data into a coupling process, the assembling techniques are here designated as spatial or FRF coupling techniques, respectively. The former is ideal for the use of FE methods, whereas the latter comprises both theoretical and experimental fields of work. The FRF coupling technique is generally referred to as the "Impedance Coupling" technique since, at the system level, it assembles mathematically the generalized impedance properties.

The application of the conceptually simple impedance coupling technique is straightforward when the components are amenable to theoretical modeling, but practical complex systems have demanded subsystem impedances to be derived from measured data. Although the models obtained via this latter approach have the advantage of reflecting in a closer way the "true" dynamic characteristics of a structure, they are contaminated by errors arising during the acquisition and analysis of measured data. Consequently, the accuracy of the dynamic properties of the assembled structure results will be somehow affected.

The experimental approach to the impedance coupling problem, herein designated as FRF coupling, was one of the main reasons that motivated a breakthrough to the development of suitable techniques and equipment to measure, assess, and analyze data. The main difficulties encountered in those applications were mainly related to the mathematical inconsistency of the measured models and to the inadequacy of experimental means to measure some terms in the FRF matrices of certain components. Mostly, those FRFs were related to rotational response measurements. Rotational responses are necessary to formulate proper constraints between connected components. Success in the prediction of results for a coupled structure is dependent on how the connection coordinates are measured and included in a coupling process. For instance, if a single connection point is assumed between

two components that respond to excitations in all three planes, it is vital to include the three rotations in addition to the three translations, in order to properly formulate the constraint conditions. In terms of response models, the FRFs related to rotational response/excitations represent 75% (or 60% if symmetry properties are assumed) of the total elements of the corresponding FRF matrix. Section 3 addresses the topic of measuring FRFs involving rotational dofs.

The FRF coupling method makes use of subsystem models derived directly from FRF data (commonly available from experimental studies but seldom from theoretical modeling). The dynamic properties of those models are synthesized in terms of the FRF matrix and generally denoted as $\boldsymbol{H}(\boldsymbol{\omega})$ (such as receptance, mobility, or accelerance matrices). The coordinates involved in the connection between components A and B should be identified and represented by the index c (and similarly i and j for the remaining ones), leading to the following partitioned FRF matrices:

$$\boldsymbol{H}^A = \begin{bmatrix} \boldsymbol{H}^A_{ii} & \boldsymbol{H}^A_{ic} \\ \boldsymbol{H}^A_{ci} & \boldsymbol{H}^A_{cc} \end{bmatrix} \text{ and } \boldsymbol{H}^B = \begin{bmatrix} \boldsymbol{H}^B_{jj} & \boldsymbol{H}^B_{jc} \\ \boldsymbol{H}^B_{cj} & \boldsymbol{H}^B_{cc} \end{bmatrix} \tag{11}$$

By invoking the constraint equations that impose that at the connection coordinates the forces obey to the action/reaction principle and that the displacements of each component A and B are the same, the FRF matrix of the coupled structure [77] turns out to be

$$\boldsymbol{H}^C = \left(\left(\boldsymbol{H}^A \right)^{-1} \oplus \left(\boldsymbol{H}^B \right)^{-1} \right)^{-1} \tag{12}$$

where the operation sign "$\oplus$" means "coupled to." Denoting by Z_{kl} the element k,l in the generalized impedance matrix $\boldsymbol{Z} = \boldsymbol{H}^{-1}$, the operation sign "$\oplus$" implies that the connectivity between the coordinates of both components must be respected, leading to the following assembling of matrices:

$$\boldsymbol{H}^C = \begin{bmatrix} \boldsymbol{Z}^A_{cc} & \boldsymbol{Z}^A_{ic} & \boldsymbol{0} \\ \boldsymbol{Z}^A_{ci} & \boldsymbol{Z}^A_{cc} + \boldsymbol{Z}^B_{cc} & \boldsymbol{Z}^B_{cj} \\ \boldsymbol{0} & \boldsymbol{Z}^B_{jc} & \boldsymbol{Z}^B_{jj} \end{bmatrix}^{-1} \tag{13}$$

The FRF matrices of each substructure (available over a frequency range of interest, which is the same for both structures) are "added" together frequency by frequency until the whole FRF matrix is completely calculated.

A refined version for the calculation of the FRF matrix of the coupled structure reduces the number of inversions to be carried out [59]:

$$\boldsymbol{H}^C = \begin{bmatrix} \boldsymbol{H}_{ii}^A & \boldsymbol{H}_{ic}^A & \mathbf{0} \\ \boldsymbol{H}_{ci}^A & \boldsymbol{H}_{cc}^A & \mathbf{0} \\ \mathbf{0} & \mathbf{0} & \boldsymbol{H}_{jj}^B \end{bmatrix} - \begin{bmatrix} \boldsymbol{H}_{ic}^A \\ \boldsymbol{H}_{cc}^A \\ \boldsymbol{H}_{jc}^B \end{bmatrix} \left(\boldsymbol{H}_{cc}^A + \boldsymbol{H}_{cc}^B \right)^{-1} \begin{bmatrix} \boldsymbol{H}_{ic}^A \\ \boldsymbol{H}_{cc}^A \\ \boldsymbol{H}_{jc}^B \end{bmatrix}^T \tag{14}$$

Herein only one inversion is required and, additionally, it is applied only to the sum of the sub-matrices whose order depends solely on the number of connection coordinates. More interior coordinates can then be included in the analysis without affecting significantly the required computational time. The result of this will be a quicker calculation of the required FRF matrix and, as in the latter approach, it will be able to deal with redundancies on the interior coordinates whenever they are present in each component.

There are several fields where one can encounter applications of FRF coupling techniques. For instance, the mechanical behavior of the human body has long been characterized using biodynamic measurements on various human body parts in several positions and postures. In the case of the interaction between a human body and a vibrating structure, the dynamics involved in the structure alone is as important as the dynamics of the human body. Thus, the use of FRF coupling to combine biodynamic measurements with the dynamic behavior of the structure is essential to understand the vibration transmission phenomena in such a complex assembly. The research work [101] presents the advantages and also the challenges of using FRF coupling techniques between a mechanical structure and biodynamic measurements.

Experimental/analytical substructuring methods have long been explored to expedite testing and analysis of built-up systems in various fields. However, many of these efforts have failed because the substructuring calculations can be very sensitive to experimental uncertainty and truncation of the subcomponent models. The work by Allen et al. [3] presents a review of the literature regarding uncertainty in experimental/analytical substructuring, highlighting the phenomena that have been observed such as inherent ill-conditioning, cross-axis sensitivity, uncertainty modeling and propagation, as well as the fact that experimental measurements may exhibit phenomena that are not physically realizable.

The other coupling method one shall be concerned with is the *modal coupling* technique, also referred to in the related literature as time domain or component mode synthesis methods. The basic philosophy is the same as the previous one, that is, it permits the use of reduced component models in order to achieve a reduced order in the final equation of motion matrices of the assembled structure. However, unlike the impedance-based methods, which take advantage on the reduction of the number of coordinates, those methods use a reduction performed on the number of modes used to describe each component model, while still accounting for all the physical dofs. By using a Ritz-type transformation, the reduced number of principal coordinates is related to the number of modes that is taken into account for the modal estimation; generally, the information relating to the higher natural frequency modes is discarded. Essentially, there are two modal coupling approaches that differ from each other according to the dynamic displacement shapes used to form the truncated

set of the natural modes. In the first approach, the elastic modes pertaining to a fixed-interface component are retained, whereas in the second one the modes are obtained by assuming the component to be vibrating in a freely supported condition at its attachment points. This being the most readily simulated condition during an experimental test, it constitutes an attractive technique for the use of combined experimental/theoretical analysis of dynamic structural systems.

The use of a set of truncated modes [140] to establish the compatibility equations sometimes leads to unacceptable errors in the prediction of the assembled system responses. Thus, for rigidly connected subsystems a more accurate definition is necessary, either by including more modes or, if these represent an unreasonable number, by providing some information about the effects of the neglected modes. Two possible ways may be used to improve the structural definition of each component; the first one, by using additional masses attached to the connection points in an attempt to generate a more realistic condition for the component when it is vibrating together with the remaining parts (the localized flexibility properties near the connection area are better represented, since more modes are brought to the frequency range of interest); the second one, by seeking to compensate for the lack of flexibility due to the truncation of the set of natural modes by using additional and important information concerning the flexibility effects of the out-of-range modes [141]. Component mode synthesis is also addressed in Sect. 4, as a model reduction technique.

A different approach to the coupling procedure has been proposed by Rixen and van der Valk [114, 115], where substructures are no longer characterized by their matrices, but rather by the impulse response on their interface. The impulse-based substructuring (IBS) method proposed in Rixen and van der Valk [114] provides a systematic way to couple components through their interface using impulse response functions obtained analytically, experimentally, or numerically. The method expresses the interface problem in a dual form, meaning that the interface forces are computed in order to enforce the interface compatibility conditions. The time response is then computed by applying a convolution product (Duhamel's integral) in each substructure.

2.2 Uncoupling

Generally, the interest of knowing the properties of one of the components leads us to the formulation of the uncoupling techniques. This situation is regularly encountered in practice in structural monitoring and vibration control techniques, where monitoring and controlling of individual (critical) components in an assembly can be very valuable. This problem arises when substructures cannot be measured separately, but only when coupled to neighboring substructures.

Reliable solutions of the uncoupling problem could lead to promising developments, both in the field of diagnostics and in the field of vibration control. Uncoupling procedures may either start with impedance-like matrices (impedance-based approach) or with mobility-like matrices (mobility-based approach).

The work [31] highlights pitfalls due essentially to lack of measured DoFs, producing ill-conditioning in the neighborhood of certain frequencies.

The uncoupling problem, that is, the identification of the dynamic behavior of a structural subsystem, starting from the known dynamic behavior of the complete system, and from information about a second component subsystem, is revisited in the general framework of frequency-based substructuring [28, 33]. Several approaches have been proposed in the literature to tackle the uncoupling problem. However, all of them present some pitfalls that have been also highlighted, such as modal truncation, lack of information on coupling DoFs (rotational DoFs), and ill-conditioning in the neighborhood of particular frequencies. It has been shown that the last problem can be circumvented by including internal DoFs in the measured dataset, of course together with coupling (or interface) DoFs. In previous papers, two frequency-based approaches were considered: an impedance-based approach and a mobility-based approach. In both approaches, the FRF matrix of the coupled system is assumed to be known at the coupling DoFs, and possibly at some internal DoFs of one subsystem. In this chapter, an approach derived through the dual formulation, within the general framework of frequency based substructuring, is developed and discussed. Possible difficulties in the use of additional internal DoFs are envisaged and investigated.

For instance, our focus can be the identification of the dynamic properties of a subsystem that works as a joint. In this case there are three main formulations [9]; let a structure C be composed of two substructures, A and B; A is divided into two parts, connected by B, which represents the joint: one of the formulations involves only the information about the connection coordinates (c), the second one requires only the information of the interior coordinates of A (i), and the third one uses a mixture of connection and interior coordinates.

Considering the first formulation, the following equation is written:

$$\boldsymbol{H}_{cc}^{B} = \left(\boldsymbol{H}_{cc}^{A} \left(\boldsymbol{H}_{cc}^{A} - \boldsymbol{H}_{cc}^{C} \right)^{-1} - \boldsymbol{I}_{cc} \right) \boldsymbol{H}_{cc}^{A} \tag{15}$$

If one cannot access the connection coordinates of the global structure C after all components being coupled, a second formulation can be used, as follows:

$$\boldsymbol{H}_{cc}^{B} = \boldsymbol{H}_{ci}^{A} \; \boldsymbol{H}_{ic}^{A} \left(\boldsymbol{H}_{ci}^{A} \left(\boldsymbol{H}_{ii}^{A} - \boldsymbol{H}_{ii}^{C} \right) \boldsymbol{H}_{ic}^{A} \right)^{-1} \boldsymbol{H}_{ci}^{A} \;\; \boldsymbol{H}_{ic}^{A} - \boldsymbol{H}_{cc}^{A} \tag{16}$$

In the third formulation, all types of coordinates can be used

$$\boldsymbol{H}_{cc}^{B} = \boldsymbol{H}_{cc}^{A} \left(\boldsymbol{H}_{ci}^{A} \left(\boldsymbol{H}_{ic}^{A} - \boldsymbol{H}_{ic}^{C} \right) \right)^{-1} \boldsymbol{H}_{ci}^{A} \;\; \boldsymbol{H}_{ic}^{A} - \boldsymbol{H}_{cc}^{A} \tag{17}$$

In both cases two and three, the number of interior coordinates should be greater than the number of connection coordinates.

An additional formulation can be written whereby the inversion process is applied to a matrix whose size depends on all the coordinates,

$$\boldsymbol{H}_{cc}^{B} = \begin{bmatrix} \boldsymbol{H}_{ci}^{A} & \boldsymbol{H}_{cc}^{A} \end{bmatrix} \left(\begin{bmatrix} \boldsymbol{H}_{ii}^{A} & \boldsymbol{H}_{ic}^{A} \\ \boldsymbol{H}_{ci}^{A} & \boldsymbol{H}_{cc}^{A} \end{bmatrix} - \begin{bmatrix} \boldsymbol{H}_{ii}^{C} & \boldsymbol{H}_{ic}^{C} \\ \boldsymbol{H}_{ci}^{C} & \boldsymbol{H}_{cc}^{C} \end{bmatrix} \right)^{-1} \begin{bmatrix} \boldsymbol{H}_{ic}^{A} \\ \boldsymbol{H}_{cc}^{A} \end{bmatrix} - \boldsymbol{H}_{cc}^{A} \tag{18}$$

An uncoupling technique presumes that a fictitious subsystem that is the negative of the residual subsystem is added to the coupled system, and appropriate compatibility and equilibrium conditions are enforced at interface DoFs. Compatibility and equilibrium can be required either at coupling DoFs only (standard interface), or at additional internal DoFs of the residual subsystem (extended interface), or at some coupling DoFs and/or some internal DoFs of the residual subsystem (mixed interface). Using a mixed interface, rotational coupling DoFs could be eliminated and substituted by internal translational DoFs. This would avoid difficult measurements of rotational FRFs. This possibility is verified in the paper [34] using simulated experimental data. A sensitivity study was performed on the uncoupling techniques taking into account the uncertainties in the dynamic properties of the components [32].

3 Measurement of Rotational Degrees of Freedom

3.1 Introduction

The study of the dynamic behavior of structures has taken on, in recent decades, a key role in engineering, even in areas as diverse as: conditioned maintenance, aerodynamics, structural modification, damage detection, fatigue life study, seismic, comfort and safety. When it is required the knowledge of the dynamic behavior of some structure, two techniques are commonly used: a numerical one, called finite element method (FEM), which requires the knowledge of the mass, stiffness, and damping properties of the elements that make up the structure under study and an experimental one, named experimental modal analysis (EMA). However, the numerical models developed using the FEM lack, in most cases, experimental validation.

One of the mathematical models generally used to describe the dynamic behavior of a structure is the response model, which relates the response to an excitation, at two given locations. The response may either be a linear (translation) or an angular (rotation) displacement. The excitation could be a force or a moment. Thus, one can consider relations between translation and force, translation and moment, rotation and translation, and rotation and moment. However, the experimental determination of any other relations, except the relation between translation and force, continues to present a major challenge for the scientific community. The biggest obstacle for the experimental determination of these quantities is the excitation of the structures with a pure moment, being the second one the corresponding measurement of

the rotational motion. It is clear that the lack of such information will lead to obtaining an incomplete experimental model; the missing information could easily represent more than 50% of the complete model. In a schematic way, and considering the possibility of 6 dofs for each measurement point, the global mobility matrix describing the FRFs can hence be subdivided by grouping together all the translational dofs (Tdofs) and all the rotational dofs (Rdofs), resulting:

$$H = \begin{bmatrix} \boldsymbol{H}_{TF} & \boldsymbol{H}_{TM} \\ \boldsymbol{H}_{RF} & \boldsymbol{H}_{RM} \end{bmatrix} \text{ with : } \quad \begin{array}{l} T \Rightarrow \text{translational response } (T_x, T_y, T_z) \\ R \Rightarrow \text{rotational response } (R_x, R_y, R_z) \\ F \Rightarrow \text{force excitation } (F_x, F_y, F_z) \\ M \Rightarrow \text{moment excitation } (M_x, M_y, M_z) \end{array} \tag{19}$$

The restriction of the structural FRF measurement to Tdofs results in the fact that only 25% of the complete mobility matrix is effectively known.

The effects of spatial incompleteness in structural coupling predictions are firstly identified, in the ends of 1960s, by Smith [129] and later by Ewins and Sainsbury [47]. The importance of assessment of Rdofs in FRF coupling has been studied by several researchers [40, 45, 52, 73, 127, 140]. The studies were unanimous in concluding that the absence of Rdofs in coupling applications could cause an underestimation of correct predictions. Urgueira and Ewins [141] and Duarte and Ewins [40] also verify that coordinate incompleteness is not the only source of error in the prediction of the dynamic behavior of a coupled system, residuals can also be a problem. This is particularly important for Rdofs at high frequencies, for which the residual terms are normally much larger than those related to Tdofs.

Also, in the fields of structural dynamic modification (SDM) and finite element Updating, it was soon understood the importance of the inclusion of Rdofs in the analysis, especially for beam-like and plate-like structures [5, 20, 30, 91, 96, 127, 128]. Avitabile and Piergentili [7] investigated the effects of truncation on the synthesized impedance used for hybrid modeling; the role of the Tdofs and Rdofs is compared, and they concluded that there is a much greater effect of the truncation in the antiresonances of the FRF of the Rdofs than of the Tdofs.

The consideration of the Rdofs seems to have a strong importance whenever one wants to validate or correct a numerical or analytical model, using data acquired experimentally on a prototype. Once the theoretical model is validated, it can be used to evaluate further project modifications. Moreover, if the modification to be implemented intends to include rotational inertias [87] or rotational stiffnesses, the rotational receptances of the unmodified system have to be obtained. Cafeo et al. [18] also verified that the combined use of translational and rotational vibration measurements may reduce the number of locations that are necessary to represent mode shapes with an accuracy similar to the one obtained with purely translational measurements.

The knowledge of Rdofs proved to be also essential in investigation fields such as:

- Identification of the dynamic characteristic of joints [79, 153]
- Identification of unknown forces from measured responses [133]
- Vibration isolation [120]
- Analysis and control of vibrational power transmissions to machinery supporting structures [67, 103]
- Determination of rigid body properties and damage detection [134, 142]
- Vehicle collision studies

As previously referred, the determination of Rdofs is a complex task with two important problems to solve: (i) the experimental measurement of rotational motion and (ii) the application of a pure moment to correctly excite the structure, at some point. The solution to these problems has been the subject of study by many researchers; since the late 1960s, great advances have been achieved and multiple experimental techniques have been developed. The principal techniques for measuring Rdofs and to apply an excitation moment to a structure are next referred, as well as their main advantages and disadvantages.

3.2 Experimental Methods for Measuring Rdofs

The experimental techniques developed to obtain Rdofs can be divided into two main groups: the indirect and direct techniques. The first group, as the name suggests, implies that the rotational responses are indirectly obtained from translational measured ones; the known techniques are (i) the block excitation technique, (ii) the mass additive technique, (iii) the finite difference technique, (iv) the use of the laser Doppler vibrometer, (v) the use of PZTs and strain gauges, and (vi) sensors using piezoelectric accelerometers. Within the second group, corresponding to the direct techniques, the measurements are obtained directly by the use of special transducers located at the measurement points. Two types are known: (i) the angular transducers and more recently the (ii) micro electro mechanical systems (MEMS).

It should be noted that there is another group of techniques, called estimation techniques based on expansion methods that will not be addressed here, because they are not considered as purely experimental techniques, since they require a finite element model of the structure. A brief review of the experimental techniques for obtaining rotational responses is given in the next section.

3.2.1 Indirect Techniques for Measuring Rdofs

Block Excitation

The use of a block excitation technique to measure the rotational receptances requires the application of a moment, at a point of the structure, to enable the measurement of the "rotation due to moment" FRFs. In most situations, the other FRFs relating translation to moment can be obtained using directly the Maxwell's "Rule of Reciprocity," implying that translation/moment FRFs are identical to the rotation/force FRFs. Smith [129] proposes a first technique to obtain the complete

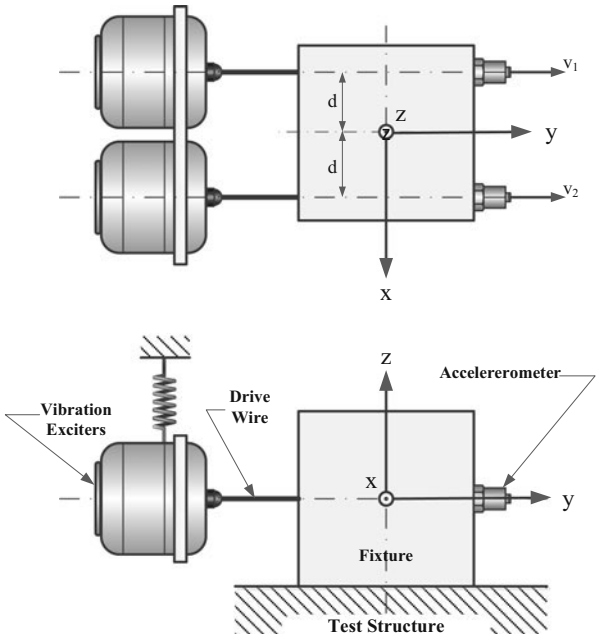

Fig. 2 Exciter block (adapted from [129])

structural mobility matrix, using a solid block attached at the measurement point and two shakers connected to that block, allowing for force and moment excitations (Fig. 2).

In 1972 the work of Ewins and Sainsbury [47] presented one of the most tested experimental techniques to measure rotational receptances, using a T-block. This block is rigidly attached to the structure at the location of interest and, by measuring two translations at two points conveniently chosen, they can be posteriorly converted into a rotation and a translation, by using simple geometric relationships. Considering that the rigid T-block is attached at point P (see Fig. 3), the kinematic relationship between the set of measured translational responses and the set of estimated translational and rotational responses at point P is as follows:

$$\begin{cases} \ddot{x}_A = \ddot{x} + s\ddot{\theta} \\ \ddot{x}_B = \ddot{x} - s\ddot{\theta} \end{cases} \quad \Rightarrow \quad \begin{matrix} \ddot{x} = \ddot{x}_p = \frac{\ddot{x}_A + \ddot{x}_B}{2} \\ \ddot{\theta} = \ddot{\theta}_p = \frac{\ddot{x}_A - \ddot{x}_B}{2s} \end{matrix} \tag{20}$$

However, measuring rotations only solves half of the problem; moment excitation may also be of interest and one can extend the above technique to relate the force f_x and the moment m_θ to the responses $\ddot{x}_p$ and $\ddot{\theta}_p$. So, performing two run tests with forces f_1 and f_2 (within the same frequency range), respectively, applied at the right and left end of the block, the following relationships can be written [77]:

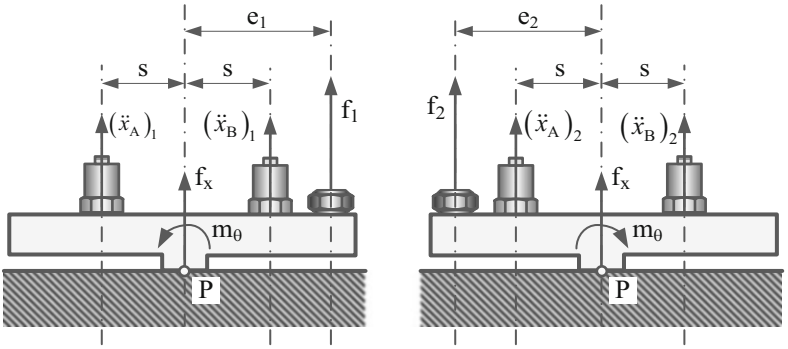

Fig. 3 T-block technique to measure the rotational response at point P (adapted from [77])

$$\text{test 1} \Rightarrow \begin{cases} f_x = f_1 - m\,\left(\ddot{x}_p\right)_1 \\ m_\theta = e_1\ f_1 - I_p\,\left(\ddot{\theta}_p\right)_1 \end{cases} \quad \text{and} \quad \text{test 2} \Rightarrow \begin{cases} f_x = f_2 - m\,\left(\ddot{x}_p\right)_2 \\ m_\theta = -e_2\ f_2 - I_p\,\left(\ddot{\theta}_p\right)_2 \end{cases} \tag{21}$$

where m and I_p are, respectively, the mass and moment of inertia of the block (including accelerometers), about point P. The acceleration values $\left(\ddot{x}_p\right)_1$, $\left(\ddot{x}_p\right)_2$, $\left(\ddot{\theta}_p\right)_1$, and $\left(\ddot{\theta}_p\right)_2$ at point P may be simply related to the measured values through Eq. (20). The receptance equation relating these quantities is

$$\text{test 1} \Rightarrow \begin{Bmatrix} \left(x_p\right)_1 \\ \left(\theta_p\right)_1 \end{Bmatrix} = \begin{bmatrix} H_{xx} & H_{x\theta} \\ H_{\theta x} & H_{\theta\theta} \end{bmatrix} \begin{Bmatrix} f_x \\ m_\theta \end{Bmatrix} = \boldsymbol{H}\,(\omega) \begin{Bmatrix} f_1 + \omega^2 m\,\left(x_p\right)_1 \\ e_1\ f_1 + \omega^2 I_p\,\left(\theta_p\right)_1 \end{Bmatrix} \tag{22}$$

$$\text{test 2} \Rightarrow \begin{Bmatrix} \left(x_p\right)_2 \\ \left(\theta_p\right)_2 \end{Bmatrix} = \begin{bmatrix} H_{xx} & H_{x\theta} \\ H_{\theta x} & H_{\theta\theta} \end{bmatrix} \begin{Bmatrix} f_x \\ m_\theta \end{Bmatrix} = \boldsymbol{H}\,(\omega) \begin{Bmatrix} f_2 + \omega^2 m\,\left(x_p\right)_2 \\ -\,e_2\ f_2 + \omega^2 I_p\,\left(\theta_p\right)_2 \end{Bmatrix} \tag{23}$$

and therefore, dividing (22) by f_1 and (23) by f_2, one obtains

$$\text{test 1} \Rightarrow \begin{Bmatrix} \left(x_p\right)_1/f_1 \\ \left(\theta_p\right)_1/f_1 \end{Bmatrix} = \boldsymbol{H}\,(\omega) \begin{Bmatrix} 1 + \omega^2 m\ \left(\left(x_p\right)_1/f_1\right) \\ e_1 + \omega^2 I_p\ \left(\left(\theta_p\right)_1/f_1\right) \end{Bmatrix} \tag{24}$$

$$\text{test 2} \Rightarrow \begin{Bmatrix} \left(x_p\right)_2/f_2 \\ \left(\theta_p\right)_2/f_2 \end{Bmatrix} = \boldsymbol{H}\,(\omega) \begin{Bmatrix} 1 + \omega^2 m\,\left(\left(x_p\right)_2/f_2\right) \\ -\,e_2 + \omega^2 I_p\ \left(\left(\theta_p\right)_2/f_2\right) \end{Bmatrix} \tag{25}$$

By suitable combination of (24) and (25) and taking into account the relationships (20) for $(x_p)_1$ and $(\theta_p)_1$, and equivalent ones for $(x_p)_2$ and $(\theta_p)_2$, the receptance matrix is found to be:

$$\boldsymbol{H}(\omega) = -\frac{1}{\omega^2}\,\boldsymbol{T}\boldsymbol{G}(\boldsymbol{\Pi} - \boldsymbol{M}\boldsymbol{T}\boldsymbol{G})^{-1} \tag{26}$$

where

$$\boldsymbol{T} = \begin{bmatrix} 0.5 & 0.5 \\ (2s)^{-1} & -(2s)^{-1} \end{bmatrix}, \quad \boldsymbol{\Pi} = \begin{bmatrix} 1 & 1 \\ e_1 & -e_2 \end{bmatrix}, \quad \boldsymbol{G} = \begin{bmatrix} (\ddot{x}_a/f)_1 & (\ddot{x}_a/f)_2 \\ (\ddot{x}_b/f)_1 & (\ddot{x}_b/f)_2 \end{bmatrix} \tag{27}$$

and

$$\boldsymbol{M} = \begin{bmatrix} m & 0 \\ 0 & I_p \end{bmatrix} \tag{28}$$

The required receptance matrix is obtained in terms of $\boldsymbol{T}$, $\boldsymbol{\Pi}$ and $\boldsymbol{M}$, which are constant for a given test configuration, together with $\boldsymbol{G}$, which incorporates data measured at the same angular frequency ω in the two test runs. The resulting receptance data have thus been fully corrected to account for the mass and inertia of the added block and transducers.

A large number of researchers have attempted to apply this technique trying to obtain the Rdofs, not only to test its performance but also for posterior application in other studies involving: structural coupling [45, 47, 48, 123, 140], structural modification [127, 128], complex damped structures [116], and others like Gleeson [54].

New techniques to obtain Rdofs using the T-block continued to be developed, like in the works by Yoshimura and Hosoya [157, 158], Maia et al. [78], Montalvão et al. [88], Silva et al. [125], Mottershead et al. [90, 91], and Mottershead et al. [91]. In Yoshimura and Hosoya [157] a T-shaped rigid block is attached to the structure at the measurement point and a set of hammer impacts are applied to several points on the T-block, resulting in a set of forces and moments applied to the fixture point, and a set of responses at the accelerometers placed on the T-block. After that, a numerical procedure makes use of the measured data to fully estimate the force and moment applied at the fixture point of the T-block, as well as the translational and rotational responses at the same point. Finally, the FRFs of the structure at the fixture point are estimated (including Rdofs) without the effect of the mass and the moment of inertia of the T-block. The same researchers [158] presented, 2 years later, a new T-block sensor, named T-square-block (T^2-block) to measure six dofs (three dofs in translation and three dofs in rotation) at some points of a car body. Maia et al. [78] propose a method based on impedance coupling techniques, in which rotational/moment receptances are estimated without having to measure them. It is also shown that neither a moment exciter nor eccentric forces applied to a rigid fixture (T-block) are needed to estimate rotational receptances. The structure is excited with a conventional shaker on a single location (a translation dof) and several sets of response measurements are taken, both in translation and rotation. This technique works perfectly when exact theoretical data is used, but fails when directly applied to real cases or with theoretical data polluted with

noise. To help improving the results, modified versions were proposed [88, 125] based upon coupling techniques, introducing a structural modification by rotating a T-block, with the force applied at its centroid. Mottershead et al. [90, 91] proposed a technique in which the T-block is treated as a structural modification at the connection point, deriving the corresponding full force and response vectors. The T-block mass and elastic properties are included in a finite element model. The receptances are estimated without any mass, inertia, or stiffness effects of the T-block, which are removed by the T-block finite element model, thus avoiding ill-conditioning problems.

The application of this technique has, as its main advantage, the possibility of moment excitation at a given point on a structure and the determination of the corresponding rotation responses. However, it is an indirect technique, that is, the rotational responses are obtained from translational ones, which makes it somehow vulnerable to ill-conditioning. Some of these particular features have been identified [75, 127, 147] and are listed below:

- The sensor (T-block and accelerometers) represents additional masses attached to the structure under test. Thus the measurement of angular accelerations on light structures should be considered carefully so that the mass loading effects caused by the sensor do not alter significantly the dynamic properties of the structure.
- The sensitivity of the sensor is directly proportional to the length of the upper arm (Eq. 20); in principle the larger this length, the more sensitive will be the sensor. However, the sensor has its own dynamic characteristics, and depending on the test frequency range, the sensor dynamics can affect the dynamics of the structure.
- Another important issue in the application of this technique is the correct attachment of the transducer to the structure, such that the behavior of the structure be transmitted to the transducer faithfully, the same being true for the transmission of the applied excitations.
- The accelerometers used to instrument the T-block should be matched in terms of sensitivities; two identical accelerometers should be used reducing the chance of inaccurate results caused by significant differences in calibration.
- The cross-axis sensitivities of the accelerometers can be very important when subtracting two FRF signals of similar size, particularly when the motion in one of the transverse directions is large. In such cases, the difference between the measured FRFs can be of the same order of magnitude as the cross-axis sensitivity component. This is the situation that may arise in determining the rotation/translation, translation/rotation, and rotation/rotation FRFs, where subtraction of measured translational FRFs is required. To minimize these effects it is necessary to align the maximum cross-axis sensitivity direction of each accelerometer with the direction of minimum transverse motion at the attachment point, something that may not be a simple task.

Another similar indirect technique for measuring the rotational mobility has been developed by Cheng and Qu [24], Qu and Cheng [105], and Qu et al. [107]

and is called "tip excitation technique (TET)"; instead of a T-block, it uses an L-shaped beam tip fixed at one point of the original structure, a flexible plane, where the rotational mobility is to be evaluated. The tip acts as a mechanical converter transforming an exciting force applied at the tip into an excitation moment applied to the original structure and reciprocally, to convert a rotational response into a translational one. The rotational compliance is evaluated using simple analytical relations that partially eliminate the effect of tip inertia on the structure. In Cheng and Qu [24] a numerical study is presented, and in Qu et al. [107] the experimental measurements were performed on a rectangular plate and the results were compared with the ones resulting from numerical simulations. It is concluded that this technique presents better results in the low to middle frequency ranges for flexible plane structures.

Mass Additive Technique

The mass additive technique to estimate rotational dofs at a measurement point was developed by Yasuda et al. [154]. This technique also requires the addition of a rigid block to the structure at a point of interest, but this time, unlike the previous one, the excitation is not directly applied to the measurement block (the added mass), to produce the moment and/or force excitation. As a consequence there is no possible estimation of direct FRFs.

The rigid body motion of the added mass is measured using six or more translational transducers (Fig. 4). After this a least-square procedure is used to compute the rigid body motions, from which the rotational and translational dofs, at the attachment point, are estimated. Next, the modal parameters are estimated using a complex exponential algorithm. Finally, a mass modification procedure is implemented to compensate for the added mass, that is, the extra mass is analytically subtracted from the process like in the block excitation technique. Yasuda et al. [154] applied this method to two structures, a cantilever beam and an automotive frame; the results obtained for the beam looked promising, but some errors have been detected for the more complex automotive frame.

This technique has been applied in various and different areas like: structural dynamic modifications [56, 64], correction of modal scaling factors [150], to determine the moments and rotations in a structure due to impact excitation [71, 133], and model updating [56].

The need for measuring multidirectional responses is becoming increasingly important in different applications; several researchers tried to develop transducers in order to measure the response of the six dofs at a point, using various linear piezoelectric accelerometers mounted on a light fixture [57, 148] or using as an acceleration sensor a piezoelectric quartz element [82].

Finite Difference Technique

In the two abovementioned methods (block exciter and mass additive technique) special fixtures with accelerometers have to be attached to the structure and their dynamic influence has to be corrected.

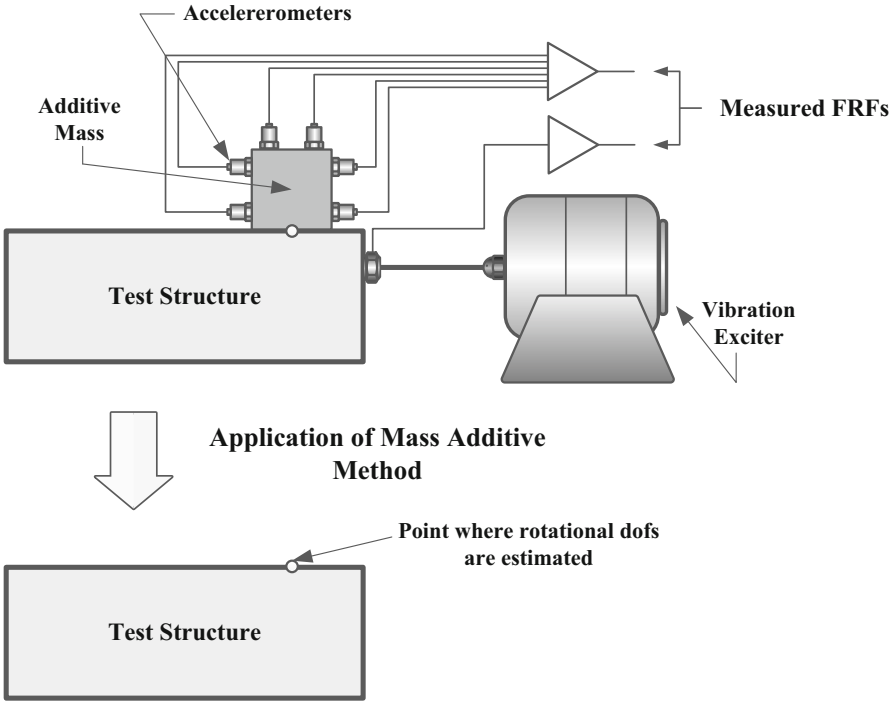

Fig. 4 Procedure for the mass additive technique (adapted from [154])

At the beginning of the 1980s, Sattinger [122] developed a method to generate experimental rotational mobility functions using conventional measurement techniques without requiring the use of special fixtures. The approach permits to represent the mobilities involving rotational responses and/or moment excitation as spatial derivatives of conventional translational mobilities; the derivatives are approximated as finite difference sums of sets of those translational values. The method is demonstrated in a set of experiments conducted on a free-free beam; good agreement was obtained between experimentally and theoretically generated versions for rotational velocity/force mobilities, although exhibiting a large amount of scatter in some frequency bands. The author believes that this scatter is due to the subtraction of nearly equal translational quantities and suggests eliminating this scatter by the application of a smoothed process, as curve fitting, to the translational data, before the subtracting operation. The derivation of rotational data could be accomplished using either first-order [23] or second-order [122] finite difference formulas. In Sattinger [122], the backward, central, and forward finite difference formulas are given, the choice between them depends on whether the location where rotation is desired is an inside, middle, or outside location, or whether it is on the positive or negative end of the global axis. The formulation of this method can also be observed in Urgueira [140], Duarte [39], or Lofrano [75].

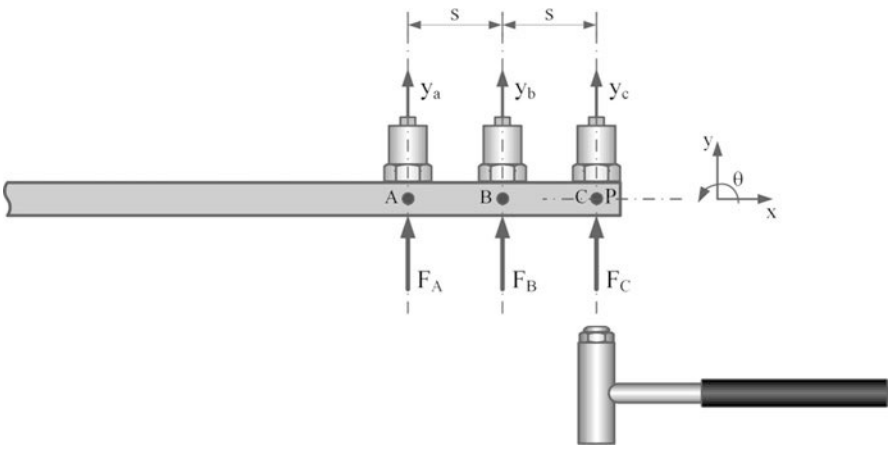

Fig. 5 Finite difference technique for Rdofs measurements (adapted from [140])

To illustrate the application of this method consider the situation presented in Fig. 5, where three (or two) accelerometers (according to the finite difference formula employed) are placed by each other, in a constant spacing s. One of the accelerometers is located at the point where rotation needs to be deduced, represented as point P, and the position of the other accelerometers are dependent on the finite difference formula employed and the direction of the global axis.

The first- and second-order finite difference transformation matrices needed for the estimation of the necessary rotational FRFs will be introduced next.

Finite Difference Transformation Matrices for First-Order Approximation

If a first-order approximation is considered, only two location sites have to be taken for the estimation of the rotational parameters, for instance, points B and C in Fig. 5. If $P = B$ and the coordinate system is the one shown in the same figure, or if $P = C$ and the coordinate system is in the opposite direction, the first-order forward (f)-difference transformation matrix is expressed as:

$$\boldsymbol{T}_{1f} = \begin{bmatrix} 0 & 1 \\ 1/s & -1/s \end{bmatrix} \tag{29}$$

If $P = C$ and the coordinate system is the one assumed in Fig. 5, or if $P = B$ and the coordinate system is in opposite direction to the assumed one, the first-order backward (b)-difference transformation matrix is expressed as:

$$\boldsymbol{T}_{1b} = \begin{bmatrix} 0 & 1 \\ -1/s & 1/s \end{bmatrix} \tag{30}$$

The accuracy of the matrices in (29) and (30) is equivalent.

Finite Difference Transformation Matrices for Second-Order Approximation

If three location sites are considered, three different formulas can be employed depending on the accelerometers and coordinate system positions, as shown in Fig. 5. The second-order forward (f)-, central (c)- and backward (b)-difference transformation matrices [23] are, respectively:

$$\boldsymbol{T}_{2f} = \frac{1}{2s}\begin{bmatrix} 0 & 0 & 2s \\ -1 & 4 & -3 \end{bmatrix} \tag{31}$$

if $P = A$ with the coordinate system assumed in Fig. 5 (or if $P = C$ with the coordinate system is in the opposite direction), or

$$\boldsymbol{T}_{2c} = \frac{1}{2s}\begin{bmatrix} 0 & 2s & 0 \\ -1 & 0 & 1 \end{bmatrix} \tag{32}$$

if $P = B$; in this case the assumed coordinate system has no importance. Finally,

$$\boldsymbol{T}_{2b} = \frac{1}{2s}\begin{bmatrix} 0 & 0 & 2s \\ 1 & -4 & 3 \end{bmatrix} \tag{33}$$

if $P = C$ with the coordinate system assumed in Fig. 5 (or if $P = A$ and the coordinate system is in the opposite direction). All the transformation matrices for the second-order approximation are of equivalent accuracy.

The set of desired FRFs related to translational and rotational coordinates, for a specific point, are determined solving the following equation:

$$\boldsymbol{H}_{est.}(\omega) = \begin{bmatrix} \boldsymbol{H}_{yy}(\omega) & \boldsymbol{H}_{\theta y}{}^{T}(\omega) \\ \boldsymbol{H}_{\theta y}(\omega) & \boldsymbol{H}_{\theta\theta}(\omega) \end{bmatrix} = (\boldsymbol{T}_{?}(\omega))\,(\boldsymbol{H}_{meas.}(\omega))\;(\boldsymbol{T}_{?}(\omega))^{T} \tag{34}$$

where $\boldsymbol{H}_{meas.}(\omega)$ contains the values of translational FRFs measured for each frequency. The subscript "?" is explained after eq. (36). The size of this matrix is related to the approximation employed and symmetry should always be considered. If a first-order approximation is chosen, two measuring points are needed, in this case points B and C, assuming that the measured matrix is symmetric, and thus,

$$\boldsymbol{H}_{meas.} = \begin{bmatrix} H_{BB} & H_{BC} \\ \text{sym} & H_{CC} \end{bmatrix} \tag{35}$$

Using the same assumptions for the second-order formulation, three measurement points (A, B, and C) are required, so at least six FRFs have to be measured to obtain the $\boldsymbol{H}_{meas.}$ matrix.

$$\boldsymbol{H}_{meas.} = \begin{bmatrix} H_{AA} & H_{AB} & H_{AC} \\ \text{sym} & H_{BB} & H_{BC} \\ \text{sym} & \text{sym} & H_{CC} \end{bmatrix} \tag{36}$$

The subscript ? used in matrix $\boldsymbol{T}_?(\omega)$ aims to emphasize that any one of the matrices in (29), (30) or (31), (32), (33) could be used depending on the order approximation used, first or second, and the point where the rotation needs to be derived. The formulation presented in Eq. (34) is generally referred as *FRF-based approach* and was used in Urgueira [140], to evaluate the use of different transducer spacing to estimate matrix in Eq. (34) in a short and a long beam. This evaluation was made simultaneously with other ones, either using the T-block approach or the data from a continuous measurement with a laser transducer.

Substituting Eqs. (35) and (29) or (30) in Eq. (34), the first-order forward (f)- and backward (b)-difference approximations can be obtained, resulting respectively in:

$$(\boldsymbol{H}_{est.})_{1f} = \begin{bmatrix} H_{CC} & -\frac{1}{s}(H_{CC} - H_{CB}) \\ \text{sym.} & \frac{1}{s^2}(H_{CC} - 2H_{CB} + H_{BB}) \end{bmatrix} \tag{37}$$

and

$$(\boldsymbol{H}_{est.})_{1b} = \begin{bmatrix} H_{CC} & \frac{1}{s}(H_{CC} - H_{CB}) \\ \text{sym.} & \frac{1}{s^2}(H_{CC} - 2H_{CB} + H_{BB}) \end{bmatrix} \tag{38}$$

A similar result occurs for the second-order forward (f), central (c), and backward (b) approximations. The development of Eq. (34) using matrix (36) and transformation matrix (34), (32) or (33) leads to:

$$(\boldsymbol{H}_{est.})_{2f} = \begin{bmatrix} H_{CC} & -\frac{1}{2s}(H_{CA} - 4H_{CB} + 3H_{CC}) \\ \text{sym.} & \frac{1}{4s^2}(H_{AA} - 8H_{BA} + 6H_{CA} + 16H_{BB} - 24H_{CB} + 9H_{CC}) \end{bmatrix} \tag{39}$$

$$(\boldsymbol{H}_{est.})_{2c} = \begin{bmatrix} H_{BB} & \frac{1}{2s}(H_{CB} - H_{BA}) \\ \text{sym.} & \frac{1}{4s^2}(H_{AA} - 2H_{CA} + H_{CC}) \end{bmatrix} \tag{40}$$

$$(\boldsymbol{H}_{est.})_{2b} = \begin{bmatrix} H_{CC} & \frac{1}{2s}(H_{CA} - 4H_{CB} + 3H_{CC}) \\ \text{sym.} & \frac{1}{4s^2}(H_{AA} - 8H_{BA} + 6H_{CA} + 16H_{BB} - 24H_{CB} + 9H_{CC}) \end{bmatrix} \tag{41}$$

Martinez et al. [85] suggest a similar process to the one proposed by Sattinger [122]; however, instead of using experimental translational FRFs directly (*FRF-based approach*), they use the modal model referred to the measured coordinates, generally derived from a row (or column) of the measured FRF matrix over a

selected frequency range encompassing k modes. The information related to the effects of the out-range modes has to be synthesized in a residual matrix $\boldsymbol{H}_{Resid.}$. Therefore, the measured response and modal models are related by

$$\boldsymbol{H}_{meas.}(\omega) = \boldsymbol{\phi}_{k_{meas}} \left(\lambda_k{}^2 - \omega^2 \right)^{-1} \boldsymbol{\phi}_{k_{meas}}^T + \boldsymbol{H}_{Resid.meas} \tag{42}$$

In order to use the finite difference approach to the translational modal parameters and to avoid modal truncation problems, a similar procedure has to be employed to the residual matrix as well. This procedure, named *Modal-based approach* can be summarized as follows:

$$\begin{aligned} \boldsymbol{H}_{est.}(\omega) &= \boldsymbol{T}_? \left(\boldsymbol{\phi}_{k_{meas}} \left(\lambda_k{}^2 - \omega^2 \right)^{-1} \boldsymbol{\phi}_{k_{meas}}^T + \boldsymbol{H}_{Resid.meas} \right) \boldsymbol{T}_?{}^T \\ &= \boldsymbol{T}_? \left(\boldsymbol{\phi}_{k_{meas}} \left(\lambda_k{}^2 - \omega^2 \right)^{-1} \boldsymbol{\phi}_{k_{meas}}^T \right) \boldsymbol{T}_?{}^T + \boldsymbol{T}_? \left(\boldsymbol{H}_{Resid.meas} \right) \boldsymbol{T}_?{}^T \end{aligned} \tag{43}$$

The main advantage of the *Modal-based approach* in relation to *FRF-based approach* proposed initially by Sattinger [122] is that the noise is removed from measured data and therefore smoother curves are obtained. This research approach is also used and reported by Maleci and Young [83] and Urgueira [140], where the modal-based approach produces better predictions than the FRF-based one.

Comparing the *finite-difference technique* (both approaches) with the *block exciting technique*, two main advantages can be easily identified:

- No special apparatus is required, only the transducers normally used in standard modal testing.
- The mass and stiffness properties of the original structure are not altered by the use of an excitation block (T-block).

However, some problems, summarized below, were identified when it is applied:

- The quality of the predictions is dependent on the *spacing* and *order used in the approximation*, and these two points are inter-related. According to Urgueira [140], increasing the approximation order for the rotation/force FRF requires a smaller spacing between the transducers, but increasing the order for the rotation/moment FRF requires a larger spacing. So, the definition of the ideal space between accelerometers is not an easy task, with a linear answer.
- The first-order approximation produces better results for the rotation/force FRFs, while the second-order approximation produces better results for the rotation/moment FRFs [41].
- The direct use of measured translational FRFs in the *FRF-based approach* normally yields unacceptably noisy rotational FRF data, because relatively small

errors in the measured data may result in large errors in the estimated responses, due to the fact that very similar quantities are subtracted. The use of regenerated FRF curves including the effects of the out-range modes (residual compensation) is recommended to solve this problem [41, 140].
- It is advisable to use similar accelerometers (mass and sensitivity) with small dimensions and mass.

Elliott et al. [43, 44] study the effects of random and bias errors when central difference finite approximation technique is used to determine the moment excitation and moment mobilities in plate and beam structures.

Liu et al. [74] present an enhanced stiffness identification method for the spindle-tool holder joint, in which the Rdofs are included. The FRFs associated to the Rdofs are determined using a finite-difference technique, to depress the influence of "modal truncation" and measurement noise; residual compensation theory is introduced to regenerate the Rdofs. An obvious improvement in the results was observed when residual compensation was used.

Laser Doppler Vibrometer

The use of the laser Doppler vibrometer (LDV) [37, 156] brought to experimental structural vibrations analysis new possibilities of measurements, impossible to obtain with the traditional vibration transducers (such as accelerometers, strain gauges), in particular measurements: on extremely lightweight objects when the local mass loading of the sensor may distort the results, or when fluid flows are studied and one wants to avoid disturbing the flow itself by the introduction of contacting transducers on structures, on hot temperatures, or even in rotating components, etc.

The laser Doppler vibrometer (LDV) is an optical velocity-measuring device based on the measurement of the Doppler shift of the frequency of laser light scattered by a moving object [84].

The advantages in the use of laser vibrometers are related to the fact that:

- The noncontact nature of the instrument makes it particularly attractive for the use in light-weight structures where the measurement interaction must be minimized.
- No loading effects at all have to be taken into account.
- The measurements can be done far from the vibrating structure, on hot or cool surfaces, in strong magnetic fields, without all the problems that a normal accelerometer would face.
- It is possible to measure a quasi-continuous line or area on the structure, thus reducing the degree of incompleteness in terms of coordinates, which sometimes is a disadvantage of experimentally derived models when compared with the theoretical ones.
- The measurements are relatively fast and easy.
- The resolution and the accuracy of the measurements are high.

- The cost of the equipment is decreasing, and the possibility to measure many points in a very short time is a very much appreciated quality.

A drawback could be the fact that the output of the laser is normally velocity and not acceleration.

The use of laser vibrometers in the measurement of vibrations begins in the 1980s, but their limited sensitivity and low signal-to-noise ratio allowed measurements only on very diffusive surfaces or by applying a retro-diffusive tape at the point of measurement; despite the referred difficulties, Oliver [98] refers to its application as a promising technique for the determination of dynamic Tdofs and Rdofs of a structure. In a work by Urgueira [140] a continuous measurement with a laser vibrometer was made on a segment of a long and a short beam, where three accelerometers and a T-block were also attached, in order to carry out an assessment of the various techniques to predict the rotational information associated with the receptance matrix.

In the early 1990s, hardware and software developments increased the performance of the instrumentation and many researches started using LDV to obtain the Rdofs.

Cafeo et al. [17] developed a non-contacting measurement approach, capable of simultaneously measuring one dynamic translation and two dynamic angular rotations (see Fig. 6). The transducer system is based on the positional measurement of two collimated light beams reflected from a planar reflective target. The light beams are created by lasers, and the locations of their respective reflections are measured with two separate two-dimensional photo-detectors. Using the geometric

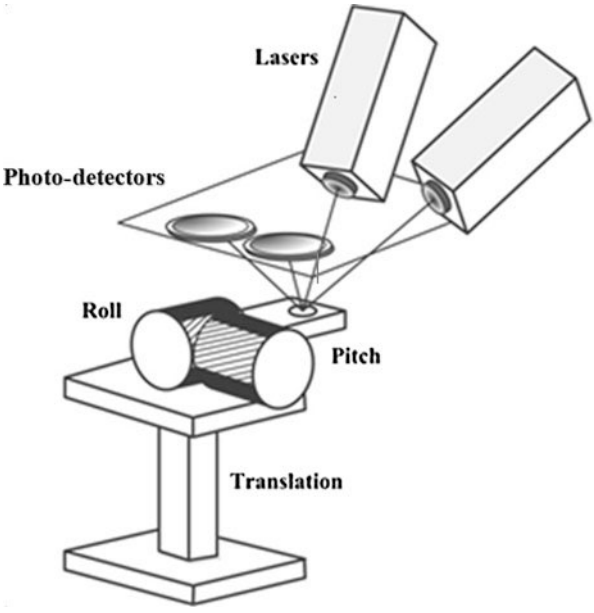

Fig. 6 Three degrees of freedom laser vibrometer (adapted from [17])

orientation between the origins of the light beams and the corresponding reflections onto the photo-detectors, vertical translation (z) as well as roll (θ_x) and pitch (θ_z) angular deflections of the planar target can be determined. The time-varying x–z coordinates' signals from the photo-detectors are digitized and then processed to estimate the three variables. The algorithm used to extract the variables from the geometric layout and photo-detector signals is explained in Trethewey et al. [139]. An evaluation of the transducer dynamic performance in a modal test environment of two structures, a cantilever beam and a printed circuit board, demonstrated the ability of the system to produce high-quality time and spectral data. The researchers used the obtained structural rotation data to refine the spatial description of mode shape, and verified that a significantly improved definition of the mode shape spatial characteristics was observed by integrating the translational and rotational modal deflections at each response measurement site [18]. Using the same technique to measure rotational data, Cafeo et al. [19] presented an SDM study with a beam element, where the modification involves the fixation of the free end of one cantilever beam; the measured rotational data are used as a database for SDM. The experimental results obtained with a real beam with dual fixed-fixed boundary conditions were compared with the SDM predictions using the experimental cantilever database, exhibiting a good correlation.

A novel non-contacting device to measure the same three dofs of vibration (translation, pitch, and roll) was proposed by Sommer et al. [130], utilizing a single laser beam reflected by a planar reflective surface target onto two transparent two-dimensional position-sensing photo-detectors (see Fig. 7). The advantage of this system over the original dual-laser beam setup [17] is the need for less hardware and smaller overall size.

Bokelberg et al. [13] presented a new laser system to simultaneously measure three translational (x, y, z) and three rotational $(\theta_x, \theta_y, \theta_z)$ displacements of a vibration object. The system is based on sensing the positions of the three collimated light beams reflected from a tetrahedral target attached to the vibration object. The dynamic position of the target is determined by using the system geometry, coordinate transformations, and kinematic closure procedures. The operational principle and experimental evaluation of this measurement technique are presented

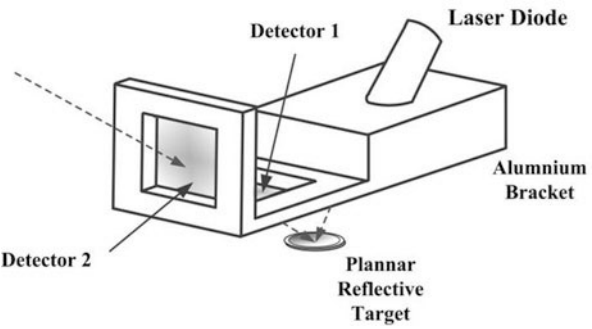

Fig. 7 Three degrees of freedom laser device (adapted from [130])

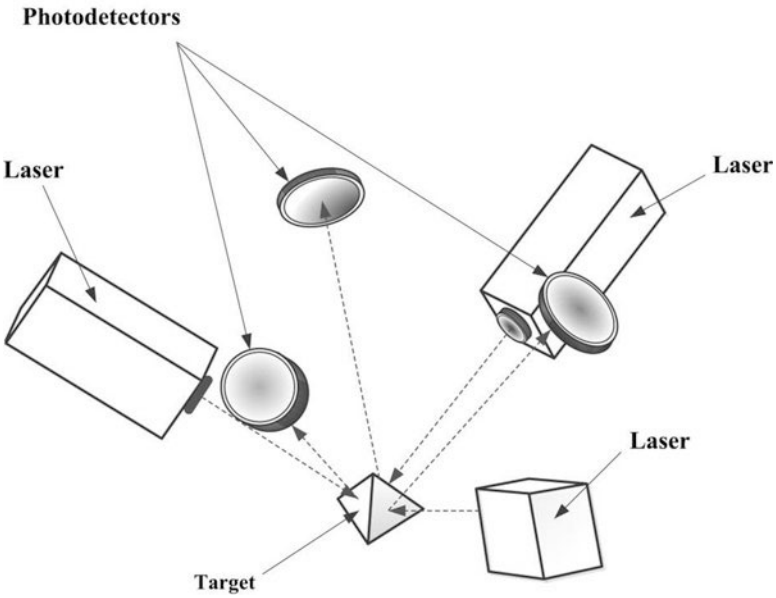

Fig. 8 Laser system to measure 6 dofs (adapted from [13])

in Bokelberg et al. [14, 15]. Figure 8 shows the conceptual design for this six degrees-of-freedom vibration measurement system. The disadvantages observed with the use of this system are: the laser system set-up must be moved to each of the desired locations for measurement, which is very time consuming when a large number of data points have to be gathered, and as a consequence of its dimensions the system is hardly portable.

The estimation of rotations from translational data using fitting functions was the approach chosen by various researchers. Two groups of fitting functions have been particularly studied: polynomials [140, 151] and splines [93, 94]. These techniques have shown considerable potential. The polynomials proved to be ideal for representing uncomplicated relationships. The main disadvantage, however, is the inability of the polynomial fits to produce acceptable results for the higher frequency modes; the results from tests show that the accuracy of the estimated Rdofs depends on the density of the original displacement measurements and also that the estimation improves with an increase in the number of measurement points between nodes. The splines, being composed of sets of polynomial pieces, turned out to be more flexible than single polynomials and capable of representing very complex relationships. The accuracy of the estimates of rotations from translational data, when spline approximations of the mode shape functions are used, depends on several factors, namely the combination of the smoothing factor and the number of knots in the fit function, and density and distribution of the measurement points on the structure.

Ratcliffe and Lieven [108] present a technique that uses the simple expedient of fitting a plane, in a least-square sense, to experimental translation data, to calculate the two out-of-plane rotations. The accuracy of the method increases when the distance between measurement points decreases, so the use of laser Doppler techniques proved to be ideal since they have the capacity of measuring a structure using a finer grid because of their speed of operation.

In 1994 two new techniques for measuring Rdofs were presented [131], using a Scanning Laser Doppler Vibrometer (SLDV); in these techniques a traditional point-by-point scanning procedure was substituted by a continuous scan along a line or around a circle on a harmonically vibrating surface, giving a modulated output which can be used to analyze structural vibration in more than one dof. Using continuous linear scanning in one dimension it is possible to extract the translation; and one angular vibration component is extracted while using circular scanning; two components of angular vibration can be derived directly from the frequency spectrum sidebands, together with the translational dofs. Interesting researches conducted by Ziaei-Rad et al. [159] and Martarelli [84] compare the experimental results obtained with the application of three techniques to obtain Rdofs on a coupled structure. Those techniques are the discrete point measurements, the continuous linear scanning, and the continuous circular scanning. The most important conclusions drawn from those works are summarized in Ziaei-Rad et al. [159]. It was found that:

- The linear and circular scan techniques offer advantages over discrete scanning in terms of time saving.
- Better results are obtained in the linear scan when short lengths are measured.
- The effects of changing radius, in the tried range, are not very significant.
- The FRF resonance peaks drop slightly when the frequency of scanning is increased, because the speckle noise always affects laser Doppler measurements.

Another technique, using Continuously Scanning Laser Doppler Vibrometer (CSLDV), for six dofs was presented by Stanbridge and Ewins [132] and named conical-scanning LDV. This technique requires performing a small radius circular scan with an SLDV on a focal lens that focuses the scanning laser beam to a point and leads to a conical scan. Two measurements have to be performed: (i) one focusing on the conical scan at a measurement point and (ii) another one intercepting that same point with a very small circle. Five of the six dofs are easily obtained: the three translations and two out-of-plane rotations. However, the lens makes the measurement of the in-plane rotation very difficult and impractical.

Giuliani et al. [53] developed a new type of scanning device, allowing the measurement of all six dofs at a given location with a single setup and a single point LDV, by combining variable small circle scans. The main aim of the research was to combine the two separated measurement approaches, performed on the previously referred technique, into a single system, based on a single point LDV in combination with a newly developed scanning head, and add the measurement of a missing in-plane rotation around a point, to provide a measurement technique that can resolve

the dynamic response of all six dofs at a point on the structure. Experimental results have shown the ability of the new scanner to distinguish between the different dofs [53] and to measure the out-of-plane deflection shapes of a specimen, bending along the three axial directions [82].

PZTs and Strain Gauge Transducers

A group of researchers developed a new technique using low-cost PZT transducers to estimate rotational quantities [10]; special reference is made to bimorph patches that are able to measure the local curvature of a structure. They provide curvature measurements from which, by interpolation techniques (single polynomial, third degree polynomials, or using the analytical modes), rotations can be determined. Despite the use of these sensors being quite simple, inexpensive, with a minimum intrusiveness due to their low weight and size, it has proven the necessity for solving a series of problems related to their amplification, bonding, and assembly to the structure, calibration, and cross-sensitivity. If all of these items are carefully considered, the results obtained using a supported beam proved to be very promising when compared to those obtained by a rotational accelerometer and by finite models.

These kinds of transducers, bimorph PZTs, present an important advantage over strain gauges in estimating curvature [66], as no geometrical and physical properties of the cross section are needed. Differently from strain gauges, bimorph PZT transducers are directly sensitive to curvature: the curvature estimation is independent of the structure to which they are attached, so that no information about the structure under test is needed.

Cicogna et al. [25] also studied the use of PZT patches (bimorph) to obtain the local curvatures on a cantilever beam and a free-free plate, and from it the rotational quantities, by interpolation techniques. A methodology based on genetic algorithms was also presented, considering the possibility of including more than one patch to find the optimal size and position of the bimorph onto beam-like structures.

3.2.2 Direct Techniques

Angular Transducers

Systron-Donner Corporation under contract to the Air Force Weapons Laboratory developed an angular instrumentation system [89], using a proper angular displacement sensor. This system uses inertial techniques to measure three axes of angular displacement with extreme accuracy over a very wide frequency range (1–2000 Hz), with no need for temperature.

Two other techniques, used on flight control and navigation, for measuring Rdofs data could be referred: the first one is based on the use of magneto-hydrodynamic sensors [136] and the second one based on the use of gyroscope sensors [1]; however, the large dimensions of these sensors prevent their use in most vibration applications.

Micro-Electro-Mechanical-Sensor (MEMS)

MEMS inertial sensors, comprising acceleration and angular rate sensors [4, 92] (i.e., micro-accelerometers and micro-gyroscopes (based on Coriolis angular rate)), are used in a wide range of areas [76, 134, 142] such as in automotive industry applications (for crash air-bag deployment systems), consumer electronics applications (such as Apple iPhones, Nintendo Wii, computers), and medical applications. They are able to measure the responses associated to all six dofs, in one go, as they can easily measure, simultaneously, three rotations and three translational motions.

A MEMS sensor is produced by micromachining techniques to form minute springs, seismic masses, and motion or force sensing elements from a silicon wafer. When the body of the accelerometer is moved by an externally applied force, the motion of the seismic mass is detected by differential capacitive, piezo-resistive, or other types of sensing elements. The signal produced is amplified, conditioned, and filtered by circuit components mounted inside the same IC package [155].

Certain types of silicones may show characteristics that reveal that they can be stronger than steel, though with only a third of the weight, allowing in recent years the building of sensors with dimensions of just a few millimeters. This is considered a great advantage, because the small size and very low weight give the possibility to insert transducers in spaces considered inaccessible for other kinds of instruments, and also to install them on smaller objects, because of the lower insertion effect, as it happens with the smartphones. It should also be stressed that the MEMS devices are cheaper when compared to other available sensors, so all these explain why the interest on MEMS technology is so high.

In the beginning, their use was limited to measurements considered of "low-quality," but during the last years MEMS technology has quickly improved, leading to sensors with higher qualities that supposedly can be used in rigorous measurement applications. Their utilization has been introduced in measurement fields, like modal analysis [11, 26, 68] or structural health monitoring [27]. Cigada et al. [26] draw attention to the fact that the metrological limits of this type of sensors are not yet well defined, and the reason is mainly due to testing costs: these sensors are so cheap that any kind of test other than gravity sensitivity check is more expensive than the sensor itself, so a true calibration for this kind of sensors does not exist so far. In order that their use becomes widespread, in those research fields, it is important to investigate and clarify the following:

- The sensor performances in measuring very low accelerations (low frequency band), where the signal to noise ratio is a critical feature
- Transverse vibration sensitivity
- Intrinsic noise
- Temperature influence

Direct Piezoelectric Rotational Accelerometers

In the last decade the first piezoelectric rotational accelerometers appeared in the market, capable of measuring directly angular accelerations [42]. However, their use in the field of experimental structural dynamics is rare when compared to the classic

translational accelerometers, mainly due to their high cost and mass modification effect on lightweight structures.

Drozg et al. [38] evaluate the performance of two direct piezoelectric rotational accelerometers to show the possibilities of their usage in structural dynamic applications. They concluded that the force-excited rotational responses measured with those two accelerometers are more accurate and reliable, compared to the indirect rotational response obtained via the T-element.

3.3 Experimental Methods for Exciting Rdofs

The excitation of structures with a pure, sufficiently powerful and well-controlled moment is a task very difficult to achieve in practice. The development of techniques that make possible the application of moments in structures has been taking place simultaneously with the development of techniques for the measurement of rotational dofs. As it happens to the techniques for measuring rotational dofs, the ones for excitation can also be divided into indirect and direct techniques. The indirect ones deduce the moment mobilities from measured force mobilities, while the direct techniques use a mechanical system to create a force couple to excite the structure under test. Further reviews of these techniques can be found in Bregant and Sanderson [16], Elliott et al. [44], and Mottershead et al. [91]

3.3.1 Indirect Techniques to Apply a Moment Excitation

The earliest attempts to measure moment receptances were indirect approaches, which made use of supports with different forms [45, 47, 107, 122]. Such supports are small rigid bodies, of accurately defined geometry, which are attached to the structure under study; the support is excited by one or various forces in different directions and/or positions. The moment excitation is determined based on the geometry of the block. Theoretically, the indirect approach poses no problem, but in practice none of these techniques succeed in applying easily a single moment component, and some of them require a complex post-analysis to extract the different excitation components.

3.3.2 Direct Techniques to Apply a Moment Excitation

The limitations observed in the application of indirect techniques led the scientific community to develop new procedures that allow the application of a pure moment. As referred in Sect. 3.2.1, Smith [129] proposed a first known technique to obtain the complete structural mobility matrix applying a crude moment exciter using two electromagnetic shakers in a configuration capable of applying a couple by using two equal and opposite forces applied to a special fixture (Fig. 2), but its acting frequency range was quite limited. Several other techniques have been proposed to apply a pure moment:

- Twin-shaker arrangements [119, 121]
- Synchronized hammers [22]

- Magneto-strictive exciters [60, 61, 102]
- Using centrifugal forces [137]

Let us make a brief summary of these methods:

Sanderson [119] constructed a moment exciter with twin shakers for the measurement of beam moment mobility. To apply the moment, two two-exciter methods are implemented using two different fixtures in the form of T-block and I-block. Their works include a theoretical study [121] and an experimental one [119] on potential bias errors, where two main types are identified. The first bias error is an error in the measurement of the moment acting on the structure, due to the rotational inertia, and it was verified that this kind of error increases with the frequency and is most prominent at resonance frequencies; the correction of this error could be easily applied if rotational inertia cancellation is applied. The second error is a bias error in the rotational velocity that can be seen to be composed of two separate parts: the sensitivity of the measurement object to false excitation and the quality of excitation. To correct these errors several proposals have been presented. A special prototype moment exciter based on magneto-strictive rods was developed by Petersson and has been described in Petersson [102]. Jianxin and Gibbs [60] studied the effectiveness of the two different twin-shaker configurations and the Petersson magneto-strictive actuator in the application of a pure moment in beam structures. They concluded that using a twin-shaker system it is not possible to achieve a pure moment excitation, the reason being that the magnitude of the forces exerted by electromagnetic shakers depends upon the structural response of the system being excited. Where cross mobility is non-zero, results reveal themselves unreliable, and it is difficult to estimate the discrepancy as the shakers are non-matching. The Petersson magneto-strictive rods actuator seems to avoid the problems of matching and setting up in the twin-shaker systems. The same conclusions were drawn by Jianxin and Mak [61] on their experimental research using a magneto-strictive rods moment exciter, where they proposed methods to improve the moment exciter to generate a pure and sufficiently powerful moment.

The method of moment excitation by synchronized hammers Champoux et al. [22] uses two impact hammers to apply a pure moment by simultaneously exciting at points at either side of a point of interest but in opposite directions. The main advantage of this method is that no additional fixtures are needed, since the two forces are applied on each side of the point of interest; however, this is only true if both sides of the test structures can be easily accessed, which often is not the case. If only one side of the structure is available, an additional T-block or I-block has to be used to transmit the couple.

Trethewey and Sommer III [137, 138] presented a device that allows the generation of a pure moment by the centrifugal forces generated by eccentric masses attached to two symmetrically connected rotating wheels (see Fig. 9). However, this system also generated an undesirable moment in an orthogonal direction; to cancel it, a second identical counter-rotating system of masses was added on top of the previous one. The major drawback of the device is its considerable weight, although other restrictions have been identified, such as the narrow frequency range,

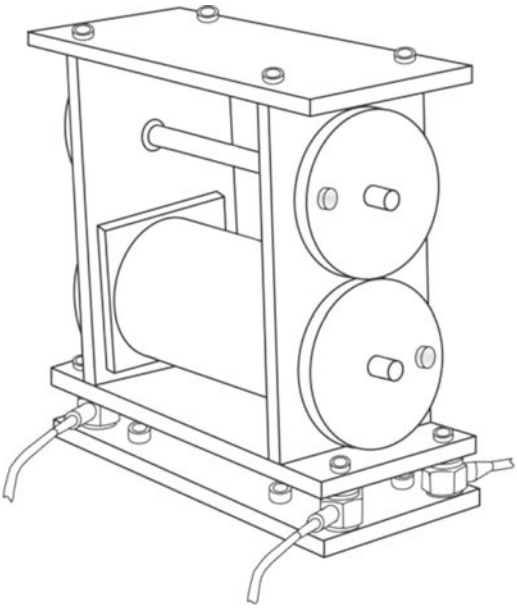

Fig. 9 Device for the generation of a pure moment by the centrifugal forces generated by eccentric masses (adapted from [138])

the limitation to harmonic excitations, and problems related to the fixture to the structure to be studied.

The error analysis previously performed, in the two-force configuration excitation arrangements, was mainly focused on the initial load of the exciters, the matching of the two forces, and the system resonance. Tao and Mak [135] also investigated the distance requirement of two-forces configuration for moment excitation.

In addition to the specific limitations of each one of the above-described methods, a main drawback is common to all of them: the large space occupied by the arrangements and the weight, which makes them unsuitable for use in many real applications.

For everything that has been said in this subsection, it is concluded that despite the fact that a lot of research work has already been accomplished, much more is required in order to create an effective system for applying a truly pure moment.

4 Condensation (Reduction) *Versus* Expansion

As the experimental data is usually collected from few coordinates and in a limited frequency range, when the comparison of numerical and experimental data is needed, the problem of model incompleteness arises. Hence, it is inevitable to deal with model incompleteness. Several methods have been proposed [77] and are being used in order to reduce the theoretical model to the test points or to expand the experimental data over the numerical model dofs.

4.1 Model Reduction

The general equilibrium equation for a given structure is

$$\boldsymbol{M}\ddot{\boldsymbol{x}} + \boldsymbol{C}\dot{\boldsymbol{x}} + \boldsymbol{K}\boldsymbol{x} = \boldsymbol{f} \tag{44}$$

If one neglects damping and defines primary p and secondary s coordinates, Eq. (44) can be partitioned as

$$\begin{bmatrix} \boldsymbol{M}_{pp} & \boldsymbol{M}_{ps} \\ \boldsymbol{M}_{sp} & \boldsymbol{M}_{ss} \end{bmatrix} \begin{Bmatrix} \ddot{\boldsymbol{x}}_p \\ \ddot{\boldsymbol{x}}_s \end{Bmatrix} + \begin{bmatrix} \boldsymbol{K}_{pp} & \boldsymbol{K}_{ps} \\ \boldsymbol{K}_{sp} & \boldsymbol{K}_{ss} \end{bmatrix} \begin{Bmatrix} \boldsymbol{x}_p \\ \boldsymbol{x}_s \end{Bmatrix} = \begin{Bmatrix} \boldsymbol{f}_p \\ \boldsymbol{0} \end{Bmatrix} \tag{45}$$

Note that forces can only act on the primary coordinates and that this subset is composed of a given number of dofs to be retained after model reduction. The selection of the retained dofs can be challenging and must be in such a way that the mode shapes can be described as well as possible.

The following subsections present some of the most referred reduction methods, with special emphasis on the transformation matrix proposed by each one. Detailed reviews on model reduction techniques have been published by Qu [104], Koutsovasilis [69], Besselink et al. [12].

4.1.1 Guyan Reduction

Introduced by Guyan [55], the Guyan or static reduction technique can be found in several commercial computational applications, although its accuracy is limited to the lower order modal properties, as it neglects the inertial terms of Eq. (45). Hence, one can state that

$$\boldsymbol{K}_{sp}\boldsymbol{x}_p + \boldsymbol{K}_{ss}\boldsymbol{x}_s = \boldsymbol{0} \tag{46}$$

and the transformation matrix of the Guyan reduction $\mathbf{T_S}$ is given by

$$\boldsymbol{T}_S = \begin{bmatrix} \boldsymbol{I} \\ -\boldsymbol{K}_{ss}^{-1}\boldsymbol{K}_{sp} \end{bmatrix} \tag{47}$$

Using the transformation matrix $\mathbf{T_S}$, the spatial model coordinates can be related to the primary ones by using the following transformation

$$\begin{Bmatrix} \boldsymbol{x}_p \\ \boldsymbol{x}_s \end{Bmatrix} = \boldsymbol{T}_S\boldsymbol{x}_p \tag{48}$$

Consequently, the reduced model matrices are given by

$$\boldsymbol{M}_R = \boldsymbol{T}_S^{\mathrm{T}}\boldsymbol{M}\,\boldsymbol{T}_S \quad \text{and} \quad \mathbf{K}_R = \boldsymbol{T}_S^{\mathrm{T}}\boldsymbol{K}\,\boldsymbol{T}_S \tag{49}$$

4.1.2 Dynamic Reduction

As the inertial terms were neglected in the formulation of the transformation matrix $\mathbf{T_S}$, the dynamic response of the reduced model is obviously exact only in static conditions. Moreover, as the excitation frequency increases, the accuracy of the reduced model responses tends to degrade. Thus, the Guyan reduction technique can be extended in order to reproduce the exact response of a structure at any given frequency ω [100]. This extension assumes harmonic excitation and it results on the modification of Eq. (47) in order to include the inertial effects at the selected frequency ω, so that the transformation matrix of the dynamic reduction technique is

$$\boldsymbol{T_D} = \begin{bmatrix} \boldsymbol{I} \\ -\left(\boldsymbol{K}_{ss} - \omega^2 \boldsymbol{M}_{ss}\right)^{-1} \left(\boldsymbol{K}_{sp} - \omega^2 \boldsymbol{M}_{sp}\right) \end{bmatrix} \tag{50}$$

and, consequently, the reduced model matrices are obtained similarly to Eq. (49).

Qu and Fu [106] present a dynamic reduction technique based on the subspace iteration method in the eigenproblem. The transformation matrix of this iterative technique is derived from the ith approximation of the first m mass-normalized eigenvectors $\boldsymbol{\Phi}_m^{(\mathrm{i})}$, such that

$$\boldsymbol{\Phi}_m^{(\mathrm{i})} = \begin{bmatrix} \boldsymbol{\Phi}_{pm}^{(\mathrm{i})} \\ \boldsymbol{\Phi}_{sm}^{(\mathrm{i})} \end{bmatrix} = \begin{bmatrix} \boldsymbol{I} \\ \boldsymbol{\Phi}_{sm}^{(\mathrm{i})} \left(\boldsymbol{\Phi}_{pm}^{(\mathrm{i})}\right)^{-1} \end{bmatrix} \boldsymbol{\Phi}_{pm}^{(\mathrm{i})} \tag{51}$$

If one considers the subspace approximation $\boldsymbol{X}_m^{(\mathrm{i}+1)}$ of $\boldsymbol{\Phi}_m^{(\mathrm{i}+1)}$, defined as

$$\boldsymbol{X}_m^{(\mathrm{i}+1)} = \boldsymbol{K}^{-1} \boldsymbol{M}\, \boldsymbol{\Phi}_m^{(\mathrm{i})} \tag{52}$$

the reduced system matrices are given by

$$\boldsymbol{M_R} = \left(\boldsymbol{X}_m^{(\mathrm{i}+1)}\right)^{\mathrm{T}} \boldsymbol{M}\, \boldsymbol{X}_m^{(\mathrm{i}+1)} \quad \text{and} \quad \boldsymbol{K_R} = \left(\boldsymbol{X}_m^{(\mathrm{i}+1)}\right)^{\mathrm{T}} \boldsymbol{K}\, \boldsymbol{X}_m^{(\mathrm{i}+1)} \tag{53}$$

4.1.3 Improved Reduction System (IRS)

The improved reduction system (IRS) technique, proposed by O'Callahan [95], develops Guyan's technique to include the contribution of the secondary coordinates' inertias as pseudo-static forces, which generates the transformation matrix $\mathbf{T_I}$,

$$\boldsymbol{T_I} = \boldsymbol{T_S} + \boldsymbol{S}\, \boldsymbol{M}\, \boldsymbol{T_S} \boldsymbol{M_R^{-1}} \boldsymbol{K_R} \tag{54}$$

where $\mathbf{T_S}$ is the transformation matrix of the Guyan reduction technique and $\mathbf{M_R}$ and $\mathbf{K_R}$ are statically reduced mass and stiffness matrices, respectively, and

$$\boldsymbol{S} = \begin{bmatrix} \mathbf{0} & \mathbf{0} \\ \mathbf{0} & \boldsymbol{K}_{ss}^{-1} \end{bmatrix} \tag{55}$$

Hence, the reduced model matrices are generated as in Eq. (49).

The transformation of Eq. (54) is a perturbation on Guyan's reduction technique and therefore some of its limitations remain, namely being exact only in static conditions. Friswell et al. [50] defined the IRS technique based on a perturbation on the dynamic reduction, where the transformation is exact for a selected non-zero frequency. This reduction technique is the dynamic IRS (DIRS) and its transformation matrix is:

$$\boldsymbol{T}_{DI} = \boldsymbol{T}_D + \boldsymbol{S}_D \boldsymbol{M}\, \boldsymbol{T}_{\mathbf{D}} \boldsymbol{M}_R^{-1} \boldsymbol{K}_R \tag{56}$$

where

$$\boldsymbol{S}_D = \begin{bmatrix} \mathbf{0} & \mathbf{0} \\ \mathbf{0} & \left(\boldsymbol{K}_{ss} - \omega^2 \boldsymbol{M}_{ss}\right)^{-1} \end{bmatrix} \tag{57}$$

The IRS technique was also modified by Friswell et al. [50] in order to improve its accuracy and is known as the iterated IRS (IIRS) technique, where the transformation matrix $\mathbf{T_I}$ is replaced by

$$\boldsymbol{T}_{II}^{(\mathrm{k})} = \boldsymbol{T}_S + \boldsymbol{S}\, \boldsymbol{M}\, \boldsymbol{T}_{II}^{(\mathrm{k}-1)} \left(\boldsymbol{M}_R^{(\mathrm{k}-1)}\right)^{-1} \boldsymbol{K}_R^{(\mathrm{k}-1)} \tag{58}$$

where the superscript (k) denotes the kth iteration, for k > 1. Note that $\boldsymbol{T}_{II}^{(0)} = \boldsymbol{T}_S$, $\boldsymbol{T}_{II}^{(1)} = \boldsymbol{T}_I$ is given in Eq. (54) and the reduced model matrices are given by

$$\boldsymbol{M}_R^{(\mathrm{k})} = \left(\boldsymbol{T}_{II}^{(\mathrm{k})}\right)^{\mathrm{T}} \boldsymbol{M}\, \boldsymbol{T}_{II}^{(\mathrm{k})} \quad \text{and} \quad \boldsymbol{K}_R^{(\mathrm{k})} = \left(\boldsymbol{T}_{II}^{(\mathrm{k})}\right)^{\mathrm{T}} \boldsymbol{K}\, \boldsymbol{T}_{II}^{(\mathrm{k})} \tag{59}$$

Further details on this technique are given in Friswell et al. [50, 51].

Xia and Lin [152] proposed a modification to the IIRS technique that leads to the following transformation matrix:

$$\boldsymbol{T}_{III}^{(\mathrm{k})} = \boldsymbol{T}_S + \boldsymbol{S}\, \boldsymbol{M}\, \boldsymbol{T}_{III}^{(\mathrm{k}-1)} \left(\boldsymbol{M}_D^{(\mathrm{k})}\right)^{-1} \boldsymbol{K}_S \tag{60}$$

with

$$\boldsymbol{K}_S = \boldsymbol{T}_S^{\mathrm{T}} \boldsymbol{K} \boldsymbol{T}_S \tag{61}$$

and

$$\boldsymbol{M}_D^{(\mathrm{k})} = \boldsymbol{T}_S^{\mathrm{T}} \boldsymbol{M} \boldsymbol{T}_{III}^{(\mathrm{k}-1)} \tag{62}$$

Note that $\boldsymbol{T}_{\boldsymbol{III}}^{(0)} = \boldsymbol{T}_{\boldsymbol{S}}$ and $\boldsymbol{T}_{\boldsymbol{III}}^{(1)} = \boldsymbol{T}_{\boldsymbol{I}}$, as for the IIRS, and the reduced model matrices are obtained similarly to Eq. (59). This technique proved to be computationally more efficient than the base IIRS [152].

4.1.4 System Equivalent Reduction Expansion Process (SEREP)

The system equivalent reduction expansion process (SEREP) was introduced by O'Callahan et al. [97], although a similar technique was proposed by Kammer [62]. This technique requires the solution of the generalized eigenproblem

$$\left(\boldsymbol{K} - \omega^2 \boldsymbol{M}\right) \boldsymbol{X} = \boldsymbol{0} \tag{63}$$

in order to obtain the modal model defined by the natural frequencies and mode shapes. The computed analytical eigenvectors must then be partitioned so that $\boldsymbol{\Psi}_{\mathrm{A}} = [\boldsymbol{\Psi}_{\mathrm{Ap}} \ \boldsymbol{\Psi}_{\mathrm{As}}]^{\mathrm{T}}$, where the subscript A refers to the analytical model. Furthermore, the Moore-Penrose pseudo inverse of $\boldsymbol{\Psi}_{\mathrm{Ap}}$ is used to map the complete analytical eigenvectors onto the secondary dofs by means of the transformation matrix $\mathbf{T}_{\mathbf{SE}}$,

$$\boldsymbol{T}_{\boldsymbol{SE}} = \begin{bmatrix} \boldsymbol{\Psi}_{\mathrm{A}p} \\ \boldsymbol{\Psi}_{\mathrm{A}s} \end{bmatrix} \left(\boldsymbol{\Psi}_{\mathrm{A}p}^{\mathrm{T}} \ \boldsymbol{\Psi}_{\mathrm{A}p}\right)^{-1} \boldsymbol{\Psi}_{\mathrm{A}p}^{\mathrm{T}} = \boldsymbol{\Psi}_{\mathrm{A}} \boldsymbol{\Psi}_{\mathrm{A}p}^{+} \tag{64}$$

and the reduced model matrices are obtained as in Eq. (49). Note that if the eigenvectors are mass-normalized, the reduced model matrices can be efficiently computed, regarding the orthogonality conditions, as

$$\boldsymbol{M}_{\boldsymbol{R}} = \left(\boldsymbol{\Phi}_{\mathrm{A}p}^{+}\right)^{\mathrm{T}} \boldsymbol{\Phi}_{\mathrm{A}p}^{+} \quad \text{and} \quad \boldsymbol{K}_{\boldsymbol{R}} = \left(\boldsymbol{\Phi}_{\mathrm{A}p}^{+}\right)^{\mathrm{T}} \boldsymbol{\Lambda} \ \boldsymbol{\Phi}_{\mathrm{A}p}^{+} \tag{65}$$

where $\boldsymbol{\Phi}$ is the mass-normalized modal matrix and $\boldsymbol{\Lambda}$ is the diagonal matrix of the squared eigenvalues.

Due to ill-conditioning issues, SEREP can only be applied if the number of primary dofs is greater or equal to the number of eigenvectors. However, as it can be derived from the SEREP formulation, the reduced model has exactly the same eigenfrequencies and eigenmodes as the full model for the modes used to form $\mathbf{T}_{\mathbf{SE}}$. Note that the IIRS technique proposed by Friswell et al. [50] converges exactly to the same solution of SEREP, avoiding the extraction of modal properties.

Kammer [63] proposed a hybrid reduction technique that combines both Guyan and SEREP formulations. The transformation matrix of this hybrid reduction technique is

$$\boldsymbol{T}_{\boldsymbol{H}} = \boldsymbol{T}_{\boldsymbol{SE}} + \boldsymbol{T}_{\boldsymbol{S}} \left(\boldsymbol{I} \text{-} \boldsymbol{\Psi}_{\mathrm{Ap}} \ \boldsymbol{\Psi}_{\mathrm{Ap}}^{+}\right) \tag{66}$$

4.1.5 Modal Truncation

Considering the modal matrix $\boldsymbol{\Psi}$, one can derive the system matrices in modal coordinates, such that

$$\boldsymbol{m} = \boldsymbol{\Psi}^{\boldsymbol{T}} \boldsymbol{M} \boldsymbol{\Psi} \qquad \text{and} \qquad \boldsymbol{k} = \boldsymbol{\Psi}^{\boldsymbol{T}} \boldsymbol{K} \boldsymbol{\Psi} \tag{67}$$

respectively, the modal mass and stiffness matrices. Note that if the mass-normalized modal matrix is used, Eq. (67) is recast as

$$\boldsymbol{\Phi}^{\boldsymbol{T}} \boldsymbol{M} \boldsymbol{\Phi} = \boldsymbol{I} \qquad \text{and} \qquad \boldsymbol{\Phi}^{\boldsymbol{T}} \boldsymbol{K} \boldsymbol{\Phi} = \boldsymbol{\Lambda} \tag{68}$$

In the modal domain, the equation of motion is completely decoupled, and therefore, it constitutes a set of linearly independent equilibrium equations related to each eigenvalue. Hence, one can obtain a reduced model just by truncation of the modal system matrices at a given mode of interest. Thus, for a truncated modal system defined by $\boldsymbol{\Phi}_{\mathbf{R}}$ and $\boldsymbol{\Lambda}_{\mathbf{R}}$, one can obtain the following reduced model matrices:

$$\boldsymbol{M}_{\boldsymbol{R}} = \left(\boldsymbol{\Phi}_{\boldsymbol{R}}^{\mathrm{T}}\right)^{-1} \boldsymbol{\Phi}_{\boldsymbol{R}}^{-1} \quad \text{and} \quad \boldsymbol{K}_{\boldsymbol{R}} = \left(\boldsymbol{\Phi}_{\boldsymbol{R}}^{\mathrm{T}}\right)^{-1} \boldsymbol{\Lambda}_{\boldsymbol{R}} \boldsymbol{\Phi}_{\boldsymbol{R}}^{-1} \tag{69}$$

Note that the reduced mass and stiffness matrices can be directly obtained from the experimental modal data, after normalization. If damping is not neglected, a second-order modal truncation must be considered, as in Koutsovasilis [69].

The use of modal truncation is the base of an efficient approach to the assembly of substructures or super-elements, the modal-based assembly (MBA), incorporated in the commercial software FEMTools (FEMtools 3.7.0, 2013).

4.1.6 Component Mode Synthesis

Developed as a modal coupling technique, one of the most accurate, although expensive, model reduction techniques is given by the component mode synthesis (CMS) methods. These methods attain a reduced order model for the substructures of a given assembled structure by reducing the number of mode shapes used to describe the dynamics of each substructure, while preserving all the physical dofs. A general CMS algorithm can be framed into three main categories: the fixed-interface, the free-interface, and the residual-flexible free interface [29, 69, 77, 141]. The choice for a specific CMS is problem dependent, although in structural mechanics the fixed-interface method is usually recommended, as it accurately retains the lower to mid frequency eigenvalues. Among several CMS hypothesis, the Craig-Bampton (CB) method [8] is perhaps the most used and therefore it is presented here.

Regarding a fixed-interface CMS method, Eq. (45) can be recast in terms of connection c and interior i dofs, as

$$\begin{bmatrix} \boldsymbol{M}_{cc} & \boldsymbol{M}_{ci} \\ \boldsymbol{M}_{ic} & \boldsymbol{M}_{ii} \end{bmatrix} \begin{Bmatrix} \ddot{\boldsymbol{x}}_c \\ \ddot{\boldsymbol{x}}_i \end{Bmatrix} + \begin{bmatrix} \boldsymbol{K}_{cc} & \boldsymbol{K}_{ci} \\ \boldsymbol{K}_{ic} & \boldsymbol{K}_{ii} \end{bmatrix} \begin{Bmatrix} \boldsymbol{x}_c \\ \boldsymbol{x}_i \end{Bmatrix} = \begin{Bmatrix} \boldsymbol{f}_c \\ \boldsymbol{f}_i \end{Bmatrix} \tag{70}$$

where $\mathbf{x}_c$ and $\mathbf{f}_c$ are the displacement and force vectors associated to the connection dofs between substructures, respectively; and $\mathbf{x}_i$ and $\mathbf{f}_i$ are the ones related to the interior dofs. Note that the connection dofs are actually the primary ones, in the sense of what was previously described.

The fixed-interface CMS algorithm is based on the assumption that the secondary dofs can be expressed in terms of both elastic and static mode shapes, considering that the connection dofs are fixed ($\mathbf{x}_c = \mathbf{0}$) and no forces are acting at the interior dofs ($\mathbf{f}_i = \mathbf{0}$). At a first stage, one may approximate the vector of interior displacements $\mathbf{x}_i$ by a linear combination of the $\boldsymbol{\Phi}_{im}$ elastic fixed-interface modes or CB modes, given by:

$$\boldsymbol{x}_i = \boldsymbol{\Phi}_{im} \quad \boldsymbol{p}_m \tag{71}$$

where $\mathbf{p}_m$ is related to the number of calculated modes (at initial stage $m = i$). However, the underlying philosophy of this reducing technique is to retain less modes, say k modes leading to a reduced modal matrix $\boldsymbol{\Phi}_{ik}$ while preserving all the physical dofs, to describe the dynamics of each substructure.

On the other hand, the vector of interior displacements $\mathbf{x}_i$ can also be approximated by using a linear combination of the constraint or static modes. In the CB method, these static modes are in fact given by the Guyan reduction, as it can be inferred from the manipulation of Eq. (70). Hence, one can relate the displacements at the interior coordinates to the connection ones, through

$$\boldsymbol{x}_i = -\boldsymbol{K}_{ii}^{-1} \boldsymbol{K}_{ic} \boldsymbol{x}_c = \boldsymbol{T}_S \boldsymbol{x}_c \tag{72}$$

Thus, connection and interior dofs can be related by the transformation matrix of the CB method $\mathbf{T_{CB}}$, derived from Eqs. (71) and (72), as follows:

$$\begin{Bmatrix} \boldsymbol{x}_i \\ \boldsymbol{x}_c \end{Bmatrix} = \begin{bmatrix} \boldsymbol{T}_S & \boldsymbol{\Phi}_{ik} \\ \boldsymbol{I} & \boldsymbol{0} \end{bmatrix} \begin{Bmatrix} \boldsymbol{x}_c \\ \boldsymbol{p}_k \end{Bmatrix} = \boldsymbol{T}_{CB} \begin{Bmatrix} \boldsymbol{x}_c \\ \boldsymbol{p}_k \end{Bmatrix} \tag{73}$$

Consequently, the reduced model matrices, for the k modes, are obtained from $\boldsymbol{T}_{CB}^{\mathrm{T}} \boldsymbol{M} \boldsymbol{T}_{CB}$ and $\boldsymbol{T}_{CB}^{\mathrm{T}} \boldsymbol{K} \boldsymbol{T}_{CB}$.

Note that the CB method can be improved by considering a more accurate approximation of the static modes. Koutsovasilis [69] proposed to replace the Guyan reduction by the IRS technique or, as it was proposed by Urgueira and Ewins [141], using the residual information of the neglected modes to improve the displacement approximation. However, one can state that the Guyan reduction can be replaced by any other more accurate technique.

4.1.7 Sum of Weighted Accelerations Technique (SWAT)

Carne et al. [21] presented the sum of weighted accelerations technique (SWAT), a force identification technique based on the concept of a modal filter. This technique uses the rigid body mode shapes in order to derive a weighting vector that separates the rigid body accelerations from the elastic response within a frequency band of interest. Hence, if one considers the transformation of generalized coordinates into physical ones, given by

$$\boldsymbol{x} = \boldsymbol{\Psi q} \tag{74}$$

the acceleration vector can be approximated by a sum of modal contributions, defined as

$$\ddot{\boldsymbol{x}} = \boldsymbol{\Psi}\ddot{\boldsymbol{q}} \tag{75}$$

By the SWAT technique, a weighting matrix $\mathbf{W}$ is derived such that a vector of rigid body accelerations $\ddot{\boldsymbol{x}}_{\mathrm{RB}}$, also known as SWAT dofs, can be extracted from the measured one:

$$\ddot{\boldsymbol{x}}_{\mathrm{RB}} = \boldsymbol{W}^{\mathrm{T}}\ddot{\boldsymbol{x}} = \boldsymbol{W}^{\mathrm{T}}\boldsymbol{\Phi}\ddot{\boldsymbol{q}} \tag{76}$$

here with mass-normalized modes. Rewriting Eq. (75) in terms of the contribution of the rigid body modes $\boldsymbol{\Phi}_{\mathrm{RB}}$ and the flexible ones $\boldsymbol{\Phi}$, one has

$$\ddot{\boldsymbol{x}} = [\boldsymbol{\Phi}_{\mathrm{RB}} \quad \boldsymbol{\Phi}] \begin{Bmatrix} \ddot{\boldsymbol{x}}_{\mathrm{RB}} \\ \ddot{\boldsymbol{x}} \end{Bmatrix} \tag{77}$$

Using Eqs. (76) and (77), it is possible to define the weighting matrix $\mathbf{W}$ that extracts only the rigid body accelerations from the measured ones, as described by Allen and Carne [2]:

$$\boldsymbol{W} = \left([\boldsymbol{\Phi}_{\mathrm{RB}} \quad \boldsymbol{\Phi}]^{\mathrm{T}} \right)^{+} \begin{bmatrix} \boldsymbol{I} \\ \boldsymbol{0} \end{bmatrix} \tag{78}$$

Note that this technique can be used as a reduction technique in the sense that the model can be replaced by its local time-dependent response [86].

On the other hand, if one truncates the elastic mode shapes to a given number of modes of interest (k), defined as the number of primary dofs to retain, as addressed by the CB method, one can relate the spatial model coordinates to the primary k ones based on Eq. (77), as

$$\boldsymbol{x} = \begin{Bmatrix} \boldsymbol{x}_p \\ \boldsymbol{x}_s \end{Bmatrix} = [\boldsymbol{\Phi}_{\mathrm{RB}} \quad \boldsymbol{\Phi}_k] \begin{Bmatrix} \boldsymbol{x}_{\mathrm{RB}} \\ \boldsymbol{x}_k \end{Bmatrix} = \boldsymbol{T}_{SW} \begin{Bmatrix} \boldsymbol{x}_{\mathrm{RB}} \\ \boldsymbol{x}_k \end{Bmatrix} \tag{79}$$

Thus, the reduced system matrices are given in a similar way to Eq. (49) and their dimension is given by the number of rigid body modes plus the number of modes of interest (k).

4.1.8 Reduction of Damped Models

Jeong et al. [58] derive a transformation matrix equivalent to the IIRS technique in the state-space formulation to be used for damped systems. The equation of motion for non-proportional damping must be reformulated in the state-space form to derive the quadratic eigenvalue problem:

$$\boldsymbol{A}\dot{\boldsymbol{y}} + \boldsymbol{B}\boldsymbol{y} = \boldsymbol{b} \tag{80}$$

with

$$\boldsymbol{A} = \begin{bmatrix} \boldsymbol{C} & \boldsymbol{M} \\ \boldsymbol{M} & \boldsymbol{0} \end{bmatrix}, \quad \boldsymbol{B} = \begin{bmatrix} \boldsymbol{K} & \boldsymbol{0} \\ \boldsymbol{0} & -\boldsymbol{M} \end{bmatrix}, \quad \boldsymbol{y} = \begin{Bmatrix} \boldsymbol{x} \\ \dot{\boldsymbol{x}} \end{Bmatrix} \quad \text{and} \quad \boldsymbol{b} = \begin{Bmatrix} \boldsymbol{f} \\ \boldsymbol{0} \end{Bmatrix} \tag{81}$$

From Eq. (80), one can write the generalized eigenvalue problem,

$$\boldsymbol{B}\tilde{\boldsymbol{\Psi}} = \boldsymbol{A}\tilde{\boldsymbol{\Psi}}\tilde{\boldsymbol{\Lambda}} \tag{82}$$

whose solutions are real or exist in complex conjugate pairs, given by

$$\tilde{\boldsymbol{\Psi}} = \begin{bmatrix} \boldsymbol{\Psi} & \boldsymbol{\Psi}^* \\ \boldsymbol{\Psi}\boldsymbol{\Lambda} & \boldsymbol{\Psi}^*\boldsymbol{\Lambda}^* \end{bmatrix} \qquad \text{and} \qquad \tilde{\boldsymbol{\Lambda}} = \begin{bmatrix} \boldsymbol{\Lambda} & \boldsymbol{0} \\ \boldsymbol{0} & \boldsymbol{\Lambda}^* \end{bmatrix} \tag{83}$$

where $\tilde{\boldsymbol{\Psi}}$ and $\tilde{\boldsymbol{\Lambda}}$ are matrices of complex conjugate pairs of eigenvectors and eigenvalues.

Rewriting Eq. (82) in a partitioned form, one has

$$\begin{bmatrix} \boldsymbol{B}_{pp} & \boldsymbol{B}_{ps} \\ \boldsymbol{B}_{sp} & \boldsymbol{B}_{ss} \end{bmatrix} \begin{bmatrix} \tilde{\boldsymbol{\Psi}}_p \\ \tilde{\boldsymbol{\Psi}}_s \end{bmatrix} = \begin{bmatrix} \boldsymbol{A}_{pp} & \boldsymbol{A}_{ps} \\ \boldsymbol{A}_{sp} & \boldsymbol{A}_{ss} \end{bmatrix} \begin{bmatrix} \tilde{\boldsymbol{\Psi}}_p \\ \tilde{\boldsymbol{\Psi}}_s \end{bmatrix} \tilde{\boldsymbol{\Lambda}} \tag{84}$$

from which one derives a transformation matrix ($\mathbf{T_{SS}}$) equivalent to the IIRS transformation given in Eq. (58):

$$\boldsymbol{T}_{SS}^{(\mathrm{k})} = \begin{bmatrix} \boldsymbol{I} \\ -\boldsymbol{B}_{ss}^{-1}\boldsymbol{B}_{sp} \end{bmatrix} + \begin{bmatrix} \boldsymbol{0} & \boldsymbol{0} \\ \boldsymbol{0} & \boldsymbol{B}_{ss}^{-1} \end{bmatrix} \boldsymbol{B}\, \boldsymbol{T}_{SS}^{(\mathrm{k}-1)} \left(\boldsymbol{B}_{R}^{(\mathrm{k}-1)}\right)^{-1} \boldsymbol{A}_{R}^{(\mathrm{k}-1)} \tag{85}$$

where the superscript (k) denotes the kth iteration, for k > 1. Note that $\boldsymbol{T}_{SS}^{(0)} = \begin{bmatrix} \boldsymbol{I} \\ -\boldsymbol{B}_{ss}^{-1}\boldsymbol{B}_{sp} \end{bmatrix}$, equivalent to the static reduction and the reduced model matrices are given by

$$\boldsymbol{A}_{\boldsymbol{R}}^{(\mathrm{k})} = \left(\boldsymbol{T}_{\boldsymbol{SS}}^{(\mathrm{k})}\right)^{\mathrm{T}} \boldsymbol{A}\, \boldsymbol{T}_{\boldsymbol{SS}}^{(\mathrm{k})} \quad \text{and} \quad \boldsymbol{B}_{\boldsymbol{R}}^{(\mathrm{k})} = \left(\boldsymbol{T}_{\boldsymbol{SS}}^{(\mathrm{k})}\right)^{\mathrm{T}} \boldsymbol{B}\, \boldsymbol{T}_{\boldsymbol{SS}}^{(\mathrm{k})} \tag{86}$$

Das and Dutt [35] proposed a modified SEREP formulated in state-space, including the gyroscopic effect and both internal and external damping. This technique is thought to reduce finite element models of rotor systems, although it can be applied to any linear system of equations.

4.2 Expansion of Measured Data

As the referred reduction methods point out, the majority of the available techniques have been developed either in the spatial or modal domains, and they can be directly used to expand the model data over the secondary coordinates. Such approach can be viewed as an inverted reduction, where the mode shape expansion is achieved by using the transformation matrices of the above referred reduction techniques. Hence, one can obtain the complete rth mode shape Ψ_r considering the expansion of Ψ_{pr}, using one of the several transformation matrices developed for model reduction purposes, such as,

$$\Psi_r = \left\{ \begin{array}{c} \Psi_p \\ \Psi_s \end{array} \right\}_r = \boldsymbol{T}\, \Psi_{pr} \tag{87}$$

If one considers not just one particular mode shape but a set of mode shapes, Eq. (87) can be recast as

$$\boldsymbol{\Psi} = \left[\begin{array}{c} \boldsymbol{\Psi}_p \\ \boldsymbol{\Psi}_s \end{array} \right] = \boldsymbol{T}\, \boldsymbol{\Psi}_p \tag{88}$$

where $\boldsymbol{\Psi}$ is a rectangular modal matrix constituted by a set of measured mode shapes $\boldsymbol{\Psi}_p$ expanded over the set of secondary coordinates.

4.2.1 Kidder's Method

Kidder [65] creates a spatial transformation using the analytical mass and stiffness matrices and the generalized eigenproblem

$$\left(\left[\begin{array}{cc} \boldsymbol{K}_{pp} & \boldsymbol{K}_{ps} \\ \boldsymbol{K}_{sp} & \boldsymbol{K}_{ss} \end{array} \right] - \omega_r^2 \left[\begin{array}{cc} \boldsymbol{M}_{pp} & \boldsymbol{M}_{ps} \\ \boldsymbol{M}_{sp} & \boldsymbol{M}_{ss} \end{array} \right] \right) \left\{ \begin{array}{c} \Psi_p \\ \Psi_s \end{array} \right\}_r = \boldsymbol{0} \tag{89}$$

From Eq. (89), the expanded mode shapes are given by

$$\Psi_r = \left[\begin{array}{c} \boldsymbol{I} \\ -\left(\boldsymbol{K}_{ss} - \omega_r^2\, \boldsymbol{M}_{ss}\right)^{-1} \left(\boldsymbol{K}_{sp} - \omega_r^2\, \boldsymbol{M}_{sp}\right) \end{array} \right] \Psi_{pr} = \boldsymbol{T}_{\boldsymbol{K}} \Psi_{pr} \tag{90}$$

where $\mathbf{T_K}$ is the transformation matrix of the Kidder's method.

Note that the expansion process is achieved mode by mode and that experimental mode shapes can be expanded over the entire model coordinates.

4.2.2 Expansion Using Analytical Modes

Perhaps the simplest approach to expand measured data is the one where the data at unmeasured dofs is directly replaced by its analytical counterpart, although numerical discontinuities may arise from this kind of procedure [77]. However, in this context, a feasible technique was introduced by Lipkins and Vandeurzen [72]. This expansion technique relies on the assumption that each mode can be obtained by a linear combination of the analytical modes. Considering the analytical modal matrix partitioned in terms of primary and secondary coordinates and selected and discarded mode shapes, one has

$$\boldsymbol{\Psi}_{\mathrm{A}} = \begin{bmatrix} \boldsymbol{\Psi}_{11} & \boldsymbol{\Psi}_{12} \\ \boldsymbol{\Psi}_{21} & \boldsymbol{\Psi}_{22} \end{bmatrix} \tag{91}$$

where the submatrix $[\boldsymbol{\Psi}_{11} \;\; \boldsymbol{\Psi}_{21}]^{\mathrm{T}}$ is related to the selected mode shapes. Hence, the expanded experimental mode shapes are generated from the following linear combination:

$$\boldsymbol{\Psi}_{\mathrm{X}} = \begin{Bmatrix} \boldsymbol{\Psi}_{\mathrm{X}_1} \\ \boldsymbol{\Psi}_{\mathrm{X}_2} \end{Bmatrix} = \begin{bmatrix} \boldsymbol{\Psi}_{11} \\ \boldsymbol{\Psi}_{21} \end{bmatrix} \boldsymbol{\upsilon} \tag{92}$$

where υ is a vector of unknown coefficients obtained in a least squares sense, as

$$\boldsymbol{\upsilon} = (\boldsymbol{\Psi}_{11})^{+} \boldsymbol{\Psi}_{\mathrm{X}_1} \tag{93}$$

and therefore the mode shapes at the secondary coordinates are computed by

$$\boldsymbol{\Psi}_{\mathrm{X}_2} = \boldsymbol{\Psi}_{21} \boldsymbol{\upsilon} \tag{94}$$

4.2.3 Expansion of Frequency Response Functions (FRF)

Rather than expand the mode shapes, the need to expand a set of measured FRFs has been addressed by several authors [16].

Silva et al. [126] used a modified version of the Kidder's expansion method in order to expand a set of measured FRFs $\mathbf{H}_{pj}(\omega)$ over the secondary model coordinates, considering that the experimental responses are due to a set of q excitations applied individually at j locations. Instead of being based on the solution of the eigenproblem, this technique is based on the notion of dynamic stiffness and it is derived from the equilibrium equation for a particular frequency, as

$$\left(\begin{bmatrix} \boldsymbol{K}_{pp} & \boldsymbol{K}_{ps} \\ \boldsymbol{K}_{sp} & \boldsymbol{K}_{ss} \end{bmatrix} - \omega^2 \begin{bmatrix} \boldsymbol{M}_{pp} & \boldsymbol{M}_{ps} \\ \boldsymbol{M}_{sp} & \boldsymbol{M}_{ss} \end{bmatrix} \right) \begin{Bmatrix} \boldsymbol{H}_{pj}(\omega) \\ \boldsymbol{H}_{sj}(\omega) \end{Bmatrix} = \begin{Bmatrix} \boldsymbol{I}_j \\ \boldsymbol{0} \end{Bmatrix} \tag{95}$$

where $\mathbf{I}_j$ is a vector of zeros except for the element corresponding to the excitation location j. From Eq. (95), the expanded FRF vector is given by

$$\boldsymbol{H}_j(\omega) = \begin{bmatrix} \boldsymbol{I} \\ -\left(\boldsymbol{K}_{ss} - \omega^2 \boldsymbol{M}_{ss}\right)^{-1} \left(\boldsymbol{K}_{sp} - \omega^2 \boldsymbol{M}_{sp}\right) \end{bmatrix} \boldsymbol{H}_{pj}(\omega) = \boldsymbol{T}_{\boldsymbol{M}} \boldsymbol{H}_{pj}(\omega) \tag{96}$$

which can also be extended to be used for damped systems, if one considers the general equilibrium equation (44).

For the sake of simplicity, from now on the explicit reference to the frequency dependence of the FRF matrix and sub-matrices will be omitted.

Avitabile and O'Callahan [6] proposed an expansion technique, in the FRF partial fraction form, written to include the effect of all the modes of the system. This method can be implemented in one of two ways: (i) one needs to synthesize the translation FRFs from the measured modal quantities through their partial fraction form and to expand them to rotational dofs using SEREP; additionally, one includes the residual effect of the unmeasured modes and the expansion of them using the dynamic expansion method; and (ii) where the synthesized FRFs are expanded to the rotational dofs using SEREP and the residual effect is related to the difference of the SEREP expansion and the dynamic one at a particular frequency. However, avoiding modal identification, one can address the straightforward expansion of the experimental rectangular FRF matrix using the transformation matrix of the modified Kidder's method ($\mathbf{T_M}$), as proposed by Silva and Maia [124] using a proper classification for each dof in the system.

As it is obvious, the expanded FRF of Eq. (96), or the ones obtained by the expansion techniques of Avitabile and O'Callahan [6], can only complete a sub-matrix of $\mathbf{H}$, related to the coordinates where the force excitation is applied. However, the rotational FRFs are required by several methods, from coupling to model updating. The work of Avitabile and O'Callahan [6] proposed a strategy to expand the set of measured FRFs in order to obtain a complete FRF matrix, as given in the work of Drozg et al. [38]. To implement such a strategy one must write the FRF matrix in the following partitioned form:

$$\boldsymbol{H} = \begin{bmatrix} \boldsymbol{H}_{pq} & \boldsymbol{H}_{pu} \\ \boldsymbol{H}_{sq} & \boldsymbol{H}_{su} \end{bmatrix} \tag{97}$$

where the subscript u is related to the non-excited coordinates, neither by forces nor by moments. Note that one has both translational and rotational dofs among the secondary coordinates and that the non-excited set of coordinates also encompasses translational and rotational dofs, respectively, identified by the subscripts s_t, s_θ, u_f, and u_τ. Thus, Eq. (97) can be rewritten as

$$\boldsymbol{H} = \begin{bmatrix} \boldsymbol{H}_{pq} & \boldsymbol{H}_{pu_f} & \boldsymbol{H}_{pu_\tau} \\ \boldsymbol{H}_{s_t q} & \boldsymbol{H}_{s_t u_f} & \boldsymbol{H}_{s_t u_\tau} \\ \boldsymbol{H}_{s_\theta q} & \boldsymbol{H}_{s_\theta u_f} & \boldsymbol{H}_{s_\theta u_\tau} \end{bmatrix} \tag{98}$$

and the complete FRF matrix can be obtained from $\mathbf{H}_{pq}$ using the following steps:

1. Expand $\mathbf{H}_{pq}$ to the secondary coordinates:

$$\begin{bmatrix} \boldsymbol{H}_{pq} \\ \boldsymbol{H}_{sq} \end{bmatrix} = \boldsymbol{T}\boldsymbol{H}_{pq} \tag{99}$$

2. Transpose the expanded FRFs:

$$\boldsymbol{H}_{pu} = \boldsymbol{H}_{sq}^{\mathrm{T}} \tag{100}$$

3. Expand $\mathbf{H}_{pu}$ to the secondary coordinates:

$$\begin{bmatrix} \boldsymbol{H}_{pu} \\ \boldsymbol{H}_{su} \end{bmatrix} = \boldsymbol{T}\boldsymbol{H}_{pu} \tag{101}$$

5 Transmissibility as a Means to Estimate the Dynamic Response

5.1 Introduction

The dynamic characteristics of a structure are often derived from a set of measured frequency response functions. However, it may happen that due to the cost related to data acquisition, or to practical reasons such as the inaccessibility of locations for measurement, certain FRFs cannot be experimentally measured. In these circumstances, it is useful to have some tools that can provide the prediction of such dynamic information. The transmissibility concept seems to play an important role to circumvent these situations.

The notion of transmissibility is presented in every classic textbook on vibrations, associated to the single degree-of-freedom system, when its basis is moving harmonically; it is defined as the ratio between the modulus of the response amplitude and the modulus of the imposed amplitude of motion.

The first attempts to extend the idea of transmissibility to a system with N dofs, that is, how to relate a set of unknown responses to another set of known responses, for a given set of applied forces, were given by Vakakis et al. [99, 143–145], although their generalization was still limited to a very particular type of N degree-of-freedom systems, one where a set constituted by a mass, stiffness, and damper is repeated several times. The works of Ewins and Liu [46] and Varoto and McConnell [146] also extend the initial concept to N degrees-of-freedom systems,

but again in a limited way, the former using a definition that makes the calculations dependent on the path taken between the considered coordinates involved, the latter by restricting the set of coordinates where the displacements are known to be coincident to the set of applied forces. An important contribution to the generalization of the transmissibility concept in frequency domain for multiple dof systems was presented by Ribeiro [109]. In this generalization, the transmissibility matrix between two sets of response functions is built from any of the mobility matrices of the structure. In most practical cases, the known (or measured) responses shall constitute one of the sets, while the other set includes the responses at any of the other coordinates. The generalization of the transmissibility concept suggests that if the transmissibility matrix can be evaluated in the laboratory or numerically beforehand, then by measuring in service some responses, one would be able to estimate the responses at the inaccessible coordinates.

The next section presents the original and an alternative formulation of the transmissibility presented by Ribeiro et al. [111]; some important properties will also be referred.

5.2 Theoretical Description

5.2.1 Fundamental Formulation

The approach proposed in Ribeiro [109] and Ribeiro et al. [111] is based on harmonically applied forces (easy to generalize to periodic ones). If one has a vector $\boldsymbol{F}_A$ of magnitudes of the excitation forces (and/or moments) at coordinates A, a vector $\boldsymbol{X}_U$ of unknown response amplitudes at coordinates U, and a vector $\boldsymbol{X}_K$ of known response amplitudes at coordinates K, then one can write:

$$\boldsymbol{X}_U = \boldsymbol{H}_{UA} \ \boldsymbol{F}_A \tag{102}$$

$$\boldsymbol{X}_K = \boldsymbol{H}_{KA} \ \boldsymbol{F}_A \tag{103}$$

where $\boldsymbol{H}_{UA}$ and $\boldsymbol{H}_{KA}$ are the receptance frequency response matrices relating coordinates U and A, and K and A, respectively. Assuming that the number of known coordinates is equal or higher than the number of applied forces, that is, $\#K \geq \#A$, one can eliminate $\boldsymbol{F}_A$ between Eqs. (102) and (103), leading to

$$\boldsymbol{X}_U = \boldsymbol{H}_{UA} \ \boldsymbol{H}_{KA}^{+} \ \boldsymbol{X}_K \tag{104}$$

or

$$\boldsymbol{X}_U = \boldsymbol{T}_{UK}^{(A)} \ \boldsymbol{X}_K \tag{105}$$

where $\boldsymbol{H}_{KA}^{+}$ is the pseudo-inverse of $\boldsymbol{H}_{KA}$. Thus, the transmissibility matrix is defined as

$$\boldsymbol{T}_{UK}^{(A)} = \boldsymbol{H}_{UA}\, \boldsymbol{H}_{KA}^{+} \tag{106}$$

Note that the set of coordinates where the forces are applied (A) need not coincide with the set of known responses (K). The only restriction is that – for the pseudo-inverse to exist – the number of K coordinates must be greater or equal than the number of A coordinates.

An important property of the transmissibility matrix is that it does not depend on the magnitude of the forces; one simply has to know or to choose the coordinates where the forces are going to be applied (or not, as one can even choose more coordinates A if one is not sure whether or not there will be some forces there and later on state that those forces are zero) and measure the necessary frequency response functions.

As previously referred, one of the requirements of this approach is that the number and locations of the dynamic loads be known. However, in real structures, it may be difficult to point out a priori the coordinates where the dynamic loads are applied; examples of these situations are the case of structures loaded by traffic or by wind. To apply the transmissibility concept to structures subjected to distributed loads, the same authors in Ribeiro et al. [110] developed a method for response prediction from a reduced set of known responses, using the transmissibility matrix.

For situations of non-harmonic excitations, as in the case of structures submitted to environmental loads, the transmissibility concept has been extended too, using the spectral densities of the response measurements [112].

5.2.2 Alternative Formulation

An alternative approach developed by Ribeiro et al. [113] evaluates the transmissibility matrix from the dynamic stiffness matrices, where the spatial properties (mass, stiffness, etc.) are explicitly included.

The dynamic behavior of an MDOF system can be described in the frequency domain by the following equation (assuming harmonic loading):

$$\boldsymbol{Z}\ \boldsymbol{X} = \boldsymbol{F} \tag{107}$$

where $\boldsymbol{Z}$ represents the dynamic stiffness matrix, $\boldsymbol{X}$ is the vector of the amplitudes of the dynamic responses, and $\boldsymbol{F}$ represents the vector of the amplitudes of the dynamic loads.

From the set of dynamic responses, as defined before, it is possible to distinguish between two distinct subsets of coordinates K and U; from the set of dynamic loads it is also possible to distinguish between two subsets, A and B, where A is the subset where the dynamic loads may be applied and B is the set formed of the remaining coordinates, where the dynamic loads are never applied. One can write $\boldsymbol{X}$ and $\boldsymbol{F}$ as

$$\boldsymbol{X} = \begin{Bmatrix} \boldsymbol{X}_K \\ \boldsymbol{X}_U \end{Bmatrix},\ \boldsymbol{F} = \begin{Bmatrix} \boldsymbol{F}_A \\ \boldsymbol{F}_B \end{Bmatrix} \tag{108}$$

With these subsets, Eq. (107) can be partitioned accordingly:

$$\begin{bmatrix} \boldsymbol{Z}_{AK} & \boldsymbol{Z}_{AU} \\ \boldsymbol{Z}_{BK} & \boldsymbol{Z}_{BU} \end{bmatrix} \begin{Bmatrix} \boldsymbol{X}_K \\ \boldsymbol{X}_U \end{Bmatrix} = \begin{Bmatrix} \boldsymbol{F}_A \\ \boldsymbol{F}_B \end{Bmatrix} \tag{109}$$

Taking into account that coordinates B represent the ones where the dynamic loads are never applied, and considering that the number of these coordinates is greater or equal to the number of coordinates U, from Eq. (109) it is possible to obtain the unknown response vector:

$$\begin{gathered} \boldsymbol{F}_B = \boldsymbol{0}, \quad \#B \geq \#U \\ \Downarrow \\ \boldsymbol{X}_U = -\boldsymbol{Z}_{BU}^{+} \, \boldsymbol{Z}_{BK} \, \boldsymbol{X}_K \end{gathered} \tag{110}$$

where $\boldsymbol{Z}_{BU}^{+}$ is the pseudo-inverse of $\boldsymbol{Z}_{BU}$. Therefore, this means that the transmissibility matrix can also be defined as

$$\boldsymbol{T}_{UK}^{(A)} = -\boldsymbol{Z}_{BU}^{+} \, \boldsymbol{Z}_{BK} \tag{111}$$

Equation (111) is an alternative definition of transmissibility, based on the dynamic stiffness matrices of the structure. Therefore,

$$\boldsymbol{T}_{UK}^{(A)} = \boldsymbol{H}_{UA} \, \boldsymbol{H}_{KA}^{+} = -\boldsymbol{Z}_{\boldsymbol{BU}}^{+} \, \boldsymbol{Z}_{BK} \tag{112}$$

Considering that the dynamic stiffness matrix for an undamped system is described in terms of the stiffness and mass matrices, $\boldsymbol{Z} = \boldsymbol{K} - \omega^2 \, \boldsymbol{M}$, one can now relate the transmissibility functions to the spatial properties of the system. To make this possible, one must bear in mind that it is mandatory that both conditions regarding the number of coordinates be valid, that is,

$$\#B \geq \#U \quad \text{and} \quad \#K \geq \#A \tag{113}$$

5.2.3 Transmissibility Properties

Observing Eqs. (104) and (106), it is possible to conclude that the *transmissibility matrix is independent from the force vector* $\boldsymbol{F}_A$. (Note that $\boldsymbol{F}_A$ is eliminated between Eqs. (102) and (103).) This means that any change verified in one of the force values, acting along with coordinates of set A, will not affect the transmissibility matrix $\boldsymbol{T}_{UK}^{(A)}$. This change can be due, for instance, to the alteration of mass values associated to coordinates A or stiffness values of springs interconnecting those coordinates. Additionally, to highlight that characteristic of matrix $\boldsymbol{T}_{UK}^{(A)}$, it can be verified from Eq. (111) that there are no coordinates A involved in the matrices $\boldsymbol{Z}$ (i.e., neither $\boldsymbol{Z}_{AK}$ nor $\boldsymbol{Z}_{AU}$). As it was presented by Maia et al. [81], this statement reinforces the previous conclusion extracted from Eq. (106) and will lead to the formulation of two properties, as follows:

Property 1. *The transmissibility matrix does not change if some modification is made on the mass values of the system where the loads can be applied – subset A.*

Property 2. *The transmissibility matrix does not change if some modification is made on the stiffness values of springs interconnecting coordinates of subset A – (where the loads can be applied).*

However, any changes in the mass values associated to coordinates A and/or any changes in the stiffness values of springs interconnecting coordinates A will affect the inertia forces and elastic forces, respectively, acting along those coordinates and thus belonging to $\boldsymbol{F}_A$.

According to properties 1 and 2, if a modification is operated on the original system, the transmissibility matrix remains constant, and therefore, it is possible to estimate the FRFs associated to the unknown coordinates without the necessity of measuring the responses on those coordinates, that is,

$$\boldsymbol{T}_{UK}^{(A)} = \boldsymbol{H}_{UA}\, \boldsymbol{H}_{KA}^{+} = \boldsymbol{H}'_{UA}\, \boldsymbol{H}'_{KA}{}^{+} \tag{114}$$

where $\boldsymbol{H}_{UA}$, $\boldsymbol{H}_{KA}$ and $\boldsymbol{H}'_{UA}$, $\boldsymbol{H}'_{KA}$ are the receptance frequency response matrices relating coordinates U and A, and K and A, for the original and the modified system. Thus, if the receptance matrix relating coordinates K and A of the modified system ($\boldsymbol{H}'_{KA}$) is known, the receptance matrix relating coordinates U and A ($\boldsymbol{H}'_{UA}$) can be estimated:

$$\boldsymbol{H}'_{UA} = \boldsymbol{T}_{UK}^{(A)}\, \boldsymbol{H}'_{KA} \tag{115}$$

5.3 Other Possible Applications of Transmissibility

The potentialities of application of the transmissibility are not limited to the determination of unmeasured FRFs, a number of other possible applications are reported in Maia et al. [81], like in structural coupling [36, 49, 70], damage detection [80, 117, 118, 160], sensor placement [149], etc.

References

1. Algrain MC, Saniie J (1991) Estimation of 3D angular motion using gyroscopes and linear accelerometers. IEEE Trans Aerosp Electron Syst 27:910–920
2. Allen M, Carne T (2006) Comparison of Inverse Structural Filter (ISF) and Sum of Weighted Accelerations (SWAT) time domain force identification methods. In: 47th AIAA/ASME/ASCE/AHS/ASC structures, structural dynamics, and materials conference 14th AIAA/ASME/AHS adaptive structures conference 7th. Structures, structural dynamics, and materials and co-located conferences. Reston: American Institute of Aeronautics and Astronautics. https://doi.org/10.2514/6.2006-1885. Accessed 24 Mar 2014
3. Allen MS, Kammer DC, Mayes RL (2010) Uncertainty in experimental/analytical substructuring predictions: a review with illustrative examples. In: Proceedings of ISMA 2010, Leuven

4. Antonello R, Oboe R (2011) MEMS gyroscopes for consumers and industrial applications. In: Minin O (ed) Microsensors. InTech
5. Avitabile P, O'Callahan J (1987) Expansion of rotational degrees of freedom for structural dynamic modifications. Presented at the 5th international modal analysis conference (IMAC V), London, pp 950–955
6. Avitabile P, O'Callahan J (2003) Frequency response function expansion for unmeasured translation and rotation dofs for impedance modelling applications. Mech Syst Signal Process 17(4):723–745. http://www.sciencedirect.com/science/article/pii/S0888327001914578
7. Avitabile P, Piergentili F (1997) Consideration for effects of rotational degrees of freedom for hybrid modeling applications. Presented at the 15th international modal analysis conference (IMAC XV), Orlando, pp 792–798
8. Bampton MCC, Craig RR Jr (1968) Coupling of substructures for dynamic analyses. AIAA J 6(7):1313–1319. https://doi.org/10.2514/3.4741. Accessed 25 Mar 2014
9. Batista FC, Maia NMM (2011) Uncoupling techniques for the dynamic characterization of substructures. In: Linking models and experiments, vol 2. Springer, New York, pp 383–392
10. Bello M, Sestieri A, D'Ambrogio W, La Gala F (2003) Development of a rotation transducer based on bimorph PZTs. Mech Syst Signal Process 17:1069–1081
11. Beskhyroun S, Ma QT (2012) Low-cost accelerometers for experimental modal analysis. In: Proceedings of the 15th world conference on earthquake engineering
12. Besselink B et al (2013) A comparison of model reduction techniques from structural dynamics, numerical mathematics and systems and control. J Sound Vib 332(19):4403–4422. http://linkinghub.elsevier.com/retrieve/pii/S0022460X1300285X. Accessed 4 Mar 2014
13. Bokelberg EH, Sommer III HJ, Trethewey MW (1993) Simultaneous measurement of six coordinate vibration: three translations and three rotations. Presented at the 11th international modal analysis conference (IMAC XI), Kissimmee, pp 522–527
14. Bokelberg EH, Sommer HJ III, Trethewey MW (1994) A six-degree-of-freedom laser vibrometer, part I: theoretical development. J Sound Vib 178:643–654
15. Bokelberg EH, Sommer HJ III, Trethewey MW (1994) A six-degree-of-freedom laser vibrometer, part II: experimental validation. J Sound Vib 178:655–667
16. Bregant L, Sanderson M (2000) Rotational degrees of freedom an historical overview on techniques and methods. Presented at the Proceedings of the international seminar on modal analysis (ISMA 25), Leuven
17. Cafeo JA, Rieker JR, Trethewey MW, Sommer III HJ (1991) Application of a three degree of freedom laser vibrometer for experimental modal analysis. Presented at the 9th international modal analysis conference (IMAC IX), Florence, pp 1161–1167
18. Cafeo JA, Trethewey MW, Sommer HJ III (1992) Measurement and application of experimental rotational degrees of freedom for mode shape refinement. Int J Anal Exp Modal Anal 7:255–269
19. Cafeo JA, Trethewey MW, Sommer III HJ (1993) On the use of measured rotational degrees-of-freedom in structural dynamic modification. Presented at the 11th international modal analysis conference (IMAC XI), pp 96–101
20. Cafeo JA, Trethewey MW, Sommer HJ III (1995) Beam element structural dynamics modification using experimental modal rotational data. J Vib Acoust 117:265–271
21. Carne TG, Bateman VI, Mayes RL (1992) Force reconstruction using a sum of weighted accelerations technique. In: 10th international modal analysis conference (IMAC X), San Diego
22. Champoux Y, Cotoni V, Paillard B, Beslin O (2003) Moment excitation of structures using two synchronized impact hammers. J Sound Vib 263:515–533
23. Chen W-H, Cherng J-S (1985) Modal synthesis via combined experimental and finite element techniques with consideration of rotational effects. J Sound Vib 103:1–11
24. Cheng L, Qu YC (1997) Rotational compliance measurements of a flexible plane structure using an attached beam-like tip, part 1: analysis and numerical simulation. J Vib Acoust 119:596–602

25. Cicogna TR, Varoto PS, Trindade MA (2008) Measurement of rotational FRFs in isotropic beams and plates using piezoceramic bimorphs and genetic algorithm optimization. Presented at the 26th IMAC: conference and exposition on structural dynamics 2008 (IMAC XXVI), Orlando
26. Cigada A, Lurati M, Redealli M, Vanali M (2007) Mechanical performance and metrological characterization of MEMS accelerometers and application in modal analysis. Presented at the conference & exposition on structural dynamics (IMAC XXV), Orlando
27. Cigada A, Lurati M, Redealli M, Vanali M (2008) Evaluation of the metrological performances of a MEMS accelerometers to the aim of their application in structural health monitoring. Presented at the conference & exposition on structural dynamics – technologies for civil structures (IMAC XXVI), Orlando
28. Cloutier D, Avitabile P (2010) Investigation on the use of various decoupling approaches. In: Proceedings of the IMAC-XXVIII, Jacksonville
29. Craig RR Jr (2000) Coupling of substructures for dynamic analyses: an overview. In: AIAA dynamics specialists conference, Atlanta, p 1573
30. Crowley SM, Mehzad J, Brown DL (1986) An investigation of structural modification using an H-frame structure. Presented at the 4th international modal analysis conference (IMAC IV), Los Angeles, pp 1268–1278
31. D'Ambrogio W, Fregolent A (2008) Promises and pitfalls of decoupling procedures. In: Proceeding of 26th IMAC, Orlando
32. D'Ambrogio W, Fregolent A (2008) Sensitivity of decoupling techniques to uncertainties in the properties. In: Proceedings of ISMA 2008, Leuven, pp 3737–3749
33. D'Ambrogio W., Fregolent A., 2009. Decoupling procedures in the general framework of frequency based substructuring. In: Proceedings of the IMAC-XXVII, Orlando
34. D'Ambrogio W, Fregolent A (2014) Are rotational DoFs essential in substructure decoupling? Dynamics of coupled structures, vol 1, Proceedings of IMAC 32
35. Das AS, Dutt JK (2008) Reduced model of a rotor-shaft system using modified SEREP. Mech Res Commun 35(6):398–407. http://www.sciencedirect.com/science/article/pii/S0093641308000451. Accessed 4 Mar 2014
36. Devriendt CMG, Fontul M (2005) Transmissibility in coupled structures: identification of the sufficient set of coupling forces. In: Proceedings of the 1st international operational modal analysis conference. Presented at the IOMAC 1, Copenhagen
37. Drain LE (1980) The laser Doppler technique. Wiley, Chichester/New York
38. Drozg A, Rogelj J, Čepon G, Boltežar M (2018) On the performance of direct piezoelectric rotational accelerometers in experimental structural dynamics. Measurement 127:292–298
39. Duarte ML (1996) Experimentally-derived structural models for use in further dynamic analysis. PhD thesis. Imperial College of Science, Technology and Medicine London, London
40. Duarte ML, Ewins DJ (1995) Some insights into the importance of rotational degrees-of-freedom and residual terms in coupled structure analysis. Presented at the 13th international modal analysis conference (IMAC XIII), Nashville, pp 164–170
41. Duarte ML, Ewins DJ (2000) Rotational degrees of freedom for structural coupling analysis via finite-difference technique with residual compensation. Mech Syst Signal Process 14: 205–227
42. Dumont M, Kinsley N (2016) Using accelerometers for measuring rotational degrees-of-freedom. Sound & Vibration
43. Elliott AS, Moorhouse AT, Pavić G (2008) Measurement of force and moment mobilities using a finite difference technique. Presented at the Acoustics' 08, Paris, pp 1808–1812
44. Elliott AS, Moorhouse AT, Pavić G (2012) Moment excitation and the measurement of moment mobilities. J Sound Vib 331:2499–2519
45. Ewins DJ, Gleeson PT (1975) Experimental determination of multidirectional mobility data for beam. Shock Vib Bull 45:153–173
46. Ewins DJ, Liu W (1998) Transmissibility properties of MDOF systems. Presented at the 16th international modal analysis conference (IMAC XVI), Santa Barbara, pp 847–854

47. Ewins DJ, Sainsbury MG (1972) Mobility measurements for the vibration analysis of connected structures. Shock Vib Bull 42:105–122
48. Ewins DJ, Silva JMM, Maleci G (1980) Vibration analysis of a helicopter plus an externally-attached structure. Shock Vib Bull 50:155–171
49. Fontul M, Ribeiro AMR, Silva JMM, Maia NMM (2004) Transmissibility in structural coupling. In: Proceedings of international conference on noise and vibration engineering. Presented at the ISMA 2004, Leuven
50. Friswell MI, Garvey SD, Penny JET (1995) Model reduction using dynamic and iterated IRS techniques. J Sound Vib 186(2):311–323. http://www.sciencedirect.com/science/article/pii/S0022460X85704518. Accessed 4 Mar 2014
51. Friswell MI, Garvey SD, Penny JET (1998) The convergence of the iterated IRS method. J Sound Vib 211(1):123–132. http://www.sciencedirect.com/science/article/pii/S0022460X97913687. Accessed 5 Mar 2014
52. Gialamas T, Tsahalis D, Bregant L, Otte D, Van der Auweraer H (1996) Substructuring by means of FRFs: some investigations on the significance of rotational Dofs. Presented at the 14th international modal analysis conference (IMAC XIV), Dearborn, pp 619–625
53. Giuliani P, Di Maio D, Schwingshackl CW, Martarelli M, Ewins DJ (2013) Six degrees of freedom measurement with continuous scanning laser Doppler vibrometer. Mech Syst Signal Process 38:367–383
54. Gleeson PT (1979) Identification of spatial models for the vibration analysis of lightly damped structures. PhD thesis. Imperial College London, University of London, London
55. Guyan RJ (1965) Reduction of stiffness and mass matrices. Am Inst Aeronaut Astronaut J 3(2):961–962
56. Helderweirt S, Van der Auweraer H, Mas P, Bregant L, Casagrande D (2001) Application of accelerometer-based rotational degree of freedom measurements for engine subframe modeling. In: 19th international modal analysis conference, IMAC XIX, pp 1298–1304
57. Ivarsson L, Sanderson MA, Troshin AG (2000) Design, theory and validation of a low mass 6-d.o.f. transducer. J Sound Vib 230:661–688
58. Jeong J, Baek S, Cho M (2012) Dynamic condensation in a damped system through rational selection of primary degrees of freedom. J Sound Vib 331(7):1655–1668. http://www.sciencedirect.com/science/article/pii/S0022460X11008959. Accessed 7 Mar 2014
59. Jetmundsen B, Bielawa RL, Flannelly WG (1988) Generalised frequency domain. J Am Helicopter Soc 33:55–64
60. Jianxin S, Gibbs BM (1998) Measurement of point moment mobility in the presence of non-zero cross mobility. Appl Acoust 54:9–26
61. Jianxin S, Mak CM (2002) Direct measurement of moment mobility and a moment excitation system. Appl Acoust 63:139–151
62. Kammer DC (1987) Test-analysis model development using an exact modal reduction. Int J Anal Exp Modal Anal 2(3):174–179
63. Kammer DC (1991) A hybrid approach to test analysis model development for large space structures. J Vib Acoust 113(3):325–332
64. Kanda H, Wei ML, Allemang RJ, Brown DL (1986) Structural dynamic modifications using mass additive technique. Presented at the 4th international modal analysis conference (IMAC IV), Los Angeles, pp 691–699
65. Kidder RL (1973) Reduction of structural frequency equations. AIAA J 11(6):892
66. Kim YY, Kang JH (1999) Strain-based rotational mode measurement in a beam. J Sound Vib 222:225–237
67. Koh YK, White RG (1996) Analysis and control of vibrational power transmission to machinery supporting structures subjected to a multi-excitation system, part III: vibrational power cancellation and control experiments. J Sound Vib 196:509–522
68. Kok R, Furlong C, Pryputniewicz J (2003) Application of MEMS accelerometers for modal analysis. Presented at the SEM annual conference & exposition on experimental and applied mechanics

69. Koutsovasilis P (2009) Model order reduction in structural mechanics: coupling the rigid and elastic multi body dynamics. PhD thesis, Technische Universität Dresden
70. Law SS, Li J, Ding Y (2011) Structural response reconstruction with transmissibility concept in frequency domain. Mech Syst Signal Process 25:952–968. https://doi.org/10.1016/j.ymssp.2010.10.001
71. Li S, Fladung W, Brown D, Bono R (1995) Indirect measurement of rotation/moment impedance functions (SAE Technical Paper No. 951271). SAE International, Warrendale
72. Lipkins J, Vandeurzen U (1987) The use of smoothing techniques for structural modification applications. In 12th international seminar on modal analysis, pp S1–S3
73. Liu W, Ewins DJ (1999) The importance assessment of RDOF in FRF coupling analysis. Presented at the 17th international modal analysis conference (IMAC XVII), Kissimmee, pp 1481–1487
74. Liu Z, Song X, Zhao Y, Cai L, Guo H, Ma J (2015) Stiffness identification of spindle-toolholder joint based on finite difference technique and residual compensation theory. Adv Mech Eng. https://doi.org/10.1155/2013/753631
75. Lofrano M (2003) Techniques to estimate the rotational frequency response functions in experimental modal analysis with applications to beam structures. PhD thesis. Escola de Engenharia de São Paulo, Universidade de São Paulo, São Paulo
76. Maenaka K (2008) MEMS inertial sensors and their applications. Presented at the 5th international conference on networked sensing systems, INSS 2008, pp 71–73
77. Maia NMM, Montalvão e Silva JM, He J, Lieven NAJ, Lin RM, Skingle GW, Todd W-M, Urgueira APV (1997) Theoretical and experimental modal analysis. Research Studies Press/Wiley, Taunton, Somerset/New York
78. Maia NMM, Silva JMM, Ribeiro AMR (1997) Some applications of coupling/uncoupling techniques in structural dynamics. Part 3: estimation of rotational FRFs using MUM. Presented at the 15th international modal analysis conference (IMAC XV), Orlando, pp 1453–1462
79. Maia NMM, Silva JMM, Ribeiro AMR, Silva PLCGC (1998) On the dynamic characterization of joints using uncoupling techniques. Presented at the 16th international modal analysis conference (IMAC XVI), Santa Barbara, pp 1132–1138
80. Maia NMM, Ribeiro AMR, Fontul M, Montalvão D, Sampaio RPC (2007) Using the detection and relative damage quantification indicator (DRQ) with transmissibility. KEM 347:455–460. ISSN: 1662–9795
81. Maia NMM, Urgueira APV, Almeida RAB (2011) Whys and wherefores of transmissibility. In: Beltran-Carbajal F (ed) Vibration analysis and control – new trends and developments. InTech
82. Maio DD, Copertaro E (2013) Experimental validation of a newly designed 6 degrees of freedom scanning laser head: application to three-dimensional beam structure. Rev Sci Instrum 84:121708
83. Maleci G, Young JW (1985) The effect of rotational degrees of freedom in system analysis (SA) via building block approach (BBA). Presented at the 3rd international modal analysis conference (IMAC III), Orlando, pp 1040–1045
84. Martarelli M (2001) Exploiting the laser Scanning facility for vibration measurements. PhD thesis. Imperial College of Science, Technology and Medicine London, London
85. Martinez DR, Miller AK, Came TG (1985) Combined experimental analytical modeling of shell/payload structures. Presented at the joint ASCE/ASME mechanics conference, AMD, 167, pp 167–194
86. Minnicino II M, Hopkins D (2004) Overview of reduction methods and their implementation into finite element local-to-global techniques. Technical report, U.S. Army Research Laboratory, Aberdeen Proving Ground, ARL-TR-3340
87. Montalvão D (2003) Determination of rotational terms of the dynamic response by means of modal analysis techniques de termos rotacionais da resposta dinâmica por técnicas de análise modal. Master thesis. Instituto Superior Técnico, UTL, Lisboa

88. Montalvão D, Ribeiro AMR, Maia NMM, Silva JMM (2004) Estimation of the rotational terms of the dynamic response matrix. Shock Vib 11:333–350
89. Morris HD, Peters RB (1980) A precision inertial angular vibration measuring system. Shock Vib Bull 50:1–10
90. Mottershead JE, Kyprianou A, Ouyang H (2003) Estimation of rotational frequency responses. Presented at the 5th international conference on damage assessment of structures (DAMAS 2003), Southampton, pp 157–165
91. Mottershead JE, Kyprianou A, Ouyang H (2005) Structural modification. Part 1: rotational receptances. J Sound Vib 284:249–265
92. Nasiri S (2013) A critical review of MEMS gyroscopes technology and commercialization status. InvenSense, Santa Clara, CA, USA
93. Ng'andu NA, Fox CHJ, Williams EJ (1993) Estimation of rotational degrees of freedom using curve and surface fitting. Presented at the 11th international modal analysis conference (IMAC XI), Kissimmee, pp 620–626
94. Ng'andu NA, Fox CHJ, Williams EJ (1995) On the estimation of rotational degrees of freedom using spline functions. Presented at the 13th international modal analysis conference (IMAC XIII), Nashville, pp 791–797
95. O'Callahan J (1989) A procedure for an improved reduced system (IRS) model. In: Proceedings of 7th international modal analysis conference, pp 17–21
96. O'Callahan JC, Chaur-Ming C (1984) Study of a structural modification procedure with three dimensional beam elements using a local eigenvalue modification procedure. Presented at the 2nd international modal analysis conference (IMAC II), Orlando, pp 945–952
97. O'Callahan J, Avitabile P, Riemer R (1989) System equivalent reduction expansion process (SEREP). In: Proceedings of 7th international modal analysis conference, pp 29–37
98. Oliver D (1988) Non-contact vibration imager for wide range of component sizes and displacement amplitudes. Presented at the 6th international modal analysis conference (IMAC VI), Kissimmee, pp 629–638
99. Paipetis SA, Vakakis AF (1985) A method of analysis for unidirectional vibration isolators with many degrees of freedom. J Sound Vib 98(1):13–23. https://doi.org/10.1016/0022-460X(85)90398-0. ISSN: 0022–460X
100. Paz M (1984) Dynamic condensation method. Am Inst Aeronaut Astronau J 22(5):724–727
101. Perrier S, Champoux Y, Drouet J-M (2013) Integrating biodynamic measurements in frequency-based substructuring to study human-structure interaction. In: Topics in experimental dynamic substructuring, vol 2, Proceedings of IMAC 31, a conference and exposition on structural dynamics
102. Petersson B (1987) On the use of giant magnetostrictive devices for moment excitation. J Sound Vib 116:191–194
103. Petersson BAT, Heckl M (1996) Concentrated excitation of structures. J Sound Vib 196: 295–321
104. Qu Z-Q (2004) Model reduction techniques: with applications in finite element analysis. Springer, London
105. Qu YC, Cheng L (1995) Rotational compliance measurement of a flexible plane structure. Presented at the 13th international modal analysis conference (IMAC XIII), Nashville, pp 948–954
106. Qu Z-Q, Fu Z-F (2000) An iterative method for dynamic condensation of structural matrices. Mech Syst Signal Process 14(4):667–678. http://linkinghub.elsevier.com/retrieve/pii/S0888327098913024. Accessed 11 Mar 2014
107. Qu YC, Cheng L, Rancourt D (1997) Rotational compliance measurements of a flexible plane structure using an attached beam-like tip, part 2: experimental study. J Vib Acoust 119:603
108. Ratcliffe MJ, Lieven NAJ (1996) Measuring rotations using a laser Doppler vibrometer. Presented at the 14th international modal analysis conference (IMAC XIV), Dearborn, pp 1002–1008
109. Ribeiro AMR (1998) On the generalization of the transmissibility concept. In: Proceedings of the NATO/ASI conference on modal analysis and testing, Sesimbra

110. Ribeiro AMR, Maia NMM, Silva JMM (2000) Response prediction from a reduced set of known responses using the transmissibility. In: Proceedings of IMAC XVIII. Presented at the 18th international modal analysis conference, San Antonio, pp 425–427. ISBN: 0-912053-67-4
111. Ribeiro AMR, Silva JMM, Maia NMM (2000) On the generalisation of the transmissibility concept. Mech Syst Signal Process 14:29–35
112. Ribeiro AMR, Fontul M, Silva JMM, Maia NMM (2002) Transmissibility matrix in harmonic and random processes. In: Proceedings of the international conference on structural dynamics modelling (SDM). Presented at the SDM, Funchal, Madeira
113. Ribeiro AMR, Fontul M, Maia NMM, Silva JMM (2005) Further developments on the transmissibility concept for multiple degree of freedom systems. Sci Bull "Politehnica" Univ Timisoara, Romania, Trans Mech 50(64):1224–6077
114. Rixen DJ, van der Valk PLC (2013) An impulse based substructuring approach for impact analysis and load case simulations. J Sound Vib 232:7174–7190
115. Rixen DJ, van der Valk PLC (2014) Impulse based substructuring as paradigm for coupled analysis of dynamic components. In: 6th European conference on computational fluid dynamics, Barcelona
116. Sainsbury MG (1976) (Experimental and theoretical techniques for the) Vibration analysis of damped complex structures. PhD. Imperial College London, University of London
117. Sampaio RPC, Maia NMM, Ribeiro AMR, Silva JM (1999) Damage detection using the transmissibility concept. In: Proceedings of ICSV 6. Presented at the sixth international congress on sound and vibration, Copenhagen
118. Sampaio RPC, Maia NMM, Ribeiro AMR, Silva JM (2001) Transmissibility techniques for damage detection. In: Proceedings of IMAC XIX. Presented at the 19th international modal analysis conference, Kissimmee, pp 1524–1527
119. Sanderson MA (1995) Direct measurement of moment mobility: part ii: an experimental study. J Sound Vib 179:685–696
120. Sanderson MA (1996) Vibration isolation :moments and rotations included. J Sound Vib 198:171–191
121. Sanderson MA, Fredö CR (1995) Direct measurement of moment mobility: part I: a theoretical study. J Sound Vib 179:669–684
122. Sattinger SS (1980) A method for experimentally determining rotational mobilities of structures. Shock Vib Bull 50:17–28
123. Silva JMM (1978) Measurement and applications of structural mobility data for the vibration analysis of complex structures. PhD thesis. Imperial College London, University of London, London
124. Silva TAN, Maia NMM (2015) Estimation of rotational frequency response functions. Presented at the 33rd international modal analysis conference (IMAC XXXIII) (ed: Allemang RJ), vol 6. Springer International Publishing, pp 35–48
125. Silva JMM, Maia NMM, Ribeiro AMR (2001) Indirect estimation of rotational frequency-response-functions. Presented at the 19th international modal analysis conference (IMAC XIX), Kissimmee, pp 1535–1542
126. Silva TAN, Maia NMM, Barbosa JI (2012) A model updating technique based on FRFs for damped structures. In: Sas P (ed) ISMA2012 international conference on noise and vibration engineering. Katholieke Universiteit Leuven, Leuven
127. Skingle GW (1989) Structural dynamic modification using experimental data. PhD thesis. Imperial College of Science, Technology and Medicine. University of London, London
128. Smiley RG, Brinkman BA (1984) Rotational degrees of freedom in structural modification. Presented at the 2nd international modal analysis conference (IMAC II), Orlando, pp 937–939
129. Smith JE (1969) Measurement of the total structural mobility matrix. Shock Vib Bull 40: 51–84

130. Sommer III HJ, Erickson MJ, Trethewey MW (1994) Single-beam laser vibrometer for simultaneous measurement of translation, pitch and roll with neural network calibration. Presented at the 12th international modal analysis conference (IMAC XII), Honolulu, pp 1196–1201
131. Stanbridge AB, Ewins DJ (1994) Measurement of translational and angular vibration using a scanning laser Doppler vibrometer. Presented at the 1st international conference on vibration measurements by laser techniques: advances and applications, Ancona, pp 37–47
132. Stanbridge AB, Ewins DJ (1996) Measurement of total vibration at a point using a conical-scanning LDV. Presented at the second international conference on vibration measurements by laser techniques: advances and applications, Ancona, pp 126–136
133. Stebbins A, Blough JR, Shelley SR, Brown DL (1996) Measuring and including the effects of moments and rotations for the accurate modeling of transmitted forces. Presented at the 14th international modal analysis conference (IMAC XIV), pp 429–436
134. Silva TAN, Almeida RAB, Urgueira APV (2018) On the use of measured rotational responses in structural dynamic analysis. J Phys: Conf Series 1106, conference 1
135. Tao J, Mak CM (2007) Error due to two-force excitation in moment mobility measurement. Appl Acoust 68:1494–1501
136. Titterton DH, Weston JL (2004) Strapdown inertial navigation technology (chapter 4.3.2). Institution of Electrical Engineers, Stevenage
137. Trethewey MW, Sommer III HJ (2002) Application of a pure moment exciter for measurement of moment-rotational dof frequency response functions. Presented at the 20th international modal analysis conference (IMAC XX), Los Angeles, pp 1153–1158
138. Trethewey MW, Sommer III HJ (2002) Measurement of rotational dof frequency response functions with pure moment excitation. Presented at the international conference on structural dynamics modelling, Funchal, Madeira, pp 81–88
139. Trethewey MW, Sommer HJ III, Cafeo JA (1993) A dual beam laser vibrometer for measurement of dynamic structural rotations and displacements. J Sound Vib 164:67–84
140. Urgueira APV (1989) Dynamic analysis of coupled structures using experimental data. PhD thesis. Imperial College of Science, Technology and Medicine. University of London, London
141. Urgueira APV, Ewins DJ (1989) A refined modal coupling technique for including residual effects of out-of-range modes. Presented at the 7th international modal analysis conference (IMAC VII), Las Vegas
142. Urgueira A, Venâncio N, Riscado P, Almeida RAB, Silva T (2018) Experimental determination of rigid body properties: an evaluation on the use of piezoelectric or MEMS tri-axial accelerometers. MATEC web conference, 148
143. Vakakis AF (1985) Dynamic analysis of a unidirectional periodic isolator, consisting of identical masses and intermediate distributed resilient blocks. J Sound Vib 103(1):25–33. https://doi.org/10.1016/0022-460X(85)90245-7. ISSN: 0022–460X
144. Vakakis AF, Paipetis SA (1985) Transient response of unidirectional vibration isolators with many degrees of freedom. J Sound Vib 99(4):557–562. https://doi.org/10.1016/0022-460X(85)90540-1. ISSN: 0022–460X
145. Vakakis AF, Paipetis SA (1986) The effect of a viscously damped dynamic absorber on a linear multi-degree-of-freedom system. J Sound Vib 105(1):49–60. https://doi.org/10.1016/0022-460X(86)90219-1. ISSN: 0022–460X
146. Varoto P, McConnell KG (1998) Single point vs multi point acceleration transmissibility concepts in vibration testing. Presented at the 12th international modal analysis conference (IMAC XII), Santa Barbara, pp 83–90
147. Varoto PS, Lofrano M, Cicogna TR, Oliveira LPR, McConnell KG (2006) Moment mobility FRF measurement techniques. Presented at the IMAC-XXIV conference and exposition on structural dynamics, St Louis, pp 1298–1304
148. Wang DH, Yuan G (2011) A six-degree-of-freedom acceleration sensing method based on six coplanar single-axis accelerometers. IEEE Trans Instrum Meas 60:1433–1442

149. Wang J, Law SS, Yang QS (2014) Sensor placement method for dynamic response reconstruction. J Sound Vib 333:2469–2482. https://doi.org/10.1016/j.jsv.2013.12.014
150. Wei ML, Zhang Q (1989) Correction of modal scaling factors using mass perturbation technique. Presented at the 7th international modal analysis conference (IMAC VII), Las Vegas, pp 830–835
151. Williams EJ, Green JS (1990) A spatial curve fitting technique for estimation of rotational degrees of freedom. Presented at the 8th international modal analysis conference (IMAC VIII), Kissimmee, pp 376–381
152. Xia Y, Lin R-M (2004) Improvement on the iterated IRS method for structural eigensolutions. J Sound Vib 270(4,5):713–727. http://www.sciencedirect.com/science/article/pii/S0022460X03001883
153. Yang K-T, Park Y (1993) Joint structural parameter identification using a subset of frequency response function measurements. Mech Syst Signal Process 7:509–530
154. Yasuda C, Riehle PJ, Brown DL, Allemang RJ (1984) An estimation method for rotational degrees of freedom using a mass additive technique. Presented at the 2nd international modal analysis conference (IMAC II), Orlando, pp 877–886
155. Yazdi N, Ayazi F, Najafi K (1998) Micromachined inertial sensors. Proc IEEE 86:1640–1659
156. Yeh Y, Cummins HZ (1964) Localized fluid flow measurements with AN He-Ne laser spectrometer. Appl Phys Lett 4:176–178
157. Yoshimura T, Hosoya N (2000) FRF estimation on rotational dofs by rigid block attachment approach. Presented at the international conference on noise and vibration engineering (ISMA 25), Leuven
158. Yoshimura T, Hosoya N (2002) FRF measurement of rotational dofs by T-block approach (Improvement of accuracy for random noise and application to a Car Body). Presented at the international conference on noise and vibration engineering (ISMA 2002), Leuven
159. Ziaei-Rad S, Martarelli M, Ewins DJ (2000) Measuring Rdofs using laser Doppler vibrometer. Presented at the international conference on noise and vibration engineering (ISMA 25), Leuven
160. Maia NMM, Neves MM, Silva, TAN (2018) Transmissibility versus damage detection. Proceedings of international conference on noise and vibration engineering (ISMA 2018), Leuven, Belgium

Linear Modal Substructuring with Nonlinear Connections

22

Peter Avitabile

Contents

Abstract

Large finite element models predominate the structural dynamic community, and inclusion of discrete nonlinear connections further complicates the models. The need for highly reduced order, computationally efficient nonlinear models is the focus of this work. System models generated from highly reduced

P. Avitabile (✉)
Structural Dynamics and Acoustic Systems Laboratory, University of Massachusetts Lowell, Lowell, MA, USA
e-mail: peter_avitabile@uml.edu

R. Allemang, P. Avitabile (eds.), *Handbook of Experimental Structural Dynamics*,
https://doi.org/10.1007/978-1-4614-4547-0_34

order components interconnected with nonlinear connection elements to predict accurate system response with efficient approaches is identified. In addition, expansion from the reduced order model to the full space of the original finite element model is shown with no degradation in the predicted full-field response for both displacement and strain for nonlinear dynamic environments.

Keywords

Nonlinear response · Nonlinear connection · Nonlinear system models · Reduced order model · Full-field expansion

Nomenclature

Matrix

[M]	Analytical mass matrix
[K]	Analytical stiffness matrix
[U]	Analytical modal matrix
$\left[\overline{M}\right]$	Diagonal modal mass matrix
$\left[\overline{K}\right]$	Diagonal modal stiffness matrix
[T]	Transformation matrix
[E]	Experimental modal vectors
[I]	Identity matrix
Ω^2	Diagonal matrix of ω^2 values

Vector

{X}	Displacement

Subscript

n	Full set of finite element DOF
a	Tested set of experimental DOF
d	Deleted (omitted) set of DOF
G	Guyan
U	SEREP

Superscript

T	Transpose
g	Generalized inverse
−1	Standard inverse
A	Component A
B	Component B

1 Introduction

The structural dynamics community routinely develops extremely large finite element models to address complicated structural systems that are used for dynamic response predictions. Many of these models are sufficiently described by linear models, but there is a large category of models that contain a variety of different

nonlinear characteristics. A sub-class of these models contains components that are connected with nonlinear coupling elements of different types (bilinear, slip-stick, gap, etc.). While the components themselves are relatively linear compared to the connection elements, the overall model becomes nonlinear, and the solution becomes more involved and requires substantial computational resources. In addition, the connection elements may have a variety of different states depending on the pressure, preload, temperature, etc. which then further complicates the analysis because there may be a variety of different cases that need to be studied and evaluated in order to determine the worst case scenario for response and strain in the system for the various dynamic events of concern.

The use of highly accurate, reduced order component models interconnected with nonlinear connection elements is very desirable in order to identify system response characteristics in an efficient manner. Further the components may also have subcomponents that are dynamically active and need to be included in the overall system response. This may be due to the need to include the subcomponent because there is a significant contribution to the system response or due to the need to have an accurate description of the subcomponent loads for detailed analysis on the subcomponent. In any event, the need for efficient reduced order models is clear. Several different approaches and techniques have been developed over the course of several years that are described herein and are useful for these applications.

The first steps in this work were done to develop linear reduced order models to form system models. Van Zandt [1, 2] developed linear reduced order component and system models to show the accuracy with extremely small order models; these were more traditional reduced order models. Butland [3–5] extended this work specifically for a Craig-Bampton component synthesis model with both analytical and experimental results. At the same time these reduced order time domain approaches were developed, there were also companion frequency domain techniques by Wirkkala [6] and Nicgorski [7–10] that complimented the time domain approaches and included both analytical and experimental approaches. In addition to the reduced order models and prediction of highly accurate time response, Chipman [11–13] extended this work in an important regard which addressed the expansion of real-time operating data collected at very small sets of measured points to a much larger space through the use of orthogonal projection functions. Initially, Chipman's work was just intended to address better visualization of real-time operating data, but then this was quickly adapted by Pingle [14–17] in order to expand the highly reduced order model to predict full field dynamic response and dynamic strain for the large set of finite element degrees of freedom. There were several important papers published by Baqersad [18–21] which clearly tied all the previous work together with linear model representations for industrial wind turbine blades where many different response scenarios were considered ultimately including a wind turbine in a rotating condition where a very small set of measurement sensors were able to adequately capture the dynamic response and dynamic strain and validated with traditional foil strain gauge measurements. Baqersad's work clearly showed the

feasibility and robustness of the approach of using a highly reduced order model for integration with measured data that is eventually used to predict full field dynamic response and dynamic strain. This starting body of work addressed linear response models for both component and system model representations and included both analytical and experimental models for these predictions.

Nonlinear models extended the concept using linear modal component and system model work as the basis for predicting system models where the connections between components are made up from nonlinear connection elements. Two approaches were taken. One utilized a physical model approach and the other utilized a modal model approach, but both provided very reduced models which makes all of the nonlinear response model computation very efficient. Thibault [22, 23] worked with highly reduced physical models that were used to generate system models with nonlinear connections. Marinone [24, 25] utilized a modal superposition approach coupled with a structural dynamic modification/system modeling approach to couple components together. The approach of structural modification relies on the ability to identify an appropriate set of modes to adequately span the space of the solution. Utilizing concepts from structural dynamic modification [26], both Thibault and Marinone developed an approach to identify the necessary modes for the analysis. Both Thibault and Marinone achieved the same accuracy in the different approaches and with significant computational savings. Thibault's approach is better suited for analytical modeling scenarios, whereas Marinone's approach works equally well with analytical and experimental data. The work performed was mainly done at the reduced order system model level. Following this work, Nonis [27–29] presented an expansion methodology that utilized uncoupled component modes to determine full field mode shapes for assembled systems. This approach [30] was adopted for the nonlinear response expansion to the finite element degrees of freedom.

Harvie [31–33] then further extended this approach to include not only full field nonlinear dynamic displacement but also full field dynamic strain to complete the picture. That work addressed all the previous work and extended the work to show that highly reduced order component models interconnected with nonlinear connections could predict both full field dynamic displacement and dynamic strain with a high degree of accuracy with extremely efficient computational models.

Obando [34–37] then directed the focus to subcomponents embedded in components used to form nonlinear system models. This work clearly showed that important subcomponent items that have significant dynamic response can be embedded into the complete system model representation without the need for specific degrees of freedom to be included and that the expansion process retained the necessary information to expand proper dynamic response information for the subcomponent in the full space.

The theory from all this work will be summarized followed by a few of the models that were developed to illustrate the techniques deployed and results obtained. The referenced papers contain many more cases evaluated as part of the work and provide further substantiation of the results shown here.

2 Theory

The theory is well documented in all the referenced papers, and only basic summary equations are presented to summarize all the work done. These mainly deal with model reduction and model expansion along with structural dynamic modification and system modeling concepts that are used throughout all this work.

2.1 Equations of Motion and Modal Space Representation

The general equation of motion for a multiple degree of freedom system in matrix form is

$$[M_1]\{\ddot{x}\} + [C_1]\{\dot{x}\} + [K_1]\{x\} = \{F(t)\} \tag{1}$$

The eigensolution can be performed to obtain the frequencies and the modal matrix. The physical system can be transformed to modal space using the modal matrix as

$$[U_1]^T[M_1][U_1]\{\ddot{p}_1\} + [U_1]^T[C_1][U_1]\{\dot{p}_1\} + [U_1]^T[K_1][U_1]\{p_1\} = [U_1]^T\{F(t)\} \tag{2}$$

which can be written as diagonal matrices of modal mass, modal damping, and modal stiffness as typically done and shown as

$$\begin{bmatrix} \ddots & & \\ & \overline{M}_1 & \\ & & \ddots \end{bmatrix}\{\ddot{p}_1\} + \begin{bmatrix} \ddots & & \\ & \overline{C}_1 & \\ & & \ddots \end{bmatrix}\{\dot{p}_1\} + \begin{bmatrix} \ddots & & \\ & \overline{K}_1 & \\ & & \ddots \end{bmatrix}\{p_1\} = \left\{\overline{F}(t)\right\} \tag{3}$$

2.2 Model Reduction and Model Expansion

The main concept behind model reduction and expansion involves the mapping between a large model containing 'n' DOF and a reduced model containing a limited 'a' set of DOF. The general transformation between the full model and reduced DOF is given as

$$\{x_n\} = \begin{Bmatrix} x_a \\ x_d \end{Bmatrix} = [T]\{x_a\} \tag{4}$$

where the full 'n' space model is made up of 'a' master DOF and 'd' deleted DOF. The transformation matrix, [T], contains the appropriate mapping information to relate the full and reduced models. By employing energy conservation principles,

the mass and stiffness of the reduced 'a' DOF can be calculated using the transformation matrix with

$$[M_a] = [T]^T [M_n] [T] \quad \text{and} \quad [K_a] = [T]^T [K_n] [T] \tag{5}$$

These reduced mass and stiffness matrices must preserve the full space model characteristics in order for them to be useful. Many model reduction schemes such as Guyan [38], dynamic [39], and IRS [40] all provide good reduced models but typically contain some distortion. Other model reduction schemes such as the system equivalent reduction expansion process (SEREP) [41], hybrid [42], and KM_AMI [43] all provide an exact representation of the full space model for the modes included in the reduced model approximation. For the work presented here, SEREP was used for the development of the reduced order model. The SEREP transformation matrix is written as

$$[T_U] = [U_n] [U_a]^g \tag{6}$$

The SEREP reduction is generally used because of its unique characteristic in that the full space mass and stiffness matrices (which are generally very large) are not needed in order to form the reduced order mass and stiffness matrices; this is not true of any other reduction scheme and provides significant benefits. The reduced matrices are given as

$$\begin{aligned} [M_a] &= [T_U]^T [M_n] [T_U] = \left[U_a{}^g\right]^T \left[U_a{}^g\right] \\ [K_a] &= [T_U]^T [K_n] [T_U] = \left[U_a{}^g\right]^T \left[\Omega^2\right] \left[U_a{}^g\right] \end{aligned} \tag{7}$$

The reduced mass and stiffness matrices are of size 'a,' but rank 'm.' Therefore when the number of retained modes is less than the number of retained DOF ($m < a$), the reduced matrices will be rank deficient. Care must be taken when dealing with the rank-deficient matrices. These are instances when KM_AMI would be used to form full ranked matrices. For the models here, full rank was maintained using $a = m$ for all cases studied.

2.3 Structural Dynamic Modification and System Modeling

For the modeling approaches used in this work, the identification of modes needed to address the structural dynamic response is needed. As the system response progresses, the different nonlinear states are tracked, and the modes needed to identify the response will change depending on the particular linear state of the system. The structural dynamic modification and system modeling procedures are used to change from one linear state to the next linear state. The modes of each component are used in linear combinations to form each of the modified states. The

physical system equations describing the coupling of one component to another component can be written as

$$\left[\begin{bmatrix}[M_n{}^A] & \\ & [M_n{}^B]\end{bmatrix} + [\Delta M_{12}]\right]\begin{Bmatrix}\ddot{x}_n^A \\ \ddot{x}_n^B\end{Bmatrix} + \left[\begin{bmatrix}[K_n{}^A] & \\ & [K_n{}^B]\end{bmatrix} + [\Delta K_{12}]\right]\begin{Bmatrix}x_n{}^A \\ x_n{}^B\end{Bmatrix} = \begin{Bmatrix}f_n{}^A \\ f_n{}^B\end{Bmatrix} \tag{8}$$

These components at the full space of the finite element model are reduced to form more efficient representation of the system components which is the work addressed by Thibault. These are then written in reduced space as

$$\left[\begin{bmatrix}[M_a{}^A] & \\ & [M_a{}^B]\end{bmatrix} + [\Delta M_{12}]\right]\begin{Bmatrix}\ddot{x}_a^A \\ \ddot{x}_a^B\end{Bmatrix} + \left[\begin{bmatrix}[K_a{}^A] & \\ & [K_a{}^B]\end{bmatrix} + [\Delta K_{12}]\right]\begin{Bmatrix}x_a{}^A \\ x_a{}^B\end{Bmatrix} = \begin{Bmatrix}f_a{}^A \\ f_a{}^B\end{Bmatrix} \tag{9}$$

Marinone developed essentially the same set of equations but from a modal space perspective and utilizes structural dynamic modification for the identification of the change of state for the system as different nonlinear characteristics occur. The basic equation describing the change in state is

$$\left[\begin{bmatrix}\ddots & & \\ & \overline{M}_1 & \\ & & \ddots\end{bmatrix} + \left[\Delta\overline{M}_{12}\right]\right]\{\ddot{p}_1\} + \left[\begin{bmatrix}\ddots & & \\ & \overline{K}_1 & \\ & & \ddots\end{bmatrix} + \left[\Delta\overline{K}_{12}\right]\right]\{p_1\} = \{0\} \tag{10}$$

where

$$\begin{aligned}\left[\Delta\overline{M}_{12}\right] &= [U_1]^T[\Delta M_{12}][U_1] \\ \left[\Delta\overline{K}_{12}\right] &= [U_1]^T[\Delta K_{12}][U_1]\end{aligned} \tag{11}$$

2.4 Mode Contribution Matrix

The number of modes necessary for the dynamic response is determined from the mode contribution matrix developed by Thibault given as

$$[U_{12}] = [U_1]^T[M_2][U_2] \tag{12}$$

The mode contribution matrix is used to determine which original mode shapes are necessary for the accurate reconstruction of each of the desired final mode shapes. If a dynamic response involves multiple system states, then the $[U_{12}]$ matrix must be computed for each configuration to determine the number of original system modes to appropriately span the space of the solution and avoid truncation. If a component mode has a high value in the contribution matrix for a certain desired system mode and that component is not included in the reduction or modes retained, then the system mode will be in error and is said to be truncated. Conversely, component modes with low contribution values for the desired system modes do not participate significantly in the system modes and therefore are not necessary to include in the solution. The mode contribution matrix is important because it can identify the minimal set of component modes that are necessary to include in a system model; retaining fewer modes in a reduced model can result in higher computational savings.

2.5 Response of Linear Components Interconnected with Nonlinear Connection Elements

The basic schematic describing Thibault's equivalent reduced model technique (ERMT) and Marinone's modal modification response technique (MMRT) to calculate the nonlinear response of the system is shown in Fig. 1; the schematic overviews both techniques. In both techniques there needs to be a clear identification of the modes needed to describe the system response in all the possible different linear states (as is typically done for any structural dynamic response model). The direct integration of equation of motion is then performed using Newmark, for instance. However, the computation time is dramatically reduced using either the reduced order models (ERMT) or mode superposition approach (MMRT). At each time step, the state of the system is checked, and if there is any change in the linear state of the system, then the model is updated to reflect the change and then the integration process is continued; if there is no change, then the integration process continues.

2.6 Expansion of Transient Time Response from Reduced Order System Models

The expansion from the reduced model to the full space model (using SEREP) is

$$\{x_n\} = \begin{Bmatrix} x_a \\ x_d \end{Bmatrix} = [U_n]\left[U_a^g\right]\{x_a\} \tag{13}$$

This equation is used for the expansion and generally is used for vector expansion. However, Chipman and Pingle have used this for the expansion of real-

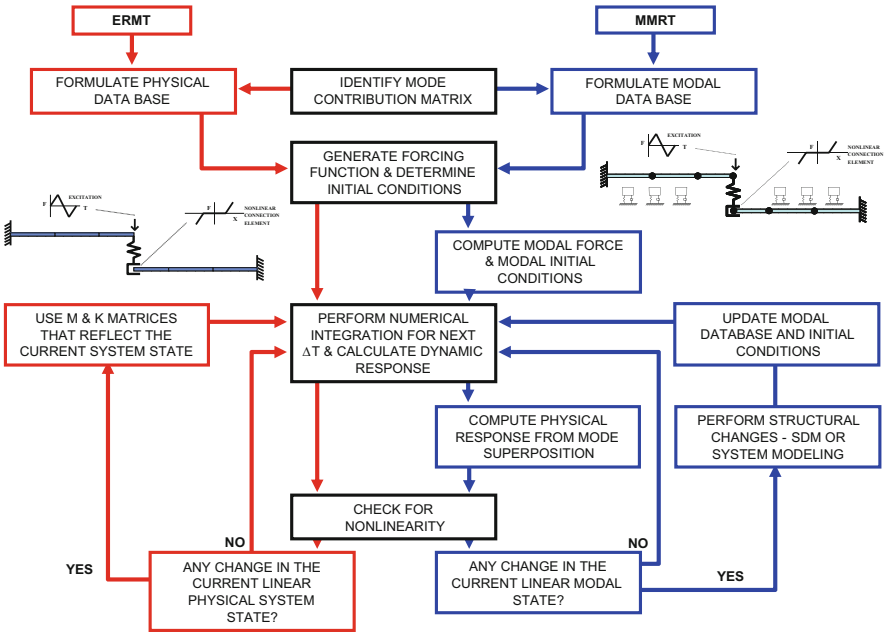

Fig. 1 Overview schematic of nonlinear response using ERMT and MMRT

time operating data for individual components. The premise being that the modes that are the primary contributors for the modal response are the same modes to use in the expansion of real-time operating data (made up from those same modal contributions). Nonis further showed that any system model that is formed from component modal representations can be expanded from reduced space to full space using that same set of uncoupled modes used to form the system model. Harvie further showed that this could be extended from linear system models to nonlinear system model response under the same premise that the modes used to form the nonlinear response are made up from various linear states. Therefore, the expansion also works for nonlinear system response when the system is comprised of linear components interconnected with nonlinear connection elements (using the uncoupled component modes from the expansion process that spans the space for all of the different nonlinear states that exist). Harvie also extended the full field expansion to identify the full field dynamic strain in conjunction with the finite element model using the full field displacements obtained at each time step.

Obando then extended the reduction and expansion process to include subcomponent (or ancillary) information embedded into the individual components; this might be a very dynamically active subcomponent (such as a circuit board, for instance) which may need significant finite element fidelity to characterize the subcomponent but then makes the component model extremely large in terms of overall model description but is critical to the overall system response.

There are several example models that have been developed for the illustration of the techniques described. In order to evaluate the results, there are two correlation tools used in the evaluations: the MAC and TRAC. The modal assurance criteria (MAC) is used to compare two deformation shapes to identify the degree of correlation; MAC values approaching 1.0 indicate very good correlation, whereas values approaching 0.0 show no degree of correlation. The test response assurance criteria (TRAC) is analogous to the MAC and is used to compare two time response traces at a particular point. The MAC and TRAC are given as

$$\mathrm{MAC}_{\mathrm{RA}} = \frac{\left[\{x_{n1}\}^{\mathrm{T}} \{x_{n2}\}\right]^2}{\left[\{x_{n1}\}^{\mathrm{T}} \{x_{n1}\}\right]\left[\{x_{n2}\}^{\mathrm{T}} \{x_{n2}\}\right]}$$

and (14)

$$\mathrm{TRAC} = \frac{\left[\{x_{n2}\}^{\mathrm{T}} \{x_{n1}\}\right]^2}{\left[\{x_{n2}\}^{\mathrm{T}} \{x_{n2}\}\right]\left[\{x_{n1}\}^{\mathrm{T}} \{x_{n1}\}\right]}$$

Note that the $\mathrm{MAC}_{\mathrm{RA}}$ is used to calculate the correlation between real-valued vectors and no complex notation is needed. In this work, the MAC is calculated between the deformation of the full space reference solution and estimated solution obtained from the reduced order model at each time step. Similarly the TRAC is used to compare the time response from the reduced order model to the time response from the full space finite element solution at each degree of freedom.

3 Test Cases

There are several test cases that were developed to illustrate the techniques identified. The earlier linear reduced order model cases are not presented here; essentially the nonlinear models presented here can all be reduced to simpler linear models. The first cases illustrate the results obtained from the approaches first developed by Thibault and Marinone. These are followed by Harvie's work which addresses nonlinear response and expansion to full space for dynamic response and dynamic strain at full field. The last cases are intended to show Obando's embedded subcomponent work.

3.1 Nonlinear Response Prediction (Thibault and Marinone)

Due to the complexity of the nonlinearities introduced into actual structural systems, a representative structure was fabricated to demonstrate the proposed technique. The laboratory structure is comprised of two cantilevered aluminum beams that are mounted to a common frame and base plate, as shown in Fig. 2. This structure was designed to be a simplified representation of a typical structural system that

Property	Beam A	Beam B
Length (in)	18	16
Width (in)	2	4
Thickness (in)	0.123	0.123
# of Elements	72	64
# of Nodes	73	65
# of DOF	146	130
Node Spacing (in)	0.25	0.25
Material	Aluminum	Aluminum
Density (lb/in^3)	0.098	0.098
Young's Modulus (Msi)	10	10

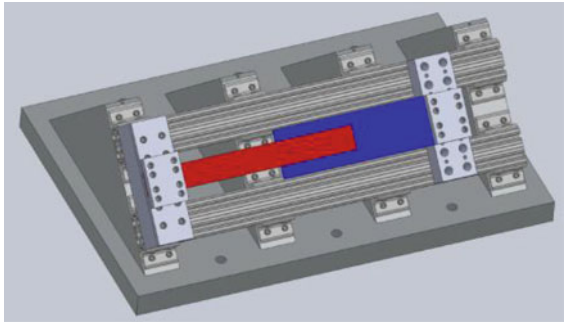

Mode #	Frequency (Hz)	
	Beam A	Beam B
1	12.915	22.625
2	84.119	141.561
3	252.339	396.604
4	519.587	776.916
5	806.163	1284.714
6	1256.551	1918.277
7	1682.965	2678.333
8	2201.360	3563.885
9	2755.524	4572.697
10	3510.011	5707.037

Fig. 2 Laboratory structure representation of contact nonlinearities (middle) with beam model characteristics (left) for Beam A and Beam B and component frequencies (right)

contains various contact and component interconnection features, such that the forced nonlinear response of the system would have similarities to real-world structures of interest.

Beam A is shown in red and Beam B is shown in blue to distinguish the two components apart from one another. Two planar beam element models were generated using MATLAB. Each beam model is clamped for 3 in of their length using translational and rotational springs to replicate the cantilevered boundary condition that is applied in the actual test fixture. Figure 2 also shows the individual beam model information (left) – dimensions, material properties, and modeling characteristics of the beam component models. Also shown is the resulting component frequencies (right) for Beam A and Beam B uncoupled from each other for the first ten bending modes of each beam component with bending about the weaker axis; torsion was not considered for this model.

The cantilevered beam component models developed were assembled into common matrix space as a linear system, which was discussed previously and is shown in Fig. 3. Note that the FEM nodes for 3 in of each beam are clamped for the cantilevered boundary condition that was applied using 10E6 lb/in translational springs and 10E6 lb-in/rad rotational springs. This was performed to simulate the boundary condition that exists on the actual test fixture, where the beams are clamped between a top plate and a base block. Translational and rotational springs were used to allow for fine-tuning of the models in order to account for possible flexibility of the test fixture if this was a concern for the cases where test data is introduced.

The full space linear component models were then reduced down to ‘a’ space using SEREP where the ADOF were selected to correspond with transducer locations on the actual tested structure. SEREP reduction was performed for the case where the number of ADOF and modes retained in the reduced order models are equal. Therefore, the selection of ADOF does not affect the reduced model characteristics. In addition, the DOF at potential contact locations was retained in the reduction process in order to formulate system models for possible contact configurations. The full space and reduced space component models are shown in Fig. 4, where the red points indicate the ADOF retained in the reduced order models and the black arrow denotes the force pulse input location, which is at DOF 105 of Beam A. Figure 4 also shows the ADOF and modes retained in the reduced

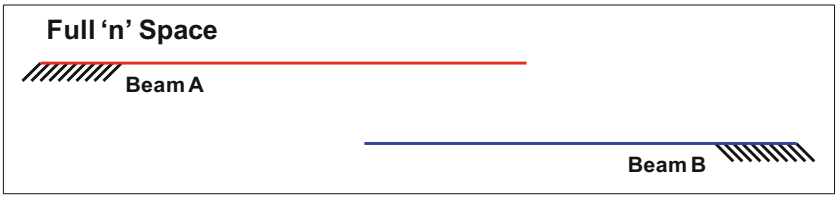

Fig. 3 Schematic of full space linear beam models

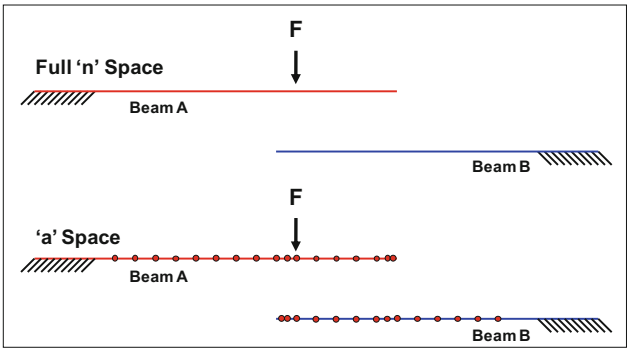

Reduced Model	# of DOF	Retained Modes	Retained DOF
Beam A 'a' Space	17	1-17	33,41,49,57,65,73,81,89,97,101, 105,113,121,129,137,141,143
Beam B 'a' Space	14	1-14	149,151,155,163,171,179,187, 191,195,203,211,219,227,235

Fig. 4 Full space and reduced models with force pulse input location

component models; note that only translational DOF were retained in the reduced component models.

An analytical force pulse was designed to be frequency band-limited, exciting modes up to 1000 Hz while minimally exciting higher-order modes. The force pulse was applied at DOF 105 of Beam A for all analytical cases studied. The force pulse input DOF was selected to avoid being located at the node of a mode, where minimal response of a particular mode could result. When computing the system response to the input force pulse using the Newmark direct integration method, the initial conditions defined at time $t = 0$ were zero initial displacement and zero initial velocity. The time step (Δt) used was 0.0001 s. An additional parameter that was used in the direct integration process was damping. For the analytical models developed in this work, the modal damping ζ, for all component modes as well as for all system modes, was assumed to be 1% of critical damping.

Although many cases were studied, the case described here consists of Beam A coming into contact with Beam B in three different configurations at two possible contact locations once a specified gap distance is closed between Beams A and B, which is 0.05 in for this case. Each system is a potential configuration of the two components depending on the relative displacements of the two beams where no contact is also a possible configuration. The spring element used at the contact locations was a 1000 lb/in translational spring and can be considered to be a relatively hard contact for the system studied in this work. The spring stiffness is applied to the full space physical model for each system configuration, and an

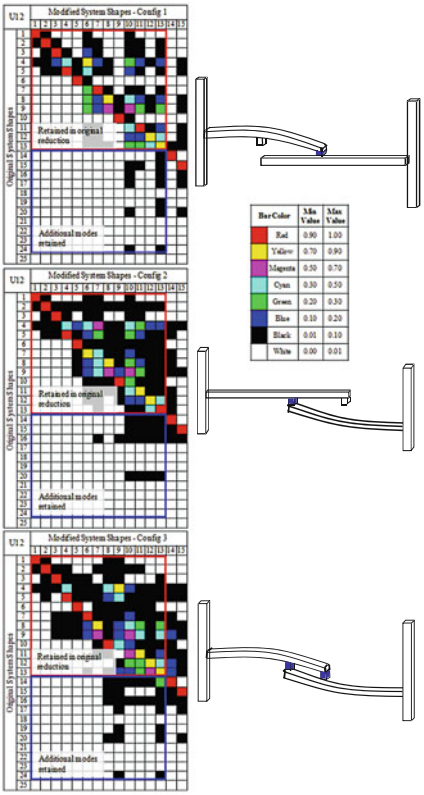

	Frequency (Hz)	Frequency (Hz)	Frequency (Hz)
	Modified System - Hard Contacts		
Mode #	Config. 1	Config. 2	Config. 3
1	21.254	15.496	36.217
2	67.744	69.517	113.686
3	127.044	119.785	228.570
4	236.020	234.136	312.678
5	338.309	325.850	339.402
6	424.257	467.087	504.557
7	532.039	527.491	532.406
8	786.594	786.040	790.327
9	809.246	828.779	833.736
10	1256.688	1257.170	1257.216
11	1294.656	1290.027	1300.104
12	1682.968	1686.002	1686.011
13	1918.723	1920.049	1920.475
14	2201.525	2202.671	2202.844
15	2683.897	2678.847	2684.381
16	2755.784	2756.010	2756.282
17	3510.464	3511.344	3511.794
18	3564.138	3563.976	3564.234
19	3948.794	3948.545	3948.795
20	4575.186	4572.697	4575.187

Fig. 5 Mode contribution and frequencies of each configuration possibility

eigensolution is computed using the modified system mass and stiffness matrices. The contact for configuration 1 occurs between DOF 141 of Beam A and DOF 191 of Beam B. The contact for configuration 2 occurs between DOF 101 of Beam A and DOF 151 of Beam B. The contact for configuration 3 occurs when both contacts for configurations 1 and 2 are closed simultaneously. The natural frequencies of the modified system configurations as well as for the unmodified components are listed in Fig. 5 along with the mode contribution matrices that are used to identify the unmodified component modes that contribute in the modified system modes for system configurations 1, 2, and 3, respectively. The mode contributions are computed using full space models such that modal truncation is not of concern. The various box colors indicate the amount that each unmodified component mode contributes in a particular modified system mode; the actual contribution ranges for each color are shown.

Although each mode contribution matrix is different, the matrices show that all potential system modes are formed from the original modal database, although the contribution from each mode changes depending on the configuration. As a result,

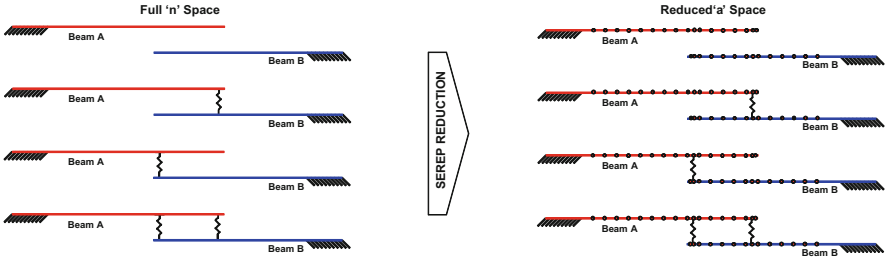

Fig. 6 Full space 'n' and reduced 'a' space models for two beams with multiple contacts

the transformation matrix that contains the original component mode shapes has the necessary information to expand any of the possible states of the system. In order to expand time response data, however, the transformation matrix used must contain an appropriate selection of modes that are needed for accurately forming the potential system modes.

For this case, three potential modified system configurations exist, which results in three separate mode contribution matrices. The 'a' space reduced model developed for this case retains 17 DOF and modes 1 to 17 of Beam A and 14 DOF and modes 1 to 14 of Beam B. The models developed for this case are shown in Fig. 6 for the full space and reduced 'a' space models. To confirm that the 31 DOF 'a' space models are sufficient for this case, the system response at DOF 141 is plotted in the time and frequency domain for the reduced model with comparison to the full space solution in Fig. 7.

The results obtained when using the 31 DOF 'a' space model can be observed to correlate very well with the full space solution in Fig. 7. Two different time correlation tools MAC and TRAC are used to quantify the similarity of the reduced model results with the full space solution. Both plots are shown in Fig. 7 where the y-axis scale for the MAC and TRAC plots is 0.999–1.0 so that the slight differences between the full space and reduced space solutions could be observed. The solution time for each model is listed with the average MAC and TRAC values in Table 1 to show the significant decrease in computation time and highly accurate results when the reduced models are used.

The solution obtained using the 'a' space model was then expanded to 'n' space using the linear transformation matrix developed in Fig. 6. Figure 8 shows the MAC and TRAC plots over the first 0.2 s (note that the TRAC is now calculated for all 276 DOF). The y-axis scale for the MAC and TRAC plots is 0.9–1.0 so that the slight differences between the full space and reduced space solutions could be observed. The 276 DOF 'a' space expanded model for the two-beam system with multiple hard contacts produces very good results as well.

The solution times for all models are listed with the average MAC and TRAC values in Table 1 to show the significant decrease in computation time, and highly accurate results are obtained when the reduced models are used. The favorable MAC and TRAC results in Table 1 show that the 31 DOF 'a' space model is sufficient

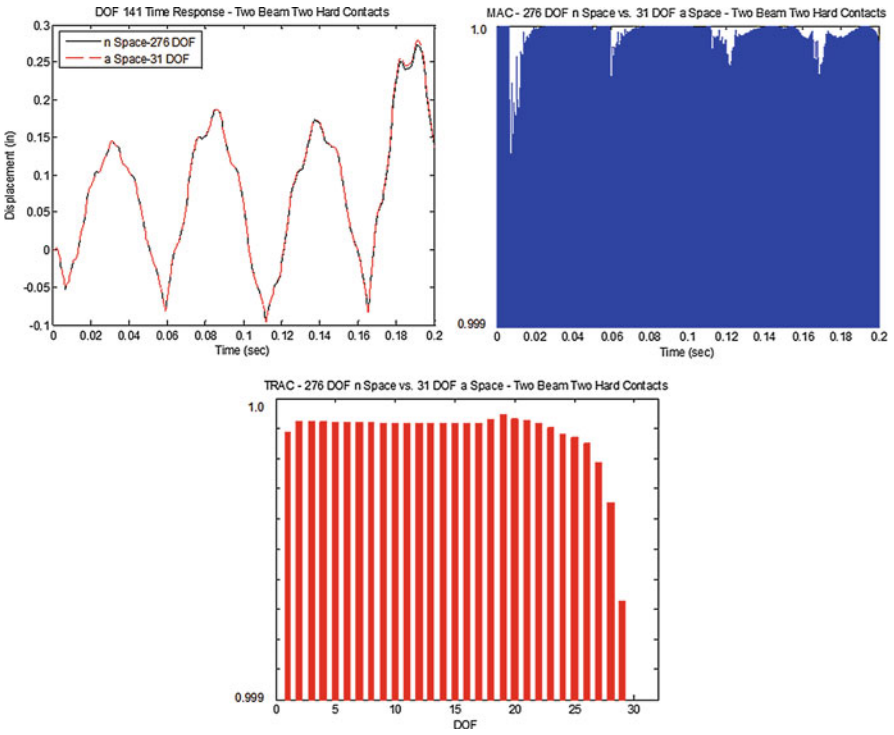

Fig. 7 Reduced model time response (DOF 141) compared to reference solution (left) with MAC of reduced order model deformed shape compared to reference deformed shape for 31 ADOF (middle) and TRAC correlation for 31 ADOF (0–0.2 s) – two beams with multiple hard contacts

Table 1 Solution times and average MAC/TRAC for two beams with multiple hard contacts – transient portion of time response (0–0.2 s)

Model	# of DOF	Solution time (sec)	Average MAC	Average TRAC
'n' space	276	88.5	0.99996	0.99958
'a' space	31	4.9		
'n' space	276	88.5	0.99996	0.99973
'a' space expanded	276	5.1		

for accurately computing the initial transient portion of the time response for this particular case. In addition, the solution time for the full space model is 88.5 s in contrast to the reduced 'a' space model, which is only 4.9 s.

Table 1 alsolists the average MAC and TRAC for each solution along with the solution time (the solution time for the expanded 'a' space is the time required to solve the 'a' space model and then expand to 'n' space). Even with the additional calculation due to multiplying the time solution by the expansion matrix, the time required is significantly reduced in comparison to the full 'n' space solution, going

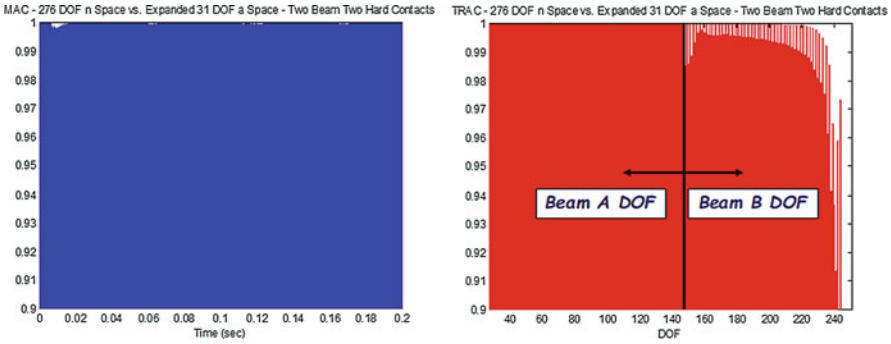

Fig. 8 MAC (left) and TRAC (right) comparisons between 276 DOF 'n' and 276 DOF 'a' expanded space models for transient portion of time response (0–0.2 s) – two beams with multiple hard contacts

from 88.5 to 5.1 s. The average MAC and TRAC have negligible improvements because the remaining error is due to truncation which is not improved by expansion of the time responses.

Table 1 shows that expanding the 'a' space time response to 'n' space yielded an accurate solution while significantly reducing the time required. Rather than solving the full space solution directly, reducing the model and then expanding the solution yielded nearly identical results at a fraction of the time.

The other key point of this case study is that the nonlinear time response was achieved using the modes of the originally uncoupled component beam models. Even though the linear mode shapes used in expanding the time responses were not identical to the mode shapes used when the configuration was in a different linear state, a separate expansion matrix for each nonlinear perturbation was not required. Because a sufficient number of modes have been used to span the space of the analytical model and all perturbed nonlinear variations of the model, the expansion does not distort the data and allows for very accurate expansion for all perturbed configurations of the two-beam system. As a result, the highly accurate expanded time solution was obtained very efficiently. In addition, an actual measured test configuration was also studied and produced results comparable in efficiency and accuracy to the analytical results presented; these experimental results are included in the references.

3.2 Nonlinear Response Prediction with Expansion for Full Field Dynamic Strain Prediction (Harvie)

A finite element model was generated using Abaqus/CAE [38]. The two-beam system, as illustrated in Fig. 8, was generated to imitate a large, complicated model to accurately demonstrate the principles at hand while maintaining a feasible model size on which reference calculations are performed; note that the diagram shown in

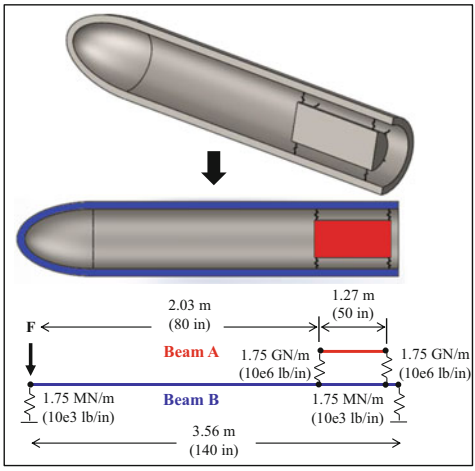

	Property	Beam A	Beam B
Geometric	Width	50.8 mm (2 in)	50.8 mm (2 in)
	Height	25.4 mm (1 in)	25.4 mm (1 in)
	Length	1.27 m (50 in)	3.56 m (140 in)
Modeling	# elements	250	700
	# nodes	251	701
	# DOF	502	1402
	Node spacing	0.2	0.2
Material	Material	Aluminum	Aluminum
	Density	7.03 kg/m^3 (2.54e-4 lb/in^3)	7.03 kg/m^3 (2.54 e-4 lb/in^3)
	Young's Modulus	68.9 GPa (10e6 psi)	68.9 GPa (10e6 psi)

Fig. 9 Physical representation of two-beam system with geometric, modeling, and material properties of two-beam system

Fig. 9 is not to scale. The main beam, Beam B, is 140 in in length and joined to the smaller Beam A, 50 in in length, using 10,000,000 lb/in translation springs; the main beam is grounded using 10,000 lb/in translation springs. The full space model contains nodes with 0.2 in spacing on each beam; therefore there are 251 nodes on Beam A and 701 nodes on Beam B. Each node contains a shear DOF and a rotational DOF to capture planar beam bending only. Details on the properties of the structure can be found in Fig. 9; note that the modeling properties are only applicable for the large N-space model.

To introduce discrete nonlinearities to the system, a gap-spring interface was used to simulate a contact; the stiffness of the spring contact is either set to a predefined stiffness value when the specified gap distance is closed or set to zero when the specified gap distance is open. The nonlinear cases have two contact locations between the beams, as shown in Fig. 10; these contact locations were chosen so that both contact springs could engage during the response. The initial gap distance was set to 0.003 in for the nonlinear cases; once again this value was chosen merely so that both contact springs would engage during the response. The three possible configurations that the beams can encounter with the springs engaged are also shown in Fig. 10 along with the frequencies for each configuration.

For all cases, a frequency band-limited analytical force pulse was utilized to excite a frequency range of roughly 400 Hz; the frequency range excited by the force pulse includes roughly 13 modes in all configurations. The use of this force pulse allows for minimal excitation of higher modes and controls the number of modes that substantially participate in the system response due to the impulse. The force was applied at the left-most node of Beam B, and the force was applied perpendicular to the beam to excite modes along the weak axis; this approximation

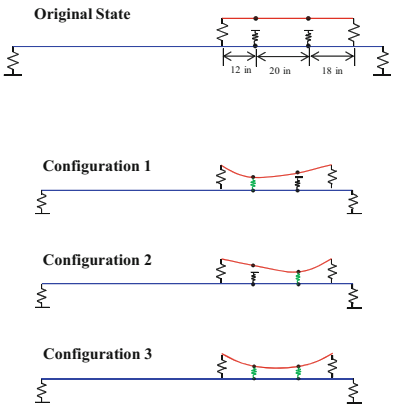

Mode	Frequency (Hz)			
	Original	Config 1	Config 2	Config 3
1	3.88	4.14	4.07	4.14
2	14.61	15.01	15.05	15.08
3	26.91	27.18	26.97	27.34
4	38.37	43.42	43.11	43.49
5	44.03	67.08	66.73	67.10
6	67.10	76.99	92.65	98.80
7	96.85	99.19	113.84	144.79
8	141.42	145.76	144.79	187.79
9	153.93	190.90	189.58	208.79
10	190.93	227.85	229.99	234.73
11	255.93	262.04	264.22	269.05
12	322.30	325.28	328.99	329.20
13	335.25	383.76	338.36	391.88
14	404.54	404.55	406.64	407.48
15	496.67	499.47	497.10	499.56
16	584.91	585.47	590.07	591.58
17	590.09	591.95	615.35	615.52
18	707.96	707.97	708.67	708.68
19	814.95	815.99	816.16	816.98
20	901.54	907.93	909.59	915.61
21	949.60	950.01	950.13	950.71
22	1078.50	1078.53	1078.71	1078.73

Fig. 10 Contact locations and configurations for nonlinear case with natural frequencies to 1000 Hz of full space system with and without hard contacts

was made to demonstrate the principles at hand and could be extended to different forcing functions and locations.

The large N-space model was reduced from 1904 modes and DOF to an n-space model with 194 modes and DOF by retaining every tenth node from the full space model. A comparison of model sizes for this reduction is shown in Fig. 11. All nodes in both models contain both shear and rotary DOF. This reduction was performed to produce a more reasonable-sized model.

The n-space model was reduced further for use with ERMT. Two model sizes, a space and aa-space, were generated for the various analyses performed. The a-space model contains 24 modes and DOF, while the aa-space model contains only 13 modes and DOF, as outlined in Fig. 11; also shown are the specific DOF and modes used in the models. The a-space model includes modes of the original system up

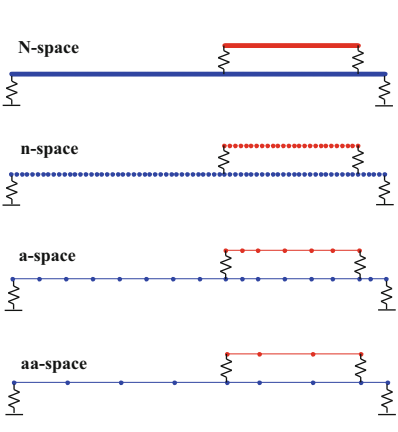

	# Nodes	# DOF	# Modes	Active DOF
N-space	952 (shear & rotary with 0.2” spacing)	1904	1904	1-1904
n-space	97 (shear & rotary with 0.2” spacing)	194	194	1-2, 21-22, 41-42, …1903-1904
a-space	24 (shear, variable spacing, max 10”)	24	24	1,101,201,301,401,501, 601,701,801,861,921, 1021,1121,1301,1341, 1401,1403,1463,1523, 1623,1723,1803,1903
aa-space	13 (shear, variable spacing, max 20”)	13	13	1,201,401,601,801, 921,1121,1301,1401, 1403,1523,1723,1903

Fig. 11 Description of full space model and reduced order models used

to approximately 1300 Hz, while the aa-space model includes modes up to only 400 Hz.

The mode contribution matrices were calculated at full space for the modified system in all configurations, and the matrices are not shown for brevity. The a-space model with 24 modes contains enough modal information to span the space of the problem for all configurations encountered.

Direct integration of the equations of motion was performed using Newmark time integration to compute the time response for all cases. Newmark integration was utilized for similarity to the solver used in Abaqus, where the Hilber-Hughes-Taylor (HHT) variation of the Newmark method is used. The damping of the system was approximated using one percent of critical damping for all modes. Proportional damping was assumed to keep a straightforward solution procedure, but a state space solution could be used to solve systems with non-proportional damping.

The full space displacements were determined using both a full space solution and the proposed efficient technique. Comparisons of the computation time and accuracy for this case are shown in Table 2. The solution time was reduced significantly by utilizing such a smaller model to solve for the response. For this case, very high accuracy was obtained using an extremely reduced model. The displacement results for the full and predicted displacement are shown in Fig. 12 along with the strain. The frequency range of the original system modes included in the reduction extends over 1300 Hz, so the energy distribution of the response is accurately captured in the frequency domain. Both the displacement and strain are predicted accurately using the reduced order model implemented in this case. The model used in the efficient technique is able to better predict the higher-order curvature in the dynamic displacement and strain response because more modes were included in the reduction. While the efficient calculation of the dynamic displacement matches nearly perfectly to the reference solution, some high-frequency content is present in the reference strain solution that is not captured

Table 2 Comparison of reduced and full solution for hard contact case with more modes

Model	# of DOF	Solution time (sec)	Average MAC	Average TRAC
Full space	1904	740.18	0.9998	0.9999
Reduced	24	0.28		

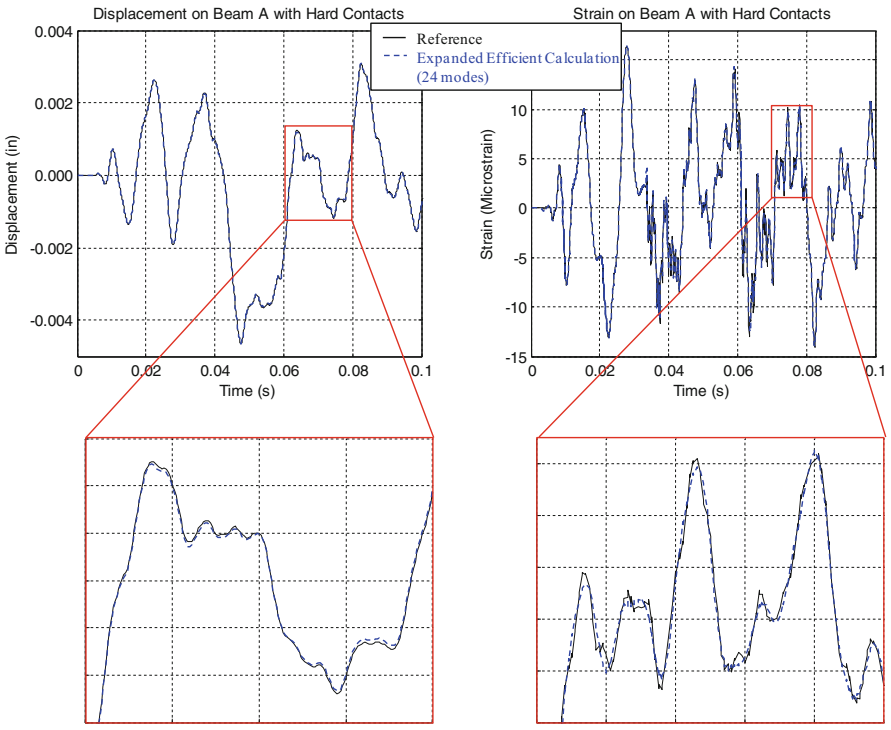

Fig. 12 Displacement and corresponding strain on Beam A for hard contact case

using the efficient calculation. The slight differences in the strain calculations can be further reduced by including even more modes in the reduced order model. The strain and displacement results calculated efficiently compare very accurately to the full space model for this case, with a solution time that is dramatically reduced compared to the full space solution.

The results obtained from this case compared very well with the full space solution because more modes were retained in the reduced solution to accurately represent the system dynamics for all possible configurations. The full solution took over 12 min to compute, but accurate strain and displacement data could be obtained in less than a second without compromising accuracy. Although the addition of hard contact springs in the system causes the necessity for additional modes to be retained in a reduced order model, the full space model can still be substantially reduced to retain only the dynamic characteristics that are necessary to the response.

3.3 Nonlinear Response Prediction with Embedded Subcomponent Models (Obando)

Further extending the models and results presented in the previous cases, this case will introduce a modally active embedded component to one of the components and will be included in the system response with no active degrees of freedom on the subcomponent with nonlinear response predicted with highly reduced component models.

Multi-component structural systems were addressed in the context of retaining embedded structural information of ancillary subcomponents for the calculation of nonlinear reduced order model time response. For linear forced response, expansion was shown to return a precise approximation of the ancillary subcomponent even in cases where the reduction does not include active DOF at that subcomponent level. The model was developed as a natural extension of the nonlinear work discussed in the last cases. A full space finite element model consisting of two systems, one of which contains a dynamically active ancillary subcomponent, were reduced to a smaller set of degrees of freedom and used for the prediction of the forced time response of the system as seen in Fig. 13. Gap-spring contact elements were introduced to generate nonlinear response between the two systems. The reduced order model (with embedded ancillary subcomponent information) was then used to calculate the response at ADOF and then to expand back to the full space finite element model and extract the predicted forced response of the ancillary subcomponent. The results for the linear and the nonlinear hard and soft contact cases will be discussed here, but further information can be found in the references. In the linear case, the SEREP model will be discussed. A reduced model was computed such that no DOF from the ancillary subcomponent (gray beam at the

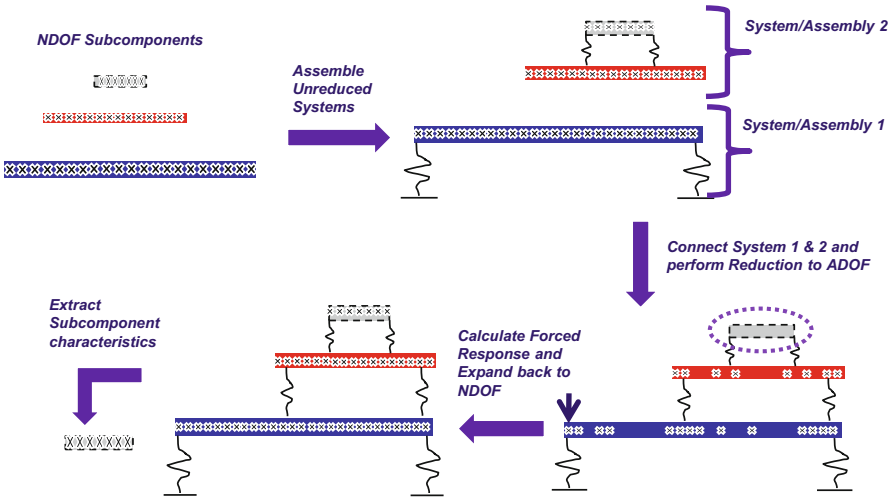

Fig. 13 Sequence for the development of reduced system response models

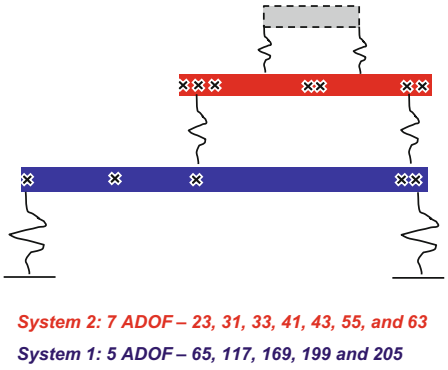

	Reference System Freq. (Hz)	SEREP Reduced System Freq. (Hz)	% Difference
Mode 1	16.8	16.8	0%
Mode 2	37.5	37.5	0%
Mode 3	68.1	68.2	0%
Mode 4	84.6	84.6	0%
Mode 5	102.1	102.1	0%
Mode 6	129.1	130.2	1%
Mode 7	210.0	211.5	1%
Mode 8	282.0	283.2	0%
Mode 9	343.0	351.2	2%
Mode 10	396.2	396.6	0%
Mode 11	477.3	2611.8	447%
Mode 12	645.3	3023.1	369%

Fig. 14 Comparison of SEREP reduced order model (12 DOF) frequencies with respect to (206 DOF) the reference solution. "x" indicates relative location of nodes in FEM

top of the red beam) was preserved in the reduction process. The model is shown in Fig. 14 and a comparison of the response as well as correlation results of the expansion process in Fig. 15.

The SEREP reduction and expansion process resulted in high correlation with full space model using only a very small fraction of the DOFs. Furthermore, the omission of the connecting DOF for the ancillary subcomponent did not yield any additional error. Addition of modes beyond the 12 modes indicated in the $[U_{12}]$ matrix in the SEREP reduced model showed large improvement from the resulting expanded model response as illustrated in Fig. 16 where expansion is used on a 17 mode and DOF reduced model. When the reduction process is successful (as it was with the SEREP and KM_AMI models), the modes selected span the space of the system response. Modes beyond the 12 indicated by the [U12] smooth the approximation of the system response and further addition of modes results in better results until the reduced 'a' space model approaches the full 'N' space solution and hence spans the whole space of the full assembled system response.

The following models expand the reduced order modeling of the three-beam system to include nonlinear response. Gap-spring contact elements are introduced to generate nonlinear response between the two systems as done in the first example shown here. However, the possibility of nonlinear contacts is introduced at the subcomponent level as shown in Fig. 17. For the first nonlinear case, four different configurations are possible (initial configuration, one configuration for each spring coming in contact, and one for both springs in contact) as seen in Fig. 17. Using the calculated $[U_{12}]$ for all configurations, the necessary number of component modes were determined in order to properly characterize the system; using the force described above, the system modes must be able to characterize the response over a 250 Hz frequency span. While this is the initial frequency range of interest for any structural dynamic study, there also needs to be a consideration for the nonlinear contacts which occur that may require a frequency range beyond that initially determined from the applied forcing function.

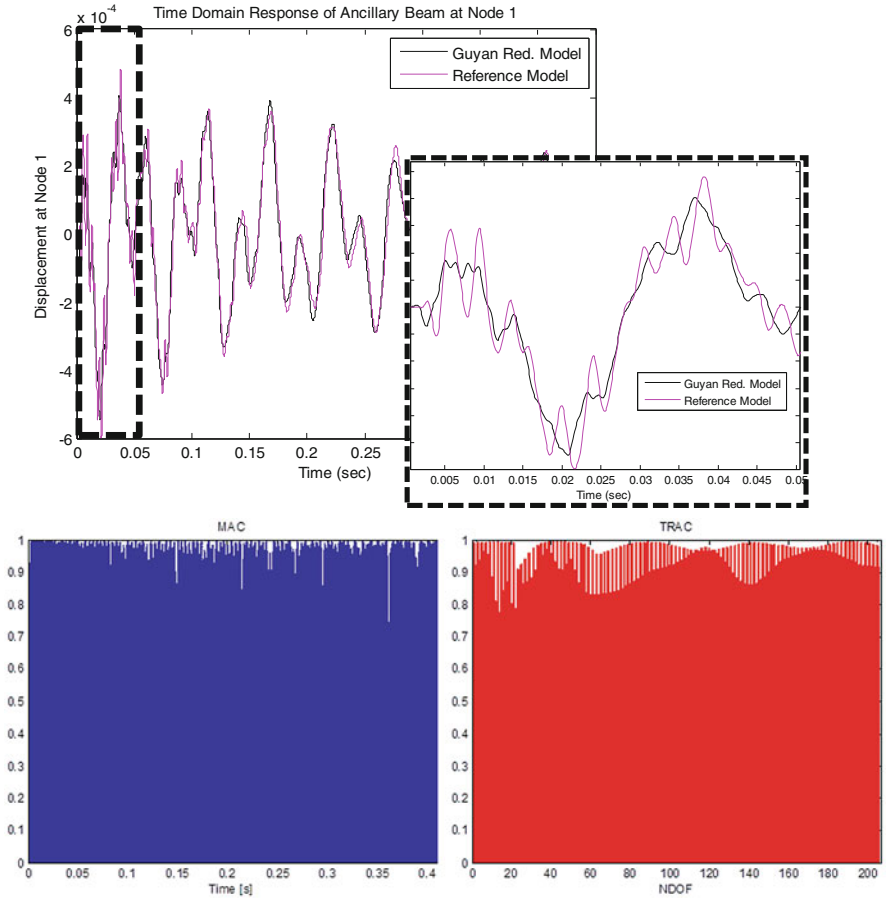

Fig. 15 Left: Comparison of time response at node 1 of the ancillary subcomponent from the expansion of a 12DOF SEREP reduced model versus the 206 DOF full space reference solution (in magenta). Zoomed in region shows the response for the first 0.1 s. Right: MAC (blue) and TRAC (red) bar plots showing the correlation of the expanded SEREP reduced model to the reference model

In these nonlinear cases, the location of the nonlinearity can have a significant effect on the accuracy of the prediction and on the number of modes (and DOF) required in the reduction/expansion process. SEREP reduction was used to reduce the active DOF of the system to an 'a' set not including DOFs on the ancillary beam. The forced responses of the reduced ADOF systems were computed. The dynamic characteristics of the ancillary subcomponent were then extracted using the system information available from the reduction process. A SEREP reduced model using 16 modes was created. Figure 18 shows the comparison of the predicted response of the expanded model and the reference model.

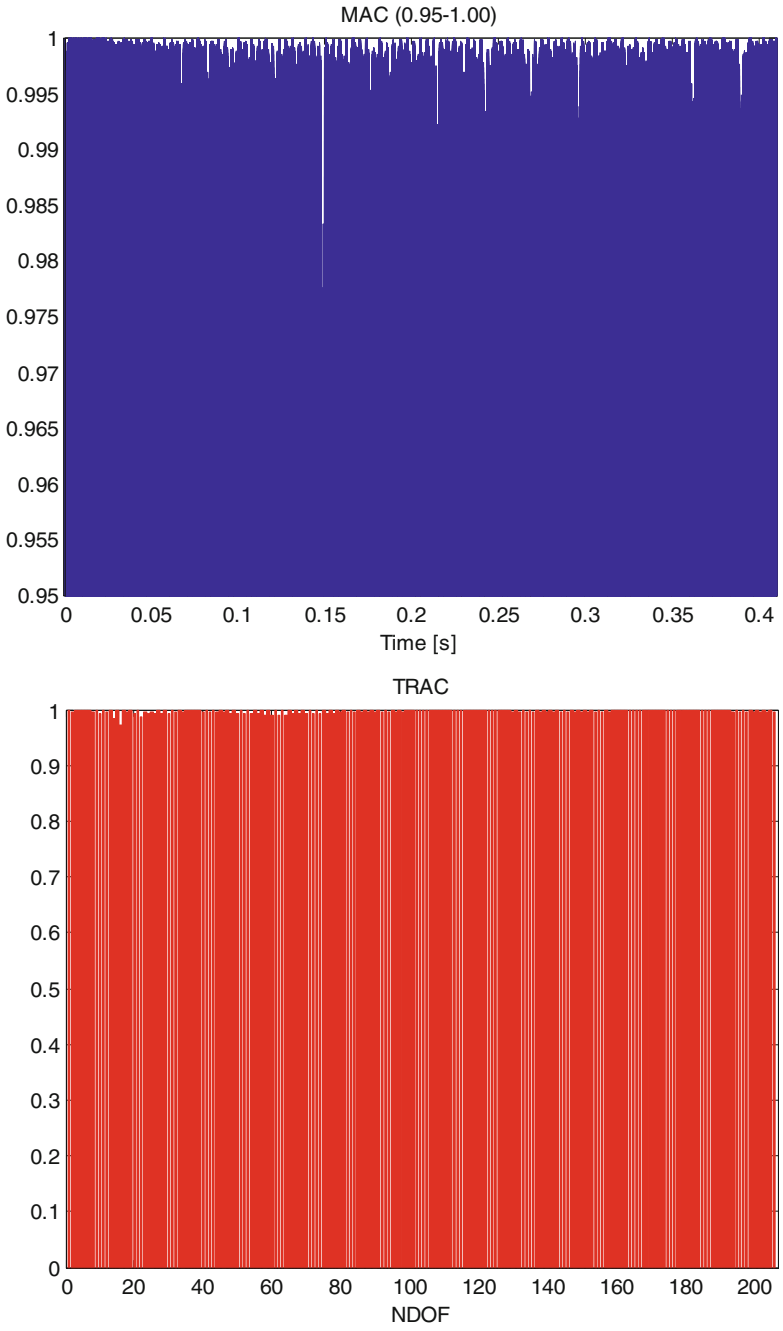

Fig. 16 MAC and TRAC plots showing correlation of the expanded 17 DOF SEREP reduced model to reference model. MAC y-axis is showing values from 0.95 to 1.0

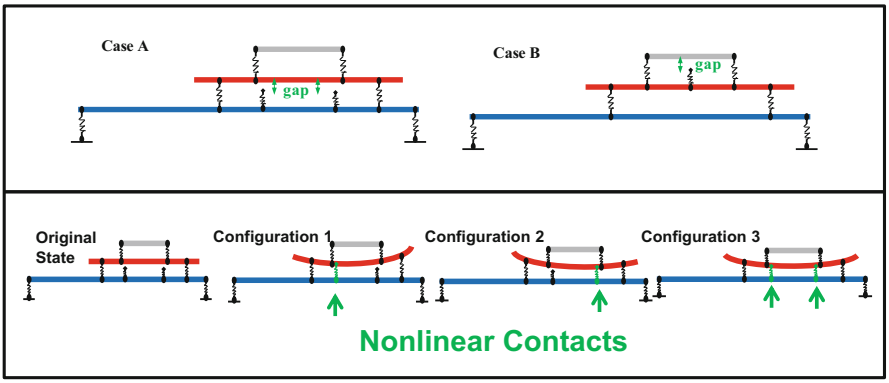

Fig. 17 Nonlinear gap-spring contact cases analyzed. The nonlinear configurations for Case A are shown. Each case indicates the closing or opening of the gap springs (in green when closed)

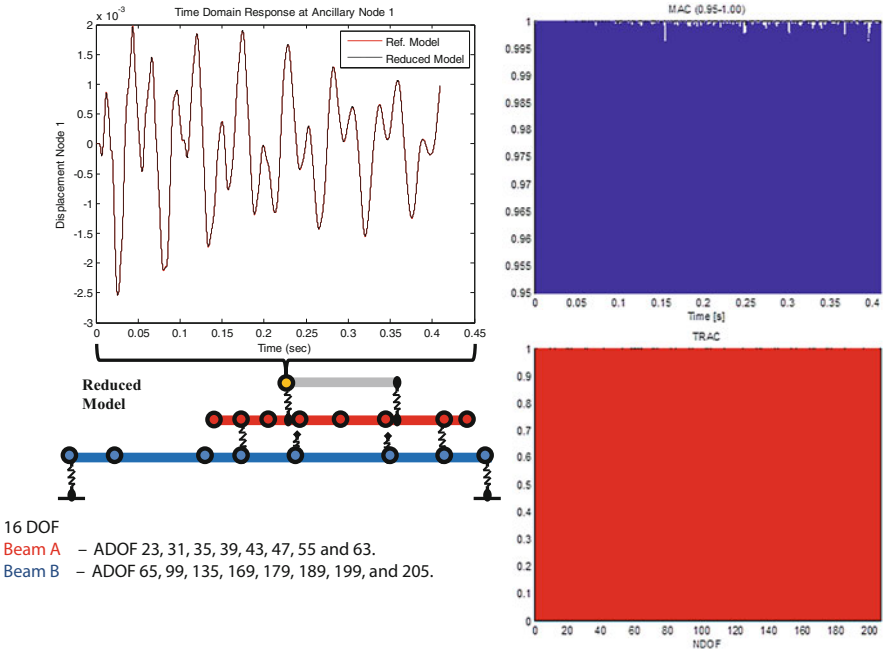

Fig. 18 Predicted response at ancillary node 1 (in yellow) from 16 DOF reduced model. MAC from 0.95–1.0 (top right) and TRAC (bottom right) correlation of models

Using 16 modes allows for the accurate prediction of up to 8 modes (which spans approximately 300 Hz) of the three-beam assembled system. Figure 19 shows the comparison of the FFT of the displacement at the left spring contact location. The FFT of the displacement at the left contact location in Fig. 19 shows no significant effect of mode truncation of the higher-order modes, and the response is an accurate

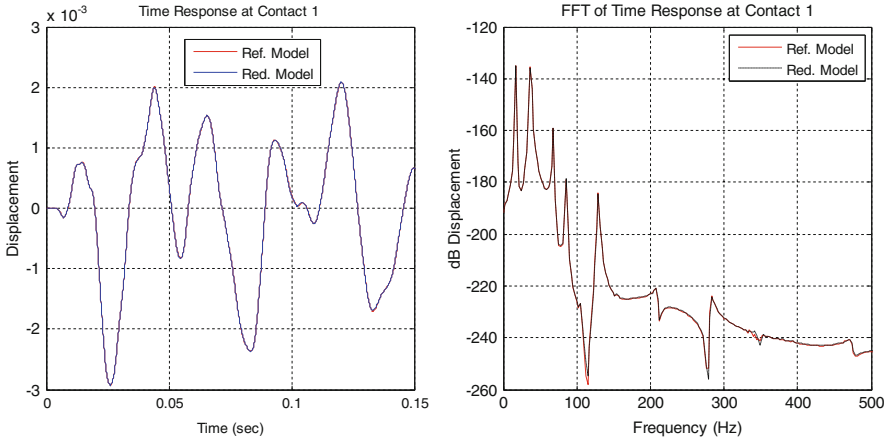

Fig. 19 Comparison of response (left) and FFT (right) of reference model and 16 mode reduced order model at spring contact location 1

approximation of the full NDOF solution. Note that no ADOF has been placed at the ancillary subcomponent or at the DOFs that connect the ancillary beam to the top beam. Nevertheless, the embedded information in the reduction process has successfully allowed the prediction of the time response at all NDOF.

The effect of higher-order modes can be exacerbated if the type of contact is a hard impact, thus producing a narrow time pulse that translates into a high-order pulse in the frequency domain. The next case will explore a hard contact spring acting at two locations of the structure. A comparison of the two types of contacts, soft and hard, can be seen in Fig. 20.

Nonlinear contacts of 10,000 lb/in were implemented instead of the soft contacts of 100 lb/in previously used. Because the hard contact excites frequencies in the range of 700 Hz, the 16 mode model previously used cannot give the best approximation of the response of the system. The selection of modes preserved in the reduction must form a linearly independent set of vectors spanning the space of the full response of the system. In other words, the selected projection vectors in the transformation matrix must be able to approximate any other vector in the space as linear combinations of the mode shape vectors preserved in the reduced space. A 21 mode and DOF model was created to better approximate the hard contact nonlinear response of the system. Figure 21 shows the correlation and response for the 21 DOF model and the reference model.

The modes used in the reduced model resulted in an accurate approximation of the response of the NDOF system. However, the effects of mode truncation could not be completely mitigated. Caution must be exercised when simply adding modes to the reduced order model since linear independence of the vectors formed in the expansion process is very important. The reduced space matrices can become ill-conditioned for certain choice and number of DOF, and the predicted response is

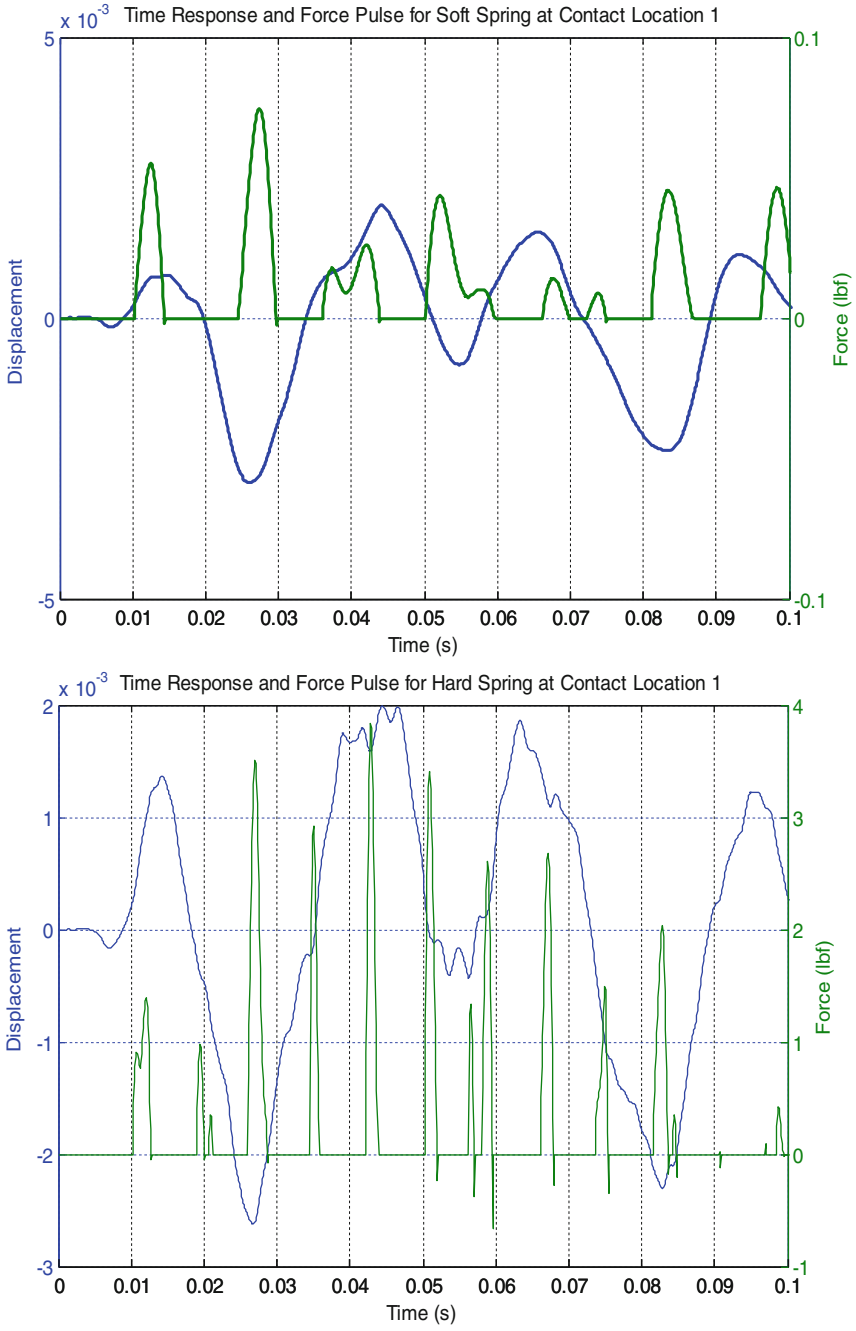

Fig. 20 Comparison of displacement and force magnitude for soft (left) and hard (right) types of nonlinear contacts at DOF 37 of the three-beam system at contact location 1 (left gap spring)

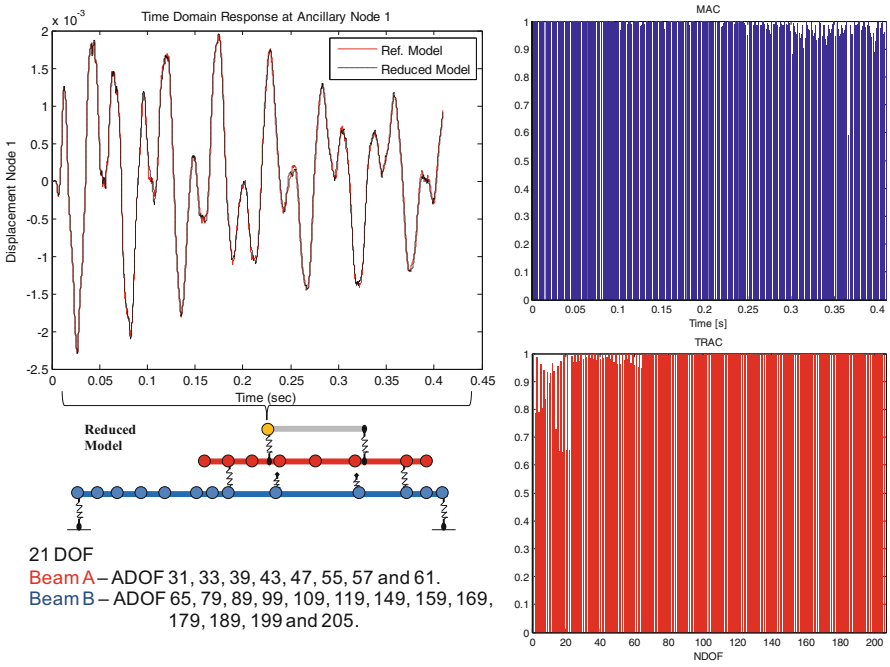

Fig. 21 Predicted response at ancillary node 1 from expansion of 21 DOF reduced order model with hard contacts. MAC (top right) and TRAC (bottom right) correlation of models

then subjected to high levels of numerical error. Figure 22 shows that the FFT and response at the contact location 1 is reasonably approximated by the reduced model of 21 modes.

The cases considered have shown that full field results can be obtained from reduced order models with subcomponent interactions from the embedded information preserved in the reduction process. Using the necessary number of modes in the reduced model to span the space of all modes of interest allows the response at the ancillary and any other DOF to be predicted accurately. The $[U_{12}]$ contribution matrix and the effect of the higher-order modes from nonlinear interactions must be taken into account as well as the linear independence and well-determined behavior of the reduced matrices in order to obtain a good approximation of the dynamic characteristics of the system. Moreover, when proper precautions are taken to reduce the N space system to 'a' space, no ADOF are needed in the dynamically active ancillary subcomponent.

Additional cases have been studied to investigate the nonlinear connection between the subcomponent and the attached component. Generally these cases produced similar results and are not presented here due to space limitations.

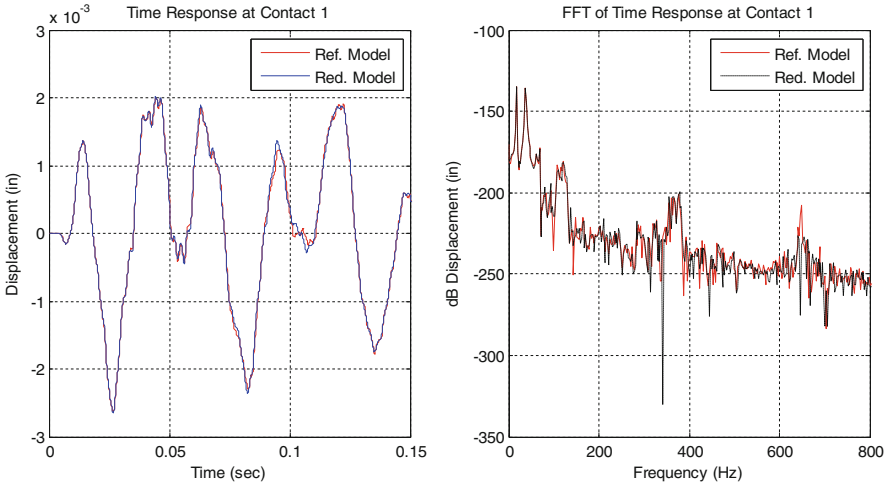

Fig. 22 Comparison of response (left) and FFT (right) of reference (in red) and expansion of 21 DOF reduced order model at contact location 1 (left gap spring)

4 Conclusions

Understanding of the linear reduction/expansion methodology showed the advantage of using reduced models for full field prediction of systems that may undergo localized nonlinear response due to component contact or coupling interactions. For these types of problems, the presence of highly nonlinear coupling elements such as hard contacts, isolation mounts, gap springs, bilinear springs, etc. is predicted with a piecewise linear approximation providing the dynamic response of the structure as a superposition of all possible configurations of the system.

For all cases considered, linear and nonlinear, high correlation values were obtained between the reference model and the predicted expanded model response from the reduced models. For such models, the computation time was greatly reduced as well as the number of DOF in the model. There was no degradation in the predicted full field dynamic response or the full field dynamic strain. The models clearly showed that very good and very efficiently calculated results could be obtained for linear components interconnected with highly nonlinear connection elements.

Author Contributions

This work has spanned several years and several student theses that are acknowledged in this section.

Van Zandt, T., Development of Efficient Reduced Models for Multi-Body Dynamics Simulations of Helicopter Wing Missile Configurations, MS, University of Massachusetts Lowell, Lowell, Massachusetts, 2004

Wirkkala, N., Efficient Method of Model Updating Using Target Definition from Impedance Based Modeling for Multi-Body Dynamics Simulations, MS, University of Massachusetts Lowell, Lowell, Massachusetts, 2004

Butland, A., A Hybrid Component Mode Synthesis Approach for System Modeling Applications, MS, University of Massachusetts Lowell, Lowell, Massachusetts, 2006

Nicgorski, D., Investigation on Experimental Issues Related to Frequency Response Function Measurements for Frequency Based Substructuring, MS, University of Massachusetts Lowell, Lowell, Massachusetts, 2006

Chipman, C., Real Time Operating Data Expansion for Improved Visualization, MS, University of Massachusetts Lowell, Lowell, Massachusetts, 2006

Pingle, P., Prediction of Full Field Dynamic Stress/Strain from Limited Sets of Measured Data, PhD, University of Massachusetts Lowell, Lowell, Massachusetts, 2010

Thibault, L., Development of Equivalent Reduced Order Model Technique for Linear Modal Components Interconnected with Nonlinear Connection Elements, MS, University of Massachusetts Lowell, Lowell, Massachusetts, 2012

Marinone, T., Efficient Computational Nonlinear Dynamic Analysis using Modal Modification Response Technique, MS, University of Massachusetts Lowell, Lowell, Massachusetts, 2012

Harvie, J., Computationally Efficient Reduced Order Models for Full Field Nonlinear Dynamic Strain Predictions, MS, University of Massachusetts Lowell, Lowell, Massachusetts, 2013

Baqersad, J., A Non-contacting Approach for Full Field Dynamic Strain Monitoring of Rotating Structures using Photogrammetry, Finite Element and Modal Expansion Techniques, PhD, University of Massachusetts Lowell, Lowell, Massachusetts, 2015

Obando, S., Use of Expansion of Highly Reduced Order Models for the Accurate Prediction of Full Field Dynamic Characteristics in the Forced Response of Linear and nonlinear Systems and Components, PhD, University of Massachusetts Lowell, Lowell, Massachusetts, 2016

Acknowledgments Some of the work presented herein was partially funded by Redstone Arsenal Award No. W31P4Q-07-P-0606 entitled "System Modeling Approaches of Helicopter/Wing/Missile Configurations," by NSF Civil, Mechanical and Manufacturing Innovation (CMMI) Grant No. 0900543 entitled "Dynamic Stress-Strain Prediction of Vibrating Structures in Operation," and by Air Force Research Laboratory Award No. FA8651-10-1-0009 "Development of Dynamic Response Modeling Techniques for Linear Modal Components." Any opinions, findings, and conclusions or recommendations expressed in this material are those of the authors and do not necessarily reflect the views of the particular funding agency. The authors are grateful for the support obtained.

References

1. Van Zandt T et al (2006) Development of efficient reduced models for rigid body dynamics simulation for helicopter missile wing combinations. In: Proceedings of the twenty-fourth international modal analysis conference, Feb 2006, St Louis
2. Avitabile P et al (2007) Development of efficient reduced models for flexible body dynamic simulation. In: Proceedings of the twenty-fifth international modal analysis conference, Feb 2007, Orlando
3. Butland A, Nicgorski D, Avitabile P (2008) A hybrid craig-bampton approach for system modeling applications. In: Proceedings of the twenty-sixth international modal analysis conference, Feb 2008, Orlando
4. Butland A, Avitabile P (2009) Component mode synthesis using reduced order test verified components. In: Proceedings of the twenty-seventh international modal analysis conference, Feb 2009, Orlando
5. Butland A, Avitabile P (2010) A reduced order, test verified component mode synthesis approach for system modeling applications. Mech Syst Signal Process 24(4):904–921
6. Wirkkala N, Avitabile P, Van Zandt T (2006) Modification of target definition for model updating using impedance based modeling for helicopter missile wing combinations. In: Proceedings of the 24th international modal analysis conference, Feb 2006, St. Louis
7. Nicgorski D, Butland A, Avitabile P (2008) Experimental issues related to frequency response function measurements for frequency based substructuring. In: Proceedings of the 26th international modal analysis conference, Feb 2008, Orlando
8. Nicgorski D, Avitabile P (2009) Conditioning of FRF measurements for use with frequency based substructuring. In: Proceedings of the twenty- seventh international modal analysis conference, Feb 2009, Orlando
9. Nicgorski D, Avitabile P (2010) Experimental issues related to frequency response function measurements for frequency-based substructuring. Mech Syst Signal Process 24(5): 1324–1337
10. Nicgorski D, Avitabile P (2010) Conditioning of FRF measurements for use with frequency based substructuring. Mech Syst Signal Process 24(2):340–351
11. Chipman CC, Avitabile P (2008) Expansion of real time operating deformations for improved visualization. In: Proceedings of the twenty-sixth international modal analysis conference, Feb 2008, Orlando. ProQuest
12. Chipman C, Avitabile P (2009) Expansion of transient operating data. In: Proceedings of the twenty- seventh international modal analysis conference, Feb 2009, Orlando
13. Avitabile P, Chipman C (2012) Expansion of transient operating data. Mech Syst Signal Process 31:1–12
14. Pingle P, Avitabile P (2010) Prediction of full field dynamic stress/strain from limited sets of measured data. In: Proceedings of the twenty-eighth international modal analysis conference, 2010, Jacksonville. Springer
15. Pingle P, Avitabile P (2011) Limited experimental displacement data used for obtaining full-field dynamic stress strain. In: Proceedings of the twenty-ninth international modal analysis conference, 2011, Jacksonville. Springer
16. Pingle P, Avitabile P (2011) Full field dynamic stress/strain estimation from limited sets of measured data. In: Proceedings of the twenty-ninth international modal analysis conference, Feb 2011, Jacksonville. Springer
17. Avitabile P, Pingle P (2012) Prediction of full field dynamic strain from limited sets of measured data. Shock Vib 19(5):765–785
18. Baqersad J, Niezrecki C, Avitabile P (2015) Predicting full-field strain on a wind turbine for arbitrary excitation using displacements of optical targets measured with photogrammetry technique. In: Proceedings of the thirty-third international modal analysis conference, Feb 2015, Orlando. Springer

19. Baqersad J et al (2015) Extracting full-field dynamic strain response of a rotating wind turbine using photogrammetry. In: SPIE/NDE, March 2015, San Diego. International Society for Optics and Photonics
20. Baqersad J, Niezrecki C, Avitabile P (2015) Full-field dynamic strain prediction on a wind turbine using displacements of optical targets measured by stereophotogrammetry. Mech Syst Signal Process 62:284–295
21. Baqersad J, Niezrecki C, Avitabile P (2015) Extracting full-field dynamic strain on a wind turbine rotor subjected to arbitrary excitations using 3D point tracking and a modal expansion technique. J Sound Vib 352:16–29
22. Thibault L et al (2012) Equivalent reduced model technique for nonlinear dynamic response. In: Proceedings of the thirtieth international modal analysis conference, Feb 2012, Jacksonville
23. Thibault L et al (2013) Equivalent reduced model technique development for nonlinear system dynamic response. Mech Syst Signal Process 36(2):422–455
24. Marinone T et al (2012) Efficient computational nonlinear dynamic analysis using modal modification response technique. In: Proceedings of the thirtieth international modal analysis conference, Feb 2012, Jacksonville
25. Marinone T et al (2012) Efficient computational nonlinear dynamic analysis using modal modification response technique. Mech Syst Signal Process 31:67–93
26. Avitabile P, O'Callahan J (1991) Understanding structural dynamic modification and the effects of truncation. Proc Int J Anal Exp Modal Anal, invited contribution 6(4):215
27. Nonis C et al (2013) Development of full space system model modes from expansion of reduced order component modal information. In: Proceedings of the thirty-first international modal analysis conference, Feb 2013, Garden Grove
28. Nonis C, Avitabile P, Obando SE (2013) System model modes developed from expansion of uncoupled component dynamic data. In: Recent advances in structural dynamics, July 2013, Pisa
29. Avitabile P, Nonis C, Obando SE (2014) System model modes developed from expansion of uncoupled component dynamic data. J Mech Eng 60(5):287–297
30. Marinone T, Thibault L, Avitabile P (2013) Expansion of nonlinear system response using linear transformation matrices from reduced component model representations. In: Proceedings of the thirty-first international modal analysis conference, Feb 2013, Garden Grove. Springer
31. Harvie J, Obando SE, Avitabile P (2013) Reduced order system model nonlinear response and expansion for full field results. In: Recent advances in structural dynamics, July 2013, Pisa
32. Harvie J, Avitabile P (2014) Computationally efficient nonlinear dynamic analysis for stress/strain applications. In: Proceedings of the thirty-second international modal analysis conference, Feb 2014, Orlando. Springer
33. Avitabile P, Harvie J, Obando SE (2014) Efficient reduced order nonlinear response with expansion for full field results. In: EURODYN 2011, Porto
34. Obando SE, Avitabile P (2014) Prediction of forced response on ancillary subsystem components attached to reduced linear systems. In: Proceedings of the thirty-second international modal analysis conference, Feb 2014, Orlando. Springer
35. Obando SE, Avitabile P (2015) Prediction of forced response using expansion of perturbed reduced order models with inexact representation of system modes. In: Proceedings of the thirty-third international modal analysis conference, Feb 2015, Orlando. Springer
36. Obando SE, Avitabile P (2015) Prediction of nonlinear forced response on ancillary subsystem components attached to reduced linear systems. In: Proceedings of the thirty-third international modal analysis conference, Feb 2015, Orlando
37. Obando SE, Avitabile P (2016) Developments in the prediction of full field dynamics for the nonlinear forced response of reduced order system models. In: Proceedings of the thirty-fourth international modal analysis conference, Feb 2016, Orlando
38. Guyan RJ (1965) Reduction of stiffness and mass matrices. AIAA J 3(2):380–380
39. Paz M (1984) Dynamic condensation. AIAA J 22(5):724–727

40. O'Callahan JC (1989) A procedure for an improved reduced system (IRS) model. In: Proceedings of the 7th international modal analysis conference. Union College, Schenectady
41. O'Callahan J, Avitabile P, Riemer R (1989) System equivalent reduction expansion process (SEREP). In: Proceedings of the 7th international modal analysis conference. Union College, Schnectady
42. Kammer DC (1991) A hybrid approach to test-analysis-model development for large space structures. J Vib Acoust 113(3):325–332
43. Marinone T, Butland A, Avitabile P (2012) A reduced model approximation approach using model updating methodologies. In: Topics in modal analysis II, vol 6. Springer, New York/London, pp 625–636

Part IV
Applications and Miscellaneous Topics

Civil Structural Testing

23

Ruben Boroschek and Joao Pedro Santos

Contents

R. Boroschek (✉)
University of Chile, Santiago, Chile
e-mail: rborosch@ing.uchile.cl

J. P. Santos
Structural Monitoring Unit, National Laboratory for Civil Engineering, Lisboa, Portugal
e-mail: josantos@lnec.pt

R. Allemang, P. Avitabile (eds.), *Handbook of Experimental Structural Dynamics*,
https://doi.org/10.1007/978-1-4614-4547-0_29

Abstract

Civil engineering structures are especially complex due to their size, geometric and physical uniqueness, intrinsic nonlinearity, and also due to the variations of their properties as a function of environmental or operational loadings and support conditions. While overloading can produce severe but recoverable changes in modal properties, in the order of 30%, environmental conditions like temperature and humidity can produce state changes, particularly in supporting soils and boundary conditions, that have been observed to impose changes of 50% on modal properties without the presence of damage. Some of these variations are abrupt while others are slow, yet regardless of their speed they impose challenges on the experimental setups and identifications techniques. The basic civil structural instrumentation is mainly based on accelerometers and displacements sensors, being their characteristics described in the present chapter. The environmental excitations are in general nonstationary and input excitations are usually not measured. So, response is generally analyzed using Operational Modal Analysis (OMA) techniques, even if Experimental Modal Analysis (EMA) have also been extensively used. The most commonly applied technique for identification is the Stochastic Identification algorithm in their covariance and data-driven versions. In order to observe the complexities of civil infrastructure, examples are given for buildings under environmental and earthquake loads and bridges under environmental and traffic loads. Identification and automatic tracking algorithm are presented theoretically and with examples.

Keywords

Civil structures · Earthquake action · Ambient vibration · Operational modal analysis · Modal identification methods · Modal estimation · Modal tracking · Cluster analysis · Stabilization diagrams · Bridge use case · Building use case

Nomenclature

$[A]$	System state matrix
a_{gi}	Base acceleration
a_P	Acceleration at position p
$a_i^{(k)}$	Average distance between the i-th object of a cluster and the remaining object of the same cluster
ADC	Analog to digital
ARX	Auto-regressive model with exogenous input
$b_i^{(k)}$	Average distance between the i-th object of a cluster and the objects assigned to other clusters
$B(P_K)$	Overall between-cluster distance measured from a partition P of k clusters
$[C]$	Observation matrix
COV	Reference to covariance-driven in SSI
C_k	k-th cluster of partition P_K
$d(x_i,x_j)$	Distance between observations i and j measured for quantity x
DAS	Data acquisition systems
EFDD	Enhanced frequency domain decomposition
EMD	Empirical mode decomposition
ERA	Eigensystem realization algorithm
FDD	Frequency domain decomposition
FFT	Fast Fourier transform
$[H]$	Hankel matrix
ITD	Ibrahim time domain decomposition
K	Number of clusters in cluster partition
$[L]$	Matrix obtained from LQ decomposition
LVDT	Linear variable differential transformer
MAC	Modal assurance criterion
MIMO	Muitiple input multiple output
MOESP	Multivariate output-error state space
MP	Mean phase
MPD	Mean phase deviation
MPC	Mean phase collinearity
Next-ERA	Natural excitation technique eigensystem realization algorithm
$[O]$	Observability matrix
P_k	Cluster partition containing k clusters
PP	Peak picking
$[Q]$	Matrix obtained from LQ decomposition
R_{XX}, R_{XY}	Cross-correlation
$SIL(P_t)$	Silhouette width of partition P containing t clusters
S/N	Signal-to-noise ratio
SHM	Structural Health Monitoring
$s_i^{(k)}$	Silhouette width of the i-th object assigned to a cluster
s_k	Silhouette width of cluster k
SSI	Stochastic subspace identification
STFT	Short-time Fourier transform
SVD	Singular value decomposition
S_{XX}, S_{XY}	Periodogram
T	Overall distance measured from a cluster partition
$[T]$	Toeplitz matrix
$[U]$	Hankel matrix of observations
UPS	Uninterruptable power supply
$v(t)$	Decay response

$W(P_K)$	Overall within-cluster distance measured from a partition P of k clusters
$\{y\}$	Response vector
$\dot{y}$, $\ddot{y}$	First and second time derivatives of y
$[Y]$	Hankel matrix of response
$\{z\}$	State space vector
β_t	Damping of mode t
γ^2	Coherence
λ	Eigenvalue
ω, f	Natural frequency of mode t
$[\Sigma]$	Singular values matrix
$[\phi]$	Modal shape matrix
$[\psi]$	Eigenvector matrix

1 Why Structural Health Monitoring (SHM) for Civil Structures

Civil engineering structures are in general large and unique. When dynamic testing is performed to a complete structure not located in laboratory, but in the field, the environmental conditions are uncontrolled and the structure is usually under operation. The sensitivity of the system to various ambient, boundary, and loading conditions, along with the restrictions for testing due to size, usage, and safety of the occupants and of the structure itself, generally requires special attention and modifications of the techniques typically applied to mechanical systems and described in other chapters. Due to their exposure to the environment and to usage, civil engineering structures exhibit slow or abrupt deterioration, damage, and collapse. The consequence of damage to these structures is not only related to loss of functionality and costly repairs. The deterioration could easily put the users and surrounding population and structures at risk.

The main challenges for dynamic testing are basically:

- *Nonlinear response*. Civil structures are inherently nonlinear due to the material used in their construction and due to their support conditions. Constituent materials are in general nonlinear even at low deformations levels. At larger deformations and extreme loads, hysteretic response is common and acceptable. Also, its boundary conditions (foundations and soils) are sensitive to environmental variations and loading history and intensity.
- *Uniqueness*. In general, each structure is unique in terms of its design, boundary conditions, construction procedures, and maintenance. Knowledge of similar structures helps understand the overall behavior, but cannot necessarily predict its particular properties and response.
- *Limited Modelling Capacity*. Numerical models are approximations that can only predict roughly the actual behavior of the structure. Nonlinear models can be developed but in general they lack basic information on the material, elements, and system hysteretic response. The typical viscoelastic models are good approximations, but they rarely represent the reality of an existing system.

Despite these characteristics, it has been possible to design, construct, and maintain these types of structures for centuries. This ability is not based on numerical models, but rather a rough understating of their actual response under varying conditions of existing similar structures.

This chapter presents the instrumentation, the identification methodologies, and on-site examples of civil testing in real structures. Laboratory and component testing are neither presented nor discussed.

2 Basic Considerations on Loading and Response

Civil structures are expected to be used for extended periods of time. A typical design considers a life span of more than 50 years for buildings and 100 years for bridges while other critical structures like dams and reservoirs can be in operation for several hundred years. Due to the long exposition to the environment and use, change of state and deterioration are common, and regular maintenance and repair and reinforcement are generally necessary. To detect these changes, a clear understanding of the structures' characteristics and responses to the environment and loading condition has to be developed. These state changes have to be distinguished between progressive and abrupt as well as recoverable and non-recoverable, to allow defining the appropriate instrumentation and procedures of detection.

Typical progressive damages consist of material deterioration (carbonation, corrosion, abrasion, etc.) or foundation modification (settlement, scouring, etc.), while abrupt changes can be related with extreme loads like overloading, freezing, blasting, extreme winds, and earthquakes, or when the structure and components reach a limit state due progressive loading.

For example, in bridge piers (Fig. 1a, b) and dams (Fig. 1c, d), it can be observed that frequency values of modes are significantly affected when the water levels rise and submerge large lengths/section of this type of structural systems.

A recent study described in Pereira, Magalhães, Gomes, Cunha, and Lemos [67], where the modal quantities of an arch dam were monitored and estimated during the first filling of the reservoir, shows that, in fact, the effect of the water level can have a significant influence on the properties of a large number of natural modes, with frequency values decreasing proportionally with the increase in water level.

3 Data Acquisition and Sensors

3.1 Sensors

Civil structure modal testing is commonly conducted using accelerometers (Fig. 2). Table 1 shows the typical accelerometer sensitivity, range, and bandwidth required for different testing conditions and excitations. In general, the DC component on the acceleration bandwidth is not required for modal testing but it is needed to detect permanent displacements due to change of state, residual displacements, or damage.

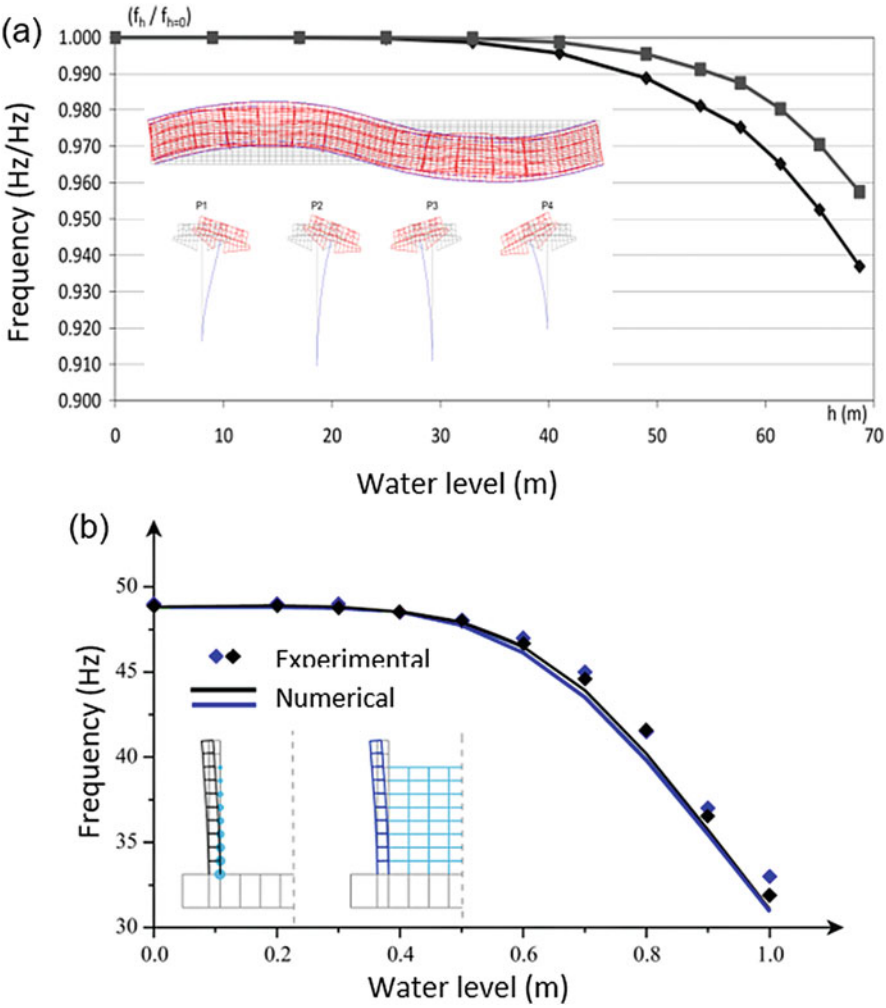

Fig. 1 Dynamic effects imposed by the water level: (**a**) changes observed in piers of a curved bridge [87], (**b**) changes observed in natural frequencies of a dam model [57]

In civil engineering, rigid systems are considered those with natural frequencies greater than 33 Hz, so higher frequencies are generally needed for component testing.

Data from spatially distributed sensors installed in civil structures must be precisely synchronized. Time lag between records of different sensors must be less than 1 ms. The lag between recordings can cause apparent complex modes on the identification [44] and in most cases can be identified from the phase between records.

Table 1 Accelerometer typical characteristics

Excitation	Bandwidth (Hz)	Range (G, +/–)	Sensitivity (G)
Impact	0.05–300	50	1e-3
Force vibration	0.05–40	2	1e-3
Ambient	0.05–40	0.25	1e-5
Earthquake	0.05–40	4	1e-3
Traffic	0.05–200	4	1e-3
Blasting	0.05–200	10 (in adjacent structure) >100 (structure close to source)	1e-3
Use	0.05–20	0.25	1e-4

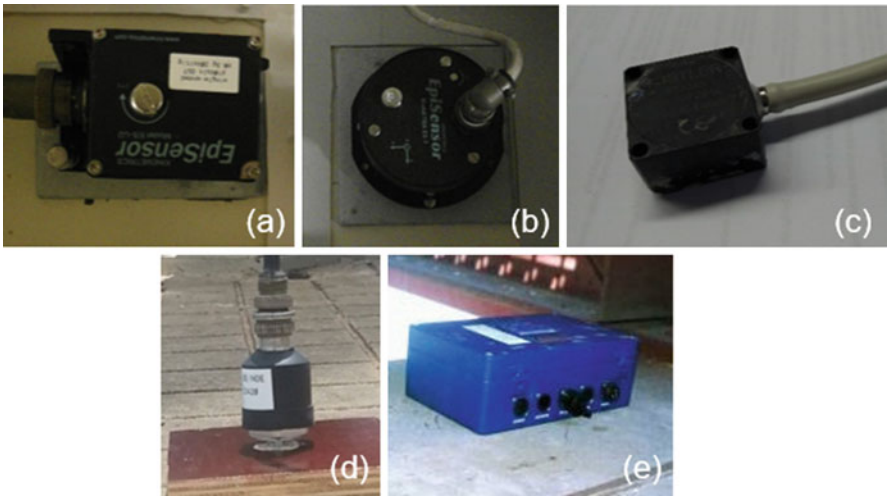

Fig. 2 Accelerometer types used in civil dynamic testing: (**a**) force balance uniaxial, (**b**) force balance triaxial, (**c**) microelectromechanical systems (MEMS), (**d**) piezoelectrical, and (e) integrated station with GPS

Due to the large dimensions of civil structures, data is usually stored locally and afterwards transmitted by cable or using cellular networks to a central storage system. The transmission of analog signals is generally avoided due to electrical contaminations and data loss. The ADC (analog-to-digital converter) and the signal conditioning units are usually installed next to the sensor, and the data transmission is made digitally and, in general, using fiber-optic medium, so as to fulfill the recommended minimum signal-to-noise ratio, which would be higher than 3.

Other sensors used in some civil dynamic testing and monitoring consist of strain gages, displacement sensors, velocity meters, tilt-meters, and image-based optical sensors. Thorough examples of sensor use can be found in ▸ Chap. 2, "Sensors and Their Signal Conditioning for Dynamic Acceleration, Force, Pressure, and Sound Applications". In this section, only a brief reference exemplifying those used in civil testing is made.

Velocity sensors and tilt-meters are capable of measuring the structural vibration speed and can be used as alternatives to accelerometers. They are based on laser or inductance, can achieve very high sensitivities, and can therefore be suitable for testing where there is need to measure vibrations with low amplitudes. However, these sensors are generally limited in capturing lower frequencies and therefore are not appropriate for slender flexible structural systems and for continuous monitoring. As a result, this type of sensors seems to be most suited for seismic movements [72].

Strain gages based on several types of transducing principles can be found in the market and in civil monitoring applications, such as resistance-based, optic-based (most common are Fiber Bragg Gratings, FBG), Carlsson or vibrating wire, with numerous solutions for mounting and fixing to civil structures, such as glue, fixed, embedded, or welded. For the purpose of modal civil testing, only the first two types, resistance (Fig. 3a, b) and optic (Fig. 3c), are capable of providing accurate dynamic data output. Regarding their mounting on civil structures, these two types of strain gages are widely available for gluing (Fig. 3a) and welding (Fig. 3b) to metallic components and for embedding in concrete (Fig. 3c).

Given the adequate signal conditioning and ADC features, these sensors are capable of providing resolutions that can be much smaller than 1×10^{-6} m/m, especially when assembling them in Wheatstone bridges. A typical use-case of Wheatstone Bridge assemblies consists of measuring flexural strain in the top and bottom flanges of Steel I-section. With the appropriate assembly, the flexural strain

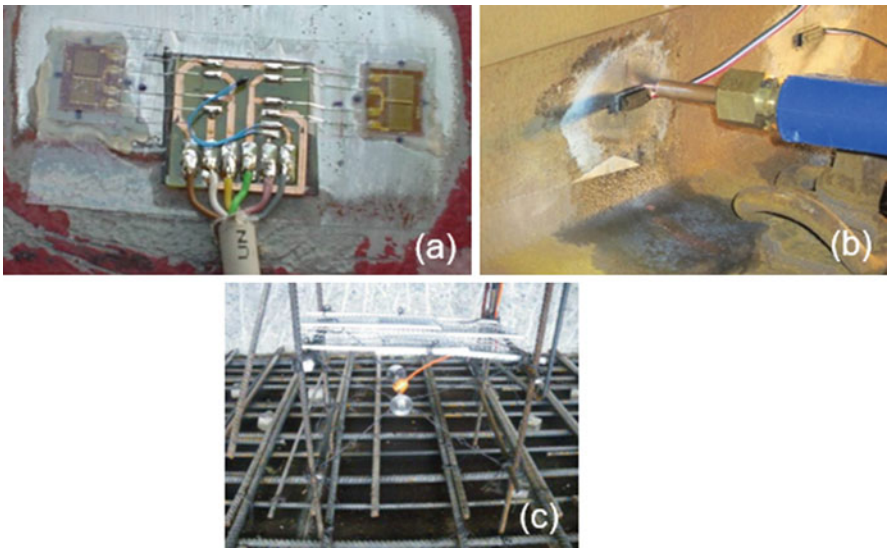

Fig. 3 Strain gages used in civil testing: (**a**) resistance-based glued, (**b**) resistance-based welded, (**c**) embedding resistance strain gage inside concrete element

can be multiplied by a factor of 2 or 4. Even if these resolutions result in smaller sensitivities to detect natural modes, when compared to the use of accelerometers, the fact that strain gages, appropriately arranged, are self-compensated for temperature effects along with their capacity to measure vibration waves with any (large) period makes them appropriate for detecting low order natural modes in large flexible civil structures, especially when these are composed of large-section elements.

Relative displacement sensors with the capacity to output accurate data at dynamic rates are also widely used in civil structural testing and generally fall into the class of LVDT (Fig. 4c), precision potentiometer, magnetostrictive (Fig. 4a, b), and optical. These types of sensors are generally fixed, or glued, to both structural nodes for which the relative displacements are to be obtained, with due care to keep rotations free at both ends. They are generally deployed between both ends of joints, bearing supports, base isolation or control devices to measure the vibrations imposed to these and also to capture the structural natural modes associated with the displacements imposed to them. Their capacity to measure vibration waves with long periods makes them particularly suitable for monitoring longitudinal mode shapes in high pier bridges such as cable-stayed and suspended ones.

Load cells generally consist of mechanical assemblies of strain gages, either resistance-based or optical, with resistant housing for high durability and force resistance. Their shapes can vary significantly so as to adapt to specific applications, such as, for example, those installed in downward end of the hangers of a bow-string

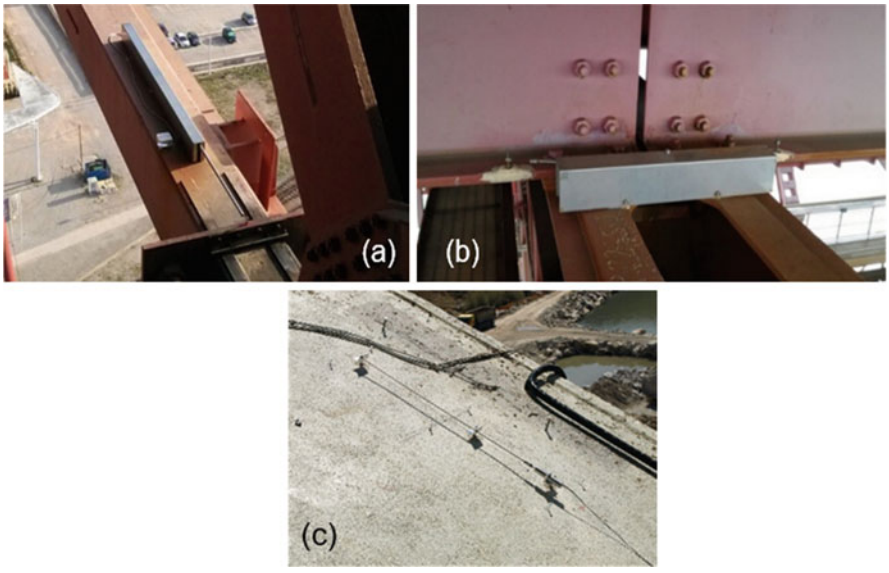

Fig. 4 Relative displacement sensors used in civil testing: (**a**, **b**) magnetostrictive sensor, (**c**) LVDT

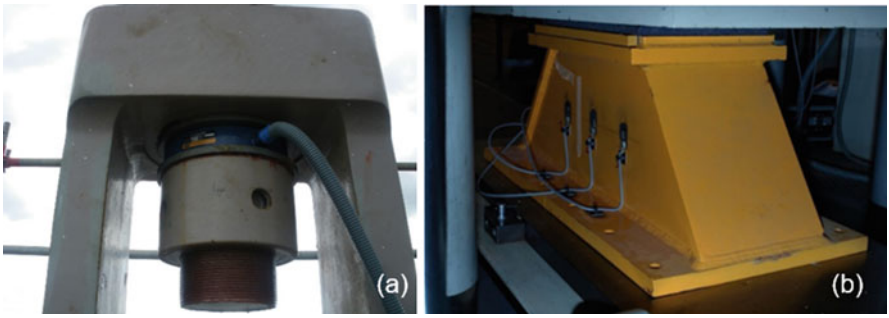

Fig. 5 Load cells used in civil testing: (**a**) standard and (**b**) specifically fabricated

bridge (Fig. 5a). When load cell solutions are not available in the market, appropriate strain gage assemblies can be defined and deployed in specific structural elements, such as the bridge bearing device shown in Fig. 5b which, after calibration, is now capable of measuring the forces applied to it. All remarks made above for strain gages apply to load cells regarding sensitivity, applicability, and ability to detect (mostly) lower order natural modes, even if characterized by very low values of frequency.

Environmental sensors are used for dynamic civil testing with the objective of measuring the effects of any demands that may influence the structural dynamic response or which may influence the structural response by changing the materials' properties or the boundary conditions.

Regarding the demands, wind is generally measured with anemometers such as the one shown in Fig. 6a or with weather stations combining anemometers with additional weather measurements, such as the one shown in Fig. 6b, c. Anemometers can be based on cups or on ultrasonic measurements (Fig. 6a–c), where the latter are more durable, precise, and require less maintenance. Water level can be measured using buoy systems, even if the newer more robust and precise ones are based on radar measurements such as the one shown in Fig. 6d and installed on the downward faces of box girders or beams.

Concerning additional actions that may change the dynamic structural response, scour is one of the most difficult conditions to measure in real bridges and can be measured using sonar-based sensors such as the one shown in Fig. 6f, which can be fixed to the upstream side of a bridge's pile header or submerged beams to detect the variation of pressure or deformation depending on the scouring level. Structural element temperature is generally measured using glued of embedded resistance thermometers such as those shown in Fig. 6e, or using thermistors, which are generally less precise and less durable than the former. Rain, hail, and humidity can generally be measured with high precision using weather stations such as the one shown in Fig. 6b.

Fig. 6 Ambient sensors: (**a**, **b**) ultrasonic anemometer from GILL Instruments, (**c**) cup-based anemometer from Vaisala, (**d**) radar-based water level sensor from OTT (**e**, fit) weather stations from VAISALA, (**f**) embedded resistance thermometers of the type PT100, (**h**) sonar sensor UDM200 for scour monitoring

3.2 Selection of Data Acquisition Systems

Data acquisition systems (DAS) must be selected based on the number of sensors (scalability), type of sensors (generality), sensitivity, stability, robustness for the environmental actions, and usage conditions. DAS could be concentrated or distributed depending on the size and level of noise present on the system. For highly electrical environmental noise, digital and optical data transmission is preferred. Typical sensitivity varies depending on the sensors, but 24 bits ADC converters are the most common. Synchronization of the different channel data is essential, and nowadays synchronization is in the order of the nanosecond or lower.

Sampling frequency is highly dependable on the parameters to be measured so flexibility on DAS per channels is higher convenient. Meteorological stations can be sampled in terms of minutes or hours and accelerations in terms of microseconds.

All connection to the DAS should consider the environmental conditions and the level of vibrations presented. Many structures require military type or bolted connectors for long-term monitoring. Connections based on friction are in general not reliable.

Voltage protection and stability is a must for long-term monitoring. Typically, UPS systems are used to stabilize, clean, and guarantee the voltage supply to the

system. See ▸ Chaps. 2, "Sensors and Their Signal Conditioning for Dynamic Acceleration, Force, Pressure, and Sound Applications", ▸ 4, "Applied Digital Signal Processing" and ▸ 5, "Introduction to Spectral and Correlation Analysis: Basic Measurements and Methods" for more detail on DAS. Vandalism is common so additional protection to the sensors and DAS should be considered.

4 Basic Procedures for SHM in Civil Engineering

Several different methods are used to identify the modal and dynamic response properties of civil engineering structures. They have been developed for more than a century, but most documented tests on real structures started to be reported in the 1950s with the development of more flexible and transportable sensing and recording systems [22, 41].

All civil structures present different levels of nonlinearity associated with constituent material, foundation conditions, and interaction between components, even if no damage is present. The nonlinearity and the need to evaluate the different states that could be present in a structure require a clear understanding of the possible excitation conditions and transitions between different response levels. Hence, key decisions for the selection of testing and analysis procedures should include:

1. Expected levels of excitation
2. Appropriate sensing and recording devices
3. Sensor locations
4. Applicable identification procedures
5. Desired identification properties
6. Representative model of the structure at each testing amplitude level

In reinforced concrete structures, the strain–stress relation is nonlinear. This nonlinearity could be elastic (recoverable) or inelastic depending on the strain levels [106] or boundary conditions. The opening and closing of micro-cracks causes an important stiffening effect and corresponding modal parameter change. If this micro-cracking is not excessive, once the loading is removed the system returns to its original stiffness. One very early example of this condition was documented by Keightley et al. when testing a dam reservoir under different periodic shaking loads [51]. The boundary condition, typically soil, is also a highly nonlinear material and highly sensitive to humidity and temperature variations [34, 36, 37]. Intrinsic energy dissipation mechanisms are also highly sensitive to amplitude [30]. These conditions require identification procedures that can capture the desired parameters and which are stable under these conditions. In general, results are valid for a specific response amplitude and environmental conditions.

Another important consideration is the differences between models' assumptions and reality. Typically, civil structures are modeled as linear viscoelastic. In practice the energy dissipation properties are mixture of different mechanisms where friction between components and radiation at foundation level also play an important role

[47, 94]. Even at very low amplitudes of vibrations, the variations in damping with amplitude are important, and at large amplitudes the response can also include hysteretic behavior among many others [4, 24]. Some numerical models have been proposed to capture the variation of damping with amplitude in buildings [45, 52, 89], but they are in general not used for the identification procedures.

This chapter presents a summary of the most common testing procedures of full structures under dynamic loads at field conditions. It presents the basic instrumentation, identification methods for system identification, response monitoring, and change of state detection.

The basic excitations considered for the identification depend on the structure size, complexity, foundation characteristics, usage, location, time for testing, and budget. The most common testing techniques are:

1. Initial conditions testing
2. Vibratory shakers
3. Ambient vibrations
4. Operational conditions
5. Extreme loading events: earthquake, blasting, wind

4.1 Initial Conditions Testing

Initial conditions, displacement and velocities, are excited by pulling [27, 56, 59], pushing [101], or impacting [60] the structure. The excitation has to be selected and applied to excite the local or the global response of the structure. Local responses are obtained when the perturbation is applied to the elements under study, like beams, columns, slabs, or walls. They are typically exited by hand systems that generate pulling or pushing, heel dropping, jumping, hammer impacting, blast impacting, and others, depending on the element characteristics and response levels desired. Global responses can be obtained by pulling, pushing, and blast impacting the structure. Several pulling mechanisms have been developed based on jacks, accompanied with quick release mechanisms (collapse mechanism [6], breakable fuse [10], etc.). Additionally, truck or heavy equipment can be used to pull the structural systems.

This type of testing is quite limited in existing structures because the level and location of loading should be carefully selected and controlled so that the response of the system is under the desired response levels. In general, the loading should be large enough to excite the structure to the desired level without damaging it. To accomplish this, a numerical model of the structure should be developed and calibrated under real conditions (typically derived from ambient test). The models are only approximations to reality, so several variations of the models are recommended to quantify, in a reliable way, the possible states that the structure or its components can reach.

To globally test a structure, it should generally not be in operation. Preparation for the test including modeling, development of loading devices, and setup of the sensors and recording system can take from weeks to months, depending on the level of response required.

The procedure applied to define the initial displacement or velocity controls the modal parameter excited. For low frequency modes, simple displacement patterns are recommended. When applying initial velocities, the impact durations should be related to the frequency of interest.

Response levels can reach high values, so response monitoring sensors should be anchored. Typical recommended acceleration sensor sensitivity is 0.001 g with a range of +/–10 g and a bandwidth between 0.05 to 20 Hz. DC components for this excitation are in general not required for acceleration. The measurement of the initial displacements or the applied impact force is generally recommended, so as to be able to obtain more information like static stiffness or inertial mass. For modal characterization, the most common procedures are Ibrahim Time Domain Decomposition (ITD), Eigensystem Realisation Algorithm (ERA), Peak Picking (PP), Short-Time Fourier Transform (STFT), and Logarithmic Decay, among others.

4.2 Force Vibration with Shaker

This type of testing is based on an excitation produced by a rotatory [43, 93, 105] or linear shaker [26]. The shaker generally produces the force by an eccentric or inertial mass. Inertial forces are in the range of +/–50 kN for practical movable systems. Due to its dimensions and at the high end of loading, the system should be anchored to the structure. The frequency band of excitation is typically between 0.2 to 15 Hz and in general has a single-frequency nature. Response levels can reach quite high values so the response monitoring sensors should be anchored. Typical recommended sensor sensitivity is 0.001 g and a bandwidth between 0.1 to 20 Hz. DC component for this vibration is not generally required.

Due to the medium and high levels of vibration that can be obtained by the shaker at resonance conditions, the structure should be nonoperative or with restrictive operations (especially in buildings). Also, the engineer responsible of the test should have previously analyzed the possible damage states that could be induced in the structure. For low levels of vibration excitations, no special care is normally needed, but for large testing loads, a set of numerical models is recommended to estimate the response.

Due to the preparatory requirements, namely the anchoring of the shaker and sensors, these procedures have very limited application. Nevertheless, the possibility of controlling the amplitude, direction, and location of the applied loading and response levels allows the observation of the structures' nonlinearities, as observed by [41, 51].

Typically, testing time could be extremely long at large amplitudes, due to the nonlinearity of the system when searching for resonance frequencies. Data analysis is relatively simple but requires extensive observation and control by the testing operators. The experimental results typically consist of acceleration, velocity, or displacement amplification response as a function of excitation frequency. Typical analysis procedures are peak picking (PP), enhanced frequency domain decomposition (EFDD), and others.

4.3 Ambient Vibrations

Ambient vibrations are produced mainly by wind, traffic, micro-tremors, and usage. In general, the excitations are not broad banded and their main energy is below 20 Hz. This bandwidth is good enough to excite the low-frequency modes of the system. Typical wind-induced drift in buildings is observed in the order of 2/1000 [95] and acceleration response amplitude in the order of 0.001 g or even lower, so sensitive accelerometers are needed. Other sources of ambient excitation could have larger amplitude so typical range is +/–0.25 g. Recommended sensor sensitivity for wind-induced vibration is 10^{-5} g and a bandwidth between 0.1 to 30 Hz. The DC frequency component for this vibration is in general not required. Due to the low level of excitation, anchorage is not required and normal friction is sufficient to keep the sensor in position, unless a permanent monitoring system is desired.

Due to the quick deployment of sensors and the extreme low risk of damaging the structure, these testing procedures are quite useful and convenient to identify the modal properties of a structure. Nevertheless, due to the extreme low-level response, the properties observed are restricted to a linear range and in general are not good predictors of higher response, especially when damage occurs.

Depending on the objective of the monitoring the density of the recording locations must be adequately chosen. If only frequency is desired, only few degrees of freedom are needed, and care should be taken not to put the sensor in a nodal point of the mode of interest. If the shape of the mode is required, then a much densely recording network is needed. The simplicity of the procedures allows the deployment of several sensors that should be properly synchronized.

For short-term recording it is not required to have a large number of recording points. In this case, one or several sensors are defined as fixed references and another set is moved around the structure to capture the response. Later the mode shape is integrated with the help of the reference point. Typical recording times for each setup are from 20 to 60 min, to obtain reliable properties.

Permanent or long-term ambient monitoring is also quite popular to detect slow and abrupt variations of modal properties. For this case the sensors should be permanently anchored and protected from the environment and the users of the structure. Long time stability of the sensors and recording system should be carefully studied for the selection of the components and synchronization between sensors. Due to the extended monitoring time, data have to be carefully analyzed before any attempt for identification or classification is done. This analysis should include at least the verification of the bandwidth of the response, the interference or contamination by periodic excitation, like motors, the occurrence of impacts to the structures, or impacts due to traffic or users. The portions of contaminated data have to be removed.

For long-term monitoring, data can be obtained in packages of shorter durations. Typically, 5–15 min are sufficient. For each data package system identification has to be performed, and later the modal properties identified have to be linked to previous obtained values. This link, in the absence of abrupt changes, can be

done using a distance metric, as the one presented in Eq. (81), which considers a normalized frequency and shape similarity (MAC) between consecutive modes and with consideration of the number of sensors. Damping is not generally used in the tracking due to its uncertainty. Example of tracking procedures from ambient vibrations can be found in [17, 49, 68].

Because of the sensitivity of civil structures to the environment, specially temperature, humidity and level of excitation, and the modal parameters vary in time [20, 32, 38, 92, 107]. Typically, modal frequency can have a daily change due to temperature of 1–2% in buildings, if freezing of soil is not present. In case of freezing, the variation on frequency can be as strong as 50%. Due to rain or high humidity the frequency change is on the order of 6%. The effects due to rain, extreme low temperatures, vary daily (temperature and radiation) and seasonal. So, to understand the magnitude and effect of the change, consistent observation periods must be considered. The relation between variations and modal properties is multivariate so the largest the observation periods the best.

The modal changes due to environmental fluctuations are quite large so if the system is required to detect deterioration, these variations can be easily masked by them. In order to increase the identification capacity of change of state, several approaches have been implemented and generally named as data normalization procedures. These consist of removing the effects of the actions, from the responses, using Principal Component Analysis [102], multilinear or nonlinear regression, neural networks [81, 107], and ARX models, among others [65].

In general, the excitation is not measured so the typical identification procedures are based on Operational Modal Analyses. Among the most used identification techniques and some references for examples of applications are PP, ERA [15], Extended Frequency Domain Decomposition [11], and Stochastics Subspace Identification [63, 62, 64].

5 Identification Methods

The identification methods used can be classified according to their basic properties:

(a) Solution space: time, frequency, state
(b) Parametric or non-parametric
(c) Direct or iterative
(d) Type of excitation

Table 2 presents the most common methods used in civil structures. There are also other methods used such as linear [78] and nonlinear time filters [76], and for others see for example Peeters et al. [66].

Table 2 System identification techniques

Name	Parametric	Domain	Excitation	Comments	Reference
Peak Picking (PP)	No	Frequency	Ambient, or colored or white noise force excitation	Easily understood and used	▶ Chap. 10, "Experimental Modal Analysis Methods"
Short-Time Fourier Transform (STFT)	No	Frequency	All type	The initial step in most identification process Best to evaluate nonlinearity of the system	[21]
Hilbert–Huang Transform	No	Time and frequency	All	Includes the possibility of nonlinear systems	[42]
Frequency Domain Decomposition (FDD)/Extended FDD (EFDD)	No	Frequency and time	Ambient, or colored or white noise force excitation	More robust tan PP	[13, 12]
Eigensystem Realisation Algorithm (ERA)	Yes	Time	Impulse		[48]
Natural Excitation Technique ERA (NeXT-ERA)	Yes	Time	Ambient		[46]
Stochastic Subspace Identification (SSI COV-SSI DATA)	Yes	Time	Ambient	Assumes properties of the unknown input excitations	[62, 99]
Multivariable Output-Error State sPace (MOESP)	Yes	Time	Input-output		[100]
N4SID	Yes	Time	Ambient -Input/output	Includes SSI and MOESP	[98]
Iterative Modal Response	Yes	Time	Earthquake	Iterative	[3]

5.1 The Fourier Transform and Time-Frequency Analysis

Among the initial steps in the identification analysis is the evaluation of its frequency content by way of the Fourier Transform (FT) and the STFT or spectrogram. The visualization of the component and its variations with time allows the user to identify the bandwidth of the signal, the presence of permanent or stationary signals, and the possible nonlinear characteristics or variation of apparent predominant signals.

The FT presents a summary of the energy for each frequency component in the whole signal. The STFT uses the FT in a relative short duration moving window, as shown in Fig. 7. The results are plotted in a 3D plot or color map, Fig. 8. The STFT uses a constant time window so careful selection of its duration shall be performed to capture the predominant frequencies and its variation with time. As indicated by Cohen [21], this transformation is redundant so it does not have an inverse. This can be overcome if the S-Transform is used instead [91]. Another alternative for some nonlinear system is the Hilbert–Huang Transform that uses the empirical mode decomposition (EMD) and the Hilbert transform to capture the variation frequency due to nonlinear responses. An example of application can be found in Shi et al. [86].

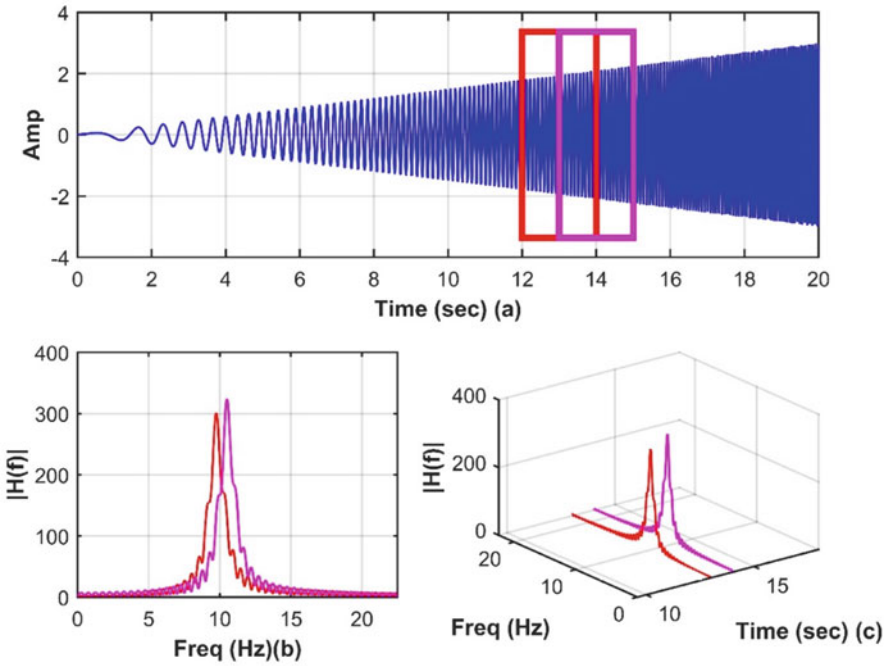

Fig. 7 Spectrogram construction. (**a**) Time series. Two windows sections to be FFT. (**b**) FFT of two windows. (**c**) 3D plot of FFT centered on the mid time of selected window. No treatment is use in this example to select the time window to reduce leakage

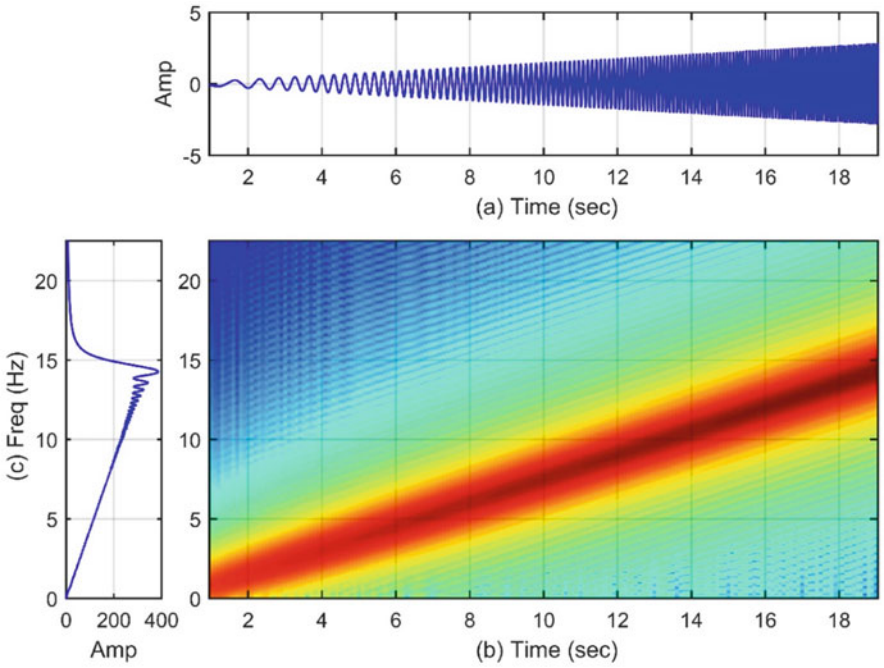

Fig. 8 Spectrogram of sine function that presents a linear varying frequency (0–15 Hz) and a linear increase of amplitude (0–3). (**a**) Time series, (**b**) spectrogram, and (**c**) Fourier transform of the whole signal

5.2 Extended Logarithmic Decay

5.2.1 Linear Adjustment of the Decay

The analysis on a single predominant frequency decaying response can be performed with and extended version of the logarithmic decay presented in Chapter 12. In this case assuming a viscoelastic one degree-of-freedom system, the decay follows the rule

$$v(t) = e^{-\beta\omega t}\left[\rho\cos\left(\omega_D t - \theta\right)\right] \tag{1}$$

Figure 9 presents the acceleration response of a wharf structure subjected to a quick release [10]. Because modes are clearly separated, the signal is band pass filtered to select the second mode. From the statistics of the zero crossing and evaluation of the linearity of the frequency, the amplitude can be evaluated (red points in Fig. 10). If all maximum absolute values of each cycle are identified and numbered, a plot can be made of $\ln(|v(t)|)$ versus its sequential number. If the resulting plot is linear, we can conclude that a viscous energy dissipation mechanism is predominant. If it presents other shape, friction or other mechanisms can be

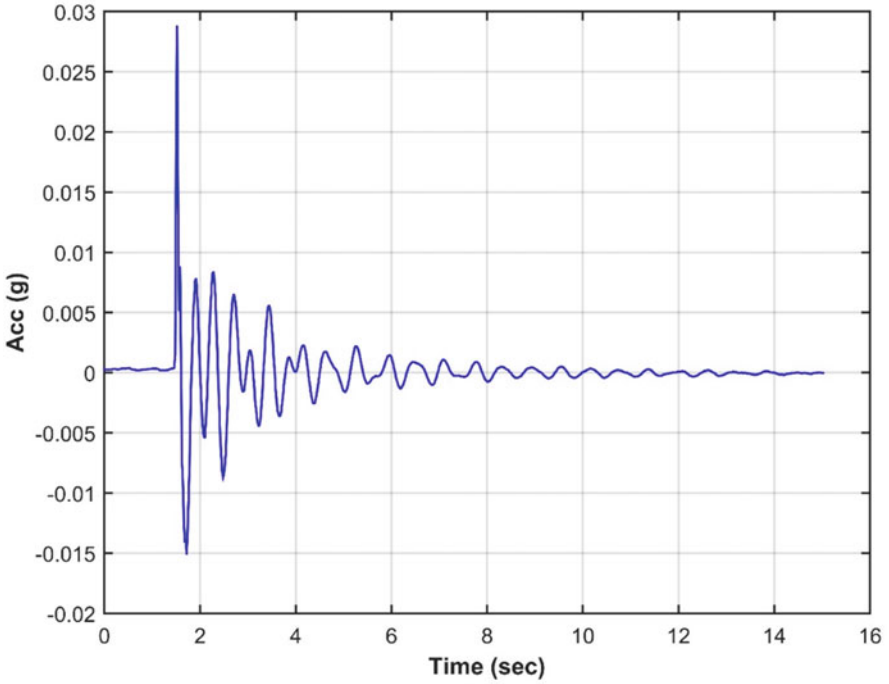

Fig. 9 Acceleration response of wharf structure. Two modes are present

detected. Due to noise, the arrangement of the data is not always linear, so a least square regression can be performed to obtain the slope, which relates to an equivalent viscous damping of the system given by Fig. 11:

$$\beta = \frac{slope}{\pi} \tag{2}$$

This procedure is not appropriate when multiple predominant decaying frequencies are present. In this case other methods like ITD and ERA are more appropriate.

5.2.2 Nonlinear Adjustment of the Decay

The decay of the response for a single observation point from a system with several degrees of freedom can be expressed as

$$v(t) = \sum_i e^{-\beta_i \omega_i t} \rho_i \cos\left(\omega_{Di} t - \theta_i\right) \tag{3}$$

where the parameters are optimized through the minimization of an error function is not recommended due to the large number of local minima, ERA and ITD are more

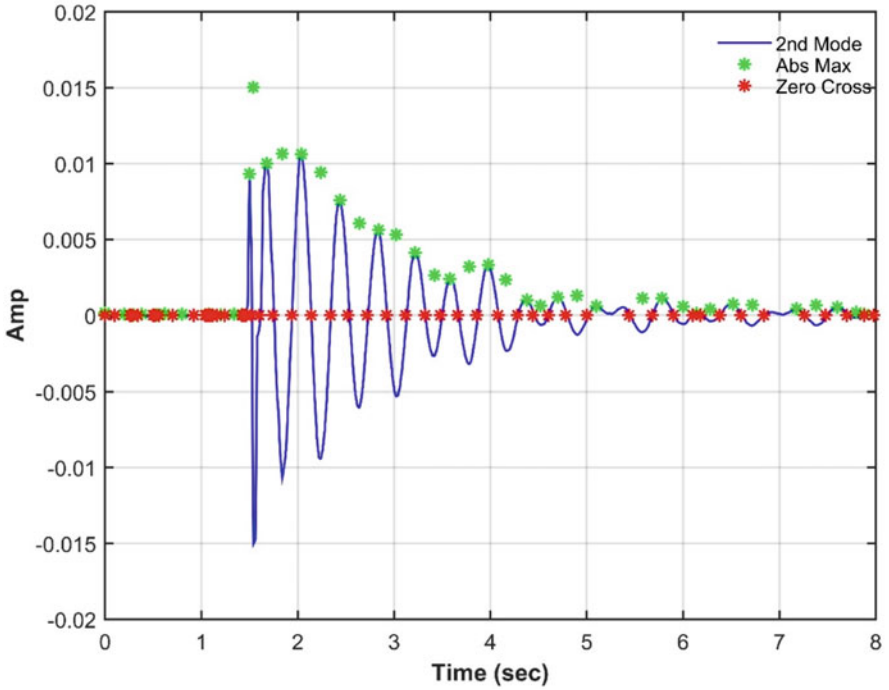

Fig. 10 Zero crossing and maximum absolute values of the second mode after extracting from original signal

appropriate methods. Nevertheless, once a close solution is found, several studies on the decay can be performed. For the original response of the initial condition test shown in Fig. 9, the nonlinear fit is shown in Fig. 12. Figure 12 presents the fitted parameters for the whole window. Figures 13 and 14 present the fit to two smaller size windows. Results of the fits are different, indicating the nonlinearity present in the response. Additionally, the error function of the fit can be used to evaluate the sensitivity of the different parameters to the error. For example Fig. 15 presents the case observed when fixing all parameters except the damping for the second mode indicating that values between 5% and 7% can give similar adjustment to the response.

5.3 Eigensystem Realization Algorithm

The method developed by JUANG and PAPPA [48] allows the parameter determination from a response decaying signal. This decaying signal can be obtained by direct experimental test (initial conditions testing) or derived from ambient vibrations (NeXT ERA, Random Decrement). See additional details of ERA in ▸ Chap. 10, "Experimental Modal Analysis Methods".

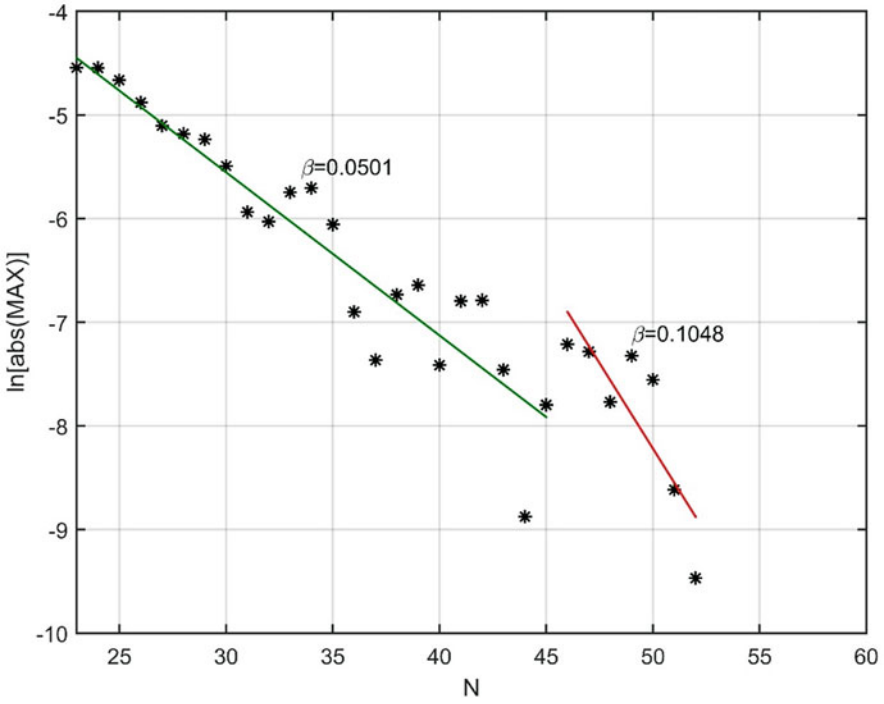

Fig. 11 Estimation of damping by least square fit to maximum absolute values

The algorithm uses the decay response of the system organized on a Hankel matrix:

$$[H_{k-1}]_{(prxqs)} = \begin{bmatrix} \underbrace{[Y_k]}_{p\times q} & [Y_{k+1}] & \cdots & [Y_{k+j}] \\ [Y_{k+1}] & [Y_{k+2}] & \cdots & [Y_{k+j+1}] \\ \vdots & \vdots & \cdots & \vdots \\ [Y_{k+i}] & [Y_{k+i+1}] & \cdots & [Y_{k+i+j}] \end{bmatrix} \begin{matrix} \\ \\ \\ \updownarrow i \end{matrix} \\ \leftrightarrow j \tag{4}$$

where p is the number of sensors, q the number of independent excitations, and i and j are the selected number of observations. There are several recommendations for defining the number of observations and the size of the problem to solve, but the number of columns should be at least twice the number of expected modal components present on the signal and the number of rows should allow the representation of the decay without including the noise portion. The stability diagram, presented in ▶ Chap. 11, "Experimental Modal Parameter Evaluation Methods" and later described below, is the most common procedure to select the representative modes.

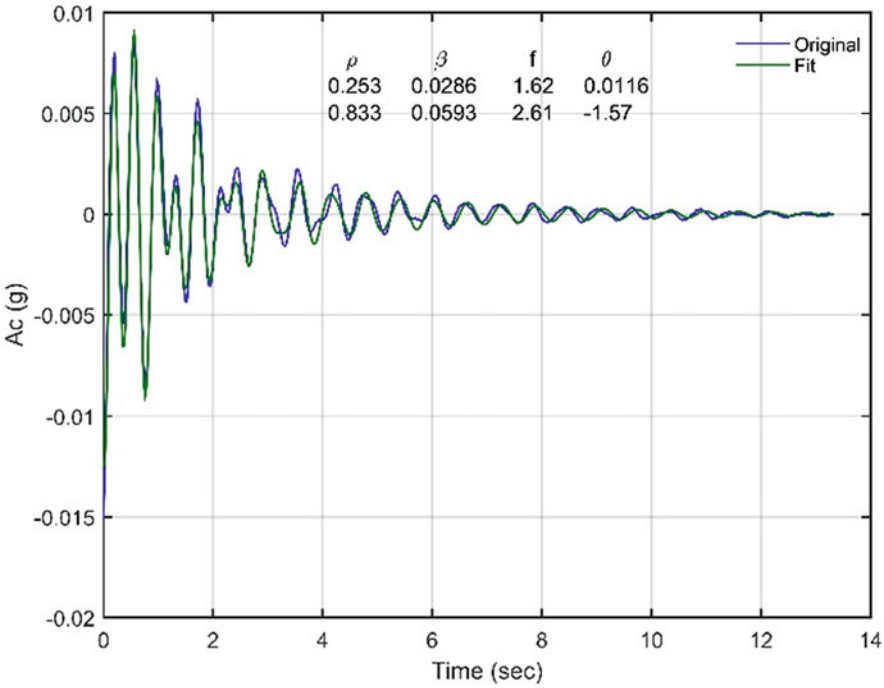

Fig. 12 Nonlinear adjustment to multimode decaying signal. Whole window

The singular value decomposition of $[H]$

$$\underset{(prxqs)}{[H]} = \underset{(prxpr)}{[U]} \underset{(prxps)}{[\Sigma]} \underset{(psxqs)}{[V]^T} \tag{5}$$

selecting a reduced number of non-null singular values.

$$\underset{(prxqs)}{[H_0]} = \underset{(prx2N)}{[U_{2N}]} \underset{(2Nx2N)}{[\Sigma_{2N}]} \underset{(2Nxqs)}{[V_{2N}]^T} \tag{6}$$

and considering

$$\underset{(pxpr)}{\left[E_p\right]^T} = \left[\underset{(pxp)}{[I]} \quad \underset{(pxp)}{[0]} \quad \cdots \quad \underset{(pxp)}{[0]}\right] \tag{7}$$

The system state and observation matrix can be found as

$$[A] = [\Sigma_{2N}]^{-1/2}[U_{2N}]^T [H_1] [V_{2N}] [\Sigma_{2N}]^{-1/2} \tag{8}$$

$$[C_d] = \left[E_p\right]^T [U_{2N}] [\Sigma_{2N}]^{1/2} \tag{9}$$

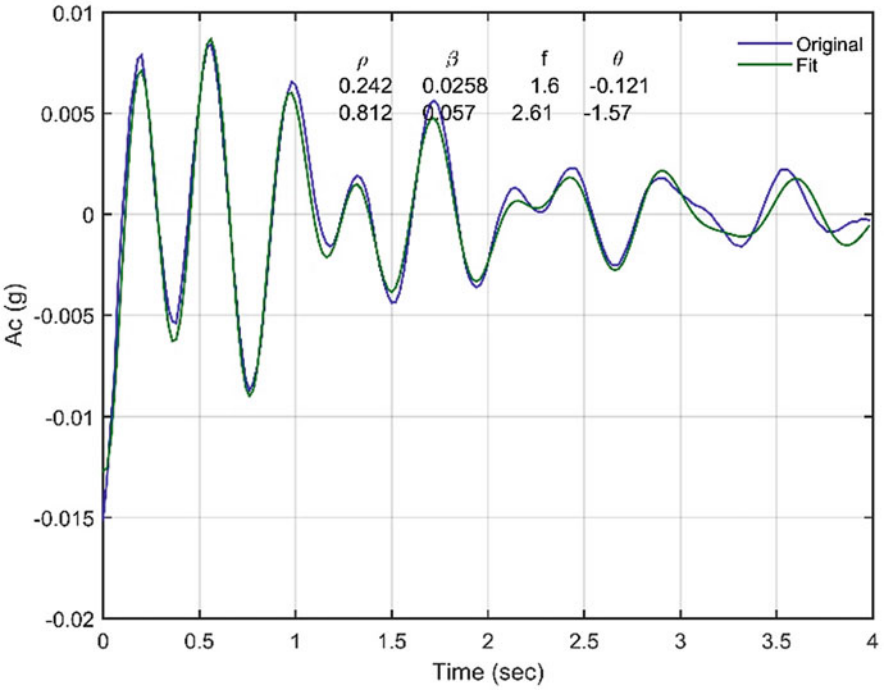

Fig. 13 Nonlinear adjustment to multimode decaying signal. Initial 4 s window

The eigenvalues and vectors of $[A]$ are

$$[A]\{\Psi_{ui}\} = \lambda_{ui}\{\Psi_{ui}\} \tag{10}$$

from which the modal shape at the observed and locations can be found as

$$\underset{(px1)}{\{\phi_{yi}\}} = \underset{(px2N)(2Nx1)}{[C_d]}\{\Psi_{ui}\} \tag{11}$$

along with the natural frequency and damping of the mode

$$\omega_i = \frac{|\ln(\lambda_{ui})|}{\Delta t}; \quad \beta_i = -\frac{\mathrm{Re}\ al(\ln(\lambda_{ui}))}{|\ln(\lambda_{ui})|} \tag{12}$$

5.4 The Periodogram

Several identification techniques are based on the power spectral estimation or periodogram. ▸ Chaps. 4, "Applied Digital Signal Processing" and ▸ 5, "Introduction to Spectral and Correlation Analysis: Basic Measurements and Methods" presents

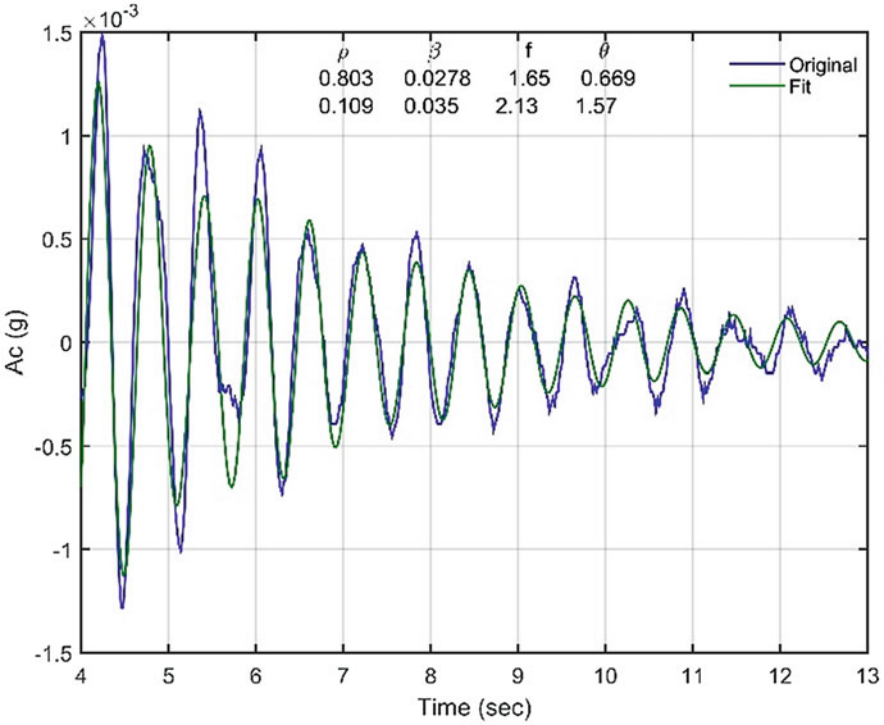

Fig. 14 Nonlinear adjustment to multimode decaying signal. Window from 4 s to end

the basic concepts of frequency domain analysis, power spectra, and periodogram. Here they are used to identify the modal properties of a system using PP, FDD, and EFDD.

Two estimators of the FRF are usually used.

$$H_1(f) = \frac{Y(f)X^*(f)}{X(f)X^*(f)} = \frac{S_{YX}}{S_{XX}} \tag{13}$$

where $Y(f)$ and $X(f)$ are the Fourier transform of the windowed signal, or

$$H_2(f) = \frac{Y(f)Y^*(f)}{X(f)Y^*(f)} = \frac{S_{YY}}{S_{XY}} \tag{14}$$

For the evaluation of $\hat{H}(f)$ we use the estimation of the periodogram

$$\hat{S}_{XX}(f) = \frac{1}{N_a}\sum_{n=1}^{N_a}(S_{XX})_n, \quad \hat{S}_{YY}(f) = \frac{1}{N_a}\sum_{n=1}^{N_a}(S_{YY})_n, \tag{15}$$

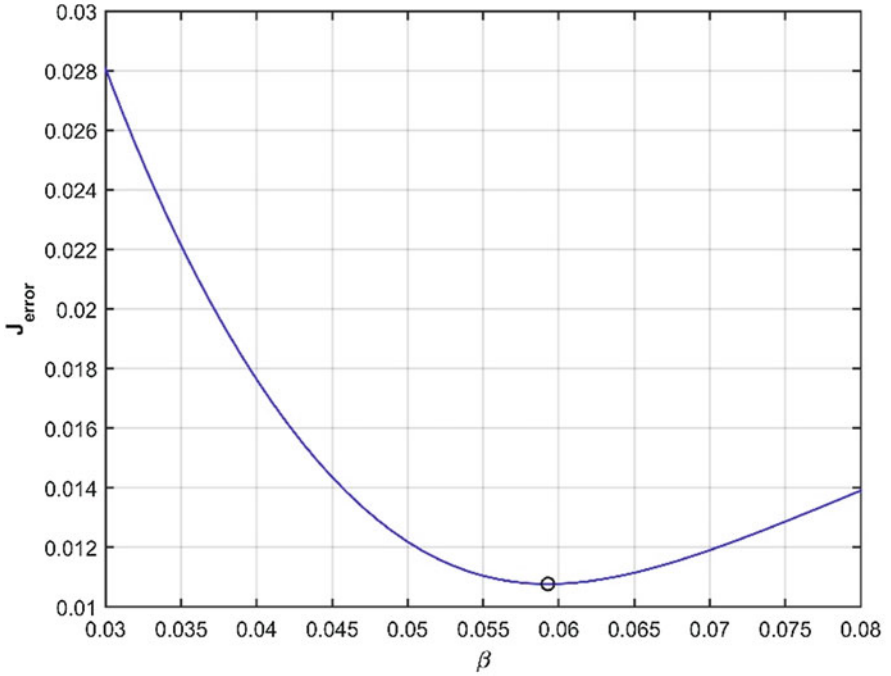

Fig. 15 Error as a function of second mode damping and optimal value for whole window

$$\hat{S}_{XY}(f) = \frac{1}{N_a}\sum_{n=1}^{N_a}(S_{XY})_n, \quad \hat{S}_{YX}(f) = \frac{1}{N_a}\sum_{n=1}^{N_a}(S_{YX})_n \tag{16}$$

The coherence in the frequency space is (see also ▸ Chaps. 5, "Introduction to Spectral and Correlation Analysis: Basic Measurements and Methods" and ▸ 6, "Frequency Response Function Estimation"):

$$\gamma^2 = \left|\hat{S}_{XY}(f)\right|^2 / \left(\hat{S}_{XX}(f)\hat{S}_{YY}(f)\right) \tag{17}$$

The coherence has values between 0 and 1. An unitary coherence reflects a clear agreement and consistent modal properties while a value lower than 1, for a given mode, can be obtained depending on:

1. Noise
2. Nonlinearity of system
3. Leakage
4. Out of phase effects

The signal-to-noise ratio can be estimated as

$$S/N = \frac{\gamma_{YX}^2}{1 - \gamma_{YX}^2} \tag{18}$$

In Fig. 16, the acceleration time series of channel 6 of the office building described in Sect. 10.1 is shown and the corresponding record shows important bursts of response. In case the signal is long enough, the high amplitude section can be removed if the remaining segments can be used to identify the structure properties. The record should be initially tested by estimating the periodogram. If clear peaks are present, in the absence of noise, they can be associated with structural properties. As an example, the power spectral density estimated by the Welch method, for all channel above ground for the TC Building, is presented in Sect. 10.1. In order to have a reliable spectrum several averages should be taken. When nonoverlapping time segments are used the uncertainty of the estimation is related by the inverse of the number of averages. The largest the number of averages, the smaller the uncertainty. This requires long records. In order to avoid leakage, the selected time segments shall be windowed. Typical window used for ambient vibrations are Hanning and Hamming. The length of the window affects the shape

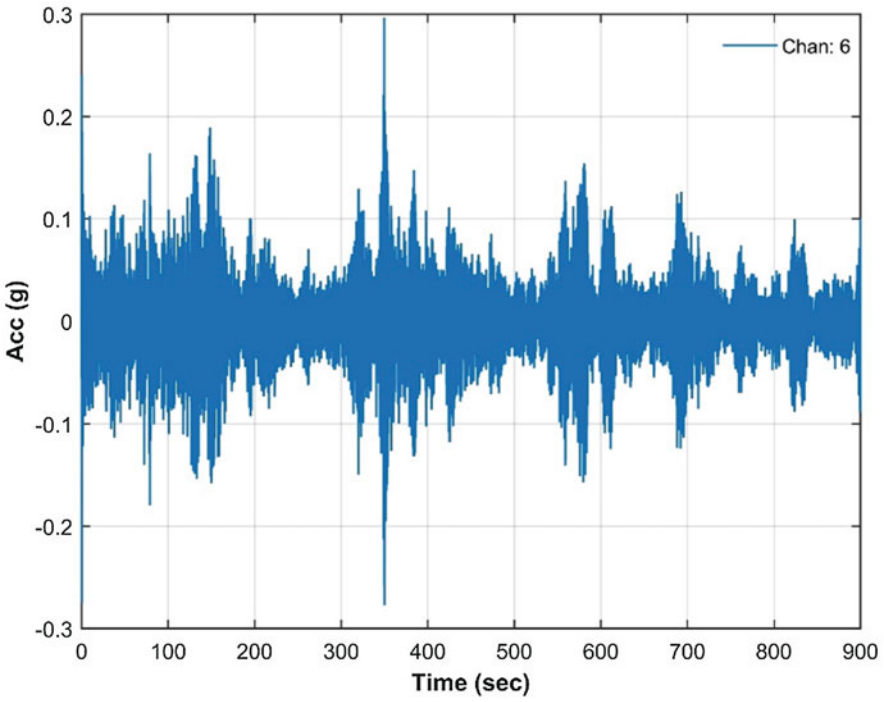

Fig. 16 Ambient acceleration response of 8 floors in an office building

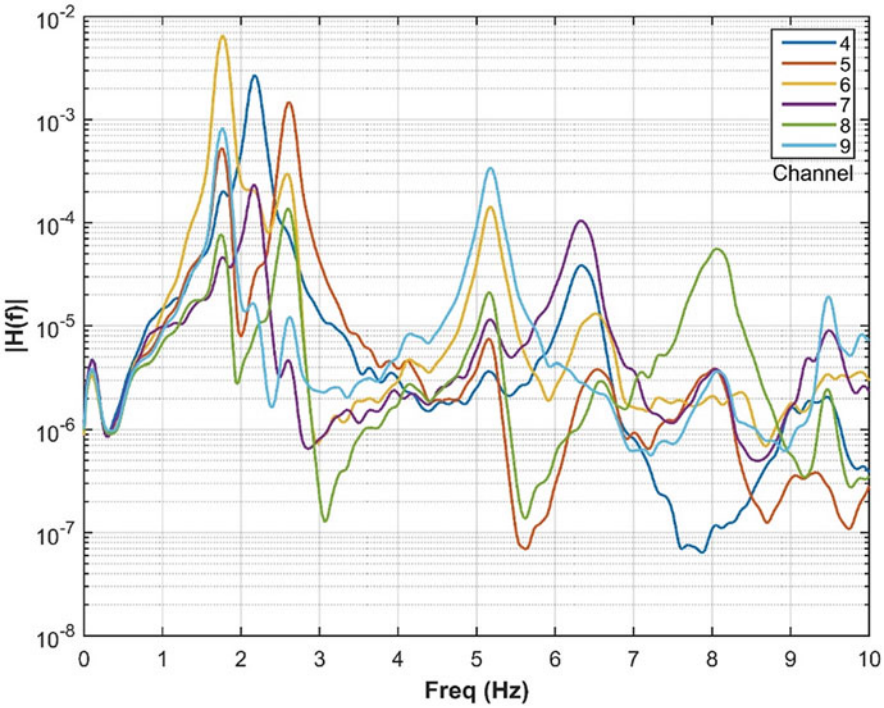

Fig. 17 Periodogram of all aboveground channels, 1–9, of an office building calculated by the Welch method

of the spectra and the identified damping. The largest the window, the smallest the effect on the damping estimation.

For typical structures with frequencies varying from 1 to 10 Hz, a window of length 20–30 s gives good results when averaged at least 30 times. This means records of more than 15 min duration must be taken. For lower frequencies, larger duration and windows are recommended.

From an initial visual inspection of Fig. 16 and of the predominant operational frequencies in Fig. 17, several peaks can be observed and, in this case, at least 8 are clearly detected. Nevertheless, not all channel presents all the peaks, because the operational response at these frequencies is small. The first three operational frequencies are 1.76, 2.17, and 2.62 Hz. Care should be taken in identifying a peak as a single modal frequency. In order to distinguish repeated frequency, the FDD methods consist of a simple procedure.

5.5 Frequency Domain Decomposition

The methods make use of this property and perform a singular value decomposition of the observed responses periodogram [12, 13]

$$svd\left(\left[S_{yy}^{+}\left(j\omega_i\right)\right]\right) = \left[U\left(\omega_i\right)\right]\left[\backslash S(\omega_i)\backslash\right]\left[U\left(\omega_i\right)\right]^{H} \tag{19}$$

If only one mode dominates the response at frequency ω_r the modal shape can be obtained as

$$\left\{\hat{\phi}_r\right\} = \left\{u_1\left(\omega_r\right)\right\} \tag{20}$$

This method allows the identification of close modes. Figure 18 presents the singular value decomposition of the estimation shown in Fig. 17. Some repeated root can be observed for frequencies close to 9.5 Hz. For damping the Enhanced Frequency Domain Decomposition, [12, 13] recommend selecting a band around ω_r, where the modal vector $\left\{\hat{\phi}_r\right\}$ is similar (MAC higher than 0.8), as shown in Fig. 19. This segment is transformed to the time domain and identification is done on the decay by different techniques, shown in Fig. 20. The damping identified by this method, in case of close modes, is not as reliable as when time domain methods are used. In the periodogram-based methods the number of points that define the

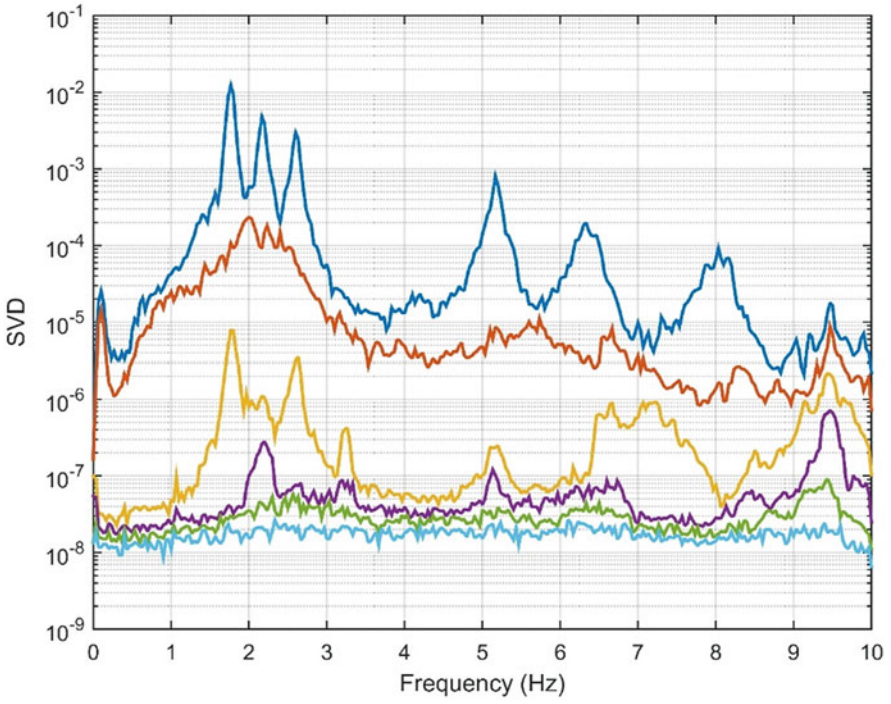

Fig. 18 Singular value decomposition of cross-spectral density matrix of 6 channels above ground

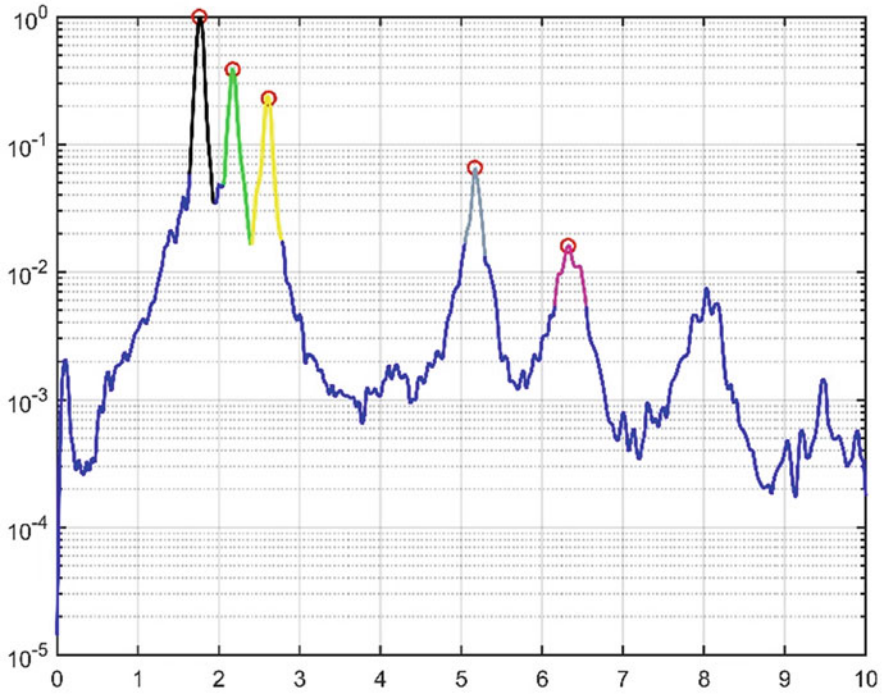

Fig. 19 Selection of frequency band for each mode to perform a damping estimation using a response function

periodogram should be large so a good resolution of the frequency of the peak is obtained.

5.6 Natural Excitation Technique ERA

The method was developed by James III et al. [46] and uses the cross-correlation of the response of structures excited by white noise with respect to a reference channel. It can be shown that cross-correlation has the same characteristics of a decaying signal of a dynamic system under initial excitations.

The cross-correlation is calculated numerically in the time or frequency domain, being in the former defined as:

$$\ddot{R}_{\ddot{y}_i \ddot{y}_j}(k\Delta t) = \frac{1}{N-k} \sum_{l=0}^{N-k} \ddot{y}_i(l) \ddot{y}_j(k+l) \tag{21}$$

For the case of one degree of freedom, the cross-correlation has the form of

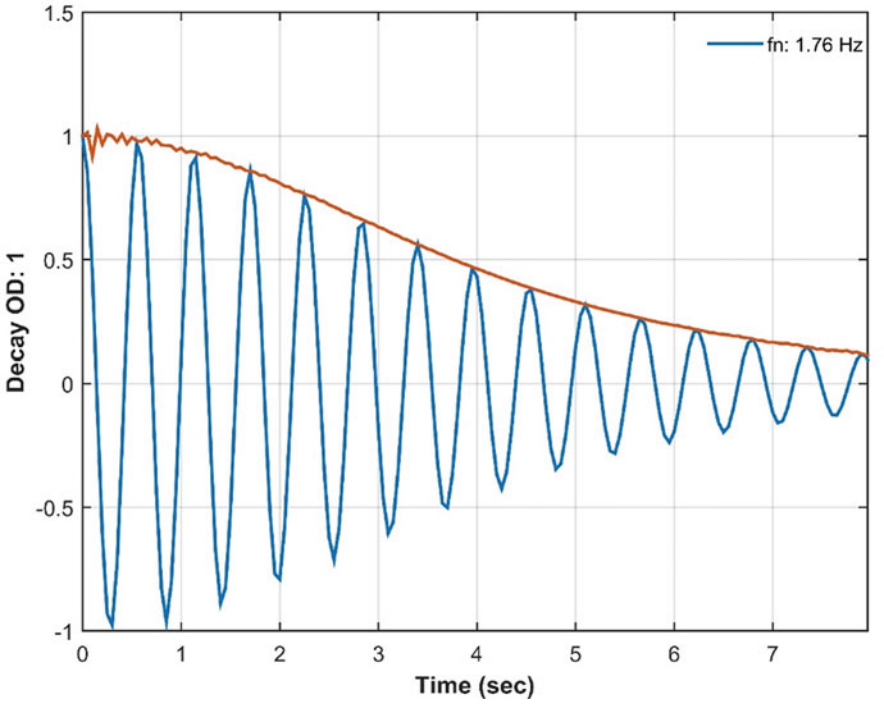

Fig. 20 Time response function for first operational mode. Envelope calculated with Hilbert transform is also shown

$$R_{yy}(\tau) = \frac{\sigma^2}{4\omega_D^3 \beta} e^{-\beta\omega\tau} \left(\frac{\beta}{\sqrt{1-\beta^2}} \sin(\omega_D \tau) + \cos(\omega_D \tau) \right) \tag{22}$$

Hence, the methodology takes the ambient response, shown in Fig. 16, and consists of obtaining its cross-correlation using a reference channel, as shown in Fig. 21. In this case we present the decaying function with respect to Channel 6. Due to the long duration of ambient records, the cross-correlation quickly diminishes to very low values associated with noise. The portion that represents the decay function should be selected and used for the analysis with ERA. The longer the period or the smaller the damping, the longer the decay signal to be selected. Several different reference sensors shall be analyzed to reduce the effect of a defective reference, which may be generated by low amplitudes at certain frequencies or by the presence of noise.

The sampling rate of the signal shall be related to expected predominant frequencies and should allow for a good representation of the decay. Extreme high sampling rates can limit the ability for modal identification and therefore down sampling the signal is generally recommended to a sampling frequency of no more than four times the maximum expected modal frequency present in the signal.

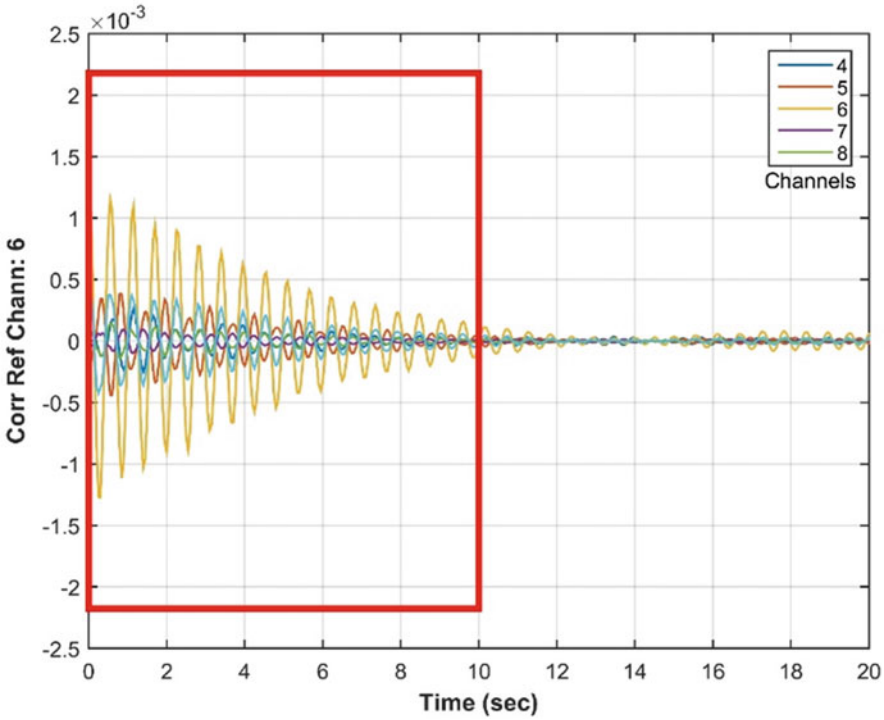

Fig. 21 IFR from correlation of response acceleration with respect to channel 6

As indicated in ▸ Chap. 11, "Experimental Modal Parameter Evaluation Methods", different model sizes should be tried to identify the most probable modal parameters. The results of the different models can be represented in a stability or consistency diagram, as shown in Fig. 22. In the stability diagram the poles comply with a set of rigid and soft criterion in order to distinguish between operational and spurious modes. Several poles could comply with these criteria. One way to select the representative pole is to construct a cluster plot of poles that comply with the criteria. In Fig. 23a, frequency damping clusters are used where it can be seen that the dispersion is mainly due to damping. Several procedures have been used to select the representative value from each cluster, but one of the best criteria is to select the pole in the densest region of the cluster. In the figure this is indicated by the red circle. The selected modal parameters are summarized in Table 3. The spread of possible results should always be kept in case needed for further analysis.

5.7 Stochastic Subspace Identification

Two SSI methods are commonly used [63]: the covariance driven (COV) and the data driven (DATA). Chapter 14 presents the description of the methods and the proper selection of the record length and number of rows in the observation matrix

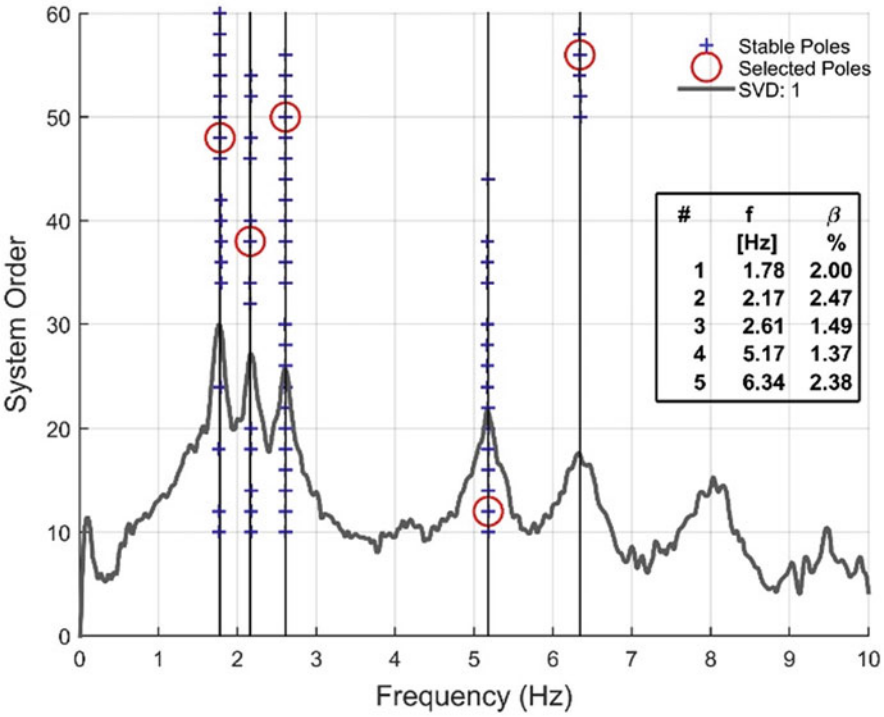

Fig. 22 Stability diagram showing poles that comply with hard and soft criteria. Identified frequency and damping is marked in red circle and shown in table. First singular value decomposition from FDD is shown in dark gray

for best results. As previously referred, care should be taken to select the appropriate length of records according to an expected number and magnitudes of the operation frequencies and damping present on the signal. The most common procedure to select the appropriate model is the construction of a stability diagram and to impose hard and soft discriminating criteria. The method of selecting a gap or jump from the singular value decomposition matrix is not practical due to the noise level present in the signals.

Theoretically, the excitation shall be white noise even if, as will be shown later, the identification can be performed adequately with color noise and even for transient event like earthquake responses.

Here SSI-COV is summarized for the key elements that are used. The methods make use of the Toeplitz matrix of the Hankel matrix of observations:

$$\left[T_{1/i}^{ref}\right] = \left[Y_f\right]\left[Y_p^{ref}\right]^T = \begin{pmatrix} \left[R_i{}^{ref}\right] & \left[R_{i-1}^{ref}\right] & \cdots & \left[R_1^{ref}\right] \\ \left[R_{i+1}^{ref}\right] & \left[R_i^{ref}\right] & \cdots & \left[R_2^{ref}\right] \\ \cdots & \cdots & \cdots & \cdots \\ \left[R_{2i-1}^{ref}\right] & \left[R_{2i-2}^{ref}\right] & \cdots & \left[R_i^{ref}\right] \end{pmatrix} \tag{23}$$

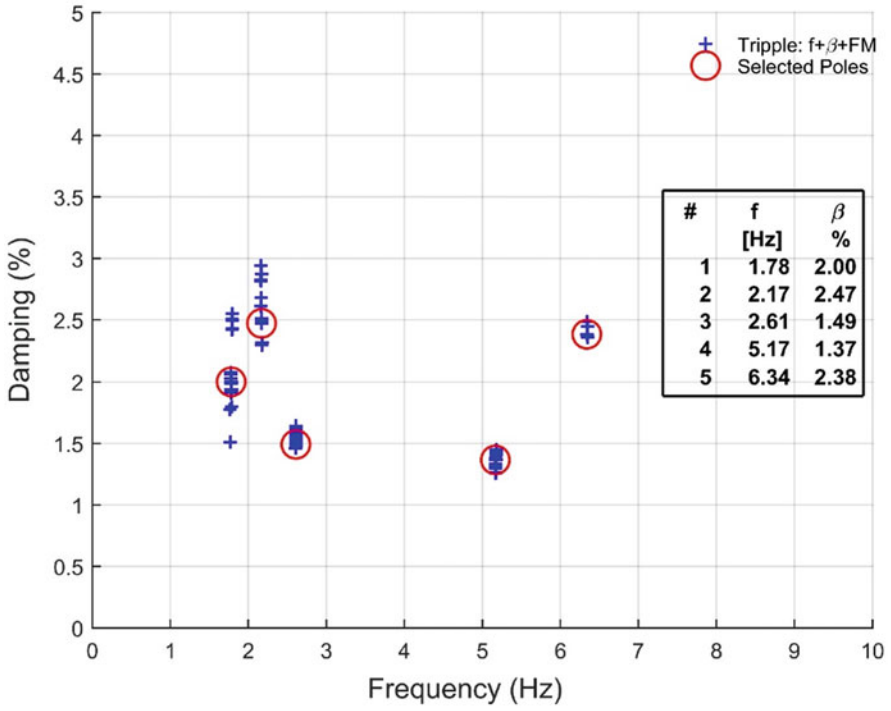

Fig. 23 Cluster of selected frequency and damping. Identified frequency and damping is marked in red circle and shown in table

Table 3 Frequency and damping derived from different methods for TC Building

Mode	EFDDFreq/Damp (Hz)/(%)	NExT-ERAFreq/Damp (Hz)/(%)	SSI-COVFreq/Damp (Hz)/(%)
1	1.76/2.26	1.78/2.00	1.77/1.69
2	2.17/2.01	2.16/2.47	2.17/2.65
3	2.62/1.76	2.61/1.49	2.60/1.91
4	5.17/1.03	5.18/1.37	5.17/1.56
5	6.32/1.57	6.34/2.38	6.32/2.20

This matrix is decomposed using singularly values to estimate the system matrix

$$\left[T_{1/i}^{ref}\right] == [U_1][S_1][V_1]^T \tag{24}$$

or

$$\left[T_{1/i}^{ref}\right] = [O_i]\left[\Gamma_i^{ref}\right] \tag{25}$$

with

$$[O_i] = [U_1][S_1]^{1/2}[T]$$
$$\left[\Gamma_i^{ref}\right] = [T]^{-1}[S_1]^{1/2}[V_1]^T \tag{26}$$

It can be shown that the discrete state matrix can be obtained by a shifted block Toeplitz matrix [62]

$$\left[T_{2/i+1}^{ref}\right] = [O_i][A]\left[\Gamma_i^{ref}\right]$$
$$[A] = [O_i]^{\dagger}\left[T_{2/i+1}^{ref}\right]\left[\Gamma_i^{ref}\right]^{\dagger} = [S_1]^{-1/2}[U_1]^T\left[T_{2/i+1}^{ref}\right][V_1][S_1]^{-1/2} \tag{27}$$

After finding $[A]$, the modal properties are obtained in a similar way as described in the ERA method section.

For the case of the TC Building, if the record length for the analysis is short, then the response could not have all modes of interest and consequently the resulting estimation may be poor. Very long record increases the computational cost and field work but does not necessarily give additional information. So careful selection of the appropriate length shall be considered. Because time domain methods require much shorter data length than frequency domain methods, the records can be split in shorter length windows and the results of each selected window can be statistically analyzed given a more stable results for the number of windows selected.

The results of the analysis of a single 15-min recording, considering 30 s and 1-, 5-, and 10-min windows, are presented in Table 4. For the 30-s duration a total of 30 windows are considered and for the 10-min window only one is considered. For the 30-s and 1-min windows not all modes are detected in all windows. In this case the average frequency and damping values are similar, but a large dispersion of the values in each window is found for the shorter windows. Table 5 shows the minimum, medium, and maximum results of the analysis of 5-min windows. Selected values are similar to those obtained by the NExT-ERA and EFDD methods, Table 3.

Table 4 Mean values damping estimate for different window length (%)

Mode	30 s	1 min	5 min	10 min
1	1.54	1.34	1.38	1.72
2	2.15	2.23	2.23	2.62
3	1.47	1.38	1.60	1.95
4	1.70	1.63	1.62	1.54
5	1.73	1.92	2.00	2.03
6	1.82	2.00	2.07	2.21

Table 5 Minimum, Mean, and Maximum Values from three 5-min independent windows

Mode	Mean frequency Min–Mean–Max	Mean damping Min–Mean–Max
1	1.76–1.77–1.78	1.17–1.38–1.69
2	2.17–2.17–2.18	1.78–2.23–2.68
3	2.60–2.61–2.61	0.98–1.60–2.23
4	5.17–5.18–5.20	1.51–1.61–1.78
5	6.32–6.35–6.37	1.71–2.00–2.38
6	8.03–8.06–8.08	1.83–2.07–2.20

5.8 Multivariable Output-Error State sPace

Multivariable Output-Error State sPace (MOESP) [100] is commonly used in civil structures when the input excitation is known. The methods transform the state space equation with known input into a decay response, to latter apply ERA.

Starting from the state space and observation equations

$$\{z_{k+1}\} = [A]\{z_k\} + [B]\{u_k\} \tag{28}$$

$$\{y_k\} = [C_d]\{z_k\} + [D]\{u_k\} \tag{29}$$

Considering the initial state $\{z_0\}$ in a recurrent formulation:

$$\{z_1\} = [A]\{z_0\} + [B]\{u_0\} \tag{30}$$

We get

$$\{z_k\} = [A]^k\{z_0\} + \sum_{i=0}^{k-1} [A]^{k-i-1}[B]\{u_i\} \tag{31}$$

In a similar way for $\{y_k\}$:

$$\{y_k\} = [C_d][A]^k\{z_0\} + [C_d]\left[\sum_{i=0}^{k-1} [A]^{k-i-1}[B]\{u_i\}\right] + [D]\{u_k\} \tag{32}$$

then

$$\begin{Bmatrix} \{y_0\} \\ \{y_1\} \\ \vdots \\ \{y_{s-1}\} \end{Bmatrix} = \begin{bmatrix} [C_d] \\ [C_d][A] \\ \vdots \\ [C_d][A]^{s-1} \end{bmatrix} \{z_0\}$$

$$+ \begin{bmatrix} [D] & 0 & \cdots & 0 & 0 \\ [C_d][B] & [D] & \cdots & 0 & 0 \\ \vdots & \vdots & \ddots & \vdots & \vdots \\ [C_d][A]^{s-2}[B] & [C_d][A]^{s-1}[B] & \cdots & [C_d][B] & [D] \end{bmatrix} \begin{Bmatrix} \{u_0\} \\ \{u_1\} \\ \vdots \\ \{u_{s-1}\} \end{Bmatrix} \tag{33}$$

if $[\mathcal{O}_s] = \begin{bmatrix} [C_d] \\ [C_d][A] \\ \vdots \\ [C_d][A]^{s-1} \end{bmatrix}$ is the extended observability matrix, and using the Toeplitz matrix, then

$$\begin{Bmatrix} \{y_k\} \\ \{y_{k+1}\} \\ \vdots \\ \{y_{k+s-1}\} \end{Bmatrix} = [\mathcal{O}_s]\{z_k\} + [\mathcal{T}_s] \begin{Bmatrix} \{u_k\} \\ \{u_{k+1}\} \\ \vdots \\ \{u_{k+s-1}\} \end{Bmatrix} \tag{34}$$

If we include the Hankel matrix of input and observations

$$\left[Y_{i,s,N}\right] = \begin{bmatrix} \{y_i\} & \{y_{i+1}\} \cdots & \{y_{i+N-1}\} \\ \{y_{i+1}\} & \{y_{i+2}\} \cdots & \{y_{i+N}\} \\ \vdots & \vdots \ddots & \vdots \\ \{y_{i+s-1}\} & \{y_{i+s}\} \cdots & \{y_{i+N+s-2}\} \end{bmatrix} \tag{35}$$

$$\left[U_{i,s,N}\right] = \begin{bmatrix} \{u_i\} & \{u_{i+1}\} \cdots & \{u_{i+N-1}\} \\ \{u_{i+1}\} & \{u_{i+2}\} \cdots & \{u_{i+N}\} \\ \vdots & \vdots \ddots & \vdots \\ \{u_{i+s-1}\} & \{u_{i+s}\} \cdots & \{u_{i+N+s-2}\} \end{bmatrix} \tag{36}$$

we reduce the equation to

$$\left[Y_{0,s,N}\right] = [\mathcal{O}_s]\left[Z_{0,N}\right] + [\mathcal{T}_s]\left[U_{0,s,N}\right] \tag{37}$$

Constructing the Hankel matrix of input and output and performing LQ decompositions, we get

$$[H] = \begin{bmatrix} [U_{0,s,N}]_{ms\ x\ N} \\ [Y_{0,s,N}]_{ls\ x\ N} \end{bmatrix} = \begin{bmatrix} [L_{11}]_{ms\ x\ ms} & [0]_{ms\ x\ ls} \\ [L_{21}]_{ls\ x\ ms} & [L_{22}]_{ls\ x\ ls} \end{bmatrix} \begin{bmatrix} [Q_1]^T{}_{ms\ x\ N} \\ [Q_2]^T{}_{ls\ x\ N} \end{bmatrix} \tag{38}$$

$$[H] = \begin{bmatrix} [U_{0,s,N}] = [L_{11}][Q_1]^T \\ [Y_{0,s,N}] = [L_{21}][Q_1]^T + [L_{22}][Q_2]^T \end{bmatrix} \tag{39}$$

with

$$[Q_i]^T [Q_j] = \begin{cases} [I] & if\ i = j \\ [0] & if\ i \neq j \end{cases} \tag{40}$$

then

$$[Y_{0,s,N}] = [\mathcal{O}_s][Z_{0,N}] + [\mathcal{T}_s][L_{11}][Q_1]^T = [L_{21}][Q_1]^T + [L_{22}][Q_2]^T \tag{41}$$

Post multiplying Equation (41) by $[Q_2]$ and considering the orthogonality relations, we get

$$[Y_{0,s,N}][Q_2] = [\mathcal{O}_s][Z_{0,N}][Q_2] = [L_{22}] \tag{42}$$

The application of singular value decomposition to $[L_{22}]$ results in

$$\begin{aligned} [L_{22}] &= \begin{bmatrix} [M_1]_{ls\ x\ n} & [M_2]_{ls\ x\ (ls-n)} \end{bmatrix} \begin{bmatrix} [\sum_1]_{n\ x\ n} & [0]_{n\ x\ (ls-n)} \\ [0]_{(ls-n)x\ n} & [\sum_2]_{(ls-n)x\ (ls-n)} \end{bmatrix} \begin{bmatrix} [N_1]^T{}_{n\ x\ ls} \\ [N_2]^T{}_{(ls-n)x\ ls} \end{bmatrix} \\ &\approx [M_1]\left[\sum_1\right][N_1]^T \end{aligned} \tag{43}$$

$$\left[\sum_1\right] = \text{diag}\,(\sigma_1 \cdots \sigma_n)\,; \quad \left[\sum_2\right] = \text{diag}\,(\sigma_{n+1} \cdots \sigma_{ls}) \tag{44}$$

By selecting n number of singular values, we get the Observability Matrix as

$$[\mathcal{O}_s] = [M_1]\left[\sum_1\right]^{1/2} \tag{45}$$

and $[A]$ as

$$[C_d] = [\mathcal{O}_s\ (1 : l, :)] \tag{46}$$

$$\begin{aligned} [\mathcal{O}_s\ (1 : (s-1)\,l, :)]\,[A] = [\mathcal{O}_s\ ((l+1) : sl, :)] \Rightarrow\ \ [A] \\ = [\mathcal{O}_s\ (1 : (s-1)\,l, :)]^+\,[\mathcal{O}_s\ ((l+1) : sl, :)] \end{aligned} \tag{47}$$

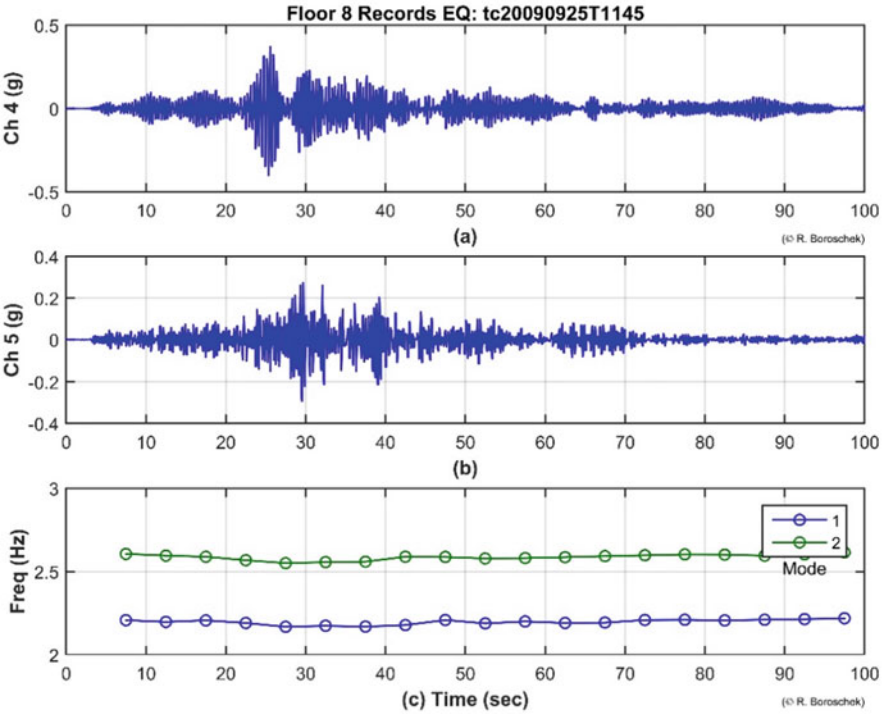

Fig. 24 (**a** and **b**) Top story record TC Building 2009 low amplitude earthquake. Record is analyzed by a sliding nonoverlapping window of 5 s. (**c**) Evolution of first predominant frequency with time

After [*A*] is found the procedure described in the ERA section is used to obtain the modal parameters.

In the TC Building more than 1700 earthquakes of different amplitudes were recorded, some of which produced damage. Figure 24 presents one of the recorded acceleration responses. The upper stories (6 channels) are analyzed considering the full record length and dividing them in 5-s length nonoverlapping windows to track an approximation to the variations of the predominant frequency. For this small amplitude response, the building is nearly elastic so no apparent change is detected. In contrary the Magnitude 8 earthquake of 2010, shown in Fig. 25, produced damage in the building, and in this case a clear reduction of the frequency is observed. This is a permanent change that later is corroborated by ambient vibrations.

5.9 Iterative Modal Identification

A modal minimization approach of an error function is an alternative to the direct MOESP method. This was initially presented in civil engineering by Beck [3] where

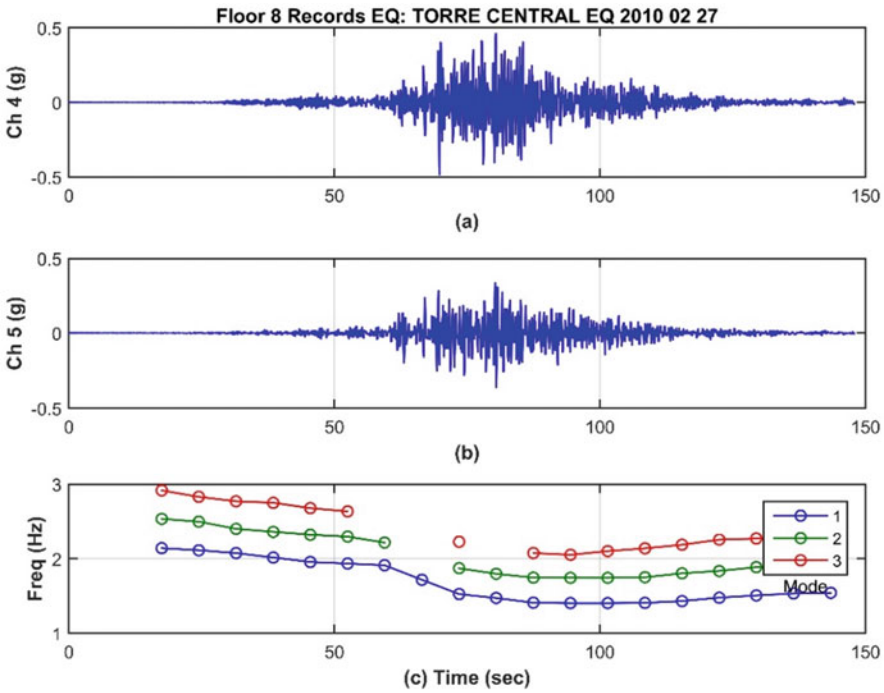

Fig. 25 (**a**,**b**) Records acquired from the TC Building 2010 damaging earthquake, analyzed by a sliding nonoverlapping window of 7s. (**c**) Evolution of first predominant frequencies over the same time period

a sequential search of modal parameters and an error function is used. This is quite a slow process; nevertheless it can provide more flexibility by controlling the modes that participate in the response, given different weighting factors to different record locations and to evaluate the shape of the error surface as a function of all independent variables. This gives important insight on the sensitivity of the parameters.

The initial dynamic modal equations used to develop the identification algorithm are

$$\ddot{y}_j(t) + 2\omega_j \xi_j \dot{y}_j(t) + \omega_j^2 y_j(t) = \sum_{i=1}^{k} L_{j,i} a_{gi}(t) \tag{48}$$

$$a_p(t) = \sum_{j=1}^{N} \phi_{j,p} \cdot \ddot{y}_j(t) \tag{49}$$

where ω_j, ξ_j, $L_{j,i}$, and $\phi_{j,p}$ are modal parameters of mode j, ω_j being the modal angular frequency, ξ_j the modal damping ratio, $L_{j,i}$ modal participation ratio for

base acceleration $a_{gi}(t)$ and $\phi_{j,\,p}$ the modal shape vector component corresponding to position p. Additionally, $y_j(t)$ and $a_p(t)$ represent modal response of mode j and estimated acceleration at position p, respectively.

Several target function can be established for the optimization problem for example [19].

$$E = \sqrt{\frac{\sum_p \alpha_p \cdot \sum_t \left(a_{0,p}(t) - a_p(t)\right)^2}{\sum_p \alpha_p \cdot \sum_t \left(a_{0,p}(t)\right)^2}} \tag{50}$$

Weight coefficients, α_p, allow to control each mode in the identification process.

The optimization is performed mode by mode, retrieving the estimated response from the target acceleration in a cyclic procedure until convergence is found.

6 Stability and Cluster Diagrams

The identification methods listed in Table 2, from which several are described in Sect. 5, are based on solutions obtained either in the time domain, in the frequency domain, or in both. Those that are reported to be more suited for modal estimation in civil structures are based on solutions obtained in the time domain [14, 48, 64], such as the SSI, the ERA, the Next-ERA, or the MOESP models (see Sect. 5). The main reason for this choice concerns the fact that while frequency and time-frequency methods estimate the existence of modes in continuous functions, time-based methods allow observing them as single-valued data objects (poles), for each of the n orders assumed for these models. The computational and theoretical simplicity associated with analyzing this type of data, when compared to the complexity associated with the analysis of continuous functions, has made researchers and practitioners choose this class of methods for civil dynamic testing. Additionally, time methods generally use less data and provide more reliable values for damping.

Even if time-based algorithms are preferable when compared to those which are frequency-based, they may still face the challenge of depending on the structure of the Hankel matrix which, in turn, depends on the model order n. In theory, the model order may be chosen as twice the number of modes needed to describe the structural system. However, this theoretical value is difficult to use in civil structural testing due to the number of spurious modes, associated with noise and other nonstructural effects, that is generally measured on site. One solution to this problem can simply consist of estimating the parameters associated with different model orders, bearing in mind that orders lower than twice the number of modes will underestimate their number while higher values will tend to generate spurious modes.

The identification of which mode estimates (or poles) can be associated with natural or spurious modes is generally conducted by choosing multiple model orders, n, from a value which clearly underestimates the system's dynamics, to one

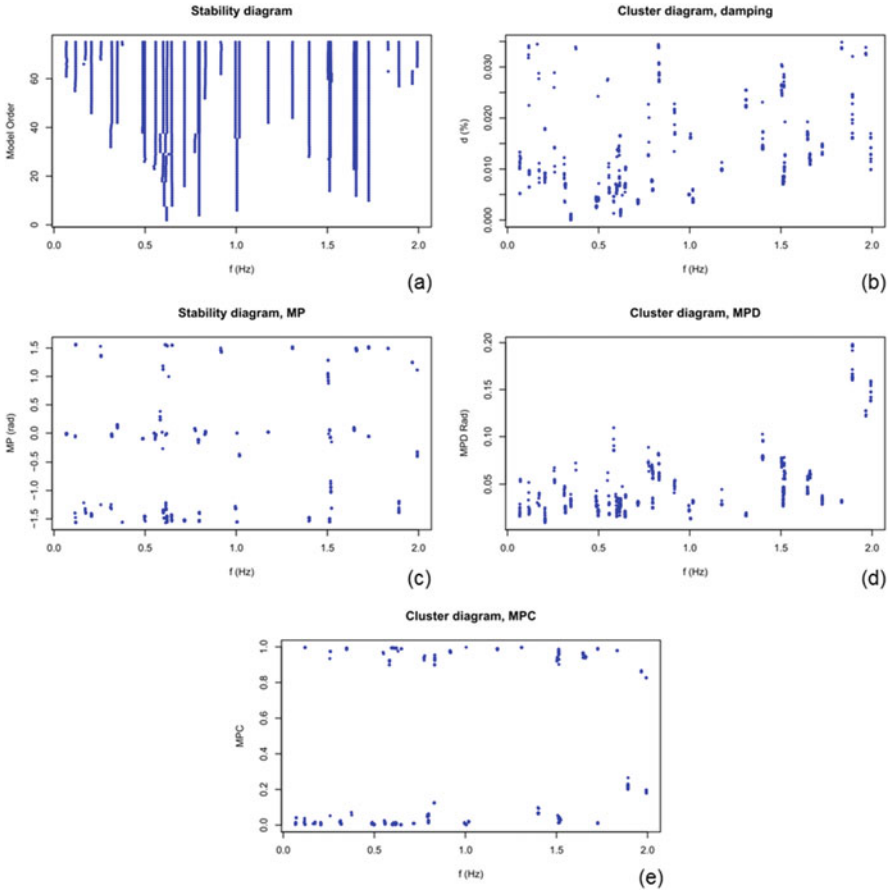

Fig. 26 (**a**) Stability diagram obtained from 1 h of data acquired on the deck of a suspended bridge and corresponding (**b**) cluster diagram (frequency vs. damping), (**c**) cluster diagram (frequency vs. MP), (**d**) cluster diagram (frequency vs. MPD), (**e**) cluster diagram (frequency vs. MPC)

which is known to produce both operational modes and noise-associated estimates. This strategy is described in Chapter 12 and known as stability diagram (already shown in Sect. 5), due to the fact that, when estimates are observed in a "frequency Vs. order" scatter plot, those associated with operational modes repeat themselves over the majority of model orders. An example of a stability diagram obtained from 1 h of monitoring data acquired on a suspended bridge is shown in Fig. 26a.

When observing the same estimates in a "frequency vs. damping" scatter plot, shown in Fig. 26b, each vertical alignment observed in the stability plot (Fig. 26a) can be observed as a tight clusters in Fig. 26b. Cluster diagrams are not necessarily drawn from "frequency vs. damping" scatter plots as the one shown in Fig. 26b. Numerous quantities associated with the coordinates of mode shapes can also be used to construct cluster diagrams, namely:

– The mean phase, MP, which can be computed as the angle of the best straight line fit of the mode shape in the complex plane. Bearing in mind the singular value decomposition of the mode shape matrix Φ, $USV^T = [\ \mathrm{Re}\ (\Phi j)\ \mathrm{Im}\ (\Phi j)\ ]$, where U and V are orthonormal columns and that V12 and V22 denote the elements (1,2) and (2,2) of the V matrix, then the MP can be obtained as [71]:

$$MP\left(\phi_j\right) = arctan\left(\frac{-V_{12}}{V_{22}}\right) \tag{51}$$

– The mean phase deviation, MPD, which measures how much each mode shape coordinate deviates from MP and can be computed simply through the scalar product between the mode shape matrix, $[\ \mathrm{Re}\ (\Phi j)\ \mathrm{Im}\ (\Phi j)\ ]^T$, and $[\ \mathrm{V}_{22} - V_{12}\ ]^T$. As a result, the MPD can be obtained as [71]:

$$MPD\left(\phi_j\right) = \frac{\sum_{i=1}^{n} \left|\phi_{ji}\right| arcos\left|\frac{Re(\phi_{ji})V_{22} - Im(\phi_{ji})V_{12}}{\sqrt{V_{12}^2 + V_{22}^2}\ \left|\phi_{ji}\right|}\right|}{\sum_{i=1}^{n} \left|\phi_{ji}\right|} \tag{52}$$

where ϕ_{ji} is the deviation of the phase from the MP and n is the number of modal coordinates.

– The mean phase collinearity, MPC, which measures how collinear, in the complex plane, mode shapes are. It lies between 0 (not collinear at all) and 1 (perfectly collinear) and can be obtained as [71]:

$$MPC\left(\phi_j\right) = \frac{\left\|Re\left(\tilde{\phi}_j\right)\right\|_2^2 + \frac{1}{\xi_{MPC}} Re\left(\tilde{\phi}_j^T\right) Im\left(\tilde{\phi}_j\right)\left(2\left(\xi_{MPC}^2 + 1\right)\ sin^2\left(\theta_{MPC}\right) - 1\right)}{\left\|Re\left(\tilde{\phi}_j\right)\right\|_2^2 + \left\|Im\left(\tilde{\phi}_j\right)\right\|_2^2} \tag{53}$$

where

$$\xi_{MPC} = \frac{\left\|Im\left(\tilde{\phi}_j\right)\right\|_2^2 - \left\|Re\left(\tilde{\phi}_j\right)\right\|_2^2}{2Re\left(\tilde{\phi}_j^T\right) Im\left(\tilde{\phi}_j^T\right)} \tag{54}$$

$$\phi_{MPC} = arctan\left(\left|\xi_{MPC}\right| + sign\left(\xi_{MPC}\right)\sqrt{1 + \xi_{MPC}^2}\right) \tag{55}$$

and where $\tilde{\phi}_j$ is the vector whose components consist of:

$$\tilde{\phi}_{ji} = \phi_{ji} - \frac{\sum_{i=1}^{n} \phi_{ji}}{n} \tag{56}$$

The cluster plots shown in Fig. 26c–e reveal the cluster sets observed in the f vs. MP, f vs. MPD, and f vs. MPC bi-dimensional spaces. The first one, Fig. 26c, reveals a clear trend exhibited by the modes shapes of this case study, to align around phase angles of 0, $\pi/2$, and $-\pi/2$, while the second, Fig. 26d, is similar, in pattern, to the one showing f vs. damping (Fig. 26b). The cluster diagram shown in Fig. 26e reveals the damping nature of the observed mode shapes of this particular case study, which are either well-aligned (MPC $\cong$ 1) and associated with proportional damping, or not collinear at all (MPC $\cong$ 0) and therefore associated with highly nonproportional damping. Regardless of the additional results and conclusions that can be obtained from these modal features, the important information underlying their density in these bi-dimensional spaces can be of importance for modal identification and experimental dynamics of civil structures under uncharacterized operational loading.

7 Modal Estimation

Civil structural dynamic testing was traditionally conducted using forced vibrations and small data acquisition periods, mostly due to the technical limitations associated with acquiring large data sets and with measuring small magnitude vibrations. Nowadays, sensors and data loggers are capable of measuring changes of one hundredth of the micro-g, where mainstream hard disk drives can store several terabytes of data and where computer processing units (CPU) can process the data in real time for dynamic feature identification. As a consequence, civil dynamic testing can be conducted continuously and autonomously for the purpose of system identification and structural health monitoring [55, 68, 82].

7.1 Distance Matrices

Diagrams such as those shown in Sect. 6 can be obtained from pairs of modal-based quantities to reveal patterns that can be directly matched to different modes. This type of patterns can, however, be obtained from each modal quantity alone by computing distances between pairs of poles. These distances between each pair of poles can be organized, in a simple manner, using distance matrices whose visualization, for example, in the form of pixel maps (as those shown in Fig. 27), allows visualizing how the modal information is organized as well the ability of each quantity to provide reliable modal estimations.

The quantification of the distances can be conducted using several metrics, from which the Minkowski distance is the simplest and well-known. It can be defined, in its relative form, as

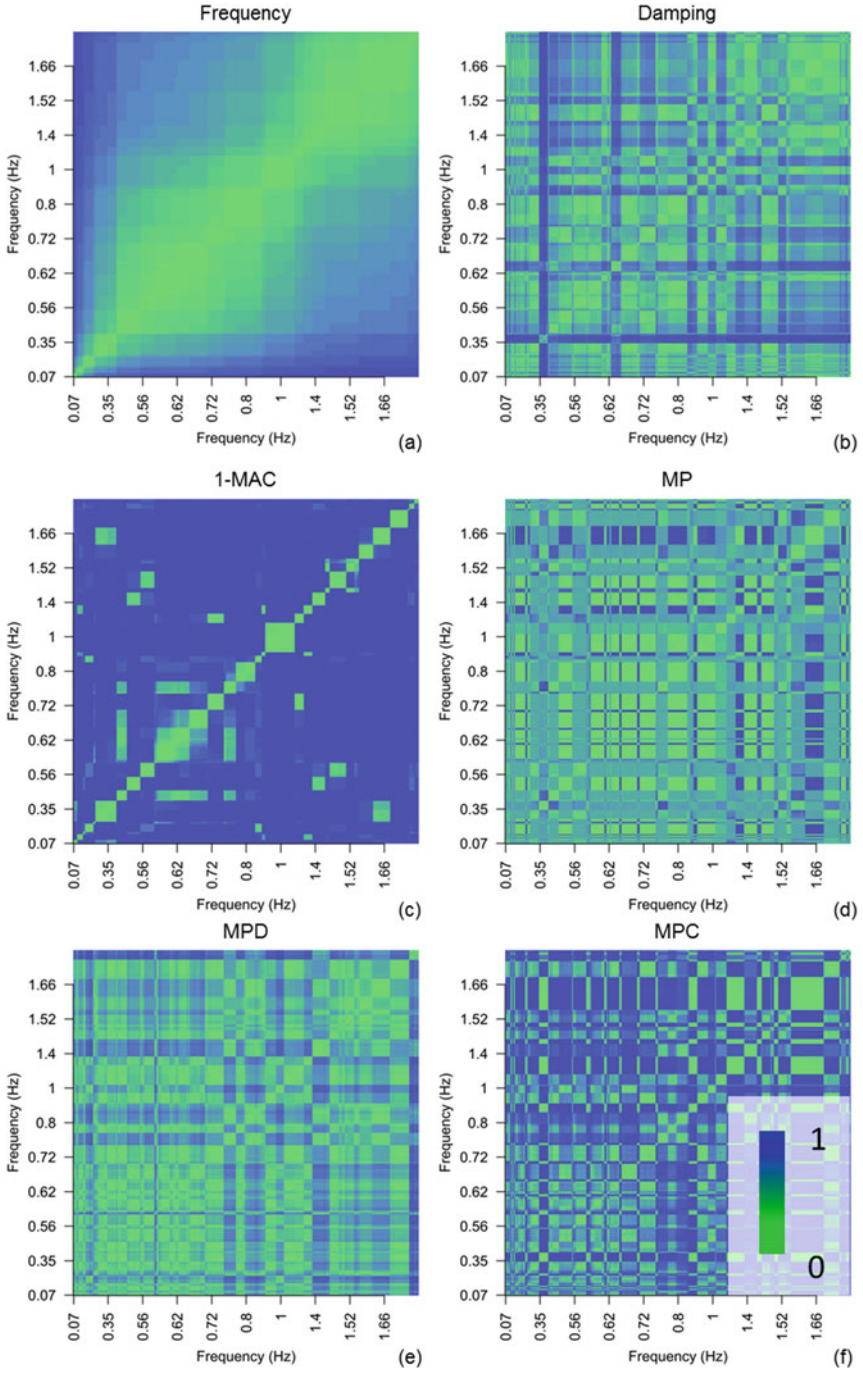

Fig. 27 Pixel plots of the distance matrices obtained from (**a**) frequencies, (**b**) damping ratios, (**c**) 1-MAC, (**d**) MP, (**e**) MPD, and (**f**) MPC

$$d\left(x_i, x_j\right) = \frac{\left(\sum_{i=1}^{n} \left|x_i - x_j\right|^p\right)^{\frac{1}{p}}}{max\ \left(\left|x_i\right|, \left|x_j\right|\right)} \tag{57}$$

where the parameter p must be taken larger than the 1. When p=1, the distance is known as Manhanttan distance and assumes the form of the absolute value of the difference between modal features. When p=2, the Minkowski distance assumes the form of the well-known Euclidean distance, or square root of sum of squares. For all matrices shown in Fig. 27, this distance with p=1 was used, with the exception of Fig. 27c, which was defined as d=1−MAC, where the MAC stands for the Modal Assurance Criterion (MAC), [1], as follows:

$$MAC\left(\phi_{iA}, \phi_{iB}\right) = \frac{\left|\sum_{i=1}^{n} \phi_{iA} \phi_{iB}^{*}\right|^2}{\sum_{i=1}^{n} \phi_{iA} \phi_{iA}^{*} \phi_{iB} \phi_{iB}^{*}} \tag{58}$$

where ϕ_{iA} and ϕ_{iB} represent modal coordinates of mode shapes A and B, respectively.

Distance matrices and their corresponding pixel plots allow observing the existence of modes through the existence of homogeneous groups estimations with distances close to zero along the main diagonal of the matrices. This is the case of the pixel plot representing the distance defined as d=1-MAC, shown in Fig. 27c, where for the structural system considered herein, a clear main diagonal comprising approximately 20 green colored groups can be observed. Along with these groups, the existence of several located far from the main diagonal can also be observed in civil testing, revealing the similarity between mode shapes with different characteristic frequencies.

When considering civil structures, there are applications where the modes are clearly well-separated in the frequency domain. In these cases, the frequency-based distance matrix can have a similar appearance as the one obtained from the MAC. There are, however, numerous civil structures where the density of modes in the frequency domain renders the frequency matrix less clearly defined along the main diagonal, as is the case of the structural system under analysis (Fig. 27a). The use of each modal feature for modal identification is therefore case dependent and must be considered for each application.

Regardless of the structural system under analysis, it must be referred that a common result obtained from civil testing of structures under operation consists in observing that the damping, the MP, the MPC, and the MPD distance matrices, exemplified in Fig. 27b, d–f, do not generally exhibit compact regions only along the main diagonal, since all these quantities repeat themselves across several distinct modes, especially when large frequency domains and numbers of modes are to be identified.

It must be referred, however, that these four modal quantities can be used for the analysis of narrow frequency domains, for distinguishing between modes with similar frequency values and whose shapes appear similar for the sensor set

installed. In these cases, the phase and collinearity can also contribute to the correct identification.

7.2 Spurious Pole Elimination Using Hard Stability Criteria

Modal estimates obtained from the time-domain identification methods can produce poles which can be associated with physical modes or with other effects influencing the dynamic test under analysis. The latter are named spurious poles (see Chapter 12) and can be characterized by not being observed across the model orders. As a result, a common procedure for distinguishing between physical and spurious poles consists of defining limits (named as hard criteria) to the values of the modal features, namely those defined in section 6 (f, d, MAC, MP, MPD, or MPC). These limits are generally in accordance with the precision requirements needed for the experimental dynamic property at hand.

Hard criteria can be seamlessly obtained from the distance values between pairs of modal estimates (shown in Fig. 27). One possible procedure for hard criteria implementation consists of analyzing the distances between poles obtained at each model order, n, with those obtained for the preceding model order, $n-1$. The algorithm associated with this type of stability criteria is based on searching if there is at least one pole j, in model order $n-1$, that meets all or a set of the following conditions when compared to pole j, of model order n,

$$d_f\,(i,\,j) \leq \lim\left(d_f\right) \tag{59}$$

$$d_d\,(i,\,j) \leq \lim\left(d_d\right) \tag{60}$$

$$d_{MAC}\,(i,\,j) \leq \lim\left(d_{MAC}\right) \tag{61}$$

$$d_{MP}\,(i,\,j) \leq \lim\left(d_{MP}\right) \tag{62}$$

$$d_{MPD}\,(i,\,j) \leq \lim\left(d_{MPD}\right) \tag{63}$$

$$d_{MPC}\,(i,\,j) \leq \lim\left(d_{MPC}\right) \tag{64}$$

where the ranges used are highly case dependent and a set of possible ranges used for the frequency, damping and MAC limits can be chosen as,

$$0.005 \leq \lim\left(d_f\right) \leq 0.05 \tag{65}$$

$$0.01 \leq \lim\left(d_d\right) \leq 0.1 \tag{66}$$

$$0.999 \geq \lim\left(d_{MAC}\right) \geq 0.95 \tag{67}$$

The application of this procedure using the limits $\lim(d_f)$=0.005, $\lim(d_d)$=0.01, and $\lim(d_{MAC})$=0.999 resulted in the new stability and cluster plots shown in Fig. 28a, b, where it can be observed that numerous poles located in non-dense regions of the cluster plot were considered spurious and therefore eliminated.

Another possible procedure based on hard stability criteria consists of checking, for each pole *j* of any order, that all or a set of the conditions shown above are met between this and all the other *i* poles present in the pole set, regardless of their order. Under this procedure, a pole is considered stable if the conditions are met between it and an arbitrary number of *s* different poles, which can be defined as a fraction of the maximum model order. The results obtained using these procedures are shown in Fig. 28c, d for an *s* value of 5 poles.

7.3 Modal Characterization Based on Parametric Procedures

Modal characterization of civil structures resorts to one of the methods shown in Sect. 5, or others, to estimate modal quantities, after which one or more steps can be taken to ensure that these estimates are free of noise or of other spurious effects [70]. Finally, each of these features can then be analyzed to characterize each of the structural modes.

The characterization of the modes may follow the manual identification of either (i) maximum values in spectra generated by frequency or time-and-frequency methods or (ii) vertical alignments in stabilization diagrams/clusters in cluster diagrams generated by time-based estimation methods.

Semi-empirical strategies may comprise the automatic or manual identification of local maxima in spectra or in histograms computed from stability diagrams [70, 73]. As alternatives to these comprise strategies, those based on curve fitting using splines, polynomial, or auto-regressive models can also be used [54, 72].

7.4 Modal Characterization Using Clustering

An alternative nonparametric class of nonparametric methods also used for civil structural testing relies in clustering algorithms, which are pattern recognition that are capable of, by themselves, labeling data simply by studying the intrinsic structure of the pole set [8, 54, 71, 84, 85]. The aim of a clustering method can be defined as the division of a data set into groups, which must be as compact and separated as possible according to a certain predefined metric. To fulfill this objective, allocation rules must be defined so that pair-wise dissimilarities between objects assigned to the same cluster tend to be smaller than those allocated in different clusters [28]. Considering a given partition containing K clusters, $P_k = \{C_1, \ldots, C_k\}$. The within-cluster distance $\mathrm{W(P_k)}$ can be defined as [39]:

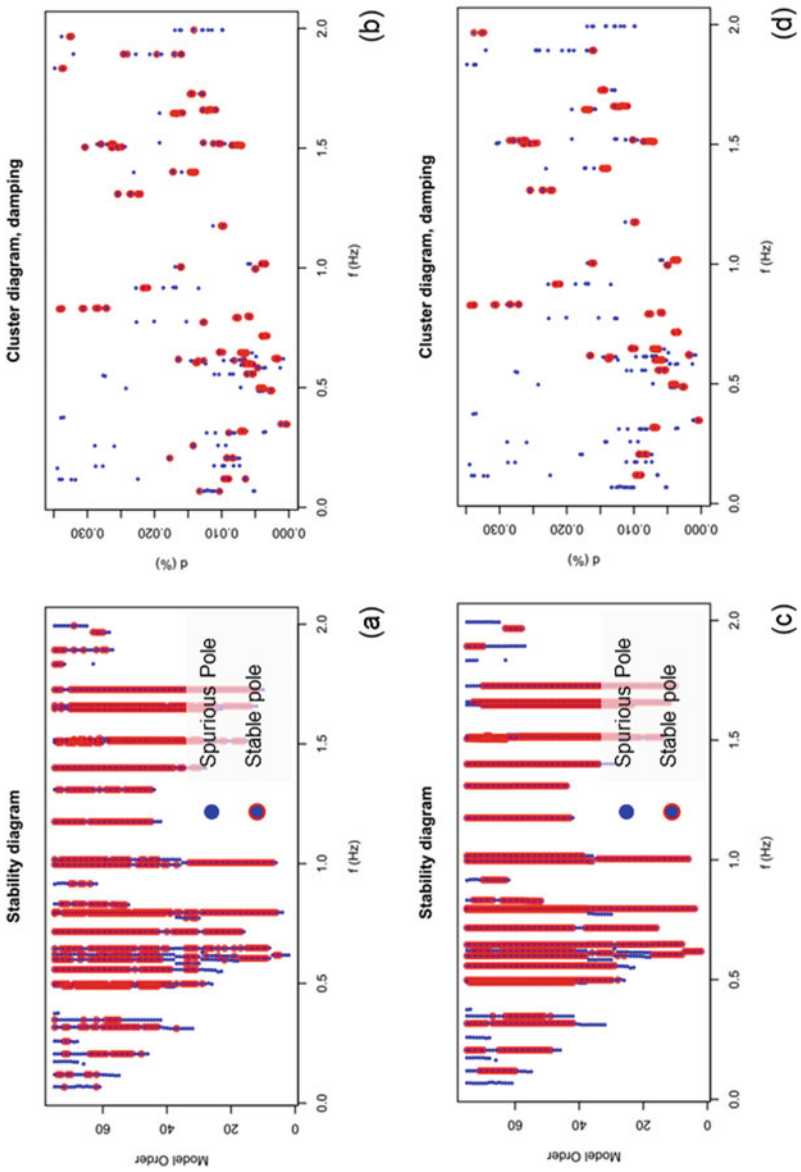

Fig. 28 Spurious pole elimination: (**a**) stability and (**b**) cluster diagrams using by-order pole elimination, (**c**) stability, and (**d**) cluster diagrams using entire-set pole elimination

$$W(P_k) = \frac{1}{2} \sum_{k=1}^{K} \sum_{C(i)=k} \sum_{C(j)=k} d_{ij} \tag{68}$$

where $C(i)$ is an allocation rule which assigns element i to cluster k, based on a distance d_{ij}. The total variation of data can be defined as in Eq.(69), where N is the total number of objects considered in the cluster analysis. Finally, the between-cluster distance $B(P_k)$ can be simply obtained by subtracting the other two defined distances, $B(P_k) = T - W(P_k)$.

$$T = \frac{1}{2} \sum_{i=1}^{N} \sum_{j=!}^{N} d_{ij} \tag{69}$$

Each cluster can be described by a prototype, which generally consists of an object of the same type as the ones being clustered. The location of each prototype can be obtained using centroids, medoids, or other representatives.

Numerous families of clustering methods can be found in the literature but the most used are the iterative and hierarchical methods, from which the k-means is the most well-known. It requires the definition of an initial set of clusters' prototypes, which is known as the initialization phase, after which each iteration starts by allocating the objects to the clusters according to an allocation rule, $c(i)$. This step is represented in Fig. 29b, where the dashed lines show the allocation of each object into the closest cluster prototype, according to the distance defined. The second step of each iteration is named representation and consists of finding the set of K prototypes that best represents the clusters defined in the allocation phase. The k-means is based on representing the clusters by their centroids (new prototypes shown in Fig. 29c). These two steps, allocation and representation, are afterwards repeated (Fig. 29d, e) until an objective function, which depends on cluster compactness and separation, reaches its global minimum value. The k-means takes the squared within-cluster dissimilarity measured across the K clusters as objective function [39].

The hierarchical agglomerative methods provide a merging hierarchy so that all partitions are defined, regardless of their number of elements [39], and starts by considering single-object clusters and, at each level of the hierarchy, merge a selected pair of clusters into a new one. This merging produces a new level in the hierarchy (which contains one less cluster). This hierarchy can be displayed in a dendrogram plot, which allows for a clear visualization of the structure of high dimensional data, such as modal features acquired from dynamic tests, in a single and unambiguous plot such as the one shown in Fig. 29g, where clusters are represented by vertical lines and hierarchy levels by horizontal lines.

Cluster merging is made, at each level, based on merging rules, among which the two simplest are the "single link" and "complete link." The first states that the two clusters containing the closest objects in a data set should be merged, the latter chooses the ones with the farthest objects. The most widely used merging rules are

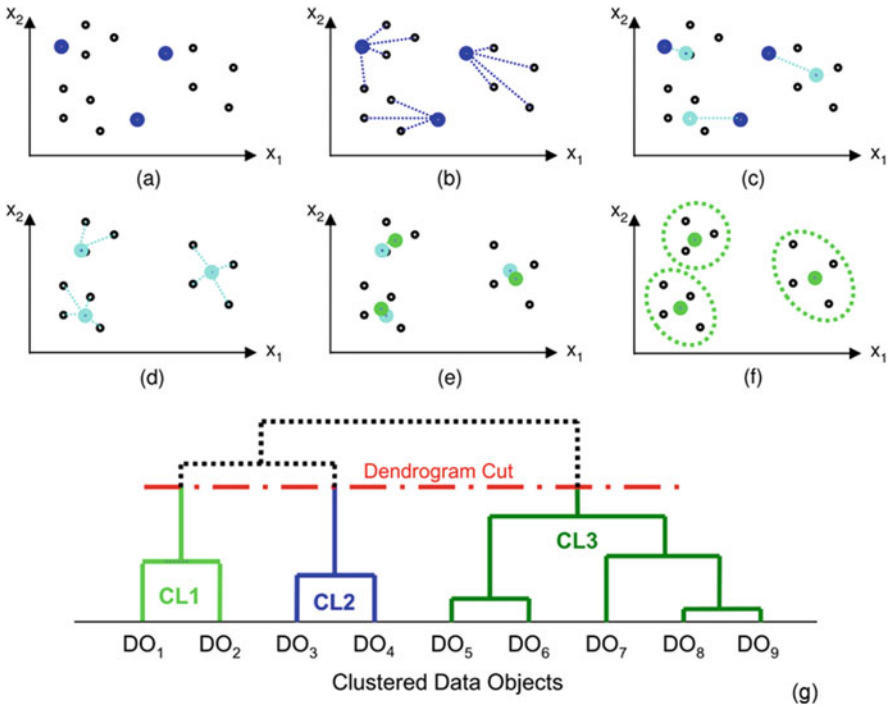

Fig. 29 K-means clustering algorithm: (**a**) initialization (three cluster prototypes to describe eleven objects); (**b**) iteration 1, allocation; (**c**) iteration 1, representation; (**d**) iteration 2, allocation; (**e**) iteration 2, representation, (**f**) final set of clusters' prototypes. Hierarchical agglomerative clustering (**g**)

the "average link" and the "ward," or "minimum variance" rule. The first defines that the pair of clusters to be merged, at each level, is the one with smaller average distance, while the "ward" rule defines that, at each level, the pair of merged clusters must generate a new partition with the smallest variance possible. From the defined agglomerative hierarchy, cluster partitions containing any number of clusters (from 1 to N) can be obtained by cutting the dendrogram plots (horizontally) between two hierarchy levels, as show in Fig. 29g.

Clustering methods, regardless of their type or nature, use distance matrices obtained between pairs of all elements being clustered as input. For modal analysis in the realm of experimental dynamics, distance metrics can consist of those obtained from the quantities presented in Sect. 6 or others considered appropriate for the application at hand Fig. 27.

To exemplify the automatic modal characterization using clustering, each of the six matrices shown in Fig. 27 was used as input in an independent hierarchical agglomerative procedure based on the minimum variance rule, without any elimination of spurious poles, and assuming that 24 modes are present in the domain [0;2] Hz. The results are shown in Fig. 30, in the form of stability diagrams overlapped

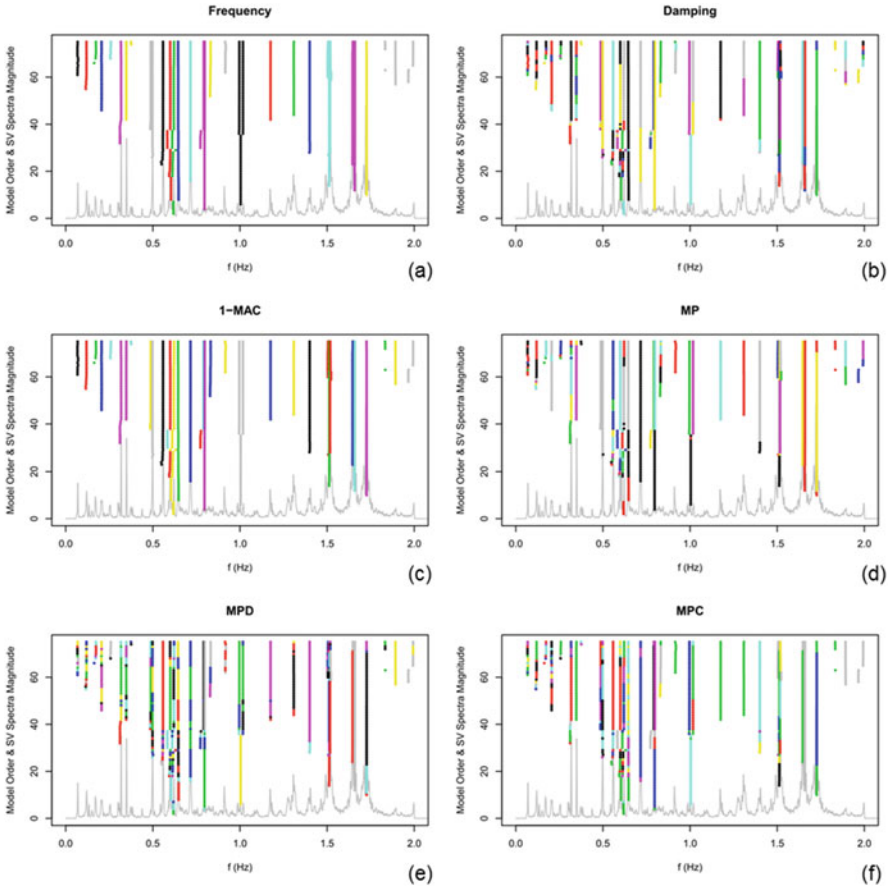

Fig. 30 Application of the hierarchical agglomerative clustering to distances metrics obtained from applying the Manhattan distance to: (**a**) frequency; (**b**) damping; (**c**) 1-MAC; (**d**) MP; (**e**) MPD; and (**f**) MPC

with the spectra of the first singular value (extracting using the method described in Sect. 5.5).

A possible criterion to analyze whether a clustering process has identified the modes adequately consists of analyzing whether it classifies each entire vertical alignment of poles as a single cluster. When conducting this analysis to the results shown in Fig. 30, it can be observed that, for the present case, the clustering processes which used frequencies and MAC as input generated more trustworthy mode classifications, when compared to the remaining ones. This conclusion is in line with the one obtained from the analysis of the distance matrices themselves, shown in Fig. 27. However, it can also be observed that even if the matrices obtained from frequencies and MAC are significantly different (Fig. 27a, c, respectively), the resulting clustering obtained from them generates similar mode configurations.

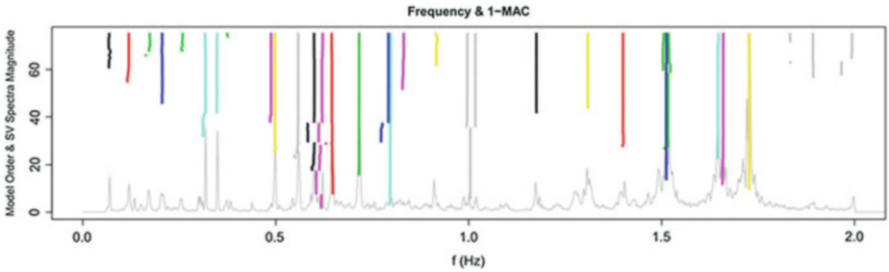

Fig. 31 Application of the hierarchical agglomerative clustering to a distance metric obtained from applying the Manhattan distance to frequency and 1-MAC of the entire pole set

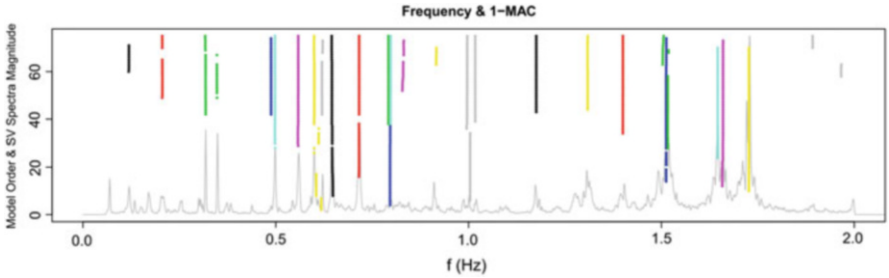

Fig. 32 Application of the hierarchical agglomerative clustering to a distance metric obtained from applying the Manhattan distance to frequency and 1-MAC of the pole set after spurious pole elimination

As an alternative to clustering based on single-feature distances, procedures using matrices obtained from several features can also be used and may prove advantageous by combining the information underlying each feature. The mode identification based on the combination of frequencies and mode shapes is exemplified in Fig. 30 for the entire pole set and in Fig. 31 for the non-spurious poles, after the elimination described in Sect. 7.2. As it can be observed, both generate trustworthy mode classifications, thus suggesting that clustering can be used both for spurious pole elimination as well as mode characterization (Fig. 32).

7.5 Assessing the Number of Modes Using Cluster Validity

Clustering algorithms are able to assign poles to any amount of predefined modes (each represented by one cluster), irrespective of whether this number of modes really exists in the structural system's dynamic response. Even though the analysis of pole allocations, such as the one shown in Fig. 31, is able to provide hints on the number of modes observed, the results may become subjective. To exemplify the problem of generating any number of clusters without knowing the real number of mode shapes in advance, Fig. 33 shows the application of clustering to the pole set analyzed so far using 5–55 clusters to represent the modes. Its analysis

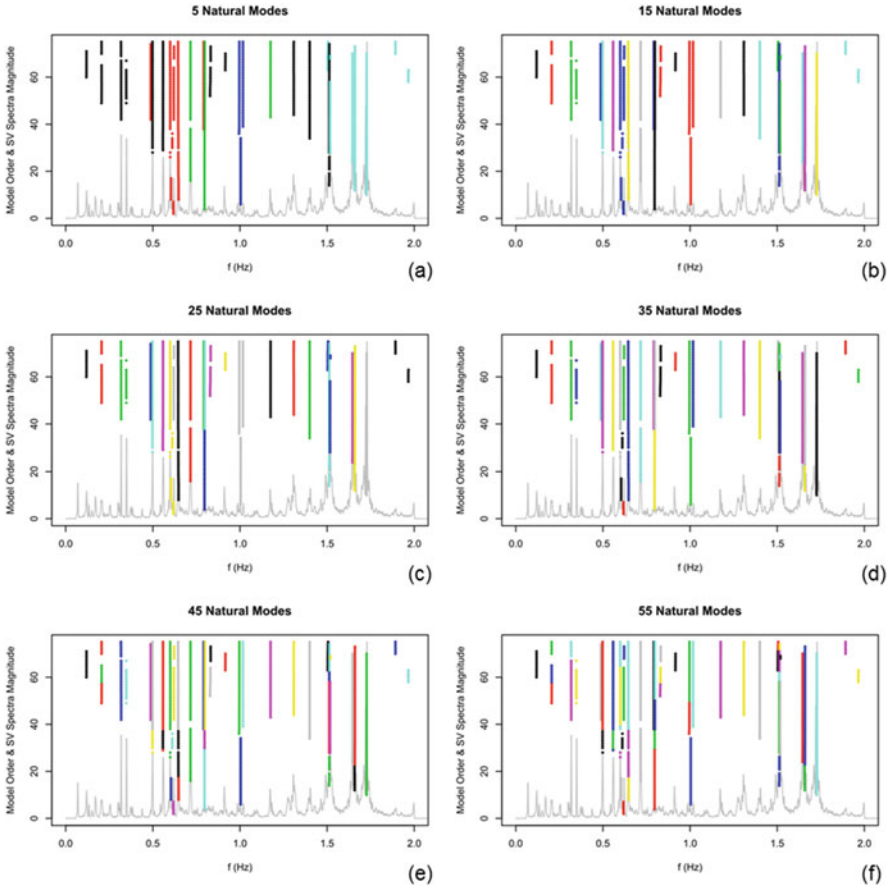

Fig. 33 Application of the hierarchical agglomerative clustering using: (**a**) 5; (**b**) 15; (**c**) 25; (**d**) 35; (**e**) 45; and (**f**) 55

allows observing that 5 or 15 modes (Fig. 33a, b) appear to be too few to represent the dynamic response of the structural system, since several different vertical alignments are classified into the same modes. However, it can also be observed that 45 and 55 clusters (Fig. 33e, f) divide several vertical alignments into different modes, and therefore might not be representing the dynamic response well.

To obtain a quantitative and objective estimation of the number of modes observed in an experimental data set, an evaluation known as cluster validity [96] may be conducted on any pole assignment. Cluster validity consists of computing indices for all possible pole classifications [58, 69] containing from k=2 modes to an arbitrary number which can be as large as the application at hand allows, and can be much larger than the number of degrees of freedom measured on site.

Each validity index provides a measure of each poles' cluster compactness and separation, regardless of the number of modes present in the evaluated

classification. The most truthful number of modes is then assessed by comparing the indices obtained from each of the evaluated partitions. Depending on each index's theoretical background, its maximum or minimum value will point out the most truthful number of clusters.

The fact that cluster validity indices are based on different theoretical backgrounds can make their ability to analyze data and point out different structural behaviors case-dependent [5, 58, 96]. For the purpose of identifying the number of modes, the Global Silhouette (SIL) index can be used [74]. To define its mathematical formulation, a pole set of N objects and K mode partitions of this set into t modes, $P_t = (C_1, \ldots, C_t)$, is considered as well as its k-th mode, consisting of M_k poles $1 \leq M_k \leq N$, defined as $C_k = \left(T_1^{(k)}, \ldots, T_{M_k}^{(k)}\right)$.

The silhouette width of the i-th object belonging to C_k is defined as

$$s_i^{(k)} = \frac{b_i^{(k)} - a_i^{(k)}}{max\left(a_i^{(k)}, b_i^{(k)}\right)} \in [-1, 1] \tag{70}$$

where $a_i^{(k)}$ is the average distance between the i-th pole of C_k and the remaining j poles assigned to the same cluster is given by

$$a_i^{(k)} = \frac{1}{M_k - 1} \sum_{\substack{j=1 \\ i \neq j}}^{M_k - 1} d_{ij}, \quad 1 \leq i \leq M_k \tag{71}$$

Similarly, the minimum average distance $b_i^{(k)}$ between object i and all the objects clustered in the remaining clusters is given by

$$b_i^{(k)} = \min_{\substack{r=1,\ldots,K \\ r \neq k}} \left(\frac{1}{M_r} \sum_{j=1}^{M_r} d_{ij} \right), \quad 1 \leq i \leq M_k \tag{72}$$

where r is any cluster of the partition $\mathrm{P_t}$ with $\mathrm{M_r}$ poles.

Finally, the silhouette index of cluster C_k, s_k, and the global silhouette index of the entire partition containing t modes, $SIL(P_t)$, are respectively given by

$$s_k = \frac{1}{M_k} \sum_{i=1}^{M_k} s_i^{(k)} \tag{73}$$

$$SIL\,(P_t) = \frac{1}{K} \sum_{k=1}^{K} s_k, \quad t = 2, \ldots, K \tag{74}$$

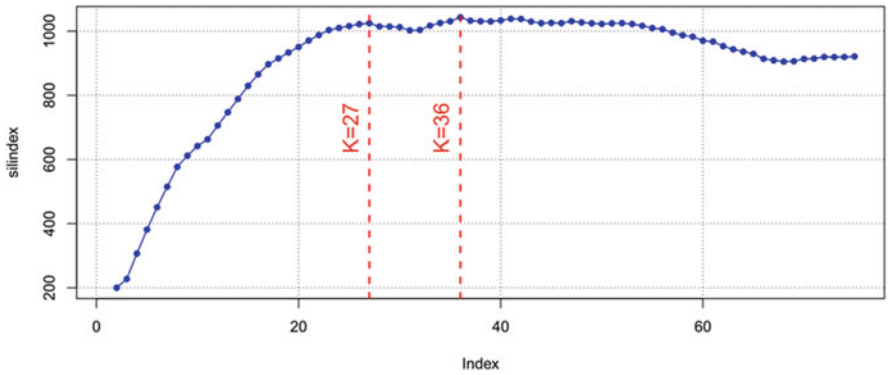

Fig. 34 SIL index obtained for cluster partitions containing K=2–75

where the higher Silhouette (SIL) corresponds to the partition exhibiting more compact and separated clusters, and thus the most truthful classification of poles into the most correct number of monitored modes. For the pole set analyzed herein, and shown in the previous figures, the maximum SIL value is obtained for K=36 modes (Fig. 34). However, it can be argued that cluster validity cannot be applied blindly without considering the context and physical problem at hand. Even if the higher value of the SIL index (or of other validity indices) might indicate the best clustering partition, its value may be too high to consider for the problem at hand. An alternative criterion consists of choosing the first local maximum, as long as it is located within a domain which is known possible for the structural system under analysis and the number of sensors deployed on site. For the example shown so far, this criterion yields K=27 modes (Fig. 34), which appear to be more in accordance with the dynamics of the structural system at hand since it leads to less splits divisions of vertical alignments in the stability diagram shown in Fig. 35b when compared to the one obtained for K=36 clusters, shown in Fig. 35a.

The maximum number of modes considered for cluster validity can also be defined as a divisor of the maximum order chosen for the modal estimation algorithm, and shown in the stabilization diagram. In Fig. 34, clustering partitions were analyzed up to the value of the maximum order, K=75.

7.6 Cluster Representatives as Mode Features' Estimates

Clustering methods and validity indices allow assessing which poles are allocated to each of the modes to characterize it according to the chosen modal features. These allocated pole subsets exhibit, however, variability and each pole by itself may not be the best representative of each mode shape. Thus, to find the best modal features characterizing each mode, accurate clusters' representatives can be obtained.

Several types of clusters representatives can be obtained, and their definition can greatly influence the result of the clustering process and its results. Both the

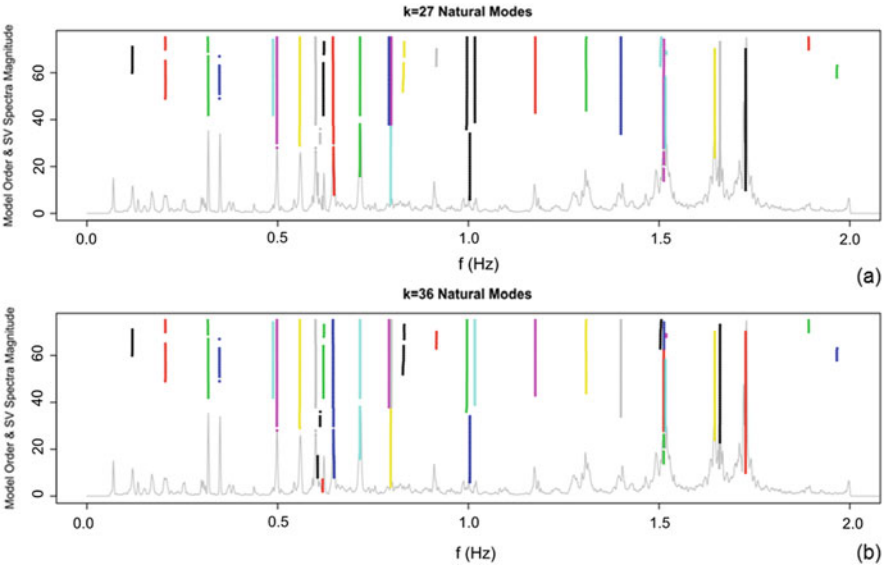

Fig. 35 Application of the hierarchical agglomerative clustering with the Manhattan distance obtained from frequencies and 1-MAC for $K=27$ and 36 clusters

k-means and the hierarchical agglomerative use the clusters' centroids (average coordinate values), computed in the p-dimensional space, where p is the number of modal features used to defined the distance matrices above described [80, 82]. Some methods such as the k-medoids use the medoids (median coordinate values) to obtain such estimates [79] and others use density-based representatives [8].

To exemplify the definition of the cluster representatives for the example shown so far, the partition comprising $K=27$ modes was considered and from it the cluster centroids were computed as representatives of each mode. These are shown as dotted lines in the stabilization diagram represented in Fig. 36a and crosses in the cluster plot represented in Fig. 36b. The corresponding mode shapes are also obtained in the same manner, from those associated with each pole. The first six shapes can be found in Fig. 37.

8 Modal Tracking

8.1 Problem Statement and Motivation

The need for modal tracking arises from structural health monitoring of civil structures, whose requirements nowadays include permanent and continuous identification of damage in an early stage, not only for ensuring safety but also for

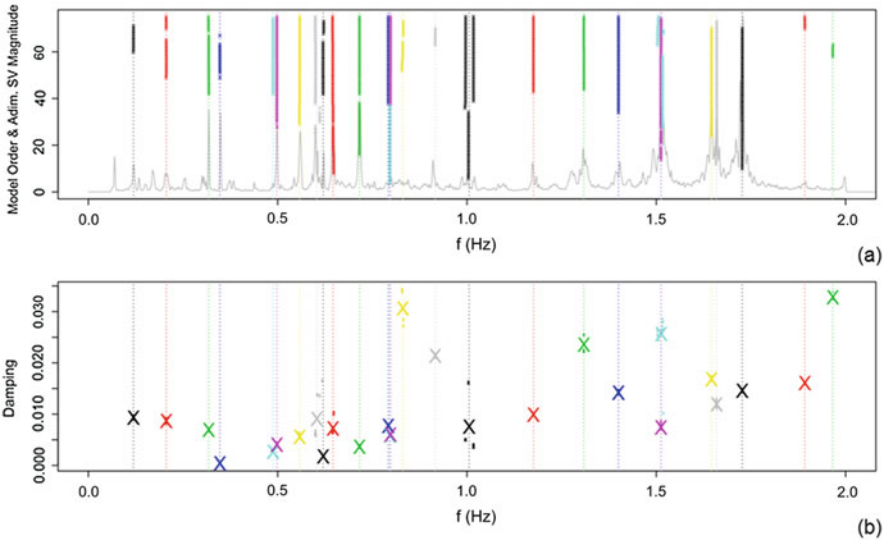

Fig. 36 Stabilization (**a**) and cluster (**b**) diagrams of the modes comprising K=27 clusters

infrastructure management [23, 79, 83]. Continuous health monitoring demands that civil dynamic testing be conducted also continuously under operation, and therefore in an automated manner [16, 49, 85].

In practice, continuous dynamic testing can be seen as a set of singular tests conducted at predefined successive time steps, taken with a time difference equal to the needs of precision and detection readiness. Each of these singular successive tests can generate a set of modes, or mode representatives, such as those shown in Fig. 36 and which, over time:

- May be associated with true modes of the structural system or with spurious estimates
- May be excited in some of the singular tests but not in others, depending on the operational and environmental loading
- May exhibit different values according to the operational and environmental loading or to changes in the structural system

For this reason, the label associated with each mode, at a certain singular test conducted at a specific time-instant, may differ when obtained in a different time-instant, on the same structural system and using the same sensor set. The task of establishing the relation between the same mode characterized in different periods of time in the same structure can be named as modal tracking. Modal tracking strategies can assume several formats and strategies, from which boundary-based tracking, where the modes' representatives are controlled by comparison against pre-known modal features, and cluster-based tracking, where natural modes'

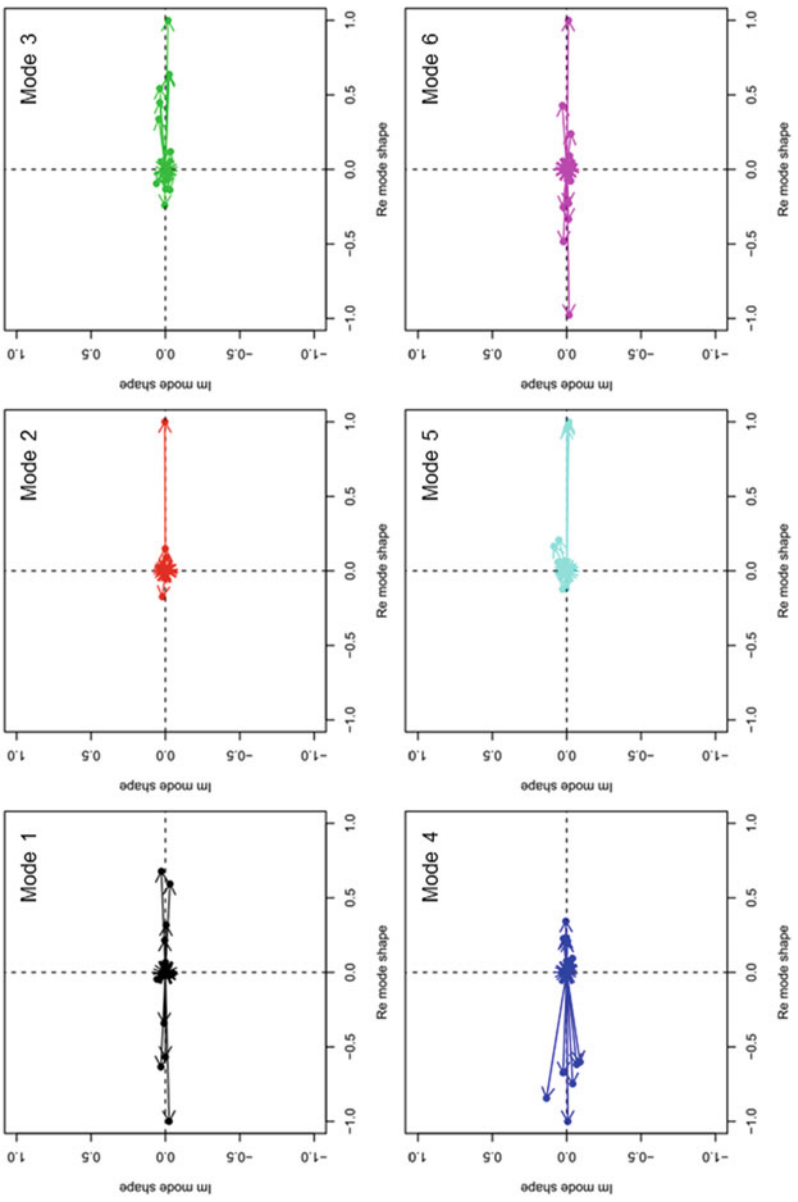

Fig. 37 Mode shapes in the complex plane

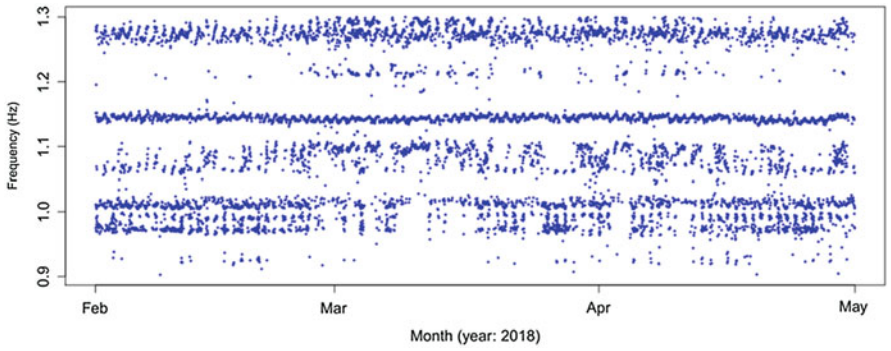

Fig. 38 Time series of modal representatives acquired hourly on a suspended steel bridge

representatives are allocated using cluster analysis and without the need for pre-known features, are popular in civil structural testing. Each of these and other strategies found in the literature has, in turn, different variants depending on the authors and the specificities of each structural system being tested [54, 85, 108]

To have examples of strategies for modal tracking, the example shown in Sect. 7 with modal estimation conducted from February to May 2018 is considered. The mode representatives were obtained hourly during this period by applying the SSI method (see Sect. 5.7) followed by cluster-based strategy described in Sect. 7. The resulting time series of modal representatives is shown in Fig. 38 for the frequency domain [0.9;1.3] Hz, where four to six near-horizontal alignments span over time, indicating that modes' frequencies are repeating themselves throughout the monitoring period under analysis. In the same plot there are, however, frequency bands with higher variability than others, indicating either important sensitivity to operational and environmental loading, or the existence of close (maybe overlapped) modes, in the frequency domain.

8.2 Tracking Based on Boundaries

The definition of boundaries for modal tracking can be used for civil dynamic testing, for the continuous safety control of operating civil structures. This type of modal tracking requires that the modal features (frequencies, damping ratios, and mode shape coordinates) of modes be known in advance and is usually based on the definition of upper and lower boundaries for each feature (f, d, MAC, MP, MPD, and MPC) and for each of the modes, identified herein with index j. These boundaries can generally be defined as,

$$f_i \in \left[\left(1-\alpha_{f,inf}\right)\ f_j;\left(1+\alpha_{f,sup}\right)\ f_j\right] \tag{75}$$

$$d_i \in \left[\left(1-\alpha_{d,inf}\right)\ d_j;\left(1+\alpha_{d,sup}\right)\ d_j\right] \tag{76}$$

$$MAC_{ij} \in \left[\left(1 - \alpha_{MAC,inf}\right); \left(1 + \alpha_{MAC,sup}\right)\right] \tag{77}$$

$$MP_i \in \left[\left(1 - \alpha_{MP,inf}\right)\ MP_j; \left(1 + \alpha_{MP,sup}\right)\ MP_j\right] \tag{78}$$

$$MPD_i \in \left[\left(1 - \alpha_{MPD,inf}\right)\ MPD_j; \left(1 + \alpha_{MPD,sup}\right)\ MPD_j\right] \tag{79}$$

$$MPC_i \in \left[\left(1 - \alpha_{MPC,inf}\right)\ MPC_j; \left(1 + \alpha_{MPC,sup}\right)\ MPC_j\right] \tag{80}$$

where $\alpha_{QUANTITY,\ sup}$ and $\alpha_{QUANTITY,\ sup}$ express the ratio between the upper or lower boundaries and the corresponding representative value of each known-in-advance mode. For simplicity, the same α value can be used for each quantity across all modes and even across features or entirely variable across modes and features and even across the time periods under analysis. Depending on the structural system and on the influence of environmental and operational actions on the mode estimation, it might be necessary to define boundaries, $\alpha_{QUANTITY}$, and reference feature values, f_j, d_j, MAC_j, MP_j, MPD_j, and MPC_j, as functions of the values assumed by the actions. Each newly arrived cluster representative, identified with the index i, can therefore be allocated into the pre-known mode j if it is within a chosen set of the boundaries represented in Eq. (75) to Eq. (80).

To exemplify the application of boundary-based modal tracking, the time series shown in Fig. 38 is considered with the objective of tracking the mode with a frequency value of approximately 1.15 Hz using as features the frequencies, the damping ratios, and the MAC values and a value of α=0.1 across for all features. The results of the tracking are shown in Fig. 39, where the mode representatives that do verify are represented in blue color whereas the remaining ones are represented in gray color.

The boundary-based tracking defined for frequency alone can be observed in Fig. 39a, where the upper and lower boundaries can be directly identified in the plot. Conversely, and in line with the results obtained for the modal estimation, the boundaries applied to damping do not produce as clear divisions in the frequency domain (Fig. 39b) since a large number of modes observed in a structural system exhibit identical damping values. Unlike for damping, the unique shape of each mode seems to produce, for the structural system under analysis, clear divisions between the representatives of a mode and those representing the remaining ones, as it can be observed by the clear time-series produced by applying the boundaries on the MAC values (Fig. 39c). This is a common result for civil structural testing, where for some structures the MAC is a useful feature for separating modes with identical frequency value. Unsurprisingly, when applying boundaries to sets of these features, for the present case study, those which include damping are less performant and those which are based on the MAC outperform the remaining ones (Fig. 39c–g).

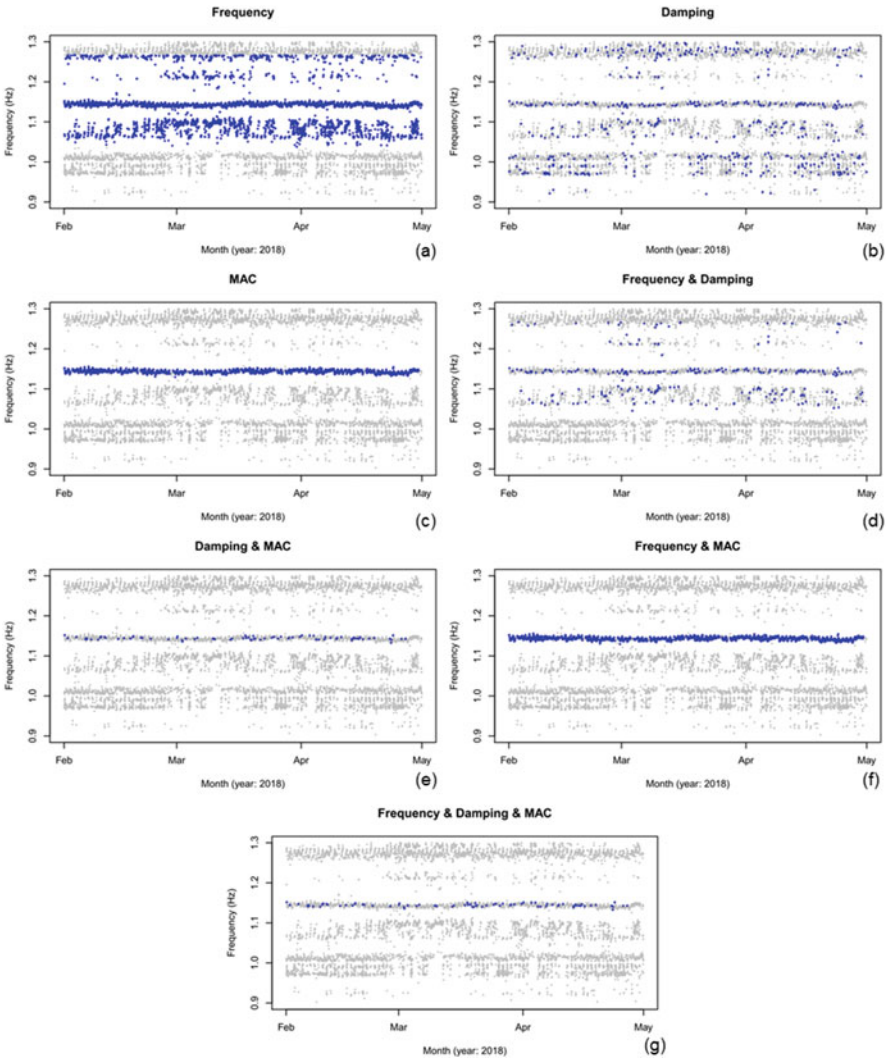

Fig. 39 Modal tracking of mode with f=1.15 Hz using α=0.1 and the following features (**a**) frequency, (**b**) damping, (**c**) MAC, (**d**) frequency + damping, (**e**) damping + MAC, (**f**) frequency + MAC, and (**g**) frequency + damping + MAC

8.3 Cluster-Based Modal Tracking

Modal tracking is based on clustering resorts to the same principles as cluster-based modal estimation, described in Sect. 7.4. As in that section, a clustering method is applied to a certain data set to allow for the best division between modes [54, 80, 85], followed by the computation of a cluster validity index [80] to ascertain

the most likely number of modes present. The difference (and additional challenge) consists of the fact that, for modal tracking, the data is dispersed through time and therefore might suffer slight variations in its inner structure, which may demand for additional procedures, depending on the structural system and on its actions' effects, such as moving-windows processes, baseline creation for posterior direct allocation, among others.

To provide an example of cluster-based tracking, the hierarchical agglomerative clustering was applied a single time to the time series shown in Fig. 38, with a cut at k=6 clusters (modes). Its results allow observing (Fig. 40) that the clustering method is capable of dividing the time series in different subsets according to the distance metrics used. When considering frequencies, the division relies mostly on the density of the representatives in the frequency domain, as it can be seen in Fig. 40a, while clustering based solely on damping generated a mixture of the modes representatives over time (Fig. 40b), as happened with boundary-based tracking. Unlike when using the frequencies and damping, the MAC-based cluster tracking (Fig. 40c) allowed observing modes with dissimilar shapes and identical frequency values, such as those observed in the frequency domain between 0.95 Hz and 1.05 Hz, in Fig. 40c, where two mode shapes were identified by the clustering methods in a dense region of representatives. These overlapped modes can be observed in large symmetric civil structures, where the MAC-based tracking assumes particular importance. The modes time series obtained by applying clustering to distances obtained from frequencies + MAC are similar to those obtained for the MAC alone, yet the addition of the frequencies as input seems to produce less miss allocations.

The application exemplified herein (Fig. 40) consists of a single-time cluster process applied to a large time-series, which can be used in practice. However, as referred in the previous paragraph, clustering can also be applied in smaller time-windows which can slide along time to consist of a baseline-free modal tracking procedure. An alternative may consist of conducting the procedure described herein for defining a baseline without pre-known knowledge of the structural system, after which the mode representatives obtained over time are compared against and allocated. Combinations of both and of other methods can also be used. Neural networks, decision trees, and other supervised classification algorithms can be used to learn the baselines defined either manually or by a clustering process such as the one described in order to improve the results of posterior allocation. When using these methods, environmental and operational actions can seamlessly be included into the process, with the possibility of large improvements in the results over time.

The assessment of the number of clusters assumes particular importance for cluster-based modal tracking and can make the difference in delivering sensitive and robust Structural Health Monitoring strategies. When too few modes are considered, different high variability of some time series can be obtained, thus leading to large confidence boundaries for safety control. This is the case of the partition containing K=4 clusters obtained from the time series shown so far (Fig. 41a) and where it can be observed that the blue cluster is allocated to representatives located in the frequency band around 1.0 Hz and in a small band characterized by f=1.3 Hz. When too many modes are considered, the appropriate clustering method may tend

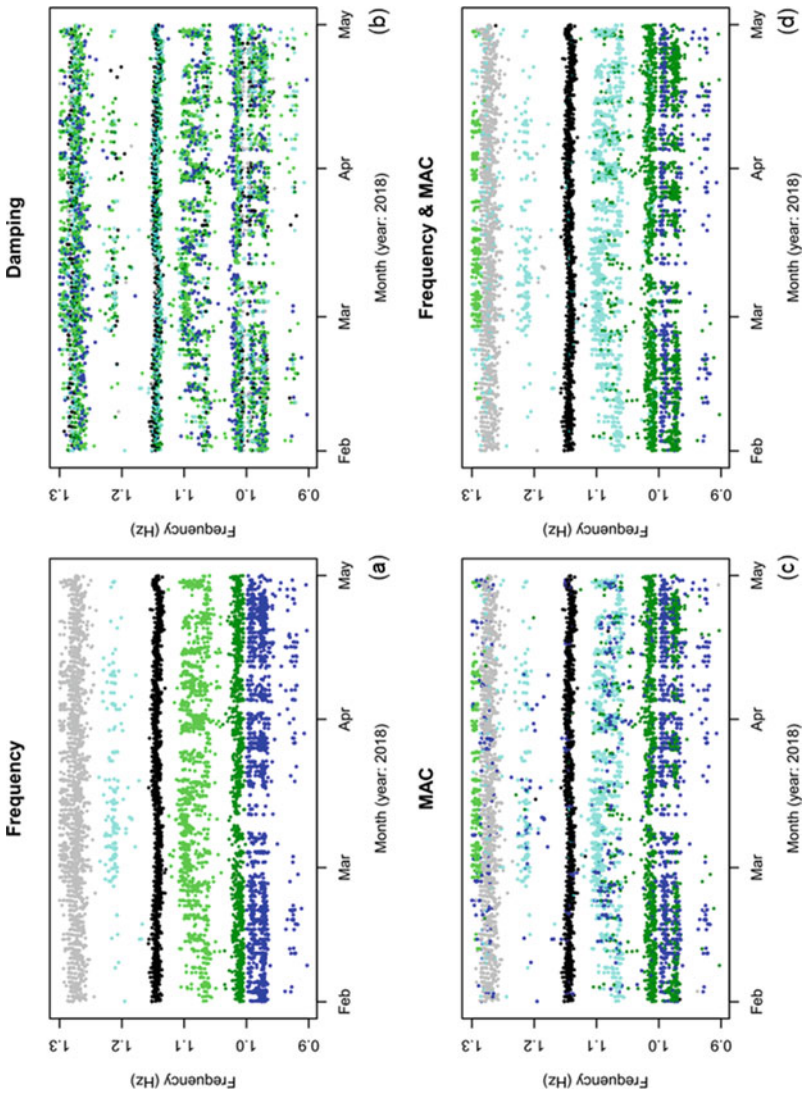

Fig. 40 Modal tracking of modes with frequencies between f=0.9 Hz and f=1.3 Hz using distance metrics obtained from (**a**) frequency, (**b**) damping, (**c**) MAC, and (**d**) frequency + MAC

to allocate the additional clusters to noise/spurious modes, thus allowing for their seamless identification and cleansing. This is clearly identifiable in the cyan cluster of Fig. 41d, which appears to be associated with a spurious mode, and in the light green cluster of the optimal partition, with the highest SIL value (Fig. 41c).

9 An Important Note to Increase the Speed of Identification

Most of the techniques use the stability diagram to select physical modes. This procedure requires the formulation of the response matrix that is later decomposed by the QR transform for different dimensions which could be quite slow. Döhler and Mevel [29] developed a methodology to compute only one QR transform and to derive the smaller dimension matrixes in a simple way speeding the process considerably.

An additional recommendation to increase the speed of the identification, when several sensors are present in a structure, is to use a small number of channels to first identify the frequency and damping and later use a larger set of sensors to identify the mode shape more densely. In order to do this, you need to apply the identification technique for the shape given the frequency and damping of the mode is known like the one presented by Caicedo and Marulanda [18]

A comparison of the methods described above can be found in Peeters and Ventura [64] and Giraldo et al. [33].

10 Application Examples

10.1 Building Excited by Ambient Vibration

There are two common testing applications, namely those based on temporary and permanent sensor arrangement.

10.1.1 Temporary Testing

The temporary arrangement can be performed by wired or wireless sensors. For identification of mode shapes, it is critical to pay attention to the synchronization between sensors. For wire systems this is typically attained by using an arrangement of analog sensors connected to a single digitization station that provide the common timing. For wireless distribution sensors, in some limited cases the sensors can be synchronized by radio frequency or others, but in general when moving between floor this is quite limited. So, the most reliable procedure for wireless-based testing is to have a very precise clock in each sensor and this clock should be synchronized at the beginning and end of the measurement and in some long duration monitoring at intermediate steps. To obtain reliable results the maximum time drift between sensor times should be smaller than 1 ms.

When a detailed mode shape is required, then two options are available, either sensors are installed in all desired location at each set up or a set of reference sensors

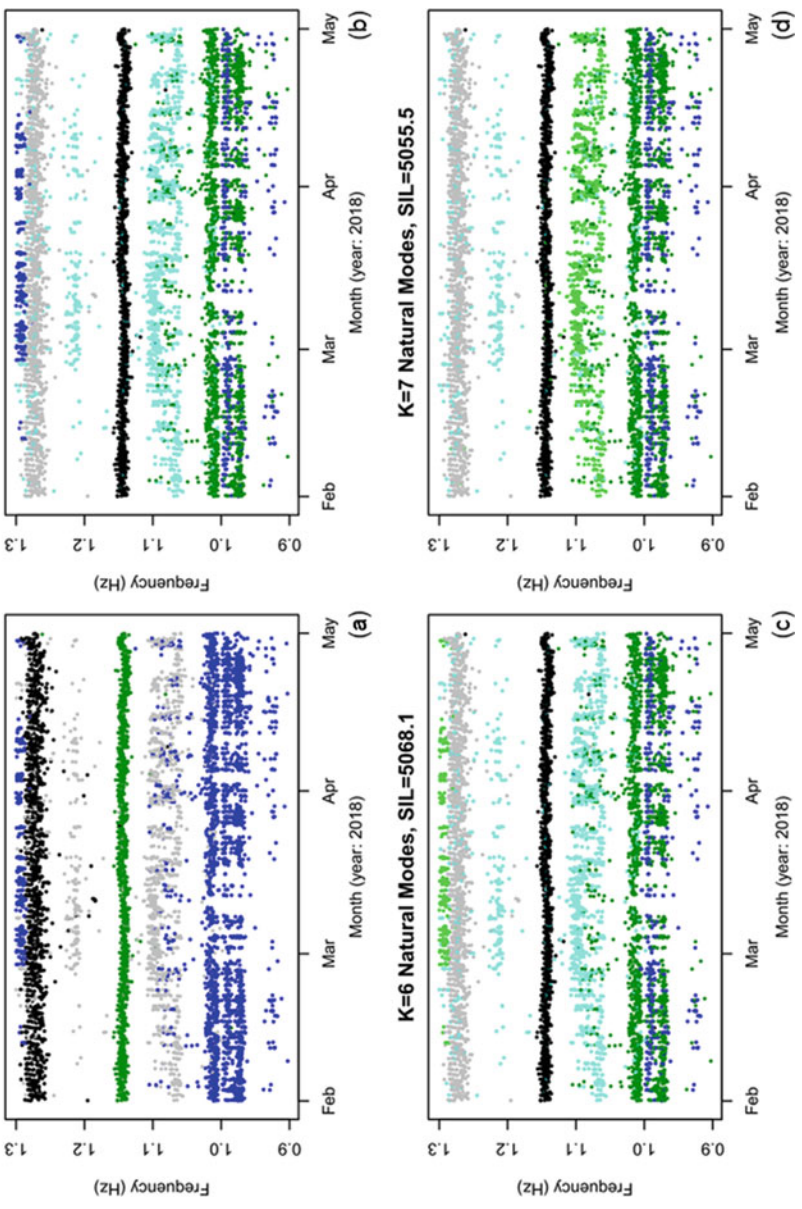

Fig. 41 Modal tracking of modes with frequencies between f=0.9 Hz and f=1.3 Hz using distance metrics obtained from frequency + MAC and a number of clusters equal to (**a**) K=4, (**b**) K=5, (**c**) K=6, and (**d**) K=7

(fixed sensors) is defined along with a set of movable or rowing sensors. In this last case a much smaller number of sensors is required and the modal shape can be reconstructed later using the reference sensors amplitude and phase. For the case of rowing sensors for each set up, the system identification procedure will provide the frequency and damping of each mode and a partial description of the shape. For several set ups there will be redundant data for frequency and damping and complimentary data for the shape. The reference and wireless rowing sensors are preferred for the procedure for long distance or highly detailed mode shapes not only because cables installation is difficult, due to physical limitations, but also due to the possibility of noise inclusion in the data.

The sensor sensitivity shall consider the level of response of the structure; nevertheless a sensitivity of $1e^{-5}$ g is generally sufficient in most cases. The bandwidth is related with the range of frequencies of interest, but for low rise structures a bandwidth between 0.5 to 15 Hz is generally sufficient. For tall buildings, a bandwidth increase to 0.01–15 Hz may be required, generally demanding for more expensive sensor sets.

Due to the low level of excitations (typically bellow 0.0005 g) and the bandwidth of interest, the sensors can be deployed directly on the surface without any permanent or temporary attachment.

Sampling frequency has to be related with modes of interest but typically 50 Hz is sufficient and 200 Hz desirable.

Duration of monitoring depends on the objective of the monitoring. When a particular environmental response is desired the duration must consider the period of the desired vibrations. Typically, measurement durations are 20–60 min. The longer time recordings allow for the evaluation of variations during the monitoring period due to possible sensitivity to the amplitude and frequency response of the structure.

The identification methods also impose requirements on the duration of the recording. Typically, the frequency domain methods require extended periods of time in order to obtain a more robust estimate of the response function. Time domain methods generally require considerable shorter recording times.

Recording building vibrations present challenges related to usage due to increased level of noise, namely people moving, causing localized slab vibration, machinery operations such as elevators, air conditioning, copy machines, printers, and electrical noise produced by illumination and communication system, among many others. Several measures can be taken to reduce their impact and one of the simplest and most effective consists of recording long periods of time and latter select sections of the recorded data that have a smaller influence of noise. Additionally, the application of procedures to reduce the noise effect by filtering and averaging is commonly used.

IT should be pointed out that buildings' modal characteristics are sensitive to amplitude of the response and environmental conditions (temperature, time of day, rain (even previous rain cycles), and weather conditions). Hence, it is very important to document and record the specific occupations levels and activity, as well as environmental conditions. The most relevant conditions are temperature, humidity

of the ground, freezing conditions and mass additions due to snow and usage. For short duration monitoring, the environmental conditions can be considered constant. Nevertheless, if the monitoring extends by hours and a sudden change of loading amplitude or weather conditions occur, this may affect the structural properties.

The best practices are to report at least the following:

(a) Building location
(b) Building structural characteristics and soil conditions
(c) Weather conditions
(d) Monitoring Time
(e) Sensor characteristics (bandwidth and sensitivity among others)
(f) Sensor locations and direction
(g) Number of recording setups
(h) Duration of each recording
(i) Sampling frequency
(j) Particular situation that occurred

Results should include

(k) Figures showing the recording signal in time and frequency space
(l) Procedures and consequence of data cleansing
(m) Filtering and decimation
(n) System identification used and their controlling parameters.
(o) Modal results including the confidence of the analyst on the results

10.1.2 Permanent Ambient Vibration Monitoring

All the comments presented for temporary ambient monitoring apply in this case; nevertheless the long-term monitoring requires several modifications on the equipment and the analysis procedures.

For this case, sensor location is fixed, so the required sensor density to describe modal shape defines the number of permanent sensors and their recording directions. In this case the sensor must be anchored to the structure to avoid motion due the normal long-term operation of the building. Cabling between sensors and central recording units or for synchronization between digital units is convenient unless other procedures are used for synchronization between especially distant sensors (now day PTP is being used). Energy must be provided permanently and a UPS system must be considered if required for continuity of operations. Special attention should be given to the selection of the recording system for long-term operations (i.e., temperature conditions and an automatic restarting).

Because for permanent continuous monitoring the data acquired can be very large, different strategies for data cleansing, conditioning, identification, tracking, storage, and referencing should be considered. All these processes must be done in real time or near-real-time. It is not reasonable nowadays to record data continuously and analyze it later.

The cleansing procedures must be able to detect at least:

(a) Periods of malfunction of the system
(b) Number of operative sensors
(c) Noise level present in each channel
(d) Procedures to discard noisy channels to avoid alterations of the identification and the tracking activities

Data conditioning must be able to process the data based on preestablished parameters or adaptive parameters.

System identification must be conducted in real-time, or use selected periods of monitoring time to perform a window system identification. Results should include description of the analysis window, the conditions of the structure, and the environment at the time of the analysis.

To handle the large amounts of data several strategies have been applied. Without been exhaustive, the following are among the most common:

(a) Obtain parameters of interest at predetermined time periods or response characteristics. Tag and storage of the derived results. Store only a subset of the original time data for post processing. Processed data is informed via electronics means (SMS, email, periodic electronic reports (daily, weekly or when a change of state is detected)).
(b) Similar to (a) but raw data is stored locally and periodically. If not required in a predefined period of time (for example a month), data is removed from the system.
(c) When allowed by the communication bandwidth, raw data is transmitted to a processing server where data is processed, made available, and stored for future analysis. In this case the cost of store raw data can be very high depending on its duration, sampling frequency, and number of channels. This procedure is recommended at the beginning of a project. After robustness of the whole process is obtained, some of the storing requirements can be relaxed but maintaining raw data allows the revaluation and the testing of new procedures.

The data is typically analyzed by using moving windows. The window length will depend on the system identification used and the robustness required for the results. For example, if methods in the time domain are used, a representative value can be obtained for an hour of measurements by performing 12 consecutive analyses in corresponding 5 min of non-overlapping data. Each 5-min data will provide information on the desired parameters and the 12 results could represent hour values with appropriate information on the dispersion of the results.

Because excitation levels are different during recordings, each analysis window could contain different modes and for a given mode its value can vary. So, a tracking strategy must be developed to link consecutive modes that are identified as the same in different time windows. This is generally solved using distance metrics strategies

as mentioned earlier, for example, in Gonzalez and Boroschek [35] the distance metric used is shown in Eq. (81), as follows:

$$d_{ref,i} = (1-\alpha)\frac{\left|f_{ref} - f_i\right|}{\max\limits_j (f_i)}\alpha \ \left(1 - MAC\left(\phi_{ref}, \phi_i\right)\right) \tag{81}$$

The distance is a combination of frequency and mode shape difference weighted by a constant that is related to the number of sensors present at the time of the analysis. For the case that no extreme events occurred between analysis windows, two modes are consider the same if the distance is less than a threshold value.

After the classification of each mode is done, using the tracking algorithm, the responses and characteristics of each identified mode can be expressed as a function of time. This collection of information will present the effect of the environment and noise. The most common effect is variation of the predominant frequency with temperature and humidity in the structure and in the foundation's surrounding soil. The variations observed in typical building can achieve up to 10% without any presence of damage and higher in the presence of soil freezing. As described previously, the continuous ambient vibrations monitoring is the most reliable procedure to detect changes of state of health on the structure so this sensitivity to environmental conditions must be considered if small changes in modal and response parameters are desired.

The most common strategy in buildings is to perform a normalization of the data by procedures previously described. When the information on the environmental variables is nonexistence or limited, removal of the induced variation can be done by a Principal Component Analysis (PCA) [102]. Alternatively, a modal parameter dependency model based on recorded environmental variables can be used. The model must consider the time lag between the response and the environmental variables. For this case ARX, MLP and others have been used [65, 81].

After data normalization, the effect of environmental variables is diminished so it is possible to detect more subtle state changes. Several procedures can be used and control charts are commonly applied [103].

One of the case studies we have been presenting is an office building. It is located in a semiarid region in Chile so it is excited by operations, wind, and earthquakes under varying environmental conditions, as shown in Fig. 42. Sensors are permanently located in the structure so evaluation of state changes can be identified and tracked automatically.

Sensors are located in three levels of the structure, shown in Fig. 43. This allows a global identification of the structure response and a limited representation of the mode shape. The sensors are of the capacitive type with a sensitivity of 1×10^{-5} g and a range of 4 g. This allows the recording of the ambient and earthquake vibrations with the same system. Sampling rate is set to 200 Hz to record the amplitudes due to earthquake motions. For ambient vibration a sampling between 50 to 100 Hz will be appropriate.

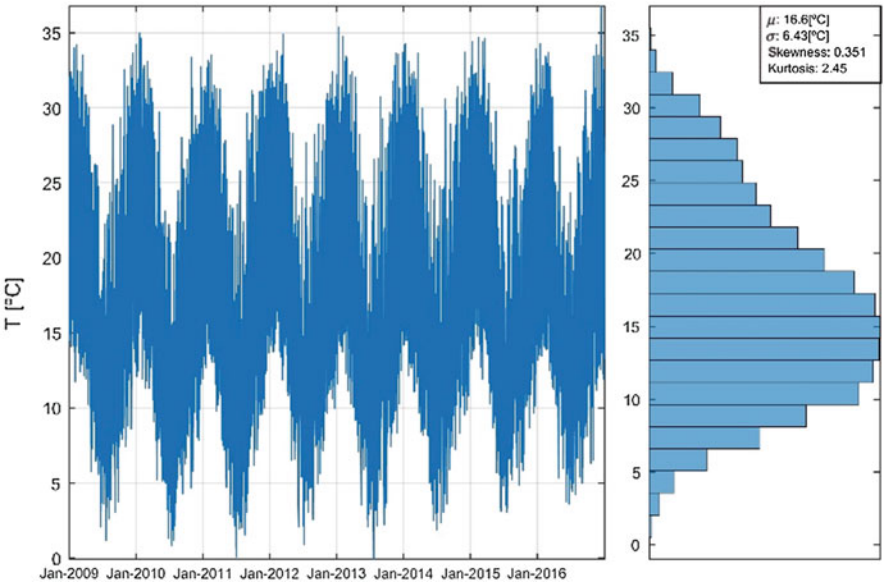

Fig. 42 Temperature variations recorded in TC Building

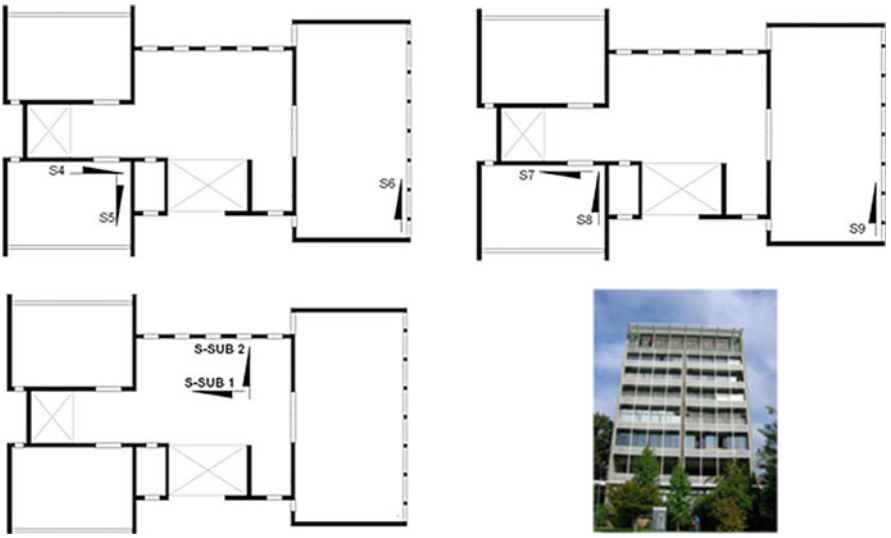

Fig. 43 TC Building

Sensors are anchored to the floor slab and they are located close to vertical structural elements to limit the effect of the slab vibrations and deformations on the DC component and its predominant frequency on the acceleration signal. Sensors are protected by a cover to avoid impact due to human activities and are located

away from doors, elevator shafts, and local permanent equipment (air conditioners and others). All sensors are wired and connect to a signal conditioning system that performs antialiasing filtering, digitizing and transferring to a local computer system. In the computer system, the data is analyzed and stored.

Data is stored using two different schemes. For ambient vibrations, 15 min records are saved to a hard drive and for earthquake events a trigger base criterion is used. For ambient vibrations the data is analyzed according to the following steps:

1. Data Cleansing. Data is automatically inspected for noise contamination, aliasing, recording errors, impacts that occur due to the use of the building and earthquakes. The earthquake records in general are not used for the ambient evaluations. The analysis uses the frequency content of the signal along with the RMS and PGA acceleration and also the value and energy evolution of the signal to identify noisy signals. An information vector is formed for the specific record, indicating which sensor data of the set is valid or not.
2. Data decimation. Data is decimated to 20 Hz for identification. Larger sampling frequencies do not contribute to the identification of modal properties and increase the computing and storage demands, as shown in Fig. 16.
3. System Identification. All aboveground channels are used for the identification. The SSI-COV data is used considering order between 20 and 100, as in Fig. 22.
4. Selection of Physical Modes. Several strategies have been developed to identify physical from spurious modes, as mentioned above. In this case a density-based criterion is used, Fig. 23.
5. Modal Tracking. When the target application is a continuous monitoring system, the mode identified in one time period should be linked to the next observations. In the absence of damage this is generally done using a distance criteria based on frequency and shape. Damping is not used because its values are highly uncertain and many modes can have similar values. A typical distance equation should consider a normalized distance and shape similarity, typically using MAC. It should also consider the number of sensors that define the mode, as shown in Fig. 44.
6. Mode Normalization. Due to the variability of environmental conditions, the properties of each mode changes with temperature, humidity, and response amplitude among others. If change of state detection is required, the influence of the this variation should be considered or removed. One possibility is to obtain the principal components of the data and remove the effects of environment, as is shown in Fig. 45 to visualize the linear relation between mode 1 and 2. Figure 46 shows the normalized frequencies. A much smaller variation is observed, allowing for more clear visualization of slow or abrupt changes. Alternatively, a model base on the environmental variables can be developed using linear multivariate regression or ARX.
7. State Change. From the normalized data a state change can be identified using control charts or other methods.

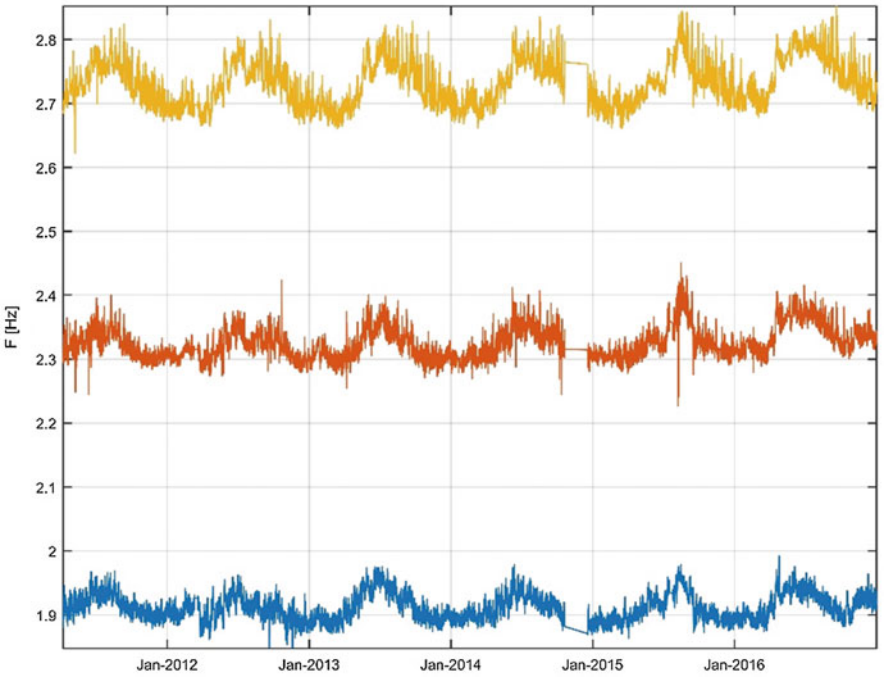

Fig. 44 First three identified and tracked frequencies

10.2 Buildings Earthquake Vibrations

Earthquake loading is characterized by transient signals with high energy between 0.05 to 30 Hz. The response in buildings is typically measured by accelerometers to capture the global behavior and, in some cases, they are complemented by strain gages and displacement meters to detect local deformation information. Tilt-meters are also used to determine residual deformations.

Similar requirements as those described for permanent ambient vibration monitoring relating to anchoring, cabling, common timing and location are needed. In addition, due to loss of power during an earthquake safe UPS and recording system are needed with a typical autonomy of 2–4 days. For the case of earthquakes, damage can be expected, so sensor location should consider all possible expected scenarios. Some guidelines are described in the following points:

1. Input recording. At the lowest basement level and at the ground surface level a minimum of three horizontal sensors are recommended to capture horizontal motions and possible wave passage causing plane rotations. Vertical sensors should be located at the end of walls and at the center of the foundation to capture vertical motions and local and global rocking.

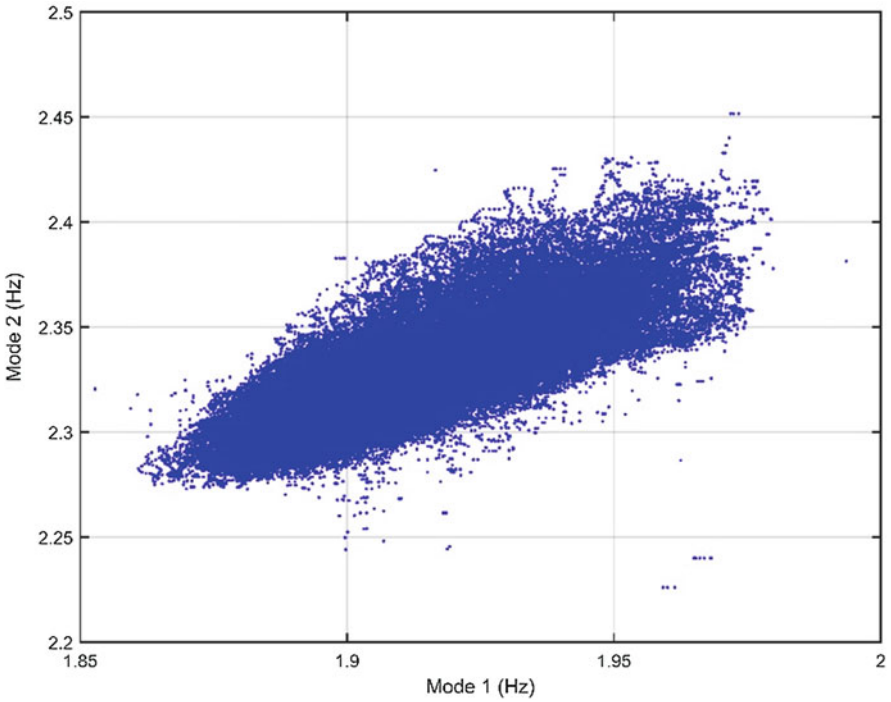

Fig. 45 Mode 1 vs. Mode 2

2. Floor displacements and rotations. To capture the motions of the floor slabs, three horizontal sensors should be installed. To capture the in-slab deformation additional horizontal sensors are needed. To capture vertical amplification and rocking, sensors should be located at opposite sides of the buildings and at borders of structural walls.
3. Storey drifts. To capture drifts the maximum number of possible floors should be instrumented. Preference should be given to the first two floors (where damage is typically concentrated) and others distributed in height.
4. Derived inertial forces. Inertial forces can be estimated based on floor accelerations. These forces can be used to estimate floor and base shear and overturning moments.
5. Vertical amplifications. In very tall buildings vertical amplification of motions is possible, so vertical sensors should be distributed in height.
6. Irregularity and damage scenarios. If predefined damage scenarios are the objective of the instrumentation, local sensor should be considered. A mix of strain and displacements sensor are common to track local responses.
7. Tilting and permanent displacement. To capture permanent displacements due to damage, acceleration sensors should have a bandwidth that contains the DC component. Integration of the acceleration signal should not filter the DC components

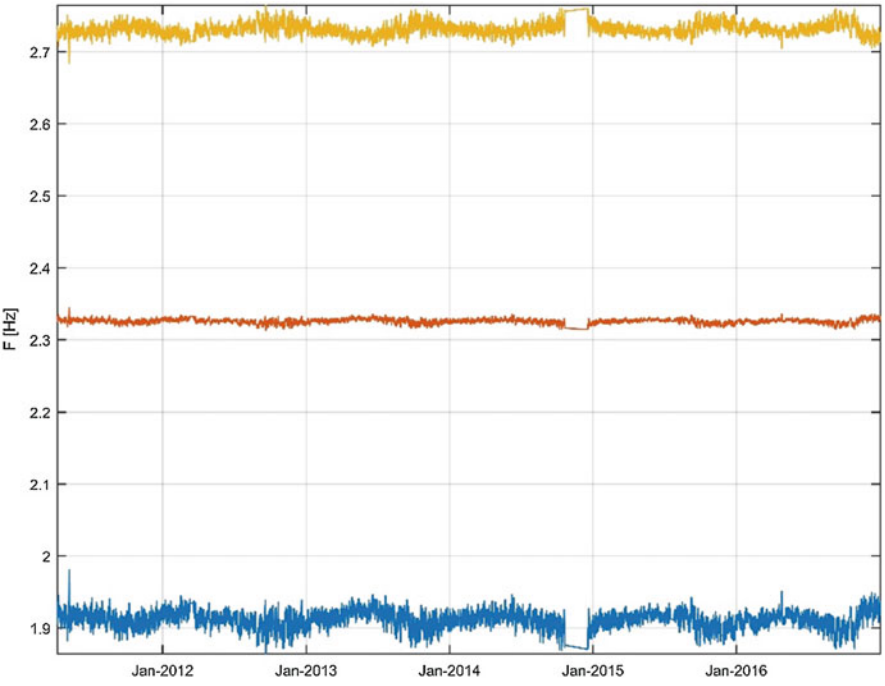

Fig. 46 Normalized frequencies

[9]. In this case accelerometers should have a very low noise, typically below 1×10^{-5} g. Tilt-meters are able to capture permanent inclinations of the structure, and they should be considered to obtain the tilt in two orthogonal directions and in more than one location in height: at ground level to detect permanent foundation rotations and upper floors to detect tilting due to structural damage.

There is a strong dependency of the modal parameters due to amplitude [40, 97], while damage can severely change the systems' responses, as shown in Fig. 25. Foundation conditions play an important role in the response, extending natural periods or increasing or decreasing the energy dissipation due to soil structure interaction [25].

Comparison of pre- and post-earthquake ambient vibration responses has been used to identify permanent modal properties changes. If the ambient vibrations are obtained immediately before and after the earthquake, the change due to environmental variables should be small (with the exception of the possible evacuation of the building). The change in periods can be an indication of the severity of the state change. Changes in predominant period below 20% (without the presence of localized damage) are related with nonstructural or light damage. Period changes between 20% and 50% can be associated with moderate damage.

The possibility of damage can be identified by the magnitude of the permanent drifts, the presence of tilting, and the level of period extension. To track the possible nonlinear response the STFT, S-Transform or regressive models [77] or windowed MIMO techniques [88] can be used.

To estimate possible damage and to correlate with design variables the acceleration and displacement at non-instrumented floors is sometimes necessary. Several schemes have been proposed to obtain drifts along the building height, even at non-instrumented floors. Typically linear or spline interpolation between floors or the use of the knowledge of the mode shape to interpolate for each modal response is used [50].

For the analysis of possible damage, displacements information are critical, particularly the relative displacement between floors or drifts. The displacements can be obtained by double integrating acceleration records. This has to be done with care in order to avoid the introduction of spurious low noise components [7, 9].

10.3 Base-Isolated Buildings

Base-isolated buildings are one of the main solutions to avoid damage in highly seismic regions. In this case the building is sitting on top of the isolators which present a high vertical stiffness and extreme low stiffness in the horizontal direction. These conditions produce a first modal shape that is similar to the seismic influence vector (constant in height). The influence vector represents the acceleration at all the degrees-of-freedom of the system assuming a rigid body motion of the structure with respect to the points of earthquake input. When the first mode has the same shape as the influence vector, the modal participation factor for all other modes is close to zero so actually the isolation layer is like an energy barrier.

The isolator can be of several types but the most common is natural rubber with or without a lead plug to increase damping capacity or steel frictional pendulum. Both isolators are highly nonlinear and do not present a viscous damping mechanism [75] so typical system identification techniques have very limited applications.

In order to record the response in this type of buildings, sensors have to have DC components. Permanent displacements are common after strong shaking. Sensors described in the earthquake response sections are the same but a concentration of acceleration and displacement sensors are needed at the interface level.

Nonlinearity is always present in the response so nonparametric identification tools like PP, spectrogram, S-Transform are appropriate [31, 59, 90]. Also MIMO techniques used in sequential windows give information, with large uncertainties, on the possible model parameters [2, 53, 61, 104].

10.4 Bridges Under Operational and Ambient Excitation

10.4.1 The Suspended 25 de Abril Bridge in Lisbon

The suspended 25 de Abril bridge (Fig. 47a), located in Lisbon, Portugal, has a total length of 2177 m, with a 1013 m long central suspended span, two 483 m lateral suspended spans, and three non-suspended spans, each approximately 100 m long (Fig. 47b). The bridge's suspension system comprises four cables, where the two main cables were installed during its construction before 1966 and the secondary ones in 1999, when the railway was installed on the bridge. Hanging from the four cables are 1344 hangers with rope-like section, divided in groups of 8 at each 168 suspended sections. Each of the two 190 m high pylons (Fig. 47d) consists of a steel truss which supports the deck at an height of approximately 70 m, while piers P2, P5, and P6 also support the deck at this height. Piers P1 and P7 connect the bridge structure to the south tunnel and to the north viaduct and are composed of concrete. These structures also include the anchorage of the main cables, while the anchorage of the secondary ones are made with concrete structures built next to each of these two piers. The bridge deck consists of a steel truss carrying 6 roadway lanes and two railway lines (Fig. 1b), comprising four main beams which span between the 200 transverse stiffening suspended frames, each of which is 11.20 m apart from the adjacent ones and also consisting of steel trusses, as it can be observed in Fig. 47c. Along with the main beams, diagonal elements span between each pair of transverse suspended frames. The roadway system consists of seven stringers supporting numerous transverse beams as well as the pavement, while the railway is supported by four stringers, one per rail.

10.4.2 Structural Monitoring System and Data

The structural monitoring system installed on the 25 de Abril Bridge acquires data from 214 measurements obtained from 171 standalone physical sensors at a rate of 500 samples/s. The quantities being measured consist (Fig. 48) of:

- Accelerations on five sections of the deck, on two sections of the pylons and on the ground at the foundations of pier P1 and the pylons, using force-balance accelerometers (Fig. 49b, c)
- Relative displacements between the piers P1, P2, P5, and P7 and the deck, using magnetostrictive displacement transducers (Fig. 49e)
- Rotations of the nodes where the cables change their angle, located on the top of piers P2 and P5, and on the pylons, using servo-inclinometers
- Stress in the mid-span of the deck's suspended spans and in three sections of each pylon, using Wheatstone bridges of resistance strain gages (Fig. 49d, f)
- Railway traffic on top of pier P1 in both railways, using rubber pads placed in between the rail and the sleepers, and instrumented with a mesh of fiber optic sensors

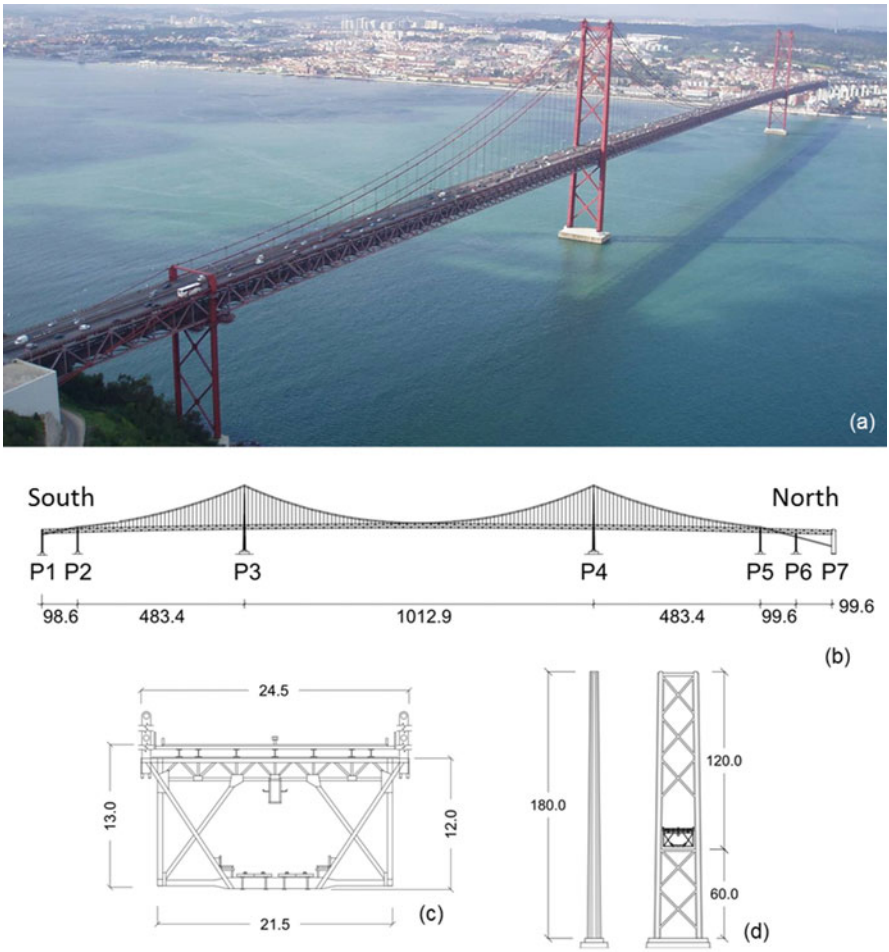

Fig. 47 The 25 de Abril bridge: (**a**) overall view, (**b**) side view, (**c**) stiffening truss section, and (**d**) tower side view

– Wind action on the mid-span and south quarter-span of the main central suspended span, using three-dimensional ultrasonic anemometers (Fig. 49g)
– Temperature in the deck and pylon sections where stress is being measured, using thermistors sharing the strain gage housing (Fig. 49d, f)

Data is being acquired from the sensors at a rate of 500 samples per second, so as to take advantage of the hardware's analog low pass filters, thus leading to over 9000 million values per day. Data is then digitally filtered to a value of 20 Hz and decimated to 50 samples per second per sensor. These samples are then kept

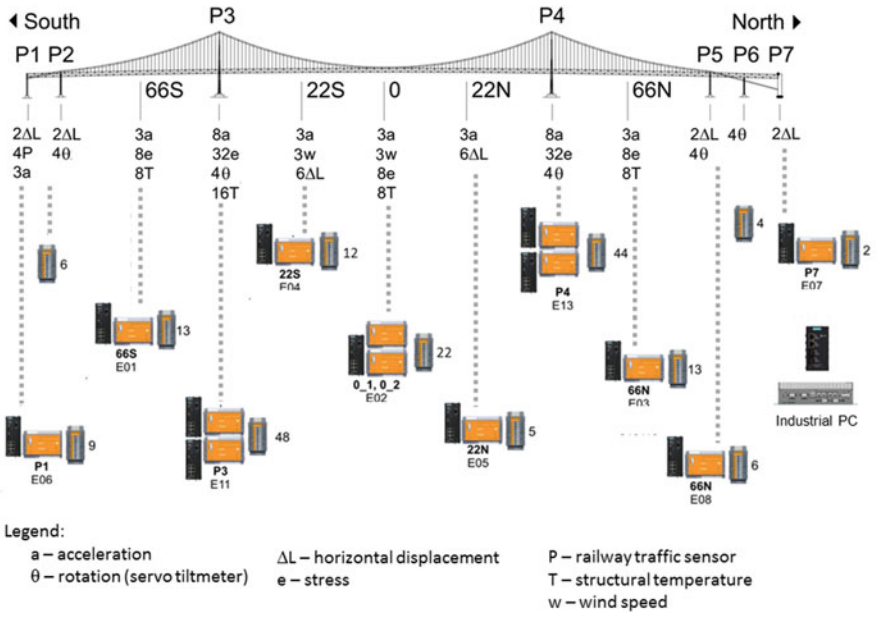

Fig. 48 Structural monitoring system of the 25 de Abril bridge

as digital inventory of the bridge's use and structural response and for Structural Health Monitoring.

For the present example, the accelerometers installed on the five cross-sections of the bridge deck and on the four sections of the pylons are considered. The instrumented cross-sections consist of those shown in Fig. 48 and named as 0, 22S, 66S, 22N, 66N ("S" stands for South and "N" for North, taken from the mid central span). Their locations consist of the center and quarters of the main span and as the center of the lateral suspended spans. The accelerometers installed on the pylons are located on their top and mid-height.

The linear character of the elements constituting long-span bridge structures, with one dimension significantly larger than the other two, motivates the conversion of the linear acceleration acquired by each sensor into section-wise accelerations associated with the vertical, longitudinal, lateral (or transversal), and rotational components of this physical quantity. This conversion can be conducted in bridge dynamic testing and has been conducted in the present example, as it can be observed in Fig. 50, which shows typical sections of the deck and pylons, where the accelerations acquired from the sensors (in blue in Fig. 50) were converted according to Eqs. (82)–(86), into the section-wise components (in green in the same figure).

$$ah = at = a1t \tag{82}$$

Fig. 49 Components of the structural monitoring system of the 25 de Abril bridge: (**a**) enclosure with acquisition, conditioning, and transmission equipment, (**b**) accelerometer housing, (**c**) accelerometer, (**d**) strain gage and thermistor housing, (**e**) magnetostrictive displacement transducer including housing, (**f**) Wheatstone bridge with thermistor, and (**g**) anemometer

$$av = (a2v + a3v)\,/2 \tag{83}$$

$$al = (a2l + a3l)\,/2 \tag{84}$$

$$ar = (a2v - a3v)\,/2 \quad \text{for the deck} \tag{85}$$

$$ar = (a2l - a3l)\,/2 \quad \text{for the pylons} \tag{86}$$

The singular value spectra of the vertical/longitudinal, transversal, and rotational acceleration components acquired on the structure are shown in Fig. 51. These were obtained by decomposing the periodogram matrix in singular values and vectors, as described in Chapter 12 and in Sect. 5.5, and allow observing that a large number of operational modes can be identified in the first and second singular values from 0 to 5 Hz. From 5 to 10 Hz, the noise generated by the road traffic increases significantly and no clear peaks are generally observed in the first two singular values. In this frequency subdomain, the last two singular values appear as those which still allow observing some modes, even if not as clearly as in the subdomain 0–5 Hz. In fact,

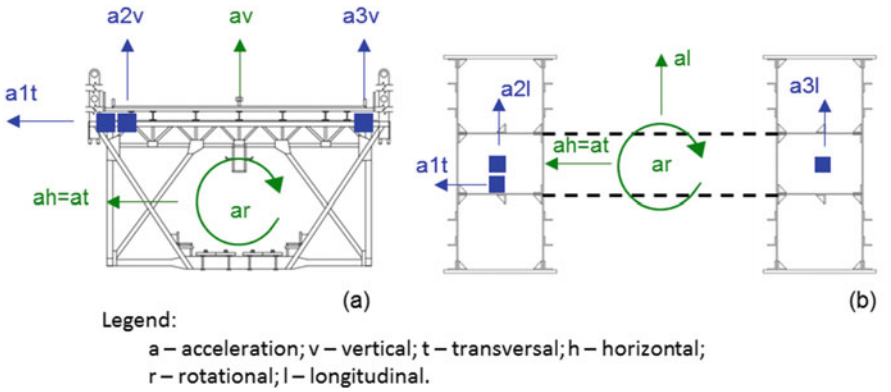

Fig. 50 Conversion of sensor acceleration into section-wise measurements: (**a**) on the deck and (**b**) on the pylons

the operational action of the traffic generates not only the baseline noise vibration shown in the SV spectra represented in Fig. 51, but it also changes the structural system being measured by adding a significant amount of mass to it, as it can be observed in Fig. 52, where the values of the RMS of the acceleration on the deck and the frequencies of the first three vertical modes are shown. By observing this plot, it can be concluded that the value of the RMS follows the amount of vehicles crossing the bridge daily, and exhibits maxima around the morning and afternoon rush hours, at the same time instants when the frequencies seem to exhibit minima. These results hint about the importance of the mass traveling on the deck on the identification of these lower order modes.

Other actions such as the railway traffic and wind are also known to be directly influencing the structural system, not only through the excitation but also by changing the properties of the materials and of the boundary conditions, as is the case of the temperature, whose influence on the latter can be of particular importance. Under these conditions, the estimation of the dynamic properties through testing can be particularly challenging and the corresponding results can exhibit very important variations observed over time.

10.4.3 Modal Estimation and Tracking

The need to conduct permanent identification in civil structures with sufficient precision, for structural health monitoring purposes, demands that the modal identification be conducted also continuously and therefore automatically. Under these constraints, the identification methods as well as the strategies for post-processing their output must be robust and precise, yet efficient. For the present case study, where a high number of modes is observed over a small frequency range, the coexistence of robustness and precision with computational efficiency can be challenging and demands for computationally efficient variants of the strategies described in Sects. 7 and 8.

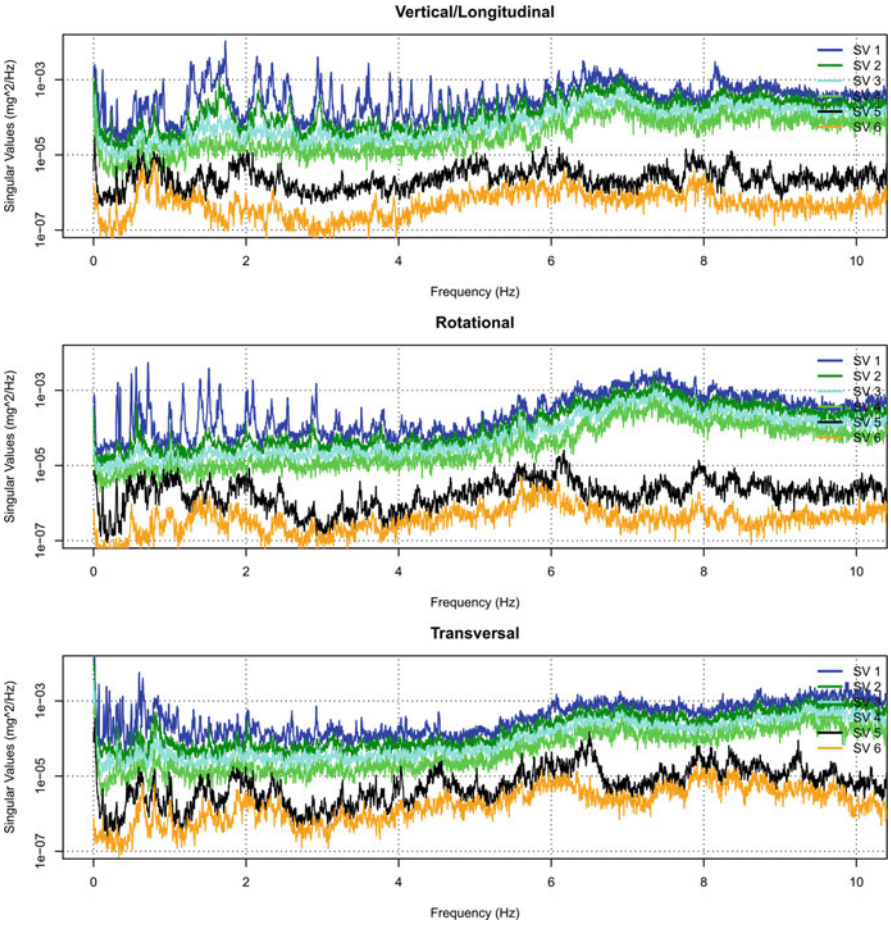

Fig. 51 Singular value spectra

When using a method such as the SSI-COV, described in Chapter 14 and in Sect. 5.7, very large values of model order, n, have to be used to detect high numbers of modes, such as the number observed in Fig. 51, for a certain frequency domain under analysis. This can be observed when trying to perform estimation using a model order of 50 in 1 h of data acquisition on the 25 de Abril Bridge, which is shown in the stability diagram of Fig. 53, where only ten modes can be observed in that frequency domain (0–10 Hz). The model order needed to appropriately capture all physical modes in this frequency domain, along with the spurious ones that will necessarily be observed, requires prohibitive amounts of time and memory. An efficient alternative which can be used consists of dividing the frequency domain under analysis into subdomains which can be as small as needed to capture all relevant physical modes. This strategy was used in the present example, where

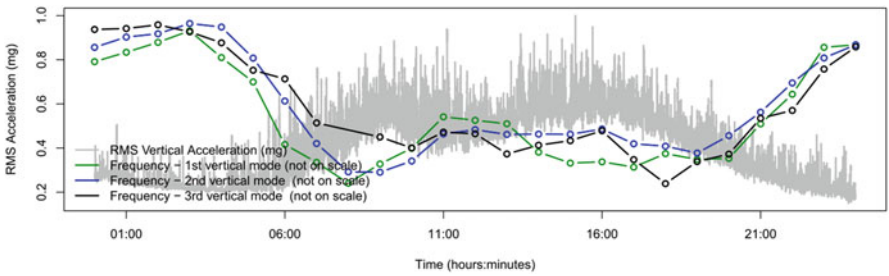

Fig. 52 RMS of acceleration on the deck and variation of the frequency values of the first three vertical modes over one day. The three frequencies are not to scale and the changes shown in the plot correspond to relative values of approximately 4% for the first two and 1.5% for the third

subdomains with a 1 Hz range were separately analyzed using the SSI-COV with a maximum model order of 50. Each of the 1 Hz frequency slices was obtained using the SSI-COV only after the application of a band-pass filter followed by decimation, so as to ensure that the process is as efficient as possible. The corresponding stability diagram is shown in Fig. 54, where a large number of modes can be identified in the vertical alignments represented in the first 6 Hz. In accordance with the conclusion obtained from the singular value spectra shown in Fig. 51, this stability diagram does not show stable vertical alignments from 6 Hz to 10 Hz, thus suggesting that poles obtained along this frequency domain are majorly related to noise, known to be generated by road traffic.

Following the calculation of the poles for the frequency domain under analysis, choice was made to perform spurious pole elimination based on hard criteria defined on the values of f, d, and MAC, chosen as 0.01, 0.05, and 0.99, respectively. The algorithm chosen for the stability verification consisted in checking whether, as each level, the poles verify all three conditions in the level immediately below. The results obtained are shown in Fig. 55 for the frequency range [0;5] Hz, whereas poles with higher frequencies were not considered given their low stability. The major motivation for performing the hard criteria verification prior to applying cluster analysis consisted in computational simplicity. Lower number of poles used as input in clustering proved important in reducing computation times, not only due to the smaller data sets but also due to easier convergence.

Using the poles considered as stable, these were considered for cluster analysis and validation. The SIL index was obtained for cluster partitions comprising from two to half of the maximum SSI order, taken as the theoretical number of modes that can be detected. Choice was made to select the cluster partition with the higher SIL value instead of the first relative maximum, so as to increase the detection incidence of each mode. The application of the hierarchical agglomerative clustering using the Ward criterion along with the SIL index allowed obtaining, for the data set acquired during 1 h and analyzed herein, the cluster representatives, taken as de centroids, shown in Fig. 56, where a large density of modes identified in the frequency range [0,5] Hz can be observed.

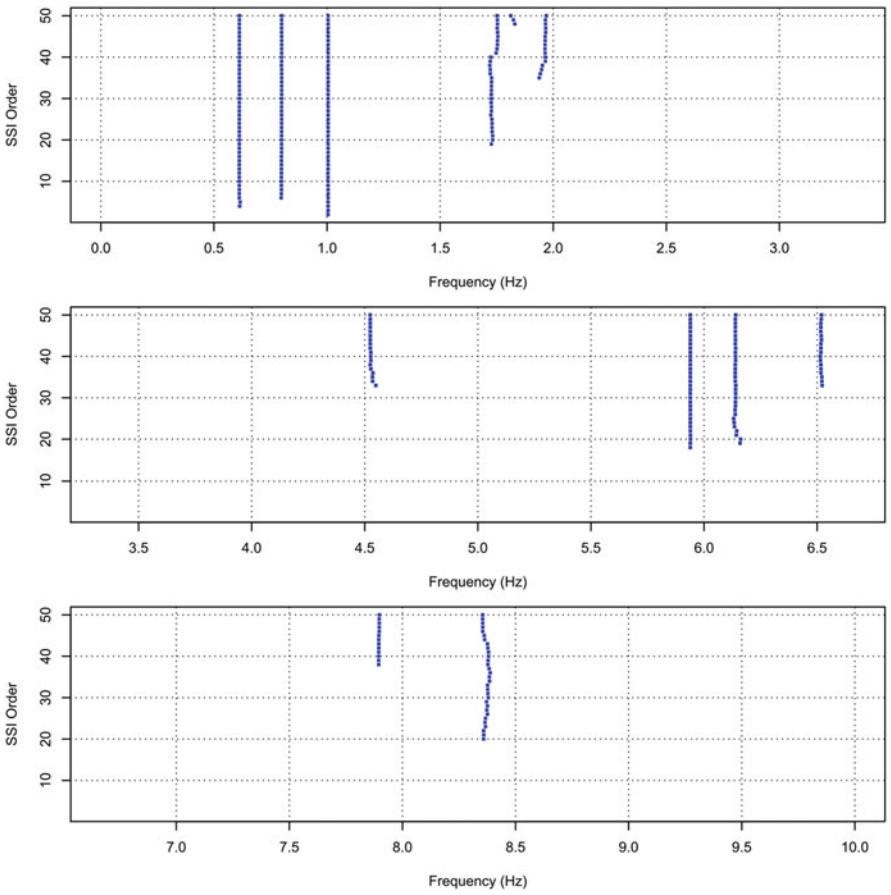

Fig. 53 Stability diagram obtained from applying the SSI to the frequency range [0;10] Hz

The time-series of cluster representatives obtained over a period of 8 months in 2018 is shown in Fig. 57, whose observation confirms the high density of modes in the range [0;5] Hz. During the period under analysis, a large number of clearly defined near-horizontal alignments over time can be observed, thus revealing modes that are repeatedly identified over time with small variability. However, large dense bands with high variability can also be observed, in which modes are not as easily distinguished.

No significant changes can be observed in the frequency values between the colder months (February and March) and the warmer ones (July and August), yet important changes are observed daily in the majority of the near-horizontal alignments, as exemplified in Fig. 52, and there are even several modes which are only detected when certain operational conditions are met, such as those with frequencies of approximately 1.5 and 3.0 Hz, which are only detected during week

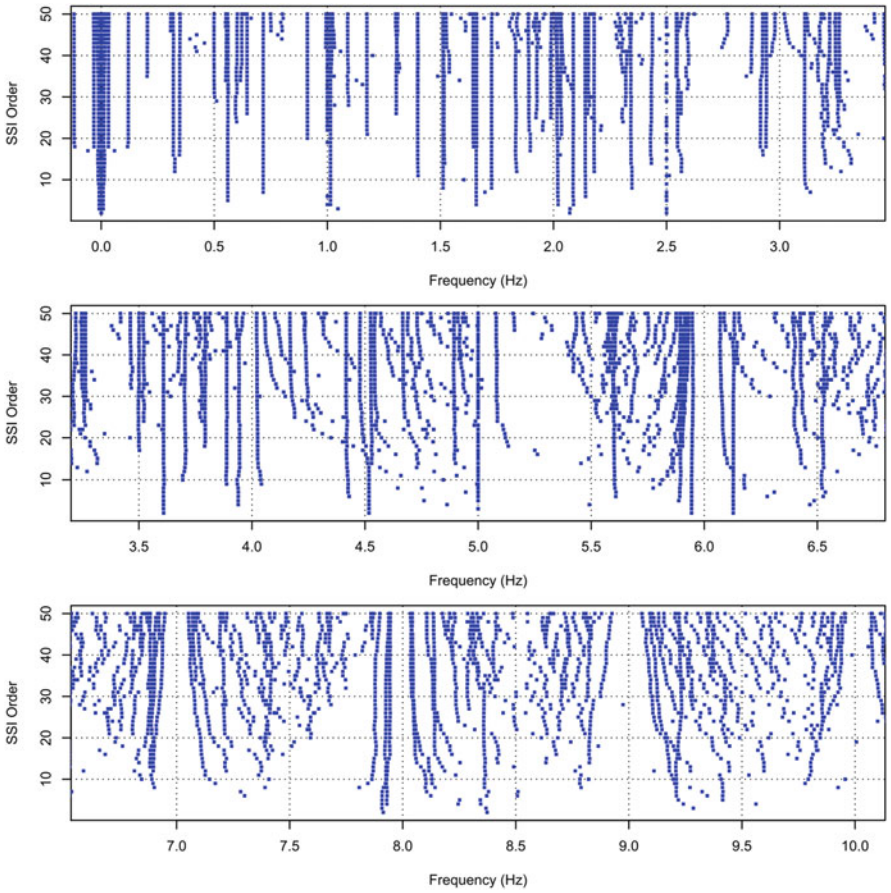

Fig. 54 Stability diagram obtained from applying the SSI to 10 frequency slices of 1 Hz

days, as it can be observed in Fig. 57. This apparent inexistence of correlation with temperature along with a strong correlation with traffic loading is not the general case in experimental bridge testing and is due to the large span and slender character of the 25 de Abril Suspended Bridge. In general, changes of approximately 5% can be observed in modal frequencies due to temperature in smaller spans, in which the influence of road traffic is also smaller. Railway bridges can be considered as an exception, regarding traffic loading, since trains crossing the bridge change the vibration regime. In these cases, one possibility consists of removing the time-series obtained during the train crossing, merging the remaining subsets of the signal using appropriate windowing functions, and in analyzing them using methods such as the SSI-COV. An alternative strategy consists of analyzing the decaying response obtained immediately after the train crossing using the ERA methods (Chapter 12 and Sect. 5.3).

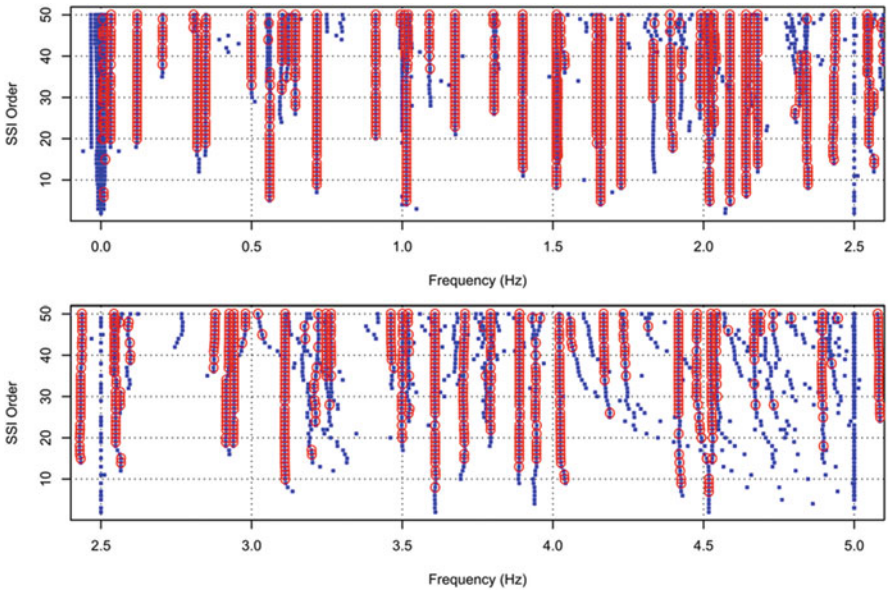

Fig. 55 Stable poles obtained using hard criteria applied to f, d, and MAC

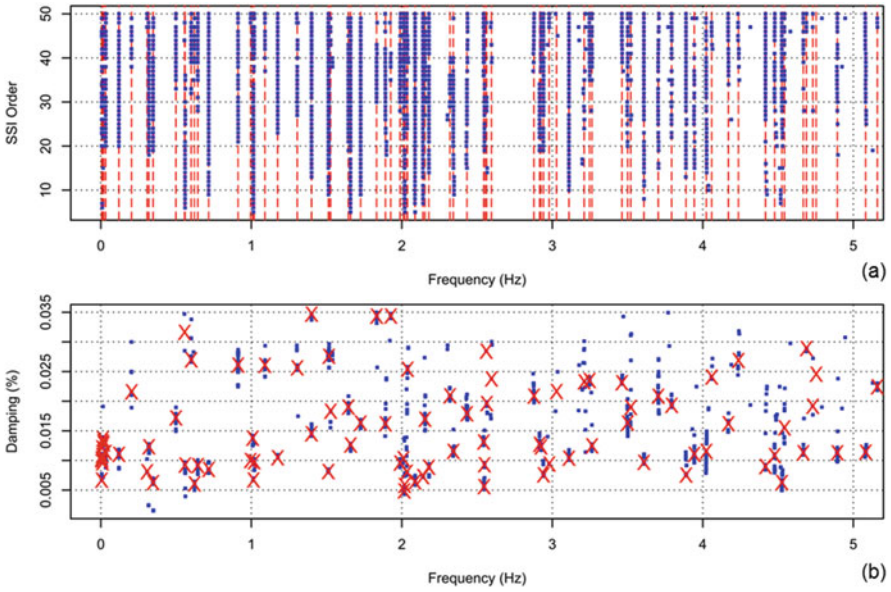

Fig. 56 Mode representatives obtained using hierarchical clustering and the SIL index and shown in: (**a**) stability diagram and (**b**) f vs. d cluster diagram

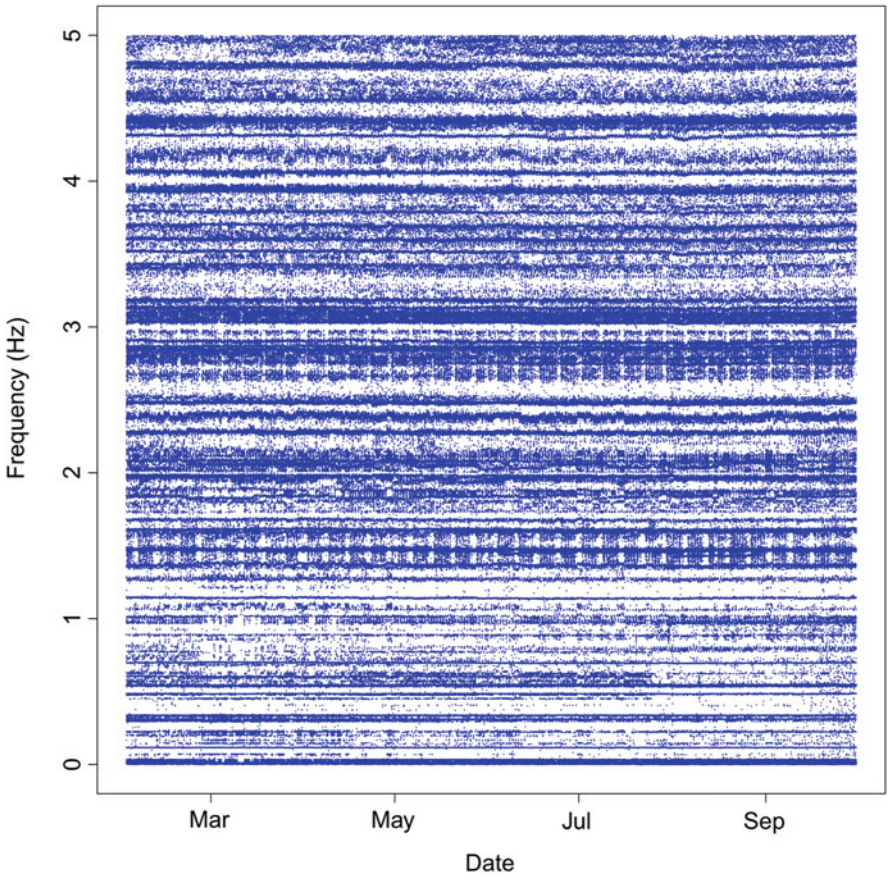

Fig. 57 Mode representatives obtained over 8 months of 2018

The modal tracking strategy used to relate the representatives of each mode obtained in different periods of monitoring time of the 25 de Abril Bridge relied also on clustering methods and on the SIL index to define a baseline reference in an unsupervised way, that is, without human intervention regarding the number of modes and their feature values. A 2-week period was selected for defining the baseline, to which the strategy described in Sect. 8.3 was applied separately for each band of 0.5 Hz. The distance matrix chosen as input was the one obtained from the frequencies and the MAC only. A total of 76 distinct modes were obtained (characterized through their clusters' centroids) and used as baseline reference to which each of the following mode representatives, obtained at posterior time instants, was compared. The allocation of each new mode into the baseline ones was conducted by calculating the distance matrix (with the same metric, based on

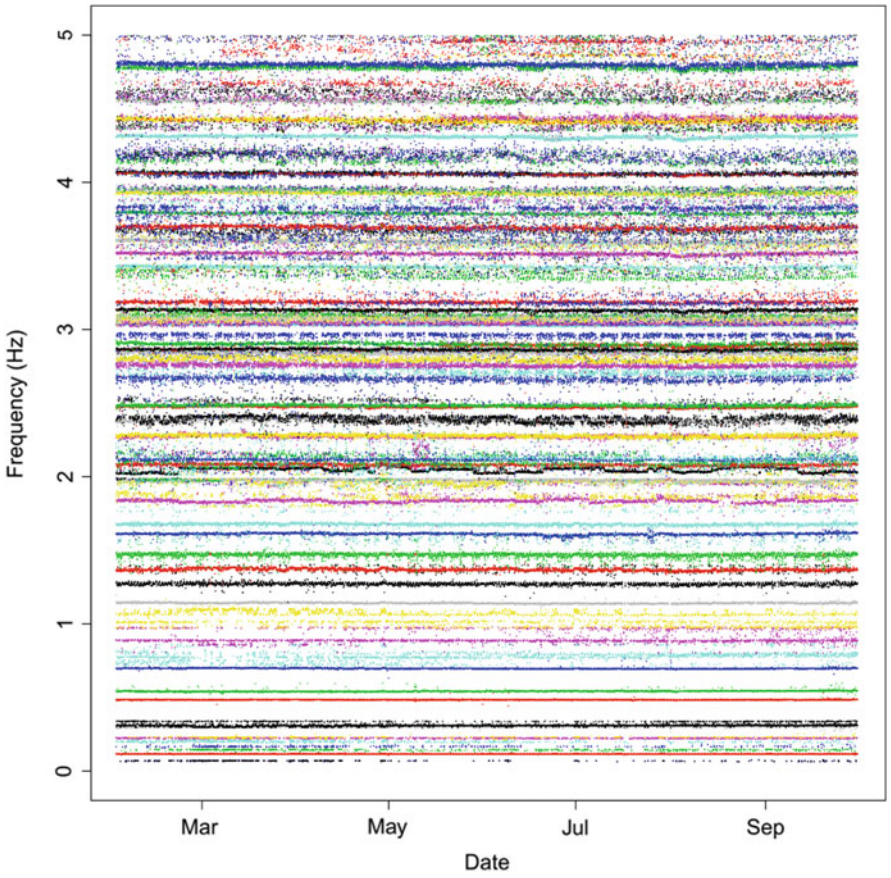

Fig. 58 Mode representatives obtained over 8 months of 2018 and colored according to the mode identification

f and MAC) between the baseline and the newly arrived modes. The newly arrived modes were then allocated into the baseline ones based on the smaller distance value found in this non-symmetric distance matrix.

The time-series of frequencies tracked for each of the 76 modes can be found in Fig. 58, where it can be readily observed that several modes exhibit smaller variability and/or higher detection incidence, thus rendering them appropriate for structural health monitoring. It can also be observed, especially for higher frequencies, that some modes are associated with noise and other effects, due to their visible variability. This disadvantage is a consequence of choosing the maximum SIL value as criterion and of choosing the maximum number of clusters equal to half the maximum SSI order. These choices resulted, however, in higher mode detection incidences over time.

11 Concluding Remarks

Testing of civil engineering structures is an old field but still exhibits limited applications. The benefits of testing, and in particular of structural health monitoring (SHM), are evident for the safety of the user and for a rational maintenance of the structural systems. A state of development has been reached where the hardware is cost effective, the software is available, and broadband communications are available with a wide coverage, robustness, and low costs.

The importance of monitoring and particularly of SHM for the recovery of infrastructure after extreme events like hurricanes and earthquakes, where the damage systems could easily outnumber the number of practitioners by a factor of 10, has already been seen in recent cases. Monitoring hardly accessible structures due to its remote location, temperature of operation, or just the difficulty and complexity of the inspection are clear benefits of the presented techniques.

To increment its use, several steps should be performed and, among these, the education of undergraduate and graduate civil engineering students on the basis of experimental techniques, and its applications to laboratory and real structures, naturally assumes particular importance. The development of academic and business public benchmark cases for the validation and promotion of the systems should also be undertaken so as to promote normalization of techniques and procedures. Finally, the development of guidelines must also be considered, not only for the users to clarify what can be gained, what is possible at this stage of developments, and what are the typical cost and reliable systems to be applied but also for the practitioners to standardize products, reduce cost, and validate results.

Acknowledgments The authors would like to acknowledge all the support given by the Department of Civil Engineering, of the University of Chile, and by the Structures Department of the Portuguese National Laboratory for Civil Engineering (LNEC).
In addition, the authors would also like to acknowledge the support given by Conicyt and Fondecyt Chile, projects 1950629, 1000912, 1070319, and the Portuguese Foundation for Science and Technology (FCT) through the SAFESUSPENSE project – POCI-01-0145-FEDER-031054 (funded by COMPETE2020, POR Lisboa and FCT).

References

1. Allemang R (2003) The modal assurance criterion – twenty years of use and abuse. Sound and Vibration 37(8):14–21. https://doi.org/10.1016/j.chemgeo.2006.02.014
2. Astroza R, Gutiérrez G, Repenning C, Hernández F (2018) Time-variant modal parameters and response behavior of a base-isolated building tested on a shake table. Earthquake Spectra 34(1):121–143. https://doi.org/10.1193/032817EQS054M
3. Beck JL (1978) Determining models of structures from earthquake records. EERL report 78-01
4. Bernal D, Döhler M, Kojidi SM, Kwan K, Liu Y (2015) First mode damping ratios for buildings. Earthquake Spectra 31(1):367–381. https://doi.org/10.1193/101812EQS311M
5. Bishop CM (2006) Pattern recognition and machine learning. pattern recognition. Springer, Berkeley

6. Bixio AR, Dolce M, Nigro D, Ponzo FC, Braga F, Nicoletti M (2001) Repeatable dynamic release tests on a base-isolated building. Journal of Earthquake Engineering 5(3):369–393. https://doi.org/10.1080/13632460109350398
7. Boore DM, Sisi AA, Akkar S (2012) Using pad-stripped acausally filtered strong-motion data. Bulletin of the Seismological Society of America 102(2):751–760. https://doi.org/10.1785/0120110222
8. Boroschek RL, Bilbao JA (2019) Interpretation of stabilization diagrams using density-based clustering algorithm. Engineering Structures 178:245–257. https://doi.org/10.1016/J.ENGSTRUCT.2018.09.091
9. Boroschek RL, Legrand D (2006) Tilt motion effects on the double-time integration of linear accelerometers: an experimental approach. Bulletin of the Seismological Society of America 96(6). https://doi.org/10.1785/0120050167
10. Boroschek RL, Baesler H, Vega C (2011) Experimental evaluation of the dynamic properties of a wharf structure. Engineering Structures 33(2). https://doi.org/10.1016/j.engstruct.2010.10.014
11. Brincker R, Ventura CE (2015) Introduction to operational modal analysis. Wiley, Chichester
12. Brincker R, Ventura C, Andersen P (2001a) Damping estimation by frequency domain decomposition. In: Proceedings of IMAC 19: a conference on structural dynamics, pp 1–6
13. Brincker R, Zhang L, Andersen P (2001b) Modal identification of output-only systems using frequency domain decomposition. Smart Materials and Structures 10(3):441–445. https://doi.org/10.1088/0964-1726/10/3/303
14. Brownjohn JMW (2003) Ambient vibration studies for system identification of tall buildings. Earthquake Engineering and Structural Dynamics 32(1):71–95. https://doi.org/10.1002/eqe.215
15. Brownjohn JMW, Magalhaes F, Caetano E, Cunha A (2010) Ambient vibration re-testing and operational modal analysis of the Humber Bridge. Engineering Structures 32(8):2003–2018. https://doi.org/10.1016/j.engstruct.2010.02.034
16. Cabboi A, Magalhães F, Gentile C, Cunha A (2011) Automated modal identification and tracking: application to an iron arch bridge. Structural Control and Health Monitoring 19(1):88–106. https://doi.org/10.1002/stc
17. Cabboi A, Magalhães F, Gentile C, Cunha Á (2017) Automated modal identification and tracking: application to an iron arch bridge. Structural Control and Health Monitoring 24(1):e1854. https://doi.org/10.1002/stc.1854
18. Caicedo JM, Marulanda J (2011) Fast mode identification technique for online monitoring. Structural Control and Health Monitoring 18(4):416–429. https://doi.org/10.1002/stc.381
19. Carreño RP, Boroschek RL (2011) Modal parameter variations due to earthquakes of different intensities. In: Conference proceedings of the Society for Experimental Mechanics Series, vol 4
20. Clinton JF, Bradford SC, Heaton TH, Favela J (2006) The observed wander of the natural frequencies in a structure. Bulletin of the Seismological Society of America 96(1):237–257. https://doi.org/10.1785/0120050052
21. Cohen L (1995) Time-frequency analysis. Prentice Hall PTR
22. Crawford R, Ward HS (1964) Determination of the natural periods of buildings. Bulletin of the Seismological Society of America 54(6A):1743–1756
23. Cremona C, Santos JP (2018) Structural health monitoring as a big data problem. Structural Engineering Internacio:1–18. https://doi.org/10.1080/10168664.2018.1461536
24. Cruz C, Miranda E (2017a) Evaluation of damping ratios for the seismic analysis of tall buildings. Journal of Structural Engineering 143(1):04016144. https://doi.org/10.1061/(ASCE)ST.1943-541X.0001628
25. Cruz C, Miranda E (2017b) Evaluation of soil-structure interaction effects on the damping ratios of buildings subjected to earthquakes. Soil Dynamics and Earthquake Engineering 100(May):183–195. https://doi.org/10.1016/j.soildyn.2017.05.034
26. Cunha A, Caetano E (2006) Experimental modal analysis of civil engineering structures. Sound and Vibration June:12–20. https://doi.org/10.1007/978-1-4020-6239-1_299

27. Cunha A, Caetano E, Delgado R (2001) Dynamic tests on large cable-stayed bridge. Journal of Bridge Engineering 6(1):54–62. https://doi.org/10.1061/(ASCE)1084-0702(2001)6:1(54)
28. Cury A, Crémona C, Diday E (2010) Application of symbolic data analysis for structural modification assessment. Engineering Structures 32(3):762–775
29. Döhler M, Mevel L (2012) Fast multi-order computation of system matrices in subspace-based system identification. Control Engineering Practice 20(9):882–894. https://doi.org/10.1016/j.conengprac.2012.05.005
30. Eyre R, Tilly GP (1977) Damping measurements on steel and composite bridges – abstract. In: Symposium on dynamic behaviour of bridges (abstract), pp 22–39
31. Furukawa T, Ito M, Izawa K, Noori MN (2005) System identification of base-isolated building using seismic response data. Journal of Engineering Mechanics 131(3):268–275. https://doi.org/10.1061/(ASCE)0733-9399(2005)131:3(268)
32. Gao W, Zhou Y (2003) Eigenvalue-based algorithms for testing positive realness of SISO systems. IEEE Transactions on Automatic Control 48(11):2051–2055. https://doi.org/10.1109/TAC.2003.819302
33. Giraldo DF, Song W, Dyke SJ, Caicedo JM (2009) Modal identification through ambient vibration: comparative study. Journal Of Engineering Mechanics-Asce 135(8):759–770. https://doi.org/10.1061/(asce)0733-9399(2009)135:8(759)
34. Gonzalez I (2013) Stochastic model updating of ballast stiffness in cold conditions. In: The 6th International conference on structural health monitoring of intelligent infrastructure
35. Gonzalez W, Boroschek RL (2019) Modal tracking on a building with a reduced number of sensors system. In: International modal analysis conference
36. González L, Boroschek R, Verdugo G (2009) Experimental study to correlate change in the structural frequency and foundation soil water content. In: Proceedings of the 17th international conference on soil mechanics and geotechnical engineering: the academia and practice of geotechnical engineering, vol 3. https://doi.org/10.3233/978-1-60750-031-5-2040
37. Guéguen P, Langlais M, Garambois S, Voisin C, Douste-Bacqué I (2017) How sensitive are site effects and building response to extreme cold temperature? The case of the Grenoble's (France) City Hall building. Bulletin of Earthquake Engineering 15(3):889–906. https://doi.org/10.1007/s10518-016-9995-3
38. Guillier B, Chatelain JL, Perfettini H, Oubaiche EH, Voisin C, Bensalem R et al (2016) Building frequency fluctuations from continuous monitoring of ambient vibrations and their relationship to temperature variations. Bulletin of Earthquake Engineering 14(8):2213–2227. https://doi.org/10.1007/s10518-016-9901-z
39. Hastie T (2011) The elements of statistical learning, data mining, inference and prediction, 2nd edn. Springer, New York
40. Haviland RW (1976) A study of the uncertainties in the fundamental translational periods and damping values for real buildings. Res. Rep. No. 5, Pub. No. R76-12, Department of Civil Engineering, MIT, Cambridge, p 115
41. Hisada T, Nakagawa K (1956) Vibration tests of various types of building structures up to failure. In: 1st World conference of earthquake engineering (WCEE)
42. Huang NE, Shen Z, Long SR, Wu MC, Shih HH, Zheng Q et al (1998) The empirical mode decomposition and the Hilbert spectrum for nonlinear and non-stationary time series analysis. Proceedings of the Royal Society A: Mathematical, Physical and Engineering Sciences 454(1971):903–995. https://doi.org/10.1098/rspa.1998.0193
43. Hudson DE (1964) Resonance testing of full-scale structures. Journal of the Engineering Mechanics Division 90:em3
44. Imregun M, Ewins DJ (1995) Complex modes – origins and limits. In: 13th International modal analysis conference, pp 496–506
45. Iwan WD, Cifuentes A (1986) A model for system identification of degrading structures. Eathquake Engineering and Structural Dynamics 14(December 1985):877–890
46. James III, G. H., Carne, T. G., Lauffer, P., J., Lauffer, J. P. (1995). The Natural Excitation Technique (NExT) for modal parameter extraction from operating wind turbines. The International Journal of Analytical and Experimental Modal Analysis, 10(4), 260–277. SAND92-1666

47. Jeary AP (1986) Damping in tall buildings – a mechanism and a predictor. Earthquake Engineering & Structural Dynamics 14(5):733–750. https://doi.org/10.1002/eqe.4290140505
48. Juang J-N, Pappa RS (1985) An eigensystem realization algorithm for modal parameter identification and model reduction. Journal of Guidance, Control, and Dynamics 8(5):620–627. https://doi.org/10.2514/3.20031
49. Kaya Y, Safak E (2015) Real-time analysis and interpretation of continuous data from structural health monitoring (SHM) systems. Bulletin of Earthquake Engineering 13(3):917–934. https://doi.org/10.1007/s10518-014-9642-9
50. Kaya Y, Kocakaplan S, Şafak E (2015) System identification and model calibration of multi-story buildings through estimation of vibration time histories at non-instrumented floors. Bulletin of Earthquake Engineering 13(11):3301–3323. https://doi.org/10.1007/s10518-015-9774-6
51. Keightley WO, Housner GW, Hudson DE (1961) Vibration tests of the Encino Dam intake tower. Technical report: Caltech EERL.1961.003. California Institute of Technology
52. Li QS, Yang K, Wong CK, Jeary AP (2003) The effect of amplitude-dependent damping on wind-induced vibrations of a super tall building. Journal of Wind Engineering and Industrial Aerodynamics 91(9):1175–1198. https://doi.org/10.1016/S0167-6105(03)00080-1
53. Loh C-H, Weng J-H, Chen C-H, Lu K-C (2013) System identification of mid-story isolation building using both ambient and earthquake response data. Structural Control and Health Monitoring 20(2):139–155. https://doi.org/10.1002/stc.479
54. Magalhães F (2010) Operational modal analysis for testing and monitoring of bridges and special structures. University of Porto, Faculty of Engineering
55. Magalhães F, Cunha Á, Caetano E (2009) Online automatic identification of the modal parameters of a long span arch bridge. Mechanical Systems and Signal Processing 23(2):316–329. https://doi.org/10.1016/j.ymssp.2008.05.003
56. Magalhães F, Cunha Á, Caetano E, Brincker R (2010) Damping estimation using free decays and ambient vibration tests. Mechanical Systems and Signal Processing 24(5):1274–1290. https://doi.org/10.1016/j.ymssp.2009.02.011
57. Mendes P (2010) Observação e análise do comportamento dinâmico de barragens de betão. Faculdade de Engenharia da Universidade do Porto
58. Milligan G, Cooper M (1985) An Examination of Procedures for Determining the Number of Clusters in a Data Set. Psychometrika 50(2):159–179
59. Moroni MO, Sarrazin M, Boroschek R (1998) Experiments on a base-isolated building in Santiago, Chile. Engineering Structures 20(8). https://doi.org/10.1016/S0141-0296(97)00086-2
60. Murray TM, Allen DE, Ungar EE (2003) Floor vibrations due to human activity. Steel Design Guide Series 11, D811(10M797)
61. Nagarajaiah S, Xiaohong S (2000) Response of base-isolated USC hospital building in Northridge earthquake. Journal of Structural Engineering 126(10):1177–1186. https://doi.org/10.1061/(ASCE)0733-9445(2000)126:10(1177)
62. Peeters B, De Roeck G (1999) Reference-based stochastic subspace identification for output-only modal analysis. Mechanical Systems and Signal Processing 13(6):855–878. https://doi.org/10.1006/mssp.1999.1249
63. Peeters B, De Roeck G (2001) Stochastic system identification for operational modal analysis: a review. Journal of Dynamic Systems, Measurement, and Control 123(4):659. https://doi.org/10.1115/1.1410370
64. Peeters B, Ventura CE (2003) Comparative study of modal analysis techniques for bridge dynamic characteristics. Mechanical Systems and Signal Processing 17(5):965–988. https://doi.org/10.1006/mssp.2002.1568
65. Peeters B, Maeck J, De Roeck G (2000) Dynamic monitoring of the Z24-Bridge: separating temperature effects from damage. In: Proceeding of the European COST F3 conference on system identification structural health monitoring, November 2015, pp 377–386
66. Peeters B, Van der Auweraer H, Guillaume P, Leuridan J (2004) The PolyMAX frequency-domain method: a new standard for modal parameter estimation? Shock and Vibration 11(3–4):395–409. https://doi.org/10.1155/2004/523692

67. Pereira S, Magalhães F, Gomes JP, Cunha Á, Lemos JV (2018) Dynamic monitoring of a concrete arch dam during the first filling of the reservoir. Engineering Structures 174(July):548–560. https://doi.org/10.1016/j.engstruct.2018.07.076
68. Rainieri C, Fabbrocino G (2014) Operational modal analysis of civil engineering structures. Springer, New York. https://doi.org/10.1007/978-1-4939-0767-0
69. Rendón E, Abundez I, Arizmendi A, Quiroz EM (2011) Internal versus external cluster validation indexes. International Journal of Computers and Communications 5(1): 158–163
70. Reynders E (2012) System identification methods for (operational) modal analysis: review and comparison. Archives of Computational Methods in Engineering 19(1):51–124. https://doi.org/10.1007/s11831-012-9069-x
71. Reynders E, Houbrechts J, De Roeck G (2012) Fully automated (operational) modal analysis. Mechanical Systems and Signal Processing 29:228–250
72. Rodrigues J (2004) Identificação Modal Estocástica Métodos de análise e aplicações em estruturas de engenharia civil. University of Porto, Faculty of Engineering
73. Rodrigues J, Brincker R, Andersen P (2004) Improvement of frequency domain output-only modal identification from the application of the random decrement technique. In: Proceedings of the 23rd international modal analysis conference
74. Rousseeuw P (1987) Silhouettes: a graphical aid to the interpretation and validation of cluster analysis. Journal of Computational and Applied Mathematics 20(1):53–65
75. Ryan KL, Polanco J (2008) Problems with Rayleigh damping in base-isolated buildings. Journal of Structural Engineering 134(11):1780–1784. https://doi.org/10.1061/(ASCE)0733-9445(2008)134:11(1780)
76. Safak E (1989) Adaptive modeling, identification, and control of dynamic structural systems. II: applications. Journal of Engineering Mechanics 115(11):2406–2426. https://doi.org/10.1061/(ASCE)0733-9399(1989)115:11(2406)
77. Şafak E (1989) Adaptive modeling, identification, and control of dynamic structural systems. I: theory. Journal of Engineering Mechanics 115(11):2386–2405. https://doi.org/10.1061/(ASCE)0733-9399(1989)115:11(2386)
78. Şafak E (1991) Identification of linear structures using discrete-time filters. Journal of Structural Engineering 117(10):3064–3085. https://doi.org/10.1061/(ASCE)0733-9445(1991)117:10(3064)
79. Santos JP (2014) Smart structural health monitoring techniques for novelty identification in civil engineering structures. PhD thesis. Instituto Superior Técnico – University of Lisbon
80. Santos J, Crémona C, Orcesi AD, Silveira P (2013a) Multivariate statistical analysis for early damage detection. Engineering Structures 56:273–285
81. Santos J, Crémona C, Orcesi A, Silveira P (2013b) Baseline-free real-time novelty detection using vibration-based symbolic features. In: EVACES'13, Ouro Preto, pp 1–8
82. Santos J, Orcesi AD, Crémona C, Silveira P (2015) Baseline-free real-time assessment of structural changes. Structure and Infrastructure Engineering: Maintenance, Management, Life-Cycle Design and Performance 11(2):145–161. https://doi.org/10.1080/15732479.2013.858169
83. Santos JP, Cremona C, Silveira P, Calado L (2016a) Real-time damage detection based on pattern recognition. Structural Concrete. https://doi.org/10.1002/suco.201500092
84. Santos J, Mata J, Cremona C, Silveira P (2016b) Detection of structural changes using symbolic representations of stochastic subspace identification estimates. In: 8th Workshop on structural health monitoring, pp 1–10
85. Santos JP, Crémona C, Silveira P (2018) Automatic modal operational analysis of a long-span suspended bridge using pattern recognition. In: 40th IABSE symposium, 19–21 September 2018, Nantes, France. Tomorrow's megastructures. IABSE, p 8
86. Shi W, Shan J, Lu X (2012) Modal identification of Shanghai World Financial Center both from free and ambient vibration response. Engineering Structures 36:14–26. https://doi.org/10.1016/j.engstruct.2011.11.025

87. Silva R, Rodrigues J (2011) Influência da altura de água nas frequências de vibração de pontes com pilares submersos. Lisbon
88. Siringoringo DM, Fujino Y (2018) Seismic response of a suspension bridge: insights from long-term full-scale seismic monitoring system. Structural Control and Health Monitoring June:e2252. https://doi.org/10.1002/stc.2252
89. Spence SMJ, Kareem A (2014) Tall buildings and damping: a concept-based data-driven model. Journal of Structural Engineering 140(5):04014005. https://doi.org/10.1061/(ASCE)ST.1943-541X.0000890
90. Stewart JP, Conte JP, Aiken ID (1999) Observed behavior of seismically isolated buildings. Journal of Structural Engineering 125(9):955–964. https://doi.org/10.1061/(ASCE)0733-9445(1999)125:9(955)
91. Stockwell RG, Mansinha L, Lowe RP (1996) Localization of the complex spectrum: the S transform. IEEE Transactions on Signal Processing 44(4):998–1001. https://doi.org/10.1109/78.492555
92. Su J, Xia Y, Ni Y, Zhou L, Su C (2017) Field monitoring and numerical simulation of the thermal actions of a supertall structure. Structural Control and Health Monitoring 24(4):e1900. https://doi.org/10.1002/stc.1900
93. Takeuchi M (1960) Vibrational characteristics of buildings, part I – vibrational characteristics of actual buildings determined by actual tests. In: Proceedings of the 2nd world conference on earthquake engineering, Tokyo
94. Tamura Y, Yoshida A (2008) Amplitude dependency of damping in buildings. In: Structures congress 2008. American Society of Civil Engineers, Reston, pp 1–10. https://doi.org/10.1061/41000(315)39
95. Tamura Y, Suda K, Sasaki A (2000) Damping in buildings for wind resistant design. In: Proceedings of the international symposium on wind and structures for the 21st century, pp 115–130
96. Theodoridis S, Koutroumbas K (2009) Pattern Recognition, 4th edn. Elsevier, London
97. Uebayashi H, Nagano M, Hida T, Tanuma T, Yasui M, Sakai S (2016) Evaluation of the structural damage of high-rise reinforced concrete buildings using ambient vibrations recorded before and after damage. Earthquake Engineering & Structural Dynamics 45(2):213–228. https://doi.org/10.1002/eqe.2624
98. Van Overschee P, De Moor B, Sista E (1994) N4SID: subspace algorithms for the identification of combined deterministic-stochastic systems. Automatica 30:75–93. https://doi.org/10.1016/0005-1098(94)90230-5
99. Van Overschee P, De Moor B, Van Overschee P, De Moor B (1996) Subspace identification for linear system: theory – implementation – applications. In: Conference proceedings of the international conference of IEEE Engineering in Medicine and Biology Society, 2008, pp 4427–4430. https://doi.org/10.1109/IEMBS.2008.4650193
100. Verhaegen M (1994) Identification of the deterministic part of MIMO state space models given in innovations form from input-output data. Automatica 30(1):61–74. https://doi.org/10.1016/0005-1098(94)90229-1
101. Ward HS, Crawford R (1966) Wind-induced vibrations and building modes. Bulletin of the Seismological Society of America 56(4):793–813
102. Yan A, Kerschen G, De Boe P, Golinval J-C (2005a) Structural damage diagnosis under varying environmental conditions – part II: local PCA for non-linear cases. Mechanical Systems and Signal Processing 19(4):865–880
103. Yan A, Kerschen G, De Boe P, Golinval J-C (2005b) Structural damage diagnosis under varying environmental conditions – part I: a linear analysis. Mechanical Systems and Signal Processing 19(4):865–880
104. Yoshimoto R, Mita A, Okada K (2005) Damage detection of base-isolated buildings using multi-input multi-output subspace identification. Earthquake Engineering and Structural Dynamics 34(3):307–324. https://doi.org/10.1002/eqe.435
105. Yousefianmoghadam S, Behmanesh I, Stavridis A, Moaveni B, Nozari A, Sacco A (2018) System identification and modeling of a dynamically tested and gradually damaged 10-story

reinforced concrete building. Earthquake Engineering and Structural Dynamics 47(1):25–47. https://doi.org/10.1002/eqe.2935

106. Zembaty Z, Kowalski M, Pospisil S (2006) Dynamic identification of a reinforced concrete frame in progressive states of damage. Engineering Structures 28(5):668–681. https://doi.org/10.1016/j.engstruct.2005.09.025
107. Zhou HF, Ni YQ, Ko JM (2011) Eliminating temperature effect in vibration-based structural damage detection. Journal of Engineering Mechanics 137(12):785–796. https://doi.org/10.1061/(ASCE)EM.1943-7889.0000273
108. Zonno G, Aguilar R, Castañ B, Lourenç PB (2018) Preliminary validation of an automatic modal identification methodology for structural health monitoring of historical buildings. International Journal of Structural and Civil Engineering Research 7(2):144–150. https://doi.org/10.18178/ijscer.7.2.144-150

Aerospace Perspective for Modeling and Validation

24

Robert Coppolino

Contents

R. Coppolino (✉)
Measurement Analysis Corporation, Torrance, CA, USA

R. Allemang, P. Avitabile (eds.), *Handbook of Experimental Structural Dynamics*,
https://doi.org/10.1007/978-1-4614-4547-0_30

Abstract

The present chapter on the Aerospace Perspective for Modeling and Validation offers an overview of generally accepted practices in the U.S. aerospace community, with emphasis on space launch systems and their spacecraft payloads. Inclusion of practices in the important U.S. aircraft community requires a more extensive document. In keeping the present chapter within the confines of "accepted practices," valuable subject matter related to scientific and technical innovations that are not yet generally accepted or peer "vetted" is considered beyond the scope of the present exposition. This chapter includes two distinct areas of subject matter, namely (1) modeling and analysis practices employed in prediction of structural dynamic behavior, and (2) integrated test-analysis practices employed in model verification, validation, and updating.

Keywords

US · Aerospace · Structural · Dynamic · Model · Validation

1 Theoretical Foundations

Review of theoretical foundations of structural dynamics is an essential preliminary step for subsequent discussions on Structural Dynamic Models (Sect. 2), and Matrix Structural Dynamic Analysis (Sect. 3). Both of these topics are products of successive (a) theoretical underpinnings from categorization (basic assumptions and approximations), (b) variational principles, and (c) the finite element method.

1.1 Categories of Dynamic Systems

Harry Himmelblau, a long-time colleague in the Southern California aerospace community, once stated that "The universe is composed of bananas and everything that's not a banana. Linear systems are the bananas, nonlinear systems are everything else." The single degree of freedom system (SDOF) model, shown in Fig. 1, serves to describe the fundamental classifications of "bananas" and "everything else."

Dynamic equilibrium of the SFOF system is described by

$$M\ddot{U} = F_L\left(U, \dot{U}, p_L\right) + F_N\left(U, \dot{U}, p_N\right) + F_E\left(t\right), \tag{1}$$

where the "linear" restoring force, F_L, is typically described in terms of two linear system parameters, $p_L = (K, B)$, as

$$F_L = -\left(B\dot{U} + KU\right), \tag{2}$$

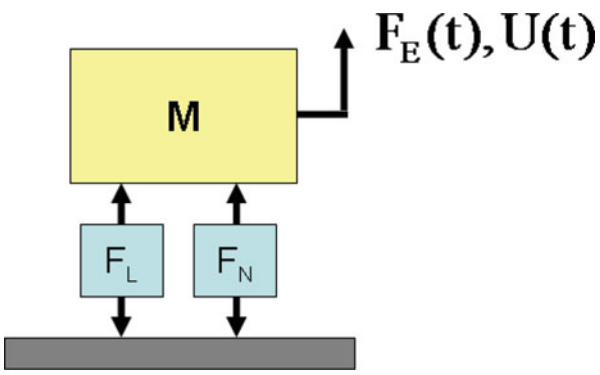

Fig. 1 SDOF system schematic

and the "nonlinear" restoring force is described in one of two general forms, namely, (a) an algebraic nonlinear function of displacement, velocity, and fixed parameters, p_N, or more generally, (b) a hysteretic nonlinear function of displacement, velocity, and evolving parameters, p_N. A typical algebraic nonlinear restoring force (cubic stiffness and "fluid" drag type dissipation) is described by,

$$F_N = -\left(B_2 \left|\dot{U}\right| \dot{U} + K_3 U^3\right). \tag{3}$$

The more general hysteretic nonlinearity is described by the evolving functional relationship,

$$(F_N\,(t + \Delta t), \{p_N\,(t + \Delta t)\}) = -N\left(U\,(t), \dot{U}\,(t), \{p_N\,(t)\}\right). \tag{4}$$

The above functional relationship describes the behavior of materials undergoing elastic-plastic deformation and structural joints that experience stick-slip frictional deformation, as well as all things not falling into the "linear" and "algebraic nonlinear" categories.

Based on the above discussion, it appears that Himmelblau's viewpoint of the universe should be modified as follows:

(a) "Bananas" are the "linear" systems described by Eq. 2.
(b) "Plantains" are the "algebraic" nonlinear systems described by Eq. 3.
(c) "All Else" are the "hysteretic," evolving nonlinear systems described by Eq. 4.

Thus Himmelblau's modified maxim is "The universe is composed of bananas, plantains and everything else." Fortunately, the majority of subject matter discussed in this chapter on the aerospace perspective for modeling and validation relates to "bananas." That being said, several very important applications falling into the other two categories will be cited herein.

1.2 Variational Principles

The entirety of the aerospace perspective for modeling and validation, regardless of "banana, plantain, or all else" categorization of the subject dynamic system, depends on variational principles. Specifically the foundational variational principles [1], in hierarchical sequence include:

1. Hamilton's Principle [2]
2. Lagrange's Equations [3]
3. The Ritz Method [4]
4. Toupin's Variational Principle [5].

Innovations due to Trefftz [6] and Galerkin [7], while generally important in twentieth-century developments in the field of structural mechanics, are of secondary significance to the above four variational viewpoints. In particular, Hamilton's Principle, Lagrange's Equations, and The Ritz Method form the overall foundation of partial differential equations of mathematical physics, finite element analysis, and matrix structural analysis. Toupin's Variational Principle provides a systematic foundation for treatment of hydroelastic dynamic systems, especially within the NASTRAN software environment [8].

1.3 The Finite Element Method

The finite element method [9], as it is widely employed in the aerospace community, is a building block approach that models structural components, represented in Fig. 2 as a classical "potato shaped" form, in terms of distributed displacement shape functions.

In matrix form, the "interior" and "boundary" displacements, U_i and U_b, respectively, relate functionally to the displacement field of the entire element, U, as

$$u\,(x, y, z, t) = \sum_{n=1}^{N_p} \Psi_{p,n}\,(x, y, z) \cdot q_{p,n}\,(t) + \sum_{n=1}^{N_h} \Psi_{h,n}\,(x, y, z) \cdot u_{h,n}\,(t), \qquad (5)$$

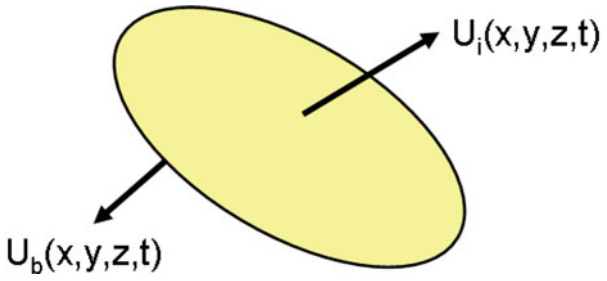

Fig. 2 Finite element

where the "Ψ_h" shape functions are associated with discrete "boundary" displacements, and the "Ψ_p" shape functions and associated generalized displacements, "q_p", relate to interior displacements (with boundary displacements set to "zero"). In matrix form, the element displacement field relates to the shape functions and displacement DOF as,

$$\{u\} = \begin{bmatrix} \Psi_p & \Psi_h \end{bmatrix} \begin{Bmatrix} q_p \\ u_h \end{Bmatrix} \tag{6}$$

Employing Hamilton's Principle and the Ritz Method (details in Reference [10]), the resulting matrix equations describing linear structural dynamic behavior of the finite element are of the form,

$$\begin{bmatrix} M_{pp} & M_{ph} \\ M_{hp} & M_{hh} \end{bmatrix} \begin{Bmatrix} \ddot{q}_p \\ \ddot{u}_h \end{Bmatrix} + \begin{bmatrix} B_{pp} & B_{ph} \\ B_{hp} & B_{hh} \end{bmatrix} \begin{Bmatrix} \dot{q}_p \\ \dot{u}_h \end{Bmatrix} + \begin{bmatrix} K_{pp} & K_{ph} \\ K_{hp} & K_{hh} \end{bmatrix} \begin{Bmatrix} q_p \\ u_h \end{Bmatrix} = \begin{Bmatrix} Q_p \\ F_h \end{Bmatrix}, \tag{7}$$

where the symmetric, positive semi-definite coefficient matrices relate to the element's mass, viscous damping, and stiffness characteristics. It should be noted that (1) the damping matrix is typically not defined on an element level and (2) element externally applied loads are typically limited to the element boundary.

Finite elements fall into three general classes [9], namely:

1. "H" elements, defined exclusively in terms of "Ψ_h" shape functions, the most common type of elements used in aerospace structural dynamics practice.
2. "P" elements, defined exclusively in terms of "Ψ_p" shape functions (which encompass the boundary).
3. The most general hybrid "H-P" elements.

The collection of all contributing finite elements for a subject structural system is described by the matrix set of equations (including additional discrete nonlinear forces),

$$[M]\{\ddot{u}\} + [B]\{\dot{u}\} + [K]\{u\} = [\Gamma_N]\{F_N\} + [\Gamma_E]\{F_E\} \tag{8}$$

where, $[\Gamma_N]$ is the nonlinear force allocation matrix for discrete nonlinear forces,$\{F_N\}$, and $[\Gamma_E]$ is the externally applied load allocation matrix associated with discrete external forces, $\{F_E\}$. The discrete, generalized displacements and velocities associated with the nonlinear forces are

$$\{u_N\} = \left[\Gamma_N^T\right]\{u\} \quad \text{and} \quad \{\dot{u}_N\} = \left[\Gamma_N^T\right]\{\dot{u}\}. \tag{9}$$

Finally, the nonlinear forces, $\{F_N\}$, are calculated employing a generalization of Eq. 4, which symbolically is represented by

$$\{F_N(t + \Delta t), \{p_N(t + \Delta t)\}\} = -\{N(\{u_N(t)\}, \{\dot{u}_N(t)\}, \{p_N(t)\})\}. \tag{10}$$

In order to clarify the logic associated with the above two dynamic system equations, let us assume that,

$$\{N\} = -[B_N]\{\dot{u}_N\} - [K_N]\{u_N\} \tag{11}$$

Such a case would result in a special form of Eq. 8 wherein

$$\begin{aligned}&[M]\{\ddot{u}\} + [B]\{\dot{u}\} + [K]\{u\} = -\left[\Gamma_N B_N \Gamma_N^T\right]\{\dot{u}\} - \left[\Gamma_N K_N \Gamma_N^T\right]\{\dot{u}\} + [\Gamma_E]\{F_E\},\\ &\text{or,}\\ &[M]\{\ddot{u}\} + \left[B + \Gamma_N B_N \Gamma_N^T\right]\{\dot{u}\} + \left[K + \Gamma_N K_N \Gamma_N^T\right]\{u\} = [\Gamma_E]\{F_E\}\end{aligned} \tag{12}$$

which consistently reduces to the appropriate linear system with additional discrete forces $\{F_N\}$.

Equations 8–10 represent a quite general finite element (matrix) set of structural dynamic equations that are employed in the aerospace industry. Two examples of widely used (locally) nonlinear applications include (a) the nonlinear Space Shuttle Orbiter payload bay attachments and (b) general launch vehicle-to-launch pad interface loads during lift-off dynamics. Specialized matrix methods widely employed in the aerospace industry are the subject of the next subsection. In a sense, the above two applications span the categories of "bananas," "plantains," and "all else."

2 Structural Dynamic Models

This section offers an overview of theoretical modal analysis of linear systems, which is the predominant basis of the Aerospace Perspective for Modeling and Validation. In spite of the complicating effects of nonlinearity, modal analysis persists in playing a role in their presence. Knowledge of the bandwidth of a system's dynamic environment is essential for determination of guidelines for construction of relevant structural dynamic models, which must adhere to "granularity" or grid spacing requirements that follow rigorous frequency-wavelength relationships.

2.1 Modal Analysis

Eigenvalues and eigenvectors associated with a linear structural dynamic system (Eq. 8) are solutions of either (a) the undamped algebraic equation.

$$\begin{aligned}&[K][\Phi] = [M][\Phi][\lambda],\ \lambda_n = {\omega_n}^2, \text{ which results from } [M]\{\ddot{u}\} + [K]\{u\} = \{0\},\\ &\{u\} = [\Phi]\cdot e^{i\omega_n t},\end{aligned} \tag{13}$$

or (b) the damped algebraic equation

$$\begin{bmatrix} -M^{-1}B & -M^{-1}K \\ I & 0 \end{bmatrix} \begin{bmatrix} \phi_V \\ \phi_u \end{bmatrix} = \begin{bmatrix} \phi_V \\ \phi_u \end{bmatrix} [\lambda], \lambda_n = \sigma_n + i\omega_n, \text{ which results from} \tag{14}$$

$$[M]\{\ddot{u}\} + [B]\{\dot{u}\} + [K]\{u\} = \{0\}, \quad \{\dot{u}\} = \{v\}, \quad \{u\} = [\phi_u] \cdot e^{\lambda_n t}, \quad \{v\} = [\phi_v] \cdot e^{\lambda_n t}$$

Nearly all traditional structural dynamics methodology employed in the U.S. aerospace industry employs undamped (real) modal analysis as a staple. However, emerging methodology is in the process of exploring potential benefits of damped (complex) modal analysis, which will not be discussed in the present chapter.

The well-known orthogonality properties of undamped normal modes (for unit generalized mass scaling) are,

$$\left[\Phi^T\right][M][\Phi] = [I], \quad \left[\Phi^T\right][K][\Phi] = [\lambda] = \left[\omega_n^2\right] \tag{15}$$

In addition, the distribution of kinetic energy for each mode is the term-by-term product,

$$\{KE_\Phi\}_n = \{[M]\{\Phi_n\}\} \otimes \{\Phi_n\}, \tag{16}$$

which has an accumulated total value of 1.0 (based on unit generalized mass mode scaling).

A truncated set of normal modes (typically selected on the basis of a dynamic frequency cut-off to be discussed in the next subsection) forms the basis of the modal coordinate transformation,

$$\{u\} = [\Phi]\{q\}, \tag{17}$$

resulting in the modal form of Eqs. 9–11,

$$\left[\Phi^T M \Phi\right]\{\ddot{q}\} + \left[\Phi^T B \Phi\right]\{\dot{q}\} + \left[\Phi^T K \Phi\right]\{q\} = \left[\Phi^T \Gamma_N\right]\{N\} + \left[\Phi^T \Gamma_E\right]\{F_E\} \tag{18}$$

$\{\ddot{q}\} + [\beta]\{\dot{q}\} + [\lambda]\{q\} = \left[\Phi^T \Gamma_N\right]\{N\} + \left[\Phi^T \Gamma_E\right]\{F_E\}$ ($[\beta] = [2\zeta_n \omega_n]$ is typically assumed diagonal),

$$\{u_N\} = \left[\Gamma_N^T \Phi\right]\{q\}, \quad \{\dot{u}_N\} = \left[\Gamma_N^T \Phi\right]\{\dot{q}\} \tag{19}$$

$$\{F_N(t + \Delta t), \{p_N(t + \Delta t)\}\} = -\{N(\{u_N(t)\}, \{\dot{u}_N(t)\}, \{p_N(t)\})\} \tag{20}$$

In the case of a linear structural dynamic system, the transient response to applied external loading involves a summation of responses of the uncoupled SDOF modal equations,

$$\ddot{q}_n + 2\zeta_n \omega_n \dot{q}_n + \omega_n^2 q_n = \left[\Phi_n^T \Gamma_E\right] \{F_E\} \tag{21}$$

2.2 Dynamic Bandwidth

Applied external loads, $\{F_E(t)\}$, imposed on integrated launch vehicle and spacecraft systems during launch and ascent typically occur within the 50–70 Hz base frequency band. The resulting dynamic stresses are generally termed "primary" structural loads. Additional "secondary" structural loads (not addressed in this chapter) that occur in a much wider frequency band are driven by acoustic and extremely brief shock environments. While U.S. government standards [11, 12] specify the primary structure frequency band for spacecraft and launch vehicle systems, the shock response spectrum (SRS) function [13] provides a rigorous basis for estimation of dynamic bandwidth.

Within the present context, the SRS function associated with a specific force time history, F(t), is the solution map for linear SDOF systems,

$$\ddot{q}_n + 2\zeta_n \omega_n \dot{q}_n + \omega_n^2 q_n = F(t)\,, \tag{22}$$

with natural frequency, $\omega_n = 2\pi f_n$, for $0 \le f_n \le f_{max}$, with a selected reference value for critical damping ratio, ζ_n. It is highly recommended that the solutions to Eq. 22 be subject to "static equilibrium" initial conditions,

$$q_n(0) = F(0)/\omega_n^2, \quad \dot{q}_n(0) = 0, \tag{23}$$

in order to suppress unwanted initial transients. The normalized displacement SRS function is defined as the following solution map,

$$SRS\,(f_n; \zeta_n) = \frac{\left|\left(2\pi f_n^2\right) q_n\,(t)\right|_{max}}{|F(t)|_{max}} \tag{24}$$

The characteristics of the normalized SRS for a typical transient force history are depicted in Fig. 3.

While the SRS peak at 10 Hz clearly indicates the dominant frequency content in the force history, the asymptotic trend for $f \ge 30$ Hz (f*) indicates the onset of quasi-static SDOF response for all modes with frequency above f*. When f* is determined as the overall maximum value for all components of $\{F_E(t)\}$, the dynamic bandwidth for response of any linear structural dynamic system subjected to such loading is rigorously established. Note that $0 \ge f \ge 50$ to 70 Hz is the generally assumed dynamic bandwidth for spacecraft and launch vehicle systems in the U.S,

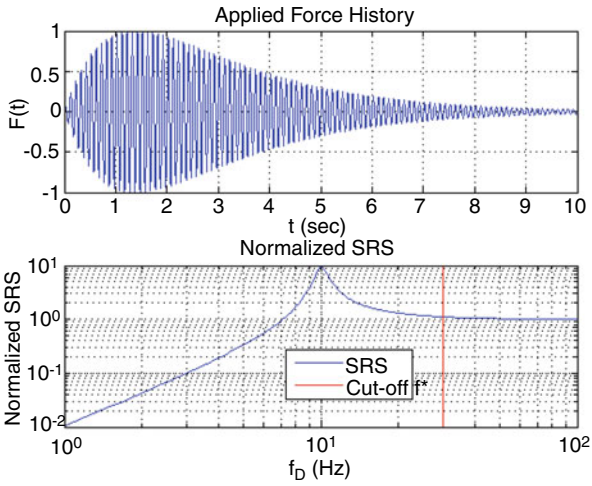

Fig. 3 Typical applied force history and associated SRS ($\zeta_n = 0.05$)

which should be reviewed and potentially revised for new systems. It must also be noted that estimation of f* is somewhat less certain when significant nonlinearities are present in a subject dynamic system.

2.3 Effective Modeling Guidelines

In order to develop a relevant dynamic model, general requirements should be addressed based on

1. Frequency band width $0 < f < f^*$, and intensity of anticipated dynamic environments, $\{F_E(t)\}$.
2. General characteristics of structural or mechanical components.

Dynamic environments are generally (a) harmonic, (b) transient, (c) impulsive, or (d) random. For all categories, the cut-off frequency (f*) is reliably determined by SRS analysis, as described in the previous subsection. The overall intensity level of a dynamic environment is described by the peak amplitude for harmonic, transient, and impulsive events, or by the statistical amplitude (e.g., mean plus a multiple of the standard deviation) for a long duration random environment. With the cut-off frequency (f*) established, the shortest relevant wavelength (L) of forced vibration for components in a structural assembly may be calculated. For finite element modeling, the quarter wavelength (L/4) is of particular interest, since it is a rough estimate of the grid spacing needed to characterize system dynamics at the cut-off frequency. Note that the actual grid spacing requirement is a function of the specific elements being used. Grid spacing (quarter wavelength) guidelines, for typical structural components, are summarized in Table 1.

Table 1 Grid spacing guidelines for typical structural components

Component	Mode type	Quarter wavelength (l/4)	Additional data
String	Lateral	$\left(\sqrt{T/\rho A}\right) / (4f^*)$	T = tension, A = area, ρ = mass density
Rod	Axial	$\left(\sqrt{E/\rho}\right) / (4f^*)$	E = elastic modulus
Rod	Torsion	$\left(\sqrt{G/\rho}\right) / (4f^*)$	G = shear modulus
Beam	Bending	$(\pi/2)\,(EI/\rho A)^{1/4}/\sqrt{2\pi f^*}$	EI = flexural stiffness
Membrane	Lateral	$\left(\sqrt{N/\rho h}\right) / (4f^*)$	N = stress resultant
Plate	Bending	$(\pi/2)\,(D/\rho h)^{1/4}/\sqrt{2\pi f^*}$	D = flexural stiffness, h = thickness
3-D Elastic	Dilational	$\left(\sqrt{E/\rho}\right) / (4f^*)$	
3-D Elastic	Shear	$\left(\sqrt{G/\rho}\right) / (4f^*)$	
Acoustic	Dilational	$\left(\sqrt{B/\rho}\right) / (4f^*)$	B = Bulk Modulus

Accurate modeling of stress concentrations, for a unified dynamic-stress model, may be addressed by employment of adaptive mesh refinement [9], or by utilization of documented stress concentration formulae [14]. If mesh refinement is utilized, the number of model degrees of freedom may increase substantially, imposing undue computational resource penalties on a model that had been appropriately designed for study of dynamic response and loads. If localized stress concentrations do not affect a model's dynamics fidelity, it is prudent to recover detailed stresses by employing (a) stress concentration formulae and/or (b) separate, detailed local or global "stress" finite element models (designed using adaptive mesh refinement).

2.4 Further Thoughts on Structural Dynamic Modeling

Additional topics of significance with regard to structural dynamic modeling which are not explicitly included in this chapter include:

(a) Damping and Joint Characterization (Misconceptions and Realities) [15]
(b) Behavior and Modeling of Non-Standard Materials [15]
(c) Fluid-Structure Interaction (Propellant Tanks) [8].

Treatment of the first two topics in the U.S. aerospace industry typically includes attempts to "fit" actual physical behavior of damping, joints, and non-standard materials (1) within the context of linear "M,B,K" modeling practices and (2) if deemed appropriate by specialized localized nonlinear models. Modeling of propellant tank fluid-structure interaction is extensively treated in the NASTRAN environment employing methodologies documented in reference [8] and further refinements/developments as well as proprietary techniques developed by U.S. aerospace corporations .

3 Matrix Structural Dynamic Analysis

The U.S. aerospace industry, specifically the launch vehicle and spacecraft community, over the past 60 years has developed and/or adopted a series of matrix structural dynamic analysis methods to address its unique modeling and validation goals. This section provides an overview of the broadly accepted methodologies, which fall into the categories of (a) model order reduction, (b) modal substructure definition, (c) component mode synthesis, (d) system dynamic response analysis including treatment of local nonlinearities, and (d) accurate estimation of local structural member loads and stresses.

3.1 Guyan Reduction

The underlying idea that defines Guyan Reduction (GR) [16] is static condensation . . . and Bob Guyan's monumental formulation was published as a one-half page technical note! The degrees of freedom describing a structural dynamic system are first separated into "analysis" and "omitted" subsets, which lead to the partitioned matrix equation (ignoring damping)

$$\begin{bmatrix} M_{oo} & M_{oa} \\ M_{ao} & M_{aa} \end{bmatrix} \begin{Bmatrix} \ddot{U}_o \\ \ddot{U}_a \end{Bmatrix} + \begin{bmatrix} K_{oo} & K_{oa} \\ K_{ao} & K_{aa} \end{bmatrix} \begin{Bmatrix} U_o \\ U_a \end{Bmatrix} = \begin{Bmatrix} F_o \\ F_a \end{Bmatrix} \tag{25}$$

If only the $[M_{aa}]$ partition of the mass matrix were non-zero, and external forces were only applied to "analysis" degrees of freedom, the relationship between "analysis" and "omitted" degrees of freedom (the GR transformation) would be

$$\begin{Bmatrix} U_o \\ U_a \end{Bmatrix} = \begin{bmatrix} -K_{oo}^{-1} K_{oa} \\ I_{aa} \end{bmatrix} \{U_a\} \tag{26}$$

In that situation, the above reduction transformation would be exact. However, when the mass matrix partitions, $[M_{oo}]$, $[M_{oa}]$, and $[M_{ao}]$, are non-zero, the reduction transformation is approximate (its columns are Ritz shape functions). Application of the reduction transformation, in a symmetric manner following the Ritz method yields, respectively, the (statically exact) reduced stiffness matrix and (dynamically approximate) mass matrix

$$\left[\overline{K}_{aa}\right] = \begin{bmatrix} -K_{oo}^{-1} K_{oa} \\ I_{aa} \end{bmatrix}^T \cdot \begin{bmatrix} K_{oo} & K_{oa} \\ K_{ao} & K_{aa} \end{bmatrix} \cdot \begin{bmatrix} -K_{oo}^{-1} K_{oa} \\ I_{aa} \end{bmatrix} = [K_{aa}] - \left[K_{ao} K_{oo}^{-1} K_{oa}\right] \tag{27}$$

$$\left[\overline{M}_{aa}\right] = \begin{bmatrix} -K_{oo}^{-1} K_{oa} \\ I_{aa} \end{bmatrix}^T \cdot \begin{bmatrix} M_{oo} & M_{oa} \\ M_{ao} & M_{aa} \end{bmatrix} \cdot \begin{bmatrix} -K_{oo}^{-1} K_{oa} \\ I_{aa} \end{bmatrix} \tag{28}$$

The reduced (approximate) matrix equation set is therefore

$$\left[\overline{M}_{aa}\right]\{\ddot{u}_a\} + \left[\overline{K}_{aa}\right]\{u_a\} = \left[-K_{ao}K_{oo}^{-1}\ I_{aa}\right]\begin{Bmatrix} F_o \\ F_a \end{Bmatrix}. \tag{29}$$

GR was initially developed to permit efficient, approximate modal analysis of structural dynamic models that were considered of excessively large order for computers in the late 1960s. Advancements in computer hardware and numerical methods have eliminated that original need. That being said, GR is still employed as a tool in modal test planning to be discussed in Sect. 4.2.

3.2 The Hurty-Craig-Bampton Method

The Hurty-Craig-Bampton (HCB) method [17, 18] continues to be the most widely applied method for definition of component substructures (also called superelements). The matrix equations of a single HCB component are a logical extension of Guyan Reduction. In a simple, direct manner, the HCB component is defined on the basis of Eq. 25, wherein the boundary degrees of freedom (which form the interface with an adjacent substructure) are the "a" subset, and the interior degrees of freedom are the "o" subset. The interior displacements, $\{u_o\}$ are expressed in terms of selected "low frequency" normal modes of the "interface-fixed" eigenvalue problem,

$$[K_{oo}][\Phi_{on}] = [M_{oo}][\Phi_{on}]\left[\omega_n^2\right]. \tag{30}$$

Therefore, the approximate relationship between physical and HCB degrees of freedom (the HCB transformation) is defined as,

$$\begin{Bmatrix} U_o \\ U_a \end{Bmatrix} = \begin{bmatrix} \Phi_{on} & -K_{oo}^{-1}K_{oa} \\ 0_{an} & I_{aa} \end{bmatrix}\begin{Bmatrix} q_n \\ U_a \end{Bmatrix} \tag{31}$$

In practice, the number of "interior" component modes included in $[\Phi_{on}]$ should be consistent with the established dynamic cut-off frequency, f*, discussed in Sect. 1.2. Application of the HCB transformation to Eq. 25, in a symmetric manner following the Ritz method yields,

$$\begin{bmatrix} I_{nn} & P_{na} \\ P_{na}^T & \overline{M}_{aa} \end{bmatrix}\begin{Bmatrix} \ddot{q}_n \\ \ddot{u}_a \end{Bmatrix} + \begin{bmatrix} \omega_n^2 & 0_{na} \\ 0_{an} & \overline{K}_{aa} \end{bmatrix}\begin{Bmatrix} q_n \\ u_a \end{Bmatrix} = \begin{bmatrix} \Phi_{on}^T & 0_{na} \\ -K_{ao}K_{oo}^{-1} & I_{aa} \end{bmatrix}\begin{Bmatrix} F_o \\ F_a \end{Bmatrix}. \tag{32}$$

The above result, compared with Eq. 29, illustrates that HCB is a mathematical extension of GR. That being noted, the two methods are typically employed for differing purposes.

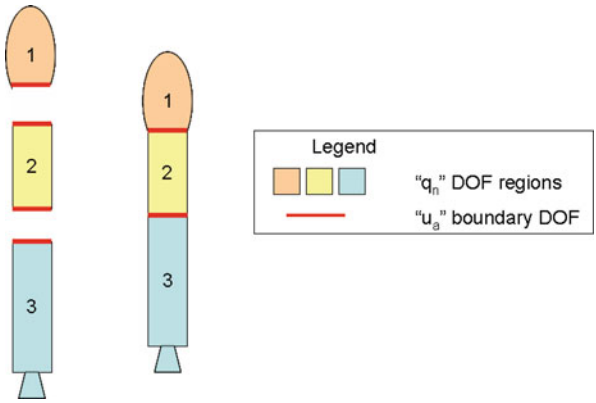

Fig. 4 Hypothetical HCB launch vehicle stack

In a sense, the HCB component can be thought of as an H-P finite element (see Sect. 1.3) with "q_n" representing the "P" degrees of freedom and "u_a" representing the "H" degrees of freedom. Considering the hypothetical launch vehicle "stack" dynamic system in Fig. 4, the assembled HCB system will adopt a "collective" matrix form conforming to Eq. 32.

On the assumption that Eq. 32 (also) represents the assembled dynamic system, the system modes, $[\Phi_{sys}]$, and modal frequencies, $[\omega_{sys}]$, (eigenvalue solution for Eq. 32) relate to the physical system DOF (Eq. 31) as follows:

$$\begin{Bmatrix} U_o \\ U_a \end{Bmatrix} = \begin{bmatrix} \Phi_{on} & -K_{oo}^{-1}K_{oa} \\ 0_{an} & I_{aa} \end{bmatrix} \begin{bmatrix} \Phi_{sys,q_n} \\ \Phi_{sys,u_a} \end{bmatrix}, \quad \text{where} \quad \begin{bmatrix} \Phi_{sys,q_n} \\ \Phi_{sys,u_a} \end{bmatrix} = \left[\Phi_{sys}\right]. \tag{33}$$

3.3 The Benfield-Hruda Method

While the Hurty-Craig-Bampton method is the most widely used approach (in the U.S. aerospace industry) for definition of integrated launch vehicle/spacecraft "component" or "superelement" dynamic models, the Benfield-Hruda (BH) method [19] endures as the most widely used method for assembly of launch vehicle/spacecraft dynamic models. The nuance of the BH method is that a "main body" substructure is defined by the matrix equation set,

$$\left[M_{aa,m}\right]\{\ddot{u}_a\} + \left[K_{aa,m}\right]\{u_a\} = \{0\}. \tag{34}$$

Assuming that the collection of HCB components (Eq. 32) "maps" onto the main body physical DOF set, the assembled dynamic system equations are,

$$\begin{bmatrix} I_{nn} & P_{na} \\ P_{na}^T & \overline{M}_{aa}+M_{aa,m} \end{bmatrix} \begin{Bmatrix} \ddot{q}_n \\ \ddot{u}_a \end{Bmatrix} + \begin{bmatrix} \omega_n^2 & 0_{na} \\ 0_{an} & \overline{K}_{aa}+K_{aa,m} \end{bmatrix} \begin{Bmatrix} q_n \\ u_a \end{Bmatrix} = \begin{bmatrix} \Phi_{on}^T & 0_{na} \\ -K_{ao}K_{oo}^{-1} & I_{aa} \end{bmatrix} \begin{Bmatrix} F_o \\ F_a \end{Bmatrix}. \tag{35}$$

The partition related to main body degrees of freedom, $\{u_a\}$, represents a main body structure "augmented" with "rigid body" substructure branches. In actuality, the branches are "rigid bodies" with locally flexible attachment DOF partitions.

A signature feature of the HB method is intermediate computation of augmented main body modes, specifically,

$$\left[\overline{K}_{aa}+K_{aa,m}\right][\Phi_a] = \left[\overline{M}_{aa}+M_{aa,m}\right][\Phi_a]\left[\omega_a^2\right]. \tag{36}$$

The intermediate stage transformation and resulting matrix dynamic equations, respectively, are

$$\begin{Bmatrix} q_n \\ u_a \end{Bmatrix} = \begin{bmatrix} I_n & 0 \\ 0 & \Phi_a \end{bmatrix} \begin{Bmatrix} q_n \\ q_a \end{Bmatrix}, \quad \text{and} \tag{37}$$

$$\begin{bmatrix} I_n & P_{na}\Phi_a \\ \Phi_a^T P_{na}^T & I_{aa} \end{bmatrix} \begin{Bmatrix} \ddot{q}_n \\ q_a \end{Bmatrix} + \begin{bmatrix} \omega_n^2 & 0_{na} \\ 0_{an} & \omega_a^2 \end{bmatrix} \begin{Bmatrix} q_n \\ u_a \end{Bmatrix} = \begin{bmatrix} \Phi_{on}^T & 0_{na} \\ -\Phi_a^T K_{ao} K_{oo}^{-1} & \Phi_a^T \end{bmatrix} \begin{Bmatrix} F_o \\ F_a \end{Bmatrix}. \tag{38}$$

The system modes, $[\Phi_{sys}]$, and modal frequencies, $[\omega_{sys}]$, (eigenvalue solution for Eq. 38) relate to the physical system DOF (Eqs. 31 and 35) as follows:

$$\begin{Bmatrix} U_o \\ U_a \end{Bmatrix} = \begin{bmatrix} \Phi_{on} & -K_{oo}^{-1}K_{oa} \\ 0_{an} & I_{aa} \end{bmatrix} \begin{bmatrix} I_n & 0 \\ 0 & \Phi_a \end{bmatrix} \begin{bmatrix} \Phi_{sys,q_n} \\ \Phi_{sys,u_a} \end{bmatrix}, \text{ where } \begin{bmatrix} \Phi_{sys,q_n} \\ \Phi_{sys,u_a} \end{bmatrix} = [\Phi_{sys}]. \tag{39}$$

The three key steps in the BH method are depicted in the hypothetical launch vehicle "stack" dynamic system below in Fig. 5, where, "I" represents the collection of HCB components (branch) and main body, "II" represents the assembled main body and "rigid" branch, and "III" represents the assembled dynamic system (Eq. 35) .

3.4 The MacNeal-Rubin Method

While the Hurty-Craig-Bampton and Benfield-Hruda methods are the most widely employed strategies for assembly of launch vehicle/spacecraft dynamic models, another approach, the MacNeal-Rubin [20, 21] (MR) method is noteworthy for its utilization in challenging situations involving localized interface nonlinearities. While there are a multitude of MR-type formulations, the present discussion focuses

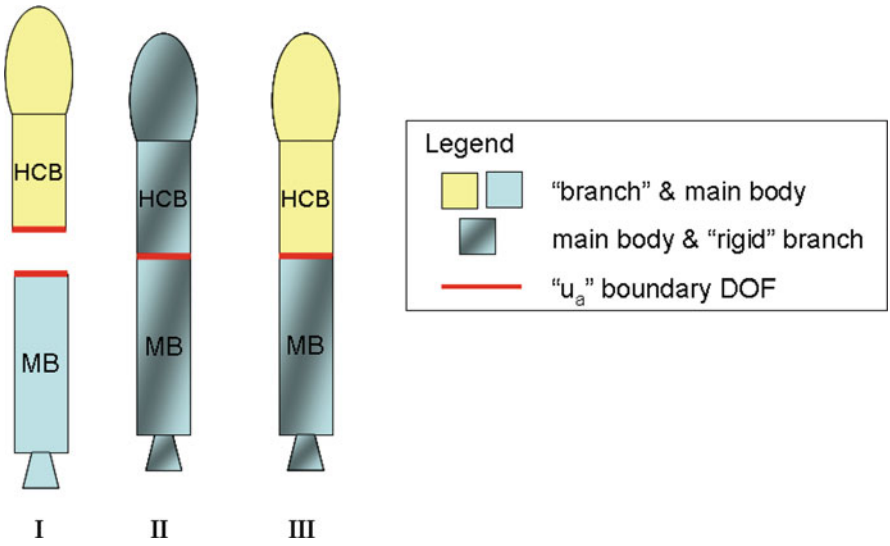

Fig. 5 Hypothetical BH launch vehicle stack

on foundational equations, which apply to the unconstrained structure (damping ignored),

$$[M]\{\ddot{u}\} + [K]\{u\} = [\Gamma]\{F\}, \tag{40}$$

MacNeal noted that "static" equilibrium of the above system associated with attachment loads is described by

$$[K]\{u_S\} = [\Gamma]\{F\} \quad \text{or} \quad \{u_S\} = \left[K^{-1}\right][\Gamma]\{F\} \tag{41}$$

In actuality, the unconstrained stiffness matrix is singular and its inverse must be conditioned in one of a variety of mechanics-mathematical techniques. One general approach, which encompasses unconstrained structures that have greater than 6 DOF singularities (rigid body motions) due to mechanisms, employs a small "shift" operator, described by

$$[K + \lambda_S M]\{u_S\} = [\Gamma]\{F\} \quad \text{or} \quad \{u_S\} = [K + \lambda_S M]^{-1}[\Gamma]\{F\} \tag{42}$$

Expressing the "static" displacements in terms of a truncated set of low frequency modes (including rigid body and mechanism modes), i.e.,

$$\{u_{s\ell}\} = [\Phi_\ell]\{q_\ell\}, \tag{43}$$

the "shifted static" displacements are

$$\{u_{s\ell}\} = [\Phi_\ell]\left[\omega_\ell^2 + \lambda_s\right]^{-1}\left[\Phi_\ell^T\Gamma\right]\{F\}. \tag{44}$$

At the heart of MacNeal's formulation [20] is the definition of residual "quasi-static" response,

$$\begin{aligned}\left\{u_{s\rho}\right\} &= \{u_s\} - \{u_{s\ell}\} = \left[[K + \lambda_s M]^{-1}[\Gamma] - [\Phi_\ell]\left[\omega_\ell^2 + \lambda_s\right]^{-1}\left[\Phi_\ell^T\Gamma\right]\right] \\ \{F\} &= \left[\Psi_\rho\right]\{F\}.\end{aligned} \tag{45}$$

Rubin's "improved" formulation [21] added a residual coefficient term associated with $\left\{\ddot{F}\right\}$ based on a MacLauren series expansion. Both MacNeal's and Rubin's formulations resulted in unorthodox, non-standard mixed displacement and force DOF dynamic equations that posed a challenge to conventional matrix structural dynamics practices.

An alternative (conventional) formulation was introduced by Coppolino [22] that employed the residual matrix, $[\Psi_\rho]$, residual "Ritz" vectors, which augment the lower frequency modes, $[\Phi_\ell]$. The augmented DOF transformation is therefore,

$$\{u\} = \left[\begin{array}{cc}\Phi_\ell & \Psi_\rho\end{array}\right]\left\{\begin{array}{c} q_\ell \\ q_\rho \end{array}\right\} \tag{46}$$

It is important to note that the residual vectors are a linear combination of the higher frequency modes of the dynamic system (and the higher frequency modes need not be known in order to form the residual vectors). Due to this property, the lower frequency modes and residual vectors are mutually orthogonal to each other, and the residual vectors are typically converted to pseudo-modes, $[\Phi_\rho]$, by solution of the following matrix equations:

$$\left[M_\rho\right] = \left[\Psi_\rho^T\right][M]\left[\Psi_\rho\right], \quad \left[K_\rho\right] = \left[\Psi_\rho^T\right][K]\left[\Psi_\rho\right], \tag{47}$$

$$\left[K_\rho\right]\left[\phi_\rho\right] = \left[M_\rho\right]\left[\phi_\rho\right]\left[\omega_\rho^2\right], \quad \left[\Phi_\rho\right] = \left[\Psi_\rho\right]\left[\phi_\rho\right].$$

Therefore, the augmented unconstrained modal transformation is

$$\{u\} = \left[\begin{array}{cc}\Phi_\ell & \Phi_\rho\end{array}\right]\left\{\begin{array}{c} q_\ell \\ q_\rho \end{array}\right\}, \tag{48}$$

and the uncoupled MacNeal-Rubin equations [22] become

$$\left[\begin{array}{cc} I_\ell & 0 \\ 0 & I_\rho \end{array}\right]\left\{\begin{array}{c} \ddot{q}_\ell \\ \ddot{q}_\rho \end{array}\right\} + \left[\begin{array}{cc} \omega_\ell^2 & 0 \\ 0 & \omega_\rho^2 \end{array}\right]\left\{\begin{array}{c} q_\ell \\ q_\rho \end{array}\right\} = \left[\begin{array}{c} \Phi_\ell^T\Gamma \\ \Phi_\rho^T\Gamma \end{array}\right]\{F\}. \tag{49}$$

The above form of the MacNeal-Rubin method is identical to uncoupled (truncated set) modal equations for an unconstrained system. However, exact static behavior is guaranteed by Eq. 49, in contrast to an approximation employing a truncated set of system modes, which typically requires many more high frequency normal modes than "residual" modes to achieve satisfactory convergence.

3.5 Application of Hurty-Craig-Bampton and MacNeal-Rubin Methodology

A prominent past application of the Hurty-Craig-Bampton and MacNeal-Rubin methods is found in space shuttle payload dynamic loads analyses. Attachment of cargo manifests in the space shuttle payload bay, as illustrated in Fig. 6, involved fittings that exhibited nonlinear stick-slip mechanical behavior.

The typical HCB cargo element (contractor) model was supplied in the following matrix form,

$$\begin{bmatrix} I_{nn} & P_{na} \\ P_{na}^T & \overline{M}_{aa} \end{bmatrix} \begin{Bmatrix} \ddot{q}_n \\ \ddot{u}_a \end{Bmatrix} + \begin{bmatrix} 2\zeta_n\omega_n & 0_{na} \\ 0_{an} & \overline{B}_{aa} \end{bmatrix} \begin{Bmatrix} \dot{q}_n \\ \dot{u}_a \end{Bmatrix} + \begin{bmatrix} \omega_n^2 & 0_{na} \\ 0_{an} & \overline{K}_{aa} \end{bmatrix} \begin{Bmatrix} q_n \\ u_a \end{Bmatrix} = \begin{Bmatrix} 0_o \\ F_a \end{Bmatrix}, \quad (50)$$

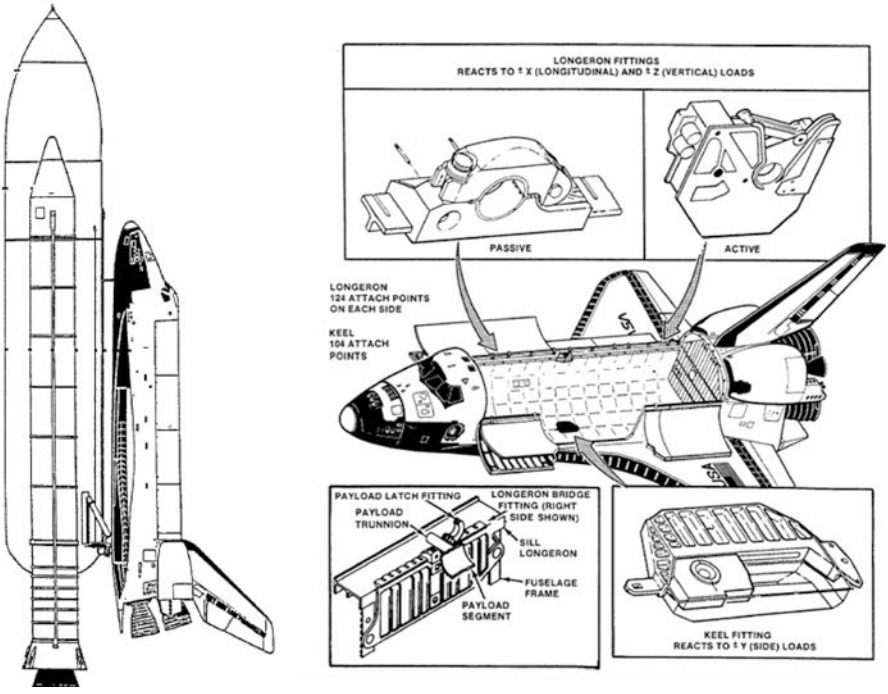

Fig. 6 Space shuttle cargo bay payload interface

where the generalized damping matrix terms were defined on the basis of cargo element engineering judgment and experimental data, if available. The nonlinear interface forces are represented by $\{F_a\}$, and the applied interior DOF forces, $\{F_o\}$, (see Eq. 32) are assumed null due to the fact that the cargo is totally enclosed within the orbiter's payload bay (Note: Payload bay acoustic loads were generally treated in a separate analysis).

The space shuttle dynamic model (often related to liftoff and abort landing configurations) was provided in a standard format, which ultimately was described by MR equations of the form,

$$\begin{bmatrix} I_\ell & 0 \\ 0 & I_\rho \end{bmatrix} \begin{Bmatrix} \ddot{q}_l \\ \ddot{q}_\rho \end{Bmatrix} + \begin{bmatrix} 2\zeta_\ell \omega_\ell & 0 \\ 0 & 2\zeta_\rho \omega_\rho \end{bmatrix} \begin{Bmatrix} q_\ell \\ q_\rho \end{Bmatrix} + \begin{bmatrix} \omega_\ell^2 & 0 \\ 0 & \omega_\rho^2 \end{bmatrix} \begin{Bmatrix} q_\ell \\ q_\rho \end{Bmatrix}$$
$$= \begin{bmatrix} \Phi_\ell^T \Gamma_e \\ \Phi_\rho^T \Gamma_e \end{bmatrix} \{F_e\} + \begin{bmatrix} \Phi_\ell^T \Gamma_a \\ \Phi_\rho^T \Gamma_a \end{bmatrix} \{-F_a\} \tag{51}$$

where the generalized damping matrix terms were defined on the basis of cargo element engineering judgment and experimental data. In addition, the distribution, $[\Gamma_e]$, and time histories of standardized external applied load transients, $\{F_e\}$, respectively were provided by the space shuttle contractor. Physical interface displacements, on the space shuttle payload bay side, were recovered via the modal transformations,

$$\{u_a\}_s = \left[\Gamma_a^T \Phi_\ell\right] \{q_\ell\} + \left[\Gamma_a^T \Phi_\rho\right] \{q_\rho\}, \quad \{\dot{u}_a\}_s = \left[\Gamma_a^T \Phi_\ell\right] \{\dot{q}_\ell\} + \left[\Gamma_a^T \Phi_\rho\right] \{\dot{q}_\rho\} \tag{52}$$

The relative displacements and velocities associated with the nonlinear stick-slip interface DOF are described by,

$$\{\Delta u_a\} = \{u_a\} - \{u_a\}_s, \quad \{\Delta \dot{u}_a\} = \{\dot{u}_a\} - \{\dot{u}_a\}_s. \tag{53}$$

Finally, the stick-slip interface forces were appropriately computed with hysteretic equations of the type,

$$\{F_a\,(t + \Delta t), \{p_a\,(t + \Delta t)\}\} = -\{N\,(\{\Delta u_a(t)\}, \{\Delta \dot{u}_a(t)\}, \{p_a(t)\})\}. \tag{54}$$

Integrated system dynamic responses associated with Eqs. 50–54 are computed by one among a variety of stable numerical integration methods.

3.6 Detailed Structural Dynamic Loads and the Mode Acceleration Method

The relationship between system dynamic response, expressed in terms of system modal DOF displacements, and detailed structural member loads and stresses (internal loads) is typically described by the matrix equation,

$$\{\sigma\} = [K_\sigma]\{u\} + [B_\sigma]\{\dot{u}\} = [K_\sigma \Phi]\{q\} + [B_\sigma \Phi]\{\dot{q}\}, \tag{55}$$

where the velocity dependent term is generally ignored. It should be noted that the modal matrix, $[\Phi]$, is associated with a truncated (base-band) set of system modes. It is a well-established fact that when the truncated mode set does not include quasi-static residual modes (see Eq. 51), serious inaccuracies in internal loads may occur. In contrast, inclusion of quasi-static residual modes automatically accounts for the quasi-static response of all higher frequency band modes, eliminating the modal truncation deficiency.

A second, more prevalent approach to recovery of internal loads, namely the mode acceleration method, was introduced in 1945 by D. Williams [23]. From a matrix viewpoint, the method is derived from the assembled physical (non-reduced order) dynamic system equations with externally applied, inertial and dissipative forces on the right-hand side. Consider a linear structural dynamic system,

$$[K]\{u\} = [\Gamma_e]\{F_e\} - [M]\{\ddot{u}\} - [B]\{\dot{u}\}, \tag{56}$$

with incorporation of right-hand side modal substitutions,

$$[\mathrm{K}]\{\mathrm{u}\} = \{\mathrm{F_{total}}\} = [\Gamma_\mathrm{e}]\{\mathrm{F_e}\} - [\mathrm{M}\Phi_\mathrm{n}]\{\ddot{\mathrm{q}}_\mathrm{n}\} - [\mathrm{B}\Phi_\mathrm{n}]\{\dot{\mathrm{q}}_\mathrm{n}\}. \tag{57}$$

It should be noted that interpretation of $[\Gamma_\mathrm{e}]\{\mathrm{F_e}\}$ as inclusive of the nonlinear forces in Eq. 8 renders the present derivation applicable to a system with local nonlinear forces.

Since the system stiffness matrix is most often singular due to a free-free condition (and sometimes mechanisms), the full set displacement DOF are separated into "relative" (l) and "reference rigid body" DOF (r) partitions resulting in,

$$\begin{bmatrix} \mathrm{K_{ll}} & \mathrm{K_{lr}} \\ \mathrm{K_{rl}} & \mathrm{K_{rr}} \end{bmatrix} \begin{Bmatrix} \mathrm{u_l} \\ \mathrm{u_r} \end{Bmatrix} = \begin{Bmatrix} \mathrm{F_{total,l}} \\ \mathrm{F_{total,r}} \end{Bmatrix} \rightarrow \begin{Bmatrix} \mathrm{u_l} \\ \mathrm{u_r} \end{Bmatrix} = \begin{bmatrix} \mathrm{I_{ll}} & \mathrm{K_{ll}^{-1}K_{lr}} \\ \mathrm{0_{rl}} & \mathrm{I_{rr}} \end{bmatrix} \begin{Bmatrix} \mathrm{u'_l} \\ \mathrm{u_r} \end{Bmatrix} \rightarrow \tag{58}$$

$$\rightarrow \begin{bmatrix} \mathrm{K_{ll}} & \mathrm{0_{lr}} \\ \mathrm{0_{rl}} & \mathrm{K_{rr} - K_{rl}K_{ll}^{-1}K_{lr}} \end{bmatrix} \begin{Bmatrix} \mathrm{u'_l} \\ \mathrm{u_r} \end{Bmatrix} = \begin{bmatrix} \mathrm{I_{ll}} & \mathrm{0_{lr}} \\ \mathrm{-K_{rl}K_{ll}^{-1}} & \mathrm{I_{rr}} \end{bmatrix} \begin{Bmatrix} \mathrm{F_{total,l}} \\ \mathrm{F_{total,r}} \end{Bmatrix},$$

where $[\mathrm{K_{ll}}]$ is the positive-definite relative stiffness matrix. Focusing on the upper partition, the mode acceleration relative displacements (akin to strains) are,

$$\left\{u'_l\right\} = \left[K_{ll}^{-1}\right]\left\{F_{total,l}\right\} = \left[K_{ll}^{-1}\right][\Gamma_e]_l\{F_e\} - \left[K_{ll}^{-1}\right][M\Phi_n]_l\{\ddot{q}_n\} - \left[K_{ll}^{-1}\right] [B\Phi_n]_l\{\dot{q}_n\} \tag{59}$$

Introducing the internal "stress" (or member load) relationship,

$$\{\sigma\} = [K_\sigma]\left\{u'_l\right\}, \tag{60}$$

the system-level mode acceleration equations become,

$$\{\sigma\} = [LTM_F]\{F_e\} - \left[LTM_{\ddot{q}}\right]\{\ddot{q}_n\} - \left[LTM_{\dot{q}}\right]\{\dot{q}_n\}, \tag{61}$$

$$[LTM_F] = [K_\sigma]\left[K_{ll}^{-1}\right][\Gamma_e]_l, \quad \left[LTM_{\ddot{q}}\right] = [K_\sigma]\left[K_{ll}^{-1}\right][M\Phi_n]_l,$$
$$\left[LTM_{\dot{q}}\right] = [K_\sigma]\left[K_{ll}^{-1}\right][B\Phi_n]_l.$$

The key advantage of the mode acceleration method is that it automatically accounts for the quasi-static response of all higher frequency modes, without the need to explicitly compute those modes. The second, vital advantage of the mode acceleration method relates to the fact that $[LTM_F]\{F_e\}$ is the quasi-static contribution to internal loads, and $\left[LTM_{\ddot{q}}\right]\{\ddot{q}_n\}$ is the system mode acceleration contribution to internal loads. The modal velocity contribution to internal loads is often neglected.

In closing the present discussion on the mode acceleration method, it should be noted that expressions for load transformation matrices are often developed by employment of Hurty-Craig-Bampton (HCB) component models, which employ expansion transformations from HCB to system modal accelerations and velocity DOF. While such an approach is employed out of necessity (HCB models based on proprietary FEMs are provided by the payload contractors to payload integration contractors), the resulting load transformation matrices should be equivalent to those described by Eqs. 56– 61.

4 Verifiction and Validation of Structural Dynamic Models

Over the past 60 years, the U.S. aerospace community has developed, refined, and standardized an integrated approach to structural dynamic model verification and validation. One name for this overall approach is the Integrated Test Analysis Process (ITAP) for structural dynamic systems, which is summarized in Fig. 7 and discussed in the immediately following subsections.

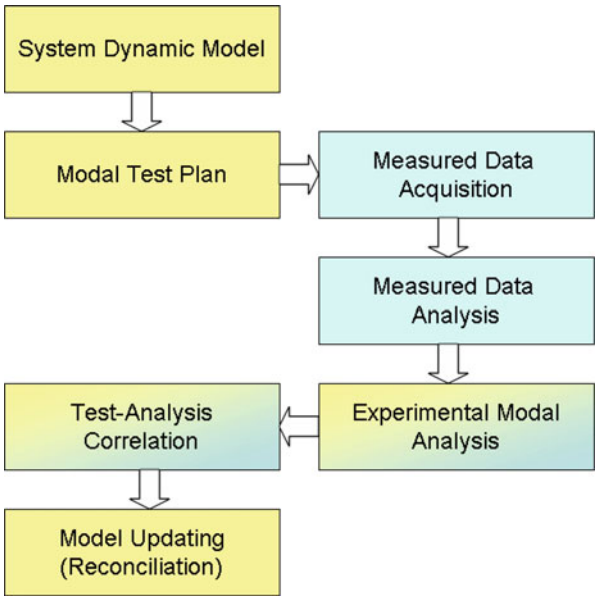

Fig. 7 Overview of the integrated test analysis process

4.1 System Dynamic Model

The system dynamic model to be verified, validated, and updated in the ITAP process should be developed employing (a) adherence to the guidelines discussed in Sects. 2.2, 2.3 and 2.4 and consistency with design documentation and engineering drawings. It is inexcusable today that "consistency" is often not practiced in many aerospace organizations, in spite of the availability of modern CAE tools that facilitate automated drawing-to-FEM consistency.

Beyond the above recommended modeling practices, a vital preliminary step in the ITAP process is initial model verification. Over the past 60 years, rigid body checks have been a standard part of the model verification process. Using a geometrically defined rigid body displacement matrix, $[\Psi_{RB}]$, the rigid body mass properties of a structure (both the complete assembly and subassemblies in unconstrained form) defined by,

$$[M_{RB}] = [\Psi_{RB}]^T [M] [\Psi_{RB}], \tag{62}$$

are correlated with reference engineering properties (total mass, center of gravity, mass moments of inertia) of the designed system. It should be noted that aircraft and space system development organizations generally include weight engineering departments which manage system mass budgets throughout the development process. The Society of Allied Weights Engineers (SAWE) was established in the U.S. in 1939 to support the weights engineering community.

The companion initial model verification calculation

$$[K_{RB}] = [\Psi_{RB}]^T [K] [\Psi_{RB}], \tag{63}$$

is employed on the structure (both the complete assembly and subassemblies in unconstrained form) to verify integrity of the modeling process. $[K_{RB}]$ must be a null matrix for an unconstrained structure. It should be noted that in special situations involving structures with "mechanisms" additional unconstrained verification calculations are required on the assembled system model (i.e., more than six stiffness free "modes").

4.2 Modal Test Planning and the Test Analysis Model (TAM)

As a general rule, the number of system model degrees-of-freedom is substantially greater than a practical number of acceleration sensor channels. Before 1965, allocation of a modal test accelerometer array was a task guided primarily by general understanding of the character of anticipated system modes. Moreover, the assembly of a system mass allocation matrix (corresponding to the test accelerometer array) was conducted on the basis of engineering experience and "expertise." The mass allocation matrix was deemed necessary for validation of test mode orthogonality, especially in aeronautical applications.

Introduction of Guyan reduction (described in Sect. 3.1) in 1965 offered a systematic strategy for definition of an appropriate test accelerometer array and system mass allocation matrix. In the context of modal test planning, the "analysis set" DOFs (Eq. 26) correspond to instrumented (accelerometer) response channels on the test article and it is assumed (based on engineering intuition) that the "omit" degrees of freedom (approximately) follow a static relationship with respect to the "analysis" set degrees of freedom. The reduced stiffness and mass matrices (corresponding to Eqs. 27 and 28) are called the test-analysis model (TAM) stiffness, $[K_{TAM}]$, and mass, $[M_{TAM}]$, matrices, respectively, within the context of the modal test plan; it should be noted that the TAM mass matrix is the more important quantity employed in the modal test plan.

Appropriateness of a selected "analysis" set may be verified by comparison of approximate modes, $[\Phi]_{TAM}$, and natural frequencies associated with the reduced eigenvalue problem (Eqs. 26–28) with the results for the exact eigenvalue problem (Eq. 25). The exact and approximate modal vectors (which use Eq. 26 as an expansion transformation) are,

$$[\Phi]_{exact} = \begin{bmatrix} \Phi_o \\ \Phi_a \end{bmatrix}_{exact}, \quad [\Phi]_{TAM} = \begin{bmatrix} -K_{oo}^{-1} K_{oa} \\ I_{aa} \end{bmatrix} [\Phi_a]_{exact} \tag{64}$$

The choice of a specific set of "analysis" degrees of freedom is acceptable if all "TAM" approximate modes and natural frequencies are "satisfactory" agreement

with the "exact" system modes and natural frequencies. A very clear example of an inadequate selection of "analysis" set degrees of freedom is discussed in Reference [24], which describes difficulties encountered in modal testing of a trim body automobile test article. In that experience, the front seats were not modeled or designated by "analysis" degrees of freedom and local seat flexing modes which coupled with overall body vertical bending motions were obscured. In response to this and other experiences, a variety of automated "analysis" DOF selection algorithms were developed. Reference [25] describes the currently accepted strategy from which other DOF selection methodologies have been developed, to be discussed in Sect. 4.4.

Utilization of Guyan reduction to designate (1) the "analysis" set degrees of freedom as the modal test accelerometer array and (2) the reduced mass matrix, $[M_{TAM}]$, as the test-analysis model (TAM) mass (allocation) matrix is the most prevalent, contemporary test planning strategy in the U.S. aerospace industry. Allocation of force excitation resources on the basis of modal gains, $\{\Phi_n\}^T[\Gamma_e]$, complements the allocated accelerometer array. Additional strain gage sensor arrays have been successfully employed by NASA/JPL [25] and others since the 1980s as part of modal survey planning and execution. Such information provides a basis for correlation and validation of load transformation matrices (see Eq. 61).

Finally, it should be pointed out that allocation of an accelerometer array may require special considerations to avoid the mapping of unwanted modes, specifically breathing modes of plate and shell subassemblies (that are not included in the target mode set). In such situations, accelerometers directed normal to a "breathing" surface should not be allocated. Moreover, if possible, tangentially oriented accelerometers should be allocated only at stiffening rings and spars to further suppress measurement of breathing modes, while focusing on "body" modes (e.g., axial, bending, and torsion modes). The above cited practice, while popular, must be employed with caution and selectively as (a) slight imperfections and manufacturing details cause mixing of "body" and "breathing" modes, and (b) suppression of sometimes important shell "bulge" modes.

In summary, the following data sets form the basis of modal test planning in the U.S. aerospace industry:

(a) TAM mass matrix, $[M_{TAM}]$, derived from appropriate application of the Guyan reduction process.
(b) TAM predicted modes and natural frequencies based on solution of the exact (unreduced) eigenvalue problem. The accelerometer array modal partition represents the predicted test modes. *It should be noted that some organizations use the Guyan reduction solution as the predicted mode set.*
(c) Applied force allocation, based on predicted mode gains to excite all target modes.
(d) Additional designated strain gages at critical locations based on pre-test flight loads analyses (the "NASA/JPL" strategy [25]).

4.3 Target Modes

Selection of a subset of significant "target" modes from the complete set of predicted modes of a test article is a practice employed by many aerospace organizations. A common, yet often inadequate approach to target mode selection involves a (significant) modal effective mass criterion (see Eq. 35). Additional target modes, however, may be selected based on modal excitations imposed on non-boundary DOF, $\left[\Phi_{on}^{T}\right]\{F_o\}$, also included in Eq. 35. In any case, the practice of focus exclusively on target modes, rather than all modes within the structural dynamic frequency band ($0 < f < f^*$) is risky due to mixing with "non-target" modes as a result of imperfections and manufacturing details.

4.4 Automated Response DOF Selection for Mapping of Experimental Modes

The difference between exact and approximate analytical eigenvectors, described in Eq. 64, is the residual displacement error matrix,

$$[R_\Phi] = \begin{bmatrix} \Phi_o + K_{oo}^{-1} K_{oa} \Phi_a \\ 0_a \end{bmatrix}. \tag{65}$$

Note that the residual error associated with the "measured" or "analysis" DOF partition is null. The modal kinetic energy distribution for the complete system is,

$$[E_\Phi] = [M\Phi] \otimes [\Phi] \tag{66}$$

where the column sum for each individual mode is unity (if the modes are normalized to unit modal mass). The residual kinetic energy matrix is now defined in a similar manner as,

$$[E_R] = [MR] \otimes [R] \tag{67}$$

Like the residual displacement error, [R], the residual kinetic energy matrix is exactly "zero" at the rows corresponding to the measured DOF. The expected characteristic that residual energy is pronounced at "omitted" yet dynamically significant DOF in any particular mode is demonstrated in the illustrative example structure along with its first six predicted modes, pictured in Fig. 8 (from Reference [26]) which follows.

Six DOFs (1,3,5,7,10,19), which are insufficient for mapping modal behavior on the "upper portion" of the bar, are first selected as response "measurement" DOFs. The residual kinetic energy associated with this selected response DOF set is illustrated in Fig. 9 as a surface with the horizontal axes corresponding to FEM DOF number and mode number, respectively. The surface clearly indicates that the

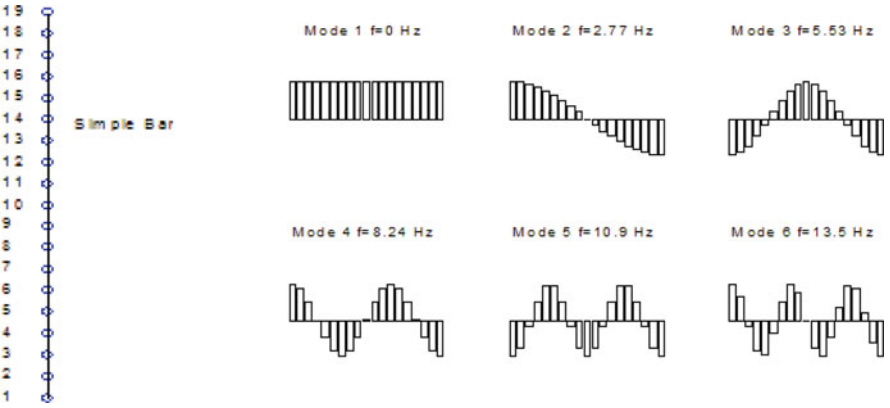

Fig. 8 Simple free-free bar structure and normal modes

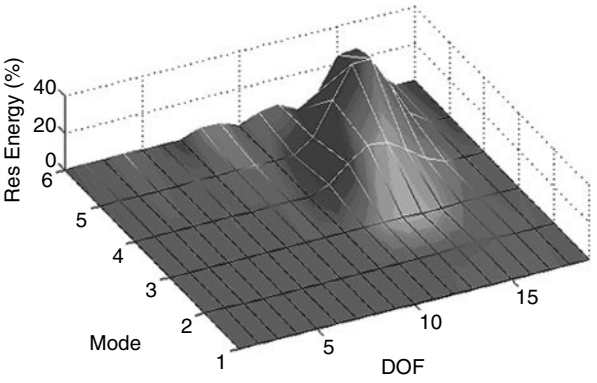

Fig. 9 Residual kinetic energy surface for the 6 DOF measured set

"measurement" DOF set is adequate for the first three modes. Pronounced residual kinetic energy terms in modes 4–6 suggest that at least two to three more DOFs on the "upper portion" of the bar structure must be instrumented to adequately map modes 4–6.

It is of interest to note the orthogonality of the approximate "measured" modes, shown below, for the present DOF selection (1,3,5,7,10,19)

$$[\mathrm{OR_{TAM}}] = \left[\Phi^{\mathrm{T}}_{\mathrm{TAM}}\right][\mathrm{M}]\,[\Phi_{\mathrm{TAM}}] = \left[\Phi^{\mathrm{T}}_{\mathrm{a}}\right][\mathrm{M_{TAM}}]\,[\Phi_{\mathrm{a}}]$$

$$= \begin{bmatrix} 100 & 10 & -1 & -55 & -58 & -46 \\ 10 & 100 & -5 & 44 & 51 & 45 \\ -1 & -5 & 100 & -18 & 3 & 29 \\ -55 & 44 & -18 & 100 & 23 & 60 \\ -58 & 51 & 3 & 23 & 100 & 33 \\ -46 & 45 & 29 & 60 & 33 & 100 \end{bmatrix} \tag{68}$$

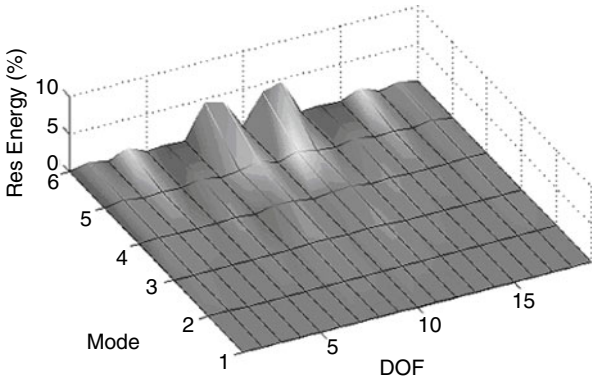

Fig. 10 Residual kinetic energy surface for the improved measured DOF set

The "acceptable" orthogonality among modes 1–3 confirms adequacy of the selected DOF set for these modes, while the extremely poor orthogonality of the remaining modes indicates a need for additional measurement DOF.

Following the recommendation for additional "measured" DOF implied by the "6 DOF based" residual kinetic energy, shown in Fig. 9, the refined residual kinetic energy (augmented with DOFs 13, 15, and 17) is

The residual kinetic energy reduces substantially as illustrated in Fig. 10. The improvement in orthogonality of "approximate" measured modes, shown below, indicates substantial improvement of the refined response measurement DOF set.

$$[\mathrm{OR}_{\mathrm{TAM}}] = \begin{bmatrix} 100 & 0 & -2 & 0 & 5 & 0 \\ 0 & 100 & 0 & 2 & 0 & -6 \\ -2 & 0 & 100 & 0 & 7 & 0 \\ 0 & 2 & 0 & 100 & 0 & 20 \\ 5 & 0 & 7 & 0 & 100 & 0 \\ 0 & -6 & 0 & 20 & 0 & 100 \end{bmatrix} \tag{69}$$

Following its introduction in Reference [26], the automated response DOF selection technique, today known as the RKE method, was applied in planning of two International Space Station (ISS) modal tests. RKE planning results for the ISS P5 modal test [27] are illustrated in Fig. 11. One noteworthy feature of the ISS P5 modal test plan was inclusion of measured DOF on the NASA/MSFC shuttle payload simulation test fixture, which had a few modes below 50 Hz.

4.5 Measured Data Acquisition, Data Analysis, Experimental Modal Analysis

Laboratory-centric tasks addressing measured data acquisition, measured data analysis, and experimental modal analysis, have undergone a high degree of and

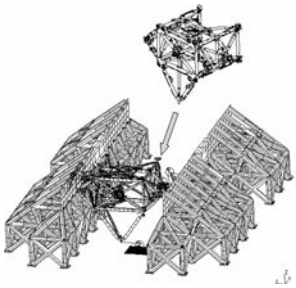

		Orthogonality Check (Normalized to 100)															
No.	Hz	1	2	3	4	5	6	7	8	9	10	11	12	13	14	15	16	17
1	18.67	100	0	0	0	0	0	0	0	0	0	0	0	0	0	0	0	0
2	19.31	0	100	0	0	0	0	0	0	0	0	0	0	0	0	0	0	0
3	24.88	0	0	100	0	0	0	0	0	0	0	0	0	0	0	0	0	0
4	28.68	0	0	0	100	0	0	0	0	0	0	0	0	0	1	0	0	0
5	29.37	0	0	0	0	100	0	0	0	0	0	0	0	0	0	0	0	0
6	30.07	0	0	0	0	0	100	0	0	0	0	0	1	0	0	0	1	0
7	34.01	0	0	0	0	0	0	100	0	1	0	0	0	0	0	0	0	0
8	34.65	0	0	0	0	0	0	0	100	0	0	0	0	0	0	0	0	0
9	35.22	0	0	0	0	0	0	1	0	100	1	1	0	0	0	0	0	0
10	35.61	0	0	0	0	0	0	0	0	1	100	0	0	0	0	0	0	0
11	37.82	0	0	0	0	0	0	0	0	1	0	100	0	-1	0	0	0	0
12	40.82	0	0	0	0	0	1	0	0	0	0	0	100	1	0	0	1	0
13	42.24	0	0	0	0	0	0	0	0	0	0	-1	1	100	1	0	-1	0
14	45.21	0	0	0	1	0	0	0	0	0	0	0	0	1	100	0	3	1
15	47.40	0	0	0	0	0	0	0	0	0	0	0	0	0	0	100	3	-1
16	50.22	0	0	0	0	0	1	0	0	0	0	0	1	-1	3	3	100	-1
17	50.41	0	0	0	0	0	0	0	0	0	0	0	0	0	1	-1	-1	100

Fig. 11 ISS P5 modal test plan predicted mode orthogonality

refinement during the past 50+ years. That being said, there are no specific standards representing aerospace industry practice in the U.S. In keeping with the intent of the present chapter, this subject matter is not addressed herein. Information on the laboratory-centric tasks is covered in other chapters in this handbook.

4.6 Modal Test-Analysis Correlation and U.S. Government Standards

The relationship between test modes, $[\Phi_{TEST}]$, and their analytical counterparts, $[\Phi_{TAM}]$, is described by the transformation,

$$[\Phi_{TEST}] = [\Phi_{TAM}]\,[COR] + [R] \tag{70}$$

where [COR] is the cross-orthogonality matrix and [R] is the residual error matrix. Employing $[M_{TAM}]$ as a weighting matrix, the least squares solution for cross-orthogonality is,

$$[COR] = [OR_{TAM}]^{-1}\left[\Phi_{TAM}^{T} M_{TAM} \Phi_{TEST}\right], \tag{71}$$

where the TAM mode orthogonality matrix (consistent with Eq. 68) is,

$$[OR_{TAM}] = \left[\Phi_{TAM}^{T} M_{TAM} \Phi_{TAM}\right] \approx [I] \tag{72}$$

It should be noted that $[OR_{TAM}]$ is exactly an identity matrix only if the "analysis" modes are the unit mass normalized modes of the Guyan reduced structural dynamic model.

An additional useful modal coherence matrix, [COH], is defined as follows,

$$\begin{aligned} \mathrm{COH}t &= \left([\mathrm{I}] - [\mathrm{OR_{TEST}}]^{-1/2}\left[\mathrm{R^T MR}\right][\mathrm{OR_{TEST}}]^{-1/2}\right) \\ &= [\mathrm{I}] - [\mathrm{OR_{TEST}}]^{-1/2}\left[\mathrm{COR^t OR_{TAM} COR}\right][\mathrm{OR_{TEST}}]^{-1/2}. \end{aligned} \tag{73}$$

It should be noted that (a) TAM mode orthogonality, (b) test mode orthogonality, (c) test-TAM mode cross-orthogonality matrices, along with (d) corresponding test-analysis natural frequency differences, represent the accepted test-analysis correlation metrics in the U.S. aerospace industry. Modal coherence, [COH], is employed by some investigators to judge the degree to which test and analysis modal clusters are linear combinations of one another; however, this metric is not widely recognized.

The following standards are imposed on space systems contractors by U.S. government agencies:

Air Force Space Command [28]

For all spacecraft modes up to 70 Hz, test mode orthogonality (unit mass normalized)

$$| \mathrm{OR_{TEST,ij}} | \leq 0.10 \ \ (10\%) \ \ \text{for} \ \ \mathrm{i} \neq \mathrm{j}$$

Test-Analysis mode cross-orthogonality (both sets unit mass normalized)

$$| \mathrm{COR_{ij}} | \geq 0.95 \ \ (95\%) \ \ \text{for} \ \ \mathrm{i} = \mathrm{j}$$

$$| \mathrm{COR_{ij}} | \leq 0.10 \ \ (10\%) \ \ \text{for} \ \ \mathrm{i} \neq \mathrm{j}$$

Difference between corresponding test and analysis modal frequencies must be less than 3%.

NASA [29]

For all significant modes, test mode orthogonality (unit mass normalized)

$$| \mathrm{OR_{TEST,ij}} | \leq 0.10 \quad (10\%) \ \ \text{for} \ \ \mathrm{i} \neq \mathrm{j}$$

Test-Analysis mode cross-orthogonality (both sets unit mass normalized)

$$| \mathrm{COR_{ij}} | \geq 0.90 \quad (90\%) \ \ \text{for} \ \ \mathrm{i} = \mathrm{j}$$

$$| \mathrm{COR_{ij}} | \leq 0.10 \quad (10\%) \ \ \text{for} \ \ \mathrm{i} \neq \mathrm{j}$$

Difference between corresponding test and analysis modal frequencies must be less than 5%.

It should be noted that the stricter standards imposed by the U.S. Air Force Space Command, particularly for spacecraft, are suited for situations in which test data is employed directly to construct a hybrid test-analysis dynamic model [30], which circumvents an often lengthy model correlation and reconciliation process.

4.7 Overview of Efficient Structural Dynamic Sensitivity Analysis

The final goal in the ITAP process involves reconciliation of the test article FEM and modal test data. While many aerospace and software organizations have custom methodologies that address the reconciliation task, there is no universally accepted approach to such an endeavor. That being said, a numerically efficient technique, namely Residual Mode Augmentation (RMA) [31] for calculation of FEM sensitivity to large parametric variation has gained acceptance in U.S. aerospace government and industry organizations.

Efficient computation of structural dynamic modal frequency and mode shape sensitivities associated with variation of physical stiffness and mass parameters is essential for (1) practical design sensitivity and uncertainty studies and (2) reconciliation of finite element models with modal test data. Sensitivity analysis procedures fall in two distinct categories, namely (a) modal derivatives for small parametric variation and (b) altered system modes associated with "large" parametric variation. The latter category is generally applicable to modal testing, which often requires significant local parameter changes at joints to effect FEM-test reconciliation. However, many investigators and commercial software packages employ estimated modal derivatives in optimization strategies, which address FEM-test reconciliation objectives.

Since the 1960s, methods for computation of modal frequency and mode shape derivatives have been developed. Fox and Kapoor [32] introduced an exact derivative formulation that required knowledge of all modes of the original system; application of the procedure when a truncated set of modes was employed produced compromised derivatives. In response to this difficulty, Nelson [33] derived an exact formulation for computation of mode shape derivatives for truncated mode sets. Efforts to refine and extend application of mode shape derivatives for finite parameter change sensitivity computations have been pursued by many investigators. However, the need for modal frequency and mode shape sensitivities that map over very large ranges for multiple parameters suggests application of alternative Ritz strategies.

The Ritz method [4] is one of the most significant developments in analytical mechanics of the past century. This method provides a logical energy formulation for consistent reduction of mass and stiffness matrices employing a set of trial vectors as a reduction transformation. Effectiveness and accuracy of the reduction process depend on selection of an appropriate trial vector set. When a truncated set of baseline system mode shapes is used as the trial vector set (popularly known as

Structural Dynamic Modification (SDM) [34], the Ritz method often produces poor estimates for the altered system. Augmentation of the truncated baseline system mode shapes with appropriately defined additional vectors, however, has been found to produce extremely accurate altered system modal frequencies and mode shapes. Quasi-static residual vectors [20], appended to a truncated set of mode shapes, were found to produce extremely accurate modes for offshore oil platform models subjected to localized alterations [35]. Residual Mode Augmentation (RMA), introduced in 2002 [27] and thoroughly discussed in Reference [31], is a procedure that defines augmented trial vectors, which are appropriate for structures subjected to highly distributed, as well as localized, alterations.

4.8 Residual Mode Augmentation (RMA)

The matrix equations describing exact free vibration of baseline and altered structures, respectively, are

$$[K_O][\Phi_O] - [M_O][\Phi_O][\lambda_O] = [0], \quad \text{and}$$
$$[K_O + p \cdot \Delta K][\Phi] - [M_O + p \cdot \Delta M][\Phi][\lambda] = [0]. \tag{74}$$

It is implicitly assumed that the stiffness and mass changes scale linearly with respect to the parameter, p. Therefore, changes in "beam" depth may not be directly applied, since the axial stiffness (AE) scales linearly with depth and the flexural stiffness (EI) scales as the cube of depth. The appropriate formulation for Eq. 74 permits linear sensitivity of "AE" and "EI" separately.

The relationship between mode shapes of the baseline and altered structures is expressed as the cross-orthogonality of orthonormal mode shape sets,

$$[\mathrm{COR}] = \left[\Phi_{\mathrm{O}}^{\mathrm{T}}\right][\mathrm{M_O}][\Phi], \tag{75}$$

where the baseline and altered structure modes are unit mass normalized.

The most fundamental Ritz approximation, used in SDM [34], employs a truncated set of low frequency eigenvalues as the reduction transformation described by

$$[\Phi] = [\Phi_{\mathrm{OL}}][\phi], \tag{76}$$

where the reduced baseline structure stiffness and mass matrices, respectively, are

$$[\mathrm{k_O}] = \left[\Phi_{\mathrm{OL}}^{\mathrm{T}}\mathrm{K_O}\Phi_{\mathrm{OL}}\right] = [\lambda_{\mathrm{OL}}], \quad [\mathrm{m_O}] = \left[\Phi_{\mathrm{OL}}^{\mathrm{T}}\mathrm{M_O}\Phi_{\mathrm{OL}}\right] = [\mathrm{I_{OL}}], \tag{77}$$

the reduced stiffness and mass sensitivity matrices, respectively, are

$$[\Delta k] = \left[\Phi_{OL}^{T} \Delta K \Phi_{OL}\right], \quad [\Delta m] = \left[\Phi_{OL}^{T} \Delta M \Phi_{OL}\right], \tag{78}$$

and the reduced altered structure free vibration equation is

$$\left[\lambda_{OL} + p \cdot \Delta k\right][\phi] - \left[I_{OL} + p \cdot \Delta m\right][\phi][\lambda] = [0]. \tag{79}$$

A well-known result of this type of trial vector reduction strategy is that the approximate altered structure eigenvalues are generally higher than results for the exact solution, and the approximate mode shapes do not closely follow the exact shapes when parametric alterations are large.

When structural alterations are well-dispersed, parametric structural changes may affect many physical degrees of freedom and require a description in terms of several independent scaling parameters, "p_i". The expressions for altered stiffness and mass matrices in such a situation are

$$[K] = [K_O] + \sum_{i=1}^{N} p_i [\Delta K_i], \quad [M] = [M_O] + \sum_{i=1}^{N} p_i [\Delta M_i], \tag{80}$$

The altered system free vibration matrix equation for this situation is

$$\left[K_O + \sum_{i=1}^{N} p_i [\Delta K_i]\right][\Phi] - \left[M_O + \sum_{i=1}^{N} p_i [\Delta M_i]\right][\Phi][\lambda] = [0], \tag{81}$$

Definition of residual vectors associated with dispersed, independent alterations of a baseline structure is accomplished by first computing the lowest frequency mode shapes of the baseline structure (Eq. 74) as well as the lowest mode shapes associated with each independent alteration of the structure.

$$\left[K_O + \bar{p}_i \Delta K_i\right][\Phi_{iL}] - \left[M_O + \bar{p}_i \Delta M_i\right][\Phi_{iL}][\lambda_{iL}] = [0] \quad (\text{for } i = 1, \ldots, N), \tag{82}$$

The selected value of each independent scaling parameter is sufficiently large to produce a substantial change in mode shapes (with respect to the baseline structure). An initial set of trial vectors that adequately (and perhaps redundantly) encompass all potential (low frequency) altered system mode shapes is

$$[\Psi] = \left[\Phi_{1L}\ \Phi_{2L} \ldots \Phi_{NL}\right] \tag{83}$$

This set of trial vectors is expressible as the sum of (a) a linear combination of baseline system mode shapes and (b) trial vectors (that are linearly independent of the baseline system mode shapes).

$$[\Psi] = [\Phi_{OL}][COR] + \left[\Psi'\right] \tag{84}$$

The cross-orthogonality coefficient matrix is determined based on the following least-squares solution.

$$\left[\Phi_{OL}^{T} M_O \Psi\right] = \left[\Phi_{OL}^{T} M_O \Phi_{OL}\right][COR] + \left[\Phi_{OL}^{T} M_O \Psi'\right] = [I_{OL}][COR] + [0], \tag{85}$$

where,

$$[COR] = \left[\Phi_{OL}^{T}\right][M_O][\Psi] \quad \text{and} \quad \left[\Psi'\right] = \left[I_{OL} - \Phi_{OL}\Phi_{OL}^{T} M_O\right][\Psi] \tag{86}$$

The "purified" trial vector set is linearly independent of the baseline system mode shapes in a manner similar to MacNeal's residual vectors, as follows:

$$\begin{aligned} \left[\Psi'^{T} M_O \Phi_{OL}\right] &= \left[\Psi^{T}\right]\left[I_{OL} - M_O \Phi_{OL}\Phi_{OL}^{T}\right] \\ [M_O \Phi_{OL}] &= \left[\Psi^{T}\right]\left[M_O \Phi_{OL} - M_O \Phi_{OL}\left(\Phi_{OL}^{T} M_O \Phi_{OL}\right)\right] \equiv [0] \end{aligned} \tag{87}$$

$$\begin{aligned} \left[\Psi'^{T} K_O \Phi_{OL}\right] &= \left[\Psi^{T}\right]\left[I_{OL} - M_O \Phi_{OL}\Phi_{OL}^{T}\right][K_O \Phi_{OL}] \\ &= \left[\Psi^{T}\right][K_O \Phi_{OL} - M_O \Phi_{OL}\lambda_{OL}] \equiv [0]. \end{aligned}$$

While the "purified" trial vector set has the above property, it includes an unnecessarily large number of vectors. An appropriate, substantially smaller set of residual vectors is identified by singular value decomposition of the generalized mass matrix.

$$[A] = \left[\Psi'^{T} M_O \Psi'\right], \tag{88}$$

The singular value decomposition process involves solution of the eigenvalue problem,

$$[A]\left[\phi_\rho\right] = \left[\phi_\rho\right]\left[\lambda_\rho\right] \qquad \lambda_{\rho 1} \geq \lambda_{\rho 2} \geq \lambda_{\rho 3} \geq \ldots\ldots \tag{89}$$

The cut-off criterion, noted below employed to define suitable reduced trial vector set, is

$$\frac{\lambda_{\rho N}}{\lambda_{\rho 1}} \leq \text{tol} = 10^{-N} \text{ (where N} \sim 4 \text{ to } 6 \text{ is usually adequate).}$$

The augmented trial vector set (replacing the reduction transformation of Eq. 76) is

$$\left[\overline{\Phi}_{OL}\right] = \left[\,\Phi_{OL}\;\Psi'\phi_\rho\,\right]. \tag{90}$$

The form of the resulting Ritz, multi-parameter sensitivity model (associated with selected values of the scaling parameters) is,

$$\left[k_O + \sum_{i=1}^{N} p_i\,[\Delta k_i]\right][\phi] - \left[m_O + \sum_{i=1}^{N} p_i\,[\Delta m_i]\right][\phi][\lambda] = [0], \text{ where} \tag{91}$$

$$[k_O] = \left[\overline{\Phi}_{OL}^T K_O \overline{\Phi}_{OL}\right],\quad [m_O] = \left[\overline{\Phi}_{OL}^T M_O \overline{\Phi}_{OL}\right],\quad [\Delta k_i] = \left[\overline{\Phi}_{OL}^T \Delta K_i \overline{\Phi}_{OL}\right],$$
$$[\Delta m_i] = \left[\overline{\Phi}_{OL}^T \Delta M_i \overline{\Phi}_{OL}\right].$$

Recovery of mode shapes in terms of physical degrees-of-freedom is accomplished with,

$$[\Phi] = \left[\overline{\Phi}_{OL}\right][\phi]. \tag{92}$$

Since its introduction in 2002 [27], RMA has exhibited the capability to accurately follow modal sensitivity trends over an extremely wide range of parametric variation. The simple cantilevered (planar) beam example, provided in Fig. 12, demonstrates typical RMA performance ("100%" is baseline). Actual cross-orthogonality checks are also excellent.

Additional recent advances and evaluations of the RMA method are found in Reference [31].

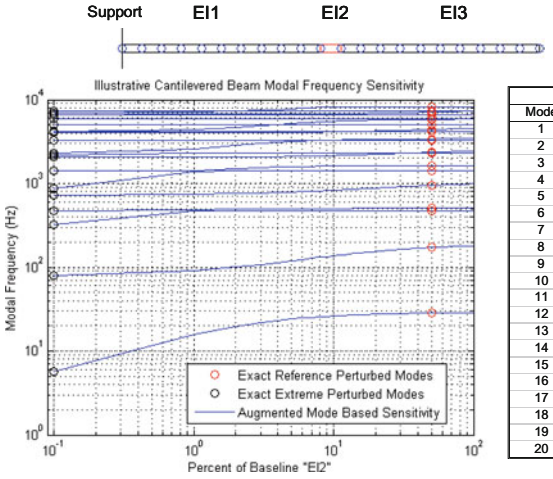

		50% EI2 Loss		99.9% EI2 Loss	
Mode	Baseline	Exact	Approx	Exact	Approx
1	28.78	28.47	28.47	5.71	5.71
2	180.39	172.40	172.40	79.86	79.86
3	467.65	467.65	467.65	320.70	320.70
4	505.11	504.82	504.82	467.65	467.65
5	989.87	950.46	950.46	733.08	733.08
6	1400.30	1400.30	1400.30	870.15	870.15
7	1636.50	1633.60	1633.60	1400.30	1400.30
8	2325.20	2325.20	2325.20	2042.60	2042.60
9	2445.00	2357.10	2357.10	2170.70	2170.70
10	3237.10	3237.10	3237.10	2325.20	2325.20
11	3416.00	3403.70	3403.70	3237.10	3237.10
12	4130.80	4130.80	4130.80	4017.60	4017.60
13	4550.00	4403.90	4403.90	4130.80	4130.80
14	5001.50	5001.50	5001.50	4201.20	4201.20
15	5844.20	5813.10	5813.10	5001.50	5001.50
16	5848.10	5844.20	5844.20	5844.20	5844.20
17	6654.20	6654.20	6654.20	6654.20	6654.20
18	7311.70	7104.70	7104.70	6668.30	6668.30
19	7427.00	7427.00	7427.00	6935.70	6935.70
20	8158.30	8158.30	8158.30	7427.00	7427.00

Fig. 12 RMA sensitivity performance for a cantilevered beam example

5 Concluding Remarks

The aerospace perspective for modeling and validation, particularly in the U.S., is primarily the product of (1) developments and applications in predictive structural dynamics and (2) evolution of an integrated test-analysis process that focuses on the goal of correlation and reconciliation of predicted and measured normal modes of structures. Practices in predictive structural dynamics employ finite element analysis (FEM) and matrix structural analysis methodologies that focus on the assumption of linear behavior of launch vehicles and their spacecraft payloads. The important area of aircraft systems, which is not covered in this chapter, incorporates unique issues associated with the coupling of structural dynamics and aerodynamics (aeroelasticity). The present state of the practice has been heavily influenced by developments in digital computer hardware and computer aided analysis (CAE) over the past 60 years.

Currently accepted best practices in the U.S. aerospace industry include:

1. Definition of linear finite element models of major components (substructures also called "superelements") that faithfully address the frequency band ($0 \leq f \leq f^*$) and intensity of dynamic environments.
2. Description of substructures in terms of component mode models, primarily employing the Hurty-Craig-Bampton (HCB) method. The MacNeal-Rubin (MR) method is rarely employed.
3. Assembly of a launch vehicle/payload system dynamic model and computation of assembled system normal modes based on the HCB or the Benfield-Hruda (BH) component mode synthesis method. The MacNeal-Rubin (MR) method is rarely employed.
4. Incorporation of local nonlinear model features in the launch vehicle/payload system dynamic model, when deemed necessary. Transient dynamic response strategies developed during the Space Shuttle program are particularly relevant; the MR method was employed in these situations.
5. Estimation of detailed structural dynamic stresses and member loads by the mode acceleration method, which (a) accounts for the quasi-static response of all modes above f* and (b) provides a systematic account of "static" and "modal" contributions to stresses and loads. Employment of MacNeal-Rubin residual "modes" is an alternative to the mode acceleration method that satisfies "a" but does not address "b."
6. Verification and validation of component structural dynamic models employing a systematic integrated test-analysis process (ITAP) that include modal test planning, measured data analysis, experimental modal analysis, and test-analysis correlation and model reconciliation.
7. Application of the residual kinetic energy (RKE) method and extensions of RKE for allocation of accelerometer resources for modal testing and test-analysis model (TAM) mass matrix definition. The TAM mass matrix is essential for conventional test mode orthogonality and test-analysis cross-orthogonality evaluations.

8. Adherence to NASA STD-5002 or SMC-C-004, which specifies minimum standards for test mode orthogonality, test-analysis cross-orthogonality, and modal frequency correspondence criteria to assure acceptable verified and validated post-test component structural dynamic models.
9. Utilization of residual mode augmentation (RMA) to enhance accuracy and reliability of structural dynamics modification (SDM) for (large multiple parameter variation) sensitivity analyses to effect component model correlation and reconciliation.

Many other excellent analytical and experimental tools are employed in structural dynamic model verification and validation, which are not uniformly accepted and standardized in U.S. aerospace community practice. It is hoped that accepted practices and standards will become more comprehensive with continuing experiences and unfolding innovations in this community.

References

1. Coppolino R (2014) Variational foundations of modern structural dynamics. IMAC XXXII
2. Hamilton WR (1835) On a general method in dynamics. Phil Trans R Soc
3. Lagrange JL (1788) Mechanique Analitique, Paris
4. Ritz W (1909) Über eine neue Methode zur Lösung gewisser Variationsprobleme der mathematischen Physik. Journal für die Reine und Angewandte Mathematik
5. Toupin RA (1952) A variational principle for the mesh-type analysis of a mechanical system. J Appl Mech 74
6. Trefftz E (1926) Ein Gegenstuck zum Ritzschen Verfahren. In: Proceedings of the 2nd International Congress of Applied Mechanics
7. Galerkin BG (1915) . . . Some questions of elastic equilibrium of rods and plates. Vestnik inzhenerov i tekhnikov 19
8. Coppolino RN (1975) A numerically efficient finite element hydroelastic analysis, vol 1: theory and results, NASA CR-2662, April
9. Zienkiewicz OC, Taylor RL, Zhu JZ (2005) The finite element method, its basis and fundamentals, 6th edn. Elsevier
10. Coppolino R (2010) Chapter 23: finite element methods of analysis. In: Piersol A, Paez T (eds) Harris' shock and vibration handbook, 6th edn. McGraw-Hill
11. Independent structural loads analysis, Air Force Space Command, SMC-S-004 (2008)
12. Load analyses of spacecraft and payloads, NASA-STD-5002 (1996)
13. Paez T (2010) Chapter 8: transient response to step and pulse functions. In: Piersol A, Paez T (eds) Harris' shock and vibration handbook, 6th edn. McGraw-Hill
14. Pilkey W, Pilkey D (eds) (2008) Peterson's stress concentration factors, 3rd edn. Wiley
15. Coppolino R (2016) Structural dynamics modeling – tales of sin and redemption. Sound and Vibration Magazine, January
16. Guyan R (1965) Reduction of stiffness and mass matrices. AIAA J 3
17. Hurty W (1965) Dynamic analysis of structural systems using component modes. AIAA J 3(4)
18. Craig R, Bampton M (1968) Coupling of substructures for dynamic analysis. AIAA J 6(7)
19. Benfield W, Hruda R (1971) Vibration analysis of structures by component mode substitution. AIAA J 9(7)
20. MacNeal RH (1971) A hybrid method for component mode synthesis. Comput Struct 1
21. Rubin S (1975) Improved component-mode representation for structural dynamic analysis. AIAA J 13(8)

22. Coppolino R (1978) Employment of residual mode effects in vehicle/payload dynamic loads analysis, Government/Industry Workshop on Payload Loads Technology, NASA CP-2075
23. Williams D (1945) Dynamic loads on aeroplanes under given impulsive load with particular reference to landing and gust loads on a large flying boat, Great Britain Royal Aircraft Establishment Reports SME 3309 and 3316
24. Coppolino RN, Borowski VJ (1997) Integrated modal testing and analysis of a body-on-frame automobile. In: Proceedings of the 15th IMAC
25. Chen JC, Garba JC (1985) Structural analysis model validation using modal test data. ASME, AMD 67:109–137
26. Coppolino RN (1998) Automated response DOF selection for mapping of experimental normal modes. In: Proceedings of the 16th IMAC
27. Coppolino RN (2002) International Space Station P5 Modal Survey: test planning through FEM reconciliation. In: Proceedings of the 20th IMAC
28. Load analyses of spacecraft and payloads, NASA-STD-5002 (1996)
29. Independent structural loads analysis, air force space command, SMC-S-004 (2008)
30. Coppolino RN (1985) Hybrid experimental/analytical dynamic models of aerospace structures. ASME, AMD 67:79–108
31. Coppolino RN (2018) Methodologies for verification and validation of Space Launch System (SLS) structural dynamic models, NASA CR-2018-219800, vol 1
32. Fox RI, Kapoor MP (1968) Rates of change of eigenvalues and eigenvectors. AIAA J 6
33. Nelson RB (1976) Simplified calculation of eigenvector derivatives. AIAA J 14
34. Avitabile P (2002) Twenty years of structural dynamic modification-a review. In: 20th IMAC
35. Coppolino R (1981) Structural mode sensitivity to local modification, SAE Paper 811044

Applied Math for Experimental Structural Dynamics

25

Chuck Van Karsen and Andrew Barnard

Contents

Abstract

Explanation of the methods, techniques, and theoretical aspects of experimental structural dynamics requires a fundamental understanding of several mathematical concepts. Data acquisition and analysis and their relationship to structural dynamics theory rely on an understanding of *domains* and *transforms*.

C. Van Karsen (✉) · A. Barnard
Mechanical Engineering-Engineering Mechanics Department, Michigan Technological University, Houghton, MI, USA
e-mail: cdvankar@mtu.edu; arbarnar@mtu.edu

R. Allemang, P. Avitabile (eds.), *Handbook of Experimental Structural Dynamics*,
https://doi.org/10.1007/978-1-4614-4547-0_32

Theoretical and computational methods in structural dynamics (modeling, correlation, parameter estimation, etc.) make use of *linear algebra* concepts and techniques. This chapter presents the fundamentals of these concepts and methods.

Keywords

Frequency response function · Transfer function · Fourier transform · Laplace transform · Impulse response function · Linear algebra · Matrix mathematics · Matrix · Singular value decomposition · Eigen problem · Eigen solution · Eigenvalue · Eigenvector · Matrix inverse

Acronyms

ω	Frequency, radians/second
f	Frequency, Hertz (cycles/second)
t	time, seconds
s	Laplace variable, radians/sec
j	$\sqrt{-1}$
a_n, b_n	Fourier Series coefficients
c_n	Fourier Series coefficients (complex form)
θ	Angle, radians
$[A$	]Matrix
$\{x\}$	Vector
$\dot{x}$	First time derivative of x
$\ddot{x}$	Second time derivative of x
$[A_{nxm}]$	Matrix consisting of n rows and m columns
σ	Eigenvalue

1 Domains and Transforms

Experimental structural dynamics uses three primary *domains* to communicate information, system properties, and characteristics of results (predicted or measured). These are the *time* , *frequency*, and *Laplace* domains. These *domains* can be thought of as coordinate systems where the choice of coordinate system depends on the characteristics of the quantity that is being described or communicated. As an example consider the following:

Suppose it is necessary to communicate the geometry of a simple cylinder by describing points in 3D space that lie on the surface of the cylinder, Fig. 1. The easiest way to accomplish this would be to use a cylindrical coordinate system. The same points could also be described using a Cartesian coordinate system as well, although it may be harder to visualize. If the point coordinates exist in cylindrical coordinates, they can be changed to Cartesian by using a *coordinate transformation*, a set of equations which relate (R, θ, Z) to (X, Y, Z). Changing back to cylindrical coordinates is accomplished by using the inverse coordinate

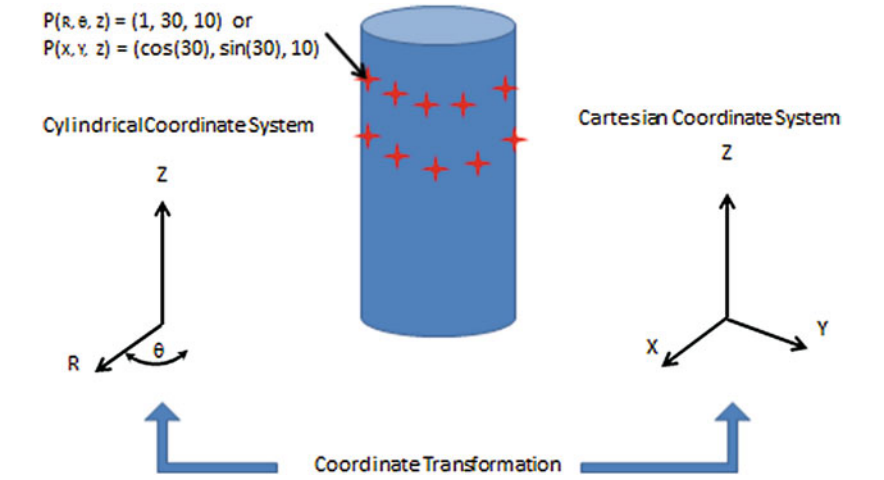

Fig. 1 Coordinate system example

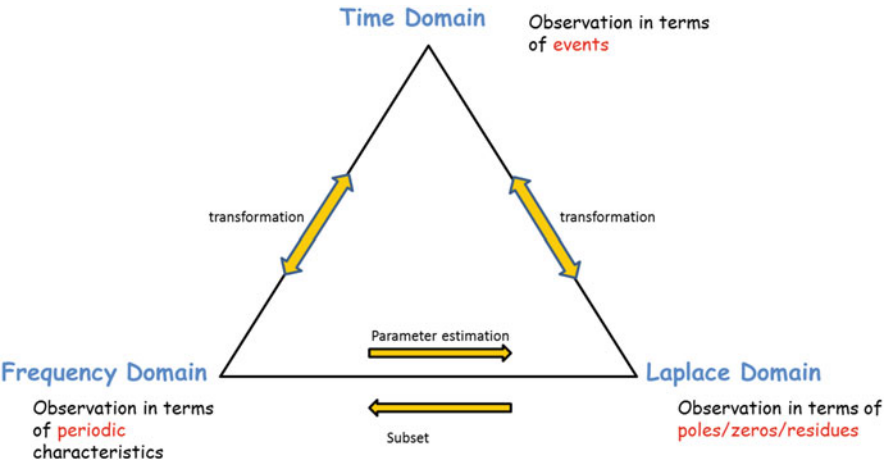

Fig. 2 Domains used in experimental structural dynamics

transformation. Information is not gained or lost with this process; it is only presented in a form that is best suited for the application.

The primary domains (coordinate systems) that are used in experimental structural dynamics are shown in Fig. 2. Experimental data is acquired in the time domain and is observed in terms of events. The fundamental laws of physics which govern structural dynamics are expressed as differential equations with time as the independent variable. Many simulation tools produce results in the time domain as well. Time (t) is typically expressed in units of seconds.

In many cases it is necessary to determine the periodic nature (frequency content) of data. This is accomplished by transforming from the time to the frequency domain using the Fourier transform. The frequency domain is complex valued having both real (cosine) and imaginary (sine) components. Information can be transformed back and forth between the time and frequency domains without any gain or loss of information. Frequency (ω) is expressed in units of radians per second. Alternatively frequency (f) can be expressed in units of Hertz (cycles per second) $\omega = 2\pi f$.

The Laplace domain is used to observe a system or structure's characteristics in terms of poles and zeros or poles and residues. This is accomplished by transforming from the time to the Laplace domain using the Laplace transform. The Laplace domain is complex valued, having both real and imaginary components. Information can be transformed back and forth between the time and Laplace domains without any gain or loss of information. The Laplace variable ($s = \sigma + j\omega$) is expressed in units of radians per second and is complex valued having a real part σ, and an imaginary part ω.

An important relationship in structural dynamics is the ratio between output of a system or structure to an input to the system or structure. This relationship is expressed as an impulse response function in the time domain, a frequency response function in the frequency domain, and as a transfer function in the Laplace domain. An example of this relationship for a single degree of freedom system is shown in Fig. 3.

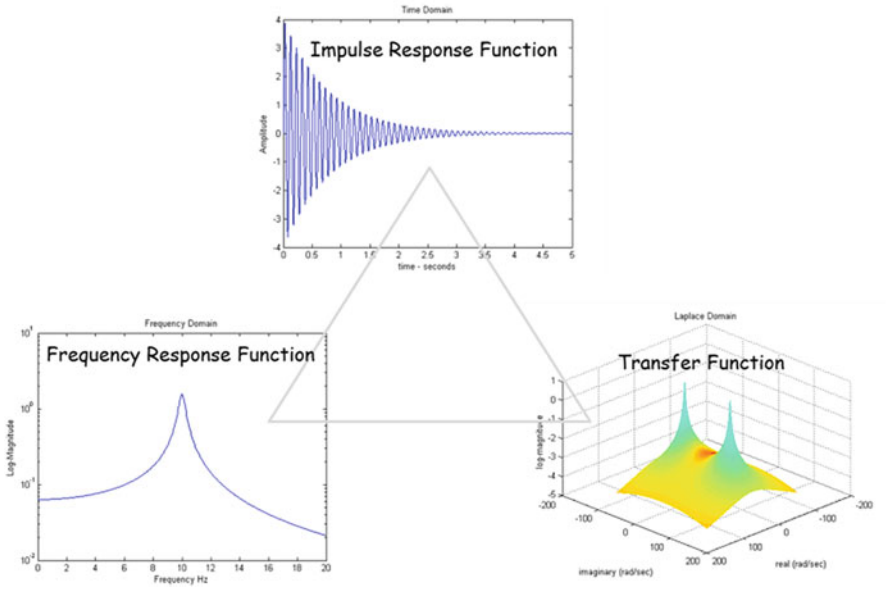

Fig. 3 SDOF input-output relationships in each domain

The mathematical descriptions of these functions in pole residue form for a single degree of freedom system are:

Impulse response function:

$$h(t) = Ae^{\lambda t} + A^* e^{\lambda^* t} \tag{1}$$

Frequency response function:

$$H(\omega) = \frac{A}{j\omega - \lambda} + \frac{A^*}{j\omega - \lambda^*} \tag{2}$$

Transfer function:

$$H(s) = \frac{A}{s - \lambda} + \frac{A^*}{s - \lambda^*} \tag{3}$$

The parameters which are characteristics of the system's input-output relationship, A, λ, are seen in each domain's mathematical description. It should be noted that the Fourier transform of the impulse response function is the frequency response function and the Laplace transform of the impulse response function results in the transfer function.

1.1 Frequency Domain

Transformation between the time and frequency domain can be accomplished in one of three ways:

1. Fourier series
2. Integral Fourier transform
3. Discrete Fourier transform (DFT)

The choice of method depends on the nature and form of the time domain information (data). The Fourier series and integral Fourier transform are used when continuous time histories are available. The DFT is used for discrete (sampled) time histories.

Any time history that is periodic with respect to time, Fig. 4, can be expressed by the following trigonometric function which is known as a Fourier series (In addition the time history must have a finite number of discontinuities within any period, it must have a finite number of maxima and minima within any period, and it must be absolutely integrable over any period. These are known as the *Dirichlet* conditions.):

$$X(t) = \frac{a_0}{2} + \sum_{n=1}^{\infty} a_n \cos(2\pi n f t) + b_n \sin(2\pi n f t) \tag{4}$$

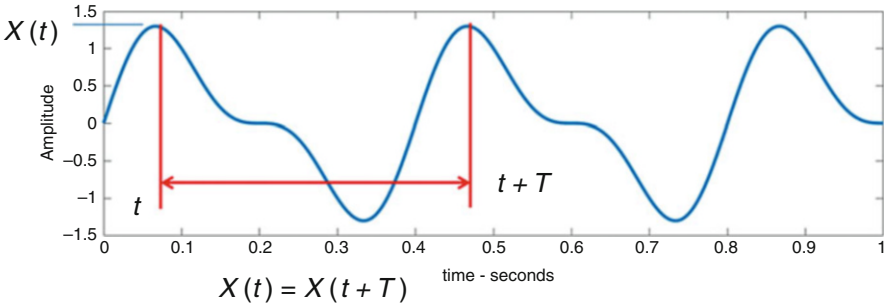

Fig. 4 Periodic time history

where:

$$f = \frac{1}{T}$$

$$a_n = \frac{2}{T}\int_t^{t+T} X(t)\cos(2\pi nft)\,dt$$

$$b_n = \frac{2}{T}\int_t^{t+T} X(t)\sin(2\pi nft)\,dt$$

The a_n and b_n coefficients provide a description of the information (data) in the frequency domain. The a_n's represent frequency content that is co-sinusoidal with respect to time t, and the b_n's represent frequency content that is sinusoidal with respect to time t.

Using Euler's identity, $e^{\pm i\theta} = \cos\theta \pm i\sin\theta$, the trigonometric form of the Fourier series can be written in complex exponential form:

$$X(t) = \sum_{n=-\infty}^{\infty} c_n e^{i2\pi nft} \tag{5}$$

where

$$c_n = \frac{1}{T}\int_t^{t+T} X(t)e^{-i2\pi nft}dt \quad \text{for } n = \pm(1, 2, 3, \ldots)$$

$$c_0 = a_0$$

$$c_n = \frac{\left(a_n^2 + b_n^2\right)^{1/2}}{2} \quad \text{for } n = \pm(1, 2, 3, ..)$$

The c_n's are complex valued with the real part representing frequency content that is co-sinusoidal with respect to time t, and the imaginary part representing frequency content is sinusoidal with respect to time t.

In either formulation the Fourier series is a simple concise method for expressing the periodic properties of time information in the frequency domain and considering experimental data or the results of a simulation all that is required is knowledge of the period (T).

1.1.1 Integral Fourier Transform

There are many situations where the time domain data is not periodic or has a finite length with no period. In order to transform these types of data to the frequency domain, it is necessary to use the integral Fourier transform.

$$\begin{aligned} X(f) &= \int_{-\infty}^{\infty} X(t) e^{-i2\pi ft} dt \quad \text{time to frequency} \\ X(t) &= \int_{-\infty}^{\infty} X(f) e^{i2\pi ft} df \quad \text{frequency to time} \end{aligned} \tag{6}$$

For a given set of time data $X(t)$, the integral Fourier transform will determine the amount of frequency content at any frequency f. The only issue is the limits on the integration. If the integration time is truncated, the frequency domain result will be incorrect. An example of this is shown in Fig. 5.

For other properties of the integral Fourier transform, see references.

Implementation and limitations of the integral Fourier transform on sampled data is presented in ▸ Chap. 4, "Applied Digital Signal Processing."

2 Linear Algebra

2.1 Basic Concepts and Definitions

The analysis of information in both the test and analytical aspects of structural dynamics requires the efficient manipulation and interrogation of large data sets, and therefore the use of matrix and vector algebra is a mandatory requirement. In this context there are fundamentally two types of problems to be solved:

Systems described by coupled algebraic expressions:

$$[A]\{x\} = \{b\} \tag{7}$$

And systems described by coupled ordinary differential equations:

$$[M]\{\ddot{x}\} + [C]\{\dot{x}\} + [K]\{x\} = \{F(t)\} \tag{8}$$

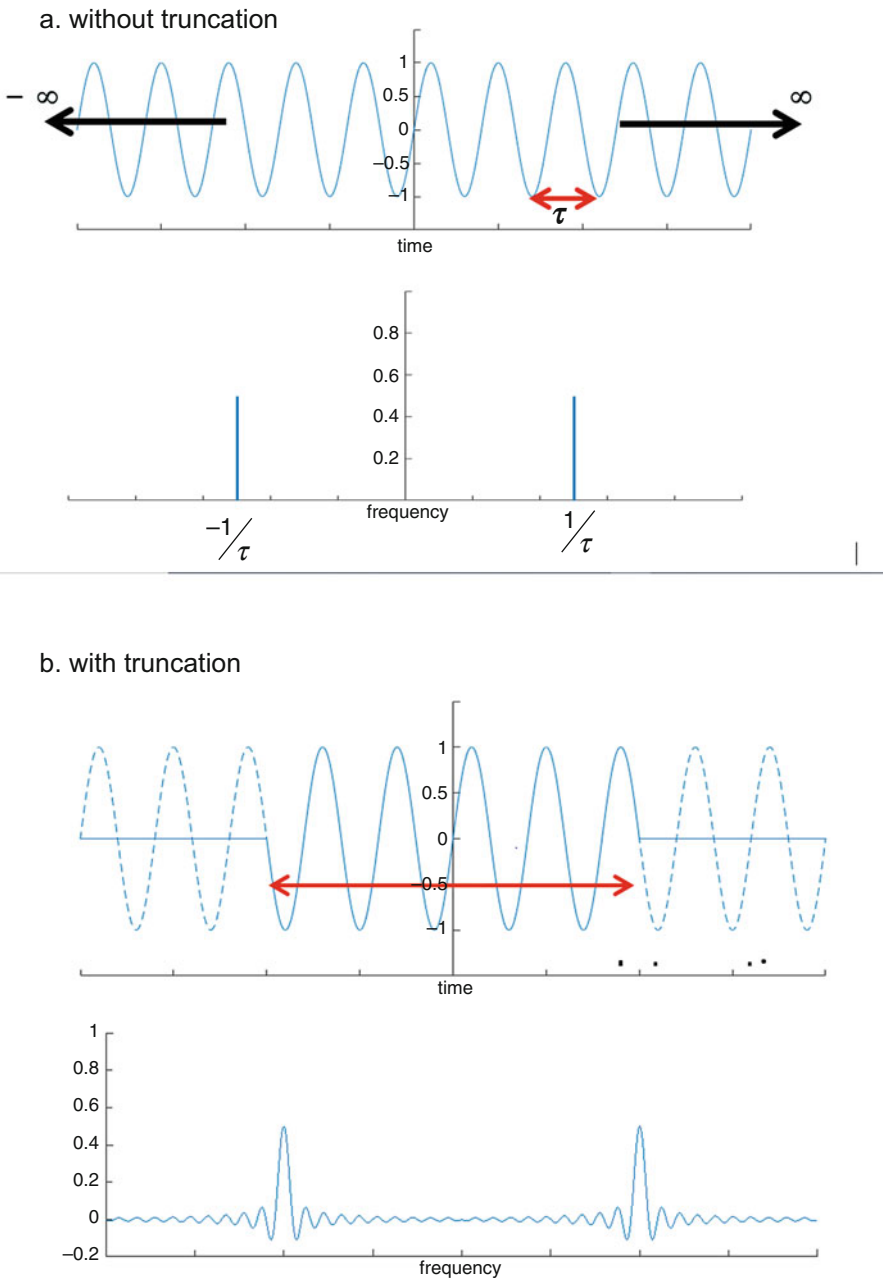

Fig. 5 Integral Fourier transform ((**a**) without truncation, (**b**) with truncation)

For systems described by matrix expressions, there are three cases which can occur:

$$[A]_{nxm}\{x\}_{mx1} = \{b\}_{nx1} \tag{9}$$

1. *Underdetermined*: $n < m$ applications include optimization, finite element model updating, and projection of data onto subspaces.
2. *Determined*: $n = m$ applications include analytical structural dynamics using finite element models.
3. *Overdetermined*: $n > m$ applications include time and frequency domain parameter estimation, least squares applications, and sensor placement algorithms.

Two basic entities are used in the language of linear algebra, a *matrix* and a *vector*. A matrix is an array of numbers or expressions. The elements of the matrix are referred to by their row/column location in the matrix.

$$[A] = \begin{bmatrix} a_{11} & a_{12} & a_{13} \\ a_{21} & a_{22} & a_{23} \\ a_{31} & a_{32} & a_{33} \end{bmatrix} \tag{10}$$

A vector is a special case of a matrix which has only one row or column.

$$\{b\} = \begin{Bmatrix} b_1 \\ b_2 \\ b_3 \\ b_4 \end{Bmatrix} \quad \text{or} \quad \langle c \rangle = \langle c_1 \;\; c_2 \;\; c_3 \;\; c_4 \rangle \tag{11}$$

A diagonal matrix has nonzero terms only on the diagonal:

$$[D] = \begin{bmatrix} d_{11} & & & \\ & d_{22} & & \\ & & d_{33} & \\ & & & d_{44} \end{bmatrix} \quad d_{nm} = 0 \;\; \text{for} \;\; n \neq m \tag{12}$$

There are several elementary rules for matrix operations.
Matrix addition:

$$[C]_{ixj} = [A]_{nxm} + [B]_{pxq} \quad i = n = p \qquad j = m = q \qquad c_{ij} = a_{nm} + b_{pq}$$

$$[A] = \begin{bmatrix} 1 & 2 \\ 3 & 4 \end{bmatrix} \quad [B] = \begin{bmatrix} 5 & 6 \\ 7 & 8 \end{bmatrix} \quad [C] = [A] + [B] = \begin{bmatrix} 1 & 2 \\ 3 & 4 \end{bmatrix} + \begin{bmatrix} 5 & 6 \\ 7 & 8 \end{bmatrix} = \begin{bmatrix} 6 & 8 \\ 10 & 12 \end{bmatrix} \tag{13}$$

Multiplication by a scalar:

$$k\,[A] = \begin{bmatrix} ka_{11} & ka_{12} & ka_{13} \\ ka_{21} & ka_{22} & ka_{23} \\ ka_{31} & ka_{32} & ka_{33} \end{bmatrix} \tag{14}$$

Multiplication of two matrices:

$$[A]\,[B] \neq [B]\,[A] \quad \text{NOT commutative} \tag{15}$$

$$([A]\,[B])\,[C] = [A]\,([B]\,[C]) \quad \text{Associative} \tag{16}$$

$$([A] + [B])\,([C] + [D]) = [A]\,[C] + [A]\,[D] + [B]\,[C] + [B]\,[D] \tag{17}$$

Matrix cancelation:

$$\begin{gathered} [A]\,[B] = [0] \quad \text{Implies one of the following;} \\ [A] = [0] \\ [B] = [0] \\ [A] \text{ and } [B] \text{ are singular} \end{gathered} \tag{18}$$

Matrix multiplication:

$$\begin{gathered} [A]_{nxm}\,[B]_{pxq} = [C]_{nxq} \text{ requirement } m = p \\ \begin{bmatrix} a_{11} & a_{12} & a_{13} \\ a_{21} & a_{22} & a_{23} \\ a_{31} & a_{32} & a_{33} \end{bmatrix} \begin{bmatrix} b_{11} & b_{12} \\ b_{21} & b_{22} \\ b_{31} & b_{32} \end{bmatrix} = \begin{bmatrix} c_{11} & c_{12} \\ c_{21} & c_{22} \\ c_{31} & c_{32} \end{bmatrix} \\ c_{21} = a_{21}b_{11} + a_{22}b_{21} + a_{23}b_{31} \\ c_{ij} = \sum_{k=1}^{m} a_{ik}b_{kj} \end{gathered} \tag{19}$$

Two special matrices are often used:

Identity matrix

$$[I] = \begin{bmatrix} 1 & 0 & 0 & 0 \\ 0 & 1 & 0 & 0 \\ 0 & 0 & 1 & 0 \\ 0 & 0 & 0 & 1 \end{bmatrix} \tag{20}$$

$1'$s on the diagonal, zeros elsewhere

Zero matrix

$$[0] = \begin{bmatrix} 0\ 0\ 0 \\ 0\ 0\ 0 \\ 0\ 0\ 0 \end{bmatrix} \quad \text{Zeros in all locations} \tag{21}$$

The transpose of a matrix is formed by interchanging rows and columns.

$$[A] = \begin{bmatrix} 1\ 2\ 3 \\ 4\ 5\ 6 \\ 7\ 8\ 9 \end{bmatrix} \qquad [A]^T = \begin{bmatrix} 1\ 4\ 7 \\ 2\ 5\ 8 \\ 3\ 6\ 9 \end{bmatrix} \tag{22}$$

If complex numbers are entities of the matrix, a Hermitian transpose (or Hermitian) is formed by interchanging rows and columns and then taking the complex conjugate.

$$[A] = \begin{bmatrix} 1-2i & 4 & 2+4i \\ 3-9i & 9 & 11-i \\ 3 & 1+i & -4-8i \end{bmatrix} \qquad [A]^H = \begin{bmatrix} 1+2i & 3+9i & 3 \\ 4 & 9 & 1-i \\ 2-4i & 11+i & -4+8i \end{bmatrix} \tag{23}$$

2.2 Transposition Rules

The following rules apply to matrix transposition :

$$\begin{aligned} &([A]+[B])^T = [A]^T + [B]^T \\ &\left[[A]^T\right]^T = [A] \\ &([A]\,[B])^T = [B]^T [A]^T \\ &([A]\,[B]\,[C])^T = [C]^T [B]^T [A]^T \end{aligned} \tag{24}$$

2.3 Special Matrix Forms

Symmetric $[A] = [A]^T$

Skew Symmetric $[A] = -[A]^T$

$$[A] = \begin{bmatrix} 1\ 2\ 3 \\ 2\ 4\ 5 \\ 3\ 5\ 6 \end{bmatrix} \qquad [A] = \begin{bmatrix} 0 & 2 & 3 \\ -2 & 0 & -5 \\ -3 & 5 & 0 \end{bmatrix} \tag{25}$$

Hermitian $[A] = [A]^H$

Skew Hermitian $[A] = -[A]^H$

$$[A] = \begin{bmatrix} 1 & 6+5i & 4i \\ 6-5i & 6 & 7-8i \\ -4i & 7+8i & 0 \end{bmatrix} \qquad [A] = \begin{bmatrix} i & 2+2i & 8 \\ -(2-2i) & 8i & -(6-3i) \\ 8 & 6+3i & 0 \end{bmatrix}$$

Diagonal terms are real — Diagonal terms are imaginary or zero (26)

2.4 Symmetric Matrix Rules

The following rules apply to symmetric matrices:

$$\begin{aligned} &[A] = [A]^T; \quad [B] = [B]^T; \quad [A][B] \neq ([A][B])^T \\ &[A] = [A]^T; \quad [C] = [B]^T [A][B]; \quad [C] = [C]^T \end{aligned} \tag{27}$$

$$\begin{aligned} &\text{Orthogonal} \quad [A][A]^T = [A]^T [A] = [I] \\ &\text{Unitary} \quad [A][A]^H = [A]^H [A] = [I] \\ &\text{Idempotent} \quad [A]^m = [A] \quad \text{any positive integer } m \\ &\text{Nilpotent} \quad [A]^k = [0] \quad \text{any positive integer } k \end{aligned} \tag{28}$$

For a Toeplitz matrix, all elements on any diagonal are equal. This matrix is often used in time domain identification techniques.

$$[T] = \begin{bmatrix} t_1 & t_5 & t_6 & t_7 \\ t_2 & t_1 & t_5 & t_6 \\ t_3 & t_2 & t_1 & t_5 \\ t_4 & t_3 & t_2 & t_1 \end{bmatrix} \tag{29}$$

A Toeplitz matrix is useful in computing the convolution of discrete data.

$$y(k) = \sum_{i=0}^{k} H(k)u\,(k-i)$$

$$\begin{bmatrix} H_0 & H_1 & H_2 & H_3 & H_4 \\ 0 & H_0 & H_1 & H_2 & H_3 \\ 0 & 0 & H_0 & H_1 & H_2 \\ 0 & 0 & 0 & H_0 & H_1 \\ 0 & 0 & 0 & 0 & H_0 \end{bmatrix} \begin{Bmatrix} u_4 \\ u_3 \\ u_2 \\ u_1 \\ u_0 \end{Bmatrix} = \begin{Bmatrix} y_4 \\ y_3 \\ y_2 \\ y_1 \\ y_0 \end{Bmatrix} \tag{30}$$

The Hankel matrix has all elements on any diagonal perpendicular to the main diagonal equal to each other. This matrix is used in the Eigensystem realization algorithm (ERA) modal parameter estimation method.

$$[H] = \begin{bmatrix} h_1 & h_2 & h_3 & h_4 \\ h_2 & h_3 & h_4 & h_5 \\ h_3 & h_4 & h_5 & h_6 \\ h_4 & h_5 & h_6 & h_7 \end{bmatrix} \tag{31}$$

In a Vandermonde matrix, the first column is 1, and successive columns are the second column raised to increasing integer powers.

$$[V] = \begin{bmatrix} 1 & v_1 & v_1^2 & v_1^3 \\ 1 & v_2 & v_2^2 & v_2^3 \\ 1 & v_3 & v_3^2 & v_3^3 \\ 1 & v_4 & v_4^2 & v_4^3 \\ 1 & v_5 & v_5^2 & v_5^3 \end{bmatrix} \tag{32}$$

This matrix occurs in curve fitting and some frequency domain parameter estimation algorithms.

2.5 Matrix Measures (Determinant and Trace)

There are two common matrix measures: determinant and trace. A determinant is only defined for square matrices and is equal to zero if the matrix is singular.

$$\begin{aligned} |[A]| &= \left| \begin{pmatrix} a_{11} & a_{12} \\ a_{21} & a_{22} \end{pmatrix} \right| = a_{11}a_{22} - a_{12}a_{21} \\ |[A]| &= \left| \begin{pmatrix} a_{11} & a_{12} & a_{13} \\ a_{21} & a_{22} & a_{23} \\ a_{31} & a_{32} & a_{33} \end{pmatrix} \right| = a_{11} \begin{vmatrix} a_{22} & a_{23} \\ a_{32} & a_{33} \end{vmatrix} - a_{12} \begin{vmatrix} a_{21} & a_{23} \\ a_{31} & a_{33} \end{vmatrix} + a_{13} \begin{vmatrix} a_{21} & a_{22} \\ a_{31} & a_{32} \end{vmatrix} \\ |[A]\,[B]| &= |[A]|\,|[B]| \qquad |[A]| = \left|[A]^T\right| \quad \left|[A]^*\right| = \left|[A]^H\right| \\ |k\,[A]| &= \left|k^n\,[A]\right| \quad \text{for } [A]_{nxn} \\ &\qquad\qquad \text{where } * \text{ indicates the complex conjugate} \end{aligned} \tag{33}$$

The trace is simply the sum of the diagonal elements of a square matrix.

$$tr\,([A]) = \sum_{i=1}^{n} a_{ii} \tag{34}$$

2.6 Vector Space

The set of all n dimensional vectors make up an n-dimensional vector space, R^n. n vectors $\{e\}_i$ in R^n are considered as linearly independent if the equation:

$$0 = a_1\{e\}_1 + a_2\{e\}_2 + a_3\{e\}_3 \ldots a_n\{e\}_n \tag{35}$$

only has a solution when all constants a_i are zero. In this case the n vectors $\{e\}_i$ span the vector space. Any n-dimensional vector $\{x\}$ can be expressed uniquely as a linear combination of the n linearly independent vectors $\{e\}_i$:

$$\{x\} = b_1\{e\}_1 + b_2\{e\}_2 + b_3\{e\}_3 \ldots b_n\{e\}_n \tag{36}$$

2.7 Vector Space Applied to Matrices

Consider this matrix equation, $[A]_{nxm}\{x\}_{mx1} = \{b\}_{nx1}$. The rank of a matrix is the number of linearly independent columns or rows rank$([A]) = r$.

$$\begin{aligned} &\text{rank}\,([A]) = m \quad [A] \text{ is full column rank}\,. \\ &\text{rank}\,([A]) = r < m, n \quad [A] \text{ is rank deficient.If } [A] \text{ is square, then it is singular.} \end{aligned} \tag{37}$$

Column space of $[A]$ is the vector space spanned by its columns.
Row space of $[A]$ is the vector space spanned by its rows.
The null space of $[A]$ is the set of vectors $\{x\}$ that satisfies $[A]\{x\} = \{0\}$.

2.8 Spectral Decomposition

In most cases a square matrix $[A]$ can be decomposed into a product of three matrices:

$$[A] = [\Phi]\,[\Omega]\,[\Phi]^{-1} \tag{38}$$

where $[\Omega]$ is a diagonal matrix of eigenvalues λ_i and the matrix $[\Phi]$ is made up of column vectors $\{\phi\}_i$ called eigenvectors. This means that $[A]$ can be diagonalized $[\Phi]^{-1}[A][\Phi] = [\Omega]$. Eigenvalues and eigenvectors satisfy the eigenvalue problem $([A] - \lambda_i[I])\{\phi\}_i$, and eigenvalues satisfy the characteristic equation $|([A] - \lambda_i[I])| = 0$.

A matrix $[A]$ is diagonalizable if it has n linearly independent eigenvectors. If $[A]$ has distinct eigenvalues, it is diagonalizable.

$$\begin{bmatrix} \phi_{11} & \phi_{12} \\ \phi_{21} & \phi_{22} \end{bmatrix}^{-1} \begin{bmatrix} a_{11} & a_{12} \\ a_{21} & a_{22} \end{bmatrix} \begin{bmatrix} \phi_{11} & \phi_{12} \\ \phi_{21} & \phi_{22} \end{bmatrix} = \begin{bmatrix} \lambda_1 & 0 \\ 0 & \lambda_2 \end{bmatrix} \tag{39}$$

Real symmetric matrices are always diagonalizable and have real eigenvalues and eigenvectors. The eigenvector matrix is orthogonal:

$$[\Phi]^T = [\Phi]^{-1} \quad \therefore \quad [\Phi]^T [A] [\Phi] = [\Omega] \tag{40}$$

2.9 Singular Value Decomposition

Any *n x m* matrix $[A]$ of rank *r* can be decomposed into a product of three matrices:

$$\begin{aligned} & & [U]_{nxn} \\ [A] = [U][S][V]^H & & [S]_{nxm} \\ & & [V]_{mxm} \\ [U] \text{ and } [V] \text{ are unitary} & & [U]^H [U] = [V]^H [V] = [I] \end{aligned} \tag{41}$$

These matrices can be partitioned such that:

$$\begin{aligned} [A] = \begin{bmatrix} [U_1] & [U_2] \end{bmatrix} \begin{bmatrix} [\Sigma] & [0] \\ [0] & [0] \end{bmatrix} \begin{bmatrix} [V_1]^H \\ [V_2]^H \end{bmatrix} \qquad & [U_1]_{nxr} \quad [U_2]_{nx(n-r)} \\ [\Sigma] \text{ is diagonal} \qquad & [V_1]_{mxr} \quad [V_2]_{mx(m-r)} \end{aligned} \tag{42}$$

As a result:

$$[A] = [U_1][\Sigma][V_1]^H \quad \Rightarrow \quad [A] = \sum_{i=1}^{r} \{u_1\}_i \sigma_i \{v_1\}_i^H \tag{43}$$

Singular values are real and satisfy the following relationship:

$$[\Sigma]_{rxr} = \begin{bmatrix} \sigma_1 & 0 & 0 & \cdots \\ 0 & \sigma_2 & 0 & \cdots \\ 0 & 0 & \ddots & \cdots \\ \vdots & \vdots & \vdots & \sigma_r \end{bmatrix} \quad \sigma_1 \geq \sigma_2 \geq \cdots \geq \sigma_r > 0 \tag{44}$$

The number of nonzero singular values is the rank, *r*, of $[A]$.

$$
\begin{aligned}
\sigma_i^2, \{u_1\}_i &\quad \text{are the eigenvalues and eigenvectors of } [A]\,[A]^T \\
\{u_2\}_i &\quad \text{are the eigenvectors of } [A]\,[A]^T \text{ with zero eigenvalues} \\
\sigma_i^2, \{v_1\}_i &\quad \text{are the eigenvalues and eigenvectors of } [A]^T\,[A] \\
\{v_2\}_i &\quad \text{are the eigenvectors of } [A]^T\,[A] \text{ with zero eigenvalues} \\
[U_1] &\quad \text{spans the column space of } [A] \\
[U_2] &\quad \text{spans the column null space of } [A] \\
[V_1]^T &\quad \text{spans the row space of } [A] \\
[V_2]^T &\quad \text{spans the row null space of } [A]
\end{aligned}
\tag{45}
$$

2.10 Eigen Solutions

Two, square, nonsingular, symmetric matrices can be decomposed into their associated eigenvalues and eigenvectors.

$$
\begin{aligned}
&[[A] - \lambda\,[B]]_{nxn}\,\{X\} = \{0\} \\
&\lambda_1, \lambda_2, \cdots \lambda_n \quad \text{are the eigenvalues,} \\
&\text{and } \{x\}_1, \{x\}_2, \cdots \{x\}_n \text{ are the associated eigenvectors}
\end{aligned}
\tag{46}
$$

2.11 Inverse Problems

2.11.1 Solution of Determined Equations

When a system of equations has as many independent equations as unknowns, a unique solution will always exist.

$$
\begin{aligned}
&[A]_{nxn}\{x\}_{nx1} = \{b\}_{nx1} \quad [A] \text{ is square, full rank and invertible} \\
&\{x\} = [A]^{-1}\,\{b\} \qquad \{b\} \text{ is alwys in the range space of } [A] \\
&[A]^{-1} \text{ is the matrix inverse of } [A]
\end{aligned}
\tag{47}
$$

The inverse of a nonsingular matrix $[A]$ is a matrix $[A]^{-1}$ that when multiplied by $[A]$ is the identity matrix.

$$
[A]\,[A]^{-1} = [A]^{-1}\,[A] = [I] \tag{48}
$$

Matrix inverses have the following properties.

$$\begin{aligned}
([A]\,[B])^{-1} &= [B]^{-1}[A]^{-1} \\
\left([A]^{T}\right)^{-1} &= \left([A]^{-1}\right)^{T} \\
\left([A]^{H}\right)^{-1} &= \left([A]^{-1}\right)^{H} \\
(k\,[A])^{-1} &= \frac{1}{k}[A]^{-1} \\
\left|[A]^{-1}\right| &= \frac{1}{|[A]|}
\end{aligned} \tag{49}$$

There are many methods for inverting a matrix. One that is particularly relevant in the field of structural dynamics is the adjoint method. The adjoint of $[A]$ is a matrix where the elements are the cofactors of $[A]$ transposed. The cofactors of $[A]$ are the signed minor determinants.

$$[A]^{-1} = \frac{\left[\text{Adjoint}\,([A])\right]}{|[A]|} \tag{50}$$

$$\text{Cofactor}([A])_{ij} = c_{ij} = (-1)^{i+j}\left|\left[M_{ij}\right]\right|$$
$$\left[M_{ij}\right] \text{ is a submatrix of } [A] \text{ obtained by deleting the } i\text{th row and } j\text{th column} \tag{51}$$

$$[A] = \begin{bmatrix} a & b & c \\ d & e & f \\ g & h & i \end{bmatrix} \quad \Rightarrow \quad [A]^{-1} = \frac{\text{adjoint}\,([A])}{|[A]|} = \frac{\begin{bmatrix} +\begin{vmatrix} e & f \\ h & i \end{vmatrix} & -\begin{vmatrix} b & c \\ h & i \end{vmatrix} & +\begin{vmatrix} b & c \\ e & f \end{vmatrix} \\ -\begin{vmatrix} d & f \\ g & i \end{vmatrix} & +\begin{vmatrix} a & c \\ g & i \end{vmatrix} & -\begin{vmatrix} a & c \\ d & f \end{vmatrix} \\ +\begin{vmatrix} d & e \\ g & h \end{vmatrix} & -\begin{vmatrix} a & b \\ g & h \end{vmatrix} & +\begin{vmatrix} a & b \\ d & e \end{vmatrix} \end{bmatrix}}{|[A]|} \tag{52}$$

2.12 LU Decomposition

LU decomposition can be used to calculate determinants and matrix inverses, and therefore it is useful in the solution of determined equations. Any nonsingular square matrix $[A]$ can be factored into the product of two matrices:

$$[A] = [L]\,[U] \tag{53}$$

$[L]$ is a lower triangular matrix, and $[U]$ is an upper triangular matrix.

$$[A] = \begin{bmatrix} 6 & -2 & -4 & 4 \\ 3 & -3 & -6 & 1 \\ -12 & 8 & 21 & -8 \\ -6 & 0 & -10 & 7 \end{bmatrix} \Rightarrow [L] = \begin{bmatrix} 2 & 0 & 0 & 0 \\ 1 & -1 & 0 & 0 \\ -4 & 2 & 1 & 0 \\ -2 & -1 & -2 & 2 \end{bmatrix} [U] = \begin{bmatrix} 3 & -1 & -2 & 2 \\ 0 & 2 & 4 & 1 \\ 0 & 0 & 5 & -2 \\ 0 & 0 & 0 & 4 \end{bmatrix} \tag{54}$$

In terms of LU decomposition, the matrix inverse is:

$$[A]^{-1} = ([L][U])^{-1} = [U]^{-1}[L]^{-1} \tag{55}$$

The determinant becomes the product of the determinants of the decomposition matrices.

$$|[A]| = |[L]|\,|[U]| \tag{56}$$

The solution to a set of determined equations can be found algebraically without the calculation of an inverse.

$$\begin{aligned} [A]\{x\} = \{b\} \quad &\Rightarrow \quad [L][U]\{x\} = \{b\} \\ [L]\{z\} = \{b\} \quad &\text{solved using forward substitution} \\ [U]\{x\} = \{z\} \quad &\text{solved using backward substitution} \end{aligned} \tag{57}$$

2.12.1 Solution of Underdetermined Equations

An underdetermined condition exists when the number of independent equations is less than the number of unknowns.

$$[A]_{nxm}\{x\}_{mx1} = \{b\}_{nx1} \quad n < m \tag{58}$$

$[A]$ is rectangular with more columns than rows and is assumed to be full-row rank. A solution will always exist, but there are an infinite number of solutions. $\{b\}$ is always in the column space of $[A]$. If $\{x\}_1$ is a solution and $\{x\}_N$ is any vector in the null space of $[A]$, then the linear combination, $\{x\}_s = \{x\}_1 + \{x\}_N$, is also a solution.

A solution is obtained in the following manner. Begin by defining a new vector $\{x\} = [A]^T\{z\}$. The original matrix equation becomes:

$$[A][A]^T\{z\} = \{b\} \tag{59}$$

Since $[A]$ is full-row rank, $[A][A]^T$ is nonsingular and can be inverted.
Solving for$\{x\}$:

$$\begin{aligned} \{z\} &= \left([A]\,[A]^T\right)^{-1}\{b\} \\ \{x\}_+ &= [A]^T\{z\} = [A]^T\left([A]\,[A]^T\right)^{-1}\{b\} \\ [A]^+ &= [A]^T\left([A]\,[A]^T\right)^{-1} \quad \text{Right Generalized Inverse of } [A] \end{aligned} \tag{60}$$

Since there are an infinite number of solutions, which solution is $\{x\}_+$, for any arbitrary solution $\{x\}_s$:

$$\begin{aligned} \{b\} &= [A]\,\{x\}_s \\ \{x\}_+ &= [A]^T\left([A]\,[A]^T\right)^{-1}[A]\,\{x\}_s = [P]\,\{x\}_s \\ [P] &= [A]^T\left([A]\,[A]^T\right)^{-1}[A] \\ \{x\}_+ &= [P]\,\{x\}_s \end{aligned} \tag{61}$$

$\{x\}_+$ is the orthogonal projection of the general solution $\{x\}_s$ onto the row space $[A]$ or the column space of $[A]^T$. $\{x\}_+$ is the minimum norm (length) solution, and $[P]$ is an orthogonal projector.

2.12.2 Solution of Overdetermined Equations

An overdetermined condition exists when the number of independent equations is greater than the number of unknowns.

$$[A]_{nxm}\{x\}_{mx1} = \{b\}_{nx1} \quad n > m \tag{62}$$

$[A]$ is rectangular with more rows than columns and is assumed to be full-column rank. $\{b\}$ may or may not be in the column space of $[A]$. If $\{b\}$ is in the row space of $[A]$, a unique solution exists. If $\{b\}$ is not in the row space of $[A]$, no exact solution exists, but an approximate solution can be found. A solution is obtained in the following manner. Begin by pre-multiplying by the transpose of $[A]$:

$$\left([A]^T\,[A]\right)\{x\} = [A]^T\,\{b\} \tag{63}$$

Since $[A]$ is full-column rank, $[A][A]^T$ is nonsingular and can be inverted. Solving for $\{x\}$:

$$\begin{aligned} &\{x\} = \left([A]^T\,[A]\right)^{-1}[A]^T\,\{b\} \\ &[A]^+ = \left([A]^T\,[A]\right)^{-1}[A]^T \quad \text{Left Generalized Inverse of} \quad [A] \end{aligned} \tag{64}$$

Combining this solution with the original equation:

$$[A]\,\{X\} = [A]\left([A]^T\,[A]\right)^{-1}[A]^T\,\{b\} = \left[\hat{P}\right]\{b\} = \left\{\hat{b}\right\} \tag{65}$$

$\left[\hat{P}\right]$ is an orthogonal projector onto the row space of $[A]$. $\left\{\hat{b}\right\}$ is the orthogonal projection of $\{b\}$ onto the row space of $[A]$.

If $\{b\}$ is in the row space of $[A]$, $\{b\} \in R[A]$

$$\begin{aligned} &\{x\} = \left([A]^T\,[A]\right)^{-1}[A]^T\,\{b\} \\ &\left[\hat{P}\right]\{b\} = \{b\} \\ &\{x\} \quad \text{is a unique solution to} \quad [A]\,\{x\} = \{b\} \end{aligned} \tag{66}$$

If $\{b\} \notin R[A]$

$$\begin{aligned} &\left\{\hat{x}\right\} = \left([A]^T\,[A]\right)^{-1}[A]^T\,\{b\} \\ &\left[\hat{P}\right]\{b\} = \left\{\hat{b}\right\} \\ &\left\{\hat{x}\right\} \quad \text{is a unique solution to} \quad [A]\,\{x\} = \left\{\hat{b}\right\} \end{aligned} \tag{67}$$

$\left\{\hat{x}\right\}$ minimizes the Euclidean norm(length) of error vector $\{e\}$.

$$\{e\} = \{b\} - \left\{\hat{b}\right\} \tag{68}$$

This solution technique is normally referred to as least squares (error) solution. Direct inversion of the normal form ($[A]^T[A]$), however, is normally not recommended to obtain the least squares solution because it is costly (computationally) and inaccurate. LU decomposition of ($[A]^T[A]$) and backward/forward substitution is faster but can also be inaccurate.

Another technique for the least squares solution which is both fast and accurate is a method which uses QR decomposition (also referred to as QR factorization). Beginning with (62), $[A]$ is uniquely factored into the following form:

$$\begin{aligned} [A]_{nxm} &= [Q]_{nxn}[R]_{nxm} \\ [Q]^T\,[Q] &= [I] \\ [R] &= \begin{bmatrix} [U] \\ [0] \end{bmatrix} \quad \text{upper triangular} \end{aligned} \tag{69}$$

Pre-multiplication by $[Q]^T$ gives:

$$\begin{aligned} [Q]\,[R]\,\{x\} &= \{b\} \\ [Q]^T\,[Q]\,[R]\,\{x\} &= [R]\,\{x\} = [Q]^T\,\{b\} \end{aligned} \tag{70}$$

Partitioning and backward substitution yields the final solution$\{x\}$:

$$\begin{aligned} \begin{bmatrix} [U] \\ [0] \end{bmatrix}\{x\} &= \begin{bmatrix} [Q_1]^T \\ [Q_2]^T \end{bmatrix}\{b\} \\ [U]\,\{x\} &= [Q_1]^T\,\{b\} \end{aligned} \tag{71}$$

2.13 Moore-Penrose Generalized Inverse

Every matrix $[A]_{nxm}$ of rank r has an mxn $[A]^+$ matrix called a generalized inverse if it satisfies the following relationships:

$$\begin{aligned} [A]\,[A]^+\,[A] &= [A] \\ [A]^+\,[A]\,[A]^+ &= [A]^+ \end{aligned} \tag{72}$$

There are an infinite number of matrices $[A]^+$ which can satisfy these conditions. If in addition $[A]^+$ also satisfies:

$$\begin{aligned} [A]^+\,[A] &= \left([A]^+\,[A]\right)^H \\ [A]\,[A]^+ &= \left([A]\,[A]^+\right)^H \end{aligned} \tag{73}$$

Then the inverse is unique and is called the Moore-Penrose generalized inverse $[A]^\dagger$. The M-P inverse is computed using singular value decomposition. Assuming $[A]$ has rank r.

$$\begin{aligned} [A]_{nxm}\{x\}_{mx1} = \{b\}_{nx1} \Rightarrow \text{SVD} \Rightarrow [A] &= \begin{bmatrix} [U_1]\ [U_2] \end{bmatrix} \begin{bmatrix} [\Sigma]_{rxr} & [0] \\ [0] & [0] \end{bmatrix} \begin{bmatrix} [V_1]^H \\ [V_2]^H \end{bmatrix} \\ [A] &= [U_1]\,[\Sigma]\,[V_1]^H \end{aligned} \tag{74}$$

The Moore-Penrose inverse is:

$$[A]^{\dagger}\,[V_1]\,[\Sigma]^{-1}[U_1]^H \quad [\Sigma]^{-1} = \begin{bmatrix} \sigma_1^{-1} & 0 & 0 & \cdots \\ 0 & \sigma_2^{-1} & 0 & \cdots \\ 0 & 0 & \ddots & \cdots \\ \vdots & \vdots & \vdots & \sigma_r^{-1} \end{bmatrix} \tag{75}$$

SVD is computationally costly, but it is accurate and stable. The nature of $[A]$ may make it difficult to determine the value of r.

The Moore-Penrose generalized inverse can solve matrix equations for any case regardless of the size and rank of $[A]$.

$$[A]_{nxm}\,\{x\}_{mx1} = \{b\}_{nx1} \Rightarrow \left\{\hat{x}\right\} = [A]^{\dagger}\,\{b\} \tag{76}$$

Case 1: Minimum norm: $n < m$ and rank$([A]) = n$.

$$[A]^{\dagger} = [A]^T\left([A]\,[A]^T\right)^{-1} \tag{77}$$

Case 2: Least squares: $n > m$ and rank$([A]) = m$.

$$[A]^{\dagger} = \left([A]^T\,[A]\right)^{-1}[A]^T \tag{78}$$

Case 3: General or rank deficient case: $r = \text{rank}\,([A]) < \min\,(n, m)$.

$$[A]^{\dagger} = [V_1]\,[\Sigma]^{-1}[U_1]^H \tag{79}$$

3 Summary

This chapter presented the details of mathematical methods discussed in other chapters of this book. When approaching structural dynamics problems, it is imperative to understand concepts of transforms and linear algebra to best approach a solution to a problem. Structural dynamics relies heavily upon mastery of the concepts presented in this chapter, some of which are subtle. Mathematics is the language and tool of the structural dynamics engineer. Using this chapter as a reference for the other chapters in this book will enable the reader to fully understand how structural dynamics methods are implemented and why certain operations are used.

References

1. Bendat JS, Piersol AG (2000) Random data analysis and measurement procedures, 3rd edn. ISBN: 0471-31733-0
2. Golub GH, Van Loan CF (2012) Matrix computations, 4th edn. Johns Hopkins University Press. ISBN-13: 978-1421407944
3. Hayek SI (2001) Advanced mathematical methods in science and engineering, 1st edn. ISBN: 0-8247-0466-5
4. Kisak PF (ed) (2016) Fourier analysis: "decomposing a waveform into a harmonic series", 1st edn. CreateSpace Independent Publishing Platform. ISBN-13: 978-1523323913
5. Kreyzig E (2004) Advanced engineering mathematics, 8th edn. ISBN: 9971-51-283-1
6. Oppenheim AV, Schafer RW (1999) Discrete-time signal processing, 2nd edn. Prentice Hall. ISBN: 0-13-754920-2
7. Spiegel MF (1974) Schaum's outline of Fourier analysis with applications to boundary value problems, 1st edn. McGraw-Hill Education. ISBN-13: 978-0070602199
8. Strang G (2016) Introduction to linear algebra, 5th edn. Wellesley-Cambridge Press. ISBN-13: 978-0980232776

Index

R. Allemang, P. Avitabile (eds.), *Handbook of Experimental Structural Dynamics*,
https://doi.org/10.1007/978-1-4614-4547-0